CONCRETE REPAIR, REHABILITATION AND RETROFITTING IV

PROCEEDINGS OF THE 4TH INTERNATIONAL CONFERENCE ON CONCRETE REPAIR, REHABILITATION AND RETROFITTING (ICCRRR 2015), LEIPZIG, GERMANY, 5–7 OCTOBER 2015

Concrete Repair, Rehabilitation and Retrofitting IV

Editors

F. Dehn
Leipzig University/MFPA Leipzig, Germany

H.-D. Beushausen, M.G. Alexander & P. Moyo
University of Cape Town, South Africa

CRC Press
Taylor & Francis Group
Boca Raton London New York Leiden

CRC Press is an imprint of the
Taylor & Francis Group, an **informa** business

A BALKEMA BOOK

CRC Press/Balkema is an imprint of the Taylor & Francis Group, an informa business

Typeset by V Publishing Solutions Pvt Ltd., Chennai, India
Printed and bound in Great Britain by CPI Group (UK) Ltd, Croydon, CR0 4YY

Published by: CRC Press/Balkema
P.O. Box 11320, 2301 EH Leiden, The Netherlands
e-mail: Pub.NL@taylorandfrancis.com
www.crcpress.com – www.taylorandfrancis.com

ISBN: 978-1-138-02843-2 (Hbk + CD-ROM)
ISBN: 978-1-315-67764-4 (eBook PDF)

Concrete Repair, Rehabilitation and Retrofitting IV – Dehn et al. (Eds)
© 2016 Taylor & Francis Group, London, ISBN 978-1-138-02843-2

Table of contents

Concrete Repair, Rehabilitation and Retrofitting IV – Dehn et al. (Eds)
© 2016 Taylor & Francis Group, London, ISBN 978-1-138-02843-2

Preface

These conference proceedings contain papers presented at the Fourth International Conference on Concrete Repair, Rehabilitation and Retrofitting (ICCRRR 2015), Leipzig, Germany, October 2015, which can be grouped under six main themes:

- Concrete durability aspects
- Condition assessment of concrete structures
- Modern materials technology
- Concrete repair, rehabilitation and retrofitting
- Performance and health monitoring
- Education, research and specifications.

A large number of papers discusses performance and assessment of innovative materials for durable concrete construction. Interesting fields, some quite new, are covered, such as self-healing techniques, high performance concretes, and strain hardening composites. The number of papers submitted on the topic of modelling and prediction of durability confirms the positive international developments towards performance-based methods for durability design and specification. Another fact that is evident from the paper submissions is that large advances have recently been made in the fields of condition assessment of concrete structures. The papers in the proceedings cover interesting new techniques for the assessment of reinforcement corrosion and its interpretation.

The majority of papers discusses recent developments in concrete repair, rehabilitation and retrofitting techniques. An important research area lies in the field of specifications for repair materials and systems. Here, an integrated approach is needed, linking assessment techniques and service life modelling to appropriate repair methods. A number of papers deals with these important issues, confirming that the industry is on the right track towards efficient and durable repairs. Based on research reports and case studies, latest developments on repair strategies and materials are presented, ranging from surface protection techniques to full-scale repairs. Numerous papers were submitted on the topic of strengthening and retrofitting, highlighting the need to cope with increasing loads and deteriorating structures and showcasing latest developments in strengthening systems.

The Fourth International Conference follows the highly successful previous International Conferences on Concrete Repair, Rehabilitation and Retrofitting. This conference is a collaborative venture between researchers from the South African Research Programme in Concrete Materials (based at the Universities of Cape Town and The Witwatersrand) and the Material Science Group at Leipzig University and The Leipzig Institute for Materials Research and Testing (MFPA) in Germany. The organization and implementation of the conference continues to embody a strong South African-German link, reflected in the excellent support given to the conference by researchers and practitioners from these two countries. However, the range of presenters at the conference continues to indicate its truly international nature. This continues to fulfill an aim of these conferences, to strengthen relationships not only between Africa and Europe but also between countries and regions from all over the world.

The backdrop, in industry and the state of national infrastructures, continues to be highly challenging and demanding. The facts remain that much of our concrete infrastructure deteriorates at unacceptable rates, that we need appropriate tools and techniques to undertake the vast task of sound repair, maintenance and rehabilitation of such infrastructure, and that all this must be undertaken with due cognizance of the limited budgets available for such work. New ways need to be found to extend the useful life of concrete structures cost-effectively. Confidence in concrete as a viable construction material into the 21st century needs to be retained and sustained, particularly considering the environmental challenges that industry and society now face.

This fourth conference also continues to seek to extend a sound base of theory and practice in repair and rehabilitation, through both theoretical and experimental studies, and through good case study literature. It also seems to the organizers that two key aspects need to be addressed currently: that of developing sound and easily applied standard practices for repair, possibly codified, and the need to seriously study the service performance of repaired structures and the repair system. In fact, without substantial effort at implementing the latter goal, much of the effort in repair and rehabilitation may prove to be less than economic or satisfactory.

All papers submitted to ICCRRR 2015 were subjected to a review process, and the proceedings contain only those papers that were accepted following this process. The review of manuscripts was undertaken by identified leading experts, acting independently on one or more assigned manuscripts. This invaluable assistance, which has greatly enhanced the quality of the proceedings, is gratefully acknowledged.

Special acknowledgements are due to the following organizations:

- Deutscher Beton- und Bautechnik-Verein e.V. (DBV)
- Deutscher Ausschuss für Stahlbeton e.V. (DAfStb)
- Deutsche Bauchemie e.V.
- International Union of Laboratories and Experts in Construction Materials, Systems and Structures (RILEM)
- International Federation for Structural Concrete (*fib*).

Finally, the editors wish to thank the authors for their efforts at producing and delivering papers of a high standard. We trust that the proceedings will be a valued reference for many working in this important field and that they will form a suitable base for discussion and provide suggestions for future development and research.

F. Dehn
H.-D. Beushausen
M.G. Alexander
P. Moyo
Editors

Concrete Repair, Rehabilitation and Retrofitting IV – Dehn et al. (Eds)
© 2016 Taylor & Francis Group, London, ISBN 978-1-138-02843-2

ICCRRR committees

LOCAL ORGANIZING COMMITTEE

F. Dehn, *Co-chairman, Leipzig University/MFPA Leipzig, Germany*
H.-D. Beushausen, *Co-chairman, University of Cape Town, South Africa*
M.G. Alexander, *Co-chairman, University of Cape Town, South Africa*
P. Moyo, *Co-chairman, University of Cape Town, South Africa*
C. Klimke, *Secretary, MFPA Leipzig, Germany*
K. Karsten, *Secretary, MFPA Leipzig, Germany*

INTERNATIONAL SCIENTIFIC AND TECHNICAL ADVISORY BOARD

Professor H. Abdelgader, *Tripoli University, Libya*
Dr. H.-P. Andrä, *LAP Consult, Stuttgart, Germany*
Professor Y. Ballim, *University of the Witwatersrand, South Africa*
Professor A. Bentur, *Israel Institute of Technology, Israel*
Professor K. Bergmeister, *BOKU Vienna, Austria*
Professor B. Bissonnette, *CRIB Laval, Canada*
Professor D. Bjegovic, *University of Zagreb, Croatia*
Professor B. Boshoff, *University of Stellenbosch, South Africa*
Professor W. Brameshuber, *RWTH University Aachen, Germany*
Mr. G. Breitschaft, *DIBt, Germany*
Professor E. Brühwiler, *EPFL Lausanne, Switzerland*
Dr. P. Castro Borges, *CINVESTAV-Mérida, Mexico*
Dr. G. Concu, *University of Cagliari, Italy*
Professor L. Courard, *University of Liège, Belgium*
Professor M. Curbach, *Technical University of Dresden, Germany*
Professor L. Czarnecki, *Warsaw University of Technology, Poland*
Professor N. de Belie, *Ghent University, Belgium*
Professor G. de Schutter, *Ghent University, Belgium*
Professor M. Di Prisco, *Politecnico di Milano, Italy*
Professor D. Fowler, *University of Texas at Austin, USA*
Professor O. Fischer, *Technical University of Munich, Germany*
Professor A. Garbacz, *Warsaw University of Technology, Poland*
Professor C. Gehlen, *Technical University of Munich, Germany*
Professor M. Grantham, *Concrete Solutions, UK*
Professor C. Grosse, *Technical University of Munich, Germany*
Dr. P. Haardt, *Federal Highway Research Institute (BASt), Germany*
Professor K. Imamoto, *Tokyo University of Science, Japan*
Professor M. Iqbal Khan, *King Saud University, Kingdom of Saudi Arabia*
Professor C.K. Leung, *UST, Hong Kong*
Professor E. Kearsley, *University of Pretoria, South Africa*
Dr. A. Klemm, *Glasgow Caledonian University, UK*
Professor E. Koenders, *TU Darmstadt, Germany*

Mr. E. Kruger, *SANRAL, South Africa*
Professor P. Lura, *EMPA, Switzerland*
Dr. J. Mackechnie, *University of Canterbury, New Zealand*
Dr. G. Marzahn, *BMVI, Germany*
Professor V. Mechtcherine, *Technical University of Dresden, Germany*
Mr. R. Morin, *Ville de Montréal, Canada*
Professor H.S. Müller, *Karlsruhe Institute of Technology (KIT), Germany*
Professor A. Nanni, *University of Miami, USA*
Dr. I. Pepenar, *ICECON GROUP, Romania*
Mr. B. Perrie, *The Concrete Institute, South Africa*
Professor G. Plizzari, *University of Brescia, Italy*
Professor R. Polder, *TNO Built Environment and Geosciences, The Netherlands*
Professor M. Raupach, *RWTH Aachen, Germany*
Professor M. Santhanam, *IIT Madras, India*
Professor J. Schnell, *University of Kaiserslautern, Germany*
Mr. N. Schröter, *Deutsche Bauchemie e.V., Germany*
Dr. A. Scott, *University of Canterbury, New Zealand*
Professor L. Taerwe, *Ghent University, Belgium*
Dr. R. Torrent, *Materials Advanced Services Ltd., Argentina*
Professor T. Triantafillou, *University of Patras, Greece*
Dr. A. Turatsinze, *LMDC Toulouse, France*
Mr. A. Van Grieken, *Van Grieken & Associates, Australia*
Professor G. Van Zijl, *University of Stellenbosch, South Africa*
Dr. A. Vaysburd, *Vaycon, USA*
Professor J.C. Walraven, *TU Delft, The Netherlands*
Dr. H. Wiggenhauser, *BAM Berlin, Germany*

Concrete durability aspects

Concrete Repair, Rehabilitation and Retrofitting IV – Dehn et al. (Eds)
© 2016 Taylor & Francis Group, London, ISBN 978-1-138-02843-2

Chloride ingress testing of concrete

D. Dunne & C. Christodoulou
AECOM Europe, Birmingham, UK

M.D. Newlands
Concrete Technology Unit, University of Dundee, UK

P. McKenna
CH2M Hill, Glasgow, UK

C.I. Goodier
School of Civil and Building Engineering, Loughborough University, Loughborough, UK

ABSTRACT: Concrete is recognised as a durable material that can provide long-term protection to embedded carbon steel reinforcement. However, effective protection can only be achieved if the mechanisms of deterioration and the durability properties of the protective material involved are fully understood. A well-known phenomenon is the ingress of chloride ions into concrete, which takes place via the solution-filled pores. These ions, combined with optimum contents of air and moisture, result in reinforcement corrosion, and subsequently, loss in functionality of a reinforced concrete element. Currently, available literature suggests that measurement of chloride ion ingress into concrete can be misleading. Reasons for erroneous measurements include: (i) continuing formation of hydration products resulting in pore refinement/pore blocking and; (ii) chloride diffusion coefficients being commonly applied as the "effective" diffusivity, which does not take into account the effect of chemical binding on the chloride ion transport process. This paper reports the findings of an investigation of different chloride test methods for measuring chloride ingress of concrete, which are currently used. This was undertaken to establish their suitability to measure this intrinsic concrete durability property. Five test methods were selected, covering the two main test method types that currently finding application: (i) electrically accelerated short-term; and (ii) naturally accelerated long-term chloride test methods. Three concrete types of CEM I, PC/FA (20–55%) and PC/GGBS (25–75%) at varying water-cement (w/c) ratios of 0.35, 0.50 and 0.65 were utilised during the investigation. This work has established that whilst all the test methods demonstrated capacities to measure chloride ingress into concrete, operator accuracy is of significant importance.

1 INTRODUCTION

1.1 *Chloride durability*

The durability of concrete structures exposed to chloride-containing solutions has being widely studied (Dunne, 2010). Nonetheless, chloride induced corrosion continues to be recognized as a major reason for the loss of durability in reinforced concrete structures. The predominant sources of these chlorides into concrete emanate from exposure to marine environments and from the application of de-icing salt on roads, parking and bridge structures. Whilst recognizing transport mechanisms, such as, capillary suction (absorption) and/or permeability, it is generally considered that long-term, diffusion is the predominant mechanism, by which chlorides are transported through concrete.

As a result, determining chloride ion diffusivity of concrete is recognised as one of the most important parameters when assessing the potential durability of concrete (Lu et al., 1995; Thomas and Matthews, 2004). Consequently, whilst all physical processes are subject to variability, it is essential that the measurement techniques which are applied to characterise this intrinsic concrete property are robust and provide a representation of the likely trends, which may be expected for a particular concrete in service.

In an effort to control this problem, there have been numerous innovations in the area of developing chloride test methods, a selection of which can be used in service life prediction models (Dunne, 2010). Whilst noting these innovations, literature suggests, that measurement of chloride ingress into concrete can be misleading (Truce, 2000,

Dhir et al., 2004). Reasons for these misleading measurements have been attributed to: continuing formation of hydration products; influence of w/c; cement type and; the chloride diffusivities in research commonly applied are "effective" diffusivities which do not take account of the effect which chemical binding has on the chloride ion transport process (Thomas and Bamforth, 1999; Perez et al., 2000; Boddy et al., 2001; Abu Hassan, 2012 and; Elfmarkova et al., 2014).

At a European level, recent developments are only now leading to CEN Technical Committee CEN/TC 51/WG 12/TG 5, issuing a draft European Standard prEN 12390-11:2013 for formal vote on behalf of TC CEN/TC 104 (CEN/EN 12390-11:2013). This test method has being designed based on several test methods (Abu Hassan, 2012).

As noted above, the 'coefficient of chloride ion diffusion' is generally used to express the resistance of concrete to this ion. Diffusion is defined as the movement of ions under a concentration gradient and is characterized by two types of coefficient: (i) the steady-state coefficient (D_{eff}) and; (ii) the non-steady state coefficient (D_{app}) respectively. Their difference lies in where D_{eff} encounters only ionic transport, whilst D_{app} takes into account binding of chlorides with cement phases. In these types of test methods, the transmission of chlorides through concrete is encouraged where high concentrations of chloride solutions are employed to initiate a concentration gradient with the concrete (Castellote et al., 2001).

As the rate of chloride ion penetration is slow, test methods have been developed to accelerate this process. These test methods, transmit chlorides through concrete, where high concentrations of chloride solutions are employed under the action of an external electric field. These methods typically provide resistivity type values or, rapid chloride migration coefficient D_{rcm}. With respect to these migration experiments, lack of agreement on their method of measurements and calculations has given rise to a large scattering of results being presented in literature (Andrade, 1993; Andrade et al., 1994; Zhang and Gjørv, 1994; NT BUILD 443, 1995; Luping, 1999; Luping, 1999a; NT BUILD 492, 1999; Schmidt-Döhl and Rostást, 1999; Castellote et al., 2001; Luping and Sørensen, 2001; Stanish et al., 2004a; Yang, 2006; Narsilio et al., 2007; aby Hassan, 2012). The first observation is where the data is presented in different dimensional units. These differences are of importance when attempts to understand the expected chloride ingress of concrete are being undertaken.

Overall, it is clear that although a great deal of research has been undertaken into test methods for assessment of chloride ingress of concrete, it is as important to understand the data which is produced and its meaning. Therefore, there is an argument that, these units of measurement are of lesser significant, and that the ability of each method to rank concretes consistently in a particular sequence is of as great importance in specifying chloride resistance of concrete. Hence promoting a movement towards a performance based approach as oppose to that of prescriptive approach.

Taking these factors into account, the aim of this research was to undertake an assessment of different currently available chloride test methods for concrete. The selected test methods would cover the two main test method forms currently finding application: (i) electrically accelerated short-term and; (ii) naturally accelerated long-term chloride test methods. This would aid in determining the suitability of these methods to establishing chloride ingress properties of concrete.

2 EXPERIMENTAL

2.1 *Materials & mix proportions*

A single sourced CEM I 42.5N cement, conforming to BS EN 197-1 was utilised, with the key characteristics of the cement are in Table 1 (BSI, 2000). In addition to Portland cement (CEM I/PC), the influence of two cement addition materials were examined in this work: (i) Fly Ash (FA); (ii) Ground Granulated Blastfurnace Slag (GGBS). The key characteristics of these addition materials are given in Table 1.

Natural sand and gravel conforming to BS EN 12620 was used as aggregate in all mixes and their properties are presented in Table 2 (BSI, 2008).

Concrete mixes were proportioned for three water-cement ratios of 0.35, 0.50 and 0.65, a total cement content of 330 kg/m^3 and single total water content of 165 kg/m^3. These constituents were proportioned in accordance with the BRE method for designing normal concrete mixes (BRE, 1997). The mix design was to achieve a consistence conforming to the S2 slump class in BS 8500-1 (BSI, 2006). Table 3 outlines the standard CEM I mix designs whilst, Table 4 outlines the addition material mix

Table 1. Cement and addition material properties.

Property measured	PC	FA	GGBS
Fineness (m^2/kg)	414†	367†	460†
Loss on Ignition, %	1.74	6.02	0.90
Particle Density, g/cm^3	3.14	2.25	2.89

†Tested by Blaine fineness method.

Table 2. Properties of aggregates.

Property measured	Natural sand 0/4 mm	Natural gravel average[#]
Shape, visual inspection	Round	Round
SSD Density[§], kg/m^3	2600	2600
LBD Density[$], kg/m^3	1680	1520
CBD Density[*], kg/m^3	1800	1610
Water Absorption,%	0.5	1.9

[#]Average of 4/10 mm and 10/20 mm aggregates.
[§]Saturated surface dry density.
[$]Loose bulk density; [*] Compacted bulk density.

Table 3. Concrete mix constituents proportions.

			Aggregates (mm)		
				Natural gravel	
w/c	Cement	Water	Natural sand 0/4	4/10	10/20
Mix constituent proportions, kg/m^3*					
0.35	470	165	600	390	785
0.50	330	165	655	415	830
0.65	255	165	685	430	855

*Super plasticizing admixture was added by weight of cement or cement and addition material.

Table 4. CEM I and binary blended cement combination concretes breakdown.

Composition of main constituents, %			
PC	FA	GGBS	Total, %
100	–	–	100
80	20	–	100
65	35	–	100
45	55		100
65	–	35	100
45	–	55	100
25	–	75	100

proportions, expressed as a percentage of the total cement contents.

The test specimens were cast in moulds and cured under damp hessian and polythene sheeting to maintain a high humidity (>95%) for 24 hours. The specimens were then de-moulded, marked for identification and cured in water at 20°C ± 2°C, in accordance with BS EN 12390-2, until time of testing (BSI, 2000).

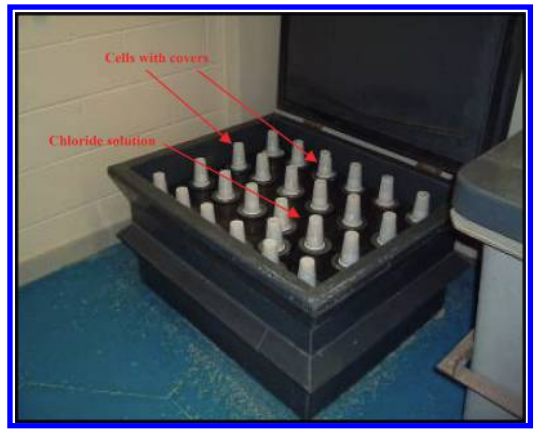

Figure 1. Steady-state chloride diffusion test method setup.

2.2 *Chloride test method procedures*

2.2.1 *Rapid chloride permeability (Method A)*

Rapid Chloride Permeability Testing (RCPT), was performed in accordance with ASTM C 1202 (ASTM, 2007). The reader should refer to this standard or the most recent version of this standard for further details.

2.2.2 *Split and spray (Method B)*

This test was performed in the same manner to that of the test method presented in Section 2.2.4, allowing the average depth of chloride penetration to be measured. Differences occurred when, at the designated testing times, the test specimens were split centrally and sprayed with a silver nitrate concentrated solution. This part of the testing procedure followed that described in Test Method C, facilitating measurement of chloride penetration depths.

2.2.3 *Rapid chloride migration (Method C)*

Rapid Chloride Migration Test (RCMT), was performed in accordance with Nordic test method (NT-BUILD 492, 1999). The reader should refer to this or the most recent version of this standard for further details.

2.2.4 *Apparent chloride diffusion (Method D)*

This test was performed in accordance with ASTM test method C1556 (ASTM, 2007). The reader should refer to this or the most recent version of this standard for further details.

2.2.5 *Effective chloride diffusion (Method E)*

A single-sided diffusion cell type test, developed by Dhir (1990), was used to study steady-state chloride ion diffusion (Figure 1). 25 mm thick

concrete specimens were taken from standard 100 mm diameter × 300 mm cylinder, after 28 days standard water curing. Twenty-four hours after air drying, these disc slices were sealed into the base of a plastic diffusion cell (110 mm diameter × 150 mm long) using silicon sealant injected to the circumferential space between the cell wall and concrete specimen.

The test cell reservoir was filled with de-ionised/distilled water and immersed in a shallow bath of de-ionised/distilled water and left for 24-hours, to allow full re-saturation of the specimen to occur. After this period the cells were filled with 840ml of calcium hydroxide saturated distilled water prior to being placed in a chloride concentrated immersion tank with an aqueous 5molar sodium chloride (NaCl) and $Ca(OH)_2$ saturated solution. Chloride ions diffused naturally through the concrete specimens until steady state was achieved. A potentiometric titration was used to measure the concentration of chlorides in each test cell at four week intervals. Once steady-state conditions were achieved after successive readings, the coefficient of chloride diffusion was calculated using a solution to Fick's First Law of Diffusion.

3 CHLORIDE TEST METHODS EVALUATION

3.1 *Background*

As alluded to previously, all physical processes are subject to variability. This variability results from natural changes in properties, differences in interactions between ingredients of materials and/or due to environmental factors. Consequently, Correlations along with undertaking an investigation into the sensitivity of each method to difference cement types were undertaken, using the two cement combination types, the PC/FA and PC/GGBS combinations.

3.1.1 *Correlations developed between test methods*

Comparison of the electrically accelerated methods demonstrated that positive linear correlations exist. These findings are presented in Table 5 where, it is seen that stronger correlations were determined at 28 days testing to that of 180 days across the three w/c's. These strong linear correlation, indicate that both methods possess a relationship to each other.

Presented in Table 6, are the coefficients when comparing chloride measurement between the naturally accelerated long-term test methods. In all cases it was observed that positive correlation exists between these test methods. Notably, it was also observed that the majority of the coefficients of determinations were above 80%. The exception being observed between Method B and E values at the 0.65 w/c.

However, it is felt that the results are a greater reflection of the high water-cement ratio as oppose to the test method. In all reality, it would be unlikely that a w/c of 0.65 would find application in a chloride containing environment. In addition, a theoretical reasoning for these differences would relate to the blocking effects of bound chlorides on the pore structure at the lower w/c, which would have had the effect of reducing the flow of chlorides.

Comparison between electrical accelerated and naturally accelerated test methods serves to evaluate whether trends exist between different test

Table 5. Correlation comparison between electrically accelerated short-term chloride test methods.

	Pearsons correlation coefficient (r)		Coefficient of determination (r^2),%	
	Test Age, Days			
w/c	28	180	28	180
0.35	0.96	0.89	0.93	0.79
0.50	0.96	0.91	0.93	0.83
0.65	0.97	0.89	0.94	0.79

Table 6. Correlation comparison between naturally accelerated long-term chloride test methods.

	Pearsons correlation coefficient (r)		Coefficient of determination (r2), %	
	Test Age, Days			
w/c	90	360	90	360
	Method B and D			
0.35	0.94	0.95	0.88	0.90
0.50	0.94	0.95	0.88	0.91
0.65	0.90	0.93	0.81	0.86
	Method B and E			
0.35	0.93	0.91	0.87	0.84
0.50	0.91	0.91	0.82	0.83
0.65	0.83	0.83	0.69	0.69
	Method D and E			
0.35	0.95	0.96	0.91	0.93
0.50	0.95	0.95	0.90	0.90
0.65	0.96	0.94	0.92	0.88

method types. These investigations established that more than 95% of the correlations were found to be as strong, as indicated by r values greater than 0.80. With the exception of the 0.50 and 0.65 w/c ratio concretes on comparison of Methods B and C, where it was observed that stronger correlations were obtained with Method A, when compared with Methods B, D and E respectively. Reasoning for the stronger correlations between Method A with Methods D and E to that of Method C is unclear from this analysis. Whilst noting this, the review established that appropriate correlations do exist between the different test method types.

3.1.2 *Variation in measured values from each test method*

The objective of this investigation was to establish whether the addition material adopted in this study (FA, GGBS) influences variations in chloride ingress measurements. CEM I (PC) was the reference concrete with the analysis performed for Methods A and C on 90 day test data, Methods B and D on 180 day chloride immersion data and Method E on the singular steady state values relative to this concrete.

On examination of the 0.5 w/c ration FA concretes, as presented in Figure where, it was established, that variation in chloride ingress measurements, were relatively consistent across test method types. Method A demonstrated increased variations from the reference concrete when compared to the Test Methods B-E. An example of this can be seen when assessing the PC/FA [BFA (35%)] concrete. Method A in comparison to the reference CEM I concrete, returned a reduction in values in the order of 35%–40%. This is in comparison to 15%–30% between the remaining test methods. These results indicate consistency amongst the latter test methods and the insensitivity of Method A to the variation in cement composition. As outlined in Table 6, with respect to Method A, it was established that this test method has the highest coefficient of variation with a value of 15%.

Similarly, the findings presented in Figure 3 demonstrates, similar trends in results for the GGBS concretes. Taking the 0.50 w/c ratio, PC65%/GGBS35% concrete to illustrate these trends, it is seen that in the case of Method A, reductions of over 60% were to that of the reference concrete, in comparison to the reaming four test methods demonstrated reductions no greater than 47%.

However, the trend in data demonstrated that variations in measurements between, Method A and the remaining four methods reduced with increasing w/c ratio. It is suggested that these findings, to a greater degree, reflect once again concrete quality at higher w/c's, rather than that of test method measurement variation.

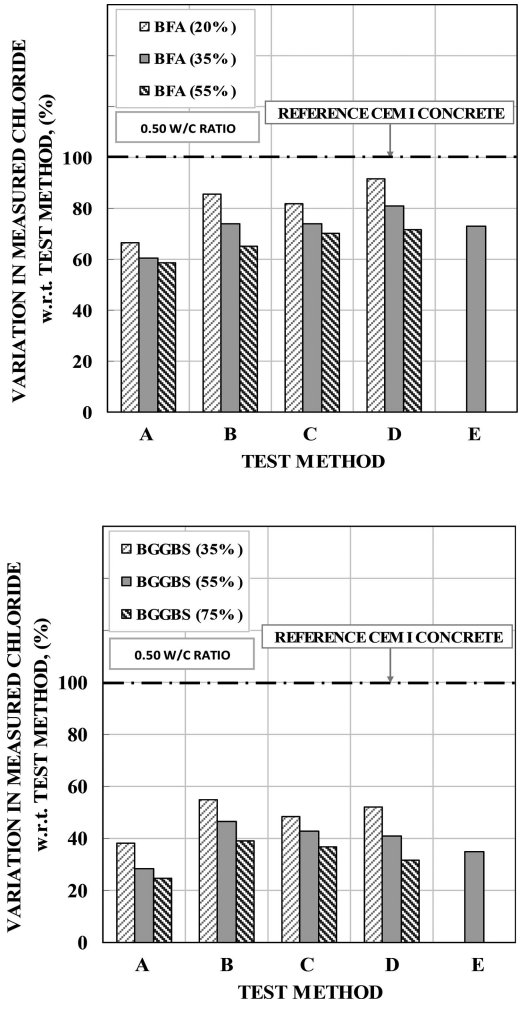

Figure 2. Chloride test methods measurement variation of Fly Ash and GGBS concrete.

4 FINAL EVALUATION OF TEST METHODS

4.1 *Ranking of test methods*

In determining the overall accuracy of a test method ISO 5725-1 (BS ISO, 1994) makes reference to both the repeatability and trueness of a test method. This repeatability term is expressed as 'precision', which is a measure of the variability observed between repeated measurements of a test method. The suitability of a test method in

performing a particular measurement is in many cases, subjective to the individual assessor.

In response to this a measured approach was applied in arriving at a consensus, as to the five chloride test methods suitability in measuring chloride ingress of concretes. The methods were assessed with respect to their simplicity, application of their measured chloride parameter, length of test and the relevance of the measured parameter of these chloride test methods to actual working life performance.

From comparison it was established, that Method C was the most consistently scoring method. On the other hand, Method D scored highest on the more critical criteria of application of measured parameter to modelling and relevance to actual chloride penetration. These are in contrast to Methods A, B and E with ratings of 14, 12 and 9 respectively. Therefore, Method D is recommended as the method most suitable for measuring chloride ingress of concrete. In particular, the measurements taken with this method will reflect expected concrete performance in working life, whilst being more appropriate to long-term durability modelling application.

The study identified that all the methods demonstrated capacities to characterise chloride ingress. Variations in magnitudes of the measured results do exist and this intensifies with increasing w/c. Nonetheless, this study has allowed each method to be ranked in the order of the most suitable for measuring chloride ingress. Method C and D were selected as being the most suitable and thereafter Methods A and B respectively, whilst Method E is deemed the fifth ranking method.

5 CONCLUSION

When determining the chloride ingress of concrete the technique applied should be robust and reliable in its measurement.

Findings from this study have demonstrated that each method has the potential for use in measuring the chloride ingress of concretes. Thereafter, each method demonstrated sensitivities to changes in w/c, albeit Method A's sensitivity reduced at the w/c of 0.65, periods of moist curing/test duration and to different cement contents and types.

Taking account of all the investigated parameters, Methods C and D are recommended as being the methods with the greatest potential for accurately measuring chloride ingress of concrete. Due to insensitivity to change in w/c and concrete composition, Method A is recommended for quality control purposes only.

REFERENCES

Abu Hassan, Z.F. 2012. Rapid assessment of the potential chloride resistance of structural concrete. PhD thesis, University of Dundee.

Andrade, C. 1993. Calculation of chloride diffusion coefficients in concrete from ionic migration measurements. Cement and Concrete Research, Vo. 23, No. 3: 724-742.

Andrade, C., Sanjuán, A. Recuero, A. & Rio, O. 1994. Calculation of chloride diffusivity in concrete from migration experiments, in non-steady-state conditions. Cement and Concrete Research, Vol. 24, No. 7: pp. 1214-1228.

ASTM C1202 - 07: 2007. Standard test method for electrical indication of concretes ability to resist chloride ion penetration.

ASTM C1556 - 04: 2004. Standard test method for determining the apparent chloride diffusion coefficient of cementitious mixtures by bulk diffusion.

Boddy, A., Hooton, R.D. & Gruber, K.A. 2001. Long-term testing of the chloride-penetration resistance of concrete containing high-reactivity metakaolin. Cement and Concrete Research, Vol. 31, No. 5: 759-765.

British Research Establishment (BRE). 1997. Design of normal concrete mixes 2nd edition, Teychnne, D.C., Franklin, R.E. & Entroy, H.C. Watford.

British Standards Institution (BSI). 1994. BS ISO 5725-1: 1994. Accuracy (trueness and precision) of measurement methods and results - Part 1. General principles and definitions.

British Standards Institution (BSI). 2000. BS EN 197-1: 2000. Cement - Part 1. Composition, specification and conformity criteria for common cements.

British Standards Institution (BSI). 2000. BS EN 12390-2: 2000. Testing hardened concrete - Part 2: Making and curing specimens for strength tests.

British Standards Institution (BSI). 2002. BS EN 12620: 2002. Aggregates for concrete.

British Standards Institution (BSI). 2006. BS 8500-1: 2006. Concrete - Complementary British Standard to BS EN 206-1. Method of specifying and guidance for the specifier, London, UK.

Castellote, M, Andrade, C. & Alonso. C. 2001. Measurement of the steady and non-steady-state chloride diffusion coefficients in a migration test by means of monitoring the conductivity in the anolyte chamber Comparison with natural diffusion tests. Cement and Concrete Research, Vol. 31, No. 10: 1411-1420.

CEN/TC 51/WG 12/TG 5. 2012-2013. prEN 12390-11:2013, Testing hardened concrete - - Part xx: Determination of the chloride resistance of concrete, unidirectional diffusion.

Chlortest. 2005. Resistance of concrete to chloride ingress - From laboratory tests to in-field performance, Guidelines for practical use of methods for testing the resistance of concrete to chloride ingress. EU funded research project under 5FP GROWTH programme, 2003-2005.

Dhir, R.K., Jones, M.R., Ahmed, H.E.H, & Seneviratne, A.M.G. 1990. Rapid estimation of chloride diffusion coefficient in concrete. Magazine of Concrete Research, Vol. 42, No. 152: 177-185.

Dhir, R. K., McCarthy, M. J., Zhou, S. & Tittle, P. A. J. 2004. Role of cement content in specifications for concrete durability: Cement type influences. Proceedings of the Institution of Civil Engineers: Structures and Buildings, Vol. 157, No. 2: 113-127.

Dunne, D.J. 2010. Chloride durability and working life investigations of cement combination concretes. PhD thesis, University of Dundee, Scotland.

Elfmarkova, V., Spiesz, P. & Brouwers, H.J.H. 2014. Determination of chloride diffusion coefficient in mortars with supplementary cementitious materials. Proceedings of the RILEM International workshop on performance-based specification and control of concrete durability, Zagreb, Croatia, 11-13 June 2014: 199-205.

Lu, X. et al, 1995, Prediction for corrosion of reinforcement and freeze-thaw of concrete, Annual report for National Clamber Scientific Research Program B, Tsinghua University. Cited: Lu. X, Application of the Nernst-Einstein equation to concrete. Cement and Concrete Research, Vol. 27, No. 2, 1997: 293-302.

Luping. T. 1999. Concentration dependence of diffusion and migration of chloride ions: Part 1. Theoretical consideration. Cement and Concrete Research, Vol. 29: 1463-1468.

Luping. T. 1999(a). Concentration dependence of diffusion and migration of chloride ions: Part 1. Theoretical consideration. Cement and Concrete Research, Vol. 29: 1463-1468.

Luping, T. & Sørensen H.E. 2001. Precision of the Nordic Test Methods for Measuring the Chloride Diffusion/Migration Coefficients of Concrete. Materials and Structures, Vol. 34, October: 479-485.

Narsilio, G.A., Li. R., Pivonka, P. & Smith, D.W. 2007. Comparative study of methods used to estimate ionic diffusion coefficients using migration tests. Cement and Concrete Research, Vol. 37: 1152-1163.

Nordisk Innovations Centre. 1999. NordTest NT-BUILD 492. Concrete, mortar and cement-based repair materials. Chloride migration coefficient from non-steady migration experiments. Nordtest, Esbo, Finland, 1999.

Pérez, B.M-., Zibrar, H., Hooton, R.D. & Thomas, M.D.A. 2000. A study of the effect of chloride binding on service life predictions. Cement and Concrete Research, Vol. 30, No. 8, 2000: 1215-1223.

Schmidt-Döhl, F. & Rostást, F.S. 1999. A model for the calculation of combined chemical reactions and transport processed and its application to the corrosion of mineral-building materials: Part 1I. Simulation model. Cement and Concrete Research, Vol. 29: 1039-1045.

Stanish K., Hooton R.D. & Thomas, M.D.A. 2004. A novel method for describing chloride ion transport due to an electrical gradient in concrete: Part 2 Experimental Study. Cement and Concrete Research, Vol. 34: 51-57.

Thomas, M.D.A. & Bamforth, P.B. 1999. Modelling chloride diffusion in concrete: Effect of fly ash and slag. Cement and Concrete Research, Vol. 29, No. 4,: 487-495.

Thomas, M.D.A. and Matthews, J.D. 2004. Performance of pfa concrete in a marine environment - 10-year results. Cement and Concrete Composites, Vol. 26: 5-20.

Truce, O. 2000. Prediction of chloride penetration into saturated concrete - Multi-species approach. PhD Thesis, Chalmers University of Technology, Göteborg, Sweden.

Yang, C.C. 2006. On the relationship between pore structure and chloride diffusivity from accelerated chloride migration in cement-based materials. Cement and Concrete Research, Vol. 36: 1304-1311.

Zhang, T. and Gjørv, O.E. 1994. An electrochemical method for accelerated testing of chloride diffusivity in concrete. Cement and Concrete Research, Vol. 24, No. 8: 1534-1548.

Concrete Repair, Rehabilitation and Retrofitting IV – Dehn et al. (Eds)
© 2016 Taylor & Francis Group, London, ISBN 978-1-138-02843-2

Concrete corrosion in an Austrian sewer system

C. Grengg, A. Baldermann & M. Dietzel
Institute of Applied Geosciences, Graz University of Technology, Graz, Austria

F. Mittermayr
Institute of Technology and Testing of Building Materials, Graz University of Technology, Graz, Austria

M.E. Böttcher
Leibniz Institute for Baltic Sea Research (IOW), Warnemünde, Germany

A. Leis
RESOURCES—Institute for Water, Energy and Sustainability, Joanneum Research, Graz, Austria

ABSTRACT: This study comprises the application of a multi proxy approach, where a strongly deteriorated Austrian sewer system was intensively investigated. Understanding the underlying reaction mechanisms leading to the deterioration by bacteriogenically induced sulfuric acid attack of concrete structures is highly complex and often not fully understood. The aim of this study is to contribute to a deeper understanding by introducing a novel approach that comprises a range of mineralogical methods, as well as hydro-geochemical analyses, analyses of gases, hydro-geochemical modelling, and microbiological analyses. An overview of the field site and analytical results will be presented. Actual causes for concrete deterioration as well as strategies for sustainable remediation will be presented and discussed.

1 INTRODUCTION

Corrosion of concrete based sewer systems due to Microbial Induced Concrete Corrosion (MICC) is a worldwide occurring issue with huge economical relevance (O'Connell et al. 2010; Yuan et al. 2013). System service-life's are reported to decrease from initially 100 down to as low as 10 years (Jensen 2009). General mechanisms of MICC are known since 1900 (Olmstead & Hamlin 1900) and can be summarized as a series of coupled redox reactions caused by bacterial activities. Within the wastewater, biotic sulfate (SO_4^{2-}) reduction occurs under anaerobic conditions, creating hydrogen sulfide (H_2S), among other sulfide species (Joseph et al. 2012; Jiang et al. 2014). Accordingly, degassing into the sewer atmosphere and subsequent diffusion into the pore structure of the concrete takes place. There, re-oxidation by Sulfide Oxidizing Bacteria (SOB), e.g. *Acidithiobacillus thiooxidans*, produces sulfuric acid (H_2SO_4), which causes the concrete deterioration to proceed.

This study aims to extend the understanding about the driving forces of MICC, using a multi proxy approach, with special focus on mineralogical phase alterations and neo-formations. Therefore, an Austrian sewer system which is urgently due for restoration, after a lifespan of only 9 years, was extensively investigated.

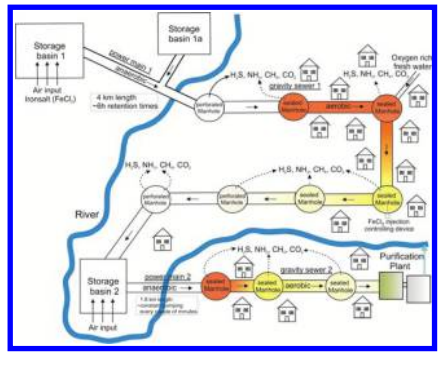

Figure 1. Schematic view of the sewer system including the two storage basins, the two power mains and the gravity sewer sections. Orange colors indicate areas of intense corrosion, while grey colors represent lower degradation degrees (Grengg et al. 2015).

2 STUDY AREA

The investigated sewer system is located near the provincial city of Graz in the south-eastern parts of Austria. It is transporting the daily wastewater flow of around 13000 persons, as well as the runoff from eventual storm events, thus it can be categorized as a combined sewer network. In 2004 two new power mains were installed, in order to secure a proper wastewater transport. Ever since community complains about odor rose and concurrently deterioration of the concrete within parts of the gravity sewers started. Figure 1 displays a schematic view of the sewer system.

3 MATERIALS AND METHODS

Solid and liquid samples from different manholes throughout the whole system were collected for further mineralogical, mechanical, biological and geochemical analyses. Long term gas observations were conducted within several manholes to measure total H_2S volumes. Additionally, drill cores form various concrete manholes were taken in order to value the concrete characteristics of the non-corroded concrete, the residual thicknesses of the manhole shafts and corrosion rates.

3.1 *Liquids*

Liquids were sampled throughout the whole sewer system for chemical analyses. On site measurements of pH, electric conductivity, O_2 concentration and redox potential were carried out. In the lab, the solutions were filtered using 0.45 µm membranes prior to alkalinity analyses by potentiometric titration with 0.005 M HCl. The concentration of dissolved components was measured by a Dionex ICS-3000 Ion Chromatograph (IC) and a PerkinElmer Optima 8300 DV Inductively Coupled Plasma Optical Emission Spectrometer (ICP-OES). A hydraulic press was used to extract the pore fluids from the deteriorated concrete, according to a modified setup of Tritthart (Tritthart 1989). The extracted pore fluids were analysed correspondingly to the methods described above. Hydrochemical modelling was carried out using the computer code PHREEQCi (version 3.1.5–9133). The minteq database was applied in order to calculate saturation indices of gypsum and anhydrite, whereas llnl database was used for bassanite (Parkhurst & Appelo 1999).

3.2 *Solids*

Deteriorated concrete was sampled from different sites and shovelled into plastic bags. The samples were dried at 40°C, and subsequently grounded, together with 10 wt.% ZnO as internal standard, for mineralogical analysis using a PANalytical X'Pert PRO diffractometer (XRD). Quantitative mineral phase identification was carried out with the PANalytical X'Pert HighScore software (version 2.2e). Secondary Electron Images (SEI) of deteriorated concrete were mugged using AuPd sputtered samples in a Zeiss DSM 982 Gemini scanning electron microscope. Thin sections of drill core samples were produced for back-scattered images (BSE), single spot analyses and elemental mapping, using a JEOL JXA-8200 Superprobe (EMPA).

3.3 *Gas phase*

Concentrations of gaseous H_2S, CH_4 and CO_2 within the sewer pipe atmosphere were measured using a Draeger 3000 gas monitor. Several long term gas measurements were installed in order to determine variations in H_2S contents.

3.4 *Bacteria analyses*

Concrete samples were taken in order to extract and identify occurrent bacteria. One gram of each sample was crushed and suspended in 1 ml 0.9% NaCl solution, before being inoculated into a 100 ml Erlenmayer flask containing 20 ml modified growth medium for the enrichment of Thiobacilli at 25–30 °C for 7 days. The Thiobacillus broth was composed after the Thiobacillus Agar 788, containing mainly thiosulfate (S_2O_3) and diverse salts (Starkley 1935). Grown bacteria were extracted and but in a hydraulic medium for selective incubation, consisting of the Thiobacillus Agar 788 plus 0.2 g precipitated sulfur powder. The DNA of emerged bacteria was used for amplification of a 298 base pair 16S rDNA fragment. Results were justified with the 16S rRNA database of Eurofinz MWG Operon.

4 RESULTS AND DISCUSSION

Redox potentials from 32 down to –320 mV were measured within the first storage basin and gravity sewer, respectively. This is indicative for a strictly reducing environment, related to intense bacterial activity within the power mains. Low oxygen levels of about 0.3 mg/l in the wastewater of the storage basins favoured the colonization of sulfate-reducing bacteria within the biofilm of the power mains. Bacteria of the genus *Desulfovibrus* and *Desulfobulbus* that occur in such environments are known to oxidize organic matter rapidly, using sulfate as electron acceptor in the absence of oxygen or nitrogen (Jensen et al. 2011; Jensen 2009). The significant

Table 1. Chemical composition of expressed pore fluids from deteriorated concrete. Electrical Conductivity (EC) and pH were measured under laboratory conditions. Saturation indices for gypsum (Gp), bassanite (Bs) and anhydrite (Anh) were calculated (Grengg et al. 2015).

Sample ID	pH	EC (mS/cm)	Na^+ (mg/l)	NH_4^+ (mg/l)	K^+ (mg/l)	Mg^{2+} (mg/l)	Ca^{2+} (mg/l)	Sr^{2+} (mg/l)	ΣFe (mg/l)	ΣAl (mg/l)	SO_4^{2-} (mg/l)	PO_4^{3-} (mg/l)	SI (Gp)	SI (Bs)	SI (Anh)
GS1-3-PF1	0.9	59.5	97.8	296	122	115	680	5.88	1527	311	13605	198	0.11	–0.84	0.10
GS1-4-PF1	0.9	64.2	91	152	266	243	584	5.69	2080	540	18139	156	0.14	–0.80	0.14
GS1-5-PF1	2.4	5.7	182	80.8	33.3	51.8	577	3.26	151	21.2	2719	0.89	0.06	–0.89	0.05
GS1-6-PF1	2.7	8.7	109	236	186	309	542	13.7	838	394	7127	3.74	0.10	–0.85	0.09
GS1-6-PF2	1.6	20.4	103	315	163	206	621	15.0	1005	305	9951	17.02	0.15	–0.80	0.14
GS1-6-PF4	1.6	18.3	75.4	370	111	126	494	3.54	643	139	7750	7.19	0.04	–0.91	0.03
GS2-1-PF1	1.0	102.0	2978	2994	1383	4322	551	14.9	15693	5720	104210	555	0.41	–0.52	0.43
GS2-1-PF3	0.7	101.0	573	210	330	990	567	4.54	2818	998	40818	161	0.11	–0.83	0.11
GS2-1-PF4	0.9	66.4	523	198	346	931	520	8.47	2943	919	32717	141	0.10	–0.85	0.09

decrease in SO_4^{2-} concentration with flow direction, from 247 to 14 mg/l verified the reduction of sulfate into sulfide speciation's due to bacterial activity. Simultaneously, the H_2S level rose up to 367 ppm in the atmosphere of the concrete based manholes. The H_2S was liberated from the wastewater into the manholes atmosphere due to changes in surrounding pressure, flow turbulences and temperature (Saracevic 2008). Gaseous H_2S is considered to be rapidly absorbed into the pore structure of the concrete where it was oxidized, either by biotic or abiotic control, over a chain of complex reactions, with H_2SO_4 as the final product (Islander et al. 1992). During early stages of MICC, acid-base reactions between CO_2, H_2S and the concrete successively caused the pH to drop from ~13.5 to ~9.5 (Joseph et al. 2012). Under the latter pH progressive colonization of the concrete pore structure by SOB occurred. With persistent decreasing pH new strains of bacteria developed and colonized the pore structure of the concrete (Alexander et al. 2013). In this study, the expressed pore fluid from the corroded concrete yielded pH values between 3.1 and 0.7, generating an extremely aggressive (micro) environment. The bacteria extracted from the deteriorated concrete were identified as *Acidithiobacillus thiooxidans* (Grengg et al. 2015). Those bacteria are known to be active until a pH of 0.2 if sulfate concentrations exceed 74 g/l (Lee et al. 2006). In our samples the sulfate concentrations were up to 104 g/l. Chemical compositions of extracted pore fluids are displayed in Table 1.

The H_2SO_4 produced triggered dissolution of the cementitious matrix and carbonatic additives, as well as massive formation of gypsum ($CaSO_4 \cdot 2H_2O$), anhydrite ($CaSO_4$), and bassanite ($CaSO_4 \cdot 0.5H_2O$). Figure 2 compares the change in

Figure 2. Change in quantitative mineralogical compounds of unaltered (grey) versus heavily deteriorated concrete (green), related to MICC, together with the weight percentage change in %. Note the strong negative correlation between the dissolution of the cementitious matrix and the carbonatic additives versus the neoformation of sulfate salts, e.g. gypsum (Gp), bassanite (Bs) and anhydrite (Anh). X-ray amorphous phases (Amph), mainly represent the CSH phases within the cement.

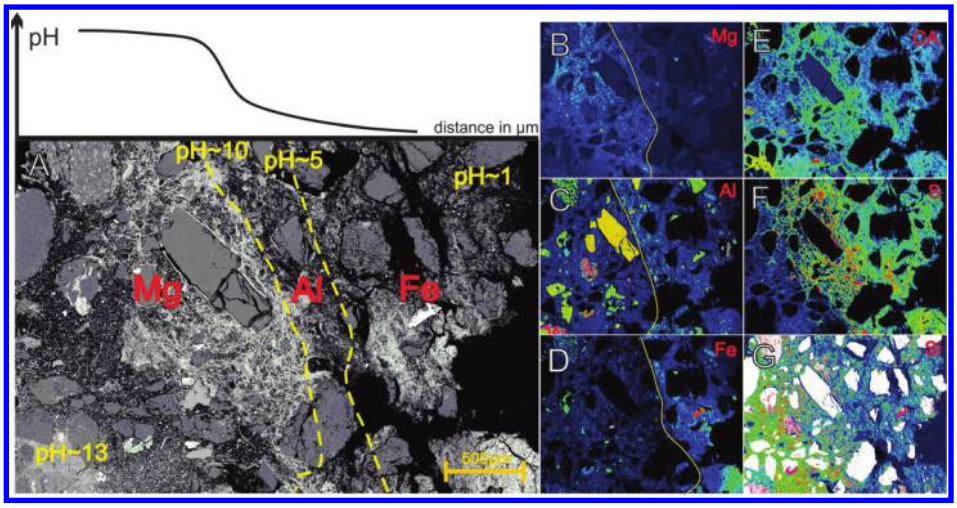

Figure 3. Displaying the pH depending dissolution and re-precipitation of Mg, Al, and Fe within a progressive corrosion front from the right to the left side (A). Mg accumulations indicate pH >10 (B) while Al is enriched in areas with pH between 5 and 10 (C). Fe enrichment can be explained by the ability of *Acidithiobacillus ferrooxidans* to reduce Fe (III) to Fe (II) and subsequent oversaturation of distinct iron bearing phases within the interstitial solutions causing precipitation (D). Additionally, concentrations of sulfur (S), calcium (Ca) and silica (Si), within the propagating corrosion front, emanating from top right to bottom left, are presented (E–G). Notice the opposing trend of Si and S enrichment.

quantitative mineralogical composition between deteriorated concrete within sewer manholes and unaltered concrete. Expected ettringite formation lacked due to its high solubility at pH values present. The intact precast concrete of drill cores, extracted from the manholes of the corroded manholes, showed compressive strengths of 88 ±11 N/mm^2 and residual thickness of 4.0 to 12.5 cm. Hence, the loss of material within heavily corroded manholes could be determined with up to 9 cm within the last 9 years (Grengg et al. 2015).

Microprobe analyses displayed gradual depletion of the Calcium-Silicate-Hydrate phases (CSH) and Calcium Hydrates (CH) within the cementitious matrix due to dissolution caused by the propagating corrosion. Simultaneously, integration of sulfur (S) into the concrete matrix proceeded, with coinstantaneous depletion of silica (Si), calcium (Ca) and magnesium (Mg) occurring. In general, the integration of S proceeded along cracks and grain boundaries of the additives, before propagating throughout the whole matrix. The dissolved ions, such as Mg, Ca, Na, or NO_3 were continuously enriched within the interstitial solutions resulting in high concentrations of Total Dissolved Solids (TDS) (Table 1). Most relevant element distributions are displayed in Figure 3 (B-G). Additionally, element mapping within thin sections of different alteration zones clearly document, beside of expected incorporation of S and coincident depletion of Si and Ca, areas where Mg, Al, and Fe accumulated. Those accumulation zones can be explained by the pH depending stability of single Mg, Al and Fe bearing phases. Mg containing phases within the cementitious matrix, got dissolved in low pH areas until oversaturation occurred, followed by its re-precipitation, as i.e. brucite ($Mg(OH)_2$) in zones of pH >10. In analogy, due to its amphoteric characteristics, Al re-accumulated as, e.g. aluminium hydroxide ($Al(OH)_3$), in areas where the pH ranged between 10 and around 5 (Appelo & Postma 2005). Fe accumulations within areas with pH <5 could be due to the activity range of the SOB species *Acidi-thiobacillus ferrooxidans* at these conditions. These chemolithrophs have the ability to use ferric iron (Fe(III)) as an electron acceptor if oxygen is limited. Hence, subsequent reduction of Fe(III) proceeded, which triggered massive dissolution of the higher soluble ferrous iron (Fe(II)), resulting in high concentration of dissolved Fe ions of up to 15.7 g/l.

Consequential, oversaturation of distinct iron bearing phases, e.g. melanterite ($FeSO_4{\cdot}7H_2O$) occurred and iron precipitation proceeded. Accumulation zones of Mg, Al and Fe are displayed in Figure 3 (A; B–D).

5 CONCLUSION

The application of a multi proxy approach, including chemical, mineralogical, mechanical and microbiological analyses, is a very powerful tool to investigate

the complex reactions induced by MICC. The deterioration of the concrete in an Austrian sewer system was clearly attributed to bacteriogenically induced sulfuric acid attack and associated formation and degassing of H_2S. The pH values below 1 created an extremely aggressive (micro)environment within the pore structures of the concrete which enhanced the decomposition of the cement matrix and its alteration into distinct calcium sulfate salts, e.g. gypsum, anhydrite and bassanite. Rapid concrete corrosion is unavoidable under such conditions and could be quantified to exceed rates of 1 cm/y.

REFERENCES

Alexander, M., Bertron, A. & De Belie, N., 2013. *Performance of Cement-Based Materials in Aggressive Aqueous Environments* 1st ed. M. Alexander, A. Bertron, & N. De Belie, eds., Ghent: Springer.

Appelo, C.A.J. & Postma, D., 2005. *Geochemistry, groundwater and pollution* Second Edi., Amsterdam: A.A. Balkema Publishers.

Grengg, C. et al., 2015. Microbiologically induced concrete corrosion: A case study from a combined sewer network. *in Revision*.

Islander, B.R.L. et al., 1992. Microbial ecology of crown corrosion in sewers. *Journal of Environmental Engineers*, 117(6), pp. 751–770.

Jensen, H.S. et al., 2011. Growth kinetics of hydrogen sulfide oxidizing bacteria in corroded concrete from sewers. *Journal of hazardous materials*, 189(3), pp. 685–91. Available at: http://www.ncbi.nlm.nih.gov/pubmed/21440988 [Accessed October 14, 2014].

Jensen, H.S., 2009. PhD thesis; *Hydrogen sulfide induced concrete corrosion of sewer networks*. Aalborg University.

Jiang, G. et al., 2014. The role of iron in sulfide induced corrosion of sewer concrete. *Water research*, 49, pp. 166–74. Available at: http://www.ncbi.nlm.nih.gov/pubmed/24326021 [Accessed October 14, 2014].

Joseph, A.P. et al., 2012. Surface neutralization and H(2)S oxidation at early stages of sewer corrosion: influence of temperature, relative humidity and H(2)S concentration. *Water research*, 46(13), pp. 4235–45. Available at: http://www.ncbi.nlm.nih.gov/pubmed/22677502 [Accessed October 14, 2014].

Lee, E.Y. et al., 2006. Removal of hydrogen sulfide by sulfate-resistant Acidithiobacillus thiooxidans AZ11. *Journal of bioscience and bioengineering*, 101(4), pp. 309–14. Available at: http://www.ncbi.nlm.nih.gov/pubmed/16716938 [Accessed September 12, 2014].

O'Connell, M., McNally, C. & Richardson, M.G., 2010. Biochemical attack on concrete in wastewater applications: A state of the art review. *Cement and Concrete Composites*, 32(7), pp. 479–485. Available at: http://linkinghub.elsevier.com/retrieve/pii/S0958946510000727 [Accessed August 27, 2014].

Olmstead, W.M. & Hamlin, H., 1900. Converting portions of the Los Angeles outfall sewer into a septic tank. *Engineering News*, pp. 971–980.

Parkhurst, B.D.L. & Appelo, C.A.J., 1999. User's guide to phreeqc (Version 2)- A computer program for speciation, and inverse geochemical calculations., (Version 2).

Saracevic, E., 2008. *PhD thesis; Zur Kenntnis der Schwefelwasserstoffbildung und -vermeidung in Abwasserdruckleitungen*. TU Wien.

Starkley, R.L., 1935. Isolation of some bacteria which oxidize thiosulfate. *Soil Sciences*, 39, pp. 197–220.

Tritthart, J., 1989. Chloride binding in cement I. Investigations to determine the composition of porewater in hardened cement. *Cement and Conrete Research*, 19(4), pp. 586–94.

Yuan, H. et al., 2013. Degradation modelling of concrete submitted to sulfuric acid attack. *Cement and Concrete Research*, 53, pp. 267–277. Available at: http://linkinghub.elsevier.com/retrieve/pii/S0008884613001749 [Accessed September 24, 2014].

Concrete Repair, Rehabilitation and Retrofitting IV – Dehn et al. (Eds)
© 2016 Taylor & Francis Group, London, ISBN 978-1-138-02843-2

One-dimensional scanning of water transport in hardened cement paste during freeze-thaw attack by NMR imaging

Z. Djuric, M. Haist & H.S. Müller
Institute of Concrete Structures and Building Materials, Karlsruhe Institute of Technology (KIT), Karlsruhe, Germany

J. Sester & E.H. Hardy
Institute for Mechanical Process Engineering and Mechanics, Karlsruhe Institute of Technology (KIT), Karlsruhe, Germany

ABSTRACT: Exposing concrete to a freeze-thaw attack in the presence of water increases the water content of the pores in relation to the pore volume (the so-called degree of saturation). Hereby the degree of saturation can significantly exceed the saturation reached by the capillary suction normally observed on concrete. Upon reaching a critical value of saturation structural damage within the concrete, i.e. the formation of cracks, will occur within only one freeze-thaw cycle. The so-called frost suction cannot be described from single classical transport laws, such as diffusion etc. In order to quantify the frost suction, it is decisive to observe continuously, non-destructive and spatially resolved the water transport during the freezing and thawing process. A suitable measurement method is the one-dimensional Nuclear Magnetic Resonance imaging technique (NMR). For this analysis method, a special set-up was used which allows a non-destructive and highly spatially resolved detection of the water uptake during the frost exposure. Thus, using this NMR technique the time-dependent progress of the water uptake in hardened cement paste during the frost attack test was investigated. Selected results will be presented in this paper.

1 INTRODUCTION

Concrete structures are exposed to various environmental exposures. One of the most relevant ones in moderate climate zones such as northern Europe is frost attack. Frost damage occurs when several unfavourable conditions are met at the same time. These conditions include numerous freeze-thaw cycles with low temperatures in combination with sufficient water influx to the building element and insufficient frost resistance of the used concrete.

The damage is characterized by the scaling of the fine mortar on the surface and a micro crack formation in the interior of the structural element (see Fig. 1). This can lead to a reduction of the strength of the concrete so that the intended service life of the building is significantly reduced.

The lifetime prediction of concrete exposed to frost strongly depends on the accuracy of the model laws applied. However, due to the complexity of the physical effects observed during freezing and thawing the formulation of time-dependent deterioration laws is extremely difficult. So far, no appropriate model for the service life prediction of the freeze-thaw attack for concrete is available. Hence, there is great need for research (Djuric et al. 2012).

Figure 1. Frost damage on a hydraulic engineering structure in Saratov (Russia).

2 PHYSICAL MECHANISMS OF FROST DAMAGE

The deterioration of concrete caused by freeze-thaw action is directly linked to the formation of ice on the concrete's surface and within its porous microstructure. During the phase change from liquid to solid, water exhibits a volume dilatation of approx. 9 vol.-%. In case the degree of water saturation in

the pores exceeds a defined critical value—the so-called critical degree of saturation S_{crit}—the pore space is not sufficient for the volume expansion of freezing water (Fagerlund 2004). The freezing water causes a burst pressure in the pores which can lead to large tensile stresses in the surrounding hardened cement paste. Exceeding the tensile strength of the cement paste, this pressure gives rise to an internal cracking and so to a progressive destruction of the concrete (Powers 1945, Helmuth 1972). Against this background, the degree of water saturation of the pore system is essential for the formation of damages within the concrete. As damages virtually occur instantaneously when the critical saturation is reached, modelling the deterioration behaviour of concrete must focus on the description of its saturation behaviour.

As can be seen from Figure 2 by comparing the water uptake of two concretes subjected to pure capillary suction or to a repeated freeze-thaw loading within the so-called CIF-Test (**C**apillary Suction, **I**nternal damage and **F**reeze-thaw Test, see (Setzer 2001a)), the water uptake resulting from freezing and thawing by far outweighs the one from classical transport processes such as capillary suction or diffusion (also see (Kruschwitz 2008)). This was explained by Setzer with the so-called "micro ice lens model", which can be illustrated using Figure 3 (Setzer 2009, Setzer 1999, Setzer 2001b).

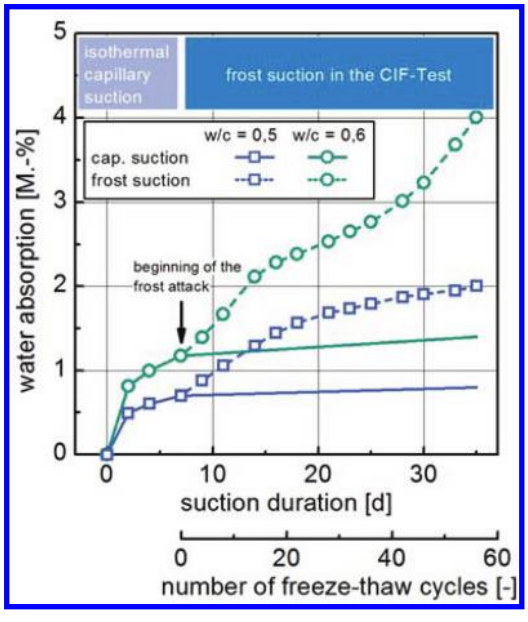

Figure 2. Water absorption of two different concretes with water/cement ratio (w/c) of 0.5 and 0.6 during capillary suction and frost suction in the CIF-Test (dashed lines: data from (Müller & Guse 2010)).

Figure 3 shows the temporal course of the temperature and the resulting strain deformation of a concrete structural element as well as the involved physical processes during the freeze-thaw action. Essential for understanding the mechanisms of freeze-thaw damaging is the fact, that the freezing temperature of water is strongly influenced by surface forces as well as the ion content of the water. As the surface forces strongly increase with reducing pore size, the freezing behaviour of the pore water thus is a function of the pore size distribution of the concrete.

For reasons of simplification, in Figure 3, concrete is considered as hardened cement paste with very fine gel pores and larger capillary pores, which are both embedded in the hydration products. During cooling below 0 °C, at first water freezes on the concrete surface (Fig. 3, stages 1 and 2) whereas the water in the gel and capillary pore system still is in the liquid state at this point (Powers 1945, Setzer 1999). If the temperature is further reduced, the water contained in the larger capillary pores begins to freeze (see Fig. 3, stage 3) whereas in the gel pores it is still in the liquid state. For stationary conditions, the capillary pores contain a defined amount of ice, whereas the remaining volume is filled by air with a specific humidity. Being in contact with the ice, the humidity of the air is strongly reduced by condensation and freezing. However, being in contact with the gel pore system, the drying of the pore-air is compensated by a transport of liquid water from the gel pores to the capillary pores and thus manifests itself macroscopically in concrete shrinkage (frost shrinkage).

Only at very low temperatures below approx. –25 °C the water which is trapped in the smallest capillary pores and in the gel pores changes its phase state and freezes (Fig. 3, stage 4, see also (Siebel et al. 2005)). This results in a pronounced volume expansion of the sample and—due to the ice pressure—to initial changes such as crack formation.

During the thawing process, at first ice contained in the gel pores and in the very fine capillary pores begins to melt (Fig. 3, stage 5). Due to the water loss the gel pores experienced during the previous freezing process in combination with the micro-structural damages of the hardened cement paste that surrounds the pores, negative pressure has been generated, which can be reduced only by water absorption, i.e. by an overall increase of the degree of saturation. This process is described as frost suction (Siebel et al. 2005, Setzer 2001b). As a prerequisite, liquid water e.g. on the concrete surface must be available at this time. This is especially true when the concrete surface is treated with deicing salts (e.g. chloride) so that the freezing point of free water at the surface is greatly reduced. As a consequence water loaded with chlorides is sucked

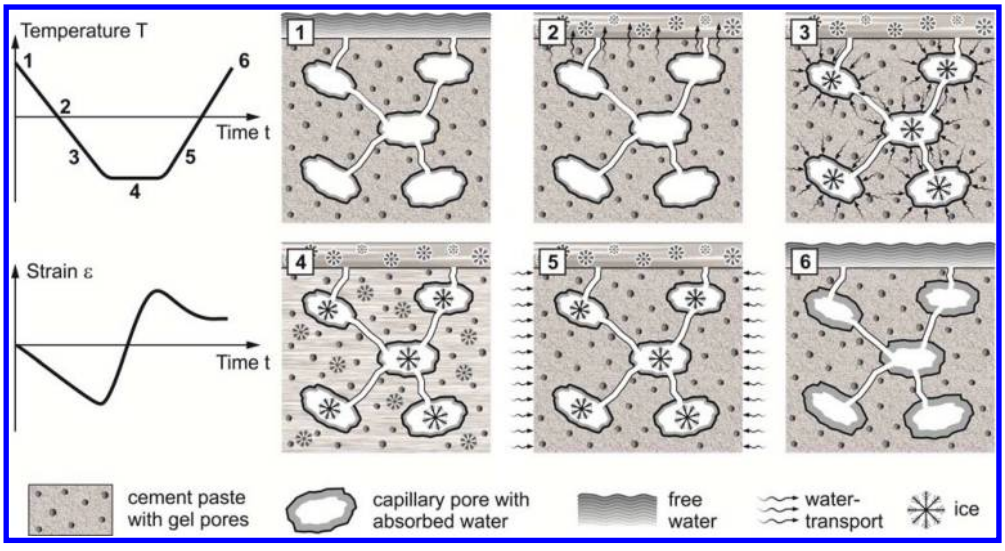

Figure 3. Schematic strain behaviour of hardened cement paste during the freeze-thaw test after repeated freeze-thaw cycles including schematic representation of physical processes in the hardened cement paste for each state.

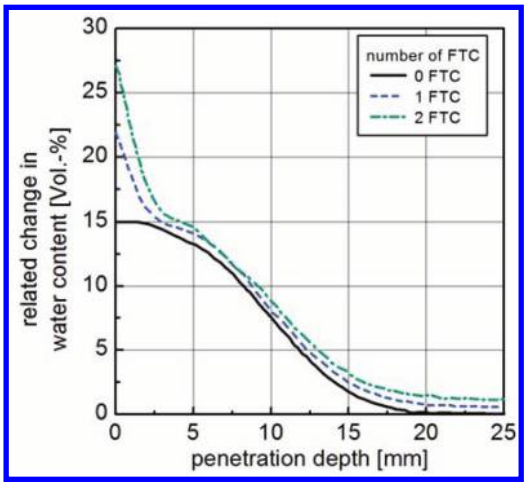

Figure 4. Related water content change in dependence of the distance from the hardened cement paste surface before and after the frost stress from a numerical calculation (Kruschwitz 2008).

into the pore system and due to diffusion effects provokes a further increase of the degree of saturation (Fig. 3, stage 6).

Structural damage of hardened cement paste on micro-level manifests itself in a remaining residual strain and in significantly increased water saturation, see e.g. (Auberg 1998).

With regard to the description of the deterioration process it is important to note, that both the saturation front and thus the deterioration are unidirectional processes, progressing from the concrete surface into the concrete. Results presented by Kruschwitz (Kruschwitz 2008) using a thermodynamic model show, that changes in the water saturation of the concrete are normally limited to the top millimetres of the concrete, see Figure 4. Experimental evidence for these results is however missing so far.

In his model Kruschwitz (Kruschwitz 2008) represents the suction process essentially by a seepage flow, and thus by a permeation process. With the numerical solution presented by Kruschwitz, changes in concrete moisture and concrete deformation due to freezing can be calculated (Kruschwitz 2008). Figure 4 shows that frost suction is of central importance particularly for the saturation behaviour of the concrete surface zone.

3 MOISTURE MEASUREMENT IN CONCRETE BY NMR METHODS

3.1 *Measurement principle of the NMR method*

The basic physical concept underlying the NMR method is the interaction of atomic nuclei with external magnetic fields (Hardy 2012). Hereby, hydrogen nuclei possess the strongest naturally occurring magnetic moment and can be well detected.

The NMR measurement setup in principle is shown in Figure 4. It consists of two permanent magnets (1), in the centre of which an open-ended

cylindrical sample space (2) is located. Within the sample space the hardened cement paste specimen (5) is exposed to a directed magnetic field (main magnetic field of strength B_0) through which an equilibrium magnetization of the sample parallel to the B_0 field is produced. The sample space itself is surrounded by a coil (3), by which the hydrogen nuclei of the sample can be excited for a short time with a high frequency field B_1, perpendicular to the B_0 field. By the superposition of these two magnetic fields B_0 and B_1, the nuclear magnetization of ^{1}H nuclei atoms is deflected from its B_0 orientation. After the B_1 field has been turned off, a precession movement of the magnetization in the sample is observed, which induces an electrical response signal in the high frequency coil, see Figure 4. The intensity of the response signal is proportional to the existing number of ^{1}H nuclei and thus with the water content of the sample. From the signal decay, information on the degree of binding and the physical state of the water can be derived.

Using this measurement technique an integral value for the water content in the sample can be obtained. For a spatially resolved—in this case depth-resolved—moisture measurement, the experimental setup was equipped with a gradient coil (4) by which the magnetic field can be varied locally in its intensity, thus encoding the measurement signal with a spatial information.

3.2 *Used NMR set-up*

For the NMR moisture measurement a BRUKER minispec mq10 NMR Analyzer apparatus was used and equipped additionally with a gradient coil system (see section 3.1). The system is connected to a computer for the detection of long running measurements. The field strength of the B_0-field is 0.235 T and is produced by a permanent magnet system.

The principle interior set-up is schematically pictured in Figure 5. Adjacent to the shown components a glass Dewar tube (inner diameter is 12 mm) with high vacuum and silver coated surface is installed (see Fig. 5). This serves as a protection against the internal temperature of 40 °C of the magnets and to ensure a one-dimensional heat transport during an in situ frost attack simulation.

3.3 *NMR pulse sequence*

To obtain a relationship between the signal intensity and the moisture content, the Free Induction Decay (FID) was measured. This is the easiest method to get a signal from the entire sample.

The spatially resolved data were measured with a Single Point Imaging (SPI) sequence with incremented encoding times (Emid & Creyghton 1985).

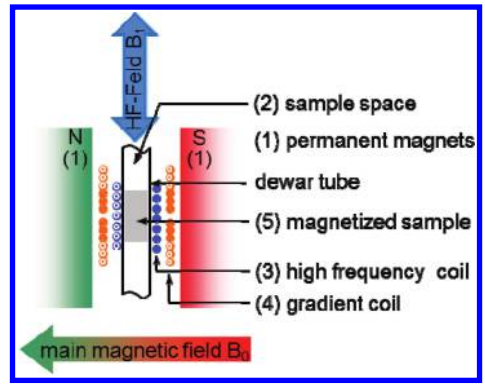

Figure 5. Schematic representation of NMR measurements with a superposed magnetic field gradient.

3.4 *Calibration*

As previously mentioned, the degree of water saturation plays an important role in view of the freeze-thaw attack. Fagerlund defines the degree of saturation as follows:

$$S = \frac{v_w}{v_p} = \frac{(m_{act} - m_{105°C}) \cdot \rho_w}{(m_{150bar} - m_{105°C}) \cdot \rho_w} \quad (1)$$

where S = degree of saturation [–]; v_w = total water volume (evaporable at 105°C) [cm³]; v_p = volume of the pores [cm³]; m_{act} = mass of the sample at the time of the examination [g]; $m_{105\,°C}$ = mass of the sample after drying at 105 °C [g]; $m_{150\,bar}$ = mass of the sample after saturation with water at 150 bar pressure [g]; and ρ_w = density of water [g/cm³] (Fagerlund 1977).

This formula was taken as a basis to convert the NMR signal into a degree of saturation.

First of all, to ensure a proportional dependency between the measured NMR signal intensity (in the considerable time domain for the intended investigation) and the water saturation, samples with different water/cement ratio and different levels of saturation were examined. For this, evacuated samples were first saturated in water under 150 bar pressure and dried slowly. Frequently the intensity of the NMR signal given by the whole sample was measured (analyzed by FID). Only at the end of the drying process the samples were dried at 105 °C and the value of the saturation degree were determined (see Eq. 1).

Figure 6 shows the dependency of the signal at the echo time of 37 µs, 52 µs, 102 and 202 µs, exemplary for four hardened cement paste samples (called calibration samples Cal1, Cal2, Cal3, Cal4) with a water/cement ratio of w/c = 0.4. As can be seen from Figure 6 the signal intensity increases linearly with

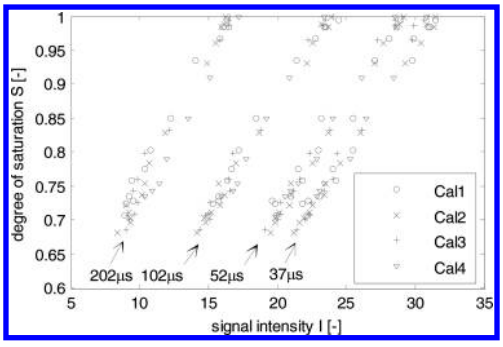

Figure 6. Degree of saturation subjected to the intensity of the NMR signal at an echo time of 37 µs, 52 µs, 102 µs and 202 µs for four equal hardened cement paste samples with w/c = 0.4 (FID measurements, every measured signal is indicated relative to the signal of a homogeneous reference sample).

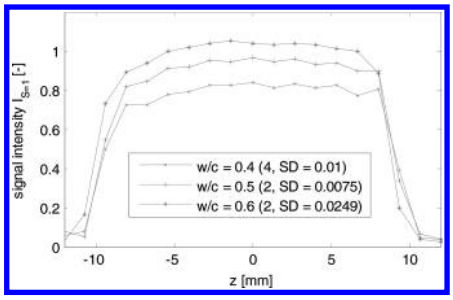

Figure 7. Signal intensity $I_{S=1}$ distributed over the longitudinal axis of hardened cement paste samples with different water/cement ratios saturated in water at 150 bar pressure at an echo time of 60 µs (the signal is indicated relative to the signal of a homogeneous reference sample). The amount of measured samples which were taken for the averaging and the standard deviation is given in brackets.

the degree of saturation. Finally, the linear dependency permits the direct calibration of the spatially resolved signal intensity (measured by SPI) into the distribution of the degree of saturation in the sample. So, the calibration was taken as follows:

$$S_{NMR} = \frac{I}{I_{S=1}} \tag{2}$$

where S_{NMR} = degree of saturation identified by the NMR; I = spatially resolved signal intensity over the sample; and $I_{S=1}$ = spatially resolved signal intensity over the saturated sample measured on equivalent samples.

In additional to the examination of the integral NMR signal intensity of saturated samples, the distribution of the water content and the NMR signal intensity, respectively, was analyzed. Figure 7 shows the results obtained from the SPI measurements of the hardened cement paste samples, for water/cement ratios of w/c = 0.4, 0.5 and 0.6, saturated in water at 150 bar pressure (S = 1). Each curve is generated by averaging the spatially resolved NMR signal intensity $I_{S=1}$ of several samples.

As can be seen from Figure 7 a spatial resolution of 1.33 mm (between adjacent data points) could be achieved in the experiments. The resolution is even better at later echo times of the signal.

The transition from air to the sample reflected in a sudden increase in signal intensity (see Fig. 7). Further, Figure 7 shows that the signal intensity decreases strongly with decreasing water/cement ratio. This is attributed to the decreasing porosity with decreasing water/cement ratio and thus to the decreasing water content in the sample and modified NMR relaxation behaviour. Further, against the background of the higher sensitivity of the NMR set-up in the center of the coil (z = 0) the distribution of the saturated sample can be assumed as homogenous.

4 EXPERIMENTAL

4.1 *Sample preparation*

For the sample preparation Portland white cement CEM I 42.5 R with a very low iron content was used and mixed to a cement paste with a water/cement ratio of w/c = 0.4. The fresh cement paste was filled in small tins and compacted shortly on a vibration table. All tins were closed airtight and rotated for 24 hours in a wheel-setup preventing sedimentation. After approx. 28 d cores of 1 cm diameter were obtained and cut to a length of 2 cm. Until the experimental investigation the samples were stored at a climate of 20 °C and 65% RH (relative humidity).

For the sealing of the generated surface—that took place one week before testing—epoxy resin in combination with glass fibers was used. Epoxy resin is suited because of the invisibly in the NMR and the possibility of applying a thin coating that is necessary due to the lack of space in the NMR Dewar tube. Further it was important to make the sealing longer than the real sample (see Fig. 8), forming a small container on top of the test surface. In this container water can be inserted preventing a water loss during the one hour lasting NMR measurements.

4.2 *Experimental investigation*

The experimental investigation of the water transport during the frost attack was performed on

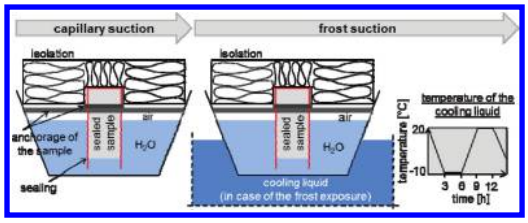

Figure 8. Experimental process of the water uptake during capillary suction (left) and frost suction (right).

hardened cement paste with a water/cement ratio of w/c = 0.4 at the age of 6 months (see section 4.1).

As the basic principle for the simulation of the practical frost-attack of hardened cement paste a modified common testing method, the "Capillary suction, Internal damage and Freeze thaw Test" (CIF-Test), was used (Setzer 2001a).

The frost testing program is subdivided into two sections:

1. capillary pre-saturation
   Getting a capillary saturated test surface, the samples were exposed to demineralized water for three days (see Fig. 8).
2. cyclic freezing and thawing exposure
   The capillary saturated samples were exposed to the frost attack (see Fig. 8) with a minimum temperature of –10 °C and 30 Freeze-Thaw Cycles (FTC).

The test set-up for the capillary suction and the frost exposure is given in Figure 8. The test specimens were placed in distilled water. For the simulation of the freeze-thaw cycles the containers equipped with test specimens were put into a liquid cooling bath of an insulated CIF-freezer. One freeze-thaw cycle took 12 hours and consisted of a 3 hour cooling from 20 °C to –10 °C and holding for 3 hours at –10 °C, 3 hours thawing and finally 3 hours holding at 20 °C. A cooling and thawing rate of 10 K/h was used.

The measurement of the moisture profile was carried out before and after the capillary suction and during the freezing and thawing exposure at intervals of two freeze-thaw cycles.

Comparing the frost suction to a capillary suction further samples were kept in the shown water container (Fig. 8, left) in a climatic chamber at a temperature of 20 °C and a relative humidity of 65%. Also at these samples the NMR measurement was done daily.

4.3 *Results*

As explained in section 3.4 the measured signal intensity profiles are normalized with respect to the signal intensity $SI_{s=1}$ of equal, but completely saturated, samples into the degree of saturation. It should be noted that all investigated samples were measured with a water film on the sample surface (section 4.1) preventing a water loss during the measurement; however for the used NMR pulse sequence this free water is not visible due to its long relaxation. Both the capillary water uptake test and the frost attack test were performed on four equal samples each (w/c = 0.4). The presented results show the mean value at each measure point of the four samples of each.

4.3.1 *Capillary suction*

The result of the time dependent and spatially resolved degree of water saturation during the capillary suction (without frost exposure) is presented in Figure 9. Here the water exposed surface is located at approx. z = 8 mm and the center of the sample is at z = 0 mm. Because of the higher sensitivity of the frequency coil in the center of the NMR machine, a slight gradient can be observed at the left and right surfaces of the sample. Further the free water on the sample surface influences the measurements in the first millimeters next to the stressed surface. Therefore the first 2 mm of the profile border area and the edges of the samples, respectively, have to be ignored (see grey area in Fig. 9).

As can be seen from Figure 9, the gradual water uptake could be closely followed with a longitudinal resolution of 1.14 mm. Before starting the capillary suction test, the samples were stored in a climatic chamber at 20°C/65% RH until reaching the hygral equilibrium state. The distribution of the saturation degree at this hygral quilibrium state is labeled 20°C/65% RH (see Fig. 9). At this time the measurement shows a homogeneous distribution of moisture throughout the sample with

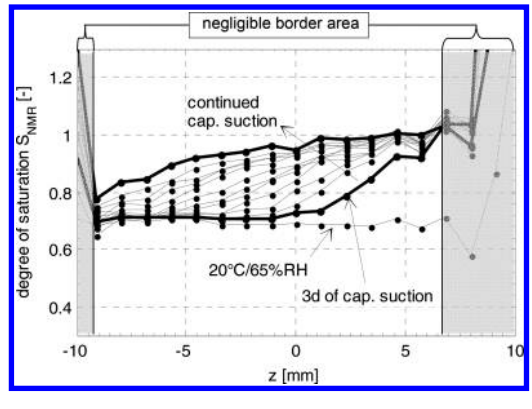

Figure 9. Averaged degree of saturation profiles distributed over the longitudinal axis of hardened cement paste samples with a water/cement ratio of w/c = 0.4 during the capillary suction (SPI with 70 µs echo time).

a saturation degree of S = 0.7. After exposing the surface (z = 8 mm) to water the degree of saturation increases in the first millimeters. The first profile after water exposure was measured after only three days of capillary suction. Here, the degree of saturation rose up to S = 0.9 in the first 5 mm. In the course of the water uptake two effects were observed. On the one hand the degree of saturation is marginally growing in the area next to the exposed surface up to S = 1.0 and on the other hand the water front is propagating slowly into the sample. After 3 weeks of the capillary water uptake the water front reached the bottom of the sample with a maximum degree of saturation of S = 0.8.

4.3.2 *Frost suction*

The longitudinally resolved increase of the saturation degree in the sample in dependence of the freeze-thaw cycles is shown in Figure 10. The resolution is 1.14 mm. Here again the exposed surface is located at about z = 8 mm and the center of the sample is at z = 0 mm. As explained above, the profile margins should remain unconsidered (see grey areas).

The homogenous distribution of moisture before the beginning of the test with a saturation degree of S = 0.7 is also given in Figure 10. After three days of capillary suction the saturation degree reached a value of S = 0.9 in the first millimeter of the exposed surface. Thereafter the freeze-thaw attack starts. The NMR measurements were performed after 2, 4, 6, 8, 14, 16, 18, 20, 22, 28 and 30 FTC. As can be seen, the cyclic exposure provokes an increase of the saturation degree that outweighs the one from the pure capillary suction (compare Fig. 10 with Fig. 9) at each measurement point of the sample. Furthermore there is a faster transportation of water into the sample. It is notable, that the saturation degree of S = 1.0 is reached after only 2 FTC and even exceeded. The reason is the dilatation of the freezing water in the pores and the related expansion of the pores. Hence, a damage of the samples can be assumed.

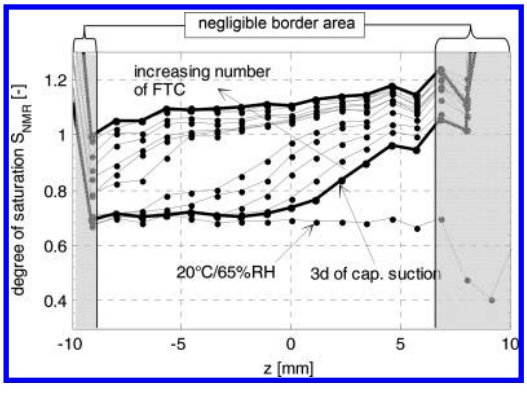

Figure 10. Averaged degree of saturation profiles distributed over the longitudinal axis of hardened cement paste samples with a water/cement ratio of w/c = 0.4 during the frost suction (SPI with 70 µs echo time).

4.4 *In situ one-sided temperature control*

For the in situ investigation of moisture profiles in hardened cement paste samples during the frost attack a NMR measurement system with a specially adapted sample head including a cooling unit was developed (see Fig. 11).

For the one-sided cooling of the hardened cement paste sample in the NMR system, a suitable thermo-electric cooling element provides the required cooling power for the needed temperature difference. On the hot side, the heat is dissipated by a heat exchanger at about 273 K. On the cold side there is an aluminum block for the heat transfer. To this, a cooling bar is attached which establishes the thermal connection to the sample. The material of the cooling bar has to be a good heat conductor without being an electrical conductor and neither being para- or ferromagnetic (silicium or ceramic).

The described set-up is then introduced into the cylindrical Dewar tube of the NMR system and the measurement is started.

Within the framework of the initial application of the presented set-up the freezing and thawing process could be followed with a very high accuracy. Intensive investigations on this are in process.

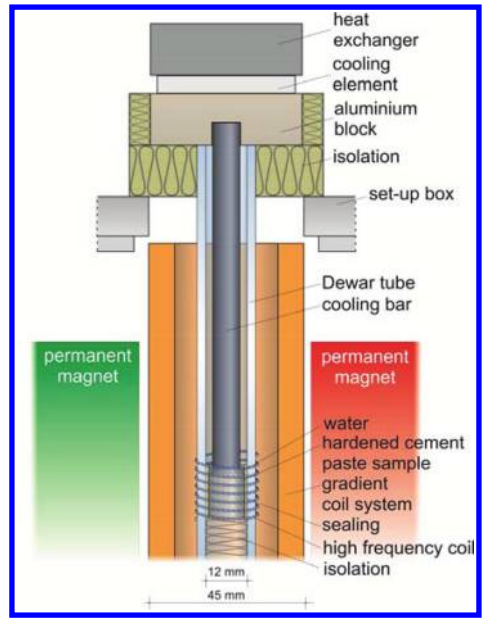

Figure 11. Setup for the in situ one-sided temperature control.

5 CONCLUSIONS

The paper presented the potential of a new NMR set-up which allows a time-dependent, non-destructive and highly spatially resolved scanning of the water transport of hardened cement paste subject to a freeze-thaw exposition.

First, to obtain accurate quantitative moisture profiles, a calibration method of the measured NMR signal for hardened cement paste had to be developed by converting the signal into a degree of saturation. The calibration and its application are shown in the paper.

Furthermore, the spatially resolved water transport due to the capillary suction and the frost suction has been investigated. The results obtained from the analysis showed that the water transport during the freeze-thaw attack is even more active than the one by capillary suction. Obtaining a saturation degree of 0.75 by capillary suction in the border area of the stressed surface, the frost suction provokes a degree of saturation of 1.0 or even higher that give a sign for the sample damage. Additional to this the water front, caused by the frost attack, penetrated further into the sample.

In conclusion, an extended NMR setup for the in situ one-sided temperature control is presented. Thereby, for the first time it is possible to observe the freezing and thawing processes and associated therewith the water transport during the freeze-thaw attack without interruption.

The presented opportunities of the developed NMR set-up are investigating in the framework of a research project at the Karlsruhe Institute of Technology (KIT). Currently further influences on the frost suction both from the concrete-technological parameters (water/cement ratio) as well as environmental conditions (temperature intensity) are examining.

ACKNOWLEDGEMENT

The investigations were realized within the scope of the project MU1368/15-1 “Quantification and modelling of the saturation behavior of hardened cement paste during the frost attack by means of innovative NMR imaging” sponsored by the German Research Foundation. The authors thank the DFG for the financial support.

REFERENCES

Auberg, R. 1998. Zuverlässige Prüfung des Frost- und Frost-Tausalz-Widerstandes von Beton mit dem CDF- und CIF-Test. Mitteilungen aus dem Institut für Bauphysik und Materialwissenschaft, Dissertation.

Djuric, Z. et al. 2012. Modelling of the saturation behavior of cement paste during freezing and thawing action. In Proceedings of the Third International Symposium on Life-Cycle Civil Engineering, (IALCCE 2012), 462–469.

Emid, S & Creyghton, J. 1985. High-resolution NMR imaging in solids. In Physical B & C 128 (1), 81–83.

Fagerlund, G. 1977. The critical degree of saturation method of assessing the freeze/thaw resistance of concrete. In Materials and Structures 10, 58, 217–229.

Fagerlund, G. 1997. Internal frost attack—state of the art. In Frost Resistance of Concrete, 321–338.

Fagerlund, G. 2004. A Service Life Model for International Frost Damage in Concrete. Lund Institute of Technology, Division of Building Materials.

Hardy, E.H. 2012. NMR Methods for the Investigation of Structure and Transport, Springer-Verlag.

Helmuth, R.A. 1972. Investigations of the Low Temperature Dynamic Mechanical Response of Hardened Cement Paste. Dept. of Civil Eng., Stanford Univ., Technical Report 154.

Kruschwitz, J. 2008. Instationärer Angriff auf nanostrukturierte Werkstoffe – eine Modellierung des Frostangriffs auf Beton. Univ. Duisburg-Essen, Cuvillier, Dissertation.

Lowke, D. & Brandes, C. 2008. Prognose der Schädigungsentwicklung von Betonen bei einem Frost-Tausalz-Angriff. In 8. Münchner Baustoff-seminar.

Model Code for Service Life Design 2006. fib Bulletin 34, Fédération Internationale du Béton, Lausanne.

Müller, H.S. & Guse, U. 2010. Zusammenfassender Bericht zum Verbundforschungsvorhaben „Übertragbarkeit von Frostlaborprüfungen auf Praxisverhältnisse“. Deutscher Ausschuss für Stahlbeton (Ed.), Berlin, Beuth, 577.

Powers, T.C. 1945. A Working Hypothesis for Further Studies of Frost Resistance of Concrete. In J. of ACI 41, 245–272.

Powers T.C. 1960. Properties of cement paste and concrete. Proc. Fourth Int. Symp. Chemistry of Cement 2, 577–609.

Sarja, A. & Vesikari, E. 1996. Durability Design of Concrete Structures. Report of RILEM Techn. Committee 130-CSL.

Setzer, M.J. 1977. Einfluss des Wassergehalts auf die Eigenschaften des erhärteten Betons. In DAfStB, 280.

Setzer, M.J. 1999. Mikroeislinsenbildung und Frostschaden. In Werkstoffe im Bauwesen—Theorie und Praxis, Eligehausen R. (Ed.), Ibidem, Stuttgart, 397–413.

Setzer, M.J. 2001a. CIF-Test—Capillary suction, Internal damage and Freeze thaw Test, Reference method and alternative methods A and B. Material and Structures 34, 9, 515–525.

Setzer, M.J. 2001b. Micro-Ice-Lens Formation in Porous Solid. In J. of Colloid and Interface Science 243, 193–201.

Setzer, M.J. 2009. Physikalische Grundlagen der Frostschädigung von Beton. In 6. Symposium Baustoffe und Bauwerkserhaltung, Tagungsband, 5–12.

Siebel, E. et al. 2005. Übertragbarkeit von Frost-Laborprüfungen auf Praxisverhältnisse. DAfStB, 560, Beuth, Berlin.

Concrete Repair, Rehabilitation and Retrofitting IV – Dehn et al. (Eds)
© 2016 Taylor & Francis Group, London, ISBN 978-1-138-02843-2

Effects of electrochemical chloride extraction on microstructure of various cement paste systems

Nguyen Thi Hai Yen, Yokota Hiroshi & Hashimoto Katsufumi
Division of Engineering and Policy for Sustainable Environment, Hokkaido University, Sapporo, Japan

ABSTRACT: The adverse effects of the long term application of electrochemical chloride extraction on binding capacity of hydrated cement products are innegligible. In this study, the influences of electrochemical chloride extraction in the microstructural properties of hydrated cement products of cement pastes were investigated in paste specimens by using a modified migration cell that was conducted with the applied current density of 4.5 A/m^2 and synthesized pore solutions used as electrolytes for 8 weeks. Three types of cement pastes were used with the water/binder ratio of 0.4; that were ordinary Portland cement, fly ash cement and blast furnace slag cement pastes. Chloride source was supplied by adding 1.5% sodium chloride. After extraction, the acid-soluble chloride content significantly reduced. Portlandite content increased proportionally with the time of extraction in ordinary Portland cement and fly ash cement pastes. Furthermore, the alteration and decomposition of C-S-H were inevitable with different rates.

Keywords: electrochemical chloride extraction; chloride removal; C-S-H gel; modified migration cell

1 INTRODUCTION

The resources of the earth are depleted day by day, including the materials for concrete, the most popular material used in construction. Therefore, the maintenance and prolongation the lifetime of an existing structure are necessary not only due to the budget issues, but also the sustainability problems for the effective using of earth materials and carbon dioxide emission. Electrochemical realkalization and Electrochemical Chloride Extraction (ECE in this paper) arose as options to solve the issue that, when the source of corrosion is extracted or eliminate out the zone around steel reinforcement, it is not clear if the corrosion process of reinforcement stops, the passive layer is repassivated or the deterioration progress could be slowdown and the performance and lifetime of the structures prolonged.

Theoretically, they are both potential methods to stop the further corrosion process and mitigate the deterioration progress of reinforced concrete structures when they are exposed to severe environments. Although they have the same principle, the results from many studies have shown out that the efficiency of fore-mentioned methods is different. Meanwhile electrochemical realkalization has been accepted widely [1–2], the effectiveness and efficiency of ECE are remaining suspicion although there were many research have been done. The feasible results of ECE on mitigating the further corrosion progress of reinforcement when it was conducted in several existing reinforced concrete structures; however, have not stopped the arguments, not only about the effectiveness and the possibility of this method on preventing the deterioration progress but also the technical term [1–14]. Moreover, the use of substitution materials has been applied widely for last some decades, but there were very few studies of the impacts of ECE on blended cement.

Therefore, in this study the impacts of ECE in chemical properties and C-S-H, the main component that affects to the binding capacity of the paste on various types of cements including Ordinary Portland Cement (OPC), Fly Ash cement (FA) and Blast Furnace Slag cement (BFS) pastes were studied.

2 EXPERIMENTAL PROCEDURE

The paste specimens were casted with the size of 40 mm by 40 mm by 160 mm in stainless steel mold and with the water-to-binder ratio of 0.4. Three types of binder were used, ordinary Portland cement, fly ash cement with 20% of fly ash and blast furnace slag cement with 40% of slag by weight of binder. The source of chloride in the pastes was supplied by adding 1.5% NaCl into mixing water during casting. The proportions of cement pastes and the composition of cement, fly

ash and blast furnace slag powders are summarized in Tables 1 and 2, respectively. To prevent the unexpected segregation of solid particles in the mix, the paste was kept mixing five minutes for two hours and a half at 15-minute intervals before pouring into the stainless steel molds. These molds were then wrapped by polyethylene film for 24 hours before the paste specimens were demoulded and immersed in saturated calcium hydroxide solution to prevent leaching of Portlandite. After curing for three months in saturated calcium hydroxide solution, the paste specimens were cut into the disks with the size 40 mm by 40 mm by 5 mm as shown in Figure 1. These disks were soaked in acetone for one day and then dried in desiccator for two days. Afterwards, they were preserved in a vacuum chamber before conducting the test in order to suppress the effect of carbonation.

To set up the extraction, the disk specimen was assembled a pair of rubber case and then held in an acrylic holder of the migration cell as shown in Figure 2. Similar to the others, the migration cell using in this test involves two transparent compartments with the acrylic holder at the middle to hold the paste disk and two electrodes to connect to the power supply as shown in Figure 3. However, some modifications on the acrylic holder so as to allow conducting the experiment on much thinner specimens in compared to the other migration cells. Therefore, the effect of the electrical current to the chemical and morphological properties of cement paste can be studied in more detail with less interference of the preparation procedure.

To simulate the extraction process in a reinforced concrete structure, synthesized pore solution with appropriate concentration of chloride ions, solution 1, was used as catholyte for first four weeks of the extraction process; afterward, the catholyte was replaced by the other synthesized pore solution that contains no chloride ions, solution 2. Solution 2 was also used as anolyte throughout the extraction process. The concentration of electrolytes and pH of them are given in Table 3 [15]. Eight migration cells were conducted for each type of binder. The electrical current density of 4.5 A/m^2 with respect to the surface area

Table 1. The proportion of cement paste (%. wt weight of binder).

	W/B	Cement	Fly ash	Slag	NaCl
OPC paste	40	100	0	0	1.5
FC paste	40	80	20	0	1.5
BFS paste	40	60	0	40	1.5

Table 2. Composition of cement and fly ash (%. wt weight of powder).

	SiO_2	Al_2O_3	Fe_2O_3	CaO	MgO	SO_3
OPC	21.5	5.65	2.53	64.9	–	1.07
FA	55.40	26.90	3.70	4.10	0.40	0.70
BFS	33.3	15.7	0.4	42.8	6.5	–

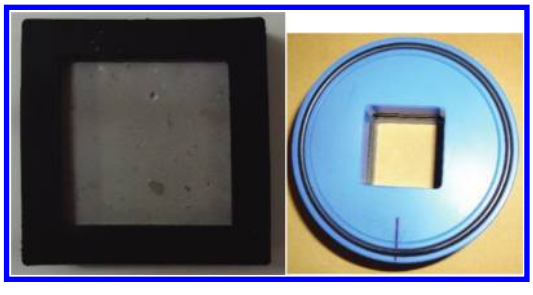

Figure 2. Rubber case and acrylic holder.

Figure 1. Cement paste specimen and paste disks using in migration cell.

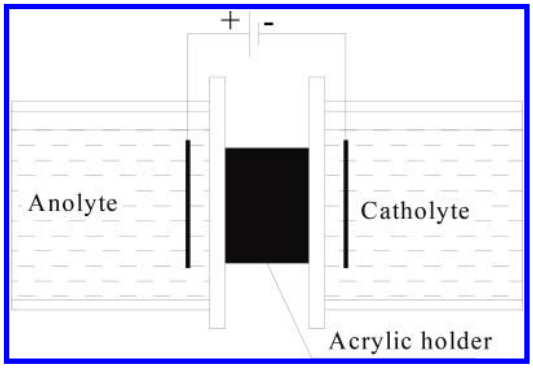

Figure 3. Schematic illustration of modified migration cell.

Table 3. Composition of electrolytes (mol/l).

Solution	1	2
KCl	0.11	0.00
KOH	0.10	0.20
NaCl	0.117	0.00
NaOH	0.15	0.10
$Ca(OH)_2$	Oversaturated	Oversaturated
pH	13.39	13.47

Table 4. Applied current and voltage for each type of cement paste.

	Current (mA)	Voltage (V)
OPC paste	4.61	2.0
FA paste	4.61	7.0
BFS paste	4.61	3.9

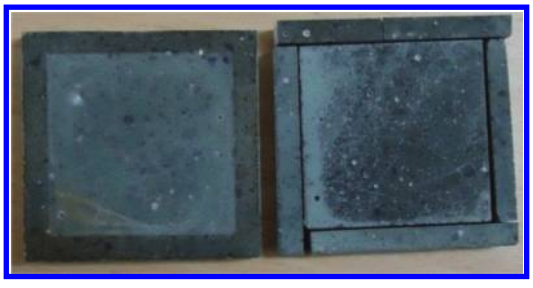

Figure 4. Disk specimens after ECE application.

of paste specimen was employed for eight weeks. The detailed current and voltage applied for each type of cement pastes were presented in Table 4. After each two-week interval of extraction, two of those eight migration cells were terminated current application. These disks were immersed in acetone within 24 hours before cutting off the edge that was held by the rubber case during extraction as shown in Figure 4. Three-quarters of this remaining were crushed and pulverized to gain the powder. Those samples were dried in desiccator for 3 days before preserving in a vacuum chamber to counteract the effect of carbonation.

Acid-soluble chloride content and water-soluble chloride content in the paste powders were determined in accordance to ASTM C1152/C1152M and ASTM C1218/C1218M, respectively. Thermal analysis was carried out to evaluate the variation in Portlandite existene in the pastes during the extraction process. Moreover, the alteration of C-S-H gels was investigated through Scanning Electron Microscope (SEM) and Energy-Dispersive X-ray Spectroscopy (EDS).

3 RESULTS AND DISCUSSIONS

3.1 *Chloride removing*

The acid-soluble chloride content profiles or total chloride content in cement paste versus the time of extraction are shown in Figure 5. As expected, when the synthesized pore solution with chloride ions—solution 1 was still used as catholyte during the first four weeks, which simulates the condition that chloride ions in pore solution around the cathode migrated towards the anode under the impact of the electrical field, the chloride content in the pastes increased. However, after the catholyte was changed to solution 2, the chloride content in the pastes significantly reduced, especially in ordinary Portlant cement and fly ash cement pastes. Based on the acid-soluble chloride content profiles, as shown in Figure 5, approximately 53% and 48% of the initial acid-soluble chloride content were released from the ordinary Portland cement and fly ash cement pastes after the current application for 8 weeks. The reduction of acid-soluble chloride in the blast furnace slag cement paste was lower: only approximately 30%.

Figure 6 shows the variation in the water-soluble chloride content during the extraction process. These results are corresponding to the acid-soluble chloride content profile as shown in Figure 5. When solution 2 was used as catholyte in the first four weeks, water-soluble chloride content increased. It followed by the significant reduction after the catholyte was replaced by solution 2. At the end of the extraction process, 68% and 53% of the initial water-soluble chloride were removed from the ordinary Portland cement and the fly ash cement pastes, while it was 35% from the slag cement paste.

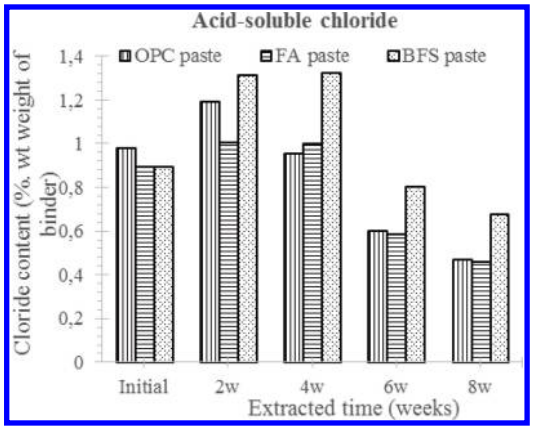

Figure 5. Acid-soluble chloride content in cement pastes versus time of extraction.

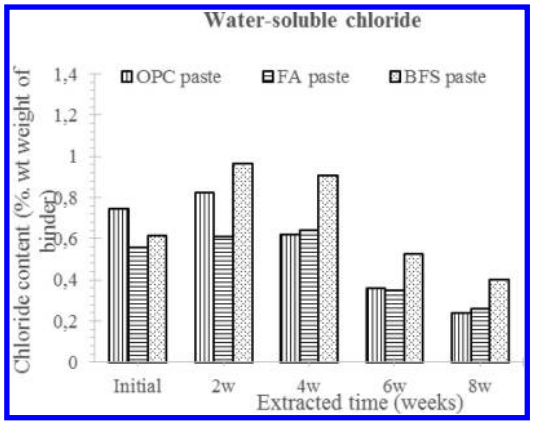

Figure 6. Water-soluble chloride content in cement pastes versus time of extraction.

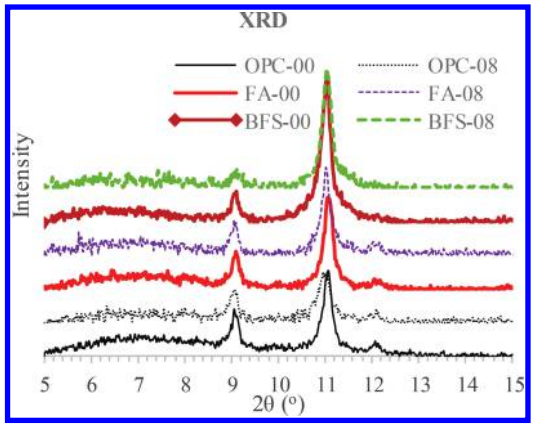

Figure 8. X-ray diffraction results on cement pastes before and after 8 weeks extraction.

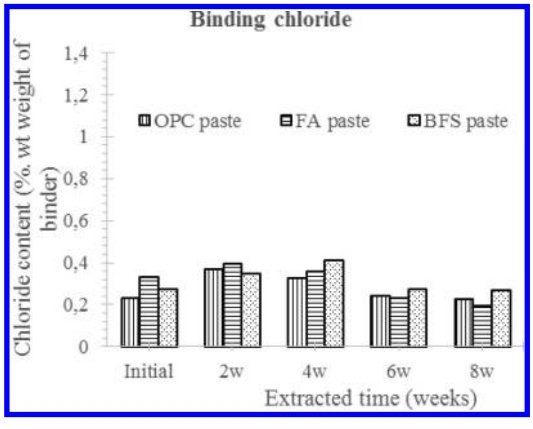

Figure 7. Binding chloride content in cement pastes versus time of extraction.

For ordinary Portland cement and blast furnace slag cement pastes, the reduction of binding chloride content during the extraction is negligible, it was approximately 7% of the initial binding chloride content at the end of the current application; on the contrary, in the case of fly ash cement paste the reduction of binding chloride is unignorable, it reached to 35% of the initial binding chloride content, as shown in Figure 7.

However, the height of the specific peak of Friedel's salt at the angle (2θ) of 11.3° from the X-ray diffraction results employed in initial paste powders (OPC-00, FA-00 and GBFS-00) and the specimens had been applied the current for 8 weeks (OPC-08, FA-08 and BFS-08) present greater reduction in ordinary Portland cement and blast furnace slag cement pastes than that in fly ash cement paste as shown in Figure 8. There was no significant difference on the height at that specific peak in the fly ash cement paste after extraction in comparison to the other types of binder. It seems that the reduction of binding chloride in the fly ash cement paste during extraction process primarily contribute from the chloride that adsorbed on the surface of C-S-H.

It is interesting here that, in this study, the aluminium oxide content in slag cement and fly ash cement are almost the same, 9.67% and 9.9% and is considerably higher than that in ordinary Portland cement. However, the efficiency of extraction process on releasing chloride in ordinary Portland cement paste and in fly ash cement paste was similar; and their efficiency was both much greater than that in the blast furnace slag cement paste. Moreover, with nearly the same content of aluminum oxide, the removal of binding chloride in the fly ash cement paste was remarkably higher than that in the blast furnace slag cement paste. This occurrence may relate to the difference on hydration mechanisms of slag cement and fly ash cement where fly ash with rather low content of calcium oxide performs as a pozzolanic admixture, meanwhile blast furnace slag acts as a cementitious material, theoretically.

3.2 *Portlandite content*

The variation of Portlandite content versus the application time of the current is shown in Figure 9.

For ordinary Portland cement, during the application of current, the Portlandite content gradually increased. A similar trend was observed in the fly ash cement pastes, except the first week of application. Nevertheless, in the blast furnace slag cement paste the Portlandite content increased in

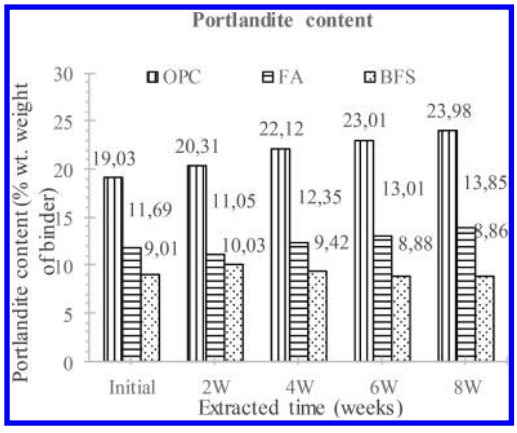

Figure 9. Portlandite content in paste specimens versus time of extraction.

the first week of extraction process, but afterwards followed by the slight reduction.

The difference in tendencies of variation of the ordinary Portlant cement and the fly ash cement pastes with the slag cement paste may concern to the alteration of their hydrated products during the application of current and the vulnerability of their hydrated products under the change of surrounding environment.

3.3 *Alteration of C-S-H phases*

Alteration of C-S-H phases after the current application also affects not only to the binding capacity of cement pastes but also its microstructure. They, in turn, impact to the diffusivity and stability of structure against the surrounding environment. Therefore, SEM and EDS were employed to investigate the alteration of C-S-H due to the application of electrical direct current.

For the ordinary Portland cement paste and the fly ash cement paste, before the extraction was applied the ratio of C/S gel phase in C-S-H phase mostly varied from 1.9 to 2.4 and 1.5 to 1.9 as shown in Figures 10 to 12. There were also some chances to meet the gel but the C/S ratio out of their values. After 8-week extraction for the ordinary Portland cement paste, there were some occasions to catch the gel that the C/S ratio was lower than its own original, 1.2 to 1.5; however, it was very easy to capture the gel that morphology was analogue to C-S-H gel but the C/S ratios were unusually greater, from 5 to 11 as shown in Figure 13.

For the fly ash cement paste, the trend was similar to the case of ordinary Portland cement paste. After 8-week extraction, the gel phase with the ratio C/S of 0.8 to 1.4 was captured. Simultaneously, the gel that morphology resembled to C-S-H

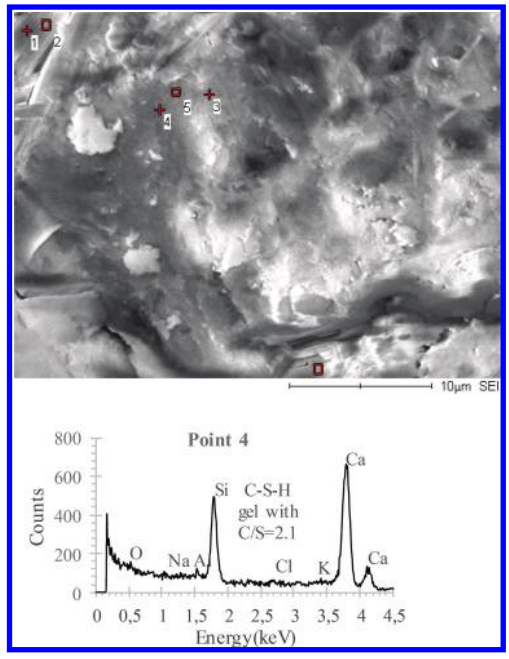

Figure 10. Bulk phase of Portlandite (points 1, 2 and 6), morphology of C-S-H gel phase with high C/S ratio (point 3 C/S = 2.4, point 4 C/S = 2.1, and point 5 C/S = 2.5) and EDS result at point 4 of OPC paste before extraction.

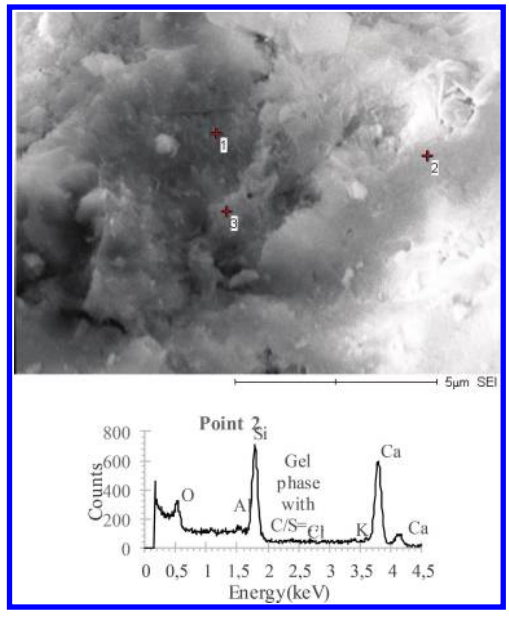

Figure 11. Morphology of C-S-H gel phase with low C/S ratio (point 1 C/S = 1.87, point 2 C/S = 1.81, and point 3 C/S = 2.03) and EDS result at point 2 of OPC paste before extraction.

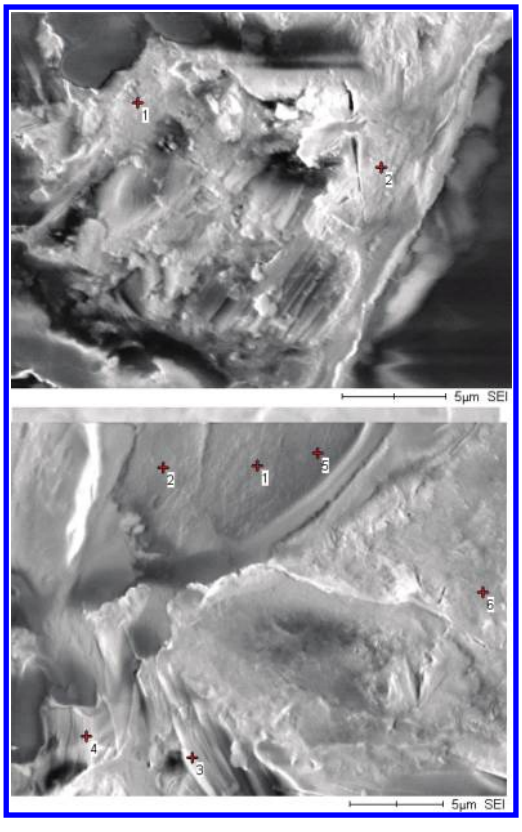

Figure 12. Morphology of C-S-H gel phase (point 1 C/S = 1.02, point 2 C/S = 1.92, point 3 C/S = 1.6, and point 4 C/S = 1.53) before extraction of FA paste.

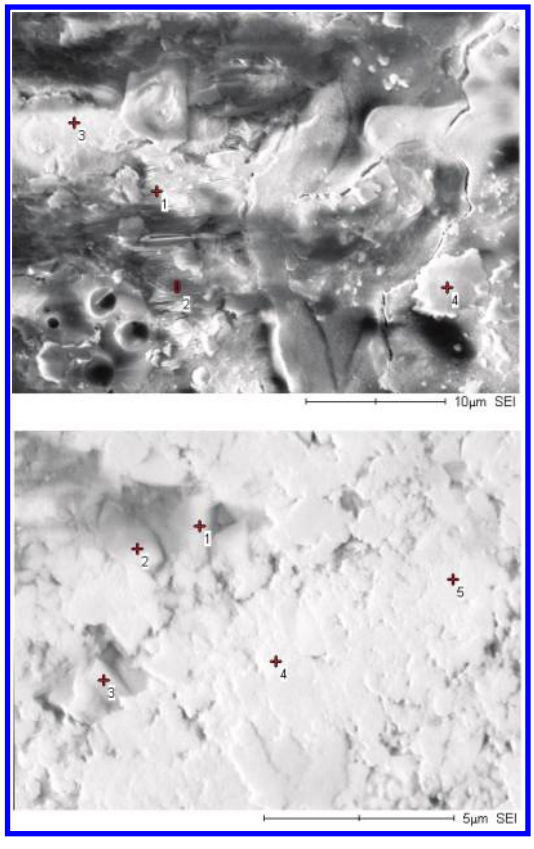

Figure 13. Gel phase of OPC paste after 8-week extraction (Up: point 1 C/S = 1.3, point 2 C/S = 2.1; Down: point 1 C/S = 8.2, point 2 C/S = 8.5, points 3 and 4: Portlandite, point 5 C/S = 5.3, and point 6 C/S = 11.2).

gel but with remarkably higher C/S ratios, was also caught; their C/S ratios varied widely from 3.5 to 9 as shown in Figures 14 and 15.

It should be noted that, the probability to capture gel with lower C/S ratio in the fly ash cement paste after 8-week extraction was greater than the gel with unusually high C/S ratio. Moreover, unlikely in the case of ordinary Portland cement paste, where there was no occurrence of silicon species that corresponded proportionally to the high C/S ratio gel, in fly ash cement paste some gels with high S/C ratio were captured after the extraction was conducted for 8 weeks as points 2 and 4 shown in Figure 15. However, it is uncertain to have a conclusion whether the high S/C gel was products of the alteration during extraction application or it was the remains of fly ash particles when it was found in both cases, before and after extraction.

In comparison to the ordinary Portland cement and the fly ash cement pastes, the C-S-H gel phase

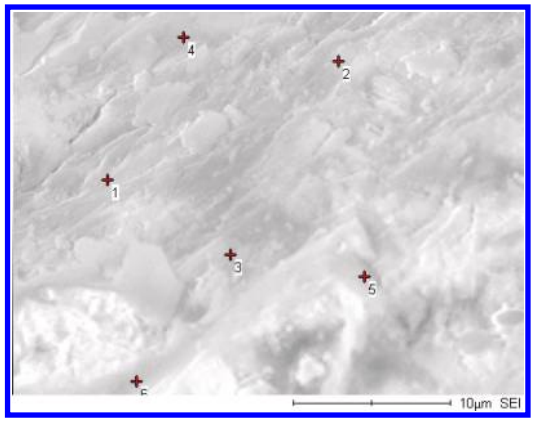

Figure 14. Gel phase of fly ash cement paste after 8-week extraction (Up: points 1 and 2: Portlandite, point 3 C/S = 1.3, and point 4 C/S = 0.92; Down: points 1, 2 and 3: Portlandite, point 4 C/S = 8.9, and point 5 C/S = 8.5).

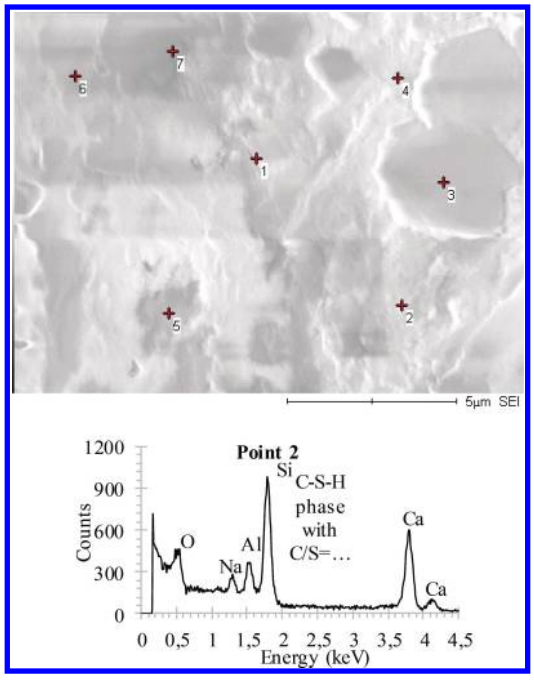

Figure 15. Gel phase with high S/C ratio (point 2 S/C = 8.8 and point 4 S/C = 5.1) in fly ash cement paste after 8-week extraction (point 1 C/S = 1.37, point 3 C/S = 0.89, point 5 C/S = 1.2).

in the blast furnace slag cement paste was rather consistent in both cases, before extraction and after the application was conducted for 8 weeks.

Before extraction, the C/S ratios of C-S-H gel phase mostly varied from 1.0 to 1.4, as shown in Figure 16. It was rarely existent of the C-S-H gel with the C/S ratio greater than 1.8. After the extraction was applied for 8 weeks, the morphology of C-S-H gel in the blast furnace slag cement paste was mostly unchanged as shown in Figure 17. However, it was likely as in the other cases, there were few cases that the gel resembled to C-S-H gel but the C/S ratio was very high as shown in Figure 18.

It is interesting to note that, the probability to capture the gel with remarkably high C/S ratio after 8-week extraction in the blast furnace slag cement paste was considerably low, it was much lower than the chance to meet that gel in the cases of the ordinary Portland cement and the fly ash cement pastes. Furthermore, the C/S ratio in this case was much greater than that in the ordinary Portland cement and the fly ash cement pastes, it mostly varied from 10 to 50; there were very few occasions to capture the gel with C/S ratio was approximately 5. Therefore, it can be considered to be small crystal of Portlandite.

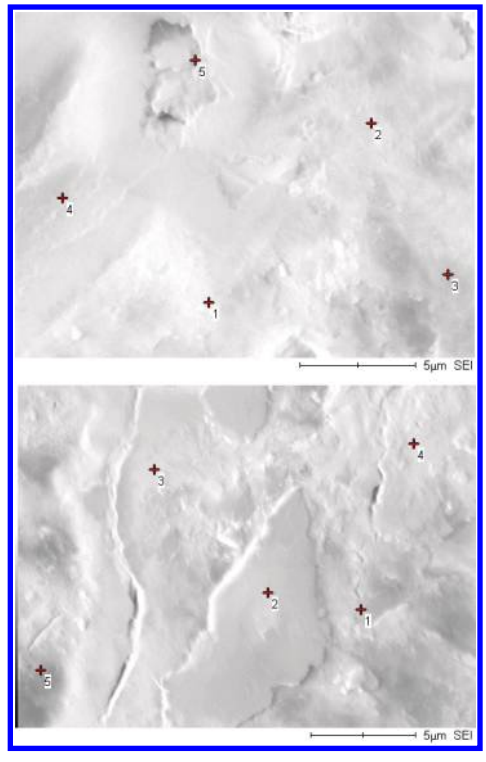

Figure 16. Morphology of C-S-H gel phase of BFS (Up: point 1 C/S = 1.25, point 2 C/S = 1.10, point 3 C/S = 1.87, point 4 C/S = 1.18, point 5 C/S = 1.26, and point 6 C/S = 1.11; Down: point 1 C/S = 1.81, point 2 C/S = 1.03, point 3 C/S = 0.99, point 4 C/S = 1.04, point 5 C/S = 1.11, point 6 C/S = 0.85, and point 7 C/S = 1.63) and EDS result of point 2 on the down figure before extraction.

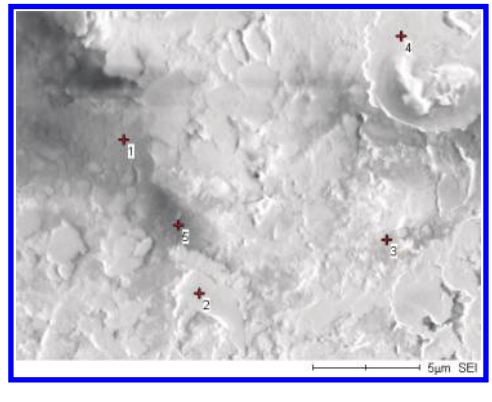

Figure 17. Morphology of C-S-H gel phase of BFS (Up: point 1 C/S = 1.26, point 2 C/S = 1.13, point 3 C/S = 1.26, point 4 C/S = 0.94, and point 5 C/S = 1.18; Down: point 1 C/S = 1.60, point 2 C/S = 1.07, point 3 C/S = 0147, point 4 C/S = 1.14, and point 5 C/S = 2.27) after 8-week extraction.

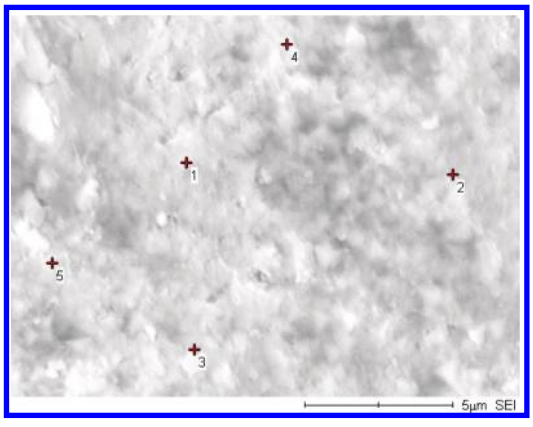

Figure 18. Gel phase with unusually high C/S ratio after 8-week extraction in slag cement paste (point 1 C/S = 7.48, point 2 C/S = 45, point 3 C/S = 47, point 4 C/S = 52, and point 5 C/S = 17.3).

4 CONCLUSIONS

Electrochemical chloride extraction is an efficient method to release chloride ions from the pastes, especially water-soluble chloride ions. It can remove approximately 50% of acid-soluble chloride ions.

There was no significant differences in reduction of acid-soluble chloride content of the ordinary Portland cement paste and the fly ash cement paste, 53% and 48%, respectively. However, the reduction of chloride content in the blast furnace slag cement paste was rather low, only approximately 30%. It was interesting that the reduction of binding chloride in the fly ash cement paste was greater than that in the ordinary Portland cement and the blast furnace slag cement pastes.

Portlandite content in the ordinary Portland cement and fly ash cement pastes gradually increased during extraction. Nevertheless, in the blast furnace slag cement paste it slightly reduced after increasing in the first week of extraction.

The alteration or even the decomposition of C-S-H gel phases in these three popular types of binder was inevitable due to the long application of electrical current. However, it seems that C-S-H gel phase in the blast furnace slag cement paste showed a more stable than that in the ordinary Portland cement and the fly ash cement pastes when they suffered the same quantity of electric current passed through.

ACKNOWLEDGMENT

This work has been supported by JSPS KAKENHI Grant Number 26630208.

REFERENCES

[1] Marcotte et al. (1999). The effect of the electrochemical chloride extraction treatment on steel-reinforced mortar Part I: Electrochemical measurements, Cement and Concrete Research 29, 1555–1560.
[2] Marcotte et al. (1999). The effect of the electrochemical chloride extraction treatment on steel-reinforced mortar Part II: Microstructural characterization, Cement and Concrete Research 29(10), 1561–1568.
[3] Ihekwaba et al. (1996). Pull-out and bond degradation of steel rebars in ECE concrete, Cement and Concrete Research 26(2), 267–282.
[4] Orellan et al. (2004). Electrochemical chloride extraction: efficiency and side effects, Cement and Concrete Research 34(2), 227–234.
[5] Siegwart et al. (2005). The effect of electrochemical chloride extraction on pre-stressed concrete, Construction and Building Materials 19(8), 585–594.
[6] Swamy et al. (2006). Effectiveness and structural implications of electrochemical chloride extraction from reinforced concrete beams, Cement and Concrete Composites 28(8), 722–733.
[7] Wang et al. (2007). Change of electrochemical property of reinforced concrete after electrochemical chloride extraction, Journal of Wuhan University of Technology—Materials Science Edition 22(4), 764–769.
[8] Yodsudjai et al. (2013). Influences of Electric Potential and Electrolyte on Electrochemical Chloride Removal in Reinforced Concrete, Journal of Materials in Civil Engineering 26(1), 83–89.
[9] Abdelaziz et al. (2009). Evaluation of the short and long-term efficiencies of electro-chemical chloride extraction, Cement and Concrete Research 39(8), 727–732.
[10] Elsener et al. (2008). Long-term durability of electrochemical chloride extraction, Materials and Corrosion 59(2), 91–97.
[11] Elsener et al. (2007). Mechanism of electrochemical chloride removal, Corrosion Science 49(12), 4504–4522.
[12] Fajardo et al. (2006). Electrochemical Chloride Extraction (ECE) from steel-reinforced concrete specimens contaminated by "artificial" sea-water, Corrosion Science 48(1), 110–125.
[13] Green et al. (1993). Electrochemical changes in chloride-contaminated reinforced concrete following cathodic polarisation, Corrosion Science 35(5–8), 1627–1631.
[14] Ismail et al. (2011). Electrochemical chloride extraction effect on blended cements, Advances in Cement Research 23(5), 241–248.
[15] Bertolini, L., & Elsener, B., & Pedeferri, P., Polder, R.P. (2004). Corrosion of steel in concrete, Prevention, Diagnosis, Repair. Wiley, VCH.

Concrete Repair, Rehabilitation and Retrofitting IV – Dehn et al. (Eds)

Study on possibility of estimation of chloride content in coastal reinforced concrete structures using electromagnetic waves

J. Nojima, M. Uchida & T. Mizobuchi
HOSEI University, Tokyo, Japan

ABSTRACT: In this study, as an evaluation method of estimation of chloride content using the electromagnetic wave, the relationship between content of chloride ions and the conductivity, which directly influences the attenuation of the reflected waveform of the electromagnetic wave based on the attenuation equation derived from the Maxwell's wave equation, was investigated in the laboratory and the applicability was verified in existing structures. As the results of applications to six existing structures which were different from used materials, conditions of mix proportion, environmental conditions and the service life, etc. using this proposed equation, it was confirmed that this estimation equation was possible to deduce the average chloride content in the cover concrete from the concrete surface to the position of reinforcement.

1 INTRODUCTION

Reinforcement corrosion caused by the presence of chloride ions around the reinforcing bars has been identified as one of the major causes of deterioration of concrete structures. The chlorides could find their way to concrete either as part of constituent materials when sea sand is used, or, by gradual permeation and diffusion as in the case of marine structures, or, cases where deicing salts are used to melt away snow on highways, etc. However, a definite understanding about any corrosion of reinforcement is very difficult unless corrosion induced cracks appear on the surface. In order to detect the deterioration caused by the chloride ions in an early stage, it is implemented generally to investigate chloride contents within concrete by carrying out chemical analysis using cores drawn from the RC structure. But, the method for carrying out to the chemical analysis using drawing cores not only gives damage partially to the concrete structure, but also is only to obtain result of analysis at the position of the drawn cores. In addition, drawing cores to estimate the chloride contents in concrete could not make it possible to investigate the changes in chloride contents over time at exactly the same place.

Thus, development of truly non-destructive tests to estimate the chloride contents in concrete could make it possible to investigate the changes in chloride concentration over time at exactly the same place, without having physically approach the structure, or causing any damage. From past studies, it was confirmed that the amplitude value of the electromagnetic waves decreases with increasing chloride contents in concrete. It has been reported that electromagnetic waves method is possible to estimate the progress of deterioration by attack of chloride ions in concrete structures. But, the attenuation of the reflected waveform of the electromagnetic wave changes by many factors such as the kind of cement, temperature and humidity in concrete and roughness of concrete surface besides content of chloride ions.

In this report, as an evaluation method of estimation of chloride content using the electromagnetic wave, the relationship between content of chloride ions and the conductivity, which directly influences the attenuation of the reflected waveform of the electromagnetic wave based on the attenuation equation derived from the Maxwell's wave equation, was investigated in the laboratory and the applicability was verified in existing structures.

2 FORMULATION OF ESTIMATION EQUATION OF CHLORIDE CONTENT USING ELECTROMAGNETIC WAVE

When the electromagnetic wave occurred to sinusoidal vibration in single angular frequency ω is assumed as one dimensional wave equation, it is possible that electric field E and magnetic field H are shown using the wave equation (1) in the following.

$$\nabla^2 E - k^2 E = 0, \quad \nabla^2 H + k^2 H = 0,$$
$$k = \left(\omega^2 \varepsilon\mu - j\omega\mu\sigma\right)^{0.5} \tag{1}$$

where, k = propagation coefficient; ε = permittivity (F/m); μ = magnetic permeability (H/m); σ = conductivity (S/m); and j = complex number.

In the propagation coefficient, the imaginary shows the attenuation coefficient which gradually attenuates with the propagation of electromagnetic wave. The electromagnetic wave attenuates at the short propagated distance, as this attenuation coefficient is bigger. Moreover, this attenuation coefficient changes by the angular frequency and the conductivity, because the magnetic permeability is 1.0 on this attenuation coefficient in case of the dielectric like concrete. Therefore, the attenuation of the electromagnetic wave at some frequencies is occurred with change of the conductivity.

In equation (1), when plane wave with polarized wave in the x direction is propagated in the z direction, the electric field is shown by following equation.

$$E = \hat{x}E_0 \exp(-jkz) = \hat{x}E_0 \exp(-\alpha z - j\beta z) \tag{2}$$

where, the imaginary β = the phase coefficient; and the real part α = the attenuation coefficient.

α and β are approximated by the following equation (3) as the value of $\sigma/\omega\varepsilon$ shown at the ratio of displacement current and conductive current becomes smaller than 1.0 in case of the dielectric medium like concrete through the electromagnetic wave (relative permittivity is 4 to 12 and frequency is about 1.0 GHz). Where, the imaginary β is the phase coefficient and the real part α is the attenuation coefficient.

$$\alpha \cong \left(\frac{\sigma}{2}\right)\sqrt{\frac{\mu}{\varepsilon}}, \quad \beta \cong \omega\sqrt{\mu\varepsilon} \tag{3}$$

In equation (2), the value of the electric field in electromagnetic wave is shown in attenuation equation of equation (4) and the electromagnetic waveform attenuates at the short propagated distance, as the attenuation coefficient is bigger because the electromagnetic waveform is exponentially decreased with advancing in the z direction.

$$|E| = |E_0|\exp(-\alpha z) = |E_0|\exp\left(-\sigma\sqrt{\frac{\mu}{\varepsilon}}\frac{z}{2}\right) \tag{4}$$

In equation (4), the characteristics of the electromagnetic wave attenuation in the medium like concrete is determined by the change of conductivity, permittivity and distance from the antenna of the radar, because the magnetic permeability in concrete does not change as the electric field is fixed.

In the past studies, it was confirm that there was high correlation in the relationship between the value of the electric field shown in the equation (4) and the value of the amplitude of the electromagnetic wave radar in aqueous solution in which the concentration of sodium chloride changed. Then, on the basis of equation (4), the relationship between amplitude values output from the electromagnetic wave radar and the conductivity, permittivity and distance from the antenna of the radar which are the characteristic of the electromagnetic wave attenuation above mentioned, is shown in equation (5). Where, permittivity and permeability are shown at dielectric constant and relative permeability.

$$|\mathrm{A}_w| = \zeta \cdot \delta_c \cdot |\mathrm{A}_0| \exp\left\{-189 \cdot \xi_t \kappa_w \sigma_{ca} \cdot (\varepsilon_r)^{-0.5} \cdot z\right\} \tag{5}$$

where, $|\mathrm{A}_w|$ = the output amplitude value of the electromagnetic wave radar; ζ = the attenuation coefficient with transmission and reflection of electromagnetic wave; δ_c = the influence coefficient on type of cement; $|\mathrm{A}_0|$ = the peculiar input amplitude value in the electromagnetic wave radar; ξ_t = the conductivity correction factor which is determined from the concrete temperature; κ_w = the conductivity correction factor which is determined from relative humidity in concrete; σ_{ca} = conductivity of concrete (S/m), ε_r is dielectric constant of concrete; and z = the propagated distance in the loss medium.

In equation (5), as the dielectric constant is about 81 for seawater while the dielectric constant is about 80 for fresh water, the dielectric constant hardly changes to the concentration of sodium chloride in aqueous solution. Therefore, the output amplitude value of the electromagnetic wave radar with changes in chloride content in the concrete is obtained from the conductivity of concrete and the distance of cover concrete in equation (5). In other words, it is possible to estimate the conductivity of the concrete using equation (6) from the temperature, the relative humidity, the dielectric constant, the output amplitude value of the electromagnetic wave radar and the distance of cover concrete in the investigation objective portion.

$$\sigma_{ca} = \frac{10^3}{2\sqrt{\varepsilon_r} \cdot c} \cdot \eta \cdot \ln\left(\frac{|\mathrm{A}_w|}{\zeta \cdot \delta_c |\mathrm{A}_0|}\right),$$
$$\eta = -\frac{1}{189 \cdot \xi_t \cdot \kappa_w} \tag{6}$$

where, c = the cover concrete (mm).

It is possible to estimate the content of chloride ions in the investigation objective portion by obtaining the relationship between the content of chloride ions and the conductivity of concrete calculated from equation (6).

3 EACH INFLUENCE FACTOR IN CALCULATION OF CONDUCTIVITY OF CONCRETE

In order to calculate the conductivity of concrete, it is necessary to obtain each coefficient in the equation (6). The coefficient of each factor prescribed from the test results in the laboratory is mentioned to the following.

3.1 *Coefficient affecting to amplitude value of electromagnetic wave*

In this study, the commercially available electromagnetic wave radar was used because it was expected that the electromagnetic wave radar of handy-type was used when considering the working efficiency and versatility in existing structures. In that case, the electromagnetic wave radiates in the air once from the output antenna of the radar, and after that is incident on other medium (concrete) from the air and after reflecting the electromagnetic wave by interfacial boundary with the different medium (reinforcing bar), the part of the electromagnetic wave penetrates through the medium. In this study, the synthesized scattering permeation coefficient which considered the transmittance at the boundary surface and the reflectivity from the reinforcing bar of the electromagnetic wave when being incident vertically to concrete from the air is established. The transmittance of the electromagnetic wave at the boundary surface with in the air and concrete (incidence and reflection) is calculated using the following equation.

$$\dot{T} = \left\{ z_0 \left(\frac{(\varepsilon_r)^{-0.5} - 1}{(\varepsilon_r)^{-0.5} + 1} \right) + 1 \right\}^2 \tag{7}$$

where, z_0 = the wave impedance (= 377Ω).

On the other hands, the attenuation ratio of each cover of concrete about the reflection from the reinforcing bar was obtained when carrying out to the measurement of the electromagnetic wave using test specimens different in the cover of concrete and making the amplitude value at the 70 mm cover of concrete the standard. The relationship between the cover of concrete and the attenuation ratio is shown in Figure 1 and the regression equation is shown in the following.

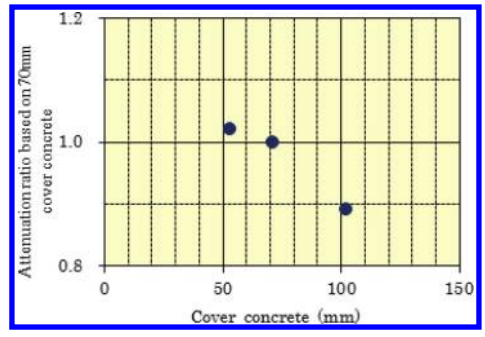

Figure 1. Relationship between cover concrete and attenuation ratio.

Photograph 1. The degree of roughness of concrete surface.

$$\lambda = -2.7 \times 10^{-3} c + 1.18 \tag{8}$$

The attenuation coefficient with the penetration and the reflection of the electromagnetic wave is shown in the following equation where influences of both of the equation (7) and (8) are considered as well as the degree of roughness of concrete surface is also considered.

$$\dot{T} = \left\{ z_0 \left(\frac{(\varepsilon_r)^{-0.5} - 1}{(\varepsilon_r)^{-0.5} + 1} \right) + 1 \right\}^2 \left(-2.7 \times 10^{-3} c + 1.18 \right) \cdot \nu \tag{9}$$

where, ν = the coefficient which shows the degree of roughness of concrete surface.

When concrete surface is in the state as shown in Photo 1 in existing structure, the output amplitude value is reduced using the coefficient ν based on the result of the laboratory test respectively.

The influence coefficient on difference of the kinds of cement was obtained from the result of the measurements of the electromagnetic wave using concrete specimens in which chloride content 1.2 kg/m^3 was mixed beforehand about the normal portland cement, the blast furnace slag cement type B and the fly ash cement type B. As the result, while the amplitude value was simi-

lar mostly even if the cover of concrete changed into normal portland cement and the blast furnace slag cement type B as shown in Figure 2, the value of the fly-ash cement type B was bigger about 20% than other cement. It seems that the conductivity falls because of decrease of various ions content in pore solution of concrete due to the absorption of fly ash. From the results shown in Figure 2, the value of output amplitude was set to 0.8 times to concrete using fly ash cement.

3.2 *Correction coefficient of conductivity by concrete temperature*

On the influence of concrete temperature, the measurement of electromagnetic wave was carried out using the test specimens which changed the curing temperature up to 5°C–30°C and from which cover concrete was different. From the results, the correction coefficient of conductivity by concrete temperature was calculated as the basis on the result of the case of 20°C curing temperature and 70 mm cover concrete. Figure 3 shows the relationship between the correction coefficient and concrete temperature. As shown in Figure 3, as the correction coefficient was only dependent on changes of the curing temperature without regard to cover concrete, the correction efficient of temperature was calculated using equation shown in the following.

$$\xi_t = 1.04 \times 10^{-2} T + 0.77 \tag{10}$$

where, T = concrete temperature (°C).

3.3 *Correction coefficient of conductivity by relative humidity in concrete*

On the influence of relative humidity in concrete, the correction coefficient was calculated based on the amplitude values in relative humidity 60%RH from the results of measurements that hygrometers were embedded in the test specimens from which water cement ratio was different and measurements of the electromagnetic waves were carried out in the thermostatic chamber in relative humidity 60%RH after curing in water. Figure 4 shows the relationship between the correction coefficient and relative humidity of concrete. As shown in Figure 4, as the correction coefficient was only dependent on changes of the relative humidity of concrete without regard to water to cement ratio, the correction efficient of temperature was calculated using equation shown in the following.

$$\kappa_w = 7.18 \times 10^{-4} \times RH^2 - 7.95 \times 10^{-2} \times RH + 3.19 \tag{11}$$

where RH = relative humidity (% RH, $60 \le RH \le 90$).

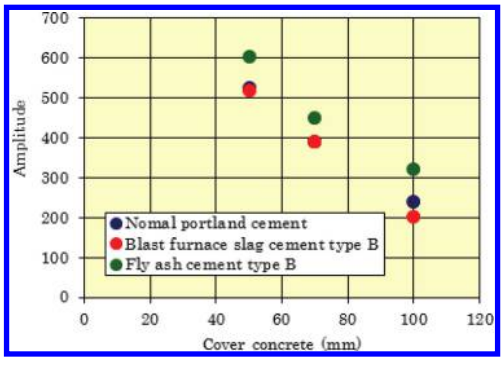

Figure 2. Relationship between cover concrete and amplitude value in each kind of cement.

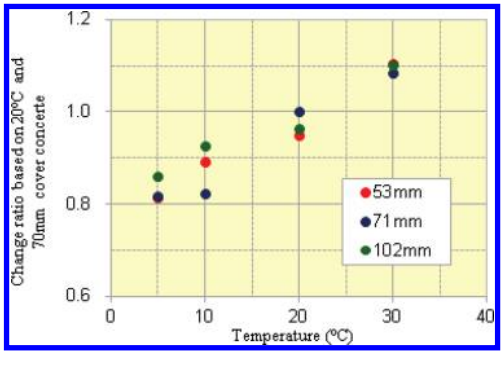

Figure 3. Relationship between concrete temperature and change ratio in each cover concrete.

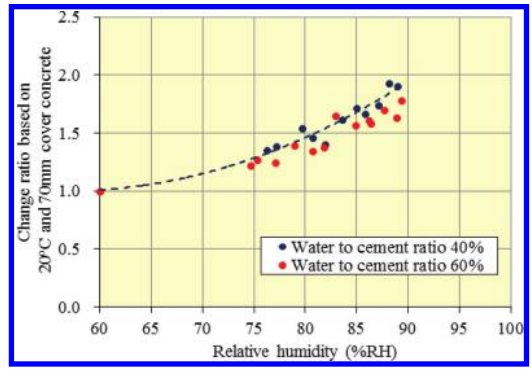

Figure 4. Relationship between relative humidity and change ratio in each water to cement ratio.

4 RELATIONSHIP BETWEEN CONDUCTIVITY OF CONCRETE AND CONTENT OF CHLORIDE IONS

4.1 *Estimation from experimental results in laboratory*

Using the equation (6) which is estimation equation of the conductivity of concrete and each correction coefficient calculated from the equation (7) to the equation (11), in the concrete specimens in which mixed content of chloride ions were varied from 0 kg/m^3 to 5.93 kg/m^3 as shown in Figure 5, the estimation of the conductivity of concrete was compared with content of chloride ions. The concrete specimens made water to cement ratio to be 50% using the blast furnace slag cement type B. For measurement of electromagnetic waves, the equipment with specifications as given in Table 1 was installed on the specimen. Measurements of the electromagnetic waves were carried out in the thermostatic chamber of relative humidity 60%RH in 20°C. The relationship between the estimated conductivity of concrete and content of chloride ions is shown in Figure 6. As shown in Figure 6, the estimated conductivity of concrete in which content of chloride ions was 0 kg/m^3 was 0.08 (S/m) which was almost similar to the value in the past study. Though, the conductivity of concrete was varied widely, the content of chloride ions tended to increase with increase in the conductivity of concrete. The regression coefficient was 0.843 and there was a high correlation relatively both of them. The relationship between the conductivity of concrete and the content of chloride ions is shown in the following.

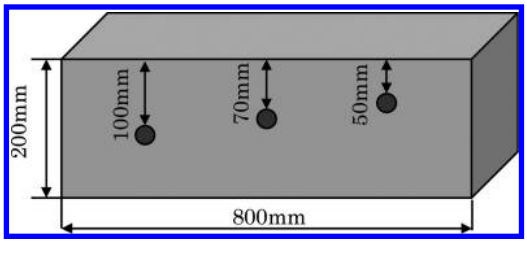

Figure 5. Test specimen.

Table 1. Specifications of electromagnetic wave measuring equipment.

Item	Specifications
Radar frequencies	1.0 GHz
Measurement method	Impulse method
Transmission voltage	17Vp-p (at load 50 Ω)
Horizontal resolution	80 mm

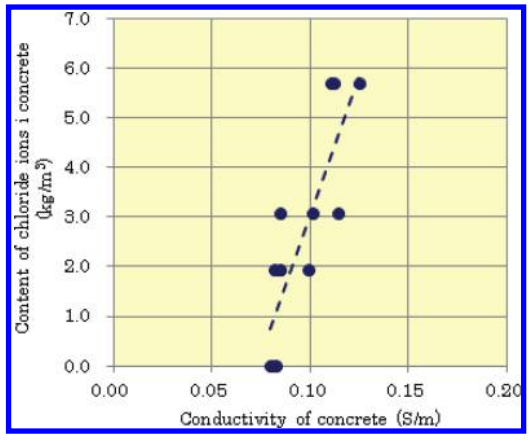

Figure 6. Relationship between conductivity of concrete and content of chloride ions in laboratory.

$$W_{cl} = 114.1\sigma_c - 8.38 \quad (12)$$

where, W_{cl} = content of chloride ions (kg/m^3).

4.2 *Estimation from field survey*

The estimation of content of chloride ions using the electromagnetic waves was carried out in the six power plants from 2010. Until now, drawn cores were collected from more than 60 positions as well as the measurements of electromagnetic wave were carried out around the drawn cores. The surveyed points were upper surface and side face of the slab featuring the piers. The number of years of service life had almost passed for more than 10 years and there was also the member which has passed for more than 50 years among them. In most of the members in the investigation object, normal portland cement and fly ash cement were used. Water to cement ratio was applied to 40% to 60%.

Based on the conditions above mentioned, the conductivity of concrete was calculated. However, concrete temperature was ambient temperature of the day in survey field and the relative humidity was 90%RH by making the assumption that the desiccation into concrete was little. The results compared with the chemical analysis of content of chloride ions drawn cores (total content of chloride ions) and estimated conductivity of concrete show in Figure 7. As the results of chemical analysis were total content of chloride ions and the conductivity of concrete was the estimation to ions in the pore solution, the total content of chloride ions which was converted into the soluble content

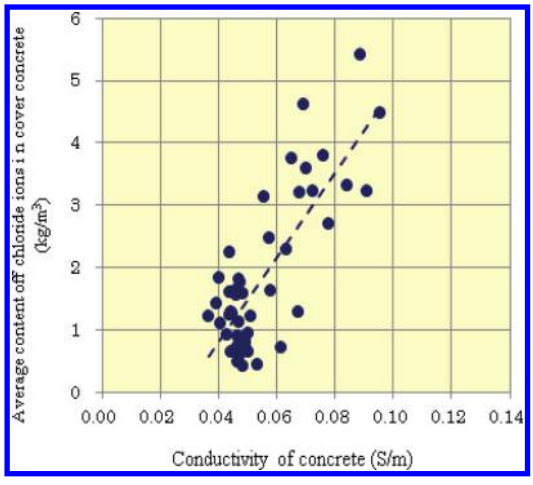

Figure 7. Relationship between conductivity of concrete and content of chloride ions in field survey.

of chloride ions with references in the past studies was used.

As shown in Figure 7, the content of chloride ions increased with the increase in the conductivity of concrete, though the calculations of conductivity of concrete were varied widely as well as the calculation results in the laboratory. The correlation coefficient was 0.790. The relationship between the conductivity of concrete and the content of chloride ions is shown in the following.

$$W_{acl} = 67.5\sigma_c - 1.88 \quad (13)$$

where, W_{acl} = content of chloride ions in field survey (kg/m^3).

From the equation (13), it was possible to estimate the average content of chloride ions in cover concrete in the non-destruction using environmental conditions and measurement results by electromagnetic wave in the field survey.

5 CONCLUSIONS

In this study, the relationship between content of chloride ions and the conductivity, which directly influences the attenuation of the reflected waveform of the electromagnetic wave based on the attenuation equation derived from the Maxwell's wave equation, was investigated and the estimated equation incorporated the factors which affect the estimation of the content of chloride ions as influence coefficient was suggested. This proposed equation was applied to 6 existing structures in which used materials, conditions of mix proportion, environmental conditions, and number of years of service life differed, and the estimation using this proposed equation was compared with results of chemical analysis of content of chloride ions. As the results, it was possible to find the availability of estimating the average content of chloride ions in cover concrete from the estimated equation proposed in this study.

For the future, the estimation method of content of chloride ions at the reinforcing bar will be also investigated, while the estimation accuracy of the content of chloride ions in concrete using the electromagnetic waves is improved.

REFERENCES

Arthur v. H: Dielectric Materials and Applications, Artech House Publishers, 1954.

Junichiro N., Mami A. & Toshiaki M. 2011, Application of an Electromagnetic Method for Evaluation of Chlorine Distribution in Concrete, NDTMS 2011.

Junichiro N. & Toshiaki M. 2011, Applicability of Electromagnetic Wave Method for Estimation of Chloride Content of Coastal Structures, Proceedings of Concrete Solutions, 4th International Conference on Concrete Repair, Design, pp. 359–368.

Jun-ichiro N., Hiroki I. & Toshiaki M. 2012, Possibility of Estimation of Chloride Content in Concrete to Existing Structures Using Electromagnetic Wave, Structural Faults and Repair.

Jun-nichiro N., Hiroki I., Mami U. & Toshiaki M. 2013, Theoretical And Experimental Study On Estimation Of Chloride Content In Concrete Using Electromagnetic Wave, Nondestructive Characterization for Composite Materials, Aerospace Engineering, Civil Infrastructure, and Homeland Security.

Jun-ichiro N., Mami U. & Toshiaki M. 2014, Basic Study for Improvement of Estimation Accuracy Content of Chloride Ions Using Electromagnetic Waves Method, Structural Faults and Repair.

Mizobuchi, T., Suda, K., Hayashi, D. & Yokozeki, K. 2005, Experimental Study on Applicability of Measuring Method of Chloride Content using Electromagnetic Wave in Reinforced Concrete Structures, The 11th International Conference on Fracture.

Concrete Repair, Rehabilitation and Retrofitting IV – Dehn et al. (Eds)
© 2016 Taylor & Francis Group, London, ISBN 978-1-138-02843-2

Lithium migration in mortar specimens with embedded cathode

L.M.S. Souza & O. Çopuroğlu
Faculty of Civil Engineering and Geosciences/Materials and Environment, TU Delft, Delft, The Netherlands

R.B. Polder
Faculty of Civil Engineering and Geosciences/Materials and Environment, TU Delft, Delft, The Netherlands
TNO Technical Sciences/Structural Reliability, Delft, The Netherlands

ABSTRACT: Alkali-Silica Reaction (ASR) is a durability problem that affects numerous concrete structures worldwide. As the reaction progresses, it might lead to deleterious expansion and cracking. The addition of lithium into fresh concrete is already acknowledged as a preventive method. In existing structures, however, lithium would need to be driven into the concrete and the most effective way is through ionic migration. For migration to occur in reinforced concrete, power is supplied between an external electrode and the rebar. If the reinforcement is the cathode, it attracts positive ions, such as lithium ions. Several studies have been conducted on the use of lithium migration as a treatment for ASR. Nevertheless, so far, there is no agreement on the conclusions. It is necessary to better understand this process order to develop a possible treatment against ASR. In this work, a preliminary investigation on lithium migration into mortar specimens with embedded cathode is presented.

1 INTRODUCTION

Concrete structures worldwide are affected by a degradation mechanism known as Alkali-Silica Reaction (ASR). Hydroxyl and alkali (sodium and potassium) ions react with siliceous components present in reactive aggregate, forming a hygroscopic gel. As the ASR gel absorbs water from the pore solution, it expands. As the process progresses, it leads to deleterious expansion and cracking of the concrete element. Even though the reaction is not completely understood, there are several preventive methods against it, such as the use of supplementary cementitious materials or lithium-based admixture. On the other hand, if the reaction is detected in an existing structure, currently, there are no definite treatments.

The addition of lithium ions to the reactive concrete mixture leads to the formation of a non-expansive ASR gel (McCoy & Cadwell 1951, Feng et al. 2010). In hardened concrete, those ions need to be transported into de cementious matrix and migration is the most effective technique. (Thomas et al. 2007, Santos Silva et al. 2008). Migration is the ionic transport mechanism where the driving force is an electric field, formed between electrodes immersed in electrolyte solutions. In cementious materials, the pore solution functions as electrolyte and reinforcement is commonly used as one of the electrodes.

For the past 20 years, numerous authors have investigated lithium migration into ASR affected concrete (e.g Page 1995, Whitmore & Abbot 2000, Thomas & Stokes 2004, Santos Silva et al. 2008, Pacheco & Polder 2010, Bentivegna et al. 2011, Liu et al. 2011, Ueda et al. 2013, Lizarazo-Marriaga et al. 2014). However, it is still necessary to fully understand the principles of lithium migration and document its effect on ASR affected concrete. It is known that the use of the reinforcement as electrode might bring deleterious effects, such as loss of bond strength between rebar and changes in the pore structure, depending on the level of current (Bertolini et al. 2013). In this paper, preliminary results on the experimental study of lithium migration with embedded cathode is presented.

2 EXPERIMENTAL

2.1 *Material and specimens preparation*

Mortar cylinders (diameter of 98 mm and 60 mm of height) were cast with a titanium mesh at 10 mm from one of the surfaces, as shown in Figure 1. The mesh was embedded to represent the situation when a reinforcement bar would be used as cathode in a structure under treatment.

The mortar mixture had a water to cement ratio of 0.5 and sand to cement proportion of 3:1. Portland cement type CEM I 42.5 N, standard

Figure 1. Specimen with embedded titanium mesh (top side).

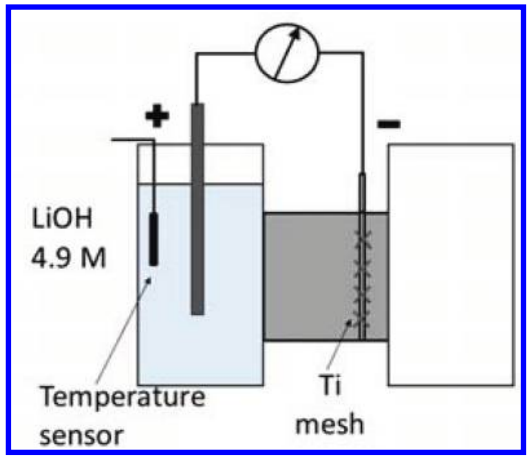

Figure 2. Diagram of the experimental set-up.

sand with D_{max} of 2.00 mm (according to EN 196 1:2005) and deionized water were used. The specimens were cured in the fog room for 36 days.

2.2 *Experimental procedure*

Lithium migration test was performed in a set-up as shown in Figure 2. Each specimen was positioned between two chambers—one with LiOH solution (4.9 M) and another that remained empty, working only as support for the specimen. The chamber with electrolyte received a titanium electrode that worked as anode. The embedded titanium mesh in the specimens were the cathode. Once an electric potential was applied between the electrodes by means of a power source, cations moved towards the cathode while anions were attracted towards the anode. Two types of cell were used. They were identical, except for the presence of ventilation holes in the type I, as shown in Figure 3.

Specimens were tested during four or eight weeks, under 15 or 25 V. Current and anolyte temperature were continuously monitored. Cell electrical resistance was measured with a multimeter at 120 Hz, in resistance mode. Resistivity was calculated by Equation 1 below:

$$\rho = R * A / L \tag{1}$$

where R = the electrical resistance (Ω); A = specimen surface area (m²); L = specimen thickness (m).

Anolyte pH was measured with pH test strips and samples were collected throughout the experiment and analysed by Inductively Coupled Plasma

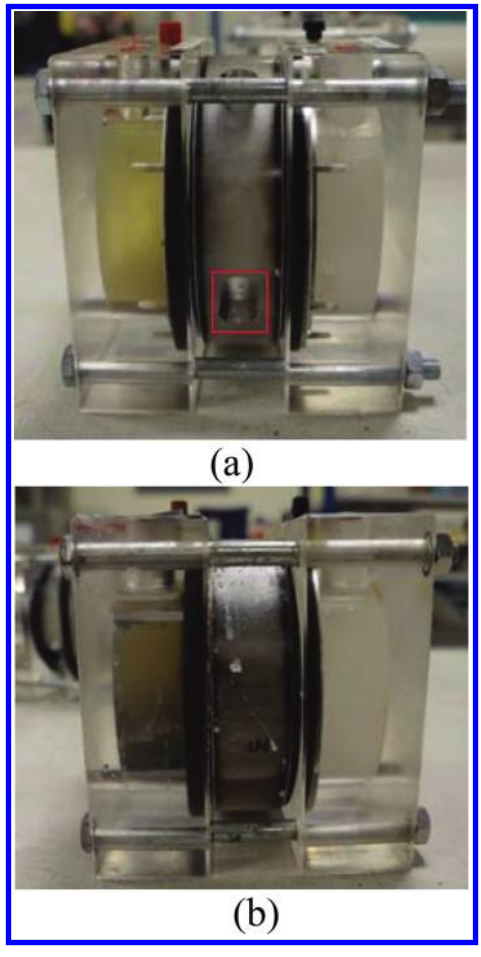

Figure 3. Ventilated cell—type I (a) and non-ventilated cell—type II (b).

(ICP), in order to obtain the concentration of sodium, potassium and lithium and calcium.

2.3 *Results and discussion*

Current density plots are shown in Figure 4. The cells under 25 V exhibited rapid increase in current density in the first hours, reaching a maximum value in less than 12 hours. Same behaviour was noted by other authors (Pacheco & Polder, 2010; Liu et al. 2011). After that, the current density dropped steadily until about day 30, when it stabilized until the end of the experiment. In the cells under 15 V, on the other hand, the current density decreased from the beginning of the experiment. When comparing the cells under the same level of voltage, it can be noted that cells in the set-up type II presented higher current density than those in the set-up type I—and the difference was more pronounced when the applied voltage was higher.

When observing the anolyte temperature behaviour of all cells in Figure 5, it can be observed that the temperature in set-ups type I were lower than those in the other cells. This happened most likely due to the presence of ventilation holes in ring around the specimen. Lower temperatures lead to higher resistivity values and, finally, to lower current densities. It is important to highlight the fact that from day 14 until day 20, the cell LiOH 4.9 M (8 w. 25V I) did not have its anolyte temperature measured due to problems with the temperature sensor. The differences between set-ups type I and II can also be observed in passing charge values, shown in Table 1. Nevertheless, the cells under higher voltage for longer exhibited higher charge, as expected.

The cell electrical resistivity values during the experiment are shown in Figure 6. Initially, the cells presented average resistivity of 35.0 (± 1.4) Ω·m. All cells exhibited increasing resistivity until the end of the experiment. The ones tested for 8 weeks showed a somewhat constant value after 4 weeks, as it was observed in the case of current density. At the end of the experiment, the current was turned off and resistance was again measured after 24 hours. Interestingly, the resistivities did not return to the initial values, indicating that the

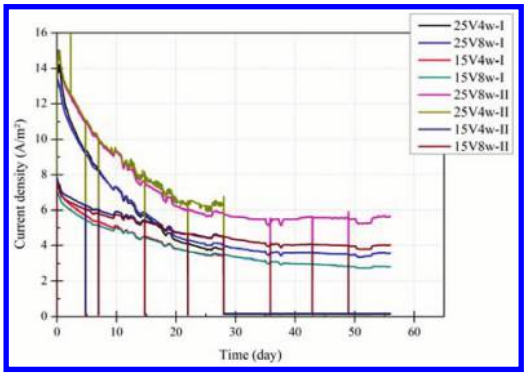

Figure 4. Current density plots.

Table 1. Charge through the specimens during experiment.

Cells	Charge (kC)
LiOH 25V 4w (I)	123
LiOH 25V 4w (II)	159
LiOH 25V 8 w (I)	186
LiOH 25V 8w (II)	253
LiOH 15V 4 w (I)	88
LiOH 15V 4w (II)	103
LiOH 15 V 8w (I)	138
LiOH 15V 8w (II)	172

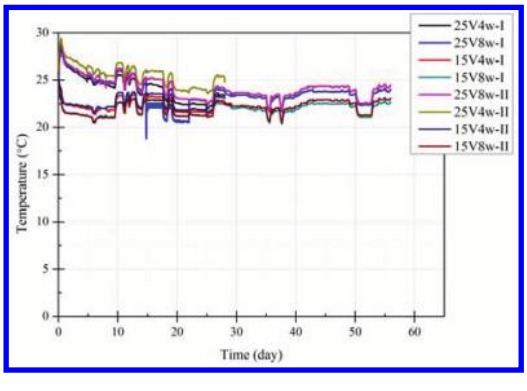

Figure 5. Temperature behavior during experiment.

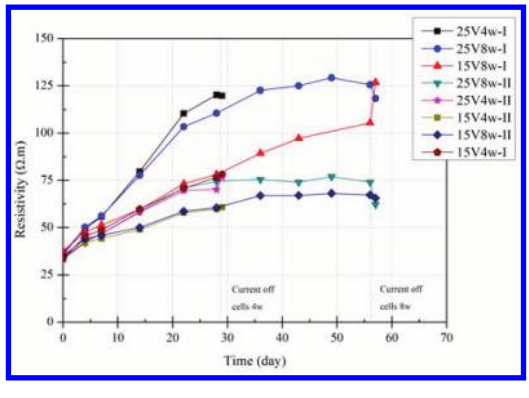

Figure 6. Resistivity variations during test.

variations during the experiment were not a mere artefact due to temperature, as seen in other work (Souza, 2015). This indicates that there were, in fact, irreversible changes in the microstructure of the specimens and/or in the pore solution composition. One possibility is that the production of H_2 on the titanium mesh in the specimens, due to cathodic reaction (Equation 2), lead to development of pressure that resulted in local debonding. Further investigation is planned in order to determine the nature of those changes. Variations in pH in anolyte are related to the anodic reaction, shown in Equation 3. Nevertheless, due to the high buffer capacity of the initial solution, the pH remained 14 throughout the test for all cells.

$$2H_2O + 2e^- \rightarrow 2OH^- + H_2 \quad (2)$$

$$2OH^- \rightarrow H_2O + \frac{1}{2}O_2 + 2e^- \quad (3)$$

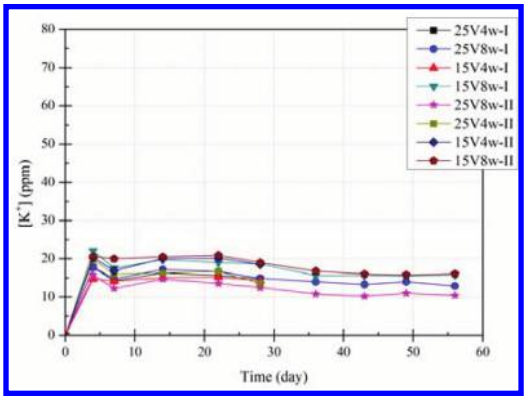

Figure 7. Potassium concentration in anolyte.

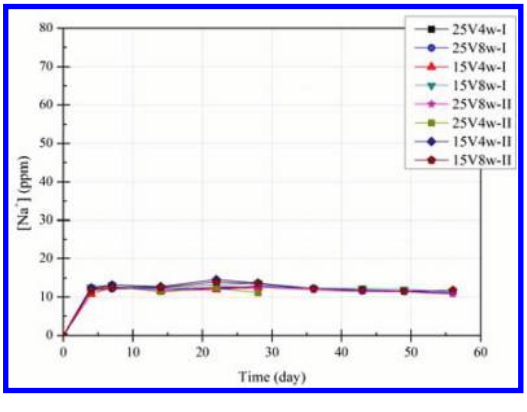

Figure 8. Sodium concentration in anolyte.

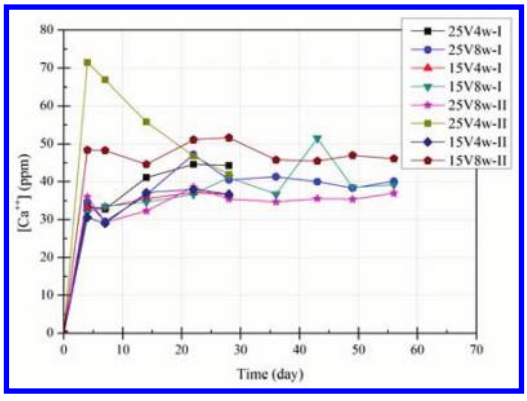

Figure 9. Calcium concentration in anolyte.

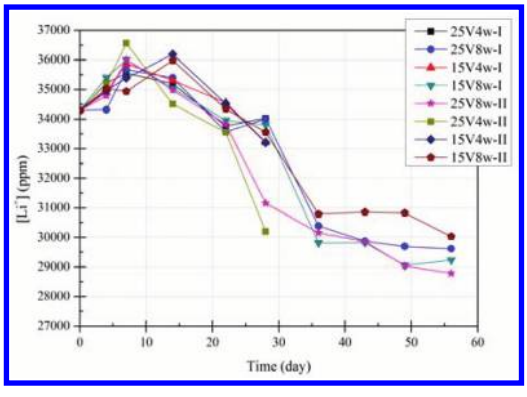

Figure 10. Lithium concentrate ion in anolyte.

Figures 7–10 show the chemical composition of the anolytes during the experiment. Sodium, potassium and calcium ions leached from the specimen by simple dissolution for the first few hours while lithium ions left the anolyte through migration into the specimen. As expected, more lithium ions were removed from anolyte when higher voltage was applied. Chemical analyses of the specimens is foreseen.

3 CONCLUDING REMARKS

Preliminary results indicate that by applying higher voltage it is possible to drive more lithium ions into the specimen, as expected. However, that voltage should be limited. Studies have shown that high current density levels (above 10 A/m²) might lead to changes of the microstructure of concrete and debonding of the reinforcing steel used as electrode (Bertolini et al., 2013). Even though it is not yet

possible to determine the cause of the irreversible increase in resistivity during the experiment, those results indicate that the magnitude of this effect depends on the applied voltage. Therefore, when using this technique as treatment against ASR, it is necessary to find the current density level that would lead to the necessary lithium penetration without causing damage to the concrete element.

This work is still in progress. Other tests, such as obtaining lithium profile in the specimens, are still needed.

ACKNOWLEDGMENT

Financial support by the Dutch Technology Foundation (STW) for the project 10971: "Modelling, non-destructive testing and Li-based remediation of deleterious Alkali-Silica Reaction in concrete structures" is gratefully acknowledged.

REFERENCES

Bertolini, L.; Elsener, B.; Pedeferri, P.; Redaelli, E. & Polder, R.B., 2013. *Corrosion of Steel in Concrete: Prevention, Diagnosis, Repair*. Weinheim: Wiley-VCH.

Bentivegna, A.F.; Giannini, E.R. & Folliard, K.J. 2012. Use of electrochemical migration to mitigate alkali-silica reaction in large scale concrete structures. In. Michael Grahtham, Viktor Mechtcherine & Ulrich Schneck (eds) *Concrete Solutions; Proc. 4th Intern. Conf. of Concrete Repair, Dresden, Germany, September 2011.* London: Taylor & Francis Group.

Feng, X.; Thomas, M.D.A.; Bremmer, T.W.; Folliard, K.J. & Fournier, B. 2010. New Observations on the Mechanism of Lithium Nitrate Against Alkali Silica Reaction. *Cement and Concrete Research* 40(1): 94–101.

Liu, C.-C.; Wang, W.-C. & Lee, C. 2011. Behavior of cations in mortar under accelerated lithium migration technique controlled by a constant voltage. *Journal of Marine Science and Technology* 19 (1): 26–34.

Lizarro-Marriaga, J.; Lozano, J.; Silva, J., Fonseca, L.; Hermida, G. & Claisse, P. A novel assessment of the electrochemical lithium impregnation. 2014. In Michael Grantham, P.A. Muhammed Basheer, Bryan Magee & Marios Soutsous (eds) *Concrete Solutions—Proceedings of Concrete Solutions, 5th International conference on concrete repair*, Belfast, Northern Ireland, September 2014. CRC Press.

McCoy, E.J. & Caldwell, A.G. 1951. New approach to inhibiting alkali-aggregate expansion. *Journal of the American Concrete Institute* 22: 693–706.

Pacheco, J. & Polder, R.B. Preliminary study of electrochemical lithium migration into cementitious mortar. 2010. In Klaas van Breugel, Guang Ye & Yong Yuan (eds) *Proceedings 2nd International symposium on service life design for* infrastructure, Delft, October 2010. Bagneux: RILEM publications.

Page, C.L. & Yu, S.W. 1995. Potential effects of electrochemical desalination of concrete on alkali-silica reaction. *Magazine of Concrete Research* 47 (170): 23–31.

Santos Silva, A.; Salta, M.; Melo Jorge, M.E.; Rodrigues, M.P. & Cristino, A.F. 2008. Research on the suppression expansion due to ASR. Effect of coatings and lithium nitrate. In Broekmans, M.A.T.M. & Wigum, B.J. (eds) *Proceedings 13th International Conference on Alkali-Aggregate Reaction in Concrete (ICAAR), June 2008, Trondheim*.

Souza, L.M.S.; Polder, R.B. & Çopuroğlu, O. 2015 Influence of anolyte on lithium migration in concrete. In Carmen Andrade, Joost Gulikers & Rob Polder (eds) *Durability of reinforced concrete from composition to protection—Selected papers of the 6th International RILEM PhD workshop*, Delft, The Netherlands, July 2013, Springer.

Thomas, M.D.A.; Fournier, B.; Folliard, K.J.; Ideker, J.H. & Resendez Y. 2007. *The use of lithium to prevent or mitigate alkali-silica reaction in concrete pavements and structures. Report from Federal Highway Administration FHWA-HRT-06-133*, Washington D.C: U.S. Department of Transportation.

Thomas, M.D.A. & Stokes, D.B. 2004. Lithium impregnation of ASR-affected concrete: preliminary studies. In Mingshu Tang & Min Deng (eds), *Proceedings 12th International Conference on Alkali-Aggregate Reaction in Concrete (ICAAR), Beijing, October 2004, 659−667*. Beijing: Beijing World Publishing Corporation.

Treatment used to mitigate Alkali-Silica Reaction in Concrete.

Ueda, T.; Baba, Y. & Nanasawa, A. 2013. Penetration of lithium into ASR-affected concrete due to electro-osmosis of lithium carbonate solution. *Construction and Building Material* 39: 113–118.

Whitmore, D. & Abbot, S. 2. 2000. Use of an applied electric field to drive lithium ions into alkali-silica reactive structures. In M.A. Bérubé, Benoît Fournier & Benoit Durand (eds) *Proceedings 11th International Conference on Alkali-Aggregate Reaction in Concrete (ICAAR), Quebec City, June 2000, 1089-1098*. Sainte-Foy: Centre de Recherche Interuniversitaire sur le Béton (CRIB).

Concrete Repair, Rehabilitation and Retrofitting IV – Dehn et al. (Eds)
© 2016 Taylor & Francis Group, London, ISBN 978-1-138-02843-2

Analysis and visualization of water uptake in cracked and healed mortar by water absorption tests and X-ray radiography

B. Van Belleghem & N. De Belie
Magnel Laboratory for Concrete Research, Department of Structural Engineering, Faculty of Engineering and Architecture, Ghent University, Zwijnaarde, Belgium
Strategic Initiative Materials (SIM), Project ISHECO within the Program "SHE", Zwijnaarde, Belgium

J. Dewanckele & V. Cnudde
Centre for X-ray Tomography, Department of Geology and Soil Science, Faculty of Sciences, Ghent University, Ghent, Belgium

ABSTRACT: Crack formation in cementitious materials is a common problem which highly accelerates the ingress of water and aggressive substances. For most structures fast crack repair may be needed, however, repair costs can be large and in some cases repair is impossible due to inaccessibility. Autonomous crack healing by means of encapsulated polyurethane is a possible solution to increase the durability of structures. Water absorption tests on mortar prisms indicate that crack healing can reduce the water absorption of mortar by 50%. Visualization of the water profile inside the specimens by means of X-ray radiography shows that healed cracks can be either completely filled with polyurethane and block the water ingress into the crack completely or the polyurethane may not fill up the whole crack but seal the crack faces. In both cases it is clearly seen on the X-ray images that the water ingress into the mortar is significantly reduced. It can be concluded that autonomous crack healing by means of encapsulated polyurethane has the potential to improve the durability of cementitious materials.

1 INTRODUCTION

Service life and durability of porous cement-based materials has become a topic of great importance because of the economic and ecological implications. Penetration of moisture is one of the most important damage mechanisms that could lead to the deterioration of building materials such as mortar and concrete. Water itself is not really harmful for most building materials, but it commonly acts as a medium for the transport of aggressive substances when it penetrates into a porous material.

Some studies use permeability as an indicator for the ability of building materials to transport water (Aldea et al. 1999, Reinhardt & Jooss 2003, Wang et al. 1997). However, when concrete is only partly saturated, capillary absorption dominates the ingress of water at early times. As capillary absorption is the dominant mechanism for water uptake in most concrete structures, this will be the topic of this investigation.

Although the capillary water absorption of sound mortar and concrete has already been studied in depth (Hall 1986, Hall 1987, Hall 1989, McCarter et al. 1992), considering concrete in a perfect, uncracked state is usually not realistic. In most cases the concrete used in structures is cracked. Cracks can significantly accelerate ingress of water into the concrete matrix. Even very fine cracks can accelerate water absorption due to high capillary forces. Wang (2014) was one of the researches that performed water sorptivity tests on cracked concrete. In his research, three different load levels were used to compare water absorption of concrete cracked by different loads. He concluded that there was no clear monotonic increase of sorptivity with the load level. Possible better parameters to evaluate the effect of cracks on water ingress are crack width and crack depth.

As cracking of reinforced concrete cannot be completely prevented and manual crack repair holds multiple disadvantages, a lot of research has been done in the past few years in order to heal the cracks autonomously. Autonomous crack healing by the use of encapsulated healing agents embedded inside concrete is one of the promising approaches in the domain of self-healing (Van Tittelboom et al. 2011). Encapsulation based self-healing materials sequester a healing agent inside discrete capsules. When a crack appears, the capsules break and the healing agent flows into the crack. One of the most important aspects of capsule based self-healing is the choice of the healing agent. A lot of different healing agents have been investigated already (Dry

2001, Van Tittelboom 2012). Polyurethane is one of these agents with a lot of promising properties. It has the ability to expand upon reaction, which makes it possible to fill large crack volumes with little encapsulated pre-polymer. It is also very flexible and available in a wide range of viscosities (Petrie 2007).

The efficiency of the healing mechanism to seal the crack autonomously can be investigated by a gravimetrical water absorption test. This method indicates the total amount of water that is absorbed after a certain amount of time. Although this is already useful information, the water profile inside the specimen cannot be visualized with this method. Especially for cracked and healed concrete, it is necessary to understand the process of water transportation and the development of water distribution inside the sample. Moisture flow in porous materials can be visualized by electrical techniques, Nuclear Magnetic Resonance (NMR) spectroscopy (Rucker-Gramm & Beddoe 2010) or radiation attenuation techniques such as X-ray or neutron radiography (Roels & Carmeliet 2006, Cnudde et al. 2008, Zhang et al. 2010, Derluyn et al. 2013, Van Tittelboom et al. 2013, Dewanckele et al. 2014). Among these methods, radiation attenuation techniques can provide the best accuracy and resolution. When an object is irradiated by an X-ray or neutron beam, the beam attenuates due to the interaction with the material and the transmitted intensity of the beam can be recorded. When a porous material is scanned in dry and wet state (before and after absorption of water), the images can be subtracted from each other to visualize the water inside the sample. In this research, X-ray radiography is used to visualize the moisture uptake in cracked and healed mortar samples.

2 MATERIALS AND METHODS

2.1 *Glass capsules*

In order to carry the healing agent and trigger the healing action, cylindrical glass capsules were used similar to the capsules used by Van Tittelboom et al. (2011). Borosilicate glass tubes with an internal diameter of 3 mm and an outer diameter of 3.35 mm were used. Due to their high brittleness, the capsules will easily break when the healing action needs to be triggered. The glass does not react with the healing agent inside and forms an airtight barrier for the agent.

2.2 *Healing agent*

A one component Polyurethane (PU) was used as healing agent. This polymer was developed within the framework of another project (SHEcon). The one component PU was preferred above multi-component healing agents, because of the risk of incomplete mixing of the different components. The viscosity of the healing agent is very important regarding a good self-healing of cracks. On the one hand the viscosity needs to be low enough so that the healing agent is able to flow in the crack, on the other hand the viscosity must be high enough to make sure that it does not leach out of the crack too much and that it is not absorbed by the matrix. The viscosity of the pre-polymer is 6700 mPas at 25°C.

The pre-polymer of the healing agent was carefully injected into the glass capsules. First, the capsules were sealed with Polymethylmethacrylate (PMMA) at one end, then the capsules were filled with the pre-polymer of the healing agent by means of a syringe with a needle. Finally, the other ends of the capsules were also sealed with PMMA and the capsules were ready to be embedded inside the mortar samples.

2.3 *Mortar samples*

To determine the influence of cracks and the efficiency of crack healing on the water absorption of mortar, samples with ordinary Portland cement mortar were prepared. A standard mortar mix was made with a composition according to EN 196-1. A mass ratio of 6:2:1 of aggregate-cement-water was taken, which gives a water-cement ratio of 0.50. The aggregate in the standard mortar mix was sand with grain size 0–2 mm.

2.3.1 *Samples without self-healing properties*

Unreinforced prismatic mortar specimens with the following dimensions were cast in wooden forms: 40 mm × 40 mm × 160 mm. For each series three samples were produced. For the uncracked reference samples, first the molds were partially filled with mortar. When this first layer was compacted on a vibration table, the molds were completely filled with mortar and vibrated again.

To create cracked mortar prisms, a non-destructive method was used to generate standardized cracks in mortar. An artificial crack was made by means of thin steel plates which were introduced into the fresh mortar upon casting and removed before complete hardening. The thin plates had a thickness of 300 µm. The crack depth was kept constant at 20 mm, which was half the height of the mortar samples. The crack length was 40 mm, so that the cracks ran through the whole width of the mortar sample. The steel plates were placed on iron rods which were fixed above the molds by using magnetic bases (Fig. 1). Prisms with one, two and four cracks were made. For the prisms with multiple cracks, the intermediate distance between adjacent cracks was kept constant at 20 mm.

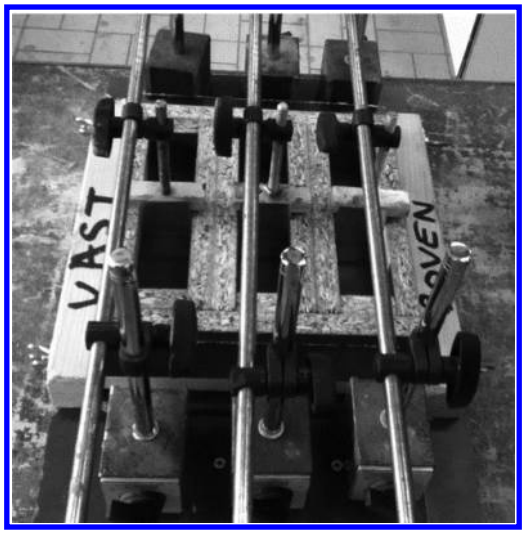

Figure 1. Standardized artificial cracks—positioning of the steel plates.

When all the steel plates were positioned in the molds, the mortar was brought into the molds in the same way as for the uncracked samples.

After casting, all specimens were placed in an air-conditioned room with a temperature of 20 ± 2°C and a relative humidity of at least 95%. After 24 hours, the metal plates were removed carefully and the prisms were demolded. Then, the prisms were stored under the same conditions until the age of 28 days.

An overview of the test series with their abbreviations and the area exposed to water during the absorption test is given in Table 1.

2.3.2 *Samples with self-healing properties*

Autonomous healing of cracks in cementitious materials by encapsulated polyurethane occurs by breaking of capsules, filled with healing agent, upon crack appearance. In this research standardized artificial cracks by means of metal plates are used. Since the self-healing mechanism needs to be triggered at the moment that the crack appears, the PU filled capsules need to break at the moment when the plates are pulled out of the mortar samples. For that reason two holes with a diameter of 3.5 mm were drilled into the thin steel plates. The capsules were then put into those holes, so that they would break when the plates are pulled out (Fig. 2).

Mortar prisms with one and two autonomously healed cracks were made (Table 1). For the prisms with one healed crack two capsules with a length of 30 mm were positioned on nylon threads so that the distance from the bottom and the sides of the

Table 1. Overview of the test specimens.

Specimen type	Abbreviation	Number of cracks	Area exposed to water (cm²)
Uncracked	UNCR-A	0	64
	UNCR-B	0	4
Cracked	CR-1	1	4
	CR-2	2	8
	CR-4	4	16
Self-healing	SH-1	1	4
	SH-2	2	8

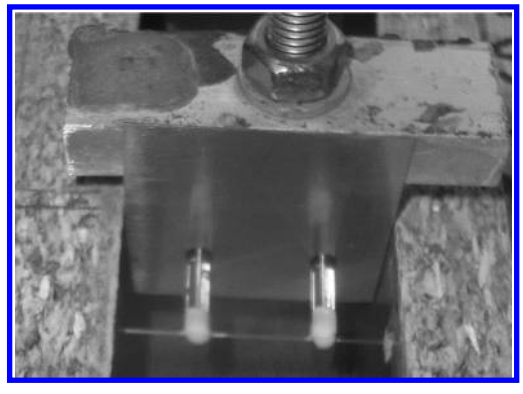

Figure 2. PU-filled capsules through steel plates.

prisms to the capsules is 10 mm. The intermediate distance between the capsules was then 20 mm. The capsules were glued on the nylon threads with PMMA to make sure they stay in the same position when mortar is poured into the molds. For the mortar samples with two healed cracks, capsules with a length of 50 mm are used that run through both metal plates. The positioning of the capsules in the molds was the same as for the prisms with one healed crack and the distance between the two cracks was again 20 mm.

When the capsules and plates were positioned in the molds, the mortar was brought into the molds in the same way as for the other samples. So first a mortar layer of 10 mm was put in the molds and compacted on a vibration table. Then the molds were completely filled with mortar. After casting, the self-healing specimens were placed in an air-conditioned room with a temperature of 20 ± 2°C and a relative humidity of at least 95%. They were demolded after 24 hours and stored in the same conditions until the age of 28 days. When the mortar samples had reached the age of 28 days, the metal plates were pulled out of the mortar. This resulted in breakage of the capsules and triggering of the self-healing mechanism.

2.4 *Crack healing*

When the glass capsules were broken due to pulling out the thin metal plates in the specimens SH-1 and SH-2, the polyurethane leaked into the crack and then hardened in the crack due to the exposure to moisture in the air. The polyurethane needs at least 24 hours to harden completely inside the crack, so the self-healing prisms were stored for two days in a climate room at a temperature of 20°C and a relative humidity of 60%.

2.5 *Specimen preparation for absorption testing*

Because the cracks in the mortar prisms are made by thin metal plates, the surface of the specimens that was not in contact with the formwork (troweled surface) is the test face during the absorption test. This surface is not perfectly flat and the outermost layer of this surface is usually more porous than the rest of the mortar. In order to exclude these effects, the outermost layer (approximately 1 mm) was cut off by water-cooled sawing. For the uncracked and cracked samples this was done at the age of 28 days, for the self-healing samples the layer was cut off after the healing took place, so after 30 days.

After removal of the outermost layer, the specimens are brought to a low and even moisture level by drying them in an oven at 40 ± 2°C until constant mass was achieved, according to the European standard NBN EN 13057. Constant mass was defined as a mass change of not more than 0.1% in 24 hours. The drying process was necessary to give all specimens an even moisture level within a short time. If the samples would not have been dried, the time to reach constant mass at a relative humidity of for example 60% would have been several months (Rucker-Gramm & Beddoe 2010, Castro et al. 2011). The drying temperature should not be much higher than 40°C, because microcracking might occur around the aggregates due to differential thermal expansion and contraction when mortar is exposed to higher temperatures. This microcracking would have a negative influence on the capillary water absorption.

To evaluate the water uptake of one or multiple cracks and the efficiency of the self-healing it is necessary that only a small zone around each crack is subjected to water during the absorption test. Therefore, the sides of the samples were partly covered with aluminum butyltape after the drying period. The tape consists of a self-adhesive rubber butylmass with a tear-resistant aluminum layer on top. The advantage to regular aluminum tape is the fact that the tape can be nicely pressed against the mortar surface in order to make it watertight. The test face of the samples was also covered with aluminum butyltape so that there was only a zone with an area of 4 cm² around each crack in contact with water (Fig. 3).

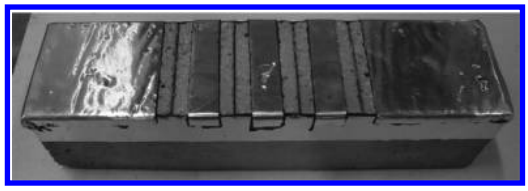

Figure 3. Test face of a mortar specimen covered with aluminum butyltape.

For the uncracked specimens, one series was taped only on the sides to evaluate uniform water uptake through the whole bottom surface of the samples (denoted UNCR-A). The other uncracked series was taped on the sides and partly on the bottom, so that a zone with an area of 4 cm² was in contact with water (denoted UNCR-B). This last series was made to compare the uncracked mortar samples to the (self-healing) specimens with one crack, because in this case all the before mentioned specimens have the same area (4 cm²) exposed to water during the absorption test.

2.6 *Water absorption test*

According to the standard NBN EN 13057, all samples were taken out of the oven and placed in a climate room at a temperature of 20°C and a relative humidity of 60% when they were dry. The samples were left in this environment for 24 hours. After that period, the absorption test started. The test faces of all specimens were placed on supports in a shallow tray containing water such that the depth of immersion of each specimen is 2 ± 1 mm. A cover is placed on the tray immediately after all specimens have been positioned in it. The water uptake into the specimens is then determined by weighing the prisms at several time intervals using a balance with an accuracy of 0.01 g. When the specimens are taken out of the tray, they are wiped with a wet cloth to remove surplus water. After weighing, the samples are immediately returned to the tray and the cover is replaced. In this research the specimens were weighed every 5 minutes during the first half hour of the absorption test and every 30 minutes during the next 8 hours. After that, the specimens are weighed again after 24, 48, 72 and 96 hours of exposure to water.

2.7 *X-ray radiography*

As previously mentioned, the water uptake inside the specimen cannot be visualized through a gravimetrical water absorption test. Because the artificial cracks in the mortar prisms run through the whole width of the specimen, a 2D water uptake situation was established. For that reason, X-ray

radiography could be used for the visualization of the time dependent water movement into cracked or healed mortar samples. For each specimen type mentioned in Table 1, an extra sample was made for X-ray radiography. The experiments were performed on HECTOR, a 240 kV micro-CT setup optimized for research (Masschaele et al. 2013). As X-ray source, a XWT 240-SE microfocus from X-RAY WorX was installed. This high power reflection tube can deliver a target power of up to 280 W for high X-ray flux, while a minimum focal spot size of 4 µm makes the system ideally suited for high resolution X-ray CT.

The radiographs were taken with an energy of 140 kV and a power of 150 W. A thin (1 mm) Cu filter was installed. For each image ten frames were taken with an exposure time of 500 ms. A magnification of 2 was obtained by placing the samples in the middle between the X-ray source and the detector. The Source Detector Distance (SDD) was 1200 mm, so the Source Object Distance (SOD) was 600 mm. Each specimen was placed on two line supports in a plastic container. Two specimens could be illuminated at the same time by placing one container on top of the other (Fig. 4). As can be seen in Figure 4, the upper container is not placed straight above the other one. Instead, the upper container is shifted a little so that both containers could be filled with water without moving them. This is very important for the analysis of the moisture content in the samples, because the wet and dry images will be subtracted from each other. When samples in the wet image are shifted just a little bit compared to the dry image the moisture content will not be clearly visible.

When the setup was ready, the samples could be illuminated a first time in the dry state. Next, the containers were carefully filled with water by means of a syringe so that the immersion of each specimen is 2 ± 1 mm. Only one minute after the water was added, a first scan of the samples in the 'wet' state could be taken. During the first half hour of water absorption process the samples were illuminated approximately every 6 seconds. After the first half hour, the samples were illuminated every 13 minutes for the next 24 hours. Afterwards, the water profile in the mortar specimens at several time intervals could be visualized with the program ImageJ by subtracting the dry image from the wet images.

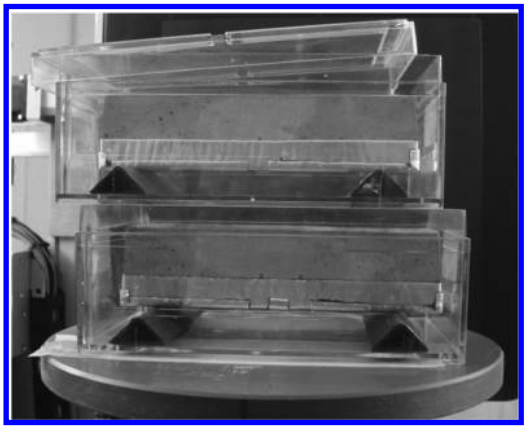

Figure 4. Setup of the specimens scanned by X-ray radiography.

3 RESULTS AND DISCUSSION

3.1 *Crack width measurements*

Before the start of the absorption test, the crack widths of all standardized cracks are measured microscopically. The width of each crack is measured 8 times along its length. The mean crack width is 283 ± 2 µm which is slightly less, but still in good agreement with the thickness of the metal plates (300 µm).

3.2 *Comparison of the water absorption between uncracked and cracked mortar*

The results of the gravimetrical water absorption test are represented in graphs where the cumulative water absorption per unit of surface area (g/cm²) is plotted in function of the square root of time ($h^{0.5}$). Firstly, the water absorption of uncracked and cracked mortar is analyzed. The results are given in Figure 5. In general, the water absorption

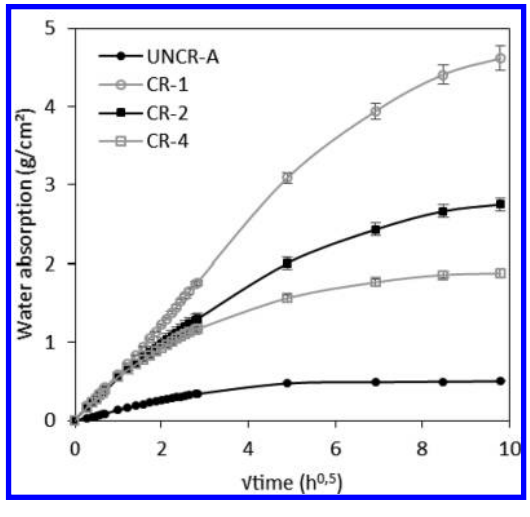

Figure 5. Water absorption curves of uncracked and cracked mortar specimens. Error bars represent the standard deviations of the mean values of 3 specimens.

of all specimens is increasing nearly linear with the square root of time during the first 8 hours of the test. This is in agreement to what is found in literature (Hall 1989, Martys & Ferraris 1997).

Looking at the results of the cracked mortar specimens, it is clear that the water absorption per unit surface area is the same during the first hour of the absorption test (Fig. 5). This is logical, because the cracks of all cracked samples are almost identical, so the water uptake of one or more cracks per unit of surface area is the same. However, after the first hour the prisms with two cracks begin to take up less water per unit surface area than the prisms with one crack. The same can be concluded for the prisms with four cracks compared to the ones with one or two crack(s). The reason that the samples with one crack take up more water per unit of surface area than the samples with two or four cracks is the fact that water can spread horizontally in the specimens from both crack faces. When two cracks are present in the sample, the surface area subjected to water is doubled and the water can only spread freely from one crack face of each crack. The horizontal water movement in the mortar zone between two adjacent cracks is limited because of the overlap of the water spread. It can be concluded that the horizontal overlap of the water spread between adjacent cracks occurs after approximately one hour of water absorption. This is also confirmed when the water front is visualized with X-ray radiography (section 3.4).

For the uncracked specimens there is a uniform water uptake in the sample and therefore almost no horizontal water movement. For that reason, the uncracked samples take up the least water per unit surface area. It can also be seen that the uncracked prisms are already completely saturated after 48 hours.

3.3 *Evaluation of the self-healing efficiency*

From the results of the water absorption test it is possible to evaluate whether a one component polyurethane is able to reduce the water absorption in cracked mortar. In Figure 6 the water absorption of the samples with one healed crack (SH-1) is compared to the water absorption of samples with an unhealed crack (CR-1) and uncracked samples with the same surface area subjected to water (UNCR-B). Figure 7 shows the comparison between the water absorption of two healed cracks (SH-2) and two unhealed cracks (CR-2).

It can be concluded from the results that the polyurethane is very well able to seal the cracks in most of the samples. After 24 hours, the mean total water absorption of the healed specimens with both one and two cracks is almost half the amount of the mean water absorption of the unhealed specimens. The mean absorption of the SH-1 specimens is even comparable to that of the uncracked mortar samples.

It should be mentioned that one of the three tested SH-1 samples showed a lower healing efficiency than the other two. This is also the reason why the standard deviation for this series is much larger than for the other sample series (Fig. 6). Microscopic images of the cracks of the SH-1 series were taken in order to verify whether the cracks were

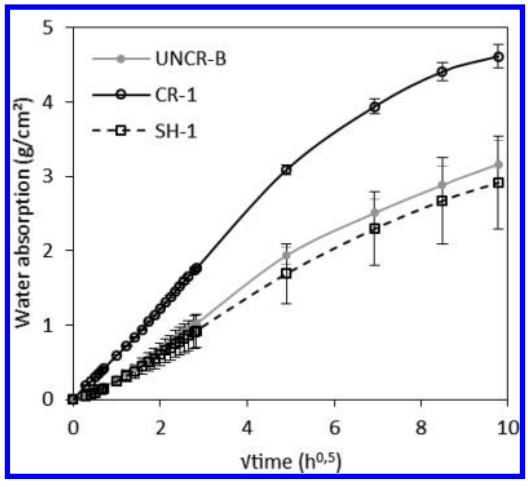

Figure 6. Comparison of water absorption between healed and unhealed specimens with one crack and uncracked samples. Error bars represent the standard deviations of the mean values of 3 specimens.

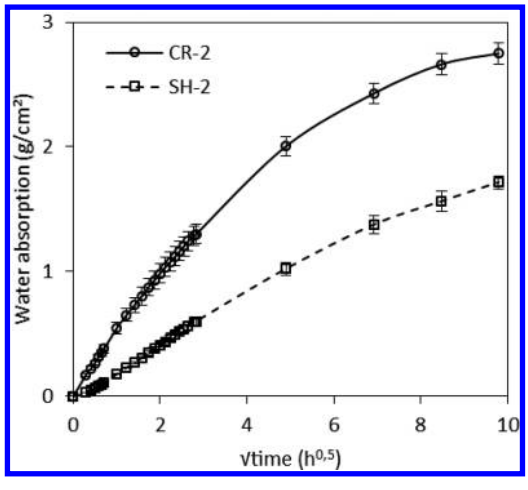

Figure 7. Comparison of water absorption between healed and unhealed specimens with two cracks. Error bars represent the standard deviations of the mean values of 3 specimens.

well sealed at the surface. From these images it was seen that at some small parts of the crack surface the polyurethane did not completely seal the crack. With the software ImageJ the length of the parts in the crack that were not sealed were compared to the total crack length. For the two SH-1 samples which showed good healing results in the water absorption test, only 4.5% and 5% of the crack length was not well sealed. For the other SH-1 sample that showed a lower healing efficiency, 18.3% of the crack was not well sealed. This may explain the fact that the water absorption of this last mortar prism was higher than for the other ones.

3.4 *Visualization of the water uptake by X-ray radiography*

By subtracting the X-ray images in the wet state (during the absorption test) from the dry state image the water profile in the mortar specimens could be visualized. In the following figures, the middle parts (width of 6.5 cm) of the different mortar samples are shown. The water inside the samples is indicated by the darker zones in the images. The darker the zones in the images, the more water is present in the sample.

In Figure 8 a comparison between the water uptake of an uncracked (UNCR-B) and cracked (CR-1) specimen is visualized. From these images it is clear that the water uptake in a specimen with a crack is very fast in the first 30 minutes of the test while there is almost no water uptake in the uncracked sample. After 8 hours, the water in the cracked specimen has already reached the top of the sample. The water front in the uncracked sample has only reached half the height at 8 hours. At 24 hours, the water in both specimens has spread over the whole middle part.

Figure 9 gives a comparison between the water uptake of an unhealed and healed specimen with two adjacent cracks. It can be seen that the images for the unhealed specimen are not very clear. This is because the sample shifted a bit during the filling of the container. When the images in the wet state were then subtracted from the dry state image, there was no perfect overlap. Despite this fact, the water front is still visible. The water front in the cracked specimen for each of the cracks in the first 30 minutes of the absorption test is very similar to the water profile for the specimen with one crack (Fig. 8). For the healed specimen on the other hand, there is very few water uptake through the cracks. This means that the cracks are very well sealed by the polyurethane. The crack on the right in the figures does not turn dark on the inside. This indicates that the crack is completely filled with polyurethane, because no water could enter. The left crack on the other hand does turn dark after 30 minutes, which indicates that the left crack is not completely filled with polyurethane. However, the water entering the mortar through the crack faces is very limited, so the crack faces are probably covered with PU for the biggest part. This clearly limits the horizontal water spread inside the mortar sample. After 8 hours, water has spread over the whole middle part of the cracked specimen. For the healed specimen the water front after 8 hours is more comparable to that of the uncracked specimen (Fig. 8).

For the specimen with four cracks, the same conclusions can be stated as for the specimen with

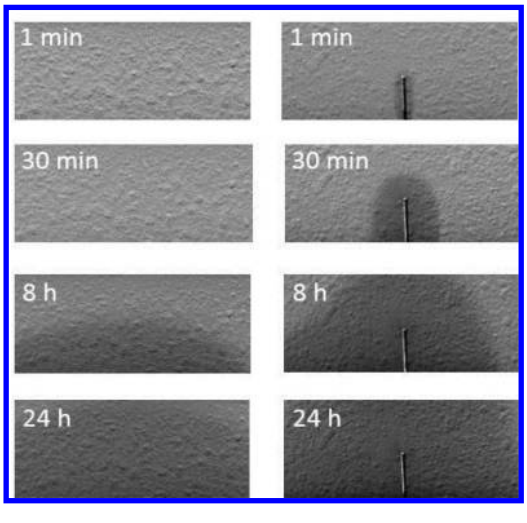

Figure 8. Visualization of the water uptake in an uncracked (UNCR-B) and cracked (CR-1) specimen.

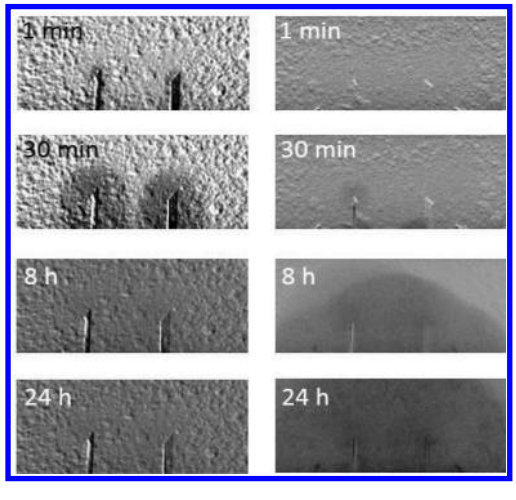

Figure 9. Visualization of the water uptake in a cracked (CR-2) and healed (SH-2) specimen with two adjacent cracks.

two cracks. The X-ray images of the specimens with multiple cracks also show that the overlap of water spread between two adjacent cracks occurs somewhere between 30 and 50 minutes of exposure time. The approximation of one hour, based on the results of the gravimetrical absorption test clearly agrees well to that.

4 CONCLUSIONS

The water absorption of sound mortar and also mortar with cracks is increasing nearly linear with the square root of time during the first 8 hours of contact with water. After one hour testing, the water uptake per exposed surface area of mortar with multiple cracks is less than for mortar specimens with one crack, because there is always a horizontal overlap of the water spread between adjacent cracks inside the specimens.

The polyurethane used in this research is a very appropriate healing agent for obtaining crack healing in cementitious materials. Although the pre-polymer of the polyurethane had a rather high viscosity, the PU was able to seal most of the cracks. The total water absorption after 24 hours of cracked specimens with one or two cracks could be reduced by 50% due to crack healing with polyurethane. The water uptake of the healed specimens was even comparable to the water uptake of uncracked samples. If the water would contain aggressive substances, the self-healing activity would greatly reduce the degradation rate and improve the durability of the structure. This finding could be used to prove that an important service life extension of structures can be achieved by self-healing cementitious materials.

X-ray radiography is a very fast and efficient non-destructive test method to visualize the water uptake in mortar. The distribution of the water profile inside the specimens could be clearly visualized at several time intervals. The images are directly obtained with good resolution in space and time. Also, the mechanism of water uptake in cracked and healed specimen could be compared. From these results it is clear that healed cracks can be either completely filled with PU and block the water ingress into the crack completely or the PU may not fill up the whole crack but seal the crack faces. In both cases the water ingress into the mortar is significantly reduced.

ACKNOWLEDGEMENTS

This research under the program SHE (Engineered Self-Healing materials) (project ISHECO: Impact of Self-Healing Engineered Materials on steel COrrosion of reinforced concrete) was funded by SIM (Strategic Initiative Materials in Flanders) and IWT (Agency for Innovation by Science and Technology). The financial support from the foundations for this study is gratefully acknowledged. The authors would like to thank Kim Van Tittelboom for critically reading the manuscript.

REFERENCES

Aldea, C-M., Shah, S.P. & Karr A. 1999. Permeability of cracked concrete. *Materials and Structures* 32(5): 370–376.

Castro, J., Bentz, D. & Weiss, J. 2011. Effect of sample conditioning on the water absorption of concrete. *Cement and Concrete Composites* 33(8): 805–813.

Cnudde, V., Dierick, M., Vlassenbroeck, J., Masschaele, B., Lehmann, E., Jacobs, P., Van Hoorebeke, L. 2008. High-speed neutron radiography for monitoring the water absorption by capillarity in porous materials. *Nuclear Instruments & Methods in Physics Research B* 266(1): 155–63.

Derluyn, H., Griffa, M., Mannes, D., Jerjen, I., Dewanckele, J., Vontobel, P. et al. 2013. Characterizing saline uptake and salt distributions in porous limestone with neutron radiography and X-ray micro-tomography. *Journal of Building Physics* 36(4): 353–374.

Dewanckele, J., De Kock, T., Fronteau, G., Derluyn, H., Vontobel, P., Dierick, M., Van Hoorebeke, L., Jacobs, P., Cnudde, V. 2014. Neutron radiography and X-ray computed tomography for quantifying weathering and water uptake processes inside porous limestone used as building material. *Materials Characterization* 88: 86–99.

Dry, C. 2001. Design of self-growing, self-sensing and self-repairing materials for engineering applications. *Proceedings of SPIE 4234*: 23–29.

Hall, C. 1986. Water movement in porous building materials—VII: the sorptivity of mortars. *Building and Environment* 21(2): 113–118.

Hall, C. 1987. Water movement in porous building materials—IX: the water absorption and sorptivity of concretes. *Building and Environment* 22(1): 77–82.

Hall, C. 1989. Water sorptivity of mortars and concretes: a review. *Magazine of Concrete Research* 14(147): 51–61.

Martis N.S. & Ferraris C.F. 1997. Capillary transport in mortars and concretes. *Cement and Concrete Research* 27(5): 747–760.

Masschaele, B., Dierick, M., Van Loo, D., Boone, M.N., Brabant, L., Pauwels, E., Cnudde, V., Van Hoorebeke L. 2013. HECTOR: a 240 kV micro-CT setup optimized for research. *Journal of physics: Conference Series* 463: UNSP 012012.

McCarter, W.J., Ezirim, H. & Emerson M. 1992. Absorption of water and chloride into concrete. *Magazine of Concrete Research* 44(158): 31–37.

NBN EN 196-1. 2005. *Determination of strength. Methods of testing cement.* European committee for Standardization. Brussels, Belgium.

Petrie, E.M. 2007. *Handbook of adhesives and sealants*: 377–423. New York: McGraw-Hill.

Reinhardt, H-W. & Jooss, M. 2003. Permeability and self-healing of cracked concrete as a function of temperature and crack width. *Cement and Concrete Research* 33(7): 981–985.

Roels, S. & Carmeliet J. 2006. Analysis of moisture flow in porous building materials using microfocus X-ray radiography. *International Journal of heat and Mass Transfer* 49: 4762–4772.

Rucker-Gramm, P. & Beddoe, R.E. 2010. Effect of moisture content of concrete on water uptake. *Cement and Concrete Research* 40(1): 102–108.

Van Tittelboom, K. 2012. *Self-healing concrete through incorporation of encapsulated bacteria- or polymer-based healing agents.* Ph.D. thesis, Ghent University, Faculty of Engineering and Architecture. Ghent, Belgium.

Van Tittelboom, K., De Belie, N., Van Loo, D. & Jacobs, J. 2011. Self-healing efficiency of cementitious materials containing tubular capsules filled with healing agent. *Cement & Concrete Composites* 33(4): 497–505.

Van Tittelboom, K., Snoeck, D., Vontobel, P., Wittmann, F.H., De Belie, N. 2013. Use of neutron radiography and tomography to visualize the autonomous crack sealing efficiency in cementitious materials. *Materials and structures* 46(1–2): 105–121.

Wang, K., Jansen, D.C. & Shah, S.P. 1997. Permeability study of cracked concrete. *Cement and Concrete Research* 27(3): 381–393.

Wang, L.C. 2014. Experimental study on water absorption by concrete damaged by uniaxial loading. *4th International Conference on the Durability of Concrete Structures*. West Lafayette, USA.

Zhang, P., Wittmann, F.H., Zhao, T. & Lehmann, E.H. 2010. Neutron imaging of water penetration into cracked steel reinforced concrete. *Physica B—Condensed matter* 405(7): 1866–1871.

Concrete Repair, Rehabilitation and Retrofitting IV – Dehn et al. (Eds)
© 2016 Taylor & Francis Group, London, ISBN 978-1-138-02843-2

Experimental study on the long-term leaching properties of CSG materials

Wei Feng, Zhongwei Liu, Jinsheng Jia & Fengling Ma
China Institute of Water Resources and Hydropower Research, State Key Laboratory of Simulation and Regulation of Water Cycle in River Basin, Beijing, China

ABSTRACT: Based on the pressing concerns in engineering, Leaching properties of the main materials in Cemented Sand and Gravel (CSG) Dam were studied. The results showed the permeability coefficient of CSG was 10^{-10} m/s and it decreased over time. The permeability coefficient reduced to about half of the initial value after 120 d. In constant hydraulic pressure, the leached Ca^{2+} was few and tended to stabilize when the leaching time reached 480 d. Internal pH of CSG continued to decrease until reached 10.0–11.5, belonging to low alkaline. The strength of material decreased obviously with the leaching of Ca^{2+}. The leached Ca^{2+} of CSG curing 1 year was very few and less than 10 mg/L, and the cumulative leaching rate was less than 0.1% after 100 d. It usually needs more than one year from the beginning of construction of CSG dam to water storage. Even if leaching occurs, the leached Ca^{2+} is very few. So the CSG materials with long curing time have good ability to resist Ca^{2+} leaching.

1 INTRODUCTION

Cemented Sand and Gravel (CSG) is a new-building dam material produced by mixing a small amount of cementitious materials, sand and gravel without screening or washing on site, paving and vibration compaction. Advantages of projects built by CSG are as follows: ①Low cement content and low temperature rising by hydration heat, leading to simple temperature controlling measures. ②Low grading demand of aggregates. Sands and gravels dug from the dam riverbed and excavation. ③Low cost. The low cement and low aggregate demand reduce the cost. ④Low environmental impacts. The CSG dams are economical, fast, safe and environment-friendly. So they have broad application potential (Raphael 1970 and Hirose 2007). In recent years, CSG dams have been used as permanent buildings in Japan, Turkey, Greece, France, Philippines and other countries (Hirose et al. 2003).

For a long time, it is believed that concrete buildings long-term immersed in natural water must suffer leakage risk. The continuous leaching of calcium oxide in concrete will affect the stability of calcium silicate, on which the strength and durability of concrete mainly depend.

CSG material, as a new dam construction material, needs low cement content (40~60 kg/m^3, total dosage of cementitious materials is less than 100 kg/m^3), so it has low strength and poor permeability resistance. Even equipped with specialized impervious body, the CSG dam still has the risk of penetration and leaching. With long-term leaching under pressure water, will the Ca^{2+} continue to leach, how the strength attenuation change when osmotic quantity reaches a certain degree. Will the CSG material be complete destroyed by large serious leaching? The above questions are the main focus of this paper.

2 MATERIALS AND METHOD

2.1 *Testing materials*

The natural gravel stone from Yongding River in west Beijing, 42.5 Portland cement and class II fly-ash were used as the raw materials of CSG. The mixtures were made into cylinders (φ 43 × 44 cm) and cubes (side length is 30 cm). The mixing proportion was shown in Table 1. A pressure leaching testing machine was adopted in the experiments and the water pressure was 0.5 MPa. Deionized water was applied on the top surface of the specimen and penetrating through the body to the bottom.

8 cubes (side length is 30 cm) and 3 cylinders (φ 43 × 44 cm) were made, and experiment was conducted on 6 cubes and 3 cylinders after curing for 43 days, and the other 2 cubes were cured for 1 year before testing. Specimens were full-graded CSG with the maximum aggregate size 150 mm.

Affected by the uniformity of CSG, each specimen showed different density, so the corrosion situation was different. 1#, 3#, 5# cube specimens and 7#, 9# cylinder specimens had been carried out broken test after leaching experiments. Other samples were still in leaching experiments.

Table 1. Mixing proportion of CSG.

Water-binder ratio	Water-cement ratio	Water consumption (kg/m^3)	Cementitious materials (kg/m^3)	Sand (kg/m^3)	Gravel (kg/m^3)	V_C (s)	Full graded specimens density (kg/m^3)	Wet sieving specimens density (kg/m^3)	Relative density (%)
0.9	1.8	72	80	584	1816	7	2543	2479	99.6

2.2 *Mensuration of pH value*

water samples were collect regularly and the volume and pH value of the water were measured according to the "Test codes for hydraulic concrete" (SL352-2006, China).

2.3 *Calculation of Ca^{2+} leaching quantity*

The leaching quantity of Ca^{2+} was determined by chemical titration method. 0.0271 mol/L of EDTA was used as the standard solution. The Ca^{2+} cumulative leaching quantity of CSG was calculated by titration as following equation (1):

$$C_{C_a} = V_1 C \times 40.08 \times 1000 / V \tag{1}$$

where C_{Ca} is the calcium concentration (mg/L); C is the concentration of EDTA standard solution (mol/L); V_1 is the volume of EDTA standard solution (ml); V is the water volume (mL).

The formula for calculating the permeability coefficient is as follows (2):

$$K = \frac{QL}{AH} \tag{2}$$

where K is permeability coefficient (m/s); Q is the average flow through the specimens (m^3/s); L is the height of specimen (m); A is the section area of specimen (m^2); H is acting water head (m) (1 MPa water pressure = 100 m water head).

3 LEACHING TEST OF CSG AFTER CURING 43 DAYS

3.1 *Effect of leaching on permeability coefficient*

The permeability coefficients of 1~9# specimens were similar as shown in Table 2 and the order of magnitude of permeability coefficient is 10^{-10} m/s. It can be concluded that CSG was in lower impermeability grade, but had minor permeability coefficient.

The cumulative permeability curves of 1#~6# cube specimens were shown in Figure 1. Table 2 showed that with the change of time, the infiltration stages were clearly divided into two-stage and 140 d was the demarcation in the seepage diachronic curve, showing good linear relation. Except the first stage of 5# had poor linearity of infiltration phase, others kept good linearity.

From Table 2, the permeability coefficient of CSG specimens can be down to the magnitude order of 10^{-10} m/s. In the first stage, permeability coefficient of 5# cube specimen indicated the maximum coefficient is 5.08×10^{-10} m/s. With the increase of time, it dropped by 55.5% in the second stage with 2.26×10^{-10} m/s. The permeability coefficient of 9# cylindrical specimen obtained the maximum value at 4.89×10^{-10} m/s. With up to the second stage, it also dropped by 68.1% at 1.56×10^{-10} m/s.

By comparison, permeability coefficient of 1–9# specimens indicated larger coefficient in the early stage. Later (after 120 days' test), permeability coefficient tended to decrease. That self-sealing phenomena was obviously appeared in the CSG.

3.2 *Variation relation of pH values in CSG leachate*

The pH value of leachate were shown in Figure 2, which indicated the pH value in CSG leachate gradually reduced in the process of leaching, ranging from 12.5 to 10.0, even below to 10.0. To some extent, the pH value of leachate also reflected the alkali content dissolved in the leachate in CSG. The initial seepage and soluble alkali quantity were larger, which reflected a higher pH value of the leachate. With the increase of time, the permeability coefficient of CSG decreased. The secondary hydration of fly ash could consumes the alkali contents. Therefore, the pH value of leachate gradually reduced and then remained stable within a certain range.

Recent studies have shown that regardless of cement or concrete, pH values generally kept above 12.5 after 2–3 years. The pH values of concrete with fly ash will decline. If pH values decreased from 12.5 to11.5, which indicated that about 90% of $Ca(OH)_2$ was absorbed by fly ash. In this test, the pH value of the leaching specimen has declined to 11.5 below, even close to 10.5. Therefore it could infer the $Ca(OH)_2$ in CSG was basically absorbed with little dissolved Ca^{2+} after 1.5 years' leaching.

Table 2. Permeability coefficient of specimens.

Specimens	1#	2#	3#	4#	5#	6#	7#	8#	9#
Size	30 × 30 × 30 cm						ϕ 43 × 44 cm		
Infiltration time (d)	142	140	135	140	140	140	121	238	58
The first stage									
Cumulative seepage (L)	64.1	67.9	72.1	64.4	102.1	49.4	53.0	85.8	44.2
Permeability coefficient (10^{-10} m/s)	3.24	3.65	3.72	3.58	5.08	2.66	3.03	2.34	4.89
Infiltration time (d)	343	358	/	346	176	343	294	223	263
The second stage									
Cumulative seeage (L)	69.9	78.7	/	58.4	51.1	45.9	31.1	45.1	61.2
Permeability coefficient (10^{-10} m/s)	1.61	1.71	/	1.34	2.26	1.06	0.70	1.28	1.56
Decreasing of permeability coefficient (%)	50.3	53.2	/	62.6	55.5	60.2	76.9	45.3	68.1

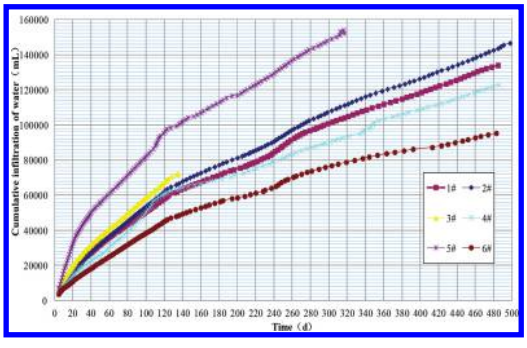

Figure 1. Cumulative seepage and time of cube specimens.

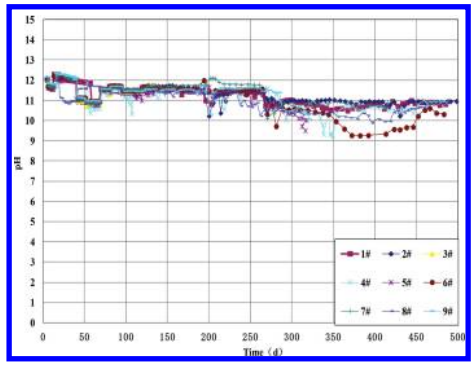

Figure 2. Development curves of pH value.

Table 3. The Ca^{2+} leaching results in the leachate of CSG specimens.

Specimens	1#	2#	3#	4#	5#	6#	7#	8#	9#
Size	30 × 30 × 30 cm						Φ43 × 44 cm		
Volume (m^3)	0.027						0.064		
Water consumption (kg)	1.944						4.598		
Cement content (kg)	1.08						2.555		
Fly ash content (kg)	1.08						2.555		
CaO content (g)	657						1555		
CaO leaching quantity (g)	14.9	15.2	13.1	10.1	20.8	10.6	10.4	9.6	15.7
CaO leaching rate (%)	2.26	2.31	2.00	1.53	3.16	1.61	0.67	0.61	1.01
The concentration of Ca^{2+} (mg/L)	9–225	9–212	39–217	8–138	13–243	4–226	9–139	4–212	4–282
Duration (d)	485	498	135	486	316	483	415	461	321

The characterization of SEM, XRD and TGA also confirmed this phenomenon.

3.3 *The leaching of Ca^{2+} in CSG material under water pressure*

After curing 43 d, the test results of leaching of cube and cylinder specimens are shown in Table 3, and Ca^{2+} was shown in the form of CaO. $Ca(OH)_2$ was the main source of dissolvable Ca^{2+}. However, the generation rate of $Ca(OH)_2$ in hydration products, as a variable, was affected by the continuous Ca^{2+} leaching, so it's difficult to accurately calculate the total amount of dissolvable $Ca(OH)_2$ in specimens, then the proportion of total CaO in cementitious materials was counted.

In the Ca^{2+} leaching process of 1~9# specimens, the accumulative leaching quality time curve in the form of CaO was shown in Figure 3. Among 1~6# cube specimens, 5# specimen had the maximum dissolved cumulative amount at 20.8 g and the proportion of total CaO in cementitious materials was 3.16% after leaching 316 d. And that in 4# specimen at 10.1 g was minimum with CaO ratio at 1.53% after 486 day's leaching. And among 7~9# cylindrical specimens, dissolved cumulative amount of CaO was 15.7 g and total CaO ratio in cementitious materials was 1.01% in 9# specimen after 321 d. While, the leaching CaO amount of 8# specimen was only 9.6 g, accounting for 0.61% after 461 d. In Figure 3, it could be observed that the cumulative leaching quality and dissolved concentrations of Ca^{2+} tended to be stable over time. After 200 d, the dissolvable Ca^{2+} was few and almost insoluble until 400 d. The microscopic analysis confirmed that crystal structure of $Ca(OH)_2$ was not observed in the hydration products of leaching specimens.

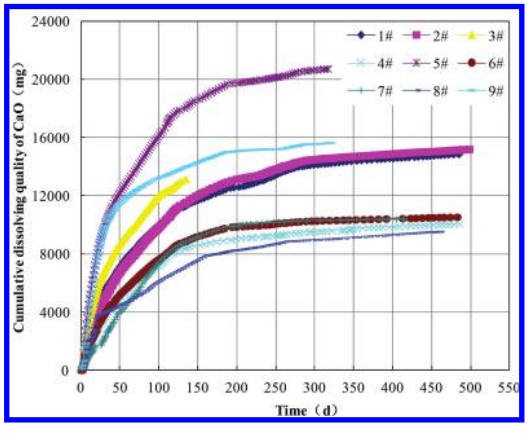

Figure 3. The CaO cumulative leaching quality and infiltration time curve.

3.4 *Strength loss of the CSG under water pressure*

Material strength was the most important property for CSG dam. After leaching, strength gradually decreased, affecting the dam safety, which has been a greatest concerned problem.

To compare the change of CSG mechanical strength in the process of Ca^{2+} leaching, broken tests were conducted by 1,3,5# cube and 7,9# cylinder specimens after leaching. The results were shown in Table 4. Other specimens remained testing to observe the effect of leaching time on strength. It could be found the strength gradually reduced with continuous leaching. After 316 d, total leaching CaO ratio of 5# specimen was 3.16% with highest leaching quantity. Comparing with standard curing specimen, the strength decreased by 61%. Through 135 day's leaching, the total leaching CaO ratio of 3# specimen was 2.0% with 31% reduction in strength. Among cylindrical specimens, total leaching CaO ratio in 9# specimen was 1.01% after 321 d, and the strength decreased by 20.1% comparing with standard curing specimen. While 7# specimen was only 0.67% after 415 d, falling by 12.8%. When total leaching CaO ratio in cementitious materials reached 3.16% at most, the strength of CSG obviously dropped to 5.5 Mpa, decreasing by 60%. But the phenomenon of CSG collapsed due to large CaO cumulative leaching quantity wasn't observed.

From Table 4, the ratio of reduction in strength and Ca^{2+} leaching quantity was not constant, which was related to specimens size, water pressure and so on. The ratio of average reduction in strength and Ca^{2+} leaching quantity was about 17%, that is, when total leaching CaO ratio was 1%, strength dropped by 17%.

Table 4. The comparison of compressive strength pre-and post leaching of full grade CSG specimens.

Specimen	1#	3#	5#	7#	9#
Size	30 × 30 × 30 cm			Φ43 × 40 cm	
Infiltration time (d)	485	135	316	415	321
Leaching rate of CaO (%)	2.26	2.00	3.16	0.67	1.01
Compressive strength (standard curing specimen) (MPa)	15.4	11.6	14.1	14.8	14.1
Compressive strength after leaching (MPa)	11.4	8.0	5.5	12.9	11.6
Reduction in strength (%)	26.0	31.0	61.0	12.8	20.1
Reduction in strength/Ca^{2+} leaching quantity (%)	11.5	15.5	19.3	19.1	17.7
Average reduction in strength/Ca^{2+} leaching quantity (%)	16.6				

4 LEACHING TEST OF CSG AFTER CURING 1 YEAR

Previous research had confirmed that CSG had certain self-sealing ability. Some studies (Hiroshi and Akira 2000, Liapichev 2003, Kazuko et al. 2005, Christophe et al.1996, Xiong et al. 2008) proved that normal concrete and roller compacted concrete both showed obvious self-sealing ability. The main reasons could be summarized as follows: (1) Hydration products absorbed water and swelled, when seepage water flowed through the pores. (2) Concrete would be further compacted due to the continual hydration of gelled material with the continuous infiltration. (3) Fine mud, clay particles etc, mixed in the seepage water would block the pore channels. (4) As the seepage path extended, $Ca(OH)_2$ concentrations continued to improve, and blocked pores by the crystal in some micro-pores.

Though the water-binder ratio was larger in CSG material (water-binder ratio in this research was 0.9), which also had the similar properties of concrete. That is, self-sealing phenomenon was appeared as the decrease of permeability coefficient That means, when the age was increasing, hydration products blocked the pores due to the cement hydration and secondary hydration of the fly ash, which further reduced permeability.

To compare the leaching performance of CSG after long curing period, experiments were carried out by 2 cubes CSG specimens (length at 30 cm), and after curing for 1 year. The water pressure was increasing to 1.2 MPa. The results of Ca^{2+} leaching were shown in Table 5. It could be concluded that the permeability coefficient of specimens, curing for 1 year, were smaller and up to 10^{-11} m/s, with very few dissolvable Ca^{2+}.

Table 5. Leaching results of cubes CSG specimens (1 year curing period).

No.	10#	11#
Size	$30 \times 30 \times 30$ cm	
Volume (m^3)	0.027	
Water consumption (kg)	1.944	
Cement content (kg)	1.08	
Fly ash content (kg)	1.08	
CaO content (g)	657	
Leaching quantity of CaO (g)	0.51	0.45
Leaching rate of CaO (%)	0.1	0.1
The concentration of Ca^{2+} (mg/L)	4–135	4–122
Duration (d)	110	117
Cumulative infiltration of water (L)	6.6	18.4
Permeability coefficient (10^{-11} m/s)	2.2	4.4

With the increase of age (more than 1 year), activity of fly ash was gradually stimulated in the CSG, and the active SiO_2 and Al_2O_3 had secondary hydration reaction with $Ca(OH)_2$, the hydration product of cement, and generated new hydration products. The new hydration products would fill the primary pores, so that the pores were refined, segmented and blocked. Hydration of fly ash consumed many $Ca(OH)_2$ and produced Calcium Silicate Hydrate gel (CSH), filling in the skeleton of $Ca(OH)_2$ crystals, which could reduce the thickness of transition zone. This was so called "self-sealing" or "self-closure" phenomena.

In Table 5, after curing 1 year, the porosity of CSG was decreasing, anti-permeability was further enhanced, and the dissolvable Ca^{2+} quantity was little. Thus, it could be concluded after long age of curing, especially over 1 year, CSG has high anti-permeability and anti-leaching (resistance to Ca^{2+} leaching). For water conservancy projects, over 1 year is needed from the beginning of construction to completion. CSG after long age curing has high resistance to leaching.

5 CONCLUSIONS

Following phenomenon would occur in CSG under the continous water pressure ①As the internal pores were filled with water, the porosity would continuously change due to the auto-compacting with the increasing age; ②$Ca(OH)_2$ in hydration products were leached, and other products might be hydrolyzed. ③Hydraulic fracturing occurred in the micro-cracks by the pressure seepage water. ④The strength of CSG was obviously decreased because of the seepage and leaching.

The experimental results showed that

1. With the increase of age, permeability coefficient of CSG was decreased, and it kept at 10^{-10} m/s 120 d later, half of the initial value. In the leaching process, activity of fly ash was stimulated gradually, and active SiO_2 and Al_2O_3 had secondary hydration reaction with $Ca(OH)_2$, the hydration product of cement. After the longest leaching duration at 485 d, the dissolved Ca^{2+} was little, and tended to be stable.

   Internal pH of CSG continued to decrease until reached 10.0–11.5, belonging to low alkaline. The strength was obviously decreased with the Ca^{2+} leaching. The total leaching CaO ratio in cementitious materials was 3.16%, reaching the maximum value. The ratio between average reduction in strength to Ca^{2+} leaching quantity was about 17%, that is, when the total leaching CaO ratio in cementitious materials was 1%, with 17% reduction in strength.

2. It usually needs more than one year from the buildup of CSG dam to water storage. After curing for 1 year, the leached Ca^{2+} of CSG is very few, which has good ability to resist Ca^{2+} leaching.

ACKNOWLEDGEMENT

This work was supported by the National Basic Research Program (973 Program) of China (Grant No. 2013CB035903) and by the National Key Technology R&D Program (2013BAB06B02).

REFERENCES

Christophe, C., Raoul, F., Jean, M.T., 1996. Leaching of both calcium hydroxide and C-S-H from cement paste: Modeling the mechanical behavior [J]. Cement Concrete Research, 8, 1257–1268.

Hirose, T., Engineering manual for construction and quality control of trapezoidal CSG dam [R]. Japan Dam Engineering Center Report, September 2007.

Hirose, T., Fujisawa, T., Yoshida H et al, 2003. Concept of CSG and its material properties [C]. Proceedings 4th International Symposium on Roller Compacted Concrete Dams, Madrid: 465–473.

Hiroshi, S., Akira, D., 2000. Leaching tests on different mortars using accelerated electrochemical method [J]. Cement and Concrete Research, 11, 1815–1825.

Kazuko, H., Shunkichi, S. et al, 2005. Effects of porosity on leaching of Ca from hardened ordinary Portland cement paste [J]. Cement Concrete Research, 35, 1764–1775.

Liapichev, Y.P, 2003. Seismic stability and stress-strain state of a new type of FSH-RCC dams [C]. Proceedings 4th International Symposium on Roller Compacted Concrete Dams, Madrid, 485–492.

Raphael, J.M, 1970. The optimum gravity dam [A]. Rapid Construction of Concrete Dams [C], ASCE:221–224.

Xiong K., He Y.L, Peng Y.F, 2008. Study on adaptability to geological faulted foundation of hardfill dam [J]. Frontiers of Architecture and Civil Engineering in China, 2(4):343–349.

Concrete Repair, Rehabilitation and Retrofitting IV – Dehn et al. (Eds)
© 2016 Taylor & Francis Group, London, ISBN 978-1-138-02843-2

Effects of resistivity on corrosion rate measurements obtained from a coulostatic monitoring device

A.N. Scott
Department of Civil and Natural Resources Engineering, University of Canterbury, New Zealand

ABSTRACT: There are a number of factors which can influence the measurement of the corrosion rate of reinforcing steel in concrete. A coulostatic device was used to estimate the rate of corrosion of steel in reinforced concrete samples with varying resistivities. The resistivity of the concrete was controlled through the addition of a micro silica binder and changes to the water/cement ratio of general purpose cement. The rate of corrosion was strongly correlated with the resistivity of the concrete and the calculated coulostatic corrosion rates ranged from 0.02 to 1.18 μA/cm^2 in steps of approximately 0.4 μA/cm^2. The corrosion rates obtained from the coulostatic technique were in reasonable agreement with gravimetric results taken after approximately 18 months of weekly cycles of salt water exposure followed by drying.

1 INTRODUCTION

There are a variety of techniques available for the determination of the rate of corrosion of reinforcing steel in concrete. Andrade and Alonso (1996) provide a fairly comprehensive summary of the principle corrosion monitoring techniques together with a range of factors which affect corrosion rates and their measurement. The most common methods for laboratory and site investigations involve some form of Linear Polarization Resistance (LPR) measurement.

The coulostatic method of corrosion rate determination is essentially an LPR technique. Unlike the common galvanostatic method which typically monitors the response of potential to an applied current over a period of minutes, the coulostatic method measures the relaxation of the potential after a known charge with a duration in the order of milliseconds is applied to the electrode. According to Glass (1995) corrosion rates are related to the time constant describing the potential decay induced by a small charge perturbation. A high corrosion current therefore will lead to a rapid decay of the potential transient whereas with a lower corrosion current the decay of the potential after the perturbation will take some time. A typical potential transient monitored over 30 seconds is shown in Figure 1.

The theoretical development and principles of the coulostatic method have been well presented in a number of sources (Glass et al 1993, Rodriguez and Gonzalez 1994, Hassanein et al 1998). A brief outline of the main features of the method and determination of corrosion rates will be presented as follows. The potential transient is described by the equation (Hassanein et al 1998):

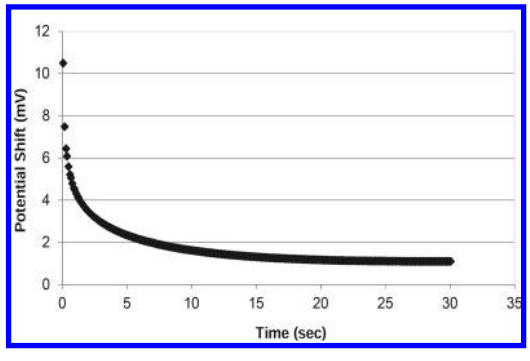

Figure 1. Potential transient of steel electrode after application of small of small charge.

$$n_t = n_o \exp\left(\frac{-t}{\tau_c}\right) \tag{1}$$

where n_t is the potential shift at time t, n_o is the initial potential shift and τ_c is the time constant. The polarization resistance R_p is then obtained from the time constant and capacitance (C) information, equations 2 and 3, with q_s being the applied charge density.

$$\tau_c = CR_p \tag{2}$$

$$C = \frac{q_s}{n_o} \tag{3}$$

Values are obtained by fitting equation 1 to the results for a curve such as that shown in Figure 1. The value of η_o is thus calculated from the fitted equation and is not a measured value. There is an apparent deviation between the fitted curve and the measured potentials immediately after the perturbation. The behaviour of the steel mortar interface is said to be modeled by the Randles equivalent circuit which places a resistor, representing the polarization resistance, in parallel with a capacitor, which represents the double layer capacitance. Rodriques and Gonzalez (1994) have suggested the standard Randles circuit is a simplification and that there should be three resistor-capacitor combinations in series accounting for the mortar cover, passivating film and finally the metal-concrete interface. The first two however are said to discharge almost instantaneously.

If potential measurements are taken approximately 0.1 seconds after the cessation of the charge, many of the very early transients should have dissipated. Any remaining early transients are unlikely to significantly affect the corrosion rate measurements as potential readings in the coulostat used for this investigation are typically taken for at least 30 seconds. Thus the overall shape of the curve and the resulting equation are still valid.

The length of the charge has been shown by Glass (1995) to have an effect on the shape of the relaxation transient with longer perturbations resulting in progressively flatter relaxation curves. The relaxation curve for perturbations of approximately 35 ms differs only marginally from those of 4.65 ms, with perturbations even up to 350 ms showing reasonable agreement.

2 EXPERIMENTAL INVESTIGATION

The corrosion rate of mild steel round bar embedded in concrete was investigated for three mix designs using a coulostatic measuring device. Three different concrete mix designs were chosen to provide a range of resistivity values. Details of the mix designs along with 7, 28 and 90 day compressive strengths are provided in Table 1.

Plain round mild steel with a diameter of 12 mm was cut into lengths of approximately 470 mm. The steel bars were wire brushed to remove any mill scale, cleaned and weighed prior to casting. The ends of the bars were covered in shrink wrap and epoxy coated to provide an exposed surface area of 120 cm^2.

Three replicate concrete prisms (460 mm long by 120 mm square) with a central mild steel round bar were cast for each mix. The cover depth for all the specimens was 40 mm. The specimens were demoulded after 24 hours and water cured under a damp hessian cloth wrapped in plastic. After 7 days the specimens were loaded under three point bending to produce one central transverse crack with a width between 0.6 and 0.9 mm. Three additional GP 0.45 specimens were cast and left uncracked to maintain passive corrosion conditions.

Table 1. Concrete mix design (kg/m^3).

	GP 0.45	GP 0.6	MS (8%)
W/C	0.45	0.6	0.45
Water	173	174	173
GP Cement	378	283	347
Microsilica	–	–	30
Sand	829	906	817
Stone (13 mm)	1051	1051	1051
SP (ml)	–	–	800
7 day strength (MPa)	51	31	51
28 day strength (MPa)	60	41	64
90 day strength (MPa)	69	48	74

SP—super plasticizer.

The sides of the cracked specimens were sealed and a plastic reservoir placed on the surface. The specimens were placed in a 21 °C climate controlled room after approximately 14 days and subjected to weekly cycles of 3 days ponding with 3.5% NaCl solution followed by 4 days drying. Tap water was used instead of NaCl for the passive control samples.

The specimens were monitored weekly for corrosion rate ($\mu A/cm^2$), potential (mV) and resistivity (kOhm.cm). The polarization resistance data was obtained by a couloustatic technique, as previously described in the introduction. The polarization resistance was converted to a corrosion rate (i_{corr}) by means of the Stern-Geary relationship as provided in equation 4 (Schiessl, 1988), with an assumed value of 26 for B as suggested by Andrade and Alonso (1996).

$$i_{corr} = \frac{B}{R_p} \tag{4}$$

After approximately 18 months the specimens were broken open and the steel bars removed. The shrink wrap was carefully removed and the bars cleaned in a solution of hydrochloric acid, antimony trioxide and stannous chloride as provided in ASTM G1-03. The average measured corrosion rates obtained from the coulostatic technique were compared to those obtained by gravimetric analysis.

3 RESULTS AND DISCUSSION

The potential measurements shown in Figure 2 for GP 0.45, GP 0.6 and MS 0.45 indicate that

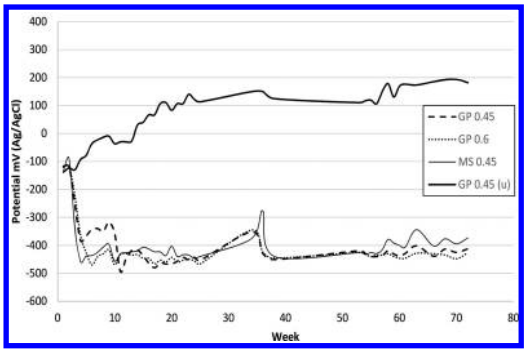

Figure 2. Average weekly potential measurements.

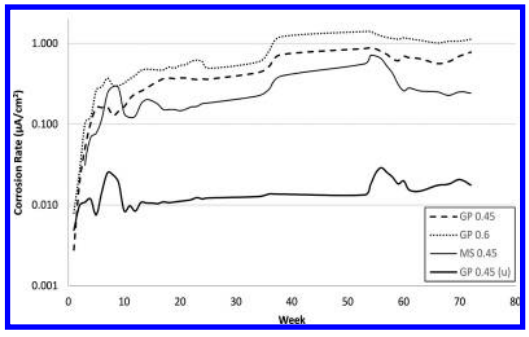

Figure 3. Smoothed averaged corrosion rate (µA/cm²).

corrosion initiated shortly after the specimens were first ponded with salt solution. In most cases active corrosion potentials were observed within 3 weeks after the start of ponding. The uncracked specimens GP 0.45(u), which were ponded with tap water, showed a gradual increase in potential and no active corrosion was observed over the course of the investigation.

The first measurement at week 1 was after cracking and before ponding with salt water. The measured corrosion rates in all cases were very low, as shown in Figure 3. The corrosion rates for GP 0.45 (U), the uncracked control, were reasonably consistent and had an average value of approximately 0.02 µA/cm² from week 38 onward. The corrosion rates for GP 0.45, GP 0.6 and MS 0.45 were 0.72, 1.18 and 0.39 µA/cm² respectively.

The mix designs were initially chosen to provide a range of concrete resistivity values which would in turn yield different corrosion rates. Figure 4 provides the relationship between resistivity and corrosion rate for the actively corroding specimens.

The uncracked specimens were intended to maintain passive conditions and provide the lowest level of corrosion which was measured at 0.02 µA/cm². There is a reasonable range of calculated corrosion rates from 0.39 to 1.18 µA/cm² in steps of approximately 0.4 µA/cm² for the actively corroding specimens. The distinct corrosion levels provide a useful comparison against actual corrosion rate as determined by mass loss measurements.

The total measured corrosion current over the investigation was calculated for each specimen based on the individual corrosion rate curves. The total charge was converted to an equivalent mass loss through the use of Faraday's law and compared to the actual mass loss calculated as the difference between the initial mass of the steel prior to casting and that measured at the end of the investigation after cleaning.

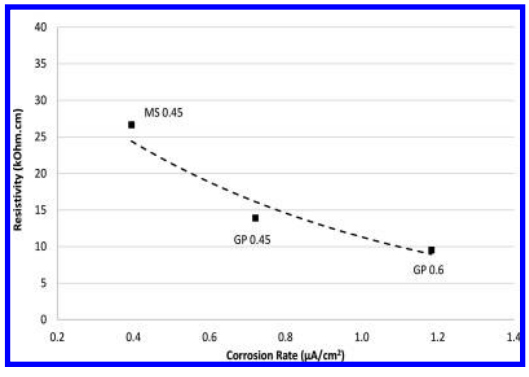

Figure 4. Relationship between corrosion rate and resistivity.

Table 2. Comparison of coulostatic and gravimetric mass loss.

	Mass loss coulostatic	Mass loss gravimetric	Percent difference
GP 0.45	0.80	0.55	+45
GP 0.6	1.27	0.75	+70
MS 0.45	0.54	0.32	+68
GP 0.45 (u)	0.02	0.03	–13

Table 2 provides a comparison between the average calculated mass loss obtained from the coulostatic corrosion rates with those of the measured gravimetric mass loss. It can be seen that the calculated coulostatic mass loss was approximately 60% greater than that obtained from gravimetric analysis for all the actively corroding specimens. The difference in mass loss between the calculated and measured non-corroding specimens was negligible.

The difference in average values are within a factor of 2 which is considered an acceptable range

of accuracy as suggested by Andrade and Alonso (1996). The results for the comparison of coulostatic and gravimetric mass loss for individual specimens is provided in Figure 5.

The resistivity of the concrete did not appear to affect the difference between the gravimetric and coulostatic mass loss. The resistivity of the MS 0.45 specimens were roughly 2.5 times greater than those of the GP 0.6 specimens yet the percentage difference between the calculated and measured mass loss was almost identical.

It can be seen in Figure 6a and 6b that the corrosion was not uniform over the entire bar length but rather localized to the region just below the cracked surface.

The coulostat, as with other LPR methods, requires the transmission of a charge from the counter electrode typically located on the surface of the concrete to the reinforcing steel. As a measurable shift in potential of a few millivolts is necessary to get an accurate estimate of the corrosion rate, a concrete with a high resistance may limit the perturbation of the reinforcing steel thus preventing the measurement of the corrosion rate. The coulostat used in this investigation allows the operator to select a given charge. The device attempts to send the required charge for up to 200 ms. If the desired level of charge is not reached after 200 ms the charging circuits are closed and the total charge transmitted is reported for use in calculating the corrosion rate.

The coulostat, as with other LPR methods, requires the transmission of a charge from the counter electrode typically located on the surface of the concrete to the reinforcing steel. As a measurable shift in potential of a few millivolts is necessary to get an accurate estimate of the corrosion rate, a concrete with a high resistance may limit the

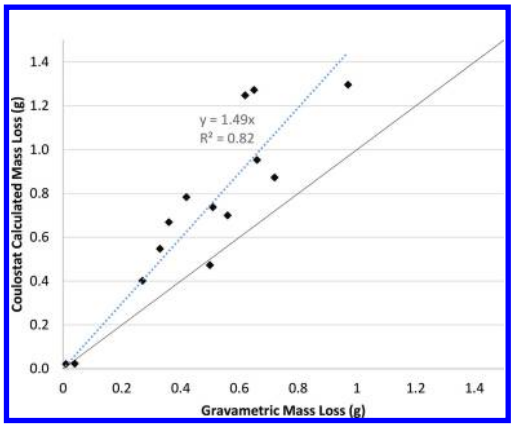

Figure 5. Comparison of measured gravimetric mass loss with coulostat calculated mass loss.

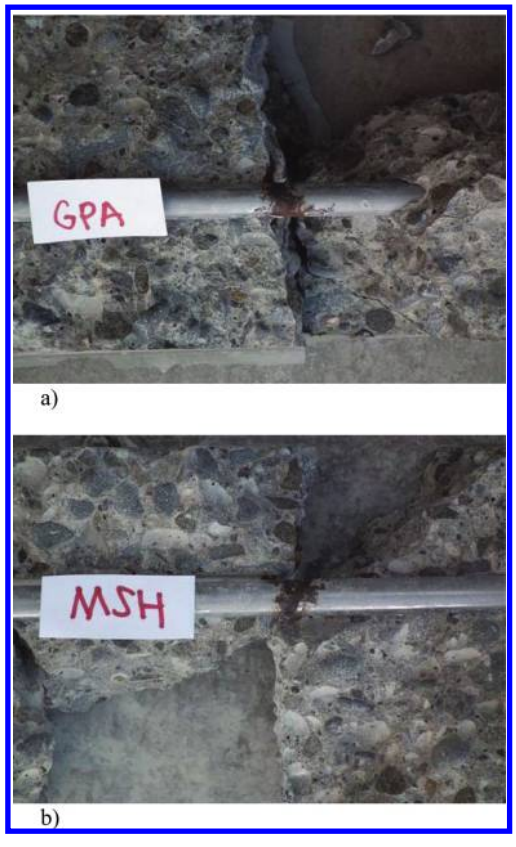

Figure 6. Extent of corrosion on: a) GP 0.45, b) MS 0.45.

perturbation of the reinforcing steel thus preventing the measurement of the corrosion rate. The coulostat used in this investigation allows the operator to select a given charge. The device attempts to send the required charge for up to 200 ms. If the desired level of charge is not reached after 200 ms the charging circuits are closed and the total charge transmitted is reported for use in calculating the corrosion rate.

A sample of coulostat results for GP 0.6 and MS 0.45 readings are presented in Table 3 along with a short period of potential measurements in Figures 7 and 8. The same charge of 0.2 millicoulombs (mC) was selected for both specimens. Despite the resistivity of the MS 0.45 specimen being approximately 4 times greater than the GP 0.6 specimen the actual transmitted charges were 0.25 and 0.23 mC respectively.

The higher resistivity of the MS specimens effectively limited its corrosion rate. As a result the initial potential shift, η_o, of MS 0.45 was more than double that of GP 0.6. Figure 7 shows the lower

Table 3. Selected coulostat corrosion measurement data.

	GP 0.6	MS 0.45
Resistivity (kOhm·cm)	11	44
Charge (mC)	0.23	0.25
η_o (mV)	20	50
Rate (μA/cm^2)	0.94	0.17

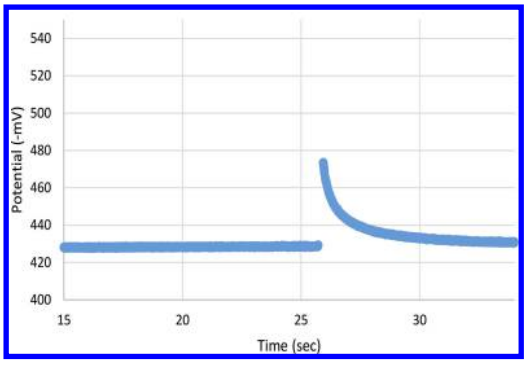

Figure 7. Potential transients for GP 0.6.

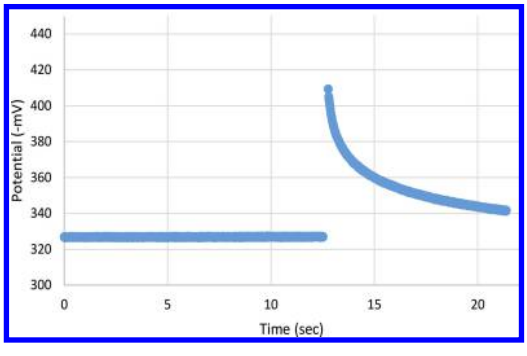

Figure 8. Potential transients for MS 0.45.

potential shift together with a fairly rapid return to pre-perturbation potentials compared to Figure 8 which displays a significantly larger potential shift and slower discharge.

In both the cases of GP 0.6 and MS 0.45 the coulostat provide a reasonable indication of the corrosion rate. While the variations in resistivity resulted in different corrosion rates the resistivity of the concrete did not adversely affect the measurement of those rates. If the resistivity of the concrete was considerably higher it is possible the coulostatic device would be unable to apply the desired level of charge within the given time, but the corrosion rate would also likely be lower thus reducing the size of the charge necessary to produce a reasonable potential shift.

4 CONCLUSIONS

The coulostat used in this investigation was able to accurately estimate the rate of corrosion for reinforcing steel embedded in concrete produced with a range of mix designs. The individual resistivity for the difference concrete varied from less than 10 kOhm.cm to over 40 kOhm.cm resulting in corrosion rates from 0.4 to 1.2 μA/cm^2 for actively corroding steel and 0.02 μA/cm^2 for passive steel. The resistivity of the concrete did not have a detrimental effect on the coulostatic corrosion measurements as concrete with both high and low resistivity showed similar variations in corrosion rates when compared to gravimetric measurements. The maximum difference between the estimated coulostatic mass loss and gravimetric measurement was 70% which is within a factor of two considered to provide an accurate representation of the actual corrosion rate.

ACKNOWLEDGEMENTS

The author wishes to gratefully acknowledge the contribution of Avinash Rao for his time and patience on this project.

REFERENCES

ASTM G1-03, 2003, Standard Practice for Preparing, Cleaning, and Evaluating Corrosion Test Specimens, ASTM International, West Conshohocken, PA, USA, pp. 18–26.

Andrade, C. Alonso, C. 1996, Corrosion Rate Monitoring in the Laboratory and On-Site. Corrosion and Building Materials, 10 (5), pp. 315–328.

Glass, G., Page, C., Short, N. and Yu, S. 1993, An Investigation of Galvanostatic Transient Methods used to Monitor the Corrosion Rate of Steel in Concrete, Corrosion Science, Vol. 35, No. 5–8, pp. 1585–1592.

Glass, G. 1995, An Assessment of the Coulostatic Method Applied to the Corrosion of Steel in Concrete, Corrosion Science, Vol 37, No. 4, pp. 597–605.

Hassanein, A., Glass, G. and Buenfled, N. 1998, The use of Small Electrochemcial Perturbations to Assess the Corrosion of Steel in Concrete, NDT&E International, Vol. 31, No. 4, pp. 265–272.

Rodriguez, P. and Gonzalez, J. 1994, Use of the Coulostatic Method for Measuring Corrosion Rates of Embedded Metal in Concrete, Magazine of Concrete Research, Vol. 45, No. 167, pp. 91–97.

Schiessl, P. (Ed.) 1988, Corrosion of Steel in Concrete: Report of the Technical Committee 60-CSC, RILEM, Chapman & Hall, London.

Concrete Repair, Rehabilitation and Retrofitting IV – Dehn et al. (Eds)
© 2016 Taylor & Francis Group, London, ISBN 978-1-138-02843-2

Study of residual protection following interruption of impressed current cathodic protection in concrete

D.W. Law & S. Bhuiyan
RMIT University, Melbourne, Vic, Australia

ABSTRACT: Impressed Current Cathodic Protection (ICCP) is a well-established technique to rehabilitate and protect corroding steel reinforcement in concrete. Recent studies have demonstrated that the protective effects of ICCP do not cease immediately after the system is interrupted, but can persist for a period of time before corrosion re-initiates. The residual effect is attributed to the beneficial effects of ICCP, where chlorides are repelled from the steel and re-alkalisation of the concrete around it occurs, thereby re-establishing passivity. This paper looks into this phenomenon of this residual effect and investigates how long it lasts and how it varies with current densities and duration of ICCP application. A number of parameters including steel potentials, depolarisation values, corrosion rates and concrete resistance were monitored for salt-contaminated reinforced concrete specimens that were subjected to ICCP and subsequently interrupted. Overall the results show that residual protection can be achieved by the application of ICCP to reinforced concrete structures. The duration and current density of the applied current both affect the duration for which this protection will remain.

1 INTRODUCTION

Reinforced concrete is the one of the most widely used construction material in the world today. However, the corrosion of steel reinforcement in concrete structures is a global problem causing billions of dollars to be spent in repairs and maintenance to keep structures in a safe and functional state. The problem has led to a range of repair and rehabilitation techniques being developed to prevent and treat the corrosion process. Amongst the various approaches developed to tackle this problem, Impressed Current Cathodic Protection (ICCP) has proven to be an effective method of stopping ongoing corrosion and preventing it from occurring in the future.

The use of ICCP has become an accepted and widely used technique for the rehabilitation of reinforced concrete structures where corrosion has been initiated by chloride ions, either from the ingress of de-icing salts or in marine environments. The use of ICCP systems is now covered by national standards around the world (BSI, 2000, NACE, 2007, AS2328, 2008). These provide information on the initial polarisation and operational parameters to ensure initial passivation and continuing protection.

The ICCP system works on the basis of shifting steel potentials to more negative values using a DC power supply in order to thermodynamically prevent corrosion from occurring. The negative potential repels chloride ions and allows the generation of hydroxyl ions at the steel-concrete interface which leads to an increase in the pH, helping restore passivity (Koleva et al., 2009, Glass and Chadwick, 1994, Broomfield, 2007). Once passivity is achieved, the applied current can be reduced to maintenance levels that sustain the passive state. The reduction in the current also assists in preserving the operational lifetime of the cathodic protection system, reducing the likelihood of acid attack at the anode.

Recent research on existing structures with ICCP applied has indicated that these systems can provide protection even after the ICCP has stopped operating (Presuel et al., 2002, Page, 1997, Broomfield and Tinnea, 1992). A recent study of 10 reinforced concrete crossbeams in the UK showed that the steel remained passive up to 3 years after the ICCP was no longer being applied (Christodoulou et al., 2010). Understanding the causes of this could have considerable benefits for the long term operation of ICCP systems and the initial energising of the system. This could include economic benefits by extending the lifetime of an ICCP system by allowing it to be de-activated (or pulsed) through its operational life and to provide a more efficient process for the initial energising of the system and passivation. In addition it may be possible to gain a better understanding of the passivation process by investigating the causes of residual protection.

Research has shown that the application of ICCP induced changes in the local environment of the steel/concrete interface, namely the removal of chloride from around the rebar and the consumption of oxygen and water in the production of hydroxyl ions, which results in restoration of steel passivity (Glass and Chadwick, 1994).

In order to study the residual effects of an ICCP system, it is necessary to monitor the changes that occur at the steel/concrete interface during the application of ICCP and following its interruption. The objective of this paper is to report on the findings of testing carried out by applying a range of current densities (20, 60, 180 and 540 mA/m^2 based on steel surface area) for different time periods (1 and 3 months). The parameters monitored included resistivity, temperature, humidity, potential and corrosion rate to determine what, if any, level of residual protection was afforded the steel.

2 METHODOLOGY

The test specimens were developed from a previous pilot study to determine the optimum configuration for the monitoring sensors (Bhuiyan et al., 2014).

The test regime included ten specimens. The specimens were made from a 100% Ordinary Portland (OP) cement mix with a nominal strength of 40 MPa. This was chosen to simulate a standard site mix. In order to initiate corrosion, 0.5% and 3% NaCl by weight of cement, was added to the mix. The 0.5% was selected to replicate levels commonly found in reinforced concrete structures, the 3% was selected to accelerate the corrosion process given the time constraints in laboratory trials. The mix design is given Table 1.

A schematic of the test specimen is given in Figure 1. The specimen is 300 × 150 × 100 mm with a ribbed mild steel bar, diameter 16 mm and length and 250 mm, with 40 mm cover. The cathodic protection current was applied via a activated titanium mesh ribbon anode De Nora Type 1—current rating of 5.5 mA/m at 110 mA/m^2). Monitoring of the specimen included an embedded Ag/AgCl electrode (Castle type LD15), a welded-tip thermocouple, a humidity sensor (Honeywell HIH4000-01) and three pairs of resistivity probes (Bhuiyan et al., 2014, McCarter et al., 2005).

Table 1. Mix design.

Constituent	Quantity (Kg/m^3)
Cement	420
Water	210
Fine aggregate	625
Coarse aggregate (7 mm)	625
Coarse aggregate (10 mm)	625
NaCl (0.5%)	2.1
NaCl (3%)	12.6

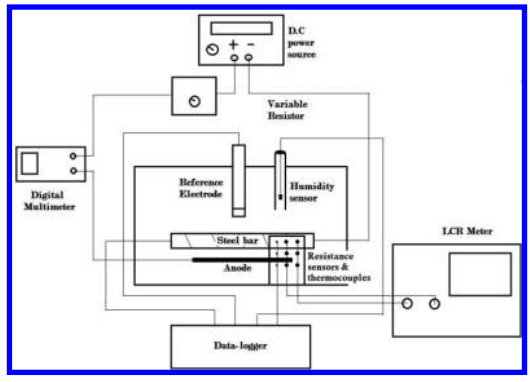

Figure 1. Schematic of test specimen.

Table 2. Test Regime ICCP specimens.

Specimen	% Cl	Current density (mA/m^2)	Duration (months)
1	3	20	3
2	3	60	1
3	3	60	3
4	3	180	1
5	3	180	3
6	3	540	1
7 (control)	3	0	–
8	0.5	20	3
9	0.5	60	1
10 (control)	0.5	0	–

After de-moulding, specimens were kept in a spray cabinet which was set to spray twice a day (every 12 hours), with each spray cycle lasting 30 minutes. The specimens for the 3% NaCl were left to corrode for 3.5 months before the Cathodic Protection (CP) was applied, the specimens with 0.5% salt were conditioned for 2 months prior to application of the CP.

The current was selected to enable a comparison between current density and total charge passed. As such current densities of 20, 60, 180 and 540 mA/m^2 were selected and durations of 1 and 3 months, Table 2. The 20 mA/m^2 was selected to replicate the maximum current density applied to structures. Previous research on accelerated corrosion of bond specimens has indicated current densities up to 200 mA/m^2 can be applied without adverse effects on the steel/concrete interface

(El Maaddawy et al., 2005), as such current densities 60 and 180 mA/m^2 were selected as appropriate for accelerated testing. Finally, due to the short time frame of the project specimens were also tested at 540 mA/m^2.

Corrosion was evaluated via the steel potential and corrosion rate measurements using Linear Polarisation Resistance (LPR). The current was applied by connecting the bar to the negative terminal of the DC power source and the anode mesh to the positive terminal, with a multimeter connected in series to the circuit to measure the current. All the probes with the exception of the resistance sensors were wired to the data-logger, which was set to sample every half hour (except during depolarisation period when a higher sampling rate was used). Manual readings had to be taken from the LCR meter (connected to the resistance sensors) as a multiplexing switch control unit was not available to automatically sample the readings between sensor pairs.

3 RESULTS

The steel potentials for the 3% NaCl specimens are given in Figure 2 and for the 0.5% NaCl specimens in Figure 3.

The results show that all of the 3% specimens have an initial potential following casting of approximately –300 mV, Ag/AgCl. During the conditioning period these potentials become slightly more positive and ranged between approximately –230 and –330 mV, indicating a moderate corrosion risk. This is attributed to the continued hydration of the concrete and a passivation on the rebar. The 0.5% specimens all have initial potentials of approximately –100 mV, Ag/AgCl, indicating a low corrosion risk. The data shows a clear difference between the 3% and the 0.5% concentrations and would suggest that corrosion may have been initiated on the 3% specimens but not in the 0.5% specimens. This is supported by the corrosion rate data, Figure 4, 3% chloride and Figure 5, 0.5% chloride.

The data shows an initially moderate to high rate of corrosion of 0.3–2.5 µA/cm^2 for the 3% specimens, which falls into the moderate to passive range 0.1–0.5 µA/m^2 over the conditioning period (Law et al., 2004). This correlates to the rise in potential during the same period and shows that some passivation of the bar is occurring and that a longer conditioning period is required to fully initiate corrosion for both the 3% and 0.5% chloride specimens. The 0.5% specimens show a similar trend with a high initial corrosion rate but that the

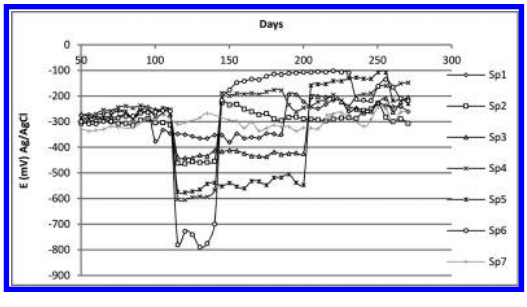

Figure 2. Steel potential vs time, 3% chloride specimens.

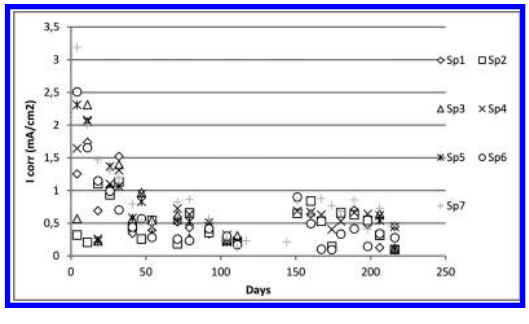

Figure 4. Corrosion rate vs time, 3% chloride specimens.

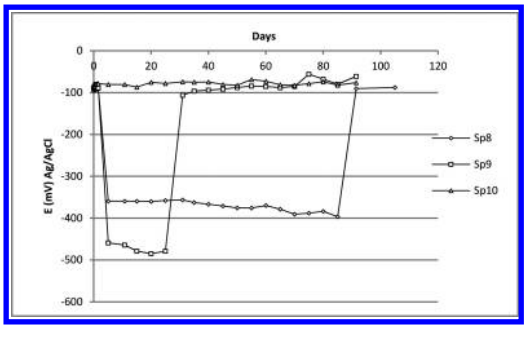

Figure 3. Steel potential vs time, 0.5% chloride specimens.

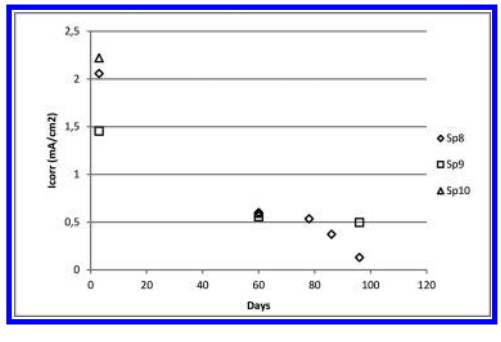

Figure 5. Corrosion rate vs time, 0.5% chloride specimens.

corrosion rate falls rapidly as the hydration of the cement leads to the passivation of the rebars.

During CP application, corrosion rate measurements were not possible due to application of the CP. Shortly after current interruption, corrosion rates show increased values, contrary to what one would expect. Similar findings were reported in literature and a few hypothesis have been put forward (Green et al., 1993):

- Steel passivation can take time, depending on the oxygen diffusion rate to the steel bar
- Alkaline attack of steel can occur at high current densities due to production of $HFeO_2^-$
- Potential soon after current interruption is close to the reversible potential of half reaction.

Following CP the corrosion rates fluctuated in the low to passive range, indicating that protection had been maintained. However, overall, corrosion rate data did not show any definitive evidence of the residual effects.

The potential and corrosion rate data indicate that the 0.5% bars are probably passive when the CP is applied, while the 3% bars probably have some low level corrosion occurring. This is further supported by visual inspections following testing, where cut sections of the concrete specimens revealed some corrosion products for the 3% specimens, but very little (negligible) for the 0.5% specimens, Figure 6.

When CP is applied, a drop in potential is observed in all specimens when the current is applied. Thus the CP is seen to be successfully polarizing the steel to more negative potentials, indicating that protection is being applied to the bars. The polarization observed shows a direct relationship to the current, as would be expected. Specimen 1, 20 mA/m^2, is polarized to approx. –350 mV, specimens 2 & 3, 60 mA/m^2, are polarized to approx. –450 mV, 4 & 5, 180 mA/m^2, are polarized into the range –550 to –600 mV and specimen 6, 540 mA/m^2, is polarized in to the range –750 to –800 mV.

A current sweep was conducted on control specimens for the 3% and 0.5% salt specimens, Figure 7. The data shows that a higher current density was required for the 3% specimens, as would be expected.

Figure 6. Visual inspection, 3% and 0.5% NaCl specimens.

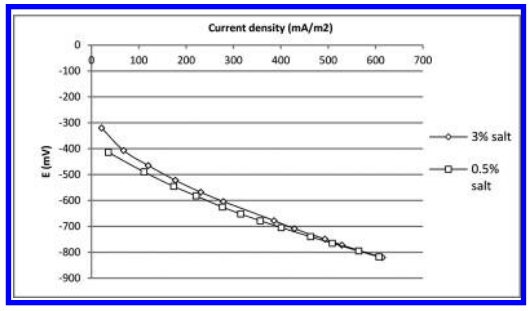

Figure 7. Current sweep, 3% and 0.5% NaCl specimens.

Table 3. 24 hour decay.

	24 hour decay (mV)			
Specimen	1 week	1 month	2 month	3 month
SP1	110	152	161	160
SP2	131	162		
SP3	168	173	188	202
SP4	285	316		
SP5	267	280	289	300
SP6	452	496		
SP8	239	237	247	268
SP9	261	324		

This current density required is related to the corrosion activity, further supporting the evidence that low level corrosion is present in the 3% specimens but that the 0.5% specimens are probably passive at the time of the application of the CP.

The potential of the control specimens at both the 3% and 0.5% chloride both remain more or less constant through the CP period and once the CP is switched off. This would indicate that even after 250 days in the wet/dry cycling corrosion has not been well established and remains at a low level, as supported by the visual inspection and corrosion rate data. This shows that for laboratory trials specimens need to be conditioned well in advance if active corrosion is to be established prior to application of CP.

In order to assess the performance of the CP instant off and 24 hour decay was monitored for each specimen after 1 week and at 1 month for all specimens and further monitored at 2 months and 3 months for the specimens with CP applied for the 3 month period. All the specimens showed similar behaviour, with all the specimens achieving the 24 hour 100 mV decay requirement, even after 1 week, Table 3.

The 24 hour decay data shows that significantly higher decay values are found for the 0.5%

specimens, SP8 and SP9, than the corresponding 3% specimens, SP1 and SP2 and SP3. Examples of the 24 decay are given in Figures 8 and 9. Similar profiles are obtained for all the specimens, with the decay values plateauing out with time, with little increase observed in the 24 hour decay value between 1 and 3 months, with SP1 even showing a small reduction. This would indicate that protection is achieved rapidly, as would be anticipated given the minimal corrosion on the bars prior to application of the current.

The 0.5% NaCl specimens displayed significantly higher depolarization values compared to the 3% specimens. Furthermore, it is observed that the percentage of change in the depolarization value between 1 week and 1 month is clearly much lower than the 3% NaCl specimens. The data shows that passivity was more readily achieved in the 0.5% specimens, as would be expected. Once the passivity is achieved little change in the decay trace is observed.

The 3% specimens shift to potentials slightly more positive to those pre-CP, while the 0.5% specimens have potentials similar to those pre-CP, Table 4.

This can be attributed to the condition of the bars and the effect of the CP. The 0.5% specimens were most likely in a passive state at the application

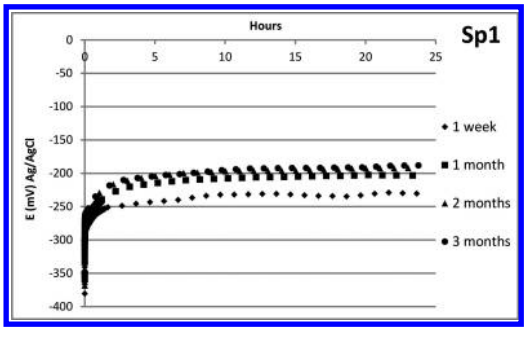

Figure 8. 24 hour decay, SP1.

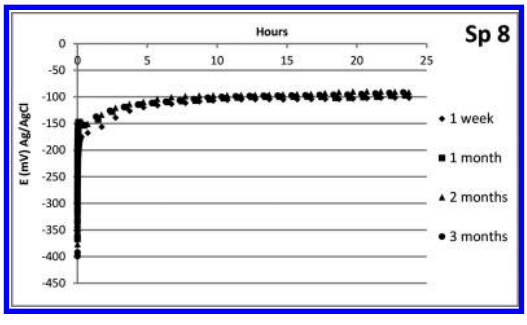

Figure 9. 24 hour decay, SP9.

Table 4. Steel potential data pre and post CP.

Specimen	Pre CP potential (mV, Ag/AgCl)	Post CP potential (mV, Ag/AgCl)	Residual protection (Days)
SP1	–249	–221	10
SP2	–282	–176	<5
SP3	–270	–209	20
SP4	–251	–187	45
SP5	–255	–205	55
SP6	–258	–145	90
SP8	–90	–90	5*
SP9	–89	–106	55*

*—on going with no drop observed to date.

of the CP, while the steel in the 3% had low level of corrosion activity and a higher chloride concentration at the bar/paste interface. The application of the CP acts to stop the corrosion and generate hydroxyl ions at the steel/cement interface and repels chloride ions from the vicinity of the bar. A combination of these two effects has resulted in the steel in the 3% specimens now being in a passive state, and hence the more positive potentials, for the 0.5% the bars were probably already passive before the application of the CP, thus potentials remain constant pre and post application.

Following the halting of the CP it can be seen that all the 3% specimens have a period of time as the potential continues to drift more positive, indicating protection is maintained (with the exception of SP2). This indicates that residual protection is being afforded to the bars, similar to that reported (Christodoulou et al., 2010, Glass et al., 2001). Results for SP2 are inconclusive as potential starts to fall almost immediately after current interruption to the control potential, however in a gradual manner rather than a sudden drop, as seen for other specimens. It is conservative to estimate that the residual protection of SP2 was less than 5 days.

The 0.5% specimens both returned to similar potentials observed prior to application of the CP. To date no change in the potentials or corrosion rates has been observed for any specimens, including the control specimen, SP10. At this point no clear evidence can be determined as to whether residual protection has been achieved. Should the specimens with CP applied remain passive beyond the control then this could be taken as indicative of additional protection being provided. This data again shows that longer conditioning periods are needed for laboratory specimens prior to applying CP.

Analysis of the potentials shows that a drop in potential is observed for the 3% specimens after a number of days, Table 4. This is indicative that the residual protection is being lost at this point.

As would be anticipated the duration of the residual protection increases with current density and, as again would be anticipated, the longer the application of the CP, at a set current density, the longer the residual protection. However, while the three month specimens do show a longer period of residual protection for the same current density, this is not a direct function of the duration, ie the three month specimens do not give three times the residual protection. The three month specimens only provide a small additional period of protection compared to the one month specimens. This would suggest that a certain level of residual protection is afforded once corrosion has been halted, and the passive layer restored. The additional protection may then be a function of the hydroxyl ions generated at the rebar and any transport of chloride ions from the vicinity of the steel. Both of these phenomena will result in changes in the Cl^-/OH^- ratio, which has been identified as a key factor in the initiation of corrosion (Glass and Buenfeld, 1997). The disruption of residual protection likely occurs when chloride ions diffuse back under the natural concentration gradient to the steel and causes depassivation.

An increase in current density shows a larger increase in the duration of the residual protection, though only the SP4, 180 mA/m^2, specimen have a proportionally longer residual period compared to SP2, 60 mA/m^2. In all other cases the residual protection does not increase at the same rate as the current density. This would further suggest that restoration of the passive layer itself is the primary factor in providing residual protection, with the charge passed then providing additional time.

It is also noted that there is no direct relationship between the total charge passed and the residual protection. SP1 and SP2 both pass the same total charge but SP1 provides a slightly longer period of residual protection. For SP3 and SP4 and SP5 and SP6 the specimen with the higher current density, but shorter CP period provides the longer residual protection. This effect also increases as the applied current density increases.

A possible explanation is that at the higher current density more of the charge is carried by the chloride ions in the pore solution. Thus at the higher current density more chloride ions are removed from the zone around the rebar, analogous with desalination. This is supported by the resistivity measurements, Figure 10. Three sensors were placed with in the specimens adjacent to the bar (P3—positioned mid-level of bar, P2 and P3 10 mm and 20 mm below P1, respectively). For clarity only the top sensor, P1, is reported, though all three sensors have very similar resistances prior to application of the CP.

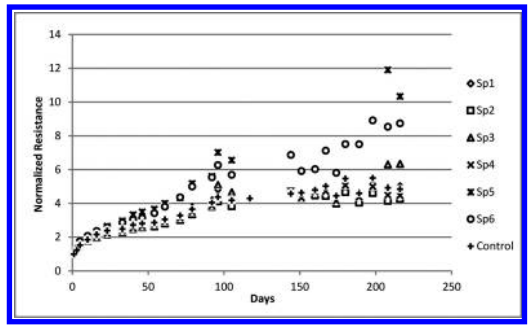

Figure 10. Normalised resistance measurements, sensor P1.

The data shows are general increase in resistance with time for all specimens, with all specimens having similar values.

The concrete resistance can be broken down into three stages; during the first week, the rate of increase in concrete is at a maximum, followed by a slower but steady increase up to approximately 100 days, after which the resistance starts to reach an almost constant state. The maximum rate of increase during the first few days after casting is due to rapid concrete hydration. As hydration continues and the specimens dry out, the resistance continues to increase. At 100 days a somewhat steady state appears to be reached. Corrosion rates taken after 100 days were also very similar for each specimen, which indicates a direct relationship with concrete resistance. This observation further supports that the high initial corrosion rates and degree of fluctuation is influenced by concrete resistance.

Following application of the CP there is a considerable scatter of the resistance observed. This is attributed to the generation of hydroxyl ions at the bar and migration of chloride ions away from the bar. This will affect the relative concentration of the ions in the pore solution at each depth. This variation can be noted from analysis of the three sensors at different depths. Examples of SP1 and SP6 are given in Figures 11 and 12.

The data shows that as the current density increases the variation in the normalized resistance between P1, P2 and P3 increases. As the resistance can be taken a measure of the ion concentration within the pore solution, this supports the hypothesis that there have been changes in the relative concentrations of the ions due to the applied current.

The resistivity in the concrete can also be affected by the temperature and the relative humidity. The fluctuations in temperature and relative humidity through the course of the experiment are shown in Figures 13 and 14.

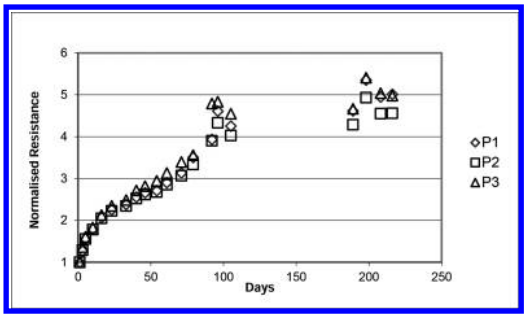

Figure 11. Normalised resistance measurements, SP1.

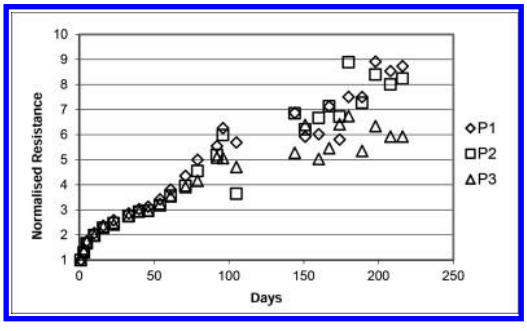

Figure 12. Normalised resistance measurements, SP1.

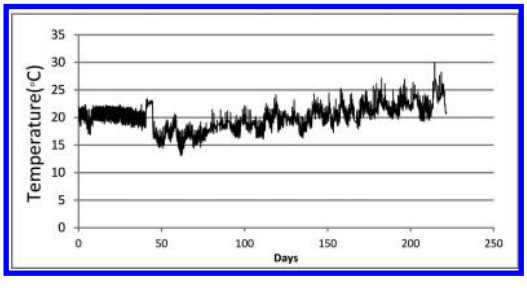

Figure 13. Temperature vs time.

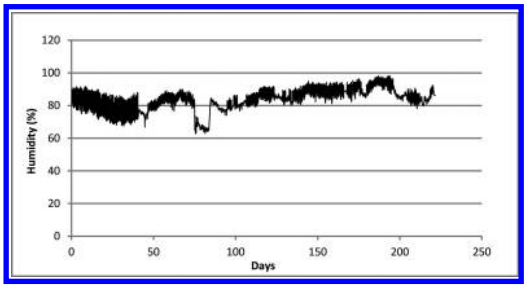

Figure 14. Relative humidity vs time.

The relative humidity remains fairly constant throughout the experiment, Fluctuations are seen due to drying and wetting cycles, but generally remains between 80–90%. These values are representative of concrete in an exposed environment and would not lead to the corrosion being under anodic or cathodic control due to insufficient moisture or oxygen to support corrosion. The drop between 75–80 days is due to a failure in the spray pump over a weekend period and is not expected to have any impact on the results as this was during the conditioning period, but could account for a drop in corrosion rates at this point.

The temperature does show some variation between 15–25 °C over the course of the experiment. This is attributed to variations in the laboratory environment reflecting the seasonal variation in the weather. Again these are changes that would be consistent with concrete in an exposed environment and are not anticipated in affecting the residual protection. The temperature variations could account for small fluctuations noted in the corrosion rate and resistances, but not in the general trends.

4 CONCLUSIONS

CP has been successfully applied to laboratory specimens, with the steel bars achieving the criteria specified for the protection of reinforced concrete structures.

Following the application of the CP residual protection was observed in all specimens with CP applied.

The duration of the residual protection increased with time of application. However, the increase in the duration of the residual protection was not linear with time.

The duration of residual protection increased with current density, though again this was not a direct relationship between the duration and current density.

In general specimens with the higher current density, but shorter CP period provided the longer residual protection.

The potential and corrosion data indicated that active corrosion had not been initiated in the 0.5% specimens during the conditioning process, while low level corrosion was occurring in the 3% specimens at the time of the application of the CP.

The resistance measurements suggested that the CP had affected the ion concentration in the pore solutions around the bar, possibly due to the production of hydroxyl ions and the removal of chloride ions in the interfacial zone.

The relative humidity and temperature in the specimens were consistent with those experienced in exposed concrete structures.

Overall the results show that residual protection can be achieved by the application of ICCP to reinforced concrete structures. The duration and current density of the applied current both affect the duration for which this protection will remain.

REFERENCES

AS2328 2008. AS 2328.5 Cathodic Protection of Metals; Part 5 Steel in Concrete. Australian Standards.

Bhuiyan, S., Law, D.W., Molyneaux, T.C.K. & Nicholls, P. 2014. The Impact Of The Interruption Of Impressed Current Cathodic Protection On The Steel/Concrete Interface. *In:* GRANTHAM, M. (ed.) *Concrete Solutions; 5th International Conference on Concrete Repair.* Belfast.

Broomfield, J.P. 2007. *Corrosion of Steel in Concrete,* London, Taylor & Francis.

Broomfield, J.P. & Tinnea, J.S. 1992. Cathodic protection of reinforced concrete bridge components. *Report ID No: SHRPCUWP92618,.*

BSI 2000. BS EN 12696; Cathodic Protection of Steel in Concrete. British Standards Institure.

Christodoulou, C., Glass, G., Webb, J., Austin, S. & Goodier, C. 2010. Assessing the long term benefits of Impressed Current Cathodic Protection. *Corrosion Science,* 52, 2671–2679.

El Maaddawy, T., Soudki, K. & Topper, T. 2005. Long-term performance of corrosion-damaged reinforced concrete beams. *Aci Structural Journal,* 102, 649–656.

Glass, G.K. & Buenfeld, N.R. 1997. The presentation of the chloride threshold level for corrosion of steel in concrete. *Corrosion Science,* 39, 1001–1013.

Glass, G.K. & Chadwick, J.R. 1994. An Investigation into the Mechanisms of Protection Afforded by a Cathodic Current and the Implications for Advances in the Field of Cathodic Protection. *Corrosion Science,* 36, 2193–2209.

Glass, G.K., Hassanein, A.M. & Buenfeld, N.R. 2001. Cathodic protection afforded by an intermittent current applied to reinforced concrete. *Corrosion Science,* 43, 1111–1131.

Green, W.K., Lyon, S.B. & Scantlebury, J.D. 1993. Electrochemical Changes in Chloride-Contaminated Reinforced-Concrete Following Cathodic Polarization. *Corrosion Science,* 35, 1627–1631.

Koleva, D.A., Guo, Z., Van Breugel, K. & De Wit, J.H.W. 2009. The beneficial secondary effects of conventional and pulse cathodic protection for reinforced concrete, evidenced by X-ray and microscopic analysis of the steel surface and the steel/cement paste interface. *Materials and Corrosion-Werkstoffe Und Korrosion,* 60, 704–715.

Law, D.W., Cairns, J., Millard, S.G. & Bungey, J.H. 2004. Measurement of loss of steel from reinforcing bars in concrete using linear polarisation resistance measurements. *Ndt & E International,* 37, 381–388.

Mccarter, W.J., Chrisp, T.M., Starrs, G., Basheer, P.A.M. & Blewett, J. 2005. Field monitoring of electrical conductivity of cover-zone concrete. *Cement & Concrete Composites,* 27, 809–817.

NACE 2007. SP0290: Impressed Current Cathodic Protection of Reinforcing Steel in Atmospherically Exposed Concrete Structures.

Page, C.L. 1997. Cathodic Protection of Reinforced Concrete—Principles and Applications. *Repair of Concrete Structures.* Norway.

Presuel, F.J., Sagues, A.A. & Kranc, S.C. 2002. Steel activation in concrete following interruption of long-term cathodic polarisation. *Corrosion 2002.*

Concrete Repair, Rehabilitation and Retrofitting IV – Dehn et al. (Eds)
© 2016 Taylor & Francis Group, London, ISBN 978-1-138-02843-2

Deterioration of service reservoirs constructed in accordance with EN 206

R. Brueckner
Mott MacDonald, Bristol, UK

C. Atkins & P. Lambert
Mott MacDonald, Altrincham, UK

ABSTRACT: EN 206 provides guidance for the design of concrete exposed to chemical attack, however, several recently constructed or refurbished service reservoirs have undergone deterioration. In contrast, reservoirs constructed more than 20 to 30 years ago do not show signs of this particular type of deterioration. The equivalent British Standard, BS 8500, and BRE Special Digest 1 concentrate on the attack of sulphate containing waters but do not cover other potentially aggressive aqueous environments.

The affected concrete surfaces have been attacked by aggressive water, transforming the surface into a mushy paste fully depleted of calcium compounds. Two further distinct zones have been observed. Zone 2 has been carbonated and Zone 3 has experienced Portlandite depletion. The initial findings are consistent with mild acid attack by ingressing moisture.

To identify the cause of the attack and allow the selection of resistant concrete mixes, a series of field experiments and investigations has been initiated at affected service reservoirs. Concrete specimens of compositions representing the recommendations of EN 206 for XA3, together with more durable mixes, have been immersed in natural waters of varying aggressiveness. The water properties have been assessed over an extended period and the rate of deterioration determined at four reservoirs.

This paper details the investigations carried out and discusses the recommendations provided in EN 206 with regards to the attack by "aggressive" drinking water in service reservoirs. It is hoped it will initiate discussion on the contents of EN206 and any further guidance required to obtain durable concrete structures.

1 INTRODUCTION

Water can be a highly aggressive medium, attacking concrete as a result of erosion or chemical attack. In general, concrete has excellent resistance to chemical attack provided an appropriate mix is used and it is well compacted. However, due to its high alkalinity, Portland Cement (PC) based concrete is not particularly resistant against strong acids or compounds which can convert to acids, as noted by Neville.

The hydration products of PC decompose during chemical attack and the newly formed products may leach out or, if not soluble, may be disruptive to the integrity of the concrete. The reactions occur when the aggressive compounds are in solution. Calcium hydroxide ($Ca(OH)_2$) is the most vulnerable compound within the cement paste, however, the Calcium-Silicate-Hydrate (C-S-H) phases can also be attacked. Calcareous aggregates such as limestone are similarly susceptible whilst siliceous aggregates are generally not attacked.

The most important factors in the corrosive attack of concrete are the amount of fluid flowing over the exposed surface of the concrete and the pH. If a significant flow rate is occurring, the attack on the concrete can be considerable even for mildly acidic conditions. However, if one of the corrosion products formed is insoluble, it can provide a protective layer on the surface of the concrete. The types of attack, depending on the pH, are shown in Table 1.

Table 1. Type of concrete attack depending on pH, Neville.

pH	Type of attack
>8.5	Largely unaffected unless very strong alkaline solutions are present
7.0–8.5	Superficial leaching of calcium hydroxide
6.0	Attack is minimal unless the flow rate is significant
5.0	Serious attack, extent depending on flow rate
<4.0	Hardened cement and calcareous aggregates are rapidly attacked

The more impermeable the concrete, the lower the rate of attack for any given exposure condition.

Most natural waters have acidities that fall into the pH range 4 to 8.5. Below pH 5 the acidity is usually due to the presence of humic acid which has limited aggression because calcium humate is almost insoluble in water and forms a protective layer on the concrete.

When natural waters containing carbon dioxide attack concrete, the calcium hydroxide and the hardened cement paste are first carbonated and then dissolved, resulting in decalcification. The two attacking species are carbonic acid, H_2CO_3, and calcium bicarbonate, $Ca(HCO_3)_2$. As calcium bicarbonate is soluble it will be removed by the aggressive water, providing sufficient carbonic acid is present to stabilise the bicarbonate formed. Calcium carbonate, whether present due to carbonation of calcium hydroxide or as limestone aggregate, and the hydrated cement phases are also attacked by carbonic acid. The end products of the attack are gelatinous forms of hydrated silica and alumina and iron hydroxides. In practice, most of the hydrated alumina and iron hydroxides are removed by the aggressive water so that the only remaining product is gelatinous silica. It is the formation of soluble calcium bicarbonate and its removal by the water that is responsible for the attack of concrete surfaces.

Non-calcareous aggregates are left standing proud of the corroded surface when attacked by soft acidic water. Many limestone aggregates will be dissolved more readily than the surrounding cement paste and may form a comparatively smooth surface. As the attack proceeds, smaller aggregates near the surface may become dislodged as the degraded surface develops. The use of calcareous aggregates increases the buffer effect at the surface and may reduce the rate of deterioration due to acid attack.

2 INTERNATIONAL GUIDANCE

Where concrete is exposed to natural soils and ground water then EN 206 provides guidance on the exposure class Chemical Attack—XA. EN 206 differentiates between XA1—slightly aggressive chemical environment, XA2—moderately aggressive environment and XA3—highly aggressive chemical environment. The exposure class is then identified using EN 206. An extract is represented in Table 2, showing the limiting values for exposure classes for chemical attack from groundwater.

The National Annex of BS EN 206 provides recommendations for the design of concrete exposed to XA environments. XA3, as the most severe exposure class, requires a minimum concrete strength of C35/45 with a maximum water-cement ratio of 0.45 and a minimum cement content of 360 kg/m^3. The German Standard DIN 1045-2 recommends the same minimum water-cement ratio of 0.45 but a lower cement content of 320 kg/m^3. Where sulphates are present, BRE Special Digest 1 is applicable for the specification of concrete in the UK. The most severe Design Sulphate class DS5 in BRE SD1 specifies the use of an ACEC Class of AC-5 that requires a Design Chemical class DC-4 plus one Additional Protective Measure (APM). DC-4 specifies a maximum w/c-ratio of 0.35 and minimum cement content of 380 kg/m^3 with a CEM II/B-V+SR or CEM III/A+SR. The APM is required to be a protective coating.

Detailed guidance is available for the specification of concrete exposed to sulphate in groundwater or soil; however, there is a lack of detailed guidance when concrete is exposed to aggressive water containing chemical species other than sulphates. Engineers are then required to advise on appropriate durable concrete mixes which may vary as the assessment is largely based on experience. Besides sulphates, acids are the most common chemical species to attack concrete. Aggressive dissolved carbon dioxide forming a mild acid can cause significant deterioration where water is considered to be soft with a low alkalinity/total hardness. Deterioration due to ammonium or magnesium is rarely encountered except in certain industrial or brownfield environments.

Table 2. Extract from EN 206.

Chemical characteristic	Reference test method	XA1	XA2	XA3
SO_4^{2-} [mg/l]	EN 196-2	≥200 and ≤600	>600 and ≤3000	>3000 and ≤6000
pH	ISO 4316	≤6.5 and ≥5.5	<5.5 and ≥4.5	<4.5 and ≥4.0
CO_2 [mg/l] aggressive	EN 13577	≥15 and ≤40	>40 and ≤100	>100 up to saturation
NH_4^+ [mg/l]	ISO 7150-1	≥15 and ≤30	>30 and ≤60	>60 and ≤100
Mg^{2+} [mg/l]	EN ISO 7980	≥300 and ≤1000	>1000 and ≤3000	>3000 up to saturation

3 WATER CHARACTERISTICS

Water generally contains dissolved gases. Oxygen is the most important of the dissolved gases. Carbon dioxide must be considered in relation to other constituents, especially calcium hardness.

The effect of carbon dioxide is closely linked with the bicarbonate content. Calcium bicarbonate requires excess carbon dioxide in solution to stabilize. The necessary concentration depends on the temperature and the other constituents of the water. With insufficient dissolved carbon dioxide, the water will be supersaturated with calcium carbonate and a slight increase in pH will tend to cause its precipitation, forming a scale on the contact surfaces. The water will usually be non-corrosive under these conditions.

If carbon dioxide is present in excess of the stabilizing equilibrium, there can be no deposition of calcium carbonate and any old deposits or calcium bearing compounds will be dissolved. The corrosiveness of water can be expressed by the Saturation Index (SI), also known as Langlier Saturation Index (LSI).

$$SI = pH - pH_s \ (pH_s = \text{saturation pH value})$$

If the SI is positive the water will be supersaturated with respect to calcium carbonate, whereas if it is negative the water is considered to be unstable and will be aggressive to calcium carbonate and calcium bearing compounds.

The Water Services Association of Australia (WSAA) states that water is considered to be potentially aggressive if it has a SI of less than –1.5. However, it should be noted that the SI only indicates the presence of a driving force and does not guarantee that scaling or dissolution will occur. Mons et al. recommend that the LSI. should be in the range –0.2 to +0.3 to avoid scaling and corrosion problems.

Another related parameter is the Ryznar Stability Index, which is given by:

$$RSI = 2pH_s - pH$$

An RSI of 6.5 to 7 indicates that water is approximately at saturation equilibrium with respect to calcium carbonate, whereas an RSI of greater than 8 is considered to be undersaturated, tending to dissolve any existing $CaCO_3$.

The corrosiveness of water can also be expressed using the Calcium Carbonate Precipitation Potential (CCPP) which is defined as the quantity of calcium carbonate that can theoretically precipitate from supersaturated water or alternatively dissolve into unsaturated waters. The degree of super or undersaturation can be calculated from the water's pH, alkalinity and Ca^{2+} concentrations and their potentials are represented in Table 3. This index is considered to be more reliable than the LSI. and RSI. as it takes account of the amount of calcium carbonate that could ultimately be dissolved to achieve equilibrium. The WSAA provides some values for the aggressiveness of water.

To obtain non-corrosive water the South African Water Research Commission under Lowenthal et al. suggests that *"The chemical state of the water needs to be adjusted to a slight state of supersaturation with respect to calcium carbonate: a precipitation potential of about 4 mg/l is recommended."* In contrast to that statement, the WSAA suggests that scaling already occurs above 0 and that water is still passive up to a CCPP value of –5.

CCPP provides essentially identical information to the LSI in a slightly expanded numerical form and is, again, a theoretical calculation based on thermodynamic data.

The hardness is one of many factors influencing the aggressive properties of water. According to Neville there are apparent trends in relation to the aggressiveness based on the hardness of water:

- Soft water is aggressive and undersaturated with respect to calcium carbonate.
- Very hard water is usually not very aggressive provided that it is supersaturated with calcium carbonate. Underground water with a low pH value and high carbon dioxide content is aggressive.
- Water of intermediate hardness frequently contains a significant amount of other constituents and there is often a tendency for a scale to be loosely formed.

The usual classification of water by hardness in according to Thresh et al. is represented in Table 4.

Water containing free carbon dioxide, such as moorland water or mineral waters, also attacks concrete but not all carbon dioxide is aggressive. Some carbon dioxide is required to form and stabilize calcium bicarbonate in the solution. Water containing low amounts of carbon dioxide, such as flowing pure water as a result of condensation, can cause surface

Table 3. $CaCO_3$ precipitation potentials.

$CaCO_3$ precipitation potential	CCPP values
Scaling (protective)	> 0
Passive	0 to –5
Mildly dissolving	–5 to –10
Dissolving (aggressive)	< –10

Table 4. Total water hardness [Thresh et al.].

$CaCO_3$ content	Total water hardness
50 ppm	Soft
50–100 ppm	Moderately soft
100–150 ppm	Slightly hard
150–250 ppm	Moderately hard
250–350 ppm	Hard
>350 ppm	Very hard

erosion. Other types of water, such as peaty water, can be very aggressive due to the low pH. All these exposure conditions result in leaching of the readily soluble calcium hydroxide and other calcium bearing compounds in the cement paste. The reaction occurs as aggressive free carbon dioxide dissolved in the pore water of the cement paste reacts with calcium hydroxide, Portlandite, to form calcium carbonate which then continues to react with free carbon dioxide to form calcium bicarbonate.

4 INVESTIGATION

In the UK, concrete is typically designed in accordance with BS EN 206, BS 8500, BRE Special Digest 1 and other current guidelines but despite compliant designs and specifications, issues with concrete durability have occurred during recent years. This was notably encountered at water service reservoirs where structures had been recently constructed or refurbished. It was observed that concrete faces started to transform into a mushy paste, fully depleted of calcium compounds, within one year after construction, see Figure 1. Reservoirs constructed in the 1970s and 1980s have, however, not experienced similar deterioration when exposed to the same water.

Following the occurrence of the surface deterioration, an investigation was initiated to assess the cause and identify appropriate and durable concrete mixes for future works. To assess the deterioration mechanism and its potential aggressiveness on the structure during its design life the following factors were considered to be most relevant:

- Composition of the attacked concrete;
- Rate of deterioration on varying mixes;
- Composition of the attacking media.

4.1 *Water composition*

The composition of the water was analysed with respect to alkalinity, calcium content, total hardness, pH, temperature, chlorides, magnesium and sulphates. Representative samples of the water were taken at the inlet and outlet of the reservoirs

Figure 1. Soft concrete surface.

Table 5. Reservoir water characteristics.

	SR1	SR2	SR3	SR4
Alkalinity [mg/l $CaCO_3$]	15	55	131	198
Calcium [mg/l Ca^{2+}]	6	41	67	107
Total Hardness [mg/l $CaCO_3$]	22	130	192	292
pH	7.6	7.2	7.3	7.6
Temperature [°C]	5.7	10.6	14.7	13.0

on at least three occasions. The results showed that the contents of chlorides, magnesium and sulphates are negligible. The water is mobile due to the operation of the reservoir. The data from inlet and outlet did not show significant differences, indicating that an obvious increase or decrease of any particular characteristic was not present. The mean results of the main characteristics are presented in Table 5.

4.2 *Concrete composition*

The concrete mix design of the attacked service reservoirs was determined using either archive information or petrographic analysis. The original concrete mix design was only available for one Service Reservoir (SR2). 4 No. concrete cores were retrieved from each of the three remaining reservoirs at representative locations from the submerged floors and walls for petrographic analysis.

The concrete was based on Portland cement, with or without pfa and ggbs, with varying cement content between 340 and 460 kg/m^3 and a water-cement ratio of 0.45 to 0.5. The aggregate generally comprised coarse limestone and siliceous sand. The detailed composition of the concrete is shown in Table 6. In the case of SR2, the Exposure and Design Chemical Class in the concrete specification

Table 6. Reservoir concrete composition.

	SR 1	SR2 (specification)		SR3	SR4
	Cast in-situ	Cast in-situ	Precast	Cast in-situ	Cast in-situ
Concrete class		C32/40	C50/60		
Cement type	CEM III/A (50%)	CEM III/A + SR	CEM III/A + SR	CEM II/B-V (30%)	CEM I
Cement content [kg/m^3]	460	Min. 360	Min. 380	340	380
w/c-ratio	0.45	Max. 0.45	Max. 0.4	0.45	0.45–0.5
Aggregate type	Limestone; siliceous sand	Limestone	Limestone	Calcareous siltstone, sandstone	Limestone

were XD2 and DC-2, respectively. The data for SR2 were obtained from the construction specification and provide the minimum/maximum requirements but not the actual mix design.

Exposure class XD2 was chosen due to the risk of chlorine in the water in a wet, rarely dry environment. In the case of suspected exposure to chemical attack, XA, BS 8500 refers to the determination of the ACEC classes, i.e. BRE Special Digest 1—Aggressive ground conditions. BS 8500 does not provide specific requirements for XA exposures other than sulphates.

Surface deterioration and weakening of the cover zone of the cores retrieved from SR3 was confirmed by petrographic analysis whereas no visible signs of deterioration could be found at SR1 and SR4. Signs of carbonation up to a depth of 2.5 mm were however observed at the cores of SR1 which is untypical for a 50% ggbs concrete that is submerged.

4.3 *Extent of deterioration*

Deterioration was visually observed at SR2 and SR3 in the form of a softened concrete surface that could easily be scraped away within 1 and 15 years, respectively (Fig. 2). The depth of deterioration within the concrete and the potential cause was assessed in more detail on the concrete core samples from SR1, SR3 and SR4. Core samples from SR2 were not retrieved as a result of the obvious deterioration after 1 year and that information about the concrete mix design was available. Both the in-situ and precast concrete elements were observed to be affected, i.e. that the C50/60 concrete with a minimum of 380 kg/m^3 CEM III/A+SR and a w/c-ratio of 0.4 was also attacked. Controlled permeability formwork was used during construction that should have provided a more resistant cover zone.

The analysis of the visually affected concrete at SR3 showed signs of surface deterioration as a result of softening and porosity enhancement.

Figure 2. Soft surface.

Three distinct zones of surface alteration, that are typical of mild acid attack, were identified which were as follows:

- Substantial porosity enhancement/calcium depletion up to a depth of 0.4 to 0.7 mm caused by exposure to mildly aggressive and mobile moisture. Portlandite and the strength providing calcium bearing phases are affected in that zone.
- Carbonation from 0.4 to 1.2 mm depth as a result of the ingress of moisture containing dissolved CO_2.
- Portlandite depletion up to 3 mm depth as a result of leaching.

4.4 *Rate of deterioration*

As a result of the insufficient data and varying concrete and water parameter it has so far not been possible to assess the rate of deterioration. However, the concrete mixes specified and designed for all four reservoirs would have satisfied the XA3 requirements of DIN 1045-2 and SR1, SR2 and SR4 would have justified the more stringent requirements of BS EN 206 for XA3.

To obtain more data and to assess the susceptibility of varying concrete mix designs, which are supposedly more demanding than the minimum XA3 exposure conditions, a testing regime was identified. This comprised the manufacture and immersion of concrete cubes into the drinking water service reservoirs which are specified to have the following parameters as outlined in Table 7.

The w/c-ratio was chosen to be 0.35 and 0.45 with a cement content of 380 kg/m^3 using OPC, CEM II/B-V and CEM III/A. Two additional mixes were selected of which one has a higher cement content of 420 kg/m^3 CEM III/A and the second represents the requirements of BS EN 206 and BRE SD1.

Higher cement contents and lower w/c-ratios were not selected to identify mixes that can be easily specified and designed on the majority of projects. 2 No. cube specimens were produced for each mix and reservoir to obtain representative results within the space available.

The cube samples were cured in a standard site manner and washed prior to initial testing and immersion. The testing included the determination of the weight loss and dimensions at the initial testing and at 3, 6, 12 and 24 months. The testing procures are highlighted in the following sections.

4.4.1 *Weight*

The weight of each cube is determined in Saturated Surface Dry (SSD) conditions prior to immersion and at the defined inspection dates. The cubes are cleaned from any surface erosion products/softened concrete and then weighted.

4.4.2 *Dimensions/erosion*

The section loss of the cubes is determined by measuring the 3 No. opposite faces at a minimum of 5 No. representative locations. The depth of erosion is specifically determined at one face where 3 No. stainless steel pins are inserted into the cube in a triangular arrangement. The erosion is measured at 1/3 and 2/3 positions between the pins to obtain at least 6 No. results from each cube.

Table 7. Concrete mixes to be investigated.

Mix	w/c-ratio	Cement content [kg/m^3]	Cement type
1	0.35	380	CEM I
2	0.35	380	CEM II/B-V
3	0.35	380	CEM III/A
4	0.45	380	CEM I
5	0.45	380	CEM II/B-V
6	0.45	380	CEM III/A
7	0.45	420	CEM III/A
8	0.45	360	CEM III/B

4.4.3 *Petrographic analysis*

Petrographic analysis is performed at representative specimens to determine the deterioration progress into the cement matrix. The overall depth of deterioration comprising the loss of cover zone due to erosion and depth of paste alterations due to ingress of aggressive water can then be determined.

5 DISCUSSION AND CONCLUSIONS

Recently constructed service reservoirs have been affected by concrete deterioration within a relative short time period. The deterioration was observed as softening of the surface cover zone and was confirmed by petrographic analysis to be the result of ingress of moisture containing dissolved carbon dioxide resulting in mild acid attack. The extent of surface softening has yet to be quantitatively identified but the modifications to the cement paste are up to a depth of 3 mm. The deterioration progress has been found to show three distinct zones:

- Zone 1 (outer zone): Zone of substantial porosity enhancement and calcium depletion where Portlandite and the strength-providing calcium-bearing phases are attacked by carbonic acid.
- Zone 2: Zone of carbonation where ingressing moisture containing dissolved carbon dioxide reacts with dissolved calcium hydroxide.
- Zone 3 (inner zone): Portlandite as the most soluble cement hydration product is dissolved by the ingress of aggressive water causing leaching of $Ca(OH)_2$.

The aggressiveness of the water was initially assessed by determining the Langlier Saturation Index (LSI), the Ryznar Stability Index (RSI), the Calcium Carbonation Precipitation Potential (CCPP) and the Water Hardness. The LSI, RSI and CCPP indices gave inconclusive results, indicating that the water at SR2 and SR3 is moderately aggressive (LSI) but still oversaturated at SR3 based on the RSI consistent with non-dissolving characteristics. Furthermore, according to Thresh et al., the Total Water Hardness (ppm $CaCO_3$) indicates slightly hard, i.e. scaling, water (100–150 ppm $CaCO_3$). However, erosion, i.e. dissolving properties, was observed at one reservoir within a year of construction. The pH was generally greater than 7.2 and did not undergo conclusive changes from inlet to outlet.

Hence, the water assessment was carried out based on the alkalinity (mg/l $CaCO_3$) that appeared to represent the deterioration observations to date. The aggressiveness of the water was identified to be higher the lower the alkalinity. Therefore the aggressiveness was categorized as follows:

Table 8. Concrete deterioration depending on mix design and water aggressiveness.

	SR1	SR2		SR3	SR4
	Cast in-situ	Cast in-situ	Precast	Cast in-situ	Cast in-situ
Cement [kg/m^3]	460 CEM III/A	Min 360 CEM III/A+SR	Min 380 CEM III/A+SR	340 CEM II/B-V	380 CEM I
w/c-ratio	0.45	0.45	0.4	0.45	0.45–0.5
Alkalinity [mg/l $CaCO_3$]	14	55	55	131	198
Total hardness [mg/l $CaCO_3$]	22	130	130	192	292
Age [years]	3	1	1	15	
Deterioration	Carbonation of outer zone	Surface softening	Surface softening	Surface softening	No deterioration

- Extremely aggressive water at SR1 (alkalinity: 14 mg/l $CaCO_3$/total hardness: 22 mg/l $CaCO_3$);
- Highly aggressive water at SR2 (55 mg/l $CaCO_3$/ 130 mg/l $CaCO_3$);
- Slightly to moderately aggressive water at SR3 (131 mg/l $CaCO_3$/ 192 mg/l $CaCO_3$); and
- Non-aggressive water at SR4 (198 mg/l $CaCO_3$/ 292 mg/l $CaCO_3$).

The cause of deterioration was found to be aggressive and undersaturated low alkaline water. It should be noted that these are initial conclusions based on the concrete mixes used during construction, water data and investigation findings to date as represented in Table 8. Conclusions regarding the susceptibility of different concrete mixes cannot yet be drawn. As a consequence, a comprehensive investigation regime has been initiated.

The 5 No. concrete mixes used at the 4 No. reservoirs were supposed to be more resistant to chemical attack/aggressive water than the minimum requirements for XA3 in accordance with BS EN 206 except the concrete of SR3. Assessing the data the water at SR3 does not appear to be particularly aggressive and could be classified as moderately aggressive conforming to an XA2 exposure class. Deterioration was however observed and confirmed.

The service reservoir exposed to the potentially most aggressive water, with an alkalinity of about 14 mg/l $CaCO_3$, supposedly had the most resistant concrete mix with 460 kg/m^3 CEM III/A and a w/c-ratio of 0.45. The petrographic analysis, however, showed that attack has commenced with signs of a 2.5 mm zone of carbonation within submerged concrete.

In this investigation it has been proposed that water aggressiveness is categorized based on the alkalinity in ranges of:

- Extremely aggressive: ≤ 50 mg/l $CaCO_3$;
- Highly aggressive: >50 and ≤ 100 mg/l $CaCO_3$;
- Moderately aggressive: >100 and ≤ 200 mg/l $CaCO_3$;
- Non-aggressive: >200 mg/l $CaCO_3$.

Concrete specimens are produced and immersed into the reservoirs so that the overall deterioration rate and susceptibility is assessed to identify more appropriate exposure classes and resistant concrete mixes. The investigation will also provide more details on the effects of the calcium content, total hardness, pH and of the aggressive carbon dioxide content.

Final conclusions and recommendations with respect to the recommendations provided in EN 206 for the chemical attack classes cannot yet be given. It is, however, evident that the current requirements are not sufficient and that EN 206 may need to be reviewed or amended in light of recent findings and observations.

REFERENCES

Lowenthal, R.E.; Wiechers, H.N.S. & Marais, G.V.R. 1986. Softening and Stabilization of Municipal Waters, Water Research Commission, South Africa.

Mons, M.N.; van Dijk, J.C.; Gatel, D.; Hesse, S.; Hofman, J.A. & Nguyen, M.L. 2006. Drinking water hardness; Reasons and criteria for softening and optimal composition of drinking water. International Symposium on health aspects of calcium and magnesium in drinking water, Baltimore, USA.

Neville, A.M. 2005. Properties of Concrete, Fourth Edition, Pearson Education Ltd. Harlow, UK.

Thresh, J.C.; Beale, J.F. & Suckling, E.V., 1943. The examination of water and water supplies. Philadelphia, USA, The Blakiston co.

Water Services Association of Australia (WSAA).

Concrete Repair, Rehabilitation and Retrofitting IV – Dehn et al. (Eds)
© 2016 Taylor & Francis Group, London, ISBN 978-1-138-02843-2

Modelling of chloride diffusion coefficient in concrete with supplementary cementitious materials

K.N. Shukla & R.G. Pillai
Indian Institute of Technology Madras, Chennai, India

ABSTRACT: Chloride ingress through diffusion is a major deterioration mechanism, making it vital to account for it in Service Life Prediction (SLP) frameworks. However, most SLP frameworks have limited provisions for the estimation of the chloride diffusion coefficient ($D_{chloride}$), a parameter with substantial influence on the chloride induced corrosion initiation. Developing a model for $D_{chloride}$ based on raw material characteristics and mixture proportions can help in the selection of materials during the planning phase of projects. This article presents the development of models for the estimation of $D_{chloride}$ based on 42 datasets collected from literature. First, the predictor variables were identified. Then, a diagnostic study was conducted to investigate the influence of each variable on $D_{chloride}$. Then, models that relate $D_{chloride}$ to the significant variables were developed. These models have Mean Absolute Percentage Error (MAPE) equal to 3.77% and Weighted Absolute Percentage Error (WAPE) equal to 1.59%, indicating reasonably good predictions of $D_{chloride}$.

1 INTRODUCTION

The durability of a Reinforced Concrete (RC) structure depends upon its interaction with numerous environmental degradation factors (ISO 15686-1:2000). The ingress of ions, liquids or gases present in the service environment into the structure can have highly deleterious effects on the durability of concrete structures. For instance, the presence of chlorides or carbon dioxide at the steel-cementitious interface would depassivate the steel in concrete, and in the presence of oxygen and water, steel can corrode (Mehta and Monteiro). Service Life Prediction (SLP) models are an alternative to the existing prescriptive approach to design. In general, these models take into account the exposure conditions and the material characteristics while assessing the comparative performances of various material systems in the structure. Suitable assumption/estimation of the complex input parameters is a huge concern in service life prediction. One such complex parameter is chloride diffusion coefficient ($D_{chloride}$). $D_{chloride}$ can be estimated based on the raw material characteristics and mixture proportions. This study aims at developing a probabilistic model for $D_{chloride}$ such that it will 'complete' the SLP framework, thereby allowing service life prediction during the actual planning stage.

Remainder of this paper presents a quick review on the $D_{chloride}$ models used in various SLP frameworks. Then, the significance of this research and model development is presented. Following this, discussions on various factors influencing $D_{chloride}$ are presented. Then, discussions on the data base generated and model development are provided. The statistics of the developed model are also presented.

2 SERVICE LIFE PREDICTION MODELS

This section presents, in brief, five existing service life prediction models (i.e. CHLODIF++, ClinConc, STADIUM®, LIFE-365™ and DuraCrete) and the equations for $D_{chloride}$. Following is the discussion on the basis of evaluation, advantages and the disadvantages of these models.

2.1 *CHLODIF++*

CHLODIF++ has been developed for new structures, for which the data on $D_{chloride}$ is not available (Oslakovic et al. 2012). In this model, $D_{chloride}$ at any time t is modelled as follows.

$$D(t) = D_{w/c} f_{init} \left[1 + 256\left(1 - \frac{RH}{100}\right)^4\right]^{-1} \times t^{-m} \qquad (1)$$

where,

$$D_{w/c} = 5 \times 10^{-13} \times e^{4.8708\left(\frac{w}{c}\right)} \qquad (2)$$

is $D_{chloride}$ based on w/c ratio, f_{inite} is the coefficient accounting for chemical and mineral admixtures, t is the age of the structure and m is the age factor. CHLODIF++ takes into account the effects of several parameters such as water-to-cement ratio, the concentration of mineral and/or chemical admixtures and super plasticizers, relative humidity, temperature, age of the structure, and the details of curing as well as cracking in predicting the service life of a structure. Hence, it can be concluded that CHLODIF++ has quite a comprehensive set of input variables. However, the $D_{w/c}$ component, which is the initial prediction of $D_{chloride}$, relies only on w/c. This simplistic assumption, unless carefully made, might lead to inaccuracies in prediction.

2.2 *ClinConc*

ClinConc is an advanced SLP model which takes into account convection, multi-ionic characteristics etc. in addition to the diffusion mechanism in modelling the ingress of chlorides (Tang 2008). It is based on a finite difference approach and uses directly measurable data as input. ClinConc considers only the diffusion of free chlorides into the concrete and therefore, to model the ingress it follows a two-step procedure. The ingress of free chlorides is modelled through Fick's second law and the distribution of total chlorides (into 'free' and 'bound' parts) is calculated on the basis of mass balance equations in combination with non-linear chloride binding models. In this model, $D_{chloride}$ is defined as follows:

$$D_0 = \frac{\left(0.8\alpha_t^2 - 2\alpha_t + 2.5\right)\left(1 + 0.59K_b\right) \times k_{TD}}{1 + k_{OH} \times K_b \times k_{Tb} \times f_b \times \beta_b \left(\frac{c_s}{35.45}\right)^{\beta_b - 1}} \times D \tag{3}$$

where, D_0 is the initial apparent diffusion coefficient, α_t is the time dependent factor for chloride binding, K_b is the binding factor, k_{TD} and k_{Tb} are the temperature factors for diffusion coefficient and chloride binding, k_{OH} is the factor describing the effects of alkalinity, f_b and β_b are chloride binding coefficients, c_s is the free chloride concentration in the surrounding environment and D is the diffusion coefficient from laboratory tests 6 months after the start of exposure. In addition to a very detailed and elaborate prediction methodology, ClinConc also offers separate treatment of material properties and exposure environment as an advantage. However, it has its own limitations. It was initially developed for submerged structures, which remain in continuous contact with seawater and therefore, has to be modified for application in the air borne chloride scenario.

2.3 *STADIUM®*

STADIUM® (Software for Transport And Degradation In Unsaturated Materials) is a concrete SLP model which uses time step finite element analysis to simulate the ingress of deleterious ions (including chlorides) in conjunction with certified lab testing to determine the service life of exposed reinforced concrete structures. STADIUM® considers the chemical and physical properties of the concrete and the effect of chloride binding in determining the transport properties of the 20+ concrete mixtures that it was developed for. STADIUM® is a commercial software package developed by SIMCO Technologies and is extensively used by the United States Navy in its port expansion projects. Being a commercial project is one of the biggest limitations of STADIUM® since its source code, governing equations and framework are not available (i.e. not an open-source software) for review and evaluation.

2.4 *LIFE-365™*

LIFE-365™ was developed by the Strategic Development Council of the American Concrete Institute through LIFE-365 consortiums I and II; and is one of the most widely used SLP models (Life-365 2012). It is freely available on the Internet as a software package. It predicts the time to initiation of corrosion using a finite difference approach to Fick's 2nd law. $D_{chloride}$ is considered to be time and temperature dependent and is modelled in the following manner.

$$D(t,T) = D_{ref} \times \left(\frac{t_{ref}}{t}\right)^m \times e^{\frac{U}{R}\left(\frac{1}{T_{ref}} - \frac{1}{T}\right)} \tag{4}$$

where, $D(t,T)$ is the diffusion coefficient at time t and temperature T, m is the age factor (also known as the diffusion decay, as defined in equation 4), D_{ref} is the diffusion coefficient at reference time $t_{ref} = 28$ days and reference temperature $T_{ref} = 293$ K, U is the activation energy of the chloride diffusion process (35000 Jmol^{-1}) and R is the universal gas constant (Life-365 2012).

$$m = 0.2 + 0.4\left(\frac{\%FA}{50} + \frac{\%SG}{70}\right) \tag{5}$$

where $\%FA$ and $\%SG$ are the percentages of fly-ash and slag in the concrete, respectively. LIFE-365™ has become widely used because of its user friendly interface, free availability and comprehensiveness. In addition to predicting service life based on user input, LIFE-365™ also generates several reports,

and suggests maintenance and repair plans. LIFE-365™ is limited by the simplifications and assumptions it makes to deal with complex phenomena. Additionally, it is developed specifically for use in North America based on a database collected primarily from North America. This limits its reliable use in other locations in the world.

2.5 *DuraCrete*

DuraCrete is complete performance based design tool, in addition to being a probabilistic SLP framework. It uses the concepts of reliability index and explicit performance requirements to overcome several limitations of the conventional prescriptive design frameworks. Unlike the other models discussed so far, which try to predict a single value of the time to initiation of corrosion, DuraCrete defines a serviceability limit state and calculates the probability of that limit state being reached. All of this can be done at user selected levels of reliability (DuraCrete 1999a). DuraCrete proposes to use $D_{chloride}$ directly measured using compliance laboratory tests or models a time dependent variation through simple power functions to arrive at an apparent diffusion coefficient, $D_a(t)$ as follows:

$$D_a(t) = D_a\left(t_{ex}\right) \times \left(\frac{t_{ex}}{t}\right)^n \tag{6}$$

where, $D_a(t)$ is the function describing the observed time dependent variation of the apparent $D_{chloride}$, t_{ex} and t are, the times at first exposure and the inspection time, respectively, and n. is the age factor. The DuraCrete framework, like many others, accepts $D_{chloride}$ as an input value that has to be derived from one of the compliance tests mentioned in the project report titled 'Compliance Testing for Probabilistic Design Purposes' (DuraCrete 1999b).

3 RESEARCH SIGNIFICANCE

The existing service life prediction frameworks suffer from insufficiencies that hinder their purpose of enabling careful selection of materials during the planning and design phase. For example, one of the major inadequacies of the LIFE-365™ framework is its incapability to accurately estimate $D_{chloride}$ based on mixture proportions and/or field tests. While others like DuraCrete accept $D_{chloride}$ as an input value obtained from a laboratory test.

Despite being carefully selected on the basis of short testing time and high accuracy of results, compliance tests are time taking and do not allow complete freedom of quickly trying a number of combinations. This problem is further accentuated by the shortage of laboratories capable of conducting compliance tests in developing nations where construction is booming. The fact that codes do not mandate compliance tests coupled with the problems faced in conducting them has resulted in tests not being carried out altogether. This issue can be addressed through the development of a probabilistic model for preliminary assessment of concrete systems that relates $D_{chloride}$ with the mixture proportions and raw material characteristics. The model should be capable of accommodating the developments in raw materials. A way of doing this is to incorporate the physical properties and chemical composition of the raw materials into the model. The beauty of this approach is that these data can be obtained from the material manufacturers. The developed model will thereby allow for the selection of durable concrete systems from the various material options available during the planning stage of projects itself.

4 DATABASE AND STATISTICAL MODELLING

As a first step in modelling $D_{chloride}$, diagnostic plots are developed to explore the effect of each variable. Then using an engineering understanding of the diffusion process and mathematical principles, the variables are classified as "critical" and "non-critical" variables. Then a probabilistic model is formulated using the critical variables.

4.1 *Database generation*

One of the most challenging aspects of developing a probabilistic model for $D_{chloride}$ was collecting data for modelling. An attempt was made to generate a fairly large and comprehensive database containing $D_{chloride}$ and all variables that might possibly affect it. About 40 literature articles on $D_{chloride}$ were extensively reviewed. Most other articles were incomplete due to the lack of data on raw materials characteristics. Only three articles were found to have complete data on raw material characteristics, mixture proportions and $D_{chloride}$, which are required for the modeling purposes defined in this article. These are Audenaert et al. 2010, Leng et al. 2000, and Ramezanianpour et al. 2014 from Belgium, China, and Iran, respectively. The developed database contains 48 cases each with 17 fields. These include both normal and special types of concretes. The database has also been designed to accommodate concrete mixes containing fillers, pozzolans and superplasticizers. Several cases of this type have also been identified and recorded.

4.2 *Critical variables*

Cement hydration mechanisms and diagnostic plots indicate that the w/b, specific surface area of binder, SiO_2 and CaO contents in the binder are important variables affecting the chloride diffusion coefficient. The possible relationships between these variables and the chloride diffusion coefficient are as follows.

4.2.1 *Water-to-binder ratio (w/b)*

This is defined as the ratio of the water content per unit volume of concrete to the total binder content per unit volume of concrete. It is also responsible for hydration of cement and the formation of C-S-H gel. The available reaction front and its movement define the properties of the C-S-H matrix through which chlorides diffuse later. w/b has the strongest correlation with diffusion coefficient among all variables considered. This is illustrated in its main effect diagnostic plot (Fig. 1).

4.2.2 *Specific Surface Area (SSA)*

Specific surface area of the binder was taken as the weighted mean of the specific surface area of each of the binder components (say, Portland cement, fly ash, etc.). Only Portland cement, fly ash and slag were considered while developing this model but the concept is applicable to other materials as well. Materials with high specific surface such as silica fume, metakaolin etc. generate fairly impervious binder matrices. An inverse relationship is expected between specific surface area and $D_{chloride}$.

4.2.3 *SiO_2 content*

SiO_2 content in binder was taken as the weighted mean of the SiO_2 contents of each of the binder components (say, Portland cement, slag, etc.). SiO_2 is the S component of the C-S-H gel reaction front, the importance of which has been discussed previously. The main effect plot of the SiO_2 is presented in Figure 2. The main effect shows a strong trend such that it can potentially become exponential through interactions with other variables.

4.2.4 *CaO content*

CaO content in binder was taken as the weighted mean of the CaO contents of each of the binder components. CaO is the C component of the C-S-H gel reaction front. On a close analysis of the data, it was found that SiO_2 and CaO in combination make up a large percentage of the chemical composition of the binder and this percentage remains fairly constant—for the modelling purposes. For the collected data, the mean of SiO_2 + CaO content is 81.71% with a standard deviation of 2.73%. Because of this reason, CaO has not been included in the model as a separate term once SiO_2 has already been considered. SiO_2 was preferred over CaO because of a stronger visible trend between $D_{chloride}$ and SiO_2.

4.3 *Variable properties*

It was observed that two distinct groups of cases existed in the database. The first group was comprised of data from Ramezanianpour (2014), and was characterized by $D_{chloride}$ greater than 10×10^{-12} m^2/s. The second group consisted of data from Audenaert (2010) and Leng (2000), and all but one values of $D_{chloride}$ were less than 10×10^{-12} m^2/s.

Table 1 shows the ranges of each of the critical predictor variables. It can be seen that the SiO_2 content is more or less similar for each data source and therefore, ranges overlap. However, the existence of two distinct groups can be explained on the basis of w/b and specific surface area values. Both high w/b and low specific surface area values

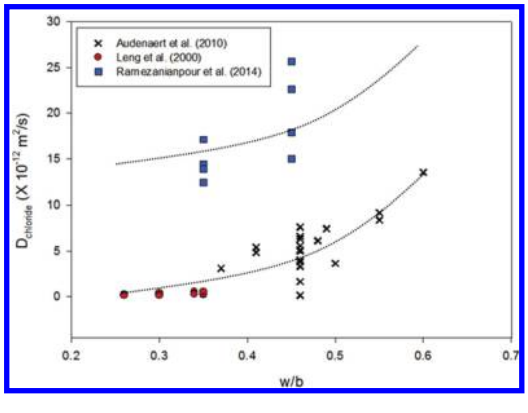

Figure 1. Diagnostic plot on the main effect of w/b on $D_{Chloride}$—a possible exponential trend.

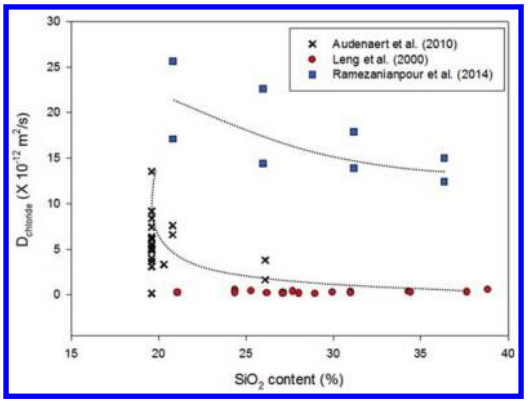

Figure 2. Diagnostic plot on the main effect of SiO_2 content in binder on $D_{chloride}$.

Table 1. Ranges of critical predictor variables, sorted according to database groups.

Group	Data source	*w/b*	SiO_2 content (%)	SSA (m^2/kg)
LSSA	Ramezanianpour (2014)	0.35 to 0.45	21.0 to 36.5	280 to 290
HSSA	Audenaert (2010)	0.37 to 0.60	19.5 to 26.0	345 to 465
HSSA	Leng (2000)	0.26 to 0.35	21.0 to 39.0	360 to 460

result in high values of $D_{chloride}$. This is because in both these situations, the cement paste is quite porous and therefore, offers less resistance to the ingress of chloride ions. For this reason, two different models were developed for two different SSA groups (< and ≥345 m^2/kg). Group Low Specific Surface Area (LSSA) consists of cases with SSA less than 345 m^2/kg (least of all high specific surface area cases) and group High Specific Surface Area (HSSA) consists of cases with SSA greater than or equal to 345 m^2/kg.

4.4 *Non-critical variables*

Initially, two groups of variables were formed based on the fields present in the database. The first group on 'mix proportions' included w/b, water, %cement, %fly ash, %slag, % filler, % fine aggregate, % coarse aggregate and binder-to-aggregate ratio. The second group on 'raw materials characteristics' included chemical composition, specific surface area and density of the binder. Following this, the critical variables were identified based on the C-S-H matrix theory. Diagnostic plots were prepared for all variables to explore any potential relations. Most variables were rejected because of their poor correlations with $D_{chloride}$, Chemical constituents other than SiO_2 and CaO were present in small amounts and are not known to have prominent effect on $D_{chloride}$. The percentage content of individual binder components (say, Portland cement, slag, etc.) would have been important had weighted mean not been considered for determining the effective chemical composition of the binder mixture. But, since weighted mean has been considered, inclusion of these is not necessary. If more information about the aggregates had been available, the aggregate percentages could have been utilized. For this study, with the C-S-H reaction front approach, these have been left out.

5 PROBABILISTIC MODELLING

5.1 *Assumptions and limitations*

The following assumptions have been made while developing the probabilistic model for estimating $D_{chloride}$.

- Specific surface area, SiO_2 content and CaO content of the binder are the same as the weighted mean of the raw material characteristics of each of the binder components.

$$x_{binder} = p_{C_1} x_{C_1} + p_{C_2} x_{C_2} + \cdots + p_{C_n} x_{C_n}$$

  where, x is specific surface area, SiO_2 content or CaO content; n is the total number of ingredients of binder; p is percentage; and C_i is binder ingredient (say, Portland cement, fly ash, etc.)
- The model is based on data collected from concrete mixtures and therefore, is not valid for mortars.
- The model is based on binders that contain either only Portland cement, Portland cement and fly ash or Portland cement and slag. Therefore, the model is not applicable for concrete mixes containing other Supplementary Cementitious Materials (SCMs).

5.2 *Model form*

A model form was developed based on the main effects and 2-way as well as 3-way interactions of the predictor variables. As a first step, specific surface area and%SiO_2 content in the binder were normalized to bring each predictor variable in the [0,1] range. This was done to properly capture the effect of each individual variable on $D_{chloride}$. Without normalizing, predictor variables with high absolute values (such as specific surface area) tend to bias the model and decrease its effectiveness and scope. A maximum Specific Surface Area (SSA_{max}) of 500 m^2/kg was assumed for normalization process. The upper limit has been selected based on the consideration that the model is being developed for concretes mixes containing only Portland cement, fly ash and slag, for which typical values of specific surface area are ≤500 m^2/kg. Another variable, SiO_2 content was expressed as percentage and therefore, has been normalized through division by 100.

Diagnostic plots were prepared for the 2- and 3-way interactions between the predictor variables. Only HSSA data were used for this purpose, mainly because the number of data sets in LSSA were too few to observe any trends.

However, it should be noted that the model form remains the same for both HSSA and LSSA models; only the coefficients change based on the data used for calibration, for which both HSSA and LSSA data were sufficient. Diagnostic plots were prepared to understand the existing trend and transform variables such that the trend resembles an exponential curve. The interactions were of the form $X:Y \sim \alpha X^{\beta} \times \gamma Y^{\delta}$. The MATLAB™ code used for model calibration executes faster if the values provided initially are close to the final value. For this purpose, starting values of β and δ were obtained through an approximate best exponential fit (Fig. 3). It should be noted that the values of β and δ so obtained only serve as starting reference points for the MATLAB™ calibration code and do not affect the final outcome in any way. The values of α and γ were kept constant and equal to 1. Final values for α and γ can be obtained through the calibration code.

After obtaining a reasonable estimate of the power terms in a 2-way interaction between SiO_2 content and specific surface area, a 3-way interaction term of the form $w/b^{\theta 1} \times (SSA_{binder}/SSA_{max})^{\theta 2} \times p_{SiO_2}{}^{\theta 3}$ was developed. A procedure similar to the 2-way interaction optimization was followed to obtain the value of each θ for a good fit. The interaction effect of w/b $(SSA_{binder}/SSA_{max})^{-0.4} \times p_{SiO2}{}^{-1}$ for Group HSSA cases resulted in a coefficient of determination (R-squared) value of 0.86 when an exponential trendline was fitted to it (Fig. 4). This was the highest R-squared value among all manually tried combinations of θ_i. These values were taken as the initial reference values for the MATLAB™ calibration code. It was also noticed that for all interaction products, the value of θ_1 remained constant and equal to 1. As a result, the following model form has been developed.

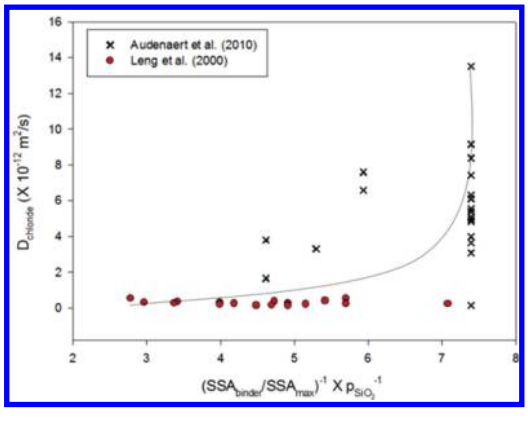

Figure 3. HSSA Group—Interaction effect of $(SSA_{binder}/SSA_{max})^{-1}p_{SiO_2}{}^{-1}$ obtained by varying values of β and δ, and visually analyzing goodness of fit.

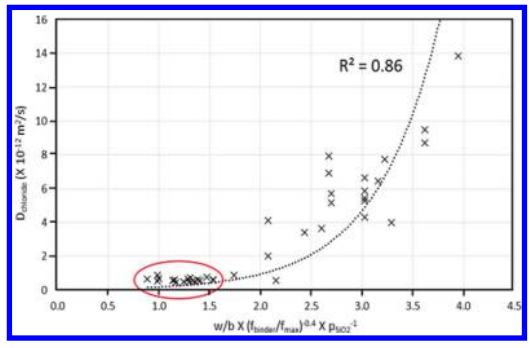

Figure 4. HSSA Group—Interaction effect of *w*/*b*, specific surface area and SiO_2 content in binder.

Table 2. Maximum Likelihood Estimates (MLE) model parameters.

Group	Statistic	θ_0	θ_1
LSSA	MLE	4.95	–0.60
	Standard deviation	0.26	0.02
	Coefficient of variation	0.05	0.03
HSSA	MLE	0.24	–0.95
	Standard deviation	0.04	0.02
	Coefficient of variation	0.15	0.02

$$D_{28,predicted} = \theta_0 exp\left\{\left(\frac{w}{b}\right) \times \left[\left(\frac{SSA_{binder}}{SSA_{max}}\right) p_{SiO_2}\right]^{\theta_1}\right\} + \sigma\varepsilon \quad (7)$$

5.3 *Model calibration and assessment*

The database of 48 cases was screened for outliers and 6 cases were removed. The model was calibrated using the remaining 42 cases. Calibration was done through a maximum likelihood estimation MATLAB™ code (Gardoni 2009). This code provides the estimates for each θ_i along with the standard deviation and coefficients of variation for each (Table 2). The code algorithm is designed to minimize the residual sum of squares. It should be noted that the Coefficient of Variation (COV) is a statistical quantity obtained for a particular dataset, can be changed and therefore, should not be used to evaluate the model. For example, COV can be reduced by the inclusion of a large number of closely spaced high leverage points in the low $D_{chloride}$ range (as ellipsed in Fig. 4). The removal of these cases during calibration results in higher COV (0.16 and 0.03, respectively for θ_0 and θ_1, in group HSSA) but the Maximum Likelihood

Estimates (MLE) remain similar in magnitude. In summary, large COV values (>0.3) might indicate problems with the MLE, but otherwise, instead of COV, quantities such as model error and MAPE/WAPE, as discussed later, should be used to evaluate the model.

The two final probabilistic models developed for estimating $D_{chloride}$ are given in Eq. (8a) and Eq. (8b).

LSSA model for $SSA_{binder} < 345\,m^2/kg$

$$D_{28,predicted} = 4.95\exp\left\{\frac{w}{b}\left[\left(\frac{SSA_{binder}}{SSA_{max}}\right)p_{SiO_2}\right]^{-0.60}\right\} + \sigma\varepsilon \quad (8a)$$

HSSA model for $SSA_{binder} \geq 345\,m^2/kg$

$$D_{28,predicted} = 0.24\exp\left\{\frac{w}{b}\left[\left(\frac{SSA_{binder}}{SSA_{max}}\right)p_{SiO_2}\right]^{-0.95}\right\} + \sigma\varepsilon \quad (8b)$$

Figure 5 illustrates the goodness of fit of the model. It can clearly be seen that most data points fall inside one standard deviation. The high leveraging effect of data cases with $D_{chloride} < 2$ (low range) can also be seen.

The posterior mean of the standard deviation, σ, of the model error can be used to evaluate the accuracy of the developed model. The values of σ for the developed LSSA and HSSA models are 0.8741 and 0.7813, respectively. To provide a more intuitive measure of the model accuracy, the Mean Absolute Percentage Error (MAPE) is also calculated for the LSSA model. The MAPE can be seen as the average error in the model expressed as a percent of the measured value and can be mathematically expressed as follows.

$$\text{MAPE} = \frac{1}{n}\left[\sum_{i=1}^{n}\left(\frac{\left|D_{i,predicted} - D_{i,28}\right|}{D_{i,28}}\right)\right] \quad (9)$$

where, $D_{i,predicted}$ is the value of $D_{i,chloride}$ predicted using the model developed and D_{28} is the value obtained from literature. The 'i' represents the individual data. The MAPE for the LSSA model is 0.0377. The MAPE has not been calculated for the HSSA model, because of the presence of a large number of $D_{chloride} < 1$ m^2/s cases in the HSSA database. The presence of small denominators can create a singularity problem. For such series, Weighted Absolute Percentage Error (WAPE) is a better estimate than MAPE. The WAPE can be mathematically expressed in Eq. (10).

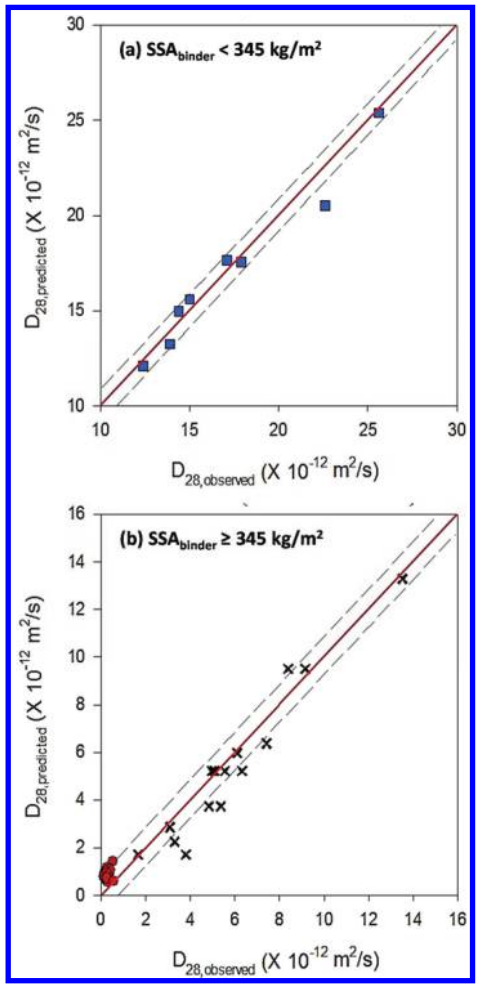

Figure 5. Correlation between the observed and predicted data on $D_{chloride}$ for the (a) LSSA and (b) HSSA models.

$$\text{WAPE} = \frac{1}{n}\left[\sum_{i=1}^{n}\left(\frac{\left|D_{i,predicted} - D_{i,28}\right|}{\sum D_{i,28}}\right)\right] \quad (10)$$

where, the terms are as defined in Eq. (8). In summary, the MAPE of 0.0377 for LSSA model and WAPE of 0.0159 for HSSA model indicate that these models can make reasonably good predictions of $D_{chloride}$.

6 CONCLUSIONS

Based on 42 data sets, collected from literature, on chloride diffusion coefficient, raw material

characteristics of binders, and mixture proportions, a probabilistic model (Eq. 11) was developed.

$$D_{28,predicted} = \theta_0 exp\left\{\left(\frac{w}{b}\right)\times\left[\left(\frac{SSA_{binder}}{SSA_{max}}\right)p_{SiO_2}\right]^{\theta_1}\right\} + \sigma\varepsilon \quad (11)$$

where,
if

$SSA_{binder} < 345 m^2/kg$, then $\theta_0 = 4.95, \theta_1 = -0.60$;

and if

$SSA_{binder} \geq 345 m^2/kg$, then $\theta_0 = 0.24, \theta_1 = -0.95$

A comprehensive and larger database for $D_{chloride}$ needs to be developed and the model should then be recalibrated and made more robust using the newly acquired data.

Although significant amount of literature exist on durability performance of various concrete systems, most of the available data sets are incomplete (i.e., data on raw material characteristics and mixture proportions are not available). This emphasizes the need to include data on raw material characteristics, mixture proportions, mixing procedures, porosity, etc. in the scientific publications on strength and durability of concrete systems. Such data sets would help developing more useful models for service life prediction.

ACKNOWLEDGEMENT

This research was carried out at the Building Technology and Construction Management (BTCM) Division, Department of Civil Engineering, Indian Institute of Technology Madras, Chennai, India. The support from BTCM colleagues and faculty in IIT Madras is highly appreciated.

REFERENCES

Audenaert, K., Yuan, Q., & De Schutter, G. (2010). On the time dependency of the chloride migration coefficient in concrete, *Construction and Building Materials,* 24 (2010) 396–402.

DuraCrete (1999a). *Design Framework*, Document BE95-1347/R0, The European Union—BriteEuRam III, Contract BRPR-CT95-0132, Project BE95-1347, 7–13.

DuraCrete (1999b). *Compliance Testing for Probabilistic Design Purposes*, Document BE95-1347/R0, The European Union—BriteEuRam III, Contract BRPR-CT95-0132, Project BE95-1347, 22–35.

ISO 15686–1:2000, (2000). Buildings and constructed assets—Service life planning—Part 1: General Principles.

Leng Faguang, Feng Naiqian, & Lu Xinying (2000). An experimental study on the properties of resistance to diffusion of chloride ions of fly ash and blast furnace slag concrete, *Cement and Concrete Research,* 30 (2000) 989–992.

Life-365 (2012). Service life prediction model and computer program for predicting the service life and life-cycle cost of reinforced concrete exposed to chlorides. URL: http://www.life-365.org/; most recently accessed on: 16 Apr 2015.

Mehta, P.K., & Monteiro, P.J.M. (2013). Concrete: Microstructure, Properties, and Materials.

Muigai, R., Moyo, P., & Alexander, M. (2012). Durability design of reinforced concrete structures: a comparison of the use of durability indexes in the deemed-to-satisfy approach and the full-probabilistic approach, *Materials and Structures* DOI 10.1617/s11527–012–9829-y.

Oslakovic, I.S., Bjegovic, D., Mikulic, D., & Krstic, V. (2012). Development of service life model CHLODIF++, *Computational modelling of concrete structures*, EURO-C, 573–578.

Ramezanianpour, A.A., Mahmoud Motahari Karein, S., Vosoughi, P., Pilvar, A., Isapour, S., & Moodi, F. (2014). Effects of calcined perlite powder as a SCM on the strength and permeability of concrete, *Construction and Building Materials,* 66 (2014) 222–228.

Tang, L. (2008). Engineering expression of the ClinConc model for prediction of free and total chloride ingress in submerged marine concrete. *Cement and Concrete Research*, 38(8), 1092–1097.

Concrete Repair, Rehabilitation and Retrofitting IV – Dehn et al. (Eds)
© 2016 Taylor & Francis Group, London, ISBN 978-1-138-02843-2

Damage risk and development in concrete pavements caused by an Alkali-Silica Reaction

A. Wiedmann, E. Kotan & H.S. Müller
Institute of Concrete Structures and Building Materials (IMB), Department Building Materials, Karlsruhe Institute of Technology (KIT), Karlsruhe, Germany

ABSTRACT: Concrete pavements underlie climatic and interfering mechanical impacts as well as additional stresses resulting from construction conditions or the construction method. An Alkali-Silica Reaction (ASR), on the other hand, leads to expansion and strain. These two combined load cases may cause cracking. The aim of this work is to investigate the macroscopic behaviour of the different exposures. For this purpose an appropriate numerical model has to be developed, which allows describing the complex interactions. By means of extensive experimental fracture mechanical examinations the temporal change of strength and deformation of concrete due to ASR is investigated. Based on this work, it will be possible to develop suitable measures to reduce the risk of cracking and possibly to prevent any damage in the future.

1 INTRODUCTION

In recent years, some cases of damage to concrete pavements have occurred in the German motorway network, which are attributed to an ASR. These damages and the related drastic degradation of durability have led to a strong increase in activity in this research area. In Germany, repairing damage caused by an ASR costs millions of euros year over year.

Figure 1 shows a typical damage as a result of ASR. The advanced damage is characterised by longitudinal cracks in the concrete pavement.

ASR in concrete means a reaction of aggregate-components with alkalis in the pore water. In this reaction, an alkali-silica gel is formed. This gel is able to swell, the increasing volume leads to cracking and finally to a concrete damage (Stark 2013).

Figure 1. Advanced stage of ASR-damage with longitudinal cracking in the concrete pavement.

The chemical and mineralogical processes that occur in an ASR have already been described in many works. Research concerning a change of material properties and cracking-mechanisms, on the other hand, is quite rare or incomplete (Bödeker 2003).

So far, above all, optical methods or ultrasonic transit time measurements have been used to ascertain the influence of ASR and the subsequent changes of the concrete structure. Mechanical parameters of damaged concrete are determined by conducting compression tests on drilling cores. This allows deducing the possible residual strength of drilling cores, which have been stored in an ASR-provoking environment. Up to now, this approach has solely been used to estimate the compression strength. Softening, on the other hand, cannot be predicted by these means. Using drilling cores is not sufficient to deduce the behaviour of an entire building element or concrete inside of a building. Additional influences are the age of the concrete and the duration of ASR. Depending on the testing age, changes of the frequency and formation of cracks occur. This leads to significant scattering, which even increases with increasing testing age (Bödeker 2003).

Thus, the deduction of results determined on drilling cores onto a building element is limited. Besides, there is no description of the determination of fracture-mechanical parameters such as fracture energy, tensile strength, stress-deformation behaviour of ASR-damaged concrete known. These parameters are essential for a realistic calculation

of formation of meso- and macroscopic cracks with the Finite Element Method (FEM).

In order to describe the behaviour of ASR-damaged concrete, numerous mathematical, numerical and rheological models have been used. Parts of these were developed using most simple boundary conditions. Thus, those are not suited for depicting the behaviour for realistic, complex conditions.

As part of a research project, which is promoted by the Federal Highway Research Institute (Bundesanstalt für Straßenwesen, BASt), numerical examinations have been conducted at the Institute of Concrete Structures and Building Materials (IMB). Thereby, a higher damage risk on the upper side of concrete pavement slabs due to combined thermal-hygral stress and traffic load has been determined (Müller et al. 2010). An additional ASR may reduce the predominant tensile stress because of its expansion increase. However, a concurrent decrease in tensile strength due to internal damage may also result. In particular, the dominating effect could not be determined, because the decrease of strength and stiffness of concrete due to ASR is scientifically unclarified or non-quantifiable. Actual cases of damage show developing cracks but give no reasons. These shall be explored as part of the present project.

2 EXPERIMENTAL INVESTIGATIONS

2.1 *Concrete raw materials and material characteristics*

To describe the realistic resistance of concrete against cracking, the temporal change of strength and deformation properties of pavement concrete under ASR and possibly loading caused by traffic is necessary. The investigation of these aspects is carried out as subproject six of research group DFG 1498 "alkali-silica reaction in concrete members at simultaneous cyclic loadings and external alkali support", which is funded by the DFG since 2011. Apart from the Institute of Concrete Structures and Building Materials (IMB), Karlsruhe, the group consists of researchers of the following institutes: Institute for Structural Mechanics (RUB), Bochum, Chair of Building Materials Technique (RUB), Bochum, Federal Institute for Materials Research and Testing (BAM), Berlin, and F.A. Finger-Institute for Building Material Science (FIB), Weimar. The aim of the experimental investigations is to determine different fracture-mechanical parameters of pavement concretes after enduring subsequent damage due to ASR. For this purpose, each individual subgroup produces reference specimens under the same conditions with centrally provided source materials of pavement concrete (Table 1). These specimens are stored at 20 °C and 65% r.h. (reference storage) to ensure identical conditions for hydration.

Experimental investigations on various reference samples yield the compressive and tensile strength, the fracture energy, the Young's modulus and the stress-deformation behaviour. Thus, the alteration of (fracture-) mechanical parameters of concrete, whose structure has been damaged by ASR, can be determined to a high precision.

The compressive strength f_c and the Young's modulus E_{c0} are determined on cylindrical samples or drilling cores. The split tension test yields a characteristic value of the tensile strength of cylindrical specimen $f_{ct,sp}$. This enables comparing the samples to drilling cores of concrete pavements. Uniaxial tensile tests on constricted, bone-shaped specimens yield the direct tensile strength f_{ct} and the Young's Modulus E_{c0}.

The extensive determination of fracture-mechanical parameters includes a description of the post-cracking behaviour. Notched prismatic specimens are suited best for these tests. For centric stress, notches are sawn on either side of the prism. The direct tensile test on these specimens yields the so called net tensile strength $f_{ct,n}$, the fracture energy G_F and the force-deformation relation. Due to the unilateral stress during ASR-provoking storage (thawing agent application, see below) it is as well suitable to determine the net flexural strength $f_{ct,fl,n}$ and the fracture energy $G_{F,f}$ in a three point bending test on unilaterally notched beam shaped specimens. Provided that the force-deformation relation is known, the post-cracking behaviour can be determined. The deformation is usually recorded via inductive displacement transducers.

2.2 *Pre-damage and ASR-provoking storage*

Pre-damage of the specimens allows the determination of (fracture-) mechanical parameters. The damaging proceeds in different subprojects. Larger-sized beams are produced, stored and subsequently mechanically pre-damaged by cyclic stress. Afterwards, alkalis are applied by fulling a

Table 1. Composition of the pavement concrete.

Setting	Designation/value
Cement	CEM I 42.5 N
Cement content [kg/m³]	360
w/c-ratio [–]	0.42
Aggregate	Granodiorite and upper rhine crushed gravel
Grading curve	A/B 22
Air pore content [vol %]	4.0–4.5

thawing agent for example. From the lager-sized beams, smaller specimens are sawn or drilled and subsequently stored under different ASR-provoking conditions. The specimen dimensions are specified by the different storage conditions. A possible scenario is the fog chamber storage in accordance to the German Alkali Guidelines (Alkali-Richtlinie 2007). The specimens are stored at a constant temperature of 40 °C and 99% r.h. over a period of nine months.

An application of the performance testing (FIB cyclic climate storage test) allows a different ASR-provoking storage. The specimens pass through various climatic exposure cycles, which include a drying phase at 60 °C, a moistening phase with fog and an alternating freeze-thaw phase. On the top side of the beam shaped prisms, a de-icing solution enables the penetration of alkalis (Stark 2013).

The aim of the experimental investigations is to determine the effect of different types of exposure and their influence on fracture-mechanical material parameters. Therefore, parameters are determined gradually, after each load case respectively the grade of pre-damage, and finally for the load combination. These parameters are continuously compared to those of a reference concrete (Fig. 2, left branch, series 1). Within this approach, the complex exposure of real concrete shall be modelled and analysed as realistically as possible.

Figure 2 shows the flowchart of the experimental investigations to determine the mechanical material properties after several exposures of the two different series 1 and 2 (each open circle symbolizes an experimental determination of mechanical properties of the pavement concrete).

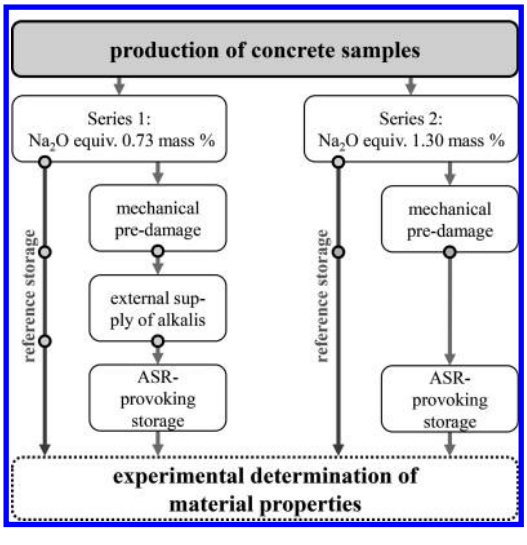

Figure 2. Flowchart of the experimental investigations to determine mechanical material properties in subject to the kind of pre-damage and the series 1 and 2.

The procedures of preliminary damage and ASR-provoking storage as described so far allow the external supply of alkalis, but do not cause a homogenous damage over the specimens' cross-sections. Therefore, a second series of specimen made of pavement concrete with boosted cement (Fig. 2, right branch, series 2) is produced. These specimens are stored under ASR-provoking conditions and tested after timed varying storage, as well. Within this method, the ASR is supposed to be homogenous over the cross-sections and the effect of the degree of damage under ASR-provoking storage on mechanical parameters can be quantified.

A comparing testing of the damage degree or characterisation with the aid of optical and physical methods (e.g. X-ray 3D-computed tomography) scanning) allows the comparison of both series. These tests are conducted in collaboration with another subproject (Weise & Wiedmann et al. 2015). Besides, the extensive characterization of damage is essential to transfer the development of the damage-degree onto the temporal development of damage caused by ASR under practical conditions.

2.3 *Determination of material properties after different impacts*

Within the scope of this paper, the experimental determination of mechanical material parameters will be described using the example of the centric tensile test after two different types of loads (combination of loads). The acquirement of these parameters is essential to develop material laws to describe the resistance of concrete in a macroscopic numerical model. As described in section 1, cracks occur when the tensile strength is reached. The remaining tensile strength is one of the relevant material characteristics which has to be determined.

At the age of 56 days, after production (series 2, internal alkali supply) and storage, the lager-sized ($27 \times 50 \times 200$ cm^3) beams were tested in a four point bending test in the laboratories of the Federal Institute for Materials Research and Testing (BAM) in Berlin. The used loads caused a mechanical pre-damage, which correspond to realistic conditions of a concrete pavement. The test set-up and further information about the mechanical stress is described in detail in Przondziono et al. 2015, Weise & Wiedmann et al. 2015. Immediately after finishing the cyclic running four point bending test, small prismatic specimens ($7.5 \times 7.5 \times 13.0$ cm^3) were obtained by sawing and send to Karlsruhe together with parallel stored reference specimens.

Figure 3 shows the schematic test set-up of a centric tensile test. The force introduction was realised by stiff and non-rotatable steel plates. Between both, the specimens were adhered with fast hardening glue consisting of two components. This test set-up ensures a stable process to determine the smooth crack development over the cross section of the specimens.

The deformation of the specimens was measured at six different positions using inductive transducers (gauge length 50 mm). The deformation velocity was about 0.03 mm/min, which means that the duration of each test was 10 minutes. Before the test the prismatic specimens were bilateral notched with a depth of $d_{n1} = 5.0$ mm.

The experiments were carried out in order to study the effect of mechanical pre-damage on the mechanical properties of concrete. Based on the force-deformation relation, the two mechanical parameters of net tensile strength $f_{ct,n}$ and fracture energy G_F were determined. Figure 4 shows the influence of a mechanically induced pre-damage on the mean stress-deformation relation

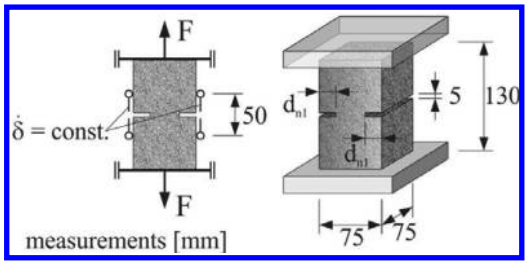

Figure 3. Schematic figure of the experimental test set-up of the centric tensile test by using bilateral notched prismatic test specimens.

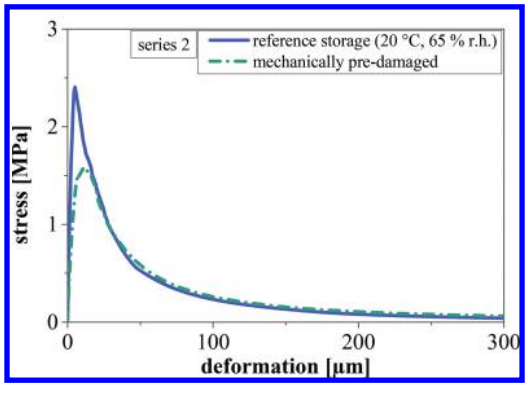

Figure 4. Influence of mechanically induced pre-damage on the mean stress-deformation relation identified in the centric tensile test by using bilateral notched specimens ($7.5 \times 7.5 \times 13$ cm³), notch depth $d_{n1} = 5.0$ mm.

of pavement concrete which was carried out as part of the DFG funded research group. Hence, the net tensile strength was reduced about 30 per cent due to the mechanically induced pre-damage. However, in contrast the fracture energy decreases only about 10 percent.

At least four successful experiments were the basis of both relationships. Further specimens of this series (series 2) will be stored within the scope of the 60 °C concrete prism test (Alkali-Richtlinie 2007) with and without mechanically pre-damage. There the specimens are stored at 60 °C over water in tightly sealed containers in a test reactor. As described above, the same parameters have yet to be determined.

So far, the specimens of pavement concrete were not damaged due to ASR, but damaged as a result of a fatigue loading. To investigate the effect of a harmful ASR on the material properties of pavement concrete, a further lager-sized beam was produced in Bochum, mechanically pre-damaged in Berlin (in the cyclic running four point bending test) and afterwards tested in the FIB cyclic climate storage test in Weimar (FIB-ccst). For that, water and a de-icing agent solution (NaCl) were used on the top side of the beams. In comparison with the obtained specimens for the 60 °C concrete test so far, the measurements of the specimens ($10 \times 10 \times 19$ cm³, depth of the notch $d_{n2} = 15.0$ mm) were adapted to the standards of the FIB cyclic climate storage test (Stark 2013).

Figure 5 shows the experimental test set-up of the centric tensile test with six inductive displacement transducers in the measuring frame. The procedure of the test corresponds to the one which was used for the smaller specimens. At least six specimens were used for every relationship.

Figure 6 shows the influence of a mechanically pre-damage and a harmful ASR on the stress-deformation relation in a centric tensile test.

First, only the influence of the mechanical pre-damage will be considered. Hereby, the net tensile strength decreases about 20 per cent after mechanical pre-damage with water on the top side of the beams. With a NaCl-solution on the top side of the beam, the mechanical pre-damage leads to a reduction of the tensile strength about 30 per cent after FIB-ccst.

Secondly, on the one hand, the net tensile strength of the pavement concrete (series 1) was reduced by almost 15 per cent due to an ASR, if you compare just the storage in FIB-ccst with water and with NaCl-solution on the top side of the beam. On the other hand, if you consider a mechanically pre-damage in combination with an ASR-provoking storage at FIB-KWL (using NaCl-solution), the tensile strength of the pavement concrete is about 40 per cent lower than the

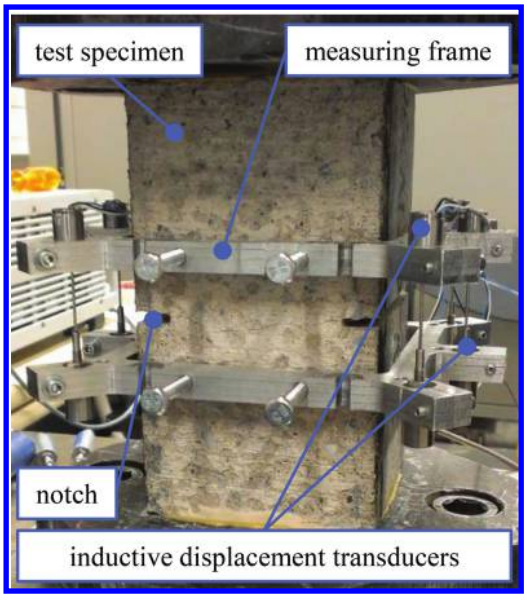

Figure 5. Experimental test set-up of the centric tensile test by using bilateral notched prismatic test specimens ($10 \times 10 \times 19$ cm^3, noth depth $d_{n2} = 15.0$ mm) after FIB cyclic climatic storage test.

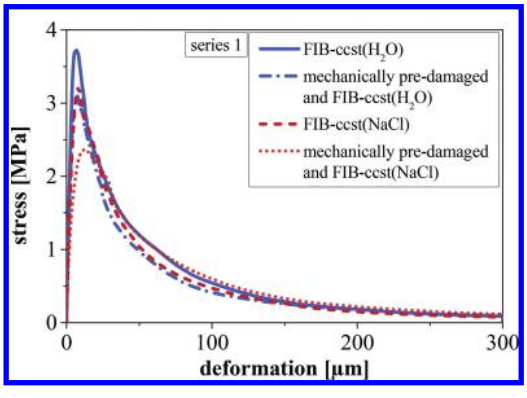

Figure 6. Influence on the mean stress-deformation relation identified in the centric tensile test by using bilateral notched prismatic test specimens ($10 \times 10 \times 19$ cm^3) (with and without mechanically pre-damage) after FIB cyclic climatic storage test (FIB-ccst), notch depth $d_{n2} = 15.0$ mm.

storage at FIB-ccst (using water on the top side of the beam).

The results of the FIB cyclic climate storage test (temporal development of expansions) for non-damaged and pre-damaged specimens of series 1 with water or NaCl-solution on the top side of the beams are depicted in Giebson 2015.

3 THEORETICAL AND ANALYTICAL INVESTIGATIONS

3.1 *Formulation of material laws (resistance)*

At first, material laws have to be formulated on the basis of the obtained experimental observations as part of theoretical-analytical analysis. This is absolutely necessary to be able to implement the time— and load-dependent stresses of concrete in terms of numerical calculations realistically. At this point the focus is on the influence of the internal damage as a result of ASR and the associated impact on all mechanical material properties. To derive the formulation of constitutive equations a sufficiently broad basis of result data from the experimental studies must be available. With the help of these studies it will be able to make statements according to the impact of ASR on the change of the strength and deformation properties of the selected pavement concrete.

3.2 *Description of the influence*

In a further step of the theoretical-analytical analysis, the quantitative description of the complex stresses of concrete pavements for the numerical analysis has to be considered. In this connection the quality of the selected stress scenarios affects the accuracy of the obtained numerical results. To describe the climatic conditions such as air temperature and relative humidity, it can be referred to already existing records of the Institute of Concrete Structures and Building Materials. In this case, the focus is on the determination of the course of zero-stress temperature also considering the manufacturing period and the construction method. The traffic load will be estimated on the current state as a quasi-dynamic load on the basis of DIN-Technical report 101 (DIN-FB 101 2009).

4 NUMERICAL INVESTIGATIONS

Using numerical analysis, both the time-dependent material properties in connection with the realistic display of the fracture mechanical behaviour of concrete influenced by the ASR (resistance), as well as the implementation of the complex stress scenarios (impacts) are realised. These eventually serve to analyse and predict the formation of macroscopic cracks in the concrete pavement and to derive measures for damage reduction and prevention in the future.

The numerical simulation is made using the finite elements program DIANA. For this purpose the numerical calculation model (Müller et al. 2010) developed at the Institute of Concrete Structures and Building Materials is refined. The composite

system of concrete carriageway shown in the model consists of concrete pavement, hydraulically bound base course, frost blanket course and corresponds to the standard structure of carriageways with concrete pavement according to RStO 12, see Figure 7.

Within the scope of the numerical analysis, primarily the upper cross-section range of the concrete carriageway, the concrete pavement, is examined, whereas the calculation models to discretise consist of unreinforced pavement concrete. Figure 8 shows the principle structure of the regarded carriageway cross section.

Due to the fact that the complex processes of the coupled moisture and heat transport in connection with cracking under consideration of rheological concrete behaviour can so far only be analysed in a two dimensional viewing, the 2D modelling will be placed in the foreground of the numerical analysis. The numerical models are made of unreinforced pavement concrete, where the material is displayed as a continuum in the first approximation. To consider the heterogeneity of the concrete, the material properties are subdued and the tensile strength (respectively the fracture energy or possibly also

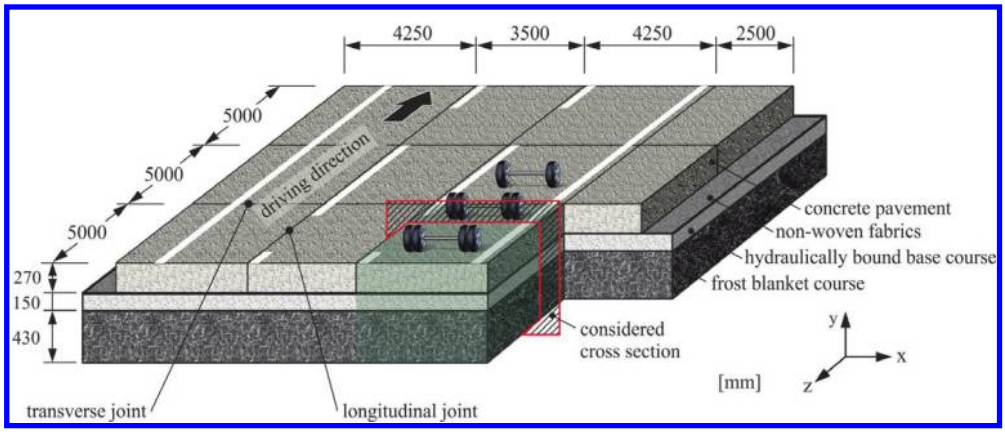

Figure 7. Schematic illustration of the considered three-lane motorway of a carriageway cross section based on (Müller et al. 2010).

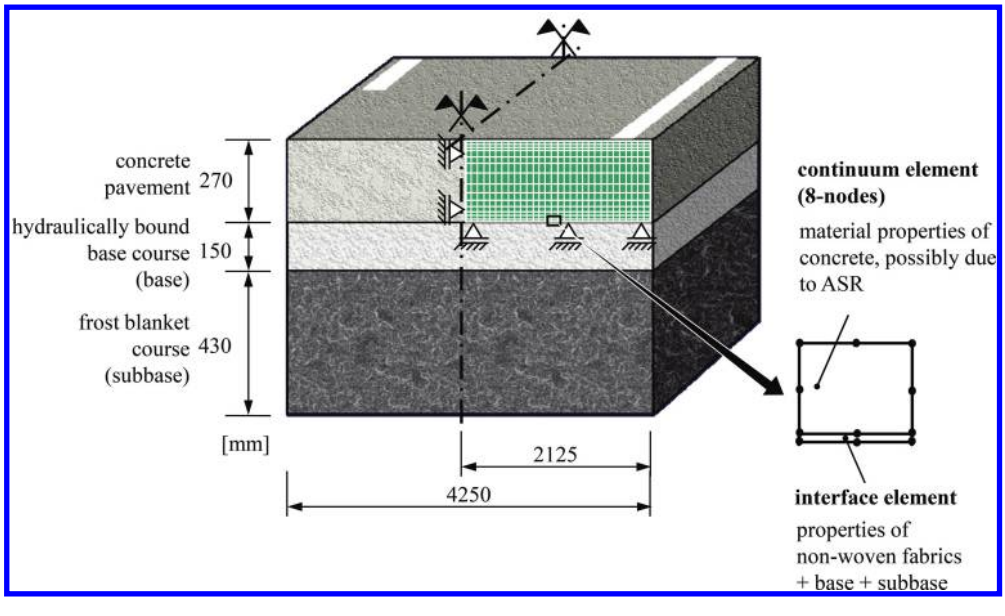

Figure 8. Schematic illustration of the considered carriageway cross section and the finite-element mesh of the regarded carriageway based on (Müller et al. 2010).

the elastic modulus), assigned to the particular element, is varied. The detailed description of the implementation of the model approach can be found in Mechtcherine 2000.

To simulate the crack formation and propagation, non-linear fracture mechanics is used. Therefore, the fracture mechanical behaviour of concrete is described following the cohesion model of Bažant and Oh (Bažant & Oh 1983). At this point, the findings gained as a result of the extensive experimental analysis that describe the change of the material properties of concrete due to ASR are applied by assigning the available and determined material properties of compressive and tensile strength as well as the elastic modulus and fracture energy to the material used in the simulation.

In parallel, it is necessary to consider the creep and shrinkage behaviour in context of the numerical analysis due to the models of the fib model Code 2010 (fib Model Code 2010), which are followed by the adaption with the help of its own performed accompany tests.

The forecast of the time course of the ASR-damage of concrete pavement initially takes place on the basis of the effective ASR-expansions with varying temperature and moisture conditions. Thus, for example, on the basis of thermic-hygric relations based on climate data, it can be estimated to what extend at which times the conditions for the ASR are given. In connection to these expansions due to ASR will take into account in the simulation, which are determined during experiments. Therefore, the conditions for the realistic simulations of temporal deformation behaviour and cracking of carriageway plate are given, which serve as basis for the development of measure to prevent broad carriageway cracks.

5 CONCLUSIONS AND OUTLOOK

In Germany a deleterious ASR causes enormous repair costs of significant economic relevance until today. To assess the durability of concrete carriageways, the description of the complex loading collective which consists of temperature and moisture changes, and also traffic and ASR is necessary. Moreover, there are influences due to manufacture and curing which have to be considered. In addition, the consequences of harmful influences such as traffic or in particular ASR on the temporal change of the strength and deformation properties of pavement concrete have to be determined.

At first, within the scope of this paper, the problems of the identification of material properties of ASR-damaged concrete in order to describe the resistance of the pavement concrete were explained. An experimental design within the DFG research group to depict the complex exposures and the related experimental determination of (fracture-) mechanical material properties was described.

Building on this, the consequences of a mechanically pre-damage and a deleterious ASR after the FIB cyclic climatic storage test on the example of the stress-deformation relation within the centric tensile strength were explicated. At this, a mechanically induced pre-damage in combination with storage in the FIB cyclic climatic storage test reduces the net tensile strength about 40 percent. Thereby realistic input values to characterise the resistance of pavement concrete towards crack formation and propagation for the future numerical calculations were determined.

Further experimental investigations will focus on the determination of additional material properties after ASR-provoked storage, especially in the 60 °C concrete prism test (Alkali-Richtlinie 2007).

Afterwards a short introduction of the proposed numerical investigations including the presentation of the used model of a concrete carriageway was explained. The proper innovation with regard to the numerical investigations will be the consideration of damage in the concrete pavement due to an ASR.

Finally, the analysis of the stress-strain behaviour and the resulting crack formation in the concrete pavement to derive measures for the future damage reduction will carried out.

ACKNOWLEDGEMENT

Further information about the DFG research group 1498 “alkali-silica reaction in concrete members at simultaneous cyclic loadings and external alkali support” can be found on the internet at http://www.for1498.sd.ruhr-uni-bochum.de. The authors wish to thank the members and institutes of the research group for the supply of pre-damaged and reference specimens and also the possibility of storage capacities, especially the DFG for funding the project.

REFERENCES

Alkali-Richtlinie. 2007. Vorbeugende Maßnahmen gegen schädigende Alkali-Reaktion in Beton. *Deutscher Ausschuss für Stahlbeton*. Beuth Verlag. Berlin.

Bödeker, W. 2003. Alkalireaktion im Bauwerksbeton. Ein Erfahrungsbericht. *Deutscher Ausschuss für Stahlbeton.* Beuth Verlag. Berlin.

Bazant, Z.P. & Oh, B.H. 1983. Crack band theory for fracture of concrete. *Materials and Structures.* Vol. 16.

DIN-FB 101. 2009. Einwirkungen auf Brücken. Beuth Verlag Berlin.

fib—International Federation for Structural Concrete. 2013. fib Model Code for Concrete Structures 2010. International Federation for Structural Concrete, Lusanne, Schweiz.

Giebson et al. 2015. Untersuchungen zur Alkali-Kieselsäure-Reaktionen in vorgeschädigten Fahrbahndeckenbetonen. *Beton—und Stahlbetonbau 110.* Heft 1, S. 13–21.

Mechtcherine, V. 2000. Bruchmechanische und fraktologische Untersuchungen zur Rissausbreitung in Beton. *Schriftenreihe des Instituts für Massivbau und Baustofftechnologie.* Universität Karlsruhe.

Müller, H.S. et al. 2010. Rechnerische Untersuchungen zur Entstehung breiter Risse in Fahrbahndecken aus Beton unter Mitwirkung einer Alkali-Kieselsäure-Reaktion. *Abschlussbericht zum Forschungsvorhaben 08.0189/ 2006/LRB im Auftrag des BMVBS/BASt.* Karlsruhe.

Przondziono, R. et al. 2015. Vorschädigungen in Beton infolge zyklischer Beanspruchungen und deren Auswirkung auf Transportprozesse im Hinblick auf eine schädigende AKR. *Beton—und Stahlbetonbau 110.* Heft 1, S. 3–12.

RStO 12—Richtlinien für die Standardisierung des Oberbaus von Verkehrsflächen. 2012. Forschungsgesellschaft für Straßen—und Verkehrswesen.

Stark, J. & Wicht, B. 2013. Dauerhaftigkeit von Beton. *Springer Verlag.* F. A. Finger-Institut. Weimar.

Weise, F. & Wiedmann, A. et al. 2015. Auswirkungen von Ermüdungsbeanspruchungen auf Struktur und Eigenschaften von Fahrbahndeckenbeton. *Beton—und Stahlbetonbau 110.* Heft 1, S. 22–33.

Concrete Repair, Rehabilitation and Retrofitting IV – Dehn et al. (Eds)
© 2016 Taylor & Francis Group, London, ISBN 978-1-138-02843-2

Reinforcement corrosion behavior in bending cracks after short-time chloride exposure

F. Hiemer, S. Keßler & C. Gehlen
Centre for Building Materials, Technische Universität München, Munich, Germany

ABSTRACT: Even if properly designed, crack formation in reinforced concrete structures is inevitable. Cracks in the concrete cover considerably reduce the barrier property against corrosion-initiating substances. Aggressive agents (e.g. chlorides) depassivate the reinforcement locally in the cracked area, which can lead to macro-cell corrosion. To protect direct driven concrete surfaces against chloride ingress such as in multi-storey car parks, German Standards recommend the application of surface coatings.

In the course of a research project, the reinforcements' corrosion behavior in cracked concrete and the influence of an applied surface protection system on the corrosion process is investigated. Therefore, basic electrochemical parameters of corrosion and its boundary conditions are recorded. The paper presents results of the short-time chloride exposure as well as first findings concerning the influence of an applied sealing on corrosion activity. Chloride contamination led to active corrosion whereas the coating not always decreased macro-cell corrosion.

1 MOTIVATION

When it comes to the durability of reinforced concrete structures, the corrosion of reinforcement constitutes one of the main issues concerning their deterioration. Besides many factors, chloride contamination stands out as one of the most important causes for reinforcement corrosion, especially in traffic structures such as bridges or car parks, which are highly exposed to de-icing salts.

Since the design principle of reinforced concrete structures is based on crack formation for activating the reinforcements' tensile capacity, cracking is an inherent characteristic of these structures. Although cracking impairs the local transport properties of the concrete cover (Šavija & Schlangen 2010), it is not yet completely understood whether cracks accelerate only the corrosion initiation process or the overall corrosion process (Yu et al. 2014).

Cracks allow a locally limited but rapid ingress of aggressive agents to the steel surface. In the case of a chloride attack this can lead to an accumulation of chlorides in the crack area. When exceeding a critical chloride content, the protecting passive layer on the steel is destroyed and therefore the reinforcement is locally depassivated. This discrete depassivation promotes the formation of macro-cell corrosion. Figure 1 schematically shows a chloride induced macro-cell corrosion in which the anodic and cathodic sub-processes are spatially separated.

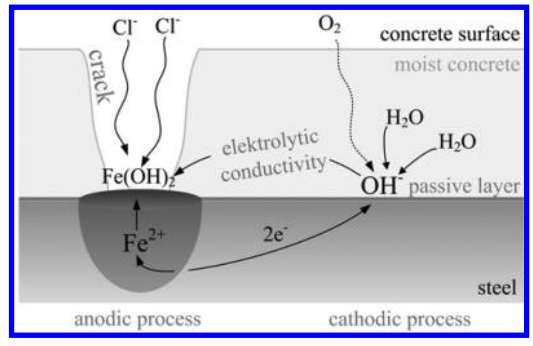

Figure 1. Schematic illustration of corrosion mechanisms in cracked reinforced concrete.

The drop of electrochemical potential on the depassivated steel surface (anode) results in a potential difference to surrounding cathodic areas. Free electrons e^- pass through the steel to the cathode where they react with water H_2O and oxygen O_2 to form hydroxide ions OH^-. The electrochemical cell is short-circuited by the electrolytic conductivity of the concretes' pore system.

The electrochemical processes can be expressed by an equivalent circuit diagram in which the sub-processes are transferred into resistances and a driving potential ΔE resulting from the potential difference, Figure 2 and Equation 1 (Raupach 1992).

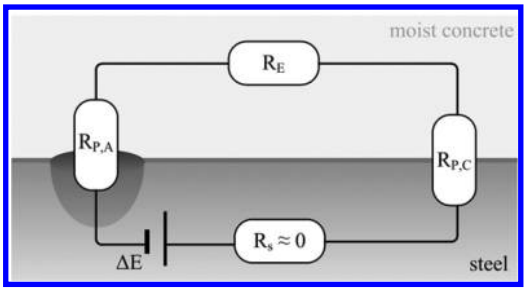

Figure 2. Equivalent circuit diagram for the corrosion of steel in concrete.

$$I_{corr} = I_{macro} + I_{micro} = \frac{\Delta E}{R_{P,A} + R_{P,C} + R_e} + I_{micro} \quad (1)$$

The quotient of the driving voltage and the sum of all system resistances describes the macro-cell corrosion current I_{macro}. Another important part of the total corrosion I_{corr} is the microcell corrosion I_{micro}. In this corrosion type the cathodic reaction takes place in immediate vicinity of the macro-cell anode, therefore contributing inseparable to the corrosion process.

Anodic polarisation resistance $R_{P,A}$ and cathodic polarisation resistance $R_{P,C}$ can be described as the interference of each sub-process, e.g. due to the charge transfer resistance in the phase boundary steel/electrolyte or an obstruction of materials supply to the respective electrode.

The electrolytic resistivity of concrete R_E is a major factor influencing active corrosion (Hunkeler 1995, Warkus & Raupach 2008). It is depending on a variety of factors originating from concrete parameters as wells as environmental influences. Besides the temperature, pore structure and the ionic composition of the pore water, the resistance is very dependent on the moisture content of the concrete (Catharin & Federspiel 1972, Schulte et al. 1978). On the one hand the desiccation of concrete diminishes the charge transport in the pore system which increases the specific electrolytic resistance of the hardened concrete. Furthermore, the size of the cathodic contributing steel surfaces is significantly reduced when the concrete is drying out (Noeggerath 1990, Warkus 2012).

These interrelations are used to protect reinforced concrete structures which are directly driven upon. The German national annex to Eurocode 2 (DIN EN 1992-1-1/NA 2013) demands the application of a crack-bridging coating or alternative concepts to avert an ongoing ingress of corrosion promoting agents.

On the one hand, the accumulation of depassivating substances such as chlorides is reduced, minimizing the risk of reinforcement depassivation. At the same time, the water intake through the concrete surface is hindered, leading to a reduction and homogenisation of the moisture content in the concrete component. Hence, the electrolytic conductivity decreases, reducing the overall corrosion rate, see Equation 1.

The planning principles for the coating of concrete structures, such as multi-storey or underground car parks, are provided in a German bulletin (DBV 2010). Therein it is recommended to coat the concrete surface after crack formation is finished, even if a short-time chloride exposure cannot be ruled out. A potentially initiated corrosion process is not expected to endanger the load bearing capacity of the structure. However, the corrosion behavior of reinforcement steel in cracked concrete is not yet clarified, nor has there been a scientifically investigation of its development after the cracked concrete surface is sealed. In addition, especially in the vicinity of a crack, the influencing factors of reinforcement corrosion, e.g. the moisture content as well as the chloride concentration, are subject to wide fluctuations.

Thus, a research project was initiated, in which reinforced concrete specimens are used to investigate the corrosion process in cracked concrete after a short-time chloride exposure. Subsequently the effect of an applied surface protection system on the corrosion situation can be determined.

In the following chapter the experimental program is presented, whereas in chapter 3 a first insight into the results of the exposure as well as on the influence of an applied coating is given.

2 EXPERIMENTAL

2.1 *Specimens*

Specimens had to be designed allowing the initiation of a defined bending crack orthogonal to a steel bar representing the depassivated anode. Besides other boundary conditions, the positioning of reinforcement elements had to ensure the electrical isolation of anodic and cathodic sub-processes in order to create a measurable macro-cell corrosion current. 19 concrete prisms with dimensions of $150 \times 150 \times 700$ mm³ were produced.

Figure 3 shows the geometry and reinforcement setup of the produced macro element specimen. The crack crossing "anode bar" is made of a reinforcement steel bar ($\varnothing = 10$ mm) and a total length of 250 mm. To define the size of the anodic area, the exposed steel surface was limited to 50 mm in the vicinity of the crack.

The steel bar sealing was made of a shrinking tube in order to reduce oxygen diffusion to non-depassivated steel surfaces outside of the crack area. Hence, cathodic reactions on the anode bar

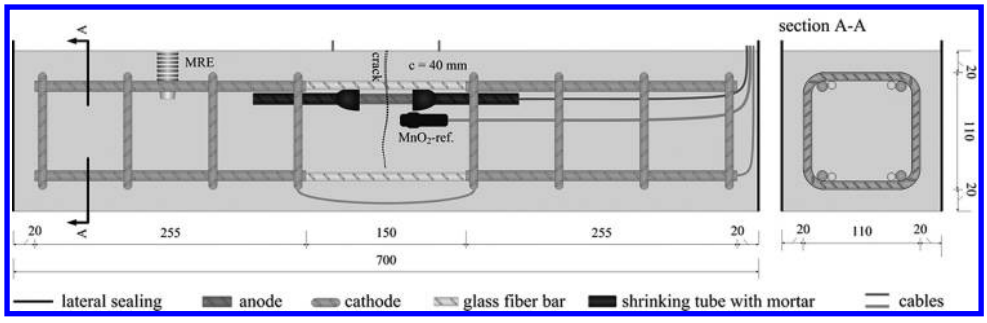

Figure 3. Geometry and reinforcement setup of the specimens, all dimensions in [mm].

can be reduced to a minimum. To prevent crevice corrosion, the transition area between the shrinking tube and the steel bar is filled with a highly alkaline mortar. According to the general rules and rules for buildings (DIN EN 1992-1-1 2011) and the corresponding exposure situation of cyclic wetting and drying in combination with chloride attack (XD3), the anode bar was fixed in the formwork with a cover depth of 40 mm.

To provide sufficient cathodic area for the corrosions process, two reinforcement cages, each consisting of four stirrups (∅ = 8 mm) and four main bars (∅ = 10 mm), were installed. The "cathode cages" were positioned outside the crack area to exclude their depassivation during the chloride exposure. In order to ensure a sufficient tensile capacity of the specimens during crack initiation, corrosion resistant glass fiber bars were integrated. Additionally, this improved the control of the crack initiation.

As anode bar and cathode cages are electrically isolated, all electrochemical measurements can be conducted on each half cell separately. For half-cell potential measurements a reference electrode (MnO_2, E_{ref} ≈180 mV_{SCE}) was fixed close to the anode area. Hence a nearly IR-drop free potential measurement of the anode is possible. Additionally, a Multi Ring Electrode (MRE) was installed on the concrete surface to determine the changes of concrete moisture due to the exposure cycles and the later coating.

In order to reproduce a realistic structural situation, the concrete composition was designed in accordance with DIN 1045-2 (2008) and the requirements resulting for a concrete component in a corresponding exposure class (XD3). A Portland cement (CEM I 32.5 R) with a content of 320 kg/m³ was used for 19 specimens. Sand and gravel with a maximum aggregate size of 16 mm was chosen. The w/c ratio was set to 0.45 and plasticizer was used to adjust a plastic consistency of the fresh concrete. The mean value of the cube strength at an age of 28 days was about 45 N/mm².

For curing, the specimens were stored for 7 days under moist jute cloths at a temperature of 20 ± 2 °C. Afterwards they were stored in a climate of 20 °C/85% RH until the age of 28 days after which the cracks were produced by three-point-bending. The crack width was adjusted to 0.3 mm which results from the permitted crack width for certain exposure conditions given in DIN EN 1992-1-1 (2011). The crack width was fixed with metal foils of 0.3 mm thickness which were inserted into the crack before the load was reduced again, Figure 4. Hence, the crack width on the concrete surface could be set precisely to 0.3 mm.

To simulate a slab structure and its one-dimensional exposition of the concrete surface, the lateral areas had to be sealed with a non-diffusive and waterproof aluminium-butyl rubber band after the crack was initiated.

2.2 *Exposure*

During the exposure only the anodes should be charged with chloride solution. Therefore, the area loaded with chloride solution was limited to the central 10 cm of the specimen. To ensure an evenly and therefore practical watering of the concrete, the outer areas were loaded only with tap water, whereas a 1.5 M.-% sodium chloride solution was used in the crack area. Figure 5 shows the finally prepared specimens.

Beginning with the first exposure all specimens are stored in a climate of 20 °C/85% RH. The concrete surface was completely wetted with chloride solution and the tap water once a week for the duration of 12 weeks. By this period of exposure, the intensity of a chloride attack by de-icing salts in the course of one winter period was simulated.

Afterwards the surface of the specimens is sealed with a two component polyurethane coating. This sealing meets the requirements of a surface protection system with high crack-bridging abilities for surfaces which are directly driven upon (OS 11

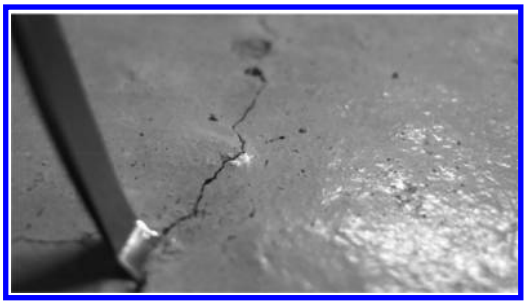

Figure 4. Metal foil keeping the crack open.

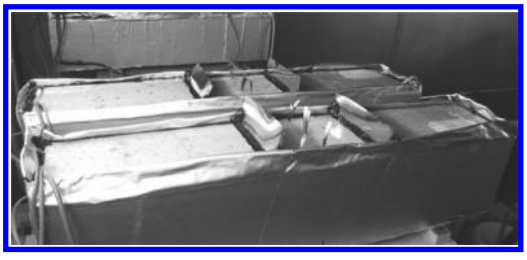

Figure 5. Specimens exposure.

according to DAfStb 2001). After the application of the coating the specimens stay stored in its climate.

2.3 *Electrical measuring setup*

Once the lateral surfaces were sealed with butyl-rubber band the electrochemical parameters were recorded periodically. Before the chloride exposure, first measurements were carried out in order to obtain values about the initial state of the specimens. The electrochemical parameters are recorded throughout the chloride exposure as well as after the coating of the specimens. Hence, the complete development of the corrosion process can be traced.

The macro-cell corrosion current I_{macro} is logged regularly every 3 hours. Cathode cages and the anode bar are short circuited through a low-resistance, high resolution ampere meter with automatic data recording. The macro corrosion current allows a time dependent assessment of the mass transfer resulting from corrosion activity.

In a weekly rhythm the short circuit is suspended leading to a depolarization of the electrodes. Subsequently the free corrosion potentials of anode and cathode can be determined. The driving voltage ΔE of the corrosion cell is derived from the difference of these potentials, giving another relevant parameter to assess the reinforcements' corrosion state. Thus, differences in corrosion activity before and after the coating application can be determined.

Additionally, multi ring electrodes, as shown in Figure 6, were installed in some of the specimens.

Starting from the exposed concrete surface a depth dependent resistivity profile is determined regularly. The continuous detection allows a qualitative evaluation of the moisture development in the surface area throughout the exposure as well as after applying the coating. Hence, the interrelation between changes in moisture distribution, and therefore in electrolytic resistance, and an eventual variation of the corrosion process can be detected.

3 FIRST RESULTS

In the following first results of the short-time chloride exposure are presented. Furthermore an insight on the influence of an applied coating is given.

3.1 *Corrosion behavior during short-time chloride exposure*

Amongst all 19 corrosion specimens eleven showed active corrosion during the twelve weeks of cyclic wetting with a 1.5 M.-% sodium chloride solution.

To evaluate the corrosion state of the crack crossing anode in those specimens, the data of the corrosion current I_{macro} as well as the free corrosion potentials of their anodes are regarded. Figure 7 contains these parameters from three characteristic specimens (PC-5, PC-12 and PC-20) representing the different situations which occurred in the case of active corrosion.

After crack initiation and before the beginning of exposure all anodic potentials were in the same magnitude at around –260 to –280 mV_{MnO2}, which indicates the passivity of the steel surface. The mean potentials of the cathodic cages, portrayed as a dotted line in the bottom diagram, range in the same order of potential and thus ensure the assumption of passivity. All cathodes showed a quite steady potential in the course of the exposure, mostly ranging at around –260 mV_{MnO2}.

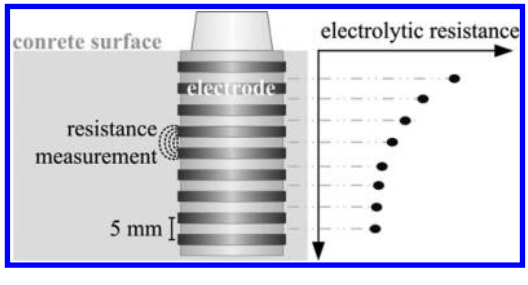

Figure 6. Scheme of a multi ring electrode.

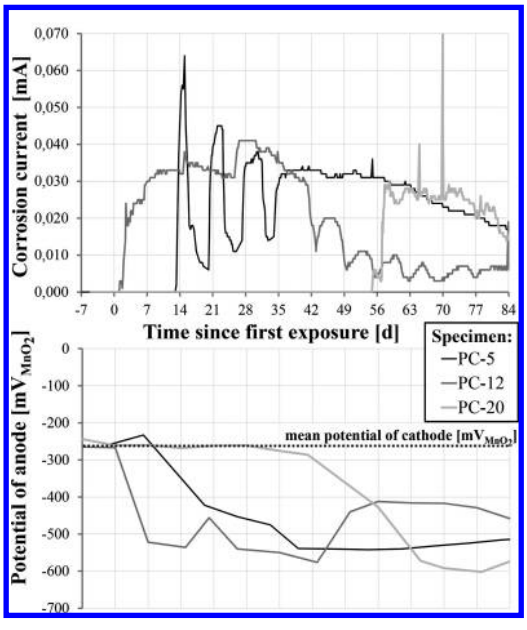

Figure 7. Macro-cell corrosion current (top) and corresponding free corrosion potentials of the anodes (bottom) of three exemplary specimens during the short-time chloride exposure.

The first situation of corrosion behavior is reflected via specimen PC-12. Only a few days after the first moistening a significant decrease of the anodic potential ($\Delta U \approx 250$ mV) indicates an immediate depassivation. This potential drop was accompanied with an instant increase of the macro-cell corrosion current. With the continuing chloride loading the potential kept dropping to a minimum of −580 mV_{MnO2} after around 42 days, creating a driving voltage ΔE between anode and cathode of about 320 mV. The corrosion current reached its maximum of 0.042 mA after 28 days when it started to decline during the ongoing cyclic loading. The descent in corrosion current is accompanied with a positive development of the anodic potential, lowering the overall driving voltage ΔE of the corrosion cell.

The second kind of corrosion behavior is represented by specimens PC-5 and PC-20. For the first-mentioned after two weeks the continuous loading with chloride solution resulted in a steadily diminishing anodic potential. Surpassing a certain potential difference ΔE between anode and cathode, a macro corrosion current was initiated which nearly came to a complete halt between every moistening. Only after five weeks of loading the corrosion current was settling on a constant level which slightly decreased until the end of exposure, whereas the anodic potential stayed constantly low at values around −520 mV_{MnO2} causing a driving voltage ΔE of around 260 mV.

Likewise, specimen PC-20 showed a delayed reaction. A decrease in potential occurred after 42 days, leading to active corrosion in form of a measurable corrosion current after two more weeks. Both, potential of the anode as well as the macro-cell corrosion current receded only a little until the end of exposure after twelve weeks.

On eight of the 19 specimens no corrosion activity could be determined, as Figure 8 exemplarily shows on specimen PC-6.

With the first chloride exposure, the anode potential tends to decrease, but the steel surface could not be depassivated. The electrodes are not polarized and no corrosion current is measured.

3.2 *Short-time influence of a concrete surface coating on chloride induced corrosion*

Of the eleven specimens that showed active corrosion during the exposure, seven corrosion processes halted before the concrete surface coating could be applied. Either this standstill occurred already during the time of exposure or the corrosion process stopped rather quickly after the exposure was ended. In this time the specimens remained in their usual climate at of 20 °C/85% RH. Of the remaining four, the electrochemical parameters obtained from three specimens (PC-3, PC-5 and PC-7) in the first twelve weeks after the coating are shown in Figure 9.

On the one hand, the anodic potentials of all three specimens remained quite low at around –400 to –450 mV_{MnO2}. On the other hand the corrosion currents had already decreased to minimum currents of 0.002 to 0.006 mA.

In the beginning, the coating of specimen PC-5 resulted in a noticeable increase of corrosion current ($\Delta I \approx 0.010$ mA), but had no noteworthy influence on its anodic potential. Only when considering the whole period of 12 weeks after

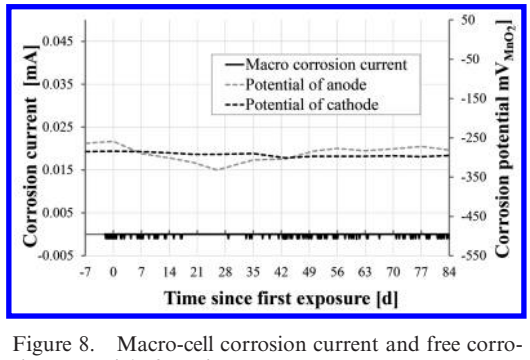

Figure 8. Macro-cell corrosion current and free corrosion potential of specimen PC-6.

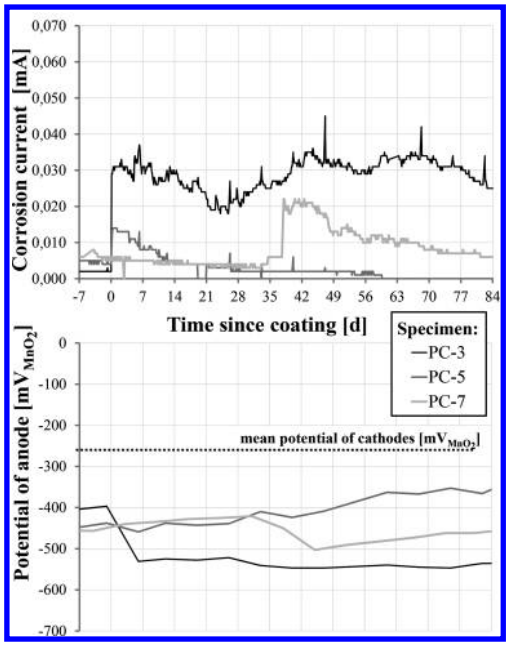

Figure 9. Macro-cell corrosion current (top) and corresponding free corrosion potentials of the anodes (bottom) of three exemplary specimens after the application of the coating.

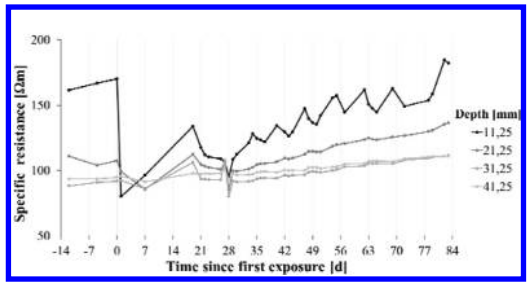

Figure 10. Depth dependent resistance profile in the uncracked concrete surface of specimen PC-1 during chloride exposure.

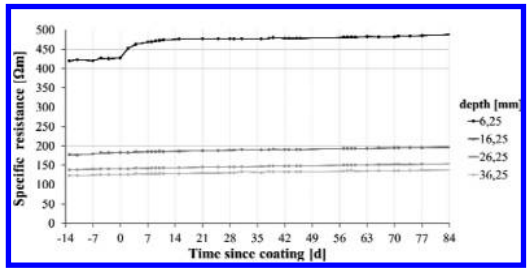

Figure 11. Depth dependent resistance profile in the uncracked concrete surface of specimen PC-1 after coating.

the coating, a constant but slow increase of the potential is detectable. After nine weeks this lead to an undetectable corrosion current, indicating a standstill of corrosion activity.

Both, specimens PC-3 and PC-7 showed a comparable behavior considering the sharp increase of the macro-cell corrosion current after the coating was applied. In specimen PC-3 the application caused an immediate reaction of the anodic potential which enlarged the driving potential by nearly 150 mV. The generated corrosion current abruptly exceeded 0.030 mA and did not decrease until the end of the investigated period. The macro-cell corrosions current of specimen PC-7 showed a delayed reaction to the application of the coating. The potential drop occurred after five weeks under sealed conditions and resulted in a current rise of about 0.020 mA. The current afterwards slowly declined but did not come to a complete halt in the period considered.

3.3 *Moisture development during exposure and after surface coating*

The depth dependent resistances of the concrete specimens were obtained with multi ring electrodes in the uncracked concrete surface. Throughout the chloride exposure, usually a distribution like shown in Figure 10 was determined.

The area close to the surface until a depth of ca. 20 mm is heavily influenced through the weekly moistening. Since the exposure was held in a constant climate of 20 °C/85% RH, a climatic variation of the resistance can be excluded. However, in deeper regions no significant influence of the resistivity and therefore the moisture balance could be found. Out of these results it can be assumed, that the concrete moisture remains sufficiently during the weekly exposure, to provide a specific resistance to enable macro-cell corrosion activity (Hornbostel 2013).

Figure 11 provides the resistance profile of the same multi ring electrode after the concrete surface was sealed with the coating.

The overall trend is slightly going upwards, resulting from the continuing hydration of the cement paste. Only in the top layer a significant influence of the concrete resistance due to the coating is detectable. In the deeper areas there is no indication, that the moisture balance is influenced in any way.

4 DISCUSSION, CONCLUSION AND OUTLOOK

The first results on the corrosion behavior in cracked concrete after a short-time chloride

exposure show that a depassivation of the crack crossing reinforcement is very likely to occur. Even only after 12 weeks of exposure to a 1.5 M.-% sodium chloride solution the anodic potentials dropped significantly leading to potential differences ΔE between anode bar and cathode cages of approximately 250–300 mV. These drops were accompanied by increasing macro-cell corrosion currents, which afterwards mostly showed a degressive progress. On the one hand this could be lead back to an increasing electrolytic resistance resulting from the continuously hydrating cement paste. On the other hand during the corrosion process oxidation products are formed that can shield the area of active corrosion. This can lead to a shortage of corrosion promoting agents, reducing their overall concentration and therefore increasing the anodic polarization resistance in the corrosion system.

Although the corrosion currents tended to decrease throughout the exposure, not all corrosion processes came to a complete halt, even not in the time after the exposure was ended. Additionally, the application of a crack-bridging surface protection system on the concrete specimens had different effects on their corrosion behavior. In some actively corroding specimens the process was halted after the coating was applied. Other specimens responded with a spontaneous sharp increase of macro-cell current, which in some of those specimens decreased afterwards. In others it remained constant over the observed period of twelve weeks after the coating. This sharp rise could be due to time dependent diffusion effects, which have led to a repeated accumulation of chlorides on the steel surface. These provoked further depassivation of the reinforcement which occurred coincidently at the same time when the coating was applied.

In order to clarify these questions as well as to completely investigate the corrosion behavior in the coated specimens further measurements have to be carried out.

Furthermore the effects of microcell corrosion have to be investigated. The previously mentioned shielding of the corroding area can affect the development of microcell corrosion (Beck 2010). In addition, there is a risk, that the sealing of the crack area can conserve a micro climate in the crack, which could endanger the load bearing capacity of a structure by maintaining microcell corrosion.

Hence, beginning with the end of the exposure some of the specimens are taken for destructive investigations. Every three months anode bars from three specimens are dismounted and the corrosion products are removed from their surface. Thus, the gravimetric mass loss can be calculated. The difference between gravimetric and coulometric mass loss, which can be calculated from of the accumulated corrosion current, enables the quantification of the microcell corrosion. Because of the ongoing destructive investigations, the time dependent development of the microcell corrosion can be assessed.

Therefore further quantification, monitoring and destructive investigation of the specimens is needed to clarify the development of the macrocell corrosion process and to determine the effects of the microcell corrosion after the coating is applied.

ACKNOWLEDGEMENTS

The authors wish to thank the German Research Foundation (DFG) for supporting this project. Furthermore we would like to sincerely thank Schöck Bauteile GmbH, Badische Stahlwerke GmbH and SCHWENK Zement KG, who provided some of the materials used in this project.

REFERENCES

Beck, M.F. 2010. Zur Entwicklung der Eigenkorrosion von Stahl in Beton. *Dissertation, RWTH Aachen, Germany*.

Catharin, P. & Federspiel, H. 1972. Der elektrische Widerstand des Betons. *Elektrotechnik und Maschinenbau, Vol. 89, No. 10, pp. 399–407.*

DAfStb Deutscher Ausschuss für Stahlbeton e. V, 2001. DAfStb Richtlinie—Schutz und Instandsetzung von Betonbauteilen (Instandsetzungsrichtlinie), Part 1–4. Berlin: Beuth Verlag.

DBV German Society for Concrete and Construction Technology 2010. DBV-Bulletin: Multi-storey and Underground Car Parks.

DIN Deutsches Institut für Normung e.V. 2008. DIN 1045-2, Concrete, reinforced and prestressed concrete structures—Part 2: Concrete—Specification, properties, production and conformity—Application rules for DIN EN 206-1, Berlin: Beuth Verlag.

DIN Deutsches Institut für Normung e.V. 2011. DIN EN 1992-1-1, Eurocode 2: Design of concrete structures—Part 1-1: General rules and rules for buildings; *German version EN 1992-1-1:2004 + AC:2010.* Berlin: Beuth Verlag.

DIN Deutsches Institut für Normung e.V. 2013. DIN EN 1992-1-1/NA, National Annex—Nationally determined parameters—Eurocode 2: Design of concrete structures—Part 1-1: General rules and rules for buildings. Berlin: Beuth Verlag.

Hornbostel, K., Larsen, C. K. & Geiker M. R. 2013. Relationship between concrete resistivity and corrosion—A literature review. *Cement & Concrete Composites, Vol. 39, pp. 60–72.*

Hunkeler, F. 1995. The resistivity of pore water solution—a decisive parameter of rebar corrosion and repair methods. *Construction and building materials, Vol. 10, No. 5, pp.381–389, 1996.*

Noeggerath, J. 1990. Zur Makroelementkorrosion von Stahl in Beton: Potential—und Stromverteilung in Abhängigkeit verschiedener Einflussgrößen. *Dissertation, ETH Zürich, Swizerland.*

Raupach, M. 1992. Zur chloridinduzierten Makroelementkorrosion von Stahl in Beton. *Deutscher Ausschuss für Stahlbeton*, *Issue 433,* Berlin: Beuth-Verlag.

Šavija, B. & Schlangen, E. 2012. Chloride ingress in cracked concrete—a literature review. In C. Andrade and J. Gulikers (eds.), *Advances in Modeling Concrete Service life: Proceedings of 4th International RILEM PhD Workshop held in Madrid, Spain, 19 November 2010.*

Schulte, C., Mader, H. & Wittmann, F.H. 1978. Elektrische Leitfähigkeit des Zementsteins bei unterschiedlichem Feuchtigkeitsgehalt. *Cement and Concrete Research, Vol. 8, No. 3, pp. 359–367.*

Warkus, J. 2012. Einfluss der Bauteilgeometrie auf die Korrosionsgeschwindigkeit von Stahl in Beton bei Makroelementbildung. *Dissertation, RWTH Aachen, Germany.*

Warkus, J. & Raupach, M. 2008. Numerical modelling of macrocells occurring during corrosion of steel in concrete. *Materials and corrosion, 59, No. 2, pp. 122–130.*

Yu, L., François, R., Hiep Dang, V., L'Hostis, V. & Gagné, R. 2015. Development of chloride-induced corrosion in pre-cracked RC beams under sustained loading: Effect of load-induced cracks, concrete cover and exposure conditions. *Cement and Concrete Research, Vol. 67, pp. 246–258.*

Concrete Repair, Rehabilitation and Retrofitting IV – Dehn et al. (Eds)
© 2016 Taylor & Francis Group, London, ISBN 978-1-138-02843-2

Physical model for structural evaluation of R.C. beams in presence of corrosion

A. Cesetti, G. Mancini & F. Tondolo
Politecnico di Torino, Torino, Italy

A. Recupero & N. Spinella
Università di Messina, Messina, Italy

ABSTRACT: Corrosion of steel in concrete is a very common degradation phenomenon observed in reinforced concrete structures. It impairs the resisting section of the bars due to the change in the nature of material, the surrounding concrete around the steel bars because of the volume expansion effect of rust and finally modifies the bond between steel and concrete. Some experimental tests are present in literature in which the structural behavior of reinforced concrete beams in presence of corrosion of longitudinal bars and stirrups was analyzed: a progressive reduction of the load bearing capacity was demonstrated with an increase level of corrosion. Furthermore a not-obvious rupture mechanism was observed due to the effect of rust formation; in particular with the increase level of corrosion a change in the type of collapse was observed. In this paper a physical model based on the theory of plasticity is employed in order to explain the residual capacity of corroded beams. The model was developed for sound structures and is able to consider the interaction between shear and bending moment: this aspect is generally neglected following the codes prescriptions for structural evaluation but could become of importance when degradation takes place and determines changes in terms of mode failure. In this model the effect of corrosion is implemented in terms of section reduction and change of basic relationship of steel, degradation of concrete; a comparison with the reliable literature data is performed.

1 INTRODUCTION

Corrosion is the most problematic issue for reinforced concrete (r.c.) structure. Hardly r.c. structures are not affected if not seriously damaged by corrosion. This phenomenon is caused by the presence of a high level of chlorides near the reinforcement and/or the occurrence of carbonation of concrete cover: these lead to a critical drop of alkalinity of concrete that expose to corrosion the steel bars. Different aspects can be addressed to corrosion of reinforcement in concrete: the reduction of the section of reinforcement, the reduction of yielding point and ductility of steel in the residual section, the loss of bond between steel and concrete and the loss of bearing capacity of cracked concrete around corroding steel, due to the expansion of the oxides, other than as an extreme consequence the spalling and delamination of the cover. These effects are responsible for the reduction of the performance of r.c. structures both in service and at ultimate conditions.

A wide literature on the structural behavior of corroded elements is available (Rodriguez et al. 1996; El Maaddawy et al. 2005; Zhu & François, 2014) and a series of mechanical models has been developed in order to simulate the effects this degradation mechanism (Coronelli & Gambarova, 2004; Toongoenthong & Maekawa, 2005). Experimental campaigns on natural and artificially corroded structures were performed in order to analyze all the aspects related to corrosion, from early cracking (Andrade et al. 1993) to bond behavior (Fang et al. 2004; Mancini et al. 2014), from deformation in service to residual ductility at ultimate conditions. As stated in Mancini and Tondolo (2014), among the tests using accelerated corrosion, it is better to refer to tests in which a limited level of current density is used in order to evaluate tests with the structural consequences of corrosion respect to the natural ones. In terms of corrosion mechanism, the reduction of the section could be considered as proportional to the current densities flowing into the reinforcement; in fact in case of electrochemical corrosion (Rodriguez et al. 1996) it can be easily calculated from the Faraday's law, taking into account the scatter due to the efficiency of the corrosion methods (El Maaddawy et al. 2003); the reinforcement being all the anodic part of the process. On the other hand in natural

conditions the loss of the section due to corrosion is determined by local corrosion mechanisms and it can be calculated by means of a direct measure with gravimetric procedure at the end of the tests.

The change of structural response of corroded reinforcement was investigated by Cairns et al. (2005) and a dataset collection has been obtained also from previous experimental campaigns. The structural effects are connected to the spatial distribution and the entity of corrosion attack on the bar.

Bond between steel and concrete, for corrosion levels higher than 2% can influence the structural behavior in a deep manner especially for unconfined structures and members. In fact, longitudinal cracking caused by corrosion and the progressive loss of confinement exerted by concrete is responsible of a change of behavior for anchorages and overlapping zones and more in general for the transfer mechanism of stresses (Cairns et al. 2005; Mancini et al. 2014), furtherly exalted if a mechanical action is present (Giordano et al. 2011) and even leads to higher deformation levels.

The cracking of concrete caused by the expansive nature of the oxides generates a loss of bearing capacity of concrete that could imply small effects in tensile zone but substantial ones in compression zone.

For all the previous listed effects corrosion of longitudinal and transverse reinforcement causes a loss of load-bearing capacity of the structural element and, in some cases, may also lead to a change of the failure mode, which modifies from ductile for bending (M) to brittle for shear (V) (Rodriguez et al. 1996). In this scenario, a model able to capture the interaction between bending and shear seems to be the very appropriate to describe the behavior of r.c. beams with corroded rebar.

2 PHYSICAL MODEL

Several contributions are present in literature on the interaction between bending and shear, following two different approaches: empirical and theoretical. The formulations of the former group are based on several test results carried out on RC members and try to provide handy equations for designers. The models that are part of the latter group, instead, start from the theory of the stress fields of Bach et al. (1978) and propose formulations valid in wide ranges of input parameters, taking into account the different internal actions (shear, bending moment and axial force).

Herein, a sectional model belonging to the theoretical group of formulations, originally proposed by Recupero et al. (2005) and in the following widely validated (Colajanni et al. 2014) against several test results on structural element having circular cross-section and also used for design (Colajanni et al. 2008), is herein adapted to provide the shear-flexure strength of specimens under corrosion effects. It allows to take into account the simultaneous presence of bending moment and shear force on the beam, for a constant value of axial force. The latter for a beam is considered equal to zero.

The adopted procedure for shear-flexure strength evaluation consists of dividing the cross-section into layers of depth y_i not identified a priori, and subjected to uniform normal σ and shear τ stress distributions to ensure the equilibrium with the internal actions N, M and V. In details, the cross-section was divided into three concrete layers having areas S_{c1}, S_{c2} and S_{c3}, and the longitudinal rebars were modeled as point elements divided into two different steel layers having area S_{s1} and S_{s2}, respectively (Fig. 1c).

With reference to the concrete element in Figure 1, obtained by two cuts, one with a plane orthogonal to the beam axis abscissa z, and another one parallel to the web concrete stress field at the abscissa z+Δz (Fig. 1a), the following equilibrium equation in the y direction can be written:

$$V^* - q \cdot z = V = \frac{A_{ws}}{s} y_3 \, \sigma_{wt} \mathrm{ctg}\theta \tag{1}$$

where V* is the shear external action at the abscissa z; θ is the distributed vertical load; σ_{wt} is the stress of the steel stirrup. Next, a new column segment is considered, obtained by cutting the element with two section planes with slope θ = 90° to the beam axis at the abscissa z and z+Δz (Fig. 1b); thus the new equilibrium equation of the column segment in the y direction reads:

$$V^* - q \cdot \Delta z = V = \sigma_{cw} \, S_{c3} \cos\theta \sin\theta \tag{2}$$

where σ_{cw} is the axial stress in the S_{c3} concrete layer. Furthermore, the expressions of the internal forces in the tension chord and in the compression chord are the following:

$$\sigma_{s1} \int_{S_{s1}} dS_s + \sigma_{s2} \int_{S_{s2}} dS_s + \sigma_{c1} \int_{S_{c1}} dS_c + \sigma_{c2} \int_{S_{c2}} dS_c = F_1 + F_2 + C_1 + C_2 = N + V\mathrm{ctg}\theta \tag{3}$$

$$\sigma_{s1} \int_{S_{s1}} y_s dS_s + \sigma_{s2} \int_{S_{s2}} y_s dS_s + \sigma_{c1} \int_{S_{c1}} y_c dS_c + \sigma_{c2} \int_{S_{c2}} y_c dS_c = M + V \, \mathrm{ctg}\theta \left(\int_{S_{c3}} y_c dS_c \Big/ \int_{S_{c3}} dS_c \right) \tag{4}$$

where σ_{ci} and σ_{si} are the axial stress of the concrete and steel related to the i-th layer, respectively; C_i and F_i the resultant forces in the concrete and the

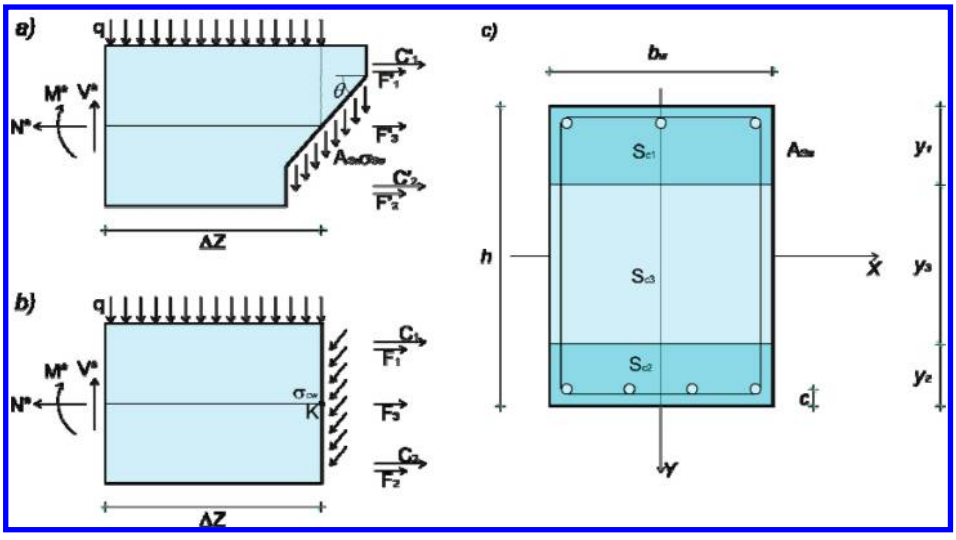

Figure 1. a) and b) external and internal forces scheme assumed; c) cross-sectional model of the beam.

steel related to the i-th layer, respectively; and y_c, y_s are the lever arms (algebraic values) calculated starting from the centroid of the cross-section.

The failure of the structural element may occur either by concrete crushing or by transversal reinforcements yielding. Using the nominal values for the steel yielding f_{ym} and for the concrete compression strength f_{cm} and $f'_{cm} = \nu f_{cm}$ [con $\nu = 0.5$, (Italian Code, 2008)], the terms related to the areas S_{c1}, S_{c2}, and S_{c3} depend on the depth of the web layers y_1, y_2, and y_3, which may vary according to the following geometrical and static conditions:

$$y_1 + y_2 + y_3 = h \tag{5}$$

$$-f_{cm} \le \sigma_{ci} \le 0 \quad i = 1, 2 \tag{6}$$

$$-f'_{cm} \le \sigma_{cw} \le 0 \tag{7}$$

$$-f_{ym} \le \sigma_{sj} \le f_{ym} \quad j = 1, 2 \tag{8}$$

The best outcome of the mathematical model is given by a linear programming method that allows to evaluate both the depth of the layers (y_1, y_2, y_3), the ctgθ, and all stresses (σ_{ci}, σ_{si}) by maximizing the element resisting actions in the respect of the plastic boundaries conditions of material strength and the geometrical restrains of the layer sizes.

3 ADAPTION OF THE MODEL TO THE CASE OF CORRODED BEAMS

The previous model should be modified according to the effect of corrosion both on concrete and steel. With this aim it is possible to simulate the reduction of the bearing capacity of cracked concrete near a corroding steel bar. In particular, according to Coronelli and Gambarova (2004), the maximum cylindrical compressive strength of concrete could be evaluated by means of the following:

$$f^*_{cm} = \frac{f_{cm}}{1 + K\,\varepsilon_1/\varepsilon_{c0}} \tag{9}$$

where K is the coefficient related to bar roughness and diameter assumed equal to 0.1, ε_{c0} is the strain at the peak compressive stress f_{cm}, ε_1 is the average tensile strain in the cracked concrete at right angles to the direction of the applied compression.

The value ε_1 can be evaluated by means of the following equation:

$$\varepsilon_1 = \left(b_f - b_0\right)/b_0 \tag{10}$$

where b_0 is the section width without corrosion crack, b_f is the increased width when corrosion cracks occur. In order to give an estimation of the increase the following equation could be used:

$$b_f - b_0 = n_{bar} w_{cr} \tag{11}$$

where n_{bars} is the number of bars in the compressed layer, w_{cr} is the total crack width for a given corrosion level that can be evaluated (Molina et al. 1993):

$$w_{cr} = \sum_i u_{i,corr} = 2\pi\left(u_{rs} - 1\right)X \tag{12}$$

where u_{rs} is the ratio volumetric expansion of the oxides, X is the corrosion depth and $u_{i,corr}$ is the

opening of the single crack. According to Molina et al. (Molina et al. 1993) u_{rs} is taken equal to 2.

In terms of modification of the stress-strain law for steel the suggestions present in Cairns et al. (2005) are here reported and used in the model:

$$f^*_{ym} = \left(1 - \alpha_y Q_{corr}\right) f_{ym} \quad (13)$$

$$f^*_{yu} = \left(1 - \alpha_u Q_{corr}\right) f_{um} \quad (14)$$

$$\varepsilon^*_u = \left(1 - \alpha_u Q_{corr}\right) \varepsilon_u \quad (15)$$

where: f^*_{ym}, f^*_{um} and ε^*_u represent yield strength, ultimate tensile strength and elongation corresponding to ultimate strength after corrosion; f_{ym}, f_{um} and ε_u represent yield strength, ultimate strength and elongation of the non-corroded bar respectively; Q_{corr} is the average cross section loss whereas α_y, α_u and α_l are empirical coefficient. The values for the empirical coefficients α are reported in Table 1 for different corrosion types.

3.1 *Comparison of proposed model with experimental data*

In this section, the experimental data collected in literature are reported and deep described, then the proposed model is used to carry out numerical analysis.

3.2 *Experimental data*

The ability of the proposed model to reproduce the shear-flexural response of corroded beams under transversal loads, has been validated by comparing the numerical results to the strength values obtained by means of failure tests performed on reinforced concrete beams subjected to corrosion effects, reported in the literature (Rodriguez et al. 1996; El Maaddawy et al. 2005; Zhu & François 2014).

The experimental tests presented by Rodriguez et al. (1996) were carried out on specimens subjected to electrochemical corrosion to study the structural behaviour of flexural elements with corroded reinforcements. The beams, having dimensions 150 × 200 × 2000 mm, were designed with high longitudinal reinforcement ratio (4ϕ12 for tensile and 4ϕ8 for compressive) and with stirrups space close to d/2 (ϕ6/85 mm), being d the effective depth of the beam. Both corroded and non corroded beams were tested up to failure, applying two symmetrical concentrated loads at 800 mm from the supports. Table 2 summarizes the main results, both in terms of service/ultimate load and average attack penetration of reinforcement.

Table 1.

Corrosion	Q_{corr} [%]	α_y	α_u	α_l
Chloride	0–25	0.017	0.018	0.06
Carbonation	0–3	0.012	0.011	0.03

Table 2. Data of specimens tested by Rodriguez et al. (1996).

Code	311	312	313	314	316	315
Days (#)	0	0	111	128	164	190
Penetration						
Tensile (mm)	0	0	0.3	0.48	0.42	0.51
Compr. (mm)	0	0	0.2	0.26	0.37	0.34
Stirrups (mm)	0	0	0.35	0.5	0.54	0.63
Service load						
δ (mm)	5.3	5.5	5.5	5.5	5.9	7.7
w (mm)	0.2	0.2	0.2	0.2	0.3	0.3
Ultimate load						
V (kN)	52.3	53.2	38.7	39	37.7	27.7
M (kNm)	38.1	38.8	28.2	28.5	27.5	20.2

An experimental study designed to investigate the combined effect of corrosion and sustained loads on the structural performance of RC beams was carried out by El Maaddawy et al. (2005). They tested a total of nine beams, each measuring 152 × 254 × 3200 mm. One beam was tested as a virgin while eight beams were exposed to accelerated corrosion for up to 310 days using an impressed current technique. Moreover, four of the nine beams were corroded under a sustained load equal to approximately 60% of the yield load of the virgin beam. The flexural reinforcement of specimens consists of two No. 15 deformed steel reinforcing bars for tensile and 2ϕ8 mm rebars for compressive. The transversal reinforcement consists of stirrups ϕ8/80 mm with a 25 mm clear cover (c) in the shear span and ϕ8/333 mm in the constant moment region. In this test campaign, corrosion was restricted to the tensile steel reinforcement placed in the middle of the specimen. Table 3 summarizes the main results, both in terms of yield/ultimate capacity and average attack penetration of tensile reinforcement.

Zhu and François (2014), recently, have presented an experimental work to investigate the influence of chloride corrosion of the reinforcing bars on the residual structural performance of RC beams. A mechanical experiment was conducted with a three-point loading system on three non corroded and four corroded beams that had been exposed to a chloride environment for 14, 23, 26 and 28 years. The specimens were cast with dimensions 150 × 280 × 3000 mm and longitudinal reinforced with 2ϕ12 for tensile and 2ϕ6 for compressive. The shear reinforcement was obtained with stirrups ϕ6/220 mm. Table 4 summarizes the main results of tests, both in terms of yield/ultimate

Table 3. Data of specimens tested by El Maaddawy et al. (2005).

Code	Virgin	CN-50	CN-110	CN-210	CN-310	CS-50	CS-110	CS-210	CS-310
Mass loss (%)	0.0%	8.9%	14.2%	22.2%	31.6%	9.7%	15.4%	22.8%	30.0%
Penetration									
Tensile (mm)	0.00	0.73	1.18	1.89	2.77	0.80	1.28	1.94	2.61
Yield capacity									
P (kN)	67.2	61.7	57.4	50.7	44.12	59.9	55.1	50.1	46.1
δ (mm)	15.6	14.4	13.9	13.0	11.7	12.3	8.9	8.4	7.4
Ultimate capacity									
P (kN)	75.0	70.2	66.8	60.0	53.3	66.1	64.6	64.2	56.9
δ (mm)	73.3	89.0	78.4	62.4	59.0	73.4	85.9	79.9	66.8
M (kNm)	37.5	35.1	33.4	30.0	31.2	33.0	32.3	32.1	28.4
V (kN)	37.5	35.1	33.4	30.0	31.2	33.0	32.3	32.1	28.4

Table 4. Data of specimens tested by Zhu and François (2014).

Code	B1T1	B2T2	B2T3	B1Cl1	B2Cl1	B2Cl2	B2Cl3
Years (#)	14	26	28	14	23	26	28
Penetration							
Tensile (mm)	0.00	0.00	0.00	0.14	0.29	0.34	0.37
Yield capacity							
P (kN)	46.0	44.1	46.0	37.0	28.2	30.0	26.0
δ (mm)	3.9	7.1	8.3	5.3	4.0	6.3	3.1
Ultimate capacity							
P (kN)	54.2	49.4	50.2	42.5	37.0	37.1	30.7
δ (mm)	80.8	79.8	73.8	23.0	37.0	39.4	21.0
M (kNm)	39.3	35.8	36.4	30.8	26.8	26.9	22.3
V (kN)	27.1	24.7	25.1	21.3	18.5	18.6	15.4

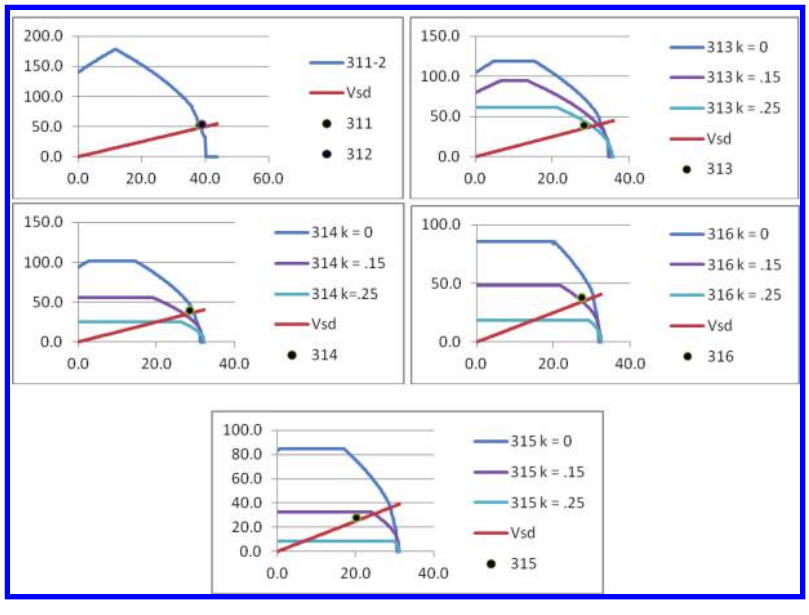

Figure 2. Interaction diagrams M-V for all specimens tested by Rodriguez et al. (1996).

capacity and average attack penetration of tensile reinforcement.

3.3 *Numerical analysis*

The numerical analysis have been carried on using the procedure already described in the previous section. In the proposed model, the concrete strength for uniaxial longitudinal stresses f_{cd1} have been evaluated neglecting the safety coefficient (set equal to 1, $f_{cd1} = f_{cm}$), while for stresses in presence of transverse load the concrete strength f_{cd2} was calculated as proposed by the Italian code (2008), assuming an effectiveness shear factor equal to 0.50 ($f_{cd2} = 0.50 f_{cd1} = 0.50 f_{cm}$).

The modelling of specimens tested by Rodriguez et al. (1996) has taken into account of the reduction of the material strength, as

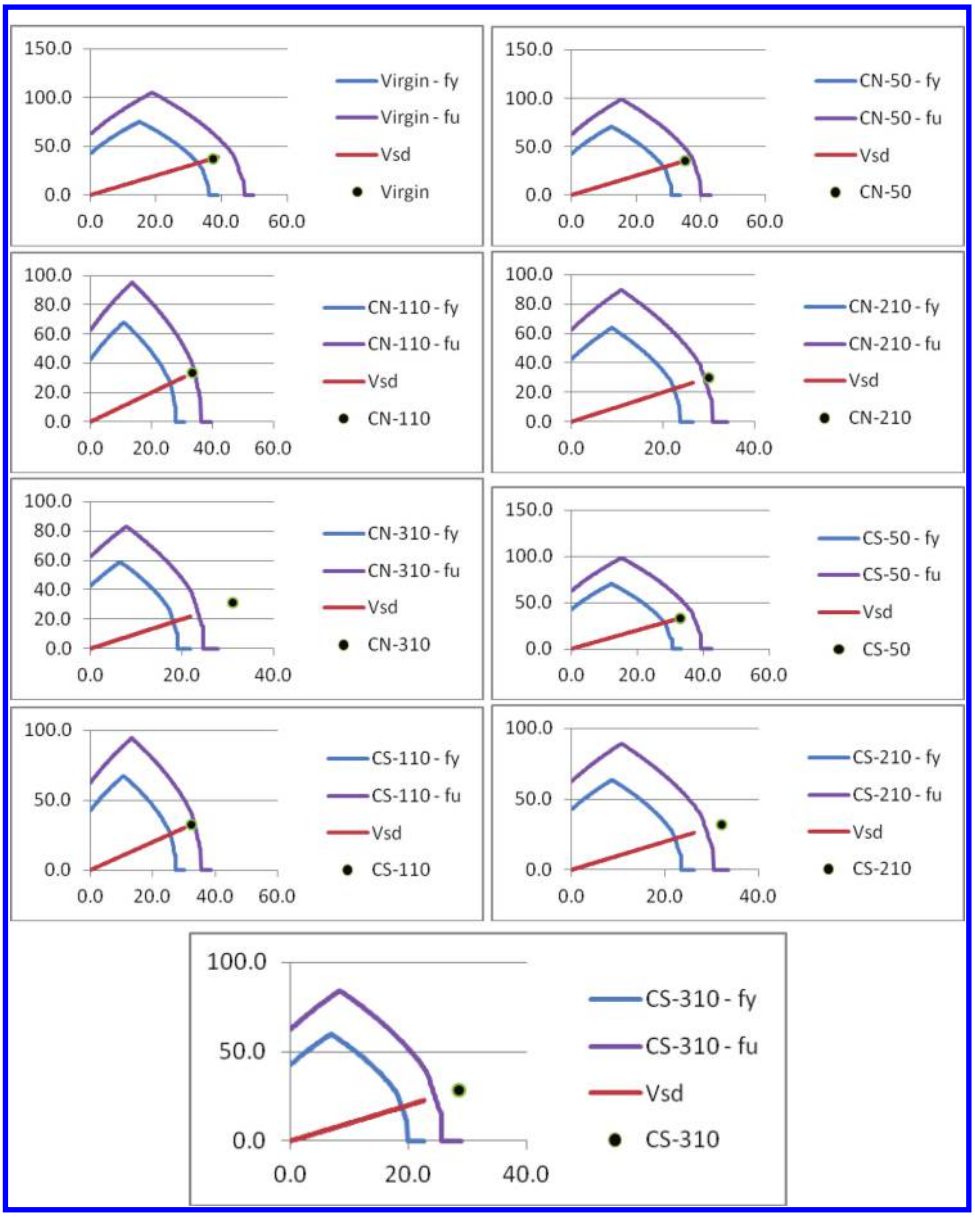

Figure 3. Interaction diagrams M-V for all specimens tested by El Maaddawy et al. (2005).

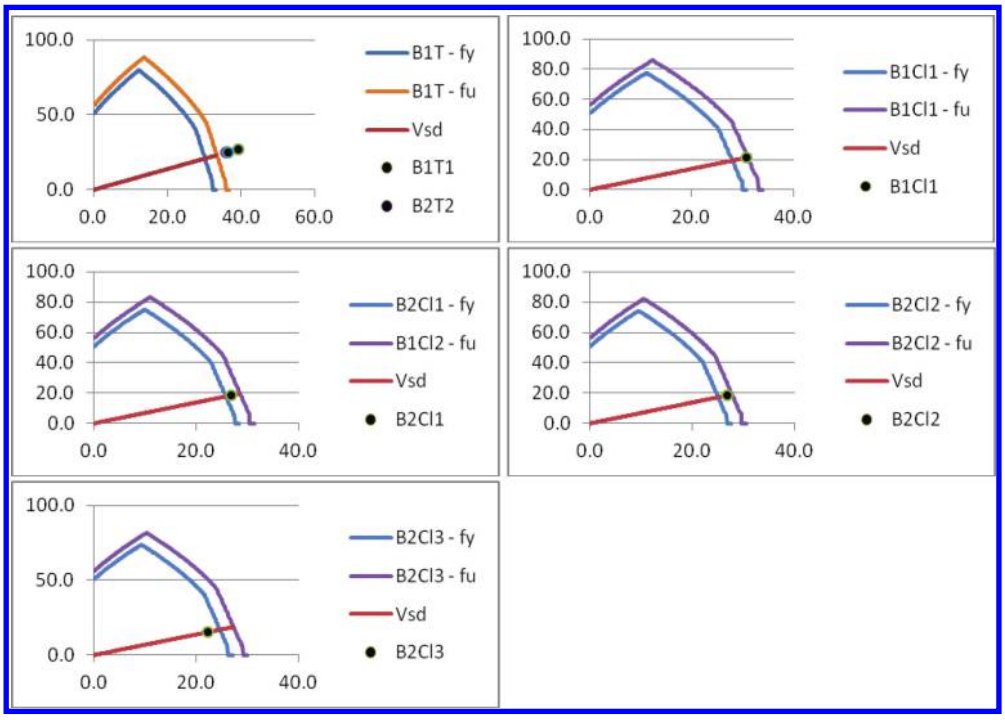

Figure 4. Interaction diagrams M-V for all specimens tested by Zhu and François (2014).

described in the previous section, and also of the rebar section of reinforcement (longitudinal and transversal). Moreover, the author provided the average and the maximum (pitting) attack penetration. Therefore, the residual bar diameter (ϕ_r) was estimated considering both the average value (μ) of attack penetration and also a greater value as function of pitting (σ). The following equation was adopted:

$$\phi_r = \phi_r - \alpha(\mu + k\sigma) \tag{16}$$

Being α a coefficient which depends on the type of the attack; and k a coefficient ranging between 0 and 0.25.

In Figure 2 the interaction diagrams *M-V* for all specimens tested by Rodriguez et al. (1996) are shown.

The experimental response of specimens tested by El Maaddawy et al. (2005) have been also reproduced with the proposed analytical procedure. In this case the tensile steel reinforcing bars were Grade 60, having yield (f_{ym}) and ultimate (f_{um}) strengths of 450 MPa and 585 MPa, respectively. Therefore, two numerical analysis for each specimen were performed, assuming as plastic limit of tensile steel stress the yield and the ultimate strength, respectively.

In Figure 3 the interaction diagrams *M-V* for all specimens tested by El Maaddawy et al. (2005) are shown.

As for the specimens tested by El Maaddawy et al. (2005), also the difference between the yield and ultimate value of tensile strength of steel reinforcing bars used by Zhu and François (2014) in their beams was remarkable. In details, the yield strength and the ultimate strength of steel were 560 MPa and 620 MPa, respectively. Therefore, also for this group of tests, two numerical analysis for each specimen were performed, assuming as plastic limit of tensile steel stress the yield and the ultimate strength, respectively. In Figure 4 the interaction diagrams *M-V* for all specimens tested by Zhu and François (2014) are shown.

In all cases, the proposed model gives an appreciable agreement with experimental results and confirm its adequate reliability for both corroded and non corroded beams.

4 CONCLUSIONS

In the present paper a plastic model for the analysis of corroded structure is employed. The model is able to take into account the interaction between shear and bending moment acting in the same

section of the r.c. element. The effects of the reduction of bearing capacity of concrete in compression and the reduction of steel section together with the modification of the constitutive law for steel due to the corrosion are implemented. Results show a good agreement between the M-V curve domains and the experimental data taken from reliable experiences available in literature. Some differences are registered; they could be addressed to the scatter of the phenomenon of corrosion. The model could be furtherly improved in order to take into account other effects of corrosion as the bond loss between steel and concrete.

REFERENCES

Andrade, C., Alonso C.M. & Molina F.J. 1993. Cover Cracking as a function of bar corrosion: Part I-Experimental test. *Materials and Structures*, 26(8): 453–464.

Bach F., Braestrup, M.W. & Nielsen, M.P. 1978. Rational Analysis of Shear in Reinforced Concrete. *in I.A.B.S.E. Proceedings*, pp.15.

Cairns, J., Plizzari, G., Du, Y., Law, D.W. & Franzoni, C. 2005. Mechanical properties of corrosion-damaged reinforcement. *ACI Materials Journal*, 102(4): 256–264.

Cairns, J., Du, J. & Law, D. 2008. Structural performance of corrosion-damaged concrete beams. *Magazine of Concrete Research*, 60(5): 359–370.

Colajanni, P., Recupero A., & Spinella, N. 2008. Design Procedure for Prestressed Concrete Beams. *Computers and Concrete*, 13(2): 235–253.

Colajanni, P., Recupero, A. & Spinella, N. 2014. Shear Strength Degradation Due to Flexural Ductility Demand in Circular R.C. Columns. *Bulletin of Earthquake Engineering*, 1–13.

Coronelli, D. & Gambarova, P. 2004, Structural assessment of corroded reinforced concrete beams: Modeling guidelines. *ASCE Journal of Structural Engineering.* 130(8): 1214–1224.

El Maaddawy, T. & Soudki, K.A. 2003. Effectiveness of impressed current technique to simulate corrosion of steel reinforcement in concrete. *Journal of Materials in Civil Engineering*. 15(1): 41–47.

El Maaddawy, T., Soudki, K. & Topper, T. 2005. Long-Term Performance of Corrosion-Damaged Reinforced Concrete Beams. *ACI Structural Journal*. 102(5): 649–656.

Fang, C., Lundgren, K., Chen, L. & Zhu, C. 2004. Corrosion influence on bond in reinforced concrete. *Cement and Concrete Research.* 34(11): 2159–2167.

Giordano, L., Mancini, G. & Tondolo, F. 2011. Reinforced Concrete Members Subjected to Cyclic Tension and Corrosion. *Journal of Advanced Concrete Technology*. 9(3): 277–285.

Italian Code, NTC. 2008. Norme tecniche sulle costruzioni, Supplemento Ordinario alla Gazzetta Ufficiale serie generale n. 29.

Mancini, G. & Tondolo, F. 2014. Effect of bond degradation due to corrosion—a literature survey. *Structural Concrete*. 15(3): 408–418.

Mancini, G., Sabia, D., Pettinato, E. & Tondolo, F. 2014. Pull-out tests in presence of high level of corrosion. *In IALCCE Fourth International Symposium on Life-Cycle Civil Engineering*, Tokyo.

Molina, F.J., Alonso, C. & Andrade, C. 1993. Cover cracking as a function of rebar corrosion. Part II—Numerical model. *Materials and Structures*. 26: 532–548.

Recupero, A., D'Aveni, A. & Ghersi, A. 2005. Bending Moment–Shear Force Interaction Domains for Prestressed Concrete Beams. *Journal of Structural Engineering*. 131(9): 1413–1421.

Rodriguez, J., Ortega, L.M. & Casal, J. 1996. Assessing structural conditions of concrete structures with corroded reinforcement. *In 4th Int. Conference on Concrete in the Service of Mankind, Concrete Repair Reabilitation and Protection*. Dundee, UK.

Toongoenthong, K. & Maekawa, K. 2005. Multi-mechanical approach to structural performance assessment of corroded RC members in shear. *Journal of Advanced Concrete Technology*, 3(1), 107–122.

Zhu, W. & Francois, R. 2014. Structural performance of RC beams in relation with the corroded period in chloride environment. *Materials and Structures*. in press.

Concrete Repair, Rehabilitation and Retrofitting IV – Dehn et al. (Eds)
© 2016 Taylor & Francis Group, London, ISBN 978-1-138-02843-2

Bond-slip model for corroded steel in concrete

A. Cesetti, G. Mancini, F. Tondolo & C. Vesco
Politecnico di Torino, Torino, Italy

ABSTRACT: Bond in concrete is of outmost importance for the definition of resisting mechanisms in reinforced concrete structures. Bond performance is directly related to both serviceability and ultimate behaviour of reinforced concrete members, because it influences the stiffness of the elements but also the ductility of the mechanical response and the anchorage capacities. In presence of corrosion bond between steel and concrete is modified according to different factors as amount of corrosion, cover/rebar diameter, strength of concrete, reinforcement characteristics influencing the mechanical response of the contact surface between the two materials. In the paper, starting from a reference bond-slip law as suggested by MC2010, a modified relationship in presence of corrosion is studied by using a numerical model specifically developed and calibrated on experimental results, coming from pull-out test of corroded specimens. These specimens are characterized by an increasing level of corrosion up to 20%, presence of confinement and use of a current density equal to 200 μA/cm^2. Different relationships are proposed for specimens with and without confinement.

1 INTRODUCTION

Corrosion of reinforcement in concrete is a very huge problem for reinforced concrete (r.c.) structures. Among the other structural effects, bond action between the two materials impairs the force transmission mechanism and obviously is of outmost importance. Modification of tension stiffening, anchorage length, ductility and bearing capacity of r.c. structures can be addressed to bond loss. Mechanical models have been developed for bond-slip relationship reproducing bond test with long (beam type) and short embedment length (pull-out). In order to study a local relationship a test setup with short embedment length is needed (Mancini & Tondolo 2014b) as RILEM (1994) type. There are plenty of models in scientific literature able to reproduce and predict the bond behaviour in pull-out tests. Fantilli et al. (2007) used an approach previously developed for the simulation of pull-out test mechanism for uncorroded smooth bars. Lundgren et al. (2012) developed an analytical model able to simulate bond-slip behaviour of corroded ribbed reinforcement. The authors introduced a model with plastic slip in the first branch of bond-slip relation. Furthermore this model is capable to take into account the effect of both corrosion and transversal confinement provided by the presence of stirrups. The effect of corrosion is simulated by means of a progressive reduction of bond-slip relationship from confined to unconfined. Other very comprehensive but complex proposals, as that one developed by Ozbolt et al. (2014) using finite element method, have been also established on the base of a coupled chemo-hygro-thermo-mechanical model.

2 PROPOSED MODEL

In this paper a new and relatively simple numerical model is proposed in order to reproduce the performance of bond in presence of corrosion with pull-out tests. In this model the equations reported in Noghabai (1998) that allows to evaluate the bar-concrete pressure due to bond action are used. Furthermore the structural effect of corrosion is taken into account. Pull-out and splitting mode failures are simulated and a comparison with experimental tests is also shown.

2.1 *Solution for the boundary value problem*

In pull-out tests the mean bond stress along the embedment length and the slip at the unloaded end of the specimen are registered. In these tests, according to the RILEM (1994) guidelines, the anchored length is short (five bar diameters) in order to avoid yielding of the reinforcement before the complete sample failure due to bond. In the anchorage zone, the mean bond stress can be calculated as follows:

$$\tau_m = \frac{P}{\pi \cdot \Phi \cdot L} \tag{1}$$

where P is the acting force, Φ is the bar diameter and L is the bonded bar length. The mean bond slip relationship is derivable from equation (1)

for a range of values of P and the corresponding slip s. The expressions that govern the problem are three:

– equilibrium equation of a generic cross section:

$$P = A_c \varepsilon_c E_c + A_s \varepsilon_s E_s \tag{2}$$

where A_c is the concrete section, ε_c is the concrete strain, E_c is the Young's module of concrete, A_s is the steel section, ε_s is the steel strain and E_s is Young's module of steel;

– equilibrium equation of a generic portion of bare bar:

$$(\varepsilon_s + d\varepsilon_s) E_s A_s - \varepsilon_s E_s A_s = \tau_s \cdot \pi \cdot \Phi \cdot dx \tag{3}$$

Taking into account that $A_s = \pi\Phi^2/4$ it is possible to obtain:

$$\frac{d\varepsilon_s}{dx} = \frac{4\tau_s}{E_s \Phi} \tag{4}$$

– compatibility equation between steel and concrete at the interface layer:

$$\varepsilon_s - \varepsilon_c = \frac{ds}{dx} \tag{5}$$

where s is the bar to concrete slip. To solve this boundary value problem it is necessary to introduce a boundary condition that is:

$$\varepsilon_{s,x=0} = \frac{P}{A_s E_s} \tag{6}$$

The problem can be solved by means of predictor corrector method for differential equation (Fantilli et al. 2007). The results give for every applied displacement at the loaded end, the value of pull-out force P, the profile of ε_s, ε_c, s and τ along the embedment length. In this way it is possible to simulate a displacement controlled test. In order to take into account the effect of the lateral pressure due to bar-concrete interaction caused both by pull-out stresses and corrosion, an extension of this model is proposed in the following paragraphs.

2.2 *Analytical model for thick-walled concrete rings*

An important issue in pull-out test is the effect of radial pressure that arises between concrete and bar when the mechanical action of bond is present; this is related to the interaction between the ribs and the surrounding concrete. This mechanism produces compressive radial stresses and consequently hoop tensile circumferential stresses that can bring to the cracking of concrete (splitting cracks). In order to take into account this effect an elastic cracked cohesive model is used. This model considers both the strength of uncracked concrete and the cohesive contribution of cracked concrete. Therefore the concrete section is divided into two parts (Fig. 1): elastic uncracked ring (external) and cracked cohesive section (internal).

This model was developed and used by several authors (Van der Veen 1990, Reinhardt 1992, Rosati & Schumm 1992, Noghabai et al. 1998). In this model a linear softening law for concrete is chosen:

$$\sigma_t = f_{ct}\left(1 - \frac{w}{w_c}\right) \tag{7}$$

Starting from an equilibrium between internal pressure (exerted by corrosion or pull-out force), and external pressure given by tensile strength of concrete, the following equilibrium can be written imposed:

$$2 p_i r_i = 2 p_{cr} r_{cr} + 2\int_{r_i}^{r_{cr}} \sigma_t(r) dr \tag{8}$$

where r_i is the internal radius (radius of rebar), r_{cr} is the cracked radius and σ_t the residual tensile

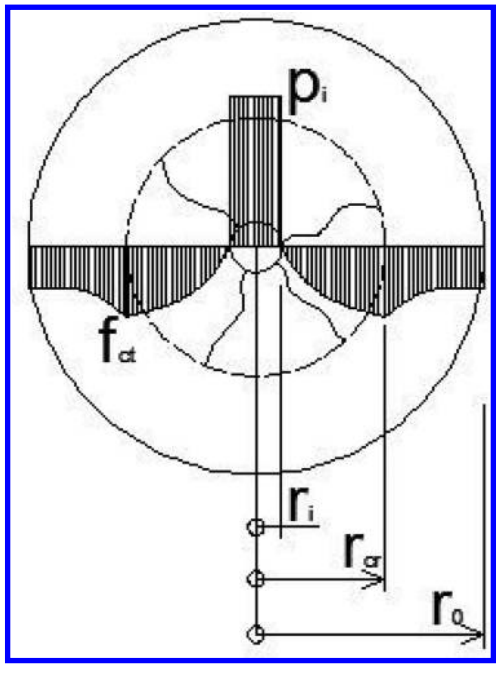

Figure 1. Elastic cohesive model representation.

stress in the cracked concrete (see Fig. 1) according equation 7. The left side of 8 is the inner pressure, whereas on the right side there is the pressure on the cracked ring and the contribute due to cohesion. In correspondence of $r = r_{cr}$ the hoop stresses (σ_t) are equal to concrete tensile strength (f_{ct}) and the tangential displacement is u_t. This displacement includes the crack width and the residual elastic deformation due to the unloading process of cracking mechanism (unloading of the bulk). Thus, in case on n cracks, the displacement is calculated as:

$$u_t(r) = 2(\varepsilon_e + \varepsilon_{cr})\pi r = \left(\frac{2\sigma_t}{E_c} + \frac{nw}{\pi r}\right)\pi r \tag{9}$$

In the surface between cracked and uncracked ring the displacement is assumed constant and equal to $u_t(r_{cr}) = 2\varepsilon_{ct}\pi r_{cr}$. Therefore in the cracked ring, rewriting with respect to the crack width:

$$n \cdot w = 2\pi\varepsilon_{ct}\left(r_{cr} - r\frac{\sigma_t}{f_{ct}}\right) \tag{10}$$

With a linear softening law for concrete it is possible to relate the displacement w_c to the fracture mechanics properties, in particular to the characteristic length $l_{cr} = E_c G_f / f_{ct}^2$, where $G_f = w_c f_{ct}/2$; it can be obtained:

$$w_c = 2\frac{l_{cr} f_{ct}}{E_c} = 2l_{cr}\varepsilon_{ct} \tag{11}$$

Now introducing equations 10 and 11 into the equation 7, it is possible to obtain:

$$\sigma_t = f_{ct}\frac{n \cdot l_{ch} - \pi \cdot r_{cr}}{n \cdot l_{ch} - \pi \cdot r} \tag{12}$$

Substituting 12 into 8 it is possible to derive the internal pressure (in the case of n cracks):

$$\frac{p_i}{f_{ct}} = \frac{r_{cr}}{r_i}\frac{r_0^2 - r_{cr}^2}{r_0^2 + r_{cr}^2} + \int_{r_i}^{r_{cr}}\left(\frac{1}{1 - \dfrac{\pi \cdot r}{n \cdot l_{cr}}} - \frac{2\pi \cdot r_{cr}}{2n \cdot l_{cr} - 2\pi \cdot r}\right)dr \tag{13}$$

With $r_i < r_{cr} < r_0$. The maximum pressure is obtained with $r_{cr} = r_{cr,crit}$, that is the greatest cracked radius value beyond which the cracking mechanism becomes unstable and propagates. One underline that relationship of equation 13 describes the internal pressure associated to every value of r_{cr}.

2.3 *The contribution of transversal reinforcement*

In order to evaluate the effect of transversal reinforcement an additional contribution must be added to the model according to the following assumptions:

- transversal reinforcement is transformed into an equivalent cylinder with an equivalent thickness,
- stresses in the cylinder are assumed to be constant,
- the steel is assumed to be a linear elastic material,
- in presence of no-circular reinforcement, an equivalent radius is evaluated.

Depending on the crack front (r_{cr}), two situations are possible: the crack front is internal to reinforcement radius (see Fig. 2) or the stirrups are inside the cracked radius. When the cylinder is inside the outer elastic ring, elastic thick walled ring theory is applicable, thereby tangential deformation can be evaluated as follows:

$$\varepsilon_t(r) = \frac{2}{E_c}\frac{p_{cr} r_{cr}^2 r_0^2}{(r_0^2 - r_{cr}^2)r^2} = \varepsilon_t(r_{cr}) \cdot \frac{r_{cr}^2}{r^2} \tag{14}$$

Therefore at transversal reinforcement level ($r = r_s$) knowing that $\varepsilon_t(r_{cr}) = f_{ct}/E_c$ the deformation of the cylinder is known. In the situation where the

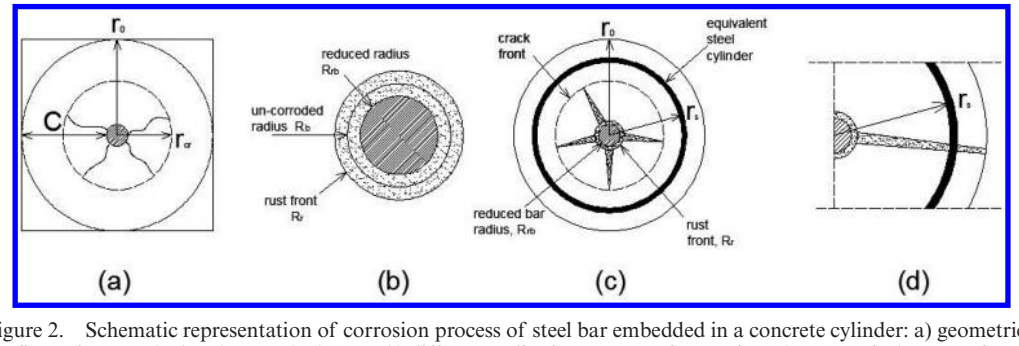

Figure 2. Schematic representation of corrosion process of steel bar embedded in a concrete cylinder: a) geometrical configuration, cracked and uncracked zones, b) different radius in presence of corrosion, c) geometrical assumption for cracks and confinement, d) truncated crack profile.

equivalent cylinder is inside the cracked section, it is possible to calculate the deformation as follows:

$$\varepsilon_t(r_s)2\pi r_s = \varepsilon_{ct}2\pi r_{cr} \tag{15}$$

Knowing that at the crack front $\varepsilon_{ct} = f_{ct}/E_c$ the eq. 15 becomes:

$$\varepsilon_t(r_s) = \frac{f_{ct}}{E_c}\frac{r_{cr}}{r_s} \tag{16}$$

Having assumed a linear elastic behaviour for steel, the global equilibrium (8) can be rewritten as follows:

$$2p_i r_i = 2p_{cr}r_{cr} + 2\int_{r_i}^{r_{cr}} \sigma_t(r)dr + 2E_s\varepsilon_t(r_s)t_{s,eq} \tag{17}$$

2.4 *Relationship between internal pressure and lateral displacement*

Pull-out mechanism induces radial displacement because of the presence of concrete struts that arise due to ribs of bars. The radial displacement can be due to the presence of oxides product or to the pull-out mechanism. Oxides products induces internal pressure in consequence of their greater volume in relation to that one of the sound metal.

Assuming that:

$$\varepsilon_t(r_i)\cdot r_i = \varepsilon_t(r_{cr})\cdot r_{cr} \tag{18}$$

and knowing that:

$$\varepsilon_t(r_i) = \frac{v}{r_i} \tag{19a}$$

where v is the imposed radial displacement and

$$\varepsilon_t(r_{cr}) = \frac{f_{ct}}{E_c} \tag{19b}$$

the cracked radius can be evaluated as follows:

$$r_{cr} = \varepsilon_t(r_i)\cdot r_i \cdot \frac{E_c}{f_{ct}} = v\cdot\frac{E_c}{f_{ct}} \tag{20}$$

Therefore imposing a radial displacement v, from 20 it is possible to evaluate r_{cr} and then form 17 the internal pressure.

2.4.1 *Radial displacement due to pull-out test*

During pull-out test the ribs of bar determine a radial displacement in the surrounding concrete; this displacement is due to the formation of sliding planes between the ribs. One remarks that the radial displacement changes because the sliding plane does not remain unchanged due to the progressive failure of concrete. One can propose that the radial displacement is related to the slip by means of the following nonlinear relationship:

$$v = v_{s_1}\cdot\left(\frac{s}{s_1}\right)^{0.4} \quad \text{for } s \le s_1 \tag{21}$$

$$v = v_{s_1} + \tan(\beta)\cdot(s - s_1) \quad \text{for } s_1 < s \le 2 \text{ mm} \tag{22}$$

$$v = v_{s_1} + \tan(\beta)\cdot(2 - s_1) \quad \text{for } s > 2 \text{ mm} \tag{23}$$

Additionally we assume that v_{s1} = 3.25*10^(–3) and tan(β) = 1.5*10^(–4). The previous parameters are set in order to fit with eq. 21 the value of maximum bond strength versus the corresponding slip registered during the test of reference specimen (uncorroded and unconfined specimen). The second branch of eq. 22 simulates the constant level of bond strength after the maximum peak; after 2 mm it is assumed that the additional slip is unable to increase radial displacement (ribs are slipping along the concrete) and then the maximum radial displacement remain constant.

2.4.2 *Radial displacement due to corrosion*

Corrosion process transforms steel into expansive oxides that induce an imposed radial displacement and consequently determine a radial pressure increase. Corrosion of bars can be expressed as a mean value in terms of attack penetration (x_{ave}). The attack penetration can be evaluated from the mass loss, assuming a homogenous cross section reduction. The phenomenon is complex because corrosion products behaves like a gel that moves through concrete pores, fills cracks when concrete is cracked and finally flow out when it reaches the external surface. Taking into account a steel bar with an un-corroded radius R_b, reduced radius R_{rb} embedded in a concrete element with a cover thickness c, the rust front reaches a radius R_r (Fig. 2). For a fixed corrosion penetration x_{ave}, it is possible to evaluate the reduced radius R_{rb} and the volume loss ΔV_s for unit length.

$$\begin{aligned} R_{rb} &= R_b - x_{ave} \\ \Delta V_s &= \pi R_b^{\,2} - \pi R_{rb}^{\,2} \end{aligned} \tag{24}$$

where ΔV_s is the volume of the oxides, evaluated by means of the volumetric expansion coefficient (α):

$$\Delta V_r = \alpha\cdot\Delta V_s \tag{25}$$

To take into account concrete porosity a theoretical porosity thickness is introduced. In this way, it is assumed that corrosion product fills the concrete pores before to give rise to an inner pressure. After the completion of the filling process corrosion starts to increase pressure producing a radial displacement equal to:

$$v_{cor} = R_r - R_b = \sqrt{\frac{\Delta V_r - \Delta V_s}{\pi} + R_b^2} - R_b \tag{26}$$

This radial displacement is valid up to concrete cracking. When concrete cracks, oxides flow into these cracks. So there is an initial volume that can be filled by corrosion oxides equal to:

$$\Delta V_{r,\max} = \left[\pi\left(R_b + h\right)^2 - \pi(R_b - x_{ave})^2\right] \tag{27}$$

where h is the equivalent thickness taking into account concrete porosity. When oxides fill up theoretical porosity thickness entirely ($\Delta V_r > \Delta V_{r,max}$), an inner pressure get started. Supposing a linear crack opening (Fig. 2) a maximum volume that fills cracks and porosity effect can be easily evaluated. When this volume is filled, iron oxides start to establish a pressure. The scenario changes when the section is completely cracked. Indeed in this case a truncated shape of crack is assumed (Fig. 2).

At this point, not all corrosion products remain in concrete, i.e. inner pressure does not increase because of the flow of oxide gel outside. Thus a relationship for the estimation volume loss is introduced:

$$\Delta V_{loss} = 1 - a^{-(x - x_{cr})^b} \tag{28}$$

where a and b are empirical parameters and x_{cr} is the attack penetration when crack appears at the external surface. The values of a and b are assumed as $a = 5$ and $b = 0.24$ by comparison of maximum radial pressure in specimens with corrosion cracks already present before the bond test.

In presence of corrosion the radial displacement calculated as previously indicated (eq. 21–23, 26) must be accounted for before the pull-out test and then three situations can occur:

- a radial displacement due to corrosion unable to produce cover cracking (v_{cr}) is reached and during the test the additional radial displacement due to the pull-out test is lower than v_{cr}: pull-out failure is registered;
- a radial displacement due to corrosion unable to produce cover cracking (v_{cr}) is reached and during the test the additional radial displacement due to the pull-out test is higher than v_{cr}: splitting failure occurs during the test;
- a certain amount of corrosion able to produce cover cracking is present. The specimen is already cracked with splitting type cracks before the starting of pull-out test.

In case of splitting failure it is assumed that the radial displacement increases steeply with the slip because of the formation of a sliding surface. This sliding surface has a slope characterized by rib depth and rib space as indicated by other authors (Tastani & Pantazopoulou 2012) and is here taken into consideration with a $v/s = 0.1$.

Furthermore, the radial displacement is updated to take into account the Poisson effect exerted by the longitudinal stress of bars.

2.5 *Local bond stress-slip relationship*

The local bond slip relationship for unconfined concrete reported in MC2010 (2010) is chosen. The relationship is described from the following equations:

$$\tau = \tau_{\max} \cdot \left(\frac{s}{s_1}\right)^{\alpha} \quad \text{for } 0 < s \le s_1 \tag{29}$$

$$\tau = \tau_{\max} - \left(\tau_{\max} - \tau_f\right) \cdot \frac{s - s_1}{s_3 - s_1} \quad \text{for } s_1 < s \le s_3 \tag{30}$$

$$\tau = \tau_f \quad \text{for } s > s_3 \tag{31}$$

where τ_{max} is the maximum bond strength, s_1 is the slip at the maximum bond strength is assumed equal to 0.5 mm, α equal to 0.4, $\tau_f = 0.5 \cdot \tau_{max}$ and s_3 is the clear rib spacing.

Even though the MC2010 indicates τ_{max} as a function of concrete compressive strength, in this paper, τ_{max} is a function of the lateral pressure according to the following failure criterion that is set to the experimental values of reference specimens (uncorroded and unconfined):

$$\tau_{\max} = c + \mu\sigma_p \quad \text{for } \sigma_p \le 25 \text{ MPa} \tag{32}$$

$$\tau_{\max} = c + \mu\sigma_{p,pl} \quad \text{for } \sigma_p > \sigma_{p,pl} = 25 \text{ MPa} \tag{33}$$

where μ is the friction angle assumed equal to 0.9, c is the cohesion assumed equal to 1.5 MPa and $\sigma_{p,pl}$ is the pressure beyond of which maximum tangential stress do not increases anymore. In this way the maximum bond strength is varying according to the lateral pressure σ_p and is different along the embedment length. In addition with the increasing value of corrosion, the value of s_1 is proportionally reduced according to the following formula in order to take into account the stiffness increase caused by corrosion:

$$s_1 = 0.5 - \frac{0.25}{50} \cdot x_{ave} \quad \text{for } x_{ave} \le 50 \text{ µm} \tag{34}$$

$$s_1 = 0.25 \text{ mm} \quad \text{for } x_{ave} \ge 50 \text{ µm} \tag{35}$$

Furthermore, for a small amount of slip, the frictional (33–34) criterion cannot take into account the chemical adhesion at the steel-concrete interface that is responsible of the stress transfer

mechanism at low value of bond. Therefore the following formulation for an higher cohesion contribution, only for small slip values, is proposed:

$$c = \mu\sigma_{p,pl} + 1.5 - \left(\mu\sigma_{p,pl}\right)\cdot\left(\frac{s}{s_1}\right)^{0.2} \quad \text{for} \quad s \le s_1 \qquad (36)$$

$$c = 1.5 \quad \text{for} \quad s > s_1 \qquad (37)$$

3 DATA ANALYSIS AND DISCUSSION

The model previously introduced is used to simulate the results of pull-out tests in presence of corrosion performed by the Authors. Complete details can be found in Mancini et al. (2014a). Both the pull-out tests for confined and unconfined samples were tested. For confined specimens, the assumption of 4 internal cracks is used whereas for unconfined specimens, 2 cracks are considered according to Noghabai (1998). Furthermore the coefficient α for the evaluation of expansive effect of the oxides is set equal to 5 within the range 1.8–6.4 as indicated by Lundgren (2002) and Pantazopoulou & Papoulia (2001). The tests have been conducted according to the suggestion reported in Mancini & Tondolo (2014b) especially for what concerns current density for the accelerated electrochemical corrosion.

In the Figure 3 the radial pressure due to an imposed radial displacement for both confined and unconfined specimens is shown. It is evident for unconfined specimens as increasing the radial displacement a pressure rise is registered but after reaching the maximum pressure when $r_{cr} = r_{cr,crit}$ and then a splitting failure occurs. For confined specimens, due to the effect of transversal reinforcement it is evident that the higher is the radial displacement, the more is the radial pressure. This increment is valid until yielding of stirrups.

In Figures 4 and 5 it is shown the bond slip behavior for unconfined and confined specimens

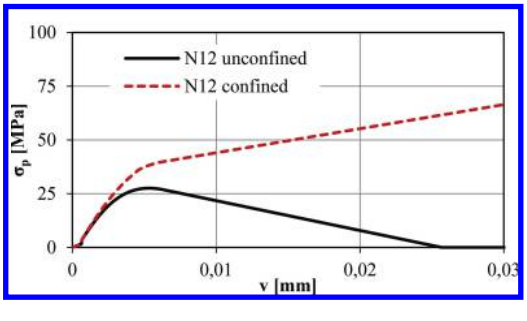

Figure 3. Radial pressure with radial displacement for confided and unconfined RILEM pull-out specimens with 12 mm diameter embedded bar.

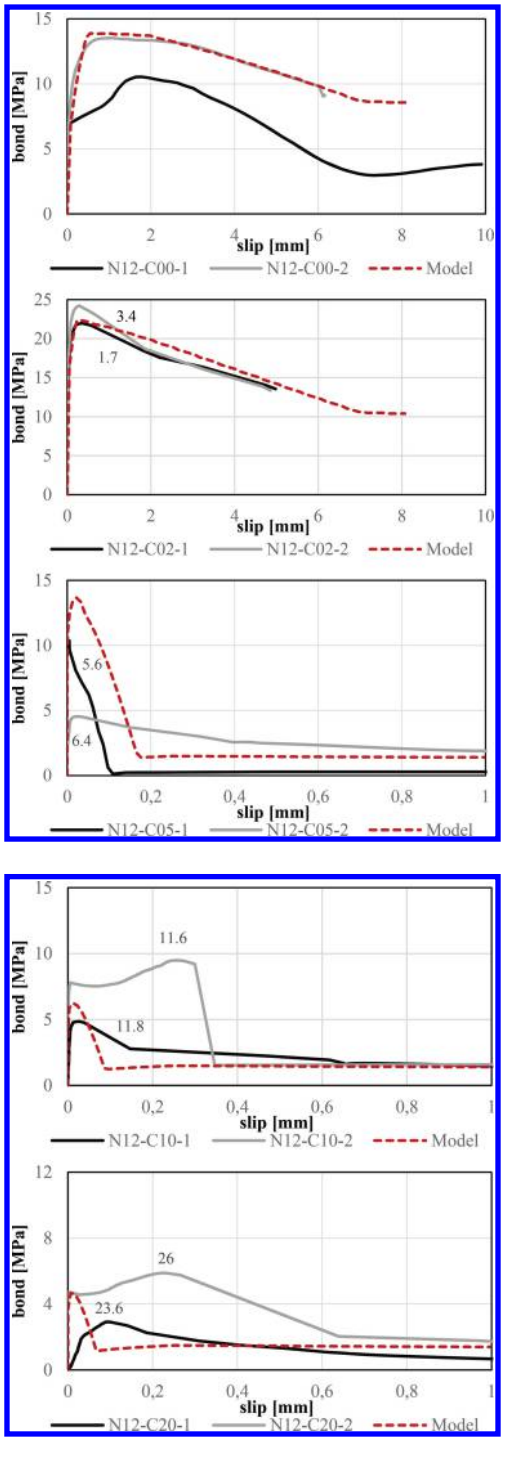

Figure 4. Bond slip curves for unconfined, uncorroded and corroded specimens with different weight loss level. The numbers near the curves indicate real corrosion in terms of weigth loss.

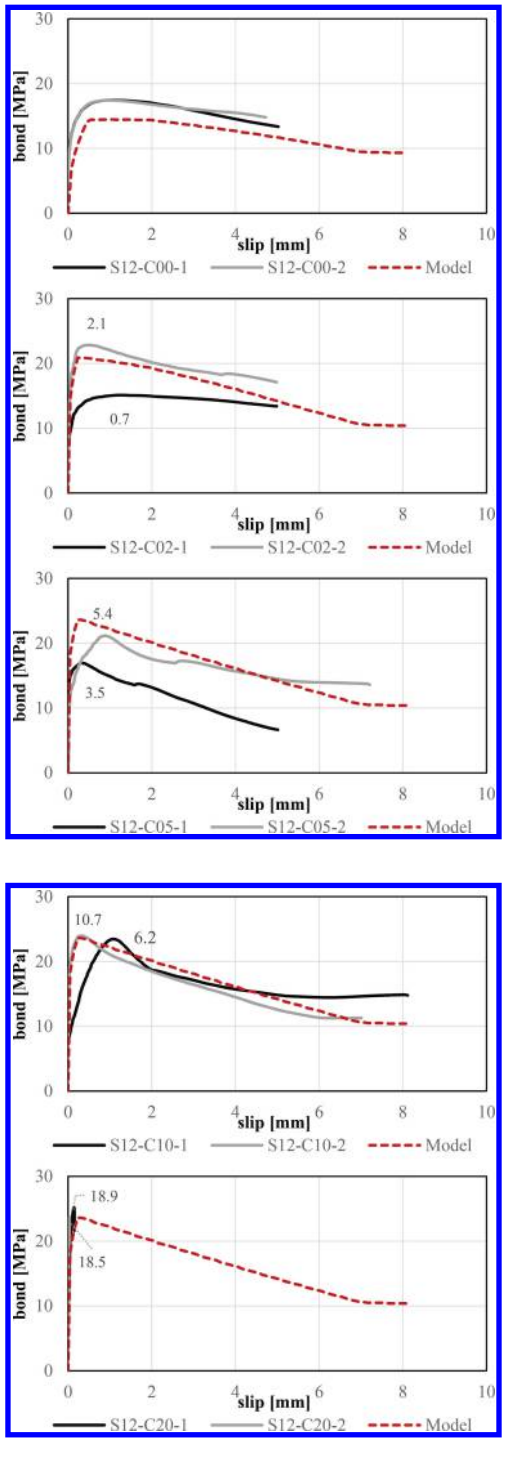

Figure 5. Bond slip curves for confined, uncorroded and corroded specimens with different corrosion levels. The numbers near the curves indicate real corrosion in terms of weigth loss.

respectively; it is possible to observe the model simulation plotted with the dashed line whereas for each level of corrosion, a black and grey experimental curves are reported. Both Figures 4 and 5 present test on specimens corroded for an estimated level equal to 0, 2, 5, 10, 20 percent of mass loss (from top to bottom of Figs. 4 and 5). Actually, the real mass loss, evaluated by means of a gravimetric procedure after the tests, is pictured for each specimen into the graphs on the corresponding curve whereas the simulation of the model refers to the estimated theoretical mass loss. It is evidenced a good agreement between the experimental and numerical curves. As reported in Mancini et al. (2014a) an anomaly can be associated with specimen N12-C00-1 probably due to a poor compaction during casting.

4 CONCLUSIONS

In the present work an analytical model able to simulate the structural behaviour of embedded steel in concrete even in presence of corrosion and transversal confinement is introduced. The model reproduces the structural scheme of pull-out RILEM bond test. It is able to take into account the effect of radial pressure due to: the mechanical action that arises between concrete and the ribs of the bar, the corrosion of the longitudinal bar and the presence of confinement. Local bond-slip relationship is related to a failure criterion in which the maximum bond strength is function of the radial pressure. Pull-out failures and splitting failures can be reproduced. An interaction between the effects of corrosion and bond action is highlighted in terms of radial pressure. This model is used to simulate the experimental results of pull-out specimens characterized by the presence of transversal confinement. The longitudinal bars of the specimens were subjected to a corrosion values ranging between 0% and 20% in terms of mass loss. The model is able to reproduce the increase of bond strength for low values of corrosion if they are unable to already crack the concrete before the bond test. A good agreement can be evidenced for all the corrosion valued both for confined and unconfined specimens. Splitting failures are properly associated to unconfined samples with a minimum values of corrosion starting from 5% whereas for all the others test a pull-out mechanism is reproduced.

REFERENCES

Fang, C., Lundgren K., Chen L. & Zhu C. 2004. Corrosion influence on bond in reinforced concrete. *Cement and Concrete Research* 34, no. 11: 2159–2167.

Fantilli, A.P, Mihashi, H. & Vallini, P. 2007. Crack profile in RC, R/FRCC and R/HPFRCC members in tension. *Materials and Structures* 40: 1099–1114.

fib, 2012. MC2010 fib model code, Bulletin no. 65–66. Lau-sanne (CH), Switzerland.

Lundgren, K. 2002. Modelling the effect of corrosion on bond in reinforced concrete. *Magazine of Concrete Research.* 54(3): 165–173.

Lundgren, K., Kettil, P., Hanjari, K.Z., Shulne, H. & Soto San Roman, A. 2012. Analytical model for the bond-slip behaviour of corroded ribbed reinforcement, *Structural and infrastructure Engineering*, 8(2): 159–169.

Mancini, G., Sabia, D., Pettinato, E. & Tondolo, F. 2014. Pull-out tests in presence of high level of corrosion. In IALCCE Fourth International Symposium on Life-Cycle Civil Engineering, Tokyo.

Mancini, G. & Tondolo, F, 2014. Effect of bond degradation due to corrosion—a literature survey, *Structural Concrete*, 15(3) 408–418.

Noghabai, K. 1998. Effect of tension softening on the performance of concrete structures. *PhD Thesis, Lulea University of Technology, Division of Structural Engineering.*

Ozbolt, J., Orsanic, F. & Balabanic, G. 2014. Modeling pull-out resistance of corroded reinforcement in concrete: Coupled three-dimensional finite element model. *Cement and Concrete Composites* 46: 41–55.

Pantazopoulou, S.J. & Papoulia, K.D. 2001. Modelling cover cracking due to reinforcement corrosion in r.c. structures. *Journal of Engineering Mechanics*. 127(4): 342–351.

Reinhardt, H.W. 1992. Bond of steel to strain-softening concrete taking account of loading rate. *Fracture Mechanics of Concrete Structures*. Elsevier, London: 809–820.

Rilem, 1994. *Recommendations for Testing and Use of Construction materials*.

Rosati, G. & Shumm, C. 1992. Modeling to local bar-to-concrete bond in reinforced concrete beams. *Bond in concrete—from research to practice.* Riga, Latvia, 3(12): 34–43.

Tastani, S.P. & Pantazopoulou, S.J. 2012. Modelling reinforcement-to-concrete bond. *In Bond in Concrete, Fouth International Symposium*, Brescia, Italy.

Van der Veen, C. 1990. Cryogenic bond-slip relationship. *Doctoral thesis, Delft University of Technology, Delft, The Netherlands*.

Concrete Repair, Rehabilitation and Retrofitting IV – Dehn et al. (Eds)
© 2016 Taylor & Francis Group, London, ISBN 978-1-138-02843-2

Pull-out tests on R.C. corroded specimens

A. Cesetti, G. Mancini & F. Tondolo
Department of Structural, Geotechnical and Building Engineering, Politecnico di Torino, Italy

ABSTRACT: The structural behaviour of reinforced concrete structures is strictly related to bond performance between steel and concrete. In the present paper, bond tests on r.c. specimens in presence of corrosion are performed in order to evaluate the damage on bond mechanism due to corrosion. The results of the tests on concrete specimens with RILEM type shape, having side of 120 mm and 160 mm, reinforced with ribbed steel bars with diameter of 12 and 16 mm, respectively with and without confinement, in presence of an increasing level of corrosion up to 20% of estimated mass loss are presented. Corrosion is applied by means of an electrochemical procedure using a current density of 200 μA/cm^2. The test results show the effect of oxidation of the steel at the interface with concrete and the change of performance in terms of bond strength.

1 INTRODUCTION

Corrosion is definitely the most important degradation mechanism for reinforced concrete (r.c.) structures. Even if designed against corrosion attack within the service life, r.c. structures very often remain in service well beyond that time so, except if an accurate maintenance is performed, corrosion is expected to appear at a certain time. Corrosion level is considered a significant parameter for evaluating the structural condition of r.c. structures. In fact, it influences not only the flexural and shear ultimate capacity, ductility and anchorage strength, but also service behaviour in terms of stresses, cracks formation and deformation (Rodriguez et al. 1994). Reinforcement corrosion modifies steel transversal section with a reduction of effective area, concrete integrity by cracking of portions around corroded bar, eventually with spalling and delamination of concrete cover, and finally the interaction between concrete and reinforcement by a bond reduction. On the other side it can be observed that the performance of r.c. structures is deeply associated to bond mechanism (Giordano et al. 2011).

A lot of experimental tests on bond between steel and concrete have been performed in the past using a very high level of current density (higher than 500 μA/cm^2), without transverse confinement and with a medium-low amount of corrosion (lower than 10% of mass loss) that does not provide information for corrosion levels over than 5%.

In order to extend the knowledge about bond in presence of corrosion, tests with a specific setup have been performed: low current density (200 μA/cm^2), confined test specimen with corroded transverse reinforcement, test performed up to a corrosion level of 20% with bar diameters of 12 and 16 mm. At the moment, the first diameter series is completed, whereas some samples of the second series are still under test.

2 PREVIOUS EXPERIMENTAL INVESTIGATIONS

A large amount of bond tests designed to investigate the issue of performance interface between steel and concrete in presence of corrosion is available in literature. Bond tests can be essentially divided into two main categories: beam and pull-out tests. In beam test, the concrete around the tensed bar is in tension, whereas the concrete results to be in compression in the pull-out one. Another classification can be associated with a long or short embedment length related to the value of the bar diameter. It could be assumed as short embedment length a length equal or lower than five bar diameters, whereas a long embedment length is attributed to a length of more than five diameter. It is important to give this distinction because for short embedment length, the average bond strength versus the slip (measured at the free edge of the bar) could be taken as representative of a local bond-slip relationship more than for long embedment length tests. A detailed survey on corrosion tests available in literature can be found in Mancini & Tondolo (2014) and in a previous paper of the same Authors (Mancini et al. 2014).

3 EXPERIMENTAL PROGRAM

3.1 *Test procedure*

Pull-out tests were carried out in order to evaluate bond slip performance for specimens under different corrosion levels. Non corroded specimens

were also tested for comparison purpose. All corroded specimens were subjected to the procedure of electrochemical corrosion: the amount of current density used was equal to 200 μA/cm^2 in line with other experimental tests performed in the past by the same Authors. This current density can be considered as an upper limit for the reliability of electrochemical accelerated corrosion methods (Mancini & Tondolo 2014). The electrical current was applied directly on both longitudinal bars and stirrups for samples were the latter were present. So it was simulated the actual conditions in r.c. structures, where the corrosion definitely affects the outer layer of reinforcement (stirrups) at least as much as the internal (longitudinal bars) one. The experimental procedure was set in the following daily steps: wet-dry cycles in order to ensure a wetness parameter $w_t = 0.75$ (Duracrete, 2000), visual inspection with evaluation and eventually measurement of corrosion crack widths. At the end of this procedure, once an expected amount of corrosion was reached for each specimen, a pull-out test was performed. Moreover, every corroded specimens was demolished in order to extract its reinforcement for a weight procedure in agreement with of G1-90 Standard (2003) and for comparison purpose with theoretical data.

3.2 *Specimens description*

The dimensions of the specimens were in line with pull-out test of RILEM standard (1994) (see Fig. 1). Reinforcement was made of a steel grade B450C. The longitudinal reinforcement had a length of about 500 mm and a 12 mm diameter for the "12 series" whereas the longitudinal reinforcement was a 16 mm diameter with a length of about 800 mm for specimens of "16 series". A common Portland cement type was used; the mix proportions, by weight of cement, sand and gravel were 1:2.6:3.7 with a maximum aggregate size of 14 mm and a water/cement ratio of 0.6. The concrete mix was poured into 120 × 120 × 120 and into 160 × 160 × 160 steel moulds. Eight concrete cubes with side 160 mm and eight cylinders with 150 mm diameter were also casted for testing cubic compression and tensile strength respectively. For all specimens 3% of NaCl by weight of cement was added to the mixture in order to accelerate corrosion process. After two days from casting, the samples were removed from the moulds and placed into water for 28 days. The 28-day cured specimens had an averaged measured strength R_c equal to 30.9 MPa and tensile splitting strength $f_{ct,sp}$ of 3.15 MPa estimated by means of an indirect test method.

In the following, Table 1 lists all the samples tested up to now during the experimental campaign.

The transverse reinforcement was made by closed stirrups with diameter of 8 mm, length equal to 352 mm and spacing of 23 mm for 12 mm bars specimens whereas for bars of 16 mm close stirrups with 8 mm diameter, length of 480 mm and spacing of 50 mm (Fig. 2) were used.

The specimen named SY-CXX-1 was characterized by the presence of transverse reinforcement (S in spite of N, that means no transverse

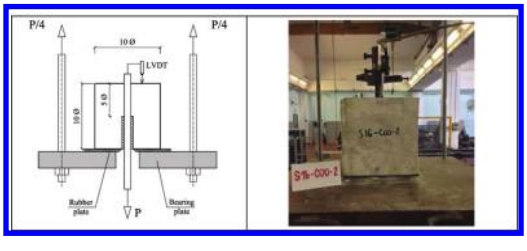

Figure 1. Overview of the specimen and testing machine.

Table 1. Samples of the experimental campaign.

Label	Transv Reinforce	Expected* Corrosion [%]	Measured* Corrosion [%]
N12-C00-1	No	0	–
N12-C00-2	No	0	–
N12-C02-1	No	2	1.7
N12-C02-2	No	2	3.4
N12-C05-1	No	5	5.6
N12-C05-2	No	5	6.4
N12-C10-1	No	10	11.8
N12-C10-2	No	10	11.6
N12-C20-1	No	20	23.6
N12-C20-2	No	20	26.0
S12-C00-1	Yes	0	–
S12-C00-2	Yes	0	–
S12-C02-1	Yes	2	0.7
S12-C02-2	Yes	2	2.1
S12-C05-1	Yes	5	3.4
S12-C05-2	Yes	5	5.4
S12-C10-1	Yes	10	6.2
S12-C10-2	Yes	10	10.7
S12-C20-1	Yes	20	18.9
S12-C20-2	Yes	20	18.5
N16-C00-1	No	0	**
N16-C00-2	No	0	**
N16-C02-1	No	2	**
N16-C02-2	No	2	**
N16-C05-1	No	5	**
S16-C00-1	Yes	0	**
S16-C00-2	Yes	0	**
S16-C02-2	Yes	2	**
S16-C05-2	Yes	5	**

*Mass reduction; **not yet measured.

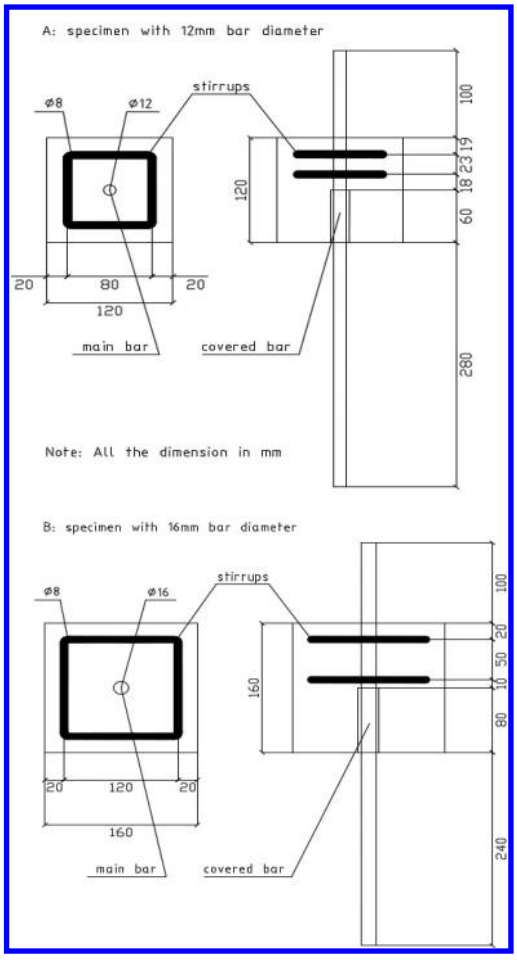

Figure 2. Detailed specimens geometry.

reinforcement), Y that corresponds to the bar diameter (12 or 16 mm) theoretical level of corrosion of XX% and it was the first sample of this type (suffix 1). In fact it was designed to have at least two specimen for each setting for comparison purpose. At time of drafting not all the specimens were tested and therefore Table 1 is not complete with all the 40 specimens; and for some tested sample the actual corrosion is not referred. As evident from Figures 1, 2, the bonded length was 5 times the bar diameter. The remaining part of bar inside the specimen was covered with plastic sleeve. Before casting, wooden spacers were used in order to give rigidity to the transverse reinforcement and ensure the proper stirrup spacing. Concrete cover was ensured through wooden sticks (see Fig. 3), of length equal to specimen side, placed on the reinforcement with cables ties. After the positioning of the sticks, the initial wooden spacers were removed.

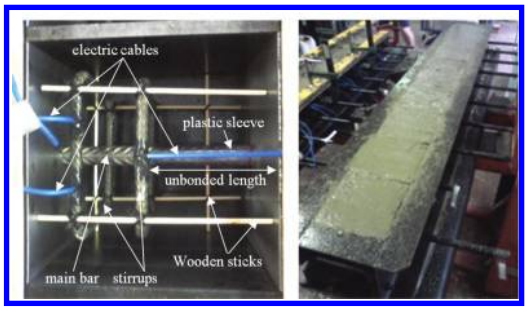

Figure 3. Reinforcement, wooded sticks and electrical connections in the formwork and casting.

The electric cables were linked to transverse and longitudinal reinforcement: they connected electrically reinforcement and ensured the proper concrete cover in the vertical plane through steel clamps (see Fig. 3).

3.3 *Accelerated corrosion method*

The accelerated corrosion process was obtained through the application of direct current on both the longitudinal bar and the stirrups (anodes) within the specimen through electrical cables fixed to the reinforcement before casting (see Fig. 3). The specimens were subjected to a current density of 200 μA/cm^2 (Fig. 4). The cathode was a stainless steel wool, fixed on a fabric that covered all the faces of the specimen (Fig. 5); it was positioned along the bonded length of the specimen.

The fabric had a double function: it kept the moisture preventing a rapid evaporation of the water used for wetting and ensured the contact between the stainless steel wool and the surface of the specimen.

The specimens, coated by the cathode, were placed inside plastic containers, were covered with a plastic top and subjected to wet and drying cycles (Fig. 5).

In order to obtain a specific value of corrosion in terms of mass loss, a prediction formula was used. Starting from Faraday's law, it is possible to obtain the time needed to reach a desired level of mass loss through the application of a current I:

$$\Delta m = \frac{M \cdot I \cdot t}{z \cdot F} \tag{1}$$

where Δm is the consumed mass of iron (in grams), M is the atomic weight of the metal (56 g for the Fe), I is the current intensity (in Ampere), t is the time (in seconds), z is the valence (2) that is the number of electrons that the iron brings into play in the redox

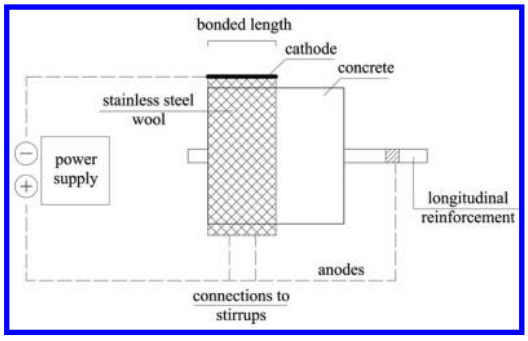

Figure 4. Scheme of corrosion for a confined specimen.

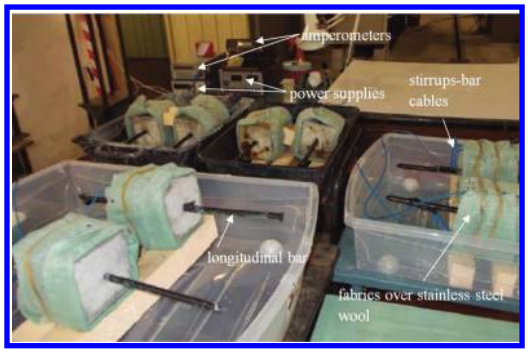

Figure 5. Accelerated corrosion system.

process, F is the Faraday constant (96500 A·s). The current intensity to use I(A) is obtained by multiplying the current density (200 μA/cm^2 max allowable value, as discussed in Mancini & Tondolo, 2014) for the lateral surface of the anodes. The initial mass of the reinforcement is calculated as the product of the mass density ρ of the iron, equal to 7.85 g/cm^3, and the volume of the same reinforcement. The different levels of corrosion are referred only to the longitudinal bar: for the given Cxx level of corrosion, so specimen with stirrups must be subjected to a time of corrosion equal to that of the specimen without stirrups. Comparison between theoretical and actual degree of corrosion can be obtained after bar weight procedure.

3.4 *Pull-out tests*

The pull-out test, in line with RILEM-recommendation, was used to determine bond efficiency. Each test was conducted under displacement control with a rate of 0.2 mm/min using a Baldwin universal testing machine with capacity of 500 kN. The relative displacement between steel and concrete was measured up to bond failure at the unloaded end. In Figure 1 both a scheme of the pull-out test and a picture of specimen S16-C00–2 are shown.

4 TEST RESULTS AND DISCUSSION

In order to study the bond between bar and concrete in presence of corrosion, the following issues are analysed:

- bond stress-slip curve and in particular maximum bond strength with different level of corrosion;
- effect of confinement on bond performance;
- comparison between theoretical and actual degree of corrosion.

The pull-out test for every specimen gives the relation τ-s (see Fig. 6) where "s" is the slip measured under the tensile force T and τ_m is the average bond stress calculated by means of the following expression:

$$\tau_m = \frac{T}{\pi \cdot \phi \cdot l_{emb}} \tag{2}$$

where l_{emb} is the embedment length and ϕ is bar diameter.

For every type of specimen, two samples were tested, except that for specimens N16-C05 and S16-C10 and for all the specimens of 16 series with 10% and 20% of corrosion, because they were not yet ready for test.

The average bond strength of uncorroded specimens of series 12 mm (Fig. 6a) was approximately equal to 17.4 MPa in presence of transverse confinement, whereas it was 12.0 MPa for specimens without stirrups. It can be observed from Figure 6a that up to 5 mm of slip only a slight reduction of bond strength is perceivable, showing a presence of ductile behaviour even if the maximum bond strength was registered for about 1 mm of slip.

In Figure 6b the results of four test in presence of estimated 2% corrosion are reported. Except for specimen S12-C02-1, that shows a marked difference in bond efficiency if compared to the uncorroded confined tests and to S12-C02-2, the other samples reveal an increase of bond strength with also a rise in terms of stiffness; the latter effect is evident from the reduced value of slip corresponding to the maximum bond strength (0.3 mm). Moreover the increase in bond strength is even more evident for specimen without stirrups than in the confined specimen. The increase of bond strength was described in previous experimental researches and summarized in fib Bulletin n°10 (2001). The reduction of bond stresses after the peak load with increasing slip is more evident for the uncorroded specimens; that is with increasing

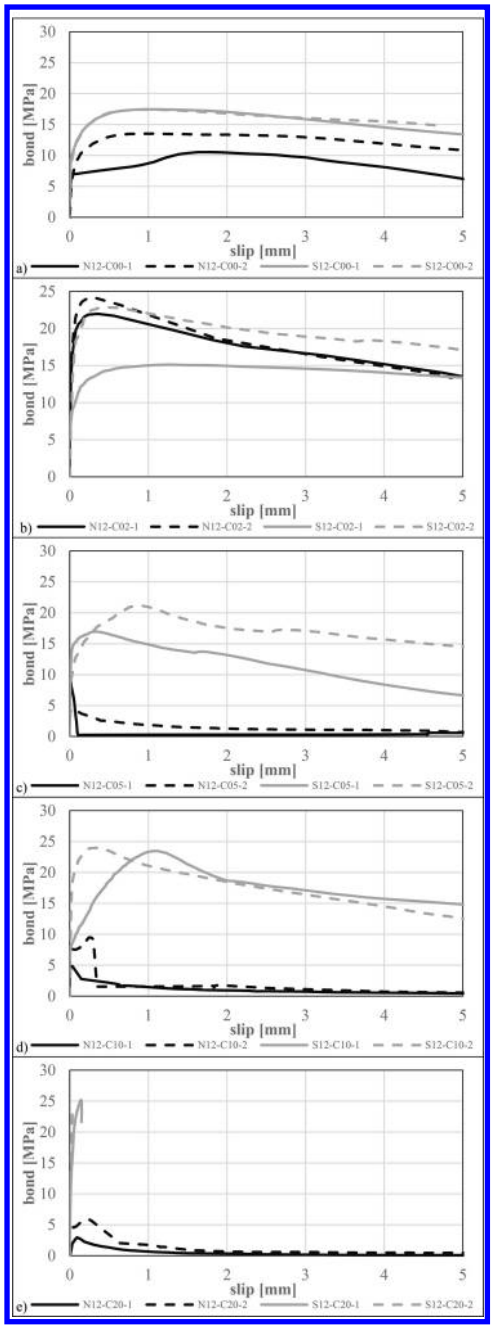

Figure 6. Bond slip curves for N/S12 series.

slip, unconfined specimens tend to reduce their bond stress in a more pronounced way then the confined specimens.

The reason for that, for unconfined specimens, is the absence of stirrups able to prevent a rapid decrease of bond. The anomalous behaviour for specimen N12-C02-1, if compared to N12-C02-2, could be explained by a low level of actual corrosion (see Table 1). The bond strength of the specimen S12-C02-2 with an expected corrosion level of 2% was 23.5 MPa for confined specimens and equal to 23.1 MPa for unconfined specimens.

The confined specimen with corrosion level 5% (Fig. 6c) had a bond strength of 19.0 MPa whereas the bond strength of specimen without stirrups was 7.4 MPa with a rapid decay of the curve due to the splitting failure. With this level of corrosion an important decay of bond efficiency is registered for unconfined specimens. This is practically due to the presence of internal and external cracks caused by corrosion, that drastically reduces the bond capacity of the specimens.

Finally, the test results with 0 to 5% of corrosion suggest that initially bond strength, due to the increase of lateral pressure exerted by the rust along the embedment length, takes advantages from it, but when corrosion level exceeds a certain value (2%) bond strength becomes smaller for unconfined specimens, by effect of the presence of longitudinal cracks caused by corrosion before the bond test.

In Figure 7 some results for specimens with 16 mm diameter bar are reported. It is evident for confined specimens the increase in bond strength efficiency associated with the progressive attack penetration (assuming theoretical values of corrosion). The unconfined specimens with 0% of corrosion show a very high value of bond strength, being the average value even higher than the average value for confined uncorroded specimens. For unconfined samples with 2% of corrosion, the splitting failure is obtained during the bond tests but they were already cracked before the bond test; they reached an average bond strength of 16.5 MPa. Another reduction of bond strength is again registered for 5% of theoretical corrosion; its value was about 8.1 MPa. Again, corrosion cracks were present before the test. For specimen actual conditions before the bond test see Figure 8.

The analysis of the two series (12 and 16 mm) reveals some similarities and also some differences in terms of structural behaviour. For both series, considering confined specimens, an increase of bond efficiency with corrosion is registered. On the other hand for series of 12 mm the bond strength for unconfined specimens for 2% of mass loss reveals an increase of bond strength and only at 5% the splitting failure is observed with a corresponding drop of bond strength; for series of 16 mm the increment at 2% is not observed, because the confinement exerted by the surrounding concrete (size effect) determined a higher value of confinement but also the appearance of stresses able to

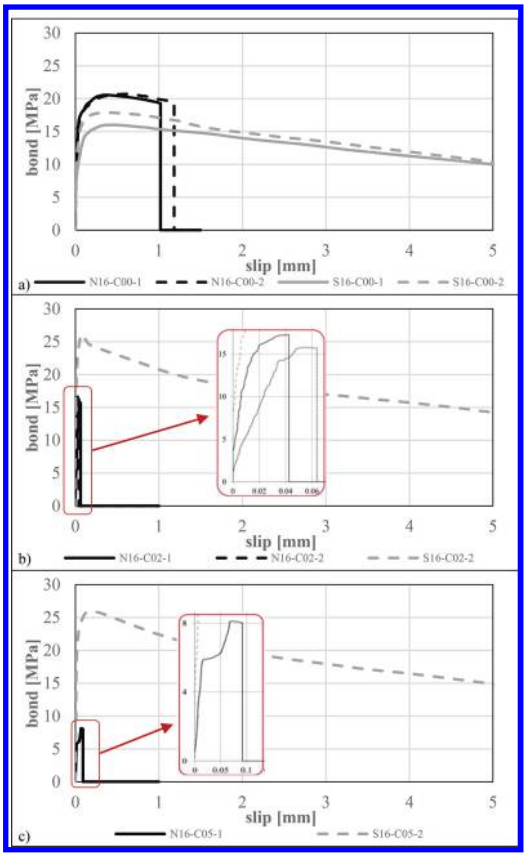

Figure 7. Bond slip curves for N/S16 series.

Figure 8. N16-C05-1 specimen after corrosion process.

reach the tensile strength and to produce splitting failure.

In Figure 8 two pictures of the specimen N16-C05-1 after the corrosion process and before the mechanical test are reported. Crack pattern visible on the surface and in particular along the rebar is very similar to that caused by splitting tensile stresses generated by bond; therefore, as described earlier, after a certain amount of corrosion, bond strength is directly reduced because cracking around the main bar is achieved earlier. Once the confining effect of the concrete is lost, there is a sudden collapse. One can be see for almost all the corroded specimens that bond strength is lower than that registered for the corresponding uncorroded specimen and it corresponds to a lower value of slip, this is due to a more stiff connection between steel and concrete caused by rust pressure effect.

The comparison between designed and measured corrosion level for longitudinal and transverse reinforcement was computed using the results of the gravimetric procedure ASTM G1-03 (2003) and comparing the final weight with the one before the test (Table 1). Predicted corrosion percentage of longitudinal bar was estimated to be reached in not confined specimens; it was obtained nevertheless the technical difficulties in measurement of very small mass variations. Actual corrosion effectiveness of longitudinal bar in confined specimens was not equal to the predicted one. Besides, stirrups reached higher corrosion levels than estimated percentages.

Unlike not confined specimens, those with transverse reinforcement already show a considerable crack pattern and rust stains at corrosion level 5%. Taking into account of low corrosion percentage, superficial rust in confined specimens is mainly due to stirrups because of their proximity to the specimen surface. Both confined and unconfined specimen types do not show delamination of concrete cover during the corrosion phase.

Unconfined specimens with 5, 10 and 20% of induced corrosion reveal longitudinal cracks that become wider during the pull-out test. This demonstrates the correlation between cracks due to corrosion and the weakening of bond transmission mechanism between steel and concrete.

5 CONCLUSIONS

In this paper bond between steel and concrete in presence of corrosion is analysed in terms of local bond-slip behaviour, by means of pull-out tests of specimen according to RILEM (1994). The experimental campaign considered both unconfined (typical Rilem configuration) and confined specimens with two closed stirrups placed along the embedment length. Two different series of specimen with bar diameter of 12 and 16 mm respectively were tested. The results of some samples of the series 16 mm are not yet available. The whole experimental campaign considers specimens with a corrosion level from 0 to 20% of bar mass loss. The corroded specimens were previously subjected to corrosion (both longitudinal bar and stirrups) up to the expected corrosion level and then subsequently mechanically tested. The electrochemical corrosion method used a relatively low level of

current density (200 μA/cm^2) so to obtain reliable data for application on real structures. The results demonstrate an important influence of the level of corrosion and in particular the key role played by the presence of stirrups for both the maximum bond strength and the global bond-slip response.

In absence of confinement exerted by stirrups, up to 2% of corrosion, an increase of bond efficiency is registered for specimens with 12 mm diameter whereas a progressive reduction of bond strength is highlighted for series of 16 mm for increasing corrosion levels. However, even for series 12 mm, a sudden reduction is measured when 5% of corrosion is reached and a reduced bond strength is evidenced. This trend is confirmed for corrosion levels of 10 and 20% of mass loss. The reduction of bond strength is obviously associated to the longitudinal crack formation due to both corrosion and splitting effect caused by the mechanical action of bond. Therefore two situations can be observed respect to the longitudinal crack in corroded specimens: it was not formed (N12-C02-1/2) both before and during the test so corrosion increases bond efficiency and then pull-out failure occurred; it was formed before the test because of corrosion and then only a residual strength is available (all the other specimens).

Confined specimens of series 12 mm showed a progressive rise of bond efficiency with increasing level of corrosion. On the other hand, the series 16 mm appears to be more sensitive to the presence of corrosion since 2% of corrosion, showing an important gain in bond efficiency that remained constant for 5% of corrosion.

REFERENCES

ASTM G1-03. 2003. Standard practice for preparing, cleaning, and evaluating corrosion test specimens.

Duracrete R4-5, 1998. Modelling of Degradation BE95-1347/R4-5, December 1998. The European Union-Brite EuRam III, DuraCrete-Probabilistic Performance Based Durability Design of Concrete Structures, CUR, Gouda.

fib 2001. Bulletin n°10, Bond of reinforcement in concrete. Lausanne (CH), Switzerland.

fib, 2012. MC2010 fib model code, Bulletin no. 65–66. Lausanne (CH), Switzerland.

Giordano, L., Mancini, G. & Tondolo, F. 2011. Reinforced concrete members subjected to cyclic tension and corrosion. *Journal of Advanced Concrete Technology*, 9(3), 227–285.

Mancini, G. & Tondolo, F. 2014. Effect of bond degradation due to corrosion—a literature survey, *Structural Concrete*, 15(3) 408–418.

Mancini, G., Sabia, D., Pettinato, E. & Tondolo, F. 2014. Pull-out tests in presence of high level of corrosion. *In IALCCE Fourth International Symposium on Life-Cycle Civil Engineering*, Tokyo.

RILEM 1994. Recommendations for the Testing and Use of Constructions Materials.

Rodriguez, J., Ortega, L.M. & Casal J. 1994. Corrosion of reinforcing bars and service life of concrete structures: corrosion and bond deterioration. *International Conference "Concrete across borders"*, Denmark.

Concrete Repair, Rehabilitation and Retrofitting IV – Dehn et al. (Eds)
© 2016 Taylor & Francis Group, London, ISBN 978-1-138-02843-2

Corrosion resistance of BS 8500 compliant concretes

C. Christodoulou & D. Dunne
AECOM Ltd., Colmore Circus Queensway, Birmingham, UK

C.I. Goodier
School of Civil and Building Engineering, Loughborough University, Loughborough, UK

R. Yea
Kier Construction, UK

ABSTRACT: Corrosion of steel reinforcement in concrete, due to the ingress of chloride ions, is the most significant form of concrete deterioration. Fresh concrete however, provides a highly alkaline environment which facilitates a protective passive oxide layer around the steel reinforcement. Modern engineering standards provide guidance to designers on the specification of concrete mixes to meet a prescribed design life. More than one cement blend may however be available to meet the specific design life for a particular exposure classification, which can occasionally lead to confusion. This work investigated the corrosion resistance of BS 8500 compliant cement combinations for a XS3 environmental exposure in order to identify relative durability performance differences. The concretes investigated contained Portland Cement (PC), Fly Ash (FA) and Ground Granulated Blastfurnace Slag (GGBS). FA and GGBS were blended in binary combinations with the PC, at levels of 28% and 51% respectively. Two water/cement (w/c) ratios of 0.35 and 0.40 were investigated, together with total cementitious contents of 380 kg/m^3, representing typical structural reinforced concrete. Specimens were cyclically exposed to a saline solution and tested for compressive strength, electrochemical potential, resistivity, and chloride ion content with depth.

1 INTRODUCTION

Corrosion of reinforcement is the most common cause of deterioration. Modern design standards aim to overcome this by means of prescribed controls such as minimum cementitious content, minimum cover, maximum water/cement ratio etc (British Standards 2006). This is generally known as a "deemed-to-satisfy approach" and assumes that the concrete composition selected will result in the desired service life (Gulikers 2014). However, such an approach is not taking adequately into consideration the significantly different performance of cementitious binders, which will ultimately control the time to onset of corrosion.

However, the ultimate choice of concrete mix design lies with the designer, who may be unfamiliar with the effect of the numerous variables which will influence the overall durability performance of the final product. Furthermore, there is a common misconception that a greater cementitious content will result in significant improvements in concrete durability as a result of a potentially greater cementitious binder capability. However, this is not rigorously proven. In fact, significant increases in cementitious content may result in thermal cracking and early age shrinkage, which will therefore reduce durability.

In addition, it is widely accepted that increasing the depth of cover provided to the reinforcement would have a beneficial effect to durability. It is not uncommon to identify cover levels of 100 mm or more in major bridge construction projects in order to achieve a service life of 120 years. However, there is usually little consideration to structural effects and stress distribution within the members, as an increase in cover in a region of high tensile stresses, may result in structural cracking.

Furthermore, the significance of the transport mechanism of ions such as chlorides is often overlooked. In fact, modern durability analysis is based on the application of mathematical modelling based on probabilistic approaches (e.g. fib 2010, Concrete Society 2004). These models are based primarily on Fick's 2nd law of diffusion, incorporating empirical factors to improve mathematical and laboratory result fitting. However, it is commonly overlooked that the primary mode of transport of external chlorides ions into concrete, is sorption, which is achieved by means of capillary suction (Christodoulou et al. 2013, Ungricht 2004).

Table 1. Permissible mix design combinations to BS8500 for XS3.

Allowable cement type	Min. cover (mm)	Max. w/c ratio	Min. cementitious content (kg/m^3)
CEM I/IIAIIB-S	55	0.35	380
CEM I/IIAIIB-S	65	0.4	380
CEM IIB-V/IIIA	45	0.35	380

Therefore, it is often the case—in particular for ordinary structures such as typical highway crossings—that the structural designer, who is also responsible for the selection of the concrete mix design, is presented with the option of a number of concrete mix designs conforming to the design standard requirements and are all "deemed to satisfy" the intended design life.

With particular reference to BS 8500 (British Standards Institution 2006), based on a design life of 100 years and an XS3 environmental exposure class (i.e. tidal, splash and spray zones), which is generally considered to be the most significant regarding durability, the following permissible mix design combinations are shown in Table 1.

Theoretically, all of the above design combinations, have a similar durability performance, despite the fact that there are infinite resultant concrete mix designs combinations due to the inclusion of secondary cementitious materials in various percentages.

The aim of this research was to undertake preliminary research on the performance of resultant concrete mix designs from the above three main design categories for an XS3 environmental exposure class, in order to establish whether there were any differences in their performance. The results of this study would assist in producing guidance notes to designers of reinforced concrete structures.

2 METHODOLOGY

The following sections provide a summary of the mix designs, specimen preparation and testing procedures used on this study.

2.1 *Concrete mix designs*

Based on the permissible design combinations, CEM I (Portland cement), CEM IIB-V (Portland cement with 21% to 35% fly ash) and CEM IIIA (Portland cement with 36% to 65% GGBS) were investigated. For the binary concrete mix designs (i.e. CEM IIB-V and CEM IIIA), the average allowable percentage of cement replacement material was used.

As the minimum concrete cover of CEM I is higher than that of the binary blends, an additional CEM I mix design with a similar minimum cover depth to CEM IIB-V and CEM IIIA was also investigated. Table 2 provides a summary of the concrete mix designs used for this research programme.

2.2 *Specimens*

For each concrete mix design, two slabs with dimensions of 300 mm wide by 500 mm long and 125 mm deep were cast, together with 6 Nr 100 mm^3 cubes. Each slab contained 2 Nr 16 mm diameter, 480 mm long ribbed reinforcing main bars, which were interconnected by 2 Nr 6 mm diameter, 295 mm long smooth transversely placed reinforcing bars (Fig. 1).

2.3 *Conditioning*

The slabs were air cured for a period of 28 days. Following this initial conditioning, they all underwent a

Table 2. Concrete mix designs.

Mix reference	Min. cover (mm)	Max. w/c ratio	Min. cementitious content	Cement replacement
CEM I (65)	65	0.4	380	N/A
CEM I (45)	45	0.4	380	N/A
CEM IIB-V (45)	45	0.35	380	28% PFA
CEM IIIA (45)	45	0.35	380	51% GGBS

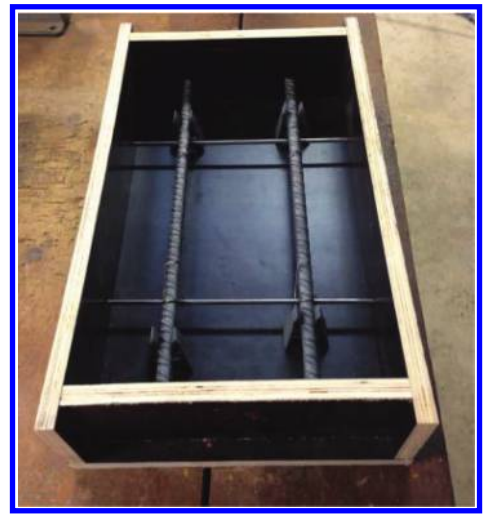

Figure 1. Typical slab arrangement.

cyclic dry and wet conditioning which aimed to replicate XS3 environmental exposure conditions. The samples were wetted with an aqueous solution of 3.5% salinity using laboratory grade sodium chloride for a period of 3 days and then allowed to air-dry within the laboratory (i.e. shielded from external environmental conditions) for 4 days. This procedure was followed over a total period of 125 days.

2.4 *Testing*

The following section provides a summary of the testing methodology employed, to determine both physical and durability characteristics.

2.4.1 *Compressive strength*

The compressive strength is a simple destructive test, where a concrete cube or cylinder is crushed under pressure to obtain a compressive strength in N/mm^2 or MPa. In the UK, this testing technique is prescribed within BS12390-3:2009. The compressive strength tests were carried out at ages of 7 days and 28 days, and also at the end of the testing programme.

2.4.2 *Electrochemical potential*

Electrochemical potential is a numeric value obtained from the potential difference generated between an anode and cathode in a corrosion cell (ASTM 2009, Concrete Society 2004, Elsener 2001, Elsener 2003, Stratful 1957). It is a long established technique with typical ranges of steel potentials for various conditions against different types of reference electrodes widely available in the public domain (DMRB 1990, Elsener 2003).

2.4.3 *Surface resistivity*

Resistivity is a 'geometrically independent property' (Hornbostel et al. 2013) that expresses the freedom for which ions can transport through the pore matrix of a concrete mass (Osterminski et al. 2012). The 4-point Wenner probe is one non-destructive, electrochemical method of ascertaining the resistivity for a mass of reinforced concrete (Polder et al. 2000, Goodier et al. 2015). The instrument functions by applying a known electrical current between the outer electrodes, with the two inner electrodes measuring the drop in voltage experienced (Berkeley and Pathmanaban 1990, Polder et al. 2000, Bertolini et al. 2004).

2.4.4 *Chloride profiles*

This particular test allows the establishment of a concentration profile for a body of concrete that has been subjected to an environment containing chloride ions. Concrete dust samples were obtained by drilling of the specimens. Chloride contents are normally expressed as a 'percentage of chloride ion by mass of dried sample' (Concrete Society, 2004). The methodology for this test is prescribed by BS EN 14629 (British Standards Institution 2007), with further technical guidance provided by Technical Report No. 60 (Concrete Society 2004).

3 RESULTS

This section describes the findings obtained from the monitoring of the specimens over a period of 125 days.

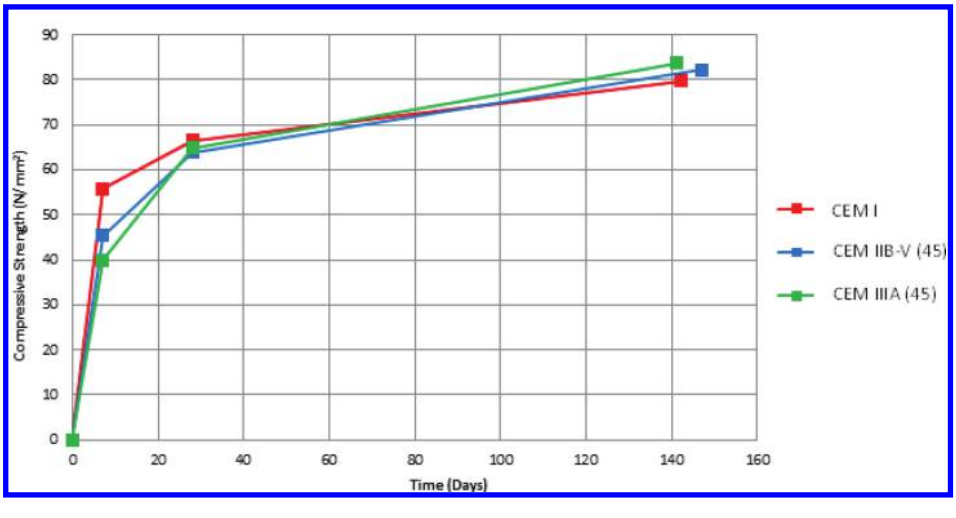

Figure 2. Compressive strength development over time.

3.1 *Compressive strength*

Compressive strength testing was undertaken on three sets of cubes for each mix design at 7, 28 and 125 days, and the results are shown in Figure 2. The generic trends exhibited by each concrete are as would be expected, with an initially rapid increase in compressive strength in all cases up to 7 days, especially for the CEM 1 mix design. The rate of compressive strength development then reduces up to 28 days and continues to reduce up to the end of the testing period.

More specifically though, it can be observed that the evolution of compressive strength for CEM IIIA (45) is the lowest both at 7 and 28 days with CEM I being the highest, as the former have the lowest amount of Portland cement. However, at 140 days this has reversed, suggesting that the rate of hydration curing of CEM III A has continued, after initial strength gain, at a faster rate than the other mix designs. This is may be attributed to a prolonged period of moist curing.

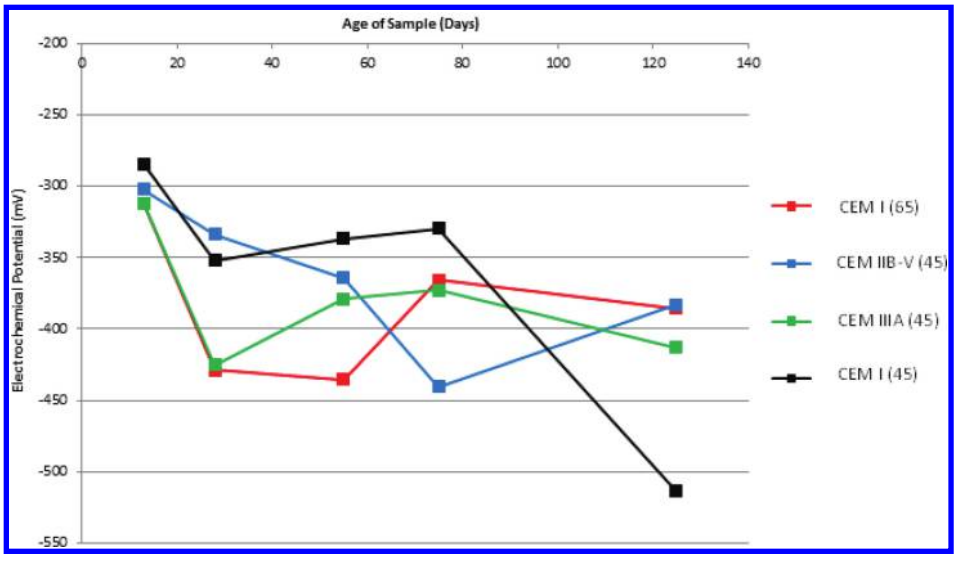

Figure 3. Potential evolution over 125 days.

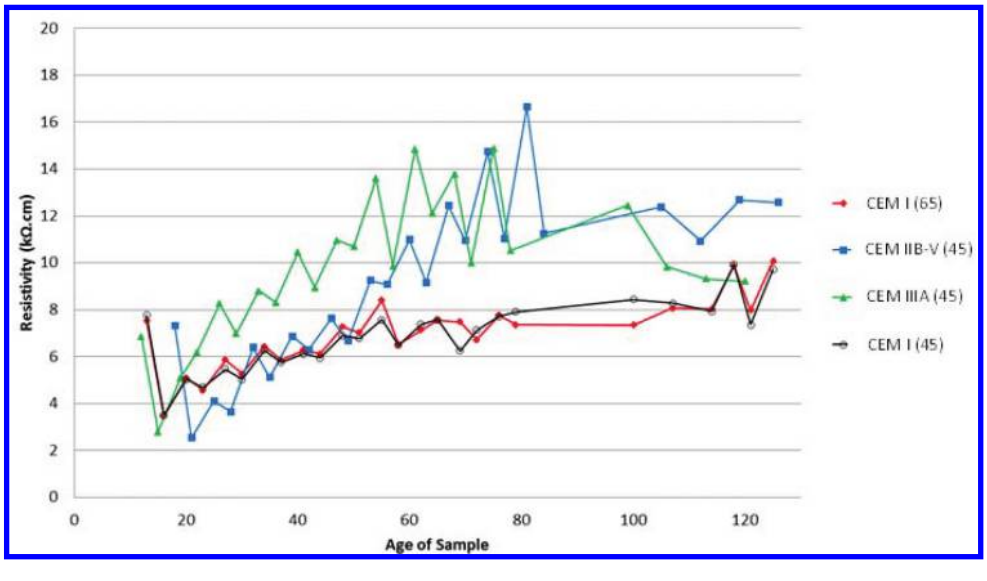

Figure 4. Resistivity evolution over 125 days.

3.2 *Electrochemical potential*

Figure 3, provides an overview of the steel potential against a silver/silver chloride electrode (Ag/AgCl) over a period of 125 days. It can be observed that in all cases there was a decline in potentials after the first exposure cycle. Most notably, the non-compliant CEM I (45) concrete exhibited a significant drop in potential at 125 days. This suggests that corrosion of the steel reinforcement may have initiated.

3.3 *Resistivity*

The evolution of resistivity over time is illustrated in Figure 4. On initial inspection, it appears that the resistivity of each concrete develops at a different rate. However, on closer review it appears that the development of resistivity of the CEM I slabs is as expected very similar.

The development of resistivity was also very similar for the CEM IIB-V and CEM IIIA concretes, which contained pozzolanic material.

The resistivity fluctuations observed are associated with readings at the start of the drying cycle following a wet one, and the end of the drying cycle.

Table 3. Corrosion risk based on surface resistivity (Concrete Society 2004).

Surface resistivity	Corrosion risk
>20 kΩcm	Low
10–20 kΩcm	Low to moderate
5–10 kΩcm	High
<5 kΩcm	Very high

However, overall resistivity has slowly increased for all concrete mix designs. Nevertheless, all readings remained at relatively low levels, normally associated with high to moderate risk of corrosion (Table 3), which may be attributed to elevated levels of chlorides at the surface of the concrete.

3.4 *Chloride profiles*

Figure 5 illustrates the results of chloride profiles based on drillings undertaken on 25 mm increments. It can be observed that, generally, all concretes exhibited relatively high chloride concentrations at the depth of reinforcement after 125 days. It is noted that there is significant variation in the chloride content of the two CEM I concretes, highlighting the inherent variability of this test method.

4 DISCUSSION

The long term durability of the available mix designs is an important consideration, as it will allow the designer to choose a blend of concrete based on the overall risk and susceptibility of a structure to XS3 environmental conditions.

The electrochemical potentials for all the mix designs have been depressed with time. This is likely to be the result of a large increase in moisture content, as strong capillary suction has drawn the additional moisture into the pore matrices of the samples. This would increase the conductivity of the electrolyte within the cover zone, allowing for an increase in corrosion intensity and a reduction in IR drop.

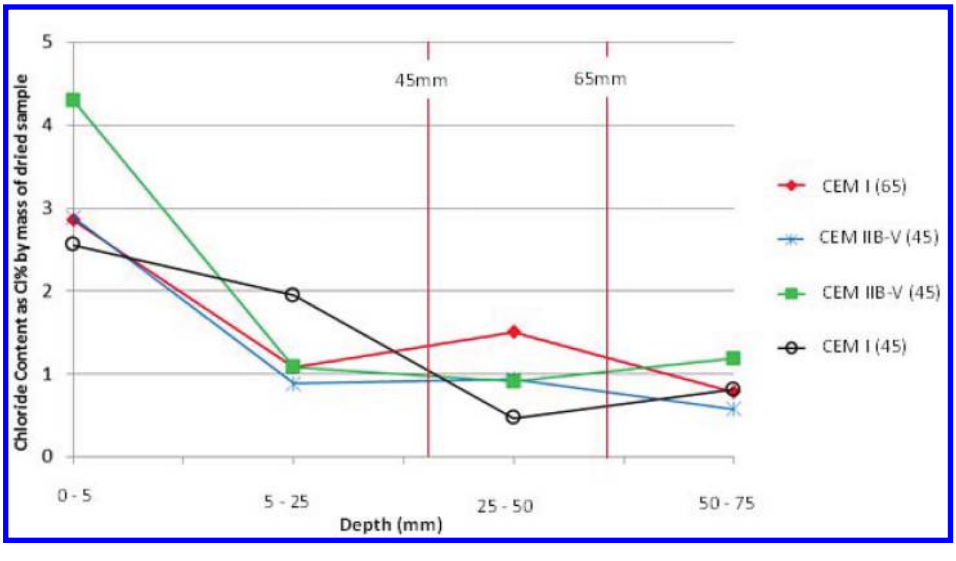

Figure 5. Chloride profiles.

It is noted that all of the electrochemical potential values for the duration of the testing remained mainly at absolute values less than –350 mV and in accordance to ASTM C-876 (ASTM 2006), suggesting that there is a 90% chance that corrosion is active in each of the concretes. However, this effect can be attributed to the significant increase in moisture which results in depressed potentials. However, the CEM I (45) mix design, which is not compliant in terms of cover to BS 8500 (British Standards Institution 2006), exhibited a steep decline in potentials at approximately 75 days, suggesting that electrochemical activity (i.e. corrosion) was taking place.

The development of resistivity appeared to be slower for CEM IIB-V (45) than the other mix designs, but increased over time, resulting in the highest resistivity overall. It is postulated that this is due to the slower pozzolanic reaction as a result of the addition of PFA and the occupation of pores with the latent production of C-S-H l. This is also exhibited by the CEM IIIA (45) mix.

Another observation is that the evolution of resistivity of CEM IIBV (45) behaves in a similar manner to CEM I (65) up until approximately 50 days. From there it diverges, and an increased rate of resistivity is observed which may be synonymous with the 'incubation period'. This infers that it has taken approximately 50 days for the pH level within CEM IIBV (45) to develop to a level where dissolution of the PFA particles may commence, and the pozzolanic reaction of these may take effect.

CEM IIIA (45) exhibited a greater increase in resistivity than CEM IIBV (45) despite the fact that it also contained pozzolanic material. It is possible that, for this to occur, the development of pH for CEM IIIA (45) has been much quicker than CEM IIB-V (45). This is in line with the findings of Glass et al. (1991) and Polder (2012).

The chloride profiles for all concretes gave mixed results, without very distinctive trends. It was observed though, that CEM I (45) had a significantly different performance than the CEM I (65) mix design at the 25–50 mm and 50–75 mm, suggesting that there may have been issues either with the production and casting of the specimens, the concrete dust sampling, or the chemical analysis.

These chloride profiles suggest however, that the conditioning methodology has presented a highly aggressive environment, given the very high level of chloride concentration even at depths of 50–75 mm.

Overall, the results of the monitoring have not yet given strong evidence which of the CEM I (65), CEM IIB-V (45) or CEM IIIA (45) offered greater durability performance characteristics. It is postulated that this is due to the fact that the specimens have thus far undergone only 9 wetting and drying cycles (i.e. 125 days) and therefore are considered to still be of a relatively young age. The conditioning cycle will be continued until all concretes demonstrate active corrosion activity by means of concrete cracking.

However, the results of the potential mapping have provided an early indication that for the CEM I (45) corrosion activity may be taking place only after 125 days of testing.

5 CONCLUSIONS

To date, the research has not yielded tangible evidence to determine which of the complaint CEM I (65), CEM IIB-V (45), CEM IIIA (45) concretes offers the best durability performance. This may be expected as design standards consider that these mix designs provide a similar level of durability. However, it is noted that the potential mapping for the non-compliant CEM I (45) mix design has given early evidence that corrosion activity may have initiated.

The resistivity of all mix designs has increased slowly over time; however, it remained low. Of particular interest was the fact that the resistivity development of CEM IIB-V and CEM IIIA was similar to CEM I for the first 50 days. However, the former exhibited a greater rate of resistivity increase following this initial period, which is attributed to the "incubation period" of the pozzolanic material, as CEM IIIA is latent hydraulic.

REFERENCES

ASTM 2009, Standard Test Method for Corrosion Potentials of Uncoated Reinforcing Steel in Concrete, American Society for Testing and Materials, West Conshohocken, Pennsylvania, USA.

Berkeley K.G.C. and Pathmanaban S. 1990, Cathodic Protection of Reinforcement Steel in Concrete. 1st edn. London: Butterworths.

Bertolini L., Elsener B., Pedeferri P., Redaelli E. and Polder R., Corrosion of steel in concrete, prevention, diagnosis, repair, 2nd Edition, Wiley-VCH, Germany, 2013.

British Standards Institution, BS EN 8500:2006, Complementary British Standard to BS EN 206, London, BSI, 2006.

British Standards Institution, BS EN 12390-3:2009, Testing hardened concrete, Parte 3: Compressive strength of test specimens, London, BSI, 2009.

British Standards Institution, BS EN 14629:2007, Product and Systems for the Protection and Repair of Concrete Structures—Test Methods—Determination of Chloride Content in Hardened Concrete. London, BSI, 2007.

Christodoulou C., Goodier C., Austin S., Webb J., Glass G., Long-term performance of surface impregnation of reinforced concrete structures with silane, *Construction*

and Building Materials, 48 (2013), pp. 708–716 DOI information: 10.1016/j.conbuildmat.2013.07.038.
Concrete Society, Technical Report 60, Electrochemical tests for reinforcement corrosion, Surrey, UK, 2004.
Design Manual for Road and Bridges, Volume 3, Section 3, Part BA 35/1990 Inspection and Repair of Concrete Highway Structures, Departmental Standard, UK, 1990.
Elsener B. 2001, Half-cell potential mapping to assess repair work on RC structures, *Construction and Building Materials*, 15, pp. 133–139.
Elsener B. 2003, Half cell potential measurements—Potential mapping on reinforced concrete structures, RILEM TC 154-EMC: Electrochemical techniques for measuring metallic corrosion, Materials and Structures 36, pp. 461–471.
fib 2010. Model code for concrete structures.
Glass G.K., Page C.L. and Short N.R. 1991. Factors Affecting the Corrosion Rate of Steel in Carbonated Mortars. *Corrosion Science*, 32(12), pp. 1283–1294.
Goodier C., Xueting C., Christodoulou C., Dunne D. and Yea R. 2015, Resistivity and water absorption of concrete, International Conference on Concrete Repair, Rehabilitation and Retrofitting, 05–07 October 2015, Leipzig, Germany.
Gulikers J., Design for concrete durability: from deemed-to-satisfy to dreamed-to satisfy, Concrete Solutions 2014: Grantham, M., Basheer, M., Magee B. and Soutsos, M. (eds): Proceedings of the International Conference on Concrete Solutions 2014. London: CRC Press, ISBN 978-1-138-02708-4.
Hornbostel K., Larsen C.K. and Geiker M.R. 2013. Relationship between concrete resistivity and corrosion rate—A literature review, *Cement and Concrete Composites*, 39(0).
Osterminski K., Polder R. and Schießl P. 2012, Long Term Behaviour of the Resistivity of Concrete. HERON, 57(3).
Polder R., Andrade C., Elsener B., Vennesland Ø., Gulikers J., Weidert R. and Raupach M. 2000, RILEM TC 154-EMC: Electrochemical Techniques for Measuring Metallic Corrosion—Test Methods for On-Site Measurement of Resistivity in Concrete. Materials and Structures, 33.
Polder R. 2012. Effects of Slag and Fly Ash on Reinforcement Corrosion in Concrete in Chloride Environment—Research from the Netherlands. *HERON*, 57(3), pp. 197–210.
Stratful R.E. 1957, The corrosion of steel in a reinforced concrete bridge, *Corrosion* 13, pp. 43–48.
Ungricht H. Wasserhaushalt und Chlorideintrag in Beton—Einfulls der Exposition und der Betonzusammensetzung. In: Ph.D. thesis. Universities of Zurich and Basel; 2004. [in German].

Concrete Repair, Rehabilitation and Retrofitting IV – Dehn et al. (Eds)
© 2016 Taylor & Francis Group, London, ISBN 978-1-138-02843-2

Variations of humidity within a relatively large ASR-affected concrete cylinder exposed to a natural environment

Hiroyuki Kagimoto
Electric Power Development Co. Ltd., Kitakyushu, Japan

Yukihiro Yasuda
JPower Design, Kanagawa, Japan

Shigeru Kinoshita
CTEC, Kanagawa, Japan

Mitsunori Kawamura
Kanazawa University, Kanazawa, Japan

ABSTRACT: In order to elucidate changes of the value of relative humidity (R.H.) related to understanding of the behavior of ASR expansion within massive concrete bodies, humidity within relatively large ASR—affected concrete cylinders (φ450 mm × 900 mm) placed in a natural environment as well as in atmospheres whose temperature and humidity had been precisely controlled, was pursued by measuring R.H. values for long periods. When changes in R.H. value with time in the concrete with ASR cracks which had been placed in dry atmospheres were followed by the re-saturation in an atmosphere of >95% R.H., the humidity up to the depth of 100 mm from surfaces increased in early stages after the beginning of re-saturating process, but a sudden rise of environmental R.H. to >95% was considerably delayed at the depth of 200 mm. It is found that permeability of near-surface regions in the concrete cylinder with reactive aggregate was increased by the formation of ASR cracks. When the concrete was exposed to natural environments whose humidity changed from 20 to 80% throughout a year, humidity within the concrete changed very slowly. R.H. values in surface-near portions up to 50 mm were smaller than 80%, but humidity in the portions deeper than 50 mm was maintained at greater than 90% R.H. The permeability of the portions up to the depth of 50 mm decreased during the first drying-re-saturating process in a drying-re-saturating repetitions regime in the laboratory. The reduction in permeability of the near-surface layer thinner than 50 mm may be due to the impregnation of micro-cracks with ASR gels in the first drying—re-saturating process.

1 INTRODUCTION

Considering that ASR surface cracks were caused by differences in expansion between near-surface and internal regions (Stark 1991, Hagelia 2004), it is necessary to understand what factors influenced ASR expansions and how expansions proceeded for elucidating the initiation of cracks and the process of their extension. Alkali leaching in near-surface regions in concrete submitted to high moisture environments and intermittently in contact with water, e.g. undergoing rain fall, reduces expansions in the near-surface regions (Lindgard et al 2012). Thus, humidity significantly influences ASR expansion, but there is few study concerning variations of humidity within ASR-affected large concrete bodies.

By conducting measurements of values of relative humidity and strains within a relatively large concrete cylinder in a dry atmosphere, we revealed that expansion had greatly decreased with reductions in humidity in near-surface regions, but a high moisture condition had been maintained in inner portions of the concrete cylinder, resulting in surface cracking (Kagimoto et al. 2011).

Surface cracks on ASR-affected concrete structures progress with time under conditions of wetting-drying repetitions in natural environments. However, few study is concerned about how internal humidity changed in the concrete structures which has undergone wetting-drying repetitions. Few study reported to what depth internal humidity was affected in the concrete structures in environmental atmosphere.

In this study, in order to reveal changes of the value of relative humidity (R.H.) for understanding the behavior of expansion within massive concrete bodies and humidity within relatively large concrete cylinders (φ450 mm × 450 mm and 600 mm) placed in natural environment as well as in atmospheres whose temperature and humidity had been precisely controlled, was pursued by measuring R.H. values with sensors embedded at various depths from the surface of the concrete cylinders for long periods.

We reported the changes in R.H. values with time at various depths from surfaces after a concrete cylinder (φ450 mm × 900 mm) which had been placed in dry atmospheres for a long time, was exposed to a moisture environment of >95% R.H. (Kagimoto et al. 2011). After that, humidity within another concrete cylinder which underwent wetting-drying repetitions in the laboratory several times were measured. Changes in internal humidity in another concrete cylinder exposed to a natural environment was also pursued. On the basis of the results obtained, we discussed the characteristics of changes in internal humidity in the concrete cylinder exposed to a natural environment in this study.

2 OUTLINE OF EXPERIMENTS

2.1 *Materials and mix proportion of concrete*

Coarse and fine reactive aggregates used were gravel and sand from the Joganjigawa river in Toyama Prefecture in Japan; non-reactive aggregates a crushed rock produced in Oume and sand from the Oigawa river in Japan. Reactive silica in the aggregates was included as opal, glass, cristobalite and tridymite. Table 1 provides the dissolved silica (S_c) and the reduction in alkalinity (R_c) obtained in the application of the standard chemical method for seeing potential reactivity of the aggregates (JIS A 1145). A low alkali cement with an equivalent percentage of Na_2O_{eq} of 0.53% was used. Expansions of mortars at 6 months measured according to JIS A 114 are also given in Table. 1. In the production of concrete, a water-reducing admixture was added to maintain a slump value of 100 mm.

The mix proportions of concrete are provided in Table 2. 5.21 kg NaOH per 1 m^3 concrete was added at a dosage level of alkali equivalent percentage of 1.8% Na_2O_{eq} in cement to promote expansion of the concrete with reactive aggregate.

2.2 *Production of concrete cylinders equipped with strain gauges and censor assembly units for measuring humidity*

At the production of a concrete cylinder (φ450 mm × 900 mm), as shown in Figure 1, acrylic rods of 30 mm in diameter by 400 mm long, which have a cylindrical protrusion (φ10 mm × 10 mm) on the end, were embedded vertically so as to make rooms for accommodating sensor assemblies to measure humidity. A figure added on each dot in Figure 2 denotes a depth of sensor assemblies from surface. About 24 hours after the placement of concrete, all of the acrylic rods extracted leaving φ30 mm × 300 mm cylindrical holes attached

Table 1. Properties of aggregate.

Physical properties	
Reactive aggregate	Non reactive aggregate
*Coarse aggregate**	*Coarse aggregate****
Density: 2.64 g/cm³	Density: 2.71 g/cm³
Absorption: 1.66%	Absorption: 0.44%
*Fine aggregate***	*Fine aggregate*****
Density: 2.61 g/cm³	Density: 2.62 g/cm³
Absorption: 1.94%	Absorption: 1.42%
Alkali reactivity of reactive aggregate	
Coarse aggregate*	Fine aggregate**
Reduction in alkalinity	*Reduction in alkalinity*
91 mmol/l	61 mmol/l
Dissolved silica	*Dissolved silica*
253 mmol/l	190 mmol/l
JIS mortar bar test	*JIS mortar bar test*
0.34%/6 months	0.38%/6 months

*Jogannji river gravel, **Joganji river sand, ***Oume crushed stone, ****Oigawa river sand.

Table 2. Mix proportion of concvrete.

Maximum aggregate size (mm)	Water cement ratio	Sand ratio	Unit content (kg/m³)			
			Water	Cement	Sand	Gravel
20	0.55	0.45	175	318	833	1,030

Figure 1. Censor assembly unit for measuring R.H. and temperature.

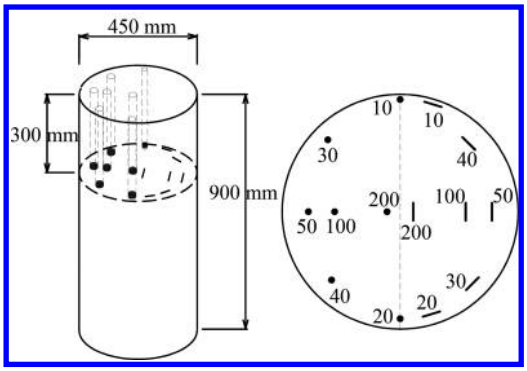

Figure 2. Positions of sensor assemblies and strain gauges in a concrete cylinder.

with φ10 mm × 10 mm cylindrical spaces on the end behind (Fig. 2). Sensors for measuring relative humidity were fixed into the holes drilled in the central portions of the other series of acrylic cylinders (φ30 mm × 40 mm) prepared in advance (Fig. 1). After these sensor assemblies were embedded into the end of φ30 mm × 300 mm cylindrical holes, mortars were poured into remaining upper portions in the holes. Thus, we can measure R.H. values in atmospheres in small rooms (φ10 mm × 10 mm) in concrete that were equilibrium with moisture states in the surrounding concretes.

Electrical strain gauges were also embedded in concrete in the circumferential direction at depths of 10, 20, 30, 40, 50, 100, 200 mm from surfaces of concrete cylinders.

Length changes with time in concrete prisms under the three different environmental conditions, >95% R.H. at 35 °C and 40 °C, 60% R.H. at 35 °C up to 73 days followed by a condition of 70% R.H. at 40 °C were measured in concrete expansion tests.

2.3 *Drying—wetting repetitions tests*

2.3.1 *Regimes of drying-wetting repetitions*

The following three drying-wetting repetitions regimes were set up for simulating drying-wetting repetitions which concrete structures usually undergo in natural environments.

Case A: This regime was instituted for seeing changes in R.H. value with time in the concrete with ASR cracks which had been placed in dry atmospheres followed by the re-saturation in the atmosphere of >95% R.H. Namely, the temperature and R.H. in the storage room were maintained at 35 °C and 60% R.H. at early stage and then raised to 40 °C and 70% R.H. at 73 days for 292 days (the drying process). After that, the environmental relative humidity had been raised to >95% R.H.

Case B: This case was set up for seeing changes in R.H. value with time within the concrete with ASR cracks when exposed to the drying-wetting repetitions after the drying process in Case A. Namely, after the drying process whose details were described in Case A, the concrete cylinders were exposed to repetitions of the drying (40 °C, 70% R.H.) and re-saturating process (40 °C, >95% R.H.) every 60 days.

Case C: Changes in humidity within a concrete cylinder made with a non-reactive aggregate exposed to a natural environment were measured. The exposure site was positioned about 3 km from the coast in Chigasaki in Kanagawa Prefecture in Japan in 2011~2013.

Case D: A reactive aggregate-containing concrete cylinder was exposed to a natural environment in the same site as in Case C.

Details of these four different cases are tabulated in Table 3.

2.3.2 *Specimens used in the experiments*

As tabulated in Table 3, the concrete specimen used in Case D was what was obtained by cutting off the upper 600 mm from the concrete cylinder (φ450 mm × 900 mm).

Measurements of R.H. values in Case A and B were made once a day for seeing changes in humidity within the concrete cylinder after a drastic change in environmental humidity.; measurements in Case C and D once a week for seeing differences in changes of humidity within the concrete cylinder throughout a year between the one with and without reactive aggregate. Measurements of humidity and strain were also once an hour for seeing changes in humidity during three days arbitrarily selected.

2.4 *Observations of internal cracks in the concrete cylinder*

After the completion of the drying-re-saturating repetition in the Case A, concrete discs about 20 mm thick were cut from the concrete cylinder with the saw. A concrete disc was divided into four fan-shaped parts. Then, they were gently dried in an atmosphere with 60% R.H. at 20 °C for about 24 hours, and then transferred to a vacuum desiccator. They were impregnated with an epoxy resin with a low viscosity containing a fluorescent dye. After the resin hardened at room temperature, cutting faces of specimens were polished with the SiC powder for observing polished faces under normal and UV light.

Table 3. Experimental condition.

	Aggregate	Specimens (mm)	Environmental conditions		Frequency of measurements	Remarks
			Drying process	Wetting process		
A	Reactive	Φ450 × 900	40 °C, 70% R.H. Duration: 292* days	40 °C, >95% R.H. Duration: 1,500 days	Once a day	The re-saturating process after the end of drying process (1 cycle only) Location of censors for measuring humidity: 10, 20, 30, 40, 50, 70, 200 mm Electrical strain gauges were also contained.
B			40 °C, 70% R.H. Duration: 315* days	40 °C, >95% R.H. Duration: 60 days		3 re-saturating—drying repetitions for 60 days after the end of drying process. Location of Humidity censor: 10, 20, 30, 40, 50, 100, 200 mm Electrical strain gauges were also embedded.
C	Non-reactive	Φ450 × 450	Natural environment Duration: 2 years		Once a week Once a hour	Natural environment condition Location of censors for measuring humidity: 25, 50, 75, 100 mm Electrical strain gauges were also embedded.
D	Reactive	Φ450 × 600	Natural environment Duration: 9 months (after the completion of exposure tests of Case A)			The upper 600 mm potions were cut off from the φ450 mm × 900 mm cylinder. Natural environment condition after the end of Case A. Location of censors for measuring humidity: 10, 20, 30, 40, 50, 70, 200 mm Electrical strange gauges were also embedded.* After finishing case A.

*35 °C, 65% R.H. for first 73 days.

3 RESULTS AND DISCUSSION

3.1 *Expansion in concrete prisms*

Changes in expansion with time in concrete prisms under the three different environmental atmospheres are presented in Figure 3. As shown in this figure, concrete prisms in > 95% R.H. at 35 °C and 40 °C started to rapidly expand about 60 days, and then expansion rates gradually decreased towards the ultimate expansion of about 3.0%. Namely, the latent period of ASR expansion was about 60 days. However, concrete prisms in an environment of changing 60% R.H., 35 °C to 70% R.H., 40 °C at 73 days continued to shrink.

3.2 *Changes in humidity within an ASR-affected concrete cylinder in the drying-re-saturating process (Kagimoto et al. 2011) (Case A)*

Figure 4 shows changes in humidity within the concrete cylinder throughout the drying-re-saturating process. It is found from this figure that the humidity in the portions smaller than 40 mm in depth gradually decreased with time, and reduction rates in humidity in the portions greater than 50 mm deep was small. As seen in this figure, humidity in the portions deeper than 100 mm was only a little influenced by the dry environments.

It is also found from Figure 4 that after the beginning of re-saturating process, increasing rates in R.H. values were different at different depths. Especially, R.H. value at the depth of 100 mm gradually increased after the beginning of re-saturating process. But, humidity at the depth of 200 mm still tended to decrease up to about 100 days, and then slowly increased towards >95% R.H. Furthermore, the increase rates in humidity at the depth of 10 mm were as small as those at the depth of 200 mm. It is not clear why the permeability of the portions up to 10 mm has been reduced.

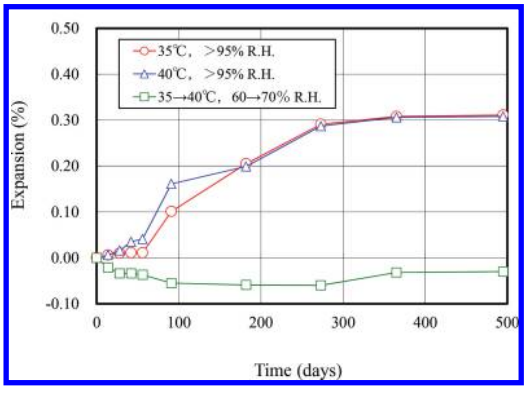

Figure 3. Expansion curves in concrete prisms (100 × 100 × 400 mm) under the three different environmental conditions.

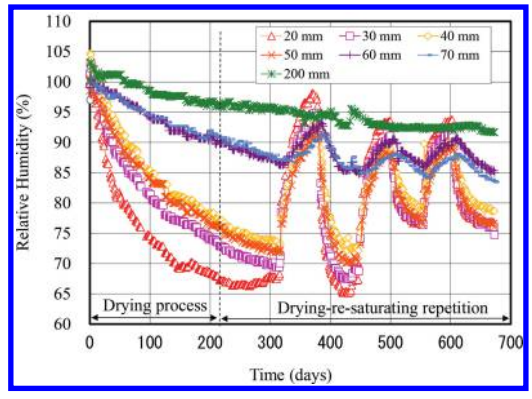

Figure 5. R.H. value vs. time curves at various depths in a reactive concrete cylinder under drying—wetting repetitions.

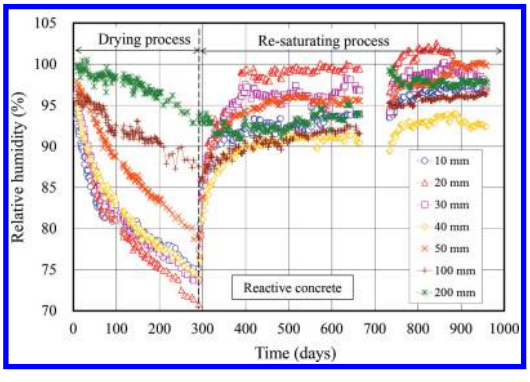

Figure 4. R.H. value vs. time curves at various depths in a reactive concrete cylinder.

3.3 *Changes in humidity within the ASR-affected concrete cylinder exposed to drying-re-saturating repetitions (Case B)*

As seen in Figure 5, R.H. values at the depths of 20, 30, 40, 50 mm changed sensitively responding to the drying-re-saturating repetitions, but R.H. at the depths of 60, 70 mm and 200 mm a little and little changed, respectively. R.H. values in the portions smaller than 70 mm depth varied in the wave-like way at regular intervals. Especially, the extent of variations of R.H. at the depths smaller 50 mm in the first drying-re-re-satulating process were greater than those in the second drying-re-satulating process. Little difference was found between the amplitude of waves in the second and the third repetition. This result indicates that the permeability of the portions up to the depth of 50 mm decreased during the first drying-re-saturating process. Micro-cracks caused by expansion of ASR gel pockets in the drying process accelerated the intrusion of water into the concrete cylinders in the re-saturating process (Kagimoto et al. 2011). The reduction in permeability of the near-surface layer thinner than 50 mm may be due to the impregnation of micro-cracks with ASR gels in the first re-saturating process, because ASR gels became viscous liquid by absorbing water during the re-saturating process and moved through micro-cracks filling them with gels (Knudsen& Thaulow 1975).

3.4 *Variations of humidity within a concrete cylinder exposed to a natural environment (Case C and D)*

Figure 6(a) shows variations of R.H. values at various depths within a non-reactive aggregate concrete cylinder exposed to a natural environment throughout a year (2012.4~2013.3). Dots in the figure denote R.H. values of the environmental atmosphere. In these areas, environmental humidity during the period of June to August is usually about 80% R.H. and reduced to smaller than about 20% R.H. in the winter. As seen in Figure 6(a), R.H. values within the concrete cylinder were higher than 90% R.H. in the summer, and reduced to about 80% in the winter corresponding to changes in environmental humidity. Around November and December in 2012, R.H. values of environmental atmospheres were reduced to 20%. Around the fall, humidity at the depth of 25 mm was 70% R.H., and throughout the winter varied up and down around a critical val ue of 80% R.H. below which ASR expansion does not occur. Figure 6(a) also shows that humidity increased with increasing depth, and for periods of the spring to the summer about 95% R.H. at the depth of 100 mm. But, R.H. values in the portions have not been smaller than 85%.

Plotting R.H. values at various depths within a reactive aggregate-containing concrete cylinder

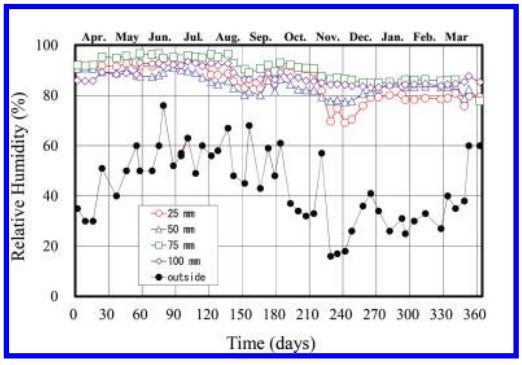

Figure 6(a). R.H. value vs. time curves at various depths in a non-reactive concrete cylinder exposed to a natural environment.

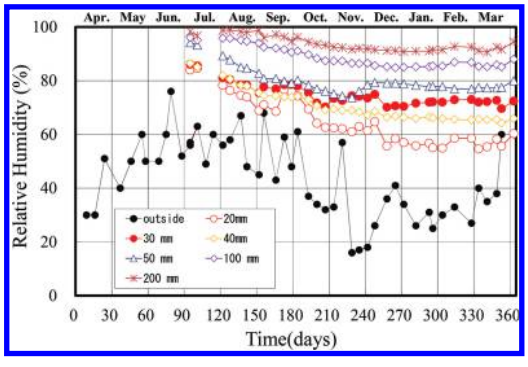

Figure 6(b). R.H. value vs. time curves at various depths in a reactive concrete cylinder exposed to a natural environment.

gives Figure 6(b). It is found from Figure 6(b) that R.H. values at the depths smaller than 50 mm in the reactive aggregate concrete cylinder were considerably low, compared with those in the non-reactive aggregate concrete cylinder in the winter. Most plots for those depths were lower than a critical R.H. value of 80%. As also seen in this figure, R.H. values at the depth of 40 mm are lower than those at the depth of 30 mm. This discrepancy may be due to incidental differences in ASR cracks patterns between the two portions at which the sensors were situated. The sensor embedded at the depth of 10 mm did not work well.

As shown in Figure 3, expansion of concrete prisms with reactive aggregate increased with time up to about 300 days in >95% R.H. A few surface cracks were found for the first time in the concrete cylinder at 150 days in the Case A (Kagimoto et al. 2011).

Surfaces cracks have developed with time and, as shown in Figure 7(a), finally tortoise shell-like

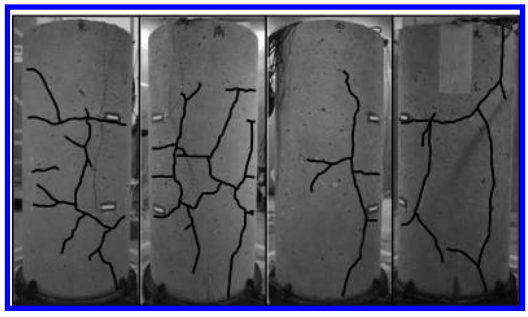

Figure 7(a). Sketches of surface cracks on a reactive concrete cylinder in the drying and re-saturating process.

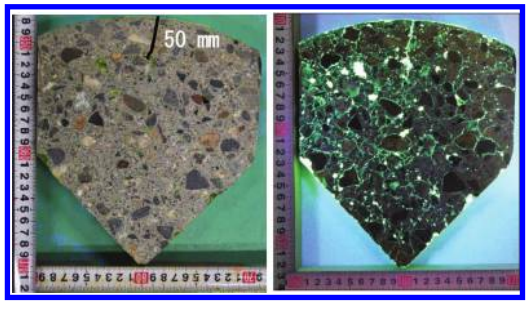

Figure 7(b). Sketches of surface cracks on a reactive concrete cylinder in the drying and re-saturating process.

cracks patterns were formed at the end of experiment in the Case A. In this figure, only cracks whose widths were greater than 0.05 mm, but many cracks smaller than 0.05 mm existed. Figure 7(b) shows photographs of the polished section of a fan shaped concrete piece taken under normal and UV light for seeing the depth of surface cracks and internal cracks patterns. It is found from this figure that a thick crack about 50 mm in length and about 1 mm wide has progressed from surfaces to inner portions. A crack seen in this figure is a part of surface cracks in the sectional direction. In addition to the thick surface crack, a number of meso-scale cracks were found in this figure. Thus, when a reactive aggregate-containing concrete cylinder was exposed to drying-wetting repetitions in a natural environment, R.H. values in the near-surface layer were sensitively in response to changes in environmental humidity. The sensitive response of R.H. values in the near-surface regions to environmental humidity is attributable to increases in permeability of the portions caused by the formation of ASR micro—and macro-cracks.

As seen in Figure 6(a) and (b), at the depths greater than 50 mm, little difference was found in variations of R.H. value between the concrete cylinders with and without reactive aggregate.

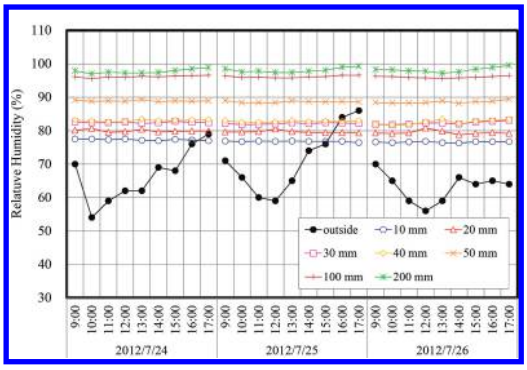

Figure 8. Daily changing of relative humidity in a reactive concrete cylinder.

These results show that water mainly moved through thick cracks only in near-surface regions (less than 50 mm in depth) in the concrete cylinders with and without reactive aggregate in response to environmental humidity.

Figure 8 shows changes in environmental humidity and humidity within the concrete cylinder during several days arbitrarily selected in the summer. As seen in this figure, environmental humidity greatly changed from 54% R.H. to 88% R.H., but internal humidity little changed even at the depth of 10 mm.

4 CONCLUSIONS

The major results obtained are as follows;

1. The humidity in the surface-near regions up to 100 mm deep increased in early stages after the beginning of re-saturating process, but effects of an arise to >95% R.H. was delayed at the depth of 200 mm in the Case A.
2. Once ASR-affected concrete underwent drying, changes in humidity within the concrete occurred for only short periods responding to changes of environmental humidity. Namely, permeability in the concrete cylinder was increased by the formation of ASR cracks.
3. When the concrete cylinder with reactive aggregate exposed to natural environments whose humidity changed from 20 to 80% R.H. throughout a year, humidity within the concrete changed very slowly. R.H. values in surface-near portions up to 50 mm were smaller than 80%, but humidity in the portions deeper than 50 mm was maintained at greater than 90% R.H.
4. Humidity of the portions up to 50 mm from surfaces was less than 80% R.H., but the humidity greater than 90% R.H. was maintained at depths greater than 50 mm in the Case A.
5. Changes in environmental humidity little influenced the humidity in the portions deeper than 50 mm even in the ASR-affected concrete cylinder in a natural environment.
6. The reduction in permeability of the near-surface layer thinner than 50 mm may be due to the impregnation of micro-cracks with ASR gels in the first re-saturating process, because ASR gels became viscous liquid by absorbing water during the re-saturating process and moved through micro-cracks.
7. R.H. values in the reactive aggregate concrete cylinder at the depths smaller than 50 mm were considerably low compared with those in the non-reactive aggregate concrete cylinder in the winter.

REFERENCES

Hagelia P. (2004). Origin of map cracking in view of the distribution of airvoids, strength and ASR-gel, Proceedings of 12th International Conference on Alkali Aggregate in Concrete, Beijing, China, pp. 870–881.

Kagimoto, H., M. Kawamura (2011). Measurements of strain and humidity within massive concrete cylinders related to the formation of ASR surface cracks, J. Cem. Concr. Res. 41 (8), pp. 808–816.

Knudsen T. and N. Thaulow (1975) Quantitative microanalyses of alkali-silica gel in concrete, Cem. Concr. Res. 5 (5), pp. 443–454.

Lindgard, J., O. Andic-Cakir, I. Fernandes, T.F. Ronning, M.D.A. Thomas (2012). Alkali-Silica Reactions (ASR): Literature review on parameters influencing laboratory performance testing. J.Cem.Concr.Res. 42 (2), pp. 223–243.

Stark D. (1991). The moisture condition of field concrete exhibiting alkali-silica reactivity, in: V.M. Malhotra (Ed.), Proceedings of the 2nd International Conference on Durability of Concrete, ACI SP-126, Montreal, Canada, pp. 973–987.

Concrete Repair, Rehabilitation and Retrofitting IV – Dehn et al. (Eds)

Influence of electrochemical lithium penetration from various kinds of lithium solution on ASR expansion of concrete

T. Ueda
Tokushima University, Tokushima, Japan

A. Nanasawa
DENKI KAGAKU KOGYO KABUSHIKI KAISHA, Niigata, Japan

M. Tsukagoshi
Tokushima University, Tokushima, Japan

ABSTRACT: Chloride attack and ASR are serious deterioration mechanisms of concrete structures respectively. Moreover, in the cases of marine environment and cold climate area, complex deterioration of these mechanisms can be observed because of the supply of sea water or de-icing salt. In this study, as a remedial measure against such a complex deterioration, electrochemical penetration of lithium from the electrolyte solution was investigated. It was clarified that electrolyte temperature greatly affected the extent of lithium penetration and the treatment at 40 °C remarkably accelerated lithium penetration into concrete compared with the case of 30 °C. Regarding the kind of lithium salt, $LiNO_3$ solution was most effective among a number of different kinds of lithium salt in the viewpoints of Li^+ penetration of into concrete and suppression of concrete expansion.

1 INTRODUCTION

Chloride attack and ASR are serious deterioration mechanisms of concrete structures respectively (JSCE 2007). Moreover, in the cases of marine environment and cold climate area, complex deterioration of these mechanisms can be observed because of the supply of sea water or de-icing salt (Habuchi et al. 2004). Complex deterioration mechanism due to both chloride attack and ASR has not been clarified yet but it would be greatly affected by the environmental temperature.

As a remedial measure against such a complex deterioration, this study tried an electrochemical penetration of lithium from electrolyte solution. It has been confirmed by many researchers that lithium salts have the effect of suppressing ASR-induced expansion of concrete (MacCoy & Caldwell 1951). Supposing the application of the lithium salts as a repair additive for concrete structures deteriorated by ASR, sufficient amounts of Li^+ must be driven into the ASR-affected concrete (Diamond & Ong 1992). Then, an electrochemical technique to accelerate the penetration of the lithium ions (Li^+) in a lithium-based electrolyte solution into concrete has been employed for the purpose of suppressing ASR-induced expansion due to Li^+ (Whitemore & Abbott 2000). However, from the results of past research work, the penetration area of Li^+ is limited around the concrete surface and it is difficult to make Li^+ penetrate into the deeper part of concrete (Ueda et al. 2006).

In this study, experimental investigations were carried out aiming to grasp the influence of kinds of lithium salts and the temperature of the electrolyte solution on migration properties of ions in concrete and ASR-induced expansion of concrete. Moreover, the protection effect against steel corrosion and the chemical composition of reaction products in concrete were also investigated.

2 EXPERIMENTAL PROGRAM

2.1 *Materials*

Mixture proportions of concrete adopted in this study were shown in Table 1. Water to cement

Table 1. Mixture proportions of concrete.

W/C (%)	s/a (%)	Content (kg/m^3)						
		C	W	S1	S2	G1	G2	NaCl
55	48	338	186	250	591	261	641	15.1

ratio (W/C) of concrete was 55% for all mixture proportions. This concrete is supposed to be damaged by the complex deterioration. Then it contained reactive aggregate and NaCl was added as the source of alkali. In order to adjust the total alkali contents as R_2O was 10.0 kg/m^3 for the acceleration of deterioration, a corresponding amount of NaCl was dissolved in the mixing water.

Ordinary portland cement (density: 3.16 g/cm^3, specific surface area: 3280 cm^2/g, R_2O: 0.56%) was used. As the fine aggregate, non-reactive fine aggregates (S1, density: 2.56 g/cm^3) and reactive aggregate (S2, density: 2.60 g/cm^3) were mixed at the pessimum weight ratio of 3:7. As the coarse aggregate, non-reactive aggregate (G1, density: 2.55 g/cm^3, G_{max}: 15 mm) and reactive aggregate (G2, density: 2.68 g/cm^3, G_{max}: 15 mm) were mixed at the pessimum weight ratio of 3:7.

2.2 *Preparation of specimens and electrochemical treatment*

Specimens prepared in this study were 100 × 100 × 300 mm reinforced concrete prisms with a steel bar φ13 SR235 (JIS number) at the center of the square section as shown in Figure 1. All specimens were cured in the wet 20 °C condition for 28 days. A part of specimens were continuously stored at the constant temperature of 20, 30 or 40 °C in the moist condition for accelerating ASR for 350 days, followed by the electrochemical treatment.

For all specimens to be subjected to electrochemical treatment, brass chips were pasted to concrete surfaces after the curing for 28 days for the measurement of concrete expansion after the electrochemical treatment. Five concrete faces of each specimen were insulated with epoxy resin coating, leaving one exposed surface before the electrochemical treatment.

After the epoxy coating, each specimen was immersed into electrolyte liquid in a plastic container, and direct electric current was supplied between rectangular shaped titanium mesh as the anode and the steel bar in concrete as the cathode. As the current density, 1.0 A/m^2 to the exposed concrete area was adopted. Treated period was 8 weeks. These conditions of the treatment were decided based on those of the conventional chloride removal method (Hondel & Polder 1992) (JSCE 2001). Kinds of electrolyte liquid and their temperature conditions are shown in Table 2. The standard temperature level of electrolyte liquid was 30 °C to accelerate the lithium penetration except the case of 40 °C $LiNO_3$ solution. Regarding the specimens stored at the constant temperature condition for 350 day, 40 °C $LiNO_3$ solution was selected as the electrolyte liquid. These specimens were kept in the moist condition and the temperature was constantly 40 °C for the acceleration of ASR after the treatment.

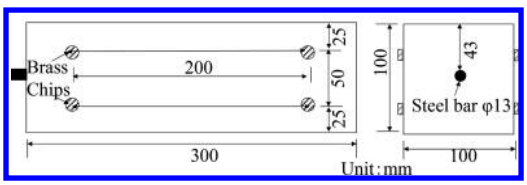

Figure 1. Outline of a RC specimen.

2.3 *Tests of specimens*

After finishing the electrochemical treatment, the distribution profiles of ion content (Cl^-, Na^+, K^+, Li^+) in the concrete specimens were measured using powder samples grinded from the cut out seven concrete plates in a specimen, as shown in Figure 2. The Na^+, K^+ and Li^+ contents were measured by means of atomic absorption spectrometry using a

Table 2. List of electrolyte.

Kind of salt	Content of salt (%)	Content of Li (%)	Temperature (°C)
LiOH	10	3.0	30
Li_2CO_3	1.2	0.22	30
Li_2SiO_4	23	2.9	30
$LiNO_3$	30	3.0	30
			40
$Ca(OH)_2$	0.2	0	30

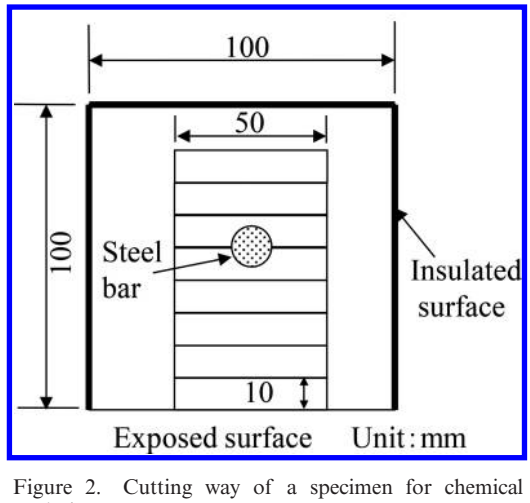

Figure 2. Cutting way of a specimen for chemical analysis.

crashed fine powder sample solved by HNO_3 solution. Cl^- content was measured according to JIS A 1154.

Specimens after the electrochemical treatment were kept in the moist and constant temperature at 40 ºC environment and the expansion rate of concrete was measured regularly by means of a contact gauge. At the same time to measure the concrete expansion, half-cell potential, polarization resistance of steel in specimens and resistivity of concrete were measured regularly. As a reference electrode for these electrochemical monitoring, saturated silver chloride (Ag/AgCl) was used. Polarization resistance was measured by the rectangular wave electric current polarization method, as the deference of impedances at 800 Hz and 0.1 Hz of electric current frequency. Resistivity was obtained as the impedance at 800 Hz of electric current frequency.

3 RESULTS AND DISCUSSIONS

3.1 *Migration of ions in concrete due to applying electrochemical treatment*

The distributions of Cl^- content in the specimens just after completing treatment are shown in Figure 3. The steel bar is located at the center (50 mm from the exposed surface) of each specimen. Although this technique is not for extracting Cl^- from concrete, Cl^- content around the steel bar is decreased by the electrochemical treatment compared with the non-treated case (N), because this technique is based on the same principle as that of desalination. Since such a side effect is expectable, this technique could be an effective repair method for concrete structures deteriorated by the complex mechanism of chloride attack and ASR. There isn't significant difference of the chloride removal effect among the some kinds of lithium salts but the rise in the electrolyte temperature from 30 °C to 40 °C improves the desalination effect in the case of $LiNO_3$.

The distributions of R_2O content in concrete specimens immediately after completing treatment are shown in Figure 4. The amount of R_2O was calculated by the following formula.

$$R_2O = Na_2O + 0.658K_2O \ (kg/m^3) \quad (1)$$

According to this figure, in the case of the specimens treated with the electrolyte at 20 °C, a great amount of R_2O accumulates around the steel bar in concrete. It is considered that such an accumulation of alkali is caused by the electrophoresis of cations (Na^+, K^+) contained in the concrete toward the steel bar as the cathode.

Like the case of Cl^- distribution, the rise in electrolyte temperature from 30 °C to 40 °C might accelerate the electrophoresis of Na^+ and K^+. Then, it can be expected that the rise in temperature would result in a larger amount of R_2O accumulation around the steel bar. However, in Figure 4, the accumulated amount of R_2O is reduced with the rise in the electrolyte temperature from 30 °C to 40 °C. Such a moderation of the alkali accumulation at the steel bar may be caused by the decrease of the transference numbers of Na^+ and K^+ in concrete with the migration of lithium-based electrolyte solution. The authors reported similar results in the past paper (Ueda et al. 2011). The reduction of the concentrated alkali at the steel bar would mean the reduction of the risk of ASR or ASR-induced expansion of the concrete around the steel bar.

Distributions of Li^+ content in the concrete immediately after treatment are shown in Figure 5. In this figure, Li^+ content around the concrete

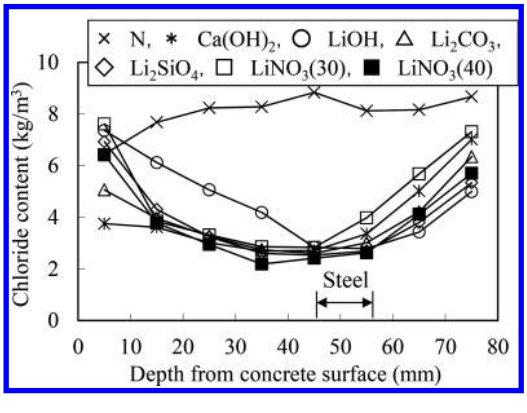

Figure 3. Distributions of chloride content in concrete after treatment.

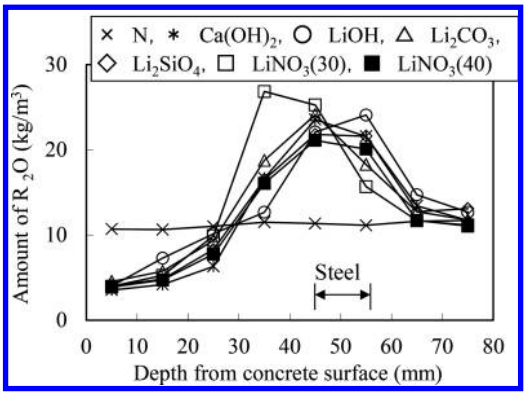

Figure 4. Distributions of R_2O content in concrete after treatment.

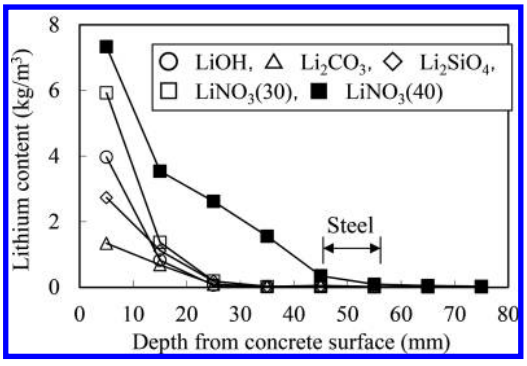

Figure 5. Distributions of lithium content in concrete after treatment.

surface increases with the electrochemical treatment. However, when the temperature of electrolyte is 30 °C, the penetration depth of lithium is about 25 mm regardless of the kinds of lithium salt. The authors already reported that it was difficult to drive a sufficient amount of Li^+ into the concrete at the depth of the steel bar by the electrochemical treatment with the LiOH electrolyte solution at room temperature (Ueda et al. 2006). On the other hand, Figure 5 shows that 40 °C electrolyte of $LiNO_3$ increase the amount and the depth of lithium penetration compared with the case of 30 °C. The authors reported similar results from the experiment using Li_2CO_3 solution as the electrolyte (Ueda et al. 2011). Further investigation is necessary to clarify the adequate conditions of the electrochemical treatment considering the concrete expansion behavior after the treatment.

3.2 *Concrete expansion after electrochemical treatment*

Variation curves of concrete expansion rate with time, which were measured in the longitudinal and the vertical direction in each concrete specimen (refer to Fig. 1), are shown in Figure 6. Each curve is the average of measured data from three specimens treated under the same conditions. The horizontal axis of this figure expresses the total period after the end of curing. N is a non-treated case, whilst the others are treated cases with different kinds of electrolyte liquid. Non-treated specimens were moved to the condition for accelerating ASR (40 °C, 95% R.H.) immediately at the end of the curing period of 28 days and values of concrete expansion rate were measured regularly. Treated specimens were subjected to conditions for ASR acceleration after completion of electrochemical treatment, at which time expansion

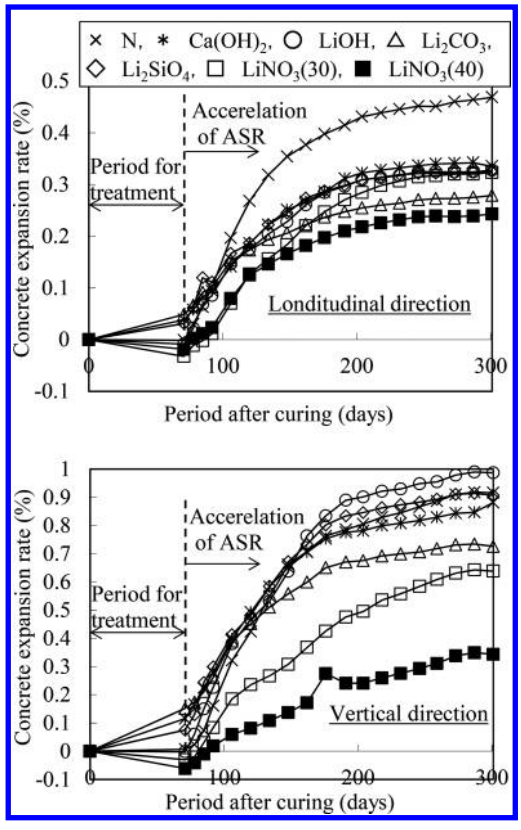

Figure 6. Variation curves of concrete expansion rate with time during the period of treatment and ASR acceleration.

measurements started. Original lengths were measured before treatment began.

In Figure 6, it can be seen that although non-treated specimen shows relatively large expansion, all treated specimens show smaller expansion rates after treatment. Such a suppression of concrete expansion would be achieved by a large amount of Li^+ contained in the concrete around the concrete's surface, as shown in Figure 5. When the electrolyte temperature is 40 °C with $LiNO_3$, concrete expansion after treatment is less than the other treated cases using electrolyte at 30 °C. It can be considered that high temperature treatment increases the risk of accelerating concrete expansion during treatment, but it also has the effect of promoting lithium penetration that may serve to suppress concrete expansion after the treatment.

As can be seen in Figure 4, a large amount of alkali accumulated around the steel bar due to electrochemical treatment and such alkali could accelerate ASR-induced expansion of concrete.

However, according to Figure 6, concrete expansion rates are not promoted by the electrochemical treatment, compared with non-treated cases. It has been reported that excessive supply of electricity, exceeding the pessimum value, does not accelerate ASR-induced expansion of concrete (Page & Yu 1995). In this study, amount of accumulated alkali around the steel bar due to treatment may exceed the pessimum value, and this may have resulted in relatively small ASR-induced expansion.

From Figure 6 (the lower one), expansion rates in the vertical direction are larger than those in the horizontal direction because concrete expansion in the vertical direction isn't confined by the embedded steel bar. However, even in this case, Li_2CO_3 and $LiNO_3$ as the electrolyte show effective suppression of concrete expansion rate. From these results, the 40 °C electrolyte of $LiNO_3$ would be most effective to use for the electrochemical method against ASR damage of concrete.

3.3 *Protection effect against steel corrosion*

Variation curves of half-cell potential with time during the period of treatment and ASR acceleration are shown in Figure 7. From this figure, the potential values of treated specimens indicate less than –1000 mV due to the influence of the cathodic polarization. However, the potential values of treated specimens gradually increase with the repassivation by the supply of oxygen after finishing electrochemical treatment. The half-cell potential of the specimen treated with $LiNO_3$ electrolyte at 40 °C, which was most effective to suppress ASR expansion, rises to the higher values than that of non-treated specimen. While, the other treated specimens don't show enough rise of potential values because of the delay of re-passivation due to the moist environment storage for accelerating ASR.

Photos of steel bars from specimens after the ASR acceleration for 300 days are shown in Figure 8. As the degree of steel corrosion was generally slight, the weight loss wasn't measured. In the case of non-treated specimen, localized adhesion of white products supposed ASR gel is observed while steel corrosion can be seen in the non-adhesion area. In this study, the amount of premixed Cl^- was about 9 kg/m^3 and the expansion rate of concrete was relatively large but in the past paper, authors reported that the progress of steel corrosion can be suppressed due to the protection effect of ASR gel in the ASR acceleration environment. Then, the situation of steel corrosion is consistence with the result of the past research (Ueda 2013). In the cases of the treated specimens using $LiNO_3$ electrolyte, there is no localized steel corrosion like the case of non-treated specimen and only slight rust can be seen hence the protection effect against steel corrosion is achieved due to applying electrochemical treatment. Since the treatment in 40 °C results in the whole adhesion of white products while 30 °C treatment results in very limited white area, the temperature of the electrolyte may affect the property and distribution of the reaction products.

3.4 *Observation and composition analysis of white products deposited inside of specimens*

Photos of inside situation around the steel bar of splitted specimens (non-treated and treated using

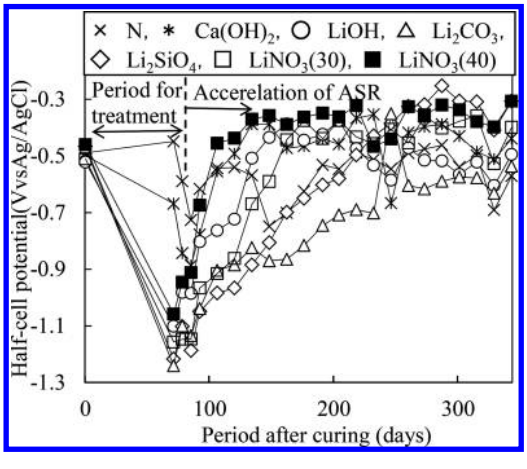

Figure 7. Variation curves of half-cell potential with time during the period of treatment and ASR acceleration.

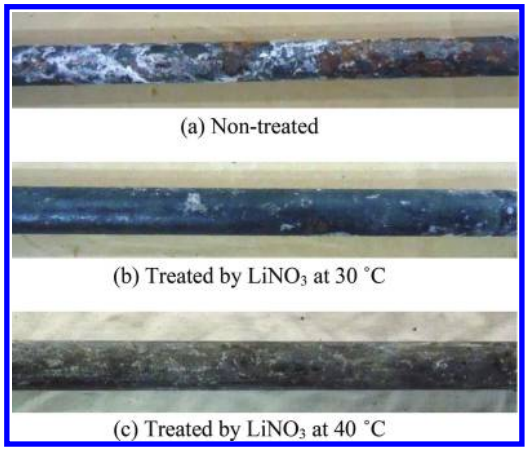

Figure 8. Photos of steel bars from specimens after the ASR acceleration for 300 days.

$LiNO_3$ electrolyte) after the ASR acceleration for 300 days are shown in Figure 9. In the case of non-treated specimen, the whole of concrete around the steel bar colored whitish while in the cases of treated specimens, there are many dots of white products filling small voids of concrete around the steel bar.

Moreover, concrete around the steel bar in the treated specimens colored dark which may be caused by the accumulation of alkali due to the electrochemical migration of ions.

SEM photos of white products observed inside of specimens (the red-line-circled parts in Fig. 9) are shown in Figure 10 and the results of composition analysis of the products are shown in Table 3. From Figure 10, in the case of non-treated specimen, the photo shows the typical ASR gel while in the treated cases, the aggregations of particles in the size of 1–3 μm are observed. Furthermore, the rise in temperature from 30 °C to 40 °C causes the smaller size of particles. Table 3 shows that the electrochemical treatment increases SiO_2 composition and decreases CaO composition, which may mean the reduction of rigidity of ASR gel. Moreover, in the case of 40 °C treatment, Li_2O is detected over 10% hence the gel containing Li^+ which will have the property of low expansion with water absorption is produced around the steel bar.

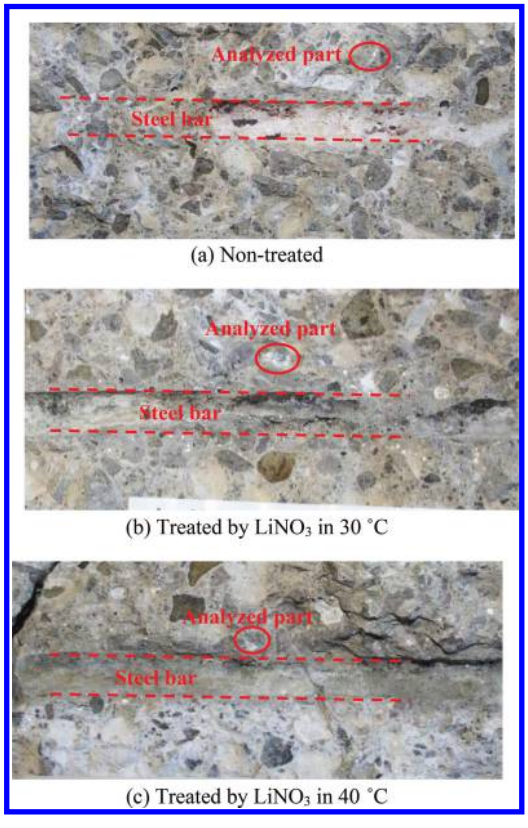

Figure 9. Photos of inside situation of specimens after the ASR acceleration for 300 days.

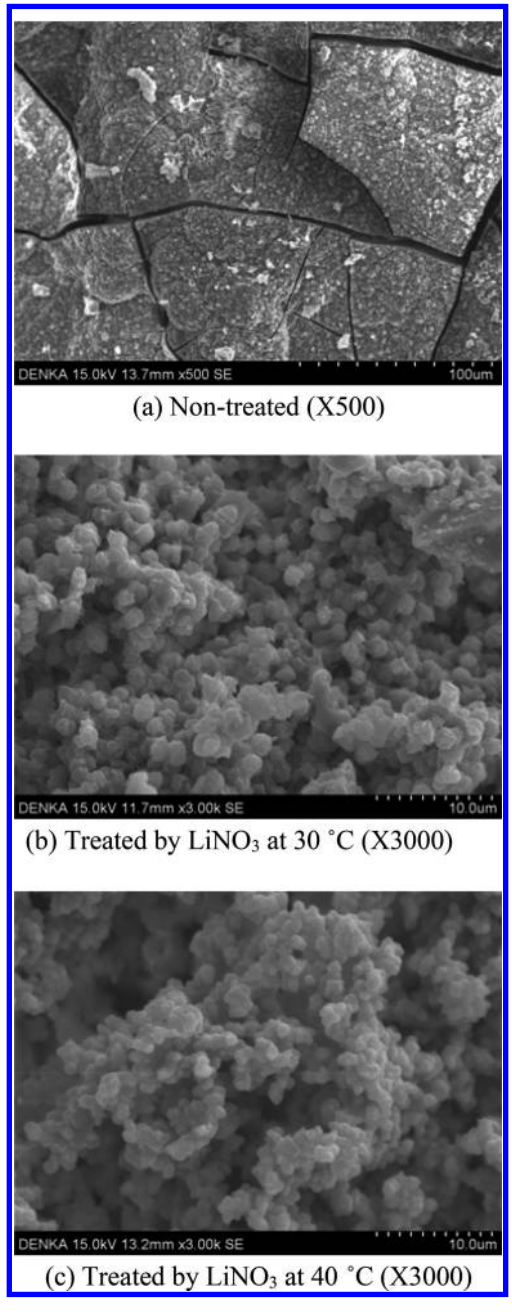

Figure 10. SEM photos of white products observed inside of specimens.

Table 3. Results of composition analysis of white products.

Name	Composition (%)				
	SiO_2	Na_2O	K_2O	CaO	Li_2O
Non-treated	69.1	8.2	0.8	21.9	<0.1
$LiNO_3$ (30 °C)	86.0	8.8	0.4	5.0	<0.1
$LiNO_3$ (40 °C)	74.8	4.9	0.4	7.6	12.3

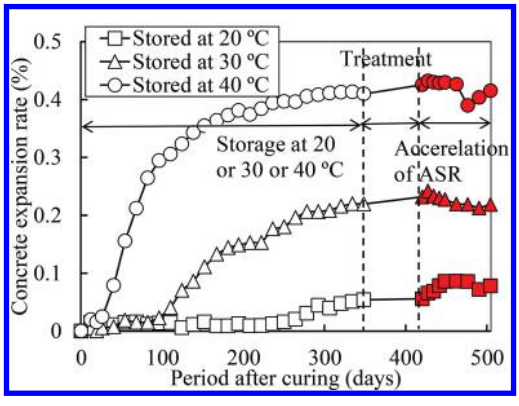

Figure 11. Variation curves of concrete expansion rate with time during the storage at the constant temperature followed by the treatment and ASR acceleration.

3.5 *Repair effect of electrochemical treatment applied to deteriorated concrete*

Variation curves of concrete expansion rate and half-cell potential of steel with time during the storage at the constant temperature for 350 days followed by the treatment and ASR acceleration are shown in Figure 11 and Figure 12 respectively.

From Figure 11, it can be seen that the storage at the higher temperature results in earlier and larger concrete expansion rate since the temperature around 40 °C strongly accelerates ASR. From Figure 12, all curves of half-cell potential show the high possibility of steel corrosion during the storage period at the constant temperature due to the heavy amount of pre-mixed chlorides.

Regarding the concrete expansion after the electrochemical treatment, Figure 11 shows that the treatment doesn't promote the concrete expansion rate due to ASR acceleration storage after the treatment regardless of the difference of the concrete expansion rate before the treatment. On the other hand, regarding steel corrosion, Figure12 shows that half-cell potential values indicate less than −1000 mV due to the strong cathodic polarization as shown in Figure 7. Moreover, the potential values of treated specimens gradually

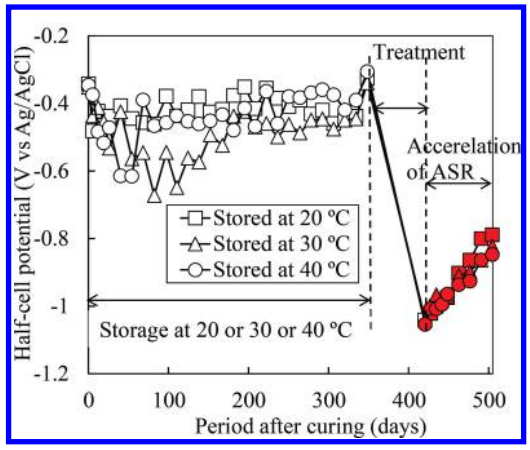

Figure 12. Variation curves of half-cell potential with time during the storage at the constant temperature followed by the treatment and ASR acceleration.

increase with the re-passivation after the electrochemical treatment during the storage in the condition for ASR acceleration, so the protection effect against steel corrosion can be expected.

4 CONCLUSIONS

This study conducted experimental investigations to grasp the complex deterioration mechanism due to chloride attack and ASR, and to confirm the effect of the electrochemical remedial measure against it. The results obtained from this study can be summarized as follows.

1. The rise in temperature of electrolyte solution from 30 °C to 40 °C remarkably accelerated the migration of Cl^- and Li^+ in concrete due to applying electrochemical treatment. Regarding the kind of lithium salt, $LiNO_3$ solution was most effective among some kinds of lithium salt contained in electrolyte solution from the viewpoint of lithium penetration.
2. The rise in temperature of electrolyte solution from 30 °C to 40 °C didn't promoted the accumulation of Na^+ and K^+ around the steel bar in concrete.
3. Regardless of conditions of electrochemical treatment, concrete expansion rate after treatment was suppressed when compared with that of the non-treated cases. It was evident that the 40 °C electrolyte of $LiNO_3$ would be more effective than other electrolytes used in this study to suppress the ASR expansion of concrete.
4. The protection effect against steel corrosion due to applying the electrochemical treatment

was confirmed by the observation of steel in concrete.

5. White products observed around steel bar in the treated specimen by 40 °C electrolyte of $LiNO_3$ contained Li_2O in the percentage of over 10%.
6. As a result of application of the electrichemical treatment after the complex deterioration of reinforced concrete, concrete expansion was not accelerated by the treatment regardless of the concrete expansion level before the treatment.

REFERENCES

Diamond, S. & Ong S. 1992. The Mechanism of Lithium Effects on ASR. *Proc. of the 9th International Conference on Alkali-Aggregate Reaction*: 269–278.

Habuchi, T. Tsuji, H. & Torii, K. 2004. Steel corrosion mechanisms caused by combined action of ASR and chloride penetration. *Annual Proc. of Japan Concrete Institute*, 26(1): 1017–1022.

Hondel, A.J. & Polder, R.B. 1992. Electrochemical Realkalisation and Chloride Removal of Concrete. *Construction Repair*: 19–24.

Japan Society of Civil Engineers. 2001. Recommendation for design and construction of electrochemical corrosion control method. *Concrete Library of JSCE* 107.

Japan Society of Civil Engineers. 2007. Standard specifications for concrete structures—2007, Maintenance.

MacCoy, W.J. & Caldwell, A.G. 1951. New Approach to Inhibiting Alkali-Aggregate Expansion. *Journal of ACI*, 22: 693–706.

Page, C.L. & Yu, S.W. 1995. Potential effects of electrochemical desalination of concrete on alkali-silica reaction. *Magazine of Concrete Research*, 47: 23–31.

Ueda, T. Yoshida, Y. Yamaguchi, K. & Ashida, M. 2006. Electrochemical migration of lithium ions into hardened concrete and ASR expansion after treatment. *Proc. of Structural Faults & Repair-2006*, CD-ROM.

Ueda, T. Baba, Y. & Nanasawa, A. 2011. Effect of electrochemical penetration of lithium ions on concrete expansion due to ASR. *Journal of Advanced Concrete Technology*, 9(1): 31–39.

Ueda, T. Kushida, J. Tsukagoshi, M. & Nanasawa, A. 2013. Influence of temperature on electrochemical remedial measure and complex deterioration due to chloride attack and ASR. *Proc. of the 3rd International Conference on Sustainable Construction Materials & Technologies (SCMT3)*, CD-ROM.

Whitemore, D. & Abbott, S. 2000. Use of an Applied Electric Field to Drive Lithium Ions into Alkali-Silica Reactive Structures. *Proc. of 11th International Conference on Alkali-Aggregate Reaction*: 1089–1098.

Concrete Repair, Rehabilitation and Retrofitting IV – Dehn et al. (Eds)
© 2016 Taylor & Francis Group, London, ISBN 978-1-138-02843-2

Effect of surface-applied inhibitors on anticorrosion performance of steel bars in sea sand concrete

Zixiao Wang, Shi Di & Zhiyong Liu
School of Civil Engineering, Yantai University, Yantai, China

ABSTRACT: Three surface-applied corrosion inhibitors (AMA, PCI-2010 and MFP) and two kinds of sea sand are used for making three water binder ratios (0.35, 0.45 and 0.55) concrete. Influences of sea sand upon the concrete strength are studied. Anticorrosion effects of corrosion inhibitors are studied in sea sand concrete by electrochemical analysis (LPR and EIS). Corrosion characteristics of steel bar surface are observed by broken test. The results show that using sea sand in concrete without any inhibitor has little or no adverse effect on 3 days and 28 days compressive strength of concrete, adding 2 wt% $NaNO_2$ in cementing material has a negative effect on the compressive strength of sea sand concrete. Compared to the anticorrosion effect of adding $NaNO_2$ in sea sand concrete, surface-applying PCI-2010 shows a similar effect. Followed by AMA, the anticorrosion efficiency is general. The anticorrosion of MFP in sea sand concrete is the worst of three inhibitors. Inhibiting efficiencies of three corrosion inhibitors are increase with the water binder ratio and the age of sea sand concrete. In the situation of concrete with high content of chloride ion in sea sand, using corrosion inhibitors have better anticorrosion performance.

1 INTRODUCTION

Due to massive growth of infrastructure construction, quantity demand of concrete and aggregate is increasing rapidly. River sand has been the most widely-used fine aggregate in concrete. But over-exploitation of river sand has led to some harmful environmental problems such as raising the level of the riverbed, lowering of the water table. As a result, the limited recourse and high prices of river sand hampers the development of construction in China.

Ascribed to convenience in mining and transportation, mature technology and lower costs [1], sea sand has great application potential in concrete construction. Especially the offshore sand is rich in estuaries of coastal areas. But the sea sand contains chloride ions that may cause steel bars corrosion and accelerate degradation of concrete structures. For preventing the steel bars in concrete from corrosion, desalinating the chloride ions in sea sand is the key problem.

In Europe, marine aggregates play a critical role in construction of coastal states, such as UK, Germany, the Netherlands, Denmark and Belgium. According to annual reports [2] of aggregates from 2002 to 2006, highest usage of sea sand in the Netherlands per year is 29.07 million m^3, usage in UK, Germany, Denmark and Belgium are 13.13, 7.57, 7.01 and 1.63 million m^3. In the UK more than 60% of the marine aggregates are used in the construction industry [3], and the proportions in the Netherlands, Denmark and Belgium are 49.2%, 59.9% and 93.8%. In Asia, since the early Meiji, sea sand was used in Japan's construction industry. According to a survey of Hiroshi Yamazaki [4], 38% investigated concrete batching plants in the coastal areas in Japan use sea sand in concrete which mixed with sodium nitrite as corrosion inhibitor. In South Korea plenty of sea sands have been used in concrete structures since 1993 and more than 70% sand in construction are sea sands [5].

To improve the durability of sea sand concrete, a traditional simple method is adding inorganic corrosion inhibitors such as nitrite in fresh concretes for the past decades [6–7]. But the nitrite is harmful to human's health and the properties of fresh and hardened concrete. Recently surface-applied corrosion inhibitor is used to delay corrosion of steel bars in concrete and prolong the service life of concrete structures [8–12]. However, very few investigations have reported the anticorrosion efficiency of surface-applied inhibitors on sea sand concrete. In this paper, anticorrosion effects of three surface-applied inhibitors on sea sand concrete are studied.

2 EXPERIMENTAL WORK

2.1 *Materials*

Table 1 presents the main technical parameters of the 42.5R ordinary Portland cement. Main parameters

Table 1. Main technical parameters of cement.

Parameters	
Density (g/cm^3)	3
Fineness (%)	1.1
Normal consistency (%)	27.6
Initial setting time (min)	185
Final setting time (min)	260
Bending strength (MPa)	4.9 (3d) 8.5 (28d)
Compressive strength (MPa)	25.5 (3d) 48.6 (28d)

Table 2. Main parameters of offshore sand.

Parameters	
Apparent density (kg/m^3)	2650
Tight density (kg/m^3)	1590
Bulk density (kg/m^3)	1460
Modulus of fineness (mm)	2.7
Content of silt content (%)	2.3
Content of clay lump (%)	0.8
Content of chloride ion (%)	0.004

of offshore sand are given in Table 2. Moreover, artificial sea sands are made up of offshore sands which fully immersed in sea water for 48 h and then dried at 100 ± 5°C. So, the only difference between two kind sea sands is the content of chloride ion. Offshore sand contains 0.004% chloride ion by weight, while artificial sea sand contains 0.12%.

Carbon steel bars of 12 mm in diameter, 70 mm in length are used as work electrodes in the tests, and the chemical composition of steel bar is 0.19% C, 0.02% Si, 0.37% Mn, 0.011% P, and 0.019% S. Both ends of the steel electrodes are masked with epoxy. Thin stainless steel sheets of thickness 5 mm and length 70 mm are used as the counter electrodes in the tests.

Three kinds surface-applied corrosion inhibitors used in the tests are as follows: an alcohol amine inhibitor (AMA), an amino carboxylic acid (PCI-2010) and water solution of monofluorophosphate (MFP). Sodium nitrite is used as Darex Corrosion Inhibitor (DCI) mixed in fresh concrete for a contrast of anticorrosion effect.

2.2 *Specimens and mixing*

Two steel electrodes and one thin stainless sheet are placed in the cubical concrete square specimen (size 100 mm × 100 mm × 100 mm). Concrete mix design compositions are given in Table 3 and Table 4.

The specimens are maintained in curing room under the standard curing condition (relative humidity is 95%, temperature is 20°C). Corrosion inhibitors are painting on one face of concrete specimens at the age of 3 days. The sketch diagram of concrete specimen is shown in Figure 1. The amount of migrating corrosion inhibitors is 200 g/m^2, in other word, 2 g per face. After the painting faces drying, specimens are still curing until the 28 days.

Table 3. Inhibition efficiency (%) values of steel bar in offshore sand concrete.

Time (d)	$NaNO_2$	PCI-2010	AMA	MFP
30	44.8	21.6	27.8	10.7
60	98.0	95.0	96.3	–
120	95.4	98.2	97.6	98.3
240	96.7	97.8	86.6	–

Table 4. Inhibition efficiency values of steel bar in artificial sea sand concrete.

Time (d)	$NaNO_2$	PCI-2010	AMA	MFP
30	49.0	41.5	96.0	66.9
60	99.7	97.3	96.6	96.0
120	98.7	98.0	21.6	96.0
240	96.7	97.6	86.8	96.9

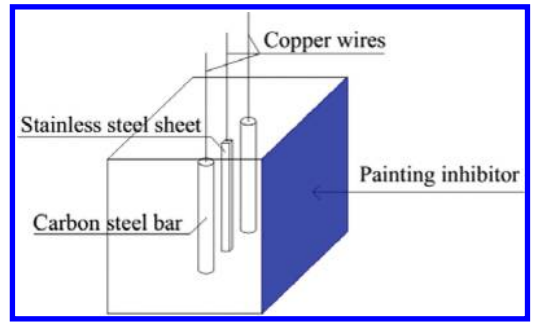

Figure 1. Sketch diagram of concrete specimen.

2.3 *Experimental techniques*

An electrochemical work station (PARSTAT 2273) is used for electrochemical analysis. The Linear Polarization Resistance (LPR) is used for evaluating the corrosion rate of steel bar in concrete. The corrosion current density (I_{corr}) quantifies corrosion behavior of work electrode [13–15]. An I_{corr} value of less than 0.1 μA/cm^2 indicates negligible corrosion of steel bar in concrete, while a value greater than 0.3 μA/cm^2 indicates active corrosion [16]. Thus, as to the steel bar in sea sand concrete,

an I_{corr} value of 0.3 μA/cm^2 is considered as the threshold criterion for corrosion initiation.

Electrochemical Impedance Spectroscopy (EIS) tests are performed on all specimens treated with inhibitors in approximately 240 days of exposure to the conventional environment. The IE% (inhibiting efficiency) is calculated by using the following formula:

$$IE\% = (R_p^{inh} - R_p)/R_p^{inh} \times 100\%$$

R_p and R_p^{inh} are the polarization resistances of steel bar with and without corrosion inhibitors, respectively.

The broken test is used to observe the corrosion characteristics on steel bar's surface in concrete. Specimens with water binder ratio of 0.55 are crushed in this test.

3 RESULTS AND DISCUSSION

3.1 *Compressive strength*

Figure 2 depicts the average compressive strength of the control concrete specimens (river sand concrete specimens) and those containing sea sand or $NaNO_2$ with different water binder ratios. The values of compressive strength are determined after 3 days and 28 days of standard curing.

When water to binder ratio is lower, the 3 and 28 days compressive strength of concrete specimens containing offshore sand or artificial sea sand is greater than that of control specimens, while the compressive strength of the sea sand concrete specimens mixing sodium nitrate is less than that of sea sand concrete specimens. The compressive strength of sea sand concrete specimens incorporating sodium nitrate decreased with the increase of water to binder ratio. In summary, the sea sand used in this study did not adversely affect the compressive strength of concrete.

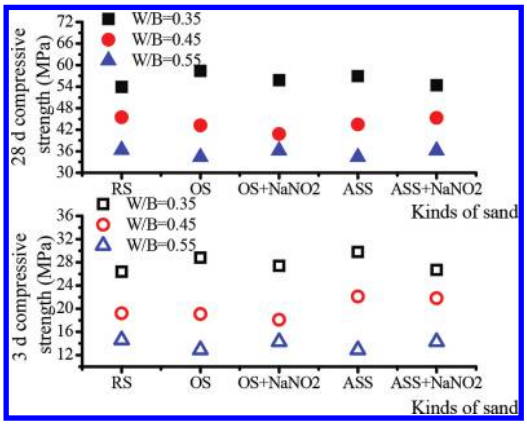

Figure 2. Compressive strength of concrete specimens at 3 days and 28 days with three water-binder ratios.

3.2 *Steel bar corrosion in sea sand concrete*

3.2.1 *Effect of water binder ratio on steel corrosion*

Figure 3 and 4 describe the change of the Rp and I_{corr} of steel bars in two kinds of sea sand concrete without the use of corrosion inhibitors. From the graphs it can be seen that steel bars have been corroded in sea sand concrete of three water binder ratios. The corrosion of steel bar is much serious in high water binder ratio concrete than in lower water binder ratios.

3.2.2 *Effect of concrete age on steel corrosion*

Moreover, Figure 3 and 4 represent that the I_{corr} of steel bar in sea sand concrete is increased with the increase of concrete age. Therefore, corrosion of steel bar in sea sand concrete is the accumulation

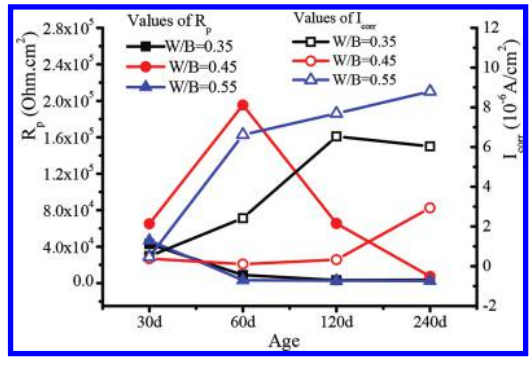

Figure 3. R_p and I_{corr} for offshore sand concrete without corrosion inhibitor at different age.

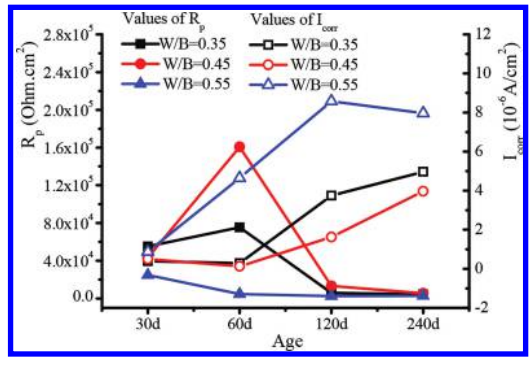

Figure 4. R_p and I_{corr} for artificial sea sand concrete without corrosion inhibitor at different age.

of time. This can explain that low content of Chloride ion in sand of concrete could also cause the corrosion of steel bar; sea sand concrete cannot be used in architectural engineering without any protection technique of steel bar corrosion.

3.2.3 *Effect of corrosion inhibitors on steel corrosion*

According to the above analysis, it is clearly that using specific technique for protecting steel bar from corrosion in sea sand concrete is necessary. In this paper, some corrosion inhibitors are used for this purpose. Figure 5 and Figure 7 are representing the R_p and I_{corr} of steel bar in two kinds of sea sand concrete with corrosion inhibitors at different age, the concrete water binder ratio is 0.55. And Figure 6 and Figure 8 are indicating the R_p and I_{corr} of steel bar in two kinds of sea sand concrete with corrosion inhibitors at different water binder ratios.

The results anticorrosion performance of AMA an alcohol amine organic inhibitor and MFP a cathodic inhibitor are as describes bellow. From the Figure 5, it can be seen that surface—applied AMA to offshore sand concrete can reduce I_{corr} of steel bar to 0.3 μA/cm² in short time, such as 120 days; but cannot prevent steel bar from

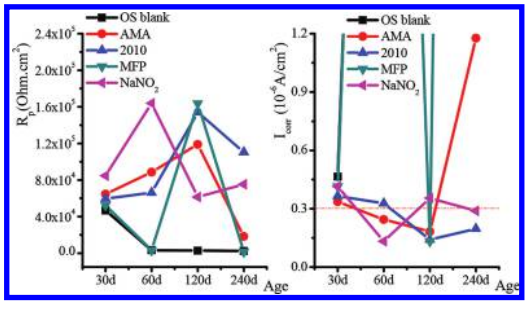

Figure 5. R_p and I_{corr} of steel bars in OS concrete specimens at different age and W/B = 0.55.

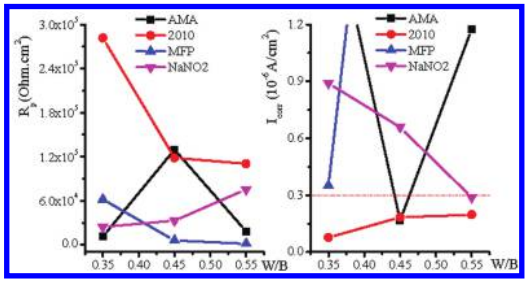

Figure 6. R_p and I_{corr} of steel bars in offshore sand concrete in different water binder ratios, at the age of 240 days.

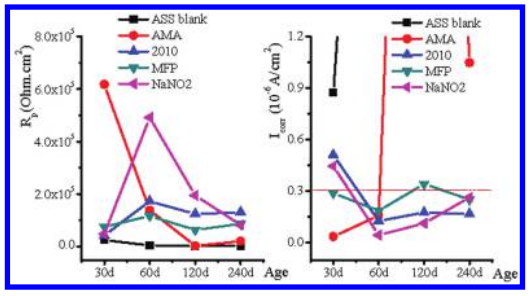

Figure 7. R_p and I_{corr} of steel bars in ASS concrete specimens at different age and W/B = 0.55.

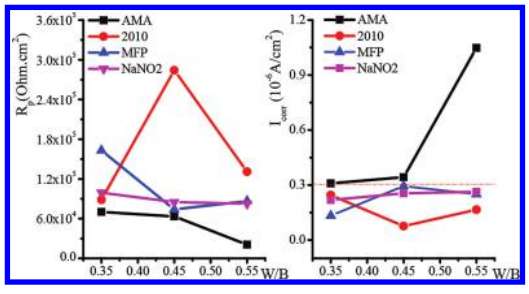

Figure 8. R_p and I_{corr} of steel bars in artificial sea sand concrete in different water binder ratios, at the age of 240 days.

corrosion at longer time. Surface—applied MFP to offshore sand concrete cannot decline I_{corr} of steel bar continuously and effectively. And according to Figure 7, surface-applied AMA to artificial sea sand concrete cannot bring the I_{corr} down over 0.3 μA/cm². Surface—applied MFP to the artificial sea sand concrete has an efficient anticorrosion property.

The R_p and I_{corr} of steel bar in sea sand concrete specimens adding 2% wt sodium nitrite are as reference values in tests. As Figure 5 and Figure 7 showing, at every time node, values of I_{corr} of steel bar in sea sand concrete surface-applying PCI-2010 are around 0.3 μA/cm², and numerical fluctuate within 20%. The I_{corr} can reduce to 0.3 μA/cm² at 240 days tests. Therefore, surface-applied PCI-2010 to two kinds of sea sand concrete has the similar anticorrosion performance with the control groups.

As to the relevance between steel bar corrosion and water binder ratios, Figure 6 and Figure 8 can explain it.

Figure 6 describes values of I_{corr} of steel bar in offshore sand concrete surface-applying PCI-2010 increase with the increase of water binder ratios of concrete, and the values of I_{corr} are all below 0.3 μA/cm² at the age of 240 days. The values of I_{corr} of steel bar in offshore sand concrete

decrease with the increase of water binder ratio. The I_{corr} of steel bar in offshore sand concrete surface-applying AMA or MFP and water binder ratios have no remarkable rule. From Figure 8, it can be seen that water binder ratio has little unwanted effect on values of I_{corr} of steel bar in artificial sea sand concrete surface-applying PCI-2010 or MFP or control group; values of I_{corr} are all lower than 0.3 μA/cm^2. But I_{corr} of steel bar in artificial sea sand concrete surface-applying AMA increases with the increase of water binder ratio.

To compare the anticorrosion effect of four kinds of corrosion inhibitors, Table 4 and Table 5 represent the values of inhibiting efficiencies of them. The order of IE of four inhibitors is as follows: PCI-2010 > $NaNO_2$ > AMA > MFP.

The results of LPR can illustrate that surface-applying PCI-2010 is an efficient technique to restrain corrosion of steel bar in sea sand concrete at the age of 240 days. Although the anticorrosion effect of PCI-2010 is decreases with the increase of water binder ratio of concrete, but isn't related to the content of chloride ion in sea sand.

For more detailed studies of the anticorrosion effect of inhibitors in long time, the results of EIS can do it. Figure 9 and Figure 10 are showing the Nyquist and Bode curves of steel bar in two kinds of sea sand concrete with or without inhibitors at the age of 240 days. As can be seen from the Figure 9 and Figure 10, values of the charge transfer resistance (R_{ct}) of steel bar in sea sand concrete without inhibitors is a very small, indicating steel bars are corroded seriously; in sea sand concrete with inhibitors, the pore resistance (R_p) of sea sand concrete and R_{ct} of steel bar increase obviously.

Firstly, comparing four inhibitors, surface-applying PCI-2010 to sea sand concrete has the highest R_p and the steel bar in it has the highest R_{ct}.

Table 5. Mix design composition (a) (applied to 1 m^3 concrete).

No.	W/B	Water/ kg	Cement/ kg	Stone/ kg	Fly ash/ kg	Slag/ kg
1#	0.35	190	393	70	80	960
2#	0.45	180	280	60	60	960
3#	0.55	170	219	40	50	960
4#	0.35	190	393	70	80	990
5#	0.35	190	393	70	80	990
6#	0.45	180	280	60	60	990
7#	0.45	180	280	60	60	990
8#	0.55	170	219	40	50	990
9#	0.55	170	219	40	50	990
10#	0.35	190	393	70	80	990
11#	0.35	190	393	70	80	990
12#	0.45	180	280	60	60	990
13#	0.45	180	280	60	60	990
14#	0.55	170	219	40	50	990
15#	0.55	170	219	40	50	990

Table 6. Mix design composition (b) (applied to 1 m^3 concrete).

No.	Super plastisizer/kg	RS/ kg	OS/ kg	ASS/ kg	$NaNO_2$/ kg
1#	696	–	–	–	10.9
2#	832	–	–	–	8
3#	892	–	–	–	6.2
4#	–	666	–	–	10.9
5#	–	666	–	10.9	10.9
6#	–	802	–	–	8
7#	–	802	–	8	8
8#	–	885	–	–	6.2
9#	–	885	–	6.2	6.2
10#	–	–	666	–	10.9
11#	–	–	666	10.9	10.9
12#	–	–	802	–	8
13#	–	–	802	8	8
14#	–	–	885	–	6.2
15#	–	–	885	6.2	6.2

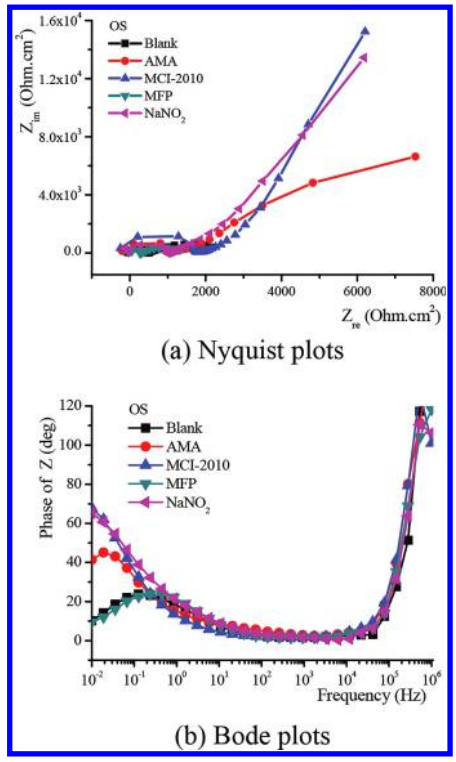

Figure 9. EIS plots for the steel in OS concrete (W/B = 0.55) with different inhibitors on 240th day.

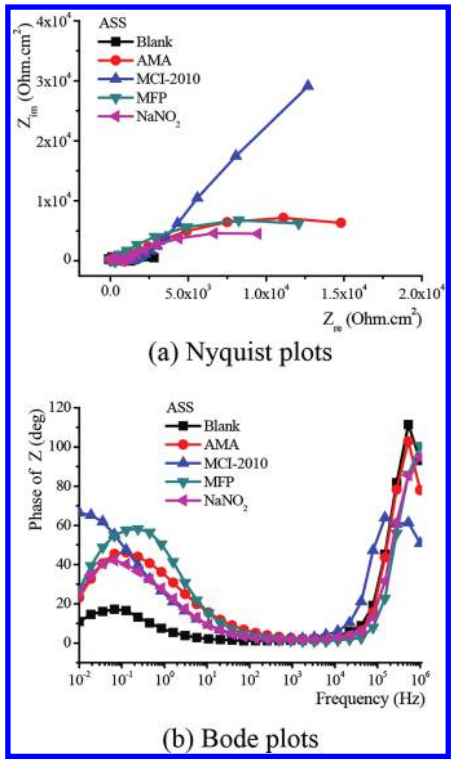

Figure 10. EIS plots for the steel in ASS concrete with different inhibitors on 240th days.

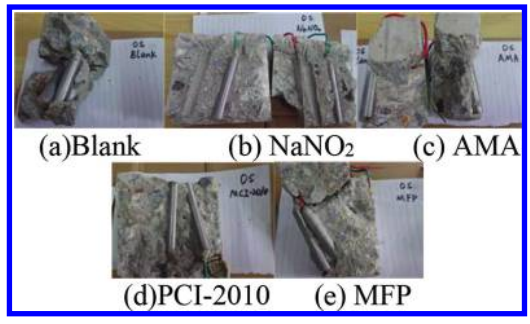

Figure 11. Surface features of steel bars in OS specimens.

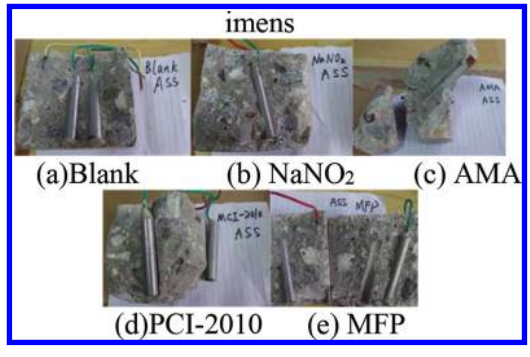

Figure 12. Surface features of the steel bars in ASS specimens.

Secondly, values of R_{ct} of steel bar in two kinds of sea sand concrete surface-applying PCI-2010 are very close, in other word, the anticorrosion effect of PCI-2010 on steel bar doesn't change with the content of Chloride ion in sea sand. And surface-applying AMA to sea sand concrete has the similar performance with PCI-2010. Thirdly, for inorganic inhibitors, the content of Chloride ion in sea sand has great influence on the change of R_{ct} of steel bar. Compared with the R_{ct} of steel bar in sea sand concrete without inhibitors, R_{ct} of steel bar in artificial sea sand concrete surface-applying MFP is twice than that in offshore sand concrete; R_{ct} of steel bar in artificial sea sand concrete adding 2% wt sodium nitrite is half of that in offshore sand concrete.

The results of EIS can again prove that the anticorrosion effect of PCI-2010 for steel bar in sea sand concrete is independent of the content of Chloride ion in sea sand.

To get more intuitive conclusions, Figure 11 and Figure 12 represent the surface corrosion characteristics of steel bar in two kinds of sea sand concrete at the age of 240 days, the water binder ratio is 0.55. From Figure 11 and Figure 12, it can be seen that steel electrodes in sea sand concrete without inhibitors or surface-applying AMA are rusting obviously. Steel electrodes in sea sand concrete surface-applying MFP are lacking luster which means large area of passive film on steel electrodes have been damaged. Furthermore, steel electrodes in sea sand concrete surface-applying PCI-2010 or adding 2% wt sodium nitrite are smooth and bright, don't have obvious rusty spots.

The results of broken test can also explain that surface-applying PCI-2010 can effectively delay the corrosion of steel bar in sea sand concrete.

3.3 *Penetrative anticorrosive mechanism of MCI*

The anticorrosion mechanism of surface-applying MCI can be concluded as follows: migrating corrosion inhibitors molecules through the concrete capillary pores penetrating the concrete cover to the surrounding of steel bar. By physical sorption or chemical combination on the surface of steel bar, MCI molecules can interrupt the cathodic and anodic reaction of electrochemical corrosion, therefore inhibiting the electrochemical corrosion of the steel bar [17]. Moreover, PCI-2010 molecules can

react with the cement hydration products, the reaction products are filled in the pores of the concrete, so hampering water and oxygen and Chloride ion from entering concrete [18]. Thus, surface-applying PCI-2010 to sea sand concrete has a superior anticorrosion effect on steel bar.

4 CONCLUSIONS

Using offshore sand or artificial sea sand in concrete has little effect on the compressive strength of concrete at the age of 7 days or 28 days. The order of IE for inhibitors in this paper is as follows: PCI-2010 > $NaNO_2$ > AMA > MFP. Surface-applying PCI-2010 to sea sand concrete has been found to be effective in inhibiting steel corrosion at the age of 240 days. Additionally, the anticorrosion effect of PCI-2010 in sea sand concrete is stable, the chloride ion content in sea sand have little effect on the anticorrosion effect. However, the anticorrosion effect of sodium nitrite in sea sand concrete is decrease with the increase of Chloride ion content in sea sand. As a result, at least surface-applying PCI-2010 to offshore sand concrete is a workable method to protect steel from corrosion in 240 days.

ACKNOWLEDGEMENTS

The authors are grateful for finical supports from the National Natural Science Foundation of China (No.51278443) and Shandong Province Natural Science Foundation (ZR2011EEM006).

REFERENCES

[1] Yin Hui-guang, Li Yan, Lv Heng-lin, Gao Quan. Durability of sea sand containing concrete: Effects of chloride ion penetration, Mining Science and Technology (China), 2011(21):123–127.
[2] Adonis F. Velegrakis, Arnaud Ballay, Serafim Poulos, Rolandas Radzevicius, Valerie Bellec, Faustino Manso. European marine aggregates resources: Origins, usage, prospecting and dredging techniques [J]. Journal of Coastal Research, 2010(51):1–14.
[3] ICES, 2005. Report of the Working Group on the Effects of Extraction of Marine Sediments on the Marine Ecosystem (WGEXT). San Sebastián, Spain 5–8 April, ICES CM 2005/E: 60: 102.
[4] Hiroshi Yamazaki. Views about using sea sand as concrete aggregate in Japan [J]. Translator: ZENG Rui-yu. Hydro-Science and Engineering (China), 1975(3):117–123.
[5] Cho Dong-Oh. Challenges to sustainable development of marine sand in Korea [J]. Ocean & Coastal Management, 2006, 49(1):1–21.
[6] Yang Chang-hui, Zhang Hang, Ou Zhong-wen, Wang Chong. Corrosion inhibitor for concrete based on seawater and sea sand. Concrete (China), 2010(11):69–72.
[7] Liu yang, Study on anticorrosion property of steel corrosion inhibitor in marine environment [D]. China, Shandong: Chinese Marine University, 2012.
[8] Sagoe-Crentsil K.K., Yilmaz V.T., and Glasser F.P. Properties of Inorganic Corrosion Inhibiting Admixtures in Steel-Containing OPC Mortars: Chemical and Electrochemical Properties. Advance in Cement Research, 1996 (4): 91–102.
[9] Gonzales J.A., Ramirez E., Bautista A., Protection of Steel Embedded in Chloride-Containing Concrete by Means of Inhibitor. Cement and Concrete Research, 1998 (28):577–589.
[10] Monticelli C., Frignani A., and Trabanelli G. A Study on Corrosion Inhibitors for Concrete Application. Cement and Concrete Research, 2000 (30): 635–642.
[11] Batis G., Pantazopoulou P., Routoulas A. Corrosion protection investigation of reinforcement by inorganic coating in the presence of alkanolamine-based inhibitor. Cement and Concrete Composites, 2003 (25):371–377.
[12] Ormellese M., Berra M.,Bolzoni F., et al. Corrosion inhibitors for chlorides induced corrosion in reinforced concrete structures. Cement and Concrete Research, 2006 (36):536–547.
[13] Network D. Manual de inspección, evaluación y diagnóstico de corrosión en estructuras de hormigón armado. Río de Janeiro: CYTED programe; 1997.
[14] Broomfield J.P. Life prediction of corrodible structures. NACE Symposium, Cambridge. 1991:14.
[15] González J.A., Miranda J. Corrosión en las estructuras de hormigón armado: Fundamento, medida, diagnosisy prevención. 2007, CSIC, Madrid, Spain.
[16] Omar S. Baghabra Al-Amoudi, Mohammed Maslehuddin, A.N. Lashari, Abdullah A. Almusallam. Effectiveness of corrosion inhibitors in contaminated concrete [J]. Cement & Concrete Composites, 2003 (25): 439–449.
[17] Liu Zhiyong, Miao Changwen, Sun Wei. Effect of Migratory corrosion inhibitors on the durability of Chloride-contaminated refeinforced concrete (II)—long-term effect, morphological and mechanismic analysis [J]. Journal of the Chinere ceramic society. Vol. 38, No.7, 2010(7):1324–1327.
[18] Yu Lei, Liu Zhiyong, Zuo Xiaobao. Migrating Corrosion Inhibitor Transporting Model in Cement Concrete [J]. Journal of the Chinere ceramic society. Vol. 42, No.11, 2014 (11):1370–1376.

Concrete Repair, Rehabilitation and Retrofitting IV – Dehn et al. (Eds)
© 2016 Taylor & Francis Group, London, ISBN 978-1-138-02843-2

Durability design of concrete mixtures for sewer pipe applications: A review of the Life Factor Method

M.W. Kiliswa, M.G. Alexander & H.-D. Beushausen
Concrete Materials and Structural Integrity Research Unit, Department of Civil Engineering, University of Cape Town, South Africa

ABSTRACT: This paper reviews certain equations that are used for calculating key parameters influencing microbially-induced concrete corrosion in sewers. The equations form the basis of the so-called Life Factor Method (LFM) that is widely used by practising engineers for corrosion prediction in Portland cement based concrete sewers that flow partly full. Under certain conditions hydrogen sulphide (H_2S) is generated in stale sewage and is readily released into the sewer headspace where it is biologically converted to sulphuric acid on the moist pipe walls. This acid attacks the concrete matrix. Thus, the key parameters in this method are the rate of H_2S oxidation on the sewer walls and the alkalinity of the concrete. Therefore, if the LFM is to be used to predict corrosion of concrete sewers with different binder systems, additional factors such as material factors must be introduced to cater for additional rate-controlling parameters that are not currently covered by the LFM.

1 INTRODUCTION

In the durability design of concrete outfall sewers which flow partly full, the alkalinity of the concrete matrix is one of the significant considerations used to predict the system's service life. The other consideration is sulphide generation forecasting within the sewer as emphasised in earlier publications (US EPA 1977). Sulphide forecasting is based on flow-slope relationships under prevailing climatic conditions, which are used to design sewer lines that will produce minimal sulphide. Sulphide exists in the stale sewage as sulphide ions (S^{2-}), hydrogen sulphide ions (HS^-), and hydrogen sulphide molecules (H_2S) both in aqueous and gaseous states, depending primarily on pH. At pH less than 7, H_2S predominates in aqueous solutions, and is readily released into the sewer headspace especially under turbulent flow conditions in partly filled sewers (Alexander & Fourie 2011). The aggressive H_2SO_4 (which attacks the concrete matrix) on the non-submerged sewer walls is biologically generated from this available H_2S. It therefore follows that durability design in sewer networks is based on interrelationships between climatic conditions, sewer hydraulics and the properties of the sewer pipe material that is exposed to H_2S. This interrelationship is expressed in certain sewer design methods such as ExtCorr, WATS, and LFM, but LFM remains the most common one in use by design engineers in predicting the corrosion rate (Kley & Caradot 2013).

2 LIFE FACTOR METHOD

The rate of corrosion of a concrete sewer can be calculated from the rate of production of H_2SO_4 on the pipe wall, which in turn is dependent upon two factors; sulphide generation within the sewage, and the rate at which H_2S is released into the headspace from the surface of the sewage stream (Boon & Pomeroy 1990). The LFM consists of a series of equations that considers these different factors.

2.1 *Sulphide generation within the sewage*

Sulphide generation generally occurs at sewage temperatures above 15°C (US EPA 1974). Pomeroy & Parkhurst (1977) assumed that the concentration of nutrients supporting Sulphate-Reducing Bacteria (SRB) (responsible for generation of sulphide) that thrive in the slime layer of the sewage is proportional to the Biological Oxygen Demand (BOD) of most municipal wastewater. BOD is dependent on sewage temperature. The quantity of available nutrients that provide energy to the SRB is measured by the 5-day BOD (BOD_5) (McLaren 1984). However, since for design purposes a seasonal or annual effect is required, sulphide generation is determined from the effective (EBOD) as shown in Equation 1 (US EPA 1985).

$$[\text{EBOD}] = [\text{BOD}_5] \times 1.07^{(T-20)} \quad (1)$$

where [EBOD] = effective [BOD_5] (mg/l); [BOD_5] = composite average BOD_5 (mg/l); T = wastewater temperature (°C).

For sewers flowing partly full, there is an air-water interface and the sewage entrains air, whereas generated H_2S (in gaseous form) escapes via this interface. This means that the sulphide accumulation in the sewage is slower than it would be in an equivalent system with the pipe flowing full. Assuming there is little or no Dissolved Oxygen [DO] in the sewage, SRB would reduce the sulphate in the sewage to sulphide [S], and [S] generation can be determined from Equation 2 (US EPA 1985).

$$\frac{d[S]}{dt} = M'\left(\frac{EBOD}{R}\right) - \frac{m[S](sV)^{0.375}}{d_m} \quad (2)$$

where d[S]/dt = rate of change of total sulphide (mg/l/); [S] = total sulphide concentration (mg/l); M′ = effective sulphide flux coefficient for H_2S generated in the slime layer when there is open channel flow in a gravity system (m/hr); EBOD = effective BOD_5 (mg/l); R = hydraulic radius of flow area (m); m = sulphide loss coefficient due to oxidation and escape into headspace; s = slope of energy grade line (m/m); V = mean flow velocity (m/s); d_m = mean hydraulic depth (m).

There will be a theoretical upper limit to the sulphide concentration in the sewage when the losses equal the [S] generation and this will occur when (Equation 3):

$$[S]_{lim} = \frac{M'}{m} EBOD(sV)^{-0.375}\left(\frac{P}{W}\right) \quad (3)$$

where $[S]_{lim}$ = upper limit for H_2S generation in an open channel gravity system (mg/l); P = wetted perimeter (m); W = flow width (m).

The limiting value of [S], $[S]_{lim}$, is approached asymptotically in a sewer flowing partly full under gravity and will not be reached under these conditions. However, when a sewer flowing partly full under gravity receives discharge from a closed system, the [S] concentration may exceed the limiting value and H_2S will be stripped rapidly from the sewage to re-establish equilibrium between gas concentrations in the sewer headspace and sewage. The downstream sulphide concentration is calculated from Equation 4 (US EPA 1985).

$$S_2 = S_{lim} - \frac{(S_{lim} - S_1)}{\log_{10}^{-1}\left[\frac{m(sV)^{0.375}\Delta t}{2.31 d_m}\right]} \quad (4)$$

where S_2 = downstream sulphide concentration (mg/l); S_1 = upstream sulphide concentration (mg/l); Δt = flow time in a given reach of sewer (hr).

Due to biological activities in the sewage, several sulphur compounds are formed but it is the gaseous H_2S that can escape causing odour and corrosion problems. Therefore, for corrosion-related analysis, it is necessary to determine the proportion of [S] formed that is dissolved, and the proportion of this Dissolved Sulphide [DS] that is H_2S. The proportion of [S] that is [DS] is variable and dependent upon sewage pH and its metals content. The proportion of [DS] that is H_2S is directly related to the pH of the sewage (Bealey et al. 1982).

As discussed above, the rate of sulphide production is influenced by several factors. It increases with increase in temperature and also depends on the concentrations of both the organic nutrients and sulphate. The rate of sulphide production can be limited by a scarcity of either sulphate or organic nutrients, and since both are consumed in the biological reactions that produce H_2S, they are required in a certain ratio (Boon & Pomeroy 1990). If there is an excess of organic nutrients, then the rate is limited by the amount of sulphate and if there is an excess of sulphate, it is limited by the amount of organic nutrients.

Equations 1 to 4 express the rate of sulphide build-up as a function of the various factors that influence generation by the slime layer and the losses by oxidation and escape to the air. As they stand, these equations are limited due to the difficulty in securing relatively accurate input information (Hvitved-Jacobsen et al. 2013). For example, absorption of oxygen at the surface of the sewage stream can be predicted if the slope, pipe size and flow quantity are known, but extra oxygen will be added at junctions, drops, and other points of turbulence. It is also difficult to predict the rate at which oxygen will be consumed.

Boon & Pomeroy (1990) stated that the practical approach to the difficulty in H_2S prediction is to consider cases in which unpredictable factors are considered favourable for sulphide build-up. That is, it will be assumed that sufficient sulphate is present so that it is not limiting, that oxygen concentration is low, that no nitrate is present, and that there is no toxic condition or other factor that inhibits the action of the slime layer. These assumptions vary in-situ even within a section of the same sewer, and their applications to different sewer environments could result in unreliable outcomes. However, under typical sewer conditions, indicative dissolved sulphide concentrations can be determined from these equations for use in estimating H_2S flux from the sewage surface.

2.2 *Hydrogen sulphide release*

When there is no equilibrium between the concentrations of gaseous H_2S in the sewage and the sewer headspace, interface movement of this gas occurs. Since H_2S concentration is invariably lower in the sewer headspace than in the sewage, its release is usually from the sewage to the sewer headspace.

Under typical sewer conditions, once [DS] in the sewage has been determined using Equations 1 to 4, the rate of H_2S release can be calculated from Equation 5.

$$\varphi_{sf} = 0.69(sV)^{0.375} J[DS] \quad (5)$$

where φ_{sf} = H_2S flux from the sewage surface (g/m^2/h); s = hydraulic gradient (m/m); V = stream velocity (m/s); J = proportion of dissolved sulphides in sewage present as H_2S; DS = dissolved sulphides in sewage (m/l).

Assuming that all H_2S escaping to the sewer headspace is oxidised on the pipe wall, the average H_2S flux can be obtained by multiplying φ_{sf} by the ratio of sewage surface width, W, to exposed wall perimeter, P', to give Equation 6.

$$\varphi_{sw} = 0.69(sV)^{0.375} J[DS]\left(\frac{W}{P'}\right) \quad (6)$$

where φ_{sw} = average H_2S flux from the sewage surface (g/m^2/h).

However, apart from the flow velocity, the rate at which H_2S is released from the sewage is also influenced by local turbulence and whether the flow is sub- or super-critical (Goyns 2013). This equation, therefore, is also limited due to the absence of additional parameters that contribute to H_2S release from the sewage.

2.3 *Corrosion rate*

H_2SO_4 that is generated on the moist sewer surfaces may react with the alkaline (acid soluble) constituents, specifically the calcareous fractions, in the concrete as shown in Equation 7.

$$H_2SO_4 + CaCO_3 \rightarrow H_2O + CO_2 + CaSO_4 \quad (7)$$

If the formation rate of the H_2SO_4 is 'low', a major part of it will react with the acid soluble components such as any PC-based binder matrix. On the other hand, if the formation rate of the H_2SO_4 is relatively 'high', part of it will trickle down the sewer walls before reaction. This 'excess' acid will reach the sewage and may react with the alkaline components therein to form sulphate ions. The liquid film on the sewer walls around the sewage daily flow level may contain these ions that could, through association, cause chemical sulphate attack on the concrete (Hvitved-Jacobsen et al. 2013).

Equation 7 shows that 1 mol of H_2S (32 g H_2S-S) resulting in the formation of H_2SO_4 has a potential for reaction with 1 mol (100 g $CaCO_3$) of cement and/or calcareous aggregate in the concrete. Based on this mass balance, a quantitative method was developed for predicting the corrosion rate of concrete in relation to the alkalinity of the concrete material and the rate of H_2S absorption in the moisture on the concrete surface. This is expressed empirically in Equation 8 (US EPA 1974).

$$r_{corr} = \frac{100}{32} \cdot \frac{\phi_{sw}}{A} \quad (8)$$

where r_{corr} = corrosion rate per unit area of the concrete surface (g/m^2/h); ϕ_{sw} = rate of H_2S absorption in the moisture at the concrete surface (g H_2S-S/m^2/h); A = alkalinity of the concrete material in units of g $CaCO_3$ per g concrete material.

If the right-hand side of Equation 8 is divided by the density of concrete, estimated to be 2.4×10^6 g/m^3, the area-based corrosion rate can be expressed as an annual corrosion rate in units of depth per time as shown in Equation 9.

$$c = 11.4 \frac{\phi_{sw}}{A} \quad (9)$$

where c = annual corrosion rate (mm/year).

In Equation 9, it is assumed that all H_2SO_4 formed on the concrete wall will react with the acid soluble portion of the concrete matrix. However, this is not usually the case and an efficiency coefficient is necessary for acid reaction based on an estimated fraction of acid remaining on the sewer wall. This can be expressed as shown in Equation 10.

$$c = 11.4k \frac{\phi_{sw}}{A} \quad (10)$$

where k = efficiency factor < 1.

For systems where ϕ_{sw} is low, the value of k approaches 1, whereas for higher values of ϕ_{sw}, k may decrease to about 0.3 (US EPA 1985).

To ensure that a sewer remains serviceable after a certain period, Equation 10 can be used together with the design life in order to determine the required additional concrete cover to reinforcing steel as shown in Equation 11.

$$Az = 11.4k\phi_{sw}L \quad (11)$$

where $z = cL$ = additional concrete cover required over reinforcing steel (mm); L = required design life of a sewer (years).

The term '*Az*' on the left-hand side of Equation 11, called the Life Factor, is used for comparing different concrete mixtures by alkalinity. The term on the right-hand side describes the conditions within the sewer in terms of sewage properties and flow characteristics, sewer headspace, and the required service life.

Studies undertaken in a 'live' sewer environment in South Africa show that Equation 11 can be accurately used in PC based concretes with siliceous aggregates. For other binder systems such as PC based concrete with calcareous aggregates or Calcium Aluminate Cement (CAC) based concretes, Equation 11 has to be modified in order to realistically predict the rates of corrosion since CAC based systems performed up to 4 times better than PC based systems due to additional rate-controlling parameters such as control of bacterial metabolism by toxicity (bacteriostatic effect) of the CAC (Goyns 2014).

2.4 *Discussion*

The LFM (Equation 10) is a sound basis for prediction of PC based concrete corrosion and is widely used (Vollertsen et al. 2011). It assumes that the rate of corrosion, c, is proportional to the flux of H_2S to the pipe wall. However, not all absorbed H_2S reacts with the alkaline parts of concrete, accounted for by the concrete alkalinity, A, and efficiency factor, k. A material constant (*11.4*) is incorporated to account for process stoichiometry and concrete density.

The flux of H_2S to the pipe wall depends on a range of conditions, the first being sulphide formation under anaerobic conditions, part of which is precipitated by metal ions (Nielsen et al. 2005). Another part becomes biologically or chemically re-oxidised in the bulk water and biofilms depending mainly on constituent concentrations, catalysts and pH (Nielsen et al. 2006; Kotronarou & Hoffmann 1991; Nielsen et al. 2008). The H_2S that is not oxidised is released to the sewer headspace where it is absorbed by moist pipe surfaces or lost in the system (Vollertsen et al. 2011). The rate of release of H_2S depends on the sewer hydraulics, pH, sewage constituents, and gaseous phase concentrations (Pomeroy & Parkhurst 1977). The transfer of H_2S to the moist pipe walls depends on the movement and turbulence in the gas phase as well as the surface conditions of the sewer pipe (Hvitved-Jacobsen 2002).

Recent attempts have been made to modify the LFM in order to account for the dynamics in the sewer environment. Kienow & Kienow (2004) reviewed this method and proposed two factors; a turbulence corrosion factor and a crown corrosion factor. These factors account for system specific corrosion rates induced by turbulence and system design.

Goyns (2014) reported that different binder systems such PC based concrete with either siliceous or calcareous aggregates, and CAC based concrete have varying rates of corrosion when subjected to microbially-induced H_2SO_4. The LFM accurately predicts this rate of corrosion in PC based concrete with siliceous aggregates.

Therefore, if the LFM is to be used to predict corrosion of concrete sewers with different binder systems, additional factors such as material factors must be introduced to cater for additional rate-controlling parameters that are not currently covered by the LFM.

2.5 *Conclusions*

From experience, the LFM, although largely deterministic, is a sound basis for corrosion prediction in PC based concrete sewer systems. However, it is limited in applications due to a combination of the dynamic conditions in sewer environments and advancement in cementitious material properties. Improved understanding of the fundamentals associated with these areas provides opportunities for refining this method through development of performance based material factors—since ultimately, it is the (concrete) sewer pipe material that is responsible for corrosion resistance or durability performance.

REFERENCES

Alexander, M.G. & Fourie, C.W. 2011. Performance of sewer pipe concrete mixtures with portland and calcium aluminate cements subject to mineral and biogenic acid attack. *Materials and Structures*. 44 (1): 313–330.

Bealey, M., Duffy, J.J., Preuit, R.B. & Stuckey, R.E. 1981. *Concrete Pipe Handbook*. Virginia: ACPA.

Boon, A.G. & Pomeroy, R.D. 1990. *The problem of hydrogen sulphide in sewers*. 2nd ed. Westminster: Acer John Taylor.

Environmental Protection Agency, Centre for Environmental Research Information. 1985. *Design manual: Odor and corrosion control in sanitary sewerage systems and treatment plants*. EPA, Cincinnati.

Goyns, A. 2014. Virginia sewer rehabilitation: Progress report 6. Pretoria: CMA.

Goyns, A. 2013. *Design manual for concrete pipe outfall sewers*. Midrand: CMA.

Hvitved-Jacobsen, T., Vollertsen, J. & Nielsen, A.H. 2013. *Sewer processes: Microbial and chemical process engineering of sewer networks*. 2nd ed. Boca Raton: CRC Press.

Hvitved-Jacobsen, T., Vollertsen, J. & Nielsen, A.H. 2002. *Sewer processes: Microbial and chemical process engineering of sewer networks*. Boca Raton: CRC Press.

Kienow, K.K. & Keinow, K.E. 2004. Evaluation of sanitary sewer sulphide, odor and corrosion potential. *Proceedings of the Pipelines 2004 International Conference*. August 1–4. San Diego.

Kienow, K.K. & Pomeroy, R.D. 1978. Corrosion resistant design of sanitary sewer pipes. *ASCE Convention and Exposition*. October 16–20. Chicago, IL. 25.

Kley, G. & Caradot, N. 2013. *Review of sewer deterioration models*. Berlin: KWB.

Kotronarou, A. & Hoffmann, M.R. 1991. Catalytic autooxidation of hydrogen sulphide in wastewater. *Environmental Science and Technology*. 25(6): 1153–1160.

McLaren, F.R. 1984. *Design manual: Sulphide and corrosion prediction control*. Virginia: ACPA.

Nielsen, A.H., Hvitved-Jacobsen, T. & Vollertsen, J. 2008. Effect of pH and iron concentrations on sulphide concentrations in wastewater collection systems. *Water Environment Research*. 80(4): 380–384.

Nielsen, A.H., Hvitved-Jacobsen, T. & Vollertsen, J. 2006. Recent findings on sinks for sulphide in gravity sewer networks. *Water Science and Technology*. 54(6): 127–134.

Nielsen, A.H., Lens, P., Vollertsen, J. & Hvitved-Jacobsen, T. 2005. Sulphide-iron interactions in domestic wastewater from gravity sewer. *Water Research*. 39(12): 2747–2755.

Pomeroy, R.D. & Parkhurst, J.D. 1977. *Progress in water technology*. London: Pergammon.

US EPA. 1985. *Design Manual: Odor and corrosion control in sanitary sewerage systems and treatment plants*. Cincinnati: EPA.

US EPA. 1974. *Process design manual for sulphide control in sanitary sewerage systems*. Washington: EPA.

Vollertsen, J., Nielsen, A.H., Jensen, H.S., Rudelle, E.A. & Hvitved-Jacobsen, T. 2011. Modelling the corrosion of concrete sewers. *12th International conference on urban drainage*. September 11–16. Porto Alegre.

Concrete Repair, Rehabilitation and Retrofitting IV – Dehn et al. (Eds)
© 2016 Taylor & Francis Group, London, ISBN 978-1-138-02843-2

Moisture exchange in concrete repair system captured by X-ray absorption

M. Lukovic, E. Schlangen, G. Ye & K. van Breugel
Section of Materials and Environment, Faculty of Civil Engineering and Geosciences, Delft University of Technology, Delft, The Netherlands

ABSTRACT: One of the main reasons for premature failure of concrete repair systems are stresses due to differential shrinkage between the old (concrete or mortar substrate) and new (repair) material. These are primarily caused by moisture exchange between the repair system and environment or moisture transport within the repair system itself. However, during the setting and hardening of the repair material, moisture exchange will also determine the development of material properties in the repair material and interface between repair material and substrate. In this paper, moisture profiles are quantified using X-ray absorption technique. The output of X-ray attenuation measurement is a spatial distribution of linear attenuation coefficients expressed as grey scale values. First, preliminary studies are performed to determine the absorption rate of the mortar substrate. Cumulative water absorption and penetration depth of the water front are monitored as a function of time. Furthermore, absorption of the substrate when water is absorbed from the top is investigated. Main advantages and drawbacks of the method are presented and compared with results from the gravimetric test. Following, moisture exchange in the repair system is investigated. In one specimen, a primer was used. When curing is stopped, drying profiles in the repair system are quantified. Knowledge about the water exchange between the repair material and the concrete substrate, which takes place at the early stage, is only the first step towards more-justified decisions about substrate preconditioning and possible use of primers and curing compounds in experiments and field practice.

1 INTRODUCTION

Moisture transport between repair material and concrete (or mortar) substrate determines the development of the interface and repair material microstructure in concrete repair systems (Zhou 2010, Courard, Lenaers et al. 2011). Capillary absorption by the concrete substrate is beneficial as it enables higher mechanical interlocking between the two materials. Yet, moisture absorption by the substrate prior to setting of the repair material also determines the resulting w/c ratio of the repair material. Therefore, if too much water is absorbed by the concrete substrate, there might be no water available for hydration of the repair material. For optimal performance of the repair system, dynamics of the moisture exchange should be well understood.

Still, this area of research remains scarcely investigated and poorly explained, as the dynamics of water exchange is very complicated and are strongly influenced by hydration of the repair material. As microstructure of the repair material is continuously changing, the diffusion coefficient of the repair material is dependent on time, initial water content and saturation state of the concrete substrate. Only a few studies on the moisture exchange in a multilayer systems when fresh, newly cast material was placed on the matured substrate have been done (Brocken, Spiekman et al. 1998, Faure, Caré et al. 2005, Kazemi-Kamyab, Denarie et al. 2012). So far, only nuclear magnetic resonance was used. Some preliminary studies on a layered "lego blocks" specimens made of freshly cast cement pastes were performed by X-ray absorption (Bentz and Hansen 2000). As both materials were freshly cast, these conditions did not directly imitate repair system. In addition, studies so far only indicated the change of moisture content (i.e. by the change of the signal or measured spectra). Yet, moisture content was not quantified.

In this paper, a possibility of using X-ray absorption method for studying the moisture dynamics in a repair system was explored. First, the rate of moisture absorption of the mortar substrate was quantified. Sample preparation and post-processing procedure for X-ray measurement data are explained. Furthermore, absorption of the substrate when a fresh repair material is cast on top of it is investigated. For improving repair performance, primers are sometimes used in the field. It is commonly assumed that the main role

of primers is to prevent water exchange between the repair and the substrate, thereby enhancing the bond strength. Therefore, in one test, commercially available primer was applied in order to investigate its role on reducing and stopping absorption of the substrate. This knowledge will enable a more justified decision about possible use of primers in future experiments and in practice.

2 MATERIALS AND METHODS

2.1 *Materials and sample preparation*

The substrate used in the study was a two year old mortar. The reason for using mortar (instead of concrete) was to minimize heterogeneity and specimen to specimen variation at the scale of investigation. A standard mortar mixture (OPC CEM I 42.5 N, water-to-cement ratio 1:2, cement-to-sand ration 1:3) was used. Small prism specimens ($18 \times 19 \times 40$ mm^3) were slowly cut with a diamond saw from bigger mortar samples. Prior to casting of the repair material, top surface of the substrate was polished to expose aggregates and minimize the influence of surface roughness. The sample is then placed in a mold and covered with aluminum self-adhesive film.

Before testing, mortar substrate was dried in the oven at 105°C until constant weight is achieved. This was done in order to remove all evaporable water and have a zero initial moisture content at the start of the experiment (Hall 1989). It has to be noted that these conditions might also trigger some microstructural changes and microcracking in the material (Ye 2003). As repair material, cement paste with OPC CEM 42.5 N and a water-to-cement ratio of 0.5 was used.

2.2 *X-ray absorption measurement*

After sample preparation, mortar substrate or repair system were placed in the Phoenix Nanotom X-ray system (CT scanner) for measuring the water exchange (Fig. 2). CT images are maps of X-ray absorption in the material (Trainor, Foust et al. 2012). Here, only a single X-ray image is taken at certain time step. The sample was kept in the same position during the whole experiment. The resulting CT images are spatial distributions of linear attenuation coefficients, expressed by GSV (grey scale value). In this paper, an attempt is made to correlate the GSV change with change in moisture content as a function of time. One way of doing this is by correlating the change of grey scale value with attenuation coefficient of water (Michel, Pease et al. 2011, Pease, Scheffler et al. 2012). There, the attenuation behavior of monochromatic x-ray is described by the Beer-Lambert law:

$$I = I_0 e^{-\mu t} \tag{1}$$

where μ is the attenuation coefficient, t is the thickness of the sample, I_0 is incident intensity. It is attenuated (i.e. absorbed and scattered) as photons pass through the specimen, resulting in transmitted intensity I. If the resulting image is a spatial distribution of the linear attenuation coefficients, expressed as a GSV, this GSV is correlated to intensity and can be used to determine the attenuation coefficient of material.

Correlating GSV change with change in moisture content is done by taking advantage of a simple physical principle. In a dry sample, X-rays are attenuated *only* by the dry material. If there is some moisture intake in a porous material, the attenuating material consists of the dry material and a thickness of water layer equivalent to the (volume) moisture content of the material. This means that, by knowing the attenuation coefficient of water, and knowing the change in GSV, the (additional) moisture content inside the material can be determined. Material was always analyzed in the middle part in order to exclude edge effects.

In order to relate the change in GSV with the change in moisture content, the following procedure was used:

– Attenuation coefficient of water can be determined based on the GSV difference of air and water (see Fig. 3). Attenuation coefficient of

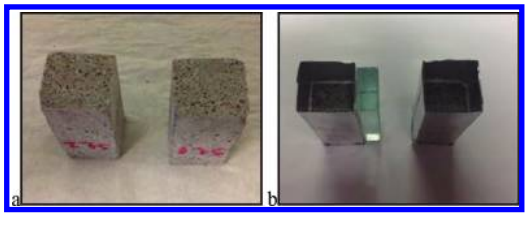

Figure 1. Sample preparation: a) samples after cutting and polishing b) samples in a mold and covered by aluminum self-adhesive film.

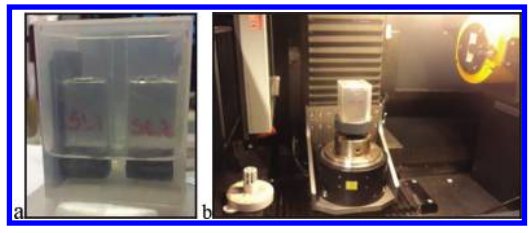

Figure 2. a) Samples prior to placing in a CT scanner b) CT scanner setup.

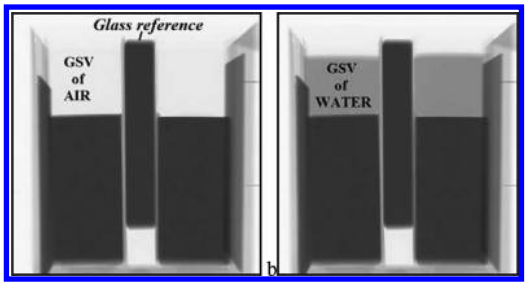

Figure 3. Difference in grey scale value a) air b) water.

water can be determined based on the following formula:

$$GSV_{water} = GSV_{air} e^{-\mu_w t_{water}} \quad (2)$$

where GSV_{water} is the greyscale value of water, GSV_{air} the grey scale value of air, t_{water} the thickness of water and μ_w is the attenuation coefficient of water. Only μ_w is unknown and can be determined.

– Once the attenuation coefficient of water is determined, GSV of the wet porous material can be correlated to GSV of the dry porous material as:

$$GSV_{wetmat} = GSV_{drymat} e^{-\mu_w t_w} \quad (3)$$

where t_w is the thickness of water layer equivalent to moisture content in sample and can be expressed as:

$$t_w = \Delta c_w \frac{t}{\rho_w} \quad (4)$$

Here, Δc_w is the change of water content [g/cm^3], t is the thickness of the sample and ρ_w is the density of water. From these equations, Δc_w can be determined as:

$$\Delta c_w = -\frac{\rho_w}{\mu_w t} \ln \frac{GSV_{wetmat}}{GSV_{drymat}} \quad (5)$$

Due to variation of the beam intensity, GSV varies even without change in the moisture content. In order to account for this effect, a reference glass was used (see Fig. 3). Subsequently, each image was calibrated according to the change of GSV in the reference glass.

Scanning parameters used in were: X-ray tube voltage 130 kV, X-ray tube current 270 µA. The spatial resolution was 30 µm/pixel.

The water attenuation coefficient was determined at the beginning of each experiment. However, as the thickness of the measured water layer and settings of the CT scanner were kept constant, the attenuation coefficient varied by 0.5% between experiments and, therefore, a constant value (0.2233 cm^{-1}) is used in all calculations. It has to be emphasized that two assumptions were made which might affect obtained results (Pease, Scheffler et al. 2012). First, the attenuation coefficient of water is taken to be independent of porous material thickness and water layer thickness. And second, Beer-Lambert law applies for monochromatic x-ray (x-ray photons of a single, consistent energy), while the x-ray source used in this study produces polychromatic x-ray photons (x-photons over a spectrum of energy levels). However, as the material properties (i.e. porosity) and material thickness were kept consistent throughout the whole experiment, and the intensity of beam was calibrated with the reference glass, it is considered that these assumptions would not considerably affect the results. In addition, measured moisture content in the specimen is compared to porosity measurements obtained by Mercury Intrusion Porosimetry (MIP) in order to check if it is in a reasonable range of values.

2.3 *MIP measurement*

In order to check the results of applied method (moisture content in the specimen), porosity of the mortar was measured. Pore size and distribution were tested by MIP. Procedure for this method is well established and detailed information can be found elsewhere (Ye 2003).

3 RESULTS AND DISCUSSION

3.1 *Absorption of the mortar substrate when water is absorbed from the bottom*

First study is done on the absorption rate of mortar (test marked as ABS-bottom). Moisture change as a function of time is given in Figure 4. Moisture profile is averaged through the thickness of the sample. Moisture profiles are given in Figure 5.

Obtained curves resemble the curves obtained by neutron radiography (Zhang, Wittmann et al. 2010) or nuclear magnetic resonance method

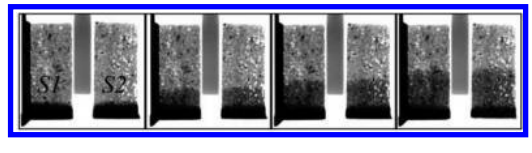

Figure 4. Qualitative representation of water change as a function of time (wetting from the bottom—ABS-bottom).

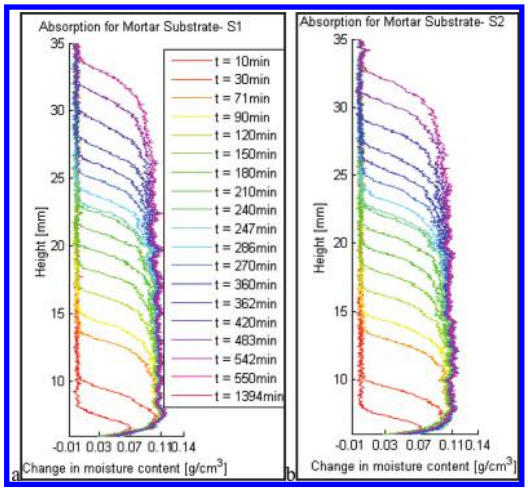

Figure 5. Moisture profiles in the left and right specimen (from Fig. 4) as a function of time (test ABS-bottom).

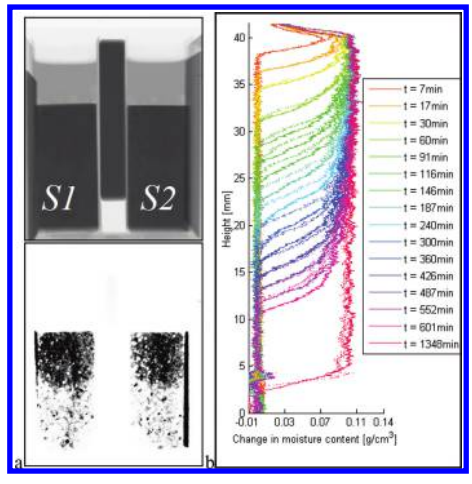

Figure 6. a) Obtained images (top-whole GSV range, bottom-chosen GSV range) b) Moisture profiles in both specimens (S1 and S2) as a function of time (test ABS-top).

(Hall 1989). This means that water profiles in mortar samples can be monitored very accurately by X-ray absorption.

3.2 *Absorption of the mortar substrate when water is absorbed from the top*

Additionally, absorption of the substrate, with a water layer on top, is investigated (tested marked as ABS-top). Water was placed at the top in order to investigate if the absorption rate would differ, as the repair material will also be cast from the top side of the substrate. Experiment setup and results are presented in Figure 6a and Figure 6b, respectively.

Inflection points of the moisture profiles (chosen at 0.05 g/cm^3) are defined as absorption profile (absorption height) and are presented in Figure 7. From Figure 7 it is observed that the absorption direction (influence of gravity) does not have significant influence on water absorption. Water absorption follows the linear function of square root within the monitored time.

The total amount of absorbed water as a function of time can be calculated by integrating moisture profile at a certain time step. These curves are given in Figure 8, and can be compared to gravimetric tests performed using same samples.

For this specimen size, results are not alike. There are a few possible reasons for this. First, due to the small specimen size and influence of cutting (possibly creating microcracks at the specimen edges), gravimetric results might show higher results than X-ray measurements. This influence is less in X-ray measurements as specimen edges

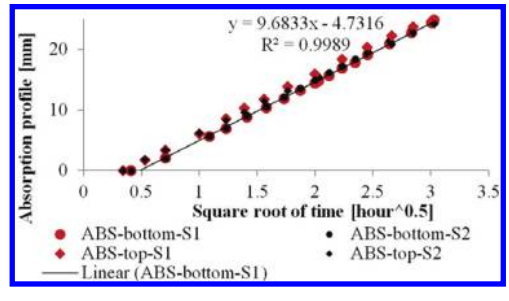

Figure 7. Absorption height in the specimens where water was absorbed from the bottom and from the top.

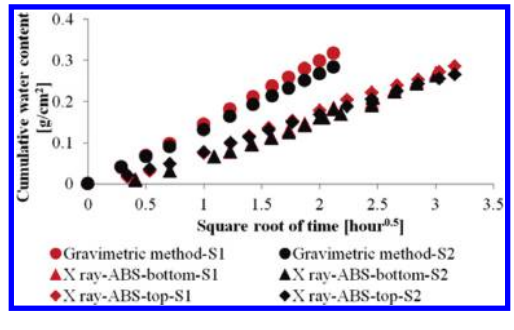

Figure 8. Comparison between moisture absorption measured by gravimetric test and by X-ray absorption.

were excluded from the analysis. Second, for this specimen size and exposed area for absorption test (around 3 cm^2), gravimetric measurement can result in large errors. Third, as discussed earlier, attenuation coefficient of water might be

somewhat lower than used in these calculations. Practically, attenuation coefficient might be lower due to interaction of material (Pease, Scheffler et al. 2012) and water and in current experiments this was not taken into account. Lower attenuation coefficient would lead to larger area and increase in calculated cumulative water content captured by X-ray absorption. In order to investigate the accuracy of the calculated attenuation coefficient and the gravimetric test, porosity measurements can be of use.

3.3 *MIP results on a substrate mortar*

Four replicate mortar samples were tested. Differential curves of all replicates are very similar and are given in Figure 9. Since it is mature mortar, the first and the second peak are very close to each other. This means that capillary pores are very fine due to the age of samples.

The average porosity of all tested samples is 12.23%, with a standard deviation of 4.17%. The average pore diameter is 0.05 µm with 8% standard deviation. The porosity measured by MIP is in accordance with the moisture content obtained by X-ray with the assumption that during absorption most of the pores are saturated (from Fig. 5 and 6 maximum moisture content is higher than 0.11 g/cm^3 and from MIP measurement, if all the pores are full, moisture content of the sample is 0.1223 g/ cm^3).

3.4 *Water exchange in a repair system*

Cement paste with a w/c ratio of 0.5 and around 15 mm thickness was cast on the top of the substrate mortar. In one case, the substrate was treated with a commercial primer prior to application of the repair material. Immediately after casting, repair systems are sealed with aluminum self-adhesive tape and placed in the CT-scanner in order to investigate the moisture exchange between repair material and concrete substrate (Fig. 10).

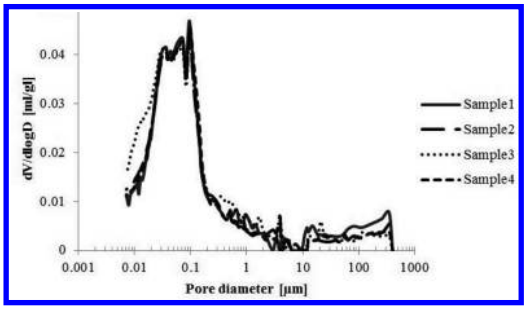

Figure 9. Pore size distribution of four replicate mortar samples.

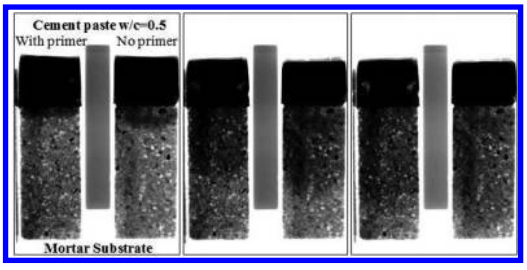

Figure 10. a) Obtained images for testing repair system (from left-immediately after putting the specimens in the CT scanner-26 min after casting, 421 min and 1283 min after casting).

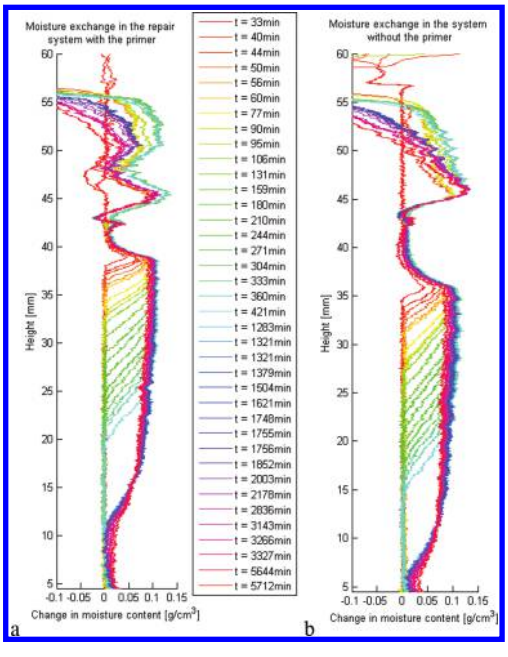

Figure 11. a) Moisture profiles in the specimen a) with the primer b) without the primer.

It is considered that the main absorbed component from the repair material is the water. Therefore, although cement slurry (and not the pure water) was absorbed by the mortar substrate, the attenuation coefficient for water is used in the calculations. This assumption, however, needs to be further investigated.

Both curves in Figure 11 start at 33 minutes, which was the time needed for casting, vibrating, sealing and placing the specimens in the CT-scanner. It seems that the primer does not reduce the rate of water absorption. However, in the beginning, the primer did slightly postpone the onset of water loss from the repair material

(Fig. 10). However, the rate of absorption seems not to be affected by the application of primer (Fig. 12). In addition, curves have a similar slope as the curves from the absorption test. This means that the cement slurry from the repair material is initially absorbed with the same speed as water. This is contradicting the assumption that, due to the higher viscosity of cement slurry compared to water, it would be absorbed slower. Therefore, as water from the repair material can be absorbed very fast, it seems that pre-saturating concrete substrate is critical factor for obtaining envisaged repair system properties.

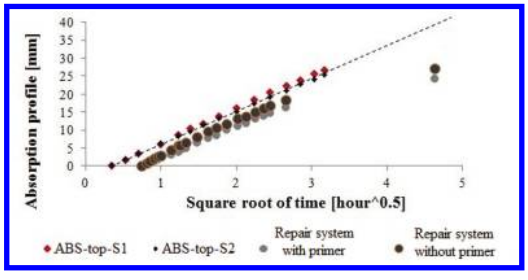

Figure 12. Absorption height in the specimens when water or repair material are absorbed from the top.

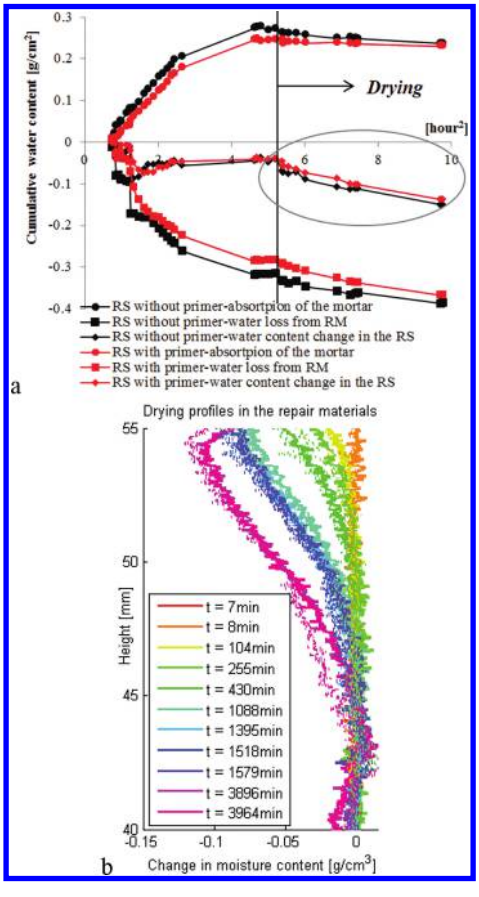

Figure 13. a) Cumulative moisture absorption in the repair system b) Moisture profiles in the repair material after exposing to drying (full line—without primer, dashed line—with primer).

If the procedure for calculating the cumulative moisture absorption based on integrating moisture profiles is applied on the repair material, the following curves are obtained (Fig. 13a). In the first 29 hours of curing, samples were sealed. In this period, the total change of moisture content in the repair system should be equal to 0 if the sealing was complete good (i.e. the amount of water that is lost from the repair material should be equal to the amount of water that is absorbed by the substrate). After 29 hours from casting, the repair systems were uncovered and exposed to drying. This can be also captured in Figure 13a. After 29 hours, the substrate still have a constant water content, which does not hold for the moisture content in the repair material. Drying profiles of the two specimens are shown in Figure 13b and they confirm that also drying profiles can be very accurately captured by X-ray absorption. In addition, both repair systems, with and without primer, show the same rate of drying. This confirms that similar amount of water was lost, leading to similar degree of hydration and therefore, the same rate of drying in two repair materials.

4 CONCLUSIONS

Based on the presented study, the following conclusions can be drawn:

- X-ray absorption can be used to predict moisture transport in porous materials very accurately and with high resolution. Both absorption profiles and drying profiles can be quantified.
- With this technique, water absorption as a linear function of square root of time could be captured.
- Applied primer did not prevent or reduce the rate of water loss from the repair material, but only delayed the onset of water loss.

Saturation level of the concrete substrate is the critical parameter for development of properties inside the repair system and its influence needs to be further investigated.

ACKNOWLEDGMENT

Financial support by the Dutch Technology Foundation (STW) for the project 10981—"Durable

Repair and Radical Protection of Concrete Structures in View of Sustainable Construction" is gratefully acknowledged.

REFERENCES

Bentz, D. and K. Hansen (2000). "Preliminary observations of water movement in cement pastes during curing using X-ray absorption." Cement and concrete research 30(7): 1157–1168.

Brocken, H., M. Spiekman, L. Pel, K. Kopinga and J. Larbi (1998). "Water extraction out of mortar during brick laying: a NMR study." Materials and structures 31(1): 49–57.

Courard, L., J.-F. Lenaers, F. Michel and A. Garbacz (2011). "Saturation level of the superficial zone of concrete and adhesion of repair systems." Construction and Building Materials 25(5): 2488–2494.

Faure, P., S. Care, C. Po and S. Rodts (2005). "An MRI-SPI and NMR relaxation study of drying–hydration coupling effect on microstructure of cement-based materials at early age." Magnetic resonance imaging 23(2): 311–314.

Hall, C. (1989). "Water sorptivity of mortars and concretes: a review." MAGAZINE OF CONCRETE RESEARCH 41(147): 51–61.

Kazemi-Kamyab, H., E. Denarie, E. Bruhwiler, B. Wang, M. Thiery, P.F. Faure and V. Baroghel-Bouny (2012). Characterization of moisture transfer in UHPFRC-concrete composite systems at early age. Second International Conference on Microstructural-related Durability of Cementitious Composites. Amsterdam, The Netherlands.

Michel, A., B.J. Pease, M.R. Geiker, H. Stang and J.F. Olesen (2011). "Monitoring reinforcement corrosion and corrosion-induced cracking using non-destructive x-ray attenuation measurements." Cement and Concrete Research 41(11): 1085–1094.

Pease, B.J., G.A. Scheffler and H. Janssen (2012). "Monitoring moisture movements in building materials using X-ray attenuation: Influence of beam-hardening of polychromatic X-ray photon beams." Construction and Building Materials 36: 419–429.

Trainor, K.J., B.W. Foust and E.N. Landis (2012). "Measurement of energy dissipation mechanisms in fracture of fiber-reinforced ultrahigh-strength cement-based composites." Journal of Engineering Mechanics 139(7): 771–779.

Ye, G. (2003). Experimental study and numerical simulation of the development of the microstructure and permeability of cementitious materials, PhD thesis, Delft University of Technology, Delft, The Netherlands.

Zhang, P., F. Wittmann, T. Zhao, E. Lehmann and Z. Jin (2010). "Visualization and quantification of water movement in porous cement-based materials by real time thermal neutron radiography: Theoretical analysis and experimental study." Science China Technological Sciences 53(5): 1198–1207.

Zhou, J. (2010). Performance of engineered cementitious composites for concrete repairs, PhD Thesis, Delft University of Technology.

Concrete Repair, Rehabilitation and Retrofitting IV – Dehn et al. (Eds)
© 2016 Taylor & Francis Group, London, ISBN 978-1-138-02843-2

Forecasting chloride-induced reinforcement corrosion in concrete—effect of realistic reinforcement steel surface conditions

U.M. Angst
ETH Zürich, Institute for Building Materials (IfB), Zürich, Switzerland

B. Elsener
ETH Zürich, Institute for Building Materials (IfB), Zürich, Switzerland
Department of Chemical and Geological Science, University of Cagliari, Monserrato, Italy

ABSTRACT: This paper presents experimental results on the effect of realistic steel surface conditions on the initiation of chloride-induced corrosion. Ten series of "as-received" reinforcement steel originating from different countries and having been subject to different exposure histories (storage, transport, handling, etc.) were studied. There were clear differences in visual appearance, which were reflected in electrochemical characterization (cyclic voltammetry). Metallographic analyses also indicated differences in terms of steel microstructure. Neither the visual appearance nor the amount of initially present rust permitted any prognosis of resistance to chloride-induced corrosion. On the other hand, martensitic steels appeared to yield lower chloride threshold values than ferritic-pearlitic microstructures.

The results illustrate the difficulties that realistic conditions cause for the concept of the critical chloride content. Given the low degree of confidence with which corrosion initiation can be predicted, the feasibility of the concept of the critical chloride content is discussed.

1 INTRODUCTION

Over the last decades, considerable efforts have been made in science and engineering to predict initiation of chloride-induced reinforcement corrosion in concrete. After it was recognized in the second half of the last century that i) initiation of pitting corrosion in alkaline concrete requires the presence of chloride and that ii) some sort of correlation exists between the risk for corrosion initiation and the chloride concentration in the concrete (Hausmann, 1967, Richartz, 1969, Vassie, 1984), the concept of the *critical chloride content* or *chloride threshold value* was born. This concept is now well-established and reflects the wide-spread belief that initiation of chloride-induced reinforcement corrosion can be predicted directly as a function of the chloride concentration. Direct evidence for this are also the extensive research efforts made over the last decades to model chloride ingress into concrete, e.g. reviewed in (Tang et al., 2012). The conceptual approach of assessing the risk of corrosion simply as a question of chlorides found its way also into national and international standards that specify tolerable chloride concentrations for produced concrete or chloride threshold values to be used in condition assessment (such as 0.4% chloride by cement weight). Given the well-known large uncertainties inherent to the critical chloride content (Angst et al., 2009), these values are relatively conservative.

The success of the described concept of reducing corrosion initiation to a mere question of chlorides was certainly favored by the fact that chloride concentrations in concrete can relatively easily be determined, both in the laboratory and on samples taken from structures, and by the simple need for a criterion, on which engineering decisions can based.

As long as concrete technology and construction methods remained relatively constant and resulted in similar concrete qualities and properties over many years, it may have been feasible to rely on long-term field experience, i.e. to design and assess structures based on past experience. However, advances in concrete technology (e.g. admixtures permitting manufacture of denser concretes) and cement production (e.g. the use of supplementary cementitious materials to improve certain concrete properties and to reduce the environmental footprint) led to significant changes in terms of concrete microstructure, pore solution chemistry, chloride binding capacity, etc. Given the absence of past experience for the majority of these

modern, non-Portlandite systems, attempts were made to determine the critical chloride content with help of accelerated testing in the laboratory. A large number of literature attempts are reviewed in (Angst et al., 2009). It is very well known that these attempts generally got bogged down in many details such as specimen design, accelerating chloride ingress, measurement methodologies, etc. As a result, literature chloride threshold values scatter over several orders of magnitude and there exists still no accepted test setup or method to determine this parameter of uttermost practical importance. One of the major challenges lies in simultaneously satisfying the general desire for a fast and reproducible method and the requirement of practice-related conditions to ensure that the results are relevant for practice.

This paper presents experimental results on the effect of realistic—generally termed "as-received"—steel surface conditions on the initiation of chloride-induced corrosion. This is here used as an example of one of the numerous degrees of freedom that exists in experimentally determining the critical chloride content. The example illustrates the difficulties that realistic conditions cause for the concept of the critical chloride content. Given the low degree of confidence with which corrosion initiation can be predicted, the feasibility of the concept of the critical chloride content is discussed.

This work was performed at the Institute of Building Materials at ETH Zurich, Switzerland, as part of the work of RILEM technical committee 235-CTC "corrosion initiating chloride threshold concentrations in concrete".

2 EXPERIMENTAL

2.1 *Materials*

Plain carbon steel reinforcement steel bars of diameter 12 mm and length 10 cm were sent to ETH Zurich from different countries. This included ten different series of reinforcement steel that were bought by participants of RILEM TC 235-CTC in their respective countries, compare Table 1. All rebar samples were type Class B according to EN 1992-1-1:2005, with the exception of series H (China). The bars from series H also had a slightly smaller diameter than 12 mm. The two series from Sweden (G and I) were supplied by different laboratories.

The rebars were sent to ETH in "as-received" condition, which means with the surface state as they were delivered from the supplier. At one end of each bar, a hole was drilled and an electrical cable connection was made with help of a screw. Thanks to the mechanical connection, there was no need for soldering or other heating of the steel that may have affected the steel and its surface.

Table 1. Designations and countries of origin of the 10 different series of as-received reinforcement steel bars tested in this work.

Designation	Country
A	Switzerland
B	Denmark
C	Germany
D	France
E	Spain
F	The Netherlands
G	Sweden
H	China
I	Sweden
J	Norway

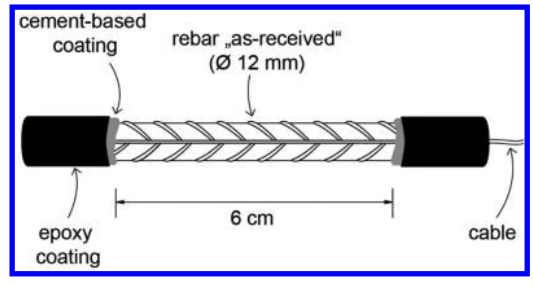

Figure 1. Schematic illustration of specimen.

Subsequently, the rebars were degreased with acetone and immediately after this, the ends of the rebars were coated with a thin (ca. 1–2 mm) layer of the cement-based product Pro Svum 05/Pro Acryl 100 supplied by the company Pro-Tex AS, Denmark. The central, uncoated and later exposed part of the rebars had a length of 6 cm. Figure 1 schematically shows the specimen geometry.

2.2 *Exposure*

For each series, two bars were prepared as described above and then vertically hanged in an exposure tank. The tank was filled with saturated calcium hydroxide solution so that the entire part of uncoated steel surface was submerged. The tank was closed with a lid to limit ingress of air and thus carbonation of the solution. The pH of the exposure solution was checked at least once per week and calcium hydroxide powder was regularly added to ensure constant buffering at pH = ca. 12.5.

All specimens were connected to a data logger. A silver/silver chloride/sat. potassium chloride reference electrode was continuously immersed in the solution at the edge of the tank. All rebar potentials

were measured at an interval of 1 h versus the immersed reference electrode.

After 42 d of exposure in sat. $Ca(OH)_2$, sodium chloride was added to the solution to increase the chloride concentration stepwise on a weekly basis. The increase in chloride concentration was always 0.01 mol/l (step height) up to 0.09 mol/l. After this, the step height was increased to 0.02 mol/l.

During all exposure experiments, the temperature remained constantly at 20–22°C.

2.3 *Measurements and methods*

Prior to preparing the samples as described in the previous section, the rebar surfaces were examined by means of reflected-light *microscopy*. From selected bars, sections were cut, polished and etched (3% nitric acid) for metallographic analyses of the microstructure.

After ca. 40 d of exposure in sat. $Ca(OH)_2$, *cyclic voltammetry* was performed on all rebars. The sweep rate was 5 mV/s and the scans were started from the open circuit potential. It was first scanned in cathodic direction with a reverse potential at –1.4 V vs. $Ag/AgCl_{sat}$; the upper reverse potential was 0.6 V vs. $Ag/AgCl_{sat}$. In total, 5 cycles were recorded.

During exposure to chloride, the potentials of the bars were monitored. A drop by at least 150 mV into negative direction was considered to indicate corrosion initiation. Normally, these drops occurred within very short time, but some of the specimens were able to recover and repassivate. These depassivation and repassivation events are well known, e.g. (Angst et al., 2011), and have also been taken into account for defining onset of corrosion in the work of RILEM TC 235-CTC. In the present study, the criterion for stable corrosion onset was that the potential of at least 150 mV more negative than the initial "passive level" was maintained for the rest of the test period, at least for 3 weeks (no repassivation).

3 RESULTS AND DISCUSSION

3.1 *Microscopy and metallography*

Already by the naked eye, clear differences between the as-received surface states of the ten different series of rebars could be seen. Figure 2 shows three selected examples that are representative for the surfaces of the ten different series of as-received rebars. Series C, D, and E were all essentially free from red or brown visible corrosion products and exhibited an almost clean metal surface. The rebars of series A, G, H, and I were partially coated (<50% of the surface) with red-brown corrosion products. Finally, series B, F, and J were severely pre-corroded and exhibited relatively thick and flaky layers of red-brown corrosion products. This arbitrary classification in "low", "intermediate" and "high" degree of pre-existing rust is also summarized in Table 2.

The metallographic analyses (Fig. 3) revealed that the rebars of series C and F exhibited an almost homogenous ferrite-pearlite microstructure over their cross-sections. Series H also shows a ferrite-pearlite microstructure, however a markedly coarser one. Series H also has a significantly higher carbon content than the steels from series C and F. The rebars belonging to all the other series had a composite microstructure with typically three zones: a ferrite-pearlite core, an intermediate layer, and a surface layer of martensite. These bars obviously underwent a thermo-mechanical strengthening process (e.g. as known under trade-names such as "Tempcore") that lead to the tempered martensite surface layer.

3.2 *Cyclic voltammetry*

Figure 4 shows two examples of clearly distinct cyclic voltammograms that are representative for all measurements (compare Figure caption). The voltammogram shown in Figure 4a exhibits a number

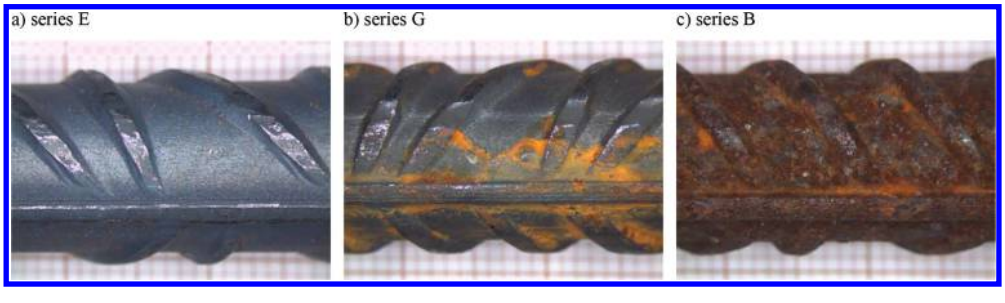

Figure 2. Optical micrographs of three selected examples of the rebars in as-received surface condition (rebar diameter = 12 mm, grid unit = mm). Figure a) is an example of a *low degree* of pre-existing rust, b) represents an *intermediate degree* of pre-existing rust, and c) a *high degree* of pre-existing rust.

Table 2. Degree of pre-existing rust on the rebar surface, microstructure of the outermost layer, and current densities of peak I during the first cycle of cyclic voltammetry, j_p, of the different rebar series.

Series	Degree of rust	Surface microstructure	j_p (mA/cm^2)
A	Intermediate	Martensite	1.64
B	High	Martensite	6.47
C	Low	Ferrite-Pearlite	1.73
D	Low	Martensite	0.64
E	Low	Martensite	1.60
F	High	Ferrite-Pearlite	4.92
G	Intermediate	Martensite	2.86
H	Intermediate	Coarse Ferrite-Pearlite	3.46
I	Intermediate	Martensite	1.99
J	High	Martensite	5.74

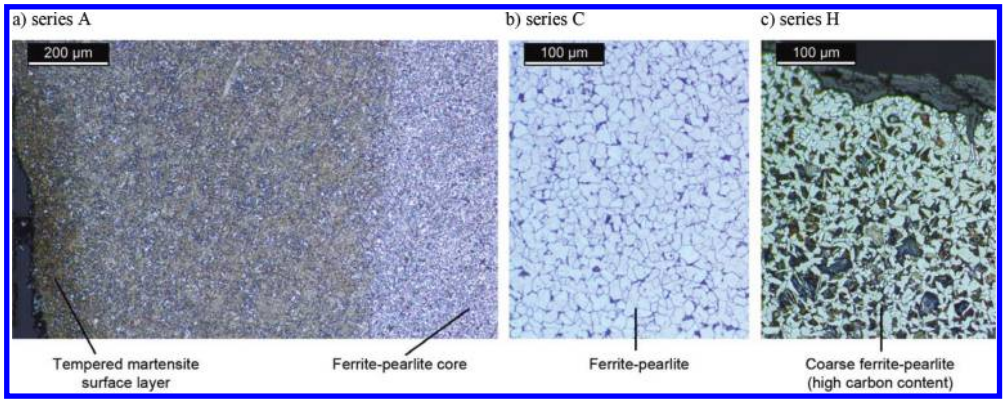

Figure 3. Metallographic sections of a) an example of a rebar with a martensite surface layer and a ferrite-pearlite core, b) an example of a rebar with homogenous ferrite-pearlite microstructure, and c) the steel from series H with a coarse ferrite-pearlite microstructure and a markedly higher carbon content than the example shown in Figure 3b.

of distinct peaks in both anodic and cathodic current direction. With increasing number of cycles, the current density, j, at these peaks increased. The peak indicated with the Roman number I at a potential close to –0.5 V vs. $Ag/AgCl_{sat}$ corresponds most likely to the conversion of Fe(II) to Fe(III) (R.S. Schrebler Guzmán et al., 1979, Ravikumar et al., 1996, Cabrini et al., 2014). The peak current density, j_p, of peak I at the first cycle is in the example shown in Figure 4a equal to 1.64 mA/cm^2.

In the voltammogram shown in Figure 4b, this peak is much less pronounced but exhibits a significantly higher current density, which also increases with increasing number of cycles run. For the first cycle, j_p is 6.47 mA/cm^2. All other peaks that were apparent in Figure 4a vanish in the blurred voltammogram measured for series B, which is representative also for series F and J. Series B, F, and J have in common that their steel surface was covered with a relatively thick layer of pre-existing corrosion products (compare Fig. 2). The much higher current densities observed in these cases during cyclic voltammetry can be ascribed to the oxidation and reduction of these corrosion products.

For simplicity, in this work, the peak current density j_p only of peak I will be evaluated. Values derived from the first cycle of cyclic voltammetry are given in Table 2, together with some information collected from the microscopic techniques described above.

There is a clear relationship between the degree of pre-existing rust on the as-received steel bars and j_p; the more corrosion products that are present on the surface, the higher is j_p. For the essentially blank rebars (series C, D, and E), j_p was in the range of ca. 0.6–1.7 mA/cm^2, while for the surface rust states classified as "intermediate" j_p was in the range of ca. 1.6–3.5 mA/cm^2, and for the highly pre-corroded surfaces j_p was in the range of ca. 4.9–6.5 mA/cm^2.

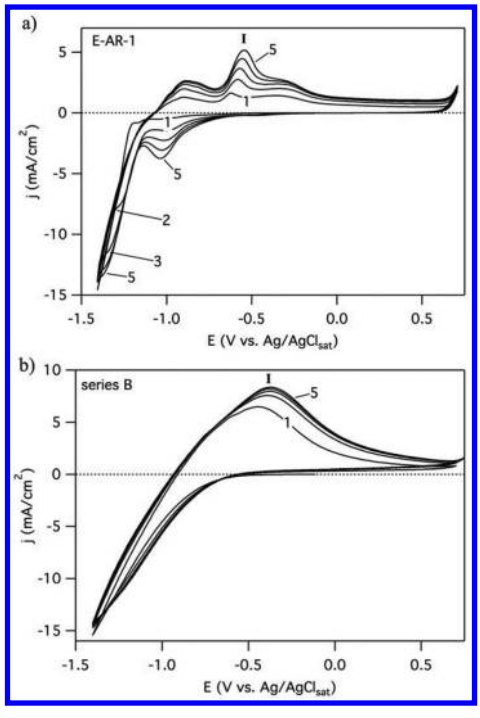

Figure 4. Cyclic voltammograms run after ca. 40 d exposure in chloride-free saturated calcium hydroxide solution. The voltammogram shown in Figure a) is representative for rebar series A, C, D, E, G, H, and I, i.e. those with low-intermediate degree of pre-existing rust; Figure b) is representative for rebar series B, F, and J, i.e. those with a high degree of pre-existing rust. Arabic numbers indicate the cycles; the Roman number the peak.

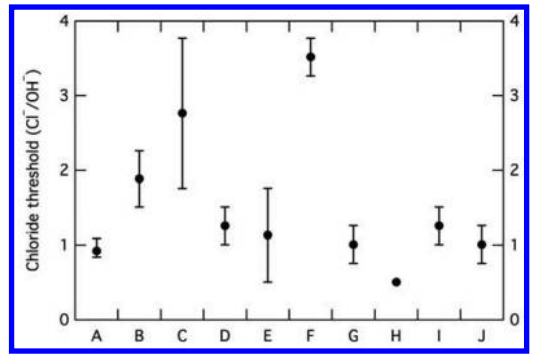

Figure 5. Chloride threshold values (min/mean/max) for each series of the as-received rebars.

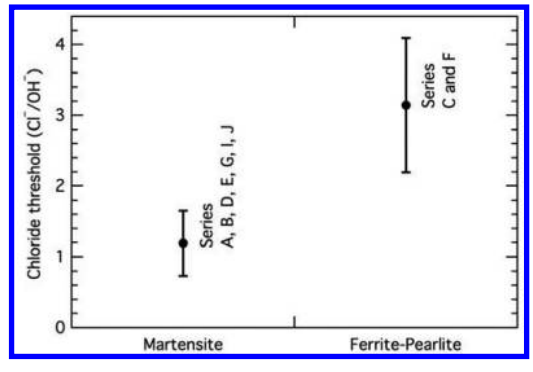

Figure 6. Chloride threshold values (mean and standard deviation) for rebars with martensite or ferrite-pearlite microstructure at the surface (compare Table 2 and Fig. 3). Series H excluded for reasons given in the text.

3.3 *Corrosion tests*

The chloride concentration in the solution when corrosion initiation was detected is regarded as the chloride threshold value. It can be expressed as ratio of chloride and hydroxide concentrations. The results of the present study are shown in Figure 5. Note that each series consisted of 2 rebars, with the exception of series A, where 3 bars were tested. Clearly, the measured threshold values scatter over a wide range. In most cases, the scatter within one series was smaller than the overall variability.

Nevertheless, comparing these results with the observations made with microscopy and electrochemical surface characterization by means of cyclic voltammetry (Table 2), one can conclude that there exists no systematic relationship between the chloride threshold value and the degree of initial pre-existing rust or j_p. Neither the amount of rust initially present on the surface nor the visual appearance of the rebars permits thus any prognosis of the corrosion behavior when exposed to chlorides.

This may be interpreted as a disagreement with various literature results that indicated that pre-corroded steel surfaces perform typically worse in terms of resistance to chloride-induced corrosion compared to clean surfaces (Mammoliti et al., 1996, Li and Sagüés, 2001, Pillai and Trejo, 2005, Manera et al., 2008). Nevertheless, in these studies, corroded samples were investigated and compared to samples from the same batch, which were treated in different ways (e.g. sandblasting, polishing, etc.) to remove the rust layers. This is thus not the same situation as when comparing steel from different producers (different countries of origin, different exposure history, etc.) where some exhibit initial rust layers and other do not—as was the case in the present study.

From this it is inferred that another parameter rather than the presence of absence of initial rust plays an important role in corrosion initiation. There is indication that the microstructure of the steel may be such an influencing factor. Figure 6 shows the observed chloride threshold

values sorted according to the type of steel microstructure that was apparent in metallographic analyses (summarized in Table 2). Concerning the ferrite-pearlite microstructures, series H was here excluded because it showed considerable differences (compared to series C and F) both in terms of microstructure (coarser) and carbon content (higher). As is apparent from Figure 5, series H initiated corrosion at significantly lower chloride concentrations than series C and F.

It appears from Figure 6 that the samples with a martensite structure at the surface generally initiated corrosion at lower chloride concentrations than did those samples with a ferrite-pearlite structure. This is in agreement with other literature results that indicated that martensitic steels are more prone to pitting corrosion than the ferrite-pearlite microstructure (Al-rubaiey et al., 2013). In this regard, however, more research work is clearly needed.

Figure 7 depicts the cumulative probability distribution of all samples tested in this work. For comparison, the well-known data from (Hausmann, 1967) are also shown in the plot. Hausmann tested bars that were initially "*cleaned and burnished to bright steel with emery paper*" (rebar length 22.9 cm, diameter 0.95 cm). This is clearly a different surface state than the as-received bars tested in the present work. Hausmann performed experiments in different alkaline solutions; Figure 7 shows only the results from saturated calcium hydroxide solution (thus comparable with the exposure conditions in the present work).

If all rebars tested in the present work are considered (circles in Fig. 7), the resulting distribution of chloride threshold values scatters considerably, in fact from Cl^-/OH^- = ca. 0.2 to almost a value of 4, thus by over one order of magnitude.

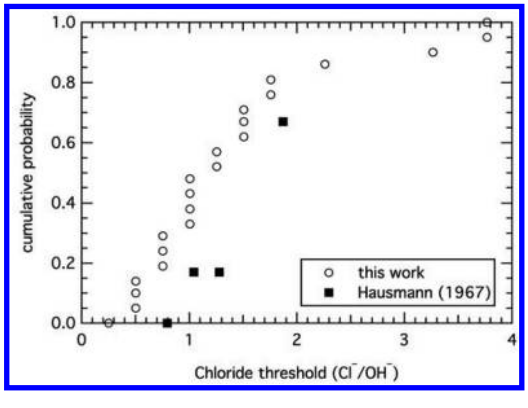

Figure 7. Cumulative probability distribution of chloride threshold values of all tested rebars, in comparison to the well-known results obtained by Hausmann (1967).

Nevertheless, it appears that more than 80% of the values are within the range Cl^-/OH^- = 0.2 to 2, and that only a small number of rebars shows a significantly better corrosion resistance.

Although Hausmann used bright steel surfaces, where all pre-existing oxides had been mechanically removed, his results are not very different from the present observations. The famous criterion derived from his work, viz. the chloride threshold value of Cl^-/OH^- = 0.6, frequently used in the literature and in service life modeling, appears in the context of both his and the present work to be a highly conservative criterion for corrosion initiation. More than 90% of the here studied specimens initiated corrosion at Cl^-/OH^- ratios higher than 0.6.

3.4 *Implications for corrosion prognosis and laboratory testing*

As one may have expected, the different as-received steel surfaces performed very differently when exposed to alkaline, chloride containing solution. A huge scatter of chloride threshold values was observed (Fig. 5), not only between the various tested series of rebars, but sometimes also within individual rebar series, i.e. even when the steel bars originated from the same batch (same metallurgy, same exposure history, etc.). There was no correlation between the degree of rust being initially present on the surface and the corrosion performance. Thus, the absence or presence of pre-existing rust on the reinforcement steel surface does not permit predicting the resistance to chloride-induced corrosion, not even qualitatively. A factor that may have a significant effect was however identified to be the microstructure (martensite vs. ferrite-pearlite) (Fig. 6).

For laboratory testing, the rebar surface is only one of the numerous degrees of freedom in the design of experiments or test methods for chloride threshold values (Angst et al., 2009). It is clearly evident that the so-called "as-received condition" cannot guarantee repeatability and reproducibility: When n rebars from the same batch are tested in alkaline solution, n different chloride threshold values are obtained. The results from Hausmann (Fig. 7) indicate that this is similarly true also if the as-received surface state is eliminated by cleaning and burnishing. The observed variability in threshold values (Fig. 7) may simply be explained by the stochastic nature of pitting corrosion initiation.

The marked extent to which the chloride threshold value scatters, however, has consequences for predicting corrosion initiation and service life modeling. This can be illustrated by the following example of a deterministic calculation of chloride ingress based on the well-known "error function approach" derived from Fick's second law of diffusion (Tang et al., 2012). For the present

purpose, the following assumptions are made: surface chloride concentration = 3.0% by weight of cement, negligible initial chloride concentration in the concrete, chloride diffusion coefficient at reference age 28 d of 2×10^{-12} m²/s, and the ageing factor = 0.3. The predicted total chloride content in the concrete was converted to free chloride concentration with help of experimental data for chloride binding reported in (Angst, 2011). A pore solution pH of 13 was assumed to calculate the ratio of chloride and hydroxide. The time to corrosion initiation was then predicted with the different threshold values shown in Figure 7 and the result is shown for two different cover depths in Figure 8. It is evident that the variability inherent to realistic rebar surface conditions such as the as-received state tested in this study leads to an enormous uncertainty in corrosion prognosis.

In reality, there are even additional uncertainties that were neglected in computing the data in Figure 8 such as the variability of concrete cover depths, chloride diffusion coefficients, and other model parameters. Moreover, the present results were determined with a setup in solution that can be considered as a homogeneous medium around the rebar. In concrete, on the other hand, further irregularities and defects arise at the steel surface such as macroscopic voids (either filled with air or with solution), cracks, aggregates, etc. These are well known to have local effects on corrosion initiation (Reddy, 2001, Soylev and Francois, 2003) and are thus expected to broaden the scatter even more.

Given these large uncertainties in present predictive modeling, one may question the benefit of a prognosis stating that corrosion will initiate sometime between 20 and 200 years after construction. It appears that the current concept of modeling chloride penetration into concrete and relating it to a chloride threshold value has a very weak predictive power. As a result, in service life design and maintenance planning, highly conservative assumptions have to be made (e.g. a chloride threshold value of $Cl^-/OH^- = 0.6$).

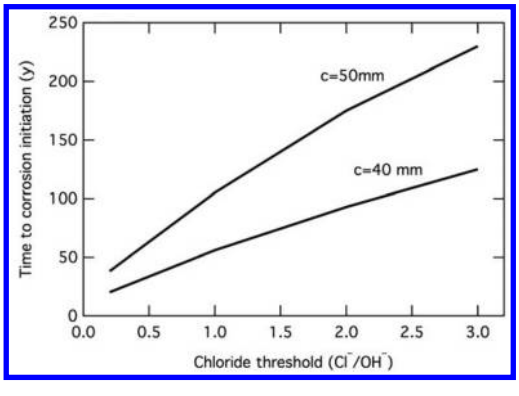

Figure 8. Uncertainty in service life predictions arising from the variability in chloride threshold values; c = cover depth. See text for model assumptions and explanations.

Clearly, the issue of corrosion initiation in concrete cannot be reduced to a question of chlorides only, and the concept of the critical chloride content needs to be replaced or enriched with a more refined approach capable of taking into account all other dominant and relevant effects. The steel surface condition can be considered as one of the many possible examples that lead to a "macroscopic variability". More refined methods are urgently needed to characterize in detail the fundamental properties and mechanisms that dictate why corrosion initiates on one rebar and not on another, although they come from the same batch, share the same exposure history and appear from the current perspective identical. Only with such an approach will it be possible to reduce the large uncertainties inherent to current concepts and models.

4 CONCLUSIONS

In this work, ten series of "as-received" reinforcement steel originating from different countries and having been subject to different exposure histories (storage, transport, handling, etc.) were studied. There were clear differences in terms of visual appearance (from almost blank to severely pre-corroded), which were reflected in electrochemical characterization after 40 d of exposure in saturated calcium hydroxide. Metallographic analyses also revealed differences in terms of steel microstructure. Corrosion testing in chloride containing alkaline solutions revealed a high scatter in terms of chloride threshold value, both within and between the tested rebar series.

No systematic correlation was observed between the chloride threshold value and the degree of initial pre-existing rust. Thus, neither the visual appearance nor the amount of initially present rust permits any prognosis of the corrosion behavior when exposed to chlorides. Only the steel microstructure seems to have a noticeable effect, i.e. rebars with a tempered martensite structure at the surface were more susceptible to pitting corrosion than steels of ferrite-pearlite microstructure.

Considering that in the present test setup, the exposure environment being a solution is homogenous, there is still a significant variability in chloride threshold value for the as-received steel bars. It is expected that the variability becomes even more pronounced when the rebars are embedded in concrete, which, being a composite material, introduces further in homogeneities at the steel/concrete interface.

Nevertheless, it was concluded that even the steel surface condition alone is a parameter that causes an enormous uncertainty in current conceptual service life modeling. The common approach of reducing the issue of predicting corrosion initiation to a mere matter of chlorides was questioned. At present, the relevant parameters are obviously not yet understood and cannot be adequately quantified. There is thus an urgent need for more refined methods to characterize in detail the fundamental properties and mechanisms that dictate why corrosion initiates on one rebar and not on another, given the same chloride concentration.

ACKNOWLEDGEMENTS

The authors acknowledge the support of the members of RILEM technical committee 235-CTC who provided the as-received rebars from their countries.

REFERENCES

Al-rubaiey, S.I., Anoon, E.A. & Hanoon, M.M. 2013. The influence of microstructure on the corrosion rate of carbon steels. *Eng. & Tech. Journal,* 31, 1825–1836.

Angst, U. 2011. *Chloride induced reinforcement corrosion in concrete. Concept of critical chloride content—methods and mechanisms*. Doctoral thesis, Norwegian University of Science and Technology, NTNU.

Angst, U., Elsener, B., Larsen, C.K. & Vennesland, Ø. 2009. Critical chloride content in reinforced concrete—A review. *Cement and Concrete Research,* 39, 1122–1138.

Angst, U., Elsener, B., Larsen, C.K. & Vennesland, Ø. 2011. Chloride induced reinforcement corrosion: electrochemical monitoring of initiation stage and chloride threshold values. *Corrosion Science,* 53, 1451–1464.

Cabrini, M., Lorenzi, S. & Pastore, T. 2014. Cyclic voltammetry evaluation of inhibitors for localised corrosion in alkaline solutions. *Electrochimica Acta,* 124, 156–164.

Hausmann, D.A. 1967. Steel corrosion in concrete. How does it occur? *Materials Protection,* 6, 19–23.

Li, L. & Sagüés, A.A. 2001. Chloride corrosion threshold of reinforcing steel in alkaline solutions—Open-circuit immersion tests. *Corrosion,* 57, 19–28.

Mammoliti, L.T., Brown, L.C., Hansson, C.M. & Hope, B.B. 1996. The influence of surface finish of reinforcing steel and pH of the test solution on the chloride threshold concentration for corrosion initiation in synthetic pore solutions. *Cement and Concrete Research,* 26, 545–550.

Manera, M., Vennesland, Ø. & Bertolini, L. 2008. Chloride threshold for rebar corrosion in concrete with addition of silica fume. *Corrosion Science,* 50, 554–560.

Pillai, R.G. & Trejo, D. 2005. Surface Condition Effects on Critical Chloride Threshold of Steel Reinforcement. *ACI Materials Journal,* 102, 103–109.

Ravikumar, M.K., Balasubramanian, T.S., Shukla, A.K. & Venugopalan, S. 1996. A cyclic voltammetric study on the electrocatalysis of alkaline iron-electrode reactions. *Journal of Applied Electrochemistry,* 26, 1111–1115.

Reddy, B. 2001. Influence of the steel-concrete interface on the chloride threshold level, PhD thesis, Imperial College, London.

Richartz, W. 1969. Die Bindung von Chlorid bei der Zementerhärtung. *Zement-Kalk-Gips,* 10, 447–456.

Schrebler Guzmán, R.S., J.R. Vilche & Arvía, A.J. 1979. The potentiodynamic behaviour of iron in alkaline solutions. *Electrochimica Acta,* 24, 395–403.

Soylev, T.A. & Francois, R. 2003. Quality of steel-concrete interface and corrosion of reinforcing steel. *Cement and Concrete Research,* 33, 1407–1415.

Tang, L., Nilsson, L.O. & Basheer, P.A.M. 2012. *Resistance of Concrete to Chloride Ingress,* Abingdon, Spon Press.

Vassie, P. 1984. Reinforcement corrosion and the durability of concrete bridges. *Proc. Instn Civ. Engrs.,* Part 1, 76, 713–723.

Concrete Repair, Rehabilitation and Retrofitting IV – Dehn et al. (Eds)
© 2016 Taylor & Francis Group, London, ISBN 978-1-138-02843-2

Effect of reinforcement corrosion on serviceability behavior of RC beams and analytical model

L. Hariche
LDMM Research Laboratory, Djelfa University, Djelfa, Algeria

M. Bouhicha
Civil Engineering Research Laboratory, Laghouat University, Laghouat, Algeria

S. Kenai
Civil Engineering Research Laboratory, Blida University, Blida, Algeria

Y. Ballim
School of Civil and Environmental Engineering, University of the Witwatersrand, Johannesburg, South Africa

ABSTRACT: Corrosion of reinforcement bars in R.C structures is one of the main causes that induce an early deterioration of a structure and reduces its service life. This paper reports results of an experimental programme to check on the effect of reinforcement corrosion on the serviceability behaviour of R.C beams under load. Four series of beams were tested (6 Beams each series, 3 corroded and 3 control), the difference between the tree first series was just in the arrangement of the reinforcement (2Y12 at the bottom of the first, 1Y16 at the bottom of the second and 3Y10 at the bottom of the third), the last one the difference was in the load. To accelerate corrosion, the beams were immersed in baths of a sodium chloride solution (3%) and an electrical current was applied to selected elements of reinforcing for periods in excess of 30 days. During these periods the beams were subjected to a 4-point load of 20 kN for tree first series and 30 kN for the fourth series.

The results show the evolution of reinforcement corrosion and central deflection under simultaneous load, the effect of the reinforcement arrangement and map cracking of the corroded beams.

1 INTRODUCTION

The success of Reinforced Concrete (RC) is due mainly to its structural versatility, long-term durability characteristics and the complementary interaction of its materials, namely the reinforcing steel and concrete. Provided that appropriate measures were undertaken in the design and the construction of a reinforced concrete structure, reinforcing steel embedded in concrete is normally protected against corrosion during the service life of the structure. However, this concrete cover protection to the reinforcement can be deteriorated by aggressive agents leading to the corrosion of the steel in concrete.

Internationally, the corrosion of reinforcing steel bars is the principal cause of early deterioration of concrete structures, leading to a reduction in residual service life. When aggressive agents reach the reinforcement due to the chloride attack or the carbonation of concrete cover, corrosion may start affecting [1]:

- the steel, due to the reduction of both the bar section and the mechanical properties [2]
- the concrete, due to the cover cracking provoked by the expansion of corrosion products [3]
- the composite action of concrete and steel, due to the bond deterioration [4].

The combined effect of increased cracking and bond slippage results in increased serviceability deflection of the beams.

Most of the research work found in the literature which tries to asses this phenomenon were based on laboratory studies. In order to reduce the time necessary for the corrosion of reinforcing bars, acceleration procedures such as impressing an electrical current on the steel or adding chloride sodium solution to the mixing water of concrete were used. Moreover, in the majority of the work reported in the literature, the corrosion of steel bars was carried out before load-testing of the RC elements. Ballim et al [5,6] point out that this testing procedure presents two main drawbacks:

- In real structures, the corrosion takes place while the structure carries load and the two effects act

synergistically to accelerate the deterioration of the structure. For example, in the case of a beam element, cracks induced by the corrosion products are widened by the effects of the applied loads (and vice versa), thus allowing greater access to oxygen and water for more rapid corrosion than if the load effects were not simultaneously imposed.

- During the corrosion process, the time-dependent effects of a sustained load on serviceability limit state behaviour are not considered. The level of corrosion related stresses and the duration and the level of external loads are both influencing factors in the deformation of the structure.

The research work reported in this paper accepts the logic of this approach to assessing the effects of reinforcement corrosion in laboratory-based studies. It was therefore considered important that a further contribution to the understanding of the effects of corrosion on structural performance should be based on an assessment of performance under simultaneous load and reinforcement corrosion conditions.

The research work involved the testing of four series of RC beams subjected to reinforcement corrosion while maintaining a sustained load. The first three series of beams were subjected to the same test conditions except that the arrangement of the bottom tension reinforcement was varied. Series 1 contained two Y12 bars (226 mm^2), Series 2 had a single Y16 bar (201 mm^2) and Series 3 contained three Y10 bars (235 mm^2). The beams in these three test series were subjected to a 4-point load of 20 kN. In the fourth test series, the tension reinforcement consisted of two Y12 bars and the beams were subjected to an increased 4-point load of 30 kN.

2 DESCRIPTION OF THE SUSTAINED LOADING TEST RIG

The sustained load test rig developed by Ballim and Reid [5] was used in this testing program. Briefly, the loading rig allows a sustained four point bending load to be applied to a simply supported reinforced concrete beam over a span of 1050 mm. The load is applied through a compressed spring, onto a spreader beam that is placed on the top of the test beam. For the samples subjected to accelerated corrosion of the tension reinforcement, the undersides of the test beams as well as the supports were located inside a plastic watertight tank containing an electrolyte (3% NaCl solution). A companion steel bar, which acts as the cathode for the accelerated corrosion process, was placed in the electrolyte solution below the beam. The same testing rig and arrangement was used for the control un-corroded samples, except that the electrolyte was replaced by plain water.

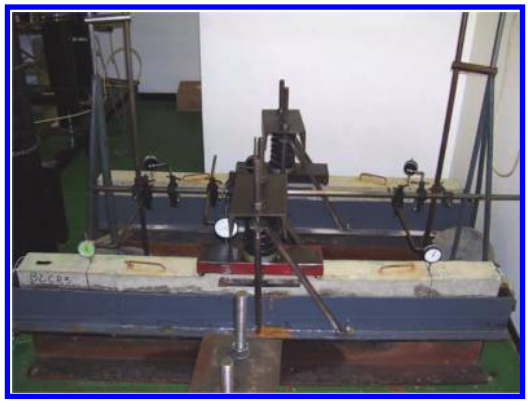

Figure 1. Compressing springs to apply the sustained load and a general view of the loaded frames.

Six loading rigs were used to allow simultaneous testing of three beams with corroding reinforcement and three un-corroded control beams. One such set of six beams constituted a single test series.

Compression of the load spring was achieved by turning the nuts on threaded rods which passed through a movable plate. The magnitude of the load was controlled by monitoring the vertical compression of the spring (see Fig. 1a). The springs were fabricated to provide a spring rate of 400 N/mm. However, for the six springs used in the experimental program, calibration procedures indicated that the spring rates varied between 406 N/mm and 436 N/mm. By using a spirit level to ensure that the movable loading plate was horizontal during loading and a Vernier depth gauge, it was possible to compress the spring to an accuracy of 0.1 mm. This translates to a load accuracy of approximately 0.05 kN. An example of a loaded test frame is shown in Figure 1b.

The central deflections of the beams as well as the deflection of the beams over the support points were measured using dial gauges attached to the main steel I-section. This allowed the central deflection of the beams to be determined relative to that of the supports. It should be noted that the supports points inside the electrolytic plastic tank were made from a hard plastic material.

3 EXPERIMENTAL PROGRAM

3.1 *Test beam dimensions and materials used*

Twenty-four beams were cast with the dimensions and reinforcing layout shown in Figure 2. The

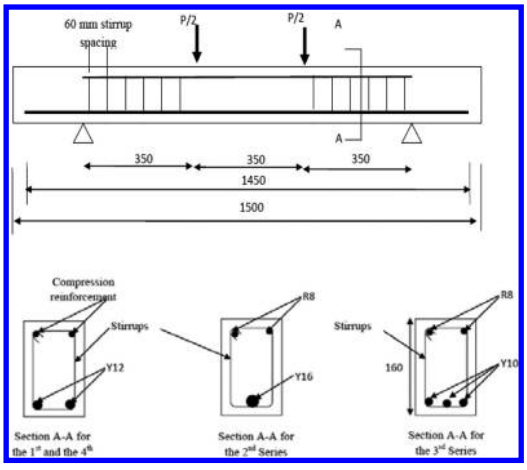

Figure 2. Dimensions and reinforcement details of the concrete test beams.

beams were divided equally into four series of six beams. In each series, the main tension reinforcing steel of three beams was subjected to accelerated corrosion while the three beams served as control, un-corroded beams. As stated before the two parameters investigated during this study were reinforcement arrangement and magnitude of loading. The first three series of beams were used to study the effect of tension steel arrangement, as shown in Figure 2. The fourth series of beams were reinforced in an identical manner as the first series but was subjected to a higher applied load than in the case of the first three series of tests. The tensile reinforcement of the beams consisted of high tensile deformed bars (Y) whereas the shear links and compression (top) reinforcement was made of mild steel bars, cut and bent as appropriate. All the reinforcing steel was obtained from the same steel mill run and a sample of the Y12 bar was tested to give a 0.2% proof stress of 596 MPa.

The shear stirrups were covered with a section of heat-shrink plastic at the points of contact with the main tension steel bar. This was done to electrically isolate the rest of the steel cage from the main tensile bars that were to be corroded by an impressed current.

The concrete mixture used to make the beams and cube samples for compressive strength testing consisted of ordinary Portland cement (CEM1), crushed sand, water and 13,2 mm crushed gravel with the proportions shown in Table 1. This concrete was designed according to guidance found in the literature [7] so as to yield a target 28-day compression strength of 47 MPa. The crushed sand used had a fineness modulus of 2.86 and its grading satisfied the SABS 1083 [8] requirements. In the

Table 1. Mix proportion of the concrete used for preparing the beams.

Cement (CEM I)	409.1 kg/m^3	
Gravel	1000 kg/m^3	w/c = 0.55
Sand	849.6 kg/m^3	Slump = 60 mm
Water	225 L/m^3	

preparation of each series of 6 beams, sufficient concrete was mixed to also prepare three 100 mm cubes for compression strength testing and three 100 mm square × 200 mm high prisms for elastic modulus measurements in accordance to BS 1881 part 121 [9]. All concrete samples were moist cured for 28 days at temperature of 22 ± 1°C.

3.2 *Instrumentation and loading of the test beams*

An insulated electrical wire was soldered to one end of each tensile reinforcement bars before casting and the soldered area was coated with a thick layer of insulating paint. This wire was held in place when the concrete was cast so that it will be exited from the top face of the beam. A galvanostatic method was used to accelerate the corrosion of the tensile reinforcement bars by connecting it to the positive terminal of a DC power supply, thus forcing the reinforcing steel to become anodic. The negative electrode was then connected to a steel rod (cathode) placed in an electrolytic solution.

The DC power supply, with a voltage limit of 30 V and a maximum current output of 3 A, was used to supply the corrosion current at a rate of approximately 150 mA/cm^2. A data logger connected to a computer was used to record the current in the reinforcing bars every hour during the test period.

After curing, the beams were placed in the loading rig for testing. The soffit of the beams was immersed in a liquid solution to a depth of approximately 30 mm. As stated before, a 3% sodium chloride solution was used for the corroded beams whereas normal tap water was used for control beams. After a soaking period of one day in solution, the beams were loaded by compressing the springs to the required level and the resulting deflections were recorded as the elastic responses to the application of load. The corrosion current was then applied to the reinforcing bars. Both the corrosion current and the applied loads were checked daily and adjusted to the set values if required. After the testing period, which generally exceeded 30 days under sustained load and simultaneous corrosion, the beams were remove from the loading rig and inspected visually for any corrosion damage that may have occurred. They were then placed in an Amsler testing machine with a load

capacity of 2000 kN and tested to failure using the same 4 point bending loading arrangement.

3.3 *Rate of corrosion calculation*

Two methods were used to estimate the corrosion rate and are given as follows:

1. Gravimetric method:
   At the end of the test programme, the main tension reinforcement bars were carefully removed from each of the corroded beams and cleaned of all adhering mortar and corrosion product. The bars were then weighed to determine the extent of corrosion. The method used for cleaning the bars was similar to that outlined in ASTM G167 [10] and involved first brushing the bar with a brass bristle brush and brass wool and then dipping it into a dilute inhibited phosphoric acid solution.
2. Faraday's law:
   This method was used to determine a theoretical relationship between the time over which the impressed current was allowed to flow and the extent of corrosion [11,12 and 5]. The corrosion is an electrochemical reaction which means it results in a production of electrons. Assuming that, the oxidation of iron to ferrous ions ($Fe \rightarrow Fe^{2+} + 2e^{-}$) represents the principal electrochemical reaction, the charge that passes the circuit at time t after the start of the impressed current can be written using Faraday's law:

$$q_t = m \cdot n \cdot F = \frac{m_c}{w} \cdot n \cdot F \tag{1}$$

where:
q_t: is the total charge passed through the circuit after time t,
m: is the number of moles of reactant consumed (or product formed),
n: is the number of electrons required to convert reactant to product,
F: is Faradays constant (96 485 C/mol).
m_c: is the mass of the original iron consumed (g),
w: is the molar mass of the iron (= 55.85 g/mol for Fe).

The charge can be determined by integrating the impressing current, I, with respect to time as follows:

$$q_t = \int_{t=0}^{t} Idt \tag{2}$$

Combining equations (1) and (2) yields the following equation, from which the mass of corrosion product can be determined at any time during the accelerated corrosion process:

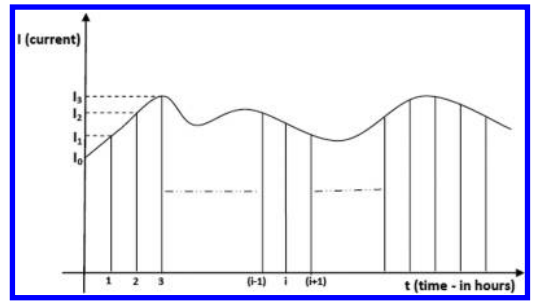

Figure 3. Illustrative current vs. time graph showing computational analysis parameters.

$$m_c = \frac{q_t w}{nF} \tag{3}$$

q_t was calculated by numerically integrating the hourly measurements of impressed current over the time of testing, using the procedure described below.

The Trapezoidal formula was used to calculate the integral numerically, using the following approach:

$$q_0 = 0 \tag{4}$$

$$q_1 = q_0 + 3600\frac{I_0 + I_1}{2} \tag{5}$$

$$q_2 = q_1 + 3600\frac{I_1 + I_2}{2} \tag{6}$$

and more generally:

$$q_i = q_{i-1} + 3600\frac{I_{i-1} + I_i}{2} \tag{7}$$

The total charge q_t can thus be estimated every hour which in turn yields the hourly lost mass of steel (m_c). If m_o is the original mass of the uncorroded bar, the hourly rate of corrosion (C_t) with reference to the original mass, is given by:

$$C_t = \frac{(m_o - m_c)100}{m_o} \tag{8}$$

However, in reality, the $Fe \rightarrow Fe^{2+} + 2e^{-}$ is not the only reaction which takes place at the anode. There are competing reactions and Faraday's law will only give a true reflection of the extent of corrosion if all the electron equivalents which have entered in the reaction are used. It is therefore necessary to determine the ratio of the charge consumed in the reaction of interest (oxidation of Fe in the reinforcing steel) to the total charge passed. This ratio is referred to as the current efficiency, N [13, 14], and was obtained by comparing the mass

of corrosion product determined from the gravimetric method to that given by Equation 3 for the total accelerated corrosion period. This value of N was then used to adjust the extent of corrosion determined using Equation 3 at various times during the corrosion process.

4 RESULTS AND DISCUSSION

4.1 *Extent of corrosion*

As mentioned above, two methods were used to estimate the rate of corrosion: gravimetric method and Faraday's law. The results obtained by the first method are summarized in Table 2. The values given by Faraday law were adjusted by multiplying them by current efficiency factor N. The values of N obtained for the series of beams tested are shown in Figure 4. The results seem to indicate that the current efficiency increases when arrangement of small diameter reinforcing bars are used.

Upon removal from the concrete, all the corroded bars generally showed pitting corrosion with some areas of more concentrated corrosion, as shown in Figure 5. This is in accordance to what was reported in the literature [14–16] and may be explained by the absence of carbonation of concrete, which would generally lead to more uniformly distributed corrosion.

The positions of the areas of concentrated corrosion can be identified in Figure 6, which shows examples of the measured diameters of the reinforcement bars at different locations along their lengths.

The pitting corrosion was observed to be focused at both the middle and the electrical connection end of the steel bars. This is most probably caused by electrical current concentration at the electrical connection end region and by higher steel stress together with increased concrete cracking in the middle section.

4.2 *Cracking patterns*

The beams were cleaned after corrosion testing and the cracking patterns as well as crack widths were measured and recorded. Typical crack patterns and crack widths are shown in Figures 7a to 7d for the four series of tests. were carried out as shown in Figure 7.

It can be seen that longitudinal cracking occurred mainly on the sides of the beams for series 2Y12 and 3Y10 while for series 1Y16 a soffit longitudinal crack was observed. The choice

Table 2. The rate of corrosion determined by Gravimetric method (mass loss).

Test series	Beam No.	Tensio bar number	Rate of corrosion (%)	Av. rate of corrosion (%)	Duration of accelerated corrosion period (days)
1	CR1	1	13.02	11.33	
		2	9.65		48
	CR2	1	11.73	11.69	
		2	11.65		
	CR3	1	11.51	12.37	
		2	13.22		
2	CR1	1	5.75	5.75	30
	CR2	1	5.96	5.96	
	CR3	1	5.94	5.94	
3	CR1	1	8.75		
		2*	5.30	6.49	
		3	5.42		
	CR2	1	4.77		55 for beam No. 3
		2*	3.40	4.43	
		3	5.13		20 for beams No. 1, 2
	CR3	1	15.20		
		2*	11.17	19.43	
		3	31.93		
4	CR1	1	7.98	9.18	
		2	10.39		
	CR2	1	5.18	6.28	32
		2	7.37		
	CR3	1	6.84	9.14	
		2	11.45		

* For the Series 3 beams, bar number 2 is the central bar.

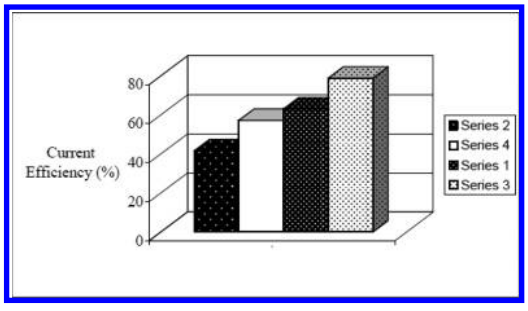

Figure 4. Current efficiency.

Figure 5. Appearance of the corroded steel.

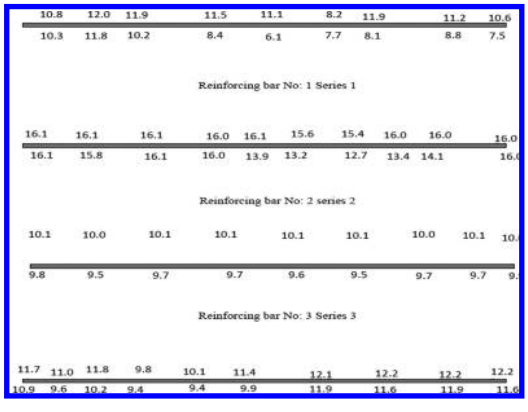

Figure 6. Diameter (in mm) of the corroded bars measured at various positions along the length of each bar after corrosion and cleaning.

of steel arrangement therefore appears to have a strong influence on the nature and extent of damage to concrete cover when the steel corrodes.

4.3 *Deflection behaviour at serviceability limits state*

a. Deflection of control beams:
The mid-span deflections of control beams where the increase in deflection is mainly due to time dependent effect such as creep. Table 3

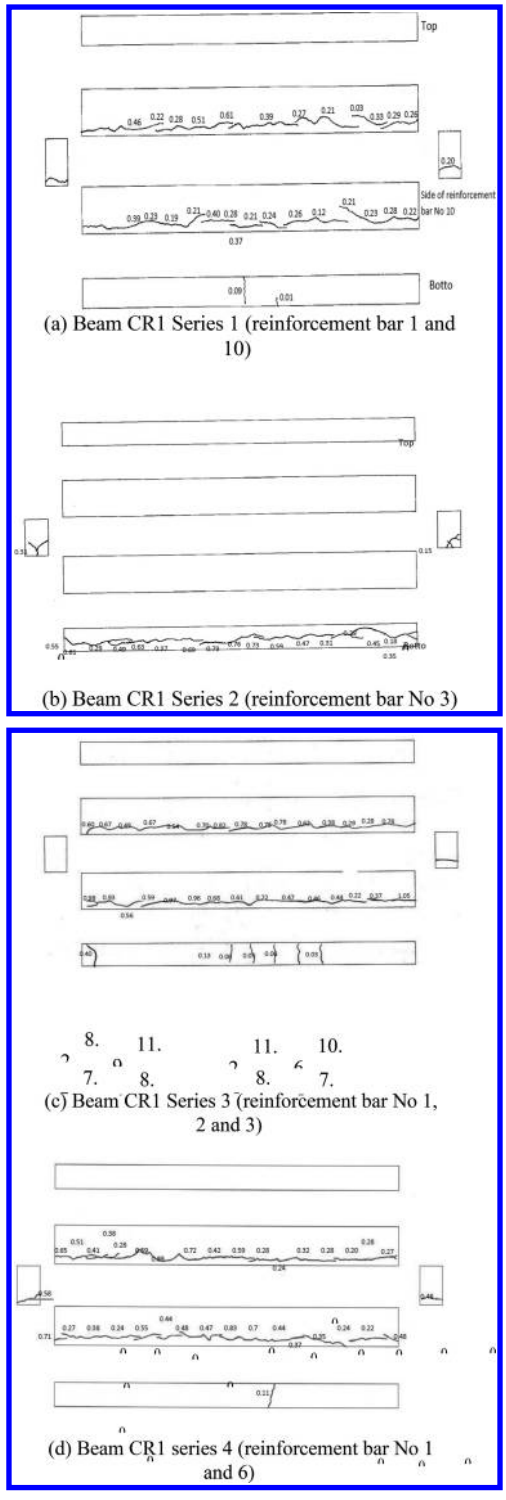

Figure 7. Cracking pattern and crack widths (in mm) for the four series of test beams.

Table 3. Percentage of deflection variation of control beams.

Series	f_c28 (MPa)	Age at the beginning of loading (days)	Loading duration (days)	% of deflection variation
Series 1	48.1	130	55	13
Series 2	45.9	30	30	30
Series 3	42.44	100	55	37
Series 4	43.79	34	32	24

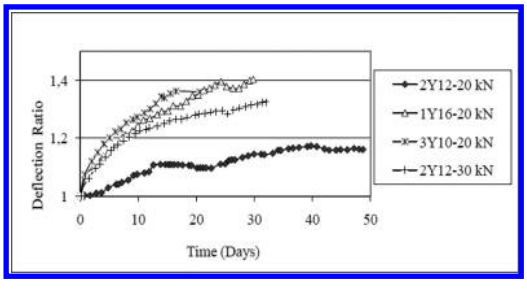

Figure 8. Mid-span deflections ration of control beam with time.

gives the relative increase in deflection at mid span, the duration as well as the age of loading and the compression strength of concrete used to make these control beams. It can be noticed that the creep effect decreases when either the strength of concrete increases [7, 17 and 18] or the age of concrete at loading increases.

b. Deflection of corroded beams:

Figures 8 and 9 show mid-span deflection variation with respectively the time and the rate of corrosion. It can be seen that deflection increases with both the time and the degree of corrosion of the tensile reinforcement. It can also be seen from these figures that the deflection of the first and the third series are more or less identical and are relatively lower than the deflection of the second series., highlighting, thus, the importance of an adequate layout of the tensile reinforcement across the beam's soffit.

The relative deflection of the corroded beams was obtained by dividing their deflections by the corresponding deflections of the control beams. The variation of the relative deflection with the rate of corrosion is shown in Figure 10 for the series of beams considered herein. Relative deflection seems first to increase linearly with the rate of corrosion, then this increase is reduced once the rate of corrosion surpasses 2 to 4%. Moreover, the curves of series one, three and four are more or less

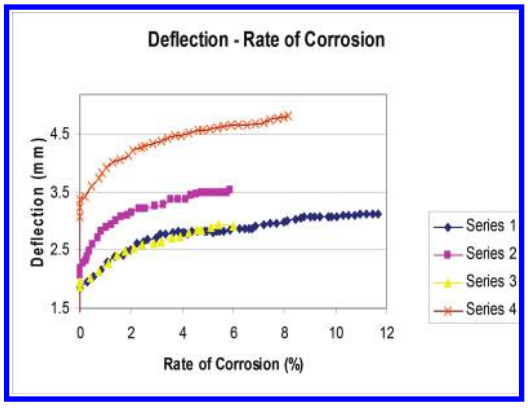

Figure 9. Mid-span deflections of corroded beams with rate of corrosion.

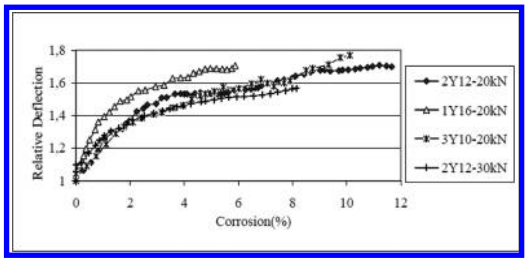

Figure 10. Relative deflections of corroded beams with rate of corrosion.

identical whereas relative deflection for series 2 is the highest for all rates of corrosion considered. Consequently, the arrangement of soffit reinforcement seems to have a great influence not only on the cracking pattern but also on the increase of the corrosion caused deflection.

5 ANALYTICAL MODELS OF THE CORROSION OF FLEXURAL BEAMS

5.1 *Rigidity and damage coefficient*

The values of the parameters, for the four points bending test, are: a = 350 mm, P = 20 kN for the three first series, and P = 30 kN for the last series. The bending moment and the deflection at mid span are given by:

$$M(L/2) = \frac{Pa}{2} \tag{9}$$

$$W(L/2) = \frac{23Pa^3}{48EI_o} = \frac{23Pa^3}{48R_o} \tag{10}$$

$R_o = EI_o$ Rigidity at the beginning of test.

$$R_o = \frac{23Pa^3}{48W_o(L/2)} \quad (11)$$

a. Controls beams:
After "t" time, the deflection increase, this is due mainly to the creep. It can be explicate by the lost in stiffness:

$$R_{Cont} = \frac{23Pa^3}{48W_t(L/2)} = R_o - \Delta R_{Creep} \quad (12)$$

ΔR_{Creep}: is the lost in stiffness due to the creep.

b. Corroded beams:
In the corrosion tests, the loading was kept constant. At "t" time of loading and accelerated corrosion, we have "c" level of corrosion, the deflection is increased, but in this case, is due to the creep and the corrosion of the reinforcement. Therefore, the corroded beam stiffness R(c) can be obtained from the above equation, and it can, also, illustrated by the lost in stiffness given by:

$$R_{Corr}(c) = \frac{23Pa^3}{48W_{Corr}(L/2)} = R_0 - \Delta R_{Creep} - \Delta R_{Corr} = R_{Cont} - \Delta R_{Corr} \quad (13)$$

where: c is the rate of corrosion.

ΔR_{Corr} is the lost in stiffness due to the corrosion, and can be calculated as:

$$\Delta R_{Corr} = R_{Cont} - R_{Corr} \quad (14)$$

It's more convenient to represent the relative lost in stiffness $\Delta R_{Corr}/R_o$ for each series.

This graph shows that the lost in stiffness is more important in the low level of corrosion, then, it stabilised. The reduction of the beam stiffness (from R_o to R(c)) is due to the well established effects of corrosion: rust staining, spilling of cover zone, reduction of bond strength and reduction of steel cross-section.

The variation of the relative rigidity $(R(c)/R_o)$ with the rate of corrosion is shown in Figure 12.

It can be seen that the loading level at service does not seem to have a significant effect on the reduction of the beam stiffness, (2Y12-20 kN and 2Y12-30 kN series of beams). However, the arrangement of the soffit reinforcement of the beam seems to have an effect, albeit a small one, on the drop of the beam stiffness after corrosion. A fit of the curves contained in Figure 14 shows that the stiffness of the beam drops sharply when the rate of corrosion is less than 2%. After this level of corrosion the drop seems to be relatively less important when the rate of corrosion is increased. The proposed bilinear model for the relative rigidity variation with the rate of corrosion is shown in Figure 12.

$$\frac{R(c)}{R_o} = -0{,}1373c + 0{,}9601 \quad \text{When } c < 2\% \quad (15)$$

$$\frac{R(c)}{R_o} = -0{,}0122c + 0{,}7152 \quad \text{When } c > 2\% \quad (16)$$

From the above equations we can also derive the damage coefficient "D(c)" [20–22], which is defined by:

$$D(c) = 1 - \frac{R(c)}{R_o} \quad (17)$$

The damage coefficient is calculated from this equation, and represented in Figure 13.

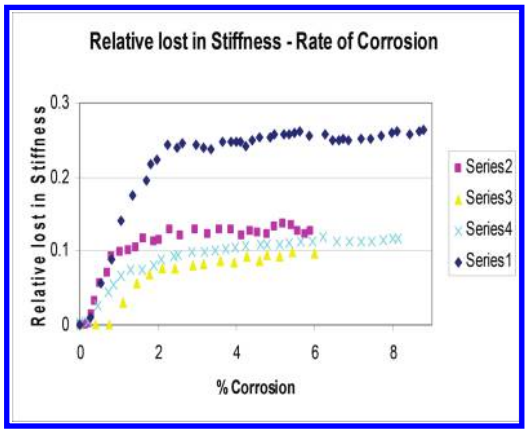

Figure 11. Relative lost in stiffness vs. rate of corrosion.

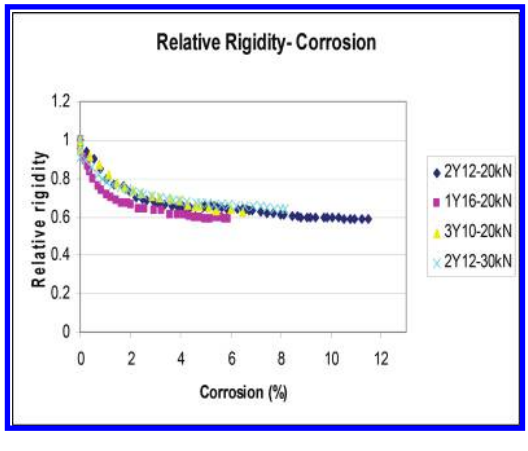

Figure 12. Relative rigidity vs. the rate of corrosion.

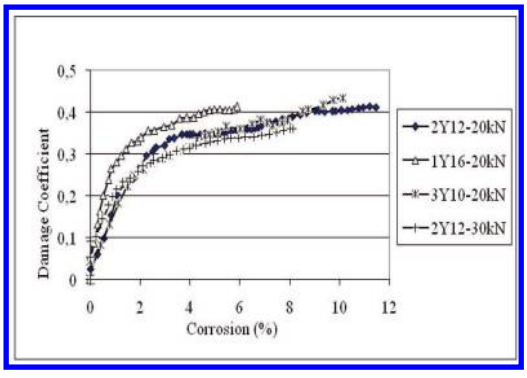

Figure 13. Damage coefficients vs. rate of corrosion.

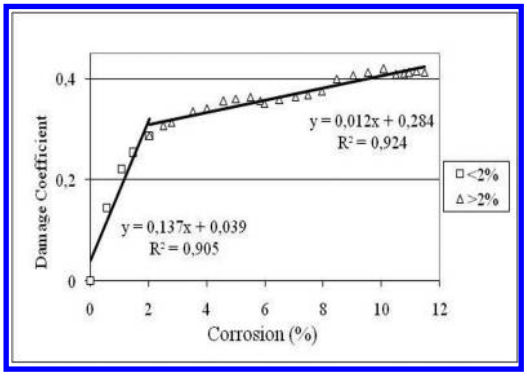

Figure 14. Average damage coefficients vs. rate of corrosion.

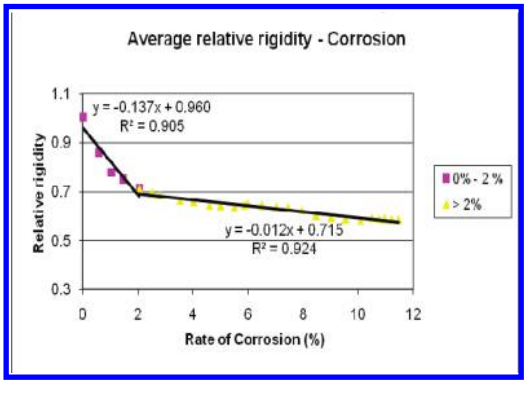

Figure 15. Proposed bilinear model.

It can be seen from Figure 13 that the damage in beam series of 1Y16-20 kN is more important than the other series. This confirms the importance of the soffit steel arrangement. Moreover, as found above in the relative rigidity analyses, a bilinear model can also be adopted for the definition of the damage coefficient in function of the rate of corrosion, Figure 14.

$$D(c) = 0{,}1373c + 0{,}0399 \quad \text{When } c < 2\% \tag{18}$$

$$D(c) = 0{,}0122c + 0{,}2848 \quad \text{When } c > 2\% \tag{19}$$

6 CONCLUSION

The following conclusions can be drawn from this experimental and analytical investigation:

1. In the process of acceleration of corrosion the current efficiency is more important for 1Y16 then 2Y12 and 3Y10. That's mean; to accelerated corrosion of small diameter steel we need more current than the big diameter steel to have the same level of corrosion. Also when there is vagabond current in RC structure there is less risk of corrosion in small diameter then the big one.
2. Conformed to the literature of corrosion [1, 14–16], the reinforces steel are corroded by pitting corrosion, because it was caused by chloride attack, and there is no carbonation of concrete.
3. From the crack on the surface of RC beams we can predict that the reinforced steel in this side is corroded. Than for perspective, it will be very interesting if we can find a relationship between the rat of corrosion and the crack width, from that we can estimate the degree of corrosion in the RC structure just from the crack width on the surface.
4. Under simultaneous load and accelerated corrosion, the deflections of the beams increase with progressive corrosion of the reinforcement. A large increase in deflection was noted during the early stages of corrosion as a result of propagation of transverse cracks on the beams caused by the flexural tension and the expansive stresses induced by the corrosion products.
5. From this investigation it was observed clearly the role of the arrangement of the steel in the section of concrete. In spite of air section of steel was nearly the same, the beams of 2Y12 and 3Y10 were more performed in deflection, curvature and rigidity then the beams of 1Y16.
6. The analytical analyses propose some correlation related to the rat of corrosion.

REFERENCES

[1] J. Rodriguez, L.M. Ortiga, J, Casal, "Load carrying capacity of concrete structures with corrosion reinforcement", Construction and Building Materials, Vol. 11, No. 4, 1997, pp. 239–248.

[2] C. Andrade, C. Alonso, D. Garcia & J. Rodriguez "Remaining life time of reinforced concrete structure; Effect of corrosion on the mechanical properties of steel" International conference on life Prediction of corrodible structures, Cambridge, UK, 1991, pp. 12/1–12/11.
[3] C. Andrade, C. Alonso, and F.J Molina "Cover cracking as a function of bar corrosion: Part 1: Experimental test", Material and Structures, No. 26, 1993, pp. 453–464.
[4] J. Rodriguez, L.M. Ortega and J. Castel, "Corrosion of reinforcing bars and service life of reinforcing concrete structure: Corrosion and bon deterioration", International conference on concrete across borders, Odense, Denmark, vol. 2, 1994, pp. 315–326.
[5] Y. Ballim, J.C. Reid "Reinforcement corrosion and the deflection of RC beam-an experimental critique of current test methods", Cement & Concrete Composites vol. 25, 2003, pp. 625–632.
[6] Y. Ballim, J.C. Reid, A.R. Kemp, Deflection of RC beams under simultaneous load and steel corrosion". Magazine of Concrete Research 53, No. 3, 2001, pp. 171–181.
[7] B. Addis and G. Owens (ed), "Fulton's concrete technology", 8th edition, Cement & Concrete Institute, Midrand, South Africa, 2001.
[8] SABS 1083. Specification for Aggregates from natural sources. South Africa Bureau of standards, Pretoria, South Africa, 1976.
[9] BS 1881: 1983, Testing concrete, Part 121 Method for determination of static modulus of elasticity in compression. London: British Standards Institution, 1983.
[10] ASTM G1-67, Recommended Practice for Preparing, Cleaning and Evaluating Corrosion Test Specimens. American Society for Testing and Materials, Philadelphia, PA, 1971.
[11] Cabrera J.G. and Ghoddousi P. The effect of reinforcement corrosion on the strength of the steel/concrete bond. Proceedings of the Conference on Bond in Concrete, Latvia, CEB, 1992, Chapter 10, pp. 11–24.
[12] Broomfield J.P. "Assessing corrosion damage on reinforced concrete structures", In Swamy RN, (editor). Corrosion and corrosion protection of steel in concrete. Sheffield: Sheffield Academic Press. 1994. P. 1–25.
[13] Macinnes D.A. The Principles of Electrochemistry. Reynolds Publishing Corporation, New York, 1939, pp. 38–39.
[14] Raharinaivo A., Arliguie G., Chaussadent T., Grimaldi G., Pollet V., Taché G., La corrosion et la protection des aciers dans le béton, Presses de l'école nationale des Ponts et Chaussées, Paris, 1998..
[15] D. Landolt, "Introduction to surface reactions: Electrochemical basis of corrosion". in P. Marcus (editor), Corrosion Mechanisms in theory and practice. 2nd Edition, Marcel Dekker, Inc New York, 2002, pp. 1–18.
[16] Bardal E., "Corrosion and Protection", Springer Verlag, London, 2004.
[17] Macginley T.J. and Choo B.S. "Reinforced concrete: Design theory and exemples", 2nd edition, Spon press Taylor & Francis group, London & New York, 2003.
[18] Ghali A., Favre R. and Elbadry M., "Concrete structures: Stresses and deformation", 3rd edition, Spon press, London & New York, 2002.
[19] Cabrera J.G, "Deterioration of concrete due to reinforcement steel corrosion", Cement & Concrete Composites 18, 1996, pp. 47–59.
[20] Capozucca R., Cerri M.N., "Influence of reinforcement corrosion—in compressive zone – on the behaviour of RC beams", Engineering Structures; vol. 25, 2003, pp. 1575–1583.
[21] R. François, A. Castel, T. Vidal, "A finite macroelement for corroded reinforced concrete", Materials and Structures, vol. 39, 2006, pp. 571–584.
[22] P.J. Sanchez, A.E Huespe, J. Oliver, S. Toro, "Mesoscopic model to simulate the mechanical behaviour of reinforced concrete members affected by corrosion", International journal of solids and structures, vol. 47, 2010, pp. 559–570.

Concrete Repair, Rehabilitation and Retrofitting IV – Dehn et al. (Eds)
© 2016 Taylor & Francis Group, London, ISBN 978-1-138-02843-2

Damage evaluation for freezing-thawing affected concrete by automated panoramic fluorescent microscope

Shuguang Li, Gaixin Chen & Guojin Ji
State Key Laboratory of Simulation and Regulation of Water Cycle in River Basin, China Institute of Water Resources and Hydropower Research (IWHR), Beijing, P.R. China

Wanqiu Xia & Dong Zhang
Jiangxi Hongping Pumped-Storage Power Plant, State Grid Xinyuan Holding Co. Ltd., Nanchang, China

ABSTRACT: The deteriorating process of concrete suffered Freezing-Thawing (FT) is a process of initiation and development of microcracks. It's very important to establish the correlation between the macroscopic properties and the microcrack characteristics to evaluate the damage extent in concrete. The first step is to quantify the microcrack characteristics such as length, width and density. Though CT or MRI is a promising tool of analyzing microcracks nondestructively, the spatial resolution of either of them is far from satisfactory to detect FT-induced microcracks. Traditional microcrack-analyzing techniques such as Scanning Electron Microscope (SEM), Optical Microscope (OM), Fluorescent Microscope (FM) are all based on a limited number of small microscopic samples 1 or 2 mm in dimension cut from concrete slices. However, the limited samples are not representative and the microscopic analysis results are not reliable because concrete is a highly heterogeneous materials composed of mortar, Interfacial Transition Zones (ITZ) and aggregates. Accordingly, this paper presented a method of acquiring panoramic microscopic images of concrete slices (10 cm * 10 cm in size) impregnated with fluorescent epoxy by Automated Panoramic Fluorescent Microscope (APFM) which is designed and developed by our team. The APFM is characterized by four automatic modules, i.e., auto-scanning module, auto-focusing module, auto-mosaicing module and auto-analyzing module. Panoramic images of the concrete slices can be obtained by APFM in about two hours, which is efficient and accurate. In addition the area, length, density of microcracks in the slices can also be extracted and analyzed in the auto-analyzing module by digital-image-processing technique once the panoramic image is obtained. The evolution of microcrack characteristics in concrete during the FT damaging process is obtained and the results show that the length density and area density of the microcracks increase with the increase of the FT damage degrees. Relationships between the mechanical properties and the microcrack density are also established. Quantitative microcrack analysis based on APFM is a promising tool in evaluating FT damage and revealing the essence of damage in concrete.

1 INTRODUCTION

Most of the hydraulic concrete structures in North China are subjected to Freezing and Thawing (FT) deteriorations. FT-damaged concrete will suffer mass loss, decreases in mechanical properties and gradual loss of durability and the concrete structures will be decommissioned soon if nothing is done to prevent the development of damage.

The precondition of maintaining and repairing FT-damaged concrete structures is to make appropriate and reliable evaluations of the FT damage in concrete. FT-damage evaluation methods include nondestructive methods, such as resonant frequency (China Institute of Water Resources and Hydropower Research, 2006; Ohtsu, 2005), ultrasonic velocity (Ohtsu, 2005; Suzuki, et al., 2010). Although the above non-destructive techniques are easy to apply, but they are all phenomenological descriptions and either can reveal the essence of FT damage in concrete, which is the initiation and propagation of microcracks (Li and Cao, 2004).

With the development of microscopy and Digital-Image-Processing (DIP) techniques, some scientists such as Ammouche (2000), Litorowicz (2006), Elzafraney and Soroushian (2005a, 2005b) and Li et al (2012, 2014, 2015) begin to quantify microcrack patterns in mortar or concrete deteriorated by mechanical loadings, Alkali-Aggregate Reaction (AAR) or other factors. However, their microscopic analyses for concrete are all based on several so-called representative microscopic images

and couldn't represent the accurate microcrack patterns in the slices. As we all know, concrete is a highly heterogeneous material because of its three-phase structure, we should obtain and analyze as many microscopic images as possible in the concrete slice to get a realistic microcrack pattern.

It is noteworthy that though CT technology seems to be a promising non-destructi ve tool to get the 3D structure of cracks in concrete through image-reconstruction, the Field Of Vew (FOV) and the spatial resolution is in a dilemma. The greater the FOV, the smaller the spatial resolution, and vice versa. It is really a huge challenge for the current CT system to detect FT-caused microcracks 10~50 μm wide in full-scale concrete specimens which are usually over 5 cm in dimension in the laboratory. For instance, Wakimoto, et al. (2008) applied x-ray laminography to assess damage in concrete specimens 7.6 cm in dimensions which had been exposed to freezing temperatures, but only microcracks about 0.1 mm~0.2 mm in width could be identified.

This paper mainly poposed a method to generate panoramic image of the microcrack pattern in the concrete slice by an Automated Panoramic Fluorescent Microscope (APFM). Then the evolutions of microcrack patterns of microcracks in concrete with the increase of FT cycles were investigated. Finally correlations between the mechanical properties and the microcrack density were established.

2 EXPERIMENTAL PROGRAM

2.1 *Materials and mixing proportion*

A series of concrete specimens with Fly Ash (FA) were produced and ordinary Portland cement with a density of 3.21 g/cm^3 was used. The density of the FA is 2.42 g/cm^3.

Natural sand was used as fine aggregates with a fineness modulus of 2.12.

Two-grade crushed gravels whose sizes were in the ranges of 5~20 mm and 20~40 mm respectively were used as coarse aggregates.

A naphthalene-based superplasticizer was introduced to obtain fresh concrete with satisfying workability. Rosin-based air-entraining agent was used for air-entrained concrete and the actual air void content in the concrete specimens is 2.0%. The mixing proportions of the two series of concrete are shown in Table 1.

2.2 *Testing procedures*

A series of prismatic, cubic and cylindrical specimens were produced for FT tests and mechanical tests according to the *Test code for hydraulic concrete (SL352-2006)* of China (China Institute of Water Resources and Hydropower Research, 2006). After being cured for 90 d in the standard curing room, all the specimens were placed in rubber sleeves filled with water and kept in the chamber of the FT testing machine. Rapid freezing and thawing methods were used and the resonant frequency tests of the specimens at different FT cycles were done according to the *Test code for hydraulic concrete (SL352-2006)* (China Institute of Water Resources and Hydropower Research, 2006), which is similar with *Standard Test Method for Resistance of Concrete to Rapid Freezing and Thawing (ASTM C 666/C 666 M-03(2008))*.

Mechanical tests were performed to get the compressive strength, the splitting-t ensile strength of those specimens subjected to different FT cycles. The dimensions of the prismatic specimens for the compressive tests and axial tensile tests were 15 cm × 15 cm × 15 cm and 10 cm × 10 cm × 55 cm, respectively. For the resonant frequency tests as well as the flexural tests the specimen dimensions were 10 cm × 10 cm × 40 cm. polymer latex significantly reduces the brittleness of concrete, and has a higher ratio of tensile strength and compressive strength.

2.3 *Freezing-thawing and mechanical test results*

FT damage degree is proposed to describe the deteriorating extent of FT cycles to concrete and it is calculated by the following formula,

$$D_{FT} = 1 - \frac{E'}{E_0}$$

where D_{FT} is the FT damage degree, E_0 is the initial dynamic modulus of elasticity of concrete and E'

Table 1. Concrete mix proportions.

			Additives (%) (kg/m^3)							
									Aggregate	
W/C	FA ratio (%)	Sand ratio (%)	Super-plasticizer	Air-entraining agent	Water	Cement	FA	Sand	5~20 mm	20~40 mm
0.52	25	34	0.65	0.0095	136	196	66	674	664	667

is the dynamic modulus of elasticity of concrete suffered certain FT cycles.

The relative dynamic modulus of elasticity and FT damage degree of the concrete specimens at different FT cycles are shown in Figure 1. It can be seen from Figure 1 that the relative dynamic modulus of elasticity decreases while the FT damage degree increases with the increase of FT cycles. the FT damage degree increases gradually to over 0.40 at 325 FT cycles.

Table 2 shows the FT damage degree, the relative compressive strength, the relative tensile splitting strength and the static modulus of elasticity of the concrete specimens F52 suffered different FT cycles. The relative mechanical properties are calculated by dividing the mechanical properties of concrete specimens suffered certain FT cycles by those specimens cured for 90 d.

It can be seen from Table 2 that the relative compressive strength, the relative tensile splitting strength and the static modulus of elasticity of the two series of concrete decrease with the increase of the FT cycles. For concrete F52 the decrease in mechanical strength is much larger. At the FT cycle 325, the relative compressive strength, the relative splitting tensile strength and the relative static modulus of elasticity are 0.54, 0.14 and 0.32, respectively. It indicates that for concrete F52, the splitting tensile strength and the modulus of elasticity are more sensitive to FT damage than the compressive strength.

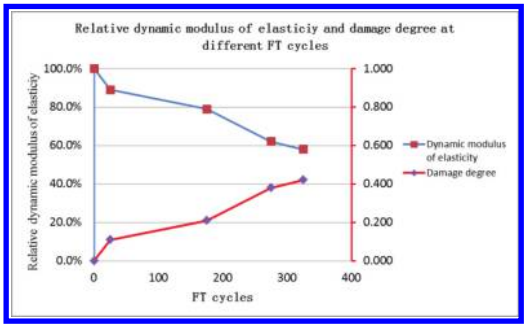

Figure 1. Relative dynamic modulus of elasticity and FT damage degree of concrete at different freezing-thawing cycles.

3 QUANTITATIVE MICROCRACK ANALYSIS

3.1 *Specimen preparation*

Fluorescent epoxy vacuum-impregnation method is used since it has little influence on the original microcrack patterns in concrete.

The concrete specimens for microscopic analysis were prepared by fluorescent epoxy vacuum-impregnation method in the following procedures:

a. Two slices of 15 mm to 20 mm thickness were cut from the middle parts of each 10 cm × 10 cm × 40 cm prismatic specimen (to reduce the effects of both ends on microcrack patterns) which had been tested for resonant frequency at different FT cycles.
b. The surfaces of the slices were ground and polished using a grinder to obtain a smooth flat surface.
c. The smooth surfaces were rinsed with water at low and high speeds to remove any leftover debris.
d. The slices were dried in an oven at a temperature of 40~50°C for 24 h.
e. The slices were placed in a plastic container and evacuated for at least 1 h at a constant pressure of 1 kPa in a vacuum chamber.
f. The plastic container inside the vacuum chamber was then filled with the epoxy resin containing fluorescent dye while maintaining the vacuum.
g. Finally, the slices were taken out from the vacuum chamber and from the plastic container, and then slightly ground to remove the excess epoxy on the surfaces once the epoxy was hardened.

Table 2. Mechanical strength of concrete F52 at different FT cycles.

	F52-0	F52-25	F52-175	F52-275	F52-325
FT cycles	0	25	175	275	325
Relative dynamic modulus of elasticity (%)	100	89	80	62	60
FT damage degree, D_{FT}	0.00	0.11	0.20	0.38	0.40
Compressive strength (MPa)	41.2	37.6	33.2	25.8	22.3
Relative compressive strength	1.00	0.91	0.81	0.63	0.54
Splitting tensile strength (MPa)	3.09	2.83	2.23	1.01	0.43
Relative splitting tensile strength	1.00	0.92	0.72	0.33	0.14
Static modulus of elasticity	38.52	33.2	25.01	15.36	12.15
Relative static modulus of elasticity	1.00	0.86	0.65	0.40	0.32

Quantitative microcrack analyses were performed by an Automated Panoramic Fluorescent Microscope (APFM) on those slices cut from the specimens tested for resonant frequencies at specified FT cycles (0, 25, 175, 275 and 325). Typical images of these slices are shown in Figure 2.

3.2 *Automated panoramic fluorescent microscope*

Besides specimen preparation, reliable quantitative analysis of microcracks requires acquisition, processing, and analysis of the microcrack images in the concrete slices. An automated panoramic fluorescent microscope was designed and developed to get a panoramic image of the microcrack pattern in the concrete automatically.

Once the microscopic specimen (the impregnated and polished concrete slice) is put on the stage, the stage will automatically move in two directions in the range of 10 cm × 10 cm and microscopic image will be taken every step and stored in the computer. To get clear images the camera can be moved along the z-direction every *m* step (*m* is set in advance and is usually 2~5). More than 4000 images will be obtained for a slice with an area of 10*10 cm and the images can be mosaicked into one panoramic view automatically by DIP technique. The specimens are scanned automatically on the stage at a magnification of 40× which was sufficient to detect microcracks as thin as 2 μm in width.

Typical panoramic images of some of the slices are shown in Figure 3. It should be noted that only 2 cm*2 cm representative regions from the panoramic images are shown in Figure 3 to make the microcracks more clearly. It can be seen from Figure 3(a)~(c) that for concrete slice F52-0 (concrete without FT cycles), only a few microcracks are observed. For concrete slices F52-175 and F52-325 (suffered 175 and 325 FT cycles, respectively), more microcracks can be observed.

Figure 2. Typical slices from concrete suffered different FT cycles. (From left to right: F52-0, F52-25, F52-175 (the first row), F52-275, F52-325 (the second row), the numbers means FT cycles).

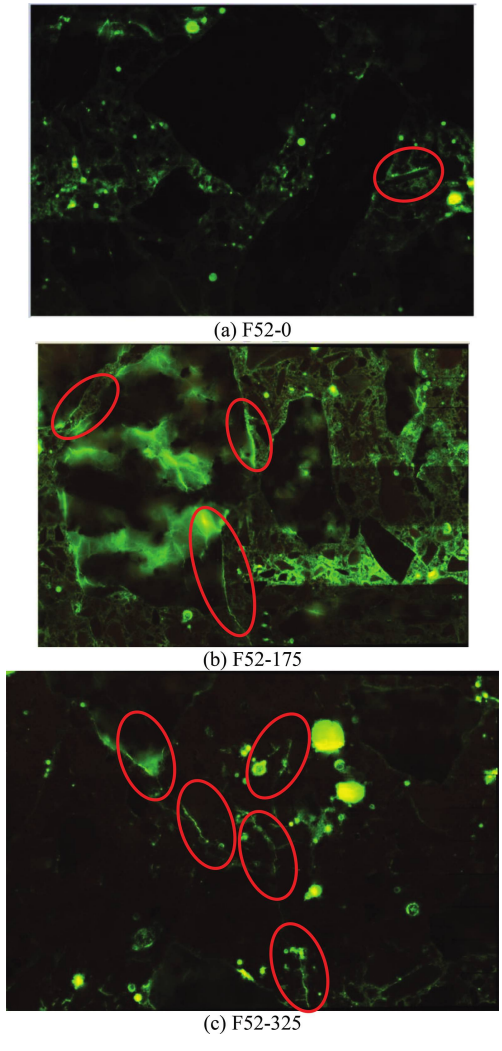

(a) F52-0

(b) F52-175

(c) F52-325

Figure 3. Typical panoramic images of different slices, microcracks are highlighted in circles.

3.3 *Quantitative analysis system of microcracks in concrete*

A MATLAB-based software package called QUANSMIC (QUantitative ANalysis System of MIcrocracks in Concrete) was developed to acquire the geometrical characteristics of microcrack patterns. It includes four modules, namely image-binarizing module, shape-analyzing module, crack-skeletonizing module and automatic-measuring module.

The original colour microscopic images containing microcracks are firstly converted into greyscale images, and then the microcracks are recognized and extracted by the image-binarizing module. Noises and voids are distinguished from the microcracks and deleted by the shape-analyzing module and then the preserved microcracks are skeletonized by the crack-skeletonizing module. Finally the geometrical characteristics such as area, length and average width of the microcracks are measured and calculated by the automatic-measuring module.

The precision of QUANSMIC was validated with several ordered specimens with shapes of known sizes and the comparisons showed that QUANSMIC has a high accuracy. Details about QUANSMIC are introduced in ref (Li et al, 2013, 2014).

4 QUANTITATIVE MICROCRACK ANALYSES OF FT-DAMAGED CONCRETE

Six microcrack characteristic parameters, namely the total length, length density, total area, area density, maximum width and average width are calculated by QUANSMIC to quantify the microcrack patterns in concrete specimens subjected to different FT degrees. They are calculated as follows:

Total length—sum of the microcrack lengths on all the microscopic images,
Length density—ratio of the total length to the observing area,
Total area—sum of the microcrack areas on all the microscopic images,
Area density—percentage of the area of the microcracks to observing area,
Average width—total area divided by the total length,
Maximum width—the maximum value of all the average microcrack widths.

4.1 *Microcrack characteristics at different FT cycles*

The length density, the area density, the average width and maximum width of matrix cracks of the concrete slices at different FT cycles are shown in Table 3. It can be seen from Table 3 that both the length density and the area density increase with the increase of the FT cycles. It can also be seen from Table 3 that for the concrete specimens with zero FT cycle (without any deterioration), either the length density or the area density of matrix cracks is at a very low level. It indicates that a few initial microcracks could be found in the undamaged concrete before any loading or deterioration. They are perhaps caused by mortar shrinkage because of the cement hydration, or resulted from the cutting and drying procedures in the processing process. Further study needs to be done to find which the exact reason is.

It can also be seen from Table 3 that both the maximum width and the average width of microcracks increase with the increase of the FT cycles. It indicates that as the FT cycles increase many new microcracks are emerging while the existing microcracks are becoming wider and wider.

4.2 *Relationships between the mechanical properties of FT damaged concrete and the microcrack characteristics*

Relationships between the relative compressive strength, the relative splitting-tensile strength and the static modulus of elasticity and the average length density are shown in Figure 4. The average length density is averaged value of two slices.

It can be seen from Figure 4 that very good quadratic correlations can be established between the relative mechanical properties and the average length density. All the squares of the correlation coefficients are higher than 0.97. It can also be seen from Figure 4 that the relative compressive strength is less sensitive to the microcrack density than the relative splitting-tensile strength and the static modulus of elasticity.

Relationship between the FT damage degree and the microcrack density is shown in Figure 5. It can be seen from Figure 5 that very good linear correlation can be established between the FT damage degree and the microcrack density.

As seen from the above results and analyses, the decreases in the mechanical properties of

Table 3. Microcrack characteristics of concrete F52 at different FT cycles.

	F52-0	F52-25	F52-175	F52-275	F52-325
FT cycles	0	25	175	275	325
Length density (mm/mm^2)	0.0008	0.031	0.04	0.07	0.072
Area density (%)	0.0015	0.061	0.052	0.115	0.132
Average width (μm)	16.2	17.8	17.9	18.2	19.3
Maximum width (μm)	16.3	22.1	23.6	24.9	31.6

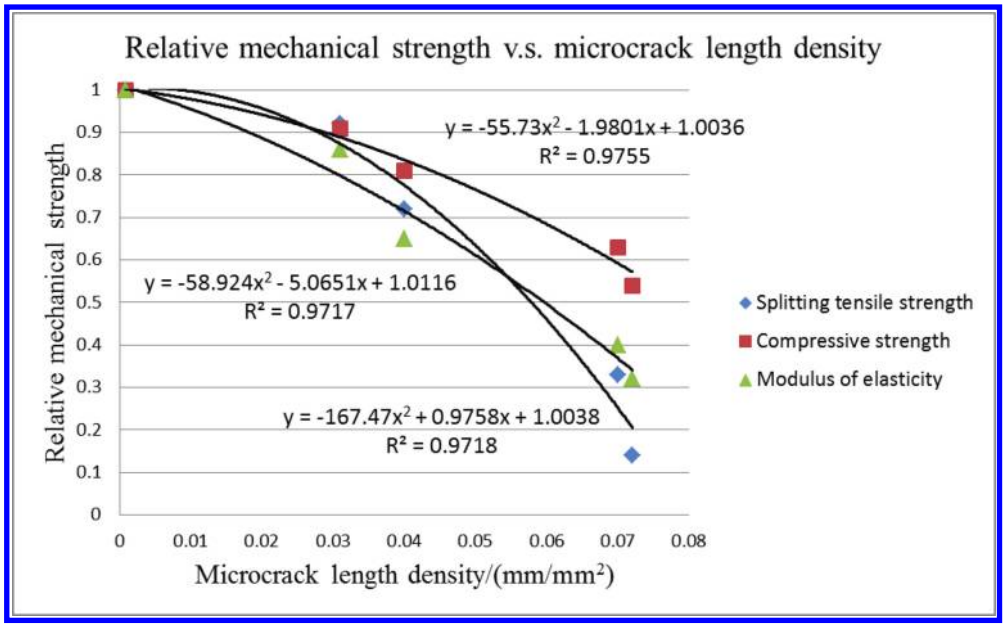

Figure 4. Relationships between the relative mechanical strength and the average length density.

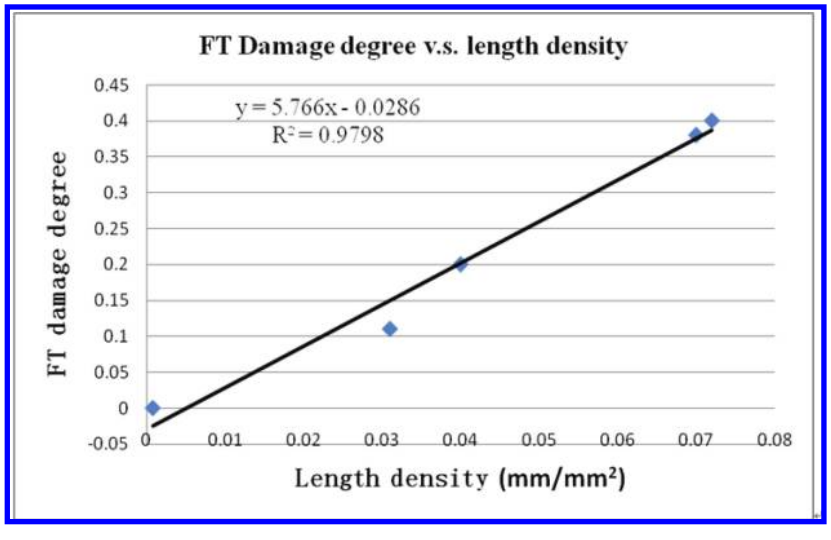

Figure 5. Relationships between the FT damage degree and the average length density.

FT-deteriorated concrete have strong correlations with the microcrack density. This indicates that instead of mechanical tests and non-destructive tests to measure the resonance frequency or the ultrasonic velocity, microcrack density obtained by quantitative microcrack analysis could be developed as a new tool to quantitatively evaluate the damage in concrete.

5 CONCLUSION

A thorough investigation based on APFL and DIP techniques was made on the development of microcrack patterns in slices cut from concrete specimens suffered different FT cycles. The following conclusions can be drawn from the results and analysis above.

a. The length density, area density, maximum width and average width of microcracks in concrete all increase with the increase of FT damage degree.
b. Quadratic correlations are established between the relative mechanical properties (including the relative compressive strength, the relative axial splitting-tensile strength and the static elastic modulus) and the average microcrack length density. All the correlation coefficients are higher than 0.97, indicating that microcrack density could be used to evaluate FT damage in concrete.

ACKNOWLEDGEMENTS

Financial support from the Major State Basic Research Development Program of China (Grant No. 2013CB035901), the National Natural Science Foundation of China (51409284), the Open Research Fund Program of State key Laboratory of Hydroscience and Engineering (2015-C-02), the State key Laboratory of Hydrology-Water Resources and Hydraulic Engineering (2014491311) and State Key Laboratory of Simulation and Regulation of Water Cycle in River Basin (IWHR-SKL-201412) are gratefully acknowledged.

REFERENCES

Akcaoglu, T., Tokyay, M., et al., 2005. Assessing the ITZ microcracking via scanning electron microscope and its effect on the failure behavior of concrete. *Cement and Concrete Research*, **35**(2): 358–363.

Ammouche, A., Breysse, D., et al., 2000. A new image analysis technique for the quantitative assessment of microcracks in cement-based materials. *Cement and Concrete Research*, **30**(1): 25–35.

China Institute of Water Resources and Hydropower Research. Test *code for hydraulic concrete (SL 352–2006*. The ministry of China, 2006. (in Chinese)

Elzafraney, M. and Soroushian, P., 2005a. Quantitative microstructural investigation of deteriorated reinforced concrete bridge deck. *Journal of Materials in Civil Engineering*, **17**(2): 159–167.

Elzafraney, M. and Soroushian P., 2005b. Sampling approach for quantitative microscopic investigation of concrete through planar and spatial measurements. *Magazine of Concrete Research*, **57**(6): 321–330.

Landis, E.N. and Nagy, E.N., 2000. Three-dimensional work of fracture for mortar in compression. *Engineering Fracture Mechanics*, **65**(2): 223–234.

Litorowicz, A., 2006. Identification and quantification of cracks in concrete by optical fluorescent microscopy. *Cement and Concrete Research*, **36**(8): 1508–1515.

Li, J.Y., Cao, J.G., 2004. *Research and application of durability in hydraulic engineering concrete*. Beijing: China Electric Power Press. (in Chinese)

Li, S. G., Chen, G. X., et al., 2014. Quantitative damage evaluation of concrete suffered freezing–thawing by DIP technique [J]. Construction and Building Materials, 2014; 69: 177–185.

Li, S. G., Chen, G. X., et al., 2013. Quantitative damage evaluation of AAR-affected concrete by DIP technique. Magazine of Concrete Research. 2013, 65(3): 332–342.

Ohtsu, M., 2005. Nondestructive evaluation of damaged concrete due to freezing and thawing by elastic-wave method, *Journal of Advanced Concrete Technology*, **3**(3): 333–341.

Suzuki, T., Ogata, H., et al., 2010. Use of acoustic emission and X-ray computed tomography for damage evaluation of freeze-thawed concrete. *Construction and Building Materials*, **24**(12): 2347–2352.

Wakimoto, K., Blunt, J., et al., 2008. Digital laminography assessment of the damage in concrete exposed to freezing temperatures. *Cement and Concrete Research*, **38**(10): 1232–1245.

Concrete Repair, Rehabilitation and Retrofitting IV – Dehn et al. (Eds)
© 2016 Taylor & Francis Group, London, ISBN 978-1-138-02843-2

Modelling the service life of concrete until cover cracking due to reinforcement corrosion

E. Bohner, M. Ferreira & O. Saarela
VTT Technical Research Centre of Finland Ltd., Espoo, Finland

ABSTRACT: The service life design of reinforced concrete structures requires material models capable of reliably describing both mechanisms of damage and the general progression of damage over time. However, most models that are currently being used only capture the process of carbonation and chloride penetration into the uncracked concrete that is at the initial phase of degradation. Typically, these models disregard the actual damage, i.e. the corrosion of the reinforcing steel. As a result, the service life design established to date only considers the end of the initiation phase of the degradation process, i.e. the onset of damage (time of depassivation or onset of corrosion) as a critical limit state. The corrosion of the reinforcement and its consequences, i.e. the crack formation and spalling of concrete, are not considered, which may lead to a substantially shorter estimated service life of the structures. Comprehensive investigations were recently undertaken on the depassivation of steel reinforcement and on crack formation in concrete which have resulted in an analytical model for corrosion-induced cracking occurring in the surface zones of structural components. This paper presents a holistic approach in which two models used for determining the time to depassivation (initiation phase) and the time to cover cracking as a result of reinforcement corrosion (propagation phase) are combined. An example is provided of a semi-infinite reinforced concrete wall which has been designed for the serviceability limit state of concrete cover cracking.

1 INTRODUCTION

Reinforced Concrete Structures (RCS) are subject to constant deterioration limiting their service life. The service life prediction of deteriorating structures is affected by the uncertainties associated with material properties, mechanical and environmental loads, damage occurrence and propagation models (Kim et al. 2013). Therefore, estimation of service life requires probabilistic models and methods to account for the uncertainties that govern the deterioration processes.

The service life design of reinforced concrete structures requires material models capable of reliably describing both mechanisms of damage and the general progression of damage over time. However, most models that are currently being used only capture the process of carbonation and chloride penetration into the uncracked concrete that is at the initial phase of degradation. Typically, these models disregard the actual damage, i.e. the corrosion of the reinforcing steel. As a result, the service life design established to date only considers the end of the initiation phase of the degradation process, i.e. the onset of damage (time of depassivation or onset of corrosion) as a critical limit state. The corrosion of the reinforcement and its consequences, i.e. the crack formation and spalling of concrete, are not considered, which may lead to a substantially shorter estimated service life of the structures. There are two distinct phases in the corrosion induced deterioration process of concrete (see Fig. 1).

The first phase (initiation) is defined as the time necessary for chloride ions to reach a critical

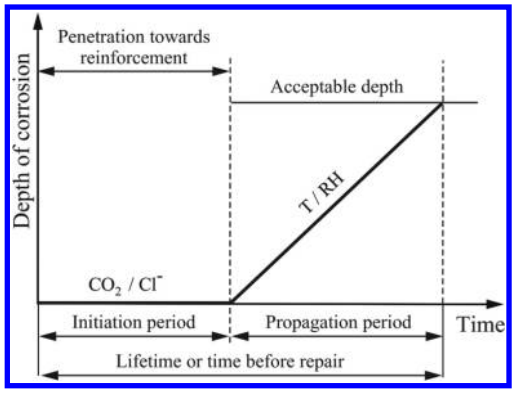

Figure 1. Schematic representation of steel corrosion in concrete (Tuutti 1982).

concentration at the depth of the reinforcement to cause its depassivation. Typically diffusion controls the process. This instant is defined as corrosion initiation. The second phase (propagation) is defined as the period of time that follows the initiation of corrosion. It can be separated in different deterioration phases, of which the first is cracking of concrete cover. Typically corrosion rate controls the process at the outset. After the appearance of the first crack, the continuous volume expansion due to rust formation as a consequence of the proceeding corrosion leads to crack propagation resulting in the spalling of the concrete cover.

In practice, it has been observed that time dependent reliability models do not consider the causational relationship between serviceability limit states, dealing with each limit state independently. As an example, corrosion initiation and propagation are usually dealt with independently, ignoring the dependency between them. Commonly the propagation phase is ignored, i.e. considered to be on the safe side (conservative approach). This might stem from the lack of models, and confidence in models for this phase. As a consequence, design decisions based upon independent time-dependent reliability models will not produce optimal outcomes.

Comprehensive investigations were recently undertaken on the depassivation of steel reinforcement and on crack formation in concrete which have resulted in an analytical model for corrosion induced cracking occurring in the surface zones of structural components (Bohner 2013).

An attempt to bridge this gap is made with a basic methodology for the probabilistic determination of service life, combining both corrosion initiation and propagation phase models. The approach takes into account the time dependency of the individual phenomena, and the relationship between both phases.

The quantitative prediction of the time to cracking is needed in the development of a holistic deterioration model for the prediction of service life. A probabilistic methodology is presented based on theoretical physical models for corrosion initiation and time from corrosion initiation to cracking of the concrete cover (time-to-cracking), and the causational relationship between them, i.e. time-to-cracking depends on the time to corrosion initiation. Based on the methodology, it is demonstrated how the models influence the estimated time to corrosion cracking considering both deterioration mechanisms involved. This approach helps to improve the prediction of durability for new or to define optimal repair strategies for existing concrete structures. The time from corrosion initiation to cracking of the concrete cover is a critical period for modelling the time to repair, rehabilitate, and replace RCS.

This paper presents a probabilistic design procedure which combines the calculation of two independent limit states for concrete deterioration: chloride induced corrosion initiation, and corrosion induced cracking of concrete. By combining the limit states, the outcome of the service life calculation is the probability of time to corrosion induced cracking, at any time starting after construction.

2 RELIABILITY ANALYSIS

2.1 *Basic reliability analysis*

In general, engineering design consists of proportioning the elements of a RCS so that it satisfies various criteria of performance, safety, serviceability, and durability under various loadings. A reliability analysis can be used to calculate the probability of failure of a limit state at any instant in time during the RCS's service life. The objective of durability design is to keep the probability of failure throughout the service life period below a certain requirement that depends on the consequences of failure. The limit state defines the conditions beyond which a specified requirement for a structure (or component) is no longer met for a certain degree of reliability (ISO/FDIS 16204:2012). Limit states are represented by the limit state equations, generally of the form $g(x) = 0$. A limit state violation (or failure) occurs when an undesirable condition for the structure is reached. The probability of occurrence of a limit state violation is a numerical measure of the chances of its occurrence, based on long term observations or subjective estimates.

The basic reliability problem considers only one load effect S resisted by one resistance R. Both R and S are described by known Probability Density Functions (PDF), $f_R(r)$ and $f_S(s)$ respectively, where any uncertainty concerning a variable is explicitly taken into account. For convenience, it is considered R and S are not functions of time. If R and S have known PDF's $f_R(r)$ and $f_S(s)$ respectively, and are expressed in the same units, then

$$p_f = P\left(R - S \le 0\right) \text{ or } P\left\{g\left(R,S\right) \le 0\right\} \tag{1}$$

where $g(x)$ is termed the limit state function, and the probability of failure is synonymous to the probability of limit state violation. The probability of failure of the joint (bivariate) density $f_{RS}(r, s)$ is given by

$$p_f = P\left(R - S \le 0\right) = \iint_D f_{RS}\left(r,s\right) dr.ds \tag{2}$$

If R and S are independent, then

$$f_{RS}(r,s) = f_R(r).f_S(s) \tag{3}$$

which leads to

$$p_f = P(R-S \le 0) = \int_{-\infty}^{\infty} \int_{-\infty}^{s \ge r} f_R(r).f_S(s)\,dr.ds \tag{4}$$

For a random variable X, the cumulative distribution function is given by

$$F_X(x) = P(X \le x) = \int_{-\infty}^{x} f_X(y)\,dy \tag{5}$$

If R and S are independent, and if $x \le y$, the solution of the probability of failure for bivariate density functions can be written in a single integral form known as the convolution integral:

$$p_f = P(R-S \le 0) = \int_{-\infty}^{\infty} F_R(x).f_S(x)\,dx \tag{6}$$

$F_R(x)$ is the probability $R \le x$ of the probability that the actual resistance R of the member is less than some value x, representing failure. The term $f_S(x)$ represents the probability that the load effect S acting on the element has a value between x and $x + \Delta x$ in the limit as $\Delta x \to 0$. By calculating the integral over all x, the total failure probability is obtained. This is schematically shown in Figure 2.

A reliability analysis can be performed by numerical integration, Monte Carlo simulation, or using approximate methods such as First Order and Second Order Reliability Methods (FORM/SORM). The numerical integration was not preferred in this case because of the large dimension and the complexity of this problem.

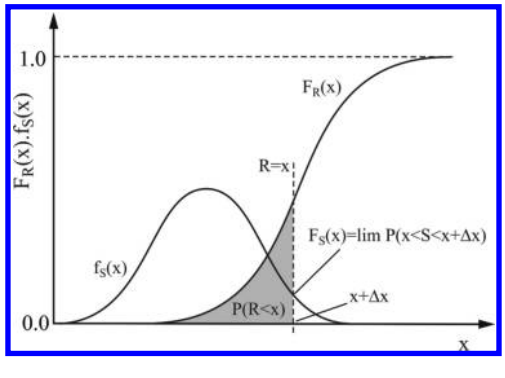

Figure 2. Basic R-S problem: $F_R(x).f_S(x)$ representation (Naess 1995).

The reliability analysis in this study was performed using Monte Carlo simulation. Even for the computing of small probabilities, the development of variance reduction techniques such as importance sampling (Thoft-Christensen & Baker 1982), and the evolution of computing power has reduced dramatically this once time consuming process. The theoretical description of this method is given in many references (Rubinstein 1981, CSEP 1995).

2.2 *Reliability analysis—combination of two limit states*

A methodology is presented which contributes to the development of reliability-based approaches for the durability design and service life prediction of RCS that combines the probabilistic determination of two limit states (corrosion initiation and corrosion induced cracking) in a single analysis, thus removing the need for one of the limit states.

By combining initiation with propagation until cracking, the combined service life covers the period from $t = 0$ until the time for the first crack with a width of a minimum of 0.05 mm to appear on the surface of the concrete. The combination includes both the processes described in Sections 3.2 and 3.3.

Assuming that corrosion is initiated at some time τ, for cracking to take place at time t the corrosion process has to have a duration of $t - \tau$. Consequently, the combined probability distribution of the time of cracking is

$$f_{i,p}(t) = \int_{-\infty}^{\infty} f_p(t-\tau \,|\, T_i = \tau)\, f_i(\tau)\, d\tau \tag{7}$$

where $f_{i,p}$ = probability of failure; $f_p(t)$ = PDF of the propagation model; and $f_i(t)$ = PDF of the initiation model.

The start of corrosion propagation process depends on the corrosion initiation process, however the mechanisms that describe each of these processes are independent of each other. Therefore the modelling and computation of this distribution can be simplified by replacing the conditional PDF with corresponding marginal probability distribution:

$$f_{i,p}(t) \approx \int_{-\infty}^{\infty} f_p(t-\tau)\, f_i(\tau)\, d\tau \tag{8}$$

The model assumes chloride ingress starts at the time of construction ($t = 0$), and that the corrosion process starts when chloride has reached a critical

threshold value at the depth of the reinforcement. Consequently,

$$f_p(t) = f_i(t) = 0 \quad \forall \ t < 0 \tag{9}$$

allowing the integration interval to be shortened.

For $t \geq 0$

$$f_{i,p}(t) \approx \int_0^t f_p(t-\tau)\, f_i(\tau)\, d\tau \tag{10}$$

A consequence of this approach is that there is no need to establish a limit state requirement for corrosion initiation, and another for cracking. By combining the calculations, only one requirement for the outcome of both needs to be defined. Furthermore, the uncertainties related to both processes, as modelled in the PDF's, are properly combined.

3 DETERIORATION MODELS

A reliability analysis begins with the formulation of a limit state function, which represents the performance of a structure or an element, in terms of a number of basic random variables. The model parameters are characterised by PDFs. Even the uncertainties associated with the model and the tests used should typically be considered. It is an assumption that the models for corrosion initiation and propagation are sufficiently validated in order to provide realistic and representative results. Conformity is checked by verifying that the specified reliability is unsurpassed in the verification of the limit state function over the service life of the structure.

The limit state function for time to corrosion initiation is defined by:

$$g_i(x,t) > 0 \Leftrightarrow C_{crit} - C(x,t) > 0 \tag{11}$$

where $g_i\,(x,\ t)$ = limit state function for corrosion initiation; C_{crit} = critical chloride content leading to depassivation [%/weight of cement or concrete]; and $C\,(x,\ t)$ = chloride concentration at depth x and time t [%/weight of cement or concrete]; and described in section 3.1.

The limit state function for time to corrosion induced concrete cracking is given by:

$$g_p(x,t) > 0 \Leftrightarrow \Delta r_{crack}(t) - \Delta r_{corr}(t_{corr}) > 0 \tag{12}$$

where $g_p\,(x,\ t)$ = limit state function for corrosion induced concrete cracking; Δr_{corr} = increase of rebar radius due to corrosion [mm]; Δr_{crack} = critical increase of rebar radius due to corrosion at time of cracking [mm]; t_{corr} = time of corrosion [years]; and described in section 3.1.

3.1 *Limit state requirements*

Designers must define the criteria for which the limit state is evaluated. There is still considerable debate as to what are the appropriate values for durability related limit states. With regards to reinforcement corrosion, this is in part due to the difficulty in practice to define a precise instant when corrosion actually starts. Values based on experience or set by conventions are required.

When defining the requirement for probability of failure (or reliability index—β), the criteria that should be taken into account are: the type of limit state (initiation of deterioration, SLS or ULS); the service life for new structures or reference period for existing structures; the consequences of failure; and, the cost of safety measures. Typical values suggested for structural design for p_f/β are for a period of 50 years 0.0667/1.5 for a serviceability limit states, and $\approx 10^{-4}$/3.8 for ultimate limit states.

In the fib Model Code for Service Life Design (2006), β = 1.3 is presented as a "recommended minimum value" for exposure class XS independent of the RC of the structure. According to the LNEC E-465 (2007), the reliability index varies according to the RC from 1.2 to 2.0 for the RC1 and RC3 class, respectively. These β-values correspond to failure probabilities of approximately 12% and 2%, respectively. There is yet no consensus as to which should be the appropriate values for the reliability index, when considering limit states associated with durability (Gulikers 2006, Ferreira & Gulikers 2007).

3.2 *Time to corrosion initiation*

The model is based on the *fib* Model Code for Service Life Design (2006) approach, which is based on the classical solution of Fick's second law with semi-infinite boundary and constant surface concentration. This model includes a time dependent apparent diffusion coefficient.

$$C(x,t) = C_0 + (C_S - C_0) \cdot \left(1 - erf \frac{c}{2\sqrt{D_{ap} \cdot t}}\right) \tag{13}$$

$$D_{ap} = D_0 \cdot \exp\left(be\left(\frac{1}{t_{ref}} - \frac{1}{t_{real}}\right)\right) \cdot k_t \cdot \left(\frac{t_0}{t}\right)^{\alpha} \tag{14}$$

where C_0 = initial chloride concentration in the concrete [%/weight of cement or concrete]; C_S = surface chloride concentration [%/weight of

cement or concrete]; c = concrete cover depth [mm]; D_{ap} = apparent diffusion coefficient [m²/s]; D_0 = diffusion coefficient at t_0 [m²/s]; α = ageing factor of diffusion coefficient [–]; t_0 = reference time [years]; t = life time [years]; t_{real} = temperature of the water/air in contact with concrete [K]; t_{ref} = reference temperature [K]; be = Arrhenius slope [–]; k_t = transfer parameter [–].

Although widely used, the model has not have been calibrated for periods longer than 30 years and has several limitations and sources of uncertainty (Gulikers 2006). Equation 13 provides an estimate of the chloride profile for a specific period of exposure time. It is applicable for 1-D situations, and not suitable for small columns and beams, especially in the regions near the edges. The model also includes a number of implicit assumptions: exposure to chloride starts at $t = 0$, i.e. immediately after casting; C_s is constant over time; and D_{ap} varies with time and temperature only, until $t = \infty$ according to Equation 14.

3.3 *Time from corrosion initiation to concrete cracking*

In order to describe the action S, which represents the propagation of corrosion, the increase of reinforcement bar (rebar) radius Δr_{corr} has to be defined. This increase is dependent on the time of corrosion and results from the reduction of the reinforcement bar radius due to corrosion in combination with the expansion of the occurred corrosion products (Eq. 15). The reduction of the rebar radius is based on the corrosion rate $\dot{x}_{corr}$. The corrosion rate can be either determined experimentally or it can be calculated by means of models, such as that of Osterminski & Schießl (2011). The expansion factor, also known as volume ratio λ, is calculated by the quotient of the volume of rust and the volume of the steel (Bohner & Müller 2012).

$$\Delta r_{corr}\left(t_{corr}\right) = t_{corr} \cdot \dot{x}_{corr}\left(t_{corr}\right) \cdot \left(\lambda - 1\right) - d_{por}\left(t_{corr}\right) \tag{15}$$

where Δr_{corr} = increase of rebar radius due to corrosion [mm]; $\dot{x}_{corr}$ = corrosion rate [mm/a]; λ = volume ratio [–]; d_{por} = function to take account of rust migration into concrete pores [mm].

Experimental investigations have shown that the initial radius increase of the corroding rebar is weakened by the migration of corrosion products into the surrounding voids and pores of the concrete. This results in a time delay of the development of corrosion induced stresses. Stress levels that are able to cause concrete cracking occur not until a certain saturation of the pores in the transition zone around the steel surface has taken place. By means of a continuous function (Eq. 16), which was derived based on physical considerations, the migration of rust into the concrete pores can be considered as:

$$d_{por}\left(t_{corr}\right) = p \cdot d_{tz} \cdot \tanh\left(\frac{\dot{x}_{corr}\left(t_{corr}\right) \cdot \left(\lambda - 1\right)}{p \cdot d_{tz}} \cdot t_{corr}\right) \tag{16}$$

where p = porosity of the transition zone accessible for corrosion products [–], valid $0 \le p < 1$; d_{tz} = thickness of the transition zone accessible for corrosion products [mm].

The action S (increase of rebar radius due to corrosion) encounters a resistance R (see Fig. 3) that derives from the concrete surrounding the rebar. It can be defined as the critical increase of rebar radius due to corrosion at the time of cracking (see Eq. 17). This threshold value depends on concrete age, concrete properties, size and shape of rebar and concrete cover thickness. Its derivation is based on the linear elastic theory for a thick-walled cylinder assuming linear viscoelastic behaviour of the concrete (Bohner 2013):

$$\Delta r_{crack}\left(t\right) = \frac{f_{ct}\left(t\right)}{E_{c,eff,D}} \cdot \frac{d_s + 2c\left(1 + c/d_s\right)\left(1 + \nu\right)}{1 + \left(\frac{3d_s + 6c}{3d_s + 4c}\right)^2} \cdot k_{nonlin} \cdot k_{local} \cdot k_{\mu} \tag{17}$$

where Δr_{crack} = critical increase of rebar radius due to corrosion at time of cracking [mm]; t = concrete

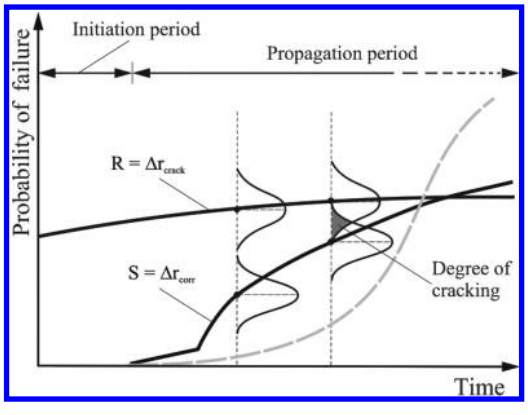

Figure 3. Schematic representation of the time dependent increase of reinforcement bar radius due to corrosion Δr_{corr} (loading S), the critical reinforcement bar radius at the time of cracking Δr_{crack} (resistance R) and the resulting failure probability (Bohner 2013).

age [a]; f_{ct} = tensile strength of concrete [MPa]; $E_{c,eff,D}$ = effective modulus of elasticity of concrete [MPa] (influence of creep, relaxation and degradation, see Müller & Kvitsel 2002); ν = Poisson's ratio of concrete [–]; d_s = rebar diameter [mm]; c = concrete cover [mm]; k_{nonlin} = factor for consideration of plasticity and cracking of concrete [–]; k_{local} = factor for consideration of a localisation of corrosion (pitting corrosion) [–]; k_μ = factor for consideration of percentage of reinforcement [–].

The model assumes that the corrosion instantly appears as uniform corrosion, covering the entire circumference of the reinforcement bar. A distinct pitting corrosion can be taken into account by assigning a value to the factor k_{local}. The complex time-dependent stress-induced deformation behaviour of concrete and its characteristic tension softening during cracking have a significant influence on the duration of the deterioration process. They are considered based on simplifying or adjunct functions, as e.g. the effective modulus of elasticity for concrete creep or the factor k_{nonlin} for taking into account the quasi-brittle cracking behaviour of concrete. For a detailed discussion of Equation 15–17 and further information on the factors k_{nonlin}, k_{local} and k_μ including the development of the model based on elastic theory for a thick-wall cylinder and its verification with experiments, see Bohner (2013).

4 RELIABILITY ANALYSIS—EXAMPLE

4.1 *Parameter distribution and values*

In the following example, a hypothetical semi-infinite reinforced concrete wall located in a XS3 environment (tidal/splash zone) according to the EN 206-1 (2006) is considered. This scenario enables the use of a 1-D analysis and diffusion being the main form of chloride transport in the concrete (convection zone not considered in this study).

To illustrate the procedure described in Section 2.2, service life calculations have been performed considering two distinct concrete qualities: a CEM I 42.5 N with w/b ratio 0.50, and a CEM III/A 42.5 R with w/b ratio 0.55. Both concretes have similar mechanical performance, but differ significantly from a chloride ingress perspective, where CEM III out performs CEM I. For each parameter, distribution type and values used are presented in Table 1 for the corrosion initiation model.

For the corrosion propagation model, two distinct corrosion rates were chosen to simulate a "fast" (3.0 µA/cm²) and a "slow" corrosion process (0.3 µA/cm²). Corrosion rate is defined by a lognormal distribution (CoV = 0.3) with an average value of 0.0035 mm/year and 0.035 mm/year for "slow" and "fast" corrosion, respectively. The remaining parameters are presented in Table 2.

Table 1. Parameter values/distributions for time to corrosion initiation calculation.

Parameter	Units	CEM I	CEM III
C_{crit}	%/wt.c	B[0.6, 0.15, 0.2, 2]	
C_0	%/wt.c	N[0.10, 0.005]	
C_S	%/wt.c	LN[2.50, 0.75]	
c	mm	LN[55.0, 10.0]	
$D_{RCM,0}$	$10^{-12} \cdot m^2/s$	LN[12.0, 4.8]	LN[4.5, 1.8]
k_t	–	C[1.0]	
b_e	K	N[4800, 500]	
T_{ref}	°C	C[20.0]	
T_{real}	°C	C[20.0]	
n	–	B[0.3, 0.06, 0.0, 1.0]	B[0.45, 0.09, 0.0, 1.0]
t_0	Years	C[0.0767]	

Distribution types: LN—lognormal; N—Normal; B—Beta; C—Constant.

Table 2. Parameter values/distributions for time from corrosion initiation to concrete cracking calculation.

Parameter	Units	CEM I	CEM III
λ	–	C[2.1]	
p	–	N[0.14, 0.02]	N[0.16, 0.02]
d_{tz}	mm	LN[0.18, 0.05]	LN[0.20, 0.05]
d_s	mm	C[16.0]	
c	mm	LN[55.0, 10.0]	
$f_{ct}(t)$	MPa	N[3.10, 0.31]	N[2.90, 0.29]
E_c	MPa	N[29300, 2000]	N[28300, 2000]
v	–	C[0.20]	
k_{nonlin}	–	C[2.3]	
k_{local}	–	C[0.70]	
k_m	–	C[1.0]	
D	–	C[0.0]	
φ	–	C[0.70]	
ρ	–	C[0.80]	

Distribution types: LN—lognormal; N—Normal; C—Constant.

4.2 *Results and discussion*

The calculation of the limit states for both individual models was performed with a direct Monte Carlo simulation based on 5000 determinations for each time step. The results are presented in Figure 4a for corrosion initiation and in Figure 4b for corrosion propagation, for both "fast" and "slow" corrosion.

The probability density function in Equation 10 was computed with trapezoidal numerical quadrature, as described by Stoer & Bulirsch (1980).

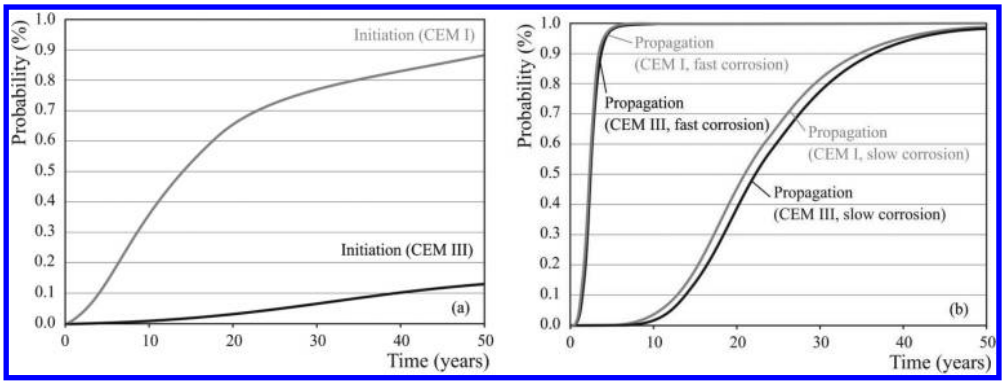

Figure 4. Probability of limit state failure for corrosion initiation (a), and corrosion propagation (b). Both CEM I and CEM III concretes are shown, as well as "fast" and "slow" corrosion processes.

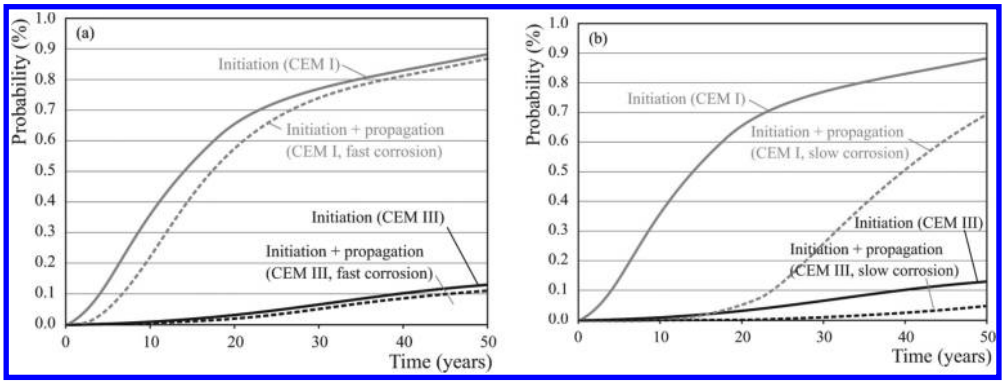

Figure 5. Probability of limit state failure for corrosion initiation and for corrosion initiation combined with corrosion propagation. In (a) the corrosion rate of the propagation model is "fast", and in (b) the corrosion rate of the propagation model is "slow".

The results are presented in Figure 5a for corrosion initiation combined with "fast" corrosion propagation, and in Figure 5b for corrosion initiation combined with "slow" corrosion propagation.

The service life obtained by combining the two individual service life calculations depends on both the quality of concrete and the corrosion rate. However, the quality of concrete, mostly determining the time to corrosion initiation, dominates as it is the precursor for the corrosion propagation phase.

Assuming a 10% probability for the limit state failure for corrosion initiation, it is normal to expect that the probability for the limit state failure for corrosion propagation should be lower since the consequences are more severe, and already damage inducing. The combination of both limit states should then be judged by the requirement for the second limit state since it is the phenomenon being observed, i.e. first cracking. A value of 7% is assumed for the limit state for corrosion propagation, for the sake of the following analyses.

If considering a "slow" corrosion (see Fig. 5b), the combination of the two limit states leads to an extension of the overall service life of the RCS of approx. 18 years, when compared with the limit state for corrosion initiation. If considering a "fast" corrosion rate (see Fig. 5a), an extension of 2 to 3 years in the service life is observed for a CEM I concrete. However, for the CEM III concrete, the combination of the two limit states results in a reduction of the overall service life of the RCS from 40 to 35 years.

This result seems contradictory because the overall service life is shortened when compared with the service life of corrosion initiation. The calculation of the combined service life takes into account the probability of each limit state occurring simultaneously, which normal service life calculations cannot account for. For a traditional

service life calculation, the limit state of propagation is always an extension of the limit state of corrosion initiation.

These results show that the choice of evaluation criteria for the limit state for corrosion initiation or for propagation cannot be chosen arbitrarily. It would be expected that a limit state for propagation results in an extension of the limit state of corrosion initiation. This raises questions regarding what are the values that should be used. Could the criteria differ based on the type of structural part, type and quality of concrete and environmental conditions?

Cairns & Law (2003) suggest that the limit state for propagation could be identical to that of the initiation because the appearance of the first crack does not affect the mechanical performance of the RCS. In this case, a combination of limit states would always result in an extension of the service life of the RCS.

There is currently not enough background information to understand the consequences of certain values, and while many values are being put forward based on those used in structural design they do not necessarily represent adequately the complexity of the deterioration mechanism and the economic consequences of limit state failure. However, the choice of limit state requirement is still relatively subjective. Could a lower reliability (higher probability of limit state failure) for cracking be considered? While the benefits for the service life design of new concrete structures, and for the remaining service life determination of existing structures, are apparent, the criteria by which the limit states are defined are not yet mature.

5 CONCLUSIONS

This paper presents a probabilistic design procedure which combines the calculation of two independent limit states for concrete deterioration: chloride induced corrosion initiation and corrosion induced cover cracking of concrete. By combining these two limit states, the outcome of the service life calculation is the probability of time to corrosion induced cracking, at any time starting after construction. The design procedure is exemplified with two qualities of concrete (CEM I and CEM III) and two corrosion rates ("slow" and "fast").

This study quantifies the impact that the propagation phase can have on the entire design service life of a RCS.

While in the past propagation models have had limitations (empirical nature, assumptions, simplifications, difficult handling, etc.), which call into question the outcome of the modelling, now the certainty behind the modelling is renewed. This is based on a new analytical time-to-cracking model (Bohner 2013) that allows for a realistic and quantitative description as well as a reliable prediction of the evolution of the damage process.

As a consequence of the probabilistic design procedure, combining the limit states of corrosion initiation and propagation, there is a theoretical probability for cracking, starting already with the construction of the RCS.

The results show that the outcome of the combined analysis depends on the criteria for limit state evaluation chosen for the service life determination. In the example presented, it is observed that the choice of a lower probability of failure for corrosion propagation than for corrosion initiation could result in a combined service life that is shorter than that determined only for corrosion initiation.

The difficulty in this analysis resides in the definition of the limit state requirement (reliability index or probability of limit state failure). There is currently not enough background information to understand the consequences of certain values, and while many values are being put forward based on those used in structural design they do not necessarily represent adequately the complexity of the deterioration mechanism and the economic consequences of limit state failure.

Despite the necessary discussion regarding the requirements for service life determination, this approach improves modelling for the entire service life of a structure, enabling cost savings possibilities through the avoidance of unnecessary repair costs by an optimised timing of the repair measures.

REFERENCES

Bohner, E. 2013. Rissbildung in Beton infolge Bewehrungskorrosion. Karlsruhe Institute of Technology (KIT), Dissertation.

Bohner, E., Müller, H.S. 2012. Analytical prediction model for concrete cover cracking due to reinforcement corrosion. In: Life-Cycle and Sustainability of Civil Infrastructure Systems, Strauss, Frangopol und Bergmeister (ed.), Taylor and Francis Group, London, pp. 442–448.

Cairns, J., Law, D. 2003. Prediction of the ultimate limit state of degradation of concrete structures. ILCDES 2003: Integrated Lifetime Engineering of Buildings and Civil Infrastructures, Rotterdam. 6 p.

CSEP. 1995. Introduction to Monte Carlo methods. Computational Science Projects, ORNL.

Ferreira, R.M., Gulikers, J. 2008. Critical considerations on the assessment of the durability (serviceability) limit state of reinforced concrete structures. Pro.11th DBMC, Istanbul, 11-14 May. pp. 1425–1432.

Fib Bulletin 34. 2006. Model Code for Service Life Design. International Federation for Structural Concrete, 206 p.

Gulikers, J. 2006. Critical issues in the interpretation of results of probabilistic service life calculations. In *International RILEM Workshop on Integral Service Life Modelling of Concrete Structures*. Univ. Minho, Guimarães, Portugal, ISBN 972-99179-2-2. pp. 195–204.

ISO/FDIS 16204:2012 Durability—Service life design of concrete structures. ISO. 40 p.

Kim, S., Frangopol, D.M., Soliman, M. 2013. Generalized Probabilistic Framework for Optimum Inspection and Maintenance Planning. *J. Struct. Eng.* 139. pp. 435–447.

LNEC E 465:2007. Betões. Metodologia para estimar as propriedades de desempenho betão que permitem satisfazer a vida útil de projecto de estruturas de betão armado ou pré-esforçado sob as exposições ambientais XC e XS. LNEC Laboratório Nacional de Engenharia Civil, Lisboa. 24 p.

Müller, H.S., Kvitsel, V. 2002. Kriechen und Schwinden von Beton. Grundlagen der neuen DIN 1045 und Ansätze für die Praxis. In: Beton- und Stahlbetonbau 97, no. 1. pp. 9–19.

Naess, A. 1995. Structural reliability. Lecture Notes Fag 37078, NTNU, Norway.

Osterminski, K., Schießl, P. 2011. Voll-probabilistische Modellierung von Bewehrungskorrosion: Ein Beitrag zur Dauerhaftigkeitsbemessung. Schlussbericht zum Teilprojekt D der DFG-FOR 537 "Modellierung von Bewehrungskorrosion", cbm, TU München.

Rubinstein, R.Y. 1981. Simulation and monte carlo method. John Wiley & Sons, New York.

Stoer, J., Bulirsch, R. 1980. Introduction to numerical analysis. Springer Verlag: Berlin.

Tuutti, K. 1982. Corrosion of steel in concrete. CBI Research. 4.82. 468 p.

Thoft-Christensen P, Baker M.J. 1982. Structural reliability theory and its applications. Springer Verlag: Berlin.

Concrete Repair, Rehabilitation and Retrofitting IV – Dehn et al. (Eds)
© 2016 Taylor & Francis Group, London, ISBN 978-1-138-02843-2

A whole of life approach to concrete durability—the CIA concrete durability series

Frank Papworth
BCRC, Perth, Australia

ABSTRACT: *fib* Model Code 2010 has introduced various methodologies for treating durability design as a whole of life requirement. The Concrete Institute of Australia (CIA) committee on durability has used the Model Code as a background for producing seven recommended practice notes that detail many of the requirements for ensuring durability is achieved by appropriate action from the planning stage through design, construction, maintenance, restoration to decommissioning. This paper shows how these various documents build to provide a whole of life durability approach. It covers deemed to satisfy requirements applicable to all concrete structure types based on standard input parameters for design life, reliability and exposure. The series includes details on project planning and good practice which if followed will increase the likelihood that the specification, design detailing and construction will be optimal to achieving the developer and community expectations regarding the long term performance of concrete structures. Also included are methods for modelling, degradation over time and crack control design. Thus the series provides what is described as a unified durability design process.

1 INTRODUCTION

Whilst research into concrete durability continues, the knowledge on exposure significance, deterioration processes, materials properties and workmanship implications has developed significantly over the last 30 years. In addition new cementitious materials, admixtures and additives have been widely introduced. Much more advanced concretes are now available. New durability design practices have also been developed, including durability modelling methods, and new methods of construction have been introduced. However, to an extent at least, these developments are not fully reflected in a clear and unified manner through the Australian Standards dealing with concrete durability requirements (e.g. modelling methods, use of fly ash, slag, silica fume, and galvanised and stainless steel reinforcement). The CIA durability series provides recommendations on durability design using a wider range of concretes and reinforcements, and details how to implement new durability design methods.

Durability requirements in Australian Standards are fragmented through different standards and their commentaries dealing with concrete durability requirements for different structure types (e.g. AS 2159 [1], AS 3600 [2], AS 3735 [3], AS 4997 [4] and AS 5100.5 [5]). Perceived conflicts between these documents (e.g. higher covers in AS 3735 than AS 3600 for the same life and exposure) might sometimes be explained by the different owner requirements (e.g. reliability required) but reasons for the differences are not given and the associated assessment methods not clearly stated. To some extent the concrete industries energy for contributing to development of durability codes is diluted through maintenance of the multitude of codes that address the same topic in variable ways.

For many concrete elements in mild exposures incorporating the proposed durability design processes may make little difference to construction requirements because existing code deemed to satisfy provisions often provide adequate performance. However, for elements in more severe exposures, guidelines that comprehensively detail how to assess owner's needs, environmental exposures and materials requirements; how to specify performance or prescriptive materials properties; and how to ensure construction is appropriate to the design will provide structures that meet their durability requirements more consistently. The durability series provides the required guidelines in seven documents:

- Z7/01 Durability—Planning
- Z7/02 Durability—Exposure Classes
- Z7/03 Durability—Deemed to Comply Requirements
- Z7/04 Durability—Good Practice Through Design, Concrete Supply and Construction
- Z7/05 Durability—Modelling
- Z7/06 Durability—Cracks and Crack Control
- Z7/07 Durability—Testing.

The durability that the owner and community require from structures will only be obtained if specific consideration is given to how durability requirements impacts on construction cost, inspections needs, maintenance requirements, aesthetics and operational and community costs. While strong emphasis is placed on achieving the design life, durability must be met long into the future, possibly well past the initial design life. The durability series will go a long way to providing the necessary tools for design and construction of durable structures based on the latest understanding of exposure, materials and deterioration process.

2 Z7/01 DURABILITY PLANNING

Whist there has been various papers published on durability planning [7,8,9,] Z7/01 is the first industry guideline on the topic. Information on processes involved in concrete deterioration are available for engineering analysis but a formal process for achieving durable structures in design, construction and operational maintenance is missing. Durability planning outlined in Z7/01 provides a system to formalise the process of achieving durability through appropriate design, construction and maintenance.

Z7/01 sets out the process of planning to achieve the required level of durability. The durability planning outcomes will be delivered in a Durability Assessment Report specific for the project. This will describe how the desired level of durability will be achieved and ensured using appropriate tools and recommendations given in Codes and Recommended Practices (e.g. CIA Z7/02-07).

A Durability Assessment Report provides a continuous link in durability objectives between design, construction and maintenance. Durability planning evaluates, explains and provides solutions for all stakeholders. Greater confidence is provided for the design and required service lives to be achieved.

Durability is provided with improved confidence when the concrete structure asset owner is actively involved starting from the project brief stating specific durability requirements. Designer and/or contractor provided durability requirements without adequate asset owner input may mean optimum functionality and whole of life cost may not be achieved. Asset owner maintenance cost and resources may be excessive to keep the asset operational or the asset owner may face rapid premature depreciation.

Concrete structures recommended to use durability planning will have durability design requirements that are complex, critical or uncertain. Durability planning is not expected for simple structures in benign exposure conditions.

The Durability Assessment Report issued will explain the durability requirements and provide details to be included in the project design reports, specifications, design drawings, asset maintenance plans and/or operation and maintenance manuals. This report may be a page for simple structures or detailed for complex or critical or structures in severe exposures. Durability checklists in tabular form provide useful project guidelines complementary to the Durability Assessment Report.

3 Z7/02 DURABILITY—EXPOSURE CLASSES

The Z7/02 committee, which comprised various durability technical experts, agreed current Australian Standard durability classes have three issues in how they deal with exposure classifications:

a. Exposure classes for different structure types, e.g. piling, marine structure, water retaining structures and general concrete structures, can have different exposures classifications according to current Australian codes. In reality the exposures are common to all concrete and use of different class types for the same exposure is confusing.
b. The same exposure class is used for different exposure types, e.g. a B2 exposure could be due to chloride exposure or sulfate exposure. This makes it difficult to provide a range of solution that will always be applicable to each exposure class.
c. The exposure classes are not in line with those used in ISO or European standards. This makes it difficult to compare Australian durability requirements with international requirements.

Hence Z7/02 provides different exposure classes for each type of exposure and applies them to concrete in all structure types. The ISO 16204 [10] exposure classes are adopted where possible but the ISO format for exposure classes is adopted in all cases.

Different projects will have different design life and reliability requirements and this also needs to be factored into the durability design. In some cases the different Australian Standards may have incorporated these aspects into the exposure classifications and this may account for why the exposures classes are different in different Australian Standards. However it is possible to allow for different life and reliability requirements for individual elements rather than forcing every project of a certain type to adopt the same life and reliability level. For example some elements of a marine structure may be highly critical and require a high reliability associated with an ultimate limit state (e.g. reliability around 4) while others may have virtually no failure consequence should they deteriorate and have a much lower reliability requirements (e.g. as low as 0.5). The same structure may only be required for 20 years or 100 years.

Further details on design life and reliability can be found in CIA's Z7/01—Durability Planning.

The base used for the exposure classification was the fib Model Code 2010 [11] and EN201 [12] as these have had extensive recent discussion from participants from all over the world. Where a departure from these documents is used in Z7/02 the reason for the departure is given. The principle reason for departures is that in Australia a broader range of exposures in some exposure types has been recognised.

The exposure classes discussed in Z7/02 are the criteria against which deemed to comply provisions in Z7/03 are defined. Hence Z7/02 can be considered a commentary on the exposures used in Z7/03. Exposure classes include:

XC—atmospheric carbonation inducing,
XS—seawater exposure,
XD—chlorides other than seawater,
XA—aggressive chemicals in ground exposure
XF—freeze thaw,
XG—exposure to liquids, vapours and gases,
XM—water migration
XX—metals in the cover zone
XR—abrasion
XI—moisture and ASR
XH—temperature and delayed ettringite fomation.

A common criticism of the first version of Z7/02 was that there was no guide to how the exposure classes in Z7/02 related to exposure classes in Australian Standards. Appendices have now been added that describe this.

4 Z7/03 DURABILITY—DEEMED TO COMPLY REQUIREMENTS

At the commencement of the task groups it was agreed that deemed to comply requirements would be prepared after the other Z7 recommended practices so that it could be based on them. Hence at the time of preparing this paper attention is only just refocussing on Z7/03. The group, set the following as the approach to be followed:

- Provide requirements for each exposure class (e.g. chloride, sulphate, acid, atmospheric gases)
- Requirements linked to cement systems including GP cement, fly ash, slag and silica fume)
- Provide guidance for galvanised and stainless steel reinforcement, prestressing and steel fibres
- Give recommendations for effect of coatings on other durability requirements
- Define significance of curing methods on other durability requirements
- Provide advice based on minimum cover.
- Incorporate reliability as a factor in determining durability requirements

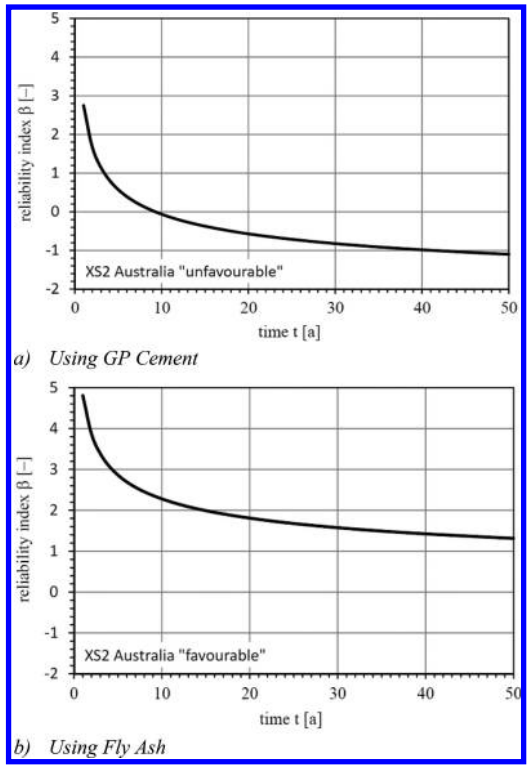

Figure 1. Reliability based on full probability analysis for a coastal structure using a 0.45 w/c ratio and 45 mm minimum cover [2].

- Design lives of 25, 50, 100 and 200 years to be considered.

Reliability design is a major new introduction to durability design although it is well know for structural design. As shown in Figure 1 reliability for chloride induced corrosion of marine and coastal structures has a steep reduction with time initially and then begins to flatten out. For most concrete the reduction between 50 years and 100 years is not high and from 100 years to 200years is even less. This is because the rate of chloride ingress is proportional to the square of the cover. It is proposed that factors will be applied to cover to allow for both design life and reliability requirements.

5 Z7/04 DURABILITY—GOOD PRACTICE THROUGH DESIGN, CONCRETE SUPPLY AND CONSTRUCTION

Australian concrete construction standards more generally focus on minimum design and material requirements and with the exception of a few more

detailed "Hand Books" standards are unlikely to provide more informative recommendations about how to design or construct a structure to get the target life expectancy. The previous edition of Z7 gave a good backbone for Z7/04 but Z7/04 authors found Z7/04 kept growing as different aspects of design, concrete supply and construction were considered.

As the title suggests, Z7/04 has applicability to more general concrete design and construction as well as concrete requiring specifically higher levels of durability. Z7/04 details areas such as

- the impact of specifications on the contract process,
- impacts of design on construction,
- details of materials requirements used in construction,
- material quality control processes,
- construction process and supervision,
- detailing issues in common structural elements that may present potential durability issues to the designer & constructor.
- reinforcement spacers and chairs. This is an area that has been demonstrated to cause weakness in durable construction and is rarely adequately specified.

The designer and durability consultant must understand the structural design and the material properties to consider how the required properties can be delivered during the construction process. There are many elements to this delivery process that impact on the final structures durability and Z7/04 provides information that helps to highlight the more critical areas of concern from design detailing through material supply to construction of the structure for all concrete construction stakeholders.

The document is intended to inform all parties involved in design and construction about the benefits of durability planning and subsequent construction control so they can deliver the expected level of maintenance and life of the structure to the asset owners. Different sections of Z7/04 deal with:

- Detailing—Poor detailing of the structure can lead to various issues and common issues are outlined. Typical details that will help overcome durability problems are provided.
- Pre-pour planning—The concrete supplier cannot know if concrete supply is fit for purpose with no awareness of where and how the concrete is to be placed. As the concrete supplier is often best placed to advise on what can be provided to overcome a particular problem part of the pre-pour planning is to introduce the supplier to the proposed pours. Many experienced concrete engineers will review the contractor's method statement and will be able to pass useful comment. Hence another part of pour planning is proper documentation of the methods to be used and dissemination of approved method statements to those that will place the concrete.
- Quality management—Lack of Quality Management throughout the production, delivery and placing process may lead to construction of a cheap but poorly performing structure.
- Concrete materials and concrete supply—Although AS1379 provides useful advice there are a number of aspects left open to the designer and these are discussed in Z7/04. Additional recommendations on issues not covered by AS1379 are also provided.
- Reinforcement Types—Reinforcements of various types are used in construction and these all impact on the potential durability of the structure.
- General construction issues—This includes placing, finishing and curing of concrete plus training issues and solutions. Lack of training is one of the most common causes of construction defects and subsequent durability issues. Even the simplest of training can save the contractor and owner huge re-work and repair costs respectively. Hence some provision in the contract should be made for the contractor's team to be adequately trained.
- Construction of different element types—Different sections of Z7/04 consider durability aspects of insitu cast, precast and sprayed concrete.

6 Z7/05 DURABILITY—MODELLING

Durability modelling is a major area of development in Europe with *fib* Commission 8 having two active task groups dealing with different aspects of modelling which support the modelling sections of fib Model Code 2010 and ISO 16204. Z7/05 has drawn on these documents in its considerations.

Durability design of a reinforced concrete structure mostly involves selecting suitable concrete compositions and related durability measures for a specific exposure condition to achieve the specified design life. There are mainly four approaches to conducting durability design as defined in *fib* Bulletin 34 [13], i.e.:

- deemed to satisfy design, i.e. complying the durability prescriptive requirements in codes,
- avoidance of deterioration, e.g. use of stainless steel to avoid potential issues with corrosion,
- partial safety factor design with deterministic modelling, and
- full probabilistic design based on stochastic modelling.

In the past, most concrete structures were designed using a 'deemed-to-satisfy' approach by following code requirements, which was predominantly established based on long term field

observations. The durability outcomes using this approach were a mixture of some successes and some failures. It was found that the failures occurred more frequently on the structures in aggressive conditions built since 1970 while structure built before that performed generally better.

Although the causes of the change in the 1970's have not been fully understood, this change has coincided with many changes including the cement characteristics (containing more C_3S and being finer), climate change (higher temperature and more C_2O in atmosphere) and construction practices (poor curing and compaction). These changes have not been reflected in the durability requirement by various Australia Standards.

Lack of long term durability data on new materials, principally cement concrete mixes and reinforcement, and change of exposure conditions, a 'deemed-to-satisfy' approach may not now be sufficiently reliable. In some case it may lead to premature failure while in others it may be overly conservative e.g. where higher performing materials are used. The avoidance of deterioration approach can reliably provide a superior durability performance. However the associated high cost discourages wide application except on some critical elements in critical projects.

An alternative durability design method, durability modelling (of either full probability design or partial factor) based on current material characteristics and known exposure parameters has a potential ability to provide a more reliable durability outcome if appropriate models and parameters are adopted. It is especially effective to predict long term performance of concrete structure in chloride laden condition and carbonation condition.

The advantage of modelling approach is that it does not rely on the observed long term information on the performance of field concrete structures and it can be adopted to more aggressive condition compared those in the codes. Such a modelling approach has been increasingly applied in durability design for major infrastructure projects in Australia and around world. Modelling is an even more effective tool to determine the remaining service life of existing concrete structures as it is based on the actual interaction of the structure and exposure.

Various models and preferred input parameters have been established and used in the past. However they produced significantly different prediction results and consequently different durability requirements even for the similar conditions and materials. Apparently, some models and associated input values must be incorrect, incomplete, and/or inappropriate for the prevailing conditions. Therefore, to achieve accurate and reliable modelling outcomes without a risk of premature durability failure or being too conservative at a high cost, it is critical to select suitable durability models and input parameters across the industry. Only by this approach can consistent durability designs be achieved with a reliable durability outcome.

The objectives of Z7/05 was to review commonly used models and their input parameters for chloride diffusion, carbonation and corrosion propagation process so as to be able to recommend the most suitable models and input parameters with their statistical distributions. However, considering the complex nature of concrete deterioration process and still insufficient researches this current guide is considered to be a working document which will be updated with more understandings and new findings in future.

7 Z7/06—CRACKING AND CRACK CONTROL IN CONCRETE STRUCTURES

The chairman for this group has undertaken a review of the current literature on crack control, including CIRIA C660 [14], and is very familiar with current code requirements. He has also been managing a significant research programme on this topic and important results will be available to feed into to the groups recommended practice note by the end of 2014.

At present, there is no Australia Standard method for calculating crack widths. The methods outlined in CIRIA C660 are often used for early-age thermal crack control and a variety of methods have been proposed for estimating the width of load-induced cracks. Irrespective of their cause, crack widths are known to vary with time and are greatly affected by temperature changes and by drying shrinkage. Most current approaches do not include the design shrinkage strain as input into the crack width calculation, and consequently, they cannot hope to accurately, or even adequately, predict final crack widths.

The mechanics associated with cracking caused by early-age thermal deformations, restraint to drying shrinkage, and external loads are all different. Whatever the cause, each type of crack is controlled by reinforcement and the width of the crack depends on the stress in the reinforcement crossing the crack. Z7/06 will provide a consistent and rational approach for predicting crack widths in concrete structures. It will provide guidance on how this approach can be used for the determination of final crack widths in a variety of common design situations, including example calculations for early-age cracks, restrained shrinkage cracks and load-induced cracks. Z7/06 will also provide guidance on the acceptable final calculated crack width (both average and maximum widths) from a durability point of view in all the various exposure

classifications and how this varies with the design life of the structure. With the calculation procedure clearly specified, limits can be placed on the maximum calculated crack width, without attempting to ensure that every crack in the actual structure meets the design requirements.

Cracking and crack control in concrete structures will fill a current void. The existing approach for crack control in AS3600-2009 is often unreliable, quite inflexible, and unrelated to the specific durability requirements of the structure. For cracks caused by the applied loads and resulting from bending and direct tension, AS3600-2009 requires that the stress in the reinforcement crossing the crack due to service loads does not exceed a specified maximum value. The maximum value depends only on the bar diameter or the bar spacing. In addition, certain detailing requirements are imposed involving maximum limits on concrete cover and bar spacing. These requirements are independent of the exposure classification, the type and importance of the structure, the mix proportions, the concrete material properties (including the shrinkage strain), the heat of hydration, etc.—all of which affect crack widths and, therefore, should be considered in the design for crack control. With regard to restrained shrinkage and temperature cracking, minimum quantities of reinforcements are specified depending on the whether a "strong", "moderate" or "minor" degree of crack control is required. Again many of the factors that affect crack widths are not considered, including the level of shrinkage or the exposure classification.

8 Z7/07 DURABILITY—TESTING

Authorship of Z7/07 was widespread, not surprisingly given the broad nature of the testing methods. Z7/07 provides guidance on performance tests for durability design and implementation. Often several test methods supply similar information. The limitations and advantages of test methods are reviewed, and recommendations provided on which test is the most suitable for project specifications.

Test methods are available to assess various aspects of durability performance through a concrete structure's life cycle including:

- Mix Acceptance Tests (including tests to validate values used in modelling)
- Tests For Quality Assurance
- Tests Where Placed Concrete is Suspect
- Tests For Condition Monitoring.

A wide range of tests designed to demonstrate the potential durability performance of concrete have been introduced over the years. This has caused some uncertainty for:

- Asset Owners: To understand what methods are available, the appropriateness of those methods to the structures' exposure, environment and life cycle, and the most cost effective testing regimes to achieve the required outcomes and level of certainty that they are looking to achieve.
- Designers: To know which tests are the most appropriate to specify and how much test data is required to ensure that the level of statistical confidence from the test results underpinning the design is appropriate.
- Contractors and Material Suppliers: To understand and have confidence in the consistency, repeatability and validity of trial data and quality control performance testing they are required to undertake for compliance with the project specification.
- Suppliers of Laboratory Testing Services: To maintain and calibrate equipment, train staff, maintain third party accreditation for the tests (e.g. perform the tests to sufficient frequency, provide regular proficiency training of staff and keep detailed records) and competitively price test methods despite some being not often specified.

Z7/07 aims to reduce the confusion and uncertainty. It provides guidance on performance tests for durability design and implementation. Often several test methods supply similar information. The limitations and advantages of these methods are reviewed, and recommendations provided on which test is the most suitable for project specifications.

Design phase durability testing requirements are recommended to be clearly specified for four stages:

- Mix trials to confirm the mix is suitable.
- Quality assurance tests as construction proceeds.
- Tests at the end of the defects liability period to create a list of items for repair.
- Tests during the design and service life including monitoring.

Construction phase materials testing and selection requirements recommended are:

- Materials testing and selection must be completed in accordance with the project specifications prior to use in the works. Additional testing is required prior to a change in supply of materials.
- Verification of concrete mix designs to meet project specification durability requirements can take considerable time, and unscheduled changes in concrete supply during construction may result in program delays. Durability testing of concrete such as chloride diffusion, water permeability, drying shrinkage, etc. may have a long test period (e.g. up to 3 months).
- Variability of durability tests must be taken into account by the durability consultant, with

specification test criteria allowing for alternative solutions to achieve the required durability if the test results do not achieve the specified values. This can be achieved by conservative durability design and/or provision for use of additional measures such as protective coatings or special additives or other measures.

Operations and maintenance phase monitoring and testing recommended are:

- Practical Completion Inspection—Prior to a structure going into service it is important to determine if any defects need to be contractor repaired and to document the initial structure characteristics and condition for future reference and comparison.
- Periodic In-Service Visual Inspection—A reactive approach to on-going maintenance be limited to visual inspections only and these may be performed on a regular or ad-hoc basis. This may be adequate provided no major defects are found and may be sufficient to prevent minor defects from becoming major ones, if appropriate, follow up repairs are performed. This approach may be suitable for minor structures and/or structures with a short design life.
- In-Service Condition Monitoring and Testing—Proactive maintenance will involve early intervention to prevent or delay the onset of corrosion initiation. This will require regular inspections or remote monitoring of embedded probes in conjunction with non-destructive testing.

If significant repairs/strengthening have been carried out, then a post-intervention inspection should be carried out along similar lines to a new structure first inspection mentioned above.

This document is intended to inform all parties involved in design, construction and maintenance about the benefits of durability performance testing and how, as part of a durability planning and implementation process, it will lead to an increased likelihood of achievement of the design life of structures and buildings.

9 CONCLUSIONS

Concrete durability is a complex topic covering a wide spectrum of inputs into design, construction and maintenance. The CIA durability series is an attempt to provide recommendations influencing durability into a consistent, conservative and comprehensive set of documents.

This has been a difficult task and has taken many years to reach even this initial stage. International work particularly that of fib Commission 5 (now 8) on the same topic, has been influential in putting the recommendations together.

The process involved workshops with industry in the early stages to assess what changes were considered necessary. Later various task groups were established to deal with specific aspects. The effort required to do this was considerable but considered worthwhile in view of the cost to the community of poor durability, the conflicts arising within different Australian Standards and differences in approaches between the various practicing durability consultants.

ACKNOWLEDGEMENTS

Although the task group chairmen were largely responsible for developing the recommended practices authorship was widespread and many have contributed to reviews. I thank the task group chairmen and members, other contributors, reviewers and all those that have contributed.

REFERENCES

[1] AS 2159–2009, “Piling—Design and installation”. Australian Standards, Sydney.
[2] AS 3600: 2009, “Concrete structures”. Australian Standards, Sydney.
[3] AS 3735–2001, “Concrete structures retaining liquids”. Australian Standards, Sydney.
[4] AS 4997–2005, “Guidelines for the design of maritime structures”. Australian Standards, Sydney.
[5] AS 5100.5–2004, “Bridge design—concrete”. Australian Standards, Sydney.
[6] Concrete Institute of Australia, Z7 Durable Concrete Structures, first published February 1990 and second edition February 2001.
[7] Papworth, F., Marosszeky M. “Durability Plans—Development and Implementation” The 22nd Biennial Conference of the Concrete Institute of Australia 2005: Issues, opportunities, innovations Sydney 2005.
[8] Green, W, Riordan G, Richardson G and Atkinson, W, “Durability assessment, design and planning—Port Botany Expansion Project”, Proc. 24th Biennial Conf. Concrete Institute of Australia, Sydney, Australia, Paper 65, 2009.
[9] Paull, R, “Concrete Durability Client Durability Requirements”, Concrete Institute of Australia, Concrete Durability Workshop, Adelaide, Brisbane, Melbourne, Perth & Sydney, June, 2009.
[10] ISO 16204:2012, Durability—Service life design of concrete structures. International Organization for Standardization (ISO), Switzerland, 2012.
[11] *fib* Bulletin 65/66: Model Code 2010—Volumes 1 and 2, March 2012. Lausanne, Switzerland, 2006.
[12] EN206–1:2000 Concrete—Part 1: Specification, performance, production and conformity.
[13] *fib* Bulletin 34: Model Code for Service Life Design. Lausanne, Switzerland, 2010.
[14] Bamforth P.B., “CIRIA C660 Early-age thermal crack control in concrete” CIRIA, London, 2007.

Concrete Repair, Rehabilitation and Retrofitting IV – Dehn et al. (Eds)
© 2016 Taylor & Francis Group, London, ISBN 978-1-138-02843-2

On the relationship between the formation factor and diffusion coefficients of Portland cement mortars

Z. Bajja, W. Dridi, B. Larbi & P. Lebescop
CEA, DEN, DPC, SECR, Laboratoire d'Etude du Comportement des Bétons et des Argiles, Gif-sur-Yvette, France

ABSTRACT: Concrete durability continues to be a subject of considerable interest, especially with the use of cement based materials on structures increasingly demanding on term of sustainability and resistance to aggressive ions penetration or radionuclide release. Diffusion is considered one of the main transport phenomena that cause migration of aggressive solutes and radionuclide in a porous media according to most studies.

In this work, two different tracers (an ion, and a radionuclide) were tested on the same formulations of mortars (w/c = 0, 4 and sand volume fractions from 0 to 60%) by the through-out diffusion, in order to determine the effective diffusion coefficients of each tracer and each formulation. The obtained results have proven the validity of the formation factor equation relating the effective diffusivity of a tracer to its diffusion coefficient in pure water.

1 INTRODUCTION

Despite the significant efforts deployed to improve the design, production and placement of concrete mixtures, the premature decay of infrastructures remains one of the main challenges facing the construction industry at the beginning of this 21st century [1]. Therefore, the durability of cement-based materials continues to receive significant international attention from both scientists and engineers.

Since these materials are porous, their durability is basically determined by their ability to resist the penetration and the transport of aggressive agents. The diffusion coefficients of ions and radionuclides in cementitious materials are the most important parameters to evaluate the state of degradation of structures.

In the framework of the storage of nuclear waste, (HTO) the liquid form of tritium, is considered as an ideal tracer for the characterization of the effective diffusivity in cementitious materials, because of its negligible interaction with the cement matrix [2] and the facility to apply Fick's law to a molecule such the HTO. However, the radioactive nature of HTO encourages looking for nonradioactive elements (generally ions) that can provide its diffusion coefficient without having to carry out tritiated water diffusion tests very expensive and dangerous.

Only diffusion in saturated porous materials is concerned in this study. Electro-diffusion and unsaturated conditions are ignored hereafter. Thus, the aim of this study is to prove the validity of the formation factor equation (Eq. 1) relating the effective diffusivity (D_e^{ion}, D_e^{rad}) in the cementitious material respectively of an ion and a radionuclide to their diffusion coefficient (D_0^{ion}; D_0^{rad}) in an infinitely diluted solution, usually in pure water at 25°C.

$$F = \frac{D_0^{rad}}{D_e^{rad}} = \frac{D_0^{ion}}{D_e^{ion}} \qquad \text{(Eq. 1)}$$

For that purpose, several formulations of mortars were tested in through-out diffusion with HTO and with lithium ion which has allowed identifying their diffusion coefficients.

2 EXPERIMENTAL PROCEDURES

2.1 *Test program*

Six different mixtures were prepared, to achieve the goal fixed previously. Mortars were manufactured from mixing Portland cement (European grade CEM I 52, 5 N CE PM-ESCP2 NF), with standardized siliceous sand CEN IN 196-1 labeled SN, and with water and the super plasticizer Glenium27 for some formulations.

These formulations were made by fixing water-to-cement ratio (w/c) and by varying the relative aggregate volume content (C_{ag}) in the objective to have different geometrical formation factors for each specimen. (Table 1) gives the proportions of the tested materials.

Table 1. Proportions of materials tested.

Mixtures ID	w/c[1]	C_{ag}[2]	Gle-27[3]
SN. 0%	0.4	0%	–
SN. 10%	0.4	10%	–
SN. 30%	0.4	30%	–
SN. 50%	0.4	50%	–
SN. 55%	0.4	55%	–
SN. 60%	0.4	60%	0.5%

[1]w/c is the water-to-cement ratio. [2]C_{ag} is the relative aggregate volume content; [3]Gle-27(%) is the weight of Glenium 27 relative to weight of cement.

Mortar specimens were mixed according to the standard mortar fabrication procedure NF EN 196-1 and were cast in PVC cylinders 70 mm in diameter and 110 mm high.

After 24 h, specimens were demoulded and conserved in lime water. They were cured in a humid chamber at T = 20 ± 1°C for a period exceeding three months, to ensure complete hydration of the material and to have a "fixed" microstructure during all the experiments.

Samples used for diffusion tests are 6 mm thick discs, obtained by underwater cutting of the central portion of each specimen. The thickness chosen for discs of 6 mm is justified for two reasons: First, a reason of representativeness, because to have reliable results, the sample must at least have a thickness three times larger than the maximum grain diameter (1,8 mm for SN). Also, a thick sample will take more time to be tested by the through-out diffusion than a fine sample. That's why, the thickness of 6 mm was chosen since it represents a compromise between the rapidity and the representativeness of the test.

2.2 *Microstructure analysis*

The microstructure of the studied materials was investigated by free water porosity and Mercury Intrusion Porosimetry (MIP) measurements.

2.2.1 *Free water porosity measurements*

Water porosity measurement is considered as a parameter of first order in the evaluation of the durability of material [3]. The experimental method [4] consists in determining water porosity by weighing the three following parameters: The sample water saturated mass M_s, the sample dried mass M_D, and M_w the sample mass when immersed in water.

Dried mass was obtained after an oven drying at the temperature of 60°C until constant weight. From these data, porosity accessible to water can be calculated as follows:

$$\varphi = \frac{M_s - M_D}{M_s - M_w} \quad \text{(Eq. 2)}$$

2.2.2 *Mercury intrusion porosimetry*

Before testing, the samples were first frozen (–195°C) by immersion into liquid nitrogen for 5 min. This quick quenching process at very low temperature allows generation of ice microcrystals that do not alter the microstructure.

After freezing, samples were introduced for 7 days in a freeze-dryer in which vacuum were kept to 10-1 Pa. This operation allows the ice trapped in the material porosity to sublimate. This freeze-drying technique is commonly used in many industrial areas like soil engineering, food industry, and biology. This technique is considered as a suitable procedure for MIP investigation on cement-based materials [5, 6]. MIP measurements have been carried out using micromeritics porosimeter with a maximum 413MPa injection pressure. The contact angle was 130° for all samples. The minimum pore access diameter reached is about 3 nm. For each specimen, two samples were tested and the results averaged.

2.3 *Through-out diffusion tests*

There are many methods of measurement of the coefficients of diffusion. Most known are natural diffusion tests, electrically accelerated tests or test of immersion in a concentrated solution. The choice of the method of measurement depends on the nature of the diffusing element but also on requirements of time. For this study the choice of the diffusing element will be on one hand a radioactive isotope (HTO) and on the other hand a solution containing lithium ions Li^+ (lithium chloride solution LiCl).

The through-out diffusion tests consist on putting the mortar sample between two compartments. The samples were sealed into position using an epoxy adhesive "Araldite" and by means of O-rings to avoid leakage.

Each compartment of 111 ± 1 ml volume is filled with saturated lime water. Then the cell is left to stand for about fifteen days to check the tightness of the cell and stabilize the sample before the test. After this period, the upstream compartment of each cell was doped with one of two species (HTO or Li^+).

The amount of elements transferred from the upstream to the downstream compartment was then followed in time by successive samplings which were analyzed by ionic chromatography device (for monitoring Li^+ ions) and by a scintillation tritium monitor for the monitoring of HTO. The lower limit of detection for the ionic chromatography is 0.18 µmol/l.

During the test, the concentration at the downstream compartment was checked not to reach

3% of the upstream concentration; otherwise, the downstream solution is drained. Therefore the upstream concentration C_0 and downstream one C_1 were maintained constant for all time (C_0 = 3.2 10^6 Bq/L; $C_1 \approx 0$) for HTO and (C_0 = 41 mmol/l; $C_1 \approx 0$) for lithium solution (LiCl).

3 RESULTS

3.1 *Water porosity and mercury intrusion porosimetry*

By increasing the sand content in mortars, the water porosity decreases (Fig. 1a).Water porosities are then compared to (1-C_{ag}) linear plot called the law of perfect dilution and which reflects the linear decrease of mortars porosity made with non-porous aggregates. It can be seen that experimental results are close to (1-C_{ag}) plot and don't breached the line except for the SN.60% mortar where water porosity value is slightly above dilution line.

This was confirmed by measurements of bulk densities by water porosimetry (Fig. 1b). The evolution according to the sand content curve presents a fall of the density at the SN.60%.

The slight increase of porosity and the decrease of bulk density in 60% sand volume fraction are correlated with an increase in air voids content within the material. Voids which can be interpreted by the presence of air bubbles. This anomaly of the SN.60% was also observed by mercury porosimetry. Figure 2 presents the pore size distribution of the tested formulations.

The curve representing the cement paste (SN.0%) shows that the diameter of the largest pores appears around 0,05µm, a threshold diameter from which percolation of capillary pores is observed. In contrast, the curves corresponding to

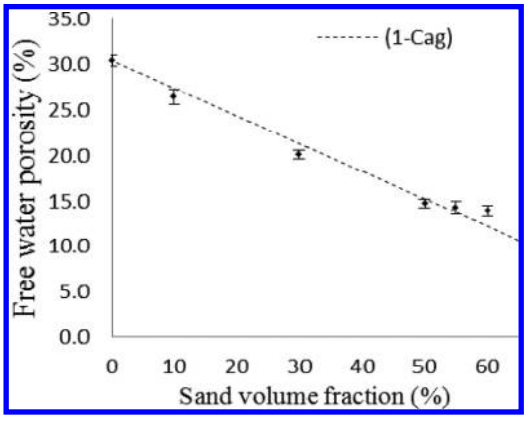

Figure 1a. Results of free water porosity measurements for tested mortars.

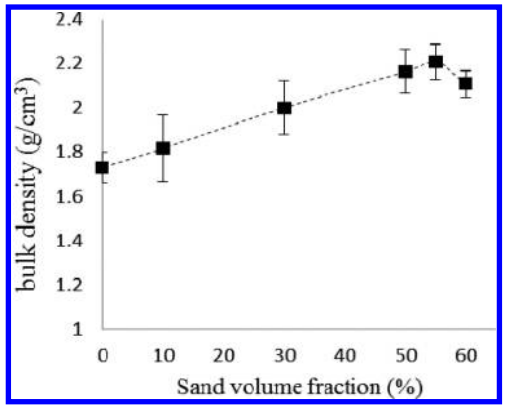

Figure 1b. Results of bulk density measurements for tested mortars.

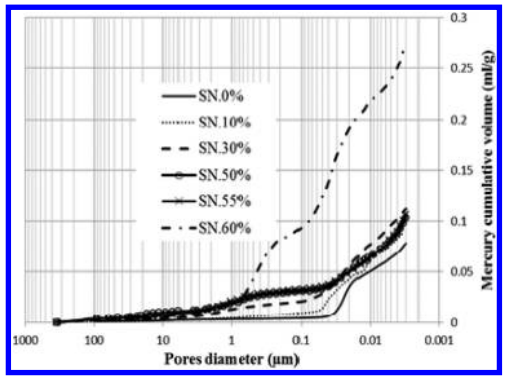

Figure 2. Pore size distribution of tested mortars.

the other formulations show that the pore distribution is characterized in particular by the appearance of larger diameters than those observed for cement paste. The addition of aggregates therefore increases the amount of larger pores (≥0,01 µm), even for mortars with only 10% of sand. This change in microstructure may be due to the formation of Interface Transition Zone aggregates/paste (ITZ) characterized by a higher porosity and its percolation [7, 8, 9]. However, this explanation is not sufficient to justify the microstructural behavior of (SN.60%) mortar.

3.2 *Diffusion tests*

3.2.1 *Lithium diffusivity in mortars*

Figure 3 shows the profile of effective diffusion coefficients of lithium ion vs. the sand volume fraction present in the formulations.

It is noticed, that with low content of sand in particular between 0 and 50%, the diffusivity of

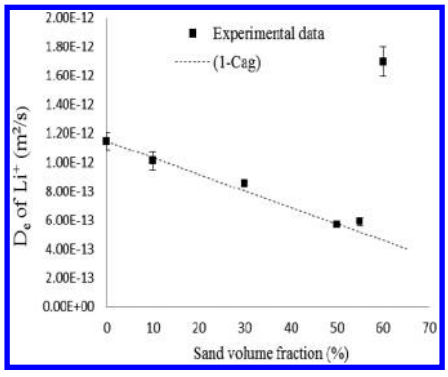

Figure 3. Effective diffusion coefficient D_e vs sand content of lithium.

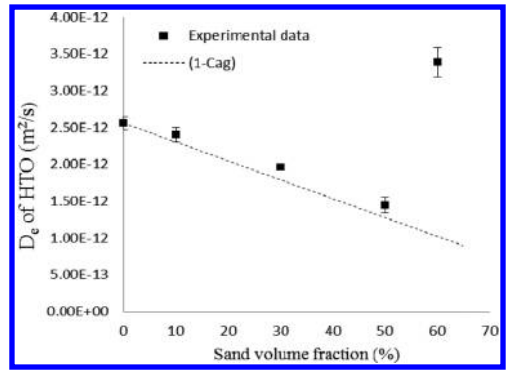

Figure 4. Effective diffusion coefficient D_e of HTO vs sand content in mortars.

lithium decreases with sand content in a perfect dilution law:

$$D_e^{mortar} = D_e^{paste} \times (1 - C_{ag}) \quad \text{(Eq. 3)}$$

With D_e^{mortar} is the diffusion coefficient of the mortar, D_e^{paste} the diffusion coefficient of the cement paste, and C_{ag}, the sand content in the mortar.

Mortar behavior becomes different starting from the formulation SN. 55%, where the diffusion coefficient varies very little compared to the mortar within 50% sand content. However, the formulation which remains the most significant is SN.60%, because its diffusion coefficient rises considerably and largely exceeds the diffusion coefficient of the cement paste.

These results observed for different formulations are in perfect agreement with the results of water porosity and mercury porosimetry. These phenomena were also noted in previous studies found in the literature such [10] and [11].

3.2.2 *Tritiated water diffusivity in mortars*

Tritium diffusion tests were carried out on the formulations SN. 0%, SN. 10%, SN. 30%, SN. 50% and SN. 60% and were repeated twice for each formulation. Both formulations SN. 55% and SN. 65% could not be tested by tritium diffusion.

Figure 4 shows the effective diffusion coefficient values according to aggregate fraction volume. The general tendency of the curve in Figure 4 is in perfect agreement with the diffusion results of lithium and with water porosity and mercury porosimetry results.

3.2.3 *Interpretation of diffusion results*

For materials with less than 55% sand volume, the effect of dilution is dominating for the two tests of diffusion with HTO and lithium. In these formulations, the ITZ layer around the aggregates exists according to the results of mercury porosimetry, but it remains isolated and does not affect diffusive characteristics of the materials.

This tendency has suddenly changed from 55 to 60% sand volume fraction, where a significant increase in the diffusion coefficient is observed. Moreover, il was noticed an increase in the mercury penetrated volume (at 0.6 µm diameter in Figure 2) revealing of the interconnection of this class of pores (0.1 to 1 µm). This interconnection created can therefore cause the formation of a percolation path within the sample which may justify this very significant increase in diffusivity. In this case, several hypotheses can be suggested to try to explain the cause of this interconnection. Among these, the interconnection of ITZ and/or the heterogeneity of the material. This last proposition means that because of the small proportion of cement present in the SN. 60%, it is possible to find some areas poor in cement but rich in water, others containing sufficient binder, and another part that may contain anhydrous in majority.

These various material microstructures can finally lead us to believe that a competitive aspect exist in mortars: on one side, the presence of nonporous sand grains tend to decrease the diffusivity but on the other the presence and the interconnectivity of ITZ are respectively at the origin of the appearance of larger pores and probably the cause of the increase of the diffusion coefficient (in the SN. 60%).

4 DISCUSSION ON THE VALIDITY OF THE FORMATION FACTOR CONCEPT

The objective of this paragraph is to compare the formation factors obtained experimentally from the results of lithium and tritium diffusion tests.

Table 2 shows experimental values of effective diffusion coefficients of each tracer within the tested formulations. Therefore, knowing the diffusion coefficients of the element "i" (D_0^i), it is possible to calculate the formation factor for each formulation using the relation:

$$F_i = \frac{D_0^i}{D_e^i} \quad \text{(Eq. 4)}$$

It is noted that the values of D_0^{HTO} et D_0^{Li} measured in an infinitely diluted solutions are respectively 2.27×10^{-9} (m^2/s) and 1.03×10^{-9} (m^2/s) [12].

The comparison between experimental formation factors gives rather close results, (Fig. 5).

Initially, formation factors (of HTO and lithium) follow the same tendency i.e. they increase with the sand content for mortars until 55% of sand, and decrease dramatically around 60% of sand.

Disparities between formation factor values measured with the two tracers do not exceed 15% for all tested formulations except the SN.60% mortar where a difference of about 25% is recorded. Regarding an uncertainty of measurements around 20% in the diffusion tests, the obtained results make it possible to validate the (Eq.1). They confirm the geometrical character of the formation factor which reflects the morphology and the connectivity of pore network of a given material. They also reveal the invariability of this parameter regarding the nature and the concentration of diffusing tracer.

Differences obtained between these factors must normally tend to zero since it is the same formulations which were tested by the two tracers. Because of some disturbances that can take place during tests, such an error exists. Among these disturbing factors, may be mentioned two possible reasons. From one perspective, it was noticed during the tests, a slight drop of temperature in the room where were placed the cells, this fall of temperature can cause a decrease in effective diffusion coefficients and thus increase the formation factor F. From another perspective, the increase in the formation factor may be due to the presence of chlorides ions in the upstream solution (solution of LiCl). These ions diffusing into mortars can involve some possible modifications in the microstructure of materials, in particular in the porosity of the hydrates. Otherwise, since hydrates porosity in CEM I based materials represents a smaller fraction of total porosity (compared to a CEM V material for example), the effect produced by chloride ions on the geometry of pores cannot be more important. In addition the concentration of chlorides ions used is quite weak, and the duration of which analyses were stopped (113 days) remain insufficient to cause modifications in the microstructure of the samples. This effect was noticed by [13] mainly for concretes containing CEMV, where the variation of formation factors is more considerable.

Finally, the omission of electrical interaction between diffusing species (ions) can also explain the disparities between formation factors obtained from HTO and ionic species diffusion tests.

Table 2. Experimental diffusion coefficients and resulting formation factors.

Mixtures ID	D_e^{HTO} (m^2/s)	D_e^{Li} (m^2/s)	F_{HTO}	F_{Li}
SN. 0%	$2.56 \cdot 10^{-12}$	$1.15 \cdot 10^{-12}$	886.72	896.43
SN. 10%	$2.40 \cdot 10^{-12}$	$1.01 \cdot 10^{-12}$	945.83	1019.80
SN. 30%	$1.96 \cdot 10^{-12}$	$8.55 \cdot 10^{-13}$	1158.16	1204.67
SN. 50%	$1.45 \cdot 10^{-12}$	$5.69 \cdot 10^{-13}$	1565.52	1810.19
SN. 55%	–	$5.90 \cdot 10^{-13}$	–	1745.76
SN. 60%	$3.39.10^{-12}$	$1.70 \cdot 10^{-12}$	669.62	605.88

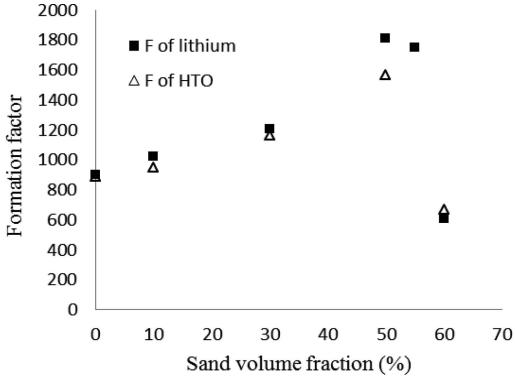

Figure 5. Comparison between formation factor of lithium, and HTO obtained experimentally.

5 CONCLUSION

With the assessment of this paper, several conclusions could be found. First, it was shown that the Eq. 1—giving the expression of diffusion coefficients of any ionic or radioactive specie from the geometrical formation factor of a material—can be validated for at least the two species tested which are lithium ion and tritiated water. This validity is conditioned by the respect of tests conditions i.e. a rather low upstream concentration of 41 mmol/l of LiCl, a fixed temperature during diffusion tests, materials formulated only with CEM I and without additions … This result is regarded as perfectly

interesting, since it will allow determining orders of magnitude of the effective diffusion coefficients of any other diffusing specie by knowing the geometrical formation factor of a material. However, to determine the formation factor, it is preferable to use tritium as a tracer, because its low reactivity with the cementing matrix, but also because it diffuses more quickly than ions (steady state starts at 10 days for HTO against 30 days for lithium ion) and thereafter, makes it possible to have the exact value of De for shorter tests durations compared to ions.

REFERENCES

[1] J.F. Young, Bridging concrete into the 21st century Proceedings of the ECI Conference on Advances in Cement and Concrete, August 21–24, Copper Mountain, CO (2003), pp. 1–8.

[2] C. Richet, Etude de la migration des radioéléments dans les liants hydrauliques—Influence du vieillissement des liants sur les mécanismes et la cinétiques des transferts, Ph.D. Thesis; Université Paris XI Orsay (1992) (in French).

[3] V. Baroghel-Bouny & Ammouche A. (2007). Sous groupe « microstructure ». In Arliguie & Hornain (Dir), Grandubé book (pp. 63–106) (in French).

[4] Grandubé book—Grandeurs associés à la durabilité des bétons—French association of civil engineering (2007).

[5] C. Gallé, Effect of drying on cement-based materials pore structure as identified by mercury intrusion porosimetry, a comparative study between oven-, vacuum-, and freeze-drying, Cem. Concr. Res. 31 (2001) 1467–1477.

[6] A. Kumar, D.M. Roy, The effect of desiccation on the porosity and pore structure of freeze-dried hardened Portland cement and slag blended pastes, Cem. Concr. Res. 16 (1) (1986) 74–78.

[7] B. Bourdette, E. Ringot, J.P. Ollivier, Modelling of the transition zone porosity, Cem. Concr. Res. 25 (1995) 741–751.

[8] D.N. Winslow, M.D. Cohen, D.B. Bentz, K.A. Snyder, E.J. Garboczi, Percolation and pore structure in mortars and concrete, Cem. Concr. Res. 24 (1994) 25–37.

[9] S. Caré, Influence of aggregates on chloride diffusion coefficient into mortar, Cem. Concr. Res. 33 (2003) 1021–1028.

[10] B. Bourdette, Prise en compte des aureoles de transition dans la characterisation et la modélisation des processus physique et chimiques d'altération, Ph.D. Thesis, Institut National des Sciences Appliqués de Toulouse (1994) (in French).

[11] E.J. Garboczi, D.P. Bentz, Modelling of the microstructure and transport properties of concrete, Cem. Concr. Res. 10 (1996), 293–300.

[12] P. Vanysek; Ionic Conductivity and Diffusion at Infinite Dilution—CRC Hansbook of Chemestry and Physics, 2000–203.158.253.140.

[13] H.R. Mercado Mendoza, Transferts aqueux à travers les matériaux cimentaires partiellement saturés. Ph.D. Thesis; University of Toulouse (2012) in French.

Concrete Repair, Rehabilitation and Retrofitting IV – Dehn et al. (Eds)
© 2016 Taylor & Francis Group, London, ISBN 978-1-138-02843-2

Resistivity and water absorption of concrete

C.I. Goodier & C. Xueting
School of Civil and Building Engineering, Loughborough University, Loughborough, UK

C. Christodoulou & D. Dunne
AECOM Europe, Colmore Plaza, Birmingham, UK

R. Yea
Kier Construction, Sandy, UK

ABSTRACT: Corrosion is a significant cause of the deterioration of reinforced concrete structures. The main cause of corrosion is the ingress of aggressive chemicals such as chloride ions from salts. However, there is a lack of knowledge and understanding regarding the relationship between compressive strength, resistivity and water absorption of different concrete types—all of which are critical parameters influencing the chloride ingress rate and development of corrosion in reinforced concrete. Concrete cubes and cylinders with varying proportions of water-cement (w/c) ratios, Pulverised Fly Ash (PFA) (10–40% replacement), Ground Granulated Blastfurnace Slag (GGBS) (20–70% replacement) and Silica Fume (SF) (5–15%) contents were cast, and tested for compressive strength, hardened density, bulk and surface resistivity, and water absorption. The results showed that increasing the PFA, GGBS or SF replacement contents significantly increased both the surface and bulk resistivity of the concrete (e.g. with the 70% GGBS replacement, up to 9 times greater when compared to the control concrete). The addition of SF or GGBS had a considerable positive effect on the water absorption (even at low dosages), lowering it by up to a factor of 10. The PFA however, had little, or even an adverse, effect on the water absorption. Cement replacements such as PFA, GGBS and SF can therefore contribute significantly to improving the resistivity of concrete, and hence the resistance of concrete to chloride ingress, and should therefore be seriously considered for the majority of concretes designed for aggressive environments.

1 INTRODUCTION

Concrete is a naturally porous material, and the size and distribution of pores in concrete varies. This depends upon the constituent materials, quality of compaction, materials used in the mix design, w/c ratio, degree of hydration, and curing (Christodoulou et al, 2013; Concrete Society, 2008). Some of these pores will form an interconnected network of pore space that, under the right conditions, can be penetrated by water, gas or ions.

The relevant transport mechanisms for the ingress of water, gases and ions are (Kropp and Hilsdorf, 1995; Christodoulou et al, 2013):

i. diffusion of free molecules or ions due to a concentration difference;
ii. permeation of gases or liquids through water saturated specimens due to hydraulic pressure difference; and,
iii. capillary suction (absorption) of liquids due to surface tension acting in capillaries.

Whilst, these mechanisms act together under natural environmental exposure conditions for atmospherically exposed concrete, capillary suction (absorption) tends to be the dominant mechanism (Christodoulou et al, 2013; Concrete Society, 2008; Kropp and Hilsdorf, 1995). Ions such as chlorides are transported into the concrete pore system by being dissolved into water, which subsequently cause corrosion of the steel reinforcement, and ultimately spalling of the surrounding concrete cover.

1.1 *Resistivity*

Resistivity is a 'geometrically independent property' (Hornbostel et al. 2013) that expresses the freedom for which ions can migrate through a pore matrix of a concrete mass. It is usually expressed in terms of $\Omega \cdot$cm, but is scaled depending on the size of values obtained (Berkeley and Pathmanaban, 1990). Resistivity is influenced by the structure of the pore matrix, and the moisture content contained within it (Polder et al., 2000; Andrade and Alonso, 2001; Bertolini et al., 2004). There is a strong inverse relationship between resistivity and corrosion rate or chloride penetration (Alonso et al., 1988; Polder

et al. 2000; Bertolini et al., 2004; Morris et al., 2004; Hornbostel et al., 2013). It must be noted, however, that this relationship cannot be described as completely proportional, as contaminants, such as chloride ions, also reduce resistivity (Hornbostel et al., 2013). For understanding the susceptibility of a hardened concrete to corrosion, it is clear measuring resistivity is important. However, there is currently no standard method of interpretation for measured values of resistivity. This has led to many differing opinions by academics; in particular with respect to corrosion prediction ranges (Table 1). There seems to be a general consensus that there is a low probability of corrosion at <10 kΩ·cm, whereas the upper boundary is less clear.

Currently, there is no standard procedure covering the use of resistivity measuring instruments within the UK, however, in the USA, AASHTO TP95-11 (AASHTO, 2011) specifies the 4-Point Wenner Probe method.

There has been much discussion among academics, over the past decade around the merits of this method, with Table 2 summarising some of the advantages and disadvantages that have been presented in various literature.

These sources describe it as convenient, quick and able to be used on many different geometries, hence is identified as a good technique for site applications (Polder et al., 2000). One disadvantage is the influence of reinforcement on the results obtained. In addition, it is repeatedly noted in literature, that if this is the only parameter utilised to assess a reinforced concrete mass, misinterpretations are likely. It would suggest, therefore, that a combination of different parameters will elicit more accurate conclusions.

1.2 *Absorption*

Absorption (and adsorption) describes the natural phenomena of a liquid being drawn into empty (or partially empty) pores by capillary attraction (Domone and Illston, 2010). This is caused by the surface tension acting within the capillaries of the pore matrix, creating an 'underpressure' (Kropp and Hilsdorf, 1995; Bertolini et al., 2004; Hunkeler, 2005). The degree as to which this occurs is influenced by many variables, including density, viscosity and surface tension of the fluid and the structure of the pore matrix present within the concrete body (Kropp and Hilsdorf. 1995; Bertolini et al., 2004).

Table 1. Comparison of reported ranges for active corrosion probability with respect to resistivity.

	Probability of active corrosion state kΩ cm		
Reference	Low	Moderate	High
Morris et al 2004	>30	10–30	<10
Pullar-Strecker 2002	>20	10–20	<10
Polder et al 2000	>50	10–50	<10
Gonzalez et al 2004	>50	20–50	<20
Elkey & Sellevoid 1995	>20	10–20	<10
Song et al 2007	>20	10–20	<10

The process of capillary suction begins with an initial absorption rate, which tends to be quick in completely unsaturated concrete, and proceeds into either a non-steady or a steady absorption rate. The type that exists is dependent on the conditions of liquid exposure. A non-steady state occurs with short exposure, while a steady state occurs with prolonged contact with the liquid (Kropp and Hilsdorf, 1995).

As capillary suction depends on the presence of air within the pore matrix, it occurs predominantly where evaporation can take place (Hunkeler, 2005). For a reinforced concrete structure, this is close to the surface.

Weight gain of simple concrete specimens can be measured, in which case the absorption (or sorptivity) is expressed as the amount of water absorbed per unit exposed surface divided by square root of time, e.g. $kg/m^2/hr^{0.5}$.

Modern designs standards aim to protect the embedded steel reinforcement by means of prescribed controls such as minimum cementitious content, minimum cover, maximum w/c ratio etc, commonly known as a "deemed-to-satisfy approach" (Dunne et al, 2015; British Standards 2006). This approach assumes that the concrete composition selected will result in the service life desired/selected, but does not fully take into consideration the significantly different performance of combinations of cementitious binders, cover, and w/c ratios (Dunne et al, 2015). One way of doing this is by properly understanding the relationship between the concrete cover properties such as absorption, resistivity and compressive strength.

1.3 *Supplementary Cementitious Materials (SCMs)*

The more common SCMs are Pulverised Fuel Ash (PFA) and Ground Granulated Blast Furnace Slag (GGBS), and are controlled within the different exposure classes of BS8500 by a range of OPC replacement percentages.

In general, for SCMs, there is a reduction in heat omitted during the early hydration process compared to that of PC, a long-term overall increase in compressive strength and, most importantly in

Table 2. Advantages/disadvantages of 4-Point Wenner Probe.

Source	Advantage	Disadvantage
Bertolini *et al.*, 2004	– Good correlation obtained between resistivity measurements at lower depths and that gained on the surface by this technique	– Interference of reinforcement can severely reduce accuracy of results
Polder *et al.*, 2000	– Quick – Allows entire concrete surface to be assessed – Can be done at any point in service life – Allows areas of high permeability to be quickly identified – Quality of workmanship achieved can be assessed at early age	– Must be used in conjunction with other NDT methods, such as potential mapping, to ensure accuracy of interpretation – Cannot be performed on buried or submerged objects
Berkeley and Pathmanaban, 1990	– Simple to complete – Non-destructive	– Is an average evaluation down to a depth dictated by the spacing of electrodes; different to resistivity at the depth of reinforcement – Interference of reinforcement can severely reduce accuracy of results – Undulating surface of concrete can effect contact
Du Plooy *et al.*, 2013	– Good repeatability of results possible – Commonly used technique – Can be used on a concrete surface of arbitrary geometry	– Must be used in conjunction with other NDT methods to ensure accuracy of interpretation – Interference of reinforcement can severely reduce accuracy of results
AASHTO, 2011	– Simple to complete – Good repeatability of results if completed by same operator – No bias on the value of resistance achieved; can only be defined in terms of test method	– Interference of reinforcement can severely reduce accuracy of results

the context of this research, an overall reduction in permeability to liquids (Bjegovic et al., 2012). This occurs as the latent production of C-S-H fills existing capillaries, acting to densify the concrete. The result is a more tortuous, discontinuous pore network for penetrating liquids and ions to follow (Schießl and Lay, 2005, p.107;). This particular attribute is clearly beneficial when considering reinforced concrete structures exposed to chloride rich environments, as the duration required for chloride ions to reach the depth of reinforcement is significantly increased. One of the advantages of these SCMs is a reduction in heat omitted during the early hydration process compared to that of PC, a long-term overall increase in compressive strength and, importantly for durability, an overall reduction in permeability to liquids (Bjegovic et al., 2012). This occurs as the latent production of C-S-H fills existing capillaries, acting to densify the concrete. The result is a more tortuous, discontinuous pore network for penetrating liquids and ions to follow (Schießl and Lay, 2005).

According to Polder (2012) however, the pozzolanic reaction of GGBS is more rapid than for PFA. This results in higher compressive strengths and reduced chloride diffusion coefficients at earlier ages. However, these are still inferior to that of OPC.

In addition to this, the chloride binding capacity of PFA and GGBS appear to be considerably different. According to Arya and Xu (1994), it was found that the chloride binding capacity of GGBS blended concrete was significantly better than PFA blended concrete, with GGBS > PFA > OPC. This, in their opinion, is due to a difference in hydroxide anion concentration, suggesting that the pH of a PFA blend develops more slowly than in a GGBS blend. Two other analyses, although not a direct comparison, do develop this idea further. Dhir et al. (1996; 1997) suggest that, in the case of PFA and GGBS, they both improve the binding capacity of the concrete by increasing the alumina content within the pore fluid. This allows for larger quantities of Friedel's salt, or bound chlorides, to be produced. It is therefore possible that a larger quantity of alumina may be found in the products of the pozzolanic reaction of GGBS than PFA, resulting in the difference in binding capacity. Glass and Buenfeld (2000b) suggest how differences in binding capacity can be quantified,

as their research suggests that high concentration gradients of total chloride ion by mass of cement suggest a high binding capacity.

It is clear that both the rate of the pozzolanic reaction and the chloride binding capacity are important when considering the penetration of chlorides, as the proportioning of cement blends have a significant effect on these intrinsic properties. Therefore, they cannot be treated in the equal nature that the current format of BS8500 would suggest.

The possible reason that this has occurred can be found in the lack of clarity presented in research based on the specification of a definitive replacement percentage of SCM to PC for a specific environment. Andrade and Buják (2013) stated that there is currently not enough evidence to 'produce a quantitative model in the case of blended cements, in particular because we do not know well how blended cements age'.

It would seem, therefore, there is a lack of specific research into the differences in intrinsic properties between different SCM blends of concrete with regards to resistance against chloride induced corrosion. This has resulted in the open ended approach to specification present within BS8500.

2 METHODOLOGY

2.1 *Mix design*

All concretes had an aggregate/cement ratio of 4, a sand/aggregate ratio of 0.5, and a cement:sand: aggregate ratio of 1:2:4.

Fine aggregate (sand) was 0–2 mm, and coarse aggregate 2–25.4 mm (Table 3). Mix 1 was PC at w/c ratios of 0.50, 0.55, 0.60 and 0.65. Mix 2 had PFA at cement replacements levels of 10–40%, Mix 3 had GGBS at cement replacement levels of 40–70%, and Mix 4 had SF at cement replacement levels of 5–15%. Mixes 2, 3 and 4 had a w/c ratio of 0.6.

All mixes contained 7.54 kg sand and 15.08 kg coarse aggregate.

Table 3. Mix designs.

Mix	W/C ratio	Water (kg)	PC (kg)	PFA, GGBS, SF (kg)
1 PC	0.5	1.89	3.77	–
	0.55	2.07	3.77	–
	0.6	2.26	3.77	–
	0.65	2.45	3.77	–
2 PFA	0.6	2.26	3.39	(10%) 0.38
		2.26	3.02	(20%) 0.75
		2.26	2.64	(30%) 1.13
		2.26	2.26	(40%) 1.51
3 GGBS		2.26	2.26	(40%) 1.51
		2.26	1.89	(50%) 1.89
		2.26	1.51	(60%) 2.26
		2.26	1.13	(70%) 2.64
4 SF		2.26	3.58	(5%) 0.20
		2.26	3.39	(10%) 0.38
		2.26	3.21	(15%) 0.57

2.2 *Casting*

The cement replacements were mixed with water for 30 seconds. Then, sand, coarse aggregate, PC and one third of the water was placed into the pan mixer and was mixed for 120 seconds. Then, the remaining water was added, and mixed for a final 120 seconds. Three 100 mm diameter × 200 mm high cylinders and six 100 mm^3 cubes were cast to BS 1881-113:2011 for each mix design. The slumps, to BS EN 12350-2:2009, were between 10 to 45 mm. The concrete was vibrated in 2 layers on a vibrating table, and then covered with plastic sheeting. The specimens were de-moulded after 24 hours, and then cured in water curing tanks at (20 ±5) °C for 28 days until testing (BS 1881-113:2011).

2.3 *Testing*

The concrete compressive strength was measured at 7 and 28 days to BS 1881-116:1983.

The resistivity of 3 cylinders per mix design was measured with a ResiPod Resistivity Meter, a 4-point Wenner probe, according to AASHTO TP95-11 (2011). Surface resistivity was measured on 4 sides of the cylinder at 0, 90, 180, and 270 degrees. The average resistivity was then calculated. The bulk resistivity was also measured for each of the 3 cylinders.

The cylinders were sawn into 25 mm high discs, then placed in an oven at (40 ± 2) °C for 7 days until a constant weight was achieved. They were placed in (2 ± 1) mm water, and weighed after 12 min, 30 min, 1 h, 2 h, 4 h and 24 h according to BS EN 13057:2002.

3 RESULTS

3.1 *Compressive strength*

The results of concrete compressive strength at 7 and 28 days is shown in Figure 1 and Table 4. As expected, for the PC concretes, for an increase in w/c ratio, there is a corresponding decrease in compressive strength. For the PFA mixes, an increase in PFA causes a decrease in compressive strength, at 7 and 28 days, as expected.

For the GGBS mixes, strength development is slower compared with PC concrete, but increases at 28 days, again as expected. Compressive strength at 7 days is similar for the SF mixes, but the higher

proportions of SF begin to manifest themselves as higher compressive strengths at 28 days.

3.2 *Resistivity*

The results for surface and bulk resistivity are presented in Table 4 and Figure 2.

3.2.1 *Effect of w/c ratio on resistivity*

With increased w/c ratio from 0.5 to 0.65 for the PC mixes, surface resistivity decreased slightly, as was expected (Castro et al., 2011). On the other hand, bulk resistivity however, remained relatively unchanged, around 30 kΩ·cm.

3.2.2 *Effect of PFA/GGBS/SF on resistivity*

The surface resistivity of the PFA concretes increased from 9.36 kΩ·cm (0% PFA) to 21.88 kΩ·cm (40% PFA), as expected (Saraswathy and Song, 2007). Bulk resistivity also increased from 30.7 kΩ·cm to 68.6 kΩ·cm respectively.

Figure 1. Compressive strength of mix designs at 7 and 28 days.

Surface resistivity of the GGBS concretes increased from 93.6 kΩ·cm (0%) to 76.63 kΩ·cm at 70%, and for bulk resistivity from 30.7 to 269.6 kΩ·cm, again as expected (McNally and Sheils, 2012).

The surface resistivity of the 15% SF concrete was 67.9 kΩ·cm, increasing from 9.36 kΩ·cm for the 0% SF mix. The bulk resistivity for SF concrete increased considerably, up to 229.1 kΩ·cm for the 15% SF, almost eight times higher than that of the PC concrete.

Table 5 shows, where surface resistivity of the PC concretes are <12 kΩ·cm, they are all classed as having a 'high' chloride ion penetrability. Additionally, the surface resistivity of the 10–40% for PFA concrete is between 11 to 22 kΩ·cm, resulting in these concretes being classed as 'moderate' for susceptibility to chloride ion penetrability. Thereafter, the GGBS, penetrability is classed as 'low-very low', whilst lastly, the addition of SF results in concretes possessing an even greater resistance to the penetrability of chloride ions.

3.3 *Water absorption*

3.3.1 *Effect of w/c ratio*

As expected, with an increase of w/c ratio, water absorption increases. Specifically, the water absorption of 0.5 w/c ratio concrete is 39 kg/m^2·h$^{0.5}$. When the w/c ratio raised to 0.65, its absorption almost doubled to 63 kg/m^2·h$^{0.5}$.

3.3.2 *Effect of PFA/GGBS/SF on water absorption*

The results for the PFA blended concretes are less conclusive, demonstrating 85 kg/m^2·h$^{0.5}$ for both

Table 4. Summary results for compressive strength, resistivity and water absorption.

	Comp. strength (MPa)				
Mix	7 d	28 d	Surf. res. kΩcm	Bulk res. kΩcm	Abs. kg/m^2/hr$^{0.5}$
W/C 0.5	36.9	45.4	9.58	31.60	38.84
W/C 0.55	32.0	39.5	9.41	29.23	47.50
W/C 0.6	25.8	34.1	9.36	30.73	59.13
W/C 0.65	20.0	25.5	7.90	29.57	62.38
PFA 10	22.3	31.4	10.69	36.50	85.57
PFA 20	19.8	25.9	13.76	43.67	57.01
PFA 30	13.8	22.8	17.49	56.23	54.70
PFA 40	10.3	20.4	21.88	68.6	85.57
GGBS 40	21.3	35.0	37.37	68.57	10.11
GGBS 50	21.6	38.9	46.52	155.9	6.56
GGBS 60	19.7	29.5	56.90	197.3	12.16
GGBS 70	18.9	31.4	76.63	269.6	9.24
SF 5	26.0	41.8	21.82	71.63	7.32
SF 10	25.6	44.5	40.30	144.2	5.35
SF 15	26.5	47.9	67.90	229.1	4.23

Figure 2. Surface resistivity and bulk resistivity of different mix design.

Table 5. Chloride ion penetrability based (AASHTO, 2011).

Chloride ion penetration	100 × 200 mm cyclinder (kΩ · cm)
High	<12
Moderate	12–21
Low	21–37
Very low	37–254
Negligible	>254

the 10% and 40% PFA replacement levels but, they dip in between. Water absorption would be expected to decrease with increasing PFA replacement, hence the 40% result could be an anomaly. Another reason could be the slow development of PFA concretes compared with traditional PC concretes, and at this 28 days the concrete matrix has not fully formed.

The water absorption for the GGBS concrete is similarly inconsistent, but all the values are lower than the reference PC concrete with a value of 59.1 $kg/m^2 \cdot h^{0.5}$.

The water absorption of the 15% SF concrete is the lowest of all the concretes at 4.2 $kg/m^2 \cdot h^{0.5}$, with 5% SF resulting in a water absorption of 7.3 $kg/m^2 \cdot h^{0.5}$, illustrating that even a very small proportion of SF is very effective at reducing water absorption.

4 CONCLUSIONS

It is clear that the concretes investigated here with a lower w/c ratio have a higher 28 day compressive strength and resistivity, and a lower water absorption.

PFA can increase resistivity with this effect increasing at higher PFA content. This is when making a comparison of concretes at equal w/c ratios and test age. The resistance of these concrete to water absorption is less clear when reviewing the current data set.

GGBS considerably increases the resistivity, with increased GGBS content being increasingly effective. Water absorption was found to decrease however, although no further overall improvements in performance were observed with increasing GGBS from 40%–70%. Taking these factors into account, GGBS seems an appropriate additive to improve concrete long-term resistivity and water absorption, even at low replacement rates.

In comparison, the addition of SF seems the ideal cement replacement to improve concrete compressive strength, resistivity and resistance to water absorption, again, even at low replacement rates.

REFERENCES

AASHTO, 2011. Standard Method of Test for Surface Resistivity Indication of Concrete's Ability to Resist Chloride Ion Penetration. TP 95–11. Washington, USA: AASHTO.

Alonso, C., Andrade, C. and Gonzalez, J.A. 1988. Relation Between Resistivity and Corrosion Rate of Reinforcements in Carbonated Mortar Made with Several Cement Types. Cement and Concrete Research, 8, pp. 687–698.

Andrade, C. and Bujak, R. 2013. Effects of Some Mineral Additions to Portland Cement on Reinforcement Corrosion. Cement and Concrete Research, 53, pp. 59–67.

Andrade, C. and Alonso, C. 2001. On-Site Measurements of Corrosion Rate of Reinforcements. Construction and Building Materials, 15, pp. 141–145.

Berkeley, K.G.C. and Pathmanaban, S. 1990. Cathodic Protection of Reinforcement Steel in Concrete. 1st edn. London: Butterworths.

Bertolini, L., Elsener, B., Pedeferri, P. and Polder, R. 2004. Corrosion of Steel in Concrete: Prevention, Diagnosis and Repair. 1st edn. Weinheim, Germany: WILEY-VCH.

Bjegovic, D., Stirmer, N. and Serdar, M. 2012. Durability Properties of Concrete with Blended Cements. Materials and Corrosion, 63(12), pp. 1087–1096.

Castro J., Bentz D., Weiss J. (2011) Effect of Sample Conditioning On The Water Absorption of Concrete. Cement and Concrete Composites. Vol. 33(8), pp. 805–813.

Concrete Society 2008. Technical Report 31, Permeability testing of site concrete. Surrey, UK.

Christodoulou, C., Goodier, C., Austin, S.A., Webb, J., Glass, G.K. 2013, Long-term performance of surface impregnation of reinforced concrete structures with silane, Construction and Building Materials, Vol.48, pp.708–716, http://dx.doi.org/10.1016/j.conbuildmat.2013.07.038, https://dspace.lboro.ac.uk/2134/13023.

Dhir, R.K., El-Mohr, M.A.K. and Dyer, T.D. 1997. Developing Chloride Resisting Concrete Using PFA. Cement and Concrete Research, 27(11), pp. 1633–1639.

Dhir, R.K., El-Mohr, M.A.K. and Dyer, T.D. 1996. Chloride Binding in GGBS Concrete. Cement and Concrete Research, 26(12), pp. 1767–1773.

Du Plooy, R., Palma Lopes, S., Villain, G. and Derobert, X., 2013. Development of a multi-ring resistivity cell and multi-electrode resistivity probe for investigation of cover concrete condition. NDT & E International, 54(0), pp. 27–36.

Domone, P. and Illston, J.M. (2010), Construction materials: their nature and behavior, 4th ed., 2010 Spon Press, London.

Dunne, D., Christodoulou, C., Goodier, C.I., Corrosion resistance of BS 8500 compliant concretes, paper submitted to 4th Int. Conf. on Concrete Repair, Rehabilitation and Retrofitting (ICCRRR), Leipzig, 05–07 Oct. 2015 paper submitted.

Elkey, W. and Sellevold, E. 1995. Electrical Resistivity of Concrete. 80. Olso, Norway: Norwegian Road Research Laboratory. Cited In: Sadowski, L. 2013. Methodology for Assessing the Probability of Corrosion in Concrete Structures on the Basis of Half-Cell Potential and Concrete Resistivity Measurements. The Scientific World Journal, 2013, pp. 1–9.

Glass, G.K and Buenfield, N.R. 2000b. The Influence of Chloride Binding on the Chloride Induced Corrosion Risk in Reinforced Concrete. Corrosion Science, 42, pp. 329–344.

Gonzalez, J.A., Miranda, J.M. and Feliu, S. 2004. Considerations on Reproducibility of Potential and Corrosion Rate Measurements in Reinforced Concrete. Corrosion Science, 46, pp. 2467–2485.

Hunkeler, F. 2005. Corrosion in Reinforced Concrete: Processes and Mechanisms. In: H. BÖHNI, ed, Corrosion in Reinforced Concrete Structures. 1st edn. Cambridge: Woodhead Publishing Ltd., pp. 1–42.

Hornbostel, K. Larsen, C.K. and Geiker, M.R., 2013. Relationship between concrete resistivity and corrosion rate—A literature review. Cement and Concrete Composites, 39(0), pp. 60–72.

Kropp J., Hilsdorf H.K. 1995 RILEM Report 12, Performance criteria for concrete durability, Taylor and Francis, Oxford, UK.

McNally C., Sheils E. (2012) Probability-based Assessment of The Durability Characteristics of Concretes Manufactured Using CEM II and GGBS Binders. Construction and Building Materials. Vol. 30, pp. 22–29.

Morris, W., Vico, A. and Vazquez, M. 2004. Chloride induced corrosion of reinforcing steel evaluated by concrete resistivity measurements. Electrochimica Acta, 49(25), pp. 4447–4453.

Polder, R. 2012. Effects of Slag and Fly Ash on Reinforcement Corrosion in Concrete in Chloride Environment—Research from the Netherlands. HERON, 57(3), pp. 197–210 Arya and Xu (1994).

Polder, R., Andrade, C., Elsener, B., Vennesland, Ø., Gulikers, J., Weidert, R. and Raupach, M. 2000. RILEM TC 154-EMC: Electrochemical Techniques for Measuring Metallic Corrosion—Test Methods for On-Site Measurement of Resistivity in Concrete. Materials and Structures, 33, pp. 603–611.

Pillar-Strecker, P. 2002. ICE Design and Practice Guide—Concrete Reinforcement Corrosion: From Assessment to Repair Decisions. 1st edn. London: Thomas Telford Publishing.

Saraswathy V. and Song H.W. (2007) Effectiveness of Fly Ash Activation on The Corrosion Performance of Steel Embedded in Concrete. Magazine of Concrete Research. Vol. 59, No. 9, pp. 651–661.

Schiell, P. and Lay, S. 2005. Influence of Concrete Composition. In: H. BÖHNI, ed, Corrosion in Reinforced Concrete Structures. 1st edn. Cambridge: Woodhead Publishing Ltd., pp. 91–134.

Condition assessment of concrete structures

Concrete Repair, Rehabilitation and Retrofitting IV – Dehn et al. (Eds)
© 2016 Taylor & Francis Group, London, ISBN 978-1-138-02843-2

An investigative study into the application of Non-Destructive Testing techniques for integrity assessment of RC piles

E. Okwori, P. Moyo & K. Matongo
Department of Civil Engineering, University of Cape Town, Cape Town, South Africa

ABSTRACT: Traditional methods of pile integrity assessment do not provide adequate information regarding the in-situ properties of RC piles. Non-Destructive Testing (NDT) methods offer the advantage of providing information regarding the in-situ integrity of RC piles in a non-evasive manner. The sonic echo method is one of the useful NDT's employed in the integrity evaluation of RC piles. However, researchers have stated that the method is not devoid of limitations, thus hindering its effective application.

This investigative study presents an experimental evaluation of the effectiveness of sonic echo technique in defect detection in RC piles. The main objectives of the study are pattern characterization of defects in piles and an identification of the more critical influence between defect size and defect location in defect detectability. Details of experimental mock-up pile specimens consist of nine piles with 0.24 m diameter and 3.22 m in length with necking, honeycombing, building defects and an undamaged pile. Findings from a comparison between wave signals of non-defective and defective piles indicate that necking, honeycombing and bulbing defects can be distinguished from each other and are clearly identifiable. Also defect detectability was observed to decrease with decreasing defect size. Conclusively sonic echo technique is observed to remain a useful method for troubleshooting problems with existing RC pile foundations and is highly effective for quality assurance of new pile constructions.

Keywords: pile integrity; non-destructive testing; low strain (sonic echo method); Reinforced Concrete (RC)

1 INTRODUCTION

Civil infrastructures such as bridges, dams, high-rise buildings, largely depend on the use of piles, for support. In addition they are used for underpinning works, for example in marine facilities as temporary platforms to facilitate construction work and especially in abnormal soil or ground conditions. Deep foundations in one way or the other play a significant role in determining safety, stability, and structural reliability of civil infrastructures, which they support. Therefore it is very crucial and important that these piles are sound and structurally intact. Because if for any reason the structural integrity of these supporting structures are in jeopardy, failure may occur. The integrity of piles may be compromised if and when they become dysfunctional from damages/defects and when they can no longer perform their intended function. Resulting from an inability to be readily accessed for repair and improvement works, quality control and remedial works become quite expensive and time consuming. This inevitably impacts negatively on the integrity of the super-structure being supported (Ernst & Taffe, 2006).

A number of factors influence the development of damages in these piles, these factors result from a combination of weak ground conditions, and pile construction and installation processes. Reinforced concrete piles in specific may be damaged or flawed due to influences such as concrete casting, long-term loading, and harsh environmental conditions (Klingmuller & Kirsch, 2002).

This influences lead to the development of flaws, namely bulbs, necks, waists, expansions, and steps amongst others in piles. The property of the piles that determines its functionality and performance, while also giving an indication of the pile's integrity, is the, piles continuity in physical dimensions and consistency of its material (Brad Hessing, 2012). A derivation in a pile's integrity may prevent it from performing its intended function; flaws/defects play a major role in causing deviations in the integrity of piles (Sellountou & Alverez, 2011), (Trivedi & Misra, 2012). In retrospect of this, the need for piles to be tested and inspected is necessary to avoid failure (Esfahari & Ramirez, 2003). To guarantee the safety of the superstructure and the end users, piles need to be tested. Their structural soundness, which includes

consistency in pile dimensions/geometry, strength and absence of flaws or defects in a pile, must be verified. Tests, which can be performed to ensure soundness of piles, include bearing capacity tests, integrity of pile tests, settlement of pile under load, load testing etc. In light of the above, various methods of testing the integrity of piles exist. These methods vary from time consuming expensive traditional methods such as static analysis, probe piles, dynamic formulae, static testing to cost effective more sophisticated methods such as low strain integrity testing methods which include (sonic echo, pulse echo, impact echo), cross hole (single hole) ultra sonic testing, gamma logging, Cross-hole Sonic Logging (CSL), Wave Equation Analysis for Piles (WEAP), CAPWAP analysis (Garland, Frank, & Mohamad, 1990).

Traditional methods of testing and quality assurance of piles largely involve visual inspections of the construction process and coring tests. This approach is effective in the detection of localized damage and flaws, but not as much in the detection of general or widespread damages. In addition, coring causes damages to the structure, which has to be repaired, and becomes a focal point for the propagation of damages and deterioration of piles. This disadvantage with the traditional methods led to use of non-destructive methods of testing of piles. These methods do not cause structural damage to the piles. The use of non-destructive methods for assessment provides information regarding the location and extent of defects in piles. Non-destructive methods are applied in the assessment of piles during quality assurance tests of new piles; troubleshooting of problems with new and existing piles, condition evaluation of older piles for retrofitting and remedial action (ASTM D5882-07, 2013). Non-destructive testing has been applied in the integrity evaluation of piles since the 19th century (Sanslone & Carino, 1997). The methods and principles applied, however, are still evolving. Some examples of non-destructive tests which are applied to the integrity evaluation of piles are: sonic echo, impact echo, log-impedance, sonic-logging, seismic echo, gamma-gamma and a host of other methods (ASTM, 2004). Non-Destructive Testing (NDT) has become an essential component of pile construction quality assurance. Its very existence has improved the front end of the quality assurance process (Hertlien & Davis, 2006). However a drawback on the use of NDT's in pile integrity evaluation is the inability of current methods in use, to provide information on the entire pile cross-section (George & Dean, 2010). Sonic echo technique among other methods is cheap, fast, reliable and provides information regarding the entire pile cross-section. Although during testing, variations in type of defect, size, and location may lead to complicated signals, which are difficult interpret.

In light of this, an experimental program is carried out to investigate the effectiveness of Sonic echo technique, in identification of defect type using sonic echo signals and an identification of the more critical influence between defect size and location. Towards increasing the understanding of variations in defect occurrence and further to help the interpretation of complicated signals during pile integrity assessments.

2 SONIC ECHO TECHNIQUE IN PILE INTEGRITY ASSESSMENT

Sonic echo technique is a non-destructive assessment technique for piles based on the principle of stress wave propagation in elastic medium. The technique was developed in the early 19th century and became commercially operational in the late 19th century (Sansalone & Streett, 1992). The technique measures the uniformity of the pile's physical dimensions and the consistently of the pile's material. The sonic echo technique also known as low-strain pile integrity testing method is conducted from the top (upper side) of the pile. Test equipment includes a hammer, receiver (geophone/accelerometer) mounted on the top of the pile, and a data acquisition system. The technique involves the generation of wave energy by means of a mechanical impact (hammer impact). The resulting compressive stress wave propagates through the pile until it arrives at the pile bottom. The compressive waves are reflected off discontinuities/irregularities or the end of the pile and the reflected wave, travels back to the pile top. The receiver measures the vibration response of the pile to impact. The data collection platform acquires, processes and displays the received outputs. Pile integrity is evaluated by identifying and analyzing the arrival times, direction and amplitude of reflections measured by the receivers in time domain. Figure 1 shows a pictorial representation of the sonic echo setup consisting of the hammer, accelerometer/geophone and the recording device/portable computer.

The results of the tests are presented as either velocity versus time (time domain) plots or acceleration amplitude versus frequency (impulse response) plots. Figure 2 shows a typical velocity vs. time plot and Figure 3 shows mobility vs. frequency plot. The presence of a defect causes apparent reflections to occur prior to the toe response in the time domain. When these reflections are of the same sign as the toe response they are usually associated with a relative decrease in impedance of the pile. When the reflections are opposite in sign to

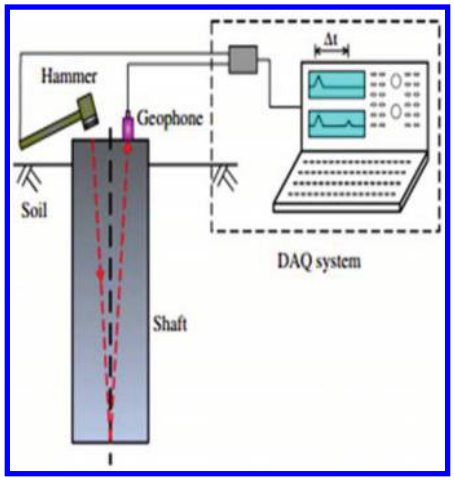

Figure 1. Sonic echo testing setup (Huang & Ni, 2012).

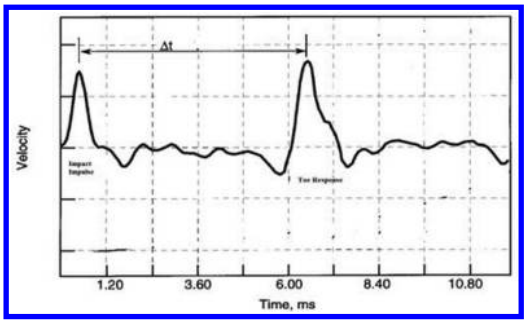

Figure 2. Velocity vs time signal trace of pile intergrity test (ASTM, 2004).

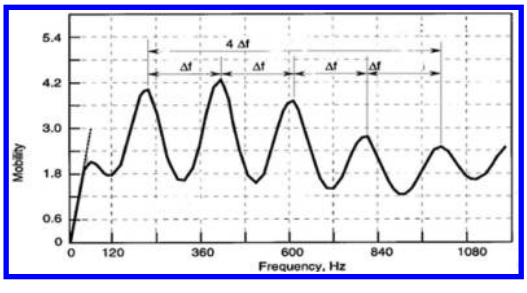

Figure 3. Amplitude vs frequency signal trace of pile intergrity test (ASTM, 2004).

the toe reflection the reflections are due to a relative increase in pile impedance.

In the frequency domain the difference between the maximum peaks on the curve is calculated and used to generate the length of the pile. The concrete quality can also be determined by measuring the difference in frequency between individual peaks. The presence of irregular peaks of unequal value as the mobility function of the frequency usually indicates a pile with change in cross-section (Jaroslaw, Lukasz, & Krzysztof, 2008).

Note: the orientation of the impact impulse is positive based on the ASTM standard orientiation. It can also negative.

2.1 *Principle of sonic echo technique*

A disturbance in a solid (reinforced concrete pile) causes the entire body of the solid to respond by accelerating linearly or angularly. The applied force causes deformations in the solid body resulting in the generation of stress waves. When the deformation is in the elastic range the applied force is rapid and changes with time. Three types of stress waves propagate in a solid i.e. Compression wave (P-waves), Shear waves and Rayleigh waves. Particle motion at wave front for P-waves is parallel to propagation direction, which produces compressive or tensile stress. For shear waves motion is vertical to propagation direction resulting in shear stress. R-wave has an elliptical particle motion. P-waves travel at the highest velocities (Sadri & Mirkhani, 2009).

The characteristics of compressive stress waves during the process of propagation in an ideal linear elastic medium i.e. reinforced concrete piles can be described by either kinematics of deformation theory (Wang, 2004). Kinematics of deformation theory is based on the propagation of one-dimensional (1D) wave, which is detailed mathematically below as in 2.2.

2.2 *1D wave propagation (kinematics of deformation theory)*

The basic assumptions which in the kinematics of deformation theory:

a. The wavelength is equal to or larger than the pile diameter
b. The pile cross section A is constant, young's modulus E and mass density are homogeneous.
c. Pile cross-sections remain plane, parallel and uniformly stressed
d. Lateral inertia effects are negligible

Consider an element along a reinforced concrete pile. Stresses acting on the element are denoted by σ and $\sigma+(\delta\sigma/\delta x)\,dx$. The unbalanced force on the element is $(\delta\sigma/\delta x)\,dx$. Let the particle displacement be denoted by U, the particle velocity by $\delta u/\delta t'$, the particle acceleration by $\delta^2 u/\delta t^2$ and the strain ε by $(\delta u/\delta x)$.

Summation of forces and stresses acting on the element are based on newtons second law of motion

force is equals the product of mass and acceleration. Figure 4 shows the diagrammatic expression of force and stresses acting on the pile element.

The summation of the stresses in the pile element using newton's second law of motion is given by

$$-\sigma_x + \left(\sigma_x + \left(\delta\sigma_x\right)/\delta x\right)dx) = \rho^* dx\left(\delta \wedge 2u\right)/\left(\delta t \wedge 2\right) \tag{1}$$

Eliminating common terms on both sides of the equation we obtain

$$\left(\delta\sigma_x\right)/\delta x = \rho\left(\delta \wedge 2u\right)/\left(\delta t \wedge 2\right) \tag{2}$$

Assuming a linear relationship between stress and strain where analyzing the wave propagation Young's modulus (E) can be used to simplify the equation

$$E = \sigma_x / \varepsilon \tag{3}$$

Since strain is the ratio of displacement to change in length $\varepsilon = \delta u / \delta x$ replacing the strain with the new modification the young's modulus becomes

$$E = \sigma_x /(\delta u/\delta x) = (\sigma_x \delta x/\delta u) \tag{4}$$

Therefore the stress $\sigma_x = E(\delta u/\delta x)$ substituting in equation 4 above the resulting equation is given by $\left(\delta \wedge 2u\right)/\delta x E = \rho\left(\delta \wedge 2u\right)/\left(\delta t \wedge 2\right)$ which may be rewritten as

$$\begin{aligned}&\left(\left(\delta \wedge 2u\right)/\left(\delta t \wedge 2\right) = E/\rho\left(\delta \wedge 2U\right)/\left(\delta x \wedge 2\right)\right)\\ &= \left(\left(\delta \wedge 2u\right)/\left(\delta t \wedge \left(2\right)\right) = c \wedge 2\left(\delta \wedge 2u\right)/\left(\delta x \wedge 2\right)\right)\end{aligned} \tag{5}$$

Which may be called one-dimensional wave equation and wave velocity $c = \sqrt{(E/\rho)}$ (may be written as $c\_1 = \sqrt{\left(\left((\lambda+2\mu)\right)/\rho\right)} = \sqrt{\left((1-\nu)E/\left((1+\nu)(1-2\nu)\rho\right)\right)}$ considering the passion ratio of the material) the equation is a second order differential. D' Alembert solution to the equation is given by

$$u(x,t) = \psi(x-ct) + \phi(x+ct) \tag{6}$$

$u(x,t)$ Represents displacement

$\psi(x-ct)$ Represents a downward traveling wave at speed c in x direction

$\phi(x+ct)$ Represents an upward travelling wave at speed c in x direction

The downward velocity at a mass point in a pile may be denoted by v_1 and is given by

$$v_1 = \frac{\delta\psi(x-ct)}{\delta t} = -\psi c \tag{7}$$

Since stress = force (p)/area (A) therefore force (p) = stress * area and stress from equation 3 is written as $\sigma = E\varepsilon$ the downward force or stress is therefore given by $P_1 = \varepsilon AE$ rewriting P_1

$$p_1 = \left(-\frac{\delta\psi(x-ct)}{\delta x}AE\right) = -\psi AE \tag{8}$$

Substituting in 8 $v_1 = p_1 c/AE$ therefore $p_1 = \left((AE/C)\,v_1\right) = zv_1$.

The upward velocity at a mass point in a pile may be denoted by v_2 and is given by $p_1 = -zv_1$.

The total velocity in the pile is given by

$$v(x,t) = \frac{\delta u}{\delta t} = \left(\frac{\delta\psi(x-ct)}{\delta t} + \frac{\delta\phi(x+ct)}{\delta t}\right) = v_1 + v_2$$

The total force in the pile is given by

$$\begin{aligned}p(x,t) &= -AE\frac{\delta u}{\delta t} = \left(\frac{\delta\psi(x-ct)}{\delta x} + \frac{\delta\phi(x+ct)}{\delta x}\right)\\ &= P_1 + P_2\end{aligned}$$

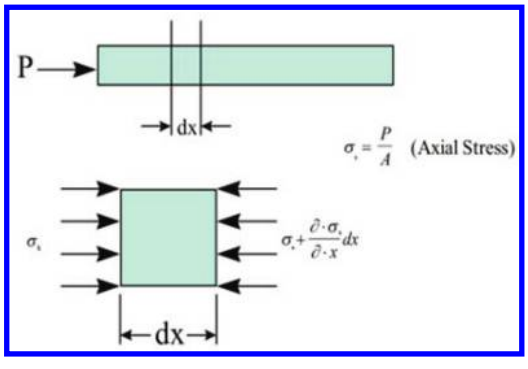

Figure 4. Cross section showing pile element with stress distribution (Jian-hua, Yuan & Liu, 1999).

3 EXPERIMENTAL INVESTIGATIVE STUDY

This investigative study is carried out by analyzing the propagation of elastic stress waves based on sonic echo testing on the surface of nine piles. The study involves comparing test results from a non-defective pile and eight defective piles. In this way the effectiveness of the sonic echo technique in detecting the type and nature of defect is assessed.

3.1 *Pile specimens*

Nine (9) reinforced concrete piles, having the same dimension, mix design, reinforcement type and

boundary conditions, were tested. The control pile (non defective) consisting of no defect, three piles with necking defects, three piles with honeycombing defects and two piles with bulbing defects. The decision of comparing tests results of the non-defective pile against the defective pile arises from the need to provide knowledge of the inner composition of pile integrity and defect nature, which are frequently affected by uncertainties.

The piles are circular with length of 3200 mm and thickness of 250 mm, and they are reinforced. Table 1 shows the defect locations and Figure 5 shows the pictorial location of the defects.

A pictorial presentation of the defects investigated are detailed in Figures 6,7 and 8.

3.2 *Test equipment*

Test equipment used in carrying out sonic echo testing on the piles include basically the following

a. Olson freedom data PC (Testing and analysis software)
b. Impulse hammer

Table 1. Table indicating defect type and location.

Defect type induced in pile	Defect location (Depth from pile top)/No. of piles per defect		
	Pile 1 (Top)	Pile 2 (Middle)	Pile 3 (Bottom)
Control pile	–	N/a	N/a
Neck	0–0.6 m	1.6 m	2.8–3.2 m
Bulb	0–1 m	1.5–2 m	N/a
Honey combing	0.4–0.8 m	2–2.4 m	2.4–2.8 m

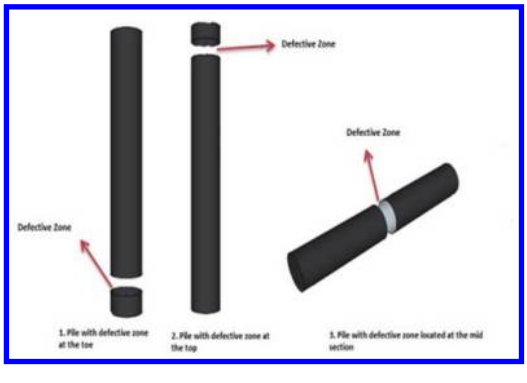

Figure 5. Showing defective zones in mock-up laboratory piles.

Figure 6. Necking defect.

Figure 7. Bulbing defect.

Figure 8. Honeycombing defect.

c. Accelerometer
d. Connection cables between receivers and freedom data pc.

3.3 *Testing parameters*

During the propagation of compressive stress waves through an elastic medium i.e. reinforced

concrete, which is used in evaluation of integrity in reinforced concrete piles through detection of anomalies. Certain properties of the stress waves are critical for identification, location of defects, assessing p6bvz sensitivity and resolution of the system to locate anomalies (Nelligan, 2013). These properties include basically wavelength, frequency and velocity of the wave. The relationship between these properties is given by

$$Wavelength(\lambda) = \frac{Velocity(v)}{Frequcncy(f)} \quad (9)$$

$\lambda : wavelength\ (m), v : velocity\ (ms), f : frequency\ (Hz)$

For reinforced concrete piles the velocity of wave propagation through the pile is fixed due to the velocity been a material characteristic of the medium. It depends on the properties of the concrete arising from type and size of aggregate, cement etc. The typically velocity of wave propagation in reinforced concrete pile varies between 3500 m/s – 4600 m/s for reinforced concrete with good quality (Finno & Gassman, 1998).

A conclusion from the relationship above indicates that an increase in frequency will lead to a corresponding decrease in wavelength. Hence during testing with sonic echo, the frequency for data sampling is critical in order to control the wavelength. The wavelength used possesses a significant effect on the probability of detecting a defect. A general principle adopted during testing states that defect size must be approximately equal to or larger than the wavelength of the propagating wave to stand a reasonable chance of detectability (Carino J, 2004). Table 2 shows the testing parameters for the piles.

The minimum detectable defect size based on the rule of thumb stated by Carino J, (2004) and the testing parameters stated in Table 2 is given as $\lambda = 0.078 \approx 0.08m$ which is less than or equal to the size of all defects been investigated in this study, which makes the sampling frequency and velocity of the stress wave suitable for the investigation.

Table 2. Testing parameters.

Parameter	Value
1 Sampling rate	20 us
2 Record size	2048
3 Number of records	3
4 Trigger level	+/–0.5
5 Trigger delay	1000
6 Wave velocity	3900 m/s
7 Filter	Low-pass filter

4 RESULTS

Results of the sonic echo tests performed on the piles shown in Figures 9, 10 and 11. It can be noticed that sonic echo is able to recognize necking, honeycombing and bulbing defects).

Necking defect details as presented below in Figure 4 showing an undamaged pile, 63% necking located between 1.5 m–2 m, 42% necking located between 0 m–0.6 m, and 23% necking located between 0 m–0.6.

Honeycombing details as presented below in Figure 10 showing wave signals of undamaged pile, 63% honeycombing located between 1.5 m–2 m, 42% honeycombing located between 0 m–0.6 m, and 23% honeycombing located between 0 m–0.6 m.

Figure 11 shows wave signals of bulbing defects details include undamaged pile, 50 % bulbing at 1.5 m–2 m, 12 % bulbing at 0 m–0.6 m.

It is assumed that the defect and toe reflection impulse magnitudes are less in relation to the

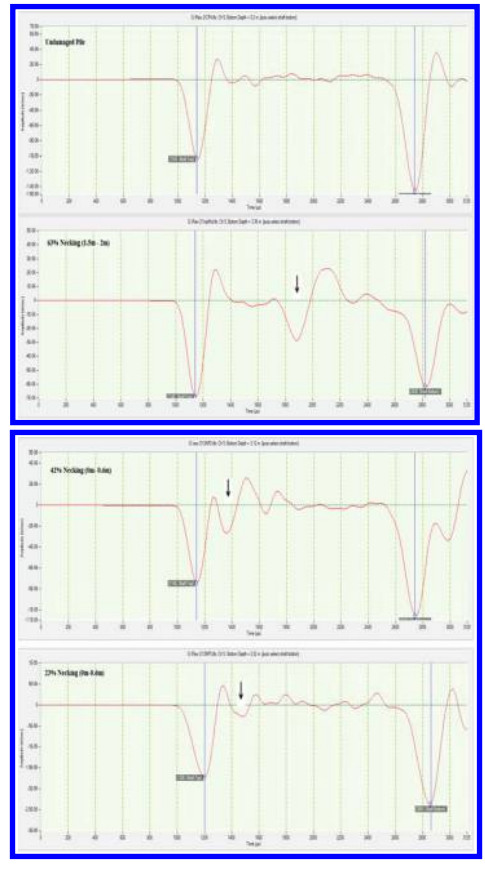

Figure 9. Comparing sonic echo signals of undamaged pile and piles with necking defects.

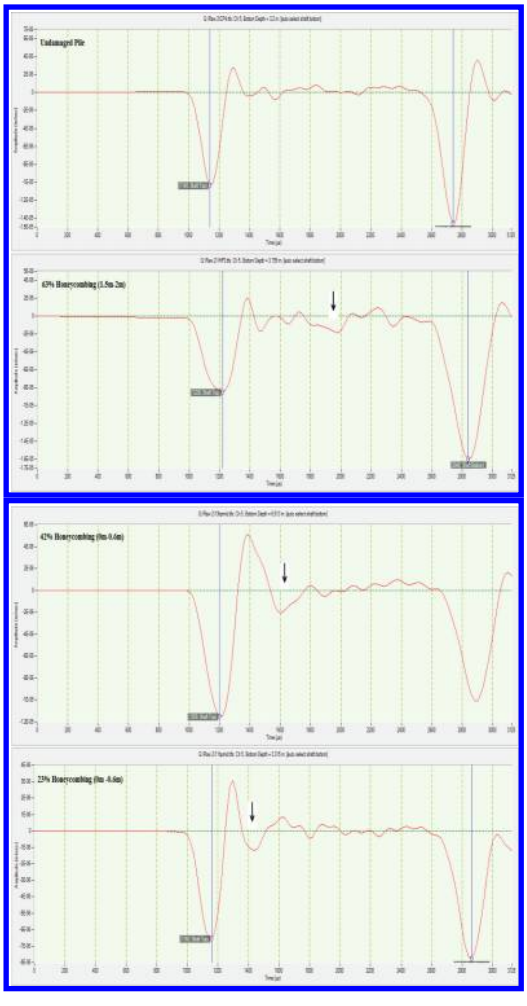

Figure 10. Sonic echo signals of undamaged pile and piles with honeycombing defects.

impact impulse magnitude in practical situations. This however does not appear exactly true when observing the above wave signals. It crucial to note that this still holds as the magnitudes of reflection are negative in sign convention resulting in the larger magnitude having a smaller amplitude parameter or value.

Following this reasoning the defect reflections and corresponding toe reflections of each necking, honeycombing and bulbing pile are calculated as a percentage of the impact impulse to show how much variation in impedance exists between necking, honeycombing and bulbing defects of various magnitudes. Figure 12 below shows the normalized defect and corresponding toe reflections from necking defects.

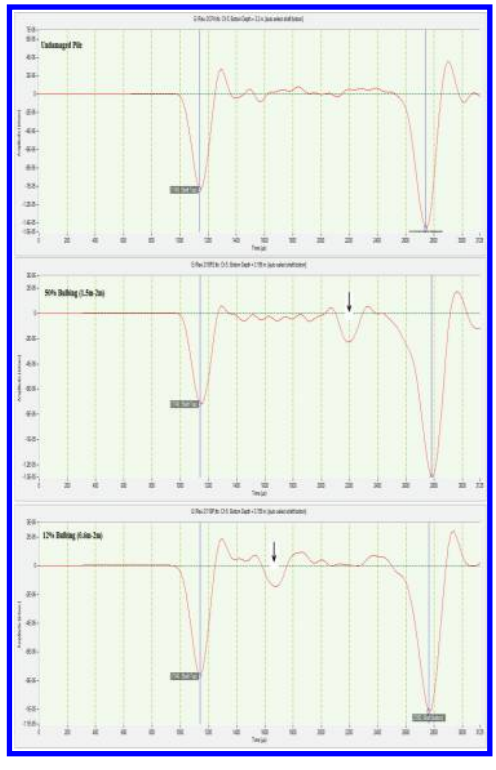

Figure 11. Comparing sonic echo signals of undamaged pile with bulbing piles.

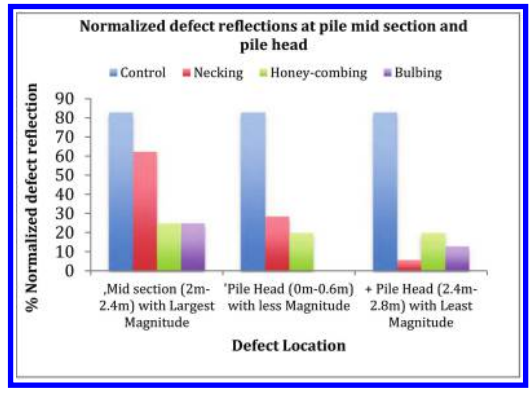

Figure 12. Normalized defect reflections from necking, bulbing, and honmeycombing piles in decseding order of magnitude.

Results from waves signals have pointed out that a negative (–) positive (+) blip (compressive tensile) signal is identified at the location of necking defects see figure 9 above, a low amplitude negative (–) blip in the wave signal is identified the

location of honeycombing defects see figure 10 above, and also a positive (+) negative (–) positive (+) blip (tension compression tension) is indicative of a bulbing defect as seen in figure 11. Simply put the variations in waves signals for the different defect can be attributed to variations of impedance resulting from a decrease/or increase in cross sectional area. From Figure 12, it can also be deduced that as defect magnitude decreases, its detectability also decreases. Indicating 4 that defect magnitude having more influence on defect detectability compared to defect location.

5 CONCLUSION

In conclusion sonic echo technique is perceived to remain a useful tool in integrity evaluation, quality assurance and troubleshooting of problems with reinforced concrete pile foundations nondestructively.

This investigative study has helped to increase knowledge regarding the detectability of defects via their patterns and also helps to improve the front end of pile integrity evaluations using sonic echo technique by identification of the more critical influence on defect detectability in piles.

REFERENCES

ASTM D5882-07. "Standard for Low Strain Impact Intergrity Testing of Deep Foundations." West Conshohocken: ASTM international, 2013.

Carino J, Nicholas. *Stress wave propagation methods.* National Institute of standards and Technology, CRC Press, 2004, 1–36.

Esfahari, Hadi Salehi, and Maria Teresa Ramirez. "Institutions, Infrastructure and Economic Growth." *Journal of development Economics*, 2003: 443–477.

Ernst, Niederleithinger, and Alexander Taffe. "Early stage wave velocity of concrete piles." *Cement & concrete composites* (ELSEVIER), 2006: 317–320.

George, Piscsaiko, and Cotton Dean. "Non—destructive Testing Methods for Drilled Shaft and ACIP Piles." 2010, 525–532.

Huang, Yan-Hong, and Sheng-Huoo Ni. "Experimental study for the evaluation of stress wave approaches on a group pile foundation." *NDT & E International* (Elsevier), 2012: 134–143.

Hertlien, Bernard, and Allen Davis. *Non Destructive Testing of Deep foundations.* West Sussex: John Wiley & sons Ltd, 2006.

Jaroslaw, Rybak, Sadowski Lukasz, and Schabowicz Krzysztof. *Non-destructive impulse response S'mash method for concrete pile testing.* Institute of Geotechnics and Hydrotechnics, Wroclaw University of Technology, DEFEKTOSKOPIE, 2008, 195–202.

Klingmuller, Oswald, and Fabian Kirsch. "A quality and safety issue for cast-in-place piles 25 years of experience with low strain integrity testing in germany: from scientific peculiarity to day to day prectise." German committe for dynamic pile testing, 2002.

Nelligan, Tom. "Ultrasonic flaw detection: Theory, practice and application." *Non-destructive testing.* Prod. Olympus. Waltham: Olympus, 2013.

Sadri, Afshin, and Koorosh Mirkhani. "Wave Propagation Concrete NDT Techniques for evaluation of structure and materials." Canada, 2009.

Sellountou, Evgenia-Anna, and Camilo Alverez. "Thermal Integrity Profiling: A Recent Technological Avancement in Intergrity Evalaution of Concrete Piles." Pile Dynamics Inc, 2011.

Concrete Repair, Rehabilitation and Retrofitting IV – Dehn et al. (Eds)
© 2016 Taylor & Francis Group, London, ISBN 978-1-138-02843-2

Studies on the key technical problems of asphalt concrete facing slabs in the upper reservoir of Huhhot Pumped-Storage Plant in North China

Shifa Xia, Yihui Lu, Zhengxing Wang & Fucheng Zhang
China Institute of Water Resources and Hydropower Research, Beijing, China
Beijing IWHR-KHL Co. Ltd., Beijing, China

ABSTRACT: Asphalt concrete facing slabs have been widely used as anti-seepage structures worldwide in Pumped-Storage Plants (PSP). In China a great many PSPs are going to be built in the next 5–10 years according to the national PSP developing plan to meet the increasing need for power and energy. Huhhot PSP which was built in 2013 in Inner Mongolia in North China where the weather is very cold, the anti-fracture property of the asphalt concrete in low-temperature is the critical issue to be solved to use asphalt concrete as seepage-proof facing slabs. In this paper, firstly the developing process of construction technology of asphalt concrete facing slab in China as well as its application in home and abroad are briefly introduced. Then three main issues in paving asphalt concrete facing slabs in Huhhot PSP, namely, the anti-fracture design for asphalt concrete slab in low temperature, the compaction technology of impermeable layer with modified bitumen and the construction technology in low temperature are addressed. Finally the technical difficulties and solutions in building the asphalt concrete facing slabs in the upper reservoir in Huhhot PSP are summarized. The success of building asphalt concrete facing slab in Huhehot project indicates that the technology is reliable and can be applied in other similar projects in China.

1 INTRODUCTION

1.1 *Applications of asphalt concrete facing slabs in PSPs*

Asphalt concrete has an excellent anti-seepage performance and deformation properties adapting to the foundation and temperature. No structural joints are needed in the construction of asphalt facing slabs thus it has a fast construction speed. Also it is nontoxic and environment-friendly, and has a good durability. Asphalt facing slabs are a good choice for the imperious body of rock-fill dams and have been used on dams since 1930s in foreign countries. Asphalt Core Rock-Fill Dams (ACRD) were considered as one of the most suitable type for high dams on the 16th International Conference on Large Dams (ICOLD) in 1988. Because of the good anti-seepage performance, excellent adaption to rough topography and variation of water level, asphalt concrete facing slabs had been used as imperious body in the upper reservoirs of PSP's [1]. It is noteworthy that all of the imperious bodies of PSP's upper reservoir in west-European have been built with asphalt concrete facing slabs since 1975. In China, this technology was first adopted in dams in 1970s, and had been applied in 26 Asphalt Concrete Facing Dams (ACFD) up to 1990. After 1990, asphalt concrete facing slabs were mainly applied as the imperious body in PSPs, such as Tianhuangping, Zhanghewan, Baoquan and Xilongchi. According to incomplete statistics, over 80 PSPs have adopted asphalt concrete facing slabs as the imperious body, and these power stations are mainly distributed in German, Sweden, Norway, France, USA, Japan and China.

1.2 *The technology development of asphalt concrete facing slab*

The development of asphalt concrete facing slab in China can be classified into 3 stages: the exploration stage, the corporation stage and the self-innovation stage.

During the exploration stage (1970~1980), because of lack of key technology related with the asphalt concrete mixing design, construction equipment and construction method, and because of the bad quality of bitumen, most of the asphalt concrete facing slabs built in this stage encountered problems of flowing-cracking and joints cracking, etc. They would lead to severe leakage and affect the safety of project. This caused many doubts to applications of asphalt concrete in projects of China, and made the development of asphalt concrete facing slab fall into a very difficult period. The construction of related-projects applying asphalt concrete almost stopped and some projects even had to replace the asphalt concrete facing slab with other type of imperious body (like Niutoushan in Zhejiang, Chebahe in Hubei).

From 1990 to early 21th century, some domestic asphalt concrete facing slab projects began to open to foreign companies and the development of asphalt concrete in China went the into corporation stage. The typical projects were Tianhuangping, Zhanghewan and Xilongchi. These projects were constructed by foreign companies or by Sino-foreign corporations, e.g., Tianhuangping were constructed by Strabag (German) and Zhanghewan and Xilongchi were constructed by Taisei (Japan). However, the key technology was still grasped by foreign companies and was not learned by China, although related Chinese companies had taken part in these construction projects. But by participating in these projects, the Chinese technicians mastered a general knowledge of the foreign advanced technology. The asphalt concrete construction technology began to step into the self- innovation stage with the progress in material technology.

The self-innovation stage lasts from 2006 to now. During this stage, in order to improve the asphalt concrete facing slab technology, the Chinese research institutes have studied the anti-seepage performance, deformability, thermo-stability, water stability and durability of asphalt concrete facing slab and applied them in Nangudong and Baoquan projects. Chinese technicians have developed an integrated technology of asphalt concrete facing slab including mixture design method with structure-stability theory as its core theory, construction technology and equipment. The technology has been used successfully. The Baoquan project was the first large asphalt concrete facing slab project which was fully designed and constructed by domestic companies. Its success plays an important role in guiding and promoting the construction of asphalt concrete facing slabs in China and ends the dependence of China on foreign companies in asphalt concrete technology.

With the improvement in the quality of domestic bitumen and in the key technology of asphalt concrete facing slabs, the ACFD projects of China have expanded from south China to north China. In north cold region, because of the low temperature, cracks are prone to occur in conventional reinforced concrete facing slabs and the water proof in the joints are prone to fail, leading to seepage through the dam. So asphalt concrete facing slab is the first choice in cold region for its good performance in resisting frozen-fracture and no joints in construction, although the unit price is relatively high. For instance, the Xilongchi project started in 2005 and the Baoquan projects started in 2006 both adopted asphalt concrete slabs as the impervious body.

The Hohhot PSP upper reservoir is located in cold region, where the annual average temperature is 1.1°C and the extreme lowest temperature is –41.8°C, which is the lowest temperature of the PSPs built and under construction worldwide. Asphalt concrete facing slab was adopted as the anti-seepage structure of the whole upper reservoir. The anti-seepage performance of asphalt concrete facing slabs is the key to success of the upper reservoir. The key technical problems and solutions are summarized in this paper.

2 KEY TECHNICAL PROBLEMS OF THE ASPHALT CONCRETE FACING SLABS OF HOHHOT PSP UPPER RESERVOIR

The Hohhot project has a lot of difference with the other domestic project in mixture design and construction controls, its difficulty are mainly in the following three points.

1. Low temperature cracking-resistance is difficult to reach. The Hohhot PSP upper reservoir is located in cold region in China, where the weather condition is very bad and air temperature is very low in winter. Asphalt facing slab is on the surface of the dam, so it bears not only the stress caused by water level change, but also the thermal stress caused by temperature difference. So, asphalt concrete slabs must have good performance of cracking-resistance in low temperature. When the water level in the reservoir falls in winter, Especially when the cold wave occurs, asphalt concrete facing slab will shrink and generate thermal stress because of the low air temperature. When the temperature of asphalt concrete is decreasing, the upper layer of the slab will shrink but the shrinkage is restrained by lower layers and foundation, thus tensile stress in the facing slab will occur. When the tensile stress is beyond the tensile strength, cracking will occur. According to the data, the lowest temperature the asphalt concrete facing slab project abroad experienced is –35°C at Oscheniksee reservoir in Austria. The dam height was 81 m and asphalt concrete facing slab was adopted as the impervious body on upstream face. A lot of cracks were found in the facing slabs leading to the dysfunction of the project after a cold wave in which the lowest temperature was almost –35°C. The extreme low air temperature of Xilongchi project in China is –34.5°C and it adopted modified bitumen and construction technology of Taisei company of Japan in building its impervious layer. The fracture temperature of the impervious layer asphalt concrete inspected on site is –39°C and Xilongchi project is running well now. The extreme low air temperature of Hohhot project is –41.8°C and the designed

fracture temperature is no greater than –43°C. There is no experience for us to refer to under such extreme condition.

2. It is difficult to make the porosity of the impervious layer less than 3%. Modified bitumen is applied in the asphalt concrete facing slabs of Hohhot PSP upper reservoir and the bitumen content is high (more than 7%). Related studies indicate that compared to unmodified bitumen, modified bitumen has a higher viscosity (Picture 1), thus a higher construction temperature is needed for the impervious layer to ensure the compaction effect. So it is difficult to meet the key requirement for porosity of the impervious layer, which is less than 3%, especially at the joints between layers. It can be seen from the on-site paving experiment that the porosity of impervious layer is difficult to reach regulated values after compaction. Most measured porosities of asphalt concrete are close to the upper limit. Some porosities of concrete at joints are even higher than the upper limit. How to solve this problem during the large scale construction is very important. Because study results and construction practice indicate that asphalt concrete will suffer leakage and poor durability when the porosity of asphalt concrete is greater than 3%, leading to the failure of the whole project finally.
3. The construction technology of asphalt concrete facing slabs in severe cold region is difficult. According to construction experience, asphalt concrete facing slabs should be paved under the conditions that the air temperature is higher than 5°C and the wind force is less than level 4 to ensure the paving quality. But in severe cold region, time for construction will be short if we exactly follow this rule, so the project schedule will be delayed. How to mixing the mixture, paving, compacting and get a qualified asphalt concrete facing slab is a challenge.

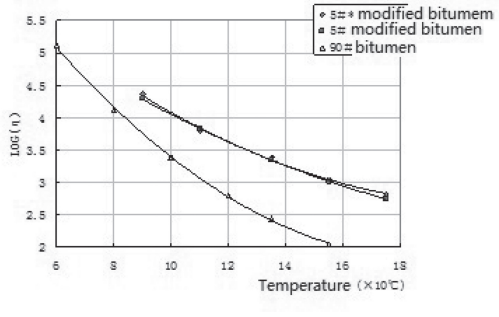

Picture 1. Viscosity-temperature curve of different bitumen.

3 SOLUTION FOR THE DIFFICULTIES

3.1 *Low temperature cracking-resistance of impervious layer facing slab*

Appropriate modified bitumen and mixing design are the solutions. Before Hohhot project, the representative modified bitumen is the one adopted in Xilongchi project. This bitumen is a product of Taisei Company of Japan, whose cracking-temperature is –38°C. This could meet the requirement of Xilongchi project but not Hohhot. Therefore, assigned by the managing company of Hohhot project, the KHL Company carried out the investigation for the newest asphalt products, and executed the total performance tests for the 13 kinds of asphalt from 4 factories. The cracking temperature of 3# modified bitumen (PetroChina), SK-2 modified bitumen (IWHR) and 5#* modified bitumen (IWHR) are –43.0°C, –45.7°C, and –47.5°C. The modified bitumen adopted in Hohhot project has a big difference with the one in Xilongchi project, as can be seen in Table 1. Together with the bitumen test, performance test and inspection analysis of the main raw materials such as coarse aggregate, fine aggregate, mineral powder were carried out. The physical and mechanical performance experiments of asphalt concrete were also carried out. Especially, through mixing design a large amount of frozen-fracture tests were adopted to select the appropriate asphalt and mixing radio to meet the requirement of low temperature cracking resistance. At last, the optimized mixing radio was recommended.

After taken these action, during the large scale construction, test results of asphalt mixture from mixer and specimen from field show that the cracking temperature of asphalt concrete of Hohhot PSP upper reservoir is –43.1°C [max], –46.9°C [min], –44.6°C [average], which meets the design requirement.

It should be noted that the test value of cracking temperature of asphalt concrete in Xilongchi project is higher than that of Hohhot project, with the average values of –39°C and –44.7°C respectively. But as shown in Table 1, we could see that the brittle point of the modified asphalt used in Xilongchi project is lower than that used in Hohhot project. This indicates that there is no explicit relation between cracking temperature of asphalt concrete and brittle point of asphalt. The mixing ratio also influences the cracking temperature of asphalt concrete. Generally after aging the softening point of asphalt will rise, but the modified bitumen adopted in Xilongchi project and Hohhot project showed reverse result that the softening point decreased after aging. As seen from the testing results, the softening point of the

Table 1. The performance of modified asphalt used in Hohhot and Xilongchi project.

Serial number	Item	Unit	Technology requirement		Test values in Xilongchi [2]	Test values in Hohhot
			Xilongchi [2]	Hohhot		
1	Penetration (25°C, 100 g, 5 s)	1/10 mm	>80	>100	98	118
2	Penetration index	–	≥–0.6	≥–1.2	6.7	3.9
3	Ductility in low temperature	Cm	≥40 (5°C)	≥70 (5°C)	64	80
4	Ductility (15°C, 5 cm/min)	Cm	≥150	≥100	103	85
5	Softening point	°C	≥50	≥45	82	65
6	Kinematic viscosity (135°C)	Pa·s	–	≤3	–	1.803
7	Brittle point	°C	≤–20	≤–22	–27.8	–25
8	Flash point	°C	>230	≥230	250.3	282
9	Density (25°C)	g/cm^3	Measured	Measured	1.020	1.000
10	Solubility	%	>99.0	≥99.0	99.4	99.8
11	Elastic recovery (25°C)	%	–	≥55	–	99
12	Separation difference	°C	–	≤2.5	–	0.2
13	Paraffin content of matrix asphalt	%	<2.3	≤2	1.6	1.4
	RTFOT					
14	Weight change ratio	%	≤1.0	≤1.0	–0.2	–0.5
15	Change of softening point	°C	<5	≤5	–5.0	–4.5
16	Ratio for penetration	%	≥55	≥50	93	109
17	Brittle point	°C	≤–18	≤–19	–21	–28
18	Ductility in low temperature (5°C)	Cm	≥25 (5°C)	≥30 (5°C)	67	65
19	Ductility (15°C, 5 cm/min)	Cm	≥100	≥80	87.7	69

Table 2. Mixing ratio for impermeable layer of Hohhot project.

Mineral aggregate gradation										
Sieve diameter (mm)	16	13.2	9.5	4.75	2.36	1.18	0.6	0.3	0.15	0.075
Pass percent (%)	100	96.6	89.3	65.4	50	37.2	27.2	17.6	14.2	11

Asphalt content (the percentage of the asphalt weight in the gross weight of asphalt and mineral aggregate): 7.3%

modified asphalt used in Xilongchi and Hohhot projects decreased 5°C and 4.55°C respectively. This phenomena needs to be further studied.

3.2 *Control of the porosity of impervious layer asphalt concrete (<3%)*

During the construction of the impervious layer asphalt concrete of Hohhot PSP upper reservoir, the following actions were taken:

1. According to the test results of pavement experiment, mixing ratio was adjusted a little. Bitumen content was reduced but river sands and mineral powder increased, so that the impervious layer is easy to compact on slope.
2. Use advanced paver machines. When paving on slope, paver with a function of 90% precompaction was used. At the fan-shaped region of reservoir's corner, the width is decreasing from top to bottom and paver with alterable paving width was used. The paving efficiency is improved and the quality is ensured.
3. Well compaction schedule. Through paving experiment, initial compaction, re-compaction, final compaction temperatures and compaction times were determined. The moving speed of vibrating roller was raised to ensure that the bitumen did not stick to the roller at high temperature.
4. Special joints treatment. Joints could be classified to hot joints and cold joints. Treatment could be divided to pre-treatment and post-treatment. Pre-treatment means using infra-red heating equipment to heat the joints before paving. In order to ensure the compaction temperature, insulating cover was used when paving at night. Post-treating means to heat those unqualified area (porosity > 3%) using infra-red equipment and compact again.

The test results of Hohhot project indicate that after these actions, porosity of impervious layer

Table 3. Standard for construction temperature and process on slope paving.

Project	Rolling process	Temperature (°C)	Rolling times	Way of rolling
Level layer	Initial rolling	>130	1	Quiet rolling
	Double rolling	>105	3	Vibration rolling when forward, Quiet rolling when backward
	Final rolling	>90	1	Quiet rolling
Impermeable layer	Initial rolling	>140	1	Quiet rolling
	Double rolling	>115	3	Vibration rolling when forward, Quiet rolling when backward
	Final rolling	>90	1	Quiet rolling

and joints was well controlled and the qualified rate reached 99%.

3.3 *Low temperature construction technology of leveling layer of Hohhot PSP upper reservoir*

The Huhehot project is located in a severe cold region, with high altitude and large wind during the whole year. According to the specified construction criterion (daily average temperature higher than 5°C, wind force lower greater than level 4), the construction time will be very short. Therefore, construction technology at low temperature should be explored. Considering safety, construction of leveling-layer asphalt concrete at low temperature was only implemented from mid September to the end of October in 2012.

3.3.1 *Reformation of mixer at low temperature*

The daily average temperature in Huhehot project is mainly lower than 5°C and the night temperature is lower than 0°C after mid September. Under this condition, in order to ensure the quality and production capacity of asphalt concrete, the mixer was reformed. The reformation including: water proof and freezing proof of aggregates, thermal insulation of pneumatic system (building air compressor room and heating device), change of fuel oil, raise of the temperature of hot aggregates and the mixture and so on. 25000 t mixtures were produced from mid September to the end of October in 2012, with the qualification rate of 100%.

3.3.2 *Paving and rolling on site*

There are five principles when paving at low temperature condition: quickly unloading, quickly transporting, quickly feeding, quickly paving and quickly rolling. Besides these, the truck should be covered with insulation materials during transportation and the surface of asphalt concrete also need to be covered after paving. The purpose is to reduce the heat loss during transportation, paving and compaction and ensure the temperature of paving and compaction. Detailed steps are as follows.

①. Temperature control. The temperature of paving and rolling must not exceed the upper limit of the standard. The truck should be covered with insulation materials during transportation to reduce the heat loss. Because of the low temperature and large wind, the temperature of asphalt concrete decrease quickly during paving and rolling. So the initial rolling should be done as quickly as possible after paving to reduce the heat loss. If the mixture could not be compacted after paving timely, it should be covered by insulation cover. The insulation should be maintained after initial rolling so the temperature of re-compaction and final compaction is enough.

②. Control of feeding car. The loading amount and speed of the car must be controlled during the low temperature construction. The amount of the mixture in the feeding car must be well controlled, ensuring the mixture was feeding uniformly (8 t each time). The feeding speed should be as quickly as possible on the premise of safety.

③. Control of the paver. Paver with high compaction capacity should be used when construction at low temperature. Before paving, the iron plate should be heated and the compaction power should be adjusted to make sure the compactness was higher than 90% after paving. Paving speed should be 1.0 m/min~1.5 m/min at the lower half of the layer. The paving speed could be properly raised at the upper half because the transportation distance is short and the supply of mixture is sufficient. The temperature of initial compaction, re-compaction and final compaction should be ensured by insulation when paving under low temperature.

The area of leveling layer constructed at low temperature in Huhehot project is about 50,000 m^2. After taking the above measures, testing results showed the qualification rate of the leveling layer

was 95%. The unqualified area was removed and re-paved in 2013.

4 CONCLUSIONS AND SUGGESTION

1. Most of the impervious body of PSP upper reservoir worldwide use asphalt concrete facing slabs, and all of them used asphalt concrete facing slab in West Europe since 1975. In China about 44.1% and 14.7% of the PSPs built and being built use reinforced concrete facing slab and asphalt concrete facing slab as impervious body, respectively. Though it seems that the reinforced concrete facing slab is preferred in China, asphalt concrete facing slab has a very broad application prospect in cold region, because of its excellent anti-seepage performance, excellent low-temperature crack resistance, deformability adapt to bad foundation and water level change, faster construction speed and similar unit price compared with reinforced concrete facing slab.
2. Modified bitumen and mixing ratio design is the key factor of the low-temperature crack resistance of asphalt concrete. The modified bitumen applied in Hohhot PSP upper reservoir represents the highest level of material properties in low-temperature crack resistance of bitumen in China. Compared with unmodified bitumen, properties of aged bitumen showed reverse rule and needs further study. The mixing design technologies of asphalt concrete have been mature domestic, yet the properties of modified asphalt should be further studied.
3. In cold regions, modified asphalt is usually adopted at impermeable layer of facing slab. However, its high viscosity and the high content could result in difficulties in compaction during the construction process. Based on the experiences of the Huhehot project, it is difficult to control the porosity of joints between strips of impermeable layer. To meet the design requirement, perfect construction technology and elaborate treatment are necessary. The construction technologies of rolling right after the asphalt paver should be further studied to improve the quality of the joints.
4. In cold regions, the construction period is short if asphalt concrete is paved strictly according to the requirements in related specifications. Therefore, construction technology of leveling layer under low temperature was explored in the Huhehot project. Such measures as low-temperature reformation of mixer, thermal insulation with quilts and quick rolling to ensure the initial rolling temperature of asphalt concrete were adopted during the construction process, which ensured the quality of mixtures and asphalt concrete after rolling compaction. The test results of the Huhehot project indicate that the qualification rate of on-stie paving and rolling quality is higher than 95%, which proves the practicability of above measures. However, the construction technologies of impermeable layers under low temperature should be further studied.

REFERENCES

[1] Qiu ru bin, comparison of anti-seepage type of pumped storage plant upper reservoir-reconsideration of the anti-seepage of asphalt concrete facing slab. Construction of pumped storage plant, 2009.

[2] Zhang hen jun, Construction experience of pampered storage plant abroad, Shanxi hydraulic science and technology, 1995.

[3] Yue yue zhen, Hao ju tao hydraulic asphalt concrete anti-seepage technology, chemical industry press.

[4] Shoichi ABE, Takehiko OKUDERA, Hiroyuki SETO, Rational design and construction of embankment and asphalt facing on the upper reservoir at Kyogoku Project, C.2, Twenty-fourth Congress on Large Dams, Kyoto, 2012.

[5] Zhang wei, construction quality control of xilongchi upper reservoir, xi'an university of science and engineering.

[6] The current situation and prospect of pampered storage plant in China http://www.chinasmartgrid.com.cn/news/20120626/369042.shtml.

[7] Lu yi hui, Xia shi fa, Hao ju tao, Design for Mix Proportion and Construction of Asphalt Concrete Facing Slab in Cold Region, CHINCOLD annual meeting and the 3th international symposium on rock-fill dam, 2013,11 Kunming.

Concrete Repair, Rehabilitation and Retrofitting IV – Dehn et al. (Eds)
© 2016 Taylor & Francis Group, London, ISBN 978-1-138-02843-2

Evaluation of sulfate damages in a tunnel concrete segments

F. Moodi & A.A. Ramezanianpour
Concrete Technology and Durability Research Center, Amirkabir University of Technology, Tehran, Iran

Q. Bagheri Chenar & M. Zaker Esteghamati
Department of Civil and Environmental Engineering, Amirkabir University of Technology, Tehran, Iran

ABSTRACT: Sulfate attack affects the durability and integrity of concrete members greatly. Sulfate ions cause expansion, cracking, strength loss and adhesion reduction in concrete components, which threatens concrete structures health. This paper discusses the devastating effects of sulfate attack in a tunnel which is located in the southwest of Iran. During tunnel excavation, a vast volume of groundwater and H_2S gas enters into the tunnel that leads to the failures in the concrete segments. In order to investigate sulfate attack hypothesis, 69 core specimens were taken and tested. Compressive strength, water absorption and electrical resistance tests were performed on 64 specimens and total number of 85 sulfate ion tests were implemented. Experimental investigations show that sulfate attack has probably happened and necessary measures should be taken to prevent damage propagation and repair damaged segments.

1 INTRODUCTION

The adverse consequences of chemical attacks on cement based materials are a growing importance topic in structural health monitoring and concrete damage researches. Chemical attacks affect the durability of concrete significantly, which determines the expected service life of concrete members (Zivica, V., & Bajza, A., 2001). According to ACI committee 201, chemical attacks are divided into six groups: 1-acidic attack 2-alkali attack 3-carbonation 4-chloride attack 5-leaching 6-sulfate attack (ACI, 1962). Increasing sources of acid attacks and cement based materials alkalinity emphasizes the importance of acidic attack (Zivica, V., & Bajza, A., 2001). Interaction of sulfate ions with cement paste matrix causes sulfate attack which threatens integrity and durability of concrete, either by expansion of cement matrix or progressive loss of strength and mass (Ghafoori, N., et al, 2008 & Mehta, P.K., 1986 & Brown, P.W., Badger, S., 2001). The three step mechanism of sulfate attack induced expansion is as followed (Ghafoori, N., et al, 2008 & Mathis, R.P., 1996 & Kosmaka, S.H., & Panarese, W.C, 1988):

1. Sulfate ions react to tricalcium aluminate in the Portland cement and forms 6-calcium aluminate trisulfate hydrate (ettringite)

$$3CaO*Al_2O_3+3(CaSO_4*2H_2O)+26H_2O \rightarrow 3CaO*Al_2O_3*3CaSO_4*32H_2O \quad (1)$$

2. Tetracalcium aluminate monosulfate-12-hydrate (monosulfoaluminate) is formed due to ettringite reaction with remaining C_3A

$$2(3CaO*Al_2O_3)+3CaO*Al_2O_3*3CaSO_4*32H_2+4H_2O \rightarrow 3\left(4CaO*Al_2O_3*SO_3*12H_2O\right) \quad (2)$$

3. Monosulfoaluminate reaction with sulfate ions produce more ettringite:

$$4CaO*Al_2O_3*SO_3*12H_2O+2\left(CaSO_4*H_2O\right)+16H_2O \rightarrow 3CaO*Al_2O_3*3CaSO_4*32H_2O \quad (3)$$

Continuous formation of ettringite leads to internal pressure, which causes expansion. Also, reaction of calcium hydroxide in existing cementitious materials with high concentrated sulfate compounds results in formation of gypsum, which will cause strength loss in concrete members (T. Thorvaldson, 1952 & E.G. Swensen, 1968 & Mehta, P.K., 2000). In 1890, Candlot and Vicat observed sulfate attack (Bellmann, F., & Stark, J., 2007). Since then sulfate attack has been reviewed extensively in literature and the effect of sulfate ions ingress in expansion, cracking and spalling of concrete structures had been studied by various authors (Chabrelie, A., 2010 & Santhanam, M., et al, 2002 & Schmidt, T., Lothenbach, B., et al, 2009 & Skalny, J., & Brown, P.W., 2002). Chemo-transport-mechanical models have been developed

to predict the behavior of cementitious materials under sulfate attack (Idiart, A.E., López, C.M., et al, 2011 & Basista, M., & Weglewski, W., 2008 & Tixier, R., Mobasher, B., 2003). Another form of sulfate attack is Thaumasite Sulfate Attack (TSA) which affects calcium silicate hydrates and transforms cement matrix into a non-adhesive mass, reducing effective cover of concrete and increasing the potential of reinforcement corrosion (Brueckner, R., Williamson, S.J., & Clark, L.A., 2012 & Thaumasite Expert Group, 1999). In concrete structures exposed to aggressive water, sulfuric acid attack may cause TSA (Oberholster, R.E., et al, 1983). Low temperature, mobile water and calcium carbonate are essential for the occurrence of TSA (Bellmann, F., & Stark, J., 2007). Early investigation of the thaumasite was carried out in 1965 by Erlin and Stark (Bellmann, F., & Stark, J., 2007) and it has a major role in some reported damage cases since then (Oberholster, R.E., 2002).

The tunnel which is discussed in this paper is located at the southwest of Iran. The length of the tunnel is over 48.7 kilometers. It will be used to carry water to agricultural lands. During construction, severe corrosion and damage in concrete segments have been observed (Figs. 1 & 2).

Figure 1. Field observations of tunnel damages.

Figure 2. Liquefaction of the concrete segments surface layers.

At severely damaged parts of the tunnel, surface layers of concrete segment were liquefied and accumulated. Because of H_2S gas high concentration (up to 1050 ppm) and strong water seepage, the idea of chemical attack involving sulfate ions was proposed. This paper discusses the experimental investigation performed on core specimens which have been extracted from tunnel concrete segments in order to evaluate the current situation.

2 MATERIALS AND METHODS

The tunnel project, which is discussed in this paper is divided in four parts and the fourth part which is 14700 meters, is evaluated. In order to assess the damage in concrete wall segments of the tunnel, two core specimens have been extracted in every 500 meters. 5 additional core specimens have been extracted from the ceiling of the tunnel in the location of severely damaged concrete segments. The total number of 69 core specimens has been evaluated as follows: Compressive strength, electrical resistance and Water absorption capacity tests have been carried out on 64 specimens. Finally, 85 sulfate ion tests have been implemented.

2.1 *Compressive strength test*

The compressive strength test has been performed to evaluate the bearing capacity of the tunnel concrete segments. The results of these tests can provide an assessment of concrete quality and damage propagation in the tunnel concrete segments. There are several standards (ACI 318-71, 1971, BS 1881: Part 120, 1983, ASTM C 42, 1999) which specify the necessary procedures regarding the determination of compressive strength of core specimens. Height to diameter ratio, reinforcements and moisture percentage influence obtained compressive strength in specimens. The diameter of extracted core specimens was 75 mm. Core specimens were placed in water for at least 48 hours. The water temperature was 20 C. After specimens had been saturated, compressive strength tests were conducted.

2.2 *Electrical resistance test*

Concrete electrical resistance is related to its permeability and environmental conditions. Higher permeability allows aggressive ions to penetrate concrete easier, which consequently increases electrical conductivity and decrease electrical resistance. Therefore a higher electrical resistance indicates a better performance against aggressive ions.

Florida method was used to measure electrical resistance of specimens (FM 5-578, 2004).

2.3 *Water absorption test*

Concrete porosity allows water containing chemical substances to leave off aggressive components. Remaining chemical substances can cause chemical attack. Therefore, evaluating porosity and permeability is a vital part of durability assessment of concrete structures. The water absorption test indicates concrete porosity and permeability by indicating its ability to absorb water (and possibly hazardous water-soluble components). Core specimens were dried in an oven at 105 C for 72 hours (BS 1881- Part 122, British Standard, 1983). Then they were carefully weighted and exposed to ambient temperature. Finally, they were submerged in water for half an hour and then weighed. The water absorption value is then calculated as the difference between specimen weights.

2.4 *Sulfate ion test*

As presented in previous sections, sulfate attack can affect concrete durability greatly. Also, bacterias change H_2S gas to sulfuric acid which reacts with the cement phase, transforming calcium hydroxide to calcium sulfate and damages concrete. Therefore, measurement of existing sulfate ion can provide an insight for evaluating concrete health conditions. Iranian concrete standard (ABA, 2000) states that water-soluble sulfate content (in the term of So_3) should not exceed than 4% of cement weight and total sulfate content should not exceed than 5% of cement weight. The total existing sulfate value is calculated as the sum of sulfate content in all of the components of concrete. "Determination of sulphate content—Test method" states that total sulfate content can be obtained by acid extraction (ISIRI 8672, 2007). It is generally accepted to use the same methods applied to aggregates and soil to cementitious materials as well. The documentations showed that cement grade used in concrete segments mixture is 425 kg/m^3. Assuming that the specific weight of the concrete was equal to 2350 kg/m^3, it is deducted that water-soluble sulfate content and total sulfate content should be less that 0.72% and 0.9%, respectively. An instrument for preparing powder samples was designed and assembled in Concrete Technology and Durability Research Center, Amirkabir University of Technology. Powder samples were prepared from specimens of tunnel inner and outside sections and were tested for both soluble and total sulfate content. Tests were performed on powder samples at every 5 mm of first 25 mm of specimen depth.

3 RESULTS AND DISCUSSION

3.1 *Compressive strength test results*

The results are presented in Figure 3. Compressive strength of 3%, 53.3%, and 43.7% of specimens were between 5–20 MPa, 20–35 MPa and 35–50 MPa respectively. Since the design value of 28-day compressive strength was 35 MPa, 56.3% of specimens had lower compressive strength than the design value. This strength loss may occur due to sulfate attack or poor construction quality. To distinguish the source of strength shortcoming, 24 core specimens were extracted from 8 segments which had already been stored in construction site. The diameter of these specimens was 101 mm. After preparing accordingly, this set of specimens has been tested. Compressive strength of all the specimens was above 35 MPa. Therefore, it can be deducted that the lack of sufficient strength is mainly due to an external agitating factor like sulfate attack.

3.2 *Electrical resistance test results*

As shown in Figure 4, electrical resistance of specimens varied between 16 to 55 kΩ-cm. According to Persian Gulf concrete durability standard, concrete corrosion due to aggressive ion ingress in concrete samples with electrical resistance bellows 5 is less likely (Persian Gulf concrete durability standard, 2006).

3.3 *Water absorption test results*

As shown in Figure 5, water absorption value for specimens varied from 3.2% to 7% with a mean value of 5%. 92% of specimens had a water absorption value over 4%. Persian Gulf concrete durability standard recommends water absorption value under 2%, which concludes a high potential for

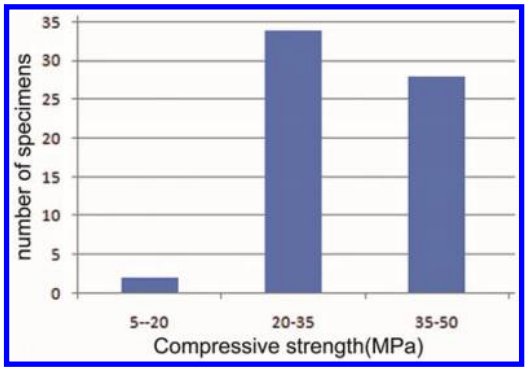

Figure 3. Compressive strength values of core specimens.

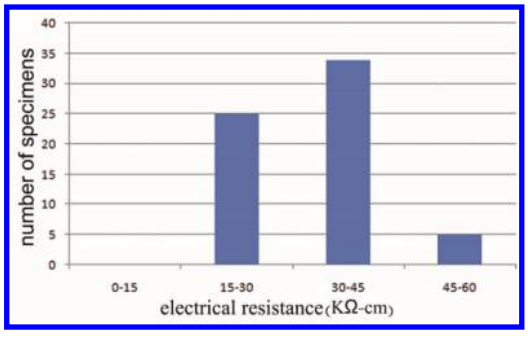

Figure 4. Electrical resistance values of core specimens.

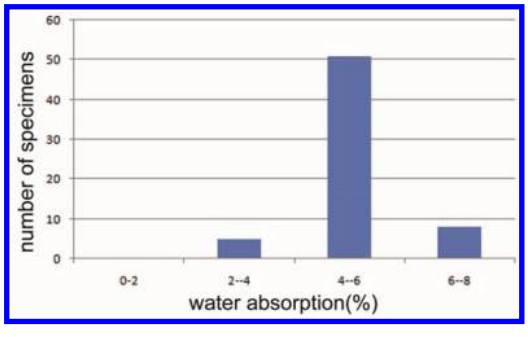

Figure 5. Water absorption values of core specimens.

concrete permeability, providing a suitable environment for aggressive ions infiltration (Persian Gulf concrete durability standard, 2006).

3.4 *Sulfate ion test results*

Figure 6 shows that, except for 3 specimens, water-soluble sulfate content in tunnel inner sections specimens is less than 72% in all depths. Also, water-soluble sulfate content deviation from the value prescribed by the standard in those 3 specimens is less than 0.1%. Because of the calcium sulfate negligible solubility these results can't be meaningful without further investigation. Therefore, acid extraction had been performed to provide total sulfate content of specimens. Figure 7 shows that the majority of specimens had total sulfate content above 0.9%. Total sulfate contents decreased by depth increment and reached to allowable value at 20 mm depth except for 4 specimens. Figures 8 & 9 show water-soluble and total sulfate contents in the specimens of the tunnel outer sections. The water-soluble sulfate content is less than 0.72% in all samples at all depths and except for 3 specimens, total sulfate content is less than 0.9% in all samples at all depths. These 3 specimens have total sulfate content more than 0.9% at 5 mm

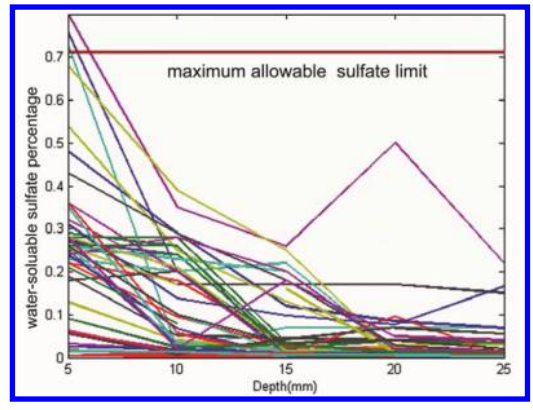

Figure 6. Water-soluble sulfate content of core specimens from inner sections of the tunnel.

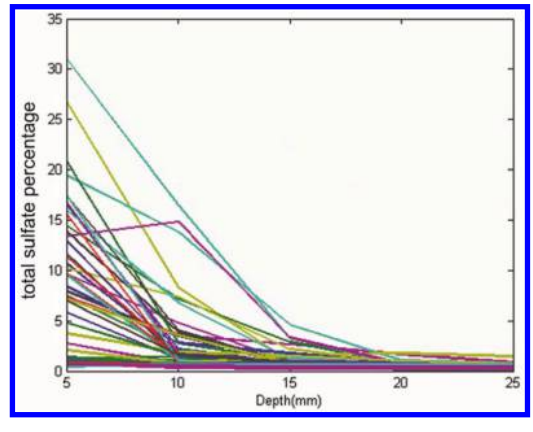

Figure 7. Total sulfate content of core specimens from inner sections of the tunnel.

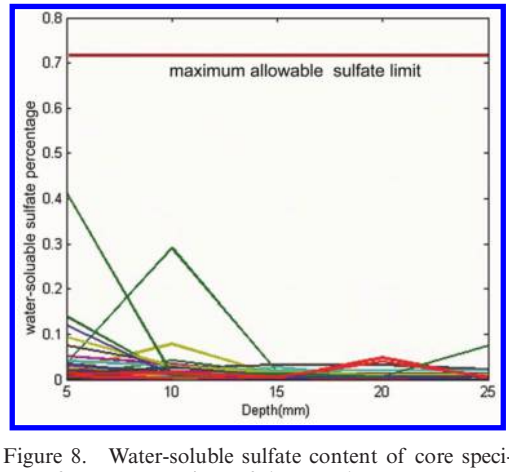

Figure 8. Water-soluble sulfate content of core specimens from outer sections of the tunnel.

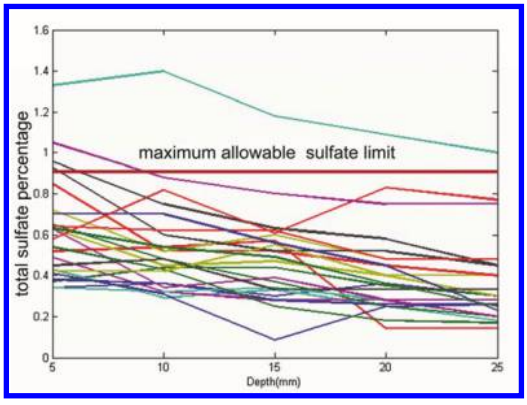

Figure 9. Total sulfate content of core specimens from outside sections of the tunnel.

depth which reach allowable total sulfate content at 10 mm depth for two of them.

4 CONCLUSION

Field observations of damaged concrete segments and H_2S gas existence inside the tunnel suggest that the mentioned tunnel suffers from chemical attack. In order to evaluate the current hypothesis 69 core specimens were taken from tunnel concrete segments and compressive strength, electrical resistance, water absorption and sulfate ion tests were performed. Results show that compressive strength was decreased, which implies that an external factor reduced specimens compressive strength. Also, specimens have high permeability which facilitates possible aggressive ion ingress. Although the water-soluble sulfate content in the tunnel inner section specimens is less than the prescribed value, total sulfate content is more than allowable value. The difference between two values is mainly due to calcium sulfate, which is the main product of sulfuric acid attack. Therefore, it can be concluded that the sulfuric acid attack which is produced by bacterias from H_2S could be the cause of tunnel segment damages. A comparison of total sulfate content between specimens from tunnel segments and segments stored in site supports this hypothesis. Stored segments have much less total sulfate content.

Also, because of sulfate ions, lime aggregates used in the tunnel concrete segments, low temperature in some parts of the tunnel and humid environment, it is possible that TSA has happened. The tunnel which is discussed in this paper is located below ground water level which helps seepage. Seepage provides the necessary water to carry chemical substances and accelerates chemical damage mechanism. Field observation of concrete Liquefaction supports TSA occurrence.

REFERENCES

Aashto, S. (1999). ASTM C 42/C 42M-99 Standard Test Method for Obtaining and Testing Drilled Cores and Sawed Beams of Concrete.

ACI Committee 201. (1962, December). Durability of Concrete in Service. In ACI Journal Proceedings (Vol. 59, No. 12). ACI.

Basista, M., & Weglewski, W. (2008). Chemically assisted damage of concrete: a model of expansion under external sulfate attack. International journal of damage mechanics.

Basista, M., & Weglewski, W. (2008). Micromechanical modeling of sulfate corrosion in concrete: influence of ettringite forming reaction. Theoretical and Applied Mechanics, 35 (1–3), 29–52.

Bellmann, F., & Stark, J. (2007). Prevention of thaumasite formation in concrete exposed to sulfate attack. Cement and Concrete Research, 37 (8), 1215–1222.

Brown, P.W., & Badger, S. (2001). Reply to the discussion by William G. Hime and Stella L. Marusin of the paper "The distribution of bound sulfates and chlorides in concrete to mixed NaCl, MgSO4, Na2SO4 attack".

Brueckner, R., Williamson, S.J., & Clark, L.A. (2012). The effects of the thaumasite form of sulfate attack on skin friction at the concrete/clay interface. Cement and Concrete Research, 42 (2), 424–430.

BS 1881—Part 122, 1983, "Method for Determination of Water Absorption", British Standard.

Chabrelie, A. (2010). Mechanisms of degradation of concrete by external sulfate ions under laboratory and field conditions.

Designation: FM 5-578, 2004, Florida Method of Test for Concrete Resistivity as an Electrical Indicator of its Permeability.

FM 5-578, 2004, Florida method of test for Concrete Resistivity as an Electrical Indicator of its Permeability, Florida Department of Transportation.

Ghafoori, N., Diawara, H., & Beasley, S. (2008). Resistance to external sodium sulfate attack for early-opening-to-traffic Portland cement concrete. Cement and Concrete Composites, 30 (5), 444–454.

Idiart, A.E., López, C.M., & Carol, I. (2011). Chemo-mechanical analysis of concrete cracking and degradation due to external sulfate attack: A meso-scale model. Cement and Concrete Composites, 33 (3), 411–423.

Iranian concrete standard, 2000, Iranian Organization of Management and Planning.

ISIRI 8672, 2007, Determination of sulphate content—Test method, Institute of Standards and Industrial Research of Iran.

Kosmaka, S.H., & Panarese, W.C. Design and Control of Concrete Mixtures, 1988. Portland cement Association, Skokie, IL.

Mathis, R.P. (1996). Freezing and thawing, deicing salt, and sulfate resistance of concrete pavers (Doctoral dissertation, Southern Illinois University at Carbondale).

Mehta, P.K. (1986). Concrete. Structure, properties and materials.
Mehta, P.K. (2000). Sulfate attack on concrete: separating myths from reality. Concrete International, 22 (8).
Oberholster, R.E. (2002). Deterioration of mortar, plaster and concrete: South-African laboratory and field case studies. In Proceedings of the first international conference on thaumasite in cementitious materials, Garston, UK (pp. 19–21).
Oberholster, R.E., Van Aardt, J.H.P., & Brandt, M.P. (1983). Durability of cementitious systems. Bames, P. Structure and performance of cements. London, 365.
Persian Gulf concrete durability standard, 2006, building and construction research center, Ministry of construction and urban development of Iran.
Santhanam, M., Cohen, M.D., & Olek, J. (2002). Mechanism of sulfate attack: a fresh look: part 1: summary of experimental results. Cement and concrete research, 32 (6), 915–921.
Schmidt, T., Lothenbach, B., Romer, M., Neuenschwander, J., & Scrivener, K. (2009). Physical and microstructural aspects of sulfate attack on ordinary and limestone blended Portland cements. Cement and Concrete Research, 39 (12), 1111–1121.
Skalny, J., & Brown, P.W. (2002). Sulfate attack on concrete. Taylor & Francis.
Standard, A.C.I. (1971). 318-71, Building code requirements for reinforced concrete.
Standard, B. (1983). BS 1881-122: Testing concrete. Method for determination of water absorption.
Standarts, B. (1983). BS 1881 Part 120 Method for Determination of the Compressive Strength of Concrete Cores. British standards.
Swensen E.G. (Ed.), 1968, Performance of Concrete, Univ. Of Toronto Press, Toronto.
Thorvaldson, T. 1952, Chemical aspects of durability of cement products, 3rd ICCC, Cement and Concrete Association, London, pp. 436±485.
The Thaumasite Form of Sulfate Attack: Risks, Diagnosis, Remedial Works and Guidance on New Construction; Report of the Thaumasite Expert Group, 1999, Department of the Environment, Transport and the Regions.
Zivica, V., & Bajza, A. (2001). Acidic attack of cement based materials—a review. Part 1. Principle of acidic attack. Construction and Building Materials, 15 (8), 331–340.

Concrete Repair, Rehabilitation and Retrofitting IV – Dehn et al. (Eds)
© 2016 Taylor & Francis Group, London, ISBN 978-1-138-02843-2

In-situ concrete strength assessment based on Ultrasonic Pulse Velocity (UPV), rebound, cores and the SonReb method

Frank Papworth
BCRC, Perth, Australia

David Corbett
Proceq, Switzerland

Reuben Barnes
PCTE, Perth, Australia

ABSTRACT: The strength of concrete in a new structure is sometimes called into question. This may be due to cylinders not being taken, poor cylinder production, transport or testing, the actual concrete strength being low or the suspicion that in-situ cylinders are not representative of in-situ concrete. Whatever the reason testing of the in-situ concrete is generally called for. This paper gives a brief outline of the key aspects of strength assessment including a review of concrete supply and testing records, extent of testing required, assessment by cores to AS 1012.14 (1) and AS 3600 (2), ultrasonic (direct and indirect methods) and rebound hammer testing and analysis of in-situ strength using cores and NDT results (including published methods such as EN 12504 (3), EN 13791 (4), BS 6089 (5) and those under consideration by RILEM). If the concrete strength is found to be low, a structural analysis has to be undertaken. The paper includes information of six projects assessed. In two, strengths were low across the whole mine site but in each case only one structure required strengthening. In another, very low strength was identified at an early stage and a risk assessment identified the structure should be replaced. In the others, strengths were found to be adequate.

1 INTRODUCTION

For many years CSTR 11 (7) was the revered document on assessment of concrete compressive strength from cores. This was updated in 1987 (8). In 2002 CIA Z11 (9) was published and became the Australian reference for assessment of core strengths as a supporting document for AS 1012.14 (1). AS1012.14 provides performance requirements on sampling, conditioning, and reporting on cores and calls on AS 1012.9 (6) as the method of testing concrete samples for compressive strength. However, in 2004 a project report on core strengths by the Concrete Society (10) provided updated information on tests from a range of samples and findings were subsequently incorporated in an updated BS 6089 (5) which is complimentary to BS EN 13791 (4), the European standard on testing concrete strength in structures. Consequently CSTR 11 (7,8), and AS1012.14 (1) and CIA Z11 (9) which are at least partly based on them, should be used with caution as some of the analysis methods have been superseded. The Concrete Society issued Advice Note 43 (11) in 2013 which summarises some of the approaches in the new European standards. In this paper some of the differences between European Standards and the methods used in Australia based on CSTR 11 are given.

BS EN 13791 now provides clear guidance on the use of ultrasonic pulse velocity and rebound hammer testing. These methods enable rapid scanning of the concrete to detect variations in strength and BS EN 13791 provides guidance on how their use can be incorporated into reducing the number of cores required. In this paper the methods are outlined with specific reference to direct and indirect UPV measurements and combined use of rebound, UPV and core strengths using the 'SonReb' method.

An outline of the strength assessment on seven projects is given in the paper to show the variety of approaches that may be appropriate. For each project a durability assessment was also undertaken but this is not included here as the paper's focus is strength and structural assessment. The methods employed for strength assessment range from reliance on 28 day cube strengths to the use of cores,

UPV and rebound testing. The subsequent analysis of the structures included a full structural analysis to determine structural reliability and risk assessment if there was a reduced reliability.

2 METHODS OF TESTING

2.1 *Cores*

To maximise the number of cores meeting code requirements and to minimise damage to the core and structure, the engineer should ensure that the coring contractor has adequate experience in using his equipment to take cores for the specified purpose. On one project in remote Botswana the contractor arrived with a brand new coring machine, no hold down anchors and 5 people. His first core failed the requirements of AS 1012.14 because the machine was not properly secured and because of stop start coring. Being a remote location it took two days to get the team working.

Before coring the reinforcement locations are carefully mapped and marked with due allowance for bar diameter. The upper reinforcement layer can generally be identified using a covermeter but this may miss saddles which may be identified using ground penetrating radar.

Assessment of core strength can be based on BS EN 13791 and BS 6089. A comparison of these with current Australian standards is given in Table 1.

2.2 *Rebound*

The original rebound hammer measured the hardness of a material by the degree of rebound. The instrument worked by firing a known mass using a standard spring loading to impact on a rod held in contact with the surface being tested. When the mass hits the rod it rebounds to an extent that depends on the hardness of the surface in contact with the rod. The original rebound hammer measured the rebound value R mechanically as a distance that the mass rebounded from the concrete surface. Extensive testing carried out in the late 1950's gave correlation curves between rebound value and concrete compressive strength.

In 2007 an electronic version of the original rebound hammer was introduced. This instrument measures rebound value (now Q) as the quotient between the velocity of the hammer mass just before and after impacting the rod. The validity of the new measurement principle has been recognized by the major standards bodies.

It should be noted that Q-values and R-values are not interchangeable. Correlation curves developed for the original rebound hammers cannot be used with Q-value and correlation curves developed for the new hammer cannot be used with the

Table 1. Australian and european standard requirements for assessing in-situ concrete strength.

	Not yet harmonised with European practice (based on CSTR 11)		State of the art documents on in-situ strength assessment
	AS 1012.14	CIA Z11	BS EN 13791/BS6089
Core diameter	75 mm	75 min or 2.5 × agg size	100 mm (increase number of cores if using diameters down to 50 mm)
Core length:diameter ratio	Close to 2:1	1 to 2 (ideally 1.9 to 2)	1 to 2
Actual strength corrections			
Correction l:d	k_1 = 1 for l/d = 2 reducing in steps to 0.87 for l/d = 1		$K_{cyl} = 2.0/(1.5 + 1/(l/d))$
Correction rebar present	–	k_2 by formula	Avoid rebar
Correction core axis	–	k_3 = 1 perp. to casting direction and 1.08 if parallel	Influence noted but UK Annex NA says no allowance to be made
Core locations limits			
Vertical pours	–	Not from top 20% up to 300 mm	Exclude top 300 mm. Core top third
Face of concrete	–	Not within 50 mm of face	Not within 50 mm of face
Number of cores where suspect batch	–	3 from each suspect batch	15 with no NDT, 9 with NDT. Move to reduce the number with NDT
Conditioning	Wet 3d or air 7d	Dry (7d) as AS 3600	Air 3d but allowance can be made for wet cure
End preparation	AS 1012.9	Sulphur cap or ground ends	Ground ends recommended
Provision for outliers	–	No	Yes
NDT assessment	–	–	UPV, pullout and rebound accepted as means of reducing core numbers

classical hammer. The manufacturer provides a strength relationship between Q values and compressive strength based on a lower 10th percentile curve. They do not provide direct relationships between Q values and R values, as testing on various types of concrete have shown that the relationship is not constant.

When assessing in-situ compressive strength using cores, EN 13791 requires at least 15 cores to be taken to establish the insitu concrete strength. The number of cores to be taken may be reduced to 9 when used in combination with NDT tests such as rebound hammer or ultrasonic pulse velocity.

In the German national annex to EN 13791 there is also the possibility to assign a compressive strength class based on rebound hammer testing alone, as in many cases, it is not allowed to take cores. EN 13791 is currently under review and there are proposals for reducing the number of cores further when used in combination with NDT testing and also to generally accept the method described in the German national annex.

Testing should be undertaken in accordance with EN 12504-2. A test location should be a minimum 100 m thick, 300 × 300 mm test area, minimum of nine readings, impact points >25 mm apart, surface clean and smooth. Nine such test locations are required for a test region as described in EN 13791. A core should also be taken at each test location to establish the correlation. The method then uses the core correlation to shift a base correlation curve upwards. The same method may be used with ultrasonic pulse velocity.

2.3 *Ultrasonic Pulse Velocity*

UPV can be determined in number of ways direct, indirect and semi-direct. Only the first two are discussed here. Direct UPV is the most reliable as the velocity is measured across the entire element and gives an average velocity for a large thickness of concrete. Direct UPV can also be measured on cores to give a direct correlation between UPV and core strength.

However in cases where access to only one face is possible a direct velocity measurement is not possible. Yaman (16) developed a method of measuring the indirect velocity over 4 head spacings (200, 250, 300 and 350 mm). This is very similar to the surface velocity method described in Annex A of EN 12504-4. The slope of a straight line plot of time vs head spacing (Fig. 1) gives an indirect velocity that is very close to the direct velocity for homogeneous specimens. The principle difference between direct and indirect UPV's is that direct measurements are largely through the bulk concrete and indirect measurements are largely through the near surface but Yaman's five point method avoids direct

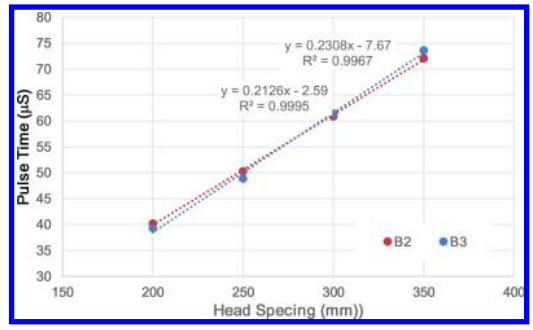

Figure 1. Indirect pulse velocity using Yaman's five point method.

surface effects such as carbonation and finishing. This is particularly useful for assessing slabs. It should be noted however, that typically concrete is an inhomogeneous material and the difference between indirect and direct pulse velocities can vary significantly if surface effects are deep.

In the indirect mode a particular issue is the low signal level compared with direct measurements. The first pulse may not trigger the timer unless the gain is suitably increased. For such measurements, it is advisable to use a waveform display to be certain of correct triggering. This may or may not be apparent from the best fit line through the four data points. Testing should otherwise be undertaken in accordance with EN 12504-4.

2.4 *SonReb*

One issue with combined use of NDT and cores for strength assessment is the number of core correlations required according to EN BS 13791. By reducing uncertainty by combining two NDT measurements the number of correlation points decreases.

Breysse (15) describes the SonReb method of combined UPV and Rebound measurement as discussed by RILEM Technical Committee TC 207-INR as follows: *"This combination has received the name of SonReb, for Sonic and Rebound. Rebound and ultrasonic pulse velocity measurements can be carried out quickly and easily. The underlying concept is that if the two methods are influenced in different ways by the same factor, their combined use can cancel the effect of this factor and improve the accuracy of the estimated strength."* Breysse gives two approaches to the combined assessment based on best fit of data but the multivariate approach A is preferred, i.e.: Approach A: $fc = aV^bR^c$ where a,b and c are constants (1.15×10^{-10}; 2.6 and 1.3 respectively); V is UPV; R rebound number.

Although standard values for a, b and c are given project specific values are determined.

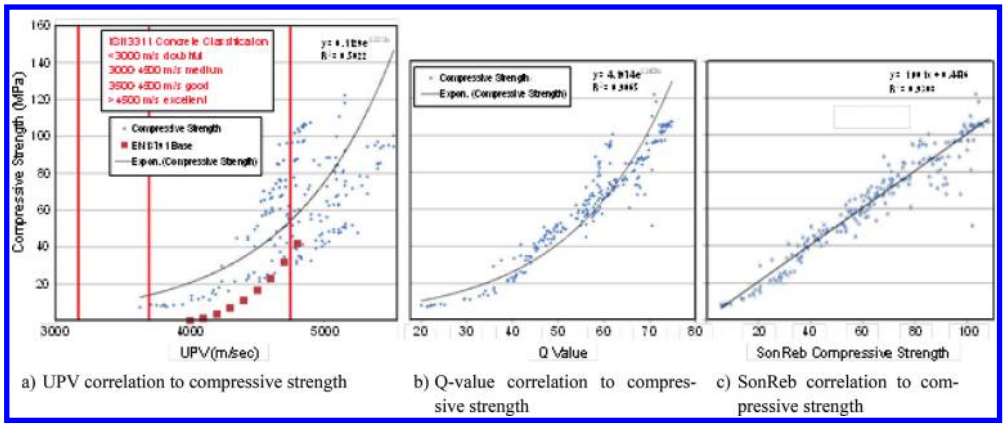

a) UPV correlation to compressive strength b) Q-value correlation to compressive strength c) SonReb correlation to compressive strength

Figure 2. Data from 240 cubes to establish SonReb calibration curves for Q value.

Generally, the SonReb method provides an increase in correlation accuracy when compared with using either the rebound method or UPV method in isolation.

The data, presented in Figure 2 was collected by the rebound hammer manufacturer to establish a SonReb curve using the Q-value. It illustrates the benefit of using the combined method. The SonReb method has been established as a national standard in several countries including Italy and China in particular and is currently being considered by the RILEM TC-249-ISC committee dealing with in-situ compressive strength estimation.

3 STRUCTURAL ASSESSMENT OF NEW CONCRETE STRUCTURES IN A GHANA MINE

Shortly after construction deterioration of the primary crusher approach slab led to a preliminary investigation of the strength of concrete. This indicated that there was cause to suspect that the strength of concrete could be lower than design. Subsequently a detailed investigation of the concrete to identify if there were any significant deficiencies in construction was undertaken.

For cores testing SANS standards were followed but as there were no SANS standards for non-destructive tests international standards were followed. The specified strengths varied and are shown together with core strength results in Table 2.

The large fraction of cores that failed the individual and average strength requirements, and the margin by which some cores failed, was a serious concern.

Rebound hammer and core testing results from the same location are shown in Figure 3. The best fit relationship is achieved at compressive strength = $2.161e^{0.043x}$ where x is the Q value. The rebound results are from the surface of slabs and

Table 2. Core test results from Ghana mine.

Element orientation	Vertical		Horizontal	
Specified strength	40 MPa	25 MPa	40 MPa	25 MPa
No of cores	3	4	–	19
No of comp. tests	3	7	–	28
Avg strength (MPa)	34.0	16.1	–	17.8
Std dev. (MPa)	–		–	6.3
% Failing ind. result	0%	57%	–	54%
% Failing avg. result	0%	100%	–	71%

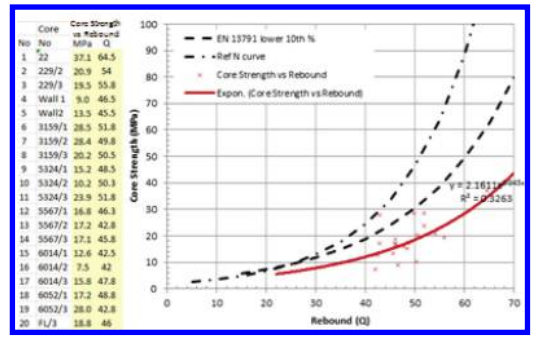

Figure 3. Core strength vs rebound hammer.

the finishing may account for why a high Q value is achieved for a given compressive strength but more likely was that carbonation had occurred hardening the surface strength. This effect means rebound results on the top of the slab are not an effective method of assessing bulk strength. Consequently the assessment was based on core strengths.

Based on the core strength tests an equivalent characteristic cylinder strength of 15 MPa was determined for the 25 MPa concrete and 25 MPa for 40 MPa concrete. The structural assessment was undertaken in conjunction with the original designers with free and unfettered access to the design calculations. Jointly with the designer critical elements were identified and checked based on the strengths of 15 MPa and 25 MPa and 10 year design life. The structural review identified all structures behaved acceptably at the actual in-situ strengths except for one tall conveyor support. Additional cores from this structure indicated there were still some concerns and hence strengthening was instigated.

4 STRUCTURAL ASSESSMENT OF NEW CONCRETE STRUCTURES AT A BOTSWANA MINE PLANT

25 MPa and 32 MPa concrete was specified for footings/slabs and walls/columns respectively but review of the cube test results showed a much lower strength was achieved in practice. Cores were taken from various locations and results were consistent with the cube results. Multiple cube results from the same batch tested at the same age were quite consistent and 7 day results were reasonably consistent at 67% of the 28 day results. This indicates that, failing an unexpected consistent error in testing, the results are a realistic and able to be used as a true indication of the strength of concrete supplied. The results are summarised in Table 3.

Compressive strengths from 2 cores taken from each of three different bases gave a characteristic in-situ cylinder strength of 17.5 MPa. This was marginally higher than the 28 day cube results and may have an improvement due to the aging.

28 rebound hammer results provided had an average cube strength of 28 MPa and a standard deviation of 5.6 MPa to give a characteristic cube strength of 18.8 MPa.

A review of the mix indicated low coarse aggregate volume and a high proportion of crushed sand. The mix would have had a high water demand and it was concluded that to achieve a workable concrete extra water would have likely been added.

Hence for the project it was determined that:

a. No further NDT testing was generally required as adequate data was available to give a reasonable estimate of the concrete strength. Originally the client had asked for more detailed NDT testing to show which elements had low strength concrete.
b. A 28 day characteristic compressive cylinder strength of 15 MPa was to be used for structural assessment of all bases except those produced between 4–9th May.
c. For the concrete poured 4–9th May the location of the concrete placed was to be identified and design undertaken for strengthening to take the full design loads.

Table 3. Summary of 28 day compressive strength test results.

Period	4th–9th May	Remainder
f'_c cube (MPa)	11	19
f'_c cylinder (MPa)	9	15

The structural assessment was undertaken of all structures by review of the original designs. This showed that in general the 15 MPa cylinder strength was adequate. The exceptions were:

a. Primary Crusher Base Slab—Development lengths up to 400 mm to short due to low strength and low cover. Strengthen to reduce stresses or effectively increase development lengths.
b. Primary Crusher Rear Wall—Will crack as applied moments are 3 times the moment capacity.

5 STRUCTURAL ASSESSMENT OF NEW CONCRETE IN AN AUSTRALIAN MINE PLANT

On this project the concrete strength was called into question when the supervisor recorded that after taking cylinders for strength assessment the concrete water was added to the mix for placement. Cores and NDT were used to establish the actual characteristic strength of 18 MPa for most elements, well below the minimum specified strength of 32 MPa.

Structural analysis was undertaken to show if these low strengths might be acceptable. A foundation slab was considered as 1 m wide strips with actual load points imposed and resisted by soil spring nodes. Although the concrete strength was only 18 MPa the authors believe that it is reasonable to extrapolate outside the range of characteristic compressive strengths of 20 MPa to 100 MPa, specified in Clause 1.1.2 of AS3600, provided that a reliable coherent set of core results can be obtained. Of note is the anchorage bond length where requirements will increase beyond those in AS3600 in highly stressed elements. The analysis undertaken indicated that although capacities were significantly reduced most parameters were predicted to be acceptable except for shear and hence a risk assessment was undertaken.

Risk is conventionally assessed by ISO 31000 (12) based on a combination of consequence and likelihood of failure. For some failure modes full probabilistic modelling can be undertaken to assess failure likelihood quite accurately. Where these methods are not possible a qualitative approach

can be followed. The consequence of structural failure can vary significantly.

Discussions with the owner identified that the increased likelihood of failure was unacceptable because when combined with the consequence of failure the risks during operations became unacceptable. Consequently the concrete was replaced.

6 STRENGTH ASSESSMENT OF A NEW AUSTRALIAN SHOPPING CENTRE FLOOR SLAB

The strength of a concrete slabs on grade had been called into question. The strength of the surface layer is highly affected by finishing and curing and hence assessment using rebound hammer testing is not recommend as the results are very dependent on near surface properties. It was agreed to undertake widespread testing using indirect ultrasonic pulse velocity to show potential variations in strength. Cores were undertake for calibration of the UPV. Rebound hammer results were also taken over a wide area to determine if it gave any further insight into concrete performance.

UPV results were taken using the five point indirect method. Results were recorded on a spreadsheet which automated a linear regression analysis to check the four results gave adequate correlation (Table 4). The velocities, and the rebound results, were plotted in a spreadsheet using conditional formatting to highlight variations (Table 5).

In the case of the rebound results there appears to be two distinct areas where the 10 percentile strengths are 24.9 and 38.2 MPa. These variations are not seen in the UPV results. The Rebound variations may be due to variations in finishing and curing of the two pours and be limited to surface effects.

The UPV results were correlated with strength and gave the following relationship:

Strength (MPa) = $8.5344e^{0.3173v}$ where v is ultrasonic pulse velocity in m/s.

Converting the UPV to strength results gave a plot of strength as shown in Table 6. The colour coding is based on highlighting areas where the strength is less than the required 32 MPa.

7 STRENGTH ASSESSMENT OF NEW COLUMNS AND WALLS OF AN AUSTRALIAN OFFICE TOWER

S65 concrete was poured in columns and stair well walls. Cylinder results were marginal and hence strength assessment was requested. An assessment of in-situ strength was undertaken using the SonReb method with UPV and rebound measurements calibrated against core strength tests. The process used for the SonReb method was:

1. Mark out reinforcement grid on the concrete surface using GPR so that UPV test results avoided the influence of reinforcement as far as possible.
2. Mark out sixteen measurement points for each element. These comprised eight pairs of measurement points precisely on opposite faces of the element. Typically four measurement points were at 0.5 m, 1 m, 1.5 m and 2.0 m above base level so that strength with height could be assessed. No significant variation was found (Fig. 4).
3. Assess the path length for the measurement points.
4. Take direct UPV measurements using digital UPV equipment with the transmitter on one face and receiver on the other for each of the eight

Table 4. Indirect UPV data for shopping centre floor slab. D is the transmitter/receiver separation and T the corresponding wave transit time.

Separation	(mm)	Result No	B1	B2	B3	B4	B5	B6	B7	B8	B9	B10	B11
D1 (mm)	200	T1 (μs)		40.2	39.3	39.2	39.6	41.6	38.7	39.9	38.2	41.4	39.4
D2 (mm)	250	T2 (μs)		50.3	48.9	49.9	51.8	49.7	49.2	49.9	49.8	50.2	52.4
D3 (mm)	300	T3 (μs)		60.9	61.4	62.9	62.1	60.3	61.3	60.1	63.7	65.9	61.4
D4 (mm)	350	T4 (μs)		72.1	73.6	73.3	73.9	74.2	72.9	72.7	72.1	73.1	72.7
		Sparkline											
		Velocity (m/sec)		4701	4318	4329	4413	4547	4356	4589	4289	4423	4571
		RSQ		0.999	0.997	0.998	0.999	0.986	0.999	0.997	0.992	0.980	0.995

Table 5. Colour coded plot of rebound and UPV test results.

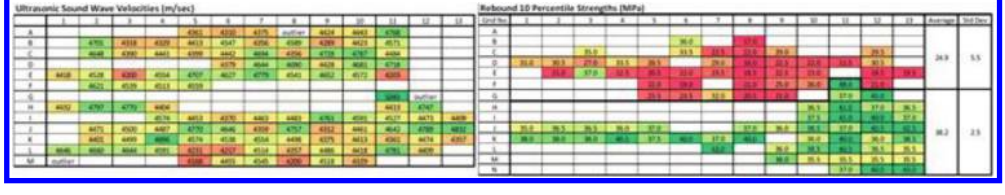

Table 6. Plot of compressive strength estimated using UPV measurements.

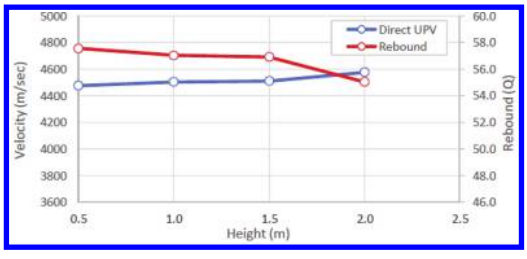

Figure 4. UPV and rebound with height for a shaft wall.

pairs of measurement points. The transmitter and receiver were then swapped at each pair of points to give sixteen direct measurements. The UPV equipment's built in measuring process takes multiple measurements to give an average of several reading for each result. Results were also verified by the strength of the received signal and only highly reliable results were recorded.

5. Prepare the concrete surface using a grinding stone at each of the sixteen points and take rebound measurements using the digital rebound hammer. Ten rebounds were used to give one Q value.
6. Enter the data in the results spreadsheet prepared for the project to verify results were sensible and consistent. The formula for strength generally used is $f_{ck} = a.V^b.Q^c$ where a, b and c are constants V is the ultrasonic pulse velocity in m/s. Q is the rebound value as given in RILEM (14).

8 STRENGTH ASSESSMENT OF 50 YEAR OLD BASEMENT COLUMNS IN AN AUSTRALIAN BUILDING

On this city centre project the building height was to be increased adding several new floors of office space. This translated to additional load in the basement columns and diaphragm wall. The existing structure had reached its 50 year design life and hence a durability and strength assessment was undertaken to confirm that the load capacity was adequate and that the structure would provide an additional 50 year life commensurate with the requirements for the new structure.

The strength assessment was in two parts. Cores were taken from walls, columns and slabs. For the more critical columns a wider assessment of strength was required. This was achieved by correlating direct UPV results with core strengths and then using UPV results to give an indication of in-situ strengths. The correlation was based on compressive strength = $1.0828e^{0.8201v}$ where v is UPV.

Piles were tested using a force vibration test as developed by Davis and Dunn (17). Testing was undertaken by measuring the response from a series of hammer blows on the concrete surface using a geophone held on the concrete surface adjacent to the hammer. Where there was no pile response the test location was moved along until a response was found. Having located the pile the test results were recorded. The received signal was put through a fast Fourier transform to give Mechanical Admittance and Frequency. Mechanical Admittance gives the load deflection curve based on wave theory. Frequency gives parameters of the pile model. Information obtained includes pile length, minimum pile diameter, presence of an end bulb, concrete modulus and safe pile load.

9 STRENGTH ASSESSMENT OF OLD SHOPPING CENTRE COLUMNS IN AUSTRALIA

Testing was undertaken on ground floor columns of a shopping centre in Queensland to assess the capacity for planned extensions. No coring was allowed in the structure and so a completely non-destructive NDT method was proposed. NDT results depend on the materials used and so cylinders made using local materials were tested to create a calibration between NDT (UPV and rebound) and cylinder strengths.

Sixteen cylinders were tested. Direct UPV measurements were taken on the cylinders and then once the cylinder has been compressed to 3.5 MPa the rebound values were taken using an original rebound hammer. The cylinders were then crushed. The calibration co-efficient were assessed using the equation proposed by Samirin (18), i.e. f'c = aR + bV4. Samarin's approach was an early form of combined ultrasonic pulse velocity and rebound for strength assessment and the SonReb equation would be recommended today. Excel's 'Solver' function was used to give the values for a and b of 1.0695 and 4.96×10^{-15} respectively. The correlation achieved was 0.973.

Ten columns were tested. Two rebound hammer tests were carried out in accordance with BS 1881:202 on each face. Two UPV measurements (BS1881:203) were taken between each of the two sets of opposing faces. Care was taken to avoid any reinforcing steel by locating this first using a covermeter. Calculated strengths are shown in Table 7.

Table 7. Calculated strength form rebound and UPV measurements.

Column	1	2	3	4	5	6	7	8	9	10
Rebound Number	47.8	54.4	52.1	51.4	53.3	49.8	50	48.5	53.6	54.8
UPV (m/se)	4457.5	4300	4298.3	4173.3	4155	4295	3776.7	4175	4207.5	4100
Calculated Strength (MPa)	53.0	59.8	57.4	56.4	58.5	54.9	54.5	53.3	58.8	60.0

10 CONCLUSIONS AND RECOMMENDATIONS

All structures are different and the structural assessment requirements will depend on the circumstances of each. Testing required is unclear until historic information available is reviewed and possibly not fully understood until some preliminary tests are under taken. An overall process to structural assessment might be:

a. Determine precisely what outcome is sought.
b. Review existing data to determine what is known about the concrete and what additional information is needed. Existing construction data may be adequate.
c. Prepare a test programme that will provide the information required. A preliminary test programme may identify if more detailed is required and if so what test methods should be used. On some structures it may be necessary to base the assessment on cores alone. On others rebound or UPV measurements, calibrated against cores or cylinders of a similar mix, may be particularly useful in providing a global assessment not practical with cores. On many structures SonReb will provide the most efficient assessment method.
d. From the strength assessment undertake a structural assessment to determine if the reliability is reduced below code requirements and if so undertake a risk assessment to determine if the risk is acceptable.

ACKNOWLEDGEMENTS

The authors wish to thank their clients for involvement in their projects.

REFERENCES

[1] Standards Australia "AS 1012.14 Method of testing concrete. Methods for securing and testing cores from hardened concrete for compressive strength" Standards Association of Australia, 1991, Homebush, Australia.
[2] Standards Australia "AS3600–2009 Concrete Structures." Standards Association of Australia, 2009 Homebush, Australia.
[3] BS EN 12504 "Testing concrete in structures., Part 1 Cored specimens—taking, examining and testing in compression, (2009) Part 2 Non-destructive testing. Determination of rebound number (2012). Part 3 Determination of pull out force (2005). Part 4 Determination of ultrasonic pulse velocity (2004). BSI, London, UK.
[4] BS EN 13791 "Assessment of compressive strength in structures and precast concrete component" British Standards Institute, 2007, London, UK.
[5] British Standards "BS6089 Assessment of in-situ compressive strength in structures and precast concrete components—complementary guidance to BS EN 13791" British Standards Institute, 2010, London, UK.
[6] Standards Australia "AS1012.9—Method of testing concrete. Methods for the determination of the compressive strength of concrete specimens" Standards Association of Australia, 1999, Homebush, Australia.
[7] Concrete Society "Concrete Testing for Strength" Technical Report 11, Concrete Society, 1976, Camberly, UK.
[8] Concrete Society "Concrete Testing for Strength" Technical Report 11, Concrete Society, 1987, Camberly, UK.
[9] CIA Z11 "The Evaluation of Concrete Strength by Testing Cores" Recomme, nded Practice Z11, Concrete Institute of Australia, 2002, Sydney, Australia.
[10] Concrete Society "In situ concrete strength. An investigation into the relationship between core strength and standard cube strength." Concrete Society. Project Report 3, 2004, Camberly, UK.
[11] Crook N. "Assessment of in-situ concrete strength using data obtained from core testing." Advice Note 47, Concrete Society, 2013, Camberly, UK.
[12] ISO "ISO 31000:2009 Risk Management" International Organization for Standardization, 2009, Geneva, Switzerland.
[13] fib "The fib Model Code for Concrete Structures 2010" Fédération internationale du béton, 2010 Lausanne, Switzerland.
[14] RILEM "NDT4 Recommendation for in situ concrete strength determination by combined non-destructive methods", Réunion Internationale des Laboratoires et Experts des Matériaux, systèmes de construction et ouvrages. 1993, Bagneux, France.
[15] Breysse D. "Main challenges of non-destructive evaluation of on-site concrete strength" Concrete Repair, Rehabilitation and Retrofitting III 2012 Taylor Franicis Group, 2012, London, UK.
[16] Yaman I.S., Inci G., Yesiler N. and Aktan H. "Ultrasonic Pulse Velocity in Concrete Using Direct and Indirect Transmission" ACI Materials Journal Nov/Dec 2001 pp. 450–45.
[17] Davis A.G. and Dunn C.S. "From theory to field experience with non-destructive vibration testing of piles." Proc. Inst. Civ. Eng. Part 2, No 59, pp. 867–875, 1974.
[18] Samarin A., and Meynink, P. "Use of combined ultrasonic and rebound hammer method for determining strength of concrete structural members," Concrete International, vol. 3, no. 3, pp. 25–29, 1981.

Concrete Repair, Rehabilitation and Retrofitting IV – Dehn et al. (Eds)
© 2016 Taylor & Francis Group, London, ISBN 978-1-138-02843-2

Impact loads on concrete bridge caps—studying load distribution for recalculation of existing bridges in the ultimate limit state

M. Niederwald & M. Keuser
University of the German Armed Forces Munich, Germany

K. Goj
Building Authority at the Bavarian Ministry of the Interior, Germany

S. Geuder
Central Office for Bridge and Tunnel Construction at the Southern Bavarian Motorway Office, Germany

ABSTRACT: Bridges have to be designed for different impact situations. The load assumptions for road bridges are covering impact loads due to the impact on vehicle restraint systems. The loadings have been increased significantly within the last decade because of rising requirements regarding the containment capacity of vehicle restraint systems. Therefore new systems were developed, which are transmitting higher impact forces into the superstructure. In case of retrofitting an existing bridge with a modern crash barrier system, this leads often to the problem of insufficient load bearing capacity of the cap and the superstructure. This paper is therefore intended to study load distribution of impact forces due to impact on vehicle restraint systems in concrete caps in order to make use of load bearing reserves. This is done to give practical advises for the recalculation of existing concrete bridges for higher impact loads according to DIN EN 1991-2 (2010).

1 INTRODUCTION

The superstructures of road bridges have to be designed for different impact situations according to DIN EN 1991-2 (2010). There are two accidental load cases, which have to be considered for vehicle leaving the road and either hitting the curb of the sidewalk or the crash barrier system, which is usually mounted onto the concrete bridge cap. Especially the load assumptions for the impact on the vehicle restraint systems have changed within the last two decades and the applied impact loads have been increased significantly. This is because of the increasing demand towards higher containment capacity according to the structural codes.

Road bridges in Germany have been equipped since the 1960s with guard rails to minimize the consequences of accidents and to keep vehicles from falling of the bridge when they are accidentally leaving the driving lane. However, spectacular accidents in the past have shown that these protective devices do not always fulfil their job and especially in the case of an impact of a heavy vehicle, such as a truck or a bus, can lead to a breakthrough through the barrier by the vehicle. Such accidents are in most cases associated with deaths involved road users and enormous property damage. Because of such severe accidents one was anxious to replace the simple steel guardrail (EDSP), which is apparently inadequate for stopping heavy vehicles, by more powerful systems. The improvement and development of vehicle restraint systems was therefore the subject of intense research (Sedlacek 2004) and as a result a number of new guardrails have come on the market, which are having a better containment capacity. The higher residing effect of the new vehicle restraint systems compared to the EDSP leads to the effect, that there must be much higher loads transmitted into the bridge superstructure in the exceptional load case of a vehicle impact on the guardrail. This has meant that in Germany the amount of connection reinforcement of ø12–40 between the cap and superstructure required by the codes for the design of new bridges was nearly tripled to ø14–20 in the year 2009 (RiZ-ING 2009).

If existing bridges are considered to be retrofitted with vehicle restraint systems with a higher containment level, it is often not possible to perform the necessary verification successfully, that the existing connection reinforcement is able to safely carry the higher impact forces. The bending and shear capacity of the bridge cantilever is often unsufficient in that case. An elaborate strengthening of the superstructure or even the

replacement of the whole bridge is then often an inevitable consequence.

In order to find ways to minimize such costly remediation in the future a study has been initiated at the University of the German Armed Forces to investigate the potential of possible load distribution of impact forces in cap longitudinal direction. First results are presented in this paper.

2 IMPACT LOADS ACCORDING TO DIN EN 1991-2 AND ITS DISTRIBUTION

As described above, there are two different impact situations according to DIN EN 1991-2 (2010), which have to be investigated. These two load cases consist of the impact of a tire on the curb of the sidewalk and the impact on the vehicle restraint system. The second one is divided into two different load assumptions for the structural design, like for example the design of the bridge cantilever, and the design of structural details such as the connection reinforcement between the concrete cap and the superstructure. The load assumptions for each mentioned impact situation are described in the following as well as the related load distribution within the cap, which is usually used in the verification in the ultimate limit state.

A detailed overview over the load assumptions for impact situations according the German structural codes in the past can be found in (Niederwald et al. 2014).

2.1 *Impact on the curb of the sidewalk*

According to DIN EN 1991-2 (2010) there should be a horizontal load applied in transverserly direction in oder to cover the stresses due to vehicle impact on the curb of the sidewalk. The horizontal load is supposed to have a value of 100 kN and it should engage 50 mm below the top surface of the curb as it is shown in Figure 1. At the same time a vertical axle load of $V = f \times 0{,}75 \times \alpha_{Q1} \times Q_{1k}$

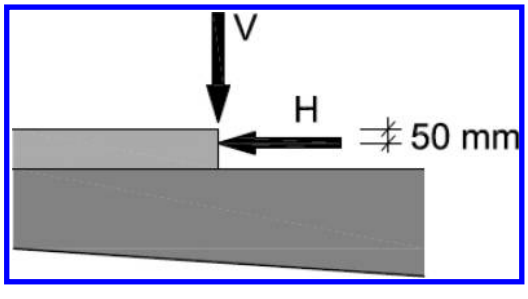

Figure 1. Impact loads on the curb of the sidewalk according to DIN EN 1991-2 (2010).

which is derived from the load model LM 1 should be applied.

The impact loads shown in Figure 1 can be distributed in the cap under an angle of 45° like it is done for the accidental loads due to impact on vehicle restraint system, which are described in the following section 2.2. Because in the codes the impact loads on the curb of the sidewalk are usually smaller than the ones for the impact on vehicle restraint system and because of the mechanism of load distribution being the same, in the following only the impact on vehicle restraint system is investigated in detail.

2.2 *Impact on vehicle restraint system for structural design*

Before new vehicle restraint systems are allowed to be used, they have to pass an impact-test according to DIN EN 1317-2 (2010). As a result of the testing the crash barriers are divided into levels, which consist of the containment level, the level of impact severity and the effective area, which describes the deformation of the guardrail. According to the guideline for passive protection devices (RPS 2009), the vehicle restraint systems installed along German motorways are supposed to have a containment level of at least H2 or H4b. How to perform such impact-tests is described in detail by Hellmich et al. (2000) and Hellmich et al. (2002).

For the structural design DIN EN 1991-2 (2010) provides equivalent loads which are derived from experimental results of such crash tests. The horizontal equivalent loads are split up into four classes A to D, which have to be chosen in dependence to the vehicle restraint system used. In class A the smallest force of 100 kN and in the class D the greatest force of 600 kN is provided. The load is acting over a length of 0.5 m transversely to the direction of traffic and 1.0 m above road surface or 100 mm below the top edge of the crash barrier, whereas the smaller of both values is decisive. Besides the horizontal force a vertical load also has to be applied, which results from an axle load of the load model LM1. The specified loadings for the structural design are shown in Figure 2.

It is a common way to distribute the impact loads with an angle of 45° like it is described in section 2.1 for the impact on the curb of the sidewalk. The effective width, over which the loads can be distributed, has to be calculated separately for the horizontal and for the vertical load, as it is shown in Figure 3. The horizontal load is getting transmitted into the superstructure by the connection reinforcement between the cap and the cantilever. Therefore, it is distributed outwards first, before it moves back to the end of the cantilever. The effective width for the horizontal load $b_{eff,nx}$ is

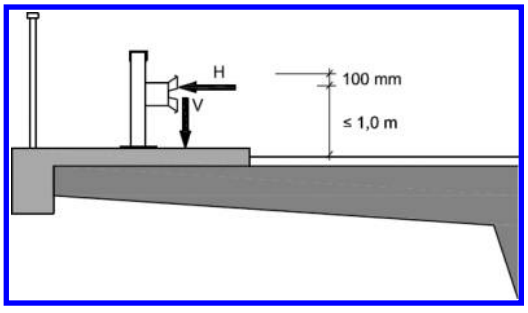

Class	Horizontal force H [kN]	Vertical force V [kN] $V = f \times 0{,}75 \times \alpha_{Q1} \times Q_{1k}$
A	100	f × 225
B	200	f × 225
C	400	f × 225
D	600	f × 225

Figure 2. Impact loads due to vehicle impact for structural design according to DIN EN 1991-2 (2010).

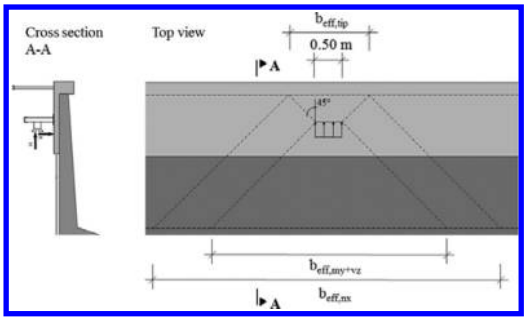

Figure 3. Load distribution of impact loads in the structural design.

therefore bigger than the effective width $b_{eff,my+vz}$ for bending moments and shear forces caused by the vertical load.

Recently the BASt (Bundesanstalt für Straßenwesen) has initiated a research project to get better insight into the values of the horizontal impact loads which have to be applied in order to reflect the vehicle impact in a safe way. First results show that the loads are significantly lower than the values which are defined in DIN EN 1991-2 (2010).

2.3 *Impact on vehicle restraint system for the local component design*

The load bearing capacity of safety barriers made of steel is limited by the plastic cross-section resistance of the post or through the maximum load capacity of the attachment to the bridge cap, taking into account the longitudinal load-bearing effect. For the local design of the bridge cap and the connection reinforcement according to DIN EN 1991-2 (2010), a load of 1.25 times the cross-sectional resistance (plastic shear force and bending moment) of the post has to be applied, engaging in the post axis at the top surface of the cap, as shown in Figure 4. As described in (BASt 2012) this approach for the design of the cap and the connection reinforcement is safe, because in the case that the anchoring of the post would have a higher bearing capacity, the post would fail prior to the attachment, and thus a further load increase would not be possible. In the opposite case, the characteristic resistance of the post will not be reached.

For the simple distance protection planks (EDSP), however, the maximum capacity is limited by a shear failure of the connection-bolts between the guardrail post and the footplate. Compared to modern vehicle restraint systems with a containment level of H2 or H4b, these loadings, which are transmitted into the superstructure of the bridge are much smaller, as shown in Table 1 (Gütegemeinschaft Schutzplanken 2014).

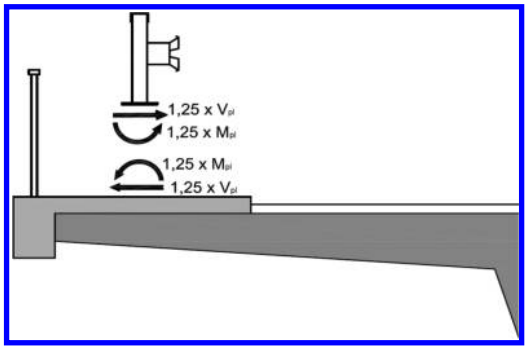

Figure 4. Impact loads due to vehicle impact for the local component design according to DIN EN 1991-2 (2010).

Table 1. Classification and characteristic resistance of vehicle restraint systems (Gütegemeinschaft Schutzplanken 2014).

	EDSP 1.33 Bw	Super-Rail Eco Bw
Containment level	H1	H2
Loading class for structural design	A	B
Characteristic resistance for local component design		
$1.25 \times V_{pl}$ [kN]	12.8	116.8
$1.25 \times M_{pl}$ [kNm]	6.4	52.5

For the verification in the local component design of the connection reinforcement between the bridge cap and the cantilever it is common to apply the impact force transmitted from the crash barrier into the superstructure as 1.25 times the characteristic resistance of a post and to distribute it over a width of 1.33 m, which corresponds to the distance between the posts in longitudinal direction. The bridge cap is therefore divided longitudinally in 1.33 m wide, independent segments (Kuhlmann et al. 2012), as shown in Figure 5.

It is obvious, that with this kind of load distribution rather high tensile forces are obtained in the connection reinforcement for modern vehicle restraint systems, listed as an example in Table 1. In the case of a retrofit of an existing bridge with a restraint system with a containment level of H2 or H4b the verification of the connection reinforcement can therefore often not be performed successfully.

This is the reason, why it is necessary to find improved models for distributing the impact loads in this design situation. When considering the effect of the load distribution in case of the local component design of the bridge cap and its connection reinforcement under impact loads according to Eurocode the question raises how often the plastic forces of the posts have to be considered. Choosing the load distribution on one single segment with the width corresponding to the distance between the posts as shown in Figure 5, this question does not matter since only the characteristic resistance of one single post is considered in the calculation.

However, if a model is used, which is supposed to capture the effect of load distribution in longitudinal direction and which is therefore much wider than 1.33 m, it must be clarified how many plastic connection forces as illustrated in Figure 4 have to be applied in order to reflect the effects of the impact event on the vehicle restraint system sufficiently. Because there are no normative regulations to be found in DIN EN 1991-2 (2010), it is necessary to analyze the load assumption first, before load distribution can be investigated.

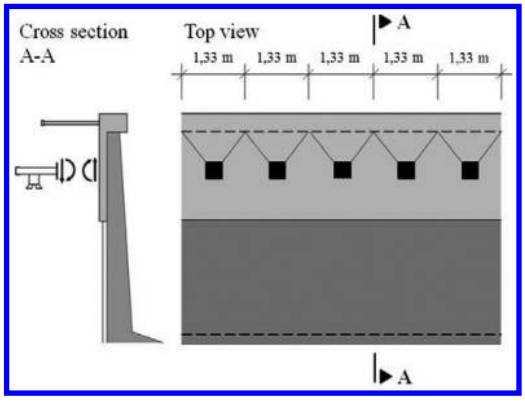

Figure 5. Load distribution of impact loads in the local component design.

3 MODIFIED LOAD ASSUMPTIONS FOR IMPACT ON VEHICLE RESTRAINT SYSTEM

In order to make use of the load distribution in longitudinal direction for the necessary verification of the connection reinforcement between the cap and the cantilever, the load assumptions for the local component design need to be clarified in the first place.

Usually the load assumption, especially for the structural design (see section 2.2), are derived from full scale impact tests. These tests are very difficult to perform and therefore very expensive. This is the reason why experimental investigations to obtain load models are no option within this study. Furthermore, there is a huge number of different vehicle restraint systems available, that would have to be tested in order to obtain a generalized load assumption.

In order to estimate the required number of post forces which have to be applied on the concrete cap, a practical solution was chosen by performing calculations based on the plastic hinge theory using a strut and tie model, which is intended to reflect the vehicle restraint system. The strut and tie model is illustrated in Figure 6. At the clamped supports of the post-rods plastic hinges are defined, which can carry forces in the amount of the characteristic resistance of the restraint system according to Table 1, right column. As an external load, the horizontal equivalent load of 200 kN for the structural design according to DIN EN 1991-2 (2010), class B is applied to the system.

The aim of the calculations is to find out how many posts have to be activated in order to carry the horizontal load from the respective load class and how many of them are reaching their plastic

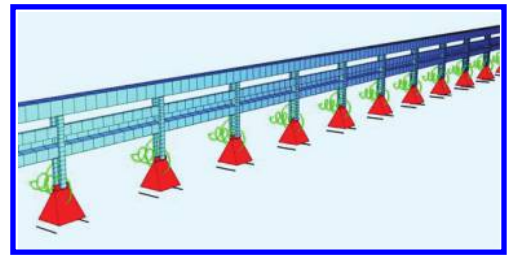

Figure 6. Strut and tie model of vehicle restraint system.

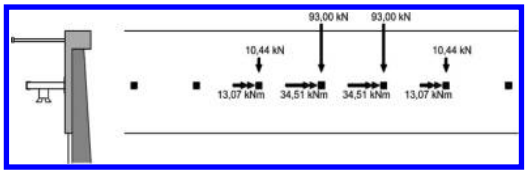

Figure 7. Reaction forces at the clamped supports of the post rods of the strut and tie model of the vehicle restraint system "Super-Rail Eco Bw".

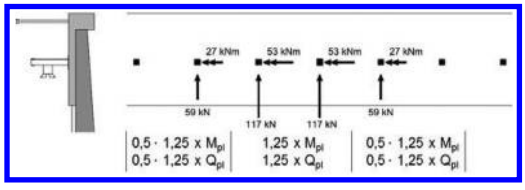

Figure 8. Proposed load arrangement for the vehicle restraint system "Super-Rail Eco Bw".

ultimate bearing capacity. For further information see (Niederwald et al. 2014).

The numerical simulations were performed so far for the vehicle restraint system "Super-Rail Eco Bw" as listed in Table 1. The reaction forces at the clamped supports of the post-rods are illustrated in Figure 7. It can be seen that the two posts close to the applied impact force are reaching their plastic shear capacity. In total four of the posts are getting loaded, while the first and the last post are applied with much smaller loads then the two in the middle.

Regarding the results from the strut and tie model as presented in Figure 7 it is possible to derive a propsal for a safe load arrangement for the investigated vehicle restraint system. The calculated reaction forces have be to be multiplied with the factor 1.25 according to DIN EN 1991-2 (2010) before they can be applied as loadings on a model for the concrete cap. The proposed load arrangement for the vehicle restraint system "Super-Rail Eco Bw" is shown in Figure 8. It can be seen, that four post forces are applied at the same time, whereby the first and the last one are only applied with 50% of the characteristic resistance of the crash barrier with respect to the lower reaction forces of the two outer posts.

4 STUDYING LOAD DISTRIBUTION OF IMPACT LOADS ON CONCRETE BRIDGE CAPS

4.1 *Finite element simulations*

In order to study the effect of the load distribution in longitudinal direction within the bridge cap finite element simulations are getting performed using a folded plate structure of the cap. The finite element model of the concrete cap is illustrated in Figure 9. The bridge cap is discretized with two-dimensional finite elements that are capable of considering the nonlinear material behavior of reinforced concrete. It is important to take realistic material behaviour into account to prevent overestimating of the stiffness of the cap and consequently overestimating the distribution of the impact loads.

The plate of the cap is elastically bedded to simulate the support on the bridge cantilever. The bedding can transmit compression forces only. In case of tension forces the bedding fails and the internal forces are getting redistributed. The connection between the cap and the superstructure at the tip of the cantilever is modeled by two nonlinear springs, which are supposed to carry the horizontal loads and also the bending moments caused by the vehicle impact. The upper spring represents the behaviour of the connection reinforcement. Upon reaching the yield strength of the reinforcement, the spring can absorb any further load and the forces are getting redistributed in longitudinal direction. The bottom spring is describing the pressure point for the rotional loadings. Its characteristics are derived from the material behaviour of the cap-concrete. The distance between the pairs of springs in longitudinal direction corresponds to the distance between the connection reinforcement.

The following results of studying the load distribution using the described model are done for two impact situations: impact in the middle of the cap and impact at the beginning of the cap.

4.2 *Distribution of modified load arrangement for the local component design situation*

For the following study of the load bearing behaviour of a concrete bridge cap the modified load arrangement presented in section 3 was applied as an external loading on the cap for two different impact situations: impact in the middle and at the beginning of the cap. In Figure 10 the deformation

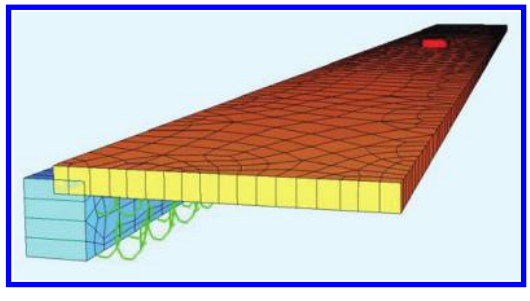

Figure 9. Finite element model of a concrete bridge cap.

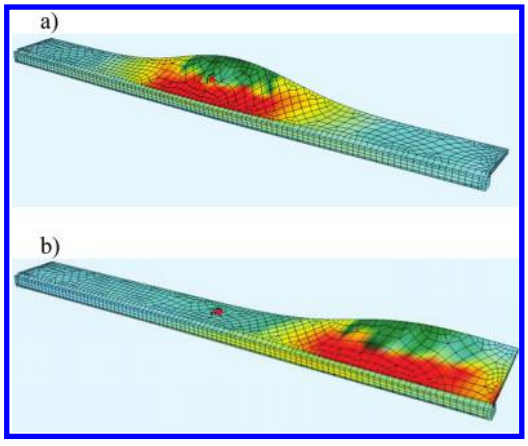

Figure 10. Deformation figures for a) impact in the middle of the cap and b) impact at the beginning of the cap.

figures for both impact situations can be seen. Note that this kind of deformation is rather unrealistic due to the fact of an axle load usually being present while the impact on the vehicle restraint system is occurring. Therefore, a lifting of the cap is rather unlikely.

The deformations figures are indicating that the impact loads are getting distributed in longitudinal direction. It is therefore possible to make use of it in terms of performing the necessary verifications of the connection reinforcement between the cap and the bridge superstructure successfully.

In order to study how the load distribution in the local component design is influenced by the geometry of the cap, a parameter study was performed, for which first results are presented in the following figures.

In Figure 11 the tension forces acting in the connection reinforcement between the cap and the bridge cantilever are plotted in reference to the length of the cap for different heights of the cap of 15, 20 and 25 cm. The results for the impact in the middle of the cap are shown in Figure 11a and the results for the impact at the beginning are plotted in Figure 11b. It can be noted, that in both impact situations the connection reinforcement reaches its yielding strength over a certain length, which is indicated by the two plateaus in Figure 11a and 11b. Regarding the curves for the impact in the middle of the cap, the connection reinforcement of the cap with a height of 25 cm is the only one for which the tension forces are slightly underneath the yielding strength. The results presented in Figure 11 indicate that the impact at the beginning of the cap becomes decisive for the load distribution within the connection reinforcement.

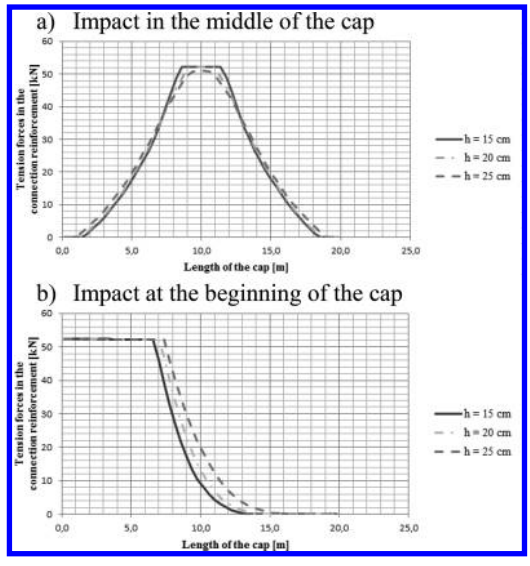

Figure 11. Tension forces in the connection reinforcement for a) impact in the middle of the cap and b) impact at the beginning of the cap.

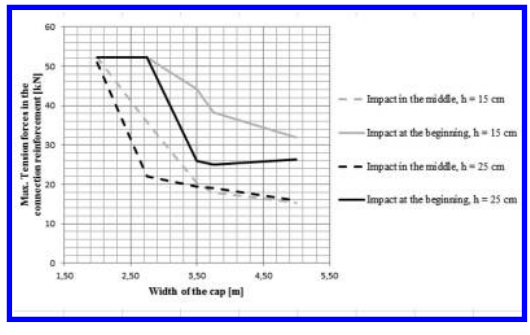

Figure 12. Maximum tension forces in the connection reinforcement for different cap widths.

The height of the cap has only little influence on the distribution for the impact in the middle of the cap, while the curves for the impact at the beginning are differing a little in the area of decreasing tension forces.

In Figure 12 the maximum tension forces acting in the connection reinforcement are plotted in reference to different cap widths ranging from 2.0 m to 5.0 m for the two impact situations and two different heights of the cap of 15 cm and 25 cm. It can be seen that with increasing cap width the maximum tension forces in the reinforcement are decreasing rather fast. This can be explained by the increasing load distribution length with increasing stiffness of the shear panel of the cap.

4.3 *Distribution of impact loads according to DIN EN 1991-2 (2010) for the structural design*

The distribution of impact loads according to DIN EN 1991-2 (2010) for the structural design situation was also investigated using the above described finite element model for the cap. The applied loads are shown in Figure 2. The study was performed with the aim to somehow modify the effective width for the bending and shear design of bridge cantilevers like it is shown in Figure 3 in order to enlarge the length of load distribution for the recalculation of existing bridges. Unfortunately, the numerical simulations showed that the chosen model for the concrete cap is not able to describe the load bearing behaviour under that kind of loadings in a realistic manner. It is therefore planned to take the influence of the bridge cantilever into account in further studies.

5 CONCLUSION AND OUTLOOK

The loadings which have to be applied due to the impact on crash barriers have been increased significantly within the last decade because of the fact of rising requirements regarding the containment capacity of vehicle restraint systems. Therefore new systems were developed, which can transmit higher impact forces into the bridge superstructure. In case of retrofitting an existing bridge with a modern crash barrier system, this leads to problems regarding the safety in the ultimate limit state. To avoid an expensive strengthening of the bridge it is helpful to take advantage of the load distribution in longitudinal direction of the bridge. Therefore, this paper studies the load bearing behaviour of existing concrete bridge caps using a nonlinear finite element simulation. First of all, load assumptions for vehicle impact according to DIN EN 1991-2 (2010) were presented. Because of a lack of normative regulation for the local component design a modified load arrangement for one specific vehicle restraint system was developed and described in section 3. The modified loadings were then used for a parameter study, which was done to investigate the influence of different sizes of bridge caps. First results showed that the effect of load distribution on the acting tension forces in the connection reinforcement is significantly. The structural behaviour of existing bridge caps will be therefore investigated in more detail in further studies. It is also planned to improve the structural model in order to take the influence of the bridge cantilever into account for the distribution of impact loads in the structural design situation according to DIN EN 1991-2 (2010).

REFERENCES

BASt. 2012. Ergänzende Kriterien zum Einsatzfreigabeverfahren für Fahrzeug-Rückhaltesysteme in Deutschland. Bundesanstalt für Straßenwesen, 09.11.2012.

DIN EN 1991-2. 2010. Einwirkungen auf Tragwerke—Teil 2: Verkehrslasten auf Brücken; Deutsche Fassung EN 1991-2:2010. DIN, Deutsches Institut für Normung e.V.

DIN EN 1317-2. 2010. Rückhaltesysteme an Straßenbrücken—Teil 2: Leistungsklassen, Abnahmekriterien für Anprallprüfungen und—Prüfverfahren für Schutzeinrichtungen und Fahrzeugbrüstungen. DIN, Deutsches Institut für Normung e.V.

Gütegemeinschaft Schutzplanken. 2014. Gütegemeinschaft Stahlschutzplanken e.V.: Stahlschutzplanken-Info 2/2014, Siegen.

Hellmich, K. & Piringer, S. & Plomer, S. & Stangl, E. & Stella, J. 2000. Krafteinwirkung auf die Kappe und den Überbau einer Brückenkonstruktion infolge eines Anprallvorganges an eine Stahlleitschiene. In *Stahlbau*, Vol. 69, No. 9, pp. 673–681.

Hellmich, K. & Brandauer, F. & Stella, J. & Stangl, E. 2002. Festlegung von auf Brücken einwirkenden charakteristischen Lasten beim Anprallvorgang gegen Rückhaltesysteme. In *Bauingenieur*, Vol. 77, pp. 13–21.

Kuhlmann, U. & Zizza, A. & Günther, H.-P. 2012. Anpralllastan an Schutzeinrichtungen auf Brücken. Anpassung der DIN-Fachberichte "Stahlbrücken" und "Verbundbrücken" an endgültige Eurocodes und nationale Anhänge einschließlich Vergleichsrechnungen. Berichte der Bundesanstalt für Straßenwesen, Heft B 88, Bergisch-Gladbach.

Niederwald, M. & Keuser, M. & Goj, K. & Geuder, S. 2014. Investigation of the load bearing behaviour of existing bridge caps subjected to accidental loads due to impact on vehicle restraint systems. In Fischer, O. & Keuser, M. & Mangerig, I. & Mensinger, M. & Siebert, G. & Yamaguchi, T. (eds.), *Proceedings of the 10th Japanese German Bridge Symposium, Munich, Germany.*

RiZ-ING. 2009. Richtzeichnungen für Ingenieurbauten. Bundesministerium für Verkehr, Bau und Stadtentwicklung, Verkehrsblatt-Verlag Borgmann GmbH & Co KG, Dortmund.

RPS. 2009. Richtlinie für passive Schutzeinrichtungen an Straßen durch Fahrzeug-Rückhaltesysteme. Forschungsgesellschaft für Straßen—und Verkehrwesen.

Sedlacek, G. & Kammel, C. & Geßler, U.J. & Bleck, W. & Myslowicki, S. & Poprawe, R. 2004. Innovative Schutzplanken aus Stahl. In *Bautechnik*, Vol. 81, No. 8, pp. 662–663.

Concrete Repair, Rehabilitation and Retrofitting IV – Dehn et al. (Eds)
© 2016 Taylor & Francis Group, London, ISBN 978-1-138-02843-2

Laser Induced Breakdown Spectroscopy (LIBS)—innovative method for on-site measurements on chloride contaminated building materials

S. Millar, T. Eichler, G. Wilsch & C. Gottlieb
BAM, Federal Institute for Material Research and Testing, Berlin, Germany

ABSTRACT: The Laser Induced Breakdown Spectroscopy (LIBS) for the investigation of element distributions and ion transportation in building materials (especially for concrete) is established at BAM. The method is a combination of laser ablation and optical emission spectroscopy. With its translation stage (lab-system) or scanner system (mobile system) the element distribution is evaluated and the heterogeneity of concrete is considered in the results. The spatial resolution of a measurement may reach 50 µm with maximum pulse frequency up to 100 Hz. The whole system is automated that minimize the time of a measurement and also the probability of errors. All elements are detectable and with the use of reference samples a quantitative analysis is possible. A validated mobile LIBS-system for on-site application on building materials is under development at BAM. The system is designed to measure the content of harmful species like chlorine, sulphur or alkalis to give the engineer a tool for the estimation of the condition of concrete structures and quality assurance during concrete repair work on-site.

1 INTRODUCTION

Concrete buildings are designed in consideration of a specific expected lifetime. Usually for reinforced concrete structures in civil engineering as e.g. multi-storey car parks a minimum life time of approximately 50 years is strived for. Environmental factors like weather, location or general exposition can force aging—and damage-processes due to deterioration of concrete and/or reinforcement. The ingress of harmful species like CO_2 or Cl^- causes corrosion of the embedded reinforcement in the concrete structure. In this case especially older constructions with insufficiently concrete cover are not able to attain the assessed life time. Laser Induced Breakdown Spectroscopy (LIBS) can be applied as a fast and reliable method in order to identify harmful species and their accompanying damage processes.

The LIBS method is a combination of material ablation, plasma formation and analysis of emitted radiation by spectroscopic methods. To generate plasma a high energy pulsed Nd:YAG-laser is focused on a surface. The radiation of the plasma is analysed by a spectrograph and in combination with a CCD-camera. As a matter of principle all elements are detectable, even light elements like hydrogen or sodium. The results can be quantified by calibration.

LIBS may be used on gases, liquids or solids. There are a lot of applications in different fields like environmental analysis, pharmaceutical investigation, biomedical investigation, forensic investigation or industrial applications like process control, recycling, sorting and quality control during manufacturing (Hahn & Omenetto 2012, Noll 2012).

At BAM LIBS has been successfully applied for investigations on distribution and transport of different ions in building materials (Wilsch et al. 2005 & 2011, Weritz et al. 2005 & 2006 and Eichler et al. 2010).

The challenge of separating aggregates and cement-matrix in studying element distributions of concrete based materials, which is e.g. wet chemical analyzes unfit to do, solves LIBS at BAM with a scanning system. Taking the heterogeneity of concrete into account is necessary and elementary, because the main transport-processes occur in the cement-matrix via pores. In damaged concrete the transport processes can be supported by cracks. With a spatial resolution of 50 µm and the aforementioned scanning technique LIBS is able to image the transport of harmful ions by cracks (Fig. 1).

The performance of LIBS is demonstrated by investigation of a number of concrete cores drilled out of a chloride contaminated parking deck. A second example illustrates the detection of the carbonation depth. LIBS as a promising technique is currently on the step from pure laboratory applications to an on-site analyse technology. In cooperation with system developers and companies a mobile LIBS-system is in development at BAM.

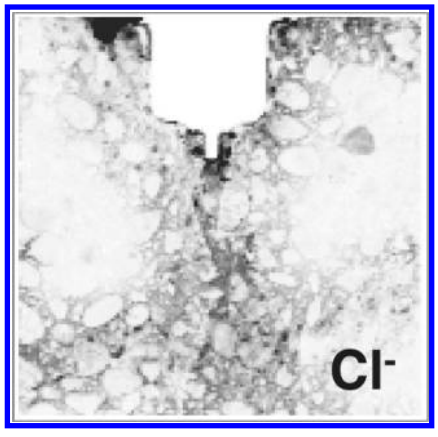

Figure 1. Chloride-ingress at a cracked concrete specimen; crack width = 350 µm; sample-size = 140 mm × 140 mm; applied with a NaCl-solution from top; darker grey represents a higher chloride content.

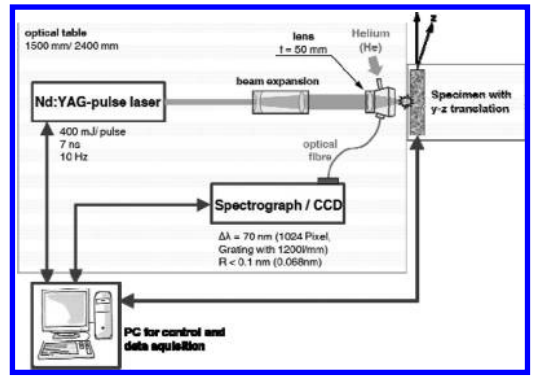

Figure 2. Experimental setup.

2 LIBS

2.1 *Experimental setup (lab-system)*

For investigations on concrete samples in the laboratory the experimental setup is shown as schematic diagram in Figure 2.

A pulsed NdYAG laser (Innolas Spitlight 600) with a output energy of 350 mJ per pulse is used at a fundamental wavelength of 1064 nm. Pulse frequencies from 10 Hz to 50 Hz can be used. The beam is guided through a beam expander and focused on the sample surface with a lens (f = 50 mm). The spot size at the surface is ≤ 0,2 mm. Due to the high energy density in the focus area plasma ignites and radiates for some µs. The light emitted from the plasma is guided by an optical fibre to a Czerny-Turner type spectrometer (Shamrock 330i). In front of the entrance slit of the spectrometer an edge filter to suppress light with wavelength below 550 nm is located. A CCD-camera (Andor Idus DV420A) is used as detector.

The investigated specimen is located on a translation stage and may be moved in a plane perpendicular to the laser beam. To remove dust and to get a lower limit of detection the environment of the plasma is purged with helium.

The setup is controlled by laboratory-written LABVIEW software. An automated measurement procedure minimises the liability to errors and enables fast analysis of samples.

2.2 *Sample preparation*

For LIBS measurements only an optically accessible surface is necessary. To get volume information, a core has to be cut in the middle. This is done by dry cutting or by cutting cooled with petroleum. The measurements are performed on the cross section of the core (Fig. 3).

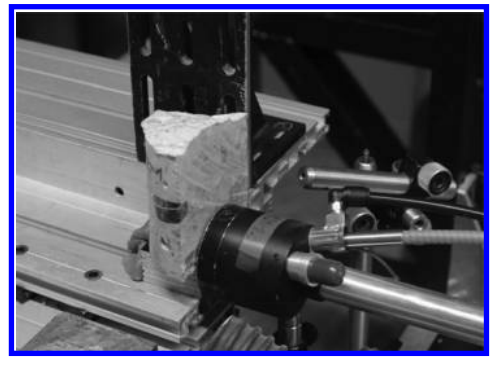

Figure 3. Translation stage with concrete core cut in the middle to do measurements on the cross section. During the measurement the specimen is moved line by line in the plane perpendicular to the laser beam.

2.3 *Measurement*

For LIBS measurements with the lab-system the sample is placed on the translation stage at a constant distance to the lens. The sample is scanned line by line. Standard measurements are made, depending on the issue, with line spacing between 0,25 mm to 2,0 mm. The interval of subsequent measurements per line is also of the same order. Using this scanning technique the heterogeneity of concrete is recorded.

The resolution of a measurement is a compromise between exact reproduction of material heterogeneity and time for a measurement. The higher the resolution is chosen the more time is needed for the measurement.

2.4 *Mobile system*

To give the engineer a tool for on-site inspections of concrete buildings, a mobile LIBS-system is in development at BAM. This mobile setup is intended to help engineers making fast statements about the actual condition, the necessity of maintenance arrangements and the durability of structures.

The setup of the mobile system is shown in Figure 4. The laser is located in the measuring head, which is fixed on a scanner system. The laser head is moved by the scanner to take the heterogeneity into account. The maximum area, which currently can be scanned, is 17,0 cm × 15,0 cm. With the help of compressed air the scanner can be fixed on vertical surfaces or even overhead. The head is connected with the control unit via a 5,00 m cable. The laser energy is 3 mJ per pulse and can run with a frequency up to 100 Hz. The plasma radiation is delivered to an optical fibre and analysed by the detection unit. To maintain laser safety regulations, a cover in connection with a brush shields the laser beam path.

2.5 *Evaluation*

The data evaluation needs some normalization procedures to eliminate interferences like fluctuations of pulse energy, surface properties or dust in the beam path. This is done by a LABVIEW based software which calculates for every element under investigation and for every point measured the peak maximum (Ix) proportional to the background (Bx) (Fig. 5). The result is an element map over the measured area which represents the color coded intensity values per point. Figure 1 shows an example of a 140 mm × 140 mm scanned surface. The image contains 19600 measurement points. A darker red represents a higher concentration of chloride.

Figure 4. Mobile scanner with fixed laser head (left) to scan surfaces and take the heterogeneity of concrete into account, connected with the control unit (right) via cable.

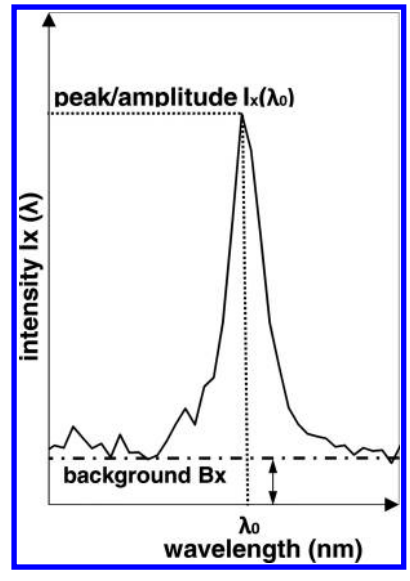

Figure 5. Normalisation of signals with proportion between peak maximum (I_x) and the background (B_x).

The software allows differentiation between measurements performed on coarse aggregates and the cement-matrix. For example by evaluation of calcium content for each point measured.

3 MEASUREMENTS AND RESULTS

3.1 *Calibration for chloride*

Durdragne et al. (1998) and Tran et al. (2001) used the spectral line at 837,6 nm in the Near Infrared Range (NIR) to detect chlorine in gases and solid organic compounds. By flushing the induced plasma with helium, influences of atmospheric elements like nitrogen or oxygen have been excluded. Another advantage of a helium purge is the increased sensitivity of the chlorine line.

LIBS is only able to detect the element chlorine, which is in pure form gaseous. In concrete normally only occur ions of chlorine (chlorides, Cl^-). Therefor the signal of the chlorine peak can be implied to the total chloride concentration in concrete samples.

A typical spectrum on a chloride contaminated specimen is shown in Figure 6. The wavelength range runs from 810 to 860 nm. Beside chlorine other elements occurring in concrete like calcium, oxygen, carbon or sodium can be detected simultaneously.

In order to quantify results a calibration is necessary. This is done by measurements on a set of reference samples with known element content

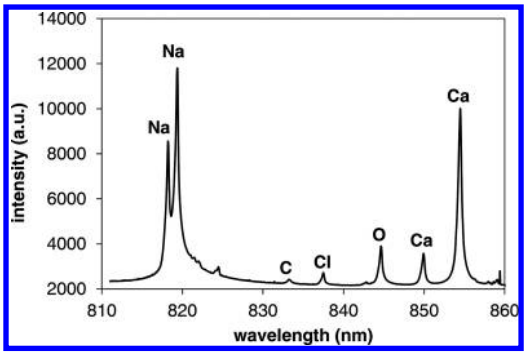

Figure 6. Typical spectrum measured on concrete in the selected NIR wavelength range. The peaks are marked with the according element symbols.

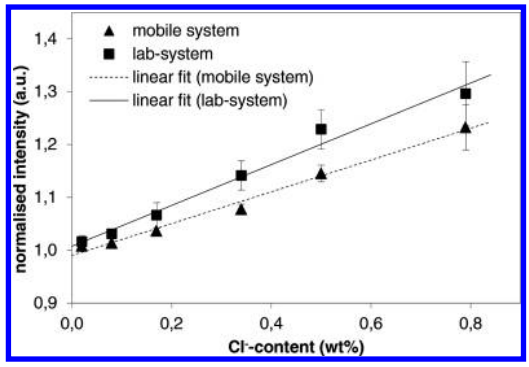

Figure 8. Calibration curves for chloride. Comparison between lab-system and mobile-system. Cl^-—content of the reference samples were analysed by wet chemical analyses.

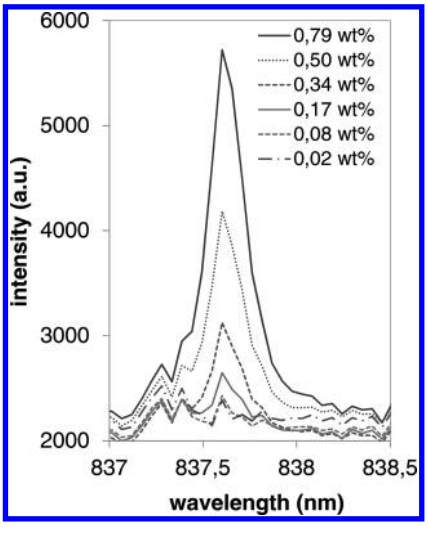

Figure 7. Rising chlorine peak at 837,6 nm with increasing chloride concentration of the reference samples.

in a similar matrix. The peak at 837,6 nm rises with an increasing concentration of chloride in the samples (Fig. 7). The concentration of chloride in the reference samples was determined by wet chemical analyses. The concentrations are indicated in wt% refer to the weighed portion.

Due to the high energy in the focus area LIBS vaporises some µg of the sample surface. Following the results of the wet chemical analysis is correlated with the normalised intensity.

As an example the calibration curves for the evaluation of quantitative values of chloride are shown in Figure 8. In the diagram the calibration curve of the lab-system is compared with the curve of the mobile setup.

The calibration curves are in a similar range and both usable for quantitative measurements. They had been made with the same spectrometer, which is usually made for lab conditions. The current work is to adapt the used settings and configurations into so-called compact spectrometer to get a more comfortable setup for on-site investigations.

3.2 *Quantitative chloride measurements*

In order to quantify results and to extract errors the calibration has to be made in the same conditions in which the measurement will be made. With the calibration curve made in the same ambient atmosphere, the results of the measurement (normalised intensities) can be converted into quantitative values. In Figure 9 (left) an element map of chloride is shown. The image shows the chloride distribution on a 40 mm × 70 mm area. The resolution (line interval/point distance) is 0,5 mm × 0,5 mm. With a pulse frequency of 10 Hz the measurement of 11200 points takes less than one hour and with 50 Hz about 12 minutes.

With the help of elements that rather occur in the cement-matrix than in the aggregates or vice versa, it is possible to exclude the coarse aggregates. These elements could be e.g. calcium or oxygen, which are detected simultaneous with chlorine in the chosen wavelength range (see Fig. 6). To which size the aggregates can be excluded depends on the chosen resolution. A comparison of ingress-profiles with and without coarse aggregates is shown in Figure 10.

To verify the results of the LIBS measurement the specimen was examined with wet chemical analyses. Therefore the concrete core was cut into 10 cm slices. These slices were grinded and the obtained floor prepared for the determination of

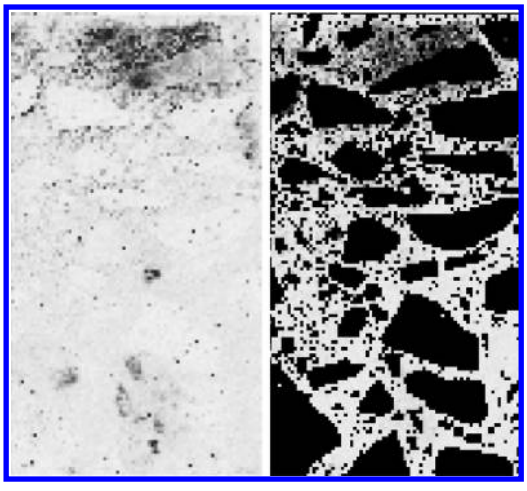

Figure 9. Left: chloride distribution on the measured surface including all measurement points. Right: chloride distribution with excluded coarse aggregates. Dark grey represents a higher chloride concentration.

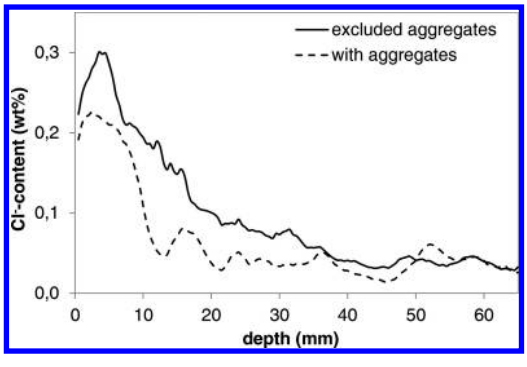

Figure 10. Comparison of ingress profiles of chlorides. The dotted line includes all measurement points and the bold shows the ingress with excluded aggregates. The measurement was made with a resolution of 0,5 mm × 0,5 mm.

the chloride concentration. A wet chemical analysis is only able to give information about the mean value concentration, which does not consider the heterogeneity of concrete. This is done by taking the ratio between cement—and aggregate-mass into account. With this estimation the mean values are adapted with a respective factor to get an element concentration according to the cement-matrix. The comparison of both methods is demonstrated in Figure 11.

While gathering the condition of concrete buildings, especially corrosion endangered concrete buildings, engineer estimate the danger of chloride induced pitting corrosion of reinforcement

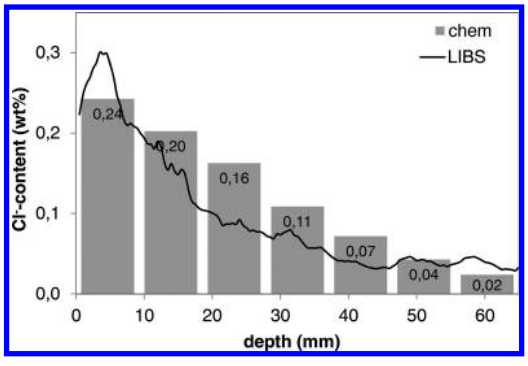

Figure 11. Comparison of wet chemical analyses and LIBS results on the same specimen.

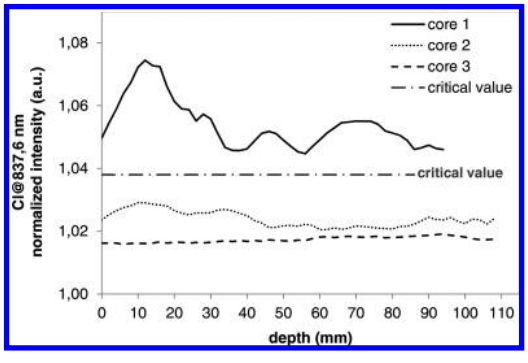

Figure 12. Comparison of the relative chloride concentration measured in correlation to the depth on the cross section of three cores. The critical chloride value at which corrosion may be initiated is marked by a line. The cores where taken from a parking garage on different positions.

by drilling cores. A comparison of relative chloride concentrations measured in correlation to the depth is displayed in Figure 12. The measurements were performed on the cross section of three different cores. The cores were taken from a parking garage on different positions.

The critical chloride value at which corrosion may be initiated is marked by the red line. Core 1 indicated by the bold marked values is in critical condition—repair work is urgently required. Core 2 has an increased chloride concentration, but not critical—monitoring of this area is necessary. And Core 3 shows no chloride values. The evaluation of these three cores takes less than one hour. Thus a large number of cores can be evaluated which form a reliable decisional basis for civil engineer.

3.3 *Carbonation depth*

The durability of reinforced concrete and prestressed steel concrete structures depends, amongst

others, on the efforts taken to maintain passivity of the reinforcement or pre-stressing steel. The passivity can not only be lost by the ingress of chloride. It can also be lost by the carbonation of concrete. The steel can lose his passivity, if the carbonation front reaches the reinforcement. With the implementation of the DIN EN 206 (previously DIN 1045), which consists of customised rules for the design of reinforced concrete buildings dependent on the exposition (e.g. thickness of concrete cover), corrosion caused by carbonation became rarely. But older buildings, which had been built with older standards, are still endangered. Mostly the concrete cover is too thin and the carbonation depth has already reached the steel.

The standard procedure to estimate the depth of the carbonation depth is the phenolphthalein test. The ingress of CO_2 entails that the pH-value of the pore solution in the concrete decreases from 12,5/14 to 6/9. By spraying the relevant area with phenolphthalein the decreasing of the pH-value can be made visible (Fig. 13, left). The region where the pH-value is > 9 becomes violet and the area where the carbonation front runs (pH-value < 9) has no color change.

With LIBS the engineer is able to detect the ingress of chloride and CO_2 with one measurement. By the evaluation of carbon, which also occurs in the wavelength range from 810 nm to 860 nm (at 833,5 nm, Fig. 6), the carbonation front became visible (Fig. 13, right).

3.4 *On-site measurements on a bridge*

In cooperation with companies and authorities BAM got the opportunity to make first measurements on a bridge with the mobile LIBS-system. The bridge is located at the North Sea and is exposed to a saline environment. The aim was to get an overview of chloride concentration in correlation to the exposure. The results of the investigation give an impression, if areas or parts of the bridge are more exposed than others.

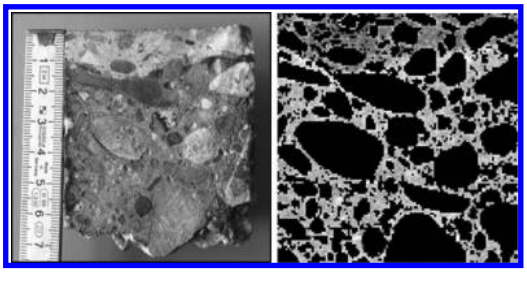

Figure 13. Comparison of phenolphthalein-test (left) and LIBS measurement by evaluating the C-signal at 833,5 nm.

Figure 14. On-site investigation on a bridge. The scanner with the laser-head is fixed with compressed air at the cantilever to estimate the chlorine concentration.

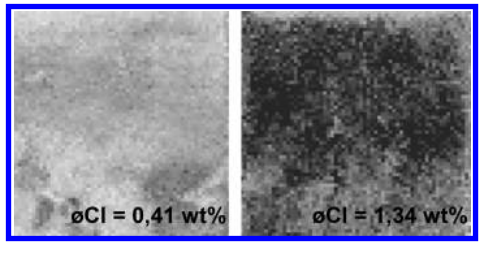

Figure 15. Two surfaces, each 140 mm × 140 mm, measured on a bridge. Resolution = 2,0 mm × 2,0 mm. Surface left was measured on the cantilever and has an average chloride concentration of 0,41%. The surface right has an average value of 1,34% and was measured on the wall (top). One measurement took about 15 min.

The investigation includes the bridge structure, including the wall (top and below), the cantilever and the floor. Altogether measurements of 23 surfaces, each 140 mm × 140 mm, were done on three days. The measurements were also made to test the functionality of the mobile system in harsh conditions. First results are shown in Figure 15. It displays that the exposure varies between different areas. The top of the wall (Fig. 15, right) is exposed to a higher chloride attack than the cantilever. The mobile system is able to detect differences of the exposure on even in rougher weather conditions. In further investigations the results of the on-site measurements will be verified on drilled cores in the laboratory.

4 CONCLUSIONS

Following conclusions may be drawn from the investigations exemplarily shown above:

- LIBS is able to measure directly on the sample surface. Compared to the standard methods

in civil engineering only a minimum of sample preparation is necessary.

- The method is able to take the heterogeneity of the material into account. Coarse aggregates can be excluded (to which size depends on the chosen resolution) by evaluating elements that rather occur in the cement-matrix than in the aggregates or vice versa, e.g. calcium or oxygen.
- With the use of reference samples quantitative results can be derived.
- LIBS allows fast measurements with saving time and man power in comparison to standard procedures in civil engineering.
- The possibility to detect several elements at the same time allows the engineer to make statements about different damage processes or their probability with one measurement. Especially for the assessment of corrosion endangered reinforced concrete buildings LIBS may is an advantage with detecting the chloride ingress and the carbonation front simultaneously.
- The technique is currently on the step from pure laboratory applications to an on-site analysis technology. The mobile system (with the appropriate detector) is able to give quantitative results, comparable to the lab-system. First measurements under rough weather conditions were shown.

The setup of rules and standards is the next step to establish LIBS as a standard procedure for chemical investigations of building materials.

REFERENCES

Durdrange l., Adam P., Amouroux J. Time resolved laser-induced breakdown spectroscopy: application for qualitative and quantitative detection of fluorine, chlorine, sulfur and carbon in air. Appl Spectrosc 1998; 52(10):1321–7.

Eichler T.; Isecke B., Wilsch G, Goldschmidt S., and Bruns M. (2010) Investigations on the chloride migration in consquence of cathodic polarization, Materials and Corrosion, 61, No.6: 512–517.

Hahn, D.W. & N. Omenetto (2012). "Laser-Induced Breakdown Spectroscopy (LIBS), Part II: Review of Instrumental and Methodological Approaches to Material Analysis and Applications to Different Fields." Appl. Spectrosc. 66(4): 347–419.

Noll, R., Laser-induced Breakdown Spectroscopy—Fundamentals and applications, 2012, Springer Verlag, Berlin Heidelberg.

Tran M., Sun Q., Smith BW, Winefordner J.D. Determination of F, Cl, and Br in solid organic compounds by laser-induced plasma spectroscopy. Appl Spectrosc 2001; 55(6): 739–44.

Weritz F., Schaurich D., Taffe A., and Wilsch G. (2006) Effect of heterogeneity on the quantitative determination of trace elements in concrete, Anal Bioanal Chem 385: 248–255.

Wilsch G., Weritz F., Schaurich D., and Wiggenhauser H. (2005), Determination of chloride content in concrete structures with laser-induced breakdown spectroscopy, Constr Build Mater 19:724–730.

Wilsch, G., Schaurich D., et al. (2011). Imaging Laser Analysis of Building Materials—Practical Examples. Review of Progress in Quantitative Nondestructive Evaluation, Vols 30a and 30b 1335: 1315–1322. References in the text: Figure 1, Figures 2–4, 6, 8a, b (not abbreviated).

Concrete Repair, Rehabilitation and Retrofitting IV – Dehn et al. (Eds)
© 2016 Taylor & Francis Group, London, ISBN 978-1-138-02843-2

Enhancing the interpretation of Torrent air permeability method results

R. Neves
Barreiro Technology School, Polytechnic Institute of Setúbal, Barreiro, Portugal

ABSTRACT: The Torrent method is a non-destructive method applicable on site, which is suitable to assess near-surface concrete air permeability and has a relevant association with the main corrosion inducing factors in reinforced concrete. Nevertheless, due to the usual scatter of gas permeability, a careful interpretation of results shall be ensued. The aim of this study was to investigate the influence of using different instruments on the air permeability coefficients, obtained according to Torrent method. The air permeability coefficient was calculated using as lower pressure value 35 mbar. The procedure led to approximate results obtained with different instruments and to a similar scatter. This contributes to improve the accuracy and reliability of air permeability assessment with the Torrent method.

1 INTRODUCTION

1.1 *Background*

The unforeseen deterioration of reinforced concrete structures has caused growing concerns on durability issues. This concern led to considerable research efforts and to developments, such as test methods capable of providing indications on concrete durability.

Onsite measurement of air permeability provides a useful approach to assess the service life of concrete structures, being useful to anticipate whether the target service life is to be achieved.

However, it is recognized that gas permeability results have considerable scatter and are sensitive to some test parameters, e.g. applied pressure (Abbas et al. 1999). This scatter and sensitiveness may impair the interpretation of air permeability test results. Moreover, according to Ho & Lewis (1987), "what is important is the recognition of test limitations so that valid interpretation of results can be made".

This study aims at contributing to improve the interpretation of results from a non-destructive method applicable on site, which is suitable to assess near-surface concrete air permeability and has a relevant association with the main corrosion inducing factors in reinforced concrete: chloride penetration (Romer & Leeman 2005) and carbonation (Neves et al. 2012) and that is considered in Swiss standard SN 505 262/1 (SIA 2013). The method was proposed by Torrent (1992) and is presented next.

1.2 *Torrent method*

The principle of the Torrent method is to first create a certain degree of vacuum in the test chamber using a vacuum pump and then cut the connection between the vacuum pump and the test chamber and measure the rate at which pressure increases in the latter. This makes it possible to calculate an air permeability coefficient kT associated with this method (Torrent & Frenzer 1995).

The calculation is possible only if one knows the flow path (RILEM TC 116-PCD 1999). In this method the air flow is unidirectional, which is possible because of a guard-ring (Fig. 1) and a pressure regulator that balances the pressure in both the test chamber and the guard-ring. This feature also prevents the air flow into the test chamber

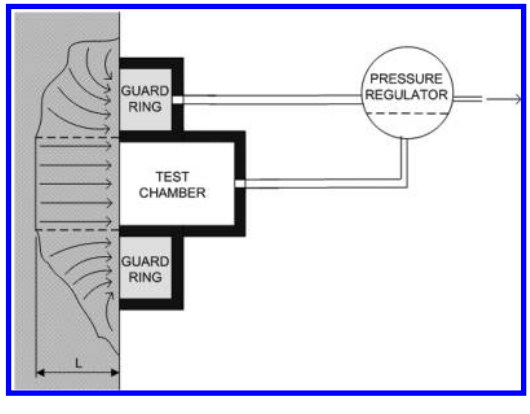

Figure 1. Sketch of the principle of Torrent method.

from coming mainly through the 'skin concrete' when the cover concrete is to be assessed.

Air permeability coefficient is calculated according to the following equation:

$$kT = \left(\frac{V_c}{A}\right)^2 \times \frac{\mu}{2 \times \varepsilon \times p_a} \times \left(\frac{\ln\left(\frac{p_a + \Delta p}{p_a - \Delta p}\right)}{\sqrt{t_f} - \sqrt{t_i}} \right)^2 \quad (1)$$

where kT = air permeability coefficient (m^2); V_c = volume of test chamber (m^3); A = cross section of test chamber (m^2); μ = viscosity of air at 20 °C ($N \cdot s/m^2$); ε = porosity of concrete (–); p_a = atmospheric pressure (N/m^2); Δp = pressure increase in test chamber (N/m^2); t_i = time at start of measurement (s); and t_f = time at end of measurement (s).

More details about the method can be found elsewhere (Torrent 1992, Torrent et al. 2007).

2 EXPERIMENTAL

2.1 *Concrete*

Four concrete mixes were prepared using 280 kg/m^3 of binder, a water-binder ratio of 0.7, limestone coarse aggregates, natural silica sand and a water reducing admixture based on modified lignosulphonates. In some of the mixes commercial corrosion inhibitor was used and a pozzolanic addition replaced Portland clinker.

The tests for this study were performed in small cylinders (150 mm diameter and 50 mm tall) sawn from larger ones (150 mm diameter and 300 mm tall). The larger cylinders were removed from molds at 24 hours and kept in tepid (20 °C) water for 7 days.

A 7-day curing period has been adopted in several research works involving air permeability tests (Ribeiro et al. 2003, Torrent 2005), including by multinational research groups (Andrade et al. 2007). Several authors have found experimentally that prolonging moist curing beyond 7 days has little influence on permeability (Dhir et al. 1987, Schonlin & Hilsdorf 1988).

They were then sawn and the test specimens were coated with a double layer of adhesive aluminum in their molded (curved) surface. After that they were kept in a laboratory chamber at 22°C and 60% RH until testing, which occurred at 28 days. The test chamber had a diameter of 40 mm and was always placed on sawn surfaces.

Each mix was sampled twice, using concrete from different batches. Each sample comprised 15 specimens. Thus, 120 air permeability measurements were carried out.

2.2 *Testing instruments*

The air permeability tests were carried out using two commercially available instruments that operates according to Torrent method: the Torrent Permeability Tester (TPT) and the Permea-Torr (PT).

Although both instruments follow the same basic operation procedures, there are some differences. A noteworthy difference is the fact that the initial testing pressure (pressure at time t_i – see Eq. 1), when testing with TPT is the lowest pressure that the system (concrete + instrument + vacuum pump) can achieve within 30 seconds, while for PT the user is able to set a value between 0 and 60 mbar, with a recommended value of 30 mbar.

Another relevant difference is the estimation of pressure variation in the test chamber. The pressure variation in the testing chamber is not only due to the incoming air flow from concrete but also to system losses. The effective pressure variation shall be the measured variation minus losses. To estimate losses a meta-test is carried out over an impermeable surface, commonly designated as calibration. The measured pressure variation is attributed to system losses.

The calibration pressure range for TPT is from the lowest pressure that the system (impermeable surface + instrument + vacuum pump) can achieve within 30 seconds to the pressure elapsed 12 minutes. As the lowest pressure achieved varies between meta-test and concrete testing and the subtraction of system losses is for corresponding time intervals, there is a shift on the subtracted pressures (losses). When testing with PT, this can be avoided as the user is able to set the lowest calibration pressure to the same value as for concrete testing.

Each sample was divided in two subsamples. The subsamples with 7 specimens were tested with TPT while the subsamples with 8 specimens were tested with PT. Contrary to what happened in other studies (Torrent 2012) each specimen was tested by only one instrument.

3 ANALYSIS

3.1 *Raw air permeability coefficients*

A total of 120 air permeability tests were carried out and grouped in 8 sets (4 mixes sampled twice). According to Neves et al. (2012), the median has shown to be a suitable parameter to represent a sample from an air permeability population. Therefore, each set of results is represented by its median air permeability coefficient (kT) in Figure 2, where the results from each instrument are also compared.

Although it can be observed that there are consistent differences in the median values of each set,

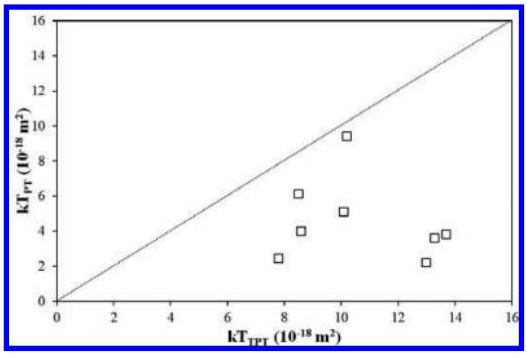

Figure 2. kT results with TPT and PT instrument.

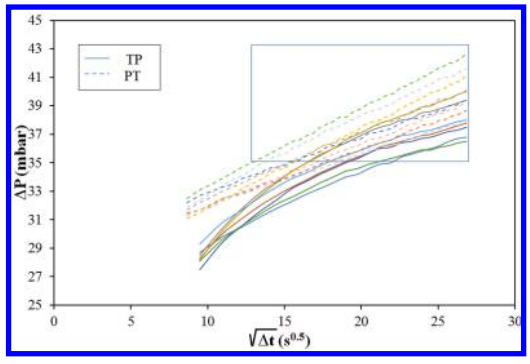

Figure 3. Pressure variation with time (example for sample Z#1).

Table 1. *P*-values of Mann-Whitney-Wilcoxon test for kT results with TPT and PT instrument.

Mix	Batch	*P*-value	Batch	*P*-value
Z	#1	$\approx 10^{-4}$	#2	0.555
I	#1	$\approx 10^{-4}$	#2	$\approx 10^{-4}$
H	#1	0.018	#2	0.028
O	#1	0.003	#2	$\approx 10^{-4}$

a statistical test of hypothesis was applied to check if results from both instruments are equivalent.

According to Neves et al. (2012) the analysis of air permeability results shall be performed assuming no particular statistical distribution of the data. Therefore, a non-parametric test, the Mann-Whitney-Wilcoxon test, was adopted to test the null hypothesis that the two populations are the same. Thus, eight bilateral tests of hypothesis were performed. According to the results presented in Table 1, at a significance level of 5%, the null hypothesis was rejected in seven of the eight tests.

As, effectively, the compared populations are the same, the reason for rejecting the null hypothesis shall be attributed to the testing instruments. Then, an empiric analysis of the test data that supported the calculation of kT was carried out. In this analysis it was found that although higher pressure variation occurred with TPT instrument, the final rate of pressure variation was similar with both instruments. Moreover, it was found that for absolute pressures less than 35 mbar, the rate of pressure variation with the square root of time (see Eq. 1) with the TPT instrument was not constant, which is in opposition to the theoretical background of the test. An example of this situation is presented in Figure 3.

Part of this deviation from the expected linearity can be explained by part of the test being run below vapor pressure, causing evaporation of water from concrete into the evacuated test chamber

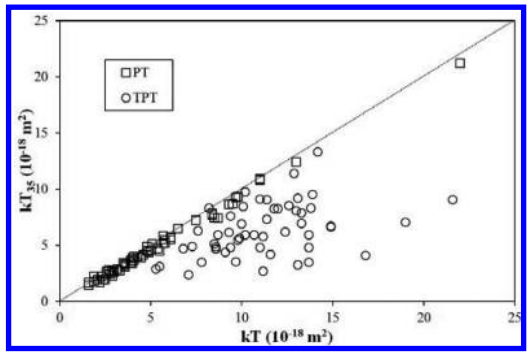

Figure 4. kT values versus kT_{35} values.

(Romer 2005). Another contributing factor may be the shift in the correction of the pressure variation (see 2.2).

3.2 *Modified air permeability coefficients*

Based on the prior analysis, the air permeability coefficients were recalculated, considering, in Equation 1, $p_i = 35$ mbar and t_i the corresponding time. The symbol for these recalculated air permeability coefficients is kT_{35}. In one of the eight sets, corresponding to the second sample of mix I (I#2), in four of the seven specimens tested with TPT, the maximum pressures reached within the test were under 35 mbar. Therefore, for these specimens, it was not possible to calculate kT_{35}.

A comparison between raw and modified air permeability coefficients is presented in Figure 4.

Similar values are found for tests carried out with PT, which was expected given the linear behavior observed in the previous analysis, as well as lower kT_{35} than kT for tests carried out with TPT. This was also expected, as the water evaporation effect (see 3.1) was cut out.

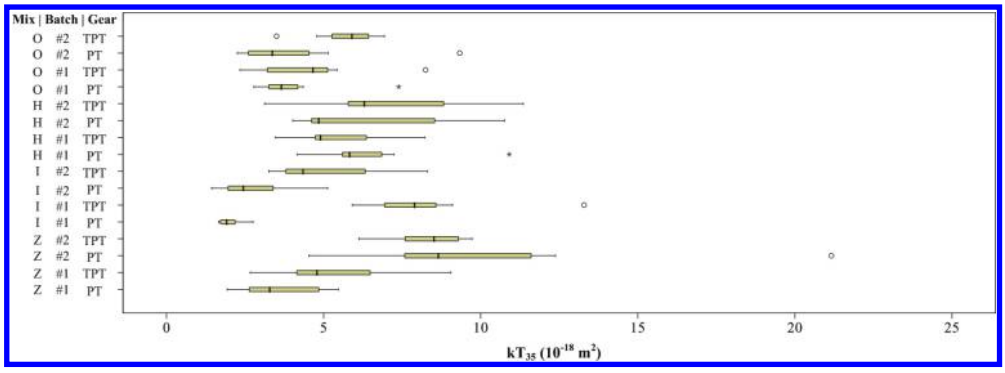

Figure 5. Boxplot for kT_{35} results.

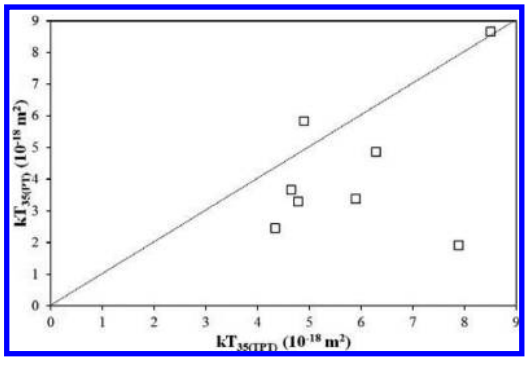

Figure 6. kT_{35} results with TPT and PT instruments.

Again assuming no particular statistical distribution, the obtained kT_{35} are displayed in boxplots (Fig. 5). Outliers, which are cases between 1.5 and 3 boxlengths from the edge of the box, are identified with a "o" mark. Extreme outliers, which are cases more than 3 boxlengths away from the edge of the box, are identified with a "*" mark. The boxlength is the interquartile range of the results (Foster 1998).

In 7 of the 16 represented sets, there are outliers, a ratio similar the one found by Neves et al. (2012). The outlier distribution between instruments is quite equitative. According to Neves et al. (2012), a single void or micro-crack, may increase air permeability by more than one order of magnitude. Thus, the found outliers shall be attributed to concrete than to testing operator or instruments.

The medians of the 8 set of results obtained with each instrument are presented and compared in Figure 6.

Contrary to what happens in Figure 2, similar median values of each set for both instruments are found. The Mann-Whitney-Wilcoxon test was applied to check if results from both instruments

Table 2. *P*-values of Mann-Whitney-Wilcoxon test for kT_{35} results with TPT and PT instrument.

Mix	Batch	*P*-value	Batch	*P*-value
Z	#1	0.121	#2	0.613
I	#1	$\approx 10^{-4}$	#2	0.133
H	#1	0.281	#2	0.463
O	#1	0.613	#2	0.054

are equivalent. According to the results presented in Table 2, at a significance level of 5%, the (null) hypothesis that the two populations are the same cannot be rejected in seven of the eight tests.

To assess whether the change on the initial testing pressure would influence the scatter of the results, and again assuming no particular statistical distribution of the data, the quartile variation coefficients for kT and kT_{35} (Eq. 2) were computed.

$$V = 100 \times \frac{Q_3 - Q_1}{Q_3 + Q_1} \quad (2)$$

where V = quartile variation coefficient; Q_3 = third quartile; and Q_1 = first quartile.

Quartile variation coefficients of raw and modified results obtained with TPT and PT instruments are presented and compared in Figure 7.

Although in some cases the scatter increased, in other cases it has decreased, being the overall balance practically nil.

However, as with the adopted procedure the range of pressure variation diminishes, it may be expected that the test loses capability to differentiate air permeability of different mixes.

The mixes used in the present study have the same water-binder ratio, a major influencing parameter on concrete permeability (Jensen & Hansen 2001). Thus, they are not suitable to assess if the adopted

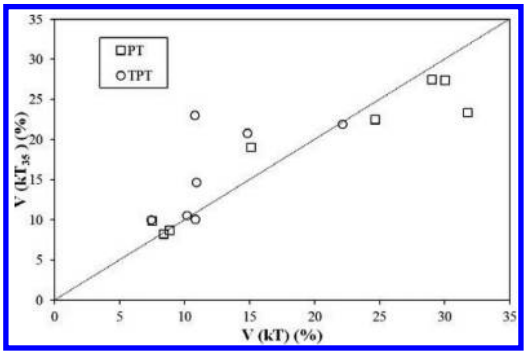

Figure 7. Quartile variation coefficients for kT and kT_{35} results.

procedure causes differentiation capability loss. To carry out this assessment, air permeability data of two mixes from a study presented by Neves (2012) were adopted.

One of the selected mixes has 290 kg/m^3 of cement CEM IV/A-V (CEN 2001) and a water-cement ratio of 0.54, while the other has 340 kg/m^3 of cement CEM IV/A-V and a water-cement ratio of 0.46. Both have limestone coarse aggregates, natural silica sand and a water reducing admixture: based on modified lignosulphonates for the first one and based on polycarboxilic ether the second.

It was not possible to calculate kT_{35} for all specimens, as in one for each mix the final pressure did not reach 35 mbar.

The Mann-Whitney-Wilcoxon test was applied to check if both mixes have the same air permeability (kT_{35}). The test returned a p-value near zero, which means that, at a significance level of 5%, or much lower, the (null) hypothesis that the two populations have the same air permeability is rejected. This is a preliminary indication that calculating the air permeability coefficient considering an initial pressure of 35 mbar does not impair its representativeness.

4 CONCLUSIONS

A comparative study of air permeability results using two different instruments for the same method in different specimens of the same sample was developed. Based on the collated data and its analysis, it was possible to found that:

- Testing with TPT instrument generally leads to higher air permeability coefficients than testing with PT instrument;
- Pressure variation has a fairly linear relationship with the square root of time when testing with PT instrument;
- When testing with TPT instrument, a fairly linear relationship of pressure variation with the square root of time is only achieved of 35 mbar onwards;
- Calculating the air permeability coefficient considering an initial pressure of 35 mbar, does not affect the air permeability coefficients when PT is applied;
- Calculating the air permeability coefficient considering an initial pressure of 35 mbar, affects the air permeability coefficients obtained testing with TPT making them equivalent to those obtained testing with PT;
- Calculating the air permeability coefficient considering an initial pressure of 35 mbar does not affect the scatter of air permeability results;
- There are preliminary indications that calculating the air permeability coefficient considering an initial pressure of 35 mbar does not impair the air permeability differentiation capacity of the method.

Thus, an adjustment of already calculated air permeability coefficients based on data obtained with TPT instrument, considering an initial pressure of 35 mbar, is advised, as it corresponds to an improvement of such air permeability assessments. Nevertheless, for less permeable concretes, the adjustment may not be possible, as testing pressure may always be below 35 mbar.

Moreover, if air permeability tests are to be carried out using TPT instrument, it is recommended to cut the connection between the vacuum pump and the test chamber when pressure reaches approximately 35 mbar and to apply the same procedure for the meta-test (calibration).

REFERENCES

Abbas, A. et al. 1999. Gas permeability of concrete in relation to its degree of saturation. *Materials and Structures* 32: 3–8.

Andrade, C. et al. 2007. Comparative test—Part I: 'Penetrability' methods. In R. Torrent & L. Luco (eds), *Non-destructive evaluation of the penetrability and thickness of the concrete cover*: 157–185. Bagneux: RILEM Publications.

CEN 2001. *EN 197-1, Cement Part—1: Composition, specifications and conformity criteria for common cements*. Brussels: CEN.

Dhir, R. et al. 1987. Near-surface characteristics of concrete: assessment and development of in situ test methods. *Magazine of Concrete Research* 39 (141): 183–195.

Foster, J. 1998. *Data analysis using SPSS for Windows—version 6: A beginner's guide*. London: SAGE.

Ho, D. & Lewis, R. 1987. A reply to discussions of the paper 'Carbonation of concrete and its prediction'. *Cement and Concrete Research* 17: 1005–1008.

Jensen, O. & Hansen, P. 2001. Water-entrained cement-based materials: I. Principles and theoretical background. *Cement and Concrete Research* 31(4): 647–654.

Neves, R. 2012. *Concrete air permeability and carbonation in structures* (in Portuguese). PhD Thesis in Civil Engineering. Lisbon: Instituto Superior Técnico-Technical University of Lisbon.

Neves, R. et al. 2012. About the statistical interpretation of air permeability assessment results. *Materials and Structures* 45 (4): 529–539.

Ribeiro, A. et al. 2003. Performance of concrete with an intended life of 50 years. *ACI Special Publication 212*: 871–890. Farmington Hills: ACI.

RILEM TC 116-PCD 1999. Concrete durability—An approach towards performance testing. *Materials and Structures* 32 (3): 163–173.

Romer, M. & Leeman, A. 2005. Sensitivity of a non-destructive vacuum test method to characterize concrete permeability. In M. Alexander et al. (eds), *Concrete repair, rehabilitation and retrofitting; Proc. inter. conf., Cape Town, 21–23 November 2005*. Boca Raton: CRC Press.

Romer, M. 2005. Effect of moisture and concrete composition on the Torrent permeability measurement. *Materials and Structures* 38: 541–547.

Schönlin, K. & Hilsdorf, H. 1988. Permeability as a measure of potential durability of concrete—Development of a suitable test apparatus. *ACI Special Publication 108*: 99–115. Farmington Hills: ACI.

SIA 2013. *SN 505 262/1, Construction en béton—Spécifications complémentaires, Annexe E: perméabilité à l'air dans les structures*. Zurich: SSIA.

Torrent, R. & Frenzer, G. 1995. *Methoden zur messung und beurteilung der kennwerte des uberdeckungsbetons auf der baustelle—Teil 2* (in German). Bern: Office Federal des Routes.

Torrent, R. 1992. A two-chamber vacuum cell for measuring the coefficient of permeability to air of the concrete cover on site. *Materials and Structures* 25 (6): 358–365.

Torrent, R. 2005. Towards a performance-based specification and conformity control of durability. In A.A. Di Maio & C.J. Zega (eds) *Structural concrete and time; Proc. fib symposium, La Plata, 28–30 September 2005*.

Torrent, R. 2012. Non-destructive air-permeability measurement: from gas-flow modelling to improved testing. *2nd International Microdurability conference, Amsterdam, 11–13 April 2012*.

Torrent, R. et al. 2007. Non-destructive methods to measure gas-permeability. In R. Torrent & L. Luco (eds), *Non-destructive evaluation of the penetrability and thickness of the concrete cover*: 35–70. Bagneux: RILEM Publications.

Concrete Repair, Rehabilitation and Retrofitting IV – Dehn et al. (Eds)
© 2016 Taylor & Francis Group, London, ISBN 978-1-138-02843-2

Combined Non Destructive Testing for concrete compressive strength prediction

G. Concu, B. De Nicolo, N. Trulli & M. Valdés
Department of Civil Engineering, Environmental and Architecture, University of Cagliari, Cagliari, Italy

ABSTRACT: Non Destructive Testing (NDT) techniques are widely used in civil engineering for evaluating materials and structural mechanical parameters such as in situ concrete compressive strength. A combination of two or more NDT techniques is generally recommended, in order to reduce errors dependent on materials, aggregate dimension and size, environmental parameters, so that the accuracy of in situ concrete compressive strength estimation is improved. An experimental campaign has been carried out on several concrete cubic specimens having different design concrete strength, with the aim of determining robust correlations between compressive strength, rebound index and ultrasonic pulse velocity and of evaluating the reliability of the proposed correlations in predicting concrete compressive strength. For this purpose, after NDT techniques have been carried out, specimens have been put through compressive test. The influence of time curing and compressive strength class has been taken into consideration.

1 INTRODUCTION

Assessing the concrete compressive strength of existing structures without affecting buildings functionality and serviceability is a very important task. A standardized procedure for determining in situ concrete compressive strength is the core extraction method (EN 12504-1, 2009) Nevertheless, this method gives partial information because cores strength is affected by: i) the location of the concrete in the structural element, ii) the core orientation, iii) the amount and distribution of moisture in the core at the time of the test, iv) the age of concrete. Italian and European regulations (Italian Building Code, 2008 and Eurocode 8—part 3, 2005) consent that core extraction is complemented by Non Destructive Testing (NDT) techniques, which estimate materials and structural mechanical parameters from non invasive measurements of other parameters empirically correlated to the mechanical ones. A combination of two or more NDT techniques is generally recommended, in order to reduce errors dependent on materials, aggregate dimension and size, environmental parameters, so that the accuracy of in situ concrete compressive strength estimation is improved (Concu, 2011, Breysse, 2012). The combination of Rebound Hammer Test (RHT) and Ultrasonic Testing (UT) is one of the most commonly used and several correlations between the rebound index I_r, the ultrasonic pulse velocity V and the compressive strength are available in literature (RILEM NDT 4, 1993, Di Leo, 1994, Gasparik, 1992, Lenzi, 2010, Tanigawa, 1984). However, these correlations should be determined by statistical regression of experimental data, and they should be calibrated through compressive tests carried out on cored samples.

In this frame, an experimental campaign has been carried out on several concrete cubic specimens having different design concrete strength in order to determine robust correlations between compressive strength, rebound index and ultrasonic pulse velocity and to evaluate the reliability of the proposed correlations for estimating in situ concrete compressive strength.

2 MATERIALS AND METHODS

The experimental campaign has been carried out on 90 standard concrete cubic specimens with a side length of 150 mm. Specimens have been casted by using three different design concrete strength (C8/10, C25/30 and C45/55) according to EN 206 and they have been sorted into three groups each made of 30 specimens. Each group is labeled as the corresponding strength class. Strength classes are defined by both the characteristic cylinder strength f_{ck} and the characteristic cubic strength R_{ck}, evaluated at 28 days of curing on cylindrical and cubic specimens respectively. UT, RHT and compressive tests have been carried out on the specimens.

2.1 *Ultrasonic testing*

NDT techniques based on ultrasonic wave propagation are used in structural diagnosis for investigating

a wide range of structures and infrastructures, and in laboratory for materials characterization, for example concrete and rock elements (EN 12504-4, 2004 and EN 14579, 2004). UT traditional application is based on measurements of the velocity V of waves propagating through the material. The velocity is obtained from the ratio l/t, where t is the time the wave needs to travel along the path of length l. V is a function of material elastic modulus, Poisson's number and density, thus it is directly related to structures elastic parameters, and indirectly to mechanical ones. UT is preferentially carried out applying the Direct Transmission Technique (DTT), in which the wave is transmitted by a transducer through the test object and received by a second transducer on the opposite side. DTT is effective as the broad direction of wave propagation is perpendicular to the source surface and the signal travels through the entire thickness of the item.

Ultrasonic measurements are affected by several factors, including: i) moisture content and temperature of the concrete, ii) water content of the concrete, iii) path length, iv) shape and size of the specimen, v) cracks, fissures and voids.

In this study the DTT has been carried out on specimens (Fig. 1) at 7, 14 and 28 days of curing and it has been performed using the ultrasonic test equipment Pundit Lab+, developed by Proceq®. The testing equipment includes:

- a pairs of standard transducers with natural frequency of 54 kHz for emitting and receiving signals;
- a unit for signals generation, acquisition and preliminary analysis;
- a PC for data storage and further signal processing;
- a dedicated software, Pundit Link, which unlocks the full capabilities of the ultrasonic test system.

The energizing signal is a square wave with high input voltage of 500 V which allows signals to be detected even if strongly attenuated.

For each specimen, eight measures of velocity have been performed. The velocity value associated with a specimen represents the mean value measured on the specimen itself.

2.2 *Rebound Hammer Test*

RHT is a surface hardness test and it is based on the principle that the rebound of an elastic mass strongly depends on the hardness of the concrete surface against which the mass strikes. When the rebound hammer plunger is pressed against the concrete surface, the spring controlled mass in the hammer rebounds. The amount of the mass rebound depends on the concrete surface hardness. (EN 12504-2, 2012).

The factors that mostly affect the rebound index I_r are: i) the type, dosage and size of aggregates, ii) the cement type and dosage, iii) surface conditions (wetting, carbonation, roughness).

In this study each specimen has been placed in a press in order to avoid movements caused by the impact of the hammer and for each face of the specimen the rebound index I_r has been measured (Fig. 2).

After performing both UT and RHT, compressive tests have been carried out on the specimens according to EN 12390-3, 2009.

2.3 *SonReb method*

The SonReb method, formerly developed by RILEM Technical Committees, performs a combination of UT and RHT measurements in order to partially reduce the uncertainties of each method and to provide a more reliable estimation of the concrete compressive strength (Concu, 2014).

The uncertainty of RHT and UT due to the various factors cited in 2.1 and 2.2 respectively, could be partially contrasted by using both methods together. The cross-examination of V and I_r is advantageous

Figure 1. Ultrasonic testing on a cubic specimen.

Figure 2. Rebound hammer test on a cubic specimen.

because I_r provides information about the concrete strength near the surface, whilst V is affected by the inner concrete properties. Moreover, some influencing factors, as moisture content and concrete age, show an opposite effect on UT and RHT (Guida, 2012, Masi, 2013, Pucinotti, 2015). Thus, the application of the SonReb method allows the influencing factors to be contained.

The relationship between concrete compressive strength f_c, V and I_r is described in the literature by several models, one of which, very commonly applied, is given by the following equation:

$$f_c = a \cdot V^b \cdot I_r^c \quad (1)$$

where a, b and c are correlation coefficients determined from the experimental data by the method of least squares. These coefficients strongly depend on the characteristics of the concrete taken into consideration. Therefore a, b and c should be calibrated on the basis of compressive strength tests carried out on cores.

3 RESULTS AND DISCUSSION

UT measurements have been carried out on cubic specimens after 7, 14 and 28 curing days in order to take the influence of the curing process into consideration. Table 1 reports the average values (V), the Standard Deviation (SD) and the Coefficient of Variation (COV) of measured ultrasonic velocity.

During the curing process an increase of ultrasonic pulse velocity can be noted for each group of specimens. As an example Figure 3 shows the variation of V for C25/30 specimens. A similar trend has been obtained for C8/10 and C45/55.

Table 2 reports the average values of rebound index (I_r) and compressive strength (f_c) measured at 28 days of curing. Cylindrical compressive strength has been evaluated from the cubic compressive strength according to the Italian Building Code.

Table 1. Variation of ultrasonic pulse velocities during the curing process.

Curing time	Strength class	V (m/s)	SD (m/s)	COV (%)
7 days	C8/10	3505	12.15	0.35
	C25/30	4270	31.85	0.75
	C45/55	4500	18.65	0.40
14 days	C8/10	3660	20.15	0.55
	C25/30	4435	15.20	0.35
	C45/55	4545	22.85	0.50
28 days	C8/10	3785	27.20	0.70
	C25/30	4520	7.40	0.15
	C45/55	4635	13.70	0.30

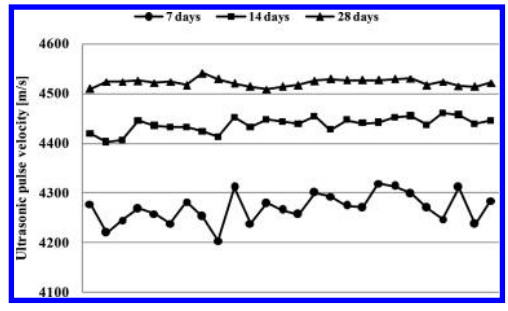

Figure 3. V variation of C25/30 specimens during the curing process.

Table 2. Rebound hammer index and cylindrical compressive strength values.

	C8/10	C25/30	C45/55
I_r	29.25	38.90	42.90
SD*	0.55	1.05	1.05
COV** [%]	1.80	2.70	2.50
f_c [N/mm²]	8.60	27.60	46.65
SD* [N/mm²]	0.35	0.45	1.55
COV** [%]	4.00	1.65	3.35

*SD = Standard Deviation; **COV = Coefficient of Variation.

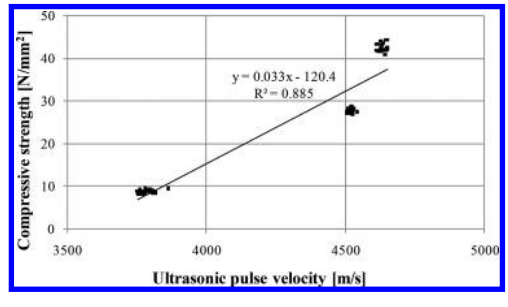

Figure 4. Correlation between ultrasonic pulse velocity and concrete compressive strength.

It can be inferred from Tables 1 and 2 that both V and I_r increase with compressive strength.

In order to evaluate the accuracy of the estimation of in situ concrete compressive strength a regression analysis between non destructive parameters and concrete compressive strength has been performed. Figures 4 and 5 show the correlations V–f_c and I_r–f_c respectively. High R^2 values have been achieved for both correlations.

The results of UT and RHT have been combined by applying the SonReb method. A double power model has been chosen according to Equation 1, and Equation 2 has been achieved. Coefficients a, b and c, shown in Table 3, minimize the sum of

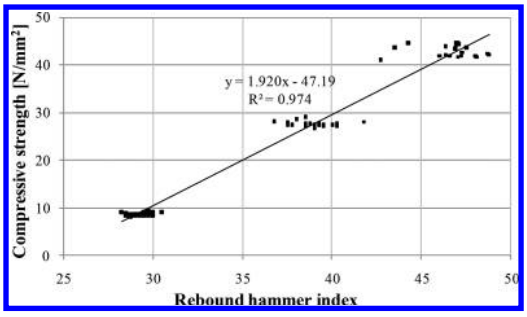

Figure 5. Correlation between Rebound Hammer Index and concrete compressive strength.

Table 3. SonReb Method: coefficients for concrete compressive strength estimation.

a	*b*	*c*
$1.10 \cdot 10^{-16}$	4.05	1.628

squared differences between theoretical and experimental concrete compressive strength.

$$f_c = 1.10 \cdot 10^{-16} \cdot V^{4.05} \cdot I_r^{1.628} \quad (2)$$

A coefficient $R^2 = 0.994$ has been achieved.

4 CONCLUSIONS

An experimental campaign has been carried out on 90 concrete cubic specimens, having different design concrete strength, aiming at determining robust correlations between compressive strength, rebound hammer index and ultrasonic pulse velocity and at evaluating the reliability of the proposed correlations for estimating in situ concrete compressive strength. UT measurements have been carried out on the specimens at 7, 14 and 28 curing days in order to take the influence of the curing process into consideration.

Throughout the achieved results the following conclusions can be drawn:

- an increase of ultrasonic pulse velocity can be noted during the curing process;
- both ultrasonic pulse velocity and rebound hammer index increase with concrete compressive strength;
- both ultrasonic pulse velocity and rebound hammer index well correlate with concrete compressive strength;
- a slight increase in R^2 coefficient can be achieved when the SonReb method is applied.

ACKNOWLEDGEMENTS

The authors would like to thank Unical S.p.A. for the support.

REFERENCES

Breysse, D. 2012. Nondestructive evaluation of concrete strength: an historical review and a new perspective by combining NDT methods. *Construction and Building Materials* 33: 139–163.

Concu, G., De Nicolo, B., Pani, L. 2011. Non-Destructive Testing as a tool in reinforced concrete buildings refurbishments. *Structural Survey* 29 (2): 147–161.

Concu, G., De Nicolo, B., Pani, L., Trulli, N., Valdés, M. 2014. Prediction of Concrete Compressive Strength by Means of Combined non-destructive Testing. *Advanced Materials Research* 894: 77–81. Trans Tech Publications, Switzerland doi:10.4028/www.scientific.net/AMR.894.77.

Di Leo, A., Pascale, G. 1994. Il giornale delle prove non distruttive 4.

EN 1998-3. Eurocode 8: Design of structures for earthquake resistance—Part 3: Assessment and retrofitting of buildings, 2005.

EN 12390-3. 2009. Testing hardened concrete—Part 3. Compressive strength of test specimens.

EN 12504-1. 2009. Testing concrete in structures. Cored specimens. Taking, examining and testing in compression.

EN 12504-2. 2012. Testing concrete in structures—Part 2. Non-destructive testing. Determination of rebound number.

EN 12504-4. 2004. Testing concrete—Part 4. Determination of ultrasonic pulse velocity.

EN 14579. 2004. Natural stone test methods. Determination of sound speed propagation.

EN 206. 2013. Concrete. Part 1: Specification, performance, production and conformity.

Gasparik, G. 1992. *Quaderno didattico*, AIPND, Brescia.

Guida, A., Pagliuca, A., Minerva, A.T. 2012. *International Journal of Geophysics*, 2012, Article ID 659612

Italian Building Code. 2008. DM 14/01/2008, Norme tecniche per le costruzioni. Suppl. Ord. n.30 alla G.U. n.29 del 4/2/2008.

Lenzi, M., Versari, D., Zambrini, R. 2010. Indagine sperimentale di calibrazione del metodo combinato SonReb, INARCOS.

Masi, A., Chiauzzi, L. 2013. An experimental study on the within-member variability of in situ concrete strength in RC building structures. *Construction and Building Materials* 47: 951–961.

Pucinotti, R. 2015. Reinforced concrete structure: Non destructive in situ strength assessment of concrete. *Construction and Building Materials* 75: 331–341.

RILEM NDT 4. 1993. Recommendation for in situ concrete strength determination by non destructive combined methods, Compendium of RILEM Technical Recommendations, E&FN Spon, London.

Tanigawa, Y., Baba, K., Mori, H. 1984. Proc. of In Situ/Nondestructive Testing of Concrete, Detroit, American Concrete Institute, SP-82: 57–76.

Concrete Repair, Rehabilitation and Retrofitting IV – Dehn et al. (Eds)
© 2016 Taylor & Francis Group, London, ISBN 978-1-138-02843-2

Estimation of concrete strength and stiffness by means of Ultrasonic Testing

G. Concu, B. De Nicolo, N. Trulli & M. Valdés
Department of Civil Engineering, Environmental and Architecture, University of Cagliari, Cagliari, Italy

ABSTRACT: The need to assess the structural condition of existing concrete structures strongly supports the development of Non Destructive Testing (NDT) techniques for evaluating the degree of decay and for predicting mechanical parameters such as strength and stiffness.

Among NDT, Ultrasonic Testing (UT) is frequently applied, because the velocity of ultrasonic signals travelling through the material is directly related to mechanical and physical parameters, e.g. dynamic elastic modulus, Poisson's ratio and density.

UT has been carried out on several concrete cores having different size and strength, and the velocity of both longitudinal and shear waves (V_l and V_s respectively) has been measured. Then the dynamic elastic modulus E_d has been derived from V_l and V_s values, according to waves propagation theory. Next, cores have been put through compression test, in order to determine the static elastic modulus E_s and the compressive strength.

Results have been analyzed and discussed.

1 INTRODUCTION

The assessment of existing concrete structures is a complex problem to deal with, especially when it concerns building of historical relevance. The evaluation of a structure real state shouldn't interfere with the condition and the functionality of the building, and should possibly involve limited costs. The need to assess the structural condition of existing concrete structures strongly supports the development of Non Destructive Testing (NDT) techniques, in order to evaluate the degree of decay and to estimate mechanical parameters such as strength and stiffness (Breysse, 2012, Concu, 2014, Puccinotti, 2015, RILEM NDT 4, 1993, Concu, 2011). Among NDT, Ultrasonic Testing (UT) is frequently applied, because the velocity of ultrasonic signals travelling through the material is directly related to mechanical and physical parameters, e.g. dynamic elastic modulus, Poisson's ratio and density (Naik, 2004).

In the past, several efforts have been made to estimate materials strength from measurements of ultrasonic waves velocity, starting from the assumption that the velocity is directly related to the elastic modulus, and the elastic modulus is directly related to the strength (Bogas, 2013, Cannas, 2013, Chavez, 2014, Khan, 2011, Yildrim, 2011). However, strength estimation is acceptable only when a direct correlation between velocity and strength is available, for example by measuring the velocity on cores extracted from the structure and then tested for strength determination. In this context, an experimental program has been started in order to better understand the correlation between compressive strength, elastic modulus and ultrasonic waves velocity.

UT has been carried out on several concrete cores having different size and strength, and the velocity of both longitudinal and shear waves (V_l and V_s respectively) has been measured. Then dynamic elastic modulus E_d has been derived from V_l and V_s values, according to waves propagation theory. Next, cores have been put through compression test, in order to determine the static elastic modulus E_s and the compressive strength.

2 MATERIALS AND METHODS

The experimental campaign has been carried out on 26 concrete cylindrical specimens having two different size: (i) diameter of 65 mm and length of 130 mm; (ii) diameter of 100 mm and length of 260 mm. Specimens have been cored from cubic specimens having a side length of 300 mm which have been casted by using different design concrete strength. The cores have been sorted into five groups, from A to E, depending on their compressive strength and their dimensions, as summarized in Table 1.

UT has been carried out on the cores in order to evaluate the dynamic modulus of elasticity. Then, measurement of both static modulus of elasticity and compressive strength has been carried out.

Table 1. Groups of specimens.

Group	Group size	f_{ck} range (N/mm^2)	Length (mm)	Diameter (mm)
A	6	5–15	260	100
B	5	20–35	260	100
C	5	45–60	260	100
D	3	5–15	130	65
E	7	30–60	130	65

2.1 *Ultrasonic Testing and dynamic modulus of elasticity*

UT traditional application is based on measurements of the velocity V of waves propagating through the material. The velocity is obtained from the ratio *l*/*t*, where *t* is the time the wave needs to travel along the path of length *l* (EN 12504-4, 2004, EN 14579, 2004).

UT has been performed by using the ultrasonic test equipment Pundit Lab+, developed by Proceq®. The testing equipment includes:

- a pairs of standard transducers with natural frequency of 54 kHz for emitting and receiving signals;
- a pairs of shear wave transducers with natural frequency of 250 kHz for emitting and receiving signals;
- a unit for signals generation, acquisition and preliminary analysis;
- a PC for data storage and further signal processing;
- a dedicated software, Pundit Link, which unlocks the full capabilities of the ultrasonic test system.

For each specimen the velocity of both longitudinal and shear waves has been calculated as the average value of five repeated measurements.

From the basic theory of propagation of ultrasonic waves on concrete (Jones, 1962) it is possible to evaluate the dynamic modulus of elasticity from V_l and V_s as follows:

$$\nu_d = \cdot \frac{V_l^2 - 2 \cdot V_s^2}{2 \cdot \left(V_l^2 - V_s^2\right)} \tag{1}$$

$$E_d = 2 \cdot \rho \cdot V_s^2 \cdot \left(1 + \nu_d\right) \tag{2}$$

where ν_d is the dynamic Poisson's ratio.

2.2 *Static modulus of elasticity and compression test*

The static modulus of elasticity E_s has been evaluated by applying the Method B described in EN 12390-13, 2013:

$$E_s = \frac{\Delta\sigma}{\Delta\varepsilon} \tag{3}$$

where $\Delta\sigma$ is the difference between the measured stresses and $\Delta\varepsilon$ is the strain difference during the test.

Furthermore, the theoretical modulus of elasticity E_t has been calculated according to the formula proposed by the Italian Building Code (DM 14/01, 2008):

$$E_t = 22000 \cdot \left(\frac{f_{cm}}{10}\right)^{0.3} \tag{4}$$

where f_{cm} is the effective cylindrical compressive strength evaluated according to EN 12390-3, 2009.

3 RESULTS AND DISCUSSION

Ultrasonic parameters V and E_d increase as compressive strength increases. The same trend is shown by E_s. Table 2 summarizes, for each group of cores, the average values of longitudinal and shear wave velocities (V_l, V_s), dynamic, static and theoretical modulus of elasticity (E_d, E_s, E_t), the Standard Deviation (SD) and the Coefficient of Variation (COV).

A regression analysis between non destructive parameters and mechanical parameters has been carried out. Figure 1 shows the correlations between the characteristic compressive strength f_{ck} and the longitudinal wave velocity V_l while

Table 2. Average values of experimental and theoretical data.

	Groups of cores				
Parameter	A	B	C	D	E
V_l [m/s]	4110	4285	4475	3510	4235
SD [m/s]	270	185	55	230	90
COV [%]	6.55	4.30	1.25	6.60	2.20
V_s [m/s]	2445	2550	2615	2085	2525
SD [m/s]	155	110	20	140	55
COV [%]	6.30	4.35	0.75	6.70	2.25
E_d [N/mm^2]	31935	35225	38050	23435	34910
SD [N/mm^2]	4555	3250	400	3745	1610
COV [%]	3.50	5.60	2.60	2.75	4.60
E_s [N/mm^2]	23460	28910	31390	28585	37300
SD [N/mm^2]	1360	835	1570	365	1275
COV [%]	5.80	2.90	5.00	1.30	3.40
E_t [N/mm^2]	26960	32935	37445	25615	35555
SD [N/mm^2]	2230	1425	880	1980	955
COV [%]	8.30	4.35	2.35	7.75	2.70

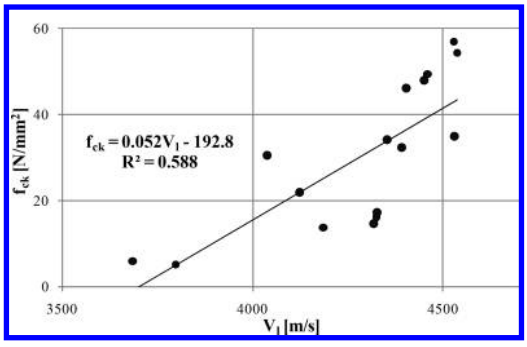

Figure 1. Correlation between characteristic compressive strength and longitudinal wave velocity for groups A, B and C.

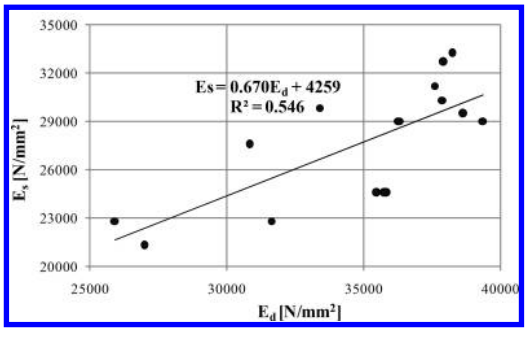

Figure 2. Correlation between static and dynamic modulus of elasticity for groups A, B and C.

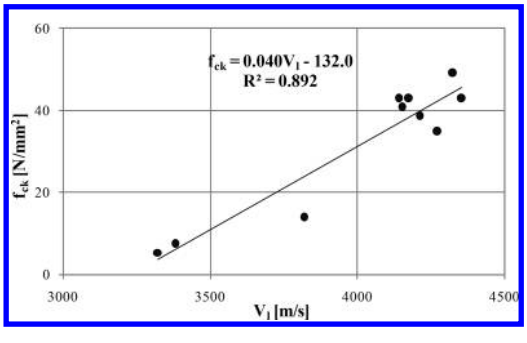

Figure 3. Correlation between characteristic compressive strength and longitudinal wave velocity for groups E and F.

Figure 2 shows the correlation between the static modulus of elasticity E_s and the dynamic modulus of elasticity E_d. Both correlations are referred to groups A, B and C (bigger cores).

In a similar way Figures 3 and 4 show the correlations f_{ck} – V_l and E_s – E_d for groups E and F (smaller cores).

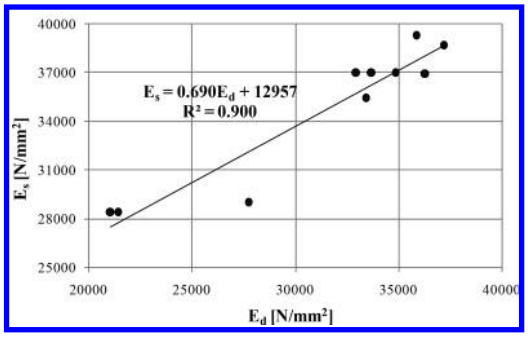

Figure 4. Correlation between static and dynamic modulus of elasticity for groups E and F.

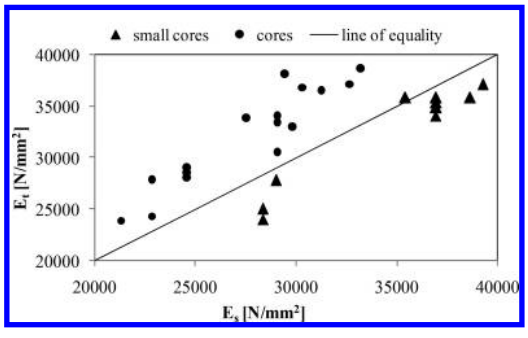

Figure 5. E_s vs E_t for each specimen.

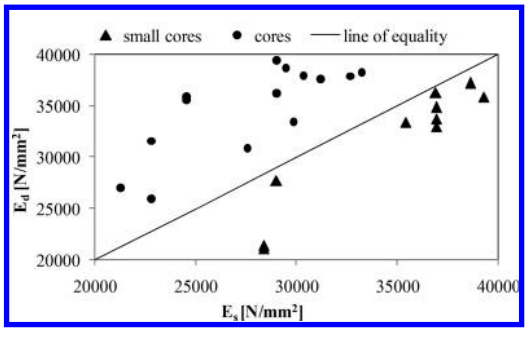

Figure 6. E_d vs E_s for each specimen.

The correlations concerning groups E and F show higher R^2 values than those concerning groups A, B and C.

Figure 5 plots E_t, the theoretical modulus of elasticity, versus E_s, experimentally measured, while Figures 6 plots E_d, derived from UT, versus E_s.

An overestimation of E_t compared to E_s can be observed for groups A, B and C (bigger cores), while groups E and F (smaller cores) show an opposite behavior (Fig. 5). Similarly, E_d is overestimated

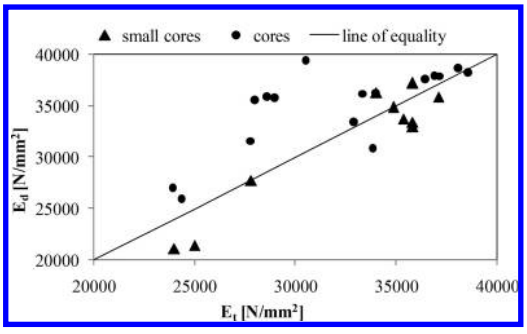

Figure 7. E_d vs E_t for each specimen.

compared to E_s for groups A, B and C, while it is underestimated for groups E and F (Fig. 6).

In Figure 7 E_d is plotted versus E_t. E_d is generally higher than E_t for bigger cores, while smaller cores show the opposite behavior.

4 CONCLUSIONS

An experimental campaign has been carried out on 26 concrete cylindrical specimens having different size. Specimens have been cored from cubic specimens having a side length of 300 mm which have been casted by using different design concrete strength.

Ultrasonic velocities of both longitudinal and shear waves propagating through the specimens have been measured in order to evaluate the dynamic modulus of elasticity. The static modulus of elasticity and the compressive strength have been experimentally determined and the theoretical modulus of elasticity has been evaluated too.

Throughout the achieved results the following conclusions can be drawn:

- as the compressive strength increases, an increase of the ultrasonic parameters (V_l, V_s, E_d) and of both the theoretical and the experimental modulus of elasticity (E_s and E_t) is achieved;
- the correlations $V_l - f_{ck}$ and $E_d - f_{ck}$ fit better for smaller cores than for bigger cores;
- when compared to E_s, both E_t and E_d show an overestimation for bigger cores and an underestimation for smaller cores;
- E_d is generally higher than E_t for bigger cores, while smaller cores show an opposite behavior.

ACKNOWLEDGEMENTS

The authors would like to thank Unical S. p. A. for the support.

REFERENCES

Bogas, J.A., Gomes, M.G., Gomes, A. 2013. Compressive strength evaluation of structural lightweight concrete by non-destructive ultrasonic pulse velocity method. *Ultrasonics*, 53: 962–972.

Breysse, D. 2012. Nondestructive evaluation of concrete strength: an historical review and a new perspective by combining NDT methods. *Construction and Building Materials* 33: 139–163.

Cannas, B., Carcangiu, S., Concu, G., Fanni, A., Forcinetti R., Montisci, A., Sias, G., Trulli, N., Usai, M. 2013. Ultrasonic Testing of Masonry Structures by Features Extraction and Self Organising Maps. *International Journal of Civil Engineering and Building Materials*, 3 (4); 166–178.

Chavez, L., Alonso, E., Martínez, W., Graff, M., Artega, J. 2014. Prediction of the Static Modulus of Elasticity Using Four non Destructive Testing. *Journal of Construction*, 13(1): 33–40.

Concu, G., De Nicolo, B., Pani, L. 2011. Non-Destructive Testing as a tool in reinforced concrete buildings refurbishments. *Structural Survey* 29 (2): 147–161.

Concu, G., De Nicolo, B., Pani, L., Trulli, N., Valdés, M. 2014. Prediction of Concrete Compressive Strength by Means of Combined non-destructive Testing. *Advanced Materials Research* 894: 77–81.

EN 12390-3. 2009. Testing hardened concrete—Part 3. Compressive strength of test specimens.

EN 12390-13. 2013. Testing hardened concrete. Part 13: Determination of secant modulus of elasticity in compression.

EN 12504-4. 2004. Testing concrete—Part 4. Determination of ultrasonic pulse velocity.

EN 14579. 2004. Natural stone test methods. Determination of sound velocity propagation.

Italian Building Code. 2008. DM 14/01/2008, Norme tecniche per le costruzioni. Suppl. Ord. n.30 alla G.U. n.29 del 4/2/2008.

Jones, R. 1962. Non Destructive Testing of Concrete. Cambridge University Press, London.

Khan, Z., Cascante, G., El Naggar, M.H. 2011. Measurement of dynamic properties of stiff specimens using ultrasonic waves. *Can. Geotech. J.* 48.

Naik, T., Malhotra, V.M., Popovics, J.S. 2004. The ultrasonic pulse velocity method. *Handbook of nondestructive testing of concrete*. CRC Press.

Pucinotti, R. 2015. Reinforced concrete structure: Non destructive in situ strength assessment of concrete. *Construction and Building Materials* 75: 331–341.

RILEM NDT 4. 1993. Recommendation for in situ concrete strength determination by non destructive combined methods, Compendium of RILEM Technical Recommendations, E&FN Spon, London.

Yıldırım, H., Sengul, O. 2011. Modulus of elasticity of substandard and normal concretes. *Construction and Building Materials*, 25: 1645–1652.

Concrete Repair, Rehabilitation and Retrofitting IV – Dehn et al. (Eds)
© 2016 Taylor & Francis Group, London, ISBN 978-1-138-02843-2

A repair quality control with elastic waves based methods vs. concrete substrate quality

A. Garbacz & T. Piotrowski
Warsaw University of Technology, Warsaw, Poland

L. Courard
University of Liege, Liege, Belgium

B. Bissonnette
CRIB—Department of Civil Engineering, Laval University, Quebec (QC), Canada

ABSTRACT: An adhesion in repair system is one of the most important factors that affect the repair efficiency. The elaboration of reliable nondestructive method for an adhesion mapping is one of the most important tasks. A majority of NDT methods mentioned in EN 1504-10 and ACI Concrete Repair Manual for assessment of concrete structures are based on propagation of stress waves. However, these investigations are rarely focused on evaluation of bond strength. Repair system is difficult to test with NDT methods because of many factors influencing stress wave propagation. In this paper the effect of a quality of concrete substrate on propagation of stress waves in repair system and their influence on possibility of the bond strength estimation is discussed.

1 INTRODUCTION

As a result of repair or protection of the building structure at least two component system: concrete substrate in contact with repair material is produced.

An adhesion in such system is one of the most important factors that affect the durability of repair (Czarnecki & Emmons, 2002). The adhesion depends on many phenomena taking place at interface zone (Courard 2005, Silfwerbrand & Beushausen 2006, Garbacz et al. 2005, Courard et al. 2011): presence of bond-detrimental layers, wettability of concrete substrate by repair materials, roughness and microcracking of concrete substrate, moisture content in concrete substrate versus repair material (i.e. cement or polymer mortar).

The above factors imply that according to the many standards and guidelines, e.g. European Standard EN 1504-10 and ACI Concrete Repair Manual (2003), the both of bond strength and bond quality should be evaluated. The pull-off test is recommended for assessment of a bond strength. The use of pull-off test, due to its semi-destructive character, is restricted by owners and managers. Therefore, the elaboration of reliable nondestructive method for an adhesion mapping is one of the most important tasks. A majority of NDT methods mentioned in EN 1504-10 and ACI Concrete Repair Manual for assessment of concrete structures are based on propagation of stress waves. Particularly ultrasonic methods (UPV), Impact Echo (IE) and Impulse-Response (IR) methods are recommended for evaluation of repair quality. Lately a combinations of NDT methods are investigated (Garbacz et al. 2013). However, these investigations are rarely focused on evaluation of bond strength.

To select the appropriate NDT method for repair quality control, the following factors should be taken into account (Carino 1997, Garbacz 2005):

- type and size of defects at the interface zone to be investigated;
- thickness of overlay;
- type of repair material (cement based or polymer composites);
- quality of concrete substrate (roughness, microcracking, saturation level).

First two factors have a major influence depend mainly on NDT method used. Type of repair material could affect a reflection coefficient. In the case of multilayer system the propagation of stress waves depends on differences in acoustic impedances of the both repair material and concrete substrate (Carino 1997). The reflection coefficient for concrete/air interface is equal nearly to 1.0—there is almost total reflection at the interface.

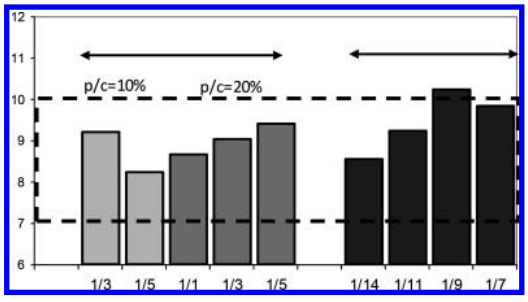

Figure 1. The acoustic impedance of tested polymer-cement and polymer (w/o Portland cement) mortars and concretes representative for commercial repair mortar; dotted line—typical range of acoustic impedances for cement concretes and mortars.

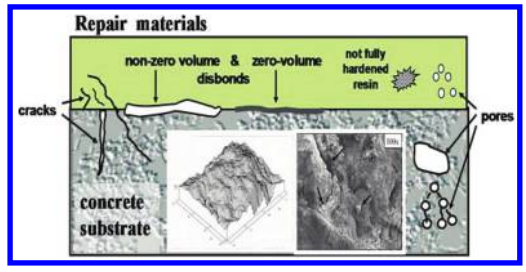

Figure 2. Sketch of possible defects in repair system and example of surface geometry of concrete substrate after milling.

Experimental investigations with IE method have shown that usually an interface is "visible" if absolute value of R coefficient is higher than +0.24 (Sansalone & Carino 1989). Garbacz (2015) showed that in the case of many commercial polymer cement (PCC) repair mortars their acoustic impedances are similar to the it can be assumed that repair material and typical concrete substrates have similar acoustic impedances (Fig. 1).

The above conclusions allow to assume that detection of flaws at the interface overlay—concrete substrate can be performed with procedures developed for "solid" concrete structures. The effect of interface should be taken into account in the case of overlays with acoustic impedance different than that for concrete substrate. e.g. pure polymer coating, asphalt pavements, etc.

The aim of this paper is to analyze of the effect of a quality of concrete substrate on propagation of stress waves in repair system and their influence on a possibility of the bond strength estimation.

2 REPAIR SYSTEM AS AN OBJECT OF NDT ASSESSMENT

Repair system is difficult to test with NDT methods because of many factors influencing stress wave propagation (Fig. 2).

Two main types of defects affecting stress wave propagation might occur in such system (Adams & Drinkwater 1997):

– adhesion type (at the interface zone: overlay-substrate): various types of "non-zero" volume disbonds (e.g., voids, delaminations) and "zero-volume" disbonds—weak adhesion areas (e.g. due to presence of dust, oil, etc.);
– cohesion type (in repair material or/and concrete substrate): porosity, cracks, honeycombing, partially non-hardened resin in the case of polymer material.

Above defects are often result of the operations that have to be performed prior to a repair as well as an application of repair material. Surface concrete treatment is used to remove deteriorated and carbonated concrete and any type of layer that causes the decrease of adhesion and to enlarge the area of contact surface by increasing surface roughness. The technique and the energy chosen induce many different profiles. It has been widely demonstrated that a surface preparation of concrete substrate can influence significantly on the microcracking level and surface roughness, the substrate saturation level and, as a consequence, it may affect the bond strength between repair material and concrete substrate.

The effect of concrete surface roughness on the adhesion is not clear. Some authors found a correlation between adhesion strength and some "roughness parameters" (e.g. Fukuzawa et al. 2001). Courard et al. (2014) have shown, using multiple regression approach, that roughness is a statistically significant variable influencing bond strength. From the other hands, a few authors (Silfwerbrand & Beushausen 2006, Garbacz et al. 2005, Bissonnette et al. 2006) conclude that surface roughness itself does not have significant influence but microcracks induced by surface treatment contribute to the deterioration of the quality of the bond.

The effect of a bond coat is also discussed. According to one opinion (Silfwerbrand & Paulsson 1998), the bond coat should be avoided because of creation of an extra plane of weakness. Moreover, bond coat could have a negative effect with very rough surfaces because it could limit a good interlocking effect between substrate and repair material. The other conclusion drawn by some authors is that a presence of bond coat can significantly increase the adhesion (Austin et al. 1995, Pretorius & Kruger 2001. Garbacz et al. 2005).

Using stress waves based methods for evaluation of bond strength needs to find answer whether the interface quality affects the stress wave propagation and if is it possible to extract from the signal any information related to the bond strength.

3 TESTED REPAIR SYSTEMS

In the framework of several project conducted at Warsaw University of Technology in cooperation with the University of Liege various repair systems different in concrete surface and interface quality, were tested. In the first stage, a commercial PCC repair mortar containing glass microfibers was applied on relatively weak concrete substrate (C20/25) subjected, prior to repair, to various surface treatments with different aggressiveness levels. As result concrete substrates with different roughness and microcracking levels (Table 1) were obtained. Surface roughness was characterized by

Table 1. SEM observation and profile analysis of the concrete substrate C20/25 after various surface preparation.

Example of surface view SEM - magnification 100x	Waviness profiles obtained with profilometer and selected parameters
No treatment 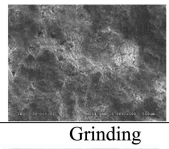	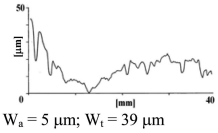 W_a = 5 µm; W_t = 39 µm
Grinding 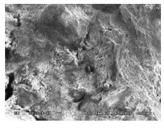	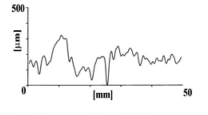 W_a = 32 µm; W_t = 219 µm
Sandblasting 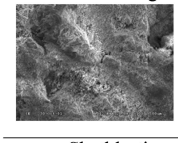	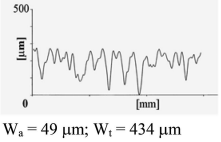 W_a = 49 µm; W_t = 434 µm
Shotblasting 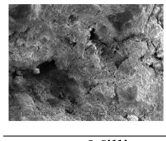	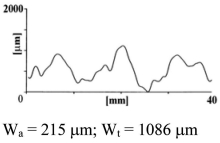 W_a = 215 µm; W_t = 1086 µm
Milling 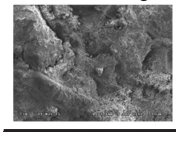	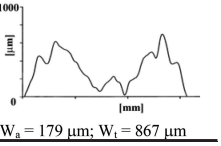 W_a = 179 µm; W_t = 867 µm

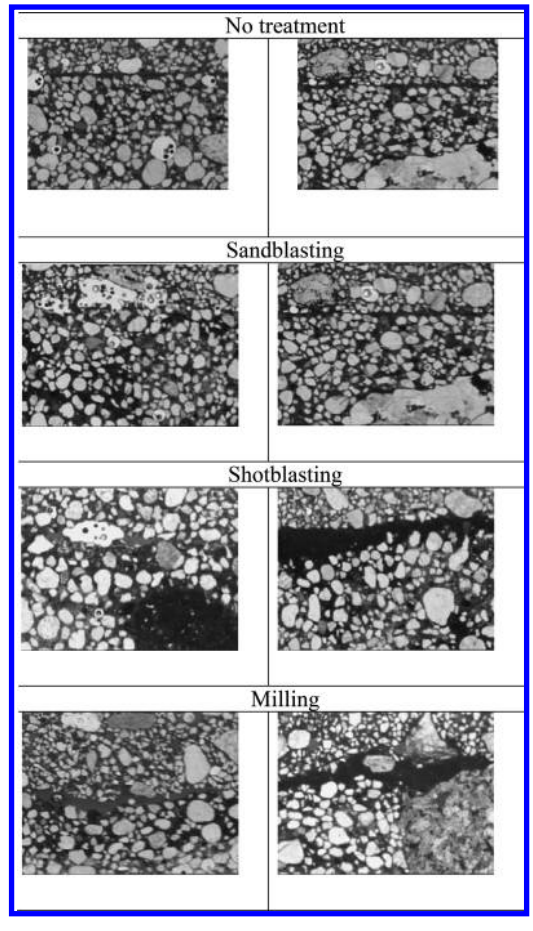

Figure 3. View of the interface between repair material and concrete substrate after various way of surface preparation without (left) and with (right) bond coat.

parameters of the waviness profile (high frequency filtration of profile) determined with a mechanical profilometer (Garbacz et al. 2005).

According to the manufacturer's technical data sheet, this mortar should be used with a polymer-cement bond coating because of its low workability (the details are given in Garbacz et al. 2005). The overlay (thickness 10 mm) was applied on the concrete substrate with and without a bond coat to obtain different air void contents and levels of compactions at the interface (Fig. 3).

4 NDT MEASUREMENTS

After 28 days of hardening, the IE and ultrasonic measurements were carried out. The IE measurements were performed with Docter test system using the impactor of 2 mm in diameter to generate

a stress wave. The same repair systems were tested further with ultrasonic pulse echo method using commercial digital ultrasonic flaw detector ULTRA CUD20 and a pair of transducers with nominal frequency of 500 kHz. This method is expected to be more sensitive to the presence of voids at interface because of shorter waves are generated. Each measurement received an A-scan consisted of characteristic peaks corresponding to the reflection from the interface.

Afterwards, the adhesion between the repair material and the concrete substrate was determined with the pull-off test (acc. EN 1542). Additionally, the quality of interface was observed on the cross-sections with light microscope.

The results of investigations can be summarized as follows. As the surface roughness increased (Fig. 4), the pull-off strength for the systems without bond coat decreased and more air voids at the interface zone were observed (see Fig. 3). In the case of system with bond coat the bond strength in repair systems were less sensitive on concrete substrate quality.

The test results indicate that there is no correlation between the pull-off strength and the P wave velocity for the repair system with bond coat (Fig. 5a). The bond coat filled irregularities of concrete substrate properly and air voids at the interface were not observed. The statistically significant relationship was obtained for systems without the bond coat—the P wave velocity increased as the pull-off strength increases. In this case, the fraction of air voids at the interface increases when the roughness increases. In both types of repair systems the pulse velocity was not correlated with the substrate roughness (Fig. 5b). The trend was found in studying the relationship between the amplitude of maximum frequency peak and the pull-off strength (Fig. 5c): as the pull-off strength increases, the amplitude value of peak decreases. Statistical significance of the relationship between the amplitude value of the highest peak and the mean waviness of surface profile (Fig. 5d) was also found but only for the repair systems without the

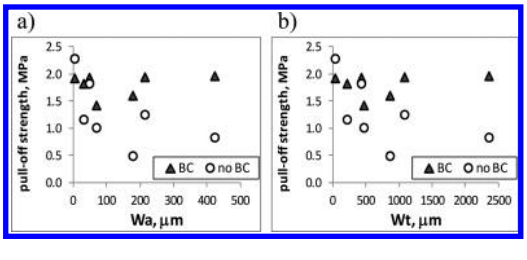

Figure 4. Pull-off strength vs. waviness parameter W_a (a) and Wt (b) for different repair systems with and without bond coat (BC).

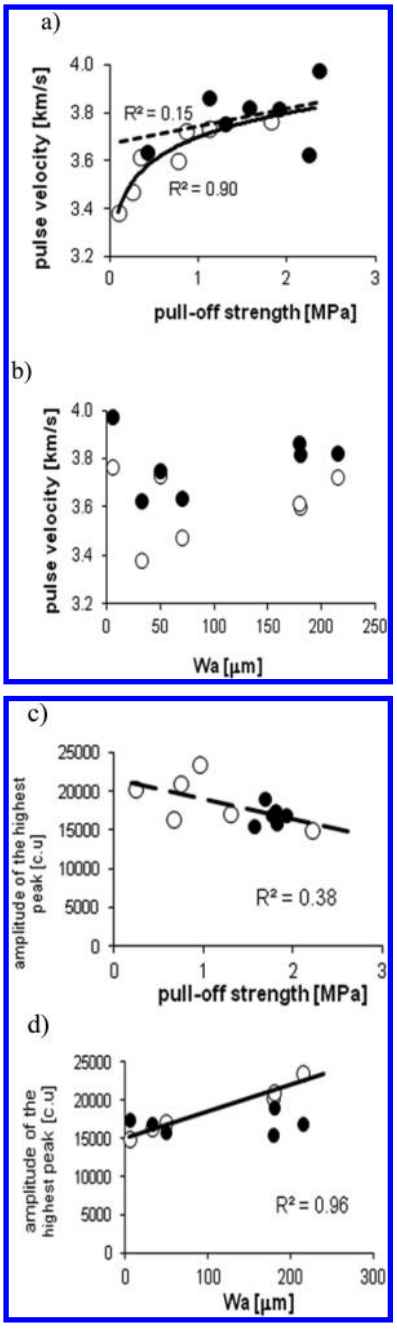

Figure 5. Relationships between parameters describing stress wave propagation and parameters describing repair system quality: pulse velocity IE vs. (a) pull-off strength, (b) mean waviness of profile, Wa; amplitude of the highest peak of frequency spectrum of ultrasonic signal (c.u.—conventional unit) vs. (c) pulse velocity IE and (d) mean waviness of profile, Wa, (concrete substrate C20/25, overlays with (•) and without (o) the bond coat; adopted from (Garbacz 2010).

bond coat, essentially because the fraction of air voids increased with the surface roughness.

The results obtained indicates that for IE method, the roughness of the concrete substrate does not affect significantly the P wave propagation through the repair system if the bond quality is sufficient (absence of large voids at the interface). The ultrasonic method is than more sensitive.

The above relationship was investigated for stronger concrete, C40/50 (Garbacz et al. 2006). Four types of surface preparation techniques were used: polishing, sandblasting, scabbling and very high pressure water-jetting. The concrete slabs ($600 \times 800 \times 130$ mm) have been covered by a self-compacting commercial PCC mortars (3-cm thick). For the repair systems, two specific ranges of the IE frequency spectrums were analyzed: around the bottom peak frequency and around frequencies corresponding to the interface. The lowest mean values of bottom peak were obtained for polishing and hydrodemolition. The amplitude of interface peak was the highest for polished samples. Scabbled and hydrodemolished samples present similar values of interface peak. The relationships between amplitudes of either bottom or interface peaks and parameters describing quality of repair systems were not statistically significant for any of the tested repair systems (Fig. 6).

Additionally the normalized frequency spectrums were characterized with RugoDS program using 3D surface profile analyzing approach (Courard et al. 2007). The number of I-E measurement from 1 to 10 was the third axe parameter (Fig. 7a) and all the statistic parameters (Fig. 7b) for 3D distribution of frequency spectrum were calculated.

There were no statistically significant relationships between the amplitude parameters of IE frequency spectrum and the pull-off strength (Fig. 8). However, the relations between statistical these parameters of frequency spectrum and parameters describing concrete substrate quality show some tendencies. Roughness and cracking influenced the minimum amplitude level, Wm, of the IE frequency profile. It was observed that as the roughness (Fig. 8b) and cracking (Fig. 8c) increased the minimal amplitude of frequency profile. This tendencies could be interpreted as an increase of noise level in the IE frequency spectrum due to roughness and cracking of concrete substrate. Similar results were obtained by Santos et al. (2011). Their Finite Element Model (FEM) simulations indicates that the roughness of a concrete substrate had relatively low influence on the ultrasonic signal

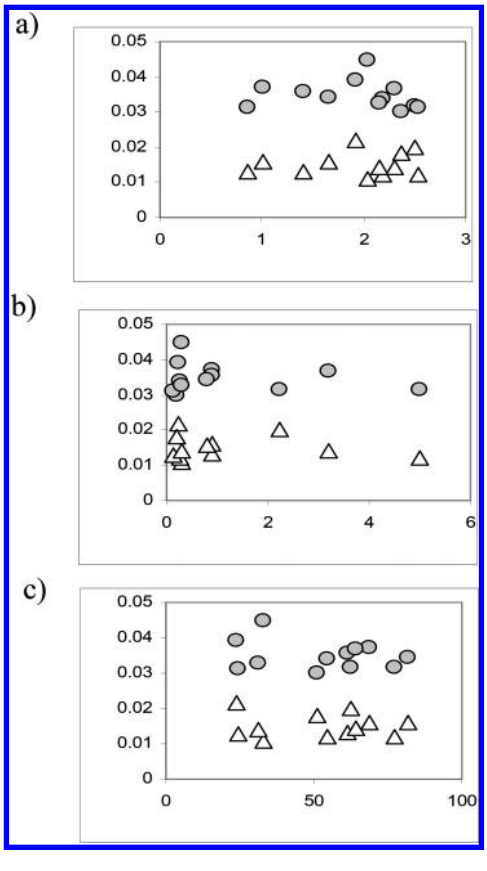

Figure 6. Amplitude of bottom (•) and interface (Δ) frequency peaks versus: (a) pull-off strength, (b) surface roughness index, SRI, (c) length of crack (adopted from Garbacz et al. 2006).

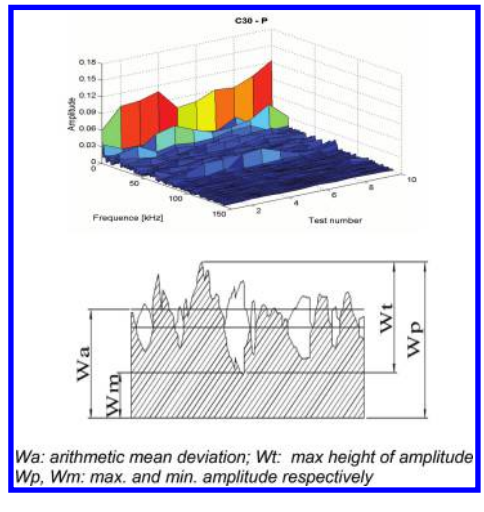

Figure 7. Example of 3-D frequency distribution and definitions of IE frequency spectrum amplitude parameters applied for characterization of impact-echo signal.

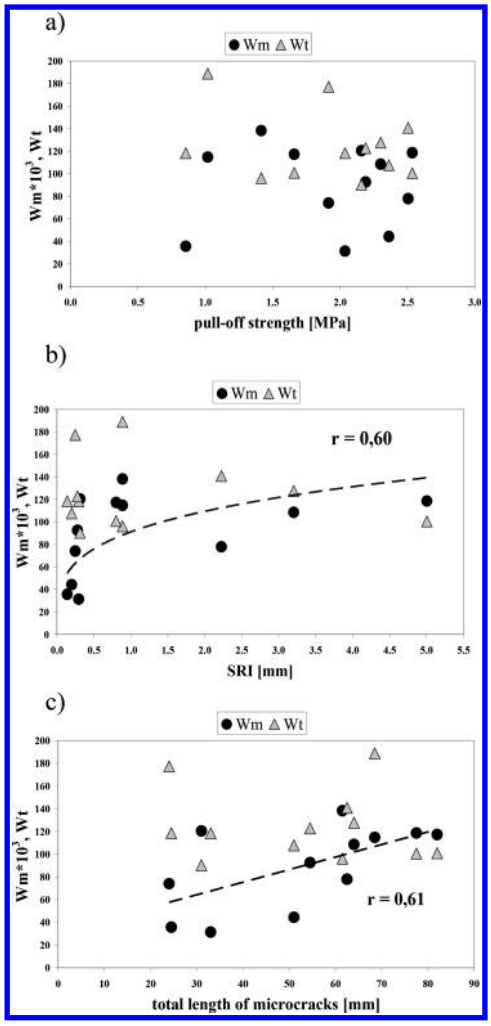

Figure 8. Maximum height of amplitude Wt, and minimum amplitude level, Wm, of 3D frequency distribution versus (see Fig.7): (a) pull-off strength, (b) surface roughness index SRI, c) total length of cracks (adopted from Garbacz et al. 2006).

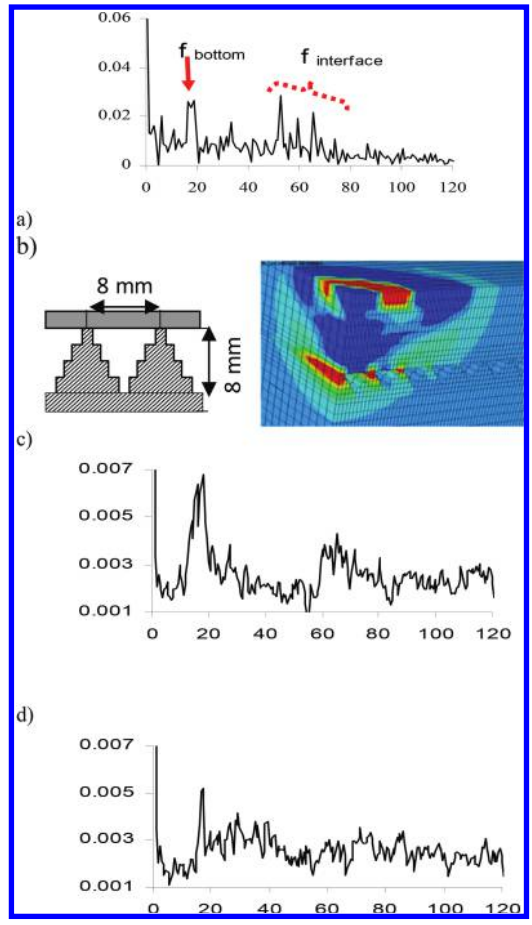

Figure 9. Typical frequency spectra for repair systems with concrete substrate after hydrodemolition: (a) experimental results for plate; FEM simulations: (b) examples of disturbance in wave propagation in the case of air voids presence at interface, (c) frequency spectrum for substrate irregularities unfilled—presence of air voids at the interface, (d) frequency spectrum for substrate irregularities completely filled (adopted from Kwaśniewski & Garbacz 2008).

amplitude as well. However, they observed that the pulse decreases in the presence of rough interfaces, due to a greater wave dispersion.

The effect of substrate roughness and presence of air voids at the interface on stress wave propagation were also investigated using FEM of repair system by Kwaśniewski & Garbacz (2008). The simulations were performed for system with the same geometry that used in the experiment. The surface geometry corresponded to real surfaces roughness obtained after sandblasting and hydro-demolition under high pressure of previously described concrete substrate.

Two extreme cases of filing of surface irregularities were modelled: completely filled and non-filled surface irregularities. The material; properties (E modulus and density) of both concrete substrate and overlay were determined experimentally. The results of simulations indicate that the presence of air voids at the interface can significantly influence the stress wave propagation. This was observed in the both of experimental (Fig. 9a) and FEM (Fig. 9b-d) frequency spectra. If surface profile irregularities are filled, the surface roughness does not significantly influence the resulting frequency spectrum (Fig. 9d).

5 SUMMARY

The multi-variants investigations showed that for the both IE and ultrasonic methods, the roughness and microcracking of the concrete substrate does not affect significantly the P wave propagation through the repair system if the bond quality is sufficient—absence of large voids at the interface. However, parameters describing roughness and microcracking of concrete substrate can be considered as important parameter for improvement of reliability of the bond strength evaluation using more complicated signal analyses (eg. wavelet approach, artificial neural networks) of stress waves resulting from NDT methods. First examples of such analyses can be found e.g. Sadowski & Hoła (2014) showed that substrate roughness is an important factor for the prediction of bond strength between the concrete layers in concrete floors using the nondestructive acoustic techniques together with artificial neural networks.

ACKNOWLEDGEMENTS

This paper was elaborated in the framework of the research projects carried out in the framework of the scientific cooperation programs between foreign agencies of Wallonia-Brussels International (Belgium), (MNiSW) Polan and Laval University, Canada.

REFERENCES

Adams R.D., Drinkwater B.W. 1997. Nondestructive testing of adhesively bonded joints, *NDT&E Int*, 30, 93–98.

Austin, S., Robins, P. and Pan, Y. 1995. Tensile bond testing of concrete repairs., Mater Struct (28): 249–259.

Bissonnette, B., Courard, L., Vaysburd, A., Bélair, N. 2006. Concrete removal techniques: influence on residual cracking and bond strength. *Concrete Int*, 28 (12), 49–55.

Carino N.J. 1997. Nondestructive Test Methods, Concrete Construction Engineering Handbook, ed. E.G. Nawy, CRC Press, 19.1–19.67.

Concrete Repair Manual. 2003. ACI International, Farmington Hills, MI, USA, pp.862.

Courard, L. 2005. Adhesion of repair systems to concrete: influence of interfacial topography and transport phenomena, *Mag Concrete Res*, 57(5). 273–282.

Courard, L. Schwall, D. Piotrowski, T. 2007. Concrete surface roughness characterization by means of optomorphology technique, Adhesion in Interfaces of Building Materials: a Multi-scale Approach, *Advances in Materials Science and Restoration AMSR No. 2.*, Aedificatio Publishers, 107–115.

Courard, L., Lenaers, J.-F., Michel F., Garbacz A. 2011. Saturation level of the superficial zone of concrete and adhesion of repair systems, *Constr. Build. Mater.*, 25, 2488–2494.

Courard, L. Piotrowski, T. Garbacz, A. 2014. Near-to-Surface properties affecting bond strength in concrete repair. Cement. Concrete Comp., 46, 73–80.

Czarnecki, L and Emmons, P.H. 2002. Repair and protection of concrete structures (in Polish). Polski Cement, Cracow.

Fukuzawa, K., Mitsui, M. and Numao, T. 2001. Surface roughness indexes for evaluation of bond strengths between CRFP sheet and concrete. In: ICPIC 2001, Xth International Congress on Polymers in Concrete, USA, p.12 (CD).

Garbacz, A. 2005. Non-destructive assessment of repair efficiency with impact-echo and ultrasonic methods—an overview, in *Concrete Repair, Rehabilitation and Retroffiting*, Taylor & Francis, 1319–1326.

Garbacz A., Piotrowski T., Załegowski K., Adamczewski G. 2013. UIR-Scanner Potential to Defect Detection in Concrete, Advanced Materials Research, 687, 2013, Ed. Ru Wang and Zhenghong Yang, Trans Tech Publications Ltd, 359–365.

Garbacz, A. 2015. Application of stress based NDT methods for concrete repair bond quality control. *Bull. Pol AcadSci-Te*, 63 (1) (in press).

Garbacz, A., Gorka, M., and Courard, L. 2005. On the effect of concrete surface treatment on adhesion in repair systems. *MagConcrete Res*. 57, 49–60.

Garbacz, A. Piotrowski, T. Courard, L. 2006. An analysis of stress wave propagation in repair systems using wavelet approach, RILEM PRO 51 (CD): Advances in Concrete through Science and Engineering, Canada.

Kwaśniewski, L., Garbacz, A., 2008, Characterization of stress wave propagation in impact-echo method using FEM models of repair systems, Challenges for Civil Construction, FEUP, Portugal, 92–93 + CD.

Pretorius, J. and Kruger, D. 2001. The influence of surface roughness on the bond strength of concrete repairs. In: ICPIC 2001, Xth International Congress on Polymers in Concrete, USA, p.13 (CD).

Sadowski Ł., Hoła J. 2014. New nondestructive way of identifying the values of pull-off adhesion between concrete layers in floors, *JCiv EngManag*, 20 (4), 561–569

Sansalone M., Carino N.J. 1989. Detecting delamination in concrete slabs with and without overlays using the impact-echo method, ACI Materials Journal 86.

Santos, P., Júlio E., Santos, J. 2011. Towards the development of an in situ non-destructive method to control the quality of concrete-to-concrete interfaces, *Eng. Struct.*, 32(1), 207–217.

Silfwerbrand, J. Paulsson, J. 1998. Better bonding of bridge deck overlays. *Concrete Int.* 20 (10): 56–61.

Silfwerbrand, J. Beushausen, H. 2006. Bonded concrete overlays—bond strength issues, Concrete Repair, Rehabilitation and Retrofitting (Eds. H. Beushausen, F. Dehn and M.G. Alexander), Taylor & Francis Group, London, 61–66.

Concrete Repair, Rehabilitation and Retrofitting IV – Dehn et al. (Eds)
© 2016 Taylor & Francis Group, London, ISBN 978-1-138-02843-2

Condition assessment of a 100-year-old RC building in Hiroshima

T. Kinose & K. Imamoto
Department of Architecture, Graduate School of Engineering, Tokyo University of Science, Tokyo, Japan

T. Noguchi
Department of Architecture, Graduate School of Engineering, University of Tokyo, Tokyo, Japan

T. Ohkubo
Department of Social and Environmental Engineering, Graduate School of Engineering, Hiroshima University, Hiroshima, Japan

ABSTRACT: Former Army Clothing Depot constructed in 1913 locates within about 2.7 km of radius from the blast of atomic bomb, and there are lots of trace of iron doors and windows at the blast center side. Walls of interior and exterior are built with masonry and the main structures such as column, beams and slabs are built with reinforced concretes. This building is one of the oldest reinforced concrete structures in Japan. Due to the above reasons, this building has high academic and historical values. Authors it was surveyed this building for the purpose of accumulation of the date which contribute preservation and repair as this building.

1 INTRODUCTION

It is well known all over the world that Hiroshima is the only country where American army dropped an atomic bomb in 1945. Intense blast and heat ray of an atom bomb almost destroyed all buildings within 2 km of radius from a blast center at present. About 80 bombed buildings are left including Atomic Bomb Dome (Photo 1) within 5 km of radius from the blast center. Former Army Clothing Depot (Photo 2) constructed in 1913 is left within about 2.7 km of radius from the blast center, and there are lots of trace of iron doors and windows at the blast center side (Photo 3). Walls of the interior and exterior are built with masonry and the main structures such as columns, beams and slabs are built with reinforced concretes. This building is one of the oldest reinforced concrete structures in Japan. Due to the above reasons, this building has high academic and historical values. Authors surveyed this building for the purpose of accumulation of the date which contribute preservation and repair

Photo 1. Atomic Bomb Dome (1945).

Photo 2. Former Army Clothing Depot.

Photo 3. Windows damaged by atomic bomb.

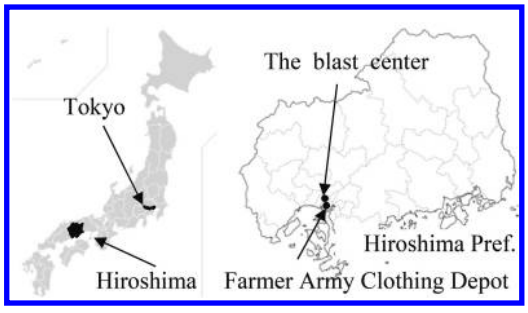

Figure 1. Location of building.

as this building. This paper deals with a condition assessment of this oldest RC building from the view point of durability.

2 EXPERIMENTAL

2.1 *Outline of buildings*

The building site includes 4 types of building, as shown in Figure 2. In this study, building No. 2 and No. 3 were surveyed. Plans and tested points are shown in Figure 3. Details of buildings such as location and year of construction (age at survey) are shown in Table 1.

2.2 *Experiments*

Following measurements were applied on the surveying.

2.2.1 *Crack investigation*

Clack width of concrete was measured with the crack scale as shown in Photo 4. The clack widths were measured at 3rd floor of the building.

2.2.2 *Re-bar corrosion*

This survey aims at preservation and needs for repair of the building. Re-bar corrosion in concrete was surveyed by visual observation. Grades of corrosion rates were classified based on the standards proposed by guideline of Architectural Institute of Japan (AIJ).

2.2.3 *Differential settlement*

Differential settlement was measured with a laser level as shown in Photo 5. The data measured in 2014 were compared with those measured in 1992.

2.2.4 *Carbonation depth and compressive strength*

Carbonation depth was measured with concrete core samples (φ75 mm) at tested points as shown in Figure 3 according to Japanese Industrial Standards (JIS) A1152 (Method for measuring carbonation depth of concrete). Carbonation velocity is based on the squar root theory shown in Equation (1). Compressive strength test was performed with core specimens after carbonation test according to JIS A1107 (Method of sampling and testing for compressive strength of drilled cores of concrete).

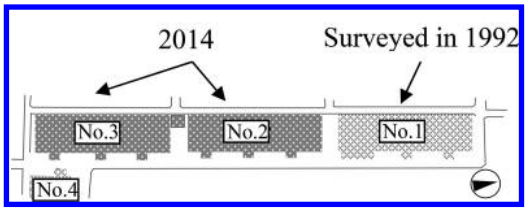

Figure 2. Site of the buildings.

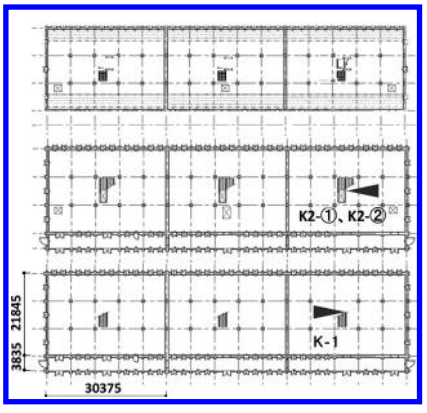

Figure 3. Plan of the building and tested point points.

$$C = A\sqrt{t} \quad (1)$$

C: Carbonation depth (mm)
A: Carbonation velocity (mm/years$^{1/2}$)
t: Age at survey (years).

2.2.5 *Environment condition*

A temperature and humidity meter was set on the surface of concrete (see Fig. 3, K-1) and changes of temperature-humidity of inner part of building was measured.

3 RESULTS AND CONFERENCES

3.1 *Crack of concrete*

Cracks were remarkable at a column on the 3rd floor of building No. 3. Slices-like cracks with constant pattern were observed at all over the column as shown in Photo 7. The average width of

Table 1. Details of building.

Name of building	Location	Notation	Detail			
			Year of construction (age at survey)	Stairs	Main structure	Main finishing material
Farmer Army Clothing Depot	Hiroshima (Hiroshima)		1913 (101 years)	3	Outside pillars, wall: Brick inner pillars, beams, slabs: Reinforced concrete	Mortor (5–10 mm)

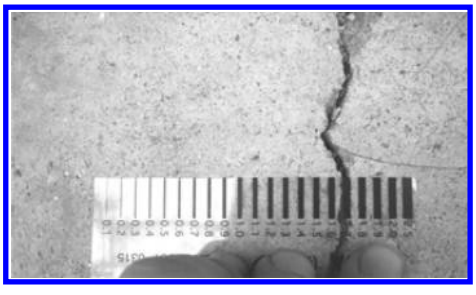

Photo 4. Crack scale.

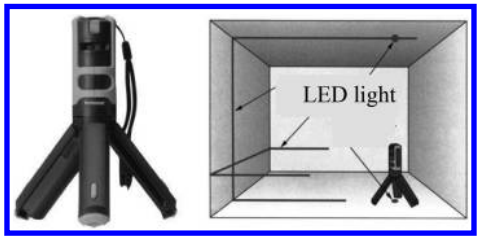

Photo 5. Laser level.

concrete cracks was about 2.2 mm. This value was much larger than crack width induced by concrete shrinkage.

3.2 *Differential settlement*

Measured lines of differential settlement with lazar level in each floor in building No. 2 are shown in Figure 4. The results on 1992 and 2014 are shown in Figures 5 to 9. The maximum differential settlement at center part of floor's ranged from 10 to 15 cm. The tendency of X axial direction was close to that of Y axial. The amount of the settlement increased by 5 to 10 cm since 1992. In this building, there were independent footing at central part of the building and connected footing by underground beams locates outer zone of the building as shown in Figure 4. This might be a reason that the amount of settlement of the inner columns was larger than that of exterior walls. Hence, tensile stress occur at the column as shown in Figure 10. In addition, it would be one of the causes of crack that diameter of column on the 3rd floor which diameter was smaller than those on the 1st and 2nd floors.

Photo 6. Crack at the 3rd floor of No. 3 depot.

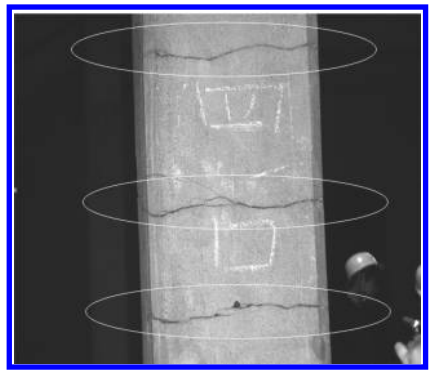

Photo 7. Detail of cutting into round slice-like crack.

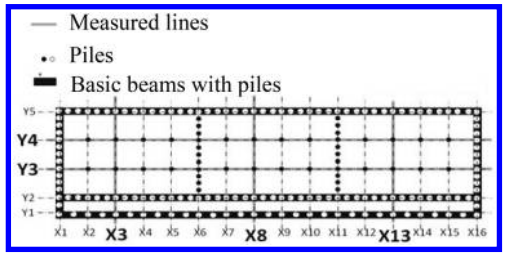

Figure 4. Measured lines of differential settlement and location of the piles and the basic beams.

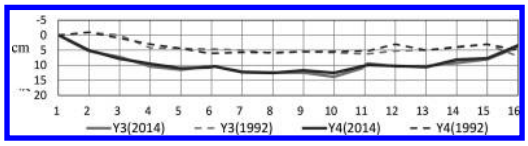

Figure 5. Amount of the settlement (No. 2, 3F).

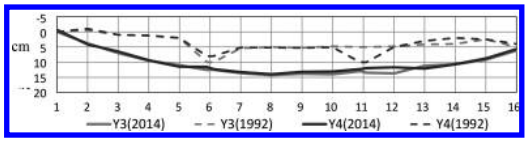

Figure 6. Amount of the settlement (No. 2, 2F).

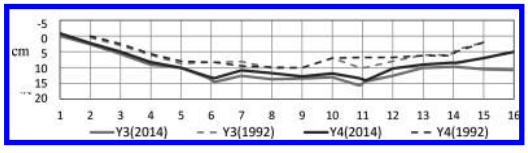

Figure 7. Amount of the settlement (No. 2, 1F).

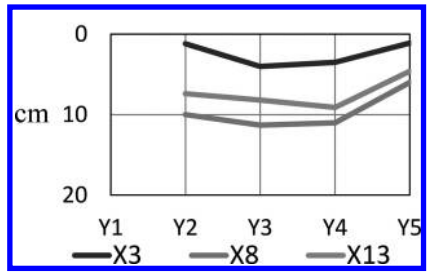

Figure 8. Amount of the settlement (No. 2, 2F).

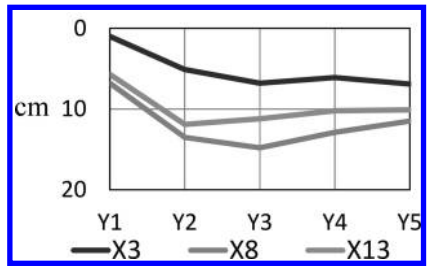

Figure 9. Amount of the settlement (No. 2, 1F).

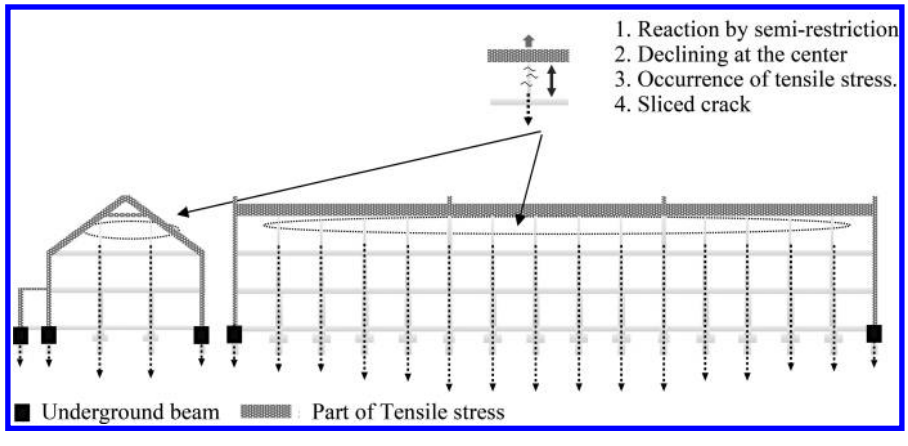

Figure 10. Mechanism of occurrence of cutting into round slice-like crack.

Table 2. Results of carbonation and compressive strength (2014, 1992).

Depot No. (year of survey)	Floor	Part	No.	Compressive strength N/mm^2	Young's modulus $\times 10^4$ N/mm^2	Carbonation depth mm	Carbonation velocity mm/year$^{1/2}$
3 (2014)	1	Beam	K1	17.9	–	93.6	9.36
	2	Beam	K2-①	–	–	60	6.00
	2	Beam	K2-②	14.9	2.29	77.3	7.73
	2	Beam	a	14.4	2.00	30	3.40
	3	Beam	b	13.2	2.25	60	6.79
2 (1992)	1	Dirt floor	c	12.7	2.38	20	2.26
	2	Slab	d	14.6	1.83	–	–
	3	Slab	e	17.5	2.54	–	–
	3	Loof	f	21.0	–	–	–

Table 3. Re-bar corrosion grade.

Grade	Re-bar corrosion conditions	Photos
1	No corrosion	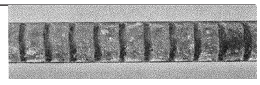
2	Slight corrosion (surface)	
3	Almost corrosion (surface) or Partical section loss	
4	Section loss as a whole	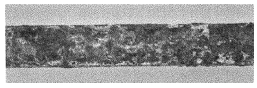
5	Section loss up to 1/2–2/3	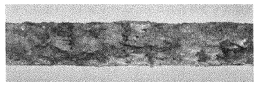

3.3 *Compressive strength and carbonation*

Test results of compressive strength and carbonation depth in 2014 and 1992 are shown in Table 2. Although the tested points are different in 2014 and in 1992, overall carbonation proceeded with time. Average compressive strength of concrete was 14.4 N/mm^2.

3.4 *Re-bar corrosion*

Re-bar corrosion rater were evaluated with exposed bars due to loss of cover concrete. Re-bar corrosion grade based on AIJ guideline are shown in Table 3. States of re-bar corrosion were classified into 5 grades. Table 4 shows the corrosion grade of re-bar of this building. It can be seen that a re-bar corrosion at a roof of 1st floor of building No. 2 quite significant due to leak of water from the crack of roof concrete as shown Photo 8. Figures 11 to 12 show relationship between carbonation depth and cover thickness of concretes of existing structures which authors previously surveyed. The tendency that the re-bar corrosion progresses remarkably at the part where cover thickness minus carbonation depth was small. On the other hands, at the point where the cover depth of concrete was large enough, re-bar corrosion cannot be observed. Corrosions of columns were slight (grade 3). This might be due to relatively moderate R.H. at indoor, as shown in Figure 13. According to the above results, frames of this building would be sound and counter measurements for the differential settlement and water leakage from roof should be necessary to conserve this building.

Table 4. Results of re-bar corrosion.

Year of survey	Depot No.	Floor	Part	Grade
2014	2	1	Roof	5
	3	1	Pedestal	3
		3	Capital	3
1992	1	1	Pillar	2
		2	Pillar	2
		3	Pillar	2
		3	Beam	3

Photo 8. A leak of water trace from the crack.

Photo 9. Exposed re-bar at 1st floor in No. 3.

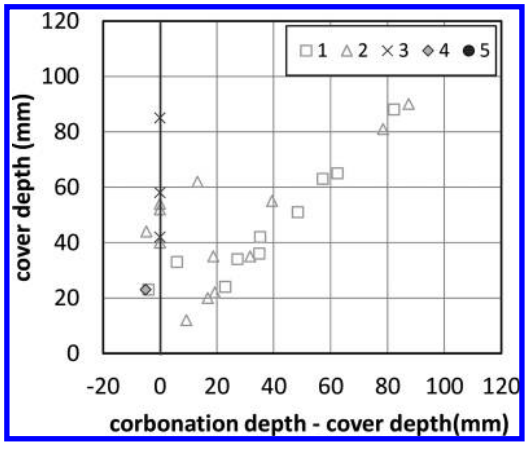

Figure 11. Relationship between a loss of carbonation and cover depth of A-D (indoor condition).

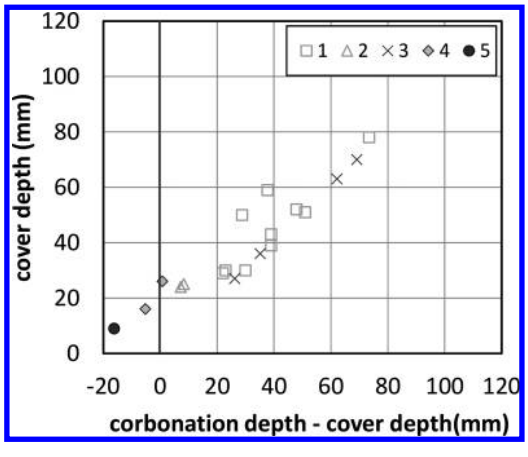

Figure 12. Relationship between a loss of carbonation and cover depth of A-D (outdoor condition).

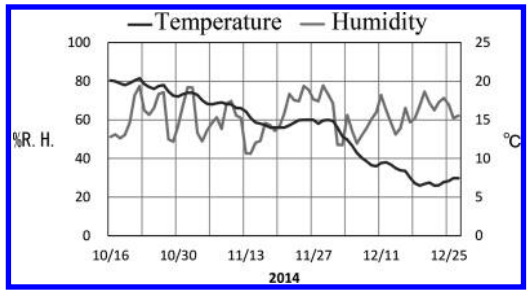

Figure 13. Temperature and humidity (indoor).

4 CONCLUSIONS

Following findings were obtained through the surveys.

1. Cracks of column were remarkable at 3rd floor of building. Sliced cracks with constant pattern were observed at all over the column.
2. The maximum differential settlement at central part of each floor ranged from 10 to 15 cm. The amount of the settlement increased by 5 to 10 cm since 1992.
3. This differential settlement might cause tensile stress induced cracks of columns.
4. Re-bar corrosion was quite significant due to water leakage. On the other hands, at the point where the cover depth of concrete was large enough, re-bar corrosion cannot be observed.
5. Frames of this building would be sound and counter measurements for differential settlement and water leakage from roof should be necessary.

ACKNOWLEDGMENT

The authors would like to thank Mr. and Mrs. Takada for their contributions to this study. This survey was performed with the co-operation of a working group from the survey of reinforced concrete structure for durability from Architectural Institute of Japan.

REFERENCES

1. Cooperative society of survey and repair of building in Hiroshima.: Report of the survey of "Former Army Clothing Depot" for strength, 1992.
2. JASS 5 (2009), Japan architectural standard specification.
3. Architectural Institute of Japan: Standard for recommendation for practice of survey, diagnosis and repair for deterioration of reinforced concrete structures, 1997.

Concrete Repair, Rehabilitation and Retrofitting IV – Dehn et al. (Eds)
© 2016 Taylor & Francis Group, London, ISBN 978-1-138-02843-2

A technical review of seven cathodic protection systems in Jersey

John Drewett
Concrete Repairs Ltd., London, UK

Kevin Davies
CorroCiv Limited, Manchester, UK

Kevin Armstrong
States of Jersey, UK

ABSTRACT: Jersey is the largest of the Channel Islands situated off the coast of France. The reinforced concrete infrastructure is in an exposed marine environment which causes durability problems due to corrosion of the steel reinforcement. Since 1996 the States of Jersey has installed seven impressed current cathodic protection systems on reinforced concrete structures to enhance durability. Three marine structures, three multi storey car parks and one airport facility have been protected using a variety of different anode systems which include titanium mesh, ribbon and discrete anodes, conductive paint and conductive cementitious. With some anode maintenance and upgrading of obsolete software systems the systems continue to operate. They continue to provide the level of corrosion protection intended and extend the effective service life and residual value of the assets.

1 INTRODUCTION

Jersey is the largest of the Channel Islands, situated off the coast of Normandy with a resident population of around 100,000. The reinforced concrete infrastructure managed by the States of Jersey suffers from steel reinforcement corrosion initiated by chloride ions from the marine environment.

In the mid-1990s the States of Jersey decided to utilise Impressed Current Cathodic Protection (ICCP) to enhance durability when the structures were repaired. On one marine repair scheme a series of trials were undertaken to assess the performance of different impressed current and galvanic anode systems available at that time.

Between 1996 and 2006 there have been seven impressed current cathodic protection systems installed on reinforced concrete structures to enhance durability. The structures are; three multi storey car parks, three marine berths and one airport landing light support facility. A range of anode systems have been used which include:

a. Discrete conductive ceramic anodes
b. Discrete MMO coated Titanium (MMO/Ti) anodes
c. Conductive cementitious overlay
d. MMO/Ti mesh with cementitious overlay
e. MMO/Ti ribbon mesh
f. Conductive paint.

The installed ICCP systems are monitored using LD15 or LD25 silver/silver chloride reference electrodes supplied by Castle Electrodes Ltd and computer control systems over the last 20 years. All these systems have been monitored since installation and there have been some maintenance works undertaken to correct problems which have arisen but the systems continue to provide corrosion protection.

2 THE PROJECTS

2.1 *London Berth, Victoria Pier*

This was the first ICCP system to be installed on the Island in 1998 after a two year trial using a range of anode systems. Fifteen anode zones were installed to protect the slab soffits, beams and columns using a combination of two anode types.

Slab soffits, beams and high level pile caps—1520 m^2 proprietary CP60 conductive mortar spray applied.

Piles, columns and low level pile caps—950 m^2 MMO/Ti mesh with a sprayed overlay.

The system is monitored using 40 No. LD25 silver/silver chloride reference electrodes and powered by a multi-channel output, remote controlled, remote-operated and monitored, DC power supply and data acquisition system.

2.1.1 *Maintenance*
In 2011 the computer controlled power and control system was replaced, as it had become obsolete and the ICCP system was reconfigured from 15 zones to 8 zones to simplify operation. No works have been necessary to the original installed anode or monitoring system after 16 years in the tidal marine environment.

2.1.2 *Future maintenance*
One zone shows a higher current output and lower driving voltage. This could be because it is a much larger zone area-wise and there may be a partial electrical short circuit in the system, but it continues to provide adequate corrosion protection.

2.2 *Green street multi storey car park*

This is a 4 storey car park in St Helier which provides a very important function, parking for 600 vehicles. As part of a £2M refurbishment in 1999 an ICCP system was installed to protect the reinforced concrete decks, columns, walls and internal faces of the parapets.

The anode system used for the deck was the Zebra Deck Anode System supplied by Protector AS in Norway complete with a wearing surface. This system is a conductive paint system applied in strip coats on the deck surface and overlaid with the wearing surface. It was the first time the system had been used in the UK. The columns and walls were protected using a conductive paint system again supplied by Protector AS with a decorative topcoat. In total 10,500 m² of deck surface and 1,600 m² of walls and columns were protected using the ICCP system.

Photograph 1. Cabling installation checks.

2.2.1 *Maintenance*
The cathodic protection system has received little maintenance since installation. One datalogger has been replaced after 14 years of service. The top deck wearing course was replaced 3 years after the system was installed after the original surface failed to sufficiently accommodate thermal movement in this location.

2.2.2 *Future maintenance*
Assessment of the life of the CP system for future years. Car park due for refurbishment in 2020.

2.3 *New North Quay*

The system was installed in 2000 to protect the deck soffit and sub-structure. The original design

Photograph 2. Zebra deck anode installed prior to deck surfacing.

Photograph 3. Overview of the Quay.

was for 34 anode zones using 1,000 m MMO/Ti mesh ribbon anodes buried in chases cut into the concrete.

The system was monitored using 16 No. LD15 silver silver chloride reference electrodes, a remote controlled central control unit and three networked substations.

2.3.1 *Maintenance*

In 2011 the obsolete computer controlled power and control system was replaced and the zoning reconfigured to 8 zones for operational reasons. The existing field wiring, AC power and telephone line were re-used.

2.3.2 *Future maintenance*

None envisaged at present except routine monitoring.

2.4 *Jersey airport*

The reinforced concrete Instrument Landing System (ILS 27) Localiser Plinth is situated at the Western end of the Jersey Airport runway overlooking St. Ouen's bay. It is located in a very harsh environment and consequently suffers from corrosion of the reinforcement due to high chloride levels from the marine environment.

An impressed current cathodic protection system was installed in 2003 to provide long term protection to the steel reinforcement in the exposed parts of the piers, beams and deck slab soffits. The anode system comprise mixed metal oxide coated titanium ribbons and proprietary MMO/Ti tubular discrete rod anodes placed in horizontal rows at regular spacing. There are two anode zones, each monitored by 4 LD15 silver silver chloride reference electrodes.

The ICCP system has been functioning correctly since the installation was completed.

2.4.1 *Maintenance*

In 2011 some minor maintenance was undertaken to re-embed some of the discrete anodes and repair some localised acidification around some of the MMO/Ti ribbon.

2.4.2 *Future maintenance*

One of the reference electrodes is providing erratic readings so may need to be replaced in the future.

2.5 *Berth no. 2, Albert pier*

An ICCP system was installed in 2005 to protect the reinforced concrete soffit, beams and columns. The selected anode system comprises 300 m of MMO/Ti ribbons chased into horizontal rows at regular spacing on the deck slab soffits and transverse beams. The longitudinal beams and columns are protected using 550 No. conductive ceramic and MMO/Ti discrete anodes. There are 4 anode zones rated at 3.0 A/15 V DC with 2 LD15 silver silver chloride reference electrodes monitoring each zone.

a. Zone 1—CP10/150 conductive ceramic discrete anodes in lower columns
b. Zone 2—CP10/150 conductive ceramic discrete anodes in mid deck beams
c. Zone 3—CP10/150 conductive ceramic discrete anodes from mid deck to top deck
d. Zone 4—Lower output Type 150 MMO/Ti ribbon in the top deck slab and transverse beams.

The power and control unit is fully automated but with a manual option for on-site interrogation if required.

2.5.1 *Maintenance*

By 2011 some of the discrete anodes had failed and so were replaced with MMO/Ti tubular anodes in acid-resistant CP15 grout.

2.5.2 *Future maintenance*

Zone 1 (lower columns) is passing no current so it seems like the DC circuit has failed and requires further investigation.

Zones 2, 3 and 4 are functioning correctly and no corrosion has been found.

2.6 *Pier road Multi Storey Car Park (MSCP)*

The States of Jersey own and operate 5 MSCPs in the main town of St Helier. Some are exposed to the marine environment and as a consequence suffer from corrosion of the steel reinforcement. ICCP Systems have been installed in 3 of the car parks to improve the durability of the reinforced concrete, extend the service life and reduce maintenance costs.

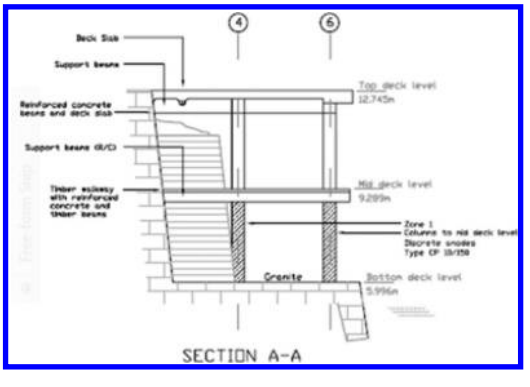

Figure 1. Cross section showing anode zoning.

Pier Road MSCP is situated in a prominent sea front position above St Helier Harbour. Specific exposed areas along the West and East sides of the car park were protected using ICCP systems. The deck slab edges and beams ends have high levels of chloride ions at the steel reinforcement so cathodic protection is being used to enhance the durability.

The anodes are all MMO/Ti durAnode 3 discrete anodes, 12,060 in total, supplied by Cathodic Protection International (CPI) in 18 zones with 108 No. LD15 silver silver chloride reference electrodes being used to monitor the system. There are 6 floors protected using in total 2130 anodes for the columns and 9930 anodes for the floor slab edge beams.

The power and control unit supplied by CPI has one central monitoring station and 3 sub stations.

The system was installed in 2005 and is functioning correctly in accordance with European Standard EN12696:2012.

2.6.1 *Maintenance*

No maintenance has been undertaken since installation. The car park has recently been refurbished incorporating a deck coating to further protect the concrete but no repairs were necessary to the ICCP nor were significant concrete repairs required in the ICCP protected areas.

2.6.2 *Future maintenance*

There is some AC interference in one zone which is closest to the AC power control electrical switch room and it is possible that the steel within the reinforced concrete is "picking up" some stray AC electrical interference. This is seen as instability in the depolarisation curves and might be corrected with filters on the monitoring control unit.

Two zones exhibit quite high current output even though the drive voltages are low (<3VDC) so there may be some short circuiting of the ICCP anode systems in these zones, possibly due to other maintenance works after the system was installed. This needs further investigation.

Overall the ICCP system is working well and providing the corrosion protection needed to enhance durability.

Photograph 4. General layout of the car park.

2.7 *Sand street Multi Storey Car Park*

In 2006 an ICCP system was installed in the car park to provide long term corrosion protection to the steel reinforcement of the longitudinal floor beams on the upper floors and the seaward facing edge columns on all floors which had been suffering extensive chloride induced corrosion. Previous concrete repairs had failed to achieve long term corrosion protection.

The anodes used were durAnode Type 3 proprietary discrete anodes supplied by CPI installed into the floor ribs and columns. A total of 12,080 anodes were installed in 5 floors decks and 864 anodes in 6 levels of columns. The system is divided into 18 zones and monitored using 126 LD15 silver silver chloride reference electrodes.

The power and control unit has one central station and 5 substations.

Since the installation the ICCP system has performed well with significant negative shifts in the steel as expected, indicative of adequate corrosion protection. The output currents are quite low and the system is operating on constant voltage output mode set at 4.0 VDC.

2.7.1 *Maintenance*

No maintenance has been undertaken since installation except one off-the-shelf low voltage power supply unit was replaced in one substation

2.7.2 *Future maintenance*

At the beginning of 2014 the system was de-energised and a fault has occurred in one substation when it was re-energised. Investigation revealed that the substation had not been re-energised correctly and was reset. It is now functioning correctly. Also two reference electrodes are possibly malfunctioning but there is sufficient redundancy in the monitoring system for this not to cause any immediate problems. This car park is due for refurbishment at the end of 2015 including a deck coating to further protect the concrete surfaces.

3 SUMMARY

Overall the seven ICCP systems have performed very well in harsh marine environments. Jersey experiences several Atlantic storms and 12 m spring tides each year and being an Island is subject to

marine blown chlorides all year round. The earlier control and monitoring units have become obsolete and were replaced but this is only to be expected with the rapid development of microprocessor–based operating systems and the newer units should be able to operate for longer periods without upgrades. All of the ICCP systems were designed to permit maintenance/upgrade of the control and monitoring units and were located in readily accessible positions to facilitate this.

The variety of anode systems used have, in the majority of cases, worked well over the last 10–17 years.

a. MMO/Ti mesh—950 m^2
b. MMO/Ti ribbon mesh—1,300 m
c. Conductive paint—12,100 m^2
d. Thoro 60 conductive cementitious—1,520 m^2
e. Discrete anodes—25,554 No.

A few–anodes have needed to be replaced but there have been no–whole system failures and there is every indication with the low voltage and currents required to achieve corrosion protection to the steel, that these anodes will continue to operate for many years with minimal maintenance.

The 252 No. silver silver chloride reference electrodes have had some failures (<3%) but on the whole have performed well over the last 17 years and with some redundancy built into the designs, these failures have not compromised the performance of the monitoring system or the ability of the ICCP system to provide the level of corrosion protection intended.

From the Client's perspective the initial investment in ICCP systems, targeted at specific corrosion problem areas has reduced the long term costs of managing these structures and has extended the effective service life and residual value. Car parking for example is a very sought after commodity in St Helier. With regular monitoring and maintenance the systems should continue to provide corrosion protection for many more years.

Concrete Repair, Rehabilitation and Retrofitting IV – Dehn et al. (Eds)
© 2016 Taylor & Francis Group, London, ISBN 978-1-138-02843-2

Corrosion survey of the bridge deck "Viadotto Colle Isarco"/"Autobahnbrücke Gossensaß" on the Motorway called "Autostrada del Brennero" in North-Italy

Roberto Giorgini
CorrPRE Engineering BV, Reeuwijk, The Netherlands

ABSTRACT: The scope of this corrosion survey was to detect and quantify zones with high corrosion probability of the normal reinforcement and if possible the prestressed tendons of a total of 8000 m^2 surface area of the upper bridge deck of the "Viadotto Colle Isarco". This viaduct is part of the A22 Motorway called "Autostrada del Brennero" and lays 10 km's south of the Austrian-Italian border in Italian territory approximately 1200 m high in the Alps. In case serious problems were found no recommendations were requested at this point of the survey due to the size and the structural complexity of the concrete structure.

Zones with high probability of corrosion were identified by the potentials measured and inspected through scarification and sandblasting. Based on this verification it was estimated an approximate 9% of the total surface area with high probability of corrosion in the prestressed tendons. This amount is based on adding up all measuring points with a potential being more negative than –450 mV divided by the total amount of measuring points. During previous inspections fractured prestressed tendons were found. All the fractures were found in the threaded region of the coupler joints but no fractures were found in corroded tendons laying in the "active" zones away from the coupler joints. Samples taken from the fractured tendons were sent to the lab for metallurgical analysis and revealed no susceptibility for hydrogen embrittlement of the steel used which has a perlitic microstructure. Fractures found in the tendons in previous inspections are most probably caused by major stress fatigue cycles from traffic loads in combination with corrosion due to the stress-sensitive couplings. Exactly similar cases (*Heerdter crossing in Düsseldorf in 1976*) were found in old reports, e.g. published in the technical report 26 "Influence of material and processing on Stress Corrosion Cracking of prestressing steel—case studies" by the International Federation for Structural Concrete (fib) in Lausanne.

1 INTRODUCTION

The goal of this project is to perform a corrosion survey of the bridge deck named "Viadotto Colle Isarco" to establish the condition of the reinforcement and if possible the prestressed tendons.

This viaduct is part of the A22 Motorway called "Autostrada del Brennero" and lays 10 km's south of the Austrian-Italian border in Italian territory approximately 1200 m high in the Alps. It is one of the longest and highest box girder bridges on the Brenner highway between Italy and Austria.

The entire viaduct measures 1028.8 mtrs in length with a cantilevered central span of 163 mtrs.

The A22 goes from Innsbruck-Austria to Modena-Italy and is approximately 360 kms long.

The surface areas indicated by the chief engineer is restricted to certain areas of the bridgedeck where the post-tensioned tendons are subject to maximum tension which can be seen from Figure 7. These maximum tension zones in combination with the high strength steel can make these tendons prone to hydrogen embrittlement if corrosion is already initiated depending on the microstructure of the steel tendons. The surface area involved was estimated at a total of 8000 m^2.

Figure 1. Location of the viaduct.

The reason for above requested corrosion survey was the concern of several Highway engineers regarding their findings during previous repairwork which was done appr. 1 year before the date of this survey.

During repairwork of the bridgedeck these engineers discovered several corroded and fractured tendons.

Figure 3, 4, 5 and 6 shows how the prestressed tendons and ducts were casted in the concrete bridge deck.

Figure 8 shows the set-up of the prestressed tendons within the ducts and Figure 9 how the repairwork was executed. It can be seen that the concrete top layer including the reinforcement bars just above the prestressed tendons has been completed removed and replaced.

Figure 10 shows several samples taken from the fractured tendons which are send to the lab for metallurgical analysis. This analysis has been performed in the laboratory of the Material-prüfungsanstalt at the University of Stuttgart.

Figure 2. "Viadotto Colle Isarco"/"Autobahnbrücke Gossensaß".

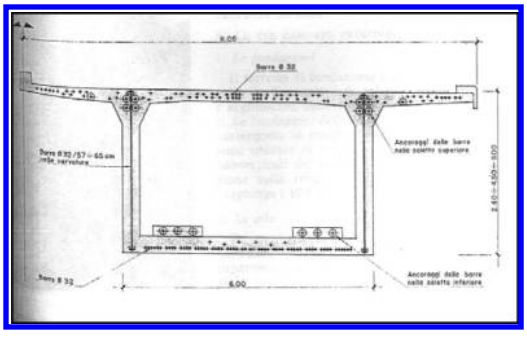

Figure 3. Cross section of the box girder bridge with the prestressed tendons.

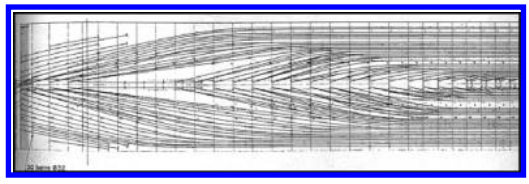

Figure 4. Top view of the prestressed tendons.

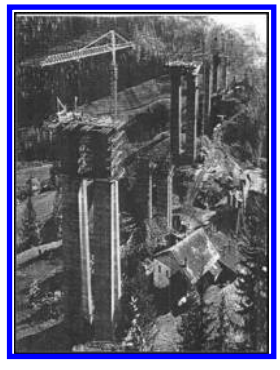

Figures 5 and 6. The bridge under construction in 1969.

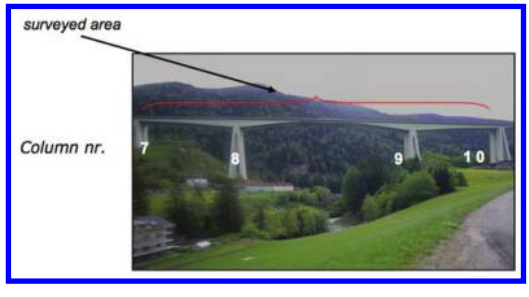

Figure 7. The zone of the construction which is subjected to the survey.

According to the designs the tendons are made of St 85/105, which is hot rolled, strained and tempered material which leads to a pearlitic microstructure after cooing from the rolling temperature[1]. Lab analysis will reveal whether the material used is in agreement with the specified material and later will be discussed the suitability of this material under these circumstances.

An important detail should be mentioned is the fact that big amounts of de-icing salts are used on this bridgedeck due to the altitude of the bridge and therefore laying in an area of long cold icy winters with temperatures easily reaching –15°C.

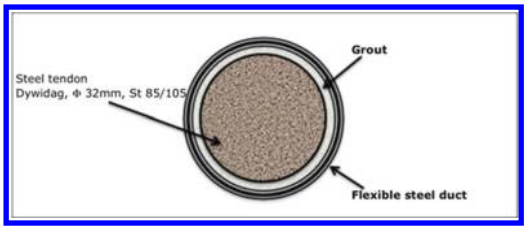

Figure 8. Prestressed steel tendons laying in a flexible steel duct filled with grout.

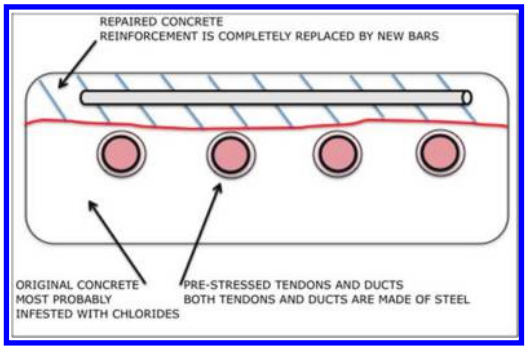

Figure 9. Situation of the bridgedeck just beneath the asphalt layer.

Figure 10. Samples taken from the fractured tendons for metallurgical analysis.

2 EXPERIMENTAL

During this inspection the following non-destructive methods were used:

1. Potential-mapping
2. Verification of zones with high corrosion probability
3. Metallurgical analysis
4. Chloride content analysis.

Steel embedded in good quality concrete is protected by an high alkaline pore water solution which, in the presence of oxygen, passivates the steel. The loss of alkalinity due to carbonation of the concrete or the penetration of chloride ions (arising from either marine or de-icing salts, or in some cases present in situ from the use of a calcium chloride additive) can destroy the passive film. In the presence of oxygen, humidity and aggressive ions in concrete, corrosion of the steel starts.

A characteristic feature for the corrosion of steel in concrete is the development of macrocells, that is the co-existence of passive and corroding areas on the same reinforcement bar forming a short-circuited galvanic cell, with the corroding area as the anode and the passive surface as the cathode. The voltage of such a cell can reach as high as 0.5V or more, especially where chloride ions are present.

2.1 *Potentialmapping*

The half-cell potential mapping method can be used for the detection of corrosion of tendons in pretensioned concrete. In this method, the differences in potential between the tendon and a suitable reference electrode placed at various points on the concrete surface are measured. The concrete surface is moistened to provide sufficient electrical conductivity.

In general, corrosion is greatest at positions of high negative potential with large potential gradients around them. With this techniques one should be aware that the rebars have to be electric continuous.

Figure 11 shows the equipment used. The device is actually the high impedance meter which has a built in software system.

In order to evaluate the corrosion and the extent to which this could result in cracking and spalling

Figure 11. Equipment used for the potential measurements.

of the concrete, it is important to gain insight in the exact locations of passive and active zones in the construction.

For this purpose the measurement has to be performed in a grid covering the entire concrete surface. During this corrosion survey the distance between each measuring point is 55 cm in transverse direction of the bridge deck and 95 cm in longitudinal direction which is determined by the equipment's characteristics.

Specifically for this project due to its expanded surface area and the limited time available, the equipment was adapted to ease but increases the speed of the measurement method.

The problem which could occur during potential mapping was the fact that the bridgedeck was covered with a 8 cm asphalt layer and often a bituminous layer between the asphalt and concrete for waterproofing is applied. This could create problems during the survey as the bitumious layer has a very high resistance. Out of experience it is known that moisturising the asphalt surface with water and soap will give very reasonable results.

So basically the equipment was modified in such a way that all procedures needed to complete the measurement could be done from a single position by one man without disturbing his position and the position of the equipment.

The equipment contains several parts which is:

Figure 11 shows the instrument measuring and storing the data. Windows based software is included which allows downloading, presenting and editing the data measured by the instrument.

It also shows two measuring wheels attached to a shaft with a 55 cm distance from each other. Each wheel containing a built-in $Cu/CuSO_4$ reference cell including a pressure vessel with hoses to wetten the wheels continuously. The measuring procedure is as following:

- Check continuity of reinforcement.
  Several random spots on the bridgedeck was chosen with a distance of approximately 30 mtrs between each spot and on those spots an hole of 10 cm through the asphalt layer was drilled down to the reinforcement. With a LCR meter the resistance between these spots was measured. The total resistance indicated by the meter minus the wiring resistance should not exceed 1 Ohm for good electric continuity between the bars.
- Making the instrument's earth-contact with the reinforcement.
  These holes drilled to the reinforcement which showed good electric continuity were used for the instrument's earth connector.
- Performing the survey (see Fig. 11); the data are automatically stored.

2.2 *Verifications of zones with high corrosion probability*

During the corrosion survey every point on the bridge deck measured was closely monitored and when potentials were measured which indicated high probability of corrosion these points were marked with chalk to eventually verify possible corrosion and possible fractured tendon.

2.3 *Metallurgic analysis*

The objective of the metallurgical analysis is to reveal possible cause of the fractured samples like hydrogen embrittlement as high strength prestressed tendons are quenched and tempered steels which are particularly susceptible to hydrogen embrittlement, and checking whether the material is in accordance with the specification.

According to the specification the pre-stressed tendons are manufactured by Dywidag and have the short name St 85/105, previous St 835/1031. These tendons are made of hot-rolled silicon-manganese-carbon steel with a pearlitic microstructure.

The analysis has been performed in the laboratory of the Material-prüfungsanstalt at the University of Stuttgart.

2.4 *Chloride content analysis*

The chloride ions may originate from the ingredients of the concrete mixture, may be mixed in as an accelerator ($CaCl_2$), or may diffuse through the hardened concrete. The most commonly used method of assessement to determine the origin of the chlorides is performing a chloride penetration profile from analysis of samples taken from different depths. The chloride profile which is the chloride content vs. concrete depth will indicate from what source the chlorides originate.

The concrete samples are collected by drilling incrementally using a 50 mm diameter percussion drill and collecting the dust, at 0–20 mm, 20–40 mm, 40–60 mm. and taking concrete samples from the direct prestressed tendon surrounding during the corrosion verifications.

3 RESULTS

3.1 *Potential mapping*

The results of the potential mapping are presented as corrosion "colour" cards in which the colour of each measuring point indicates the potential range. Figure 12 indicates the four zones in which the results of the corrosion survey are devided and presented.

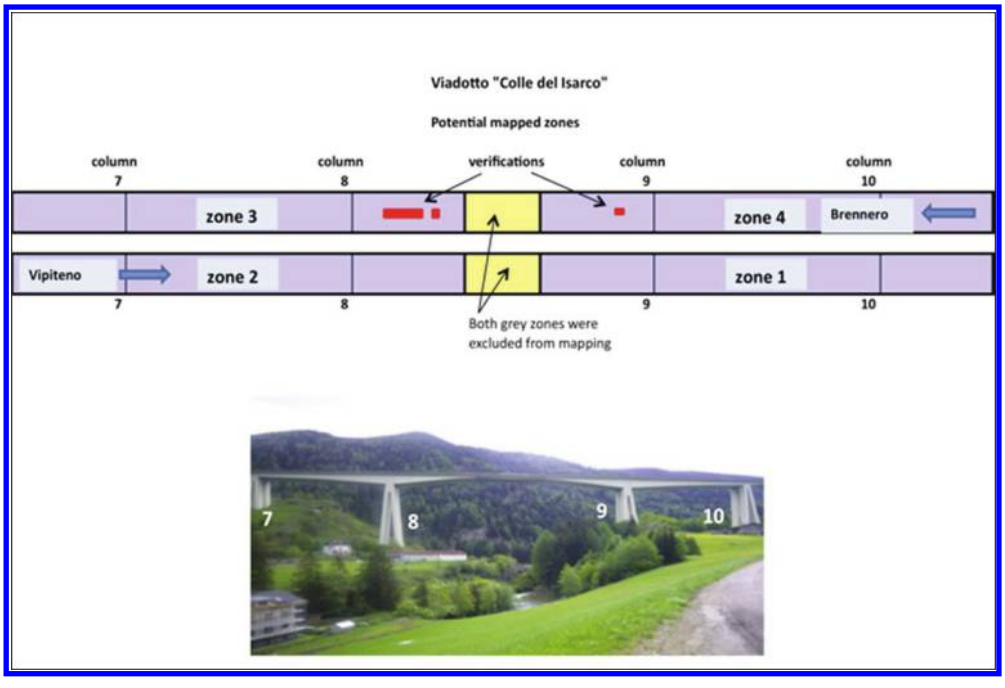

Figure 12. Zones in which the colour cards are devided.

Colour range: the green and yellow colours indicate low probability of corrosion. The difference between the colours green and yellow should be found in the humidity-difference in the concrete. Points represented by the yellow colour contain most probably higher concentrations of humidity within the concrete. The red colour indicates points with a higher probability of corrosion. The stronger the color in the colour cards, the more negative is the corrosion potential.

3.2 *Chloride content analysis*

Results are presented in Table 1.

The exact locations of the samples taken are found in the "colour cards" presented.

4 DISCUSSION

Steel embedded in good quality concrete is protected by the high alkalinity pore water which, in the presence of oxygen, passivates the steel. This electrolyte is mainly a saturated solution of $Ca(OH)_2$ (pH = 12), but the presence of alkaline cations as K^+ or Na^+ in the cement raw materials can induce an increase of pH in the pore solution up to 14.

Previous studies[2] indicated the presence of Fe_3O_4 (magnetite) and g-Fe_2O_3 (g-hematite) and a redox process:

$$3Fe_3O_4 <=> 4g\text{-}Fe_2O_3 + Fe^{2+} + 2e^-$$

taking place in the outer layer of the passive film.

This passive film or protection can be removed only through carbonation of the concrete or if a critical chloride content at the steel surface is exceeded (depassivation), allowing the reinforcement to corrode where a sufficient supply of moisture and oxygen at the steel surface are available.[3]

These reactions leads to the development of regions of differing electrochemical potentials and resulting in current flow within the concrete. The current flow in the concrete is accompanied by an electrical field which can be measured at the concrete surface as can be seen in Figure 13, resulting in equipotential lines that allow the location of the most corroding zones at the most negative values.

The potentials in this electrochemical circuit can be measured at the concrete surface with a measuring-electrode. This measuring method is performed in the same way as measuring the redox-potentials in a galvanic cell, a "half-cell" or reference cell/electrode is used with a sponge for the conductive contact. Using a good high-impedance voltmeter (to avoid polarization effects of both the rebar and the reference electrode), of which one pole is earthed to the reinforcement. The potential of the reference-electrode in relation to the reinforcement can be read.

Table 1. Results chloride analysis.

		sample	cement	cement	Cl- cement
		nr	type	% m/m	% m/m
1	0 - 20mm	1-1	portland	31,2	0.07
2	20-40mm	1-2	portland	31,8	0.08
3	40-60mm	1-3	portland	31,0	0.09
4	0 - 20mm	2-1	portland	33,6	0.08
5	20-40mm	2-2	portland	30,0	0.08
6	40-60mm	2-3	portland	33,3	0.08
7	0 - 20mm	3-1	portland	32,3	0.15
8	20-40mm	3-2	portland	15,1	0.07
9	40-60mm	3-3	portland	14,7	0.12
10	0 - 10mm	4-1	portland	12,3	0.09
11	10-20mm	4-2	portland	33,4	0.09
12	20-30mm	4-3	portland	30,0	0.06
13	0 - 20mm	5-1	portland	33,0	0.12
14	20-40mm	5-2	portland	34,3	0.16
15	40-60mm	5-3	portland	34,9	0.21
16	0 - 20mm	6-1	portland	34,7	0.57
17	20-40mm	6-2	portland	34,0	0.05
18	40-60mm	6-3	portland	34,2	0.03
19	0 - 20mm	7-1	portland	30,8	0.15
20	20-40mm	7-2	portland	29,8	0.19
21	40-60mm	7-3	portland	33,3	0.45
22		8	portland	35,2	0.07
23		9	portland	35,8	0.07
24		10	portland	34,5	0.07
25		11	portland	32,0	0.18
26		12	portland	33,2	0.31
27		13	portland	33,9	1.66
28		14	portland	33,9	0.86
29		15	portland	35,7	0.79
30		16	portland	33,6	0.90
31		17	portland	32,3	0.44
32		18	portland	35,5	1.56
33		19	portland	34,1	0.72
34		20	portland	31,9	0.65
35		21	portland	34,4	1.06
36		22	portland	34,4	0.80
37		23	portland	36,7	1.18

The absolute values obtained in this way can be influenced by many factors, which are rather difficult to determine and therefore often give cause for criticism as for the correct interpretation of the measured values. This because the ASTM-standard, as showed in the table, only indicates regular conditions in which corrosion can or cannot be expected.

This standard doesn't discuss the possible interpretations of the measured values in case of altered situations, such as e.g. low potential gradients, carbonation, humidity changes and the specific resistance changes of the concrete. So care should be taken during the interpretation of the values.

The total surface area of approximate 8000 m^2 has been potential mapped of which 25% of the

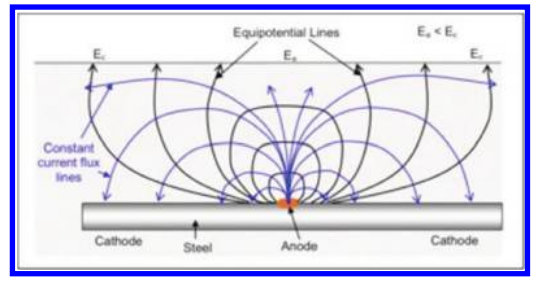

Figure 13. Potentials can be measured on the concrete's surface due to the equipontial lines.

total surface area showed areas which resulted in values being more negative than –350 mV [CSE]. However this does not need to mean that at those locations all the prestressed tendons are corroding.

As shown in Figure 9 reinforcement bars are positioned above the prestressed tendons, so it could be possible that the potentials indicate a situation of active reinforcement bars but passive tendons. Although the chance to encounter such a situation is very small due to the fact that almost the whole surface area of the bridge deck has been restored completely including replacement of the reinforcement bars by new passive bars.

Knowing this fact and seeing the very negative potentials at certain areas we feared that a particular situation could occur at these locations which is called macro corrosion cells, which could accelerate the corrosion rate of the prestressed tendons.

The prestressed tendons are located in the original concrete with relatively high chloride contents as can be seen from the chloride analysis.

These tendons are under tension and for structural safety reasons the concrete surrounding these tendons cannot be restored. However the restored top-layer of the bridge-deck exists of fresh high alkaline concrete with passive bars. These passive bars are more likely to be prone to the oxygen reduction reaction due to their position than the passive tendons as can be seen in Figure 14. This oxygen reduction reaction will most probably accelerate the corrosion reaction of the active tendons.

This can only be checked visually by destructive verification of zones with high corrosion probility. By scarifying the concrete to the depth of the tendons we were able to verify these zones. We kept these verifications to a very limited quantity due to the amount of energy involved during the scarification which may cause mechanical damage to the corroded and possible weakened tendons.

After scarification and sandblasting we inspected these areas. Clearly can be seen from

Figure 24 the highly corrosive tendons and very passive reinforcement bars laying on top of it. Several corrosion pits seen in the bars have a depth of 6mm which indicates severe chloride attack.

Regarding chloride attack there is a general agreement in the literature that chloride ions lead to depassivation, but the exact mechanism is not well understood.

It is also generally agreed that a critical concentration of chloride ions that leads to depassivation exists, but there is little agreement on an exact quantitative amount of chloride required for depassivating plain carbon steel.

The critical chloride content or chloride threshold concentration is the concentration of Cl^- ions that is sufficient to cause active corrosion or induce pitting given enough time.

The critical chloride content is most commonly expressed as *total chloride content relative to the weight of the cement (Cl-% m/m cement)*. The main reason for this is the fact that the determination of total chloride content in an existing structure is relatively simple and well documented in standards.

Many national and international recommendations like RILEM, CEB and CUR report a critical chloride content of 0,4% Cl^- m/m cement. Basically it means that the chloride contents above this value will most probably initiate corrosion and pitting.

Early studies by Hausmann[7] in 1967 indicated a $[Cl^-/OH^-]$ ratio of 0.63, above which the chloride-induced corrosion takes place faster than passive film repair by hydroxyl ions, based on simulated pore solution chemistry at a pH about 13.5.

However other studies, for example done by Diamond[8] indicated that in typical cement pastes, the $[Cl^-/OH^-]$ ratio at which risk of corrosion is significant drops as low as 0.3.

The concentration of chloride that causes depassivation depends heavily on other variables such as oxygen concentration, pH, rebar surface conditions, presence of other ions in the pore solution, and various concrete properties including type of aggregate, concrete additives, mix design, moisture level, and air content[5].

A passive film will contain relatively numerous flaws and defects, even when formed on a metal of high purity depending on its micro-structure. Chloride ions penetrate the oxide layer at these defects due to dissolution of the more reactive species in the oxide layer. Regardless of mechanism, corrosion initiation is a localized phenomenon caused by a sufficient concentration of chloride ions.

According to some studies[6] localized pitting attack is caused by sufficient chloride ion concentration and will preferentially occur at regions of low dissolved oxygen content.

The initial oxide film formed on steel in concrete is $Fe(OH)_2$, which is then converted to either ferrous (Fe^{2+}) or ferric (Fe^{3+}) oxide (also known as y-FeOOH). Although y-FeOOH is the more stable of the two oxides, it forms more slowly. Because these conversions are never complete, chloride ions may compete with the conversion of $Fe(OH)_2$ to y-FeOOH by the following reaction:

$$Fe(OH)_2 + 6Cl^- <=> FeCl_6^{3-} + 2OH^- + e^-$$

The chloride complex formed in this equation is soluble in the surrounding pore solution and, therefore does not provide protection against corrosion of the rebar surface. Pore solutions containing sufficient chloride concentrations will promote localized areas of depassivation on the rebar surface where the ferrous oxide has not been converted to y-FeOOH, even if the pore solution pH is above 11.5.

When analysing the chloride content of the samples a difference can be seen between the restored top-layer of the bridge-deck and the original concrete beneath this restored layer.

Table 1 shows the results of the chloride content. Samples 1 to 21 are taken from the concrete cores drilled in the top layer of the bridge-deck and samples 22 to 37 are taken from the concrete pieces of the original concrete around the prestressed tendons.

Clearly can be seen that samples taken from the restored bridge deck (1–23) have a much lower chloride content than the samples taken form the original concrete (22–37). Although the first 20 mm already show a small increase of chloride content compared to the values form 20–60 mm depth. This indicates that the process of chloride ingress is actually still ongoing due to the use of deicing salts almost 6 months a year.

Specifically the samples taken from the concrete surrounding the prestressed tendons show chloride contents exceeding 1% m/m cement. This indicates a high probability of chloride initiated corrosion.

4.1 *Susceptibility of prestressed steel*

In the case of prestressed steel used for the tendons, the presence of very small amounts of hydrogen can lead to irreversible damage. Therefore the susceptibility of the steel to hydrogen is of enormous importance.

During the corrosion process, hydrogen atoms are released from the water and then absorbed by the steel. In prestressing steels, hydrogen under mechanical stresses can create pre-cracks in critical structural areas such as grain boundaries. These cracks may grow and result in fracture. Atomic hydrogen released on the steel surface can be absorbed and enriched by diffusion in multi-axially stretched plastic zones, crack tips, corrosion pits and precipitates in the steel structure.

The susceptibility of prestressed tendons to hydrogen embrittlement depends on the chemical composition of the steel, the production process and subsequent treatment (e.g., thermal treatment). All types of prestressing steels (hot-rolled, quenched and tempered, cold-deformed steel) can be used without fear of corrosion problems if optimal characteristics are achieved.

Steel types where the majority of the grain boundaries are perpendicular to the applied forces are most at risk. This group includes, hot-rolled and quenched and tempered steels. In the latter case, the austenite grain boundaries are of concern. In the case of cold-formed wires and strands, the deformed grain boundaries run predominantly in the direction of the applied force. This explains why, in the presence of high hydrogen supply, cold-drawn wires and strands manufactured from these types of wires perform better than hot-rolled and quenched and tempered steel.

Substantial variability in susceptibility to H-SCC can be observed in different types of steel, depending on composition and/or thermal treatment. Sensitivity of steel microstructures to hydrogen embrittlement increases in the following order: perlitic grades, quenched and tempered, bainitic steels formed by continuous cooling, and finally martensitic microstructure[1]. Because of the high sensitivity of martensitic steel, it is not used where there is any risk of hydrogen-induced stress corrosion cracking. Prestressed steels with bainitic structures have resulted in numerous structural failures and the use of this steel in construction is no longer permitted.

Cracks may occur in partially prestressed concrete structures. Since such cracks tend to open and to close under the influence of a superimposed fatigue stress, a number of factors must be considered and these are discussed below.

Cracks can occur in concrete due to fatigue loading displacements between the tendon and the injection mortar or the steel duct.

The "verification" zones where severe corrosion was found indicated no cracks in the tendons. This fundamentally indicates that the steel used is not susceptible for hydrogen embrittlement. The steel used is St 85/105 (32 mm tendons) and has a perlitic microstructure. Perlitic steel is known for its low susceptibility for hydrogen embrittlement. This is proved by the metallurgic lab analyses performed by MPA (University of Stuttgart).

However previous inspections showed cracks in the tendons. Actually the samples given by the Highway Agency and sent to the lab for analysis were samples cut out from the fractured tendons. Remarkably these fractures were located in the very close vicinity of the coupler joints. A detailed sketch of these coupler joints can be seen in Figure 16.

Figure 17 shows the exact location of the fractures which were all in the threaded region of the coupler joints. The inspection report of the Highway Agency also indicated the high chloride content found in these areas were the fractured tendons were located.

As indicated previously heavily corroded parts of the tendons which were not in the close vicinity of the coupler joints as seen in Figure 17 showed no fractures. These facts directed us to the coupler joints in combination with chlorides as the possible cause of the fractures in the threaded region of the tendons. Previous studies[9] of problems with pre-stressed coupling joints indicated that couplers may crack as a result of imposed stresses.

Imposed stresses could be non-uniform sun heating and low amount of reinforcement which crosses the coupling joint to elevate stress concentrations in the joints.

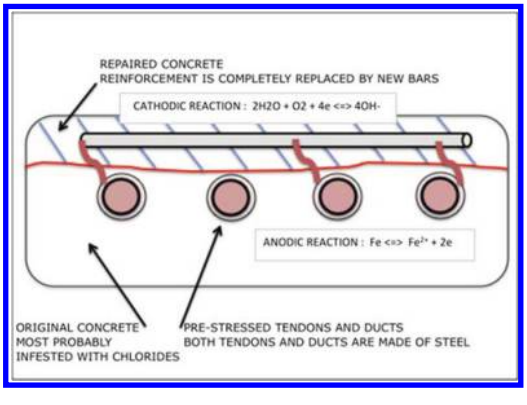

Figure 14. Possible macro corrosion cell occurring and accelerating the corrosion rate of the tendons.

Figure 15. Despite heavily corroded tendons and 6 mm deep "pits", no fractures in the tendons were found at locations away from the couplers.

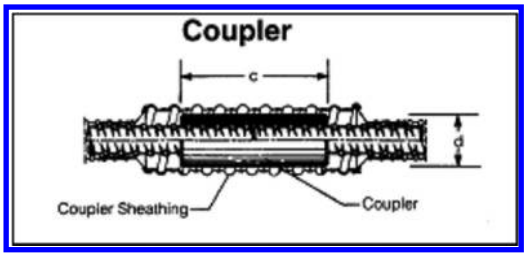

Figure 16. Typical Dywidag tendon coupler.

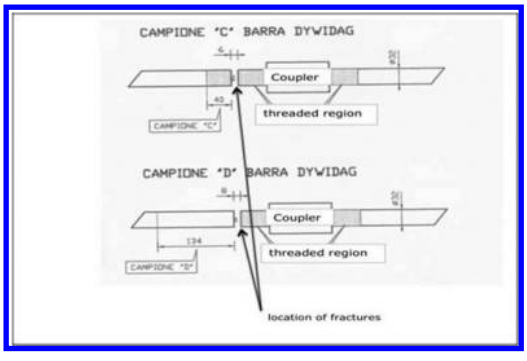

Figure 17. Location of fractures were in the threaded region of the coupler.

In these particular situations the joints will suffer major stress fatigue cycles from traffic load which also led to prestressing steel fractures owing the stress sensitive couplings.

A similar situation of fatigue failure of prestressed tendons in the coupling joint region was discovered at the "Heerdter crossing" in Düsseldorf in 1976, until then unrecognized, and indicated as a weakness of prestressed concrete structures[10].

Two separate prestressed concrete bridges form a flyover at the Heerdter crossing. The bridge decks were cast in place as continuous single-hollow-core girders. As the longitudinal prestressed, single smooth tendons made of 26 mm diameter bar of steel grade St 85/105 by Dywidag were used.

At section joints the tendons were coupled with threaded connections exactly the same as used in the bridge deck "Viadotto Colle Isarco".

In 1976 on one of the bridges flyovers, increased crack widths were clearly visible in the bottom plate at several coupling joints in the curved region. The coupling joints at this location were formed as indented joints with 8 up to 12 tendons located there. At the indentations the concrete was cracked right through in the extension of the course of the main joint and nearly all prestressed tendons were broken due to corrosion fatigue in the threaded region of the coupling joints.

Investigation further revealed that the unforeseen cracking of the coupling joints or in the close vicinity of it occurred predominantly as the result of imposed stresses due to non-uniform solar heating. The cracking of the coupling joints imposed consequential effects in turn on the prestressed steel. The unforeseen cracking was combined with an insufficient amount of reinforcement placed over the coupling joints and a large fatigue load caused by the traffic.

Due to this uncovering DIN 4227 was developed and specifically part 1 describes the risk of fatigue fracture from coupling joints which depends greatly on the amount of reinforcement which crosses the coupling joints. The minimum acceptable longitudinal reinforcement which goes through the coupling joints has been significantly increased. The reinforcing steel bars with their ribs limit the movement in the joints and reduce the range of alternating stresses. In this way they reduce the fatigue loading on the couplings.

5 CONCLUSION

Potential mapping of appr. 8000 m^2 of concrete surface area of the upper bridge deck of the Viadotto "Colle Isarco" indicated heavily corroded prestressed tendons due to chloride ingress proved by the lab analysis of the concrete samples. The corroded zones showed pits up to 6 mm deep. The total zone with possible corrosion is estimated on 9% of the total surveyed surface area. This amount is based on adding up all measuring points with a potential being more negative than –450 mV divided by the total amount of measuring points.

However no fractures were found in those "active" zones away from the coupler joints.

The steel St 85/105 used for the prestressed tendons has the perlitic microstructure and is not susceptible for hydrogen embrittlement as proved by the metallurgic analysis performed in the laboratory of the Materialprüfungsanstalt at the University of Stuttgart.

Fractures found in the tendons in previous inspections are most probably caused by major stress fatigue cycles from traffic loads in combination with corrosion due to the stress-sensitive couplings.

It is well known that a corrosive environment will reduce the fatigue strength of prestressing steels and reduce therefore maximum allowable stress fatigue cycles of the prestressed tendons.

Exactly similar cases (*Heerdter crossing in Düsseldorf in 1976*) were found in old reports, e.g. published in the technical report 26 "Influence of material and processing on Stress Corrosion Cracking of prestressing steel—case studies" by

the International Federation for Structural Concrete (fib) in Lausanne—Switzerland. Case history search discovered that the steel tendons used in this construction were exactly the same: St 85/105 and fractures were found in the threaded region of coupling joints due to corrosion fatigue.

REFERENCES

[1] Durability of concrete and cement composites, Chapter 6, page 187–246 Degradation of prestressed concrete, Nuernberger, Sawade, Isecke.

[2] Materials Science, Volume 192–194 (1995), pp 891–898, Passivation of reinforcing steel in concrete, C. Andrade, P. Merino, X.R. Novoa.

[3] Corrosion of steel in the area of cracks in concrete, Chapter 2, page 13, M. Raupach, "Corrosion of reinforcement in concrete construction". published by SCI, 1996.

[4] Corrosion and Corrosion Control. Uhlig, and Greene, N. D. Wiley, New York, 1985.

[5] Testing of selected metallic reinfocing bars for extending the service life of concrete bridges: testing in solutions, Scully, Marks and Hurley. Virginia Transportation Research Counsil.

[6] Steel Corrosion in Concrete, A. Bentour, S. Diamond, and N. Berke. E & FN Spon, London, 1997.

[7] Hausmann, D. A. Steel Corrosion in Concrete. How Does it Occur? Journal of materials protection, Vol. 11, 1967, pp. 19–23.

[8] Diamond, S., "Chloride Concentrations in Concrete Pore Solutions Resulting from Calcium and Sodium Chloride Admixtures," Cement, Concrete and Aggregates, Vol. 8, No. 2, Winter 1986, pp. 97–102.

[9] Corrosion induced failures of prestessing steel, Nurnberger, Ott-Graf-Journal, Volume 13, 2002.

[10] Technical report 26 by the International Federation for Structural Concrete (fib) in Lausanne—Switzerland, "Influence of material and processing on Stress Corrosion Cracking of prestressing steel—case studies".

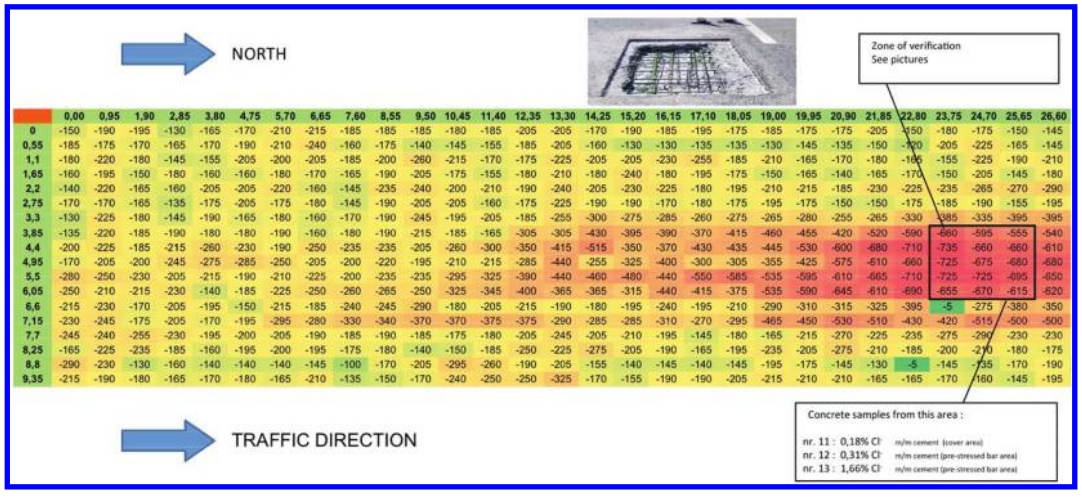

	0,00	0,95	1,90	2,85	3,80	4,75	5,70	6,65	7,60	8,55	9,50	10,45	11,40	12,35	13,30	14,25	15,20	16,15	17,10	18,05	19,00	19,95	20,90	21,85	22,80	23,75	24,70	25,65	26,60
0	-150	-190	-195	-130	-165	-170	-210	-215	-185	-185	-185	-180	-185	-205	-205	-170	-190	-185	-195	-175	-185	-175	-175	-205	-150	-180	-175	-150	-145
0,55	-185	-175	-170	-165	-170	-190	-210	-240	-160	-175	-140	-145	-155	-185	-205	-160	-130	-130	-135	-135	-130	-145	-135	-150	-120	-205	-225	-165	-145
1,1	-180	-220	-180	-145	-155	-205	-200	-205	-185	-200	-260	-215	-170	-175	-225	-205	-205	-230	-255	-185	-210	-165	-170	-180	-165	-155	-225	-190	-210
1,65	-160	-195	-150	-180	-160	-160	-180	-170	-165	-190	-205	-175	-155	-180	-210	-180	-240	-180	-195	-175	-150	-165	-140	-165	-170	-150	-205	-145	-180
2,2	-140	-220	-165	-160	-205	-205	-220	-160	-145	-235	-240	-200	-210	-190	-240	-205	-230	-225	-180	-195	-210	-215	-185	-230	-225	-235	-265	-270	-290
2,75	-170	-170	-165	-135	-175	-205	-175	-180	-145	-190	-205	-205	-160	-175	-225	-190	-190	-170	-180	-175	-195	-175	-150	-150	-175	-185	-190	-155	-195
3,3	-130	-225	-180	-145	-190	-165	-180	-160	-170	-190	-245	-195	-205	-185	-255	-300	-275	-285	-260	-275	-265	-280	-255	-265	-330	-385	-335	-395	-395
3,85	-135	-220	-185	-190	-180	-180	-190	-160	-180	-190	-215	-185	-165	-305	-305	-430	-395	-390	-370	-415	-460	-455	-420	-520	-590	-660	-595	-555	-540
4,4	-200	-225	-185	-215	-260	-230	-190	-250	-235	-235	-205	-260	-300	-350	-415	-515	-350	-370	-430	-435	-445	-530	-600	-680	-710	-735	-660	-660	-610
4,95	-170	-205	-200	-245	-275	-285	-250	-205	-200	-220	-195	-210	-215	-285	-440	-255	-325	-400	-300	-305	-355	-425	-575	-610	-660	-725	-675	-680	-680
5,5	-280	-250	-230	-205	-215	-190	-210	-225	-200	-235	-235	-295	-325	-390	-440	-460	-480	-440	-550	-585	-535	-595	-610	-665	-710	-725	-725	-695	-650
6,05	-250	-210	-215	-230	-140	-185	-225	-250	-260	-265	-250	-325	-345	-400	-365	-365	-315	-440	-415	-375	-535	-590	-645	-610	-690	-655	-670	-615	-620
6,6	-215	-230	-170	-205	-195	-150	-215	-185	-240	-245	-290	-180	-205	-215	-190	-180	-195	-240	-195	-210	-290	-310	-315	-325	-395	-5	-275	-380	-350
7,15	-230	-245	-175	-205	-170	-195	-295	-280	-330	-340	-370	-370	-375	-375	-290	-285	-285	-310	-270	-295	-465	-450	-530	-510	-430	-420	-515	-500	-500
7,7	-245	-240	-255	-230	-195	-200	-205	-190	-185	-190	-185	-175	-180	-205	-245	-205	-210	-195	-145	-180	-165	-215	-270	-225	-235	-275	-290	-230	-230
8,25	-165	-225	-235	-185	-160	-195	-200	-195	-175	-180	-140	-150	-185	-250	-225	-275	-205	-190	-165	-195	-235	-205	-275	-210	-185	-200	-210	-180	-175
8,8	-290	-230	-130	-160	-140	-140	-140	-145	-100	-170	-205	-295	-260	-190	-205	-155	-140	-145	-140	-145	-195	-175	-145	-130	-5	-145	-135	-170	-190
9,35	-215	-190	-180	-165	-170	-180	-165	-210	-135	-150	-170	-240	-250	-250	-325	-170	-155	-190	-190	-205	-215	-210	-210	-165	-165	-170	-160	-145	-195

Results corrosion survey: Zone 3a of the bridge deck with verified locations of the prestressed tendons.

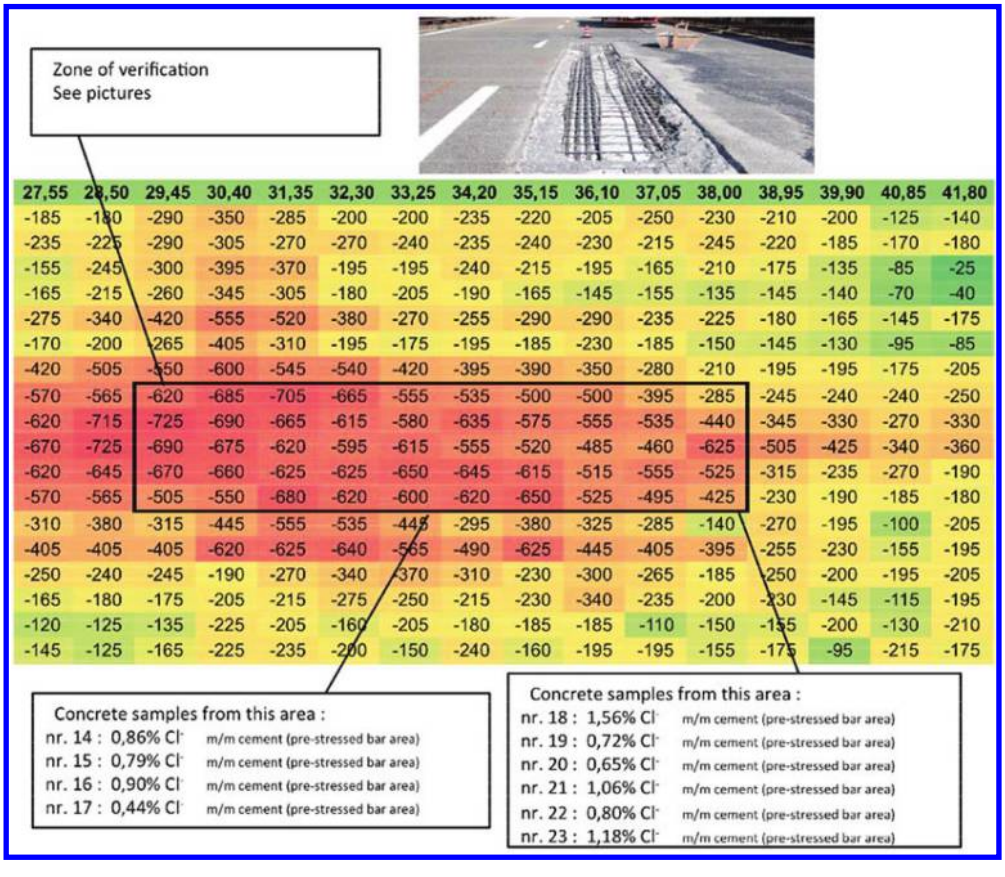

27,55	28,50	29,45	30,40	31,35	32,30	33,25	34,20	35,15	36,10	37,05	38,00	38,95	39,90	40,85	41,80
-185	-180	-290	-350	-285	-200	-200	-235	-220	-205	-250	-230	-210	-200	-125	-140
-235	-225	-290	-305	-270	-270	-240	-235	-240	-230	-215	-245	-220	-185	-170	-180
-155	-245	-300	-395	-370	-195	-195	-240	-215	-195	-165	-210	-175	-135	-85	-25
-165	-215	-260	-345	-305	-180	-205	-190	-165	-145	-155	-135	-145	-140	-70	-40
-275	-340	-420	-555	-520	-380	-270	-255	-290	-290	-235	-225	-180	-165	-145	-175
-170	-200	-265	-405	-310	-195	-175	-195	-185	-230	-185	-150	-145	-130	-95	-85
-420	-505	-550	-600	-545	-540	-420	-395	-390	-350	-280	-210	-195	-195	-175	-205
-570	-565	-620	-685	-705	-665	-555	-535	-500	-500	-395	-285	-245	-240	-240	-250
-620	-715	-725	-690	-665	-615	-580	-635	-575	-555	-535	-440	-345	-330	-270	-330
-670	-725	-690	-675	-620	-595	-615	-555	-520	-485	-460	-625	-505	-425	-340	-360
-620	-645	-670	-660	-625	-625	-650	-645	-615	-515	-555	-525	-315	-235	-270	-190
-570	-565	-505	-550	-680	-620	-600	-620	-650	-525	-495	-425	-230	-190	-185	-180
-310	-380	-315	-445	-555	-535	-445	-295	-380	-325	-285	-140	-270	-195	-100	-205
-405	-405	-405	-620	-625	-640	-565	-490	-625	-445	-405	-395	-255	-230	-155	-195
-250	-240	-245	-190	-270	-340	-370	-310	-230	-300	-265	-185	-250	-200	-195	-205
-165	-180	-175	-205	-215	-275	-250	-215	-230	-340	-235	-200	-230	-145	-115	-195
-120	-125	-135	-225	-205	-160	-205	-180	-185	-185	-110	-150	-155	-200	-130	-210
-145	-125	-165	-225	-235	-200	-150	-240	-160	-195	-195	-155	-175	-95	-215	-175

Results corrosion survey: Adjacent surface of zone 3a with verified locations.

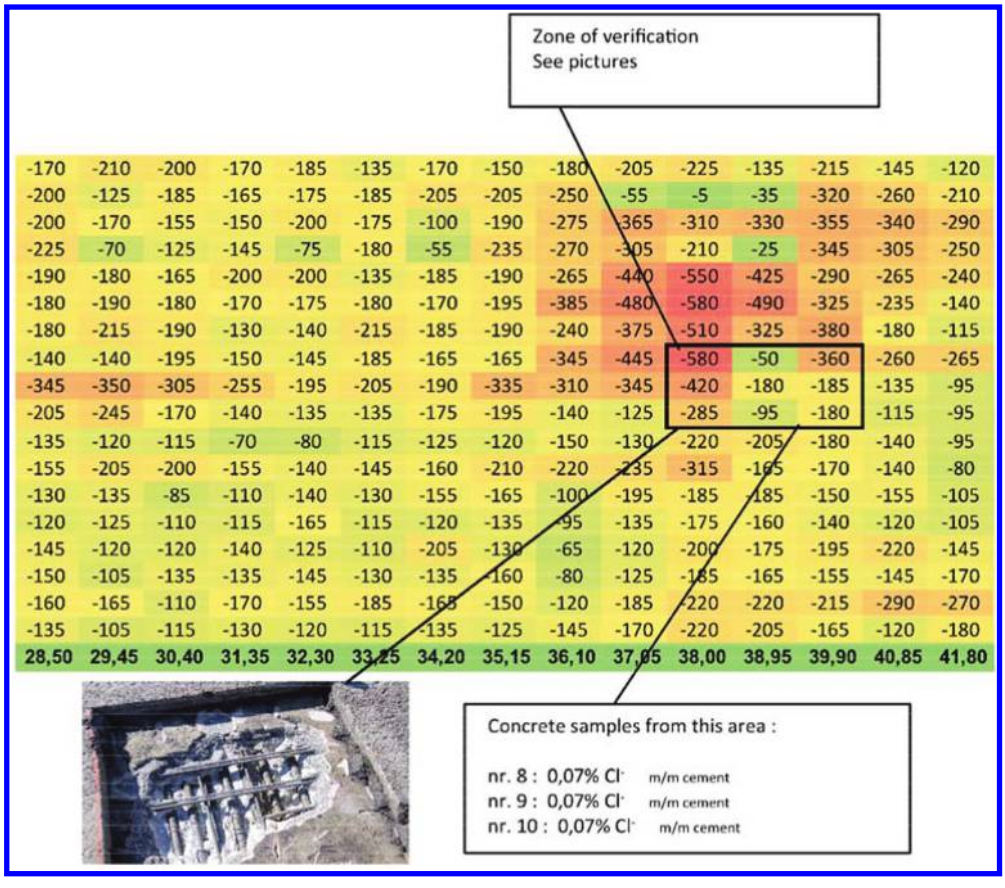

Results corrosion survey : Zone 4 with verified locations.

Concrete Repair, Rehabilitation and Retrofitting IV – Dehn et al. (Eds)
© 2016 Taylor & Francis Group, London, ISBN 978-1-138-02843-2

Mechanical performance of deep beams damaged by corrosion in a chloride environment

Linwen Yu
Université de Toulouse, UPS, INSA, France
LMDC, Toulouse, France
Department of Civil Engineering, CRIB, Université de Sherbrooke, Québec, Canada

Raoul François
Université de Toulouse, UPS, INSA, France
LMDC, Toulouse, France

Richard Gagné
Department of Civil Engineering, CRIB, Université de Sherbrooke, Québec, Canada

Vu Hiep Dang
Faculty of Civil Engineering, Hanoi Architectural University, Hanoi, Vietnam

Valérie L'Hostis
CEA Saclay, CEA, DEN, DPC, SECR, Gif-sur-Yvette, France

ABSTRACT: Two beams with dimensions $3000 \times 280 \times 150$ mm were exposed to a chloride chamber for 27 and 36 months, corrosion of the reinforcements in the beams were accelerated by wetting and drying cycles. Two deep beams were taken from each long beam. Mechanical test were applied on the four deep beams. Then corrosion maps, cross-sectional loss of tensile reinforcements and diameter loss of stirrups were depicted. The results showed that corrosion distributed quite randomly on the reinforcements. The beams with light corrosion on tensile reinforcements failed in shear mode. Severe corrosion of tensile bars lead to the flexure failure of deep beams.

1 INTRODUCTION

Corrosion is the upmost threat for the durability of reinforced concrete structures exposed in a marine environment. Structural performance and serviceability of reinforced concrete structures is affected by corrosion from several aspects, cross-sectional loss of reinforcements, disbonding between concrete and reinforcements caused by the expansion of corrosion products, and brittle performance of corroded reinforcements.

Numerous of studies (Alsulaimani et al., 1990; Du et al., 2013; Zhu and François, 2014a) have been carried out on the mechanical performance of corroded reinforced concrete beams. However, most of the existing studies were focused on the slender beams. Due to the different load transfer mechanisms in slender beams and deep beams, it is quite necessary to investigate the mechanical performance of deep beams damaged by corrosion. Wang et al. (Wang et al., 2011, 2012) studied the shear behavior of reinforced concrete beams damaged by partial length corrosion on tensile reinforcements. Xia et al. (Xia et al., 2011) and Higgins et al. (Higgins et al., 2012) carried out some experiments on the shear performance of beams damaged by corrosion on stirrups. However, normally not only tensile reinforcements or stirrups are damaged in the corrosion damaged RC structural elements in-service. And all the investigations mentioned above accelerated corrosion with impressed current, which lead to different corrosion distribution comparing with natural corrosion (Yuan et al., 2007).

Zhu and François (Zhu et al., 2015, 2013) studied the mechanical performance of deep beams corroded in a climate accelerated environment. At the same time, the mechanical performance of uncorroded beams were also tested to highlight the impact of corrosion on the mechanical performance of deep beams. The cracking pattern after failure, the failure mode and span to effective depth ratio of all the beams were investigated in their research.

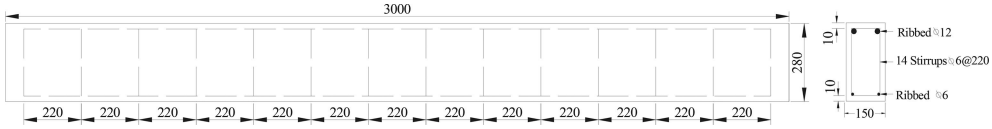

Figure 1. Layout of the RC beams type Bs (all dimensions in mm).

In this paper, some deep beams were corroded in the same environment as that in the studies of Zhu and François (Zhu et al., 2013, 2015). Then the mechanical performance of beams with different span to effective depth ratios (1.55, 1.94 and 2.03) and different corrosion degrees were studied in order to enrich the experiment results and try to get some more knowledge on the mechanical performance of deep beams damaged by corrosion.

2 EXPERIMENTAL CONTEXT

A batch of beams with dimensions 3000 × 280 × 150 mm, which a sufficient size to be representative of the real structure conditions, were cast at Laboratoire Matériaux et Durabilité des Constructions (L.M.D.C.) in Toulouse in 2010. All the beams were divided into two groups named type As and type Bs according to the different reinforcement layouts. The beams were stored in a confined chamber with chloride environment under service load so as to simulate the real structures in service. After a certain period of corrosion, the corroded beams were taken out of the chamber and bending test was applied on the full scale beams. During the bending test, the broken section and cracks induced by bending were mainly concentrated in the middle of the full scale beams. The two ends of full scale beam were undamaged and were cut to form two short span beams in order to study the shear performance of corroded beams. In this study, four short span beams, extracted from two beams of type Bs (Bs02 and Bs04), were investigated here.

2.1 *Reinforced concrete beams*

The beams of type B were reinforced with ordinary reinforced steel (yield strength = 500 MPa). The concrete cover is 10 mm and the arrangement of steels is shown in Figure 1. The diameter of tensile bars is 12 mm, while that of compressive bars and the stirrups is 6 mm. It worth noting that there were no hooks on the longitudinal bars at the ends. The composition of the concrete is shown in Table 1. The actual water/cement ratio was fine adjusted in order to obtain a slump of 70 mm. The average compressive strength of concrete was 45 MPa by the test of cylindrical specimens (110 × 220 mm) at 28 days.

Table 1. Concrete composition and cement composition.

Mix composition		
Rolled gravel (silica + limestone)	5–15 mm	1109 kg/m^3
Sand	0–5 mm	745 kg/m^3
Portland cement: OPC (CEM I)		364 kg/m^3
Water		182 kg/m^3

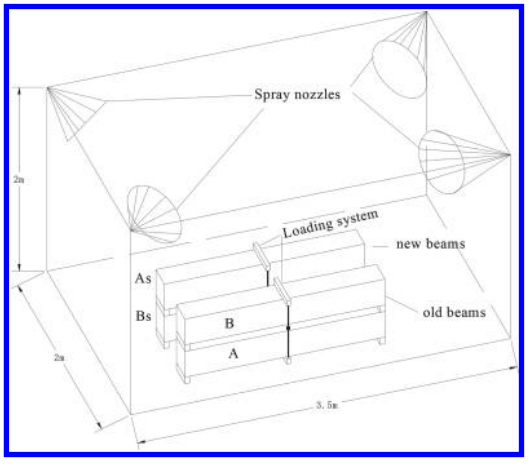

Figure 2. Loading system and exposure condition.

2.2 *Loading of the beams*

One type A beam and one type B beam were loaded together with the loading system shown in Figure 2. The beams were loaded at two different levels. Level 1 loading (M_{ser} = 13.5 kN·m) was designed according to the Serviceability Limit State (SLS) requirements in an aggressive environment based on an indirect limitation of crack width. Level 2 loading (M_{ser} = 21.2 kN·m) was designed according to Ultimate Load Limit state (ULS) in a non-aggressive environment. For beam Bs02, the bending moment was M_{ser} = 13.5 kN·m (corresponding to a point load of 20 kN), while the bending moment of Bs04 was M_{ser} = 21.2 kN·m (corresponding to a point load of 30 kN).

2.3 *Exposure environment*

Once the beams were loaded, they were stored in a confined chamber as shown in Figure 2. Salt fog

(35 g/L of NaCl, corresponding to the salt concentration of sea water) was generated by four spray nozzles located at each upper corner of the chamber. The exposure condition was wetting-drying cycle with two days of spraying and then 2 weeks of drying, and the temperature was the same as the natural environment of south west France, with monthly-average temperatures ranging from 5.1°C to 21.3°C.

3 EXPERIMENT RESULTS AND DISCUSSION

Beam Bs02 and beam Bs04 were taken out of the confined chamber after being exposed in the chloride environment for 36 and 27 months respectively. Corrosion maps were depicted, afterwards bending test was carried out on the two full scale beams.

3.1 *Dimension of the short span beams*

As stated in last section, damage occurred only in the middle of the full scale beams. So the short span beams were extracted at two ends of the full scale beams. In order to consider the effect of different span/effective depth ratios on the mechanical performance of corroded RC beams, short span beams with different span lengths were extracted. The length of both short span beams extracted from beam Bs04, named as Bs04-A and Bs04-B, was 1200 mm. The net span was 1000 mm and the span/effective depth ratio was 1.94. The two short span beams extracted from beam Bs02 were named as Bs02-A and Bs02-B. The length was 1250 and 1000 mm respectively. The net span was 1050 and 800 mm respectively while the span/effective depth ratio was 2.03 and 1.55 respectively. The dimensions of the four short span beams are presented in Figure 3. The hatched zone stand for the part damaged in the bending tests and was discarded.

3.2 *Cracking maps of short span beams*

Full scale beams Bs04 and Bs02 were taken out of the chloride chamber after 27 and 36 months of exposure respectively. Cracking maps of the two full scale beams were depicted before bending test. A video microscope was used to measure width of cracks, including transverse cracks and longitudinal cracks, in the beams. The accuracy of the video microscope was 0.01 mm and the magnification was between 25 to 175 times. On the cracking maps, the black lines represent bending cracks, while the red lines represent corrosion cracks. The standard lines represent cracks whose width are smaller than 1.0 mm while the bold lines represent cracks those are wider than 1.0 mm. The blue hatched zone means spalling of concrete cover.

On beam Bs04-A, there were more corrosion cracks around the front tensile bar, although the exposure environment and the concrete cover depth were the same for the front bar and the back bar. For most of cracks, the crack width was smaller than 1.0 mm. The maximum crack width was about 1.4 mm, which located near to the left end of the beam. For beam Bs04-B, there was no much difference on the crack distribution around the front bar and the back bar. The maximum crack width was about 0.9 mm, which located in

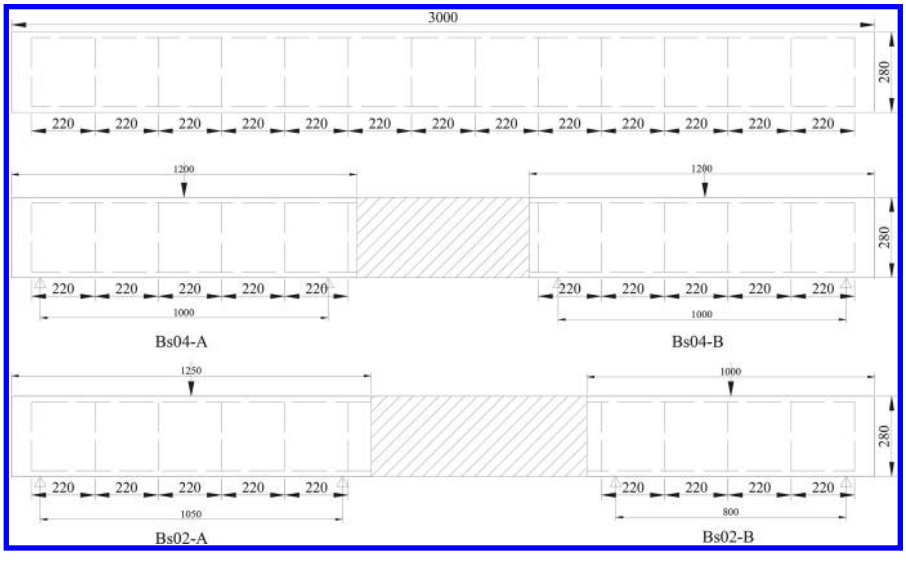

Figure 3. Dimensions of the four short span beams (in mm).

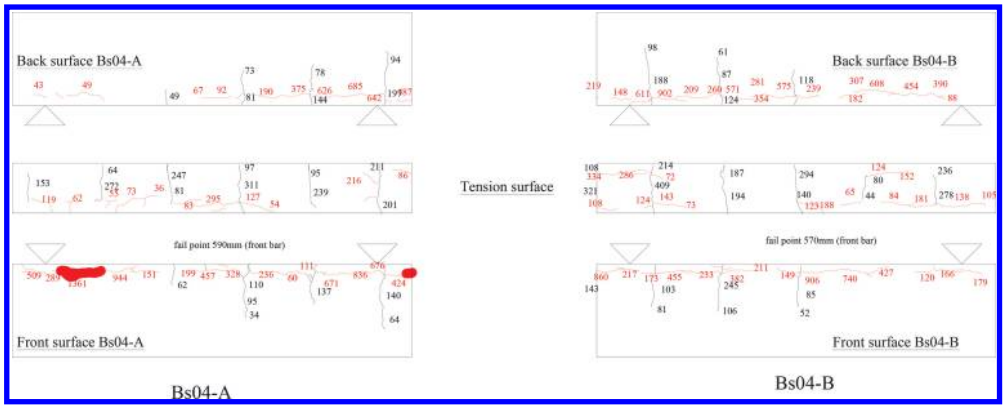

Figure 4. Cracking maps of Bs04-A and Bs04-B.

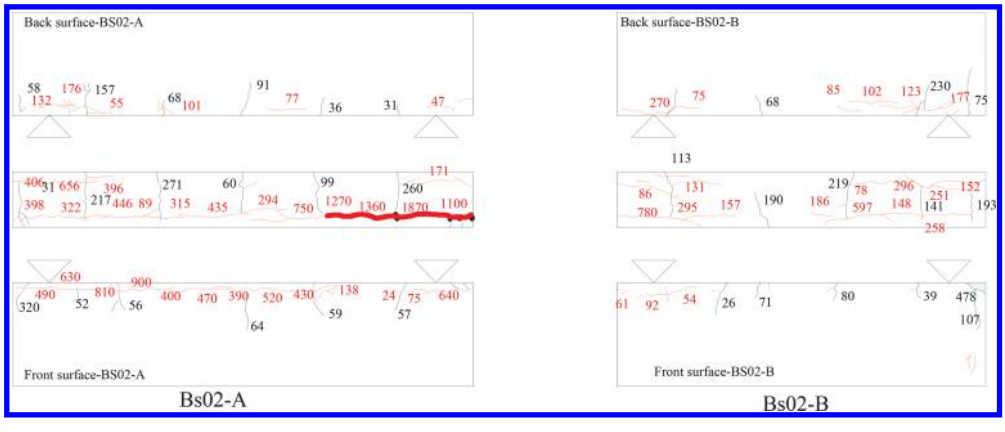

Figure 5. Cracking maps of Bs02-A and Bs02-B.

the middle of the front bar and on the left end of the back bar.

There were much more cracks on the front side of beam Bs02-A than on the back side. The widest crack was located on the right side, which is closed to the central part of the original full scale beam. And the most large crack width was about 1.9 mm. The situation on beam Bs02-B was quite different. There were much fewer cracks on both front and back sides of beam Bs02-B than Bs02-A. Most of the cracks were distributed on the tensioned surface. There were nearly no cracks on the central part of beam Bs02-B. It is particularly worth noting that there was some spalling occurred on the right end of beam Bs02-B.

3.3 *Corrosion maps*

After the mechanical test, tensile bars were extracted out and cleaned with Clark's solution (ISO 8407) to remove the corrosion products. The corrosion distributions on the tensile bars were described in detail. General corrosion and pitting corrosion areas were depicted with different stamps. General corrosion areas were covered by the blue hatched lines while pitting corrosion areas were covered by the solid blue zones. The red points on the steel bars of beam Bs04-A and Bs04-B stand for the failure point during the mechanical tests.

As presented in Figure 7, almost all the surface of tensile bar in beam Bs04-A and Bs04-B was corroded. The situation of beam Bs02-A and Bs02-B was quite different, there are some zones uncorroded on the back tensile bar of beam Bs02-A and Bs02-B. It corresponded to the areas without corrosion cracks in Figure 6. Although the corrosion time of beam Bs02-A and Bs02-B was longer than that of beam Bs04-A and Bs04-B, the corroded area was a bit smaller.

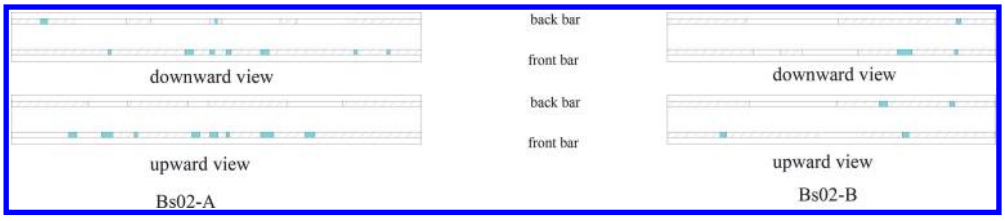

Figure 6. Corrosion maps of beam Bs02-A and Bs02-B.

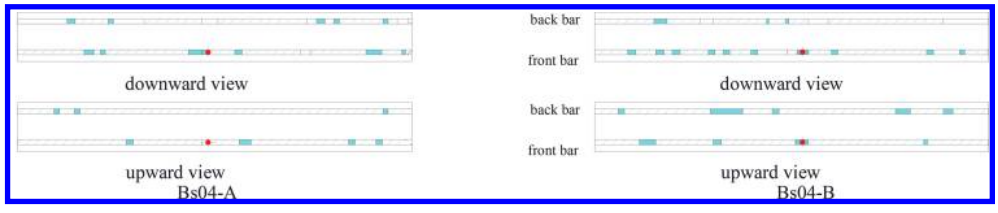

Figure 7. Corrosion maps of beam Bs04-A and Bs04-B.

3.4 *Cross-sectional loss of tensile bars and diameter loss of stirrups*

Gravimetric method was used to calculate cross-sectional loss of corroded steel bars. Due to the irregular distribution of corrosion, steel bars were cut into short pieces of different lengths according to the corrosion pattern. The length of each piece was measured with vernier calipers with a precision of 0.02 mm. The weight was measured on a balance with a precision of 0.01 g. the loss of cross-section was then calculated with Equation (1). The original mass of the short sections can be calculated with Equation (2):

$$\Delta A_s = \frac{m_0 - m}{m_0} \cdot A_s \tag{1}$$

$$m_0 = \rho \cdot A_s \cdot L \cdot \tag{2}$$

where ρ (g/cm^3) is the density of the steel bar, considered to be 7.85 g/cm^3; L is the length of each short section; ΔA_s is the average loss of cross-section of the corroded bars over the short section length; A_s is the nominal cross-section of the steel bars; m is the residual mass of the short sections of corroded bar; and m_0 is the nominal mass of the steel bars.

The cross-sectional loss of tensile bars embedded in beam Bs04-A and Bs04-B is presented in Figures 8(a) and 8(b) respectively. Figures 9(a) and 9(b) show the cross-sectional loss of tensile bars in beam Bs02-A and Bs02-B.

For beam Bs04-A, the maximum cross-sectional loss was 36.7%, which located on the front bar and was about 560 mm from the left end.

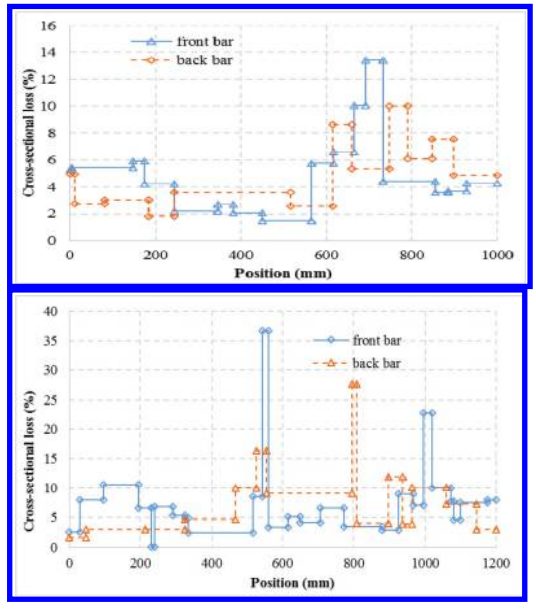

Figure 8. Cross-sectional loss of beam Bs04-A and Bs04-B.

It corresponded to the failure point of this beam during the mechanical test. The situation of beam Bs04-B was similar, the maximum cross-sectional loss was 39.0% and located on the front bar, about 560 mm from the right end. It also corresponded to the failure point during the mechanical test.

The cross-sectional loss of front bar in beam Bs02-A was much higher than that of back bar, which agrees with the cracking maps. In Figure 4,

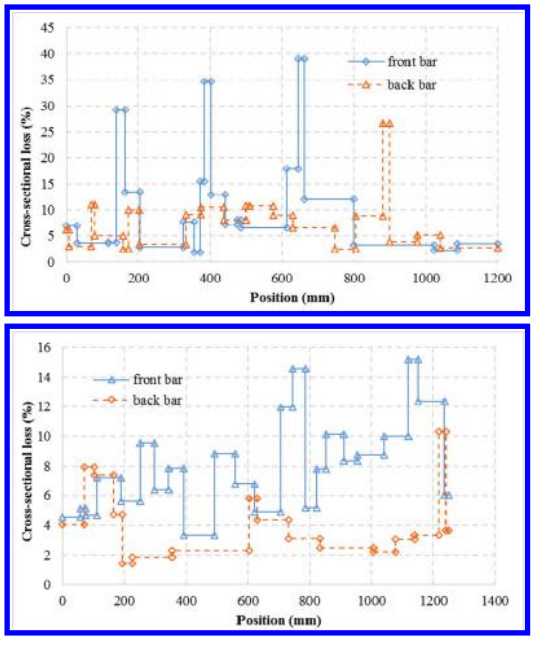

Figure 9. Cross-sectional loss of beam Bs02-A and Bs02-B (in percentage).

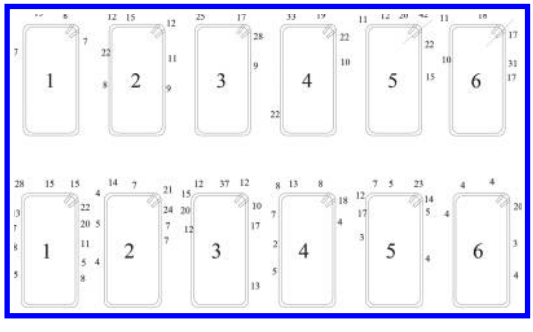

Figure 10. Diameter loss of stirrups in beam Bs04-A and Bs04-B (in percentage).

we can find there are much more corrosion cracks around the front bar than the back bar. It could be concluded that corrosion cracks can reflect corrosion degree to some extent. Different from beam Bs04-A and Bs04-B, the maximum cross-sectional loss was not in the middle of the beam but was close to the right end. The maximum cross-sectional loss of tensile bar in beam Bs02-B was about 13.4% and it was also not in the middle.

The stirrups in the beams were also corroded. A vernier caliper was used to measure the residual diameter of stirrups, then the diameter loss in percentage was calculated. The results are presented in Figures 10 and 11. It is obvious that corrosion was

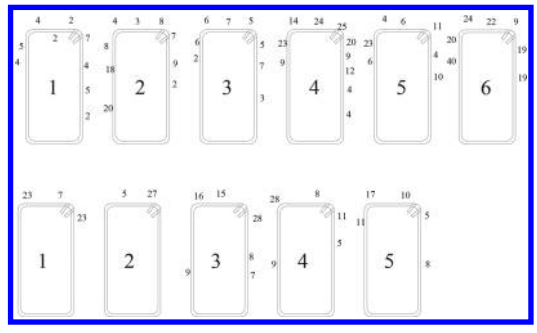

Figure 11. Diameter loss of stirrups in beam Bs02-A and Bs02-B (in percentage).

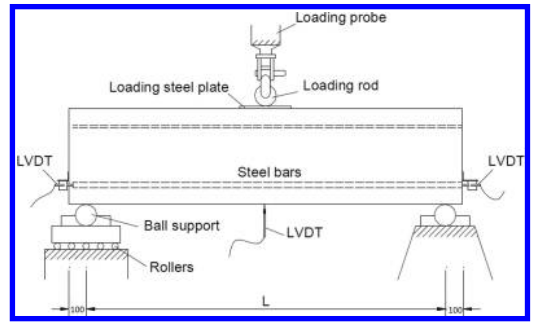

Figure 12. A schematic of mechanical test setup.

concentrated on the top of all the stirrups. Two reasons are contributed to this phenomenon. Firstly, more chloride solution was sprayed on the top surface of the beams, it results in more corrosion on the top of the stirrups. Secondly, the top surface was tensioned during the storage. Thus chloride was more permeable through the top surface.

3.5 *Mechanical tests of beams*

Short span beams were loaded with a three-point loading equipment. The beams were loaded at a constant rate of 0.5 kN/s until failure. The mid-span deflection was recorded with a digital sensor with an accuracy of 0.01 mm. Other four digital sensors with the same accuracy were placed on each end of the two tensile bars to record the slip during the mechanical test. The anchorage length of all the beams was 100 mm. A schematic of the test setup is presented in Figure 12.

The pictures of beam Bs04-A and Bs04-B after mechanical test are shown in Figures 13(a) and 12(b) respectively.

For beam Bs04-A and Bs04-B (a/d = 1.94), cracks induced by loading initiated in the middle of the two beams. The initial cracks propagated vertically

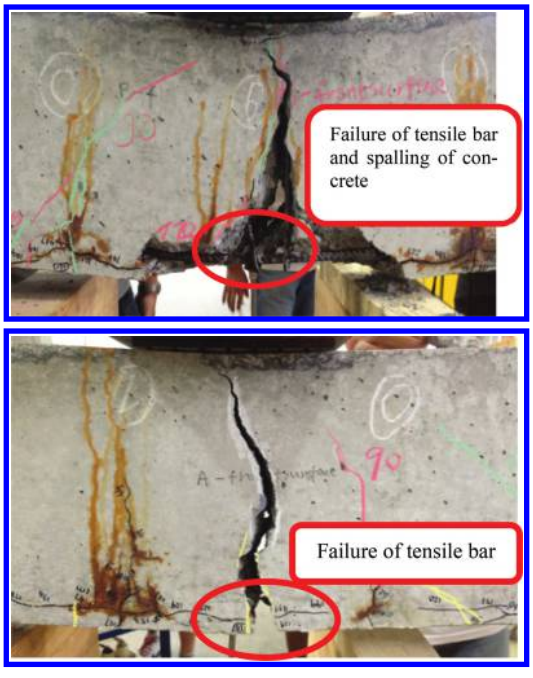

Figure 13. Failure of beam Bs04-A and Bs04-B.

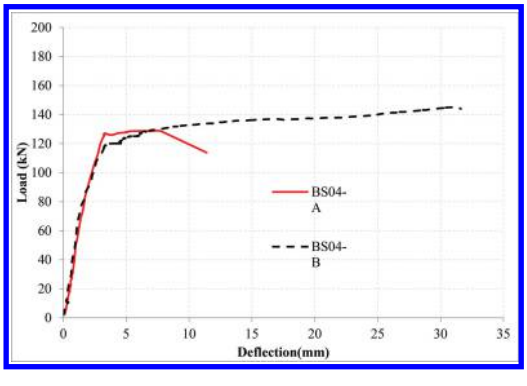

Figure 14. Load-deflection curves of beam Bs04-A and Bs04-B.

upward to the loading point with the increase of loading. The main crack became wider with the increase of load. Shortly after the load reached the peak, beam Bs04-A failed suddenly due to the failure of front tensile bar closed to the middle of the beam. For beam Bs04-B, the crack pattern was nearly the same as that of beam Bs04-A, and it also failed due to the rupture of a tensile bar. Comparing with beam Bs04-A, however, beam Bs04-B experienced a much longer yield period before failure. It could be reflected on the load-deflection curves of the two beams, which are presented in Figure 14.

There was another difference between beam Bs04-A and Bs04-B, some concrete cover in the middle span spalled before the failure of beam Bs04-B while there was no concrete delaminated on the beam Bs04-A. Before the loading test, the maximum crack width in the middle of beam Bs04-B was 0.9 mm, which was greater than the value on beam Bs04-A, 0.46 mm.

Figures 15(a) and (b) present the pictures of beam Bs02-A and Bs02-B after mechanical test.

For beam Bs02-A (a/d = 2.03), an inclined crack with a slight angle was formed on the right of the mid-span. Some concrete cover on the right part spalled with the increase of loading. Finally, the beam failed due to the rupture of two stirrups and the disbonding between concrete and steel. As presented in Figure 10(a), there were obvious pitting corrosion at the failure points on the stirrups, the diameter loss of stirrups at the failure points was 42% and 17% respectively. For beam Bs02-B (a/d = 1.55), a crack with a slight angle was formed on each side of the mid-span. Concrete cover on both sides except in the mid-span spalled with loading increasing. Finally the beam failed due to the disbonding between concrete cover and steel reinforcement. Both the two beams failed in a brittle way, the loading-deflection curves are presented in Figure 16.

Although beam Bs02-A had a greater span to effective depth ratio than beam Bs04-A and beam Bs04-B, it failed in a shear failure mode while beam Bs04-A and Bs04-B failed in a flexure mode. It could be contributed to different corrosion degree

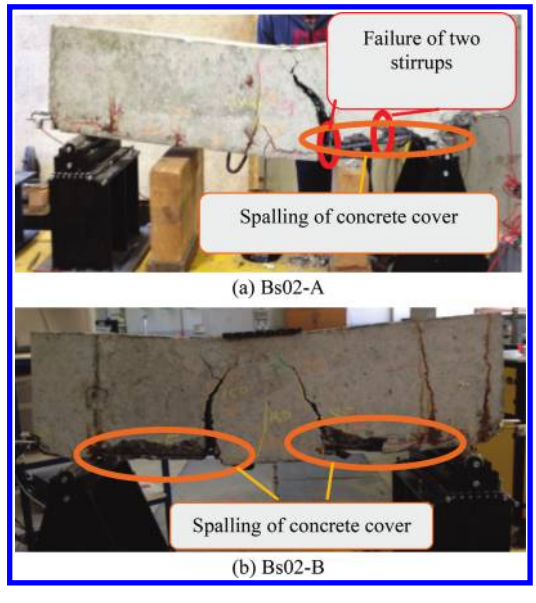

Figure 15. Failure of beam Bs02-A and Bs02-B.

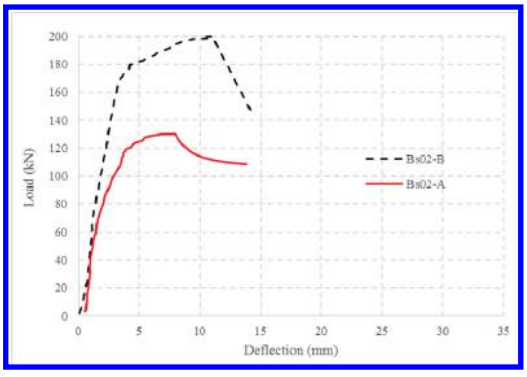

Figure 16. Load-deflection curves of beam Bs02-A and Bs02-B.

on the tensile bars. As presented in Figures 8(a), 8(b) and 9(a), we can find the corrosion degree on the tensile bars of beam Bs04-A and Bs04-B was more severe than that on beam Bs02-A. The maximum cross-sectional loss of tensile bars in beam Bs04-A and Bs04-B was 26.6% and 22.8% respectively, both of them located closed to the middle of the beams. The maximum cross-sectional loss of tensile bars in the middle of the beam Bs02-A was only 6.3% and the load capacity did not decrease as that of Bs04-A and Bs04-B.

Due to the serious corrosion on tensile bars of beam Bs04-A and Bs04-B, the tensile bars yielded before the formation of diagonal cracks. Finally the two beams failed due to the rupture of tensile bars in the flexural manner.

It worth particularly noting that, the ultimate deflection of beam Bs04-B was significantly higher that beam Bs04-A although their failure mode was the same and their maximum cross-sectional loss of tensile bar was very close. A possible reason is that the residual ductility of corroded tensile bar was quite different. Zhu and François (Zhu and François, 2013b, 2014b) confirmed that the residual ductility depends on both corrosion degree and the geometry of residual cross-section.

4 CONCLUSION

The following conclusions can be drawn:

1. Corrosion distributed quite randomly on the reinforcements.
2. The corrosion of reinforcements could change the failure mode of the reinforced concrete beams from shear to flexure. Two corroded beams, Bs04-A and Bs04-B, failed in flexure due to the serious corrosion on the tensile reinforcements. The maximum cross-sectional loss of tensile reinforcements in the two beams was 26.6% and 22.8% respectively.
3. Although the failure mode and ultimate load of beam Bs04-A and Bs04-B were nearly the same, significant ductility was presented on the two beams. The possible reason is the different ductility of corroded tensile reinforcements. Ductility of steel bar depends on both corrosion degree and geometry of residual cross-section.

REFERENCES

Alsulaimani, G., Kaleemullah, M., Basunbul, I., Rasheeduzzafar, 1990. Influence of Corrosion and Cracking on Bond Behavior and Strength of Reinforced-Concrete Members. Aci Struct. J. 87, 220–231.

Du, Y., Cullen, M., Li, C., 2013. Structural effects of simultaneous loading and reinforcement corrosion on performance of concrete beams. Constr. Build. Mater. 39, 148–152. doi:10.1016/j.conbuildmat.2012.05.006.

Higgins, C., Farrow, W.C., Turan, O.T., 2012. Analysis of reinforced concrete beams with corrosion damaged stirrups for shear capacity. Struct. Infrastruct. Eng. 8, 1080–1092. doi:10.1080/15732479.2010.504213.

Wang, X.-H., Gao, X.-H., Li, B., Deng, B.-R., 2011. Effect of bond and corrosion within partial length on shear behaviour and load capacity of RC beam. Constr. Build. Mater. 25, 1812–1823. doi:10.1016/j.conbuildmat.2010.11.081.

Wang, X.-H., Li, B., Gao, X.-H., Liu, X.-L., 2012. Shear behaviour of RC beams with corrosion damaged partial length. Mater. Struct. 45, 351–379. doi:10.1617/s11527–011–9770–5.

Xia, J., Jin, W., Li, L., 2011. Shear performance of reinforced concrete beams with corroded stirrups in chloride environment. Corros. Sci. 53, 1794–1805. doi:10.1016/j.corsci.2011.01.058.

Yuan, Y., Ji, Y., Shah, S.P., 2007. Comparison of two accelerated corrosion techniques for concrete structures. Aci Struct. J. 104, 344–347.

Zhu, W., François, R., Coronelli, D., Cleland, D., 2013a. Effect of corrosion of reinforcement on the mechanical behaviour of highly corroded RC beams. Eng. Struct. 56, 544–554. doi:10.1016/j.engstruct.2013.04.017.

Zhu, W., François, R., 2013b. Effect of corrosion pattern on the ductility of tensile reinforcement extracted from a 26-year-old corroded beam. Adv. Concr. Constr. 1, 121–136.

Zhu, W., François, R., 2014a. Corrosion of the reinforcement and its influence on the residual structural performance of a 26-year-old corroded RC beam. Constr. Build. Mater. 51, 461–472. doi:10.1016/j.conbuildmat.2013.11.015.

Zhu, W., François, R., 2014b. Experimental investigation of the relationships between residual cross-section shapes and the ductility of corroded bars. Constr. Build. Mater. 69, 335–345. doi:10.1016/j.conbuildmat.2014.07.059.

Zhu, W., François, R., Cleland, D., Coronelli, D., 2015. Failure mode transitions of corroded deep beams exposed to marine environment for long period. Eng. Struct. 96, 66–77. doi:10.1016/j.engstruct.2015.04.004.

Concrete Repair, Rehabilitation and Retrofitting IV – Dehn et al. (Eds)
© 2016 Taylor & Francis Group, London, ISBN 978-1-138-02843-2

Literature overview on the application and limitations of stress wave propagation theory for conditional assessment of concrete structures and elements

E. Okwori
Department of Civil Engineering, University of Cape Town, Cape Town, South Africa

ABSTRACT: The deterioration and damage of concrete structures has become a prominent problem in recent decades preventing concrete structures from achieving their design specifications. Therefore the need to develop efficient methods to understand the nature of the deterioration and damage mechanisms effectively is essential to providing solutions to mitigate deterioration and damages in concrete structures. This paper presents an overview, which provides information regarding the application of stress wave propagation theory in Non-Destructive conditional Evaluation (NDE) of concrete structures. Current trends, technologies and some limitations to the application of the theory, and illustrate the need for further research to improve the efficiency and applicability of the theory in NDE of concrete structures.

1 INTRODUCTION

Concrete as a construction material has been used for many decades and is regarded as one of the most economical and durable construction materials, if and when it is designed and placed properly. Used in various forms, such as reinforced concrete, pre-stressed concrete, shortcrete and many more. Despite the economy of usage and versatility of concrete as a construction material it experiences premature deterioration, which prevents it from achieving its intended design function. Some of the causes of deterioration and damage include construction errors, design errors, deterioration resulting mostly from environment conditions, overloading amongst others (Beushausen & Alexander, 2009).

Testing of concrete structures has become imperative as a result of deterioration and damages. Increasing the understanding of the deterioration process and developing strategies to cub deterioration. As such traditional testing methods of concrete structures were used in the paste to determine the status and durability of concrete structures against deterioration and damage. Which largely approached it from the prescriptive perspective usually involving the specification of strength, water cement ratio and such structures were usably tested by compressive, flexural and tensile strength tests. These tests though effective in estimation of strengths of concrete structures have disadvantages, which include but are not limited to the following.

I. Results do not provide real-time immediate evaluation of concrete structures
II. Concrete specimens used for testing differ from actual structure and do not provide a direct reflection of the state of the structure. As strength depends on the size and shape of the properties of the specimen.

Therefore to overcome these limitations and others not stated. The development of non-destructive testing methods to assess the status of concrete structures and the use of more performance-based approaches to durability of concrete structures became imperative. Also the repair and rehabilitation/restoration of serviceability of concrete structures after failure or at stages of extreme deterioration is often very expensive. Therefore conditional assessments of concrete structures are required periodically, to determine the status of the structure before failure or stages of extreme deterioration in order to optimize/reduce maintenance cost and extend the design/service life of concrete structures. A crucial aspect of conditional assessment is the determination of the cause or root of deterioration/failure mechanism in concrete structures. Which involves the application traditional and modern non-destructive testing of techniques to assess concrete structures (Verma, Bhadauria, & Akhtar, 2013). NDT's involve the application of various principles and instrumentation to access the condition of the concrete structures. Stress wave propagation techniques form part of the non-destructive testing principles

commonly applied in the evaluation of concrete structures. To detect the condition of a structure based on the assessed condition in comparism with threshold values of inherent properties of the structure. The suitability and applicability of the stress wave propagation methods depends on the knowledge and expertise available.

Hence the need for new and innovative research into the use of stress wave propagation methods for assessment of concrete structures is critical for better practice and efficient and effective use of the technique.

2 STRESS WAVE PROPAGATION THEORY IN NON-DESTRUCTIVE EVALUATION OF CONCRETE STRUCTURES

The research leading to the development and application of stress wave propagation methods in concrete structures stems from the early 20th century with L.H Donnell in 1930 till the development of the most widely used wave equation analysis program by GOBLE and RAUSCHE in 1976, which is still currently in use (Hussein & Goble, 2004). The principle of application of stress wave propagation in concrete structures is based on inducing a short duration mechanical impact generated by action of small steel balls or a hammer against the surface of a concrete structure. This causes the generation of low frequency stress waves or disturbances, which propagate into the structure. The disturbances generated propagates in various wave forms namely compressive stress waves (P-wave), shear waves (S-wave) and Rayleigh (R-wave), the P-wave is the fastest and may be used for quantification of damage and strength, it propagates at a normal to the testing surface while S-wave propagates perpendicular to the surface and R-wave propagate along the surface parallel to the testing surface and may be used for quantification of surface related anomalies (ACI COMMITTEE 228, 1998). This stress waves or disturbances are sensitive to change in impedances or boundary between dissimilar media along the concrete structure, as a result the stress waves are reflected by anomalies and external surfaces (Nicholas, 2004).

Surface shifts caused by reflections from the waves are recorded by an accelerometer or transducer, which is located adjacent to the impact location. The resulting shift versus time signals are recorded and presented in the time domain (amplitude versus time) and may also transformed into frequency domain (frequency versus time) using Fast Fourier's Transforms (FFT). Multiple reflections of stress waves between the impact surface, flaws and other external surfaces produce transient resonances which may be identified in the spectrum and used to evaluate the integrity of the structures and determine the location of flaws or anomalies. In conditional assessment the transient resonance response patterns are produced by the waveforms and spectra, more specifically the spectra that provides information about the existence and location of flaws in existing structures. In quality control applications the dimensions and geometry of the cross-sections of structures for each of the geometrical forms encountered in concrete structures (plates, circular, rectangular, columns and beams (rectangular, circular, I &T shaped beams and columns etc)) may be identified by stress wave propagation methods.

3 1D AND 3D DIMENSIONAL STRESS WAVE PROPAGATION THEORY

Stress waves, which propagate in concrete structures, may be utilized for a variety of applications, ranging from damage assessment to routine quality assurance. Forms of stress waves used are basically either 1D (One dimensional) or 3D (Three dimensional) waves. 1D wave propagation theory also known as the kinematics of deformation theory as illustrated by (Jian-hua, Yuan, & Liu, 1999) stems from newton's second law of motions, which stated the force acting on a body is proportional to its mass and acceleration is produced. Based on this law, with considerations about the summations of stress acting on a unit cross section of concrete and its material properties that the second order differential equation governing 1D wave propagation is based

$$\frac{\delta^2 u}{\delta t^2} = c^2 \frac{\delta^2 u}{\delta x^2} \tag{1}$$

where C represents the speed of the wave and is given by

$$c = \sqrt{\frac{E}{\rho}} \tag{2}$$

where E is young's modulus and ρ is mass density of the concrete material. The solution the above second order differential equation also known as D'Alemberts equation is given as

$$u(x,t) = \psi(x - ct) + \phi(x + ct) \tag{3}$$

Which illustrates and describes the motion of a 1D wave in a linear elastic medium such as concrete.

3D wave propagation theory on the other hand is based on theory of elasticity as illustrated by (Wang, 2004). The theory of elasticity is based on

stress and displacement constants, poission's effect and interface conditions in a medium. The governing the equation, which illustrates the behaviour of 3D waves in a linear elastic medium, is described by Navier-strokes equation.

$$(\lambda + \mu)\nabla\nabla k + \mu\nabla^2 k = \frac{\rho\delta^2 k}{\delta t^2} \quad (4)$$

4 STRESS WAVE PROPAGATION METHODS USED IN EVALAUTION OF CONCRETE STRUCTURES

Some of the most common stress wave propagation techniques utilized in the evaluation of concrete structures as described by nicholas (2004), are briefly described below with an insight into their applications and limits.

1. **Ultrasonic Pulse Velocity:** This method involves the measurement of the travel time of an ultrasonic pulse passing through concrete by generating a pulse with a transducer and creating a complex system of waves. Which comprises of longitudinal and compressive waves and a receiving transducer that detects the signals (Ohtsu, Yoshiara, Uchida, Saeki, & Iwata, 2003).
   Applications: Some of the applications of ultrasonic pulse velocity include determination of concrete compressive strength (Ohtsu, Yoshiara, Uchida, Saeki, & Iwata, 2003), the uniformity and quality of concrete, identification of cracks and voids, evaluation of the effectiveness of crack repairs in concrete etc (ASTM C597, 2009).
   Using the velocity and attenuation coefficient of the ultrasonic velocity pulse. Stress wave theory is used for the estimation of fresh and hardened properties of concrete. Application in determination properties of dynamic poisons ratio, dynamic young's modulus (Tesfamariam & Martin-perez, 2010). Application in the determination of hardened concrete properties includes strength development.
   In the assessment of the durability condition of deteriorating or aging structures applications based on pulse velocity method include fire damage, alkali-silica reaction, detection and monitoring of crack growth, corrosion induced spalling and delamination, freeze and thaw.
   In the repair of concrete infrastructures applications include epoxy inject repair and FRP encased concrete.
   Reliability and limitations in application: A variety of factors affect the wave velocity. As such the extraction of cores from the structure for confirmation of results may sometime be necessary. Some factors, which influence and limit the application of ultrasonic pulse velocity method include
   1. The coupling conditions of the transducers. Which highly affect the amplitude of the wave and disturb the attenuation evaluation and velocity estimation.
   2. The nature of the lateral boundaries of the structure or element may generate waves, which convert the apparent P-wave reflections.
   3. The presence of reinforcement bars in concrete may accelerate or scatter waves. Depending on the orientation of the reinforcement bars.
2. **Pulse Echo**: Involves the propagation of stress waves in a medium, initiated by a transmitter and is reflected by anomalies or interfaces and reflect waves measurement may be recorded by the same transmitter or a second transducer located near the first. The receiving transducer produces output results of the medium in time-domain waveform known as A-scan and longitudinal section known as B-scan, and a depth or parallel section to the surface known as C-scan.
   Applications: Applications of pulse echo include measuring slab thickness, pavement thickness and wall thickness also measurement of pile length in one direction and the location of surface open cracks in submerged structures.
   Reliability and limitations in application: The reliability of this method may be verified by calibration at a point of known thickness in the structure, or measurement of the wave velocity through an extracted core of known diameter and measuring the wave velocity of subsurface waves. Some of the limitations include.
   1. The method is sensitive to air-filled layers in concrete and during encounters, total reflection or scattering of the wave occurs. Also this also occurs with aggregates, which possess large surface areas and could be interpreted as a defect.
3. **Impact Echo:** Also known as sonic echo in certain circumstances of application the principle of impact and sonic echo are the same the distinction between this two is the bad of frequency been application which testing. Testing typically involves the propagation of low frequency stress pulse in a structure, originated from a mechanical impact, which moves along the structure in spherical wave fronts.
   This impulse consists of P and S waves. The arrival of a reflection arising from this impulse at the surface resulting from reflections of internal interfaces or external boundaries usually signifies an anomaly or the end of the structure. A transducer measures these arrival reflections.

In this method the wave propagates through the structure in all directions and a reflection may arrive from many directions.

Applications: Mostly used primarily for pile integrity testing due to the boundary of the pile serving a guide to confine wave energy and reduce attenuation, others include thickness determination of slabs, pavements, tunnel linings and general geometry of structural elements.

Reliability and limitations in application: The reliability of the method may be determined by calibration with a structure with known thickness. Some of its limitations include

1. The interface interaction between the stress waves with internal anomalies depends on the wavelength and dimensions of the anomaly.
2. Longer contact periods with concrete surface may be recorded resulting in lower frequency input signal with longer wavelength, due to the nature of concrete surface.
3. Assumption of a single velocity for all structures may generally yield in accurate estimates of thickness. As the velocity of propagation in a particular structure or structural element depends on the elastic modulus, area and mass density of that structure or structural element.

4. **Impulse Response Method:** This method measures the transient dynamic (impedance) response of concrete structures, which similar in comparison to impact echo method. The dynamic response of the structure is generated by a mechanical impulse using a hammer with a load cell to generate the wave energy in the structure, with a transducer located in the vicinity of impact to monitor the vibrations from the impact as a force-time function known as time domain.

   The impulse response is a function of the material properties of a structure and a deviation is the bases for identification of anomalies by the method. Response of structures may also be interpreted or presented in the frequency domain.

   Applications: Primarily used in the integrity evaluation of deep foundations or piles.

   Reliability and limitations in application: Reliability or verification of results in contention in this method can be carried out by extraction of cores from the structure. A limitation of this method is that it does not provide depth or thickness estimates for concrete structures but relative parameters from which this can be inferred. It however measures the quality of concrete.

5. **Spectral Analysis of Surface Waves (SASW) Method:** The SASW method involves the propagation of transient surface stress pulse in a concrete member. Generated by a mechanical impact and monitored by two transducers. This method basically measures the propagation of R-waves due to its ability to produce larger particle motion amplitudes compared to P and S waves. The R-wave propagates entirely in the top most layer of a concrete member.

   Applications: The SASW method may used to determine a variety of properties in a concrete structure including the wave speed profiles, stiffness profiles, the method may also be used in monitoring the curing of concrete slabs and evaluation of thickness and damage and location of repairs.

   Reliability and limitations in application: This method uses the application of surface to evaluate thickness of slabs, pavements etc a limitation to this method is the presence of cracks, voids or delaminated area will prevent the accurate estimation of the thickness. The method requires contact with the concrete surface, which may not always be accessible, or surface may be rough or moist which may affect results.

6. **Ground Penetrating Radar Method:** Also known as GPR, uses electromagnetic waves that propagate through concrete structures for testing. This electromagnetic waves are sensitive to the dielectric and conductivity properties of concrete and this forms the basics for identification of anomalies and determination of properties of concrete, as an electromagnetic wave which encounters an interface of dissimilar dielectric constant part of it energy is reflected from the interface and the rest is transmitted through. Generally the larger the difference in dielectric constant the greater the magnitude of reflections. One of the standardized methods of performing this test can be found in ASTM D4748 (Sadri & Mirkhani, 2009).

   Applications: GPR method is capable of detecting delamination, and voids in concrete. It also has the potential for monitoring cement hydration and strength development in concrete. As well as identification of position rebar in reinforced concrete etc.

   Reliability and limitations in application: Similar to most methods reliability or validation of results can be done by extraction of cores from the structures. Plans/as built drawings may also be utilized to support the interpretation of results. Some of the limiting factors of this method include.

   1. The difference in contrast between material properties to be investigated must be sufficient, as without such contrast the boundary between the materials will not reflect the GPR data.

2. Velocity variations due to material properties of a structure may lead to errors in thickness evaluations. Since it is generally common practice when using this method to assume a uniform velocity for a structure.
3. Electrical conductivity is key amongst other factors, which cause attenuations of GPR signals with materials. As GPR signals in conductive materials leads to stray currents, which reduce the depth of penetration of GPR signal.

5 LIMITATIONS TO THE USE OF ONE DIMENSIONAL STRESS WAVES THEORY

Some of the limitations to the 1D stress wave propagation theory identified from literature include but may not be limited to the following.

1. Attenuation of waves: Attenuation phenomenon occurs in concrete structures when tested with methods or techniques, which utilize stress waves as their fundamental principle. Its occurrence happens in a circumstance where the wave front moves away from the point of impulse and as it moves it becomes larger with increase in distance. It may be typical to assume no energy is lost in this circumstance but (Amir, 2009) states that the energy per unit area of the front decrease with distance and the rate of this decrease typically depends on the shape of the wave front. E.g. in spherical wave fronts the wave energy changes inversely to the square of the distance from the origin. Consequently this implies that if damage, length changes, or thickness changes, occur in a structure at such a point where the attenuation effect occurs. The energy of the wave may be too weak to produce a quantitative reflection owing to attenuation effect therefore limiting the ability of 1D stress waves in damage, thickness or length predictions.
2. Multi-reflections: Multi-reflections are occurrences which results from the oscillation of R and S waves along the surface of the concrete structures been tested. Which interferes with the reflection of the P—wave, rendering the thickness or length predictions inaccurate/invalid. Also it may occur where there is more than one defect in a structure (Chai, Phoon, & Zhang, 2010).
3. Damped and undamped one-dimensional stress wave theory: (Warrington, 2013) States that D'Alemberts equation that governs the propagation of 1D wave propagation in linear elastic media such as concrete assumes and is based on undamped conditions. Therefore when conditions become damped inaccurate predictions are obtained. (Warrington, 2013) Further suggested that telegrapher's equation takes into consideration damped and undamped conditions therefore providing a more suitable explanation for 1D stress wave propagation in concrete structure.
4. Noise: Amir (2009) described noise as a negative influence on physical measurements. Its magnitude in relation to signals from low stress wave reflections influences the credibility of results. Measurements are the means through which stress wave technique obtains information from structures. Some of the factors which cause noise influence during testing include.
    1. Presence of surface Rayleigh waves which cause osscilations from constant reflections and interfer with reflections which cause noise which can erronously mask or appear as presence of defects.
    2. Sharp decrease in cross sectional area of pile at the bottom, which creates regular reflections which are repetitive in character which act as medium-frequency noise.
    3. Protusions at the concrete surface during testing which break to create noise during impact.
    4. Undirected hammer blow impacts may also lead to the production of high-frequency noise when contact is made with reinforment bars.
    5. False negatives/false positives: False negatives may be described as a situation where a concrete structure is wrongly diagnosed as sound while it is damaged or defective while false positive may also be described as the vice vassal situation of a false negatives (Gordon, 2004). Arising from improper application and or improper interpretation of data. This may usually lead to a situation where a damaged concrete member is incorporated into a structure as sound, which affects the performance, safety and durability of the structure. Which may lead to catastrophic occurrences in terms of cost and safety. On the flip side it could also be a situation where an undamaged or sound member of structure is subjected to unnecessary repairs and remedial work leading to damage induction and high construction costs.

6 COMBINATION OF STRESS WAVE PROPAGATION TECHNIQUES FOR IMPROVEMENT IN ASSESSMENT OF CONCRETE STRUCTURES

The reliability of most of the stress wave propagation methods discussed, mainly have been validation by means of core extraction or a combination of two methods to validate a particular parameter

being investigated, by comparing the results from the two tests. However just comparing results from two NDT stress wave methods to validate or improve the results may not be enough to improve the results as various factors have various effects on both methods as described by (Breysse & Garnier, 2012). The major methods which users of NDT combination techniques use are:

1. Comparison of results obtained by two or more methods to confirm measurements and identify variations. Examples include ultrasonic, impact echo and impulse response for conditional assessment of buildings, radar and pulse echo for defect detection in slabs, radar and impact echo for detection of damage in bridge decks, radar and ultrasonic for hydraulic structures.
2. Comparison of results obtained by two or more methods to improve and aid interpretation of results. This usually needs some method of analysis i.e. image analysis, statistical analysis to provide confirmations. Examples include radar, impact echo and ultrasonic for quality control of concrete rail tracks, surface waves and electrical conductivity for detection of cracks of slabs.
3. The utilization of a quick method for rough estimates and mapping, and verified by a slow method in problematic areas identified by the first. Examples include ultrasonic, radar and thermography of assessment of corrosion development through periodic inspection in slabs.

Although the aim of combining these method is to achieve

a. Accuracy of estimation of properties
b. Determine relevance of physical explanations and diagnosis
c. Reduce the time to obtain results.

The influences of external and environmental factors play a significant role in causing variability, which affect the aim of combining techniques. An illustration of how external factors influence the variability of test results of combining techniques is considering a case amongst a other cases can be observed from the Figure 1 below which illustrates the measurement of capacimetry (permittivity) of concrete using radar, ultrasonic, infrared thermography and electrical resistivity. The figure below illustrates the variation in the three methods with a regression curve, which exhibits a parabolic shape.

As result of this variations Breysse and Garnier (2012) have proposed an ambitious but more functional method of combining NDT techniques known as the the inversion method which involves the combination of two method such that the first methods measures or estimates a parameter which can be corrected by the second measurement value.

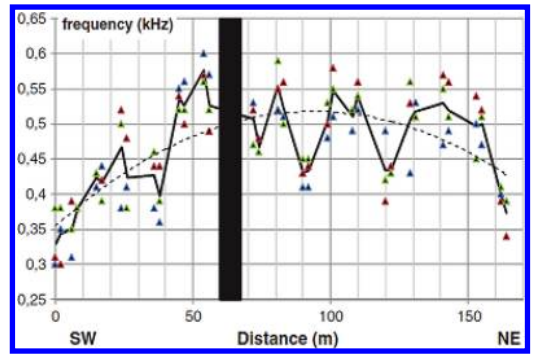

Figure 1. Variation in combining technique with regression curve (RILEM, 2012).

An ideal case description of this combining technique would be to have a structure with an influential parameter (R) which possesses a unique relationship with a given NDT parameter value (I) therefore I may be expressed as a function of R

$$I = f(R)$$

And the inversion will be expressed as $R = f^{-1}(I)$ providing the value of the R parameter. However the practical application is never as simple. This technique helps to achieve better estimations and measurements through

1. Ensuring when the first method is sensitive to two influential parameters the second is sensitive to one or the two, which enables inversion to occur and more functional measurements of the parameter.
2. Also ensuring that if the initial method is sensitive to one influential parameter, but having a particular bias factor, measuring a second parameter, which is sensitive to that bias, can reduce the effect of the bias.

An example of this combining technique, which has been used, is called the "SonReb" which combines the use of rebound number to provide the initial assessment of concrete strength, which is corrected with ultrasonic pulse velocity.

This inversion method is termed ambitious due to its difficulty in feasibility during practical applications as well as possessing its own limitations. But it remains a more functional approach to the application of combining techniques.

7 FUTURE TRENDS

Future trends incorporated or which can be incorporated into the applications of stress wave propagation methods to reduce/eliminate limitations and produce effective and quantitative results include.

1. Scanning technique: A significant number of non-destructive testing methods are beginning to incorporate scanning mechanisms in to their principles and technological set-up. Stress wave propagation methods also incorporating scanning mechanism in to their set-up this saves time and produces more accurate data about the status of an entire p structure as opposed to data from a localized points in structures.
2. 3D tomographic testing: This uses the application of stress waves with Synthetic Aperture Focusing Technique (SAFT) to build 3D visualizations of the geometry of the concrete structure in contention to show internal disturbances. Particularly 3D tomographic testing uses typical stress wave testing method such pulse echo, ultrasonic pulse etc with imaging reconstruction software capable of producing images such as those obtained from medical radiology profession using Magnetic Resonance Imaging (MRI) techniques. Although due to the heterogeneous nature of concrete this is not a straight forward process, therefore a combination of images from various data points to reconstruct an image the depicts the concrete internal microstructure by using spatial averaging of a large number of single measurements per unit area under testing with an array of low frequency, short pulse transducer and a mathematical algorithm that uses 3D SAFT (Michaux & Grill, 2014).
3. Wave Modeling: Modeling of waves propagation increases the understanding regarding the behaviour of wave propagation in a heterogeneous material like concrete and prediction of possible characteristics of anomalies in practical applications.

8 CONCLUSIONS

The continuous advancement in technology prompts a continuous improvement in the use of stress wave propagation methods in concrete structures for conditional assessment of concrete structures. The techniques described present quick, efficient and reliable methods for conditional assessment of concrete structures without causing damage to structures.

REFERENCES

ACI COMMITTEE 228. (1998). *Non—destructive test methods for evaluation of concrete in structures*. American Concrete Institute.

Amir, J.M. (2009). *Pile intergrity Testing*.

ASTM C597. (2009). Standard test for pulse velocity through concrete.

Beushausen, H., & Alexander, M. (2009). Concrete Repair. In C. a. Africa, & G. Owens (Ed.), *Fulton's Concrete Technology* (Nineth Edition ed., pp. 393–412). Midrand, South Africa: Cement & Concrete Institute.

Breysse, D., & Garnier, V. (2012). Non destructive assessment of concrete structures: combination of different techniques for addressing new challenges. *Reliability and limits of single and combined techniques, RILEM State-of-art-report 1*, pp. 335–358.

Chai, H.-Y., Phoon, K.-K., & Zhang, D.-J. (2010). Effects of Source on Wave Propagation in Pile Integrity Testing. *Journal of Geotechnical and Enviromental Engineering*.

Gordon, C. (2004). Quality assurance of bored pile foundations. *New Civil Engineer*.

Hussein, M., & Goble, G. (2004). A brief history of the application of stress wave theory to piles current practices and future trends in deep foundations. In J.A. Hussien (Ed.), *Current practices and future trends in deep foundations (GeoTrans)* (pp. 186–201). American Society of Engineers (ASCE).

Jian-hua, Y., Yuan, J.-x., & Liu, M.-g. (1999). Assessment of pil integrity by low strain stress wave method. *HKIE Transactions*, 6:1,42–49.

Michaux, C., & Grill, M. (2014). *NDT 3D tomographic testing cases on concrete and national hertigae buildings.* In Situ SA Rue de la Cimenterie, Site MecanArbed, Luxemburg.

Nicholas, J.C. (2004). Stress Wave Propagation Methods. In J.C. Nicholas, *Non Destructive Testing methods.* CRC Press LLC.

Ohtsu, M., Yoshiara, T., Uchida, M., Saeki, H., & Iwata, S. (2003). Estimation of concrete properties by elastic wave method. *Non-destructive testing in Civi Engineeing (NDT-CE 2003)*.

RILEM. (2012). Non-Destructive Assessment of Concrete structures: Realiability and limits of single and combined techniques. *STAR 207-INR.*

Sadri, A., & Mirkhani, K. (2009). Wave Propagation Concrete NDT Techniques for evaluation of structure and materials. Canada.

Tesfamariam, S., & Martin-perez, B. (2010). *Stress Wave Propagation for Evaluation of Reinforced Concrete structures*. The University of Britsh Coloumbia & *University of Ottawa. Canada: Woodhead Publishing limited.*

Verma, S.K., Bhadauria, S.S., & Akhtar, S. (2013). Review of Non-destructive Testing Methods for Conditional Monitoring of concrete structures. *Journal of Construction Engineering*.

Wang, H. (2004). *Theoretical Evaluation of Embedded Plate Like and Solid Cylindrical Concrete Structures With Guided Waves*. Northwesthern University, Civil and Enviromental Engineering, Evanston, Illinois.

Warrington, D.C. (2013). *Persistent Issues in the Wave Equation for Piling for Both Forward and Inverse Mehtods.* Retrieved April 5, 2013, from Vulcan Iron Works inc and Pile Driving Equipment: Vulcanhammer.

Concrete Repair, Rehabilitation and Retrofitting IV – Dehn et al. (Eds)
© 2016 Taylor & Francis Group, London, ISBN 978-1-138-02843-2

Concrete cultural heritage in France—inventory and state of conservation

E. Marie-Victoire & M. Bouichou
Laboratoire de Recherche des Monuments Historiques, Champs-sur-Marne, France

T. Congar & R. Blanchard
Cercle des Partenaires du Patrimoine, LRMH, Champs-sur-Marne, France

ABSTRACT: Concrete being a major construction material of the 20th century, more and more buildings and structures are listed as historical. This cultural heritage, even if it could appear "young" with respect to more ancient constructions such as medieval or antic monuments, is decaying, partly due to incipient construction technology knowledge and partly to environmental aggressive conditions. To try to cope with this problematic, a European project named REDMONEST, gathering 3 countries (Belgium, France and Spain), was launched in 2014, through the European JPI-CH platform. Within this project, 3 research axes will be addressed: inventory, diagnosis and conservation treatments of concrete cultural heritage. One of the first steps of the project was to carry out a survey to make a precise inventory and to evaluate the state of decay of these monuments. In this paper the results obtained in France will be presented, showing a considerable amount of structures, with a great variety of construction periods and building uses (apartments, churches, industries …). Data on their main pathologies and current state of conservation will be discussed. Finally, potential diagnosis tools and conservation strategies will be put into perspective.

1 INTRODUCTION

Concrete is the most used building material in the world today. Due to its performances and ability to be cast, but also to the vast panel of color and textures it can provide, concrete has stimulated architectural innovation and creativity. Therefore, numerous countries are now considering concrete architecture as cultural heritage. Nevertheless, this architecture is decaying, due to a combination of lack of knowledge of concrete construction technology for the most ancient monuments, and environmental aggressive conditions. But only few specific research and developments were dedicated to decays, diagnosis and restoration or conservation of ancient concretes, as concrete construction is often considered as short-life construction, renewable, and rarely as heritage.

The purpose of the REDMONEST project, supported by the European JPI-CH platform was first to establish a "snapshot" of the concrete cultural heritage listed in the 3 countries partners (Belgium, France and Spain), in terms of architecture typologies and pathologies. The second step will be to test or develop diagnosis tools and warning sensors adapted to monitor the previously identified pathologies. Finally some conservation treatments will be evaluated on emblematic demonstration sites in each of the 3 countries partners.

In this paper, the data collected concerning the French listed cultural heritage will be first presented. Then outlooks dealing with diagnosis and conservation strategies will be discussed.

2 FRENCH MONUMENTS MADE OF CONCRETE OR CONTAINING CONCRETE

2.1 *Survey: scope and protocol*

The aims of the survey were to identify national and international classification criteria (Jamiot et al., 2003), but also to make an inventory of the listed constructions partly or completely made of concrete, with when possible information on their state of conservation.

Two steps were considered. First the existing national and international databases and bibliographies (Toulier, 1997) were explored. Then a set of multilingual forms was elaborated in order to collect more data especially on specific decays. In France, these forms were sent to a panel of 169 architects, conservators and curators working in the field of cultural heritage. Two hundred

forms were returned and a dedicated database was built. The national averages presented in this paper are the result of the compilation of the regional data collected.

2.2 *Global amount of listed monuments*

The first results of the survey performed in France, evidenced a strong policy of protection of buildings and structures partly or completely made of concrete, introduced in the 1990ies (Fig. 1), leading to an increase of the amount of listed monuments from 41 in 1970 to 816 in 2015.

2.3 *Period of construction*

Most of the listed monuments (58%) were erected between the 2 world wars (Fig. 2).

2.4 *Typologies*

Twelve typologies of monuments were identified, with a predominance of domestic or sacred architecture (Fig. 3). Thus 60% of the list consists

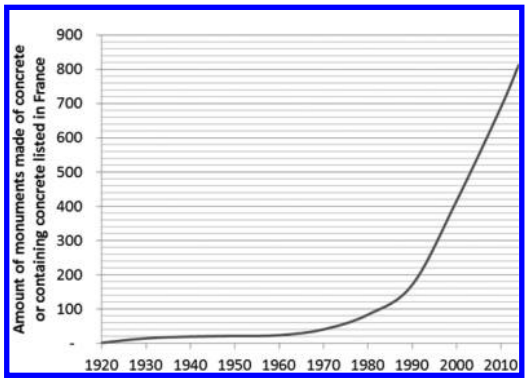

Figure 1. Increasing amount of monument completely or partially made of concrete listed in France.

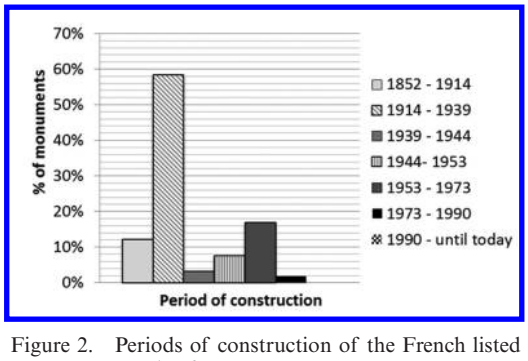

Figure 2. Periods of construction of the French listed monuments made of concrete.

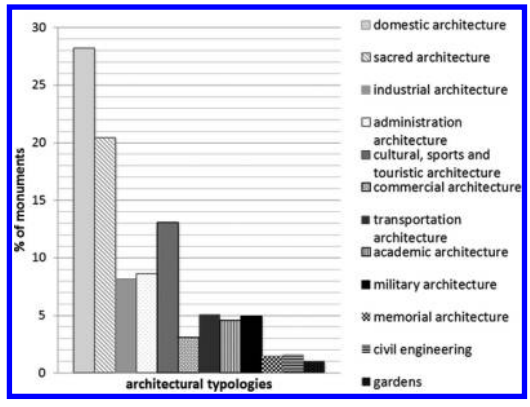

Figure 3. Typologies of monuments made of concrete identified in France.

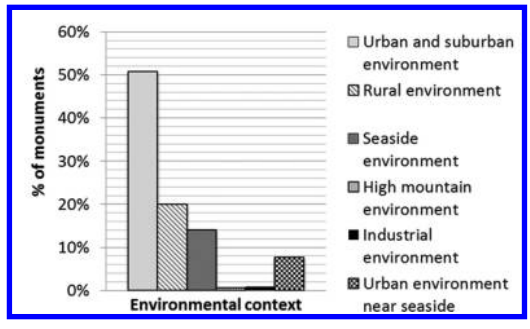

Figure 4. Environmental context of the French listed monuments made of concrete.

in: 150 houses or villas; 50 collective buildings; 150 churches, chapels, cathedrals; 25 theaters, movie theaters, museums; 25 hotels and casinos; 12 train-stations; 33 schools, high schools and universities; 33 blockhouses.

2.5 *Environmental context*

A majority of the monuments are located in urban and suburban environments (51%), when only 14% are siting in seaside environment, 8% being submitted both to urban and seaside environment (Fig. 4).

3 STATE OF CONSERVATION AND MAIN PATHOLOGIES

3.1 *State of conservation*

Based on 175 answers to a questionnaire submitted to architects and curators in charge of this cultural heritage in France, more than 60% of these

monuments are in a good or in a satisfactory sate of conservation, but 20% are considerably damaged or endangered (Fig. 5).

A finer analysis of the answers reveals that façades, structures and roofs are the parts of the monuments the most affected by damages (Fig. 6).

3.2 *Main pathologies*

Two types of decays were identified on the ancient concrete monuments examined: superficial ones and deeper degradations.

Considering the superficial degradations, 3 forms emerged: superficial sulfate reaction combined with black dirt deposits; biological covering; and erosion and lixiviation (Marie-Victoire et al., 1996; Marie-Victoire et al., 2010).

The deeper degradations were mainly due to carbonation induced corrosion.

3.2.1 *Superficial sulfate reaction and black dirt deposits*

As most of the monuments are located in urban environment, without surprise, in clear correlation with urban pollution (heating oil, automobile exhaust emissions …), they are affected by black dirt deposits. The thickness of these deposits can vary from less than one millimeter to real black crusts of more than one centimeter (Figs. 7–8), with a typical bubon-shaped surface, evidenced by binocular observations (Fig. 9). Even if superficial, the back dirt deposits can damage the readability of a façade and in a more evident way the legibility of a sculpture (Fig. 10).

In addition, the analysis of some black crusts evidenced the presence of soot deposits (Fig. 11), embedded in a gypsum mat (Fig. 12). Sulfates concentration profiles performed on several monuments located in urban environments revealed that this sulfate pollution is not only superficial, as it can affect significantly (concentrations by weight of cement higher than the 4% threshold

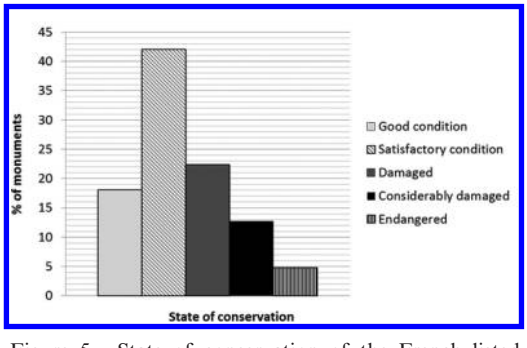

Figure 5. State of conservation of the French listed monuments made of concrete. General evaluation.

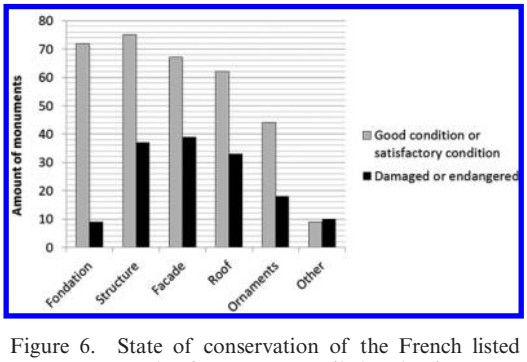

Figure 6. State of conservation of the French listed monuments made of concrete. Detailed evaluation.

Figure 7. Example of black dirt deposits with different morphologies and thickness. Left picture: Saint-Joseph Church (Le Havre, 1951–1957). Right picture: Le Signal (Le Havre, 1959–1960).

Figure 8. Example of Black crust collected on Saint-Jean de Montmartre church, (Paris, 1894–1904). Locally its thickness exceeds 1 cm.

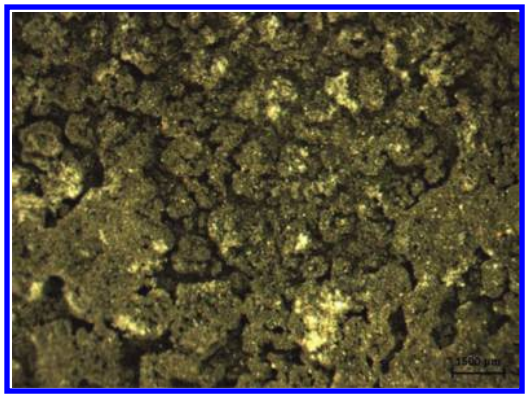

Figure 9. Binocular view of a black crust collected on a Saint-Jean de Montmartre church, (Paris, 1894–1904), revealing a typical bubon-shaped surface.

Figure 10. High relief made of concrete from Palais de Chaillot (Paris, 1934–1937). Black dirt deposits are affecting the sculpture legibility.

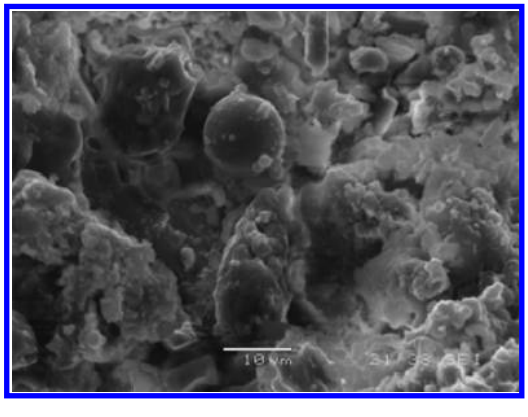

Figure 11. SEM view of a black crust evidencing the presence of a round-shaped soot (G = X500).

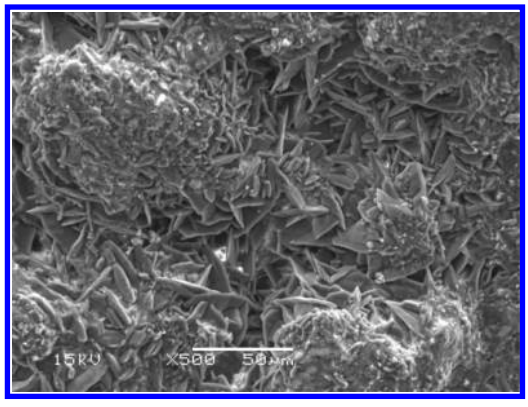

Figure 12. SEM view of a black crust evidencing the presence of a gypsum mat (G = X500).

Figure 13. Dense biological covering affecting the façades of the ATM towers (Ivry-sur-Seine, 1963–1967). The biological covering is mainly composed of algae and lichens.

recommended by the EN 197-1 standard) the concrete on thicknesses higher than one centimeter.

3.2.2 *Biological covering*

The second type of superficial alteration consists in biological covering. From a light veil of algae to the growth of mosses, it can vary in species and intensity, lichens being the most common (Figs. 13–14).

As black dirt deposits; biological covering can clearly affect the readability of an architecture, as shown on the left picture of Figure 15, a veil of green algae covering a large part of the north façade; or of a sculpture (Fig. 15, left picture) as evidences the yellow lichen growing on the top of a sculpture on the right picture of Figure 15. But the problem is not only aesthetical. Thus SEM observations of a cross section perpendicular to the surface of a monument covered with lichens

Figure 14. Dense biological covering observed on the Jeanne Hachette center (Ivry-sur-Seine, 1970–1972). Locally some thick blooming mosses were growing.

Figure 15. Examples of biological covering affecting the readability of an architecture or of a sculpture. Left picture: Saint-Nicaise church (Rouen, 1934–1937) covered with green algae. Right picture: Sculpture of Robert Tatin's Museum (Cossé le Vivien, 1962–1983), covered with a thick biological deposit; and especially with yellowish lichens affecting the legibility of the sculpture.

evidenced the impact of roots growth in superficial loss of cohesion (Fig. 16, Bouichou et al., 2010).

Finally, biological covering is clearly favored by the surface roughness and the porosity of the concrete.

3.2.3 *Erosion and lixiviation*

The third superficial decay mechanism observed on historic concrete is erosion, often associated to lixiviation. This combined action of wind and more or less acidic rain results in the loss of the superficial skin of the concrete, revealing the aggregates on smooth surfaces (Fig. 17) and increasing the loosening of the aggregates on rough ones.

Either in the case of architectural concrete cast in wooden panels, or in the case of sculptures, this skin erosion can lead to the loss of original details (Fig. 18).

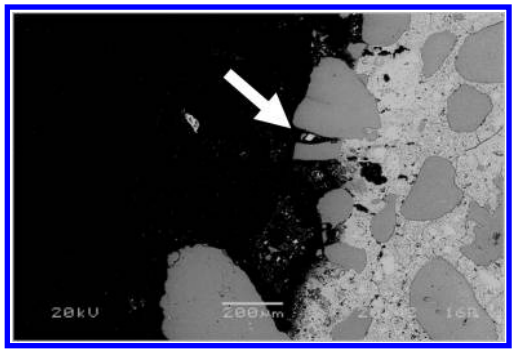

Figure 16. SEM view of a cross section perpendicular to the concrete surface, sampled on Jeanne Hachette center (Ivry-sur-Seine, 1970–1972). The growth of the roots of a lichen clearly contributed to the aggregate fracture.

Figure 17. Wall of the city of Grenoble (end of 19th century). The erosion and lixiviation phenomena revealed the presence of aggregates and therefore evidenced that it was not cut stone, but fake stones made of natural-cement-based concrete.

Figure 18. Monumental head sculpted in a concrete block by Carlo Sarabezolles for the bell tower of Notre-Dame des Missions church (Epinay-sur-Seine, 1932). Left picture: view of 1933. Right picture: view of 2009 evidencing a loss of sculpted details due to erosion/lixiviation.

3.2.4 *Carbonation induced corrosion*

Now the most frequent decay mechanism encountered on historic concrete is obviously carbonation induced corrosion (Neff et al. 2007).

Carbonation is an ineluctable chemical reaction that occurs between some hydrates (portlandite, calcium-silicate-hydrated …) of the cement paste and atmospheric carbon dioxide (Marie-Victoire et al., 2006; Thiéry, 2006). This reaction induces the transformation of Portlandite into Calcite (Fig. 19), which leads to a decrease of pH of the concrete from initial values of 12–14, to values lower than 9. It means that if the concrete was initially protective for steel rebars, when carbonated it becomes potentially corrosive, depending on the availability of enough oxygen and water.

The decays begin to occur when the carbonation reaches the rebars level. At that point the age of the concrete is of importance, for several reasons:

– First the most ancient concretes are often also the more porous (as superplasticizers were not common), which eases the penetration of carbon dioxide,
– Secondly, the concrete construction knowhow was not always mastered. Thus it is usual to encounter low concrete cover, honeycombing, or cement leakage. Theses construction defects clearly facilitate both the progression of carbonation and the consequent corrosion process,
– Thirdly, the type of cement is critical. Effectively the survey has demonstrated that a majority of monument were built between the two world wars. For a lot of them, slag cements which are easier to carbonate as they contain less Portlandite, were employed.
– Fourthly, the survey evidenced that a majority of the French monuments are located in urban environment, where the levels of carbon dioxide in the atmosphere are often higher than in rural areas, which again favors the carbonation reaction.
– Finally the period of contact between concrete and carbon dioxide is of course higher for the most ancient monuments.

As a consequence considerable depths of carbonation were measured on ancient concretes (Fig. 20). Thus several monuments exhibited total

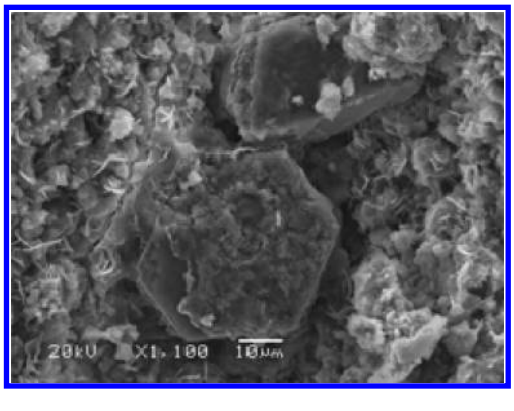

Figure 19. SEM view showing the on-going carbonation of portlandite crystals (right photo. G = x1100). ONERA wind tunnel (Meudon, 1932–1934).

Figure 20. *Maison du Brésil* located in the vicinity of the Parisian beltway (Paris, 1957–1959). Phenolphthalein test on a core indicating a 4 cm carbonation depth.

Figure 21. Wind tunnel erected between 1932 and 1934 to test aerodynamic performances of big size models (Meudon, 1932–1934). Due to the wind tunnel activity the concrete walls were carbonated on their entire thickness. In this monument, impressive corrosion facies were observed.

Figure 22. Carbonation induced corrosion can generate spalling, which means important loss of original material, but also a possible impact on the artwork understandability. Left picture: Keith Haring mural of Necker's Hospital (Paris, 1971). Right picture: High-relief of the bell tower of Dinan train station (Dinan, 1931).

carbonation on the entire depth of walls, which means a carbonation depth up to 10 cm and sometimes even higher (Marie-Victoire et al., 2006; Hergenroeder, 2003).

But carbonation is only a problem in reinforced concrete. Thus artificial stones from the end of the 19th century, which are not reinforced, are often very well preserved, except a superficial erosion phenomenon (Fig. 17).

When the carbonated concrete is reinforced, generalized corrosion can take place leading to expansive corrosion products formation (Neff et al., 2007) and consequently to spalling (Fig. 21).

This carbonation induced corrosion phenomenon, as a consequence, can lead to important loss of original material, which is problematic in the field of cultural heritage. The two examples presented in Figure 22 show that when reinforced concrete artwork are concerned, their legibility can be strongly impacted.

4 OUTLOOKS: DIAGNOSIS AND CONSERVATION STRATEGIES

The first part of the survey of the Redmonest project, dedicated to an inventory, revealed that hundreds of reinforced concrete monuments are listed in France. Due to the French policy of protection of 20th century cultural heritage this amount is increasing every day. The preliminary results of the Belgian and Spanish surveys, also indicate that a noticeable amount of concrete construction tend to be listed.

A second part of the survey, not developed in this paper, was dedicated to evaluate the needs of the persons in charge of the maintenance of this atypical cultural heritage in terms of information and training. The first results indicate that they are expecting information about concrete pathologies and conservation/restoration treatment in order to establish maintenance strategies.

There is therefore a real need of research in order to better understand the specific decays of this new cultural heritage, but also to determine how to monitor this decays and finally to develop tailored restoration and conservation solutions.

As the most common, but also the most deleterious source of decay identified on reinforced concrete French cultural heritage was carbonation induced corrosion, the next steps of the project will targeted on this specific pathology.

Thus, the second step will be dedicated to corrosion and conditions leading to corrosion (presence of water …) on site diagnosis. Two types of tools will be considered: embedded sensors (humidity, corrosion …) and non-destructive monitoring systems either usual as the electrochemical panel of devices (Andrade, 2001), traditionally used for concrete diagnosis (potential and resistivity mapping, polarization resistance measurements), or newly developed (evanescent-field-dielectrometry-based moisture monitoring (Olmi, 2006) …).

The last step of the project will focus on conservation treatments orientated on corrosion problematics. Hence water-repellent treatments will be tested on several iconic monuments spread in France, Belgium and Spain. In parallel, a PhD study has started in Belgium, in the University of Liège, to test in controlled laboratory condition the performances of several families of hydrophobic treatments when applied to delay corrosion in reinforced concrete (Courard, 2014).

5 CONCLUSION

The survey performed as preliminary step of the European Redmonest project evidenced that concrete is now making part of the cultural landscape, as it is encountered in quite an amount of monuments listed either in France, Belgium or Spain.

This first series of results concerning the main pathologies observed on ancient concrete, targeted the next steps of the project to diagnosis and conservation strategies focusing on rebars corrosion evaluation and treatment.

ACKNOWLEDGMENTS

The authors would like to thank the European Commission and the French Ministry of Culture and communication for their financial support to the REDMONEST project. They would also

like to thank the partners of the project (CSTC, Limelette, Belgium; Ulg, Liège, Belgium) and more particularly the leader: IETcc (Madrid, Spain) for their technical support.

REFERENCES

Andrade C., Alonso C., 2001, On-site measurements of corrosion rate of reinforcements. Construction and Building Materials, Vol. 15, pp. 141–145.

Bouichou M., Marie-Victoire E, François A., Bousta F., & Orial G., 2010, Elimination of biological covering on concrete: tests in situ of different techniques, *In* Concrete under severe conditions: environment and loading: proceedings of the 6th international conference (CONSEC'10), Mérida, Yucatan, Mexico, 7–9 June 2010/ed. by Pedro Castro-Borges, Eric I. Moreno, Koji Sakai, Odd E. Gjorv, Nemkumar Banthia, pp. 1181–1188.

Courard L., Lucquiaud V. & Al., 2014, Evaluation of the durability of hydrophobic treatments on concrete architectural heritage, Hydrophobe VII, Lisbon, 11–12 September 2014, 9p.

Hergenroeder M., Rackwitz R., 1991, Investigations on the statistics of carbonation depths in concrete, 2nd International RILEM/CEB symposium on quality control of concrete structures, Ghent, 1991, pp. 451–460.

Jamot F., Marx J., Audibert M., Denante S., 2003, La protection des immeubles au titre des Monuments historiques, Manuel méthodologique, Ministère de la culture et de la communication—Direction de l'architecture et du patrimoine, 2003, Paris, 269p.

Marie-Victoire E. & Al., 1996, Les altérations visibles du béton: définition et aide au diagnostic, 1996, Champs-sur-Marne, Ed. Cercle des Partenaires du Patrimoine.

Marie-Victoire E., Cailleux E., Texier A., 2006, Carbonation and historical buildings made of concrete, *In* Journal de physique IV, Proceedings of NUCPERF 2006: Corrosion and long term performance of concrete in NPP and waste facilities, 27–30 March 2006, Cadarache, France, EFC Event 284, vol. 136, November 2006, p. 305–318.

Marie-Victoire E., Texier A., 2010, Béton et monuments historiques. De l'architecture à la sculpture, In Anticorrosion et durabilité dans le bâtiment, le génie civil et les ouvrages industriels. Presses polytechniques et universitaires romandes, Lausanne, 2010, pp. 389–404.

Neff D., Marie-Victoire E., L'Hostis V., Cailleux E., Vincent L., Texier A. & Al, 2007, Preservation of historical buildings: understanding of corrosion mechanisms of metallic rebars in concrete, *In* METAL 2007: Study and conservation of composite artefacts, Interim meeting of the ICOM-CC Metal WG, Amsterdam, 17–21 September 2007, ed. C. Degrigny, R. Van Langh, I. Joosten, B. Ankersmit, p. 30–35.

Olmi R., Bini M., Ignesti1 A., Priori S., Riminesi C. and Felici A., 2006, Diagnostics and monitoring of frescoes using evanescent-field dielectrometry, Measurement science and technlology, Vol. 17, pp. 2281–2288.

Thiéry M., 2006, Modélisation de la carbonatation atmosphérique des matériaux cimentaires, Ouvrage d'art OA52, Etudes et recherches des Laboratoires des Ponts et Chaussées, Laboratoire des Ponts et Chaussées, Paris, Mars 2006, 337p.

Toulier B., 1997, Histoire, techniques et architecture du béton armé en France, In Monumental, n°16, Editions du patrimoine, Paris, Mars 1997, pp. 6–19.

Concrete Repair, Rehabilitation and Retrofitting IV – Dehn et al. (Eds)
© 2016 Taylor & Francis Group, London, ISBN 978-1-138-02843-2

The development of a new Dutch guideline for the conservation of historic concrete (URL 4005)

H.A. Heinemann
Department Building Solutions, Bartels Engineering, Apeldoorn, The Netherlands

ABSTRACT: Conservation of historic concrete is a growing field. Although several aspects overlap with concrete repair, differences in their aims and properties of modern and historic concrete require different approaches. On an academic and governmental level, these additional requirements have been acknowledged. Iconic concrete structures received much attention during their conservation. Parallel, several less known historic concrete buildings have been repaired with less support for research and execution of the works. In many cases, works were carried out by repair companies directly without advice from independent surveyors. These projects gave indication that more support is needed in practice, stressing the need for surveys, explaining the aspects of concrete conservation, and how to identify a suitable concrete conservation company. Therefore, a new guideline for concrete conservation is being developed in the Netherlands. In this paper, the background of the guideline, its aims and scope, but also obstacles during its development are described.

1 INTRODUCTION

In recent years, concrete conservation has been emerging as an own discipline from concrete repair. The relationship between the two fields is still strong, as they use similar approaches, techniques and repair materials. Yet what differs is on the one hand the diverging aims of concrete conservation and repair, and on the other hand the properties of historic concrete (Heinemann, 2013). However, many of these demands are discussed on an academic or governmental level, and have not yet been disseminated sufficiently to practitioners or owners.

In the meantime, many historic concrete buildings have been repaired in the Netherlands. The success of the interventions varies. Some show premature failure of repairs as the properties of the historic concrete were not fully understood (Heinemann et al. 2008, Fig. 1), others involve a large scale removal of historic material (Heinemann, 2013, Fig. 2), others received wide international recognition (Backer, et al., 2005, Fig. 3).

Influencing factors are for example the condition of the historic structure, the experience with historic concrete of the involved parties, availability of independent surveys, and last not least the chosen repair approach. Noteworthy is that in Dutch practice, condition assessments are not always carried out prior to repair, and decisions on repair strategies are often made by concrete repair companies. Owners have thereby difficulties to evaluate the state-of-conservation of the historic concrete, the proposed intervention and the necessity of pre-investigations. Even if an independent survey with repair advices exists, it is for laymen difficult to evaluate an alternative proposal offered by a repair company.

Figure 1. Premature failure of a crack repair due to thermal movement of plain concrete (Fort Bezuiden Spaarndam, part of the Defense Line of Amsterdam, 1897–1901, UNESCO World heritage site, intervention 1998, situation 2006).

Figure 2. Large-scale removal of historic concrete during repair (circumambulation passageway Pilgrimage church, Brielle, H. Goossens (reconstruction), E.J. Margy, 1912).

Figure 3. Example of an architectural icon from the modern movement (Van Nelle factory, J.A. Brinkman and L.C. van der Vlugt, 1926–1931, situation 2008).

As a reaction towards the increasing number of concrete conservation projects and to improve their quality, a guideline for the conservation of concrete is currently being developed: the *URL 4005 Conservation of historic concrete*. Initially, this guideline was supposed to come into effect in the Netherlands by January 2015. Due to unexpected obstacles and the recentness of the field, requiring more attention, its release is delayed. In this paper, the background, aims, and obstacles of developing such a guideline are discussed.

2 THE DUTCH UITVOERINGSRICHTLIJN (URL, GUIDELINE)

A *uitvoeringsrichtlijn* (URL) is a Dutch guideline which defines construction works. For restoration works for monuments separate URLs exist. These are managed by a Dutch foundation for the quality of heritage care, the *Stichting Erkende Restauratiekwaliteit Monumentenzorg* (ERM).

URLs are drafted by an expert committee including practitioners, government agencies, material suppliers, surveyors and architects. Until now, URLs exist for traditionally used materials in historic buildings, such as brick, timber or thatched roofs (ERM 2014a, 2014b, 2014b). To follow these guidelines can be a requirement to receive subsidies for maintenance works of monuments.

In these guidelines the additional requirements for assessment, conservation aims, execution of repairs, properties of repair materials and intended outcome are described. Contrary to normal repair guidelines, the cultural heritage values and different types of historic material are explicitly addressed. For the URL for historic concrete, the synergies between historic research and material investigation are endorsed in order to develop suitable conservation strategies. But also practical aspects such as trial repairs, and methods and degree of concrete removal are considered.

Although many of these aspects seem self-evident, in practice they are often neglected due to ignorance, or limited time and financial budgets. With the guideline, it is expected that the quality of concrete conservation will improve as the additional demands are outlined and stakeholders supported to define suitable conservation strategies.

3 CONCRETE CONSERVATION PRACTICE

3.1 *Definition of historic concrete*

Concrete was (re-)introduced as a building material in many European countries in the middle of the 19th century. Initial areas of application of plain concrete were military and hydraulic structures. The breakthrough of reinforced concrete was in the 1870s. At the beginning of the 20th century, reinforced concrete became widely accepted for civil structures. With the advances in production, concrete technology and architectural exploration, concrete established itself as a universally applicable material in the late 1930s (for example Fig. 4). After the Second World War, reinforced concrete

Figure 4. Prefab column made with coloured concrete and specially chosen aggregates, now showing cracks and leaching, indicating ASR (Giraffe compound, Zoo Blijdorp, Rotterdam, S. van Ravesteyn, 1940).

Figure 5. Several railway station built during the post—war reconstruction period were made with pre-fab concrete elements, other which special aggregates and surface finishes (for example railway station Enschede, H.G.J. Schelling, 1950).

had become a main building material (Heinemann, 2013).

In order to decide whether the URL is applicable or not, it has to be defined whether the concrete in question can be considered as historic. This determination is influenced by several parameters. A pragmatic solution is to link the term with the status of the concrete structure, for example when a building is listed and concrete dates from the original construction period, we tend to consider it as historic.

As a building has to be at least 50 years old to be listed as a national monument in the Netherlands, such an approach can be rather arbitrary from a material point of view, as it does not considered construction history and the differences of historic concretes. It is not differentiated whether a concrete is comparable to modern concrete, or reflecting previous, maybe even archaic steps, in the development of concrete.

For example, a 1960s structures might be made with a ground granulated blast furnace slag cement, normal aggregates (gravel, sand), the mix design based on a w/c factor, and the reinforcement in form of a mesh. In principle the concrete is comparable to modern concrete. A pre-stressed concrete structure dating from the same period however might be one of the first of a new structural principle. Here, we could encounter the effects of trial-and-error, searching for better details. From a material history point of view, the latter case might be of a higher value.

Limiting the definition to specific period/age would exclude many technical novelties from the 1960s onwards. On the other hand, it would be too exhaustive, as it would cover aged concrete structures which are not considered of historical value, for example most of our infrastructure which was built prior to the 1970s.

Concluding, historic cannot be used as a synonym for being listed as a monument or associated with a minimum age. Instead, the historical context has to be considered (e.g., construction time, former concrete technology) and the heritage values attributed to the concrete in question.

This requires an understanding of the construction history of concrete, including the evolution of

concrete technology, material development, architectural and structural application, and historic and geographical context. Thereafter, the historic concrete can then be evaluated whether it is also of historic significance and hence valuable.

For example, early concrete buildings are often listed for their pioneering characters, and the material of a high value. The construction of many architectural icons of the Modernist Movement relied on the achievements of civil engineers and concrete technologists of the previous decades. Here, the material properties might be of less historic interest, and more the structural design and impact on the spacious feeling appreciated. For the Post-war period, the high professional level of concrete design and pre-fab construction allowed a quick reconstruction, whilst exploring the possibilities of mass production.

3.2 *Properties of historic concrete*

Whereas heritage values are an interpretation of the historic structure by a society, the properties of historic concrete can be measured objectively. Due to the changes in constituents used, mix design, application, and underlying standards, the properties of historic concrete are manifold. Factors are, amongst others, the sophistication of concrete technology and production, insight into concrete durability and fields of application. Material aspects are hereby amongst others the variations in thickness of the concrete cover, the porosity, vulnerability to freeze-thaw damage and the use of deleterious constituents. The properties of historic concrete are also influenced by its age and accompanied material changes, degradation, repairs, neglect or changes to the structure itself.

3.3 *Possible conservation aims*

Its varying roles during history are reflected in the reasoning why a historic concrete building is listed as monument. In the Netherlands, following categories of values are applicable for listing buildings (Ministerie voor Onderwijs Cultuur en Wetenschap, 2011; RDMZ, 1991):

- Aesthetical values
- Scientific significance
- Cultural-historical value
- Uniqueness
- Integrity and recognisability
- Values of building groups
- Architectural historical values.

Conservation should aim to preserve the characteristics and materials of the historic building which represent these values. In case of aesthetical values, this is very often linked to the façade of a building, and the colour and texture of the concrete. For the scientific significance or cultural-historical values, this can also mean that a very early reinforcement system can be of high value.

Following international conservation charters (e.g. ICOMOS, 1964), conservation aims to preserve the original structure (and material) in its current state. Modifications, (partial) replacements, or restoration, are considered less desirable. A total reconstruction of elements or an entire building is generally seen as objectionable and could lead to an unlisting of a monument.

The URL ERM 400 for criteria for the evaluation of maintenance and conservation of monuments (ERM, 2013) reflects this philosophy in its hierarchy of different options in its so-called "conservation ladder" (Table 1).

Together with case specific heritage values and material properties, the boundary conditions can vary strongly per conservation project and result in diverging conservation aims despite similar origin of material properties and encountered degradation.

3.4 *Concrete conservation practice*

The aforementioned aspects are mainly discussed on a political, management and academic level. In conservation practice, additional obstacles exist originating in the recentness of the field. Whereas for iconic conservation projects (e.g. Meurs & van Thoor, 2011; Backer, et al., 2005) conservation aims and possible conservation strategies are discussed by several stakeholders, decisions based on reports and trials, the conservation of most historic concrete buildings is less publicly monitored.

No generally accepted standards exist which clarify when to speak of concrete repair or of concrete conservation. Instead, higher aesthetical demands are often considered as the main aspects of concrete conservation. That such practice neither reflects the principles nor the complexity of historic concrete conservation and concrete repair has been addressed previously (Heinemann, 2013).

Whereas the definition of concrete conservation is one aspect of discussion, the conservation

Table 1. "Conservation ladder" according to URL ERM 400.

1. Conservation/maintenance
2. Repair
3. Renewal
a. Copy
b. Imitation
c. Improvement

process itself is neither clarified. In practice, it is not required to carry out a technical survey of a historic structure prior to repair. Due to the newness of the topic, not all controlling authorities or architects coordinating conservation work are always sufficiently trained to evaluate the suitability of a proposed intervention. The owner can directly contract a company of choice to carry out the supposedly necessary repair works, assuming that the company is sufficiently competent to choose an appropriate repair technique. The choice of a repair technique can be biased, influenced by the preference and specialisation of the repair company. In addition, no certificates and standards exist to identify concrete repair companies specialised in concrete conservation.

For concrete repair companies the lack of independent technical surveys is not always welcomed. Yet due to financial and time pressure, and competition, they cannot always insist on technical surveys. As a consequence, the quality of the restoration works and the preservation of historic relevant material can be at stake.

Whether the above mentioned approach is a theoretical or incidental problem cannot be answered yet satisfactorily. A comprehensive overview of the long-term performance of repairs of historic concrete, such as previously done for normal repair works (Tilly & Jacobs, 2007) does not exist. Isolated case studies (Heinemann, 2013) identified several weak links in the conservation process, such as wrong diagnosis, lack of knowledge, or postponing interventions. These factors can lead to the use of incompatible repair techniques or unnecessary loss of historic material.

A cause is the little synergy between the field of concrete repair and construction history. By better understanding the peculiarities of historic concrete, former state-of-the-art and the consequences for durability, investigations could be better targeted and the suitability of repair techniques better evaluated.

4 DEVELOPMENT OF THE URL FOR CONCRETE CONSERVATION

The demand for more support for the execution of concrete conservation had been recognised by all parties involved in the conservation process. In 2013 it was decided to develop a URL especially for historic concrete. Aims were to distinguish the more challenging concrete conservation from normal concrete repair, and enhance the quality of concrete conservation.

The committee for the development of the URL, were the author makes part of, was chosen based on their experience with the conservation of historic concrete and/or development of URLs. The committee consists of architects, concrete repair companies, surveyors, academics, and representatives of the Dutch Cultural Heritage Agency.

As a starting point, the problems and wishes known from practice were outlined. One finding was that many aspects related to technical surveys, such as the need of a damage assessment and choice of a compatible repair strategy, are only discussed during the contracting phase with the concrete repair company, and not in a previous planning phase. Therefore, the URL should stress the need and benefits of carrying out a technical survey by an independent party prior to the repair works.

Planners required more legal support when deviating from normal concrete repair standards and certified repair materials. They were not covered by common practice despite knowing the advantages of their custom-made solutions. Discussions arose whether a overview of possible repair mortars and their mix design for some historic concretes was helpful or not, as these could be misunderstood as universally applicable for historic concrete. On the other hand, they could give guidance by showing previous best practice. As a spin-off a database should be created to show under which conditions which repair technique performed well. Furthermore, objective criteria were needed to compare and evaluate possible techniques. In this context, the URL should demand to carry out trial-repairs.

Other practical difficulties were the narrow mindset of what people considered as concrete conservation, namely mainly repairs with higher aesthetical demands or repairs of very poor concretes. A better discussion of possible conservation demands and suitable repair strategies was wished for. Fundamental knowledge gaps on concrete durability and historic concrete by the parties involved in concrete conservation were observed likewise.

The range of topics and problems reflected that more structure and guidance is needed in the entire process of concrete conservation, starting from correct and in-depth historical and technical surveys, the importance of mock-ups, and to criteria to evaluate the durability of a proposed conservation technique. The challenge for the URL is now to focus of what it can cover, and which topics need other tools to increase the quality of concrete conservation.

4.1 *Scope of the URL*

A main challenge of the development of a guideline is to clearly determine and follow its goal. As many aspects of concrete conservation are still under development, the temptation exists to integrate all

demands in one document. Especially as currently no other tools are being developed which could address related problems.

The initial aim of the URL was to offer guidance regarding the preparation and execution of historic concrete conservation works. The expectation is to increase the level of proficiency of concrete repair companies and the quality of concrete conservation works.

The URL will cover the most common repair techniques, such as patch repair, sprayed concrete, and injection, application of coatings and surface treatments, and special techniques such as cathodic protection. A neutral consideration of common and less common techniques for concrete conservation was considered relevant. The choice should be case-based, depending on the underlying damage cause, the properties of the concrete and conservation aim.

Within the field of concrete conservation, a preference for patch repairs can be observed. Coatings are sometimes disliked for their visual impact, and the suitability of electrochemical techniques is sometimes doubted due to the configuration of the reinforcement. In addition, electrochemical repair techniques require planning by experts, and the underlying principles of these techniques are not always known by non-repair experts.

As the underlying degradation mechanisms and technical principles of repair are the same for normal and historic concrete, standards for repair are commonly applied in conservation practice. As they reflect years of practice, using them consciously for conservation is justifiable.

In the URL for the conservation of historic concrete, reference will be made to existing standards for concrete repair, such as the NEN-EN 1504:2004 (2004), and its Dutch supplements for concrete repair, injection and cathodic protection (CUR recommendation 45, 1996, CUR recommendation 56, 1997; CUR recommendation 117, in press).

Awareness of the situations when concrete repair standards do not apply is, however, necessary. The reason can be very fundamental, such as emphasising to preserve cultural-historical values instead of maintaining the functionality of a structure. More detailed questions are the application of alternative repair mortars compatible with historic concretes such as lime-trass cement with broken bricks as aggregates.

The chapters of the draft of the URL include inspection and consultancy in one part, and the execution of the works in another part. These will be outlined in the following sections.

4.1.1 *Inspection and consultancy*

In the URL, two types of surveys are addressed, namely technical and (construction) historical surveys. The first is commonly carried out after incidents or during normal periodic inspections. The later is usually written in order to list a building or to evaluate its heritage value.

Normally, historical reports of concrete buildings focus on the architect and the underlying reinforcement system (e.g. Monier or Hennebique), and material historical aspects are not addressed. The demands for construction historical research as outlined in the URL go further than the standard historical reports, as the clearly demand information on the type of concrete (e.g. plain concrete, decorative concrete), the properties of the concrete surface, the colour and how it was achieved (e.g. pigments, grounded stone), the composition of the concrete (e.g. binder, type of aggregates) and the type of reinforcement (e.g. type of ferrous metal, geometry, reinforcement system).

The demands towards technical inspections are similar to those of normal technical surveys of concrete, besides that the surveyor should have knowledge of historic concrete and affinity for conservation.

An advice for conservation should be based on both, the technical and historical survey. The potential of combining these two reports is not commonly used. By doing so the conservation aim can be better translated into technical demands, for example a maximal degree of concrete removal due to importance of the original concrete, balancing the technical minimum requirements and preservation of original material. By explaining the choice of a repair strategy and importance of the concrete, the alertness during the repair could increase. Together, these steps should lead to a clear description of the works.

4.1.2 *Execution of works*

The URL describes the quality of the works and the qualifications of the contractor. Besides common Dutch certificates for concrete repair for both the middle and higher management, they have to have experience with the conservation of historic concrete. As no certificates exist especially for concrete conservation, this is done by means of a portfolio.

The execution of the works should consider normal aspects of concrete repair, such as the safety of the structure during repair. Additional demands are for example to communicate with the surveyors during the intervention when the historic reinforcement is visible in order to document it, or not to remove historic reinforcement without a constructive function. Awareness whether new reinforcement can be welded to the historic reinforcement is advised, as not all historic ferrous metals are weldable (De Bouw, 2010). For the surface finish, the effects of different formworks and colour changes

of repair mortars during time (humidity, biological growth) should be considered.

Due to the properties of the historic concrete and the heritage values to preserve, a chosen repair strategy might not always be the technical most durable solution. In order to identify premature failure of a repair, an inspection and maintenance plan is recommend in the URL. The works, materials used and frequency of future inspections and repairs should be documented and made available for the owner.

The demands towards the materials used for repair, and how to limit the choice of alternative materials by the contractor, are still under discussion, and were one of the obstacles encountered in the process.

5 OBSTACLES

The introduction of the URL was initially planned for January 2015. During its development, obstacles were encountered in order to embed the URL in the existing guidelines, avoid loop-holes and to focus on its main aim.

One loop-hole was to give construction companies the opportunity to deviate from proposed repair strategies and materials. This does not mean that construction companies are considered to chose incompatible materials or not capable to recognize maybe a flaw material choice in a survey. In such cases, it is expected that surveyor and repair companies communicate in order to find a better solution. Yet the bigger threat is that a suitable repair advice is overruled. Instead, a different material might be applied, which might have been chosen without considering the material properties, conservation aims and underlying damage cause. Laymen such as owners might not be able to evaluate the risks and benefits from alternatives.

Another obstacle is the recentness of the field, the lack of other guidelines related to concrete conservation, and involvement of stakeholders without knowledge of (historic) concrete during conservation. This tempted to incorporate too much information and demands in the URL, turning it into an unreadable document.

Currently, the URL is being critically reviewed whether it fulfils its initial aims, namely to give support for conservation works and to increase the quality of concrete conservation. Aspects which were considered relevant, yet not part of the scope of the URL, such as the quality of historical and technical inspections, will have to be discussed in different settings.

6 CONCLUSIONS

The development and introduction of a guideline for the conservation of historic concrete is a welcomed signal within the conservation field. It shows that historic concrete is being acknowledged as a historic material, requiring equal care and investigation as traditional materials encountered during conservation. Yet, due to the recentness of the field, it cannot rely on the practical experience to identify best practice or loop-holes.

During the development of the URL, underlying problems within the conservation field frequently surfaced. Many of these problems originate from the aspect that no training exists for concrete conservation, explaining the varieties and properties of historic concrete, the consequences for durability and options for conservation. Most available experience is case-based and generic knowledge is limited.

The introduction of the URL can push the concrete conservation market, by requesting sound research prior to repair works, and by creating awareness that concrete conservation involves more than normal concrete repair.

REFERENCES

Backer, A.M., Camp, D. & Dicke, M., 2005. *Van Nelle—Monument in progress*. Rotterdam: Uitgeverij De Hef.

CUR Civieltechnisch Centrum Uitvoering Research en Regelgeving, 1996. *CUR aanbeveling 45. Kathodische bescherming van wapening in beton-constructies*.

CUR Civieltechnisch Centrum Uitvoering Research en Regelgeving, 1997. *CUR aanbeveling 56. Injecteren van scheuren in beton-constructies met kunsthars injectievloeistoffen*.

CUR Civieltechnisch Centrum Uitvoering Research en Regelgeving, in press. *CUR aanbeveling 117. Specialistische instand-houdingtechnieken—repareren van beton.*

De Bouw, M., 2010. *Brussels Model Schools (1860–1920). Structural Analysis of the Metal Roof Trusses*. Brussel.

English Heritage, et al., 2012. *Practical Building Conservation: Concrete*. Ashgate Publishing, Ltd.

ERM Stichting Erkende Restauratiekwaliteit Monumentenzorg, 2013. *Beoordelingsrichtlijnen Onderhoud en Restauratie Monumenten (BRL ERM 4000)*. Gouda: ERM.

ERM Stichting Erkende Restauratiekwaliteit Monumentenzorg, 2014a. *URL 4001 Timmerwertk (Timberworks)*. Gouda: ERM.

ERM Stichting Erkende Restauratiekwaliteit Monumentenzorg, 2014b. *URL 4003 Historisch Metselwerk (Historic brick)*. Gouda: ERM.

ERM Stichting Erkende Restauratiekwaliteit Monumentenzorg, 2014c. *URL 4004 Rietdekken (thatched roofs)*. Gouda: ERM.

Heinemann, H.A., van Hees, R., & Nijland, T. (2008). *Concrete: Too young for conservation?* In D'Ayala, D. & Fodde, E. (Eds.), Structural Analysis of Historic Construction, Bath. Taylor & Francis Group.

Heinemann, H.A., 2013. Historic Concrete From concrete repair to concrete conservation. Delft: Delft Digitalpress.

ICOMOS International Council on Monuments and Sites, 1964. *International Charter for the Conservation and Restoration of Monuments and Sites (The Venice Charter 1964)*.

Meurs, P. & van Thoor, M.T., 2011. *Zonnestraal Sanatorium: The History and Restoration of a Modern Monument*. Rotterdam: Nai Publishers.

Ministerie voor Onderwijs Cultuur en Wetenschap, 2011. *Monumentenwet 1988 (Heritage act 1988)*.

NEN-EN 1504:2004. *Products and systems for the protection and repair of concrete structures*—Delft: Nederlands Normalisatie-instituut.

RDMZ Rijksdienst voor de Monumentenzorg, 1991. Handleiding Selectie en registratie Jongere Stedebouw en bouwkunst (1850–1940). Zeist: RDMZ.

Tilly, G. & Jacobs, J., 2007. *Concrete repairs. Performance in service and current practice*. Watford: IHS BRE Press.

Concrete Repair, Rehabilitation and Retrofitting IV – Dehn et al. (Eds)
© 2016 Taylor & Francis Group, London, ISBN 978-1-138-02843-2

Evaluation of moisture and gas permeability of surface treated concrete and its application to historical reinforced buildings in Japan

Kei-ichi Imamoto & Chizuru Kiyohara
Tokyo University of Science, Tokyo, Japan

Kaori Nagai
Nihon University, Tokyo, Japan

Maiko Misono
Constec Engineering, Co., Japan

ABSTRACT: Surface-impregnation materials and coating agents would be effective in keeping the authenticity of historical reinforced concrete buildings. This study investigates the effect of the surface-impregnation materials and coating agents in preventing the moisture and gas ingress into concrete. The following conclusions were obtained: (1) surface-impregnation materials did not change the appearance of concrete and did not prevent the progress of carbonation. (2) Surface-coating agents changed the appearance of concrete, but they had a significant effect on the prevention of carbonation ingress. (3) A good agreement was found between air permeability and carbonation progress. Based on these findings, the surface e-impregnation agent was applied to the National Museum of Western Art of Japan which is one of the important cultural landmark of Japan.

1 INTRODUCTION

Around the world, there are many different varieties of historical legacies, and we face a common challenge of their maintenance. In this contex, conservation and repair work have an important role to play in the preservation of these historical structures. In Japan, 'Keeping the original structure' is advertency, and its policy is applied to historical structures made from various materials such as, stone, wood, and steel.

On the other hand, in Japan, it has been more than 100 years since concrete construction has been used, therefore, the need to develop a conservation method for concrete has arisen. However, at present, it is difficult to evaluate the efficacy of repairing materials, because their aging properties are not well understood.

In this study, authors focus on surface-impregnation materials and coating agents that would not change the appearance of concrete. Authors investigated the applicability of these agents in the conservation of historical reinforced concrete buildings (Misono, 2013). As mentioned previously, in Japan, 'Keeping the original structure' is advertency when conserving and repairing historical buildings. Therefore, authors verify the durability of surface-impregnation materials and coating agents in aggressive environments.

2 EXPERIMENTAL APPROACH

2.1 *Concrete specimen*

In this study, concrete samples with a water-cement ratio of 60% were prepared. The mixture composition is given in Table 1. Specimens were cured in

Table 1. Mixture proportion of concrete.

		Unit amount (kg/m^3)					
				G		S	
W/C (%)	Sand percentage (%)	W	C	G1	G2	S1	S2
60	48.5	172	287	613	266	655	289

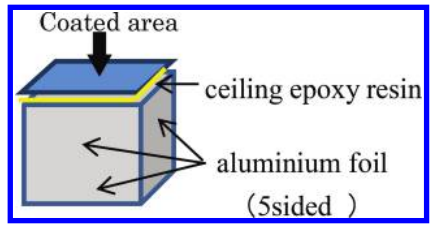

Figure 1. Schematic drawing of a structural specimen.

Table 2. Types of impregnations and surface coatings.

Type	Main component	Symbol	Construction technique			
			Pretreatment	Frequency	Dilution	Application quantity [kg/m^2]
Surface-impregnation materials	Silane, siloxane	SS-1	Dry	1	–	0.2
		SS-2	Dry	1	–	0.2
	Silane	S-1	Dry	2	–	0.3~0.4
		S-2	Dry	2	–	0.6
		S-3	Dry	2	–	0.9
	Silicate	K-1	Wet	3	–	0.35
		K-2	Wet	2	○	0.15~0.1
	Acrylic, sodium, potassium	AKN	Dry	1	–	0.28
Surface-coating agents	Aqueous acrylic, silicon	E-AS	Dry	3	–	0.1~0.15
	Fluorine	E-F	Dry	3	○	0.1~0.15
No application	–	N	–	–	–	–

water of 20 °C for 28 days and then in air with 60% R.H. at 20 °C and for 28 days. They were then stored in a climate controlled chamber with the following conditions: 20 °C, 60% R.H., and 5% CO_2 concentration.

Two types of blocks with dimensions of 10 × 10 × 40 cm and 15 × 15 × 10 cm were prepared for the carbonation test and heat and moisture deterioration test, respectively, Figure 1 shows an outline of the specimens. The details of surface impregnation and coating are shown in Table 2. Impregnation and surface coating were applied to the specimens in accordance with their specifications.

2.2 *Outline of experiment*

2.2.1 *Accelerated carbonation test*

The carbonation depth in concrete was obtained accordance with JIS A 1153 at 8, 15 and 26 weeks.

2.2.2 *Heat and moisture deterioration*

The specimen was exposed to 100 cyclic heat rays and water sprinkling. The protocols of heat rays and water sprinkling cycles are shown Figure 2.

2.3 *Measurement items*

2.3.1 *Gloss level retention*

The gloss level of the specimen surface was measured at six points using a gloss checker that complied with JIS K 5600-47.

2.3.2 *Color difference*

The color phase, brilliance, and chromaticity of the surface were measured using a color-difference meter. The measurements were conducted for three

Photo 1. Left: heat rays; right: water sprinkling.

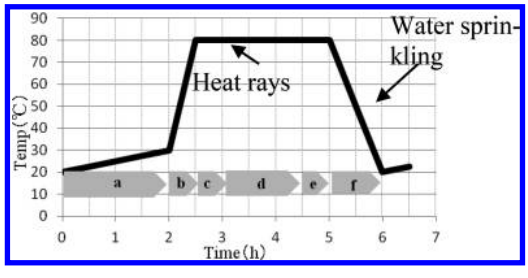

Figure 2. Protocol of heat deterioration.

parts of the concrete surface, and ΔE was calculated using Eq. (1).

$$\Delta E = (\Delta a^2 + \Delta b^2 + \Delta L^2)^{1/2} \quad (1)$$

where ΔL denotes luminosity (in compliance with JIS Z 8729), and Δa and Δb are differences in chromatic coordinates.

2.3.3 *Moisture content*

Moisture content was measured using a ceramic sensor embedded at 2 cm depth from the concrete surface at step 'e' shown in Figure 2.

2.3.4 *Coefficient of air permeability*

Air permeability was measured using a Torrent permeability tester shown in Photo 2. Air permeability was evaluated by changes in pressure in the inner chamber of the tester. All the excess air flowing into the outer chamber was evacuated. Thus, the air flow into the inner chamber was unidirectional and unaffected by unwanted ingress of air along the concrete skin (Torrent, 1992).

2.3.5 *Coefficient of moisture adsorption*

Water vapor adsorption was measured for 14 days in chamber with 100% R.H. after heating of specimens at 105 °C for 48 h. The moisture adsorption ratio was calculated using Eq. (2).

$$c = \frac{C}{C0} \tag{2}$$

where c denotes the coefficient of moisture adsorption (%), C denotes the total amount of water vapor adsorption (g), and C0 denotes amount of water vapor adsorption after heating at 105 °C (g).

2.3.6 *Contact angle*

The contact angle of a moisture particle on the concrete surface was measured using a microscope, as shown in Figure 3.

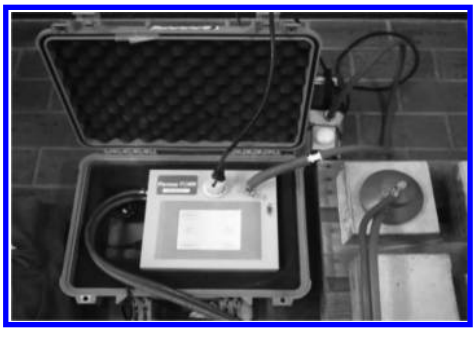

Photo 2. Measuring device.

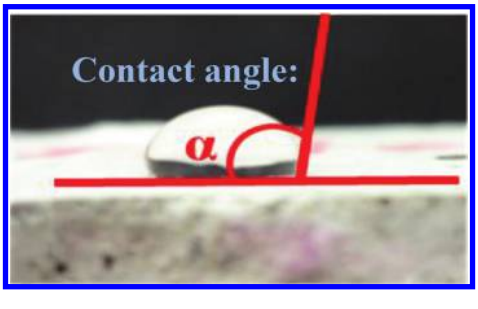

Figure 3. Contact angle of a moisture particle.

3 RESULTS AND DISCUSSION

3.1 *Gloss level retention and color difference*

Figures 4 and 5 show the results for gloss level retention and color difference. Regarding the gloss level, the surface-coating agents (E-AS, E-F) showed relatively high gloss levels. In contrast, the surface-impregnation materials except K-1, K-2, and AKN exhibited values close to that of reference concrete with no treatment. Regarding the gloss level retention, glossiness reduced overall after the accelerated carbonation test and heat and moisture deterioration test. In particular, there was a large difference in the glossiness of E-F before and after acceleration. Photo 3 shows the appearance of the coating agent E-F. It can be observed that popping bubbles occurred at the concrete surface owing to heat damage. This deterioration result in the reduction in the glossiness of E-F.

There was no clear difference in the colors the surface-coating agents and surface-impregnation materials. Therefore, gloss level retention was chosen as the color change index.

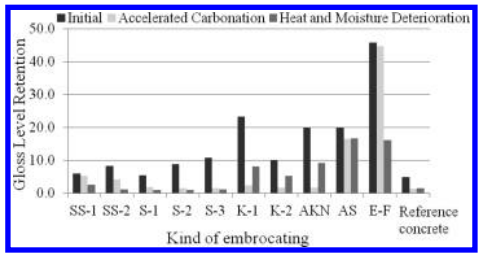

Figure 4. Gloss level retention.

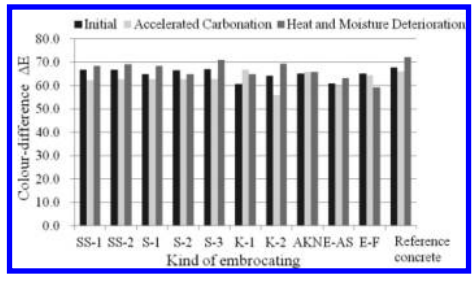

Figure 5. Colour-difference (ΔE).

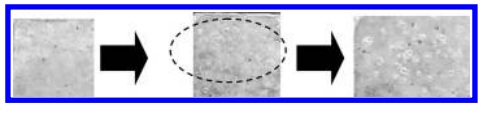

Photo 3. Change in the surface of concrete specimen using coating agent E-F.

3.2 *Moisture content*

Figure 6 shows changes in the electrostatic capacity of ceramic sensors embedded in the concrete samples after the heat and moisture deterioration tests. The change in the electrostatic capacity was then converted into moisture content (Yuasa, 1997), as shown in Figure 7. It can be seen that the surface-impregnation materials S-2 and S-3 effectively prevented moisture ingress into concrete.

3.3 *Coefficient of air permeability*

Figure 8 shows changes in the air permeability of concrete 30 days before and after heat deterioration. The air permeability of concrete with the surface-impregnation materials was higher than that of reference concrete. This might be due to the effect of water evaporation from concrete with the surface-impregnation materials. On the other hand, the air permeability of the surface-coating agents was lower than that of reference concrete.

S-2 and S-3 exhibited higher air permeability after heating. This might be due to the prevention of moisture ingress and allowance of moisture evaporation, which dries concrete. Other specimens using both surface-impregnation materials and surface-coating agents exhibited decreased air permeability because of the increase in the moisture content of concrete through cyclic water sprinkling.

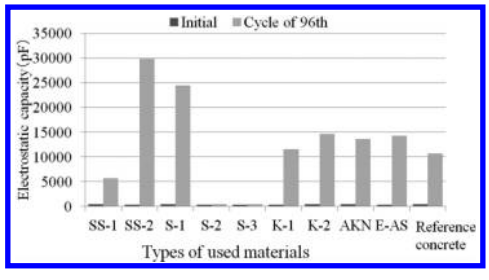

Figure 6. Change in the electrostatic capacity of ceramic sensor.

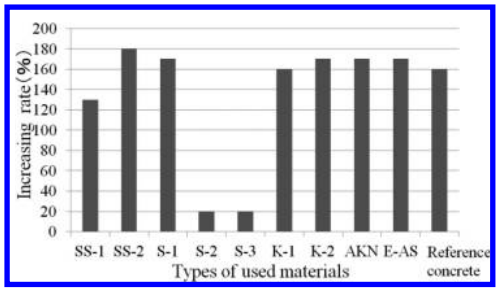

Figure 7. Increasing rate of moisture content.

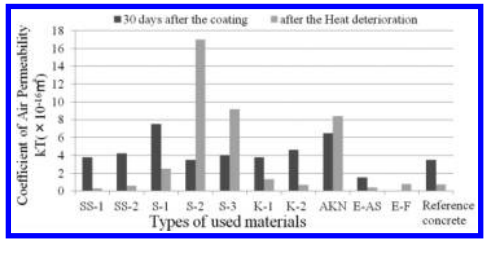

Figure 8. Change in the coefficient of air permeability.

3.4 *Depth of carbonation*

Figure 9 shows changes in the carbonation of concrete. It is clear that the surface-impregnation materials did not prevent carbonation; on the other hand, the surface-coating agents effectively prevented carbonation. After changes in carbonation due to heat and moisture deterioration, K-1 showed relatively reduced carbonation. This might be due to the reaction and generation of C-S-H from silica gel on the surface of concrete by water sprinkling.

Figure 10 shows the relationship between the depth of carbonation and air permeability of the concrete 30 days after the coating. It can be seen that a slight agreement was obtained between them. This means that air permeability might be a parameter for evaluating the preventive effects of carbonation.

Figure 11 shows the relationship between the electrostatic capacity and air permeability of concrete at 30 days after the coating. The agreement between these parameters was poor. Hence, it will be necessary to apply other methods for evaluating the prevention effects of the moisture.

3.5 *Coefficient of moisture adsorption*

Figure 12 shows changes in the coefficient of moisture adsorption. The difference between the coefficients of surface-impregnation materials and surface-coating agents was not significant. It can be seen that the coefficient of moisture adsorption of all the used materials was less than that of reference concrete. It can be expected that the

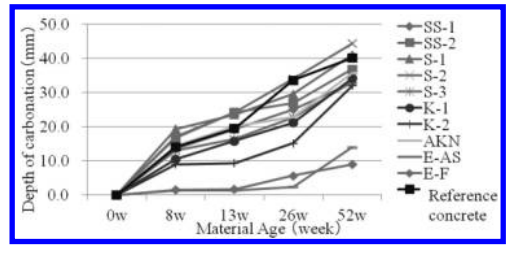

Figure 9. Changes in carbonation after heat and moisture deterioration.

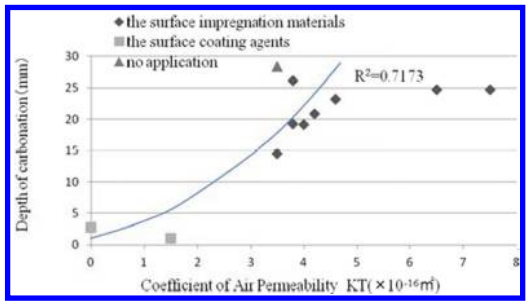

Figure 10. Relationship between carbonation depth and air permeability.

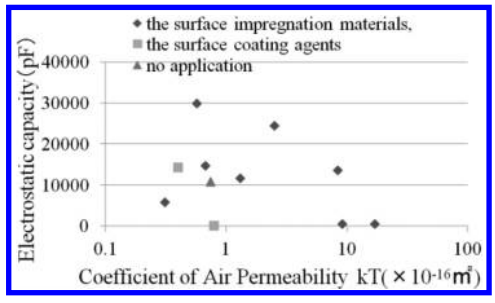

Figure 11. Relationship between electrostatic capacity and air permeability.

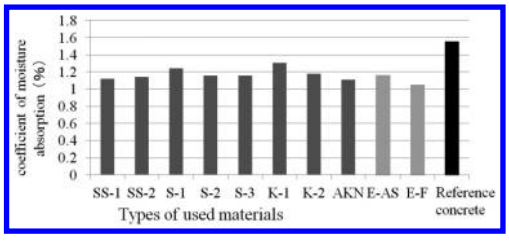

Figure 12. Change in the coefficient of moisture adsorption.

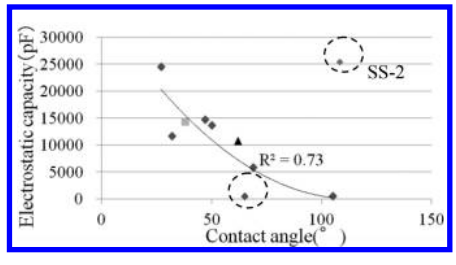

Figure 13. Relationship between electrostatic capacity and contact angle.

Table 3. Characteristics of each material.

Type	Symbol	Gloss-level retention	Colour difference	Carbonation control	Percolation control of water
Surface-impregnation materials	SS-1	○	A	–	–
	SS-2	–	A	△	△
	S-1	○	D	–	△
	S-2	–	A	–	◎
	S-3	–	A	–	◎
	K-1	△	C	△	–
	K-3	–	D	△	–
	AKN	△	D	–	–
Surface-coating agents	E-AS	△	C	◎	–
	E-F	△	D	◎	–

◎: Excellent
○: Good
△: Not effect
–: No tendency

A: Equal to the reference concrete.
B: Mostly equal to reference concrete.
C: Not similar to reference concrete.
D: Quite different to reference concrete.

impregnation and surface coating materials are preventive of the moisture vapor.

3.6 *Contact angle*

Figure 13 shows the relationship between the electrostatic capacity and contact angle of liquid water. It can be seen that there was a good agreement between them except for one of the surface-impregnation materials (SS-2).

With regard to SS-2, liquid water required a long time to be soaked into concrete than in the case of material (SS-1). It has been confirmed that the contact angle of SS-2 decreased with time. This means that the contact angle might be a parameter for evaluating the preventive effect of moisture ingress.

Table 3 summarizes the characteristics of the surface-impregnation materials and coating agents used in this study.

4 APPLICATION TO NATIONAL WESTERN MUSEUM (NMWA) IN JAPAN

4.1 *Outline of the NMWA*

The NMWA (Photo 4) was constructed in 1959 with concrete design strength of 18 MPa. Further details of the building and specifications of the concrete mixture are listed in Table 4. Round bars with yield strength of 235 MPa were used for reinforcement.

4.2 *Condition assessment with NDT*

The National Museum of Western Art (NMWA) is an important cultural landmark of Japan. In order to maintain the authenticity of the building, non/minor destructive test methods (NDT/MDT) were performed. A combination of a small core sampling test and a non-destructive on-site air permeability test was performed to determine the carbonation progress of the concrete structures and also to minimize the impact on the concrete appearance. The method described here is known as the 'Torrent Permeability Tester' and was developed in Switzerland. This tester has two advantages: (1) The spurious air entering through preferential paths (e.g. micro cracks or extremely porous outer skin) is absorbed by the outer chamber, and thus, it does not affect the measurements, and (2) This method is entirely non-destructive without unsightly spot on the concrete surface.

Photo 4. Appearance of the NMWA.

Table 4. Details about NMWA.

Location	Ueno Tokyo
Completion	29 May 1959
Designer	Le Corbusier
Assistant designer	Junzo SAKAKURA, Kunio MAEKAWA, and Takamasa YOSHIZAKA
Structural design	YOKOYAMA structural design office
Contractor	SHIMIZU Corporation
Ground area	1,587 m^2
Total floor area	4,353 m^2
Height	11.46 m
Type of structure	Reinforced concrete 3 stories

Figure 14 shows the relationship between the carbonation velocity based on the square root theory and the air permeability coefficient (kT) of concrete. It can be seen that a good agreement can be obtained between them and the air permeability tester can be considered to be a suitable tool for estimating the carbonation progress of concrete in a non-destructive manner. Based on this finding, concrete carbonation significantly proceeded as shown in Figure 15 (Imamoto, 2012).

4.3 *Application of surface-impregnation agent to NMWA*

Figure 16 shows changes in the coefficient of moisture adsorption. It can be seen that the coefficient of moisture adsorption of all the used materials was less than that of reference concrete. It can be

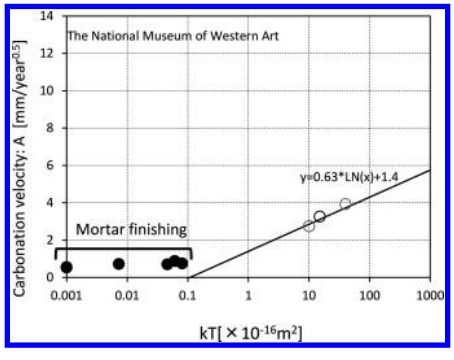

Figure 14. Relationship between carbonation and air permeability.

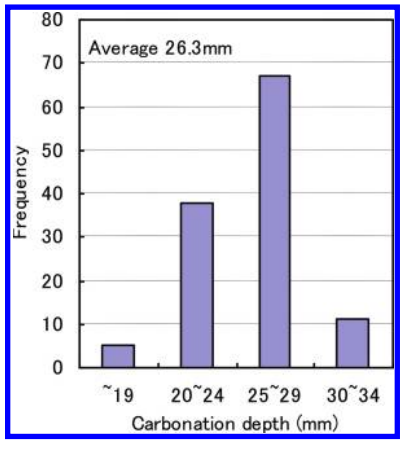

Figure 15. Distribution of carbonation depth.

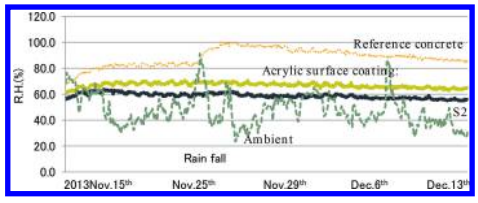

Figure 16. Changes in the coefficient of moisture adsorption.

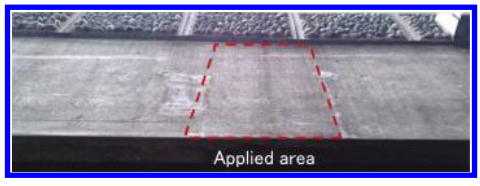

Figure 17. Applied area of impregnation agent.

Figure 18. Surface electric resistivity test.

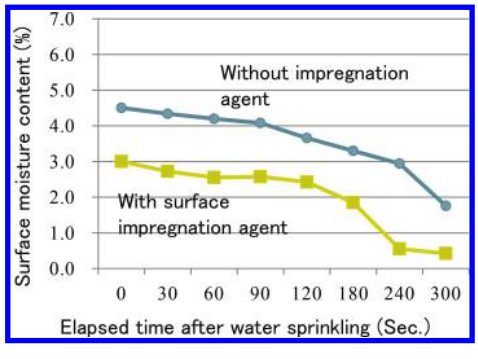

Figure 19. Change in electric resistivity after water sprinkling.

expected that the impregnation (S2) described previously was effective to prevent the ingress of moisture vapor into concrete. Also, Figure 17 shows applied area of impregnation agent. It can be seen that no change of appearance was confirmed.

As described in Figure 13, effectiveness of impregnation agent was confirmed with the estimation of contact angle. Hence, authors evaluated the effectiveness of impregnation agent on-site with surface electric resistivity after water sprinkling as shown in Figure 18.

Figure 19 shows change in electric resistivity after water sprinkling. The surface resistivity decreased by the application of the impregnation agent. It can be seen that the impregnation agent well prevented the ingress of moisture which caused steel corrosion of carbonated concrete. In this study, authors showed an example way to conserve the carbonated RC building.

5 CONCLUSIONS

An approach towards to conserve a historical RC building in Japan was introduced.

1. A non-destructive on-site air permeability test was useful for assessing carbonation pf concrete.
2. The surface-impregnation materials did not change the appearance of concrete, but the surface-impregnation materials allowed carbonation to proceed.
2. The surface-coating agents changed the appearance of concrete, but they also effectively prevented carbonation progress.
3. The surface-impregnation materials with silicate prevented the progress of carbonation by heat ray exposure and water sprinkling.
4. A good agreement was found between air permeability and carbonation progress.
5. Contact angle might be a parameter for evaluating the preventive effect of liquid moisture ingress.
6. Impregnation agent well prevented the ingress of moisture which caused steel corrosion of carbonated concrete of NMWA.

REFERENCES

Imamoto, K. A. Tanaka and M. Kanematsu, Non-destructive assessment of concrete durability of the National Museum of Western Art in Japan, Second International Conference on Microstructural-related Durability of Cementitious Composites, Amsterdam, Holland, (CD-ROM), 2012.4.

Misono, M. K. Imamoto and K. Nagai, Evaluation of moisture and gas permeability of surface treated concrete under accelerated weathering conditions, Rehabilitation and Restoration of Structures, Proceedings of an International Conference held at IIIT Madras, Chennai, India, pp.625–634, 2013.2.

Torrent, R.J. A two-chamber vacuum cell for measuring the coefficient of permeability to air of the concrete cover on site, Mater. & Struct., Vol.25, No.150, pp.358–365, July 1992.

Yuasa, N., Kasai, Y. and Matsui, I., 'Measuring method for moisture content in hardened concrete using electric properties of a ceramic sensor', Journal of Structure Concrete Eng., AIJ, (498), (1997) 13–20.

Modern materials technology

Concrete Repair, Rehabilitation and Retrofitting IV – Dehn et al. (Eds)
© 2016 Taylor & Francis Group, London, ISBN 978-1-138-02843-2

A new restrained shrinkage test for HPC repair materials

A. Reggia, F. Macobatti, F. Minelli & G.A. Plizzari
DICATAM, University of Brescia, Brescia, Italy

S. Sgobba
CTG S.p.A., Bergamo, Italy

ABSTRACT: Concrete performance traditionally refers to compressive strength and workability. Recently, High Performance Concrete evidenced the possibility of enhancing other material properties. Among these, resistance to shrinkage cracking is gaining more attention among practitioners, due to its strict relation to durability requirements. Shrinkage cracks occur in restrained structures: for this reason, material characterization should be made on the basis of a restrained shrinkage test. The ring test is an easy-to-use tool since one can measure the time-to-cracking of a concrete mix. Focus of this paper is to critical discuss the current standard test procedure and, then, to introduce a novel and enhanced testing set-up with the aim to reduce the time-to-cracking and to allow the measure of the post-cracking performance of the material being investigated. The work presents the results of the new test performed on High Performance Concrete, Fiber Reinforced Concrete with the additional use of Internal Curing.

1 INTRODUCTION

Repairing, maintaining and retrofitting existing Reinforced Concrete (RC) structures and infrastructures arises today not only as a possible perspective, but also as a necessity for the growth and development of our cities. In particular, the need to upgrade infrastructures to the increasing demand of traffic and to the performance requirements introduced by new technical regulations requires the development of innovative materials and technologies for the rehabilitation and retrofitting of existing structures. Among new materials, the use of High Performance Concrete (HPC) for structural reinforcement may be advantageous because, on one hand, it has a high chemical-physical compatibility with the substrate and, on the other, for the possibility to apply the reinforcing material in layers of a reduced thickness with a small increase of weights. However, in the design of such interventions, the volumetric compatibility between the structure and the repair material must be considered.

Tensile stresses may be generated in a cement-based repair material when its volumetric changes are prevented by the elements to be restored, such as in the case of partial depth repairs, jacketing and overlays of existing Reinforced Concrete (RC) infrastructures. Volumetric changes are a result of several factors such as moisture loss, chemical reactions and temperature variations taking place in concrete. When the induced tensile stresses exceed the current value of tensile strength of the repair material, they may result in cracking. Hence, early-age cracking of the repair material due to restrained shrinkage can be considered as a critical issue in repairing and retrofitting existing RC infrastructures with cement-based materials. Cracks allow water and chemical products to penetrate into the new layer, resulting in a premature deterioration of the repair and leading to a reduction of the expected service life of the structure.

During the last few years, concrete technologists have been studying the mechanisms governing the early-age cracking of reinforced concrete members, especially after the diffusion of HPC, material with a low water-cement ratio that have an high potential with regards to the restrained shrinkage cracking. Despite an increased tensile strength, HPC develops higher stress rates and early-ages of cracking, due to a fast development of shrinkage deformation and a high elastic modulus of the material (Wiegrink et al. 1996). As concrete is characterized by a poor tensile strength (with respect to the compressive strength), a short randomly distributed fiber reinforcement has been shown as one of the more effective techniques in controlling shrinkage cracking of concrete members (Grzybowski & Shah 1990). The addition of fibers increases the material toughness and, thus, the energy required to the development of the cracking process. After cracking occurs, fibers bridge across the crack resulting in smaller crack widths and higher stress transfer. The effectiveness

of Fiber Reinforced Concrete (FRC) in controlling shrinkage cracking is largely influenced by the type, volume, geometry and toughness of fibers.

Conventional laboratory tests for HPC and FRC (e.g. UNI EN 12390-3:2009, EN 12390-13:2013 and UNI EN 14651:2007) provide useful information both on elastic and fracture properties (e.g. compressive strength, elastic modulus and residual tensile strengths respectively) but cannot be used to estimate the actual shrinkage cracking potential of a given concrete mixture. Free shrinkage tests (e.g. UNI 11307:2008, ISO 1920-8:2009, DIN 1045 and ASTM C157/C157M-08) can be used to assess the dimensional variations due to hydration process (i.e. autogenous shrinkage) and exchange of water with the surrounding environment (i.e. drying shrinkage) in free conditions, but do not provide any information on the cracking risk of concrete because no tensile stress is induced in the specimen. In particular, the possibility of evaluating the effect of fibers results limited because their presence become relevant only after the formation of cracks.

Therefore, assessment of shrinkage cracking potential of concrete should be determined by means of a restrained shrinkage test that can consider both the effect of restraint conditions (i.e. degree of restraint) and the effect of time-developing material properties. Many studies have been carried out during the last three decades, mainly using three types of test: linear test (Paillere et al. 1989, Banthia et al. 1993, Kovler 1994, Bloom & Bentur 1995), plate test (Kraai 1985) and ring test (Swamy & Stavrides 1979, Kovler et al. 1993, See et al. 2003, He et al. 2004, Shah & Weiss 2006). The latter provides a nearly constant degree of restraint through an axis-symmetric specimen geometry. In this type of test, a concrete specimen is cast around an inner steel ring, which provides a restraint to the shrinkage of concrete. The steel ring is also used to evaluate the induced tensile stresses in concrete through the measure of the steel deformation with strain gauges: a sudden drop in the steel ring deformation is interpreted as the failure of the concrete ring.

The standard methods based on the ring test, AASHTO PP 34-99 (1999) and ASTM C1581/C1581M (2009), have been developed to determine the cracking tendency of concrete through the measure of the time-to-cracking, as the time required to the concrete specimen to crack in a controlled environment. In addition, the ASTM standard provides an analytical method to calculate the stress rate in the concrete ring from the measure of the deformation in the steel ring. In the ASTM standard, the cracking tendency of a given concrete mixture is determined on the bases of four performance classes defined by the time-to-cracking and the stress rate. Hence, the standard test methods can be considered valuable tools for the evaluation of the influence of composition and material properties of concrete on cracking sensitivity. However, the lack of a direct measure of the crack opening limits the usefulness of the test method to the evaluation of the pre-cracking behavior (e.g. time-to-cracking and stress rate) and does not allow any consideration on the post-cracking performance of the material. In particular, without a measure of the crack width, the effect of fibers cannot be easily evaluated after cracking and their effect on the strain deformation of the steel ring is hard to interpret.

The present work aims to be part of a broader research path that takes away from the studies of Swamy & Stavrides (1979) and continues with the research of Shah and others (Grzybowski & Shah 1990, Shah & Weiss 2006), up the definition of the current technical standards. The goal of the work is to continue the route with an additional effort to make the test more suitable for its use as a reference standard for HPC and FRC. For this reason, this research has two specific objectives: the first is the reduction of the time-to-cracking, through the increase of the degree of restraint of the test set-up; and the second is the need to measure the crack opening by means of the predetermination of its location. As already evidenced by previous researches (Cangiano et al. (2012), Reggia et al. (2012) and Reggia (2013)) both objectives are achieved with the introduction of a preformed notch in the concrete ring that, on the one hand, increases locally the degree of restraint and, on the other, allows to place a transducer for the measuring of the crack opening. The proposed change of the test method aims at developing a sufficiently robust testing technique able to emphasize the role of concrete as well as that of fibers (from which it is reasonable to expect a significantly different behavior in relation to restrained shrinkage cracking). The work presents the results of a recent experimental campaign conducted on HPC and FRC with the additional use of Internal Curing (IC). The effects of the addition of an hybrid reinforcement of steel and polypropylene fibers and pre-wetted Light Weight Aggregates (LWAs) are discussed with reference to the risk of cracking (evaluated through the determination of the time-to-cracking) and to the development of the cracking process (with the calculation of the crack opening rate).

2 EXPERIMENTAL TESTING

2.1 *Testing set-up*

The testing set-up of the notched ring test consists of a steel ring with a thickness (t_s) of 25,4

mm, with an outer diameter (D_{os}) of 330 mm and a height (h) of 152 mm. The outer diameter of the concrete (D_{oc}) is 420 mm. The cross section of the concrete ring is 45 × 152 mm. Unlike standard ring test methods (ASTM), the new configuration introduces a preformed notch 15 mm deep with an angular profile of 90°, as shown in Figure 1. Hence, the reduced section of the concrete ring is 30 × 152 mm. The outer surface of the steel in contact with concrete, is perfectly smooth and polished to limit the friction between the two materials. Furthermore, the friction is limited between the sample and the support base. The outer mold is made with a polytene tube and the base is made of a polytene panel.

The specimen geometry is designed to provide a Degree Of Restraint (DOR) able to generate cracking in the concrete ring in the first few days after the placing of concrete. In fact, degree of restraint represents the portion of the deformation due to shrinkage which is converted into concrete tensile deformation. The greater the degree of restraint, the greater the system's ability to induce shrinkage cracking: 100% represents the perfectly restrained condition, while 0% represents the free shrinkage condition. The DOR can be easily expressed by the following formula proposed by See et al. (2003):

$$DOR = \frac{A_s \cdot E_s}{A_c \cdot E_c + A_s \cdot E_s} = 84\% \quad (1)$$

where A_s = area of the cross section of the steel ring (3861 mm^2); E_s = modulus of elasticity of steel (210 GPa); A_c = area of reduced cross section of the concrete ring (4560 mm^2); E_c = modulus of elasticity of concrete (35 GPa).

Table 1 summarizes the dimensions of the specimens used in the AASHTO, ASTM, CTG (according to Cangiano et al., 2012) and in the proposed notched ring tests. The introduction of a steel ring with a greater thickness determines an increased value of the DOR, equal to 77%. The presence of a reduced cross-section in the notch raises locally the value of the DOR_n up to 84%. The proposed testing set-up develops a greater DOR than standard methods, with an increment of +34% with respect to the AASHTO standard and +20% to the ASTM standard. Therefore a reduction of the time-to-cracking is reasonably expected. The CTG ring has a slightly greater DOR_n, equal to 88%, thanks to a larger thickness of the steel ring. Note that the values of DOR must be interpreted as reference values, calculated considering a constant value of the elastic modulus of concrete equal to 35 GPa. According to equation (1), changes in the value of the modulus of elasticity, due to the progress of hydration process or variation in the mixture composition, are reflected in slightly different values of the DOR.

Table 1. Ring test specimens dimensions and degrees of restraint.

		AASHTO	ASTM	CTG	Notched ring test
D_{oc}	mm	457	405	375	420
D_{ic}	mm	305	330	255	330
D_{os}	mm	305	330	255	330
D_{is}	mm	279,6	304	185	279,6
t_c	mm	76	37,5	60	45
t_s	mm	12,7	13	35	25,4
t_n	mm	–	–	30	30
h	mm	152	150	105	152
DOR	%	50	68	78	77
DOR_n	%	–	–	88	84

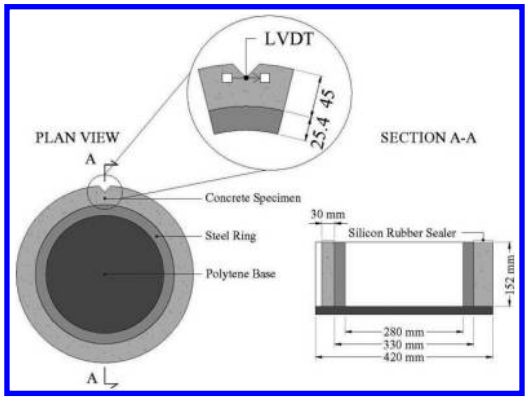

Figure 1. Notched ring test set-up.

2.2 *Testing procedure*

Concrete is mixed according to the specification given in UNI EN 12390-2:2009. First aggregates, cement and silica fume are putted in the mixer, then water and superplasticiser. After reaching the desired workability, HPC is removed from the mixer and poured in the formworks. Then, fibers are gradually added ensuring an uniform distribution. In the end, the FRC is extracted from the mixer and poured in the molds. In the case of IC, the pre-wetted LWAs are added with the other aggregates and the mixing procedure of HPC is followed. At the end of each mixing phase, the workability of the fresh mixes is measured according to UNI EN 206:2006 with the Abrams cone.

After casting, specimens are covered with a previously wetted burlap, to protect specimens from evaporation during the first 24 hours. After 24 hours the outer formwork of the ring is removed

Figure 2. LVDT at the tip of the notch (CTOD): HPC-2 specimen at 21 days.

and the upper surface of the concrete ring is sealed. By this, evaporation could occur only through the lateral surface of the ring, since both the lower and the upper surface of the ring are sealed. The ring test monitoring begins at casting and is conducted under controlled environmental conditions for three weeks. The specimens are placed in a climate controlled chamber with a constant temperature T and a constant relative humidity RH. To increase the rate of shrinkage, temperature is set to 20±1 °C and relative humidity to 50±5%. According to ASTM specification.

2.2.1 *Monitoring*

Within each steel ring one strain gauge is mounted at concrete notch to measure the deformations induced by shrinkage of concrete ring. The strain gauge is connected directly to a data acquisition system and to a computer to record the data at intervals of 15 minutes immediately after casting. The formation of the crack in the notch can be identified by a sudden drop of the deformation measured by the strain gauge placed at the notch. In addition, a Linear Voltage Displacement Transducer (LVDT) is placed on the tip of the notch (Crack Tip Opening Displacement—CTOD) on the upper surface of the specimen (Fig. 2). The transducer is applied directly on the surface of concrete using a thin layer of a quick-hardening ethyl cyanoacrylate based adhesive. The LVDT is connected directly to the data acquisition system for continuous monitoring 24 hours after casting.

3 MATERIALS AND MIX DESIGN

3.1 *Mix design*

The High Performance Concrete (HPC) under investigation consists of C70/85 concrete, with a cement content of 547 kg/m^3, a silica fume content of 159 kg/m^3 and a water/binder ratio of 0,22. The concrete mixture without fibers is designed to have consistency class S5, provided by the use of superplasticiser with a dosage of 19 l/m^3. The Hybrid Fiber Reinforced Concrete (HyFRC) is made on the basis of the HPC with the addition of 25 kg/m^3 of steel fibers and 8 kg/m^3 of polypropylene fibers corresponding to volumetric percentages V_f of 0,32% and 0,88% respectively, giving a total volumetric percentage of 1,20%. The Internally Cured Hybrid Fiber Reinforced Concrete (ICHyFRC) is made on the basis of the HyFRC by replacing the 52% volume of sand with a pre-wetted LWA. The design and the consistency classes of HPC, HyFRC, and ICHyFRC mixes under investigation are reported in Table 2.

The cement type is CEM II/A LL-42.5R. It is a Portland cement with limestone type II with high normalized resistance and high initial resistance. The silica fume is a dry densified microsilica powder designed to increase concrete compressive strengths.

In the experimental campaign two different types of fibers are used together: a steel fiber and a polypropylene fiber (Fig. 3). Steel fibers are hook-ended macro-fibers 30 mm long with a diameter of 0,35 mm. The tensile strength is greater than 2500–3000 MPa. The polypropylene fibers are corrugated polypropylene macro-fibers 29 mm long with a diameter of 0,75 mm. The tensile strength is

Table 2. Mix design and workability of HPC, HyFRC and ICHyFRC (Macobatti, 2015).

		HPC	HyFRC	ICHyFRC
Cement 42.5R	kg/m^3	547	547	547
Silica Fume	kg/m^3	159	159	159
Total binder	kg/m^3	706	706	706
Water	kg/m^3	154	154	154
Superplast. content	l/m^3	19,3	22,6	22,5
Polyprop. fiber content	kg/m^3	–	8	8
Steel fiber content	kg/m^3	–	25	25
Sand 0–4 mm	kg/m^3	868	862	510
Gravel 4–10 mm	kg/m^3	651	643	637
LWA 0–5 mm	kg/m^3	–	–	207
Density	kg/m^3	2395	2390	2237
Water/binder ratio		0,22	0,22	0,22
Aggreg./binder ratio		2,14	2,09	1,90
Superplast./ binder ratio		0,04	0,04	0,04
Slump	mm	240	230	150
Consistency class		S5	S5	S3

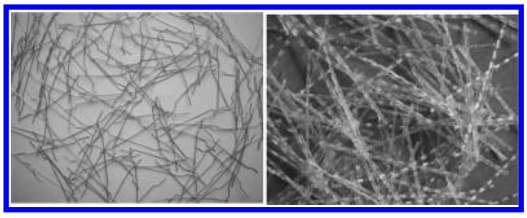

Figure 3. Steel fibers (left) and polypropylene fibers (right).

Table 3. Chemical and physical characteristics of fibers.

	Steel fiber	Polypropylene fiber
Material	Steel	Polypropylene
Shape	Hooked	Corrugated
Density	7850 kg/m^3	910 kg/m^3
Length L	30 mm	29 mm
Equivalent diameter ϕ	0,35 mm	0,75 mm
Aspect ratio L/ϕ	85,7	31,2
Tensile strength	2500–3000 MPa	400–450 MPa

400–450 MPa. The main chemical-physical characteristics of the fibers are listed in Table 3.

The low w/b ratio and the presence of fibers may reduce workability of concrete at the fresh state. To overcome this problem without changing the w/b ratio, a high-range water reducer based on second generation polycarboxylate is used.

Natural aggregates of silica source are also used. Two aggregate types with diameters ranging between 0 and 10 mm are used and sorted according to size of the grains see Table 2. The LWA is made from plastic clay heated and expanded in a rotary kiln at a temperature of about 1100 °C. The aggregate size distribution of LWAs is between 0,5 and 5 mm in order to have the same gradation of the sand replaced. The density of grains of LWA is 1150 kg/m^3. The absorption at 24 hours is 10%. To determine particle size distribution the Bolomey curve is used, taking into consideration the binder content, the maximum diameter of the aggregates and the desired workability of the mixture. The aggregates/binder ratio is 2,14, 2,09 and 1,90 for HPC, HyFRC, and ICHyFRC respectively. Further details can be found in Macobatti (2015).

3.2 *Internal curing*

Internal curing is defined as the supply of water throughout a freshly placed cementitious mixture using internal reservoirs, via pre-wetted LWA, that readily release water as needed for hydration or to replace moisture lost due to self-desiccation. Thanks to random dispersion of LWA the water released into the element is more uniform than water penetrated with external curing. Mixture proportioning with internal curing provides the necessary additional water to prolong the time during which saturated conditions are maintained within the hydrating cement paste. The maintenance of these saturated conditions will both contribute to an increase in the achieved degree of reaction of the cementitious materials and also minimize the development of autogenous shrinkage contributing to early-age cracking. Equation (2) provides the relationship between the water demand of the hydrating mixture and the supply that is readily available from the internal reservoirs (Bentz & Weiss 2011): the left-hand side of the equation represents the water demand of the concrete mixture and the right-hand side represents the water being supplied.

$$C_f \cdot CS \cdot \alpha_{max} = S \cdot \Phi_{LWA} \cdot M_{LWA} \quad (2)$$

where C_f = binder factor of the concrete mixture, equal to 706 kg/m^3; CS = chemical shrinkage of the binder at 100% of the reaction, assumed equal to 0,064 (Bentz & Weiss 2011); α_{max} = expected maximum degree of reaction for the binder, equal to (w/b)/0,36 = 0,61; M_{LWA} = mass of LWAs replacing the Normal Weight Aggregates NWAs, equal to 207 kg/m^3; S = saturation level of LWAs relative to a quantified "pre-wetted" condition, equal to 1; and Φ_{LWA} = measured sorption capacity of the internal reservoirs equal to 10%.

4 EXPERIMENTAL RESULTS

For each material under investigation, the following tests have been conducted: 3 compression tests according to UNI EN 12390-3:2009 at the age of 28 days; 3 test for the determination of the secant elastic modulus according to EN 12390-13:2013 at the age of 28 days; 3 three point bending tests according to UNI EN 14651:2007 at the age of 28 days; 2 free shrinkage measurements according to ASTM C157/C157M-08; and 2 restrained shrinkage tests according to the notched ring test method herein presented.

4.1 *Mechanical characterization*

The HPC has consistency class S5 and strength class C80/95, with a slump of 240 mm and a cubic compressive strength of 101,5 MPa respectively. The HyFRC has consistency class S5, with a value of slump equal to 230 mm, and a strength class C80/95, with a cubic compressive strength of 104,1 MPa. The ICHyFRC has lower consistency class

S3 and strength class C80/95, with a slump of 150 mm and a cubic compressive strength of 97,6 MPa. The average value of secant elastic modulus in compression is 36 GPa in HPC, 37 GPa in HyFRC and 31 GPa in ICHyFRC. The average values, the standard deviation and the coefficient of variation of compressive strength and elastic modulus are reported in Table 4. The average values of the limit of proportionality (i.e. the modulus of rupture) and the residual tensile strengths f_{Rj} according to UNI EN 14651:2007 are reported in Table 5.

4.2 *Free shrinkage*

The free shrinkage of concrete is performed measuring the relative dimensional changes of axial prismatic specimens with nominal dimensions of 75 × 75 × 285 mm according to ASTM C157/C157M-08. These measurements allow the estimation of the potential volumetric contraction of shrinkage of concrete during the drying phase without any type of constraint. During the test, the samples are stored in a climatic chamber at a temperature of 20±1 °C and relative humidity of 50±5%. For each batch, two specimens are casted and the measurements of the specimens are performed at 24 hour intervals during the 21 days after casting. The measurements are made using an analogic comparator mounted at the top of a steel support. Before reading the axial variation, the reference bar is put in a suitable frame in order to set the initial zero. The free shrinkage of concrete mixes have been monitored during the execution of the restrained shrinkage test. The values of free shrinkage deformation are reported in Table 6 at 7, 14 and 21 days. The percentage differences compared to HPC are reported in brackets for HyFRC and ICHyFRC.

Table 4. Compressive strength and secant elastic modulus in compression at 28 days: average values (R_{cm}, E_{cm}), standard deviation (σ) and coefficient of variation (CV).

	$R_{cm}(28)$ (MPa)	σ (MPa)	CV (–)	$E_{cm}(28)$ (GPa)	σ (GPa)	CV (–)
HPC	101,5	4,7	0,05	36	3	0,07
HyFRC	104,1	2,8	0,03	37	4	0,09
ICHyFRC	97,6	1,1	0,01	31	3	0,09

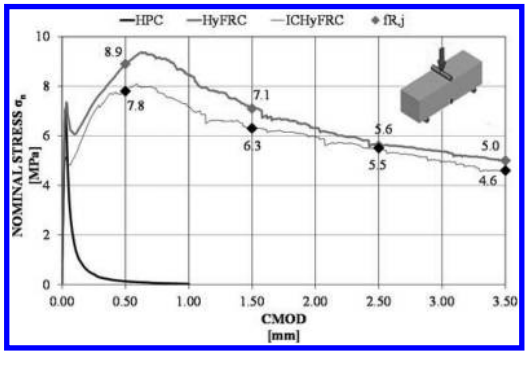

Figure 4. Three point bending test: mean curve of HPC, HyFRC and ICHyFRC.

Table 5. Limit of proportionality and residual tensile strengths at 28 days: average values (f_{Lm}, f_{R1m}, f_{R2m}, f_{R3m}, f_{R4m}).

	f_{Lm} (MPa)	f_{R1m} (MPa)	f_{R2m} (MPa)	f_{R3m} (MPa)	f_{R4m} (MPa)
HPC	7,1	–	–	–	–
HyFRC	7,4	8,9	7,1	5,6	5,0
ICHyFRC	5,2	7,8	6,3	5,5	4,6

4.3 *Restrained shrinkage*

Figure 5 and Figure 6 show the results of notched ring tests.

The behaviour of HPC is very clear and characterized by a rapid development of the steel strain deformation up to its peak value, at 3,4 and 3,0 days for the two samples. After the peak, a sudden and clear drop in the steel strain with the cracking of the concrete ring is observed. In the

Table 6. Free shrinkage of concrete mixes at 7, 14 and 21 days.

	$\varepsilon_{c,sh}(7)$ (μm/m)	$\varepsilon_{c,sh}(14)$ (μm/m)	$\varepsilon_{c,sh}(21)$ (μm/m)
HPC	440 (ref.)	522 (ref.)	590 (ref.)
HyFRC	365 (–17%)	448 (–14%)	512 (–13%)
ICHyFRC	290 (–34%)	426 (–18%)	435 (–26%)

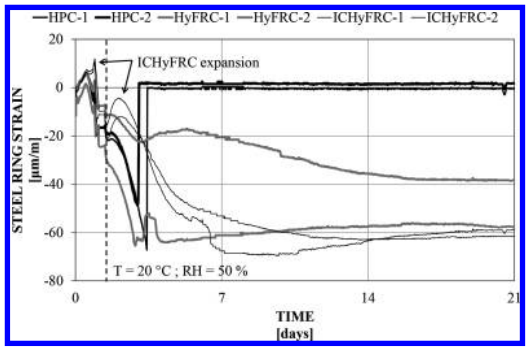

Figure 5. Notched ring test: steel rings strains.

following days a variation in the steel deformation is no longer observed. The crack opening, measured at the tip of the notch, initially increases with a slow rate but, after cracking, rapidly increases to 1,460 and 1,609 mm at 7 days whereas 1,525 and 1,655 mm at 21 days. After this initial period the crack reaches a steady state with a partial recovery of the opening.

The HyFRC samples show a similar performance, compared to HPC, in the pre-cracking phase, reaching the cracking at 3,3 and 2,8 days (Fig. 5). After cracking, the steel strain continues to increase (HyFRC-1) or reaches a stationary state with no release of deformation (HyFRC-2). After cracking, the CTOD changes the rate of growth reaching the values of 0,078 and 0,264 mm at 7 day whereas 0,111 and 0,367 mm at 21 days. The effect of fibers can be seen in the absence of a drop in the steel strain, due to the capacity of fibers to transfer tensile stresses across the crack, and to the reduction of the crack opening, due to the ability of fibers to counteract the cracking process.

The performance of ICHyFRC shows a more gradual development of steel strains with an unclear transition between pre-cracking and post-cracking phase. Cracking may be identified by a change in the crack opening rate, at 4,0 and 3,5 days. The crack opening development is less pronounced than in the other materials reaching the values of 0,097 and 0,131 mm at 7 days whereas 0,148 and 0,199 mm at 21 days.

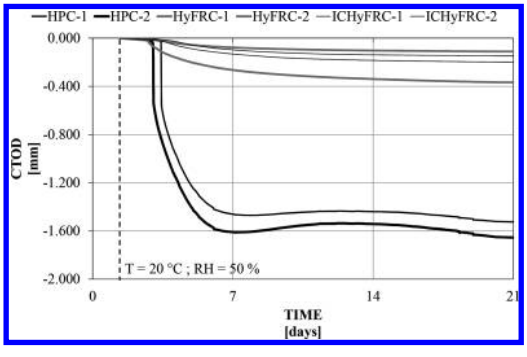

Figure 6. Notched ring test: cracks openings (CTOD).

4.4 *Shrinkage cracking performance indexes*

The resistance to restrained shrinkage cracking can be defined on the basis of two experimental measurements: the cracking initiation time or time-to-cracking (T_c); and the crack opening rate (v_c).

The time of initiation of the cracking process T_c is intended as the time interval between the exposure of the material to the environment which determines the shrinkage and the time in which a sudden variation of the crack opening (or a variation in the rate of crack opening) is measured. The rate of crack opening v_c is defined as the ratio between the increment of the crack opening after a predetermined period of time, i.e. the average velocity of cracking in a given time:

$$v_c(t) = \frac{w(t) - w(T_c)}{(t - T_c)} \text{ with } t > T_c \quad (3)$$

where $w(T_c)$ = relative displacement between the faces of the notch at the incipient cracking; $w(t)$ = crack opening after a predetermined period of time; $(t - T_c)$ = period of time of observation with $t > T_c$.

T_c can be related to the likelihood of the cement matrix to crack due to restrained shrinkage: the more the material is prone to cracking, the more T_c will be short. The time-to-cracking is influenced by the time development of shrinkage and mechanical properties of concrete. In particular, concretes characterized by a rapid development of shrinkage and elastic modulus will be characterized by short T_c (e.g. HPC), while materials with a slow

Table 7. Performance indexes: time-to-cracking (T_c) and crack opening rate (v_c).

Material	Tc (days)	$v_c(7)$ (μm/day)	$v_c(14)$ (μm/day)	$v_c(21)$ (μm/day)
HPC-1	3,4	399	133	85
HPC-2	3,0	393	137	90
Mean value	3,2 (ref.)	396 (ref.)	135 (ref.)	88 (ref.)
HyFRC-1	3,3	16	8	5
HyFRC-2	2,8	59	29	19
Mean value	3,1 (–3%)	38 (–90%)	18 (–87%)	12 (–86%)
ICHyFRC-1	4,0	25	12	7
ICHyFRC-2	3,5	29	15	10
Mean value	3,8 (+19%)	27 (–93%)	13 (–90%)	9 (–90%)

development of shrinkage or a gradual development of the elastic modulus will be characterized by longer T_c (e.g. ICHyFRC).

The rate of crack opening v_c defines, instead, the material's ability to counteract cracking: the lower v_c, the higher the material ability to control the cracking process. This parameter depends largely by the shrinkage and by the residual strength of the material after cracking. For instance, concretes characterized by a brittle post-cracking behaviour will experience high v_c (e.g. HPC), while concretes characterized by high residual strength will be identified by a slow development of the cracking process (e.g. HyFRC and ICHyFRC). The above mentioned parameters are given in Table 7. Figure 7, Figure 8 and Figure 9 show the values of T_c, $v_c(7)$ and $v_c(21)$ graphically. Moreover, Table 7 also reports mean value for the three materials and, in brackets, the percentage differences of HyFRC and ICHyFRC compared to HPC.

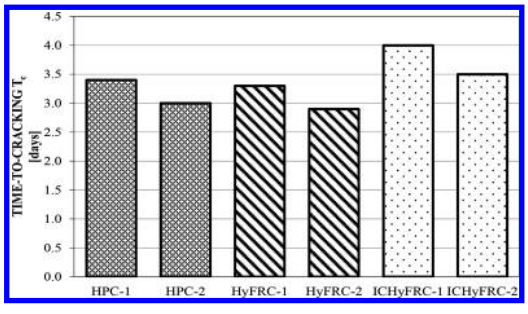

Figure 7. Time-to-cracking of concrete mixtures.

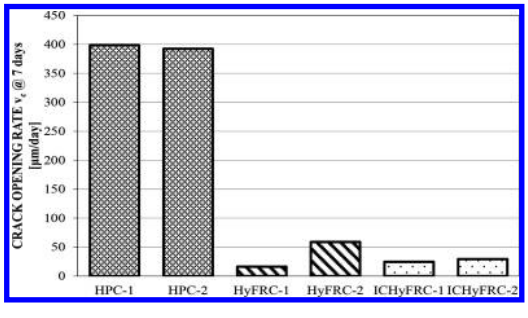

Figure 8. Crack opening rate of concrete mixtures at 7 days.

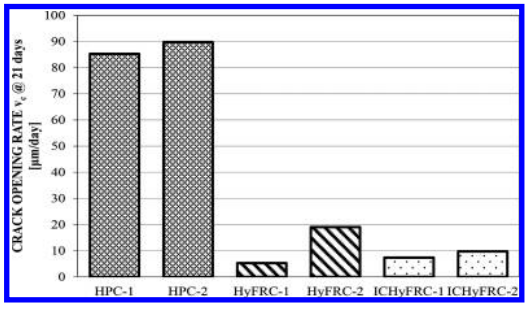

Figure 9. Crack opening rate of concrete mixtures at 21 days.

5 CONCLUDING REMARKS

Based on the experimental study herein conducted, the following conclusions can be drawn:

- The evaluation of cracking sensitivity of HPC and FRC under restrained shrinkage can be performed by means of a restrained ring test with an innovative methodology characterized by a higher DOR and having a notch. The presence of a reduced section allows to achieve three important results: an expected reduction of the time-to-cracking, due to an higher DOR, in comparison with that required for the same material tested with the standard ring test AASHTO and ASTM; the possibility to make more accurate measurements of the crack opening and its development in time; and the opportunity to collect not only qualitative but also quantitative results on the cracking process determined by restrained shrinkage, such as crack opening and crack opening rate.
- The restrained shrinkage behavior can be determined both by the evaluation of the deformation of the ring in steel and by assessment of the crack opening in the notch. The deformations measured in the ring steel allow an easy evaluation of the time-to-cracking, generally associated with a sudden decrease of the deformations of the ring. The development over the time of the crack opening is used to estimate the average crack opening rate at predetermined time intervals. From the results of the tests conducted it is possible to determine not only the sensitivity to cracking of the concrete, depending to the cement matrix, but also to evaluate the resistance to the restrained shrinkage cracking, due to the presence of the fibrous reinforcement.
- The effect of the addition of hybrid fibers resulted in a limited decrease in the time-to-cracking comparing HPC with HyFRC. This effect may be due to the small decrease in the tensile strength of the fiber reinforced material. Moreover, the addition of fibers results in a significant decrease in the rate of crack opening, caused by an increase of the capacity of fiber reinforced concrete to counteract the advance of the cracking process. This effect is particularly

evident for the speed of growth of the crack evaluated at 7 and 21 days.

– Internal curing causes an increase in the time-to-cracking of mixtures. In this case the time-to-cracking increases from 3,4 and 3,0 days (HPC) to 4,0 and 3,5 days (ICHyFRC). This effect may be due to the lower rate of free shrinkage, accompanied to an expansion during the first hours after casting and a lower elastic modulus. In addition, the presence of fiber reinforcement gives the same benefits shown for the HyFRC.

ACKNOWLEDGMENTS

A special mention goes to Prof. J. Weiss, Purdue University, for his valuable assistance in defining the mixtures herein utilized. Thanks are due to Grace, BASF, LaMatassina and Laterlite for the materials supply. The contribution of Barbara Bassanesi, Silvia Bettoni and Federico Pedretti for the mechanical characterization of HPCs is gratefully acknowledged. The laboratory assistance of technician at DICATAM Augusto Botturi, Domenico Caravaggi, Andrea Del Barba and Luca Martinelli is also greatly appreciated.

REFERENCES

AASHTO PP 34–99 1999. Standard Practice for Estimating the Cracking Tendency of Concrete. Washington DC, USA: American Association of State Highway and Transportation Officials.

ASTM C1581/C1581M 2009. Standard Test Method for Determining Age at Cracking and Induced Tensile Stress Characteristics of Mortar and Concrete under Restrained Shrinkage. West Conshohocken, PA, USA: ASTM International.

Banthia, N., Azzabi, M., & Pigeon, M. 1993. Restrained shrinkage cracking in fibre-reinforced cementitious composites. *Materials and Structures* 26(7): 405–413.

Bentz D.P. & Weiss W.J. 2011. Internal Curing: A 2010 State-of-the-Art Review. Gaithersburg, MA, USA: National Institute of Standards and Technology NIST.

Bloom, R., & Bentur, A. 1995. Free and restrained shrinkage of normal and high-strength concretes. *ACI Materials Journal* 92(2): 211–217.

Cangiano, S. Sgobba, S. Plizzari, G.A. Minelli, F. & Reggia, A. 2012. Characterization of cracking behaviour of concrete under restrained shrinkage through ring test (in italian). *CTE congress proceedings*.

Grzybowski, M., & Shah, S.P. 1990. Shrinkage cracking of fiber reinforced concrete. *ACI Materials Journal 87*(2): 138–148.

He, Z., Zhou, X., & Li, Z. 2004. New experimental method for studying early-age cracking of cement-based materials. *ACI Materials Journal* 101(1): 50–56.

Kovler, K., Sikuler, J., & Bentur, A. (1993). Restrained shrinkage tests of fibre-reinforced concrete ring specimens: effect of core thermal expansion. *Materials and Structures* 26(4): 231–237.

Kovler, K. 1994. Testing system for determining the mechanical behaviour of early age concrete under restrained and free uniaxial shrinkage. *Materials and Structures* 27(6): 324–330.

Kraai, P.P. 1985. A proposed test to determine the cracking potential due to drying shrinkage of concrete. *Concrete construction* 30(9): 775–778.

Macobatti, F., 2015. Experimental and numerical study of early-age cracking in retrofitting of existing RC structures. *PhD Thesis (in press)*.

Paillere, A., Buil, M., & Serrano, J.J. 1989. Effect of Fiber Addition on the Autogenous Shrinkage of Silica Fume. *ACI Materials Journal* 86(2): 139–144.

Reggia, A., Minelli, F., & Plizzari, G.A. 2012. Suitable Restrained Shrinkage Test for Fibre Reinforced Concrete: A Critical Discussion. In 7th RILEM International Conference on Cracking in Pavements: 615–624. Delft: Springer.

Reggia, A., 2013. Characterization of the Shrinkage Behavior of High Performance Cement Based Materials for Structural Rehabilitation. *PhD Thesis*. Roma: ARACNE editrice.

See, H.T., Attiogbe, E.K., & Miltenberger, M.A. 2003. Shrinkage cracking characteristics of concrete using ring specimens. *ACI Materials Journal* 100(3): 239–245.

Shah, H.R., & Weiss, J. 2006. Quantifying shrinkage cracking in fiber reinforced concrete using the ring test. *Materials and structures* 39(9): 887–899.

Swamy, R.N., & Stavrides, H. 1979. Influence of fiber reinforcement on restrained shrinkage and cracking. *ACI Journal proceedings* 76(3): 443–460.

Wiegrink, K., Marikunte, S., & Shah, S.P. 1996. Shrinkage cracking of high-strength concrete. *ACI Materials Journal 93*(5): 409–415.

Concrete Repair, Rehabilitation and Retrofitting IV – Dehn et al. (Eds)

Studies on creep deformation of ultra-rapid-hardening cement-type bonded anchor

S. Ando & T. Tamura
Sumitomo Osaka Cement, Chiba, Japan

K. Nakano
Chiba-Institute of Technology, Chiba, Japan

T. Tanuma
Urban Renaissance Agency, Kanagawa, Japan

ABSTRACT: Creep deformations of ultra-rapid-hardening cement-type post-installed bonded anchors were measured. The influences of the sustained load magnitude, steel bar diameter, and type of anchor were studied for an embedment length of seven times the nominal diameter. It was estimated that creep failure would not occur within 50 years for an inorganic-type post-installed bonded anchor at a stress level of 0.33. The displacement of D19 bars was larger than that of D13 bars at the same stress level. For organic-type anchors, the displacement changed mostly at a stress level of 0.55 as the test duration increased, so the creep limit was considered to be approximately 0.55. The relationship between the time to creep failure and the stress level was determined for the different types of anchors tested. The slope of the line for the time to creep failure versus the stress level for the inorganic post-installed bonded anchor type was about half of that for the cast-in-place anchor type.

1 INTRODUCTION

The collapse of the ceiling of the Ted Williams Tunnel in South Boston, Massachusetts, USA occurred on July 10, 2006. The National Transportation Safety Board released a report about the accident that attributed the major cause of the collapse to epoxy creep. In Japan, concrete ceiling panels inside the Sasago Tunnel collapsed on December 2, 2012. It has been a concern that the ceiling panels' post-installed anchors used may have deteriorated during long-term use.

When equipment is attached to a concrete structure, post-installed anchors are essential for successful construction. Post-installed anchors can be positioned exactly and are easy to install. More than 500 million post-installed anchors are used annually in Japan. Thus, the safety of post-installed anchors is an important subject.

However, there has been little research on the tensile creep behaviour of post-installed bonded anchors in Japan. The creep behaviour of post-installed anchors of polyester resin was studied by Yano et al. (1981), and that of anchors of epoxy ester was studied by Nakano et al. (2011). The creep behaviour of organic-type bonded anchors is summarised in *Anchorage in Concrete Construction* (Eligehausen et al. 2006).

Nevertheless, few studies have focused on the creep behaviour of inorganic-type post-installed bonded anchors.

This study was conducted to investigate the creep behaviour of ultra-rapid-hardening cement-type post-installed bonded anchors. The influences of the sustained load magnitude, steel bar diameter, and type of anchor were examined in this study.

2 EXPERIMENTAL MATERIALS AND METHODS

2.1 *Anchor materials*

Table 1 lists the materials and mix proportions of the post-installed bonded anchors used in the tests.

The post-installed bonded anchors were of the cartridge type, in which the raw materials are enclosed in a steel pipe.

The inorganic-type anchor contains ultra-rapid-hardening cement, sand, and other materials in a cartridge. Water is poured into the top of the cartridge, and the materials are mixed by a special mixer in the cartridge. They are then injected into a drilled hole.

The organic-type anchor is formed by mixing a base agent containing bisphenol A epoxy resin, bisphenol F epoxy resin, and a hardening

Table 1. Anchor materials.

Type of anchor	Materials		Mix proportions
Inorganic-type post-installed bonded anchor	Base agent Ultra-rapid-hardening cement Quartz sand	Hardening agent Water	Base agent: hardening agent 100:38
Organic-type post-installed bonded anchor	Bisphenol A epoxy resin Bisphenol A epoxy resin Quartz sand	m-Xylene diamine Aliphatic polyamine Quartz sand	3:1

Table 2. Properties of concrete and anchor materials.

Type of anchor	Concrete compressive strength (N/mm^2)	Static elastic modulus (kN/mm^2)	Bonded anchor compressive strength (N/mm^2)	Static modulus of elasticity (kN/mm^2)
Inorganic-type post-installed bonded anchor	24.3	28.4	62.4	25.0
Organic-type post-installed bonded anchor	24.3	28.4	109.0	2.7

Table 3. Material specifications of deformed bar.

Type of anchor	Deformed bar	Type	Yield strength (N/mm^2)	Static modulus of elasticity (kN/mm^2)
Inorganic-type post-installed bonded anchor	D13	MK785	791	190
	D19	USD685	936	210
Organic-type post-installed bonded anchor	D13	MK785	791	190

agent containing m-Xylene diamine and aliphatic polyamine in a mixing nozzle.

2.2 *Material properties*

Table 2 lists the properties of the concrete and the anchor materials. The material specifications of the deformed bars used in the bond strength tests and creep tests are listed in Table 3, and the specimen shapes are shown in Figure 1. The compressive strength and static modulus of elasticity of the concrete were measured using 100 × 200-mm cylinder specimens, and those of the inorganic-type anchors were measured using 50 × 100-mm cylinder specimens. Concrete was placed into steel pipes to prevent tensile cracking. The steel pipes were 216 mm in outer diameter and 4.5 mm in thickness. D13 and D19 reinforcing bars were used for the anchors. The embedment length was seven times the nominal diameter of the steel bar. The D13 was connected to M14 by flash butt welding. Similarly the D19 was connected to M24. The diameters of the anchor holes were

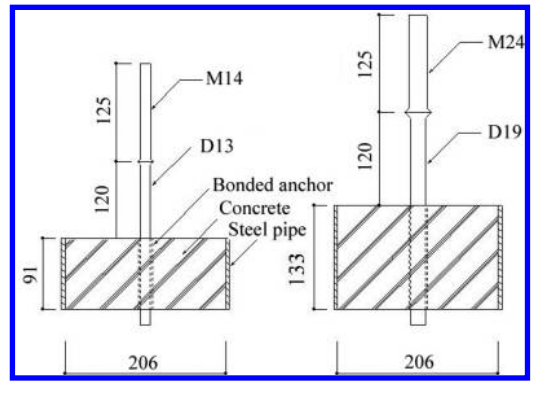

Figure 1. Specimen shapes (all dimensions in mm).

18 mm for the D13 bars and 24 mm for the D19 bars.

When the concrete was 28 days of age, anchor holes were drilled using a diamond core bit, anchor materials were placed in the holes, and the

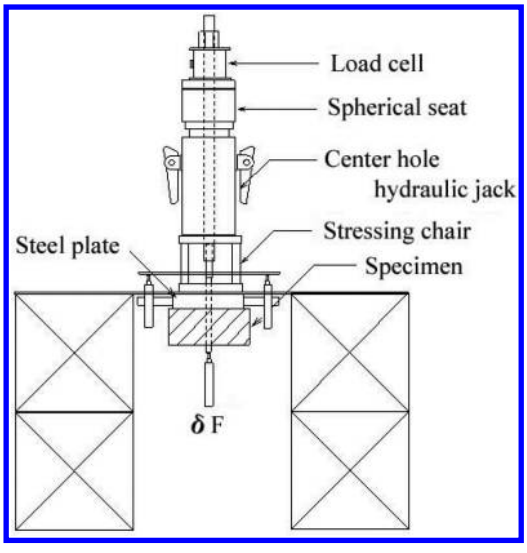

Figure 2. Bond strength test apparatus.

deformed bars were inserted. The deformed bars penetrated the test specimens.

2.3 *Bond strength*

Bond strength tests were carried out when the concrete reached an age of more than three months, to avoid the concrete compressive strength being too high. The bond test apparatus is shown in Figure 2.

A steel plate was set on the specimen to produce bond failure. The steel plate had an outer diameter of 180 mm, an inner diameter of 30 mm for the tests on the D13 bars, and an inner diameter of 38 mm for the tests on the D19 bars.

Each specimen was loaded using the centre hall jack. The load and the displacement of the free end were measured.

2.4 *Creep test device*

The creep test apparatus is shown in Figure 3. A specimen was placed in the upper part of the apparatus, and a sustained load was applied with a spring. After the spring was compressed with the hydraulic jack, the bolt in the lower part of the apparatus was tightened. When the load applied by the hydraulic jack was removed, the specimen was subjected to sustained loading.

The tests were carried out at 20°C and 60% relative humidity. The steel plate was positioned as in the bond strength test. After a load with a magnitude 0.33 times the ultimate load magnitude was

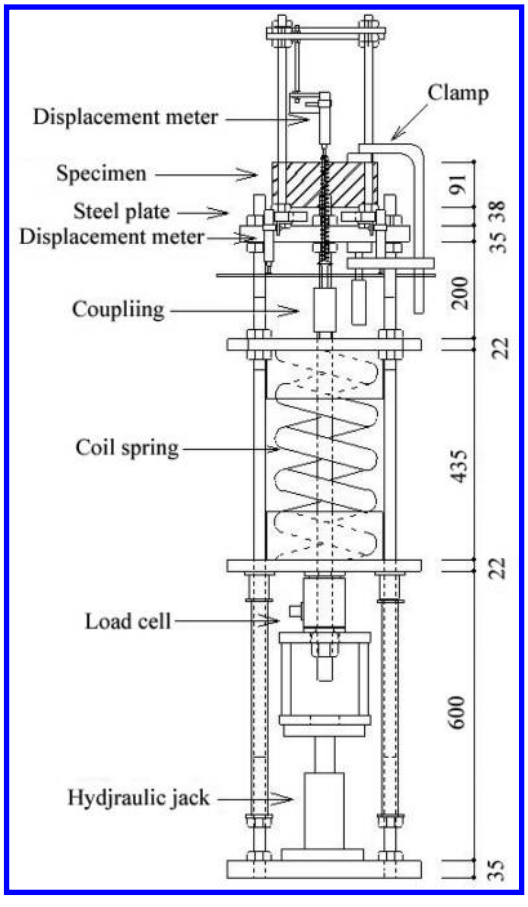

Figure 3. Tensile creep test apparatus (all dimensions in mm).

applied repeatedly, sustained loading was applied at the target load level.

The creep test conditions are listed in Table 4. The three types of anchors were prepared: the Cast-In-Place anchors (CIP), the Inorganic-type Post-Installed Bonded anchors (InPIB), and the Organic-type Post-Installed Bonded anchors (OrPIB).

To investigate the influence of the sustained load magnitude, sustained loads were applied at magnitudes of 0.33 to 0.95 times the ultimate load magnitude. In each test, the load magnitude and the displacement of the anchor at the free end (δF in Fig. 2) were measured.

For stress levels (sustained load/ultimate load) below 0.66, the sustained load was removed after three months. For stress levels greater than 0.66, the sustained load was maintained until creep failure.

Table 4. Experimental conditions.

Specimen	Type of anchor	Sustained load (kN)	Stress level	Deformed bar	Embedment length (mm)
CIP-D13-0.33	Cast-in-place anchor	15.3	0.33	D13	91
CIP-D13-0.65		29.1	0.63		
CIP-D13-0.69		32.0	0.69		
CIP-D13-0.86		39.8	0.86		
InPIB-D13-0.35	Inorganic-type post-installed bonded anchor	32.8	0.35	D13	91
InPIB-D13-0.53		49.0	0.53		
InPIB-D13-0.69		64.7	0.69		
InPIB-D13-0.80		74.4	0.80		
InPIB-D13-0.90		84.5	0.90		
InPIB-D13-0.93		87.3	0.93		
InPIB-D13-0.95		89.0	0.95		
InPIB-D19-0.34	Inorganic-type post-installed bonded anchor	71.1	0.34	D19	113
InPIB-D19-0.50		106.1	0.50		
InPIB-D19-0.66		140.7	0.66		
OrPIB-D13-0.49	Organic-type post-installed bonded anchor	59.7	0.49	D13	91
OrPIB-D13-0.54		65.7	0.55		
OrPIB-D13-0.63		75.2	0.61		

* Sustained load/ultimate load.

3 RESULTS

3.1 *Bond strength*

The bond strength test results are shown in Table 5 and Figure 4. The bond strengths ($\tau b1$) were calculated using the following equation.

$$\tau b1 = \frac{P\max}{\pi \cdot da1 \cdot 1b} \quad (1)$$

where $\tau b1$ = the bond strength, $P\max$ = the ultimate load, $da1$ = the nominal diameter of the deformed bar, and $1b$ = the embedment length.

The average bond strength of the CIP-D13 anchors was 12.7 N/mm^2, and that of the InPIB-D13 anchors was 25.7 N/mm^2, or approximately twice as high as that of the CIP-D13 anchors.

This can be considered an indicator that the compressive strength of the inorganic-type anchor is more than twice as high as that of the cast-in-place concrete anchor. The average bond strength of the OrPIB-D13 anchors was 33.8 N/mm^2, which is approximately 1.25 times that of the InPIB-D13 anchors.

The average displacement of the CIP-D13 anchors at the time of the ultimate load was approximately 0.8 mm, that of the InPIB-D13 anchors was 0.3–0.5 mm, and that of the OrPIB-D13 anchors was 1.1–1.8 mm. After the InPIB-D13 anchors reached the ultimate load, the displacement decreased rapidly. In contrast, the displacement of the OrPIB anchors increased rapidly at a load level more than 100 kN before the ultimate load.

The displacements of the InPIB-D19 anchors at the time of the ultimate load were in the range of 0.06–0.11 mm, which is much smaller than the range for the InPIB-D13 anchors.

3.2 *Creep test*

3.2.1 *Comparison between cast-in-place anchor and inorganic-type post-installed anchor*

The results of the creep tests of the CIP-D13 and InPIB-D13 anchors are shown in Figure 5.

The higher the sustained load was, the larger the displacements of the CIP-D13 and InPIB-D13 anchors were, and the displacements increased with the duration of loading. Stress levels below 0.63 did not produce creep failure in the CIP-D13 anchors within 91 days. However, at a stress level of 0.69, creep failure occurred at 172 days, and at a stress level of 0.86, creep failure occurred at 3.55 days. In contrast, little variation in the displacement of the InPIB-D13 anchors with load duration was observed at stress levels below 0.53. At a stress level of 0.80, creep failure occurred at 168 days, at a stress level of 0.90, creep failure occurred at 197 days, at a stress level of 0.93, creep failure occurred at 0.64 days, and at a stress level of 0.95, creep failure occurred after only 5 minutes.

Table 5. Results of bond strength tests.

Specimen	Compressive strength of concrete (N/mm^2)	Anchor (mm)	Drilled hole (mm)	Embedment length (Mm)	Ultimate load (kN)		Bond strength (N/mm^2)		Displacement at ultimate load (mm)	
		da1	da2	Lb	Pmax	Average	$\tau b1$	Average	σF	Average
CIP-D13	24.3	12.7	–	91	43.5	46.2	12.0	12.7	0.83	0.81
					46.5		12.8		0.84	
					48.5		13.3		0.76	
InPIB-D13	24.3	12.7	18	91	102.2	93.5	28.2	25.7	0.48	0.35
					89.0		24.5		0.27	
					89.2		24.6		0.30	
InPIB-D19	24.3	19.1	24	133	210.3	211.9	26.4	26.6	0.06	0.08
					204.8		25.7		0.07	
					2207		27.7		0.11	
InPIB-D13	24.3	12.7	16	91	121.7	122.7	33.5	33.8	1.29	1.40
					126.4		34.8		1.15	
					119.9		33.0		1.77	

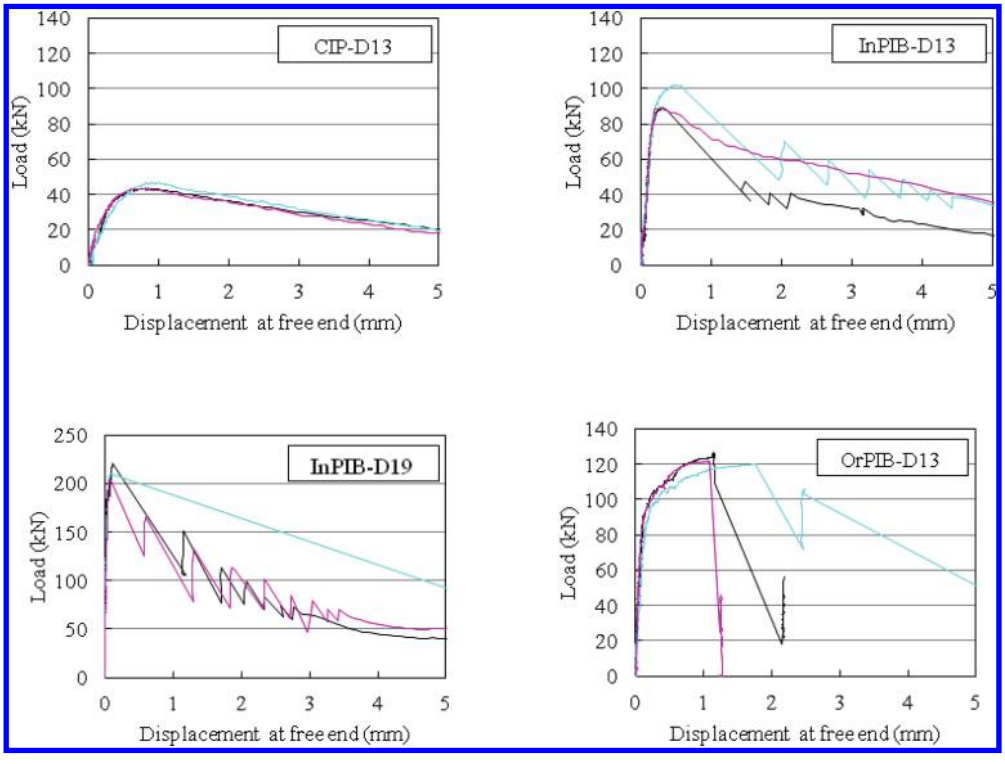

Figure 4. Load and displacement at free end.

The displacement at the time of the creep failure of the CIP-D13-0.69 anchor was 1.1 mm, and that of the InPIB-D13-0.80 anchor was 1.2 mm. These displacements at the time of the creep failure were 2–3 times greater than that measured in the bond strength test. The displacement at the time of the creep failure of the InPIB-D13-0.95 anchor was 0.58 mm, and that of the InPIB-D13-0.93 anchor was 0.63 mm. The displacement at creep failure increased as the duration of loading increased.

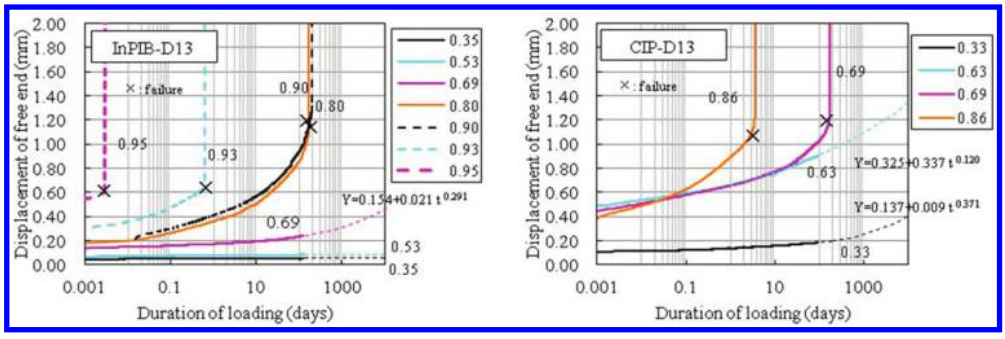

Figure 5. Creep deformation of cast-in-place anchors and post-installed anchors.

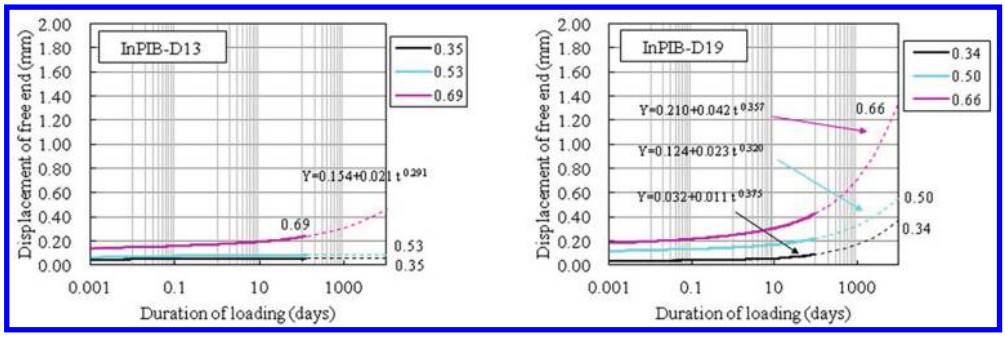

Figure 6. Creep deformation of D13 and D19 anchors.

The displacements measured in these tests were extrapolated using equation (2) to estimate long-term creep deformations:

$$S(t) = So + a \cdot t^b \tag{2}$$

where So = the initial displacement under the sustained load at $t = 0$ and a and b are constants (tuning factors).

The displacement of the CIP-D13-0.63 anchor was estimated to be 1.15 mm at 5 years and 1.23 mm at 10 years. Because creep failure of the CIP-D13-0.69 anchor occurred at 1.1 mm, it is presumed that creep failure of the CIP-D13-0.63 anchor would occur after several years.

The displacement of the CIP-D13-0.32 anchor was estimated to be approximately 0.5 mm at 50 years. The displacement of the InPIB-D13-0.33 anchor remained largely unchanged with increasing loading duration. Therefore, it is presumed that creep failure will not occur within 50 years for either the CIP-D13-0.32 anchor or the InPIB-D13-0.33 anchor.

3.2.2 *Influence of deformed bar diameter*

As the test results for the D13 and D19 bars in Figure 6 show, for the same stress level, the displacements of the D19 bars were larger than those of the D13 bars. In addition, the displacement of the InPIB-D19-0.34 anchor and the InPIB-D19-0.50 anchor gradually increased with increasing loading duration.

By extrapolation, the displacement of the InPIB-D19-0.34 anchor at 50 years was estimated to be 0.43 mm, that of the InPIB-D19-0.50 anchor was estimated to be 0.65 mm, and that of the InPIB-D19-0.66 anchor was estimated to be 1.60 mm.

In contrast, the displacement of the InPIB-D13-0.69 anchor was estimated to be 0.52 mm at 50 years, which is smaller than that estimated for the InPIB-D19-0.66 anchor.

Although the embedment lengths of the D13 and D19 bars were seven times of nominal diameter, the displacements of the D19 bars were larger.

Because the loads sustained by the D19 bars were large, it was presumed that the load magnitude rather than the stress level influences the creep deformation.

3.2.3 *Comparison between inorganic-type and organic type*

The test results for the InPIB-D13 and OrPIB-D13 anchors are shown in Figure 7.

The initial displacement of the OrPIB-D13-0.55 anchor was large, and the deformation also increased with increasing loading duration more than that of the OrPIB-D13-0.50 anchor. Furthermore, the deformation of the OrPIB-D13-0.50 anchor was smaller than that of the OrPIB-D13-0.55 anchor. Thus the creep limit of the OrPIB-D13 anchors is considered to be approximately 55%.

For the OrPIB-D13-0.63 anchor, creep failure occurred at 1.14 days. Although the displacement at the time of the ultimate load was approximately 1.2 mm, the displacement before the failure of the OrPIB-D13-0.63 anchor was approximately 3.5 mm. As with the CIP-D13 and InPIB-D13 anchors, the displacement at the time of the creep failure of the OrPIB-D13 anchors was approximately three times as large as that at the time of the ultimate load.

Accordingly, it is presumed that the displacement at the time of creep failure becomes larger than that at the time of the ultimate load as measured in a bond strength test.

The sustained load applied to the OrPIB-D13-0.64 anchor was 75 kN, and that applied to the InPIB-D13-0.80 anchor was 74 kN. Under essentially the same load, creep failure of the OrPIB-D13-0.64 anchor occurred at 1.14 days, and that of the InPIB-D13-0.80 anchor occurred at 168 days. The displacement of the InPIB-D13-0.53 anchor

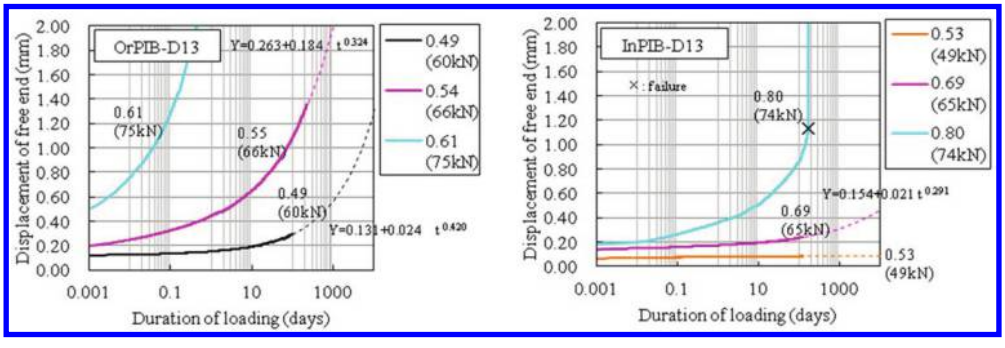

Figure 7. Creep deformation of inorganic-type and organic-type anchors.

Table 6. Displacement difference between 0 days and 91 days and time to failure.

Specimen	Sustained load (kN)	Stress level	Displacement at free end: Duration of loading: 0 days (mm)	91 days (mm)	Diff. (mm)	Measured time to failure (days)	Estimated time to failure (days)
CIP-D13-0.33	15.3	0.33	0.06	0.19	0.13		295146
CIP-D13-0.65	29.1	0.63	0.12	0.94	0.82		1028
CIP-D13-0.69	32.0	0.69	0.14	1.02	0.88	172	
CIP-D13-0.86	39.8	0.86	0.38			3.55	
InPIB-D13-0.35	32.8	0.35	0.05	0.05	0.00		
InPIB-D13-0.53	49.0	0.53	0.06	0.08	0.02		
InPIB-D13-0.69	64.7	0.69	0.14	0.23	0.09		477973
InPIB-D13-0.80	74.4	0.80	0.16	0.84	0.68	168	
InPIB-D13-0.90	84.5	0.90	0.23	0.92	0.69	197	
InPIB-D13-0.93	87.3	0.93	0.31			0.64	
InPIB-D13-0.95	89.0	0.95	0.52			0.00285	
InPIB-D19-0.34	71.1	0.34	0.04	0.09	0.05		
InPIB-D19-0.50	106.1	0.50	0.12	0.22	0.10		
InPIB-D19-0.66	140.7	0.66	0.19	0.43	0.24		
OrPIB-D13-0.49	59.6	0.49	0.12	0.29	0.17		
OrPIB-D13-0.54	66.9	0.55	0.20	1.06	0.86		
OrPIB-D13-0.63	75.2	0.61	0.35			1.14	

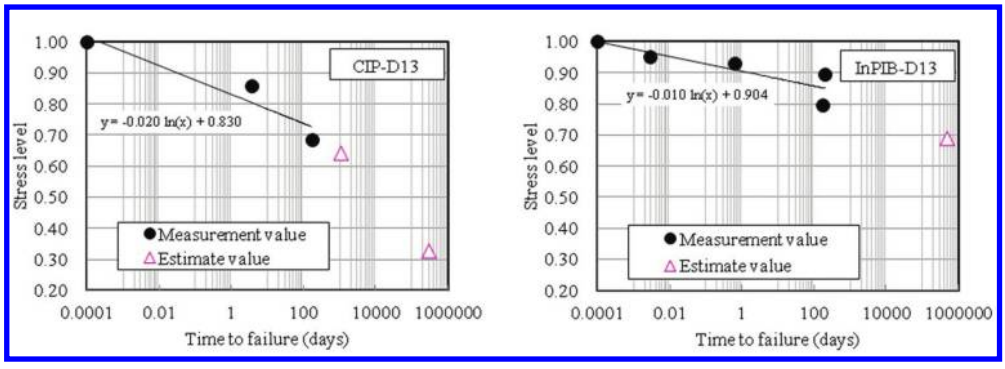

Figure 8. Time to creep failure versus stress level.

at 91 days was 0.08 mm, and that of the InPIB-D13-0.69 anchor was 0.23 mm. Furthermore, the increase in deformation with increased duration of loading was small.

Although it is presumed that the creep limit of the OrPIB-D13 anchors is approximately 55%, the creep limit of the InPIB-D13 anchors is considered to be larger than that of the OrPIB-D13 anchors, because the time to creep failure is long at a stress level of 0.80 and the deformation of the InPIB anchors at a stress level of 0.69 was smaller than that of the OrPIB anchors.

3.2.4 *Estimated creep failure time*

The displacement, stress level, and time to creep failure are shown in Table 6.

By extrapolation, the displacement at creep failure was estimated to be 1.1 mm for the CIP-D13-0.33, CIP-D13-0.65, and InPIB-D13-0.69 anchors.

The relationship between the duration of the sustained load and the stress level is shown in Figure 8.

Approximate expressions for the time to creep failure versus stress level were obtained from the creep test results and were evaluated. The slope of the line for the InPIB-D13 anchors was about half of that for the CIP-D13 anchors. These results suggest that at high stress levels, InPIB-D13 anchors are less likely to experience creep failure than CIP-D13 anchors.

Relationships between the stress level and the difference between the displacement at 0 days and that at 91 days are shown in Figure 9.

For the InPIB-D13 anchors, the variation in displacement became quite large at a stress level of approximately 0.70. The displacement of the OrPIB-D13 anchors became large at a stress level of approximately 0.50–0.55.

Assuming that the creep limits of the different types of anchors are represented by the inflection

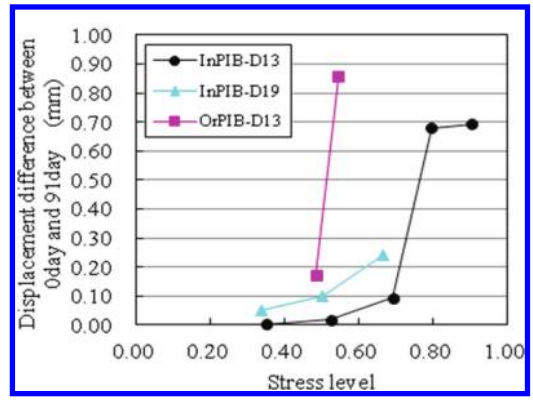

Figure 9. Displacement difference versus stress level.

points of the displacement curves in Figure 9, the creep limit of the InPIB anchors is considered to be approximately 0.70, and that of the OrPIB anchors is approximately 0.50–0.55. Compressive creep failure of concrete is known to occur at a stress level greater than 0.70, which is consistent with these results. It is likely that the creep limit of an inorganic-type anchor will be higher than that of an organic-type anchor.

4 CONCLUSIONS

The creep deformation of ultra-rapid-hardening cement-type post-installed bonded anchor was studied, and the influences of the sustained load magnitude, deformed bar diameter, and anchor type were examined for an embedment length of seven times the nominal diameter.

At a stress level of 0.33, the displacement of the inorganic-type post-installed bonded anchor remained nearly unchanged under sustained loading for 91 days. This suggests that at a stress level of

0.33, creep failure of an inorganic type post-installed bonded anchor will not occur within 50 years.

At stress levels greater than 0.80, creep failure occurred within 200 days, and the displacement at the time of creep failure increased as the time to creep failure increased.

In comparing D13 and D19 bars, the displacements of the D19 bars were found to be larger than those of the D13 bars at the same stress level and the same embedment length ratio, which was seven times the nominal diameter.

Because the sustained loads on the D19 bars were high, the displacements of the D19 bars were larger than those of the D13 bars.

For organic-type anchors, for which the displacement differential increased with increasing test duration increase, the creep limit is considered to be approximately 0.55. The displacement at the time of creep failure was 3.5 mm, which was larger than that for the inorganic-type anchors. However, the displacement at the time of creep failure was 2–3 times that measured in the ultimate loading test.

For the inorganic anchor type, the slope of the line of the time to creep failure versus the stress level was approximately half of that for the cast-in-place anchor type. Therefore, at high stress levels, creep failure is less likely to occur in an inorganic type of anchor than in a cast-in-place anchor.

REFERENCES

Elighausen, R., R. Mallee, and J.F. Silva (2006). *Anchorage in Concrete Construction.* A Wiley Company.

European Organisation for Technical Approvals (2008). *ETAG 001, Part Five, Bonded Anchors*, p. 25.

Nakano, K., Y. Matsuzaki, and T. Sugiyama (2011). Study on Long-term Allowable Stress for Post-installed Anchor Part3-Experiment on Tensile Creep Deformation, *Architectural Institute of Japan, Summaries of Technical Papers of Annual Meeting*, The conformation IV, pp. 639–640.

National Transportation Safety Board (2006). *Highway Accident Report: Ceiling Collapse in the Interstate 90 Connector Tunnel, Boston, Massachusetts, USA*, July 10, 2006.

Yano, A., S. Suigaya, and Y. Matuszaki (1981). Study about capacity *Technical Papers of Annual Meeting*, pp. 1517–1518.

Concrete Repair, Rehabilitation and Retrofitting IV – Dehn et al. (Eds)
© 2016 Taylor & Francis Group, London, ISBN 978-1-138-02843-2

Assessment of the use of Arcelor Mittal electric arc furnace slag as coarse aggregates in concrete production

D. Maharaj & A. Mwasha
University of the West Indies, Kingston, Jamaica

ABSTRACT: Arcelor Mittal electric arc furnace slag is a byproduct from the steel making process. Locally, it is generated in great amounts and when produced, it is left in stockpiles at the production site. The use of this industrial by product in the construction industry could be beneficial in minimizing natural resource depletion and the high environmental impacts caused by concrete production. As such, this study focuses on the effectiveness of using Arcelor Mittal electric arc furnace slag as coarse aggregates in the making of concrete. However, since the electric arc furnace slag is an industrial by product, a comprehensive knowledge of its characteristics is required. Therefore, this paper examines the physical, mineralogical and chemical properties of electric arc furnace slag. The feasibility of using electric arc furnace slag in the concrete was examined by conducting compressive and tensile strengths of concrete mixtures using replacement ratios of 0%, 15%, 30%, 45%, 60%,75% and 100% of the slag as coarse aggregates. The findings indicate that the compressive and tensile strengths of the concrete achieved using the different ratios of the slag is comparable to that using purely natural aggregates. Therefore, the utilization of Arcelor Mittal electric arc furnace slag in concrete production is an efficient means of reducing the costs and environmental impacts.

1 INTRODUCTION

Due to increasing cost of raw materials and the continuous reduction of natural resources, the use of waste materials could be a potential alternative in the construction industry (Pellegrino, 2009). The continued and expanding extraction of natural aggregate causes serious environmental problems which lead to irremediable deterioration of rural areas. Quarrying of aggregates alters land topography and causes potential environmental problems such as erosion (Manso, 2006). Aggregates occupy approximately 70% of the volume of concrete and the properties of the concrete produced are dependent on the characteristics of the aggregates used.

The use of the industrial by products as aggregates is not only adding extra aggregate sources but also reduces environmental pollution [3]. One such industrial by product which could be beneficial to the construction industry is electric arc furnace slag. Electric arc furnace slag is a by product from the steel making industry. It is generated in electric arc furnaces which utilizes scrap iron to produce steel. As such, the quality of the electric arc furnace slag generated depends on its origin. Therefore, the properties of concrete produced using electric arc furnace slag is significantly influenced by its physical and chemical characteristics.

Qasrawi (2009) found that the tensile and compressive strengths of concrete increased with an increase in the electric arc furnace slag content of the concrete mixes. The results from other studies conducted by Pellegrino (2011), Abu-Eishah (2011) Manso (2006) showed that the compressive and tensile strengths of concrete containing electric arc furnace slag as aggregates were higher than when putely natural aggregates were used.

Locally, electric arc furnace slag is generated at 300,000 tonnes annually (Arcelor Mittal Steel, 2008). The Arcelor Mittal electric arc furnace slag is left in stockpiles at the production site when it is generated and this results in serious environmental problems.

The purpose of this study is to analyse how the mechanical properties of concrete vary by changing the content of the electric arc furnace slag in the concrete mixtures.

2 MATERIALS AND METHODS

The concrete mixtures which were formulated consisted of water, aggregates and cement.

2.1 *Aggregates*

The two types of aggregates used in this study are quartz and electric arc furnace slag. Quartz were used as fine and coarse aggregates whereas

the electric arc furnace slag were used as coarse aggregates in the concrete mixtures.

2.2 *Cement*

Blended cement was used in the concrete mixtures. This type of cement was obtained from a local cement factory (Trinidad Cement Limited) and is manufactured using a burned mixture of limestone, clay using 30% fly ash.

2.3 *Methods*

In the process of evaluating the effect of different percentages of electric arc furnace on the strength of concrete, it is necessary to deduce the physical, chemical and mineralogical composition of the natural aggregates and the electric arc furnace slag.

2.3.1 *Determination of the physical properties of the aggregates*

The physical properties were analyzed by performing a sieve analysis of the aggregates and doing specific gravity and water absorption tests of the aggregates.

Samples of the fine natural aggregates and the electric arc furnace steel slag were taken according to BS 812: Part 102:1984. The gradation (size distribution) of the aggregates was performed using the ASTM C33 limits.

The gradation curves of the natural aggregates (quartz) and the electric arc furnace slag are shown in Figure 1, Figure 2 and Figure 3 respectively.

Figure 1 shows the grading of the fine natural aggregates according to the ASTM C33 upper and lower limits. From Figure 1, the ASTM C33 upper and lower limits are represented by the solid lines.

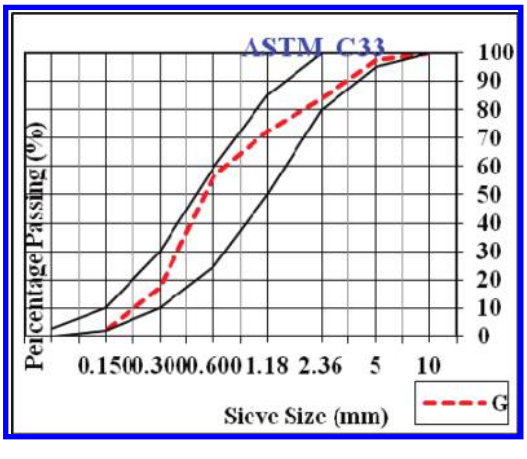

Figure 1. Gradation of the natural fine aggregates according to ASTM C33 Limits.

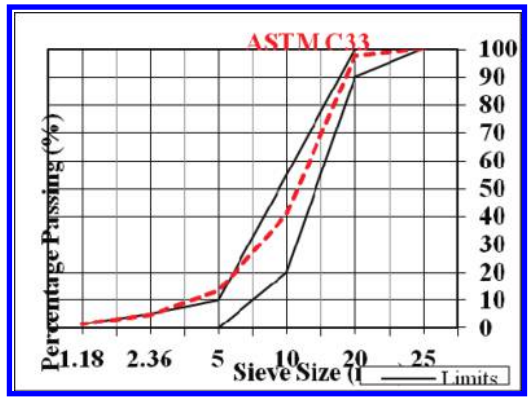

Figure 2. Grading of the coarse natural aggregates according to ASTM C33 limits.

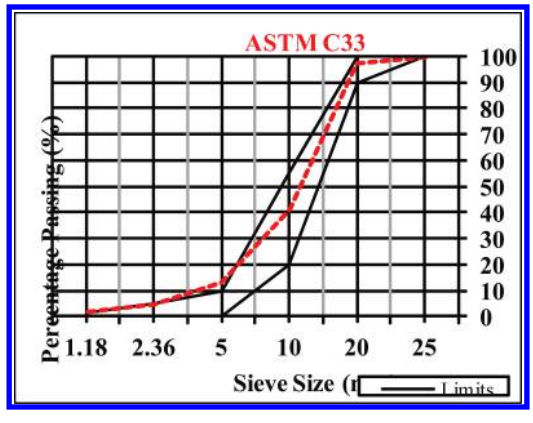

Figure 3. Grading of the electric arc furnace slag (coarse aggregates).

These limits specify the size distribution for each sieve size. Based on this graph, the grading of these aggregates falls within the range of the upper and lower limits of the ASTM C33 standards and as such, meet the gradation requirements.

Figure 2 illustrates the grading of the coarse natural aggregates according to the ASTM C33 standards in which the representative sample size was within the range of the specification for the 10 mm and 20 mm sieve size. However, the coarse aggregates were out of the boundary for the 5 mm sieve size. The graph shows that 51% of the aggregates pass through the 20.0 mm and 0.3% of the aggregates pass through the smallest sieve size which is 0.150 mm. There is evidence of continuous grading occurring between the upper and lower limits with a decrease in the percentage of the aggregates passing through the respective sieve

Table 1. Specific gravity values of natural aggregates and electric arc furnace slag.

Sample	Specific gravity on an oven dried basis	Specific gravity on a saturated surface dried basis	Apparent specific gravity	Water absorption
Natural aggregate	2.60	2.61	2.62	0.32
Electric arc furnace steel slag	3.39	3.44	3.56	1.44

sizes. However, there is some indication of possible gap grading between 0.15 mm and 0.30 mm sieve sizes since the same percentage of the aggregates pass through these sieve sizes.

Figure 3 illustrates the size distribution of the slag according to the ASTM C33 standards in which the gradation of the aggregates was within the upper and lower limits. Based on Figure 8, 95.1% of the aggregates pass through the 20.0 mm. However, the grading showed that 0.3% of the aggregates pass through the smallest sieve size which is 0.150 mm.

2.4 *Determination of the specific gravity, water absorption of the natural aggregates and the electric arc furnace steel slag*

The specific gravity and the water absorption tests of the natural aggregates and the electric arc furnace steel slag were conducted according to BS 812:Part 2:1975 (1984). The results from these two tests illustrated in Table 1 shows that the electric arc furnace slag has a higher specific gravity than the natural aggregates. This indicates that it is acceptable for use in concrete structures.

2.5 *Identification of the chemical elements and minerals present in electric arc furnace slag*

The determination of the chemical elements present in the electric arc furnace slag was done using a Bruker—Axs XRay Spectrometer Model SRS 3400. An ELTRA CS 2000 carbon/sulphur Determinator was used to deduce the percentage of carbon and sulphur present.

Table 2 illustrates the atomic number and the corresponding percentage composition of the elements present in the electric arc furnace slag. It can be seen that oxygen is the most dominant element present in the electric arc furnace slag with an average concentration of 36.250%. However, the second highest elemental concentration is calcium with an average of 21.115% and an atomic number of 20. Additionally, the element which has the highest atomic number is iron and its concentration in the electric arc furnace slag was 19.910%.

Table 2. Chemical elements present in the electric arc furnace slag.

Elements present	Atomic number of elements	Percentage composition of elements by weight (%)
Oxygen	8	36.250
Calcium	20	21.115
Iron	26	19.910
Silicon	14	9.571
Magnesium	12	6.815
Aluminium	13	3.035
Carbon	6	1.147
Manganese	25	0.809
Titanium	22	0.477
Phosphorous	15	0.235
Sodium	11	0.145
Sulphur	16	0.140
Vanadium	23	0.101
Total	211	99.75

2.5.1 *Identification of the minerals present in fine natural aggregates and electric arc furnace slag*

The identification of the minerals present in the fine natural aggregates and the electric arc furnace steel slag was done using x ray diffraction analysis. This was conducted using a Philips X-ray diffractometer model PW/1840, with Ni filter, CuKa 30 mA.

Figure 4 and Figure 5 display the type of minerals present in the natural aggregates and the electric arc furnace slag respectively. It is evident that quartz and mica are the two minerals present in the natural aggregates and the minerals present in electric arc furnace slag are calcite, quartz, kirschsteinite and merwinite.

2.6 *Mix proportions of concrete varied percentages of electric arc furnace slag*

Concrete mixtures were prepared for 0.4 water to cement ratio using percentage of electric arc furnace slag 0%, 15%, 30%, 45%, 60%, 75% and

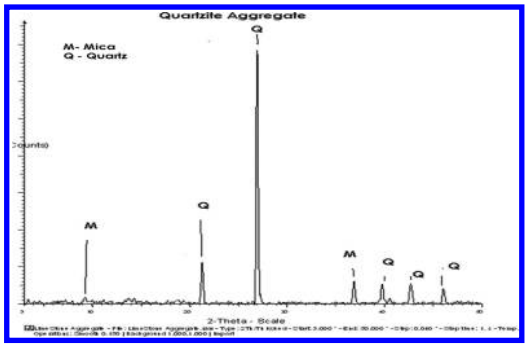

Figure 4. Minerals present in quartz aggregate.

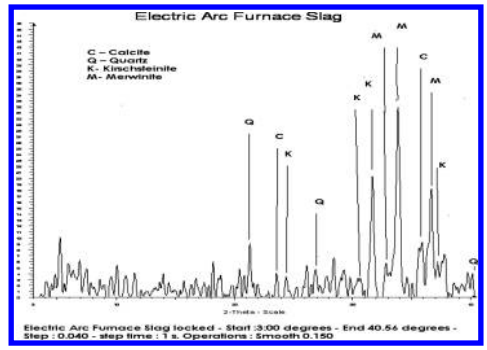

Figure 5. Minerals present in electric arc furnace slag.

Table 3. Mix proportions using varied percentages of electric arc furnace slag.

Ratio of electric arc furnace slag	Mass of fine natural aggregates (Kg)	Mass of coarse aggregates (Kg) electric arc furnace slag	Mass of water (Kg)	Mass of cement (Kg)
0%	21.5	26.3	6.4	15.9
15%	43.35	7.65	6.8	17
30%	35.7	15.3	6.8	17
45%	28.05	22.95	6.8	17
60%	20.4	30.6	6.8	17
75%	12.75	38.25	6.8	17
100%	0	51.0	6.8	17

Table 4. Slump height and density of concrete mixtures.

Ratio of electric arc furnace slag	Height of slump (mm)	Density of fresh concrete (kg/m^3)
0%	0	2340
15%	5	2358.20
30%	15	2404
45%	30	2514.90
60%	50	2567.20
75%	20	2709
100%	190	2783.60

100%. The mix designs of the concrete mixtures are described in Table 3.

Table 3 and Table 4 illustrate the mix proportions and the measurements of the concrete mixtures respectively.

1. The workability of the concrete mixtures was tested by conducting slump tests as described in ASTM C143.
2. The fresh density of all the mixes was measured according to ASTM C138.
3. For each concrete mixture, ten cubes and ten cylinders were prepared and cured in a water bath in the laboratory at 20 °C for a twenty four hour period.
4. The concrete samples were de-molded from the cubes and cylinders after the twenty four hour period.
5. The compressive strength of the concrete was tested using the cubical specimens and was conducted according to ASTM C39 and the tensile split test was performed according to ASTM C496 on the cylindrical concrete samples.

3 RESULTS AND DISCUSSION

3.1 *Evaluation of the tensile and compressive strengths of concrete containing different percentages of electric arc furnace slag*

For each percentage of electric arc furnace slag, ten samples of concrete mixtures were prepared. The average compressive and tensile strengths were tested.

By observing Table 5, the average compressive strength for the different percentages of the electric arc furnace slag, it could be deduced that it did not

Table 5. Average compressive strength using different percentage of electric arc furnace slag.

Percentage of slag	Average compressive strength (Mpa)	Coefficient of variation
0	57.2	0.081
15	51.7	0.15
30	50.4	0.12
45	59.8	0.11
60	58.7	0.12
75	64.6	0.14
100	51.4	0.11

Table 6. Average tensile strength using different percentages of electric arc furnace slag.

Percentage of slag	Average tensile strength (Mpa)	Coefficient of variation
0	3.3	0.59
15	3.3	0.15
30	3.3	0.19
45	3.3	0.12
60	3.4	0.14
75	3.6	0.15
100	3.2	0.15

increase as the percentage of electric arc furnace slag increased in the concrete mixtures.

By observing Table 6, it could be deduced that the tensile strength did not increase as the percentage of electric arc furnace slag increased in the concrete mixtures. Instead, the compressive and tensile strengths of concrete achieved using electric arc furnace slag were similar to using purely natural aggregates.

Additionally, the results from this analysis are similar those attained by the researchers Qasrawi (2009), Pellegrino (2011) and Manso (2006). These researchers have conducted related experiments and found that using electric arc furnace slag produced similar compressive and tensile strengths of concrete as when purely natural aggregates were used.

4 CONCLUSIONS AND RECOMMENDATIONS

Based on the study presented in this research, the following deductions were made:

1. The strengths achieved using the different ratios of electric arc furnace slag is comparable to that using purely natural aggregates.
2. The findings from the strength tests indicate the potential of cheaper and more environmentally friendly concrete production.

REFERENCES

Arcelor Mittal Steel. 1969. "*Transforming Steel Tomorrow*." Accessed December 29th, 2013. http://www.corporatearcelormittal.com.

ASTM C143/C143M. 2005. *Standard Test Method for Slump of Hydraulic-Cement Concrete*. ASTM International.

ASTM C39/C39M. 2003. *Standard Test Method for Compressive Strength of Cylindrical Concrete Specimens.* Annual Book of ASTM Standard. Vol. 04.02.

ASTM C 496. 1996. *Standard Test Method for Splitting Tensile Strength of Cylindrical Concrete Specimens* ASTM International.

Manso JM, Polanco JA Losañez M, González JJ. *Durability of concrete made with EAF slag as aggregate*. Cem Concr Compos 2006; 28:528–34.

Pellegrino C., Gaddo V. *Mechanical and durability characteristics of concrete containing EAF slag as aggregate*. Cem Concr Compos 2009. 31:663–71.

Qasrawi, H., Shalabi F., Asi, I. *Use of low CaO Unprocessed steel slag in concrete as fine aggregates*. Construction and Building Materials. 2009. 23.1118–1125.

Concrete Repair, Rehabilitation and Retrofitting IV – Dehn et al. (Eds)
© 2016 Taylor & Francis Group, London, ISBN 978-1-138-02843-2

Self compacting grout and concrete: How it is produced and why it is needed

H.S. Abdelgader & A.S. El-Baden
Department of Civil Engineering, Faculty of Engineering, University of Tripoli, Tripoli, Libya

ABSTRACT: Using non-traditional concrete in engineering applications such as the construction of nuclear reactor shields, dams, massive under water bridge piers and repairs of building foundations etc., have been considered as an efficient solution to overcome challenges of limitations of the use of normal conventional concrete. Such new types of concretes which have been developed and produced are completely dissimilar from the conventional concrete in the method of mixing, handling, pouring, consolidation, behaviors, cost etc. Based on the technology of ready-mixed Self-Compacting Concrete (SCC), two types of concrete been introduced and named as: Two-Stage Concrete (TSC) and Rock-Filled Concrete (RFC), where a Self-Compacted Grout (SCG) injected or poured to fill the void space of preplaced or Self-Compacted Aggregate (SCA) or rocks. By other words, TSC (Pre-placed Aggregate) unlike Normal Concrete (NC), it is made by first placing the coarse aggregate in the formwork and then injecting a grout consisted of sand, cement and water to fill the voids between the aggregate particles. The main benefits of the method are widely appreciated as Low heats of hydration, high compressive strengths and density, economic savings, practically no mass shrinkage, low coefficient of thermal expansion, excellent bond to existing structures. Similarly, the construction technology of RFC mainly consists of two processes: filling the working space with large scale rock mass and pouring the SCC into the pre-packed rock body. Less cement in the composite, which results in less heat of hydration, makes the temperature control of RFC much easier, and this new construction method leads to fast construction speed, high concrete quality and improves the economics and environmental performance of massive concrete structures. Generally, the properties of two-stage concrete are thus influenced by the properties of the coarse aggregate, the properties of the grout, and the effectiveness of the grouting process. This paper illustrates the importance, advantages and special requirements of introducing TSC in the concrete industry field. Also, it demonstrates results from research work conducted in the last decade to address TSC in terms of grout property requirements and some important mechanical properties.

1 INTRODUCTION

Normal conventional concrete is one of the most widely used construction materials in transportation and infrastructure projects among many other applications. The quality of concrete produced is highly influenced by its placement technique during manufacturing (Neville 1981, Neville & Brooks 1987). These techniques involve free-fall gravitational placement, pumping, belt conveyors, tremie, and preplaced aggregate concrete ……etc. The goal when applying any of these techniques is to place concrete into the formwork with minimum segregation, minimum honeycombing and maximum possible homogeneity of the concrete constituents (ACI-318 2008). Placing concrete underwater is a challenging task due to the risk of high washout of the concrete constituents while placement thus resulting in low quality concrete. To overcome such problem, underwater concreting can be performed by using dewatering, caissons, tremie and anti-washout admixtures (ACI-304 2005). Concrete shrinkage and consequently shrinkage cracking has been a growing concern. This has been the case in modern concrete work due to the use of higher content of cementitous materials, mineral admixtures, low water-to-cement ratio and extended exposure to severe conditions during service; all of which may contribute to increasing in concrete. Minimizing shrinkage can take place by adequate mix proportions, thorough curing and the use of shrinkage compensating cement (Abdelgader 1999). On the other hand, using non-traditional concrete in engineering applications has been considered as an efficient solution to overcome challenges of limitations of the use of normal conventional concrete. Such new types of concretes which have been developed and produced are completely dissimilar from the conventional concrete in the method of mixing, handling, pouring,

consolidation, behaviours, cost …….etc. Based on the technology of ready-mixed Self-Compacting Concrete (SCC), two types of concrete been introduced and named as: Two-Stage Concrete (TSC) and Rock-Filled Concrete (RFC), (ACI-304 2005). In this paper we will consider the TSC in more details as will be seen in the next subtitles.

What is the TSC? As the name would suggest TSC is produced through a two-stage process. Firstly washed coarse aggregate is placed into the formwork in-situ. Later a specifically designed grout is introduced into the form from the lowest point under gravity pressure to fill the voids, cementing the aggregate into a monolith (Abdelgader 1996), see Figure 1.

2 GENERAL ASPECTS OF TSC

2.1 *Advantages*

TSC differs from conventional concrete in having higher percentage of coarse aggregates which are placed in direct contact with each other resulting in fewer voids that are to be filled with the mortar/grout. This low percentage of voids and direct contact of aggregate particles should have a positive impact on the concrete properties both on short and long terms. Its main advantages could be summarized as the following (ACI-304 2005 & Abdelgader 1996):

- Less shrinkage leading to less cracking
- Easier placement in difficult placement conditions
- Adequacy for underwater construction and repair
- Super mechanical and durability properties
- Ability for placement at remote locations
- Good environmental impact
- Reasonable cost.

2.2 *Technical background*

Mechanically TSC acts in a fundamentally different way under external stress to traditional concrete where the concrete matrix absorbs, distributes and resists the stresses. Due to this point-to-point contact in TSC all the stress is passed first through the stone skeleton then, after deformation of the stone particles, the grout both restrains the aggregate and transfers the loads (Nowek et al. 2007), as shown in Figure 2. The strength of TSC is a function of a number of variables, including the aggregate strength and the strength of the grout, in addition to further variables such as: water to cement ratio (w/c), cement to sand ratio (c/s) ….etc. (Abdelgader 1999).

2.3 *Application of TSC*

TSC is used where placing conventional concrete is extremely difficult, such as:

- Constructions include massive reinforcement steel and embedded items
- Underwater repairs.
- Concrete and masonry repairs, such as when spalling had occurred exposing the embedded reinforcement.
- Applications where shrinkage and heat of concrete must be kept to a minimum, such as dams.
- Applications where heavy weight aggregate used such as in the construction of nuclear reactors-shields.
- In large volume foundations where there are particular technical considerations such as concerns over thermal cracking, mass shrinkage and cold joints.

2.4 *Materials used*

Similar to conventional concrete almost all materials such as: cement, sand, coarse aggregate, water,

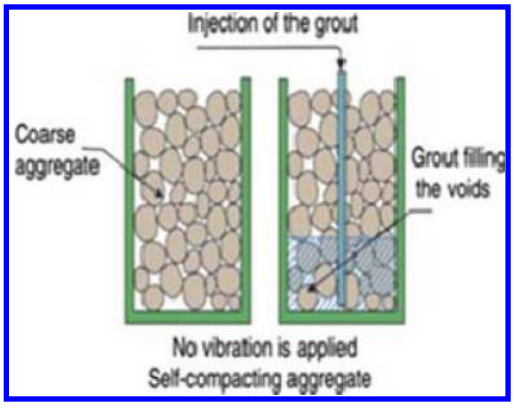

Figure 1. Self compacting grout technology.

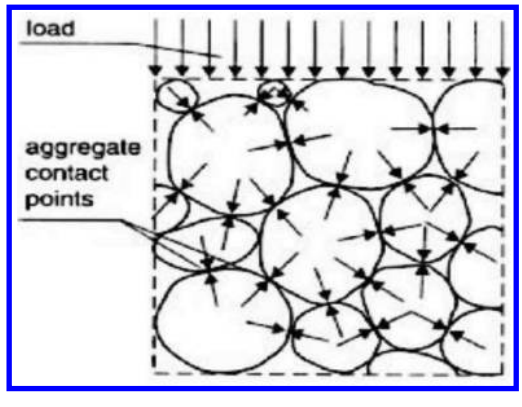

Figure 2. Stress transfer mechanism in TSC.

pozzolana additives, admixtures and fibres, that comply with specifications can be used in TSC (ACI-304 2005).

2.5 *Grout properties and flow*

The grout typically consists of sand, cement, water, pozzolana, plasticizer/super-plasticizer and air entraining agents (for anticipated freeze and thaw problem, if required). Good quality of TSC grout is characterised by high fluidity, low sedimentation, good viscosity, intensive hydration and a notable increase in the cement particles surface. The characteristics of the grout are affected by water content, sand grading and content, cement, pozzolana, and the types and amounts of admixtures. For each mixture there are optimum amounts of fillers and admixtures which produce the best pumpability or consistency. The pozzolana and the plasticizer/super-plasticizer are used to impart flow-ability to the grout and acted on both the mechanical and rheological properties of the grout (Abdelgader et al. 2003). The injection is achieved by pumping the grout through vertically mounted rigid pipes which almost reach the bottom of the section to be cast. As the grout is pumped into the form the injection pipes are slowly raised. Injection of grout into small units can be achieved by pumping into the bottom of the formwork at different elevations, (ACI-304 2005). Mathematically the description of propagation is very difficult. General empirical equation of propagation curve has been derived, (Abdelgader et al. 2012), and described in Equation1 as follows:

$$Y = \alpha/\{(bx^2+)*[(\gamma/t) - (1/\beta) + 1]^{(1/2)}\} \quad (1)$$

where α = thickness of stone layer (m); $\beta = (a \times b \times f)$; a = parameter dependent of mixture fluidity.; b = parameter dependent of stone: shape, size, kind of grain, surface, number and relation of fraction; f = Environment of construction; $\gamma = (c \times d \times e)$; c = parameter dependent of efficiency of flushing pipe (m^3/min.); d = parameter dependent of perforation; e = parameter dependent on the kind of excavation bottom; t = time (min.); x = distance from flushing pipe (m); y = level of mixture in stone (m).

3 EXPERIMENTAL INVESTIGATIONS

3.1 *Materials*

The cement used was ordinary Portland cement Type I with 28-days compressive strength of 41 MPa and Blaine fineness of approximately 3500 cm^2/g. Cement properties conformed to ASTM standards (ASTM-C150 1994). The fine aggregate used was natural beach sand of specific gravity 2.63 and maximum size of 1.18 mm. Coarse aggregate used was angular basalt of specific gravity 2.69, crushing value of 20.74%, abrasion value of 23.81%, and absorption value of 23.81%. Grading curves for both fine and coarse aggregate are presented in Figures 3 and 4, respectively. Both fine and coarse aggregate properties were found in accordance with ASTM standards (ASTM-C33 1997). The super plasticizer used in the grout was a naphthalene–formaldehyde derivative, trade name 'SikaMent-163' and was mixed at the rate of 2% by weight of cement. The expanding agent, trade name 'Intraplast-Z' was an aluminium powder-based admixture; this was also used at the rate of 2% by weight of cement.

3.2 *Mixture proportions and sample preparation*

Three different proportions of sand–cement ratio (c/s), 0.5: 1, 1: 1 and 1.5: 1, with varying water-cement ratios (w/c) of: 0.38, 0.55 and 0.80, were tried to determine the optimum mix proportions,

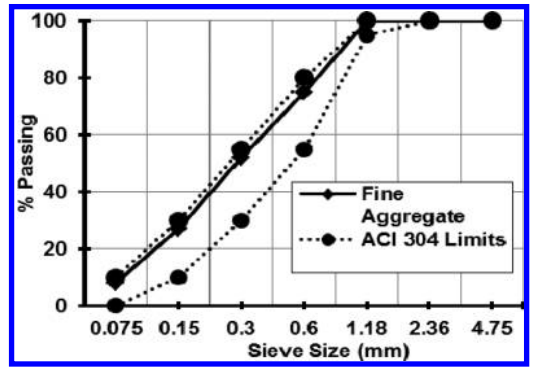

Figure 3. Sieve analysis results of fine aggregate.

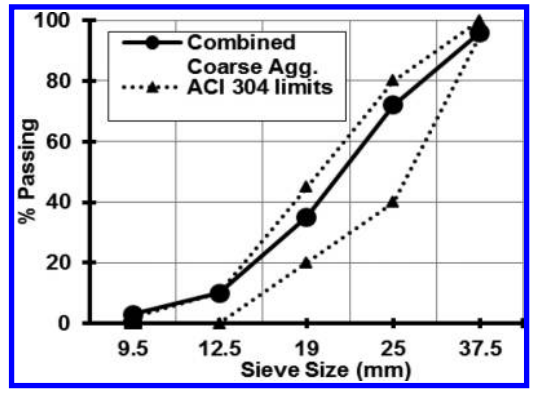

Figure 4. Sieve analysis results of coarse aggregate.

as shown in Table 1. A total of 360 standard concrete cylinders (150 mm × 300 mm) were tested in unconfined compression and tension at 28 days.

3.3 *Consistency discussion*

To measure consistency, both a flow cone and flow table tests were conducted (ASTM-C230 2001 & ASTM-C939 2010), as shown in Figure 5. Fluidity results are presented in Table 2 and 3. Tests on consistency demonstrated that the higher c/s ratio of 1.5 required much more water, whereby the flow cone depends on the time of flow while the flow table depends on the propagation of flow. For example, the w/c ratio 0.38 in the plain grout and expanding admixture at all c/s ratios is the minimum ratio to obtain grout; it was not possible to penetrate all voids in the aggregate skeleton and higher pumping pressure was required to inject the grout. As a result of low w/c and high c/s ratios, the concrete specimen has a honeycombed structure with partial binding of the aggregate skeleton. Grout containing superplasticiser admixture at a w/c ratio of 0.38 and a c/s ratio of 1.5, on the other hand, filled visual voids and created a smooth surface of the sides and ends of each cylinder (Abdelgader et al. 2008).

Table 1. Grout mix proportions.

w/c	*c/s*	Cement (Kg/m^3)	Sand (Kg/m^3)
0.38	0.5	295	590
	1	421	421
	1.5	525	350
0.55	0.5	282	564
	1	407	407
	1.5	338	338
0.8	0.5	265	530
	1	396	396
	1.5	490	326

Figure 5. Flow cone and flow meter setup.

3.4 *Compressive strength discussion*

The compressive strength (fc') of TSC was tested with and without admixture at 28 days. Sample of results is shown in Table 4. Based on the results, a relation for fc' has been assumed, according to the design algorithm presented [14]. Equation (2) is an empirical equation derived from the experimental data for prediction of compressive strength of TSC (fc') as the following:

$$fc' = A + B * (w/c) + C * (w/c)^D + E * (c/s) \quad (2)$$

where: fc' represents the estimated compressive strength of TSC, w/c is the water-to-cement ratio and c/s is the cement-to-sand ratio. A, B, C, D and E are regression coefficients presented in Table 5. Compressive strength without admixture was found to be lower than compressive strength with admixture (super plasticiser). The possible reason for this decrease in strength was the low fluidity of the grout. When high fluidity of grout was used (achieved by using super plasticiser at high w/c ratios), the compressive strength of TSC did not increase. The quality of TSC depends not only on the strength of grout but on its ability to expand while fluid and remove the traces of bleed water that collect under aggregate particles (King 1959 & ASTM-C494 2004).

With this idea of an expanding admixture, a blend of special metallic aluminium powder expansion agent was used in the grout. The strength data, show that when using the expanding admixture the compressive strength of TSC was significantly increased. Super-plasticiser and expanding admixture were used together among the four types of grouts.

The compressive strength was found to have the highest strength. This could be attributed to the

Table 2. Flow table test results in centimeters (cm).

w/c	*s/c*	Without admixtures	Super-plasticizers	Expanding admixtures	Expanding admixtures and super-pl.
0.38	0.5	0	4	4.5	5
	1	0	5.5	5	6
	1.5	3	6.5	5.5	7
0.55	0.5	8	9	8	10
	1	9	10	10	12
	1.5	10	11	12	14
0.8	0.5	15	1	15	16
	1	16	18	16	17
	1.5	17	19	17	18

Table 3. Flow cone test results in seconds (sec.).

w/c	*s/c*	Without admixtures	Super-plasticizers	Expanding admixtures	Expanding admixtures and super-pl.
0.38	0.5	0	155	158	153
	1	0	151	153	148
	1.5	180	146	150	148
0.55	0.5	94	91	86	80
	1	90	87	84	75
	1.5	85	83	83	70
0.8	0.5	40	31	32	30
	1	37	29	31	31
	1.5	35	28	30	29

Table 4. Average compressive strength results (MPa).

w/c	0.38		0.55			0.8	
s/c	0.5	1	0.5	1	1.5	0.5	1
Without adm.	–	–	16	18	21	14	15
Super-palsticizer	16	17	18	20	21	14	16
Expanding admixture	15	17	17	18	20	17	18
Expanding adm. and super-plasticiers	19	19	19	20	23	18	19

Table 5. Regression results for equation (2).

Type of grout	A	B	C	D	E	Correlation coefficient
Without adm.	–4	11	4	–2	4	0.883
Super-palsticizer	44	–33	–3.3	–1.7	2	0.944
Expanding admixture	–14	–40	68	0.5	3	0.891
Expanding adm. and super-plasticizers	–26	–88	127	0.5	1.9	0.66

following: (a) higher fluidity of grout using super plasticiser (which enables the grout to fill all the voids between aggregate particles) (b) expansion effect of grouts using expansion admixture to minimise bleeding and settlement of grout.

3.5 *Tensile strength discussion*

The tensile strength (*ft*) of TSC was investigated at 28 days. Table 6 shows the values of experimental tensile strength in splitting mode. Equation (3) is an empirical equation derived from the experimental

Table 6. Average tensile strength results (MPa).

w/c	0.38		0.55			0.8	
s/c	0.5	1	0.5	1	1.5	0.5	1
Without adm.	–	–	2.2	2.4	2.6	1.8	2.3
Super-palsticizer	1.7	2.0	2.4	2.7	2.8	2.2	2.4
Expanding admixture	1.6	1.9	2.4	2.6	2.8	2.3	2.6
Expanding adm. and super-plasticizers	1.8	2.1	2.8	2.9	3.4	2.4	2.6

Table 7. Regression results for equation (3).

Type of grout	A	B	C	D	E	Correlation coefficient
Without adm.	–0.3	1.2	0.6	–1.3	0.5	0.833
Super-palsticizer	–13	–25	39	0.5	0.3	0.86
Expanding admixture	–12	–23	36	0.5	0.4	0.96
Expanding adm. and super-plasticizers	9.8	–7.4	–1.4	–1.4	0.4	0.855

data for prediction of tensile strength of TSC (ft) in (MPa).

$$ft = A + B * (w/c) + C * (w/c)^D + E * (c/s) \quad (3)$$

where, *ft* represents the estimated tensile strength of TSC, *w/c* is the water-to-cement ratio and *c/s* is the cement-to-sand ratio.

Table 7 shows the values of the regression coefficients. No cause was apparent for the relatively high tensile strength. However, it is believed that the amount of coarse aggregate, method of placement and the greater mechanical interlocking among the particles could be responsible for the high tensile strength. Failure in tension was restricted principally as a result of the line of fracture which was occurred through the mortar and coarse aggregate.

3.6 *Compressive-tensile strength relationship*

From the results it appears that there is a good correlation between the compressive strength and tensile strength of TSC.

As the compressive strength increased with grout, the tensile strength was also found to increase in the same manner.

In the present work, however, Equation (4) was developed by regression analysis to relate tensile strength (*ft*) to compressive strength (*fc′*). The relationship between the compressive strength and the tensile strength of different grout proportions is shown in Figures 6 to 9 for different admixtures.

$$ft = A + (B) \times fc' + (C) \times (fc')^D \quad (4)$$

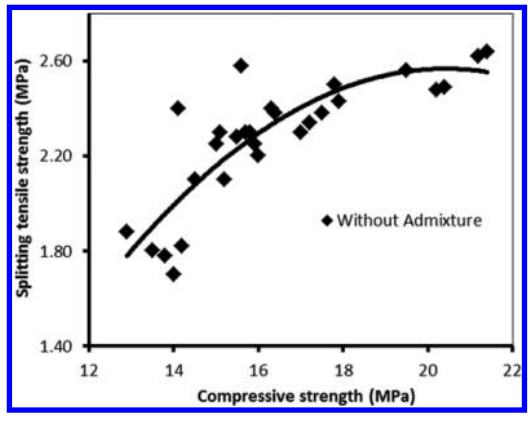

Figure 6. Compressive strength versus tensile strength.

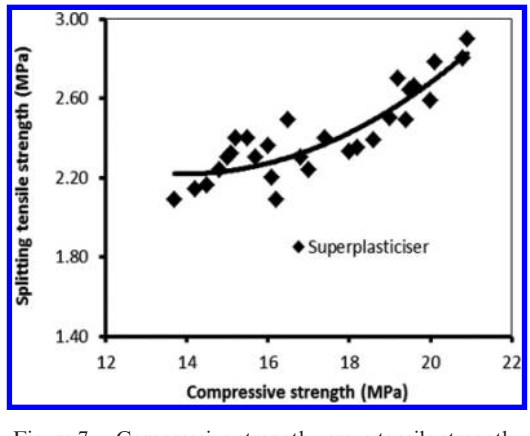

Figure 7. Compressive strength versus tensile strength.

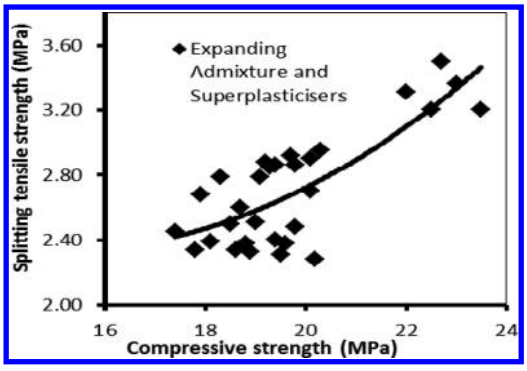

Figure 8. Compressive strength versus tensile strength.

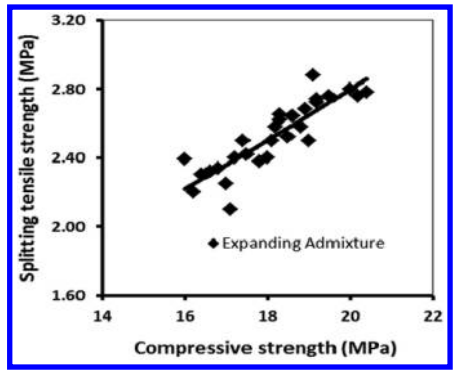

Figure 9. Compressive strength versus tensile strength.

Table 8. Regression results for equation (4).

Type of grout	A	B	C	D	Correlation coefficient
Without adm.	–50	–0.4	38	0.1	0.724
Super-palsticizer	40	0.4	–32	0.1	0.8
Expanding admixture	–4.3	–0.3	1.82	0.6	0.721
Expanding adm. and super-plasticizers	163	1.2	–132	0.1	0.68

where: *ft* is tensile strength and *fc*` is the compressive strength. Table 8 shows the values of the regression coefficients.

4 CONCLUSIONS

- As the method of placement in TSC is entirely different from that of NC, a suitable admixture is necessary to satisfy the requirement for the pumping ability of grout. The expanding admixture was found to be the most suitable admixture as it provided higher fluidity with minimum bleeding.
- The compressive strength and tensile strength of TSC was tested with and without admixture at 28 days for all grout proportions. On the basis of the results, a correlation between the strength and grout proportions was statistically derived.
- The fractured specimens of TSC showed that a large proportion of failures occurred by cracking through the coarse aggregate particles.
- The authors believe that there are many aspects of TSC that require clarification through further theoretical and experimental studies such as: energy dissipation, failure mechanism and cracking, shrinkage, creep and other time dependent deformations.

REFERENCES

Abdelgader, H. 1999. How to design concrete produced by a two-stage concreting method. Journal of Cement and Concrete Research 29(3): 331–337.

Abdelgader, H.S. 1996. Effect of quantity of sand on the compressive strength of two-stage concrete. Magazine of Concrete Research 48(2): 353–360.

Abdelgader, H.S., & Górski, J. 2003. Stress-strain relations and modulus of elasticity of two-stage concrete. ASCE Journal of Materials in Civil Engineering: (4), 251–255.

Abdelgader, H.S, El-Baden, A.S., Ahmed S. & Fahema, A.H. 2012. Concreting methods that produce low carbon. Proceeding of The International Conference on Sustainable Built Environment: Kandy-Sir Lanka.

Abdelgader, H. & Elgalhud, A. 2008. Effect of grout proportion on strength of two-stage concrete. Structural Concrete Journal: 163–170.

ACI Committee 318. 2008. Building code requirements for reinforced concrete. American Concrete Institute: Detroit: Michigan: USA.

ACI Committee 304. 2005. Guide for the use of preplaced aggregate concrete for structural and mass concrete applications. American Concrete Institute: Farmington Hills: Michigan: USA: 21–24.

ASTM-C150. 1994. Specification for portland cement. American Society for Testing and Materials: Philadelphia: Pennsylvania.

ASTM C33. 1997. Specification for concrete aggregates. American Society for Testing and Materials: Philadelphia: Pennsylvania.

ASTM C230. 2001. Standard specification for flow table for use in tests of hydraulic cement. American Society for Testing and Materials: Philadelphia, Pennsylvania: 129–133.

ASTM C939. 2010. Standard test method for flow of grout for preplaced aggregate concrete (flow cone method). American Society for Testing and Materials: Philadelphia, Pennsylvania: 134–136.

ASTM-C494. 2004. Standard specification for chemical admixtures for concrete. American Society for Testing and Materials: Philadelphia: Pennsylvania.

King J. 1959. Concrete by intrusion grouting: Handbook of heavy construction. McGraw-Hill, New York.

Neville, A. 1981. Properties of concrete. London. Pitman Books Limited

Neville, A. & Brooks, J. 1987. Concrete technology. London: Longman Scientific and Technical.

Nowek, A., Kaszubski, P., Abdelgader, H.S. & Gorski, J. 2007. Effect of admixtures on fresh grout and two-stage (pre-placed aggregate) concrete. Structural Cement Journal of the FIB 8(1): 201–215.

Concrete Repair, Rehabilitation and Retrofitting IV – Dehn et al. (Eds)
© 2016 Taylor & Francis Group, London, ISBN 978-1-138-02843-2

Research and development of polymer modified self compacting concrete used for replacement of large area deterioration concrete

Xiangzhi Kong, Gaixin Chen, Shuguang Li, Guojin Ji & Sijia Zhang
State Key Laboratory of Simulation and Regulation of Water Cycle in River Basin, China Institute of Water Recourses and Hydropower Research, Beijing, P.R. China

ABSTRACT: A lot of concrete dams and their ancillary buildings need to be repaired because of freezing and thawing, scour and erosion. For large area concrete repair, replacement of concrete is a good choice, especially when the depth of the repairing area exceeds 6 inches. But this method has some disadvantages in some aspects, compared with the cement or polymer mortar. For example, the durability, interface bond strength, and the complicated repair procedure. In this study we developed a Polymer Modified Self Compacting Concrete (PMSCC) which can achieve self compaction without any vibration. Experimental results show that the tensile strength of the PMSCC is 3.63 MPa at 28 days, the ultimate tension strain is 179 microstrain increased by 54.3% compared with Portland cement self compacting concrete, and the relative dynamic modulus of elasticity is 97% after 300 times freezing and thawing circles. Simulation test shows that the interfacial bond strength between new and old concrete is higher than 1.56 MPa without any adhesives. In addition, finite element analysis results show that appropriate setting joints could effectively avoid thermal cracks during the operation stage. PMSCC has the features of "high anti-crack ability, good durability and high bond strength" which is suitable for the replacement of large area deterioration concrete, especially for the dam upstream concrete.

1 INTRODUCTION

For concrete repair, there are lots of materials and techniques could be selected, but people are most concerned about the durability of patching materials, bond strength between the new and old concrete as well as the integrity of structure after repairing. Therefore, to determine the repair scheme we must take account of the particularities of the projects and its adaptation of the plans. Replacement with new concrete will not change the building structures, and the patching materials could be in accordance with the constitutive relation and the deformation properties in the maximum range to improve the integrity of structures. The building restores to its initial profile after repair.

Polymer cement concrete (known as polymer Modified concrete), due to the accumulation film formation effect of polymer material, has many excellent properties, such as tensile strength, bonding strength, water resistance and durability, etc., while its porosity must be reduced. Therefore, we use a non-air entraining acrylic latex as the modifier. The concept of self-compacting concrete was first proposed by a Japanese scholar named Okamura in 1986. Afterwards, self-compacting concrete became popular all over the world because of its unique construction superiority, good strength and durability.

The paper is aiming at development a polymer modified self-compacting concrete used as replacement concrete for the old structure, using the improvement effect of polymer latex on cement based materials and the construction superiority of self-compacting concrete. It will be suitable for the replacement of large area freezing-thawing or erosion damaged hydraulic concrete, as well as the strengthening and reinforcement of the beams, columns and other building components with unsatisfied strength or density.

2 MATERIALS AND CONCRETE MIX PROPORTION

Cement: ordinary Portland cement (P.O 42.5);

Mineral admixture: class II and F fly ash;

Fine aggregate: limestone manufactured sand with a fineness modulus of 2.63 and dust content of 18.7%;

Coarse aggregate: natural gravel with a maximum aggregate size of 20 mm;

Polymer: non-entraining acrylic emulsion with solid content of 47%,

Fiber: 6 mm polypropylene fiber;

Chemical admixture: high-performance water reducing agent.

Table 1. Concrete mix proportions (kg/m^3).

No.	Water	Cement	Fly ash	Sand	Stone	Acrylic emulsion	Water reducer	Fiber
SCC	180	300	200	825	767	–	6.5	0.45
PMSCC-1	123	300	200	765	711	100	6.0	0.45
PMSCC-2	123	400	100	777	693	100	6.0	0.45

Concrete mix proportions are shown in Table 1. There are three mix proportions including normal Self-Compacting Concrete (SCC) and polymer modified self-compacting concrete (PMSCC-1 and PMSCC-2). Concrete samples are made without vibration. Curing Method is 7 days wet curing plus 21 days dry curing.

3 EXPERIMENT RESULTS AND DISCUSSION

3.1 *Fresh concrete*

The Fresh concrete of PMSCC can be seen in Photo 1. It has a good workability and stability. Its slump flow is over 660 mm and the extension time T500 is less than 2 s, which has reached SF2 class and VS2 grade level filling ability specified in JGJ/T 283. It can be used for structures which have more reinforcement or buildings with high requirement for concrete appearance.

Photo 1. Polymer Modified Self-Compacting Concrete.

3.2 *Hardened concrete*

Test results of compressive strength, tensile strength, and modulus of elasticity are listed in Table 2. Compared with SCC, the compressive strength of PMSCC-1 which has only 9.4% solid polymer (percentage of all binding materials, in mass) is 31.8 MPa reduced by 12.8 MPa, direct tensile strength is 3.19 MPa reduced by 0.02 MPa, and modulus of elasticity is 23.1GPa reduced by 7.5GP. For the PMSCC-2, the compressive strength is 37.0 MPa reduced by 7.6 MPa, tensile strength is 3.63 MPa increased by 0.42 MPa, and elastic modulus is 23.5GPa reduced by 7.1GPa. Thus, we confirm that adding polymer latex significantly reduces the brittleness of concrete, and has a higher ratio of tensile strength and compressive strength.

Ultimate tension strain is in response to the ultimate deformation ability of concrete under tensile stress, which is tested according to DL/T 5150. Trying to increase the ultimate tension strain of concrete can reduce the cracks due to shrinkage or temperature stress. For the thin layer replacement concrete, trying to increase its ultimate tension strain could reduce the interface stress between old and new concrete and decrease the risk of cracking effectively. The results show that ultimate tension strain of PMSCC is significantly improved after adding latex. At 28 days, ultimate tension strain of PMSCC-1 is 147 με increased by 26.7% compared with SCC. Ultimate tension strain of PMSCC-2 is 179 με increased by 54.3%.

Concrete durability tests were performed according to ASTM C 803, ASTM C 666 and ASTM C 1202. From the test results in Table 2, we confirm that PMSCC has good durability and corrosion resistance which attribute to the following two reasons: First, polymer particles can reduce the porosity of slurry, with significant effects especially for sealing connection pores; second, the polymer film has good waterproof performance.

Autogenous volume change, although it may occasionally be an expansion, is usually shrinkage and is entirely a result of chemical reaction within the concrete and aging, which has a great effect on concrete anti-crack ability. Test results show that, at 28 days, 90 days, the autogenous volume deformation of PMSCC-1 is expansion, while the autogenous volume deformation of SCC is shrinkage. Till 160 days, they are all getting to be shrinkage, and the value is 4 με and 44 με respectively. Obviously, PMSCC has less autogenous volume shrinkage than SSCCC (Fig. 1).

Dry shrinkage of hardened concrete is usually occasioned by the drying and shrinking of the

Table 2. Hardened concrete properties.

	Compressive strength (MPa)		Tensile strength (MPa)		Modulus of elasticity (GPa)		Ultimate tension strain (millionths)		Permeability coefficient ($m/s \times 10^{-12}$)	DF	Ability to resist chloride ion penetration (coulomb)
No.	7d	28d	7d	28d	7d	28d	7d	28d	28d	28d	28d
SCC	25.0	44.6	2.57	3.21	25.5	30.6	111	116	0.5	90	–
PMSCC-1	22.1	31.8	2.27	3.19	18.1	23.1	137	147	0.7	95	–
PMSCC-2	29.0	37.0	2.90	3.63	20.1	23.5	170	179	0.3	97	820C

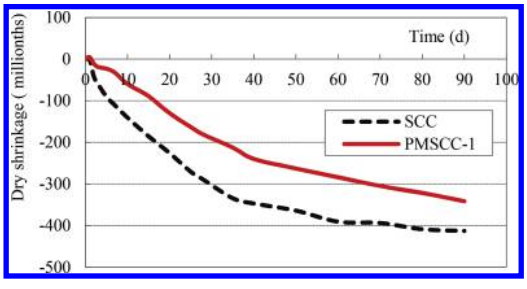

Figure 1. Autogenous volume deformation of concrete.

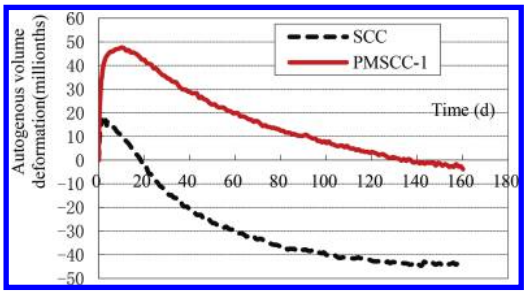

Figure 2. Dry shrinkage of concrete.

cement gel that is formed by hydration of Portland cement. Test results show that dry shrinkage of PMSCC-1 is 289 με at 28 days, and is significantly smaller than the dry shrinkage of SCC (Fig. 2).

For thin layer replacement concrete, trying to reduce the autogenous volume shrinkage and the dry shrinkage could significantly reduce decrease its cracks and the interface shear stress between new and old concrete, and improve the integrity of structures after repairing.

Regarding the modifying mechanism of polymer on cement mortar and concrete, the current consistent view is: the improvement effect is achieved through the film, which is formed by polymer with higher cohesive strength, within the cement paste or the transition zone of cement paste and aggregate; cement hydration is performed simultaneously with the polymer, finally forming the interpenetrating network structure which cement paste and polymer film mutually intertwined. For the polymer modified self-compacting concrete, its compressive strength decreased, but the ratio of tension and compression significantly increased; elastic modulus significantly decreased, plasticity increased; due to the formation of the polymer film and the plugging effect on connection gap in concrete. Frost resistance, permeability, and the resistance to chloride ion penetration of concrete are all improved significantly. In addition, the modification can significantly reduce the autogenously volume deformation and the dry shrinkage of concrete because of the water retention property of polymer film. In summary, PMSCC used as replacement concrete has features of "self-compacted, high anti-crack ability, good durability", which could effectively reduce the interface stress between the new and old concrete and improve the integrity of repair structure.

3.3 *Bond strength between new and old concrete*

Using replacement concrete to repair or to reinforce damaged concrete structure, maximally guarantee the similarity of repair materials and old concrete in terms of performances and deformation, but the interfacial bond strength is often smaller than the bond strength of mortar. Therefore, people are more concerned about the bonding issue between new and old concrete. Here a examination was performed, which is to simulate the repair of concrete beam and column with the PMSCC (Photo 2). Two concrete prisms with the size of 400 mm × 400 mm × 1600 mm, which suffered freeze-thaw damage, are selected as samples to be repaired. Remove the surface frosted concrete exposing fresh surface and clean with water. Install sheet steel form around the samples, assuring the repair layer thickness between 70 mm and 80 mm. Pour Polymer-Modified Self-Compacting Concrete (PMSCC-2) into the gaps. Note that there is

Photo 2. Concrete samples before and after repair (a1)and (a2) before repair, (b) after repair.

Table 3. Bond strength between new and old concrete.

Sample diameter (mm)	Load (KN)	Pull strength (MPa)		Note
		Single	Average	
141.7	24.5	1.56	2.27	Sub-layer old concrete broken
	38.9	2.47		The interface of new and old concrete break off, there is aggregate at the broken surface
	30.6	1.94		
	49.3	3.12		The interface break, the broken section has the aggregate less than 20 mm
93.6	16.0	2.33	2.26	The pull head and the concrete bonding surface broken
	15.6	2.26		
	18.4	2.67		Lower layer old concrete broken, there is aggregate greater than 40 mm at the broken section
	12.3	1.78		

not any interface adhesives. Removed forms after 7 days. The surface condition of the concrete sample is shown in Photo 2.

After maintenance 28 days, conduct pullout tests to test the bond strength between new and old concrete. The test results and section position description are shown in Table 3.

For the diameter of 141.7 mm, the maximum pullout strength is 3.12 MPa, the minimum pullout strength is 1.56 MPa, and the average value is 2.27 MPa. For the diameter of 93.6 mm, the maximum pullout strength is 2.67 MPa, the minimum pullout strength is 1.78 MPa, and the average value is 2.26 MPa. Observation the pull sections: the minimum pull strength specimen is broken at the locations of foundation concrete. In light of this, PMSCC has good bond strength with the foundation concrete, the interfacial bond strength is not less than 1.56 MPa, and the average is above 2.26 MPa.

For the new and old concrete interface without planted-bar, the interface adhesion has three kinds: mechanical engaging forces, Van der Waal's forces and chemical acting force. PMSCC assure a high bond strength with the foundation concrete from the following three aspects: firstly, polymer modified self-compacting concrete has a lot of bonding materials, the growth of a lot of hydration products which mix to the interspaces in the old concrete surface to form a dense structure, can significantly improve the mechanical engaging force of the new and old concrete interface; secondly, the accumulation effect of the polymer particles can significantly improve the Van der Waal's force of the interface; thirdly, foundation concrete surfaces need no interface agent, the use of high adhesive material of polymer modified self—compacting concrete, and the incorporation of fly ash, improve the chemical forces of the interface by the hydration reaction of adhesive materials between the old and new concrete.

4 SIMULATION

A numerical simulation of a patch repair system with PMSCC is presented. The repair system consists of a 0.08 m thick(h1) repair layer cast over a 0.4 m thick(h0) and 0.4 m wide(w) substrate as shown in Figure 3. Simulation of four different lengths is done and the length (L) is 0.4 m, 0.8 m, 1.2 m, and 1.6 m respectively.

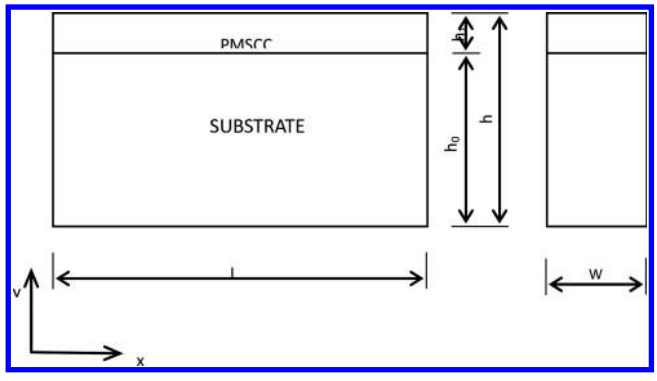

Figure 3. Patch repair system.

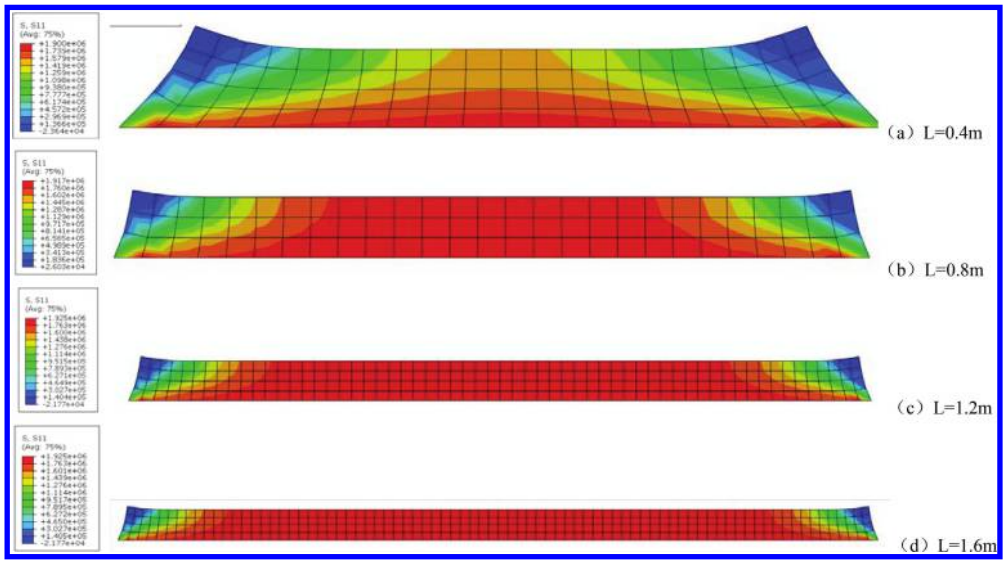

Figure 4. Maximum principal stresses for PMSCC (+ tensile, – compressive).

The thermal and mechanical characteristics of the repair layer are as follows:

Modulus of elasticity: $E_1 = 23.5 \times 103$ MPa
Poisson's ratio: $\mu_1 = 0.167$
Thermal expansion coefficient: $\alpha_0 = 4.3 \times 10^{-6}$ °C$^{-1,}$
$\alpha_1 = 7.7 \times 10^{-6}$ °C^{-1}
Simulation of the temperature drop: $\Delta T = -20$ °C.

The stress inside the PMSCC is due to the repair material and the substrate with different coefficients of thermal expansion, and the deformation is constrained. Therefore, simulation is only for the repair layer, and the repair body bottom in the direction normal is to the fixed constraint. The repair layer is discretized using four-node isoparametric element. Figure 4 is the repair layer the maximum principal stress distribution nephogram.

It can be seen from Figure 4 that there exists larger stress in the interface between the PMSCC and the substrate, with the increase of patch length, the maximum principal stress is also increasing. When the repair layer is greater than 1.2 m in length, the maximum principal stress does not increase anymore. Length of the repair layer (L) is 0.4 m, 0.8 m, 1.2 m and 1.6 m; the maximum principal stress is respectively 1.90 MPa, 1.92 MPa, 1.93 MPa and 1.93 MPa. The maximum principal stress is lower than the tensile strength of the repair material PMSCC, also lower than the interface bond strength.

It is confirm that a reasonable set of joints determined by numerical simulation can effectively reduce the cracking risk of the repair material and the Interface delamination. For PMSCC used as

concrete replacement, the length of repair layer can be greater than 1.2 m.

5 CONCLUSION

In this study we have successfully produced the polymer modified self-compacting concrete with non-entraining acrylic latex, which is suitable for the old concrete repair by replacement. Performances test and simulations experiment results show that the concrete has the features of "self-compaction, high plasticity, high anti-crack ability, good durability and corrosion resistance", and has good bond strength with the foundation concrete. Finite element analysis results show that appropriate setting joints could effectively avoid cracks appearing of the PMSCC during the operation stage.

ACKNOWLEDGEMENTS

The authors are grateful to the National Basic Research Program (973 Program) of China (2013CB035901) and the National Key Technology R&D Program (2013BAB06B02) for their financial support.

REFERENCES

ACI Committee 546. Concrete Repair Guide, ACI 546R-96 (Reapproved 2001).

ACI Committee 548. Polymer-Modified Concrete. ACI 548.3R–03.

Andrea Dimmig—Osburg, Kay A. Bode, Weimar. Translated by Chen Xufeng. Discussion on Development prospects of Polymer Cement Concrete (PCC)—Composition, Role and Application of PCC.

ASTM C1202–12 Standard Test Method for Electrical Indication of Concrete's Ability to Resist Chloride Ion Penetration.

ASTM C666/C666M-03(2008) Standard Test Method for Resistance of Concrete to Rapid Freezing and Thawing.

ASTM C803/C803M-03(2010) Standard Test Method for Penetration Resistance of Hardened Concrete.

DL/T 5150–2001 Test code for Hydraulic Concrete.

Han Juhong, Zhao Guofan. Study on Rupture Properties Test of New and Old Concrete Bonding Interface. (In chinese).

JGJ/T 283–2012. Technical Specification for Application of Self-Compacting Concrete. (In chinese).

Liu Yunhua, Xie Youjun. The Study Status of Self-Compacting Concrete. [J]. Journal of Silicate, Vol.35, No. 5, May 2007. (In chinese).

Xie Huicai, Li Gengying. Formation Mechanism of New and Old Concrete Interfacial Adhesion [J]. Silicate Bulletin, 2003 03. (In chinese).

Zhong Shiyun, Yuan Hua. Polymer Applications in Concrete. [M]. Chemical Industry Press, Publishing Center of Materials Science and Engineering, 2003, 03, Beijing. (In chinese).

Concrete Repair, Rehabilitation and Retrofitting IV – Dehn et al. (Eds)
© 2016 Taylor & Francis Group, London, ISBN 978-1-138-02843-2

Using steel fibered high strength concrete for repairing continuous normal strength concrete bending elements

K. Holschemacher
University of Applied Sciences, Leipzig, Germany

I. Iskhakov & Y. Ribakov
Ariel University, Ariel, Israel

ABSTRACT: Using Steel Fibered High Strength Concrete (SFHSC) for repairing normal strength concrete bending elements has been previously proved to be effective for statically determined beams. After repairing using this method a beam becomes a two-layer element that consists of SFHSC in the compressed zone and Normal Strength Concrete (NSC) without fibers in the tensile one. The present study is focused on experimental investigation of statically non-determined Two-Layer Beam (TLB). A two-span TLB was tested under concentrated loads acting in the middle of each span. The concrete classes for NSC and SFHSC were selected based on the results of previous studies. An optimal steel fibers' content for the SFHSC was 40 kg/m^3. The tests were focused on investigating the load-deflection relationships, bonding between the SFHSC and NSC layers, transfer of shear between the layers and Poisson deformations in the SFHSC layer. The tested beam exhibited proper behavior under the design load. After the design load was achieved the forces were further increased. The test has demonstrated that when the load was about 150% of the design value cracks propagated through the whole NSC layer, but not appeared at the SFHSC one. The experimental data, obtained in the frame of this study, proves that SFHSC is a very effective material for repairing existing NSC structures.

1 INTRODUCTION

Concrete structures repairing can be carried out for restoring the original structural shape and strengthening the damaged elements. There are different techniques for retrofitting and strengthening of reinforced concrete structures.

Known methods include steel plate bonding, external pre-stressing, section enlargement, and reinforced concrete jacketing. Although the first two methods increase the elements load bearing capacity and also disposed to corrosion (Banu & Taranu, 2010). Strengthening by section enlargement can be performed by adding a new concrete layer to the structural element. The most important issue in this case is to ensure proper bonding between the concrete of the existing element and that, applied for its strengthening.

Thanoon et al. (2005) have studied the structural behavior of cracked reinforced concrete one-way slab, repaired using five techniques: cement grout, epoxy injection, ferro-cement layer, carbon fibre strip and section enlargement. The efficiency of the selected repair and strengthening techniques and their effects on the structural behavior had been analyzed. All techniques were found to be able to enhance the structural capacity of cracked concrete slabs.

Ultra High Performance Fiber Reinforced Concrete (UHPFRC) is effective for rehabilitation of existing concrete structures (Oesterlee et al., 2009). A thin layer of UHPFRC, casted on existing Normal Strength Concrete (NSC) element, increases its load bearing capacity and serviceability.

This idea was further validated (Bruhwiler & Denarie, 2008). It combines protection and resistance functions of UHPFRC with NSC. The rehabilitated full-scale structures have also significantly improved durability.

The authors have demonstrated before that roof beams, in which a part of their section comes above the slab, and subjected to aggressive surrounding environment, can be repaired using the idea of two-layer bending elements (Iskhakov & Ribakov, 2007). In such beams the damaged part is replaced by a steel fibred high strength concrete (Iskhakov et al., 2013).

The optimal fiber weight ratio is selected based on the ductility level requirements (Iskhakov & Ribakov, 2011). Steel fibers have little effect on beams' elastic deformations, but increase the ultimate ones, due to the additional energy dissipation potential of fibers.

A method for obtaining the class of Steel Fibred High Strength Concrete (SFHSC) and the load bearing capacity of simple supported beams after retrofitting was proposed (Iskhakov et al., 2011). With this aim experimental investigations were carried out. SFHSC cubic and cylindrical specimens as well as short two-layer beams, made of NSC in the tensile zone and SFHSC in the compressed one, were tested. These experimental results together with those, obtained by Bruhwiler & Denarie (2008) and Oesterlee et al. (2009), show a promising way for using SFHSC for repairing damaged beams and slabs.

A logical extension of the authors' previous work (Iskhakov et al., 2013) is repairing of a Continuous Two-Layer Beam (CTLB), which is a focus of the current study. As it was mentioned above, the roof beams are subjected to aggressive surrounding environment that causes sufficient damage to NSC and corrosion in the reinforcing steel. A similar problem is relevant for roof one directional slabs.

From the technological viewpoint, repairing the upper zone of a continuous structure is a rather easy task. A more complicated problem is repairing the bottom zone of the structure. The problem can be solved using a number of methods, like replacing the old damaged structure by a new two-layer one, using temporary columns to unload the middle supports with negative bending moments, etc. The present work is focused on experimental investigation of CTLB, assuming that the first methodology is used.

2 AIMS AND SCOPE

In the recent years two-layer concrete beams with NSC in the tensile zone and SFHSC in the compressed one was intensively investigated theoretically (Iskhakov & Ribakov, 2011). Simple supported full-scale TLB were tested (Iskhakov et al., 2014). A logical extension of these tests is experimental investigation of a Continuous Two-Layer Beam (CTLB), which is a focus of the current study.

The experimental study on full-scale continuous TLB is based on results of previous theoretical investigations (Iskhakov & Ribakov, 2011). An optimal fiber content in the HSC layer, obtained by testing small-scale specimens (Holschemacher et al., 2012), was used.

The experiments are aimed at studying the role of steel fibers in the HSC layer to provide a basis for developing design provisions for RC CTLB. An additional issue studied in this work is the influence of the bending moments with different signs on the CTLB behavior.

SFHSC was casted just in the compressed section zone according to the bending moments' diagram

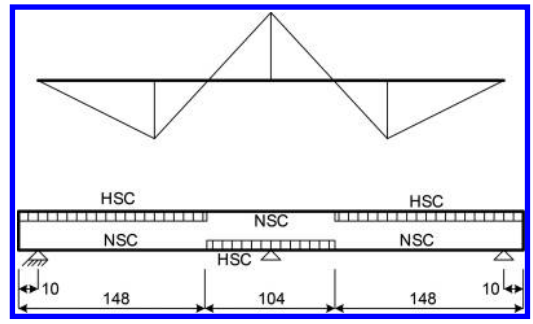

Figure 1. CTLB bending moments diagram and corresponding NSC and SFHSC layers layout.

(Fig. 1). Interaction between the concrete layers in longitudinal direction of the continuous beam is studied. The concept of selecting the SFHSC layer depth, equal to that of the compressed section zone was also verified.

3 EXPERIMENTAL PROGRAMM

The investigation included testing of the following specimens:

- 3 NSC and 3 SFHSC cubes to obtain the compression strength;
- 3 NSC and 3 SFHSC cubes to obtain the splitting tensile strength;
- 3 SFHSC cylindrical specimens for obtaining the modulus of elasticity;
- a full scale CTLB was tested under five-point loading.

The steel fibres, used in this study, were like at the previous research stages—straight fibres with end hooks. Their ultimate tensile strength was 1100 MPa. The fibres have a length of 50 mm and a diameter of 1 mm. The number of fibres per kg is 3150. The applied fibres weight ratio was 40 kg/m^3.

Additionally to the fibres, the following materials were used for preparing the concrete mixture:

- Portland cement CEM II/A-LL 42.5 N with granulated slag and limestone between 6 and 20%, density of 3.05 kg/dm^3 for HSC and Portland cement CEM I 42.5 N—for NSC;
- fly ash with density of 2.3 kg/dm^3 and grain between 2 and 290 μm;
- poly-carboxylic ether-based super-plasticizer with a density of about 1.07 kg/dm^3;
- long-term retarder with a density of 1.17 kg/dm^3;
- natural sand with a fraction size of 0 to 2 mm;
- two different types of gravel with fraction sizes of 2 to 8 mm and 8 to 16 mm.

Sand and gravel had a specific density of 2.65 kg/dm^3.

The beam was reinforced with normal ductile steel bars with an ultimate strain of 25 ‰. The modulus of elasticity, yield strength, and ultimate strength of the reinforcing steel were 200 GPa, 500 MPa, and 525 MPa, respectively. A detailed reinforcement scheme of the beam is shown in Figure 2.

Concrete compressive and splitting tensile strengths were measured for six 15 cm cubes—three for NSC and three for SFHSC. The SFHSC elasticity modulus was found by testing three cylinders with a height of 20 cm and a diameter of 15 cm. Results of these tests are presented in Tables 1–4.

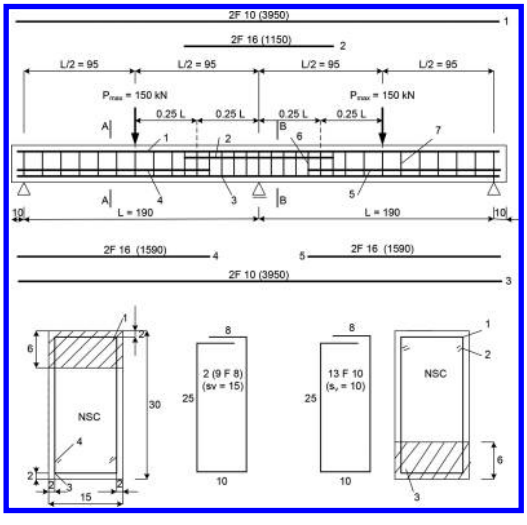

Figure 2. The CTLB reinforcement scheme.

The CTLB was tested under five-point loading. Before testing the beam between the outer supports was divided into 19 sections, the length of each one was 20 cm. The external forces were applied using a manually activated actuator.

The following measuring devises were installed on the beam:

- two LVDTs for measuring the deflections under each concentrated load;
- one LVDT for measuring the middle support uplift;
- three LVDTs for measuring horizontal shear deformations between the NSC and SFHSC layers;
- three LVDTs for measuring vertical shear deformations between the NSC and SFHSC layers;
- two LVDTs for measuring the Poisson deformations in the upper SFHSC layers;
- two load cells under the concentrated forces.

The loads were applied by steps and at each step cracks openings were measured. Additionally, the interaction between the concrete layers was controlled.

At the first and second steps the load corresponded to 50% and 100% of the calculated cracking moment, respectively. The deflection at the middle of each span for both steps was less than 1 mm. The third load step corresponded to 1 mm deflection in the middle of each span and to beginning of crack formation. The following load steps were 2, 3, 4, 5, 8, 10 and 14 mm. For loading steps, corresponding to mid span deflection from 10 mm to 14 mm, crack formation has almost completed.

During the external loads application, cracks' appearing and opening were recorded. The first cracks appeared at the third load step, when the mid span deflections were 1 mm. The cracks

Table 1. Margin settings for A4 size paper and letter size paper.

Specimen	Weight [kg]	l [cm]	b [cm]	h [cm]	ρ [kg/dm^3]	Load [kN]	f_{cm} [MPa]
1	8.0470	15.1	15	15	2.369	889.7	39.28
2	7.9505	15.1	15	15	2.340	855.7	37.78
3	8.1050	15.25	15	15	2.362	896.8	39.21

Table 2. Compressive strength of SFHSC cubic specimens.

Specimen	Weight [kg]	l [cm]	b [cm]	h [cm]	ρ [kg/dm^3]	Load [kN]	f_{cm} [MPa]
1	8.3251	15.15	15	15	2.442	1862.3	81.95
2	8.3150	15.15	15	15	2.439	1814.8	79.86
3	8.1376	15	15	15	2.411	1735.0	77.11

Table 3. Splitting tensile strength of SFHSC (FWR = 40 kg/m³).

Specimen	Weight [kg]	l [cm]	b [cm]	h [cm]	ρ [kg/dm³]	Load [kN]	f_{cm} [MPa]
1	8.3399	15	15.25	15	2.431	202.8	5.67
2	8.4623	15	15.4	15	2.442	190.2	5.27
3	8.4282	15	15.2	15	2.464	187.3	5.26

Table 4. Modulus of elasticity of SFHSC.

Specimen	Weight [kg]	l [cm]	b [cm]	h [cm]	ρ [kg/dm³]	E_m [N/mm²]
1	3.8494	15	15	20.2	1.078	39513
2	3.8061	15	15	20.05	1.074	38669
3	3.8546	15	15	20.2	1.080	39221

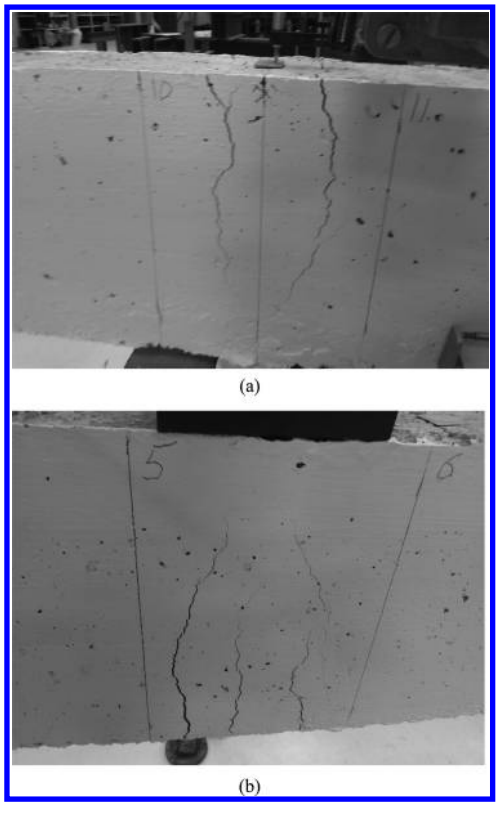

Figure 3. Crack patterns in the tested beam: a—above the middle support; b—in the mid span.

appeared above the middle support, where the maximum negative moment appears. The width of the cracks was 0.05 mm. When the mid span deflections reached the value of 14 mm (about 1/140 of the span), the maximum cracks' width was 2.5 mm.

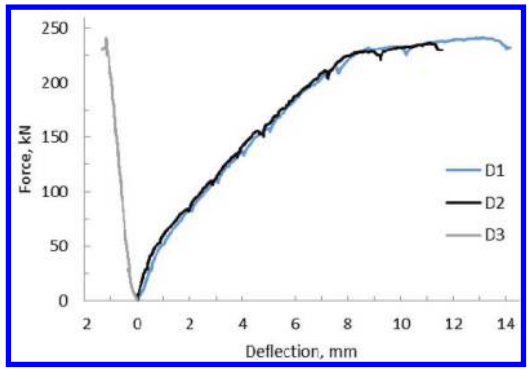

Figure 4. Load—deflection curves in the middle of the spans (D1 and D2) and the middle support uplift (D3).

A crack with maximum width appeared at the same section. It is obvious that this stage corresponds to the CTLB failure.

A typical crack patterns above the middle support and in the mid span of the beam is shown in Figure 3. Section 5 is subjected to the maximum positive bending moment. The cracks propagate up to the SFHSC layer. It proves the assumption that the SFHSC layer depth in continuous beams should be equal to that of the compressed zone.

Experimentally obtained deflections at the mid spans of the beam and above the middle support are given in Figure 4. The graph demonstrates an elastic—plastic behavior of the beam at the post-cracking range. Thus, it experimentally confirms that, as for simple supported TLB (Iskhakov et al., 2014) also for the investigated continuous beam, proper selection of steel fiber content allows achieving the desired ductile behavior, in spite that the beam's compressed zone is made of brittle HSC. The force-deflection lines on the graph are

smooth. It demonstrates that there is proper interaction between the SFHSC and NSC layers.

The maximum Poisson strain in SFHSC was $0.2 \cdot 10^{-3}$ that corresponds to the HSC properties. It should be noted that the maximum One of the aims of the present study was analysis of SFHSC and NSC layers' interaction in horizontal and vertical directions. Six LVDTs were installed for this reason—three for measuring horizontal deformations between the layers and other three—for vertical ones.

The border between the SFHSC and NSC layers corresponds to the neutral axis of the CTLB section therefore the above-mentioned deformations correspond to pure shear. The maximum horizontal deformations' values are about 2‰ in both spans. This deformation corresponds to elastic-plastic deformation of compressed concrete. Therefore, at pure shear non-linear deformations can appear in concrete. At the same time, the deformations near the middle support are minimal and are practically negligible.

The maximal values of vertical shear deformations are about 50 times lower than the horizontal ones. It proves that there is no de-bonding between the layers and that the CTLB withstands the design load. It should be noted that these deformations are approximately equal at the beam spans and above the middle support.

4 CONCLUSIONS

The study focused on testing a continuous two span two-layer reinforced concrete beam for verifying the suitability of a TLB idea for repairing continuous RC beams.. The main aim of the study was testing the behavior of an RC CTLB under positive and negative bending moments.

Solution for the problem of the SFHSC layer thickness and its location along the continuous beam, which is very important for repaired elements, was found: the thickness of the layer is equal to the section compressed zone depth and length of the layer corresponds to the distance between the zero values in the bending moments' diagram.

Interaction of SF HSC and NSC layers was studied to prove the efficiency of such beams for real structures that require repairing.

The CTLB was designed according to previously developed methodology. No horizontal or vertical cracks between the layers appeared up to the ultimate limit state. It proves that such methodology is effective for repairing continuous RC beams.

Thus, continuous two-layer RC beams correspond to all requirements of existing design codes and recommended for practical application as effective and economical method for repairing bending structures.

REFERENCES

Banu D. & Taranu N. 2010. Traditional solutions for strengthening reinforced concrete slabs. *Buletinul Institutului Politecnic Din Iasi,* Publicat de Universitatea Tehnica "Gheorghe Asachi" din Iasi, LVI (LX), Fasc. 3.

Bruhwiler E. & Denarie E. 2008. Rehabilitation of concrete structures using ultra-high performance fiber reinforced concrete, *Proceedings of the Second International Symposium on Ultra-High Performance Concrete,* March 5–7, Kassel, Germany.

Iskhakov I. & Ribakov Y. 2011. Two-layer beams from normal and fibered high strength concrete, *6-th International Structural Engineering and Construction Conference,* Zurich, Switzerland, June 21–26.

Iskhakov I., Ribakov Y., Holschemacher K. & Mueller T. 2011. Using steel fibred high strength concrete for repearing normal strength concrete beams and slabs. In Grantham M., Mechtcherine V. & Schneck U. (eds) *Concrete Solutions 2011—Dresden.* CRS Press (Tailor & Francis Group, A Balkema Book), 681–687.

Holschemacher K., Iskhakov I., Ribakov Y. & Mueller T. 2012. Laboratory tests of two-layer beams consisting of normal and fibered high strength concrete: ductility and technological aspects, *Mechanics of Advanced Materials and Structures,* 19, 513–522.

Iskhakov I., Ribakov Y., Holschemacher K. & Mueller T. 2013. High performance repairing of reinforced concrete structures. *Materials & Design*, 44, 216–222.

Iskhakov I., Ribakov Y., Holschemacher K. & Mueller T. 2014. Experimental Investigation of Full Scale Two-Layer Reinforced Concrete Beams, *Mechanics of Advanced Materials and Structures,* 21 (4), 273–283.

Oesterlee C., Bruhwiler E. & Denarie E. 2009. Structural behaviour of composite elements combining reinforced ultra-high performance fibre-reinforced concrete (UHPFRC) and reinforced concrete, *Beton und Stahlbetonbau*, 104 (8), 462–470 (in German).

Thanoon A., Jaafar M.S., Razali M., Kadir A. & Noorzaei J. 2005. Repair and structural performance of initially cracked reinforced concrete slabs. *Construction and Building Materials*, 19 (8), 595–603.

Concrete Repair, Rehabilitation and Retrofitting IV – Dehn et al. (Eds)
© 2016 Taylor & Francis Group, London, ISBN 978-1-138-02843-2

Investigations on the suitability of technical textiles for cathodic corrosion protection

Amir Asgharzadeh & Michael Raupach
Institute of Building Materials Research, RWTH-Aachen University, Germany

Detlef Koch
Koch GmbH, Kreuztal, Germany

ABSTRACT: Cathodic Protection (CP) is a widely used method to protect steel reinforcements against corrosion. In the course of the last half century, it has been established as a proven system for repairing corrosion-affected reinforced concrete structures, which have mainly been damaged by chloride-induced corrosion. The impressed current anode system for the protection of steel in concrete is latest state of technology. The CP anodes can be embedded in mortar, as coating or distinct anode on the repair structure surface and exposed to external current. In this way, the potential of carbon steel is shifted in cathodic direction and the anodic dissolution of carbon steel is suppressed. The current densities on the surface of the reinforcement play a key role in the shifting of the potential in cathodic direction. Nowadays, Mixed Metal Oxide coated Titanium (MMO) is used as an anode material for CP due to its high durability under anodic polarization. Also other materials such as carbon fibers are being studied. Carbon textiles in combination with mortar, which provide high mechanical properties and are also conductive, have not been studied systematically so far. In this paper investigations are described, which have been carried out in order to evaluate the capabilities of different carbon-textile anodes and different mortar mixtures for the cathodic protection of steel in concrete. In order to evaluate the polarization behavior of carbon-textile in mortar, galvanostatic experiments were performed. Based on these experiments, current density-potential-curves were derived.

1 INTRODUCTION

In order to protect constructions in aggressive environment and restrict the cross-sectional reduction of the reinforcement, repair actions are required. Raupach (2001) To achieve this objective, it is necessary to inhibit one of the two partial reactions (anodic/cathodic) of the corrosion process. Cathodic Protection (CP) is allocated to the process, which suppresses the anodic partial reaction. An advantage of CP is that chloride contaminated concrete does not have to be removed and almost non-destructive repair is still possible. Raupach (1992).

Figure 1 illustrates the principle of CP as follows: By embedding an inert anode, the reinforcement is applied selectively via a DC source with an impressed current. Raupach (1992) This current causes an excess of electrons in the reinforcement which makes the reinforcement act as a cathode. Thereby, the corrosion processes are reduced to an acceptable level.

To prevent the anodic dissolution of iron, a CP system for uncoated steel in concrete buildings is typically operated at current densities between 2 mA/m^2 to 20 mA/m^2. DIN EN ISO 12696 (2012).

If the component, however, is continuously saturated with water or for preventive CP, a current density of 0.2 mA/m^2 to 2 mA/m^2 can be considered.

1.1 *Textile reinforced concrete*

Textile reinforced concrete is a composite system of cement based concrete with glass or carbon

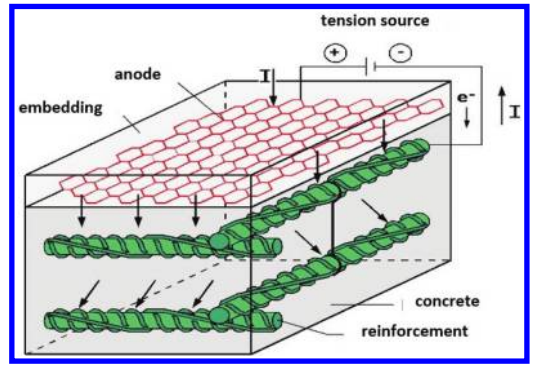

Figure 1. Concept of cathodic protection with an inert external-current-anode according to Boehni (1990).

fiber meshes as a reinforcing material. By using this material, it is possible to achieve low component thicknesses. This is due to the durability of textile reinforced concrete, as no thick concrete cover in the range of 2–5 cm such as for reinforced concrete is necessary.

Conventional CP systems located on the market function with MMO coated titanium as anode material. However, the use of technical textiles as anode material would have advantages to this material. Compared to traditional repair measures, the use of Textile Concrete is considered to be more environmentally friendly and the repair of a corrosion-damaged component could be more resource-efficient and cost-effective. Furthermore, textile reinforced concrete has several considerable advantages regarding serviceability and durability compared to traditional steel reinforced concrete.

2 EXPERIMENT SETUP AND TEST PROCEDURE

The test setup presented in Figure 2 was selected to simulate a component surface. The undermost layer of concrete containing reinforcement (here: MMO coated titanium), while the subsequent layer of concrete simulates the concrete cover. To simulate the reinforcement the MMO coated titanium was used, because this material can produce a homogeneous electric field due to its chemical inertness and reticular structure. Carbon Textile is applied onto the component surface by means of a specially developed mortar. Thus, a renovation of a corrosion-damaged concrete component is simulated. For the measurements suitable reference electrodes were required. Electrolyte bridges were placed in the specimens to be able to connect external reference electrodes to the specimen (Fig. 3). This electrolyte bridge was filled for a later connection with silver-silver chloride solution.

The following chart, (Table 1), provides an overview of the textile meshes, and the following images show the textiles in detail and their installation into the specimen.

After the Textile anodes were applied to the concrete base, the test specimens were cast with the special mortar. This mortar layer had a thickness of 15 mm and formed finely to the surface of the test specimens (see Fig. 2). Three different mortars were tested. In combination with the four anode materials a total of 12 specimens were made. The following chart, (Table 2), gives an overview of the mortar properties.

When the specimens had matured, they were connected to a potentiostat. The carbon textiles act as a working electrode, while the MMO coated titanium was connected as a counter electrode (see Fig. 8). Galvanostatic tests with stepwise increased applied electrical currents were carried out. Here, the potentials of the working electrode were measured against the reference electrode. The current densities

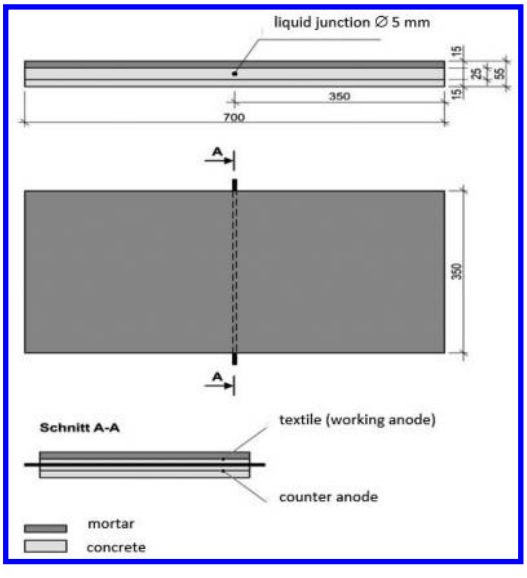

Figure 2. Detailed drawing of the specimen—dimension [mm] according to Henkel (2014).

Figure 3. Installed liquid junction (left), concrete base plate (right) according to Henkel (2014).

Table 1. Properties of the textiles.

Textile	Material/ structure	Coating	Mesh width (0°/90°) (mm)
1	Carbon/single mesh	Styrene-butadiene-rubber	14/8
2	Carbon/single mesh	Epoxy	20/20
3	Carbon/double mesh	Styrene-butadiene-rubber	15/15
4	Carbon/single mesh	Styrene-butadiene-rubber	14/13

Table 2. Overview of the mortar properties.

Mixture	Mortar mixture	Water	Water-reducing admixture	Special aggregate	Compressive strength [N/mm²]	Density [kg/dm³]
B	X	X	No. 1	X	110.3	2.37
C	X	X	–	–	77.6	2.26
D	X	X	No. 2	X	118.2	2.40

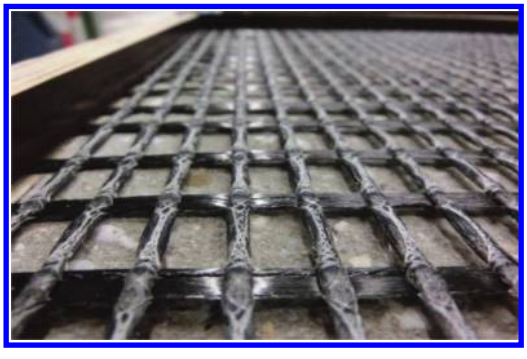

Figure 4. Textile 1 according to Henkel (2014).

Figure 5. Textile 2 according to Henkel (2014).

Figure 6. Textile 3 according to Henkel (2014).

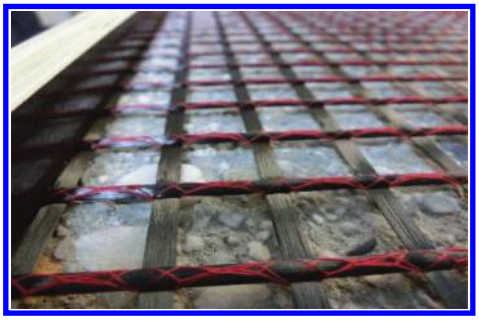

Figure 7. Textile 4 according to Henkel (2014).

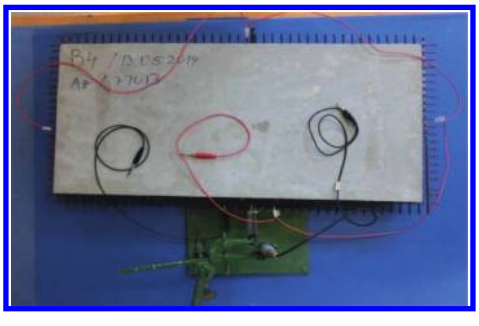

Figure 8. Complete test specimen according to Henkel (2014).

in detail, were 0 mA/m² (open circuit potential); 1 mA/m²; 3.2 mA/m²; 10 mA/m² und 20 mA/m².

Following each stage, instant-off potential measurements were performed. This procedure ensured that IR drop compensated potentials were measured, and that the actual polarization of the anode material is not overrated. Following the last instant-off measurements, the depolarization was determined. The duration of the intervals were chosen sufficiently large (12 h), so that the recorded potentials began to approach a limit where almost no changes were detected.

3 RESULTS

Figure 9 shows an exemplary curve of the galvanostatic stages experiment of the specimen B1.

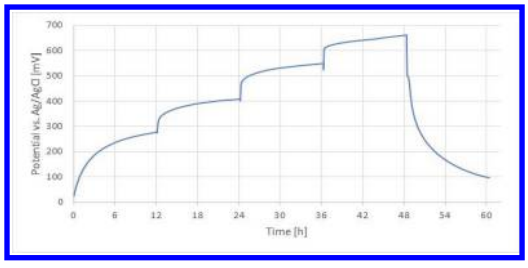

Figure 9. Galvanostatic test by progressive current densities—specimen B1 according to Henkel (2014).

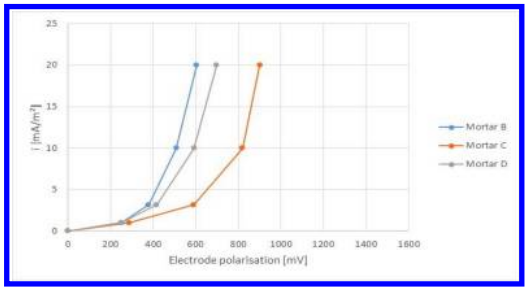

Figure 10. Current density-potential-curve textile 1 Henkel (2014).

The four stages in the various current densities can be clearly seen, and that the potential values stabilize after 12-hour depolarization's measurement. The IR drop can also be seen in the graph. After 36 hours, the galvanostatic test is completed with 10 mA/m^2 related to concrete surface.

To evaluate the galvanostatic stage testing with relation to the CP, current density versus potential curves were generated, as the following four Figures 10–13 show for the different embedding mortars and textiles. It can be seen, from the comparison of the curves, which combination of mortar and carbon textile requires the lowest voltage to achieve a current-density of 10 mA/m^2.

On the basis of the measurements for textile 1, mortar B is the most appropriate. In textile 3 and 4, mortars B and D have almost identical results. In textile 4, the difference of polarization of textiles in mortars C, B, and D is still less than 100 mV, and in textile 3 several hundred millivolts. The significantly deviating course of the measurement curves of textile 2 can be explained to the epoxy coating. This represents an increased resistance compared to Styrene-Butadiene (SBR) coating, so the conductivity of the textile decreases.

The evaluation with respect to the three tested mortar mixtures has shown that mortars B and D, with each textile, have almost identical polarization properties. Accordingly, they have the lowest

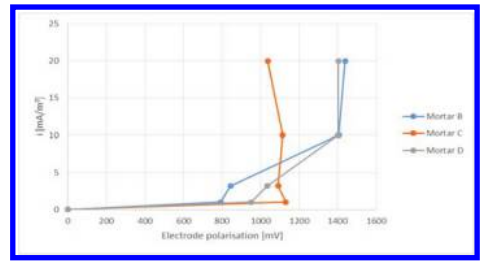

Figure 11. Current density-potential-curve textile 2 Henkel (2014).

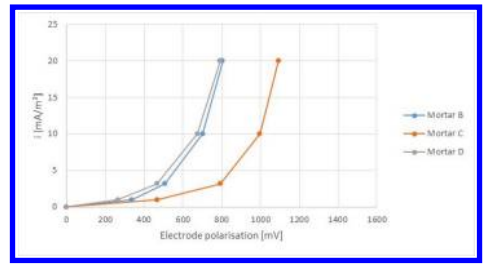

Figure 12. Current density-potential-curve textile 3 Henkel (2014).

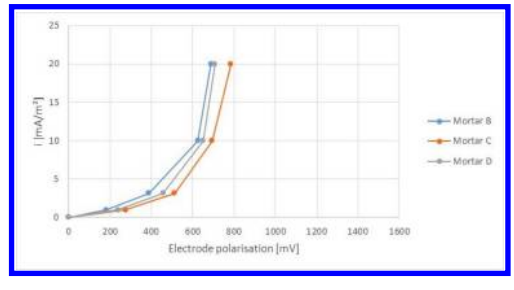

Figure 13. Current density-potential-curve textile 4 Henkel (2014).

voltages needed to achieve the same protective current density.

The lowest values in absolute terms are among the systems B1, B4 and D4.

In this work, these combinations were favored for further investigation. Benefits can result due to the different properties of the anode materials in practice. While textile 1 is on rolls, the textile 4 is supplied in mats.

4 CONCLUSIONS

The results of the experiments carried out within this study led to the following conclusions.

Carbon textiles are suitable as an anode material for the CP.

The SBR-impregnated materials revealed a significantly better polarization behavior compared to the EP-impregnated textiles.

The double mesh textile structure of the textile type 3 has been found to not be as advantageous compared to the single mesh structures of the textile types 1 and 4.

All investigated mortars can be used as embedding material for CP. The conductive hard aggregate used in B and D takes considerable benefits for the conductivity and compressive strength of the mortar.

5 OUTLOOK

This study has shown, that carbon textiles are generally suitable to be used as anodes for CP. Based on these results further investigations are required to shows the durability of carbon textiles.

ACKNOWLEDGMENT

The investigations have been carried out at the RWTH-Aachen University in cooperation with Koch GmbH for the project “cathodic corrosion protection with textile concrete”, supported within from AiF ZIM (Central Innovation Programme) initiated by Federal Ministry for Economic Affairs and Energy. We would like to thank to AiF for the support of this interesting project.

REFERENCES

Baeckmann, W. v. 1999. Historische Entwicklung des elektrochemischen Korrosionsschutzes. In W. v. Baeckmann, W., *Handbuch des kathodischen Korrosionsschutze*: 1–14. Weinheim: Wiley-VCH.

Boehni, H. 1990. Grundlagen der Korrosion und des elektrochemischen Korrosionsschutzes. *Korrosion und Korrosionsschutz*. Schweizerischer Ingenieur- und Architektenverein.

Deutsches Institut für Normung e.V. 2012. DIN EN ISO 12696 Kathodischer Korrosionsschutz von Stahl in Beton. Berlin: Beuth Verlag GmbH.

Henkel, P. 2014. Bachelorthesis. Untersuchung zur Bestimmung der Eignung technischer Textilien für den kathodischen Korrosionsschutz. Aachen: Institute of Building Materials Research of RWTH-Aachen University

Raupach, M. 1992. Kathodischer Korrosionsschutz im Stahlbetonbau: Instandhaltungsverfahren fuer Spezialfaelle. *Beton* 42: 674–676.

Raupach, M. 2001. Korrosionsschutzverfahren fuer Stahlbetonbauwerke: Entwicklung und Tendenzen. Restoration of Buildings and Monuments, 25. Aachener Baustofftag.

Concrete Repair, Rehabilitation and Retrofitting IV – Dehn et al. (Eds)
© 2016 Taylor & Francis Group, London, ISBN 978-1-138-02843-2

The evaluation of concomitant use of Metakaolin and Limestone Portland Cement to durability of HPC Concrete

A.A. Ramezanianpour
Head of Concrete Technology and Durability Research Center, Amirkabir University, Tehran, Iran

Nima Afzali
Master of Engineering of Construction Management, Amirkabir University of Technology, Tehran, Iran

ABSTRACT: Nowadays, the importance of the durability in concrete structures is more than the other factors like the compressive strength. Reinforced concrete structures, which are exposed to harsh environments are expected to last over long periods of time. For that important reason, a durable structure needs to be produced. Especially for reinforced concrete structures, one of the major forms of environmental attack is chloride penetration, which leads to corrosion of the reinforcing steel and a subsequent reduction in the strength, serviceability of the structure. This may lead to early repair or replacement of the structure. The ability of chloride ions to penetrate the concrete must then be known for design and quality control purposes. A common method of preventing such deterioration is to prevent chlorides from penetrating the structure by using additives like High Reactivity Metakaolin (HRM) in the system. Metakaolin is highly processed kaolinite clay that has been heat-treated under controlled conditions. Based on the important researches, also using appropriate portions of limestone contributes to improve compressive strength and permeability of concrete, But using 15% of limestone in concrete has severe effects on durability.

Which is unique In this paper is, the simultaneous effects of different percentages of Metakaolin (10%, 12.5%, 15%) with Type 1-425 Portland Cement containing 15% limestone at a high performance concrete (>60 MPa) have been evaluated.

In order to produce appropriate limestone cement, additional tests like Alpine Sieve, Bending test, and Compressive Strength, etc. have been carried out in this investigation. Results of using a high reactivity Metakaolin in high-performance concrete in adjacent with excessive amount of limestone, and the relative influences on the Compressive Strength, Impermeability, Electrical Resistance, and RCMT indexes (Rapid chloride Migration Test) are just some important factors presented in this paper.

1 INTRODUCTION

As it is obvious today, too many experiments have been carried out on the properties and applications of Limestone powder and Metakaolin in various types of concretes according to the durability, repairing or retrofitting purposes during our own time. Evaluation of physical properties and durability of such concretes against chloride attack and measurement of chloride ion penetration are some well-known experiments.

In this investigation after implementation of comprehensive experiments for evaluation of physical, chemical, and mechanical characteristics of applied materials, concomitant use of Metakaolin and Limestone Portland Cement to durability of HPC Concretes containing low water-cement ratio 0.31 and excessive cement paste has been evaluated. The maximum size of aggregate 12 mm selected, and proportion of sand to coarse aggregate was 3/1. This selection applied due to strengthening the appearance of cement paste and pozzolans' role and reduction of aggregate influences in probable weakness of concrete micro-structure. On the other hand, researchers reported conflicting views due to application of limestone powder in concrete. Since the reported conclusions in this article show the high rate of water absorption of applied limestone powder, then use of metakaolin in such HPC concrete caused a reduction of compressive strength and also durability at early ages in all the experiments. However, pozzolanic activity of Metakaolin is obvious during 7–90 days, the proper effect of this material observed in 90 days in comparison with control specimens.

2 LITERATURE REVIEW

2.1 *Application of limestone powder*

Before the 1980s, limestone powder was applied as an inert filler but recently, the results show that

calcium carbo-aluminate hydrates precipitate during the hydration of Portland Limestone Cement and also have an important role in an interaction between (C_3S) and ($CaCO_3$). Even though the $CaCO_3$ accelerates the hydration of C3S and modifies the Ca/Si ratio of C–S–H but limestone powder does not show pozzolanic activity and, never produce any C–S–H gel consequently. Limestone powder shows several physical effects such as, dilution effect, filler effect and heterogeneous nucleation in concrete micro-structure.

European Standard (EN 197-1-2000) has permitted up to 5% limestone as a minor additional constituent and also identifies four types of PLC containing 6–20% limestone. ASTM Standard (C150-04) also allows up to 5% of limestone, and both codes declare that calcium carbonate ($CaCO_3$) content calculated from the calcium oxide content should be more than 70% by mass.

Ramezanianpour et al. (2009) indicated that Portland Limestone Cement concretes containing up to 10% limestone, generally have lower depths of water penetration than OPC concretes, and PLC concretes containing more than 10% limestone show greater depths of water penetration and these are related with the filler effect, heterogeneous nucleation and also the dilution effect respectively.

Commonly, it is accepted that the fineness of the limestone is a factor that effects on setting time of cement pastes, but there are many contradictory comments about this issue. Vu et al. (2001) declared that for cement pastes of different fineness and C3S contents at 0% and 5% limestone replacements, the Initial and final setting times were found to decrease as fineness increased. El-Didamony et al. (1995) reported that increase of limestone decreased the setting time of cement pastes and reported approximately 70 min decrease in initial setting time for 20% replacement of limestone. On the other hand, Guemmadi et al. (2005) found that the setting time of pastes varied with the fineness, but no clear trend has been observed. Moir and Kelham (1997) found that increased fineness causes longer initial set times at 20% limestone replacement. Furthermore Tsivilis et al. (1999) found a minor decrease in set times when replacement increases.

2.2 *Application of metakaolin for durability of concrete*

Kaolinite clays, undergo thermal treatment and transform into Metakaolin. Metakaolin is one of the high reactivity pozzolans and being used in various industries widely. The results from many studies declare the positive influence of this material on improvement of bending and compressive strength, reduction of water penetration, creep of concrete and increase of resistivity against chloride attack.

$$MK[Al_2Si_2O_7] + CH + H \rightarrow CSH, C_4AH_{13}, C_3AH_6, C_2ASH_8 \quad (1)$$

Higher alumina contents, such as MK, tend to have higher pozzolanic capacities because formation of C-A-H has a high CH demand. The following relation (2) is a view of cement hydration and pozzolanic reaction after production of CH in adjacent of water. The reactivity of metakaolin highly depends on produced CH in the system, presence of adequate mixing water, the amount of C3 A in cement and also the amount of MK replacement.

Portland Cement

$$C_3S + H \xrightarrow{\text{fast}} C \cdot S \cdot H + CH$$

Portland · Pozzolan Cement

$$\text{Pozzolan} + CH + H \xrightarrow{\text{slow}} C \cdot S \cdot H \quad (2)$$

Poon et al. (2001) reported that degree of pozzolanic reaction was higher at the level of 5% MK than the levels of 10% and 20% for all ages which it is due to the greater amount of cement, and a higher concentration of CH, which is available for reaction with the pozzolan.

Frías and Cabrera (2000) evaluated the amount of CH content in MK pastes via DTA and TGA and declared the Increasing of CH content until 7 days in all replacements. After this procedure consuming of CH content until 90 days in all replacements observed and again, slight increasing of CH content has been reported. Based on another research from Shvarzman et al. (2003) and also Arikan et al. (2003) the positive influence of MK in micro structure improvement reported, but they have mentioned that Pozzolanic reactions, filler effects, accelerating effects in hydration, dilution, and also distribution effect is impossible to be considered separately!

Vaishali et al. (2011) worked on cubes of 15 cm size and cured for 28 days and then tested for measuring the compressive strength values of High-Performance Concrete (HPC) produced with MK and eventually declared that in various w/c ratios from 0.3 to 0.5, the replacement of 10% MK shows the best results. Furthermore, in RCPT test (Rapid Chloride Penetration Test) showed that the minimum charge passed (coulombs) is related to the w/c = 0.3 and replacement of 30% MK.

Courard et al. (2003) also confirmed that an appropriate amount of MK replacement, has positive influence on chloride attack and electrical resistivity behavior.

3 EQUIPMENTS AND INSTRUMENTS

Calibrated compressive strength apparatus, Wenner apparatus for measurement of electrical resistivity, Rapid Chloride Migration Test (RCMT) apparatus for measurement of the none-steady-state migration coefficient, and also general casting and curing vessels and molds.

4 PROCEDURE OF EXPERIMENTS

4.1 *Description of the tests and standards*

In this experimental program more over the tests carried out on the materials, the mortar and concrete specimens evaluated by the explained tests in this section.

For production of new cement which applied in all the concrete specimens (LPC) Limestone Portland Cement, which contains 15% limestone powder, Normal Consistency (ASTM C-305), Initial and Final Setting time (ASTM C-187-98), Bending and Compressive Strength on mortar specimens have been implemented then, the obtained results were compared with Original Portland Cement (OPC type 1-425) specimens.

It will be mentioned that for evaluation of MK physical reactivity index, separate experiments based on (ASTM C-109) were conducted by measurement of compressive strength on mortar specimens containing (OPC).

The Long-term water absorption test based on (ASTM C-642-97) was conducted on cylindrical Concrete Specimens with 100 mm diameter, 50 mm thickness, and more than 800 gr weight.

Evaluation of Surface Electrical Resistivity was implemented by Wenner apparatus based on (ASHTO T08) on cylindrical concrete specimens with 100 mm diameter and 200 mm height.

Calculation of the none-steady-state migration coefficient was implemented by (RCMT) apparatus based on (NT Build 492) on cylindrical concrete specimens with 100 mm diameter and 50 mm thickness. The following formula (3) explains the required variables.

$$D_{nssm} = \frac{0.0239(273+T)L}{(U-2)t}\left(x_d - 0.0238\sqrt{\frac{(273+T)Lx_d}{U-2}}\right) \quad (3)$$

U: Absolute value of the applied voltage, V;
T: Average value of the initial and final temperatures in the anolyte solution, °C;
L: Thickness of the specimen, mm;
x_d: Average value of the penetration depths, mm;
t: Test duration, hour.
D_{nssm}: Migration coefficient, $\times 10^{-12}$m^2/s.

Figure 1 shows the arrangement of RCMT apparatus setup. The catholyte solution which is 10% NaCl by mass in tap water (100 g NaCl in 900 g water) and the anolyte solution which is 0.3 N NaOH in distilled or de-ionized water (approximately 12 g NaOH in 1 liter water) were prepared for the apparatus.

4.2 *Preparation of specimens*

All the mixing, curing, and casting procedures and other preparation methods were based on mentioned international codes. The specimens were cured in lime-water at the temperature of 18–20 °C until the test day.

4.3 *Experimental program*

- Evaluation of MK physical reactivity index in (OPC) mortar Specimens
- Production of new cement (LPC 15% Limestone powder) by (OPC) type 1–425
- Comparison of (LPC) characteristics with (OPC) characteristics by evaluation of mortar specimens.
- Evaluation of MK influence in durability of concrete specimens containing (LPC) with different percentages of MK replacement.

For evaluation of Compressive Strength and also durability characteristics of concrete specimens, 4 different mixture designs containing 0%, MK as

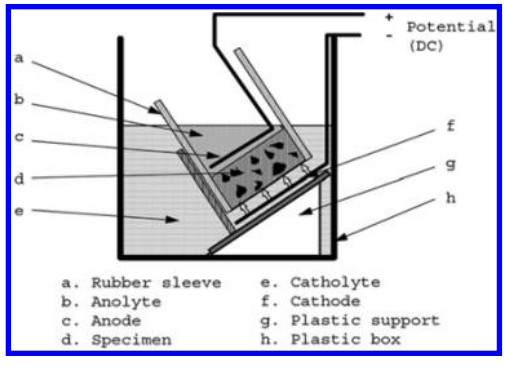

Figure 1. Schematic picture of (RCMT) apparatus.

Table 1. Alpine sieve test.

No	Material	Remained on 90 micron %
1	OPC	4.3
2	LPC	4.1

the control specimens, 10%, 12.5%, 15% MK were selected. The cement used for all the concrete specimens was just LPC (15% limestone powder).

4.4 *Applied materials*

The required lime stones for production of (LPC), were crushed and grinded based on the amount of remained cement particles on 90 microns Alpine Sieve as shown in Table 1.

Metakaolin (MK) used as the high reactive pozzolan and supplementary for Limestone Portland cement in concrete specimens. Table 2 shows the XRF results of MK compositions.

Fine aggregates have been twice washed and also the maximum size of coarse aggregates in concrete mixture design was 12 mm. It will be noted that, the proportions of aggregates in all concrete mixtures were 75% fine aggregates to 25% coarse aggregates. Table 3 presents the physical specifications of fine and coarse aggregates.

For better distribution and mixing procedure, the third generation of carboxylic super-plasticizer has been applied in the concrete system. The commercial name of this product was TamCem 23SSR. The amount of replacement was 0.4% of binder materials' weight.

W/Binder ratio was 0.31 and the mixing water used in this experimental program tap water, which has appropriate conditions for using in a concrete mixture.

4.5 *Reactivity of applied metakaolin*

For evaluating the physical reactivity of metakaolin in the test program, the compressive strength of cubic mortar specimens containing 15% metakaolin at 7 and 28 days in comparison with the type I-425 Portland cement used as an index. The cubic specimens were in 5 cm dimensions.

The sand to cement content was 3/1 by weight and the amount of water to cement ratio was (0.5). Also the fineness modulus of the sand used was 2.98 and the designed mixtures for the mortars are in Table 4.

The index of increasing compressive strength by 15% of metakaolin in comparison with control specimens for 7 days obtained 0.97 and for 28 days specimens 1.095 acquired.

4.6 *Analyses and results*

In this section more over an evaluation of implemented experiments a comprehensive discussion of the test results will be carried out. The results presented in Table 5 is related to the comparison of physical characteristics of mortar and cement paste specimens obtained from OPC and LPC.

Table 2. Metakaolin XRF results.

Contents	SiO_2	AL_2O_3	Fe_2O_3	MgO	CaO	TiO_2	K_2O	Na_2O
%	59.12	33.84	2.27	0.37	2.45	0.18	0.54	0.37

Table 3. Physical characteristics of aggregates in mortar and concrete.

Aggregates	Water absorption ratio	Density gr/cm^3	Maximum size
Fine	2.2	2.55	
Coarse	1.8	2.58	12 mm

Table 4. Mixture design for one litter of mortar.

	Proportions (gr/litter)	
Materials	OPC	15% MK
Sand	1667	1667
Cement	556	472
Metakaolin	0	83
Water	278	278

Table 5. Physical properties of cement pastes.

			Setting time (min)			Bending strength (Mpa)			Compressive strength (Mpa)		
No.	Specimen	Code	Initial	Final	Normal consistency %	3 days	7 days	28 days	3 days	7 days	28days
1	OPC	343	180	219	24	5.3	6.9	7.7	27.8	36.8	46.4
2	LPC	343/1	131	155	24	4.9	6.5	7.6	25.7	34.1	43

For producing the new cement (LPC) which contains 15% limestone replacement with OPC, it was mandatory to test the new LPC in comparison with OPC physical characteristics. As mentioned in this article, there are too many diverse views that contradict each other about the role of limestone on the setting time of pastes, But in this report, obviously 27–30% reduction in setting time was observed by 15% replacement of limestone, which emanates from water absorbent activity of particles.

Also because, a similar fineness assumed for limestone and cement particles as reported in section (4.4) Table 1 the lime stones were grinded till the remained amount on the 90 micron alpine sieve stayed on 4.1–4.3%. A similar consistency with 24% water that obtained for OPC and LPC, could be another index for the same fineness of the new cement particles. In this report the bending strength of LPC mortar at 7 & 28 days was approximately similar to OPC, But for compressive strength at 28 days, 7.3% reduction was observed as shown in Table 5 and Figure 2.

The following Table 6 represents the concrete specimens' mixture design which the compressive strength test and durability tests such as long-term water absorption, electrical resistivity and chloride migration coefficient have been carried out.

In these mixtures for achieving the HPC concrete with compressive strength more than 60 Mpa at 28 days, 530 kg of LPC, which contains 451 kg cement and 79 kg limestone with W/B ratio 0.31 has been selected. Table 6 shows the design mixture proportions of concretes. The amount of Superplasticizer to achieve the slump between 7–10 cm acquired 0.4% of the LPC weight.

For evaluation of compressive strength, the cubic concrete specimens of 10 cm dimensions, cured in lime water until the test days. As shown in Figure 3 with growing the age, the compressive strength increases and the differences between the compressive strength of mixtures containing MK compared with the control specimens' decrease. Finally, ***In 90 days***, MK10 & MK12.5 have more strength than control specimens. In some cases, the OLPC (control specimen) has more compressive strength even in 90 days age in comparison with MK15%. It's due to, when we encounter with the concretes in very low W/B ratios (0.31 in this program), the amount of strength gaining because of clinker reactions is very high especially in type I-425 cement and the concrete has a more integrated structure and lesser porosity and the influence of MK in adjacent with dilution effect doesn't show a considerable reactivity in obtaining compressive strength and structure improvement, and dilution effects as a weakness. However, based on reactivity measurement test of this type of metakaolin (w/c = 0.5) the reactivity factor in 28 days reached to 1.095 of the control specimens. On the other hand it seems that because of existence of limestone powder as the high water absorbent nucleuses (based on Setting Time test results) in the system that contains very low w/b ratios, and the particles lose water gradually, the velocity of MK pozzolanic reactions will be reduced.

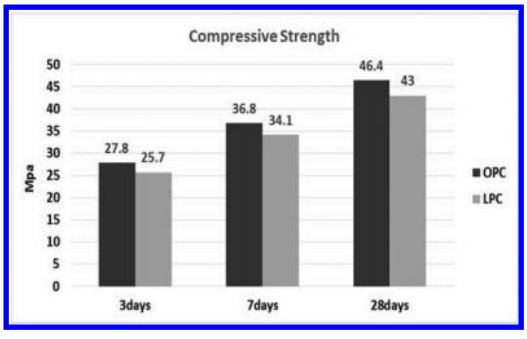

Figure 2. Compressive strength of mortar specimens.

Table 6. Concrete mixture designs for 1 m^3 volume of concrete.

Materials (Kg)	Control 0%	MK10%	MK12.5%	MK15%
Coarse agg.	410.5	410.5	410.5	410.5
Fine agg.	1216	1216	1216	1216
LPC	530	477	464	451
MK	0	53	66	79
Water	164	164	164	164
Agg. water absorption	22.2	22.2	22.2	22.2
Super plasticizer	2.12	2.12	2.12	2.12

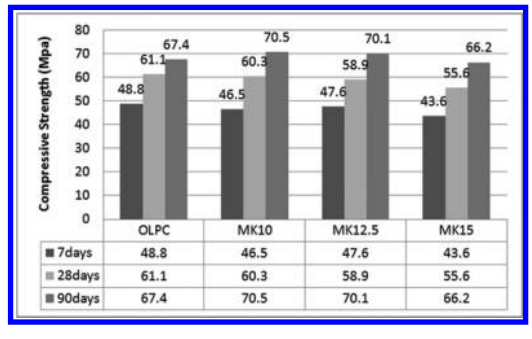

Figure 3. The compressive strength of mixtures at various ages.

As it is clearly visible, finally the role of Mk shows itself in improvement of the compressive strength in MK10 and MK12.5 in 90 days. The maximum of obtained strength related to MK10 with 70.5 Mpa.

The activity of MK especially in very low W/C ratios, relates to the appropriate proportions of the water content of cement paste, C-H production in the system, and amount of replacement of MK, particularly when a high-water absorbent material like limestone exists. In unsuitable situations, higher replacements of MK never show appropriate activity. Figure 4.

The long-term water absorption test approved the statements in the other form. Water absorption experiment for all mixture designs carried out on 3 cylindrical specimens with 10 cm diameter and 5 cm thickness cut. As it is observed in Figure 5 generally with growing the specimens' ages, the amount of water absorption in all specimens is reduced. This phenomenon is natural and shows the hydration progress and reduction of porosity in the system. The large amount of percentages of water absorption (more than 5%) and also the small amount of changes in water absorption of various samples toward each other as shown in the following figure, is due to the existence of excessive cement paste in the micro structure of concrete and also containing a large amount of limestone powder 15%, which acts as the ultrafine water absorbent particles in this system, and a long period of time.

Results show the increase of water absorption at higher level of replacements of MK in the system at early ages. The dilution effect of MK has an important role in weakness of structure in 28 days age. With reduction of clinker in the system which has a very low W/C ratio plays a more important role in structural strength, especially at early ages. The porosity increases then higher water absorption is observed as discussed.

The amount of water absorption reduced in MK10 and approximately in MK12.5 in 90 days age when compared with OLPC, But in MK15, the effect of dilution is more than the pozzolanic reactivity and demonstration of growth toward OLPC is observed. The least water absorption observed in MK10 in 90 days age at about 5.54%.

The Figure 6 represents the amounts of Surface Electrical Resistivity of designed mixtures in different ages. Based on these results, on control specimens with growth of the sample ages, and improvement of micro structure and also completion of hydration reactions the resistivity improves. When the amount of clinker reduces in this system, the porosity increases even though in the other way the amount of ionized clinker concentration also reduces in the system but obviously the effect of micro structure and water penetration in reduction of resistivity (accelerating ions movement) until 28 days age overcomes the other issues especially due to excessive cement paste existence in designed concretes. The measurement of all specimens implemented when they were saturated.

The results in Figures 6 and 7 show that with visible growth of MK influence through 28–90 days ages, the measurements in 90 days age, shows the proper effect of using any replacement of MK

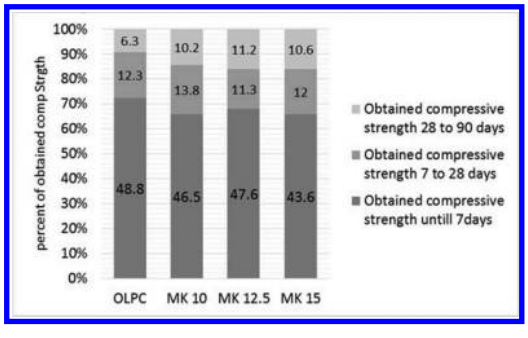

Figure 4. Compressive strength gaining for various mixtures.

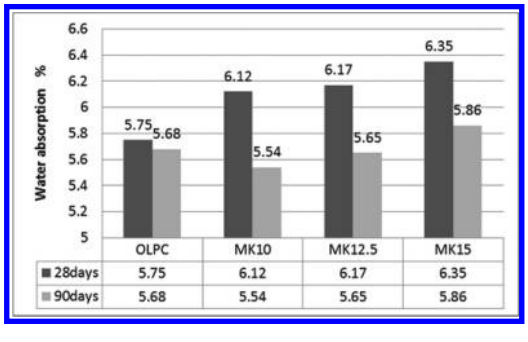

Figure 5. Water absorption test results.

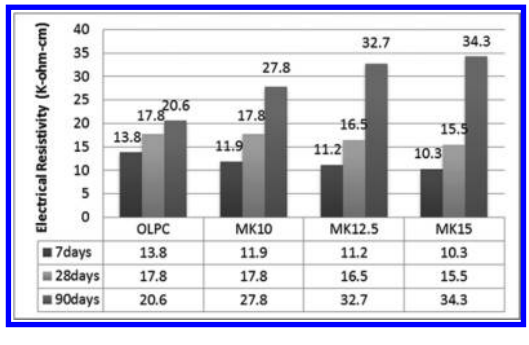

Figure 6. Electrical resistivity of specimens.

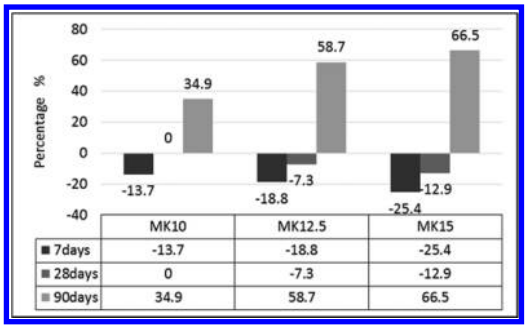

Figure 7. Percent of resistivity growth in comparison with control specimens.

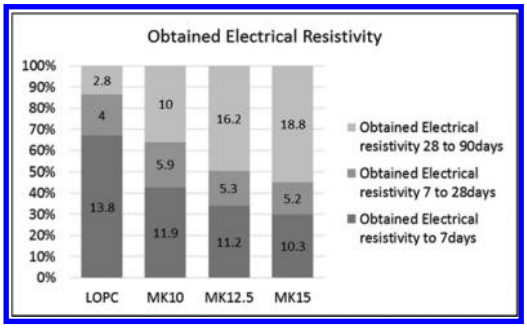

Figure 8. Obtained electrical resistivity till 90 days age.

in improvement of the electrical resistivity. More completion of pozzolanic reactivity, reduction of ion consistency, and refining the micro structure and also consuming the OH^- ion by reactive SiO_2 reactions, and on the other hand, dilution effect of more MK replacements, cause resistivity increasing in older ages. Then MK15% at 90 days has the best resistivity. It's necessary to be mentioned that, using more coarse aggregates and increasing the maximum size of Aggregates and also applying lesser cement in concrete have proper influences on growth of electrical resistivity.

The Figure 8 represents Obtained electrical resistivity till 90 days age for more comprehensive evaluation.

One of the most important issues on reinforced concrete structures, is the corrosion of steel bars due to chloride ion existence. This corrosion usually increases the bar volume and cause cracks and spalling of the concrete. Eventually, there is no way but destruction of the concrete structure.

The migration coefficient in RCMT also depends on the micro structure of the concrete and the conductivity of the pore fluid (OH^- ion). When in control specimens, the ages increases, due to improvement of micro structure, a reduction in the migration coefficient is visible. Perhaps the small changes emanating from excessive amount of cement paste in the system, but clearly when the metakaolin affects the system at 28–90 days ages, especially at 90 days age measurement, we could see more considerable reduction in all replacements of metakaolin. The compressive strength results, water absorption results and electrical resistivity conclusions, all are showing the fact that until 28 days of age the replacement of more metakaolin in this high-performance concrete cause weaker micro structure in the system. This phenomenon is also visible in RCMT results.

Based on the Figure 9 the worst Migration Coefficient observed in 28 days of age for MK15 equal to 14.05 and the lowest coefficient obtained also at 90 days of age for MK15. It's because of reactivity of metakaolin which consumes the $Ca(OH)2$ in the system and by consuming the OH^- ions, the conductivity of the pore fluid and consistency of ions in the system are reduced. In all percentages of replacement, the effect of MK in improvement of concrete against chloride ion migration at 90 days age is obvious. Furthermore Figure 10 represents the Reduction of the

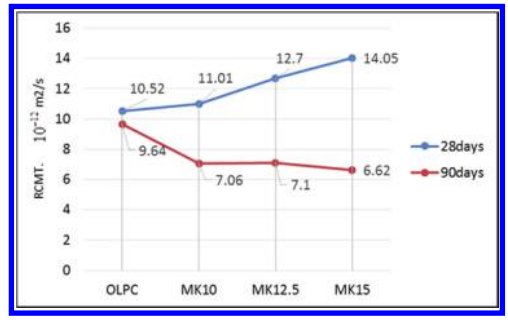

Figure 9. Migration coefficient of RCMT test.

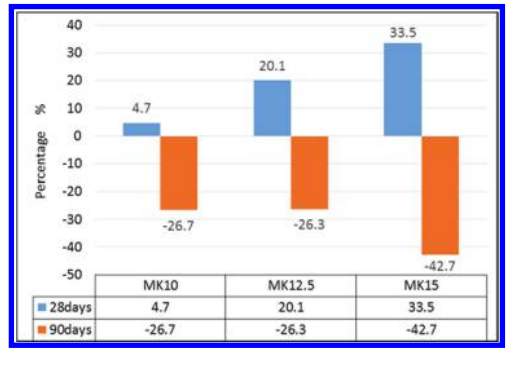

Figure 10. Reduction of migration coefficient compared to control samples.

migration coefficient compared to control samples for a clear comparison.

5 CONCLUSIONS

All replacement levels of Mk caused growth of migration coefficient and weakness of electrical resistivity at 28 days of age, which is emanating from dilution effect and reduction of clinker in the system.

The clinker reactions in very low W/C ratio demonstrate more powerful activity in improvement of structure toward pozzolanic activities.

Based on all the stated results, applying metakaolin in lower replacement amounts, for concretes containing low w/b ratios is recommended.

Also the effect of limestone water absorption on the reduction of MK activity at early ages for durability of concrete specimens should not be neglected particularly for situations of retrofitting and repair of structures and presence of low reactivity pozzolans.

Existence of excessive cement pastes even in High-Performance Concretes (HPC) cause reduction of electrical resistivity and severe weakness against electro-chemical attacks due to increasing the ion consistency in concrete.

The activity of MK, especially in very low W/C ratios, relates to appropriate proportions of the water content of cement paste, C-H production within the system, and amount of replacement of MK, particularly when a high-water absorbent material like limestone exists. In unsuitable situations, higher replacements of MK never show appropriate activity.

REFERENCES

Arikan, M. et al. 2003 "Development of cement and concrete additives based on thermally activated kaolin". TUB_ITAK project proposal_IC¸TAG; 680:55.

Courard, L. et al. 2003 "Durability of mortars modified with metakaolin", Cement and Concrete Research, 33(9): 1473–1479.

El-Didamony, H. et al. 1995. "Limestone as a retarder and filler in limestone blended cement", Ceramics—Silikaty, 39, 1, 15–19.

Frías, M. & Cabrera, J. 2000, "Pore size distribution and degree of hydration of metakaolin-cement pastes", Cement and Concrete Research; 30(4): 561–569.

Guemmadi, Z. et al. 2005. "Iinfluence of limestone fillers on the mechanical performances of cement pastes", Proc Intl Conf on Cement Combinations for Durable Concrete, 339–350.

Hooton R.D. et al. "Portland-Limestone Cement" Cement association of Canada: State-of-the-Art Report and Gap Analysis for CSA A 3000".

Moir, G.K., and Kelham, S., 1997. "Developments in the manufacture and use of Portland limestone cement," ACI Special Publication SP 172–42, pp. 797–819.

Poon, C.S. et al. 2001 "Rate of pozzolanic reaction of metakaolin in high-performance cement pastes", Cement and Concrete Research; 31(9): 1301–1306.

Ramezanianpour, A.A. et al. 2009 "Influence of various amounts of limestone powder on performance of Portland limestone cement concretes" ELSEVIER *Cement & Concrete Composites* 31: 715–720.

Shvarzman, A. et al. 2003 "The effect of dehydroxylation/amorphization degree on pozzolanic activity of kaolinite", Cement and Concrete Research; Vol. 33(3);

Tsivilis, S. et al. 1999a. "A study on the parameters affecting the properties of Portland limestone cements." Cement and Concrete Composites, 21, 2, 107–116.

Tsivilis, S. et al. 1999b. "The effect of clinker and limestone quality on the gas permeability, water absorption and pore structure of limestone cement concrete." Cement and Concrete Composites, 21, 2, 139–146.

Vaishali. et al. 2011 "Chloride-Ion permeability studies of metakaolin based high performance concrete" International Journal of Engineering Science and Technology".

Vu, D.D. et al. 2001 "Strength and durability aspects of calcined kaolin-blended Portland cement mortar and concrete", *Cement and Concrete Composites*; 23(6): 471–478.

Concrete Repair, Rehabilitation and Retrofitting IV – Dehn et al. (Eds)
© 2016 Taylor & Francis Group, London, ISBN 978-1-138-02843-2

Polymer modified high performance concrete as structural repair material of existing structures

K.D. Zavliaris
Greece

ABSTRACT: In many instances concrete structures need to be either repaired because of degradation or strengthened for upgrading. Among the available techniques, utilization of Polymer Modified High Performance Concrete (PMHPC) and mortar (PMHPM) can be used as repair and strengthening method as is stated and discussed in this paper.

The structural performance of PMHPC and PMHPM is controlled by the cement type, the presence of pozzolans in the mix, the type and size of aggregates, the W/C ratio, the type and content of Polymer and the type and content of fibers.

From design considerations point of view the shear transfer and slip across interface, the effect of shrinkage and the combined action of steel bars and fibers are important and must be taken into account.

Finally a comparison of PMHPC and normal cement concrete in terms of strength, durability and cost is made which can serve as selection guide for the repair materials and techniques.

1 STRUCTURAL REPAIRS

Concrete is a durable structural material used widely across the globe in both infrastructure and buildings in a variety of load bearing systems, reinforcement types and construction methods. In many instances, however, there is need for repairing, strengthening and general upgrading concrete structures as a result of degradation, damage, change of use or increased loads of the structure.

As repair is termed the restoration of the initial (maiden) mechanical properties i.e the ultimate capacity and the stiffness of the structural member. Repair techniques involve injections, replacement of damaged reinforcement and patching.

On the other hand strengthening aims at upgrading the mechanical properties by utilization of a great variety of methods and materials, namely:

- Jacketing by means of:
  - Cast in Place Concrete
  - Shotcrete
  - High Performance concrete or mortar
  - Modified High Performance concrete or mortar
  - Polymer Concrete, all reinforced by
    - Ordinary steel bars or meshes
    - Steel fibers in a variety of geometry
    - Non-metallic fibers in different forms i.e. individual fibers or textiles, with a wide range of materials and geometry
- Glued steel plates
- Glued fiber reinforced polymers
- Bonded external mineral fiber reinforced mortars
- External post stressing.

2 HIGH PERFORMANCE CONCRETE AND MORTAR

The term High Performance Concrete (HPC) and High Performance Mortar (HPM) implies that the corresponding mixtures possess high workability, high durability and high ultimate strength,

From a structural point of view the crucial characteristics are: strength, ductility and durability.

As far as the strength of concrete is concerned a typical Classification is:

Normal Strength Concrete (NSC): 20–50 MPa
High Strength Concrete (HPC): 50–100 MPa
Ultra High Strength Concrete (UHPC): 100–150 MPa
Special Concrete > 150 MPa.

2.1 *Mechanical behaviour*

Generally, HPC exhibits the following features in comparison with NSC: more linear stress-strain curve, increased strain corresponding to the maximum stress, steeper post-peak domain and ultimate deformation decreased with increasing strength, s. Figure 1.

The Elastic Modulus Ec for normal weight HPC with: 21 MPa < fc < 83 MPa can be given as:

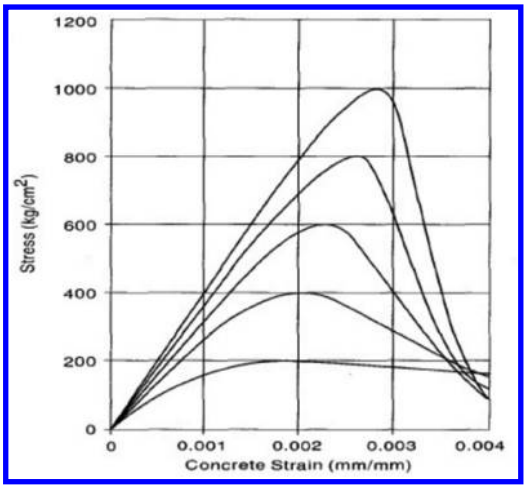

Figure 1. Stress–Strain relationship of HPC, after [6].

Table 1. HPC proportioning and time dependent strength after [3].

Units per m³	Mix number					
	1	2	3	4	5	6
Cement, Type I, kg	564	475	487	564	475	327
Silica fume, kg	—	24	47	89	74	27
Fly ash, kg	—	59	—	—	104	87
Coarse aggregate SSD (12.5 mm crushed limestone), kg	1068	1068	1068	1068	1068	1121
Fine aggregate SSD, kg	647	659	676	593	593	742
HRWR Type F, liters	11.6	11.6	11.22	20.11	16.44	6.3
HRWR Type G, liters	—	—	—	—	—	3.24
Retarder, Type D, liters	1.12	1.05	0.97	1.46	1.5	—
Water to cementing materials ratio	0.28	0.29	0.29	0.22	0.23	0.32
Fresh concrete properties						
Slump, mm	197	248	216	254	235	203
Density, kg/ m³	2451	2453	2433	2496	2459	2454
Air content, %	1.6	0.7	1.3	1.1	1.4	1.2
Concrete temp., °C	24	24	18	17	17	23
Compressive strength, 100 x 200-mm moist-cured cylinders						
3 days, MPa	57	54	55	72	53	43
7 days, MPa	67	71	71	92	77	63
28 days, MPa	79	92	90	117	100	86
56 days, MPa	84	94	95	122	116	—
91 days, MPa	88	105	96	124	120	92
182 days, MPa	97	105	97	128	120	—
426 days, MPa	103	118	100	133	119	—
1085 days, MPa	115	122	115	150	132	—
Modulus of elasticity in compression, 100 x 200-mm moist-cured cylinders						
91 days, GPa	50.6	49.9	50.1	56.5	53.4	47.9
Drying shrinkage, 75 by 75 x 285-mm prisms						
7 days, millionths	193	123	100	87	137	—
28 days, millionths	400	287	240	203	233	—
90 days, millionths	573	447	383	320	340	—
369 days, millionths	690	577	520	453	467	—
1075 days, millionths	753	677	603	527	523	—

Ec = 3320 √fc + 6900 MPa where fc is the compressive strength of concrete.

Durability properties are related to the resistance of concrete to permeation of water and chemical ions. HPC generally exhibits better durability characteristics than NSC, which can be further improved by modification with polymers.

Shrinkage of HPC is reported to be slightly different from that of NSC, according to [6].

2.2 *Materials*

Crucial for achieving higher strength while maintaining good workability, is the selection of cement in terms of its chemical compatibility with additives, finesses and chemical composition. Low C3A cements result in improved rheology of mixture.

The low water/cement ratio causes desinfication in both the matrix and interfacial zone, thus, the aggregates may become the weak link of the system. Therefore, there is need for their careful selection from chemical and physical point of view. A general rule is the higher the strength to achieve the smaller the maximum size of aggregates.

Fine pozzolanic materials are extensively used, the most common being microsilica. The requirements on workability with low water/cement factor can be satisfied by special superplasticizers among which polycarboxylate ethers are very common.

2.3 *The importance of early strength in structural repairing*

An important aspect of the structural repair materials is that of early development of the strength since in many instances there is an element of urgency in the interventions to be carried out. From this point of view HPC exhibits very interesting features as can be seen from Table 1.

3 POLYMER MODIFICATION OF CONCRETE /MORTARS

Polymer Modified Cement Concrete (PMCC) mixtures are those in which a water soluble or emulsified polymer is added during mixing. As the concrete cures, hardening of polymer also occurs, forming a continuous matrix of polymer throughout the concrete.

The polymers in use are latexes, redispersible polymer powders, water-soluble polymers, liquid resins, and monomers. The most commonly used are: Styrene-Butadiene Rubber (SBR) latex, Ethylene-Vinyl Acetate (EVA), Polyacrylic Ester (PAE) and Epoxy (EP) resin.

For all PMCC it is very important that both cement hydration and polymer film formation (coalescence of polymer particles and the polymerization of resins) proceed parallel to yield a monolithic matrix phase with network structure in which the cement hydrate phase and polymer phase interpenetrate. In polymer-modified mortar and concrete structures, aggregates are bound by such co-matrix phase, resulting in superior properties compared with conventional cementitious composite.

The above model, explains why the properties of ordinary cement mortar and concrete are generally improved to a great extent by latex modification. It is generally considered that plain hardened cement paste mainly has an agglomerated structure of calcium silicate hydrates and calcium hydroxide bound together by the weaker van der Waals forces,

and therefore, microcracks occur easily in the paste under stress. This leads to poor tensile strength and fracture toughness of normal cement mortar and concrete. By contrast, in the latex-modified mortar and concrete, it appears that the microcracks are bridged by the polymer films or membranes which prevent crack propagation, and simultaneously, a strong cement hydrate-aggregate bond is developed [1].

The shrinkage properties of PMC and PMM are strongly dependent on the type of polymer and to lessen degree to P/C after [1].

For SBR modified concrete and mortars these rates rates are slightly less of that of ordinary concrete and mortar subject to P/C rate.

3.1 *SBR (styrene butadiene rubber) modified concrete*

SBR Polymer is the most widely used in concrete. SBR properties after [9] are shown in Table 2.

Table 2. Properties of SBR, after [9].

Physical state	Milky white liquid
Total solids (by weight of weight of polymer)	40%
Specific gravity	1.01
PH	10.5
Mean particle size	0.17 microns

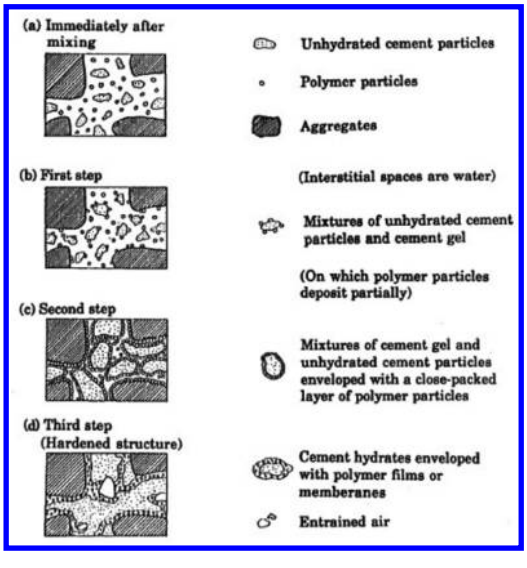

Figure 2. Simplified model of formation of polymer–cement co-matrix after [9].

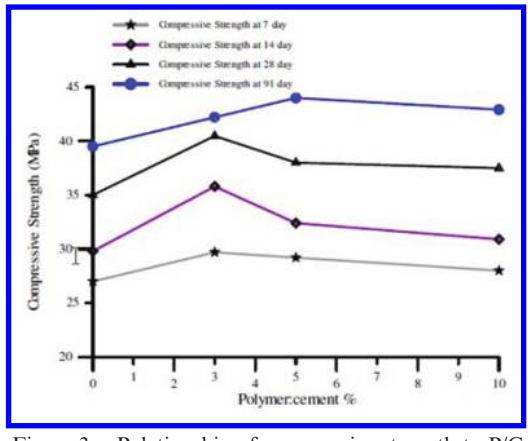

Figure 3. Relationship of compressive strength to P/C ratio of PMC after [1].

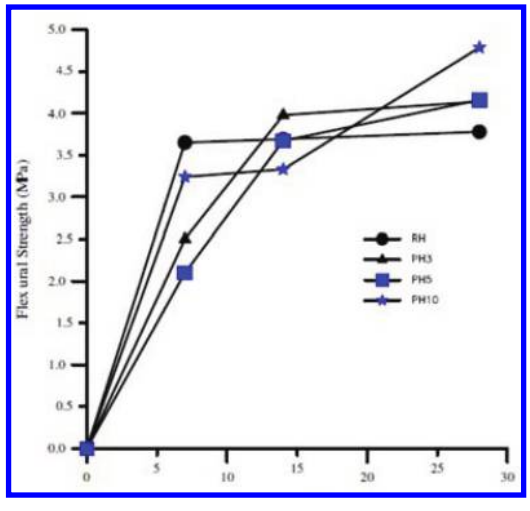

Figure 4. Relationship of Flexural strength to P/C ratio of PMC after [1] RH: C/P = 0%—PH3:C/P = 3%—PH5: CP = 5%, PH10:C/P = 10%.

In SBR modified Concrete and Mortars high adhesion between the polymer films and cement hydrates is established which results in enhancement of flexural and compressive strength and higher durability of PMC, PMM.

3.2 *Mechanical properties of SBR modified concrete*

In the following tables the influence of SBR modification on the main mechanical properties of concrete is illustrated.

On the other hand the improvement of durability by the addition of polymer in the matrix in

terms of reduction in the depth of carbonation is illustrated in the following Figure 5.

3.3 *Effect of polymer modification on the reinforcement of fibre reinforced concrete*

One of the reasons to Polymer modify HPC is to increase the adhesion of concrete to both the reinforcement steel and concrete substrates, [9].

The same effect applies on the fibers added to HPC in order to rectify its brittleness characteristics, Figure 6, and results in increased flexural strength, subject to the type of fibers, the type of polymer and P/C ratio, according to [10].

3.4 *Mix proportioning of PMC or PMP*

The polymer/cement ratio (the weight ratio of the amount of total solids in a polymer latex to the amount of cement in a latex-modified mortar or concrete mixture) is the controlling factor for achieving the strength requirements for the tensile and flexural strength and those for adhesion on the substrate of latex-modified mortar and concrete.

The mix proportions of most latex-modified concretes depend on many factors. Crucial are the polymer-cement ratio of the latex-modified concrete with range from 5 to 15%, and the water-cement ratio with values from 30 to 50%.

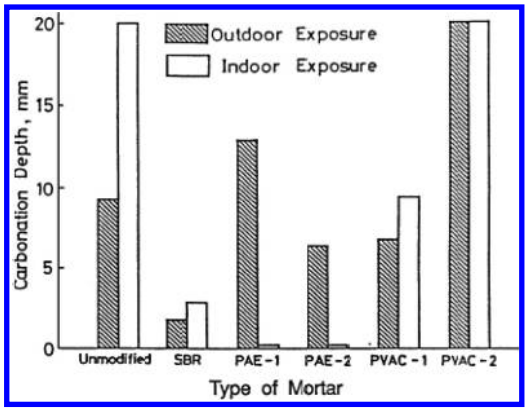

Figure 5. Reduction of depth of carbonation of PMC as function of the type of polymer, after [9].

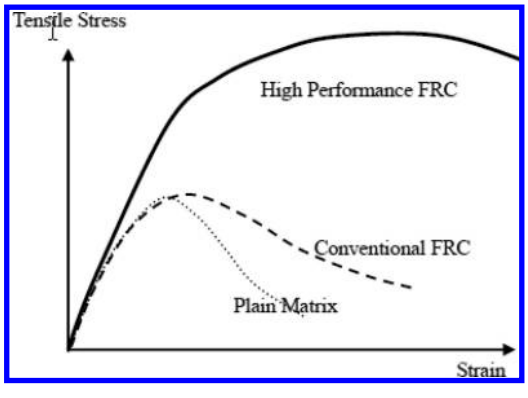

Figure 6. Improvement of Compressive behavior of HPC by addition of fibers, after [4].

4 THE BOND BETWEEN HPC AND ORDINARY CONCRETE SUBSTRATE

In structural repairs of concrete, the bond between repair materials and concrete substrate is of vital importance. It depends on a range of controlling factors such as interface properties, properties of repair concrete and curing and environmental conditions.

Interface properties involve the degree of roughness and cleanliness of the substrate along with the laitance on it. The critical characteristics of the repair concrete apart from its strength are the workability which determines the ability to fill the voids and cavities of the interface, the content of cementitious material, the degree of the polymer modification and its compaction. There are some quite different methods for measuring the bond strength, the most common of which are illustrated in the following Figure 7 along with test results of concrete mixes with varying SBR content;

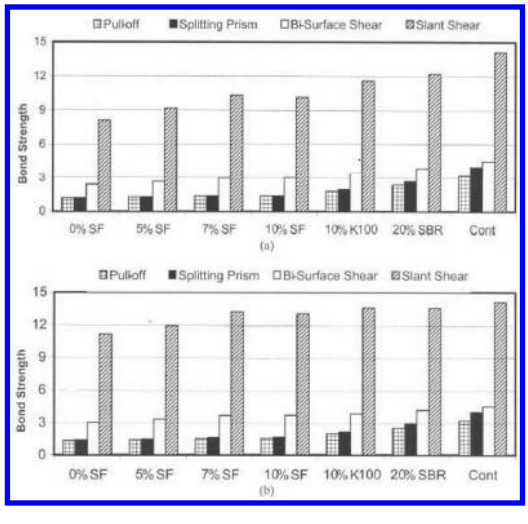

Figure 7. Measured bond strength by different methods for (a) low roughness—(b) high roughness substrates with varying contents of SBR and K100 (cyano-acrylate resin) after [8].

Table 4. Ultimate shear bond strength between HPC (78 MPa)—NSC (40 MPa) after [7].

Surface Finish	All Specimen		"Not So Rough" Specimen		"Intermediate" Specimen		"Rough" Specimen	
	Average [psi]	Standard Deviation [psi]	Average [psi]	Standard Deviation [psi]	Average [psi]	Standard Deviation [psi]	Average [psi]	Standard Deviation [psi]
Broom	498	27	498	27	N/A	N/A	N/A	N/A
As-Placed	667	87	632	75	672	83	711	65
Rake	821	107	752	99	816	68	882	96

Tables 5. Ultimate slip and shear strength between HPC (78 MPa)—NSC (40 MPa), after [7].

Table 5-5: Two-Point Load Results

Beam	Specimen ID	Failure Mode	Failure Load [kip]	Interface Slip at Failure [in]
8	A4.1	Horiz. Shear	27.9	0.0281
9	A4.3	Horiz. Shear	34.4	0.0064
10	B4.3	Horiz. Shear	32.2	0.0105
11	M10.2	Horiz. Shear	33.9	0.0124
12	M10.3	Flexure-Shear	39.2	0.0084
13	R2.2	Horiz. Shear	28.1	0.0133
14	R2.3	Horiz. Shear	33.6	0.0114
15	R4.2	Horiz. Shear	32.4	0.0107
16	R4.3	Horiz. Shear	37.9	0.0090
17	R10.2	Horiz. Shear	37.4	0.0121
18	R10.3	Horiz. Shear	34.9	0.0119
19	S4.2	Horiz. Shear	25.5	0.0176
			Average	0.0127

Table 5-6: Horizontal Shear Stress at Failure for Two-Point Load [psi]

Beam	Specimen ID	From Strain C/Lb_v	Elastic VQ/Ib_v	ACI V/b_vd_v	AASHTO V/b_vd_v
8	A4-1	482.2	863.2	698.4	846.6
9	A4-3	814.0	1060.8	860.7	1043.2
10	B4-3	915.6	993.2	804.6	975.3
11	M10-2	1075.0	1067.0	848.4	1028.4
12	M10-3	1288.0	1248.1	981.1	1189.2
13	R2-2	639.0	850.6	703.7	852.9
14	R2-3	1182.0	1015.1	840.2	1018.4
15	R4-2	1348.0	1001.0	811.1	983.2
16	R4-3	1245.0	1165.9	948.1	1149.2
17	R10-2	1054.0	1141.3	934.3	1132.5
18	R10-3	1194.0	1073.6	873.1	1058.3
19	S4-2	787.4	787.9	637.5	772.7
	Average	1002.0	1022.3	828.4	1004.1

In every join of repair concrete with substrate three phases are involved: the substrate-the interphase (the bond zone)—and the repair concrete, or mortar.

Independently from the magnitude of the strength of both concrete layers, existing and new, the interface is the weak link of the system due to discrepancies in the properties of the two layers, namely differences in modulus of elasticity, in the stage of shrinkage and creep which cause interfacial strain across the interface.

As far as the bond between HPC and Normal Cement Concrete (NSC) is concerned, Tables 4 and 5, as is reported in [7], are indicative of the magnitude of the shear bond strength and the corresponding slip at the interface between 78 MPa HPC and 40 MPa NSC.

5 THE INFLUENCE OF POLYMER MODIFICATION ON THE BOND BETWEEN ORDINARY CONCRETE SUBSTRATE AND HPC

The adhesion of SBR modified mortar and concrete to concrete substrate improved, due to presence of polymer, is of high importance for the enhancement of the bond between concrete substrate and HPC. The adhesion depends mainly on

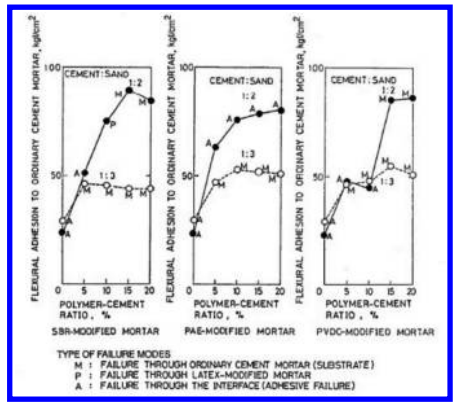

Figure 8. Effect of polymer/cement ratio on adhesion of PMM after [9].

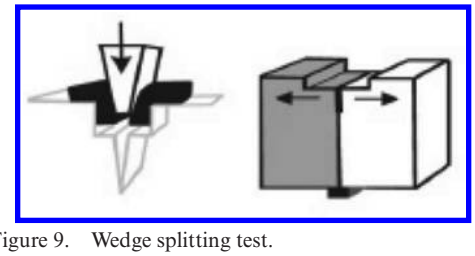

Figure 9. Wedge splitting test.

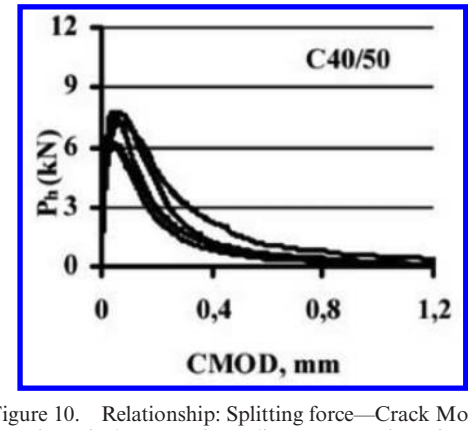

Figure 10. Relationship: Splitting force—Crack Mouth Opening Displacement for ordinary NSC 40/5,0 after [5].

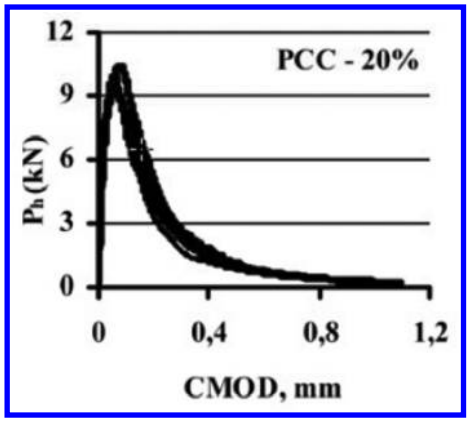

Figure 11. Relationship: Splitting force—Crack Mouth Opening Displacement for the same mix NSC 40/50 modified with 20% polymer modification, after [5].

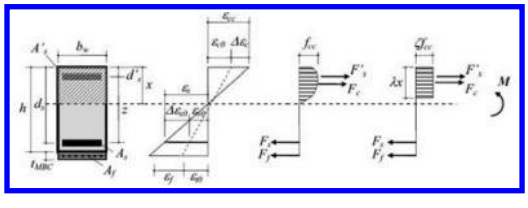

Figure 12. Internal forces of a strengthened beam simplified after [2].

the properties of substrate and polymer-cement ratio, the effect of which is shown in Figure 8 and Figures 9, 10, 11.

6 DESIGN CONSIDERATIONS

In the case of repair in which, the initial structural member regains its original stiffens, from the point of view of design the shear stresses across the interface must be calculated and checked whether they are safely transferred. On the other hand in the case of strengthening the structural performance of strengthened member is that of composite action, Figure 12. The ultimate capacity of the repaired member must be calculated taking into consideration the mechanical properties of both repair and substrate material, the volume changes and the shear and slip across the interface as per above sections 2, 3, 4 and 5.

7 COMPARISON TABLE

The following table of comparison of PMHPC—NSC—Shotcrete—HPC is drawn, upon their compressive and flexural strength, their durability expressed in terms of depth of carbonation and their bond strength to NSC substrate.

The cost was calculated by consideration of prices of materials, in the South—East Mediterranean and Middle East countries. The selection criterion is that of cost normalized with respect to the relative values of the mechanical properties, bond and durability.

n.	Type of repair material	Compr.Streng th ratio (1)	Tens.Strength ratio (2)	Durability ratio (3)	Bond toNSC ratio(4)	Cost (Euro/m3)	Comparison cost value **normalized** with respect to variables
		Variable 1	Variable 2	Variable 3	Variable 4		
1	NSCC	1,22	1,5	1,5	2,5	50	343
2	SHOTCRETE	1,15	1,35	1,2	1,4	160	417
3	HPC	1	1,15	1,15	1,4	68	126
4	PMHPC	1	1	1	1	120	120

Variables		
(1)	Compr.Strength ratio :	1/√(fci/fc4)
(2)	Tens.Strength ratio :	fti/ft4
(3)	Durability ratio :	dur 1/dur4
(4)	Bond toNSC ratio :	bi/b4
	Cost (Euro/m3) :	Direct cost

REFERENCES

[1] Al-Hadithi Abdulkader "Flexural, Impact and Thermal Properties of Polymer Modified Concrete", Ministry of Higher Education And Scientific Research. University of Technology. Building and Construction Depart. Iraq 2005.

[2] Blanksvärd T. Strengthening of concrete structures by the use of mineral based Composites. Luleå University of Technology Department of Civil, Mining and Environmental Engineering Division of Structural Engineering SE-971 87 Luleå. Sweden. 2009.

[3] Burg, R.G., and Ost, B.W., Engineering Properties of Commercially Available High-Strength Concretes (Including Three-Year Data), Research and Development Bulletin RD104, Portland Cement Association, 1994, 62 pages.

[4] Büyüköztürk O, Lau D. High Performance Concrete: Fundamentals and Application. Department of Civil and Environmental Engineering, Massachusetts Institute of Technology. Cambridge, Massachusetts. 2002.

[5] Chmielewska B. Adhesion Strength and Other Mechanical Properties of SBR Modified Concrete. International Journal of Concrete Structures and Materials. Vol. 2, No. 1, pp. 3~8, June 2008.

[6] Khadiranaikar R.B. High Performance Concrete. Bagalkot. India 2011.

[7] Kovach J.D, Naito C. Horizontal Shear Capacity of Composite Concrete Beams without Interface Ties. PCI/PITA RESEARCH PROJECT. ATLSS REPORT NO. 08–05. June 2008.

[8] Momayez A. Ramezaniapour A.A et al. Experimental Investigations of the Methods of Evaluating the bond strength between concrete substrate and repair materials. FACI. The University of Arizona.Tuscon.2002.

[9] Ohama. Y. HANDBOOK of polymer modified mortars. Properties and Process Technology. College of Engineering Nihon University Koriyama, Japan. NOYES Publications 1995.

[10] Xu Hanfeng. Properties of fiber reinforced concrete with latex modification. Faculty of Graduate Studies. Department of Civil Engineering. University of British Coumbia. 2003.

Concrete Repair, Rehabilitation and Retrofitting IV – Dehn et al. (Eds)
© 2016 Taylor & Francis Group, London, ISBN 978-1-138-02843-2

A new approach for internal curing of high performance concrete to reduce early-age volume variations

P.A. Savva & M.F. Petrou
University of Cyprus, Nicosia, Cyprus

ABSTRACT: Cement hydration and particles flocculation are responsible for concretes solidification. Several physiochemical mechanisms are activated from the moment that cement comes in contact with water until the material becomes solid. An ideal maturing period for concrete would be a stress-free situation. However, due to the aforementioned mechanisms it is almost impossible for concrete to maintain the same volume from its very first moment until solidification. These mechanisms will develop differential volume variations within the structure of the material which will yield in stress development. Since the material in the early-age will not be able to develop adequate strength, it will crack due to these stresses. The objective of this research is to develop an internal curing approach which will focus on reducing these volume variations in order to prevent early-age cracking. Attention is given on delivering additional water within the materials' structure using existing constituents of the mixture. High Absorptive Normal Weight Aggregates (HANWA) have been employed to deliver water for Internal Curing (IC) within the materials' structure. In order to evaluate the results, concrete mixtures including dry and saturated HANWA have been compared with ordinary (low-absorptive) Normal Weight Aggregates (NWA). Furthermore, mixtures including NWA and Superabsorbent Polymers (SAP) have been tested. The mixtures have been compared in terms of autogenous shrinkage, compressive strength, chloride diffusivity and vacuum porosity. Finally, two curing methods have been employed in order to assess the effectiveness of external curing on such dense concrete mixtures.

1 INTRODUCTION

Autogenous shrinkage could be described as the bulk or external shrinkage of a sealed, isothermal cementitious material without being subjected to external forces (RILEM TC 225-SAP 2012), whereas chemical shrinkage, which is likely to occur after the rigid skeleton formation, is considered as the total shrinkage or internal and external deformation (Schröfl et al. 2012). Prior to setting, the material is not able to withstand internal voids due to poor strength that causes the material to collapse over the voids. However, when the material develops adequate strength, the formation of voids due to chemical shrinkage is inevitable. Chemical shrinkage occurs because the hydrated materials occupy less space than the unhydrated constituent materials. For typical cement, chemical shrinkage is estimated at approximately 8–10 ml volume reduction per 100 g of cement reacted and ~22 ml volume reduction for 100 g silica fume reacted.

In normal strength concrete, autogenous shrinkage does not manifest itself in such a scale to be risky for the materials quality. Advances in concrete technology the last decades have brought new materials in use. High strength concrete, high performance fiber reinforced concrete and ultra high performance fiber reinforced cementitious composites are materials with superior performance (HPC), characterized by their high compressive strength and low permeability. Their performance is attributed to the improved packing of the constituent materials, which alongside reduction in water content result in a denser matrix as opposed to conventional concrete. Shortage in water due to low w/b ratio increases the early-age shrinkage which is a result of chemical shrinkage and self-desiccation (Schröfl et al. 2012).

Self-desiccation is governed by two physical mechanisms. The reduction of disjoining pressure will cause the material to contract, whereas, the meniscus formation within the pore will cause tension in the pores fluid (Laplace's Law). The disjoining pressure will be greater when the RH is high and therefore a drop in RH will reduce the disjoining pressure causing shrinkage (Lura et al. 2003). The availability of water within the pores will prevent RH drop and disjoining pressure reduction. Pores partially filled with water within the materials structure cause the creation of water-air menisci and RH drop (Kelvin's Law) (Lura et al. 2003). The water-air menisci will result in tension

stress development within the pore fluid and consequently the surrounding material will develop compressive forces to restore equilibrium (Barcelo et al. 2005; Schröfl et al. 2012; Lura et al. 2003). The surrounding compressive stress will lead to further contraction.

It is therefore understandable that in order to prevent self-desiccation additional water should be provided. Since the w/b ratio increase is not possible in HPC, other methods have to be employed. Several methods that have been proposed include the addition of internal reservoirs in order to replenish the consumed water and maintain the RH at high levels, Shrinkage Reducing Agents (SRA) to reduce pore fluid's surface tension and expansive minerals to counteract shrinkage (Sant et al. 2011).

The dispersion of water reservoirs have been a well established method to reduce early-age shrinkage and self-desiccation.

2 BACKGROUND

In order to prevent self-desiccation in a concrete mixture, it is necessary to maintain RH at high levels. The density of HPC which yield to depercolated capillary pores hinders the diffusion of the external moisture throughout the material's structure restricting its access (Sant et al. 2011). Therefore, in order to reach the inner core of the material's body dispersed water reservoirs have to be incorporated. It is implied that the better dispersion will result in uniform water utilization throughout the materials matrix and thus IC will be more effective. Two well established methods of IC are the use of SAPs and LWAs. Both methods though weaken the material, either by causing additional porosity or due to the introduction of mechanically weak materials.

Zhutovsky & Kovler have reported that concrete's mechanical and durability deterioration is inevitable since a porous and mechanically weak material is introduced (Zhutovsky & Kovler 2010). Byard has reported that internally cured mixtures' compressive strength slightly decrease in comparison with the corresponding control (CTRL) mixtures' (Byard et al. 2012). A Round-Robin Test (RRT) conducted by 13 different laboratories across the world has used the same mix design but local aggregates and examined the effect of including SAPs in concrete. The majority of the researchers have reported a decrease in compressive strength for concretes including SAP. Nevertheless, in some cases, an improvement has been observed (Mechtcherine et al. 2013). In the contrary, research reports claim that compressive strength reduction is not a subsequent of SAPs inclusion in concrete (Lura et al. 2006). A further investigation supports that the consistent reduction in HPCs compressive strength could be surpassed by a proper design, regarding the dosage and the curing of each mixture (RILEM TC 225-SAP 2012). It continues suggesting that the interest has to be focused on achieving IC without affecting other properties of the material.

Furthermore, other properties of the material are affected by the introduction of IC. Young's Modulus (YM) and flexural strength seems to deteriorate due to insufficient stiffness and increased porosity (Zhutovsky & Kovler 2010; Byard et al. 2012; Mechtcherine et al. 2013). Additionally, in NWA mixtures the permeability is governed by the cement paste permeability. In mixtures including LWAs the permeability may be influenced by the properties of LWAs. A reduction in permeability and diffusivity can be expected in IC mixtures due to extended hydration that leads in capillary pores discontinuation. However, in both SAPs and LWAs IC methods, additional porosity is expected to be introduced in the mixture (RILEM TC 196-ICC Rep 41-6 2007).

3 RESEARCH SIGNIFICANCE

The technique of Self Curing Concrete (SCUC) or Internal Curing (IC) as it is widely known has arisen at the beginning of the last decade (Jensen & Hansen 2000) and much advancement have been achieved since. It is an on-going research topic and it attracts great attention since the advantages of establishing an IC technique are both short and long term. Improved performance during the structures service life as well as extended life-cycle is only two of the main benefits that contribute to a less expensive construction and maintenance cost ensuring environmental sustainability.

The ideal IC method should be able to reduce the autogenous shrinkage of HPC without compromising any other properties.

The effort of this research has been focus on establishing IC in HPC without reducing any other properties of the material. HANWA exhibit high absorption capacity that benefits IC and sound mechanical properties that ensure the mixtures serviceability.

4 EXPERIMENTS

Five mixtures with low w/b ratio (0.25) have been intensively designed to increase autogenous shrinkage (Table 1). In order to reduce or diminish autogenous shrinkage three IC mediums have been employed. HANWA in two different states (SSD and DRY) and two types of SAPs were compared. The HANWA has been introduced in two

Table 1. Mix constituents (kg/m^3).

	CTRL	HANWA SSD	HANWA DRY	SAP T1	SAP T2
CEM	864	864	864	864	864
Water	216	216	216	216	216
Coarse	854	854	854	854	854
Sand	499	344	344	228	228
SP	0,09%	0,05%	0,05%	0,04%	0,23%
SAP	–	–	–	1,5	1,7
IC water	–	44,0	44,0	44,0	44,0
Slump	70	100	85	85	80

Table 2. Aggregates properties.

	ρa (g/cm^3)	WA_{24}	FM	Fraction
NWA	2,74	1,1%	–	4/10
HANWA	2,30	5,2%	–	4/10
SAND	2,63	1,2%	2,12	0/4

different conditions in order to clarify whether a Saturated-Surface Dry (SSD) condition would affect the materials performance as opposed to dry state (DRY). The SAPs have been employed in order to compare their effectiveness as opposed to the HANWA. The HANWA and NWA properties are presented in Table 2. The utilized SAPs were poly (acrylic acid) partial sodium salt for T1 and poly (acrylic acid), partial potassium salt, slightly cross-linked for T2. The polymers were tested in suspended pore solution using the teabag method and it was concluded that there absorbing capacity was 29 g/g for SAP-T1 and 26 g/g for SAP-T2. Therefore, the amount of SAP required to carry the necessary quantity of IC water was 0.18% and 0.2% with respect to cement mass for T1 and T2 respectively.

The aggregates water absorption at 24 hours (WA_{24}) was calculated according to (EN-1097 2013) (Table 2). The mixtures slump has been measured in fresh state concrete whereas tests on compressive strength and vacuum porosity at 3, 7, 28 and 90 days and rapid chloride permeability at 7, 28 and 90 days have been conducted in hard state. Additionally, in order to assess whether external curing would have any effect on such dense mixtures, two methods of curing have been employed. One series of specimens have been immersed in a water tank with constant temperature (23 ± 1°C) whereas another series have been wrapped with polyvinyl chloride membrane and stored in a room with controlled temperature (23 ± 1°C).

Finally, the HANWA effectiveness had to be validated in terms of IC prior implementing them in HPC. Castro has reported that an effective IC

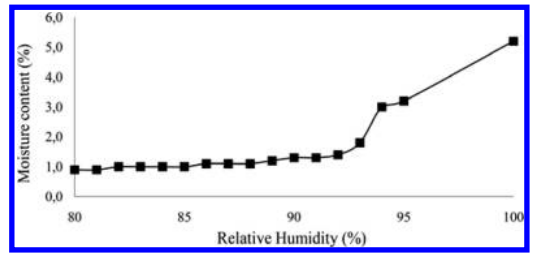

Figure 1. HANWA desorption properties.

aggregate would have larger pores than cement pores (Castro et al. 2011). An indirect way to check aggregates suitability is by calculating the aggregates ability to release moisture at high RH-levels. HANWA-SSD has been placed in an environmental chamber and exposed to gradually RH decrease where its mass loss was recorded (Fig. 1). Figure 1 indicates that HANWA release the majority of its moisture content (80%) at high RH levels (85%) and therefore it could be utilized for IC.

5 RESULTS

5.1 *Autogenous shrinkage*

After the mixtures were mixed one prismatic specimen from each batch was wrapped in membrane and stored in controlled environment. After the specimens were solidified two rectangular sections (7 mm × 35 mm) of membrane at the specimen's opposite faces were removed using a surgical blade and the free surface was covered with epoxy resin. After the resin was solidified, 30 mm strain gauges were attached at each side and the specimens were wrapped again in order to protect the specimens and the gauges from external moisture. The employed method ensured that the measured deformations would represent only longitudinal displacements of the specimen, and no moisture exchange would occur.

As explained above, insufficient water in the materials pores would increase autogenous shrinkage. It is therefore justifiable that the CTRL mixture exhibits the higher autogenous shrinkage (Fig. 2). The decrease in autogenous shrinkage regarding the IC mixtures indicates that the IC water has been successfully delivered to the mixture increasing RH and reducing the materials shrinkage. Mixtures HANWA-SSD, HANWA-DRY and SAP-T2 have managed to reduce significantly autogenous shrinkage whereas SAP-T1 fully diminished it. HANWA-SSD and HANWA-DRY curves are almost identical. This implies that the state of HANWA prior entering the mixture does not affect their effectiveness. Finally, SAP mixtures seem to exhibit the lowest autogenous shrinkage. It was anticipated that the specific polymers would perform very efficiently at the first days because at the age of two hours the polymers are providing the majority of their water back to the mixture (Fig. 3).

The main reason for conducting a tea-bag test on SAPs was to evaluate the polymers absorption capacity in order to modify the mix design accordingly. However, Schröfl has reported that SAPs who observe an early desorption such as the SAPs used in this research (Fig. 3), are likely to be effective for internal curing only at early-ages (Schröfl et al. 2012).

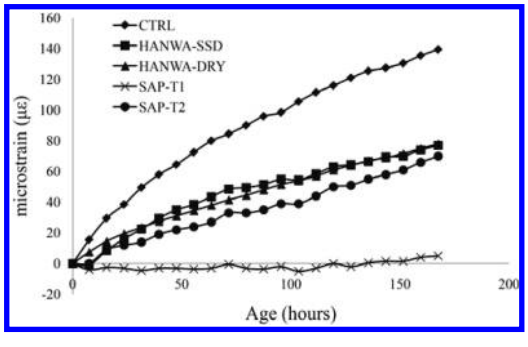

Figure 2. Autogenous shrinkage.

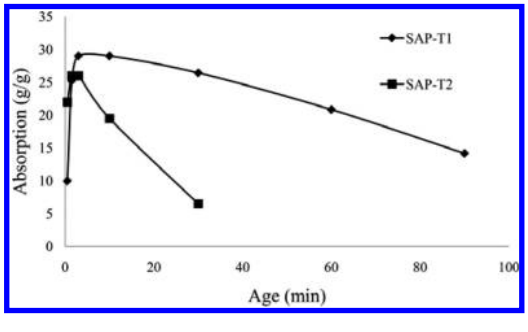

Figure 3. SAPs absorption rate in pore fluid.

5.2 *IC effect on workability*

The mixtures workability has been checked with respect to the required amount of polycarboxylate polymer superplasticizer (SP) added to the mixture (Fig. 4). HANWA-SSD, HANWA-DRY and SAP-T1 mixtures have exhibited similar rheological behavior. The CTRL mixture required higher amount of SP in order to fulfill the slump requirements (100 ± 30 mm) whereas SAP-T2 mixture required a very high amount of SP in order to retain its workability. It has to be mentioned that the aggregates (HANWA-NWA) have been checked using image analysis software (ImageJ (Ferreira & Rasband 2012)) in order to check their circularity. The measurements were expressed as percentage (0: min-1: max) where a completely circular particle is indicated by the value of 1.0. As the measurement approaches 0.0, it indicates an increasingly elongated shape. The measurements have been conducted on a minimum of 75 particles from each batch and both aggregates exhibit similar degree of circularity (HANWA: 0.61, NWA: 0.64). It can be concluded that the different behavior is exclusively attributed to the IC mediums. HANWA-SSD, HANWA-DRY and SAP-T1 seem to benefit the mixtures workability whereas the CTRL and SAP-T2 mixtures require higher amount of SP due to the lack of water. It has to be concluded though that the workability variations caused by SAP strongly depend on the polymers absorption capacity, absorption rate and the additional water entered the system (RILEM TC 196-ICC Rep 41-5 2007).

5.3 *Rapid Chloride Permeability (RCP)*

The RCP test was conducted based on ASTM C1202 (ASTM C 1202-2009). The experiment

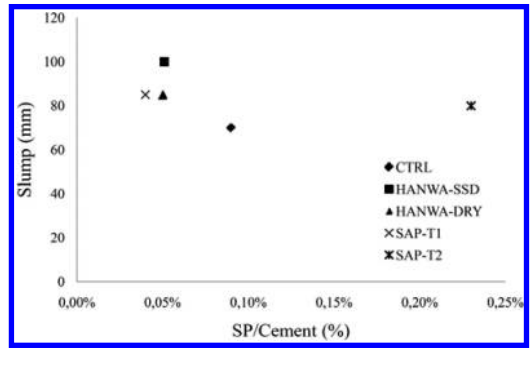

Figure 4. Mixtures' workability.

consists of measuring the amount of chloride ions passed through 50 mm thick cylindrical concrete specimens. The specimen's sides are immersed in sodium chloride and sodium hydroxide and a potential difference of 60V is maintained. The total charge passed in coulombs relates the resistance of the specimen to chloride ion penetration. Each specimen has been conditioned according to the standard.

Based on Table 3 the CTRL mixture exhibits the lowest permeability value. The specific mixture includes NWA and no IC agent. The highly dense microstructure due to the constituent materials yields in a refined pore network. Several conclusions can be drawn by observing the evolution of RCP reduction in Table 3. Observing the RCP reduction all the mixtures exhibit a similar reduction (~65%) from day 7 to day 90 except SAP-T2. The specific mixture seems to suffer a very early-age water exhaustion and therefore their contribution was diminished after the first days of the materials life-cycle. Furthermore, the curing method does not seem to highly affect the results. However, it is worth noticing that all the specimens extracted from the water curing method were consistently exhibiting slightly lower charge pass. Besides the CTRL mixture, the HANWA-SSD mixture observes the lowest RCP values at 90 days. It is believed that the specific mixture will be able to utilize IC water to the mixture even at late ages, in contrast to other methods that are likely to utilize their water content at early-ages. Finally, the SAP-T1 and the HANWA-DRY mixture seem to perform very well, whereas SAP-T2 has the poorest contribution to the materials performance.

5.4 *Vacuum porosity*

The specimens have been kept in a sealed chamber where the pressure was removed. Afterward they were subjected to vacuum for 24 hours before being immersed in water. After 24 hours their immersed and saturated mass was recorded before being placed in an oven with constant temperature of 105°C. After constant mass was reached the dry mass of the specimens was recorded and the porosity of each specimen was extracted. It has to be noted that the results correspond to a single test conducted on a different specimen at each time interval.

The porosity values of the mixtures are presented in Table 4. The CTRL mixture has the lowest porosity in comparison with the IC mixtures. Implementing IC has specific disadvantages. One of these is the porosity increase which leads to a reduced compressive strength at the very early-age. SAPs mixtures have exhibited high porosity at early-ages, which was anticipated. The expected reduction of porosity at 28 days is not reflected in the results. This is attributed to the fact that the specific polymers utilized in this research are likely to exhaust their IC ability at early ages. The space occupied by the polymers particles remain empty and it is added up to the total porosity. Finally, the HANWA-SSD mixture exhibits a superior performance in terms of porosity values as well as pore sealing. The assumption that the specific IC medium would be able to provide IC water even at later ages is enhanced by the results of porosity. It is noticeable here that the membrane curing method seems to be slightly more effective than water curing method. Furthermore, the HANWA-DRY mixture in this case seems to perform poorly. It seems that the specific mixture does not absorb the total quantity of added water, increasing the w/b ratio and the porosity.

5.5 *Compressive strength*

The compressive strength of the CTRL mixture was expected to obtain the highest value due to the lack of IC materials which result in additional porosity and weak porous mediums (Table 1). In fact up to the age of 28 days the CTRL seems

Table 3. RCP results (Coulombs)—M: Membrane curing method, WC: Water curing method.

	7 Days		28 Days		90 Days	
	M	WC	M	WC	M	WC
CTRL	3695	3228	2352	2088	1378	1168
HANWA-SSD	5850	5736	3022	3978	2137	1974
HANWA-DRY	5433	4576	4410	3556	2202	1606
SAP-T1	6554	6249	3831	3714	2198	2228
SAP-T2	4972	5100	4258	3648	2333	2314

Table 4. Vacuum porosity.

	3 Days	7 Days	9 Days	28 Days
	Membrane cured specimens			
CTRL	12,5%	11,4%	9,4%	8,2%
HANWA-SSD	14.8%	14.0%	13.7%	12.7%
HANWA-DRY	15.5%	14.7%	16.6%	17.1%
SAP-T1	17.5%	15.2%	15.3%	14.5%
SAP-T2	17.3%	16.3%	15.2%	14.7%
	Water cured specimens			
CTRL	12.8%	12.0%	9.9%	8.2%
HANWA-SSD	15.6%	14.8%	14.1%	13.6%
HANWA-DRY	15.1%	15.0%	15.6%	16.3%
SAP-T1	18.0%	16.2%	15.6%	14.2%
SAP-T2	17.4%	16.7%	15.3%	15.0%

Table 5. Compressive strength (all values are in MPa).

	3 Days		7 Days		28 Days		90 Days	
	f_{cm}	SD	f_{cm}	SD	f_{cm}	SD	f_{cm}	SD
Membrane cured specimens								
CTRL	84,6	3,9	82,1	7,4	93,2	4,5	88,5	14,8
HANWA-SSD	76,2	3,8	76,7	0,7	80,3	3,2	86,1	3,4
HANWA-DRY	71,8	1,1	67,6	5,3	75,6	3,8	75,9	3,9
SAP-T1	62,6	4,1	72,9	2,3	80,4	5,1	81,7	1,6
SAP-T2	66,0	4,7	67,3	5,4	81,6	8,1	78,8	7,4
Water cured specimens								
CTRL	71,7	8,8	79,7	12,6	80,9	19,6	75,0	17,6
HANWA-SSD	76,6	2,4	75,0	4,0	74,9	9,0	81,5	3,9
HANWA-DRY	62,7	5,2	73,0	2,6	74,3	2,6	74,4	5,2
SAP-T1	66,3	4,1	71,1	2,0	80,2	5,4	92,9	4,1
SAP-T2	58,8	8,9	66,5	7,2	84,7	4,9	78,6	6,2

to develop high strength. However, at the age of 90 days in both methods of curing, the CTRL mixture exhibits a loss in compressive strength. Due to the high Standard Deviation (SD) it cannot be concluded that the material suffers a reduction. This is attributed to the fact the pore water is likely to be depleted in its majority. Also, the external water curing cannot reach the inner core of the material to continue hydration, due to its low permeability. The HANWA-SSD mixture seems to continue developing high compressive strength. This is attributed to the extended hydration which was anticipated because of the dispersed IC sources of water. The specific mixture's compressive strength at the age of 90 days seems to overcome the CTRL mixture. Furthermore, the compressive strength of HANWA-SSD mixture and HANWA-DRY do not justify the argument that the aggregates would fully absorb the additional water during the mixing. Consequently, partial amount of the additional water seems to participate in the w/b ratio.

Additionally, at the early-ages, the SAP mixtures have observed reduced compressive strength. Nevertheless, despite the early-age water exhaustion, the SAP-T1 mixture at the age of 90 days seems to recover its loss in compressive strength and overcome the CTRL mixture. The specific mixture is highly benefited at the early-age due to the autogenous shrinkage reduction without suffering any damage in compressive strength. It has to be mentioned that the mixture exhibit a notable difference with regard to the difference in curing method. The membrane cured specimens do not exhibit any strength evolution at the age of 28 to 90 days whereas the water cured specimens behave very differently. SAP-T2 mixture, exhibits a very well behavior up to the age of 28 days, where its strength evolution is adequate. The specific mixture seems that it has reached the maximum of its compressive strength up to the age of 28 days, regarding both curing methods, since from 28 to 90 days it suffers a slight fall. This has probably happened due to the polymers exhaustion along with the additional water that would enhance extended hydration. It has to be noticed that external curing does not seem to benefit the mixture with respect to its compressive strength. This is attributed to the dense pore network of the specimens where the externally source of water cannot reach the inner core of the specimens. It has to be mentioned that the results represent the average of 3 cubic specimens of dimensions $100 \times 100 \times 100$ mm.

6 DISCUSSION

A conclusion can be drawn comparing SAPs-T1 porosity and RCP regarding the contribution of the polymers to the mixtures performance. Although the RCP is greatly decreased during the first 90 days of the mixtures life-cycle, its porosity is observing only a slight reduction. It has to be mentioned that the SAPs polymers' size do not exceed 1 mm. It has been also reported that the most effective particles size is nearly 100 μm in swollen state (Jensen & Hansen 2002). Therefore, the size of the particles contributes to an even dispersion within the materials matrix contributing to an effective IC. The fact that SAPs will be fairly dispersed would be beneficial for the pore network sealing. On the other hand, the SAPs exhaustion will contribute to an additional porosity.

Furthermore, the mixtures including IC agents have observed a great improvement in their properties up to the age of 28 days. All mixtures but

HANWA-SSD have exhibited minor improvements in their properties between 28 and 90 days.

It has been mentioned above that the HANWA-SSD releases the 80% of their moisture content at high RH levels. Consequently, the rest of 20% of the aggregates moisture is held by the aggregates within their structure. The water extracted at the early-ages of the mixture through the HANWA-SSD will contribute to an increased degree of hydration at the aggregates adjacent space. This will reduce the surrounding porosity and the remaining water extraction from the aggregates body will require a lower RH. Additionally, the small pores of the HANWA will also require lower RH in order to provide the water. It is therefore concluded that the specific mixture will be able to provide IC water to the mixture at late ages when RH will drop further, increasing the degree of hydration.

7 CONCLUSIONS

The objective of this research was to evaluate the effectiveness of using HANWA as an IC agent without compromising the mechanical properties of HPC. The HANWA-SSD concrete mixture has been compared with mixtures including SAPs. The results indicate that the HANWA-SSD mixture has performed very well in reducing autogenous shrinkage. Additionally, it managed to maintain good mechanical and durability properties at both early and late-age.

In order to establish the mechanisms supported in this paper, the research on the specific topic is on-going.

REFERENCES

ASTM C 1202, 2009. Standard Test Method for Electrical Indication of Concrete's Ability to Resist Chloride. *Annual Book of ASTM Standards*, pp.1–6.

Barcelo, L., Moranville, M. & Clavaud, B., 2005. Autogenous shrinkage of concrete: A balance between autogenous swelling and self-desiccation. *Cement and Concrete Research*, 35, pp.177–183.

Byard, B.E., Schindler, A.K. & Barnes, R.W., 2012. Early-Age Cracking Tendency and Ultimate Degree of Hydration of Internally Cured Concrete. *Journal of Materials in Civil Engineering*, 24(August), pp.1025–1033.

Castro, J. et al., 2011. Absorption and desorption properties of fine lightweight aggregate for application to internally cured concrete mixtures. *Cement and Concrete Composites*, 33(10), pp.1001–1008. Available at: http://dx.doi.org/10.1016/j.cemconcomp.2011.07.006.

EN-1097, 2013. Tests for mechanical and physical properties of aggregates Part 6: Determination of particle density and water absorption.

Ferreira, T. & Rasband, W., 2012. ImageJ User Guide. *IJ 1.46r*, p.137. Available at: http://rsbweb.nih.gov/ij/docs/guide/146–30.html [Accessed February 10, 2015].

Jensen, O.M. & Hansen, P.F., 2000. Water-entrained cement-based materials I. Principle and theoretical background., 31, pp.1–13.

Jensen, O.M. & Hansen, P.F., 2002. Water-entrained cement-based materials II. Experimental observations., 32, pp.973–978.

Lura, P. et al., 2006. Compressive strength of cement pastes and mortars with superabsorbent polymers. In *RILEM conference on Volume Changes of Hardening Concrete: Testing and Mitigation*. Lyngby, pp. 117–126.

Lura, P., Jensen, O.M. & Van Breugel, K., 2003. Autogenous shrinkage in high-performance cement paste: An evaluation of basic mechanisms. *Cement and Concrete Research*, 33, pp.223–232.

Mechtcherine, V. et al., 2013. Effect of internal curing by using superabsorbent polymers (SAP) on autogenous shrinkage and other properties of a high-performance fine-grained concrete: results of a RILEM round-robin test. *Materials and Structures*, 47, pp.541–562. Available at: http://link.springer.com/10.1617/s11527–013–0078–5.

RILEM TC 196-ICC Rep 41–5, 2007. *State of the Art Report of RILEM technical committee Internal curing of concrete* K. Kovler & O.M. Jensen, eds., Bagneux, France: RILEM Publications S.A.R.L.

RILEM TC 196-ICC Rep 41-6, 2007. *State of the Art Report of RILEM technical committee Internal curing of concrete* K. Kovler & O.M. Jensen, eds., Bagneux, France: RILEM Publications S.A.R.L.

RILEM TC 225-SAP, 2012. *State of the Art Report of RILEM tecnical committee Application of Superabsorbent Polymers (SAP) in Concrete Construction V*. Mechtcherine & H.-W. Reinhardt, eds., Springer Dordrecht Heidelberg London New York.

Sant, G., Bentz, D. & Weiss, J., 2011. Capillary porosity depercolation in cement-based materials: Measurement techniques and factors which influence their interpretation. *Cement and Concrete Research*, 41(8), pp.854–864. Available at: http://dx.doi.org/10.1016/j.cemconres.2011.04.006.

Schröfl, C., Mechtcherine, V. & Gorges, M., 2012. Relation between the molecular structure and the efficiency of superabsorbent polymers (SAP) as concrete admixture to mitigate autogenous shrinkage. *Cement and Concrete Research*, 42, pp.865–873.

Zhutovsky, S. & Kovler, K., 2010. Durability Aspects of Internally Cured High., (August).

Concrete Repair, Rehabilitation and Retrofitting IV – Dehn et al. (Eds)
© 2016 Taylor & Francis Group, London, ISBN 978-1-138-02843-2

Real-scale testing of the efficiency of self-healing concrete

K. Van Tittelboom, D. Snoeck, E. Gruyaert, B. Debbaut & N. De Belie
Magnel Laboratory for Concrete Research, Ghent, Belgium

J. Wang
Magnel Laboratory for Concrete Research, Ghent, Belgium
Laboratory of Microbial Ecology and Technology, Ghent, Belgium

A. De Araújo
Magnel Laboratory for Concrete Research, Ghent, Belgium
Polymer Chemistry and Biomaterials Group, Ghent, Belgium

ABSTRACT: After several years of research in the Magnel Laboratory (Belgium) to obtain concrete with self-healing properties, the most promising mechanisms were tested on a larger scale. Instead of small mortar samples with self-healing properties, real-scale self-healing concrete beams (150 mm × 250 mm × 3000 mm) were made and the efficiency of autonomous crack repair was evaluated over time after loading the beams in four-point bending. In addition to a reference beam without self-healing properties, a beam with encapsulated polyurethane and a beam containing superabsorbent polymers were investigated. While for the beam with polyurethane, crack repair is obtained as the healing agent is released as soon as cracks damage the embedded capsules, the superabsorbent polymers absorb water which intrudes into the cracks, immediately blocking the crack through swelling and later on by continued hydration and precipitation of calcite. The efficiency of both self-healing approaches was compared by measuring the reduction in water ingress into the cracks and by measuring the crack width reduction over time.

1 INTRODUCTION

Concrete is a frequently used construction material because of its low cost, freedom of design, high compressive strength, … However, while concrete has a high compressive strength, its tensile strength is rather limited. Due to this, concrete often contains cracks within the tensile zones. Although these cracks do not threaten the structural integrity, as reinforcement is provided within these zones to carry the tensile stresses, they do harm the durability of the structure. Via these cracks aggressive agents can enter the matrix and cause concrete degradation e.g. by sulfate attack, chloride ingress, carbonation, … This may lead to further widening of the cracks and degradation of the reinforcement steel due to corrosion, which can finally result in structural problems. Therefore, it is important that cracks are repaired. However, manual crack repair is expensive and not always feasible because of eventual inaccessibility of cracks.

In 2001, when White et al. (2001) published their paper in Nature about self-healing in polymer based materials, research on the development of self-healing materials gained a real boost. Also attempts were taken to implement self-healing properties inside cementitious materials. Actually, cementitious materials do already have the natural ability to repair damage to a certain extent (Edvardsen 1999). If water enters into concrete cracks and gets into contact with unhydrated cement particles, these can further hydrate and result in crack closure. If both water and carbon dioxide are present, crack closure can be obtained when leaching calcium hydroxide reacts with carbon dioxide to form calcium carbonate crystals. However, as the natural, so called autogenous, crack healing mechanism is limited to small cracks (Reinhardt & Jooss 2003), many attempts have been made to engineer concrete in order to obtain an improved, autonomous, crack healing efficiency.

Some approaches rather promote the autogenous crack healing ability by limiting the crack width through the addition of polymeric fibers (Li & Yang 2007) or by the use of shape memory alloys (Jefferson et al. 2009) which return to their original shape, and thus result in crack closure, upon heating. Other approaches promote the autogenous healing ability by providing an extra amount of water through the use of superabsorbent polymers (SAPs) (Lee et al. 2010, Snoeck et al. 2012). If SAPs are embedded in the concrete

matrix, they absorb water entering via the cracks. The initial swelling action of the SAPs blocks the cracks against further ingress and slow release of the absorbed water, later on, leads to further hydration and calcite precipitation. In other approaches, calcite precipitation is intensified by the addition of micro-organisms to the matrix (Jonkers 2011, Wang 2014). Upon water ingress via the cracks these organisms start to consume available nutrients and precipitate calcium carbonate to close the crack. Next to these self-healing approaches, capsule-based (Dry 2000, Van Tittelboom et al. 2011) and vascular based (Dry 2001, Pareek & Oohira 2011) mechanisms are reported, in which autonomous crack repair is obtained by release of a, mostly polymer based, healing agent from embedded capsules or from a vascular system. Release of the agent is triggered through breakage of the capsules or the tubes at the moment of crack formation.

In the Magnel Laboratory (Belgium), we started our research on self-healing cementitious materials in 2008. A number of the above mentioned self-healing approaches have been investigated, resulting in diverse self-healing efficiencies. For this study, the most promising approaches were selected to be applied and tested on their efficiency on a larger scale.

2 MATERIALS

2.1 *Self-healing mechanisms*

The first self-healing approach which was tested on a larger scale, consisted of the incorporation of encapsulated polyurethane. The polyurethane based healing agent, was a one-component, air-curing agent with a viscosity of 3536 mPas at 25°C. Although this agent was developed within the framework of another project, it was supposed to meet the requirements in order to obtain efficient self-healing in the large scale concrete beams. This means that the healing agent should remain fluid until capsule breakage, although it should be very reactive to harden as soon as the capsules break and the agent, flowing into the cracks, comes into contact with moisture from the surrounding matrix. In addition, the viscosity of the agent should not be too high, so it is easily released from the capsules and it easily flows into the crack, while at the other hand the viscosity should not be too low, to prevent complete absorption of the healing agent by the surrounding matrix, which would lead to an empty crack. The healing agent was encapsulated by tubular glass capsules with an inner diameter of 3 mm, an outer diameter of 3.35 mm and a length of about 50 mm. To fill these tubes with the healing agent, first, one end of the tubes was sealed by means of methylmethacrylate (MMA) glue. Then the polyurethane was injected into the tubes by means of a syringe with a needle after which the second end was sealed again with MMA. These brittle capsules were embedded inside the concrete matrix to obtain self-healing properties. As soon as cracks appear in the hardened concrete matrix, the brittle glass capsules crossed by one of these cracks, will break. Due to capillary action, the healing agent will be released from the capsules and will be drawn into the crack. There, the agent will contact moisture inside the pores of the cementitious matrix causing a foaming reaction and hardening of the agent, finally leading to autonomous crack repair.

The second self-healing approach which was ready to be tested on a larger scale, consisted of the use of hydrogels or SAPs. The bulk-polymerized SAPs which were used within this study, were obtained from the company SNF Floerger. They were synthetized from a cross-linked copolymer of acrylamide and acrylate, and had particle sizes less than 600 µm. This self-healing mechanism is not immediately activated at the moment cracks appear but requires water or moisture ingress into the cracks to become active. When water enters into the cracks, contact with the SAP particles near the crack surface will result in immediate swelling of the particles and thus blockage of the crack. However, over time the particles will release their water content again so the crack blocking effect will be gone but on the other hand the slowly released water will become available to the cementitious matrix and will result in permanent crack closure by further hydration of unhydrated cement particles and calcium carbonate precipitation of leached calcium hydroxide if also carbon dioxide is available within the crack.

2.2 *Concrete beams with(out) incorporated self-healing mechanisms*

One reference beam (code: REF) without self-healing properties was prepared in order to evaluate autogenous healing and to note the additional healing efficiency in the case a self-healing mechanism was embedded. Moulds with dimensions of 150 mm × 250 mm × 3000 mm were used for both the reference beam and the beams with self-healing properties. Preparation of the moulds consisted for the REF beam in placement of the reinforcement bars. As the beams were casted upside down (because later on they would also be loaded in opposite direction) the reinforcement bars were positioned at the upper side of the mould in such a way that the concrete cover on top of the bars would be 20 mm. In total fours bars with a diameter of 10 mm were equally divided over the width of the mould.

To cast the real scale concrete beam with embedded polyurethane (code: SHC-PU), in total 350 capsules, filled with polyurethane, were prepared. Positioning of the tubes within the mould was done by means of a network of wires attached through the walls of the mould 10 mm below the top. Every 40 mm over the complete length of the beam, except the 160 mm at the ends, a wire was used to connect the one side of the mould with the other (Fig. 1A and B). Glass tubes were glued onto this network of wires by means of MMA glue. Each time, five capsules were placed with an intermediate distance of 46 mm and at both capsule ends there was 5 mm overlap with the wires. The next row was then arranged in an alternating way compared to the previous row. Next to the network of capsules, this beam also contained four reinforcement bars with a diameter of 10 mm. These were positioned underneath the network of capsules at the same position as in the reference beam.

The self-healing approach relying on the swelling and thus blocking effect of SAPs (code: SHC-SAP) did not require additional preparation compared to the reference beams, as the SAPS are added to the concrete upon mixing. It can already be mentioned that the superfluity of additional preparation is an advantage of this self-healing approach compared to the approach with embedded capsules.

After preparation of the moulds, concrete mixes were made. It was decided to cast all beams with self-compacting concrete as vibration of the concrete by means of a needle would be almost impossible for the beam containing the network of wires with capsules. The composition of the concrete mix which was used for each of the beams is shown in Table 1. All ingredients were mixed in a Zyklos 200 litre mixer. The mixing procedure was as follows: sand, gravel, cement, limestone filler (and SAPs) were mixed properly. Subsequently, the needed amount of water was added under continuous mixing. After one minute of mixing, superplasticizer (Glenium 51) was added steadily while mixing persisted. The moulds of the beams were covered with a plastic foil after casting of the beams. The moulds of the beams were removed after six days, then the beams were further stored at room temperature until the time of testing.

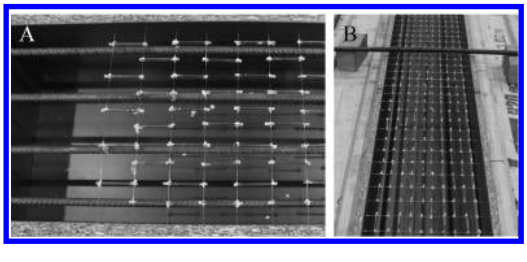

Figure 1. Placement of capsules, filled with polyurethane, on a network of wires which is connected to the sides of the mould (A and B).

Table 1. Composition of the concrete mixes.

	Composition [kg/m³]/[l/m³]		
Components	REF	SHC-PU	SHC-SAP
Sand 0/5	853	853	853
Gravel 2/8	370	370	370
Gravel 8/16	328	328	328
CEM I 52.5 N	300	300	300
Limestone filler	300	300	300
Water	165	165	207
Glenium 51	3.33	3.00	12
SAP	–	–	3

3 METHODS

3.1 *Crack formation*

In order to create multiple cracks, the beams were loaded in four-point bending. To facilitate performance of the water ingress measurements (see 3.3.1), the beams were loaded in upward direction (Fig. 2). The distance between both loading points amounted to 1000 mm. The metal rollers, used to exert the line loads, were placed symmetrically with regard to the middle of the beam. The rollers of the supports were positioned at the ends of the beam. For one of both supports the displacement was fixed in all directions, while the other one was free in x-direction. To ensure that the load was exactly the same in each of both loading points and that the load values increased at the same speed, one jack was used and the force exerted by this jack was transmitted to both rollers by means of a metal beam (Fig. 2). The exerted force was measured with a load cell. Next to the exerted load, the deformation of the beam was recorded during four-point bending. The curvature of the beam was measured by means of five Linear Variable Differential Transformers (LVDT's, Fig. 2). All LVDT's were positioned at the bottom side (compression zone) of the beam. Making use of the coordinate system shown in Figure 2, they were placed at the following x-positions: LVDT1 at 0 mm, LVDT2 at 800 mm, LVDT3 at 1500 mm, LVDT4 at 2200 mm and LVDT5 at 3000 mm. As the concrete composition and thus the concrete strength varies for the different beams under investigation (REF: 58.4 ± 0.9 N/mm², SHC-PU: 59.2 ± 0.4 N/mm², SHC-SAP: 47.7 ± 0.5 N/mm²), not the load or the curvature, but the average crack width was used to control the four-point bending

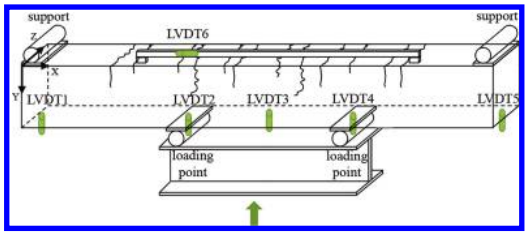

Figure 2. Setup of the four-point bending test with indication of the coordinate system, rods represent the position of the LVDT's, the arrow indicates the load position and direction.

test. Therefore, a measurement frame with a length of 1400 mm was positioned at the top of the beam (tensile zone), symmetrically with respect to the middle (Fig. 2). The total displacement within the area covered by this measurement frame was measured by an LVDT (LVDT6), which was connected to the frame in horizontal position. The measured displacement is mainly caused by the formation of cracks and further crack opening and partly by strain of the concrete matrix. Supposing that the contribution of concrete elongation is rather limited, the value measured by this LVDT represents the total crack opening within the zone covered by the measurement frame. Division by the total amount of cracks seen within this zone, results in the average crack width.

At the moment of crack formation, beams were loaded in four-point bending until the average crack width amounted to 250 μm. Note that this value is an overestimation of the real crack width, measured by means of microscopy, as both the strain of the concrete and the total crack width are taken into account when measuring the deformation in the zone covered by the measurement frame. Once this value was reached, the deformation of the beams were fixed and the jack was taken away during the seven weeks period of crack healing.

3.2 *Crack healing*

For the beam with encapsulated polyurethane (SHC-PU), crack formation triggered breakage of the capsules, release of the healing agent and subsequent crack repair when the healing agent came into contact with moisture in the concrete matrix. For the other self-healing approach under investigation (SHC-SAP) contact with water is needed in order to activate the mechanism. As contact with water also induces autogenous crack healing, the natural mechanism of crack healing which is inherent to concrete, it was decided to bring all beams (REF, SHC-PU and SHC-SAP) in contact with water. In this way all beams would exhibit, to some extent, autogenous crack healing and the influence of this effect is filtered out when results are compared. Bringing the beams into contact with water in order to obtain autogenous healing and to activate the self-healing approach with SAP, was done by giving the beams a shower with water four times a day during one minute for a time span of six weeks. Therefore, a plastic tube containing holes, over the complete length of the tube, was positioned in the middle above each of the beams (Fig. 3). At given times, water was pumped through the tubes so it was spraying over the top surface of the beams. As water was subsequently flowing along the sides of the beams, the side surfaces became also wet during each showering cycle. Water which was not absorbed by the cracks or by the concrete matrix was collected, by means of plastic foil, in basins which were positioned underneath the beams.

3.3 *Evaluation of the healing efficiency*

3.3.1 *Crack width reduction*

The initial widths of the cracks in the beams were measured by means of optical microscopy. For each crack, along the whole length of the beam, crack width measurements were performed at 9 positions. 2 measurements at each side of the beam and 5 more measurements of the width at the top surface of the beam. For the beam with encapsulated polyurethane, it was seen immediately that part of the cracks were filled up by polyurethane. During the seven weeks healing period for all of the beams, crack widths became lower due to autogenous (and autonomous) crack healing. Therefore, crack widths were measured a second time after six weeks spraying with water and the crack width reduction over time was calculated.

3.3.2 *Reduction in water ingress*

In order to evaluate the self-healing efficiency, the reduction in water ingress due to crack healing was

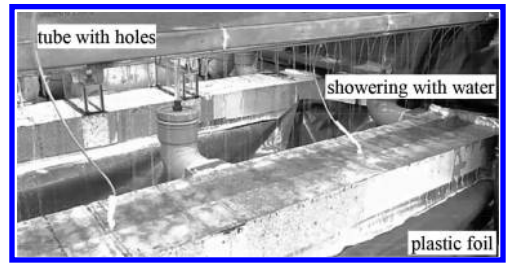

Figure 3. Showering of the concrete beams with water in order to induce autogenous crack healing and trigger the self-healing mechanism based on the use of embedded SAPs.

measured. After crack formation, plastic basins were glued onto each of the beams, covering 3 zones with a selected crack. The basins were made out of polyvinylchloride and had inside dimensions of 50 mm × 230 mm (Fig. 4). The height of the basins amounted to 100 mm. At the top of the basins two holes were provided. One was used for water supply and closed during the test by means of a plug. In the second hole, a pipette was positioned with a length of 400 mm and an inner diameter of 12 mm. This pipette was used for accurate following of the water flow inside the crack during the test. At the bottom of the basin an outlet was provided for fast release of the water after finishing the water ingress test. During the measurement, the sides of the cracks, selected for water ingress, were sealed by means of self-adhesive aluminum butyl tape in order to prevent the water intruding via the crack at the top from leaching out of the crack via the sides of the beam.

Water ingress was calculated using equation 1.

$$k = \frac{aT}{At} \ln\left(\frac{h_0}{h_f}\right) \quad (1)$$

with

k = coefficient reflecting the water ingress [m/s]
a = cross-sectional area of the pipette [m²]
A = contact area of water with beam [m²]
T = height of beam [m]
t = time [s]
h_0 and h_f = initial and final water head (sum of water height in basin and pipette) [m].

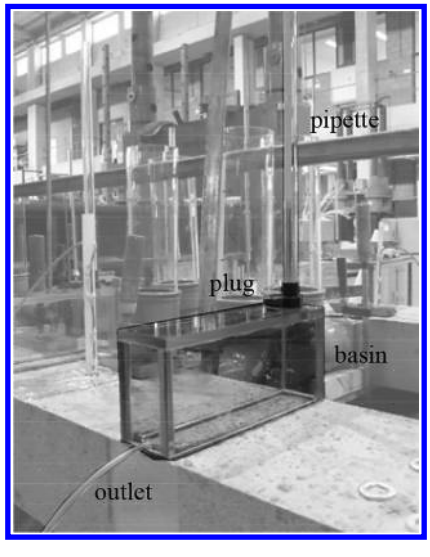

Figure 4. Setup used to measure the water ingress into the cracks.

Water ingress measurements were performed immediately after crack formation and were repeated after crack healing.

4 RESULTS

4.1 *Multiple crack formation*

The aim was to investigate whether an improved crack healing efficiency was obtained for the beams with the implemented self-healing approaches (SHC-PU and SHC-SAP) compared to the reference beam (REF). As the crack healing efficiency, particularly the contribution of autogenous healing, depends on the crack width, we aimed for a similar crack width for all of the beams under investigation. Therefore, the beams were not loaded until a predefined load was reached, but they were loaded until an equal average crack width of 250 µm was reached. The SAP beam had a lower strength as the SAP particles act as flaws, thus stress initiators (Yao et al. 2011). In Table 2 it can be seen that the number of cracks within the zone covered by the measurement frame (Figure 2) differed for each of the beams, being 20, 22 and 24 for the REF, SHC-PU and SHC-SAP beam, respectively. Due to this, the loading and thus also the elongation of the beams within the middle zone was different. For the REF beam and the SHC-PU beam, the elongation in the middle zone is represented as the sum of two values as the loading was performed in two stages. However, for each of the beams the average crack width (obtained by dividing the total elongation in the middle zone by the number of cracks in the middle zone) amounted to approximately 250 µm.

In Figure 5 the vertical displacement measured by the LVDT's positioned along the length of the beams is given. For the REF beam and the SHC-PU beam, the displacement is shown as the sum of two bars as these displacements were obtained in two separate loading stages. It can be clearly seen that for LVDT1 and LVDT5, which were placed close to the supports, the measured displacement was very little, as expected. For LVDT2 and LVDT4, placed symmetrically with regard to the middle position of the beam, a similar

Table 2. Multiple crack formation by four-point-bending.

Beam	# cracks in middle zone [–]	Elongation of middle zone [mm]	Average crack width [µm]
REF	20	4.01 + 1.10	256
SHC-PU	22	4.00 + 1.55	252
SHC-SAP	24	5.94	248

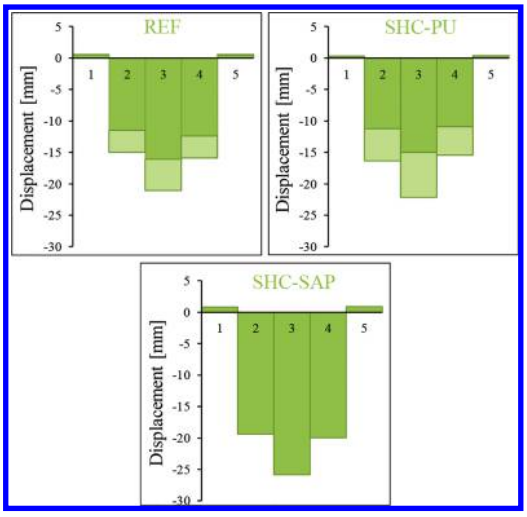

Figure 5. Vertical displacement of the beams at the position of LVDT1, LVDT2, LVDT3, LVDT4 and LVDT5.

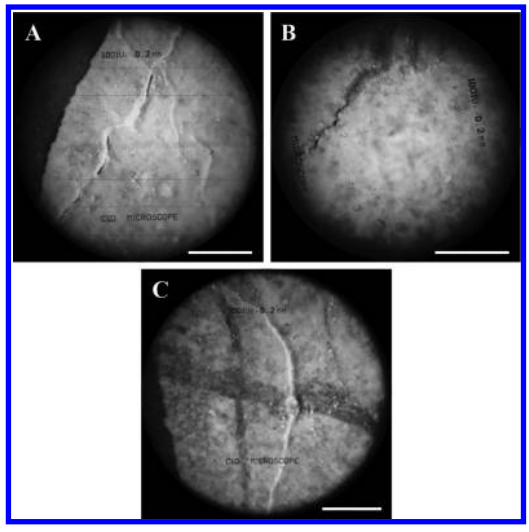

Figure 6. Micrograph of a healed crack inside the reference beam (A), the beams with encapsulated polyurethane (B) and the beams with superabsorbent polymers (C). The white line in the pictures represents a distance of 1 mm.

negative value for the displacement was measured. As the y-axis is oriented downward (Fig. 2), negative values are obtained for the deformation of the beam loaded in upward direction. The highest negative value was seen in the middle of the beam (LVDT3). As for the SHC-SAP beam more cracks were detected in the middle zone, and thus loading was continued for a longer time, higher absolute values for the displacement were registered. While for the REF beam and the SHC-PU beam the displacement in the middle of the beam amounted to –20.76 mm and –22.91 mm, for the SHC-SAP beam this value amounted to –25.84 mm.

4.2 *Visualization of crack closure by microscopy*

Due to cyclic exposure of the cracks to water for a period of six weeks, cracks showed some autogenous healing. In Figure 6A it can be seen that for the REF beam some crack healing was noticed, however, this remained limited to the smaller cracks. White precipitates, connected to the crack faces, can be seen. For narrower cracks this led to complete crack healing, however, for larger crack widths we noticed that for the REF beam no complete crack healing could be obtained. This confirms that the natural, autogenous, crack healing mechanism is limited to healing of smaller cracks.

For the beam with encapsulated polyurethane (SHC-PU), the highest portion of crack healing occurred at the moment of crack formation and capsule rupture. However, due to the six weeks spraying with water some additional autogenous healing closed the cracks. This is shown in Figure 6B. While the upper part of the crack is filled with polyurethane healing agent, it can be seen that the lower part is partly filled with calcium carbonate crystals.

In the beam with superabsorbent polymers improved crack healing was noticed. This can be clearly seen in Figure 6C. In this case more complete crack healing was obtained and also larger cracks could be more completely filled.

4.3 *Crack closing ratio*

The crack closing ratio was calculated as the difference in crack width before and after healing divided by the original crack width. This evaluation procedure only takes into account the amount of healing obtained during the six weeks showering period and not the extent of immediate healing of the beam with encapsulated polyurethane (SHC-PU). Cracks were divided into different categories, based on the original crack width, and crack closing ratios were calculated for each category of each test series.

What immediately can be seen from Figure 7 is that smaller cracks are more likely to be healed compared to wider cracks. For crack widths within the range of 0 to 50 µm, healing ratios within the range of 40 to 80% were obtained, while for the cracks within the largest crack width range (200 to 250 µm), healing ratios only amounted to 10 to 30%. A gradual decrease of the healing ratio for

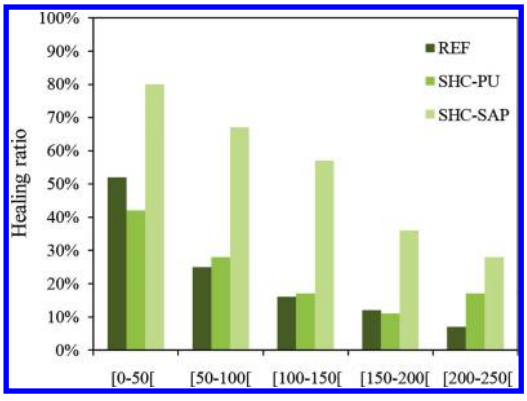

Figure 7. Crack healing ratio obtained within each crack range and for each of the test series under investigation.

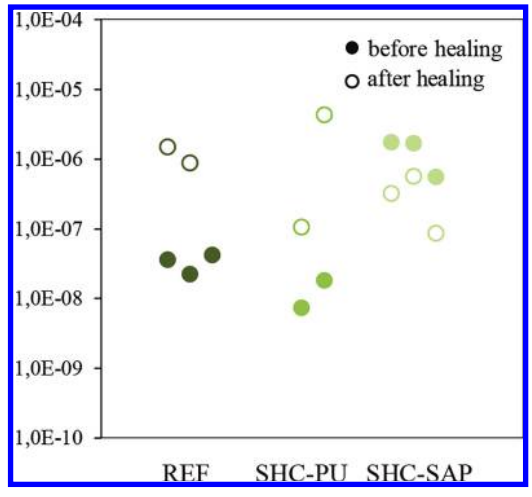

Figure 8. Water ingress into three (some results are missing) selected cracks for each test series measured before and after the healing period.

each test series can be seen with increasing crack width range. A second very clear finding is that the healing ratio for the beam with embedded SAP particles (SHC-SAP) is considerably higher compared to the healing ratios which are obtained for the two other test series under investigation (REF and SHC-PU, having almost the same healing ratios for each range).

This finding clearly indicates that the addition of SAPs to the concrete matrix promotes crack healing when the crack faces are exposed to water. Due to the addition of SAP, a healing ratio of 80% was obtained for cracks within the smallest crack width range. But also for the largest range, about 30% healing was obtained when SAPs were added to the matrix. Although no improved healing ratio is noticed when the SHC-PU beam is compared with the REF beam, this does not mean that healing was inefficient for this series. The healing efficiency of the SHC-PU beams is just not reflected by this experiment as at the time of the initial crack width measurement, autonomous healing already occurred for the SHC-PU beam. This experiment only shows the amount of additional autogenous crack healing which occurred during the seven weeks healing period with six weeks showering.

4.4 *Decrease in water ingress*

As can be seen from Figure 8, before crack healing, the water ingress into the cracks of the beam with embedded SAPs was clearly higher compared to the ingress into the other series (REF and SHC-PU). This is due to the fact that the SAP particles within the matrix of this beam attract an additional amount of water. However, this will result in a beneficial effect later on, as the water, absorbed by the SAPs, will be released to the surrounding cementitious matrix and result in further hydration and calcium carbonate precipitation. When these newly formed crystals are precipitated inside the cracks this results in an increased autogenous crack healing efficiency. This improved healing efficiency is partly represented by the results shown in Figure 8. While for the REF beam and the beam with encapsulated polyurethane (SHC-PU) higher water ingress values were obtained after healing, the SHC-SAP beam showed lower water ingress. We believe this should be attributed to healing of the cracks as for the SAP series crack closure was also shown from the microscopic analysis. The fact that higher water ingress was measured for the two other test series (REF and SHC-PU) is in contradiction with our expectations. However, we believe that this finding is due to the fact that the saturation state of the beams at the moment of the water ingress measurements was different before and after healing. Moreover, these water ingress measurements were very difficult to perform as for some of the selected cracks water was not only intruding in the concrete matrix via the crack but also leaked out of neighboring cracks. This makes it very difficult to draw sound conclusions from this test.

5 CONCLUSIONS

From this study it can be concluded that both self-healing approaches under investigation have some potential to be applied on real scale. However, the use of encapsulated polyurethane requires much more preparation to fill the tubes and position them in the moulds compared to the addition of

SAPs. Therefore, current research focusses on the development of encapsulation materials with properties evolving over time. So at first they should be flexible and survive concrete mixing while later on the capsules should become very brittle to break at the moment of crack formation. Use of this type of capsules would strongly decrease the time needed for preparation of concrete elements containing encapsulated healing agent. This is subject to further research.

With regard to healing, the approach making use of embedded SAP seems to result in the highest healing efficiency. Crack closure was obviously enhanced through the addition of SAPs to the concrete matrix. This was less clear for the beams with embedded polyurethane, however, the healing efficiency of this approach was not reflected by the crack width measurements. While it was hard to prove a good healing efficiency from the water ingress measurements, after crack formation release of polyurethane from the capsules inside the cracks was clearly noticed.

ACKNOWLEDGEMENTS

This research under the program SHE (Engineered Self-Healing materials) (project SECEMIN: Self-healing cementitious and mineral building materials) was funded by SIM (Strategic Initiative Materials in Flanders). The authors would like to thank this foundation for their financial support.

REFERENCES

Dry C. (2000). Three designs for the internal release of sealants, adhesives, and waterproofing chemicals into concrete to reduce permeability. *Cement and Concrete Research* 30 (12), pp. 1969–1977.

Dry C. (2001).Design of self-growing, self-sensing, and self-repairing materials for engineering applications. Paper presented at the Smart Materials Conference, pp. 23–29.

Edvardsen C. (1999). Water permeability and autogenous healing of cracks in concrete. *ACI Materials Journal* 96 (4), pp 448–454.

Jefferson A., Joseph C., Lark R.J., Isaacs B., Dunn S., Weager B. (2010). A new system for crack closure of cementitious materials using shrinkable polymers. *Cement and Concrete Research* 40 (5), pp. 795–801.

Jonkers H.M. (2011). Bacteria-based self-healing concrete. *Heron* 56 (1/2), pp. 1–12.

Lee H.X.D., Wong H.S., Buenfeld N.R. (2010). Potential of superabsorbent polymer for self-sealing cracks in concrete. *Advances in Applied Ceramics* 109 (5), pp. 296–302.

Li V.C., Yang E.H. (2007). Self healing in concrete materials. In: van der Zwaag S (ed) Self healing materials: An alternative approach to 20 centuries of materials science, Springer, pp. 161–193.

Pareek S., Oohira A. (2011). A fundamental study on regain of flexural strength of mortars by using a self-repair network system. Paper presented at the 3rd International Conference on Self Healing Materials, Bath, UK, 27–29 June 2011, pp. 46–47.

Reinhardt H-W., Jooss M. (2003). Permeability and self-healing of cracked concrete as a function of temperature and crack width. *Cement and Concrete Research* 33 (7), pp. 981–985.

Snoeck D., Van Tittelboom K., Steuperaert S., Dubruel P., De Belie N. (2014). Self-healing cementitious materials by the combination of microfibres and superabsorbent polymers. *Journal of Intelligent Material Systems and Structures* 25(1), pp. 13–24.

Van Tittelboom K., De Belie N., Van Loo D., Jacobs P. (2011). Self-healing efficiency of cementitious materials containing tubular capsules filled with healing agent. *Cement and Concrete Composites* 33(4), pp. 497–505.

Wang J., Soens H., Verstraete W., De Belie N. (2014). Self-healing concrete by use of microencapsulated bacterial spores. *Cement and Concrete Research* 56, pp. 139–152.

White S.R., Sottos N.R., Moore J., Geubelle P., Kessler M., Brown E., Suresh S., Viswanathan S. (2001). Autonomic healing of polymer composites. *Nature* 409, pp. 794–797.

Yao Y., Zhu Y., Yang Y. (2011). Incorporation of SAP particles as controlling pre-existing flaws to improve the performance of ECC. *Construction and Building Materials* 28(1) pp. 139–145.

Concrete Repair, Rehabilitation and Retrofitting IV – Dehn et al. (Eds)
© 2016 Taylor & Francis Group, London, ISBN 978-1-138-02843-2

Sprayed textile reinforced concrete layers for a durable protection of waterway engineering structures

C. Morales Cruz & M. Raupach
Institute of Building Materials Research (ibac), RWTH Aachen University, Germany

ABSTRACT: At the Institute of Building Materials Research (ibac) of the RWTH Aachen University, DURTEX, a durable, watertight, and crack-bridging protective textile reinforced concrete layer, was developed for restoring concrete, steel reinforced concrete or natural stone structures. A pilot application includes the surface repair of a pillar of the *Weir Horkheim* in Heilbronn-Horkheim where promising first results under real conditions were achieved (Orlowsky et al. 2011, Orlowsky et al. 2012, Morales Cruz et al. 2014a). This pilot application is vital for the joint research project between public administration partners, industry partners and research institutes of the RWTH Aachen University. It seeks to further develop and create procedures for the surface repair of hydraulic structures with low strength concrete surfaces. The paper at hand provides an overview of the function principle of DURTEX. Furthermore, the components of the developed DURTEX-protective layer, with which a crack-bridging up to 0.3 mm has been achieved, are presented. Additionally, the practical implementation of the developed application methods on the boiler house of the power generating plant *eins energie in sachsen* is introduced. To conclude, first results of an inspection three months after the completion of the sample surfaces are presented.

1 INTRODUCTION

The results of the inspections of hydraulic structures carried out by the Federal Office of Hydraulic Engineering (BAW) have shown that many hydraulic structures show an increased maintenance demand. In several cases, unreinforced tamped concrete hydraulic structures show not only low concrete strengths, but also cyclic opening movement joints and cracks. Considering the upcoming repair measures and taking the different concrete properties of the existing waterway engineering structures into consideration, four "old concrete" classes were created (A1–A4). These concrete substrates are classified depending on their compressive and surface strength (see Table 1).

Table 1. Classification of the concrete substrates according to the ZTV-W LB 219.

		Old concrete class			
Characteristic values	Unit	A1	A2	A3	A4
Compressive strength	N/mm²	≤10	>10	>20	>30
Surface strength (arithmetic mean)		–	≥0.8	≥1.2	≥1.5
Surface strength (lowest single value)		–	≥0.5	≥0.8	≥1.0

The permissible surface repair methods of waterway engineering structures are presented in Table 2. For the surface repair of such structures anchored, steel-reinforced concrete or sprayed-concrete layers are allowed. Alternatively, non-anchored, unreinforced concrete, mortar, sprayed-concrete or sprayed-mortar layers, which are connected over adhesive strength to the concrete substrates, can be used. In the few cases when these structures are not exposed to water or rear water penetration, surface protection systems can be applied.

A disadvantage of steel-reinforced concrete or sprayed concrete is the high layer thickness, which is required for the necessary corrosion protection of the steel reinforcement. The associated increase in the component cross-section can be problematic for the repair of hydraulic structures, such as floodgates and weir structures, since the inside space is often limited.

For the old concrete classes A2–A4 it is allowed to produce thinner ($20 \leq d \leq 60$ mm), unreinforced, non-anchored layers by using sprayed-mortar/concrete systems (ZTV-W LB 219 copy 2013). So far, only a few (four in total) unreinforced sprayed mortar/concrete systems are listed in the "Compilation Hydraulic Engineering" for the repair of the old concrete class A3, and only one is listed for the repair of the old concrete class A2. In addition to the limited availability of unreinforced surface repair systems, cyclically opening cracks

Table 2. Permissible protection and repair systems according to the ZTV-W LB 219.

Old concrete class	Sprayed-concrete concrete d ≥ 90 mm		Sprayed-mortar/ concrete 20 ≤ d ≤ 60 mm	Polymer modified cement concrete 10 ≤ d ≤ 60 mm	Surface protection systems
A1	X	X*	–	–	–
A2	X	X	S-A2**	–	–
A3	X	X	S-A3**	–	X*
A4	X	X	S-A4**	X*	X

*Only under certain condition (see ZTV-W LB 219); **the compression strength and deformation behavior of the sprayed mortar/concrete surface repair systems must be adapted to the corresponding old concrete class.

and joints in the concrete substrates, which lead to a "break-through" of the cracks in the repair system and in a reduction of the intended service life due to water penetration, possibly resulting in spalling of the repair layer, hinder the use of unreinforced sprayed-mortal/concrete systems.

In cooperation with industry partners and research institutes of the RWTH Aachen University, two non-anchored surface repair systems (S-A2 and S-A3) for substrates without water pressure as well as two anchored systems (S-A2 and S-A3) for substrates with gap water pressure (up to 50 kN/m²) are being investigated within the framework of the transfer project T09, which is funded by the German Research Foundation (DFG) *Textile Reinforced Sprayed Mortar Layers for the Surface Repair of Waterway Engineering Structures*.

In order to comply with the permissible layer thickness of 60 mm for sprayed-mortar/concrete layers, so-called technical textiles can be used as reinforcement material. Technical textiles are biaxial fabrics made from AR-Glass fiber or Carbon rovings and have mesh sizes from 5 to 38 mm. The combination of technical textiles with a cement-bound matrix is known as textile reinforced concrete "TRC".

To achieve a fine crack distribution with sufficiently small crack widths and to provide a sealing effect, a de-bonding area must be created along the sides of the joint or crack in the supporting surface (see Fig. 1). The de-bonded area creates a free expansion length in the protective layer. The number and width of the resulting cracks in the protective layer mostly depend on the type of textile reinforcement, the width of the de-bonding area, and the bonding behavior between the cement matrix and textile reinforcement. Since the de-bonded area is much smaller than the total bonded area, it can be assumed that the durability of the protective layer is not negatively influenced by any local de-lamination between the supporting surface and the protective layer. The combination of the properties of the protective layer

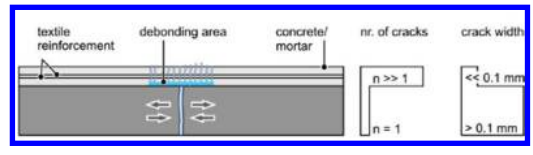

Figure 1. Schematic drawing of the textile reinforced concrete DURTEX-layer. The crack width and the number of cracks on the DURTEX-layer and supporting surface are presented—the de-lamination zone is exaggerated on purpose.

"durable, watertight and crack-bridging" and the material TRC frame the acronym DURTEX. The individual components of the DURTEX protective layer are:

- concrete or sprayed mortar/concrete,
- textile reinforcement,
- de-bonding area,
- anchorage (if necessary).

The fundamental suitability of the DURTEX protection layer, with respect to the transfer of the crack opening of the substrate into many fine cracks on the protective layer surface, has already been demonstrated in laboratory studies on textile reinforced cement mortar mixtures (Büttner et al. 2013).

2 MATERIALS

Within the framework of this project, two dried sprayed polymer-modified concrete mixtures (S-A2 and S-A3) were developed for the surface repair of the old concrete classes A2 and A3 (Morales et al. 2014c). Starting points for the development of the sprayed concrete mixtures are the requirements according to the leaflet "Spritzmörtel/Spritzbeton nach ZTV-W LB 219, Abschnitt 5, (MSM) Ausgabe 2012" and the limitations of the layer thickness in (ZTV-W LB 219 copy 2013). With the chosen grain size of 6 mm, the total layer thickness

can range from 20 mm to 60 mm. Aspects such as a low elastic modulus, the low shrinkage values with highly developed micro-crack formation ability, as well as a high adhesiveness value were pursued (see Table 3).

During this project various textile structures have been tested, including: AR-Glass and carbon fibers, impregnated with SBR (Styrene-Butadiene Rubber) or EP (Epoxy), as 2D and 3D structures. In Figure 2, two commercially available textile reinforcements, which were favored in the studies, are presented.

Since the goal of the DURTEX-protective layer is to increase the durability and not to strengthen the load bearing capacity of the substrate, the focus was on improving the bonding behavior between textile reinforcement and sprayed polymer-modified concrete mixtures. Current studies investigate possible surface modification processes. First results on subsequent sand dusted epoxy-coats show an increase of the adhesive strength between cement-matrix and textile reinforcement.

In the conducted studies, the width of the de-bonded area varied between 12 and 22 cm along the crack of the supporting system. So far, hydraulic materials (polymers such as epoxy resins or polyurethanes) and various one-sided adhesive tapes were tested. The effectiveness of the de-bonding materials was tested in adhesive tensile strength tests. For the use on the construction site, tapes are suitable because of the uncomplicated and fast application and good de-bonding performance (see Fig. 4, left). Cementitious materials can be used to de-bond wide and scrawly cracks in substrates (see Fig. 4, right).

Table 3. The characteristic values of the surface repair systems.

Characteristic values	Units	Old concrete class	
		S-A2	S-A3
Compressive strength, 28d	N/mm²	26.8	29.7
Ultimate flexural strength, 28d		6.5	6.3
Shrinkage, 28d	mm/m	–0.52	–0.51
Elastic modulus (static), 28d	N/mm²	21500	23500

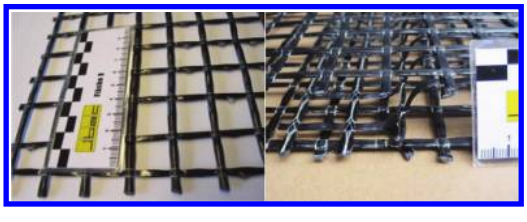

Figure 2. EP impregnated carbon textiles. Left: 2D textile, right: 2 Layers of the 2D textile at a distance of 20 mm.

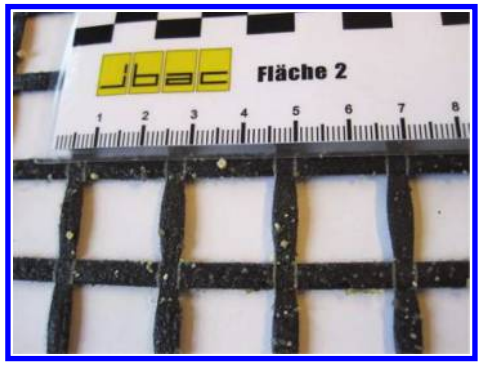

Figure 3. EP impregnated carbon structures with a subsequent sand dusted epoxy-coat.

Figure 4. De-bonding materials. Top: acrylic-adhesive with HDPE-film, bottom: cement-based coat (StoCrete FB).

3 EXPERIMENTS

In order to quantify the interaction between the sprayed polymer-modified concrete and the textile reinforcement, extensive studies on the composite system are required. Both, the load-bearing capacity as well as the crack-bridging ability of the textile reinforced protective layer are relevant and need to be investigated. In order to test the mechanical properties—load bearing capacity and the crack-bridging ability—two different experimental set-ups are required (Büttner et al. 2013, Morales et al. 2014c). The load bearing capacity of DURTEX is investigated in uniaxial tensile tests as described in (Orlowsky et al. 2011), while the determined failure loads are used as part of a structural design. The crack distribution and the crack spacing hint at the bonding behavior of the textile reinforcement and the sprayed polymer-modified concrete.

At ibac, the crack-distributing ability of DURTEX is quantified with the test set-up shown in Figure 5 (Morales et al. 2014b). This test set-up is based on the crack-bridging examination of surface protection systems according to (DAfStb, 2001). However, the dimensions were adjusted to the materials and test specimen ($70 \times 10 \times 9$–12 cm³).

The aim of the crack-bridging experiment (see Fig. 5) is the quantification of crack-distributing properties of the DURTEX-layer with a defined crack opening of the supporting surface. By converting the crack opening of the supporting surface into much smaller cracks in the protection layer (goal: $w \leq 0.1$ mm), it is possible to achieve water tightness (in a technical sense). The crack-distributing ability of the protective layer is influenced by the textile reinforcement, the cement matrix as well as by the de-bonding width.

When testing the crack-distributing ability of the protection layer two points have to be considered. First, the crack-bridging test must be carried out under uniaxial tensile stresses of the protective layer (perpendicular to the cracked supporting surface) and must be conducted as such, in order to avoid an unintended bending. Secondly, the goal to measure the number of cracks and their widths ($w \leq 0.1$ mm) on the protective layer continuously during the test is only possible when using measuring instruments with a high resolution (e. g. digital close range photogrammetry). The photogrammetric measuring process is divided in two phases: the image recording and image analysis phase (Morales et al. 2014b). At ibac, a photogrammetric measuring system of the company GOM is used. The 3D video measuring system ARAMIS® is able to measure the deformation of the sample in real time without contact. The ARAMIS® Systems can only detect sufficiently structured surfaces. Therefore, a stochastic pattern is sprayed onto the testing surface (see Fig. 6). In addition to measuring the deformation of the protective layer during the crack-bridging test, the tensile load and the crack opening on both sides of the crack on the supporting surface were measured with inductive displacement sensors (see Fig. 6). This allowed the subsequent analysis of the number of cracks, the crack spacings and the individual crack widths on the surface of the DURTEX-layer. Furthermore, the effectiveness of the DURTEX-layer at any

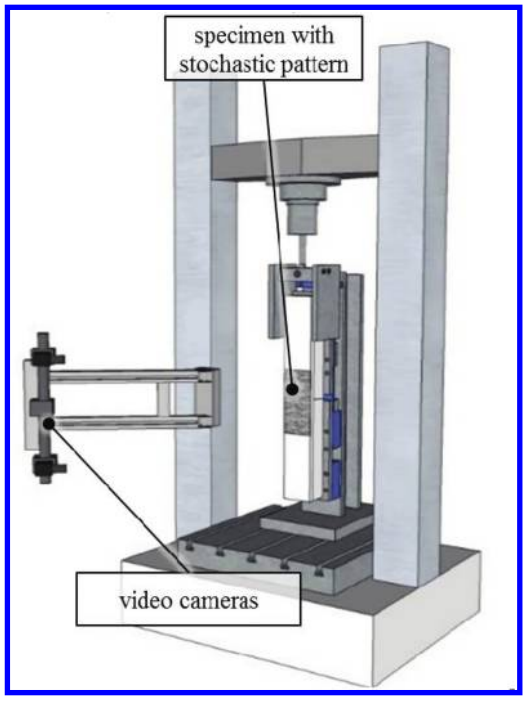

Figure 5. Test setup including the image recording ARAMIS® System.

Figure 6. Close-up of the crack-bridging specimen, the stochastic pattern on the testing surface as well as the inductive displacement sensor.

crack width opening of the supporting surface can be determined and compared.

The second phase of the photogrammetric measuring process, the image analysis phase, is also carried out with ARAMIS®. An example is presented below.

4 RESULTS

The crack bridging test is a realistic simulation of crack movements occurring in the structure. Figure 7 shows an exemplary analysis of the crack-bridging test done with ARAMIS® for a DURTEX protection developed during this project. The following materials were selected:

- two 2D layers of an EP impregnated carbon textile reinforcement
- a sprayed polymer-modified concrete mixture (S-A2)
- and a 12 cm wide de-bonding tape.

Figure 7 displays that a crack opening of the supporting surface of 0.5 mm leads to the formation of four cracks on the protective layer within the de-bonding area. The mean crack-width is 0.12 mm.

Additionally, Figure 7 provides evidence that the goal to deform the specimen uniaxially has been achieved. The measured deformation (with the inductive displacement sensors) corresponds to the sum of the single crack widths in the protective surface (see Fig. 7, bottom left).

Taking the existing measurement data into account, a maximum crack width opening of 0.6 mm of the substrate was set as basis for this project. The measurements at Weir Horkheim, which faced natural weathering conditions for more than two and a half years, showed a maximum crack opening of the substrate of 0.28 mm. Thus, the requirements of this project are on the safe side. In order to achieve the goal of crack widths of $w < 0.1$ mm on the protective layer at a crack opening of 0.6 mm of the substrate, the width of the de-bonding material can be increased e. g. to 20 cm. However, a controlled crack distribution with crack widths $w < 0.1$ mm, with a 0.3 mm crack opening in the substrate with the developed DURTEX protective layer is possible with the 12 cm de-bonding width. Further experiments are underway.

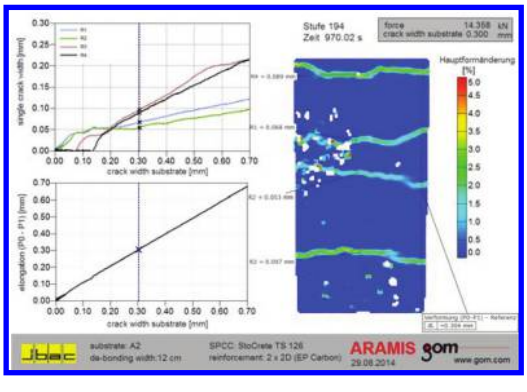

Figure 7. Analysis of the crack-bridging test with ARAMIS®. Top left: individual cracks over the crack opening of the concrete body; bottom left: sum of the cracks in the protective layer over the crack opening of the concrete body; right: visualization of individual cracks in the measuring field.

5 IMPLEMENTATION OF THE DURTEX CONCEPT—EINS ENERGIE IN SACHSEN

The testing of the two practice-applicable methods ("layer by layer" and "one step") under real construction conditions were tested on a 20 m² wall of a boiler house of the power generating plant *eins energie in Sachsen*. However, the sample surface presented neither cyclic opening movement joints, nor cracks.

In cooperation with the companies Massenberg und StoCrete, a total of four sample surfaces, with a sprayed polymer-modified concrete mixture (S-A2) and carbon textile reinforcement, were created in November 2014. In Figure 8, the setup of the four sample surfaces is presented.

The sample surfaces 2 and 3 were created using the layer by layer method. First, a 10 mm thick layer of sprayed concrete is applied, followed by the manual placement of the first layer of textile reinforcement. These two steps are repeated and finalized with a top layer (sprayed concrete). This results in a good bond between technical textiles and sprayed concrete.

In sample surface 4, one production step is reduced as a result of the special textiles used (see Fig. 2, right). Due to the spacing between the two 2D-layers, the total layer thickness was increased. The mesh size of the textile reinforcement and the spacing between the two 2D-layers are crucial for ensuring an adequate penetration of the sprayed concrete. Disregarding this will lead to flaws and so-called "spray-shadows".

The setup of the sample surfaces 2, 3 and 4 is not suitable for substrates with gap water pressure, since they require an anchored protection layer to the substrate. Therefore, a second method (single layer spraying) was developed in the context of this project. By using either textile spacers or anchors, the technical textiles can be set in place, reducing

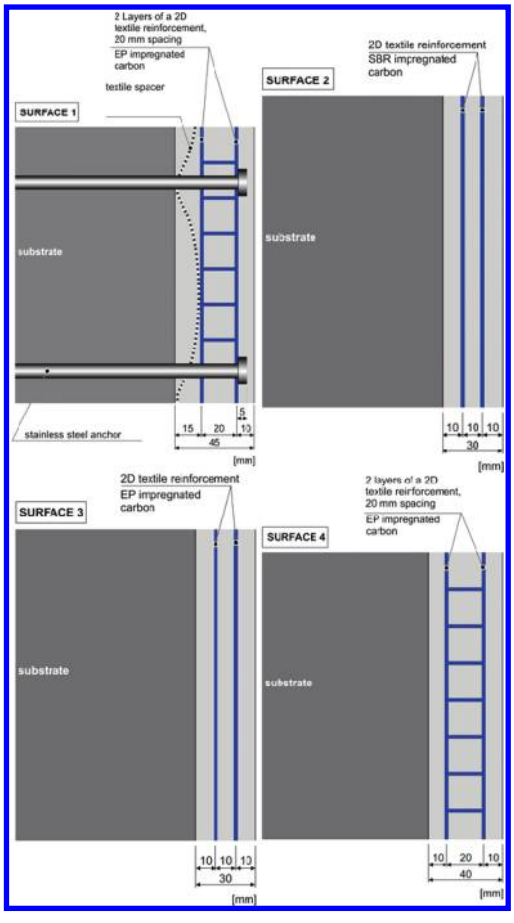

Figure 8. Setup of the four sample surfaces.

the concrete spraying steps to one (see sample surface 1). However, this method leaves less space for inaccuracies. In order to prevent flaws or spray shadows, it must be assured that the rovings of the technical textiles are located directly above one another.

The general condition of the four sample surfaces was examined in February 2015, three months upon their completion. First results show that the adhesive tensile strength of all four sample surfaces complies with the requirements of the BAW (BAW Merkblatt 2012).

6 CONCLUSION

In the publication at hand, the concept of a textile reinforced, flexible protective layer to repair concrete surfaces with moving cracks in concrete structures durably was presented. The results can be summarized as follows:

- The protective layer DURTEX is capable of deforming itself as well as absorbing the movements and the loads acting from the substrate.
- The crack-bridging test set-up allows a uniaxial tensile test of the protective layer.
- The optical inspection and analysis of the protective layers when using ARAMIS® allows the continuous measurement of the deformation and the crack widths of the protective layer.
- A controlled crack distribution with crack widths $w < 0.1$ mm at a 0.3 mm crack opening in the substrate with the developed DURTEX protective layer has been shown.
- Two practice applicable methods under real construction conditions were developed and tested during this project.

Within the framework of this project, the use of textile reinforced concrete for the repair of hydraulic structures will be further investigated. Current studies examine the change in the crack-bridging properties of the DURTEX-layer under cyclic and permanent load, combined with rear water pressure.

REFERENCES

BAW Merkblatt 2012, Spritzmörtel/Spritzbeton nach ZTV-W LB 219, Abschnitt 5.

Büttner, T. & Morales Cruz, C. & Raupach, M. 2013. Dauerhafte Schutzschichten aus Textilbeton für Bauwerksoberflächen im Wasserbau. *Bautechnik,* Volume 90, Issue 8, pages 485–490.

Morales Cruz, C. & Raupach, M. & Westendarp, A. & Bruder, S. 2014a. Untersuchungen an einer vier Jahre alten Schutzschicht aus textilbewehrtem Spritzbeton am Wehr Horkheim. *Beton 64,* Nr. 10, pages 390–395.

Morales Cruz, C. & Raupach, M. 2014b. Untersuchungen zur kontrollierten Rissverteilung textilbewehrter Schutzschichten. *Restoration of Building and Monuments*, Issue 20, Nr. 6, pages 405–412.

Morales Cruz, C. & Raupach, M. 2014c. Textile Reinforced Sprayed Mortar for the Repair of Hydraulic Engineering Structures. *Structural Faults and Repair*, Issue 2014.

Orlowsky, J. & Raupach, M. & Westendarp, A. 2011. Textilbewehrte Spritzmörtel zur Instandsetzung von Wasserbauwerke. *Beton 61*, Nr. 12: pages 486–490.

Orlowsky, J. & Raupach, M. 2012. Textile reinforced sprayed mortar for the repair of hydraulic engineering structures. *Concrete Repair, Rehabilitation and Retrofitting III,* pages 1065–1070.

ZTV-W LB 219, 2013. Zusätzliche Technische Vertragsbedingungen—Wasserbau für Schutz und Instandsetzung der Betonbauteile von Wasserbauwerken.

Concrete Repair, Rehabilitation and Retrofitting IV – Dehn et al. (Eds)
© 2016 Taylor & Francis Group, London, ISBN 978-1-138-02843-2

Production and fresh properties of powder type self—compacting concrete in Sudan

O.M.A. Daoud & T.M. Kabashi
Building and Roads Research Institute, University of Khartoum, Khartoum, Sudan

ABSTRACT: This paper presents the results of an experimental study conducted to produce powder type self-compacting concrete in Sudan. The primary objective of the study is to conduct an exploratory work towards the development of a suitable SCC mixes in the hot climate of Sudan, with special consideration focus on solving problems related to satisfactory segregation resistance, filling, and passing abilities thorough conducting a series of trial mixes. In addition, the paper investigates different fresh properties of SCC and their interrelations at the fresh state. Different tests were carried out to characterize raw materials. All necessary modifications in proportioning and mixing are mentioned. Mixing procedure adopted in the study is well explained. Different successful SCC mixes were produced and their fresh properties were studied. Some reliable statistical relations between fresh properties of SCC were developed and presented. Comparisons of these relations with previously published relations showed that in spite of the different material type, proportions, humidity, environmental and climatic conditions, the overall performance of the fresh self-compacting concrete mixes achieved, demonstrated same pattern. The effects of fly ash content and super plasticizer dose on fresh properties of SCC are also highlighted. Results also showed that marginal high strength concrete could be produced with same constituent proportions.

1 INTRODUCTION

A recent innovation in construction industry that makes use of advance technology of both mineral and chemical admixtures is Self-Compacting Concrete (SCC). Sudan is one of the developing countries that face many problems in the field of construction and infrastructures; one solution of these problems is towards employment of self-compacting concrete, which overcomes the problem of non-skilled labor, saves time, and solve durability problems. The application of SCC in Sudan is very rare because of lack of research and published data pertaining to locally produced SCC. Therefore, there is a need to conduct studies, further researches, and investigations to get the knowledge of SCC and to be aware about its all aspects; starting from selection of suitable constituents including superplasticizer, mineral admixtures, mix proportion optimization, assessment of the fresh state and hardened state properties to produce it successfully (Kabashi & Daoud, 2014).

2 MATERIALS USED

2.1 *Cement*

Ordinary Portland cement (Type I) was used. The chemical analysis of cement is presented in Table 1.

2.2 *Fly ash*

Class F Fly ash obtained from Zouxian power plant was used. The chemical analysis of fly ash is presented in Table 2.

Table 1. Chemical analysis of cement.

Test	% by mass
Loss on ignition at 1000°C	4.63
Silica as SiO_2	19.53
Aluminum oxide as Al_2O_3	5.66
Ferric oxide as Fe_2O_3	3.20
Calcium oxide as CaO	58.37
Magnesium oxide as MgO	2.67

Table 2. Chemical analysis of fly ash.

Test	% by mass
Loss on ignition at 1000°C	1.61
Silica as SiO_2	49.78
Aluminum oxide as Al_2O_3	36.63
Ferric oxide as Fe_2O_3	3.71
Calcium oxide as CaO	4.00
Magnesium oxide as MgO	1.04

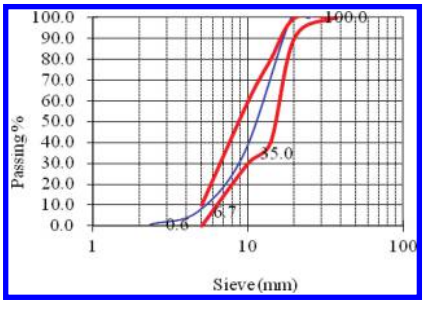

Figure 1. Particle size distribution of coarse aggregates using BS jacket.

Table 3. The physical properties of fine aggregates.

Test conducted	Result
Specific gravity	2.65
Total water absorption	0.5%
Fineness modulus	2.36

Table 4. Sieve analysis of fine aggregates.

BS sieve size (mm)	Retained weight (g)	Percentage retained by weight	Percentage passing by weight
10.0 mm	0	0	100
5.00 mm	1.8	0.262	99.74
2.36 mm	5	0.728	99.27
1.18 mm	78.3	11.41	88.59
600 µm	321.7	46.86	53.14
300 µm	556.14	81.01	19
150 µm	660.01	96.14	3.86
PAN	686.53	$\sum = 236.41$	

2.3 *Coarse aggregates*

Natural crushed igneous stones with maximum size 20 mm processed from the local quarries of Toryia Mountain were used as coarse aggregates (Fig. 1). The average values of specific gravity and absorption were 2.87 and 1.1%, respectively.

2.4 *Chemical admixtures*

Sikament®—R2004 complies with ASTM C-494 Type G and BS 5075 part 3 was used. It is a modified synthetic dispersion brown liquid with density of 1.2 ± 0.005 kg/l at 20° C.

2.5 *Fine aggregates*

Locally available natural sand was used as fine aggregate. The sand used was classified as class M according to BS 882:1992. Physical properties of sand and sieve analysis are presented in Table 3–4 respectively.

3 EXPERIMENTAL WORK

3.1 *Mixing procedure*

A fixed mixing procedure takes 10 minutes was adopted and carried out throughout this research using a drum type concrete mixer. In order to achieve maximum super plasticiser efficiency, dispersion of the powder, and to avoid balling effect; the concrete was mixed in the following way:

1. Powder (including cement and/or fly ash) and aggregate (fine and coarse) were mixed for one minute;
2. The 1st part (80%) of mixing water was added slowly while mixing and mixed for another one minute;
3. The 2nd part (20%) of mixing water with super plasticizer dissolved in it was added slowly while mixing for another 1 minute;
4. Mixing was continued for a further 2 minutes;
5. The mix was allowed to rest for 3 minutes;
6. The mix was remixed for 2 minutes and discharged for testing.

Figure 2. Slump flow test.

3.2 *Mix proportions*

Table 5. Mix proportioning.

Trial mix. no.	Total powder content (kg/m³)	Cement (kg/m³)	FA (kg/m³)	Sand(S) (kg/m³)	C.A (kg/m³)	S/C.A ratio	Water (kg/m³)	W/P ratio	SP (L/m³)
1	528	528	–	950	792	1.20	190	0.36	8
2	528	528	–	793	898	0.88	212	0.4	9
3	536	536	–	910	803	1.13	198	0.37	8
4	536	536	–	910	803	1.13	198	0.37	8.8
5	550	550	–	901	763	1.18	200	0.36	13.3
6	550	550	–	858	820	1.05	200	0.36	8.8
7	550	550	–	858	820	1.05	200	0.36	10
8	550	550	–	858	820	1.05	200	0.36	8.7
9	550	465	85	858	820	1.05	200	0.36	10
10	550	465	85	858	820	1.05	200	0.36	8.7
11	550	465	85	858	820	1.05	200	0.36	6
12	550	465	85	858	820	1.05	200	0.36	7.3
13	550	415	135	858	820	1.05	200	0.36	8.75
14	550	415	135	858	820	1.05	200	0.36	7.3
15	550	415	135	858	820	1.05	200	0.36	6
16	550	355	195	858	820	1.05	200	0.36	5
17	550	355	195	858	820	1.05	200	0.36	6.7
18	550	355	195	858	820	1.05	200	0.36	6

4 RESULTS AND DISCUSSION

4.1 *General*

The results of fresh properties tests of trials been performed during experimental work is presented in Table 6, while the succeeded trials that satisfied self-compacting properties were selected and shown n separate in Table 7. The slump flow of selected mixes obtained ranged from approximately 650 mm to 750 mm indicated good deformability (Fig. 2). The slump flow obtained categorized as SF2, which is suitable for many normal applications (e.g. walls, columns). Test results of this research indicated that all selected SCC mixes shown in Table 7 meet the requirements of allowable flow time and categorized as VS1/VF1 (Fig. 3); the selected mixes has similar slump flow times of average 2 seconds. Consequently all selected mixes has good flowability even with congested reinforcement, and the addition of fly ash did not affect the slump flow time. As indicated by the J-ring results (Fig. 4), all mixes exhibited good passing ability and no blockage was exhibited in any of the mixes. All selected mixes displayed good resistance to segregation categorizes as SR2. The values obtained in this study are in agreement with the results reported by other researchers.

The first trial conducted has failed because of incompatibility of the trial constituent's proportions; sand content was too much. The trial resulted in high amounts of bleeding and segregation. In the second trial the constituent proportions were adjusted; Fine aggregate content was reduced to 793 kg/m³, and coarse aggregate was increased to 898 kg/m³. Water and SP were also increased to 212 kg/m³ and 9 l/m³ respectively, while cement content kept constant at 528 kg/m³. In spite of this, a considerable amount of bleeding and segregation were also noticed. Consequently all proportions were readjusted in the third trial; cement content and Fine aggregate content were increased to 536 kg/m³ and 910 kg/m³ respectively. Coarse aggregate, water, and SP were reduced to 803 kg/m³, 198 kg/m³ and 8 l/m³ respectively to be within the guidelines typical ranges. The third trial showed good results, but the V-funnel time after 5 minutes was not within the recommended limits, furthermore, the slump flow time achieved the maximum recommended value (5 sec.), so both results indicate relatively high viscosity. Therefore in the fourth trial the super plasticizer dosage was increased to maintain adequate viscosity. Some of the workability characteristics were obtained, but from a visual sight of view and according to the result obtained from screen stability test the segregation index was 10.2%, it seems that SCC mix would be prone to segregation. Thus to proceed towards achieving homogenous powder type SCC mix, the cement content was increased to 550 kg/m³ in trial number five. The coarse aggregate and

Table 6. Fresh properties tests results.

Mix. ID.	Slump flow test		J-ring test			V-funnel test		GTM screen stability test %
	Dia. (mm)	$T_{50\,cm}$ (s)	Dia. (mm)	$T_{50\,cm}$ (s)	B_j (mm)	$T_{10\,s}$ (s)	$T_{5\,min.}$ (s)	
1	–	–	–	–	–	–	–	–
2	–	–	–	–	–	–	–	–
3	–	–	735	5	0.85	9	12:50	–
4	745	3:40	735	5	1.4	6	7	10.2
5	775	3:30	–	–	–	–	–	–
6	590	3:50	570	4:30	2.1	5	6:02	4.5
7	731	2:35	720	3:23	1.5	6	6:27	–
8	730	2	660	2:58	1.1	6:30	7	4.9
9	810	3:30	805	2:52	1.1	8	8:12	39
10	775	2:08	760	2:55	1.03	8	8:30	17.8
11	495	–	–	–	–	–	–	–
12	700	2	670	2:51	1.1	6	6:19	8.2
13	800	1:48	755	2	1.03	4:22	5	33
14	767	3	705	3:50	1.03	7:20	8:54	15.7
15	690	2	680	2:10	1.65	6:21	7	8.1
16	480	–	–	–	–	–	–	–
17	750	–	–	–	–	–	–	–
18	660	2	653	2:34	1	6	6:10	5.1

Table 7. Fresh properties tests results of selected SCC mixes.

Mix. ID.	Slump flow test		J-ring test			V-funnel test		GTM screen stability test %
	Dia. (mm)	$T_{50\,cm}$ (s)	Dia. (mm)	$T_{50\,cm}$ (s)	B_j (mm)	$T_{10\,s}$ (s)	$T_{5\,min.}$ (s)	
CM	730	2	660	2:58	1.1	6:30	7	4.9
SCC 15%	700	2	670	2:51	1.1	6	6:19	8.2
SCC 25%	690	2	680	2:10	1.65	6:21	7	8.1
SCC 35%	660	2	653	2:34	1	6	6:10	5.1

Figure 3. V-funnel test.

Figure 4. J-ring test.

fine aggregate contents were decrease to 763 kg/m^3 and 901 kg/m^3 respectively, while water and SP dosage were increased to 200 kg/m^3 and 13.3 l/m^3 respectively. The trial has failed because of high dosage of super plasticizer used. In the next trial, the coarse aggregate and fine aggregate contents readjusted to 820 kg/m^3 and 858 kg/m^3. This amounted to 50% of its solid volume and 46% by volume of mortar in concrete, respectively as recommended by rational mix design (Liu, 2009).

The w/p ratio was kept constant at 0.36 and SP was reduced to 8.8 l/m^3. This trial satisfied self-compactability requirements, but low slump flow value of 590 mm was obtained. Therefore in the trials number seven and eight super plasticizer dosage was varied to satisfy the optimum slump flow value in addition to the other required characteristics of SCC. Both trials gave good results, but mix number eight was adopted as a reference or control mix to study the effects of using fly ash class F to replace cement in SCC mixes. Different percentage of 15%, 25% and 35% fly ash class F replaced cement were used. In the succeeding trials (nine, ten, eleven, and twelve) 15% of fly ash class F was used to replace cement. All proportions were kept constant as in the control mix, except SP dosage varied to satisfy self-compactability requirements. Trial number nine has failed; segregation occurred because of high dosage of super plasticizer (10 kg/m^3) used. The obtained segregation index (SI) was very high about 39%. Therefore in order to control Segregation the SP dosage was reduced to 8.7 l/m^3 in trial number ten. But this resulted in inhomogeneous mix with lower value of SI about 17.8%. Therefore, more reduction in SP dosage was used in trial number eleven towards getting a homogenous mix with SI less than 15%. SP dosage of about 6 l/m^3 was used, but the trial failed due to the low dosage of SP used. Slump flow of 495 mm lower than recommended was obtained. The SP dosage was increased again to 7.3 l/m^3, this time the trial succeeds and satisfactory results were obtained. The following trials (thirteen, fourteen, and fifteen) examined the effects of 25% fly ash class F replacing cement. Trial number thirteen failed due to segregation, (SI) was very high 33%, so the SP dosage was reduced in trial number fourteen which achieved SI equal to 15.7%. A further reduction in SP dosage was done in trial number fifteen which successfully gave the required results. 35% of fly ash class F replaced cement was used in trial mixes number sixteen, seventeen, and eighteen. Using either low (5 l/m^3) or high (6.7 l/m^3) dosage of SP as used in trails number sixteen and seventeen respectively resulted in failure trial, while using optimum dosage of super plasticizer (6 l/m^3) could control segregation and resulted in successful mix satisfying self-compactability requirements as achieved in trial number eighteen.

4.2 *Effect of percentage of fly ash on workability*

The addition of fly ash resulted in reduction of super plasticizer dosage; the increase in fly ash content was associated with a decrease in SP dosage as shown in Figure 5. A linear relationship in the form of $Y = -0.083x + 8.6$ with $R^2 = 0.92$ was obtained. Therefore for a given w/p, addition of fly ash generally results in a reduction of super plasticizer dosage for a similar workability (flow diameter). Similarly, for the same workability, increasing the water/powder ratio reduces the amount of super plasticizer dosage required. This confirms the conclusion from Douglas (2004). The increase in workability referred to the spherical particle shape of fly ash that led to better particle packing; consequently a reduction in the water requirement or increase the consistence of the concrete.

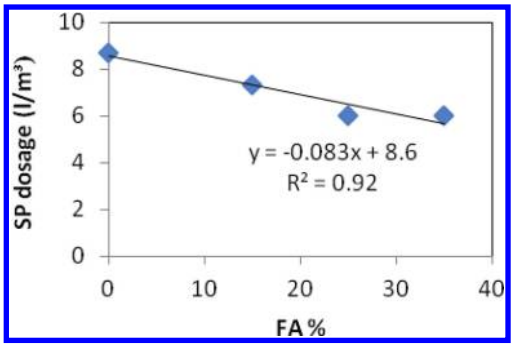

Figure 5. Relationships between super plasticizer dosage and fly ash content.

Furthermore the results obtained from J-ring and V-funnel achieved times ($T_{50\,cm}$, $T_{10\,s}$, and $T_{5\,min}$) were lower than that of control mix indicating high workability and high filling ability obtained using fly ash. All mixes showed good passing ability as indicated by the step height parameter (Bj), and it seems that the addition of fly ash did not make any difference. It was noticed that from the results obtained of J-ring test, the flow spread (Fd) increases as the fly ash content increases indicating good deformability, except the flow spread of SCC 35% decreases. The selected mixes has similar slump flow times $T_{50\,cm}$ (average 2 seconds), that means the addition of fly ash did not affect the slump flow time. While the results obtained by J-ring test shows difference which can be attributed to the confinement effect imparted by the ring. J-ring times increases as the fly ash content increases indicating good filling ability, except J-ring $T_{50\,cm}$ of SCC 35% decreases. Although all constituents' proportions of the 25% FA SCC mix and 35% FA SCC were the same, we found that the increasing the replacement ratio from 25% to 35% adversely affect the workability and resulted in low filling ability as indicated by slump flow test and J-ring test results, this confirms the statement "high levels of fly ash may produce a paste fraction which is so cohesive that it can be resistant to flow" stated by the European guidelines for self-compacting concrete, (2005). In spite of this the results obtained were still within the acceptance range. The screen

stability test also resulted in lower SI value for 35% FA SCC than that for 25% FA SCC, which indicate better segregation resistance for 35% FA SCC mix compared to 25% FA SCC mix.

4.3 *Relationships between key characteristics of the SCC*

The relationships between key characteristics of the SCC; Filling ability, Passing ability, and Segregation resistance were studied. The analysis presented was compared to a previous research performed by Liu (2009).

4.3.1 *T500 time vs. V-funnel time*

European guidelines for self-compacting concrete (2005) mentioned that T50 cm and V-funnel time are both related to viscosity. The data obtained shows a linear relationship between T50 cm and V-funnel times as shown in Figure 6, and this confirms the conclusion from Liu (2009). If a straight line is fit fitted to the data an equation in the form of $Y = 0.41x - 0.051$ could be obtained with an $R^2 = 0.99$ indicating a Strong correlation.

4.3.2 *Filling ability vs. passing ability*

The relationship between filling ability and passing ability was demonstrated by plotting Slump flow vs. step height of J-ring as shown in Figure 7. It is obvious that the higher slump flow the lower chance of blocking. The readings for slump flow and spread of J-ring approximately the same that is why mix stability has to be considered. It seems that as the slump flow decreased the step height of J-ring increased, as a result the tendency to blocking increased. Blocking criteria was unlikely to occur in this research as indicated from test results. The maximum value obtained for step height (Bj) was equal to 2.1 mm which is far from 10 mm the maximum acceptable value.

The relationship between filling ability and passing ability could also demonstrated by plotting

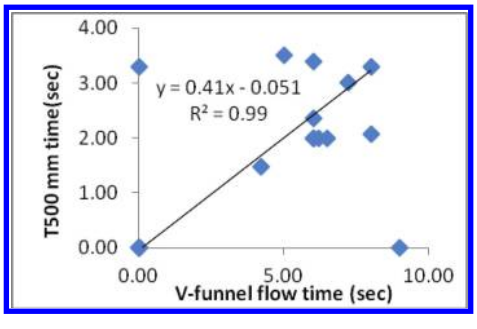

Figure 6. Relationships between T500 time and V-funnel time.

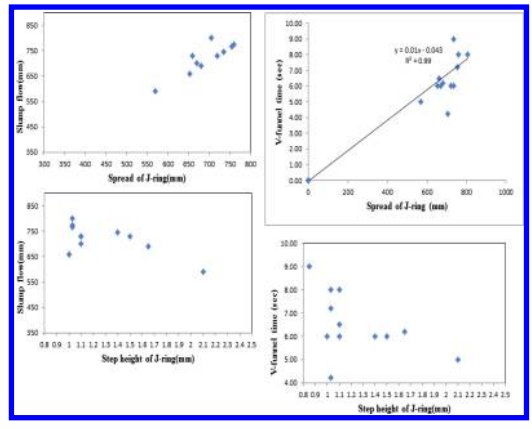

Figure 7. Slump flow and V-funnel time vs. J-ring results.

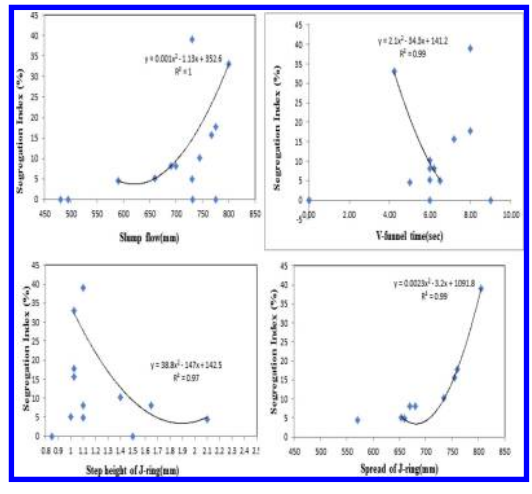

Figure 8. Segregation vs. slump flow, V-funnel time, step height and spread of J-ring.

V-funnel time vs. spread and step height of J-ring as shown in Figure 7. A reliable correlation between V-funnel time vs. spread of J-ring; an equation in form of $Y = 0.01x - 0.043$ with $R^2 = 0.99$ was obtained. The distribution of data showed that most data have slump flow in the range of 600 mm–800 mm with v-funnel time lies in range of 6–9 sec, and step height of 0.85 to1.65 mm; which confirms good filling and passing abilities according to European guidelines of SCC (2005).

4.3.3 *Segregation*

Figure 8 displays the relationship between segregation resistance and filling ability. Statically strong correlation with $R^2 = 1$ obtained between slump flow and segregation index in form of

$Y = 0.001x^2 - 1.13x + 352.6$. It is clear that for slump flow values greater than 700 mm, the segregation index increased sharply. Another reliable relationship between segregation resistance and filling ability was obtained using V-funnel test results. As shown in Figure 8 an equation in a form of $Y = 2.1x^2 - 34.3x + 141.2$ with $R^2 = 0.99$ is obtained. Generally the higher V-funnel time means low viscosity, therefore low chance of segregation to occur. Most trial mixes have V-funnel time about 6 sec., but different segregation index due to different content of fly ash. The relation between fly ash content and segregation is proportional. It was noticed that as fly ash content increase the segregation index increases. Determination of optimum dosage of super plasticizer helped in controlling stability of SCC.

Furthermore, statistically good correlation was obtained between segregation resistance and passing ability as presented in Figure 8. Segregation index decreased with increased in the step height of J-ring; and increased with increased in spread of J-ring. SCC mixes had high segregation risk as indicated by screen stability test, while blocking did not occur as shown from J-ring test result.

Finally it could be concluded that filling ability, passing ability and segregation resistance are interrelated and interdependent, and the trend is similar to the results obtained by Liu (2009). But it is clear that filling characteristics control segregation resistance more than passing ability. And both the spread and the step height of J-ring are equally related to slump flow and V-funnel time; it seems that yield stress introduced by slump flow had same effect as viscosity introduced by V-funnel time on passing ability.

5 CONCLUSIONS

1. Powder type SCC has been successfully produced, using class F fly ash replaced cement up to 35% without the need of a Viscosity Modifying Agent (VMA).
2. SCC is very sensitive to small changes in constituent materials, so it requires careful attention during all production stages.
3. The main constituents ratio of selected trial mixes used in this research were: powder content of 550 kg/m^3, W/P ratio of 0.36, S/CA ratio of 1.05, water content of 200 l/m^3, with various dosages of super plasticizer.
4. As the replacement percentage of fly ash increased the workability increased for a constant W/P ratio.
5. As the replacement percentage of fly ash increased the tendency to segregation enormously increased. Reducing dosage of super plasticizer to the required level that satisfied the key properties of SCC, has led to homogenous mix with appropriate consistency.
6. A reliable empirical correlation between the required super plasticizer dosage and the fly ash content was obtained.
7. It was found Filling ability, passing ability, and segregation resistance are interrelated and interdependent.
8. In spite of the difference in materials type, proportions, humidity, environmental and climatical conditions, the overall behavior of constituents if the self compactability requirements achieved demonstrated same pattern.
9. The fresh properties observed for all of the selected fly ash mixes were good and within acceptance range as compared to the control mix.

REFERENCES

Douglas, R.P. 2004. Properties of Self-Consolidating Concrete Containing Type F Fly Ash. Degree of Master of Science in Civil Engineering, Portland Cement Association (PCA) & Research and Development Information (R&D), PCA R&D Serial No. 2619.

EFNARC. 2002. Specifications and Guidelines for Self-Compacting Concrete, EFNARC, UK (www.efnarc.org), pp. 1–32.

EN 12350-8. (2007). Testing fresh concrete—Part 8: Self-compacting concrete—Slump-flow test.

EN 12350-9. (2007). Testing fresh concrete—Part 9: Self-compacting concrete—V-funnel test.

EN 12350-11. (2007). Testing fresh concrete—Part 11: Self-compacting concrete—Sieve segregation test.

EN 12350-12. (2007). Testing fresh concrete—Part 12: Self-compacting concrete—J-ring test.

Kabashi, T.M. (2014). Production and Properties of Powder-type Self-Compacting Concrete in Sudan. M. Sc. Thesis, Building and Road Research Institute, University of Khartoum, Sudan.

Liu, M. 2009. Wider application of additions in self-compacting concrete. Degree of Doctor of Philosophy, Department of Civil, Environmental and Geomatic Engineering, University College London.

The SCC European Project Group. 2005. The European guidelines for self-compacting concrete: specification, production and use.

Concrete Repair, Rehabilitation and Retrofitting IV – Dehn et al. (Eds)
© 2016 Taylor & Francis Group, London, ISBN 978-1-138-02843-2

Utilization of polypropylene fibre reinforced cement composites as a repair material: A review

A. Baricevic, M. Pezer & N. Stirmer
Faculty of Civil Engineering, University of Zagreb, Zagreb, Croatia

ABSTRACT: Environmental and structural loads cause stresses, deformations, and displacements in structures. According to the building codes, they have to be designed and built to safety resist all those actions during entire service life. When deteriorated, structures must be repaired and strengthen so that during usage they do not represent a risk for the users. Due to the low expenses and good mechanical characteristics, cement-based composites are often used for repairs. In structures susceptible to shrinkage and/or exposed to specific load conditions, used cement-based composites are improved with polypropylene fibres. These composites have many beneficial characteristics; like as reduced occurrence of microcracks, positive effect on autogenous, plastic and restrained shrinkage, increased resistance to spalling during the fire, accessible price etc. Due to those characteristics, they are often used for repair of slabs, pavements and concrete overlays. Detailed state-of-the-art is presented and encompasses both fresh and hardened state properties. Also, a possibility for further improvement of repair materials is discussed.

1 INTRODUCTION

Environmental and structural loads cause stresses, deformations, and displacements in structures. According to the building codes, they have to be designed and built to safely resist all those actions during entire service life. When deteriorated, structures must be repaired and strengthen so that during usage they do not represent a risk for the users.

Major issues during repair are the bond quality between substrate concrete and overlay, stresses caused by differential shrinkage and durability of the repaired structure (Silfwerbrand 2006). A good bond also prevents salt and contaminated water to flow through the interface having access to both the substrate and the overlay. Absence of micro cracking, absence of laitance layer, cleanliness, compaction, and curing are the main factors affecting bond (Silfwerbrand 2006). When choosing a repair material basic requirement is its compatibility to the substrate concrete. Repair material and substrate should be similar in terms of stiffness or flexibility, measured by modulus of elasticity, in terms of thermal expansion, and other mechanical and durability properties. All important properties for the quality repair are included in Table 1.

Due to the low expenses and good mechanical characteristics, cement-based composites are often used for repairs. In structures susceptible to shrinkage and/or exposed to specific load conditions, used cement-based composites are improved with polypropylene fibres. In such cases cement-based composites are improved with polypropylene fibres.

Table 1. Desired properties of repair material (Bjegovic 2015).

Property	Importance	Relation between repair materials (S) and substrate concrete (B)
Shrinkage	1	S < B
Tensile strength	2	S > B
Modulus of elasticity	3	S ≤ B
Toughness	4	S > B
Thermal expansion	4	S ≤ B
Creep	5	S ≥ B
Compressive strength	6	S ≤ B

Detailed state-of-the-art analysis on properties of such repair materials is presented in this paper. A short discussion on their possible improvements with ecologically sustainable materials is shown.

1.1 *Why polypropylene fibres?*

Today different types of fibres are available on market, from steel and polymer as well as fibres produced from different recycled materials. Their role is to distribute stresses between damaged and undamaged cross sections during entire service life of structures. During design phase, depending on their properties, fibres are selected based on their future application (Table 2).

Polymer fibres from different origin; polypropylene, nylon, polyethylene, carbon or aramid fibres have found their application in fibre reinforced concrete (Hannant 1978). Within this paper, properties of cement composites with PP fibres are discussed as these fibres are most frequently used due to their low price, inert behaviour in alkaline environment and ease dispersion in cement matrix (ACI 544.5R-10 2010).

Polypropylene fibres are produced in an extrusion process in which the material is hot drawn through a die. Desired shape and size of the cross section together with surface appearance of both monofilament and fibrillated fibres are formed on the mouthpiece (Hannant 1978; Seferovic 2002).

Main difference between fibrillated and monofilament is in their appearance, Figure 1. Fibrillated fibres look like a hair net or fishing net when opened, while monofilament fibres are produced in continuous filaments called a tow (ACI 544.1R-96 2009). Multifilament fibres are consisting of many continuous filaments or strands, as opposed to monofilament, which is one strand (ACI 544.1R-96 2009).

According to the European regulations, PP fibres are divided in two classes (EN 14845-2:2006):

Table 2. Influence of fibre type on desired property (Lambrechts 2009).

Property	Steel fibres	Polymer micro fibres	Polymer macro fibres
Plastic shrinkage	+	+++	+
Drying shrinkage	+++	0	–
Impact resistance	+++	+	++
Crack width (LSS)	+++	0	0
Post-cracking behaviour (ULS)	++	–	–
Spalling in fire	0	+++	0
Fatigue resistance	+++	0	+
Fire resistance	+	–	0
Visual appearance	+	+	+
Corrosion resistance	+	+	+

Legend: + positive, – negative, 0 without influence.

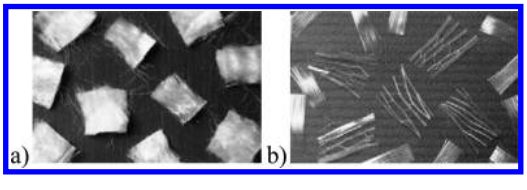

Figure 1. Polypropylene fibres: a) monofilament fibres; b) fibrillated (mesh) (ABC Polymer Industries 2014).

Table 3. Properties of various types of polypropylene fibres (Ideker & Banuelos 2014).

Fibre type	Length (mm)	Youngs moduls (GPa)
Macro fibre	25–50	5–10
Micro fibre	6–25	3–5

- Class I (micro fibres—monofilament and fibrillated) – diameter < 0.3 mm,
- Class II (macro fibres)—diameter > 0.3 mm, geometric characteristic similar to steel fibres.

Characteristics of both micro and macro fibre types are presented in Table 3. Microfibers are dispensed in small doses from 0.6 to 1.0 kg/m^3 or 0.1% by volume and at the same time macro fibres are dosed in higher amounts, from 4 to 7 kg/m^3 (Leung et al. 2005; ACI Education Bulletin E2–00 2006). Extensive research of Myers et al. (Myers et al. 2008) showed that maximum amount of PP fibres is 3 kg/m^3 for micro and 9 kg/m^3 for macro fibres. At the same time, micro fibres with lengths below 25 mm are used more often (Newman & Choo 2003). Namely, microfibers reduce appearance of cracks during plastic shrinkage in the early age period when the strength of concrete is still very small. The cracks are formed when tensile stresses reach the tensile strength. Increased strength and strain capacity during first 12 hours and thus reduced appearance of cracks is assured by addition of micro fibres (Ideker & Banuelos 2014). This is of great importance for the durability of concrete; as in such way penetration of aggressive substances from the environment is reduced (Sanjuhn & Moragues 1997). On the other hand, macro fibres are typically used for improvement of the strength and strain carrying capacity, and for control of shrinkage due to drying (ACI 544.5R-10 2010).

2 CEMENT COMPOSITES WITH POLYPROPYLENE FIBRES

2.1 *Plastic shrinkage*

Plastic shrinkage presents a major concern during repair of deteriorated structures (Ghoddousi & Javid 2010). Slabs, pavements and concrete overlays are especially susceptible to plastic shrinkage cracking (Naaman et al. 2005), Figure 2. Usage of low modulus polymer fibres is shown to be very effective in these circumstances as their modulus of elasticity is higher compared to the modulus of concrete during first 24 hours of hardening (Fig. 3).

At lower dosage rates, PP fibres are very effective in controlling plastic shrinkage cracking and the fibrillation process greatly enhances the bonding between the concrete and the PP fibres. This is very important because plastic shrinkage cracks can lead to the development of larger cracks as drying shrinkage occurs. It is well known that cracking control is essential for the development of more durable and long-lasting structures (Naaman et al. 2005).

Two most important parameters for control of plastic shrinkage are the volume fraction of fibres and their diameter (ACI 544.5R-10 2010; Naaman et al. 2005; Banthia & Gupta 2006). By increasing diameter and fibre volume an adequate control of plastic cracks is achieved (ACI 544.5R-10 2010; Naaman et al. 2005; Sanjuhn & Moragues 1997). In such way is possible to reduce the occurrence of cracks by 10% if an appropriate volume fraction (0.2%) and diameter of fibres is used (ACI 544.5R-10 2010). Thinner and longer fibres are streamlined than thicker and shorter, while more effective control is achieved with fibrillated rather that monofilament fibres (Banthia & Gupta 2006). By combining different lengths (6–20 mm) of multifilament fibres, higher influence on plastic shrinkage is achieved compared to mixes with only one fibre length (Myers et al. 2008).

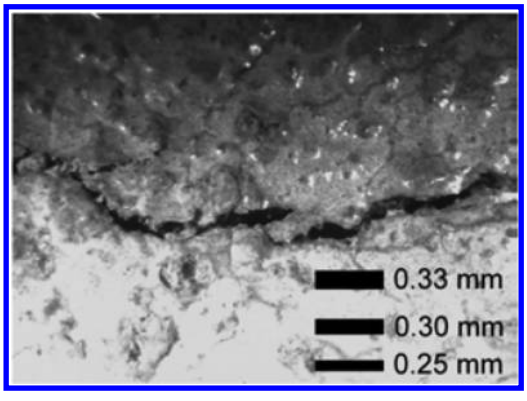

Figure 2. Typical example of maximum crack width in plain concrete (Naaman et al. 2005).

2.2 *Autogenous shrinkage*

Polypropylene fibres have positive influence on the autogenous shrinkage (Saje et al. 2012; Saje et al. 2011), therefore is possible to establish a relationship between the amount of PP fibres and shrinkage values. Investigation on influence of different PP fibre (length 12 mm) volumes shown that for 0.25, 0.5 and 0.75% of fibres, autogenous shrinkage decreases progressively for 5, 15 and 26% respectively in relation to the plain concrete after 24 hours (Saje et al. 2012). Additional influence on early autogenous shrinkage can be achieved with usage of pre-moistened PP fibres and corresponding reduction of designed water (Saje et al. 2011). This is because moistened fibres do not absorb water needed for hydration.

On contrary, Myers et al. (Myers et al. 2008) concluded that PP fibres have a minor or no impact on autogenous shrinkage.

2.3 *Drying shrinkage*

Based on up to date experimental results, PP fibres have minor or don't have effect on the drying shrinkage. Only, addition of 0.1% of PP fibres by volume has beneficial effect on the drying shrinkage, while higher contents can have adverse effect (Aly et al. 2008; Sadrmomtazi & Fasihi 2010). Due to their small modulus of elasticity compared to the modulus of elasticity of hardened concrete, higher

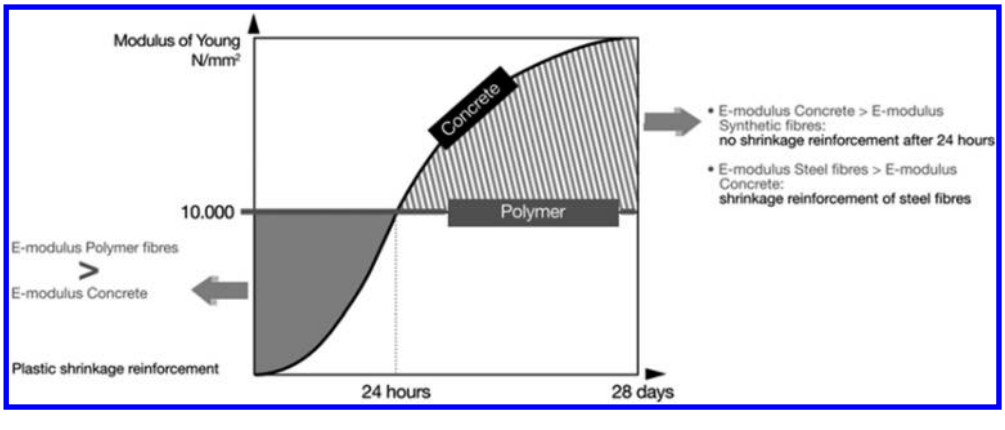

Figure 3. Strengthening of cement composites using polymer fibres during first 24 hours (Lambrechts 2009).

contents of PP fibres do not have further influence (Myers et al. 2008; Ideker & Banuelos 2014).

Their positive effect is expressed in the case of composites with recycled aggregates, where addition of 0.25% by volume (length/diameter = 10/0.035 mm) assures 6% reduction of shrinkage compared to the reference mix without fibres (Mesbah 2000). Added in higher volumes (0.5 to 1%), they cause 5 to 6% increase of drying shrinkage in relation to the same mix without the PP fibres (Mesbah & Buyle-Bodin 2000; Sadrmomtazi & Fasihi 2010).

Influence of the fibre diameter on drying shrinkage is shown on Figure 4. Smaller diameter has a more positive effect in composites with monofilament fibres 0.1% (Lamour et al. 2005), while fibrillated fibres better control shrinkage compared to multifilament fibres of same length (Kumar et al. 2013).

2.4 *Restrained shrinkage*

Restrained shrinkage is usually determined using steel ring method. Dimensions of such rings are different, depending on the composition of the studied mixes. The width of the concrete ring, together with the thickness of the steel mould has major influence on the developed stresses, and is determined according to the maximum aggregate size, type of fibres, length and diameter of fibres, the quality of the matrix and etc. (Swamy & Stavrides 1979; Folliard et al. 2003; Lamour et al. 2005; Ideker & Banuelos 2014).

Unlike other types of shrinkage, available literature data for the restrained shrinkage mostly follows the same trend. Polypropylene fibres have a positive impact on reducing the crack width, and thus the value of restrained shrinkage (ACI 544.5R-10 2010). Multiple cracking displayed by hardened composites with 2% PP fibres by volume during restrained shrinkage tests indicate their ability to distribute induced strains (Swamy & Stavrides 1979; ACI 544.1R-96 2009). The value of their contribution depends on type, diameter and shape of

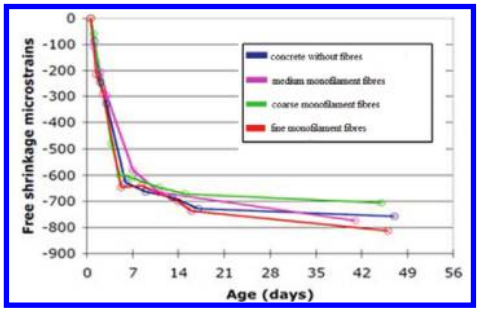

Figure 4. Free shrinkage evolutions (Lamour et al. 2005).

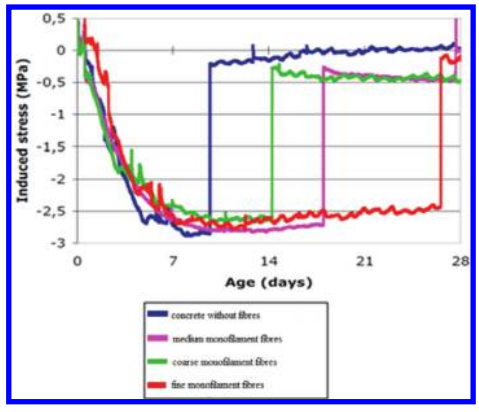

Figure 5. Stress evolution in the restrained shrinkage test (Lamour et al. 2005).

used fibres. Monofilament fibres with diameter 18 µm showed higher influence on restrained shrinkage than fibres with lager diameters (30 µm and 36 µm) (Lamour et al. 2005). Investigation of monofilament and sinusoidal-shaped high performance fibres (length 5.1 cm) showed greater contribution of monofilament fibres (Folliard et al. 2003). For comparison, cracks in plain concrete appeared after 36 days, in concrete with sinusoidal fibres after 202 days, while for concrete with monofilament fibres crack did not occurred even after 600 days. Achieved behaviour is result of better anchoring ability of monofilament fibres, which results in better stress distribution. Difference in time of crack occurrence is considered to be a result of used large quantity of PP fibres (8.9 kg/m^3).

2.5 *Tensile strength*

Addition of micro and macro PP fibres assures increase of tensile strength (Song et al. 2005, Ramezanianpour et al. 2013; Patel et al. 2012, Gencel et al. 2011). Increase is present when micro fibre content is kept below 1.5 kg/m^3, if used in higher contents PP fibres cause a decrease of tensile strength (Ramezanianpour et al. 2013). For example, increase of 9.7% compared to the plain concrete is achieved with 0.6 kg/m^3 of PP fibres (Song et al. 2005). Longer PP fibres assure higher strengths for the same volume fraction (Vairagade & Kene 2013).

2.6 *Modulus of elasticity*

The addition of fibrillated polypropylene fibres in quantities varying from 0.1 to 2.0 percent by volume has no effect on the static modulus of elasticity compared to ordinary concrete without fibre addition (ACI 544.1R-96 2009).

2.7 *Flexural strength and toughness*

Incorporation of PP fibres in fibre reinforced cement composites slightly increases the value of the flexural strength compared to the composites without fibres (ACI 544.1R-96 2009; Skazlic 2003; Sadrmomtazi & Fasihi 2010). Optimum fibre content is considered 0.3% by volume, as any further increase in quantity causes a decrease of flexural strength. Performed studies have shown, that in respect to the plain concrete, addition of 0.91 kg/m^3 of monofilament fibres of circular cross section and smooth surface (length/diameter = 12/0.037 mm) or fibrillated PP fibres (length/diameter = 12/0.45 mm) assure 9.48 and 13.40% increase in flexural strength.

Improved post-cracking behaviour and energy absorption capacity of composites is assured even with very small amounts of polypropylene fibres (0.1% by volume) (Johnston 2001). Value of the improvement is dependent on the PP fibre properties; i.e. type of fibres, content, fibre/ matrix adhesion, quality of the composite matrix. According to the previous research, composites with fibrillated PP fibres achieve better results that those with monofilament fibres.

2.8 *Creep behaviour*

If high stress level is maintained, polymer fibres behave viscously and creep, even exhibiting creep rupture (ACI 544.5R-10 2010). Investigation of macro fibres (length 40 mm, diameter 0.8 mm) confirmed significant tensile creep, even at levels as low as 30% of the fibre capacity (Babafemi & Boshoff 2015). For example, tensile creep failure occurs within 10 days for specimens loaded at 60% and within less than a day for specimens loaded at 70% of residual strength (Babafemi & Boshoff 2015). Performed tests indicated that creep of macro synthetic fibre concrete is not only considerable, but also leads to creep failure at service loads (Fig. 7) (Lambrechts 2009).

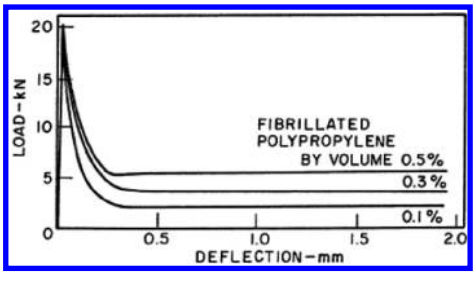

Figure 6. Load deflection curves obtained with toughness testing by bending samples of reinforced concrete with different amounts of polypropylene fibres with a length of 19 mm (Johnston 2001).

2.9 *Resistance to spalling*

During exposure to elevated temperatures, explosive cracking of concrete elements may occur. This behaviour often appears during early stages of fire, most often within first 30 minutes of standard fire test. It results with spalling of concrete layers thick from 25 to 100 mm and can embrace area up to 1 m^2, Figure 8. In such way, loss of protective concrete layer, sometimes up to the reinforcement, may lead to decreased bearing capacity of concrete elements.

Presence of PP micro fibres has positive impact on the behaviour of concrete during elevated temperatures. Due to their chemical composition, polypropylene fibres melt at temperatures above 165˚C. It is this melting that is believed to facilitate the reduction in the internal stresses in the concrete that cause the explosive spalling (Smith & Atkinson 2010, Jelcic Rukavina et al. 2014). However, they can have negative effect on concrete's residual mechanical properties since they significantly decrease the residual compressive and tensile strength of concrete. It is therefore recommended to use PP fibres as part of a total spalling protection design method in combination with other materials such as external thermal barriers (Sideris & Manita 2013).

2.10 *Compressive strength*

Investigation of influence of different volumes of polypropylene fibres (approximately 6 mm length)

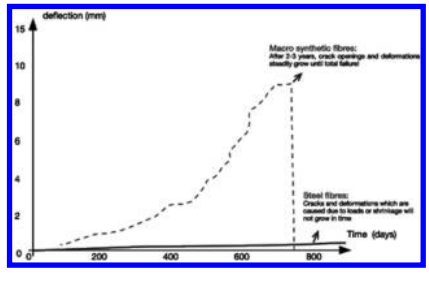

Figure 7. Influence of polymer macro fibres on creep (Lambrechts 2009).

Figure 8. Test samples from CTRL testing—plain concrete and concrete with PP fibres (Smith & Atkinson 2010).

on the values of compressive strength showed that increase in PP fibre volume has minor effect on the compressive strength values (Seferovic 2002; Bayasi & Zeng 1994; Sadrmomtazi & Fasihi 2010; Skazlic 2003; Kumar et al. 2013; ACI 544.1R-96 2009). Positive effect on the compressive strength was obtained with addition of 0.1% of PP fibres, while higher volumes (from 0.3 to 0.5%) caused a decrease of the same value. Cited authors note that increase of strength in the case of small fibre volumes (up to 0.1%) is caused by fibres ability to bridge cracks as uniformly distributed PP fibres, prevent further opening of initial cracks and their coalescence in macro cracks.

For higher volumes, one should be aware that incorporation of small diameter fibres into the mix makes compaction more difficult, and hence, more entrapped air stays in the final mix (Leung et al. 2005). Therefore, a certain decrease of compressive strength is present for mixes with higher contents of PP fibres (above 0.5% by volume) (ACI 544.1R-96 2009). An increased amount of entrapped air, presence of segregation and reduced workability, all caused by no homogenous distribution of PP fibres, have negative effect on hardened concrete properties. To avoid such cases, proper relationship between maximum aggregate size and fibre length is inevitable.

Although, results available in the literature are various, a general conclusion regarding behaviour during fracture can be adopted. After reaching compressive strength, no decomposition of the specimens is perceived and further bearing capacity is present, what implies higher ductility of composites reinforced with PP fibres, as such behaviour is not characteristic of ordinary concrete (ACI 544.1R-96 2009).

2.11 *Fresh state properties*

Properties of fibre reinforced mixes in fresh state are depended on geometric characteristics of fibres, i.e. length/diameter. To achieve homogeneous distribution, it is necessary to pay attention on the dependence between maximum aggregate size and length of fibres.

Small quantities of PP fibres in mix (length < 25 mm, fibrillated or monofilament) may increase the cohesion and prevent sedimentation due to their interlocking characteristics (ACI 544.1R-96 2009). But higher volumes of fibres require modification of the mix proportions to accommodate the increased surface area of the fibres and to prevent negative effects on workability and air content (ACI Education Bulletin E2-00; Bayasi 1994; Myers et al. 2008). Fibrillated fibre has less influence to reduction of workability than multifilament fibre of the same volume content (length max 15 mm) (Kumar et al. 2013). Macro fibres have minor influence on workability than micro fibres (Myers et al. 2008). However, an adequate workability can be obtained even with addition of 0.3% micro fibres or 2% macro fibres (Skazlic 2003; Myers et al. 2008). To have a workable mixture, increase in sand content while decreasing the coarse aggregate content is required. At the same time a high-range water-reducing admixture, rather than additional water, should be used to adjust slump loss.

Simultaneously, mixing time should be optimized, as too short mixing time can cause insufficient separation of fibres, while too long mixing causes damage of fibres and has influence on shape coefficient. Both can have adverse effect on the properties of concrete in the hardened state (Grdić 2011; Skazlic 2003). Optimal mixing time is considered to be 5 minutes (Nili & Afroughsabet 2010).

3 POSSIBILITY OF FURTHER IMPROVEMENT OF REPAIR MATERIALS

Using PP fibre in concrete has many benefits. However, surface smoothness, chemical structure and hydrophobic properties, result in poor adhesion characteristics between fibres and cement matrix (Wang et al. 2006). All that, presents a severe limitation of their usage in high performance applications so further improvement of their interfacial strength with matrix is need. Modifying fibre surface by roughening assures improved adhesion in fibre/matrix interface (Lopez-Buendia et al. 2013). Following treatments are used up to date: wet chemical treatment, flame treatment, mechanical indentations, cold plasma treatment and alkaline surface treatment and alkaline precursors (Singh et al. 2004; Lopez-Buendia et al 2013; Flekoglu et al. 2009; Fialova et al. 2012).

With the development of environmental awareness, there is a growing interest to find alternatives for waste management. Waste tires present a specific waste whose removal from the environment is inevitable due to many reasons such as health issues, accidental fires, etc. One of the innovative solutions is to utilize products obtained by waste tyre recycling in concrete (rubber granules, steel fibres or polymer fibres). Since the dimensions and composition of Recycled Tyre Polymer Fibres (RTPF) obtained from waste tyres are similar to dimensions of PP fibres, a concept involving replacement of manufactured fibres with RTPF is investigated, Figure 9. Based on the limited literature data (Serdar et. al 2013; Serdar et al. 2014; Bjegovic et al. 2010; Mavridou 2011, Project Anagennisi 2014), RTPF can be used as substitution of PP fibres, as they do not induce negative effects on concrete mechanical properties, but do enhance concrete behaviour regarding autogenous and restrained shrinkage. Further optimization is needed for their usage as repair material.

Figure 9. Recycled tyre polymer fibres—by products of mechanical recycling of waste tyres.

4 CONCLUSIONS

The addition of PP fibres in general has significant influence on specific concrete properties. The main contribution of PP fibres is their beneficial effect on autogenous, plastic and restrained shrinkage of cement composites together with increased resistance to spalling during the fire. Due to those characteristic they are often used in repair materials.

By improving interfacial strength between PP fibres and the cement matrices, further improvement of such materials is possible. Surface treatments like wet chemical treatment, flame treatment, mechanical micro-pitting, cold plasma treatment and alkaline surface treatment and alkaline precursors on PP fibres contribute to the improvement of fibre/concrete adhesion in fibre-reinforced concrete. Other possibilities for improvements include usage of secondary raw materials such as recycled tyre polymer fibres. Their usage has positive effects on shrinkage behaviour, especially autogenous and restrained shrinkage, but further optimization is needed.

ACKNOWLEDGEMENTS

The research presented is part of the project "Anagennisi—Innovative Reuse of all Tyre Components in Concrete" funded by the European Commission under the 7th Framework Programme Environment topic.

REFERENCES

ABC Polymer Industries: http://www.abcpolymerindustries.com/concrete-fibers.php; 25.09.2014.

Aly, T., Sanjayan, J.G., Collins, F. 2008. Effect of polypropylene fibers on shrinkage and cracking of concretes. *Materials and Structures*, 41(10), 1741–1753.

ACI 544.5R-10. 2010. *Report on the Physical Properties and Durability of Fiber-Reinforced Concrete.* Reported by ACI Committee 544. 5R-10.

ACI 544.1R-96. 2009. *Report on Fiber Reinforced Concrete*. Reported by ACI Committee 544.1 R-96.

ACI Education Bulletin E2-00. 2006. *Reinforcement for concrete—materials and applications*. Developed by Commitee E-701, Materials for Concrete Construction.

EN 14845–2:2006. *Test methods for fibres in concrete–Part 2:* Effect on concrete.

Babafemi, A.J. & Boshoff, W.P. 2015. Tensile creep of macro-synthetic fibre reinforced concrete (MSFRC) under uni-axial tensile loading. *Cement & Concrete Composites*, 55, 62–69.

Banthia, N. & Gupta R. 2006. Influence of polypropylene fiber geometry on plastic shrinkage cracking in concrete, *Cement and Concrete Research*, 36(7), 1263–1267.

Bayasi, Z. & Zeng, J. 1993. Properties of Polypropylene Fiber Reinforced Concrete. *ACI Materials Journal*, 90, 6, 605–610.

Bjegovic, D. 2015. Lectures from subjects of graduate study-course–Materials Science: Technology of Repairs and Strengthening, University of Zagreb, Faculty of Civil Engineering, Zagreb.

Bjegovic, D., Lakusic, S., Serdar, M., Baricevic, A. 2010. Properties of concrete with components from waste tyre recycling. In Srumova Z, Sruma V (eds), *Concr. Struct. Challenging Times*: 134–40. Praha, Czech: Concrete Society (CBS) and CBS Servis, s.r.o.

Felekoglu, B., Tosun, K., Baradan, B. 2009. A comparative study on the flexural performance of plasma treated polypropylene fiber reinforced cementitious composites. *Journal of Materials Processing Technology*, 209, 5133–5144.

Fialova, M., Moravek, T., Kopkane, D., Rahel, J., Stahel, P., Černak, M. 2012. Polypropylene fibers modified by atmospheric pressure plasma as reinforcement for concrete. *In Conference proceedings NANOCON 2012*: p. 174–178, 5 pp. Brno: TANGER spol s.r.o.

Folliard, K. et.al. 2004. *Evaluation of Alternative Materials to Control Drying Shrinkage Cracking in Concrete Bridges*. Research Report, Center for Transportation Research, The University of Texas at Austin.

Gencel, O., Ozel, C., Brostow, W., Martınez-Barrera, G. 2011. Mechanical properties of self-compacting concrete reinforced with polypropylene fibres. *Materials Research Innovations*, 15, 3, 216–225.

Ghoddousi, P. & Javid A.A.S. 2010. Plastic Shrinkage Evaluation of Self-Consolidating Concrete as Repair Materials Based on Restrained and Free Strain Measurements. Khayat K.H., Feys D. (eds), *Design, Production and Placement of Self-Consolidating Concrete, Proceedings of SCC2010, Montreal, Canada, September 26–29, 2010*, Rilem bookseries, Volume 1., 295–306.

Grdić, Z. 2011. *Concrete Technology*, Nis, Civil Engineering and Architectural Faculty, University of Nis. (in Serbian).

Hannant, D.J. 1978. *Fibre Cements and Fibre Concretes*, Chichester, New York, Brisbane, Toronto, John Wiley & Sons.

Ideker, J. & Banuelos, J. 2014. *The use of synthetic blended fibers to reduce cracking risk in high performance concrete*. Final Report, Oregon Department of Transportation, Oregon.

Jelcic Rukavina, M., Bjegovic, D., Seferovic, E. 2014. Influence of high fire temperatures on fibre reinforced concrete. In Milanko, V., Laban, M., Mračkova, E. (eds), *Book of Proceedings of 4th International Scientific Conference on Safety Engineering (Fire, Environment, Work Environment, Integrated Risk) and 14th International Conference on Fire and Explosion Protection*, 21–28, Novi Sad: Higher Education Technical School of Professional Studies.

Johnston, C.D. 2001. *Fiber-reinforced cements and concretes*. Singapore, Gordon and Breach Science Publishers.

Kumar, R., Goel, P., Mathur, R. 2013. Suitability of Concrete Reinforced with Synthetic Fiber for the Construction of Pavements. *In Third International Conference on Sustainable Construction Materials and Technologies*, Kyoto, Japan.

Lambrechts, A. 2009. Steel- and Synthetic Fibre reinforced Concrete, Which fibre to use for which application and why?, Bekaert, http://www.ribaproductselector.com/Docs/6/17706/external/COL717706.pdf, 08.03.2015.

Lamour, V., Moranville, M., Chaignon, J. 2005. Effect of low volume polypropylene fibers on early age cracking of concrete. In Banthia N., Uomoto T., Bentur A., Shah S.P. (eds), *Proceedings of the third international conference on construction materials: performance, innovations and structural implications*. Vancouver: The University of British Columbia.

Leung, C.K.Y., Lai, R., Lee, A.Y.F. 2005. Properties of wet-mixed fiber reinforced shotcrete and fiber reinforced concrete with similar composition. *Cement and Concrete Research*, 35, 4, 788–795.

Lopez-Buendia, A.M., Romero-Sanchez, M.D., Climent, V., Guillem, C. 2013. Surface treated polypropylene (PP) fibres for reinforced concrete. *Cement and Concrete Research*, 54, 29–35.

Mavridou, S. 2011. Utilization of Textile Fibres from Worn Automobile Tires in Cement based mortars. *Global Nest Journal*, 13(2), 176–181.

Mesbah, H.A. & Buyle-Bodin, F. 2000. Efficiency of polypropylene and metallic fibres on control of shrinkage and cracking of recycled aggregate mortars. *Construction and Building Materials*, 13(8), 439–447.

Myers, D., Kang, T.H., Ramseyer C. 2008. Early-age propertis of polymer fibre-reinforced concrete. *ACI Materials Journal*, 7, 9–14.

Naaman, A.E., Wongtanakitcharoen, T., Hauser, G. 2005. Influence of Different Fibers on Plastic Shrinkage Cracking of Concrete. *ACI Materials Journal*, 102, 1, 49–58.

Newman, J. & Choo, S.B. 2003. Advanced Concrete Technology, 1st ed, Oxford, Butterworth-Heinemann, Elsevier.

Nili, M. & Afroughsabet, A.V. 2010. The effects of silica fume and polypropylene fibers on the impact resistance and mechanical properties of concrete. *Construction and Building Materials*, 24, 927–933.

Patel, P.A., Desai, A.K., Desai, J.A. 2012. Evaluation of engineering properties for polypropylene fibre reinforced concrete. *International Journal of Advanced Engineering Technology*, III, I, 45–45.

Project Anagennisi. 2014. *D4.1: RTPF reinforced concrete*. FP7 Project: Innovative Reuse of all Tyre Components in Concrete.

Ramezanianpour, A.A., Esmaeili, M., Ghahari, S.A., Najafi, M.H. 2013. Laboratory study on the effect of polypropylene fiber on durability, and physical and mechanical characteristic of concrete for application in sleepers. *Construction and Building Materials*, 44, 411–418.

Sadrmomtazi, A., Fasihi, A. 2010. Influence of polypropylene fibers on the performance of nano-SiO2-incorporated mortar. *Iranian Journal of Science and Technology, Transactions of Civil Engineering*, 34, 4, 385–395.

Saje, D., Bandelj, B., Sustersic, J., Lopatic, J., Saje, F. 2012. Autogenous and Drying Shrinkage of Fibre Reinforced High-Performance Concrete. *Journal of Advanced Concrete Technology*, 10, 59–73.

Saje, D., Bandelj, B., Sustersic, J., Lopatic, J. 2011. Shrinkage of polypropylene fibre reinforced high performance concrete. *ASCE Journal of Materials Civil Engineering*, 23, 941–952.

Sanjuan, M.A., Moragues, A. 1997. Polypropylene fibre reinforced mortar mixes: Optimization to control plastic shrinkage. *Composites Science and Technology*, 57, 6, 655–660.

Seferovic, E. 2002. Polypropylene fibers in the support work for the Sveti Rok tunnel. *Gradjevinar—Journal of the Croatian Assocoation of Civil Engineers*, 54 (9), 535–539.

Serdar, M., Baricevic, A., Bjegovic, D., Lakusic, S. 2014. Possibilities of use of products from waste tyre recycling in concrete industry. *Journal of Applied Engineering Science*, 12(1), 89–93.

Serdar, M., Baricevic, A., Lakusic, S., Bjegovic, D. 2013. Special purpose concrete products from waste tyre recyclates. *Gradjevinar—Journal of the Croatian Association of Civil Engineers*, 65, 793–801.

Sideris, K.K. & Manita P. 2003. Residual mechanical characteristics and spalling resistance of fiber reinforced self-compacting concretes exposed to elevated temperatures. *Construction and Building Materials*, 41, 296–302.

Silfwerbrand, J.L. 2006. Bonded concrete overlays—Research needs. In Marchand, J., Bissonnette, B., Gagné, R., Jolin, M., Paradis, F. (eds), *Proceedings of the second International RILEM Symposium on Advances in Concrete through Science and Engineering*: 193–206. Qubec City, Canada: RILEM Publications S.A.R.L.

Singh, S., Shukla, A., Brown, R. 2004. Pullout behaviour of polypropylene fibers from cementitious matrix. *Cement and Concrete Research*, 34, 1919–1925.

Skazlic, M. 2003. *Hybrid high performance fibre-reinforced concrete*. M.S Thesis, Faculty of Civil Engineering, University of Zagreb.

Smith, K. & Atkinson, T. 2010. PP fibres to resist fire induced concrete spalling. Tunneltalk, http://www.tunneltalk.com/Polypropylene-fibres-Nov10-Resistance-to-concrete-spalling-under-fire.php, 08.03.2015.

Song, P.S., Hwang, S., Sheu, B.C. 2005. Strength properties of nylon and polypropylene fiber reinforced concretes. *Cement and Concrete Research*, 35, 1546–1550.

Swamy, R.N., Stavrides, H. 1979. Influence of Fiber Reinforcement on Restrained Shrinkage and Cracking. *ACI Journal Proceedings*, 76, 3, 443–460.

Vairagade, V.S. & Kene, K.S. 2013. Strength of Normal Concrete Using Metallic and Synthetic Fibers. *Procedia Engineering, Chemical, Civil and Mechanical Engineering Tracks of 3rd Nirma University International Conference,* 51, 132–140.

Wang, W., Wang, L., Shi, Q., Yu, H., Chen, T., Wang, C., Sun, T. 2006. Progress of the Surface Modification of PP Fiber Used in Concrete. *Polymer-Plastics Technology and Engineering*, 45, 29–34.

Concrete Repair, Rehabilitation and Retrofitting IV – Dehn et al. (Eds)
© 2016 Taylor & Francis Group, London, ISBN 978-1-138-02843-2

A novel technique for self-repair of cracks of reinforced concrete structures

S. Pareek
College of Engineering, Nihon University, Koriyama, Fukushima-ken, Japan

ABSTRACT: Cracks in RC structures are one of the most prominent reasons for the durability loss by corrosion of reinforcing steel by forming channels for CO_2, water and Cl^- ions to penetrate into the concrete easily. The objective of this research work is to develop a self-repair system for cracks of reinforced concrete structures by using a network system. In this study, the regain of flexural strength of ordinary cement mortars by the self-repair system using a repair material for injection in the network system is proposed. In addition to this, the influence of viscosity of the repair material injected in the network on the regain of flexural strength by self-repair system was also evaluated. From the test results, it was found that the repair material with a lower viscosity was more effective as a repair material and showed a remarkable regain of flexural strength of mortar specimens.

1 INTRODUCTION

Cracking in Reinforced Concrete (RC) structures is an inevitable phenomenon, which may occur due to tensile loads, shrinkage and or thermal loads etc. These cracks in RC structures are one of the most prominent reason for the durability loss by corrosion of reinforcing steel by forming channels for CO_2, water and Cl^- ions to penetrate into the concrete easily. The service life span of RC structures is drastically shortened by these cracks in concrete. In order to repair these cracks, a periodical inspection to detect these cracks by engineers and technicians is a highly time and cost consuming. In addition, the crack inspection of RC structures such as nuclear facilities and highly elevated bridges and building structures involves extreme risk and substantial cost for the inspection and repair of such RC structures.

The objective of this research work is to develop a self-repair system for cracks of reinforced concrete structures by using a network system. Figure 1 shows the autonomic self-healing or self-repair system used in this study to repair the cracks and the strength regain was obtained at the first (before crack repair) and the second loading (after crack repair). In this study, the regain of flexural strength of ordinary cement mortars by the self-repair system using a repair material in the network system and the storage period of the repair material in the network was taken into consideration. In addition to this, the influence of viscosity of the repair material injected in the network on the regain of flexural strength by self-repair system was also evaluated. In order to prolong the storage period of the repair material in the network, several types of surface treatment techniques were applied and tested.

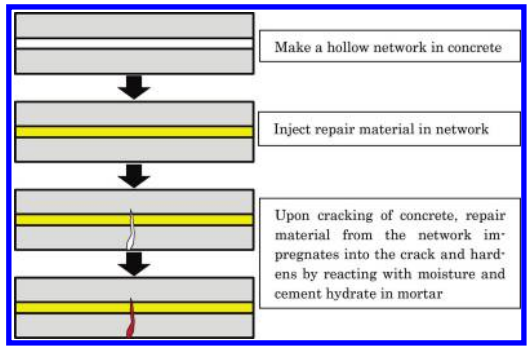

Figure 1. Concrete self-repair system.

Compared to existing crack self-repairing and self-healing techniques, the epoxy injection network has the following advantages: (1) Different from the self-repairing methods using brittle containers or tubes for adhesives, the proposed self-repair process is feasible for onsite concrete casting. (2) Different from the autogenic self-healing techniques, full strength recovery can be achieved in a shorter time period without the necessity of water.

2 TESTING PROGRAM

2.1 *Mortar specimens with network*

Figure 2 shows the dimensions of the cement mortar specimens prepared by using ordinary Portland

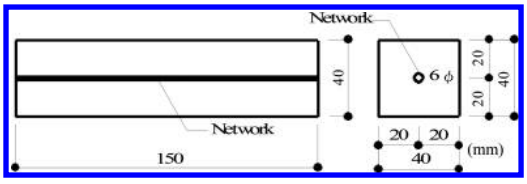

Figure 2. Outline of test specimen.

Table 1. Properties of epoxy resin.

Type of Epoxy Resin	Hardening Mechanism	Thixotropic Index	Specific Gravity	Viscosity (mPa・s,23℃)
A	Moisture Sensitive	6.5	1.07	14000
B		2.2	1.07	1900
C		1.0	1.15±0.05	150±100

Table 2. Properties of network surface treatment materials.

Identification	Density (g/cm^3)	Average Penetration Depth (mm)	Viscosity (mPa・s)
B1	0.880	5～10	0.95
B2	0.882	5～10	1.0～10
B3	0.885	5～10	1.2
P1	1.02	9.0	200
P2	—	7.0～9.0	200
P3	1.06	6.9	200

cement and sand with a ratio of 1:3 (by weight) and a water-cement ratio of 72%. The networks were installed by using smooth steel bars placed in the center of the cross-sections which were removed after the hardening of the mortars.

2.2 *Materials for crack injection and network surface treatments*

Table 1 shows the properties of the 1-component epoxy resins used for injection into networks for self-repairing of cracks and Table 2 shows the properties of surface treatment materials for the networks. The three types of epoxy resins A, B and C with different viscosities were used for injection. For the surface treatment of networks 3 types of barrier penetrants B1, B2 and B3 and 3 types of polymer dispersions P1, P2 and P3 were used to prolong the storage time of epoxy resins in the networks. Apart from this, the epoxy resin C was also used for the surface treatment (EC).

2.3 *Testing procedures*

Mortar specimens with hollow network in the center of the cross-section were prepared and subjected to two sets of test program.

1. Mortar specimens were prepared having a hollow network in the specimens and loaded to develop by using a fully-automatic load controlled machine to generate cracks of 0.05~0.20 mm. Photo 1 shows the mortar specimen with crack injection system into the network. Figure 3 shows the test program to investigate the effect on epoxy resin as repair material by pre- and post-injection, and curing conditions on the regain of flexural strength at 2nd loading (after crack self-repair). In addition to this, viscosity of the epoxy resin on the crack self-repair was also taken into consideration.
2. Figure 4 illustrates the test program to investigate the storage time period of epoxy resin in network. In order to prolong the storage of epoxy resin in the network, several types of surface treatments inside the network were done to prevent the hardening of epoxy resin in the network.

The two types of curing conditions in the first test program were normal cure and accelerated cure. The normal cure was 7d dry cure [20°C, 60% R.H.] + 7d moist cure [20°C, 90% R.H.] + 7d dry cure [20°C, 60% R.H.] a total of 21d and accelerated cure was 5d dry cure [20°C, 60% R.H.] + 4h autoclave [50°C]+ 20h dry [50°C] + 1d dry cure [20°C, 60% R.H.] a total of 7d respectively. All the specimens in the second test program for network surface treatments were subjected to accelerated cure

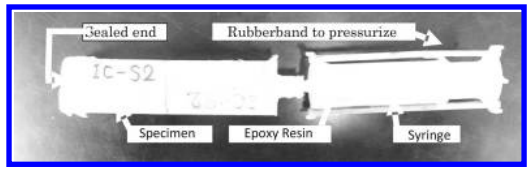

Photo 1. View of crack injection system.

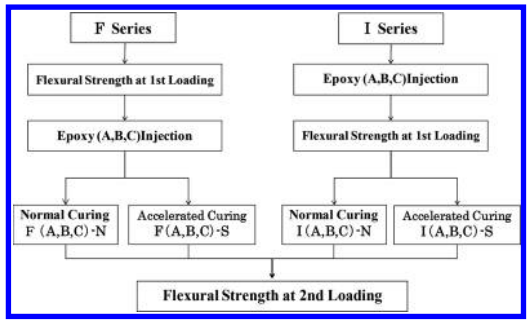

Figure 3. Test program to investigate the basic conditions of repair material and curing conditions.

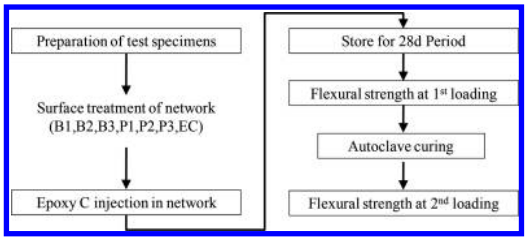

Figure 4. Test program to investigate the storage time of material in network.

Table 3. Flexural strength test results and regain of flexural strength of test specimens.

Type of Specimen	Curing Condition	Dimensions (cm)	1st Loading		2nd Loading		Regain of Strength (%)
			Max.Load (kN)	Flexural Strength (N/mm^2)	Max.Load (kN)	Flexural Strength (N/mm^2)	
FA-N	Normal	4×4×15	2.51	5.88	0.16	0.39	6.6
FB-N	Normal		2.83	6.62	0.38	0.86	13.0
FC-N	Normal		2.54	5.94	2.10	4.91	82.7
FA-S	Autoclave		3.21	7.52	0.29	0.61	8.1
FB-S	Autoclave		2.86	6.71	1.04	2.47	36.8
FC-S	Autoclave		3.21	7.49	3.00	7.04	94.0
IA-N	Normal		2.39	5.65	0.44	1.02	18.1
IB-N	Normal		2.54	5.98	0.74	1.74	29.1
IC-N	Normal		2.40	5.62	2.41	5.65	100.5
IA-S	Autoclave		2.32	5.44	0.11	0.26	4.8
IB-S	Autoclave		2.73	6.41	0.66	1.56	24.3
IC-S	Autoclave		2.75	6.45	3.01	7.06	109.5

to test for the regain of flexural strength. For all the test specimens, regain of flexural strength was obtained by the following equation:

$$C = \frac{B}{A} \times 100[\%] \begin{cases} \text{A: Avg. flexural strength at 1st loading} \\ \text{B: Avg. flexural strength at 2nd loading} \\ \text{C: Regain of flexural strength} \end{cases}$$

3 TEST RESULTS AND DISCUSSIONS

3.1 *Effect of curing condition and viscosity*

Table 3 and Figure 5 shows the results of the effect of pre- and post-injection, curing condition and viscosity of epoxy resin on regain of flexural strength of mortars of the first test program. Epoxy resin C showed a flexural strength regain of 80% or more irrespective of the pre- or post-injection of epoxy resin and curing conditions. In comparison, epoxy resin A and B with higher viscosities showed a poor regain in flexural strength,

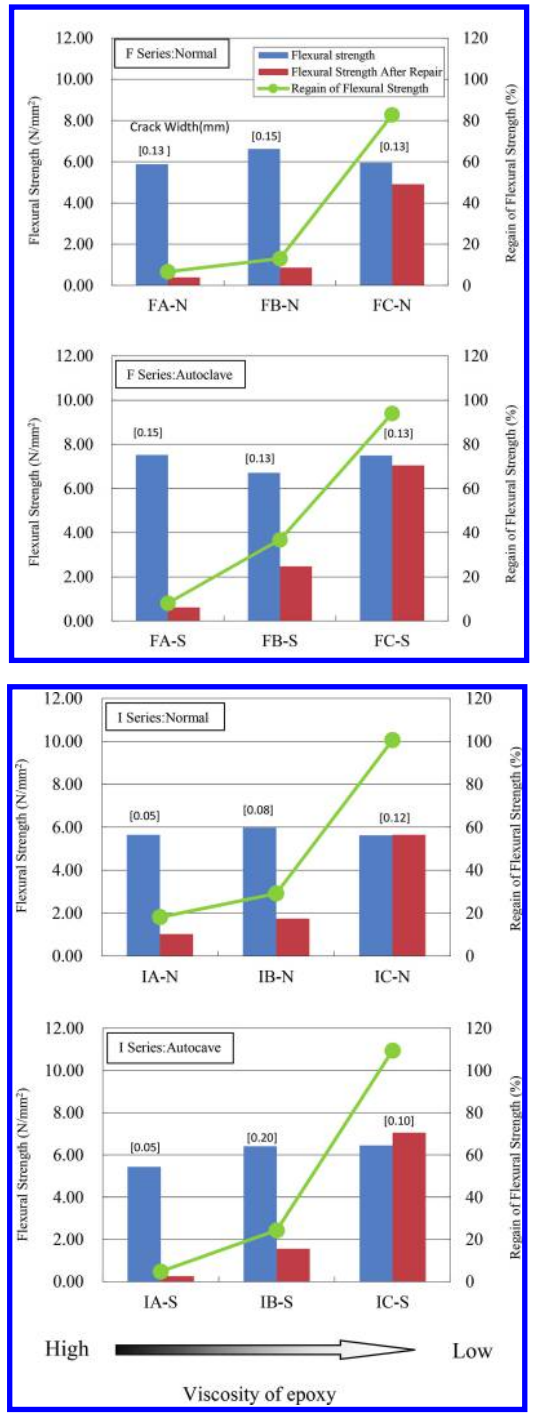

Figure 5. Influence of viscosity and curing condition of epoxy resin on regain of flexural strength.

which may be accounted due to the smaller crack widths for poor impregnation into the cracks and insufficient self-repairing. The influence of viscosity is distinctly seen by the decrease in viscosity and the increase in regain of flexural strength. Furthermore, in regards to the normal and accelerated curing condition on the regain of flexural strength, accelerated curing showed better results for the I-series (pre-Injection of epoxy resin in network) in comparison to the F-series (post-injection after First loading).

3.2 *Effect of surface treatments of network*

Table 4 and Figure 6 give the regain of flexural strength of specimens after self-repair. The network of the mortar specimens were treated by different barrier penetrants (B1, B2 and B3), polymer dispersions (P1, P2 and P3) and Epoxy resin (EC) respectively in order to prolong the storage time of epoxy resin in the networks to prevent the hardening by the interaction of moisture and alkali of cement hydrates. Remarkable regain of flexural strength after self-repair of cracks was observed for B1, B2 and EC treated networks, which prevented the moisture and alkali from coming into contact with the 28d stored epoxy resin in the networks. Barrier penetrants B1 and B2 have excellent water and moisture repellency which prevents the stored epoxy resin from coming in contact and hardening

Table 4. Flexural strength test results and regain of strength of test specimens at 28d storage after injection of epoxy resin.

Type of Specimen	Curing Condition	Dimensions (cm)	1st Loading		2nd Loading		Regain of Strength (%)
			Max.Load (kN)	Flexural Strength (N/mm²)	Max.Load (kN)	Flexural Strength (N/mm²)	
P1-a	Autoclave	4×4×15	2.67	6.26	0.27	0.63	10.1
P1-b			2.73	6.40	0.18	0.42	6.6
P1-c			2.85	6.68	0.04	0.09	1.3
P2-a			2.90	6.80	0.09	0.21	3.1
P2-b			2.81	6.59	0.43	1.01	15.3
P2-c			2.72	6.37	0.89	0.89	14.0
P3-a			2.67	6.26	0.39	0.91	14.5
P3-b			2.51	5.86	0.30	0.70	11.9
P3-c			3.16	7.41	0.41	0.96	13.0
B1-a			2.69	6.30	1.78	4.17	66.2
B1-b			2.83	6.63	3.28	7.69	116.0
B1-c			2.41	5.65	1.74	4.08	72.2
B2-a			2.83	6.63	1.18	2.77	41.8
B2-b			2.36	5.53	2.32	5.44	98.4
B2-c			2.86	6.70	1.74	5.62	83.9
B3-a			2.68	6.28	0.08	0.19	3.0
B3-b			3.32	7.78	0.24	0.56	7.2
B3-c			2.83	6.63	0.03	0.07	1.1
EC-a			3.15	7.38	1.97	4.62	62.6
EC-b			2.69	6.30	2.99	7.01	111.3
EC-c			3.19	7.48	1.48	3.42	45.7

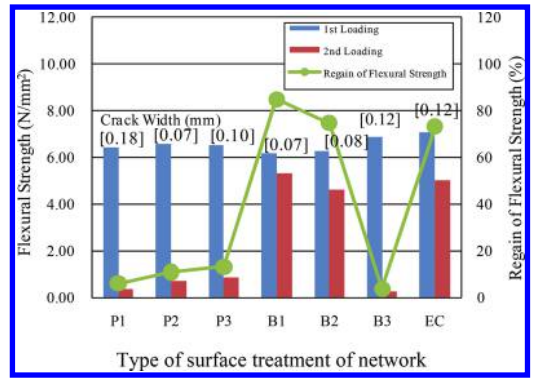

Figure 6. Influence of surface treatment of network on regain of flexural strength after 28d storage.

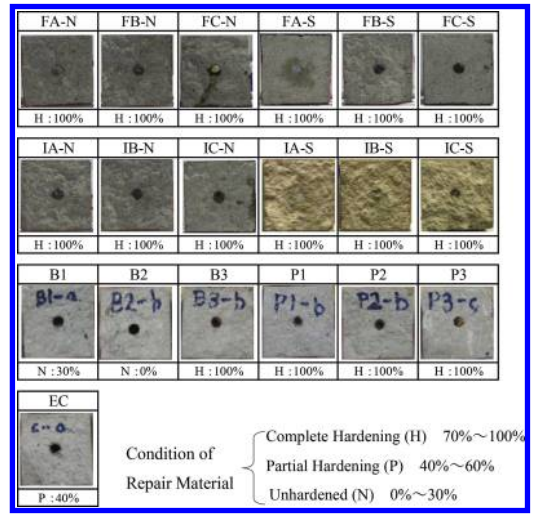

Photo 2. Cross section of specimens and condition of epoxy resin in network.

remaining in liquid state to heal the cracks at second loading after 28d storage. In case of Epoxy resin (EC) treated network an epoxy coating layer is formed in the network which functions as a glass tube and prevents the moisture from coming in contact with the epoxy resin. However, the regain in flexural strength showed large variation with the highest values exceeding 100% and the lowest value of up to 40% likely due to non-uniform coating layer in the network to prevent the penetration of moisture into the epoxy resin. On the other hand, surface treatments of network by P1, P2, P3 and B3 did not show any effectiveness in preventing the penetration of moisture to the epoxy resin in the network resulting in complete hardening and no regain in flexural strength.

Photo 2 shows the fractured cross sections of the specimens with the network. The ratio of hardened epoxy resin area to the total area of the cross section of the network was graded in three patterns as complete hardening (H:70%–100%), partial hardening (P:40%–60%) and unhardened (N: 0%–30%) shown in the Photo 2. The specimens of F and I series with untreated surface network showed complete hardening of the epoxy resin in the network due to reaction of the moisture of the mortars with the epoxy resin in the network. The specimens with surface treatment of network by B1 and B2 showed almost no hardening whereas network treated with EC showed partial hardening of the epoxy resin due to the formation of non-uniform coating layer formed in the network.

4 CONCLUSIONS

From the test results, it was found that the epoxy resin with a lower viscosity was more effective for self-repairing of cracks and showed a remarkable regain of flexural strength of mortar specimens. Furthermore, the internal network surface treatment techniques by barrier penetrants B1, B2 and epoxy resin EC helped to increase the after 28d storage period of the epoxy resin for the self-repair of cracks.

REFERENCES

Dry, C. 1994. Matrix cracking repair and filling using active and passive modes for smart timed release of chemicals from fibers into cement matrices Smart Mater. Struct. 3: 118–123.

Dry, C. and McMillan W 1996. Three-part methylmeth-acrylate adhesive system as an internal delivery system for smart responsive concrete Smart Mater. Struct. 5: 297–300.

De Rooij, M., Van Tittelboom, K, De Belie, N. and Schlangen, E., (Eds.) 2013. Self-healing phenomena in cement based materials: State-of-the-art report of RILEM technical committee 221-SHC (Dordrecht Heidelberg New York London: Springer).

JCI-TC075B. 2009. Technical committee report on autogenous-healing in cementitious materials (Japan Concrete Institute) (In Japanese).

JCI-TC091A. 2011. Technical committee report on self-healing/repairing technology in cement-based materials (Japan Concrete Institute) (In Japanese).

Concrete Repair, Rehabilitation and Retrofitting IV – Dehn et al. (Eds)
© 2016 Taylor & Francis Group, London, ISBN 978-1-138-02843-2

The effectiveness of corrosion inhibitors in reducing corrosion in chloride contaminated RC structures

P.A. Arito & H.-D. Beushausen
Concrete Materials and Structural Integrity Research Unit, Department of Civil Engineering, University of Cape Town, Cape Town, South Africa

ABSTRACT: This paper presents the results of an investigation into the effectiveness of a corrosion inhibitor using reinforced concrete beam specimens with three different binder types. Active corrosion in the specimens was induced by cyclic (2 weeks) drying and immersion of test specimens in a salt solution. Three levels of corrosion, namely: low (<0.5 μA/cm^2), moderate (0.5–1.0 μA/cm^2) and high (>1.0 μA/cm^2) were induced in the specimens. The effectiveness of the corrosion inhibitor was monitored over a duration of 134 weeks from their time of application. The assessment of the effectiveness of the corrosion inhibitor was done with respect to corrosion rate, Half-Cell Potential (HCP) and concrete resistivity measurements. The test results show that corrosion rates and HCPs decreased significantly in all the specimens in which the corrosion inhibitor was applied, indicating that the inhibitor was successful in lowering the risk of corrosion damage to the specimens.

1 INTRODUCTION

Corrosion of steel is the major cause of deterioration of RC structures. It results when the passive layer of γ-Fe_2O_3 (gamma iron oxide) formed on the surface of steel during cement hydration breaks down. The breakdown of the protective passive layer on the reinforcing steel commonly results from the ingress of chloride ions and/or carbon dioxide from the exposure environment as well as stray currents. The corrosion of steel in Reinforced Concrete (RC) structures results in negative socio-economic effects, poor aesthetics as well as reduction in the service life.

The most common techniques that have been used to control the corrosion of steel in RC structures comprise: patch repairs, corrosion inhibitors, electrochemical techniques (e.g. cathodic protection, electrochemical chloride extraction, etc.), coating the reinforcement and concrete surface treatment. Corrosion inhibitors are chemical substances that decrease the corrosion rate when present in the corrosion system at suitable concentration, without significantly changing the concentration of any other corrosion agent (Mackechnie and Alexander, 2001; Söylev and Richardson, 2008). They are a good alternative to other corrosion protection methods or classical repair methods due to their lower cost and easy application.

Corrosion inhibitors control corrosion in RC structures through a combination of the following mechanisms (Trepanier et al., 2001; Trejo et al., 2009): delaying the onset of corrosion by reducing the rate of ingress of chlorides, increasing the chloride threshold value for corrosion initiation, reducing the rate of corrosion once it is initiated, influencing the degree to which chlorides are chemically bound in the concrete cover, and by influencing the electrical resistance and chemical composition of the concrete system. Corrosion inhibitors can be mainly classified in three different ways (Söylev and Richardson, 2008): according to their application methods, according to their mechanism of protection, or their content.

Migrating Corrosion Inhibitors (MCIs) can be classified into three groups according to the electrochemical mechanisms (Bjegovic et al., 2000; Söylev and Richardson, 2008): anodic, cathodic and mixed.

This paper presents the results of an investigation into the effectiveness of a chloride inhibitor (Protectosil(R) CIT, an advanced corrosion inhibitor for steel reinforced concrete based on organo-functional silanes) in reducing corrosion of steel in RC beams specimen that are exposed to a chloride contaminated environment.

2 EXPERIMENTAL SET UP

The effectiveness of the corrosion inhibitor was assessed using reinforced concrete (RC) beam specimens (150 × 150 × 380 mm). Three binder types—100% CEM I 42.5N (PC), 50/50 PC/GGBS and 70/30 PC/FA—were used. All specimens had a constant water:binder ratio of 0.50 and cover of

20 mm. The specimens were made to conform to ASTM G-109 specifications. The specimens were exposed to a controlled laboratory environment; with the average temperature and relative humidity ranging between 23 ± 2° C and 50 ± 4% respectively. The selection of the aforementioned parameters is based on commonly used concretes in South Africa for structures that are exposed to marine environments. PC concretes were used as control specimens. Corrosion rates, half-cell potential and concrete resistivity were measured bi-weekly over a period of 134 weeks except for the period during the application of the corrosion inhibitor (i.e., between week 62–66).

2.1 *Test materials, mix design, casting and curing*

The RC beam specimens were made using the following materials:

i. CEM I 42.5N,
ii. Fly ash (class F),
iii. Ground granulated blastfurnace slag (GGBS),
iv. Klipheuwel sand was used as a fine aggregate (Fineness Modulus = 2.7; relative density = 2.65),
v. Greywacke was used as a coarse aggregate (CBD = 1570 kg/m^3; relative density = 2.7).

A summary of the concrete mix proportions that were used to make the test specimens, and some selected concrete properties, are presented in Table 1.

For each binder type, and water:binder ratio, 6 beams (3 with the corrosion inhibitor applied after inducing corrosion and 3 without the corrosion inhibitor applied after inducing corrosion) were cast resulting in a total of 18 beams. The specimens without the corrosion inhibitor were used as reference specimens. The specimens were cast and de-moulded after 24 hours. The de-moulded specimens were thereafter cured in a water bath maintained at a temperature of 23 ± 2° C for a period of 28 days. Three 100 × 100 × 100 mm concrete cubes were also cast and cured in the same water bath. The cubes were used to determine the compressive strength of the various concrete mixes according to SANS 5863.

Table 1. Summary of concrete mix proportions and selected concrete properties.

Binder composition	100% PC	50/50 PC/GGBS	70/30 PC/FA
Material (kg/m^3)			
w/b ratio	0.50	0.50	0.50
Mix label	PC-50	SL-50	FA-50
PC (CEM I 42.5N)	370	185	259
GGBS	–	185	–
Fly ash	–	–	111
Fine aggregate: 2 mm max.	827	827	827
Coarse aggregate: 13 mm	1040	1040	1040
Water content	185	185	185
28-day compr. strength (MPa)	49.3	45	39
Slump (mm)	58	72	94

2.2 *Inducing active corrosion*

After 28 days of water-curing, active corrosion rate ($i_{corr} \geq 0.1$ µA/cm^2) was induced in the specimens by exposing them to two cycles of 2-week drying at 70° C followed by a 2-week submersion in a 3% NaCl salt solution). After active corrosion was induced in all the specimens (at the end of the second cycle), the specimens were then subjected to a cyclic 2-week wetting with 3% NaCl solution followed by a 2-week drying until steady corrosion rates were recorded. This was attained between week 45 and 62 in the different specimens. The average corrosion rates in the specimens before the application of the corrosion inhibitor depicted three levels of corrosion rate, namely: low (<0.5 µA/cm^2), moderate (0.5–1.0 µA/cm^2) and high (>1.0 µA/cm^2).

2.3 *Application of corrosion inhibitor*

The corrosion inhibitor (Protectosil(R) CIT) was applied to the specimens after 62 weeks of corrosion when the corrosion rates showed minimal fluctuation with time.

i. The corrosion inhibitor was applied in three coats. Each coat was applied by spraying the corrosion inhibitor onto the concrete surface.
ii. A period of 24 hours was allowed between successive coats to enable the corrosion inhibitor to penetrate deep into the concrete (as advised by the supplier).
iii. After the last (third) coat, a period of 14 days elapsed before resuming corrosion rate, half-cell potential and resistivity monitoring.
iv. According to the supplier, the protection from the corrosion inhibitor is fully developed after 14 days from the time of application of the last coat.

2.4 *Corrosion monitoring*

Corrosion monitoring comprised the measurement of the following: corrosion rate, half-cell potential and concrete resistivity in all the test specimens. Corrosion rate was measured bi-weekly

using the Gecor 6™. The Gecor 6™ is a commercial corrosion rate measurement instrument that uses a linear polarization resistance technique to quantify the corrosion current density. Half-Cell Potential (HCP) was measured bi-weekly against a silver/silver chloride (Ag/AgCl) reference electrode as specified in the ASTM C 876. Concrete resistivity was measured bi-weekly using the 4-point Wenner probe technique (Gowers and Millard, 1999). The resistivity measurements were taken at the end of the wetting period when the surface of the specimens was in a saturated but surface dry condition. Corrosion rate, half-cell potential and concrete resistivity measurements were not taken during the application of the corrosion inhibitor (week 62–66).

3 RESULTS AND DISCUSSIONS

3.1 *Corrosion rate*

Corrosion rate refers to the amount of metal wastage produced by a unit surface area of metal when referred to a specific period of time (Andrade et al., 2004). Corrosion rate measurements are the only reliable method of measuring the actual corrosion activity in RC structures. Thus, quantitative information pertaining to the corrosion rate of steel in concrete is important for the identification of actively corroding zones, the evaluation of repair methods, the control of repair work on site, service life prediction and structural assessment of corroding structures.

The time development corrosion rate trends for the different concretes are presented in Figures 1–3. In the figures, 'time zero' corresponds to the first reading taken after active corrosion was induced in the beam specimens.

From the Figures 1–3, it is evident that the corrosion rates induced in the specimens is dependent on the type of binder. Specimens that were cast using PC/GGBS and PC/FA attained corrosion rates that were lower than those cast using plain PC; despite the fact that all the test specimens were subjected to similar conditions while inducing corrosion. These observations are consistent with the commonly held view that Supplementary Cementitious Materials (SCMs) perform best with respect to corrosion control (Arito et al., 2012). The beneficial effects of SCMs in reducing corrosion can be attributed to the refined, less continuous pore structure that leads to a decrease in permeability and chloride solidification (Asrar et al., 1997; Trejo et al., 2009). Thus, concretes made from SCMs have a lower permeability and electrical conductivity than those made from PC. Their use would, therefore, result in a reduction in the rate of corrosion. Polder and Peelen (2002) reported that slag and fly ash in concrete delays the onset of corrosion by slowing down the ingress of chloride. Asrar et al. (1997 and 1999) have also reported on the improved corrosion protection and durability that is associated with the use of microsilica in concrete.

The average corrosion rates after the application of the corrosion inhibitor were computed from

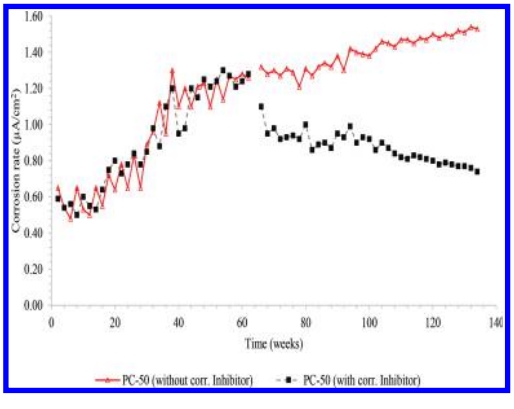

Figure 1. Corrosion rate trends in PC-50 specimens.

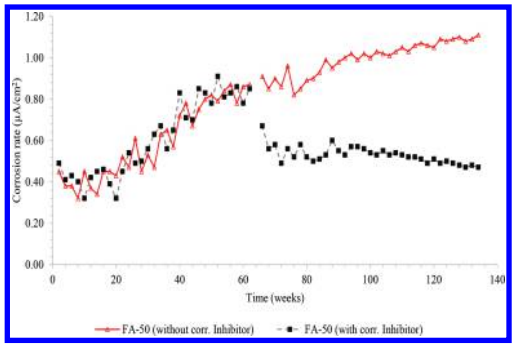

Figure 2. Corrosion rate trends in FA-50 specimens.

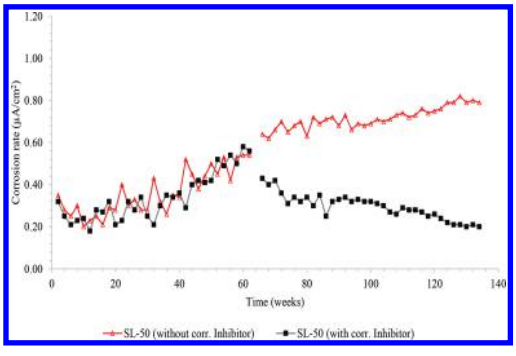

Figure 3. Corrosion rate trends in SL-50 specimens.

the corrosion rate measurements made between weeks 128 and 134—i.e., when the measured corrosion rates had stabilized. From Figures 3–6, it can be inferred that the application of corrosion inhibitors decreased corrosion rates significantly in all test specimens. The average corrosion rates decreased as follows during the test period: PC specimens (39%), PC/FA specimens (43%) and PC/GGBS (60%). A summary of the average corrosion rates before and after the application of the inhibitor in the various test specimens is presented in Table 2.

From Table 2, it is evident that corrosion rates increased in specimens without an inhibitor. Thus, it can be inferred that the inhibitor resulted in a reduction in corrosion rates. The corrosion rates in specimens without an inhibitor increased by: 25% in PC specimens, 32% in PC/FA specimens and 60% in PC/GGBS specimens. Whereas the experimental setup could not facilitate the direct comparison of corrosion rates across specimens made using different binders, owing to the fact that different corrosion rates were induced in each series of test specimens initially, it can be observed

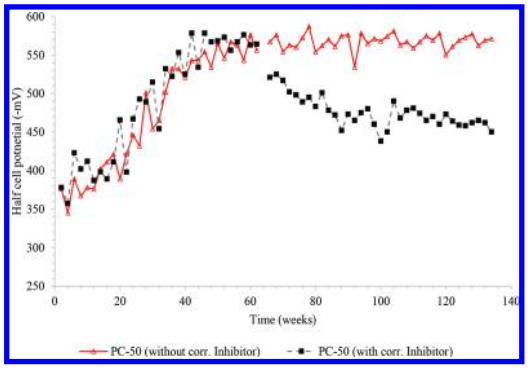

Figure 4. Half-cell potential trends in PC-50 specimens.

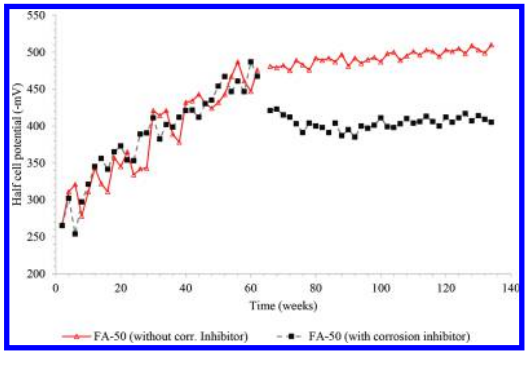

Figure 5. Half-cell potential trends in FA-50 specimens.

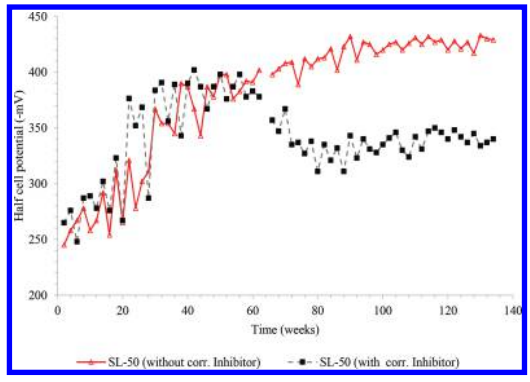

Figure 6. Half-cell potential trends in SL-50 specimens.

Table 2. Summary of average corrosion rates in test specimens.

	Corrosion rate (μA/cm²)	
Specimen ID	Week 62	Week 134
PC-50		
Without inhibitor	1.22	1.53
With inhibitor	1.25	0.76
FA-50		
Without inhibitor	0.83	1.10
With inhibitor	0.83	0.48
SL-50		
Without inhibitor	0.50	0.80
With inhibitor	0.52	0.21

that specimens that were made using PC/GGBS experienced the greatest percentage reduction in corrosion rates. The level of corrosion rates in the test specimens before and after the application of the corrosion inhibitors changed as follows: corrosion in plain PC specimens reduced from 'high' corrosion rate to 'moderate-to-high' corrosion rate (i.e., from 1.25 μA/cm²–to 0.76 μA/cm²), corrosion rates in PC/FA specimens reduced from 'moderate-to-high' corrosion rate to 'low' corrosion rate (i.e., from 0.83 μA/cm²–0.48 μA/cm²) and corrosion in PC/GGBS specimens reduced from 'moderate-to-low' corrosion rate to 'low' corrosion rate (i.e., from 0.52 μA/cm²–0.21 μA/cm²). An interpretation of the aforementioned corrosion rates can be obtained in Broomfield, 2007.

While it has been generally observed, and reported in similar and other corrosion-related studies, that specimens made using plain PC tend to experience a higher percentage reduction in corrosion rates than in specimens made using blended cements, with all other factors held constant (Arito, 2012; Arito et al., 2012; Arito et al.,

2013); the higher percentage reduction in corrosion rate observed in PC/GGBS specimens than in PC specimens that were used in this study contradict the predominant view. The inhibitors in this study seem to be more effective in mitigating corrosion in specimens whose levels of corrosion are in the following order: low, moderate and high respectively. An explanation of this phenomenon could not be obtained based on the tests that were undertaken. Nevertheless, a more comprehensive and accurate explanation of this phenomenon could be obtained after an investigation of various specimens made using different binder types and exposed to similar initial corrosion conditions.

3.2 *Half-Cell Potential*

The Half-Cell Potential (HCP) (also known as open-circuit potential, rest potential or corrosion potential) is the electrochemical potential, measured in Volts, between a sacrificial black steel working electrode and a reference electrode (Trejo et al., 2009). Any surface (typically a piece of metal) on which an electrochemical reaction takes place will generate an electrochemical potential difference when it is in contact with an electrolyte (Myrdal, 2007). Thus, the measurement of corrosion potential (or half-cell potential) is one of the simplest ways of assessing the severity of corrosion or the presence of electrochemical activities that take place on the rebar surface.

Half-cell potential measurements, in the form of potential maps, are used in condition assessment and repair work. While half-cell potential maps have been reported to help in indicating the probability of reinforcement corrosion (Bjegovic et al., 2000; Ahmad, 2003; Song and Saraswathy, 2007), they can also be used to determine the precise location of corroding zones. On the contrary, potential maps do not provide information on the corrosion rate or the amount of steel lost. Thus, they ought to be interpreted carefully. The time development half-cell corrosion potential trends for the different concretes are presented in Figures 4–6.

From Figures 4–6, it can be observed that the Half-Cell Potential (HCP) trends are similar to those for corrosion rate in Figures 1–3. More specifically, the induction of corrosion in the specimens resulted in a decrease in HCP values (i.e., HCP values become more negative); an observation that is consistent with literature findings. HCP values that are more negative are a potential indicator of a higher rate of corrosion (Bjegovic et al., 2000), especially in systems that are not subjected to cathodic protection. Similarly, from Figures 4–6, it can be inferred that the application of the inhibitor resulted in an increase in HCP values (i.e., HCP values became less negative). An increase in HCP values as a result of the addition of inhibitors would imply a reduction in corrosion rates—a phenomenon that corroborated the results from the corrosion rate measurements.

The HCP values of the test specimens were less negative than those of the control specimens throughout the entire experiment by approximately 100 mV. The most negative HCP values in specimens without an inhibitor were observed in the following order: plain PC, followed by PC/FA and finally PC/GGBS. These observations are consistent with most literature on corrosion.

3.3 *Concrete resistivity*

Electrical resistivity measurements have been used to indirectly evaluate concrete diffusivity, the degree of concrete saturation and its aggressiveness, and the size and tortuosity of the pores in a concrete system (Polder et al., 2000; Grantham, 2003; Broomfield, 2007). Thus, resistivity measurements can be used to assess the ease with which corrosion currents flow through concrete. Moreover, resistivity can be related to the corrosion rate and the susceptibility to penetration by chloride. Low resistivity spots within a structure, for example, could indicate the possible locations where chloride penetration will be quickest. In addition, it has been observed that corrosion rate is inversely proportional to concrete resistivity (Polder, 2001; Morris et al., 2002; Polder and Peelen, 2002). This inverse relationship between resistivity and corrosion rate, however, may vary with the concrete composition. The time development concrete resistivity trends for the different concretes are presented in Figures 7–9.

From Figures 7–9, it can be seen that the application of the corrosion inhibitor did not affect concrete resistivity. The specimens that were made using plain PC exhibited low resistivity. Specimens that were made using PC/FA and PC/GGBS,

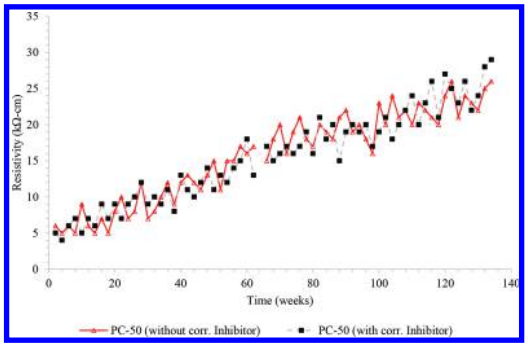

Figure 7. Concrete resistivity trends in PC-50 specimens.

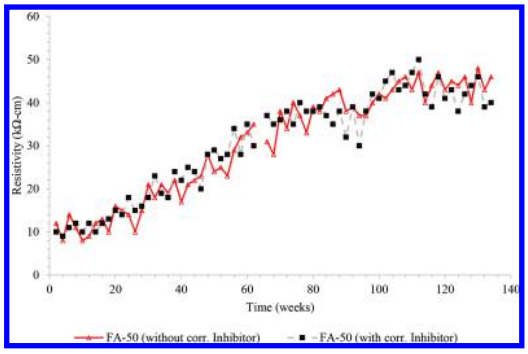

Figure 8. Concrete resistivity trends in FA-50 specimens.

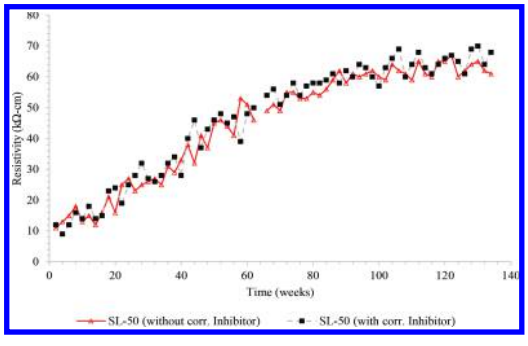

Figure 9. Concrete resistivity trends in SL-50 specimens.

however, exhibited high resistivity. The trends in the resistivity values that were observed vis-à-vis the binder type are consistent with literature on corrosion. Similarly, the fact that specimens that were made using plain PC concrete experienced corrosion rates that were higher than those made from PC/FA and PC/GGBS mixes is consistent with literature.

The increase in the concrete resistivity with time could be attributed to the reduction in the amount of pore water as a result of cement hydration. The increase in resistivity reduces the rate at which electrons and ions move from the anode to the cathode within the corrosion macrocell in the embedded steel. The reduction in the rate at which the electrons move could consequently contributes to the reduction in corrosion rate, though to a slight extent.

4 CONCLUSIONS

The effectiveness of a commercial corrosion inhibitor, was investigated by carrying out accelerated corrosion experiments in the laboratory. A modified version of ASTM G109 test method was used. The test results show that corrosion rates not only decreased in the specimens with low corrosion rates (<0.5 μA/cm^2) but also in those with moderate (0.5–1.0 μA/cm^2) and high (>1.0 μA/cm^2) corrosion rates. Corrosion rate and half-cell potential measurements showed very good agreement in determining the effect of the corrosion inhibitor, confirming that both methods yielded valid results. The corrosion inhibitors used in this study therefore show good potential for application in the prevention of damage related to chloride-induced reinforcement corrosion.

ACKNOWLEDGEMENTS

The authors would like to express their sincere acknowledgements to Mr. Peter Horn (of Evonik Industries, Germany), Mr. Stephen De Klerk (of BASF South Africa (Pty) Ltd) and Dr. Mike Otieno (of the University of the Witwatersrand, South Africa) for their support and contribution towards the success of this project.

REFERENCES

ASTM-C876-91. (1999). Standard test method for half-cell potentials of uncoated reinforcing steel in concrete, ASTM International, West Conshohocken, PA 19428–2959, USA.

ASTM-G109. (2007). Standard test method for determining effects of chemical admixtures on corrosion of embedded steel reinforcement in concrete exposed to chloride environments. ASTM International, West Conshohocken, PA 19428–2959, USA, 6 pp.

Ahmad, S. Reinforcement corrosion in concrete structures, its monitoring and service life prediction—a review. Cement & Concrete Composites, 25, (2003), pp. 459–471.

Andrade, C., Alonso, C., Gulikers, J., Polder, R., Cigna, R., Vennesland, Ø., Salta, M., Raharinaivo, A., and Elsener, B. RILEM TC 154-EMC: 'Electrochemical techniques for measuring metallic corrosion' recommendations. Test methods for on-site corrosion rate measurement of steel reinforcement in concrete by means of the polarisation resistance method. Materials and Structures/Matériaux et Constructions, Vol. 37, November 2004, pp 623–643.

Arito, P. A. Discrete sacrificial anodes and their use in service life extension of chloride contaminated reinforced concrete structures, MSc (Eng.) Dissertation, University of Cape Town, November 2012.

Arito, P.A., Beushausen, H., Alexander, M.G., and Otieno, M.O. (2012). The use of discrete sacrificial anodes in reducing corrosion rate in chloride contaminated concrete. International Conference on Concrete Repair, Rehabilitation and Retrofitting III—Alexander et al. (Eds), Taylor and Francis Group, London, pp. 999–1002.

Arito, P.A., Beushausen, H., Alexander, M., and Otieno, M. (2013). The use of sacrificial anodes in extending the service life of RC structures in South Africa. International Conference on Advances in Cement and Concrete Technology in Africa, Uzoegbo and Schmidt (Eds), BAM Federal Institute for Materials Research and Testing, pp 1081–1088.

Asrar, N., Malik, A. U., Ahmad, S, and Andijani, I. N. Corrosion protection of rebars in concretes. Second Acquired Experience Symposium on Desalinisation Plants O&M, SWCC, Al-Jubail, Sept. 29–Oct. 3 1997, pp 1456–1477.

Asrar, N., Malik, A.U., Ahmad, S., and Mujahid, F.S. Corrosion protection performance of microsilica added concretes in NaCl and seawater environments. Construction and Building Materials, 13, (1999), pp. 213–219.

Bavarian, B., and Reiner, L. Improving durability of reinforced concrete structures using migrating corrosion inhibitors, NACE International, Corrosion, 2004, Paper No 04323, 11 pp.

Bjegovic, D., Miksic, B.A., and Stehly, R.D. Test protocols for migrating corrosion inhibitors (MCI) in reinforced concrete. Materials and Corrosion 51, 2000, Pp. 444–452.

Broomfield, J. P. (2007). Corrosion of Steel in Concrete: Understanding, Investigation and Repair, 2nd Edition, Taylor and Francis, 277pp.

Evonic Industries, Protectosil® CIT, Corrosion Inhibitor Treatment, Product Data and Test Information, 4 pp.

Gowers, K. R. & Millard, S. G. (1999). Measurement of concrete resistivity for assessment of corrosion severity of steel using Wenner technique. ACI Materials Journal, Vol. 96(5), pp. 536–541.

Grantham, M. (2003). Diagnosis, inspection, testing and repair of reinforced concrete structures: Advanced concrete technology—Testing and quality. Newman, J., and Choo, B.S. (Eds), Elsevier, Butterworth Heinemann, pp. 6/43–6/54.

Mackechnie, J.R., and Alexander, M.G. (2001). Repair principles for corrosion-damaged reinforced concrete structures. Research monograph No. 5, Department of Civil Engineering, University of Cape Town, pp. 5–36.

Morris, W., Vico, A., Vazquez, M., and de Sanchez, S. R. Corrosion of reinforcing steel evaluated by means of concrete resistivity measurements. Corrosion Science, 44, (2002), pp. 81–99.

Myrdal, R. (2007). The electrochemistry and characteristics of embeddable reference electrodes for concrete. Woodhead Publishing Limited, Cambridge, England, 26pp.

Polder, R., Andrade, C., Elsener, B., Vennesland, Ø., Gulikers, J., Weidert, R., and Raupach, M. RILEM TC 154-EMC: Electrochemical techniques for measuring metallic corrosion. Materials and Structures/ Matériaux et Constructions, Vol. 33, December, 2000, Pp. 603–611.

Polder, R.B. Test methods for on site measurement of resistivity of concrete—a RILEM TC-154 technical recommendation. Construction and Building Materials, 15, (2001), Pp. 125–131.

Polder, R.B., and Peelen, W.H.A. Characterisation of chloride transport and reinforcement corrosion in concrete under cyclic wetting and drying by electrical resistivity. Cement & Concrete Composites, 24, (2002), pp. 427–435.

Sanchez, M., and Alonso, M.C. electrochemical chloride removal in reinforced concrete structures: Improvement of effectiveness by simultaneous migration of calcium nitrite. Construction and Building Materials, 25, (2011), pp. 873–878.

SANS-5863 (1994) Concrete tests—compressive strength of hardened concrete, South African Standard Code of practice, First revision.

Söylev, T.A., and Richardson, M.G. Corrosion inhibitors for steel in concrete: State-of-the-art report. Construction and Building Materials, 22, 2008, Pp. 609–622.

Song, H. -W., and Saraswathy, V. Corrosion monitoring of reinforced concrete structures—A review. Int. J. Electrochem. Sci., 2, (2007), pp. 1–28.

Trejo, D., Halmen, C., and Reinschmidt, K. (2009). Corrosion performance tests for reinforcing steel in concrete. Technical report, Report No. FHWA/TX-09 /0–4825–1, Texas Transportation Institute, 232pp.

Trepanier, S.M., Hope, B.B., and Hansson, C.M. Corrosion inhibitors in concrete Part III. Effect on time to chloride-induced corrosion initiation and subsequent corrosion rates of steel in mortar. Cement and Concrete Research, 31, (2001), pp. 713–718.

Concrete Repair, Rehabilitation and Retrofitting IV – Dehn et al. (Eds)
© 2016 Taylor & Francis Group, London, ISBN 978-1-138-02843-2

Protection against biogenic sulfuric acid corrosion—development of a sprayed polymer concrete

Robert Schulte Holthausen & Michael Raupach
Institute of Building Materials Research, RWTH-Aachen University, Germany

ABSTRACT: Concrete sewage systems can be severely damaged when attacked by biogenic sulfuric acid corrosion. While minor aggressive exposures can be accounted by using a high sulfate resistant cement, higher concentrations of acid (pH 3.5) require the protection of concrete surfaces. A number of different linings and coatings have been used in sewage systems throughout the decades, such as Polymer Concrete (PC) and or manually applied ceramics and inorganic glass. However, these have been limited to newly constructed pipes and manholes as well as local repair. In cooperation with Massenberg GmbH, the Institute of Building Materials Research of RWTH Aachen University developed a new way of applying PC for the rehabilitation of damaged concrete surfaces of sewage systems; by dry spraying an epoxy mortar on concrete, layers with an average thickness of 20 mm on vertical and overhead surfaces were successfully produced. The dry sprayed PC was examined for its overall performance such as strength, adhesion, thermal expansion, and wear. A special focus has been put on the diffusion properties and the durability in an acidic environment. Based on these positive laboratory results, a first practical application in a waste water structure is currently underway.

1 INTRODUCTION

Changes in population density in Germany have increased the aggressiveness of waste water. (Kampen et al. 2011). Reduced amounts of waste water increase dwelling times and require longer transit distances. At the same time, involuntary leakage of groundwater into the sewage system is prevented and by this, higher concentrated waste water is generated. At the same time, decreased amounts of runoff in such structures allow the rehabilitation using coatings and linings that are reducing the cross section of canals.

One severe consequence of these changes is the increasing attack of waste water structures by sulfuric acid, formed in a two step process. First sulfides in the waste water are biologically converted to hydrogen sulfide, that degasses into the atmosphere of the canal and accumulates in the biofilm at the crown of the canal. In a second step, hydrogen sulfide is biologically converted into the highly corrosive sulfuric acid, causing a severe acid attack on concrete especially in the canal crown. In some cases, pH-values of 1 and below were measured in the biofilm in the crown (Kampen et al. 2011), which can lead to corrosion rates of 10 mm per year. These high rates entail the destruction of waste water structures in short periods of time and imply the immediate need for action. One of the most effective ways of preventing such an attack is a proper ventilation of the structure, purging the atmosphere and preventing the formation of sulfuric acid. Unfortunately, this is accompanied by a strong sulfur odor, resembling that of rotten eggs, which commonly can not be accepted in inhabited areas. PH-Values, found in waste water structures, the corresponding intensity of attack on concrete and possible protective measures are listed in Table 1.

While moderate attacks from waste water down to a pH-value of 3.5 can be prevented by improved concrete technology such as increasing compaction and concrete quality, and using a high sulfate resistance cement, higher acid concentrations inevitably lead to a dissolution and spalling of the cementitious matrix.

Table 1. pH-value, intensity of attack and protective measures in waste water structur.

pH-value in the crown of the canal	Intensity of attack on concrete	Protective measures
13 to 6	Mild	None, suitable concrete
6 to 3.5	Moderate	Cement with high sulfate resistence, high quality concrete
3.5 to 0	Severe	Lining or coating essential

In these cases, protective coatings or linings have to be used, separating the concrete from the highly corrosive waste water such as:

- linings
  - high density polyethylene
  - tube liner, GFRP (glass fiber reinforced plastic)
  - ceramics
  - polymer concrete
  - inorganic glass panels and sheets
- coatings applied manually
  - silicate based mineral mortar
  - polymer/polymer concrete
- sprayed coatings
  - Sprayed Glass
  - Sprayed Polymer Concrete.

Acid resistant materials used are thermoplastic polymers such as polyethylene or inorganic layers e.g. made of glass. (Orlowsky & Raupach 2010) These are applied as prefabricated panels or linings, mounted onto the concrete surface. Protective coatings usually include high performance resins such as epoxy, polyester or polyurea. (Liebscher & Gillar 2011) While the application of such coatings is rather inexpensive, they bear the risk of delamination due to rear water pressure, especially on local imperfections in the substrate. Another widely used approach to protect concrete surfaces from aggressive waste water are thicker layers of filled polymers, also known as Polymer Concrete (PC). PC was able to show its excellent durability even in highly aggressive environments such as waste water structures over several decades. (Bloomfield 1994) The main drawback until now was the limitation to newly built structures or local repair, since up to now no proper technology for large scale application on site existed.

In order to meet this challenge, Massenberg GmbH and the Institute of Buildings Materials Research joined forces to develop a new application method for polymer concrete in a dry spraying process. The project was funded by the German Federal Ministry for Economic Affairs and Energy (BMWi). In correspondence to Sprayed Polymer Cement Concrete (SPCC), this new material is named Sprayed Polymer Concrete (SPC). (Schulte Holthausen et al. 2014)

1.1 *Development of a dry spraying process for PC*

Dry spraying is a commonly used method to apply cementitious materials in layers from several millimeters up to a few centimeters in thickness. With dry spraying, a mixture of cement, aggregates, and, if necessary, further dry components are transported by an airstream from a spraying concrete machine, through a hose to the nozzle. While passing the nozzle, water is added—sprayed into the stream of dry components. The mixture is shot onto the surface causing parts of the material to adhere. In the beginning, larger aggregates bounce back, forming the so called rebound, leaving behind a layer of mostly cement paste on the surface. Thus forms a thin sticky layer, allowing larger aggregates to adhere until a layer of sufficient thickness is reached. The compaction of the material is usually excellent due to the rebound, producing dense and high quality surfaces. On the other hand, the addition of water, dosed by hand by the nozzleman, and the uncontrolled rebound make it difficult to maintain exact control of the composition of the material and calls for an improved quality assurance on site.

The dry spraying of a PC shows several analogies to dry spraying of cementitious mortar. Here, the aggregates are transported through a hose and the polymer binder is added at the nozzle. An important factor, determining the PCs overall quality, is the homogenization of aggregates and binder. Furthermore, the relation of the aggregates grading curve and the viscosity of the binder largely affects the applicability of the PC. To assure the proper homogenization, Massenberg GmbH developed a new nozzle unit, making use of a complex geometry of spray jets inside the nozzle, allowing complete coverage of the aggregates while using a minimum amount of epoxy resin. Similar to SPCC, the possibility of varying binder content and uncontrolled rebound increase the necessity for proper quality assurance. (Schulte Holthausen & Weichold 2014)

The rehabilitation of waste water structures using SPC includes the following steps (Schulte Holthausen et al. 2014):

- Removing all concrete having
  - a sulfide contend greater than 1 wt-% with respect to the total concrete mass
  - a mean pull-off strength of less than 1.5 N/mm² and less than 1.0 N/mm² as smallest value
  - a pH-value below 10, tested with phenolphthalein
- Rebuilding the pipes original cross section by applying an alkaline SPCC to ensure the loadbearing capacity and rebar protection
- Applying a protective layer of SPC with a thickness of approx. 20 mm.

Figure 1 illustrates the procedure for the rehabilitation of a waste water structure with the machinery for dry spraying and the layers applied.

1.2 *Specimen preparation and methods used*

All specimens were fabricated in a dry spraying process at a spraying station, built for this purpose. The station was standing covered, yet open to the

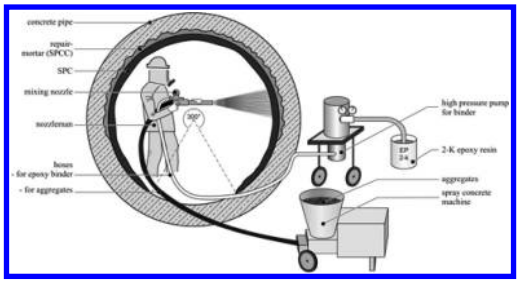

Figure 1. Schematic illustration of the procedure of dry spraying of a SPC inside of a sewage duct.

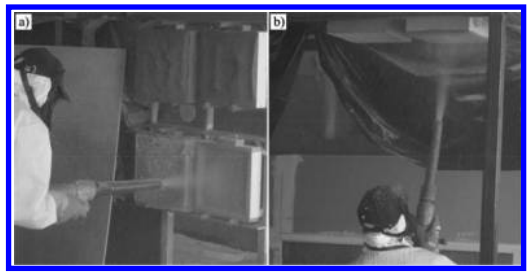

Figure 2. Fabrication of SPC specimens a) in moulds and b) on a concrete substrate overhead.

outside at Massenberg GmbH. Temperature and humidity during spraying varied from between 5 to 25 °C. All specimens were made in a total of three days, distributed over one year. Between every fabrication day, the information gained on the mortar quality was iteratively incorporated into the fabrication process. Figure 2 illustrates the spraying process, fabricating specimens on a vertical surface and over head.

As substrates, concrete specimens with dimensions of 300 × 300 × 100 mm³ according to DIN EN 1766 (MC 0.40) with a water/cement-ratio of 0.4, and a maximum aggregate-size of 8 mm were used. The specimens were partly wetted, to simulate a potentially moist concrete substrate inside a waste water structure. Second, moulds with the inner dimensions 270 × 270 × 60 mm³ were used for the investigation of pure SPC specimens.

The parameters, varied for the SPC production, were:

- different grading curves of dried quartz aggregates between 0.1 to 4 mm
- type and amount of resin. The resin was a commercial, solvent-free epoxy for concrete-surface protection
- spraying angle to the surface
- orientation of surface (vertical wall and overhead ceiling)
- spraying pressure and nozzle mixing unit.

While concrete specimens with a SPC layer were mostly used for adhesion testing, the mortar sprayed into the moulds was cut to appropriate sizes for further testing.

The testing methods included:

- Testing the materials consistency
  - binder content as residue on ignition
  - change in grain size composition by sieving
  - density
- Mechanical testing
  - compressive and tensile strength on cubes with an edge length of 40 mm referring to DIN EN 12190 and DIN EN1542
  - Young's modulus on cylinders with a diameter of 45 mm and a length of 140 mm referring to DIN EN 13412
  - for abrasion resistance using the so called "Böhmescheibe" according to DIN EN 13892
  - for creep resistance referring to DIN EN 13584 with a compression load of 25% of the maximum strength
- Testing for adhesion to the concrete substrate by pulling of steel cylinders with a diameter of 50 mm, referring to DIN EN 1542.
- Permeation and its influence on mechanical properties of water and a solution of water and 10% sulfuric acid by immersion of cubes with an edge length of 40 mm. Following the immersion, the compression strength was tested.
- In order to quantify the ingress of sulfuric acid into the specimen, non-destructive measurements by single-sided Nuclear Magnetic Resonance (NMR) were conducted, aiming to determine the spin-lattice relaxation in a depth profile from to specimens surface up to a depth of 2 mm.

The last two measurements were of particular importance to allow an estimation of the durability under biogenic sulfide corrosion attack.

2 RESULTS

2.1 *Results of overall performance*

An overall outline of the SPC's properties is given in Table 2. Even though the nozzleman was instructed to partly produce binder rich, as well as lent specimens, the binder content reached values in a comparably small variation between 14 and 21 wt-%; all following investigations showed that this range of content is uncritical for the desired material properties. A high loss of larger aggregates was measured due to rebound. The mortar density varies between 2.01 and 2.03 g/cm³ indicating a proper compaction; using the densities of resin and aggregates, a total pore volume between 0 and 3 vol.-% can be estimated for the SPC.

Table 2. Results from the laboratory testing of SPC specimens.

Test method		Results	
Property	Norm	Unit	Value
Material consistency			
Binder content	Residue on ignition	[wt-%]	14 to 21
Change in grain size	DIN EN 12192-1:2002	Loss of larger grains	
Mortar density	DIN EN 12190:1998	[g/cm³]	2.02
Mechanical properties			
Compressive strength	DIN EN 12190:1998	[N/mm²]	90 to 105
Tensile strength	DIN EN 1542:1999	[N/mm²]	12 to 16
Young's modulus	DIN EN 13412:2006	[N/mm²]	13 500 to 18 000
Wear resistance	DIN EN 13892-3:2004	[cm³/(50 cm²)]	8 to 10
Creep deformation	DIN EN 13584:2003	[mm/m/d]	0.039
Hygroscopic properties			
Coefficient of sorption	DIN EN 13057:2002	[kg/(m²d$^{0.5}$)]	0.001
Diffusions resistance μ_{H2O}	DIN EN ISO 7783:2012	–	3440
Thermal properties			
Thermal expansion α_T	DIN EN 1770:1998	[10^{-6} 1/K]	32
Adhesion			
Pull of strength	DIN EN 1542:1999	[N/mm²]	>3.5 average >2.6 minimum
Durability in 10% sulfuric acid (28-day immersion)			
Coefficient of sorption	DIN EN 13057:2002	[kg/(m²d$^{0.5}$)]	0.002 to 0.006
Change in compressive strength	DIN EN 12190:1998	[%]	−7.5 to +4
Ingress of acid	By NMR spinlattice relaxation	[mm]	0.8 to 1.5

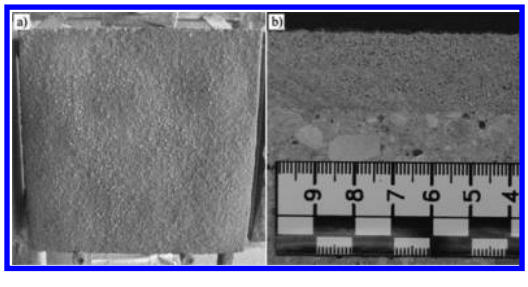

Figure 3. (a) Surface of dry sprayed polymer concrete specimen, (b) cut through the specimen, SPC applied to concrete substrate.

Figure 3 gives an impression of the reached surface quality as well as the layer composition of the material.

Mechanically, the SPC shows very good properties. With compressive and tensile strengths greater than average cementitious mortars and concrete, the SPC is expected to withstand all usual exposures. Wear resistance is in the range of cementitious mortars. The creep deformation was evaluated using a four element Burgers model (Ritchie 1965) as long term, viscous creep. Values around 0.04 mm/m/d indicate, that the layer of SPC should not be taken in account for long term loading capacity.

A critical parameter for the durability of linings and coatings is proper adhesion to the substrate. Especially for some epoxy binders, a moist concrete substrate can hamper the proper adhesion. However, in this case, an epoxy was used that is known to adhere to damp concrete surfaces. The results from pull off tests gave 2.6 N/mm² as smallest value and an average of 3.5 N/mm² for all 65 individual values. This clearly proves that adhesion, even on moist substrates, is not a problem for this SPC and holds true for vertical as well as overhead surfaces. Furthermore, the influence of a permanent moist substrate was tested by immersion of cylindrical specimens having a layer of SPC on a layer on concrete for three months in water. No significant reduction of pull-off strength was notable.

2.2 *Results for diffusion properties and durability*

Among the economic and fast application of the SPC, its durability and its impermeability in moist and acidic environments are properties of major importance. Such properties can only be tested properly under real-life conditions; accelerated

tests under intensified conditions only give an estimate on performance. For this, cubic specimens with a edge length of 40 mm were immersed in water and in a solution of water and 10% sulfuric acid for 28 days at 20 °C and the mass uptake was measured. As reference, specimens were stored at 21 °C and 65% relative humidity. Afterwards, the specimens were dried at 40 °C until a constant mass was reached and were then tested for compressive strength. The coefficient of sorption was derived from the mass uptake, following the law of square-root of time, according to DIN EN 13057.

Figure 4a and 4b illustrate the compression strength and coefficient of sorption for reference and immersed specimens for four different mortars, differing in type of epoxy binder and binder content. In general, comparatively high compressive strengths greater than 80 N/mm² and at the same time very low coefficients of sorption of around 0.001 $kg \cdot m^{-2} \cdot h^{-0.5}$ were found for all samples. The SPC shows an slightly increasing strength and decreasing sorption with increasing binder content. The SPC made with epoxy binder EP2 shows higher compressive strength and sorption, which is in good agreement with the results on the pure binder material (not shown). Immersion in acid increases sorption for all materials, especially for SPC made with EP2.

To further investigate the influence of sulfuric acid, single-sided Nuclear Magnetic Resonance (NMR) measurements using a NMR MOUSE (Mobile Universal Surface Explorer) (Blümich et al. 2008) were conducted. This method is based on monitoring the de—and refocusing of spins in hydrogen nuclei. Here, the spin-lattice (T_1) relaxation was measured, indicating a number of material properties such as molecular mobility and magnetic impurities in the material. The depth profiles shown in Figure 5 were recorded in 0.1 mm steps starting at the specimens surface up to a depth of 2 mm.

Specimens, having been stored in air or immersed in water show a constant value for T_1 relaxation of around 130 ms from the surface into the specimens

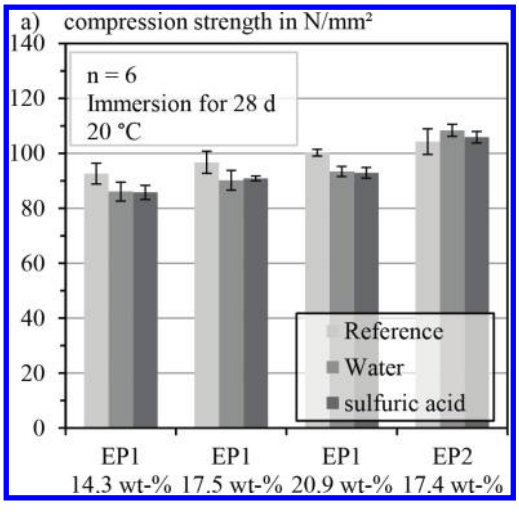

Figure 4a. Results for specimens stored in air, immersed in water and 10% sulfuric acid for 28 days at 20 °C for compression strength.

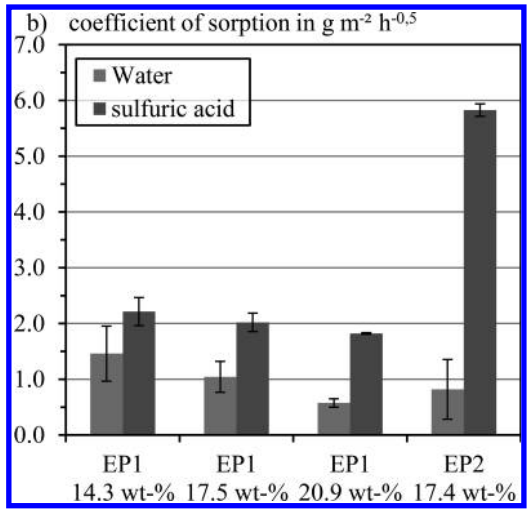

Figure 4b. Results for specimens stored in air, immersed in water and 10% sulfuric acid for 28 days at 20 °C for coefficient of sorption (error bar is showing standard deviations).

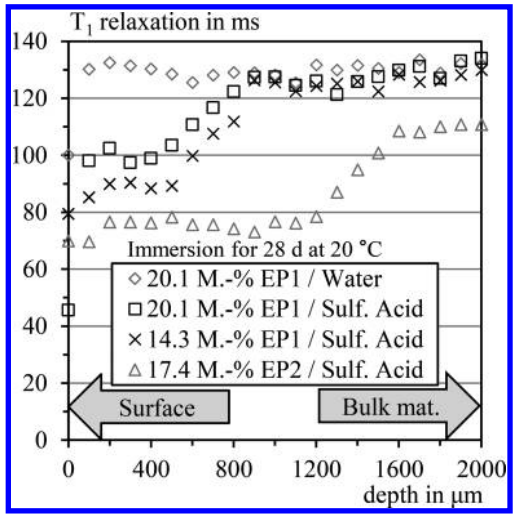

Figure 5. NMR spin-lattice-relaxation profiles through the first 2 mm from surface of SPC-specimens after the immersion in water and sulfuric acid for 28 days.

bulk material. On the other hand, specimens having been immersed in sulfuric acid show a decrease of T_1 relaxation of around 30% at the surface up to a depth of several hundred micrometers. Moreover, SPC made from EP2 generally has a shorter T_1 relaxation around 110 ms but shows the same effect of reduced T_1 relaxation at the surface. These results agree well with the results for the sorption coefficient. Specimens having greater sorption coefficients show a greater depth of the reduced T_1 relaxation as well. This effect is consistent in further specimens and indicates that a correlation between ingress of sulfuric acid and the depth for the reduction of T_1 relaxation can be found. The reason for this effect is still under investigation and is part of our ongoing research.

3 CONCLUSIONS

In a cooperative effort, the Institute of Building Materials Research and Massenberg GmbH successfully developed a new polymer concrete and a method for its application. By dry spraying the material, a dense polymer concrete can be produced which adheres well to concrete surfaces. The wide range of tests done on the material show its good mechanical properties its technical impermeability and durability in moist and acidic environments. In particular, the sorption of the materials under investigation was very low, indicating the possibly good protection of the concrete substrate from the aggressive canal atmosphere. Furthermore single sided NMR measurements were introduced, aiming at non-destructive evaluation of the ingress depths of sulfuric acid.

Since fall 2014, SPC specimens are tested under real-life biogenic sulfide corrosion conditions in sewage canals in Germany in a first practical application. Results are expected in fall 2015 and will be part of an upcoming publication.

ACKNOWLEDGMENT

We would like to thank the German Federal Ministry for Economic Affairs and Energy (BMWi) for funding of this project within the ZIM program.

REFERENCES

Bloomfield, T. Abwasserkanäle und—leitungen aus Polymerbeton, Tiefbau Ingenieurbau Straßenbau 36 (1994), No. 10, pp. 30–43.

Blümich, B. & Perlo, J. & Casanova, F. Mobile Single-Sided NMR, Progress in Nuclear Magnetic Resonance Spectroscopy 52, (2008) pp. 197–269.

Kampen, R. & Bose, T. & Klose, N. Betonbauwerke in Abwasseranlagen—Planung, Bau, Instandhaltung, Bau+Technik GmbH, 2011.

Liebscher, M. & Gillar, M. (2011) Sanierung von Abwasserschächten—Untersuchung von Materialien und Systemen zur Abdichtung und Beschichtung—Institut für Unterirdische Infrastruktur (IKT) Forschungsbericht.

Orlowsky, J. & Raupach, M. Biogene Schwefelsäurekorrosion in Abwasseranlagen—Mechanismen und Schutzmöglichkeiten: Biogenic Acid Sulphur Corrosion in Waste-Water Plants—Mechanisms and Possibilities of Protection, Aachener Schriften zur Stadtentwicklung (2010), No. 14, 11. Kölner Kanal und Kläranlagen Kolloquium 2010, pp. 8/1–8/9 ISBN 978-3-938996-07-2.

Ritchie, P. Physics of Plastics. London: Iliffe Books, 1965.

Schulte Holthausen, R. & Stahl, H. & Raupach, M. Spritzbarer, säurebeständiger Epoxidharzmörtel für die Instandsetzung von abwassertechnischen Anlagen, Restoration of Buildings and Monuments 2014, pp. 311–323, Aedificatio, ISSN0947-4498.

Schulte Holthausen, R. & Weichold, O. Single-Sided Nuclear Magnetic Resonance as a Non-Invasive Tool to Evaluate Sprayed Polymer Concrete, Proceedings of the Conference on the Rehabilitation and Reconstruction of Buildings (CRRB 2014), ISBN-13: 978-3-03835-506-9.

Concrete Repair, Rehabilitation and Retrofitting IV – Dehn et al. (Eds)
© 2016 Taylor & Francis Group, London, ISBN 978-1-138-02843-2

Colloidal nanosilica application to improve the durability of damaged hardened concrete

M. Sánchez & M.C. Alonso
Institute of Construction Sciences "Eduardo Torroja" (IETcc—CSIC), Madrid, Spain

I. Díaz & R. González
Autonomous University of Nuevo León, Monterrey, Mexico

ABSTRACT: Nowadays, ageing of existing concrete structures exposed to highly aggressive environments is one the highest concerns for the construction industry. In this context, developing sustainable, efficient and secure technologies for the repair and maintenance of such structures rises as a challenge to assure their service life. In present paper, a non-invasive repair method, based on the application of colloidal nanosilica on the concrete surface, is proposed. Two mechanisms to force the nanosilica penetration have been considered: capillary suction and migration. The ability of colloidal nanosilica to consolidate the cementitious matrix has been confirmed; nanosilica promotes the decrease of capillary pores not only filling the pores but also interacting chemically with the substrate to form new gels, which seem to evolve with time in presence of the appropriate humidity conditions.

1 INTRODUCTION

Nowadays, one of the greatest challenges for construction industry is the need to deal with the high amount of aged concrete constructions presenting different type and level of damage. A huge investment is required in repairing activities to guarantee the performance of concrete infrastructures. In this sense, traditional repair methods, based on removing the damaged part of the structure and substituting by new materials are not only highly expensive but also, often risky for workers.

Looking for novel solutions, environmentally friendlier, non-invasive for the structures and non-risky for the workers should be a requirement for the construction industry. In last decades, advanced methodologies based on removing the aggressive instead of the polluted bulk of the concrete (carbonated or chloride contaminated concrete). These technologies, Electrochemical Chloride Extraction (ECE) and/or Electrochemical ReAlkalization (ERA), are based on applying an electrical field between the steel rebar, connected as cathode, and an external anode located on the concrete surface (Polder, 2003). Also the simultaneous penetration of corrosion inhibitors during these electrochemical treatments has been proposed to improve the efficiency of electrochemical repair technologies (Sánchez, 2011). Currently, other alternatives, based on incorporating electrically charged nanoparticles through concrete pores under the action of an electric field are being also assessed as further stage during electrochemical repair treatments.

The migration of silica nanoparticles covered with nanoalumina as further stage of a ECE treatment to seal the concrete surface protecting it against new penetration of aggressive has been also proposed (Cárdenas, 2006). The viability of the treatment was confirmed by detecting an increase on the steel rebar protection after this type of treatment through corrosion current measurements (Cárdenas, 2009).

Also the viability of promote the migration of colloidal nanosilica under the action of an electric field, showing a compatible interaction between the nanosilica and the cementitious substrate, has been confirmed (Sánchez-Moreno, 2013). A decrease of the total porosity, with a refinement of the capillary pores is observed with this type of treatment. The reactivity of the nanosilica is proposed by these authors (Sánchez, 2014) forming C-S-H gels with high silicon content. A maximum penetration depth of 2 mm was reached after the treatment of nanosilica migration.

In order to evaluate the influence of the transport mechanism on the efficiency of the treatment on densifying and protect the surface against a further aggressive penetration, two different treatments are proposed in the present study: migration under the action of the electric field (M) and capillary suction through a previously dried mortar surface (CS).

2 EXPERIMENTAL PROCEDURE

2.1 *Materials and samples*

Mortar OPC samples were fabricated for the study of repair treatments with colloidal nanosilica. Siliceous sand with a chemical composition of 98% SiO_2 was used in the fabrication of the mortar. Deionised water was employed in order to avoid the intrusion of other ions in the mix that could interfere with the posterior analysis. A cement/sand ratio of 1/3 and a water/cement ratio of 0.5 were used for the mortar fabrication. Similar mortar samples but substituting the siliceous sand for a calcareous sand with similar size distribution were selected for studying the chemical interaction between the penetrated nanosilica and the cementitious matrix without interference of the siliceous aggregate in the chemical analysis.

Cylindrical samples of 7.5 in diameter and 15 cm were prepared. The samples were cured for 7 days within a humid chamber under controlled conditions (98 ± 2% relative humidity and 21 ± 2 ºC). After curing, the cylindrical samples were cut in thinner slices, 5 cm thick, which were submitted to the nanosilica penetration treatments.

A commercial solution of colloidal nanosilica, Bindzil 301, was used for the superficial treatments on the hardened mortar surface. As indicated by the product data-sheet (Bindzil 301 data sheet), the amorphous silica nanoparticles are discrete, spherical and monodispersed. A slight superficial negative charge is promoted by modifying the nanoparticles with a reactive epoxy silane. A diluted solution of with 15% nanosilica was prepared for the superficial treatments.

2.2 *Treatment methodologies*

Two different methods have been assessed to promote the transport of the colloidal nanosilica through the concrete pores: Migration (M) and Capillary Suction (CS). Before the treatment with nanosilica, the hardened mortar samples were preconditioned, as described below for both methodologies considered.

2.2.1 *Migration treatment*

Before migration treatment, mortar samples were saturated in water under vacuum conditions in order to assure the transport of silica nanoparticles by migration under the applied electric field.

During testing, an external anode and cathode were located on both surfaces of the mortar slice, as shown in scheme included in Figure 1. Stainless steel meshes were used as electrodes. A tank with the colloidal nanosilica solution was located on the mortar surface in contact with the cathode, in order to promote the migration of the negatively charged particles towards the opposite side of the mortar sample, connected as anode, were a tank with distilled water were located to assure the electrical contact in the system. A voltage of 12 V was applied between both electrodes and maintained for 3 days.

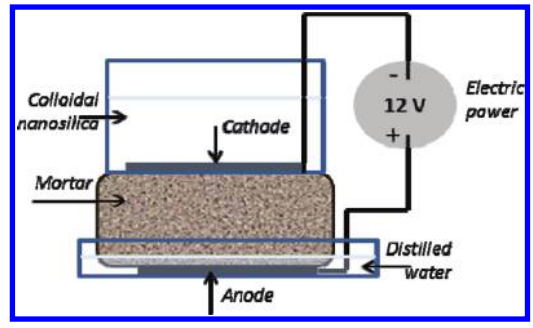

Figure 1. Arrangement scheme for migration treatment.

After finishing the treatment, the handled samples were cured in an environment with high humidity, stored in a closed box with water in the bottom, in order to allow the nanosilica reacting with the cementitious substrate, forming the new phases that fill the pores and consolidate the solid matrix.

2.2.2 *Capillary suction treatment*

Before capillary suction of colloidal nanosilica diluted solution, mortar samples were dried at controlled conditions (25°C, 30% RH) until constant weight in order to favor the transport by suction of the nanosilica solution.

The arrangement was similar than in the case of migration but without the connection of the electric field. In this case, also two electrodes were located at both sides of the mortar slice, in order to take periodical measurements of the resistivity across the sample, as defined in next section.

The treatment with colloidal nanosilica penetrating by capillary suction was carried out in 5 cycles defined by 2 days of nanosilica penetration (tank filled with the solution) and 5 days of drying at the laboratory atmosphere (tank empty).

2.3 *Sealing efficiency characterization*

2.3.1 *Indirect sealing parameters*

Resistivity measurements were carried out following the arrangement defined in the Spanish standard for direct measurements (UNE 83988-1:2008). An a/c current was applied between the electrodes located at both sides of the samples (32 mV_{rms} at 1 kHz) to obtain the ohmic resistance (R_{ohm}) value. Each value was obtained as the mean value of 5 measurements.

The resistivity (ρ) is estimated multiplying the cell constant (k), as defined in equation (1):

$$\rho = k \cdot R_{ohm}$$
$$k = \frac{S}{L} \quad (1)$$

where S is the area of the sample in contact with the electrodes and L is the thickness of the mortar slice.

After the migration treatment, the resistivity of the mortar samples was monitored during the 28 days of storage under high humid conditions. In the case of capillary suction treatment, resistivity measurements were carried out during the 28 days of treatment; the measurements were obtained in high humid conditions, just before empty the tank for starting each drying stage.

2.3.2 *Direct sealing parameters*

After the migration treatment, the effective chloride diffusion coefficient was determined at the age of 28 days after finishing the treatment, using an accelerated test defined in the Spanish standard (UNE 83987:2009). The effective chloride diffusion coefficient was estimated under stationary conditions, forcing the migration of chloride through the pores of the treated mortar under the action of an external electric field (12 V). Similar arrangement than the described in (Andrade, 1993) was used for characterizing the chloride transport. The treated mortar was located in a migration cell with two external electrodes located at both sides of the sample. A 1 M chloride diffusion filled the tank with the cathode (catholyte) and distilled water the tank with the anode (anolyte). The chloride migration was forced from the catholyte to the anolyte by applying a constant voltage of 12 V. The conductivity of the anolyte was periodically measured until reaching almost constant values. The chloride concentration was estimated from equation (2):

$$Cl^- = 10^{-3} \cdot (-1.71 + (11.45 \cdot C_{25})) \cdot V_a \quad (2)$$

where Cl^- = chloride amount in the anolyte (in mol); C_{25} = conductivity of anolyte at 25°C (in mS/cm); and V_a = anolyte volume (in l).

The effective chloride diffusion coefficient at steady state conditions (D_{eff}) can be obtained from the modified Nernst-Planck equation (3):

$$D_{eff} = \frac{A \cdot R \cdot T \cdot l}{z \cdot S \cdot F \cdot Cl^- \cdot \gamma \cdot \Delta\phi_{ss}} \quad (3)$$

where A = slope in the lineal region $Cl^-(t)$ response (mol/s); R = 1.9872 cal/mol · K; T = mean temperature in anolyte during the test (K); l = thickness of the mortar sample (cm); z = 1; S = area of the sample exposed to the chloride solution (cm^2); F = 23,060 cal/V_{eq}; Cl^- = initial concentration of chloride in catolyte (mol/cm^3); γ = 0.657; $\Delta\phi_{ss}$ = weighted mean value of the effective voltage between both sides of the sample during the treatment, obtained in the stationary period (V), that is, during the period of Cl^- vs t linear response.

After the capillary suction treatment with colloidal nanosilica, the coefficient of water absorption (K) and the mortar effective porosity (ε_e) were estimated following the procedure described in the Spanish standard for determining the absorption of water by capillarity (UNE 83982:2008). This test was carried at the end of the treatment (30 days total length).

Previously to the water absorption test, the lateral surface of the samples was painted to avoid penetration of water through the lateral areas and the treated samples were pre-conditioned under controlled conditions (20 ± 2°C, 65% RH) until reaching constant weight. Then, the treated surface was on a recipient with a thin layer of water (about 5 mm) and the sample was periodically weight until 72 hours of testing.

Two stages can be distinguished when representing the mass-profit (Q) versus $t^{0.5}$: a lineal behavior during the early hours, corresponding to the water absorption through the capillary pores (stage 1), and an almost constant response due to the filling air pores by diffusion (stage 2).

The water capillary absorption coefficient (K) can be estimated from equation (4):

$$K = \frac{(Q_n - Q_0)}{10 \cdot A \cdot \sqrt{t_n}} \quad (4)$$

where Q_n = weight of the sample at saturation, i.e., at the end of the stage 1 (g); Q_0 = weight of the sample before starting test (g); A = section of the sample (cm^2); t_n = time (min) needed to reach saturation, i.e., time at the end of stage 1.

2.4 *Nanosilica/cementitious matrix interaction*

The reactivity of the nanosilica with the cementious matrix was evaluated by characterizing the chemical composition of treated mortars after 7 and 28 days of finished the migration treatment by BSE/EDX with a JEOL JSM-6360 LV. The C/S of C-S-H gels was estimated as a qualitative indicator of this chemical interaction.

This analysis was carried out on mortar samples fabricated with calcareous sand to avoid the interference of siliceous sand on the chemical analysis of the hydrated phases in the cementitious solid matrix.

3 RESULTS AND DISCUSSION

3.1 *Efficiency of colloidal nanosilica migration treatment*

3.1.1 *Evolution of indirect sealing parameters*

In Figure 2 the evolution of the resistivity during the post-treatment period, from the finishing of the migration treatment until 28 days of curing under high humidity conditions, has been represented. Two samples are represented in order to evaluate the measurement repeatability. A good correlation between both samples can be observed from Figure 2.

The electrical resistivity (ρ) is an indirect measurement of the pore connectivity in the cementitious matrix of concrete. After the nanosilica migration treatment, a significant increase of the resistivity is registered with the time of curing in high-humid conditions. An evolution of the interaction between the penetrated nanosilica and the cementitious matrix, forming new products that consolidate the substrate, could justify this increase. After 7 days of post-treatment curing, the resistivity of the mortar sample treated with colloidal nanosilica tends to stabilize, maintaining a non-significant variation until 28 days of post-treatment curing. It seems that the most relevant part of the interaction between the nanosilica and the treated substrate takes place during the first 7 days of post-treatment curing under high humidity conditions.

3.1.2 *Direct sealing parameters: Chloride transport resistance*

The efficiency of the migration treatment in protecting the mortar samples against the further penetration of chloride was analyzed and the value of the effective chloride diffusion coefficient was estimated at the age of 28 days after finishing the treatment.

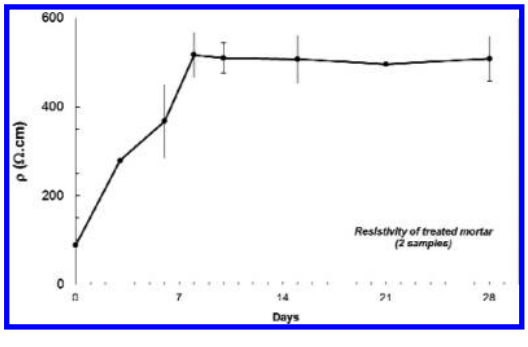

Figure 2. Resistivity evolution of treated mortar samples during the period of curing after the migration treatment finished.

In Figure 3 the evolution of chloride in the anolyte during the accelerated migration test for estimating the effective chloride diffusion coefficient (D_{eff}) applying equations (2) and (3) is included. A non-treated mortar sample, stored under the same humid conditions than the treated ones has been included as the reference case.

The estimated values for D_{eff} are included in Table 1 for both treated and reference mortar samples. The decrease of D_{eff} in treated mortar samples at the age of 28 days after finishing the treatment with colloidal nanosilica migration confirms the effectiveness of the treatment in hindering a further penetration of aggressive. A significant reduction in D_{eff} has been registered in both treated samples (>65%).

3.2 *Efficiency of colloidal nanosilica capillary suction treatment*

3.2.1 *Resistivity measurements*

In Figure 4 the evolution of the resistivity during the treatment of colloidal nanosilica penetration by capillary suction mechanism has been represented. The resistivity measurements were taken during the treatment, at the end of each stage of product application, that is, just before removing the

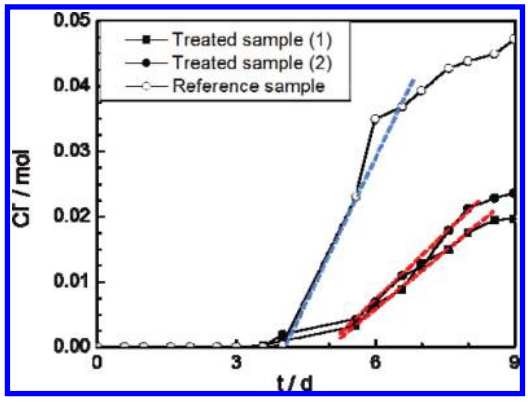

Figure 3. Evolution of chloride in the anolyte during chloride migration test. Colored lines: stationary-state period.

Table 1. Effective chloride diffusion coefficient in treated samples after the colloidal nanosilica migration treatment.

	D_{eff} (10^{-8} cm²/s)	% decrease
Treated sample 1	1.33	76
Treated sample 2	1.99	65
Reference sample	5.62	

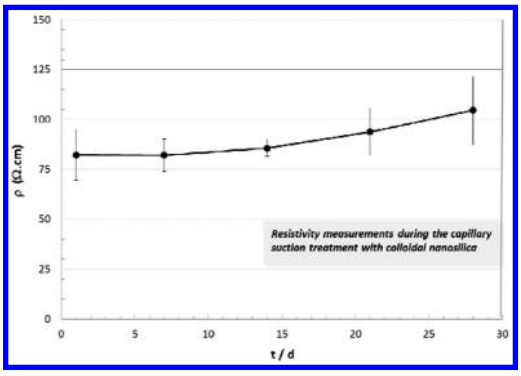

Figure 4. Resistivity evolution of treated mortar samples during the cycles of capillary suction treatment for nanosilica penetration.

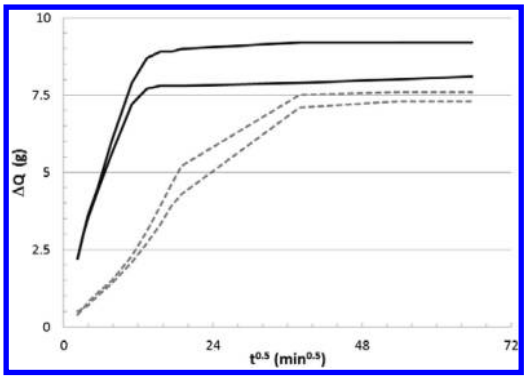

Figure 5. Increase of mass during test for characterizing the capillary water absorption coefficient after the nanosilica penetration by capillary suction.

solution for starting the dry step of each cycle. Three samples were considered in order to evaluate the repeatability of the measurements and the mean value is included in Figure 4.

A gradual increase of resistivity is registered during the capillary suction treatment for nanosilica transport, mainly after the 3rd cycle of the treatment (15 days).

3.2.2 *Water absorption measurements*

In Figure 5 the increase of mass (ΔQ) the two tested samples after the capillary suction treatment with nanosilica penetration has been represented. Two non-treated mortar samples at the same age were also tested as reference cases.

The two typical stages of this type of testing can be distinguished:

– Stage 1: water absorption through the capillary pores. Corresponds to the linear region of the graph, until the stabilization of the mass increment.
– Stage 2: almost constant response due to the filling air pores by diffusion.

Longer periods for the stage 1 are registered for the treated mortar samples indicating a slower water absorption by capillarity. Also lower increase of mass are measured for the treated samples, confirming the higher resistance against the water penetration from the treated surface.

In Table 2 the values estimated for the coefficient of water absorption (K) are resumed for both treated and reference cases. A significant decrease on this coefficient is obtained for mortar samples after the treatment with penetration of colloidal nanosilica by capillary suction.

Table 2. Coefficient of water absorption (K) and mortar effective porosity (ε_e) after capillary suction.

	K (kg/m^2 min$^{0.5}$)
Treated sample 1	$6 \cdot 10^{-4}$
Treated sample 2	$5 \cdot 10^{-4}$
Reference sample	$2 \cdot 10^{-3}$
Reference sample	$2 \cdot 10^{-3}$

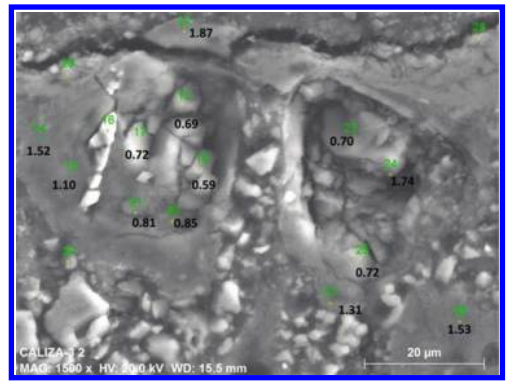

Figure 6. Micrograph of the nanosilica/solid phases interaction at the age of 28 days after finishing the migration treatment. Depth: 100 µm from treated surface.

3.3 *Colloidal nanosilica/cementitious matrix interaction*

3.3.1 *After migration treatment*

In Figure 6 one micrograph of the interaction between the penetrated nanosilica and the cementitious solid matrix of calcareous mortar, at the age of 28 days after finishing the treatment, is included. The micrograph shows a region near to the treated

surface (about 100 µm depth). The black numbers indicate the C/S ratio analyzed by EDS.

The presence of C-S-H gels enriched in silicon is observed, as previously stated in (Sánchez, 2014). A nucleus with lower C/S ratio (0.6–0.7) appears surrounded by C-S-H with higher C/S ratio (0.80–1.10). The typical values traditionally observed in a conventional C-S-H gel (1.5–1.8) are observed out the nucleus silicon-enriched.

Thus, the incorporation of the nanosilica to the cementitious matrix can be expected to occur by chemical reaction with the calcium compounds of substrate, giving the formation of new solid phases that evolve with the hydration during the curing period of treated samples in high humid conditions.

3.3.2 *After capillary suction treatment*

In Figure 7 one micrograph of the interaction between the penetrated nanosilica and the cementitious solid matrix of calcareous mortar, after the treatment with penetration of colloidal nanosilica by capillary suction, is included.

The micrograph shows a region near to the treated surface (about 100 µm depth). The black numbers indicate the C/S ratio analyzed by EDS.

In this case the presence of a nucleus enriched in silicon compounds is also observed; the C/S ratio in this region presents lower values (0.07–0.60) when comparing with the mortar after nanosilica migration treatment (Fig. 6). Furthermore, in the case of nanosilica penetration by capillary suction, the increasing gradient of C/S ratio is not clear, and the presence of "conventional" C-S-H gels around the nucleus with enriched silicon composition is not identified.

The hypothesis of an earlier stage of hydration of the new C-S-H gels incorporating the penetrated nanosilica might justify these observations. The colloidal nanosilica would penetrate through the mortar pores but the long periods of dried conditions would hinder the reactivity of nanosilica with the calcium compounds of the substrate, and thus, the evolution of the new products should be slower than in the case of nanosilica migration test.

Nevertheless, further studies focused on evaluate the evolution of C-S-H gels after the different treatments, considering several ages of post-curing both in high and low humidity conditions are being carrying out in order to go in depth in the definition of the action mechanisms of colloidal nanosilica when enters in contact with a hardened cementitious matrix.

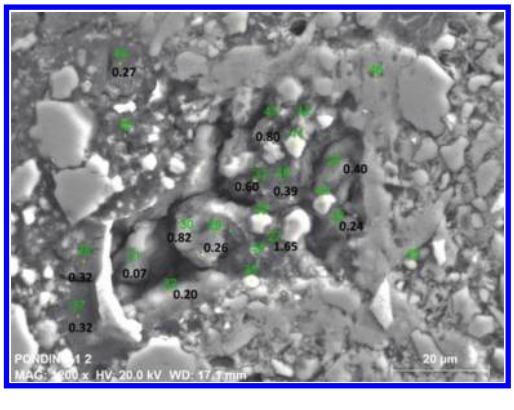

Figure 7. Micrograph of the nanosilica/solid phases interaction at the age of 28 days after finishing the capillary suction treatment. Depth: 100 µm from treated surface.

4 CONCLUSIONS

- Two different treatments are successfully proposed to promote the transport of colloidal nanosilica from the surface of mortar samples: electrical migration and capillary suction.
- In both applied treatments, an increase of resistivity has been observed after the nanosilica penetration, as an indirect indicator of the cementitious matrix consolidation after the treatments.
- The treatments of nanosilica penetration have shown to be effective in hindering the further entrance of chloride and water.
- The presence of humidity seems to be a critical factor controlling the chemical interaction between the nanosilica and the hardened cementitious matrix.

ACKNOWLEDGEMENTS

Authors acknowledge ZEUS QUÍMICA S.A. the material supply. M. Sánchez also acknowledges the Spanish Ministry of Economy and Competitiveness (MINECO) her "Juan de la Cierva" postdoctoral position (JCI-2011-09572).

REFERENCES

Andrade, C. 1993. Calculation of chloride diffusion coefficients in concrete from ionic migration measurements. *Cement and Concrete Research* 23: 724–742.

BINDZIL 301 Datasheet: http://www.dbbecker.com/images/stories/MarketingFolder_BrianMorris/DBB_Technical_DataSheets/EKA_NOBEL/PDS_BCC301.pdf.

Cardenas, H. & Struble, L. 2006. Electrokinetic nanoparticle treatment of hardened cement paste for reduction of permeability. *J. Materials in Civil Engineering* 18: 554–60.

Kupwade-Patil, K., Gordon, K., Xu, K., Moral, O. & Cardenas, H. 2009. Electrokinetic nanoparticle treatment of hardened cement paste for reduction of permeability. In Limbachiva & Kew (eds). *Excellence in Concrete Construction through Innovation*: 365–371. London: Taylor & Francis.

Polder, R. 2003. Electrochemical maintenance methods. In Cigna, R., Andrade, C., Nürnberger, U., Polder, R., Weydert, R., Seitz, E. (eds), *Corrosion of steel in reinforced concrete structures, final report*: 115–145. Brussels: European Commission.

Sánchez, M. & Alonso, M.C. 2011. Electrochemical chloride removal in reinforced concrete structures. Improvement of effectiveness by simultaneous migration of calcium nitrite. *Construction and Building Materials* 25: 873–878.

Sánchez, M., Alonso, M.C. & González, R. 2014. Preliminary attempt of hardened mortar sealing by colloidal nanosilica. Construction and Building Materials 66: 306–312.

Sánchez-Moreno, M. Alonso M.C., Díaz, I. & González, R. 2013. Improvement of hardened concrete durability by nanosilica electromigration. In De Belie, Van der Zwaag, Gruyaert, Van Tittelboom & Debbaut (eds), *Proc. 4th International Conference on Self-Healing Materials ICSHM 2013*: 70–74. Ghent: Magnel Laboratory for Concrete Research.

UNE 83982. 2008. Concrete durability. Test methods. Determination of the capillary suction in hardened concrete. Fagerlund method.

UNE 83987:2009. Concrete durability. Test methods. Measurement of chloride diffusion coefficient in hardened concrete. Multiregime method.

UNE 83988-1. 2008. Concrete durability. Test methods. Determination of the electrical resistivity. Part 1: Direct test (reference method).

Concrete Repair, Rehabilitation and Retrofitting IV – Dehn et al. (Eds)

Combined influence of slag composition and temperature on the performance of slag blends

O.R. Ogirigbo & L. Black
Institute of Resilient Infrastructure, University of Leeds, West Yorkshire, UK

ABSTRACT: This study has investigated the influence of GGBS chemical composition on the strength and transport properties of slag blends under different temperature conditions. Two slags having Ca/Si ratios of 1.05 and 0.94 respectively were used to partially replace a CEM I 52.5R at 30%. Various tests including compressive strength, sorptivity, chloride ingress and chloride binding were carried out on mortar and paste specimens to measure the performance of the slag blends against a CEM I 42.5R at 20 and 38°C. The mortar specimens were cured for 28 days before exposure to a 3% sodium chloride solution. The results obtained showed that temperature had more influence on the performance of the slag blends than the variation in chemical composition. The slag with the higher Ca/Si ratio had better chloride binding and chloride resistance, and this was attributed to its higher alumina content.

1 INTRODUCTION

Concrete is the most widely used construction material in the world with consumption rates up to 11 billion metric tonnes every year. This is as a result of its ability to resist penetration of water when used in marine environments, good fire resistance properties, versatility in forming various shapes, abundance of raw materials and low manufacturing and maintenance costs (Mehta and Monteiro, 2006). One consequence of concrete's popularity is that it is responsible for about 5–7% to total global CO_2 emissions (Bye, 2011).

Over recent decades, it has become common practice to use Secondary Cementitious Materials (SCM) such as GGBS, fly ash, silica fume, to partially replace Portland cement in the making of concrete. When they are used as additives, these SCMs have been shown to improve certain properties of concrete such as workability, durability and long—term strength.

As the drive to reduce global CO_2 emissions continues, there would be much more demand for these SCMs. However, slag composition may vary from site to site, and so variability in chemical composition is worthy of attention.

There are standards which regulate the use of these SCMs. For example, BS EN 197-1:2011 stipulates that for GGBS the $(CaO + MgO)/SiO_2$ ratio by mass must exceed 1 (EN197-1:2011). However, work done by several authors has shown that these oxide (basicity) ratios may not be an accurate predictor of slag reactivity and performance. A study by (Mantel, 1994) investigating the hydraulic activity of five different slags concluded that there was no clear correlation between the basicity ratios and the properties of the slags.

This work focuses on the impact a change in chemical composition of GGBS may have on its performance in different temperature conditions.

2 EXPERIMENTAL PROGRAMME

2.1 *Materials*

Two CEM I cements (CEM I 42.5R and CEM I 52.5R) designated as C42.5R and C52.5R were used for the study. Two slags (S1 & S2) having similar physical properties but different chemical compositions were used for the study. Both were combined with the C52.5R at 30% replacement level. The performance of the slag blends were measured against the C42.5R. The chemical composition of the slags and cements, as determined by XRF and some physical data are shown in Table 1.

2.2 *Details of mixes and curing conditions*

A mixture of mortar and paste samples was used throughout this study. Compressive strength, sorptivity and chloride penetration depth were determined on mortar samples, while bound chloride content was determined from paste samples. For all the tests, samples were prepared using a water:binder (w/b) ratio of 0.5. All samples were cured at temperatures of 20 and 38°C and at a relative humidity of 99%.

Table 1. Properties of cementitious materials.

Property	Unit	C42.5R	C52.5R	S1	S2
LOI 950°C	%	2.20	2.54	(+1.66)	(+0.40)*
SiO_2	%	19.71	19.10	36.58	40.14
Al_2O_3	%	5.08	5.35	12.23	7.77
MnO	%	0.03	0.03	0.64	0.64
Fe_2O_3	%	2.97	2.95	0.48	0.78
CaO	%	63.16	62.38	38.24	37.90
MgO	%	2.19	2.37	8.55	9.51
SO_3	%	2.97	3.34	1.00	1.47
Glass	%	na	na	99.3	97.1
Blaine	cm^2/g	3510	5710	4490	4090
Density	g/cm^3	3.23	3.18	2.94	2.95

*The sample was oxidized with HNO_3 before the determination of LOI.

3 TEST METHODS

Unconfined Compressive Strength (UCS) tests were conducted in accordance with (EN196-1:2005). $40 \times 40 \times 160$ mm mortar prisms were cast and split in the middle after a period of 24 hours to produce $40 \times 40 \times 80$ mm samples for testing. Mortar samples were cured at 20 and 38°C so as to investigate the influence of temperature on the strength performance of the slag blends.

Sorptivity was determined using similar methods to those used by (Güneyesi and Gesoğlu, 2008). 50 mm mortar cubes were cured for 28 days at 20°C and 38°C, and dried to constant mass in an oven at 50°C. The sides of the samples were coated with paraffin and placed in a trough of water, with the water level kept at about 5 mm from the base of the samples. The mass of the specimens were recorded at predetermined times (1, 4, 9, 16, 25, 36, 49 and 64 mins). At each of these times, the mass of water absorbed by each specimen was obtained, and from this the sorptivity coefficient (k) was calculated using the following expression:

$$k = \frac{Q}{A\sqrt{t}} \quad (1)$$

where:
Q amount of water absorbed in cm^3
t time in seconds
A cross-sectional area of the specimen that was in contact with the water in cm^2
k sorptivity coefficient in $cm/s^{1/2}$.

The depth of chloride ion penetration was measured by exposing 50 mm mortar cubes to a 3% sodium chloride solution after they had been initially cured for 28 days. The samples were withdrawn periodically, at 14, 28, 56 and 90 days, to determine the depths of chloride ion penetration. The withdrawn samples were split in half and the surfaces of the freshly split samples were sprayed with a 0.1M silver nitrate ($AgNO_3$) solution. The presence of free chlorides was indicated by the formation of a white precipitate of silver chloride (AgCl), while in the absence of free chlorides the reaction between silver nitrate and portlandite resulted in a brown coloration, due to the formation of silver hydroxide. Thus, by linear measurements from the edge of the specimen up to the colour change boundary, the depth of free chloride penetration could be determined.

Bound chloride content was measured using the method developed by (Luping and Nilsson, 1993). Paste samples were prepared and cured in sealed plastic moulds for a period of 8 weeks. The central portions of the cured samples were wet-crushed and water-sieved to particles ranging in size from 0.25 to 2.0 mm. The particulate samples were vacuum dried in a desiccator at room temperature to remove most of the water, then stored in a desiccator with decarbonized air at 11% RH kept by saturated LiCl solution for 14 days. About 20 g of the particulate sample dried at 11% RH was put in a plastic cup and filled with approximately 50 ml of a given concentration of NaCl solution saturated with $Ca(OH)_2$. The cup was sealed and stored at temperatures of 20 and 38°C for a period of 6 weeks to attain equilibrium. After equilibrium was reached, the chloride concentration of the resulting solution was determined. Knowing the initial concentration of the NaCl solution, the content of bound chlorides was determined using the expression:

$$C_b = \frac{35.45V\left(C_i - C_f\right)}{W} \quad (2)$$

where:
C_b bound chloride content in mg/g-sample
V volume of solution in ml
C_i initial concentration of the chloride solution in mol/l
C_f equilibrium concentration of the chloride solution in mol/l
W weight of the dry sample in g, which is calculated from the difference in weight of the sample dried in a desiccator at 11% RH and in an oven at 105°C.

4 RESULTS AND DISCUSSION

4.1 *Compressive strength*

The compressive strength results obtained at 20 and 38°C for all mixes is shown in Figure 1. At 20°C, the C42.5R mix had higher early strength

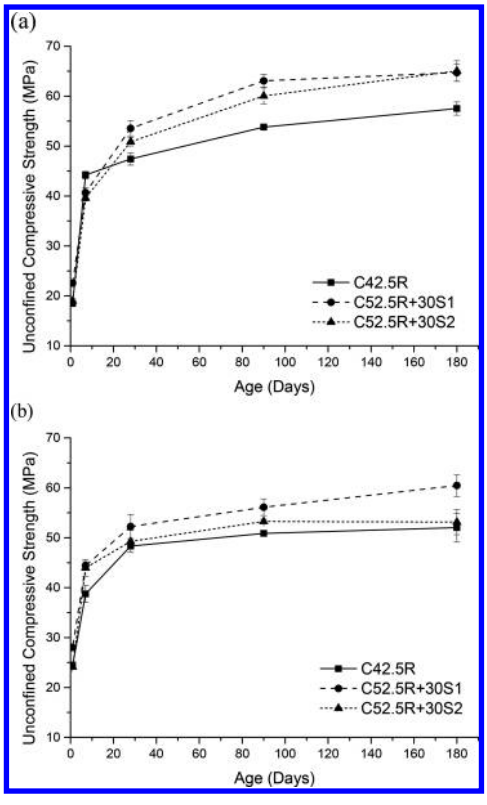

Figure 1. Compressive strength development at (a) 20°C and (b) 38°C.

gain up to 7 days but this trend reversed at 28 days and beyond with the slag blends having higher strengths. Slag 1 had a higher basicity ratio than slag 2 and was expected to perform better but the difference in their strength performance was minimal especially at later ages. This is in agreement with results obtained by (Mantel, 1994).

The high temperature curing at 38°C as shown in Figure 1b increased the early strength of the samples up to 7 days but there was minimal strength gain beyond 28 days as compared to 20°C. This shows the deleterious impact of high temperature curing on the later-age strength development as observed previously (Barnett et al., 2006, Brooks and Al-kaisi, 1990). The slag blends showed better strength performance than the C42.5R at all ages. Also, at 38°C there was a clear distinction in the strength performance of the slag blends with slag 1, the more basic of the 2 slags, performing better than slag 2 at all ages.

4.2 *Sorptivity*

The 28-day sorptivity data are shown in Table 2. Increasing the curing temperature from 20°C to 38°C resulted in an increase in sorptivity of the C42.5R sample by about 140%, compared with an increase of about 90% for the slag blends.

Table 2. Effect of curing temperature on sorptivity.

	Sorptivity, k (cm/s$^{1/2}$) × 10^{-3}	
	20°C	38°C
C42.5R	4.12 ± 0.08	9.94 ± 0.07
C52.5R + 30S1	2.08 ± 0.05	3.96 ± 0.07
C52.5R + 30S2	3.32 ± 0.09	6.36 ± 0.04

High temperature curing results in a high initial rate of hydration, retarding subsequent hydration. This produces a non-uniform distribution of hydration products compared with the case of a lower curing temperature (Brooks and Al-kaisi, 1990). This explains the increase in sorptivity at the higher curing temperature of 38°C.

At 20°C, the sorptivity of the slag 2 blend was 60% higher than that of the slag 1 blend suggesting that the slag 1 blend has a finer microstructure and is more resistant to the penetration of water. While the curing at 38°C increased the sorptivity of the slag blends by about 90%, the difference between the sorptivity of the slag 2 blend compared to that of the slag 1 blend was relatively the same as at 20°C.

4.3 *Depth of chloride penetration*

The depth of chloride ion penetration measured for samples which had been cured for 28 days before exposure to 3% sodium chloride solution is shown in Figure 2.

From both plots, it can be seen that the slag blends performed better at resisting chloride ingress than the C42.5R mix. As was observed in the results obtained from the sorptivity test, there was a negative impact of high temperature curing on the resistance to chloride ingress. Increasing the temperature from 20°C to 38°C resulted in an increase of about 45% in the chloride ion penetration depth of the C42.5R mix after 90 days of exposure. For the slag 1 and slag 2 blend, the increase was 30% and 50% respectively. This is in line with results obtained previously (Detwiler et al., 1991, Al-Khaja, 1997).

As the duration of exposure increased, the depth of chloride ion penetration also increased. However, the increase was more pronounced at 38°C. At 20°C, the difference between the average chloride penetration depth after 28 and 90 day exposure was 3 mm for the C42.5R mix, and about 1 mm for the slag blends. However, at 38°C the difference was about 8 mm for the C42.5R mix, 2 mm and 4 mm for slag 1 and slag 2 blends respectively.

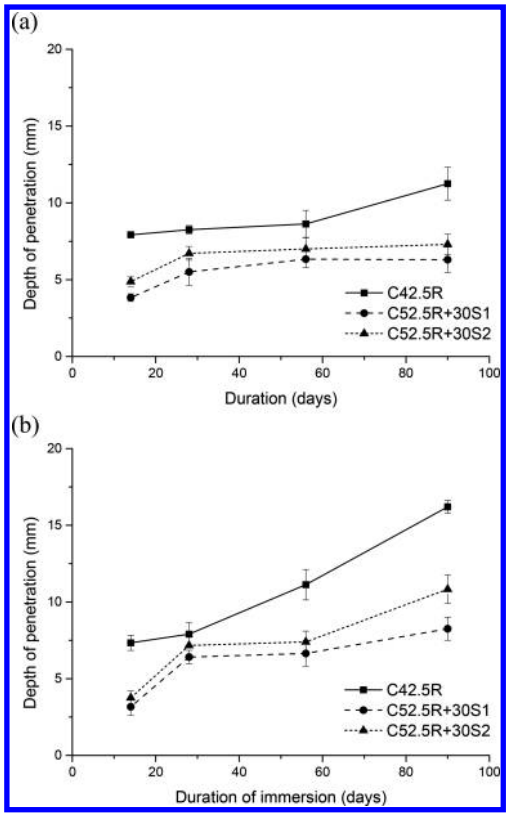

Figure 2. Depth of chloride ion penetration at (a) 20°C and (b) 38°C.

4.4 *Chloride binding capacity*

The bound chloride content obtained for samples exposed to 6 different concentrations of sodium chloride solution (0.1, 0.3, 0.5, 1.0, 2.0 and 3.0 M) at 20°C is shown in Figure 3. The chloride binding capacity of the mixes was obtained using Freundlich's binding isotherm (shown in Equation 3), as this gave the best fit to the data.

$$C_b = \alpha C_f^{\beta} \tag{3}$$

The chloride binding coefficients α and β obtained for the mixes is shown in Table 3.

From Figure 3, the bound chloride content increased as the concentration of the sodium chloride solution increased. The slag blends had higher chloride binding capacities than the C42.5R mix. This explains the lower chloride penetration values obtained for the slag blends as compared with the C42.5R mix.

The chloride binding capacity of the slag 1 blend was slightly higher than that of the slag 2 blend,

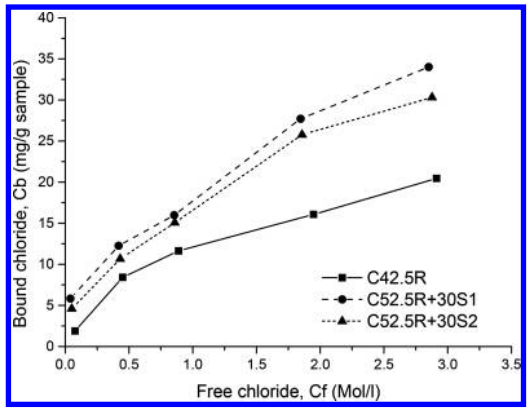

Figure 3. Chloride binding relationship for all mixes at 20°C.

Table 3. Chloride binding coefficients at 20°C.

Mix	α	β	Adj. R^2
C42.5R	11.74	0.52	0.965
C52.5R + 30S1	19.47	0.53	0.976
C52.5R + 30S2	17.48	0.54	0.986

and was in agreement with the results obtained for the depth of chloride penetration. The higher chloride binding capacity of slag 1 blend could be attributed to its higher alumina content, as had previously been observed (Thomas et al., 2012).

The effect of temperature on chloride binding was also investigated. Figure 4 shows the bound chloride content for the mixes at 38°C while Table 4 shows the corresponding chloride binding coefficients.

Evaporation occurred at rates ranging from 6–8% at 38°C and this was corrected for using the method adopted by (Zibara, 2001) as shown in Equations (4–6). The correction is based on two assumptions:

- The ratio of the initial and equilibrium volume of the chloride solutions is equal to the ratio of the initial and equilibrium weight of the chloride solutions
- The evaporation does not affect the equilibrium between the bound and free chlorides

$$\frac{V_i}{V_{ee}} = \frac{W_i}{W_{ee}} \tag{4}$$

$$C_e \times V_i = C_{ee} \times V_{ee} \tag{5}$$

$$C_e = C_{ee} \times \frac{V_{ee}}{V_i} = C_{ee} \times \frac{W_{ee}}{W_i} \tag{6}$$

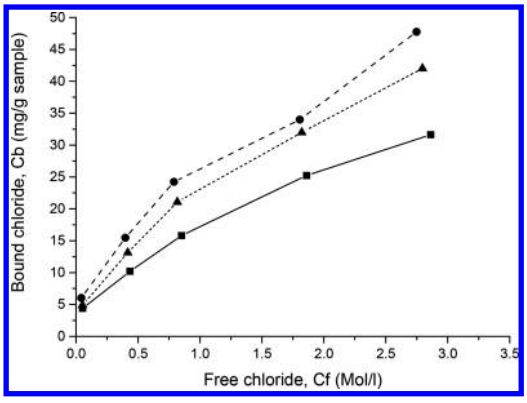

Figure 4. Chloride binding relationship for all mixes at 38°C.

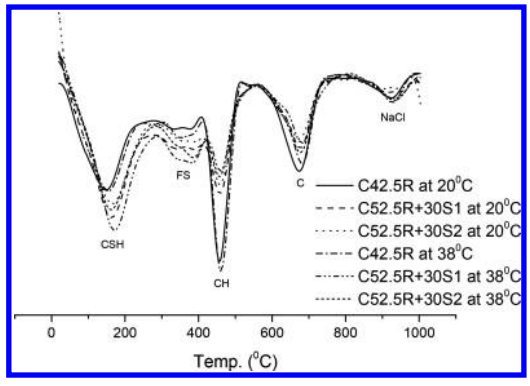

Figure 5. DTG plots showing peaks of Freidel Salt (FS) for all mixes at 20 and 38°C.

Table 4. Chloride binding coefficients at 38°C.

Mix	α	β	Adj. R^2
C42.5R	17.49	0.56	0.995
C52.5R + 30S1	26.46	0.55	0.984
C52.5R + 30S2	23.00	0.58	0.997

Increasing the temperature from 20°C to 38°C increased the bound chloride content for all the mixes. There was an increase of about 49% in the chloride binding coefficient (α) of the C42.5R mix as against 36% and 32% for slag 1 and slag 2. One would expect this to reflect in the chloride ingress resistance, but the results shown in Figure 2 showed that increasing the temperature from 20°C to 38°C increased the depth of chloride ion penetration.

DTG plots obtained from thermal analysis carried out on the test samples at the end of the exposure period are shown in Figure 5. The plots show increased peak due to Friedel Salt (FS) for the samples that were exposed at 38°C, which agrees with the results of the chloride binding experiment.

This is in agreements with results obtained previously (Panesar and Chidiac, 2011). In a study by (Loser et al., 2010) on the chloride resistance of concrete and its binding capacity, they pointed out that chloride binding is related to the degree of hydration of the cement and of the mineral admixtures. The higher chloride binding capacity observed at the higher temperature of 38°C can be attributed to the effect of temperature on the degree of hydration. The higher temperature of 38°C may lead to a higher degree of hydration as shown in the compressive strength results, hence greater chloride binding. The higher temperature of 38°C may also result in a coarser and a more open microstructure, hence the greater depths of chloride ion penetration and water sorptivity.

Chloride binding capacity may not be a good indicator of performance relating to resistance to chloride ingress as shown by the results obtained from this study. However, there was a strong correlation between the results obtained for sorptivity and depth of chloride ion penetration.

5 CONCLUSIONS

From the results obtained from the study, the following conclusions are drawn:

- High temperature curing enhances the early strength development of slag blends but not the later strength.
- The strength and transport properties of slag blends are better than that of neat systems especially at high temperature conditions.
- High temperature curing increases the rate of chloride ingress. However, this has a greater effect on slags of lower reactivity.
- The alumina content of slags tends to enhance their chloride binding and their ability to resist chloride ingress, but not necessarily their strength.
- High temperature exposure can increase the chloride binding capacity but this does not necessarily mean that there would be an improved resistance to chloride ingress.

ACKNOWLEDGEMENT

The authors would like to acknowledge the Petroleum Technology Development Fund (PTDF) for providing the funds for this research.

REFERENCES

Al-khaja, W.A. 1997. Influence of temperature, cement type and level of concrete consolidation on chloride ingress in conventional and high-strength concretes. *Construction and Building Materials,* 11, 9–13.

Barnett, S.J., Soutsos, M.N., Millard, S.G. & Bungey, J.H. 2006. Strength development of mortars containing ground granulated blast-furnace slag: Effect of curing temperature and determination of apparent activation energies. *Cement and Concrete Research,* 36, 434–440.

Brooks, J.J. & Al-kaisi, A.F. 1990. Early strength development of Portland and slag cement concretes cured at elevated temperatures. *ACI Materials Journal,* 87, 503–507.

Bye, G.C. 2011. *Portland cement*, London, ICE publishing.

Detwiler, R.J., Kjellsen, K.O. & Gjørv, O.E. 1991. Resistance to chloride intrusion of concrete cured at different temperatures. *ACI Materials Journal,* 88, 19–24.

EN196-1:2005 Determination of strength. *Methods of testing cement.* Brussels: BSI.

EN197-1:2011 Composition, specifications and conformity criteria for common cements. Brussels: BSI.

Güneyesi, E. & Gesoğlu, M. 2008. A study on durability properties of high-performance concretes incorporating high replacement levels of slag. *Materials and Structures,* 41, 15.

Loser, R., Lothenbach, B., Leemann, A. & Tuchschmid, M. 2010. Chloride resistance of concrete and its binding capacity—Comparison between experimental results and thermodynamic modeling. *Cement and Concrete Composites,* 32, 34–42.

Luping, T. & Nilsson, L.-O. 1993. Chloride binding capacity and binding isotherms of OPC pastes and mortars. *Cement and Concrete Research,* 23, 247–253.

Mantel, D.G. 1994. Investigation into the hydraulic activity of five granulated blast furnace slags with eight different portland cements. *ACI Materials Journal,* 91, 471–477.

Mehta, P.K. & Monteiro, P. 2006. *Concrete: Microstructure, properties and materials,* New York, McGraw-Hill.

Panesar, D. & Chidiac, S. 2011. Effect of Cold Temperature on the Chloride-Binding Capacity of Cement. *Journal of Cold Regions Engineering,* 25, 133–144.

Thomas, M.D.A., Hooton, R.D., Scott, A. & Zibara, H. 2012. The effect of supplementary cementitious materials on chloride binding in hardened cement paste. *Cement and Concrete Research,* 42, 1–7.

Zibara, H. 2001. *Binding of external chlorides by cement pastes*. PhD, University of Toronto.

Concrete repair, rehabilitation and retrofitting

Concrete Repair, Rehabilitation and Retrofitting IV – Dehn et al. (Eds)
© 2016 Taylor & Francis Group, London, ISBN 978-1-138-02843-2

The construction of the bridge over the Vaal River in Warrenton—a case study

Tiago Massingue
The South African National Roads Agency Limited SOC (SANRAL), South Africa

ABSTRACT: The construction of the bridge over the Vaal River in Warrenton replaces an existing low level bridge that had been in operation for 83 years. From an economic perspective, the new bridge offers significant improvements in terms of living conditions to the people of Mahareng as during the rainy season they were deprived from crossing the Vaal River for approximately six weeks. Specific objectives outlined during the design stage, highlighted to the following improvements over the existing low level bridge:

- providing an extra lane capacity, improving traffic flow in both directions,
- providing new pedestrian footpaths and thus enhancing safety,
- providing safer road shoulders for bicycles crossing the bridge,
- improved discharge capacity during high floods of the Vaal River,
- reducing the risk of floods which have in the past affected the local community in Warrenton,
- improving the economic development for Warrenton,
- enhancing the overall traffic flow and safety on the N18 as a National Road.

The existing low level bridge was to be demolished in order to accommodate the new one. However the existing legislation in South Africa [Section 34 Act 25, 1999—South African Heritage Resources Agency] outlines that any structure that is in existence for over 60 years must be protected in terms of heritage requirements. Therefore, while the above objectives were still justified, Structural Retrofitting for altered service conditions was to be given to the old structure in order to preserve its historical significance. The Project has shown at the end that new and old can come together in a proactive bridge development interface. Critics argue that the old bridge has enhanced the significance of the new one. Additional benefits were gained by means of job creation, training programs and the SMME development in the area. This is a positive South African story about the development of bridge infrastructure projects as part of the South African National Roads Agency's mandate to promote and develop road network of the country.

1 INTRODUCTION

The South African National Roads Agency SOC Limited (SANRAL) is mandated to provide and manage a sustainable national road infrastructure, to minimize the cost of transport and to stimulate economic growth. These objectives may include, from time to time, the need to upgrade existing or build new structures, where necessary, to improve traffic flow and the safety of road users. It is within this context that SANRAL has identified the need to construct a new bridge on National Route 18 Section 1 (N18-1), in proximity and downstream of the existing single lane, low level bridge across the Vaal River at Warrenton in the Northern Cape Province.

The original bridge over the Vaal River in Warrenton opened for traffic on the 29 October 1931, was designed by the Office of the Chief Inspector of Roads at the Cape Provincial Administration and constructed by Mr. Marshall. This low level bridge has the following dimensions: 55 Spans of 16 m each and 2.5 m height.

To accommodate pedestrians on the single carriageway bridge of 3 m width, 1 m × 0.6 m precast concrete side sidewalks were provided and painted in yellow for aesthetics.

With some geometric constraints the low level bridge has been used for 83 years. The type of constraints during its existence included a limited bridge cross section allowing one direction of

traffic flow at a time and overtopping by floods as per the Table 1, below, and the associated repair costs immediately after floods passed through.

Table 1, shows that the highest discharge of 4194 cumecs after 1931 was recorded in 1988. The consequence of such flood and recently confirmed particularly with the 2010 recent floods, is that adjacent communities were not able to access the Municipality of Warrenton where there is a predominance of economic activities. This from the National Roads Agency perspective was an unattainable situation and needed to be permanently addressed.

From an economic perspective, the new bridge offers significant improvements in terms of living conditions to the people of Mahareng Municipality. Specific objectives were outlined during the design stage and are highlighted below:

- provide an extra lane to improve traffic flow in both directions,
- provide new pedestrian footpaths and thus enhance safety,
- provide safer road shoulders for bicycles to cross the bridge,
- improve discharge capacity during high floods of the Vaal River,
- reduce the risk of floods which have in the past affected the local community in Warrenton,
- improve the economic development of Warrenton,
- enhance the overall traffic flow and safety on the N18 as a National Road.

Site investigations revealed that the existing low level bridge had to be demolished in order to accommodate the new one. However, legislation in South Africa [Section 34 Act 25, 1999—South African Heritage Resources Agency] requires that any structure that has been in existence for over 60 years must be protected in terms of heritage requirements. Therefore, while the above objectives were justified, Structural Retrofitting for altered service conditions was to be given to the old structure in order to preserve its historical significance. The Project has shown at the end that new and old can come together in a proactive bridge development interface.

Table 1. Record of worst flood over 83 years of the low level bridge performance.

Number	Year	Discharge (m^3/s)
1	1957	3568
2	1988	4194
3	1996	2359
4	2010	2749

The construction of new bridge, over the Vaal River in Warrenton.

Comments received suggested that the old bridge has enhanced the significance of the new one.

1.1 *Scope overview*

The project is located on the northern outskirts of Warrenton in the Northern Cape Province, in the Frances Baard District Municipality. Warrenton as shown in Annexure A, resorts under the Magareng Local Municipality.

This paper entails the construction of a new bridge (Bridge No. B0067) and the associated road works for the realignment of National Route 18 Section 1 (N18-1) across the Vaal River at Warrenton, in proximity to and downstream of an existing single lane, low level river bridge, (Bridge No. B2284) on N18-1. The total length of realignment of N18-1, inclusive of the new bridge which has a length of 368 m, was 1.48 km.

Work undertaken in terms of the contract included:

- Establishment of the contractor,
- The provision of offices, laboratories and housing for the engineer's site personnel,
- The accommodation of traffic. The existing low level river bridge remained in use for the accommodation of traffic throughout the construction of the project,
- The relocation of existing electrical (Eskom and Municipal) and telecommunication services,
- The construction of roads works,
- The construction of surface drainage,
- The construction of subsoil drainage,
- The construction of the new Bridge B0067 across the Vaal River,
- The rehabilitation of the existing low level bridge, which was retained due to the historic significance thereof,
- Ancillary work consisting of:
  - The installation of service ducts;
  - The construction of segmental block paved sidewalks;
  - The construction of gabion erosion protection, including the protection of approach fills to the new bridge across the Vaal River;
  - The erection of guardrails;
  - The erection of fencing;
  - The relocation of existing road signs and the erecting of new road signs;
  - The application of road markings;
  - The establishment of grassing;
  - Finishing of the road and road reserve and the treatment of the old road;
- The erecting of the following at the existing low level bridge across the Vaal River:
  - Bollards to prevent vehicular access to the bridge;

- Information signs regarding the use of the bridge;
- The construction of a segmental block paved rest area on the Warrenton side of the Project. A commemorative plaque providing a brief background of the existing low level bridge and new bridge was erected at the rest area. A blocked paved walkway was constructed from the rest area to the existing low level bridge:
  - The erecting of the overhead lighting over an 800 m length of the project, including across Bridge no. B0067.

2 THE NEW ROAD AND BRIDGE DESIGN CRITERIA

The new design criteria is based on the South African design requirements in terms of the following:

- overall bridge alignment and project limits,
- access roads to the new bridge,
- the Technical Recommendations for Highways (THR 4 Road Category and THR 7 for Bridges),
- the design speed,
- the level of service, and,
- the road cross section.

The details of the design criteria and scoping requirements are discussed below.

Horizontal alignment:
- 2 no. horizontal curves.

Vertical alignment:
- dictated by bridge deck soffit design level:
- based on SANRAL design criteria
- designed for 1:50 recurring flood with 1.6 m freeboard
- maximum road gradient: 2.6%
- 0.5% gradient across new bridge
- fill height at bridge approaches:
- maximum height: 4.5 m
- new cutting north of Vaal River:
- maximum depth: 2.5 m
- material between new and existing cutting to be removed.

Pavement design:
Surfacing: Asphalt—from commercial sources
Base: Crushed, graded stone—from commercial sources
Sub base: Cement stabilized natural gravel—from cutting and/or commercial sources
Selected layers: Natural gravel—from cutting and/or commercial sources.

Surface drainage:
- Prefabricated culverts
- Side inlets, downpipes and stilling basins on high fills, with gabion erosion protection
- Concrete lined open drains with stilling basins, with gabion erosion protection.

Subsurface drainage:
- in cuttings
- perforated UPVC pipes with crushed stone and sand backfill concrete outlet structures.

Ancillary road works:
- gabion erosion protection, including bridge approach fills
- guardrails
- fencing
- road signs
- road markings
- finishing.

Accommodation of traffic during construction:
- on surfaced temporary deviations and existing road existing low level bridge to remain in use.

Bridge Dimensions:
Length:
- overall length: 368 m
- 16 no. spans × 23 m long.

➢ *Cross-sectional dimensions:*
- overall width: 14.76 m
- 2 × 3.7 m wide lanes
- 1.5 m wide surfaced shoulders
- 1.5 m wide sidewalks: separated from traffic lanes by concrete barriers with concrete pedestrian handrails.

Substructure:
Foundations:
- reinforced concrete foundations
- anchored into rock with epoxy grouted bars.

Abutments:
- 2 no. abutments
- reinforced concrete, wall type, with splayed wing walls.

Piers:
- 15 no. piers
- reinforced concrete, twin wall type, rounded piers with supporting beams for deck.

Superstructure (deck):
- precast beams with reinforced concrete diaphragm beams
- reinforced concrete deck slab
- concrete barriers separating traffic lanes and pedestrian sidewalks
  pedestrian sidewalks with provision for utility services
- precast concrete pedestrian handrails.

Overhead lighting:
- installation of overhead street lighting.

3 HYDROLOGICAL STUDIES

3.1 *Deterministic and emperical flood estimation methods*

Flood peaks were estimated using the Regional Maximum Flood (RMF) and the Standard Design Flood (SDF) methods for recurrence intervals ranging from 1:10 years to 1:200 years. Flood peaks for these methods are summarized in Table 2.

3.1.1 *Regional maximum flood*

The Vaal catchment extends across the flood region with a K-value of K = 3,4. Using the Franco-Rodier equation on which the RMF peaks are based yields a value of 11,713 m^3/s. Maximum recorded values within this regions reveals that at the Bloemhof dam, a value of 6140 m^3/s was recorded during the 1988 floods (88/03/15) in the area. At the Kimberly water works, a value of 5410 m^3/s was recorded in Feb 1894. These have been reported in the technical report titled, "Regional Maximum Flood Peaks in Southern Africa" Report No TR137 by Mr Z Kovacs of the Department of Water Affairs and Forestry.

3.1.2 *Summary of deterministic and empirical flood peak calculations*

A summary of the calculated flood peaks are shown in Table 2.

The RMF estimate of 11713 m^3/s should be viewed as an approximate upper limit of the flood peak for this catchment against which the other flood estimation methods can be compared. As this is a very large catchment, the Rational and SDF methods should idealize the required flood peaks. The Empirical method seems to overestimate the flood peaks for most of the recurrence intervals. The recorded data (1940–2007) from gauging station C9H008, including the floods of 1988, were statistically analyzed to provide more certainty about the varying deterministic and empirical flood peak flow estimates.

Table 2. Comparison of calculated peak flows.

Return period	Rational	Empirical	SDF (basin 8)	RMF
1:2	1023		358	
1:5	1615		1228	
1:10	2163	4412	2062	
1:20	2922	5992	3084	
1:50	4543	8297	4783	5922*
1:100	6452	10536	6392	7062*
1:200	7520		8286	8363*
RMF (return period not defined)				11713

*50,100 and 200 year flood peaks based on QT/RMF ratios calculated during the study.

3.1.3 *Catchment characteristics*

The New bridge location falls in Drainage Region C of the Department of Water Affairs (DWAF Main Drainage Regions) with a catchment area of 117 613 Km^2. The surface hydrology of the catchment consists mainly of the Vaal River and its major tributaries namely the Vet, Vals, Renoster and Wilge Rivers. The length of the longest watercourse namely the Vaal River, from its origin near Breyton in Mpumalanga to the defined bridge location is approximately 1089 km.

A network of dams also forms part of the catchment area. The Bloemhof Dam is situated approximately 100 km upstream of the new bridge location. Further upstream some of the major dams in the system are the Vaal Dam and Grootdraai Dam in the Vaal River, Skerknsfontein Dam in the Wilge River, Allemanskraal Dam in the Sand River and the Erfenis Dam in the Vet River.

4 BRIDGE HYDRAULICS

4.1 *Input data and analysis method*

In compliance to Chapter 8 of SANRAL Drainage Manual, 5th Edition, the Bridge hydraulic Analysis, was based on the following design Parameters:

- Road Classification: Class 2 (Regional Distributor)
- Design Frequency: 1:50 years
- Design Flood: 4200 m^3/s
- Freeboard, FD: 1.6 m.

The HEC-RAS River Analysis System was used for calculation of the flood lines and bridge hydraulics, with the following data input:

- Steady Flow analysis method: Chèzy
- Roughness Coefficient based in the Drainage Manual a roughness of 0.4 m was used for the Chèzy Analysis. The presence of rocks in the riverbed was taken into consideration in determining the roughness coefficient.
- An estimated downstream riverbed slope of 0.002 m/m was used. The slope is defined as the slope at the downstream cross section, which is 1 km downstream from the existing low-level bridge.

The bridge hydraulics of the following proposed bridge locations was determined.

Location A: the new bridge is located 10 m downstream of the existing low flow, with the existing bridge position.

Location B: the new bridge is located 20 m downstream of the existing low flow, with the existing bridge position.

Location C: the new bridge is located 10 m downstream of the existing low flow, without the existing bridge position.
Location D: the new bridge is located 20 m downstream of the existing low flow, without the existing bridge position.

4.2 *Recommended bridge deck soffit level*

The 1:50 yr Water Surface (WS) elevations at the bridge locations discussed above can be summarized as per the table below:

Location	Bridge upstream WS elevation (m)	Bridge downstream WS elevation (m)
A	1171.83	1171.98
B	1171.84	1171.97
C	1171.83	1171.98
D	1171.84	1171.97
Average	1171.835	**1171.975**

The recommended bridge deck soffit level is thus as provided below:

Maximum WS elevation at the bridge	Freeboard	Minimum bridge deck soffit level
1172	+ 1.6 m	= 1173.60

For a schematic indication of the bridge deck soffit level refer to Annexure B.

5 DETAILED DESCRIPTION OF THE MAJOR WORKS

5.1 *Road works*

5.1.1 *Horizontal and vertical alignments*

(a) Horizontal alignment

The horizontal realignment of N18-1 included two horizontal curves, namely:

- a curve with a radius of 80 m, located between km0.849 198 and km0.933 025, on the Warrenton side of Bridge no. B0067, and
- a curve with a radius of 720 m, located between km1.399 423 and km2.087 845, on the Jan Kempdorp side of the project.

Bridge no. B0067 is located on a straight alignment, between the abovementioned curves.

(b) Vertical alignment

The vertical realignment of N18-1 included four vertical curves with lengths ranging from 150 m to 300 m.

The maximum gradient is 2.795%, through a cutting north of the Vaal River, and the minimum gradient is 0.5%, which is also the gradient maintained across Bridge no. B0067 towards Warrenton.

Maximum fill heights on the approaches to Bridge no. B0067 are approximately 4.5 m above natural ground level. The maximum height above river bed of the deck of Bridge no. B0067 is approximately 9 m. North of the Vaal River, the vertical realignment resulted in a cutting with a maximum depth of approximately 2.5 m.

5.1.2 *Cross-sectional elements*

(a) N18-1

The realignment of N18-1 was constructed to a bituminous surfaced, two lane, single carriageway standard.

In Warrenton, where the realignment of N18-1 joins onto the existing alignment of N18-1 (Margareta Prinsloo Street), the road width was tapered to join onto the existing road width of 18.4 m.

Over the extent of the intersection of N18-1 and provincial roads MR923 and DR3405 the road width is also to be adjusted to accommodate exclusive right turn lanes to these respective provincial roads.

Cross-sectional elements of the realignment of N18-1 were as follows:

- 2×3.7 m wide bituminous surfaced lanes
- 1.5 m wide bituminous surfaced shoulders adjoining the lanes
- a total nominal bituminous surfaced width of 10.4 m
- a camber of 2%, except where the road is in super elevation in the curve located between km1.399 423 and km2.087 845
- 1.5 m wide sidewalks adjacent to surfaced shoulders, on either side of Bridge no. B0067, between Joubert Street in Warrenton and the intersection of N18-1 with provincial roads MR923 and DR3405.

On the approach fills to Bridge no. B0067, a Type B1 semi mountable kerb-and-channelling combination was constructed between the surfaced shoulder and the sidewalk. In these instances, the 300 mm wide cast in situ concrete channelling was incorporated into the 1.5 m wide bituminous surfaced shoulder.

Through the cutting north of the Vaal River, sidewalks were constructed at the bituminous surfaced level of the road to facilitate drainage. Concrete edge beams were constructed between the 1.5 m wide bituminous surfaced shoulder and the block paved sidewalk. On the Warrenton-bound lane, concrete edge beams were also constructed on the outer edge of the block paved sidewalk. On the Jan Kempdorp-bound lane, a 1.5 m wide V-shaped

Type F concrete lined open drain was constructed adjacent to the outer edge of the sidewalk.

Sidewalks were constructed to a 2% fall, sloping away from the bituminous surfaced shoulder

- guardrails were erected in sidewalks, adjacent to kerb-and-channelling combinations, on the approach fills to Bridge no. B0067, and adjacent to the surfacing over the extent of sidewalks between Bridge no. B0067 and the intersection of N18-1 with the provincial roads.

Guardrails were also erected on the outer edges of sidewalks, as pedestrian safety measures, over the longitudinal extents of the wingwalls of Bridge no. B0067

- on the approach fills to Bridge no. B0067, an 800 mm wide gravel shoulder was constructed adjacent to the outer edge of the sidewalks
- fills were constructed to a nominal side slope of 1V: 1.5 H
- cuttings were excavated to a nominal slope of 1V: 2 H
- in situ material remaining between the Warrenton-bound lane of N18-1 and the cutting on the existing alignment of N18-1 was removed and shaped to form a continuous surface towards the upper edge of the cutting on the existing alignment of N18-1.

(b) Intersecting roads, streets and accesses

Cross-sectional elements for intersecting roads, streets and accesses were as follows:

Joubert Street:
- 2 × 3.4 m wide bituminous surfaced lanes, and bituminous surfacing over the extent of the bell mouth of the intersection with N18-1
- Type B1 semi-mountable kerb-and-channelling combination over the extent of the bell mouth.

Warren Street:
- 2 × 3.4 m swide bituminous surfaced lanes with 0.3 m wide bituminous surfaced shoulders over the extent of bituminous surfacing, and bituminous surfacing over the extent of the bell mouth of the intersection with N18-1
- Type B1 semi-mountable kerb-and-channelling combination over the extent of the bell mouth
- 8.4 m wide gravel wearing course over the extent of gravel surfacing.

Commemorative plaque- and rest area access:
- 2 × 3.4 m wide segmental block paved lanes and bituminous surfacing over the extent of the bell mouth of the intersection with N18-1
- Type B1 semi-mountable kerb-and-channelling combination over the extent of the bell mouth and the sidewalk leading to the rest area.

Main Road (MR) 923:
- 2 × 3.7 m wide bituminous surfaced lanes with 1.7 m wide bituminous surfaced shoulders over the extent of bituminous surfacing, and bituminous surfacing over the extent of the bell mouth of the intersection with N18-1;
- 800 mm wide Type C cast in situ concrete mountable kerbs over the extent of the bell mouth
- 8 m wide gravel wearing course over the extent of gravel surfacing.

District Road (DR) 3405:
- 2 × 3.7 m wide bituminous surfaced lanes with 1.7 m wide bituminous surfaced shoulders over the extent of bituminous surfacing, and bituminous surfacing over the extent of the bell mouth of the intersection with N18-1
- 800 mm wide Type C cast in situ concrete mountable kerbs over the extent of the bell mouth.

5.1.3 *Pavements*

(a) N18-1

The pavement of N18-1 consisted of the following:

- Bituminous surfacing:
- 40 mm thick continuously graded, medium grade, asphalt surfacing, manufactured with 60/70 penetration grade bitumen
- Base:
  150 mm thick type G1 crushed stone base compacted to 88% of apparent density
- Subbase:
  50 mm thick type C4 stabilised natural gravel compacted to 96% of modified AASHTO density
- Upper selected layer:
  150 mm thick type G6 natural gravel compacted to 95% of modified AASHTO density
- Lower selected layer.

150 mm thick type G7 natural gravel compacted to 93% of modified AASHTO density.

(b) Intersecting roads, streets and accesses

The pavements for the bituminous portions of intersecting roads were as described for N18-1.

The pavements for the gravel portions of intersecting roads consisted of the following:

- Gravel wearing course:
  150 mm thick type G7 natural gravel compacted to 95% of modified AASHTO density
- Upper selected layer:
  150 mm thick type G6 natural gravel compacted to 93% of modified AASHTO density.

(c) Roadbed preparation

Roadbed preparation consisted of the compaction of the in situ material to 90% of modified AASHTO density.

(d) Stabilization of upper selected layer

The upper selected layer was stabilized and compacted to 95% of modified AASHTO

density over limited lengths of 80 m and 50 m, respectively, at the beginning and end of the cutting, and at the abutments of Bridge no. B0067. 17

(e) Bituminous surfacing on bridge deck
Bituminous surfacing on the deck of Bridge no. B0067 consisted of a nominal 50 mm thick continuously graded, medium grade, asphalt, first placed as a levelling layer with a nominal thickness of 10 mm, followed by a 40 mm thick wearing course. A tack coat was applied to both the concrete surface of the bridge deck and to the asphalt levelling layer.

5.1.4 *Surface drainage*
(a) Culverts
Culverts consist of prefabricated pipe culverts with cast in situ reinforced concrete head-and wingwalls where required.

(b) Surface drainage
Surface drainage consisted of the following:

- a Type B1 semi-mountable precast concrete kerb and cast in situ concrete channelling combinations on the approach fills to Bridge no. B0067
- reinforced concrete side inlets with 300 mm diameter corrugated metal downpipes and stilling basins, in Type B1 kerb-and-channel combinations, on the approach fills to Bridge no. B0067
- a 900 mm base width × 600 mm deep, trapezoidal shaped, cast in situ reinforced concrete canal, with stilling basin, extended by means of gabions up to the Warrenton abutment of Bridge no. B0067, leading from Warren Street towards the Vaal River
- a 1.5 m wide Type F, V-shaped, cast in situ concrete lined open drain with stilling basin, in the cutting on the Jan Kempdorp-bound lane of N18-1, north of the Vaal River
- 800 mm wide Type C cast in situ concrete mountable kerbs at the intersection of N18-1 and provincial roads MR923 and DR3405
- a cast in situ reinforced concrete field inlet, which drains into a stormwater pipe leading towards the trapezoidal canal, at the intersection of N18-1 and Warren Street

5.2 *Bridge no. B0067*

5.2.1 *Locality*
Bridge no. B0067 is located on the north western outskirts of Warrenton. The longitudinal centre of the bridge is at km1.124 on N18-1.

The bridge crosses the Vaal River at an angle of approximately 88° to the direction of flow and approximately 6.8 m to 19.8 m downstream of the low level bridge.

5.2.2 *Geology*
The bridge is located on andesitic lava of the Allanridge Formation of the Platberg Group, Ventersdorp Supergroup. Exposures of this rock are present within the streambed of the Vaal River. Alluvial gravels and boulders, overlying the andesite bedrock, are also evident in the streambed.

5.2.3 *General description*
Bridge no. B0067 is concrete structure consisting of a cast in situ reinforced concrete substructure, founded on rock, and a superstructure comprising a beam-and-slab type deck consisting of pretensioned, pre-stressed beams and a cast in situ reinforced concrete slab. 18.

The bridge is 368 m long between abutments, consisting of 16 × 23 m spans, and has a skew angle of 0°. The overall deck width is 14.76 m, including sidewalks.

5.2.4 *Foundations*
The bridge is founded directly on hard rock andesite, on mass concrete, by means of spread footings. Footings are anchored into the rock by means of Y32 bars which were drilled and grouted into the rock.

5.2.5 *Substructure*
The two abutments consist of reinforced concrete wall type abutments with splayed wingwalls.

The fifteen (15 no.) piers consist of twin, reinforced concrete, Y-shaped wall type columns with rounded ends and cross beams to support the superstructure.

Both the abutments and piers were constructed with fluted (recessed) surface finishes, which were treated with protective coatings.

5.2.6 *Superstructure*
The superstructure consists of nine (9 no.) pretensioned, pre-stressed beams per span, with transverse diaphragm beams, and a cast in situ reinforced concrete slab.

The overall deck width of 14.76 m provides for the following:

- 2 × 3.7 m wide traffic lanes
- 1.5 m wide road shoulders on either side of the traffic lanes
- 1.5 m wide sidewalks on either side of the bridge, separated from the road shoulders by means of Type F cast in situ concrete parapets. Sidewalks are provided

6 GENERAL APPLICATIONS

National Water Act 1998:

- Section 21(c): Impeding or diverting the flow of water in a watercourse

- Section 21(i): Altering the bed, banks, course or characteristics of a watercourse

An additional rest area with tables and parking facilities was also provided to enhance the social component of the project.

Construction Methodology.

7 PROJECT OUTPUTS

At the end of the construction process the following road and bridge construction outputs were achieved:

- 144 Precast Beams
- 27.2 tonnes per beam
- 16 Prestressing Strands
- Total length presstressing Strand in Beams approximately 59.04 km
- Total Length Rebar in Beams: approximately 209.4 km
- Elastomeric Bearings: 288
- Total Volume Concrete in Bridge: approximately 6295 m^3
- Total Area Formwork (Temporary and Permanently): Approx 10350 m^2
- Mass of Total Structure: Approx 16000 tonne.

8 PROJECT MILESTONES/ ACHIEVEMENTS

8.1 *Sanral strategy for socio-economic development*

In line with the South African Government's Policy to address poverty related issues the South African National Roads Agency includes the following in its projects:

- Labour Intensive Methods
- The Contract Participation Goals (CPG)
- Training & Skills transfer Programs, and
- The Socio-Economic Development
- Environmental Control & Mitigation Actions.

By investing in the above additional benefits are gained by means of job creation, the SMME development in the area as well as training programs. The construction of the bridge over the Vaal River in Warrenton has become a positive story in terms of the overall development of bridge infrastructure projects in South Africa, for the following reasons.

8.2 *Job creation*

- A number of persons employed has varied during contract period, dependent on requirements. The maximum number of persons employed per month was in the order of 145.
- Of the above on average 50% of persons employed were local and representing local communities.
- The proportion of persons-hours in terms of employment throughout the project duration was: Male: 255884 and Females: 38392.
- The value of employment of local persons was in the order of R5.6 million.
- The value of employment of all persons was: Male: R10.9 million and for Female was R1.1 million, totaling overall R12 million.

8.3 *Targeted enterprises (SMME and BE)*

- Employment varied during contract period, dependent on requirements. The maximum number of targeted enterprises during any month was 7.
- The type of services delivered included:
  - Steel fixing,
  - Relocation of electrical services,
  - Transport,
  - Gabion construction,
  - Fencing activities,
  - Security Services,
- The Value of employment to SMMEs was in the order of R9.4 million.

8.4 *Training and skills transfer*

A substantial effort was made on site to train local labour in order to equip them with the required skills for doing the bridge construction and works related activities.

These have included:

Engineering skills

- Basic Concrete Skills,
- Basic Reinforcing Skills
- Laying of precast kerbs
- Installation of concrete culverts
- Installation of gabions and reno mattresses.

A total of 60 people were trained in this regards.

Generic skills

- Applying the Organization and Health Safety (OHS)—Act in Construction Environment,
- The Traffic Management on Site,
- The environmental Induction.

A total of 393 people were trained in these areas.

Entrepreneurial skills

- Business Appreciation Skills
- Estimating and Tendering processes
- Safety.

A total of 19 people, 14 from the seven companies employed and 5 selected from the labourer have benefitted from the training process.

Professionally accredited companies were appointed by SANRAL for all the above activities.

8.5 *The socio-economic development*

The overall cash injection into the communities during the construction period through the implementation of strategic objectives and project components amounted to R21 million. The spin-offs in terms of long-term development to the area remain to be quantified but the safety of road users and people living in the area has significantly improved since the bridge opening in February 2013.

8.6 *Environmental control and mitigation actions*

The following issues were relevant for environmental compliance:

- The area where the bridge was constructed was considered an important spawning area for fish species within the region. This was especially pertinent as the presence of both the Vaalharts Weir and the Bloemhof Dam means that upstream access was not possible to migrating fish. SANRAL therefore had to ensure that the habitat would not suffer transformation due to the construction activities and that all site disturbances would be reinstated.
- As the habitat associated with the bridge site would be readily utilised by fish as spawning beds SANRAL had to make considerable effort to ensure that construction activities in the water course (e.g. pier footings) during autumn and winter seasons when the river's flow is also at it's lowest, as this was also be advantageous for the construction of the works.
- In addition to the implementation of the Environmental Management Plan (EMP), which by law is a contractual requirement, an independent Environmental Control Officer (ECO) was assigned by SANRAL to monitor, audit and report on the implementation of the EMP, both during the construction phase and the subsequent watercourse rehabilitation.
- The bridge design and construction was undertaken in a manner such as not to impact on the longitudinal connectivity of the aquatic habitat, and the migratory access was maintained as this was considered vital to the ongoing conservation of fish within the region.
- The footprint of the development during the construction phase was retained as small as possible by limiting construction vehicles and plant to designated roadways only.
- Destruction of the riparian habitat through the unnecessary clearing of vegetation was avoided.
- Dumping of any excess rubble, building material or refuse was prohibited within the riparian habitat. Dumping of materials only took place at designated and properly managed sites.
- Adequate toilet and ablution facilities were provided for all construction personnel to negate informal ablutions taking place within riparian zones.
- Fires within the riparian zones were prohibited.

9 POSITIVE IMPACTS/CONCLUSION

- Reduction of possibility of flooding of river crossing
- Elimination of traffic diversion during floods
- Access to Warrenton improved
- Provision of two lane, uninterrupted traffic flow
- Improved safety for pedestrians and cyclists
- Reduction in road user costs
- Elimination of economic loss to Warrenton during flooding
- Reduction of maintenance costs for SANRAL.

By doing this Project SANRAL was not only able to fulfill its stated objective to develop and manage the national roads network, but through Structural Retrofitting for altered service conditions was able to improve road safety, while at the same time would preserve the historical significance of the old structure. The Project has shown that the new and old can live together by the proactive interface of this bridge infrastructure project.

Annexure A: Bridge location.

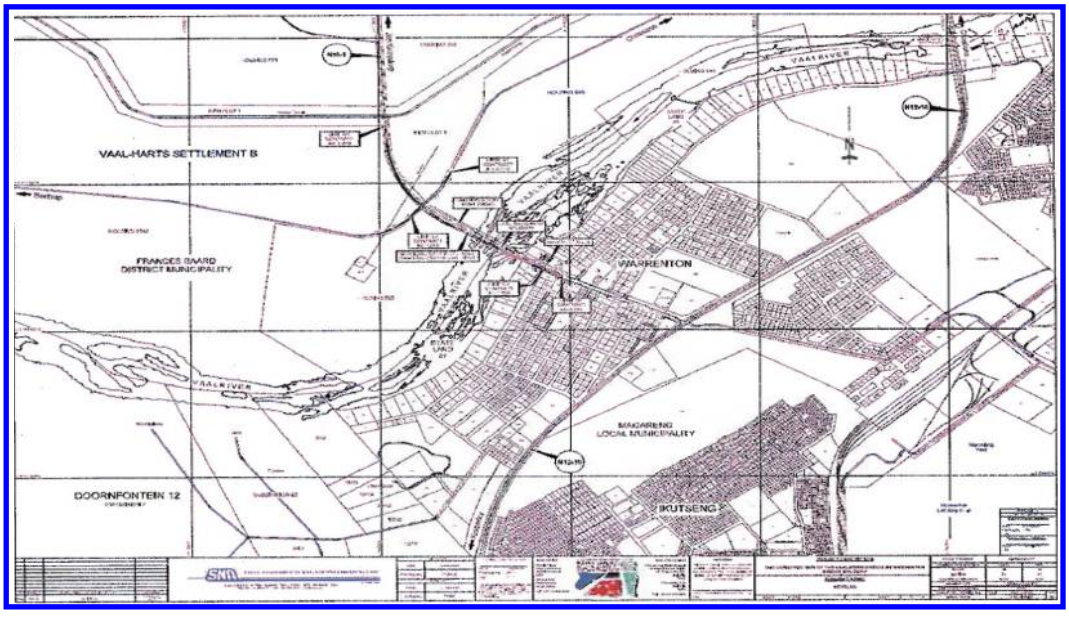

Annexure B: Flood hydrology and bridge hydralulics.

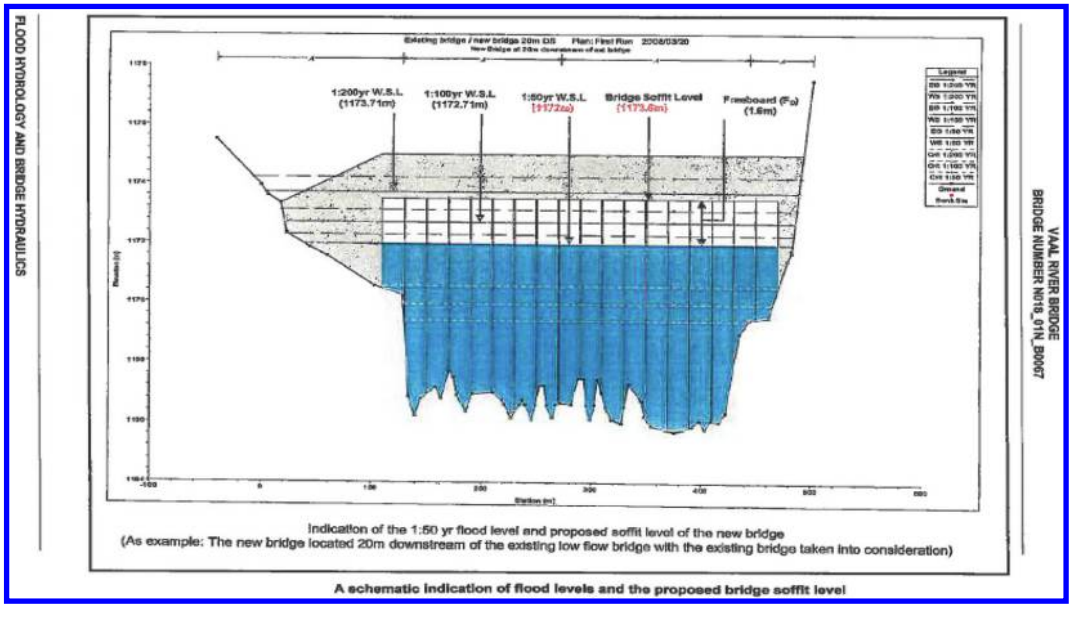

Bridge photos

Low level bridge built in 1931.

The old and new bridges: 1931–2014.

Floods 2010—Road & bridge cut off 6 weeks.

The new bridge 2013/2014.

Low level bridge—reduced cross section.

New bridge 2013/2014.

Maintenance & safety challenges after 2010 floods.

New bridge: retrofitting for altered service conditions.

Appendix A

Date	Report/document title	Author(s)
July 2011	CONTRACT No: N.018-010-2007/1—The Construction of a bridge and associated road works across the Vaal River in Warrenton: Volumes 1, 2, 3, 4, 5, 6 & 7.	The Regional Manager—SANRAL: J C Van Der Walt: Project Manager—Tiago Massingue—SANRAL, Edwin Kruger, Bridge Network Manager—SANRAL, Supervision Engineer: J J Opperman SNA Civil Structural Engineering
1996	The Technical Recommendations for Highways (THR 4 Road Category)—THR6:1996	COLTO—Committee of Land and Transport Officials South Africa
1999	South African Heritage Resources Agency—[Section 34 Act 29, 1999]	GOVERNMENT NOTICES, South African Heritage Resources Agency
1993	Department of Environmental Affairs National Water Act 1998: Section 21 (c); Section 21 (i)	GOVERNMENT NOTICES, DEPARTMENT OF ENVIRONMENTAL AFFAIRS AND TOURISM
1993	Occupational Health and Safety Act, 1993 Construction Regulations, 1993, Act No. 85 of 1993	GOVERNMENT NOTICES, DEPARTMENT OF LABOUR
2014	Occupational Health and Safety Act, 1993 Construction Regulations, 2014 Act No. 85 of 1993	GOVERNMENT NOTICES, DEPARTMENT OF LABOUR
2000	Preferential Procurement Policy Act 2000 Treasury Regulations—Act 5 of 2000, (PPPFA)	GOVERNMENT NOTICES, DEPARTMENT OF TREASURY
December 2003	The Broad-Based Black Economic Empowerment Act—Act 53 of 2003 (B-BBEEA)	GOVERNMENT NOTICES, DEPARTMENT OF TREASURY
October 2008	Flood Hydrology and Bridge Hydraulics Final Report	SNA CIVIL & STRUCTURAL ENGINEERS
December 2011	Revised PPPFA Regulations December 2011—Alignment of PPPFA goals with B-BBEE objectives	GOVERNMENT NOTICES, DEPARTMENT OF TREASURY

Concrete Repair, Rehabilitation and Retrofitting IV – Dehn et al. (Eds)
© 2016 Taylor & Francis Group, London, ISBN 978-1-138-02843-2

Numerical study on effect of ductility in the flexural capacity enhancement of RC beam strengthened with FRP

A. Kashi & M.Z. Kabir
Department of Civil and Environmental Engineering, AmirKabir University of Technology, Iran

F. Moodi
Concrete Technology and Durability Research Center, AmirKabir University of Technology, Iran

ABSTRACT: The repair, rehabilitation and strengthening of Reinforced Concrete (RC) beams is a challenging engineering problem. Flexural strengthening of these members is achieved by attaching FRP strengthening system to the tension face of a flexural member. Previous studies have demonstrated by attaching externally bonded fabric of Carbon Fibre Reinforced Polymer (CFRP) laminate to the tension side of reinforced concrete beams can increase stiffness and maximum load of the beams. In this report, a finite element model was posted out to examine the effect of ductility on the flexural capacity enhancement of RC beams after attaching CFRP. Two cases of RC beam (552 mm × 305 mm × 6840 mm) were analysed by FE modelling. The field of longitudinal flexural rebar has been dissimilar in these two types of the beam. The total area of flexural rebar in series A beams is more than series B. Modelling of three point bending experiment for control beams (without attaching CFRP) showed that beam in type B is more ductile than type A. By applying CFRP on the tension face of the beams, the gain in maximum flexural load of the specimens reached values of approximately 8.8% and 13.4% in type A beam and 35% and 46% for type B beam respectively, for 1 mm and 2 mm thickness of CFRP. The results showed applying the FRP system in a more ductile beams, will be more efficient than the beams by low ductility.

1 INTRODUCTION

FRP composites have been used in structural engineering for both new construction and for repair and strengthening of existing structures. Strengthening of members, where the original structure's strength or ductility is increased from the loads or displacements for which it was originally designed. This increase may be necessitated by the desire to make the structure compatible with existing building codes (for example because of seismic retrofitting) or may be desired due to changes in use of the structure.

Flexural strengthening of concrete members such as beams, slabs, walls, and columns has been the most popular usage of FRP where the flexural capacity has not been sufficient. Few decades ago, steel plates have been used to enhance flexural strength of RC structures by externally bonding such heavy plates to the tension zone of RC structures. During the last three decades, externally bonded Fiber Reinforced Polymer (FRP) composite systems have been accepted by civil engineers and were considered as efficient substitutes for the steel plates rehabilitation option due to their various advantages such as lower weight and ease of application as well as corrosion resistance. Many researchers have shown that the structural performance of the externally bonded FRP systems to RC structures depends on bond between concrete and FRP. Therefore proper preparation of concrete surface and curing of adhesive at the time of FRP installation are crucial for structural performance (Bank, 2006).

Flexural capacity of RC beams will be improved after attaching FRP system on the tension face of members. The behavior of reinforced concrete beams was studied by Kachlakev and Miller. For the finite element models, the flexure, shear, and flexure/shear strengthened beams have had higher load carrying capacities than the control beam by 37%, 16%, and 105%, respectively. The experimental FRP-strengthened flexure, shear, and flexure/shear beams have had capacities greater than the control beam by 45%, 45%, and 104%, respectively (Kachlakev, et al., 2001). Other research showed, the stiffness of the CFRP-retrofitted beams have been increased compared to that of the control beams and installing externally bonded CFRP plates have resulted in an increase in maximum flexural capacity. The increase in maximum load of the retrofitted specimens have reached values

of about 23% for retrofitting in shear and between 7% and 33% for retrofitting in flexure. Moreover, retrofitting have shifted the mode of failure to be brittle (Taleb Obaidat, et al., 2010).

However the flexural capacity of RC beams will be improved after installing FRP laminate, ductility of these members will be decreased. This despite the fact that ductility of a structural system, its components, and the constituent materials has always had special importance in the design of structures especially against earthquake. It is now well established that externally bonded Fiber-Reinforced Polymer (FRP) composites which are bonded to concrete structures for strengthening and repair works can prematurely deboned in generally a brittle manner (Bank, 2006). Al-Saidy found that the ultimate deflection of RC beams after strengthening by CFRP sheets have been decreased to a level below the control beam and the use of transverse straps (U-shaped CFPR sheet) anchored the flexural CFRP sheet and prevented any delamination at concentrated loads. The U-shaped straps have been more effective in beams with higher rate of corrosion (Al-Saidy, et al., 2010). The result of four-point bending tests on slabs, determined by attaching two layers of FRP sheet under that, ductility have been decreased in comparison with using only one layer of FRP (Pela, et al., 2011). Oehlers showed in his research, plated beam had a shorter softening plateau due to the combined effect of concrete crushing and plate debonding, whereas the unplated RC beam had a long ductile plateau as the steel bar was able to strain harden considerably, while the concrete was softening (Oehlers, et al., 2008).

In this paper, a finite element model was carried out to find out the effect of ductility on the flexural capacity enhancement of RC beams after attaching CFRP.

2 MATERIAL PROPERTIES

2.1 *Concrete elements*

Concrete elements have been defined as a solid element. In concrete, cracking model has been used to define properties after yielding steel bars. Before yielding bars, concrete's behavior was simply isotropic. It means before plastic limit, slope of stress/strain curve in both tension and compression was changed linearly. Poison's ratio, density of the concrete, modulus of elasticity, compressive strength and tension strength of concrete are summarized in Table 1.

After occurring damage in both tension and compression, Concrete Damage Plasticity (CDP) model has been developed. In this model, after yielding bars, if force is removed, the residual plastic strain is found by a rebound function of the modulus of elasticity. This rebound function is modified by damage parameters of CDP model. Additionally, microstructure of concrete must be identified in FE model. So the parameters, dilation angle Ψ, flow potential eccentricity m, initial biaxial/uniaxial ratio σ_{c0}/σ_{b0}, the ratio of the second stress invariant on the tensile meridian k_c and viscosity parameter μ should be defined. The values of these parameters are shown in Table 2.

2.2 *Rebar elements*

Beam element has been used to define rebar within the concrete. The node of rebar elements was embedded and constrained within the nodes of the concrete elements. General metal elasticity parameters within elastic strain below the yield stress, were defined as a rebar property. Modulus of elasticity E_s, yield stress f_{ys} and ultimate stress f_{us} are the most important parameters for rebar properties (summarized in Table 3). Metal elasticity was defined as a stress/plastic-strain relationship, where the initial value for stress corresponds to the maximum stress in which plastic strain is zero.

2.3 *FRP elements*

Generally the FRP composite are anisotropic materials, it means the properties are different in all directions. In this study the main direction was x direction and the properties in y direction were the same as in those in the z direction, so it was assumed that FRP is the orthotropic material. Additionally, linear elastic properties were defined for FRP laminates. In finite element model, shell element was used to model FRP laminates.

Table 1. Concrete properties.

ν	ρ (kg/m³)	E_c (MPa)	f_c (MPa)	f_r (MPa)
0.2	2400	34300	43.5	3.13

Table 2. General concrete damaged plasticity parameters.

Ψ	m	σ_{c0}/σ_{b0}	k_c	μ
31	0.1	1.16	0.67	0

Table 3. Rebar properties.

E_s (MPa)	f_{ys} (MPa)	f_{us} (MPa)
200000	415	620

Table 4. Material properties for FRP composite.

FRP type	Elastic modulus (MPa)		Poison's ratio		Shear modulus (MPa)		Ultimate strength (MPa)					
							Shear		Compressive		Tensile	
CFRP (carbon/ epoxy)	E_1	144700	v_{12}	0.3	G_{12}	5200	S_{12}	77	C_1	1200	T_1	1500
	E_2	9650	v_{13}	0.3	G_{13}	5200	S_{13}	77	C_2	250	T_2	50
	E_3	9650	v_{23}	0.45	G_{23}	3400	S_{23}	38	C_3	250	T_3	50

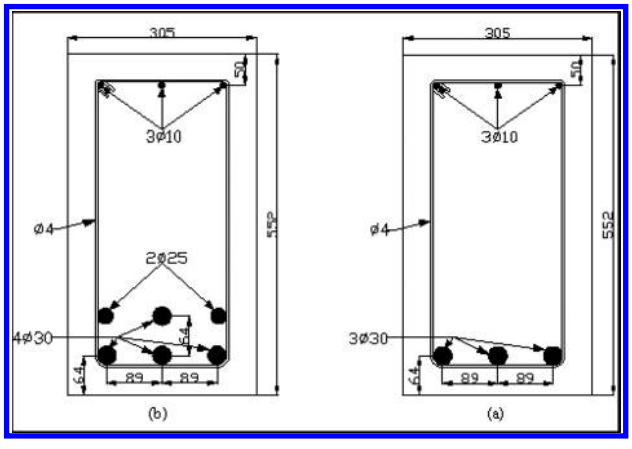

Figure 1. Beams cross section (a) Group B (b) Group A.

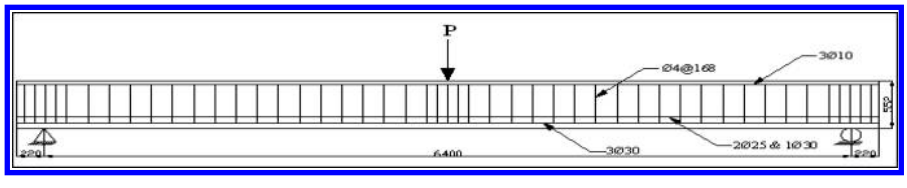

Figure 2. Beam span and loading test.

FRP type, elastic modulus, tensile strength and compressive strength of the FRP composite in three directions, shear modulus and shear strength of the FRP composite for three planes and major Poisson's ratio are the necessary data for FRP modelling. The properties of FRP are summarized Table 4. In Table 4, direction 1 is the same as the fiber direction (main direction) while the 2 and 3 directions are perpendicular to the 1. Thickness of each layer of CFRP has been assumed 1 mm.

3 BEAM TEST

3.1 *The geometry of the beams*

In this study two types of RC beam were analysed by FE modelling. The dimensions of the full-size beams have been similar in the both of the beams (305 mm*552 mm*6840 mm), but the area of longitudinal flexural rebar has been dissimilar in these two types of the beam. Total area of the flexural rebar in beam A and B, is 2826 mm² and 981 mm², respectively. The span between the two supports was 6400 mm. Cross section of types A and B beam are shown in Figure 1, also Figure 2 shows spanning the length and loading procedure of the beams.

3.2 *Beam strengthening*

The soffit of two types of the beam was strengthened with CFRP laminates, 305 mm wide 6840 mm lengths and different thickness. Four groups were defined in each type. Series A were included control beam (without strengthening) and strengthening by 1 mm, 2 mm and 3 mm of CFRP. In series B, in addition

of control beam, strengthening was done with 0.5 mm, 1 mm and 2 mm of CFRP. As mentioned before, the thickness of each layer has been 1 mm.

3.3 *Loading test*

A simple single point beam load test, was chosen for this research (Fig. 2). Beams were loaded at 40 MPa increments to a point near ultimate, then subsequently were loaded at 20 MPa increments until failure. Beams were supported and loaded on plate rollers allowing for free rotation. A 2.5 cm thick steel plate, modelled, was added at the support location in order to avoid stress concentration problems. This provided a more even stress distribution over the support area. Moreover, a single line support was placed under the centerline of the steel plate to allow rotation of the plate.

4 RESULT AND DISCUSSION

4.1 *Group A beams*

As it was mentioned in previous sections, the beams in series A consisted of control beam and strengthened beams by 1, 2, 3 layers of CFRP. It should be noted that because the total area of the flexural rebar in control beam A was more than type B, series A beams were less ductile than type B. Figure 3 illustrates the differences in load-deflection behavior of the four beams in series A. The ultimate flexural load (Pu) of control beam and strengthened beams by 1, 2 and 3 layers of CFRP had been 399.1 (KN), 434.8 (KN), 456.5 (KN) and 473.5 (KN), respectively. So strengthening by 1 mm, 2 mm and 3 mm CFRP have higher load carrying capacities than the control beam by 8.5%, 13.4%, and 17%, respectively. It means the flexural capacity of the strengthened beams increases with the increase of CFRP layer numbers. In addition, the first cracking load (Pc) and steel yielding load (Py) of the beams are increased by increasing the layer number. The values of Pu, Py and Pc and their corresponding displacement are summarized in Table 5.

The behavior of the control beam shows, after yielding of steel bars, concrete crushing was occurring. By strengthening of the beam, the failure behavior of the beams was not changed, it means before that CFRP was ruptured, compressive stress damaged concrete. Maximum stress, tension in CFRP laminate has been 489 (MPa), 446 (MPa) and 437 (MPa) for 1, 2 and 3 layers strengthened beams, respectively, when crushing was occurring, so the whole capacity of the CFRP was not used. This behavior is because of the total area of flexural bars, these beams were stronger in tension than compression because of existing more flexural bars.

By reducing the area of the flexural steel bars, the beams becomes weaker in tension, so the role of CFRP will be bolder than the past (in series B beams).

4.2 *Group B beams*

To understand more about the effect of CFRP in strengthening of the beam, group B beams was

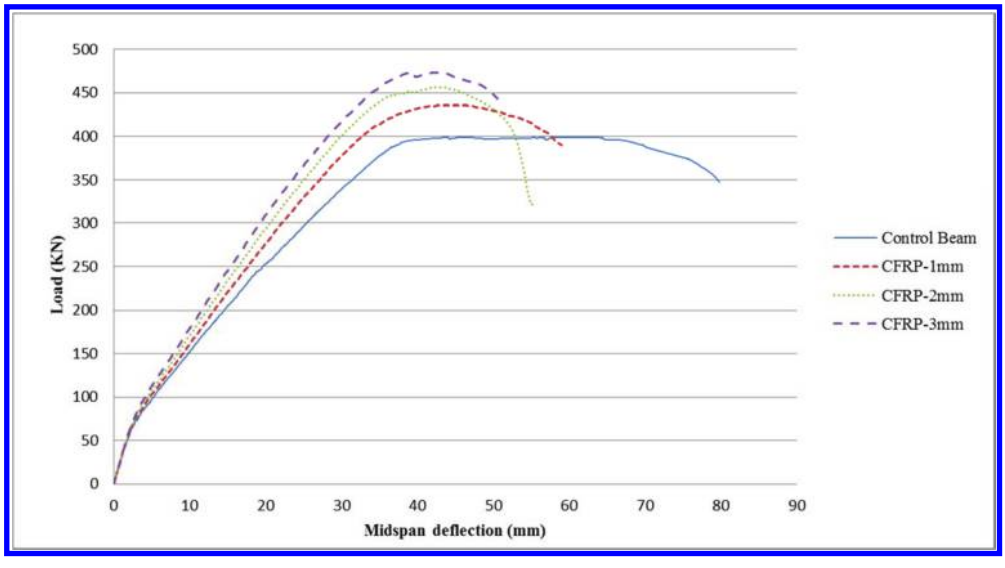

Figure 3. Comparison between load–deflection curves for type A beams.

Table 5. Result of FE modeling for beams in type A.

Beams	Pc* (KN)	Py** (KN)	Pu*** (KN)	Dc* (mm)	Dy** (mm)	Du*** (mm)	Failure monitoring
Control beam	62.4	384	399.1	2.32	36.01	60.5	First steel yielding then concrete crushing
1 mm-CFRP	69.26	422	434.8	2.57	36.6	43.12	First steel yielding then concrete crushing
2 mm-CFRP	71.1	453.8	456.5	2.45	40.7	42.83	First steel yielding then concrete crushing
3 mm-CFRP	79.9	473.5	473.5	2.91	42.64	42.64	First steel yielding then concrete crushing

*Pc and Dc are corresponding to load and displacement which concrete start cracking.
**Py and Dy are corresponding to load and displacement which bars start yielding.
***Pu and Du are corresponding to load and displacement in failure.

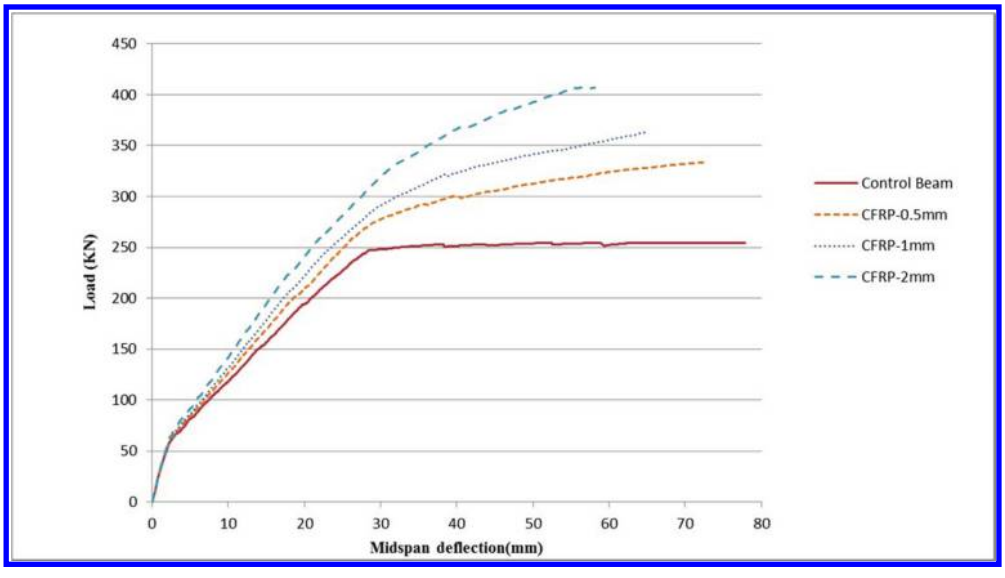

Figure 4. Comparison between load–deflection curves for type B beams.

introduced and analysed. By reducing the area of flexural steel bars from 2826 mm² (in group A) to 981 mm² (in group B) the contribution of laminates will be highlighted. Figure 4 illustrates the differences in load-deflection behaviour of the four beams in series B. The ultimate flexural load (Pu) of control beam and strengthened beams by 0.5, 1 and 2 layers of CFRP had been 254.3 (KN), 333.4 (KN), 363 (KN) and 406.9 (KN), respectively. It shows strengthening by 0.5 mm, 1 mm and 2 mm CFRP have had a higher load carrying capacities than the control beam by 26.9%, 35.2%, and 46.1%, respectively. The values of ultimate flexural load Pu, steel yielding load Py, first cracking load Pc and their corresponding displacements are summarized in Table 6.

The failure behavior of the control beam in group B is similar to control beam in group A. Table 6 shows, after yielding of steel bars, concrete crushing was occurring. The failure mode of the beam has been changed by attaching 0.5 mm CFRP. In this beam, after yielding of steel bars, stress in CFRP sheet has been reached to the ultimate value and CFRP rupture was occurred before concrete crushing. But by using more layers of CFRP (1 mm and 2 mm) the failure mode was changed to crushing concrete after steel bar yielding. Maximum stress, tension in CFRP laminate was 1086 (MPa) and 781 (MPa) for 1 mm and 2 mm CFRP, respectively. So it was concluded that the strengthening of group B beams by 0.5 mm CFRP was the most beneficial state in comparison to other strengthened beams in this study.

Table 6 Result of Fe modelling for beams in type B.

Beams	Pc* (KN)	Py** (KN)	Pu*** (KN)	Dc* (mm)	Dy** (mm)	Du*** (mm)	Failure monitoring
Control beam	43.6	247	254.3	1.55	28.88	77.94	First steel yielding then concrete crushing
0.5 mm-CFRP	52.6	270	333.4	1.93	28.2	72.49	First steel yielding then then CFRP rupture
1 mm-CFRP	55.8	287.1	363	2.03	29.15	64.89	First steel yielding then concrete crushing
2 mm-CFRP	62.9	319.18	406.9	2.31	29.93	58.02	First steel yielding then concrete crushing

*Pc and Dc are corresponding to load and displacement which concrete start cracking.
**Py and Dy are corresponding to load and displacement which bars start yielding.
***Pu and Du are corresponding to load and displacement in failure.

4.3 *Comparison between group A and B*

Result of FE modelling for group A beams (Table 5) shows, according to the equation (1), the ductility of control beam in this series is 1.68. By attaching CFRP laminate, ductility will be reduced to 1.17, 1.05 and 1 for 1 mm, 2 mm and 3 mm thickness of CFRP. Additionally enhancement of load carrying capacities for 1 mm, 2 mm and 3 mm CFRP had been 8.5%, 13.4%, and 17%, respectively, according to pervious sections.

In the other hand, according to Table 6 the ductility of the control beam in group B was 2.69 and strengthening by 0.5 mm, 1 mm and 2 mm CFRP reduced ductility to 2.57, 2.22 and 1.93, respectively. Moreover the increasing of flexural capacities had been 26.9%, 35.2%, and 46.1% for 0.5 mm, 1 mm and 2 mm CFRP, respectively. By comparing these two types of the beams, it was concluded that flexural capacity enhancement of RC beams in group B is more than RC beams in group A, it's because of the ductility of control beam. In type B, control beam was more ductile than type A, so the role of CFRP in strengthening will be bolder on series B beams.

$$\mu = \Delta u/\Delta y \quad (1)$$

where μ = ductility; Δu = ultimate displacement and; Δy = yielding displacement.

5 CONCLUSION

The paper investigated the flexural behaviour of RC beams which had differente ductility and retrofitted with CFRP. The following conclusions are drawn from this numerical study:

1. By strengthening of RC beam in group A, the flexural capacities have been increased 8.5%, 13.4%, and 17%, and ductility decreased 35.7%, 46.1% and 50.7% respectively, for 1 mm, 2 mm and 3 mm CFRP thickness. In addition, by attaching CFRP sheets, the yielding of steel bars was postponed in comparison to control beam.
2. In type B, the total area of flexural steel bars was 55% decreased. A similar process was seen in group B beams. So the enhancement of flexural capacity was 26.9%, 35.2%, and 46.1% and ductility reduction was 4.5%, 19.1% and 32.9% for 0.5 mm, 1 mm and 2 mm CFRP strengthening, respectively.
3. By comparison, between series A and B, it was found that the effect of CFRP in increasing of flexural capacities, was higher in a more ductile beams. On the other hand by reduction of ductility the effect of CFRP becomes lower.

REFERENCES

[1] Bank, C. 2006. *Composites for construction.* New Jersey: John Wiley & Sons, Inc.
[2] Kachlakev, D. and Miller, T. 2001. Finite element modeling of reinforced concrete structures strengthened with FRP laminates. *Oregon Department of Transportation Research Group*. Washington, DC.
[3] Taleb Obaidat, Y., Heyden, S., Dahlblom, O., Abu-Farsakh, G. and Abdel-Jawad, Y. 2010. Retrofitting of reinforced concrete beams using composite laminates. *Construction and Building Materials,* vol. 25, pp. 591–597.
[4] Pela, L., Aprile, A. and Benedetti, A. 2011. Experimental study of retrofit solutions for damaged concrete bridge slabs. *Composites: Part B,* vol. 43, pp. 2471–2479.
[5] Oehlers, D., Griffith, M. and Mohamed Ali, M. 2008. Ductility components and limits of FRP-plated RC structures. *Construction and Building Materials,* vol. 23, pp. 1538–1543.
[6] Al-Saidy, A., Al-Harthy, A., Al-Jabri, K., Abdul-Halim, M. and Al-Shidi, N. 2010. Structural performance of corroded RC beams repaired with CFRP sheets. *Composite Structures,* vol. 92, pp. 1931–1938.

Concrete Repair, Rehabilitation and Retrofitting IV – Dehn et al. (Eds)
© 2016 Taylor & Francis Group, London, ISBN 978-1-138-02843-2

Study of the crack pattern and its evolution by DIC of RC beams externally reinforced with TRC and CFRP

S. Verbruggen, T. Tysmans, J. Wastiels & S. De Sutter
Department of Mechanics of Materials and Constructions, Vrije Universiteit Brussel, Brussel, Belgium

ABSTRACT: Textile Reinforced Cements (TRC) are emerging as an external reinforcing material for concrete structures. Especially the high fibre volume fraction TRCs are investigated by researchers as an alternative for the already established Carbon Fibre Reinforced Polymer (CFRP) strips due to their high mechanical performances, their advantages related to fire safety and their relatively low cost. The application of an external bending reinforcement on a reinforced concrete beam will considerably influence the cracking behaviour of this beam, with potential benefits for the concerning serviceability limit state. An extensive experimental study of this influence and the difference between the different reinforcing materials (CFRP and TRC) is performed in this paper. To measure the crack pattern and its evolution, this paper presents the use of the Digital Image Correlation (DIC) technique. Based on these DIC measurements the bending cracking behaviour of reinforced concrete beams with spans of 0.6 and 2.3 meters is studied. For the small scale beams, the paper shows that the TRC-reinforced beams exhibit a similar crack pattern and evolution to the CFRP-reinforced beams, while for the larger scale beams the TRC-reinforced alternative exhibits a more favourable cracking behaviour. The effectiveness of the DIC measuring technique to monitor the cracking behaviour of externally reinforced concrete beams is hereby also demonstrated.

1 INTRODUCTION

In the past decades, the interest in externally reinforcing concrete structures has significantly increased resulting in uses like stay-in-place formwork or strengthening and repair applications. This interest is translated in a vast amount of research (CEB 2006, Alexander et al. 2012, Guadagnini), as well as in a large number of practical applications (ECC, Sika). Composites, e.g. carbon fibres imbedded in an epoxy matrix (CFRP—Carbon Fibre Reinforced Polymers) are mostly used as a reinforcing material. External reinforcement is actually one of the few applications where composites have truly known a breakthrough in civil engineering (Bank 2006).

Despite the established value of the CFRP material, other composites are emerging as reinforcing materials, like the Textile Reinforced Cement/concrete (TRC) composites, mainly because of their advantages related to fire safety and their reduced cost. Even though papers investigating the use of TRC as an external strengthening or repair material in shear (Triantafillou et al. 2006, Brückner et al. 2006, Blanksvärd et al. 2009, Contamine et al. 2011, 2013) as well as in bending (Taljsten 2007, Bisby 2009, Ombres 2011, 2012, D'ambrisi 2011) show promising results, most of them admit that additional developments are needed to meet the same loadbearing performance as the CFRP solution. For manufacturing reasons most of these studies use an open grid textile structure, resulting in a typical fibre volume fraction of 5%. Increasing this fibre volume fraction would result in an increased loadbearing capacity. In order to achieve this higher fibre volume fraction, we impregnate dense fibre textiles with a fine grained cementitious matrix, resulting in a fibre volume fraction of about 20%. Previous studies on the same high fibre volume fraction TRC already demonstrated the possibilities of this composite material as an external reinforcement (Verbruggen et al. 2012, 2013, 2014).

Still, comparison of the material tensile stress-strain behaviour shows that even with these high fibre volume fractions we are not able to even approach the tensile capacities of CFRP (Fig. 1).

This discrepancy in ultimate stress between both reinforcing materials results in a considerably larger TRC cross-section, needed to achieve a similar ultimate limit state capacity of the externally reinforced beam. This aspect might indicate that apart from the previous advantages like the fire safety, the main benefit of the (high fibre volume fraction) TRC external reinforcement should be found in cases where a serviceability limit state is dominant.

Therefore this paper investigates the influence of external TRC bending reinforcement on the

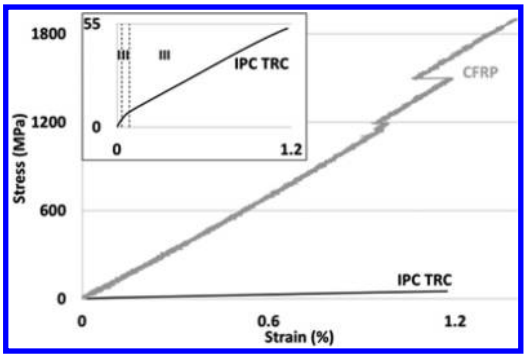

Figure 1. A significant difference in tensile strength is obtained between CFRP and TRC.

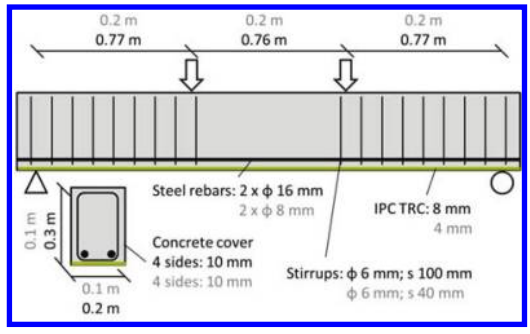

Figure 2. Two different beam geometries are tested.

cracking behaviour, and thus the concerning serviceability limit state in steel-reinforced concrete beams. The study is based on bending tests, monitored with Digital Image Correlation (DIC) to follow the crack pattern evolution.

2 EXPERIMENTAL PROGRAM

2.1 *Specimen types and test set-up*

In order to study the cracking behaviour in bending, externally reinforced beams are tested under four point bending with third point loading. Two different beam scales are investigated: small scale beams with a span of 0.6 m (indicated in grey in Fig. 2) and larger scale beams with a span of 2.3 m (indicated in black in Fig. 2). For each geometry both a TRC and CFRP externally reinforced alternative, together with a reference non-externally reinforced beam are tested. For the larger scale beams only one specimen per type is produced, for the smaller scale beams three reference specimens and four of each external reinforcement type are investigated. Only one representative beam of each type will be presented in an attempt to preserve an overview and considering the great similarity in the experimental results (Verbruggen 2014). The beam geometry and the specification of the internal reinforcement are summarized in Figure 2.

The global loadbearing behaviour, visualized in the load-deflection curves, is obtained out of load measurements by the testing bench and displacement measurements with a Linear Variable Differential Transformer (LVDT).

Both TRC and CFRP external reinforcement are glued onto the concrete using a two-component epoxy glue (PC 5800/BL produced by ECC (ECC 2009)). A pretreatment of the concrete surface, prior to placing the external reinforcement, is performed in order to remove the laitance layer, such that the aggregates are exposed.

2.2 *Materials*

2.2.1 *Concrete*

The concrete material characteristics of both beam geometries are described in Table 1. These material characteristics are experimentally determined at the age of testing of the beams. The compressive strength (Table 1) is the cylindrical strength calculated from tests performed on cubic shaped specimens. The young modulus can be calculated from the compressive strength. All calculations are based on (CEN 2004, BIN 1973).

2.2.2 *Steel reinforcement*

The traditional steel reinforcement consists of ribbed bars made of S500 steel, of which the material characteristics were not experimentally derived, so the standard values of 500 MPa for the yield stress and 200 GPa for the young modulus are assumed.

2.2.3 *TRC*

The TRC matrix material used in this study is Inorganic Phosphate Cement (IPC) (European Patent Office 2000) (commercially available under the name Vubonite (www.vubonite.com)). This cementitious material is developed at the Vrije Universiteit Brussel (VUB) and can be combined with standard E-glass fibres due to its neutral pH after hardening. IPC consists of a combination of wollastonite powder with a phosphoric acid liquid, in mass proportions of 82/100. This combination hardens at room temperature and becomes a strong, durable, heat resisting and fire-safe material. Using the hand layup production technique the IPC matrix is reinforced with 8 (0.6-m-span beams) or 16 (2.3-m-span beams) randomly in-plane oriented fibre textiles, being chopped strand mats Vetrotex M5, with a surface density of 300 g/m². This results in a thickness of about 4 mm (0.6 m span beams)

Table 1. Concrete material properties.

	0.6 m span	2.3 m span
Compressive strength	33.9 MPa	35.0 MPa
Young modulus	33.8 GPa	34.0 GPa
Modulus of rupture	4.8 MPa	5.3 MPa

Table 2. IPC TRC material properties.

Tensile strength	58.4 MPa
Ultimate strain	1.2%
Young modulus stage I	12.5 GPa
Young modulus stage III	4.8 GPa

or 8 mm (2.3 m span beams) and a fibre volume fraction of 21.0%. The non-linear tensile stress-strain behaviour of IPC TRC is illustrated in the top left corner of Figure 1. Table 2 summarises the material characteristics of the IPC TRC based on ten tensile tests.

For all beam geometries the IPC TRC is applied over the full width and length of the bottom surface.

2.2.4 *CFRP*

For the CFRP a constant thickness of 1.2 mm, a tensile strength of 2210 MPa and a Young modulus of 143 GPa were obtained.

A 63 mm and a 30 mm wide strip is applied in the middle of the beam width for the 0.6 m and 2.3 m span beams respectively.

3 DIGITAL IMAGE CORRELATION

Digital Image Correlation (DIC) is an optical, non-contacting measuring technique, enabling the possibility to determine the displacement- and deformation field of the specimen's surface under any type of loading condition. Prior to testing a speckle pattern of black spots on a white background is applied on the specimen's surface. Out of grey scale pictures taken during testing by two charge-coupled device cameras of this speckle pattern, a 3D image can be created. The measurements are based on the comparison of a reference image, generally in the unloaded stage, with the images taken at the different load steps. The comparison is done by searching for the same group of neighbouring pixels (called a subset) in both the reference and the loaded images. This comparison results in the displacement, represented in the centre of the subset. By moving the centre point of this subset over the whole image, in steps of a certain amount of pixels (called the step size), the full displacement field can be calculated. Out of a square grid of displacement points (called a strain window), the strain can be derived and represented in the centre of the strain window. Again by repetition the whole strain field can be obtained. (Sutton et al. 2009)

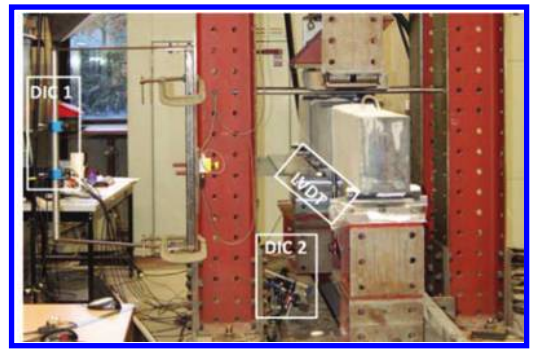

Figure 3. Two DIC systems are used to monitor the cracking behaviour of the beams.

The DIC technique is a valuable and promising tool to identify and monitor the crack pattern of concrete beams with externally bonded reinforcement. This can be done in a quantitative and qualitative way as cracks cause a discontinuity in the displacement and strain fields, which are both measured or calculated by DIC. Many recent studies apply a similar image processing technique to monitor concrete structures (Ferrier et al. 2003, Avril et al. 2004, Contamine et al. 2013, Tsangouri et al. 2013).

To monitor the crack pattern, two DIC systems are applied. One pair of DIC cameras (DIC 1 in Fig. 3) follows the side edge of the beam and another pair of cameras (DIC 2 in Fig. 3) the bottom edge. Both systems are set up in such a way that the entire or the central area of the constant bending moment zone (0.2 m for the 0.6 m span beams and 0.4 m for the 2.3 m span beams) can be measured. The analysis is done using the VIC3D-2009 software package from Correlated Solutions where a subset size of 31 (0.6 m span beams) or 21 (2.3 m span beams) pixels, a step size of 5 pixels and strain window size of 11 are used. Figure 3 illustrates the full test set-up and measuring equipment for the 2.3 m span beams.

4 RESULTS AND DISCUSSION

4.1 *0.6 m span beams*

The experimental results and their discussion are based on the load-deflection and failure behaviour, after which the cracking behaviour obtained with DIC measurements is introduced.

4.1.1 *Load-deflection behaviour*

The load-deflection behaviour of a reference, an IPC TRC and a CFRP reinforced smaller scale beam is compared in Figure 4. Just as in previous studies using IPC TRC external reinforcement, the initial high stiffness of both externally reinforced beams is retained 60% longer (15 kN) than the one of reference beam (9 kN) (Verbruggen et al. 2012, 2013, 2014). Due to the presence of a greater total amount of reinforcement, the post-cracking stiffness of the strengthened beams is higher than the one of the non-externally-reinforced reference beam. The load increase of respectively 47.6% and 59.8% as a consequence of the presence of external IPC TRC and CFRP reinforcement indicates the effectiveness of the external reinforcing technique.

The reference beam fails by steel yielding and concrete crushing at a load of 49.0 kN. Both the IPC TRC and CFRP-reinforced beams fail by steel yielding and concrete crushing, closely followed or preceded by debonding at flexural or mixed flexural and shear cracks (IPC TRC: 72.3 kN and CFRP: 78.3 kN). Both failure mechanisms clearly develop simultaneously during loading. The pictures of the failed specimens and the DIC results (Fig. 5) indicate the debonding at flexural cracks by the difference in vertical displacement between the external reinforcement and the concrete substrate. The experimental failure modes and ultimate loads are quite comparable for both reinforcing materials, enabling a further comparison of both beam types.

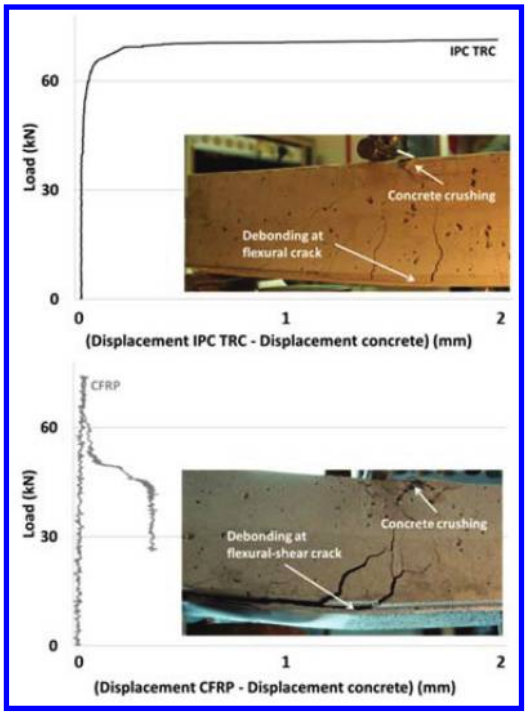

Figure 5. Both externally reinforced beams fail by steel yielding and concrete crushing, closely followed or preceded by debonding at flexural or mixed flexural and shear cracks.

4.1.2 *Cracking behaviour*

The cracking behaviour of the beams is studied based on the DIC measurements of the side and bottom surfaces in the zone of constant moment.

Figure 6 shows the relative horizontal displacement versus the horizontal position on the beam for different load steps at a height of typically 2 mm in the concrete. The vertical discontinuities indicate a sudden increase in horizontal displacement, and thus a crack in the concrete. The graph of the reference non-externally-reinforced beam is cut off at a displacement of 2 mm to keep a comparable overview with the externally reinforced beams. Its total horizontal displacement at the maximum load of 49.0 kN equals 4.1 mm. An overview of the plotted cracks and their numbering is given in the top left corner of each graph. This overview corresponds to the apparent strain field of the beam at its maximum load. Here a crack is defined as a difference in horizontal displacement larger than 0.02 mm at the maximum load over a horizontal interval of 5 mm, which is not adjacent to another crack interval.

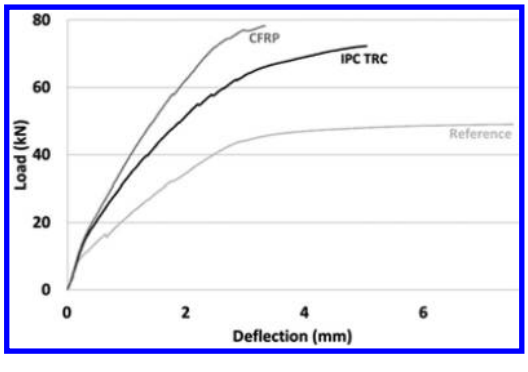

Figure 4. Both externally reinforced beams retain the initial stiffness longer and reach a higher ultimate load compared to the reference beam.

Adding external reinforcement to an internally-reinforced concrete beam increases the number of cracks, but this number is similar for the IPC TRC and CFRP reinforcing material: the reference beam shows four cracks, the CFRP and IPC TRC reinforced beams seven. Additionally, at a comparable load step the total horizontal displacement (and thus crack width) is much higher for the reference beam compared to the externally reinforced alternatives (e.g. at 40 kN the total displacement is 1.06 mm for the reference beam, 0.47 mm for the IPC TRC and 0.48 mm for the CFRP

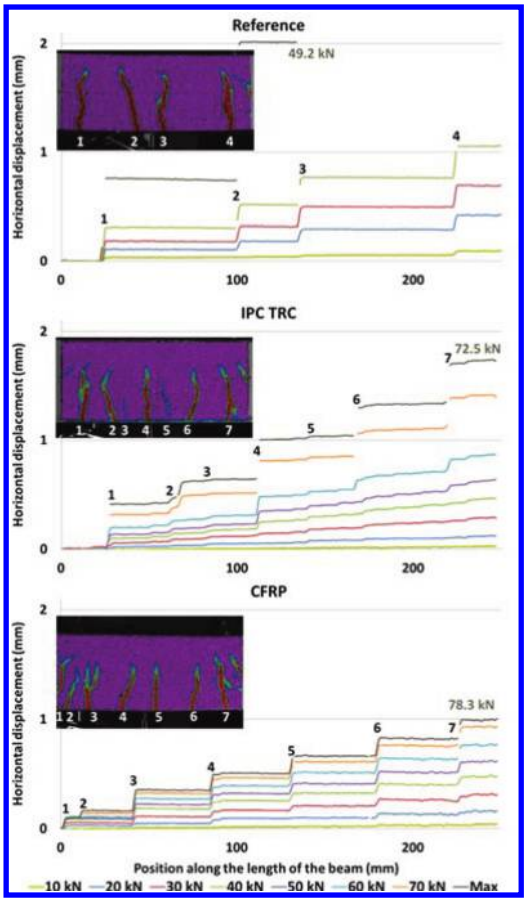

Figure 6. External reinforcement on a RC beam increases the number of cracks and reduces the crack width.

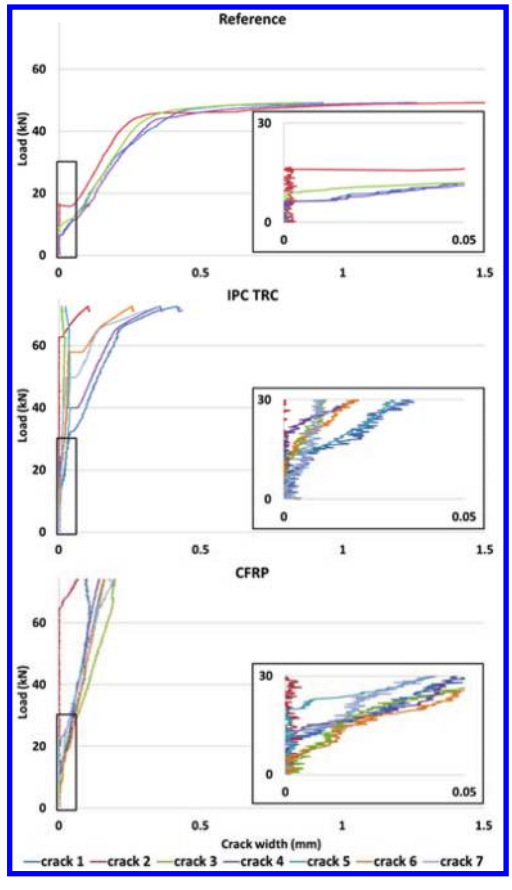

Figure 7. Despite the retention of initial high stiffness, the cracks in an externally reinforced RC beam nucleate at the same load as those in the reference RC beam.

reinforced beam). Both above findings result in a lower crack width for each individual crack for the externally reinforced beam. This can reduce moisture penetration and thus favourably influence the durability of the passive reinforcement, regardless the type of external reinforcement.

The evolution of the crack widths with increasing load illustrates the influence of an external reinforcement patch on the initiation and growth of the cracks (Fig. 7). All cracks present in the beams are represented and indicated with the same numbering as in Figure 6. The individual crack width evolution again indicates that the presence of an external reinforcement results in a significant smaller crack opening (maximum 1.5 mm for the reference beam compared to 0.2 mm for the CFRP en 0.4 mm for the IPC TRC reinforced beams).

To clarify the onset of the crack development, the lower right corner shows a zoom of this curve for loads from 0 kN to 30 kN and crack widths from 0 mm to 0.05 mm. All beam types exhibit already at least one crack at a load of about 7 kN, even when the initial high stiffness does not reduce until a higher load (15 kN) is applied (Fig. 4). For both externally reinforced beam types the crack nucleation is a gradual process, where most of the cracks start to form between 7 kN and 26 kN and one or two cracks even at a higher load, while for the reference beam all cracks nucleate between 6 kN and 16 kN with a sudden increase in crack width for a constant load. The simultaneous crack nucleation together with the moderate crack width increase for the externally reinforced beams results in the retained high uncracked stiffness. This confirms the conclusions for non-internally-reinforced beams drawn in (Verbruggen et al. 2012, 2013, Verbruggen 2014).

The retention of initial high stiffness is the consequence of the smaller crack widths due to the crack bridging capacity of the external reinforcement.

This crack bridging is indicated in Figure 8 for the IPC TRC reinforced beam, where he horizontal displacements in the zone of constant moment measured in the concrete (at the side of the beam—black curve), and measured in the external reinforcement (at the bottom of the beam—grey curve), are compared (at the maximum load of 72.5 kN). The vertical discontinuities (cracks) in the curve of the concrete are not present in the curve of the external reinforcement, even though both curves exhibit a comparable slope.

Figure 9 compares the evolution of the average crack width of all cracks present in the zone of constant moment in the concrete beams with an increasing load. Both externally reinforced beams exhibit a clearly smaller average crack width compared to their reference specimen. Up to a load of around 65 kN the average crack width of the IPC TRC reinforced beam is slightly lower than the one of the CFRP reinforced alternative. At a load of about 60 kN the individual (Fig. 7) as well as the total crack width (Fig. 6) increases for the beam externally reinforced with IPC TRC. The latter is probably due to the debonding between the IPC TRC and the concrete substrate at flexural cracks, which clearly develops around a load of 60 kN, as indicated in Figure 5.

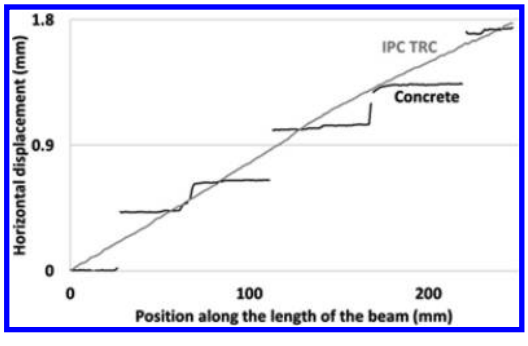

Figure 8. Even though the overall slope of the horizontal displacement versus position curves is comparable, the discontinuities (cracks) in the curve of the concrete are not present in the one of the external reinforcement.

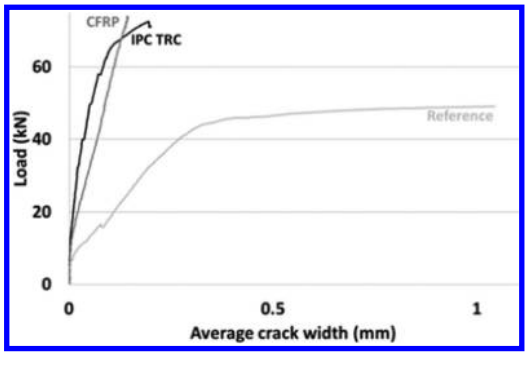

Figure 9. The average crack width of the externally reinforced beams is significantly smaller than the one of the reference beam.

4.2 *2.3 m span beams*

To exclude possible scale effects related to the small scale specimens, similar experiments are performed on a limited number of larger scale beams.

4.2.1 *Load-deflection behaviour*

Figure 10 represents the load-deflection behaviour of the 2.3 m span beams, where the externally CFRP and IPC TRC-reinforced beams, reach a comparable ultimate load of 192 kN and 209 kN respectively, compared to 152 kN for the reference beam. Even though the IPC TRC reinforcement results in a retention of the initial high stiffness compared to the reference non-strengthened specimen (50 kN versus 35 kN—increase of 43%), the CFRP alternative loses its high stiffness at the same load as the reference beam. This could be due to the fact that the amount and the contact width of the CFRP (30 mm) is to small compared to the width of the concrete substrate (200 mm).

Figure 11 indicates the different failure modes occurring during testing in the IPC TRC reinforced beam: steel yielding and concrete crushing, debonding at flexural cracks and debonding at the end anchorage. The debonding at flexural cracks is indicated by the difference in vertical displacement between the external reinforcement and the concrete substrate, which already starts around 80kN, but suddenly increases at 165 kN. For the CFRP-reinforced beam on the other hand, failure is only determined by debonding at flexural cracks.

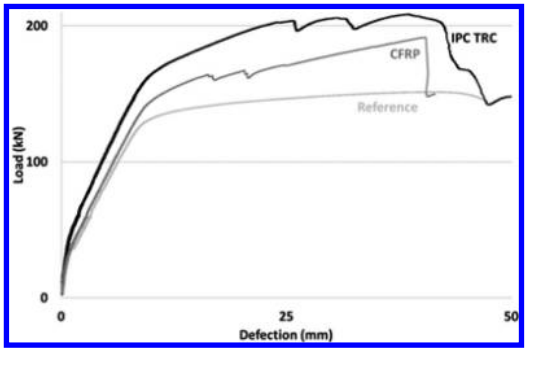

Figure 10. The IPC TRC reinforcement results in a retention of the initial high stiffness compared to the reference non-strengthened specimen and the CFRP alternative (50 kN versus 35 kN—increase of 43%).

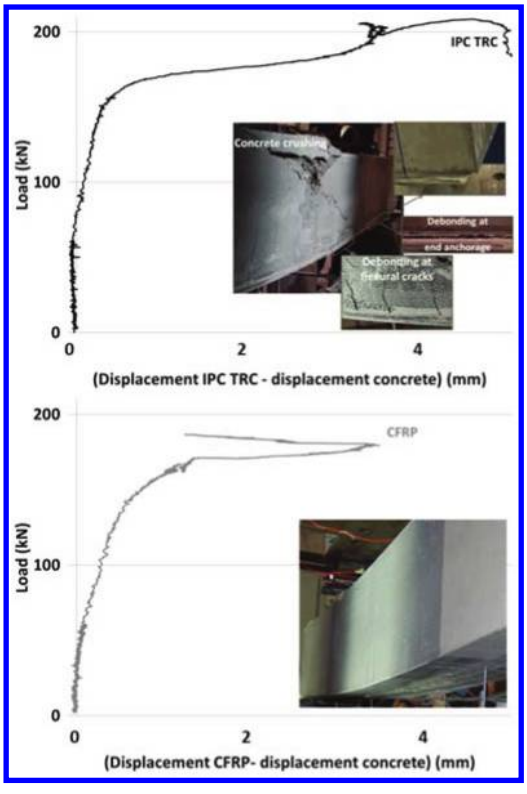

Figure 11. The IPC TRC reinforced beam exhibits several failure modes, while the CFRP reinforced alternative fails by debonding.

The different failure modes between both externally reinforced beams may be explained by the larger contact area between the IPC TRC reinforcement and the concrete substrate, which not only avoids peeling-off, but also precludes better the crack extension and opening.

4.2.2 *Cracking behaviour*

Similarly to Figure 6, Figure 12 plots the horizontal displacement over the length of the beam together with an overview of the cracks. Due to a to large displacement of the reference beam the pictures of the last load steps (from 140 kN onward) cannot be correlated correctly and so no reliable results can be retrieved. Adding external reinforcement to a RC beam increases the number of cracks: two for the reference beam, three for the CFRP-reinforced beam and seven for the IPC TRC counterpart. Contrarily to the very similar cracking behaviour of the IPC TRC and CFRP-reinforced 0.6 m span beams, where the same number of cracks is obtained, the larger scale IPC TRC-reinforced beam has more than double the amount of cracks with a comparable total displacement as

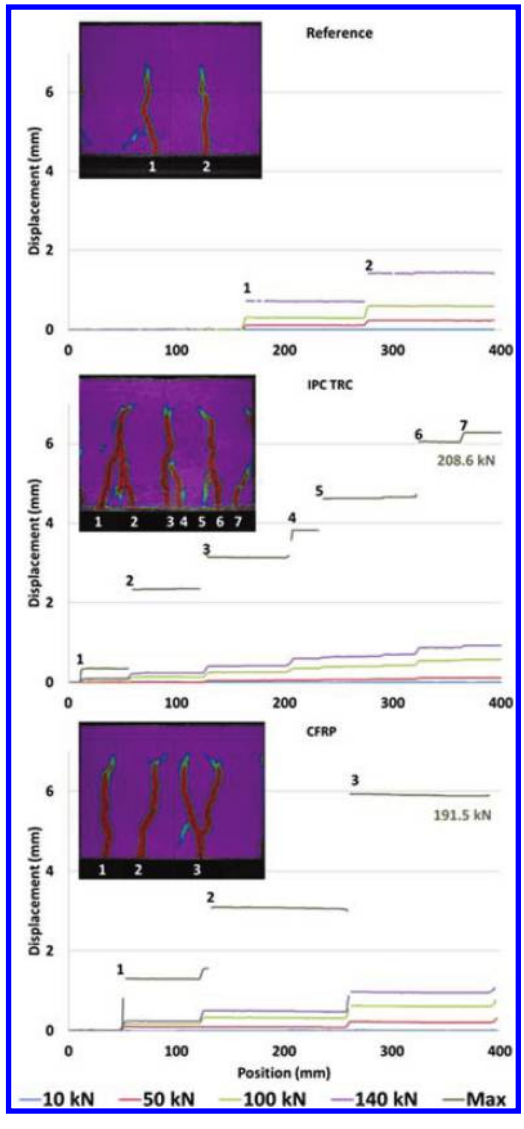

Figure 12. Contrarily to the smaller scale beams, the IPC TRC reinforced beam exhibits more cracks compared to the CFRP alternative.

the CFRP-reinforced alternative. The combination of a larger amount of cracks with a comparable total displacement results in a lower crack width for each individual crack. This difference with the smaller scale beams is probably due to the larger discrepancy in contact area between the external reinforcement and the concrete substrate (small scale: 100×600 mm^2 versus 63×600 mm^2; medium scale: 200×2300 mm^2 versus 30×2300 mm^2).

Figure 13 represents the individual crack width evolutions for all cracks identified by the

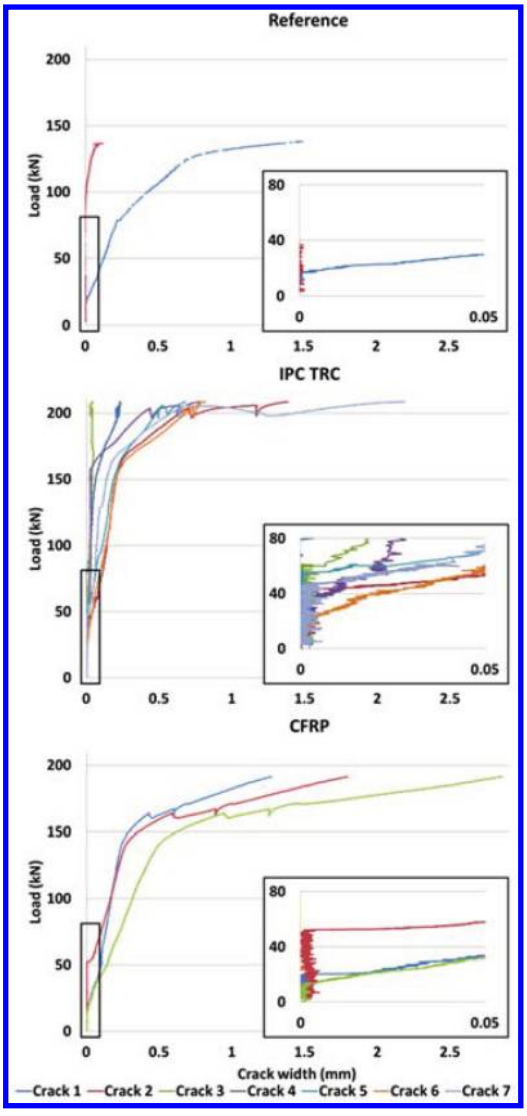

Figure 13. The crack openings in the IPC TRC-reinforced beam are lower and their development is more gradual compared to the CFRP alternative.

discontinuities in de horizontal displacements (Fig. 12), with a zoom on the onset of the crack development in the lower right corner (similar to Fig. 7 for the smaller scale beams). At lower load steps (up to 165 kN—start of the clear debonding of the IPC TRC (Fig. 10)) the individual crack widths of the IPC TRC-reinforced beam are significantly lower than the ones of the CFRP-reinforced counterpart, confirming the observations from Figure 10. Also does the IPC TRC-reinforced beam exhibit a more gradual and slow crack opening development, whereas the CFRP-reinforced beam even exhibits a sudden increase in crack width for a constant load. These differences between both reinforcing materials are probably due to the more efficient crack bridging with a larger contact width between the reinforcement and the concrete substrate. This might expose an advantage of IPC TRC over CFRP, as a larger cross-sectional area and thus contact width with the concrete is needed to meet the same load-bearing capacity as a CFRP-reinforced beam due to the lower strength of the IPC TRC.

5 CONCLUSIONS

Compared to CFRP strips and depending on the set-up and the failure modes, IPC TRC as a reinforcing material can offer several advantages related to the cracking and damage behaviour of a concrete beam. These advantages originate mainly from the lower strength and stiffness of the IPC TRC, which leads to a larger cross section (and thus contact width) than the one necessary with CFRP to meet a similar ultimate load.

The DIC measuring technique proved a valuable tool to measure the cracking behaviour of externally reinforced concrete beams. This is the consequence of the broad spectrum of possible quantitative and qualitative results, obtained by performing these DIC measurements on the side and the bottom surfaces of the specimens.

ACKNOWLEDGEMENTS

Research partially funded by a scholarship of the Institute for the Promotion of Innovation through Science and Technology in Flanders (IWT-Vlaanderen) and by the Brussels Capital Region through the Innoviris Strategic Platform Brussels Retrofit XL.

The authors gratefully acknowledge the cooperation with the company TRADECC, trough the delivery of the epoxy glue and CFRP.

REFERENCES

Alexander M.G., Beushausen H.-D., Dehn F. & Moyo P. (Editors) 2012. *Proceedings of Concrete repair, rehabilitation and retrofitting III (ICCRRR)*. Cape Town, South Africa: CRC Press, Taylor & Francis Group.

Avril S., Ferrier E., Vautrin A., Hamelin P. & Surrel Y. 2004. A full-field optical method for the experimental analysis of reinforced concrete beams repaired with composites. Compos part A-appl s; Vol. 35; pp. 873–884.

Bank L.C. 2006. *Composites for construction: Structural Design with FRP Materials*. Hoboken, New Jersey: John Wiley & Sons, Inc.

BIN (Belgisch instituut voor de normalisatie) 1973. Proeven op beton; Drukproef; addendum 1. Belgische Norm, Brussels.

Bisby L.A., Roy E.C., Ward M. & Stratford T.J. 2009. Fibre reinforced cementitious matrix systems for fire-safe flexural strengthening of concrete: Pilot testing at ambient temperature. Proceedings ACC, NGCC; Chesterfield, U.K.

CEN (Comité Européen de Normalisation) 2004. Eurocode 2: Design of concrete structures—Part 1–1: General rules and rules for buildings. ENV 1992-1-1.

Blanksvärd T., Täljsten B. & Carolin A. 2009. Shear strengthening of concrete structures with the use of mineral-based composites. J compos constr; Vol.12, No. 1; p. 25–34.

Brückner A., Ortlepp R. & Curbach M. 2006. Textile reinforced concrete for strengthening in bending and shear. Mater struct; Vol. 39; p. 741–748.

Brückner A., Ortlepp R. & Curbach M. 2008. Anchoring of shear strengthening for T-beams made of Textile Reinforced Concrete (TRC). Mater struct; Vol. 41; p. 407–418.

CEB-FIP 2006. *fib bulletin 35; Retrofitting of concrete structures by externally bonded FRPs with emphasis on seismic applications*. Lausanne, Switzerland; ISBN 2-88394-075-4.

Contamine R., Si Larbi A. & Hamelin P. 2011. Evaluation of the TRC (Textile Reinforced Concrete) solutions in the case of RC beams shear strengthening. Proceedings ICSHCC2; Rio de Janeiro, Brazil; p. 89–95.

Contamine R., Si Larbi A. & Hamelin P. 2013. Identifying the contributing mechanisms of Textile Reinforced Concrete (TRC) in the case of shear repairing damaged and reinforced concrete beams. Eng struct, Vol. 46, p. 447–458.

D'Ambrisi A. & Focacci F. 2011. Flexural strengthening of RC beams with cement-based composites. J compos constr; Vol. 15, No. 5; p. 707–720.

ECC. Referentielijst Opgelijmde wapening. http://www.ecc-belgium.be/.

European Patent Office 2000. EP 0 861 216 B1, Inorganic Resin Compositions. Their Preparation And Use Thereof.

Ferrier E., Avril S., Hamelin P. & Vautrin A. 2003. Mechanical behaviour of beams reinforced by externally bonded CFRP sheets. Mater struct; Vol. 36; pp. 522–529.

Guadagnini M. (Chair of the action) 2013–2017. *COST Action TU1207: Next Generation Design Guidelines for Composites in Construction*. http://tu1207.eu/.

Ombres L. 2012. Debonding analysis of reinforced concrete beams strengthened with fibre reinforced cementitious mortar. Eng fract mech; Vol. 81; p. 94–109.

Ombres L. 2011. Flexural analysis of reinforced concrete beams strengthened with a cement based high strength composite material. Compos struct; Vol. 94; p. 143–155.

Sika. Sika at work projects. http://aus.sika.com/.

Sutton M.A., Orteu J.J. & Schreier H.W. 2009. Image correlation for shape, motion and deformation measurements. Basic concepts, theory and applications. Springer Science+Business Media; New York, USA; ISBN 978-0-387-78746-6.

Täljsten B. & Blanksvärd T. 2007. Mineral-based bonding of carbon FRP to strengthen concrete structures. J compos constr; Vol. 11, No. 2; p. 120–128.

TRADECC 2009. PC 5800/BL. http://norborn.no/wp-content/uploads/2011/12/PC-5800-BL-TD.pdf.

Triantafillou T.C. & Papanicolaou C.G. 2006. Shear strengthening of reinforced concrete members with Textile Reinforced Mortar (TRM) jackets. Mater Struct, Vol. 39; p. 93–103.

Tsangouri E., Van Tittelboom K., Van Hemelrijck D. & De Belie N. 2013. Visualization of the healing process on reinforced concrete beams by application of Digital Image Correlation (DIC). Proceedings HPSM6; New Forest, UK; pp. 1–12; ISBN 978-1-84564-720-9.

Verbruggen S., Wastiels J., Tysmans T., Remy O. & Michez S. 2012. The influence of externally bonded longitudinal TRC reinforcement on the crack pattern of a concrete beam. Proceedings ICCRRR, Cape Town, South Africa, p. 1259–1265.

Verbruggen S., Wastiels J., Tysmans T. & Puystiens S. 2013. Comparison between TRC and CFRP as external reinforcement for plain concrete beams. Proceedings ICCM19; Montreal, Canada; ISBN: 978-0-9696797-1-4; p. 2252–2260.

Verbruggen S., Tysmans T. & Wastiels, J. 2014. TRC or CFRP strengthening for reinforced concrete beams: An experimental study of the cracking behaviour. Eng Struct, Vol. 77, p. 49–56.

Verbruggen S. 2014. Reinforcement of concrete beams in bending with externally bonded textile reinforced cementitious composites. PhD thesis, Vrije Universiteit Brussel.

Concrete Repair, Rehabilitation and Retrofitting IV – Dehn et al. (Eds)
© 2016 Taylor & Francis Group, London, ISBN 978-1-138-02843-2

Intelligent, multifunctional textile reinforced concrete interlayer for bridges

C. Driessen & M. Raupach
Institute of Building Materials Research, RWTH Aachen University, Aachen, Germany

ABSTRACT: In bridges, which show defective sealing, chloride ions can migrate into the concrete, catalyse the corrosion of the reinforcement and thus threaten the durability of the construction. The corrosion of the reinforcement can only be seen on the surface of the bridge when a high degree of impairment is already reached. Consequently, at that state, comprehensive building operations are necessary, which lead to traffic obstructions and thus to economic losses. In the context of the joint research project "Intelligent, multifunctional textile reinforced concrete surface for bridges – SMART-DECK"– an innovative, multifunctional and thin interlayer will be developed, which will provide three functions: an all-over real-time humidity-monitoring; a preventive cathodic corrosion protection, which can be adjusted by sections and a strengthening reinforcement of bridges with an insufficient load-bearing capacity.

1 INTRODUCTION

1.1 *The joint research projcet*

"Smart Deck" is a joint research project of seven partners from industry and science. The project is sponsored by the BMBF and is planned to be finalized within three years.

1.2 *Underlying idea*

In the context of the project an innovative, multifunctional and thin (approx. 30 mm) interlayer for bridges will be developed, which will provide significant benefits in comparison to the state of the art for new bridge constructions as well as for existing bridges. SMART-DECK is based on textile reinforced concrete and will provide three functions: an all-over real time humidity-monitoring; a preventive cathodic corrosion protection, which can be adjusted by sections and a strengthening reinforcement of bridges with an insufficient load-bearing capacity. By means of the monitoring system damages in the sealing layer are recognized early and, combined with the cathodic corrosion protection, traffic obstructions are prevented.

The renewing of the bridge deck sealing has not to be carried out immediately after an alarm value has been reached, but can be postponed to periods with little traffic. All three functions—the monitoring system, the preventive cathodic corrosion protection and the reinforcement—are realized by textile reinforcement, which consists of carbon meshes and a new developed mortar. Thus it is possible that Smart—Deck does not increase the dead load of the structure or at least not significantly. The aim of Smart-Deck is to extend the durability of bridge constructions and reduce economic losses which emerge from traffic delays because of comprehensive building operations. Furthermore despite the higher initial investments the life cycle costs of bridges can be reduced due to fewer maintenance intervals.

2 THE TREE FUNCTIONS OF SMART DECK

2.1 *The monitoring system*

The interlayer will be divided into sections, which are arranged transverse to the lane. Each section builds a separate sensor. Two technical textile layers are arranged with a spacing of 15 mm. The electrical resistivity between the two layers is measured. When the sealing starts to leak and water permeates into the interlayer, a drop in the measured electrical resistivity is detected and the operator of the bridge construction receives a note about the leakage. It is planned to monitor the condition of the sealing in real time. Therefore all relevant data are transmitted via internet or mobile radio and are presented in a simple form e.g. in a color scheme. By now, sensors for the monitoring of humidity in constructions or sensors which help to estimate the probability of corrosion exist, but these sensors work only discrete at the point of installation (Raupach 2013). The monitoring of a complete construction would need a high number of sensors, which is not an economic solution.

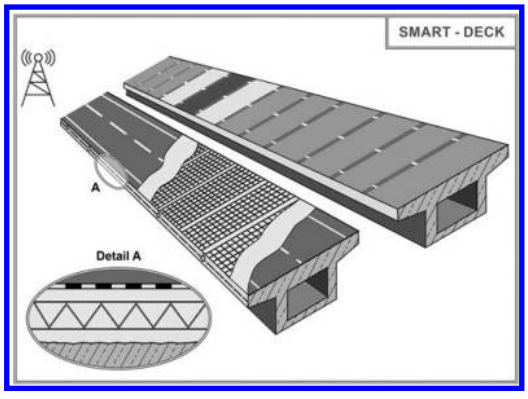

Figure 1. The intended structure of Smart-Deck.

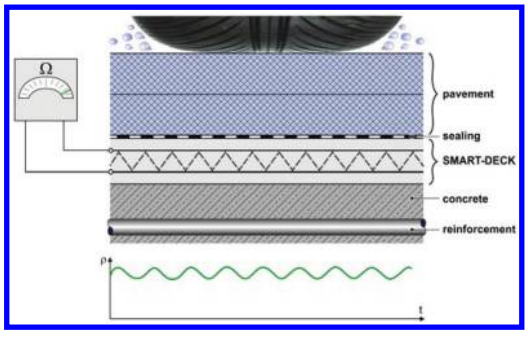

Figure 2. The monitoring system.

2.2 *The cathodic corrosion protection*

When an event of damage in the sealing is detected and when it is impossible to fix the defective sealing without delay in traffic, the cathodic corrosion protection can be switched on. Thus the constructional measures of the bridge deck sealing can be postponed to periods with less traffic or to that point of time when a renewing of the sealing is planned anyway. With a rectifier an electrical field is generated between the carbon and the reinforcement, which disables chloride migration into the construction. Thus the depassivation of the steel is prevented. Nowadays systems for cathodic corrosion protection are not used on lanes and bridges because of cost concerns: primarily due to the fact that the sealing has to be removed to install the anodes and moreover the established impressed current anodes are expensive.

2.3 *Reinforcement by the technical carbon textiles*

In the course of the project the strengthening effect of the textile reinforcement to the transverse load-bearing capacity will be examined. Due to the reinforcement of the flexural tension zone, the crack formation is reduced, so it is expected that the transverse load—bearing capacity will reach a higher level.

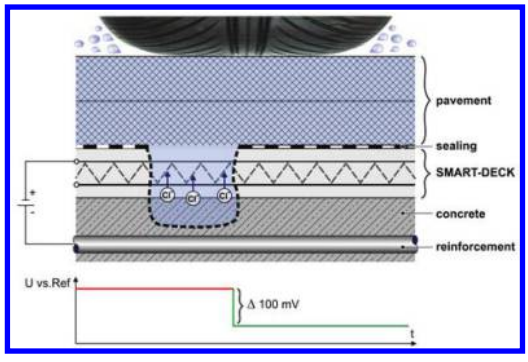

Figure 3. The cathodic corrosion protection.

3 EXPERIMENTAL PROGRAM

3.1 *Development of the mortar mixture*

To investigate the electrical resistivity of the mortar experiments with alternating current between at least two layers of carbon textiles will be performed.

3.1.1 *Relationship between electrical resistivity and humidity*

To develop a well-working monitoring system one has to examine the properties of the mortar in regard to the relationship between electrical resistivity and humidity on the one hand. To receive a finely graduated humidity-monitoring it is necessary that the mortar has a high sensitivity for humidity, which means that the mortar should have a wide range in resistivity-values at different points of moisture content. On the other hand for the cathodic corrosion protection a low electrical resistivity of the mortar would be advantageous. In order to reach these objectives a suitable pore structure has to be found. In this context capillary pores with low constrictivity and tortuosity could help to achieve the intended properties (Reichling 2012).

3.1.1.1 Test specimen production and test method

The structure of the test specimen can be seen in Figure 4. The electrical resistivity between the meshes is measured with alternating current. Therefore the specimens are stored under water until the measured resistivity values stay constant. The measured values and the weight of the

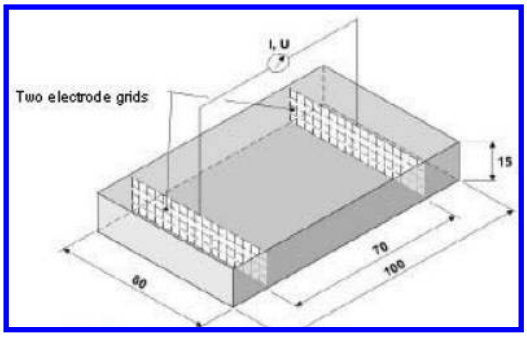

Figure 4. Test Specimen for resistivity examinations.

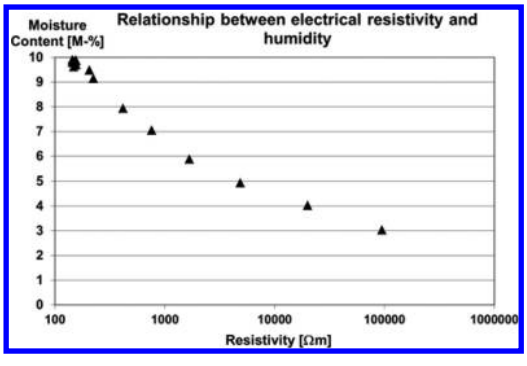

Figure 5. Relationship between electrical resistivity and humidity.

specimens are recorded. Afterwards the specimens are dried to reach low water contents. Starting at these contents, different moisture contents are being adjusted through the addition of different amounts of water. The specimens are being packed vapour resistant to reach a homogenous distribution of the water. After two weeks the specimens are being unpacked and weighed. The resistivity is being measured before the specimens are dried again until they reach a constant weight and are being weighed again. Based on this data the relationship between humidity and resistivity values can be calculated. The AC resistance is converted with a cell constant into a resistivity.

In the following diagram the relationship between humidity and electrical resistivity of one kind of mortar used in the project is shown. The objective is to modify this mortar or to develop a new mortar to receive a higher drop in the resistivity values and thus a better detectability of damages in the sealing. However even with the existing difference in electrical resistivity values at different moisture contents one can already assess the condition of the sealing.

Additionally, criteria have to be worked out defining which humidity values or otherwise which

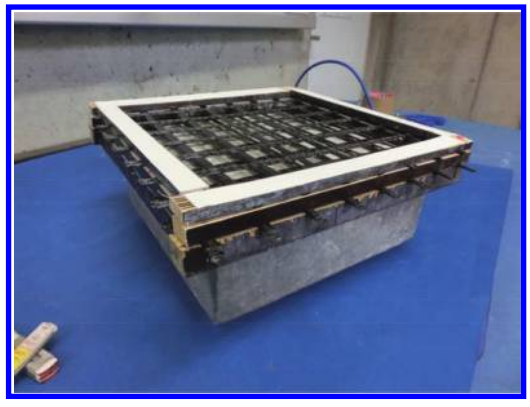

Figure 6. Specimen with carbon textiles before the mortar was filled in.

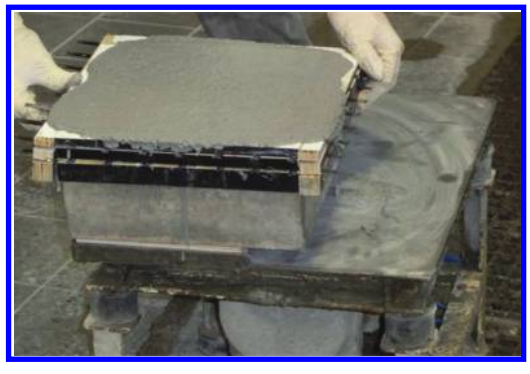

Figure 7. Specimen with carbon textiles and mortar at the wacker plate.

drop of electrical resistivity defines the level of risk for the bridge construction. It has to be examined which size of defective sealing should reasonably be detected. Therefore numerical simulations are being used to analyze the influence of scale effects and temperature. If the measurements mentioned above will not allow conclusions concerning the humidity values and resulting the risk for corrosion impedance-spectroscopy measurements will be used. At a defined risk level the cathodic corrosion protection will be switched on automatically.

3.2 *Selection of the technical textile*

The polarization behavior of different types of technical carbon textiles is being examined. Therefore specimen with matured concrete (approx. two years) with a counter electrode in form of a titanium mesh and a reference electrode were used to apply layers of mortar and textile reinforcement.

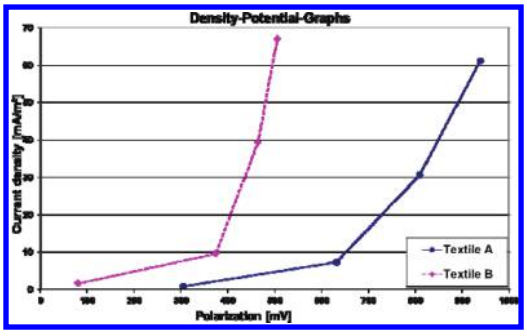

Figure 8. Density-Potential-Graphs of technical carbon textiles with different mesh widths.

Two layers of carbon textile reinforcement were fixed with a spacing of 7.7 mm and 22.5 mm respectively to the substrate concrete at the formwork. Then mortar was poured into the formwork and filled up to a level of 7.5 mm above the textile layer.

Previous studies show that technical carbon textiles with a small mesh width reach even at a low level of polarization (400 mV) a current density of 20 mA/m², which is sufficient for the cathodic protection of steel in concrete. In the diagram below Textile A has twice as many rovings as Textile B, which leads to a greater surface and therefore to higher current densities at the same level of polarization.

Another aspect is the durability of the system in respect to the carbon. Experiments are planned, to find out whether in case of a permanent polarization of the carbon an oxidation of the carbon takes place. This could lead to a reduced durability of Smart Deck. Due to the low current densities which are needed for a preventive cathodic corrosion protection, possibly no significant oxidation of the carbon occurs. In addition the influence of the dispersions and coatings of the textile reinforcement on the polarization properties of the carbon will be tested.

3.3 *Development of the electronic components*

For the functionality of the system, it is important to do researches on the frequency response of the system, so that it is possible to acquire data on the drop of resistivity in case of a defective sealing without electrode polarization. Therefore electrochemical impedance spectroscopy will be used. The measuring frequency is adjusted to the impedance of the mortar.

4 CONCLUSION AND OUTLOOK

4.1 *Conclusion*

The following conclusions can be drawn at the actual state of the project:

- One of the tested mortars showed already a clear difference in electrical resistivity values at different points of moisture contents. Thus the intended concept for the monitoring should be feasible.
- It is possible to reach polarization values which are high enough for the cathodic protection with low current densities using technical carbon textiles.
- Investigations on the strengthening effect of the technical carbon textiles are being examined at the Institute of Structural Concrete (IMB).

4.2 *Outlook*

After the development of all components for the three functions, the system will be applied on a bridge construction to test the collaboration of the different functions.

ACKNOWLEDGEMENT

The authors would like to thank the BMBF for sponsoring the project and the project executing organization, "VDI Technologiezentrum GmbH (VDI TZ)" for the support. (http://www.eurovia.de/standort/17866-niederlassung-bauwerksinstandsetzung).

The project partners:

Eurovia Beton GmbH, Niederlassung Bauwerksinstandsetzung, Hofheim-Wallau (Projektkoordinator); Bundesanstalt für Straßenwesen, Bergisch-Gladbach; FTA GmbH, Albstadt; Massenberg GmbH, NL Bürstadt; Sto SE & Co. KGaA, Stühlingen; Institut für Massivbau (IMB), RWTH Aachen.

REFERENCES

Raupach, M.; Gulikers, J.; Reichling, K.: Condition Survey with Embedded Sensors Regarding Reinforcement Corrosion. In: Materials and Corrosion 64 (2013), Nr. 2, S. 141–146 ISSN 1521-4176.

Reichling, K.; Weichold, O.; Raupach, M.: Was verrät uns der elektrische Widerstand über den Beton? What do we Learn About the Electrical Resistivity of Concrete? In: Restoration of Buildings and Monuments 18 (2012), Nr. 5, S. 265–274 ISSN 1864-7251.

Concrete Repair, Rehabilitation and Retrofitting IV – Dehn et al. (Eds)
© 2016 Taylor & Francis Group, London, ISBN 978-1-138-02843-2

Preliminary investigation of flexural strengthening of RC beams using NSM iron-based shape memory alloys bars

H.N. Rojob & R. El-Hacha
University of Calgary, Calgary, Alberta, Canada

ABSTRACT: The applications of Shape Memory Alloys (SMA) in structural engineering field are limited to small scale projects and not adapted in practical application due to its high cost. Recently, the iron-based SMA (Fe-SAM) is being developed. The inexpensive constitutive materials of the Fe-SMA and the availability of mass production facilities of steel products makes this material more suitable for large scale structural engineering applications than the most common SMAs (i.e. NiTi). SMA is mainly characterized by the Shape Memory Effect (SME) phenomenon. The SME represents the ability of the SMA to recover part of the inelastic strain through heating. This paper reports on the flexural performance of $2000 \times 305 \times 150$ mm RC beam strengthened with Fe-SMA tested under four point bending setup. The pre-strained Fe-SMA bar was anchored inside a groove cut on the tension side of the RC beam and then heated up to 350°C, where the transformation from martensite to austenite phase occurred causing a prestressing force developed in the Fe-SMA bar that counteracts the applied loads. The results revealed a significant increase in the yielding and ultimate loads. Furthermore, the ductility of the beam was significantly improved.

1 INTRODUCTION

As the strengthening and rehabilitation of structures become vital tools to solve the deterioration issues of reinforced concrete structures, researchers are looking for more practical, efficient, and economical techniques. The application of innovative materials such as Fiber Reinforced Polymers (FRPs) was widely used in the past few decades, especially in the area of flexural strengthening of reinforced concrete (RC) beams (Lamanna, et al., 2001; El-Hacha & Rizkalla, 2004; Baky, et al., 2007). For flexural strengthening, the FRPs are typically applied as Externally Bonded (EB) sheets/plates/strips, Near Surface Mounted (NSM) strips/bars, or Mechanically Fastened (MA) strips/plates at the tension face of the RC beams/slabs. The use of FRPs shows a superior performance relative to the conventional rehabilitation materials (i.e. steel and concrete). The application of FRPs reinforcement in the form of strips, sheets, plates, and bars is considered to be a passive strengthening technique in the sense that these materials will not be active unless a further deformation or deflection is induced in the beam, which means that this type of strengthening is meant to improve the ultimate capacity of the beams. In some cases it is essential to improve the performance of the RC beams at service loads to reduce deflection and cracking. To achieve that, researchers introduced the application of prestressing FRPs where the FRP elements are prestressed against the structural members in the form of active strengthening (El-Hacha and Soudki, 2013; El-Hacha & Gaafar, 2011, El-Hacha et al. 2001).

More recently, Shape Memory Alloys (SMA) have been attracting the researchers from different fields due to their superior properties. Besides the material superelasticity, corrosion and fatigue resistivity, SMAs are mainly characterized by the Shape Memory Effect (SME) phenomenon. The SME represents the ability of the SMAs to recover part of the inelastic strain through heating. The recovered strain in this transformation can be utilized to introduce stresses to structures. The most common SMA is made of Nickel and Titanium (NiTi). Due to the high cost of the NiTi, it wasn't widely used in large-scale civil engineering applications. A newly developed Iron-based SMA (Fe-SMA) with considerably lower cost, and high recovery stress of 200–400 MPa, is considered to be a suitable choice for structural engineering applications (Awaji, 2014; Dong, et al., 2009; Li, et al., 2013).

The approach proposed herein adopts the NSM technique for flexural strengthening of RC beams using Fe-SMA bars. The pre-strained Fe-SMA is to be anchored in a grove cut on the tension side of the RC beam, followed by heating above the activation temperature. Because the bar is restrained from

both ends through steel anchors, no strain will be recovered. Instead, the heating process will cause a prestressing force in the Fe-SMA bar that counteracts the applied loads on the beam, and eventually improve the serviceability and ultimate behaviors. In this case the SMA does not require any jacking system or sophisticated anchorage tools. The ongoing research project studies the behavior of concrete beams strengthened with Fe-SMA bars under different loading and environmental conditions. This paper reports on the behavior of RC beam strengthened with Fe-SMA bar under monotonic loading tested at room temperature.

2 BACKGROUND

The SMAs in general are characterized by two main distinct properties, namely; the pseudo-elasticity and the Shape Memory Effect (SME). These properties are attributed to the temperature and stress dependent phase transformation. Martensite phase exist at low temperatures, and the high symmetry phase called Austenite phase at high temperature. The uniqueness of SMAs is attributed to the martensite transformation which occurs by shear lattice distortion and not by atom diffusion. In absence of load, the martensite transformation (also called forward transformation) starts at temperature value M_s (martensite start) until temperature M_f (martensite finish) at which all the material transforms into martensite form. The reverse transformation (from martensite to austenite) starts when the material is heated in absence of stress at a temperature marked as A_s (austenite start). The material will totally transform to austenite at A_f (austenite finish) as shown in Figure 1. During the cooling process below M_f, the twining process prevents any macroscopic shape change, where multiple variants coexist in a phase called twinned martensite. The martensite variants can be forced to orient (detwin) in a one dominant variant through mechanical loading. The detwinning process takes place at a stress level σ_s (detwinning start) and finishes at stress level σ_f (detwinning finish) causing macroscopic inelastic strain. Upon heating the SMA material while in the detwinned martensite phase above A_f the detwinned martensite phase transforms to the parent austenite phase causing recovery of the inelastic strain. This process is called the Shape Memory Effect (SME) as presented in Figure 2 (Lagoudas, 2008; Cismasiu, 2010). The SME can be utilized to apply stresses to structures by having the ends of the SMA material restrained. In this case, no recovery strain will occur, alternatively, a recovery stress will develop. It is worth mentioning that part of the inelastic strain is induced through a slip deformation (movement

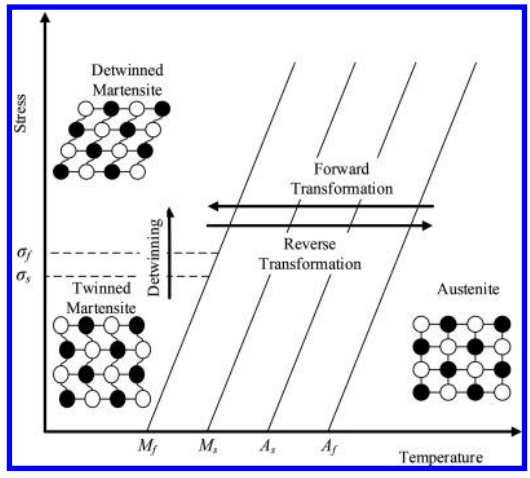

Figure 1. Phase diagram of SMA, after Lagoudas (2008).

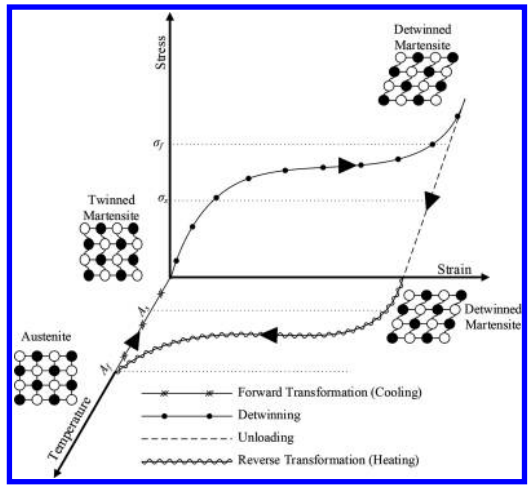

Figure 2. Shape memory effect of SMA, after Lagoudas (2008).

of dislocations). This type of strain causes a reduction in the shape recovery ratio (recovered strain to initial strain) depending on the type of SMA (Awaji, 2014).

3 EXPERIMENTAL PROGRAM

The experimental program of this research project consists of testing seven (150 × 305 × 2000 mm) rectangular RC beams in total. The beams are divided in three sets according to the testing conditions. The first set involves the testing of two beams strengthened with NSM Fe-SMA bars

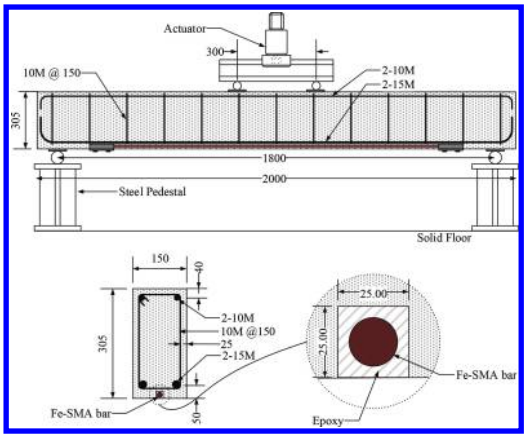

Figure 3. Geometric details of the RC beam strengthened with Fe-SMA bar.

and one control unstrengthened beam. The two strengthened beams in the first set vary based on the thermo-mechanical training of the Fe-SMA bar (i.e. no training, one cycle training). The beams in the first set will be tested at room temperature under monotonic loading. In the second set, one control unstrengthened beam and one strengthened beam will be tested after being exposed to sever environmental conditions. The third set consists of one control unstrengthened beam and one strengthened beam tested under cyclic loading. This paper reports on the results of the RC beam strengthened with NSM Fe-SMA bar without thermo-mechanical training tested monotonically at room temperature. Figure 3 shows the geometric details of the RC beam. The beam is 2000 mm long with 1800 mm span length, and cross section of 150×305 mm. The beam was designed according to CSA 23.3–04 such that no shear failure will occur. Therefore, 10M two-legged stirrups were provided at spacing of 150 mm. The beam was reinforced with two 15M bars in tension and two 10M bars in compression with total steel cross-sectional area of 400 mm^2 and 200 mm^2, respectively. The average yield and ultimate strengths of the steel reinforcements were 458 MPa and 619 MPa, respectively. The average compressive strength of the concrete at the day of testing was 40 MPa.

3.1 *Preparation of the Fe-SMA bar*

The beam was strengthened with 1000 mm long and 14.3 mm diameter Fe-SMA manufactured by Awaji (2014). The stress-strain curve of the Fe-SMA bar is shown in Figure 4. The Fe-SMA bar was initially strained to 6% as shown in Figure 5. The bar was threaded using NF 6/19″ threading tape on both ends as presented in Figure 6. The

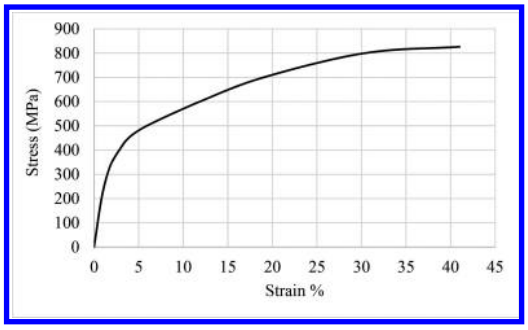

Figure 4. The stress strain curve of the Fe-SMA bar (Awaji, 2014).

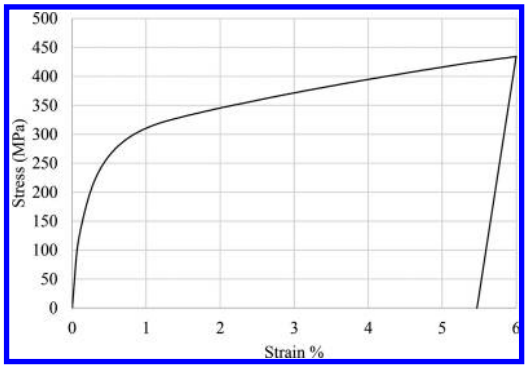

Figure 5. The application of 6% strain to the Fe-SMA bar.

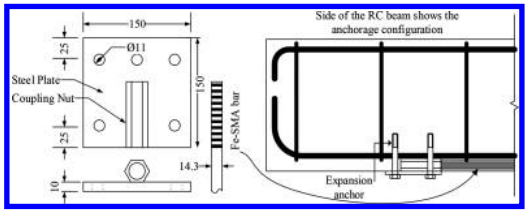

Figure 6. Details of the anchorage set.

bar was then connected to the steel coupling nuts at both ends. The coupling nuts were then welded to 10 mm thick steel plates as shown in Figure 6. The bar was then embedded inside a groove cut on the tension side of the RC beam. The steel plates were anchored to the RC beam using Carbon Steel Kwik Bolt 3 Expansion anchor produced by Hilti Inc. (2011) as shown in Figure 6.

3.2 *Heating procedure*

A flexible resistive heating tape was wrapped around the Fe-SMA bar. The bar was then heated

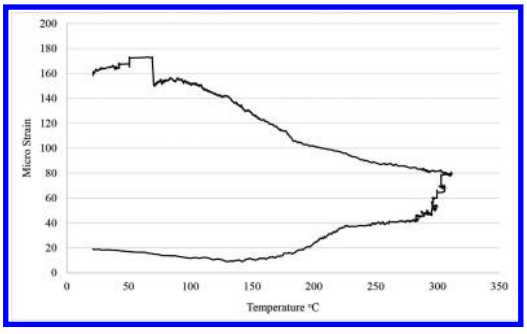

Figure 7. Concrete strain at the level of tension steel during the heating process (Noting that the beam was flipped over to facilitate the heating process).

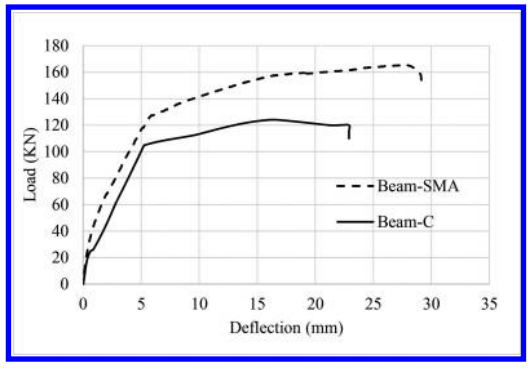

Figure 9. Load-deflection curves of Beam-C (Hadiseraji & El-Hacha, 2014), and Beam-SMA.

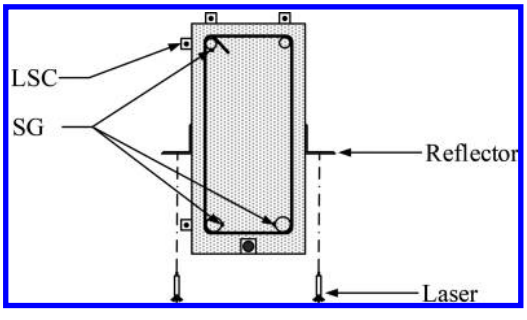

Figure 8. Locations of the strain gauges (SG), LSCs, and laser transducers at the mid-span of the beam.

Figure 10. Flexural cracks at the mid-span of Beam-SMA.

to 350°C. The strain in the concrete at the level of tension steel was monitored during the heating process. A slight reduction in the strain was initially observed as shown in Figure 7 due to the thermal expansion behavior of the Fe-SMA bar. Once the temperature reached the activation temperature of the Fe-SMA bar (150°C), the strain started to increase. In the cooling stage, further compression strain in the concrete was observed caused by the removal of the thermal expansion effect. After the beam cooled down, the groove was filled with epoxy adhesive produced by Sika (2012).

3.3 *Bending test*

The beam was tested monotonically on four point bending setup as shown earlier in Figure 3. The beam was instrumented with four Linear Strain Conversion (LSC) at the mid-span of the beams as presented in Figure 8 to monitor the stain at the concrete surface (two LCSs were placed on the side of the beam in which one of each is mounted at the level of the longitudinal bottom and top steel; and two LCSs were mounted at the top of the beam to measure the strain in the concrete in compression). Two strain gauges (SG) were installed on the tension steel and one was installed on the compression steel. Two laser transducers were used to monitor the vertical deflection at the mid-span of the beam.

4 RESULTS AND DISCUSSION

The strengthened beam failed in a ductile failure mode by crushing of concrete after the yielding of the steel reinforcement and Fe-SMA bar, respectively. The load mid-span deflection curve of the beam strengthened with NSM Fe-SMA bar (Beam-SMA) is presented in Figure 9 along with the control beam (Beam-C) tested by Hadiseraji & El-Hacha (2014). Figure 10 shows the flexural cracks at the mid-span of Beam-SMA. Figure 11 shows the distribution of strain across the depth of Beam-SMA at the mid-span at the cracking load, yielding load, and ultimate load.

Table 1 shows a summary of the testing results. The results indicate that the flexural performance of the strengthened beam was improved. The yielding load and the ultimate load were increased by 22% and 33%, respectively. More importantly,

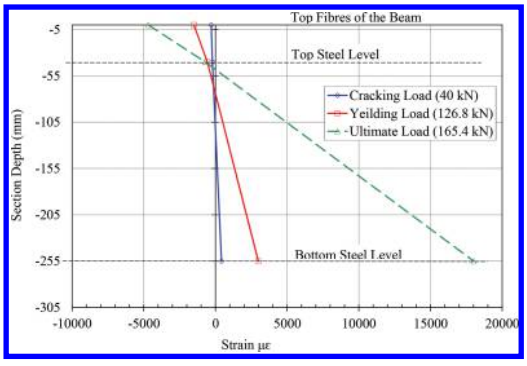

Figure 11. Strain distribution across the depth of Beam-SMA at the mid-span at different loading levels.

Table 1. Summary of the test results of: Beam-C (Hadiseraji & El-Hacha, 2014) and Beam-SMA.

	Beam-C	Beam-SMA	%Δ
Cracking load: P_{cr} (kN)	19	40	111
Yielding load: P_y (kN)	104	126.8	22
Ultimate load: P_u (kN)	124	165.4	33
Deflection at yield: Δ_y (mm)	5.3	5.7	7
Deflection at ultimate: Δ_u (mm)	18.0	27.5	53
Deformability index	3.4	4.8	43
Energy dissipated (kN.mm)	1534	3777	146

the ductility was significantly improved. The ductile behavior of the Beam-SMA was reflected by the 43% increase in the deformability index (the deformability index was calculated as the ratio of deflection at ultimate load to the deflection at yield load), and the 146% increase in the total dissipated energy over Beam-C (the total dissipated energy was computed as the total area under the load deflection curve up to the ultimate load).

5 CONCLUSIONS

The test results revealed the feasibility and effectiveness of the Fe-SMA bars in flexural strengthening of RC beams. The advantages of such smart material over the FRPs are the easiness of applying the prestressing force and the high ductility of the material that allows for a ductile failure mode. It is worth mentioning that the Fe-SMA bar was used without thermo-mechanical training. The application of thermo-mechanical training will result in an improvement in the mechanical performance of the Fe-SMA bar and eventually enhances the flexural capacity of the strengthened beam. The research project is ongoing and results will be presented in future publications.

ACKNOWLEDGMNETS

The authors would like to acknowledge the University of Calgary and the Natural Sciences and Engineering Research Council of Canada (NSERC) for their financial support towards this research project.

REFERENCES

Awaji. 2014. Shape Memory Alloy. (Awaji Materia Co. Ltd) Retrieved Dec 27, 2014, from http://www.awaji-m.jp/english/r_and_d/about.html#alloy

Baky, H.A., Ebead, U.A., & Neale, K.W. 2007. Flexural and Interfacial Behavior of FRP-Strengthened Reinforced Concrete Beams. *Composite for Construction*, Vol. 11, No. 6, pp. 629–693.

Cismasiu, C. 2010. *Shape Memory Alloys*. Rijeka, Croatia: Sciyo.

Dong, Z., Klotz, U.E., Leinenbach, C., Bergamini, A., Czaderski, C., & Motavalli, M. 2009. A Novel Fe-Mn-Si Shape Memory Alloy With Improved Shape Recovery Properties by VC Precipitation. *Advanced Engineering Materials*, Vol. 11, No. 1–2, pp. 40–44.

El-Hacha, R., & Soudki, K. 2013. Prestressed near-surface mounted FRP reinforcement for concrete structures—a review. *Canadian Journal of Civil Engineering*, Vol. 40, No.11, pp. 1127–1139.

El-Hacha, R., & Gaafar, M. 2011. Flexural strengthening of reinforced concrete beams using prestressed, near-surface-mounted CFRP bars. *PCI Journal*, Vol. 56, No. 4, pp. 134–151.

El-Hacha, R., & Rizkalla, S.H. 2004. Near-Surface-Mounted Fiber-Reinforced Polymer Reinforcements for Flexural Strengthening of Concrete Structures. *ACI Structural Journal*, Vol. 101, No. 5, pp. 717–726.

El-Hacha, R, Wight, R.G., & Green, M.F. 2001. Prestressed fibre-reinforced polymer laminates for strengthening structures. *Progress in Structural Engineering and Materials Journal*, No. 3, pp. 111–121.

Hadiseraji, M., & El-Hacha, R. 2014. Strengthening RC beams with prestressed near-surface mounted CFRP stip. CICE 2014 Conference, 20–22 August 2014. Vancouver, BC, Canada.

Hilti Inc. 2011. Kwik Bolt 3 Carbon Steel. Retrieved 01 08, 2015, from https://www.hilti.ca/anchor-systems.

Lagoudas, D.C. 2008. *Shape Memory Alloys*, Modeling and Engineering Applications. Texas, USA: Springer Science.

Lamanna, A.J., Bank, L.C., & Scott, D.W. 2001. Flexural Strengthening of Reinforced Concrete Beams Using Fasteners and Fiber-Reinforced Polymer Strips. *ACI Structural Journal*, Vol. 98, No. 3, pp. 368–376.

Li, K., Dong, Z., Liu, Y., & Zhang, L. 2013. A newly developed Fe-based shape memory alloy suitable for smart civil engineering. *Smart Materials and Structures*, Vol. 22, pp. 1–7.

Sika. 2012. Product Data Sheet: Sikadur 32. (Sika Inc.) Retrieved June 2014, from https://can.sika.com/

Concrete Repair, Rehabilitation and Retrofitting IV – Dehn et al. (Eds)

Preliminary experimental investigation of reinforced concrete columns confined with NiTi SMA wires

K. Abdelrahman & R. El-Hacha
University of Calgary, Calgary, Alberta, Canada

ABSTRACT: Strengthening concrete columns through confinement techniques is commonly used to enhance the structural performance of the concrete. Recently, an innovative strengthening technique that utilizes smart materials termed Shape Memory Alloys (SMA) have been introduced. The SMA possesses unique characteristic properties that lie in their ability to undergo large deformations and return back to their original shape through stress removal or heating. This paper aims to investigate the use of SMA in the form of wires to actively confine the concrete. The preliminary investigation includes characterizing the material properties of the SMA wire relevant to the confinement application. In this case, namely the tensile properties and the recovery stress test was conducted. The experimental testing conducted to determine appropriate splicing connection for the SMA wire is also presented. Finally, a preliminary experimental study was conducted to determine the effectiveness of utilizing SMA wires to actively confine the concrete. The test results showed significant enhancement in the strength and ductility of the SMA confined concrete, when compared to the unconfined concrete specimen.

1 INTRODUCTION

Recent catastrophic failures due to earthquakes revealed the vulnerability of our infrastructure. Investigations conducted on these structures revealed that the main cause of failure was associated with the collapse of the concrete columns that lead to progressive failure of the structure. Thus, it is now imperative that repair and strengthening strategies of concrete columns is crucial to ensure the safety of the public and revive our current infrastructure to become structurally reliable to withstand future earthquake events.

Traditional strengthening and repair methods such as concrete casing and steel jacketing are considered ineffective, as the strengthening material suffer from the same deterioration effect as the parent material. On the other hand, the use of non-corrosive and light-weight materials such as Fibre Reinforced Polymers (FRP) become passively engaged and confines the concrete column only after significant damage is encountered by the concrete. Thus, there is a critical need to develop smart and innovative strengthening strategies for concrete columns.

Recently, a new class of smart materials termed Shape Memory Alloys (SMA) have been introduced as a strengthening material to enhance the structural performance of concrete columns. The SMA's possess unique thermo-mechanical properties and material characterization that overcome the shortcomings of the abovementioned confinement methods. The SMA used in the form of wires, when wrapped around the column can actively confine the concrete by utilizing its unique thermo-mechanical properties. Thus, the main objective of this paper is to investigate the possibility of actively confining the concrete columns using SMA wires, which is the first phase of a currently ongoing research study undertaken by the authors to study the influence of eccentric loading conditions on SMA confined concrete columns.

In this paper, a background information on SMA's and a brief literature review on the very limited research studies related to SMA confined concrete is presented. Followed by the experimental testing conducted to characterize the material properties of the SMA wires, specifically the tensile properties and the recovery stress characteristics. Also included in this paper is the splicing connection test performed to determine an appropriate method to connect splices of the SMA wires. The main objective of this paper was approached by conducting a preliminary experimental study, which consisted of actively confining concrete columns using SMA wires, and comparing its structural performance with an unconfined concrete column.

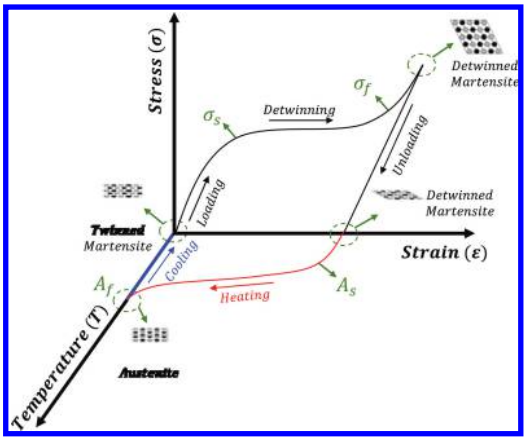

Figure 1. Shape memory effect of the SMA (after Lagoudas, 2008).

2 BACKGROUND INFORMATION ON SMA

Shape Memory Alloys (SMA) are commonly referred to as smart materials for their ability to take large deformations (up to 8%) and return to their original shape upon heating or unloading. These unique properties of SMA occur due to phase transformation of the material between the austenite and martensite phases. The austenite and martensite phases are related to the high temperature and low temperature state of the material. The SMA's are characterized by four distinctive temperatures: austenite start temperature (A_s), austenite finish temperature (A_f), martensite start temperature (M_s), and martensite finish temperature (M_f).

Recovering the original shape of the SMA after being deformed beyond its elastic limits through unloading is referred to as super-elasticity, and through heating is characterized as the Shape Memory Effect (SME). In this paper, only the SME phenomenon will be discussed due to its relevancy to the confinement application mechanism. To better describe this phenomenon, the thermo-mechanical loading path in a combined stress-strain temperature space is schematically shown in Figure 1. Under a stress-free state, loading the material in its martensitic form results in a linear elastic stress-strain response until the minimum detwinning stress (σ_s) is reached. After this point, the SMA experiences a yielding plateau due to a detwinning process characterized by a zone of large strains and low stiffness. The detwinning finish stress (σ_f) marks the completion of the detwinning process and is usually followed by an increase in the stiffness depending on the type of the SMA. At this stage, unloading the SMA would approach a state of zero stress with retained deformation in the material. Recovering the original undeformed state of the material occurs by heating the SMA above the austenite finish temperature (A_f). This triggers the SME of the SMA, which is characterized by phase transformation from martensitic to austenitic. Subsequent cooling of the SMA would transform the material back to its martensitic state, and the entire cycle can be repeated (Fig. 1).

3 LITERATURE REVIEW

The conceptual idea of utilizing the SME of the SMA as a confinement strategy to enhance the performance of the concrete was first proposed by Krstulovic-Opara & Thiedeman (2000). This innovation comprised of embedding post-tensioned SMA fibres in the cementitious composites of high and normal-strength concrete cylinders. The test results reported in this study showed enhancement in the strength and ductility of the tested cylinders. Through the aforementioned study, Janke et al. (2005) realized the potential of utilizing SMA as a form of external strengthening strategy to actively confine the concrete. Experimentally investigating this concept was first performed by Choi et al. (2008), where the authors studied the ability of Ni-Ti SMA in the form of martensitic and austenitic wires to externally confine concrete cylinders. The findings reported in this study were considered as a major breakthrough as it verified experimentally the success of concrete confinement using SMA wires, by quantifying the enhancement in the structural performance of the SMA confined concrete. The effectiveness of utilizing Ni-Ti SMA wires to actively confine concrete cylinders was also studied by Andrawes et al. (2010), Destrebecq & Balandraud (2010), Mirzaee et al. (2010) and Zuboski (2013). The findings of these test studies also confirmed the superior structural performance of the concrete specimens confined with the SMA wires.

Choi et al. (2010) investigated the use of NiTiNb SMA wires to externally confine concrete cylinders. The test data showed that the NiTiNb SMA wires increased the compressive strength and ductility of the cylinders. They also found that the NiTiNb wires were more effective in increasing the peak strength and dissipating energy than the NiTi wires.

Further experimental investigation was conducted by Shin & Andrawes (2010), where the research focus was aimed at comparing the performance of SMA confined concrete cylinders with that of the cylinders wrapped with the conventionally used Glass Fibre Reinforced Polymers (GFRP) sheet. The test results showed a significant

increase in the strength and ultimate strain of the SMA actively confined concrete cylinders over the conventional GFRP wrapped concrete cylinders. The authors also proposed a new hybrid active/passive confinement technique that comprised of SMA spirals plus GFRP/epoxy sheets (SMA-GFRP). The study showed that the hybrid SMA-GFRP confinement technique exhibited a superior performance over the conventional passive confinement technique. This research investigation clearly showed the potential of using SMA spirals solely or as a supplementary confinement technique along with FRP wraps.

Tran et al. (2014) conducted a similar research investigation as Choi et al. (2008), where concrete cylinders were actively confined using Ni-Ti SMA wire in its martensitic state, and passively confined using the SMA wire in its austenitic state. Their comparison between using SMA wire through active and passive confinement mechanism showed that the stiffness, strength and ductility were significantly improved in the case of active confinement.

In light of the very limited research studies conducted on SMA confined concrete, it is clearly recognizable that this active confinement technique has a great potential to significantly enhance the structural performance of concrete columns.

4 SMA MATERIAL COMPOSITION AND CHARACTERIZATION

The main elements that compose the SMA wire selected for this study were Nickel (*Ni*) and Titanium (*Ti*) with an atomic percentage of 48% and 37%, respectively. The SMA wires had a round cross-sectional diameter of 1.9 mm that could provide a linear strain recovery up to 6.3% when heated above the A_s temperature of 60°C. The SMA wires have been supplied by the manufacturer in its martensitic pre-strained form in cut lengths of 2.4 meters. According to the manufacturer, the ultimate tensile strength, elastic modulus, and strain at failure of the SMA wire were 818 MPa (±50 MPa), 462 MPa (±5 MPa), and 41% (±5%), respectively.

5 TENSILE TESTING OF SMA WIRE

During the confinement procedure, the SMA wire is initially utilized in its pre-strained martensite form. After which, the application of heat triggers the SME of the SMA wire transforming the wire into its austenite state that actively confines the concrete specimen through a reactive force induced by restraining the SMA wire. Thus, the tensile characteristics of the SMA wire were determined in its martensite and austenite state.

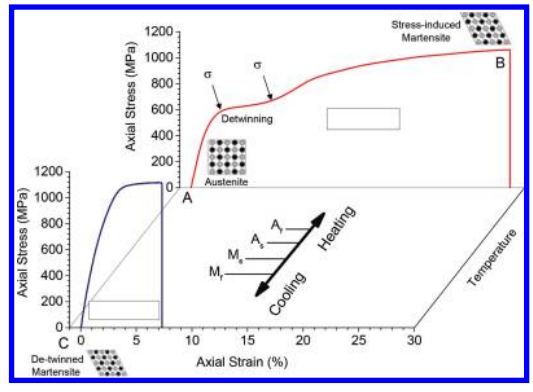

Figure 2. Stress-strain behaviour of the SMA wire in the martensite and austenite phases.

The SMA wires were shipped by the manufacturer in their martensitic state and the tensile test performed at this stage will determine the martensitic tensile properties of the SMA wire. In order to determine the austenitic tensile properties, the SMA wire was heated via electrical current above the austenite transformation temperatures (>60°C). The SMA wire was left to cool down to room temperature (≈22°C) and due to its unique thermo-mechanical properties, the martensitic SMA wire was now transformed to its austenite phase and can sustain this phase at room temperature. At this point, the tensile testing of the SMA wire will determine its austenitic tensile properties.

The gauge length of the SMA specimen used to determine the tensile characteristics of the wire was 300 mm. Three specimens were tested at each state (martensite and austenite) of the SMA wire for repeatability purposes. A tensile displacement control mode was applied at a rate of 4.5 mm/sec until failure. The stress-strain characteristics of the SMA wire in the martensite and the austenite phases are shown in Figure 2. For clarity purposes, the result of only one specimen in each phase was included in the figure, however, the results of all the tested specimens is summarized in Table 1. Typical stress-strain behaviour of the SMA wire in the martensite and the austenite phases were achieved. The martensitic SMA wire showed a linear stress-strain relationship up to the yield point, after which the stiffness reduced significantly defined by a region of increasing axial strain accompanied with a slight increase in the stress until failure. For the austenitic SMA wire, an increase in the stiffness was noticed after the yield point accompanied with increasing stress and deformation until failure.

Table 1. Summary of the experimental tensile testing of the SMA wire.

Properties	UOM*	T-1	T-2	T-3	Avg.	(±Std)
	Martensite Phase					
Yield Stress	MPa	720	660	650	677	(±38)
Yield Strain	% 1.3	2	1.6	1.5	1.77	(±0.3)
Ult. Tensile Strength	MPa	1100	1101	1117	1106	(±9.5)
Elongation	%	7.4	7.8	7.3	7.5	(±0.3)
	Austenite Phase					
Yield Stress	MPa	500	520	560	527	(±25)
Yield Strain	%	2	2.2	1.9	2	(±0.12)
Ult. Tensile Strength	MPa	1079	1082	1062	1074	(±8.8)
Elongation	%	36	37	29	34	(±3.6)

* UOM = Unit of Measurement; Std: Standard deviation.

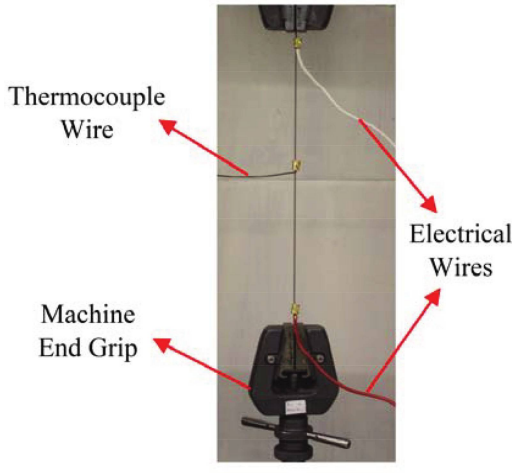

Figure 3. Recovery stress test of the SMA wire.

6 RECOVERY STRESS TEST

Quantifying the amount of recovery stress generated to actively confine the concrete column is paramount for column design purposes. The recovery stress mechanism of the SMA wire is activated by heating the material above the austenite finish temperature (A_f) of 120°C. There are several methods reported in the literature to induce heat to the SMA wire, among which, the most common methods include the use of a torch, an oven, or an electrical current. A key factor to the success of implementing SMA confinement strengthening technique is to ensure that the practicality aspect is satisfied. Accordingly, the heating methods using a torch or oven are considered to be impractical and have been discarded. Thus, the use of an electrical current was selected in this research study as the heating source to the SMA wire. This heating method is easily applicable and ensures uniform flow of heat through the material. In addition, the control parameters such as the voltage, current, heating temperature and the time required to the heat the SMA wire are easily controllable and adjustable compared to the other heating techniques.

Once the heating source of the SMA wire was determined, the recovery stress can now be examined. This investigation was conducted using a Tinius Olsen testing machine with a load capacity of 20 kN. The testing protocol involved restraining the SMA wire using the end grips of the machine. Then, an electrical current was passed through the SMA wire triggering the SME mechanism, and since the wire was restrained, a recovery stress was generated in the wire. The recovery stress was calculated from the reaction force measured using the load cell in the machine. The temperature of the SMA wire was monitored using a thermocouple. The set-up of the recovery stress test is shown in Figure 3.

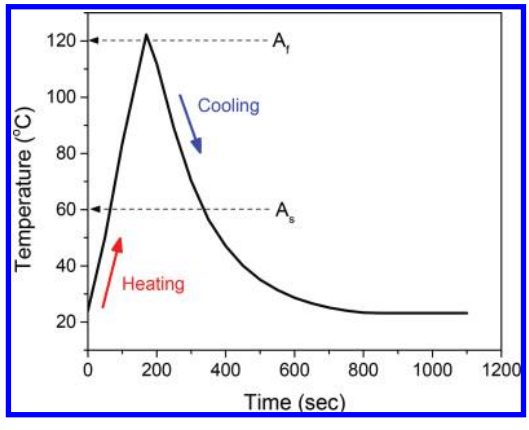

Figure 4. Temperature versus heating time of the SMA wire.

The recovery stress test was conducted on three SMA specimens measuring 40 cm in length. For clarity purposes, the test results for one sample was graphed in Figures 4–6. The recovery stress test was initiated by heating the SMA wire via electrical current above the austenite finish temperature (A_f) and then the wire was left to cool back to room temperature. The desired temperature of 120°C was reached within 3 minutes from heating the SMA wire (Fig. 4). As the temperature of the SMA wire increased, the generated recovery stress also increased linearly until a yield point

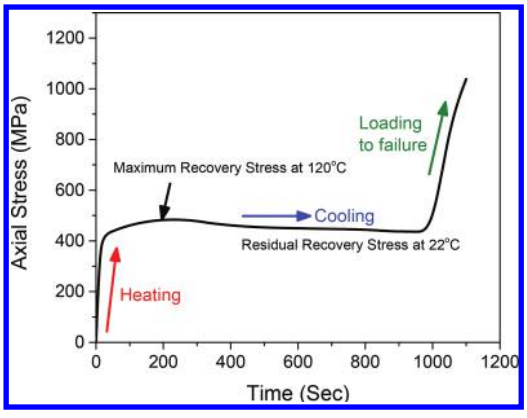

Figure 5. Axial stress versus time for the SMA wire recovery stress test.

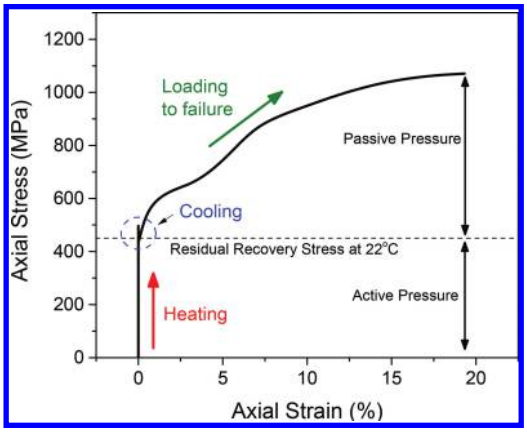

Figure 6. Axial stress versus axial strain for the SMA wire recovery stress test.

was reached corresponding to the austenite start temperature (A_s) at 60°C. After which, the recovery stress increased at a slower rate with the increase in temperature until the desired temperature of 120°C was reached, corresponding to A_f. Terminating the heat source caused a gradual drop in the maximum recovery stress attained until it eventually stabilized at room temperature, representing the residual recovery stress of the SMA wire (Fig. 5). For one of the tests, the SMA wire was then loaded to failure to determine the total confinement pressure. The total confinement pressure of the SMA wire is generated through active and confinement mechanisms. The active confinement pressure produced by the SMA wire is triggered by the SME, and the passive confinement pressure applied by the SMA wire is generated during the axial compressive loading of the SMA confined concrete. The testing protocol shown in Figure 6 allowed

Table 2. Maximum and residual recovery stress of the SMA wire.

Parameter	UOM*	T-1	T-2	T-3	Avg	(±Std)
Maximum Recovery Stress	MPa	579	584	581	581	(±2.7)
Residual Recovery Stress	MPa	486	483	486	485	(±1.6)

* UOM = Unit of Measurement Std: Standard deviation.

to quantify the generated active and passive confinement pressure of the SMA wire. The summary of the recovery stress test results is presented in Table 2. Accordingly, the maximum recovery strain attained by the SMA wire was 581 MPa, the recovery stress then converged and became stable at a value of 485 MPa at room temperature.

7 ANCHORAGE SYSTEM

For shipment and pre-straining purposes, the SMA wires have been supplied by the manufacturer in cut lengths of 2.4 meters. In addition to the need to anchor the SMA wire at the ends of the specimens, the use of a splicing connection was also necessary to ensure continuity of the SMA wire across the height of the specimen. Three splicing mechanisms that included the use of sleeves, welding the SMA wires, and U-clamp connections were considered. The advantages and disadvantages of each splicing connection system were evaluated and in some cases were experimentally investigated.

The first splicing type connection investigated was welding splices of the SMA wires. Theoretically, the heat produced from the welding process would alter the thermo-mechanical properties of the SMA wire that could potentially trigger the SME of the wire, thus, the welding type connection was discarded. The second type of splicing connection investigated involved the use of sleeve anchors. A preliminary experimental investigation was conducted to evaluate the effectiveness of the sleeve anchors as a potential splicing connection adopted for this study. The load transfer mechanism of the sleeve anchors were investigated by connecting two splices of the SMA wire using varying number of sleeve anchors subjected to tensile loading. The test results showed immediate slippage of the SMA wires with up to five sleeves anchors used at the splicing connection. Thus, the use of the sleeve anchors as a splicing connection was discarded. Finally, the use of the U-clamp anchors as a splicing connection was investigation by conducting a similar experimental study to

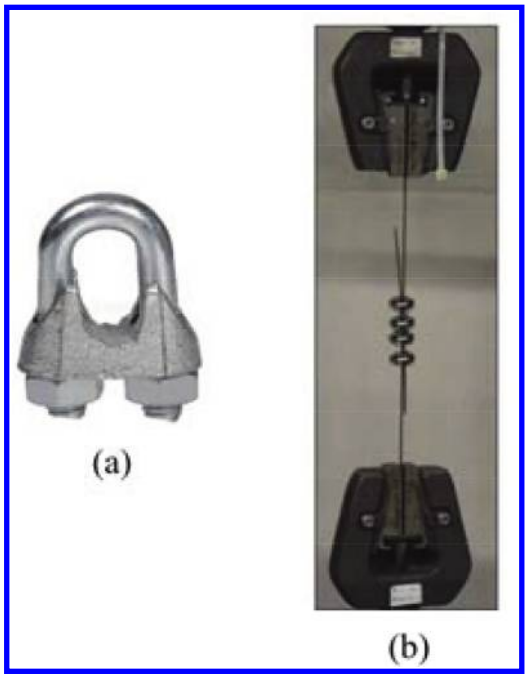

Figure 7. (a) U-clamp anchor, and (b) tensile testing of the splicing connection using four U-clamp anchors.

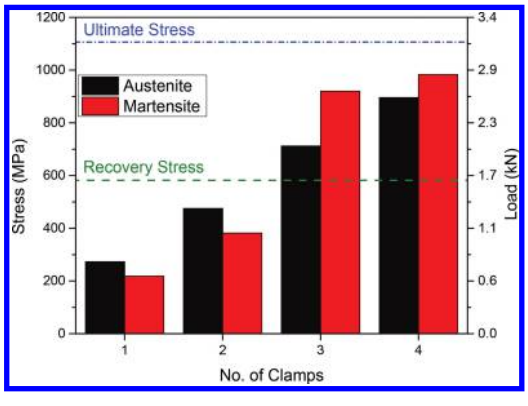

Figure 8. U-clamp anchorage test results of the SMA wire.

the sleeve type connection. Based on the dimension and application of the SMA wire, the type of U-clamp anchors selected in this study had a wire rope size of 3.175 mm (1/8 inches) and were made from malleable iron (Fig. 7a). The number of U-clamp anchors were varied (up to four U-clamp anchors) at the splicing connection to obtain the desired results (Fig. 7b). The splicing connection test was conducted on the SMA wire in its martensite and austenite phases.

A summary of the U-clamp anchorage experimental investigation is shown in Figure 8. To ensure the success of the splicing connection, the used connection should be able to transfer forces equivalent to the active and passive confinement forces developed during the confinement process and the axial compressive loading of the concrete column. The test results indicate that the corresponding stress obtained from using four U-clamps exceeded the maximum recovery stress and nearly reached the ultimate stress of the SMA wire. Thus, the type of splicing connection adopted in this research study consisted of four U-clamp anchors.

8 EXPERIMENTAL TEST RESULTS OF THE SMA CONFINED CONCRETE

Once the material characterization and the test parameters of the SMA wires were defined, a preliminary investigation was conducted to study the experimental behaviour of the SMA confined concrete. The main purpose of this investigation was to:

1. test the validity of the developed electrical circuit system as an appropriate heating system
2. determine the success of thermally triggering the active confinement mechanism of the SMA wire
3. investigate the performance of the U-clamp splicing connection system
4. quantify the enhancement in the strength and ductility of the actively confined SMA wrapped cylinder

8.1 *Test set-up and instrumentation*

The concrete cylinders used in this study measured 100 mm in diameter and 200 mm in height. The cylindrical specimens were subjected to uni-axial compression at a loading rate of 10 kN/sec to failure. One cylinder was confined with the SMA wire at a pitch spacing of 10 mm and the other cylinder was left to act as a control specimen. The test cylinders were instrumented with conventional foil strain gauges to measure localized axial and hoop strains. The detailing of the instrumentation configuration is shown in Figure 9.

The pre-strained SMA wires shipped at their martensite phase provided flexibility and ease of operation. The SMA confinement procedure of the concrete cylinder was initiated by coiling the SMA wire with two turns at one end of the cylinder. The SMA wire was then fixed and tightened to the concrete cylinder using four U-clamp anchors. Under a constant tensile force, the SMA wire was wrapped around the concrete cylinder at

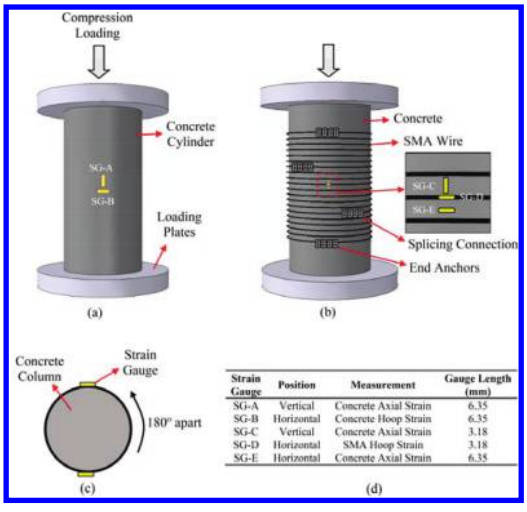

Strain Gauge	Position	Measurement	Gauge Length (mm)
SG-A	Vertical	Concrete Axial Strain	6.35
SG-B	Horizontal	Concrete Hoop Strain	6.35
SG-C	Vertical	Concrete Axial Strain	3.18
SG-D	Horizontal	SMA Hoop Strain	3.18
SG-E	Horizontal	Concrete Axial Strain	6.35

Figure 9. Instrumentation detailing; instrumentation set-up of (a) unconfined, and (b) SMA confined concrete cylinder; (c) location of the strain gauges; and (d) summary of the strain gauges installed.

a pitch spacing of 10 mm. At the opposite end of the cylinder, the SMA wire was also coiled with additional two turns and tightened to the concrete cylinder with U-clamp anchors. The intermediate splices of the SMA wires were connected with four U-clamps to ensure continuity of the SMA wire across the height of the cylinder. The end product of the SMA confined concrete is shown in Figure 10.

8.2 *Heat application using electrical current*

The selected heat source for this research investigation was supplied via electrical current. The developed circuit used to generate the electrical current was composed of the following components: a thermocouple sensor, a variable auto transformer (VAT), a voltmeter, an Amp meter, and an electrical shunt (Fig. 11). The thermocouple sensor was connected to the SMA wire to monitor the temperature. The VAT was used to adjust the required voltage supply to maintain an electrical current of 15 Amps. The voltage readings from the VAT were constantly verified using a voltmeter connected to the circuit. The maximum current capacity of the Amp meter available for use was 10 Amps, which was below the generated electrical current of 15 Amps. Thus, in order to monitor the current in the circuit, an electrical shunt was installed. The main purpose of the electrical shunt was to create a path of least resistance. The resistivity of the electrical shunt was 0.005 Ω. The voltage drop across

Figure 10. SMA confined concrete cylinder.

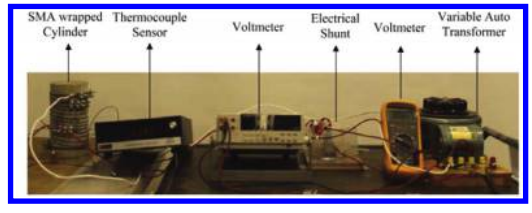

Figure 11. Components of the electrical circuit used to heat the SMA confined concrete cylinders.

the shunt was measured, from which the electrical current was determined using Ohm's law.

Once the SMA wires were wrapped around the concrete specimen, the electrical wires from the developed circuit were connected to the ends of the SMA wire (Fig. 11). This method would ensure evenly distributed heating of the SMA spirals. Once the electrical circuit was complete, the VAT was switch on to generate the electrical current required to heat the SMA wire. At the instant the thermocouple sensor measured the target temperature of 120°C, the voltage supply was cut and the SMA wrapped cylinder was left to cool to room temperature. This point marks the transformation of the wire from the martensite to the austenite

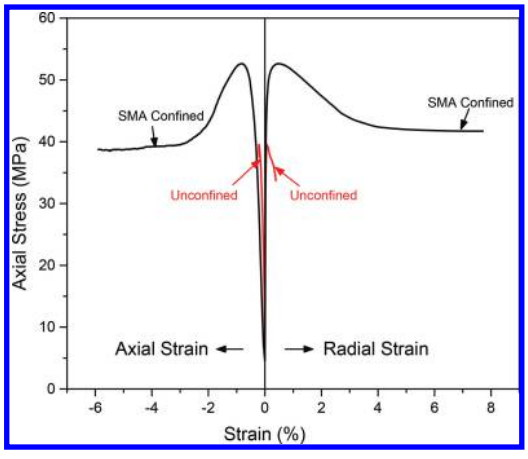

Figure 12. Test results of unconfined and SMA confined concrete cylinders.

phase, and also completes the active confinement procedure of the concrete cylinder.

8.3 *Test results*

The main objective of this section is to validate and access the investigated parameters, which include the heating system via electrical current, the end anchorage and splicing connections, and accessing the recovery stress generated to actively confine the concrete cylinder using the SMA wires. The success of the confinement technique can be determined preliminarily by quantifying the strength and ductility gain of the SMA wrapped cylinder. A summary of the experimental test data is graphically presented in Figure 12. A brief assessment of the experimental data show significant enhancement in the strength and ductility of the SMA confined concrete cylinder, when compared to the control cylinder. The actively confined SMA wrapped cylinder experienced an increase in the ultimate strength, axial strain and radial strain by factors of 1.4, 28, and 20, respectively, compared to the unconfined concrete cylinder. The SMA confined concrete possesses almost a linear stress-strain relationship up to the maximum strength, after which a gradual decrease in the strength is recorded until the failure of the specimen. The behaviour of the stress-strain curve after the yield point critically relies on the recovery stress, and the pitch spacing of the SMA wire. Using SMA wire that exhibit high recovery stress accompanied with low pitch spacing can result in an ascending slope with strength and ductility enhancement after the yield point is reached. It should be noted that the strain gauge mounted on to the SMA wire immediately

Figure 13. Failure mode of the SMA confined concrete cylinder.

detached during the initial loading stages of the specimen. Difficulties were encountered bonding the strain gauge to the SMA wire due the high curvature and the small cross-sectional diameter of the SMA wire.

The failure mechanism of the SMA confined cylinder was very ductile. The concrete cylinder remained intact despite the high axial deformation and radial strains recorded. At failure, the SMA wire fractured at the mid-height section followed by the formation of a diagonal crack across the height of the concrete cylinder (Fig. 13). The fracture of the SMA wire indicates the efficiency of the developed splicing connection to transfer forces effectively between splices of the SMA wires. This also means that the SMA wire experienced very low or negligible slippage at the splicing connection. In addition, the use of U-clamp anchors were capable of connecting splices of the SMA wire without inducing high stress concentrations that could result in potential premature failure of the wire at the connection point.

9 SUMMARY

The main objective of this paper was to investigate the feasibility and effectiveness of actively confining concrete using the SMA wires. The objective was approach by characterizing the material properties

of the SMA wire and determining certain parameters such as the splicing connections and the heating system required to achieve the innovative confinement technique. The test results of the conducted preliminary experimental investigation clearly showed the enhanced structural performance of SMA confined concrete over the unconfined concrete specimen. The outcome of this study verified the success of actively confining the concrete specimens with the SMA wires. Thus, the research study undertaken by the authors can be further progressed towards its main objective of investigating the behaviour of eccentrically loaded reinforced concrete columns actively confined using SMA wires.

ACKNOWLEGEMENTS

The authors are grateful for the financial support provided by the University of Calgary towards this research project.

REFERENCES

Andrawes, B., Shin, M. & Wierschem, N. 2010. Active confinement of reinforced concrete bridges using shape memory alloys. *Journal of Bridge Engineering ASCE* 15(1): 81–89.

Choi, E., Nam, T-H., Chung, Y-S. & Park, T. 2008. The behaviour of concrete cylinders confined by shape memory alloy wire. *Smart Materials and Structures* 17: 10pp.

Choi, E., Nam, T-H., Yoon, S-J., Cho, S-K. & Park. J. 2010. Confining jackets for concrete cylinders using NiTiNb and NiTi shape memory alloys wires. *Physica Scripta T139*: 4pp.

Destrebecq, J-F. & Balandraud, X. 2010. Interaction between concrete cylinders and shape memory wires in the achievement of active confinement. *Materials with Complex Behaviour, Advanced Structural Materials* 6: 19–34.

Janke, L., Czaderski, C., Motavalli, M. & Ruth, J. Applications of shape memory in civil engineering structures—overview, limits and new ideas. *Materials and Structures* 38: 578–592.

Krustulovic-Opara, N. & Thiedeman, P.D. 2000. Active confinement of concrete members with self-stressing composites. *ACI Materials Journal* 93(3): 297–308.

Lagoudas, D.C. 2008. Shape memory alloys, modeling and engineering applications. *Springer Science + Business Media, LLC*: 435pp.

Mirzaee, Z., Motavalli, M. & Shekarchi, M. 2010. Experimental investigation of compressive concrete elements confined with shape memory Ni-Ti wires. *Fracture Mechanics of Concrete Elements and Concrete Structures—Assessment, Durability, Monitoring and Retrofitting of Concrete Structures*, Korea Concrete Institute, Seoul: 1173–1178.

Shin, M. & Andrawes, B. 2010. Experimental investigation of actively confined concrete using shape memory alloys. *Engineering Structures* 32: 656–664.

Tran, H., Balandraud, X. & Destrebecq, J.F. 2014. Improvement of the mechanical performances of concrete cylinders confined actively or passively by means of SMA wires. *Elsevier Urban & Partner*: 8pp.

Zuboski, G.R. 2013. Stress-strain behaviour for actively confined concrete using shape memory alloys. *Master of Science Thesis*, The Ohio State University, USA, 213pp.

Concrete Repair, Rehabilitation and Retrofitting IV – Dehn et al. (Eds)
© 2016 Taylor & Francis Group, London, ISBN 978-1-138-02843-2

Chillon Viaduct deck slab strengthening using reinforced UHPFRC: Full-scale tests

D. Zwicky
School of Engineering and Architecture Fribourg (HEIA-FR), Institute of Construction and Environmental Technologies (iTEC), University of Applied Sciences of Western Switzerland (HES-SO), Fribourg, Switzerland

E. Brühwiler
Laboratory of Maintenance and Safety of Structures (MCS), Civil Engineering Institute (IIC), Swiss Federal Institute of Technology Lausanne (EPFL), Lausanne, Switzerland

ABSTRACT: The Chillon Viaduct, built by prestressed box girder segmental construction, was constructed in the late 1960s. Recent examination of structural performance showed that punching of wheel loads through the deck slab is prevailing, though structural safety requirements currently can be fulfilled. Furthermore, the box girder concrete is prone to Alkali Silica Reaction (ASR). The chosen strengthening measure is adding a layer of ultra-high performance fiber reinforced concrete additionally reinforced with steel rebars (R-UHPFRC) on the top surface of the deck slab, also serving as waterproofing layer. This paper reports on full-scale tests up to failure on specimens representing zones between and above the girder webs, respectively. The goal was to determine the impact of the strengthening layer on ultimate resistance and failure modes. This paper is complemented by a second contribution on finite element analyses of the tested specimens.

1 INTRODUCTION

The twin Chillon Viaduct, situated next to the world-famous Chillon Castle on Swiss National Highway A9/E27 on the east end of Lake Geneva, was conceived by Jean Muller and designed by Jean-Claude Piguet. The viaduct was built in the late 1960s. The variable height box girder structure, spanning between 92 m and 104 m over a total length of 2'210 m, was built by prestressed segmental construction with epoxy-glued joints which was a world novelty at the time.

Recent examination of the structural performance showed that the prevailing failure mode at Ultimate Limit State (ULS) is punching of wheel loads through the only 18 cm thick deck slab, though structural safety requirements currently can be fulfilled. Further investigations revealed, however, that the concrete is prone to alkali silica reaction (ASR). The latter is expected to lead to concrete shear strength reduction in the future, with an adverse impact on punching resistance.

As the replacement of the waterproofing on the deck slabs was planned for 2014–15, its combination with a strengthening intervention was investigated. The chosen strengthening consists in casting a 40 to 50 mm thin layer of ultra-high performance fiber reinforced concrete, additionally reinforced with steel rebars (R-UHPFRC), on the top surface of the deck slab. Due to the R-UHPFRC layer, ultimate resistances in shear and bending and fatigue resistances of the deck slab were significantly increased, exceeding the expected concrete strength reduction in the future. The UHPFRC layer also serves as waterproofing layer, leading to reduction of the concrete humidity and thus of further ASR development.

This paper reports on full-scale failure tests on specimens representing zones between and above the webs of the box girder, respectively. The goal was to verify the expected increase in ultimate resistance due to the R-UHPFRC layer, as expected through analytical models. This paper is complemented by an additional paper (Sadouki et al. 2015) on finite element analyses for reproduction of test results.

2 FULL-SCALE TESTS

2.1 *Objective*

The mandate by the Swiss National Road Authority FEDRO to the first author was to perform and evaluate failure tests on full-scale specimens representing potentially prevailing zones of the unstrengthened and the strengthened deck slab,

including material tests. The primary objective of the full-scale tests was to determine the impact of the strengthening layer on ultimate resistance and failure modes, in particular with regard to punching failure.

Final layouts of test specimens and test set-ups were developed in close collaboration with the second author. Fabrication of test specimens was projected by the structural engineering company and the construction company mandated for the rehabilitation works on the viaduct.

2.2 *Test specimens*

2.2.1 *Interaction of punching shear and bending*

According to Swiss code SIA 262 (2013) and other international codes (e.g. fib MC 2010b) for concrete structures as well as underlying research (Muttoni et al. 2013), the punching resistance of a concrete slab without transverse reinforcement interacts with the exploitation of the available bending resistance. The deck slab of the Chillon Viaduct is reinforced with different rebar diameters in the zones over the webs and in the zones between the webs of the box girder.

With this in mind, a test series A for slab specimens submitted to positive bending and a test series B submitted to negative bending were performed. One test series consisted of three unstrengthened specimens (e.g. specimens As1 to As3) and three strengthened specimens (e.g. specimens B+1 to B+3), to explore variability of test results.

2.2.2 *Simulating ASR effects*

In agreement with the client, it was decided to simulate the expected adverse effects of ASR on concrete shear strength by producing test specimens with a reduced compressive strength, targeting a strength class C20 (fib MC 2010a).

2.2.3 *Positive bending—test series A*

Test series A was designed to represent the deck slab between the box girder webs submitted to positive bending moments. As the weight of the test specimens had to be limited due to lifting gear capacities at iTEC's Structural Laboratory, the specimen width was selected to approximately represent a length of the real deck slab which is delimited by zero bending moments.

The test specimens are supported on two edges of 3 m length. The inferior reinforcement layer, governing for positive bending resistance, consists of ductility class B rebars (fib MC 2010a) Ø14 with 125 mm spacing and a nominal concrete cover of 20 mm. Longitudinal inferior reinforcement is Ø12 with 125 mm spacing while superior reinforcement layers are constructive (Ø10/250 and Ø8/250, respectively).

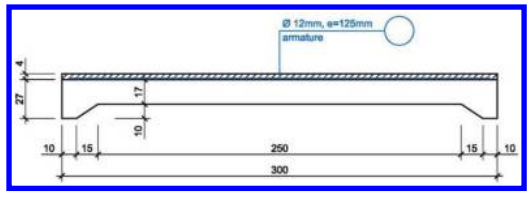

Figure 1. Test series A specimens, dimensions in cm.

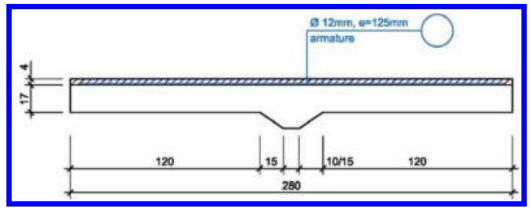

Figure 2. Test series B specimens, dimensions in cm.

Figure 1 shows the specimen geometry including the R-UHPFRC strengthening layer. Note that the slab thickness of 18 cm is reduced by approx. 1 cm due to interface roughening by high-pressure jetting. The strengthening layer is provided with only one transversal reinforcement layer of Ø12/125, put directly onto the slab face.

2.2.4 *Negative bending—test series B*

The specimens for test series B, representing the zones near the girder webs with negative bending moments, are produced on the same basis as series A. Figure 2 shows the geometry including the R-UHPFRC strengthening layer. Governing superior reinforcement of the deck slab consists of Ø16 rebars spaced at 125 mm with 20 mm nominal concrete cover.

These test specimens are supported on a line support at the middle of the slab only. The haunch represents the geometry of the real deck slab next to the webs.

2.2.5 *Fabrication of test specimens*

Concreting of the test specimens took place near the construction site, with the goal to simulate realistic on-site concreting conditions, Figure 3.

2.3 *Material properties of test slab concrete*

Mechanical properties of the test specimens were determined the same day as the full-scale test. Material properties of the reinforcement steel were not tested.

2.3.1 *Compressive strength*

Compressive strength of the test slab concrete was determined on four cylinders Ø150 mm and 300 mm

Figure 3. Concreting the R-UHPFRC strengthening layer.

Table 1. Test slab concrete compressive strength.

	Age	AVG*	COV**	Min.	f_{ck}***
Specimen	Days	MPa	%	MPa	MPa
As1	44	21.0	3.1	20.1	13.0
As2	50	22.0	3.7	21.1	14.0
As3	55	23.1	3.1	22.5	15.1
A+1	48	19.9	3.3	19.2	11.9
A+2	54	20.6	1.6	20.4	12.6
A+3	60	21.3	3.5	20.2	13.3
Bs1	46	24.1	2.9	23.1	16.1
Bs2	53	27.0	1.5	26.6	19.0
Bs3	55	28.0	1.8	27.5	20.0
B+1	102	23.0	6.2	21.4	15.0
B+2	105	29.3	1.8	28.9	21.3
B+3	110	30.1	2.1	29.7	22.1

*average; **coefficient of variation; ***characteristic value.

height per test slab. Table 1 shows the results where the characteristic compressive strength f_{ck} is determined according to Swiss Standard SIA 269/2 (2011), where the average and minimum value have to be known (SN EN 13791 2007).

Apart from the last two specimens, the characteristic concrete strength was below the targeted C20 grade (fib MC 2010a), section 2.2.2. The very low COVs indicate a consistent fabrication of test slabs.

2.3.2 *Young's modulus*

Young's modulus of the test slab concrete was determined on three cylinders Ø150 mm and 300 mm height per test slab specimen, Table 2.

The average young's modulus E_{cm} of concrete is related to the average compressive strength f_{cm} by.

$$E_{cm} = k_E \sqrt[3]{f_{cm}} \quad (1)$$

Table 2. Young's modulus of deck slab concrete.

	Age	AVG	COV	$k_{E,exp}$
Specimen	Days	MPa	%	–
As1	44	23'840	5.0	8640
As2	50	24'534	4.3	8755
As3	55	25'228	7.7	8860
A+1	48	22'067	3.5	8140
A+2	54	21'667	2.7	7905
A+3	60	22'076	0.9	7965
Bs1	46	25'153	2.2	8710
Bs2	53	26'118	4.3	8705
Bs3	55	26'761	3.4	8815
B+1	102	26'229	7.1	9225
B+2	105	29'093	2.8	9435
B+3	110	29'527	4.6	9490

where k_E = coefficient depending on the aggregate material (SIA 262 2013).

For alluvial gravel aggregates, k_E varies between 10'000 and 12'000 and for crushed lime aggregates, k_E varies between 8'000 and 10'000 (SIA 262 2013). Considering the measured average values of compressive strength, experimental values $k_{E,epx}$ vary between 7'900 and 9'500, Table 2, principally SIA 262 (2013). The values tend to increase with age, i.e. for slab specimens B+. For test series As, A+ and Bs of comparable age, the experimental values of k_E vary between 7'900 and 8'850. The low coefficients of variation also confirm a homogenous test slab production.

2.3.3 *Tensile strength*

Tensile strength of test slab concrete was determined by double-punch test (Chen 1970) on four cylinders Ø150 mm and 150 mm height per slab specimen.

Average values vary between 2.1 MPa and 2.7 MPa, COVs between 3% and 10%, also confirming a homogenous test slab production. In comparison to calculated values (fib MC 2010a), referring to compressive strength, the measured tensile strengths are 10% to 50% higher.

2.4 *Material properties of UHPFRC*

Quality control of the UHPFRC consisted in flexural tensile and compressive strength testing.

2.4.1 *Flexural tensile strength*

Flexural tensile strength was determined in four-point bending tests on three prisms $40 \times 40 \times 120$ mm^3 per test slab and was calculated according to elasticity theory of stresses, Table 3.

Table 3. UHPFRC flexural tensile strength.

	Age	AVG	COV
Specimen	Days	MPa	%
A+1	48	41.3	21.8
A+2	54	34.8	12.6
A+3	60	37.9	18.9
B+1	102	47.1	6.5
B+2	105	45.6	3.9
B+3	110	47.1	12.9

Table 4. UHPFRC compressive strength.

	Age	AVG	COV
Specimen	Days	MPa	%
A+1		N/A	
A+2	54	153	1.7
A+3	60	188	3.1
B+1	102	204	6.1
B+2	105	201	3.8
B+3	110	197	3.4

The average values correspond to a usual quality of UHPFRC but vary considerably from one specimen to another; in particular, for specimen A+2. The coefficients of variation are rather high and imply an inhomogeneous fabrication quality.

This is explained by the rather stiff (thixotropic) fresh UHPFRC that was used to withstand slopes of up to 7% on the viaduct. Such a mix needs to be cast using a finishing machine providing some vibration, as was done on the viaduct. However, the UHPFRC specimens were fabricated manually. They are thus not entirely representative for the UHPFRC cast on the viaduct, i.e., leading to lower strength values and significantly higher variability of results when compared to the corresponding values obtained during the on-site application.

2.4.2 *Compressive strength*

The measured compressive strength values of the UHPFRC are given in Table 4.

The average compressive strengths are at the upper limit of expected values of 150 MPa to 200 MPa. The low coefficients of variation imply a rather good fabrication quality for this specimen geometry, seemingly less affected by the fabrication process than the smaller flexural specimens, section 2.4.1.

This confirms, one the one hand, the influence of the casting method applied with UHPFRC, in particular, in the case of thixotropic fresh properties, and on the other hand, the low variability of UHPFRC properties determined from test specimens if these are correctly fabricated.

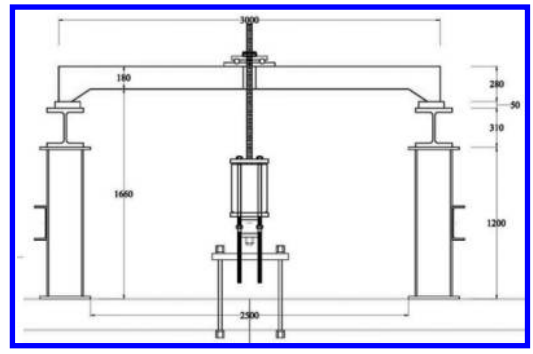

Figure 4. Test set-up for positive bending, dimensions in mm.

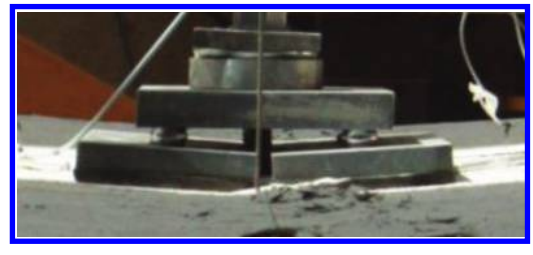

Figure 5. Device for introduction of concentrated force.

2.5 *Test set-ups*

2.5.1 *Positive bending*

Test specimens A for positive bending are supported on neoprene strips on two edges, Figure 4. One concentrated force is applied at the upper face at mid-point of the test slab by a steel rod and a hydraulic jack anchored to the strong floor.

The concentrated force is applied on a 0.4×0.4 m^2 surface, simulating the contact surface of a wheel load (SIA 261 2014). The application device is designed such that it can follow local curvatures, Figure 5.

Measurements, primarily targeting to follow the overall force—deflection response of test specimens, include the force as well as vertical deflections at the centerlines of the supports and next to the force point at mid-span.

The tests were performed under actuator displacement control at quasi-static displacement rate.

2.5.2 *Negative bending*

The test rig for specimens B, representing the deck slab zones next to the girder webs with negative

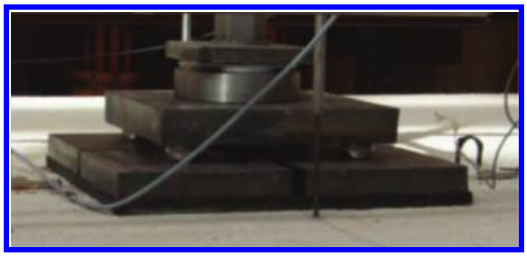

Figure 6. Test set-up for negative bending, dimensions in mm.

bending, consists of a central line support with a neoprene strip and two concentrated forces applied symmetrically to the centerline, Figure 6. The force application devices are the same as in the positive bending tests.

The distance between the edge of the web haunch and the edge of the force corresponds the double of the effective slab depth. As the expected ultimate forces are considerably higher in this test series, each concentrated force is applied by two steel rods, each equipped with a hydraulic jack and connected by a force distribution steel profile which transfers the jack forces to the force application device.

Measurements cover the applied forces as well as vertical deflections next to the web haunches, under the applied forces and at the free edges of the test slab.

3 TEST RESULTS AND COMPARISONS

The empirical evaluation of test results targeted at identifying the influence of the R-UHPFRC strengthening layer, in comparison to the unstrengthened specimens, on the overall structural behavior, ultimate resistance, failure modes, potential residual resistance and deformation capacity.

3.1 *Test series A—inner slab zones*

Figure 7 shows overall deformation behaviors of unstrengthened and strengthened specimens.

The failure mode of the unstrengthened specimens As is associated with yielding of the flexural reinforcement followed by concrete crushing, i.e. a highly ductile rupture. Maximum forces F_u and associated mid-span deflections w_u vary little, Table 5.

3.1.1 *Effect of the R-UHPFRC layer*

The overall responses of the strengthened specimens show that specimen A+2 behaved quite differently from the others, Figure 7(b).

It could be identified prior to the test that the strengthening layer was already delaminated, Figure 8, potentially due to insufficient preparation of the interface or inadequate UHPFRC quality. It was therefore decided to treat the associated test results with reserves, particularly with regard to recommendations to be formulated.

Specimens A+1 and A+3 behaved similarly. Ultimate bearing force is attained by delamination of the strengthening layer on large surfaces. It may be suspected that interface bond strength of specimen A+3 was of somewhat lower quality as the substrate concrete usually has a lower tensile strength than the bond strength at the interface.

Both specimens, A+1 and A+3, showed residual capacities associated with flexural failure of the test slab. The second drop in residual capacity is associated with interface rupture between concrete slab and strengthening layer over the remaining surfaces. Table 6 shows ultimate failure forces and associated mid-span deflections for test series A+.

Ultimate resistance is increased due to the UHPFRC strengthening layer by 61% (A+1), 19% (A+2) and 53% (A+3), respectively, in comparison to the average resistance of test series As.

Residual capacities amount to approximately 90% of the ultimate force or 153% (A+1), 115% (A+2) and 137% (A+3), respectively, of the average ultimate force of the unstrengthened specimens.

Deformation capacity is assessed by the deflection associated with the respective ultimate force. Reference is made to a nominal deflection-to-span ratio of $w_u/L = 1/40$ that may be considered as a ductile deformation behavior limit (SIA 262 2013). The average ultimate deflection of the unstrengthened specimens As shows good deformation capacity ($w_{u,avg} = L/46$).

For specimen A+1, the deformation capacity is slightly increased ($w_u = L/41$) while it decreases considerably ($w_u = L/71$) for specimen A+3. In the latter case, however, deformation capacity reduction is associated to premature delamination of the strengthening layer. Test specimen A+2 also shows a reduced deformation capacity ($w_u = L/64$) at maximum force.

At attaining residual capacity, the strengthened specimens exhibit 164% (A+1), 96% (A+2) and 106% (A+3), respectively, of the average deformation capacity of the reference specimens.

3.2 *Test series B—slab zones adjacent to webs*

Figure 9 shows the overall force—deflection response of unstrengthened and strengthened specimens, considering in each case the slab side where failure occurred.

Ultimate resistance of the unstrengthened specimens was attained by tensile shear failure along an

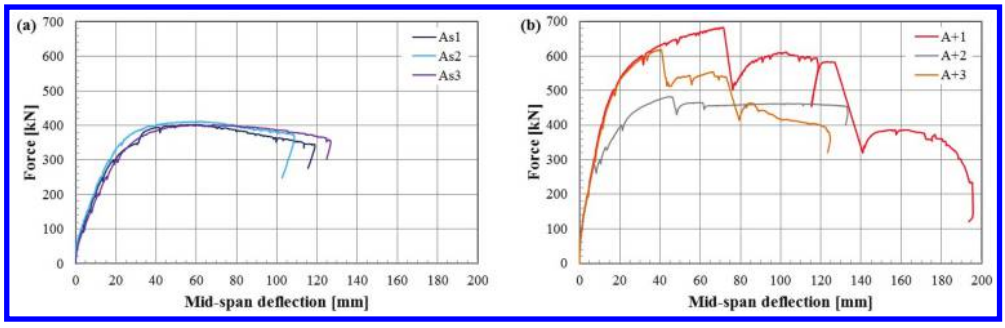

Figure 7. Overall force—deflection response of test specimens A – (a) unstrengthened and (b) strengthened specimens.

Table 5. Maximum force and deflection of specimens As.

Specimen		As1	As2	As3	AVG	COV
F_u	kN	403	412	401	405	1.4%
w_u	mm	58.0	63.1	66.7	62.6	7.0%

Figure 8. Delamination of R-UHPFRC layer prior to testing.

Table 6. Maximum force and deflection of specimens A+.

Specimen		A+1	A+2	A+3
F_u	kN	653	483	619
w_u	mm	71.2	45.0	40.6

inclined crack starting from the edge of the force introduction point and extending towards the edge of the web haunch, Figure 10.

Attaining maximum force was followed by a softening behavior, Figure 9(a). Ultimate force and associated deflection at force introduction points vary little, Table 7.

3.2.1 *Effect of the R-UHPFRC layer*

The overall responses of the strengthened specimens were similar, Figure 9(b).

Reaching ultimate resistance was related to interface rupture between slab concrete and strengthening layer on extended surfaces, presumably by fracture in the concrete just below the UHPFRC layer where this failure usually takes place if the interface surface is properly prepared and the UHPFRC has an appropriate consistency. At this stage, no sign of shear failure in the deck slab could be observed.

Post-peak behavior was of a softening type, followed by a second drop in resistance capacity (at a deflection of approx. 25 mm) where a visible delamination close to the strengthening layer could be observed. Increasing deflections beyond this point also resulted in a shear failure, as observed for As test specimens.

Ultimate resistances of test specimens B+ vary little but associated deflections at force introduction points show rather large variation, Table 8. This is also associated with a considerably stiffer response of these specimens at lower force levels, Figure 9(b).

Due to the UHPFRC strengthening layer, ultimate resistance increased by 53% (B+1), 48% (B+2) and 55% (B+3), respectively, in comparison to the unstrengthened specimens As and vary little.

The deformation capacity of the unstrengthened specimens is rather small with w_u/L = 1/187 on the average. The strengthened specimens show reduced deformation capacity up to 50%.

Assessment of deformation capacity is refined as ultimate force values are increased considerably but failure is reached at similar deformation. Reference is made to a ductility index $D_s = w_u/w_y$ where w_y corresponds to a nominal yield deflection which is determined by scaling the deflection at 40% ultimate force, considered to be the end of the elastic stage, to the ultimate force level. The higher the ductility index, the more important is the deformation capacity. Often, a minimum of D_s = 3 is required for ductile structural behavior.

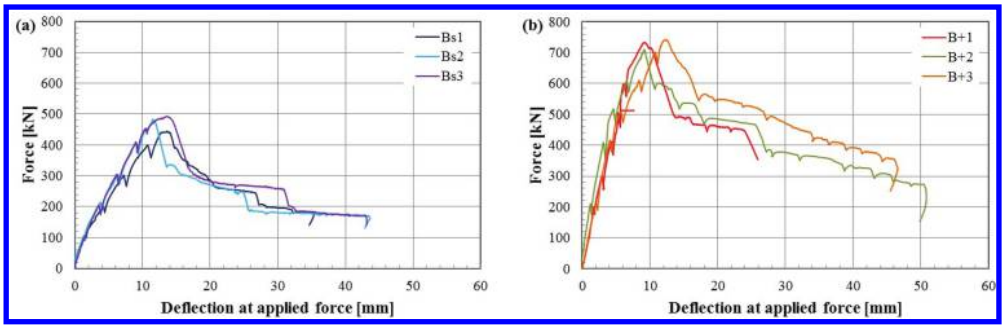

Figure 9. Overall force—deflection response of test specimens B – (a) unstrengthened and (b) strengthened specimens.

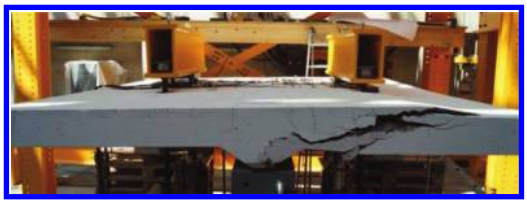

Figure 10. Shear failure of test specimens Bs.

Table 7. Maximum force and deflection of specimens Bs.

Specimen		Bs1	Bs2	Bs3	AVG	COV
F_u	kN	460	483	493	479	3.5%
w_u	mm	13.6	11.5	13.6	12.9	9.3%

Table 8. Maximum force and deflection of specimens B+.

Specimen		B+1	B+2	B+3	AVG	COV
F_u	kN	733	710	741	728	2.2%
w_u	mm	9.1	9.2	12.5	10.3	19%

With this approach, D_s = 1.56 is found on the average for the unstrengthened specimens Bs. The strengthening layer applied in test series B+ changes ductility indices to D_s = 1.30 (B+1), D_s = 1.85 (B+2) and D_s = 1.74 (B+3), respectively, corresponding to a decrease of 17% for specimen B+1, and increases of 18% (B+2) and 12% (B+3) for specimens B+2 and B+3, respectively. Applying the strengthening layer improves ductility of the slab to some extent but deformation capacity still remains limited.

4 CONCLUSIONS AND OUTLOOK

The results of this study allowed to give the following conclusions and recommendations to the client:

4.1 *General conclusions*

- Punching failure could not be observed in any of the tests.
- Failure forces of the unstrengthened specimens vary between about 400 kN and 480 kN which are about three times the characteristic value of wheel loads as given by codes.
- Casting a 40 mm layer of reinforced UHPFRC increases ultimate resistance by at least 50%, provided that the interface is properly prepared and that the stiffness of the fresh UHPFRC mix is appropriately chosen.
- Since failure modes in the tests were associated to premature delamination of the strengthening layer, improved resistance would be obtained by proper preparation of the interface.

4.2 *Failure at inner slab zones*

- Slab zones between the box girder webs, submitted to positive bending moments, fail with moderate to normal ductility, i.e. announcing failure by major deflections.
- Residual resistance capacity of strengthened inner slab zones is still considerably higher than that of unstrengthened. Bending failure is observed, preceded by major deformations.

4.3 *Failure in slab zones adjacent to girder webs*

- Slab zones adjacent to girder webs, submitted to negative bending moments, show limited deformation capacity, strengthened or unstrengthened.

– In unstrengthened slab zones, failure is associated with shear failure in an inclined crack through the substrate concrete slab.
– In strengthened slab zones, failure is related to R-UHPFRC layer delamination. No sign of shear failure of the substrate concrete slab could be observed at this stage.
– Deformation capacity (ductility) is slightly improved by the presence of the R-UHPFRC strengthening layer.

4.4 *Outlook*

The full-scale tests confirmed that also an unstrengthened slab undergoing strength reduction due to ASR would not fail by punching of a wheel load. Furthermore, this kind of failure would only imply local damage to the slab which could be rehabilitated relatively easy.

Nevertheless, the client decided to strengthen the deck slabs of the Chillon Viaduct by means of an R-UHPFRC layer due the following advantages:

– The strengthening layer also serves as a waterproofing layer.
– The R-UHPFRC strengthening considerably increases the flexural stiffness of the deck slab, thereby reducing fatigue stresses in the (potentially ASR-affected) concrete and the reinforcing bars.
– The strengthening layer also provides a strength reserve for future traffic development and axle loads.
– In view of future interventions to rehabilitate and improve further highway bridges, the UHPFRC works on the Chillon Viaduct allowed to gain important experience.

Casting of the R-UHPFRC strengthening layer on the 2.1 km long Chillon Viaduct was performed during five weeks, ending in September 2014. Structural design of the R-UHPFRC strengthening was performed using analytical resistance models which were validated by non-linear finite element modelling, see Sadouki et al. (2015), in turn being calibrated to the present test results.

ACKNOWLEDGEMENTS

The authors wish to express their gratitude to the client and his panel of experts for the pleasant collaboration in this interesting project.

The first author also sincerely thanks his research associates (Yannick Plüss, Joel Mabboux, Loïc Chopard, Steve Dubois, Médéric Berguerand, and Anthony Fridez) and the technical staff at iTEC's Structural Laboratory (Damien Roy, Jean-Paul Andrey, Dominique Delaquis, and Yanis Schaller) for their rigorous and accurate work provided in the preparation, execution and evaluation of the full-scale tests and their results.

REFERENCES

Chen, W. 1970. Double-punch test for tensile strength of concrete. *ACI Journal*, 67(12):993–995.

fib MC. 2010a. *Model Code 2010 – Final draft, Volume 1*, bulletin no. 65, Lausanne: International Federation for Structural Concrete (fib).

fib MC. 2010b. *Model Code 2010 – Final draft, Volume 2*, bulletin no. 66, Lausanne: International Federation for Structural Concrete (fib).

Muttoni, A.; Fernández Ruiz, M.; Bentz, E.; Foster, S. & Sigrist, V. 2013. Background to fib Model Code 2010shear provisions—part II: punching shear. *Structural Concrete* 14(3):204–214.

Sadouki, H.; Brühwiler E. & Zwicky, D. 2015. Chillon Viaduct deck slab strengthening using reinforced UHPFRC: Numerical simulation of full-scale tests. *Proc. International Conference on Concrete Repair, Rehabilitation and Retrofitting (ICCRRR 2015), Leipzig, 5–7 October 2015*.

SIA 261. 2014. *Actions on structures* (in German or French). Zurich: Swiss Society of Engineers and Architects.

SIA 262. 2013. *Concrete structures* (in German or French). Zurich: Swiss Society of Engineers and Architects.

SIA 269/2. 2011. *Existing structures—concrete* structures (in German or French). Zurich: Swiss Society of Engineers and Architects.

SN EN 13791. 2007. *Assessment of in-situ compressive strength in structures and precast concrete components.* Zurich: Swiss Society of Engineers and Architects.

Concrete Repair, Rehabilitation and Retrofitting IV – Dehn et al. (Eds)

Chillon Viaduct deck slab strengthening using reinforced UHPFRC: Numerical simulation of full-scale tests

H. Sadouki & E. Brühwiler
Laboratory of Maintenance and Safety of Structures (MCS), Civil Engineering Institute (IIC), Swiss Federal Institute of Technology Lausanne (EPFL), Lausanne, Switzerland

D. Zwicky
School of Engineering and Architecture Fribourg (HEIA-FR), Institute of Construction and Environmental Technologies (iTEC), University of Applied Sciences of Western Switzerland (HES-SO), Fribourg, Switzerland structure

ABSTRACT: Recent examination of structural performance of the Chillon Viaduct in Switzerland built in 1969, showed that punching failure mode of the deck slab is prevailing, though structural safety requirements currently can be fulfilled. Since the concrete is prone to Alkali Aggregate Reaction (AAR), the viaduct was strengthened by adding a layer of ultra-high performance fiber reinforced cement composite material additionally reinforced with steel rebars (R-UHPFRC) on the top surface of the deck slab. To validate the strengthening method, full-scale tests up to failure on specimens representing zones between and above the girder webs were conducted, as presented in a companion paper. This full paper reports on the results from non-linear Finite-Element Analysis (FEA) of the experimental results, targeting at verifying the effectiveness of the strengthening method using R-UHPFRC and at calibrating the FEA model with respect to the verification of the ultimate resistance and the structural safety level of the strengthened deck slab of the Chillon Viaduct. It is shown that 3D FE-analysis effectively simulates with sufficient accuracy the structural behavior of the tested slab elements.

1 INTRODUCTION

The Chillon Viaduct located on the Swiss National Highway on the East end of the Lake of Geneva, was constructed in the late 1960s. Recent structural assessment showed that the governing failure mode at Ultimate Limit Sate (ULS) is punching of wheel loads through the 18 cm thin deck slab, though structural safety requirements currently can be fulfilled.

Further investigations revealed that the concrete is prone to alkali aggregate reaction (AAR). The latter is expected to lead to significant concrete strength reduction in the future, with an associated reduction in punching shear resistance. After devising different measures for strengthening the structure, it has been decided to consolidate the viaduct by adding, on the previously hydro-jetted top surfaces of deck slabs, a 40 to 50 mm thick layer of Ultra High Performance Fiber Reinforced cement-based Composite material (UHPFRC) which is additionally reinforced by steel rebars.

The choice of UHPFRC as a strengthening material, was motivated (1) by its outstanding mechanical properties, namely high tensile and compressive strengths and a its important deformation capacity due to the high amount of incorporated steel fibres in the cement-based matrix of the material, as well as (2) by its very low porosity implying minimized moisture exchange and ingress of aggressive chemical substances such as chloride ions from the surrounding atmosphere. Consequently, the latter property (low porosity) will have beneficial effects on a further evolution of the AAR (because of lack of water supplies) and on corrosion of reinforcement of steel rebars (Brühwiler & Denarié, 2008).

To validate this novel strengthening method, an experimental program has been carried out including a series of full-scale tests on instrumented composite RC – R-UHPFRC slab elements representing zones between and above the girder webs of the viaduct (Zwicky D. et al., 2013). Main test results are presented in a companion paper to this conference (Zwicky & Brühwiler, 2015).

The present paper reports mainly on the results of numerical simulation of the tests as obtained by non-linear finite-element analysis (FEA) targeting at verifying the effectiveness of

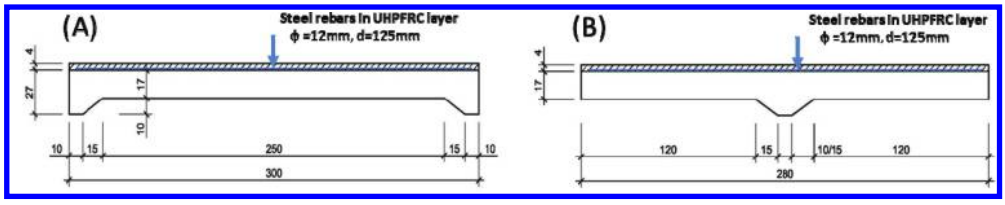

Figure 1. Cross section views of the geometry of the R-UHPFRC/R-C composite slabs for series A and B; dimensions in cm (Zwicky et al., 2013).

the strengthening method using R-UHPFRC and at calibrating the FEA model with regard to the verification of the ultimate resistance and structural safety of the strengthened deck slab of the viaduct.

2 BRIEF DESCRIPTION OF THE EXPERIMENTAL PROGRAM

For an easy reference in the rest of the sequel, the experimental program is briefly described in this paper: Full details are given in the test report (Zwicky et al., 2013) and in the companion paper (Zwicky & Brühwiler, 2015).

Two series of nearly square-shaped (3.0×2.8 m) slabs were tested. Series A (positive flexure mode of the slab between the two webs of the viaduct's box girder) consisted in 3 composite RC – R-UHPFRC slabs linearly supported at two opposite sides, as shown in Figure 1 A. The force acted at the center of the slab until failure.

While in case of series B (negative flexure mode referring to transverse cantilever slab bending), the 3 composite slabs are linearly supported along the center line, as shown in Figure 1B, and loading was performed by applying two symmetrical concentrated forces, each one located in the center of the half part of the slab.

In parallel, in order to determine the ultimate resistance of the un-strengthened slab and to compare with UHPFRC-strengthened slabs, for both test series, three companion monolithic RC slabs were also tested.

Deflections and local deformations as function of measured force were recorded at different locations.

3 FINITE ELEMENT MODELLING

A three dimensional non-linear finite element was used for analyzing the structural behaviour of the tested slabs. Finite volume elements (brick elements) with 20 nodes were employed to represent the geometry of the structure, consisting of RC monolithic slab elements and composite R-UHPFRC – RC slab elements, steel loading plates and supporting beams. The model was elaborated using the non-linear finite element analysis software DIANA (DIANA, 2010) with its graphical pre— and post-processors FEMGEM and FEMVIEW, respectively. The validation of the FE model was accomplished by comparison of numerical results with those recorded from instrumented test specimens (Zwicky et al., 2013), [(Zwicky & Brühwiler, 2015).

Taking advantage of the two-way symmetry of the all slab elements, namely, geometry of the slabs, supporting beams, loading setup and boundary conditions, a quarter only of the specimens was modeled. Figure 2 shows the FE mesh of a typical R-UHPFRC – RC slab element of Series A, supporting beam and bearing steel plate (left-side of the figure) and the adopted finite element type. A perfect connection between the concrete substrate and the UHPFRC overlay was assumed in the model; this assumption is fully justified by the fact that experimental evidence reveals that delamination of the UHPFRC layer does not occur provided that the surface of the substrate was prepared according to common rules before casting the UHPFRC. In fact, if the tensile strength of the UHPFRC and of the interface between UHPFRC and substrate concrete is larger than the tensile strength of the substrate, any cracking mechanism in the post-peak regime of R-UHPFRC – RC specimens would occur in the bulk material of the concrete substrate underneath the interface.

Boundary conditions were defined as follows: nodal displacements on the planes of symmetry AA'BB' and BB'G'F'C'C were restrained in the normal directions to their respective surfaces. All nodal displacements of the basis of the supporting beam were restrained in y-axis (direction of gravity). Loading has been carried out by imposing an incremental vertical force on the central node of the steel loading plate (point B in Figure 2).

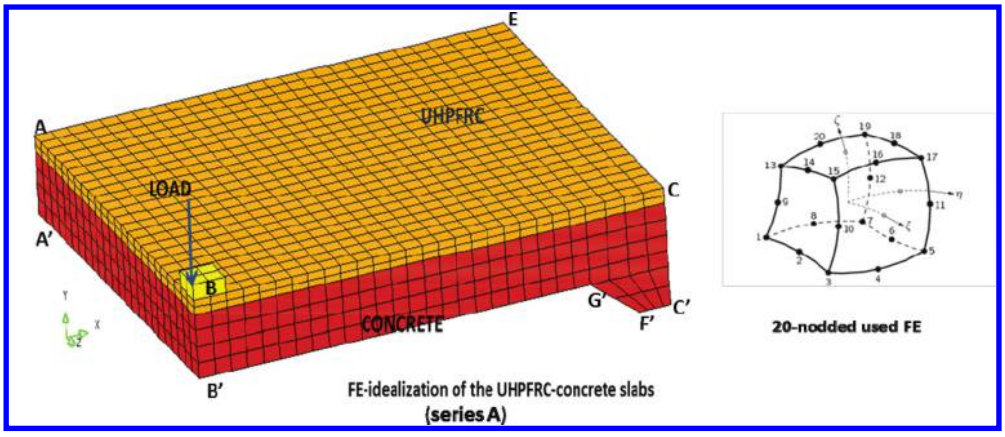

Figure 2. 3D FE-model (one quarter of the full slab): geometry, mesh, loading setup, support and boundary conditions (left-side) and the 20-nodded brick finite element used in the mesh (right-side).

4 CONSTITUTIVE MODEL FOR CONCRETE AND UHPFRC

Crack formation and propagation is undeniably the most important non-linear phenomenon in concrete structures. A great deal of effort has been dedicated in the past years to develop realistic fracture mechanics models and to implement them in computer FE-codes for predicting behavior of concrete structures subjected to complex mechanical and/or physical conditions.

Generally two approaches are often used in finite element codes to model crack propagation in the tensile regime in concrete and cement-based materials, namely the discrete and smeared crack concept (Bazant & Planas, 1998; Rashid, 1968; Rots, 1991; Rots & Blauwendraad, 1989). The first concept models a crack as a geometrical discontinuity, whereas the second one assumes a cracked element to be a continuum, but with modified material properties.

Discrete crack concept reflects more realistically the cracking phenomenon (discontinuity in the continuum, local separation in two surfaces) but it is laborious numerically if the crack path is not known in advance. This is generally the case in most concrete structures. Owing to the non-predefined crack path, nodes of FE-mesh at which tensile stress exceeds a given threshold must be disconnected from the original mesh and new nodes must be created in the damaged area. Thus, the main disadvantage of the discrete crack approach is that the topology of the FE mesh changes continuously as the crack (or cracks) propagates. Consequently permanent re-meshing of the structure is required.

The smeared crack approach assumes that the cracked element remains as a continuum. This allows for a description in terms of tensile stress-strain relation (including strain-hardening and strain-softening). The concept is very attractive not only because it preserves the topology of the original FE mesh, but also it does not impose restrictions with respect to the crack orientation of the crack planes (Rots & Blauwendraad, 1989). A crack initiates as soon as tensile stress at a given point, reaches the tensile strength of the material. The latter concept was used in the present analysis. In addition, the "multidirectional non-orthogonal crack" version elaborated by (De Borst and Nauta, 1985) was applied. In this approach, several cracks are allowed to form at the same integration point with a given threshold angle between cracks.

The total strain ε is decomposed into an elastic part ε_e and an inelastic part (crack strain) ε_{cra}, as formulated by Eq.(1) This decomposition is illustrated in Figure 3 for a typical UHPFRC undergoing strain-hardening and strain-softening. Also secant unloading and reloading methods adopted in the model are depicted in the same figure.

$$\varepsilon = \varepsilon_e + \varepsilon_{cra} \tag{1}$$

This decomposition approach has many advantages, because other important nonlinear phenomena, such as creep or relaxation (ε_{cre}), temperature variation (ε_T), drying and/or endogenous shrinkage and swelling due to an expansive reaction (e.g. Alkali-Aggregate-Reaction (AAR)) ($\varepsilon_{shr,sw}$) can easily be introduced in decomposition as formulated in Eq. (2).

$$\varepsilon = \varepsilon_e + \varepsilon_{cra} + \varepsilon_{cre} + \varepsilon_T + \varepsilon_{shr,sw} \tag{2}$$

These advantages are very important for analyzing the structural behavior of real concrete

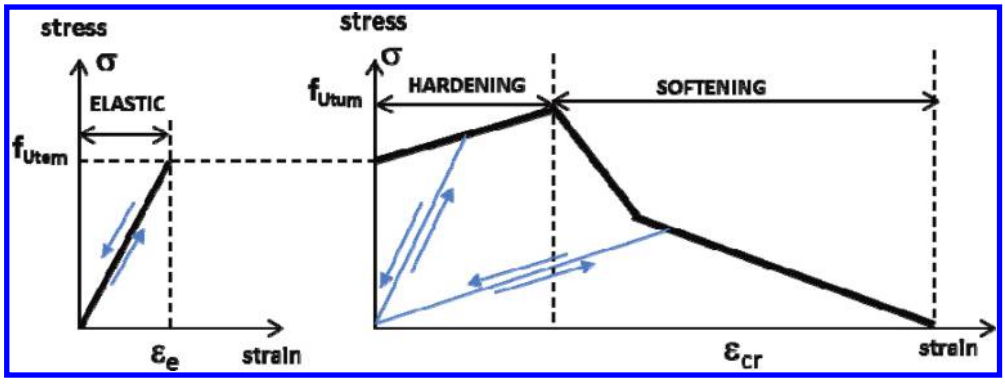

Figure 3. Subdivision of the tensile stress-strain diagram of a typical UHPFRC in its elastic domain (before onset of cracking) and its hardening-softening domain. Blue arrows represent the secant unloading and reloading.

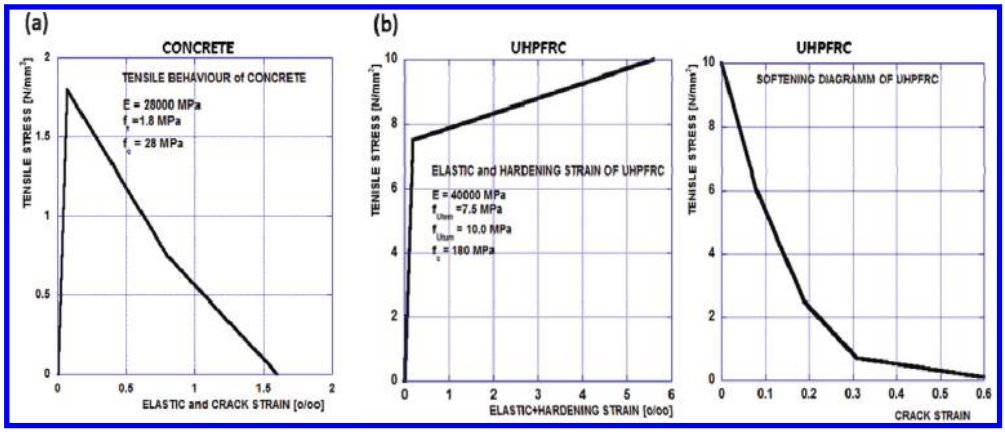

Figure 4. (a) Total tensile stress-strain diagram of the concrete; (b) tensile elastic and hardening stress-strain part and tensile stress-softening part of the UHPFRC (H707).

structures, such as the Chillon Viaduct, by taking into account not only its interaction with surrounding atmosphere (temperature, relative humidity, chemical substances) but also the influence of other phenomena such as swelling induced by AAR.

5 MATERIAL PROPERTIES USED IN THE MODEL

Material laws of concrete of the monolithic RC-slabs and of the substrate of the composite slabs which were used in the numerical simulations are given in Figure 4a, while those of the UHPFRC (named H707) are depicted in Figure 4b. In order to achieve the best agreement between numerical and experimental force-deflection responses, material properties introduced in the analyses were slightly different from those measured (Zwicky et al. 2013), [(Zwicky & Brühwiler, 2015). A value of 0.2 for the Poisson's ratio was taken for both materials.

Young's modulus and Poisson's ratio of all steel rebars were set to 210 GPa and 0.3, respectively. Yield strength for steel reinforcement rebars was set to 500 MPa. Rebars were assumed perfectly adherent to the surrounding material and following an elastic-plastic constitutive law taking hardening into account.

6 NUMERICAL RESULTS AND MODEL APPRAISAL

6.1 *Slabs of Series A (positive bending)*

Typical stress distributions in composite slabs (series A) in the linear elastic regime (before onset of crack formation) are shown in Figure 5. Stresses

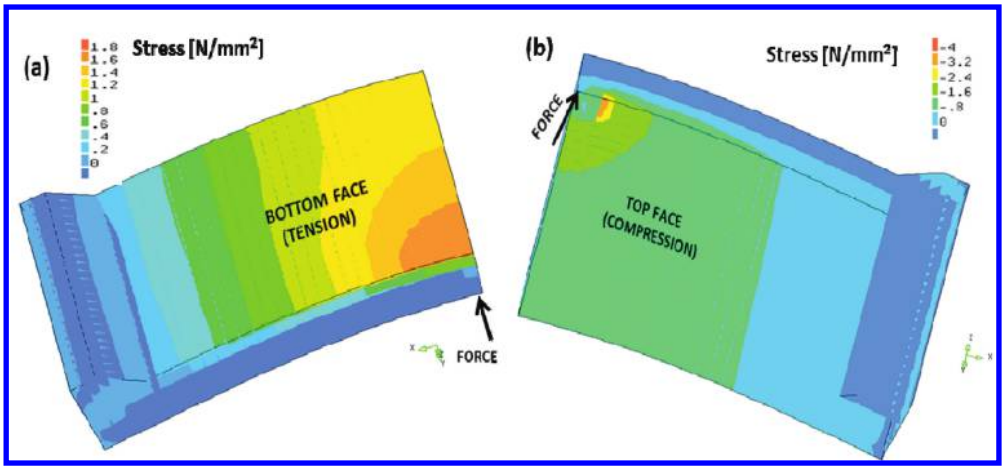

Figure 5. Stress distributions in linear elastic regime; (a) bottom face in traction, (b) top in compression; figures are shown in an exaggerated deformed shape.

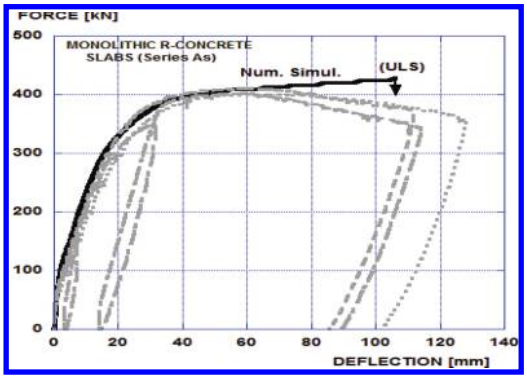

Figure 6. Comparison between experimental force-deflection curves of the three monolithic RC slabs (series A) (grey dashed curves) and the predicted one by the numerical model (black solid curve).

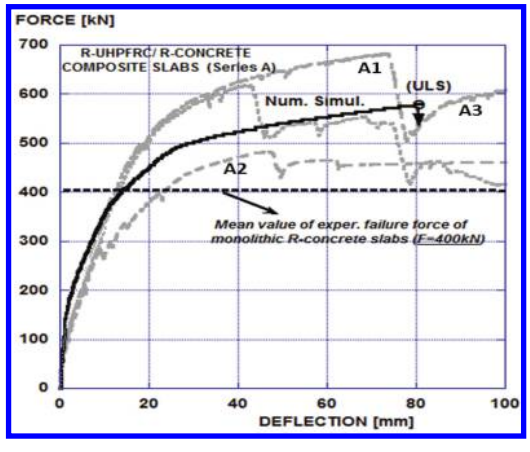

Figure 7. Comparison between experimental force-deflection curves of the three RC/R-UHPFRC composite slabs (series A) (grey dashed curves) and the predicted one by the numerical model (black solid curve).

are expressed in N/mm^2, (positive sign: tension, negative sign: compression). Figure 5a shows stress distribution of the bottom (concrete substrate) of the quarter composite slab which is in the tensile regime. Highest tensile stresses are localized in the central zone under the force, while the top face (UHPFRC-overlay) is in a state of compression, as shown in Figure 5b.

Figure 6 shows a comparison between the computed and experimental force-deflection responses of the three monolithic R-concrete slabs of series A (grey dashed curves) and the slab response predicted by the numerical model (black solid curve). We can notice that the model gives the expected good agreement between simulated and measured force-deflection curves.

In the simulation, the ULS (ultimate limit state) is defined as the last converged force step. At this loading stage, no more convergence of the numerical solution could be achieved even by using much smaller force-steps or by enhancing the convergence criteria.

Figure 7 shows the comparison between the measured force-deflection curves (grey dashed curves) of the three composite slabs (series A) and the simulated one (black solid curve).

Firstly, we can observe significant differences in the experimental force-deflection responses of the three specimens. Slabs A1 and A3 show a similar behaviour until a deflection of roughly 40 mm,

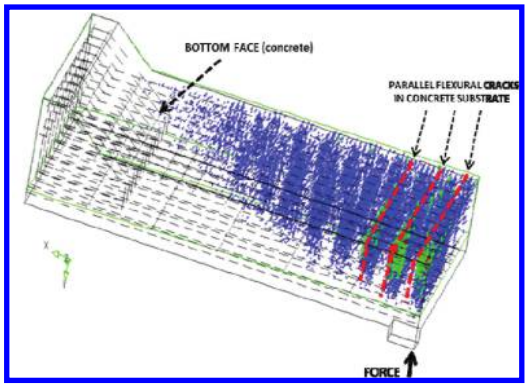

Figure 8. Crack pattern of analysed composite slab (series A).

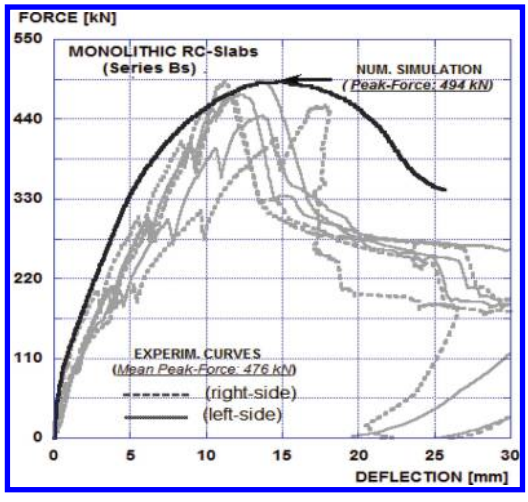

Figure 9. Comparison between experimental force-deflection curves of the three RC monolithic slabs (series B) (grey solid curves for the left part of slabs and grey dashed for the right part) and the predicted one by the numerical model (black solid curve).

then a sudden drop of the force arises at a deflection of 73 mm for the slab A1 and of 45 mm for the slab A3. This abrupt drop was induced by a sudden detachment of the UHPFRC-overlay which was due to improper UHPFRC casting on the substrate prepared by high pressure water jet, as identified after the test. Slab A2 shows a much lower structural response throughout the test. Again, this was due to insufficient or inexistent bond between concrete and UHPFRC due to improper UHPFRC casting. Consequently, Test A2 had to be discarded.

Compared to the experimental results, the computed force-deflection curve underestimates the force values by about 15% while the deflection values are well predicted.

Overall, numerical results show that strengthening slabs by means of UHPFRC increases the peak force by 45%, while experimental test revealed an increase of 47% (based on the mean value of the three specimens). The increase in resistance due to the UHPFRC-reinforcing layer is significant.

Figure 8 shows crack patterns obtained by the numerical model; cracking is represented by crack-strain distribution (coloured small bars). This picture is retreated by superimposing red-hick dashed lines on the crack-strain distribution, in order to highlight major flexural macrocracks. A good degree of similarity was observed between predicted and experimental crack patterns.

6.2 *Slabs of Series B (negative bending)*

The force-displacement response obtained by the numerical model for monolithic RC slabs subjected to negative bending (series B) is shown in Figure 9 by the solid black curve. For comparison, the recorded experimental responses obtained from the 3 monolithic RC-slabs are given in the same figure.

In the pre-peak regime, the predicted curve exhibits a slightly stiffer behaviour than the experimental ones. In the post-peak regime, the predicted response shows a rather ductile behavior, while the recorded experimental post-peak responses show rather rapid force-drop after reaching the ultimate resistance.

Anyway, a good agreement is achieved between the predicted ultimate resistance (495 kN) and the mean experimental value (479 kN).

Figure 10 gives a comparison between the numerical and experimental force-deflection responses of the RC/UHPFRC composite slabs of series B.

The computed peak-force (848 kN) is found to be 16% higher than the mean experimental value (728 kN). Compared to the experimental results, the computed force-deflection curve overestimates the force values while the deflection values are well predicted.

Figure 11 shows the resulting 3D crack-opening distribution in the post-peak domain, for an imposed deflection of 20 mm (corresponding to a force of 570 kN, see Figure 10). Red and green coloured symbols correspond to cracks with large openings; while blue coloured symbols represent micro-cracks with a very small opening or cracks in unloading state (see Figure 3) or even closed cracks.

Figure 12 gives a side view of the crack opening distribution of the corner (2-3-4-4') of the

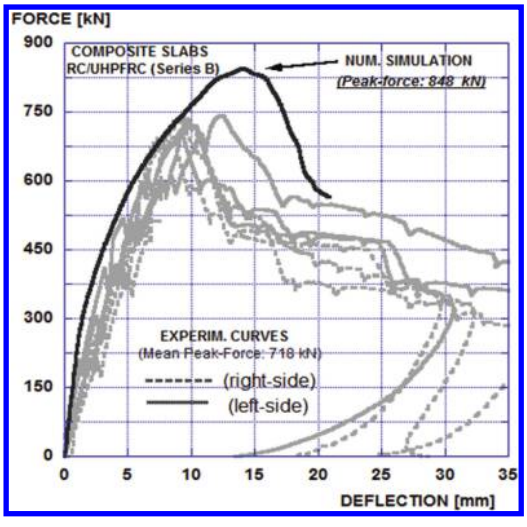

Figure 10. Comparison between experimental force-deflection curves of the three RC/UHPFRC composite slabs (series B) (grey solid curves for the left part of slabs and grey dashed for the right part) and the predicted one by the numerical model (black solid curve).

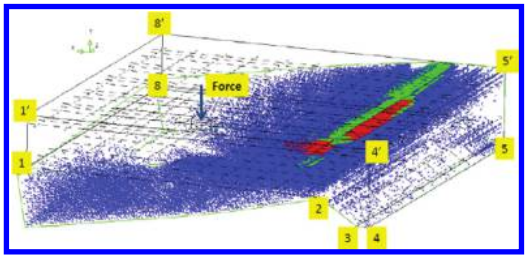

Figure 11. Perspective representation of the crack opening distributions (composite slab series B, deformed shape) in the post-peak domain (force = 570kN, deflection = 20 mm (see Fig. 10).

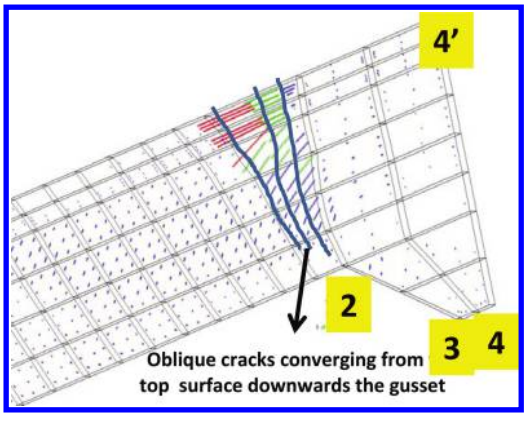

Figure 12. Visualisation of crack pattern of the corner of the composite slab (series B), at the same force level as in Fig.11.

composite slab. Three dominant oblique cracks are distinguished; they are highlighted by solid blue lines. This cracking stage corresponds to force and deflection values identical to those of Figure 11 (post-peak domain). It must be outlined that these cracks started to form already in pre-peak regime.

Overall, numerical results show that strengthening of the slab elements by means of UHPFRC increases the peak force by 45%, while experimental test revealed an increase of 47% (based on the mean value of the three specimens). The increase in resistance due to the UHPFRC-reinforcing layer is significant

7 CONCLUSIONS

The strengthening method of bridge deck slabs by means of an UHPFRC overlay has been validated by a specific experimental program which is presented in a companion contribution (Zwicky & Brühwiler, 2015). This paper presents results of a non-linear finite element analysis of the structural and cracking behavior of composite UHPFRC/concrete slabs subjected to loading similar to loading of real bridge decks.

The results of the non-linear 3D-numerical modelling of three monolithic concrete slabs and three UHPFRC/concrete composite slabs show good agreement between experimental findings and the slab response as obtained by the numerical model, both in terms of force-deflection responses and cracking patterns. The model confirms that the failure is essentially governed by the flexural mode, as observed experimentally.

In accordance with the experimental results, the computed results show that the UHPFRC layer increases significantly the resistance of concrete slabs.

In summary, 3D FE-analysis has proven to effectively simulate with sufficient accuracy the structural behavior of the tested slab elements.

This numerical model can be further used to explore the structural behavior of structures like bridges or industrial buildings subjected to different loadings and environmental conditions like temperature variation, creep/relaxation, drying shrinkage, alkali silica reaction-induced swelling or ageing effects. This validated model was used to design the strengthening of the deck slab of the Chillon Viaducts.

ACKNOWLEDGEMENTS

The authors wish to express their gratitude to the client and his panel of experts for the pleasant collaboration in this interesting project.

REFERENCES

Bazant, Z.P. & Planas, J. (1998), Fracture and Size effect in Concrete and other Quasibrittle Materials, CRC Press, Boca Raton, Florida, and London, U.K.

de Borst R. & Nauta P. (1985): Non-Orthogonal Cracks in a Smeared Finite Element Model. Eng. Comp., 2, pp. 35–46.

Brühwiler E. & Denarié E. (2013), Rehabilitation and strengthening of concrete structures using Ultra-High Performance Fibre Reinforced Concrete, Structural Engineering International, Volume 23, Number 4, November 2013, pp. 450–457.

DIANA (2010), Finite Element Analysis, User's Manual, release 9.3., TNO BV, Delft, The Netherlands.

Rashid Y.R. (1968): Analysis of Prestressed Concrete Pressure Vessels, Nuclear Eng. and Design, 7(4), pp. 334–344.

Rots J.G. (1991), Smeared and Discrete Representations of Localized Fracture, International Journal of Fracture, Vol. 51, pp. 45–59.

Rots J.G. & Blauwendraad J. (1989), "Crack models for concrete: Discrete or smeared: fixed, multi-directional or rotating? In: HERON, 34 (1).

Zwicky D. et al. (2013), Essais sur dalles "Chillon" renforcées au BFUP armé, Technical report (in french), University of Applied Sciences HEIA-FR, iTEC, Fribourg, Switzerland.

Zwicky D. & Brühwiler, E. (2015), Chillon Viaduct deck slab strengthening using reinforced UHPFRC: Full-scale tests, Proc. International Conference on Concrete Repair, Rehabilitation and Retrofitting (ICCRRR 2015), Leipzig, 5–7 October 2015.

Concrete Repair, Rehabilitation and Retrofitting IV – Dehn et al. (Eds)
© 2016 Taylor & Francis Group, London, ISBN 978-1-138-02843-2

Strengthening of existing reinforced concrete beams using ultra high performance fibre reinforced concrete

Andreas P. Lampropoulos & Spyridon A. Paschalis
University of Brighton, Brighton, UK

Ourania T. Tsioulou & Stephanos E. Dritsos
University of Patras, Patras, Greece

ABSTRACT: The efficiency of the technique of strengthening existing structures using Ultra High Performance Fibre Reinforced Concrete (UHPFRC) has been investigated in this study. The uniaxial stress-strain relationship in tension and the compressive strength characteristics have been determined by direct tensile and compressive tests respectively. These results have been used for the constitutive modelling of UHPFRC. The model in tension is consisted of several linear parts, including strain hardening followed by a significant post crack energy absorption softening branch. Finite Element method has been used for the modelling of strengthened reinforced concrete beams with UHPFRC layers and a parametric study has been conducted on beams strengthened with UHPFRC layers and jackets. The efficiency of this technique is highlighted and the performance of strengthened beams with UHPFRC layers is compared to respective specimens strengthened with additional concrete layers reinforced with steel bars.

1 INTRODUCTION

The addition of reinforced concrete layers and jackets for the earthquake strengthening of existing beams and columns is one of the most commonly used techniques in earthquake prone areas. This application can considerably improve the strength and stiffness of existing elements. There are several published experimental and theoretical studies where the behaviour of strengthened beams has been investigated (Trikha et al. 1991, Cheong & MacAlevey 2000, Altun 2004, Tsioulou & Dritsos 2011, Tsioulou et al. 2013). In case of elements strengthened with additional concrete layers, an important parameter which affects the durability and the performance of the strengthened elements is the concrete shrinkage of the new concrete (Yuan & Marosszeky 1994, Silfwerbrand 1997, Denarie & Silfwerbrand 2004, Abbasnia et al. 2005, Beushausen & Alexander 2006, Beushausen & Alexander 2007, Zhou J. et al. 2008, Lampropoulos et al. 2012). The use of UHPFRC could potentially provide improved durability and resistance due to the superior mechanical properties and due to the reduced shrinkage strain values.

The main aim of the current study is to investigate the performance of strengthened elements with UHPFRC. Ultra High Performance Fiber Reinforced Concrete is a relative new cementitious material with high steel fibre content characterized by superior mechanical properties. Kang et al. (2010) and Yoo et al. (2013) examined the effect of the steel fibers amount on the flexural strength of UHPFRC and it was found that the flexural strength increased with the fiber volume ratio while the ductility was decreased. Kang et al. (2010) presented an inverse analysis to determine the tensile fracture model of UHPFRC and a trilinear tensile fracture model of UHPFRC tensile softening model is proposed. The orientation and distribution of the fibres in the mix is an important parameter for the mechanical properties of UHPFRC. Kang & Kim (2011) investigated the effect of the fiber orientation on the tensile behavior of UHPFRC. Theoretical approach was presented together with direct tensile tests and the pre and post-cracking tensile behaviour of UHPFRC was examined. According to this study (Kang & Kim 2011) the effect of the fiber orientation distribution was found to be negligible in the pre-cracking behaviour, but this significantly affected the post-cracking behaviour (Kang & Kim 2011).

There are very limited studies on the application of UHPFRC for the earthquake strengthening of existing structures (Farhat et al. 2007, Bruhwiller & Denarie 2008). Farhat et al. (2007) investigated the shrinkage, the thermal cycling, and the fatigue of UHPFRC used for the retrofitting of concrete beams. The volume of fibres in this research (Farhat et al. 2007) was high (8%) which deviates from the

quantity normally used in UHPFRC. The results indicated that due to the high volume of the fibres in the mix, the cyclic thermal loading did not affect the mechanical properties. Farhat et al. (2007) used epoxy based adhesive to bond the strips to the initial specimens. Shear failure was prevented and the failure load was increased up to 86%. Bruhwiller & Denarie (2008) examined various other applications of UHPFRC. UHPFRC was used for the rehabilitation of a crash barrier wall of a highway bridge, a bridge pier and industrial floors.

From the existing literature, even if the application of UHPFRC for the strengthening of structures seems to be a quite promising technique, the performance of strengthened with UHPFRC elements has not been extensively studied. In the present study, experimental data have been used for the numerical modelling of UHPFRC, and the results of a numerical parametric study on strengthened beams will be presented. The performance of the strengthened with UHPFRC elements are compared to respective elements strengthened with additional RC layers and the efficiency of additional UHPFRC layers and/or jackets is highlighted.

2 BEAMS STRENGTHENED WITH ADDITIONAL RC CONCRETE LAYERS

2.1 *Experimental investigation*

In the current study the results of a previous experimental investigation on beams strengthened with additional reinforced concrete layers (Tsioulou et al. 2013) have been used. The initial beams have a length of 2200 mm and rectangular cross section of 150 mm by 250 mm. The reinforcement consists of 2H12 B500 in the tensile side with a cover of 25 mm. Strengthening has been performed by adding a new concrete layer of 50 mm thickness in the tensile side with 2H12 B500 and concrete cover of 25 mm. The additional concrete layer has been placed along the whole length of the beam and the interface between the old and the new concrete has been roughened using an air chipping hammer (Figure 1).

In this study (Tsioulou et al. 2013), the effect of the interface treatment has been examined and it has been proved that the performance of the specimens with adequate interface treatment is considerably improved compared to the response of the initial beam. The load deflection results of the Initial Beam (IB) and the strengthened beam with a RC layer and a well roughened interface (STL_RC) are presented in figure 2.

Based on these results, the maximum load capacity of the strengthened specimen is significantly increased and the yield load has been found to be 223% of initials' beam yield load (Tsioulou et al. 2013).

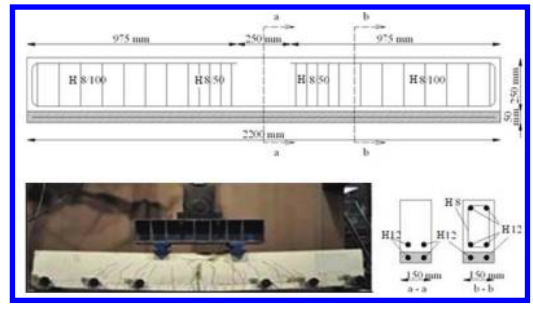

Figure 1. Geometry of beams strengthened with additional reinforced concrete layer (Tsioulou et al. 2013).

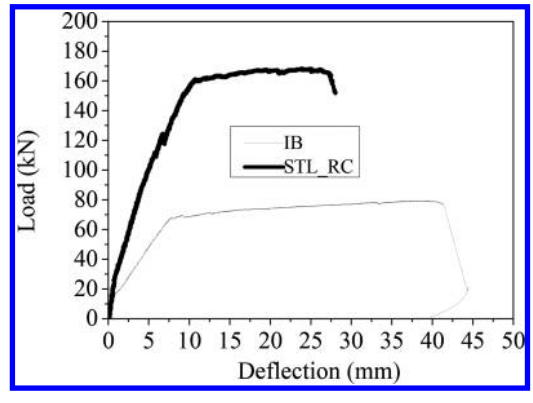

Figure 2. Load displacement results of the strengthened and the initial beams (Tsioulou et al. 2013).

2.2 *Numerical analysis of strengthened beams with RC layers*

In this section, the results of the numerical investigation of the initial beam (IB) and the strengthened beam with RC layer (STL_RC) are presented. Finite element software ATENA (Cervenka et al. 2013) has been used and the concrete has been simulated with an eight-node element, with nonlinear behaviour and softening branches in both tension and compression. The model proposed by CEB-FIP Model Code 1990 (1993) has been adopted for the modelling of concrete in compression. In tension, linear ascending branch and exponential softening branch based on the fracture energy needed to create a unit area of a stress free crack has been used (Cervenka et al. 2013). For the simulation of steel bars, linear elements with bilinear behaviour have been used. The interface has been simulated with special 2D contact elements with a coefficient of friction equal to 1.5 and cohesion 1.9 MPa. The shrinkage effect has not been taken into account in this study. The numerical model of concrete, steel reinforcement, and beam-layer interface are presented in figure 3.

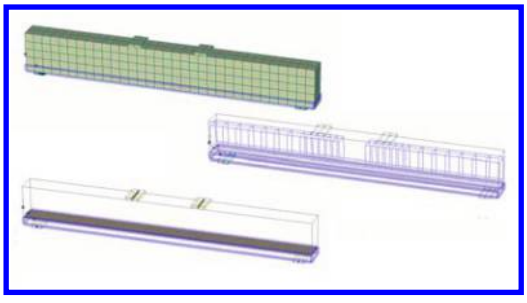

Figure 3. Numerical models for the simulation of concrete, steel and interface.

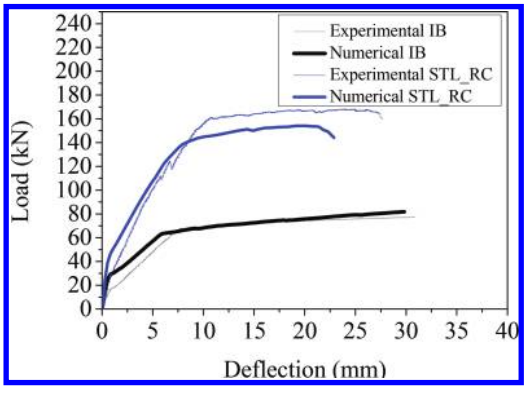

Figure 4. Numerical versus experimental results for IB and STL_RC.

Analyses have been performed for the strengthened beam with additional reinforced concrete layer in the tensile side (STL_RC) and the Initial Beam (IB), and the results are compared to the respective experimental (Figure 4).

The results indicate that the numerical model can accurately predict the response of both the initial and the strengthened beam. The same method will be used for the numerical modeling of the strengthened specimens with UHPFRC.

3 BEAMS STRENGTHENED WITH ADDITIONAL UHPFRC LAYER/JACKET

3.1 *UHPFRC Material preparation*

UHPFRC is a material with enhanced strength in tension and compression and significantly high energy absorption in the post-cracking region. Its mix composition is not much dissimilar from that of normal strength concrete. One of the main characteristics of UHPFRC is the enhanced homogeneity which is achieved by using only fine aggregates. In the mix design of the present study silica sand with maximum size of particles of 500 μm has been used together with silica fume in order to improve the rheological properties. A high steel fibre content has been used (3%), which is equivalent to the steel reinforced of specimen (STL_RC) for layer of 50 mm thickness.

Table 1. Mix design for UHPFRC (Hassan et al. 2012).

Material	Mix proportions (kg/m^3)
Cement (52.5 N)	657
GGBS	418
Silica fume	119
Silica Sand	1051
Superplasticizers	59
Water	185
3% Steel fibres (13 mm length and 0.16 mm diameter)	236

The mix design is presented in Table 1 and this is based on a previous experimental investigation (Hassan et al. 2012).

For the preparation of UHPFRC the dry ingredients were mixed first for 3 minutes, then the water and the superplasticizer were added to the mix and at the end the steel fibers were added gradually. The specimens were cured in a steam curing tank at 90°C for 3 days.

3.2 *Compressive and direct tensile tests and numerical modeling*

The standard cube compressive tests have been conducted and the compressive strength was found to be equal to 164 MPa. For the tensile strength, direct tensile tests have been carried out (Figure 5).

The tests have been performed under displacement control and a constant loading rate of 0.007 mm/sec has been used. The strain/crack opening have been measured using LVDT over a gauge length of 105 mm. A number of 6 identical specimens have been tested under tension and these results together with the average stress–strain curve are presented in figure 6.

For the numerical modelling of UHPFRC, finite element software ATENA has been used (Cervenka et al. 2013). The material properties adopted in the models are based on the experimental results of compressive and tensile tests. A compressive strength of 164 MPa and modulus of elasticity equal to 57.5 GPa have been used. The model in tension is linear up to a tensile strength of 11.5 MPa and, after the end of the elastic part, the stress-strain presented in figure 7 has been adopted for a characteristic size equal to 2 mm.

Figure 5. Experimental setup for the direct tensile testing of dog-bone specimens.

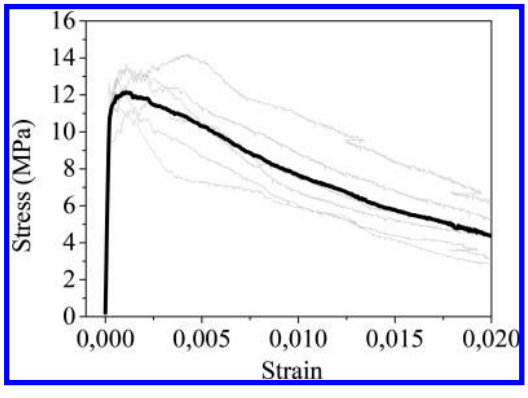

Figure 6. Stress-strain experimental results of direct tensile tests.

The numerical model and the strain and crack distribution at the maximum load value are presented in figure 8.

The results of the analyses are compared to the experimental results of the dog bone specimens and the results are presented in figure 9.

It is evident from the results presented in figure 9 that the numerical model described in the current section can accurately predict the response of UHPFRC under tension. This model has been adopted for the numerical modeling of the strengthened with UHPFRC layer/jacket beams.

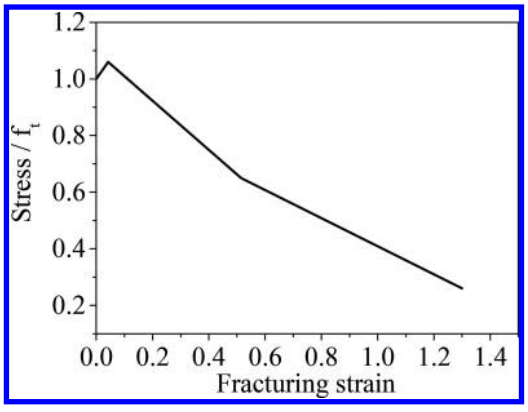

Figure 7. Tensile stress strain behavior adopted in the numerical model for the simulation of UHPFRC.

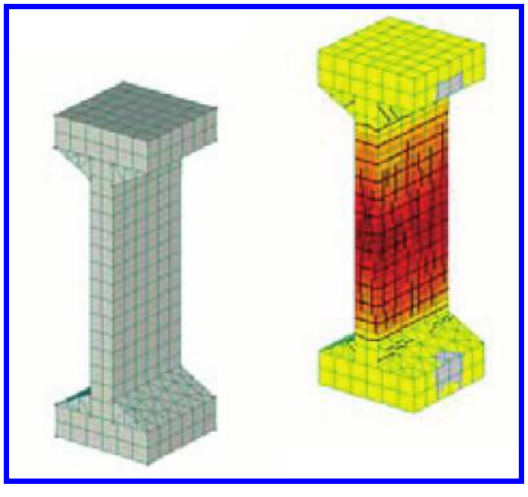

Figure 8. Finite element model and strain/crack distribution in the direct tensile test specimens.

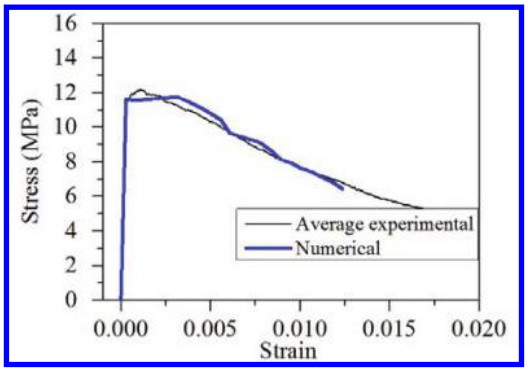

Figure 9. Numerical versus experimental results for the direct tensile tests.

3.3 *Numerical modelling of the strengthened beams with UHPFRC layer and three side jackets*

For the numerical modelling of the initial beams, the same procedure with the investigation presented in section 2.2 has been used. For the simulation of the additional UHPFRC layer, the material properties presented in section 3.2 have been implemented.

Three different types of models have been examined, one with an additional layer in the compressive zone (SCL_UHPFRC), one in the tensile (STL_UHPFRC), and another one with a three side jacket (S3SJ_UHPFRC) (Figure 10). In all the examined cases a 50 mm thick layer or jacket has been used. The performance of the strengthened beams with UHPFRC layers in the tensile and in the compressive zone are compared to respective results of strengthened elements with additional RC layer in the tensile side (STL_RC) and normal plain concrete (40 MPa compressive strength) in the compressive zone (SCL_NC).

The results of the various strengthening techniques are compared to the initial beam's results, and the load-deflection distributions are presented in figure 11.

The results presented in figure 11 indicate that the addition of UHPFRC layers/jackets can considerably improve the strength and the stiffness of the existing structures. In case of beam strengthened with additional UHPFRC layer in the tensile side (STL_UHPFRC), the stiffness is significantly increased but the yield and the maximum load values are lower compared to the respective load values of the beam with additional RC layer (STL_RC). In case of beam strengthened with UHPFRC in the compressive zone (SCL_UHPFRC), both strength and stiffness are considerably improved compared to the respective specimen with additional normal strength concrete layer (SCL_NC). The results of the beam strengthened with a three side UHPFRC jacket (S3SJ_UHPFRC) are characterized by superior performance compared to all the other examined specimens.

The yield and the ultimate bending moment (M_y and M_u) for all the examined cases have been calculated using the results of figure 11 (Table 2).

The increment of yield and ultimate moments for all the examined techniques as percentage of the respective values of the initial beam (100*ΔM/M) is presented in figure 12.

The addition of UHPFRC layer in the compressive or in the tensile side can contribute to 20–30% increment of yield and ultimate moment, while in case of a three side UHPFRC jacket the respective increment is 160–170%. When comparing the specimens with the additional layer in the tensile

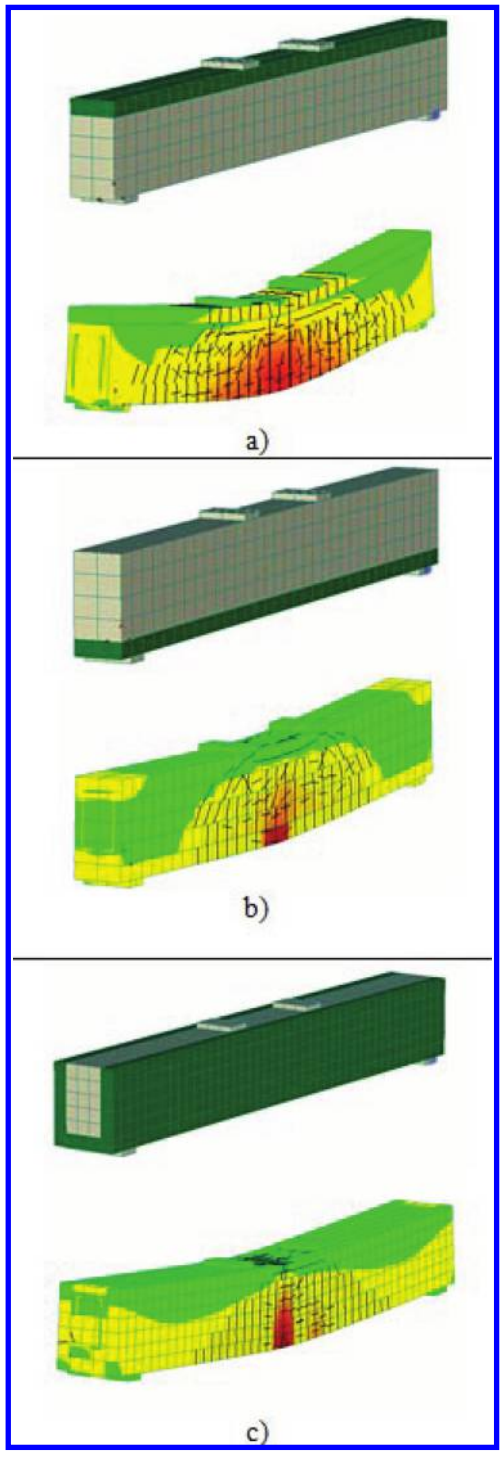

Figure 10. Finite element models and crack patterns of beams strengthened with UHPFRC a) in the compressive side, b) in the tensile side, and c) three side jacket.

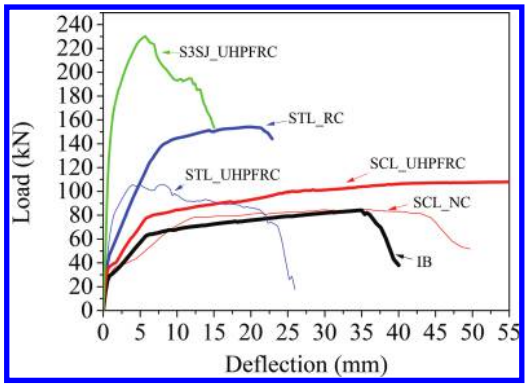

Figure 11. Numerical load-deflection results for beams strengthened with various techniques.

Table 2. Yield and the ultimate bending moment values of the examined specimens.

Specimen	M_y (10^3 Nm)	M_u (10^3 Nm)
IB	24	32
SCL_UHPFRC	29	41
STL_UHPFRC	30	40
SCL_NC	29	32
STL_RC	52	58
S3SJ_UHPFRC	63	86

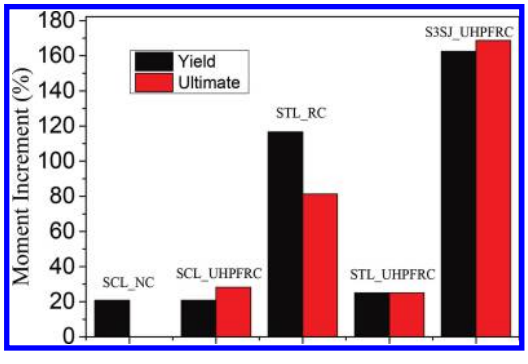

Figure 12. Moment increment for the examined techniques.

zone with RC and UHPFRC, it can be observed that the specimen with the additional RC layer shows better performance compared to the respective strengthened beam with UHPFRC.

A further parametric study has been conducted for the specimens with additional UHPFRC layer in the tensile side (STL_UHPFRC) using various UHPFRC tensile strength values. In the current study 8 MPa, 12 MPa and 16 MPa tensile strength

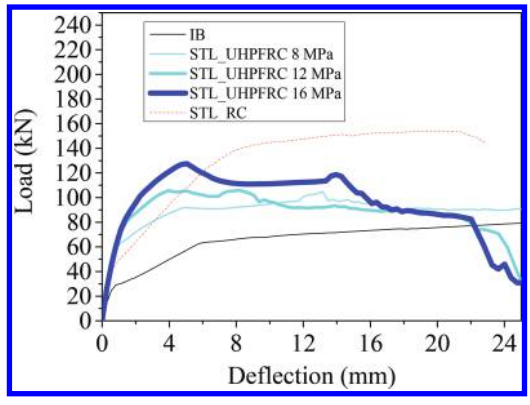

Figure 13. Parametric study results using different values for the tensile strength of UHPFRC.

values have been used and the numerical results are presented in figure 13 together with the results of STL _RC specimen.

The results of figure 13 indicate that there is a significant increment of the ultimate moment Mu when higher tensile strength values are used. As the tensile strength of UHPFRC is increased, the maximum strength of STL_UHPFRC is approaching the ultimate strength of STL_RC. However, it may worth mentioning that in all the examined specimens with UHPFRC, the stiffness is higher compared to the respective specimens strengthened with conventional strengthening techniques with normal plain and reinforced concrete layers.

4 CONCLUSIONS

In this paper an extensive numerical investigation on beams strengthened with UHPFRC layers/jacket has been presented. The numerical results are compared to respective results of specimens strengthened with normal plain and reinforced concrete. For the constitutive modeling of UHPFRC, experimental results have been used to calibrate and validate the numerical model.

The following conclusions have been drawn regarding the efficient of the strengthening technique:

- The addition of UHPFRC layers in the tensile side considerably improves the stiffness of the strengthened element. Yield and maximum load values are lower compared to the respective load values of beam strengthened with RC layer.
- In case of beams strengthened with UHPFRC in the compressive zone, the strength and stiffness increment is higher with respect to the specimens strengthened with normal strength concrete.

- The examined specimen with three-side jacket is characterized by superior performance compared to all the other examined cases.
- From the numerical results, the yield and ultimate moment increments for all the examined methods have been calculated. In case of beam strengthened with additional UHPFRC layer either in the compressive or in the tensile side, 20–30% increment of the yield and ultimate moment has been observed. The respective increment in case of three side UHPFRC jacket has been found to be in the range of 160–170%.
- A parametric study has also been presented on strengthened beams in the tensile side with different UHPFRC tensile strength values. The main conclusion is that the tensile strength is improved as the tensile strength of UHPFRC is increased.

The overall conclusion of this study is that the application of UHPFRC can considerably enhance the performance of existing reinforced concrete beams in terms of stiffness and yield & maximum strength. Further experimental and numerical investigation is required in order to take into account concrete shrinkage effect and investigate the durability of the examined technique.

REFERENCES

Abbasnia R., Godossi P. & Ahmadi J. 2005. Prediction of Restrained Shrinkage Based on Restraint Factors in Patching Repair Mortar. *Cement and Concrete Research*: 35: 1909–1913.

Altun, F. 2004. An experimental study of jacketed reinforced concrete beams under bending. *Construction and Building Materials* 18:611–618.

Beushausen H. & Alexander M.G. 2006. Failure Mechanisms and Tensile Relaxation of Bonded Concrete Overlays Subjected to Differential Shrinkage. *Cement and Concrete Research* 36: 1908–1914.

Beushausen H. & Alexander M.G. 2007. Localised Strain and Stress in Bonded Concrete Overlays Subject to Differential Shrinkage. *Materials and Structures* 40: 189–199.

Bruhwiller E., Denarie E. 2008. Rehabilitation of concrete structures using Ultra-High Performance Fibre Reinforced Concrete. *The Second International Symposium on Ultra High Performance Concrete*, *Kassel, 5–7 March 2008*. Germany.

CEB-FIP. 1993. Model Code 1990. Thomas Telford, London. UK.

Cervenka V., Jendele L., & Cervenka J. 2013. ATENA Program Documentation: Part 1 Theory, Czech Republic, Prague.

Cheong, H.K. & MacAlevey, N. 2000. Experimental behaviour of jacketed reinforced concrete beams. *ASCE Journal of Structural Engineering* 126:692–699.

Denarie E. & Silfwerbrand J. 2004. Structural Behaviour of Bonded Concrete Overlays. *Proceedings of the International RILEM Workshop on Bonded Concrete Overlays, Stockholm, 7–8 June 2004*. Sweden.

Farhat F.A., Nicolaides D., Kanelopoulos A. & Karihaloo B.L. 2007. High performance fibre-reinforced cementitious composite (CARDIFRC) – Performance and application to retrofitting. *Engineering Fracture Mechanics* 74(1–2): 151–167.

Hassan, A., Jones, S. & Mahmud, G. 2012. Experimental test methods to determine the uniaxial tensile and compressive behaviour of ultra high performance fibre reinforced concrete (UHPFRC). *Construction and Building Materials* 37: 874–882.

Kang S.T., Lee Y., Park Y.D. & Kim J.K. 2010. Tensile fracture properties of an Ultra High Performance Fiber Reinforced Concrete (UHPFRC) with steel fiber. *Composite Structures* 92(1): 61–71.

Kang S.T. & Kim J.K. 2011. The relation between fiber orientation and tensile behavior in an Ultra High Performance Fiber Reinforced Cementitious Composites (UHPFRCC). Cement and Concrete Research 41(10): 1001–1014.

Lampropoulos A., Tsioulou O. & Dritsos S. 2012. Biaxial Stress due to Shrinkage in Concrete Jackets of Strengthened Columns. *ACI Materials Journal* 109 (3): 331–340.

Silfwerbrand J. 1997. Stresses and Strains in Composite Concrete Beams Subjected to Differential Shrinkage. *ACI Structural Journal* 94(4): 347–353.

Trikha, D., Jain, S. & Hali, S. 1991. Repair and strengthening of damaged concrete beams. *Concrete International: Design and Construction* 13(6):53–59.

Tsioulou, O. & Dritsos, S. 2011. A Theoretical Model to Predict Interface Slip due to Bending. *RILEM Materials and Structures* 44(4): 825–843.

Tsioulou, O., Lampropoulos, A. & Dritsos, S. 2013. Experimental investigation of interface behaviour of RC beams strengthened with concrete layers, *Construction and Building Materials* 40: 50–59.

Yoo Y., Shin H.O., Yang J.M. & Yoon Y.S. 2013. Material and bond properties of Ultra High Performance Fiber Reinforced Concrete with micro steel fibers. *Composites Part B: Engineering* 58:122–133.

Yuan Y. & Marosszeky M. 1994. Restrained Shrinkage in Repaired Reinforced Concrete Elements. *Materials and Structures* 27 (7): 375–382.

Zhou J., Ye G., Schlangen E, & Breugel K. 2008. Modelling of Stresses and Strains in Bonded Concrete Overlays Subjected to Differential Volume Changes. *Theoretical and Applied Fracture Mechanics* 49: 199–205.

Concrete Repair, Rehabilitation and Retrofitting IV – Dehn et al. (Eds)
© 2016 Taylor & Francis Group, London, ISBN 978-1-138-02843-2

"Integralization" with new UHPC decks for existing motorway bridges

P. Hadl & R. della Pietra
Institute of Structural Concrete, Graz University of Technology, Graz, Austria

M. Reichel
König und Heunisch Planungsgesellschaft, Leipzig, Germany

N.V. Tue
Institute of Structural Concrete, Graz University of Technology, Graz, Austria

ABSTRACT: Ultra-High Performance Concrete (UHPC) has a high potential for the repair and retrofitting of existing bridges. A thin UHPC layer of a few centimeters can replace the waterproofing as well as the asphalt pavement. Due to its excellent durability properties a longer service life of bridge decks made of UHPC can be expected. Therefore, the life-cycle costs decrease. This paper presents the application of UHPC in the renovation of Steinbach-bridge, a motorway bridge in Austria. For this pilot project more than 40 m³ UHPC were produced in a ready-mix concrete plant and cast on site. Within this project a successful transfer of laboratory findings into practical productions under site conditions was achieved. Currently, the behaviour of the structure is observed by a monitoring system. This innovative solution can thus make a significant contribution to the reduction of the life-cycle costs for the renovation and retrofitting existing bridge structures.

1 INTRODUCTION

Bridge decks generally provided with a replaceable layer made of asphalt, which require an additional waterproof arrangement and have a limited service life. The basic idea of using UHPC for the retrofitting of existing bridges is to create a monolithic connected and maintenance-free bridge deck for conventional concrete bridges. In addition to a durable and waterproof surface, the UHPC also participates in the load transfer, and enhances the bearing capacity.

Previous investigations confirmed that UHPC is suitable for sealing due to its excellent packing density and durability properties (Charron et al. 2004). This contribution concentrates on the development of a UHPC mixture for the application in the pilot project Steinbach-bridge with special focus on the concrete technology, related experimental testing and the construction work.

1.1 *Pilot project—Steinbach-bridge*

Steinbach-bridge, as shown in Fig. 1, is a two-span motorway bridge located in Upper-Styria on the S6 Semmering highway between the exits Mürzzuschlag East and West. It was built in 1980 and refurbished in 2013 to provide further serviceability as well as to enhance its bearing capacity caused by increasing service loads. The application of UHPC as bridge deck within this refurbishment was a pilot project in bridge renovation and upgrading in Austria.

The superstructure has a regular plate cross section with ordinary reinforcement. It is nearly 14 m wide and has two traffic lanes and a service lane. The damage of the concrete and reinforcement were caused by leaking sealing and leaking of expansion joint. As a result, water flags, sinter and large concrete spalling could be seen at the abutment walls. Moreover, the concrete of some benchings was partially free. Figure 1 shows the plan view of Steinbach-bridge.

Figure 3 illustrates the monolithic connected UHPC topping with a thickness of 7 cm. Preliminary studies have shown that the optimal solution regarding durability and bearing capacity was an "integralization" of the existing bridge. That means that both ends of the deck were connected with the abutments by the UHPC-layer as illustrated in figure 4. Such a sulution is not yet covered by the Austrian Guideline for Research on Road, Railway and Transportation (RVS 2012) but approved in this individual case.

Figure 1. Steinbach-bridge.

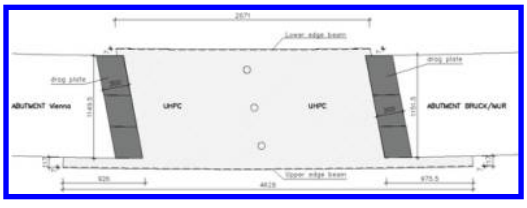

Figure 2. Plan view of Steinbach-bridge (dimensions in mm).

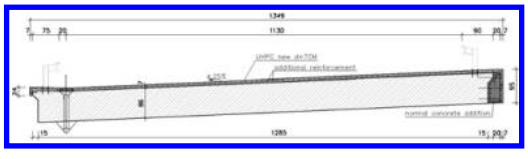

Figure 3. Cross-Section after renovation.

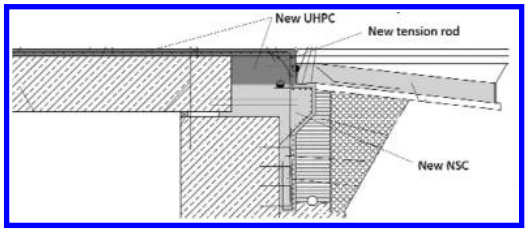

Figure 4. Principle of "integralization".

2 CONCRETE TECHNOLOGY

UHPC is a cement-based material with compressive strength ≥ 150 MPa and high resistance to many physical or chemical attacks. But it also has a brittle failure and requires therefore the addition of organic or metallic fibers to increase the ductility (Leutbecher 2007). In this project a UHPC with micro steel fibers was used.

2.1 *Requirements on UHPC topping for bridge decks*

In general, the use of UHPC as road surface requires a uniform quality of the concrete with special regard to the avoidance of any structural density defects on the surface. Those defects can result in the penetration of chloride-containing water in the concrete followed by the corrosion of steel fibers and reinforcement. Additionally, a sufficient and carefully executed compaction is also essential to guarantee resistance against freeze and thaw damages as well as high wear resistance.

The crack widths on the UHPC bridge deck surface were limited by using ordinary reinforcement (rebars Ø 10 mm, spacing 10 cm) in transverse and longitudinal direction with a concrete cover of 3.5 cm in combination with micro steel fibers (amount 90 kg/m³).

As mentioned above, the bridge has a superstructure cross slope of 4.25% and a longitudinal slope of 0.5%. The consistency of the UHPC has to enable a sufficient compaction while keeping the cross slope.

Furthermore, a concrete compressive strength > 150 MPa is necessary to ensure the bond between old and new concrete without dowels.

Finally, the UHPC surface must fulfill requirements regarding grip and flatness according to the Austrian Guideline for Research on Road, Railway and Transportation (RVS 2007). For this purpose the surface must be milled 3 days after casting by a milling machine. Grooves of the milling shall be carried out in the longitudinal direction as usual for conventional concrete roadways.

2.2 *UHPC mixture*

The used UHPC with steel fibers was developed by the Institute of Structural Concrete at Graz University of Technology. As binder, Nanodur Compound 5941 (manufactured by Dyckerhoff) was used. It contains cement to additive in mass relation 59 to 41. By this premix, the production of UHPC in ready-mix concrete plants can be considerably simplified. On the one hand only one silo is required to store the binder and on the other hand the homogenization of the fine particles is easier. Therefore, the use of mixer with low mixing intensity is possible. Further constituents of the UHPC are quartz sand (0.6–1.2 mm), basalt split (2–4 mm), water, superplasticizer, retarder and steel fibers with a length of 13 mm and a diameter of 0.2 mm.

2.3 *Material properties*

The fresh concrete properties were tested on site according to the Austrian standard for testing fresh concrete ÖNORM EN 12350 (Österreichisches Normungsinstitut 2009). The slump with and without compaction as well as the fresh concrete temperature and the processing time were determined, as shown in Table 1.

Table 1. Fresh UHPC properties.

slump (without compaction)	39 ± 2 cm
slump (without compaction)	48 ± 3 cm
fresh concrete temperature after mixing	16 ± 2°C
air temperature 06:00	4°C
air temperature 14:00	8°C
processing time	>2 h

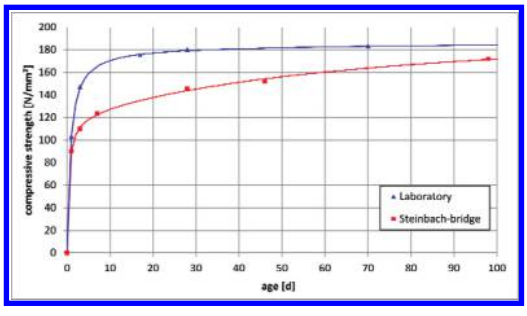

Figure 5. Development of concrete strength over time.

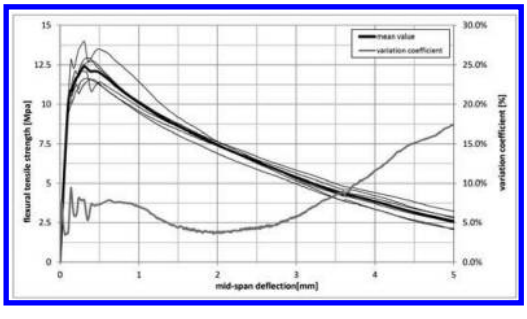

Figure 6. Bending behaviour after 28d.

The specimens to determine the hardened concrete properties were cast on site simultaneously with the bridge structure. The specimens were stored outside under approximately the same conditions and air temperature as on site. Three days after casting temperatures under 0°C were measured on site. Due to the low air temperature, the strength of concrete develops much slower than under laboratory conditions. Figure 5 compares the concrete strength development under laboratory and site conditions and figure 6 shows the bending test results on standard beams after 28d according to the Austrian Guideline for Fiber Concrete (Österreichische Vereinigung für Beton—und Bautechnik 2008). The elastic modulus after 28d was 51.000 [N mm²].

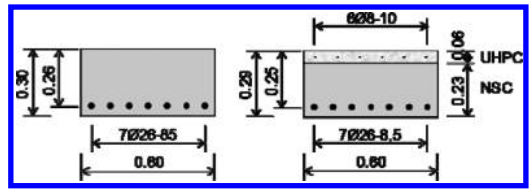

Figure 7. Cross section of specimen SV-01 (left) without and SV-02 and SV-03 (right) with UHPC topping.

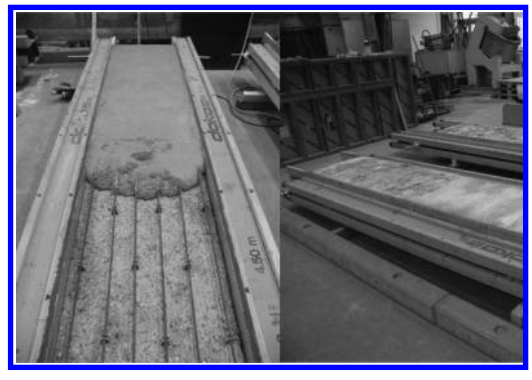

Figure 8. Casting of UHPC layer (left); Completed specimens SV-02 and SV-03 (right).

3 EXPERIMENTAL TESTING

Because of missing experience with the large amount of UHPC used in this project as ready-mix concrete, extensive experimental investigations were necessary for the transfer from production under laboratory conditions to on site conditions.

The experimental tests were performed on 3 beams of normal concrete (C30/37) with l × b = 3.2 × 0.6 m and a height of 0.3 m in case of the reference beam (SV-01) and 0.24 m NSC + 0.06 m UHPC in case of the compound system to be investigated (SV-02 and SV-03). Those two beams were blasted with high-pressure water before complementing them with the UHPC layer. The specimens were used for testing the manufacturing of the superstructure cross slope as well as the shear capacity and the bond strength between the old and new concrete. The cross sections of test beams are illustrated in figure 7.

3.1 *Superstructure cross slope*

The 6 cm UHPC layer of SV-02 and SV-03 was cast under a slope of 2.5 and 4.5% in order to test the stability of the superstructure cross slope during the compaction. At the same time, the consistency and the viscosity of the fresh UHPC were adjusted by accompanying experiments. Figure 8 shows the cast of the UHPC layers.

Figure 9. 4-point bending test.

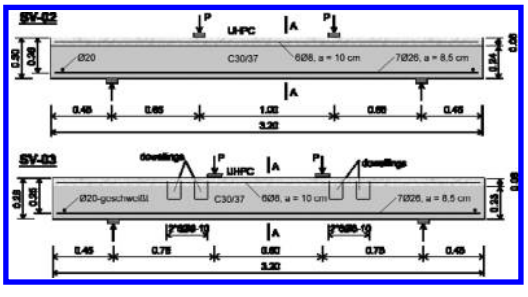

Figure 10. Test setup SV-02 and SV-03.

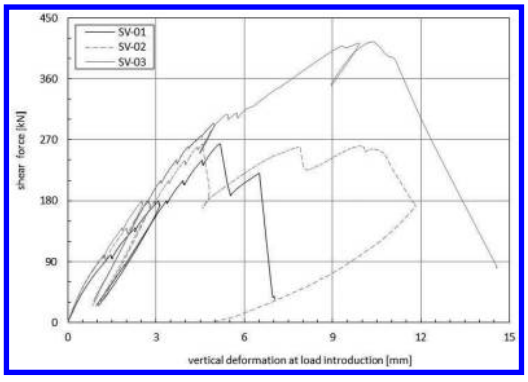

Figure 11. Load-deformation curves (static load only).

Figure 12. Tensile bond strength tests.

3.2 *Shear capacity*

The shear capacity was investigated with customized 4-point-bending tests according to Figure 10. The bending failure was excluded in all specimens through a high longitudinal reinforcement ratio of 2.4% and a shear slenderness of 3.

The specimens with UHPC topping (SV-02 and SV-03) are slightly stiffer and reach the ultimate load of the reference test (SV-01). Furthermore, test specimen SV-03 shows significant increase of the ultimate load because of its dowelling in the shear field between the load introduction area and the support area.

All specimens failed by overloading the maximum shear capacity. The formation of a decisive shear crack was observed in each specimen. In specimens with topping, the shear crack crossed the shear joint with no failure along the joint. Further, the measured relative deformations between normal concrete and UHPC topping in the bond joint were negligible small. Thus, the bond property between normal concrete and UHPC topping under shear stress can be classified as excellent. Therefore a dowelling of old concrete and UHPC was not required in the field area of the bridge.

3.3 *Bond strength*

The bond strength between normal concrete and UHPC was quantified by a tension test. In total eight cores of beam SV-02 were tested with the procedure illustrated by Figure 12. To take into account a possible preliminary damage due to the shear test loading, different sampling points were considered (four cores were located inside and four outside of the bearing area). All specimens showed a centric tensile failure within the normal concrete whereas the bond joint showed a bond strength at least of this magnitude.

3.4 *Freeze-thaw resistance*

The freeze-thaw resistance of the developed UHPC mixture was confirmed by experiments according

to the Austrian standard ONR 23303 (Österreichisches Normungsinstitut 2010). The specimens correspond to XF4. As expected, the test showed also a corrosion of the exposed fibers on the surface. Further details of those results are not discussed in this contribution.

3.5 *Surface requirements for roadways*

Without any post-treatment the UHPC surface is quite smooth and unsuitable as road surface. In order to fulfill the requirements regarding roughness and flatness according to the Austrian Guideline for Research on Road, Rail and Transportation (RVS 2007) the following options were investigated:

- High water pressure blasting
- Milling
- Retarder
- Sprinkle of basalt split

The laboratory experiments showed that the use of a milling machine provides the most effective opportunity. It does not affect the construction process significantly and requires only minimal site equipment. Furthermore, a possible unevenness due to the casting process can be compensated. Other methods could not meet the road surface requirements in the same quality.

4 CONSTRUCTION WORK

4.1 *Production in the ready mix concrete plant*

The production of UHPC was performed in a conventional ready-mix concrete plant. The used plant mixer corresponds to a simple plate mixer without separate mixing tools and single mixing speed. During the production of UHPC the mixing intensity has great influence on the fresh and hardened concrete properties. To transfer the test results from laboratory to site conditions, extensive mixing experiments were carried out in advance in the ready-mix concrete plant.

To avoid detected problems during microfiber addition in the plant mixer, a fiber dosage machine was developed. It adds fibers continuously and directly in the mixer, after the concrete reaches its yield point.

4.2 *Casting*

A total amount of 40 m³ UHPC was required for the bridge deck. The casting was achieved by a crane bucket as the viscous flow behavior of the UHPC as well as the low production capacity of the mixing plant did not allow the use of a concrete pump. In addition, the low production capacity of the mixing plant did also not allow a continuous casting over the whole width. Due to this, the bridge deck was cast in two sections with a longitudinal construction joint in the middle axis of the superstructure. Figure 13 illustrates this context.

Figure 13. Casting of the bridge with crane bucket and manufacturing the construction joint.

Because of the high viscosity of the UHPC, its compaction required a placement in two layers. The previous layer with a maximum height of 3.5 cm was needed to guarantee the bond quality with the NSC as well as a suitable compaction over the whole height of the UHPC. As shown in Figure 14, the previous layer was compacted by a wet screed, whereas the second layer and the production of the surface was carried out by a vibrating beam.

During the production it turned out, that especially the lateral completion along the long side (see Figure 3) of the bridge caused problems during casting. Due to the high viscosity of the UHPC and the small thickness of 7 cm it was difficult to cast and compact these elements. For future projects, height and thickness of the lateral completion should be coordinated. However, the production of the cross slope could easily be achieved with the knowledge of previous investigations. In detail, the large steel fiber content, the high amount of coarse basalt split 2/4 mm and the longitudinal reinforcement also blocked the leveling efforts of the fresh UHPC.

Figure 14. Compacting the first layer with wet screed and the second layer with vibrating beam.

4.3 *Milling*

The road surface has been milled after casting with a conventional milling machine. The milling depth was 3–4 mm, so that any possible unevenness from the UHPC placement was smoothed. After milling micro steel fibers are visible on the surface and protrude from the concrete. Preliminary investigations showed that theses protruding fibers impose no risk for the damages of the tire of vehicles. Later they will corrode through the application of road salt. Figure 15 shows the milled surface and the finished bridge.

5 CONCLUSION AND RECOMMENDATIONS

The present paper introduces the first application of UHPC as road surface in Austria. For this purpose a suitable UHPC with micro steel fibers was developed. The pilot project Steinbach-bridge illustrates the potential of this UHPC application regarding its material benefits and its practicability. Within this project a successful transfer of laboratory findings into practical production under site conditions was achieved.

The challenge of this UHPC application was primarily defined by an extensive production of 40 m³ concrete in the ready-mix concrete plant

Figure 15. Finished bridge deck and final road surface after milling.

with limited technical possibilities. Extensive investigations and experiments in the laboratory in the mixing plant were necessary. A comprehensive training of the construction company guaranteed the fulfillment of the desired concrete placement requirements. This project showed that the UHPC technology allows also the use as construction site concrete with the conventional equipment of a construction company. The gained knowledge in terms of concrete technology and construction work is very valuable for future projects.

Finally, this project benefited from an innovative cooperation between concrete technologists, structural designers and construction site.

REFERENCES

Charron J-P. et al., 2004. Permeability of Ultra-High Performance Fibre Reinforced Concrete under high stresses. RILEM Symposium Advances in Concrete Through Science and Engineering, Evanston, USA.

Leutbecher, T., 2007. Rissbildung und Zugtragverhalten von mit Stabstahl und Fasern bewehrtem Ultrahochfesten Beton (UHPC), PhD Thesis TU Kassel, Kassel, Deutschland.

Österreichisches Normungsinstitut. 2009. *ONR 23303: Prüfung von Frischbeton*, Wien, Austria.

Österreichisches Normungsinstitut. 2010. ÖNORM 12350: *Prüfverfahren Beton—Nationale Anwendung der Prüfnormen für Beton und seiner Ausgangsstoffe,* Wien, Austria.

Österreichisches Normungsinstitut. 2011. *Eurocode 2: Bemessung und Konstruktion von Stahlbeton—und Spannbetontragwerken*, Wien, Austria.

Österreichische Vereinigung für Beton—und Bautechnik. 2008. *Richtlinie Faserbeton*, Wien, Austria.

RVS Richtlinien & Merkblätter. 2007. *RVS 08.17.02: Deckenherstellung*, Wien, Austria.

RVS Richtlinien & Merkblätter. 2012. RVS 15.02.12: *Dauerhaftigkeit von Brücken—Grundlagen für die Berechnung von Lebenszykluskosten*, Wien, Austria.

Concrete Repair, Rehabilitation and Retrofitting IV – Dehn et al. (Eds)
© 2016 Taylor & Francis Group, London, ISBN 978-1-138-02843-2

Structural strengthening of a shop-house for use as a medical centre

C.C. Lim & Y.C. Chua
Public Works Department, Kuala Lumpur, Malaysia

ABSTRACT: A 5-storey shop-house unit was procured by the Ministry of Health Malaysia for conversion into a Medical Centre. The 8-year old reinforced concrete building was inspected, assessed and re-evaluated structurally to determine the design adequacy and functionality for use as a medical centre with respect to BS8110 and loading requirements to BS6399. A comprehensive material test was carried out on the building to determine the in-situ concrete strength, yield strength of reinforcement bars, verification of as-built structural details and the level of concrete deteriorations. The results from structural assessment show that the existing reinforced concrete structure requires extensive strengthening for use as a Medical Centre due to structural deficiency in original design and detailing. This paper presents the structural capacity evaluation of the building based on in-situ test results. The building was found to be structurally inadequate and required strengthening using Carbon-Fibre Reinforced Polymer (CFRP). In some areas, structural enlargement is necessary to address deflection issue. CFRP was used to enhance flexural and shear capacities of the structure. Consideration was also made to protect CFRP against damage by fire.

1 INTRODUCTION

A 5-storey shop-house unit was procured by the Ministry of Health Malaysia for conversion into a Medical Centre. The 8-year old building was formerly built and completed by a private developer but was never in use before it was procured by the Ministry of Health Malaysia. The building was inspected, assessed and re-evaluated structurally to determine the design adequacy and functionality for use as a medical centre with respect to design code BS8110 and loading criteria to BS6399. Unfortunately, as-built drawings, which are crucial for structural evaluation, were not available except for some as-tendered drawings. Hence, a detailed investigation, comprising a comprehensive material test on the structure including verification of as-built structural details, was necessary.

2 CONDITION SURVEY AND MATERIAL TESTS

A general visual survey was first made on the building before developing a detailed material tests plan for the structure. The objectives of the material tests plan are to evaluate the in-situ concrete strength and quality, to verify the as-built structural details and to assess the level of concrete deteriorations. Destructive and non-destructive test methods were used to determine the in-situ concrete strength, carbonation depth, in-situ concrete cover and corrosion probability of reinforcement bars. In addition, verification of as-built reinforced concrete details by means of on-site dimensional survey and exposure of existing reinforcements were carried out. The test results were subsequently used for structural integrity and capacity evaluations.

3 STRUCTURAL DESIGN CHECK

Information from the as-built details was reliably used to develop a 3-D model of the building structure. Design was checked against two limit state conditions, i.e., Serviceability Limit State (SLS) and Ultimate Limit State (ULS). Structural capacity was computed and checked against the maximum load effects under ULS. Crack widths and deflections were computed from maximum load effects under service load condition. Structural design, load combinations and load intensities are in accordance with BS8110 and BS6399. Live load and superimposed dead load intensities are generally higher for building used as medical centre than for shop or residential unit. For the medical centre, typical load intensity between 3.0 to 5.0 kPa was considered for public areas, file-storage rooms and designated areas for heavy equipment installation.

Table 1. Summary of test results.

	Slab	Beam	Column	Remarks
Average in-situ cover (mm)	22	22	NA*	Comply with 25 mm nominal cover specified.
Average carbonation depth (mm)	21	19	NA*	
Area of steel corrosion (Half-cell potential reading >95% corrosion probability	NA*	3%	NA*	No serious corrosion detected.
Average core comp. strength (MPa)	28.4	24.6	20.6	Comply with Grade 25 concrete.
Verification of reinforced concrete details	Some missing tension rebars for hogging moment	Rebar generally comply	Rebar generally comply	Structural dimensions generally comply.

* NA = Not available

4 RESULTS AND DISCUSSION

4.1 *Material test results*

In general, the overall structure is found to be in good condition. The building was never used since completion. All structures are fully plastered except for the soffit of the slabs. No sign of serious concrete defects (spalling, delamination or structural crack) except for some hairline cracks on the slabs and plaster due to shrinkage. Table 1 shows the summary of all test results. As-constructed reinforced concrete details gathered from the site are compared with the as-tendered drawings.

About 68 locations for in-situ cover measurement and 25 locations for carbonation test were carried out randomly at site on beams and slabs. Average in-situ cover was within acceptable range of the specified nominal cover of 25 mm. However, the average carbonation depth between 19–21 mm is rather high for an 8-year old building with Grade 25 concrete. Carbonation rate in concrete may be affected by climatic conditions, for example, relative humidity, temperature, efficiency of curing, etc. Warmer climate may accelerate the rate of carbonation in concrete. Based on a study (Chiew et al) conducted on buildings exposed to a similar environmental condition as in Malaysia, a carbonation depth of about 15 mm is estimated for building made with Grade 25 concrete. Generally, the carbonation front has not gone significantly beyond the level of steel reinforcement for this 8-year old building.

Readings from half-cell potential measurement do not indicate significant level of reinforcement corrosion in many parts of the structure. Field exposure of reinforcements at selected locations in the building, confirmed the test results.

The average in-situ concrete compressive strengths are within acceptable limit of BS6089 for Grade 25 concrete. The in-situ concrete compressive strength ranges from 12.5 MPa to 36.0 MPa with a mean strength of 25.0 MPa and standard deviation of 5.7 MPa. Hence, the estimated in-situ characteristic cube compressive strength was 15.6 MPa, i.e., a value having less than 5% risk of not complying. Evidence from rebar exposure at site indicates that main reinforcements are mostly high tensile bars. The characteristic yield strength is 460 MPa which is typical of the stock available in the local market.

The as-constructed structural details are generally in compliance with the as-tendered drawings. However, the slab is found to be 100 mm thick. It is deemed relatively "thin" compared to normal slab thickness of about 125–150 mm. The material test also reveals that some slabs do not have tension reinforcements to resist hogging moment at the support. Discrepancies between the as-constructed beam layout plan and the as-tendered drawing are also detected.

4.2 *Structural analysis*

The results of a 3-D frame analysis for bending moment, shear and axial forces are shown in Table 2, 3 and 4 respectively. Summaries of SLS check on crack width and deflection are shown in Table 5 and 6. These are results extracted from some critical components of the structure.

At ULS, some beams and slabs at designated areas for heavy load intensities, eg. equipment, file storage, water tanks, do not have adequate flexural and shear capacities. There are some slab panels with missing top reinforcement bars for hogging

Table 2. Summary of bending moment check at ULS.

Structure	Bending Moment (kNm) Max.	Capacity	Ratio*	Remark
Beam 1 $0.225 \times 0.6 \times 7.1$ m	214	126	1.70	Not OK.
Beam 2 $0.225 \times 0.6 \times 3.7$ m	165	83	1.99	Not OK.
Beam 3 $0.3 \times 0.6 \times 5.8$ m	180	669	1.31	OK.
Beam 4 $0.3 \times 0.75 \times 12.1$ m	280	262	1.07	Not OK.
Beam 5 $0.225 \times 0.6 \times 3.0$ m	123	90	1.37	Not OK. (Note: Zero capacity due to missing bars for hogging moment)
Slab 1 $10.1 \times 0.1 \times 4.5$ m	23–12.7	21 0	1.10 0	
Slab 2 $10.4 \times 0.1 \times 3.0$ m	8.8-26	21 0	0.42 0	

* Ratio = Ratio max. bending moment / moment capacity

Table 3. Summary for shear check at ULS.

Structure	Shear (kN) Max.	Capacity	Ratio*	Remark
Beam 1 $0.225 \times 0.6 \times 7.1$ m	162	189	0.86	OK.
Beam 2 $0.225 \times 0.6 \times 3.7$ m	140	377	0.37	OK.
Beam 3 $0.3 \times 0.6 \times 5.8$ m	120	137	1.31	Not OK.
Beam 4 $0.3 \times 0.75 \times 12.1$ m	280	262	1.07	Not OK.
Beam 5 $0.225 \times 0.6 \times 3.0$ m	123	90	1.37	Not OK.
Slab 1 $10.1 \times 0.1 \times 4.5$ m	23	21	1.10	Not OK.
Slab 2 $10.4 \times 0.1 \times 3.0$ m	8.8	21	0.42	OK.

* Ratio = Max. shear / shear capacity

Table 4. Summary of axial force check at ULS.

Structure	Size (m)	Axial Force (kN) Max.	Capacity	Ratio*	Remark
Column 1	0.3×0.6	1,000	8,100	0.12	OK.
Column 2	0.6×0.6	3,700	12,600	0.29	OK.

* Ratio = Max. axial force / axial force capacity

moment resistance which require full strengthening. Otherwise, they would have been sufficiently reinforced. Columns have been designed conservatively.

Table 5. Summary of crack width check at SLS.

Structure	Crack Width (mm) Max.	Allowable	Remarks
Beam 1 $0.225 \times 0.6 \times 7.1$ m	0.78	0.30	Not OK.
Beam 2 $0.225 \times 0.6 \times 3.7$ m	1.13	0.30	Not OK.
Beam 3 $0.3 \times 0.6 \times 5.8$ m	0.07	0.30	OK.
Beam 4 $0.3 \times 0.75 \times 12.1$ m	0.53	0.30	Not OK.
Beam 5 $0.225 \times 0.6 \times 3.0$ m	0.87	0.30	Not OK.
Slab 1 $10.1 \times 0.1 \times 4.5$ m	0.97	0.30	Not OK.
Slab 2 $10.4 \times 0.1 \times 3.0$ m	1.11	0.30	Not OK.

Table 6. Summary of span-depth ratio at SLS.

Structure	Span-depth ratio Actual	Allowable	Remarks
Beam 1 $0.225 \times 0.6 \times 7.1$ m	12.79	23.66	OK.
Beam 2 $0.225 \times 0.6 \times 3.7$ m	6.73	25.76	OK.
Beam 3 $0.3 \times 0.6 \times 5.8$ m	10.55	25.00	OK.
Beam 4 $0.3 \times 0.75 \times 12.1$ m	17.29	21.84	OK.
Beam 5 $0.225 \times 0.6 \times 3.0$ m	5.46	27.80	OK.
Slab 1 $10.1 \times 0.1 \times 4.5$ m	64.29	20.94	Not OK.
Slab 2 $10.4 \times 0.1 \times 3.0$ m	42.86	20.30	Not OK.

At SLS, the crack width and deflection of some critical beams and slabs exceed the allowable limits. Clearly, the slab has to be thickened to address both SLS and ULS conditions.

4.3 *Structural strengthening*

Structural strengthening is essentially needed to fulfil both the ultimate and serviceability requirements of BS8110. The slab thickness is increased to 160 mm by an additional 60 mm thick reinforced concrete overlay. It corresponds to an increase in the effective depth of the slab. CFRP laminates, 50 mm × 1.2 mm thick, are installed to the slab soffit at 500 mm centres. Both CFRP strengthening and 60 mm thick overlay are necessary to address three issues pertaining to design inadequacy of the slab for higher imposed load intensities, i.e., to enhance flexural and shear capacities, to keep deflection within limit and to provide a sufficient 25 mm cover to reinforcements. Strengthening details are shown in Figures 1 to 4.

Beams do not have deflection issue. They are strengthened to enhance moment and shear capacities by means of CFRP laminate and wrap respectively. CFRP laminate, 100 mm wide × 1.2 mm thick, are bonded to the beam by epoxy resin at

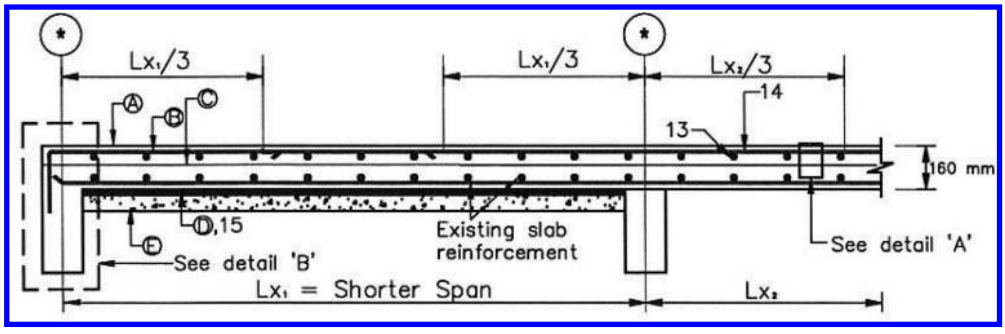

Figure 1. Typical slab strengthening with CRFP and 60mm reinforced concrete overlay.

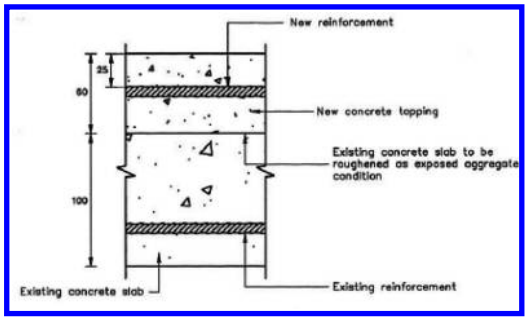

Figure 2. Typical slab strengthening with CRFP and 60mm reinforced concrete overlay.

the soffit and top surface. While CFRP wraps of 0.27 mm thick are bonded to the beam by epoxy resin at the soffit and top surface. While CFRP wraps of 0.27 mm thick are installed on both vertical sides and soffit of the beam in the form of a "U". The "U" is made continuous from the top of one side of the beam, around the beam bottom, and terminates at the top of the other side of the beam. The ends of the "U" are extended into the compression zone of the beam and terminate at one-third (1/3) of span from the support. Typical details of beam strengthening are shown in Figures 3 and 4. All columns are adequate in bending and axial compression.

Surface preparation is an important aspect prior to CFRP installation. All plasters on beams were removed and existing concrete inspected. Any defective concrete (such as cracks, honeycombs) were repaired accordingly. For example, cracks were sealed by epoxy injection. Honeycomb concrete was pressure grouted. Concrete surface was cleaned from loose particles and laitance using a disc grinder. Uneven surface was level off with epoxy putty. All sharp corners at beam were rounded off to achieve a 12 mm radius to avoid causing damage to CFRP wrap.

4.4 *Fire protection to CFRP*

CFRP is particularly susceptible to damage caused by high temperatures that may take place in the event of fire. When the ambient temperature exceeds the glass transition temperature of the resin in the CFRP material, both strength and stiffness of the CFRP strengthened structure are reduced. Hence, CFRP should be protected against damage by fire in the same way reinforcements are protected.

A two-component thixotropic epoxy based impregnating resin primer was applied onto the fully installed CFRP laminate or wrap. Dry silica sand was broadcast on the wet primer to provide a mechanical bond for the final layer of fire protection mortar. Subsequently, light wire mesh was installed over the primer to prevent debonding of mortar. Finally, a 40 mm thick vermiculite fire protection mortar was sprayed over the entire CFRP area.

5 CONCLUSIONS

CFRP has been successfully used to rehabilitate and strengthen an existing 5-storey reinforced concrete commercial building for use as a Medical Centre.

The structure has been strengthened to address the structural deficiency in the original design and detailing. Structural strengthening is essential to fulfil both the ultimate and serviceability design requirements of BS8110 and loading criteria of BS6399. For a Medical Centre, the live load intensity as required in the Code is higher than for a commercial building. Accordingly, both flexural and shear capacities of the structure have been enhanced. Slab has been thickened to keep deflection within limit. A sufficient 25 mm cover to reinforcements for durability and fire protection is ensured.

ACKNOWLEDGEMENT

The authors would like to thank the Director-General of Public Works Department Malaysia and the

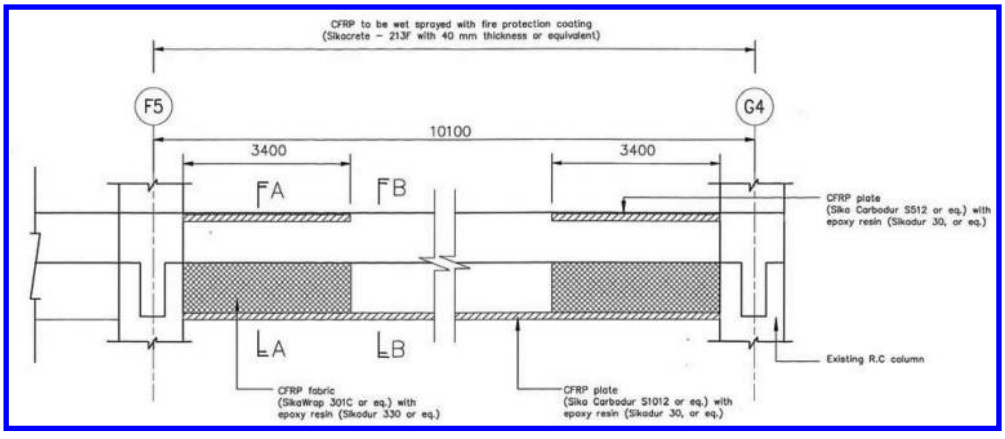

Figure 3. Typical beam strengthening with CFRP for flexure and shear.

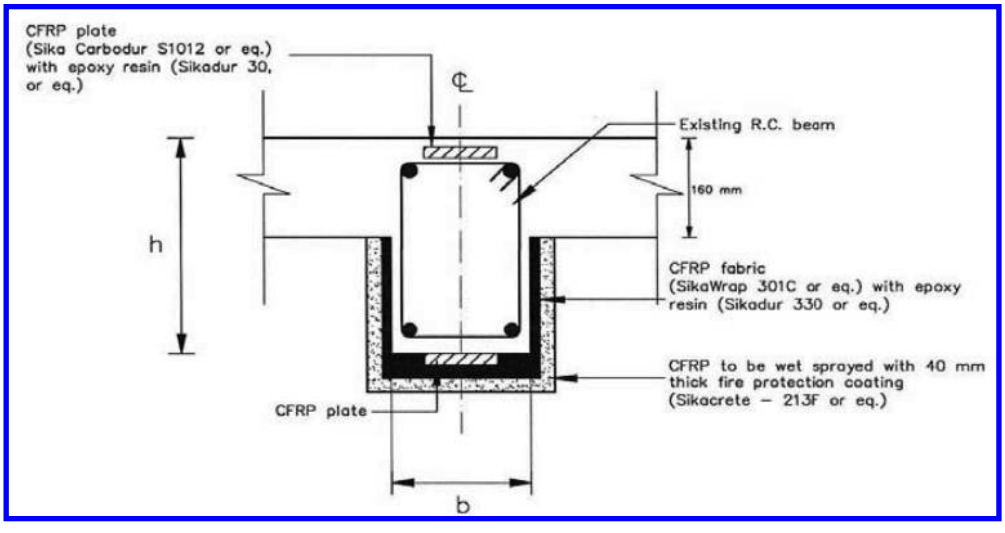

Figure 4. Typical cross-sectional details of beam strengthening.

Senior Director of Civil and Structure Engineering Branch of PWD Malaysia for their permissions to publish this paper.

REFERENCES

ACI440R-96 (1996), State of the art report on fiber reinforced plastic reinforcement for concrete structures. Detroit: American Concrete Institute.

ACI440F-99 (1999), Guidelines for the selection, design and installation of fiber reinforce polymer (FRP) systems for externally strengthening concrete structures. Detroit: American Concrete Institute.

BS6399 Part 1: 1996, Loading for Buildings—Code of Practice for Dead and Imposed Loads. London: British Standards Institution.

BS8110 Part 1: 1997, Structural Use of Concrete—Code of Practice for Design and Construction. London: British Standards Institution.

Chiew, S.P., Lay, K.S. & Ho, N.Y. (1993), Rate of carbonation in existing concrete building structures, 2nd International Conference on The Concrete Future, Kuala Lumpur.

CNR-DT (2004), Guide for the design and construction of externally bonded FRP systems for Strengthening existing structures. National Research Council, Advisory Committee on Technical Recommendation for Construction.

IKRAM Engineering Services Sdn. Bhd., (2012), Material Test Report on Klinik Kesihatan (Jenis 3) Kota Damansara, Petaling Jaya, Selangor.

Concrete Repair, Rehabilitation and Retrofitting IV – Dehn et al. (Eds)
© 2016 Taylor & Francis Group, London, ISBN 978-1-138-02843-2

Overall precision uplift rehabilitation technology for uneven settlement of concrete structure of slab ballastless track

Xinguo Zheng, Jing Liu & Shuming Li
Railway Engineering Research Institute of China Academy of Railway Sciences, Beijing, China

Weichang Xu, Zhiyuan Zhang & Youneng Wang
Shanghai Railway Bureau, Shanghai, China

Fei Cheng & Xihua Wen
Shanghai-Hangzhou Railway Passenger Dedicated Line Co., Ltd., Shanghai, China

ABSTRACT: The concrete slab ballastless track is an advanced track structure with high stability and integrity. It has been widely used in many high speed railway lines all over the world. However, when the foundation of ballastless track appears large uneven settlement deformation especially in roadbed section, compared with ballast track which can be restored by increasing the ballast under the sleepers simply, the smoothness of concrete slab ballastless track can only be restored by adjusting the thickness of the base plates of fastener system accordingly. But if continuous settlement deformation exceeds the specified adjustable range of fastener system, the smoothness of concrete slab ballastless track cannot be restored timely and completely, and then the speed of passing trains has to be limited to ensure the safety. To solve this problem only just using daily skylight time (only 4 hours every day), we systematically studied a complete set of new overall precision uplift rehabilitation technology including special grouting materials, dedicated miniaturization equipment and construction processes through a series of indoor reduced scale tests and field full scale simulations with real concrete slabs. And combined with field practices, the overall precision uplift rehabilitation technology for concrete slab ballastless track had been studied and developed. Results indicated this technology could not only restore the smoothness of settlement concrete slab ballastless track effectively and accurately, but also recover the adjustable range of the fasteners just in daily skylight time without disturbing the following operation of the railway lines. We introduced the overall precision uplift rehabilitation technology as well as the mechanism and accuracy of overall uplift, properties of grouting materials, construction process and field application effects, respectively. These will provide valuable and useful references for the rehabilitation of concrete slab structure occurred differential settlement.

Keywords: Grouting; Uplift; Concrete structure; Ballastless track; Rehabilitation; Settlement

1 INTRODUCTION

The concrete slab ballastless track is an advanced track structure with high stability and integrity. It has been widely used in many high speed railway lines all over the world [1–2]. There are currently more than 10,000 kilometers of the slab ballastless track railway, both in operation and in construction. The slab ballastless track commonly includes the rail, fastener, concrete track slab, cement emulsified asphalt mortar layer, and concrete bottom slab [3]. However, when the foundation of ballastless track appears large differential settlement deformation especially in roadbed section, compared with ballast track which can be restored by increasing the ballast under the sleepers simply, the smoothness of concrete slab ballastless track can only be restored by adjusting the thickness of the base plates of fastener system accordingly. But if continuous settlement deformation exceeds the specified adjustable range of fastener system, the smoothness of concrete slab ballastless track cannot be restored timely and completely, and then the speed of passing trains has to be limited to ensure the safety. The limit seriously affects the operation of high speed railways in some differential sunken concrete structure sections of ballastless track line.

To solve this problem only just using daily skylight time (only 4 hours every day), we systematically studied a complete set of new overall precision

uplift rehabilitation technology including special grouting materials (the polyurethane-yielding two-component liquid injection mixture), dedicated miniaturization equipment and construction processes through a series of indoor reduced scale tests and field full scale simulations with real concrete slabs. And combined with field practices, the overall precision uplift rehabilitation technology for concrete slab ballastless track had been studied and developed. We had created a new set of technology and engineering practice to uplift the concrete structure of ballastless track successfully, with no negative effect on existing railway operation. The grouting materials is injected in the ground at discrete locations under the concrete bottom slab to correct differential settlement and to apply compactive forces to the foundation layer. The two components of the foam, which mix as they are injected through a grouting pipe. The expansion pressure it exerts is used to lift the ballastless track structure, remediating a differential settlement problem without excavation. Therefore, the track smoothness can be restored quickly and accurately. This new technology had been applied successfully to the settlement rehabilitation for the ballastless track of Shanghai-Hangzhou high-speed railway.

This paper introduces this new grouting uplifting technology for concrete structure of ballastless track from the grouting materials, construction process, practical application and uplifting mechanism. These will provide valuable and useful references for the rehabilitation of concrete slab structure occurred differential settlement.

2 GROUTING MATERIAL

The grouting material applied is a kind of polyurethane-yielding two-component ("A" and "B") liquid injection mixture. After mixing, the material will gel and react to form the resulting polyurethane solid foam within a short time (see Figure 1). The one component "A" is composed of polyisocyanate prepolymer mixture without any VOC (volatile organic compounds). The other component "B" is composed of polyols and catalysts mixture such as polyetherpolyols and tertiary amines without any VOC. The polyurethane grouting is based on three dimensional network solid polymer with high strength that is produced with generation of heat and increase of volume when the liquid isocyanate compound is mixed with a liquid polyol compound [4–5]. This solid foam is able to expand and form different volumes as needed. Therefore, the technical information on the chemical and physical behaviors of the liquid injection materials and those of the polyurethane solid foam application are supposed to be very important for an effective

Figure 1. Hardened concretion of the grouting materials.

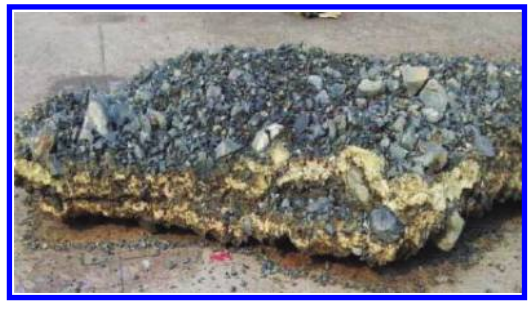

Figure 2. Sandwich structure of grouting material foam layer and graded broken stone layer.

application of this grouting material. Compared with other grouting materials, the grouting material has the following features [6–8]:

1. Designed to efficiently develop hydraulic lift
   The hydraulic uplifting for concrete structure of ballastless track is largely realized by the expansibility of the grouting materials. The hydraulic uplifting force is determined by the foaming ratio (or volume expansion) which can be controlled precisely by the.
2. High ability of permeation, diffusion and filling
   With a certain grouting process, the diffusion diameter can reach up to more than 5 meters and it has a certain volume expansion too (the free expansion ratio can reach up to 20:1). The filling ability is outstanding, meanwhile, it can compact the foundation substructure (Namely, graded broken stone layer) in the filling range to form the sandwich structure (see Figure 2).
3. Filling range controllable
   After the mixture of grouting materials, the liquid state will transform into plastic state and then the solid state within a short time. Thus, the filling range is easy to adjust by controlling the reaction speed of two component grouting materials. Therefore, it is more convenient to

construction with no need to set special curtains to prevent the slurry from overflow.

4. Low density and weight
   The structure density formed by this grouting material is around 100 kg/m3~300 kg/m3, far less than the water density. So compared with cement grouting materials, it does not increase the additional structural load significantly.
5. Fast in setting and hardening, fast in strength development
   The grouting material can reach up to more than 90% of the design strength just within 15 minutes, which can completely meet the strength requirements for railway line operation. As a result, the traffic can be resumed in time after the uplifting of concrete structure.
6. High volume stability
   It almost has no volume shrinkage after the hardened structure formed and will have the feature of a perfect elastomer before 80% of the failure load.
7. High durability
   The hardened grouting materials possess a high durability property with high water proof, frost resistance and chemical erosion resistance.

3 PRACTICAL APPLICATION

Located at Shanghai, Jinshan North Station, its railway line was designed to be 2 lines of track. Due to the differential settlement of the roadbed, the concrete structures of slab ballastless track sunken obviously. Therefore, two tracks had serious problems with the smoothness within a range of more than 300 meters. The maximum settlement of some sections even exceeded 100 millimeters. The railway speed in this sunken section of this line had to be limit to 160 km/h.

In September, 2014, the settlement ballastless track of Jinshan North Station was rehabilitated by this overall grouting uplifting technology. During rehabilitation, when the grouting equipment operated smoothly and the materials reached a stable physical and mechanical performance, the grouting uplifting rehabilitation was carried out according to the specified grouting procedure. The electronic level was adopted to monitor the rail elevation change and the total station was adopted to monitor the center line mis-alignment of concrete structure. When the uplifting height reached the expected height, stop grouting and the high-strength non-shrinking cement material was used to block up the injection holes. It only took 60 days to fulfill this repair work of this sunken section. The concrete structure had no cracking due to uplifting construction. The accuracy of uplifting elevation for the ballastless track structure can be up to ±1 mm. The rehabilitation (only 4 hours every day) had not disturbed the following operation of the railway line next day.

Figure 3. Comparison of the elevation of the track before and after uplifting rehabilitation (Note: the below pink line represents the track elevation before rehabilitation, the above yellow line represents the track elevation after rehabilitation).

After rehabilitation, the smoothness of the track was improved significantly (see Figure 3 for the track elevation comparison before and after the grouting uplifting rehabilitation). Moreover, the adjustable range of the fasteners was restored. The maximum uplifting height of the concrete structure was up to 82 millimeters (No cracking during uplifting rehabilitation). The railway speed in this section had recovered to the design speed of 250 km/h and the dynamic response of the ballastless track in this section showed normally.

4 UPLIFTING MECHANISM

Based on the field practices, the uplifting mechanism of this overall presion uplift rehabilitation was analyzed. During the overall grouting uplifting of ballastless track concrete structure, the grouting materials is filled into the space between the concrete bottom layer and the surface layer of graded broken stone foundation bed (see Figure 4) through the special grouting equipment, under a certain grouting pressure. The uplifting is realized by the expansibility of the grouting materials and the hydraulic transmission effect resulting from the grouting materials and grouting pressure. The uplifting can be divided into two stages, namely the filling & compacting stage and the uplifting & filling stage.

In the filling & compacting stage, the grouting materials will fill and compact the gaps such as the ones between the supporting layer and graded broken stone layer or those inside the graded broken stone layer. And the track structure will not be uplifted at this stage.

In the uplifting & filling stage, the filled grouting materials and the grouting pressure from grouting equipment will cause hydraulic transmission effect.

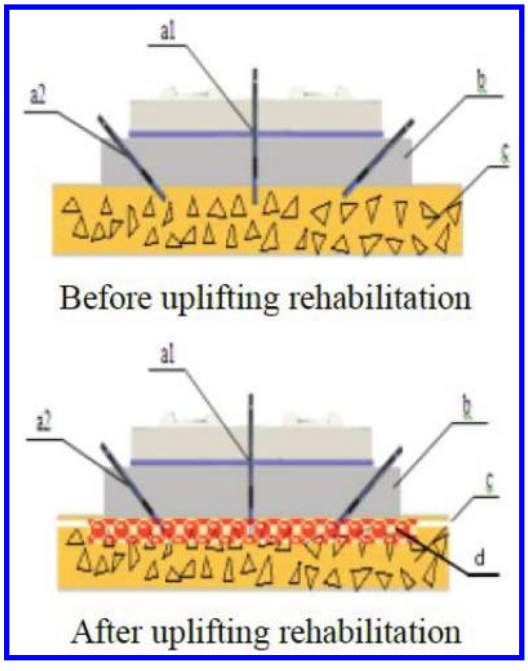

Figure 4. Uplifting mechanism and comparison of ballastless track structure before and after uplifting rehabilitation (Note: a1/a2—grouting pipes, b—concrete bottom slab, c—graded broken stone layer, d—polyurethane solid foam layer).

Meanwhile, the volume expansion from the grouting material solidification will cause expansive uplifting forces. With the effects of these two factors, the concrete structure can be uplifted continuously and stably, and the gaps between concrete structure and graded broken stone layer due to uplifting can also be filled completely and densely.

5 CONCLUSION

The overall grouting uplifting rehabilitation technology for ballastless track has the advantages of rapid restoration, good effect, simple construction, no disturbing railway line operation and little destruction to the existing concrete structure. It is also a rapid, simple and practical method to rehabilitate the ballastless track of the settlement section in a manner that can neither affect the track structure stress adversely nor affect the traffic safety, which is promising in the settlement rehabilitation of the ballastless track in operation just using daily skylight time (only 4 hours every day). The accuracy of uplifting elevation for the ballastless track structure can be up to ±1 mm. The properties of this two component grouting materials and the resulting solid foam are very versatile and with stringent quality control, this uplift rehabilitation technology can be more effectively and successfully applied to many other construction projects.

ACKNOWLEDGEMENT

This research was supported by China Railway Corporation Science and Technology Research and Development Program under Grant No. 2013G008-D, National Basic Research Program of China (973 Program) under Grant No. 2010CB736102 and China Academy of Railway Science Foundation under Grant No. 2010YJ75 and No. 2014YJ017 and Shanghai Railway Bureau Foundation under Grant No.HHKZ2013-01.

The authors are grateful to Prof. Yongjiang Xie, Zhenting Li and Yonghua Wang for their useful comments and suggestions. The authors are also grateful to Shuming Li, Dejun Yang, Zhicai Weng and Zhi Zeng for their support with material preparation and field experiments.

REFERENCES

[1] Zheng X.G., Liu J. et al.,"Preparation of Cement Emulsified Asphalt Mortar for CRTSII Slab Ballastless Track", Railway Engineering, (8), 2009, pp 121–124 (in Chinese).
[2] Jin, S.H., Chen, X.F. et al., "Key technologies of CA mortar for slab track", China Railway Science, 27(2), 2006, pp 20–24 (in Chinese).
[3] Zeng, Z., Zheng, X.G.et al., "Construction technology of cement-emulsified asphalt mortar used in CRTS II ballastless slab track", Railway Engineering, (9), 2009, pp 97–100 (in Chinese).
[4] O. Buzzi, S. Fityus, Y. Sasaki et al., "Structure and properties of expanding polyurethane foam in the context of foundation remediation in expansive soil", Mechanics of Materials, 40, 2008, pp 1012–1021.
[5] Seo D, Youn J.R., "Numerical analysis on reaction injection molding of polyurethane foam by using a finite volume method", Polymer, 46, 2005, pp 6482–6493.
[6] Byung-Sik Chun, Dong-Seong Ryu., "A Study on Applications of Polyurethane Injection Material for Ground Improvement", Jounal of Civil Engineering, 4(2), 2000, pp 113–118.
[7] Aksoy CO., "Chemical injection application at tunnel service shaft to prevent ground settlement induced by groundwater drainage: a case study", International Journal of Rock Mechanics and Mining Sciences, 45, 2008, pp 376–383.
[8] Ahmet Varol, Suleyman Dalgıc., "Grouting applications in the Istanbul metro Turkey", Tunneling and Underground Space Technology, 21, 2006, pp 602–612.

Concrete Repair, Rehabilitation and Retrofitting IV – Dehn et al. (Eds)
© 2016 Taylor & Francis Group, London, ISBN 978-1-138-02843-2

Axial compression testing of an emergency-retrofitted shear-damaged RC column

K. Nakada & M. Kochi
University of the Ryukyus, Okinawa, Japan

S. Arakaki
Kozo Factory Co., Ltd., Fukuoka, Japan

H. Karwand & M.Z. Noori
Former PEACE Participant of Japan International Corporation Agency, Tokyo, Japan

ABSTRACT: This study aims to develop a manual emergency retrofitting technique for use in damaged Reinforced Concrete (RC) buildings. It is important that the emergency retrofitted RC column is able to sustain the vertical load and the lateral force as one of the vertical load carrying members. In this respect, lashing belts comprising a ratchet buckle and an aramid fiber belt were used as the emergency retrofitting method of choice. In this study, the residual axial compression capacity of shear-damaged RC columns, and the recovered axial compression capacity of shear-damaged RC columns emergency-retrofitted using lashing belts are investigated and discussed.

1 INTRODUCTION

This study aims to develop a manual emergency retrofitting technique for use in damaged Reinforced Concrete (RC) buildings. Emergency seismic retrofitting is indispensable for rehabilitating damaged RC buildings immediately after earthquakes. The emergency retrofitting technique needs to be simple to use and fast to apply to mitigate further possible damage in relation to aftershocks in RC buildings that have already been damaged. In this study, lashing belts comprising a ratchet buckle and an aramid fiber belt were used as the emergency retrofitting method of choice.

A previous study confirmed that flexural failure occurred at a high lateral confining pressure with high ductility in a shear-damaged RC column emergency-retrofitted by lashing belts (Nakada et al. 2013). This is attributed to the concrete blocks in the damaged RC column being united as confined concrete, and active confinement occurring in relation to the lashing belts. Furthermore, lashing belts provide a shear strengthening effect. In relation to active confinement, a past study by the authors revealed that the seismic retrofitting technique using an aramid fiber belt enhanced the compressive strength of the confined concrete by up to 1.31 times compared with the compressive strength of non-retrofitted specimens (Nakada et al. 2008).

In general, the failure of vertical load carrying members causes the collapse of buildings. In this study, the residual axial compression capacity of shear-damaged RC columns and the recovered axial compression capacity of shear-damaged RC columns emergency-retrofitted by lashing belts were investigated. In the test, the damage level of the RC column, the epoxy resin repair and the laterally retrofitting by lashing belts are considered. The experimental procedures used are as follows: 1) a shear-critical RC column was damaged by cyclical lateral forces under a constant axial load and 2) a universal testing machine was used in the axial compression tests conducted on the shear-damaged RC column and the emergency-retrofitted RC column. In this paper, the results of axial compression tests using twelve specimens are discussed.

2 TEST PLAN

The retrofitting details of the test specimens are shown in Table 1. The RC column specimens used in this test were square with cross-sectional dimensions of 250×250 mm^2 with a total height of 900 mm (Figure 1). The height of the RC column test section was 500 mm, with a shear span-to-depth ratio (M/VD) of 1.0. The longitudinal reinforcement ratio (p_g) of the specimens was 1.36% (diameter = 10 mm; number of rebars: 12), and the shear reinforcement ratio (p_w) of

Table 1. Details of specimens.

No.	Series	Specimen (AC13-)	${}_c\sigma_B$ (MPa)	Damage level	W_{cr} (mm)	epoxy resin	${}_As$ (mm)	ε_{pt} (μ)	σ_r (MPa)	N_{max} (kN)	N_{max}/N_0
1	1	D3	21.2	III	1.5	-	-	-	-	1128	0.75
2		D3e			1.4	apply				1435	0.95
3		D4-1		IV	5.0	-				384	0.25
4		D4-2			3.5					455	0.30
5		D4e-1			3.5	apply				1011	0.67
6	2	N1	26.5	-	-	-	-	-	-	1849	-
7		N2								1785	-
8		6L'					63	800	0.69	1930	1.06
9		D2		II	0.3		-	-	-	1658	0.91
10		6LD4		IV	4.0		63	800	0.69	1319	0.73
11		6LD4e			5.0					1167	0.64
12		D4e-2			5.0	apply	-	-	-	1613	0.89

Notes: ${}_c\sigma_B$ = compressive strength of concrete cylinder, W_{cr} = residual crack width after shear failure test, ${}_As$ = interval of lashing belt, ε_{pt} = initial strain of lashing belt, σ_r = lateral confining pressure, N_{max} = max axial load, N_0 = max axial load of non-damaged RC column.

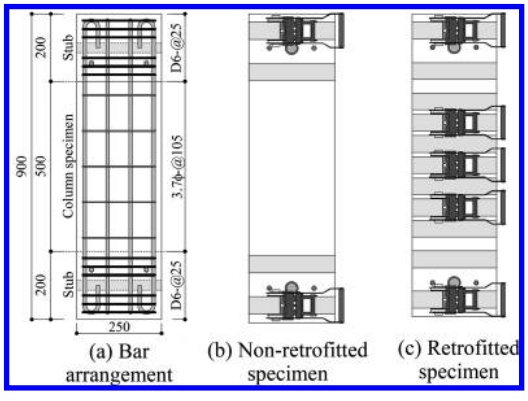

Figure 1. Column specimen [unit: mm].

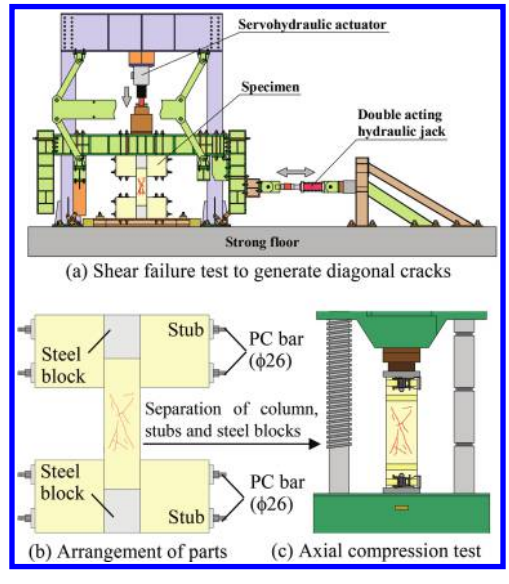

Figure 2. Test setup and loading procedure.

the specimens within the height of the test section was 0.08%. Closely spaced hoops were arranged at the top and bottom region of each specimen within a length of 200 mm, resembling a stub, to ensure that the damage occurred to the central part of the column. These RC columns are classified as being shear-critical columns. To avoid the bleeding effect, horizontal casting of concrete was performed in all specimens. The test setup and loading procedures are shown in Figure 2. Steel blocks, each with cross sectional dimensions of 250×250 mm^2 and a height of 300 mm were connected to the top and bottom of the column specimen, and the united specimen with concrete stubs was set on a loading apparatus. The contact surface of the RC column and the steel blocks of the stubs were firmly connected with epoxy resin and PC bars (with diameters of 26 mm), and these were to be integrated (Figure. 2). The shear-critical RC columns were then damaged by cyclic lateral forces under a constant axial force ratio of 0.2 (shear failure test), on the assumption that earthquakes cause shear-damage to RC columns (Figure. 2). To control the shear-damage level during the loading test, column specimens were retrofitted using aramid fiber belts with wide spacing intervals of 100 mm. The damage status of each RC column in the shear failure test was classified at a damage level between II and IV, as defined by the Japan Building Disaster Prevention Association (JBDPA 2002) (Table 2). Although the residual lateral displacement attempted to revert to zero following the shear failure test, it remained at a high damage level in the damaged-columns. The column specimen, the four concrete stubs, and the two steel blocks were separated for the axial compres-

Table 2. Criteria of damage level (JBDPA 2002).

Damage level	Damage state
I	Crack width is under 0.2 mm.
II	Crack width is about 0.2–1.0 mm.
III	Crack width is about 1.0–2.0 mm and cover concrete peels off small.
IV	A lot of cacks beyond 2.0 mm generate and cover concrete peels off, and steel reinforcement appears.
V	Cover concrete ruptures and backling of the rebars generate. It is impossible to sustain live and dead loads.

sion test, which was performed in a universal testing machine. To investigate the retrofitting performance using the lashing belt, epoxy resin, and pre-stressing, the resin was injected into the shear cracks on the four damaged column specimens at a low pressure using several injectors, and after it had hardened, the axial compression test was conducted.

Two series of specimens were considered. In Series 1, the residual axial compression capacity of the shear-damaged RC column and the recovered axial compression capacity of the repaired RC columns were investigated, and the laterally retrofitted RC columns were then considered in Series 2. The top and bottom regions of the column specimens were retrofitted in the same manner as the central part of the column. To avoid stress concentration, the four corners of the RC columns were chamfered using an aramid fiber belt with a radius of 20 mm to avoid stress concentration. After applying oil, the RC column was then retrofitted using lashing belts. The lashing belt device includes a ratchet buckle combined with an aramid fiber belt (width of belt = 50 mm). The mechanical properties of the steel and fiber reinforcements are shown in Table 3. The test parameters of these specimens include the following: the damage level (II–IV), the lateral confinement using the lashing belts, and the conditions wherein epoxy resin repair was applied and wherein it was not applied. The lateral confining pressure of the RC column was used as the introductory value in the practical RC column section, which was assumed to have a cross sectional dimension of 600×600 mm^2, a lashing belt interval of 63 mm, and an initial tension strain of 1800 μ. The lateral confining pressure (σ_r) is expressed as follows:

$$\sigma_r = (2_A a)/(b \cdot {}_A s) \cdot {}_A E \cdot \varepsilon_{pt}, \quad (1)$$

where ${}_A a$ is the cross section of the aramid fiber belt (56.2 mm^2), b is the column width, ${}_A s$ is the lashing belt interval, ${}_A E$ is Young's modulus of elasticity of the aramid fiber belt, and ε_{pt} is the initial tension strain. The compression strain of the RC column was measured in two places using eight transducers (Figure. 3).

Table 3. Mechanical properties of materials.

Reinforcement		a (mm^2)	σ_y, σ_u* (MPa)	E (GPa)
Rebar	D10	71	389	175
Hoop	3.7ϕ	11	334	205
Hoop	D6	32	479	180
Aramid fiber belt	t = 0.572mm	28.6	2060*	118

Notes: a = cross-section area, σ_y = yield strength of steel, σ_u = ultimate strength of fiber reinf., E = Young's modulus of elasticity.

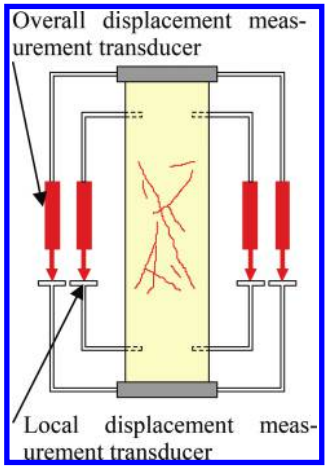

Figure 3. Axial strain measurement setup.

3 TEST RESULTS AND DISCUSSION

3.1 *Axial load–axial strain relationship of shear-damaged RC column*

The observed cracking patterns, residual crack width, and damage level after the shear failure test are shown in Table 4. Photo 1 shows the shear-damaged RC column after the shear failure test. There was no buckling of the longitudinal reinforcement in any specimen. The axial load (N/N_0)–axial strain (ε_c) relationships are shown in Figure 4, where the axial load of the non-damaged specimen N1 is divided by the maximum axial load N_0 of itself; and the axial load of specimen D2 in Series 2 is divided by the average values of N_0 of specimen N1 and N2 (1817 kN). The axial loads of specimens D3, D4-1, and D4-2 are divided by the calculated value of N_0, which considers $N_0 = N_s + N_c$, where N_s is the yield load of the rebar, and N_c is the axial load of the concrete using $0.89_c \sigma_B$.

Table 4. Observed cracking patterns after shear failure test.

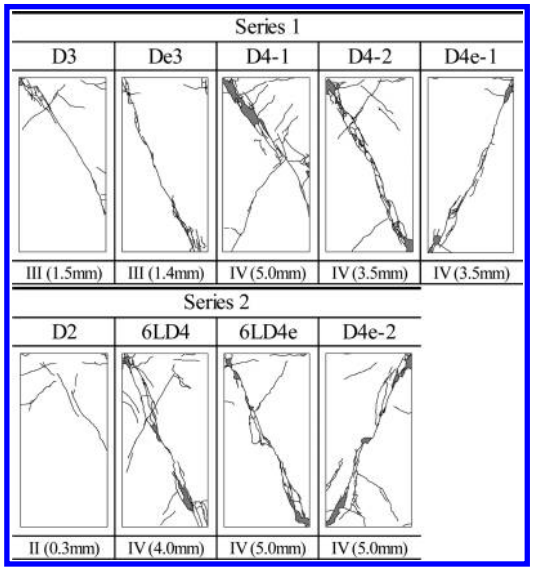

Notes: II–IV = damage level, () = max crack width (depth side).

Photo 1. After shear failure test.

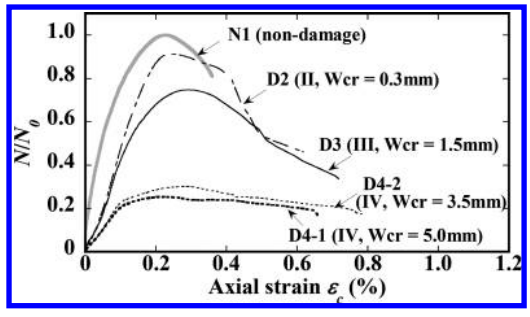

Figure 4. N/N_0 versus ε_c of damaged columns.

Photo 2. After axial compression test (D4-1).

The axial strain in specimens D4-1 and D4-2 developed diagonal cracks (Photo 2). Judging from the strain gauges in specimens D4-1 and D4-2, the yielding of the longitudinal reinforcement, located at the diagonal cracks at the top and bottom of the column, caused a reduction in axial stiffness at around 0.2 N_0. The maximum axial load of specimens D4-1 and D4-2 was 0.25–0.30 N_0 (Figure 5), and the axial load gradually decreased after reaching a maximum value. Buckling of the longitudinal reinforcement at the diagonal cracks was confirmed after the test. Specimens D3 and D2, which had damage levels of III and II, respectively, showed maximum axial loads of 0.75 N_0 and 0.91 N_0, respectively (Figure 5). Newly generated cracks were confirmed in specimen D2.

3.2 *Axial load–axial strain relationship of repaired RC column*

The test results of specimens D4e-1, D4e-2 (damage levels IV), and D3e (damage level III), which were repaired using epoxy resin, are shown in Figures 6 (a) and 6 (b) respectively. Specimens N1, D4-1, D4-2, and D3 are also shown in Figures 6 (a) and (b). In Figure 6, the axial load of specimen D4e-2 is divided by the average value of the maximum axial load of specimen N1 and N2, and the others are divided by the calculated value of N_0. In Figure 6 (a), a recovered maximum axial load of 0.67 N_0 and 0.89N_0 were confirmed in specimens D4e-1 and D4e-2, which had been repaired using epoxy resin. These values are 2.4–3.2 times higher

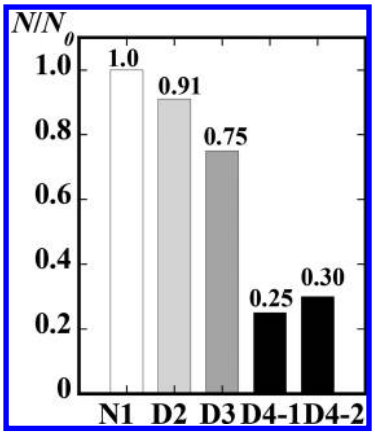

Figure 5. N/N_0 of each specimen.

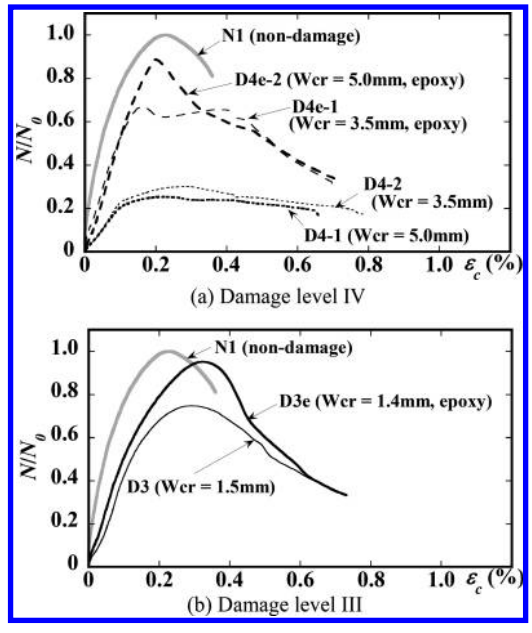

Figure 6. N/N_0 versus ε_c of damaged columns repaired by using epoxy resin.

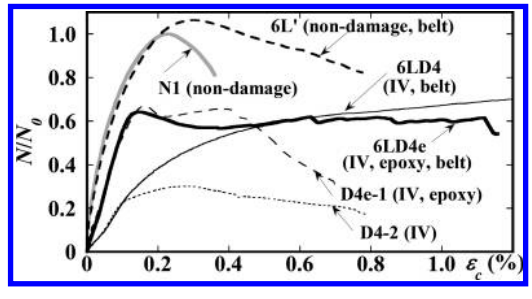

Figure 7. N/N_0 versus ε_c of damaged columns retrofitted by lashing belts.

than the residual axial load of shear-damaged RC column specimens D4-1 and D4-2. In addition, the axial rigidity also recovered considerably. In specimen D4e-1, it was observed that the axial load increased after first decreasing around the initial peak point. The epoxy resin injected into the diagonal cracks was also determined to be broken at the initial peak point. Furthermore, yielding of the longitudinal reinforcements occurred at the second peak point, followed by buckling. In contrast, however, in specimen D4e-2, which had a slightly larger damage status and a residual crack width of 5 mm (compared to specimen D4e-1 with a crack width of 3.5 mm), a large axial load and compression yielding of the longitudinal reinforcements at the top and bottom of the column was confirmed. Therefore, the epoxy resin was suggested to be successfully injected into specimen D4e-2. In Figure 6 (b), specimen D3e with a damage level of III showed a maximum axial load of $0.95N_0$. Thus, the effect of repair is greater in specimens that suffered greater damage.

3.3 *Axial load-axial strain relationships of damaged specimen retrofitted laterally*

Figure 7 shows the test results of shear-damaged RC column specimens 6 LD4 and 6 LD4e, which attained damage level IV and were laterally retrofitted using lashing belts. Specimen 6 LD4 was retrofitted using lashing belts only, and specimen 6 LD4e was additionally repaired using epoxy resin (as well as retrofitted by lashing belt pre-stressing). Specimen 6 L' was a retrofitted non-damaged specimen. In Figure 7, the axial load of specimen 6 LD4 can be seen to gradually increase with the compressive strain, due to the passive confinement in relation to the increasing tension strain of the lashing belts. In specimen 6 LD4e, however, the axial rigidity was greatly recovered and the axial load gradually increased after the peak point in relation to the passive confinement effect of the lashing belts. An increase and then a decrease of the axial load were confirmed after a compressive strain of 0.6%, and it was considered that the ratchet buckle had been damaged because a similar result was seen in relation to the strain of the belt. In specimen 6 LD4e, therefore, it is considered likely that the resultant maximum axial load was mainly related to the effect of the epoxy resin repair, due to the low lateral confining pressure by the lashing belts at the peak point of the axial

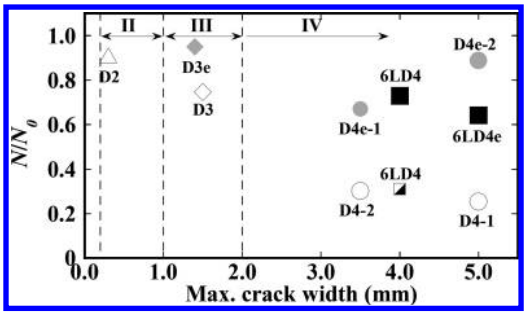

Figure 8. Residual and recovered axial compression capacity of damaged columns at various damage levels.

load–axial strain relationship. Furthermore, axial rigidity and compressive strain at the peak point can be improved by simultaneously using epoxy resin repair and external retrofitting with lashing belts.

3.4 *Relationship between crack width and axial load*

Figure 8 shows the relationship between the residual crack width after the shear failure test and the residual axial load ratio N/N_0. All data with a variety of residual drift angles are shown in Figure 8. Although it is believed that the residual axial load is affected by the residual drift angle, to control this in the shear failure test and understand the influence of residual lateral displacement on the vertical load will be the subject of future studies. The maximum axial load of specimen 6 LD4 at the end of the axial compression test, and the axial load corresponding to the axial strain at the maximum axial load of specimen 6 LD4e are shown in Figure 8. In Figure 8, the residual axial load of shear-damaged RC columns is seen to decrease with an increase in the residual crack width. There are large differences between the residual axial load ratio N/N_0 of specimens D3 and D4-2, but there is only a slight difference between those of specimens D4-2 and D4-1. It is indicated that although slightly-damaged concrete can carry most of the axial load, seriously-damaged concrete with a large crack width results in a diminished load-carrying capacity; therefore, the longitudinal reinforcements sustain the greater part of the residual axial load. A residual axial load N/N_0 of 0.6–0.9 was obtained by repairing with epoxy resin, as shown in Figure 8. By applying lateral confinement with lashing belts, a residual axial load N/N_0 of 0.6–0.7 was confirmed, regardless of whether the epoxy resin repair has been applied. However, the residual axial load (N/N_0) of 6 LD4 at the compressive strain of the maximum axial load in 6 LD4e was smaller than that of specimen 6 LD4e and was also at the same level as the shear-damaged specimens D4-1 and D4-2.

4 CONCLUSIONS

The main results of this study are summarized in the following points:

1. The residual axial compression load of shear-damaged RC columns was 91% of the compression capacity of a non-damaged RC column at damage level II, 75% at level III, and 28% at level IV.
2. At damage levels III and IV, a residual axial compression load N/N_0 of 0.67–0.95 was obtained by epoxy resin repair.
3. By applying lashing belts only, the axial load gradually increased during the loading test and a low axial rigidity was confirmed.
4. Using both epoxy resin repair and lashing belts for lateral confinement, there was a significant recovery of the axial compression capacity, axial rigidity, and compressive ductility.

ACKNOWLEDGEMENTS

The authors wish to acknowledge Mr. Tsuneo Sunagawa, the technician at the Faculty of Engineering, University of the Ryukyus, for his valuable technical assistance. The authors would like to thank Enago (www.enago.jp) for the English language review.

REFERENCES

Architectural Institute of Japan. 1990. *Ultimate Strength and Deformation Capacity of Buildings in Seismic Design.* (In Japanese).

Architectural Institute of Japan. 2010. *AIJ Standard for Structural Calculation of Reinforced Concrete Structures.* (In Japanese).

Nakada, K., Maeda, K., Morishita, Y., & Teruya, H. 2013. Experimental investigations of shear-damaged RC columns externally retrofitted by lashing belts prestressing *Proc. of the Japan Concrete Institute* (JCI) 35(2): 103–108. (In Japanese).

Nakada, K. & Yamakawa, T. 2008. Compressive behavior of RC column confined externally by aramid fiber belt prestressing. *Journal of structural and construction engineering*, AIJ 73(600): 1617–1624. (In Japanese).

The Japan Building Disaster Prevention Association. 2002. *Damage Level Assessment Criteria and Guidelines for Rehabilitation of Earthquake Damaged Reinforced Concrete Buildings.* (In Japanese).

Concrete Repair, Rehabilitation and Retrofitting IV – Dehn et al. (Eds)
© 2016 Taylor & Francis Group, London, ISBN 978-1-138-02843-2

Rehabilitation of corrosion-aged concrete T-girders with textile-reinforced mortar

T. El-Maaddawy
United Arab Emirates University, Al Ain, United Arab Emirates

A. El Refai
Laval University, Quebec City, Canada

ABSTRACT: This paper examines the effectiveness of using Textile-Reinforced Mortar (TRM) as an innovative technique for rehabilitation of severely corrosion-damaged Reinforced Concrete (RC) T-girders. A total of six RC beam specimens, 3200 mm long each, with a T-shaped cross section were constructed and tested under four-point bending. Prior to testing, five specimens were subjected to accelerated corrosion for 5 months that corresponded to an average measured mass loss of 22% in the tensile steel bars. Corrosion was induced in the tensile steel reinforcement in the middle third of the specimens to resemble a flexure-critical corrosion-damaged RC beam. Four corroded specimens were repaired with the TRM system whereas one corroded specimen was not repaired and one specimen was neither corroded nor repaired to act as a benchmark. The TRM system consisted of carbon or basalt fiber grid (textile) embedded into a cementitious non-shrink mortar. The repair scheme consisted of TRM layers internally embedded within the corroded region of the beam or a combination of internally embedded and externally bonded TRM layers. Corrosion damage significantly reduced the flexural capacity and ductility of the unrepaired beam. The basalt TRM system could not restore the original flexural capacity of the beam whereas the carbon TRM repair system fully restored the capacity. Doubling the amount of the internally embedded TRM layers slightly increased the flexural strength gain but reduced the beam ductility. The use of carbon TRM layers internally embedded within the corroded region together with TRM layers externally bonded along the beam span was more effective in improving the flexural response than the use of internally embedded TRM layers alone. Textile-reinforced mortar can be considered a very promising alternative for rehabilitation of corrosion-aged RC structures.

1 INTRODUCTION

Reinforced Concrete (RC) structures in the Arabian Gulf and worldwide suffer from extensive corrosion due to the harsh environment and/or use of deicing-salt (Almusallam et al. 1996, El-Maaddawy et al. 2005, Mangat & Elgarf 1999). Traditional methods of repairing corrosion-damaged RC structures involve the replacement of the corroded bars and the substitution of the deteriorated concrete layers with new concrete. One of the most appealing techniques for rehabilitation of such structures is the use of ferrocement as external reinforcement where steel mesh is embedded in concrete before being layered with cement mortar. Despite the advantages of this method in improving the structure's strength and ductility, the presence of the steel mesh triggers the resumption of corrosion after repair. Other methods implicate the use of epoxy-bonded fiber-reinforced polymers sheets attached externally to the concrete surface. Many researchers have reported the success of increasing the strength of corrosion-damaged beams by using epoxy-bonded composite sheets (Bonacci & Maalej 2000, El-Maaddawy & Soudki 2005, El-Maaddawy et al. 2007). However, numerous concerns have been raised concerning the performance of the epoxy-bonded composite systems in case of fire and other exposure hazards, the toxicity nature of epoxy, and its poor thermal compatibility to the base concrete.

The present study is proposed to challenge the shortcomings of these traditional methods. It proposes a new rehabilitation technique for the corrosion-damaged RC structures that utilizes newly produced carbon and basalt fiber textile grids embedded between cement-based mortar layers as shown in Figure 1. The system is referred to as Textile-Reinforced Mortar (TRM). This repair technique overcomes the shortcomings of ferrocement where corrosion activity can be completely mitigated after strengthening owing to the

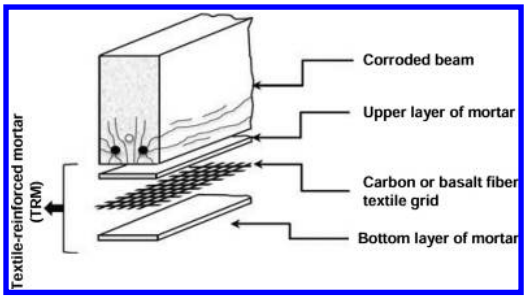

Figure 1. Flexural strengthening with TRM system.

anticorrosive nature of the textile grid used in reinforcing the cement mortar. The technique also surmounts the epoxy-bonded fiber-reinforced composite system that lacks fire resistance as the textile reinforcement is shielded between the mortar layers. In addition, the compatibility between the TRM and the concrete substrate is inherited since both materials have the cement as a common "base".

The viability of the TRM system to improve the flexural response of undamaged RC beams has been demonstrated in few recent studies (D'Ambrisi & Focacci 2011, Elsanadedy et al. 2013, Hashemi & Al-Mahaidi 2010, Hashemi & Al-Mahaidi 2012). Nevertheless, the effectiveness of the TRM system to improve the flexural response and restore the load capacity of corrosion-damaged RC beams has not been investigated. This research work aims at filling this gap and providing insight into the performance of corroded beams repaired with TRM layers.

2 EXPERIMENTAL PROGRAM

2.1 *Test matrix*

The test matrix is given in Table 1. The experimental program comprised testing of six RC T-beam specimens. One specimen was neither corroded nor repaired to act as a benchmark, one specimen was corroded but not repaired, and four specimens were corroded then repaired using different TRM schemes. Specimens D-2Ci and D-4Ci were repaired with two and four carbon TRM layers, respectively, internally embedded within the corroded zone. Specimen D-4Bi was repaired with four basalt TRM layers, internally embedded within the corroded region. The repair of specimen D-2Ci-2Ce comprised two carbon TRM layers internally embedded within the corroded zone and two carbon TRM layers externally bonded to the tension face along the beam span.

Table 1. Test matrix.

	TRM repair scheme		
Specimen	Material	Internally-embedded	Externally-bonded
Control	–	–	–
D-NR	–	–	–
D-2Ci	Carbon	2	–
D-4Ci	Carbon	4	–
D-4Bi	Basalt	4	–
D-2Ci-2Ce	Carbon	2	2

*D = damaged; NR = not repaired; 1, 2, and 4 = number of TRM layers; C and B = Carbon and Basalt textiles, respectively; i = internally embedded within the corroded zone; e = externally bonded on tension face along the beam span.

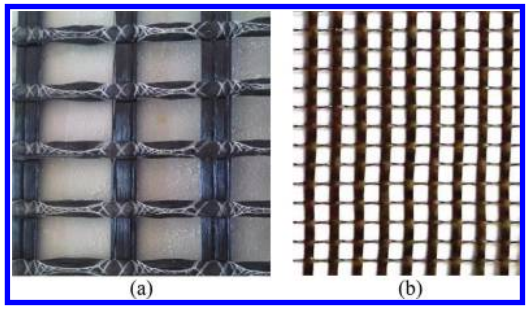

Figure 2. Textile reinforcement. (a) carbon textile grid. (b) basalt textile grid.

2.2 *Materials*

The average cylinder concrete compressive strength was 25 MPa. The yield strengths of the tensile and compressive steel reinforcement were 538 and 345 MPa, respectively. Two types of textile grids made of carbon and basalt fibers were used in this study as shown in Figure 2. The textile grid was made of joint carbon fiber bundles (rovings). The longitudinal carbon rovings were spaced at a distance of 10 mm whereas the transverse rovings had a spacing of 18 mm. The basalt rovings were spaced at a distance of 5 mm in both longitudinal and transverse directions. Table 2 lists the mechanical properties of the textile grids as provided by the manufacturers. The cementitious matrix was a non-shrink metallic aggregate mortar produced by BASF and commercially known as Embeco® 885. The mortar had a compressive strength, flexural strength, and modulus of elasticity of 62, 7.9, and 25 MPa, respectively (data obtained from the manufacturer data sheet).

Table 2. Properties of textile grids used in repair.

Property	Type of textile	
	Carbon	Basalt
Weight (g/m^2)	609	250
Tensile strength (MPa)	3800	1040
Modulus of elasticity (GPa)	230	10
Elongation at break (%)	1.25–1.6	10.3

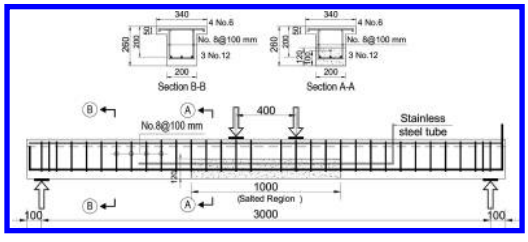

Figure 3. Details of the test specimen.

2.3 *Test specimens*

The geometry and details of reinforcement of a typical test specimen is shown in Figure 3. The test specimens were designed to resemble a flexure-critical corrosion-damaged T-beam with a corroded zone restricted to the middle third of the span. The test specimens had a length of 3200 mm and effective span of 3000 mm. The cross-section was T-shaped having a web width of 200 mm, flange width of 340 mm, total depth of 260 mm, and effective depth of 200 mm. The tensile steel consisted of three 12 mm diameter deformed bars whereas the compressive steel consisted of four 6 mm diameter plain bars. Double-leg 8 mm diameter deformed steel stirrups were provided at a spacing of 100 mm to avoid shear failure. The stirrups located within the corroded zone were epoxy-coated. Contact locations between the shear stirrups and the longitudinal steel reinforcement were isolated. The lengths of the tensile steel bars located outside the corroded region were also epoxy-coated.

2.4 *Accelerated corrosion aging*

A constant current density of 200 μA/cm^2 was impressed by means of external power supplies through the tensile steel bars that acted as anode and an internal cathode in the form of a stainless steel tube placed longitudinally at a distance 100 mm from the bottom soffit of the beam. To promote corrosion and depassify the steel in the corroded region, the concrete mix used to cast the middle third of the beam up to a height of 120 mm, measured from the soffit of the beam, had a 3% NaCl (salt) by weight of cement. The beams were then subjected to wet-dry cycles for 5 months. The wet-dry cycles consisted of 2 days of wet phase followed by 2 days of dry phase. During the wet phase, water mist was sprayed on the beams by means of fogging compressed air mist nozzles. The specimens were encased in a polyethylene cover during the wet phase to control the interior humidity.

2.5 *Repair methodology*

The repair works included edge conditioning, removal of deteriorated concrete, undercutting of exposed bars, surface cleaning of steel, roughening of concrete substrate, and application of the TRM layers. The beams were placed upside down with the beam soffit placed at the top to facilitate the repair work. The edges of the corroded region were saw-cut at 90°. The deteriorated concrete layers were removed using a chipping hammer. The corroded steel reinforcing bars were exposed and a concrete layer of approximately 30 mm below the bars was removed. A high-pressurized water jet was used to remove the rust and clean the surface of the steel bars. The concrete substrate was then roughened using the high-pressurized water jet. The corroded bars and concrete substrate were then cleaned of dust and loose particles using a high-pressure air jet. A grooved area of 1200 mm long, 200 mm wide, and 100 mm deep was therefore prepared for the TRM application.

The grooved area was moistened for two days using wet burlaps prior to the placement of TRM layers. The grooved area was then filled with mortar of sufficient depth that covered the exposed steel bars. The textile grids, precut to the desired lengths, were then placed and fully impregnated in the mortar using hand pressure. Successive layers of mortar and textile were then applied until the desired number of layers was achieved. A final top layer of mortar covered the last textile grid flush with the beam's soffit. The repaired areas were then covered using wet burlaps and plastic sheets for 24 hours to minimize water evaporation and to avoid the formation of initial cracks along the repaired area. The repaired areas were then cured using wet burlaps for 28 days then left air-cured for approximately two weeks prior to testing. Figure 4 shows the beams after surface preparation and TRM application.

2.6 *Test set-up and procedure*

The specimens were tested to failure in four-point bending configuration under displacement control at a rate of 1.5 mm/min. The beam span between supports was 3000 mm whereas the shear span was 1300 mm (Figure 3). The load was applied using a servo hydraulic MTS actuator of 500 kN capacity. A spreader steel beam was used to spread the load

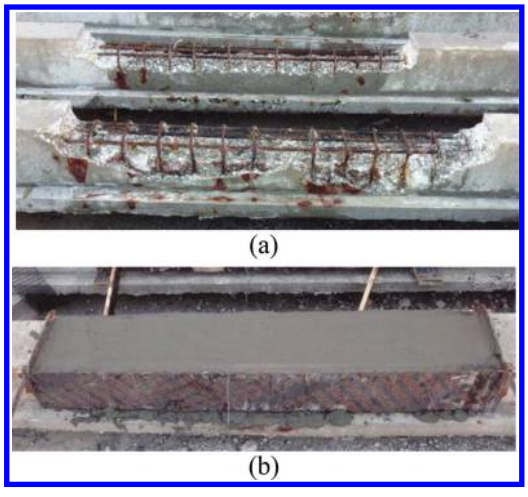

Figure 4. TRM repair. (a) surface preparation. (b) TRM application.

equally to two loading points 400 mm apart. The applied load was recorded by means of a load cell placed between the actuator and the spreader beam. A linear variable displacement transducer (LVDT) was attached to the bottom soffit of the beam at mid span to record the beam deflection. All beams were instrumented at midspan with a 60 mm long strain gauge bonded to the top surface of concrete and 5 mm long strain gauges bonded to the tensile steel bars at midspan. The measuring instruments were connected to a 30-channel data acquisition system to record the readings.

3 EXPERIMENTAL RESULTS

3.1 *Corrosion cracking and mass loss*

Significant deterioration was observed in all corroded beams at the end of accelerated corrosion aging. Rust stains and longitudinal cracks were noticeably observed at the level of the tensile steel reinforcing bars. The corrosion crack width observed in the test specimens was on average 1.8 mm with a minimum of 1.2 mm and a maximum of 3 mm. The typical corrosion crack pattern observed in the corroded beams is shown in Figure 5. After testing the beams to failure, three steel samples, 150 mm long each, were extracted from the corroded bars of each beam, cleaned of rust according to the chemical cleaning procedure of the ASTM G1-03 (2011), then weighed to determine the tensile steel mass loss caused by corrosion. Several corrosion pits were observed on the surface of the corroded samples. The tensile steel mass loss was on average 22% with a minimum of 20% and a maximum of 25%.

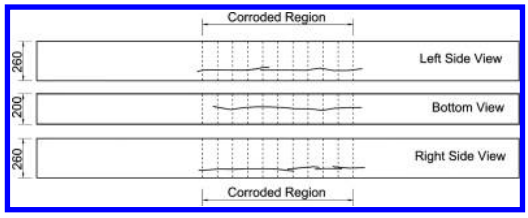

Figure 5. Typical corrosion crack pattern.

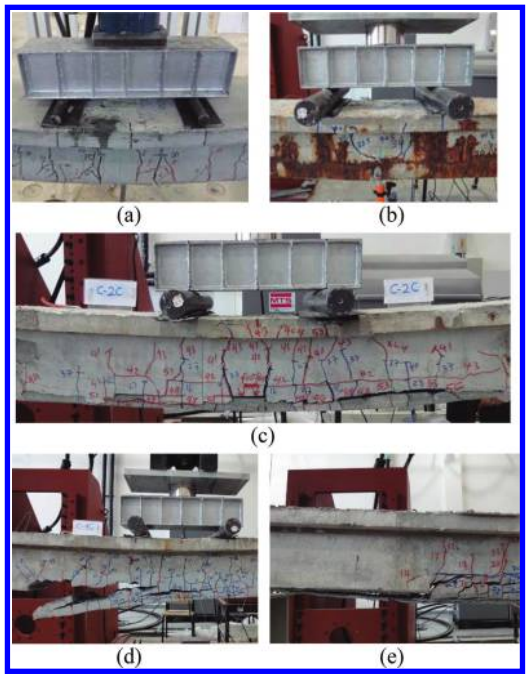

Figure 6. Failure modes. (a) concrete crushing. (b) fracture of tensile steel. (c) intermediate flexure crack-induced interfacial debonding. (d) concrete cover separation. (e) mixed flexure-shear crack-induced interfacial debonding/concrete cover separation/local concrete crushing.

3.2 *Failure mode*

The failure modes of the tested beams are shown in Figure 6. The control specimen exhibited a conventional flexural mode of failure that was initiated by yielding of the tensile steel followed by crushing of concrete at the compression face. Specimens D-NR and D-4Bi failed by fracture of the tensile steel without crushing of concrete. Specimens D-2Ci and D-2Ce failed by yielding of the tensile steel followed by intermediate flexure crack-induced interfacial debonding at the mortar/textile interface. In this failure mode, debonding at the mortar/textile interface was initiated at a flexure crack in the constant moment region or under one of the

load points then propagated towards the ends of the TRM layers. Specimen D-4Ci failed by yielding of the tensile steel followed by peeling of the concrete cover (i.e. concrete cover separation). In this failure mode, failure was initiated by the formation of an inclined crack at the vicinity of the TRM reinforcement. This crack progressed horizontally towards the midspan along the tension steel reinforcing bars causing the separation of the concrete cover. Specimen D-2Ci-2Ce failed by yielding of the tensile steel followed by intermediate flexure-shear crack-induced interfacial debonding at the mortar/textile interface. Debonding was initiated at the mortar/textile interface of the externally bonded TRM layers due to the formation of a flexure-shear crack at the vicinity of the TRM reinforcement. The debonding propagated towards the ends of the externally bonded TRM layers. As the load progressed, an inclined crack developed at the vicinity of the repaired region then progressed horizontally towards the midspan causing concrete cover separation. Local concrete crushing at the top surface of concrete was also observed at the onset of failure of specimen D-2Ci-2Ce.

3.3 *Load-deflection response*

The load-deflection responses of the tested specimens are depicted in Figure 7. From this figure, it can be seen that corrosion damage and cracking significantly reduced the load capacity and ductility of the unrepaired beam but had insignificant effect on the beam stiffness. The effectiveness of the TRM repair system to improve the flexural response of the corroded beams and restore the original load capacity of the beams was highly dependent on the type of the textile reinforcement and number/distribution of the TRM layers within the beam span. The basalt TRM repair system was not effective in improving the flexural response whereas the internally embedded carbon TRM layers fully restored the load capacity and ductility, expect for specimen D-4Ci where only 90% of the ductility was restored. The use of carbon TRM layers internally embedded within the corroded region together with TRM layers externally bonded along the beam span was more effective in improving the flexural response than the use of internally embedded TRM layers alone. Detailed analysis of the test results in terms of strength and ductility are presented in the following sections.

3.4 *Strength analysis*

The strength results are summarized in Table 3. The yield and ultimate loads of the corroded beams are compared to those of the control specimen. Corrosion of steel reinforcement significantly

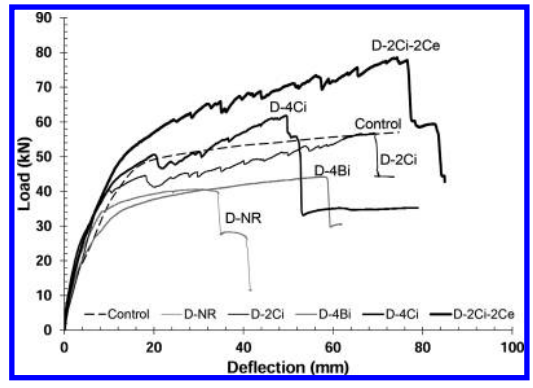

Figure 7. Load-deflection response.

Table 3. Strength results.

	Load values		Load ratio*	
Specimen	Yield (kN)	Ultimate (kN)	Yield	Ultimate
Control	47	57	–	–
D-NR	34	41	0.72	0.72
D-2Ci	40	57	0.85	1.00
D-4Ci	44	62	0.94	1.09
D-4Bi	34	44	0.72	0.77
D-2Ci-2Ce	48	79	1.02	1.39

*With respect to those of the control beam.

reduced the yield and ultimate loads of specimen D-NR relative to those of the control specimen. A 22% average tensile steel mass loss resulted in approximately 28% reduction in the load capacity. The reduction in load capacity was greater than the reduction in the average steel mass loss caused by corrosion because of the presence of corrosion pits on the surface of the steel bars, which resulted in fracture of the tensile steel shortly after yielding without crushing the concrete. The use of two layers of internally embedded carbon TRM restored approximately 85% of the beam yielding load but fully restored the ultimate load. Increasing the number of carbon TRM layers further increased the yielding and ultimate loads. The yielding load of specimen D-4Ci was approximately 94% of that of the control specimen whereas its ultimate load exceeded that of the control specimen by approximately 9%. This demonstrated the effectiveness of the carbon TRM system in improving the flexural response and restoring the load capacity of corroded RC beams. The use of four layers of internally embedded basalt TRM had no effect on the yielding load but slightly increased the ultimate load relative to those of specimen D-NR.

The basalt TRM repair system could not restore the load capacity of the control beam. The load capacity of specimen D-4Bi was approximately 7% higher than that of specimen D-NR yet 23% lower than that of the control specimen. The inferior performance of specimen D-4Bi can be attributed to the reduced modulus of elasticity of the basalt textile reinforcement. Specimen D-2Ci-2Ce exhibited superior performance relative to all specimens. The yielding load of specimen D-2Ci-2Ce was approximately 9% higher than that of specimen D-4Ci and almost equal to that of the control specimen. The ultimate load of specimen D-2Ci-2Ce was approximately 27% higher than that of specimen D-4Ci and 39% higher than that of the control specimen. The flexural response of specimen D-2Ci-2Ce outperformed that of its counterpart specimen D-4Ci because of the increased development length of the two externally bonded TRM layers, which delayed the debonding of the TRM layers, separation of the concrete cover, and hence allowed the beam to develop a high load capacity.

3.5 *Ductility performance*

Large deflection before failure would provide ample warning of structural distress. The beam ductility is the capacity of the beam to sustain large deformation before failure without a significant drop in load after yielding of the tensile steel reinforcement. The ductility index is defined as the ratio of the beam deflection at ultimate load to the deflection at yielding load. Deflections of the tested specimens and their ductility indexes are given in Table 4. The ductility indexes of the corroded specimens are compared to that of the control specimen.

The ductility index of the corroded-unrepaired specimen D-NR was approximately 24% lower than that of the control specimen. The deflection of specimen D-NR at ultimate load was 60% lower than that of the control specimen. This can be attributed to the premature failure of specimen D-NR by fracture of the tensile steel without crushing of concrete. The deflection of specimen D-2Ci at ultimate load was approximately 92% of that of the control specimen but its ductility index exceeded that of the control specimen by approximately 50%. Doubling the amount of the carbon TRM layers reduced the deflection at ultimate load and the ductility. The deflection of specimen D-4Ci at ultimate load was approximately 67% of that of the control specimen whereas its ductility index was approximately 91% of that of the control specimen. Although the ductility index of specimen D-4Bi was almost equal to that of the control specimen, its deflection at ultimate load was approximately 23% lower. The deflection of specimen D-2Ci-2Ce at ultimate load was almost equal tot that of the control specimen but its ductility index was 35% higher. These results demonstrated the viability of using externally bonded TRM layers in combination with the internally embedded layers to improve both the load capacity and ductility.

Table 4. Ductility results.

Specimen	Deflection values		Ductility index	Ductility index ratio*
	Yield (mm)	Ultimate (mm)		
Control	16.3	75	4.6	-
D-NR	8.6	30	3.5	0.76
D-2Ci	10	69	6.9	1.50
D-4Ci	12	50	4.2	0.91
D-4Bi	12.6	58	4.6	1.00
D-2Ci-2Ce	12	74	6.2	1.35

*With respect to the ductility index of the control beam.

4 CONCLUSIONS

The flexural response of severely corrosion-damaged RC beams repaired with TRM systems has been investigated in this study. Based on the test results, the following conclusions can be drawn:

- The reduction in load capacity of RC beams caused by corrosion was greater than the reduction in the tensile steel mass loss. A 22% average tensile steel mass loss resulted in approximately 28% reduction in the load capacity. The corroded-unrepaired beam failed prematurely by fracture of the tensile steel shortly after yielding which resulted in approximately 60% reduction in the deflection at ultimate load and 24% reduction in the ductility.
- All corroded beams repaired with TRM systems failed by yielding of the tensile steel followed by intermediate crack-induced interfacial debonding, except specimens D-4Bi and D-4Ci that were repaired with four basalt and four carbon TRM layers, respectively, internally embedded within the corroded region. Specimen D-4Bi failed by fracture of tensile steel whereas specimen D-4Ci failed by concrete cover separation. In both cases, yielding of the tensile steel preceded failure of the beams.
- The effectiveness of the TRM repair system to improve the flexural response of the corroded beams was highly dependent on the type of the textile reinforcement and number/distribution of the TRM layers within the beam span.

– The basalt TRM repair system could not restore the original load capacity of the corroded beam due to its low modulus of elasticity. On the contrary, two internally embedded carbon TRM layers fully restored the original load capacity of the beam.
– Increasing the amount of the internally embedded carbon TRM layers from two to four further increased the flexural strength to a level higher than that of the control specimen yet reduced the beam ductility.
– The use of carbon TRM layers internally embedded within the corroded region together with TRM layers externally bonded along the beam span was more effective in improving the flexural response than the use of similar amount of TRM layers internally embedded within the corroded zone.

ACKNOWLEDGMENTS

The authors would like to express their gratitude to the UAEU for financing this project under the UAEU-NRF reviewed grant no. 31 N121.

REFERENCES

Almusallam, A., Al-Gahtani, A.S., Aziz, A.R., Dakhil, F., and Rasheeduzzafar (1996). Effect of reinforcement corrosion on flexural behavior of concrete slabs. *Journal of Materials in Civil Engineering*. 8(3): 123–127.

Bonacci, J.F. & Maalej, M. (2000). Externally bonded fiber-reinforced polymer for rehabilitation of corrosion damaged concrete beams. *ACI Structural Journal*. 97(5): 703–711.

D'Ambrisi, A. & Focacci, F. (2011). Flexural strengthening of RC beams with cement-based composites. *Journal of Composites for Construction*. 15(5): 707–720.

El-Maaddawy, T., Soudki, K, and Topper, T. (2005). Long-term performance of corrosion-damaged reinforced concrete beams. *ACI Structural Journal* 110(5): 779–790.

El-Maaddawy, T.A. & Soudki, K.A. (2005). Carbon-fiber-reinforced polymer repair to extend service life of corroded reinforced concrete beams. *Journal of Composites for Construction.* 9(2): 187–194.

El-Maaddawy, T., Soudki, K., and Topper, T. (2007). Performance evaluation of carbon fiber-reinforced polymer-repaired beams under corrosive environmental conditions. ACI Structural Journal. 104(1): 3–11.

Elsanadedy, H.M., Almusallam, H.M., Alsayed, S.H., and Al-Salloum, Y.A. (2013). Flexural strengthening of RC beams using textile reinforced mortar—experimental and numerical study. *Composite Structures*. 97: 40–55.

Hashemi, S. & Al-Mahaidi, R. (2010). Investigation of bond strength and flexural behavior of FRP strengthened RC beams using cement-based adhesives. *Australian Journal of Structural Engineering*. 11(2): 129–139.

Hashemi, S. & Al-Mahaidi, R. (2012). Flexural performance of CFRP textile-retrofitted RC beams using cement-based adhesives at high temperature. Construction and Building Materials. 28: 791–797.

Mangat, P.S. & Elgarf, M.S. (1999). Flexural strength of concrete beams with corroding reinforcement. *ACI Structural Journal*. 96(1): 149–158.

Concrete Repair, Rehabilitation and Retrofitting IV – Dehn et al. (Eds)
© 2016 Taylor & Francis Group, London, ISBN 978-1-138-02843-2

Dismantling of damaged PSC damaged suspended span of Varsova Bridge across Vasai Creek on NH-8, Mumbai, India

M.L. Gupta
IRB Infrastructure Developers Ltd., Mumbai, India

D.A. Bhide
Design, IRB Infrastructure Developers Ltd., Mumbai, India

P.B. Dongre
IRB Infrastructure Developers Ltd., Mumbai, India

ABSTRACT: The existing Varsova Bridge across Vasai Creek, called as Bassein Creek Bridge when constructed, was opened to traffic in 1968. It is in Mumbai Ahmedabad section of NH-8, about 35 Km from Mumbai. Major cracks were noticed in the West side girder of the penultimate span from Mumbai end on 12th December 2013. The site was inspected for assessment of the damage. It was decided to replace the said span with composite steel girder. The real task was to dismantle the existing PSC span without any debris falling in the creek and working in a very restricted work area as well as within a very short period. This paper discusses the replacement done accounting for the constraints imposed from the design and construction of the existing structure, formulating replacement scheme, design of new structure, dismantling the damaged PSC span and its replacement with composite deck, steel girders and concrete deck slab.

1 BRIDGE DETAILS

The Bridge is 555.32 m long with 8 spans. The span arrangement is 48.46 + 2 × 57.3 + 2 × 114.6 + 2 × 57.3 + 48.46 m. The main spans from central three piers were built with balanced cantilever construction. These are with single cell box girder. The cantilever construction was continued in adjacent penultimate spans with overhangs of 8.84 m each. These overhangs support suspended spans of 48.46 m. Suspended spans as well as end spans are with two nos., pre-cast post tensioned girders with in-situ deck slab. Thus the bridge has 6 spans continuous module for a length of 458.4 m. Overall deck width is 10.77 m. Rocker and rocker cum roller bearings are used at all the locations. Thin plate piers are provided at all locations. Except at penultimate foundation locations, only a single row of bearings is provided over all piers. All foundations are with cassions.

Each girder of all 4 simply supported spans was strengthened with 20 nos. of 12.7 mm dia. External single strand tendons. (Figures 1–2).

2 THE DAMAGE

Existing girder on West side suspended span of penultimate span on Mumbai end developed wide cracks at center (Figure 3). Cracks were predominant on one side of central diaphragm. The major crack was about 150 mm wide at the bottom flange. It progressed towards top and away from center. Crack had branched out while progressing. A large portion of concrete was missing at the crack location. The reinforcement and internal prestressing cables were exposed at the crack location (Figure 4). Some of the prestressed wires of internal cables were snapped. At top of deck, a perceptible kink was observed in railing, directly above the location of the crack. Some cracks were observed in intermediate diaphragm at one of the deviator blocks for external tendons. The suspender plates of deviator block at this location were also twisted.

Obviously the damaged girder remained in position due to external prestress provided and a complete collapse of span was averted.

Figure 1. Elevation showing external pre-stressing.

Figure 2. Bottom view of external pre-stressing.

Figure 3. Cracks in damaged girder (Elevation of girder).

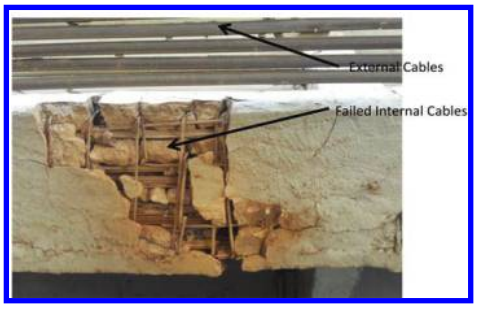

Figure 4. Cracks in damaged girder (soffit of girder).

3 LIMITATIONS IMPOSED BY EXISTING STRUCTURAL SYSTEM

The drawings for the existing bridge were not easily available. The details of external pre-stress applied to simply supported spans were available with the Authority. The details of the cable profile of the continuous structure, central 4 continuous spans with overhangs were also available. The original contractor was able to retrieve the drawings of the simply supported spans.

Some startling facts emerged from the available details. The articulations supporting 48.46 m long suspended spans were prestressed. Dimensions of the articulations were just sufficient to place bearings. As such no space was available to provide any sort of supporting arrangement at this end. The rocker bearings over articulations were with fully anchored rag bolts. The bottom plates could not be removed without breaking articulations. The cantilever overhangs of continuous module were pre-stressed in longitudinal direction. Any increase in the load over the articulations was clearly ruled out.

The span preceding overhang had majority of the cables at top. Unfortunately details of cable layout at bottom were not available. No anchorages for bottom cables were seen inside the span. It was then concluded that the bottom tension was probably catered by un-tensioned reinforcement. This led to conclusion that any reduction in load in cantilever will induce unfavorable tensile moment at bottom of the said span.

The penultimate pier supported two equal simply supported spans. The dead load effects were balanced on the pier and pier cap. The pier cap had cantilevers that supported the span. Any change in reaction of new structure would induce unbalanced loads and cause some overstress in pier cap as well as pier and cassion foundation at this location. In absence of the detailed drawing it was not possible to determine the allowable extent for change in loads.

From the foregoing findings it was concluded that "The load on articulations as well as at other end had to be matched to that of existing structure.", else some undesirable stresses would be induced in the supporting structures. Since the existing bridge is more than 50 years old it was prudent not to overstress any of the components.

The equipment for dismantling had to be erected over damaged and existing structure. Obviously the same had to be designed in such a way that the induced forces would be within the live load effects so as not to overload the structure at any stage.

4 LIMITATIONS IMPOSED BY LOCATION OF THE BRIDGE

The bridge is within tidal zone. The navigation clearance is provided in central span only. The deck had almost 3% slopes towards abutments. As such the head room below the damaged span from high tide level was extremely limited for any equipment to operate. The bed in creek comprises of very soft marine clay, about 6 to 8 m deep. Providing any sort of supports from bed was therefore ruled out.

5 DISMANTLING SCHEME

Supporting the deck from bottom was ruled out due to bed stratum as well as low restricted head room. The support therefore had to be from the top of deck. Available draft, especially at low tide condition was too small to float crane with sufficient capacity. Restricting operations during high tide would have required much larger construction time than available. Deployment of any barge mounted crane was ruled out.

Another option was to erect launching girder across the damaged span. The launching girder would have enabled to remove the intact girder as a whole. The damaged girder in longitudinal direction was stable but the crack at center would have rendered it unstable in transverse direction while removal, especially so in absence of deck slab or diaphragms. These were providing the lateral stability to damaged girder and preventing its collapse. In addition the difficulties in availability of the launching girder, taking it across the existing end span as well as damaged span, need for side shifting of existing girders below launching girder ruled out use of any launching girder.

This led to proposal of erecting girders exactly over each of the existing girders and suspending the segments of existing girders from the erected girders. Thus use of two steel girders was obvious to fit the same. The use of concrete girders was ruled out as weight of full concrete deck with present code provisions would be excessive. The present code provisions required a three girder system with thicker components resulting in significantly heavier structure. The dimensions of old structure were quite thin compared with present code requirements, e.g. web thickness, cable spacing etc. The support arrangement for new deck on existing bearings would also be impractical for three girder system. Concrete structure, within weight limits and complying with present codes was not possible. Only viable option was steel girder with concrete deck slab. Only two girders could be used enabling simpler seating on bearings.

Use of composite deck with two steel girders was then finalized as it facilitated both dismantling as well as permanent structure.

6 DISMANTLING SEQUENCE

The major steps were as below (Figure 5 Shows schematic sequence).

6.1 Remove the services/utility cables laid over footpaths

6.2 Cut the footpaths and part of the cantilever slab, keeping the flanges of the precast girders intact along with deck slab over them

6.3 Remove existing bituminous wearing coat

6.4 Assemble steel girders in the approach, in line with intact girder of the damaged span

6.5 Launch the steel girder over intact girder across the damaged span

6.6 Support this girder beyond diaphragm at articulations of cantilever overhang on one end, in line with girder/webs and over beams on other end

6.7 Side shift 1st girder to place it over the damaged girder

6.8 Launch 2nd girder across the intact span. Fix cross diaphragms/bracings for lateral stability

6.9 Lift the girders to ensure clear headroom of 1.5 m for working space

6.10 Erect the suspension system for cut segments of girder/deck.

6.11 Remove he deck in between girder flanges and cross diaphragms, except in central portion of span as these were necessary for lateral stability

6.12 Cut girder segments about 3 m long and weighing 10t each, on an average

6.13 Remove the cut segments with a moving trolley over main steel girders and strand jacks mounted over the trolley

6.14 Lower the cut segments in the barge stationed below

6.15 Retrieve the embedded parts of the bearings from cut segments. Clean all the components and re-assemble at locations

6.16 Lower the main girders over assembled bearings

6.17 Erect shuttering for the deck slab and cast the same. Follow this with casting of raised footpaths and parapets

6.18 Fix expansion joints, lay bituminous wearing coat and open to traffic

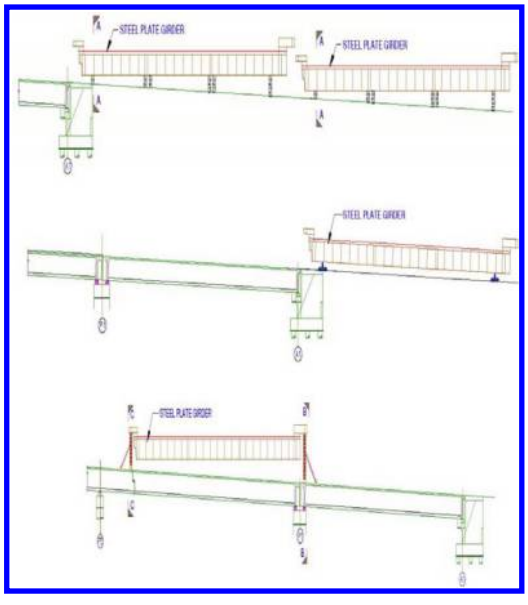

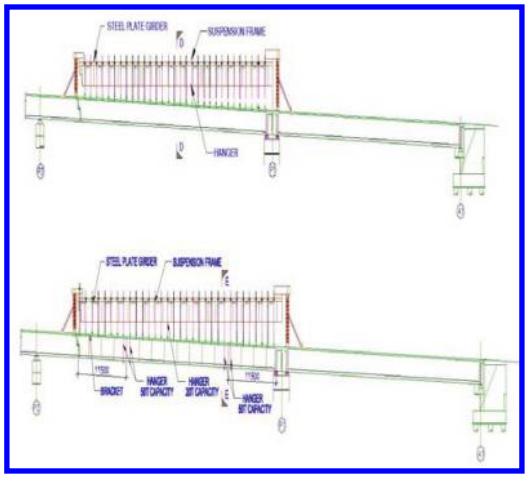

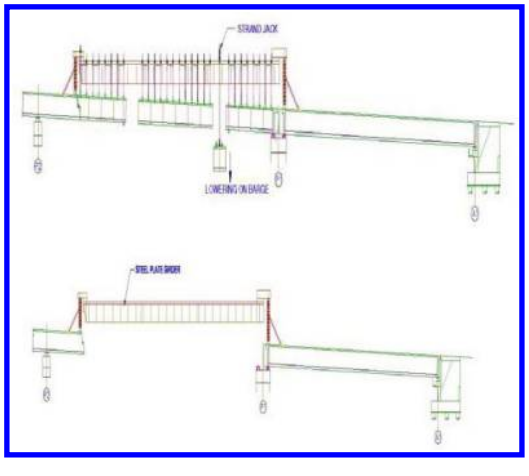

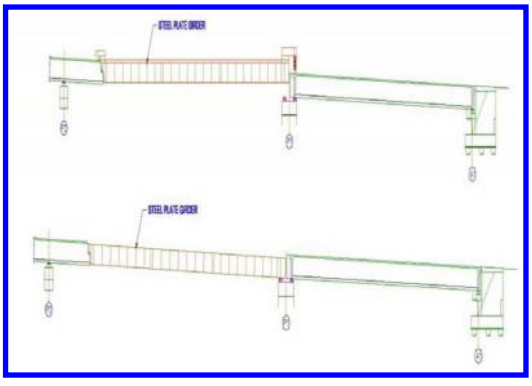

Figure 5. Schematic arrangements for construction sequence.

7 DETAILING OF NEW STEEL GIRDERS

Since the existing bearings were to be used it was prudent to adopt the overall depth of new structure same as existing structure. An assessment of load that can be safely rolled over intact girder was made. Accordingly steel girders and concrete slab were dimensioned for permanent structure. Medium tensile steel of grade E350 BR was used for main girders and of grade E250 BR for other components to control weight. All joints, except at splice locations were welded. HTS, grade 8.8 bolts were used for splicing.

The web depth of the girder of 2.45 m was chosen to suit the available plate width of 2.5 m. In order to match weight of old and new structure solid raised footpath configuration and deck slab for full deck width was retained. The overall deck dimensions at articulation end were kept exactly same as old structure, enabling direct connection of bearings at that end. This arrangement resulted in overall depth of the deck as 160 mm less than the existing structure. Therefore a block of welded plates to connect the bearings at pier end to the girder was provided.

8 TEMPORARY SUPPORT ARRANGEMENT OF GIRDERS

The temporary supports were provided over webs/girders of adjacent spans so as to transfer load directly to girders & bearings. To facilitate this, brackets from top flange was provided at either ends. These brackets were bolted to top flanges for easy removal before casting of deck slab. (Figure 6)

The temporary supports for the girders were in form of trestles at each end (Figure 7). Trestles

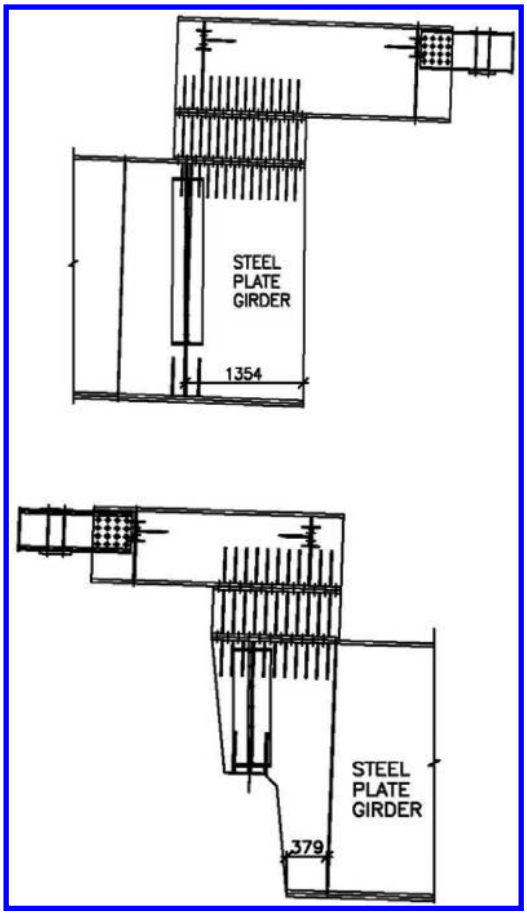

Figure 6. Bracket arrangements for lifting and lowering of main girders.

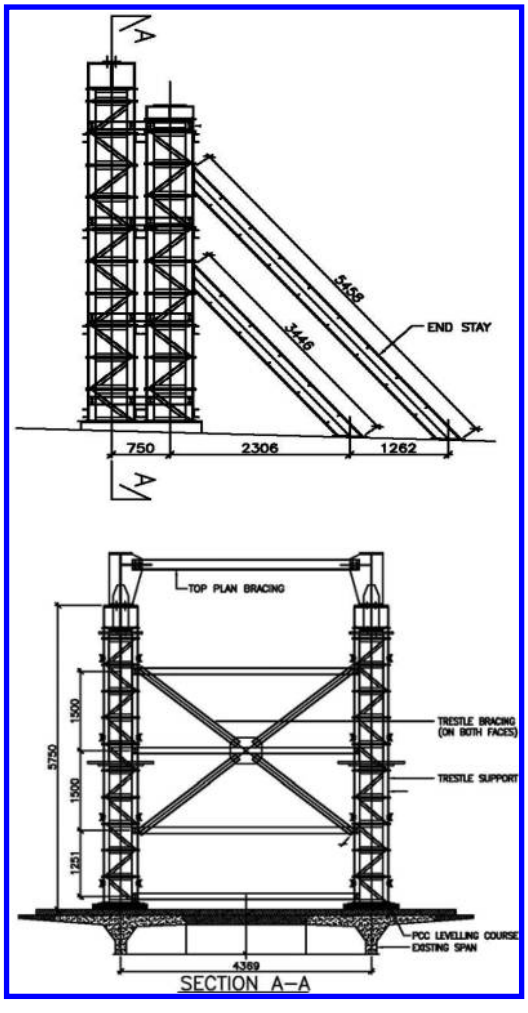

Figure 7. Trestles for supporting main girders during dismantling of damaged girder.

were made in pieces that could be easily handled for raising and lowering. Two trestle arrangements were necessary as temporary supports during raising & lowering operations were unavoidable.

9 SUSPENDING ARRANGEMENT FOR HOLDING CUT SEGMENTS

Basic arrangement for suspending cut segments of the girders was with pair of beams across the two main girders for each of the segments, weighing about 10t. Beams were spaced at 1.5 m C/C with respect to corresponding segment that was to be held. Thus four suspenders were planned for each of the segments. Each of the suspenders was designed to carry half the load of the segment at working stress level. (Figure 8)

Since the girders were with external pre-stress as well as some residual pre-stress in damaged girder and full in intact girders, each of the segments of L/4 length resulting from first cuts were expected to act one unit. Therefore the suspenders on either side of first cuts were designed to carry load of the said length of the girder. (Figure 9)

The suspenders held the girder segments through beams connected to segment at top of slab. Each beam was connected to segment through two bolts drilled and socketed in deck slab. Six nos. of trial anchors were tested for pull out load varying from 14t to 18t.

The slab and diaphragm panels were comparatively light, weighing about 2.5t. These were suspended directly from the girders. The removal

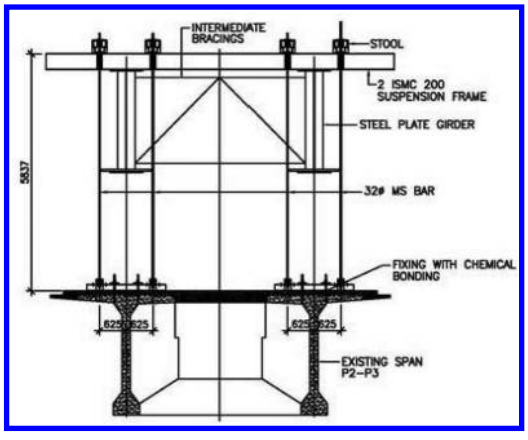

Figure 8. Suspending arrangement of cut segments.

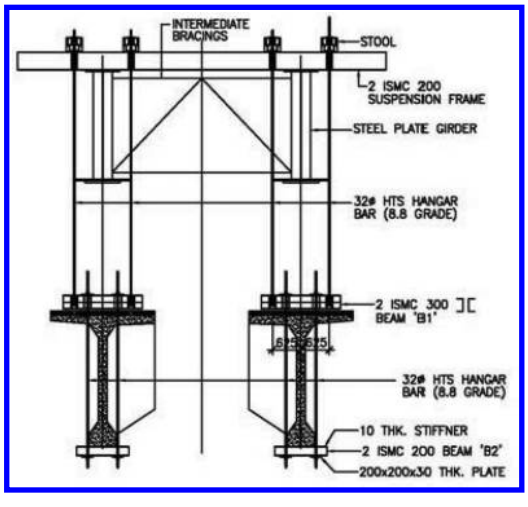

Figure 9. Suspending arrangement of cut segments at L/4 location of girders.

of cut segment was planned with moving trolley over steel girders. Four strand jacks, two on either side of each girder were mounted on trolley. The strands were connected to beams on girder segments through hooks and segments were lowered on to the barge below. For slab and diaphragm segments, the same were held in position by middle pair of jacks and then cut & lowered.

10 PROCEDURE FOR DISMANTLING OF DAMAGED SPAN

The cantilever footpaths along with some part of deck slab, till edge of flange of original precast girder were cut in segments of 2.5 to 3 m length. These segments were initially supported with crane on deck. Same was later replaced with a 50t crane on adjacent span as deformations of damaged girder were observed with crane on deck. The slab in between girders was cut in two stages. Firstly transverse cuts were completed for segments prior to launching of the steel girders. Individual segments of slab were cut with support from launched steel girders. Diaphragms were cut after damaged main PSC girder was cut into segments.

Existing precast girders weighed about 180 T each with in-situ slab over their flanges. Initial cuts were planned at L/4 location. These were in two stages, first cutting bottom bulb and web followed by top flange. The 20 nos. of strands for external pre-stress were to be cut sequentially during this.

After completing first two cuts and cutting strands of external pre-stress, the cutting of girder in 3 m long segments was allowed as per site convenience.

Diaphragms were cut in parallel to the activity of cutting smaller segments of first girder. Slabs and diaphragms panels were held through anchor bolts at 4 locations for slab panel and 2 locations for diaphragm panels. No suspenders were provided for these but held directly from movable trolley on girders.

11 REMOVAL OF EXISTING DAMAGED SPAN

11.1 *Cantilever footpaths and part of deck slab*

A 50t capacity crane was mobilized for holding segments. A careful study and check was made to decide the position of the crane and its outriggers to maintain the loads transferred within carrying capacity of the deck.

11.2 *Installing and testing anchor bolts*

As a precaution and ensuring the workability and capacity of the anchor bolts and existing slab concrete, it was decided to install six nos. of test anchor bolts. As per the design of the anchor bolts of 150 mm anchor depth for 20 mm dia. HTS anchor bolts were necessary.

Five anchors were tested for 13.6t load each while one was tested till 18t load. (Figure 10)

11.3 *Fabrication, erection, launching and positioning of main steel girders*

A track with 52 Kg rails was laid in line with intact girder of the span over approach of the bridge and over intact girder to transport the steel girders in damaged span. The steel girders were erected over trolleys on rails.

Figure 10. Photo showing pull out testing of anchors in progress.

Figure 11. Main girders launched over the damaged span.

Girders were launched over the damaged span one after the other. First girder after launching across the span was side shifted. The support to girder was over the diaphragms of the span so as no load was to be transferred to damaged girder. The second girder was then launched in similar way. Cross diaphragms and bracings were installed. The girder assembly was then lifted to its desired position over trestles to support cut segments of the damaged span. The assembly was raised and maintained in horizontal alignment. (Figures 11–12). Movable trolley was erected over track to launch the girders.

11.4 *Removal of intermediate slab and diaphragm panels*

The intermediate slab panels were removed, starting from one end.

11.5 *Removal of segments of the girders*

The cutting was done with diamond studded wire saw in conjunction with concrete saw whenever

Figure 12. Main girders launched over the damaged span.

required. The cut was from bottom upwards. First two cuts were at L/4 positions.

Unexpectedly, wire saw was getting frequently stuck while cutting the webs. This appeared to be due to pre-stress from external as well as internal cables. This slowed down the progress quite significantly which lead to grossly underestimating the overall time.

Prior to start of the initial cuts suspenders of the proposed segments were tightened and tightening was continued, prior to cutting of each of the external strand set, as well as after cutting them. Suspenders on either side of the cut were invariably found to be tight indicating the load transfer to them and three segments spanning across them, as predicted.

After completion of first main cuts further cutting was continued at two locations in the girder till all segment was complete. For removal of the segments, the lifting beams were attached to segments. These beams were connected to overhead jacks on trolley. The jacks then lowered the segments in the barge positioned below the segment for transporting them to dump yard. (Figures 13–14)

While lifting and lowering the last segment at Mumbai end, anchor bolts in the concrete failed one after the other. Fortunately the piece was on pier cap and was laterally held hence it did not fall in the creek but got settled on cap. The saddle plate of rocker cum roller bearing at this end slipped into the creek. Rollers were fortunately held by bottom plate and remained in dangling position. The segment and rollers were secured over cap with wooden wedges immediately. All dismantling operations were without any untoward incident. (Figure 15)

Figure 13. Lowering in progress.

Figures 14. Lowering of girder segments by partly completed.

Figure 15. Lowering of existing damaged girders completed and last segment lowered in the barge.

12 RE-FIXING OF BEARINGS AND LOWERING OF STEEL GIRDERS

The top plates of the rocker bearings were removed from cut segments. All the plates were cleaned and inspected. Only surface rusting and some dried grease stains existed. These were thoroughly cleaned and installed. A new saddle plate was manufactures for the one that fell in creek. The bolts connecting bearings to girders were removed. Existing bolt threads were inspected and new bolts manufactured to suit the same for the required length. The shear pins in rocker bearings were also removed and replaced with new.

The main steel girders were provided with slotted holes in bottom flanges to pass the bolts connecting bearing plates and to fasten them. This enabled fixing of bearings quite smoothly to the new girders.

Steel girders were then lowered in position. The rocker bearings at one end were aligned and matched with existing bottom plates, embedded in articulations. The rollers of the bearings on other end were set at required position for ambient temperature for resting the rocker assemblies over them.

13 COMPLETING BALANCE ACTIVITIES

The uncertain and unfamiliar activities for replacement of the span were almost over. Casting of deck slab and providing other miscellaneous items however became a challenge on account of very small time left for the same. However these were completed quite fast. The bridge was opened to traffic within 10 days lowering the steel main girders in position.

14 CREDITS

14.1 *Owner: National Highway Authority of India*

14.2 *Independent engineer: Intercontinental Consultants & Technocrats Pvt. Ltd*

14.3 *Executed by: IRB Surat—Dahisar Tollway Pvt. Ltd. (Subsidiary of IRB Infrastructure Developers Ltd.)*

14.4 *Design Consultant: STUP Consultants Pvt. Ltd*

ACKNOWLEDGEMENTS

The Authors express sincere thanks to NH division, Public Works Department, Government of Maharashtra, Gammon India Ltd. (Designer and Contractor of original Bridge) and Mr. D K Kanhere, Retired CE, PWD, Government of Maharashtra for making available the original drawings and valuable information on old structure and repairs.

Concrete Repair, Rehabilitation and Retrofitting IV – Dehn et al. (Eds)
© 2016 Taylor & Francis Group, London, ISBN 978-1-138-02843-2

Repair and retrofitting of two mega liter post tensioned, precast concrete tanks for molasses storage

J.H. Strydom
SMEC South Africa, Pretoria, South Africa
The University of the Witwatersrand, Johannesburg, South Africa

B.H. Schlebusch
SMEC South Africa, Pretoria, South Africa

ABSTRACT: In this paper, retrofitting and repair of post tensioned, precast concrete molasses storage tanks, constructed in Durban, South Africa, is presented. The two mega litre precast concrete tanks were constructed to store molasses for a yeast manufacturing plant. The tank floors consist of a post tensioned concrete slab. Vertically pre-stressed concrete panels, post tensioned horizontally, form the walls of the tanks and a tarpaulin roof is used to protect the molasses from the environment. Both tanks had significant defects and could not be certified to hold molasses. These included, insufficient grout strength, backward bending, omitted post tensioning cables, sliding of panels and structural defects in precast panels. The tanks were repaired by carefully retrofitting external pre-stressed cables to the precast panels. Stressing forces are transferred to the precast panels by means of X-Anchors. A concrete curtain wall was cast on the interior to provide a durable leak proof system. A Sika combiflex bandage was used to ensure a watertight movement joint on the inside of the tank. The repair of each tank was completed within two months.

1 INTRODUCTION

Convectional cast in-situ concrete tanks provide a suitable choice for storing liquids such as water and molasses. In recent years, the use of precast concrete increased in many fields of civil engineering mainly due to shorter construction periods. Precast concrete has been applied in constructing bridges, and highway pavements for numerous years. Precast concrete panels have recently been used in the construction of storage tanks (Karbaschi and Goumdarzizadeh 2011). The fabrication of precast concrete components allows greater flexibility to reduce on-site personnel and increase the use of local unskilled labor (Hjorteset, et al. 2013).

Tanks constructed by using precast elements generally have two shapes; rectangular or circular. The use of the precast concrete panels instead of conventional in-situ concrete, considerably increases the speed and precision of construction (Karbaschi and Goumdarzizadeh 2011).

In the field of precast or preptressed concrete, numerous research papers and handbooks have been published (Khaloo 2003). Only a few publications are available for precast concrete tanks. One of the major papers published on the subject involves the study of seismic retrofitting of numerous precast rectangular and cylindrical tanks in New Zealand (Taylor and Wright 2003). Karbaschi and Goumdarzizadeh 2011 investigated the effect of the height to diameter ratio, post tensioning force value, liquid level and installing position of tendons on seismic response of the tank. Karbaschi and Goumdarzizadeh 2011 found that adding post tensioning cables is an efficient method for decreasing opening joints of wall panels in horizontal earthquake motions.

Post tensioning systems are widely used in structures. These systems are grouped in two categories namely bonded and un-bonded systems (Bijan O 1994). Un-bonded tendons do not form a bond along its length with the concrete as it is protected from corrosion with a plastic sheathing as well as a grease layer as indicated in Figure 1. Stresses in the tendons are transferred via anchors provided at the ends. Bonded tendons on the other hand form a continuous bond with the concrete surrounding it thus allowing for stress transfer.

SMEC South Africa was appointed to design six tanks, which would be used for molasses storage by a yeast company in Durban South Africa. Molasses, is a viscous by-product of the refining of sugarcane or sugar beets into sugar and has a density of 14 kN/m^3 which is 40% more dense than that of water.

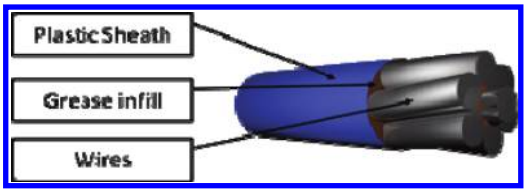

Figure 1. Un-bonded strand indicating the plastic sheathing and grease infill (Adapted from Bijan O 1994).

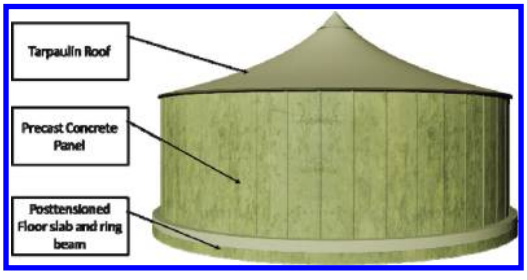

Figure 2. 7 m High, 21 m diameter, molasses storage tank.

Each tank consists of a post tensioned cast in-situ base slab. Pre-stressed, precast panels form the wall of the tank. The tanks are covered by a tarpaulin roofs supported on a steel poles as indicated in Figure 2.

Construction of two of the tanks were stopped due to major defects present which included missing un-bonded strands, defects in precast panels and the as-built geometry of the tanks. These defects where mainly due to poor construction. Although defects were present in two of the six tanks, only one tank is presented as the defects and remedy of the two tanks are similar.

In this paper the design of the tank walls is provided. Defects present after construction are discussed in detail. The remedy which included carefully retrofitting of external pre-stressing cables to the tank is also presented.

2 DESIGN OF THE WALLS

The entire tank was designed by SMEC, however, only the design of the walls is the focus of this paper as it is the most complex part of the tank.

The tank has an internal diameter of 21.0 m, is 7 m high and comprises of 44 precast panels. 26 un-bonded strands were used, in sleeves provided in the panels, to stress the panels together. Stressing buttresses were placed at panels 1 and 23.

The limit state design method was used to design the tank. The tank was designed in accordance with:

- The South African Standard Code of Practice—Structural Use of Concrete: SABS 0100-1 Edition 2.2 (2000) and;
- The British Standard Code of Practice for—Design of Concrete Structures for Retaining Aqueous Liquids: BS 8007:1987.

Design loading is in accordance with SABS 01060-1989 as amended 1990, 1991 and 1993. The following design loading was used:

- Live Load – Molasses 14,0 kN/m^3 and;
- Dead Load – Reinforced concrete 24 kN/m^3.

The precast wall panels comprise of vertically prestressed concrete class 50/19, with Young's modulus of 34 GPa. Prestressing steel is low relaxation super grade with a minimum characteristic strength (CS) of 1770 MPa and complies with BS 5896. The Young's modulus of the prestressing steel is 195 GPa.

The unbounded strands used to prestress the panels horizontally were stressed such that the pressure at the joints is more than 1.5 MPa when the tank is full. The width of the seal between the panels is 70 mm.

The following losses are present: steel relaxation of 2.5%, losses in the jack of 4% during stressing, long term creep loss of 0.83%, shrinkage loss of 2.58%, wobble and friction loss of 32.5% and wedge slip of 8 mm after seating of the wedge.

3 DEFECTS PRESENT AFTER THE CONSTRUCTION OF THE TANK

After a site investigation to ascertain the conditions of the tank constructed, it was clear that the tank was not fit to be used for molasses storage. The defects present in the tank are discussed next.

3.1 *Grout between panels*

The grout between the panels has two main functions:

1. To evenly transfer the stresses from one panel to the other.
2. To act as a water proofing barrier once the tank is in use.

Cube results for the grout used between the panels were not provided by the contractor. As a number of grout mixes were made and because the grout was in development phase, it would be expected that more than one batch of concrete cubes would be tested. It is vital that cube results are obtained as the structural integrity of the

Table 1. Cables that was not installed in the tank.

Number of cables Half of Tank	Tank Left	Right
Design	26	26
Installed	24	22
Cables not all around		4

tank cannot be determined without the results. It is important to note that since the grouting layer between the panels is thin (2 mm – 8 mm), it was not possible to confirm the compressive strength of the as-built grout without the cube results.

The grout between the must be applied at equal thickness to avoid a stress concentration in isolated areas of the precast panels as stresses are transferred from one panel to the next. From the investigation it could not be ascertained whether the grout was applied evenly.

3.2 *Stressing of un-bounded strands*

The strands are stressed in two stages. The initial stressing is performed after the construction of all panels. Final stressing is only performed once the grout between the precast wall panels has reached 30 MPa.

The final stressing of the tank was not completed as a number of cables where not installed in the tank as summarized in Table 1.

It is important to note that all cables are crucial to ensure adequate compressive stress at the joints. It was thus critical that the contractor installed all the cables as per the SMEC design.

3.3 *As-built geometry of the tank*

The geometry of the tank is of utmost importance. If the panels are not installed circular, as per the construction drawings, large stresses can be experienced between subsequent panels. With reference to Figure 4, dimension O, is calculated to be 110 mm for this tank. If this dimension is not within tolerance a stress concentration will be experienced at the interface between the two panels. The minimum allowable dimension for O is 53 mm and the maximum is 289 mm. If the dimension is less than 53 mm, two adjacent panels are almost horizontal to one another and a phenomenon named backward bending is experienced.

The as-built dimension O for each subsequent panel is provided in Figure 4.

It is apparent that panel 33-34-35 is not within tolerance. The final stressing of the tank could not commence before the panels were moved to

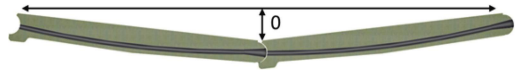

Figure 3. Geometry of the precast panels. O is the dimension from the horizontal reference line to the panel joint.

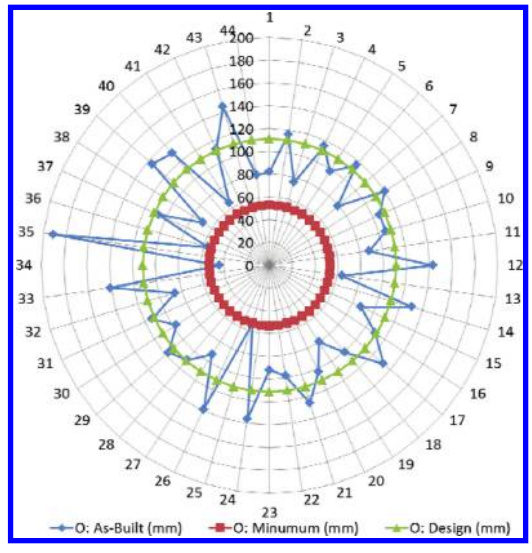

Figure 4. As-built of dimension 0 for the tank.

the correct position. The process of moving panels after the grout has hardened is very delicate. The risk of creating leaks is inevitable as the grout cracks when the panels are moved. Grout must therefore be replaced by pressure grouting, which is a specialist task.

3.4 *Sliding of the panels*

The precast panels slide on a ceramic tile as the grout between the panels settles during initial stressing and shrinks elastically during final stressing. It can be seen in Figure 5, that an adequate sliding surface was not provided. Defects in the precast panel were introduced by a restraint in sliding.

3.5 *Defects in precast panels*

The 50 MPa, vertically stressed precast concrete wall panels forms an integral part of the tank. The integrity of these panels is of great importance to ensure the longevity of the structure.

Figure 6 shows an opening cut into a precast panel to allow the stressing cable to pass through a blocked joint between two panels. This defect is at the bottom part of the tank, where the pressure is at a peak.

Figure 5. Crack of panel due to sliding restraint during stressing.

Figure 6. Defects of precast wall panels.

4 IMPLEMENTATION OF THE REPAIR OF TANK BY RETROFITTING

The repair of the tank was vital due to the high demand for molasses storage in South Africa. SMEC was appointed by the yeast company to design a solution that would allow the tank to be used for molasses storage as soon as possible. The designed solution is discussed in the following section.

4.1 *Curtain wall*

The defects of the tank was severe. Numerous remedies and retrofitting were required to repair the tank. Missing cables could not be fitted afterwards as cable ducts were blocked by grout in the joints. Due to the holes in the panels as well as missing

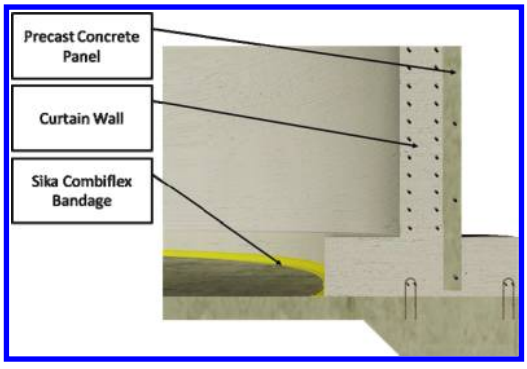

Figure 7. Isometric section of the retrofitting of a curtain wall.

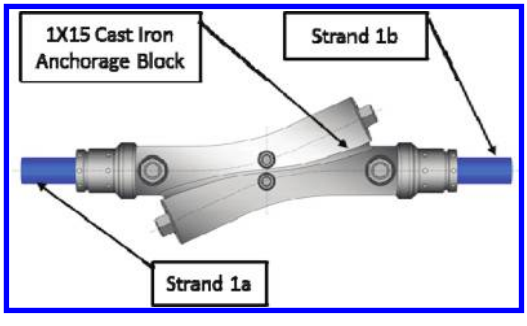

Figure 8. Freyssinet 1 × 15 Anchor known as an X-Anchor (as adapted from the Freyssinet Catalogue).

cables, a curtain wall was constructed on the inside of the tank. The curtain wall acts as a waterproofing barrier and forms a composite section with the precast panels. A sketch of the curtain wall is provided in Figure 7.

The precast panels were utilised as the external shutter during construction of the curtain wall.

A Sika Combiflex bandage was installed at the nib of the curtain wall to prevent leaks when the plinth moves during the daily use of the tank.

4.2 *X-anchors*

Three external stressing cables were installed to withstand pressure of fresh concrete during the casting of the curtain wall. The cables were further required to resist the loading of the filled tank during daily use.

The three external cables were anchored using Freyssinet X anchors. A diagram of an X-anchor is provided in Figure 9.

The external cables were guided with clips as indicated in Figure 9. Sliding plates were provided

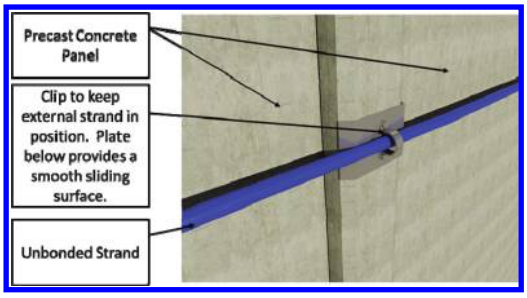

Figure 9. External stressing cables. The plate clip combination provides a smooth sliding surface.

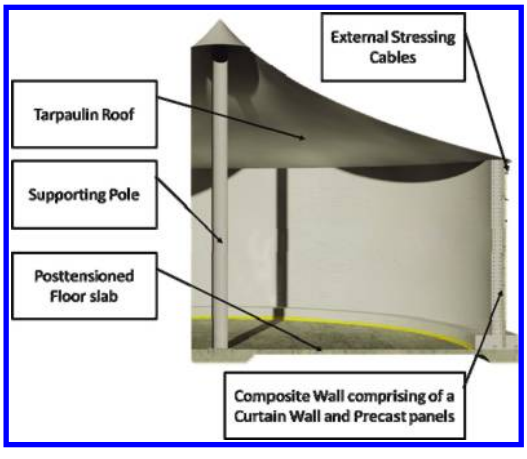

Figure 10. Section indicating external stressing cables and tented roof.

to prevent the plastic sheath from damage during installation.

A section of the repaired tank is provided in Figure 10. The external stressing cables were installed and the curtain wall was cast before the tarpaulin roof was added. The roof covered the tank to protect the molasses from the elements.

A water test was conducted in accordance with BS8007 to ensure that the tank was watertight before it was approved for molasses storage. The entire retrofitting operation was completed in two months. A photo of the repaired tank in use is provided in Figure 11.

5 CONCLUSION

A number of defects were present in the tank. The defects included, grout strength, backward bending, missing cables, roughened sliding surface for precast panels and defects in the precast panels.

Figure 11. Repaired 2ML molasses storage tank.

The tank was repaired by retrofitting external stressing cables to withstand the pressure of the molasses during the daily use. A curtain wall was used as a composite membrane to prevent leaks and to act as a structural support. The external cables were anchored with X-Anchors supplied by Freyssinet. A Sika combiflex bandage provided a leak proof movement joint on the inside of the tank. Retrofitting and repair of the tank was completed in two months. A water test indicated that the tank was watertight and ready for molasses storage.

ACKNOWLEDGEMENTS

A word of acknowledgement to Anchor Yeast for the appointment to design the repair for of the two tanks. Technical input as well as the supply of excellent construction products from both Sika and Freyssinet was vital for the project. Acknowledgment of the contractor Afristruct Projects for the quality of works during the construction of the repair.

REFERENCES

373, ACI Committee. Design and Construction of Circular Prestressed Concrete Structures with Circumferential Tendons. Manual of concrete practice, Reported by ACI Committee, n.d.

Bijan O, A. Unbonded and Bonded Post-Tentioning Systems in Building Construction. A Design and Performance Review, Pos-Tentioning Institute, Arizona: PTI Technical Notes, 1994.

Bladon, S. "Repair Techniques for Prestressed Concrete Tanks." Maintenance Tips, Micham, n.d.

Hjorteset, K, M, W Wernli, M, W Lanier, K, A Hoyle, and H, O William. "Development of large-scale precast, prestressed concrete liquefied natural gas storage tanks." PCI Journal, 2013.

Karbaschi, M E, and R and Hedayat, N Goumdarzizadeh. "Efficiency of Post-Tensioning Method for Seismic Retrofitting of Precast Cylindrical Concrete Reservoirs." World Academy of Science, Engineering and Technology, 2011.

Khaloo, A R. Design of pre-stressed concrete structures. Tehran: Sineh Sorkh publications, 2003.

Minehane, J, M, and D, B O'Rourke. "Response of Precast Prestressed Concrete Circular Tanks Retaining Heated Liquids." ACI structural journal, 2014: 247–254.

Takeuchi, H, S Taketomi, and S Samukawa. "Renovation of a concrete water tank in chiba prefecture, japan, Nanni, A;." 2004.

Taylor, R G, and P D Wright. "Innovative seismic retrofit of concrete water supply tanks." Pacific Conference on Earthquake Engineering. 2003.

Wernili, M, Ghorbani I, and M Oesterle. "Effect of differential creep and shrinkage on prestressed composite concrete sections." PCI/NBC, 2013.

Concrete Repair, Rehabilitation and Retrofitting IV – Dehn et al. (Eds)

Repair and widening of the Nels River Bridge on road R37 in South Africa

R.G. Miller & R. Nel
ARQ (Pty) Ltd, South Africa, Pretoria, South Africa

E.J. Kruger
South African National Roads Agency (SOC) Ltd (SANRAL), Pretoria, South Africa

ABSTRACT: This paper deals with the repair, strengthening, improvement and widening of the Nels River Bridge situated in the Mpumalanga province of South Africa. The paper outlines the design complexities and discusses the solutions and the construction techniques followed that resulted in a successful project.

1 INTRODUCTION

The Nels River Bridge is located on Road R37 between Sabie and Nelspruit in South Africa (GPS co-ordinates 25° 17' 26.32"S 30° 46' 1. 74"E). This bridge was unique in that it comprised two arched balanced cantilevers connected with a mechanical hinge in the centre. The hinge mechanism was on the verge of failure for a second time prompting the bridge owner and client to implement a major rehabilitation of the bridge.

This bridge is critical for access across the river and complete failure would force detours of about 30 km.

In the final solution adopted the mechanical hinge connection was fully eliminated and the deck made continuous. When the bridge was repaired it was also widened from 9.1 m to 12.4 m between parapets.

This paper presents details of the repair, strengthening, improvement and widening of the bridge. The design challenges, the solutions implemented and the construction techniques followed are discussed.

2 BRIEF DESCRIPTION OF THE ORIGINAL BRIDGE

The original bridge essentially comprised two balanced cantilever structures connected by a hinge in the centre as depicted in figure 1. The hinge mechanism allowed rotation and longitudinal movement but restrained differential vertical translation.

The 4 span bridge, comprised an arched concrete box girder type deck, as depicted in figure 2. The box girder deck contained a significant number of post tensioned cables, longitudinal and transverse with very little plain reinforcement. The fourth span on the Sabie side, isolated by an expansion joint, comprised a plain reinforced concrete solid slab type deck.

3 HISTORY OF THE BRIDGE REPAIR AND WIDENING PROJECT

The original Nels River Bridge, built in 1969, is depicted in the photograph, figure 3.

Over the first 20 years the central mechanical hinge deteriorated significantly over time with the result that in 1989 it needed to be totally reconstructed and strengthened.

However, the new hinge, in spite of being substantially heavier and more robust, also deteriorated over the next 22 years and in 2011 the joint mechanism was again found to be at the point of failure with the bridge vibrating unacceptably with high deflections under traffic. Severe concrete spalling had occurred in the deck soffit at the hinge connection. The deck revealed signs of failure with the result that the bridge owner decided as a precautionary measure to reduce the roadway over the bridge to a single lane with severe speed restrictions.

Following a tender process consulting engineers were appointed to provide the detailed assessments with recommendations for repair and widening of the bridge. They were also contracted to provide the detailed designs and drawings, facilitate the construction tenders and to monitor the construction.

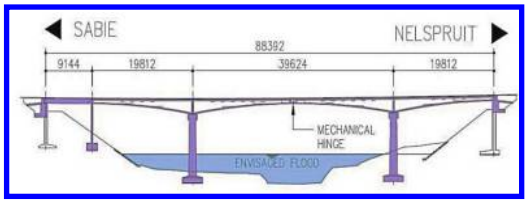

Figure 1. Section of the original Nels River Bridge.

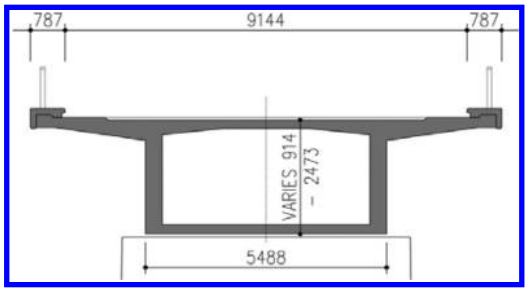

Figure 2. Cross section of the original deck

Figure 3. Side view of the original Nels River Bridge.

4 THE MECHANICAL HINGE

The central hinge connection comprised structural steel plates with slotted holes and steel pins of 90 mm diameter. As previously mentioned it allowed for rotations and longitudinal movements but provided a restraint to vertical differential translations. Refer also to figure 4.

The capacity of the bridge deck would be severely compromised should the restraint to vertical differential translations fail. This is depicted in figure 5.

An additional problem was that the existing bridge had deflected downwards at the hinge joint over the years probably due to creep. This formed a significant vertical kink in the road at the joint enhancing the dynamic load effects from heavy vehicles passing over the bridge at speed.

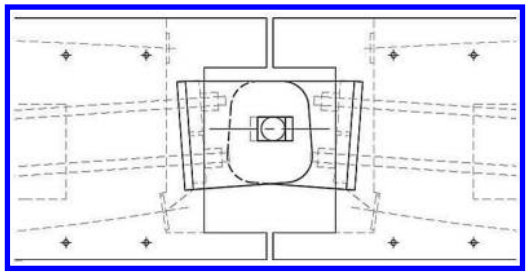

Figure 4. Schematic of the mechanical hinge.

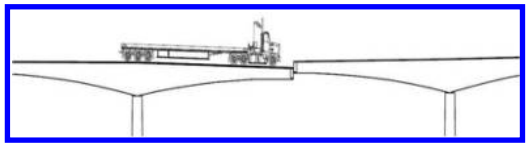

Figure 5. Vertical movements at hinge connection.

5 CLIENT REQUIREMENTS

The client's requirements for the bridge rehabilitation were the following:-

- Eliminate the mechanical hinge connection by making the deck continuous.
- Widen the bridge from 9.1 m to 12.4 m.
- Correct the road vertical alignment over the bridge.

The design methodology needed to consider that at least one traffic lane had to be kept open over the bridge during construction. Total road closures, if absolutely necessary were allowed for short periods only and the frequency of these were to be kept to an absolute minimum.

6 SOLUTIONS INVESTIGATED

Several solutions were investigated to comply with the client's brief:-

Option 1, widening on one side only, as depicted in figure 6. This option had the negative effect of having to re-align a significant part of the approach roads as well as requiring false-work in the river.

Option 2, widening on both sides, as depicted in figure 7. This option provided aesthetically the best solution and with the new slab over the old deck the re-alignment of the road could readily be implemented.

Option 3, replacement of the old bridge with a new bridge, as depicted in figure 8. An economic version of this option was one incorporating precast beams. However, this option required a new

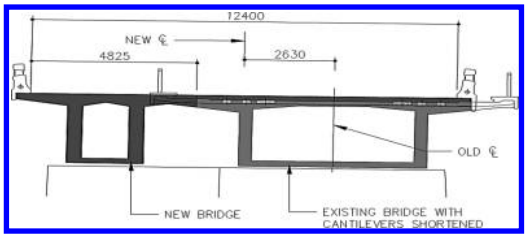

Figure 6. Option 1 – widening to one side only.

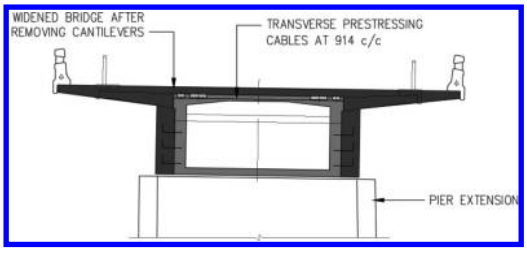

Figure 7. Option 2 – Widening to both sides.

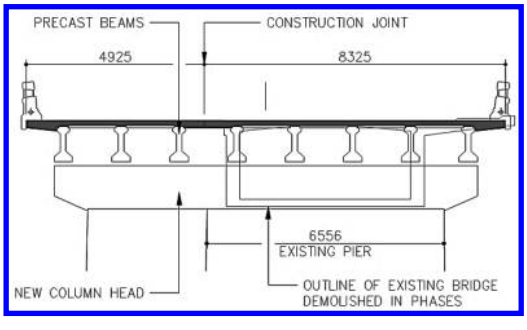

Figure 8. Option 3 – replacement of old bridge with new bridge.

pier in the middle of the river which would have been problematic from an environmental point of view. Option 3 also turned out to be the most expensive option.

From the three options, option 2 was adopted as it was cost effective and retained the form of the bridge from both an aesthetic and historic perspective.

7 ENVIRONMENTAL ISSUES

An environmental impact assessment is a statutory requirement when construction work is to take place within or near a river or waterway. The possible effects of the proposed construction on the river must be assessed.

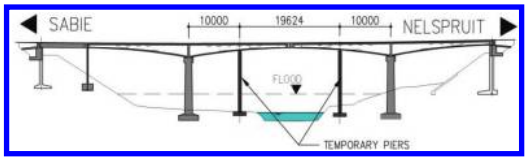

Figure 9. Temporary supports introduced on the river banks.

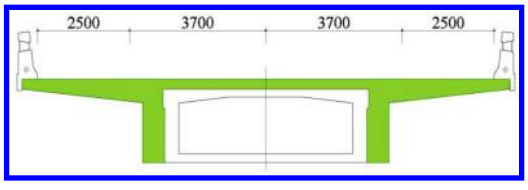

Figure 10. First deck widening / strengthening design.

The rehabilitation of the deck design required temporary supports during construction to enable the deck to carry the necessary construction loadings as well as to keep the vibrations of the deck to an acceptable level. A single, centrally placed concrete column on a spread footing, constructed in the river would have provided the best solution. This proposal was submitted to the environmental authorities but was rejected because it required the temporary deviation of the river for the purpose of constructing the temporary support foundations.

A revised design comprising two 14 m high temporary concrete support columns (see figure 9) constructed on the sides of the river, without river deviation, was then submitted and accepted.

8 INITIAL DECK DESIGN

The initial solution required that the cantilevers be cut off along the edge of the existing box girder and reconstructed in accordance with the new dimensions to allow for 2.5 m wide shoulders and 3.7 m wide lanes i.e. a width of 12.4 m between parapets (see figure 10).

The existing box girder was widened with 600 mm wide post tensioned beams on either side with new cantilevers. This beam and slab configuration would be continuous over the full length of the bridge thus eliminating the problem of the central hinge.

A slab with varying thickness was constructed on top of the deck in order to increase the section stiffness, as well as to correct the road alignment.

Figure 11. Transverse cable in Nels deck on left. Example of suitably bonded cable on right.

Figure 12. Cores introduced in deck cantilever

9 CHANGES DURING CONSTRUCTION

After construction started a core, passing through the transverse stressing cables running from cantilever tip to cantilever tip, was extracted from the bridge deck. It revealed that these cables were not bonded as they should have been (see figure 11).

Since the bridge was still under traffic the cantilevers on the one side could no longer be removed as this would affect the structural integrity of the cantilever on the other side. This methodology was deemed too risky and it was decided to revise the design in a way that did not require the removal of the cantilever.

After input from the contractor the design was changed to enable the existing cantilevers to be kept with no increase in construction cost. In order to achieve continuity with the top slab and side beams, 150 mm diameter cores were drilled through the cantilever between the transverse and longitudinal cables (see figures 12 and 13).

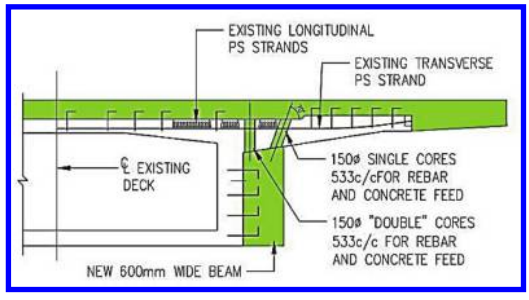

Figure 13. Revised design—cores linking new beam and slab.

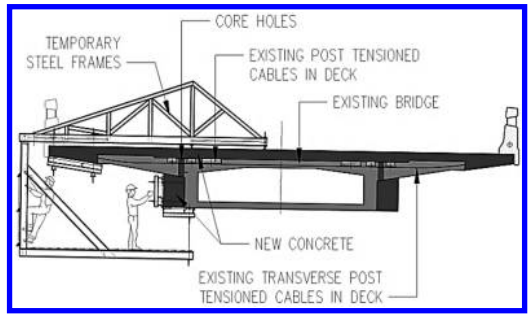

Figure 14. Deck construction methodology.

10 CONSTRUCTION

10.1 *Construction period*

Construction on the Nels River Bridge commenced on the 11th of March 2013 after having received the "Record of Decision" from the environmental authorities which stated that construction could proceed within specific environmental constraints.

The construction period was originally set at 12 months. However, due to delays the period was extended to 14 months.

10.2 *Construction methodology*

Between the designer and the contractor it was decided to construct the deck in specific steps using frames attached to and cantilevering over the side of the deck. Figure 14 provides a schematic of the procedure.

The frame support structures where costly and a limited number were manufactured to construct only about a third of the bridge length at a time on one side. Once the first third was constructed the frames would be moved towards to the second third etc. During construction there were numerous heavy trucks, carrying timber logs produced in the area, passing over the bridge throughout the day and night. The possibility of staging from the ground was therefore considered undesirable, not only due to the height involved and the river below, but also because of the differential deflections of the old bridge vs. the new concrete supported by "fixed" staging. Refer also to figure 15.

10.3 *New beams under the cantilever*

A proprietary self-levelling concrete product was used for the side beams under the cantilevers. This

Figure 15. View of bridge showing one set of temporary supports and the support frames hanging from the deck.

Figure 16. Deck construction frames and platforms.

highly flowable concrete was introduced through the core holes and well compacted concrete with strengths in excess of 60 MPa were achieved.

Care had to be taken that the shutter system was suitably sealed to prevent the flowable concrete mix from leaching out through small gaps and openings.

Two high capacity post tensioned stressing cables were provided within the beam located beneath the cantilever. These were stressed once the required concrete strengths had been achieved.

During the first placement of concrete in the beams, traffic was allowed over the bridge. This caused vibrations resulting in gaps forming in the shutter system and significant amounts of concrete leaching out. It was decided that traffic would need to be restricted during the critical concreting and curing stages. Heavy vehicles were allowed to cross one at a time at walking speed during concreting. This solved the problem but caused some traffic delay periods during curing.

10.4 *Central Hinge*

The central hinge needed to be made continuous and required special attention.

A special access frame was manufactured as depicted on the photograph in figure 16.

Continuity was achieved by dowelling steel bars into the bottom of the hinge area, by providing reinforcement continuity in the new slab over the top and the provision of the post-tensioned cables running continuous within the new beams across the central joint.

10.5 *Change in bridge continuity*

Removing the central joint of the bridge in effect made the bridge continuous for a greater length than originally designed for. The deck was supported on the piers by means of high strength concrete hinges. The piers were thus subjected to additional forces as a result of the expansion and contraction of the deck due to temperature variations. These forces were checked and found to be within design norms.

It was expected that some horizontal cracks could form near the bottom of the piers. However, this did not occur either during construction or thereafter. It transpired that the old central hinge or expansion joint was always butting or open by a few millimetres only. As a result the deck continuity did not result in significant additional forces in the piers.

At one stage it was considered to modify one of the piers to incorporate a hinge at the bottom just above the foundation. However, this solution was omitted once the behaviour of the bridge as a whole was observed.

11 CHALLENGES

11.1 *As built drawings*

The old "as-built" drawings were fortunately available. They were still in the old imperial system and not very legible. Significant time was needed to study the important information they provided i.e. most dimensions, stressing forces, reinforcement etc.

11.2 *Beam reinforcement*

The construction of the new beam underneath the existing deck cantilever caused a special problem with the reinforcement. The confined space under the cantilever called for special reinforcement detailed to the varying beam dimensions. However, the soffit of the existing cantilever was uneven and the reinforcement, planned in accordance with the

Figure 17. Soffit of deck showing new beam and widened pier head.

Figure 18. Elevation of bridge with new Parapets.

old "as-built" drawings, did not fit as had been hoped. A significant number of bars needed to be modified on site or moved to other positions. This cost the contractor quite a significant amount of extra time.

11.3 *Additional failure of the central hinge during construction*

During construction and whilst there was a lot of activity on the bridge, another portion of concrete at the central hinge spalled when a heavy truck passed over the bridge weakening the hinge considerably.

This resulted in a marked increase in vibrations of the deck under heavy vehicles making workers feel extremely uncomfortable. The contractor decided to move his workers from the deck as he felt that there were unsafe working conditions.

In order to stabilize the deck an emergency stabilizing upstand beam was introduced on top of the deck, straddling the joint, allowing the contractor to proceed with his work.

Figure 19. Roadway over the rehabilitated bridge.

11.4 *Concrete placement*

Placing the beam concrete was also a challenge. The beam concrete had to be poured through the 150 mm diameter core holes and as discussed in paragraph 10.3, was done using a self-levelling concrete product. This was poured into sealed timber formwork with varying panel sizes, purpose made to follow the arched shape of the deck. These panels needed to be well fitted and "water tight" which proved to be a challenge to the contractor.

12 CONCLUSIONS

This project was challenging and through the cooperation between the client, consulting engineer and contractor a successful widening of the bridge and elimination of the problem hinge joint resulted.

The maintenance of stability during the various stages of construction, whilst at the same time carrying heavy vehicle traffic, was obviously a most important requirement of the project and was carried out with success.

Figures 17 to 19 provide photographs of the completed bridge.

13 DESIGN AND CONSTRUCTION TEAM

Client/Bridge Owner: SANRAL (SOC) Ltd
Consulting Engineer: ARQ (Pty) Ltd
Contractor: Stefanutti Stocks (Pty) Ltd

ACKNOWLEDGEMENTS

Acknowledgement is given to SANRAL who gave permission to submit this paper.

Concrete Repair, Rehabilitation and Retrofitting IV – Dehn et al. (Eds)
© 2016 Taylor & Francis Group, London, ISBN 978-1-138-02843-2

Evaluation of repair mortar materials for old monuments in southern India

S. Divya Rani, Madhubanti Deb, Manu Santhanam & Ravindra Gettu
Department of Civil Engineering, Indian Institute of Technology Madras, Chennai, India

ABSTRACT: Mortar samples from three historical monuments in the southern Indian state of Tamil Nadu were evaluated using X-ray diffraction, Scanning electron microscopy, and Fourier transform infrared spectroscopy for their mineralogical and morphological characteristics. The results show that the lime used is of a non-hydraulic type. Additionally, several studies were performed on lab based mortars to access the parameters of compatibility to check the suitability of different renders. From the testing of lab based samples, it was observed that, for studying the compatibility of repair mortar, parameters like modulus of elasticity and capillarity coefficient play a significant role as they help to judge the rigidity and porosity of the mortar. While cement mortar proves to be very rigid for old masonry substrate, plain lime mortar is very porous. For all properties studied, the lime mortar mix with organic additives gave optimum results.

1 INTRODUCTION

There are several masonry structures of historical significance in India that require conservation. Lime binders were commonly used for the construction of masonry buildings before the large scale introduction of Ordinary Portland Cement. When modern binders are used for the repair of these structures, a lot of compatibility issues arise between the repair mortar and the substrate. The characterization of mortar used in original construction is vital for formulating a new repair mortar which is compatible with the existing structure. Groot et al. [1] state that the most effective way to characterise a mortar is to use a combination of techniques. Middendorf [2] has formulated a flowchart for the characterization of historic mortars in agreement with most of the researchers. X-ray diffraction, Scanning electron microscopy with Energy dispersive X-ray analysis, Petrographic analysis (Thin Section), Thermo gravimetric analysis and Mercury intrusion porosimetry are the commonly used techniques to understand the microstructural information of historic mortars. The characteristics of lime mortar are influenced by the binder type, i.e. whether hydraulic or non-hydraulic, the aggregate type and other additives that are added to improve the performance and durability of the mortar [3–6]. Traditionally, aggregates were sourced locally, using whatever materials were available. In India, builders have used a wide variety of organic materials in lime mortar for enabling several desired properties, which makes the system more heterogeneous compared to the rather standard hydraulic binders used in Europe. Jute fibres, jaggery, gallnut powder, pulses and cereals, milk products, palm candy, aloe vera, animal hair, oils and fats, egg whites etc. are some of the commonly used traditional additives [4–6]. Traditional manufacturing and mixing techniques are also found to vary widely, creating wide ranging effects on the performance of the material. Bindiganavile and Suresh [5] characterized historical mortar samples from the late 18th C. in Srirangapatna, a town near Mysore in southern India and concluded that they were lime-mortar samples with significant MgO content. Their results confirm the use of natural fibres, most likely derived from animal sources in one of the sites investigated. Unfortunately there is not much information in literature about the ancient technology of mortar preparation. Traditional masons employed different additives to reach the desired properties based on the knowledge passed on by generations or by intuition and such knowledge and experience are extinct today. In the present study, historic mortars from three different structures are characterized to give a technical insight into the formulation of repair mortar.

While designing a repair mortar, it is essential to weigh different physical factors according to their importance. For the same, several compatibility studies have been carried out in this field to assess some parameters of compatibility to check the suitability of different renders. It is widely accepted that the lime binders have greater permeability

than OPC, enabling them to reduce moisture entrapment by their inherent 'breatheability'. According to Penas [3], the compressive and flexural strength of mortar containing air lime as binder is less than mortar containing hydraulic lime. The dynamic modulus of elasticity is low and therefore the render will not transmit high stresses on the substrate but at the same time it is high enough to assure sufficient durability. Higher value of modulus of elasticity indicates higher rigidity and therefore the incapability of the mortar to accommodate masonry movements without degradation. The mortars have high capillarity coefficient suggesting fast absorption of water but at the same time they have high value of water vapour permeability, indicating that the mortar will dry fast. Thirumalini et al. [4] studied the effect of adding the juice of natural materials like gallnut and jaggery to the mortar and suggested that treating lime mortar with 5% of herbal juices provides greater flexural, tensile and compressive strengths by 1.6, 3, and 2–5 times respectively. For the lab based investigation in the present study, gallnut and jaggery are used as organic additives as these are reported to have been used widely in southern India.

2 MATERIALS AND METHODS

2.1 *Characterisation of historic samples*

The historic mortar samples were collected from the following temple sites, (i) Veetrirundha Perumal temple at Veppathur village near Thanjavur in Tamil Nadu which is 2000 years old (ii) Sri Kolavilli Ramar Temple in Thiruvelliyankudi village, near Kumbakonam in Tamil Nadu, where the temple complex is said to be 2000 years old and (iii) Brihadisvara Temple at Gangaikondacholapuram in Tamil Nadu, which is one of the great living Chola temples and a UNESCO World heritage site, built 1000 years ago. Representative samples were collected and stored in air tight containers. Samples were air dried and powdered to a size less than 75 µm for X-ray diffraction analysis (XRD). For Fourier Transform Infrared Spectroscopy (FT-IR), samples were prepared by grinding a known mass of solid with dried KBr. The resulting powder was then pressed at 2000 psi for 5 min to produce a pellet for analysis. The wave number ranges analysed were from 400 cm^{-1} to 4000 cm^{-1}. Broken chunks were used for Scanning Electron Microscopy (SEM) and Energy Dispersive X-ray Analysis.

2.2 *Study on simulated mortars*

For the lab based investigation, a pure lime mortar, cement mortar and a lime mortar mix with organic additives was prepared. The lime used for the mortar preparation was procured from Pollachi, Tamil Nadu, which confirmed to class C lime upon testing. The cement used is Ultratech OPC (Ordinary Portland Cement) grade 55. Raw jaggery and gallnut powder were added as organic additives. The sand used is standard sand conforming to IS 650–1991. Modulus of Elasticity, Water Sorptivity, Compressive and Flexural strengths were tested at 14, 28 and 56 days as per the relevant standards The cement/lime to sand ratio was 1:3 and the mortar was mixed with the specified quantity of water/jaggery and gallnut juice i.e., 0.5 and 0.7 water to cement/lime ratio for cement mortar and lime mortar respectively. The cubes were demoulded after 1 day of casting for cement mortar and cured in lime solution until the required age of testing. The lime mortar cubes were demoulded after 3 days of keeping them in air. Later they were air cured at 25°C and 65% RH until the required age of testing.

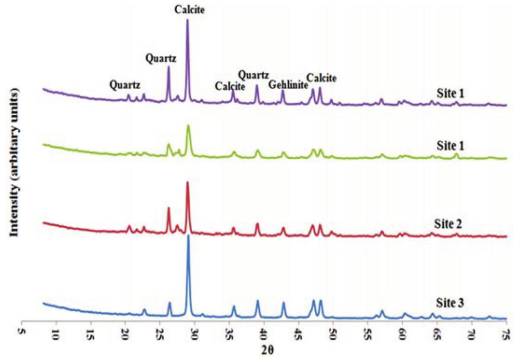

Figure 1. Diffractogram data of mortars from 3 different historic sites.

3 RESULTS AND DISCUSSION

3.1 *X-ray diffraction*

Figure 1 shows the x-ray diffractogram of historic samples compared among each other. The presence of calcite ($CaCO_3$) is clearly evident in all the samples and other minor peaks contribute to the silicates present in aggregates. The peak at 43 °2θ could be of gehlinite (C_2AS), however the other peaks of gehlinite could not be observed. There is no amorphous hump indicating the absence of any calcium silicate hydrate. Also, larnite and portlandite peaks are absent. These observations lead to a conclusion that the lime used was non-hydraulic in nature.

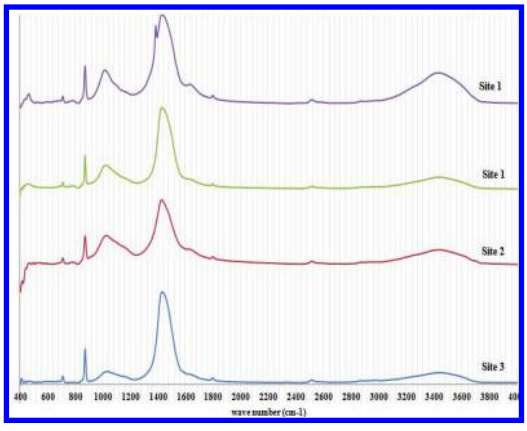

Figure 2. FT-IR spectra of mortars from 3 different historic sites.

3.2 *Fourier Transform Infrared Spectroscopy*

The FT-IR absorption spectrum of the same samples is shown in Figure 2. The bands at 712, 875 (C-O bend), 1440 (C-O stretch), 1790, 2515 and 2854 cm^{-1} correspond to calcium carbonate forms. Band at 3200–3600 cm^{-1} are due to O-H stretch bond, which could be due to the presence of moisture. The broad peak at 1000–1200 cm^{-1} can be attributed to polysaccharides or sucrose, which could possibly indicate the presence of an organic additive.

3.3 *Scanning electron microscopy*

The photomicrographs obtained from SEM analysis are presented in Figure 3(a-f). Depending on whether the lime is non-hydraulic or not, the compounds may be calcite or calcium silicates and aluminates. The dominant presence of calcite crystals can be seen in all the samples (highlighted in the images). Other minor elements present are Si, Al, Fe, Mg, Na and K. As the XRD analysis also suggests the lime to be non-hydraulic, the conclusion may be that most of the compound is in calcite form and the silica and alumina are from the aggregates. Also, the lime could be inherently impure which imparts a feeble amount of hydraulicity. The increased porosity of the matrix is another observation; dark regions in the image indicate pores or voids.

3.4 *Study on lab based specimens*

The results of lab based specimens are presented in Table 1. From the results it can be seen that the compressive and flexural strength of cement mortar is much higher than the lime mortar mixes. From

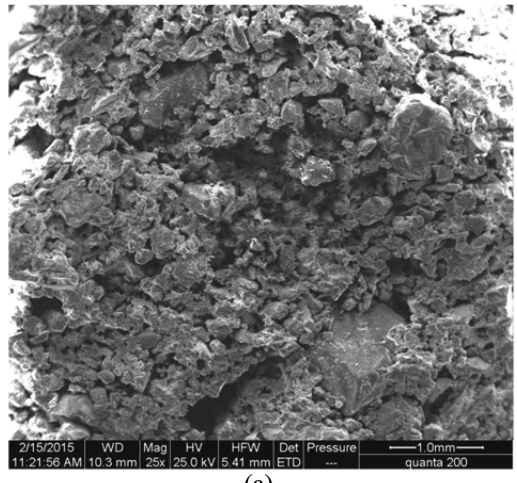

(a)

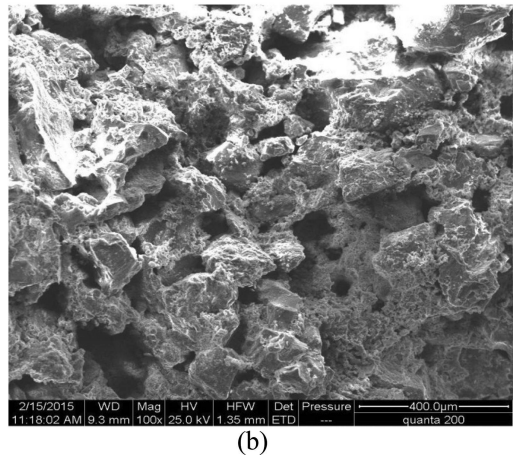

(b)

Figure 3. SEM micrographs showing features of calcite deposition, indicating non-hydraulic lime.

the studies of Penas [3] it is stated that the ideal range for repointing mortar to be used in conservation works should be between 0.6–3.0 MPa for compressive strength and 0.4–0.8 MPa for flexural strength. Thus, cement mortar can be found to be stronger than the substrate rendering it unfit for the purpose. Both the lime mixes have compressive strength in the prescribed range and can be considered suitable for repair of historic masonry. Also, as per Rodriques and Grossi [7], the compatibility risk is the highest in case the strength is more than 50% of the strength of the value prescribed in literature. In this case, the cement mortar shows highest risk in terms of compatibility and both the lime mixes satisfy the condition with minimum risk of incompatibility.

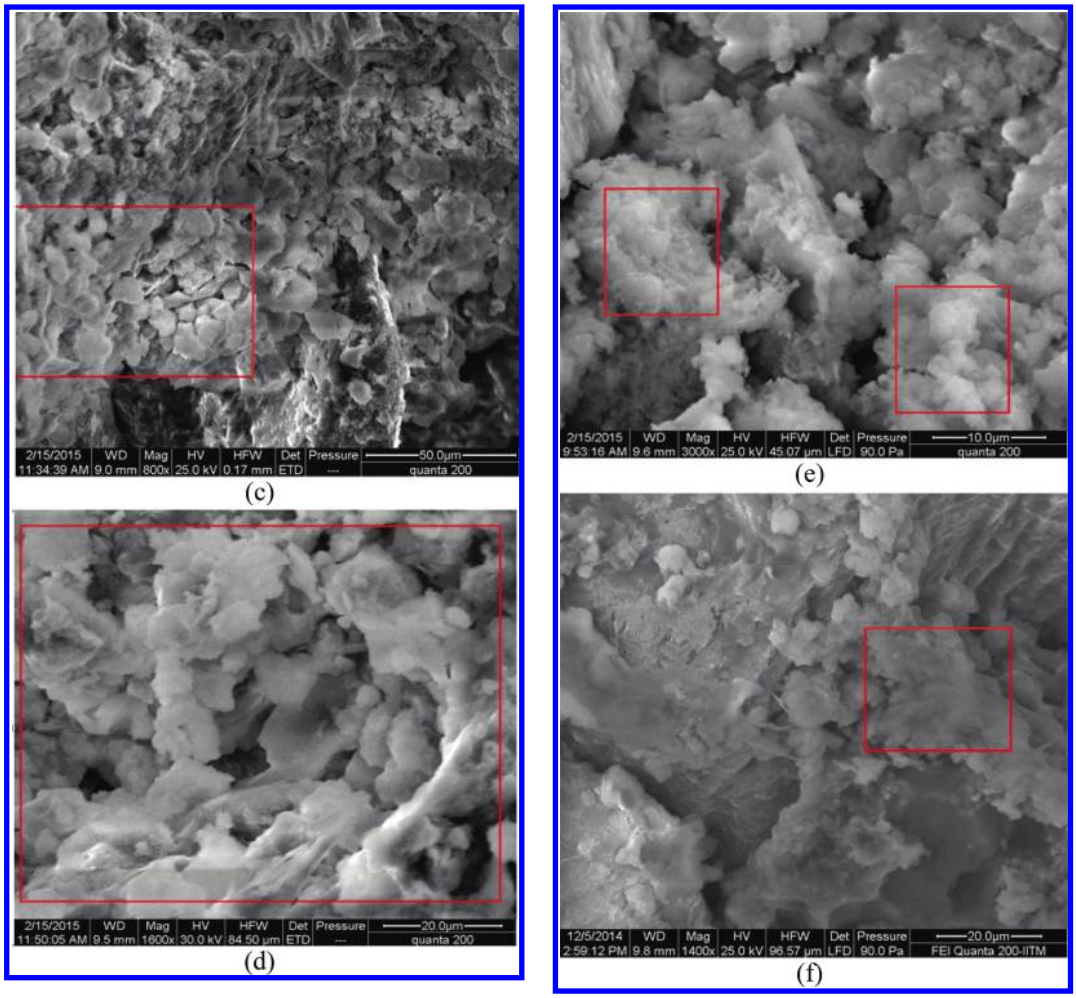

Figure 3. *Continued.*

The capillarity coefficient of lime mortar mix with additives has values within the prescribed range that indicates an optimum amount of porosity compatible with the substrate material. Similar to the previous case, cement mortar shows high risk in terms of compatibility. In this case, the plain lime mix also shows high risks of compatibility as the value is higher than 50% of the prescribed value. However the value for the lime mix with jaggery falls under lower compatibility risk category. The dynamic modulus of cement mortar is very high suggesting that the matrix is too rigid. The values for both the lime mixes are within the prescribed limit and thus they are fit for using as repointing mortar in conservation works. The compatibility risk is the highest in case the strength is more than 50% of the prescribed value. Similar to the previous cases, in this case also cement mortar shows the highest risk in terms of compatibility and the plain lime mortar and lime mortar with additives show lower risks of incompatibility.

4 CONCLUSIONS

The salient conclusions drawn from the study are as follows:

- The historic samples studied are lime mortar samples and the lime is found to be non-hydraulic in nature.
- The lab based studies prove that the cement mortar is very rigid for old masonry substrate, and plain lime mortar is very porous.

Table 1. Results of lab based investigations on mortar.

	CS *	FS **	CC ***	DM ****	SM *****
Plain Lime Mortar					
14	0.90	0.90	8.10	6.90	4.10
28	1.10	1.30	8.50	5.80	3.50
56	1.30	1.80	8.20	7.40	4.50
Lime Mortar with Additives					
14	1.20	0.40	1.40	9.20	5.50
28	1.45	1.20	1.85	20.70	6.40
56	1.65	2.50	1.30	12.20	7.30
Cement Mortar					
14	31.0	8.50	0.50	42.0	25.0
28	39.5	9.50	0.60	44.0	26.50
56	49.0	10.80	0.45	48.0	29.00

*CS – Compressive Strength (MPa)
**FS – Flexural Strength (MPa)
***CC – Capillarity Coefficient (kg/m^2.√hr)
****DM – Dynamic Modulus of Elasticity (GPa)
*****SM – Static Modulus of Elasticity (GPa)

- Cement mortar is stronger than the two mixes of lime mortar tested. However, it was observed that for studying the compatibility of mortar with the substrate, strength parameter does not play an important role. For compatibility studies, parameters like modulus of elasticity and capillarity coefficient play a more important role as they help to judge the rigidity and porosity of the mortar.
- The lime mortar mix with jaggery and gallnut powder gave optimum results and lower risk of incompatibility, which indicates that the organic additives used traditionally helped in optimising strength, flexibility and porosity of the matrix.

REFERENCES

[1] Groot, C.J.W.P., Bartos, P.J.M., Huges, J.J., *Historic Mortars: characteristics and tests-concluding summary and state of the art*, University of paisley, 12–14th May, 1999.

[2] Middendorf, D., Baronio, G., Callebaut, K., Huges, J., "Chemical-mineralogical and physical-mechanical investigations of old mortars", *Technical Report—RILEM TC 167-COM: Characterisation of old mortars with respect to their repair*, 2010.

[3] Penas, F.E. (2008), "Hydraulic lime mortars for wall renderings." <https://fenix.tecnico.ulisboa.pt/publico/department/thesis.do?method = showThesisDetails&selectedDepartmentUnitID = 1911260507879&thesisID = 2353642203634>, (June, 2014).

[4] Thirumalini, P., Ravi, R., Sekar, S.K. and Nambirajan, M., "Study on the performance of lime mortar used in ancient temples and monuments in India", *Indian Journal of Science and Technology*, 4(11), 2011, pp. 1484–1487.

[5] Bindiganavile, V. and Suresh, N., "Characterization of Historical Lime Mortar from 18th Century Relics in Srirangapatna, India", *International Conference on Rehabilitation and Restoration of Structures,* Indian Institute of Technology, India, 12th-16th February, 2013.

[6] Karandikar M. V and Khadilkar S. A, " Durable mortar and concrete through use of natural materials with biopolymers—A review", *Indian Concrete Jounal-Special Issue-Future Cements*, July 2014, pp 84–100.

[7] Rodriques, J.D. and, Grossi, A. (2007). "Indicators and ratings for the compatibility assessment of conservation actions." *Journal of Cultural Heritage,* 8(1), pp 32–43.

Concrete Repair, Rehabilitation and Retrofitting IV – Dehn et al. (Eds)

Selection procedures for concrete repair—patch repair and cathodic protection in atmospheric zones

F. Papworth, J. Dyson & M. Marosszeky
BCRC, Australia

ABSTRACT: There are many systems for patch repair and for Cathodic Protection (CP) of concrete structures and the specifier is often unclear what systems should be used under which circumstances. This paper provides methodologies for selecting the appropriate systems. The first selection is whether cathodic protection will be used as part of the repair approach. Key factors are the extent of current and future corrosion, the significance of having to breakout contaminated concrete, design life of the repair, required reliability, access for maintenance and funds available. Where patch repairs are to be undertaken a decision has to be taken on structural aspects of the repair, control of incipient anodes and how to ensure the repair will meet the design life requirements. For situations where CP is attractive a system to select the system that best meets the client needs has been developed in line with two key themes: cost and suitability. Cost considers initial and maintenance cost. Suitability includes reliability, installation speed, customer friendliness, flexibility and aesthetics. A weighting system is given to each component. The paper describes the CP selection method and outlines how it was applied for the evaluation of one project. The paper includes an outline of the benefits of different anodes.

1 INTRODUCTION

Although Cathodic Protection (CP) systems for above ground structures have been used for over 30 years in Australia many designers and contractors involved in small to medium sized concrete repair projects consider it a complex and expensive method and give it no consideration for projects they manage. Owners of these project are even less informed and rely entirely on the designer or contractor who they consider the expert. Hence on many projects no consideration is given to the life cycle cost savings, better structural outcome or improved performance and repair reliability that cathodic protection can provide. The paper provides some insight into these benefits and explains how parties not experienced in cathodic protection might consider its application.

The term cathodic protection is sometimes misused and applied to any system where an anode is installed to polarise the reinforcement, regardless of the extent of that polarisation. Cathodic protection is defined in ISO 12696 (International Standards 2011) and specific requirements are listed for achievement of cathodic protection. Other terms such as cathodic prevention and corrosion control are sometimes used to describe anode systems that provide low levels of polarisation. The meaning of these terms are discussed.

Current codes dealing with cathodic protection of concrete above ground provide little guidance on how to select anode systems. ISO 12696 Appendix C (International Standards 2011) and AS 2832.5 Appendix D (Standards Australia 2002) give a little information on anode types and Concrete Society TR 73 Appendix A and B (Concrete Society 2011) provides significantly more information but none compare systems or provide a means of selecting the most appropriate anode. Similarly, text books on corrosion of steel in concrete (Broomfield 2007; Chess & Broomfield 2014) outline some advantages of different anode systems but do not provide a systematic approach to selecting the most appropriate anode for a project. A summary of the different anodes systems based on these references and the authors experience is given in Appendix 1.

In many cases this means CP contractors offer the cheapest solution available to them, which may not be the cheapest solution available or the solution that best meets the client's needs. In this paper an approach is outlined that systematically identifies what will best suit the client's overall needs. The system is relatively simple and can be easily managed by a non-CP expert. The system can incorporate any anode system in a non-prejudicial way so that the client will be sure of getting the best system for his project if the system is followed.

2 SELECTING THE REPAIR APPROACH

When reinforcement corrodes and causes concrete to crack, spall or delaminate, the repair designer has to determine the approach to adopt for inspection and repair. Typically the first step is to determine if the issue will only ever be localised or if it is a much wider future problem. This can be determined using visual inspection, drummy testing, electrical potential measurement and cover testing.

Commonly chloride ingress, carbonation and cover are relatively uniform and hence initial distress will be followed by widespread distress. On a bridge deck in Western Australia delaminations increased from 20% to 80% in the two years between first inspections and letting a repair contract. Conversely on a LPG tank in Western Australia a few lower cover bars caused distress but cover distribution assessment identified the probability of wider future corrosion was low. Hence, testing is always required to identify the extent of repair required.

One of the most common techniques for assessing the extent of corroding reinforcement is to test the reinforcement's electrical potential. Although taking measurements is simple interpretation of the results requires great care. Various misinterpretations have been identified on Australian projects:

a. Highly negative potentials interpreted as being due to corrosion. Concrete had been cast in permanent PVC forms before exposure for testing. No causes of corrosion were apparent so this, and the formwork type, should have led to the conclusion that low potentials were due to oxygen starvation.
b. Potentials in the range +50 to –150 mv $CuSO_4$ interpreted as indicating corrosion due to high potential differentials. The results were for passive steel in uncontaminated concrete.
c. Potentials in the range –300 to –350 mv $CuSO_4$ interpreted as indicating no corrosion as the potential differences were low. The potentials were active corrosion in carbonated concrete.
d. Potentials of –150 mv $CuSO_4$ on a new water tank interpreted as the tank requiring CP because potentials were approaching –200 mv which would indicate a heightened corrosion risk. Potentials were in the passive range.

In each case those taking the potentials took the measurements correctly but did not consider the exposures effect on anodic and cathodic polarization curves when assessing the results.

Once testing has been undertaken the first step in the repair decision process can be made. Repairs to only evidently distressed concrete is only likely to be an acceptable approach if:

– Corrosion initiation is localised (e.g. low cover areas),

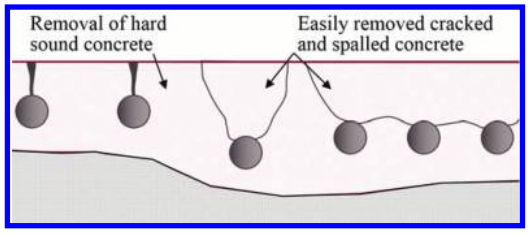

Figure 1. Typical area of concrete breakout where no cathodic protection is employed. Breakout of sound concrete behind reinforcement is highly expensive.

– There is a wider problem but the owner accepts additional repairs will become necessary in a relatively short time frame. This may occur if the immediate maintenance budget is limited.
– The structure has a short design life requirement, hence short-term holding repairs are adequate.

Where a long term repair is required and chloride ingress or carbonation is widespread then the decision becomes whether to use cathodic protection to eliminate the break out of sound but chloride contaminated/carbonated concrete or to break out around actively corroding reinforcement to remove sound but chloride contaminated/carbonated concrete (Figure 1).

Breakout of sound concrete can be a noisy process disturbing tenants and lead to expensive structural support requirements. If impressed current (ICCP) or sacrificial anode (SACP) cathodic protection are used, only loose concrete needs to be removed. ICCP gives a 50+ year design life but has high cost for design and maintenance while SACP has a 15–20 year life and low design and maintenance requirements.

3 TYPES OF REPAIR SYSTEMS

3.1 *Patch repair*

Typically patch repairs require breakout behind the reinforcement to remove chloride contaminated concrete. With no testing for the extent of chloride activated reinforcement beyond the distressed area conventional practice is to breakout 150 mm beyond the evident area of corrosion. The repair would typically include an isolation coating or zinc rich coating on the reinforcement.

3.2 *Patch repair plus incipient anode protection*

Similar to above (3.1) but low powered sacrificial anodes are incorporated around the edge of the patch to prevent corrosion of incipient anode areas (refer Section 4). Because the anodes do not

provide cathodic protection breakout and patching around the bar is still required with all the associated issues.

3.3 *Patch repair plus local cathodic protection*

In this technique higher powered cathodic protection sacrificial anodes are embedded within the repair patches to provide local cathodic protection. This means that breaking out behind the bars is not required. They also provide incipient anode protection. The repair is still localized as the anodes only protect for a limited area around the patch. Protection can be extended by using discrete sacrificial anodes with high output.

3.4 *Sacrificial anode cathodic protection*

There are various sacrificial anodes systems (surface applied, discrete and embedded) that provide high enough polarization to give cathodic protection in accordance with CP code requirements. The zinc of such anodes is consumed much faster than the lower power output anodes used for cathodic prevention. Hence a significantly higher zinc mass is required for the same life.

These systems are very simple to install as they require little monitoring. On small projects a risk analysis can be used to determine whether any monitoring is appropriate. Generally it is not as the systems are used to minimize cost and monitoring provides no great benefit. On larger projects it is likely that monitoring of a limited number of areas would be appropriate to validate the system performance.

3.5 *Impressed current cathodic protection*

The typical repair approach where there is widespread corrosion activation is to patch the corrosion damaged areas (no breakout of sound contaminated concrete required) and apply impressed current cathodic protection (ICCP) to all actively corroding areas. The systems are expensive to design, install and maintain but because they have a long life and proven performance they are frequently the repair system of choice for major projects.

4 CATHODIC PREVENTION

Over 30 years ago it was identified that when just visibly distressed areas were patched the areas around the patch failed a short time later. This is called the 'incipient anode' or 'halo effect'.

To provide protection to the incipient anodes low powered sacrificial anodes were introduced.

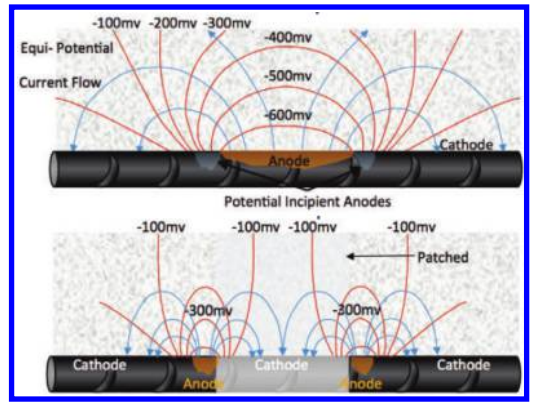

Figure 2. The top sketch shows the potential field for an anode area surrounded by an area of slightly more positive potentials. At this stage the anode cathodically protects the surrounding area that would otherwise be anodic. The lower sketch shows the same bar after repair has passivated the previously anodic area such that the surrounding area becomes the new anode.

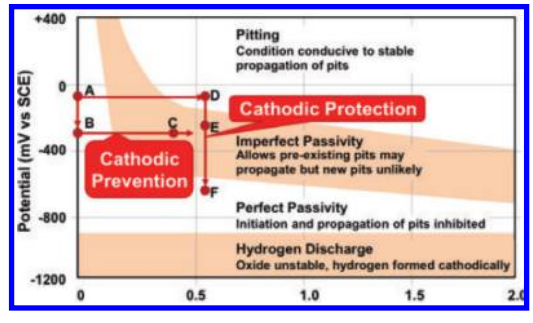

Figure 3. Sergi's (Sergi 1999) simplification of Bertollini's (Bertollini 1993) two domains of electrochemical behaviour of steel in concrete explaining the significance of reinforcement polarisation on corrosion control—cathodic prevention and cathodic protection.

These replaced the once anodic but now passivated reinforcement as the polarizing agent and gave a degree of protection to the incipient anode. Figure 2 diagrammatically explains this process. There is some debate about the incipient anode process as another theory suggests potential incipient anodes, i.e. cathodic zones, would generate hydroxyl ions and chloride ions would be drawn to the anode. In theory this could make the incipient anode areas quite passive but in the authors practical experience the process outlined in Figure 2 generally applies.

Cathodic prevention and cathodic protection are two very different processes used in different circumstances (see Section 3). The processes are described in Figure 3. For cathodic prevention a

small shift in the potential of uncorroded reinforcement (incipient anodes) leads to an increase in the chloride activation level (A → B → C). If the anodes have sufficient power to polarize the reinforcement a little more they will provide a little slowing of the corrosion rate, sometime referred to as corrosion control, but this is not cathodic protection. The same small shift in potential for corroded rebar would not fully protect the active steel (D → E). A much higher shift (D → F) is required to give cathodic protection to corroding reinforcement.

5 CATHODIC PROTECTION

Cathodic protection systems supply negatively charged electrons to the reinforcement that cause a shift in electrical potential to a more negative potential. This potential shift can be measured using reference cells embedded in the concrete.

ISO 12696 (International Standards 2011) provides general information on what inspection measures should be employed and lists general repair consideration, i.e.:

- designed, tested and installed to meet its intended life
- monitoring using reference electrodes to show the system complies with standard potential shift criteria
- anode current densities not to exceed design values

The two main types of cathodic protection systems are Impressed Current Cathodic Protection (ICCP) and Sacrificial Anode Cathodic Protection (SACP). Major differences between ICCP and SACP systems are shown in Table 1.

Table 1. Major differences between ICCP and SACP.

	SACP	ICCP
Current availability	Anode consumption rate limited	Virtually limitless.
Reinforcement polarisation	Limited (no hydrogen embrittlement risk	Variable depending. Should be limited to mitigate hydrogen embrittlement, particular in prestressed concrete.
Monitoring cost	Low. No monitoring.	High, hence not as suitable for remote areas.

6 COMMON CP SYSTEMS

SACP, or galvanic anode, systems typically cost more for the anodes relative to ICCP systems and have a shorter design life of 15–20 years (hence may need replacing). However, they have significantly lower design, installation and monitoring costs compared to ICCP systems.

Typically SACP systems are more cost effective for shorter (≤20 yr) design lives or smaller repair areas where the cost of design, wiring, control system and maintenance make ICCP system uneconomic. ICCP systems are more cost effective for longer design lives or larger repair areas.

To give some perspective Roads and Maritime Services in NSW state they have many issues with bridges in NSW and ideally they would roll out ICCP systems. However, due to budgetary constraints they are developing SACP systems with a 15–20 year life as they cannot afford ICCP systems.

There are many different ICCP and SACP systems available. Types of cathodic protection systems include:

- Surface applied sacrificial anodes.
- Internal sacrificial anode systems.
- Mixed Metal Oxide (MMO) ribbon mesh
- Net MMO anode systems.
- MMO Sawtooth ribbon anode systems.
- Discrete/tube anodes.
- Lightweight surface mounted MMO anodes.
- Conductive coating ICCP systems.

7 CP SYSTEM COMPARISON

The authors have developed a procedure for system comparison to assist the designer in selecting the most appropriate system for a particular project.

7.1 *Evaluation process*

The evaluation process has four steps:

1. Establish owner preferences. The designer determines the owners' values in regards reliability, speed of installation, intrusiveness during installation, flexibility and aesthetics.
2. Review CP systems. A five point scale is used to assess each of the acceptance criteria and a weighting applied that is specific to the project (Table 2).
3. Indicative pricing. The systems that best meet the client preferences are then priced to give a dual assessment (Table 3).
4. Specification. The systems that are both economic and meet the client needs are incorporated into the CP specification so that they can be priced by the market.

A ranking and weighting approach is applied to the acceptance criteria. This is designed to determine how well the system meets the building owner's requirements for the structure. These criteria fall into two broad categories—suitability and cost.

7.2 *Suitability factors*

Suitability factors are assessed first and any anodes not meeting the owners preferences are discarded. Remaining systems are then assessed based on both factors.

Reliability – Systems that have inbuilt resistance to acid generation get a high score. Mesh and durAnode4 score reasonably high due to their robustness and proven performance. Ribbon anode reliability would be improved if acid proof grout were used. Reliability has a high weighting as owners will be opposed to systems that are disruptive and costly in the future.

Install Speed – Owners prefer to have work completed quickly. However this has low weighting compared to reliability.

Customer Friendly – Noise and dust are the primary consideration. This has low weighting compared to reliability.

Flexibility – Flexibility is of principle interest in determining the ease to which a system can be adapted to a situation. For walls with global application this has a low weighting. For soffits where systems may need to follow cracks it has a higher ranking.

Aesthetics – Weighting depends on the type of structure, context and owners preference.

7.3 *Cost factors*

It can be tempting for owners to focus predominantly on initial cost particularly when available budget is limited, but maintenance cost is also considered to enable whole of life (life cycle) cost to be assessed.

Initial Cost – The cheapness of each system is calculated. Because the ranking is based on broad cost bands effects of minor inaccuracies are removed and, if there were no significant difference in cost between anode systems, they would all rank the same, i.e. the ranking is based on a cost scale rather than a relative scale. This is given a high weighting as initial cost has higher significance than maintenance costs that are sometime in the future.

Maintenance Cost – This is a broad classification of the estimate of maintenance cost. Hence there are only minor variations associated with possibility of needing to replace anodes. If galvanic anodes need replacing at short intervals the maintenance cost might be higher. As ICCP systems require six monthly inspection none of the systems has a low maintenance cost.

The aim of this CP system comparison method is not to enable a final CP system decision based solely on the weighted Cost and Suitability scores but rather to act as an informative guide to assist owners/stakeholders in making a decision. Where anode systems are shown to be positive or negative on the cost or acceptance scores the reason behind that score should be reviewed to ensure the scores give a reasonable impression of the anode acceptance.

8 PROJECT CASE STUDY

On a recent project where large areas of reinforced concrete structural elements required cathodic protection to achieve a future service life of 40+ years, the authors compared ICCP systems available for each type of structural element (slabs, columns, walls, beams) using the system described in Section 7. SACP systems were excluded from the comparison due to the long service life requirement and large extent of cathodic protection coverage.

8.1 *Weighting factor*

To combine the various acceptance criteria a weighting system is used to describe the relative importance of each item. The weighting is developed for each project, and possibly each element, from the discussions with the owners. The weighting for the case study is given in Table 2.

8.2 *ICCP anode systems*

There are a multitude of anode systems available but the number readily available in Australia is limited. Principle systems being marketed were compared for the project. All anodes were Mix Metal Oxide (MMO) coated titanium. This is the standard material used in CP systems but there are limited manufacturers that produce high quality products. The anodes are described below.

Table 2. Acceptance criteria weighting system.

Item	Acceptance criteria	Weighting
A	Initial Cheapness	10
B	Maintenance Cheapness	5
C	Reliability	7
D	Initial Speed Application	3
E	Customer Friendliness	4
F	Flexibility	3
G	Aesthetics	3

Sawtooth ribbon – This solid ribbon is bent to create ridges and troughs at close centres. It can be installed in small saw cut slots. It could have been suitable for all locations on the project as it is reliable and has low cost per linear meter due to material and installation methods. The drawback is the number of slots and hence high lineal meterage required.

Ribbon mesh – This is a fine mesh to create a high surface area. Like saw tooth ribbon it is grouted into slots in the concrete. The slot can be a saw cut but sometimes the depth would be too great and it is cast in a reamed slot. The ribbon is highly reliable in atmospheric exposures. Where installed in splash or tidal zones grout resistivity variations along the anode line can lead to localized current dumping. This can lead to acidification locally and failure.

Expanded mesh or net – Mesh can be applied over the entire concrete surface. The surface area is less critical in this case and so the net grillage can be more open. This more open nature is important as after pining the net to the concrete surface it is covered with a mortar to make the ionic connection to the concrete substrate. The systems are highly reliable except that application of the mortar layer can be difficult in splash and tidal zones.

Discrete / Tube anodes – These anode are generally lengths of ribbon mesh shaped to go into a hole drilled in the concrete. Tubes and star shapes provide high surface areas and this minimizes the number of anodes required to achieve a set level of current output. As the anodes are buried in the concrete they are very reliable including wet areas.

Cassette – Essentially this is a surface mounted ribbon mesh. The mesh is enclosed in a totally corrosion resistant tray with concrete contact via a felt pad. It has a high speed of installation so can be highly cost effective. Being acid resistant it can be reliably used in wet areas. Its drawback is that it is cannot be made to look attractive and hence is generally only used in basements, bridges, tunnels, wharves and industrial structures

corroDisc R – This surface mounted precast mesh anode in an acid resistant mortar is suited to all exposure zones as its output is high, it is simply installed and is reliable. Aesthetically it is rated lower than fully embedded systems but the anodes can be applied in a pattern to make the overall appearance suitable for most structures.

durAnode4 – This is a small diameter tube anode system that is simple to install due to the small diameter hole required. It is also a well-developed system in terms of control (inbuilt resistor), installation (grouting system) and reliability (proprietary) connection system.

Table 3. Ranking system.

a) Cheapness class		b) Ranking method	
Limit ($/m)	Classification	Classification	Ranking
<300	Very High	Very Low	1
<350	High	Low	2
<400	Moderate	Moderate	3
<450	Low	High	4
>450	Very Low	Very High	5

Table 4. Anode ranking for columns.

	Cost		Suitability				
Anode type	Init	Maint	Rel	Spd	Frnd	Flex	Asth
Tube Anode	2	3	2	3	3	4	5
Cassette	4	3	5	5	5	3	3
CorroDisc	5	3	4	4	5	4	4
durAnode4	3	4	4	4	4	5	5

Table 5. Weighted ranking of acceptance criteria (columns).

	Cost		Suitability				
Anode type	Init	Maint	Rel	Spd	Frnd	Flex	Asth
Tube Anode	20	15	14	9	12	12	15
Cassette	40	15	35	15	20	9	9
CorroDisc	50	15	28	12	20	12	12
durAnode4	30	20	28	12	16	15	15

8.3 *Analysis for elements to be protected*

The results and conclusions from the comparison for each element are described below.

Costs are ranked for an element type based on broad classifications of cheapness. To give a scoring system where a high number is a positive, low cost is considered as highly cheap and would get a ranking of 5. Table 3a) shows the ranking system as developed for the columns. The cost bands are not fixed but are developed to cover the range of costs expected for each element type.

The ranking method in Table 3b) is applied to cost (cheapness) and suitability factors. A high number for both factors is positive.

Columns

The Table 3 ranking system for each acceptance criteria was applied for applicable anode type as shown in Table 4.

The rankings were than multiplied by the weightings in Table 2. The result is shown in Table 5.

Table 6. Cheapness and suitability comparison (columns).

Anode Type	Tube Anode	Cassette	Corro Disc	Dur-Anode4
Cheapness	35	55	65	50
Suitability	62	88	84	86

Table 7. Weighted ranking of acceptance criteria (Beams).

Anode Type	Cost		Suitability				
	Init	Maint	Rel	Spd	Frnd	Flex	Asth
MMO Mesh	50	20	28	12	8	6	9
Sawtooth Rib	30	20	21	9	12	9	15
Ribbon Mesh	10	15	21	6	8	9	12
Cassette	20	15	35	15	20	9	9
CorroDisc	50	15	28	12	16	12	12
durAnode4	30	20	28	12	16	15	15

Table 8. Cheapness and suitability comparison (Beams).

	Mesh	Saw	Rib	Cass	Corro	dur4
Cheapness	70	50	25	35	65	50
Suitability	63	66	56	88	80	86

The ranking of the anodes based on cost and suitability is shown in Table 6.

The weighted comparison of CP systems for use on columns suggested that the Corrodisc surface mounted system scores highest on lifecycle cost, however where the owner preferred an embedded/internal CP system, the durAnode4 system also scored highly overall.

Walls

The approach used for columns was also used for walls. However different anode systems were applicable. The analysis is shown in Tables 7 and 8.

The weighted comparison of CP systems for use on the walls suggests that the Expanded Mesh with sprayed mortar overlay scores highest on lifecycle cost, whereas the Cassette and durAnode4 systems score were highest in terms of acceptability. The CorroDisc CP system was likely to be the most suitable system if both cost and suitability are considered equally.

Beams

The same system was applied for the beams. The analysis is shown in Tables 9 and 10.

Table 9. Weighted ranking of acceptance criteria (Beams).

Anode Type	Cost		Suitability				
	Init	Maint	Rel	Spd	Frnd	Flex	Asth
Tube Anode	20	15	14	9	12	12	62
Cassette	40	15	35	15	20	9	88
CorroDisc	50	15	28	12	20	12	84
DrAnode4	20	20	28	12	16	15	86

Table 10. Cheapness and suitability comparison (Beams).

Anode Type	Tube Anode	Cassette	Corro Disc	Dur-Anode4
Cheapness	35	55	65	40
Suitability	62	88	84	86

Table 11. Weighted ranking of acceptance criteria (Soffits).

Anode Type	Cost		Suitability				
	Init	Maint	Rel	Spd	Frnd	Flex	Asth
Ribbon Mesh	10	15	21	6	8	9	12
Sawtooth Rib	50	20	21	9	12	9	15
Cassette	40	15	35	15	20	9	9
CorroDisc	40	15	28	12	20	12	12
durAnode4	20	20	28	12	16	15	15

Table 12. Cheapness and suitability comparison (Soffits).

Anode Type	Rib	Saw	Cass	Corro	dur4
Cheapness	25	70	55	55	40
Suitability	56	66	88	84	86

The weighted comparison of beam CP systems suggests that if a surface mounted system is aesthetically acceptable, the Cassette and CorroDisc systems could both be considered whereas if the owner prefers an internal system, the durAnode4 system appears to be more suitable overall than the discrete/tube anode system.

Slab Soffits

The analysis for slab soffits is shown in Tables 11 and 12.

For the comparison of CP systems for use on slab soffits, it can be seen that the Sawtooth ribbon system scored highest in terms of lifecycle cost, whereas the Cassette system scored highest in terms of suitability, closely followed by the other lightweight surface mounted anode system analysed (CorroDisc) and the durAnode4 system. Therefore depending on the owner's preference, the weighted comparison would indicate that either the Sawtooth ribbon or Cassette system would be most suitable for application to the slab soffits.

CONCLUSIONS

There are a wide variety of CP systems available in Australia but use is limited because many repair system designers and contractors are unfamiliar with the methods. Sacrificial anode cathodic protection systems are simple and inexpensive to design and install and will be suited to many small to medium sized projects where impressed current systems may be to complex and expensive.

The wide range of ICCP systems available are not being widely used to their best advantage because of a range of vested interests and a lack of a clear method for assessing which system is the most appropriate to a client needs. The paper provides a system for undertaking such an assessment in an unbiased way so that clients can clearly see that the system selected will fill their requirements. Use of such selection procedures is likely to increase client understanding of cathodic protection and, by removing the mystique, make it more commonly accepted.

ACKNOWLEDGEMENTS

The authors wish to thank their clients for involvement in their projects.

REFERENCES

Bertollini. L. Bolzoni. F. Cigada. A. Pastore. T. Pedeferri. P. 1993 *"Cathodic Protection of New and Old Reinforced Concrete Structures".* Corros Sci., 35 (1993) 1633–1639.

Broomfield, J.P 2007. *Corrosion of Steel in Concrete. Understanding, Investigation and Repair.* Abingdon. Taylor and Francis.

Chess P.M. & Broomfield J.P. 2014. *Cathodic Protection of Steel in Concrete and Masonry.* Abingdon, Taylor and Francis.

Concrete Society. 2011. *Technical Report 73 Cathodic Protection of Steel in Concrete. Camberly.* Concrete Society.

International Standards. 2011 *ISO 12696 Cathodic Protection of Steel in Concrete.* Geneva. International Standards.

Sergi, G. & Page, C.L. 1999 *Sacrificial Anodes for Cathodic Protection of Reinforcing Steel Around Patch Repairs Applied to Chloride Contaminated Concrete.* Proc. Eurocorr '99 European Corrosion Congress, Aachen

Standards Australia. 2002 AS 2832.5 *Cathodic Protection of Metals. Part 5: Steel in Concrete Structures.* Sydney. Standards Australia International.

Appendix 1. Summary Comparison of Different Anode Types.

Assessment Factor	Impressed Current Anodes for Cathodic Protection										Sacrificial Anodes			
	Surface Coating			Mixed Metal Oxide Coated Titanium							Cathodic Protection			Cath. Prev.
	Graphite in Polymer Binder		Metallic	Ribbon Mesh		Net (Coarse)	Mesh (Fine)	Ribbon	Discrete		Surface Sht	Discrete	Embedded	Embedded
	Silicate Binder	Chlorinated rubber bind.	Thermal Spray Zinc	Embed in Slots	Surf. Mount. Inert Case	Mortar (e.g. Shotcrete)	Precast Surf. Mount	Saw Tooth	Star & tube fab. from rib.	Small dia. Int. Resistor	Zinc (pH5 Cl- activator)	Zinc (pH5 Cl- activator)	Zinc (pH5 Cl- activator)	Zinc (LiOH activator)
System Characteristics														
Cathodic Prot.	Yes	Yes	Yes	Yes	Yes	Yes	Yes	Yes	Yes	Yes	Yes	Yes	Yes	No
Zinc Mass	-	-	-	-	-	-	-	-	-	-	High	High	High	Low
Current Output	Low-V.High	Low-V.High	Low-V.High	Low-V.High	Low-V.High	Low-V.High	Low-V.High	Low-V.High	Low-V.High	Low-V.High	High	Moderate	Moderate	V.Low
Design life	25 years	15 years	15 years	50 years	50 years	50 years	50yrs	50yrs	50 years	50 years	15-30 years	15-30 years	15-30 years	10-20 years
Reliability - Wet	Coat Dep.	Coat Dep.	Moderate	Low-Mod	High	High	High	Low-Mod	High	High	N/A	High	High	High
Reliability - Dry	High	High	High	High	High	High	High	High	High	High	High	High	High	High
Anode Maint. Wet	Coat Dep.	Coat Dep.	Low	Mod-High	Low	Low	Low	Mod-High	Low	Low	N/A	Low	Low	Low
Anode Maint. Dry	Mod	Mod	Mod	Low	Low	Low	Low	Low	Low	Low	Low	Low	Low	Low
Cont. Sys, Maint.	High	High	High	High	High	High	High	High	High	High	Low	Low	Low	Low
App. Qlty Issues	Limited	Limited	High (coating thick)	Mod (grouting)	Low	High (overlay)	High (overlay)	Mod (grouting)	Moderate (grouting)	Low	Mod (coating)	Low	Low	Low
Usage (World Wide)	Current & extensive in Europe	Historic & limited	Current & moderate in USA	Current & Extensive (worldwide)	Current & Extensive (EU/Aust.)	Current & Extensive (worldwide)	Current & Extensive (worldwide)	Current & Moderate (Europe)	Moderate/ Low (Europe/ Aust.)	Current & Extensive (worldwide)	Current & Extensive (EU/Aust.)	Current & Extensive (EU/Aust.)	Current & Extensive (EU/Aust.)	Current & Extensive (worldwide)
Capital Cost	Moderate	Moderate	Moderate	High	Low	Mod	Mod	Mod-High	Mod-High	Mod	V.Low	Low-Mod	Low	V.Low
Available in Aust.	Yes	No	No	Yes	Yes	Yes	Yes	Yes	Yes	Yes	Yes	Yes	Yes	Yes
Suit. Low Cover	Yes	Yes	Yes	No	Yes	Yes	Yes	No	Yes	Yes	Yes	Yes	Yes	Yes
Suited areas size	Mod-large	Mod-large	Mod-large	Mod-large	Mod-large	Large	Small -Mod	Mod-large	Mod-large	Small-large	V.Small-Mod	V.Small-Mod	V.Small-Mod	V.Small-Mod
Lightweight	Yes	Yes	Yes	Yes	Yes	No	No	Yes	Yes	Yes	Yes	Yes	Yes	Yes
Exposure Zones														
Wearing surfaces	Yes	Unknown	Unknown	Yes	No	Yes	Yes	Yes	Yes	Yes	No	Yes	Yes	Yes
Suit. Splash Zone	No	No	No	Mod	V.High	Low-Mod	Mod-High	Mod	High	V.High	No	V.High	V.High	V.High
Suit. Tidal Zone	No	No	No	Poor	Mod-High	Low-Mod	Mod-High	Mod	High	V.High	No	V.High	V.High	V.High
Conc. Surf. Cond.	Sound	Sound	Excellent	Sound	Step limit	Sound	Sound	Sound	Any	Any	Sound	Any	Any	Any
Steel exposure	No	No	No	No	OK	No	No	No	No	No	OK	OK	OK	OK
Client Considerations														
Noise of install	Low	Low	Low	High	Low-Mod	Mod	Low	Mod	High	Mod	Low	Mod	Low	High
Structural Impact	Low	Low	Low	Low	Low	Mod-High	Low	Low	Low-Mod	Low	Low	Low-Mod	Low	Mod-High
Aesthetics	Excellent	Excellent	Excellent	Excellent	Poor	Moderate	Mod-High	Excellent	Excellent	Excellent	Excellent	Excellent	Excellent	Excellent
Installation Speed	Mod	Mod	Fast	Slow	Fast	Fast	Fast	Fast	Fast	Fast	Fast	Fast	Fast	Fast

Concrete Repair, Rehabilitation and Retrofitting IV – Dehn et al. (Eds)
© 2016 Taylor & Francis Group, London, ISBN 978-1-138-02843-2

Experience with installing an Impressed Current Cathodic Protection (ICCP) system on the multi-story car park of the Allianz Arena in Munich, Germany

Hernani Esteves
Ed. Züblin AG, Essen, Germany

Paul Chess
CPI FORCE, Essex, UK

Sebastian Mayer, Ronny Stöcklein & Rajko Adamovic
Ed. Züblin AG, Essen, Germany

ABSTRACT: In the end of April 2005, the new Allianz Arena in the north of Munich was opened as the home ground of the two soccer clubs FC Bayern Munich and 1860 Munich. The stadium has seats for more than 71,000 visitors. Along with the opening of the stadium, Europe´s largest multi-story car park at a soccer stadium was completed. In 2014, concrete repair works were undertaken on approximately 800 column sockets in the car park in order to prevent further corrosion activity on the reinforcement of the concrete columns and the foundations of the columns in the 1st floor. The requirements for the repair were both to enhance the lifespan of these columns for another 50 years and to reduce mechanical and environmental impact during the repair work. After carefully evaluating several repair options, cathodic protection was chosen to be the most economic and most suitable solution /1/.

1 INTRODUCTION

1.1 *Situation*

During technical inspections in the multi-story car park of the Allianz Arena in 2013, the first visual signs of corrosion in numerous column sockets were detected. Further material testing showed raised chloride contents in the concrete in a great number of column sockets. Even though cracks and spalls due to corrosion were minor, the client requested a repair method in order to maintain the function and durability of the car park for another 50 years.

1.2 *Concept*

Based on the technical inspection, the planning engineers came with a concept of cathodic protection (CP) with the target to protect selected column sockets in the car park in the long term from corrosion damage. Seven column types led to different CP layouts with MMO ribbon mesh anodes and MMO discrete anodes. Generally, MMO ribbon mesh anodes were installed at the concrete surface and provided current mainly to protect the reinforcement and the steel elements nearest to the concrete surface. The MMO discrete anodes provided current deeper into the structure. These anodes in rod form are mounted into the concrete in previously drilled holes. When the anode is fixed, the holes are filled with a special grout to connect the anode to the concrete. The design current density for the ICCP system at all column sockets was 15 mA/ m^2 steel surface in accordance with the specifications.

On column type 4, discrete anodes of different length and current output were chosen, depending on the geometry of the columns and its reinforcement steel surface and the foundation layout. At column type 3, the ICCP system was designed to protect both the reinforcement of the column feet as well as the steel starter bars of the column in the foundation. The cathodic protection at the column feet of column type 1, 2 and 3 begins 23 cm beneath floor level and reaches up to 50 cm above floor level (figure 1). ICCP on column type 4 reaches from floor level up to 40 cm above the ground.

On columns types 5 to 7, ribbon mesh anode is fixed to the concrete surface by plastic plugs. The ribbon mesh anode is wrapped around the column socket as a horizontal ring. The socket was protected from the floor level up to a height of 40 cm above the floor, using three anode rings in order to provide the intended current density (figure 2).

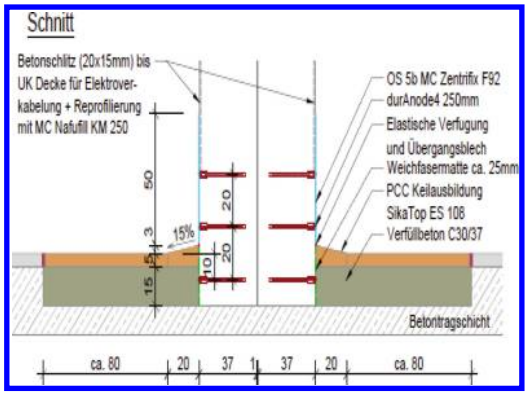

Figure 1. ICCP set-up on column type 4 with MMO discrete anodes /2/.

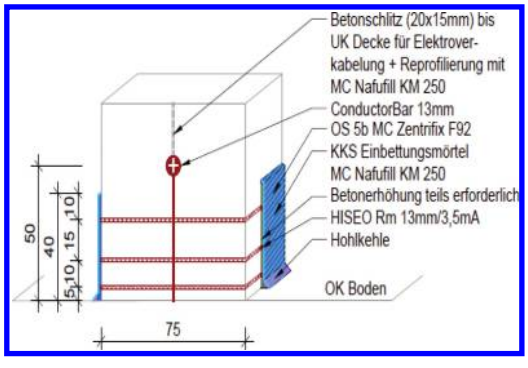

Figure 2. ICCP set-up on column type 5, 6 and 7 with MMO ribbon mesh anodes /2/.

2 INSTALLATION PROCESS

2.1 *Continuity of reinforcement*

When applying a cathodic protection system, it is highly important that all steel members and steel elements within the concrete are electrically connected. That way, the entire reinforcement forms one unit and can be connected with the negative pole of a DC power unit. Due to ICCP, the steel will be polarized and no single member or steel element will be exposed to stray currents. Continuity was considered achieved if the resistance between two points was less than 1 Ohm or less than 1 mV potential difference /3/. In the multi-story car park of the Allianz Arena, several hundred column feet were treated with ICCP. Continuity between all columns was measured between each other. In cases where there was no continuity, the isolated element was welded to the reinforcement cage.

2.2 *Sensors, cathode connections and anodes*

Prior to the anode installation at the columns, all required openings (e.g. for cathode connections and reference electrode installation) and slots for cables, primary anodes were established according to the ICCP layout. Then all slots and openings as well as the prepared concrete surfaces were washed and cleaned. Then cathode connections and monitoring cathode connections were welded to the exposed rebars in the openings. Further, 50 reference electrodes were placed into the concrete next to rebar in order to monitor and to control the ICCP system in the car park of the Allianz Arena. All power and monitoring cables were positioned in the prepared slots and fixed with plastic plugs. Finally, the function of all components was controlled using multi-meter instruments and LCR meter (L = inductance, C = capacitance, R = resistance). When all results were satisfactory, the openings and slots were closed with a CP optimized mortar.

Depending on which type of anode will be installed at a column, the preparations on the concrete slightly varied prior the anode installation. When discrete anodes were used, holes were drilled into the concrete on exactly predefined positions and with an exact drill depth to ensure a current distribution as calculated in the design. Furthermore, the exact position was located with a rebar scanner which was free of rebars and steel elements connected to the reinforcement. This way, short circuits generated by rebar contact with the anode rod were avoided. Besides the advantage of a current distribution deep into the structure, discrete anodes represent an invisible ICCP solution on a structure as the anode rods are mounted into the concrete in holes. The primary anode made of coated titanium wire runs in a slot in the concrete and electrically connects all discrete anodes on a column socket with a specially developed anode connection. After the installation process, both primary anode and discrete anodes are invisible; no extra layer of concrete and no changes in the shape of the column indicate the installation of ICCP. When using ribbon mesh anodes, the concrete surface must be cleaned thoroughly prior to anode installation. When the anode is fixed to the concrete surface, a vertically installed primary titanium strip as part of the anode connection crosses all anodes. In the crossing, spot welding electrically connects the primary anode and secondary anode. Finally a layer of ICCP approved shotcrete completely covers the anode assembly around the column. The system is able to catholically protect the reinforcement and steel elements in the column socket.

Figure 3. Cathode connection by welding to an exposed rebar in an opening at the column socket. After welding, the connection point was electrically insulated with an epoxy resin.

2.3 *Cabling, power supply and communication*

In a cathodic protection system, the entire area to be treated is subdivided into protection zones with similar conditions. The target is to create zones provided by one DC power supply unit each with an even current distribution and a balanced level of protection as the demand of current will be the same in the entire zone.

In the multi-story car park in Allianz Arena however, no large surfaces are treated with ICCP. Instead of this, a number of several hundred column feet represent a huge bundle of small protection elements spread over large distances and three floors of the parking. Each column is provided separately, equipped with a control box for revision and further adjustments. With this set-up, resistors can be placed at each control box on each column to allow the system providing even current to many columns despite them being in the same zone. Due to the long distances in this project, voltage drop in the power cabling was actively considered. With the target to reduce cable length to an acceptable extent, three separate cabinets were placed in the car park at different locations. In ICCP station 1 (master cabinet), the controller of the ICCP was had a modem and a telephone landline for remote communication, next to a number of power supply units. In ICCP station 2 (slave cabinet 1) and ICCP station 3 (slave cabinet 2), power supply and reference electrode monitoring units were installed. Each station had a separate local electricity supply. The PSUs in station 2 and 3 were connected to station 1 in order to receive the commands of the controller. All monitoring data was collected by data acquisition modules and transferred via data bus to the controller. All data was recorded and

Figure 4. Column socket with discrete anodes (compare Figure 1).

Figure 5. Cabling at the ceiling of the car park; cable boxes at each column for revision and system modification.

formed a basis for system monitoring and control. When a computer is connected to the controller on site by LAN or remotely by telephone line, all data can be displayed both in numbers and figures in various ways. The system enables the user to adjust voltages, data record cycles, alarms, upload of documentation related to the project and more.

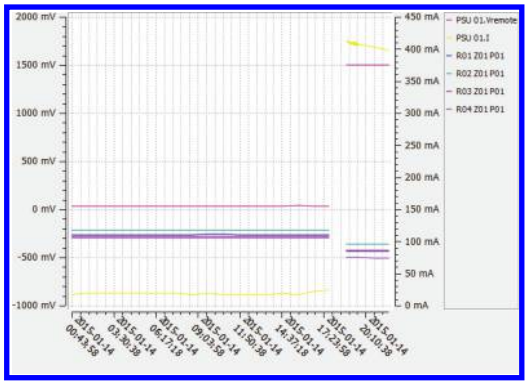

Figure 6. Polarization effect of the reinforcement after commissioning in protection zone 1 with a voltage of 1.5 V, detected by reference electrode no. 1, 2, 3 and 4 /4/.

3 COMMISSIONING AND MAINTENANCE

3.1 *Commissioning*

In January 2015, the ICCP system was energized according to chapter 9 of the standard EN 12696. By applying a small voltage to all protection zones, the polarization effect on the steel reinforcement measured by the reference electrodes was observed carefully. Aiming for a detailed data record during the commissioning, the data refresh rate of the system was set high in order to display a detailed track record of the polarization the currents and the voltage of each of the zones. When it was clear the system was behaving well and no unexpected effects which could indicate problems, the voltage was increased stepwise with the aim to carefully polarize the steel to reach full cathodic protection according to the protection criteria of EN 12696.

3.2 *Maintenance*

A certified CP specialist and a certified CP company have signed a 10 year arrangement for this system. This company is both in charge of service and maintenance of the system.

In the multistory car park in Allianz Arena, a service contract was signed parallel with the commissioning of the system to make sure the system is maintained from the beginning. The contract includes both the procedure of the replacement of defective components, an annual visual inspection as well as an annual service report. This report reflects data and events of the last 12 month and records if changes in the settings or further adjustments of the system will be necessary.

This way, the client receives a regular status record of his structure which confirms year by year the durability of a high-quality concrete repair.

4 CONCLUSIONS

In the car park of the Allianz Arena in Munich, a cathodic protection system has been successfully installed at the early stages of corrosion damage which was detected only 10 years after opening the car park in 2005. The system will provide a significant life enhancement to the structure. Different anode installations have been made to most effectively protect the various column designs in the car park.

A technically complex ICCP solution designed by the engineering office Schießl Gehlen Sodeikat GmbH in Munich with a tailor-made solution for the Allianz Arena car park was executed by specialists of the contracting company Ed. Züblin AG. An innovative power supply set up has been adopted allowing individual control of each of the columns while offering an electronic package despite the wide geographic spread of the installation.

Finally, a close cooperation between the client Allianz Arena München Stadion GmbH, the engineering office and the contractor was the key to complete this challenging project successfully, in time and with a happy client.

REFERENCES

Engineering office Schiessl Gehlen Sodeikat 2014. KKS Instandsetzung Pendelstützen PH Allianz Arena, *Leistungsverzeichnis14/042*, 04-01-2014, München.

Ed. Züblin AG, Department of Concrete Repair, Kathodischer Korrosionsschutz 2014. Layout Kathodisches Korrosionsschutzsystem, Stützenübersicht, *Instandsetzung Pendelstützen Parkhaus Allianz Arena*, No. 0001H, 2015-01-13, Essen.

EN 12696: 2012 *Cathodic protection of steel in concrete*, Beuth Verlag GmbH 2012, Berlin.

Ed. Züblin AG, Department of Concrete Repair, Kathodischer Korrosionsschutz 2014. CAPSYS project manager, Copyright 2011 Ed. Züblin AG, Version 3.3.0, Essen

Concrete Repair, Rehabilitation and Retrofitting IV – Dehn et al. (Eds)
© 2016 Taylor & Francis Group, London, ISBN 978-1-138-02843-2

Application of cathodic protection on 30 concrete bridges with pre-stressing steel: Remaining service life extended with more than 20 years

A.J. van den Hondel
Vogel Cathodic Protection, Zwijndrecht, The Netherlands

E.L. Klamer
Royal HaskoningDHV, Nijmegen, The Netherlands

J. Gulikers
Rijkswaterstaat, Utrecht, The Netherlands

R.B. Polder
TNO, TU Delft, Delft, The Netherlands

ABSTRACT: In view of long term maintenance of its infrastructure facilities the Dutch Highway Administration (Rijkswaterstaat) has repaired over 1.500 heads of prestressed beams and provided them with cathodic protection (CP). The heads of these beams showed moderate to severe damage due to reinforcement corrosion caused by the penetration of chlorides from leaking joints, which required adequate intervention on the short term. By means of cathodic protection the corrosion process has been halted, so that the risk of further degradation of the beams and possible failure of the pre-stressing steel tendons has been minimized. In addition, the concrete repairs in the chloride contaminated parts of the beams will be durable.

1 INTRODUCTION

1.1 *Cause*

Routine inspections of various bridges in and over a number of highways revealed that a significant number of bridges showed serious damage at the ends of the prestressed concrete beams supporting the decks. A large number of these beams exhibited cracks and spalling of the concrete cover as well as rust stains at the end of the beam. It was identified that the bridges affected by this problem were built between 1965 and 1976. The decks of these bridges are supported by so-called prefabricated 'contact-beams', i.e. prestressed concrete T-shaped beams, which were also prestressed as a group in transverse direction. This structural solution results in a bridge deck without necessitating a structural concrete layer on top (Fig. 1).

Further investigations showed that the cause of this damage was reinforcement corrosion initiated by chlorides. Due to leakage through the joints, the heads of the beams were exposed to wet conditions and during winter months to run-off water contaminated by chlorides from de-icing salts. Even though the concrete quality of the prefabricated beams was high, demonstrated by carbonation depths which did not exceed 4 mm, the deep penetration of chlorides combined with a moderate concrete cover thickness (with an average of about 25 mm) had eventually resulted into corrosion of the outer mild steel reinforcement. As a consequence, the concrete cover was spalling, particularly in the corners behind the support blocks and near the anchors of the pre-stressing steel tendons (Fig. 2).

1.2 *Structural risks*

The beams are prestressed with a DYWIDAG system, which consists of 3 to 6 tendons per beam. These tendons are anchored with a steel plate and a nut. Since there was a risk for the pre-stressing system to be corroded, a destructive study was performed by SGS Intron to investigate the condition of the anchors. A part of the concrete behind the anchor was removed by hydro-jetting in order to have a better impression of the effects of corrosion. The results from this inspection showed that the anchors were corroded. However, this was mainly superficial corrosion without significant material loss (Fig. 3).

Figure 1. Typical bridge in the project with 'contact-beams'.

Figure 2. Concrete damage and corrosion of mild steel reinforcement.

Investigations into the structural consequences of the material loss, resulting in a reduction of the concrete and reinforcement section, and of the (mathematical) failure of one of the tendons were conducted by Royal HaskoningDHV. It was concluded that the decrease of the reinforcement cross-section had not resulted in an unsafe structure at the time of inspection, but that further corrosion had to be stopped, in particular to maintain the concrete cover around the pre-stressing anchors and tendons. The computations also showed that for the beams with a limited number of tendons (3 or 4), failure of one of the bars could already lead to the collapse of a beam. Taking into account the serious structural consequences, the urgent recommendation was given to stop further corrosion at short notice and beams with 3 or 4 pre-stressing tendons should be the first to be treated.

1.3 *The solution*

Rijkswaterstaat, in collaboration with TNO, Royal HaskoningDHV and SGS Intron, designed

Figure 3. Surface corrosion of an anchor of a pre-stressing tendon.

a conceptual solution in which the leaking joints were to be replaced to stop the supply of water, contaminated with chlorides in the winter due to the use of de-icing salts.

However, it was clear that with this measure further corrosion of the reinforcement could not be stopped due to the significant levels of chloride contamination already present. The removal of all the contaminated concrete proved to be not feasible because of the anchoring forces of the tendons in the beams at contaminated and damaged areas.

In order to avoid the complete demolition of the bridges, it was decided to start a procurement procedure for the replacement of the expansion joints, the removal of damaged concrete of the selected beams in the affected zone of the first meter from the head of the beam, the repair of the damaged concrete sections with suitable mortars, and to provide these sections with CP of the steel reinforcement (mild steel, tendons and anchors). Part of the design was that beam heads with corrosion damage would be protected and also adjacent beam heads would be provided with CP.

While the long-term processes of maintenance and monitoring of the CP systems had to be secured, the innovative solution of introducing 20 years of maintenance and monitoring explicitly in the contract was established. As a result, the mild steel and the pre-stressing steel will be effectively protected against corrosion for at least 20 years.

Experiences obtained by Rijkswaterstaat with the application of CP on concrete structures during the past 20 years, had learned that the

involvement of the local governmental authority after completion of a rehabilitation project can decrease rapidly. As a result, the functioning of the CP system was not checked. In the past, this has led to systems that were prematurely disabled or disconnected or did not seem to work over time. Such situations occurred despite the fact that the regulations (e.g. NEN-EN-ISO 12696) require a minimal demand for a semi-annual electrical test and an annual visual inspection.

Eventually, Rijkswaterstaat decided to prescribe an impressed current CP system (ICCP) in the tender documents in order to obtain sufficient certainty about the degree of protection.

2 CATHODIC PROTECTION

2.1 *CP*

Cathodic protection is a technique to inhibit corrosion of steel to a negligible rate by lowering the potential of the metal to be protected. Cathodic protection is divided into galvanic systems (GCP) and systems with impressed current (ICCP).

2.2 *GCP*

In galvanic systems, a sacrificial anode (e.g., zinc or aluminum) is provided, which has a lower rest potential than possible corroding reinforcing steel. The direct coupling of the metallic reinforcement with the less noble anode material results in a galvanic cell in which the anode material goes into solution. In this reaction, electrons are released at the anode which are transported to the reinforcement steel where the iron anodic reaction is inhibited while the cathodic reaction is stimulated.

The advantage of such a system is that it is relatively cheap compared to a CP system with impressed current because there is no requirement for a power source and wiring.

The disadvantage of a galvanic CP system is that in advance it is difficult to accurately predict the extent to which the reinforcement, pre-stressing tendons and anchors will be protected. It is not (easily) possible to control, or to modify, the system after application in order to obtain more or less protection. In addition the anode material is literally consumed as the anodes are sacrificial, making the life span limited.

2.3 *ICCP*

In a CP system with impressed current the reinforcement steel is protected against corrosion using an external power source. Through coupling of the mild steel reinforcement, the pre-stressing tendons and anchors with an external adjustable direct current power supply to an inert anode, a protective current is forced to flow to the steel reinforcement (mild steel, tendons and anchors).

The advantage of such a system is that the level of protection can be controlled by adjusting the voltage or current output.

However, a potential risk of an impressed current system is that it can result in very negative potentials at the steel surface, in particular the pre-stressing steel. In such a situation so-called 'over-protection' occurs as in the cathodic reaction (very small) hydrogen atoms are formed. These atoms can penetrate the pre-stressing steel and eventually combine to form (much larger) hydrogen molecules. This results in (additional) mechanical stresses in the crystal structure of the pre-stressing steel.

In combination with the already present high mechanical stress levels in the pre-stressing steel, this may lead to brittle failure of pre-stressing steel.

Typically, systems based on impressed current are more expensive than galvanic CP systems. However, impressed current systems are more sustainable and have better options for control and monitoring.

2.4 *Monitoring*

In order to measure the level of protection of the mild steel reinforcement and the pre-stressing tendons, including the anchors, pseudo-reference electrodes (so-called decay probes) were installed in every beam to measure the changes in steel potential. In accordance with NEN-EN-ISO 12696 the reinforcement steel is sufficiently protected if the depolarization of the steel (the shift of the steel potential to more positive values) in the first 24 hours after the (temporary) switch-off of the CP system, is at least 100 mV. Here, with the aid of measuring cells (type activated titanium, Ti*), the depolarization is measured with respect to the so-called "instant-off" potential, i.e. the potential at the steel surface immediately after the switching-off of the applied voltage (Fig. 4).

In order to prevent hydrogen embrittlement of pre-stressing steel every beam is additionally equipped with special measuring cells (type Ag/AgCl) which are placed at the reinforcement or tendons closest to the concrete surface with the applied anode. These ('true reference') cells are stable over time and can be used to measure the absolute potential over a long period of time. In order to prevent hydrogen embrittlement, NEN-EN-ISO 12696 prescribes that the steel potential must always be less negative than -900 mV (with respect to an Ag/AgCl/0.5 M KCl reference electrode).

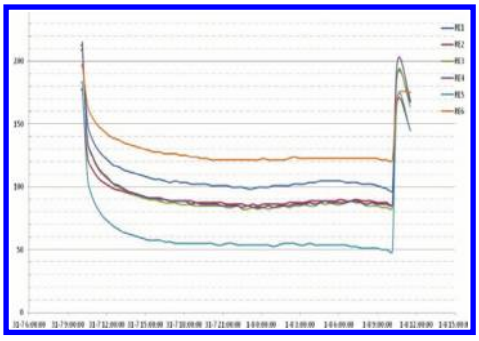

Figure 4. Example of a depolarization measurement (after 1 year of operation).

Figure 5. Severely damaged beam head after removing delaminated concrete.

The challenge for the CP engineer is to find a voltage at which sufficient protective current is supplied to all the steel in the chloride contaminated concrete section in the head of the beam in order to obtain a minimum of 100 mV depolarization in this area, but without the absolute potential at the pre-stressing steel surface to become more negative than -900 mV. At this point the limitation for the absolute potential at the pre-stressing steel surface is leading. In almost every beam equipped with a CP system (98.7%) it was demonstrated at the start-up of the systems that both criteria could be met. At the remaining 1,3% of the beam heads initially depolarization was (a little) less than 100 mV, as otherwise the absolute potential would be too negative at the pre-stressing steel. After some time (1 to 6 months) the current demand of the systems had declined and the voltage was adapted to a level that these beam heads could meet both criteria as well.

3 EXECUTION PHASE

3.1 *Scope and preparations*

The contract was ultimately awarded to the consortium Mourik/Salverda. After replacing the expansion joints by Salverda, Mourik subsidiary and CP specialist company Vogel Cathodic Protection started their operation including concrete repair and application of CP at the heads of the selected beams (starting with a first selection of almost 1.200 beams but in the end resulting in more than 1.500 CP installations on beam heads).

The first step was to remove all loose concrete parts. In some beams it was found that the concrete was affected to such an extent that at the bottom only a pyramid-shaped pressure area directly above the support remained (Fig. 5).

If a large decrease (>10%) of the concrete contact surface area was revealed during restoration of the damage, an assessment of the structural safety was made by Royal HaskoningDHV, after which the beam head was eventually restored in compliance with a prescribed procedure.

3.2 *Repair and installation of CP*

After removal of all delaminated and spalled concrete parts, the reference electrodes (RE's) for monitoring were accurately placed by drilling holes close to either the reinforcement or close to the tendons: 2 (sometimes 3) reference electrodes were placed in every beam (Fig. 6).

In every beam also 2 metallic connections to the steel were made in every beam by welding in order to provide a cathodic connection and a second connection for measuring purposes. Cable slots were milled in the concrete surface of the beam in order to make the system more durable, less visible and less vulnerable. All cables outside the surface of the beams were concealed in stainless steel pipes.

Next the concrete was repaired with a repair mortar suitable for the application of CP, which generally means without polymers and with an electrical resistivity after hardening comparable with that of the surrounding concrete.

Especially the restricted work space, the deep position of the beam heads at abutments, and the fact that at some locations the execution had to take place at night, complicated the repair work (Fig. 7).

After curing of the repair mortar a conductive coating (the CAST^{3+} system, a 2-component aluminum-silicate polymer filled with carbon) was applied as a (secondary) anode to the concrete surface of the beam head (Fig. 8). In this coating a primary current carrying anode (a CuNbPt-wire) was incorporated.

This type of anode was chosen because of the long-time experience with the material in similar conditions, the durability of the conductive coating in relation to the requested lifetime of 20 years,

Figure 6. Accurately placing the RE's for measuring sufficient protection and avoiding overprotection.

Figure 7. Restricted work space for concrete repair and CP installation.

good practical experience, and the advantages of a conductive coating with regard to the application in the restricted work space between the beam heads. Taking into account this tight working space it was chosen to apply the coating by spraying it on the concrete surface in 2 layers.

The reference electrodes and the connections for both anode (1) and cathode (2) were installed and connected per 2 or 3 beam heads to a decentralized power supply and monitoring unit (Fig. 9).

This unit was connected with a data cable and power cable to the central measuring and control unit (Fig. 10). The decentralized units collect and store the measurement results for the connected beams and these results can be approached, read, collected and programmed remotely through the modem in the central control unit. Furthermore, the voltage applied on the CP system can, depending on the results of the measurements, be adjusted remotely as well, per every decentralized unit (through the modem in the central unit). The data and power cables are concealed in stainless steel pipes.

Figure 8. Applying the conductive coating (CAST^{3+} system).

Figure 9. As-built CP system with 4 decentralized power supply and monitoring units.

Figure 10. CP system with central measuring and control unit and solar panels.

The power of the CP system is, at most locations, provided by a double battery, which is fed by solar panels (Fig. 11). At four locations an exception was made due to the local conditions (shade, buildings, afforestation, pipelines). Here the CP systems are connected to the main electric grid.

Figure 11. Solar panels.

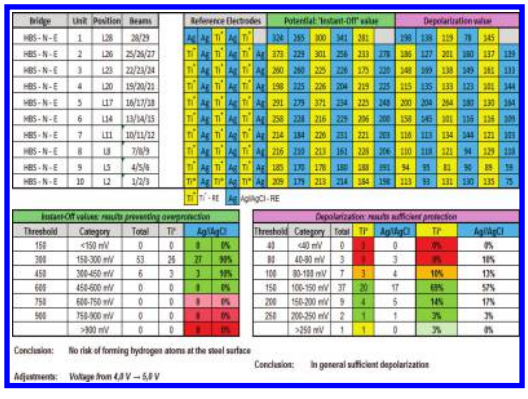

Bridge	Unit	Position	Beams	Reference Electrodes	Potential: 'Instant-Off' value					Depolarization value				
MBS - N - E	1	L28	28/29	Ag Ag Ti* Ag Ti*	324	265	300	341	281	198	138	119	78	145
MBS - N - E	2	L26	25/26/27	Ti* Ag Ti* Ag Ti* Ag	373	329	301	256	233	278	186	127	201	160	137	139
MBS - N - E	3	L23	22/23/24	Ti* Ag Ti* Ag Ti* Ag	260	260	225	226	175	220	148	169	138	149	181	133
MBS - N - E	4	L20	19/20/21	Ti* Ag Ti* Ag Ti* Ag	198	325	226	204	219	225	115	135	133	123	101	144
MBS - N - E	5	L17	16/17/18	Ti* Ag Ti* Ag Ti* Ag	291	279	371	234	225	248	200	204	264	187	130	164
MBS - N - E	6	L14	13/14/15	Ti* Ag Ti* Ag Ti* Ag	258	228	216	225	206	200	158	145	101	156	136	109
MBS - N - E	7	L11	10/11/12	Ti* Ag Ti* Ag Ti* Ag	214	184	226	231	221	203	116	113	134	144	121	101
MBS - N - E	8	L8	7/8/9	Ti* Ag Ti* Ag Ti* Ag	216	210	213	161	228	206	110	118	121	94	129	110
MBS - N - E	9	L5	4/5/6	Ti* Ag Ti* Ag Ti* Ag	180	170	178	180	188	191	94	85	82	90	89	58
MBS - N - E	10	L2	1/2/3	Ti* Ag Ti* Ag Ti* Ag	209	179	213	214	184	198	113	93	131	130	135	75

Ti* - RE Ag/AgCl - RE

Instant-Off values: results preventing overprotection

Threshold	Category	Total	Ti*	Ag|AgCl
150	<150 mV	0	0	0%
300	150-300 mV	53	26	49%
450	300-450 mV	6	3	50%
600	450-600 mV	0	0	0%
750	600-750 mV	0	0	0%
900	750-900 mV	0	0	0%
	>900 mV	0	0	0%

Depolarization: results sufficient protection

Threshold	Category	Total	Ti*	Ag|AgCl	Ti*	Ag|AgCl
40	<40 mV	0	0	0%	0%	0%
80	40-80 mV	3	0	0%	0%	10%
100	80-100 mV	7	3	43%	10%	13%
150	100-150 mV	37	20	54%	69%	57%
200	150-200 mV	9	4	44%	14%	17%
250	200-250 mV	2	1	50%	3%	3%
	>250 mV	1	1	0%	3%	0%

Conclusion: No risk of forming hydrogen atoms at the steel surface

Conclusion: In general sufficient depolarization

Adjustments: Voltage from 4,0 V → 5,0 V

Figure 12. Example of the survey depolarisation values per bridge.

4 EXPERIENCES AND RESULTS

The first CP systems are now running for over 2 years. The measurements on the CP system illustrate that the reinforcement is well protected, as is confirmed by depolarization values of the Ti*-potential decay probes (≥ 100 mV) (Fig. 12).

Also, the pre-stressing tendons, which receives less protective current due to its deeper position compared to the steel reinforcement, are in general sufficiently protected. This is confirmed by the depolarization values of the Ag/AgCl ('true reference') electrodes. The risk for over-protection, and therefore hydrogen embrittlement, of the pre-stressing steel appears to be nil. In none of the measurements an absolute steel potential ('instant-off' value) is found that exceeds the criterion of –900 mV (the most negative value measured is above, i.e. less negative than, –600 mV).

Lastly, the necessary amount of protective current is found to be relatively small. After the start up of the system, initially a relatively large (protective) current was measured. After a couple of weeks or months the current consumption decreased to approximately 10–30% of the initial starting level. A further reduction is expected as the steel is protected by the CP system for a longer period of time and the conditions surrounding the steel are becoming less corrosive and gradually more steel becomes repassivated.

5 CONCLUSIONS

The execution phase of all 30 bridges within the project was completed in August 2014. The first bridges were completed and commissioned in December 2012.

Severe corrosion of pre-stressing tendons and anchors could, in time, have had major adverse effects on the structural safety of the bridges. With the chosen solution of replacing the leaking joints to create waterproof expansion joints, in order to stop the supply of water and chlorides (de-icing salts), and to protect the reinforcement and pre-stressing steel through cathodic protection, the structural safety of the beams is restored and the remaining service life of the bridges is extended by at least 20 years. With this solution the use of radical reconstruction measures could be avoided.

As the beams are prestressed, special precaution had to be taken in order to avoid the occurrence of hydrogen embrittlement of the pre-stressing tendons. The CP system applied on the beams has to give enough protection to the steel in order to prevent corrosion and at the same time overprotection has to be avoided at all times.

As a result over 3000 reference electrodes were installed in the 1500 beams to assure corrosion protection and avoid hydrogen embrittlement simultaneously. So far with good results.

An aspect of most importance in this consideration is that the owner of the infrastructure (Rijkswaterstaat) has in advance introduced into the contract that the maintenance and monitoring of the CP systems will be performed by the contractor for a period of 20 years.

Because the concrete damage was manifested at a large number of prefabricated beams, it was possible to apply a "standard" approach to a large number of bridges within the project. In principle, the applied approach is suitable for application to similar structures. In view of possible follow-up projects, the operation of the CP systems and the results of the monitoring in the coming years will be critically evaluated.

Concrete Repair, Rehabilitation and Retrofitting IV – Dehn et al. (Eds)
© 2016 Taylor & Francis Group, London, ISBN 978-1-138-02843-2

Towards improved cracking resistance in concrete patch repair mortars

P.A. Arito, H.-D. Beushausen & M.G. Alexander
Concrete Materials and Structural Integrity Research Unit, Department of Civil Engineering, University of Cape Town, Cape Town, South Africa

ABSTRACT: The failure of patch repair mortars as a result of restrained shrinkage cracking is responsible for the reduced service life in both concrete repairs and patch repair materials. Cracking in patch repair materials is dependent on important material properties such as tensile relaxation, magnitude of restrained shrinkage deformations, elastic modulus, tensile strength, etc. Many researchers have studied the effects of various mix design parameters and constituents on each of the aforementioned material properties. However, information regarding the effect of simultaneously varying multiple mix design parameters and constituents on the cracking performance of patch repair mortars is scanty. This paper reviews the effects of various mix design parameters—binder type, binder content, water content, water:binder ratio, chemical admixtures and curing—on the crack-determining material properties of patch repair materials.

1 INTRODUCTION

Concrete patch repair mortars (PRMs) are intended to extend the service life of deteriorating concrete structures. To achieve this, PRMs are expected to possess a wide range of properties such as cracking resistance, durability and aesthetics, among other performance requirements. The aforementioned PRM properties depend to a large extent on its mix design parameters. The selection of mix design parameters for a particular PRM mix, however, is a complex process because the developed PRM needs to address constructability, service life issues, an understanding of the owner's (user's) concepts and engineering and performance requirements (ICRI, 1996) within a reasonable and an affordable budget.

The performance of PRMs in service is affected by its constituent materials. Thus, the selection of mix design parameters ought to be done with care. The selection of mix design parameters also ought to be founded on a proper understanding of the influence of various mix design parameters, and their corresponding interactions, on the desired performance requirements. The interactions that exist among mix design parameters—which are key to durability and cracking resistance in PRMs—are complex and poorly understood (Mehta and Monteiro, 2006). The subsequent subsections attempt to elucidate the individual influence of binder-related parameters, water content, water:binder ratio, chemical admixtures and curing on the cracking of PRMs.

2 BINDER-RELATED PARAMETERS

2.1 *Binder content*

Cement content affects important crack-determining material properties such as shrinkage. Increasing the cement content, at a constant water:cement ratio, results in a corresponding increase in shrinkage. However, at a given workability, which approximately means a constant water content, shrinkage is unaffected by an increase in the cement content, or may even decrease, because the water:cement ratio is reduced and the material is, therefore, more capable of resisting shrinkage (Neville, 2007). A reduction in cement content results in a corresponding reduction in heat of hydration and shrinkage.

2.2 *Binder type*

The type of binder and its particle size influence important crack-determining material properties such as water requirement, tensile strength, tensile relaxation and shrinkage. Thus, the type of binder used to make a PRM would influence its susceptibility to cracking. The Concrete Society (1992) reports that the influence of cement type and composition on long-term drying shrinkage is minimal. However, they acknowledge that the type of cement is important as far as it affects the water content of a particular mix. Tazawa and Miyazawa (1995) report that alumina cements and high early-strength cements exhibit early autogenous shrinkage, which could ultimately lead to large shrinkage deformations. Al-Gahtani and Khan (2003), while comparing shrinkage in cementitious materials

made from blended and Portland cement, report that greater early-age drying shrinkage is experienced in specimens made from blended cement than those made from Portland cement. The tendency of blended cements to undergo early-age cracking, however, is highly sensitive to the curing period.

Supplementary cementitious materials (SCMs) such as fly ash, silica fume and slag, have also been used in PRMs. They have been reported to modify the kinetics of hydration, minimise the heat of hydration, as well as improve the performance with respect to durability, mechanical strength, elastic modulus, tensile strength and creep and relaxation to varying degrees (Khan et al., 2000; Langan et al., 2002; Lawrence et al., 2003). Limestone fillers accelerate both chemical shrinkage and hydration (Bouasker et al., 2008; Nepomuceno et al., 2013); thus, their incorporation into PRM mixes could increase their susceptibility to cracking, others factors being constant.

The use of fly ash and slag results in: reduction in the amount of water required to achieve a given consistency, improved workability, reduced heat of hydration, reduced tensile strength at early ages, reduced rate of strength gain, reduced wetting expansion, reduced thermal volume changes, reduced contraction cracking, reduced porosity and improved durability. The reduction in the volume of water required to achieve a given consistence further reduces the propensity to drying shrinkage; which would consequently reduce the possibility of cracking as a result of drying shrinkage. Similarly, the reduction in the heat of hydration is desirable because it reduces the susceptibility of cracking due to thermally-induced stresses. A reduction in tensile strength, however, is undesirable. PRMs ought to have a high tensile strength in order to resist the tensile stresses that are associated with restrained shrinkage.

The volume of fly ash in a mix dictates the magnitude of drying shrinkage that would be experienced in the cement-based material in its hardened state. Drying shrinkage is reduced when fly ash is used in correct quantities; and is increased when excessive amounts are used (Uys, 1983; Banthia and Gupta, 2009). While there lacks a clear definition of 'the correct quantity' of fly ash that could be used in a mix; it is important to know that parameters such as the pozzolanic activity of the fly ash, the richness of the mix, the character and grading of the aggregates, the water:binder ratio and the material properties that the fly ash is intended to improve inform the optimum proportions of fly ash that can be used to replace cement (Uys, 1983; Lam et al., 1998). Banthia and Gupta (2009), further report that the increase in cracking in mixes that contain fly ash could be attributed to their lower initial matrix strength as well as the greater amount of water available for evaporation. The increased amount of water available for evaporation would increase shrinkage; consequently increasing the susceptibility of a mortar made from fly ash to crack.

Uys (1983) and the Concrete Society (1992) have also reported that GGBS and fly ash produce materials with a high modulus of elasticity and reduced creep at later ages. The high modulus of elasticity and reduced creep properties are undesirable in PRMs and tend to offset the benefits of reduced water content and shrinkage. The Concrete Society (1992) however reports that the magnitude of these negative effects, on an overall scale, are clearly insignificant when compared to other factors that govern cracking due to long-term drying shrinkage.

While SCMs such as condensed silica fume (CSF) and fly ash (FA) have been clearly understood to contribute to an enhanced durability in cementitious materials; there is a lack of a common understanding of the role of these SCMs on other important crack-determining properties like tensile strength. There are contradictory reports on the contribution of CSF to tensile strength—an observation that has also been reported by Toutanji et al (1999).

The densification of the microstructure of a cement-based material by adding CSF reduces the rate of moisture loss (Neville, 2007; Alexander and Beushausen, 2009). The densification of the paste is also responsible for the improved modulus of elasticity and bonding in cement-based mixes that contain CSF. The fact that the densification of the paste reduces the rate of moisture loss could, therefore, imply that drying shrinkage takes place at a slower rate in CSF mixes. However, it has been observed that there is no substantial difference between the magnitude of the final shrinkage in separate but identical specimens made using CSF and other binders.

The use of blast furnace slag cements reduces the heat of hydration, increases the rate of bleeding (at replacement levels that are greater than 60%), slows the rate of setting and large shrinkage, lowers the early-age tensile strength and reduces creep (Concrete Society, 1992; Kanna et al., 1998). Other properties that influence crack-determining properties of cement-based materials containing slag comprise: slag content and fineness. The fineness of blast furnace slag, for example, has been reported to influence the magnitude of early age shrinkage (Tazawa and Miyazawa, 1995); with Tazawa et al (1989) attributing the rate of drying of slag to its specific surface and the type of slag. At shorter curing times, an increase in specific surface area of slag in concrete results in a decrease in drying shrinkage and vice versa.

3 WATER CONTENT

The water requirement of a mix is the quantity of water required to obtain a neat cement paste of certain consistency. It is an important crack-determining parameter in cement-based materials; and is dependent on the properties of materials used in a mix such as the specific surface area, cement type, aggregate morphology, size and packing as well as the volumetric proportion of fine material.

For given materials and conditions, the higher the water content, the higher the drying shrinkage and the greater the tendency for mortar mixes to crack. High water contents also reduce the mechanical properties of the hardened material as well as increases shrinkage and creep deformations.

4 WATER:BINDER (W/B) RATIO

The hydrated cement paste is the major source of shrinkage and relaxation in cement-based materials. It plays an important role as far as shrinkage-induced cracking is concerned. The water:binder ratio is directly related to the pore system of the paste. The porosity of the paste, and its associated interconnectivity, influences important crack-determining material properties like: tensile strength and elastic modulus. While the relationship between the water:cement ratio and compressive strength, as described by Abram's law, is direct and well established; its relationship with cracking is quite complex and incorporates other factors inter alia.

Uys (1983) reports that increasing the water:binder ratio increases the potential for shrinkage; with the effect being more pronounced with a decrease in the aggregate content by volume. Banthia and Gupta (2009)—while investigating the effect of water:binder ratio, sand:cement ratio and other parameters on cracking in cementitious materials—further report that increasing the water:binder ratio decreases the total amount of heat evolved, increases the rate of evaporation as well as delays the occurrence of first crack. They also report that lower water:binder ratios result in low crack areas and small crack widths. The movement of water within the porous paste sets up tensile and hygral stresses which are a function of the water:binder ratio. These stresses result in volumetric changes (e.g. expansion and contraction) within the paste.

A reduction in the water:binder ratio, for example, would result in pastes that are characterised by low creep—because the pastes are strong and stiff—and with a high tensile strength. A high tensile strength is desirable in terms of resistance to tensile stresses that could culminate into cracking. Furthermore, pastes with high water:binder ratios contain more free water and are therefore more susceptible to drying shrinkage. The susceptibility of the paste to shrinkage-induced cracking can, thus, be reduced by lowering its water:binder ratio, other factors being equal. The extent to which the water:binder ratio can be reduced, however, ought to be considered carefully via a vis the susceptibility of a material to experience autogenous shrinkage that results from mixes with low water binder ratios.

5 CHEMICAL ADMIXTURES

The extent to which an admixture will affect shrinkage in a cementitious material depends on its intended use (Uys, 1983). An admixture may either increase or decrease drying shrinkage and creep slightly if it is used to effect a saving in cement by reducing the water and cement content while maintaining workability and minimal strength in a mix. Admixtures could also be used to increase strength by reducing the water content while maintaining the same cement content and workability. This use could result in effects that are similar to the first category of use; except that the magnitudes would be slightly reduced because of small reductions in paste content. In the second category of use, there is no significant influence on creep as long as the increase in strength afforded by the admixture is taken into account when testing all the cementitious materials at the nominal stress/strength ratio (Uys, 1983).

Despite the fact that the effect of admixtures on many material properties are well established, Uys (1983) and The Concrete Society (1992) report that it is difficult to predict their influence on the creep of a given mix. This difficulty is premised on the fact that the influence of an admixture on creep is highly specific and depends on many factors such as: method of proportioning, cement type, admixture composition, age at loading and the environment before and after loading. Also, the complexity in understanding the exact effect of an admixture on the properties of a mix is based on the fact that the influence of a particular admixture would depend on the length of the drying period. Thus, that there is no single admixture that can produce mixes of optimum quality under all conditions. It is imperative, therefore, that the influence of various types of admixtures on crack-dependent material properties such as shrinkage, elastic modulus, tensile strength, etc. be investigated.

The influence of water reducing admixtures on crack-determining material properties such as shrinkage has not been clearly defined; thus rendering it to many contradictory views. On the

one hand, it has been reported that plasticisers increase shrinkage slightly—by 10% to 20%. However, the effect of the plasticisers on shrinkage is indirect because their use may result in a change in the water content or in the cement content of the mix, or in both, and it is the combined action of these changes that influences shrinkage. Tazawa and Miyazawa (1995), on the other hand, report that superplasticisers reduce shrinkage; and have attributed this phenomenon to the effect of the superplasticisers on the rate of hydration.

Shrinkage reducing admixtures (SRAs) are organic-based formulations that reduce the surface tension of the mix water in the capillary pores of a cement-based material. The reduction of the surface tension in the capillary pores reduces the tension stresses/forces within the matrix of the material that would lead to drying shrinkage. SRAs reduce both the rate and overall magnitude of shrinkage. The extent to which SRAs reduce shrinkage in cement-based materials, however, depends on the internal relative humidity of the material, the porosity of the paste, amongst other factors (Saliba et al., 2011). Generally, SRAs do not result in significant changes in flexural strength. However, they have been reported to increase tensile strength at 28 days (Gopinath, 2010). Banthia and Gupta (2009), Gopinath (2010) and Carlswärd (2006) report that SRAs reduce autogenous shrinkage, reduce the potential for mortars to crack as well as delay their time to first crack. This phenomenon could be attributed to the lowering of the rate of tensile stress development within the mortar specimens by SRAs.

Other admixtures that could influence the crack-determining properties of PRMs are drying shrinkage inhibitors (Tazawa and Miyazawa, 1995) and retarding admixtures. Retarding admixtures may allow more shrinkage to be accommodated in the form of plastic shrinkage as well as increase the extensibility of concrete; therefore reducing the susceptibility of cementitious materials that are made from them to crack (Neville, 2007). Accelerating admixtures increase the long-term drying shrinkage of cementitious materials (Uys, 1983; Concrete Society, 1992).

6 CURING

Curing refers to the process of maintaining a satisfactory moisture content and a favourable temperature in cement-based materials during the period immediately following their placement so that the hydration of cement may continue until the desired properties are developed to a sufficient degree to meet the requirements of service (Perrie, 1994; Taylor, 2014). The two main objectives of curing are: to prevent excessive loss of moisture and to control the temperature for a period sufficient to achieve the desired requirements of service.

Curing is essential to the production of high quality cement-based materials. The benefits that can be gained from adequate curing, in light of the thrust of this paper, comprise: increased tensile strain capacity and volume stability (Concrete Society, 1992; Perrie, 1994; Taylor, 2014). An increase in the tensile strain capacity is a desirable material property because it implies that a material can undertake a greater amount of tensile strains without failing in comparison to materials with a low tensile strain capacity. Also, improved volume stability is desirable. Materials that are volumetrically stable are less susceptible to cracking. The volume stability minimises the possibility of shrinkage-induced stresses that could result in cracking. Adequate moist curing also delays the advent of shrinkage and increases tensile strength (Kronlöf et al., 1995; Neville, 2007; Alexander and Beushausen, 2009); with Kovler et al (1999) further reporting that the effect of curing is more pronounced on tensile strength than on compressive strength.

Wasserman and Bentur (2013), in a study comparing various curing techniques, report that water and wet fabric curing are more effective than curing compounds with respect to strength generation. They also found out that the use of curing compounds—in comparison to moist/water curing—does not provide a very effective sealing of the concrete surface towards the loss of moisture to the environment. The lack of an effective sealing results in relatively inferior material properties (e.g., lower strengths, higher penetration and carbonation values).

There are at least two contradictory views regarding the influence of the duration of curing on crack-determining material properties. On the one hand, Neville (2007) reports that the duration of curing is not an important parameter as far as shrinkage is concerned. Other researchers, on the other hand, report that prolonged water curing, when all other factors are held constant, results in greater shrinkage; with the increase in shrinkage being attributed to the reduction in volume of the unhydrated cement particles—which restrain shrinkage. Appa Rao (2001) reports that an increase in the duration of curing decreases the ultimate drying shrinkage. This observation has been premised on the understanding that hydrated cement pastes can restrain a large fraction of their shrinkage without cracking because they have sufficient strength; with their strength being attributed to the little water that is contained within their matrix. The duration of curing also affects the interfacial bond strength. Wong et al (1999), for example, report that the interfacial bond strength of high volume fly ash increase

proportionally with an increase in curing age. An improved interfacial bond strength is a favourable material property. An improved interfacial bond helps in enhancing the stress transfer between the two interfaces as well as delays the propagation of cracks within the interface.

7 CONCLUSIONS

The influence of various mix design parameters on cracking in PRMs has been presented. For PRMs to be effective with respect to resistance to cracking, it is imperative that the relationships and synergies that exist within the aforementioned mix design parameters are investigated, and the information obtained from such investigations is harnessed and applied into the design and development of PRMs. Also, there are many contradicting views regarding the influence of various mix design parameters on crack-determining material properties. These contradicting views tend to complicate the process of selecting optimal mix design parameters that would guarantee the realisation of effective PRMs. A more holistic investigation into the combined influence of the aforementioned mix design parameters on crack-determining material properties in PRMs, therefore, is necessary. A holistic investigation will provide valuable information that would dictate the process of designing PRMs that are effective with respect to resistance to cracking.

ACKNOWLEDGEMENTS

The authors wish to acknowledge with gratitude the University of Cape Town and the Carnegie Corporation of New York for the financial support for this research. Financial support from the University of Cape Town was in the form of a Research Associateship.

REFERENCES

Al-Gahtani, A., and Khan, M.M. Drying shrinkage characteristics of plain and blended cements. Proceedings of the sixth CANMET/ACI International conference on recent advances in concrete technology, 2003, Bucharest, Romania, Pp. 133–143.

Alexander, M., and Beushausen, H. (2009). Deformation and volume change of concrete. Fulton's concrete technology, 9th Edition, Midrand South Africa, Gill Owens (Ed), Pp. 111–154.

Appa Rao, G. Long-term drying shrinkage of mortar—influence of silica fume and size of fine aggregate. Cement and Concrete Research, 31, 2001, Pp. 171–175.

Banthia, N., and Gupta, R. Plastic shrinkage cracking in cementitious repairs and overlays. Materials and Structures, 42, 2009, Pp. 567–579.

Bouasker, M., Mounanga, P., Turcry, P., Loukili, A., and Khelidj, A. Chemical shrinkage of cement pastes and mortars at very early age: Effect of limestone filler and granular inclusions. Cement and Concrete Composites, 30, 2008, Pp. 13–22.

Carlswärd, J. (2006). Shrinkage cracking of steel fibre reinforced self-compacting concrete overlays: test methods and theoretical modelling. PhD Thesis, Department of Civil and Environmental Engineering, Luleå University of Technology. 250 pp.

Concrete Society. (1992). Concrete Society Technical report No. 22 – Non-structural cracks in concrete, 3rd Edition. Concrete Repair Manual, Second Edition, Volume 1. Published jointly by American Concrete Institute, Building Research Establishment, The Concrete Society and The International Concrete Repair Institute, 2000, Pp. 507–551.

Gopinath, R. (2010). Effect of shrinkage reducing admixtures on the properties of cement mortars. MSc. Thesis, Indian Institute of Technology, Madras. 228pp.

ICRI. (1996). Technical guidelines: Guide for selecting and specifying materials for repair of concrete surfaces. Guideline No. 03733. Concrete Repair Manual, Second Edition, Volume 1. Published jointly by American Concrete Institute, Building Research Establishment, The Concrete Society and The International Concrete Repair Institute, 2000, Pp. 835–868.

Kanna, V., Olson, R.A., and Jennings, H.M. Effect of shrinkage and moisture content on the physical characteristics of blended cement mortars. Cement and Concrete Research, Vol. 28, No. 10, 1998, Pp. 1467–1477.

Khan, M.I., Lynsdale, C.J., and Waldron, P. Porosity and strength of PFA/SF/OPC ternary blended paste. Cement and Concrete Research, 30, 2000, Pp. 1225–1229.

Kovler, K., Schamban, I., Igarashi, S., and Bentur, A. Influence of mix proportions and curing conditions on tensile splitting strength of high strength concretes. Materials and Structures, Vol. 32, August-September 1999, Pp. 500–505.

Kronlöf, A., Leivo, M., and Sipari, P. Experimental study on the basic phenomena of shrinkage and cracking of fresh mortar. Cement and Concrete Research, Vol. 25, No. 8, (1995), Pp. 1747–1754.

Lam, L., Wong, Y.L., and Poon, C.S. Effect of fly ash and silica fume on compressive and fracture behaviours of concrete. Cement and Concrete Research, Vol. 28, No. 2, 1998, Pp. 271–283.

Langan, B.W., Weng, K., and Ward, M.A. Effect of silica fume and fly ash on heat of hydration of Portland cement. Cement and Concrete Research, 32, 2002, Pp. 1045–1051.

Lawrence, P., Cyr, M., and Ringot, E. Mineral admixtures in mortars Effect of inert materials on short-term hydration. Cement and Concrete Research, 33, 2003, Pp. 1939–1947.

Mehta, P.K.., and Monteiro, P.J.M. (2006). Concrete: Microstructure, properties and materials. Third edition. Tata McGraw Hill, 660pp.

Neville, A.M. (2007). Properties of concrete, 4th Edition, Pearson Prentice Hall, Pp. 412–481.

Nepomuceno, M., Oliveira, L., and Lopes, S.M.R. Methodology for mix design of the mortar phase of self-compacting concrete using different mineral additions in binary blends of powders. Construction and Building Materials, 26, 2012, Pp. 317–326.

Perrie, B.D. The testing of curing compunds for concrete. Department of Civil Engineering, University of the Witswatersrand, Johannesburg, 1994, MSc dissertation.

Saliba, J., Rozière, E., Grondin, F., and Loukili, A. Influence of shrinkage-reducing admixtures on plastic and long-term shrinkage. Cement and Concrete Composites, 33, 2011, Pp. 209–217.

Tazawa, E., Yonekura, A., and Tanaka, S. (1989). Drying shrinkage and creep of concrete containing granulated blast furnace slag. Fly ash, silica fume, slag, and natural pozzolans in concrete. Proceedings of the Third international conference, Trondheim, Norway, 1989, SP-114 Volume 2. Malhotra, V.M (Ed). Published by the American Concrete Institute, Detroit. Pp. 1325–1343.

Taylor, P.C. (2014). Curing concrete. CRC Press, Taylor and Francis Group, 181pp.

Tazawa, E.-I., and Miyazawa, S. Influence of cement and admixture on autogenous shrinkage of cement paste. Cement and Concrete Research, Vol. 25, No. 2, 1995, Pp. 281–287.

Toutanji, H.A., Liu, L., and El-Korchi, T. The role of silica fume in the direct tensile strength of cement-based materials. Materials and Structures, Vol. 32, April 1999, Pp. 203–209.

Uys, A.J. (1983). The influence of fly ash pn the strength, elastic modulus, shrinkage and creep of concrete made with Cape Town aggregates with particular reference to Alkali-aggregate reaction. University of Cape Town, MSc Thesis. 438 pp.

Wasserman, R and Bentur, A. Efficiency of curing technologies: strength and durability. Materials and Structures, Vol. 46, 2013, Pp. 1833–1842.

Wong, Y.L., Lam, L., Poon, C.S., and Zhou, F.P. Properties of fly ash-modified cement mortar-aggregate interfaces. Cement and Concrete Research, 29, 1999, Pp. 1905–1913.

Concrete Repair, Rehabilitation and Retrofitting IV – Dehn et al. (Eds)
© 2016 Taylor & Francis Group, London, ISBN 978-1-138-02843-2

Reinforcement corrosion in separation cracks after injection with PUR

M. Kosalla & M. Raupach
RWTH Aachen University, Aachen, Germany

ABSTRACT: In separation cracks in RC elements (e. g. park decks), a short-term chloride exposure can already cause reinforcement corrosion. It is questionable, if a deep injection of the crack as an exclusive procedure is sufficient for effectively stopping the corrosion process.

For investigating the corrosion activity during the chloride exposition and after the crack maintenance, cracked beams with crack-crossing reinforcement were fabricated. The cracks have been grout injected with PUR after a winter season of six month with a periodic chloride exposure. The anodic (element) current was recorded both before and after the injection. More than one year after the injection, the measurement stopped and the crack-crossing rebars were removed from the specimens and visually investigated.

During chloride exposure the measured current flows were very high (sometimes > 200 μA). After the injection they slowly decreased and dropped nearly to zero in the next winter period. In the following summer the current flows increased just marginally, which seems to be mostly uncritical. The visual inspection mostly indicates a structurally insignificant degree of damage, because the loss of cross-section is just in exceptional cases more than 10%. So the combination of the previous slight damage and the low corrosion activity after the injection suggests a sufficient effectivity of the crack treatment. But since higher corrosion rates for worst case considerations are not excluded, it is recommended by the authors to install a monitoring system.

1 INTRODUCTION

In RC structures cracks are an usual and mostly regular effect of load transfer. In parking structures depending on the specific crack characteristics cracks can rapidly cause considerable corrosion problems due to winterly chloride exposure, which require repair works. Thereby separation cracks are crucial special cases, in which high corrosion rates are expected.

Regarding crack repairs there is no consensus among experts, which repair methods are suitable, for ensuring a durable structural safety with non-critical degradation rates of the reinforcement. In German practice it is currently discussed, how to repair a separation crack at new constructions after short-termed chloride exposure over one winter period. Partially standard solutions like a complete replacement of chloride containing concrete are desired. According to the DBV-Merkblatt "Parkhäuser und Tiefgaragen" (parking decks and basement garages) (2010) [1] a crack injection without any further pre-treatment or concrete replacement is sufficient, for reducing the corrosion rate to a technically tolerable extent.

Also economic aspects lead to preventing an expensive concrete replacement. So it is economically important to clarify, if a crack injection or even just a superficial sealing of a crack is possibly sufficient, for durably stopping the corrosion process respectively dropping the corrosion rate to a technically tolerable extent.

2 INVESTIGATIONS

The aim of the investigations was to check the effectivity of the crack injection with polyurethane (PUR) as a repair method, after development of a separation crack and subsequent short-termed chloride exposure over one winter period, respectively to determine the grade of effectivity. Hence, twelve beam specimens with a separation crack in the middle and crack-crossing reinforcement were fabricated. The corrosion element currents were monitored over the chloride charged winter period and after the crack repair as well. Thereby the cycle of chloride solution exposure as well as the treatment of the upper specimen surface was varied, for determining the influences of exposure intensity and different moisture transfer conditions. The specimens were stored under outside conditions without direct rain impact over the entire investigation time, for practically simulating the boundary conditions of a tween deck and for ensuring a defined and controllable moisture and chloride supply.

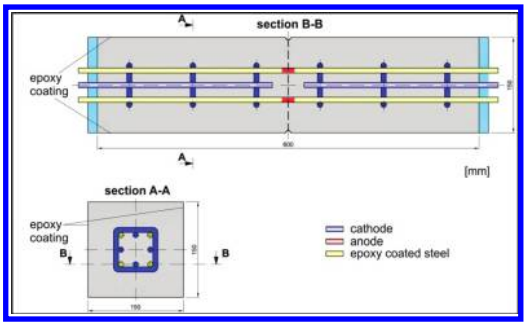

Figure 1. Specimen structure and reinforcement configuration.

Table 1. Test schedule.

1	2	3
Specimen	Surface Protection	NaCl – exposure
S.1–1	Coating system applied after crack injection	weekly
S.1–2		every second week
S.1–3		every fourth week
S.1–4		every eighth week
S.2–1	No coating system applied	weekly
S.2–2		every second week
S.2–3		every fourth week
S.2–4		every eighth week
S.3–1	Coating system applied before cracking	weekly
S.3–2		every second week
S.3–3		every fourth week
S.3–4		every eighth week

2.1 *Specimens*

The cracked beams had a length of 60 cm and a cross-sections area of 15 × 15 cm^2. The crack was built in the middle of the beam and had a target crack width of 0.3 mm. Four crack-crossing reinforcing bars are placed longitudinally over the entire beam and are arranged in a square base considering the profile. Further longitudinal rebars and stirrup reinforcement—electrically encoupled from the crack-crossing rebars—were integrated in the beam on both sides of the crack, for providing a sufficient cathodic area.

For characterizing the corrosion behavior of the steel, the individual element currents from any crack-crossing anodic rebar to the residual cathodically acting reinforcement cage was monitored continuously. The crack-crossing rebars were coated with an epoxy resin besides the crack area, for avoiding huge magnitudes of self-corrosion by preventing the steel surface area from acting cathodically. The lateral concrete surfaces of the specimens as well as these at the end of the bulk were also sealed with an epoxy resin, for avoiding moisture transfer with the environment, so the boundary conditions of a plain construction element were fulfilled.

For the concrete a PC with slag and fly ash admixtures was used. As reinforcement ripped steel bars with a diameter of 8 mm has been applied. The concrete cover was set to 40 mm, for fulfilling all requirements of German and international guidelines for XD3-concrete ([2], [3], [4], [5]), which is regularly used for decks.

2.2 *Investigation schedule*

The investigations were separated in three test series, each with four specimens. In Series 3 a rigid surface protection system was applied on the upper surface in young concrete age, which systematically got ripped, when opening the crack. The surface of Series 1 got coated with the same system after the chloride exposure period and the crack repairs. The surface of Series 2 stayed untreated during the entire investigations (table. 1). The chloride exposure period had a duration of 26 weeks. The specimens in the particular test series were varying in their exposure intensity (table. 1).

The exposure cycles and electro-chemical measurements were started exactly 28 d after concreting. A wet-drying-cycle took one week and the specimens were exposed to a 3.0% NaCl-solution in the crack area on a given day for three times, each for one hour in every regular exposure week, while the residual upper surface was exposed to tap water (fig. 2), for gaining a practical moisture distribution in the specimen.

Once the exposure period in the winter had ended, the specimens were disconnected from the measurement setup, for grouting the crack with a polyurethane based injection resin by means of a hose pump and adhesive packers (fig. 3), until the injection material was pressed out over the complete length of the upper crack side (fig. 4). After application of the surface protection system for Series 1, the measurement of the element currents was continued for further 16 months, for observing the reaction, when a significant increase of the temperature occurs in the second summer after crack repair.

After termination of the current measurements, concrete samples for the chloride analysis in the crack area were drawn by cuttings and polishings and the crack-crossing anodic acting rebars were removed from the specimens for visual investigations. After an absolute visual assessment, the shortened rebars were visually recorded by a

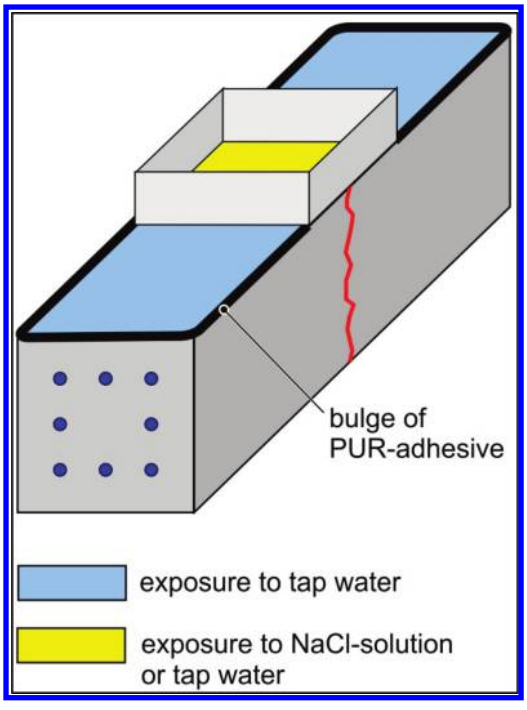

Figure 2. Exposure conditions.

Figure 3. Crack injection by means of a hose pump.

3D-Scanner by means of optical triangulation and structured light stripe method [6]. In modeling processes 3D-reproductions were made for evaluating the corrosion-induced damaged surface and the extent of cross-section reduction. For existing conditions the quantification of these characteristics is stamped by inaccuracies. The anodic acting surface was mostly underestimated and the cross-section loss was overestimated.

Figure 4. Complete injection of the crack.

3 RESULTS

3.1 *Electrochemical measurements*

By means of the development of element currents over the investigation time, the development of deterioration can be estimated, so that the effectivity of the crack repair method can be evaluated. During the exposure period the highest currents have been observed. Thereby a high fluctuation is observable due to the different exposure states and a temperature effect is noticeable. The element currents during exposure nearly reached 200 µA. But also there were observable huge fluctuations between the single anodes of one specimen, without showing a clear pattern regarding the various positions of the rebars. Thus, it is most likely, that the variations are due to a random scattering, probably caused by irregular inner cracking. Already during the chloride exposure, an influence of the exposure intensity on the element currents can be recognized.

After the injection in spring 2013, a significant decrease of the element currents was determined for all specimens. The decreasing tendency continues in spite of the temperature increase in the summer months. In the following winter period the majority of currents drop next to zero (fig. 5). For some anodes, currents around 1 µA were measured. In few exceptional cases, maximal values of 4–6 µA were observed.

As expected few element currents lightly increased again, when the temperature exceeded 20°C for longer periods (June 2014). But the average current in June 2014 is just marginal higher than in January. Thus, it cannot be assumed, that the currents generally re-increase due to summer temperatures. Most rebars, which are still indicating an active corrosion process in winter, are showing a recovery of the corrosion currents, but not in a critical extent.

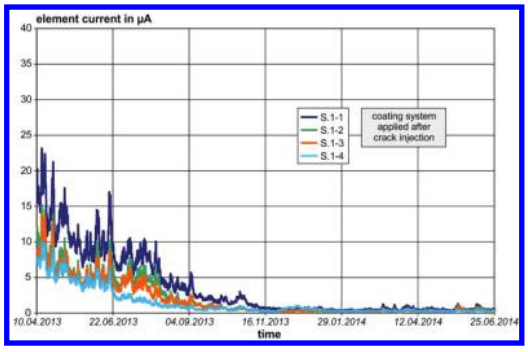

Figure 5. Element currents after the crack injection (series 1).

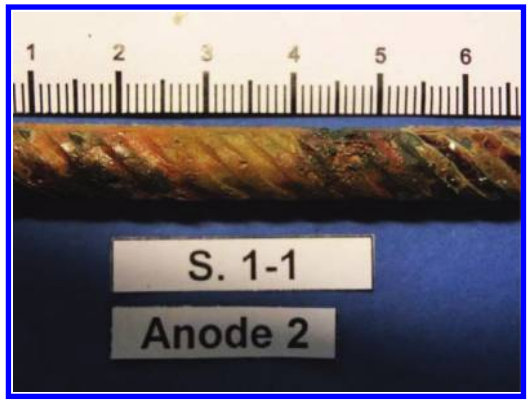

Figure 6. Various colourations in the crack area.

3.2 *Visual inspection of the removed rebars*

By the removal of the crack-crossing reinforcement bars it was recognized, that nearly all rebars were extensively discoloured brownish—both in the uncoated crack area as well as in the epoxy coated area besides the crack. Firstly it seemed to be clear, that a large part of the uncoated area of 2 cm length was affected by corrosion-induced deterioration and that additionally subsurface corrosion processes occurred in adjacent areas, so that the anodically acting area was larger than the uncoated surface. Partially small defects in the coating (cracks, peeling) were observed. Thus, either the chloride containing solution could have reached these areas over transfer processes or the corrosion products themselves have been transported. Due to the mechanical load during cracking and crack opening, inner micro cracks could have been built in the coating and in the concrete of the crack area, which have supported the transport processes. However, this could not be checked by the performed investigations. It is also possible, that the path of crack was not straight, so the inner crack could have been some centimeters besides the target crack position.

After removal of the adhesive corrosion products by chemical cleaning, it became clear, that just a small part of the uncoated area was affected by deep pitting corrosion. Thus, the actually anodically acting surfaces could not be determined exactly and it is questionable, if the entire colouration is actually caused by corrosion products. It is more probable, that the coating itself has discoloured by chemical reactions. After chemical cleaning, different types of colouration were observed on the steel surface (fig. 6). This indicates the presence of different types of corrosion products, formed by different environmental conditions during the test period.

The decisive aspect of the visual investigations was the observation, that the degradation grade of the rebars cannot be considered as critical in any case regarding structural safety. Just in exceptional cases the state could be called marginal. There is no immoderate loss of material observable and the corrosion pits are not such deep, that a decisive loss of cross-section occurs. According to visual judgement, the cross-section reduction is at most lightly over 10% and mostly clearly lower than 10%.

3.3 *Mensuration of the corroded rebars*

The attained results of the 3D-mensuration of the rebars have to be regarded with caution and cannot be classified as fully reliable. A pre-mensuration of the rebars before the tests started was not possible, the removal of the rebars caused deformations and partially additional damages and the surface condition was affected by the coating and by colouration effects. Thus, there are several possible sources of errors existing. table 2 shows the results of the analysis exemplary for Series 3:

By means of the size of the corroded surface areas, element currents actually should be recalculated in corrosion densities, for evaluating and classifying the corrosion rates, respectively the rates of material loss. Indeed these recalculations occurred exemplary for the values of table 2 (as well as another example with the assumption of an anodically acting surface of 2 cm rebar length), but the correctness of these calculations has to be treated with care, because the determined values by means of the 3D-modelation just concern the area affected by clear pitting corrosion and light uniform corrosion is not taken into account. However, it is suspected, that the area, affected by the anodic sub-process, is clearly larger than calculated. This is also indicated by the visual inspections. Thus, a deeper interpretation of the calculated current densities does not make sense.

Table 2. Results of the 3D-mensuration of the corroded rebars.

Specimen, anode	Corroded steel surface	Max. cross-section loss
-	mm²	%
1	2	3
S. 3-1, A1	38	< 2,3
S. 3-1, A2	25-30	< 9,3
S. 3-1, A3	20	< 14,9
S. 3-1, A4	5-6	< 3,1
S. 3-2, A1	8	< 2,5
S. 3-2, A2	15	< 5,3
S. 3-2, A3	70-75	< 9,9
S. 3-2, A4	8	< 2,1
S. 3-3, A1	8-10	-*
S. 3-3, A2	30-40	< 7,9
S. 3-3, A3	10	< 4,5
S. 3-3, A4	20-25	-*
S. 3-4, A1	15-20	< 3,7
S. 3-4, A2	< 5	< 4,9
S. 3-4, A3	10	n. b.
S. 3-4, A4	1	< 4,1
*The anodes A1 and A4 of specimen S. 3-3 were not digitally analysed		

Table 3. Chloride contents in the depth of the concrete cover.

Specimen	Sample depth	Chloride-content
-	mm	wt.-%/cem
1	2	3
S. 1-1	30 - 45	1,55
S. 1-2		1,50
S. 1-3		0,94
S. 1-4		0,53
S. 2-1		1,19
S. 2-2		0,96
S. 2-3		0,74
S. 2-4		0,55
S. 3-1		1,44
S. 3-2		1,45
S. 3-3		0,70
S. 3-4		0,58

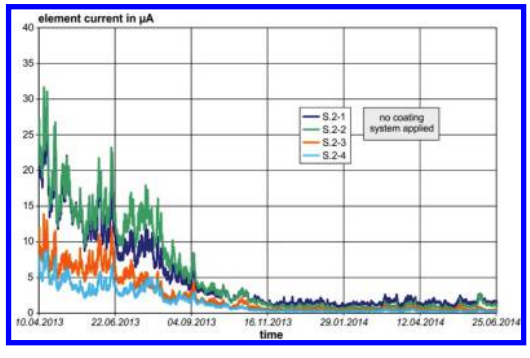

Figure 7. Element currents after the crack injection (series 2).

3.4 *Chloride analysis*

The chloride contents of the concrete cover depth in the crack area are listed in table 3. No decisive gradient in the chloride profiles has been obtained by the analysis of the cutting samples.

The comparative analysis of the polishing samples did not lead to large deviations.

4 ASSESSMENT OF THE RESULTS

4.1 *Influence of the exposure intensity*

By means of the results of the electrochemical measurements of element currents a significant influence of the exposure intensity on the corrosion behavior of the crack-crossing reinforcement is ascertainable. With increasing chloride exposure time the average and maximal element currents increase by trend. This already becomes very clear by considering the current developments in series 1 (fig. 5). series 2 (fig. 7) and series 3 (fig. 8), which show the same trend. The latter both furthermore show a significant difference between the exposure every two and every four weeks. Both higher intensities as well as both lower intensities are here nearly on the same level. This possibly indicates a marginal, critical chloride load existing, whose excess should lead to a more critical consideration of the repair method and the installation of a monitoring-system.

Also the visual investigations show a lower degradation grade with lower exposure intensity. Of course this is directly coupled with the lower chloride content in the concrete (table 3).

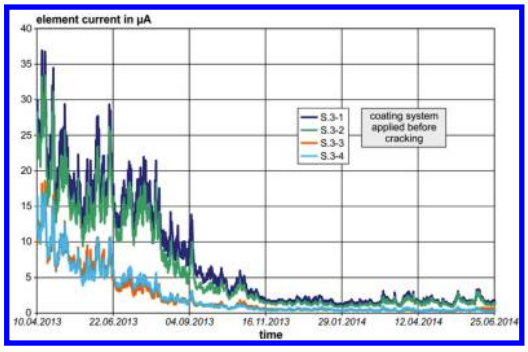

Figure 8. Element currents after the crack injection (series 3).

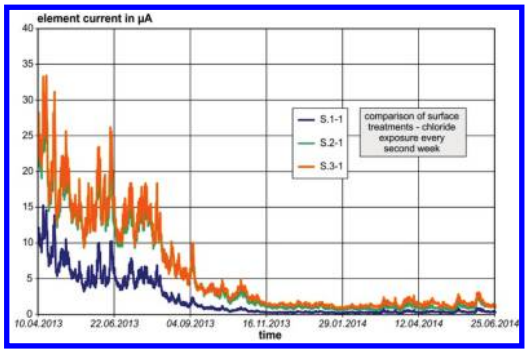

Figure 9. Comparison of the three test series (high chloride load).

4.2 *Influence of the treatment of concrete surfaces*

When comparing the three test series it is notable, that for high chloride loads both element currents and degradation grades are lowest in Series 1. Series 2 and 3 do not show more than marginal deviations in this regard (fig. 9). It is furthermore noticeable, that there is quasi no deviation between the three series regarding a lower chloride load. The overall damage seems to be the highest in Series 2, although the chloride contents in the concrete are obviously lower (table 3).

5 CONCLUSIONS AND OUTLOOK

Considering the corrosion pits and cross-section reductions in the crack area, it is noticeable, that the overall damage at the steel resulting from the exposure period over one winter and the following 15 months in most cases cannot be classified as critical state regarding bearing strength. Regarding additionally the considerable decrease of element currents after the crack repair by PUR-injection, it is obvious, that the main part of damage occurred during the chloride exposure period with an open crack in the winter. This indicates, that the deterioration process—exactly the material loss rate—decreases to a negligible magnitude after crack injection. These findings are at least valid for the assumption of a nearly stable or increasing extent of anodically acting area on the steel surface. In other cases the significance of the element current in principle is not given anymore, because for the calculation of the material loss and cross-section loss rate, the decisive value is the current density. Due to the huge uncertainties regarding the anodically acting surfaces, the in this way calculated current densities do not have significance themselves.

The basic findings and most important influencing factors on corrosion activity and effectivity of the PUR-crack injection can be reflected in the following conclusions:

- By the crack injection the corrosion activity of the crack-crossing reinforcement bars significantly decreases immediately and furthermore with time.
- Considering the development of corrosion activities over the entire investigation time, the main damage must be allocated to the exposure period with an open crack.
- The steel deterioration has to be classified as uncritical, nearly without exception.
- Higher chloride exposure intensities cause a higher chloride load and furthermore higher corrosion rates (element currents).
- There is an influence of surface treatment recognizable, but it is hard to explain. The lowest element currents occur, when the surface protection system is applied shortly after the crack injection.

It is not excluded, that a significant cross-section loss occurs after a PUR-crack injection under non-beneficial conditions. Thus, the repair method for cracks should always be combined with the application of a monitoring-system, for controlling the corrosion currents.

So it has still to be clarified, if the results are transmittable into cases with a practical incomplete injection, various injection materials as epoxy resin, various boundary conditions as wet or moving cracks or other repair methods like superficial sealing methods. Furthermore the transmissibility into aged parking constructions with former binders and concrete covers is to check.

REFERENCES

[1] Deutscher Beton—und Bautechnik-Verein; DBV; DBV Merkblattsammlung: Merkblatt Parkhäuser und Tiefgaragen (Fassung September 2010) Berlin: Deutscher Beton—und Bautechnik-Verein, e.V., 2010.

[2] Bundesanstalt für Straßenwesen; ZTV-ING: Zusätzliche Technische Vertragsbedingungen und Richtlinien für Ingenieurbauten ZTV-ING. Teil 3: Massivbau. Abschnitt 1: Beton. Stand: März 2002. Dortmund: Verkehrsblatt, 2002.

[3] DIN 1045-2: Tragwerke aus Beton, Stahlbeton und Spannbeton; Teil 2: Beton – Festlegung, Eigenschaften, Herstellung und Konformität; Anwendungsregeln zu DIN EN 206-1:2001.

[4] DIN EN 1992-1-1: Eurocode 2: Bemessung und Konstruktion von Stahlbeton – und Spannbetontragwerken – Teil 1-1: Allgemeine Bemessungsregeln und Regeln für den Hochbau; Deutsche Fassung EN 1992-1-1:2004 + AC:2010.

[5] DIN EN 206-1: Beton—Teil 1: Festlegung, Eigenschaften, Herstellung und Konformität; Deutsche Fassung EN 206-1:2000.

[6] Harnisch, J.: Zum zeitabhängigen Verhalten elektrochemischer und morphologischer Kenngrößen bei der chloridinduzierten Korrosion von Stahl in Beton: Investigations Into the Time Dependent Behaviour of Electro-Chemical and Morphological Parameters Regarding the Chloride Induced Corrosion of Steel in Concrete Aachen, Technische Hochschule, Fachbereich 3, Dissertation, 2012.

Concrete Repair, Rehabilitation and Retrofitting IV – Dehn et al. (Eds)
© 2016 Taylor & Francis Group, London, ISBN 978-1-138-02843-2

Maintenance of concrete pavements with thin-layered new concrete

Amela Cokovik & Rolf Breitenbücher
Institute for Building Materials, Ruhr-University Bochum, Bochum, Germany

ABSTRACT: In consideration of continuously increasing traffic and high exposure to freeze-thaw and deicing salt, maintenance and repair works of concrete pavements become of crucial importance. An alternative method to the conventional replacement of the entire concrete structure is the application of thin-layered new concrete. For this procedure, only the upper part of the existing pavement, which is impaired, is removed and will be replaced by a thin layer of new concrete. The crucial factor here is the bonding bahaviour between the lower layer (old concrete) and the thin layer of new concrete. The objective of this study at the Institute for Building Materials (Ruhr-University Bochum) is to investigate the influence of cyclic loading and freeze-thaw-cycles with deicing salts on the bonding properties of such concrete layers. Herein, a number of parameters are varied including the moisture condition of the old concrete, the application of adhesion primer, consistency of new concrete etc. The results acquired within the project so far have shown that the moisture condition of the old concrete does not play a significant role. Furthermore, the application of adhesive primer is only useful for concrete with a stiff consistency since the adhesive strength increased only slightly using concrete with a soft consistency.

1 INTRODUCTION

Concrete pavements are exposed to a number of stresses during their service life, mostly resulting from traffic and climate conditions. In consideration of continuously increasing traffic the durability requirement of concrete pavements becomes more and more significant. At the same time, the surface properties concerning texture and noise reduction have to be fulfilled.

In this context, maintenance and repair of concrete pavements become of crucial importance. Thereby, the main aim is to find the most economically efficient construction method through minimizing life cycle costs without affecting the functionality and quality of concrete pavements.

Usually, maintenance of concrete pavements is conducted through the renewal of the damaged concrete road. An alternative method to the conventional replacement of the entire concrete structure is the renewal of the upper part of the existing pavement, which is impaired. Herein, the milled old concrete provides the base course layer.

In case of the so-called "Whitetopping" a thin concrete layer, usually a fiber-reinforced, low-shrinkage high performance concrete is applied to an existing asphalt pavement. For conventional Whitetopping concrete, paving thicknesses amount to 200 to 260 mm. For Thin-Whitetopping (TWT) an overlay of more than 100 mm and less than 200 mm is commonly used. The thickness of Ultra-Thin Whitetopping (UTW) is usually equal to or less than 100 mm. [2][3][4][13][14][15].

The counterpart to Whitetopping is the so-called "Blacktopping" consisting of a thin asphalt layer (maximum 40 mm thickness) that is applied to a concrete base course layer. [1][10][11].

The maintenance of concrete pavements with a thin layer of new concrete is a relatively new field of work. In this context, the upper part of the existing pavement, which is impaired, is removed and will be replaced by a thin layer of new concrete. The crucial factor here is the bonding behaviour between the lower layer (old concrete) and the thin layer of new concrete which largely depends on the mechanical and rheological properties of both concretes as well as the surface conditions und roughness of the structural joint.

First pilot projects have been carried out in Austria on the motorway A14 Rheintal and the A1 between Salzburg Center and Salzburg West. The concrete pavement on the A 14 showed insufficient grip on the surface and the concrete pavement on the A1 showed chipped edges. The repair of both sections has been conducted according to the "NÖBI"-method [12]. Thereby, the near-surface damaged concrete pavement was milled off and the surface conditions were restored by applying a new concrete layer without using an adhesive primer. The maintenance was realized in 2009 and 2010. So far, no damages could be detected.

The objective of this study at the Institute for Building Materials (Ruhr-University Bochum) is

to investigate the influence of cyclic loading and freeze-thaw-cycles with deicing salts on the bonding properties of such concrete layers. Herein, a number of parameters are varied including the moisture condition of the old concrete, the application of adhesion primer, the consistency of the new concrete etc.

2 EXPERIMENTAL PROCEDURE

2.1 *Parameter variation and experimental matrix*

Within the scope of the research project, large concrete beams with dimensions of 180 × 50 × 27 cm³, consisting of a lower layer (old concrete, thickness around 20 cm) and a thin top layer (new concrete, thickness approx. 7 cm) were produced.

The variations of the large concrete beams are described in the following table (Table 1).

The compressive strength of the old concrete generally amounted to approximately 60 N/mm² with the exception of VB-7, which amounted to 80 N/mm². Furthermore, the moisture condition of the bond area (structural joint) was varied by producing a dry or moist surface.

The composition of the new concrete was varied by adding shrinkage reducing agents (concrete composition M2) to a conventional concrete composition with exposed aggregate surface (concrete composition M1). In addition, the consistency was adjusted to class F4 by appropriate dosage of superplasticizer.

In case of the large concrete beams H-1 to H-5, polymer modified adhesion primer was used. For that matter, all new concretes were produced with a stiff consistency (C1/C2) and using a shrinkage reducing agent (SRA) with the exception of H-1, which was produced without SRA.

The exposure time of the adhesive primer after application was generally about 20 to 30 minutes. Only for H-5 the exposure time was set to 2 hours. The application of the adhesion primer was conducted at an ambient temperature of approximately 20°C.

Table 1. Overview.

Large concrete beams		Moisture condition of structural joint		new concrete			
				concrete composition		consistency	
		dry	moist	M1	M2	C1	F4
Without adhesion primer	VB-1		x	x			x
	VB-2	x		x			x
	VB-3		x		x		x
	VB-4		x		x	x	
	VB-6	x			x		x
	VB-7		x		x		x
With adhesion primer	H-1		x	x		x	
	H-2		x		x	x	
	H-3	x			x	x	
	H-5		x		x	x	

2.2 *Composition of concrete*

Within the scope of this research, two characteristic concrete mixtures complying the requirements of the TL Beton-StB 07 [16] were used. The old concrete represented a characteristic base-layer-concrete with a maximum grain size of 22 mm (basalt grit) with a cement content of 360 kg/m³ and a w/c-ratio of 0.42. For the large concrete beam VB-7 a cement content of 380 kg/m³ and a w/c-ratio of 0.33 were used.

The mixture proportions of both concretes are displayed in Table 2.

The new concrete represented an exposed-aggregate-concrete with a maximum grain size of 8 mm (basalt grit) with a cement content of 430 kg/m³ and a w/c-ratio of 0,42. The consistency class F4 was adjusted by appropriate dosage of superplasticizer. Both concretes contained air-entraining agent in the appropriate dosage.

2.3 *Production and storage of the large concrete beams*

In total, 14 concrete beams consisting of old concrete with dimensions of 180 cm × 50 cm × 20 cm were produced consecutively. At the minimum age of 28 days the surface of the concrete beams was roughened using high pressure water jets (2000 bar).

Around ten months after production of the concrete beams the corresponding new concrete layer

Table 2. Mixture proportions.

		old concrete	new concrete
cement	kg/m³	360	430
type of cement	[-]	CEM I 42.5 N (sd)	
w/c-ratio	[-]	0.42	0.42
consistency	[-]	C1/C2	C1/C2, F4
air content	[Vol.-%]	4.0–4.5	5.0–5.5
max. grain size	[mm]	22	8
Rhine Sand 0/2 mm	[Vol.-%]	28	30
Basalt grit 2/8 mm	[Vol.-%]	15	70
Basalt grit 8/16 mm	[Vol.-%]	27	–
Basalt grit 16/22 mm	[Vol.-%]	30	–

was applied (Figure 1). Therefore, the structural joint was adjusted to a dry or moist condition. The bonding surface (structural joint) of beams H-1 to H-5 was additionally treated using an adhesion primer.

2.4 *Cyclic loading of large concrete beams and freeze thaw exposure*

At the age of 56 days (after production) the concrete beams were stressed cyclically in 4-point-flexural-tests (Figure 2) with up to 1.000.000 load cycles.

For the cyclic loading a stress level $\sigma/f_{fl} = 0.4$ was set. The load range ($\sigma_{max} - \sigma_{min}$) was defined by 1 MPa; corresponding with the flexural stress caused by an 11.5-t-axle.

Subsequent to the cyclic loading, drilling cores with a cross-section dimension of d = 100 mm and d = 150 mm were taken from the unstressed reference area ("Reference") and the maximum stressed area ("Cyclic loading") (Figure 3).

Some of the drilling cores taken from the maximum stressed area (800 mm × 500 mm) were additionally exposed to freeze/thaw-attack based on a modified CDF-test [6] before the investigation of the bonding properties. This test included a capillary suction period of 7 days followed by 28 freeze-thaw-cycles according to the temperature cycle in Figure 4. These specimens are further referred to as "Cyclic loading+ FT-attack".

2.5 *Investigations on structural joint and bonding properties of old and new concrete*

The compressive strength was determined on cubes with a side length of 150 mm according to DIN EN 12930-3 [7] at the age of 28 and 56 days for old and new concrete. The roughness of the structural joints was determined using the so called "Sand Volumetric Technique (SVT)" according to Kaufmann [8]. In addition, the surface tensile strength of the structural joints was determined according to DIN EN 1542 [5] before concreting.

The adhesive strength between old and new concrete was determined according to DIN EN 14488-4 [9]. For this purpose, 40 mm thick steel stamps were attached to the front sides of the drilling cores. The tests were carried out on a servo-hydraulic testing machine (capacity 250 kN), whereas the tensile load was transmitted by eyebolts and hooks into the steel stamps (Figure 5). The testing speed amounted to about 0.8 mm/min.

The adhesive shear strength was determined according to the shear test by Leutner [17]. In this test setup, shear stress was applied to the bond area between the old and the new concrete. Therefore,

Figure 1. Production of the concrete beams.

Figure 2. Test setup for simultaneous testing of six beams in a 4-point-flexural-test.

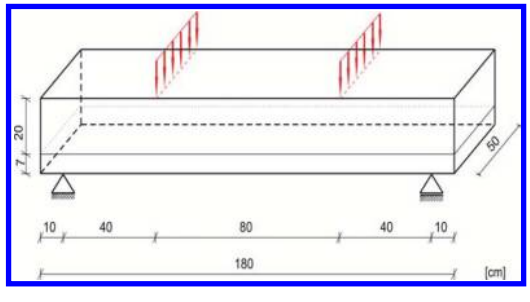

Figure 3. Test setup for cyclic loading of concrete beams (180 × 50 × 27 cm³).

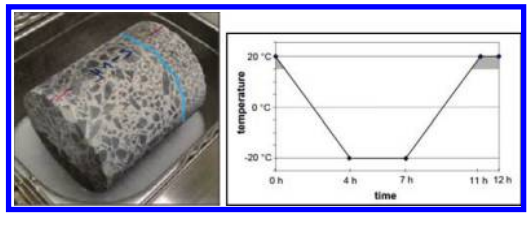

Figure 4. Left: freeze/thaw-attack on drilling core (structural joint marked in light blue); right: temperature cycle for one freeze-thaw cycle.

Figure 5. Investigation on the adhesive strength of drilling cores consisting of old (thickness approx. 140 mm) and new concrete (thickness approx. 60 mm).

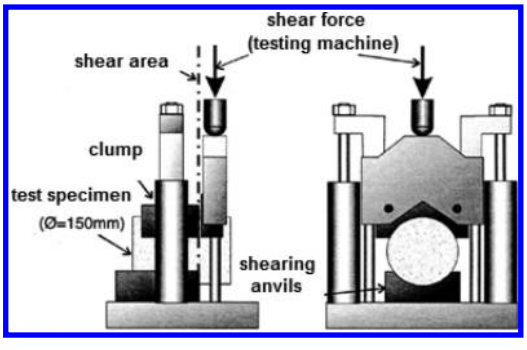

Figure 6. Test setup for shear test according to Leutner [17].

only the old concrete has been fixated in the test machine and the stress was applied perpendicular to the drilling core, as close as possible to the bond area (see Figure 6). The testing speed amounted to about 0.6 mm/min.

3 RESULTS

3.1 *Surface roughness and surface tensile strength*

The roughness of the structural joints was determined on eight different measurement points using finest sand with a volume of 50 cm³. As can be seen from Table 3, the surface roughness varied from 1.4 mm to 2.5 mm. The average surface tensile strength was determined by four single values and varied between 1.77 N/mm² and 3.55 N/mm².

Table 3. Surface roughness and surface tensile strength.

	Average surface roughness in mm	Average surface tensile strength in N/mm²
VB-1	2.5	2.88
VB-2	1.8	3.55
VB-3	2.0	1.70
VB-4	1.8	2.23
VB-6	2.3	1.77
VB-7	1.7	3.42
H-1	1.7	3.27
H-2	1.4	2.22
H-3	1.5	2.57
H-5	1.8	2.98

Table 4. Average compressive strength (56 d) in N/mm².

	Average compressive strength in N/mm²	
	Old concrete	New concrete
VB-1	57.6	74.7
VB-2	60.7	77.2
VB-3	61.8	73.5
VB-4	58.2	68.4
VB-6	63.7	67.0
VB-7	85.9	66.9
H-1	58.2	65.1
H-2	68.1	67.7
H-3	60.7	68.0
H-5	54.7	61.6

3.2 *Compressive strength*

The results of the compressive strength tests are given in the following Table. According to it, the compressive strength of the old concrete varied between approx. 55 and 64 N/mm² (with exception for VB-7) and 62 and 77 N/mm² for the new concrete.

3.3 *Bonding properties*

3.3.1 *Influence of the moisture condition of the structural joint (old concrete)*

Figure 7 represents the average adhesive strength as well as the adhesive shear strength of the large concrete beams VB-1 und VB-2, which were produced with new concretes with a consistency class of F4 and using a shrinkage reducing agent (SRA).

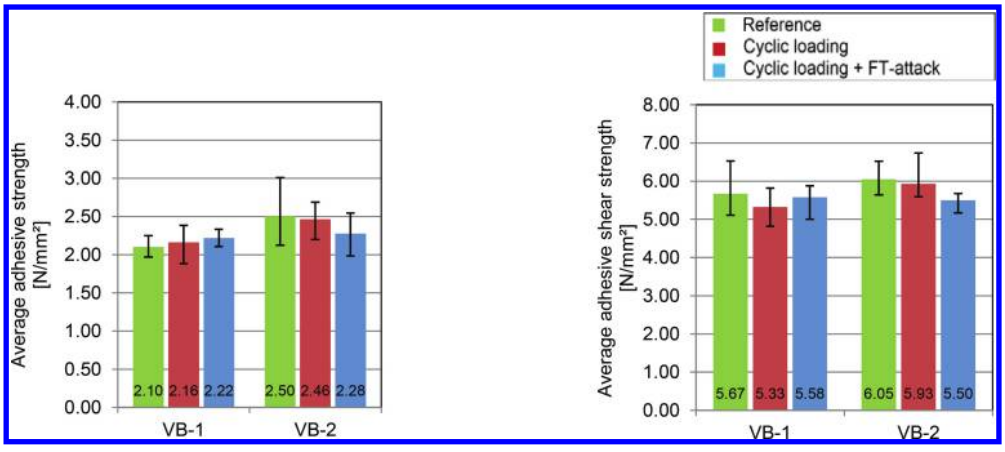

Figure 7. Average adhesive strength (left) and adhesive shear strength (right) of VB-1 and VB-2 (without adhesive primer, without SRA, consistency F4); **VB-1: moist condition** and **VB-2: dry condition (structural joint).**

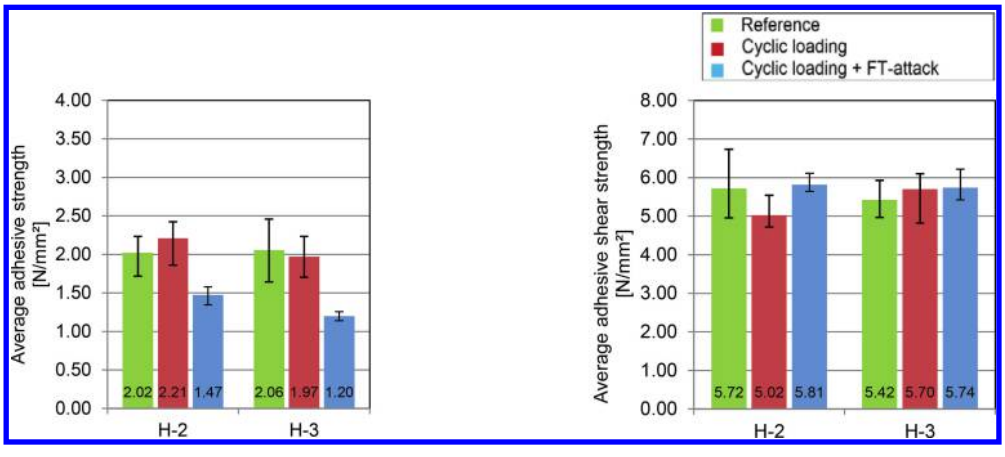

Figure 8. Average adhesive strength (left) and adhesive shear strength (right) of H-2 and H-3 (with adhesive primer, consistency C1/C2, New Concrete with SRA); **H-2: moist condition** and **H-3: dry condition (structural joint)**.

In this case, only the moisture condition of the structural joint (old concrete) varied between moist condition for VB-1 and dry condition for VB-2.

As can be seen from Figure 7 (left), concrete beam VB-2 attained up to 19% higher average adhesive strength compared to concrete beam VB-1. A difference between the test specimens "Reference" and "Cyclic loading" was not observed at this point. The testing after an additional freeze/thaw-attack ("Cyclic loading + FT-attack") resulted in almost identical average adhesive strengths of 2.22 N/mm² for VB-1 and 2.28 N/mm² for VB-2.

Within the adhesive shear test, VB-2 (dry condition) showed up to 11% higher average adhesive shear strength in comparison to VB-1 (Figure 7 right). For the latter specimens "Cyclic loading" showed approximately 6% less adhesive shear strength than the corresponding "Reference".

For VB-2 the adhesive shear strength decreased only by approximately 2%. The specimens "Cyclic loading + FT-attack" attained almost identical adhesive shear strengths with 5.58 N/mm² (VB-1) and 5.50 N/mm² (VB-2). Concluding, a dry condition of the structural joint only showed an improvement of the bonding properties of specimens "Reference" and "Cyclic loading".

The following Figure 8 displays the results of the bonding strength tests of concrete beams H-2 und H-3, which were produced using an adhesive primer before application of the new concrete layer. The new concrete was produced in a stiff consistency with the addition of SRA. In accordance to VB-1

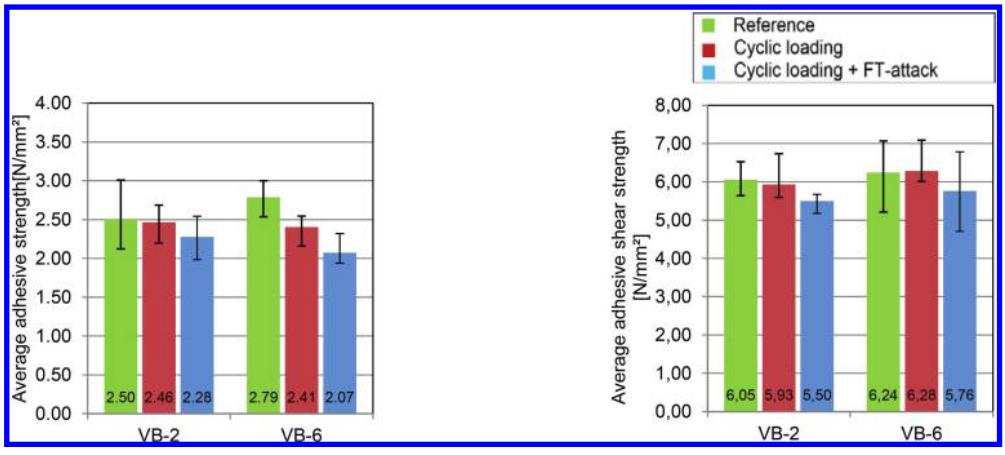

Figure 9. Average adhesive strength (left) and adhesive shear strength (right) of VB-2 and VB-6 (dry condition of structural joint, without adhesive primer, consistency class F4; **VB-2: new concrete without SRA** and **VB-6: new concrete with SRA**.

and VB-2, the structural joint of H-2 was adjusted to a moist condition and H-3 to a dry condition.

As shown in Figure 8 (left), the specimens "Reference"

revealed almost the same adhesive strength with 2.02 N/mm² for H-2 and 2.06 N/mm² for H-3. The specimens "Cyclic loading" and "Cyclic loading + FT-attack" of H-2 (moist condition) achieved up to 22% higher average adhesive strengths compared to H-3.

Compared to the corresponding reference specimens, the average adhesive strength of the "Cyclic loading + FT-attack" specimens decreased significantly by about 27% for H-2 and about 42% for H-3. In contrast to the previous fracture patterns, the specimens "Cyclic loading + FT-attack" fractured entirely in the new concrete.

Concrete beams, which were produced using an adhesive primer, new concrete with a stiff consistency (C1/C2) and using a shrinkage reducing agent (SRA), reached higher adhesive strengths on a structural joint with a moist surface condition during the application of the top layer.

The results of the adhesive shear strength tests for H-2 and H-3 are given in Figure 8 (right). Therefore, no clear correlation between the average adhesive shear strength and the moist condition of the structural joint (old concrete) was determined. For example, the reference specimens of H-2 showed an up to 5% higher strength (5.72 N/mm²) in comparison to H-3 (5.42 N/mm²). With regard to the specimens "Cyclic loading", the adhesive shear strength of H-2 decreased to 5.02 N/mm² whereas for H-3 it showed an increase to 5.70 N/mm² in relation to the corresponding reference. The specimens "Cyclic loading + FT-attack" attained almost identical adhesive shear strengths with 5.81 N/mm² (H-2) and 5.74 N/mm² (H-3).

3.3.2 *Influence of shrinkage reducing agent (SRA) in new concrete*

Figure 9 shows the bonding strengths of VB-2 and VB-6. Herein, the new concrete was applied with a consistency class of F4 on a structural joint with a dry surface. In contrast to VB-2, the new concrete of VB-6 was produced using SRA.

The average adhesive strength of the reference specimens of VB-6 amounted to 2.79 N/mm² and was approximately 12% higher compared to VB-2, while for the "Cyclic loading"-specimens nearly identical adhesive strengths, with 2.41 N/mm² and 2.46 N/mm², were determined (Figure 9, left). It also became clear, that the additional freeze/thaw-attack of the specimens "Cyclic loading" caused a higher decrease of the adhesive strength of VB-6. With regard to its reference specimens it was reduced by about 26% (to 2.07 N/mm²), while VB-2 showed a decrease of roughly 9% (to 2.28 N/mm²).

Within the adhesive shear test it was shown, that VB-6 generally attained higher adhesive shear strengths compared to VB-2. For the "Reference" the shear strength was about 3% higher and for the "Cyclic loading" approximately 6% higher than VB-2. With regard to "Cyclic loading" the additional freeze/thaw-attack caused a decrease of the average adhesive shear strength of about 8%.

The results indicate that the use of SRA in concrete beam VB-6 increased the adhesive shear strength, whereas the adhesive strength was not significantly affected by the use of SRA.

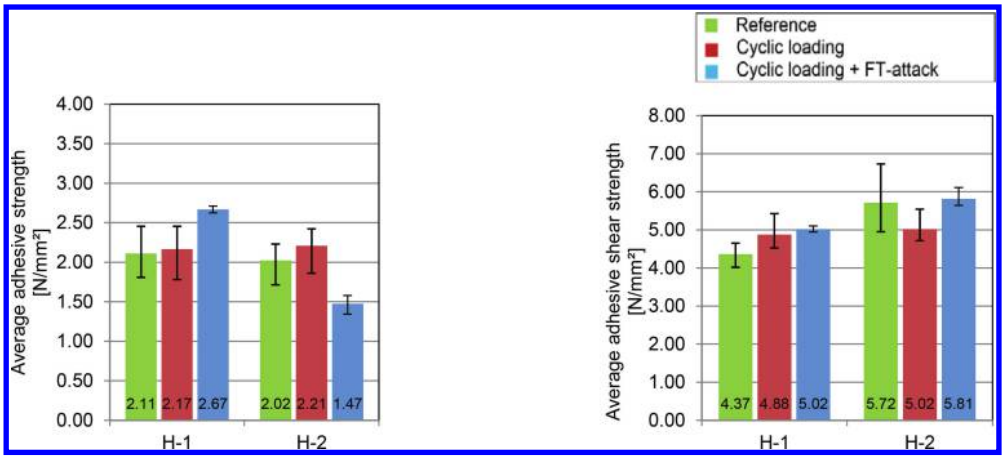

Figure 10. Average adhesive strength (left) and adhesive shear strength (right) of H-1 and H-2 (moist condition of structural joint, without adhesive primer, consistency C1/C2); **H-1: new concrete without SRA** and **H-2: new concrete with SRA**.

Compared to the large concrete beams VB-2 and VB-6, beams H-1 and H-2 were produced using an adhesive primer as well as a new concrete with a stiff consistency. H-2 furthermore included SRA in the new concrete mixture, whereas H-1 did not.

The results of the adhesive strength tests for H-1 and H-2 depicted, that the "Reference" and "Cyclic loading" specimens showed no significant difference in adhesive strength (Figure 10, left). These specimens consistently showed a fracture in the old concrete and the bond area. As displayed in Figure 10, the additional freeze/thaw-attack caused a contrary behaviour. While H-1 showed an increase of adhesive strength of approximately 27% with respect to the "Reference", the adhesive strength of H-2 decreased by about 28% (to 1.47 N/mm²). In contrast to H-1 these specimens fractured within the new concrete, which possibly suggests an insufficient air void system in the new concrete with SRA.

As the results of the adhesive shear test (Figure 10, right) indicate, concrete beam H-2 (including SRA) tested an adhesive shear strength approximately 31% higher than the concrete beam H-1 (without SRA). In both cases, the additional freeze/thaw-attack caused an increase of the adhesive shear strength, for H-1 about 4% and for H-2 about 16% with respect to the "Cyclic loading" - specimens.

3.3.3 *Influence of adhesive primer/ exposure time of adhesive primer*

The following Figure 11 (left) shows the average adhesive strength of VB-4 and H-2.

Herein, the structural joint was moistened before application of the new concrete. Furthermore, the new concrete was produced with a stiff consistency (C1/C2) and using a shrinkage reducing agent (SRA). In contrast to H-2, an adhesive primer was applied on the structural joint of VB-4.

The results of the adhesive strength test show that VB-4 reached up to 7% higher adhesive strength compared to H-2. As previously observed, the test specimens "Cyclic loading + FT-attack" fractured in the new concrete, whereas the reference specimens and "Cyclic loading" fractured entirely in the old concrete resp. in the bond area. Compared to the corresponding "Cyclic loading" specimens, the freeze/thaw-attack caused a decrease of the average adhesive strength of approximately 33%.

The results of the shear test show, that VB-4 (without adhesive primer) attained about 3% to 8% higher average adhesive shear strength compared to H-2 (with adhesive primer).

Contrary to the expectations, the adhesive shear strength of specimens "Cyclic loading + FT-attack" increased by about 5% for VB-4 (5.44 N/mm²) and about 16% for H-2 (5.81 N/mm²) with regard to the corresponding specimens "Cyclic loading".

Figure 12 shows the influence of the exposure time of adhesive primer on the bonding properties by means of concrete beams H-2 und H-5. In both cases the adhesive primer was applied on the structural joint that was moistened. However, the exposure time of the adhesive primer amounted to 30 min. for H-2 and approx. 120 min. for H-5.

As the results indicate, the average adhesive strength of the reference specimens with 2.02 N/mm² and 1.97 N/mm² were almost identical. For the specimens

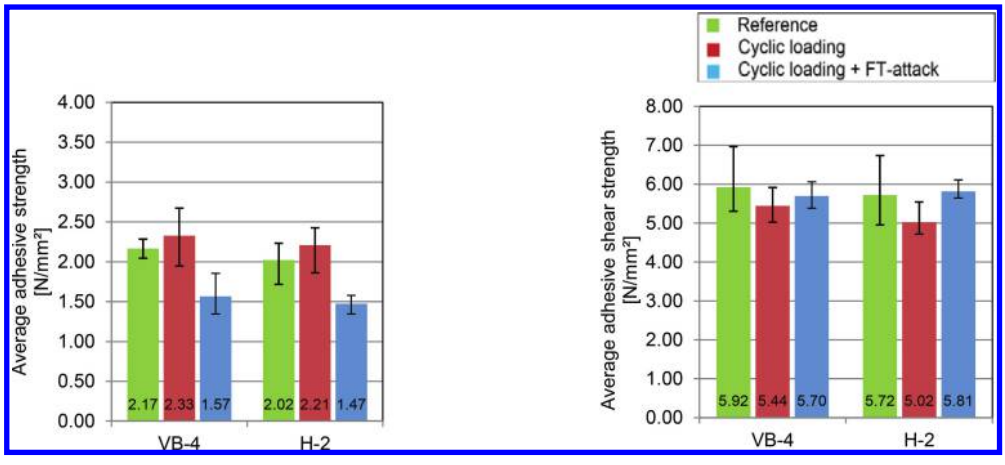

Figure 11. Average adhesive strength (left) and average adhesive shear strength (right) of VB-4 and H-2 (moist condition of structural joint, new concrete with SRA, consistency C1/C2); **VB-4: without adhesive primer and H-2: with adhesive primer**.

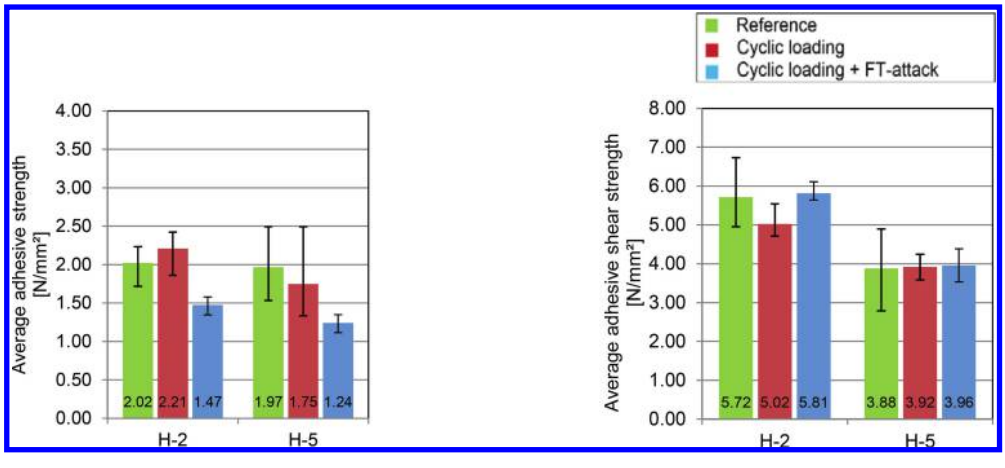

Figure 12: Average adhesive strength (left) and adhesive shear strength (right) of H-2 and H-5 (moist condition of structural joint, new concrete with SRA, consistency C1/C2**; H-2: exposure time approx. 0.5 h** and **H-5: exposure time approx. 2 h**.

"Cyclic loading" an average adhesive strength of 2.21 N/mm² was determined for H-2. H-5 showed a lower adhesive strength (1.75 N/mm²). The additional freeze/thaw-attack led to a decrease of the average adhesive strength by about 33% (to 1.47 N/mm²) respectively by about 29% (to 1.24 N/mm²).

As previously stated, the test specimens "Cyclic loading + FT-attack" fractured entirely in the new concrete, whereas the specimens "Reference" and "Cyclic loading" fractured in the old concrete as well as in the bond area.

A possible influence of the exposure time of the adhesive primer became apparent within the results of the adhesive shear strength tests. In comparison to H-2, the extended exposure time of approx. 2 hours led to a significant increase of the adhesive shear strength for beams H-5 by up to 32% in comparison to H-2.

The cyclic loading as well as the cyclic loading and the freeze/thaw-attack showed no despicable influence on the average adhesive shear strength.

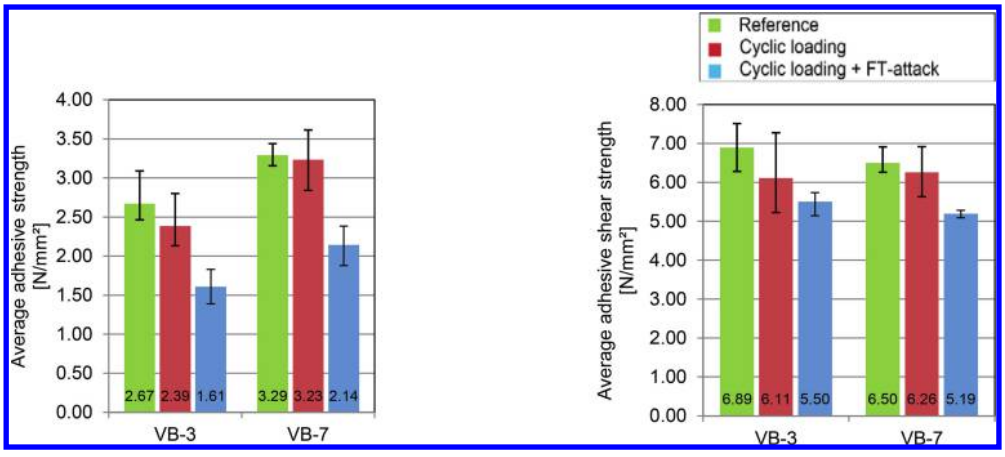

Figure 13. Average adhesive strength (left) and adhesive shear strength (right) of VB-3 and VB-7 (moist condition of structural joint, without adhesive primer, new concrete with SRA, consistency F4); **VB-3: compressive strength of old concrete approx. 62 N/mm²** and **VB-7: compressive strength of old concrete approx. 85 N/mm²**.

3.3.4 *Influence of the compressive strength of the old concrete*

Figure 13 shows the results of the bonding properties of VB-3 und VB-7, which differ from in the compressive strength of the old concrete, with approx. 85 N/mm² for VB-7 and approx. 62 N/mm² for VB-3. The results of the adhesive strength tests show that VB-7 attained up to 35% higher adhesive strength compared to VB-3. Furthermore, higher decrease of the adhesive strength after cyclic loading and after cyclic loading and freeze/thaw-attack was determined for VB-3. For example, the adhesive strength of the specimens "Cyclic loading" decreased by about 11% and "Cyclic loading + FT-attack" by about 40% with respect to the reference.

The results of the adhesive shear strength test (Figure 13, right) indicate that—contrary to the expectations—the average adhesive shear strength of VB-3 was up to 6% higher (6.89 N/mm²) than of VB-7 (6.50 N/mm²). Based on this, a positive influence of the compressive strength of the old concrete on the adhesive shear strength was not determined.

4 CONCLUSION

In this paper, relevant investigations on bonded systems produced with old concrete and a thin-layered new concrete were conducted.

Herein, a number of parameters were varied including the moisture condition of the structural joint (old concrete), the application of adhesion primer, the consistency of new concrete etc. The bonding properties between the concrete layers were determined by the adhesive strength as well as the adhesive shear strength on drilling cores.

On the basis of these investigations the pre-treatment of the structural joint and special measures during the application of the thin-layered new concrete for concrete pavement can be defined in order to ensure a durable bonding between old and new concrete.

The results acquired within the project so far have shown, that the moisture condition of the structural joint (old concrete) does not play a significant role in the bonding behaviour. Furthermore, the application of adhesive primer is only useful for concrete with a stiff consistency since the adhesive (shear) strength increased only slightly using new concrete with a soft consistency. An extended exposure time of the adhesive primer decreased the bonding properties significantly.

REFERENCES

[1] Ehrlich, N., Hersel, O.: Straßenbau heute—Betondecken, Schriftenreihe der Zement—und Betonindustrie.
[2] Eid, J.: Theoretische und experimentelle Untersuchungen dünner Betondecken auf Asphalt (Whitetopping), Dissertation 2012.
[3] Eid, J., Freudenstein, S.: Whitetopping—eine Versuchsstrecke. Betontechnologie, Bauausführung und Bewertung der Ergebnisse, Beton, Jg.: 62, Nr.11, 2012, Seite 432–438.
[4] Eid, Jochen; Freudenstein, S.: Whitetopping—Erprobungsstrecke im Zuge einer Erneuerung Straße + Autobahn, Jg.:63, Nr.6, 2012.
[5] DIN EN 1542, Measurement of bond strength by pull-off; version 1999.

[6] DIN CEN/TS 12390-9, Freeze-thaw resistance—Scaling; version 2006.
[7] DIN EN 12390-3, Testing hardened concrete – Part 3: Compressive strength of test specimens; version 2009.
[8] DIN EN 13036-1, Road and airfield surface characteristics – Test methods – Part 1: Measurement of pavement surface macrotexture depth using a volumetric patch technique; version 2010.
[9] DIN EN 14488-4, Testing sprayed concrete – Part 4: Bond strength of cores by direct tension; version 2008.
[10] Hersel, O., Kampen, R., Peck, M.: Nachhaltige Bauweise für die Zukunft: Dünne Asphaltbeläge auf Betondecken, Aktuelles zu Betonstraßen und zur Verkehrsinfrastruktur, update 2/12.
[11] Kampen, R.: Dünne Asphaltbeläge auf Betondecken (DAB) – nachhaltige Verkehrsflächen für die Zukunft, Bauingenieur, Jg.: 87, Sondernr., 2012.
[12] NÖBI – Neue österreichische Betondeckeninstandsetzungsmethode DI Stefan Spalt, ASFINAG Baumanagement GmbH, Österreichischer Betonstraßentag 2012, Betonstraßenbau: heute und morgen.
[13] Riffel, S.: Eine zukunftsfähige Sanierungsmethode mit Beton: Whitetopping; Fachbeitrag Straßenbau 06/2009.
[14] Schmerbeck, R.; Riffel, S.; Wolf, T.: Whitetopping—Erprobungsstrecke im Zuge einer Erneuerung, Bauportal, Seite 467–471, Jg.: 122, Nr.8, 2010.
[15] Werner, R.: Whitetopping—die weiße Alternative zur Sanierung von Asphaltbelägen, update 4/2005.
[16] TL Beton-StB, Technische Lieferbedingungen für Baustoffe und Baustoffgemische für Tragschichten mit hydraulischen Bindemitteln und Fahrbahndecken aus Beton, Forschungsgesellschaft für Straßen—und Verkehrswesen, Ausgabe 2007.
[17] TP Asphalt-StB, Technische Prüfvorschriften für Asphalt – Teil 80: Abscherversuch, Ausgabe 2007, FGSV, Köln.

Concrete Repair, Rehabilitation and Retrofitting IV – Dehn et al. (Eds)
© 2016 Taylor & Francis Group, London, ISBN 978-1-138-02843-2

Important factors in the performance, durability and repair of concrete façade elements

A.N. van Grieken
van Grieken & Associates, Melbourne, Australia

ABSTRACT: Concrete elements continue to feature prominently in many facades. The application of these elements in terms of geometry, finish, function and integration with other façade elements is only limited by the architectural creativity, the engineers' ingenuity and the contractors' resourcefulness.

The disparity in the durability of concrete façade elements is linked to a number of key factors which include amongst others, exposure conditions, composition of the protective concrete covers to the reinforcement, and the surface geometry and finish. In addition, movements are a common cause of defects and are often not adequately anticipated and allowed for in the design and construction. These movements include shrinkage, reversal thermal movements and deflections.

The diagnosis of defects requires tests and an adequate understanding of all relevant factors. The selection, specification and undertaking of repairs and preventative remedial works, needs to be based on this understanding of the defects and their causes, and solutions which meet the required durability. Other important commercial considerations to achieve a successful repair project, include repair quantities, and minimising access and public protection costs.

This paper examines the key durability and performance factors related to concrete façade elements and the most important corresponding repair and protective works considerations. These are based on more than 30 years of involvement with concrete facades investigations and repair projects across Australia.

1 INTRODUCTION

Many existing and new facades feature prominent concrete elements. The application of these elements in terms of geometry, finish, function and integration with other façade elements is only limited by the architectural creativity, the engineers' ingenuity and the contractors' resourcefulness.

The choice between insitu reinforced concrete elements (IRE) and precast concrete elements (PCE) is based on many factors. In most cases, both are acceptable options and structurally possible.

There is no limit to the structural use of PCE in the form of load bearing elements, including wall panels and columns and spanning elements such as beams and lintels.

Their speed of erection and high off-site quality is a major benefit. Where the architect requires a high quality finish, for example, a polished surface which highlights carefully selected aggregates of varying size and colour, this can only be achieved with PCE.

On the other hand IRE offers many benefits and can also be finished to a very high standard. This includes a Melbourne building which features off-form white, concrete facades with smooth expressed ribs and features.

The cost to construct and the speed of erection are usually the key considerations.

Whilst many IRE and PCE have stood the test of time and have remained prominent elements in the performance and appearance of the facades, others have not.

The disparity in the durability of concrete façade elements is linked to a number of key factors, which include amongst others, exposure conditions, composition of the protective concrete covers to the reinforcement, and the surface geometry and finish. In addition, movements are a common cause of defects and are often not adequately anticipated and allowed for in the design and construction. These include shrinkage, creep, reversal thermal movements and deflections.

Where defects or deficiencies have developed, it is imperative that these are diagnosed and analysed to identify the cause or causes. Investigations may only require simple observations and tests, or advanced NDT tests.

In parallel, it is important to have an understanding of the construction, exposure and load conditions, movements due to loads, including deflections and creep, amongst others.

This understanding of the defects and their causes is required to identify, select and specify

suitable solutions, to meet the required durability. Frequently, the diagnosis is easier than specifying the cure!

In addition to technical requirements, commercial and site factors are important in successful repair projects, including repair quantities, and minimising noise and disruption and access costs.

2 UNIQUE DURABILITY FACTORS

Concrete façade repairs will be durable when adequately designed for their function and exposure condition. The main durability factors, such as depths and quality of concrete covers and depths of carbonation are well researched and documented.

The most severe façade exposure conditions include salt laden air and salty rain. Many facades and structural elements exposed to such environments have a checkered history. Furthermore, the very presence of carbon dioxide in the air is a constant threat, particularly in wetter and warm humid climates Thus uncoated concrete needs to be dense, have adequate covers and well-constructed to survive undamaged.

However, in addition to the above, there are less obvious and unique conditions and factors which can influence the durability, some of which are described below.

2.1 *Surface finish*

It appears that in addition to the widely studied main depth of carbonation factors, the composition and texture of the surface are additional factors.

It appears that smooth polished exposed aggregate surfaces (photo 1) and surfaces with densely spaced exposed quartz aggregates, carbonate at a relatively lower rate. This is seen in Table 1, where depth of carbonation tests on façade elements to five buildings are listed.

The rather low results of less than 6 mm are from a 27 year old building where the facades feature precast and insitu concrete columns. The surfaces feature densely spaced exposed aggregate, a majority of which is quartz (photo 2).

Equally, low results were obtained at the 23 year old Building 5, which is clad with precast concrete panels with polished exposed aggregate surfaces.

Table 1 provides a summary of details and results.

2.2 *Surface geometry*

Ledges, rebates in the faces and water 'drips' at the base of beams, slabs are typically highly vulnerable areas.

Table 1. Depth of carbonation (DOC) examples.

	Approx Age			F'c Range	DOC Range
Build	Years	RCE	PCE	Mpa	mm
1	27		√	50–62	<6
		√		35–45	<2
2	26		√	14–17	
3	24	√		42–55	0–20
			√	32–35	0–18
4	24		√	12–21% Cement	1–15
5	23		√	35–39	AV;1–11

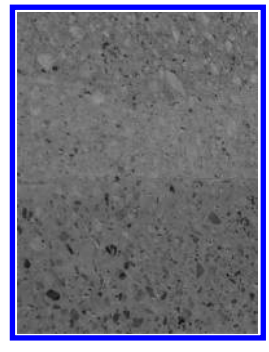

Photo 1.

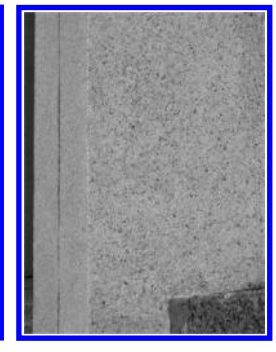

Photo 2

Photo 3.

Photo 4.

Water collects and seeps into horizontal surfaces such as ledges, creating a wet/dry, semi 'tidal' condition, which is the danger zone in marine structures. Water also adheres to the underside of beams and wall openings and is absorbed by osmosis.

In parallel with the above, concrete covers may be reduced at feature rebates (photo 4) and at 'drips' (photo 3), which potentially decreases the durability due to the increased probability of corroding reinforcement.

2.3 *Movements*

The term 'movements' is used generically in this paper, as it covers many forms of movement with possible corresponding defects. Amongst others:

- *Deflections:* cause cracking and end rotations.
- *Shrinkage and Creep* in the form of vertical and horizontal shortening: cause a range of defects including face spalling and cracking. This includes post-tensioned elements which can cause structural but also significant non-structural damage.
- *Thermal*: reversal expansion and shortening can result in defects similar to shrinkage/creep.

In general, over time buildings shorten, predominantly due to self-weight, beams deflect, and post-tensioned floors shorten due to creep. The latter can continue for many years and well beyond some expectations.

Differential thermal loads and/or thermal movements are a particular concern where PCE elements are, or become, rigidly locked in place and connected.

2.4 *Other*

A. Spalling has occurred at locations of concentrated water run-off on otherwise durable facades. These include short outlets on the face of balcony balustrades, the base of vertical architectural grooves and the base of window mullions.
B. The orientation of the façade is a significant factor as exposure conditions will vary accordingly. Hotter facades dry out faster; predominant rain directions create more frequent and more severe wetting.
C. Facades bombarded by 'salt laden' aerosols are less durable than those on the opposite leeward side of the building.
D. Furthermore, differences have been noted at local façade areas such as at corners where negative local wind pressures create drier, vacuum-like conditions.

In summary, the diagnosis of defects and conditions needs to take all of the above into consideration. Rarely are defects contributable to a single cause.

3 IMPORTANT FACTORS IN SUCCESSFUL REPAIRS AND REPAIR PROJECTS

3.1 *Technical*

High quality repair materials and methods alone may not be sufficient to achieve durable repairs.

Photo 5.

Photo 6.

Whilst it is imperative to fully understand the causes of the defects before designing the repair, the old adage to 'design around the problem' is applicable in many cases. In addition to generic repairs, specific targeted repairs may be required.

For example, additional movement accommodation capacity may need to be introduced and the local geometric configuration may need to be altered. Protective treatments are required where the development of future defects is likely, and where the repairs and existing concrete are not likely to resist to the exposure conditions.

Following are some examples:

A. Cracks and spalls may develop where PCE elements are rigidly connected to the façade structure. This was the case at a building where the facades featured heavy long-span precast concrete sunhoods. The cast-in projecting steel connections were welded to rigid steel supports. A combination of thermal stresses and deflections caused cracking and spalling (photo 5). Durable repairs require one end to be freed in addition to concrete repairs, as concrete repairs alone cannot resist the significant local stresses at these rigid connections.

   In another case, many precast concrete balustrades at a large number of public buildings developed cracks at connections. Not only were these connections fully locked in, the supporting floor was precast. The combination of movements and corresponding stresses caused cracking, which precipitated reinforcement corrosion and spalling (photo 6).
B. At highly vulnerable recessed drips with very low concrete covers, at the underside of concrete elements (for example, photo 3), it may be better to repair and infill these and add a small element to create a positive drip.
C. Not all repair projects are driven by concrete defects. Glass etching due to alkaline contaminated run-off water is a common problem.

Photo 7.

Photo 8

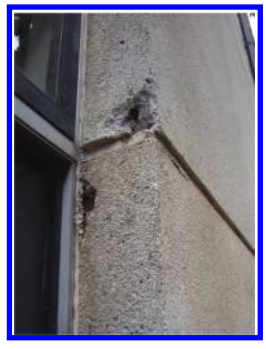

Photo 9.

Photo 10.

Rainwater may become more alkaline after passing over concrete surfaces, particularly where these are porous. The resulting glass etching, which can only be treated by buffing the glass with proprietary compounds, will re-appear if the cause of the problem is not addressed.

Impregnating silane treatment of the concrete surfaces above the windows was a very successful and very durable 'repair' at one high-rise building. As this will alter the appearance, trials are required.

D. In another case, a significant number of spalls developed on surfaces of polished PCE façade panels to a highrise CBD building. Close examination revealed that these were generally not due to corroding reinforcement, and the presence of small white particles at the apex of the conical spalls (photos 7 and 8).

As a result, in addition to concrete covers, carbonation and chloride content tests, petrographic examinations were carried out on thin sections. Furthermore, concrete specimens and the white aggregates were subjected to scanning electron microscopy (SEM) and energy-dispersive x-ray (EDX) analysis. This revealed that the white aggregates at the centre of the spalls are composed of Periclase(MgO) and Brucite [Mg(OH)2)], the latter a hydration product of Periclase. The hydration process is expansive and the likely cause of the spalling.

Clearly, conventional repairs are not applicable in this case, and as the spalling to date may be the 'tip of the iceberg', preventative remedial works are required.

E. Straightforward repairs to concrete walls can become more complicated at windows. Corroding fasteners to the concrete walls can precipitate cracks and spalling, which in turn causes the wall reinforcement to become exposed, corrode and the concrete to spall (photo 9).

Photo 11.

Photo 12.

In this case, the repairs need to include replacement of fasteners. In addition, repairs at windows need to avoid breaching waterproofing flashings, avoid altering the design of the water proofing such as, for example, and need to maintain pressure equalized cavities, drainage paths and weep-holes. Needless to say, that during the works, the interiors need to be protected against water ingress.

F. Delaminated veneers (photo 10) can effectively reduce concrete covers and require large areas of render to be removed and concrete to be repaired where reinforcement has corroded (photo 11). In other areas injection rebonding will not only re-attach these veneers, but also restore the 'protective layer of concrete'.

G. The inclusion of galvanic anodes can prevent the formation of insipient corrosion and has no visual impact. For facades this is the preferred approach as the more traditional cathodic protection requires wiring, a power source and monitoring which is often not practical, particularly at PCE, and isolation of metallic elements.

H. Clever formwork (photo 12) can be repetitive, produce an acceptable line and finish and allow the mortar to cure properly.

Photo 13.

Photo 14.

Photo 15.

Photo 16.

3.2 *Commercial*

A. *Quantities* are the most contentious and challenging aspects of façade repair projects. The optimum approach is to undertake a detailed survey of all concrete façade elements. As this is often not cost effective, the alternative is to survey a percentage and extrapolate the findings or to adopt a rates based contract. However, the latter leaves the owner with an unknown final cost.

B. *Noise and disruption* due to impact equipment is another major challenge. For example, in one case, jack hammering at Level 4 of a 60 storey building, was clearly heard in offices at the upper levels, as such sounds readily transmit through concrete structures. Legal courts, medical practices, entertainment buildings where musicians practice during the day, hotels, hospitals and the list goes on, have a very low noise tolerance. Some can neither tolerate daytime nor night-time noise. Hydro demolition, diamond drills and other 'lower' noise equipment will be required in addition to negotiations, understanding and goodwill.

C. *Communication*. Building occupants expect and need to be regularly informed about the repair works with the aim to minimize disruption, protect privacy etc.

D. *Access*. Inevitably, access and access equipment requires consent from apartment owners and building tenants. This may prove to be very difficult and limiting and needs to be resolved before the contract is signed. Some projects require access to private balconies (photo 13) for emergency access, daily access and even for the supporting frames for the swing stages.

E. *Public Protection* is usually in the form of a street level gantry. However, as photo 14 shows, footpath gantries only offer limited protection. Thus, as a minimum, the works need to be undertaken such that these become contained local work sites at the repairs and/or the façade is contained as a whole by scaffold and mesh.

3.3 *Expect the unexpected*

Unlike 'green field' new construction projects, repair projects have a higher probability of the unexpected.

This includes latent conditions, material complications and natural events. Following are some case examples:

- Live electrical copper conduits were uncovered during the removal of concrete at PCE façade panels. The corroding reinforcement which caused the spalling was not far away!
- Unique weather circumstances resulted in a plague of beetles. These repeatedly landed in large numbers, on the wet coating to the repaired facades (photo 15).
- Heritage concrete facades and façade elements are always challenging. At a major public heritage building, rubble, plaster and large voids were found behind heavily cracked precast concrete (photo 16). This required replacement with matching precast concrete elements which were constructed to meet heritage requirements in terms of materials, texture, colour and connections. Again trials were the key to success.

3.4 *Quality Assurance*

Quality Assurance starts from day one on-site to the completion. This needs to include a range of components.

- Trials allow the client to see and approve the proposed outcomes, and hold points enable the designer/specifier to inspect and study the critical stages of the works. It is particularly difficult to achieve an acceptable finish to repairs on the face of polished precast concrete surfaces.

Photo 17.

Photo 18.

Photo 19.

Photo 20.

Photo 1 in Section 1 shows a good example of a matching repair. Multiple trials are usually required with different aggregate and matrix blends at exposed aggregate surfaces (photo 17).

– Pull-off tests provide a quantitative evaluation of the quality and the bonding of the repairs (photo 18). However, these are difficult to undertake at irregular surfaces and geometries.
– Humidity, surface temperature and moisture content tests before coating are required by coating manufacturers. (photo 19).
– Monitoring quantities at agreed 'hold points' will avoid disputes, particularly at large projects with large and geometrically complex repairs (photo 20).

Finally there is no substitute for regular site presence and chats with and feedback from the tradespersons, as the most successful projects are carried out as a team.

4 CONCLUSION

Concrete façade repair projects are complex and involve many aspects. An adequate understanding of the cause of the defects, solutions which eliminate or accommodate these causes, experienced specialist contractors and a bit of luck are required for successful repair projects.

Concrete Repair, Rehabilitation and Retrofitting IV – Dehn et al. (Eds)
© 2016 Taylor & Francis Group, London, ISBN 978-1-138-02843-2

Evaluation of shear bond test methods of concrete repair

V.D. Tran, K. Uji, A. Ueno, K. Ohno & B. Wang
Tokyo Metropolitan University, Tokyo, Japan

ABSTRACT: An experimental and theoretical study were performed to evaluate the shear bond strength of the interface between concrete substrate and repair material in 5 types of test. Up to now, there are many different tests to estimate the strength but their results varies significantly. Based on the result of 63 specimens, it could be indicated that: this shear bond strength depends not only on the internal features of specimens, but greatly on test method. The experiment that exists only purely shear stress at the interface always gives the smallest result. Especially, the change of bond plane's angle in Shear Slant Test generates a larger compressive stress components at the interface; therefore the highest value of bond strength was obtained in this test. In the later part, calculations based on the shear friction theories could clarify more details about the differences of results.

1 INTRODUCTION

After the booming era in the development of infrastructure in the middle of the last century, there are more and more concrete constructions facing deteriorating situations. Instead of replacing, repairing and strengthening these structures is a better solution in both economic and environmental viewpoint. Therefore, the task of the civil engineer now is to find out an efficient method for restoring the aged constructions and at the same time, ensure the highest level of safety operation.

One of the most common measures for repairing old concrete structures is to remove the bad surface layer, clean rust of corroded reinforcement, and then overlay by a suitable material. For that reason, the good adhesion between attached material and concrete substrate is an important factor affecting the success of concrete repairs (Czarnecki 2009). To increase the bond between two parts, the usual technique is to create a rougher substrate surface or add a bonding agent (Julio et al. 2005). Although many types of test have been developed to estimate the shear bond strength of the interface, until now no accurate prediction of this value has been unified. Therefore, it is still difficult to use these results for practical application (Austin et al. 1999).

As we all know, concrete is a highly complex heterogeneous material, each specimens is not exactly the same as others. Moreover, the pattern of each test method to obtain this value is entirely different. Consequently, the shear bond stresses vary significantly between different tests. These evidences prove one thing the shear bond stresses depend on not only the characteristics of these materials and the interface's conditions, but also the test methods (Momayez et al. 2005, Santos et al. 2011).

In this study, the shear bond strength was evaluated through experimental and theoretical study. Five types of tests were conducted. The differences of each test model which lead to the dissimilar results are discussed and thereby giving us an overview about test method to obtain this strength. In the remaining part of this paper, the theoretical calculations are presented to some degree make clear of the difference in the results of these tests.

2 EXPERIMENTAL INVESTIGATION

The experimental study had the main purpose of evaluating the influence of test methods on the shear bond strength between concrete substrate and repair mortar. Simultaneously, the correlation between this strength and the interface roughness is also discussed. There are five kinds of test carried out, namely, Direct shear test (DST), Push-off test (POT), Bi-surfaces shear test (BSST), Slant shear test (SST) and Punching shear test (POT) (Uji et al. 2007). The difference in stress state, such as purely shear stress, compressive-shear stress or a change of bond plane's angle caused varying results.

During the test, AE censors are attached on the surface of all specimens. Therefore, failure processes can be monitored by the acoustic emission (AE) method and analyzed by SiGMA (Simplified Green's functions for Moment tensor Analysis) procedure (Ohtsu 1991).

2.1 *Testing procedure*

Figure 1 shows the experimental model of each test with all detail dimensions. There are many ways to classify these tests in a group with the same characteristics. In this paper, based on the stress state at the substrate surface, DST and BSST are belonging to the group that bond strength only relates to purely shear stress. In contrast, with POT and PST, their testing frame models refrain horizontal deformation of the specimens that could generate a compression component at the interface. The last one, SST is the test whose bond plane angle is not perpendicular with external load causing the change of stress direction at the interface.

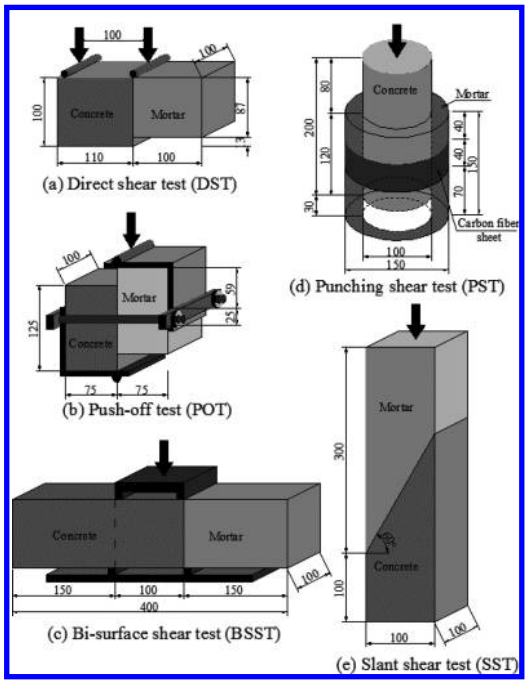

Figure 1. Shear bond test methods.

Table 1 presented the mix proportion of substrate concrete. Repair material is the premixed type which does not include polymer and fiber. Compressive strength of mortar is higher than substrate concrete. The mechanical characteristics of hardened concrete substrate and repair mortar are given in Table 2.

A total of 63 specimens were created, in which DST, PST and SST each has 15 samples divided to 3 types of interface roughness level; POT and BSST has 9 specimens each also divided to the 3 different surface types. Substrate concretes were casted and cured in standard condition until 14 days before being attached by repair mortar. After that, the specimens were continued being cured. Shear test would be carried out from 28 days age of the substrate.

Figure 2 displays the images of the concrete substrate in three types of roughness index: Smooth (S-type), Medium (M-type) and High (H-type). In all test, by using the set retarder sheets, which can adjust the setting time of cement, the surfaces of concrete substrate had been prepared for three different roughness levels. The set retarder sheets were pasted on the mold's surface, which contact directly with the M&H-type substrate surface before casting.

Table 1. Mixture proportion of base concrete.

Maximum aggregate size (mm)	Slump (mm)	Water Cement ratio (%)	Air content (%)	Unit content (kg/m^3)			
				Water	Cement	Fine Aggregate	Coarse Aggregate
20	80	58.0	4.5	174	300	821	985

Table 2. Mechanical properties of base concrete and repair material.

	Concrete substrate			Repair mortar		
	Compressive strength	Tensile strength	Elastic modulus	Compressive strength	Tensile strength	Elastic modulus
	(N/mm^2)	(N/mm^2)	(kN/mm^2)	(N/mm^2)	(N/mm^2)	(kN/mm^2)
Direct shear test	37.7	2.98	26.6	62.7	5.05	30.0
Push-off test	37.1	2.80	26.7	62.0	4.60	26.4
Bi-surfaces shear test	33.2	3.00	25.3	58.6	4.20	27.1
Punching shear Test	36.5	3.18	26.7	68.7	3.63	32.0
Slant shear test	41.4	3.25	27.7	66.3	4.09	30.7

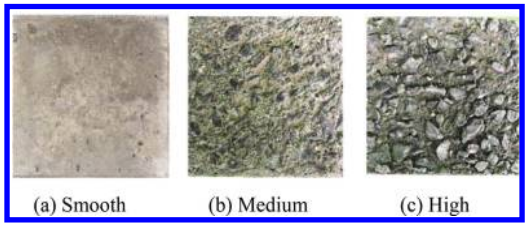

Figure 2. Three types of surface texture.

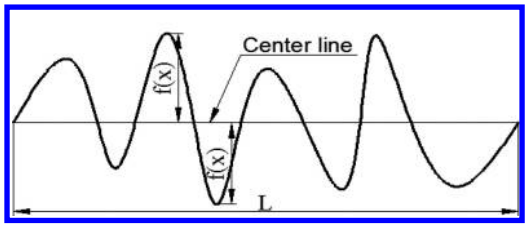

Figure 3. The center line average roughness.

After one day, these surfaces were treated by wire brush and sprayed water in different degree to create the desired roughness levels. The roughness index were measured by laser displacement transducer and qualified by the centerline average roughness method (Ohno et al. 2011). The method is calculated by the following equation:

$$R_a = \frac{1}{L}\int |f(x)|dx \quad (1)$$

Where R_a = center line average roughness (mm) which consider as the roughness index of the surface; L = length of the surface; $f(x)$ = height from center line. (Fig. 3).

2.2 *Test results*

Table 3 presents the average values of roughness in each types and the corresponding average shear bond strength. It should be mentioned that the result in Table 3 is only the value when failure mode of test was adhesion failure at the interface. It means that the plane of failure is along the interface. Especially, with PST's bond strength, the numbers inside ( ) present the average values which were not clearly adhesive failure results. In Figure 4, the imprecise values of PST are also put inside ( ).

The shear bond strength of all methods was calculated by dividing the maximum load at failure by the bond area; for SST, the bond area is a slope surface. Figure 4 illustrates more details about the correlation between the roughness index and the bond shear strength of all specimens.

Table 3. Tests results.

	Average roughness		Average shear strength
	Type	Value	(N/mm²)
Direct shear test	Smooth	0.05	0.51
	Medium	0.38	2.11
	High	0.85	2.77
Push off test	Smooth	0.1	2.59
	Medium	0.64	3.53
	High	0.99	5.00
Bi-surface shear test	Smooth	0.08	0.51
	Medium	0.47	2.43
	High	0.95	3.50
Punching shear test	Smooth	0.07	1.65
	Medium	0.36	5.33 (6.18)
	High	0.63	(6.95)
Slant shear test	Smooth	0.17	5.30
	Medium	0.49	15.41
	High	0.7	–

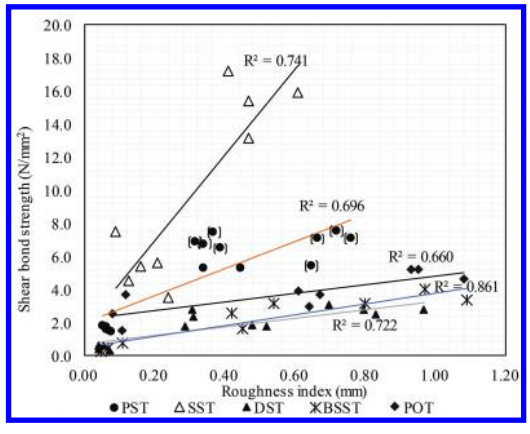

Figure 4. Relation between the roughness index and the shear bond strength from test results.

2.3 *Discussions about the results*

As can be seen from Table 3 and Figure 4, the highest values of shear bond strength in all same roughness level are belonging to SST. The following high values occurs in the PST and POT. Two remaining tests, DST and BSST have the similar and much lower values. Moreover, obviously, roughness level of the interface has a profound effect on the shear bond strength. Increasing roughness of the interface surely would lead to rising of shear bond strength. However, the outcomes of each test differ significantly, making it hard to choose an accurately value of bond strength between old and new

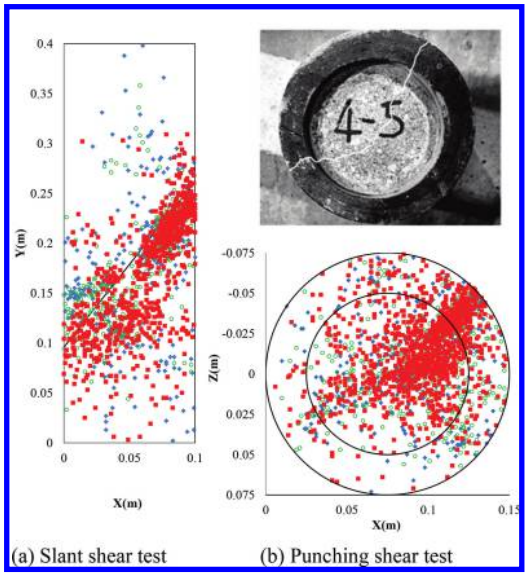

Figure 5. Results of SST and PST.

concrete. In the experimental study, SiGMA analysis was applied to obtain AE signals that made the fracture zone inside of all specimens could be visualized easily.

SST is one of the most popular tests used to obtain this value because of its simplicity. It is said that this test method is so sensitive to variation in bond strength that it could present consistent results (Santos 2011). However, same as many previous studies (Julio et al. 2004, Momayez et al. 2005), SST always gives the highest bond strength in comparison with others in the same surface's condition and material's characteristics. This can be attributed to the slope of bond plane cause high compressive stress on the surface. This compressive stress would generate higher interlock and friction forces at the interface (Santos et al. 2012). In this study, the value obtained from adhesive failure was recorded only in the S-type specimens and 4 out of 5 samples of M-type. With higher roughness level, the failure mode of the specimens turns to cohesive failure mode, which is related to these materials' compressive strength (Fig. 5a).

PST, classified to the category of bond test that stress at the interface is the combination of shear stress and compressive stress. The compressive stress is produced by the restraint comes from repair material outer ring and carbon fiber sheet when loading. Therefore, the results of this test are also high with regard to another test methods. Moreover, the slip phenomenon between two materials only occurred clearly in all smooth roughness specimens and two out of five of the

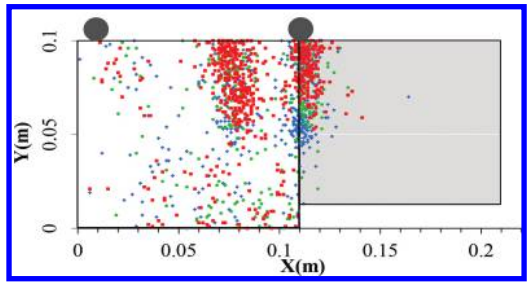

Figure 6. Results of DST in H-type specimen.

M-type. In other specimens, failure concentrated on a specific area of specimen, not all of interface (Fig. 5b). Therefore, these unclear results could not be considered as the shear bond strength. The reason maybe because this area is the weakest part of the specimens or the value of external force at this moment exceeds splitting tensile strength of the material.

DST is the simplest test that can get purely shear bond strength. 14 of 15 specimens failed at the interface. As can be seen in Figure 4, the bond strength values achieved in this method is moderately small. Furthermore, the growth of shear bond strength in the relationship with the increment of roughness level is not as much as in others method. Especially, in H-type specimens, flexural cracks appeared at the middle span of substrate concrete that would reduce the accuracy of its results. It means shear stress did not work effectively at the interface. The reason may come from a small eccentricity in loading position (Fig. 6).

With the intention to eliminate bending crack occurs as in DST, we continue carrying POT experiment with the special frame support. Two L-shaped steel plates combined with 2 bolts, tightened by hand, help to keep external loading only acting in the vertical direction at the interface. Consequently, all samples were failed at the interface. However, according to the AE results (Figs. 7a, b), shear stress seems to work well in S and M-type specimens. With H-type cases, AE events did not concentrate only at the interface. Indeed, during testing process of this method, it is difficult to keep the specimen in stable condition. Only a small eccentricity of external force, the interface would be deviated from the vertical direction and thus, generates a rotation moment in this testing sample (Fig. 7d). The existence of crack that were highlighted by pen in Figure 7c as well as the AE analysis results are clear evidences for this problem. Simultaneously, the restrain of two fixed bold at the middle of the specimens may cause the bond strength results in this test method become higher

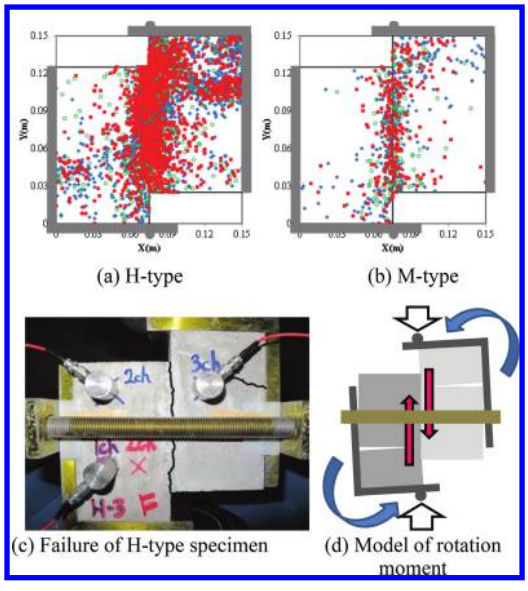

Figure 7. Results of POT.

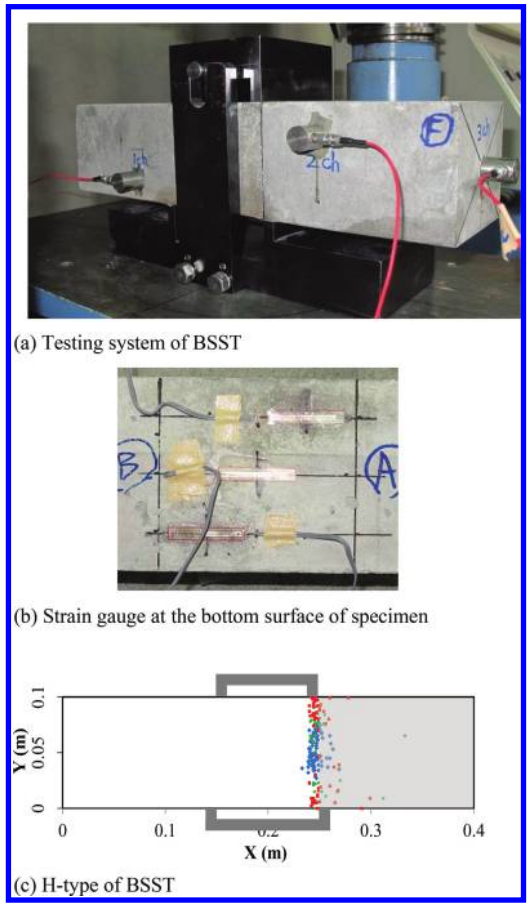

Figure 8. Results of BSST.

than in those of DST. For these reasons, this test method may not be suitable to estimate shear bond strength of bi-materials.

BSST testing systems is better in consideration of stability problems of specimen during loading. Moreover, with two loading positions as in Figure 8a, the testing system in BSST can reduce the influence of flexural phenomenon in the specimens. Additionally, to estimate the equality of loading's transmission at two locations, strain gauges were attached on the underneath surface to measure longitudinal strain (Fig. 8b). In fact, in this test method, all specimens failed at the interface. The external loading destroyed the weakest part of this concrete sample and the results of strain showed that 2 loading points are equal during testing process. The shear bond strengths obtained in this method are as small as those in DST, simultaneously the trend line of correlation between this strength and the roughness index are also similar. Although the distribution of the external loading in 2 positions need to be studied more, this test method is shown as a reliable method to evaluate purely shear bond strength between old concrete and repair material.

3 THEORETICAL ANALYSIS

Theoretical analysis in this study based on the shear-friction theory, which has been developed for almost 50 years with many researches (Santos et al. 2012). A saw-tooth model is used to exemplify the macro texture of the interface between concrete substrate and repair material (Fig. 9a).

To simplify, all saw-tooth at the interface is exactly the same. The width b depends on number n of teeth on length L of the surface. Angle α is an inclination of the saw-tooth. Based on trigonometry formula, the height $h = (b/2)\tan\alpha$ (2). According to Equation 1, the value of surface roughness average $R_a = h/2$ (3) (Fig. 9b).

It is assumed that in every saw-tooth always exist two bonding components on the surface to restrain slip between 2 parts, namely adhesion and friction (Austin et al 1999). The first term "adhesion" is mainly granted by the chemical bond connection of mortar and aggregate (the pure shear strength). The second term "friction" is contributed by friction force that resisting the relative motion of mortar on the aggregate's surface. If external loading exceeds total of restrained forces,

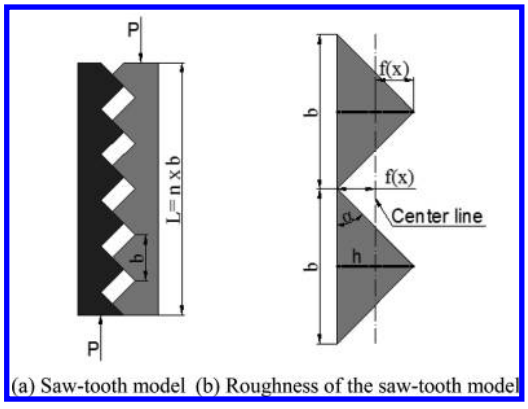

Figure 9. Saw-tooth model.

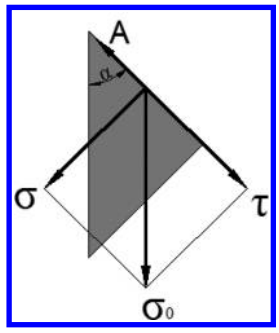

Figure 10. Force diagram in Group 1.

the shear failure will occur like a slip phenomenon between two materials. However, if the external stress goes over shear strength of these materials, shear failure would also happen due to the breaking of the saw teeth. In each type of test, the normal stress appears and varies because of external force or the change of bond plane's angle. And this is the main reason make the results of each tests is significantly different.

These 5 tests can be divided to 3 groups: Group 1: purely shear stress, Group 2: shear-compress stress and SST. DST, BSST belong to the first group; POT, PST are in the second one, SST is the one that comparatively different with others.

3.1 *Group 1: Purely shear stress group (DST, BSST)*

In the group, there is only an external force in the vertical direction. This external stress σ_0 could be analyzed to normal and tangential components at the saw-tooth's surface (Fig. 10). Slip phenomenon will start if the following condition is satisfied:

$$\tau \geq \mu\sigma + A \tag{4}$$

Where τ = the tangential external stress at the interface; μ = coefficient of friction; σ = the external normal stress at the interface; A = the adhesion strength (the pure shear strength);

As can be analyzed in Figure 10

$$\begin{cases} \tau = \sigma_0 \cos\alpha \\ \sigma = \sigma_0 \sin\alpha \end{cases}$$

The delamination will occur if

$$\sigma_0 \geq \frac{A}{(\cos\alpha - \mu\sin\alpha)} \tag{5}$$

And

$$(\cos\alpha - \mu\sin\alpha) > 0 \tag{6}$$

Equation 4 can be understood that if this condition is not satisfied (angle α is large or value μ is big), a mortar saw-tooth cannot slip on the aggregate surface. In other words, if loading continues increasing, the saw-tooth would fracture by shear stress or cohesive failure would happen in two materials. It also means that at a certain value of angle α (or R_a), the increment of roughness could not make the bond stronger.

DST and BSST are the typical types of this group. Neglecting the deviation of external force in DST and the distribution of loading to two positions in BSST, their force diagrams at each saw-tooth are exactly the same as in Figure 10.

3.2 *Group 2: Shear-compress stress group (POT, PST)*

In POT, besides the basis external stress as in DST, at the interface, another normal stress component C appears to restrain the horizontal deformation of the samples (Fig. 11). This frame system not only causes initial compression force but also makes the normal stress increase more and more when external loading rises. Therefore, the friction force at the interface also grows and the results of shear strength in this experiment are always higher than that in the previous one. We can see more details in the following formulas.

C is lateral stress caused by the fixed bolts and can analyze to normal stress C_n and tangential stress C_t at saw-tooth's surface. Based on Hooke's law for linear isotropic material, C can calculate as:

$$C = \gamma\sigma_0 + C_0 \tag{7}$$

Where γ = the Poisson ratio of material and C_0 = the initial compression force.

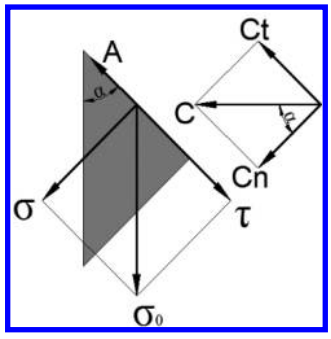

Figure 11. Force diagram in Group 2.

Equation (4) will become:

$$\tau \geq \mu(\sigma + C_n) + A + C$$

With

$$\begin{cases} \tau = \sigma_0 \cos\alpha \\ \sigma = \sigma_0 \sin\alpha \end{cases}$$

And

$$\begin{cases} C_n = C\cos\alpha = (\gamma\sigma_0 + C_0)\cos\alpha \\ C_t = C\sin\alpha = (\gamma\sigma_0 + C_0)\sin\alpha \end{cases}$$

The delamination will occur if

$$\sigma_0 \geq \frac{C_0(\mu\cos\alpha + \sin\alpha) + A}{(\cos\alpha - \mu\sin\alpha - \mu\gamma\cos\alpha - \gamma\sin\alpha)} \quad (8)$$

And

$$(\cos\alpha - \mu\sin\alpha - \mu\gamma\cos\alpha - \gamma\sin\alpha) > 0 \quad (7)$$

In PST, the force diagram is similar with this one in POT but the restrained compression force is caused by the Carbon fiber sheet and the holding force of outer ring mortar. Because tensile strength of mortar is much smaller than tensile strength of Carbon fiber sheet, the failure will occur when external stress exceeds total of the resistance ones or it reaches the value of splitting tensile of mortar material.

3.3 *Slant shear test*

The SST is one of the most common type of bonding test in which the interface is under combined state of compression and shear stresses. The angle of failure plane with horizontal direction is 60°. The change of bond plane's angle makes the projection of external force on the perpendicular direction of saw-tooth's surface increase. For that reason, the friction stress goes up and makes the value of bond shear strength in this type of test always much higher than the others (Fig. 12).

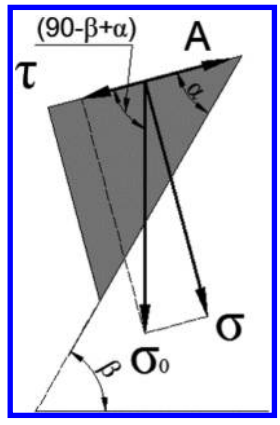

Figure 12. Force diagram in SST.

The external stress now is:

$$\begin{cases} \tau = \sigma_0 \sin(\beta - \alpha) \\ \sigma = \sigma_0 \cos(\beta - \alpha) \end{cases}$$

Equation (2) becomes:

$$\sigma_0 \geq \frac{A}{(\sin(\beta - \alpha) - \mu\cos(\beta - \alpha))} \quad (10)$$

And

$$(\sin(\beta - \alpha) - \mu\cos(\beta - \alpha)) > 0 \quad (11)$$

3.4 *Prediction of the shear bond strength in correlation with roughness index*

The equations above (Eq. 4, 8, 10) can be used to predict failure stress of each test. The right side of these equations is the minimum value of external stress σ_0 which should be achieved to cause slip phenomenon at the interface. In the following part of this paper, these equations will be calculated by specific parameters to compare with the experimental results.

Based on the laboratory results described earlier, the adhesion strength, A, could be determined as the values obtained in the purely shear test group (DST, BSST) in S-type specimens as 0.5 N/mm^2. The internal friction coefficient is considered as

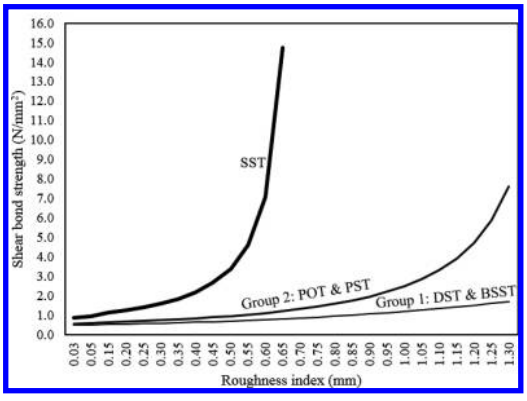

Figure 13. Relation between the roughness index and the shear bond strength from theoretical calculations.

the value for friction between cement concrete and dry gravel, as 0.6. It is assumed that the width of a saw-tooth b = 5 mm and the surface roughness average R_a vary in corresponding with the angle α (See Eq. 2&3).

In POT, the Poisson ratio the specimen's material can be determined as 0.2 of concrete material. The initial compression force C_0 could be neglected.

It should be noted that in order to create the chart about the relation between roughness index of the interface and shear bond strength is logical, firstly we should attend to the conditions in Equation 6, 9, 11. More importantly, the limits of material strength should be considered carefully. For example, the external stress cannot exceed the shear strength of concrete material (appropriately 14–17 N/mm^2). Or in PST, the specimen would fracture because of splitting tensile strength (as 3.63 N/mm^2 in Table 2).

As a result, the estimation results of three groups are presented in the Figure 12. These curves reflected comparatively similar with the laboratory results. The bond strength computed in SST is still the highest and has a high degree of sensitivity to roughness level of the interface. With these assumed parameters, the result in SST quickly reaches the limit value of material strength and switches to a different form of destruction. POT and PST's results are higher than those in group 1 due to the impact of compressive components.

4 CONCLUSION

The bond strength is significantly change depend on type of test method. Depending upon on the practical application, we can choose the appropriate type of test method.

From experimental and theoretical results, it is obvious to say that roughness level has a great influence on shear bond strength. However, from a certain limit of roughness, increment of roughness would become meaningless, because the failure would not occur at the interface but turn to cohesive failure of material.

From the theoretical calculations, it is now clear why the compress-shear stress state tests always give higher results than others and SST presents the highest. In the purely shear bond test group, BSST is the most suitable one because this test is not only simple but also more stable.

ACKNOWLEDGEMENTS

This research was supported by Asian Human Resources Fund from Tokyo Metropolitan Government.

REFERENCES

Austin, S., Robins, P. & Pan, Y., 1999. Shear bond testing of concrete repairs. *Cement and Concrete Research 29*: 1067–1076.

Czarnecki, L., 2009. Adhesion—A challenge for concrete repair, *Concrete Repair, Rehabilitation and Retrofitting II*: 935–940.

Julio, E.N.B.S., Branco, F.A.B. & Silva, V.D., 2005. Concrete to concrete bond strength: influence an epoxy based bonding agent on roughened substrate surface. *Magazine of Concrete Research* 57(8): 463–468.

Julio, E.N.B.S., Branco, F.A.B. & Silva, V.D., 2004. Concrete to concrete bond strength: Influence of roughness of the substrate surface. *Construction and Building Materials 18:* 675–681.

Momayez, A., Ehsani, M.R., Ramezanianpour, A.A. & Rajaie, H., 2005. Comparison of methods for evaluating bond strength between concrete substrate and repair material. *Cement and Concrete Research 35:* 748–757.

Ohno, K., Kurohara, S., Uji, K. & Ueno, A., 2011. Failure process in shear bonding strength test between existing concrete and repair material by acoustic emission technique. *Proceedings of International RILEM Conference on Advances in Construction Material through Science and Engineering*: 385–391.

Ohtsu, M., 1991. Simplified Moment Tensor Analysis and Unified Decomposition of AE Source. *Journal of Geophysical Research* 96(B4): 6211–6221.

Santos, P.M.D., Julio, E.N.B.S., 2012. A state-of-the-art review on shear friction. *Engineering Structures 45*: 435–448.

Santos, P.M.D., Julio, E.N.B.S., 2011. Factors affecting bond between new and old concrete. *ACI Material Journal V.108(4):* 449–456.

Uji, K., Satoh, K. & Kobayashi, A., 2007. Effects of retrofitting method using CFRP grid on shear behavior of existing concrete members. *Proceedings of the 8th International Symposium on Fiber Reinforced Polymer Reinforcement for Concrete Structures*.

Concrete Repair, Rehabilitation and Retrofitting IV – Dehn et al. (Eds)
© 2016 Taylor & Francis Group, London, ISBN 978-1-138-02843-2

Structural repair approach for reinforcement corrosion in concrete building structure: An application case

G. Gallina, M. Graziosi & A. Imbrenda
Proges Engineering S.r.l., Rome, Italy

ABSTRACT: The reinforcement corrosion in concrete building structures is one of great problem in preservation, durability and life services extension of existing building. The knowledge of structural safety level of building damaged by corrosion effects is necessary to estimate the residual service life. A probabilistic approach based on Beyesian Belif Network applied on experimental data (carbonatation concrete level) combined with the typological geometrical features of the building allow to estimate the residual services life of the building, through the lost resistance of elements. All this data permit the evaluation of best repair approach and to obtain a services life extension. The procedure data drive structural design repair choice. The study carried out show the application on a seven stories office building 56 years old. Each floor is 2000smq. Columns-beams frame forms a façade structural system. High level of reinforcement corrosion damage was evident on many structural elements. The experimental tests on reinforced concrete elements was carried out to know the carbonatation level. The structural repair is carried through rust remove, process of rebars passivation and FRP application. The service life extension is calculated for repaired structures. The study shows the potentiality of the method (the opportunity of an integral approach in this field) and limits of the approach (evaluation of confidence range in experimental data).

1 OVERVIEW

1.1 *Field*

Preservation of the real estate is one of the topics of greatest interest to those who manage them. The issue is very important both for the preservation of life and for the economic impact that structural maintenance interventions have. An important part of the real estate consists of buildings with reinforced concrete structure. In Italy, most of the reinforced concrete buildings were built in a period from the end of Second World War to the early 70s. Reinforced concrete structures of the buildings of this period have often shown problems of degradation due to corrosion of the reinforcement bars, which prompted the subsequent studies and research, which introduced the durability requirements among the criteria for a project. In this context, those who manage real estate assets will often have to decide whether to take action to repair the structures or defer interventions.

At present there are no easy use tools that allow, case by case, to quantify the damage and then evaluate the decisions to take.

1.2 *Aim*

The study proposes a methodology for assessing the probability of collapse. This determination, which can be specialized for each building, allows to have a significant datum on the basis of which make decisions about repairs.

2 BACKGROUND

2.1 *Carbonation induced corrosion*

As is known one of the major causes of corrosion is the carbonatation of concrete. The process of penetration of carbon dioxide into the concrete leads to a change of the pH causing the depassivation of the bars and their subsequent oxidation. Carbonatation is ruled by numerous factors and this causes extreme variability of the phenomenon even in apparently similar conditions. It is clear, in fact, that carbonatation both strongly depends on environmental weather conditions and material peculiar features (especially water/cement ratio, porosity, etc.). Thus the advancing front of carbonatation (defined as the area of interface between the carbonated concrete and that not carbonated) varies greatly not only according to life time of the structure but also, and just as significantly, according to the parameters given above.

2.2 *Corrosion impact on structural resistance*

Corrosion has direct and indirect effects on the resistance of reinforced concrete structures. The

direct and indirect causes are both determined by the fact that the iron oxide has a molecular size greater than the non-oxidized material and this causes expulsion of the crystal lattice with consequent detachment of the rust. The direct effect of this detachment is, of course, loss of reinforcing section. While the indirect effects are mainly two: the increase in volume determines internal coactions to concrete with the progressive formation of cracks up to reach the expulsion of the concrete cover; rust formation causes loss of bond between bar and concrete. However cracks induced by the formation of rust cause themselves greater exposure of the bars and a consequent increase in the oxidation rate.

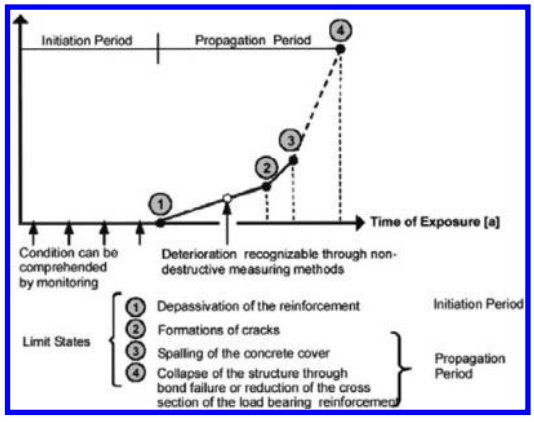

Figure 1. Typical deterioration levels for a stell reinforce concrete structure suffering from corrosion (fib 2006).

3 KEY QUESTION

3.1 *When is indispensable to act*

In most cases, the decision whether to intervene is taken after that the marks of corrosion are evident. It often happens that the decision is taken long after that there were phenomenon of spalling and therefore that the structure lies long after the end of its useful lifetime. And yet, at present, codes and recommendations do not provide explicitly a time when is indispensable to act; the fact that the structure does not report clear signs of structural instability leads to delay action.

In order to overcome this uncertainty, it is appropriate trying to quantify the risk associated with the decision not to intervene, in order to clarify who owns or manages real estate properties which are the risks assuming such decisions.

4 SOLUTION APPROACH PATTERN

4.1 *Probability of collapse: Main depending variables*

Structural deterioration due to corrosion of the bars depends on, as seen, many variables. Some of these are related to the structure itself (quality of concrete, water cement ratio, porosity, concrete cover thickness, etc.), others are completely independent from it (temperature, humidity, etc.). In addition to this we have to consider that the probability of collapse is significantly influenced by the occurrence of loads and in particular of that seismic (load not considered in the design phase for most of existing buildings). Derivatively the probability of failure will be conditioned by the depth of carbonation and the subsequent oxidation level of the bars that affects sections resistance.

The description above makes clear that the probability of failure comes from interrelation of various stochastic variables some of which are completely independent and others are conditioned one from each other or dependent.

4.2 *Analysis method: Bayesian and frequentist approach*

Modelling physical problems involving stochastic uncertainty has two main approaches: the classical probabilistic and the so-called frequentist one.

The first one cannot consider all the available data at the same time, but can explain the correlations observed taking into account uncertainties. Bayesian nets are tools which allow such an approach.

In the frequentist approach, means, coefficient of variations and probability distributions are probabilistic parameters obtained from the objective result of experimental observations. This approach can be defined as "the framework upon which uncertainty is modeled and incorporated into service life models of reinforced concrete structures" (Sudret 2008). But as quantifying the probabilistic information required to carry out a frequentist-based approach isn't always possible, a structure specialist can give an opinion that can be quantified in a knowledge-based model to get predictions about the remaining lifetime of structure.

Everything a structure expert obtains from previously acquired experience contribute to develop probabilistic information that give a ground to the knowledge-based approach. A Bayesian belief network (BBN) (in which is condensed Bayesian view), incorporates the specialist knowledge, to develop causal links among variables and to assign subjective probability to those relations. So natural knowledge of the specialist is used to develop the causal network and the BBN is useful for physical-based models not easily available.

This study introduces a knowledge-based BBN model to estimate carbonatation rate and to determine the beginning of corrosion. Environmental weather conditions, design information and in situ non-destructive testing measurements can be combined with proposed BBN model to define the possibility of corrosion induced by carbonation.

The application of Bayesian Network seems to be the most appropriate instrument to take correct account of these interconnections and achieve, easily, the determination of a failure probability.

4.3 *Bayesian net*

The Bayesian Networks are nowadays one of the most complete and coherent tool for the acquisition, the representation and the utilization of knowledge in condition of uncertainty. The uncertainties in a BBN model are reflected through subjective probabilities.

A Bayesian Network specifies a multivariate probability distribution over a set of random variables (probabilistic model) through two components:

- A directed acyclic graph (DAG), the structure, in which the nodes represent the random variables and the arcs, directed arrows between nodes, represents causal link between the connected variables;
- A set of local probability distributions, each of them is associated to a random variable and conditioned to the set of its parents in the graph. In the case of a variable with no parents, the conditional probability structure reduces to the unconditional probability (UP)_ of that variable.

Bayesian nets graphs topologies encapsulate assumptions about dependencies and conditional independencies, over a set of variables, making them graphically intuitive and explicit. Markov properties for acyclic graphs states that every node (variable) is "conditionally independent from any of its non-descendants, given the values of their parents" namely:

$$p(e|a, p(e)) = p(e|p(e)) \quad \forall \; a \in V \setminus d(e) \tag{1}$$

where d(e) is the set of descendants of e.

This rule allow to manipulate in an efficient way the joint probability distribution factorized by the chain-rule decomposition; the main advantage is the drastically decreasing in computing effort when carrying out or updating marginal distributions as new information is available. The joint distribution is simplified as explained below:

$$\begin{aligned} &p(x1, x2, x3, \ldots .xn) = p(x1|x2, x3 \ldots xn) \ldots \\ &\ldots p(x2|, x3 \ldots .xn)p(x3|\ldots . .xn)p(xn) \Rightarrow \\ &\Rightarrow (\textit{graph topology}) \Longrightarrow \prod p(xi \mid p(xi)) \end{aligned} \tag{2}$$

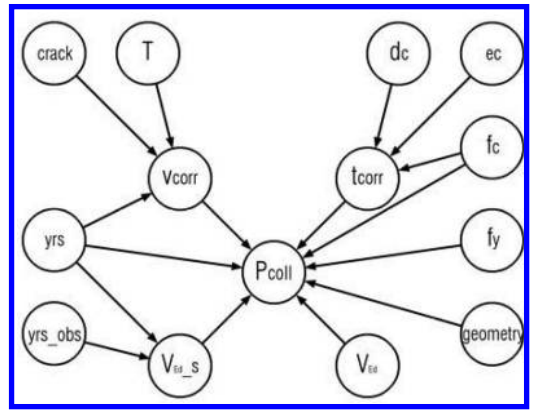

Figure 2. The BBN for probability of failure.

The main task of BBN is in handling efficiently with the implication of Bayes' theorem. In a BBN analysis, for n number of mutually exclusive hypotheses Hi, i = 1, ..., n, and a given evidence E, the up dated probability is computed as

$$P(Xj|E) = P(E|Xj)P(Xj)/\sum i\, P(E|Xi)P(Xi) \tag{3}$$

where:

p(H|E) = one's belief for hypothesis H upon observing evidence

E, p(E|H) = likelihood that E is observed if H is true, P(H) = probability that the hypothesis holds true, and p(E) = probability is the probability that the evidence takes place.

The efficacy of a BBN is realized in its flexibility to capture top-down inference, observing the cause or parent and inferring the possible effect or child and bottom-up inference, observing the effect child and inferring the possible cause parent.

Fundamentally, a BBN is used to update probabilities when new information is available. The network supports the computation of the probabilities of any subset of variables given evidence about any other subset.

4.4 *Probability of collapse bayesian net*

the goal of the proposed BBN model is to assess the structural reliability evolution over time accounting both for major accredited stochastic models concerning deterioration processes of RC structures and probabilistic description of static ad seismic loads adopted by Italian design code.

The phenomenology takes into account is very complex and requires the design of three different levels of submodels. They can be summarized as follows:

1. Model for estimating the progress of the carbonation front for the detection of corrosion

Table 1. Nomenclature.

Pcoll	Probability of failure
V_{Ed}	Shear caused by vertical loads
V_{Ed_s}	Shear caused by seismic loads
tcorr	Time from the beginning of the corrosion
vcorr	Corrosion rate
crack	Parameter opening of cracks
yrs	Time from the construction of the structure
yrs_obs	Time of observation
geometry	Geometric dates of the structure
dc	Concrete cover depth
fc	Compressive strength of concrete
fy	Yield strength
T	Temperature
ec	Exposure class

onset seen as time range necessary to the face to cross the concrete cover and to depassivate the reinforcements.
2. Model relating to the corrosion rate which, together with data relating to the propagation time of the corrosive phenomenon, helps to predict residual reinforcement area for a fixed age of the building.
3. Model for defining the conditioned probability of shear structural collapse for the element considered.

The complete model consists of the interactions of the three sub-models. The Bayesian model proposed can be thought of as a whole formed by a number of submodels each dedicated to the probabilistic description of the phases that contribute to the definition of the entire inferential process.

Each sub-model catches the causal dependencies of a given variables of output as a function of the physical parameters that most influence it highlighting the conditional independence on the basis of a priori knowledge of the phenomenon.

The output of a submodel may represent the input of one or more submodels provided that in the graph there is a directed link from the first to the second ones. In our case, for example, the output of the submodel dedicated to carbonation, concerning the moment at which the carbonation front equals the concrete cover, provides an input data for the estimation of the level of corrosion when is known the corrosion rate.

Since all the variables involved can take discrete values depending on the number of ranges in which is divided the corresponding domain of variation, the probabilistic dependency relationships are defined with tables that contain the values of probability of a node as a function of all possible configurations of the ascending nodes (nodes from which starts an arc pointing to the node of interest).

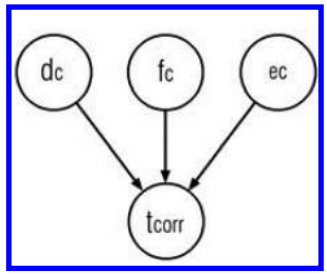

Figure 3. Sub model BBN for determine the probability of time the beginning of the corrosion.

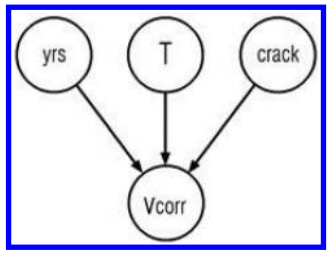

Figure 4. Sub model BBN for propagation of corrosion.

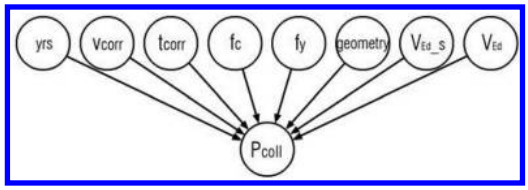

Figure 5. Sub model BBN for probability of failure.

4.5 *Mathematical model*

4.5.1 *Carbonatation model*

Several models have been developed in order to model carbonatation process. DuraCrete (2000b) proposed the following model for the progress of the carbonation front:

$$x_{ca} = \sqrt{2k_{e,ca}k_{e,ca}k_{t,ca}c_{s,ca}R_{ca}^{-1}}\sqrt{t}\left(\frac{t_0}{t}\right)^{n_{xa}} \quad (4)$$

Where:

R_{ca} – expresses the effective resistance of concrete to carbonation and is strongly influenced by the concrete composition. R_{ca} can be approximated as normal variable with mean ad std depending on w/c ratio [$kgCO_2/m^3/mm^2/yr$]

$$R_{ca}^{-1} \sim N(\mu_{Rca^{-1}}, \sigma_{Rca^{-1}}) \quad (5)$$

$c_{s,ca}$ – Surface Concentration of Carbon Dioxide.

Table 2. Grade parameter R_{ca}.

Grade	w/c ratio	distribution	μ_{Rca-1}	σ_{Rca-1}
45	0.45	Normal	25	2.23
40	0.55	Normal	5	0.38
35	0.55	Normal	15	0.89
25	>0.55	Normal	35	1.75

In this work $c_{s,ca}$ is approximated by a normal random variable with

$$\mu_{C_{s,ca}} = 6 \cdot 10^{-4} \text{ and } CoV = 0.17. \quad \text{(Li, 2004)}$$

$k_{e,ca}$ – The environmental parameter represents a ratio between observations made in an actual climate and observations made in a reference climate. The value $K_{e,ca}$ can be approximated as lognormal random variable.

$$k_{e,ca} \sim \ln N(\lambda_{e,ca}, \zeta_{k,ca}) \quad (6)$$

n_{ca} – Age Factor for Carbonation – The diffusion coefficient will increase with age, what is expressed by the age factor nca, which follows a betadistribution.

$$n_{ca} \sim \text{Beta}(q_{n_{ca}}, r_{n_{ca}}, a_{n_{ca}}, b_{n_{ca}}) \quad (7)$$

$k_{c,ca}$ – Execution Parameter for Carbonation takes execution influences upon the effective diffusion coefficient into account. The final results based on observations of concrete elements are listed below.

$k_{t,ca}$ – Test method parameter assumed here as deterministic and equal to 1.

Table 3. Environment parameter $k_{e,ca}$.

Enviroment	Distribution	$\lambda_{e,ca}$	$\xi_{k,ca}$
LAB	Deterministic	–	–
OS	Lognormal	–0.207	0.299
OUS	Lognormal	–0.198	0.266

LAB – fixed indoor humidity and temperature conditions
OS – outdoor sheltered by rain
OUS – outdoor unsheltered

Table 4. Environmen parameter n_{ca}.

Enviroment	Distribution	$q_{n_{ca}}$	$r_{n_{ca}}$	$a_{n_{ca}}$	$b_{n_{ca}}$
LAB	Deterministic	–	–	–	–
OS	Beta	0.850	1.290	0.0	0.5
OS	Beta	0.554	0.491	0.0	0.5

Table 5. Curing parameter $k_{c,ca}$.

Curing	Distribution	$\frac{q_{k_{c,ca}}}{\lambda_{k_c}}$	$\frac{r_{k_{c,ca}}}{\zeta_{k_c}}$	$a_{k_{c,ca}}$	$b_{k_{c,ca}}$
1	s. Lognormal	2.52	0.84	0.45	–
3	s. Lognormal	0.87	1.03	0.88	–
7	Deterministic	1.00	–	–	–
28	Beta	1.86	1,10	0.35	1.00

4.5.2 *Corrosion model*

The corrosion rate Vcorr can be modeled empirically. The corrosion rate is expressed as product of local influencing factors, material parameters (DuraCrete (2000b)), and a load induced crack factor as specified below.

$$V_{corr} = \frac{m_0}{\rho} \cdot cr_{fc} \quad (8)$$

Where:

V_{corr} – corrosion rate [mm/yr]

c_{rfc} – Crack factor – it accounts for the influence of cover cracking on corrosion rate (Otieno M. et al. 2011).

Pre-corrosion cracking and crack characteristics can considerably affect both corrosion initiation and its propagation. The influence of cracking on corrosion may vary depending on concrete quality, concrete resistivity, crack dimensions, crack distribution, crack self-healing and crack orientation. According to the Figure 6, in this work, crack factor is assumed as a discrete variable that randomly switches between 3 values depending on crack width.

ρ – is the concrete resistivity given by:

$$\rho = \rho_0 \left(\frac{T_{Hydr}}{t_0} \right)^{n_r} k_{T,r} k_{RH,r} \quad (9)$$

Where:

t_{Hydr} – time of hydration [mm/yr]

t_0 – reference time (1 yr) [yr]

m_0 – parameter which represents a constant for corrosion rate versus resistivity based on Faraday's law. [µmΩm/yr] (Nilsson, Lars-Olof and Gehlen 1998) propose to use a constant m_o = 822 for the time being.

ρ_0 – potential concrete resistivity for a reference environment. It can be approximated as a normal

Table 6. Crack parameter.

Crack	cr_{fc}
0.0–0.3 mm	1.00
0.3–0.7 mm	2.47
> 0.7 mm	3.71

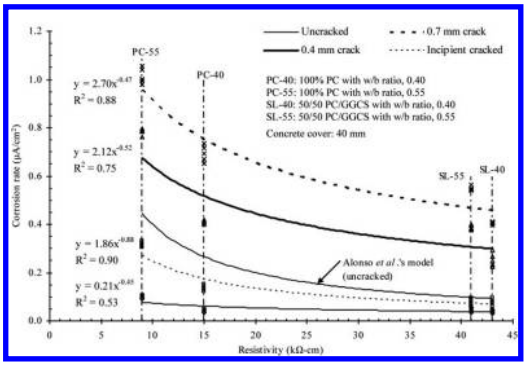

Figure 6. Effect of cracking, concrete quality and resistivity on corrosion current (Otieno M. et al. 2011).

random variable with a mean of 77 Wm and a standard deviation of 12 Wm.

$$\rho_0 \sim \mathrm{N}(\mu_{\rho_0}, \sigma_{\rho_0}) \tag{10}$$

n_r – age factor of the concrete resistivity. This parameter is determined as a normal random variable with a mean of 0.23 and a standard deviation of 0.04.

$$n_r \sim \mathrm{N}(\mu_{\rho_0}, \sigma_{\rho_0}) \tag{11}$$

$k_{T,r}$—Temperature Factor for Resistivity. it can be approximated by

$$k_{T,r} = \left(\frac{1}{1 + K(T-20)} \right) \tag{12}$$

in which parameter K is the temperature dependence of the conductivity and approximated by:

$k_{RH,r}$ Humidity Factor for Resistivity. The humidity factor $k_{RH,r}$ is different for OS and OUS conditions. We have considered only the OUS condition that characterizes our case study.

$$k_{RH,r} \sim \text{shifted } \ln\mathrm{N}(\lambda_{k_{RH,r}}, \zeta_{k_{RH,r}}, a_{k_{RH,r}}) \tag{13}$$

With: $\lambda_{k_{RH,r}} = 0.62, \quad \zeta_{k_{RH,r}} = 0.33, \quad a_{k_{RH,r}} 0.79$

Table 7. Temperature parameter.

Temperature	Distribution	ρ_k	σ_k
T > 20	Normal	0.073	0.015
T = 20	Deterministic	1	–
T > 20	Normal	0.025	0.001

4.5.3 *Loads model*

According to the Poisson model (Cornell, 1968; Stein and Wysession, 2003), probability of n earthquakes of interest occurring in an area or along a fault during an exposure time (t) in year is:

$$p(n,t,\tau) = \frac{e^{-t/\tau}(t/\tau)^n}{n!} \tag{14}$$

where τ is the average recurrence interval (or average recurrence rate, 1/τ) of earthquakes equal to or greater than a specific magnitude (M). The probability that no earthquake will occur is:

$$p(0,t,\tau) = e^{-t/\tau} \tag{15}$$

The probability of at least one (one or more) earthquake equal to or greater than a specific magnitude (M) occurring within t years is

$$p(n \geq 1,t,\tau) = 1 - p(0,t,\tau) = 1 - e^{-t/\tau} \tag{16}$$

The expression above can be used to calculate risk, expressed as X percent P_E in t years, for a given average recurrence interval (τ) of earthquakes of a certain magnitude (M or peak ground acceleration) orgreater. For example, for an average recurrence interval of about 975 years,corresponding to a peak ground acceleration of 0.108 g at the site of interest (Rome Lon.12,4813, Lat.41,9804), the risk that the area will be struck by at least one such event is about 5 percent probability in 50 years. Eq. 3 can also be used to calculate the average recurrence interval τ of earthquakes with a certain magnitude (M) or greater for a given P_E in a specific time.

5 APPLICATION CASE

5.1 *Building and structure damage description*

The bank offices building was designed in 1954 and the construction end in 1959. The building have three underground level and eight level upside. Plan shape is approximately rectangular with a internal court and a overhang part for each of edge.

The building have a RC structure: two big cores (for staircase and elevators) and the façade system, from second level to seventh level, composed

Figure 7. Corroded rebar.

Figure 8. Detail of spalling.

by a RC frame structure (columns 20×37 cm and beams). Each floor have a surface of 2000sqm.

The RC frame structures are completely exposed and since 1979 there are evidence of cracks in columns. In 2004 a FRC was applied on the exposed structures later the firsts spalling events. In 2012 there are the first cover FRC detachment and a experimental tests are carried out to study the situation and take a decision.

5.2 *Experimental tests data*

The experimental tests was carrier out to have real data on carbonatation, corrosion and concrete resistance.

The experimental test have confirm the carbonation induced corrosion phenomena of RC structures.

Table 8. Experimental tests.

Test	Number test
Cylindrical spacement strength test	58
Carbonation test	127
Rebar mass ass loss measurement	100
Cover concrete measurement	127

5.3 *Evaluation of collapse probability*

The observation of RC structures state and the results of experimental tests make clear the necessity to repair the exposed structures. The own require a quantification of the risk of collapse.

In the case study attention have been limited to shear failure mechanism of columns. The structure has very low ductility mainly due to the insufficient shear reinforcement. The shear resistance has bean estimated applying EC2 formulation reported below.

$$V_{Rd3} = (\tau_{Rd} k(1.2 + 40\rho_l)0.15\sigma_{cp})b_w d + \frac{A_{sw}}{s} 0.9 d f_{ywd} \tag{17}$$

The output of the BBN implemented through the open source package Kevin P. Murphy "The Bayes Net Toolbox for Matlab", gives the evolution over time of the probability that the resistance will fall below both the shear force due to static load, whose lower bound is fixed to 5% percentile value of dead and live loads (characteristic value according to Italian design code NTC 2008), and the shear due to seismic estimated as in 4.5.3. Static and dynamics load have different statistically independent nodes in the BBN dag (directed acyclic graph). It follows from above it makes more sense to talk about the risk that a design verification of strength is not satisfied rather than an actual failure probability.

Figure 9. represents the sensitivity analysis carried out varying each time only one input parameter in order to assess its influence compared with the a priori knowledge. The analysis is based on design geometrical information and extends from the "birth" of building to the hundredth year of age.

Several scenarios have been considered each one characterized by an increasing amount of information. In this way it is possible to assess the impact of a posteriori knowledge on the time probability curve.

The probability curves are carried out by the actual state of the building approximately 50 year after its construction

yrs_obs = 50 yrs

Follows a step by step description of the BBN updating as shown in Figure 10.

Phase 0 – only design a priori knowledge dc = 2 cm

Phase 1 – large cracks detected during visual inspection: high crack factor

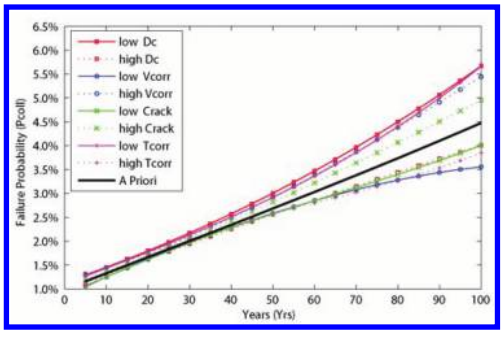

Figure 9. BBN Sensitivity analysis.

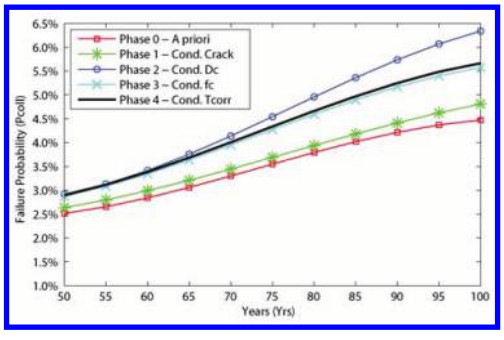

Figure 10. Failure Probability curves with increasing level of knowledge.

Phase 2 – a concrete cover significantly lower than the design one is measured dc = 0,5 cm

Phase 3 – high concrete class have been noticed from text on cylindrical specimens of the building Rck 40

Phase 4 – Ph indicator at cover depth gives high carbonation level that is closely related to short initiation period.

5.4 *Concrete structures repair*

The structural repair is carried through rust remove, process of rebars passivation and FRP application. The FRP wraps allow the refurbishment of lost stirrups section and a reactivation of the bond between concrete and steel rebar. Before of the application of FRP, a migratory corrosion inhibitor was applied to protecting and passivate the rebars.

6 CONCLUSION

The paper shows that the bayesian net are an easy method to evaluate the probability of collapse in application case too.

The bayesian net are a very good method to synthesize a great number of stochastic variability and build an adequate model of physical phenomena.

In the application case, the opportunity to build an a priori evaluation jointed to data tests produce a valid collapse probability.

Next steps on this research pattern are the use of bayesian net to define a focused experimental tests.

REFERENCES

Broomfield J. P. 2007. *Corrosion of Steel in Concrete: Understanding, Investigation and Repair. second edition.* London, UK: Taylor & Francis.

Cornell C.A. 1968. *Engineering seismic risk analysis: Bull. Seismol. Soc. Am.*, 58, p.1,583-1,606.

D.M. 14.01.2008 *Norme Tecniche delle Costruzioni* (Italian design code) (In italian).

Eurocode 2 ENV1992-1-1 Designe of concrete structures Part 1-1: General rules and rules for buildings.

Fib (2006). *Model code for Service life design.* Model code, Bullettin 34. Crete D. 2000b. *Statistical Quantification of the Variables in the Limit State Functions.* Research Project No. BE95-347/R9. The European Union: Brite EuRamIII.

Hackl J. 2013. *Generic Framework for Stochastic Modeling of Reinforced Concrete Deterioration Caused by Corrosion.* Master's Thesis, Norwegian University of Science and Technology Department of structural engineering.

Kuter A. 2009. *Management of Reinforcement Corrosion: A Thermodynamic Approach*. PhD Thesis. Lyngby, Denmark: Technical University of Denmark.

Li, Ying 2004. *Effect of Spatial Variability on Maintenance and Repair Decisions for Concrete Structures*. PhD Thesis. Delft, Netherlands: Delft University of Technology.

Malioka V. 2009. *Diss. ETH Condition Indicators for the Assessment of Local and Spatial Deterioration of Concrete Structures.* Surrey University, UK.

Murphy K.P. 2001. *The bayes net toolbox for matlab.* Department of Computer Science University of California.

Nilsson, Lars-Olof and Gehlen 1998. *Statistical quantification of the environmental parameters in the corrosion rate model*. DuraCrete Report No 4.1.8. Draft 4. The European Union: Brite EuRam III.

Otieno M., Beushausen H. & Alexander M. 2011 *Prediction of Corrosion Rate in RC Structures—A Critical Review.* Department of Civil Engineering, University of Cape Town, South Africa.

Richardson M.G. 1988. *Carbonation of reinforced concrete: Its causes and management.* CITIS Ltd., Dublin, Ireland.

Slanzi D. 2005. *Reti Bayesiane: Approcci per la Selezione del Modello* (in italian). MT, Università degli studi di Padova.

Stein S., Wysession M. 2003. *An introduction to seismology, earthquakes, and earth structure: Maldem*, Mass., Blackwell Publishing.

Tesfamariam S. & Martín-Pérez B. 2008. *Bayesian Belief Network to Assess Carbonation-Induce Corrosion in Reinforced Concrete.*

Webster M. P. 2000. *The assessment of corrosion-Damaged concrete structures*. School of Civil Engineering Birmingham, B 15 2TT,UK.

Concrete Repair, Rehabilitation and Retrofitting IV – Dehn et al. (Eds)
© 2016 Taylor & Francis Group, London, ISBN 978-1-138-02843-2

Electro Active Repair of concrete for improved durability of conventional repair

R.B. Polder
TNO Technical Sciences, Delft, The Netherlands

M.R. Geiker
NTNU, Department of Structural Engineering, Trondheim, Norway

ABSTRACT: Chloride induced reinforcement corrosion is increasing due to aging of concrete infrastructure. Conventional repairs have poor durability and many fail after less than 10 years. For conventional repair chloride contaminated concrete is removed, steel is cleaned and new concrete is applied. Leaving chlorides, e.g. in pits, corrosion may re-activate and the repair fails. The authors have invented a pre-treatment for conventional repair, called Electro Active Repair (EAR) for electrochemical removal of chlorides from corrosion products and pits. After removal of contaminated concrete, a temporary material and a temporary anode are installed and cathodic current is applied for 24 hours. Next, temporary materials are removed and repair is executed as usual. A European patent was granted and a worldwide patent applied for. The principle was confirmed in laboratory experiments. A cementitious material was placed between NaOH and $FeCl_2$ solutions. More than 90% of the chloride was removed from the catholyte ($FeCl_2$) in 20 hours at 8 A/m^2 and the pH increased from 3 to 12, which will prevent re-activation of corrosion and consequently improve the durability of the repair. The method has the advantage that it fits in the conventional repair process.

1 INTRODUCTION

Chloride induced corrosion of reinforcement in concrete is a growing problem due to aging of infrastructure exposed to de-icing and marine salts. Increased numbers of concrete structures need repair of damage and protection against chloride induced corrosion, e.g. [Polder et al. 2012]. The majority of repairs follow the conventional method: removal of chloride contaminated concrete, cleaning of the steel to bright metal and application of new concrete [EN 1504-10]. In practice, conventional repairs have poor durability and it appears that their life is limited: according to a Europe-wide survey, about 50% of repairs fail within ten years [Tilly & Jacobs, 2007; Tilly, 2011]; similar observations were made in a Dutch study [Visser & Zon 2012]. Failure of conventional repairs is due to various mechanisms, including mechanical and corrosion related factors. Other causes of repair failure may be: inadequate condition evaluation (cause of corrosion or other degradation) [Vaysburd et al. 2012], or inadequate repair specification [Snover et al. 2012]. Setting aside other causes, corrosion related factors of repair failures are: insufficient removal of contaminated concrete; insufficient cleaning of the affected reinforcing steel; and electrochemical effects (incompatibility, incipient anodes or "patching" effects) between repaired and surrounding non-repaired places where chlorides are present. In such cases, the chlorides left behind in concrete, corrosion products, and corrosion pits reactivate the corrosion process. Consequently, the loss of steel cross section continues and new cracking results, necessitating new repairs.

Removing chlorides and cleaning of steel is not critical for electrochemical methods for corrosion protection of steel in concrete [Bertolini et al. 2013]. Cathodic protection (CP) works by passing a low direct current to the reinforcing steel, suppressing corrosion. CP is being applied on a wide scale and long working lives can be obtained [Polder et al. 2014]. However, continuous current flow must be secured and specific monitoring must be carried out over the remaining life of the structure. In particular the obligation to monitor is seen as a disadvantage by many owners. Electrochemical chloride extraction (desalination) works by passing a high current for a period of up to several months, removing chloride ions from the concrete (and from pits) [Polder & Hondel 2002]. The main disadvantage is the long period of execution of the non-permanent repair process and the

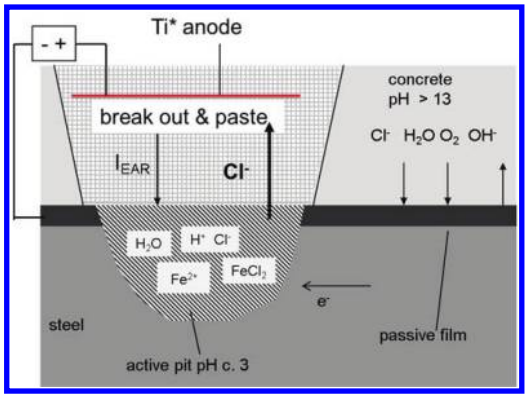

Figure 1. Principle of EAR, showing break out with temporary material ('paste'), temporary anode (Ti* anode) and current application (I_{EAR}), which removes chloride from corrosion pit.

uncertainty of when the process can be stopped without compromising the effect and without causing major changes of the concrete microstructure [Castellote et al. 1999].

The authors propose to improve the conventional method of concrete repair by adding a step in which a direct current is applied for a short period of time. This additional step is called Electro Active Repair (EAR). It causes electrochemical removal of chlorides from the steel surface, from corrosion products and corrosion pits. The overall repair process then becomes as follows. After removal of spalled concrete, a temporary material is placed in the excavation, a temporary anode is installed and a cathodic current is applied to the steel for a short time (24 hours). This is illustrated in Figure 1. The temporary material can be a cementitious material or an ion conductive gel or paste. Following steps are removal of temporary materials, removal of contaminated concrete and conventional repair as usual. A European patent has been granted in 2014 and a worldwide patent has been applied for. The method has the advantage that it fits in the conventional repair process. Monitoring is not necessary. The additional cost is expected to be moderate. Applying the invented pre-treatment to conventional repair is expected to increase the life of repairs and consequently reduce the life cycle cost of corrosion affected structures.

2 BACKGROUND

Pitting of reinforcing steel is caused by accumulation of chloride ions at the steel surface, exceeding the (local) threshold [Angst et al. 2011]. When the pit develops, more chloride ions are attracted that auto-catalyse the iron dissolution reaction. Iron chloride ($FeCl_2$) and iron (hydr)oxides are the main constituents of the pits. Because the iron (hydr)oxides are poorly soluble, the liquid contains a concentrated solution of $FeCl_2$, with a low pH; pH values were suggested of about 2 [Pacheco et al. 2011, Polder et al. 2011], which was attributed to HCl. However, the pit solution also contains a rather high concentration of $FeCl_2$. After intentionally contaminating concrete near steel bars with chloride, chloride contents of corrosion products have been observed of 3.5 to 7% of chloride ion by mass of corrosion product [Polder & Hondel, 2002]. High levels of 3% chloride by interaction volume have been found by SEM/EDS, corroborating such high chloride contents [Wong et al. 2010], see also [Scheiner & Hellmich 2007]. This can be interpreted as corresponding to a solution of approx. 2.5 mole/l of $FeCl_2$ or 5 mole/l of Cl.

The pH of $FeCl_2$ solutions of low concentration (below 0.1 mole/l) is in the range of 4 to 5 [Gayer & Wootner, 1956]; no data were found on concentrated solutions. A pH of 3 was found in the experiments described below. $FeCl_2$ will buffer the pH at about 4 or lower, which is highly corrosive. The buffer capacity is proportional to the concentration.

Summarising, active corrosion pits contain a solution with a pH between 2 and 4. A low pH is buffered by $FeCl_2$ at about pH 3 to 4. Consequently, for effective repassivation by obtaining a high pH (preferably above 10), the majority of chlorides need to be removed from the pit solution. The target level of reduction of the chloride concentration for successful treatment was set at 90%. This is what the present invention aims at and what the experiments have documented to be achievable within the parameters set.

3 EXPERIMENTAL CONFIRMATION

The principle of the proposed method was confirmed in laboratory experiments. They will be reported briefly here and in more detail elsewhere [Geiker & Polder 2015]. A cementitious material was placed between NaOH and $FeCl_2$ solutions as anolyte and catholyte, respectively, using activated titanium electrodes for applying a voltage. More than 90% of the chloride was removed from the catholyte ($FeCl_2$) in 20 hours at 8 A/m^2 and the pH increased from 3 to 12. Such a reduction of chloride concentration and increase of pH will suppress re-activation of corrosion and consequently improve the durability of the repair.

4 APPLICATION

Practical cases where EAR can be applied will vary widely in a number of parameters, such as orientation and amount of spalls. For example, on a horizontal surface the temporary material can be a liquid contained in a pond. On a vertical surface, the temporary material must be a paste or a gel that sticks to the concrete, or a vertical container must be formed and filled with liquid. If the amount of spalls is low (say 5% of the surface), the anode is placed on the original surface without the risk of short-circuiting. The temporary material is only placed in the spalls. In order to have a reasonably uniform current distribution, the temporary material needs to have similar resistivity as the concrete. If the extent of spalling and the degree of exposure of the reinforcement are high (say 50 to 100%), the anode must be physically separated from the rebar to prevent short-circuiting, using for example polymer strips or wooden battens. Similarity of resistivities may be less critical; nevertheless it should be controlled within certain boundaries. Application of the temporary material can be by casting or spraying, depending on orientation and/or containment type. The material should not dry out (increase in resistivity) or needs to be wetted. The material would preferably be recoverable and re-usable (after removing the chloride). At present we are working with industry to develop such a material.

Out of many possible combinations of parameters, two example cases have been selected to illustrate the application.

5 CASE STUDIES

Two hypothetical case studies are presented. They represent two extremes in terms of the amount of concrete damage (spalls) that is present when the repair is designed. Many cases will be somewhere in between. The cases will be described in terms of starting situation, information available, preliminary repair steps, EAR application and follow up steps to complete the repair process. As part of the description, the background is given, including possible repair/protection options and arguments for/against each of them. The overall background is that corrosion has been initiated in a bridge substructure due to penetration of chloride ions from de-icing salts or sea water.

5.1 *Case 1 – bridge abutment*

5.1.1 *Background*

This case has widespread corrosion initiation and pitting, but damage to concrete so far is limited. It is the abutment of a bridge supporting a monolithic bridge deck, where leakage through an overlying expansion joint has brought chloride containing water from de-icing salts (XD3 according to EN 206) onto the concrete surface. Corrosion initiating chloride levels have penetrated slightly behind the rebars, causing multiple corrosion pits. The amount of concrete damage (cracking and spalling) is limited, about 5% of the total surface. The owner has identified the corrosion problem based on a visual inspection that signalled some cracks and spalls; subsequently chloride sampling and potential mapping have been carried out, which have identified widespread chloride induced corrosion initiation across the top horizontal surface of the abutment. Further development of damage is to be expected in a few years. The affected area is 1 m deep by 15 wide, see Figure 2. Sketches of details are shown in Figure 3.

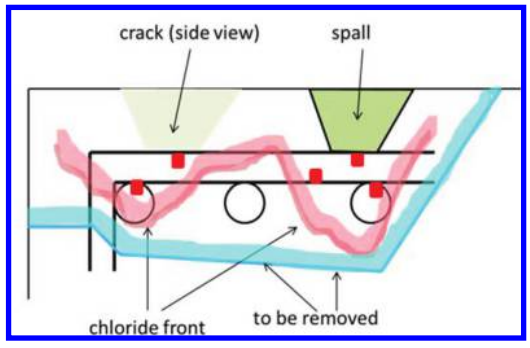

Figure 3. Sketch of details of chloride penetration and rebar layout, with examples of pitting (red squares) and cracking/spalling (concrete damage) as well as concrete removal (not to scale).

5.1.2 *Options, abutment*

Options for protection and repair are:

- do nothing,
- cathodic protection (CP),
- electrochemical chloride extraction (ECE),
- conventional repair; and
- conventional repair+EAR.

Doing nothing causes considerable loss of concrete cross section and rebar diameter in 5 to 10 years, with possible implications for structural safety and serviceability; this is not acceptable to the owner.

With CP, the cracked and spalled areas need to be repaired; then an anode is installed and connected to a power source; and a monitoring system (sensors) is installed. Due to limited working space, an anode based on conductive coating is most suitable, which has a limited life (about 15 years).

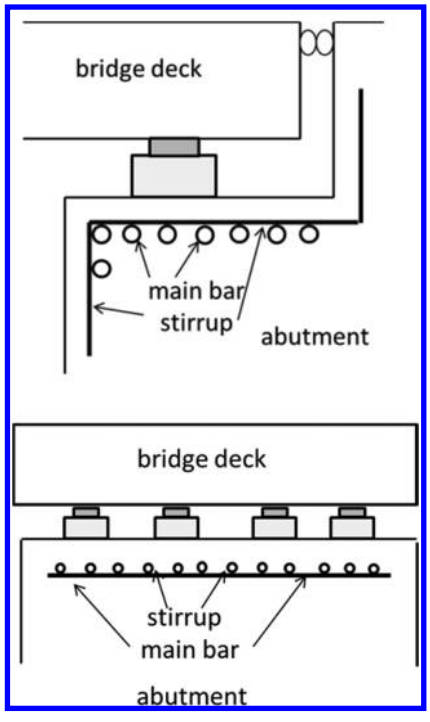

Figure 2. Case 1, Sketch of bridge abutment, longitudinal cross section of 1 m deep (top), transverse cross section of 15 m wide (bottom) (not to scale).

Operation of CP involves maintenance by electrical checks (every 6 months or more often) and visual inspection once per year. The cost of maintenance over 25 years may be as high as 50% of the initial cost of installing CP [Polder et al. 2014]. Furthermore, the owner would rather like to continue his usual policy of visual inspection every five years than having to monitor annual testing reports.

Electrochemical chloride extraction (ECE) needs several months of treatment to be sure that (nearly) all chloride is removed. A potential problem is the question when the treatment can be stopped; this requires repeated testing for (remaining) chloride and involves uncertainties due to erratic penetration of chloride (location of sampling). A drawback for the owner is that ECE is not available on the local market as a routine technique. This causes uncertainties about price levels and about the quality of the final result.

For conventional repair, significant amounts of concrete need to be removed, in principle all chloride contaminated concrete (say at least 10 mm behind the rebars); and the rebars exposed by concrete removal need to be completely cleaned of corrosion products and chloride contained in them by grit blasting (this requires significant removal on the side of the bars). Concrete removal and repair may have to be done in consecutive parts for structural reasons (or additional support has to be provided to the deck). Then, new concrete is placed. This technique fits in the routine concrete maintenance policy of the owner. However, a drawback is the narrow working space, which will hinder proper execution (removal, cleaning). Thus, there is a significant probability that chlorides are left and the repairs will fail within 5 to 10 years, corrosion will reactivate and rebar diameter loss will continue. This may compromise structural safety and serviceability. New repairs will then be necessary, potentially including the need to install new reinforcement, which will considerably increase the magnitude and cost of the intervention and include the need to stop traffic using the bridge for some time.

For conventional repair with EAR, in principle the same amount of concrete needs to be removed as with conventional repair. The treatment by short-term application of current takes away the aggressiveness from the corroding steel and its immediate vicinity. The life of the repair depends mainly on the mechanical properties of the repair/substrate interface; it may be as long as 25 years. The small damaged areas need temporary repair with a material with an electrical resistivity matching that of the parent concrete. This requires that the concrete resistivity is measured (e.g. using a four-point resistivity probe). Companies applying EAR should have materials with known resistivity available. The successive steps are described in a following section.

5.1.3 *EAR application, abutment*

The following steps need to be taken with repair plus EAR. Concrete resistivity must be measured for matching the resistivity of temporary repairs. The surface area of the reinforcement (top mesh) in the area to be treated needs to be calculated; this is typically 1 m^2 of steel surface for 1 m^2 of concrete surface. Steel continuity needs to be checked beforehand; if not continuous, a step should be added for making the steel continuous. However, usually continuity is present in civil engineering structures built after 1945.

- Clean the concrete surface (of oil, dust etc)
- Break out spalls and make temporary repairs with resistivity-matched material (mortar, paste, gel)
- Apply the EAR steps
  - Make 2 rebar connections as far apart as possible within the area to be treated, check for continuity
  - Form ponds on horizontal concrete surface by placing shutter walls, of typical size a few m^2 (“zones”)

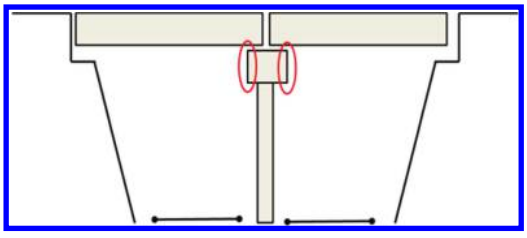

Figure 4. Case 2, sketch of bridge with support beam with areas with corrosion and spalling indicated.

- Place anode mesh (activated titanium) in ponds
- connect anode and cathode (rebar) cables to power unit
- fill ponds with liquid (saturated $Ca(OH)_2$)
- switch on current at 5 A/m^2 of steel surface; NB the total current would be about 75 A for a total of 15 m^2 of concrete surface, separated in about 5 zones
- monitor current for each zone; increase voltage if current is below 2 A/m^2, decrease voltage if current is above 8 A/m^2
- switch off at a total charge of 40–120 Ah/m^2(steel surface)
- remove power unit, cables, liquid, anodes, pond walls

– Remove concrete down to the required depth; NB for structural reasons, it may be necessary to do so in smaller parts of say one-fifth of the width of the abutment (OR take off traffic and/or provide temporary support)
– Clean newly exposed concrete surface
– Apply repair material and cure for 7 days or according to standards.

5.2 *Case 2 – bridge cross beam*

5.2.1 *Background*

This case concerns a bridge cross beam with widespread corrosion induced spalling over more than half the vertical surfaces of a cross beam supporting a bridge deck. Leakage of an overlying expansion joint has exposed the concrete to chlorides from de-icing salts. Corrosion initiating chloride levels have penetrated behind the rebars, causing multiple corrosion pits and heavy spalling. The owner has identified a corrosion problem based on a technical inspection that observed large spalls; subsequently spalled areas have been removed in order to avoid pieces falling off onto the traffic lanes below. Further development of corrosion and damage is to be expected in a few years, seriously compromising the load bearing capacity. The affected area is 1 m high by 15 wide, see Figure 4. This case is based on a real case (in The Netherlands) that was discovered and subsequently repaired in 2012/13.

5.2.2 *Options, bridge cross beam*

Options for protection and repair are:

– do nothing,
– cathodic protection (CP),
– electrochemical chloride extraction (ECE),
– conventional repair; and
– conventional repair+EAR.

Pros and cons are the same as for case 1, with additional factors; only those will be mentioned.

Doing nothing will likely compromise structural safety and road user safety and is not acceptable.

With CP, two layers of shotcrete need to be applied (one filling excavations, the second to embed the anode). The total weight added is relatively high, which requires structural recalculation. The system has a long life, but high initial cost plus considerable cost of maintenance. As for case 1, the owner prefers only routine visual inspections.

ECE needs long treatment to be successful. The surface needs repair (20–30 mm shotcrete) before ECE can be applied. Consequently, the cost will be relatively high. The new shotcrete may be contaminated by chlorides extracted from deeper layers, which may compromise durability by back diffusion. As for case 1, when to stop the treatment presents uncertainties and the unavailability in the local market presents an economic risk.

For conventional repair, significant amounts of concrete need to be removed behind the rebars, i.e. in principle all chloride contaminated concrete; then the exposed rebars need to be completely cleaned of corrosion products and adhering chlorides (the back of rebars will be hard to reach). Concrete removal needs to be done in parts for structural reasons (and probably additional support must be provided). Then, shotcrete is applied, filling up the cavities and providing new cover, up to 30–40 mm over the rebars. This technique fits in the routine concrete maintenance policy of the owner. However, the location amidst busy traffic will put pressure on execution time and thus tends to reduce time for concrete removal and steel cleaning. As a result, it is likely that chloride contaminated concrete and corrosion products will be left. Thus, there is a significant probability that the repairs will fail within 5 to 10 years, corrosion will reactivate and rebar diameter loss will continue. This may compromise structural safety and serviceability. New repairs will then be necessary, potentially including the need to install new reinforcement, which will considerably increase the cost of the (next) intervention and include the need to stop traffic using the bridge for some time.

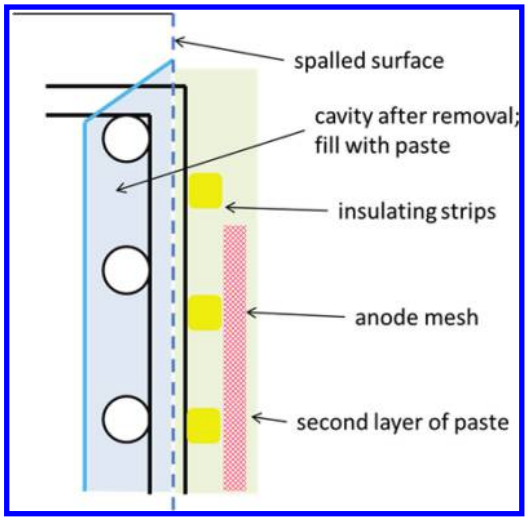

Figure 5. Repair + EAR with concrete removed first, then EAR (then repair).

For repair with EAR, in principle the same amount of concrete needs to be removed as with conventional repair. However, the current application will take away the aggressiveness from the corroding steel and its immediate vicinity. The life of the subsequent repair depends mainly on the mechanical properties of the repair/substrate interface; it may be as long as 25 years. The successive steps are described in the following section.

5.2.3 *EAR application, bridge cross beam*

The following steps need to be taken with repair plus EAR. The surface area of the outer reinforcement in the area to be treated must be known and the steel must be continuous.

Repair + EAR (Figure 5)

- Remove concrete down to the required depth; NB for structural reasons, it may be necessary to do so in smaller parts of say one-fifth of the length of the beam (OR take off traffic and/or provide temporary support)
- Apply the EAR step
  - Make 2 rebar connections on opposite ends of the beam, check for continuity
  - Fill cavities behind and around bars with electrolyte paste (paper pulp, gel)
  - Install insulating strips across rebars
  - Install titanium mesh anode in anode zones of a few m^2 typical size with cables at two opposite ends of the mesh
  - apply second layer of sponge or paste
  - connect anode and cathode (rebar) cables to power unit
  - wet paste with liquid (saturated $Ca(OH)_2$)
  - switch on current, total current is about 75 A for 15 m^2 of surface
  - monitor current (as case 1)
  - switch off at a total charge of 40–120 Ah/m^2 (steel surface)
  - remove power unit, cables, liquid, anodes, paste
- Clean new concrete surface
- Apply repair material and cure.

As an alternative, EAR can be applied before contaminated concrete is removed.

6 CONCLUDING REMARKS

It is proposed to apply a direct current to rebars in repair areas for a short period of time, which will remove chlorides from corrosion products including pits and from concrete adjacent to the rebar. This treatment, called Electro Active Repair (EAR), is an additional step to conventional repair. The authors expect that adding this treatment will increase the durability of repairs. For two hypothetical cases, differing in orientation and amount of damage, it has been described how EAR can be applied in practice. Arguments have been give why other options are not attractive and EAR provides a better solution.

REFERENCES

Angst, U., Elsener, B., Larsen, C.K., Vennesland, Ø., 2011, Chloride induced reinforcement corrosion: Rate limiting step of early pitting corrosion, Electrochimica Acta, 56, 5877–5889.

Bertolini, L., Elsener, B., Pedeferri, P., Polder, R.B., 2004, Corrosion of Steel in Concrete: Prevention, Diagnosis, Repair, Wiley-VCH Verlag GmbH & Co. KGaA, Weinheim, ISBN 3-527-30800-8, 392 pp.

Castellote, M., Andrade, C., Alonso, C., 1999, Changes in pore size distribution due to electrochemical chloride migration trials, ACI Materials Journal, 96 (3), 314–319.

Gayer, K.H., Wootner, L., 1956, The Hydrolysis of Ferrous Chloride at 25°, JACS 78, 3944–3946.

Geiker, M.R., Polder, R.B., 2015, Experimental support for new Electro Active Repair method, in preparation.

Pacheco, J., Polder, R.B., Fraaij, A.L.A., Mol, J.M.C., 2011, Short-term benefits of cathodic protection of steel in concrete, Proc. Concrete Solutions, Dresden, Eds. M. Grantham, V. Mechtcherine, U. Schneck, Taylor and Francis, London, 147–156.

Polder, R.B., Hondel, A.W.M. van den, 2002, Laboratory investigation of electrochemical chloride extraction of concrete with penetrated chloride, HERON, Vol. 47 (3) 211–220.

Polder, R.B., Peelen, W.H.A., Stoop, B.J.Th., Neeft, E.A.C., 2011, Early stage beneficial effects of cathodic protection in concrete structures, Materials and Corrosion, Vol. 62 (2), 105–110.
Polder, R.B., Leegwater, G., Worm, D., Courage, W., 2014, Service life and life cycle cost modelling of Cathodic Protection systems for Concrete Structures, Cement and Concrete Composites, 47, 69–74.
Scheiner, S. Hellmich, C., 2007, Stable pitting corrosion of stainless steel as diffusion-controlled dissolution process with a sharp moving electrode boundary, Corrosion Science, 49, 319–346.
Snover, R.M., Vaysburd, A.M., Bissonette, B., Burke, D.F., 2012, Random thoughts on concrete repair specifications' Ills and treatment prescriptions, ICCRRR III, Cape Town, Alexander et al. (eds.), Taylor & Francis.
Tilly, G.P., Jacobs, J., 2007, Concrete repairs—performance in service and current practice, IHS BRE Press, Bracknell.
Tilly, G.P., 2011, Durability of concrete repairs, in Concrete Repair, a practical guide, ed. M.G. Grantham, Taylor and Francis, 231–247.
Vaysburd, A. M., Emmons, P.H., Bissonette, B., 2012, Concrete repair as an engineering task: An approximate solution to an exact problem, ICCRRR III, Cape Town, Alexander et al. (eds.), Taylor & Francis.
Visser, J.H.M, Zon, Q. van, 2012, Performance and service life of repairs of concrete structures in The Netherlands, ICCRRR III, Cape Town, Alexander et al. (eds.), Taylor & Francis.
Wong, H.S., Zhao, Y.X., Karimi, A.R., Buenfeld, N.R., Jin, W.L., 2010, On the penetration of corrosion products from reinforcing steel into concrete due to chloride induced corrosion, Corrosion Science, 52, 2469–2480.

Concrete Repair, Rehabilitation and Retrofitting IV – Dehn et al. (Eds)
© 2016 Taylor & Francis Group, London, ISBN 978-1-138-02843-2

A quantitative approach to the concept of concrete repair compatibility

B. Bissonnette
CRIB, Department of Civil Engineering, Laval University, QC, Canada

F. Modjabi-Sangnier
SNC-Lavalin, Montreal (QC), QC, Canada

L. Courard
GeMMe Building Materials, ArGEnCo Department, University of Liège, Liège, Belgium

A. Garbacz
Warsaw University of Technology, Warsaw, Poland

A.M. Vaysburd
Vaycon Consulting, Baltimore, MD, USA

ABSTRACT: The work reported in this paper is part of a wider research program intended to provide the repair industry with improved fundamental knowledge to implement rational design methods and rules for repairs. In that regard, there is a strong need to study the fundamental relationships and parameters that underlie the repair compatibility concepts, in particular those relating to dimensional compatibility. In the first part of the paper, classical formulas derived for thick cylindrical specimens were used to analyze the tensile stress buildup in annular restrained shrinkage test specimens, taking into account the restraining conditions of the investigated ring test method and the individual concrete properties/phenomena determined experimentally (elastic modulus, creep coefficient, drying shrinkage deformation). By comparing the ring test results with the calculated tensile stresses, the validity and accuracy of the theoretical approach could be appraised. A quantitative approach for the evaluation of the performance of concrete repair in terms of dimensional compatibility was then developed. Derived from the basic strain balance approach (ratio between the total deformability in tension and the drying shrinkage deformation), a parameter referred to as dimensional Compatibility Index (CI) was introduced in order to analyze the evolution of dimensional compatibility as a function of time for a given concrete mixture, taking into account the actual degree of restraint in the element. Compatibility Index evolution curves were calculated for various repair concrete mixtures in order to highlight material behavior relating to composition parameters and temperature. As it requires the evaluation of a limited number of individual properties that are for most readily available (i.e. strength, elastic modulus, shrinkage), the Compatibility Index expressed in terms of deformation carries a lot of potential as a relatively simple and convenient analytical tool for assessing the cracking sensitivity of concrete repair materials. Overall, it can be stated that a good correlation was found between the ring test results and the tensile stress values calculated based on individual concrete properties / phenomena and that the proposed calculation method lays ground for evaluating quantitatively the dimensional compatibility of repair materials and defining suitable performance criteria.

1 INTRODUCTION AND SCOPE

In the field of civil engineering, repair and rehabilitation have drawn significant attention in the recent years. Even though engineers have been repairing deteriorated structures for many years now, the rate of unsuccessful concrete repairs remains unacceptably high. Because of the lack of knowledge gained on the influence of certain fundamental parameters, the achievement of durable repairs is reduced in some circumstances to merely a "*hit or miss*" process.

The aim of concrete repairs is to prolong the useful service life of an existing structure, to restore its load-carrying capacity and stiffness, and/or to strengthen its members. A prerequisite to achieve adequate composite action is lasting bond between the existing substrate and the newly-cast material. In this respect, compatibility between the repair material and the existing concrete is of critical

importance. In fact, the level of compatibility will generally determine whether a repair project is a success or a failure, and whether or not a repaired structure is durable.

The importance of dimensional compatibility between existing concrete and repair materials has been addressed conceptually by various authors (Emberson & Mays, 1990; Plum, 1990; Pigeon & Saucier, 1990; Emmons & Vaysburd, 1993, 1995; Cusson, 1995; Morgan, 1996; Pigeon & Bissonnette, 1999; Vaysburd *et al*., 2015). Experimental studies have then confirmed the significant role played by creep in the global dimensional balance and the risk for cracking, especially shrinkage-induced cracking (Morgan, 1996; Pigeon & Bissonnette, 1999; See *et al*., 2003). One of the most significant findings is that tensile creep appears to be more sensitive than shrinkage to certain mix design parameters (Pigeon & Bissonnette, 1999), which opens up the possibility of designing materials in view of optimizing their creep to shrinkage ratio. Moreover, a correlation between tensile creep and shrinkage was observed, a trend that could be taken advantage of in both calculations and the identification of performance criteria for repair materials.

One of the main challenges to be faced now lies in evaluating quantitatively compatibility and determining what it requires under given circumstances (characteristics of the structure to be repaired and the environment). So far, even though the concepts have been described in great detail by a number of authors, there are still no reliable criteria or design rules, fundamental or empirical, available to engineers. Some interesting empirical approaches have been suggested, for instance the *stress performance margin* (Marosszeky, 1992), which consists of an index meant to compare the cracking sensitivity of various repair materials, or the *USACE*'s tentative *Performance criteria for repair materials* (Emmons *et al*., 1993), which summarizes the limit values a material should exhibit in selected test procedures for shrinkage and cracking. Those indices and criteria are certainly a step in the right direction, but they lack a fundamental basis, as they do not address explicitly compatibility.

Besides, for the compatibility approach to become accessible to the industry, simple and reliable characterization tests are needed. Various test procedures (*ring* test, *beam curling* test, *box* test) have been developed in recent years for the evaluation of the cracking sensitivity of repair materials (Morency *et al*., 2005). Some of those so-called performance tests could become key tools for the identification of performance criteria, provided that clear relationships with both the basic material properties and the composite repair behavior are established.

Recently, laboratory and field studies have demonstrated the potential and benefits of different innovative materials or products like shrinkage-compensating concrete, self-consolidating concrete, and shrinkage-reducing admixtures. In order to perform successful repairs with such materials on a consistent basis (optimization and robustness of repair materials), it is needed to quantify their key compatibility properties and determine what is the sensitivity of those properties to the mixture composition and constituents.

2 OBJECTIVES AND PROPOSED APPROACH

The work reported in this paper is part of a wider research program intended to provide the repair industry with improved fundamental knowledge to implement rational design methods and rules for repairs. In that regard, there is a strong need to quantify and correlate the relevant aspects of dimensional compatibility in order to consistently achieve repair works that do not undergo harmful cracking and loss of bond with time. Ultimately, the objective is to provide the industry with performance criteria and guidelines.

More specifically, this paper summarizes the work achieved to relate quantitatively the individual dimensional compatibility-related properties (notably elastic properties, creep, drying shrinkage) to the corresponding stress and strain values recorded in an annular restrained shrinkage test, commonly referred to as the *ring* test. In the first part of *the program, classical formulas* derived for thick cylindrical specimens were used to analyze the tensile stress buildup in restrained shrinkage test specimens. A quantitative approach for the evaluation of concrete repair with a single dimensional compatibility *parameter, the* compatibility index, was then developed. *Compatibility index* evolution curves were finally calculated for a range of repair concrete mixtures in order to validate the approach and highlight material behavior relating to composition parameters and temperature.

3 MECHANICAL ANALYSIS OF THE RING TEST EXPERIMENT

The dimensional balance inside a repair is governed by the volume changes and mechanical properties of the repair material, together with the level of restraint provided by the existing structure. Thus, in order to evaluate the restrained shrinkage cracking sensitivity of materials, the analysis must take into account the combined effect of these properties and phenomena.

This complex task can be simplified by addressing the evolution of the stress state in a simple

restrained-shrinkage element such as that used in ring-type tests (Fig. 1). In this type of experiment, the tested material is cast around a rigid steel ring, which opposes the shrinkage deformations that occurs after setting and curing. The actual level of restraint provided by the steel ring depends on the respective geometrical and material stiffnesses of the two annular bodies (steel and concrete rings) in contact with each other. The internal stresses that develop in the system are determined by monitoring the deformations in the steel ring with strain gages.

On the basis of the theory of elasticity and a given geometry of the annular test device, it is possible to calculate the circumferential stresses developing in the annular concrete sample due to drying shrinkage restrained by the inner steel ring (Fig. 2). Classical formulas derived for thick cylindrical specimens were used to estimate the tensile stress buildup in restrained shrinkage test specimens, taking into account the individual concrete properties and phenomena determined experimentally (drying shrinkage deformation, creep coefficient, elastic modulus), as well as the restraining conditions of the investigated ring test specimen. A similar approach has been proposed by Hossain & Weiss (2006). Although the principle of superposition of deformations is not rigorously valid in cement-based materials, mostly due to ageing effects, from a design standpoint, the accuracy of the quantitative evaluation it provides is satisfactory enough from an repair design engineering standpoint, as demonstrated by its extensive use in handbooks and building codes.

While the actual deformation and stress gradients across the thickness of the specimens are considered in the calculations, the analysis of the results is based on the average stresses. The evolution of the average shrinkage-induced stress ($\sigma_{c\,avg.}$) over time can be calculated with equation 1, where

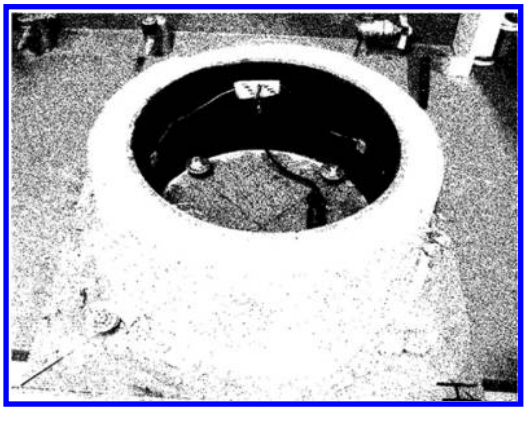

Figure 1. Example of ring test specimen (ASTM C1581) to study the restrained-shrinkage behavior of mortar and concrete mixtures.

ε_{fs} is the concrete free shrinkage, E_c and E_s are the elastic moduli of concrete and steel, ϕ_c is the creep coefficient of concrete, ν_c and ν_s are the *Poisson's* ratios of concrete and steel, and a, b, and c, are the internal, interfacial and external radii of the composite steel-concrete ring specimen.

$$\sigma_{c\,avg.}(t) = \frac{b(b+c)}{c^2-b^2}\,\frac{\varepsilon_{fs}(t)}{\left[\frac{1}{E_s}\left(\frac{b^2+a^2}{b^2-a^2}+\nu_s\right)+\frac{1+\phi_c(t)}{E_c(t)}\left(\frac{b^2+c^2}{c^2-b^2}-\nu_c\right)\right]} \quad (1)$$

By comparing the ring test results with the calculated tensile stresses, the validity and accuracy of the theoretical approach could be appraised.

Figure 3 shows ring test results obtained for an ordinary repair concrete (OPC), together with two self-compacting repair concrete mixtures produced with a slag-based ternary binder (SCC-ST) and a fly-ash-based ternary binder (SCC-FT) respectively. On each diagram, the calculated theoretical stress evolution with and without stress relaxation (lower and upper solid red lines respectively) and the experimental stress recorded over time in the ring test (solid blue line) are presented together with the corresponding tensile strength evolution curve (black line).

The pink areas between the red lines on the graphs of Figure 3 correspond to the theoretical stress relaxation potential of the concrete. By comparing the shaded areas in the two diagrams (= area between the tensile strength curve and the lower red line), it can be concluded that the OPC and SCC-ST mixtures are much less sensitive to shrinkage cracking than the SCC-FT mixture. In fact, in diagram c), both the theoretical tensile stress (including relaxation) and the recorded stress curves reach or get close to the tensile strength curve quite rapidly, whereas in diagrams a) and b), the recorded stress remains much lower, coinciding more or less with the relaxed stress curves.

Overall, a good correlation was found between the ring test results and the tensile stress values

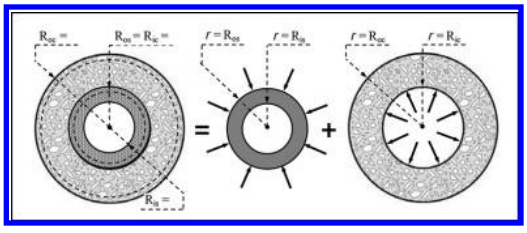

Figure 2. Basic analysis of the restrained shrinkage test specimen (mechanical equilibrium) and geometrical parameters.

calculated based on individual concrete properties/ phenomena. The level of correlation was particularly high when the test specimens (beams, rings) were partially sealed such as to obtain the same drying surface/volume ratio (S/V) in the various experiments. Based on the collected data and observations, it can be asserted that the calculation method that was developed provides a good basis for analyzing quantitatively the dimensional compatibility of repair materials.

4 QUANTITATIVE ASSESSMENT OF DIMENSIONAL COMPATIBILITY

The aforementioned mathematical formulas were further used to define a quantitative parameter for the evaluation of the performance of concrete repair in terms of dimensional compatibility. Derived from the basic strain balance approach (ratio between the total deformability in tension and the drying shrinkage deformation), the dimensional *compatibility index* (CI) was thus introduced in order to analyze the evolution of dimensional compatibility as a function of time for a given concrete mixture, taking into account the actual degree of restraint in the test specimen.

The dimensional *compatibility index* can be expressed in terms of deformation, thus allowing to relate explicitly to the various individual properties and phenomena involved in the material's response in restrained shrinkage conditions (strength, elastic modulus, creep, drying shrinkage), as well as to the degree of restriction of the element. For the latter, constants are calculated, based upon the respective geometry and mechanical properties (*Poisson*'s ratio) of both the restraining device and the test specimen. The time-dependent expression takes the following general form, where f_t is the concrete tensile strength, α_r is the instantaneous elastic restraint, and α'_r is the creep-dependent restraint:

$$C.I.(t) = \frac{\left[\frac{f_t(t)}{E_c(t)} + \phi_c(t)\varepsilon_{fs}(t)\alpha_r(t).\frac{C_c}{C_g}\alpha'_r(t)\right]}{\varepsilon_{fs}(t)\alpha_r(t)}$$

$$C_g = \frac{b(b+c)}{c^2-b^2} \quad C_c = \frac{b^2+c^2}{c^2-b^2} - v_s \quad C_s = \frac{b^2+a^2}{b^2-a^2} \qquad (2)$$

$$\alpha_r(t) = \frac{C_g}{\left(\frac{C_s}{E_s} + \frac{C_c}{E_c(t)}\right)E_c(t)}$$

$$\alpha'_r(t) = \frac{C_g}{\left(\frac{C_s}{E_s} + \frac{C_c(1+\phi_c(t))}{E_c(t)}\right)E_c(t)}$$

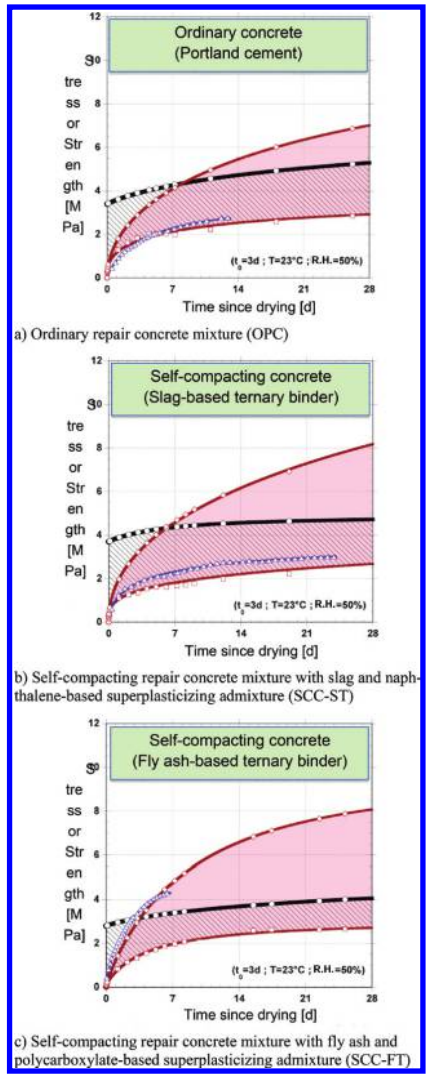

Figure 3. Comparative development of recorded and theoretical tensile stresses in AASHTO PP34 ring tests for a reference repair concrete (OPC) and two self-compacting repair concrete mixtures (SCC-ST, SCC-FT) exposed to drying at 50% R.H. at the age of 3 days (*note: solid blue line: stress recorded in the ring; lower and upper solid red lines: theoretical average concrete stress, with and without stress relaxation respectively; solid black line: tensile strength of the concrete*).

As it requires the evaluation of individual properties that for most are readily available (i.e. strength, elastic modulus, and drying shrinkage), the *compatibility index* carries much potential as a relatively simple and convenient analytical tool for assessing the cracking potential of concrete repair materials.

The CI parameter can alternatively be expressed in terms of stress. The compatibility index is then calculated as the ratio between the sum of the tensile strength (f_t) and total stress relaxation ($\Delta\sigma_{relaxation}$) in given restraining conditions, and the averaged elastic stress ($\sigma_{elastic}$) induced by restrained drying shrinkage.

5 EXAMPLES OF MATERIAL TENDENCIES REVEALED WITH THE COMPATIBILITY INDEX

The CI evolution allows to assessing whether the concrete can withstand shrinkage-induced cracking over time, taking into account the various phenomena involved and their complex interaction. *Compatibility index* evolution curves were calculated for different repair concrete mixtures in order to highlight characteristic material behavior relating to specific composition parameters and temperature (Modjabi-Sangnier, 2010).

The diagram presented in Figure 4 shows the evolution of this index for the same three concrete mixtures tested in the ring experiments (Fig. 3). Typically high at early age, the CI value is observed to decrease gradually with the ageing process, with quite steep decreasing rates in the first few days. During the drying period considered (0 to 28d), the CI values of the shrinkage-compensating (SCC) mixture produced with a slag-based ternary binder and the reference ordinary concrete (OPC) mixture are significantly higher than those determined for the fly-ash-based SCC mixture, especially in the first two weeks of drying. In other words, the two former mixtures seem to exhibit much more early-age dimensional compatibility than the SCC-TF repair mixture. The ring tests stress development curves on the diagrams of Figure 3 reveals show good agreement with the trends revealed by the CI curves. As a matter of fact, the rapid increase in tensile stress recorded for the SCC-TF rings is consistent with the much steeper decreasing rate of the CI value observed in Figure 4.

As already indicated, the CI curves can be used to compare the compatibility of different concrete mixtures and to identify specific material tendencies. In a recent investigation by Modjabi-Sangnier (2010), the comparison of results for a range of repair mixtures and curing conditions has shown that dimensional compatibility is very sensitive to certain composition variables and to temperature in the early stages of hydration. For instance, test results generated in this study remarkably show that a given binder/plasticizer agent combination can yield quite different conclusions depending on the curing temperatures. While some combinations exhibit more interesting characteristics at low curing temperatures with respect to compatibility and the cracking risk, others show exactly the opposite, as shown on the graph of Figure 5.

Based upon comprehensive experimental work by Modjabi-Sangnier (2010), it can be concluded that the composition parameters and the thermal conditions during the setting and hardening period may influence the susceptibility to cracking of a cementitious material undergoing restrained shrinkage and thereby need to be taken into account in the identification of performance criteria for dimensional compatibility.

Further investigations will address the identification of performance criteria, based on the CI approach, as well as the possibility to extract all the relevant information with a limited amount of tests (e.g. mechanical properties, length change and ring tests).

6 CONCLUSION

The proposed compatibility index appears as a quite promising analytical tool for predicting the performance of repair materials in terms of shrinkage-cracking resistance. Compatibility index data were determined for a range of repair materials and confronted with ring test results. The comparison showed good correlation, the mixture classification determined on the basis of *compatibility index* calculations being consistent with the classification based on the shrinkage-induced stresses recorded experimentally.

The *compatibility index* provides a sound basis for the identification of dimensional compatibility criteria. Such performance criteria are much awaited in the repair industry, to assist both the development of crack-resistant materials and the issuance of improved materials specifications.

ACKNOWLEDGMENTS

This project has been financially supported by the *Concrete Research Council* of the American Concrete Institute (ACI), the Natural Sciences and Engineering Research Council of Canada (NSERC), the Québec FR-QNT Research Fund, and the industrial partners of the NSERC *Industrial Chair on Durable Repair and Optimized Maintenance of Concrete Infrastructures* at Laval University (BASF Building Systems, City of Montreal, City of Québec, Euclid, Holcim, Hydro-Québec, Kerneos, King Packaged Materials, Lafarge, Ministry of Transportation of Québec, W.R. Grace & Co.), and through Scientific Cooperation Programs of the Polish, Québec and Wallonia–Brussels governments.

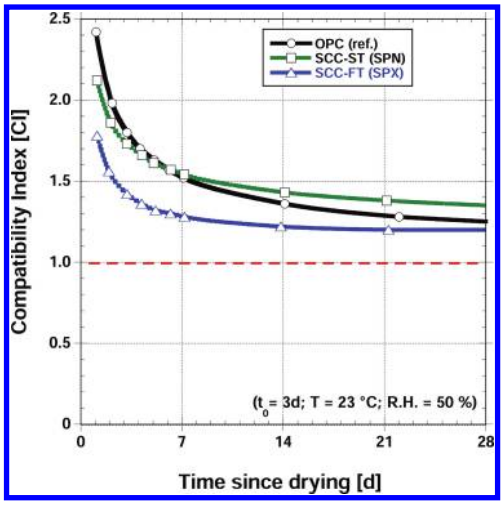

Figure 4. Evolution of the compatibility index (CI value) with time for a reference repair concrete (OPC) and two self-compacting repair concrete mixtures prepared with a slag-based ternary cement (SCC-ST) and a fly ash-based ternary binder (SCC-FT), exposed to drying at 50% R.H. at the age of 3 days.

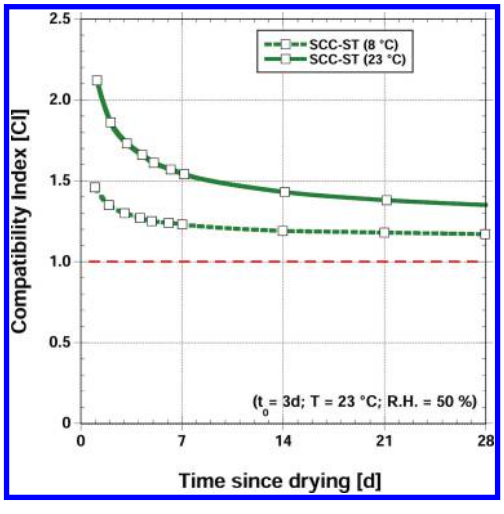

Figure 5. Evolution of the compatibility index (CI value) with time for a self-compacting repair concrete mixtures prepared with a slag-based ternary cement (SCC-ST) and, exposed to drying at 50% R.H. at different temperatures, starting from the age of 3 days.

REFERENCES

AASHTO PP34. 2005. Standard practice for estimating the cracking tendency of concrete, American Association of State and Highway Transportation Officials, Washington, DC, 5 p.

ASTM C1581. 2009. Standard test method for determining age at cracking and induced tensile stress characteristics of mortar and concrete under restrained shrinkage, Annual Book of ASTM Standards, Concrete and aggregates, volume 04.02, ASTM, West Conshohocken, PA, USA, 7 p.

Cusson, D. 1995. Durable concrete patches, *Construction Canada*, **37**(4), pp. 34–39.

Emberson, N.K. & Mays, G.C. 1990. Significance of property mismatch in the patch repair of structural concrete—part 1: properties of repair systems, *Magazine of Concrete Research*, **42**(152), pp. 147–160.

Emmons, P.H. & Vaysburd, A.M. 1993. Compatibility considerations for durable concrete repairs, *Transportation Research Record* 1382, pp. 13–19.

Emmons, P.H. & Vaysburd, A.M. 1995. Performance criteria for concrete repair materials—Phase I, U.S. Army Corps of Engineers, Technical Report REMR-CS-47, Washington (DC), April, 123 p.

Emmons, P.H.; Vaysburd, A.M.; McDonald, J.E.; Poston, R.W. and Kesner, K.E. 1993. Selecting durable repair materials: performance criteria, *Concrete International*, **22**(3), pp. 38–45.

Hossain, A.B. & Weiss, J. 2006. The role of specimen geometry and boundary conditions on stress development and cracking in the restrained ring test, *Cement and Concrete Research*, **36**(1): p. 189–199.

Marosszeky, M. 1992. Stress performance in concrete repairs, *International Conference on Rehabilitation of Concrete Structures*, Melbourne, pp. 467–474.

Modjabi-Sangnier, F. 2010 Approche quantitative de la notion de compatibilité des bétons de réparation autoplaçants (Quantitative approach of the compatibility concept applied to self-compacting repair concretes), *PhD* thesis, Laval University, 240 p. (*url*: http://www.theses.ulaval.ca/2010/27477/)

Morency, M.; Vaysburd, A.M.; von Fay, K.F. and Bissonnette, B. 2005. Development of a test method to evaluate cracking tendency of repair materials—CREEP Phase I Report, Research Report 2004-1, U.S. Bureau of Reclamation, Denver (CO), USA, March.

Morgan, D.R. 1996. Compatibility of concrete repair materials and systems, *Construction and Building Materials*, **10**(1), pp. 57–67.

Pigeon, M. & Bissonnette, B. 1999. Tensile creep and cracking potential of bonded concrete repairs, *Concrete International*, **21**(11), pp. 31–35.

Pigeon, M. & Saucier, F. 1992. Durability of repaired concrete structures, Advances in Concrete Technology, ed. V.M. Malhotra, pp. 741–773.

Plum, D.R. 1990. The behavior of polymer materials on concrete repair and factors influencing selection, *The structural engineer*, **68**(17), pp. 337–345.

See, H.T.; Attiogbe, E.K.; Miltenberger, M.A. 2003. Shrinkage cracking characteristics of concrete using ring specimens, *ACI Materials Journal*, **100**(3), pp. 239–245.

Vaysburd, A.M.; Bissonnette, B. & von Fay, K.F. 2015. Compatibility issues in design and implementation of concrete repairs and overlays, Report No. MERL-2014–87, Bureau of Reclamation, U.S. Department of Interior. 134.

Concrete Repair, Rehabilitation and Retrofitting IV – Dehn et al. (Eds)
© 2016 Taylor & Francis Group, London, ISBN 978-1-138-02843-2

The compatibility in concrete repair—random thoughts and wishful thinking

A.M. Vaysburd
Vaycon Consulting, Baltimore, MD, USA

B. Bissonnette
CRIB, Department of Civil Engineering, Laval University, QC, Canada

K.F. von Fay
U.S. Bureau of Reclamation, Denver, CO, USA

R. Morin
City of Montreal, Montreal, QC, Canada

ABSTRACT: The durability of repaired concrete structures and their useful service life depend on many factors. One of the critical factors is the achievement of compatibility in such a composite system. As a prerequisite for meeting the repair service life objectives, the compatibility/incompatibility issues should be analyzed and adequately addresses at the design stage of the project. Despite the number of publications on durability and service life of repaired concrete structures, fundamental discussion and guidance on compatibility issues are lacking. The opinions and recommendations issued on the subject are in some cases confusing, misleading or incorrect, regrettably leading to fallacies about compatibility in the practicing community. This paper is an attempt to raise and discuss some critical issues concerning the compatibility of concrete repair composite systems. Ambiguities and misconceptions in the current understanding of fundamental compatibility considerations in concrete repairs (dimensional compatibility, electrochemical compatibility and permeability compatibility) are addressed. The authors share their random thoughts on what we know, what we do not know, what we need to know.

1 INTRODUCTION

Considerable progress in knowledge of the engineering aspects of concrete repair technology has been achieved during the last twenty-five years. Nevertheless, we are still facing instances of repair structures gross deficiencies and inability in too many cases to meet the objectives of the designed service life.

The issue of compatibility in engineered repair composite systems is usually being ignored or misinterpreted by design engineers. The main reason is the lack of knowledge in this critical area, misleading guidance, and overall confusion among practicing engineers.

It is somehow astonishing to the authors, considering the significance of the problem and the thousands of studies on durability and service life of repaired structures that have been reported, that more questions than answers on compatibility subject still remain.

Certainly one reason is the lack of interest in the subject on the part of many concrete technologists, engineers, researchers and other specialists, who maybe find compatibility too mundane to study and address adequately. A search for the word "compatibility" in textbooks and concrete repair publications ordinarily draws black.

We all understand the negative results of incompatibility on repair performance. But knowing the results without clear understanding of the fundamental causes is no more satisfactory than postulation without verification. Seeking answers without the wherewithal to find them is equally frustrating.

The purpose of this paper is in no ways intended only to criticize the "conventional wisdom". The authors fully realize that a good musician is far superior to the best music critic.

The paper is an attempt to discuss some critical issues concerning the compatibility in concrete repair composite systems. The following ambiguities in the current understanding or misunderstanding of compatibility issues in concrete repair are discussed: dimensional compatibility, electrochemical compatibility and permeability compatibility.

Authors share their random thoughts on that we know, what we think we know, what we do not know, what we need to know and why.

2 CONCEPT OF COMPATIBILITY

The Webster's Dictionary provides the following definition of "compatibility" in general: *"the capacity of two or more entities to combine or remain together without undesirable after effects: mutual tolerance."*

Compatibility in repair systems is defined as the balance of physical, chemical and electrochemical properties and volume changes between the repair and existing substrate, which ensures that the composite repair system withstands the stresses induced by all loads, chemical effects, electrochemical effects and restrained volume changes without distress and deterioration over a designed period of time. Compatibility factors to be addressed in concrete repair are shown in Figure 1.

3 DIMENSIONAL COMPATIBILITY

One of the most important compatibility requirements is dimensional (deformational) compatibility. Hewlett (1993) defined the phenomenon of dimensional compatibility as "stable interfacial coexistence". Achieving dimensional compatibility in a composite repair system is a task of appropriate material selection and system behavior *vis-a-vis* getting along well together (Vaysburd, 2006).

The essence of dimensional compatibility can be formulated as follows:

- Drying shrinkage of the repair material relative to the substrate;
- Thermal expansion or contraction differences between repair and substrate materials;

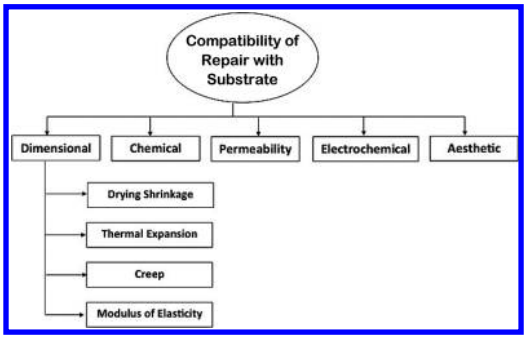

Figure 1. Compatibility factors in concrete repair (adapted from Vaysburd and Emmons, 2006).

- Differences in modulus of elasticity, which may cause unequal load sharing and strains resulting in interface stresses;
- Differences in creep;
- Relative fatigue performance of the phases in composite repair system.

The listed differences may result in initial tensile stresses that either cause cracking of the repair material or debonding at the repair substrate interface (the transition zone). Both of these will negatively affect the durability and load-carrying capacity of the repaired structure.

In the course of the discussion concerning compatibility, it is necessary to mention that some concrete repair "prophets" proclaimed that only repairing "*like with like*" can offer a durable solution and that the repair material to be compatible with existing concrete should have "composition and properties similar to the substrate concrete" (Vaysburd, 2006).

Many repairs to concrete structures are necessitated by inadequate quality of concrete leading to extensive shrinkage cracking, alkali-silica reaction, sulfate attack, etc. To follow the "*like with like*" recommendations, one has to use similar "junk" as repair material. Design engineer faced with such misleading interpretation of "dimensional compatibility" may specify repair materials with properties as close to those of the existing substrate concrete as possible. This is not only illogical, but harmful. The temptation to seek parity of properties, to avoid property mismatches between repair material and substrate is intuitively strong, but it definitely contradicts the general definition of compatibility and the definition of compatibility in concrete repair. It must be recognized that in some instances, it is desirable to select gross disparity of repair material properties.

The lack of understanding of the nature of "dimensional compatibility" in particular is the source of many failures in practice. Besides, the mistaken search for "parity" or "*like with like*" will often exclude from specifications groups of materials that are very useful and even necessary for certain applications, such as polymer mortars and concretes. The authors wish to emphasize the need for a clear appreciation of dimensional compatibility in concrete repair and appreciation in this context of those material properties that may well provide the key to successful and durable use of polymer-based materials for concrete repair.

An integral part of this appreciation is the assessment of the likely consequences of any "mismatch" of properties e.g. thermal coefficient of expansion, modulus of elasticity and creep, etc. For many applications, the repair success depends on recognizing and overcoming a potentially

destructive mismatch, either by use of appropriate polymer type of by application procedures. A point which is completely overlooked is that the apparent mismatch due to the viscoelastic nature of polymers can in fact result in beneficial stress relaxation due to the high creep that may help in preventing a potentially destructive stress buildup, which may occur due to shrinkage and temperature cycling during service.

During service life, incompatibilities in the form of dissimilar strength and moduli of elasticity between repair and substrate concrete can create difficulties, while drying shrinkage of repair materials may reduce longer-term structural efficiency by either inducing high tensile strains in the repair, or due to cracking that may reach the repair/substrate interface. Also, creep of the repair material under sustained stress may render the load-sharing capacity of the repair less effective with time.

The goal of the repair designer must be to engineer the composite repair system in such a way that the inevitable property mismatches will not lead to failure before the service life objectives are met.

It is important to emphasize that property mismatches between the substrate and the repair material is to some extent unavoidable.

Variability exists in properties of existing concrete, repair materials and internal and exterior environments. Occasionally, these different sources of variability cancel each other, but generally, as a rule, they are more likely to be cumulative. There is no way to avoid variability—nature abhors identities, variation being the rule—there is no such thing as uniformity in the physical world.

4 ELECTROCHEMICAL COMPATIBILITY

It is widely accepted that the driving force for the phenomenon of corrosion in repair systems is generally attributed to the electrochemical incompatibility between the repair and substrate. The electrochemical incompatibility is defined as the imbalance in electrochemical potential between different locations of the reinforcing steel because of their dissimilar environments caused by a repair (Gu *et al*., 1997). The dissimilar environments can be due to the differences in physical properties, chemistry and internal environments. A holistic model of concrete repair failure is presented in Figure 2.

To provide adequate resistance to aggressive actions, it is necessary to foresee how a given repaired structure will deteriorate. This in turn helps show how such deterioration is prevented or, more realistically, how to ensure a sufficiently slow deterioration process.

In other words, the aggressiveness of the existing internal (i.e. inside the structure) and exterior environments, their interaction and the possible changes caused by the repair should be given comprehensive consideration at the design stage. Such analysis is necessary in order to achieve electrochemical compatibility and fulfill the required durability and structural safety of ageing infrastructure.

Of the durability/service life problems of concrete repair, the most important but least known are the issues related to electrochemical compatibility. The authors recognize that precise analysis of electrochemical compatibility is very difficult, if not impossible. The difficulties are mainly due to three factors:

1. The existing structure has its unique internal environment caused by ageing, weathering, and chemical/electrochemical changes and activities, which necessitated the repair. As previously mentioned in this article, the existing concrete substrates are different from each other in age, quality, and service exposure.
2. The application of a repair alters the internal environment. The exterior environment depends largely on the structure's geographical location (e.g. temperature, relative humidity, rainfall levels and soil types) and the human activity nearby

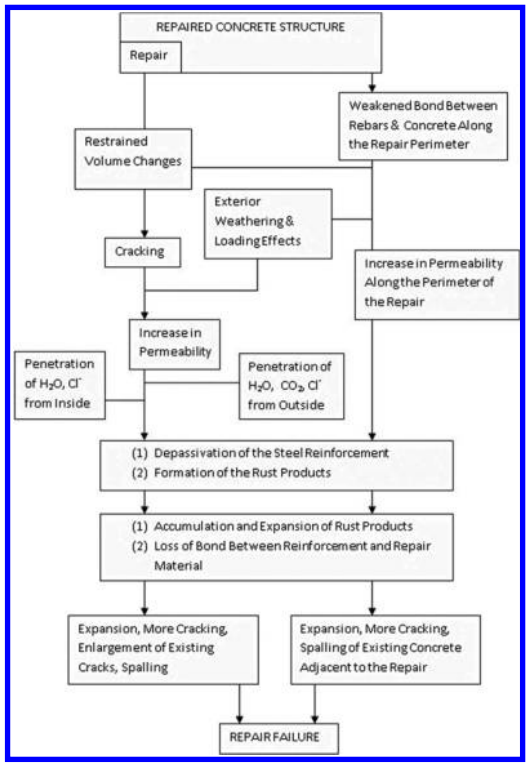

Figure 2. Holistic model of concrete repair failure (Vaysburd, 2006).

(e.g. prevailing winds and industrial—or traffic-generated pollution). The internal environment exists within the structure and, in addition, is created by the engineered repair design.

3. In repair systems, the internal environment is a moving target, constantly changing due to the existence of the internal transport mechanism (in addition to the exterior transport described earlier). Water with dissolved salts may be put into movement by temperature and/or pressure gradients. Dissolved substances can also travel by diffusion in water-saturated concrete with a stagnant water phase, provided that there is a concentration gradient. Finally, ions will migrate in an electric field, providing electrical conductivity in a repair system.

The major problem with many repaired concrete structures is continuation (or even acceleration) of reinforcing steel corrosion. When reinforced concrete is repaired, some of the chloride-contaminated concrete may be left in place, which results in the repair material having a different moisture, oxygen, and chloride content than the surrounding concrete. Strong corrosion cells may be established, resulting in spalling of the repair itself or of the surrounding area, a phenomenon often referred to as the "*halo*" or "*ring*" effect.

There is a direct link between durability and electrochemical compatibility. With a complex composite system such as a concrete repair, the interaction between aggressive exterior and internal environments becomes a major factor in progressively cumulative damage.

The combined effects of the several critical diverse environments along the electrically continuous rebar (in addition to stress field gradients) significantly add to the complexity of the problem. The influence of the repair phase on the existing surrounding material, the change in chemical composition, the distribution of aggressive agents, the presence of oxygen, moisture and admixtures, and other factors related to the repair's electrochemical properties can in fact all be critical.

Unless the repair project provides for "global" cathodic protection, the risk of corrosion is omnipresent. Therefore, performing a repair that will last successfully without problems for 10 to 15 years is not an easy task to achieve. The design engineer must be realistic and honest when setting out project objectives.

A successful repair project is not permanent; rather it is when the "defeat" occurs after the design objectives have been reached. These objectives should be based on rational engineering compatibility analysis, knowledge from observations and through trial and error. In the words of famous mathematician Jacob Bronowski (Bronowski, 1956), "*a good prediction is one which defines its area of uncertainty; a bad prediction ignores it*."

Among various factors affecting compatibility in concrete repair composite systems, the electrochemical compatibility is the most complex and critical factor for adequate performance of concrete repair jobs. It is difficult to predict how a repair will affect the electrochemical activity within a concrete structure, because it is a function of a variety of parameters such as the nature of repair materials, the condition of the substrate, the change in potentials, the exterior and internal (inside the system) environments and their interaction, and mass transport processes. The risk of corrosion and even its acceleration due to electrochemical incompatibility between the "old" and "new" portions of the repair system is virtually always present unless cathodic protection is implemented.

Unfortunately we still do not know enough today how to address reliably the issue of electrochemical compatibility and therefore to predict the future service life of a repaired concrete structure. Vaysburd *et al*. (2012) stated, "(…) *beware of the 'experts' who come up with and exact number of future service life of the repaired structure. After all, we are still subject to the mathematical and scientific laws of probability.*" The design engineers have to do their best in "durability planning" stage of the project, including electrochemical compatibility and related future service life."

5 PERMEABILITY COMPATIBILITY

Permeability of repair materials is one of the properties of importance in achieving compatibility and durability in repair projects. The majority of repair publications strongly recommend using low permeability materials in repair situations. If the use of low permeability concrete in new construction is a key to achieving durability, this rule does not necessarily apply to concrete repairs, where the situation is more complex. Unfortunately, in the case of repairs there is no "rule of thumb". There are "horses for courses", each situation is different and requires to being accurately analyzed and addressed.

The use of low permeability repair materials regardless of repair specifics can lead to unsuitable choices, incompatibility problems and eventual repair failures. Durability of the repair can be negatively affected in many situations when repair and substrate have different, incompatible permeability.

This concept may, in some cases, lead to a false sense of security and unsuitable materials incapable of providing lasting performance can be specified. Engineering analysis and judgment is

needed on defining what degree of permeability of repair materials shall be recommended for different repair situations. Most likely, there is no single recommendation as to whether materials with very low permeability or materials having compatible permeability with the existing concrete, are more effective. It depends, in the authors' view, on particular transport mechanism in the repair system. Transport of substances through and in the repair systems is a very complex process, consisting of a combination of liquid flow through macrocracking and microcracking systems, capillary transport, diffusion and osmotic effects. The exact contribution of each process needs to be quantified in each particular situation. The effects of such variables as location of the repair in the structure, chemical environment in the composite repair system, amount and distribution of cracks in both materials (substrate and repair), temperature, moisture and stresses need to be considered.

Even when incompatible permeabilities between repair material and substrate are justified, it must be acknowledged that a few "through" cracks in repair can drastically offset the benefit of a low permeability repair material. Microcracks in substrate and repair with wider cracks in both repair phases will play a much greater role in reducing durability than the permeability of the repair itself. Cracking is one of the most critical factors in the overall permeability and durability of repaired structures.

6 CONCLUSION

1. The phases in concrete repair composite system must be compatible to meet the design service life objectives. Rational compatibility analysis must be undertaken prior to detailed design to ensure the highest likelihood of success.
2. At the present time, there is still no reliable accepted design methodology addressing the compatibility issues and providing guidance to the practicing engineer towards achieving successful repair project.
3. Among the various factors affecting compatibility in concrete repair, the electrochemical compatibility is the most complex and critical factor for adequate performance of concrete repair projects. The risk of corrosion developing or even accelerating due to electrical incompatibility between the "old" and "new" phases of the system is almost inevitable unless cathodic protection is implemented.
4. Better understanding of compatibility/incompatibility issues in concrete repair composite systems will allow the repair professionals to "silt the grain from the husk" in the design of concrete repair projects.

REFERENCES

Bronowski, J. 1956. Science and Human Values, Julian Messner, Inc., New York, USA, 94 p.

Emmons, P.H.; Vaysburd, A.M. & McDonald, J.E. 1993. Some compatibility problems in repair of concrete structures—A fresh look, *Proceedings of the Third International Colloquium on Material Science and Restoration*, Esslingen, Germany, pp. 836–857.

Gu, P.; Beaudoin, J.J.; Tumidajski, P.J. & Mailvaganam, N.P. 1997. Electrochemical incompatibility of patches in reinforced concrete, *Concrete International*, **19**(8), pp. 68–72.

Hewlett, P.C. 1993. Concrete: the material of opportunity, *Concrete 2000*, Vol. 1, Dhir, R.K. and Jones, M.R. (eds.), London, E. & F.N. Spon, pp. 1–22.

Vaysburd, A.M. 2006. Durability of repaired concrete structures—The battle for survival, *Proceedings of the Second International Symposium on Advances in Concrete through Science and Engineering*, Quebec City, Canada, pp. 207–224.

Vaysburd, A.M. & Emmons, P.H. 2006. Concrete repair—A composite system: philosophy, engineering and practice, *International Journal for Restoration of Buildings and Monuments*, **12**(5/6), pp. 423–435.

Vaysburd, A.M.; Emmons P.H. & Bissonnette, B. 2012. Concrete repair as an engineering task: an approximate solution to an exact problem, *Proceedings of the International Conference on Concrete Repair, Rehabilitation and Retrofitting*, Cape Town, South Africa.

Concrete Repair, Rehabilitation and Retrofitting IV – Dehn et al. (Eds)
© 2016 Taylor & Francis Group, London, ISBN 978-1-138-02843-2

Influence of the interface mechanisms on the behavior of strengthened with reinforced concrete or steel existing RC slabs

Marina Traykova
Department of Reinforced Concrete Structures, University of Architecture, Civil Engineering and Geodesy, Sofia, Bulgaria

Raina Boiadjieva
Department of Structural Mechanics, University of Architecture, Civil Engineering and Geodesy, Sofia, Bulgaria

ABSTRACT: Extending the life of the existing structures is the base of the sustainable design. The reinforced concrete slabs are usually subjected directly to different actions and overloading and very often are seriously damaged.

The reinforced concrete and the steel jackets are one of the most popular techniques in the retrofitting practice for reinforced concrete slabs. The quality of the load transfer and the behavior of the strengthened slabs are related to the type of the interface mechanisms: mechanical interlocking and adhesive bonding, friction, dowel action of reinforcement and/or connectors crossing the interface. The choice of interaction mechanisms depends on the type of the member and of the type of loading.

Based on different numerical models, the influence of the type of the interface mechanisms on the behavior of the slabs is presented.

Finally, some general conclusions for the effectiveness of the techniques for connection and their contribution on the load bearing capacity and the deflections of the strengthened slabs are given.

1 INTRODUCTION

The reinforced concrete and steel jackets are one of the most popular techniques for retrofitting of existing reinforced concrete slabs. The connections between concrete layers with different ages and between the existing reinforced concrete and new steel elements and the solution of these connections are decisive for the behavior of the strengthened slabs.

According Model Code 2010 the main parameters for the load bearing capacity in the case of concrete-to-concrete load transfer are: interface roughness, cleanliness of surface, concrete strength and concrete quality, inclination of the shear forces, bond conditions, ratio of reinforcement, crossing the interface. Concrete to steel interfaces according Model Code 2010 play a governing role with regard to the design of strengthening with steel sheeting and profiles for different reinforced concrete elements. Interaction between concrete and steel components can be classified as follows: adhesion between two materials, frictional interlock, mechanical interlock and dowel action provided by anchor devices and systems.

This subject has been continuously studied over time, a justifiable attention that has provided several research projects since the 60´s. As a consequence, there is a large number of design expressions nowadays, which are included in several standards and documents. These equations, which assess the behavior and/or resistance characteristics through the use of variable parameters, were calibrated in order to obtain design values similar to those from empiric tests.

From the several analyzed studies (for example Bruno Baleia Casal) and from its evolution in recent years, one may conclude that the shear resistance in the interface of concrete layers with different ages is indeed a phenomenon where many simultaneous effects may be identified. Similar are the problems with interface concrete to steel.

2 SUMMARY AND ANALYSIS OF THE MAIN INTERFACE MECHANISMS

The combination of these mechanisms is complex and varies with the various intervention factors. The most important factors for the shear transfer mechanisms (concrete to concrete; concrete to steel) can be summarized in the following:

2.1 *Interface roughness*

The interface roughness has a determinant role for realization of shear mechanism. There are several methods to measure and specify the roughness of a concrete surface. The sand patch method, based on a quantitative approach, is certainly one of the best known. This method consists of pouring a defined volume of fine sand on the contact surface. Then, the subsequent measurement of the covered area diameter permits the roughness calculation. The advantage of this method is the simplicity and quickness. Nevertheless, recent advanced methods have been developed, in which some innovative processes to measure roughness are presented. Their increased complexity requires laboratory investigations—contact methods (mechanical contact profilometer) and non-contact methods (laser triangulation, photogrametry-digital imaging).

Finally for the design purposes, the surface roughness has to be classified into different categories depending on the roughness R_t Model Code 2010.

Regarding the surface treatment, there are several techniques to assign roughness to an interface: a surface prepared with a steel brush, a surface treated with sandblasting and a partially chipped surface. According to the pull-off and shear tests, the conclusion is that the more efficient technique is the treatment with sandblasting, followed by the treatment with a steel brush, the chipped surface and the casting without treatment, respectively in descending order of efficiency.

2.2 *Adhesive bonding and mechanical interlocking*

The shear strength by adhesion and mechanical interlocking can significantly contribute to the overall shear resistance. The appropriate roughness, the clean surface and the grade and the quality of concrete, which are usually parameters considered in shear stress calculation, are the main connection influencers. The adhesive bonding and the mechanical interlocking are sensitive to any contamination of the surface.

2.3 *Dowel action*

Dowel action refers to the bending resistance of connectors crossing the interface. A shear slip along the interface leads to a lateral displacement between upper and lower connector ends, thereby inducing bending stresses in these bars. These stresses are superimposed by axial tensile forces due to the openings of the joint. The interaction of tensile forces and bending leads to a reduction of the maximum possible dowel action.

2.4 *Shear friction*

The friction force is a function of the normal force across the joint, depending of the roughness of the interface. To analyze and quantify this mechanism, it's possible to use the shear friction model, original developed by Birkeland and Birkeland or the aggregate interlock model, developed by Walraven and Reinhardt.

2.5 *Bond of metal sheeting*

The use of metal sheeting is a common solution for strengthening. The interaction between the concrete and the steel element has a strong influence on the overall behavior of the slab. Usually the mechanical connecting devices are recommended to prevent the relative sleep between the two components.

2.6 *Mechanical interlock*

For strengthening post-installed devices into drilled holes are usually applied. The following mechanisms can be activated: friction, mechanical interlock, bond, dowel action.

2.7 *Final considerations*

The shear mechanism can be described as a combination of various effects:

- The adhesion is the first mechanism to be developed. The maximum shear strength is achieved at reduced values of slip.
- The contribution of each mechanism (adhesion and friction) depends mainly on the amount of transversal reinforcement.
- With the increase of slip, the reinforcement bars will be also subjected to bending. Thus, the contribution of dowel action will take place.
- The interaction of friction and dowel action depends essentially on the interface roughness, the expected slip and the anchorage of the reinforcement. Friction will prevail if a roughened surface and a good reinforcement anchorage is provided.

3 NUMERICAL EXAMPLE

3.1 *Parameters of the task*

The case study in the numerical example is a real design situation and represents a reinforced concrete one—way spanning continuous beam slab. The thickness of the slab is 10 cm. The existing reinforcement is according Figure 1. New imposed load is provided with value 10 kN/m2. Two design solutions for strengthening are presented: with an additional concrete layer and with steel sheeting.

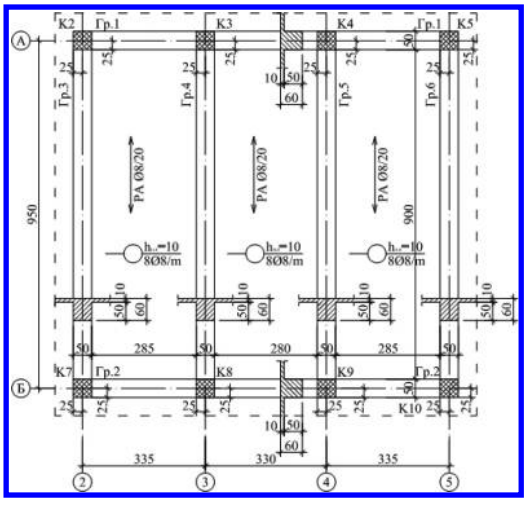

Figure 1. Existing reinforced concrete slab.

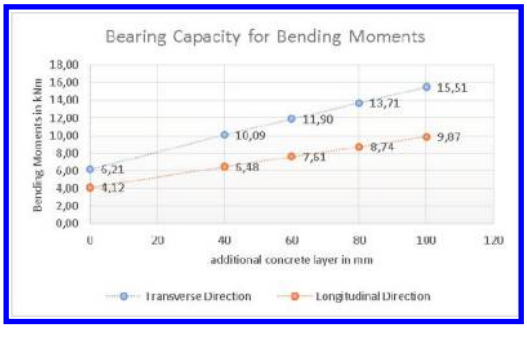

Figure 2. Bearing capacity for bending moments.

In Figure 1 the following symbols are used: "К"- column; "Гр." – beam; "РА"- distribution reinforcement.

The investigation is addressed to the following parameters:

– in case of design solution with additional concrete layer—interface roughness characteristics, arrangement of connectors and the reinforcement ratio crossing the interface;
– in case of design solution with steel sheeting - number (spacing) and type of anchors, interface between the existing reinforced concrete surface and the new steel sheeting.

3.2 *Modeling*

The numerical analysis is performed using the program SAP2000 based on the Finite Element Method. All models are developed in

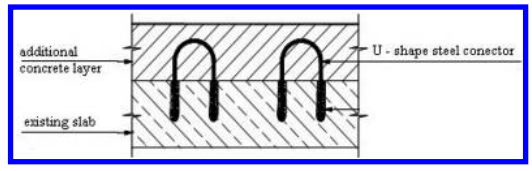

Figure 3. Solution with additional concrete layer.

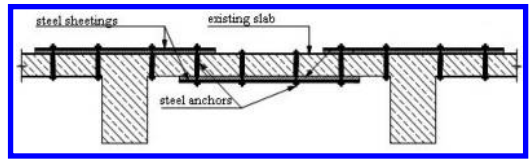

Figure 4. Solution with steel sheeting.

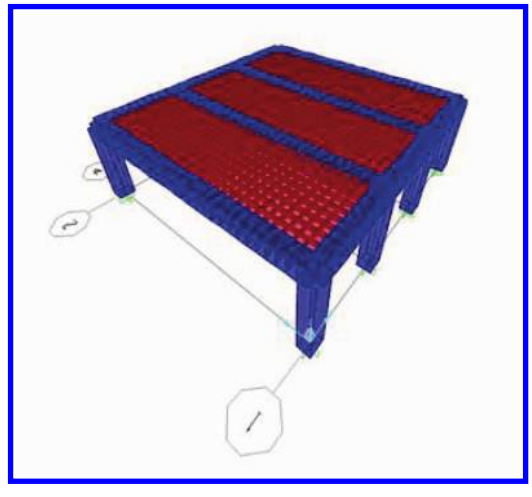

Figure 5. Solution with additional concrete layer – 3D model.

linear-elastic formulation of the problem. In the case of design solution with additional concrete layer the slab is modeled by multi-layer shell elements. The beams are modeled by linear (frame) finite elements positioned in their geometric center.

Several numerical models are developed to obtain the most reliable identification of actual behavior and bearing capacity of the strengthened slab. They are focused on the joint work of the different concrete layers and the most adequate reflection concrete-to-concrete connection.

In the case of design solution with the steel sheeting the slab is modeled by shell (area) elements. The beams are modeled by linear (frame)

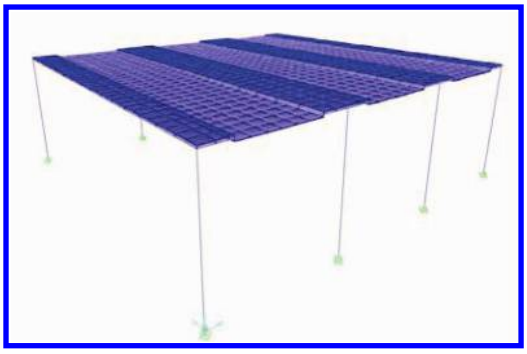

Figure 6. Solution with steel sheeting – 3D model.

finite elements positioned in their geometric center. The steel sheeting is modelled by shell elements positioned in geometric level of this strengthening. The connection concrete-to-steel is with anchors modeled in the example with stiff elements.

4 CONCLUSIONS

The analysis of the final results can be summarized in the following main conclusions:

- The amount of reinforcement bars that crosses the interface as well as the roughness of the interface are the two parameters of main importance of the shearing mechanism. The shear strength increases accordingly to the increase of the steel ratio and the roughness.
- During the reinforcement design it is important to evaluate the evolution of the building construction process and the load actions.
- When strengthening with additional concrete layer, it's very important to carry out a global solution for the slab and the beams. Increasing only the stiffness of the slab has unfavorable effect on the deflections.
- The variations of the thickness of the interface layer, in the case of additional concrete layer, show an insignificant influence on the numerical results.
- Increasing the stiffness of the interface layer between the existing and the new concrete layer, leads to a serious reduction of the deflections in the strengthened slab.
- Strengthening with steel sheeting (regardless of the changes in the different parameters) has no special contribution to the deflection of the slab and the final deflections are very similar to the deflections before the strengthening. These results are expected in view of the fact that the proposed model is not enough accurate for the real process of deformation.
- The solution with steel sheeting is more sensitive for the bending moments.
- The position and the number of anchors for the steel sheeting have significant influence on bearing capacity for the bending moments of the strengthened slab.
- Finally the proposed results and conclusions require a validation with real experimental results. The experiments will give an additional opportunity to find more precise values of the different parameters.

REFERENCES

Casal, B.B., 2011, Connections Between Concrete Layers with Different Ages, Dissertation, Civil Engineering Department, Instituto Superior Técnico, Universidade Técnica de Lisboa, Portugal EN 1992-1-1:2004.

FIB Model Code for Concrete Structures 2010.

SAP2000, Version 16.0.0, Computers and Structures Inc., 2013.

Traykova, M.D., 2014, Rehabilitation and Strengthening of Buildings, Amadeus Print, Sofia, Bulgaria (in Bulgarian).

Concrete Repair, Rehabilitation and Retrofitting IV – Dehn et al. (Eds)
© 2016 Taylor & Francis Group, London, ISBN 978-1-138-02843-2

Fundamental approach for the concept of concrete repair compatibility

L. Courard
University of Liège, Liège, Belgium

B. Bissonnette
Laval University, Québec, Canada

A. Garbacz
Warsaw University of Technology, Warsaw, Poland

ABSTRACT: Before being translated in terms of physical, mechanical and chemical of materials, the initial step for evaluating compatibility is interface creation. The thermodynamic properties of the materials as well as transport mechanisms—diffusion, capillary succion—at the interface and roughness of the concrete substrate are acting from the beginning and influencing the durability of the bond strength. A review of the main parameters influencing bond development is presented on the base of the equilibrium of the surface free energies of liquid and solid, applied to the concept of repair mortars, coating and hydrophobic treatments..

1 INTRODUCTION

Repair works quality is depending on a lot of factors dealing with properties of the repair materials, the surface preparation of the substrate, the environment and the worker's qualification.

First of all however, it is important to verify the physico-chemical compatibility of concrete substrate and repair materials.

Surface analysis, in conjunction with surface science and applied science is a major activity contributing to the knowledge of interfacial phenomenons and, more generally, to our daily well-being through improvements in health, consumer products, environment, … (Kinloch 1987).

But we have to define exactly what we mean through "surface analysis". In its simplest sense, we require analysis of the elemental composition of the outermost atom layer of a solid. Having defined that, the next request will be for detailed knowledge of the chemical binding state, precise sites of atoms in relation to crystal structure, surface homogeneity and the state of absorbates.

Surface free energy (Hawkins et al. 1930) is a direct measurement of intermolecular forces. The free energy in surface layer is the result of the attraction of the bulk material for the surface layer and this attraction tends to reduce the number of molecules in the surface region resulting in an increase of intermolecular distance. This increase requires work to be done and returns work to the system upon a return to a normal configuration: this explains why free energy exists and why there is a surface free energy (Zisman et al. 1950).

Before being translated in terms of physical, mechanical and chemical of materials, the initial step for evaluating compatibility is interface creation. The thermodynamic properties of the materials as well as transport mechanisms—diffusion, capillary succion—at the interface and roughness of the concrete substrate are acting from the beginning and influencing the durability of the bond strength.

2 NEAR TO SURFACE CHARACTERISTICS

2.1 *Principles of adhesion*

The concept of adhesion has firstly to be clearly defined because of the "duality" of the term: *"on one hand, adhesion is understood as a process through which two bodies are brought together and attached—bonded—to each other, in such a way that external force or thermal motion is required to break the bond. On the other hand, we can examine the process of breaking a bond between bodies that are already in contact. In this case, as a quantitative measure of the intensity of adhesion, we can take the force or the energy necessary to separate the two bodies"* (Kinloch 1987).

Adhesion has therefore two different aspects, according to whether our interest is mainly (1) in the conditions and the kinetics of contact or (2)

in the separation process. The intensity of adhesion will depend not only on the energy that is used to create the contact, but also on the interaction existing in the interface zone. Generally speaking, mechanism of adhesion has to be considered from two origins: specific adhesion and mechanical interlocking (Courard 2000).

When the materials are in contact, the effective area, that means the surface where contact really exists, will be a fundamental parameter to be taken into account to explain the adhesion process. This is the result of the wetting procedure of the solid body by the liquid phase. The wetting procedure can be explained as follows: the surface energies of the solid and the liquid interact each other and a change of the energy conditions occurs due to surface decrease of liquid/vapour and solid/vapour interfaces while a new interface (liquid/solid) is created (Dann 1970). At this point of view, contact angle is an interesting representation of this phenomenon: the lower is the contact angle, the better is the spreading on the surface and the more effective will be the inter-molecular interactions at the interface (Kamusewitz et al. 1985).

The investigation concerning the behaviour of the interface between repair systems and concrete substrate have shown that quality of concrete substrate is important factor affecting adhesion in repair system and has to be evaluated prior to repair. Knowledge about synergetic effects of parameters characterizing surface quality (surface roughness, microcracking, wettability) is fundamental for concrete repair compatibility (Courard 2002).

2.2 *Microstructure of the substrate*

The physical properties are fundamental for the knowledge of the interactions at the interface. A lot of notions may be defined such as opened and accessible porosity, relative impregnation ratio or water absorption. Capillary action test seems to be very accurate to describe the behaviour of the concrete "skin" in contact with the new layer (Courard 1999) and its ability to anchor the repair material in the superficial porosity of the substrate. By means of Mercury Intrusion Porosimetry, it is possible to define the concrete skeleton and estimate the specific surface, the porous volume and the mean radiuourard 2005). But the most interesting information is the porous volume as a function of the diameter; it will be so possible to evaluate theoretically the maximum quantity of liquid each type of pore will be able to absorb (Courard et al. 2003a). Based on the law of Washburn the calculation imposes to take into account the presence of the Interfacial Transition Zone (I.T.Z.) in order to be able to correlate theory and experimental observations. The microscopical observations may be useful to determine ITZ values. These investigations will allow to calculate a coefficient of capillarity, that will take into account properties like connectivity, accessibility of the pores, tortuosity, …

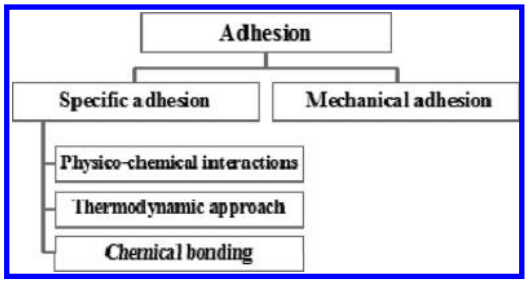

Figure 1. Principles of adhesion.

On the other hand, the nature and the concentration of the binder as well as the conditions of setting reaction are important for microscopical interpenetration: the first phenomenon observed when the new layer is laid down on the concrete substrate is the wetting of the solid surface by the liquid. The wetting is depending on two main aspects (Comyn 1992): thermodynamic (there is wetting) and kinetic (wetting has to happen as quick as possible). The kinetic aspect is physically based on the Washburn's law and is given by Equation 1.

$$l^2_p = r \cdot \gamma_L \cdot \cos\theta \cdot t / 2\eta \quad (1)$$

where l_p is the variation of penetration height, η the viscosity of the liquid (N/m².s), r the radius of the pore (m), γ_L the superficial tension of the liquid (N/m), θ the contact angle and t the time (s).

If one can represent concrete by a porous material with parallel capillaries of different radius, perpendicular to the liquid surface, physic's laws clearly show that the liquid will be absorbed with a higher force (equation of Laplace) for fine capillaries but at a higher speed and in higher quantity (equation of Washburn) for big capillaries. The Washburn's relation shows also that the penetration height increases when the viscosity of the liquid decreases, the contact angle decreases and the superficial tension of liquid increases.

Many remarks may be formulated about the use of Washburn's law (Courard 2000):

- the shape of the pore will influence the results (circular or bottle-ink for example);
- the contact angle value is not constant and depends on time and temperature;
- the pollution of the concrete surface may modify the kinetics of contact;
- the viscosity is also depending on time.

It consequently seems to be fundamental to define clearly the conditions of application in order to be able to optimise the behaviour of the liquid laid on the concrete substrate. The continuous interaction between the two bodies shows also that it is illusory to choose one without the other. These considerations indicate moreover the importance of the state of saturation of the concrete substrate before repair product application (Sasse et al. 1983).

Diffusion will also occur at the interface when contact is created. Due to its porous structure and assuming it is water saturated, diffusion of ions may happen from the interstitial solution of the cement slurry or the PCC and CC mortars to the water present into the porous skeleton of the concrete and inversely. Ionic movements will participate to the creation of chemicals bonds or, at least, to chemical interactions between the substrate and the new layer; they can contribute to the development of "chemical" anchorages (Courard et al. 2003b).

3 THERMODYNAMIC COMPATIBILITY

3.1 *Thermodynamic equilibrium*

The superficial tension of a liquid determines its ability to wet a solid surface: an efficient spreading of the liquid on the solid increases the effective surface of contact and promotes adhesion (Courard et al. 2011). The second law of thermodynamics indicates that a system of two phases is stable if local energy is minimum.

For the creation and the stability of the interface between concrete and new layer, one makes the hypothesis that this minimisation of the interfacial energy corresponds to a maximum of resistance and durability of the joint (Courard 1999).

The relation between contact angle and free energies of liquid and solid is defined according to the law of Young-Dupre (Fig. 2) given by Equation 2:

$$\gamma_S = \gamma_{SL} + \gamma_L \cdot \cos\theta \quad (2)$$

where γ_S is the surface free energy of solid, γ_L the surface free energy of liquid and γ_{SL} the surface free energy liquid/solid. The best spreading of liquid on the solid surface may be expressed by many criteria (Gutowski 1985):

- minimisation of contact angle: the lower the contact angle, the better the spreading. Some additives may modify the interactions into the interstitial solution of the cement slurry, binder layer or mortar. The effects of the use of admixtures are a low decrease of viscosity and a more large decrease of contact angle values;

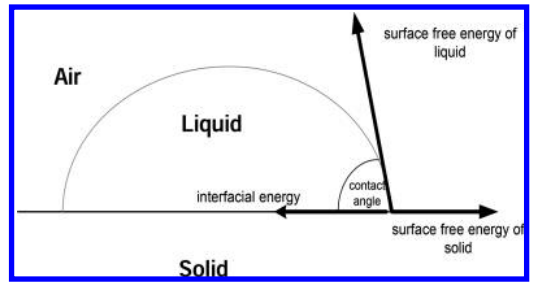

Figure 2. Wettability of a solid surface by a liquid—Young Dupré equation.

- free energies criteria: it is possible, from the Young-Dupre equation to conclude that, for a fixed value of γ_L, an increase of the difference $\gamma_S - \gamma_{SL}$ is favourable for the wettability of the surface. This criteria is however low attractive due to the difficulty to determine γ_S and γ_{SL}. Another criteria is to say that γ_L has to be the highest as possible to obtain the lowest value of the contact angle θ;
- minimization of interfacial energy or maximization of the work of adhesion. The work of adhesion represents the work necessary to separate the two bodies. These criteria are not really applicable to the situation of the creation of an interface, when liquid is spread on solid; they are more related to the resistance of the interface solid/solid, after setting or polymerization of the liquid phase.

For the analysis of the creation of the interface, it seems that the more representative criterion is the contact angle because this is a direct representation of the wettability of the surface. It is a necessary but not a sufficient condition to guarantee the efficiency of the bond.

3.2 *Relation between thermodynamic parameters and adhesion*

Some relations were found (Gutowski 1987) between the shear strength of metallic plates or glass fibres with resin and thermodynamic parameters:

$$\tau = f_1(\gamma_{SL}/\gamma_L^C) \text{ or } \tau = f_2(\gamma_S/\gamma_L^C)$$

where γ_L is the superficial tension of the liquid phase after hardening.

However, it is very difficult to establish such as relation between concrete and repair products due to several reasons (Possart et al. 1993):

- test devices used to measure adherence are generally not able to make distinction between the

contribution of adhesion forces and loss of viscoelastic or plastic energy into concrete or the new layer;
- thermodynamic considerations on the stability of the interface solid/solid may be correlated with adherence only if rupture happens at the interface;
- the measurement of the contact angle θ with goniometer is very imprecise due to the unhomogeneity and porosity of the support. This measurement is the base for the calculation of γ_S, γ_{SL} and W_A. More precision could be eventually obtained by working on powders.

For the analysis of the creation of the interface, it seems that the more representative criterion is the contact angle because it is a direct representation of the wettability of the surface. It is a necessary but not a sufficient condition to guarantee the efficiency of the bond (Possart et al. 1992).

4 INFLUENCING PARAMETERS

4.1 *Water*

Water is a dramatic parameter influencing the durability of repair works through the modification of surface properties of materials. The influence of temperature or relative humidity of the ambient atmosphere before the application and during the curing of the new layer are relatively well-known. It is quite common to observe:

- disturbances in the setting process;
- insufficient absorption of the binder by the substrate, due to water excess in the substrate or untimely evaporation of the solvents;
- untimely creep and/or thermal creep, in addition of setting creep, ...

Coatings are designed to protect concrete against environmental aggression. Water is one of the aggressive parameters able to deteriorate the concrete structure. When water comes between the polymeric system and the concrete substrate (Courard et al. 2003), thermodynamic equilibrium is modified, in respect with particular values of surface free energies of materials. From a theoretical point of view, this means a simple generalisation of the law of Young and Dupré (Courard 2000), relatively to a new interface liquid-liquid (Equations 3 and 4). Contact angle is in this case a visible effect of the interaction between the two liquids to conquer solid surface. But what happens with spreading conditions? When equilibrium is attempted and if there is no spreading of one liquid to the detriment of the second one, equilibrium of forces means:

$$\gamma_{SA} = \gamma_{SB} + \gamma_{AB} \cdot \cos\theta \quad (3)$$

or

$$\gamma_{SA} - \gamma_{SB} = \gamma_{AB} \cdot \cos\theta \quad (4)$$

where γ_{SA}, γ_{SB}, γ_{AB} and θ are interfacial tensions between solid S and liquids A and B, interfacial tension between liquids A and B, and contact angle of these liquids on the solid surface, respectively.

It is possible to show (Kinloch 1987) that the liquid with the higher tension of adhesion ($\gamma_x \cdot \cos\theta_x$) will expulse the other one from the surface. The calculation of the work of adhesion (Equation 5) can also give interesting conclusions, taking into account the variation of surface free energies in presence of water:

$$W_{x(L)} = \gamma_{x(L)} \cdot (1 + \cos\theta_{x(L)}) \quad (5)$$

The work of adhesion is an "evaluation" of adhesion and observation of Table 1 clearly indicates the loss of adhesion when water is present at the interfaces between acrylic or epoxy resins and concrete.

Thermal creep will also be produced if the application is realised in too thick layers. The degree of saturation of the substrate has also a great importance. In the example given hereafter, a PCC mortar—with dry and wet slurries—is applied on sandblasted concrete slabs characterized by different saturation levels. The adhesion strength changes in a clock-shape as a function of the water saturation level of the substrate (Table 2). The adhesion is relatively weak for low saturation levels (<50%); it reaches classical values for saturation levels between 55 and 75%. After that, we observe a decrease of the adhesion strength (>90%).

A weak saturation level produces a disturbance into the setting process of the cement while a too high saturation level acts on the attractive forces, the porosity, the kinetics of contact and, finally, the adhesion properties. One must also note that the best adhesion values are reached for a large scale of saturation levels, so that it doesn't sensitively depend on the variation of water content, except for extremal conditions.

4.2 *Microroughness*

The surface treatment of concrete substrate is important in order to promote mechanical adhesion (Trende et al. 1998). The main problems arise from co-lateral effects of the treatment, especially due to micro-cracks parallel to the surface (Bissonnette et al. 2006). After treatment, concrete surfaces present fractal topography. As for any fractal object, it is possible to break up this surface or this profile in a sum of sub-profiles. Each sub-profile can be differentiated in terms of wavelengths; there

Table 1. Calculation of work of adhesion for interfaces without (W_A) and with (W_{AL}) water.

Interface	W_A (mJ/m²)	W_{AL} (mJ/m²)
Mortar/concrete	87.8	No sense
Acrylic/Concrete	74.1	22.7
Acrylic/Acrylic	80.4	53.7
Acrylic/Hydrophobic treatment	52.2	66.7
Epoxy/Concrete	79.6	21.8
Epoxy/Epoxy	92.4	53
Epoxy/Hydrophobic treatment	56	42.2

Table 2. Adhesion of a mortar on concrete substrate vs. saturation level of concrete substrate and slurry.

Adhesion (N/mm²)		
Saturation level	with dry slurry	with wet slurry
50	0.83	2.32
52	2.80	2.14
55	2.09	2.89
70	2.75	2.65
90	3.54	3.36
93	2.13	3.06
97	1.81	2.58
100	1.43	1.48

is however no limit or precise criterion to validate the choice of decomposition method.

As mechanical interlocking is one of the basic mechanisms of the adhesion process, it is fundamental to be able to characterize the "roughness" of the substrate. Depending on local conditions of the specific building various types of surface treatments can be applied and a wild spectrum of shape and roughness can be induced (Garbacz et al. 2006).

4.3 *Human factors*

Operational factors will also induce difference in the results, depending on the tools, the competence of the worker and the manner in which he will perform the repair work. Figs. 3 and 4 show microscopical views of interface between a concrete slab and a PCC mortar applied in the same environmental conditions and from the same bag. The first worker (A) choose the techniques of pressure and smoothing while the second (B) only pressed the mortar without any finishing (12). The first view (Fig. 3) shows a lot of cracks parallel to the interface, at the interface or in the mortar, while the second is representative of a good continuity at the interface with a good spreading of air bubbles. The finishing operation (A) has induced a partial unsticking of the repair material.

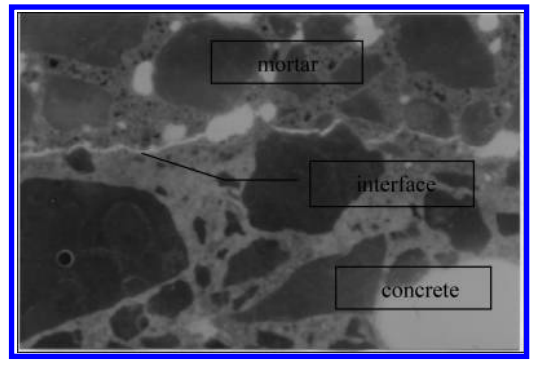

Figure 3. Microscopical view of interface between a concrete slab and a PCC mortar (operator A).

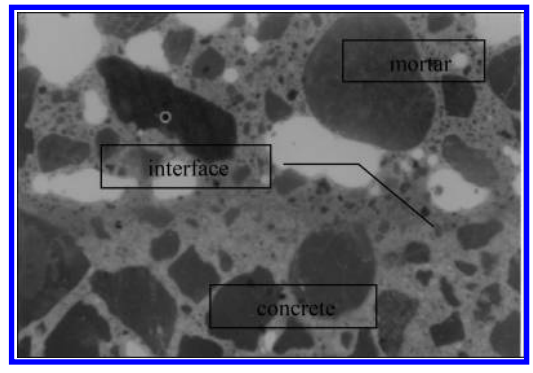

Figure 4. Microscopical view of interface between a concrete slab and a PCC mortar (operator B).

This is representative of possible destruction of the interface due to human action: forces developing adhesion have been destroyed by application conditions.

5 CONCLUSIONS

If there is creation of an interface, it means that there is a potential and mutual interaction between the two bodies. A physiological transposition of the situation would let us say that it is a case of partiality (from Latin word "*appetentia*"): this term describes the instinctive desire to all what is able to satisfy a need or something instinctive. Its application to the interface between concrete and a new layer summarizes all the parameters—physical, chemical and mechanical properties—of the substrate, the new layer and the environment that will influence the creation and the stability of this interface. Finally, that will lead to the macroscopical effect and sign of the efficiency of the cohesion: bond strength.

Compatibility between the different materials appears to be of prime importance: shrinkage, rigidity, surface roughness, viscosity, temperature, creep … etc, will make the contact effective or not and allow interactions between the materials. But the first step remains the contact that has to be created in a very short: this is the *repair speed dating*!

ACKNOWLEDGMENTS

This project has been financially supported by the Natural Sciences and Engineering Research Council of Canada (NSERC), the Québec FQRNT Research Fund and the industrial partners of the Industrial Chair on Durable Repair and Optimized Maintenance of Concrete Infrastructures at Laval University (BASF Building Systems, City of Montreal, City of Québec, Euclid, Hydro-Québec, King Packaged Materials, Lafarge, Ministry of Transportation of Québec, St-Lawrence Cement, W.R. Grace & Co. Support was also provided by the Belgium (Wallonia Brussels International) and Quebec governments through the Wallonie-Bruxelles-Québec Scientific Cooperation Program as well as Belgium – Poland (MNiSW) Scientific Cooperation Program.

REFERENCES

Bissonnette, B., Courard, L., Vaysburd, A. and Bélair, N. (2006) Concrete removal techniques: influence on residual cracking and bond strength. Concrete International, 28(12), 49–55.

Comyn, J. (1992) Contact angles and adhesive bonding, International Journal of Adhesion and Adhesives 12(3), 145–149.

Courard, L. How to analyse thermodynamic properties of solids and liquids in relation with adhesion? in: ISAP '99, 2nd International Symposium on Adhesion between Polymers and Concrete (Eds Y. Ohama and M. Puterman, Rilem Publications), Dresden, Allemagne (1999), 9–20.

Courard, L. (2000) Parametric Study for the Creation of the Interface between Concrete and Repair Products, Materials and Structures 33, 65–72.

Courard, L. (2002) Evaluation of thermodynamic properties of concrete substrates and cement slurries modified with admixtures, Materials and Structures 35, 149–155.

(a) Courard, L. and Degeimbre, R.. (2003) A capillary suction test for a better knowledge of adhesion process in repair technology. Can. J. Civil Eng., 30(6), 1101–1110.

(b) Courard, L., Darimont, A., Degeimbre R. and Wiertz, J. (2003) Hygro-thermal application conditions and adhesion. In: ed. P. Seidler, Technische Akademie Esslingen, Fifth International Colloquium Indust-rial Floors '03, Ostfildern/Stuttgart, Germany, 37–142.

Courard, L., Michel, F. and Martin, M. (2011) The evaluation of the surface free energy of liquids and solids in concrete technology. Construction Building Materials 25(1), 260–266.

Dann J.R. (1970) Forces involved in adhesive process. I. Critical surface tensions of polymeric solids as determined by polar liquids. Journal of Colloïd Interface Science 32(2), 302–331.

Fiebrich M.H., "Scientific aspects of adhesion phenomena in the interface mineral substrate-polymers", in Proceedings of 2nd Bolomey Workshop, Adherence of young and old Concrete (ed. F.H. Wittman, Aedificatio Verlag, Unterengstringen, 1994),25–58.

Garbacz, A., Courard, L. and Kostana, K. (2006) Characterization of concrete surface roughness and its relation to adhesion in repair systems. Mater. Charact. 56, p.281–289.

Gutowski, W. (1985) Physico-chemical Criteria for Maximum Adhesion. Part I: Theoretical Concepts and Experimental Evidence. Journal of Adhesion 19, 29–49.

Gutowski, W. (1987) The relationship between the strength of an adhesivebond and the thermodynamic properties of its components. International Journal of Adhesion and adhesives 7(4), 189–98.

Harkins, W.D. and Jordan, H.F. (1930) A method for the determination of surface and interfacial tension from the maximum pull on a ring, Journal of American Chemical Society, 52, 1751–72.

Kamusewitz, H. and Possart, W. (1985) The static contact angle hysteresis obtained by different experiments for the system PTFE/water, International Journal of Adhesion and Adhesives 5(4), 211–15.

Kinloch, A.J. (1987) Adhesion and Adhesives: science and technology, Chapman and Hall, London.

Possart, W. and Kamusewitz, H. (1992) Some thermodynamic considerations concerning the usual interpretation of wetting on solids, International Journal of Adhesion and Adhesives 12(1), 49–53.

Possart, W. and Kamusewitz, H. (1993) The thermodynamics and wetting of real surfaces and their relationship to adhesion, International Journal of Adhesion and Adhesives 13(2), 77–84.

Sasse, H.R. and Fiebrich, M. (1983) Bonding of polymer materials to concrete. Materials and structures 16(94), 293–301.

Tabor, D. (1981) Principles of adhesion—Bonding in cement and concrete. in Adhesion problems in the recycling of concrete, (Editor P. KREIJGER), NATO Scientific Affairs Division, 63–90.

Trende, U., and Büyüköztürk, O. 1998. Size Effect and Influence of Aggregate Roughness in Interface Fracture of Concrete Composites, ACI Materials Journal, V.95 (4), p.331–338.

Zisman, W.A. and Fox, H.W. (1950). Journal of colloid science 5, 514.

Concrete Repair, Rehabilitation and Retrofitting IV – Dehn et al. (Eds)
© 2016 Taylor & Francis Group, London, ISBN 978-1-138-02843-2

Strengthening/retrofitting of coupling beams using advanced cement based materials

M. Muhaxheri, A. Spini, L. Ferrara & M. di Prisco
Department of Civil and Environmental Engineering, Politecnico di Milano, Milano, Italy

M.G.L. Lamperti
European Commission, Institute for the Protection and Security of the Citizen, Ispra, Italy

ABSTRACT: In this paper the effectiveness has been assessed of an upgrading/retrofitting system for coupling beams (span-to-depth ratio equal to 1.5) not designed to resist earthquake actions. The proposed retrofitting technology employs either High Performance Fiber Reinforced Cementitious Composites (HPFRCCs) or Textile Reinforced Cementitious Composites (TRCCs). 14 mock-ups of coupling beam units, scale 1:2, have been casted and subjected to either monotonic or cyclic loading tests. The different resisting mechanisms in conventional plain and reinforced concrete coupling beams have been first of all investigated (tensile strength of concrete in plain concrete coupling beam; strut-and-tie mechanisms in coupling beams reinforced with only longitudinal bars; enhancement of the aforementioned mechanism due to stirrups). The influence of the boundary conditions due to the shear wall shafts on the coupling beam spanning between, has been investigated. Longitudinal and transverse reinforcement have been designed to comply only with EC2 minimum requirements for non-seismic design situations. In a second stage the effectiveness of the upgrading/retrofitting techniques has been checked testing non- and pre-damaged coupling beams. In the latter case two different drift levels have been selected for pre-damage, namely 1% and 2%, respectively meant as representative of ductility demand for SLS and ULS. Results highlight the effectiveness of the proposed upgrading/retrofitting techniques, which, also in view of their ease of execution and reduced invasiveness, can stand as a reliable alternative to other more commonly employed ones.

1 INTRODUCTION

The lateral resistance of medium and high rise buildings relies on a system of reinforced concrete (r/c) shear walls, which due to architectural requirements, such as door or window openings, consist of individual shafts connected by deep "coupling beams". Since the Alaska earthquake, in 1964, in which excessive damage in coupling beams was observed, interest has continuously raised on the importance of a correct design of coupling beams. As a matter of fact, because of their geometry (low span to depth ratio) they hardly can be designed through usual Bernoulli "beam" theory models. Early studies by (Paulay, 1971) showed that a dedicated, dense and not seldom complicated reinforcement arrangement is required in order to provide good transfer of forces: This should consist of diagonal crossing bars, further tied by stirrups to avoid their premature buckling under repeated loadings. These provisions were later accepted also by international design codes, such as ACI 318 and Eurocode 8. As a matter of fact, in most of the existing buildings, which were built before the codes enforced such kind of reinforcement, the aforementioned provisions may have not been respected. Because of updated code provisions and revised seismic zonation, together with increased sensitiveness to safety of private and public buildings, there is an increasing concern for retrofitting or upgrading coupling beams in shear walls which may have suffered damage from previous accidental events, deterioration due to environmental actions, or because of the necessity to increase their bearing capacity, in case simply to comply with new design provisions.

Several techniques have been investigated to this purpose over the past years such as:

- r/c conventional concrete jacketing (Mihaescu et al. 1990) which results not adequate as it requires a excessive sectional enlargement to comply with durability constrains for reinforcement;
- application of bolted steel plates (Su et al, 2005). In this last case, despite the good performance measured in laboratory experimental

investigations, this technique is quite unpractical, since it requires prior identification of the position of reinforcing steel bars as well as the prearrangement of holes for bolts, which may result in a damage of the element and in an increased labour cost.

High Performance Fibre Reinforced Cementitious Composites (HPFRCCs) due to their enhanced mechanical performance, mainly for their peculiar tensile behaviour, in recent decades have attracted a great attention among research and engineers community as strengthening/retrofitting solution of existing r/c structures, e.g. slender beams (Martinola et al. 2010; Triantafillou et al 2005, Meda et al. 2014), slabs (Weiland et al. 2006) and shear walls (Preti and Meda, 2015) or even as a complete replacement of conventional r/c exactly in the case of coupling beams (Canbolat et al.2005; Lequesne, 2011), which would be otherwise characterized by densely congested reinforcement, which would be unpracticable to detail.

In this paper the use of High Performance Fiber Reinforced Cementitious Composite (HPFRCC) and Textile Reinforced Cementitious Composite (TRCC) as detailed hereafter has been explored as an upgrading/retrofitting solution for poorly designed or damaged coupling beams. 14 mock-ups of coupling beam units, scale 1:2 featuring minimum longitudinal and transverse reinforcement according to Eurocode 2 prescriptions, were casted and subjected to either monotonic or cyclic loading tests. The different resisting mechanisms in conventional plain and reinforced concrete coupling beams were first of all investigated (tensile strength of concrete in plain concrete coupling beam; strut-and-tie mechanisms in coupling beams reinforced with only longitudinal bars; enhancement of the aforementioned mechanism due to stirrups). The effectiveness was then investigated of the upgrading/retrofitting techniques has been checked by testing non- and pre-damaged coupling beams. Two different drift levels were selected for pre-damage, namely 1% and 2%, respectively meant as representative of ductility demand for SLS and ULS.

Results, analyzed in terms of load bearing and energy dissipation capacity, highlight the effectiveness of the proposed upgrading/retrofitting techniques, which, also in view of their ease of execution and reduced invasiveness, can stand as a reliable alternative to other more commonly employed ones.

The application to the case of a five storey r/c shear wall was finally addressed through numerical analyses also to study the effectiveness of tailored retrofitting/upgrading alternatives.

2 EXPERIMENTAL PROGRAMME

Experimental mock-ups have been designed making reference to a shear wall containing a typical door opening, 900 mm wide (equal to the length of the coupling beam) and 2.1 m high. Assuming an inter-storey height equal to 2.7 m, this has resulted in a depth of the coupling beam equal to 600 mm and hence in a span to depth ratio of 1.5. The coupling beam specimen was hypothesized to be "poorly designed". To comply with maximum load capacity of testing equipment, a scale ratio 1:2 was adopted. The specimen hence had the following dimensions (length × depth × width): 450 mm × 300 mm × 100 mm. Reinforcement was designed to satisfy the minimum reinforcement requirement prescribed by design codes for non-seismic design situations and consisted of 2 + 2 ϕ8 mm longitudinal bars (upper and lower) and ϕ6 mm stirrups spaced at 100 mm. Yield strength of employed steel was equal 569 N/mm^2 and 552 N/mm^2 respectively for longitudinal and transverse reinforcement.

In total 14 specimens were casted in a precast plant, along with their day by day production and all along one week. Specimens were casted with a normal strength concrete and cube companion samples for each casting batch were also casted and tested for compression strength at each coupling beam testing age. Average measured cube strength was equal to 36.6 N/mm^2 with significant fluctuations which will be later called to explain some apparently contradictory experimental results.

The experimental campaign performed involved tests on "non-retrofitted" coupling beam specimens, through which the influence of the different resisting contributions (concrete tensile strength, longitudinal and transversal reinforcement) as well as on retrofitted ones was studied. As for the first part, the programme consisted of tests on two plain concrete coupling beams, two beams reinforced only with longitudinal bars and further two with both longitudinal and transverse reinforcement detailed as above. Only monotonic tests were performed on plain and longitudinally-only reinforced mock-ups whereas one monotonic and one cyclic test were performed on the mock-ups with both longitudinally and transverse reinforcement.

As for the tests on retrofitted/upgraded specimens, two "repairing" materials were employed, namely a HPFRCC and a TRCC. With for the latter case only two "upgraded" specimens were tested (the TRCC was applied to undamaged mock-ups), for the former both cases of upgraded and retrofitted specimens were considered. Besides two undamaged (upgraded) specimens, also four retrofitted ones were tested, two of which were pre-damaged at 1% drift level and two at 2% drift level. The pre-damage drift levels were selected as

Table 1. Mix design of employed HPFRCC.

Constituent	dosage (kg/m^3)
Cement type I52.5R	600
Slag	500
Siliceous sand 0–2 mm	982
Water	200
Superplasticizer	33
Straight steel fibers (l_f = 13 mm; d_f = 0.16 mm)	100

Table 2. Property of the employed AR-glass fabric.

Warp wire spacing (mm)	4.9
Warp (Tex)	2 × 640
Warp filament (μm)	14
Weft wire spacing (mm)	7.1
Weft (Tex)	1200
Weft filament (μm)	19

representative of SLS and ULS behaviour. For each couple of nominally identical retrofitted and/or upgraded mock-ups one monotonic and one cyclic test was performed.

For the cyclic test protocol, the load was applied, under displacement control, at successive 0.5% drift increments, with full load reversal. Three cycles for each drift level on either side were performed, to assess the stability of the cyclic response.

As a first retrofitting option, a 20 mm thick layer was applied of a HPFRCC was applied. The composition of the material, first suggested in (di Prisco et al. 2008) and then extensively studied in (Ferrara et al. 2011, 2012) is shown in Table 1. Because of the self-levelling ability of the material the application was simply done by pouring it into suitable formworks. As a second option, a 6 mm thick layer of TRCC, selected from a previous investigation (Colombo et al. 2013). The material consisted of the same matrix of the HPFRCC, with the maximum aggregate size cut to 0.6 mm, and reinforced with an alkali resistant glass fabric, whose property are summarized in Table 2 A lay-up application technique was chosen in this case. In all cases the strengthening was applied on the lateral and bottom surfaces of the coupling beam, which were previously sandblasted for improved bond, considering that the real situation the extrados is not accessible.

In order to reproduce realistic boundary conditions the testing set-up shown in (Fig. 1-a) was designed. Two jacks with maximum load capacity of 400 kN and stroke length of 200 mm were used to applied the load to the specimen in either

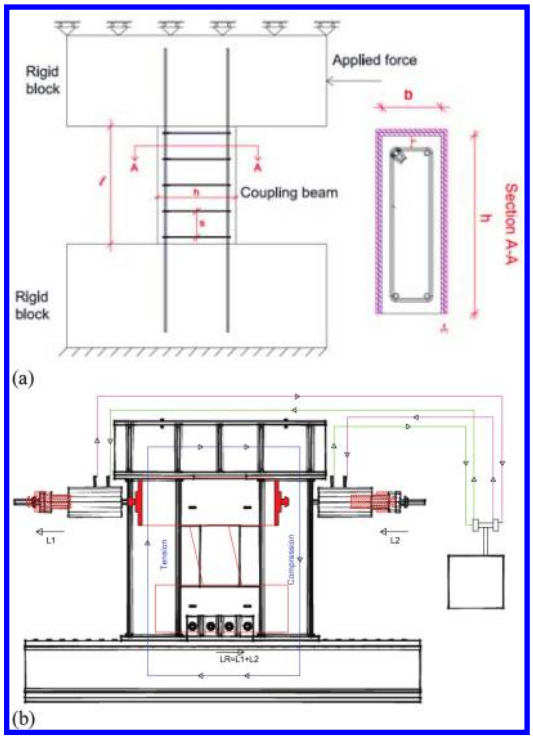

Figure 1. Schematic representation of the test mock-up with intended boundary conditions (a) and of the test set-up (b).

direction to simulate a cyclic loading. A hydraulic pump was used to generate the pressure in piston of the jack. The pump has two sets of inlet and outlet of the oil. Through two extensions and four tubes it was possible to create a closed loop of oil flow between the two jacks. This system allowed to effectively implement and apply to the specimen a cyclic loading path with two jacks counter acting each other (Fig. 1-b). The load was transferred to the specimen by means of a Dywidag bar which was connected to the jacks and passed through the specimen; the force collected by the bar from the jacks was then applied to the specimen via 30 mm thick steel plates. Through this system a compressive load is always applied to the specimen and the preparation time and cost are reduced to the minimum.

The steel structure "framing" the test specimen, has been conceived to apply, thanks to the high stiffness of its vertical and horizontal members, a loading condition characterized by pure shear loading with neither expansion in the longitudinal direction of the coupling beam nor rotation of the top (and bottom) blocks. These have to be meant as representatives of the wall shafts which are connected

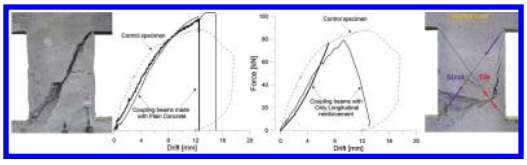

Figure 2. Load-drift curves and crack patterns at failure for plain concrete coupling beams (left) and for coupling beams with only longitudinal reinforcement (right).

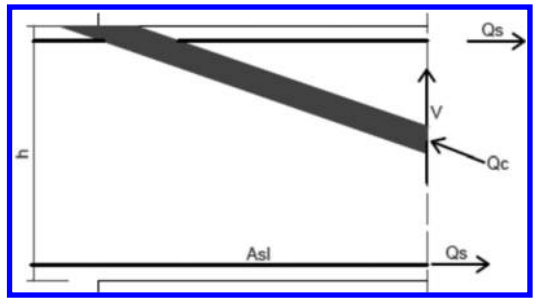

Figure 3. Schematic of the strut and tie mechanism activated in coupling beams with only longitudinal reinforcement (half of the coupling beam is shown for the sake of symmetry).

by the coupling beam. The reproduced boundary conditions hence make reference to rigid wall shafts with symmetrical stiffness on either side of the coupling beam, which can be hence considered as fully fixed at its edges.

3 EXPERIMENTAL RESULTS: ANALYSIS AND DISCUSSION.

As from the description of the experimental test program provided in the previous section, of the 14 tested mock-ups two were made of plain concrete, with neither longitudinal nor transverse reinforcement, and two were reinforced only with longitudinal bars (2 + 2 Monotonic tests were p8). Monotonic tests were performed on these four mock-ups first of all to verify the suitability of the designed testing apparatus. Moreover, the whole set of data, once compared to the measured monotonic behaviour of the mock-ups reinforced with both longitudinal and transverse reinforcement, allows to have a deeper insight into the different resisting mechanisms which governed the load bearing capacity of the coupling beams, *e.g.*, concrete tensile strength, strut and tie mechanisms, stirrup confinement effect.

The load vs. drift curves highlight good repeatability for tests on nominally identical specimens (Figure 2). The following remarks hold:

the plain concrete specimens exhibited an abnormally high load bearing capacity. A possible explanation was sought and, in the authors' opinion, found, in the daily fluctuations of the concrete compressive strength as measured at each coupling beam testing age on the companion casted cube specimens. For the plain concrete coupling beams this was equal to 48 N/mm^2, which is significantly higher than the one measured on companion cube specimens for the longitudinally-only reinforced mock-ups (31 N/mm^2), as well as for the one containing both longitudinal and transverse reinforcement (35 N/mm^2). The different measured compressive strengths resulted into different estimated tensile strengths of the concrete, as from EC2 formulae, ranging from about 3.5 N/mm^2 for plain concrete mock-ups to less than 3 N/mm^2 in the other cases. The failure mode of plain concrete mock-ups clearly features one diagonal crack (Figure 2) which likewise clearly highlights the dominant, if not exclusive, role of the concrete tensile strength in governing the load bearing capacity. This 20% tensile strength difference results into an equal difference on the load bearing capacity;

– the mock-ups containing only longitudinal reinforcement, besides a strength lower than plain concrete ones, as justified above, also featured no ductility at all. The presence of longitudinal reinforce-ment should have activated a (diagonal) strut and (longitudinal) tie mechanism, the load bearing capacity of which should have been governed by the yielding of longitudinal bars, which would have also been able to impart a certain amount of ductility to the coupling beam behaviour. According to the force equilibrium scheme (Figure 3), the load bearing capacity of the coupling beam can be evaluated as the minimum value between the one related to the yielding of the longitudinal reinforcement A_{sl}:

$$V_{Rds} = 2\ A_{sl}\ f_y/\lambda = 57\ kN \quad (1)$$

and the one due to the crushing failure of the strut:

$$V_{Rdc} = 0.4\ bh\ f_c\ /(1 + \lambda^2) = 64\ kN \quad (2)$$

where b is the thickness of the beam and λ its slenderness *l*/*z* (with *l* beam span and *z* inner lever arm assumed equal to 0.84 h). For the actual concrete compressive strength f_c and steel yielding strength f_y both calculate values resulted quite lower than the experimentally measured ones, which required more careful interpretation. It has to be remarked that the activation of the strut and tie mechanism

Figure 4. Crack pattern and failure detail of monotonically tested beam with longitudinal and transverse reinforcement.

can only be possible if longitudinal deformation, as also from the yielding of the bars, is allowed. The employed experimental set-up on its hand (Figure 1b) prevents any elongation in the aforementioned direction. This constraint may have most likely resulted into the development of a parasite longitudinal compression force, which had a twofold effect. On the one hand it reduced the tensile action in the longitudinal ties, preventing them from yielding and thus increasing the load bearing capacity. On the other hand, by adding an additional compressive stress field, it progressively modified the inclination of the diagonal strut, making it up to almost sub-vertical, as also confirmed by the observed crack pattern at failure. The latter occurred by crushing of the strut, because of the prevented yielding of longitudinal reinforcement, as explained above, and was therefore rather brittle.

The presence of a minimum transverse reinforcement (see the curve labelled as "control specimen" in Figure 2) led to an only limited increase of the load bearing capacity, thus confirming the prevailing effect of the mechanism explained above, where the resistance of the sub-vertical strut would scantly sense the present of the small and quite largely spaced stirrups. Anyway, even the provided minimum amount of transverse reinforcement was able to impart to the mechanism a certain ductility and allow the development of a more regular crack pattern up to the failure, which once again occurred by crushing of the compressive strut (Figure 4).

The experimental load bearing capacity was well captured by Level III approach of Model Code 2010. Through a stress and strain field analysis based on Modified Compression Field Theory, this sums the contribution of stirrups and the one of concrete struts, and evaluated the inclination of the latter at failure by means of an iterative procedure.

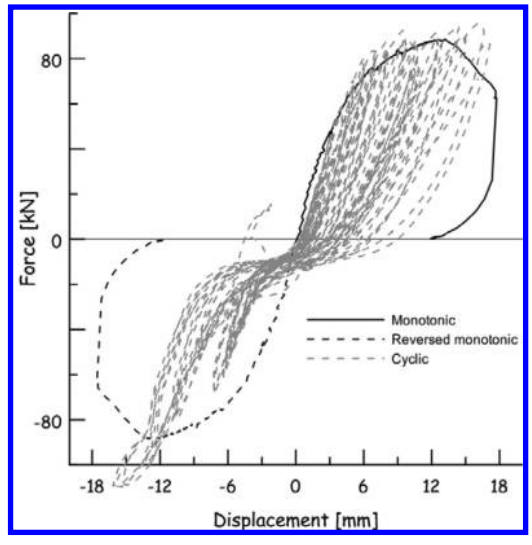

Figure 5. Cyclic and monotonic load drift curves for coupling beam with longitudinal and transverse reinforcement.

With reference to the cyclic tests performed on a nominally identical mock-up, i.e. with both longitudinal and transverse reinforcement, monotonic curve matched reasonably well the skeleton of the cyclic response (Figure 5). This was characterized by a lack of symmetry, mainly with reference to the cycle stiffness, most likely due to the accumulation of some irreversible damage since from the early cycles, which affected the stiffness recovery upon load reversal, as also obtained and explained by other authors (Canbolat et al., 2005; Lequesne, 2011). It can be furthermore observed that the response is quite stable for the threefold repetition of equal amplitude cycles and that the energy dissipation inside each cycle is fairly limited. This matches reasonably well with the failure mechanisms, as inferred above from the crack pattern observation, which appear to be mainly governed by concrete strut crushing. As a matter of fact in cyclic tests, the applied load reversal led to the formation of inclined cross cracks (Figure 6). The failure was anticipated and occurred once again because of crushing of the inclined compression struts at their corner bottoms and was also accompanied by the onset of buckling of longitudinal bars, left exposed by the cover spalling and not sufficiently laterally restrained by the largely spaced stirrups.

With reference to the tests performed on retrofitted beams, employing either the HPFRCC or the TRCC technique, a synopsis of their efficiency can be glimpsed from the force-drift curves obtained

Figure 6. Crack pattern and failure detail: cyclically tested coupling beam with longitudinal and transverse reinforcement.

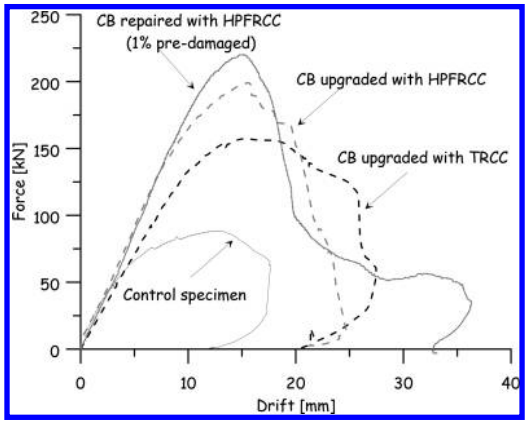

Figure 7. Comparison of the experimental results under monotonic loading considering different upgrading/retrofitting techniques.

from monotonic tests on retrofitted mock-ups and compared to the reference one (Figure 7).

The 20 mm thick HPFRCC jacketing was able to increase the load bearing capacity of about 2.5 times with respect to the control specimen, no matter whether it was applied to a virgin or a pre-damaged specimen. As a matter of fact, in the latter case (retrofitted specimen) the performance was even a little bit higher than in the former (upgraded specimen). It can be reasonably hypothesized that, because of some local de-bonding across the cracks between the *subgrade* pre-damaged specimen and the applied retrofitting jacket could have helped in better spreading the "underlying" localized damage into a larger zone in the top layer, thus better exploiting the performance of the retrofitting material. Anyway, in the case of HPFRCC, the improvement of ductility is fairly limited and a somewhat abrupt load decay was observed after the attainment of the peak. This could have been due to some delamination, caused by high bond shear stresses induced by the significant stiffness of the retrofitting layer and which could have been initiated by some early detachment caused by the quite high shrinkage (mainly autogeneous) of the HPFRCC. Anyway, the spreading of the damage (localized in the underlying specimen – Figure 8a) into some kind of multiple cracking in the retrofitting later was observed (Figure 8b). The failure always occurred because of crushing of the compressive strut, which formed in the retrofitted mock-up and whose strength could also benefit from the confinement effect provided by the HPFRCC jacket. This led to cover spalling in the only possible direction (one of the short sides of the coupling beam was not jacketed, representing

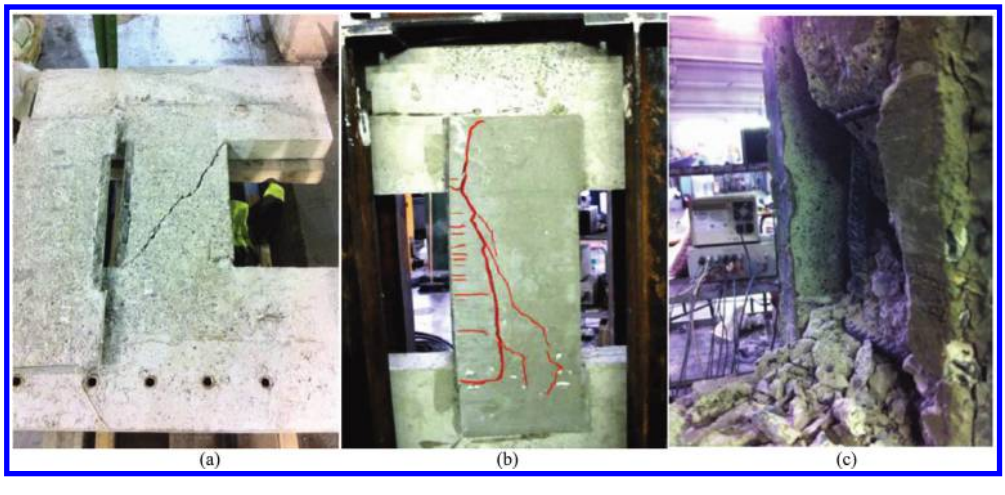

Figure 8. Localized damage (diagonal crack) into the "subgrade" retrofitted specimen (a), multiple cracking in the HPFRCC jacketing layer (b) and failure detail of the HPFRCC retrofitted coupling beam (c).

Figure 9. Crack pattern at failure for TRCC retrofitted specimen.

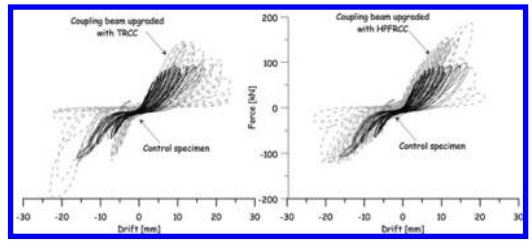

Figure 10. Cyclic force-drift curves for coupling beam specimens upgraded with TRCC (left) and HPFRCC (right), as compared to the performance of the cyclically tested reference specimen.

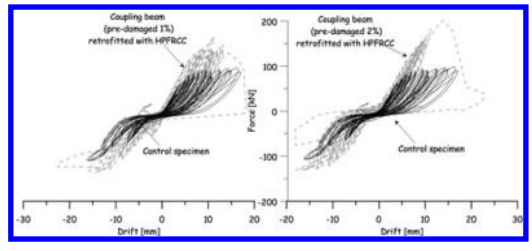

Figure 11. Cyclic force-drift curves for coupling beam specimens retrofitted with HPFRCC after a 1% (left) and a 2% drift damage (right), as compared to the performance of the cyclically tested reference specimen.

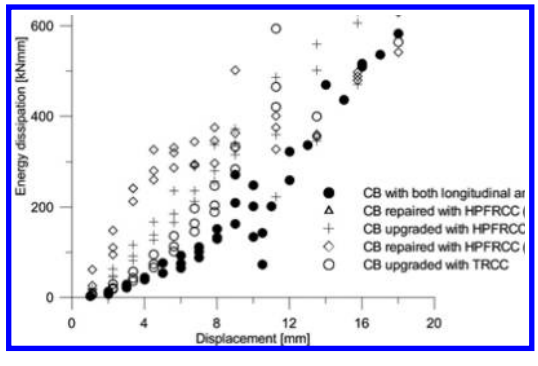

Figure 12. Energy dissipation trend along the cyclic tests.

the extrados not accessible in the real practice), followed by remarkable buckling of the bare longitudinal bars between the largely spaced stirrups and concrete crushing (Figure 8c).

On the other hand, the 6 mm thick TRCC retrofitting layer, provide a less remarkable increase in the load bearing capacity (which was anyway about 1.8 times higher than the reference control specimen), and was able to enhance in a quite evident way also the ductility of the retrofitted specimen. This could also be attributed to a better bond, either triggered by the manual application technique or by the lower shear stresses caused by the lower stiffness of the layer, which made it possible the dramatic multiple cracking which was observed before the failure (Figure 9).

The enhancement of the load bearing capacity and ductility performance provided by the two different employed retrofitting materials and techniques have been confirmed also by the results of cyclic tests performed both on upgraded (Figure 10) and retrofitted specimens (Figure 11). It has to be remarked that for the latter case only specimens retrofitted with HPFRCCs were manufactured and tested, after having been previously damaged up to two drift levels, respectively equal to 1% and 2%.

In order to better understand the cyclic performance of the tested coupling beams in terms of energy dissipation capacity, a specific analysis is carried out. The results, as plotted in Figure 12, first of all show that the values of energy dissipation of the control specimen represent a kind of lower limit for the other tests. Moreover, as a general feature, cycles at same drift level showed similar magnitude as the first cycle, confirm the stability of the response for the threefold repetition of equal amplitude cycles. With reference to the efficacy of the specific retrofitting techniques, it evidently appears that whereas HPFRCC performs better for smaller amplitude cycles, the performance of TRCC becomes dominant for higher amplitude cycles, as a further confirmation of the better ductility enhancement.

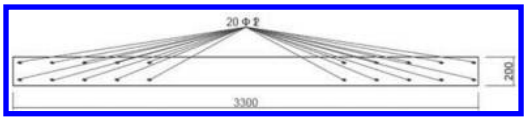

Figure 13. Geometry and reinforcement details of the hypothesized shear wall cross section.

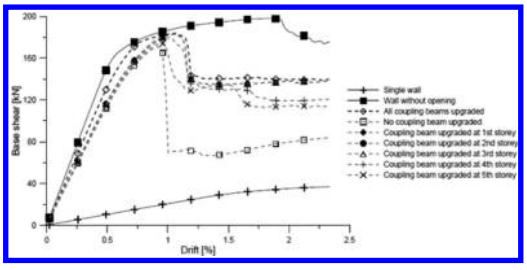

Figure 14. Push-over curves for different retrofitting options for the numerically analysed shear wall, as compared to the performance of uncoupled two-shaft wall and monolithic wall with no opening.

4 STRUCTURAL APPLICATION EXAMPLE

The efficacy of the retrofitting techniques, as tested and discussed, has been finally applied, in a numerical example, to address their use to a true structural application dealing with a 5 storey shear wall, featuring the geometry and reinforcement details shown in Figure 13. The non-reinforced part is where the opening is considered, spanned over by a coupling beam, which resulted 600 mm deep × 900 long and reinforced with 2 + 2ϕ8, as the tested mock-ups. A retrofitting option like the one tested with HPFRCC was considered, to be applied either to all the coupling beams at each storey or, separately, once at each different storey.

Numerical push-over analyses were performed by using the software MIDAS-GEN and the results (Figure 14) highlight, on the one hand, the efficacy of the employed retrofitting technique in getting back, even if not completely, to the behavior of a monolithic shear wall. On the other hand, the significance also appears of a tailored retrofitting, applied only to coupling beams at "selected" storeys.

5 CONCLUSIONS

A series of experimental tests on coupling beams, either non retrofitted or upgraded/retrofitted with advanced cement based materials was performed and the results have been herein analyzed.

In a first set of tests the role of different resisting mechanisms (concrete tensile strength, longitudinal and transverse reinforcement) was investigated, together with the influence of the boundary conditions on the development of such mechanisms. The reliability of design provisions in Model Code 2010 when applied to this kind of structural elements was also checked. The representativeness of monotonic tests, which matched well with the envelope of cyclic test curves, was confirmed.

A second set of experimental tests consisted of coupling beams upgraded or repaired with HPFRCC. The use of this upgrading/repair solution leads to enhanced performance both under monotonic and cyclic loadings. However, a loss of stability was always observed after the attainment of the peak load. This could be attributed to the increased interface deterioration between the subgrade mock-up and the HPFRCC layer, which resulted in some delamination at failure. It has been interestingly observed on monotonic tests that the specimens with increased pre-damage level performed even better in terms of load capacity. This could be explained by that the cracks present on damaged specimens, make the HPFRCC more effective at spreading the damage over a wider zone in the HPFRCC retrofitting layer, thus better benefiting from its unique behaviour in tension. Anyway, while quite easy to be applied, because of the high fluidity of the material, the delamination problems, as also due to the quite high autogeneous shrinkage of the material, still represent a drawback to be solved for spreading the use of this retrofitting technique into current engineering practice.

The final set of experimental test performed on coupling beams upgraded with TRCC, once again shows improvement of the load bearing capacity, even if not so high as for HPFRCCs. Moreover, the cyclic tests showed a more stable response after maximum load capacity. While less prone than HPFRCC to delamination problems, the technique requires a higher care during the application.

Both the proposed upgrading techniques have hence been proved to be reliable and feasible; investigation on the effectiveness of coupled solutions, employing e.g. a shrinkage compensated or internally cured HPFRCC reinforced with a glass textile mesh will be investigated in the forthcoming developments of this study.

Finally, the efficacy of one of the proposed retrofitting techniques was assessed, via a simple numerical example with reference to the structural behaviour of a 5-storey shear wall and the engineering significance of a selected coupling beam retrofitting was demonstrated.

ACKNOWLEDGEMENTS

The research was financially supported by the Italian Department of Emergency Management through the ReLUIS project "Development of new materials for seismic retrofitting".

REFERENCES

ACI 318-05 2005. Building Code Requirements for Structural Concrete and Commentary. American Concrete Institute.

Canbolat B.A., Parra-Montesinos G.J., Wight J.K.. 2005. Experimental study on seismic behavior of high performance fiber-reinforced cement composite coupling beams. ACI Structural Journal, 102 (1): 159–166.

Colombo, I.G., Magri, A., Zani, G., Colombo, M., di Prisco, M. 2013. Textile Reinforced Concrete: Experimental investigation on design parameters. Materials and Structures, 46(11): 1933–1951.

di Prisco, M., Lamperti, M.G.L., Lapolla, S., Khurana, R.S. 2008. HPFRCC thin plates for precast roofing, Proc. of Second Int. Symp. on Ultra High Performance Concrete, Kassel Germany: 675–682.

Ferrara, L., Ozyurt, N., di Prisco, M. 2011. High mechanical performance of fibre reinforced cementitious composites: The role of "casting-flow induced" fibre orientation. Materials and Structures 44 (1): 109–128.

Ferrara, L., Faifer, M., Muhaxheri, M., Toscani, S. 2012. A magnetic method for non destructive monitoring of fiber dispersion and orientation in steel fiber reinforced cementitious composites: part 2: correlation to tensile fracture toughness. Materials and Structures, 45(4): 591–598.

Lequesne, R.: (2011). Behavior and design of high-performance fiber-reinforced concrete coupling beams and coupled-wall systems. Ph.D. Thesis, University of Michigan, USA. 298 pp.

Martinola, G., Meda. A., Plizzari, G.A., Rinaldi, Z. 2010. Strengthening and repair of RC beams with fiber reinforced concrete, Cement & Concrete Composites, 32, pp 731–739.

Meda, A., Mostosi, S. and Riva, P. 2014. Shear strengtheneing of reinforced concrete beam with HPFRCC jacketing. ACI Structural Journal, 111 (5): 1059–1068.

Mihaescu, A., Tudor, D., Ciuhandu, G., Ianca, S. 1990. Research on the repair and strengthening of coupling beams in coupled shear walls damaged after earthquakes. In Proceeding of the 9th ECEE, Moscow.

Paulay, T. 1971. Coupling beams of reinforced concrete shear walls. Journal of the Structural Division, ASCE, 97 (ST3): 843–861.

Preti, M. and Meda, A. 2015. RC structural wall with unbonded tendons strengthened with HPFRC. Materials and Structures 48 (1–2): 249–260.

Su R.K.L., Zhu Y. 2005. Experimental and numerical studies of external steel plate strengthened reinforced concrete coupling beams. Eng. Structures, 27(10): 1537–1550.

Triantafillou, T. and Papanicolau, C. 2005. Textile reinforced mortars (TRM) versus fiber reinforced polymers (FRP) as strengthening materials of concrete structures. In Proceedings FRPRCS7: 99–118.

Weiland, S., Ortlepp, R., Curbach, M. 2006. Strengthening of predeformed slabs with textile reinforced concrete. In Proc. 1st international congress *fib*.

Concrete Repair, Rehabilitation and Retrofitting IV – Dehn et al. (Eds)
© 2016 Taylor & Francis Group, London, ISBN 978-1-138-02843-2

Cyclic behaviour of R.C. column with corroded reinforcement repaired with HPFRC jacket

S. Mostosi
Tecnochem Italiana S.p.A., Italy

A. Meda & Z. Rinaldi
"Tor Vergata" University, Rome, Italy

P. Riva
University of Bergamo, Italy

ABSTRACT: The reduction in the useful service-life of reinforced concrete structures, mainly due to reinforcement corrosion, is a cause of concern for several RC buildings. The corrosion damage, often, makes necessary to define strengthening techniques allowing for recovering the initial capacity of the structure. Furthermore, the reduction of strength and ductility, due to corrosion, can jeopardize the behaviour for horizontal loads. In this research, the technique based on the use of High Performance Fiber Reinforced Concrete (HPFRC) jackets with thickness of 30–40 mm, is considered and applied on RC corroded columns. Three full-scale experimental cyclic tests were performed. Besides the reference specimen, one column was tested after the rebars artificial corrosion, and the last one, after the reinforcement corrosion, was strengthening with 40 mm thick HPFRC jacket. The tests were performed up to failure by applying cyclic horizontal loads of increasing amplitude for verifying the performances of the proposed solution.

1 INTRODUCTION

The lack of durability, typically related to reinforcement corrosion, is a cause of concern in several Reinforced Concrete (RC) buildings, particularly when low strength concrete is used. A retrofit intervention on these structures should have the scope not only to restore the original bearing capacity but also to ensure an adequate durability to the structure.

The feasibility of using High Performance Fiber Reinforced Concrete (HPFRC) for strengthening RC structures has been investigated by several researchers in the last few years (Li et al., 2000, Banthia & Bindiganavile, 2001, Alaee & Karihaloo, 2003, Martinola et al., 2010, Beschi et al., 2011, Kobayashi & Rokugo, 2013, Meda et al., 2014). In particular, the effectiveness of the adoption of a jacket in fiber reinforced concrete for the strengthening of existing columns subjected to seismic action has been demonstrated in (Beschi et al., 2011)

The possibility of applying this technique on corroded RC columns is investigate herein. The problem of structural element corrosion is amplified when low strength concrete is adopted (typical of the '60 and '70 buildings), as high carbonation or chloride penetration may accelerate the rebar chemical attack. In these structures, the lack of bearing capacity due to the use of poor materials in combination with the possible corrosion of the reinforcement may be of serious concern. A high performance fiber reinforced concrete jacket can be adopted for repairing or strengthening corroded columns with the aim of ensuring adequate bearing capacity to the structures after the intervention. Furthermore, due to the compactness of the HPFRC concrete matrix and the reduced crack opening, the jacket can protect the existing column and increase the durability of the system, as highlighted in (Resplendino & Toulemonde, 2010, Wanga et al., 2014).

In order to investigate the proposed solution, full-scale tests on columns subjected to cyclic loads have been performed. In particular, three specimens with the same geometry and materials are designed, cast and tested. The first one is the un-corroded reference column, the second one is corroded and the last one is firstly corroded and then repaired with a 40 mm thick HPFRC jacket. The results show the effectiveness of the proposed solution.

2 EXPERIMENTAL TESTS

2.1 *Specimens geometry*

Three columns have been cast for the experimental campaign, named UC (Un-Corroded), C (Corroded) and CR (Corroded and Repaired). Figure 1 shows the specimens geometry and reinforcement. The columns have a 300 × 300 mm square section and a height of 1600 mm. The longitudinal reinforcement is made of four ϕ16 mm rebars, while the transverse reinforcement is made of ϕ8 mm closed stirrups spaced at 300 mm. The longitudinal rebars (in Tempcore steel) exhibited an average yield strength equal to 520 MPa and an average maximum strength equal to 620 MPa.

The geometry of the column foundation (1300 × 600 × 500 mm) is shown in Figure 1.

All the specimens were cast with concrete from the same batch, characterized by a mean cubic compressive strength equal to 20 MPa.

Two of the columns (C and CR) were subjected to an artificial corrosion of the longitudinal rebars. Since the aim of the paper was the evaluation of the bending behaviour of the columns, the stirrups were coated in order to avoid their corrosion.

2.2 *Artificial corrosion*

The longitudinal reinforcement of the columns has been corroded up to a theoretical level equal to 20% in terms of mass loss. The corrosion was obtained with an accelerated process through electrolytic cells (Fig. 2) with the columns dipped in a 3% saline solution. A preliminary campaign was organized with the aim of obtaining the required corrosion in the rebars, and to check the corrosion morphology, the influence of the corrosion on the steel constitutive relationship, and the effect of the concrete in the rebar corrosion process. An in depth description of this campaign can be found in (Meda et al., 2014).

Based on the obtained results, the corrosion process was assessed. The saline solution (3% NaCl), necessary for the accelerated electrolytic corrosion, was contained inside a PVC Ø500 mm pipe, placed around the column as shown in Figure 2, and fixed to the foundation through specific sealing products. The current intensity was equal to 0.5 A for each bar. The four Ø16 embedded bars represent the anodes, while four Ø10 diameter steel bars, placed inside the pipe, worked as cathodes (Fig. 2).

The time necessary to obtain the desired corrosion level, (20% in mass loss), was evaluated with the Faraday's law, suitably modified in order to account for the concrete presence, based on the preliminary tests on embedded specimens (Meda et al., 2014). Figure 3 shows the two columns C and CR, after the corrosion. It can be noticed a typical crack pattern due to the rust expansion, with longitudinal cracks, close to the steel rebars, often involving the whole specimen length.

2.3 *HPFRC jacket application*

One of the two corroded column (specimen CR) was prepared for the HPFRC jacket application. To this aim the following steps were followed:

– the deteriorated cover in correspondence to the four longitudinal bars was removed and the reinforcement was manually cleaned to eliminate the corrosion products;

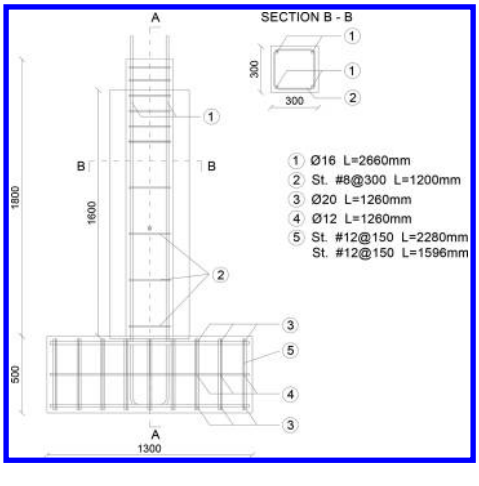

Figure 1. Geometry of the specimens.

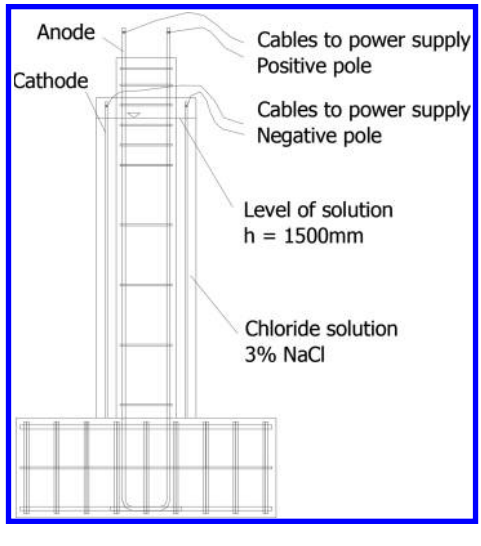

Figure 2. Accelerate corrosion process.

Figure 3. Specimen after corrosion process—crack pattern; a) specimen C; b) specimens CR.

Figure 4. Specimen CR; a) before jacket cast;) after jacket cast.

– a 80 mm deep pocket was made in order to ensure the connection of the jacket with the foundation, as made in previous researches (Beschi et al., 2011) (Fig. 4a);
– the surface of the column was sandblasted in order to obtain a roughness of about 1 mm to ensure the adhesion between the old concrete and the HPFRC jacket (Martinola et al. 2010).

Finally, a jacket having a thickness of 40 mm has been cast with a HPFRC with almost self-levelling rheology.

The high performance fiber reinforced concrete adopted is characterized by an average compressive strength, measured on cubes of about 130 MPa. The uniaxial tensile strength, measured on dog-bone specimen (Fig. 5a) is of about 6 MPa,

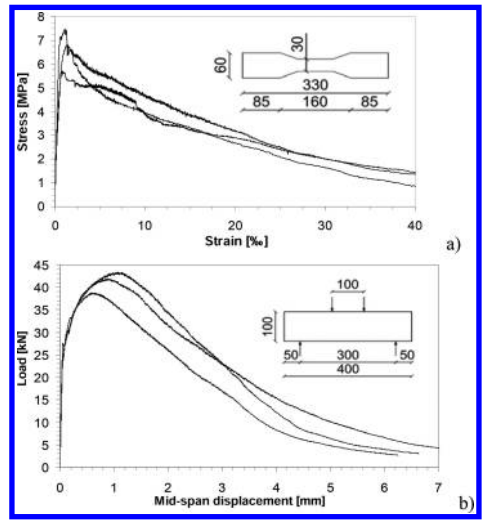

Figure 5. HPFRC tensile strength; a) tensile test; b) flexural test.

while the flexural load, measured on small beams (Fig. 5b) is about 42 kN (nominal stress equal to 12.6 MPa). Straight steel fibers having a length of 15 mm and a diameter of 0.175 mm with a volume content of 1.2% were used.

The HPFRC material was prepared in a vertical axis mixers and was cast in moulds without vibration. Since curing was carried out at ambient temperature and humidity, the column was wrapped with a plastic sheet in order to limit water evaporation.

3 TEST SET-UP AND RESULTS

3.1 *Test set-up*

The three columns were subjected to cyclic tests in the Laboratory of the University of Bergamo.

The column foundation was anchored to the laboratory strong floor with two steel profiles and four pre-tensioned high strength rebars. An axial load of 400 kN was applied with two hydraulic jacks and monitored by a pressure transducer. A self-balanced system allowed applying the axial load to the column (Fig. 6). The horizontal cyclic load, applied at a height of 1.5 m from the column foundation connection, was given by means of an electro-mechanical jack fixed to the reaction wall of the laboratory. The jack was linked to the column by means of a hinged bar system in which a load cell was placed (Fig. 6).

In order to measure the horizontal displacements, potentiometric transducers were placed on the

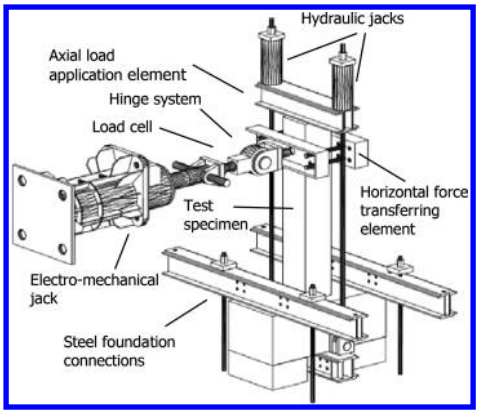

Figure 6. Test set-up.

column at the level of the load application (1.5 m from the foundation extrados). A series of potentiometric transducers placed on one of the column faces measured the rotations at the column base. Two LVDT devices register possible slip movements of the foundation. Finally, a pressure transducer was connected to the pump for the axial load monitoring. After the axial load application, the specimens were subjected to horizontal cyclic displacements of increasing amplitude, up to the failure.

The loading history was assigned according to the document (ACI, Committee 372, 2006) which defines the standard test procedure for full-scale moment-resistant elements. Once defined the drift (δ/h), as the ratio between the horizontal displacement at the load application point (δ) and the height (h), the guide line suggests to perform three complete cycles for each drift with an intermediate unloading cycle between a triplet and the following one. The initial drift (equal to 0.15%) was chosen for capturing the elastic behaviour of the specimen. Details of the horizontal displacement history are reported in Figure 7.

4 RESULTS

4.1 *Undamaged column (UC)*

The results related to the Un-Corroded specimen (UC) are summarised in the load-drift diagram shown in Figure 8. The first horizontal cracks formed for a displacement of 4.50 mm (drift equal to 0.30%). The specimen behaviour was almost linear up to a drift of 0.75%. Below a 1% drift, the cracks were approximately horizontal with a spacing almost coincident with the stirrup spacing.

The extension of the cracked zone was about 700 mm from the foundation intrados. The maximum loads, measured for positive and negative

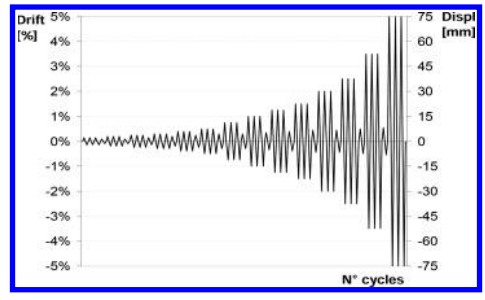

Figure 7. Loading history.

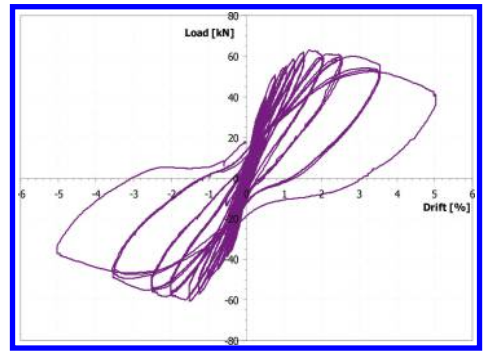

Figure 8. Reference uncorroded specimen UC: Load—drift relationship.

cycles, were equal to 63 and 61 kN, respectively. The related drifts were equal to ±2%. In the following cycles, a progressive strength degradation was observed, up to a value of about 40 kN (approximately 64% of the maximum load), related to a 5% drift. At this point, the test was stopped, due to the cover spalling and concrete crushing observed at the column base, involving a zone with a height approximately equal to the section side. Moreover, the buckling of one of the reinforcing bars was observed.

4.2 *Corroded column (C)*

The results related to the corroded specimen (C) are summarised in the load-drift diagram shown in Figure 9. The first cracks appeared for a displacement equal to 3.75 mm (0.25% drift). The maximum measured positive load was equal to about 44 kN for a drift of 1.0%, while the maximum negative one was about 46 kN for a drift of 1.25%. A significant strength reduction was observed after the cycles at 1.5% drift. The strength related to the last cycle, corresponding to a drift of 2.5%, was about 36 kN, corresponding to 78% of the maximum measured load.

Horizontal cracks located at the base, within an extension of about 700 mm from the base of the foundation appeared for cycles ranging from

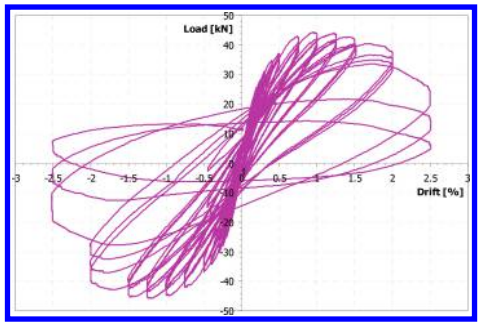

Figure 9. Corroded specimen C: Load—drift relationship.

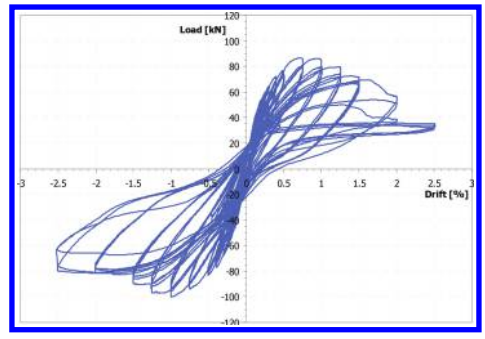

Figure 10. Corroded Reinforced specimen CR: Load—drift.

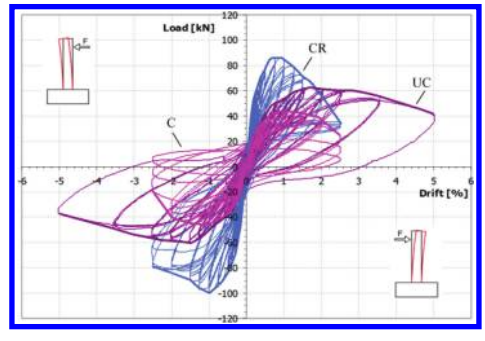

Figure 11. Load-drift relationships: comparisons.

a drift of 0.25% to 1.00%, growing in number and extension. The vertical cracks, due to corrosion, visibly opened for the cycle corresponding to a drift of 1%. Cover spalling occurred for a drift of 2%. The test was stopped at a drift equal to 2.5%, after the complete crushing of the concrete. The buckling phenomenon of all the reinforcement bars was clearly noted. At the end of the tests, the four steel rebars were cleaned and weighted. The measured mass losses, equal to 22.6%, 18.7%, 20.6% and 24.1% for the four bars, highlighted the effectiveness of the corrosion process in providing the foreseen corrosion level (20% mass loss).

4.3 *Jacketed column (CR)*

The results related to the corroded and repaired column specimen (CR) are summarised in the load-drift diagram shown in Figure 10. The first cracks appeared for a displacement of 4.5 mm (0.30% drift). The maximum recorded positive load was about 86 kN with a drift of 0.75%, while the maximum negative load was about 100 kN with a drift of 1%. In the following cycles, a significant strength reduction of the column occurred.

Horizontal cracks appeared for cycles ranging from a drift of 0.30% to 0.75% located at the base, within an extension of about 600 mm from the base of the foundation. From a drift of 0.75%, the cracks development in the external jacket was stable, while a local damage of the HPFRC jacket at the column-foundation interface. The progressive pinching of the cycles for drift values higher than 1.5% is related to the detachment of the HPFRC layer at the base, whereby the contribution of the tensile strength of the jacket layer at the base is progressively lost, and a rocking mechanism takes place at the column base. The column has reached the collapse during the third cycle corresponding to a drift of 2%, due to the rupture of one of the longitudinal rebars for positive drift. In order to gain further knowledge of the specimen behaviour, it was decided to perform even the cycles of 2.5% drift, since for negative drifts the load was still high. The test was stopped at the second cycles equal to a drift of 2.5%, when the second reinforcing bar failed. At the time, the collapse load was equal to 82 kN, corresponding to 82% of the maximum strength reached for positive displacement values.

4.4 *Comparison*

The load-drift diagrams, measured for all the specimens are compared in Figure 11. The corroded column shows a decrease of the maximum strength of about 26% (rebar corrosion of about 20%) and a marked decrease of deformation (up to 50%) with respect to the undamaged one. Furthermore, the sharp reduction of stiffness, occurring during the test of the corroded specimens, in the last two cycles, has to be remarked.

The results obtained from the jacketed specimen showed the effectiveness of this technique for strengthening columns with corroded longitudinal rebars. The maximum load for both positive and negative drifts is higher than the peak load reached by the undamaged specimen.

The maximum load measured for negative drifts, the direction in which the strengthening specimen

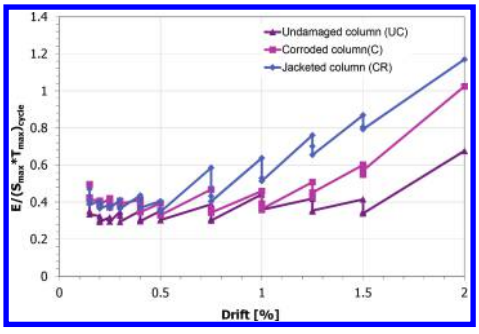

Figure 12. Dissipated energy.

showed a correct failure mode, is increased of about 65% and 118%, if compared to those of the undamaged and corroded columns, respectively. A comparison between the experimental results of the three specimens has been further performed in terms of dimensionless dissipated energy, with respect to the "elastic energy", defined as the product of the maximum force (F_{max}) for the related displacement (δ_{max}), as shown in Figure 12. For the sake of comparison, the reported results are limited to a 2.5% drift (ultimate value in the CR specimen).

The specimen with a fiber reinforced jacket (CR) shows a better behavior in terms of energy dissipation. For cycles related to high drifts (0.75% –1.00%) the energy dissipated by the CR specimen is increased of about 50% with respect to the UC (reference, uncorroded specimen) and is higher than 30% with respect to the C (corroded) one. It is observed that the dissipated energy for the strengthened columns during the cycles triplets is stable, proving the validity of the proposed rehabilitation technique.

5 CONCLUSIONS

The influence of the rebar corrosion on the cyclic behavior of rc columns and the effectiveness of the application of a thin HPFRC jacket as a repair technique have been discussed in the paper, on the basis of three full-scale tests. The analysis of the obtained results allows drawing the following remarks:

– the corrosion phenomenon can strongly affect the global behaviour of columns subjected to cyclic loads. In the tested case (characterized by rebar corrosion of about 20% in mass loss) a reduction of about 30% of the ultimate force and mainly a reduction of ultimate displacement of about 50% was detected, together with a significant stiffness decrease in the last cycles. Therefore, the corrosion phenomenon can strongly affect the local (plastic hinge properties) and global behaviour of structures in seismic zones and can significantly change their failure modes;
– with the application of a high performance jacket it is possible to increase the bearing capacity of the column with corroded rebars reaching a maximum strength greater than the one of the undamaged element. This technique is suitable for strengthening existing RC structures characterized by low concrete strength, low reinforcement ratio, concrete damage and corrosion of rebars.

Finally, the proposed technique can be easily used in structural applications as it allows strengthening R/C elements by means of a thin jacket (40 mm). Furthermore, a curing at ambient temperature and humidity is sufficient to grant the development of the full strength and a simple sandblasting ensures a good bond between substrate and HPFRC.

REFERENCES

ACI Committee 374. 2006 Acceptance Criteria for Moment Frames Based on Structural Testing and Commentary.

Alaee F.J., Karihaloo B.L. 2003. Retrofitting of Reinforced-Concrete Beams with CARDIFRC, ASCE—*Journal of Composite Construction*, 7 (3): 174–86.

Banthia N, Bindiganavile V. 2001. Repairing with hybrid-fiber-reinforced concrete. *Concrete International* 23(6): 29–32.

Beschi, C., Meda, A., Riva, P. 2011. Column and joint retrofitting with high performance fiber reinforced concrete jacketing. *Journal of Earthquake Engineering*, 15(7): 989–1014.

Kobayashi K., Rokugo K. 2013. Mechanical performance of corroded RC member repaired by HPFRCC patching, *Construction and building materials* 39:139–147.

Li, V.C., Horii, H., Kabele, P., Kanda, T., Lim, Y.M. 2000. Repair and retrofit with engineered cementitious composites. *Engineering Fracture Mechanics*. 65(2–3): 317–334.

Martinola G., Meda A., Plizzari G.A., Rinaldi Z. 2010. Strengthening and Repair of R/C Beams with Fibre-Reinforced Concrete. *Cement and Concrete Composites*, 32(9): 731–739.

Meda, A., Mostosi, S., Riva, P. 2014a. Shear Strengthening of Reinforced Concrete Beam with High-Performance Fiber-Reinforced Cementitious Composite Jacketing. *ACI Structural Journal*, 111(5).

Meda, A., Rinaldi Z., Riva, P., Mostosi, S. 2014b. Experimental evaluation of the corrosion influence on the cyclic behaviour of R.C. columns. *Engineering structures*. 76: 112–123.

Resplendino, J., Toulemonde, F. 2010. *Designing and Building with UHPFRC*, Wiley-ISTE, November, 814 pages.

Wanga, W., Liub, J., Agostini, F., Davy, C. A., Skoczylas, F., Corvez, D. 2014. Durability of an Ultra High Performance Fiber Reinforced Concrete (UHPFRC) under progressive aging. *Cement and Concrete Research. 55*: 1–13.

Concrete Repair, Rehabilitation and Retrofitting IV – Dehn et al. (Eds)
© 2016 Taylor & Francis Group, London, ISBN 978-1-138-02843-2

Concrete hinge bearing replacement: A case study of concrete hinge collapse and broader implications for concrete hinge bearings under seismic effects

R.K. Dickson
SMEC South Africa Consulting Engineers, South Africa

E.J. Kruger
The South African National Roads Agency SOC Limited, South Africa

ABSTRACT: In February 2012, several concrete hinge bearings collapsed under one of the spans of the Kakamas Bridge on National Route 14 over the Orange River in the Northern Cape, South Africa. The bridge was immediately closed to traffic by the South African National Roads Agency SOC Ltd (SANRAL), after a span settled by approximately 100 mm. Four out of six concrete hinge bearings had collapsed at one pier. Emergency repair works were carried out to replace all 180 of the existing concrete hinge bearings and new elastomeric bearings were installed as a retrofit to the existing bridge. This paper provides a case study of the collapse of concrete hinge bearings and the broader implications for concrete hinge bearings under seismic load effects. The paper describes a method of bearing replacement as a retrofit to existing bridges with concrete hinge bearings.The bridge consists of fifteen simply-supported spans of 24 m, comprised of post tensioned I-girders, constructed in 1962. The concrete hinges were found to have been overstressed. Inspection revealed splitting cracks of up to 3 mm in the concrete bearings, displacement and spalling to numerous bearings. During the investigation it was found that the area had experienced an earthquake in December 2011 of magnitude 5.0 on the Richter scale and classified VI to VII on the Modified Mercalli Scale, as well as an "earthquake swarm" in the area in which 600 earthquakes were recorded in the magnitude range 0.5 to 5.0, from 2008 to 2012. It was found that the concrete hinge bearings had been severely damaged under earthquake loads and were vulnerable to collapse in seismic events.

1 INTRODUCTION

In February 2012, several concrete hinge bearings collapsed under one of the spans of the Kakamas Bridge on National Route 14 over the Orange River in the Northern Cape, South Africa. The bridge was immediately closed to traffic after a span settled by approximately 100 mm. Four out of six concrete hinge bearings had collapsed at one pier, the two remaining bearings were split and severely damaged.

The bridge consists of fifteen simply-supported spans of 24 m, comprised of post tensioned I-girders, constructed in 1962. It is a strategic link N14 over Orange River, and is a critical link during harvest, as well as carrying high volumes of local pedestrian traffic.

2 CAUSE OF COLLAPSE

Following the collapse, a full inspection was done of all the remaining concrete hinge bearings. From inspection of the remaining bearings, it was clear that the concrete hinges had been displaced and rotated about their hinge points. Rotations of up to 1/11 were measured (substantially in excess of the recommended 1/20 limits). Numerous concrete hinges exhibited cracks of up to 2 mm in the throat of the hinges. In addition, splitting cracks up to 3 mm wide and spalls were noted on the worst-affected bearings.

The concrete hinge bearings had been overstressed and once cracked were in danger of collapse.

2.1 *Earthquake swarm in Augrabies/Kakamas*

Local residents around the bridge site reported experiencing a lot of earthquakes and tremors. They highlighted a larger earthquake which occurred on 18 December 2011. The Council for Geoscience has confirmed that an earthquake of magnitude 5.0 on the Richter scale occurred in the area on 18 December 2011, with an epicentre 17 km from the bridge, near Augrabies Falls, at a depth of 5 km.

The Council for Geoscience have further reported that: "Augrabies has recently (~2008) been experiencing what is termed an earthquake swarm i.e. a large number of earthquakes occurring in a relatively short space of time with no discernible 'main shock'. Only 9 earthquakes had been recorded in the Augrabies area during the period 1988 to 2007 (magnitude range 1.5 to 4). However, since the earthquake swarm began in 2008 the number increased rapidly in number to over 600 earthquakes recorded in the magnitude range 0.5 to 5.0." A map showing the cluster of earthquake epicentres in the area around the bridge is given in Figure 3.

Figure 1. Collapsed concrete hinge bearings.

Figure 2. Elevation of Orange River Bridge with collapsed hinge bearings.

2.2 *Relative magnitude of Dec 2011 earthquake*

The 18 December 2011 earthquake is listed for comparison with historically recorded earthquakes in South Africa in the table below. It ranks in the top six largest earthquakes in South African history (see Table 1). The 18 December 2011 earthquake is classified to have a severity rating of VI to VII in terms of the Modified Mercalli scale. This is equivalent to a Peak Ground Acceleration of up to

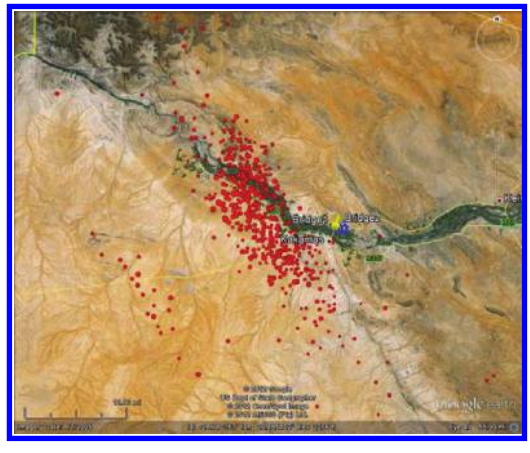

Figure 3. Earthquake epicentre locations in Augrabies/Kakamas area.

Table 1. Comparison with Notable Earthquakes.

Date	Magnitude Richter	Location	Depth km	Notes
2010-11-13	4.8	Vanderbijlpark	10	–
2011-12-28	4.9	Klerksdorp	10	–
2011-12-18	**5.0**	**Augrabies/Kakamas**	**5**	–
2003-03-05	5.3	Klerksdorp	–	–
1970-04-14	5.7	Ceres	–	Aftershock
1969-09-29	6.3	Ceres	–	12 Deaths
1932-12-31	6.3	St Lucia (KZN)	–	–
1809-09-05	6.3(est)	Milnerton, (Cape Town)	–	–
Other notable recent earthquakes:				
2010-09-04	7.1	Canterbury, (New Zealand)	10	0 Deaths
2011-03-11	9.0	Tōhoku, Japan (with tsunami)	30	15,000 Deaths

0.1 g, which means that the structural load effect of the 18 December 2011 earthquake was up to 3.3 times higher than the design earthquake load effect required to be resisted in terms of the South African bridge design code, TMH7.

2.3 *Earthquake damage to bearings*

The damage to the collapsed bearings at Pier 9 is illustrated in Figures 4 to 6. The most likely cause of the bearing collapse is that the bridge bearings were severely cracked and damaged due to earthquake loading associated with the 18 December 2011 earthquake (magnitude 5.0); and also the "earthquake swarm" of over 600 earthquakes, which has occurred in the area between 2008 and 2012. It is therefore, a likely scenario that the bearings were severely compromised by earthquake and then collapsed at Pier 9 under the passage of heavy vehicles.

Figure 4. Splitting collapse of concrete hinge bearing at Pier 9.

Figure 5. Collapsed concrete hinge bearing at Pier 9.

Figure 6. Splitting collapse of concrete hinge bearing at Pier 9.

3 EMERGENCY REPAIR AFTER COLLAPSE

The Client immediately initiated a make-safe response to collapse. This emergency repair required rapid mobilisation of a bridge designer and a contractor to carry out bridge jacking, and bearing replacement. Being a national route, the client applied pressure to have the road re-opened to traffic within 2 weeks, because the collapse occurred in the middle of agricultural harvest season. The alternative route involved a 50 km detour on unsurfaced minor roads, which was dangerous for heavy vehicles.

The road was ultimately re-opened to traffic within 2½ weeks after the collapse. In this repair contract, the bridge deck was jacked up and supported on temporary supports, then opened to traffic whilst bearings were removed and replaced with elastomeric bearings on new plinths in the following weeks.

3.1 *Temporary support solution for rapid response*

The Client, Engineer and an experienced bridge Contractor, who fortunately was working on an adjacent site some 60 km away, met on site the day after the bridge collapse to collaborate and engineer a temporary support solution which could be implemented rapidly using materials and plant which could be obtained at short notice. As engineers, the team was required to come up with unusual alternative solutions in a very limited time. The engineer was required to take into account broader issues than just the bridge repair, including economic impact for the period of the bridge closure and risk to public safety on alternative routes.

An unusual solution was devised, which did not require time-consuming access and propping from river level (10 m below the deck). Temporary structural steel supports were designed with simple steel supporting beams installed under the bridge deck, which were suspended from larger I-girders spanning above the deck and propped off the centre of the piers (Fig. 7). With temporary supports installed at deck level, the risk to temporary supports due to flood damage (during the high February flood season) was minimised.

The temporary support solution allowed simplified and rapid fabrication of structural steel elements from hot-rolled sections, so that the temporary supports could be installed in the shortest possible time. Once installed, the temporary support system allowed traffic to be accommodated between the temporary support I-girders at low speed through a single reduced lane-width. The lane width was deliberately kept very narrow so as to make sure vehicles travelled at slow speed as can be seen in Figure 8. This meant that the Contractor could proceed to remove and replace the failed bearings without the new bearing plinth and bearing installation delaying the re-opening of the bridge to traffic.

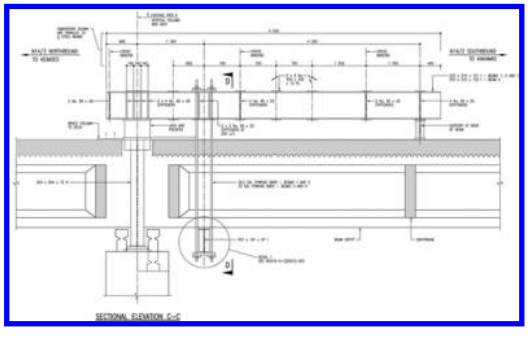

Figure 7. Temporary support solution: Girders above deck.

Figure 8. Limited width temporary accommodation of traffic.

4 COMPLETE BRIDGE BEARING RETROFIT

4.1 *Condition of concrete hinges*

Following the initial collapse, a complete inspection was done of all the remaining 174 concrete hinge bearings accessed using an Under Bridge Inspection Unit. It was found that several of the remaining concrete hinge bearings had been displaced by up to 40 mm. This resulted in rotations about the hinges of up to 1/11 (0.089 radians), which is double the recommended limit set out in the French code for concrete hinge design. The compressive working stress in the throats was determined to be approximately 30 MPa under full traffic. However, due to displacement and cracking through the throats, it is estimated that compressive stresses of up to 95 MPa have developed in these hinges.

Crack widths of up 2 mm were measured in the throat of the hinges. In addition, splitting cracks of up to 3 mm were found on the side faces of the hinges (see Fig. 9 & 10). It was clear from the cracking and visible displacement o that the hinges had been overstressed and there was a risk of further bearing collapses.

4.2 *Replacement of hinges as a retrofit*

The poor, to severely damaged condition of the remaining bearings informed the decision by the client to replace all of the remaining 174 bearings in a second six-month contract. This was carried

Figure 9. 2 mm Crack in throat of hinge: Pier 3.

out in another contract to retrofit modified bearing plinths and elastomeric bearings to the entire bridge. In the second contract, the contractor opted to use more simplified temporary supports, consisting of steel beams overhanging the top of the wall-type piers, which supported simple beams under the concrete I-girders (Fig. 11). Although more access was required in very confined spaces under the deck, this method allowed traffic to be more freely accommodated on the bridge during construction.

The complete bearing replacement retrofit contract was successfully carried out on programme and within budget. Figure 12 below illustrates a typical pier after the complete bearing retrofit.

Figure 10. 3 mm Cracks and spalling to side of hinge: Pier 6.

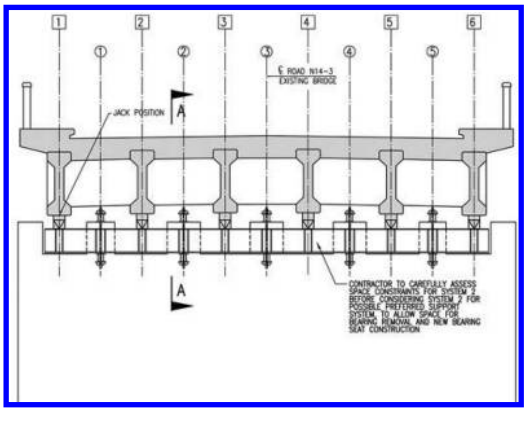

Figure 11. Typical section: Temporary support solution used for full bearing replacement project, with steel beams supported off pier.

Figure 12. Completed bearing replacement.

5 BROADER IMPLICATIONS FOR CONCRETE HINGE BEARINGS

5.1 *Concrete hinge details used at Kakamas*

The Kakamas Bridge on National Route 14 over the Orange River was constructed in 1962, however no record drawings are available.

From inspection of the removed concrete hinge bearings, it is concluded that the Kakamas Bridge hinges were based on the Mesnager and Freyssinet concrete hinge design that were in wide use in 1950's and –60's. The hinges were constructed with dowels through the throat region. However, unlike the Freyssinet hinges, the bearings use on the Kakamas did not taper the concrete hinge at the throat in the transverse direction.

Concrete hinges were first pioneered through Mesnager's work circa 1910, using reinforced concrete hinges. This was taken further by Freyssinet, who recognised that using the tri-axial state of stress in the concrete throat, the resulting compression strength of the concrete throat was significantly higher than first thought. In 1965, Fritz Leonhardt developed a computational model, nomenclature and design rules for concrete hinges still used today.

5.2 *Concrete hinges susceptible to seismic damage*

In 1962, the year of construction of the Kakamas Bridge, bridges in South Africa were conventionally not designed for earthquake load effects. Had earthquake loading with Peak Ground Accelerations of up to 0.1 g been a consideration, such concrete hinge bearings would not have been used.

Whilst it is debatable what level of vibration could cause the failure of concrete hinges, they are not robust when subject to large longitudinal displacement and do not accommodate any lateral displacement whatsoever. A major consideration is

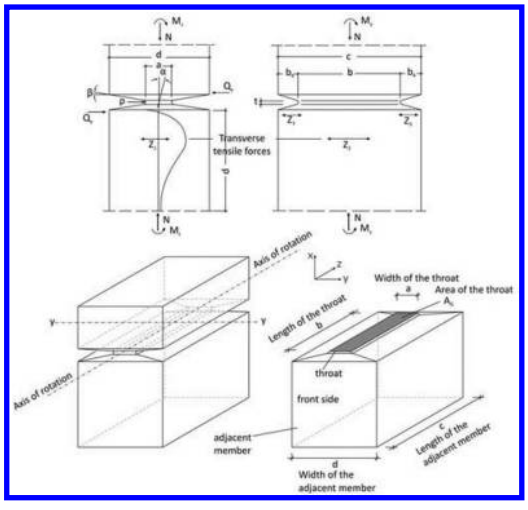

Figure 13. Nomenclature from Fritz Leonhardt (ref Marx, S, Schacht, G, 2010).

the physical height of the concrete hinge required to create double rockers able to accommodate longitudinal displacement. For the Kakamas Bridge, the double rockers hinges were 800 mm high. In the event of a bearing splitting failure, this 800 mm height represents a large potential energy which can suddenly be released in an earthquake.

The client has found from inspection of the Kakamas Bridge bearings and others at the Great Fish River that this form of concrete hinge bearing (without a transverse taper at the throat) has suffered cracking and spalling to the transverse side faces. In addition, cracking in the throat section of the hinges has been observed. This cracking and spalling is consistent with the mode of failure and collapse at the Kakamas Bridge.

As a risk mitigation measure, the Client will carry out close up inspections of all bridges with concrete hinge bearings in the national bridge network in South Africa. In the case of the Great Fish River Bridge on National Route 2, the existing concrete hinge bearings will be replaced by retro-fitting with elastomeric bearings as part of a bridge widening project.

6 CONCLUSIONS

Following the collapse of a series of concrete hinge bearings at the Kakamas Bridge over the Orange River, it was found that these bearings had suffered damage after an earthquake "swarm" in the area, which included a 5.0 magnitude earthquake. After the collapse, the remaining bearings were found to be cracked and severely damaged after seismic events and normal traffic loading.

The primary mechanisms of deterioration of these concrete hinge bearings was cracking and spalling of the faces of the bearings. When subjected to longitudinal displacements, the bearings had also cracked through the throat of the hinges and split under applied vertical loads. In the remaining bearings which had not collapsed, cracks of up to 2 mm were measured in the throats of the hinges and splitting cracks of up to 3 mm were measured on the transverse side faces of the bearings.

In this rehabilitation project, existing damaged concrete hinge bearings were successfully replaced after 50 years' service. The concrete hinge bearings were replaced with elastomeric bearings and seismic restraint blocks to comply with modern standards. This rehabilitation project demonstrated that bearings can be replaced in an emergency in extremely short time frames, given effective collaboration with an experienced Client, Engineer and Contractor.

ACKNOWLEDGEMENTS

The authors acknowledge the collaborative efforts which helped make this work possible:

- Client: South African National Roads Agency SOC Limited (SANRAL);
- Consulting Engineer: SMEC South Africa (previously t.a. Vela VKE);
- Contractor for initial emergency repair contract: Botes & Kennedy Manyano
- Contractor for balance of bridge repair contract: Haw & Inglis Civil Engineering

REFERENCES

BE5/75, 1975. Technical Memorandum (Bridges) Rules for the Design and Use of Freyssinet Concrete Hinges in Highway Structures.

BS 5400-9.1: 1983. Steel, Concrete and Composite Bridges—Part 9: Bridge Bearings.

Marx, S & Schacht, G, 2010. Concrete Hinges—Historical Development and Contemporary Use. *Proc. 3rd fib International Congress-2010*.

Concrete Repair, Rehabilitation and Retrofitting IV – Dehn et al. (Eds)
© 2016 Taylor & Francis Group, London, ISBN 978-1-138-02843-2

Seismic reinforcement of the URM by FRP system

O. Simakov
CJSC "Prepreg-SKM" Moscow, Russia

G. Tonkikh
FCSHT RSRICDE, Moscow, Russia

O. Kabancev
Moscow State University of Civil Engineering, Moscow, Russia

A. Granovsky
Central research Institute of Building Constructions V.A. Kucherenko, Moscow, Russia

ABSTRACT: This paper presents the results of experimental studies of natural samples of masonry, reinforced by a system of external reinforcement FibArm (FRP system) with warping. The result determined the effectiveness of this method of reinforcement, and defined qualitative and quantitative indicators, and the mechanism of destruction of the samples. According to the results of numerical simulation data analysis the method of calculation was developed, which calculates with sufficient accuracy the increase of the load bearing capacity of masonry reinforced by external reinforcement.

1 INTRODUCTION

It is commonly known that masonry operates on compressive stresses and takes much worse tensile, shearing and bending forces. Unlike conventional masonry work environment when it mostly takes static compressive loads with small eccentricities, at seismic impacts in the masonry walls have got a diverse mix of dynamic loads (including those which provoke bending, shearing, and tensile). That is why during earthquakes stone buildings receive the greatest damage compared with other types of buildings of modern construction. However, while meeting the requirements of work performance and meaningful measures aimed at improving the seismic resistance of buildings with load-bearing stone walls, they can be sufficiently earthquake resistant.

One of such measures is a device of external reinforcement with materials based on carbon fibers. This system is used for a long time; there are a number of standards and regulations. At the same time there are significant areas for which there is no numerical description of the load bearing capacity increase. This work exactly is devoted to resolve one of these issues.

2 TESTS

2.1 *Test configuration*

Consequences of earthquakes have been analyzed to determine the most vulnerable structures in stone buildings. These studies have showed that piers have the most significant impact on the overall seismic resistance buildings. The main damage of the stone walls includes inclined cracks in piers, arising at different directions of horizontal seismic load action.

The process of deformation of brick masonry of piers is divided into three stages, following one after another with increasing magnitude of the horizontal forces:

Stage I: Seismic forces are small; piers operate with a window header throughout the entire area of their contact, and vertical load from an upper one to the lower one is transmitted at all levels of the pier throughout its horizontal section.

Stage II: In horizontal areas of horizontal of the piers on the top and bottom levels of the adjacent openings there are cracks, and the contact between the lower and upper masonry is broken. In this stage, the transfer of vertical and horizontal loads

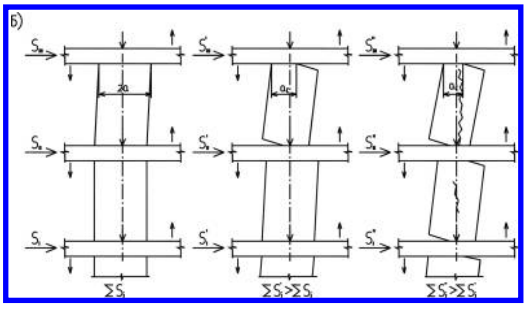

Figure 1. The pier operation configuration.

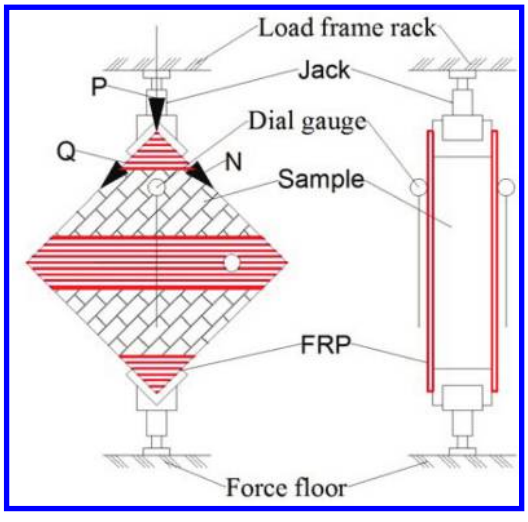

Figure 2. Test configuration.

to mentioned sections is carried out only along the length a_c <2a (where a is half width of the pier). At an alternating horizontal load the bonding is broken due to the cracking when the sign of the load is changed alternately on both sides of the pier.

Stage III: The length of the compression area is reduced and there is emerged a diagonal crack in the pier.

The same pier at different floors of the building (Fig. 1) can be in various stages of deformation, due to changes in values and ratios of vertical and horizontal forces, as well as possible differences in terms of strength and stiffness of the piers.

Taking into account the above mentioned and the analysis of various test configurations a configuration has been selected in which the compressive load is transferred along one of the diagonals (Fig. 2). In this case, the principal tensile stresses are predicted, and good repeatability of the experiment is also provided.

2.2 *Experiment samples*

During the planning phase of the experiment the following samples were selected:

Series I (S-I)—check samples of brick masonry without reinforcement, in amount of 3 pcs.;

Series II (S-II)—experimental samples of brick masonry, reinforced by a carbon one-directional tape FibARM Tape 230/300. The number of samples in the series is 3 pcs.;

Series III (S-III)—experimental samples of brick masonry, reinforced by a carbon one-directional tape FibARM Tape 530/300. The number of samples in the series is 3 pcs.;

Series IV (S-IV)—experimental samples of brick masonry, reinforced by three carbon one-directional tapes FibARM Tape 230/300. The distance between the tapes is 200 mm. The number of samples in the series is 1 pce;

Series V (S-V)—experimental samples of brick masonry, reinforced by a carbon two-directional cloth FibARM Twill 240. The number of samples in the series is 1 pce;

Series VI (S-VI)—experimental samples of brick masonry, reinforced on both sides by three carbon one-directional tapes FibARM Tape 230/300. The distance between the tapes is 200 mm. The number of samples in the series is 2 pcs.;

Series VII (S-VII)—experimental samples of brick masonry, reinforced on both sides by a carbon two-directional cloth FibARM Twill 240. The number of samples in the series is 2 pcs.

Experiment samples of **series I (S-I)** are fragments of masonry with dimensions 1060 × 1060 × 250 mm without reinforcement. Brick of brand M100 was used for laying. A solution was used made in the laboratory as a brick mortar, with the same composition (C:S:W—1:5:1.2) as of brand M75. Additives were not used in the production of the masonry that can increase the adhesion of the solution with a brick. Cubes of 70.7 × 70.7 × 70.7 mm were filled for each batch to determine the exact brand solution at the time of the test.

All samples are made of solid masonry with chain system of brick pattern. Experimental samples are prepared in the laboratory by an average bricklayer. In addition all seams both horizontal and vertical are completely filled. The samples were made without pointing of external horizontal and vertical joints. The surface quality of the samples meets the requirements for the application of the composite material without preliminary preparation with a repair leveling compound.

2.3 *Testing method*

Static load testing has been carried out by specialists of FGBU All-Russia Research Institute for Civil Defense and Emergency (FC) in the laboratory of the Central research Institute of building constructions V.A. Kucherenko, division of OJSC SRC "Stroitelstvo".

Load frame rack is a metal box frame structure. Static load is created using an oil-pumping station with electric motor, with manual valve and two cargo bilateral hydraulic jacks. The hydraulic jack the pump and pressure gauge was calibrated before testing.

The load on the sample was applied in steps of 10% of the breaking load in the stage of loading, and of 5% at the stage close to the fracture. Stress was maintained at each step for 3 minutes followed by fixation of deformations.

For metrological assurance of testing dial gauges were used with a scale of 0.01 mm, on the basis of 800 mm, located along the diagonals, and an accelerometer. The dial gauges were installed on both the brick surface and the application of composite materials.

2.4 *Results of testing*

During the tests there were determined:

– Compressive and tensile deformation of masonry;
– Rupture load.

Destruction of samples of series I

The nature of all fractures is unstable; it is practically instantaneous fracture of the sample with a single crack.

Destruction schemes are presented in Fig. 3.

Destruction of the reinforced samples.

The destruction of all the samples occurred according to the scheme, similar to the scheme of destruction of the control samples: there was one crack along the compressed diagonal, i.e. upon masonry achieved limits on the main tensile stresses.

The nature of all the destructions is unstable; it is almost instantaneous fracture of the sample. Deformability of the reinforced samples compared to the control series is not increased.

There is a rupture of carbon fiber from the masonry surface with a surface layer of bricks and the mortar.

Schemes of the reinforced samples destruction of the series are presented in Fig. 5.

The values of the bearing capacity of masonry without reinforcement and with reinforcement are presented in Table 1.

The results of the expansion of efforts into compression and shearing are given in Table 2.

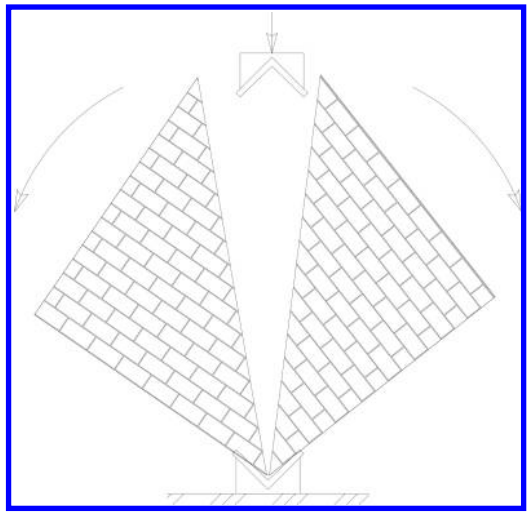

Figure 3. Destruction scheme of the sample S-I.

Table 1. Bearing capacity of masonry of the samples.

Series	The series number	P, kgf	Average P, kgf	Increase in P,%
S-I	S-2	50060	50392	0,00%
	S-3	50724		
S-II	S-II-1	63978	66120	31,22%
	S-II–2	66630		
	S-II–3	67754		
S-III	S-III–1	70119	71322	41,53%
	S-III–2	73041		
	S-III–3	70806		
S-IV	S-IV–1	74766	76506	51,82%
	S-IV–2	77865		
	S-IV–3	76887		
S-V	S-V–1	84588	84570	67,82%
	S-V–2	85863		
	S-V–3	83261		
S-VI	S-VI–1	99303	99400	97,25%
	S-VI–2	101545		
	S-VI–3	97351		
S-VII	S-VII–1	102915	102471	103,3%
	S-VII–2	104511		

The experiment found that all the reinforced samples after reaching the maximum load were subjected to unstable (instantaneous) fracture. With the destruction of the reinforced samples of series II-VI there was a rupture of carbon fiber from the masonry surface with the surface layer of bricks and the mortar. The destruction of the reinforced samples of series VII was accompanied by a rupture of carbon cloth along one direction of the

Table 2. Evaluation of shearing forces of the samples.

Series indentification number	P, kgf	Q, kgf	Increase in shearing force	
			Q, kgf	%
S-I	50392	35288	–	–
S-II	66120	46303	11015	31.21
S-III	71322	49945	14657	41.53
S-IV	76506	53576	18288	51.82
S-V	84570	59223	23935	67.82
S-VI	99400	69608	34320	97.25
S-VII	102471	71758	36470	103.35

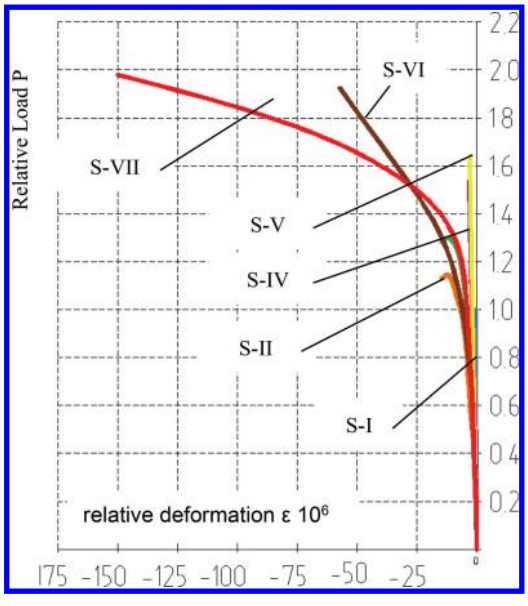

Figure 4. Deformation of masonry (compression).

fibers, and the fiber rupture begins to develop from the end and go to the cloth center.

In this case, the samples deformation process is of the unstable nature. The load on the samples during the testing was performed up to complete destruction of the sample.

According to the results of static tests the generalized diagram of masonry are built in relative values (Fig. 4–5), featuring by an increased load bearing capacity of the reinforced samples, depending on the application parameters. Relative deformations were obtained by dividing the absolute values of the length by the measurement base length (800 mm); the relative loads by load bearing capacity of samples of series I (51,195 kgf).

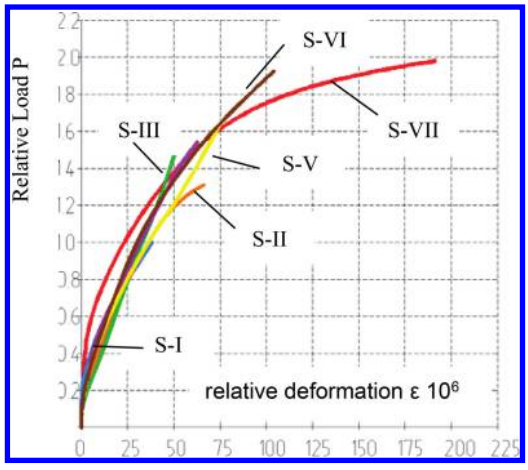

Figure 5. Deformation of masonry (elongation).

3 METHODS OF CALCULATION

As a result of the analysis of the data obtained during the experiment and computer numerical simulation a method was developed calculating the load bearing capacity of reinforced masonry piers (in the external reinforcement).

Coefficient of external reinforcement k is taken as the reinforcement rate, equal to:

$$k = \frac{A_{a_i}}{A_k} \cdot b_{fib} \cdot \delta_{fib} \cdot R_{fib} \cdot n \qquad (1)$$

where, A_k is surface area of the masonry, m^2:
b_{fib} is width of carbon fiber, m:
δ_{fib} is thickness of the one layer tape, m:
R_{fib} is average value of carbon fiber tensile breaking stress, Pa:
n is number of carbon fiber layers.

The resulting value of increasing shearing force of reinforced masonry with respect to the standard, defined as the projection of the vertical load onto the horizontal axis of the sample, can be determined by the following dependence:

$$Q = \left(0.35 \cdot \ln\left(k + 80\right) - 0.53\right) \cdot Q_0 \qquad (2)$$

where Q_0 the load bearing capacity of masonry without reinforcement, is taken to be equal to the load bearing capacity with the action of the principal tensile stresses according to a formula:

$$Q_0 \le \frac{\mathrm{R_{tq}hL}}{\nu_2} \qquad (3)$$

where h is the thickness of the wall; L is the length of the reinforced wall area; ν is the irregularity

coefficient of the shearing forces in the cross section. For rectangular cross sections ν is allowed to take 1.5; R_{tq} is design resistance to the masonry shear fracture, compressed by design force N, defined with an overloading coefficient of 0.9 by the formula:

$$R_{tq} = \sqrt{R_{tw}(R_{tw} + \sigma_0)} \quad (4)$$

where R_{tw}, the design resistance to the principal tensile stresses, is determined by test results or according to the regulatory documents; σ_0 is tension of compression by force N, equal to:

$$\sigma_0 = \frac{0{,}9N}{Lh} \quad (5)$$

The developed method of calculation with sufficient accuracy determines the load bearing capacity of the reinforced masonry. Within the analysis carried out the experimental data was compared with the calculated results according to the proposed method. The results of the calculation are presented graphically in Figure 9.

As we can see, the proposed dependence with sufficient accuracy for practical calculations, with a margin of 15%, describes the change in the strength and geometric features of reinforcement of the experiment samples of masonry with composite materials. In addition, this dependence, in our opinion, may also be suitable for other cases of reinforcement, namely for reinforcement of masonry over the entire surface in several layers.

4 CONCLUSIONS

1. The external reinforcement systems based on carbon fibers (FibArm products of CJSC "HC "Composite", Russia) are effectively included in the operation of masonry, and allows the load bearing capacity of masonry on the principal tensile stress for 30–120% depending on the reinforcement parameters (physical and mechanical features of the composite, area of reinforcement relatively to the total structure surface area, thickness and number of number of reinforcement layers). At the same time obtained schemes of destruction indicate the need for cautious and informed approach to the appointment of safety factors in order to prevent unstable fracture.
2. The developed method with sufficient accuracy for practical calculations determines the increase in shearing force of masonry due to use of external reinforcement FibArm.
3. It is reasonable to carry out additional studies to expand the scope of the external reinforcement system FibArm by using other parameters of the reinforcement and determining the maximum safety factor for different structures.

REFERENCES

[1] SP 14.13330.2014 «SNiP II-7-81* «Seismic building design code».
[2] SP 15.13330.2012 «SNip II-22-81 «Masonry and reinforced masonry structures».
[3] STO 2256-002-2011 System of externally bonded reinforcement by polymer composites FibArm for maintenance and strengthening building structures. General requirements. Technology.
[4] TU 1916-018-61664530-2013 Carbon bonds for system of externally bonded reinforcement FibArm Tape. CJSC «Prepreg-ACM».
[5] TU 1916-019-61664530-2013 Carbon bidirectional bonds for system of externally bonded reinforcement FibArm Tape. CJSC «Prepreg-ACM».
[6] TU 2257-047-61664530-2014. Epoxy two-component binder FibArm Resin 230+ for externally bonded system FibArm. CJSC « Prepreg-ACM ».
[7] TU 2257-048-61664530-2014. Epoxy two-component binder FibArm Resin 530+ for externally bonded system FibArm. CJSC « Prepreg-ACM ».
[8] Kabancev O.V., Tonkikh G.P. ect. Manual for the evaluation of seismic stability and seism reinforcement combined buildings with bearing walls of masonry. Moscow, 26 CNII MO Rus, 2002.
[9] Tonkikh G.P., Kabancev O.V., Koshaev V.V. The experimental method for reinforcement of buildings masonry concrete applications. «Earthquake engineering. Safety of construction» No 6, 2005.
[10] Tonkikh G.P., Kabancev O.V., Koshaev V.V. Experimental studies of the bearing capacity of masonry at the main loads. «Earthquake engineering. Safety of construction» No 6, 2007.
[11] Tonkikh G.P., Kabancev O.V., Simakov O.A., Baev S.M. Experimental study of seismic reinforcement masonry exterior concrete applications. «Earthquake engineering. Safety of construction» No 2, 2011.

Concrete Repair, Rehabilitation and Retrofitting IV – Dehn et al. (Eds)
© 2016 Taylor & Francis Group, London, ISBN 978-1-138-02843-2

Influence of surface concrete preparation on adhesion properties of repair materials

M. Skazlic
Faculty of Civil Engineering, University of Zagreb, Zagreb, Croatia

K. Mavar
Institute IGH, Zagreb, Croatia

A. Baricevic
Faculty of Civil Engineering, University of Zagreb, Zagreb, Croatia

ABSTRACT: The research programme was designed to present the performance of repair on horizontal surfaces through trial works on models, such as for example on bridge concrete slabs whose deteriorated surface layer needs to be removed and the pavement slab reshaped by applying the repair system procedure. The aim of the investigation was to determine optimal technology for the concrete surface preparation and the type of repair material which meets the new adhesion criteria ($f_a \geq 2.0$ N/mm^2). Pull-off testing, roughness measurement and microscope analysis were used for evaluation of applied repair systems.

1 INTRODUCTION

During life time, structures are exposed to different environments. Penetration of aggressive agents, into concrete protective layer leads to degradation of reinforced structures. Extensive deterioration due to agents such as chlorides is often found on roadways, were solutions with high chloride concentrations are used to prevent freezing. In such cases, repair is mandatory to maintain an adequate serviceability.

On Figure 1 deterioration of bridge deck caused by leaking of chloride solution through different layers of pavement presents a typical case. Usually, degradation is retained in concrete protective layer.

One of the most common forms of concrete structure repairs pertains to the procedure of removing damaged or contaminated concrete, as well as to its rehabilitation with repair mortars or concretes. The repair procedure usually takes place in the zone of the reinforcement protective layer, and consists of a number of stages as follows: surface preparation (using well-known technologies for removing concrete layers and for preparing for the application of new layers, Figure 2), application of the bonding coat, and application of repair material in accordance with the conditions of placing a new reshaped layer by using repair mortars and concretes.

Figure 1. Deterioration of bridge deck slab.

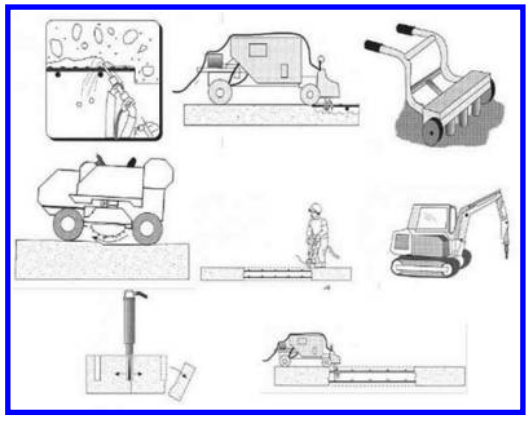

Figure 2. Available technologies for removal of damaged concrete (Emmons, 1993).

Removing concrete mainly refers to the removal of damaged or contaminated concrete, but in some cases even healthy concrete is removed to assure proper repair. Chosen procedure needs to be efficient, safe, cost-effective, and should minimize damage of the persisting concrete. If should be taken into consideration, that different technological process have diverse influence on structure due to the operational forces during concrete removal. Accordingly, most important criteria for process selection is the "soundness of underlying concrete", i.e. reduced appearance of micro cracks (Radic 2008).

2 EXPERIMENTAL PROGRAM

In this paper an investigation was carried out to evaluate influence of damaged concrete quality, concrete removal technology and type of repair material on the quality of repair works. Pull-off testing, roughness measurement and microscope analysis of microstructure were used. The obtained results were analysed according the new criterion for adhesion between the repair concrete and existing concrete of 2.0 N/mm^2 set in European standards. Up to date, proper repair was considered when adhesion using pull off method was 1.5 N/mm^2.

Trial works have been conducted on the total of 6 models of concrete slab shapes with dimensions 120 × 80 × 15 cm. Blocks are differentiated according to concrete quality of the surface, i.e. 3 concrete slabs are made of concrete class C25/30 (mark B) and 3 concrete slabs are made of concrete class C35/45 (mark A).

The following parameters have been varied in the experimental program:

– quality of the substrate concrete,
– concrete surface preparation technology and
– type of material for rehabilitation.

2.1 *Surface preparation technologies*

The concrete protective layer was removed from concrete slab models at the age of 28 days. Three different technologies were used for concrete removal, i.e. for surface preparation:

a) water under high pressure or hydrodemolition (mark HD), Figure 3a,
b) mechanical pneumatic removal of concrete (mark PH), Figure 3b,
c) wet sandblasting (mark PJ), Figure 3c.

2.2 *Composition of repair materials*

Different types of concretes were used for repair: without additives and bonding coat, with silica fume without bonding coat, with latex with and without the bonding coat.

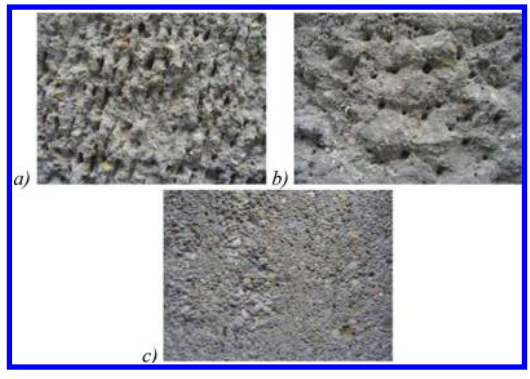

Figure 3. Surface preparation of concrete model slabs: a) with water under high pressure (hydrodemolition), b) by mechanical pneumatic removal of concrete, c) by wet sandblasting.

Table 1. Composition of repair materials.

Components	OC	SFC	LMC
Cement	400	370	400
Water	160	148	160
Superplastisizer	4	3.7	–
Silica fume	–	30	–
Latex	–	–	80
Aggregate	1822	1851	1658

Cement CEM I 42.5R, gravel aggregate fractions 0–4 mm and 4–8 mm, superplasticiser based on polycarboxylate ether, latex polymer additive, silica fume and water have been used for the preparation of repair concretes. The bond coat used with the mixture marked LMC+ is made of a latex/water/cement/sand mixture in a 1:2:2:2 ratio. Composition of repair materials can be found in Table 1.

Concrete preparation for the over layer has been conducted by mixing concrete in a laboratory, and by placing it onto the previously prepared surfaces of concrete substrate. Four squares have been placed on each block of concrete (divided into four quarters). All repair concretes have been applied onto the previously wetted concrete surface (by spraying with water mist).

In this way six different slabs (marks: AHD, BHD, APH, BPH, APJ, BPJ) were prepared with three different technologies of concrete removal (HD, PH, PJ) for each existing concrete quality (A and B), Figure 4.

Curing of repair concretes marked OC and SFC was carried out by wetting over a 7-day period,

while concretes marked LMC i LMC+ were cured first two days only. This difference in concrete curing is a consequence of adding latex as a polymer additive.

2.2.1 *Research methods*

Properties of concrete substrate, quality of prepared surface and performed rehabilitation were tested according to following standards:

- compressive strength (HRN EN 12390–3),
- static modulus of elasticity (HRN U.M1.025),
- pull-off test (HRN EN 1542).

Figure 4. Placement of repair concrete on prepared surface of concrete substrate (left) and overview of model slabs (right).

Roughness of the substrate concrete was investigated using calliper method. Microscope structure analysis was used for assessing quality of interface between exiting and repair concrete.

2.3 *Results and discussion*

2.3.1 *Properties of repair materials*

Tables 2 present the repair concrete properties. It is evident silica fume has positive influence on compressive strength, modulus of elasticity and tensile strength values, whereas adding latex effects on decrease of those properties if compared to the ordinary repair concrete.

Table 2. Properties of repair concrete in hardened state.

Property	OC	SFC	LMC
Compressive strength after 28 days (N/mm^2)	59.7	63.8	44.9
Static modulus of elasticity (GPa)	33.9	36.2	20.2
Pull-off tensile strength (N/mm^2)	4.50	4.68	3.68

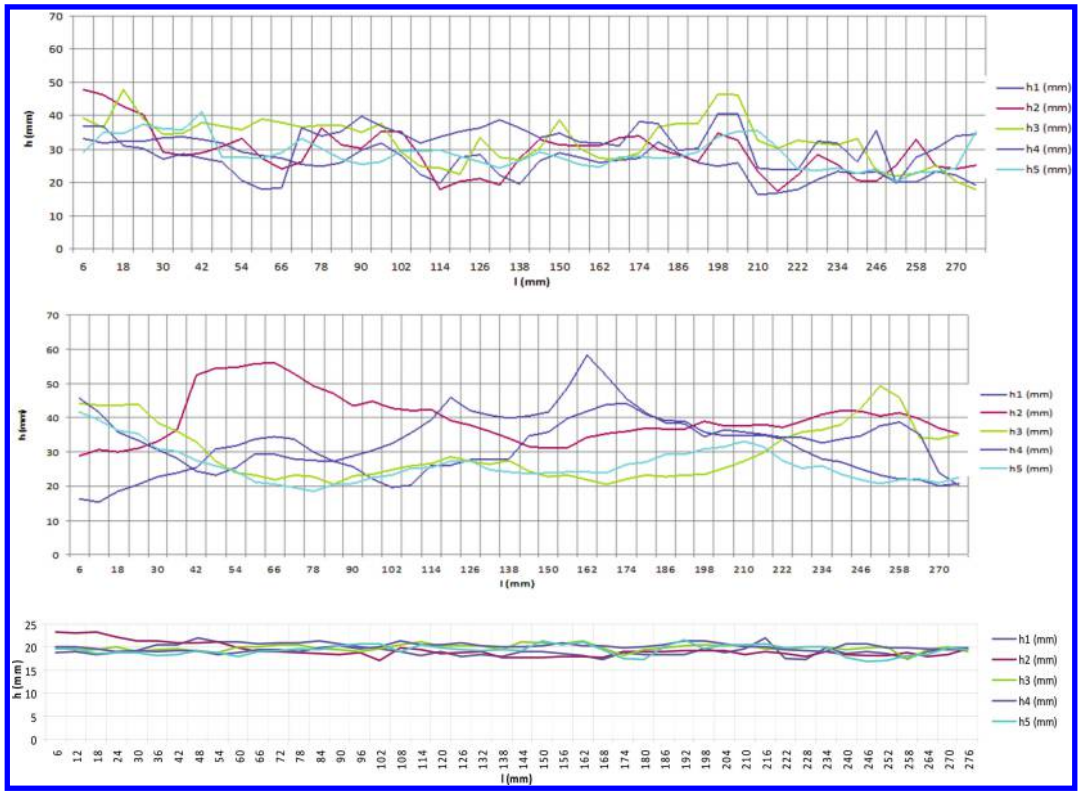

Figure 5. A presentation of logged roughness profiles for all three types of surface treatment (on concrete blocks—series A): a) by hydrodemolition, b) by mechanical pneumatic technology, c) by sandblasting.

Table 3. Statistical analysis values of measured roughness for all 6 concrete surfaces.

Type of surface	HD	HD	PH	PH	PJ	PJ
Block mark	A*	B**	A	B	A	B
Standard deviation σ_{hr} (mm)	6.29	8.00	8.72	8.28	1.13	0.85
Range between -2σ to $+2\sigma$ (mm)	25.1	32.0	34.9	33.1	4.5	3.4

*C35/45, **C25/30.

2.3.2 *Roughness of treated top surfaces*

After concrete protective layer was removed from concrete slab models, roughness of treated top surfaces was measured using a calliper. Results are presented in terms of selected roughness profiles and averaged roughness values for each slab (Figure 5, Table 3).

The test results indicate that minimal roughness is obtained by sandblasting, and maximal roughness when using a mechanical pneumatic technology.

2.3.3 *Adhesion properties of repair concretes*

After laying a repair concrete overlay, it is necessary to examine the achieved adhesion between new and old material. Testing is performed using pull off method, together with visual inspection of interface, at different ages of repair material.

According to the standard (HRN EN 1542:2001), a small metal plate is glued on repair material and after sometime a force is applied until failure. Test results include both the force value and visual observation of the failure zone.

When rehabilitation is made using repair mortars or concretes, a failure can occur in concrete substrate, on the contact between new and old material, within the repair material, in glue layer between the metal plate and repaired surface, or by combining all previous fracture modes

The mode of fracture and the value of achieved adhesion give important information about the properties of repair system, i.e. the quality of repair concrete and its bond with old concrete.

With the aim to gain a better insight into the development of bond strength during time, adhesion tests were performed at the repair concretes age of 28 and 90 days. Figure 6 shows the example of the adhesion testing implementation. An overview of adhesion average values obtained from all tests is presented in Table 4 (Mavar & Skazlić 2012, Skazlic & Mavar 2013).

It is evident from Table 4 that adhesive strength increases with time for all repair systems. According to (Bonaldo et al. 2005) excellent adhesion values were achieved with surface treatment performed

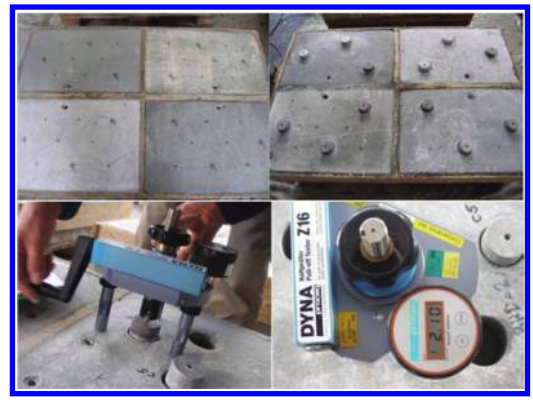

Figure 6. Surface preparation and pull off adhesion testing.

Table 4. An overview of average values of achieved adhesion on surface concretes type A and B.

Slab mark	Average values of adhesion (N/mm^2) at specified repair concrete age	
	28 days	90 days
AHD	2.53	3.28
BHD	2.28	3.19
APH	1.12	0.98
BPH	0.38	0.69
APJ	3.09	3.55
BPJ	2.66	2.85

by hydrodemolition (HD) and sandblasting (PJ), regardless of the type of repair system, even though the actual roughness of sandblasted surfaces is significantly lower. With mechanical pneumatic technology (PH) surfaces roughness is high, but the achieved adhesion is significantly lower, which indicates that there are other factors which influence the roughness test results. It is visible that only surface treatments by hydrodemolition and sandblasting satisfy the criteria of adhesion (≥ 2 MPa) after 28 and 90 days for both used concrete substrate qualities. This is due to the presence of micro cracks in underlying concrete, when surface is prepared by pick-hammer.

Interface between old concrete and repair material is examined using optical microscope. Figure 7 shows the microstructure of the interface between damaged and repair concrete for different technologies of concrete removal and repair systems.

Sandblasting process is applied on Figure 7a were repair system consists from bonding coat and con-

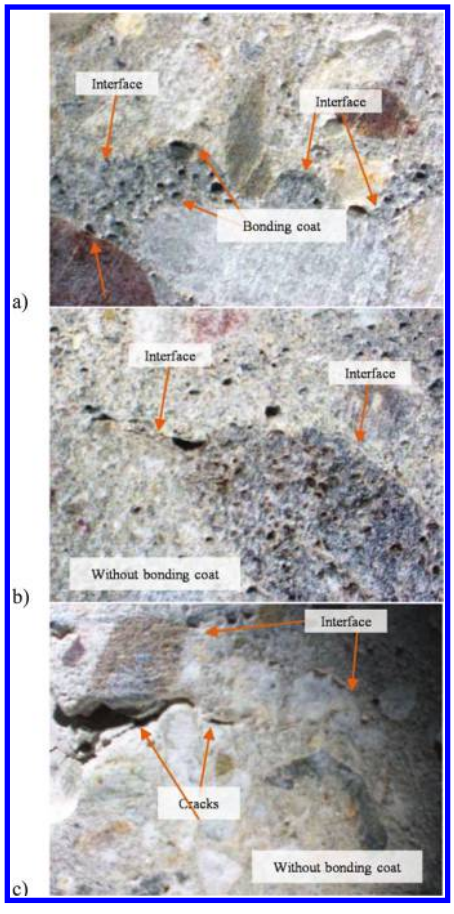

Figure 7. Interface of old (type A) and repair concrete for different technological process of concrete removal: a) sandblasting, b) hydrodemolition, c) mechanical pneumatic technology.

crete with latex. In the case showed on Figure 7b, concrete removal was performed by hydrodemolition and as repair system concrete with silica fume was applied without any bonding coat. In both cases, it is evident that a good quality interface bond was established, whereby in case 7a bonding layer was clearly expressed. Figure 7c shows a repair system were concrete surface was prepared by mechanical pneumatic technology and concrete with latex was used as repair material. Interface area is of lower quality compared to previous two cases, as micro cracks are present in underlying concrete.

2.3.4 *Correlation between concrete surface roughness and adhesion values*

Visual inspection and measurements of roughness imply an evident difference between used surface preparation technologies, and their impact on the interface quality bond. Here, only macro roughness is measured as this represents an engineering level and has a major influence on the adhesion properties of repair systems (Garbacz, et al. 2005, Albers et al. 2006, Naderi 2005, Fagerlund 2004, Saccani & Magnaghi 1999).

Based on the accomplished results (Figure 8), relationship between surface roughness and adhesion can be established:

a) In relation to individual adhesion results

It was shown that surface concrete preparation by hydrodemolition and sandblasting gives equal adhesion values, regardless of the degree of surface roughness. Although highest roughness is achieved with mechanical pneumatic technology, obtained adhesion values are much lower.

b) In relation to the set adhesion criteria ($f_a > 2{,}0$ N/mm^2)

This requirement is met when surface of substrate concrete was prepared by hydrodemolition and sandblasting, which is not the results of measured roughness. In case when surface preparation was done using mechanical pneumatic technology prescribed quality was not assured, despite high surface roughness.

2.3.5 *Influence of bonding coat on the quality of interface between substrate and repair system*

During experimental work, bonding layer was only applied within repair system labelled LMC+ (LMC system with bonding coat). After detailed examination of adhesion values for all tested repair systems, following was concluded:

- concrete with addition of latex when used with bonding coat (LMC+) has 40% better
- adhesion if compared with the same repair material without bonding layer (LMC),
- concrete with addition of latex when used with bonding coat (LMC+) has similar adhesion as concretes with addition of silica fume (SFC) without bonding layer.

3 CONCLUSIONS

Based on the results of conducted experimental research following conclusion are made regarding adhesion properties of repair material:

- The quality of concrete substrate has minor influence on the adhesion of repair system. Its influence is pronounced only in case when surface is prepared using mechanical pneumatic technology, due to the appearance of micro cracks in underlying layer.
- The roughness of substrate has no direct effect on the accomplished adhesion of repair system, but presence of micro cracks in existing concrete

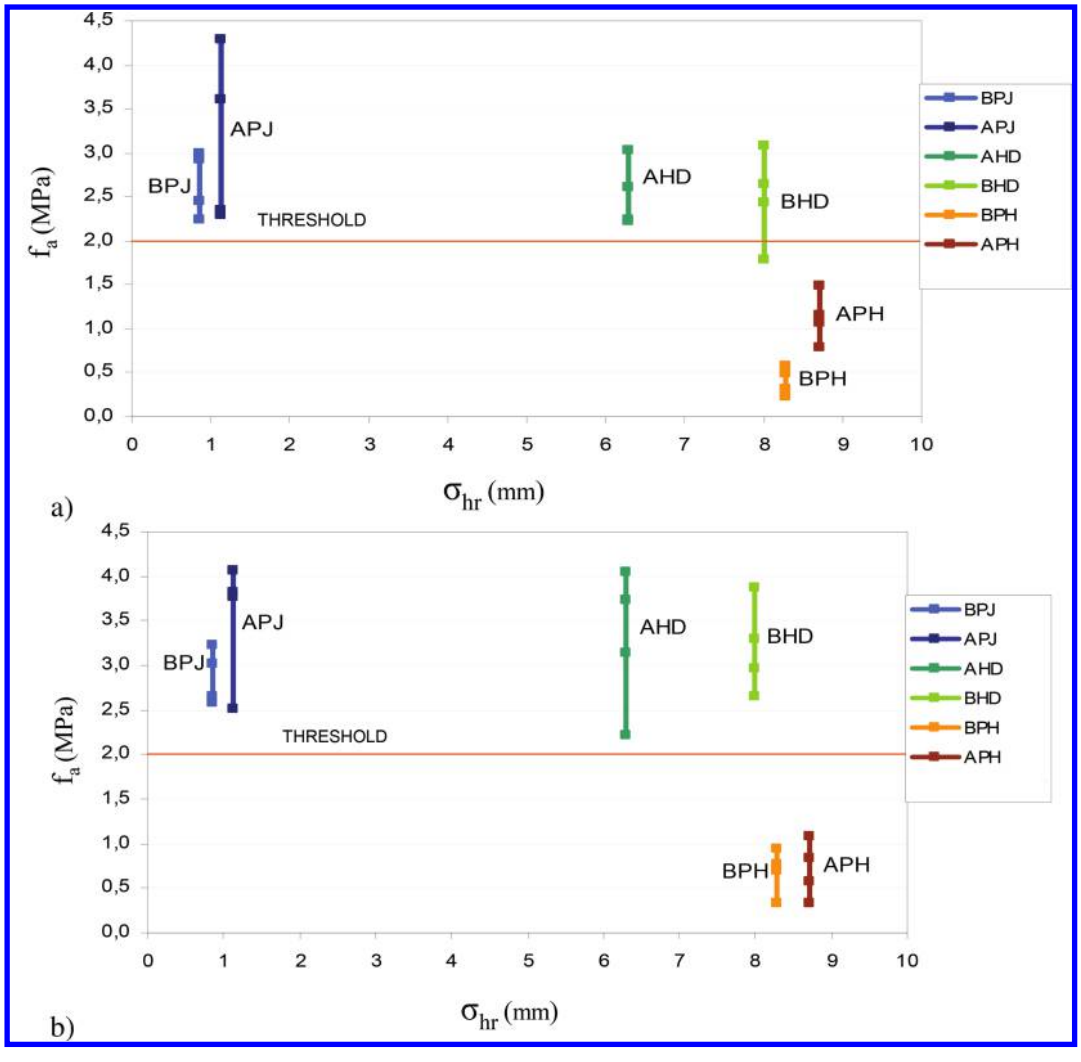

Figure 8. Relationship between the values of achieved adhesion for both substrates types and surface roughness for all tested surface preparation technologies: a) at 28 days, b) at 90 days.

found to be important. Surface preparation using mechanical pneumatic technology is therefore considered inappropriate.

– Adhesion of repair system is increased with its age.
– At the age of 28 day, adhesion requirement ($f_a > 2.0$ N/mm^2) is achieved by following repair systems:
  - Concrete with addition of silica fume without bonding layer,
  - Concrete with addition of latex when bonding coat is applied.

REFERENCES

Emmons, Peter H. 1993. Concrete Repair and Maintenance Illustrated: Problem Analysis; Repair Strategy; Techniques, RS MEANS, Kingston, MA.

Radić and others 2008. *Concrete structures 4: Repair works*, chapter: Methods for repair of concrete structures, Croatian University edition

HRN EN 1542: 2001 Products and systems for the protection and repair of concrete structures—Test methods—Measurement of bond strength by pull-off.

Bonaldo E., Barros J.A.O., Lourenco P. B. 2005. Bond Characterization between Concrete Substrate and

Repairing SFRC Using Pull-off Testing, *International Journal of Adhesion & Adhesives* 25, 463–474.

Garbacz A., Gorka M. and Courard L. 2005. Effect of concrete surface treatment on adhesion in repair systems, *Magazine of Concrete Research* 57(1), 49–60.

Albers A., Nowicky L., Enkler H.-G. 2006. Development of a Method for the Analysis of Mixed Fraction Problems. *Int. J. of Applied Mechanics and Engineering* 11(3), 479–490.

Naderi Mahmood 2005. Friction-transfer test for the assessment of in situ strengthened adhesion of cementitious materials. *Construction and Building Materials* 19, 454–459.

Fagerlund G 2004. Strategy for maintenance and rehabilitation in concrete structures, Work Package 2.3: evaluations of alternative repair and upgrading options: Final Report—REHABCON Manual, Div of Building Materials LTH, Lund university.

Saccani A., Magnaghi V. 1999. Durability of epoxy resin-based materials for the repair of damaged cementitious composites. *Cement and Concrete Research* 29, 95–98.

Mavar, K., Skazlic M. 2012. Influence of construction technology on the adhesion of remedial concrete *Gradevinar: Journal of the Croatian Association of Civil Engineers*, 7, 545–552.

Skazlic M., Mavar K. 2013. *Optimum Concrete Surface Preparation For Repair Works*, Proceedings of the Fourth International Workshop on Performance, Protection and Strengthening of Structures under Extreme Loading (ed. Suresh N, Banthia N.), India.

Concrete Repair, Rehabilitation and Retrofitting IV – Dehn et al. (Eds)
© 2016 Taylor & Francis Group, London, ISBN 978-1-138-02843-2

Management of the M4 Elevated Section substructures

C.R. Hendy & C.T. Brock
Atkins, Epsom, UK

A.D.J. Nicholls
Connect Plus (M25) Ltd., UK

S. El-Belbol
Highways Agency, UK

ABSTRACT: The M4 Elevated Section in West London is a 1.9 km concrete viaduct structure providing a major arterial route into London. An intervention model bringing together structural assessment and forecast deterioration, corrosion modeling and cracking has been developed to prioritise structural rehabilitation of the substructure crosshead beams. To evaluate residual strength an initial assessment of crossheads was undertaken, which identified a deficiency in tensile capacity at the ends of the crosshead cantilevers compared to current demands. Further assessment has been undertaken, including three dimensional strut and tie, non-linear finite element analysis and plastic analysis, to confirm public safety with continued trafficking of the structure, and to determine the need for strengthening.

Additionally extensive monitoring of the crossheads has been implemented including mapping of all cracks, and remote crack monitoring to safeguard the substructures and allow early interventions. The long term maintenance strategy brings together strengthening and cathodic protection concrete preservation methods with removal and repair of concrete delamination.

This paper discusses the development of the prioritisation process including deterioration modeling, together with the extended structural analysis to formulate a strengthening programme for these substructures.

1 INTRODUCTION

1.1 *Overview of the elevated structure*

The M4 motorway in West London is supported on an elevated reinforced concrete viaduct 1.9 km in length. The elevated section carries the M4 dual two lane motorway above and parallel to the A4 dual carriageway, forming a major arterial route in to central London. The structure incorporates 103 concrete crossheads supporting the mainline and a further 23 crossheads supporting the Junction 2 slip-roads.

The elevated structure comprises simply supported decks, typically with 16.2 m span lengths, formed of pre-stressed concrete beams with an in-situ concrete deck. The substructures are typically single pier reinforced concrete with cantilever crossheads supporting the decks via elastomeric bearings. The crossheads incorporate nibs that extend out from the lower section of the crosshead cantilevers, forming the bearing shelves. The central section of the crosshead extends up to the top of deck level and directly supports the carriageway between spans. Asphaltic plug deck joints are provided between decks above the upstand.

1.2 *Strategic management principles*

The M4 Elevated Section forms part of the M25 Design Build Finance and Operate (DBFO) contract. The DBFO concessionaire is Connect Plus, who have a contract with the Highways Agency to maintain the project network for the 30 year contract duration.

The key contractual obligation for Connect Plus is to hand back the M4 Elevated Section at the end of the 30 year contract in a no worse condition than that agreed at a condition assessment completed at contract commencement. The success in achieving these requirements will be measured through expenditure and lane closure tests where it is required that any works in the 15 years following contract completion should not exceed 125% of those measured in the final 15 years of the contract.

To achieve these requirements it is essential to understand the current condition of the crossheads,

Figure 1. General view of the M4 Elevated Substructures.

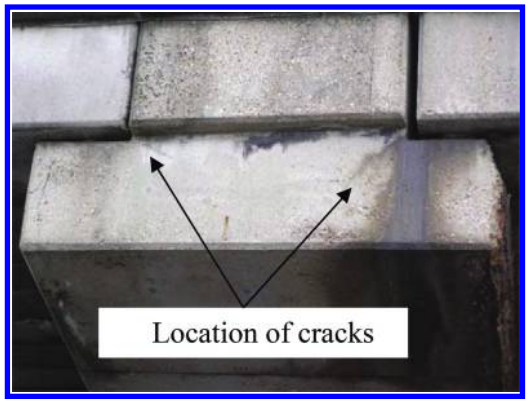

Figure 2. Location of cracks at crosshead cantilever ends.

its change with time and external factors such as drainage. It was therefore necessary to develop a strategy for the management of the M4 elevated substructures over a 45 year period.

The objective of the strategy was to maximise the operation of the assets and optimise total spend by evaluating the appropriate points at which interventions should be undertaken. Availability of the highway was a key factor because the contract includes financial penalty for periods of unavailability. The best theoretical strategy for the M4 elevated was initially found to be to schedule maintenance works interventions only where they became necessary to maintain structural capacity. However, as discussed in section 2, it soon became clear all crossheads first needed strengthening to meet current demands and this needed to be implemented ahead of operation of the long-term maintenance strategy. Other considerations affected long-term maintenance prioritisation including ease of access to different crossheads and control of other risks to public safety such as that posed by spalling concrete.

The time when refurbishment would become necessary was determined. This process brought together corrosion modeling to estimate the degree of reinforcement corrosion and strength loss with the overall structural assessment. From chloride sampling taken from the M4 elevated crossheads the corrosion modeling evaluated the time duration for the level of chlorides to reach 0.3% of cement content at the depth of reinforcement. This threshold level was considered to be the point where active corrosion of the reinforcement was instigated and an assumed rate of corrosion was applied to the affected bars (BRE 2009).

To develop the long-term maintenance strategy it was necessary to put in place a system to prioritise intervention. A scoring system was therefore developed considering primary deterioration indicators on which each substructure could be evaluated. This considered in particular:

- structural capacity compared to demand
- predicted deterioration rate (based on chloride levels and half-cell survey results)
- concrete delamination extents
- crack extents
- existence or otherwise of cathodic protection
- traffic management requirements, access issues and disruption to the travelling public.

Each of these characteristics was weighted depending on the level to which they dictate the intervention prioritisation of the substructures. A threshold level was determined representing a level of deterioration where intervention is necessary and a time to intervention for each crosshead, and an indicative works programme was produced.

1.3 *Current condition*

The crosshead substructures have been suffering from extensive corrosion and concrete delamination caused by salt water ingress (from winter maintenance) through deck joints, evidenced by extensive water staining. As part of continued maintenance strategy to the structure, several rehabilitation and prevention methods have been employed including removing large areas of delaminated cover concrete, concrete repair, and the application of cathodic protection and netting. Site testing has confirmed the chloride concentration is significantly in excess of the 0.3% threshold associated with high risk of active corrosion occurring (up to a maximum of ~8%). The presence of reinforcement corrosion is further supported by half-cell potentials taken from the structure exceeding –350 mV (CET Safehouse 2012), indicating a greater than 90% probability of corrosion occurring.

Some cracking has occurred on many of the crosshead ends concentrated at the re-entrant corners. This location acts as a halving joint and is subject to high stress concentration, therefore some degree of cracking is expected. However the crack

extents needed to be carefully monitored. In some locations the cracking has propagated between the re-entrant corners to 'join up'. This behavior indicates a progress loss of concrete tensile strength and subsequent transfer of loading on to the available vertical reinforcement which is of concern as discussed in section 2.1.

Due to the shape of the crossheads, it is impossible to inspect the condition of the concrete faces adjacent to the deck ends. Principally testing has focused on the accessible vertical faces and crosshead soffits, both of which are typically in poor condition. It is considered possible that conditions at the inaccessible faces are suffering at least the same level of corrosion as the visible faces.

1.4 *Deck joints*

Water penetration through the deck expansion joints has been reported since the mid 1980s. A programme of expansion joint replacements to all crossheads has recently been completed which involved removing the life expired Asphaltic Plug Joints (APJ) and replacing these with high modulus asphaltic plug joints with improved whole life cost performance. The original design had a discrete APJ above each expansion joint. The replacement joints extend over both expansion joints across the full width of the crosshead.

Provision for subsurface drainage in the joints was improved but subsequent surveys have shown significant amounts of water continuing to penetrate the deck joints, probably beneath the surfacing and under the joint, resulting in on-going contamination of the crossheads. An additional problem is that the APJ extends only between kerblines; water can thus penetrate through the verges and central reserve.

1.5 *Control of concrete spalling*

Significant areas of concrete delamination are present on the elevated substructures. The potential for delaminated concrete to fall on to the A4 dual carriageway directly beneath the M4 elevated section has been taken seriously and carefully assessed to mitigate this risk.

To overcome the risk from falling concrete, a netting system has been installed around the crosshead cantilevers. This netting is designed to catch the full cover concrete without significant deflection or damage to the netting occurring. Additionally a regular regime of delamination surveys has been put in place to identify areas of deteriorated concrete before they become delaminated from the substructures. These delamination surveys are carried out on a three month basis with interim six weekly surveys carried out on crossheads with the worst rate of delamination particularly during the winter months where the risk of delamination is greater due to freeze-thaw action. Further mitigation is provided through regular walk through inspections examining the netting for any captured concrete, which would indicate acceleration in deterioration.

Figure 3. Concrete delamination on crosshead cantilever faces.

Loss of concrete section has also exposed large areas of reinforcement as shown in figure 3, exposing reinforcement to accelerated atmospheric corrosion.

2 SUB-STANDARD STRUCTURE MANAGEMENT STRATEGY

2.1 *Initial structural assessment*

An initial assessment of the crosshead structures was undertaken based on record drawings to determine live load capacity and its sensitivity to reinforcement corrosion. The assessment demonstrated that the majority of each crosshead was able to carry 40 tonne assessment loading, but the light vertical reinforcement in the end 3 m of each cantilever was overstressed. The location of the bearing shelves below the top of the crosshead, where the main flexural reinforcement is provided, necessitates load transfer up to this reinforcement. The vertical reinforcement provided at the ends of the cantilevers was found to be inadequate to cater for current loading demands. Additionally, current codified minimum reinforcement requirements were not met. This made the presence of cracks as shown in Figure 2 a concern.

2.2 *Management strategy formulation*

Following the conclusions of the initial structural assessment a rigorous management regime was implemented in accordance with BD 79/06 (Highways Agency 2006). This regime included a thorough examination of the likelihood and

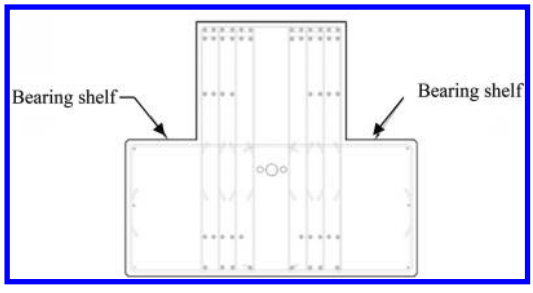

Figure 4. Existing reinforcement within the crosshead cantilevers.

implications of non-intervention, together with instigating a detailed inspection regime focusing on the ends of the crossheads where the start of any potential failure mechanism would first manifest itself. The management regime focused on a risk based approach to protecting public safety, putting in place defined trigger levels in the event any evidence of structural deterioration was identified.

The following actions were undertaken to ascertain the optimum management strategy for the M4 elevated substructures:

- Extended analysis considering three dimensional strut and tie analysis, non linear concrete modelling and considerations of reinforcement strain hardening.
- Assessment of ductility of potential failure mechanisms and hence the amount of warning these would give.
- Detailed inspection of the substructures at cantilever ends to identify evidence of initiation of a failure mechanism.
- Analysis of the impacts and disruption to the travelling public in the event of emergency closure, including the elevated accident risk associated with traffic diversions.
- Design and procurement of contingency measures to be mobilised immediately in the event evidence of accelerated structural deterioration was identified.

2.3 *Refined structural analysis*

Refined analysis was undertaken to optimise the predicted load carrying capacity of the crossheads and to inform behaviours mechanism. Extended analysis considering both strut and tie modeling and non-linear concrete modeling was undertaken.

The strut and tie analysis considered optimisation between two load paths available at the end of the crosshead. The first load path represented the transfer of load vertically from the bearing locations to the flexural reinforcement at the top of the crosshead section (refer to diagram 5).

The second strut and tie load path considered took advantage of concrete compression struts in the lower portion of the crosshead to transfer the bearing loads to the bent up bars closer to the pier. This load path reduces the load required to be carried on the vertical links but requires a tensile tie to be available directly below the bearing shelves. Record drawings indicate there is only one 25 diameter bar located at the top of the nibs which could provide this resistance. However cover meter surveys confirmed that the bars curtailed without end anchorage as indicated on the record drawings.

The load capacity of the crosshead cantilever ends was optimised by superimposing the resistances provided by both load paths. However the contribution of the second load path is limited by the contribution of the longitudinal tension bar within the nibs, therefore it was not possible to generate significant benefits over and above the predictions of the initial analysis.

In tandem a non-linear concrete model of the crossheads was developed to investigate potential strength benefits and to provide greater certainty as to how a failure mechanism would ultimately develop. The model incorporated all reinforcement and considered a rigid connection to the concrete, therefore not taking in to account bond characteristics. The analysis was performed in Abaqus using its 'concrete damaged plasticity' model for concrete behavior. The analysis considered tensile cracking, tension softening and compressive crushing of the concrete.

This analysis showed that for relatively small tensile concrete characteristic strength (~1 N/mm^2) the concrete was able to transfer the bearing loads and remained uncracked at the end of the cantilever. Model failure scenarios occurred at the cantilever root at a much higher load than applicable. This was not considered realistic because the model did not properly take account of the potential brittle fracture of the concrete arising from high stress concentrations at the crack tip, nor the presence of pre-existing shrinkage cracks or voids.

To reduce the influence of concrete tensile strength, the analysis was re-run for lower concrete tensile strengths which then gave very similar results to the strut and tie approach, as would be expected since it ignores concrete tensile strength. For low concrete strengths, cracks propagate at the crosshead ends under lower loading conditions, resulting in redistribution of force to the vertical bars in the crosshead ends and ultimately ductile failure at a load lower than that required. For higher concrete strengths, failure occurs above the required load but is governed by concrete tensile failure and is hence brittle. This resistance model could not be relied upon and hence adequate strength of the crossheads could still not be demonstrated.

2.4 *Consideration of overall failure mechanism and strain hardening*

The refined analyses in section 2.3 still focused on the crosshead in isolation and not the potential for any redistribution of load to elsewhere in the structure upon localised failure. To understand the additional reserve of strength, the combined superstructure and substructure was considered as a single structural system.

A ductile failure, ignoring concrete tensile strength, occurring anywhere in the final 3.0 m of a crosshead cantilever was considered. This part of the crosshead supports the verge, 600 mm hard strip and a proportion of the inside traffic lane (the M4 motorway having no hard shoulder in this location). In the event the cantilever ends displace, and support is lost to the outer deck bearings, the deck itself can span transversely due to the presence of end diaphragms and concrete infill between the beams. In reality, the ductility of the vertical steel in the crossheads means that the two mechanisms can be superposed, thus adding strength in excess of the predictions of section 2.3.

Reinforcement test data also concluded the ultimate steel strength is greatly in excess of the yield strength by 45% as a minimum. When strain hardening was additionally considered it was possible to demonstrate that the full traffic loading could be carried at the ultimate limit state, albeit with significant plastic deformation and damage occurring to the crosshead cantilever and adjacent decks leaving the structure unserviceable and very expensive to repair.

Whilst this gave confidence overall collapse would not occur, a residual concern that lumps of concrete might spall under the high strains and fall on to the A4 below was considered. This risk was however mitigated by the presence of the protective netting described in section 1.5.

In light of this analysis and mitigation, the overall risks to public safety from continued operation in the short to medium term were considered to be low if suitable monitoring was also put in place as discussed in section 3. However, it was concluded strengthening was required to maintain adequate reliability long-term. This is discussed in section 4.

3 STRUCTURAL MONITORING

A detailed regime of structural monitoring was put in place to identify early signs of structural deterioration to allow intervention before damage occurs.

Monitoring has been implemented on a risk based approach with focus being on the piers showing the greatest cracking. A series of trigger levels was defined based on risk level. DEMEC studs have been installed at all re-entrant crack locations and a 3 monthly programme of re-measurement has been implemented. Where cracking extends the full distance between re-entrant corners the affected crossheads are classed as high risk and real time monitoring devices have been installed over the cracks. These devices take regular measurements of displacements parallel and perpendicular to the cracks and the data can be remotely access through a web based portal. The monitoring data is constantly interrogated to identify any signs of progressive deterioration through steady increasing crack length and width.

Typically the monitoring shows a very high correlation with temperature affects, with both daily and seasonal changes observed. Various methods have been used to remove these temperature affects with varying degrees of success. They do not prevent long term trends being identified, which in the case of some crossheads do show progressive crack increase.

Trigger levels for crack width (based on localised reinforcement yielding) have been set. If they are exceeded, temporary interim strengthening measures have been designed and fabricated and are available to be installed rapidly. In accordance with the requirements of BD 79, strengthening of all the deficient regions is programmed within three years.

4 STRENGTHENING AND PROTECTION

To provide adequate reliability over the residual life of the structures, localised strengthening is required to the piers. It was essential to produce a cost-effective solution which would additionally have minimum impact on the travelling public during installation. The strengthening method additionally was developed to minimise any deterioration of the recently replaced expansion joints (thereby not inadvertently leading to greater water ingress of reinforcement corrosion).

The strengthening comprises installing, by drilling and fixing, new reinforcement both transversely and vertically to supplement load path 1, shown in Figure 5, at the ends of the cantilevers. The requirement not to damage the expansion joints or close the M4 during the works meant the vertical bars could not be anchored on the top of the crosshead. Therefore the vertical bars are resin anchored as high as feasible in the concrete section and additional longitudinal reinforcement installed where the vertical bars are fully anchored. This combination of additional reinforcement provides a truss system to transfer the bearing loads at the ends of the cantilevers to the sections of greater reinforcement. To minimise disruption to the traffic on the A4 below, all works were undertaken during nighttime.

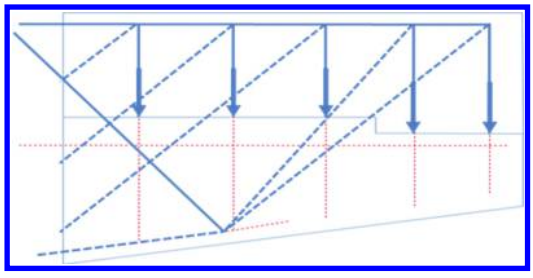

Figure 5. Strut and tie analysis load path 1.

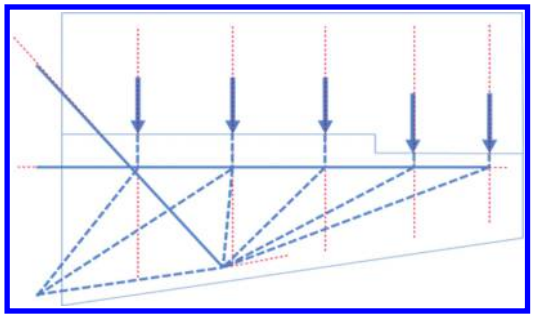

Figure 6. Strut and tie analysis load path 2.

As the crosshead concrete is contaminated with high levels of chlorides the maintenance strategy needed to take future corrosion of reinforcement in to consideration. To address chloride induced corrosion, stainless steel reinforcement has been specified which has enhanced protection for high chloride environments. Additionally, resin grout has been specified both to take advantage of its greater bond strengths and its chemical isolating properties. Fully grouting the additional reinforcement will minimise the risk of chloride attack and the stainless steel will further mitigate the extent of future deterioration.

A key issue in the strengthening installation was the drilling of holes for new reinforcement insertion without damaging the existing reinforcement. This led to the need for both a prescriptive drilling protocol, requiring core holes to be abandoned and relocated in some situations, together with the addition of temporary external longitudinal pre-stress applied by pre-stressing bars anchored to a steel frame at each end of the crosshead. This pre-stressing force supplemented load path 2 shown in Figure 6 (by increasing the resistance of the horizontal tie member) and thus provided mitigation against damaging the sparse existing vertical reinforcement during drilling. The layout of core holes was carefully designed to minimise the potential for hitting reinforcement and 3D modeling proved helpful in this regard as discussed in section 6.

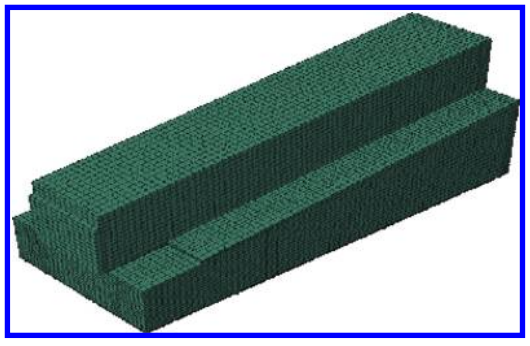

Figure 7. Non-linear finite element crosshead modelling.

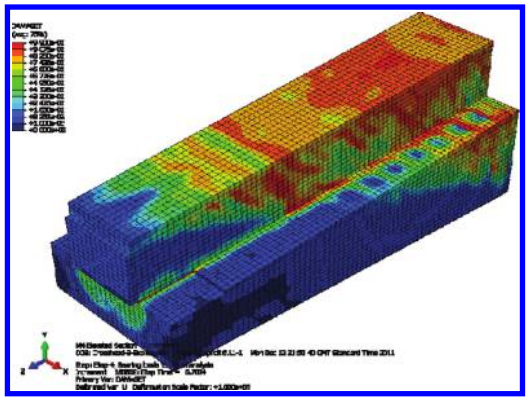

Figure 8. Non-linear finite element crosshead analysis.

5 CORROSION PROTECTION

A key consideration in the maintenance strategy was the link between the assessed capacity of the structure and the forecast deterioration due to chlorides. As such, a choice had to be made whether to carry out significant concrete repairs, potentially several times during the contract period to meet the handback requirements discussed in Section 1.2, and beyond, or to resume the installations of cathodic protection and arrest deterioration. Installation of cathodic protection was evaluated as the optimum cost solution, arresting structural deterioration from corrosion and also localised spalling of concrete.

An impressed current protection system has been designed to deliver protection to the reinforcement locations identified as at risk of corrosion and was trialed first at crosshead 82. This comprises discrete anodes installed below the bearing shelves to provide protection to the vertical and transverse bars. This location is particularly at risk of corrosion resulting from water ingress through the cracks propagating from the re-entrant corners. Additionally discrete anodes have been designed to

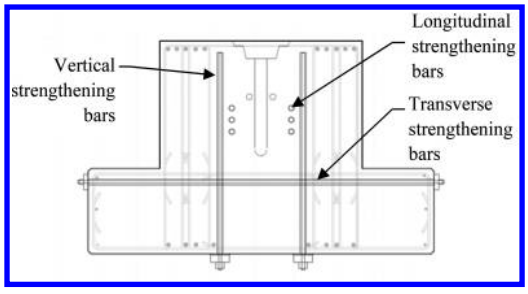

Figure 9. Strengthening reinforcement to be installed within the crosshead cantilevers.

Figure 10. Laser scan image of the M4 Elevated Section.

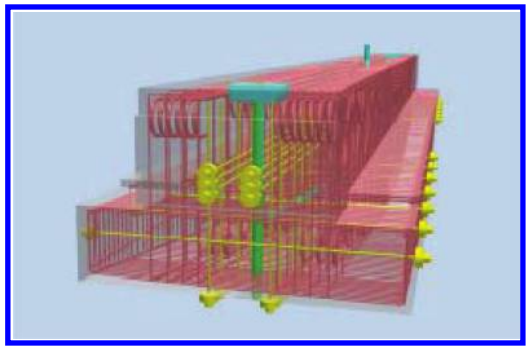

Figure 11. Image of crosshead showing existing and strengthening reinforcement.

be installed in longitudinal cores located at the top of the crossheads to deliver protection to the main flexural reinforcement. These cores are undertaken from both ends of the crosshead and discrete anodes secured with cementitious grout. Finally a cathodic protection ribbon system is specified to the accessible faces of the crossheads. The ribbon system is installed in chases cut in to the concrete, removing the requirement for a spray applied cementitious overlay and maximising future durability. While the stainless steel strengthening bars do not explicitly need protection against chloride induced corrosion, these bars are made electrically continuous with the rest of reinforcement and connected to the negative side of the cathodic protection system to prevent stray current induced corrosion.

Cathodic protection is combined with removal and repair of delaminating concrete. Areas of delaminated or spalled concrete are first removed and concrete repair material 'tied' in to the existing reinforcement cage. Incorporating combined repair and cathodic protection removes the need to remove chloride impregnated concrete, minimising the break-out and repair extents. The anticipated design life of concrete repairs only (without cathodic protection) is considered to be short (approximately 5–10 years) at which time further repair works would become necessary.

Measures to address water ingress through the expansion joints are also being developed to mitigate the exposure of the crossheads to chloride contaminated water. This includes re-waterproofing the central reserve service trough and implementing drainage improvements to capture water before it reaches the expansion joints.

6 BUILDING INFORMATION MODELLING

Building Information Modelling (BIM) was used during the interim planning and strengthening design phases and continues to be used for ongoing asset management of the crossheads.

The geometry of all the crossheads and the surrounding carriageway below the viaducts was laser scanned and a 3D model created from the point cloud data. This provided valuable measurements of the as-built structure to cross-check against the record drawings. It also allowed standby contingency emergency temporary propping systems (for use in the event that monitoring trigger levels were exceeded) to be visualised and developed such that their founding locations on the A4 carriageway below had the minimum impact on traffic flows and safety.

At the detailed design phase for the strengthening, as-built reinforcement was incorporated into the 3D models. This model was then used to route virtual core holes for the new reinforcement and cathodic protection anodes through the crosshead in locations to minimise clashes with existing reinforcement.

The BIM model also contains numerical and visual attached data relevant to the ongoing asset management of the viaducts. Each crosshead is split into smaller uniquely referenced surfaces to which condition data is attached including:

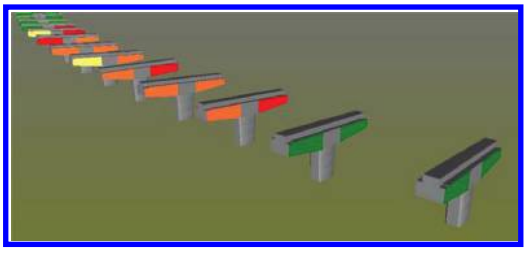

Figure 12. BIM environment showing variation in chloride levels.

- chloride levels
- half cell readings
- strength utilisation
- estimated reinforcement section loss
- crack widths
- presence of spalling and exposed reinforcement

The data can be viewed numerically or by colour scale in Navisworks (see Figure 12) and an embedded deterioration model in the source data allows predictions of this condition data to be viewed with time.

The crosshead as a whole has further attached data which can similarly be viewed including:

- contractual Condition PI score
- maintenance prioritisation score
- proposed maintenance plan and intervention date
- inspection reports and defect diagrams
- as-built information

Aspirationally, the model will be developed to include full details in 3D of all existing and new reinforcement together with details of the cathodic protection systems. Additionally all defects will be added directly to the model so they can be viewed live rather than through attached

7 CONCLUSION

Water ingress through the M4 elevated section deck joints has resulted in very high levels of chloride impregnation with an associated high risk of reinforcement corrosion actively occurring.

The original scope of the maintenance strategy was to predict a future time to intervention, bringing together structural capacity and corrosion modeling. A management strategy in accordance with BD 79 has been instigated, which has considered further analysis including strut and tie and non-linear concrete modeling to understand to extents of this deficiency and the anticipated consequences of not intervening. Plastic analysis incorporating the post-yield behavior of the reinforcement and transverse contribution of the decks was used to justify continued trafficking of the structure together with rigorous monitoring to identify structural deterioration early. However, strengthening is required to maintain long-term performance.

A comprehensive prioritisation process has been developed, including deterioration modelling, to formulate a programme both for the short term strengthening and longer term intervention requirements for these substructures. Concrete rehabilitation methods have been evaluated and a programme of cathodic protection combined with concrete repairs has been developed on a risk basis to meet the handback requirements discussed in Section 1.2.

A BIM model was developed to assist a standby emergency propping and strengthening design and to provide a visual representation of the maintenance strategy, allowing the user to see how the substructures deteriorate over time and when intervention is required. Additionally the BIM model provides an interactive and intuitive record system.

REFERENCES

ACI 222R-01. 2001. Protection of Metals in Concrete Against Corrosion, American Concrete Institute, Farmington Hills, MI, USA.

BRE Digest 444–2, 2009. Corrosion of steel in concrete.

CET. 2012. M4 Elevated Crossheads Visual Monitoring Results—October 2012.

Clear K.C. 1976. Time-to-Corrosion of Reinforcing Steel in Concrete Slabs, Federal Highway Administration, PB 258 446, Vol. 3.

Concrete Society TR54. 2000. Diagnosis of deterioration in concrete structures—identification of defects, evaluation and development of remedial actions.

Concrete Society TR 61. 2004. Enhancing reinforced concrete durability

Highways Agency. 2006. BD79/06: Design Manual for Roads and Bridges Volume 3: Section 4: Part 18. The Management of Sub-Standard Structures.

Hillerborg, A., M. Modeer, & P. E. Petersson. 1976. "Analysis of Crack Formation and Crack Growth in Concrete by Means of Fracture Mechanics and Finite Elements," Cement and Concrete Research, vol. 6, pp. 773–782.

Lee, J., & G. L. Fenves. 1998. "Plastic-Damage Model for Cyclic Loading of Concrete Structures," Journal of Engineering Mechanics, vol. 124, no.8, pp. 892–900.

Lubliner, J., J. Oliver, S. Oller, & E. Oñat. 1989. "A Plastic-Damage Model for Concrete," International Journal of Solids and Structures, vol. 25, pp. 299–329.

Nokken, M., Boddy, A., Hooton, R.D., & Thomas, M.D. 2006. Time dependent diffusion in concrete—three laboratory studies, Cement and Concrete Research, Vol. 36, pp. 200–207

Yong Ann, K.. & Song, H. 2007. Chloride threshold level for corrosion of steel in concrete, Corrosion Science vol. 49, pp. 4113–4133.

Concrete Repair, Rehabilitation and Retrofitting IV – Dehn et al. (Eds)
© 2016 Taylor & Francis Group, London, ISBN 978-1-138-02843-2

Modern technique and concrete technology used to conserve a unique marine heritage breakwater

S. Hold
Civil & Structural Engineering C. Eng.

ABSTRACT: The channel island of Jersey has one major commercial port which is not only vital for the island's daily supplies but also the main port of entry for the important tourist trade. All of St Helier Harbour is protected from the south-westerly prevailing wind and waves by the Hermitage Breakwater started in 1874.

The damage to the surface protection of the precast blocks and joints on this south-west facing section of the wall of the pre-1887 construction was seen to have significantly deteriorated after the Feb/March 2014 storms.

Using petrography from concrete core samples it was found that DEF (Delayed Ettringite Formation) was present which meant that the blocks, once they had sustained surface damage had a residual capacity when coming in to contact with sea water as the outer concrete was worn away had the ability to 'heal itself'.

1 THE HISTORY AND SIGNIFICANCE OF THE BREAKWATER

The breakwater from Elizabeth Castle to Hermitage Rock and then beyond out to the Plate Rock was a concept in the 1850s for the construction of a grand harbour in St. Helier, Jersey.

Previous large scale breakwaters in the Channel Islands and in particular Jersey, such as St. Catherine's, had utilised dressed quarried stone mass granite blocks for outer walls with a soft inner core of secondary material. The initial engineering design for Hermitage Breakwater entailed constructing blocks of concrete and aggregate in the same form and shape as the mass granite blocks and by using this method regular geometry and lower costs were achieved (Fig. 3).

The location of the breakwater and harbour proved to be in an extremely vulnerable part of the southern Jersey coast and the arm of the harbour from the La Collette rocks was abandoned early in construction (Figs. 1 and 4). The main sheltering arm from the Hermitage Rock out to the Plate Rock was started in 1856, utilising the external block wall and 'soft core' method but with successive cross walls forming cells. The manmade blocks of concrete were cast in pits in the ground to form the shape of mass granite blocks (Fig. 3).

The method proved very difficult out from Hermitage rock as the water level deepened and exposure to the south-west prevailing weather and swells increased (Fig. 4).

In 1876 the cross wall method was abandoned and a new design of solid blocks, referred to as 'slice block', was constructed and built end over end. This method produced a 'solid' wall formed from a tessellated interlocking block arrangement

Figure 1. Hermitage breakwater and St Helier harbour.

Figure 2. SW face of pre 1876 Hermitage breakwater.

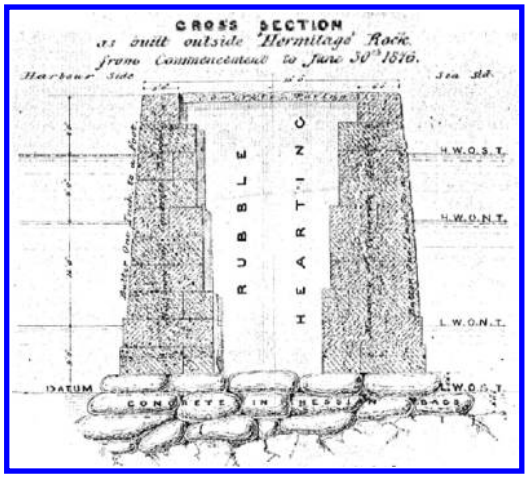

Figure 3. Original cross wall design 1850s.

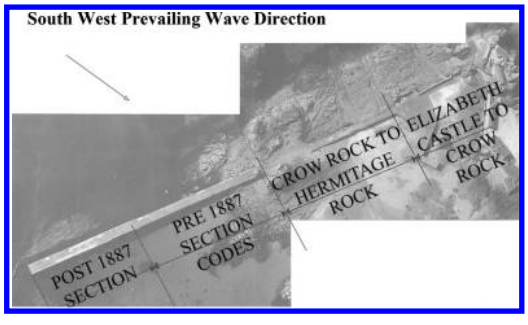

Figure 4. Elizabeth Castle, Hermitage rock and the pre 1876 and post 1876 length of breakwater.

Figure 5. A construction record of the slice block method.

with granite outer facing blocks for durability (Fig. 5).

However, even using this new, solid and more robust construction method, it was still not possible to complete the full breakwater out to Plate Rock and the project was abandoned in 1880.

The significance of the Hermitage breakwater in the modern era is that it provides essential shelter to the whole of the modern current St. Helier Harbour complex and has stood the test of time,

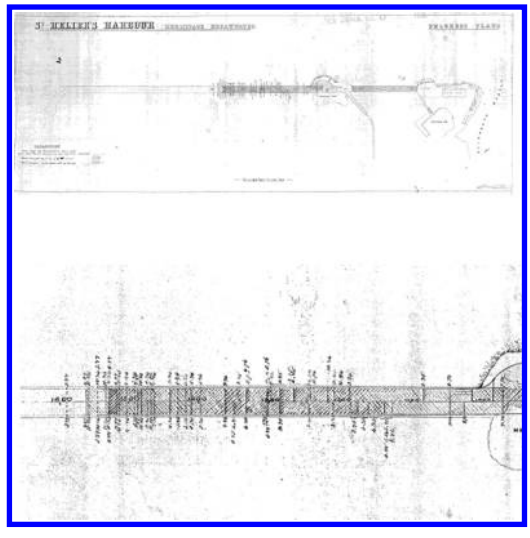

Figure 6. Site progress drawing from 1876 showing halted method.

reducing swells and wave impacts from the south-west.

2 ARCHIVE CONSTRUCTION INFORMATION

Research was undertaken in 2005 to locate historical information revealed the methods described in the previous paragraphs. Such sources were the Maritime Museum, Société Jersiaise and other historical archives. Interestingly, also discovered were the progress notes and drawings from during construction which show a dramatic slowing up of the pre- 1876 cross wall method as progress gets further away from Hermitage rocks (Fig. 6) shows the process becoming slower and slower and it was then understandable that regularised progress is made using the different solid tessellated 'slice block' arrangement.

It is not exactly known, or recorded, why this new method was halted some 200 m from Plate Rock but the inference is that once again conditions in this location proved far too aggressive for even the new construction method.

3 HEALTH CHECK SURVEY

The Transport & Technical Services Department (T&TS) in Jersey required in 2005 that a 'health check' to be carried out upon Hermitage Breakwater. This was to be undertaken at low tide/high tide to record the current conditions at that time. T&TS had over many years been carrying out

Figure 7. Surface loss 2005.

'a little maintenance often' and the 2005 survey proved that this approach had enabled such an important, significant heritage structure to be well maintained with little, other than surface defects being identified (Fig. 7).

The 2005 survey was updated in 2013 and some further deterioration of the pre-1876 block surfaces and joints was observed (Fig. 8). These were noteworthy because wave energy impact on air pockets formed at the opening joints would produce large 'exploding' forces in the concrete around the opening of the joints that in turn would accelerate the deterioration. In 2014 an underwater survey found little or no deterioration below low water but it was observed that there are one or two loose or unused 'slice blocks' at the base end of the breakwater, which were preventing, or acting against, scour in this 11.5 tidal environment.

In 2013 a digital asset register was set up to record the current condition of the structure and in particular the deterioration of the blocks from Hermitage out to the post-1876 section (Figs. 9 and 10). The storms of February and March 2014 were of such a magnitude that they constituted a 'trigger event' and therefore the 2013/14 survey was updated in the specific area of most abrasion

Figure 8. Pockets at block joints from 2013 survey.

Figure 9. Survey report, LiDAR model of 2013.

damage in and around the south-west part of Hermitage Breakwater of the pre-1876section. This survey showed that the pockets that were identified in 2013 had indeed become larger and some new pockets were discovered using a drone survey. A more detailed investigation was then instructed in terms of obtaining intrusive data information of the condition and make up of the blocks and the core material behind them.

4 PRODUCTION OF THE DATA ASSET MANAGEMENT SYSTEM

The data monitoring system is basically a 'layered' information map of the structure recorded at a specific time. The structure itself is very large but by homing in on specific photographed areas, the

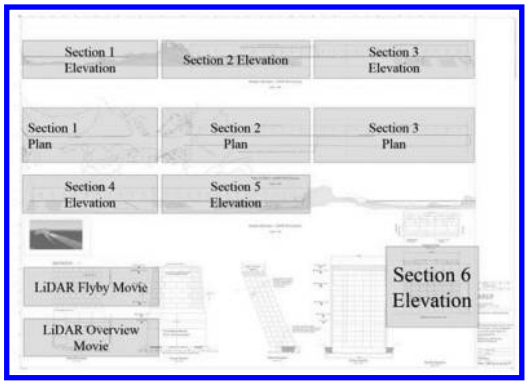

Figure 10. Digital asset form of monitoring the breakwater.

current condition can be 'benchmarked' so that in the future, either visually or by photographs or drones, the block can be assessed at any time to track deterioration. The call up of information includes a LiDAR flythrough virtual model and production of accurate geometry drawings from the LiDAR model that act as a benchmark for future monitoring.

5 FUTURE MONITORING USING LIDAR MODEL OVERLAYS

The principle of monitoring mass masonry heritage breakwaters in Jersey has been established; in particular for Gorey Pier. Here localised movements of areas of this irregular maritime heritage granite wall structure was assessed after 'trigger events'. The original LiDAR model from 2009 had superimposed another LiDAR model of 2011 and discrepancies of areas of movement were identified as well as their magnitude (Fig. 11). Just as importantly, areas that had not moved during the trigger event were also identified thus allowing to focus to repair elements on areas that had been identified as susceptible. In this way, the LiDAR monitoring model set up for Hermitage Breakwater in 2014 forms the benchmark for similar future monitoring of the breakwater geometry and the digital asset photographs the rates of specific areas of deterioration of this breakwater.

6 THE TRIGGER EVENTS IN MARCH 2014

This specifically identified that more joints had lost material at the junction between perpendicular and horizontal bed joints of the precast concrete large aggregate blocks forming outer walls. The surface 'crust' of concrete in many areas had

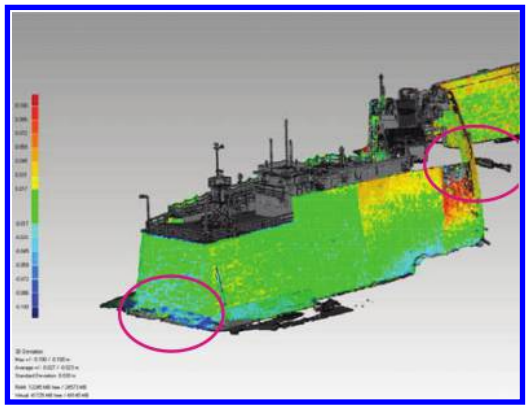

Figure 11. Gorey Pier LiDAR models superimposed showing movements.

Figure 12. Loss of surface and other pockets at joints.

also been abraded away exposing the large aggregate and cement matrix (Fig. 12). More worryingly, the detailed study from the LiDAR model and the drone survey indicated that some areas not identified in previous monitoring in 2005 and 2013 had formed. The newly identified openings had become enlarged in areas beyond normal visual data gathering range but were observable from the drone survey.

7 THE DESIGN CONCEPTS FOR PROTECTION OVERLAY

Similar heritage structures forming Jersey coast defences had been given a reinforced concrete overlay protection. At St. Ouen's sea wall for example an abrasion resistant 5 km length of armour reinforced concrete had been overlaid on the WWII concrete defence wall. This provides protection

Figure 13. St. Ouen's sea wall Atlantic waves impact from S.W.

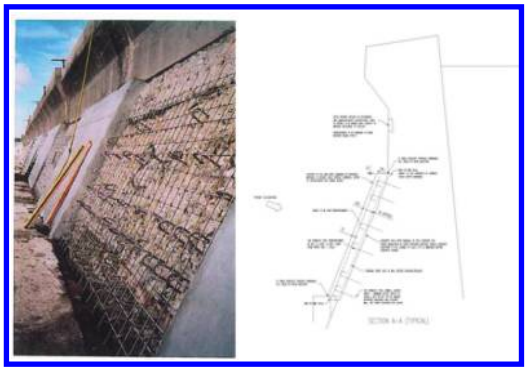

Figure 14. St. Ouen's sea wall overlay.

against the aggressive Atlantic environment and the gravel and rocks on the beach causing the abrasion (Figs. 13 and 14).

Another similar overlay protection was used in Jersey at the foundations of the St. Helier Marina where the same blocks originally produced for Hermitage Breakwater pre-1876, which had not been used, were then used to provide the foundations for the North Quay (Fig. 15). It is assumed that these are the blocks that were not used for the Hermitage Breakwater i.e. they were left over and redundant when the method was abandoned and were then used for the foundations of the North Quay but here were less susceptible to deterioration in the benign marina environment. However, in 2013 it was necessary to overlay the loose and degrading concrete blocks at the base of the North Quay which had had a layer of spray concrete applied previously that was also delaminating. A similar concrete overlay protection was applied to this marina foundation area and the formwork was indented to give the appearance of blocks for aesthetic reasons (Fig. 15).

Therefore, the project for protecting the vulnerable area of the south-westerly hermitage breakwater

Figure 15. Concrete overlay on marina block foundation left over from the Hermitage construction.

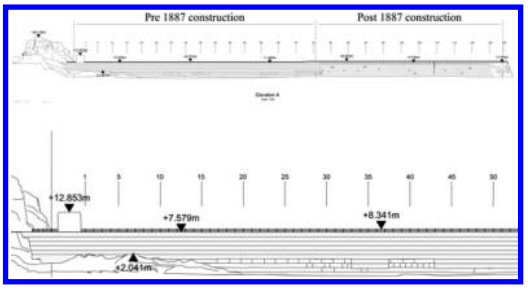

Figure 16. Extent of overlay envisaged.

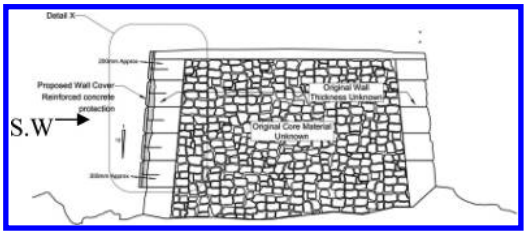

Figure 17. Overlay concept at Hermitage Pre 1876 blocks.

with a similar overlay concept was developed (Figs. 16 and 17). This was discussed with Heritage consultants and Planners who felt that it would be necessary for such a Heritage Monument to have the concrete overlay protection of the same colour and visual effect as the concrete and aggregates of the original breakwater construction.

To achieve this it was then necessary to obtain samples of the Hermitage concrete facing blocks. It was also necessary to determine the actual thickness and constituent materials together with the strength of these blocks and from cores. Only archive drawings were available from the construction era (Fig. 3) so it was not clear if the soft core material inside the crosswalls had deteriorated or had been washed out.

Figure 18. Scale and length of core 1: note size of aggregate.

Figure 19. Scale and length of core 2: note size of aggregate.

8 THE SITE INVESTIGATION AND TAKING CORES

Two horizontal concrete cores were taken in the area to be overlaid to identify the mix, type of aggregate and the reasons for the deterioration of the concrete blocks surface (Figs. 18 and 19).

It was discovered using petrography at incremental depths (Fig. 20) from the cores that as the depth of section progressed, Delayed Ettringite Formation (DEF) in the cement matrix had occurred in and around the large aggregate. This means that parts of the cement matrix within the body of the blocks had not hydrated or reacted to form concrete. This was possibly due to no contact, or limited contact, with water during the original casting process by hand but the implications were that if successive layers of cement matrix are being degraded by abrasion and salt attack from the sea then the Delayed Ettringite Formation (DEF) will

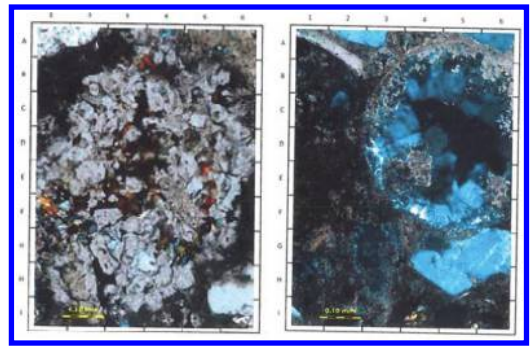

Figure 20. Petrographic slides used to determine concrete constituents at different depths.

then take place once the new layer comes in contact with the sea water. Therefore in this context, there is a kind of 'self-healing' mechanism available to the overall thickness of the blocks. Small pilot hole drilling was also carried out to determine the thickness of the blocks and the depth down to the soft core from deck level. These investigations showed that there had been no core loss due to 'wash out' (where core material is washed out through open joints) and the core fill was sand and rock fragments mixed.

9 PROTECTION SOLUTION SCALED DOWN

There then became a reduced need for the concrete overlay to protect against a breach in a storm and rapid loss of loose core fill from within the cells. However, the pockets or voids at joints still were providing air entrapment possibilities and explosive forces under wave pressures still needed to be dealt with. Therefore, as an alternative to the full scale concrete overlay concepts (Fig. 16 and 17), a design to repair the damaged pockets was produced (Figs. 21, 22 and 23). This smaller scale maintenance work could be constructed using T&TS direct labour from cradle access. In this way, significant savings were made for the long term maintenance of the structure.

10 FUTURE MONITORING

The Breakwater, as can be seen in the photographs (Figs. 1 and 2), has protected the harbour of St. Helier for over 120 years. It has suffered a few abrasions and impact damage in that period but remains a robust marine breakwater. However, the advent of sea-level rise inevitably means that in the not too distant future significant storm waves are

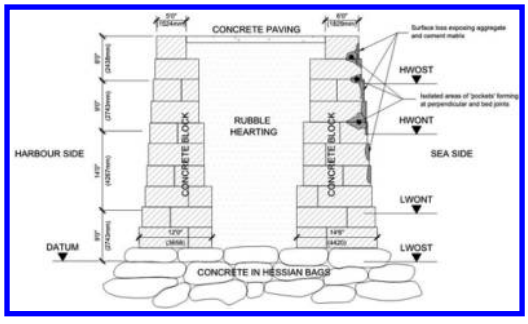

Figure 21. Existing damage.

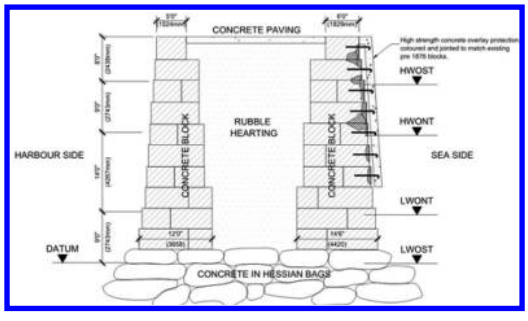

Figure 22. Overlay solution.

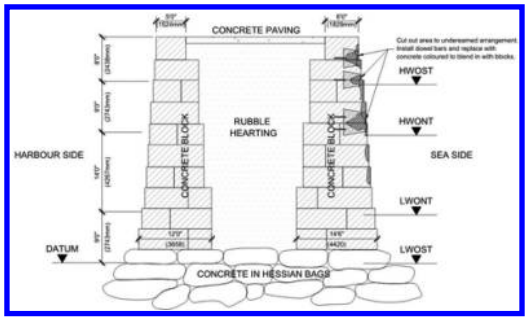

Figure 23. Repair pocket only solution.

likely to pass directly over the Breakwater and thus threaten St. Helier Harbour itself (Fig. 24). The monitoring set up in 2014 will be a benchmark for future data gathering in order to determine when major intervention will be necessary to both protect and raise this magnificent Heritage marine engineering structure.

Figure 24. Hermitage breakwater in background under water in 2008.

ACKNOWLEDGEMENTS

With thanks to the States of Jersey Transport and Technical Services engineers Kevin Armstrong, Mick Johnson and Jamie Mason.

REFERENCES

Goda.Y Ed. World Scientific. Random seas and design of maritime structures, advanced series on ocean engineering—Volume 15.

Dr, Muller G, Wolters. G. ICE Proceedings Coastlines, Structure and Breakwaters 2005. *Failure Mechanism for Blockwork Breakwaters*.

Overtopping Manual—http://www.overtopping-manual.com/calculation-tool.html

Muller G., Alsop W., Bruce T. Kartenhaus, A., Pearce A. and Sutherland J. (2007) *The occurrence and effect of wave impacts*, Proc I.C.E., Maritime Engineering 160pp 167–173, Thomas Telford.

Hold S., (2009) Repair of St. Catherine's Breakwater Roundhead. ICE 2009 Proceedings.

Maritime Museum

Sociéte Jersiaise

Concrete Repair, Rehabilitation and Retrofitting IV – Dehn et al. (Eds)
© 2016 Taylor & Francis Group, London, ISBN 978-1-138-02843-2

Some conclusions of durability and behavior of structural rehabilitation solutions applied to deteriorated reinforced concrete elements after ten years of intervention

G. Croitoru
Telekom RMC, Bucharest, Romania

A. Popaescu
Transilvania University Brasov, Romania

ABSTRACT: This case study analyzed the durability and the behavior in service in difficult conditions of reinforced concrete structural elements rehabilitated 10 years ago.

This structure ("Turbines Hall") is part of a great objective with function of electric and thermal power plant. Structure construction (columns, beams and reinforced concrete floors) started in 1967 and is currently in operation.

The service conditions are difficult: local there are recesses of technological steam and major values of humidity maintains the evolution of the corrosion of reinforcement.

Causes leading to the need for structural rehabilitation in 2004 were: deterioration from durability, faulty from execution and deterioration from operating in service.

The main solutions for structural rehabilitation were: strengthening with reinforced concrete, strengthening with laminated profiles and repairs with special mortars.

This study aims to analyze in the terms of the durability the behavior of reinforced concrete structural elements rehabilitated in the three main solutions.

1 INTRODUCTION

1.1 *General information on the structure*

Structure analyzed is "Turbines Hall" and is part of a great objective with function of electric and thermal power stations.

This great industrial objective is one of the first important investments in the sector of electric and thermal power stations, built in Romania since 1960 years.

For structure "Turbines Hall" construction started in 1967 and is currently in operation (almost 50 years in service).

This structure is type industrial hall.

Dimensions of the building are significant: transversal 39.00 m and longitudinal 135.00 m.

In general, structural elements were designed to support very heavy loads of technological equipments.

Local inside building are placed technological equipments which produce vibrations within the structural elements.

1.2 *Information on specific operating and service*

In time, the service conditions were generally difficult: local there are recesses of technological hot steam, water leakage from technological pipes and major values of humidity in some areas of the building maintains the evolution of the corrosion of reinforcement.

It is very important to mention the inefficiency of ventilation system inside "Turbines Hall" during service.

2 TYPES OF DETERIORATIONS

2.1 *Presentations*

The main types of deterioration in reinforced concrete structural elements of "Turbines Hall" construction was observed (in 2004 year):

- deterioration from durability;
- faulty from execution and deterioration from operating, in service.

2.2 *Deterioration from durability*

Deterioration from durability were manifested as follows:

- intense corrosion of reinforcement until detachment of corrosion products led to complete disintegration;

Figure 1. Deterioration from durability at reinforced concrete floors. Maximum level of deterioration led to the disintegration of reinforcement.

Figure 2. Deterioration from durability at beams. Maximum level of deterioration led to the disintegration of reinforcement.

– cracks and dislocations of concrete cover due to corrosion of reinforcement.

At reinforced concrete floors the maximum level of deterioration led to complete disintegration of reinforcement and dislocations of concrete cover due to corrosion of reinforcement on the large surfaces (see Figure 1).

At beams the maximum level of deterioration led to complete disintegration of reinforcement (longitudinal and stirrups) and dislocations of concrete cover due to corrosion of reinforcement (see Figure 2).

At columns the maximum level of deterioration led to intense corrosion of reinforcement (longitudinal and stirrups) and local dislocations of concrete cover due to corrosion of reinforcement.

2.3 *Faulty from execution and deterioration from operating in service*

Faulty from execution and deterioration from operating (in service) are much lower as compared with deterioration from durability but their number is nevertheless significantly.

Faulty from execution and deterioration from operating (in service) were manifested as follows:

– segregation of concrete in especially at columns;
– interventions on horizontal structural elements (especially at beams and reinforced concrete floors in some areas of the building).

3 ANALYSIS DESIGN

3.1 *General conclusions*

Following the verifications through calculation of structure result conclusions:

– for both types of frames (transversal and longitudinal) in terms of the initial dimensioning of the reinforced concrete elements and the loads taken into account, their load capacity is adequate;
– only if a reduction of approximately 45–50% of the section reinforcement beams and floors in stretched area (due to corrosion) their bearing capacity was insufficient;
– in cases where the degradation of reinforcement due to corrosion reached 50% of the initial section, was necessary to strengthen affected element.

4 STRUCTURAL REHABILITATIONS

4.1 *Main level of deteriorations in structural elements*

Maximum level:

– reduction over 50% of the section reinforcement led to complete disintegration because intense corrosion of reinforcement;
– dislocations of concrete cover due to corrosion of reinforcement on the large surfaces of the elements.

Major level:

– reduction 25–50% of the section reinforcement due to partial disintegration because intense corrosion of reinforcement;
– dislocations of concrete cover due to corrosion of reinforcement on the large surfaces of the elements.

Medium level:

– reduction under 25% of the section reinforcement due to minimal disintegration because corrosion of reinforcement;
– starting dislocations of concrete cover due to corrosion of reinforcement on the local surfaces of the elements.

Minimal level:

– starting corrosion of reinforcement;
– cracks and starting dislocations of concrete cover on the local extent.

4.2 *Types of solutions for structural rehabilitation*

The main types of solutions for structural rehabilitation (in 2004 year) are presented as follows.

In Maximum level of deteriorations (usual case):

– strengthening with reinforced concrete, see Figure 6;

In Maximum level of deteriorations (in zone with heavy loads of technological equipments):

– strengthening with laminated profiles add reinforced concrete;

In Major level of deteriorations case:

– partial strengthening with reinforced concrete, see Figure 8;

In Medium level of deteriorations case:

– partial strengthening with reinforced concrete or repairs with special mortars (e.g. epoxy type)

In Minimal level of deteriorations case (concrete cover):

– repairs with special mortars (e.g. epoxy type), see Figure 4;

4.3 *Additional measures*

Complementary of solutions for structural rehabilitation have adopted the following technological measures:

– improving the ventilation system into the entire building;
– eliminate water leakage from technological pipes;
– eliminate the emission of technological hot steam;
– eliminate major values of humidity inside "Turbines Hall".

5 ANALYSIS OF DURABILITY IN SERVICE OF STRUCTURAL REHABILITATIONS

5.1 *Specific of service*

In time (2004–2014 years), additional measures complementary of solutions for structural rehabilitation (see 4.3 Chapter) were not efficient.

In these conditions, in some areas of the building, the service conditions were generally difficult.

5.2 *Analysis of structural rehabilitation solutions in good conditions in service case*

For "Turbines Hall" good conditions in service are characterized by:

– a good ventilation system of the building;
– complete elimination of water leakage from technological pipes;
– complete elimination the emission of technological hot steam;
– maintaining within normal limits for humidity values.

Following analysis of behavior in service of structural rehabilitation solutions in good conditions in service case (2004–2014), result conclusions:

– new deteriorations from durability have been not observed;

Figure 3. Medium level of deterioration at reinforced concrete floors. It's necessary repairs with special mortars (2004).

Figure 4. Repairs reinforced concrete floors with special mortars. Good conditions in service case (2004–2014).

Figure 5. Major level of deterioration at beams. It's necessary strengthening with reinforced concrete (2004).

Figure 6. Strengthening beams with reinforced concrete. Good conditions in service case (2004–2014).

– behavior in service was in generally good, in according to the expectations (see Figure 4 and Figure 6);

5.3 *Analysis of structural rehabilitation solutions in bad conditions in service case*

Generally, inside the building, the service conditions were difficult.

For "Turbines Hall" bad conditions in service are characterized by:

– inefficiency ventilation system of the building;
– water leakage from technological pipes;
– the emission of technological hot steam in some areas;
– major values of humidity inside the building for long periods of time.

Following analysis of behavior in service of structural rehabilitation solutions in bad conditions in service case (2004–2014), result conclusions:

Figure 7. Strengthening beams with reinforced concrete. Bad conditions in service case (2004–2014): restarting the corrosion of reinforcement and new cracks in strengthening beams.

Figure 8. Strengthening beams with reinforced concrete. Bad conditions in service case (2004–2014): new cracks in strengthening beams.

– new deteriorations from durability have been observed:
– behavior in service was not good contrary to expectations (see Figure 7 and Figure 8);

Causes of this situation are the following:

– in some areas of the building the service conditions were continued to occur;
– the emission of technological hot steam, water leakage from technological pipes and major values of humidity have contributed to restarting and maintains the evolution of the corrosion of reinforcement.

The result of this new process are the following:

– there are cases in which the restarting of the corrosion of reinforcement led to the emergence of new cracks in consolidation beams (local situation), see Figure 7 and Figure 8.

6 CONCLUSIONS

The result of analysis of durability and behavior in service of structural rehabilitation solutions applied to reinforced concrete elements in difficult conditions for use are the following:

- for structure "Turbines Hall" construction started in 1967 year;
- this structure is currently in operation (almost 50 years in service);
- in time, the service conditions were generally very difficult (mainly major values of humidity inside the building);
- the main types of deterioration in reinforced concrete structural elements of "Turbines Hall" construction was: deterioration from durability (Major) and faulty from execution and deterioration from operating, in service;
- major contribution to deterioration from durability was confirmed by the conclusions of the technical expertise;
- the main solutions for structural rehabilitation (in 2004 year) were: strenghtening with reinforced concrete, strenghtening with laminated profiles and repairs with special mortars (e.g. epoxy type);
- even though have been used high quality materials for structural rehabilitation elements, conditions in service has led in many cases to restarting of the corrosion of reinforcement;
- there are situations where restarting of the corrosion of reinforcement led to the emergence of new cracks in strengthened beams;
- analysis of durability of structural rehabilitation solutions applied to reinforced concrete elements for 10 years in service (2004–2014) concludes that ensuring of good conditions in service is very important even for strengthened structural elements.

REFERENCES

CEB Bulletin Nr. 183 (1989)—Durable Concrete Structures. Design Guide.

CEB Bulletin No. 243 (1998)—Strategies for Testing and Assessment of Concrete Structures—Popaescu A. (co-author) Lausanne.

GM 018 (2003). Guide to investigate and diagnose of the reinforced concrete and steel structures placed in aggressive environments (in Romanian).

Popaescu, A. (2004). Technical expertise for reinforced concrete floor, columns and beams of the turbine hall of an electric and thermal power station.

Popaescu A. & Deaconu O. (2005). Rehabilitation of a grain concrete silo constructed by slip form method. The International Conference ICCRRR, Cape Town, South Africa, Taylor & Francis/Balkema, Leiden, The Netherland.

SR EN 1992-1-1 (2004). Eurocode 2. Design of concrete structures—Part 1-1: General rules and rules for buildings.

Concrete Repair, Rehabilitation and Retrofitting IV – Dehn et al. (Eds)
© 2016 Taylor & Francis Group, London, ISBN 978-1-138-02843-2

Case study for the repair of Berths 4 & 6 in Guernsey

John Drewett
Concrete Repairs Ltd., London, UK

Kevin Davies
CorroCiv Limited, Manchester, UK

Paul Segers
CH2M Hill, Birmingham, UK

ABSTRACT: Guernsey is one of the main Channel Islands situated off the coast of France and the Berths are an essential part of the Island's infrastructure. In 2008/9 a detailed condition assessment of the quay structures was commissioned by Guernsey Harbours for new loading conditions and to extend the service life of the assets. Detailed assessments of the reinforced concrete and metallic structures were undertaken and from the results a rehabilitation performance specification prepared for the repair works. The repairs to the two Berths included the design and installation of both impressed current and galvanic cathodic protection systems to enhance the durability of the structures in the severe marine environmental exposure. The contract is one of the largest marine repair and cathodic protection systems ever installed in Europe and is due to be completed in Spring 2015.

1 INTRODUCTION

Guernsey is one of the main Channel Islands situated off the coast of Normandy and has a population of 65,000. The marine berths are in the town of St Peter Port and are an essential part of the Island's infrastructure.

The port operators are Guernsey Harbours and in 2007 they commissioned a review of Berths 4, 5 & 6 which included a structural condition survey of the facilities and this was undertaken by CH2M HILL. Berth 5 is a granite quay which had a suspended concrete slab which has been replaced under another contract and berth 6 is a concrete encased steel structure within the quay walls, which were built circa 1860. Berth 4 is a reinforced concrete suspended deck supported on piles and was built in the 1970's over the existing granite dockyard.

The report recommended that the existing rail-mounted cranes be replaced with two modern mobile, wheeled, harbour cranes and that associated refurbishment and strengthening work to quay structures be carried out.

In 2008/09 the commission was extended to produce a detailed defect assessment specification and tender package which identified the methods and extent of the structural investigation and testing required. CRL Surveys Ltd were awarded the contract for the site investigation and testing which commenced in 2010, under the supervision of CH2M HILL. The findings of the site investigation confirmed the feasibility of a 50 year life extension and the original rehabilitation methodology proposed.

2 INVESTIGATION METHODOLOGY

The investigation methodology included preliminary structural checks to confirm that the original structural capacity would accommodate the dynamic loading associated with the new mobile cranes and the static loading associated with the new storage and stacking approach.

The detailed site investigation to evaluate, quantify and select an appropriate rehabilitation approach included:

2.1 *Reinforced concrete structure assessment*

2.1.1 *Primary assessment*

The primary assessment included 100% visual assessment, detailed structural measurements and hammer-rap surveys to all reinforced concrete structural elements.

The visual assess included the following specific investigations:

a. Any previously repaired areas;
b. Visible defects associated with deterioration (as in the classification system outlined above, as

Photograph 1 & 2. Showing the general arrangement of berth 4 consisting of reinforced concrete columns, beams and deck.

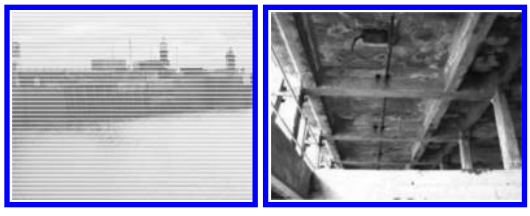

Photograph 3 & 4. Showing the general arrangement of berth 6 consisting of steel beams encased in concrete with a reinforce concrete deck.

Table 1. Example of initial damage classification.

Class	Condition
1	Clean sound concrete with no evidence of deterioration
2	Some corrosion staining and minor cracking etc. No significant spalling or hollowness
3	Large areas of heavy corrosion staining. Some minor cracking and spalling
4	Corrosion evident accompanied by cracking and spalling
5	Severe cracking and spalling, extensive areas of steel exposed

well as any construction related defects including but not limited to; cracking, honeycombing, and deteriorating construction joints);

c. Embedded metallic components other than reinforcement;
d. Presence of surface coatings.

The findings were recorded onto pre-approved defect record sheets as CAD drawings supplemented with high resolution photographic evidence. A damage classification assessment establishing a series of broad classifications as detailed in Table 1, was used to identify the extent and location of secondary detailed sampling and investigation requirements.

The initial assessment also provided an initial estimate of the extent of concrete repairs required to reinstate the elements and the CAD files were included into the rehabilitation tender package to assist the contractors with their pricing and tendering.

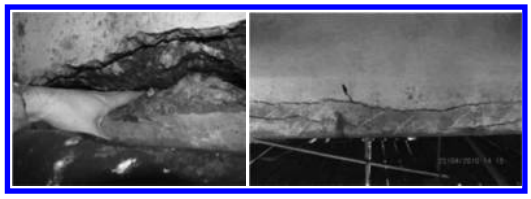

Photograph 5 & 6. Primary assessment showing deteriorated concrete to primary beams of berth 4.

2.1.2 *Secondary detailed sampling and investigation*

The locations for the secondary investigation were selected to represent a uniform distribution of test results across the structures and at specific locations identified by structural specialists.

The following secondary testing was implemented:

a. Electrical continuity survey to evaluate the feasibility of electrochemical repair options;
b. Half cell potential survey;
c. Exploratory concrete breakouts in all classes (Table 1) to assess the condition of the steel, including accurate assessment and measurement of the steel section loss;
d. Chloride ion content and depth profiling and carbonation testing drillings;
e. Concrete core samples;
f. Reinforcement steel sample extraction.

2.1.3 *Laboratory assessment*

Laboratory assessment of the collected samples included the following:

a. Concrete compressive strength assessment;
b. Petrographic evaluation of concrete from cores and cement content estimates;
c. Chemical and mechanical evaluation of reinforcement steel;
d. Weldability and carbon equivalent of the reinforcement steel.

2.1.4 *Data analysis and findings for reinforced concrete elements*

The test results were analysed to determine the appropriate rehabilitation and repair method, as summarised below.

2.1.4.1 Mechanical

The mechanical properties of the concrete and reinforcement as well as the bar diameter and spacing were used to confirm the original design and structural loading classification. The degree of

concrete deterioration and section loss were used to justify remedial action to ensure the original structural capacity was maintained.

Weldability of the reinforcement was determined and welding was selected for reinforcement replacement where section loss exceeded the maximum allowable threshold, to limit the extent of concrete repairs and concrete breakout.

2.1.4.2 Chemical

Chloride ion content and carbonation depth profiling identified that the main deterioration mechanism in the reinforced concrete was chloride induced corrosion of the reinforcement steel and that the chloride concentration at the steel exceeded the accepted threshold limits of 0.4 wt% chloride-to-cement in the majority of the test locations. This finding supported the use of electrochemical treatment as proposed originally.

A number of soffit areas were identified to be just below the chloride threshold which could enable alternative control measures to be used, such as barrier coatings. However, it was decided that a single uniform protection system, based on electrochemical treatment, was more attractive for the 50 year life extension requirement.

2.1.4.3 Compatibility with electrochemical treatment

The investigation did not identify significant levels of embedded tying wire in the cover zone that could adversely affect the electrochemical treatments. Existing concrete repairs would need to be removed as part of the rehabilitation process as their integrity could not be guaranteed and to ensure compatibility with the chosen electrochemical treatments.

2.2 *Metallic structure assessment*

2.2.1 *Primary assessment*

The primary assessment included the following:

a. 100% visual assessment above water;
b. 100% visual diver survey recorded on video;
c. Detailed structural measurements to all metallic structural elements;
d. The presence of any residual protective coatings;
e. If residual protective coatings were present, dry film coating thickness, adhesion and heavy metal contamination evaluation;
f. The presence and degree of section loss;
g. Residual metal thickness and pit depth measurement.

The findings were recorded on the defect record sheets and CAD drawings supplemented with high-resolution photographic and video evidence.

Photograph 7 & 8. Secondary assessment showing exploratory break out.

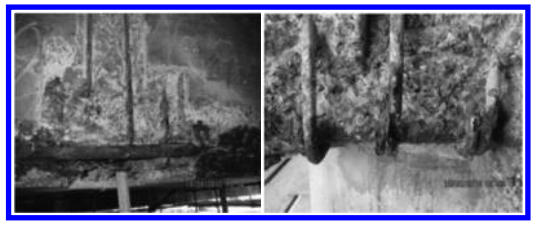

Photograph 9 & 10. Secondary break out showing reinforcement diameter, spacing and percentage section loss.

2.2.2 *Secondary assessment*

The secondary assessment included the following:

a. Microbiological sampling to assess the risk of Accelerated Low Water Corrosion (ALWC) and susceptibility to microbial assisted/induced corrosion;
b. Metal sample removal and laboratory assessment to identify the physical, mechanical and chemical properties of the steel as well as the weld ability by determination of the carbon equivalent and micro-structure;
c. Sea water resistivity at high and low water.

2.2.3 *Data analysis and findings for metallic elements*

The test results were analysed to determine the appropriate rehabilitation and repair method, as summarised below.

2.2.3.1 Mechanical

The mechanical properties of the metallic elements were used to confirm the original design and structural loading classification and confirm suitability for direct galvanic anode attachment. Weld ability of the metallic elements was confirmed, which enabled specification and development of welded plating repairs and direct welding of galvanic cathodic protection anode assemblies.

2.2.3.2 Chemical and Biological

No existing coatings were identified on any of the metallic components, coating of metallic areas above mean tide level was recommended.

Microbiological activity was confirmed, cathodic protection was recommended for protection of all

Photograph 11 & 12. Primary assessment of metallic components and wall thickness measurements.

areas below mean tide level and the cathodic protection criteria of –0.9V Ag/Ag seawater which is expected to prevent and control ALWC risk was specified.

3 THE REHABILITATION SPECIFICATION

In 2011 CH2M HILL were commissioned to prepare a detailed rehabilitation performance specification and associated tender package which was issued to four pre-qualified contractors in 2011/12.

The contract scope of works issued to tender was as follows:

a. Repair all cracked and spalling areas of concrete for berth 4 & 6
b. Design and install a combination of impressed current and galvanic cathodic protection for the reinforced concrete elements of berth 4 & 6 based on a minimum 25 year operational design life
c. Carry out welded plate repairs to steel fenders and sheet piling as required
d. Prepare and coat all exposed steel fenders and sheet piling above mean tide level
e. Replace fendering system
f. Design and install a galvanic cathodic protection system to protect all steel fenders and sheet piles.

The rehabilitation contract was awarded to Concrete Repairs Ltd (CRL) in 2012 with a scheduled start date on site in 2013 after approval of the cathodic protection design.

At tender stage CRL submitted a fully compliant bid in accordance with the performance specification and this was subsequently developed further in conjunction with CH2M HILL during the detailed design stage.

4 CONCRETE REPAIR DESIGN

There were significant areas of cracked and spalling concrete identified during the detailed investigation that required repair prior to the ICCP installation. Primarily these repairs were to the primary and secondary downstand beams.

In order to facilitate the repairs and avoid using temporary supports CRL undertook a structural analysis with an assumed construction loading of 1.5 KN/m². This confirmed that it was acceptable to break out and repair the concrete on alternate beams without propping, using a planned repair sequence which limited beam repairs to 2 m long sections.

The beam repairs were undertaken by using hydro-demolition techniques to remove defective areas of concrete and reinstating using a pre-bagged flowable high performance repair concrete compatible with the ICCP system. This repair approach was selected due to the high reinforcement density of the beams which prevented the use of sprayed concrete repairs.

Following concrete removal, localised welding repairs were carried out to the reinforcement at areas exceeding the allowable section loss tolerance. Electrical continuity of the reinforcement was also achieved on site by arc welding an 8mm reinforcement bar to the parent reinforcement.

The repair areas of the beams were shuttered and recast using a Putzmeister P13 to pump the repair material. The soffits which contained a much lower steel density than the beams, were repaired using a dry sprayed concrete mortar. In total some 80m³ of concrete repairs were undertaken.

5 CATHODIC PROTECTION DESIGN

CRL engaged Kevin Davies, CorroCiv, who is a Level 3 EN15257 Certified Senior Cathodic Protection Engineer, to undertake the CP design and manage the commissioning and monitoring of the installed systems. The system was designed in accordance with BS EN ISO 12696:2012, BS EN ISO 13174:2012 and the Works Information.

Acting on behalf of the Client, Paul Segers from CH2M HILL reviewed and commented on all cathodic protection designs and provided site audits during the installation and commission phases of the works.

There were 5 specific areas to be protected.

5.1 *Berth 4—RC components above + 2.00M OD (ICCP and GACP)*

This is the largest area of the cathodic protection systems extending to approximately 4,200 m², which was originally specified as 57 independent anode zones. CorroCiv optimised the zoning during the design with a final design detailing of 34 independent anode zones (extending to 140 m² each). The anode zones were split into a combination of

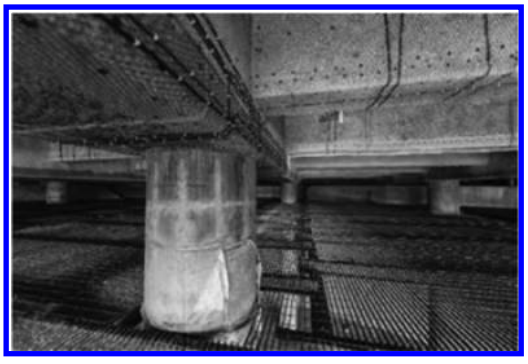

Photograph 13. Berth 4 mesh anode on beams and soffits and ribbon anodes in columns.

two primary beams and the interconnecting soffits and secondary beams between the primary beam members.

The selected anode system was a mixed metal oxide coated titanium mesh (MMO/Ti) fixed to the concrete surface and overlaid with a sprayed cementitious overlay nominally 20 mm thick.

As there is a movement joint on gridline 13 where the primary beam is actually a half joint the primary beam was protected using two anodes systems; the normal MMO/Ti mesh and the overlay and ~1 m long discrete anodes drilled into the sides of the beam. Discrete anodes were also utilised to protect the front edge of the berth in one short length where access was difficult. Inaccessible (for repair) areas along the landward side of berth 4 were protected using small discrete galvanic anodes in a concrete infill.

For the columns which were subject to tidal influence (MMO/Ti) discrete ribbon anodes installed into cut chases within the cover concrete were selected to aid installation and overcome tidal constraints.

5.2 *Berth 4—RC components below +2.00m OD (GACP)*

The reinforced concrete columns and existing crane foundations below +2.0mOD were protected using conventional seawater galvanic aluminium alloy anodes

A total of 3072 kg of aluminium anode was installed across 16 of the 39 columns and 684kg of aluminium anode was installed onto one of the two existing crane foundations to provide cathodic protection for the 25 year design life.

The anodes were fixed to individual columns using bracelet supports which were clamped to the columns at the lowest possible location below mean tide +0.24mOD. Localised electrical continuity connection to the reinforcement was achieved following concrete removal and arc welding a connection plate between the anode bracelet and the reinforcement. Electrical continuity between columns fitted with anodes and columns without anodes was achieved by the existing residual electrical continuity between elements, supplemented with dedicated electrical continuity bonding where required.

5.3 *Berth 4—Metallic fenders and Knuckle—sheet steel piling +0.24mOD (GACP)*

The existing fender and sheet steel piles were protected with a combination of conventional seawater galvanic aluminium alloy anodes which provided galvanic cathodic protection below mean tide level +0.24mOD and a high performance glass flake epoxy protective coating system for protection of tidal and atmospherically exposed areas above mean tide level.

A total of 3420 kg of aluminium anode was installed across the 16 fenders and a total of 2622 kg of aluminium anode was installed onto the sheet piles associated with the Knuckle to provide cathodic protection for the 25 year design life.

5.4 *Berth 6—RC deck slabs above +2.50m OD (ICCP)*

This area of the deck slab extended to approximately 320 m2 and was divided into 4 independent anode zones. The selected anode system was a mixed metal oxide coated titanium mesh fixed to the concrete surface and overlaid with a sprayed cementitious overlay 20 mm thick.

5.5 *Berth 6—Concrete encased steel I beams below +2.50m OD (GACP)*

A distributed standard aluminium anode system was used to protect the 8 concrete encased steel columns with a 25 year life expectancy. In total 12×50 kg anodes were required to provide adequate protection using bracelet supports similar to Berth 4.

5.6 *Cathodic protection monitoring system*

The installed CP systems are monitored using monitoring clusters consisting of one manganese manganese dioxide (Mn/MnO_2) reference electrode, one silver silver chloride 0.5M potassium chloride (Ag/AgCl 0.5M) reference electrode and one monitoring connection to the steel. Each monitoring cluster was connected to a 3 core monitoring

Photograph 14. Berth 4 Junction box and cable tray arrangement.

cable which was routed to the individual junction boxes and encapsulated within the sprayed concrete overlay.

The electrode clusters were pre-potted in CP grade repair mortar prior to installation to reduce the risk of poor electrical contact. The position of the clusters was determined by undertaking half-cell potential surveys of the reinforced concrete to identify the most anodic areas in each zone. The clusters were embedded in the concrete and wired back to the junction boxes with sufficient redundancy so that the monitoring system remains effective for the service life.

5.7 *Cabling and cable management*

In order to install the ICCP system in phases, to enable continued port operations the ICCP design included below berth junction boxes, so that the ICCP components could be installed and terminated according to the phased program. All the cabling back to the junction boxes was embedded within the concrete or anode overlay. All cable connections were made within the junctions boxes, which were special IP68 rated for submersion in water to a depth of one metre. From the junction boxes shipping multicore cables run on 316L stainless steel cable tray, mounted under the berth, back to the electrical switching station where they are connected to the centralised power and control system.

The DC positive feeders to the uncoated titanium conductor bars feeding the MMO/Ti mesh run in ring circuits from the junction boxes. For testing purposes the anode system is split at gridline 'd' so there are in effect two half zones making up a single ICCP anode zone.

The DC negative connectors are made off site and required only welding of the connector to the exposed steel with sufficient redundancy to ensure durability. The DC positive feeder connectors were made on-site within a portable workshop requiring only titanium to titanium spot welding beneath deck.

Photograph 15. Transformer rectifier with 5 power zones.

5.8 *Power and control units*

With 34 impressed current anode zones and 372 reference electrode inputs this is a large and quite complex ICCP installation which required a high performance power and control unit.

CRL selected Rectifier Technologies to manufacture and supply the control equipment. To reduce the size of the cabinets the ICCP system was divided into 7 power cabinets and a single control cabinet. The modular CP rectifier uses switch mode technology which ensured the DC power output units were small and highly efficient. The reference cells were buffered by differential multiplexers with high impedance (>100MΩ) and inherent surge protection. Six power cabinets and the control unit were installed in the electrical switch room and the seventh, at berth 6, was linked with a fibre optic cable to the control cabinet.

Photograph 16 & 17. Quality control and pre commissioning checks.

Photograph 18 & 19. Steel coatings and new fenders.

6 THE SITE WORKS

With the ICCP design agreed the work on site commenced in March 2013 with a 104 week contract programme for completion in early 2015.

The berth has a 10 m (30′) tidal range and as an island in the English Channel closer to France than England there were significant logistical challenges to complete such a large marine repair contract.

Normally fixed scaffold access platforms would be used provide a safe working environment but for such a long contract period in a remote marine location CRL decided to use a semi-permanent construction comprising; steel brackets fixed to the piles with a steel frame supporting a fixed steel mesh floor platform.

To facilitate access under Berth 4 when the berth was in use, a temporary access hole was cut through the deck.

The electrical continuity survey for Berths 4 & 6 identified areas of electrical discontinuity in the soffits because the Omnia precast panels were not well-connected and some steel reinforcement in the individual panels was also isolated.

To overcome the problem, chases were cut in the panels in both directions using hydro demolition to expose the steel reinforcement and additional reinforcement bars were welded in to reinstate the continuity. Additional continuity reinforcement was also required in some repair areas where the corrosion was severe.

The contract was programmed for the concrete repair works under the new crane locations to be completed first to facilitate the possibility of using the berth if there was an issue with Berth 5. Berth 4 was repaired and the CP installation completed followed by Berth 6 and the Knuckle.

Work on Berth 6 was delayed when the paint on the concrete encased steel frame was found to contain lead. This was analysed and a safe method of working agreed to remove the concrete and exposed paint using hydro demolition. The steel work was then encased in an anti-crack mesh and sprayed mortar overlay.

The galvanic CP system was installed using a team of divers who also repaired the steel sheet piling on the knuckle. Redundant fittings on the sheet piling were removed, the steel thickness checked and defective areas repaired using welded 12mm thick plates.

All exposed steelwork associated with the fenders above mid-tide level was grit blasted and thoroughly washed to remove the salt deposits followed by the application of four-coat epoxy coating system supplied by Corroless.

The fendering on berth 4 consisted of 15 steel H piles with Hidac rubber fender units at the top and vertical rubber high density low friction facing plates. These were replaced as part of the overall refurbishment contract.

7 COMMISSIONING

Commissioning of the ICCP and GACP system was planned in stages as the phased construction works were completed. The first phase to be commissioned was Phase 2 which stretched from gridline 5 through to gridline 9. Phase 1 from gridline 14 through to 22 was commissioned next, followed by Phase 3—the remaining areas.

Commissioning comprised; detailed testing of each core of the multicore cables interlinking the below deck junction boxes with the control units in the electrical switch room to prove correct connection, electrical continuity of the DC negative and DC positive cabling, electrical separation of the anode and cathode in each zone and stability of the steel potentials measured against the embedded reference electrodes. The monitoring system was then energised and put into a recording programme at 6-hourly inputs to establish baseline potential data for a few weeks with the DC power disconnected from the anodes.

Energisation involved; reconnecting the switches that physically disconnect the DC positive output feeders at the terminal rails and energising the DC outputs to each zone in turn. Initial output limits

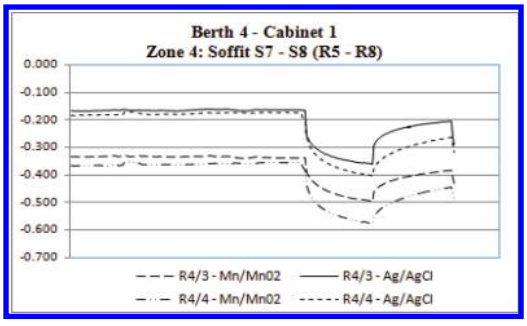

Figure 1. Zone 4 energisation graphs showing base, on and off potential.

were set at 2 A and 5 VDC. In all cases the circuit resistances were such that the 2 A output current was reached first. Driving voltages were lower than 3 VDC.

The steel potentials were recorded as the ICCP was applied (polarisation) and left on for an hour or so. The DC outputs were then switched off for another hour or so to allow the steel potentials to recover (depolarise) whilst recordings were made on a more frequent basis. In all cases the steel potentials became decidedly more negative against the two reference electrodes in the clusters when the ICCP system was applied (polarisation) and less negative (depolarisation) as it was removed. This is as expected and proves that even after a short period of time the ICCP system achieved its requirements. The graph shown below is typical of the potential shifts recorded during preliminary commissioning, in this case Zone Z4, deck soffit and secondary beams between gridlines S7–S8.

Figure 1 shows early indication of the success of applying ICCP to Zone Z4 – Deck soffit and secondary beams. Polarisation can be seen as the ICCP system is energised after off (as-found) potentials were recorded at 6-hourly intervals for a few weeks beforehand. Depolarisation can be seen as the ICCP was de-energised and then polarisation again as the system was re-energised and left operating.

Note: Mn/MnO_2 reference electrodes should show the same steel potential as approximately 180 mV more negative than as measured against an Ag/AgCl reference electrode, hence the 'offset' in the readings above.

8 SUMMARY

This has been one of the largest marine repair and cathodic protection systems ever installed in Europe. The technical and logistical details have been challenging for all the project team but the scheme has been successful to date

The impressed current and galvanic cathodic protection systems are functioning correctly in accordance with BS EN ISO 12696 and 13174. During the next 12 months the impressed system will be adjusted to its optimum operating performance. With such a large and quite complex system there will be some minor maintenance required, but providing this is undertaken and the system regularly monitored we are confident that the 25 year design life will be achieved.

Concrete Repair, Rehabilitation and Retrofitting IV – Dehn et al. (Eds)
© 2016 Taylor & Francis Group, London, ISBN 978-1-138-02843-2

Southern Europe pipeline: New life of a 1960s pipeline

C. Chanonier & C. Raulet
Diadès, Vitrolles, France

F. Martin & C. Carde
LERM, Arles Cedex, France

J. Resplendino
Setec TPI, Vitrolles, France

ABSTRACT: As part of the re-commissioning of the PL1 pipeline that supplies refineries and petrochemical sites on the Fos-Lyon-Karlsruhe axis, DIADES project managed, on behalf of SPSE, the studies into and the works relating to the reinforcement/rehabilitation and seismic compliance of a footbridge permitting the aerial crossing of the floodplain of the Durance. This study is based on the structural diagnosis performed by the laboratory of the LERM. This bridge, located south of Avignon, is a structure of eight prestressed isostatic spans with a total length of about 300 m. The main objectives of this project included its capacity to respect seismic compliance, taking into account the re-evaluation of seismic hazard in France. This work was carried out through a fully removable additional prestressed coupling to ensure the heavy maintenance of the pipeline. Using an original example of design and execution to make it possible to sustain the structure during the seismic compliance works, this presentation shows the value of the additional prestressing in the rehabilitation of existing structures, by emphasizing the importance of the diagnosis phase, focusing on the existing prestressing. It emphasizes the reliability of the various assumptions which are helpful for reinforcement dimensioning; these assumptions are based on the results of the pathological analysis of the structure including various structural investigations and inspections.

1 INTRODUCTION

The Society of South European Pipeline (SPSE) ensures the supply of petrochemical refineries by a Fos-Lyon-Karlsruhe (769 km) pipeline that spreads over 3 countries (France, Switzerland and Germany). The current transportation of around 23 million tons per year, represents in "Tons per Kilometers" more than 30% of crude oil pipeline transportation in Europe. Other pipelines complete the European network, which is able, from the Mediterranean Sea, the English Channel and the North Sea, to ensure the supply of all the refineries in the heart of Western Europe.

Given the environmental issues, it was decided by SPSE to compare how the current state and future evolution of this pipeline state could supply refineries in Eastern France and West Germany. To this end, an inspection program was carried out on the 40-inch pipeline; operating minimally, and the rehabilitation of the equipment of the 34 inch pipeline was launched in parallel, in order to once again exploit it.

As part of this restoration, the issue of aerial crossing of the Durance arose very quickly. Indeed, under Article 9.1 of the Decree of 4 August 2006 that regulates pipeline safety, governmental consent is required to maintain the aerial structure. The review of the consent file is based in particular on a structural assessment of the durability of the structure.

Also, SPSE has asked DIADES, in collaboration with LERM, to carry out a structural diagnosis of this structure. This analysis was completed by the study and evaluation of the conformity of the structure in two respects: static and seismic resistance. Investigations (structure, materials and geotechnical) and static and dynamic recalculations as part of the diagnosis have led to a reinforcement and rehabilitation of the structure through the use of external prestressing.

2 BRIEF PRESENTATION OF THE STRUCTURE

The structure under study, located in the territory of the municipality of Noves (13) is an aerial prestressed concrete bridge crossing the floodplain of the Durance, over a length of 284 m[l]. It consists

of a 12-metre span and 8 34-metre prestressed spans. The structure consists of a U-shaped covered bridge whose underside was created in 1962, 20 cm above the highest water level of the Durance. The section is 1.85 m high and has an outer width of 1.70 m. In addition, the covered bridge is coated with reinforced concrete slabs to protect the pipe from external aggressions.

Figure 1. View of the structure before the operation.

The structure is prestressed longitudinally withy post-tensioned cables positioned in the bores of the U. The structure supports the pipeline via 3 supports placed respectively at 1/6, 1/2 and 5/6 of each span.

With regards to these supports, the structure presents massive piles and two types of plate, and the massiveness of the piles can be explained by strong hydraulic constraints. The alternating arrangement of two types of plate based on 2 or 3 pickets allows a kind of longitudinal articulation of the entire structure.

3 DIAGNOSIS OF THE STRUCTURE

The diagnosis was made on the basis of a program of structural investigations, to design and manage the repair and reinforcement project of the structure. Depending on the identified disorders and the contents of the structure folder, structural investigations have been defined (investigations on materials, measurement of residual tensions) to ensure the reliability of the necessary assumptions for diagnosis and ultimately provide the basis for defining the rehabilitation works.

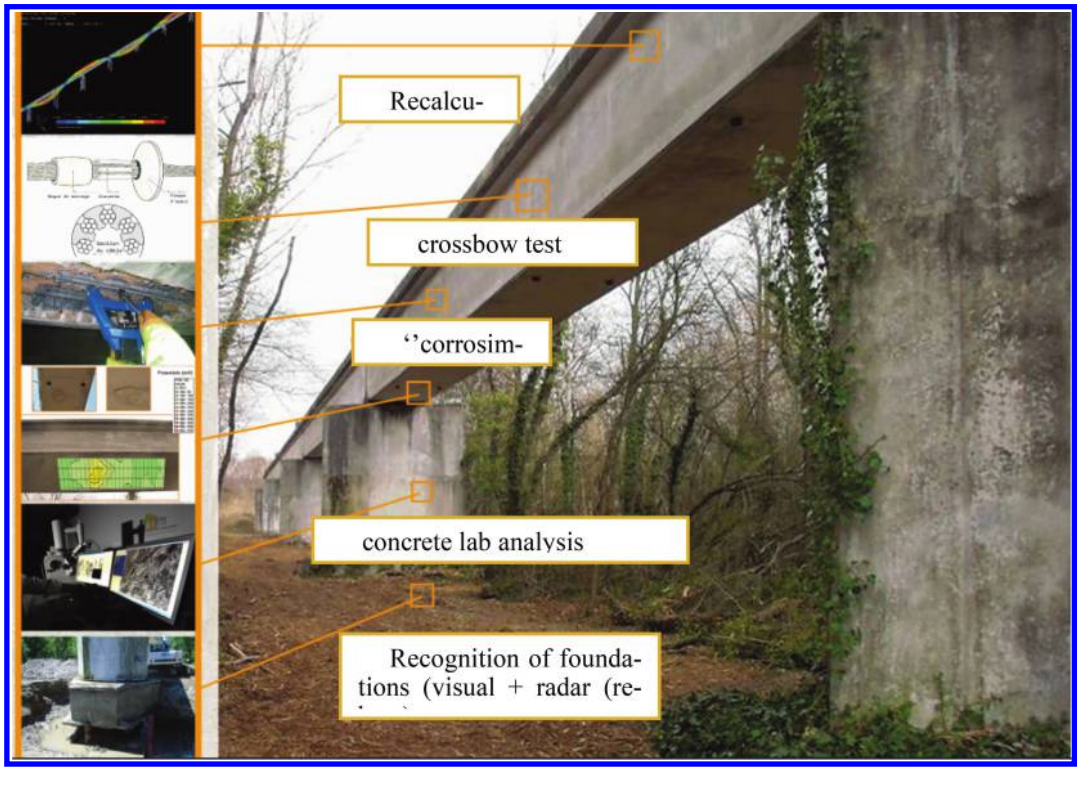

Figure 2. Representation of the main investigations for diagnosis.

3.1 *Challenges for static recalculation of the structure depending on its state of aging*

The accuracy of structural diagnosis, including the audit of the load-bearing capacity of the structure lies in the reality and representativeness of retained assumptions. Indeed, the structural diagnosis of the structure based on in situ and laboratory structural investigations optimizes assumptions for recalculation, including geometric and intrinsic characteristics of the materials, the determination of the residual prestressing, thereby reducing the uncertainty inherent in different prestressing losses (concrete flow and relaxation of cables).

3.2 *Method of existing prestressing*

The existing prestressing was conducted by GTM C.02 type 75 tons cables.
According to the document [1], the main features of these cables are:

- Diameter: 32.5 mm
- Cable section: 500 mm²
- Coefficient of friction per unit of angle: 0,10
- Coefficient of friction per unit of length: $0{,}2.10^{-2}$
- Back of the anchor cone: $0{,}1.10^{-2}$ m
- The maximum tensioning force: 82.5 t
- Young's module: 196 000 MPa
- Relaxation loss in 1000 hours: 9%

The 75 t (82.5 t in characteristic value) C.02 frame is made with 7 strands of 7 threads of 3.6 mm diameter, fixed at their ends by two anchoring devices.

It can be implemented either in the formwork before the concrete is poured or after the concrete has hardened, in a sheath arranged in the prestressed beam during its execution. In the first case, the armature must be isolated from the fresh concrete by a sealed metal tube.

After tensioning the strands are coated with a cement grout injected through an orifice in the bearing plate of one of the anchorages.

3.3 *Structural investigations program*

With regards to the existing pretensioning, possible investigations are limited and do not allow a perfect characterization of the state of the existing pretensioning. The main investigations on existing pretensioning are visual inspection, radiography, opening windows including endoscopic control inside sheaths, removal of grout for laboratory analysis and implementation of the crossbow test (principle recalled below) to set the residual stress of the existing cable.

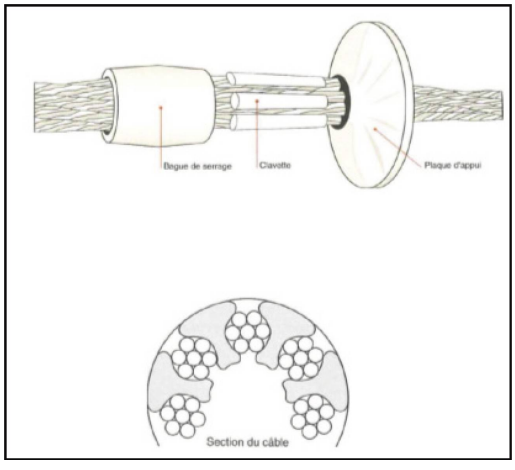

Figure 3. Overview of the anchorage system of a GTM cable type C.02.

Figure 5. Development of a crossbow test.

In fact, to accurately assess the behaviour of the structure, it is essential to determine the residual tension in the cables. By experience and given the context that requires a decision on the stability and durability of the structure, only the tests with a crossbow have been made. These tests are called destructive because they require to uncover the cable by a limited demolition of the surrounding concrete, but they do not damage the cable being tested.

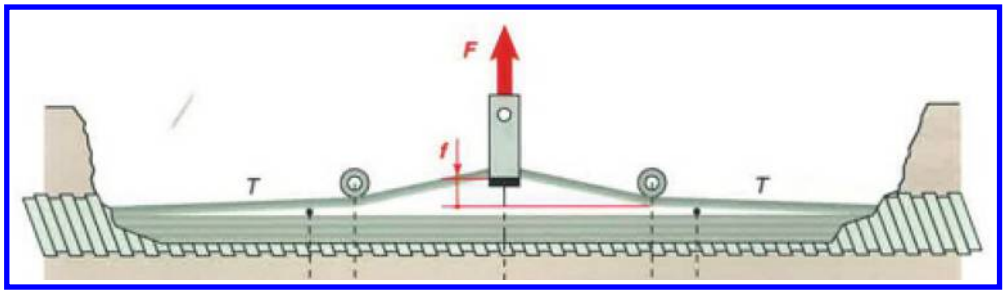

Figure 4. Principle of the test with a crossbow.

The diagnosis, on the pretensioning part, required the following steps:

– Identification of existing cable routes,
– selection of representative areas for crossbow testing
– window opening to uncover the cable
– conducting test with crossbow.

The reliability of this phase is closely related to the representativeness of the investigations. This representativeness depends on the nature of the investigations, their location and the number of tests.

In the case of diagnosis and when reinforcement dimensioning is necessary for the resumption of seismic forces by the footbridge, the number of trials and their locations were chosen to limit window openings while providing sufficient structural data. Ten crossbow trials were performed on different sections and different spans. The small difference between results helped to ensure good representativeness of the values considered in the different structural analyses.

3.4 *Tracings of existing cables*

The input data on the geometry of the existing pretensioning proved incomplete: only primers cable routes at the anchors were represented in execution plans in our possession.

Also, it was necessary to locate the geometry of the cables on each beam. The geophysical radar technology developed by LERM allowed precise positioning of each sheath with sub-centimetre accuracy.

3.5 *Crossbow test method*

The crossbow test is used to estimate the residual stress in prestressed bars, wire or strand.

The principle of the test is based on the change in the stiffness of the frame which is characteristic of the tension of the cable or strand. Thus, this test involves imposing an arrow on the frame and testing to measure the force required to achieve the

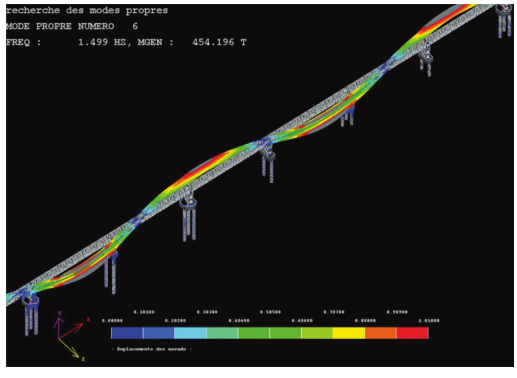

Figure 6. View of the general model—modal analysis of the structure.

arrow strength. It is performed according to the guide [3].

It should be noted that the results are not instant. After the completion of on-site measurements, a calibration phase in the laboratory on the same type of cable should be conducted to determine, by extrapolation, the measured residual stresses. The following figures illustrate this process.

During these tests, the following were also noted:

– the condition of the sheath at the time of opening of the window,
– the quality of the grouting at the opening of the sheath,
– condition of visible prestressing wires before or after release of the grout, a sample of this being carried out systematically for potential analysis. In the case where a void is revealed at the time of opening of the sheath, a video-endoscopy is performed.

With regards to the structure supporting the pipeline, no default has been detected by these controls.

The tests carried out have revealed a significant difference between the measured tension and the theoretical tension defined in the notes to calculate the

time of the order of 15% with a standard deviation of 13%. Given this observation, the residual capacity of the apron of the bridge has been appreciated by a recalculation based on the measured residual stresses. This difference between the residual tension and the theoretical tension can be explained by poor understanding at the time of construction of the phenomena of concrete flow and relaxation cables and non-consideration of phasing. These points are included in the circular referenced [2].

3.6 *Conclusions on the structural analysis of the structure*

The structural analysis was conducted using the Pythagore software (www.pythagore.setec.fr) that allows such dynamic structural analysis and modeling of prestressing cables by taking into account the different angular deviations, and construction phasing of the structure.

Diagnosis of structure has highlighted the fact that the structure showed no significant pathology and that all elements of the existing prestressing were in a good state of preservation.

The calculation of the bearing capacity of the structure under operating phases showed that the structure was able to be used under normal conditions. Sensitivity analysis, including the identification of surges in existing cables and a visit of the structure under operation was carried out in parallel in order to ensure the reliability of assumptions.

The seismic analysis of the structure confirmed the risk of independent spans clashing and also identified the need for mid span reinforcement in case of a vertical descending seism.

4 REHABILITATION PROJECT AND REINFORCEMENT OF THE STRUCTURE

4.1 *Specific maintenance of the structure*

The specific maintenance interventions recommended to sustain the structure include the cleaning of the interior of the structure, repairing sealing and patching degraded concrete, mainly located in the right side beams/ slab junction, as well as a treatment of cracks.

The diagnosis has also highlighted the need to replace the support devices and the bosses to sustain the structure and secondly to allow the transition from horizontal stresses between the apron and the piles under seismic force.

4.2 *Issues of seismic reinforcement*

The choice of spectrum to be applied to the structure is based on the importance of the structure

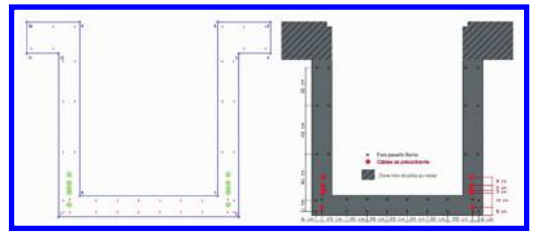

Figure 7. Section under CDS calculation surges in existing cables (here before repair).

and environmental issues of the site. The structure is in the flood plain of the Durance, in a "moderate" seismic risk area according to the annex to articles R563-1 to R563-8 of the Environmental Code as amended by Decree N°. 2010–1254 and n° 2010–1255 of 22 October 2010 and by the Order of 22 October 2010. The nominal acceleration used is 1.6 m/s². In addition, an important factor equal to 1.4 is applied to the regulatory spectrum to reflect the social and economic importance of the structure and its role in national and European society.

This regulatory spectrum was then supplemented by specific recommendations based on a specific study by BRGM. This new spectrum is then applied to the structure by a multimodal analysis that includes identifying and quantifying the significant difference in stiffness between the piers based on two piles, and piers based on three piles, depending also on the roof of the substratum.

The risk of clashing under seismic force (longitudinal displacement of ±6 cm) of the existing structure was confirmed by the analysis. The fact that each span is supported on a flexible pile and on a stiff pile naturally led to propose to couple the spans between them to allow the resumption of longitudinal stresses and prevent the risk of clashing. The durability of the internal prestressing cannot be 100% guaranteed, and the use of external prestressing is needed to improve the recovery of the descending vertical stresses under seism, the tracing of the prestressing has been optimized to sustain the structure by compensating for any any defect in the existing prestressing.

4.3 *Choice of combined static and dynamic capacity*

The dynamic reinforcement of the structure was planned from the start, with a concern for the sustainability of the project. Indeed, it seemed appropriate to take advantage of dynamic reinforcement to sustain the structure. Among the techniques

discussed, the additional external prestressing technology has been adapted to the problematic because it also reduces any electrical surges in the wires in some load cases. Post-critical calculations based on the actual position of the cables have been made. The study of tension in class III BPEL cables was performed with the Sétra's CDS software. It is based on an accurate record of the position of passive cables and rebars produced by LERM and is illustrated in Figure 7.

The sections have been verified, both at static and dynamic states, to ensure that they not only enable the prestress of the coupling span but also the transfer of force under seismic pressure, incorporating additional loss due to the possible future failure of some existing cables, by increasing the tension of the prestressing.

4.4 *Retained reinforcement solution (prestressing, piles and foundations)*

The reinforcement solution adopted for the tendering process is the coupling of the spans. For reasons of thermal expansion, the coupling of all spans is not possible. Thus, some spans are coupled together and uncoupled spans are connected by dynamic mechanical devices (lock-up device) thereby eliminating the risk of clashing in seismic events. In fact, these devices allow the slow movement caused by to thermal effects and block the rapid displacement caused by seismic movements. The additional external prestressing maintains these couplings in all load cases.

The reinforcement solution changes the static diagram of the structure and requires the local reinforcement of certain parts of the structure. To reinforce some pile footings, the use of composite materials has been preferred to other techniques, including the use of shotcrete to limit the increase in the weight of the structure and therefore the seismic stresses to be transferred.

4.5 *Disassembly & possibility of resuming reinforcement to replace the pipeline or evolution in the integrity of the prestressing*

The Client wanted to take advantage of these reinforcement interventions to sustain the structure in overcoming any future loss of preload. The use of additional external prestressing of a greased and sheathed monostrand type was preferred, leaving it possible to adjust the effective tension for the duration of the use of the structure.

For reasons of operation and maintenance, access to the pipeline must not be disturbed. Thus, all new elements, including prestressing, are removable to facilitate any further intervention to the pipeline.

5 MAIN PHASES OF WORK

The works and design studies were made by the company Freyssinet. The main tasks were as follow:

- Flushing and cleaning of the structure,
- Excavation of span 8 in order to ensure the accessibility to the structure,

Figure 8. Reinforcement of the pier bases with composites.

Figure 9. View of the structure after repair.

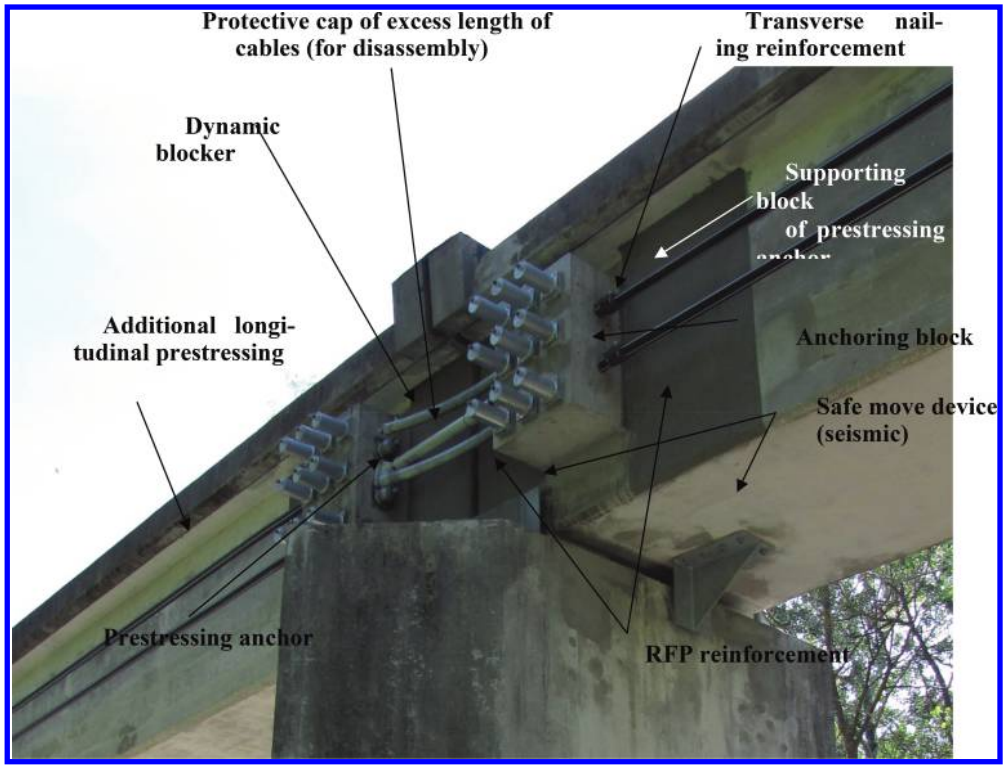

Figure 10. Detail of a beam anchor and works carried out to the extremities of the span on P3 pier.

– Rehabilitation of the seal,
– Laying the jacking beams and jacking of independent aprons,
– Renewal of support and replacement of support bosses
– Routine and specific maintenance referred to above,
– Implementation of the anchor beams for the additional external prestressing,
– Reinforcement with composites of the extremities of the deck, and of the anchor beams in particular,
– "Rigid" coupling of spans 1,2,3–4,5 and 6,7,8 to reduce the risk of clashing during possible seismic event,
– Tensioning of prestressing,
– Computer-assisted jacking of coupled spans after tensioning of additional prestressing,
– Reinforcement of the "rigid" piers, based on three piles, with composite materials with UV protection
– "Mechanical" coupling between spans A (1 + 2 + 3), B (4 + 5) and C (6 + 7 + 8) using dynamic blockers.

The work took about 9 months including a month and a half of preparation time. With regards to carrying out the prestressing, the implementation of 12 hammer beams took about one month of intervention. The tensioning of the cables was carried out in three days.

The works were properly executed, due, in particular, to the provision of clear and precise implementation procedures, identifying all critical stages, identifying all intermediate controls: expected theoretical values and acceptable ranges.

The additional prestressing reinforcement required *a posteriori* computer-aided jacking of coupled spans to rid supports of distortions inherent in the prestressing of the structure.

6 CONCLUSION

The rehabilitation of an existing structure, by means of external prestressing, stresses the need for reliable assumptions that include the determination of actual residual stresses, not estimated on the basis of the fixed losses. These should form the

basis for the definition and the "true conception" of the reinforcement required. This example also highlights the value of prestressing and composites in reinforcement and preventive maintenance of assets, in particular if seismic compliance settings are required.

This type of rehabilitation requires a thorough structural diagnosis and mastery of the technical prestressing processes. The technical development has enabled to achieve a "modular" and "removable" solution to adapt as well as possible to the structural needs of the structure without changing the exploitation of the structure and by ensuring ease of monitoring and overcoming potential defects in internal prestressing concrete.

7 PARTICIPANTS

The participants for this mission are:

- Client: *SPSE*,
- Structural Diagnosis: *DIADES + LERM,*
- Project management: *DIADES*,

Contractor: *FREYSSINET*,

- Execution consultants: *FREYSSINET International*
- External Composites inspection:

LRPC Autun

- Technical Control: *VERITAS*
- CSPS (Health and Safety coordination): *APAVE*.

REFERENCES

[1] Extract from Circular No. 82 of 28 December 1966, Official Bulletin of the Ministry of Equipment, Special Issue No. 66–24., Text No. 857.

[2] Circular No. 141 of 1953, preliminary instructions regarding the use of prestressed concrete—October 26, 1953.

[3] Guidance LCPC—Residual stress measurement of prestressing cables using the Crossbow—ref: GTARBA—November 2009.

[4] Article Review Works No. 882—July–August 2011—Diagnosis and repair of a significant structure of the South European Pipeline, from page 30.

[5] Technical Guide LCPC—Methodological guide on monitoring and auscultation—VIPP—October 2001.

[6] AFGC Guide—Methodology of non-destructive evaluation of the state of deterioration of concrete structures—September 2005 COFREND.

[7] Maintenance and Repair of Bridges—Bridges and Roads Press—July 1997.

Concrete Repair, Rehabilitation and Retrofitting IV – Dehn et al. (Eds)
© 2016 Taylor & Francis Group, London, ISBN 978-1-138-02843-2

Innovative subsequently applied shear strengthening techniques for RC members

N. Randl & P. Harsányi
Carinthia University of Applied Sciences, Austria

ABSTRACT: In a research project in cooperation with the HILTI Corporation and SIKA Austria, funded by the Austrian Research Promotion Agency FFG, the Austrian Railway Company ÖBB and the Austrian motorway operator ASFINAG, new strengthening methods for shear deficient bridges are being developed and tested. To test the strengthening effect in shear, a number of 12 T-shaped RC-beams with a length of 5.4 m and a height of 0.6 m were designed. The specific design and detailing were done in such a way that shear failure predominated even after the application of the strengthening systems. In the experimental campaign, two different types of strengthening systems were subjected to shear loading until failure. Special attention was laid not only on the increase of the shear strength, but also on serviceability requirements like crack opening. The successful use of a modern digital image correlation system provided the basis for the analysis of the crack pattern and the shear degradation.

1 INTRODUCTION

1.1 *Research significance*

The increase in traffic loads over the past decades, the on-going updating of design codes and also paradigm shifts lead to the fact that currently a substantial number of existing bridge structures do not fulfill the required safety level concerning the shear bearing capacity.

While flexural strengthening of RC structures has become a routine task in building construction, the retrofitting of shear deficient members is still a demanding topic for the following reasons:

- There are currently no harmonized recommendations for RC shear design itself available, therefore the design of shear strengthening is even more disputable.
- While flexural strengthening is oriented in the longitudinal direction of a structural member and usually applied over larger sections, local shear retrofitting requires transfer of forces and activation of the system over very short distances.

Therefore, although there exists a variety of techniques for subsequent strengthening of RC structures, there is still lack of knowledge on the efficiency of available shear repair methods. In addition, the majority of studies focus on rectangular cross sections which represent in many cases not the most relevant situation in practice (Etman 2011).

2 DESCRIPTION OF APPLIED STRENGTHENING TECHNIQUES

2.1 *Main targets*

Most existing techniques require also construction activities on the top side of the structure which in turn leads to restrictions of the traffic flow. The avoidance of such restrictions was one of the main targets in this project. Other decisive criteria were the efficiency of the applied strengthening method, economic aspects, the simplicity of the installation process and the avoidance of significant adjustments of the member's cross section. In a literature study performed in advance several existing solutions such as through-ties or shotcrete had been evaluated, however in most cases one or two of the above mentioned criteria are violated. Moreover, special attention was paid to suitability behavior, meaning especially that instant activation of the strengthening elements without the necessity of significant deformations of the structure should be achieved.

Finally the focus was placed on two promising methods fulfilling the requirements: shear strengthening with Carbon Fiber Reinforced Polymer (CFRP) sheets and post-installed undercut anchor rods. For both strengthening techniques, prototypes have been developed and produced in cooperation with the Hilti Corporation and SIKA Austria. One reason for testing two methods was the applicability for different cross sections: While the intended CFRP sheets can be easily and mainly

applied on rectangular or T-shaped bridge girders, the post installed anchors are in addition also suitable for installation in slab bridges.

Several researchers have already raised the question of interaction of conventional cast-in reinforcement and applied strengthening system (Bukhari et al. 2010, Khalifaa & Nanni 2002). Though this point is justified, in the present study the beam sections dedicated to shear failure were not provided with any cast-in shear reinforcement such as stirrups. The reason therefore is that on one hand the potential strength gain is easier to identify and on the other hand the relevant Austrian infrastructure operators classified none—or low-shear reinforced members like slabs or prestressed girders as most critical structural systems.

2.2 *CFRP sheets with end anchorage*

Numerous researchers have already proven the efficiency and usefulness of applying CFRP sheets to strengthen existing RC structures in shear. If the cross section of a structure allows for it, full wrapping around of the CFRP sheets would be the easiest way to ensure maximum effectiveness and strength gain. However, in practical situations this method is usually not feasible either due to cross sectional shapes other than rectangular or with respect to the required traffic interference. Therefore the CFRP sheets are usually bonded only to the sides or to sides and bottom of the RC member in a U-shaped constellation. The usually observed failure mode will then be lateral delamination, i.e. de-bonding, of the CFRP ends from the concrete (Belarbi et al. 2012).

Therefore the decisive factor with this type of strengthening is the CFRP's ability to transfer its extraordinary strength to the concrete member (Ozden et al. 2014, Triantafillou & Matthys 2013). Premature de-bonding hinders the full utilization of the available tensile strength of the CFRP and the overall strengthening effect is limited. Therefore some researchers already pointed out the importance of an end anchorage of the CFRP to the concrete (Kalfat et al. 2013, Manos & Katakalos 2013). However, even then the full capacity cannot be used if the anchorage is not designed in an appropriate way: The best efficiency can be reached by anchoring the CFRP ends directly to the compression zone of the RC member, thus enabling the formation of a truss model that makes use of the full available depth of the cross section. For example the proposed anchorage constellation shown in Figure 1 represents a quite typical approach, but does not allow for complete activation of the whole cross section in shear.

In order to rectify the mentioned deficits, in the present study a new and very simple end-anchorage

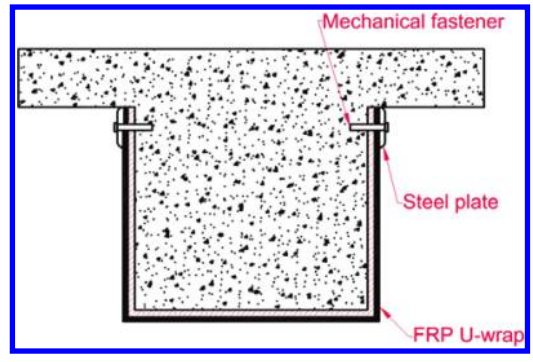

Figure 1. Example of standard FRP-anchorage.

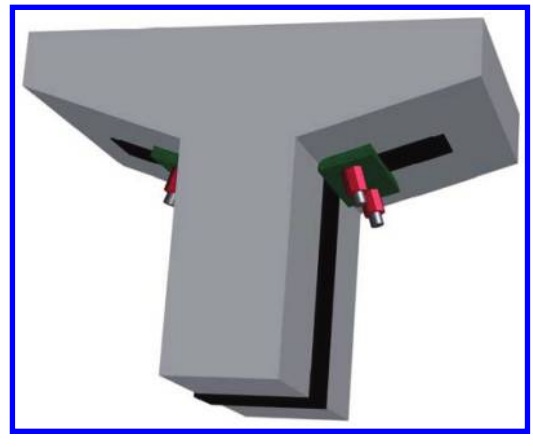

Figure 2. Outline of CFRP-strengthening in the present test series.

system has been designed which allows a direct load introduction into the compression zone: A steel plate $300 \times 150 \times 30$ mm is fixed to the upper flange of the T-section by means of rapidly curing bonded anchors (Fig. 2). Along the plate edge oriented to the wedge between web part and upper flange of the concrete cross section, the plate is rounded with a radius required to allow for a smooth CFRP redirection.

2.3 *Post-installed undercut anchors*

The basic technique of strengthening shear deficient beams by applying post-installed reinforcement has been investigated successfully by Randl & Kunz (2009). In this former test series, ten reinforced concrete beams had been tested in shear, provided with inclined reinforcing bars post-installed from the soffit of the beams. The reinforcing bars had been installed in mortar-injected boreholes and anchored with metal plates at the accessible bar end at the bottom of the beams. The

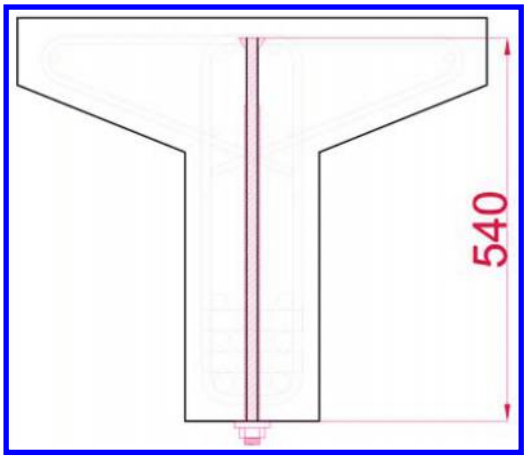

Figure 3. Outline of post-installed undercut anchor used in the present test series.

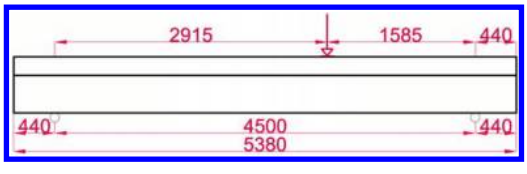

Figure 4. Test setup and side view of T-beam.

test results confirmed that post-installed reinforcing bars can significantly increase the beam shear resistance, provided they are situated properly and adequate injection mortars are used.

In the present study, in cooperation with the Hilti Corporation, a new anchorage system especially designed for this type of application was developed. The anchor is set vertically into the predrilled hole and the load is then introduced by the local end anchorage inside the structure by means of a self-undercutting expansion sleeve. This working principle allows for a concentrated load introduction at the end of the anchor even in cases where the shear crack passes quite close to the end in an unfavorable way. In addition a tubular sleeve around the whole length of the inner threaded rod enables the subsequent prestressing of the anchor rod. The introduction of a prestressing force is advantageous for serviceability behavior as well as in case of fatigue loading.

Since the anchors are set from the soffit of the RC member, traffic disturbances can be avoided to a large extent. As the anchors can be prestressed, they are activated even before additional loads act. The fact that the load introduction is concentrated via the keying effect in a single point leads to higher resistance and to less sensitivity against cracks crossing the anchorage zone as compared to other

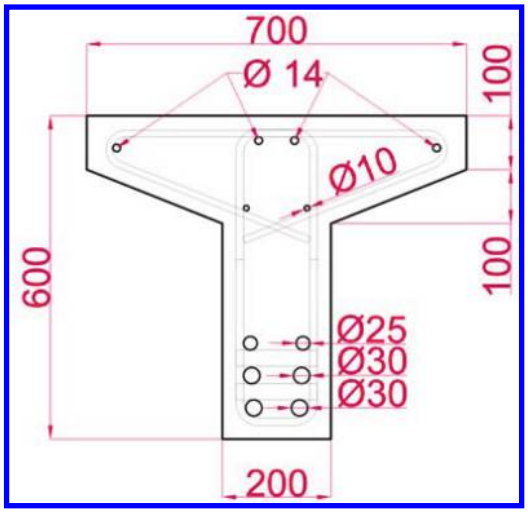

Figure 5. Reinforcement layout and geometry of T-shaped cross section.

strengthening systems such as bonded anchors or concrete screws where the load is introduced over a certain part of the element length.

3 EXPERIMENTAL CAMPAIGN

3.1 *Test setup*

Standard RC beams will usually fail first in bending and not in shear. Therefore an adequate setup and shape of the cross section had to be chosen to end up in a typical shear failure. The test specimen was a single span beam, with the load introduction at a distance of 1.585 m from the support. Taking into account the span of 4.5 m, the shear span-to-depth ratio a/d was 3.2 (with an effective depth to the bottom reinforcement d = 494 mm).

The beams were designed in such a way that premature flexural failure could be avoided even in the case of very high shear load bearing capacities due to the applied strengthening. Therefore an over-reinforced T-shaped cross section was designed, with four bars of 30 mm diameter and two bars of 25 mm diameter as longitudinal tensile reinforcement provided at the bottom of the beam (Fig. 5). The steel was a high grade S670/800 type in order to achieve maximum flexural resistance with a still reasonable reinforcement degree. As top reinforcement, only four bars of 14 mm diameter and two bars of 10 mm diameter were foreseen in order to create a stable reinforcement cage.

No stirrup reinforcement was provided in the beam sections between load introduction and closest support. On the other hand, in order to ensure

shear failure within the short span between load introduction and support, stirrups of 12 mm diameter at 190 mm spacing were applied between load introduction and farther beam support.

3.2 *Material properties of test specimen*

Hereafter, the material properties of the test specimens themselves without strengthening equipment are described. The properties of the attached strengthening systems are addressed below in the description of the application and type of strengthening.

The beam specimens were made of normal strength concrete C30/37. The mean concrete strength measured on 150 mm cubes on the day of testing was 43.5 N/mm^2.

The longitudinal reinforcing bars provided at the bottom of the beams had a nominal yield strength of 670 N/mm^2 with an average value 10% above. All other types of used reinforcement, i.e. longitudinal top bars and stirrups, were made of standard steel B550 B.

3.3 *Testing procedure*

In order to account for the fact that existing structures have already been subject to numerous loadings during their lifetime, a preloading phase was applied first: based on an estimation of the design failure load of the non-strengthened beam according to EC2, the SLS-load level was derived at 90 kN. Therefore at the very beginning, even before application of the strengthening system, each beam was subjected to 10 load cycles between 5 kN and 90 kN. During the cyclic loading, deformations as well as crack propagation were recorded, the latter one by means of visual control and use of a crack magnifier, in two tests also by using a digital image correlation system.

After finalization of the cyclic preloading, the specimens were ready for the installation of the strengthening system. In the last step, having passed through the required curing time (see following chapter), the strengthened specimens were finally tested until failure.

3.4 *Application and type of strengthening*

After the preloading phase, all specimens except for the reference test no. 1 were provided with an adequate strengthening. An overview of applied strengthening methods and tested constellations is given in the following Table 1. All strengthening elements were installed at a constant spacing of either 190 or 380 mm, in one case 570 mm.

In the case of CFRP sheets, all sheets were provided with end anchorages as illustrated in Figure 2. Only in test no. 2, in fact the same basic anchorage principle, but an alternatively formed steel element with a tear-like shape to wrap around the CFRP sheet was used. However, as this more complex and costly end anchorage did not lead to a higher strength gain compared to the simple solution shown in Figure 2, finally only the steel plate anchorage was tested.

Table 1. Applied strengthening systems.

Test No.	Type	Strengthening System	Spacing/ number [mm]/-
1	Reference	None	-/-
2	CFRP_4-2*	CFRP, 2 layers	190/4
3	CFRP_4-2	CFRP, 2 layers	190/4
4	PUAnc_7	Post-inst. anchor	190/7
5	CFRP_4-1	CFRP, 1 layer	190/4
6	PUAnc_4	Post-inst. anchor	380/4
7	PUAnc_7	Post-inst. anchor	190/7
8	CFRP_4-2	CFRP, 2 layers	190/4
9	CFRP_3-1	CFRP, 1 layer	570/3
10	PUAnc_4	Post-inst. anchor	380/4
11	CFRP_4-1	CFRP, 1 layer	190/4
12	PUAnc_4	Post-inst. anchor	380/4

* Alternative shape of end anchorage.

The varied parameters in the tests with CFRP sheets were the number of glued CFRP-layers in one sheet (either one layer or two layers, one glued upon the other) and the number resp. distance of the single sheets. In tests with undercut anchors, only the number resp. distance of installed anchors was varied (Table 1).

All CFRP sheets were fully bonded to the concrete beam surface. The CFRP sheets had a width of 100 mm and a nominal thickness of 1.3 mm. The average tensile strength of a laminated single-layer sheet with a width of 100 mm was 143 kN. Related to the total laminate thickness of 1.3 mm, Young's modulus of elasticity was close to 100 GPa and the strain to rupture 1.10%.

The undercut anchors, on the other hand, had an embedment depth of 540 mm. Taking into account the required drilling depth of 550 mm, the remaining concrete thickness at the top side of the beam was 50 mm. The material of the threaded rod was a strength class 8.8 steel. The steel rod was provided with a metric screw thread size M 12.

Both strengthening techniques were applied according to the recommendations of the two suppliers Sika and Hilti: Concerning the CFRP sheets, first of all 100 mm wide strips were cut from the 300 mm wide unidirectional carbon fiber fabrics. The cut fabrics were bonded to the concrete surface and saturated with a roller-applied epoxy-based resin. Finally the end anchorage plates were tied

to the flange by tightening screws to pre-installed threaded rods (Fig. 2). Before testing these beams, a 7-day curing time had to be concluded.

The undercut anchors were installed in pre-drilled holes of 22 mm diameter which had before been filled with a high strength injection mortar. In the last phase of the setting process, the anchors were driven into the concrete by means of an appropriate hammer drill to produce the undercut. Afterwards they were immediately prestressed by applying a defined torque moment of 60 Nm. As the curing time of the resin in this case at 20°C room temperature was only 45 minutes, the test could usually be performed already on the same day.

Comparing the strength of one element each of both different techniques, the tensile resistance of a U-wrapped 1-layered CFRP sheet reaches 2 x 143 = 246 kN while one single undercut anchor yields 70 kN (contribution of prestressed rod) plus the capacity of the tubular sleeve. Assuming full bond and load introduction of the ribbed tubular sleeve to the surrounding concrete, together with the sleeve the overall tensile resistance of the anchorage system reaches about the double of the threaded rod, i.e. 140 kN. However, concerning the sleeve contribution it has to be mentioned that the full activation of the steel sleeve is only possible if the bond length is sufficient, which means that the critical shear crack does not cross the anchorage close to its end.

3.5 *Applied measurement instrumentation*

Conventional and typical measurement instrumentation for the analysis of shear failure was installed: Along the web in the zone of the expected compression field, strain gauges were glued to the concrete surface and inclined LVDTs were applied. Moreover the vertical displacements were measured by LVDTs. In addition strain gauges were glued on top of the concrete beam and also to the longitudinal reinforcement in order to record the compression and tension strains due to bending.

Apart from the conventional measurement devices, a digital image correlation system (DIC) was used to track the displacement of each point in the shear loaded zone. DIC enables in consequence the visualization of the crack formation process and the crack propagation as well as derivation of crack widths at each load stage.

4 TEST RESULTS

4.1 *Failure modes*

All specimens exhibited typical shear failure modes, flexural failure was never decisive. During the first stage of loading, the stiffness was nearly equal for all specimens. During the preloading phase the full crack pattern due to bending developed already, with an average crack distance of about 200 mm. The first slightly inclined shear cracks with an inclination of roughly 70° to the horizontal axis appeared at the reference beam at a load level of about 130 to 140 kN, at the strengthened beams consistently at a much higher load level around 220 to 250 kN (this increase is in-line with the observations made in (Ozden et al. 2014). The shear cracks developed in between the strengthening elements, forming thereby, together with the CFRP sheets or the post-installed undercut anchors, a typical truss-like structure.

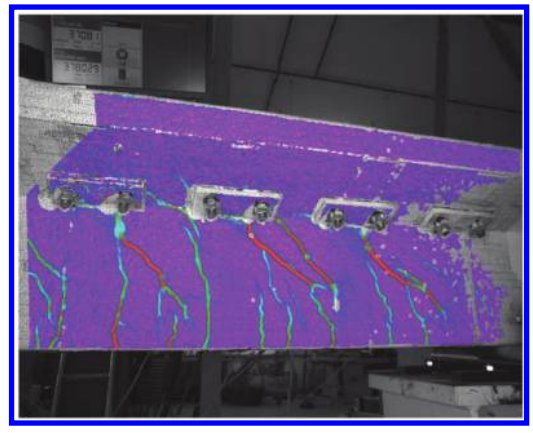

Figure 6. Crack pattern of beam 8 at 370 kN derived from digital image correlation method.

At a load level of 300 to 350 kN the inclination of the propagating shear cracks started to decline to an angle between 30° and 45° to the horizontal axis (Fig. 6). At the reference beam this was followed quickly by the formation of a continuous critical shear crack and, having passed through the flanged section, soon led to final failure (Fig. 7). In contrast, the strengthened beams showed hardly any loss in stiffness as the strengthening elements were increasingly activated. Only when the load level reached about 80 to 90% of the ultimate load, the rather flat main crack started to propagate through the whole cross section. Nevertheless, some further load increase was still possible due to the delay of the opening of this crack caused by the retaining strengthening elements.

Finally, in the case of one-layered CFRP sheets or undercut anchors, failure occurred due to rupture of the CFRP (Fig. 8) or the anchor rod (Fig. 9). In the case of two-layered CFRP-sheets, concrete failure in compression together with extensive spalling was observed so that the full ultimate capacity of the CFRP sheets was not reached.

Figure 7. Side view of reference beam after shear failure.

Figure 9. Critical shear crack at beam no. 6.

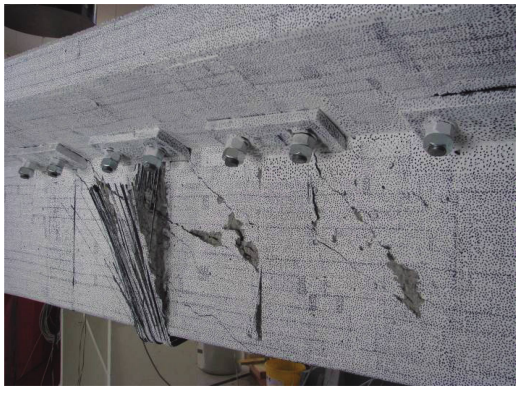

Figure 8. Rupture of CFRP sheets at beam no. 5.

Table 2. Test results.

Test no.	Type	f_{cm} [N/mm²]	F_{max} [kN]	V_{max} [kN]	$F_{max}/F_{max,1}$
1	Reference	44,5	370,9	285,3	1,00
2	CFRP_4-2*	45,7	813,8	612,8	2,15
3	CFRP_4-2	46,4	957,4	719,0	2,52
4	PUAnc_7	42,6	681,7	515,1	1,81
5	CFRP_4-1	41,1	831,3	625,8	2,19
6	PUAnc_4	43,3	612,0	463,6	1,62
7	PUAnc_7	41,2	714,4	539,3	1,89
8	CFRP_4-2	43,1	961,4	722,0	2,53
9	CFRP_3-1	40,5	752,1	567,2	1,99
10	PUAnc_4	44,5	515,0	391,9	1,37
11	CFRP_4-1	37,9	853,5	642,2	2,25
12	PUAnc_4	51,1	500,4	381,1	1,34

* Alternative shape of end anchorage.

4.2 *Load increase*

The reference beam reached an ultimate load of 370.9 kN, corresponding to a back-calculated maximum shear force $V_{max,1}$ = 285.3 kN. The derived shear force takes into account the effect of the self-weight of the beam itself.

All strengthened beam specimens exhibited a significant load increase due to the applied strengthening elements. An overview of the recorded loads, the according maximum shear forces and the load increase with respect to the reference beam is given in Table 2. Figure 10 depicts load-displacement curves of the different investigated constellations.

The most substantial load increase was reached with the CFRP-sheets with two layers (beams 3 and 8). As failure in that case was due to spalling and bursting of the concrete struts in compression, the full capacity of the four CFRP-sheets could not be totally utilized. Nevertheless, the shear enhancement reached a very high factor of 2.53. The same constellation, i.e. four sheets, but with only one CFRP-layer, led to brittle rupture of the CFRP-sheets at a load level 2.22 times above the reference load of beam no. 1.

In comparison, the undercut anchorage yielded somewhat lower, but still impressive load enhancements when taking into account the rather small cross section of each rod. While the shear capacity was nearly doubled (enhancement factor 1,85) with the application of seven post-installed anchors, a number of four rods still led to an average increasing factor of 1.44, however with a somewhat increased scatter (beams no. 6, 10 and 12).

5 CONCLUSIONS

A number of twelve shear-deficient T-shaped RC beams were tested until failure to evaluate the effectiveness of two different shear strengthening

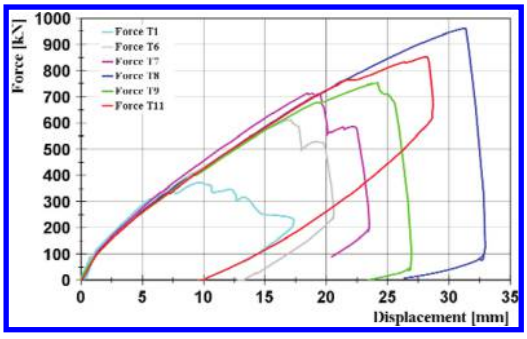

Figure 10. Load versus displacement curves of beams no. 1, 6, 7, 8, 9 and 11.

systems: application of U-shaped CFRP sheets (100 mm in width) with a special end anchorage in the flanged section and alternatively subsequent installation of prestressed self-undercutting anchor rods. Apart from the non-strengthened reference beam, 6 beams were provided with four (in one case three) 1- or 2-layered CFRP sheets and five beams with four to seven post-installed undercut anchors.

All twelve beam tests exhibited typical shear failure, with the following main observations:

- The end anchorage of the CFRP sheets by means of a steel plate fixed to the compression flange proved very effective. While the application of 2-layered CFRP sheets led to failure of the concrete strut in compression, constellations with 1-layered CFRP sheets ended up with rupture of the CFRP.
- Both tested strengthening techniques exhibited a satisfying load enhancement in shear. With the CFRP sheets the load gain was, depending on the number of sheets and layers, between 100% and 150%. The application of post-installed anchors, on the other hand, yielded a 40% load increase with four and 85% with seven anchor rods.
- The shear cracks developed in between the strengthening elements, forming thereby together with the CFRP sheets or the post-installed undercut anchors a typical truss-like structure. The formation and opening of the critical shear crack was retained due to the strengthening elements.

In the next phase of the project, the load increase by the applied strengthening elements will be further reflected with existing design models predicting the overall shear strength. In accordance with Bukhari et al. (2001), an approach that adds the individual contributions to the overall resistance seems most reasonable; however, the respective investigations are currently still ongoing.

ACKNOWLEDGEMENTS

The authors express their sincere gratitude to the Austrian Research Promotion Agency (FFG), the Austrian Railway Company ÖBB and the Austrian motorway operator ASFINAG for the funding of this research project. Likewise the support by the industrial partners Hilti Corporation and SIKA Austria and the fruitful exchange with Jakob Kunz (Hilti), Guenther Grass and Rainer Planer (both SIKA) is gratefully acknowledged.

REFERENCES

Belarbi, A., Bae, S.-W., Brancaccio, A. 2012. Behavior of full-scale RC T-beams strengthened in shear with externally bonded FRP sheets. *Construction and Building Materials* 32: 27-40.

Bukhari, I.A., Vollum, R.L., Ahmad, S., Sagaseta, J. 2010. Shear strengthening of reinforced concrete beams with CFRP. *Magazine of Concrete Research* 62(1): 65–77.

Etman, E. 2011. External bonded shear reinforcement for T-section beams. *Structural Concrete* 12 (3): 198–209.

Kalfat, R., Al-Mahaidi, R., Smith, S.T. 2013. Anchorage Devices Used to Improve the Performance of Reinforced Concrete Beams Retrofitted with FRP Composites: State-of-the-Art Review. *Journal of Composites for Construction* 17 (1): 14–33.

Khalifaa, A. & Nanni, A. 2002. Rehabilitation of rectangular simply supported RC beams with shear deficiencies using CFRP composites. *Construction and Building Materials* 16: 135–146.

Manos, G.C. & Katakalos K.V. 2013. Investigation of the Force Transfer Mechanisms for Open Hoop FRP Strips Bonded on R/C Beams with or without Anchoring Devices. *Open Journal of Civil Engineering* 3: 143–153.

Ozden, S., Atalay, H. M., Akpinar, E., Erdogan, H., Vulas, Y. Z. 2014. Shear strengthening of reinforced concrete T-beams with fully or partially bonded fibre-reinforced polymer composites. *Structural Concrete* 15 (2): 229–239.

Randl, N. & Kunz, J. 2009. Biegeschubversuche an Stahlbetonbalken mit nachträglich eingemörtelter Querkraftbewehrung. *Beton—und Stahlbetonbau.* 104 (11): 229–239.

Triantafillou, T. & Matthys, S. 2013. Fibre-reinforced polymer reinforcement enters fib Model Code 2010. *Structural Concrete* 14 (4): 335–341.

Concrete Repair, Rehabilitation and Retrofitting IV – Dehn et al. (Eds)
© 2016 Taylor & Francis Group, London, ISBN 978-1-138-02843-2

Development of a multi-disciplinary graduate course on rehabilitation of structures

T. El-Maaddawy
United Arab Emirates University, Al Ain, United Arab Emirates

ABSTRACT: This paper describes the development of a multi-disciplinary graduate course on rehabilitation of structures. The course is offered for graduate students by the Civil and Environmental Engineering department at the United Arab Emirates University. The course offers practical tips, design details, and case studies collected by the author upon comprehensive research and outreach activities. The course comprises two modules. Module I is about condition assessment and conventional repairs whereas Module II is about innovative strengthening with composites. Active-learning and problem-solving strategies are adopted in teaching the course. Cooperative learning and collaboration are prompted throughout students' group work. Self-learning, and inquiry-based learning are inspired throughout a research paper assignment and laboratory project. Students are exposed to real-life problems and hands-on training. They conduct research, analysis, and comparisons. Students are asked to present and critique recent research on assessment and rehabilitation of structures, report findings and submit technical reports. Course outcomes that are observable, measurable, and capable of being understood by students, faculty, external agencies, and stakeholders are developed and mapped to the graduate program outcomes. Quantitative (direct) and qualitative (indirect) assessment tools are developed to evaluate the level of attainment of course outcomes. The quantitative assessment tools used to assess the level of attainment of course outcomes include homework assignments, exams, laboratory project, research paper, and presentation. The qualitative assessment tools include students and faculty self-perceptions surveys.

1 INTRODUCTION

The necessity of maintaining the national development of the United Arab Emirates (UAE) has placed increasing demands upon the government and private sectors to secure proper infrastructures, transportation networks, residential and industrial complexes. To help meet those demands, the department of Civil and Environmental Engineering (CEE) at the United Arab Emirates University (UAEU) has established a Master of Science (M.Sc.) graduate program in Civil Engineering (CE), leading to M.Sc. degree in CE. The graduate program is designed to provide the community and industry with distinguished national manpower and highly qualified civil engineers for the sustainable development of the country. The program also trains students intending to purse their Ph.D. in CE. Graduates of the program are anticipated to provide the link between the advancements in civil engineering sciences and corresponding applications. The program covers various CE disciplines including structural engineering, geotechnical engineering, construction management, highway and transportation, water resources, environmental engineering, and surveying. The program has two modes of enrolment, namely "Thesis" and "Non-Thesis". The program degree requirements are given in Table 1. The "Thesis" option requires successful completion of at least 30 credit hours, among which 6 credit hours of Master's Research Thesis that should be completed over a minimum of two semesters. The thesis is defended orally to a committee as stipulated by the UAEU Graduate Studies policy and regulations. The "Non-Thesis" option requires successful completion of at least 33 credit hours. Classes are usually scheduled after 5 pm during weekdays to meet the needs of working part-time students from the industry.

The graduate studies committee of the CEE department at the UAEU, chaired by the author, has developed a set of graduate program outcomes at the MSc level that are in compliance with the QF*Emirates* (2012). The graduate program outcomes adopted by the CEE department at UAEU are given in Table 2. The outcome-based education concept has been implemented in several engineering programs worldwide (Wahab et al. 2011, Arshada et al. 2012). Systematic assessment of program learning outcomes is essential for obtaining accreditation by various accrediting organizations (QF*Emirates* 2012, Osman et al.

Table 1. Program degree requirements.

Courses	Thesis option (credit hours)	Non-thesis option (credit hours)
Core	12	12
Electives	12	21
Research thesis	6	0
Total	30	33

Table 2. Graduate program outcomes (POs).

Outcome	Description
PO1	Demonstrate understanding of highly specialized civil engineering principles, concepts, and methodologies
PO2	Evaluate the performance of advanced civil engineering systems and components through the use of applicable research principles, analytical methods and modelling techniques
PO3	Conduct advanced applied research to develop innovative solutions for highly complex civil engineering problems through the use of appropriately selected research methodologies and modern engineering tools
PO4	Apply advanced multidisciplinary problem-solving approaches to critically analyze contemporary, sophisticated, and highly complex civil engineering problems
PO5	Present and critique highly complex civil engineering issues and communicate effectively at a high level of proficiency
PO6	Demonstrate leadership and management of professional activities and ethical issues in highly complex civil engineering projects
PO7	Appreciate the social, environmental, ethical, economic and commercial considerations and professional responsibilities affecting highly complex civil engineering projects

2012, El-Maaddawy 2015). Results of assessment of program outcomes obtained from the courses can be used to evaluate the overall achievement of program outcomes and make decisions pertaining to curricular and program development (Afida et al. 2011, Lindholm et al. 2009). Such decisions can greatly improve the program competencies and student learning.

The graduate program educational objectives are set to (1) provide graduate students with a clear and comprehensive understanding of advanced civil engineering principles, (2) train graduate students on addressing contemporary, sophisticated, and complex civil engineering issues or projects by utilizing or applying multidisciplinary problem-solving approaches and using modern engineering tools, (3) serve the life-long learning needs of the engineering community and develop their attitudes to acquire further learning experiences and motivate them to get engaged in Ph.D. or advanced training programs, (4) provide efficient and productive research environment to carry out fundamental and advanced applied research to address civil engineering problems in general and regional and national problems in particular, (5) provide the community and industry with quality technical assistance and highly qualified national manpower to lead the national industrial development plans, (6) enrich the collaboration in research and graduate studies between the UAE University and the national and industrial sectors in the country and worldwide, and (7) provide a solid foundation for establishing a national research center for the CE discipline in the country.

Table 3. Course modules and topics.

Module	Topic
Condition assessment and conventional repairs	Defects and Deterioration Repair Procedure and Materials Structural Condition Assessment Structural Strengthening and Stabilization
Innovative Strengthening with Composites	Principles of Strengthening with Composites Flexural Strengthening with Composites Shear Strengthening with Composites Column Strengthening with Composites

2 COURSE DESCRIPTION

The graduate course developed in this paper is entitled Rehabilitation of Structures, and has a subject code of CIVL 616. It is an elective course with 3 credit hours. The course offers practical tips, design details, and case studies collected by the author upon comprehensive research and outreach activities. The course consists of two modules. Each module encompasses four topics. Module I is about condition assessment and conventional repair whereas Module II is about innovative strengthening with composites. Course modules and topics are summarized in Table 3.

3 DEVELOPMENT OF COURSE OUTCOMES

Undergraduate courses generally contribute to the knowledge component with a less emphasis on skills and competencies. In contrast, for graduate

Table 4. Course learning outcomes for CIVL 616.

Outcome	Description
CO1	Demonstrate understanding of damage mechanisms and principles of structural strengthening
CO2	Identify causes of defects, cracks, damage and deterioration of concrete structures
CO3	Conduct condition assessment of structures through inspection, field examination, laboratory testing, and the use of appropriate analytical techniques and problem-solving approaches
CO4	Perform analysis and design of reinforced concrete elements strengthened with advanced composites using appropriate problem-solving approaches and international code provisions
CO5	Develop an appropriate repair strategy for a deficient structure taking into consideration the social, economic and commercial aspects
CO6	Present and critique recent research on assessment and rehabilitation of structures
CO7	Report findings and communicate effectively with pees and clients

courses, there is an increased emphasis on students' ability to use and apply the knowledge and how they develop skills and associated competencies. The program outcomes are, typically, broad in scope since they specify knowledge, skills, and competencies the students are expected to attain upon successful completion of the program. On the contrary, the course outcomes are narrower in scope than the program outcomes.

The learning outcomes of the graduate course CIVL 616, given in Table 4, are developed. The course outcomes specifically describe what students will know and be able to do at the completion of the course. The statement of each course outcome begins with an action verb describing knowledge, skills, or competencies. Each outcome is observable, measurable, and capable of being understood by students, faculty, external agencies, and stakeholders.

4 TEACHING METHODOLOGY

Problem-solving and active learning strategies are adopted in teaching this course, where students are actively engaged in the learning process. The philosophy of teaching and learning through meaningful authentic problem solving that clarifies course concepts has been adopted rather than contrived examples. In the problem solving-based learning, a problem related to the subject is first displayed, typically, through video clips and/or real-life pictures from which lecture's objectives are identified and formulated. Complex problems are broken down into sub-problems. For the students to learn it, the problem and/or sub-problem solutions are broken down into steps during which active questions are frequently asked for problem solving to provide open discussions thus promoting critical thinking and brainstorming debate among students. Students are typically engaged in several hands-on class activities to apply the knowledge gained throughout the lecture time. Experimental learning has also been adopted in teaching this course where students are actively engaged in hands-on experimental work and data collection. In the laboratory sessions, students work in groups to inspire cooperative investigation and collaboration and to accentuate the spirit of teamwork. Each group is asked to submit a written report and deliver an oral presentation to enhance students' technical writing and communication skills. To engage students in higher-order thinking skills, they are asked to make analysis, comparisons and evaluation of test results. To promote self-learning, students are required to discuss and critique original and recent journal articles, describing a major scientific advancement in a research area related to condition assessment and rehabilitation of existing structures. To inspire cooperative and engaged learning and develop student communications skills, students are asked to work in groups, make presentations, submit reports and participate in discussions.

5 DEVELOPMENT OF ASSESSMENT TOOLS

Quantitative (direct) and qualitative (indirect) assessment tools have been developed to evaluate the level of attainment of course outcomes. The quantitative (direct) assessment tools used to assess student learning throughout the course included homework assignments (individual assessment), exams (individual assessment), laboratory project (group assessment), research paper (group assessment), and presentation (individual/group assessment).

The qualitative (indirect) assessment tools adopted in this study included student assessment of course survey where a questionnaire survey is developed and distributed on all students to fill out at the end of the course. In the questionnaire, students are asked to rate their level of achievement of course outcomes from *very low* to *very high* on a 5-point scale. The course instructor rates also his expected level of attainment of course outcomes at

the end of the course from *very low* to *very high* on a 5-point scale.

The homework assignments and exam questions have been carefully designed to directly measure the level of achievement of one or more specific course outcomes.

5.1 *Laboratory project*

The laboratory project is designed to assess the level of attainment of course outcomes CO3, CO4, and CO7. The main objectives of the laboratory project are to expose students to the following activities:

- Hands-on training on nondestructive tests and electrochemical techniques for structural condition assessment and corrosion monitoring.
- Hands-on training on strengthening of concrete columns with Carbon Fiber-Reinforced Polymers (CFRP).
- Application of analytical approaches for prediction of load capacity of concrete columns wrapped with CFRP.
- Comparative analysis with predictions of international guidelines and standards.
- Data analysis, report findings and effective communications with pees and clients.

The students are divided into groups, each of a maximum of three students. The project is divided into two phases. In Phase I, students perform corrosion monitoring of steel reinforcing bars in concrete prisms subjected to wet-dry cycles. Measurements of corrosion monitoring are taken once a week on three locations along the length of the concrete prism. In Phase II, students conduct nondestructive testing, strengthening, and destructive testing on concrete columns. Schematics showing test specimens employed in the laboratory project are given in Figure 1. Tests of Phase I include:

- Covermeter survey to estimate depth of concrete cover.
- Half-cell potential using Galva Pulse GP-5000®.
- Corrosion rate with linear polarization technique using Galva Pulse GP-5000®.
- Concrete resistance using 4 probe Wenner Resistivity meter.

For specimens of Phase II, the following tests are conducted prior to wrapping with CFRP:

- Schmidt hammer test.
- Ultrasonic pulse velocity test.
- Bulk concrete resistivity using Giatec RCON™ electrical resistivity meter.

Strengthening of concrete columns with CFRP include surface preparation, cutting of carbon fiber fabric sheets, mixing of epoxy adhesive, application of epoxy and wrapping of impregnated carbon fiber fabrics. The CFRP wrapping includes an overlap of 50 mm in the lateral direction. Eventually, the concrete columns are tested to failure under uniaxial compression. The following measurements are recorded during the structural test to failure and discussed in the technical report submitted by the students.

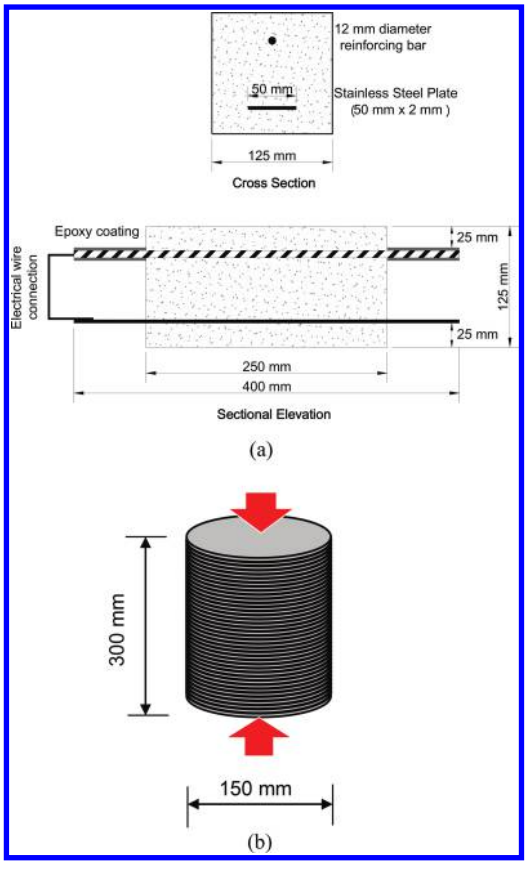

Figure 1. Test specimens for the laboratory project. (a) Phase I. (b) Phase II.

- Load capacity.
- Longitudinal strain.
- Lateral strain in CFRP-wrapped columns.

Students perform a comparative analysis between the experimental results and analytical predictions of international guidelines and standards (ACI 440.2R, Intelligent Sensing for Innovative Structures Canada Educational Module 2004).

5.2 *Research paper*

The research paper assignment is designed to assess the level of attainment of course outcomes

Table 5. Mapping of COs to POs for CIVL 616.

COs	Program outcomes (POs)							Assessment tools*
	PO1	PO2	PO3	PO4	PO5	PO6	PO7	
CO1	√							HW + EM
CO2	√							HW + EM
CO3	√	√		√				HW + LB
CO4	√	√		√				HW + EM + LB
CO5	√	√		√			√	HW + EM
CO6					√	√		RS + PR
CO7					√	√		RS + LB + PR

*HW = Homework assignments, EM = Exams, LB = Lab project, RS = Research paper, PR = Presentation.

CO6 and CO7. In the research paper assignment, students are asked to perform the following tasks:

- Present and critique recent research on assessment and rehabilitation of structures.
- Report findings and communicate effectively with pees and clients.

In this activity, students discuss and critique original and recent journal articles, describing a major scientific advancement in a research area related to condition assessment and rehabilitation of existing structures. Students are required to make presentations, submit reports and participate in discussions. The following list of suggested topics is given to students to help them in selecting their research paper topic.

- Service life predictions of deteriorated concrete structures
- Monitoring of corrosion activity and measurements of corrosion rates
- Condition assessment and evaluation techniques
- Structural Health Monitoring (SHM) and damage detection
- Strengthening of concrete structures with innovative composite systems
- Seismic-retrofitting and shake table tests of concrete structures

6 ASSESSMENT METHODOLOGY

Outcomes of each course in the program contribute to the program outcomes in a different way and to a different extent. The course outcomes must contribute to the achievement of one or more of the program outcomes. The collective learning across all courses enables students to achieve the program outcomes. The learning outcomes of the course CIVL 616 are mapped to the program outcomes as shown in Table 5. The assessment tools used to measure the level of attainment of each course outcome are also given in the same table.

Results of the quantitative assessment along with the faculty and student qualitative assessments are integrated in a course assessment form in an effort to obtain realistic assessment for the level of attainment of course and program learning outcomes. In the course assessment form, the course outcomes are linked to the relevant program outcomes. Also, each course outcome is linked to prespecified direct assessment tools. Results of students' work such as homework assignments, exams, laboratory reports, research paper, and presentations along with students and faculty self-perceptions of level of attainment of course outcomes are used as input data in the analysis.

7 CONCLUSIONS

The graduate course CIVL 616 on rehabilitation of structures offered by the CEE department at the UAEU is developed and described in this paper. The course offers practical tips, design details, and case studies collected by the author upon comprehensive research and outreach activities. Active-learning and problem-solving strategies are adopted in teaching the course. Self-learning, and inquiry-based learning are inspired throughout a research paper assignment and laboratory project. Cooperative learning and collaboration are prompted throughout students' group work. Students are exposed to real-life problems and hands-on training. They conduct research, analysis, and comparisons. They present and critique recent research on assessment and rehabilitation of structures, report findings and submit technical reports. Course outcomes are developed and mapped to the CEE graduate program outcomes. Direct and indirect assessment tools are developed. The direct assessment tools include exams, homework assignments, laboratory project, research paper, and presentations. The indirect assessment tools include students and faculty self-perceptions surveys.

REFERENCES

ACI 440.2R-08 (2008). Guide for the design and construction of externally bonded FRP systems for strengthening concrete structures. Farmington Hills, MI.

Afida, A., Hamimi Fadziati, A.W., Norhana, A., Ahmad Ashrif, A.B., Hafizah, H. (2011). Assessment of student program outcomes through a comprehensive exit strategy. Procedia—Social and Behavioral Sciences, 18: 33–38.

Arshada, I., Razalia, S., and Mohamed, Z. (2012). Programme outcomes assessment for civil & structural engineering courses at University Kebangsaan Malaysia. Procedia—Social and Behavioral Sciences, 60: 98–102.

El-Maaddawy (2015). Assessment of learning outcomes of reinforced concrete design courses: UAEU experience. 7th International Forum on Engineering Education (IFEE2015). Quality Assurance in Engineering Education. 17–19 March, Sharjah, UAE.

Intelligent Sensing for Innovative Structures Canada Educational Module No. 4 (2004). An introduction to FRP-strengthening of concrete structures. ISIS Canada. Section 2S, Canadian Network of Centres of Excellence on Intelligent Sensing for Innovative Structures. Winnipeg, Manitoba, Canada.

Lindholm, J. A. (2009). Guidelines for developing and assessing student learning outcomes for undergraduate majors, 1st Edition.

Osman, S., Jaafar, O., Badaruzzaman, W., and Rahmat, R. (2012). The course outcomes (COs) evaluation for civil engineering design II course. Procedia—Social and Behavioral Sciences, 60: 103–111.

QF*Emirates* (2012). Qualifications Framework Emirates Handbook, National Qualifications Authority (NQA). Abu Dhabi. UAE.

Wahab, H., Ayob, A., Zaki, W., Hussain, H., Hussain, A., Mokri, S. (2011). Program outcomes measurement and assessment processes.. Procedia—Social and Behavioral Sciences, 18: 49–55.

Concrete Repair, Rehabilitation and Retrofitting IV – Dehn et al. (Eds)
© 2016 Taylor & Francis Group, London, ISBN 978-1-138-02843-2

Design of externally bonded FRP systems for strengthening of concrete structures

T.A. Mukhamediev & V.R. Falikman
Scientific Research Center "Construction", Moscow, Russia

ABSTRACT: The new Russian Code of Practice (the Code) labeled "Strengthening of Concrete Structures using Composites. Design Rules" has been developed and approved. The developed Code establishes general provisions on calculation and design of concrete structures, which have been restored or enhanced by external reinforcement elements (fabrics, tapes, laminates, etc.) made of FRP using carbon (CFRP), aramid (AFRP) or glass (GFRP) fibers. The scope of the Code covers various methods used for making strengthening (plate or sheet bonding, over or under-laying, jacketing, etc.). The Code provides also guidance on rate setting of the strength and deformation characteristics of composite materials, design of externally bonded reinforced concrete structures based on strength of normal and sloping to the longitudinal axis of the structure sections, on the width of normal cracks opening, and on deflections. The paper presents the design-level dependences adopted in the Russian Code for strengthening concrete structures using composite materials, and the results of comparing the calculated data with the data of experimental research.

1 INTRODUCTION

For the recent 10–15 years in Russia and abroad the amount of work relating to rehabilitation of various purpose buildings with the aim to extend their life cycle has been essentially increased. Composite materials on the basis of glass, basalt and carbon fibers (FRP) are widely used to strengthen various structures. The efficiency of their use depends on the fact that their strength and deformation characteristics (rupture resistance, elasticity modulus and elongation at fracture) greatly differ from similar characteristics of standard materials (metal, concrete, mortar etc.) used to the same purposes. Besides, the composite material specific weight is 4–5 times less than that of steel and they can be used to strengthen structures of any shapes. These materials have small thickness (from 0.1 to 2 mm), are easily prestressed and are easily repairable, when necessary. They are durable and have a high endurance limit. Strengthening with FRP use is a less labor-intensive and energy-consuming process as compared with other strengthening methods.

In the worldwide practice the composite materials have become widely used, first of all, to recover bearing capacities and to strengthen building components of various engineering structures, industrial and civil buildings, bridges, pipes, storage bunkers, wharfages, various purpose tunnels, urban underground structures; they are also used to restore architectural monuments.

The most popular forms of composite materials used for strengthening are variously woven linen, strips, sheets or plates (lamellas, laminates). The volume fraction of reinforcing fibers in the polymer matrix varies from 25–35% in linen to 50–70% in strips. In addition, composite materials are used to make column casings and solid frames to strengthen tunnel linings.

Just few studies and insufficient documented experience in the field of using composites to strengthen of reinforced concrete structures, as well as unavailability of the regulatory framework complicate the problem facing design engineers and relating to evaluation of the adopted design solution reliability referring to structural strengthening with composite materials and their wide use in construction practice.

Specialists from Scientific Research Institute for Concrete and Reinforced Concrete after A.A. Gvozdev (NIIZhB) and Triada Holding JSC with participation of a number of specialized organizations have produced the Code of Practice "Strengthening of reinforced concrete structures using composites. Design rules" (hereinafter—the Code). It was enacted by the Ministry of Construction of the Russian Federation on 1 September 2014.

The Code establishes the requirements to analysis and design of reinforced concrete structures rehabilitated or strengthened with external reinforcement in the form of fabrics, strips and

laminates made from composite materials using carbon (carbon fiber-reinforced plastics, CFRP), aramid (organoplastics, AFRP) or glass (glass fiber plastics, GFRP) fibers (externally bonded FRP reinforcement). The Code scope is limited by reinforced concrete structures from ordinary and fine-grain concrete that falls under the guidelines of the Russian Code 63.13330.2012 [1].

The new Code comprises guidelines on regulation of composite material strength and strain characteristics, on the analysis of composite-strengthened structures for the strength of their sections, being normal and oblique to a structure longitudinal axis, for the normal crack opening width and deflections. The Code formulates structural requirements and short guidelines on the strengthening process technology and quality control also.

The Code embraces reinforced concrete structures strengthened along normal sections by means of external reinforcing in the direction of the longitudinal axis or by means of external reinforcing of a casing in the lateral direction, as well as the structures strengthened with stirrups along oblique sections.

2 CHARACTERISTICS OF COMPOSITE MATERIALS

Standard design values of composite material strength and strain characteristics are defined according to their specifications with account of experimentally established features of strengthened structure failures. The experimental studies show that exhaustion of bearing capacities of bending structure normal sections strengthened with external composite reinforcement may appear not only due to the full use of strength properties or concrete compressed zone failure, but also due to premature breakaway of strengthening elements. To rule out the failures of this type when defining the composite material strain characteristics the Code, as the foreign codes also, has introduced restriction of the design maximum permissible strains for strengthening elements. Thus, in transition from a guideline value of the composite material tensile strength to a design one, an additional decreasing coefficient γ_{f2} is introduced taking into account of the composite material and concrete bond apart from reliability and operating condition factors. According to the test results the bearing capacity of flexural structures failed due to strengthening element breakaway depends on not only strength and strain characteristics of composite materials and concrete in the strengthened structure, but also on the total thickness of the strengthening element. The relationship for coefficient γ_{f2}, accounting for these features, is taken from the ACI 440.2R-08 [2].

One of the features of composite material properties is reduction of their tensile strength with increase of the period under stress. With the first group limit state design of strengthened structures under action of only sustained dead loads this feature is taken into account by adding the decreasing coefficient of load duration to the composite material tensile strength. This coefficient is accounted for only in the analysis of sustained dead load increment after structural strengthening and is introduced instead of partial safety for materials.

According to few experimental studies including those of composite polymer reinforcement the ratio of long-time and short-time strengths is: for GFRP—0.29…0.55, for AFRP—0.47…0.66 and for CFRP—0.79…0.93. Given that by the moment of strengthening a part of sustained load has been already applied to the structure, the Code prior to accumulation of experimental data assumed the lowest values of the decreasing coefficient in the aforementioned intervals.

Since the values of commercial composite material strength and strain characteristics differ, the Code does not present their standardized numerical values. Standardized values of characteristics have to be established according to the specimen test results with 0.95 of cumulative probability, while the design values—with account of all above-listed safety factors and operating condition coefficients.

3 ULTIMATE LIMIT STATE DESIGN (THE FIRST GROUP OF LIMIT STATE)

The methods of strengthened structure design assumed in the Code are formulated with account of the initial stress and strain state of a structure prior to its strengthening. The values of the initial relative strain of steel reinforcement ε_s^0 and the initial relative strain ε_b^0 of the concrete compression face strengthening of flexural and eccentrically compressed structures are recommended to be defined by the elasticity theory ratios but with account of concrete inelastic properties under compression and crack absence or presence in the structural section tensile zone.

Ultimate limit state design procedures for strengthened structures are developed basing on design models given in the Code 63.13330.2012. As in the Code 63.13330.2012, the basic design method relating to normal section strength of a reinforced concrete structure strengthened with external reinforcement is assumed as the deformation model design method, while for special cases of structural cross-section shapes and force impacts it is allowed to use the breaking stress method.

The design relationships to consider behaviors of composite strengthened structures are assumed on the basis of the test result analysis using foreign code recommendations. The accumulated experimental base used for verifying design relationships assumed in the Code comprised test specimens tested by foreign and domestic researchers.

3.1 *Normal section strength design by the breaking stress method*

The relationships for normal section strength design of flexural and eccentrically compressed structures by the breaking stress method are established proceeding from the prerequisites of the Code 63.13330.2012 and the additional constraint:

$$R_f \le (\varepsilon_{s2} - \varepsilon_s^0) \cdot E_f, \quad (1)$$

where ε_{s2}—limit value of steel reinforcement relative strain assumed by the guidelines of the Code 63.13330.2012.

The value of the compressed zone boundary relative height ξ_{Rf}, at which the element limit state occurs simultaneously with reaching the value of stress in the composite material equal to the design value of resistance R_f, is established with account of the initial stress and strain state of the structure prior to its strengthening:

$$\xi_{Rf} = \frac{\omega}{1 + \frac{\varepsilon_{fu} + \varepsilon_b^0}{\varepsilon_{b2}}}, \quad (2)$$

where ω—characteristic of the concrete compressed zone assumed for ordinary concretes of up to and including B60 classes equal to 0.8, for high-strength concretes of B70…B100 classes and fine-grain concretes – 0.7;

ε_{fu}—design value of composite material limit relative strains calculated at design value of its tensile strength;

ε_{b2}—relative strains of compressed concrete at stresses R_b, assumed according to the guidelines given in the Code 63.13330.2012.

The relationships for normal section design of flexural and eccentrically compressed structures by the breaking stress method are assumed in the form presented in the Code 63.13330.2012 for structures with steel reinforcement but with account of strengthening elements. The scope of recommendations on the breaking stress design method for eccentrically compressed round section strengthened structures is limited by the Code 63.13330.2012 requirements to steel reinforcement arrangement.

Under violation of condition (1) the normal section strength design of flexural and eccentrically compressed structures is carried out ignoring the existing steel reinforcement.

3.2 *The normal section strength design by deformation model*

For the normal section strength design basing on the nonlinear deformation model the general system of physical ratios presented in the Code 63.13330.2012 is assumed that establishes the relation of forces with curvatures and relative strain of the element longitudinal axis. In this regard the stiffness coefficients in the Code system of physical ratios are established with account of strengthening elements and the linear relationship between their axial stresses and relative strains.

The normal section strength design of strengthened structures on the basis of the deformation model is carried out in two stages.

At the first stage the structural stress and strain state design is carried out ignoring the effect of the strengthening system on acting loads prior to strengthening. As a result of the design, one defines the initial values of the section longitudinal axis curvature and concrete relative strains and existing steel reinforcement to be further accounted for at the second design stage.

At the second stage the normal section strength design is performed with account of strengthening elements and the initial stress and strain state of the structure.

When using two-linear or three-linear deformation curves of concrete and steel reinforcement, the normal section strength design basing on the deformation model is carried out proceeding from the conditions in the Code 63.13330.2012 and the additional condition:

$$\varepsilon_f - \varepsilon_{bt}^0 \le \varepsilon_{fu}, \quad (3)$$

here ε_f—relative strains in external reinforcement from a composite material.

The described procedures of flexural element design were verified by the test specimen design. The normal section strength design of test specimens was carried out by both the breaking stress method and the deformation model method. Altogether 397 bending test specimens and 401 compression test specimens were included in the processing.

For bending test specimens the failure due to composite rupture or concrete compressed zone deterioration was detected in 58 cases, the failure due to detachment of the composite end portions—in 186 cases, and the failure due to composite breakaway in the beam middle—in 153 cases.

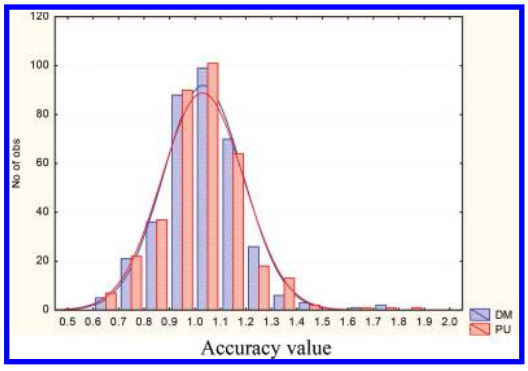

Figure 1. Design precision ratio distribution for flexural test specimens (DM—deformation model design; PU—breaking stress method design).

Figure 1 presents the results of flexural specimen design in the form of the design precision ratio distribution as a ratio of the test specimen bearing capacity actual value and the design value. The average value of the design precision ratio was 1.03 with the standard deviation 0.16. The mean difference of design results obtained by the deformation model and by the breaking stress method was 2%.

3.3 *Strength design of casing-strengthened compressed structures*

The section strength design of compressed elements strengthened with composite casings is carried out by the breaking stress method or using the deformation model with account of concrete strength increase in the three-dimensional stress state.

Basing on the test result processing the design values of concrete compression strength in the axial direction are recommended to be defined by formula

$$R_{b3} = R_b + k_{ef} \cdot k_e \cdot R_f \cdot \mu_f, \quad (4)$$

in which k_{ef} and k_e- casing efficiency factor and coefficient considering the presence of ruptures over the casing height, respectively. The coefficients are recommended to be calculated according to the relationships given in ACI 440.2R-02 [3], which are assumed in a somewhat adjusted form.

In strength design of eccentrically compressed elements of the rectangular and round sections the design relationships have parameter R_{b3} and ξ_{R3}, to be determined with account of the concrete three-dimensional stress state, instead of R_b and ξ_R

$$\xi_{R3} = \frac{\omega}{1 + \frac{\varepsilon_{s,el}}{\varepsilon_{b3}}} \quad (5)$$

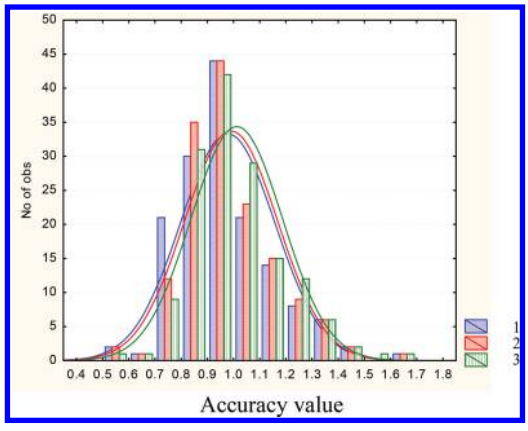

Figure 2. Distribution of design precision ratios for rectangular section test specimens under compression. (1—without k_{ef} and k_e product limitation; 2—with limitation by value 0.55; 3—with limitation by value 0.5).

$$\varepsilon_{b3} = \varepsilon_{b2} + 2\mu_f \frac{R_{f,n}}{E_b} \quad (6)$$

The design procedure was verified by correlation of the bearing capacity design and test values of specimens strengthened with composite casings and brought to compression tests. In total there were 249 specimens with round sections and 152 specimens with rectangular sections.

The rectangular section test specimens were designed with and without limitation of $k_{ef} \cdot k_e$ coefficients product. By the design results it is established that the higher design precision is achieved under limitation of these coefficients product by the value of 0.5. In this case the value of the design precision ratio was 1.01 with the standard deviation 0.17 (Fig.2).

For test round section test specimens it is found out that the mean value of the design precision ratio is 1.09 with the standard deviation 0.18 (Fig.3).

3.4 *Strength design of oblique sections*

The strength design of sections being oblique to the element longitudinal axis and strengthened with external composite reinforcement in the form of bilateral, trilateral or closed stirrups, is carried out using the strength of a concrete strip between oblique cracks, oblique sections under action of lateral forces and oblique sections under action of bending moments.

The strength design of a concrete strip between oblique cracks is recommended to be carried out according to the guidelines of the Code 63.13330.2012 without considering the behavior of composite stirrups.

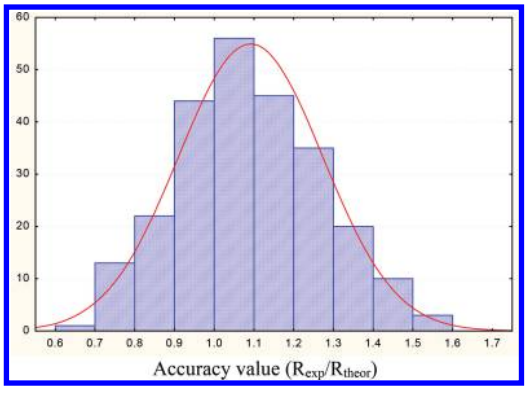

Figure 3. Distribution of design precision ratios for round section test specimens under compression.

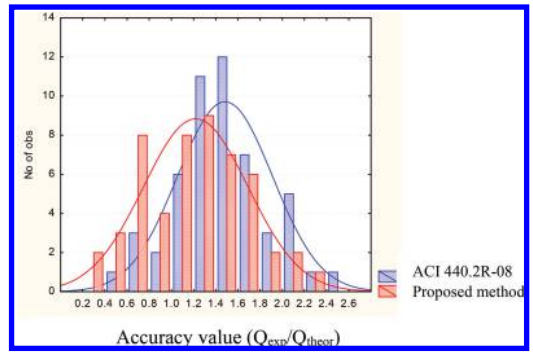

Figure 4. Distribution of the strength design precision ratios for oblique sections under lateral forces.

The oblique section design is recommended to be carried out by the procedure described in the Code 63.13330.2012, but with account of additional internal force Q_{fw} in strengthening elements that cross the oblique crack.

The relationship to determine Q_{fw} can be defined by formula

$$Q_{fw} = \psi_f \frac{A_{fw} \cdot R_{fw} \sin\alpha \cdot C_{fw}}{s_f}, \quad (7)$$

where

ψ_f—coefficient accounting for the stirrup adhesion pattern and assumed equal to:

– for closed stirrups – 0,95;

– for bilateral and trilateral stirrups– 0,85;

C_{fw}—oblique section projection length assumed equal to:

$$C_{fw} = \frac{C \cdot (h_{fw} - a)}{h}; \quad (8)$$

C—oblique section projection length assumed in calculation of forces Q_b and Q_{sw};

h_{fw}—lateral sirrup adhesion height;

A_{fw}—section area of composite lateral stirrup;

R_{fw}—design value of tensile strength for composite materials in strength design of sections being oblique to the element longitudinal axis.

With the presence of lateral steel reinforcement in the existing structure the value of C in formula (8) is assumed to be equal from h_0 to $2h_0$, while in absence of reinforcement—equal to h.

According to the data of experimental studies, when strengthened structures fail along the oblique section, the stresses in composite stirrups do not reach limit values of the material tensile strength. Moreover it is established that the limit value of the lateral force taken up by composite strengthening elements depends to a greater extent on reliability of their bond with a primary structure. Having this in mind, the Code established limitation of their tensile strength design value in the form assumed in ACI 440.2R-08 [2].

The oblique section design of reinforced concrete elements strengthened with stirrups under action of bending moments is recommended to be carried out by the procedure in the Code 63.13330.2012, but with account of additional internal force M_f in strengthening elements that transverse an oblique crack. Moment M_f taken up by transverse composite elements that cross the oblique section is assumed equal to:

$$M_f = 0{,}5 \cdot Q_{fw} \cdot C \quad (9)$$

The oblique section strength design procedure for reinforced concrete structures strengthened with composite materials was verified by the data of foreign experimental studies.

The experimental base used for design comprised 52 test specimens in the form of simple beams strengthened with composite materials in support sections. The beams were tested for action of one or two point forces; the shear span was from $1.5h_o$ to $3.5h_o$. Strengthening of beam oblique sections was performed in the form of closed (26 specimens), trilateral (14 specimens) and bilateral (12 specimens) stirrups made from all-over laps or individual strips. A part of test specimens was made with steel lateral reinforcement.

Comparison of the specimen bearing capacity design values over an oblique section with experimental values is presented in Figure 4. The mean value of the design precision ratio was 1.21 with the standard deviation 0.47. The figure gives the design results obtained by the procedure in ACI 440.2R-08 for correlation. In this case the mean value of the design precision ratio was 1.48 with the standard deviation 0.43.

One failed to detect essential effects of any parameters of test specimens on their strength along an oblique section (strengthening patterns and extents, concrete class, transverse steel reinforcement availability and quantity, etc.). Therefore, taking account of the statistical treatment results in the strength design of oblique sections strengthened with composite materials, the Code recommends assuming the following constraint:

$$Q_s + Q_{fw} \le 2{,}5 R_{bt} \cdot b \cdot h_0. \quad (10)$$

4 SERVICE LIMIT STATE DESIGN (THE SECOND GROUP OF LIMIT STATE)

In conformance with Code 63.13330.2012 requirements to the second group limit state designs presented in the Code comprise the crack formation design, the crack opening design and the strain design.

The experimental studies of crack resistance and stiffness of structures strengthened with external composite reinforcement was much less attended than their strength studies. According to the limited test data, the strengthening of flexural elements with external composite reinforcement provides their stiffness increase, reduction of normal crack opening width, and some increase of the crack formation moment.

Because of the fact that experimental studies performed in Russia and abroad are apparently insufficient, the Code recommendations on the second group limit state design of strengthened structures proceed from the guidelines for steel-reinforced structures and direct consideration of strengthening element stiffness.

The procedure given in Code 63.13330.2012 is adopted for the crack formation design of strengthened flexural structures. In the simplified method of crack formation moment design of structures with rectangular, T–shaped and H–shaped cross-sections the value of the section elastoplastic resistance for the outer concrete fiber is determined with account of strengthening elements. In the deformation model design the values of stiffness coefficients in the system of physical correlations are determined in the Code with account of strengthening elements, while the relationship between their longitudinal stresses and relative strains is assumed as a linear one. The crack formation moment is defined from solution of the system of physical correlations under relative strains of concrete at the element tensile face due to external load effect that are equal to the limit value under tension.

The crack opening width design, when cracks are normal to the element longitudinal axis, is recommended to be performed in conformance with the guidelines given in Code 63.13330.2012, while assuming the element section geometric characteristics in the design relationships with account of external composite reinforcement.

In the simplified method of deflection design of strengthened elements the geometric characteristics of element sections in the design relationships are defined with account of external composite reinforcement.

In the deformation model design of deflections the values of stiffness coefficients in the system of physical correlations in the Code are determined with account of strengthening elements, while the relationship between axial stresses and relative strains in external reinforcing elements are assumed in the form of:

$$\sigma_{fk} = \frac{E_f \cdot \varepsilon_{fk}}{\psi_{fk}}, \quad (11)$$

where

$$\psi_{fk} = 1 - \frac{1}{1 + 0{,}8 \frac{\varepsilon_{fk,crc}}{\varepsilon_{fk}}}. \quad (12)$$

where $\varepsilon_{fk,crc}$—relative strain of the external reinforcing element in the section with a crack immediately after normal crack formation;

ε_{fk}—averaged relative strain of the external reinforcing element.

5 CONCLUSIONS

Development, acceptance, implementation and application of the present Code initiate the appearance of the regulatory document for all professionals engaged in the sphere of industrial and civil engineering as well as in the transport industry; the document regulates the basic methods of external reinforcing in maintenance and strengthening of RC structures; allows objectively assessing the characteristics of composite grids and fabrics and defining their suitability for use in construction in conformance with their fields of application; ensuring interchangeability of similar domestic and foreign products; facilitating harmonization of Russian, international and European documents on technical regulation and standardization in construction.

The Code will permit to find a sound approach to revision of a number of structure strengthening

and repair designs in cast-in-situ and precast construction. Its social efficiency is based on the fact that the formulated requirements to reinforced concrete structure strengthening and rehabilitation and the calculation and design methods presented for their implementation are oriented to ensuring safety of buildings and structures, while their cost-effectiveness is ensured by a set of rational structural solutions for reinforced concrete structure strengthening and rehabilitation.

ACKNOWLEDGEMENT

The authors are grateful to S.I. Ivanov, Cand. Sc. (Eng.), and D.V. Kuzevanov, Cand. Sc. (Eng.), for calculations performed in the course of the Code preparation.

REFERENCES

1. Code of Practice 63.13330.2012. "Concrete and Reinforced Concrete Structures. General Provisions". Updated version of SNiP 52-01-2003. Ministry of Regional Development of the Russian Federation, 2012.
2. ACI 440.2R-08 "Guide for the Design and Construction of Externally Bonded FRP Systems for Strengthening of Concrete Structures," American Concrete Institute, 2008.
3. ACI 440.2R-02 "Guide for the Design and Construction of Externally Bonded FRP Systems for Strengthening of Concrete Structures," American Concrete Institute, 2002.

Concrete Repair, Rehabilitation and Retrofitting IV – Dehn et al. (Eds)
© 2016 Taylor & Francis Group, London, ISBN 978-1-138-02843-2

Conservation and restoration of exposed cement concrete structures in habitable buildings: A case study of historic cement concrete surfaces at Chandigarh

J.S. Ghuman & Janbade Prafulla Tarachand
Chandigarh College of Architecture, Chandigarh, India

ABSTRACT: Early concrete buildings in India and especially in Chandigarh are threatened by deterioration. Effective protection or maintenance is the key to sustain good health & durability of exposed cement concrete structures. This calls for creating awareness, consistent attention for repair or replacement of the sensitive deteriorated façade, taking effective continues preventive treatment of CC exposed surface in habitable buildings. This also calls for creating a trained work force.This paper tries to identify those parameters of the cement concrete properties and analyze them for conservation aspects. Though the analysis is qualitative and an attempt has been made to quantify it and thus making open for empirical understanding. The interpretations drawn could be the first step towards the goal of having explicitly described strategy for future course of suitable actions in use for conservation project. Chandigarh-City Beautiful is a unique expression of urbanism in the machine age civilization, use of natural building material, exposed cement concrete construction and the citizen's faith to sustain its Architectural Heritage. Chandigarh Administration College of Architecture, Research Cell Study, focuses on grading, maintenance, and effective treatment of the exposed cement concrete *surface texture* of buildings in the City Landscape. It also focuses on norms-standards and construction code for sustainable conservation of exposed cement concrete *surface textures*, to ensure, a healthy work and living environment in habitable buildings. Part-II of this study "Grading and Restoration of Corbusier's Concrete" covers the demonstration exercise undertaken for conservation of exposed concrete structures and surface textures in CCA Building.

Keywords: Historic cement concrete Conservation, Historical monument Conservation, Urban conservation, heritage management, Architectural conservation, and Material characterization.

1 APROACH—METHODOLOGY

1.1 Early exposed cement concrete building structures in India, especially in Chandigarh City are rapidly deteriorating, due to non-maintenance & upkeep of its surface texture. In the last 61 years, the external and internal exposed surface texture of cement concrete buildings has either changed or damaged, due to weathering action, environment pollution, effects of carbonation, or its unsatisfactory treatment and upkeep. The exposed cement concrete surfaces of the city heritage buildings are in decay, with fissures, fine hair cracks, surface moisture, deposit of salts, infested with microbial agents, insects, mites, moths, cob webs etc. The age old myth, that: exposed cement concrete surfaces do not require maintenance, no longer holds good.

The research covers listing of heritage RCC structures, in depth study of the exposed cement concrete structures in the Chandigarh College of Architecture (CCA) building, study of options & alternatives for preventive treatment of CC façade and restores healthy conditions in the interior of the habitable buildings.The study conceptual framework refers to: 1) Historical evaluation of CC, 2) Listing of heritage building structures in urban design, Chandigarh City, 3) Qualitative analysis, identification, grading & classification of damaged RCC structure, 4) Qualitative application of silicon based, polymer based or petroleum based material for conservation & restoration of the texture in RCC structures 5) Study of the structure of CCA building, development of skills & techniques ineffective & healthy maintenance of the structure & texture of cement concrete in habitable buildings. The research focuses on the absence of satisfactory skills & techniques in the effective management, maintenance & upkeep of RCC exposed surfaces in heritage buildings, including the Chandigarh College of Architecture (CCA) building. The cement concrete surface in the building interiors are subject to decay, develop

fissures, fine hair cracks, exposed steel reinforcement and is infested with micro biological harmful insects, mites, moths, repeated reappearance of cocoons, cobwebs etc. The study & demonstration exercise focus on creating awareness on conservation, restoration, maintenance & upkeep of deteriorating condition of cement concrete structures. It also aims to ensure healthy living conditions in heritage buildings.To systematically evolve viable techniques & skills, ways & means to sustain maintenance &upkeep of cement concrete structures in heritage buildings and ensure a healthy work & living environment in Chandigarh City urban landscape. This paper tries to identify those parameters of the cement concrete properties and analyze them for conservation aspects. Though the analysis is qualitative and an attempt has been made to quantify it and thus making open for empirical understanding. The interpretations drawn could be the first step towards the goal of having explicitly described strategy for future course of suitable actions in use for conservation project. Chandigarh-City Beautiful is a unique expression of urbanism in the machine age civilization, use of natural building material, exposed cement concrete construction and the citizen's faith to sustain its Architectural Heritage. Chandigarh Administration College of Architecture, Research Cell Study, focuses on grading, maintenance, and effective treatment of the exposed cement concrete *surface texture* of buildings in the City Landscape. It also focuses on norms-standards and construction code for sustainable conservation of exposed cement concrete *surface textures*, to ensure, a healthy work and living environment in habitable buildings. Part-II of this study "Grading and Restoration of Corbusier's Concrete" covers the demonstration exercise undertaken for conservation of exposed concrete structures and surface textures in CCA Building.

1.2 This calls for creating awareness to assess the extent of damage of concrete structures and surfaces, its repair and its effective treatment. The CCA Building demonstration exercise covered in this paper refer to "grading, for repair or maintenance or preventive treatment of exposed c.c. surface textures in buildings." Creating a data bank on graded concrete surface textures, constituting a team of physical planners, architects and engineers with trained-skilled work force, formulating a maintenance schedule will help improve safe & healthy work-living environment in habitable buildings.

1.3 The CCA Research Cell study covers, in-depth investigation of the exposed cement concrete structures and surfaces in buildings. It also aims to identify options-alternatives for preventive treatment of the controlled building façade and the exposed cement concrete roof surface of the CCA Building to restore its healthy texture, namely:

I. Truthfulness of material and construction code
   - **i.** Historic evaluation, type-properties and application of modern cement concrete in the construction industry.
   - **ii.** Quantify & qualify norms, standards, IS Code for sustainable cement concrete structures.
   - **iii.** Identify scanning-mapping techniques of damaged concrete building structures.

II. Grading-Restoration of Corbusier's Concrete, Demonstration Exercise
   - **i.** Chandigarh City Heritage, Corbusier's cement concrete building structures in the City Landscape.
   - **ii.** Study the CCA building structure, develop skills & techniques for conservation of exposed cc surface texture.
   - **iii.** Application of silicon, polymer or petroleum based products to ensure sustainable maintenance of the concrete surface texture.

1.4 The interpretations drawn in this paper is a step to explicitly evolve a strategy for suitable future course of action and sustainable conservation of heritage buildings in the Chandigarh City Landscape.

2 CORBUSIER'S CONCRETE: CHANDIGARH CITY LANDSCAPE

2.1 Beginning early in 1908, Mon's Le Corbusier spent his life time to perfect skills in use of reinforced cement concrete in high rise building. He successfully executed housing projects in Marseilles, France. Thereafter in early 1950's, he embarked upon his life time achievement project, the New Capital City-Chandigarh in East Punjab. The Charter-Edict laid-out by Le Corbusier enlightens the citizens on its basic urban design concepts and architecture with a view to protect its inheritance in the growth-development of the city. He introduced "Modern Age Architecture" and "Truthfulness in use of Building Materials" i.e. fusion of exposed cement concrete, bricks and stone in city planning. He pointed out that "The Age of Statues is Gone", commemoration of events to be confined to suitably placed bronze plaques.

2.2 Le Corbusier's Master Plan for Chandigarh City infused a balance of the basic Garden City concept with multi-storey high-rise buildings on

Figure 1. Chandigarh Master Plan—Phase I, II & III 1966.

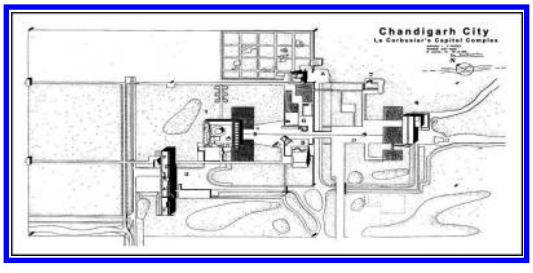

Figure 2. Capitol Complex Chandigarh by Le Corbusier.

a human scale. Despite the geopolitical-administrative changes in 1966, Chandigarh City has sustained the inherited urban form, city landscape and architectural concepts. The city is planned to breathe the sublimated spirit of art in buildings to provide places for all human activities for citizens to live a full and harmonious life with nature.

2.3 Capitol Complex in the N-E of the city is the seat of Governance with the High Court, the Assembly Building and the Administrative Secretariat in multi-storey high rise cement concrete structures. The inter-weaning open space of 1 km x 0.5 km with the Geometric Hill is laid with vast cement concrete pavement as open space for the people. The "City Landscape" blends and harmonises with the multi-storey high-rise concrete structures.

Areas of special architectural interest

2.4 Certain areas of Chandigarh are of special architectural interest where harmony and unified composition of building is regulated by architectural and zoning controls. Construction of buildings along V-2 central (Dual carriage-ways,

Figure 3. View of Assembly Building in Capitol Complex Chandigarh: Unmaintained concrete surface texture due to decay and carbonation.

Figure 4. View of RCC Building, Sector 17, Chandigarh: Damaged surface texture due to decay and carbonation.

Madhya Marg and Uttar Marg, where sky-line heights, character and architecture of buildings as planned is not to be altered. Beyond V-2 along the dual carriage way, areas are reserved for cultural, health and educational institutions. City Centre The central plaza in Sector-17 was designated by Le Corbusier as "Pedestrians Paradise". Architectural façade, cement concrete surface texture of buildings in the City Centre is not to be altered. All exposed cement concrete RCC buildings (individual private ownership) show signs of damage and decay due to weathering action and carbonation. The red sand stone flooring in the front covered corridors is also damaged / altered and is unfit for use of pedestrians.

Conservation of damaged concrete surfaces

2.5 Conservation of Le Corbusier's work in multi-storey modern cement concrete habitable structures 1952–67, deterioration of the concrete edifices in the Capitol Complex and the city landscape has been having the attention of Chandigarh (UT) Administration. Attention on this was also focused by the College of Architecture Chandigarh and the Foundation Le Corbusier Paris, France in its International Seminar held on 11th to 13th Feb, 2002 in Chandigarh.

Figure 5. PGI Nehru Hospital Building Sector-12, Chandigarh: Damaged exposed concrete façade.

2.6 Mr. Puranjit Singh, Chief Engineer Chandigarh Administration introduced the Ultrasonic Pulse Velocity Test at selected locations in the Assembly building to assess the soundness of concrete. The criteria for qualitative assessment of the concrete quality is based on IS: 13311 (Part-1). The results reveal Ultra-Sonic Pulse Velocity of more than 3.5 km/sec at undamaged areas, indicating a good quality of concrete. The poor velocities at other locations; less than 3.0 km/sec could be due to cracks and/or damage of cover concrete due to reinforcement corrosion and/or due' to honeycombing. The "Schmidt Hammer Test" for measurement of the strength / quality of the concrete was also carried out as per IS: 13311 (Part-2) at select locations in the Assembly building in Chandigarh's Capitol Complex. During the tests, a hollow sound was noticed at some of the locations, depending on the extent of de-lamination and surface deterioration. Except for some light damage of honeycombed areas, the concrete of the Assembly building exhibits good surface hardness and structural stability.

2.7 Efforts to repair the damage by the Chandigarh Administration were also initiated by involving the Central Building Research Institute, Roorkee. They recommended an extra cover on all the decayed surfaces. Since such an action would have altered the original character and texture of these buildings and impaired their authenticity, these recommendations were not accepted. Local maintenance engineers, thereafter decided to clean the affected surface with steel brushes and apply silicon coating on all external concrete surfaces of the Secretariat building. This application is effective, although the life of such treatment has not been technically proved and effects on the strength of concrete are yet to be studied.

2.8 The condition of the PGI and the University Campus Buildings with exposed concrete façade require both repair and treatment of its surface texture for a healthy work-living environment.

2.9 The Chandigarh UT Administration also engaged the services of the Associated Cement Co. research team to conduct an on-site "Non-destructive Test" and analysis of concrete for buildings in Chandigarh. The ACC team recommended comprehensive restoration methods. Their preliminary report has shown a generally good surface hardness of concrete, but problems such as inadequate concrete cover, honeycombing and signs of atmospheric corrosion with an advanced level of distress do exist at some places. The ACC team has also recommended experimental restoration technique to be tried on the affected area of the porch. This specifically relates to:

- Changing the entire waterproofing on the roof of the Assembly portico to prevent further deterioration.
- Removing damage or loose/carbonated concrete surfaces by wire brushes and de-rusting corroded reinforcing bars.
- Application of an epoxy bond coat followed, after applying migratory corrosion inhibitors on prepared concrete surface.
- Additional reinforcement to be provided wherever reinforcing steel has degenerated due to corrosion.
- Grouting with Polymers/Ordinary Portland Cement mix, to treat the cracks or damaged concrete surfaces.
- Repair of damaged concrete structures and application of preservative coating on exposed concrete surface.

3 PHYSICAL ASSESSMENT AND GRADING OF C.C. SURFACE TEXTURE IN BUILDINGS

3.1 Grading of building material i.e. cement, gravel, sand, water etc. is specifically covered by Bureau of Indian Standards, Concrete Codes: IS 456–1957, 1964, 1978, 1994 and IS Code: 456–2000. The grading of concrete is with respect to its strength-hardness, workmanship, design of concrete mix, use of shuttering material including vibrators in laying of concrete & compaction, inspection and hardness-slenderness testing requirements in the design of building structural members including solid slabs, beams etc. No Norms and Standards have been laid in the IS Code: 456–1978, 1994 & 2000 for grading of exposed cement concrete "surface texture". This comprises of "< 0.5 to < 1 mm thick crust" hardened concrete slurry of cement and fine sand grains, constituting the exposed concrete surface.

Table 1. Physical assessment of the area of external exposed façade and the concrete surface texture of cement concrete building structures in Chandigarh City Landscape.

Cement Concrete Building Structure and Architectural Controlled Façade (Exposed Concrete Surface Texture)	External Exp. c.c. Facade	Internal Exposed Concrete	Gross Exposed Concrete	Damaged Concrete Structure (in m^2)		Damaged Untreated Surface Texture (in m^2)	
	(m^2)	(m^2)	(m^2)	Area	% age	Area	% age
Capitol Complex	158938.93	635755.73	794694.67	8025.00	1.01%	794694.67	100%
Assembly Building	34690.20	138760.80	173451.00	2601.77	1.50%	173451.00	100%
Secretariat Building	40471.90	161887.60	202359.50	2428.31	1.20%	202359.50	100%
High Court Building	25439.48	101757.92	127197.40	1526.37	1.20%	127197.40	100%
Hall of Shadows Building	289.09	1156.34	1445.43	17.35	1.20%	1445.43	100%
Geometric Hill	231.27	925.07	1156.34	5.78	0.50%	1156.34	100%
Open Concrete Pavement	57817.00	231268.00	289085.00	1445.43	0.50%	289085.00	100%
City Centre, Sector-17	180389.04	721556.16	901945.20	18394.48	2.04%	901945.20	100%
SCO Concrete Façade	52035.30	208141.20	260176.50	7805.30	3.00%	260176.50	100%
Govt. Buildings Concrete Façade	11563.40	46253.60	57817.00	1734.51	3.00%	57817.00	100%
Office and Hotel Complex	28908.50	115634.00	144542.50	1806.78	1.25%	144542.50	100%
Museum and Arts College, Sector-10	40471.90	161887.60	202359.50	3237.75	1.60%	202359.50	100%
College of Architecture, Sector-12	1156.34	4625.36	5781.7	109.85	1.90%	5781.7	100%
PGI Campus, Sector-12	46253.60	185014.40	231268.00	3700.29	1.60%	231268.00	100%
Punjab University Campus, Sector-12	2890.85	11563.40	14454.25	231.27	1.60%	14454.25	100%
Administrative Block	2312.68	9250.72	11563.40	185.01	1.60%	11563.40	100%
Gandhi Bhawan	578.17	2312.68	2890.85	46.25	1.60%	2890.85	100%
Punjab, UT and other Govt. Off. Bldg. Façade, Sector-10	46253.60	185014.40	231268.00	3700.29	1.60%	231268.00	100%
SCO Bldg. Concrete Façade, MM, Sector-9	37002.88	148011.52	185014.40	4255.33	2.30%	185014.40	100%

Physical assessment of exposed C.C. surfaces

3.2 A study of the physical condition and characteristics of exposed cement concrete structure and surface texture was carried out for the i) assembly, high court & secretariat government buildings in the capitol complex, ii) museum & college of arts government buildings in sector 10, iii) engineering, college of architecture, post-graduate institute, university campus and other buildings in sector 12, iv) UT Chandigarh Secretariat and other government-private buildings along the Jan Marg, v3 road from sector 22 to the capitol complex, v) cement concrete façade in government & private buildings in city centre, sector 17 and vi) brick & cement façade of private buildings along the Madhya Marg v2 road. The condition of the structure and surface texture, its coverage is given in Table No. 1.

ST 1: Glossy shiny, lustrous bright silver grey or beige colour.

ST 2: Soft, fine to touch in silver grey colour partial change in colour of concrete surface texture due to carbonation etc.

ST 3: Smooth free from irregular surface particles, in steel or processed wood shuttering or moulding with carbonation and change in concrete surface texture colour.

ST 4: Coarse medium or small granular surface, with surface voids, carbonation, change in concrete surface colour.

ST 5: Course rough or large granular surface, generally seen in rough wood shuttering, carbonation and total change in concrete surface texture colour.

3.3 It is noted that the RCC building structures do not show major signs of structural damage, corrosion of embedded steel bars. However the exposed concrete surface texture of both the external and internal surfaces show sign of marginal damage of the concrete, fine hair cracks, water seepage and decay due to deposit of salt, algae etc. It is also noted that both the external or internal exposed surfaces of all concrete buildings are badly effected due to air pollution, effects of carbonation and change of the concrete surface texture-colour.

This calls for grading of the exposed cement concrete surfaces, effective maintenance and treatment to sustain the surface texture for a healthy work-living environment in buildings.

Grading of concrete exposed surface texture

3.4 The word "texture" is co-related to many varied or different characteristics of concrete surfaces in building structures. It predominantly refers to construction skills or techniques, grade & quality of the cement, sand & gravel in the concrete mix, tools & instruments used in laying of the cement concrete i.e. steel or wood shuttering. The texture in cement concrete structures is constituted by the physical form, shape, size & composition, colour, or finish of exposed cement concrete surfaces in habitable buildings. The key factors for a healthy or quality cement concrete texture are;

- A smooth and soft glossy surface texture
- Free of pitting, blisters, surface voids or damage.
- Free of dis-colouration due to pollution or other causes.

3.5 The study of Corbusier's concrete buildings in the Capitol Complex and other parts of the city show a distinct and high quality of glossy or smooth concrete surface texture. The exposed concrete surface in privately constructed buildings in Sector-17 City Centre and other parts of the city is either rough or coarse and is not compatible to the concrete surface texture of Corbusier's concrete buildings. ***Surface Textures (ST) are graded*** to facilitate sustainable restoration of differently placed exposed cement concrete surfaces, namely;

4 MAINTENANCE AND UPKEEP OF CONCRETE SURFACE TEXTURES

4.1 Conservation, restoration & maintenance of cement concrete structures of heritage buildings in Chandigarh City is undertaken by the Public Works Department, either with its own trained workers or through the private agencies as a specific job, on item rate basis. There are no norms, standards or specifications laid out in the Indian Standards or CPWD codes of practice to ensure satisfactory maintenance & upkeep of the heritage buildings on a regular, annual or daily basis. There is no standardized material for treatment of exposed concrete surfaces or adequate equipment, tools or instruments for maintenance & upkeep of concrete structures. No provision for permanent fixtures in the heritage buildings has been made to enable conservation, restoration or maintenance works for the exposed concrete surfaces in buildings.

4.2 Maintenance and upkeep of concrete surface texture of exposed external surfaces is subjected to weathering action. The exposed external surfaces require silicon or polymer based waterproof treatment. Alternately, household disinfectants in petroleum base were found suitable for treatment of internal exposed concrete surfaces to sustain its texture. The maintenance and upkeep of exposed concrete surface is generally carried-out by;

- ***Dry or Wet Process***: cleaning the Cement Concrete surface infested with dust and cobwebs, etc. with water and brush.
- ***Optional, use mechanical or manual dry or wet process*** i.e. air or sand blasting, or steel or coir fibre brush for cleaning the concrete surface to remove carbonation.
- ***Mechanical or manual process*** i.e. compressed air pump with a spray gun to dry and clean the Concrete Surface.
- ***Protect & treat:*** **all concrete surfaces** with silicon or polymer based product or petroleum based product i.e. a mixture of sulphur free Diesel (low lubricant) 50% + Kerosene (absence of olefin lubricant) 40% + 10% household insecticide-disinfectant (by volume) with a 4" paint brush or a compressed air pump spray gun.
- ***Ensure fire and other safety requirements:*** including use of silicone hand gloves, face mask, protective glasses etc. when treating or applying the aforesaid indigenously prepared mixture.
- ***Allow free flow of air & ventilation:*** in the room or interior portion of the building before occupying it.

5 CONSERVATION OF CCA BUILDING: DEMONSTRATION EXERCISE

5.1 The construction of the Chandigarh College of Architecture Building was completed in 1963. The RCC parabolic roof is laid on wood formwork. It therefore has a coarse or rough texture. Water proofing of the roof top was carried out by the Chandigarh Administration Engineering Deptt. in 2005–06. Though the roof water seepage has stopped, the exposed concrete roof ceiling surface has hair cracks fissures, salt deposits and the surface voids of exposed concrete is infested with harmful insects, moths, mites and microbes.

5.2 The exposed concrete building façade and the entrance porch wall was constructed in September 1963. Sun shade full size panel was drawn on a ground platform with 4" thick frame work. It was filled with sand and 1% of cement. Complete shuttering pattern was drawn and carved out in wooden formwork and anchored properly to hold the shuttering panels by using bolts at every 3'-0" (1.0 m) distance.

Figure 6. Chandigarh College of Architecture: Building façade concrete surface texture carbonation.

Figure 8. CCA Faculty Room sky light concrete dome.

Figure 7. CCA Faculty Room exposed concrete roof.

Figure 9. CCA Faculty Room surface dry process manual cleaning.

Surface texture of exposed cement concrete roof

5.3 The gross exposed concrete roof surface area and the external exposed c.c. façade of the CCA Building is 5781.70 m^2 The internal exposed concrete roof surface of a faculty room having 325 sq ft (30.19 m^2) was selected for the demonstration exercise to restore and treat its surface texture with petroleum based product. The external exposed c.c. façade is not covered in this exercise as it was partially restored with silicon / polymer based product by the Chandigarh Administration Engineering Department.

5.4 The exposed roof surface has fine hair crack, fissures, roof water seepage, salt deposit and is infested with cobwebs, insects and microbes. Over a long time period, the infested roof surface also effects the sensitive surface texture of the exposed concrete roof. It corrodes the roof surface texture to accumulate loose dust & sand, creating unhealthy work and living environment in the building.

Figure 10. CCA Faculty Room roof surface: Wet process cleaning.

Dry Process cleaning of exposed C.C. roof surface

5.5 Dry process cleaning of the coarse roof surface was skilfully carried-out with wire brush, so as not to damage the concrete surface texture. Application of excessive pressure on wire brush damaged the surface texture (ST) and exposed the concrete. The exercise helped remove the dust and loose sand infested with mites-microbes. The "Dry Process" manual cleaning had to be handled skilfully to protect the surface texture crust from damage.

Wet process cleaning of exposed C.C. roof surface

5.6 The wet process cleaning with sponge and water helped further remove the loose dust and sand from the concrete roof surface. The process also helped to minimize moisture to protect corrosion of steel bars embedded in the concrete.

Treatment of C.C. surface texture

5.7 Use of petroleum based products in the treatment of exposed cement concrete surfaces is evaluated vis-à-vis the use of lubricants at the time of laying of concrete on steel or wood formwork or mouldings. Petroleum based lubricants are healthy and are compatible when in contact with concrete and helps to develop a glossy of fine or smooth surface texture. It also helps concrete to breath in the process of its chemical reaction in its setting or hardening on the formwork or moulding and its safe dismantling. It is also noted that the application of the petroleum based products added with compatible household insecticides on exposed cement concrete surface helps in sustaining a healthy surface texture of concrete in habitable buildings.

5.8 The treatment of exposed cement concrete surface texture is regulated with a balanced use of lubricant to avoid its excessive accumulation on the concrete surface. Low sulphur diesel with or without blended biodiesel and low lubricant content proportionately mixed with household insecticide was found most suitable for treatment of exposed cement concrete surface in habitable buildings. The following products have been experimented for its application in the treatment of the exposed cement concrete roof surface in the CCA Building.

i) ***Low Sulphur Diesel:*** Petroleum-derived diesel is composed of about 75% saturated hydrocarbons (primarily paraffin-lubricant)), and 25% aromatic hydrocarbons (including naphthalenes and alkylbenzenes). It has excellent lubricant rust preventive properties, appearance-clear golden colour, flash point-low flammability compared with other petroleum fuel. The lubricating property in Diesel is compatible to cement concrete surface textures as base ingredient with household insecticides.

ii) ***Kerosene:*** A hydrocarbon liquid, commonly used as low flammable fuel (37 to 65°C) in cooking and lighting. The major components of all kerosenes are; straight chain alkanes and naphthenes (cycloalkanes), which normally account for at least 70% by volume. Aromatic hydrocarbons do not normally exceed 25% by volume of kerosene streams. Olefin (lubricant-paraffin) is usually not present or < 5% by volume, dry cleansing effect on exposed concrete surface.

iii) ***Turpentine:*** A fluid obtained from pines trees composed of terpenes, mainly the monoterpenes alpha-pinene and beta-pinene with lesser amounts of carene, camphene, dipentene, and terpinolene. It is an organic solvent used in spirit paint work. Its vapour damages the skin, eyes and respiratory system, as well as the central nervous system when inhaled. Being combustible, it also poses a fire hazard.

iv) ***Phenyl:*** Derived from benzene (C_6H_6), related to a vinyl group is a aromatic product with carbon bonding. Phenyl compounds are hydrophobic, tends to resist oxidation and reduction. It is not compatible to petroleum base due to sedimentation of carbon particles in Phenyl.

v) ***HP Finit:*** A household insecticide, very effective in knocking down & killing both flying and crawling insects like cockroaches, bed bugs, mites, mosquito, its larvae, Silverfish etc. HP Finit earlier marketed as *FLIT*, (Pyrethrum 0.05%, Malathion 1.0%) in Kerosene base is environmentally friendly. It is a compatible mix with other petroleum products.

vi) ***Rust Preventives:*** Contain corrosion inhibitors, HP RUSTOP 286 process moderate water displacement characteristics, oil type non-combination lubricant cum Rust Preventive. Physiochemical properties are, appearance-clear, flammable flash point 190, kinetic viscosity @ 40°C – 167 to 175.

vii) ***HP Spray Oil-E:*** Non phytotoxic having excellent wetting characteristics, used in dose of 2 to 3% emulsion with water in apple orchards to control damage from organic pasts, physiochemical properties, appearance-clear, colour ASTM-6, kinetic viscosity at 40°C – 19, and is biodegradable.

5.9 Application of petroleum products was carried-out to ascertain its effect on exposed concrete surfaces. It is noted that high lubricant content in rust preventives oil, is not compatible to treatment of exposed cement concrete surface. It is also noted that biodegradable oil spray used in apple orchards is also not compatible to exposed cement concrete surfaces. Inflammable turpentine used in varnish-spirit polish for wood surfaces is also not compatible to its application on exposed cement concrete surface. These products are therefore ruled-out for protective treatment of exposed c.c. surfaces.

5.10 Application of the other petroleum products was studied to ascertain a desirable mix suitable for protective treatment of exposed cement concrete surfaces. It is also noted that application of diesel or kerosene as petroleum base material, phenyl or finit as household insecticide on their own is not compatible for protective treatment of the exposed concrete surface to ensure a healthy work-living environment in buildings. Proportionate mix of the aforesaid petroleum products (by volume) were used for protective treatment of the exposed cement concrete roof surface in the CCA Building.

Figure 11. Petroleum based products for treatment of exposed concrete surface texture, i) Diesel in large green bottle container, ii) Phenyl household insecticide, iii) Turpentine Oil, iv) Kerosene in blue colour and v) Finit household insecticide in Kerosene base.

Figure 12. Application of petroleum base mix in restoration-treatment of roof surface in faculty room CCA Building.

i. Diesel 50% + Kerosene 45% (petroleum base products) + Phenyl 5% household insecticide (hydrophobic benzene).

ii. Diesel 50% + HP Finit 50% household insecticide in Kerosene base (totally petroleum based product).

5.11 It is noted that though diesel and kerosene petroleum product mix reduce the lubricant oil content by 50%, clear transparent light gold colour oil, the phenyl 5% by volume (household insecticide) add to its turbidity with carbon particles settling down in the glass (Figure 11). This was discarded to avoid carbon particles effecting the exposed cement concrete surface texture-colour. Alternately the petroleum product mix of Diesel 50% and HP Finit 50% household insecticide in Kerosene base has a clear transparent mix for protective treatment of the exposed c.c. surface.

Petroleum product mix application on roof surface

5.12 The treatment-application of the petroleum product mix of Diesel 50% + HP Finit 50% household insecticide in kerosene base on the exposed cement concrete roof surface was carried-out manually with a hand paint brush and by pressure pump spray. The manual process with paint brush was found satisfactory. The mechanical process (air pressure pump with spray gun) was found more suitable for the coarse concrete roof with exposed surface voids.

6 COST EFFECTIVE RESTORATION

6.1 The cost of dry and wet process cleaning of both external and internal exposed concrete surfaces is generally the same. It is noted that comparatively cleaning of the external surfaces require erection of scaffolding. However the cost effectiveness of treatment of external exposed surfaces with silicon base or polymer based products is estimated at USD 2.59 (Rs. 160/-) per m^2. It is 2 times more as compared to application of petroleum based products works-out to USD 1.30 (Rs. 80/-) per m^2. Its application by manual or mechanical processes does not show much variation. The cost of the dry and wet cleaning process, both may manual or mechanical works-out to USD 0.62 (Rs. 40/-) per m^2. The use of petroleum based mix for complete manual restoration of the internal concrete roof surface with mechanical pump-spray gun used in the CCA Building demonstration exercise works-out to USD 1.71 (Rs. 106/-) per m^2 i.e. approximately Rs. 10/- per sq ft.

7 FINDINGS AND CONCLUSIONS

7.1 Physical assessment and grading of exposed cement concrete surface texture (Table 1) show that the damage of concrete structures in the Capitol Complex is approximately 1.01% as compared to private owned concrete buildings in Sector-17 (2.04%) and along Madhya Marg Sector-9 (2.3%). It is also noted that the damage of exposed concrete surface texture is predominantly due to structural alterations and faulty repair of the building façade. Effort need to be made to protect, conserve and restore the truthfulness of material in the controlled building façade in the Chandigarh City Landscape.

7.2 The dry, wet, chemical cleaning process, for exposed concrete surfaces, both manual or mechanical has to be viewed as unique or specific for varied structural conditions or surface textures. The mechanical cleaning process through high air or water pressure with or without chemical additives should be avoided to avoid damage of the concrete structure or the fragile surface texture. Mechanical sand blasting cleaning process, invariably damages

the fragile exposed concrete surface texture and should be generally avoided, unless absolutely necessary for cleaning of the voids in rough or coarse exposed concrete surfaces.

7.3 The "Wet Process" of manually cleaning the concrete roof surface with sponge and water achieved excellent / outstanding results in restoration of the roof surface texture. It helped remove dust and loose carbon particles left behind in the dry process. It also helped to strengthen the fragile roof concrete surface texture. The appropriate cleaning methods and treatment for cement concrete surfaces based on the graded textures to determine the most effective method is recommended as follows:

Table 2. Cost effective restoration of exposed cement concrete surface texture.

Restoration (Nature of Work)	External Surfaces cost/m^2	Internal Surfaces cost/m^2
Dry process cleaning:		
i) Manual including cost of scaffolding	USD 0.32 (Rs. 20/-)	USD 0.29 (Rs. 18/-)
ii) Mech. sand blasting	USD 0.32 (Rs. 20 /)-	USD 0.32 (Rs. 20/-)
Wet process cleaning:		
i) Manual sponge & water	USD 0.32 (Rs. 20/-)	USD 0.29 (Rs. 18/-)
ii) Mech. PP washing	USD 0.32 (Rs. 20/-)	USD 0.32 (Rs. 20/-)
Surface Treatment Material		
i) Petroleum based mix	USD 0.65 (Rs. 40/-)	USD 0.65 (Rs. 40/-)
ii) Silicon or polymer based product	USD 1.62 (Rs. 100/-)	— —
Surface Treatment Application		
i) Manual	USD 0.65 (Rs. 40/-)	USD 0.32 (Rs. 20/-)
ii) Mech. PP spray	USD 0.97 (Rs. 60/-)	USD 0.48 (Rs. 30/-)

7.4 The petroleum product mix of i) Low Sulfur Diesel 50% ii) HP Finit 50% household insecticide in kerosene base oil, proved very effective in restoring the exposed concrete surface texture. Difficulty was experienced in the application of the petroleum product mix with pressure pump spray gun. The spray gun nozzle is not designed for spray on horizontal roof surfaces, due to oblique angle of the oil cup vis-à-vis the spray gun nozzle.

7.5 The petroleum based product mix treatment (Figure 13) is very effective in the restoration of the exposed concrete roof surface. The mix has the right proportion of lubricants in its contents to restore the texture and colour without damaging the fragile concrete crust surface texture. It is also noted that the mix is effective in sustaining the concrete surface texture.

Figure 13. CCA Building faculty room "roof surface" showing, conserved and protected surface texture after restoration and treatment.

Table 3. Recommended effective cleaning and treatment process for exposed cement concrete graded surface texture.

Graded surface texture	Recommended	Surface treatment
ST 1: Glossy, lustrous silver grey or beige colour.	Dusting, cleaning with soft cotton fibre dry mopper and clean portable water without any additives	Clear wax or petroleum jell, polish mix with diesel or kerosene
ST 2: Soft, fine to touch in silver grey colour	Coir or soft brush dry process with nylon sponge and water without any additives	Petroleum base proportionate mix with insecticide
ST 3: Smooth free from irregular surface voids or particles	Coir or soft brush dry process with nylon sponge and water without any additives	Petroleum base proportionate mix with insecticide
ST 4: Coarse medium or small granular surface, with surface voids	Wire brush, low pressure sand or water blasting mechanical process or wet process	Petroleum base proportionate mix with insecticide
ST 5: Course rough or large granular surface voids	Wire brush, low pressure sand or water blasting mechanical process or wet process	Petroleum base proportionate mix with insecticide

REFERENCES

i) Celebrating Chandigarh, Proceedings of Conference 50 Years Chandigarh 9–11 January 1999, Published by Chandigarh Perspectives, Chief Architect and Sec. Urban Development Department, Chandigarh Administration, UTSecretariat, Sector-9, Chandigarh-India.

ii) Corbusier's Concrete, Challenges of Conserving Modern Heritage, Kiran Joshi, Editor, Proceedings of Seminar on Conservation of Le Corbusier's Work in Concrete, Chandigarh 11–13 February 2002.

iii) Draft Master Plan Chandigarh 2031, Department of Architecture and Urban Planning, Chandigarh UT Administration, http://chandigarh.gov.in/.

iv) Conservation of Concrete Structures in Buildings: Prof. Jagjit Singh Ghuman, Guest Lecture Cum Workshop on "Cultural Heritage Conservation: Towards A New Paradigm" 2nd and 3rd May, 2013, CCA Auditorium, Chandigarh.

v) Cleaning History Masonry: Rehabilitation Standard No. 7—Part 1, State Historical Society of IOWA.

vi) The Investigation and Repair of Historic Concrete, Susan Macdonald, Assistant Director, NSW Heritage Office, Locked Bag 5020, Parramatta, NSW 2124.

vii) The Investigation and Repair of Historic Concrete, Susan Macdonald, Assistant Director, NSW Heritage Office, Locked Bag 5020, Parramatta, NSW 2124.

viii) Rehabilitating Corbusier's Capitol, Puranjit Singh, Former Chief Engineer Chandigarh UT Administration, Chandigarh 11–13 February 2002 Proceedings of Seminar on Conservation of Le Corbusier's Work in Concrete.

ix) IS 456, Indian Standard Code of Practise for Plain and Reinforced Concrete, Bureau of Indian Standards, Manak bhawan, 9 Bahadur Shah Zafar Marg, ND—110002.

x) CPWD Specifications, 1966/AMD 2002, on Roofing Finishing. Repairs to Buildings, Dismantling, Demolition and Miscellaneous Building Works. Vol. 2 Nabhi Publication.

Concrete Repair, Rehabilitation and Retrofitting IV – Dehn et al. (Eds)
© 2016 Taylor & Francis Group, London, ISBN 978-1-138-02843-2

Investigations into the cause and consequence of incipient anodes in repaired reinforced concrete structures

C. Christodoulou
AECOM Ltd., Colmore Circus Queensway, Birmingham, UK

C.I. Goodier
School of Civil and Building Engineering, Loughborough University, Loughborough, UK

G.K. Glass
Concrete Preservation Technologies, University of Nottingham Innovation Lab, Nottingham, UK

ABSTRACT: The incipient anode (or halo) effect often occurs on repaired reinforced concrete structures. The diagnosis of this problem is widely reported in literature to be macrocell activity. It is deemed that the cause of incipient anodes is the loss of the natural cathodic protection provided by the corroding steel to the steel in the parent concrete adjacent to the patch repair. This diagnosis however, is based on very limited data. Indeed recent potential measurements on field structures repaired with cementitious proprietary materials have provided data that suggests that macrocell activity is not a *cause* of incipient anode formation but is instead a *consequence*. Alternative mechanisms that may cause incipient anode activity include repair/parent material interface effects, residual chloride contamination within the parent concrete, and/or vibration damage to the steel/parent concrete interface during repair area preparation. The aim of the work presented here was to assess the impact of macrocell activity on the formation of incipient anodes around the perimeter of repairs in patch-repaired reinforced concrete structures. Data was collected from a major multi-storey car park and a bridge structure both located in the UK. The analysis challenges the widespread view that macrocell activity is a cause of incipient anode formation. Indeed this work illustrates that the data supporting the existing diagnosis is not convincing and suggests that macrocell activity is primarily a consequence of incipient anode formation and the cause is more likely to be a result of other factors.

1 INTRODUCTION

Corrosion of steel reinforcement affects many concrete structures. Patching is a common repair technique that involves the removal of physically deteriorated concrete (usually by hydro-demolition or jack hammer), cleaning the steel reinforcement within the patch and finally restoring the concrete profile with a proprietary repair mortar by hand, trowel, spray or other means (Dugarte and Sagues 2009, Christodoulou et al. 2011, Christodoulou et al. 2013, Christodoulou et al. 2014a, Concrete Society 2000, Concrete Society 2009). This process aims to protect the repaired area and makes the steel within the repair area passive by removing the previously corroding anodic area (Page and Sergi 2000, Broomfield 2007). However, in many cases further corrosion induced deterioration has been observed in the parent concrete in the immediate area surrounding the patch repairs, sometimes even within a few months following completion of the repair process (Nounou and Chaudhary 1999). This phenomenon is known as incipient or ring anode formation, or the halo effect (Dugarte and Sagues 2009, Page and Sergi 2000, Broomfield 2007, Bertolini et al. 2013).

Page and Treadaway (1982) introduced the incipient anode concept with the observation that the redistribution of anodic and cathodic sites following concrete repair may affect future corrosion risk. Since then the incipient anode concept has developed and been described in a variety of ways.

Bertolini et al. (2013) state that, *"If only concrete near the corroded reinforcement is replaced, the attack may start in the areas near to those repaired because they no longer benefit from the cathodic polarisation and, moreover, pitting corrosion may even be stimulated by anodic polarization from the repassivated steel in the repaired zone"*.

Concrete Society (2011) states that, *"The repair of only those sites which are actively corroding in*

a chloride-contaminated structure is likely to stimulate corrosion at sites adjacent to the repair. This phenomenon is known as the incipient anode, ring anode or halo effect".

Whereas British Standards Institution (2012) states that, [When] *"an anode develops on reinforcing steel in concrete, particularly due to chloride attack, it provides "natural" cathodic protection to the adjacent steel." When this anodic site is repaired it "allows the previously "naturally cathodically protected" adjacent areas to start corroding"*.

Many of the references above suggest that a contributing factor to incipient anode formation is the loss of the natural cathodic protection provided by the corroding steel to the steel in the parent concrete adjacent to the patch repair. However in some cases it is suggested that patch repairs stimulate corrosion as a result of enhanced macrocell activity, where anodes and cathodes separated possibly at a considerable distance from one another are formed.

The aim of the current work was to assess the impact of macrocell activity on the formation of incipient anodes around the perimeter of repairs in patch-repaired reinforced concrete structures. A multi-storey car park and a bridge, both constructed of reinforced concrete provided empirical data. This paper considers site-obtained data, together with data published previously by others (Christodoulou et al. 2013).

2 METHODOLOGY

This section describes the details of the structures selected and the testing regime employed.

2.1 *Structures*

A large multi-storey reinforced concrete car park (MSCP) in the East Midlands, UK and a 180m long multi-span reinforced concrete bridge in North Scotland, UK, were used for site trials to identify evidence for the formation of incipient anodes adjacent to concrete patch repairs. Both structures were approximately 40 years old and had suffered extensive chloride-induced corrosion damage. The structural arrangement of the MSCP was a one-way spanning ribbed slab. The typical thickness of the slab between ribs was only 80 mm and was lightly reinforced, primarily with 8 mm steel mesh. The maximum cover to the reinforcement was only 20 mm, although there were several areas, usually at the overlap locations, where cover was reduced to around 10 mm or less.

The structural arrangement of the reinforced concrete bridge structure consisted of 18 equal simply-supported spans with a total bridge length of approximately 180m. The supports consisted of steel piles connected with a reinforced concrete pile cap, supporting prestressed concrete beams with lightly reinforced concrete infill making up the deck.

Both structures were in an advanced stage of concrete deterioration and reinforcement corrosion as a result of the use of de-icing salts, the bridge structure was also exposed to an aggressive marine environment. For the car park, deterioration affected primarily the decks, the parapets and the soffits around the areas of leaking expansion joints. For the bridge structure, concrete deterioration affected primarily the reinforced concrete pile caps due to water leaking through the joints and the ends of the prestressed concrete beams which were resting on top of the pile caps.

All areas of concrete deterioration where broken up, by jack hammer on the MSCP and hydro-demolition on the bridge, the steel cleaned by rotary steel wire brushes and repaired with proprietary cementitious materials as described in Section 2.3.

2.2 *Testing*

The testing involved potential mapping, carbonation measurement and chloride profiling.

2.2.1 *Chloride analysis*

Historical data was available for chloride concentration profiles throughout the MSCP over the period 1997 to 2008. The data illustrated that for the depth band of 0–25 mm (where reinforcement was located) at least 85% of the test locations exceeded the suggested threshold of 0.3% by weight of cement (Design Manual for Road and Bridges 1990).

For the reinforced concrete bridge, 27 dust samples were taken in total, at depths of 25 mm to 125 mm at 25 mm increments, from the prestressed concrete beams and from the reinforced concrete pile caps. Chloride content of the samples was determined by an independent laboratory to BS 1881, Part 124 (Design Manual for Road and Bridges 1988). The chloride concentration of only one dust sample was below the suggested threshold 0.3% by weight of cement. Concentrations of up to 1.89% by weight of cement were identified even at depth bands of 75–100 mm.

2.2.2 *Potential mapping*

The performance of the repairs was assessed by means of surface potential mapping in which the steel potential was measured against the potential of a reference electrode (Concrete Society 2004, American Society for Testing and Materials 2009, Christodoulou et al. 2010 Christodoulou et al. 2014b, Dodds et al. 2014). A portable Ag/AgCl/0.5M KCl reference electrode was primarily

used for the testing together with a high impedance multi-meter. Direct steel reinforcement connections were not always possible and in some cases only relative values could be obtained. Notes within the Figures identify whether the steel potential values are relative or absolute values.

Following reinstatement of the patches, the area was allowed to cure for at least 10 days before undertaking surface potential mapping with frequency of testing set at approximately 10 day intervals. The spacing used for the potential mapping was on a grid of 50 mm by 50 mm in order to easily identify the formation of macrocells.

2.3 *Repair materials*

Details of the repair materials are included in Table 1, alongside a description of their chemical base and characteristics.

3 RESULT

3.1 *Multi-Storey Car Park (MSCP)*

Potential mapping results for a concrete patch repair using material type A after a period of 30 days are shown in Figure 1. It can be observed that following repair the potentials of the steel within the repair area have been pushed to more negative values.

The surface potential mapping results before and 30 days after a concrete patch repair using material type A are shown in Figure 2. Following repair, it can be observed that the potentials of the steel within the repair area were pushed to very negative values and remained more negative than the potentials of the steel in the parent concrete for the first 30 days. In addition, it can be observed that the potentials of the steel in the parent concrete were also affected.

Figure 3 illustrates the potential monitoring of a repair using Material A over a period of 246 days. The early age results (15 days) show that the steel potentials within the patch repair were depressed to very negative values as a result of the fresh alkalinity provided by the repair mortar. The steel potentials shifted to less negative values as the age of the patch repair increased, however, at no point within the 246 days of monitoring did the potentials of the steel within the patch rise above the steel potentials in the parent concrete.

Similar behavior was observed for all the patch repairs monitored as part of this work, confirming consistency on the results obtained.

Material	Structure type	Repair location	Chemical Base & Characteristics
A	MSCP	Deck	Shrinkage compensated, pourable, polymer modified concrete, trowel finished
B	Bridge	Soffits and vertical faces	Shrinkage compensated, dry sprayed, polymer modified micro-concrete, trowel finished

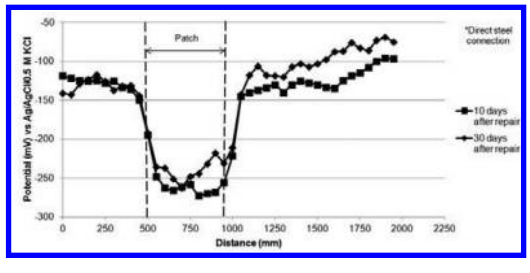

Figure 1. Potential mapping monitoring of material type A on car park deck repair.

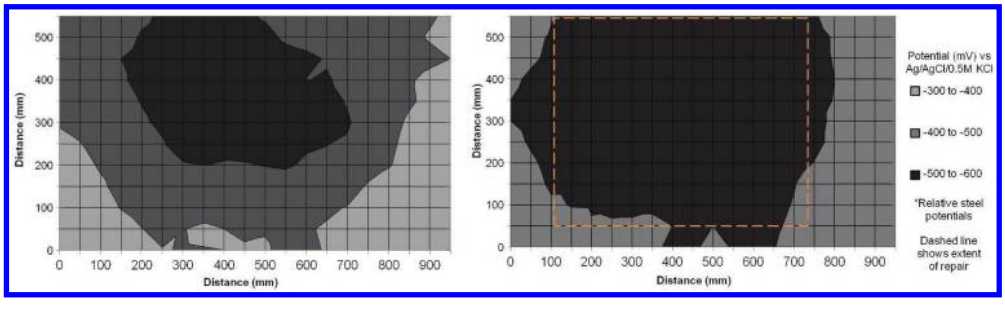

Figure 2. Surface potential mapping on car park repair (a) before and (b) 30 days after repair with material A. Dashed line in (b) illustrates extent of patch repair.

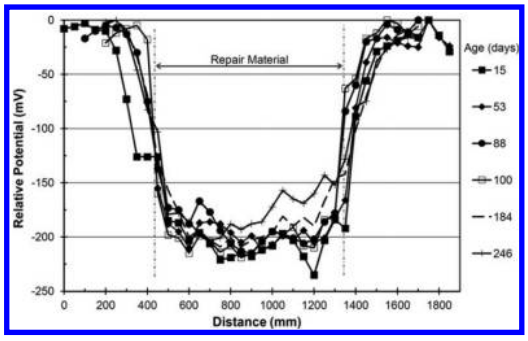

Figure 3. Evolution of average potential readings through the patch repair with material A as a function of time.

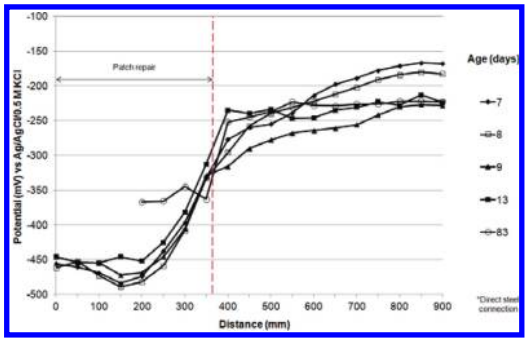

Figure 4. Potential mapping monitoring on a bridge repair with material type B.

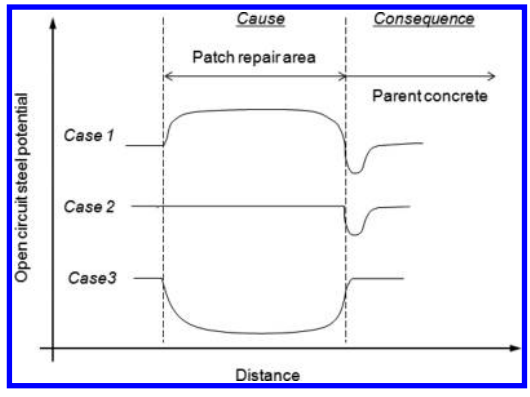

Figure 5. Three cases of potential changes between parent and repair concrete.

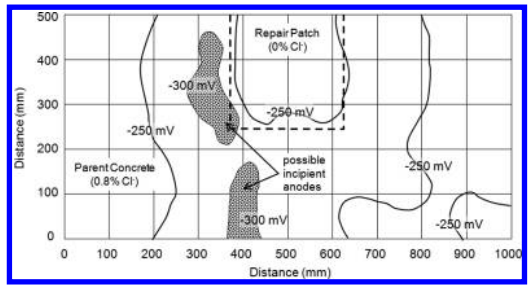

Figure 6. Open circuit steel potentials of a slab following 2 months of conventional patch repair (potential vs Standard Calomel Electrode) (Page and Sergi 2000).

3.2 *Bridge structure*

Similar behavior was observed for all the patch repairs from the bridge structure too and a random sample of the monitoring data is reported here.

Figure 4 illustrates the potential monitoring on a bridge repair using material type B. The potentials of the steel within the patch repair remained more negative than the potentials of the steel in the adjacent parent concrete over a period of 83 days.

4 DISCUSSION

4.1 *Cause or consequence*

Figure 5, illustrates three cases of steel potential changes between parent concrete and repair material. The effect of an incipient anode on the steel in the parent concrete adjacent to the repair is represented by the potential plot for cases 1 and 2.

Case 1 represents the traditional textbook understanding of the cause of incipient anode formation (Page and Sergi 2000, Broomfield 2007).

In this hypothesis, the steel within the repair passivates as a result of the alkalinity of the fresh repair material, the absence of chlorides and the abundance of dissolved oxygen in the pore solution of the freshly mixed concrete or repair mortar.

The steel potential in the repair rises above the passive steel potential in the parent concrete resulting in a macrocell that induces passive film breakdown and causes an incipient anode to form adjacent to the repair.

Case 2 represents the laboratory data (Page and Sergi 2000) which provided some initial support for macrocell induced incipient anode formation. In this example a concrete slab was cast and then repaired under laboratory conditions. The reported data showed two possible areas of incipient anode formation. Only one of these was located adjacent to the repair area (Figure 6). This would suggest that the residual chloride content was sufficient on its own to cause corrosion. In addition, the potential of the steel in the repaired area did not substantially differ from the potential of the steel in the parent concrete. The formation of new corrosion

sites adjacent to the repaired area should be no different to that at other locations on the structure. The data only shows that some natural cathodic protection that may have been provided by a previously corroding area of steel to adjacent steel was removed in the repair process.

The benefit provided by this natural cathodic protection is questionable because corrosion of a steel anode results in expansive products that cause disruption to the surrounding concrete [19–20]. This may be the reason why reinforcement corrosion tends to spread laterally along the steel bars in conditions that also result in expansive corrosion products as opposed to forming deep pits as is the case for passive metals in other environments including steel in water saturated concrete.

A related observation has been made in relation to the influence of a macrocell caused by coupling stainless steel to steel in concrete. The impact of a stainless steel/mild steel couple on inducing corrosion on the mild steel has been reported to be no different to that of a passive mild steel/mild steel couple and did not increase the corrosion damage reported on the mild steel (Bertolini et al. 1998, McDonald 1995). By the same argument, it is unlikely that a macrocell formed by coupling the steel in the repair area to steel in the parent concrete will have any substantial impact on inducing additional corrosion on the steel in the parent concrete.

Case 3 represents the findings of the present study of two full scale reinforced concrete structures, after being patched with three cementitious proprietary repair materials. The steel in the patch appears has a more negative potential than the steel in the parent concrete. Although potentials shifted to more positive values with time, they were always more negative than the potential of the steel in the parent concrete, as evidenced by Figures 1 to 4. Such an observation is not unique and has also been made by Cleland et al. (1997), and by Morgan (1996).

Some possible reasons for the case 3 behaviour include the build-up of the oxide film or that a membrane or streaming potential exists between the parent and the patch concrete (Schiegg et al. 2009, Angst et al. 2009). However, they do not dominate the time dependence to the extent that steel potentials in the repaired area rises above that in the parent concrete over time. Thus, the data from this study, like that of Cleland et al. (1997) and Morgan (1996) provide no evidence to indicate that macrocell activity is a cause of incipient anode formation in aged concrete structures repaired with proprietary repair materials. This suggests that, on balance, macrocell activity is a consequence, not a cause, of incipient anode formation in these circumstances.

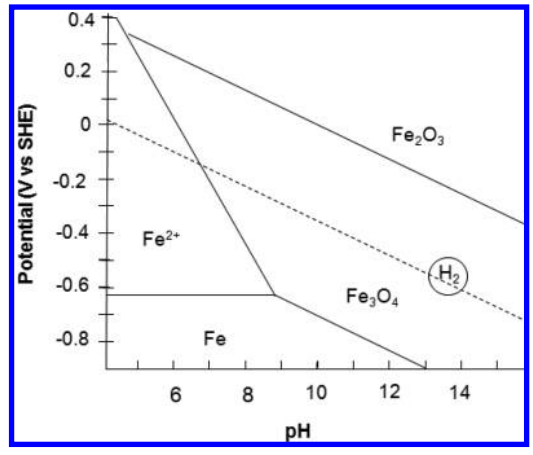

Figure 7. Modified Pourbaix diagram for the stability of iron (Pourbaix 1990).

4.2 *Factors affecting potential*

The pH of the environment can have a strong impact on equilibrium potentials with a higher pH resulting in more negative equilibrium potentials (Figure 7). A change in pH from 12 to 13 will result in a 60 mV drop (against the standard hydrogen electrode) in the equilibrium potentials between iron and its products and in the equilibrium potential for the oxygen and hydrogen reactions (Pourbaix 1990). Fresh repair concrete may well have a higher pH than aged concrete because the reaction between hydroxide and silica within the concrete or between hydroxide and carbon dioxide in the air will tend to reduce the pore solution pH to that of one of the more abundant buffering solid phases present.

The change in pH between the repair material and the parent concrete can also give rise to a membrane potential. This results due to diffusion of hydroxide ions from the patch repair to the parent concrete and a resulting build-up of charge on the walls of the pore system at the repair interface (Glass and Buenfeld 2000). A residual charge on the pore walls at the repair interface results from dissimilar dissolution of the solid phase and represents a membrane. The effect of the charge results in positive and negative ions diffusing at very different rates through the pore system and induces a membrane potential. Studies on membrane potentials in concrete suggest that large membrane effects are transient.

Passivity and oxygen availability affect the anodic and cathodic kinetics. Oxygen is consumed to passivate the steel in the repaired area. Proprietary repair materials may have a low permeability

that restricts oxygen access and increase resistance. In addition, Morgan (1996) concluded that the use of polymer, styrene butadiene or acrylic modified cement mortars did not affect corrosion of steel in adjacent unrepaired areas.

4.3 *Cracks and the repair material interface*

Cracks may occur at the interface between the parent concrete and the repair material following patch repair of concrete structures. The presence of such cracks can be attributed to drying, or plastic shrinkage, thermal or stiffness incompatibility, poor curing, surface preparation or a combination of these (Concrete Society 2000, Concrete Society 2010). Admixtures can be used to increase the volume of the repair material during early age hardening of shrinkage compensated materials. However, the material will often undergo an S-shaped expansion-contraction cycle (Szilágyi et al. 2007). Although close to zero, net unrestrained shrinkage can be achieved in such shrinkage compensated materials; there may be some limited retained shrinkage which can give rise to crack because the early expansion part of the cycle is restrained by the parent concrete.

Chadwick (1993), examined the corrosion protection afforded by single cast, cast in two halves and patch repaired specimens. He observed a major reduction in the corrosion protection for the latter two types of specimens and suggested that it is not necessary for chlorides to be present in the parent concrete for incipient anodes to form at the interface. He suggested that it is only necessary to expose the repaired concrete element to a chloride contaminated environment as the interface between the two concrete or mortar materials provides easier access for chloride penetration.

Thus, the interface between repair material and parent concrete may provide a path for chlorides to penetrate preferentially into the substrate. The extent of this effect will be dependent on surface preparation, application techniques, curing, material properties and compatibility with the parent concrete. The presence of visible cracks may be obscured by trowel finishing the repair, or a coating (if applied).

Crack formation in reinforced concrete structures and its relationship to corrosion has been established by a number of studies (Raupach et al. 1996, Schiessl et al. 1997). In particular, it has been shown that the reinforcement within and around the crack zone will start to corrode first. Chadwick (1993) also observed that the presence of construction joints in the same material resulted in corrosion initiating at lower chloride levels and concentrated at the joint interface.

4.4 *Incipient anode formation*

As just described, factors that may cause incipient anodes to form include repair material interface effects, residual chloride contamination and damage to the steel-concrete interface during repair preparation. Furthermore, cracks and interfacial effects between parent concrete and repair material provide an easier path for the chlorides to penetrate into the substrate. The parent concrete may have a higher permeability than the new repair material and this will aid the diffusion process.

The parent concrete is also likely to have some residual chloride contamination that may promote corrosion. The preparation of the repair area usually requires the mechanical removal of concrete that can cause damage to (or defects at) the interface between the unexposed steel and the parent concrete adjacent to the repair area. This increases the corrosion risk by lowering locally the chloride threshold level (Glass et al. 2007).

The repair of corroding areas removes the anode in this location and any "sacrificial" cathodic protection effects that were previously applied to the steel in the surrounding regions. However, it has been suggested that the detrimental effect of a corroding steel anode in concrete probably outweighs any beneficial effects that were provided previously by such an anode (Bertolini et al. 1998, Christodoulou et al. 2013). In other words, a corroding steel anode causes more damage than it prevents.

5 CONCLUSIONS

While the incipient anode effect often occurs on repaired reinforced concrete structures, potential measurements taken on structures repaired with a variety of proprietary repair mortars over a period of up to 250 days suggest that macrocell activity does not stimulate incipient anode formation. No evidence was found from potential measurement data obtained in this work to support the hypothesis that macrocell activity is a cause of incipient anode formation.

The use of cementitious proprietary repair materials may permanently depress steel potentials within the repair area. Reasons for this include the common low permeability and high pH of these types of materials. A high pH in an area of repair would result in a negative shift in steel potentials because equilibrium potentials of steel in concrete are more negative at the high end of the pH range.

Cracks can develop at the repair/substrate interface even when using shrinkage compensated repair materials, which may provide an easier path for chlorides to penetrate into the substrate. This is due to the fact that the shrinkage compensated

material undergoes an "S" shaped strain curve, even in an unrestrained case where no net strain occurs, which can result in shrinkage during the final phase. The extent of these cracks will be dependent upon surface preparation, application techniques, material properties, adhesion between the repair material and parent concrete and curing conditions. Such cracks may be obscured by trowel finishing of the repair, or a coating (if applied).

An increased number of incipient anodes adjacent to areas of concrete repair may arise from one or more of the following reasons:

- chlorides may enter the concrete through the interface between the parent and repair material,
- parent concrete adjacent to the repair area may have an above average level of residual chloride contamination that is sufficient on its own to cause corrosion, and/or
- preparation of a repair area may result in vibration damage at the steel interface with the adjacent parent concrete.

REFERENCES

Abreu C.M., Cristobal M.J., Montemor M.F., Novoa X.R., Pena G. and Perez M.C., Galvanic coupling between carbon steel and austenitic stainless steel in alkaline media, *Electrochim. Acta* 47 (2002) 2271–2279.

American Society for Testing and Materials, ASTM C 876–2009, Standard Test Method for Corrosion Potentials of Uncoated Reinforcing Steel in Concrete, West Conshohocken, Pennsylvania, USA, 2009.

Angst U., Vennesland Ø. and Myrdal R., Diffusion potentials as source of error in electrochemical measurements in concrete, *Mat. and Struct.* 42 (2009) 365–375.

Bertolini L., Elsener B., Pedeferri P., Redaelli E. and Polder R., Corrosion of steel in concrete, prevention, diagnosis, repair, 2nd Edition, Wiley-VCH, Germany, 2013.

Bertolini L., Gastaldi M., Pedeferri M.P., Pedeferri P. and Pastore T., Proceedings of the International Conference on Corrosion and Rehabilitation of Reinforced Concrete Structures, Orlando, USA, 1998.

British Standards Institution, BS 1881-124:1988 Testing concrete, Methods for analysis of hardened concrete, London, BSI, 1988.

British Standards Institution, BS EN ISO 12696:2012, Cathodic protection of steel in concrete, London, BSI, 2012.

Broomfield J.P., Corrosion of steel in concrete: understanding, investigation and repair, 2nd ed., Taylor and Francis, UK, 2007.

Chadwick R., Performance of concrete repair materials as corrosion protection for reinforcement, PhD thesis, University of Surrey, 1993.

Christodoulou C., Glass G., Webb J., Austin S. and Goodier C., Assessing the long term benefits of Impressed Current Cathodic Protection, *Corr. Sci.* 52 (2010) 2671–2679, DOI:10.1016/j.corsci.2010.04.018,http://hdl.handle.net/2134/7674.

Christodoulou C., Glass G., Webb J., Austin S., and Goodier C., A new approach for the patch repair of car parks using galvanic anodes, Concrete Solutions 2011, 4th International Conference on Concrete Repair, 26–28 September 2011, Dresden, Germany, ISBN 978-0-203-13468-9, https://dspace.lboro.ac.uk/2134/8825.

Christodoulou, C. Goodier, C.I., Austin, S.A., Webb, J. and Glass, G.K., Diagnosing the cause of incipient anodes in repaired reinforced concrete structures, *Corrosion Science*, 69 (2013), pp. 123–129, http://dx.doi.org/10.1016/j.corsci.2012.11.032, https://dspace.lboro.ac.uk/2134/11351.

Christodoulou C, Goodier C, Austin S, Webb J, Glass G (2014a), A new arrangement of galvanic anodes for the repair of reinforced concrete structures. *Construction and Building Materials*, 50, pp. 300–307, https://dspace.lboro.ac.uk/2134/13593, http://dx.doi.org/10.1016/j.conbuildmat.2013.09.062

Christodoulou, C., Goodier, C.I., Austin, S.A., Site performance of galvanic anodes in concrete repairs, Grantham, M., Basheer, M., Magee B. and Soutsos, M. (eds). Concrete Solutions 2014b: Proceedings of the International Conference on Concrete Solutions 2014. London: CRC Press, ISBN 978-1-138-02708-4, 1-3/09/14, https://dspace.lboro.ac.uk/dspace-jspui/handle/2134/16552.

Cleland D.J, Yeoh K.M. and Long A.E., Corrosion of reinforcement in concrete repair, *Constr. Build. Mater.* 11 (1997) 233–238.

Concrete Society, Technical Report 54, Diagnosis of deterioration in concrete structures, Surrey, UK, 2000.

Concrete Society, Technical Report 60, Electrochemical tests for reinforcement corrosion, Surrey, UK, 2004.

Concrete Society, Technical Report 69, Repair of concrete structures with reference to BS EN 1504, Surrey, UK, 2009.

Concrete Society, Technical Report 22, Non-structural cracks in concrete, Surrey, UK, 2010.

Design Manual for Road and Bridges, Volume 3, Section 3, Part BA 35/1990 Inspection and Repair of Concrete Highway Structures, Departmental Standard, UK, 1990.

Dodds, W., Christodoulou, C., Goodier, C., Austin, S., Performance evaluation of galvanic anodes through laboratory testing and on-site monitoring, In: Bjegovic D., Beushausen H. and Serdar M. (eds): Proceedings of the RILEM International workshop on performance-based specification and control of concrete durability, RILEM PRO 89, 11–13 June 2014, Zageb, Croatia, pp. 175–182, ISBN 978-2-35158-135-3, https://dspace.lboro.ac.uk/2134/15296.

Dugarte M. and Sagüés A.A., Galvanic point anodes for extending the service life of patched areas upon reinforced concrete bridge members, Contract No. BD544–09, Final Report to Florida Department of Transportation, Tampa, Florida, USA, September 2009.

Glass G.K. and Buenfeld N.R., Chloride-induced corrosion of steel in concrete, Prog. Struct. Engng. Mater. 2 (2000) 448–458.

Glass G.K., Reddy B. and Clark L.A., Making reinforced concrete immune from chloride corrosion, Proceedings of the Institution of Civil Engineers, *Constr. Mater*. 160 (2007) 155–164.

Marriaga J.L. and Claisse P., Effect of the non-linear membrane potential on the migration of ionic species in concrete, *Electrochim. Acta* 54 (2009) 2761–2769.

McDonald, Sherman M.R., Pfeifer D.W. and Virmani Y.P., Stainless steel reinforcing as corrosion protection, *Concr. Int.* 17 (1995) 65–70.

Lau K. and Sagüés A.A., Corrosion of steel in locally deficient concrete, Contract No. BD544-31, Final Report to Florida Department of Transportation, Tampa, Florida, USA, February 2009.

Morgan D.R., Compatibility of concrete repair materials and systems, *Constr. Build. Mater*. 10 (1996) 57–67.

Nounou G. and Chaudhary Z.U.L., Reinforced concrete repairs in beams, *Constr. Build. Mater*. 13 (1999) 195–212.

Page C.L. and Sergi G., Developments in cathodic protection applied to reinforced concrete, *J. Mater. Civ. Eng*. 1 (2000) 8–15.

Page C.L. and Treadaway K.W.J., Aspects of the electrochemistry of steel in concrete, *Nature* 297, (1982) 109–115.

Pourbaix M., Thermodynamics and corrosion, *Corr. Sci.* 30 (1990) 963–988.

Qian S., Qu, D. and Coates G., Galvanic coupling between carbon steel and stainless steel reinforcements, *Can. Metall. Q*. 45 (2006) 475–484.

Raupach M., Chloride-induced macrocell corrosion of steel in concrete—theoretical, background and practical consequences, *Constr. Build. Mater*. 10 (1996) 329–338.

Schiegg Y., Büchler M. and Brem M., Potential mapping technique for the detection of corrosion in reinforced concrete structures:Investigation of parameters influencing the measurement and determination of the reliability of the method, *Mat. and Corr.* 60 (2009) 79–86.

Schiessl P. and Raupach M., Laboratory studies and calculations on the influence of crack width on chloride-induced corrosion of steel in concrete, *ACI Mater. J*. 94 (1997) 56–62.

Szilágyi K., Zsigovics I. and Szautner C., Advanced shrinkage compensation of concretes by a combined admixture system, Építőanyag 59 (2007).

Zhao Y., Yu J., Y. Wu Y. and Jin W., Critical thickness of rust layer at inner and out surface cracking of concrete cover in reinforced concrete structures, *Corr. Sci*. 59 (2012) 316–323.

Performance and health monitoring

Concrete Repair, Rehabilitation and Retrofitting IV – Dehn et al. (Eds)
© 2016 Taylor & Francis Group, London, ISBN 978-1-138-02843-2

Experimental in-situ investigation of the shear bearing capacity of pre-stressed hollow core slabs

G. Schacht
MarxKrontal GmbH, Hannover, Germany

G. Bolle
Hochschule Wismar, Wismar, Germany

St. Marx
Insitut für Massivbau, Leibniz Universität Hannover, Germany

ABSTRACT: As a result of bad quality sealing, moisture and de-icing agents penetrated into pre-stressed hollow core slabs of the top floor in a freely exposed parking garage. Caused by the chlorides the slabs showed especially heavy damage in the support regions near the joints. The theoretical shear bearing capacity according to the technical approval of these slabs was strongly questionable because of the damage. With the help of an experimental loading test in-situ the influence of the damage on the shear bearing capacity of the slabs with different damage-levels could be determined. The experimental results allowed a secure evaluation on how many slabs had to be replaced or could be repaired.

For the experimental investigation of the shear bearing capacity of the hollow core slabs a combination of Photogrammetry, Acoustic Emission Analysis and section-wise curvature measurement was used to determine the beginning shear damage on a very low level during the test. The comparison of the results of the different measuring techniques allowed a clear identification of the damage processes and increased the information quality about the bearing condition of the slabs during the experimental investigation significantly. With the results of the loading tests it was concluded how many slabs had to be replaced and which could further be used.

1 INTRODUCTION

The condition of the existing infrastructure is an important location factor for every country. Different experts have estimated the worth of the existing stock of structures in Germany to 20–25 trillion Euro [1]. During lifetime, structures are exposed to permanent aging and deterioration. Because of the large number of existing structures, it is obvious that not all of them can be replaced only because the proof of a sufficient load bearing capacity according to today's code requirements is not successful. The lack of financial capacities and resources along with the idealistic value of the structures are reasons, why civil engineers are today more and more asked to preserve existing structures and ensure their bearing safety.

The evaluation of the load bearing safety of existing structures, on principle, requires a different approach than for new structures. The structure already exists and its geometry and structural characteristics can only hardly be influenced. Apart from the investigation and assessment of the material properties a main focus lies on the evaluation of the bearing capacity and bearing safety.

Often a theoretical proof of the bearing capacity and serviceability of existing structures is not successful because of missing information on the construction, damages or uncertainties about the material properties and the loading history. In such cases an experimental investigation of the bearing safety (loading test) is an alternative method for a secure and economic determination of the bearing safety of existing structures. In most cases it is therewith possible to evaluate the bearing characteristics realistically. Hidden reserves can be detected so that expensive strengthening or even a replacement are not necessary. Prerequisite for an experimental investigation of the load bearing safety is, that the test must not cause any kind of damage that affects the future use or durability of the structure (secure determination of the ultimate test load). Yet, such criteria only exist for ductile failure modes of reinforced concrete structures. Therefor loading test of reinforced or pre-stressed concrete structures with low ductile failure modes

(e.g. reinforced concrete elements without shear reinforcement, pre-stressed concrete structures) can only be carried out in exceptional cases. For such structural elements already a small structural change can cause an intolerable damage, an inadmissible loss of pre-stressing or even a reduction of the bearing capacity. The aim of a research project funded by the initiative "Zukunft Bau" of the German Bundesministerium für Bau—und Raumordnung [2] aimed to close this gap of knowledge, to investigate brittle failure modes and develop ultimate test load criteria.

2 DESCRIPTION OF THE TASK

2.1 *City-Center Greiz, initial situation*

The City-Center in Greiz was built in the late 1990s and is a prefabricated pre-stressed concrete construction. In the two lower floors of the four storey building (Figure 1) stores and restaurants are placed and the two upper floors are used for parking. Both parking decks are ventilated and the upper deck is also freely exposed to the weather.

During lifetime several defects and damages of the sealing of the slabs between the upper and lower parking decks have been detected. These defects caused the penetration of water and deicing agents into the concrete of the pre-stressed slabs. This moisture penetration led to visible damages (spalling, corrosion) on the lower surfaces of the slabs (Figure 2).

The damages concentrated close to the supports of the slabs and investigations of the chloride contamination in these areas showed high and critical values of chloride. In connection with the bad visual condition of the support areas, temporary steel frames were erected to strengthen the support areas (Figure 3) [3].

Figure 1. The City-Center Building in Greiz, Germany.

2.2 *Rehabilitation concept and material investigations*

The bad condition of the slabs and the temporary steel strengthening were no satisfying situation for the owner of the City-Center and he engaged the authors and the Ingenieurbüro für Bauwerkserhaltung Weimar to develop a rehabilitation concept.

In the course of the inspection of the damaged slabs numerous material investigations were carried out. Additional to the visual inspection, the extent and progress of the corrosion of the pre-stressing reinforcement was determined by Potential Measurements, the moisture penetration, the chloride contamination as well as the carbonation progress were investigated. These material investigations allowed a classification of the slabs according to their damage level into three groups (low, medium and heavy damage). The results showed that the heavily damaged slabs were not able to fulfill the requirements of durability because of the high moisture penetration and chloride contamination.

Figure 2. Moisture penetration through the joints between the slabs.

Figure 3. Steel girder construction to strengthen the supports.

For the repair of the material damages a concept was developed that included the renewal of the parking deck sealing and a coating of the bottom surfaces of the slabs.

More difficult was the evaluation of the bearing safety of the pre-stressed hollow core slabs because of the severe damages. For a bending failure at mid span a sufficient safety margin between first cracking and yielding of the pre-stressing strands could be guaranteed because a damage of the strands or an excessive loading would lead to large deflections and would be accomplished by extensive cracking which could be detected during regular inspections.

In contrast the evaluation of the shear bearing safety and the anchorage of the pre-stressing strands was more complicated because of the damages at the supports. The shear failure of hollow core slabs is brittle and it must be feared that the failure happens in the moment the first shear cracks would appear. A theoretical proof of the shear bearing safety was not possible because the influence of moisture and chloride couldn't be quantified. The temporary strengthening of the supports of slabs was also not able to prevent a sudden shear failure.

Because the shear bearing safety couldn't be proven, theoretically all questionable slabs had to be renewed, which was also no satisfying solution for the owner. Therefore it was decided, that all slabs with heavy damages had to be exchanged. To determine whether slabs with a medium damage degree also had to be replaced or not, a loading test was planned, with which a representative amount of slabs with medium damage were tested to evaluate their shear bearing safety.

3 EVALUATION OF THE SHEAR BEARING SAFETY

3.1 *Load bearing behavior of precast and pre-stressed hollow core slabs*

Pre-stressed hollow core slabs are prefabricated concrete slabs, which allow long spans and a rapid construction progress because of the pre-stressing in the pre-tensioning bed and the low self weight. They are produced industrially in 100 m till 200 m long strips and saw-cut into the needed lengths. The slabs can be produced up to 16 m span with heights of 150 till 400 mm [5]. The slabs consist of plain concrete with several pre-tensioned strands. The pre-stressing with immediate bond is initiated into the concrete over the so called transfer length from the end of the slabs. Hollow core slabs are built without any un-tensioned reinforcement, because it would disturb the industrial casting process.

Hollow core slabs are flexure dominated elements and have a very high bending resistance due to the pre-stressing and the high concrete quality. In case of overloading a bending failure is clearly announced through extensive crack development along the element span. With increasing load the cracks grow further into the compression zone where they branch apart and constrict the height of the compressive zone. The failure is caused by yielding and finally the rupture of the strands. Does cracking spread out into the support areas it is possible that the cracks develop in the transfer length (area of partial pre-stressing) and lead to a sudden failure of the anchorage of the strands.

Under single loads near the support there is also a danger that shear cracks develop when the principal tensile stress reaches the tensile strength of the concrete and these shear cracks rapidly spread into the compression zone and to the anchorage and therewith cause a sudden shear failure. In experimental investigations [6] also shear compression failures have been observed.

The theoretical proofs of the serviceability and bearing capacity of hollow core slabs are regulated by DIN EN 1168 [7], [8]. According to [7] the shear bearing capacity has to be determined for two situations: for sections with bending cracks according to [9] and for section without bending cracks by a limitation of the diagonal principal tensile stresses according to [7].

The hollow core slabs of the City-Center had a span of 7.07 m and a height of 200 mm. The theoretical shear bearing capacity was determined according to [7] to $V_{Rd,c} = 66.80$ kN. The theoretical shear strength was the basis for the planning of the experimental loading test and the aim test load.

3.2 *Planning the experimental evaluation of the shear bearing safety*

For experimental evaluations of the bearing safety a self-secured hydraulic loading system is used, with which the structure can controllable be loaded in the decisive sections. Contrary to loading tests with mass-forces, "self-secured" means that the applied force is automatically and immediately reduced when unexpected growths of deformation occur as non-linear reactions of the structure. In this case the oil pressure in the hydraulic jacking system automatically decreases and the slab is unloaded. Furthermore, the reaction forces due to the loading are re-anchored at the supports and the cycle of force is closed directly at the tested element, without influencing other construction elements.

The deformations of the load-tested element are simultaneously measured. Loading and deformation measurements are presented online on a

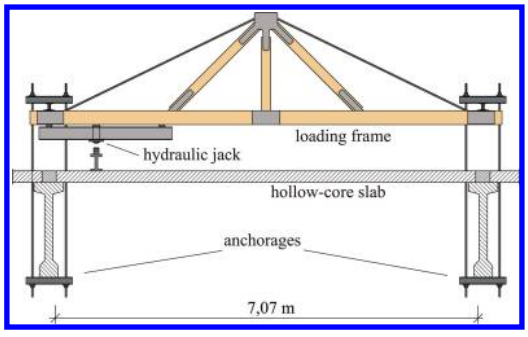

Figure 4. Experimental setup with loading frame.

Figure 5. setup of the photogrammetric deformation measure-ment in the support region.

computer during the test and are evaluated with the criteria defined in the German guideline for load testing [10] or criteria, which are specific for the tested structure. The load is stepwise increased in defined loading and unloading cycles till the aim test load *ext* F_{aim} or the ultimate test load *ext* F_{lim} is reached. The aim test load represents the required loads (characteristic loads) and all partial safety factors. The ultimate test load is maximum load which does not yet cause any damage to the investigated structure, that reduce the future load bearing safety or serviceability. This load must not be exceeded during a loading test.

In the investigations the ultimate test load at first and then the load reserve till failure were to be determined. Therewith the ultimate shear strength and information about the dominating failure mode should be gained. This was very important to clarify the margin of safety between characteristic and failure load. All load-tested slabs were replaced after the tests and to prevent a collapse during the tests, a scaffolding was erected underneath the slabs.

The experimental setup was planned according to the regulations given in DIN EN 1168 [7], Appendix J, which defines loading conditions for shear testing. The load has to be applied as a line load at a distance of $2.5 \cdot h$ from the support. Figure 4 shows the experimental setup with the loading frame, the application of the load and the re-anchorage at the supports.

The special character of this experimental evaluation of the load bearing safety of hollow core slabs was that the expected failure mode was a brittle shear failure. To be able to detect even smallest structural changes or deformations before the failure takes place, a combination of different measuring techniques was applied [2]. Additionally to conventional deformation measurements with inductive displacement transducers, which were used to measure the deflection, the concrete strain in the compression zone and the change of the slab thickness (vertical deformation), inclination sensors to determine the section-wise curvature, Acoustic Emission Analysis (AE) and the photogrammetric measuring technique have been used.

This should ensure, that already smallest structural changes, which indicate a non-linear bearing condition and therewith a beginning damage, should be detected at a very low level. Figure 5 and 6 show the application of the different measuring techniques (AE sensors were placed on the bottom surface of the slab).

3.3 *Theoretical considerations of safety*

Because of the great amount of damaged slabs it was impossible to experimentally investigate all of the questionable slabs to determine the shear bearing safety. Therefor a limited number of slabs were chosen which represented a characteristic sample of the whole population of the damaged slabs. In total 5 characteristic slabs (two with heavy and three with medium damages) were tested and the results of these tests used as the basis for an overall evaluation of the shear bearing safety of all slabs of the City-Center.

Prior to testing the slabs had to be cut free along their longitudinal joints to exclude any positive influence of load transfer to the neighbored slabs. Additionally the mortar joints at the supports and the additional concrete layer on top of the slabs were removed.

The aim test load was determined with the theoretical values of the shear bearing capacity. The test loads were calculated with the characteristic design loads according to [7], with a characteristic self weight of 2.81 kN/m, an additional dead load of 1.09 kN/m, a live load of 10 kN/m and a single live load of 10 kN. Additionally to the partial safety factors according to DIN EN 1991-1-1

Figure 6. setup of different deformation measurement techniques to monitor the shear section during load testing.

Figure 7. Testing area and taken out hollow core slabs.

Figure 8. broken-off concrete in the damage support area.

[11], further safety factors were applied to cover the uncertainties of transferring the results of the characteristic sample of slabs to the whole population of the slabs of the City-Center, that have not been tested directly.

To consider the deviation in geometry and material strength of the not directly tested slabs the partial safety factor for unreinforced concrete $\gamma_c = 1.80$ and for the deviation of the system characteristics and additional transmission factor of $\gamma_t = 150$ was chosen.

Because the self weight of the slab is fully deterministic and activate during the test, it need not be considered in the calculation of the external test loads. The shear force under design loads is $V_{Ed} = 45.85$ kN. Considering all mentioned safety values for the transfer of the test results, the aim test load is $V_{aim} = 1.5 \cdot 1.8 \cdot V_{Ed} = 123.80$ kN. The design value of the shear resistance is $V_{Rd} = 66.80$ kN and the most probable shear load at failure without any safety factors and with mean values of the material strengths is $V_{R,calc} = 163.75$ kN.

4 EXPERIMENTAL EVALUATION OF THE SHEAR BEARING SAFETY

4.1 *General information*

The loading tests were executed under normal traffic on the parking deck, only the area with the slabs to be tested was closed for public to ensure the safety of the users. Figure 7 shows the testing area with the prepared specimens.

Some slabs were taken out ahead of the tests to enable an undisturbed access to the specimen. These taken out slabs showed the full extent of the damage of the support regions caused by moisture and chlorides. The support area of the slabs with heavy damage broke off when lifting the slabs and remained on the pre-stressed girders (Figure 8). The anchorage of the pre-stressing strands was totally destroyed (Figure 9).

Three of the taken out hollow core slabs were brought to the laboratory of the University of Applied Science Neubrandenburg for further tests. The results will be reported in a later publication.

4.2 *Execution of the loading tests in-situ*

The test load was applied at a distance of $2.5 \cdot h$ from the support [7]. A steel profile girder was used to distribute the load over the whole width of the slab and a flat rubber layer assured the even load transfer from the steel girder into the concrete slab.

The load was applied according to the loading regime shown in Figure 10 with six increasing load cycles up to the aim test load. After the aim test load was reached an additional load cycle on service load level was performed before increasing the load slowly but steadily until failure of the slab.

Figure 9. loss of bond at the end-anchorage of the prestressing stands.

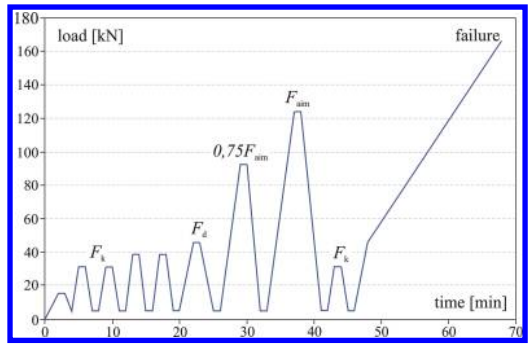

Figure 10. Principal loading regime.

Table 1. Summary of the test results.

No.	Degree of damage	Cracking load [kN]	Failure load [kN]	Failure mode
1	heavy	60	75.5	Anchorage
2	heavy	100	162	Shear-Tension
3	medium	100	154	Shear-Tension
4	medium	110	166	Shear-compression
5	medium	90	137	Shear-Tension

4.3 *Results*

4.3.1 *Shear bearing capacity*

The results of the loading tests confirmed the decision to exchange all slabs with heavy damages. The first tested slab (heavy damage) failed before the aim test load was fully applied. The second slab with heavy damages and all slabs with medium damages carried the aim test load successfully and without any signs of distress. This proved that the results (including the additional partial safety factors) could be applied to all other hollow core slabs of the City-Center. Moreover all slabs (except the first one) failed after extensive flexural cracking and an appropriate announcement of the ongoing damage process. The results of the tests are summarized in table 1.

4.3.2 *Announcement of failure*

Besides the evaluation of the shear bearing safety of the hollow core slabs, a special focus was put on the identification of a clear indication of a beginning damage in the shear section and a measureable announcement of the beginning shear failure.

In this section the results of the different applied measuring techniques are analyzed and evaluated in respect to the detection of the beginning shear failure. Exemplarily the results for the second slab with heavy damages are presented, but the principal statements are valid for all slabs.

The load was increased stepwise according to the loading regime shown in figure 10. At about 92 kN a bending crack started to develop and during the phase of constant load this crack continued straight into the compression zone. The photogrammetric evaluation shows the chronological crack propagation (Figure 11).

The load-deflection-diagram (Figure 12) shows a reduction of the bending stiffness at about 100 kN. At that time the photogrammetric pictures already show the extension of the crack clearly, even though at that time it doesn't influence the load-deflection-behavior of the slab, because the macro crack hasn't fully developed.

Under increasing load up to the aim test load of 123.8 kN the slab shows a flexure-dominated bearing behavior with increasing plastic deformations (see Figure 12).

At 105 kN beginning non-linear deformations can be detected in the measurements of the vertical deformation of the slab thickness. The vertical measurement V2 shifts from tension to compression at 120 kN. This can be explained with a change in the inner load transfer and the formation of a compression strut in the area of V2 (Figure 13). At first the vertical compression increases with further loading, but at about 150 kN a second shift can be detected and V2 now shows tensile extension and therewith a subsequent crack opening.

The change of the inner load transfer was characteristic for all slabs and could also be seen in the measured compression strain at the top of the slab. At 120 kN all measured strains show a change in the progression of the curve—which show that the linear elastic beam theory is not valid anymore. The measured strains show a drift or plastic delays into the direction of tensile strains in the compression zone (Figure 14).

The photogrammetric evaluation confirms the change of the inner load transfer at 120 kN.

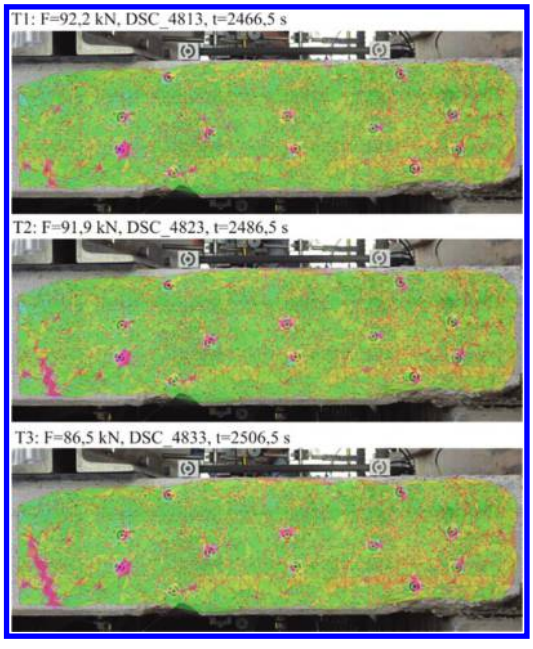

Figure 11. Photogrammetric evaluation for the time-steps T1, T2 and T3.

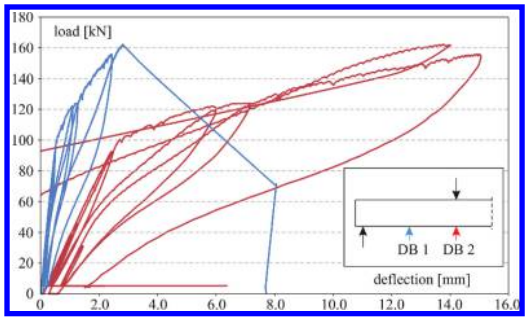

Figure 12. Load-deflection-diagram.

Figure 16 shows the crack development at four different load-levels. The allocation of the pictures to the loading regime is shown in Figure 15.

In Figure 16 a great increase of tensile strain (red triangle = $\varepsilon_1 = 1.003$) in the height of the pre-stressing strand and in the area of the anchorage are shown. Because the photogrammetric system was only two-dimensional it could not be clarified whether the high measured tensile strains are caused by a deformation in the third direction or whether they are cause by high tensile strains in the strands. At a load of 162 kN a shear crack suddenly develops and leads to the failure of the slab.

The Acoustic Emission Analysis shows a good correlation with the other measuring results. First

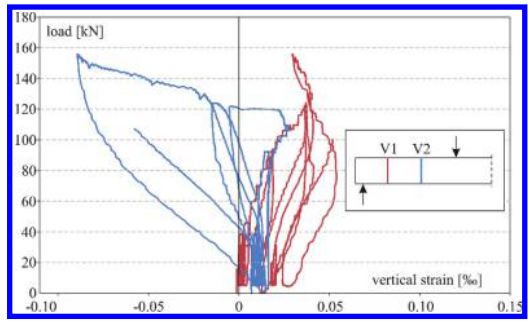

Figure 13. Vertical deformation measured through the slab.

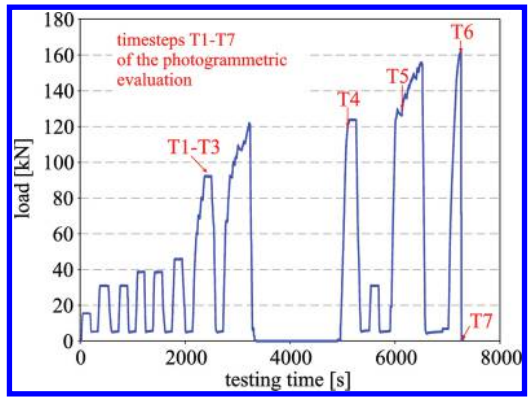

Figure 14. Assignment of the photogrammetric evaluation to the loading regime.

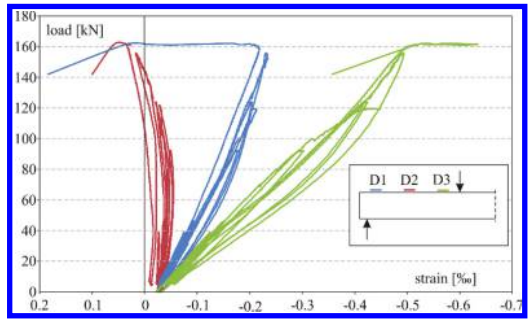

Figure 15. Concrete strain in the compression zone.

AE activity could be detected at the moment the bending crack begins to develop. This confirms the great potential of AE Analysis for the evaluation of the bearing behavior of pre-stressed structural elements. The allocation of AE signals to the bending and shear area clearly shows the shift of the cracking activity from mid span into the shear section. Up to a load of 120 kN the AE activity at the

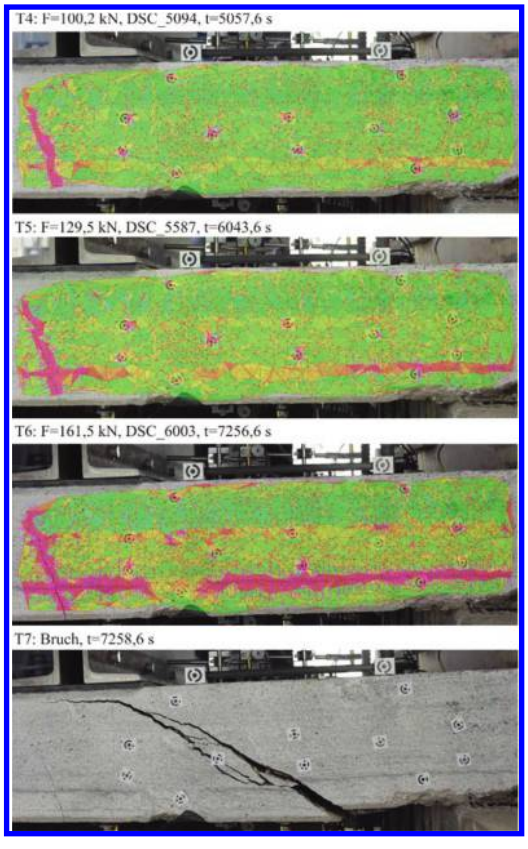

Figure 16. Photogrammetric evaluation for T4-T7.

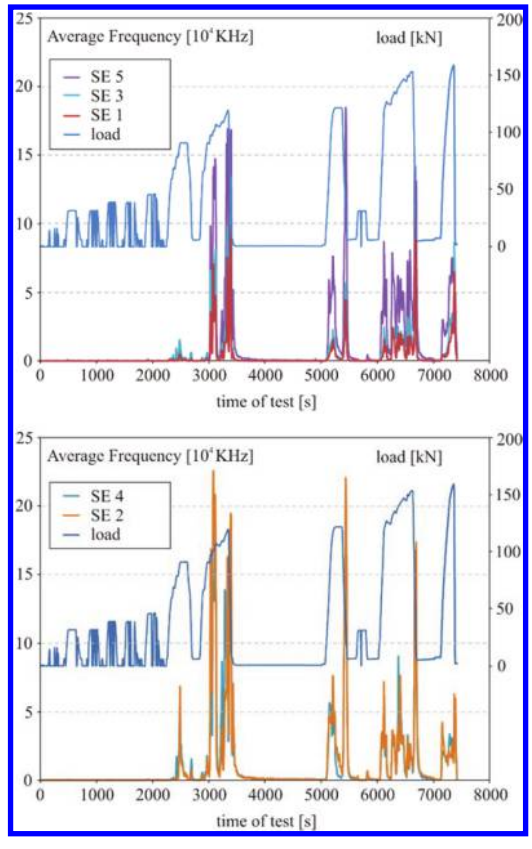

Figure 17. Development of the AE parameter Average Frequency during the load test, sensors 1,3,5 in the shear section, sensors 2 and 4 in the flexure section of the slab.

sensors 2 and 4 (bending section) is greater and at higher loads with the shear crack development the sensors 1, 3 and 5 near the support show higher signals. Figure 18 shows the measured AE signals evaluated for the parameter Average Frequency compared to applied load.

Clear indication of an irreversible damage of the slab are the especially high signals during unloading, which can be assigned to friction processes inside the cracks and bond deformations at the supports.

5 CONCLUSIONS

Based on the results of the loading tests to determine the shear bearing safety, the number of slabs that had to be replaced could considerably be reduced compared to the results of the theoretical calculations. With the help of the loading test most of the slabs could be preserved and only the heavily damaged slabs were replaced.

The loading tests proved a sufficient shear bearing safety of the medium damaged slabs. The results of the tests on five slabs could be transferred to the whole population of slabs because sufficient margins of safety were considered in the calculation of the aim test load.

The experimental investigation showed that the use of a combination of different measuring techniques allows an improved evaluation of the actual bearing behavior even for brittle failure modes with only small structural deformations before failure. The applied measuring techniques of AE Analysis, photogrammetry, inclination sensors and vertical deformation measurements allowed an early detection of beginning damage processes in the shear section of the hollow core slabs. The results are also valuable for the development of indicators for the secure detection of the ultimate test load.

These indicators have to be verified in further experimental investigations and will be developed to criteria which allow a secure definition of a beginning shear damage during load testing.

REFERENCES

Curbach, M. 2009. Brücken und die Aufgabe des Erhalts. *Beton—und Stahlbetonbau* 104, p. 133.

Marx, S. & Schacht, G. & Koschitzki, R. & Maas, H.-G. & Bolle, G. 2011. *Versuchsgrenzlastindikatoren bei Belastungsversuchen*. Abschlussbericht. Forschungsinitiative Zukunft Bau, Dresden: Eigenverlag.

IBW, 2011. Ingenieurbüro für Bauwerkserhaltung Weimar GmbH (ed.) *1. bis 3. Untersuchungsbericht—Greiz City-Center, Pardeck*, unpublished.

Diener, J. 2011. *Statische Berechnungen zur Tragfähigkeit der Spannbetonhohlplatten des City-Center Greiz.* Ingenieurbüro für Baustatik und Grundbau, Erfurt, unpublished.

Fellinger, J. & Stark, J. & Walraven, J. 2005. Shear and anchorage behaviour of fire exposed hollow core slabs. *HERON* 50 (4).

Walraven, J. & Merckx, P. 1983. The bearing capacity of prestressed hollow core slabs. *HERON 28* (3).

DIN EN 1168, 2009. *Betonfertigteile—Hohlplatten.* Berlin & Köln: Beuth Verlag GmbH.

DIN EN 1168, 2011. *Betonfertigteile—Hohlplatten.* Berlin & Köln: Beuth Verlag GmbH.

DIN EN 1992-1-1-Eurocode 2, 2012. *Bemessung und Konstruktion von Stahlbeton—und Spannbetontragwerken—Teil 1–1: Grundlagen und Anwendungsregeln für den Hochbau*, Berlin: Beuth Verlag.

DAfStb, 2001. *Richtlinie für Belastungsversuche an Betonbauwerken*. Berlin: Beuth Verlag.

DIN EN 1991-1-1-Eurocode 1, 2012. *Einwirkungen auf Tragwerke—Teil 1-1: Allgemeine Einwirkungen auf Tragwerke*, Berlin: Beuth Verlag.

Concrete Repair, Rehabilitation and Retrofitting IV – Dehn et al. (Eds)
© 2016 Taylor & Francis Group, London, ISBN 978-1-138-02843-2

Monitoring chloride concentrations in concrete by means of Ag/AgCl ion-selective electrodes

Yurena Seguí Femenias, Ueli M. Angst & Bernhard Elsener
Institute for Building Materials (IfB), ETH Zürich, Zurich, Switzerland

ABSTRACT: This work investigates the applicability of Ag/AgCl ion-selective electrodes for the non-destructive measurement of chloride concentrations in concrete.

Sensitivity to potential interfering ions and stability of the Ag/AgCl membrane in neutral and alkaline solutions are presented. The results indicate negligible interference by fluoride, sulfate, and hydroxide, but considerable interference by bromide and sulfide. In completely chloride-free alkaline solutions, the ion-selective electrodes are not stable over time, but they become again functional as soon as chlorides arrive at the sensor.

It is concluded that the studied ion-selective electrodes are applicable for monitoring the free chloride concentration in the pore solution of concrete structures exposed to chloride-bearing environments. The applicability in concrete containing blast furnace slag or other sulfide sources is however questioned.

1 INTRODUCTION

In non-carbonated concrete with low or no presence of chlorides, the steel reinforcement is passive due to the alkaline environment provided by the hydration of cement. The passive layer protects the steel from corrosion. However, this passive layer can be destroyed when a certain concentration of chlorides reaches the reinforcement (chloride-induced corrosion). Chloride-induced corrosion is the principal cause of premature failure in reinforced concrete structures worldwide (Elsener et al., 2004).

Common methods for determining chloride content in concrete are based on destructive sampling and do thus not allow continuous information at identical locations over time (Elsener et al., 2003, Atkins et al., 1996); therefore, a non-destructive technique that permits continuous measurement of the chloride content is of high interest. For this purpose, the use of Ag/AgCl ion-selective electrodes (ISEs) is a promising solution. The Ag/AgCl exhibit a Nernstian electrochemical potential as a function of the chloride ion activity in solution (Koryta, 1972, Janata, 1989, Bard et al., 2002); thus, for concrete, the Ag/AgCl ISE allows measuring the free chloride content in the pore solution. However, ISEs are also sensitive to other species that can form compounds normally of lower solubility with the constituent ion (Ag^+ for the Ag/AgCl ISE).

The sensitivity in environments containing interfering species and the stability at high pH of Ag/AgCl ISEs are thus two crucial factors regarding the applicability of the Ag/AgCl ISEs in concrete.

This paper investigates the stability of the Ag/AgCl ISE at high pH values and the interference arising from the presence of bromide, sulfate, sulfide, fluoride, and hydroxide. The use of the Ag/AgCl ISE in concrete is discussed.

2 THEORETICAL BACKGROUND

2.1 *The silver/silver chloride ion-selective electrode*

The Ag/AgCl ISE used in this work consists of silver covered by a layer of silver chloride. The Ag/AgCl ISE used belongs to the category of ion selective electrodes with solid ion exchangers (Koryta, 1972).

The potential E of the Ag/AgCl ISE is given by the Nernst law as a function of the chloride ion activity in solution (Angst et al., 2009). However, the Ag/AgCl ISE responds to the primary ion (chloride ion) with a Nernstian behavior only above a minimum concentration of it (i.e. detection limit) (Koryta and Stulik, 1983, Morf et al., 1974). Furthermore, the ISE is also sensitive to other species that can form precipitates of lower solubility with the constituent ionic specie (Koryta and Stulik, 1983, Atkins et al., 2001). This interference is traditionally considered with the selectivity coefficients, $K^{pot}_{Cl^-,Y}$ (with Y standing for the interfering specie) included in the Nikolsky-Eisenman equation (Koryta and Stulik, 1983, Janata, 1989):

$$E = E^0_{Ag/AgCl} - \frac{RT}{F}\ln\left(a_{Cl^-} + \sum\left(K^{pot}_{Cl^-,Y}\cdot a_Y^{-1/Z_Y}\right)\right) \quad (1)$$

where R is the gas constant, T the absolute temperature, F the Faraday constant, a_{Cl^-} the activity of the chloride ion, $E^0_{Ag/AgCl}$ the standard potential of the silver/silver chloride electrode (Haynes, 2013–2014), a_Y is the activity of the interfering ionic specie and z_Y its charge.

2.2 *Influencing parameters*

The potential E of the Ag/AgCl ISE depends on the chloride activity, the temperature and the sensitivity to other species.

- Chloride activity

In concentrated solutions, ions deviate from ideality as a consequence of the high ionic strength. This phenomenon is taken into account by the use of the ionic activity a_x, which is related to the concentration c_x of a specie X by the activity coefficient γ_x (Haynes, 2013–2014):

$$a_X = \gamma_X \cdot {c_X}/{c_0} \tag{2}$$

where c_0 is the standard state composition (generally chosen as 1 mol · L^{-1} (Haynes, 2013–2014)).

- Interfering species

Many silver salts have very low solubilities (Haynes, 2013–2014); therefore, in their presence, the ISE is likely to be affected. The AgCl membrane responds mainly to Cl^-, Br^-, I^-, OH^-, and S^{2-} (Angst et al., 2009, Janata, 1989, Atkins et al., 2001, Klasens and Goossen, 1977). According to equation (1), the potential of the ISE will exhibit a Nernstian behavior when the following relation is satisfied (Angst et al., 2009):

$$a_{Cl^-} >> \sum\left(K^{pot}_{Cl^-,Y} \cdot a_Y^{-1/z_Y} \right) \tag{3}$$

- Temperature

The effect of temperature has in detail been addressed in other studies and data is available to make corrections in this regard (Angst et al., 2009, Shreir, 1994).

3 EXPERIMENTAL

3.1 *Electrodes, instruments and materials*

3.1.1 *Silver/silver chloride ion-selective electrode*

The used Ag/AgCl ISE is an industrial ISE consisting of a silver wire coated with silver chloride deposited by anodizing. The tip of the ISE was additionally dipped in a melt of AgCl in order to achieve a more stable membrane (Angst et al., 2009, Elsener et al., 2003).

Table 1. Calibration solutions and corresponding liquid junction potentials for the Ag/AgCl/sat. KCl.

NaCl concentration	NaOH concentration	$E_{junction}$ at 20°C
(mol · L^{-1})	(mol · L^{-1})	(mV)
0.002	–	–3.7
0.010	–	–2.9
0.100	0.010	–1.2
0.100	0.100	0.7
0.100	1.000	8.4
0.500	–	0.1
0.500	0.010	0.3
0.500	0.100	1.5
0.500	1.000	8.4
1.000	–	1.2
1.500	–	1.9
4.000	–	4.2

3.1.2 *Potentiometric measurements*

The potential of the ISEs was measured versus the silver/silver chloride/saturated potassium chloride (Ag/AgCl/sat. KCl) reference electrode (+0.197 V versus SHE).

The measurements were performed with a PGSTAT 30 Autolab potentiostat/galvanostat (Metrohm Autolab, Utrecht, the Netherlands) with high input impedance (> 100 GΩ) connected to a Windows PC for data acquisition. The program for data acquisition was Autolab Nova v.1.10. All the experiments were carried out at room temperature (20–21 °C).

3.2 *Methods*

3.2.1 *Calibration in solution*

The Ag/AgCl ISEs were calibrated in neutral and alkaline solutions that contained known concentrations of sodium chloride ranging from 0.002 to 4 mol · L^{-1}.

It should be noted that when the reference electrode is immersed in the measured solution, a liquid junction potential $E_{junction}$ (Bard et al., 2002) establishes at its interface and adds arithmetically to the measured potential. In this work, liquid junction potentials $E_{junction}$ were calculated according to the Henderson equation (Bard et al., 2002) to correct the measured potential $E_{measured.}$. For this calculation, it is considered that the KCl concentration is 4.16 mol · L^{-1} when saturated in water at room temperature (Haynes, 2013–2014). The used solutions and the liquid junction potentials calculated are presented in Table 1.

The chloride activity was calculated according to equation (2). Mean activity coefficients ($\gamma_{NaCl\pm}$) for sodium chloride in neutral solution were obtained

Table 2. Mean activity coefficients $\gamma_{NaCl\pm}$ and activity coefficients of the chloride ion γ_{Cl^-} used in this work. Values of pH other than 7 were obtained by addition of sodium hydroxide. The values of $\gamma_{NaCl\pm}$ are taken or interpolated from (Haynes, 2013–2014). The values of γ_{Cl^-} are interpolated from (Vera et al., 2000).

	Value	NaCl concentration	pH
		(mol · L^{-1})	
$\gamma_{NaCl\pm}$	0.952	0.002	7
$\gamma_{NaCl\pm}$	0.903	0.01	7
$\gamma_{NaCl\pm}$	0.770	0.1	7
$\gamma_{NaCl\pm}$	0.681	0.5	7
$\gamma_{NaCl\pm}$	0657	1	7
$\gamma_{NaCl\pm}$	0.663	1.5	7
$\gamma_{NaCl\pm}$	0.668	2	7
$\gamma_{NaCl\pm}$	0.815	4	7
$\gamma_{NaCl\pm}$	0.874	5	7
γ_{Cl^-}	0.740	0.1	≈12
γ_{Cl^-}	0.727	0.1	≈13
γ_{Cl^-}	0.603	0.1	≈14
γ_{Cl^-}	0.642	0.5	≈12
γ_{Cl^-}	0.637	0.5	≈13
γ_{Cl^-}	0.585	0.5	≈14

from the data provided by Haynes *et al.* (Haynes, 2013–2014). The activity coefficients of the chloride ion (γ_{Cl^-}) in the solutions containing sodium hydroxide were interpolated from the data given by Hidalgo *et al.* (Vera et al., 2000). In this case, the effect of the accompanying ions was neglected and activity coefficients were calculated considering the total hydroxide concentration. The data are provided in table 2.

The calibration curves were obtained by linear regression analysis:

$$E = E_{\text{measured}} - E_{junction} = m \cdot \log a_{Cl^-} + b \quad (4)$$

For the case of pH neutral solutions, it was assumed that $\gamma_{NaCl\pm} \approx \gamma_{Cl^-}$ (Angst et al., 2009).

3.2.2 *Sensitivity to interfering species*

The effect of the possible interfering species was investigated for the case of hydroxide, bromide, sulfate, fluoride and sulfide. These were considered the main species that could cause interference to the Ag/AgCl ISEs response in concrete pore solution and seawater exposure (Elsener et al., 2003, Atkins et al., 2001, Chen, 2006, Švegl et al., 2006).

The Ag/AgCl ISEs were first immersed in NaCl solutions. The concentration of the interfering specie was increased stepwise when the potential became stable over time (few minutes—for the addition of hydroxide, sulfate, and fluoride—or few days—for the addition of bromide, and sulfide). For the study of the fluoride, sulfate and bromide interference, the experiments were started in 0.01 mol · L^{-1} NaCl solutions, and the concentration of interfering specie was increased up to 0.04 mol · L^{-1} The addition of bromide caused the Ag/AgCl ISE potential to significantly decrease, and the experiments were repeated with the sensors immersed in 0.1 mol · L^{-1} NaCl solution.

Table 3. Solutions used for the study of the sensitivity to interfering species of the Ag/AgCl ISE.

NaCl concentration	Concentration range of	
(mol · L^{-1})	interfering specie (mol · L^{-1})	Interfering specie
0.05	0.1–1.7	OH^-
0.1	0.1–1.6	OH^-
0.2	0.1–1.5	OH^-
0.3	0.1–1.6	OH^-
0.5	0.1–1.6	OH^-
0.01	0–0.4	Br^-
0.1	0–0.3	Br^-
0.01	0–0.04	F^-
0.01	0–0.04	SO_4^{2-}
0.1	0–0.01	S^{2-}
1	0–0.008	S^{2-}

The silver sulfide has an especially low solubility (Haynes, 2013–2014). It was thus expected that the Ag/AgCl ISE potential would be affected in presence of already little sulfide with respect to chloride, and the experiments were done with the sensors immersed in 0.1 mol · L^{-1} and 1 mol · L^{-1} NaCl solutions.

The use of Ag/AgCl ISE in concrete seems to be a promising solution to monitor chloride changes and some studies have already been done (Angst et al., 2009, Elsener et al., 2003, Atkins et al., 1996). For this reason, the hydroxide inference was treated separately and in more detail. The experiments were always started with 0.1 mol · L^{-1} NaOH solutions to simulate the alkalinity of the concrete pore solution. It has been reported that light may have an effect on the kinetics reactions of hydroxide (Crowell et al., 2004). The experiments were thus carried out avoiding exposure to daylight to simulate the concrete pore solution.

The ISEs were immersed in the solutions containing increasing amounts of the possible interfering species for a total of two months. The solutions used and the concentration ranges of interfering specie are given in Table 3.

The measured potential, E_{measured}, was corrected according to equation (4) with regard to the liquid junction potential, E_{junction}.

Table 4. Solutions used for the study of the long-term stability at high pH of the Ag/AgCl ISE.

NaCl initial concentration (mol · L^{-1})	NaOH concentration (mol · L^{-1})	NaCl addition after 60 days (mol · L^{-1})
0	0.01 (pH ≈ 12)	0.1mol · L^{-1}
0	0.1 (pH ≈ 13)	0.1mol · L^{-1}
0	1 (pH ≈ 14)	0.1mol · L^{-1}
0.1	0.01 (pH ≈ 14)	–

Once the experiments were finished, the Ag/AgCl ISEs that were immersed in the solutions containing bromide, fluoride, sulfate, and sulfide were returned to the original NaCl solutions, i.e. without the interfering specie present. The potential was measured again after one month of immersion in the interfering ion-free solution.

3.2.3 *Long-term stability at high pH*

The stability of the Ag/AgCl ISEs at high pH in the absence of chloride was investigated over a period of 60 days. Erlenmeyer flasks were filled to the very top with NaOH solutions and closed with a rubber plug through which the ISEs were inserted via drilled holes. The flasks were additionally sealed with silicon grease to avoid evaporation and/or carbonation of the solution.

After 60 days of immersion, 0.1 mol · L^{-1} NaCl was added to the chloride-free alkaline solutions. The solutions used for the long-term stability experiments are given in table 4.

The measured potential, $E_{measured}$, was corrected according to equation (4) with regard to the liquid junction potential, $E_{junction}$.

4 RESULTS AND DISCUSSION

4.1 *Calibration in solution*

The calibration curve according to equation (4) is shown in figure 1.

The Ag/AgCl ISEs exhibited a Nernstian behavior with slope of –57 mV (figure 1), in good agreement with the values reported in previous works (Elsener et al., 2003, Angst et al., 2009). The ISE exhibits a Nernstian behavior in the interference-free solutions for the whole range of chloride concentrations tested; it can be then concluded that the detection limit of the chloride ion in aqueous neutral solution is lower than 0.002 mol · L^{-1}, in agreement with the results reported by Angst *et al* (Angst et al., 2009). Furthermore, the standard deviation of the ten individual potential readings is always below 2 mV.

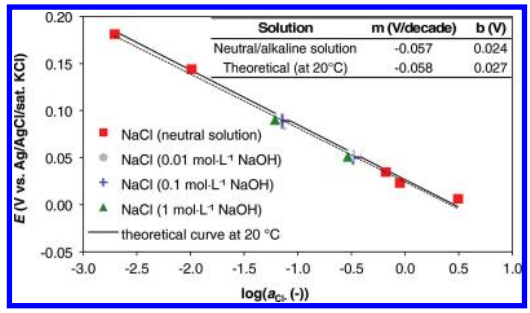

Figure 1. Calibration curve of the Ag/AgCl ISE in neutral and alkaline solutions. The mean values were obtained form ten individual readings. The standard deviation is always less than 2 mV, thus, smaller than the symbols. The parameters of the linear regression analysis are also given with the theoretical values (considering constant room temperature of 20°C (Angst et al., 2009, Shreir, 1994)).

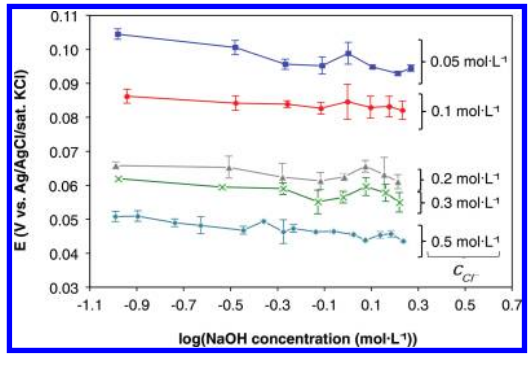

Figure 2. Ag/AgCl ISE mean potential values (from five individual readings) as a function of the logarithm of the NaOH concentration. The error bars indicate the standard deviation (≤5 mV) from the individual readings.

4.2 *Applicability of Ag/AgCl ISEs in concrete*

Figure 2 shows the potential E of the Ag/AgCl ISEs immersed in alkaline solutions containing sodium chloride as a function of the logarithm of the hydroxide concentration.

From figure 2, it can be seen that the potential E of the Ag/AgCl ISEs is overall plateau for the whole range of concentrations tested. The range (difference between the largest and smallest observed potentials) is 10 mV and it is found for the ISEs immersed in the solution containing 0.05 mol · L^{-1} NaCl.

When it comes to chloride-induced corrosion, a concentration ratio chloride to hydroxide $c_{Cl^-}/c_{OH^-} = 0.6$ is sometimes considered as threshold value for corrosion initiation (Hausmann, 1967).

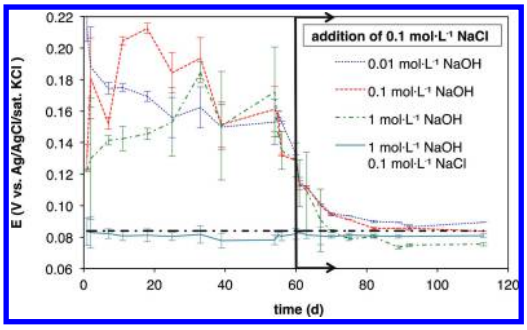

Figure 3. Ag/AgCl ISE mean potential values (from ten individual readings) as a function of time. The dot dash thick line represents the potential for a solution 0.1 mol · L^{-1} NaCl obtained from the calibration curve (section 4.1). The error bars indicate the standard deviation from the individual readings.

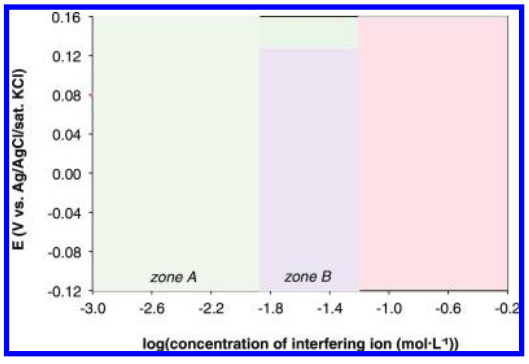

Figure 4. Ag/AgCl ISE mean potential values (from ten individual readings) as a function of the logarithm of the interfering specie in 0.01 mol · L^{-1} NaCl solution (for bromide, fluoride and sulfate) and 0.1 mol · L^{-1} NaCl solution (bromide). The error bars indicate the standard deviation from the individual readings. The zones defined in the graph (zone A, zone B, zone C) schematically represent the effect of the different interfering species on the Ag/AgCl ISE response (compare text).

As it is apparent from figure 2, no interference is expected even for clearly lower ratios c_{Cl^-}/c_{OH^-}. Thus, the Ag/AgCl will permit to detect chloride concentrations much below levels considered critical for corrosion initiation even at high pH.

Nonetheless, the instability of the Ag/AgCl ISE at high pH with no or low amount of chlorides has also been questioned (Elsener et al., 2003, Angst et al., 2009, Švegl et al., 2006). Figure 3 shows the potential E of as a function of time, before and after addition of chloride (at t = 60 days) for the chloride-free solutions.

In absence of chloride, the potential of the Ag/AgCl ISEs shows high scatter between the individual sensors (figure 3). For the Ag/AgCl ISEs immersed in chloride-free alkaline solutions (figure 3), the measured potential values were comprised between 140 mV and 120 mV vs. $Ag/AgCl_{sat}$ after 60 days of immersion.

In alkaline environments in absence or low content of chlorides, the AgCl precipitate undergoes the following reaction (Biedermann and Sillén, 1960):

$$AgCl_{(s)} + OH^- \rightleftarrows \tfrac{1}{2}\, Ag_2O_{(s)} + \tfrac{1}{2}\, H_2O + Cl^- \qquad (5)$$

The potential shift observed to more negative values is probably due to the continuous formation of Ag_2O; potentials of ~144 mV vs. $Ag/AgCl_{sat}$ at room temperature and pH ≈ 14 are reported in the literature if the ISE membrane is considered to be completely covered with Ag_2O (Angst et al., 2009, Pargar et al., 2014, Biedermann and Sillén, 1960).

It is also worth mentioning that the color of the solutions turned brown-black with time, being more pronounced for the solutions that contained higher NaOH concentrations. This color change may also be related to the transformation of AgCl into Ag_2O. This was already observed by Angst *et al.* (Angst et al., 2009).

The possible formation of Ag_2O (equation (5)) could also explain the oscillations in the Ag/AgCl ISE potential shown in figure 2, especially at the lowest chloride concentrations.

It was finally observed that the ISEs recover fast as soon as they come into contact with chloride (right part in Figure 3). The temporal scatter and instability are also considerably reduced. Thus, the possible formation of silver oxide is reversible, as already reported by other authors (Angst et al., 2009, Pargar et al., 2014). The adherence of the Ag_2O to the ISE surface (questioned by Angst *et al.* (Angst et al., 2009)) could however be an issue for the long-term stability because of the reversibility of the AgCl formation. This aspect should deserve further attention.

4.2.1 *Exposure in environments containing interfering species*

Figure 4 shows the potential E of the Ag/AgCl ISEs immersed in 0.01 mol · L^{-1} NaCl (bromide, fluoride and sulfate) and in 0.1 mol · L^{-1} NaCl (bromide) as a function of the logarithm of the concentration of the possible interfering specie (bromide, fluoride, and sulfate).

Regarding the bromide interference, it can be seen that for very small bromide concentrations, the Ag/AgCl ISEs exhibit an overall stable potential independent on the bromide content (figure 4).

However, small amounts of bromide exert a large effect on the response of the Ag/AgCl ISE; the potential shifts to more negative values and the standard deviation increases, reaching values up to 25 mV. For bromide concentrations higher than 0.05 mol · L^{-1}, the potential *E* linearly depends on the bromide concentration for both chloride concentrations tested.

When returned back to the original NaCl solutions, the ISEs did not regain the initial potential values. It has also to be noted that the immersed tip of the ISEs turned green after the bromide addition.

Concerning the fluoride and sulfate interference, up to a fluoride concentration of 0.02 mol · L^{-1}, the ISE potential can be considered to be unaffected. At fluoride concentrations higher than 0.025 mol · L^{-1}, however, a small decrease in the potential is observed. For sulfate, the potential remains almost unaffected to—at least—a concentration of 0.04 mol · L^{-1}. Moreover, when returned back to the original NaCl solution (fluoride—and sulfate-free), the ISEs exhibited potentials equal to those initially registered in the absence of the interfering specie within a few minutes.

To illustrate the effect of the interfering species on the ISE response, figure 4 is schematically divided in three different zones (zone A, zone B, and zone C).

In zone A (figure 4), the Ag/AgCl ISE behaves as an ideal chloride sensor; it exhibits a stable potential independent of the interfering specie (Angst et al., 2009, Koryta, 1972, Rhodes and Buck, 1980). This is the case for fluoride and sulfate (for the whole range of concentrations tested) and for very low concentrations of bromide (plateau part). It is in this range where the Ag/AgCl ISE is suitable for field measurements without interference. The effect of the ions in solution on the chloride activity should however be taken into account (compare Figure 1).

When the concentration of the interfering specie increases (zone B in figure 4), the response of the ISE is altered and it shows a potential determined by the simultaneous action of the primary (chloride) and interfering ion. The interference is due to the replacement of the chloride by the interfering specie on the surface of the ISE (Rhodes and Buck, 1980, Koryta, 1972). This phenomenon can be clearly seen for the case of bromide: the significant potential decrease and the high standard deviation are an indication of the above-mentioned surface coverage process. The color change of the tip of the ISEs also evidences the surface coverage with silver bromide (green).

At sufficiently high concentrations of interfering specie, the ISE surface becomes totally covered by the salt formed between the silver and the interfering specie and acts as an ISE sensitive to this specie (Rhodes and Buck, 1980, Hulanicki and Lewenstam, 1977) (zone C in figure 4). This can be observed for the case of bromide. The ISEs virtually exhibit Nernstian slope after a certain threshold of concentration.

In addition, once the interfering specie is removed from the solution, the Ag/AgCl ISE should ideally behave again as a pure chloride sensor (zone A in figure 10). For the bromide interference, this was reported by Atkins *et al.* (Atkins et al., 2001). However, the ISEs tested in this work did not completely recover. In this study, the ISEs were immersed in the solutions containing bromide for about 2 months, whereas Atkins *et al.* immersed them for only 15 minutes (Atkins et al., 2001). It is believed that the disagreement with respect to the results reported by Atkins *et al.* (Atkins et al., 2001) is due to the kinetics of the transformation of AgBr back into AgCl. In fact, Rhodes *et al.* (Rhodes and Buck, 1980) reported that the kinetics of the transformation of the AgBr back into AgCl is at least 200 times slower than the conversion of AgCl into AgBr. Thus, prolonged exposure to the interfering specie may significantly impair the functionality of Ag/AgCl ISEs.

The response of the Ag/AgCl ISE will be on one of the three zones of figure 4 depending on how severe is the interference and the experimental conditions (Koryta, 1972, Lindner and Umezawa, 2008, Hulanicki and Lewenstam, 1977, Rhodes and Buck, 1980). The severity of the interference is commonly taken into account with the selectivity coefficients (see equation (1)) (Lindner and Umezawa, 2008, Janata, 1989, Koryta and Stulik, 1983, Morf et al., 1974, Morf, 1981). The theoretical models for estimating selectivity coefficients are traditionally based on the assumption that thermodynamic equilibrium is established and the kinetics of the reactions are neglected. However, it is believed that both thermodynamics and kinetics contribute to the selectivity of ion-selective electrodes. This has already been suggested by other authors (Hulanicki and Lewenstam, 1982, Reinsfelder and Schultz, 1973).

Therefore, it appears that the theoretical models for predicting the Ag/AgCl ISE response in presence of interfering ions are not suitable for mid to long-term exposure. In this work, the exposure time of the ISE to the possible interfering species was two months. Although this is clearly longer than in other laboratory studies, field exposure times will be even far longer. Currently, we do not have any data indicating whether exposure times on the order of a few months (this work) are sufficiently long to represent field exposure times (in order of years or decades). Nevertheless, given the actual results, the following can be concluded.

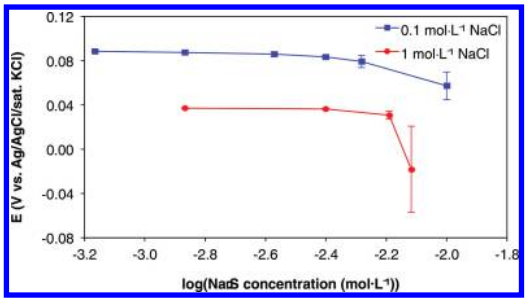

Figure 5. Ag/AgCl ISE mean potential values (from ten individual readings) as a function of the logarithm of the Na_2S concentration. The error bars indicate the standard deviation from the individual readings.

If concrete structures are exposed to seawater, bromide, sulfate, and fluoride interference could be a potential error source. The bromide, sulfate and fluoride concentrations in seawater are approximately $8.7 \cdot 10^{-4}$, $2.9 \cdot 10^{-2}$ and $7 \cdot 10^{-5}$ mol · L^{-1} respectively (Dickson and Goyet, 1994). At those concentrations (shown with arrows in figure 4), no interference was found for the ISEs immersed in 0.1 mol · L^{-1} NaCl (bromide) and in 0.01 mol · L^{-1} NaCl (fluoride, sulfate). Furthermore, from figure 4, it becomes apparent (for the bromide interference) that the ISEs can tolerate slightly higher concentrations of interfering specie when the chloride content is also higher. The chloride concentration in seawater is around 0.5 mol · L^{-1} NaCl. Thus, no significant interference from bromide is expected for seawater exposure.

4.2.2 *Blast furnace slag*

The ions present in pore solution of hydrating slag cement are principally the same as those in Portland cement, with a remarkable amount of sulfide ion in the pore solution (Chen, 2006, Gruskovnjak et al., 2008, Lothenbach et al., 2012). The sulfide interference is thus discussed in this section.

Figure 5 shows the potential E of the Ag/AgCl ISEs immersed in 0.1 mol · L^{-1} and in 1 mol · L^{-1} NaCl as a function of the logarithm of the sulfide concentration.

Sulfide interference is particularly severe. Relatively small amounts of sulfide cause high potential shifts (figure 5). For sulfide concentrations above 0.006 mol · L^{-1}, the potential of the ISEs significantly decreased for both tested chloride concentrations ($\Delta E > 20$ mV for 0.1 mol · L^{-1} NaCl and $\Delta E > 50$ mV for 1 mol · L^{-1} NaCl). The standard deviation also increased significantly at this sulfide concentration.

When returned back to the original NaCl solutions, the ISEs did not regain the initial potential values. It has also to be noted that the immersed tip of the ISEs turned black and decreased its thickness after the addition of sulfide for both tested chloride concentrations. The significant potential decrease, the high standard, and the color change of the tip of the ISEs evidences the progressive surface coverage with silver sulfide (black), as it was similarly observed for the bromide interference.

Lothenbach *et al.* (Lothenbach et al., 2012) observed that the sulfide concentration in CEM III/B 42.5 L containing 59% of slag increases during the first month of reaction and remains rather constant thereafter; concentration of about 0.008 mol · L^{-1} of sulfide were found after one month of reaction. From figure 5, it can be seen that the ISE potential is strongly affected at those concentrations.

In super sulfated cements (SSC) (Lothenbach et al., 2012, Gruskovnjak et al., 2008), even higher sulfide concentrations are found. Gruskovnjak *et al.* (Gruskovnjak et al., 2008) reported concentrations of about 0.1 mol · L^{-1} of sulfide after approximately one month of reaction.

Therefore, it seems that the applicability of the Ag/AgCl ISE in concretes with mid-high amounts of slag will be impaired by the presence of sulfide. For the concretes containing mid-low amounts of blast furnace slag (CEM III/A), it could be possible that the amount of sulfide in solution remained low enough. However, the hydration of cement containing slag is not well understood (Gollop and Taylor, 1996, Taylor, 1997).

It is also important to notice that the ISEs probably tolerate higher concentrations of interfering specie when the chloride content is also higher (figure 4); thus, in absence of chloride, the ISEs potential shown in figure 5 is probably shifted to more negative values at lower sulfide concentrations. Moreover, it should be noted that part of the chlorides will be bound by some of the hydrated cement phases (Luping and Nilsson, 1993) and the ratio chloride/sulfide can be reduced as the amount of Portland cement is increased.

In addition, the decrease in the thickness of the Ag/AgCl ISEs after the sulfide addition questions the adherence of the potential formation silver sulfide on the ISE membrane and the later reaction back into AgCl. Thus, the sensors could be damaged before chloride arrival.

5 CONCLUSIONS

The Ag/AgCl ISEs measure the free chloride content in the concrete pore solution by exhibiting a Nernstian electrochemical potential as a function of the chloride ion activity.

The sensitivity of the Ag/AgCl ISE to interfering species has been carefully studied: while negligible interference was found for fluoride, sulfate, and hydroxide, the interference is relatively severe for bromide and sulfide. Nevertheless, due the high chloride/bromide concentration ratio in seawater, the interference of bromide is considered negligible for applications related to seawater exposure.

In chloride-free alkaline solutions, the ISEs were unstable over time—probably due to transformation reactions with the environment. Upon addition of chloride, however, the sensors responded again according the Nernst's law.

Based on the current experimental observations, it was concluded that the studied Ag/AgCl ISEs are feasible for practical monitoring of the chloride concentration in concrete exposed to chloride-containing environments. An exception is concrete with high contents of blast furnace slag, where the presence of sulfide could strongly disturb the measurements. For the case of low to mid content of blast furnace slag, further research regarding the kinetics and the hydration is needed to evaluate the severity of the sulfide interference. Another open question is the long-term time evolution. If the sulfide concentration decreases with time and embedded ISEs are able to recover, they may after years/decades be functional again when chlorides start arriving at depths corresponding to common reinforcement steel cover depths.

REFERENCES

European Standard EN 197–1. Cement—Part 1: Composition, specification and conformity criteria for common cements. European Committee for Standardization, Brussels, Belgium; 2000.

Angst, U., Elsener, B., Larsen, C. K. & Vennesland, Ø. (2009) Potentiometric determination of the chloride ion activity in cement based materials. J. Appl. Electrochem., 40, 561–573.

Atkins, C. P., M.A. Carter & Scantlebury, J. D. (2001) Sources of error in using silver/silver chloride electrodes to monitor chloride activity in concrete. Cem. Concr. Res., 31, 1207–1211.

Atkins, C. P., Scantlebury, J. D., Nedwell, P. J. & Blatch, S. P. (1996) Monitoring chloride concentrations in hardened cement pastes using ion selective electrodes. Cem. Concr. Res., 26, 319–324.

Bard, A. J., Stratmann, M., Gileadi, E., Urbakh, M., Calvo, E. J., Unwin, P. R., Frankel, G. S., Macdonald, D., Licht, S., Schäfer, H. J., Wilson, G. S., Rubinstein, I., Fujihira, M., Schmuki, P., Scholz, F., Pickett, C. J. & Rusling, J. F. (2002) Encyclopedia of electrochemistry. IN WILLEY (Ed.

Biedermann, G. & Sillén, L. G. (1960) Studies on the hydrolysis of metal ions. Part 30. A critical survey of the solubility equilibria of Ag_2O. Acta Chem. Scan., 14, 717–725.

Chen, W. (2006) Hydration of slag cement—Theory, modeling and application (PhD thesis). Enschede, University of Twente, The Netherlands.

Crowell, R. A., Lian, R., Shkrob, I. A., Bartels, D. M., Chen, X. & Bradforth, S. E. (2004) Ultrafast dynamics for electron photodetachment from aqueous hydroxide. J. Chem. Phys., 120.

Dickson, A. G. & Goyet, C. (1994) Handbook of methods for the analysis of the various parameters of the carbon dioxide system in sea water, Washington.

Elsener, B., Bertolini, L., Pedeferri, P. & Polder, R. P. (2004) Corrosion of steel in concrete, Weinheim.

Elsener, B., Zimmermann, L. & Böhni, H. (2003) Non destructive determination of the free chloride content in cement based materials. Mater. Corros., 54, 440–446.

Gollop, R. S. & Taylor, H. F. W. (1996) Microstructural and microanalytical studies of sulfate attack: IV. Reactions of a slag cement paste with sodium and magnesium sulfate solutions. Cem. Concr. Res, 26, 1013–1028.

Gruskovnjak, A., Lothenbach, B., Winnefeld, F., Figi, R., Ko, S. C., Adler, M. & Mäder, U. (2008) Hydration mechanisms of super sulphated slag cement. Cem. Concr. Res, 38, 983–992.

Hausmann, D. A. (1967) Corrosion of steel in concrete. How does it occur? J. Mater. Prot., 6, 19–23.

Haynes, W. M. (2013–2014) Handbook of chemistry & physics, Boca Raton.

Hulanicki, A. & Lewenstam, A. (1977) Interpretation of selectivity coefficients of solid-state ion-selective electrodes by means of the diffusion-layer model. Talanta, 24, 171–175.

Hulanicki, A. & Lewenstam, A. (1982) Variability of selectivity coefficients of solid-state ion-selective electrodes. Talanta, 29, 671–674.

Janata, J. (1989) Principles of chemical sensors, New York, Plenum Press.

Klasens, H. A. & Goossen, J. (1977) The iodide interference with silver chloride electrodes. Anal. Chim. Acta, 88 (1), 41–46.

Koryta, J. (1972) Theory and applications of ion-selective electrodes. Anal. Chim. Acta, 61, 329–411.

Koryta, J. & Stulik, K. (1983) Ion-selective electrodes, Cambridge.

Lindner, E. & Umezawa, Y. (2008) Performance evaluation criteria for preparation and measurement of macro—and microfabricated ion-selective electrodes (IUPAC Technical Report). Pure Appl. Chem., 80.

Lothenbach, B., Le Saout, G., Ben Haha, M., Figi, R. & Wieland, E. (2012) Hydration of a low-alkali CEM III/B–SiO2 cement (LAC). Cem. Concr. Res, 42, 410–423.

Luping, T. & Nilsson, L. O. (1993) Chloride binding capacity and binding isotherms of OPC pastes and mortars. Cem. Concr. Res., 23, 247–253.

Morf, W. E. (1981) The principles of ion-selective electrodes and of membrane transport, New York.

Morf, W. E., Kahr, G. & Simon, W. (1974) Theoretical treatment of the selectivity and detection limit of silver compound membrane electrodes. Anal. Chem., 46 (11), 1538–1543.

Pargar, F., Koleva, D. A., Koenders, E. A. B. & Breugel, K. V. (2014) The importance of chloride sensors sta-

bility in monitoring ageing phenomena in concrete structures: Ag/AgCl electrodes performance in simulated pore-water environment. AMS 14: Proceedings of the 1st Ageing of Materials & Structures Conference, Delft, The Netherlands.

Reinsfelder, R. E. & Schultz, F. A. (1973) Anion selectivity studies on liquid membrane electrodes. Anal Chim Acta, 65, 425–435.

Rhodes, R. K. & Buck, R. P. (1980) Competitive ion-exchange evaluation of the bromide interference on anodized silver/silver chloride electrodes. Anal. Chim. Acta, 113, 67–78.

Shreir, L. (1994) Corrosion control. IN SHREIR, L., JARMAN, R. A. & BURSTEIN, G. T. (Eds.) Corrosion. third ed. Oxford.

Švegl, F., Kalcher, K. & Kolar, M. (2006) In-situ detection of chlorides in capillary water of cementitious materials with potentiometric sensors. Eighth CANMET/ACI International Conference on Recent Advances in Concrete Technology, 235.

Taylor, H. F. W. (1997) Cement chemistry, London.

Vera, G. D., Hidalgo, A., Climent, M. A., Andrade, C. & Alonso, C. (2000) Chloride-ion activities in simplified synthetic concrete pore solutions: the effect of the accompanying ions. J. Am. Ceram. Soc., 83 [3], 640–644.

Concrete Repair, Rehabilitation and Retrofitting IV – Dehn et al. (Eds)
© 2016 Taylor & Francis Group, London, ISBN 978-1-138-02843-2

Structural health monitoring of the Scherkondetalbrücke: A semi integral concrete railway bridge

S. Marx
Institute of Concrete Constructions, Leibniz Universität Hannover, Hannover, Germany

M. Wenner
Marx Krontal GmbH, Hannover, Germany

ABSTRACT: Semi integral bridges are characterized by the monolithic connection between the superstructure and the piers. Thereby every element of the structure participates to the transfer of forces due to traffic loads. Simultaneously, high constraining forces due to thermal variation, creep, shrinkage or settlements appears. These forces have to be accurately taken into account when designing the bridge and should be reduced through an advantageous distribution of the stiffness, especially in the substructure. The construction of semi integral bridges in the case of long viaducts is an innovation, also on international scale. In order to limit the risks associated with this non-definitively regulated type of structure and in order to collect experience about the calculation assumptions, the authorities required an extensive monitoring of the bridges. In this paper, a few results of the long-term measurements on the Scherkondetalbrücke will be presented.

1 INTRODUCTION

On the High-Speed Railway Line between Erfurt and Leipzig (Germany), long railway viaducts have been designed and executed as semi integral structures for the first time in Germany. This type of bridges is very stable by dynamical excitation and is very robust against overcharge due to the redundancy of the structure. Compared to conventional railway bridges, semi integral bridges can be executed much slender and allow a considerable liberty in the esthetical design process.

Due to the disappearing of bearing devices and joints, semi integral bridges necessitate low maintenance and provide a longer lifetime expectation. The reliability of such bridges and their lifetime can be observed for example by the Gmündertobelbrücke (see Figure 1) and on several other realized bridges in the beginning time of reinforced and prestressed concrete.

However, the absence of adjustment possibilities in the case of settlements and the high constraint forces due to temperature variation, creep and shrinkage are a handicap of semi integral bridges. These particularities have to be taken into account in a very early phase of the design process and need to be considered very accurately in order to achieve a robust and durable construction.

Experiences with long semi integral bridges are missing and guidelines are just being drafted. Furthermore, the actual calculation model for semi integral bridges is very complex due the variation of parameters as the soil stiffness or material characteristics. In order to provide security for the taken assumptions in the calculation and to collect experience with the comportment of semi integral bridges, the supervising authority required the monitoring of several bridges on the High-Speed Railway Line Erfurt—Leipzig. The monitoring includes the measurement of the long-term behavior as well as the comportment under High-Speed traffic. In this paper, results of the long-term monitoring of the Scherkondetalbrücke over a period of 5 years will be presented.

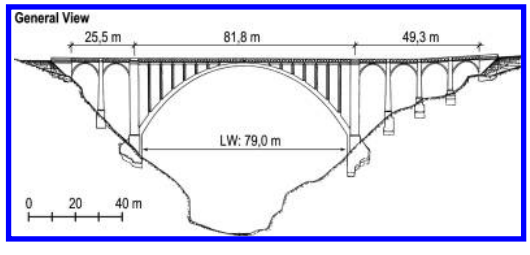

Figure 1. Gmündertobelbrücke, build 1908. (Marx & Wenner 2015).

2 THE SCHERKONDETALBRÜCKE

2.1 *The structure*

The High-Speed Railway Line Erfurt—Leipzig crosses the valley of the Scherkonde close to Krautheim, about 15 km in the north of Weimar.

To bridge the 35 m deep valley, a 576.5 m long viaduct had to be build.

In the last decades, the most High-Speed railway bridges in Germany has been build according an overall planning, as simple supported box girder with spans of 44 m. In the case of the Scherkondetalbrücke, an alternative tender has been assigned and the semi integral bridge represented in Fig. 2 has been realized. The chosen structure allows a much better integration of the viaduct in the landscape through very slender columns and the haunched superstructure (see Fig. 3). Furthermore, the maintenance costs could be lowered by minimizing the number of bearings. The abutment in the axis 0 and the piers in axis 1a to 10 are monolithically fixed with the superstructure. In the axis 11, 12 and 13, bearings have become necessary because of the increasing constraining forces due to the distance to the fixed point.

2.2 *The construction method*

By connecting the piers and the girder to an integral system between the axis 0 and 10, huge longitudinal displacements combined with constraint forces are introduced at the top of the piers. These displacements are generated half by strains due to prestressing, creep and shrinkage and half by strains due to temperature variation. Prestressing, creep and shrinkage exclusively cause a shortening of the girder, which develops for the most part in the first months after concreting. In the case of the Scherkondetalbrücke, the application of a smart construction sequence permitted to reduce the effects of these unidirectional displacements and allowed to optimize the dimension of the piers.

By placing the fixed point of the structure during the construction in the axis 13 and by realizing the girder span by span from east to west (see Figure 2), the construction sequence transformed the shortening of the girder in a negative deflection of the piers. By transferring the fixed point in axis 0 after the concreting of the last span, the direction of the deflection has been inversed and permitted to eliminate the constraint forces almost completely due to prestressing, creep and shrinkage.

3 MONITORING CONCEPT

3.1 *Reasons and background of the measurement*

With the realization of several semi integral bridges between Erfurt and Leipzig, a very new conceptual design for railway bridges has been realized in the net of the DB AG. In the phase of the execution design, many investigations, considering the variation of multiple parameters and their effects on the forces in the structure have been performed. Additionally, a monitoring is required, principally to determine the real behavior of the structure and to compare the results with the previsions. By developing the monitoring concept, two main aims have been followed:

1. Measurement of the longitudinal deformations of the superstructure
2. Measurement of the section curvature on the pier head

3.2 *Conception and realization of the long-term measurements*

The long-term behavior of both superstructure and piers is mostly dependent on the temperature vari-

Figure 3. Photograph of the Scherkondetalbrücke (Photo: Ludolf Krontal).

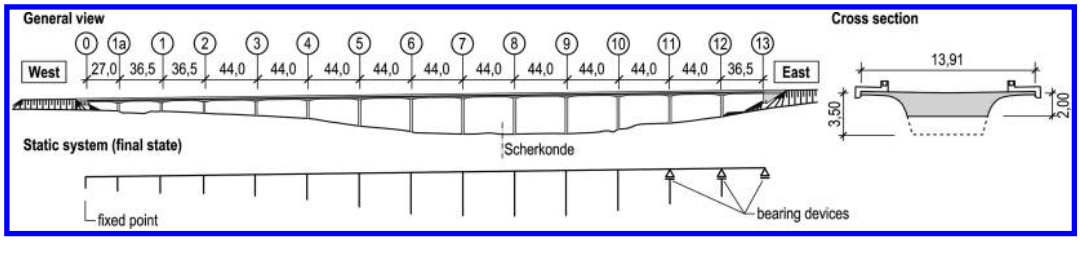

Figure 2. General view of the Scherkondetalbrücke and static system.

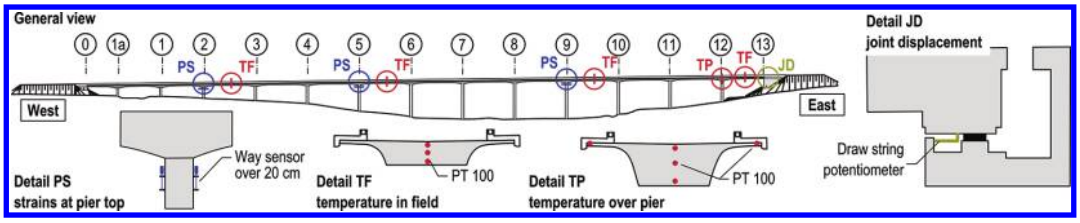

Figure 4. Concept for the monitoring at the Scherkondetalbrücke.

ations and the time-delayed concrete strains of the girder. To be able to differentiate the part of each factor in the measured effects, the temperature is measured in five sections along the girder (see Figure 4). The temperature sensors PT100 have been installed in the formwork before concreting, so that the temperature development in the early age of the concrete could be recorded. The sensors are distributed over the section height and width (see Figure 4) so that the temperature profile in the massive section can be approximated and the average temperature can be calculated.

In axis 13, the displacement of the joint between the girder and the abutment is measured with a draw string potentiometer (see Figure 4). According to geodesic measurements, the displacements of the fixed point axis 0 are negligible, so that the measured joint displacements correspond exactly with the length variation of the superstructure.

To determine the solicitation in the pier head, sensors on both western and eastern sides of the piers have been installed. The measurements are performed in the axis 2, 5 and 9 in order to collect information for different pier lengths, thicknesses and distances to the fixed point. The strains are measured on the surface of the pier, about 2 m under the bottom of the girder with a way sensor recording the relative displacement between two corners, spaced by 20 cm. (see Figure 4 and 5). In order to compensate undesired temperature effects, the gap between the corners is bridged by an invar rod.

The installation of the sensors have been performed parallel with the construction of the bridge. The first measurements could be started before the piers and the girder have been connected to an integral system.

All measures are performed once an hour. In order to guarantee a reliable monitoring of the structure behavior, high requirements to the long term stability and to the compensation of temperature effects of the measurement devices are made.

The company *Ingenieurbüro für Bauwerkserhaltung Weimar GmbH* installed the measuring system and is performing the data acquisition since 2009.

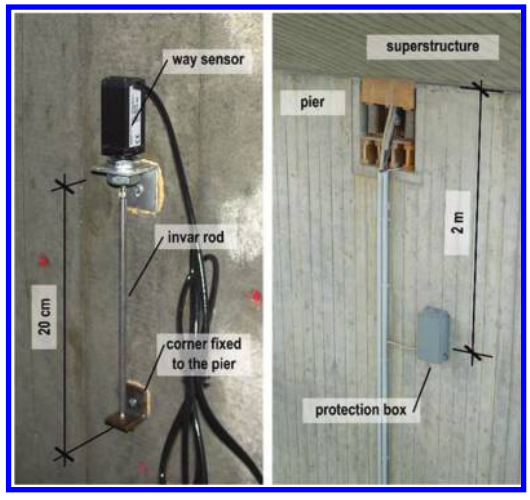

Figure 5. Sensor system for the measurement of concrete strains at the pier head.

4 RESULTS OF THE MEASUREMENTS

4.1 *Effective temperature*

The daily and yearly fluctuation of the air temperature as well as the solar radiation on the structure influence the temperature variation and its distribution in the cross section of the superstructure. For the design of the bridge, the linear component ΔT is calculated as the difference between an average temperature of the superstructure T_e and the neutral temperature T_0. Over the section height and width, an important temperature gradient can be observed. To analyze the strains due to temperature, the "effective" temperature has to be determined based on the measured datas. In this case, the effective temperature has been calculated as a weighted average of the measuring points:

$$T_e = \sum_i c_i \cdot T_i \tag{1}$$

Based on a multiple linear regression, the coefficients have been determined so that the course of

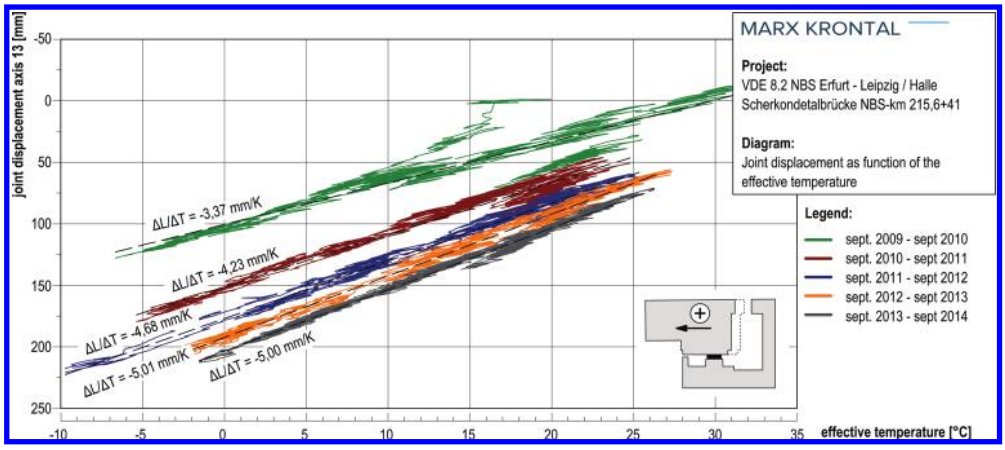

Figure 6. Joint displacement as function of the effective temperature.

the effective temperature coincide with the course of the deformation of the superstructure measured in axis 13. To minimize the disruptive effect of strains due to creep and shrinkage, a small period of two month in the last autumn has been taken as basis for the determination of these coefficients. The best fit in the field between axis 9 and 10 was reached by the following coefficients:

$$T_e = 0.29 \cdot T_{upper} + 0.35 \cdot T_{center} + 0.36 \cdot T_{bottom} \qquad (2)$$

The analysis in the other fields shows that the determined formula is valid over the entire bridge length.

4.2 *Temperature coefficient*

Since the assumption, that the abutments in axis 0 and 13 can be considered as fixed, has been verified and that the retention force do to the piers is negligible, the strains in the superstructure can be determined from the measured joint displacements ΔL in axis 13. From the beginning of the measurement to August 2014, the structure was only subjected to climatic loads. The appearing strains in the superstructure can be attributed to temperature variations and time-delayed concrete deformations and can be expressed by the following formula:

$$\varepsilon = \frac{\Delta L}{L_T} = \left(\alpha_{Tr} + \alpha_{Ta}\right) \cdot \Delta T + \varepsilon_{cc} + \varepsilon_{cs} \qquad (3)$$

where L_T = 576.5 m; α_{Tr} = "real" thermal coefficient; α_{Ta} = "apparent" thermal coefficient; ε_{cc} = creep strain and ε_{cs} = shrinkage strain.

By the composite material concrete, the thermal coefficient has to be differentiated in a real and an apparent part (Taferner et al. 2009). The real part is dependent from the kind, the composition and the proportion of the aggregates while the temperature, the age and the humidity of the concrete condition the apparent part.

By converting Equation 3, the thermal coefficient can be determined:

$$\alpha_T = \alpha_{Tr} + \alpha_{Ta} = \frac{\Delta L}{L_T \cdot \Delta T} + \frac{\varepsilon_{cc} + \varepsilon_{cs}}{\Delta T} \qquad (4)$$

As shown in Figure 6, the measured joint displacement is directly proportional to the temperature variations measured in the girder. The shorter the considered period or the older the concrete, the pronounced is the linearity between displacement and temperature. By performing a linear regression between ΔL and ΔT for a period of 1 year, 5 years after concreting, the strains due to creep and shrinkage are negligible compared to the temperature strains (see Figure 6). The thermal coefficient of the real structure can be determined according to Equation 5:

$$\alpha_T = \alpha_{Tr} + \alpha_{Ta} = \frac{5{,}00}{576.5 \cdot 10^3} = 8.7 \cdot 10^{-6}\ 1/K \qquad (5)$$

With increasing age of the concrete, the lines in Figure 6 get more and more parallel and the offset from one year to the next gets smaller, so that the determined thermal coefficient gives a very good approximation of the real temperature behavior of the superstructure.

The measured coefficient is about 13% smaller than the one assumed in the codes for the design of concrete bridges. Similar investigations performed on further viaducts showed, that the measured

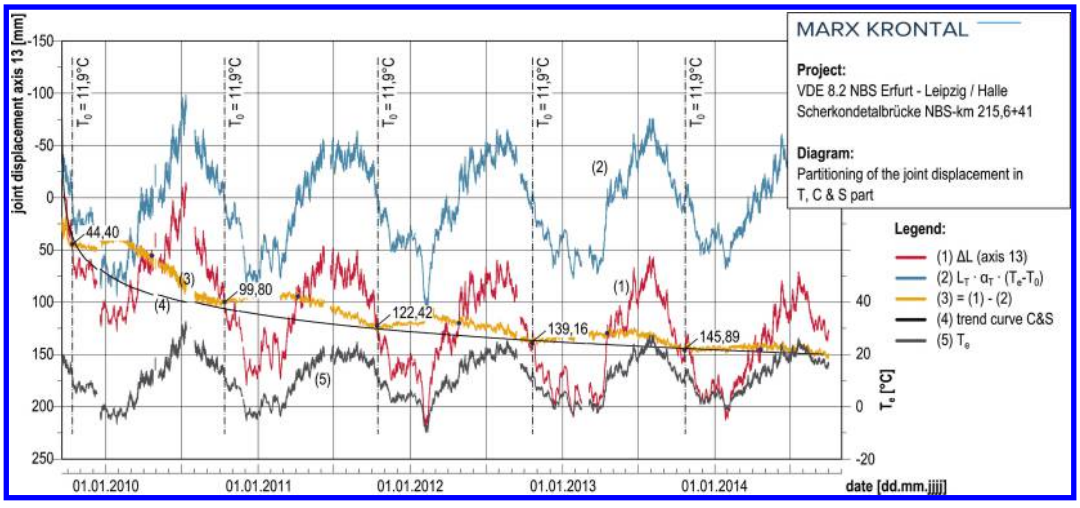

Figure 7. Partitioning of the joint displacement in temperature, creep and shrinkage part.

thermal coefficients varies between $8.0 \cdot 10^{-6}$ and $13.0 \cdot 10^{-6}\ 1/K$. This scatter band corresponds very well with the investigations of (Dettling 1962) for usual aggregates and normal concrete mixtures.

4.3 *Longitudinal deformations due to temperature, creep and shrinkage*

As shown in the last section, the longitudinal displacements are mainly caused by temperature variation and by creep and shrinkage in the first years after completing the bridge. In order to distinguish the influence of both temperature and time-delayed strains, the temperature strains have been calculated from the measured temperature variations and from the determined thermal coefficient (see Figure 7).

By subtracting the temperature part from the measured joint displacements, the strains due to creep and shrinkage can be determined.

The observed qualitative tendency corresponds to the expected trend. The irreversible displacements are equal to 55 mm in the first, 23 mm in the second, 17 mm in the third and 7 mm in the fourth year. By extrapolating the observed behavior from the five first years with a logarithmic approximation, an irreversible and unidirectional displacement due to creep and shrinkage of 210 mm can be predicted for the end value after 100 years. This measurement-based approximation confirms the calculated value according the assumptions from EN 1992.

Besides the long-term increasing of these time-delayed deformations, their seasonal development can be observed in Figure 7. The irreversible deformations develop "slower" in the cold winter month between October and February (see curve (3)) than by temperatures higher than 10°C. This seasonal difference is very pronounced in the first years and becomes smaller with increasing concrete age. The essential cause of this non-monotonous strain-development can be attributed to the influence of temperature and humidity on the concrete material characteristics. The thermal coefficient as well as the creep and shrinkage behavior are dependent from the age and from the environmental conditions. According to the code, the influence of temperature can be taken into account using the effective concrete age. The variable relative humidity can be considered in the calculation of the autogeneous shrinkage and by the calculation of the creep coefficient. By taking into account all the possibilities offered by the code to consider variable environmental conditions, it is possible to reproduce the shape of the measured curve (3), but the development of the calculated curve based on the material model of Eurocode considerably underestimates the measured one and remains monotonous. The older the concrete, the better the accordance between the model and the real object.

4.4 *Bending of the pier heads*

The monolithically fixed piers of semi integral bridges are subjected in the design process as well as by the construction to high requirements. Traffic loads generate normal forces and bending moments in the piers. However, the most of the solicitation in the piers is due to the longitudinal displacements of the superstructure. The constraint forces generated by a displacement of the pier top are primarily dependent on the pier length, on its bending

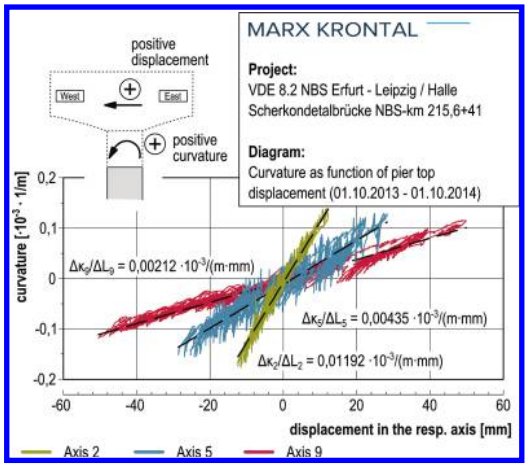

Figure 8. Curvature as function of the pier top displacement in axis 2, 5 and 9 for the period from October 2013 to October 2014.

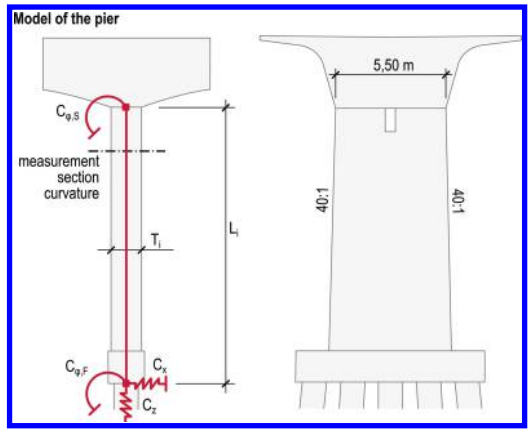

Figure 9. Model of the pier.

stiffness as well as on the bedding condition of the foundation.

The pier length is predetermined by the geometry of the valley. In order to reduce the constraint forces in the piers, the construction of the foundation and the pier section must be optimized during the design.

The choice of single-row pile foundations and thin concrete walls (1,0 to 1,5 m thick) contributed to a reduction of the solicitation in the case of the Scherkondetalbrücke. Furthermore, the chosen construction method (see section 2.2) permitted to reduce the effect of time-delayed displacements. With all these optimizations, all the piers until axis 10 could be fixed monolithically to the girder. In the axis 11 and 12, the distance to the fixed point was too big, so that the ratio between pier length and impacting displacement required the use of bearings.

In order to draw conclusions from the influence of the bedding conditions of the foundation and from the cracking of the concrete section, measurements of the strains have been performed in the area of the pier top in axis 2, 5 and 9. By measuring the strains on both east and western side of the section, the curvature can be determined and compared to the calculated ones.

The longitudinal strains in the superstructure are assumed constant over the bridge length. The displacement of the girder on each axis can be determined proportionately to the distance to the fixed point based on the measured displacement in axis 13. In the Figure 8, the measured curvature in the pier top is represented as function of the longitudinal displacement of this pier.

The measured curvature is linearly proportional to the displacement in the three monitored axis. This proves that the longitudinal displacement of the superstructure is the leading solicitation in the pier. The length of the piers are 11.73 m in axis 2, 23.95 m in axis 5 and 32.55 m in axis 9. The measurement data in Figure 8 show that the longer the pier is, the lower the gradient of the curvature by a unit top displacement is. Thus the pier length increase with increasing distance to the axis 0 (see Figure 2), the utilized capacity for bending moments is similar in each axis (see Figure 8). This attests that the chosen structure geometry is optimal for the topography of the Scherkonde valley.

Furthermore, the linear trend of the curves shows that no cracks seems to be present in the monitored pier area of about 20 cm. The measured data are not disturbed by local singularities and can be taken as basis to evaluate the resistant parameters (bending stiffness distribution along the pier and stiffness of the foundation).

In the calculation, the piers are included in the complete structure model. For the comparison between measured and calculated curvatures, a detailed model of the pier has been developed (see Figure 9). The concrete pier is modelled as a beam. The width variation of 40:1 and the hole under the girder are considered in the stiffness distribution. The continuity of the prestressed superstructure is modelled by a torsion spring $C_{\varphi,S}$. The foundation and the interaction soil/foundation is modelled by two linear springs (C_x and C_z) and by a torsion spring $C_{\varphi,F}$.

The moments and the corresponding curvature have been calculated with a linear elastic material model for the reinforced concrete and the foundation stiffness is based on mean values of the soil

Table 1. Comparison between measurement and calculation with $\Delta\kappa_i$ variation of curvature in axis i; ΔL_i longitudinal displacement in axis i.

Axis	2	5	9
Length L_i [m]	11.73	23.95	32.55
Thickness T_i [m]	1.10	1.50	1.50
$\Delta\kappa_i$ / ΔL_i calculated [$\times 10^{-3}$·1/m·mm]	0.02133	0.00530	0.00313
$\Delta\kappa_i$ / ΔL_i measured [$\times 10^{-3}$·1/m·mm]	0.01192	0.00435	0.00212
Difference	–44%	–18%	–30%

bedding conditions. The results of the comparison are summarized in Table 1.

In all three axis, the measured curvature, and consequently the constraint force in the pier head, is lower than the calculated one. This difference can be attributed to a softer behavior of the foundation than expected. Another cause can be a local decreasing of the bending stiffness on the pier top, for example due to a cracked section. In order to attribute precisely the causes, further investigations are necessary. Nonetheless, the results of measurement are favorable for the solicitation of the piers. Especially cyclic displacements due to the yearly temperature variation, which cannot be reduced through the creeping of the piers, leads to lower constraint forces than estimated in the design.

Since the system has a very stiff fixed point in axis 0, the effect of larger forces under traffic loads due to this softening will not affect the structure safety.

5 CONCLUSION

The performed monitoring over the last 5 years on the Scherkondetalbrücke delivered important data for the understanding of the behavior of long semi integral bridges and permit to verify the safety of the structure.

The measurement of the bridge temperature and of the joint displacements permit to describe the thermal behavior of the superstructure and to control the appearing time-delayed concrete deformations.

In the case of the Scherkondetalbrücke, a thermal coefficient of $8.7 \cdot 10^{-6}\,1/K$ could be determined. Measurements on several other concrete bridges show that the thermal characteristics of concrete fluctuate between $8.0 \cdot 10^{-6}$ and $13.0 \cdot 10^{-6}\,1/K$. These observations demonstrate the influence of the used aggregates and of the receipt of the concrete mixture on the material characteristics. Since temperature is a leading action for the calculation of long semi integral bridges, this scatter band has to be taken into account by designing this type of structures.

The results of the investigated bridge also show that the material models in the code provide a good approximation of the long-term development of creep and shrinkage strains. The seasonal development of these strains is obviously very sensitive to variation of environmental conditions as temperature and relative humidity. The material models in the norm are currently not able to explain this seasonal behavior, but this yearly variations does not affect whether the serviceability nor the bearing capacity of the structure.

The measured curvature in the monolithic fixed piers permit to draw conclusions on the long-term solicitation of the piers. The results confirm that the chosen geometry is optimal for the site topography. A comparison with the design assumptions indicates that the structure reacts "softer" than expected. This behavior is favorable for the structure in terms of constraint forces due to temperature, creep and shrinkage.

The performed monitoring confirms that semi integral bridges are reliable structures. The experiences derived from the results allow to identify actual inaccuracies and to specify the design basics for future projects.

REFERENCES

Marx, S. & Wenner, M. 2015. Integrale und semintegrale Bauweise. In G. Mehlhorn, & M. Curbach (eds), Handbuch Brücken: 102–111. Springer.

Taferner, J., Keuser, M. & Bergmeister, K. 2009. Integrale Konstruktionen aus Beton. In Betonkalender 2009 Teil 2, Ernst & Sohn, Berlin.

Dettling, H. 1962. Die Wärmedehnung des Zementsteines, der Gesteine und der Betone. Phd-Thesis, Technische Hochschule Stuttgart.

Concrete Repair, Rehabilitation and Retrofitting IV – Dehn et al. (Eds)
© 2016 Taylor & Francis Group, London, ISBN 978-1-138-02843-2

Maintaining and monitoring durable cathodic protection systems applied on 30 concrete bridges with prestressing steel

R.N. ter Maten
Vogel Cathodic Protection, Zwijndrecht, The Netherlands

A.W.M. van den Hondel
Cathodic Protection Advice, Capelle aan den IJssel, The Netherlands

ABSTRACT: This paper describes the experiences of maintenance and monitoring of an innovative project which involves Cathodic Protection (CP) systems which are applied on 30 concrete bridges in the Netherlands. As the concrete beam heads that where protected contain the prestressing anchorages, special care was taken for sufficient protection of the steel without over-protecting any part of the prestressing steel in order to avoid hydrogen embrittlement. The project was executed in 2012 and 2013 and involved a total of over 1.500 prestressed beams heads with a total of more than 3.000 reference electrodes, which will be monitored for 20 years. The organisation for this long-term project was set up to secure a continuing work method so the structures will (safely) be maintained in the coming decades. This organisation, the technical challenges, and results of the maintenance and monitoring of the first two years, which show interesting results with regard to the application of ICCP on prestressed concrete structures, are presented.

1 INTRODUCTION

1.1 *Preface*

This paper describes the experiences of the maintenance and monitoring of an innovative cathodic protection project named 'Liggerkoppen' (which translates to 'beam heads'). The application phase of the project is covered in the paper 'Application of durable cathodic protection systems applied on 30 concrete bridges with prestressing steel' as presented on ICCRRR 2015.

While the long-term processes surrounding the maintenance and monitoring of the Cathodic Protection (CP) systems had to be secured, the innovative solution of adding 20 years of maintenance and monitoring to the contract was established. This paper describes the organizations and the experiences of the maintenance and monitoring phase of this long-term project and the first results from the monitoring of the first 2 years.

1.2 *Paper structure*

Chapter 2 includes, in short, the project history including the preliminary investigations, the damage assessment, and the final choice for cathodic protection as solution for the durability problems. Chapter 3 includes the current project status, the long-term challenges, and a brief description of the applied CP system. Chapter 4 describes the innovative approach of adding 20 years to the contract and the subsequent advantages for all parties involved. Chapter 5 illustrates the technical challenges for the severe amount of data to be obtained and analysed. In chapter 6 and 7 the results of the first period of almost two years of measurements (monitoring) and maintenance are discussed which show interesting results with regard to the application of ICCP on prestressed concrete structures.

2 PROJECT PAST

2.1 *Project cause*

During inspections of various bridges in and over a number of highways the Dutch Highway Administration (DHA: 'Rijkswaterstaat') observed that a significant number of bridges showed severe damage at the ends ('heads') of their beams. Research showed that the cause of this damage was chloride initiated reinforcement corrosion. Because of leakage through the joints the heads of the beams were exposed to desalination salts (containing chloride) and humid conditions. Penetration of chlorides in combination with insufficient concrete cover has initially led to corrosion of mild steel reinforcement and consequential concrete damage. Because of the presence of pretension, usually 3 to

6 prestressing steel bars per beam, the structural risks were considered. Further inspection found that the anchorage showed surface corrosion, fortunately without significant material loss. However, the urgent recommendation was given to stop further corrosion at short notice in order to maintain structural integrity.

2.2 *Solutions*

Rijkswaterstaat, in collaboration with several research offices, designed a principal solution in which the leaking joints were to be replaced to stop the supply of water and chloride contaminated deicing salts.

However, by this measure further corrosion of the reinforcement can not be avoided because of the chloride-contamination of the concrete. The removal of all the contaminated concrete proved to be infeasible because of the anchoring forces of the pre-stressing.

In order to avoid the demolition of the bridges, it was decided to establish a call for tender for the replacement of the expansion joints, removal of damaged concrete of the affected beams over the first meter, and to repair and to provide these areas with CP. While the long-term processes surrounding the maintenance and monitoring of the Cathodic Protection (CP) systems had to be secured, the innovative solution of adding 20 years of maintenance and monitoring to the contract was established.

2.3 *Cathodic protection*

The advise for, and design of, a Impressed Current Cathodic Protection (ICCP) system followed from the demand for the service life of the bridges to be extended with at least 20 years. Therefore, Rijkswaterstaat decided to prescribe an Impressed Current CP system (ICCP) in the tender documents in order to obtain sufficient certainty about the degree of protection. In addition to the replacement of the expansion joints, it was prescribed to apply cathodic protection on the heads (first meter) of the beams which already shown chloride initiated damage and/or chloride contamination and to he the beams which are adjacent.

With the application of the CP system the corrosion of the reinforcement is inhibited to a negligible rate by lowering the potential of the reinforcement. The result is that further degradation and the change of possible failure of the mild and prestressed steel is removed and the concrete repairs will endure much longer than without a CP system.

Because of the greater sustainability and the better opportunities for control and monitoring in the operational phase Rijkswaterstaat decided to select the option of impressed current cathodic protection over a possible galvanic ('sacrificial-anode') system.

Figure 1. As-built CP system with conductive coating and decentralized power supply and monitoring units.

While the beams are prestressed, special precaution was taken in order to avoid possible hydrogen embrittlement ('overprotection') of the prestressed steel bars. Applied on the beams, the CP system has to provide sufficient protection for the steel in order to prevent corrosion, and at the same time overprotection had to be avoided at all times.

2.4 *Impressed current cathodic protection system*

The contract was ultimately awarded to the consortium Mourik—Salverda. After replacing the expansion joints by Salverda, Mourik daughter and CP specialist company Vogel Cathodic Protection started their operation including concrete repair and application of CP at the heads of the selected beams.

Based on the set demands in the tender documents, a CP system was designed based on a conductive coating as anode system. The applied conductive coating consists of a graphite filled aluminosilicate matrix (non cementitious binder) with good strength, adhesion and long term durability when used as an anode. As a primary anode a platinum clad copper wire was used (CuNbPt). Each beam head has its own connection tot the reinforcement steel (since there typically was no electrical continuity between beams). Each beam head was equipped with (2 or 3) reference electrodes for monitoring purposes (Fig. 1).

On the surface near to the mild steel reinforcement an activated titanium decay probe was placed in the original, non-repaired, concrete. For the selection of this location the most likely corroding area was selected as determined by potential

mapping. This was typically near the joint, at the bottom side of the beam.

Near the prestressing steel a true reference electrode (silver chloride electrode) with a long lifetime expectancy was placed. For the selection of the electrodes locations the prestressing steel was located on the 'worst case' when considering overprotection risks, so as near to the anode system as possible. On these locations, by drilling towards the cable ducts and continuously measuring the cover thickness in the bore hole (depth probe with concrete cover meter), the reference-electrodes where placed at 10 mm of the prestressing steel. This depth was typically approximately 200 mm, which is also the distance to the anode system. Also 2 connections to the steel were made in every beam by welding in order to provide for a cathodic connection in the CP system of the beam and a second connection for measuring purposes. Cable slots were milled in the concrete surface of the beam in order to make the system more durable, less visible and less vulnerable. All cables outside the surface of the beams are concealed in stainless steel pipes.

The CP system was designed to be operated on solar power with a battery back-up. In the design of capacity, for both the solar power and the battery back-up, the tender documents specified an up-time over 90% on a yearly basis. In effect this means designing for power consumption under poor production circumstances during winter time (The Netherlands is located approximately 51° latitude on the Northern hemisphere).

Furthermore, the tender documents specified the ability for remote control of the CP systems. Due to the large number of reference electrodes there is a strong need to limit the amount of cabling involved by placing power supplies near to each beam. In order to do so, in general 3 beam heads are grouped to a zone (typically 4–5 m^2 of protected surface) with a decentralized, remote controlled power supply.

3 CURRENT PROJECT STATUS

The 'Liggerkoppen'-project was executed in 2012 and 2013 on prestressed beams in 30 concrete bridges of the Dutch Highway Administration (DHA: Rijkswaterstaat) which are spread over 22 locations in the east of the Netherlands.

The number of beams which are equipped/provided with impressed current ('active') cathodic protection varies from merely 3 to over 170 beams per bridge (Fig. 2). In total the project involves an amount of over 1.500 prestressed beams of the total amount of almost 6.000. Every beam is designed as separate 'field' (or pseudo-zone) and contains at least two reference cells (occasionally three cells where placed for evaluation purposes), a titanium 'decay' probe and a 'true reference' cell. This leads to a sum of over 3.000 reference cells, which will be monitored according to the NEN-EN-ISO 12696:2012 Standard.

Figure 2. Example of as-built CP system at abutment on 27 beams with 9 decentralized power supply and monitoring units.

While the long-term processes surrounding the maintenance and monitoring of the CP systems had to be secured, the innovative solution of adding 20 years of maintenance and monitoring to the contract was established. As a result of the multi-year contract the structures will (safely) be maintained by the contractor in collaboration with the client in the coming decades.

4 PROJECT ORGANIZATION

During a preliminary assessment of the possible risks and their effect on the function of the CP systems, several key factors of possible failure where determined. These threats are either technical and focus on the system itself, or procedural, due to the organizational challenges for maintaining anything technically complex for a period of 20 years.

The technical threads were dealt with in specifying minimum demands for anode durability, technical provisions for control, and integrated quality control procedures during all phases of the execution and maintenance period. Specific demands where made on the long term performance of the CP system and the monitoring therefore involves at least two depolarisation measurements per year and an annual visual inspection, but with special emphasis on large scale evaluations in year 4, 9 en 14 of the total project. As mentioned, the long-term processes surrounding the maintenance and monitoring of the Cathodic Protection (CP) systems had to be secured. Experiences from Rijkswaterstaat with the application of CP had

taught that the involvement of the local administration after execution of the project can decrease rapidly. As a result, the functioning of the CP system was not observed. In the past, this has led to systems that were prematurely disabled or which overtime did not get the attention needed to function as intended. This despite the fact that the regulations like NEN-EN-ISO 12696:2012 prescribe a minimal demand for an annual visual inspection and at least two depolarisation measurements per year.

During a period of 20 years organisations will change, both on the side of the owner (Rijkswaterstaat) and the side of the contractor. While the execution of the work itself can easily be organised in a project based structure, the maintenance and monitoring is a 20 year process having different organisational demands. Special care was taken to avoid the loss of information on the side of Rijkwaterstaat in the transition from 'project' (execution phase) to 'process' (20 year maintenance). This resulted in intensive exchange of information at the end of the execution phase.

Evaluating the execution and transition phase, the assessed risks and threats proved to be valid. Without the attention demanded for the maintenance period following on the execution, this project would easily have become too complex to handle in the 'low attention' phase of 20 years monitoring. At this point, it has been rewarding to see a vital installation being taken care of to function as intended for decades to come.

5 TECHNICAL ASPECTS

As described before; the total project is remotely controlled at 22 locations, including 30 bridges, with CP on 1.500 beam heads, which are spread over 500 zones, and have a total of more than 3.000 reference cells. This will give enormous amounts of data, which have to be acquired, processed, evaluated and reported during a period of 20 years.

Frequently the status of each zone is checked (so-called 'on' measurements), confirming the good operation of the hardware which are especially important due to the fact that these CP systems operate on solar power (Fig. 3). These measurement typically generate data of set voltage, applied voltage, applied current, and the on-potentials of the reference electrodes: typically 4.500 numbers per measurement. Combined with a weekly interval for measuring, this will result in 234.000 numbers per year (4.7 million during the total maintenance period).

In order to establish the fact that no overprotection occurs, another type of measurement (so-called 'instant off' measurement) is performed in which the on-potentials of the individual reference electrodes as well as the behaviour in the instant of shutting off the protective current, in the first second, is measured. This typically results in 33.000 numbers per measurement. Combined with a weekly interval for measuring, this will result in 1.7 million numbers per year (34 million during the total maintenance period).

Figure 3. Central measuring and control unit and solar panels.

To prove sufficient protective current a full depolarisation over a period of 24 hours is performed according to NEN-EN-ISO 12696:2012. Although a minimum of two measurement per year are required in the standard, in the first two years 4 measurements a year are prescribed for this project. Each measurements results in 216.000 numbers, totalling up to 864.000 numbers for the first two years, and 432.000 for the subsequent years (9,5 million during the total maintenance period).

Obviously, the acquisition and processing of the data is challenging and demand automated procedures. Based on automatic processes on a yearly basis all general results are published and statistically treated. Specific measurements that could indicate problems, i.e. failure, insufficient protection or over-protection, are reported without delay on an individual basis. Acceptable outcomes (within bandwidths) are specified in the software to reduce the workload without risking neglect or ignorance of important results.

6 MONITORING

The results of the monitoring during the first two years are promising. All bridges and beam heads show sufficient protection, while no risk of over-protection was observed for this first period.

Typically the initial current density at start up of the zone is very high (50–100 mA/m^2), but drops rapidly to normal values (below 20 mA/m^2). Within a few weeks to not more than 6 months the current density needed for sufficient protection decreases to an average of 1–2 mA/m^2. At the same time this current output requires a steady increase of applied cell voltage (cathode to anode) from an initial 2 volts to values in the range of 3–7 volts. There is a variation between locations, but only minor variations within one bridge. It was therefore decided that, for the time being, all zones within one bridge are operated at the same set voltage.

As a result of the numbers shown above it can be concluded that the apparent system resistance increases. As observed, the instant-off potential at the anode shows a sharp increase from an initial value of 0,2–0,5 volts to values stabilising on approximately 1,8–2,2 volts. Therefore, part of the increase in system resistance is due to semi-permanent polarisation of the anode. Other factors resulting in increased system resistance are assumed to be oxygen consumption and drying out of the concrete after replacing the joints and the application of the conductive coating presenting a barrier to moisture absorption.

Initial measurements of depolarisation show high depolarisations which are well over the minimum requirement of 100 mV according to NEN-EN-ISO 12696:2012, with little variation over beams with active corroding steel and beams included in the project where the protection is more or less preventive (the adjacent beams). Over time this tends to reduce to values from 100–250 mV depolarisation, with no structural difference between protected and prevented sides. This might be due to the repassivation of the active corroding steel, resulting in comparable micro-environments in all beams. The difference between the monitored mild steel reinforcement and the monitored deep locations near the prestressing steel is present at start up, but tends to disappear over time. At some locations there is no significant difference between the behaviour of the reinforcement at typically 35 mm depth and the reinforcement at 200 mm depth. This was unexpected, but shows a deep penetration of sufficient protective current in a heavily reinforced, high quality concrete which is dense, and has a low permeability.

As an example various results are represented in the figures 4 to 6 below. It is noted that some reference electrodes do not meet with the 100 mV depolarisation criterion (criterion 8.6.b from NEN-EN-ISO 12696:2012). Some reference electrodes are dysfunctional, some are placed very deep in order to assess the absence of overprotection at the prestressing steel (up to 40 cm of depth), and some show instant off potentials at very low levels at which depolarisation tends to be too slow

Figure 4. Example cathodic depolarization for a typical viaduct.

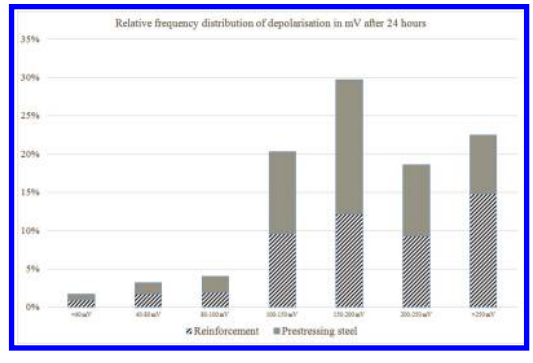

Figure 5. Overall data for frequencies (for degree) of depolarization.

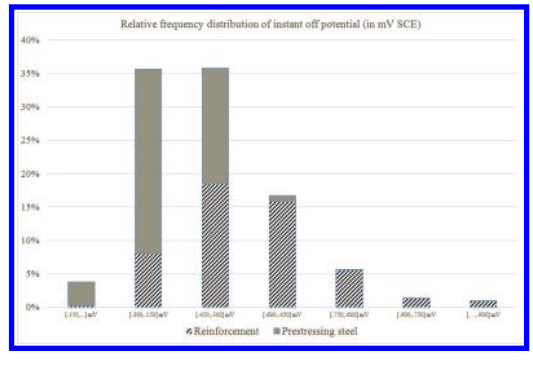

Figure 6. Overall data for frequencies exclusion of hydrogen embrittlement.

to meet criterion 8.6.b but those locations do meet criterion 8.6.a from NEN-EN-ISO 12696:2012. As the number of reference electrodes failing was very small and functional reference electrodes were present at all sites, it was decided not to replace any defective reference electrodes until future maintenance is year 4 or 9.

7 MAINTENANCE

During visual inspections several minor defects from the execution and the maintenance period where detected and dealt with. There are no signs of aging, as expected during this relatively short period, but some evaluated risks have proven to be valid. These observations where related to:

- A single incident of maintenance performed by a third party on a protected site resulted in a few small damages of the conductive coating, some water induced damage on two power supplies and large scale pollution of the surface. These issues where dealt with and resolved.
- At a few locations theft of solar panels and batteries caused temporary shutdown of the systems. After replacement measures were taken to avoid further theft.
- At three locations stainless steel cabled ducts where unintentionally shorted with the anode and corroded as anodes for protecting the reinforcement steel of the abutment beneath the protected beam heads.

All observed problems proved to be self-explanatory and unproblematic to deal with.

Over 10 years of practical experience with the specific conductive coating exists in the Netherlands. At these locations, presently significant signs of aging and failure of the anodes is observed or reported. At the same time there are signs of aging process in specimens subjected to accelerated aging tests in the laboratory. Despite the general expectancy to have a long lasting, durable anode system, within the project described above, some maintenance is expected at the scheduled full scale visual inspections in years 4, 9 and 14. For this purpose the conductive coating is not covered with a top coat, in order to facilitate easy maintenance.

8 PROSPECTIVE AND CONCLUSIONS

Cathodic Protection (CP) is a successful technique to guaranty structural integrity by which corrosion of reinforcement is inhibited to a negligible rate by lowering its potential. In a project named 'Liggerkoppen' (which translates to 'beam heads') 30 concrete bridges in the Netherlands are provided with a Impressed Current Cathodic Protection system. The project was executed in 2012 and 2013 in commissioned by the Dutch Highway Administration ('Rijkswaterstaat'; DHA).

While the long-term processes surrounding the maintenance and monitoring of the CP systems had to be secured, an innovative solution was established which included 20 years of maintenance and monitoring, which will be performed according to NEN-EN-ISO 12696:2012. As a result of the multi-year contract the structures will (safely) be maintained by the contractor in collaboration with the client in the coming decades.

Due to chloride initiated corrosion, caused by leakage through the joints in combination with insufficient concrete cover, numerous beams were damaged and it was urgent to find a solution to stop further corrosion at short notice in order to maintain structural integrity. Distributed over the 30 bridges, a total of over 1.500 prestressed beam heads are provided with a conductive, graphite filled aluminosilicate, coating as anode system.

Each beam head is equipped with (2 or 3) reference electrodes for monitoring purposes, which results in a total of more than 3.000 reference electrodes. Near the prestressing steel a true reference electrode (silver chloride electrode) with a long lifetime expectancy was placed. Special care could therefore be taken for sufficient protection of the steel without overprotecting any part of the prestressing steel in order to avoid hydrogen embrittlement.

Due to the large number of beams per bridge, beam heads were grouped to zones with decentralized power supplies to limit the cabling. The CP systems are powered with solar power with a battery back-up with a up-time over 90% on a yearly basis. The CP-systems are, as tender documents specified, remotely controlled.

During a preliminary assessment of the possible risks and their effect on the function of the CP systems, key factors of possible failure where determined. These threats are either technical, which focus on CP-systems, or procedural, due to the organizational challenges for maintaining anything technically complex for a period of 20 years.

The procedural challenges are dealt with for special care was taken to avoid the loss of information on the side of Rijkwaterstaat in the transition from 'project' (execution phase) to 'process' (20 year maintenance). Evaluating the execution and transition phase, the assessed risks and threats proved to be valid. Without the attention demanded for the maintenance period following on the execution, this project would easily have become too complex to handle in the 'low attention' phase of monitoring. At this point, it has been rewarding to see a vital installation being taken care of to function as intended for decades to come.

The technical threads were dealt with in specifying minimum demands for anode durability, technical provisions for control, and integrated quality control procedures during all phases of the execution and maintenance period. Specific demands where made on the long term performance of the CP system and the monitoring therefore involves at least two depolarisation measurements per year

and an annual visual inspection, but with special emphasis on large scale evaluations in year 4, 9 en 14 of the total project.

The status of the zones are frequently monitored, confirming the good operation of the hardware, sufficient protection of the reinforcing steel and the absence of overprotection at the prestressing steel. This results in large sets of data (48 million during the total maintenance period) which have to be processed and evaluated.

The acquisition and processing of the data is challenging and demands automated procedures. Based on automatic processes on a yearly basis all general results are published and statistically treated. Specific measurements that could indicate problems, i.e. failure, insufficient protection or over-protection, are reported without delay on an individual basis. Acceptable outcomes (within bandwidths) are specified in the software to reduce the workload without risking neglect or ignorance of important results.

The results of the monitoring during the first two years are promising. All bridges and beam heads show sufficient protection, while no risk of over-protection was observed for this first period. Typically the initial current density at start up of the zone is very high but drops rapidly to normal values. At the same time this current output requires a steady increase of applied cell voltage (cathode to anode) from an initial 2 volts to values in the range of 3–7 volts. It can be concluded that the apparent system resistance increases.

Initial measurements of depolarisation, to prove sufficient protection, show high depolarisations which are well over the minimum requirement of 100 mV with little variation over beams with active corroding steel and beams included in the project where the protection is more or less preventive. Over time this tends to reduce to values from 100–250 mV depolarisation, with no structural difference between protected and prevented sides. This might be due to the repassivation of the active corroding steel, resulting in comparable micro-environments in all beams. The difference between the monitored mild steel reinforcement and the monitored deep locations near the prestressing steel is present at start up, but tends to disappear over time.

During visual inspections several minor defects from the execution and the maintenance period where detected and dealt with. There are no signs of aging, as expected during this relatively short period, but some evaluated risks have proven to be valid. All observed problems proved to be self-explanatory, were not related to the CP technique itself, and were unproblematic to deal with.

With the application of the CP system the corrosion of the reinforcement is inhibited to a negligible rate by lowering the potential of the reinforcement. The result is that further degradation and the change of possible failure of the mild and prestressed steel is removed and the concrete repairs will endure much longer than without a CP system.

Concrete Repair, Rehabilitation and Retrofitting IV – Dehn et al. (Eds)
© 2016 Taylor & Francis Group, London, ISBN 978-1-138-02843-2

Case studies in the practical application of pulse echo technology

D. Corbett
Proceq SA, Switzerland

ABSTRACT: Although it has been around for several years, the use of ultrasonic pulse echo technology for the assessment of concrete structures is not widely understood. This paper will demonstrate the practical application of this technology by means of a number of real case studies. It will show what information can be uniquely obtained from a structure with this method and will also show how it is complementary to other non-destructive measurement techniques. It will also demonstrate the limits of the technology as it is equally important to understand what it cannot do.

1 INTRODUCTION

One of the key areas of development in Non-Destructive Testing (NDT) of concrete in recent years has been in imaging using tomography methods. There is a real need to see the internal structure of the concrete element, be it the reinforcement structure, the location of post-tensioning cables, the presence and extent of delaminations or honeycombing. Ground penetrating radar, eddy current and impact echo instruments have all been used for this purpose. Each technology has its advantages and disadvantages, yet none of them, used independently can provide all of the information required. A combination of instrumentation is necessary to build up a more complete image of the internal structure of the concrete element. Pulse echo technology is an additional string to the bow of the NDT specialist. The following case studies show what kind of information it can provide.

2 CASE STUDY ONE—PRECAST CONCRETE ELEMENTS

2.1 *The testing issue*

Precast elements are becoming ever more popular for multi-functional floor systems, heating and cooling purposes and in constructions where the weight of the element is critical. In this case the subject was a multi-storey car park. A cross section of the element is shown in Figure 1. The polystyrene blocks reduce the amount of concrete that is cast in place.

The 70 mm layer is the precast concrete and the 310 mm layer is the cast in place concrete. Each element was 13.5 m long and there were approximately 70 such elements on each floor. The floors of the car park were seen to be sagging in several areas and it was suspected that the cast in place concrete had not bonded correctly with the precast element, causing delaminations that had seriously weakened the structure. This was confirmed in a few locations by taking cores. The problem faced on site was how to determine the extent of the delaminations by non-destructive testing. Traditional pulse velocity measurements were out of the question due to practical considerations. GPR had been tried without success as that technology is only able to detect delaminations if they are filled with water or some kind of sealant such as epoxy. Pulse echo technology only requires access from a single side and is ideally suited to detecting delaminations due to the difference in the acoustic impedances of concrete and air, which means there is an almost total reflection from any air gap.

2.2 *Trial tests with pulse echo technology*

Pulse echo B-Scans were carried out on the underside of the ceiling, directly on the precast concrete using the Pundit PL-200PE instrument from Proceq.

Cores taken close to supporting columns had shown no evidence of delaminations. The first measurement was made with a fine grid of 2.5 cm

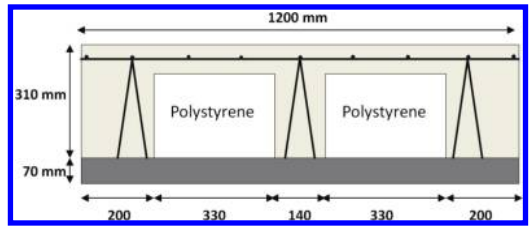

Figure 1. Cross section of precast element.

Figure 2. Pundit PL-200PE Pulse Echo Instrument.

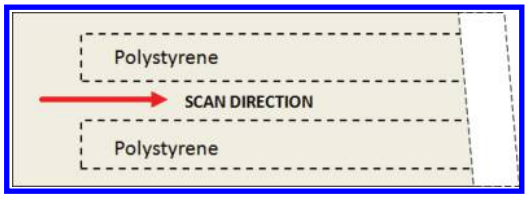

Figure 3. Positioning of initial scan.

moving outwards from one of the support columns as shown in Figures 3 and 4.

Over the first 45 cm of the scan, the back wall can be seen clearly. This is what you would expect if the bond between the precast element and the cast in place concrete is good. After this, to the right of the scan there is clear evidence of a delamination. The depth of the delamination is at 10 cm.

The shear wave pulse velocity of 2888 m/s was determined using an automatic pulse velocity estimation function that performs a surface measurement over a known distance. This is a similar procedure to the method defined in ASTM C1383 [1] for impact echo. There is currently no international standard for pulse echo technology applied to concrete testing. The method assumes that the pulse velocity at the surface is the same throughout the concrete element being measured. Generally this is not true and certainly not in an element such as this with two different types of concrete. That is the reason the distances are slightly overestimated. In this case it would be a simple matter to correct the pulse velocity as the actual element thickness is known, however as the object of the exercise is to locate delaminations it is irrelevant.

The next step was to make a scan perpendicular to the first scan at a location that was suspected of being a delamination from the first scan.

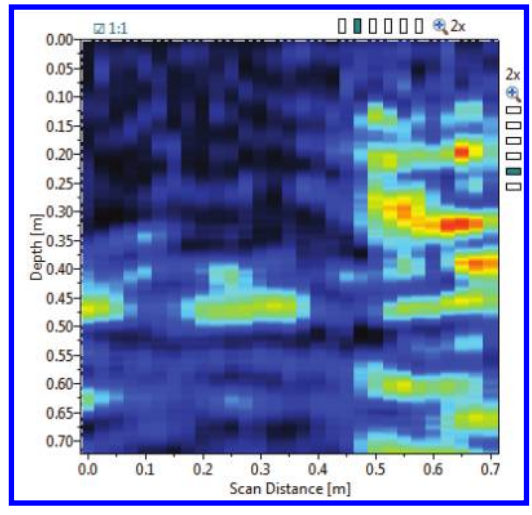

Figure 4. Initial B-scan.

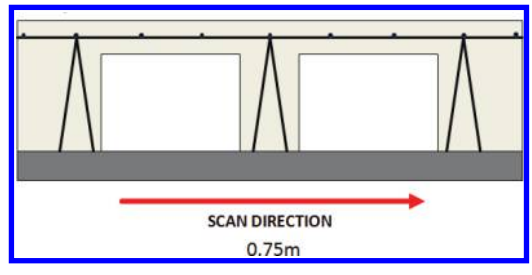

Figure 5. Positioning of second scan.

Here we can see that there is no difference in the echo when scanning over the concrete polystyrene section and the precast/cast in place concrete section. A strong echo from the polystyrene is expected as it has a much lower acoustic impedance (approximately 2.5) to that of concrete (approximately 9). On the other hand, strong echo in the area between the two polystyrene blocks can only be explained by a delamination.

2.3 *Larger scale scan*

Encouraged by the initial results it was decided to undertake a larger scale scan again in the direction indicated by Figure 3, this time using a 10 cm spacing between A-Scans.

Here it can clearly be seen that the delamination begins around 20 cm from the beginning of the scan and continues up to 1.6m. After that the back wall becomes visible again indicating a good bond between the precast and cast in place concrete.

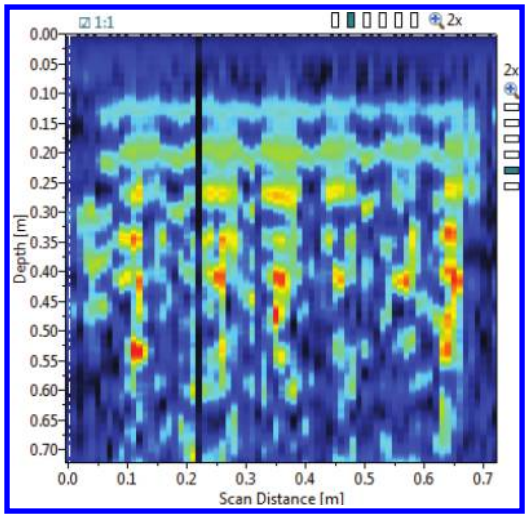

Figure 6. Perpendicular B-scan.

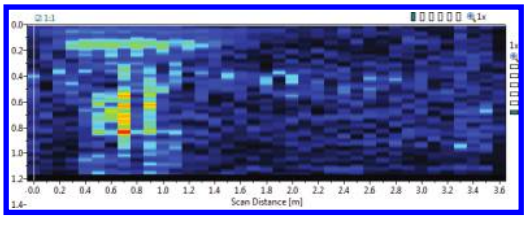

Figure 7. Large scale scan.

In order to verify the findings perpendicular control scans were made both in the area with the delamination and also in the area where it was believed there was a good bond.

The control scans provide the final evidence. In figure 8 the delamination is clear as there is no difference between the echo from the polysterene and the precast/cast in place bond.

In figure 9 the bond is good. On either side we see the echo from the polystyrene blocks and in the centre we see the reflection from the back wall indicating a good bond between the precast and cast in place concrete.

2.4 *Summary*

For this application, pulse echo technology is clearly the answer allowing the extent of the delaminations to be assessed non-destructively. Depending on the size of the delaminations, larger grids may be used to save time. Verification is always possible using a finer grid in cases of doubt.

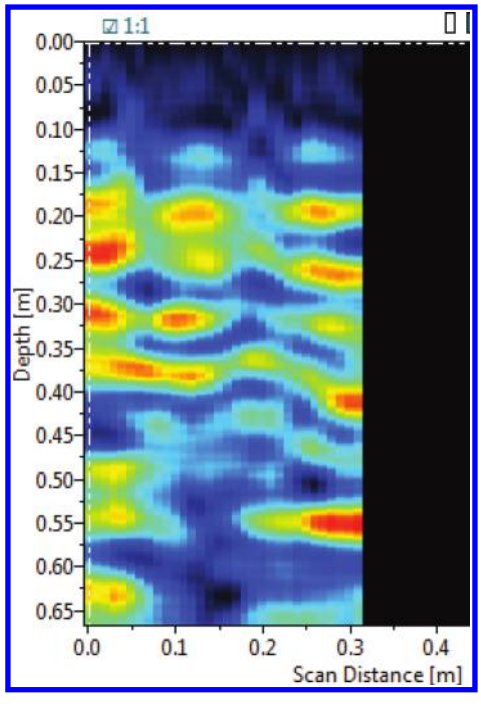

Figure 8. Control scan over delamination.

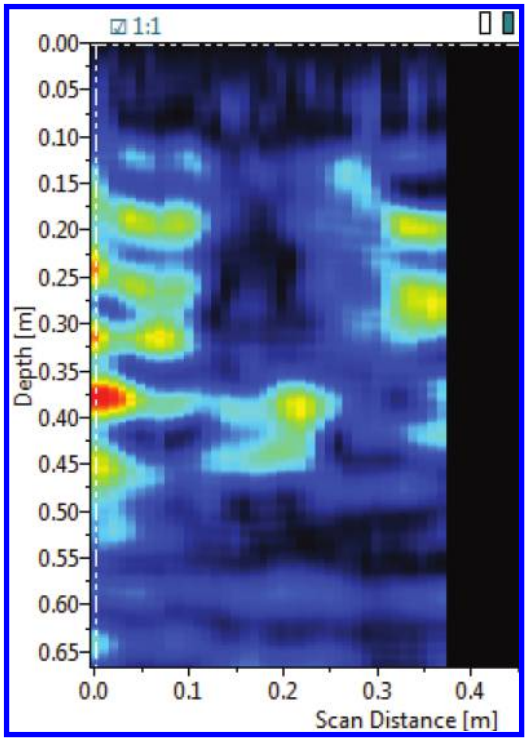

Figure 9. Control scan over good bond.

3 CASE STUDY TWO—CONTROL OF POOR CONCRETE POUR

3.1 *The testing issue*

The next case study is concerned with the construction of a large office building in Zurich. Like many similar structures the building had to be constructed as cheaply as possible and for this reason cheap materials and a low cost workforce was employed.

Figure 10 shows the cause of the suspected problem. There are built-in air ducts with a gap below of only 8–9 cm into which the concrete should flow during pouring. In this concrete layer there are also rebars and tubes for electric lines. Concrete with 32mm aggregate was used and it was suspected that it did not flow not properly and that it had not been compacted properly, leading to the creation of large voids. This was confirmed in a few locations using destructive methods. The task was to try to determine the location of further voids non-destructively.

Figure 10. Void area below air duct with rebars and service cable ducts.

Figure 11. Pulse echo measurement.

3.2 *Pulse echo scan results*

Once again it was necessary to measure on the ceiling.

The initial scan was made on a known 'bad' spot. The results are shown in Figure 11.

In this location there was no clear echo at all. Compare this image with the next scan, figure 13,

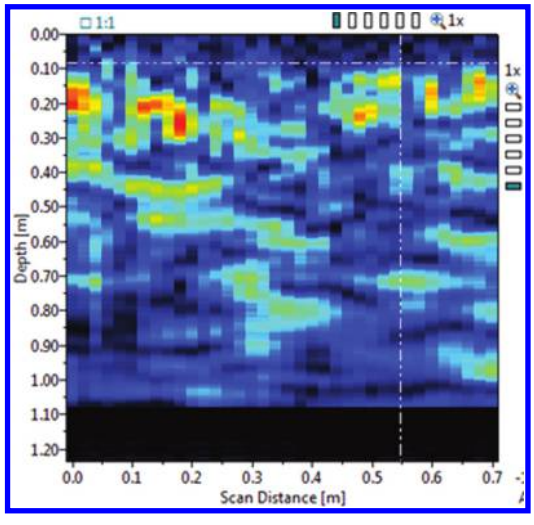

Figure 12. B-scan on a known bad spot.

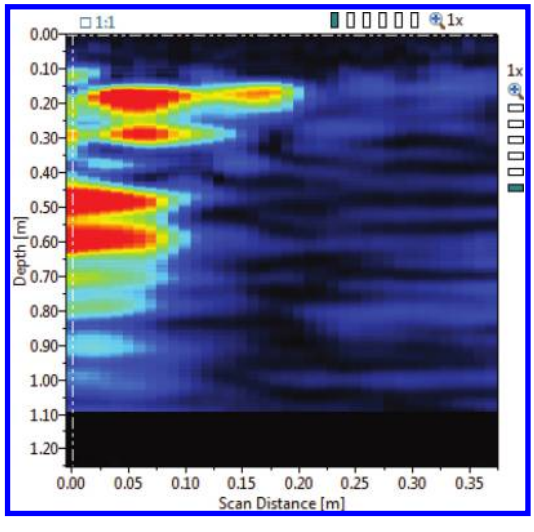

Figure 13. B-scan on a known good location.

which was made a known good location. The left side of the scan shows the reflection from an air duct at a depth of about 10 cm. The right side of the scan has no clear reflection except for a very weak echo from the back wall at around 80 cm. This was a clear indication that the pulse echo technology could differentiate between areas with and without voids. It also shows one of the limits of the technology. The Pundit PL-200PE uses a 50 kHz dry contact shear wave transducer. The maximum penetration depth is typically in the range 50 cm – 1m depending on the quality of the concrete and the amount of reinforcing steel.

At locations where the concrete had flowed and been compacted properly, the air ducts could be clearly identified at the correct depth with the correct width. An example of this can be seen in figure 13.

3.3 *Summary*

Pulse echo technology is very useful for distinguishing voids. It is very useful always in such applications to be able to measure on known good and bad locations to be certain that the interpretation of the B-scans is correct.

4 CASE STUDY THREE—LOCATING POST TENSIONING CABLES

4.1 *Description of the test*

Locating post tensioning cables can be problematic. They are generally beyond the range of eddy current instruments and if there is too much reinforcing steel present it can also be a problem for GPR. Tomographic surveys with impact echo have been used for this application. The aim of this test was to see if it was possible to locate such cables using pulse echo technology.

B-Scans were carried out from the below, perpendicular to the route of the cable. Figure 14 shows the profile of the cable. Figures 15 and 16 show the resulting B-Scans made at 90 cm and 360 cm from the end of the cable.

In Figure 15 the PT cable is clearly visible at a depth of about 25 cm. There is also a clear shadow of the cable on the back wall at a depth of 50m. Figure 16 shows the scan at 360 cm from the end.

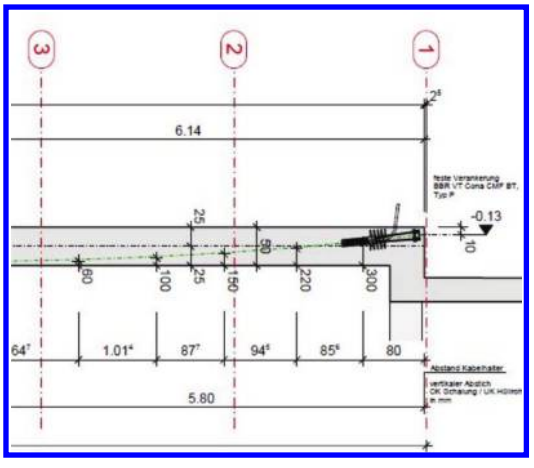

Figure 15. Profile of post-tensionin cable.

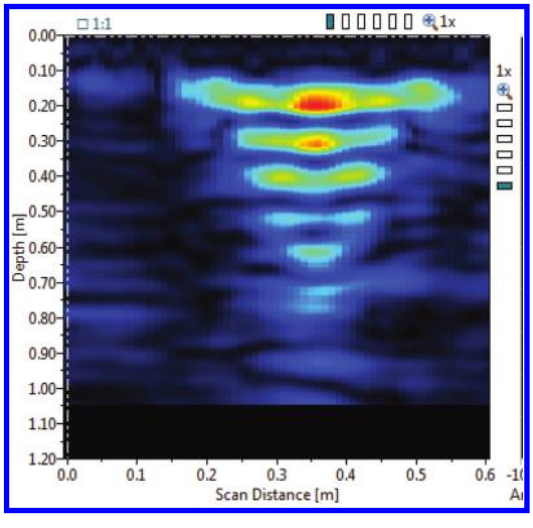

Figure 14. B-Scan over an air duct.

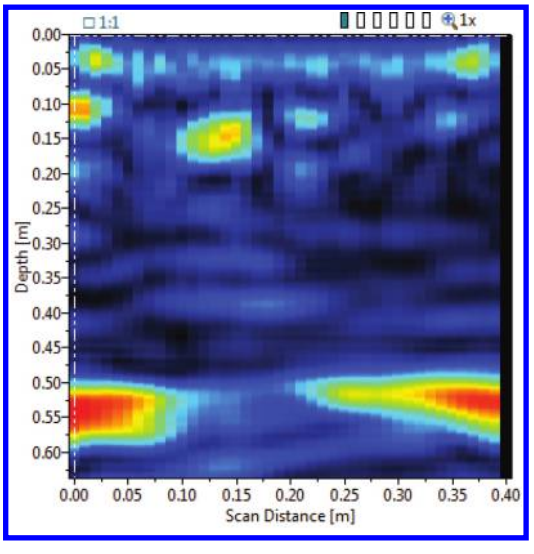

Figure 16. B-Scan over PT cable 90cm from end.

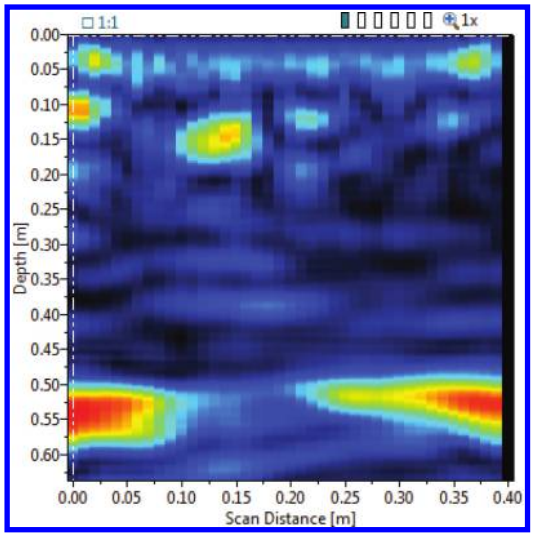

Figure 17. B-Scan over PT cable 360 cm from end.

Here again the PT cable can be clearly seen at a depth of about 10 cm and once again there is a corresponding shadow on the back wall.

4.2 *Summary*

The location of post tensioning cables proved to be very simple using pulse echo technology. It was very easy to recognize the cable and also to determine its depth at various positions along its length, allowing a check of correct installation.

5 CONCLUSION

Pulse echo technology is ideally suited for locating voids and delaminations, in particular where access is limited to a single side. While it does not have the penetration depth of impact echo technology, for structural applications where the thickness of the elements does not exceed about 1m, it provides a much clearer image of the internal defects. It is not suitable for identifying rebars. Indeed one of its advantages is that it is able to see beyond rebar layers to identify large, deeper objects such as post-tensioning cables.

REFERENCE

[1] ASTM C1383-98a, Standard Test Method for Measuring the P-Wave Speed and the Thickness of Concrete Plates Using the Impact-Echo Method, ASTM International, West Conshohocken, PA, 1998, www.astm.org.

Concrete Repair, Rehabilitation and Retrofitting IV – Dehn et al. (Eds)
© 2016 Taylor & Francis Group, London, ISBN 978-1-138-02843-2

Corrosion rate measurements in concrete—a closer look at the linear polarization resistance method

U.M. Angst & M. Büchler
Swiss Society for Corrosion Protection (SGK), Zurich, Switzerland

ABSTRACT: This paper discusses the theoretical background of the commonly used Linear Polarization Resistance (LPR) method and focuses particularly on the severe discrepancy between theory and practice when the method is applied to macro-cell corrosion, which is the typical morphology in the case of chloride-induced reinforcement corrosion. Despite the fundamental inapplicability of the LPR method, it has from literature results long been known that an—empirical—relationship between the corrosion rate and the polarization resistance exists. Experimental results on the current distribution between cathodic and anodic areas during external polarization are presented and discussed with respect to the concept of "current confinement". As a perhaps unconventional view, it is here argued that the lateral current spread-out should not be regarded as a problem, but that this is in fact one of the reasons for the "apparent applicability" of the LPR method to macro-cell corrosion.

1 INTRODUCTION

The rate at which steel corrosion occurs in reinforced concrete is an essential parameter for assessing the residual service life of a structure and thus for maintenance planning. However, determining corrosion rates *reliably*, particularly on site, is not straightforward. As a result, it is common practice to conservatively schedule repair work relatively soon after corrosion has initiated.

Also in service life predictions, the propagation stage is often not taken into account, primarily because of the low confidence in current, mostly empirical predictive models for the corrosion rate (Raupach, 2006, Otieno et al., 2011). The practice of neglecting the propagation stage, however, does not permit holistic assessments of new (innovative) solutions in terms of their cost-effectiveness and environmental impact. For developing new, sustainable cement types, for instance, it is crucial to not only reduce their environmental footprint at the time of manufacture but to also ensure long service lives. Particularly systems that tend to exhibit lower alkalinity, compared with traditional Portland cement concrete, may lead to corrosion initiation relatively early. Nevertheless, if they have at the same time denser microstructures and higher electrical resistivity, long service lives may still be reachable in practice—given low corrosion rates and thus extended propagation stages.

It is thus essential to enhance future predictive models for the corrosion propagation stage. The large uncertainties in current models can be traced to insufficient theoretical grounds, but also to the lack of reliable experimental data on the corrosion rate of structures and laboratory specimens under certain exposure conditions. In short, reliable and preferably non-destructive corrosion rate measurements play an important role at the engineering decision taking level, and form the basis for research aiming at refining predictive models for the corrosion propagation stage.

There exist a variety of experimental methods to determine the corrosion rate such as electrochemical procedures, gravimetric (weight loss) measurements or other approaches (McCafferty, 2010). For reinforcement steel embedded in concrete, only electrochemical methods permit *non-destructive* measurements of instantaneous corrosion rates. These are typically based on applying an external polarization current to excite the system and recording the system response. A number of approaches including alternating current and direct current techniques have been proposed, but the by far most common method in corrosion science in general is the so-called *linear polarization resistance* (LPR) method.

This paper discusses the theoretical background of this method and focuses particularly on the severe discrepancy between theory and the conditions in practice when the method is applied to localized corrosion, which is the typical morphology in the case of chloride-induced reinforcement corrosion. Some of the considerations are highlighted with selected experimental results that were obtained in a recent research project performed at the Swiss

Society for Corrosion Protection, funded by the Swiss Federal Roads Administration, the support of which is here greatly acknowledged (Angst and Büchler, 2015, Angst and Büchler, (in press)).

2 EXPERIMENTAL

2.1 *Materials*

The experimental results presented in this paper were obtained in a setup consisting of a large plastic container filled with aqueous solution and two layers of steel mesh (Fig. 1). While the steel mesh simulated the reinforcement steel in a concrete slab, the aqueous solution simulated the concrete. Different solution conductivities were achieved by mixing demineralized and tap water; for the results shown in this paper, the electrical resistivity of the solution was 240 Ohm m. The container was 1 m in length and width and had a height of 0.4 m. The cover depth was adjusted by filling the container to different levels. In addition, the slab thickness could be varied by adjusting the distance between the two steel meshes.

The upper and lower steel meshes were made of smooth stainless steel bars with a diameter of 6 mm and a spacing in both directions of 7 cm. The steel meshes were divided in individual zones that were electrically isolated from each other to permit measuring the individual flow of current through these zones.

At the very center of the upper steel mesh, a small plain carbon steel disc was fixed (Fig. 1). The circular disc was embedded in an isolating epoxy adhesive to electrically isolate it from the stainless steel mesh; the exposed surface area was 1 cm^2. In the pH neutral solutions, this carbon steel disc corroded actively and was thus used to simulate a local anode.

2.2 *Methods and measurements*

All zones of the stainless steel meshes and the plain carbon steel disc were electrically connected by copper wires. A macro-cell situation was established by short-circuiting these. Additionally, the currents flowing in the macro-cell and to the different cathodic steel mesh zones were recorded with data loggers.

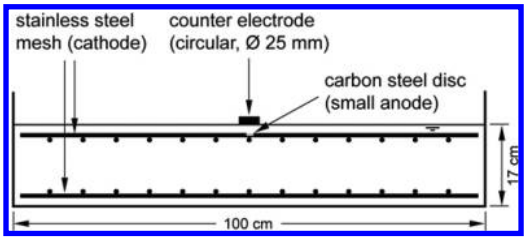

Figure 1. Schematic setup simulating a reinforced concrete slab with a small anode and a large cathodic mesh forming a macro-cell. Electrical resistivity of solution = 240 Ohm m.

Reference electrodes were positioned at different locations in the aqueous solution to measure the potential of the macro-cell. In contrast to concrete, where only the outer surface is accessible, the solution permitted positioning some of the reference electrodes close to the steel mesh.

A variety of counter electrode geometries (shape, size) were tested. These consisted of stainless steel and they were placed on the upper level of the aqueous solution to simulate the practical situation of a counter electrode being placed on the concrete surface. In the scope of the present paper, the counter electrode was cylindrical with an outer diameter of 25 mm. In its center, a small hole permitted positioning a reference electrode on the solution surface.

The macro-cell—i.e. all steel mesh zones and the supposed anode disc short-circuited—was polarized by injecting a given constant current from the counter electrode with help of a laboratory galvanostat/potentiostat. During this external polarization, the potential of the macro-cell was simultaneously measured vs. the reference electrodes being present at different locations. Additionally, the fractions of polarization current flowing through the different zones of the macro-cell were recorded. All measurements included the time-evolution during polarization.

3 THE LINEAR POLARIZATION RESISTANCE (LPR) METHOD

3.1 *Theory*

The linear polarization resistance method relies on the Stern-Geary equation (Stern and Geary, 1957, Stern and Weisert, 1959) that states an inverse proportionality between the corrosion current, I_{cor}, and the so-called polarization resistance R_p:

$$I_{cor} = \frac{B}{R_p} \tag{1}$$

While B can here be regarded as a constant, the polarization resistance is defined as the slope of the potential-current relationship in close vicinity of the corrosion potential, E_{cor}, where this curve is approximately linear (Fig. 2). Thus, $R_p = \Delta E / \Delta I$. The polarization resistance can experimentally be determined by imposing a current ΔI and measuring the resulting shift in potential ΔE, or vice versa. A requirement for the Stern-Geary equation to hold is that the excursion from the corrosion potential is limited and does not leave the quasi-linear range

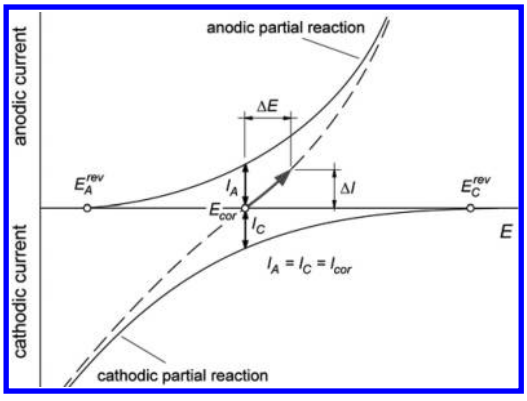

Figure 2. Current-potential relationship of uniform corrosion, which forms the basis of the mixed potential theory and thus the LPR method.

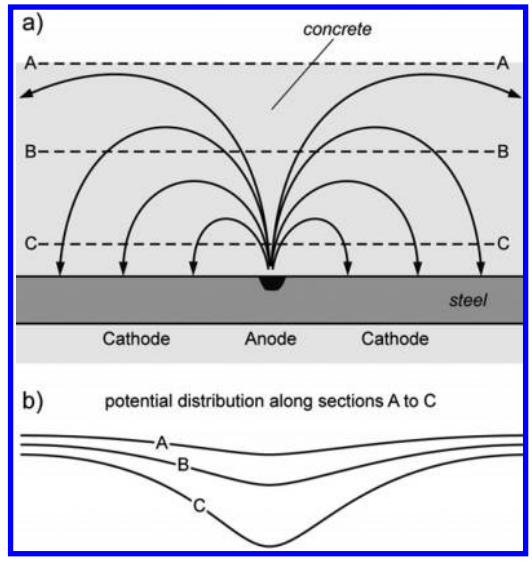

Figure 3. a) Schematic illustration of macro-cell corrosion, arrows = current field lines; b) apparent steel potential vs. a reference electrode positioned along the three sections A, B, and C indicated in Fig. 3a.

of the current-potential curve. Typically, this is in the order of 10–15 mV.

Equation (1) was derived on the basis of the so-called *mixed potential theory*, which was postulated in the first half of the last century by Wagner and Traud (Wagner and Traud, 1938). One fundamental aspect of the mixed potential theory is that the corrosion morphology is uniform, i.e. it is assumed that cathodic and anodic partial reactions occur at microscopically small locations that are uniformly and randomly (with time) distributed across the metal surface. This assumption permitted to establish the concept of the *mixed potential* that corresponds to the corrosion potential E_{cor} in Fig. 2, to which both the anodic half-cell and the cathodic half-cell are polarized in the corrosion process. It is worth mentioning that due to the negligibly small ohmic drop in the electrolyte, anodic and cathodic sites are at the very same potential, E_{cor}.

This potential can be measured with a reference electrode and an important aspect is that the position of the reference electrode with respect to the uniformly corroding metal does not affect the measured value. Wagner and Traud also postulated that cathodic and anodic partial reactions can be superimposed, i.e. that their respective current densities at a given potential can be summed. The consequence of this is that a total current-potential curve exists (dashed line in Fig. 2), which crosses the potential axis at E_{cor}, thus the net current at the mixed potential is zero.

3.2 *The question of applicability in case of localized corrosion*

In many practical situations, the corrosion morphology is not uniform. This is particularly true for chloride-induced reinforcement corrosion in concrete, where local anodes (corrosion pits) interact galvanically with typically much larger cathodic zones (Bertolini et al., 2004). Owing to the large area ratio cathode:anode, high rates of local loss of steel cross section may occur. Being able to quantify these is essential—both for research and practice.

Figure 3 shows a schematic illustration of so-called *macro-cell* corrosion. The term macro-cell is common to describe localized corrosion in concrete (Raupach, 1992). It indicates that the galvanic cell formed between the anode (pit) and the cathode is macroscopic, i.e. that the distances may be up to several decimeters (Brem, 2004).

Due to the finite conductivity of the electrolyte (the alkaline solution in the pore system of the concrete), the ohmic drop in the galvanic cell is not negligible and thus anodic and cathodic sites have *different potentials*. The direct consequence of this is that a well-defined, unique mixed potential in the sense of the theory by Wagner and Traud and as shown in Fig. 2 does for the case of macro-cell corrosion—or localized corrosion in general—not exist.

The flow of macro-cell current in the electrolyte is in Fig. 3 schematically shown by arrows. Along these current field lines, the potential in the electrolyte decreases from the anode towards the cathode. If the reinforcement steel bar is connected to a voltmeter and the potential is measured versus a reference electrode placed somewhere in the electrolyte (for instance at the concrete surface, indicated by the dashed line A-A in Fig. 3), the recorded

potential depends on the position of the reference electrode. The closer the reference electrode is positioned to the anodic site, the more negative will the recorded potential (with respect to the reference electrode) become. This is schematically shown in Fig. 3b. In fact, this effect of the location of the reference electrode on the measured potential forms the basis of the classical understanding of potential measurements in concrete as a well-established, non-destructive method to locate corroding areas (Elsener et al., 2003, Schiegg et al., 2007).

To sum up, the following critical points are given in localized corrosion situations:

1. A **mixed potential** according to the theory of Wagner and Traud does in macro-cell corrosion **not exist**.
2. Instead, the potential of the reinforcement steel bar measured vs. a reference electrode **depends strongly on the position** of the reference electrode.

This implies that upon polarization of the macro-cell from an external counter electrode (no matter where this counter electrode is located), any change in potential that can be recorded, ΔE, is dependent on the location of the reference electrode.

This is apparent from the experimental measurement results shown in Fig. 4. The macro-cell shown in Fig. 1 was polarized with a galvanostatic current pulse (60 µA) and the potential was recorded over time with two reference electrodes. With the reference electrode that was situated directly above the anode (in the center of the circular counter electrode), a clear transient was registered and a steady-state polarization ΔE of approx. 30 mV became apparent. With the reference electrode somewhat distant from the counter electrode (here 20 cm lateral distance), i.e. positioned above the cathodic reinforcement steel mesh, only a small polarization, ΔE, below 5 mV was recorded. In principle, this observation is not surprising, because the polarization current densities reaching the steel at these two locations is also different, i.e. it is lower, the larger the distance to the counter electrode (see section 5).

Nevertheless, the essential question now is: which of the two ΔE is the correct one? Since $R_p = \Delta E / \Delta I$, also the polarization resistance is a function of the position of the reference electrode. The difficulty is that *there exists no correct position for the reference electrode* in such a situation and as a result, there is no correct ΔE to be used for computing R_p. Any value depends largely on the position of the reference electrode and there is no fundamentally sound way to argue that a certain position of the reference electrode, for instance as close to the anode as possible, is the correct one.

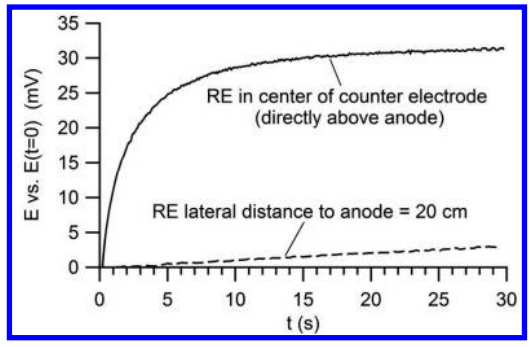

Figure 4. Potential transients during galvanostatic polarization of the macro-cell shown in Fig. 1, recorded with Reference Electrodes (RE) positioned at two different locations (initial IR jump removed).

These considerations render the application of the Stern-Geary relationship according to eq. (1) in order to derive the corrosion current highly questionable. Fact is, that owing to the absence of a well-defined, unique mixed potential, the Stern-Geary relationship is in the case of macro-cell corrosion fundamentally not valid.

3.3 *Experience*

Nevertheless, several laboratory investigations have shown a certain agreement between the LPR method and other corrosion rate measurements.

In the late 1970s, Andrade and González performed a comparison between gravimetric weight loss measurements and the LPR method (potentiodynamic scans, no corrections for *IR* drop made) on small mortar specimens without and with mixed-in chlorides and concluded that there was adequate agreement between these techniques (Andrade and González, 1978). The LPR method was reported to underestimate the corrosion rate by a factor of max. 2–3; the proportionality factor B in eq. (1) was suggested to be 26 mV for actively corroding steel.

A similar study comparing gravimetric measurements with the LPR method was reported by (Law et al., 2004). Reinforced mortar specimens were exposed to chloride ingress (and some to accelerated carbonation) and instantaneous corrosion rates were frequently measured with the LPR method (potentiostatic mode, equilibrium time = 30 s, *IR* drop corrections made manually) and integrated over time. The constant B was assumed at 25 mV for actively corroding steel. In this work, the LPR method was found to overestimate the gravimetric weight loss by a factor of typically 1.5–3, in extreme cases by a factor of 5.

Liu and Weyers used two different instruments to determine corrosion rates once a month over a period of 5 years in roughly 1 m^2 large reinforced concrete slabs, contaminated with mixed-in chlorides and stored outdoors (Liu and Weyers, 2003). At the end, gravimetric metal loss measurements were performed and compared to the electrochemical measurements (integrated over time). The two devices employed both the LPR method, one with and one without a guard ring. Unfortunately, limited details were given with respect to the measurement procedure, but apparently, both devices used potentiodynamic linear polarization, but there were significant differences e.g. with respect to the geometry and B values used. Nevertheless, the results obtained with these methods showed that the instrument with the guard ring underestimated the (gravimetric) corrosion rate by a factor of 5, while the method without guard ring led to an overestimation by a factor of approx. 3.

Nygaard et al. compared two commercial instruments (Nygaard et al., 2009). Reinforced concrete slabs were manufactured with different levels of mixed-in chlorides. The concrete specimens contained segmented steel bars that permitted measuring current densities before and during external polarization on all individual segments. This allowed to quantify the macro-cell corrosion current, which was then compared to the results of the LPR method. Both instruments include a guard ring for current confinement (compare section 5). It was concluded that for localized, i.e. macro-cell, corrosion the two devices underestimated the true corrosion rate roughly by a factor of 2–10.

To sum up, different procedures for obtaining the polarization resistance were used in different studies, and also different constants B were assumed when applying the Stern-Geary equation. Whereas some of the authors concluded that the LPR method underestimates the true corrosion rate, by factors ranging from 2 to 10, other authors concluded that the LPR method overestimates the true corrosion rate, by factors ranging from 1.5 to 5. Naturally, part of this variability may be explained by the different experimental parameters in these different studies. Nevertheless, there seems to be some general agreement in the literature that the LPR method is in principle feasible to determine corrosion rates of macro-cell corrosion in concrete.

4 THEORETICAL DISCREPANCY VS. PRACTICAL APPLICABILITY

Application of the LPR method to macro-cell corrosion can from a theoretical viewpoint not be justified (as explained in section 3.2). Nevertheless, there seems to be some sort of practical applicability of the method (as apparent from experimental studies summarized in section 3.3). One may thus conclude that despite the fundamental difficulties with the method for the case of localized corrosion, an inversely proportional relationship between the corrosion rate and an apparent "polarization resistance" can still be observed. It is, however, important to note that due to the absence of theoretical grounds, this relationship is entirely empirical.

In a recent publication by the present authors, experimental measurements and theoretical considerations allowed to explain the reasons for this empirical agreement (Angst and Büchler, (in press)). This can be illustrated by assuming that the reference electrode can be placed in close adjacency of the anodic site (e.g. in the pit). Upon application of an external polarization current, a certain fraction of this current will flow through the anode and a certain fraction will flow through the cathode. The relative fractions depend on the position of the counter electrode and on the distribution of ohmic resistances in the electrolyte and at the metal/electrolyte interfaces. Assuming that the fraction of polarization current flowing through the anode is known, ΔI_A, and that the reference electrode permits recording the polarization of the anodic half-cell alone, ΔE_A, (i.e. its true potential rather than a position-dependent one in the electric field somewhere in the electrolyte), the corrosion current can be calculated with an equation derived in (Angst and Büchler, (in press)):

$$I_{cor} = \frac{\beta_A}{2.3} \cdot \frac{\Delta I_A}{\Delta E_A} \tag{2}$$

This equation is similar but not identical with the Stern-Geary expression. Given that the corrosion process is under activation control and that the Tafel slope of the anodic partial reaction, β_A, is known, eq. (2) permits a fundamentally correct calculation of the corrosion current, I_{cor}. Analogously, an equation can also be derived for the cathode.

Nevertheless, the parameters ΔI_A and ΔE_A are usually not measureable for practical reasons. The polarization current flowing through the anode cannot be measured because the anodic site is in direct electrical contact with the cathodic metal. The true polarization of the anode cannot be measured because it is impossible to position the reference electrode in close proximity of the anodic site. In a setup such as the one shown in Fig. 1, however, this is possible.

Examining eq. (2), the second part, ΔI_A / ΔE_A, may be regarded as the inverse of a polarization resistance of the anode alone. It was in (Angst and Büchler, (in press)) with help of experimental data

shown that although the correct equation (2) and the fundamentally inapplicable equation (1) are different, they may under certain conditions yield similar results. The explanation for this is that in eq. (1) both the denominator (R_p) and the numerator (B) are in measurements underestimated so that these two errors have a certain compensating effect. In other words, although the Stern-Geary equation is in the case of macro-cell corrosion fundamentally not valid, two compensating errors cause the result to be close to the correct one. The extent to which this is possible, is however strongly dependent on the conditions, such as the geometrical configuration, the kinetics of the partial reactions, etc. Nevertheless, these considerations are able to explain why despite the fundamental inapplicability of the Stern-Geary equation, practical experience as described in section 3.3 revealed a certain "apparent applicability".

5 THE ISSUE OF "CURRENT CONFINEMENT"

5.1 *The question of the polarized area*

One of the problems with localized corrosion, as opposed to uniform corrosion, is that the area where iron dissolution occurs (the anodic area), does not correspond to the reinforcement steel area. Equation (1) yields a current, I_{cor}, rather than a current density. In order to quantify the corrosion rate, e.g. in terms of sectional loss over time, the area A of the anodic site(s) needs to be known. Only this permits conversion of I_{cor} to a current density, i.e. $i_{cor} = I_{cor} / A$. This area is usually unknown.

Another difficulty is that when a relatively small counter electrode is used to polarize reinforcement steel of almost infinite lateral dimensions, the polarization current spreads out laterally and decreases with distance from the counter electrode. This was early recognized and treated e.g. by (Feliu et al., 1988). Many attempts have since been made to confine the flow of the polarization current in the concrete, e.g. reported in (Feliu et al., 1990, Liu and Weyers, 2003, Wojtas, 2004, Nygaard et al., 2009). These approaches include the use of a so-called guard ring, positioned around the counter electrode, which is claimed to force the polarization current injected from the counter electrode to flow directly between the counter electrode and the reinforcement steel bar rather than to spread out laterally. However, the benefit of guard rings has long been disputed in the literature (see e.g. (Nygaard, 2008)).

The general motivation for current confinement approaches is to control—and thus to know—the area, which is polarized during the measurement. In this context, is important to mention that the area of the anodic sites is in macro-cell corrosion *never* the same as the corroding area. In fact, the corrosion process includes both anodic and cathodic partial reactions and although they may occur on different metal surfaces, they both belong inherently to the corrosion process. A second potential misconception about the LPR method is that the polarized area should ideally be identical with the anodic zone. Remember that the LPR method is based on polarizing the superposition of the cathodic and the anodic partial reactions, i.e. moving along the total current-potential curve (dashed line in Fig. 2), which becomes quasi-linear close to E_{cor}. Even if all polarization current flew exclusively through the anodic zone, the Stern-Geary equation would still not yield the correct corrosion current.

5.2 *The question of self-confinement*

The conceptual reasoning of forcing the polarization current to a defined area of the reinforcement steel assumes that i) it is actually possible to limit the area subject to the measurement, and ii) that this eliminates one of the main shortcomings of applying the LPR method to macro-cell corrosion.

However, the polarization current cannot be forced to a certain steel area, but it finds its way according to the resistances in the system. This includes both ohmic resistances in the electrolyte, determined by geometrical factors such as distance and conductivity, and charge transfer resistances at the metal/concrete interface. For a more detailed discussion in this regard, it is referred to (Nygaard, 2008, Nygaard et al., 2009, Angst and Büchler, (in press)).

A number of studies were performed with setups including segmented rebars or separated zones of steel surface that allowed measuring the distribution of polarization current within the macrocell (Elsener, 2002, Nygaard, 2008, Nygaard et al., 2009, Angst and Büchler, (in press), Angst and Büchler, 2015). There is a general agreement that in typical setups where the counter electrode is relatively small and close to the anode, the current density reached at the anode during polarization is much higher than at the cathode. This led to the so-called concept of "self-confinement", in which the mentioned distribution of current densities is interpreted in the sense that most of the polarization current flows through the anode "due to its lower polarization resistance". However, this view ignores that typically, the area of the cathodic zones is considerably larger than at the anode. In fact, the data reported in (Elsener, 2002, Nygaard,

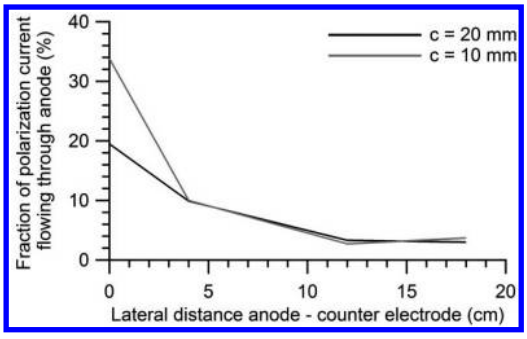

Figure 5. Fraction of polarization current passed though the anode after 30 s galvanostatic polarization of the macro-cell shown in Fig. 1. Plotted as a function of lateral distance between the counter electrode and the anode; c = cover depth.

2008, Nygaard et al., 2009, Angst and Büchler, (in press), Angst and Büchler, 2015) reveals in good agreement that the total current—as opposed to current density—flowing through the anode is typically smaller than the current flowing through the cathode. This can be explained by the much larger surface area of the cathode.

This is apparent from the experimental measurement results plotted in Fig. 5 that shows the fraction of the applied polarization current that was passed through the anode (no guard rings used). Even if the counter electrode was positioned directly above the anode, not more than 35% of the applied current reached the anode. If the counter electrode was positioned slightly laterally distant from the anode, this figure decreased to below 10%.

To conclude, in most geometrical configurations of practical relevance, the applied polarization current is predominantly passed through the cathodic rather than the anodic steel surfaces. This should, however, not be considered as a problem. In fact, it is one of the causes giving rise to the error appearing in the denominator of eq. (1) and finally leading to an "error compensating effect" and thus an "apparent applicability" of the LPR method to macro-cell corrosion, as discussed in section 4.

6 CONCLUSIONS

From theoretical considerations and selected experimental results, the following major conclusions can be drawn:

- Owing to the absence of a well-defined *mixed potential* according to Wagner and Traud, the Stern-Geary relationship and thus the LPR method is in the case of macro-cell corrosion fundamentally not valid.
- Upon polarization of a macro-cell, any recorded change in potential, ΔE, depends strongly on the position of the reference electrode. Since *there exists no correct reference electrode position*, any measured value of ΔE, and thus the polarization resistance, becomes arbitrary.
- Despite this fundamental difficulty with the LPR method, literature results indicate that there exists still an inversely proportional relationship between the corrosion rate and the "apparent polarization resistance". Due to the absence of theoretical grounds, however, this relationship must be regarded as entirely empirical.
- Experimental results of the current distribution between cathodic and anodic parts of a macro-cell during external polarization indicated that the polarization current flows predominantly through the cathodic metal surfaces. It has in the past been attempted to counteract this by "current confinement" and "guard ring" approaches. However, it was in this paper discussed that the lateral current spread-out should not be considered as a problem, but that it is in fact one of the reasons for the empirical "apparent applicability" of the LPR method to macro-cell corrosion.
- Finally, further research work should concentrate on characterizing in more detail the conditions (e.g. geometrical configurations) under which the empirical relationship between corrosion rate and apparent polarization resistance still holds. Alternatively, successful research attempts to develop a measurement method for macro-cell corrosion rates that eliminates the shortcomings of the LPR method, e.g. by avoiding the need to rely on the Stern-Geary relationship, would present a major advance for science and engineering.

REFERENCES

Andrade, C. & González, J. A. 1978. Quantitative measurements of corrosion rate of reinforcing steels embedded in concrete using polarization resistance measurements. *Materials and Corrosion,* 29, 515–519.

Angst, U. & Büchler, M. 2015. Optimizing and validating methods for the determination of the corrosion rate in reinforced concrete (AGB project 2012/013).

Angst, U. & Büchler, M. (in press). On the applicability of the Stern-Geary relationship to determine instantaneous corrosion rates in macro-cell corrosion. *Materials and Corrosion*.

Bertolini, L., Elsener, B., Pedeferri, P. & Polder, R. 2004. *Corrosion of steel in concrete,* Weinheim, Wiley VCH.

Brem, M. 2004. *Numerische Modellierung der Korrosion in Stahlbeton.* Doctoral thesis, ETH Zurich, Switzerland.

Elsener, B. 2002. Macrocell corrosion of steel in concrete—implications for corrosion monitoring. *Cement & Concrete Composites,* 24, 65–72.

Elsener, B., Andrade, C., Gulikers, J., Polder, R. & Raupach, M. 2003. Half-cell potential measurements—potential mapping on reinforced concrete structures (RILEM TC 154-EMC recommendation). *Materials and Structures,* 36, 461–471.

Feliu, S., González, J.A., Andrade, C. & Feliu, V. 1988. On-site determination of the polarization resistance in a reinforced concrete beam. *Corrosion Engineering,* 44, 761–765.

Feliu, S., González, J.A., Escudero, M. L., Feliu (Jr), S. & Andrade, M. C. 1990. Possibilities of the Guard Ring for Electrical Signal Confinement in the Polarization Measurements of Reinforcements. *Corrosion,* 46, 1015–1020.

Law, D.W., Cairns, J., Millard, S.G. & Bungey, J. H. 2004. Measurement of loss of steel from reinforcing bars in concrete using linear polarisation resistance measurements. *NDT&E International,* 37, 381–388.

Liu, Y. & Weyers, E. W. 2003. Comparison of guarded and unguarded linear polarization CCD devices with weight loss measurements. *Cement and Concrete Research,* 33, 1093–1101.

McCafferty, E. 2010. *Introduction to Corrosion Science,* New York, Springer.

Nygaard, P. V. 2008. Non-destructive electrochemical monitoring of reinforcement corrosion. Technical University of Denmark, DTU.

Nygaard, P. V., Geiker, M. R. & Elsener, B. 2009. Corrosion rate of steel in concrete: evaluation of confinement techniques for on-site corrosion rate measurements. *Materials and Structures,* 42, 1059–1076.

Otieno, M.B., Beushausen, H.D. & Alexander, M.G. 2011. Modelling corrosion propagation in reinforced concrete structures—A critical review. *Cement & Concrete Composites,* 33, 240–245.

Raupach, M. 1992. Zur chloridinduzierten Makroelementkorrosion von Stahl in Beton, Berlin, Beuth Verlag GmbH.

Raupach, M. 2006. Models for the propagation phase of reinforcement corrosion—an overview. *Materials and Corrosion,* 57, 605–613.

Schiegg, Y., Büchler, M. & Brem, M. Year. Potential mapping technique for the detection of corrosion in reinforced concrete structures: Investigation of parameters influencing the measurement and determination of the reliability of the method. *In:* Proc. EUROCORR '07, 2007 Freiburg im Breisgau, Germany. European Federation of Corrosion.

Stern, M. & Geary, A. L. 1957. Electrochemical polarization. I. A theoretical analysis of the shape of polarization curves. *Journal of the Electrochemical Society,* 104, 56–63.

Stern, M. & Weisert, E. D. 1959. Experimental observations on the relation between polarization resistance and corrosion rate. *Proceedings of the American Society for Testing and Materials,* 59, 1280–1290.

Wagner, C. & Traud, W. E. 1938. Über die Deutung von Korrosionsvorgängen durch Überlagerung von elektrochemischen Teilvorgängen und über die Potentialbildung an Mischelektroden. *Z. Elektrochem. Angew. Phys. Chem.,* 44, 391–402.

Wojtas, H. 2004. Determination of corrosion rate of reinforcement with a modulated guard ring electrode; analysis of errors due to lateral current distribution. *Corrosion Science,* 46, 1621–1632.

Concrete Repair, Rehabilitation and Retrofitting IV – Dehn et al. (Eds)

Impact of chloride redistribution on the service life of repaired concrete structural elements

A. Rahimi, T. Reschke & A. Westendarp
Federal Waterways Engineering and Research Institute (BAW), Karlsruhe, Germany

C. Gehlen
Centre for Building Materials (cbm), Technische Universität München, Munich, Germany

ABSTRACT: This paper presents a probabilistic approach to estimating the residual service life of concrete structural elements after repair. In particular, the presence of a residual contamination in the remaining concrete layer and how the redistribution of the residual chlorides affects the determination of the service life are considered. The approach presented in this paper has been validated with the aid of analytical calculations and numerical investigations.

1 INTRODUCTION

A large proportion of the activities in the construction sector concern existing structures. Numerous existing reinforced concrete structures have aged in the course of time and the functionality and even the loadbearing capacity of those that have been subject to high stress have been impaired. Concepts for estimating the residual service life are needed to enable existing structures to be assessed. If the residual service life calculated with the aid of such concepts is too low and repairs are necessary, it needs to be asked to what the extent the repairs extend the service life of the structure concerned. Instruments for estimating the residual service life prior to repair and subsequently assessing the post-repair durability are not available at the present time.

A traditional and feasible repair measure is the application of cement-based repair mortars or concretes. Depending on the depth of chloride penetration and the chloride concentration in the structural element, the concrete cover is removed either partially or completely, as are deeper areas behind the reinforcement if necessary, and replaced with repair material. The objective of such repairs is either to maintain passivity or repassivate the reinforcing steel as well as enhance the resistance of the element to further chloride penetration.

Partial removal of the concrete cover may be appropriate for economic, execution—or construction-related reasons or also as a preventive measure etc. In such cases, it must be asked whether the remaining concrete layer has to be free from chlorides or to what extent it may still be contaminated with chlorides and how the residual contamination will affect the residual service life of the concrete structural element after repair (i.e. after the concrete cover has been partially removed and replaced with a repair material).

As shown in Figure 1, the residual chloride gradient will be redistributed through both the new layer and the remaining layer over time. The chloride concentration at the rebar surface changes as a result and may at times exceed the initial value (even without the additional ingress of external chlorides). If the repaired structural element is again exposed to chlorides, the residual contamination

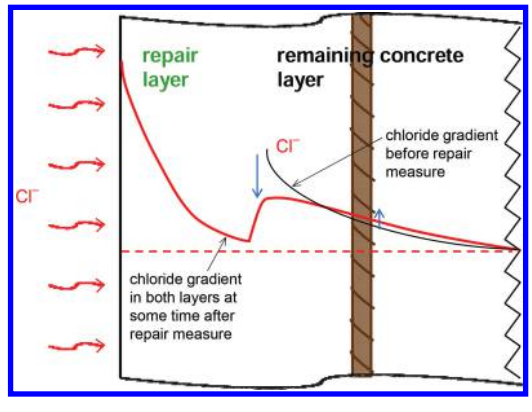

Figure 1. Chloride ingress and redistribution in a repaired concrete element (2-layer system) with residual chlorides.

will generally result in the chloride content at which corrosion is initiated being exceeded at the rebar surface at an earlier point in time.

With the aid of a pragmatic approach and numerical investigations, boundary conditions for the residual chloride gradient were specified in *Rahimi et al. (2015)*. These are the conditions that need to be satisfied if depassivation of the reinforcing steel owing to the redistribution of the residual chlorides in the remaining concrete layer is to be prevented. (Depassivation occurs when the critical chloride content C_{crit}, at which corrosion is initiated, is reached at the rebar surface). In this case, the ingress of external chlorides is ruled out. The boundary conditions concerned are as follows:

1. The maximum residual chloride content must not exceed 2.0% by weight of binder.
2. There should be a distance of at least 10 mm between the surface of the reinforcing steel and the depth at which the critical chloride content C_{crit}, at which corrosion is initiated, is reached.

Adopting a conservative approach, the favourable effect of the age of the structural element at the time of the repair measure on the chloride penetration resistance of the remaining concrete was not taken into account and any possible extraction of the residual chlorides by capillary suction and by being washed out of the new, fresh repair layer was disregarded.

The two criteria mentioned above therefore need to be considered when specifying the minimum depth to which the concrete cover has to be removed. When calculating the residual service life of structural elements repaired in this way, the chloride transport in a 2-layer concrete cover and the redistribution of the residual chloride gradient also need to be taken into consideration.

An approach for estimating the residual service life of repaired structural elements with residual contamination was presented in *Rahimi et al.* (*2014.01*) (see also section 3.2) and was based on the calculation of the service life of new structures. However, the chloride content at the rebar surface was the only element of the residual contamination that was taken into consideration. The chloride gradient and its redistribution were disregarded. In this paper, it is first discussed whether, and if so to what extent, disregarding the chloride redistribution affects the estimation of the residual service life of concrete structural elements.

To facilitate understanding of the paper, the methodology of the performance-based probabilistic service life design of new structures is briefly explained first (section 2) as it will be referred to later on in this paper when its application to existing structures is discussed.

2 SERVICE LIFE DESIGN OF NEW CONCRETE STRUCTURES

In order to satisfy the requirements for the durability of concrete structures the deemed-to-satisfy provisions, which are based on practical experience, have to be complied with. These rules are given in current standards and guidelines. Performance-based probabilistic design models are being developed as a contrast to the prescriptive methodology of standards. The "*fib* Model Code for Service Life Design, *fib* Bulletin 34 (2006)" and later "*fib* Model Code for Concrete Structures (2010)" as well as ISO 16204:2012 present a full probabilistic concept for the service life design of uncracked concrete structures for the case of chloride-induced corrosion. The concept is based on the following:

- definition of limit states
- models that are able to describe the time-dependent transport and deterioration mechanisms
- statistical definition of actions
- measurement and statistical quantification of structural element resistances
- assumed permissible failure probabilities

The *limit state* is determined by the initiation of reinforcement corrosion and reached when a critical chloride content is exceeded at the rebar surface, disrupting the passive layer protecting the rebar. At the end of the initiation period, no corrosion-induced deterioration will yet have occurred in the structure. High corrosion rates are observed in marine environments in general so that the deterioration period is comparatively short. Moreover, there is as yet no commonly used model to describe the mechanism of reinforcement corrosion and its effect on structures. Therefore, the deterioration period is disregarded in this concept and the service life is considered as the initiation period.

To assess the initiation period, a *mathematical model*, equation (1), is used to estimate the time— and depth-dependent chloride concentration $C(x,t)$ in the concrete based on the error function solution of Fick's second law of diffusion in its one-dimensional form:

$$C(x,t) = C_0 + (C_{S,0} - C_0) \times \left[1 - erf \frac{x}{2 \times \sqrt{k_e \times D_{app}(t) \times t}}\right] \quad (1)$$

where C_0 is the initial chloride content (wt.-%/c), $C_{S,0}$ is the chloride content at the surface (wt.-%/c), erf stands for error function, x is the depth with a corresponding content of chlorides $C(x, t)$ (mm), t is the time (years), k_e is the environmental variable (–) and $D_{app}(t)$ is the apparent chloride diffusion coefficient at time t (m²/s).

It can be concluded that the rate at which chlorides penetrate concrete is governed by the diffusivity of the concrete (material) and the concentration of the chloride load (environment).

This diffusion-controlled assessment of chloride ingress is only a simplification since other transport mechanisms are involved in the chloride ingression into concrete, in particular capillary absorption and permeation. However, in structures with concrete cover depths greater than approx. 30 mm, diffusion becomes the most effective and important mechanism with regard to the initiation of corrosion in concrete structures.

The transfer parameter k_e is introduced in order to take the impact of the external temperature T_{real} on the diffusion rate of chlorides into account, simplifying the calculations by using the Arrhenius equation as follows:

$$k_e = \exp\left\{ b_e \left(\frac{1}{T_{ref}} - \frac{1}{T_{real}} \right) \right\} \tag{2}$$

where b_e is the temperature coefficient (K), T_{ref} is the reference temperature (for laboratory tests) (K) and T_{real} is the temperature of the structural element or the ambient air (K).

The apparent chloride diffusion coefficient $D_{app}(t)$, which represents the material resistance from t_0 to t as a constant, is subject to considerable scatter and tends to decrease with increasing exposure time. This implies that $D_{app}(t_2) < D_{app}(t_1)$ with $t_2 > t_1$. $D_{app}(t)$ is usually determined through the "chloride profiling method" described in *NT BUILD 443:1995* and *CEN/TS 12390-11:2010*. Chloride profiles can either be taken from existing structures or from test samples stored under conditions similar to those expected in practice. As this method is both very time-consuming and costly, a simplified approach for determining $D_{app}(t)$ is introduced in "*fib* Model Code for Service Life Design, *fib* Bulletin 34 (2006)". In this approach, $D_{app}(t)$ is calculated as follows:

$$D_{app}(t) = D_{RCM}(t_0) \cdot \left(\frac{t_0}{t} \right) \alpha \tag{3}$$

where $D_{RCM}(t_0)$ is the chloride migration coefficient at the reference point of time (m^2/s), t_0 is the reference point of time (s) and α is the ageing exponent (–) and introduces the decrease of $D_{app}(t)$ over time.

$D_{RCM}(t_0)$ is simply determined by the Rapid Chloride Migration (RCM) test method (NT Build 492 1999, BAW Code of Practice MCL 2012). In this approach, the RCM test replaces the costly diffusion test. The condition for adopting this approach is, however, that considerable field data for concretes similar to the design concrete is available to enable the ageing exponent α, i.e. the decrease of $D_{app}(t)$ over time, to be estimated.

Table 1. Input parameters for the reliability analysis in Figure 2.

Parameter	Distribution & values
$D_{RCM}(t_0)$ [$.10^{-12}$ m^2/s]	ND (10.0/2.0)
t_0 [s]	constant 2,419,200 (28 d)
ageing factor α [–]	βD (0.30/0.12/0/1)
T_{ref} [K]	constant 273
T_{real} [K]	ND (283/5)
b_e [K]	ND (4800/700)
d_c [mm]	ND (60/6)
$C_{S,0}$ [wt.-%/c]	LND (3.0/1.4)
C_{Crit} [wt.-%/c]	βD (0.60/0.15/0.2/2)

Although the ageing exponent is dependent on the exposure conditions, binders have characteristic ageing exponents. *Gehlen (2000)* quantified the ageing exponent of concretes consisting of three different types of cement. Detailed explanations of this approach and recommended values for ageing exponent are published in *Gehlen (2000)*, *fib Bulletin 34 (2006)* and *Rahimi et al. (2014.09)*.

The limit state equation is obtained by comparing the chloride content in the concrete cover (position of rebars) calculated at the time t, i.e. $C(x{=}d_c, t)$, and the critical chloride content C_{crit} (eq. (4)).

$$g(X,t) = C_{crit} - C(d_C, t) \tag{4}$$

Although only free chloride ions that have dissolved in the pore solution of the concrete result in depassivation of the reinforcement, the overall chloride content is included in the model as it is difficult to determine the free chloride content in the concrete. The critical chloride content C_{crit} has to be quantified statistically and inserted into the model. Some stochastic values for the input parameters are recommended in *fib Bulletin 34 (2006)* (see also Table 1). A reliability analysis is performed using the limit state equation (4) and by specifying a minimum reliability index β. There is a correlation between the reliability index β and the probability of failure p_f. EN 1990:2002 and ISO 2394:1998 give recommendations for the reliability index for serviceability limit states depending on the expense and effort required to reduce risk from $\beta = 0$ to $\beta = 1.5$.

The diagram in Figure 2 is an example of a reliability analysis used to predict the service life of

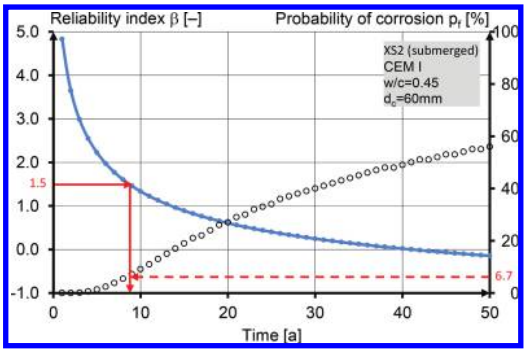

Figure 2. Development of reliability index and probability of chloride-induced depassivation of reinforcing steel over time of a marine structural element.

a structural element (CEM I (Portland cement), w/c = 0.45, d_c = 60 mm). A target reliability index of β = 1.5 (p_f = 6.7%) is expected only after a 9-year period of exposure to a marine environment (submerged), confirming that concretes made with Portland cement are unsuitable for use in conditions in which they are exposed to chlorides. The input parameters are illustrated in Table 1. The reliability analysis was performed using the STRUREL program.

This model is applied during the design stage of new structures by inserting input parameters of the material properties, of the cover depth and of actions into equation (1).

The model for service life design of (new) concrete structures for chloride-induced depassivation of the reinforcing steel has only been described here to the extent that is necessary to understand the discussion of the repair of concrete structural elements later on in this paper (sections 3 and 4). The principle of probabilistic service life design has been explained in detail in *fib bulletin 34 (2006)* and *Gehlen (2000)*, for example.

The model can also be used to assess the durability of existing structures and to predict their residual service life by determining the current material properties and the actual actions statistically and inserting them into the model. However, some modifications are required in order to model the residual service life design after a repair measure, e.g. application of repair mortars since the chloride ingress model first has to be adapted to a 2-layer model in which both the repair layer and the remaining concrete layer are considered. The possible effect of the redistribution of the residual chlorides on the service life has to be considered in particular where the remaining concrete layer contains residual chlorides, which is the subject of this paper.

3 SERVICE LIFE DESIGN OF REPAIRED CONCRETE MEMBERS CONTAINING RESIDUAL CHLORIDES

3.1 *Mathematical description of chloride transport in 2-layer systems*

The chloride transport in a concrete structural element can be described mathematically as follows for cases in which the concrete cover is partially removed and replaced with a repair material and if the remaining concrete does not contain any residual chlorides:

$$C_{new}(x,t) = C_{s,0}\sum_{n=0}^{\infty}\alpha^n\left\{erfc\frac{(2n+1)\cdot d_{c,new}+x}{2\sqrt{k_e\cdot D_{app,new}(t)\cdot t}} - \alpha\cdot erfc\frac{(2n+1)\cdot d_{c,new}-x}{2\sqrt{k_e\cdot D_{app,new}\cdot t}}\right\} \quad (5)$$

$$C_{remain}(x,t) = \frac{2k\cdot C_{s,0}}{k+1}\cdot\sum_{n=0}^{\infty}\alpha^n\cdot erfc\frac{(2n+1)\cdot d_{c,new}+k\cdot x}{2\sqrt{k_e\cdot D_{app,new}\cdot t}} \quad (6)$$

with:

$$k = \sqrt{\frac{D_{app,new}}{D_{app,remain}}} \quad (7)$$

$$\alpha = \frac{1-k}{1+k} \quad (8)$$

where $D_{app,new}(t)$ and $D_{app,remain}(t)$ are the apparent chloride diffusion coefficients of the repair material and the remaining concrete respectively and $d_{c,new}$ is the thickness of the repair layer. The chloride concentration in the layer of repair material $C_{new}(x, t)$ is described using equation (5) and that of the remaining layer of concrete $C_{remain}(x, t)$ using equation (6). The boundary conditions for the new layer are a constant surface chloride concentration ($C_{s,0}$ = const.) and an equilibrium concentration at the interface ($C_{new}(x = 0, t) = C_{remain}(x = 0, t)$).

This mathematical formulation is based on the diffusion equation for semi-finite composite media developed by *Carslaw & Jaeger (1959)* and *Crank (1975)* which has been modified to fit the model for new structures, i.e. 1-layer systems (eq. (1)).

Any interfacial resistance at the repair material/concrete layer interface is disregarded here. The interfacial resistance can be caused by the incoherence of the pore structure of the two materials (pore blocking) and by the high proportion of impermeable aggregates in both layers. In this case, the boundary condition of the equilibrium concentration at the interface is not satisfied in the

above approach and the chloride transport is modelled using other, similar mathematical equations (*Crank 1975*).

In cases in which the remaining concrete layer contains residual chlorides, these will be redistributed in both layers, as shown in Figure 1. The redistribution of the residual chlorides cannot be described mathematically by the error function solution of Fick's second law of diffusion as the required boundary condition of a constant concentration at the phase boundary, $\partial Cs/\partial t = 0$, no longer applies. The corresponding convolution integral, assuming that the apparent chloride diffusion coefficient D is the same for both layers and the residual chloride profile follows Fick's law of diffusion, is shown in equation (9). The integral does not provide a closed-form solution, i.e. it cannot be expressed as a finite number of known functions.

$$C(x,t) = \frac{1}{\sqrt{4\pi D \cdot t}} \int_{x}^{\infty} e^{-\frac{(x-y)^2}{4D \cdot t}} \cdot C_{S,0} \cdot erfc\left(\frac{y}{\sqrt{4D \cdot t}}\right) a \tag{9}$$

The interval x to ⊥ indicates the boundaries of the remaining concrete layer, $C_{s,0}$ is the residual chloride content at the interface.

In this case, it is not possible to model the chloride transport in the element mathematically in a way that is generally valid.

3.2 *Hypothetical approach*

One of the most important preconditions for predicting the service life of a structure is the availability of mathematical models to describe the relevant transport and/or deterioration mechanisms (see section 2). As explained in the previous section, there is no mathematical formulation for the chloride transport in repaired concrete structural elements containing residual chlorides. Nevertheless, a simplified approach to estimating the residual service life of such repaired elements is presented below.

The mathematical model used is the diffusion equation proposed by *Carslaw & Jaeger (1959)* (eq. (5) and (6)). The residual chloride content at the surface of the reinforcement C_r is determined/specified. The limit state is taken to be the point at which a chloride content defined as the difference between the critical chloride content and the residual chloride content ($C_{crit} - C_r$) is reached at the surface of the reinforcement due to the ingress of external chloride ions. The gradient of the residual chloride profile and its redistribution are not taken into account. The procedure described above is illustrated in Figure 3.

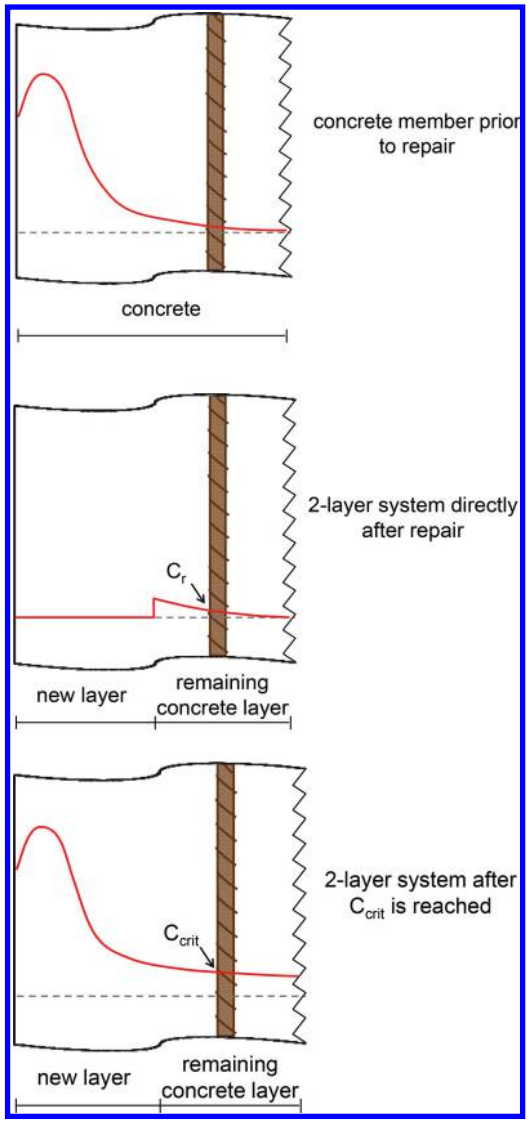

Figure 3. Schematic representation of the chloride profiles in a concrete structural element before and after repair.

The limit state equation for the reliability analysis is, by analogy to the 1-layer system (eq. 4), as follows:

$$g(X,t) = (C_{ctir} - C_r) - C(d_{c,new} + d_{c,remain}, t) \tag{10}$$

where $d_{c,new}$ and $d_{c,remain}$ are the thickness of the (new) repair layer and that of the remaining concrete layer between the surface of the reinforcing steel and the repair layer respectively.

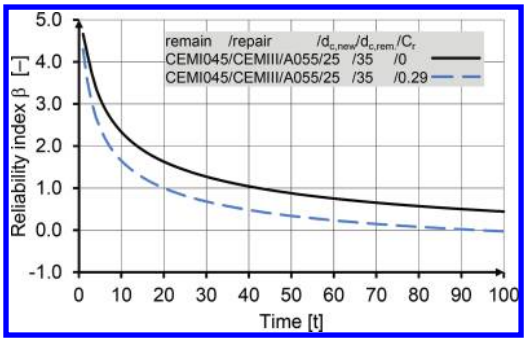

Figure 4. Development of reliability index over time. Prediction of the service life after repair using the simplified approach presented in this paper.

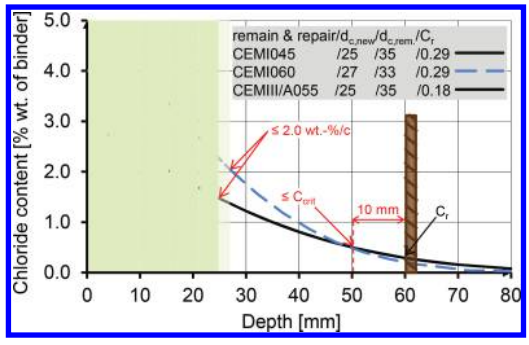

Figure 5. Residual chloride profiles for the calculations in Figure 6.

Using this approach, a reliability analysis was performed for a typical 2-layer system comprising a 25 mm thick layer of repair material made of CEM III/A concrete (GGBS cement) and a 35 mm thick remaining layer made of CEM I (OPC) concrete (same case as in Figure 1, i.e. 25 mm of the concrete cover is removed and replaced with a repair material after approx. 20 years' exposure). The gradient of the residual chlorides is shown in Figure 5 and the result of the reliability analysis in Figure 4. The residual chloride content at the surface of the reinforcement C_r is 0.29 wt.-%/c. By analogy to the 1-layer system, a beta distribution with a mean value of 0.6 wt.-%/c was assumed for the critical chloride content (cf. section 2, Table 1). By way of comparison, the case in which the remaining concrete layer does not contain any residual chlorides (C_r = 0) was also considered. The desired reliability index of $\beta = 1.5$ is achieved after 14 years (C_r = 0.29) and 23 years (C_r = 0) respectively.

In the next section it will be shown to what extent disregarding the redistribution of the residual chloride gradient affects the service life prediction established using the introduced approach.

3.3 *Actual consideration of the chloride redistribution in reliability analysis*

Section 3.1 introduced a convolution integral for the mathematical description of the redistribution of the residual chloride gradient over time (eq. (9)). The integral only applies if both the repair layer and the remaining concrete layer are made of the same material ($D_{app,new} = D_{app,remain}$). However, the integral does not provide a closed-form solution. A solution of this type can be approximated by the Rieman integral, for example.

Three case studies will now be considered. For each case, the residual service life after repair is calculated in two ways: once using the simplified approach (section 3.2) and once considering the redistribution of the residual chlorides by way of comparison. The residual chloride profiles and materials are shown in Figure 5. Each design case was calculated for the same type of action (submerged, C_{s0} = 3.0 wt.-%/c, T_{real} = 10°C). The formulation used to calculate the time—and depth-dependent chloride concentrations for the design case with the residual chloride profile shown in Figure 5, where $C_r = 0.18$ (dashed line), and which was determined using the Rieman integral is as follows (generated by means of Maxima software):

$$-(erf(\frac{x+107}{2\sqrt{D}\sqrt{t}})+5erf(\frac{x+97}{2\sqrt{D}\sqrt{t}})+15erf(\frac{x+87}{2\sqrt{D}\sqrt{t}})+$$
$$24erf(\frac{x+77}{2\sqrt{D}\sqrt{t}})+125erf(\frac{x+67}{2\sqrt{D}\sqrt{t}})+$$
$$240erf(\frac{x+57}{2\sqrt{D}\sqrt{t}})+450erf(\frac{x+47}{2\sqrt{D}\sqrt{t}})+$$
$$710erf(\frac{x+37}{2\sqrt{D}\sqrt{t}})-1570erf(\frac{x+27}{2\sqrt{D}\sqrt{t}})-$$
$$1570erf(\frac{x-27}{2\sqrt{D}\sqrt{t}})+710erf(\frac{x-37}{2\sqrt{D}\sqrt{t}})+$$
$$450erf(\frac{x-47}{2\sqrt{D}\sqrt{t}})+240erf(\frac{x-57}{2\sqrt{D}\sqrt{t}})+$$
$$125erf(\frac{x-67}{2\sqrt{D}\sqrt{t}})+24erf(\frac{x-77}{2\sqrt{D}\sqrt{t}})+$$
$$15erf(\frac{x-87}{2\sqrt{D}\sqrt{t}})+5erf(\frac{x-97}{2\sqrt{D}\sqrt{t}})+erf(\frac{x-107}{2\sqrt{D}\sqrt{t}})-$$
$$2000C_{S,0}\cdot erf(\frac{x}{2\sqrt{D}\sqrt{t}}))/2000 \qquad (11)$$

where $D = D_{app}(t)$.

It can be seen from the β-t runs in Figure 6 that the curves only differ significantly in the initial

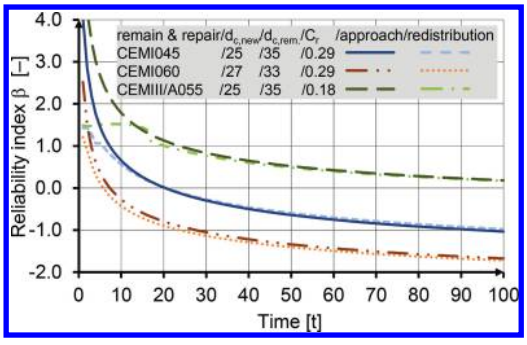

Figure 6. Prediction of service life after repair—Effect of the redistribution of the residual chlorides.

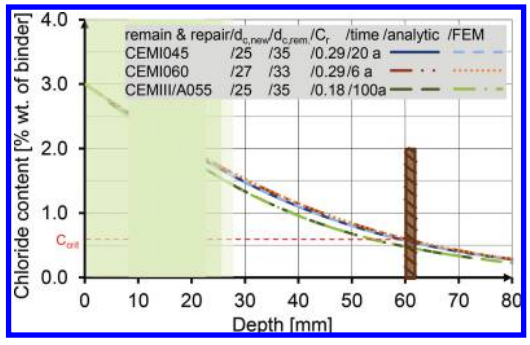

Figure 7. Chloride profiles in repaired elements. Comparing the analytical approach with FEM.

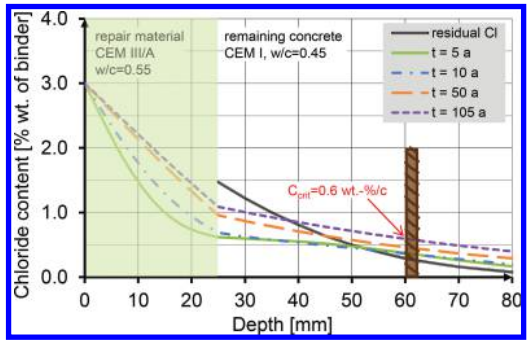

Figure 8. Chloride profiles over time in a repaired element. Calculated by FEM.

phase (i.e. in the first few years after repair). The curves subsequently converge almost entirely, indicating that the assumed approach delivers reliable results. The much lower initial reliability index in the detailed method (taking account of the chloride redistribution) is due to the significant initial reduction of the gradient of the residual chlorides which results in the chloride concentration close to the rebar surface already being increased before any significant ingress of external chlorides occurs.

The favourable effect of the age of the concrete structural element at the time of repair on the chloride penetration resistance of the remaining concrete is not taken into consideration in the calculations to obtain conservative results. Based on this assumption, the uncertainty described above directly after repair (high reliability indices) was assumed to be negligible.

The results of the numerical investigations of the diffusion-controlled chloride transport in a 2-layer system used to validate the approach described here are presented in the following section.

3.4 *Comparative numerical investigations*

The chloride ingress and redistribution in a 2-layer system were investigated using the COMSOL Multiphysics® software. The chloride penetration was considered to be by diffusion only and described using Fick's law. The mechanisms are modelled in the programme by means of differential equations and solved using the Finite Element Method (FEM). The calculations in this section are based on a mean value approach (deterministic), that is, $\beta = 0$.

First of all, the plausibility of applying the analytical approach to take account of the redistribution of the residual chlorides with the aid of the Rieman integral (Section 3.3, Figure 6) was examined. The chloride profiles calculated with the aid of this integral as shown in Figure 6 are compared with the results of the FEM calculations in Figure 7. The time selected for each profile was the service life calculated for a reliability index of $\beta = 0$ (i.e. deterministic approach) in Figure 6. The results demonstrate a perfect correlation between the analytical and numerical calculations.

The chloride profile after 100 years is shown for the case in which a CEMIII/A material with a $w/c = 0.55$ is used although the reliability index at this time is still greater than zero (see Figure 6). It can also be seen from Figure 7 that C_{crit} has not yet reached the rebar surface after a period of 100 years.

The design case calculated using the simplified approach in Section 3.2, Figure 4, is examined numerically in Figure 8. The chloride profiles after 5, 10, 50 and 105 years after repair were calculated numerically. The critical chloride content, taken as $C_{crit} = 0.60$ wt.-%/c in the reliability analyses, is reached at the rebar surface after a period of 105 years. This period of time, which is taken as the service life of the concrete structural element after repair, was calculated as 94 years when the simplified approach was used (Figure 4, $\beta = 0$). This

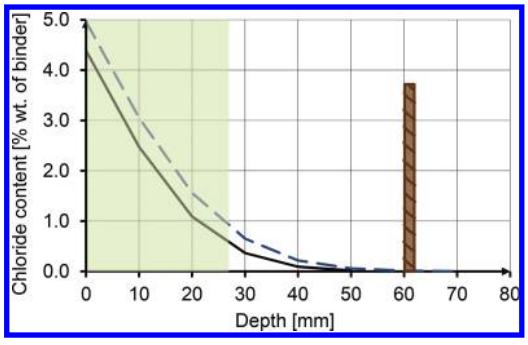

Figure 9. Examples of design cases; the residual chloride profiles do not exhibit any chloride concentration at the rebar surface.

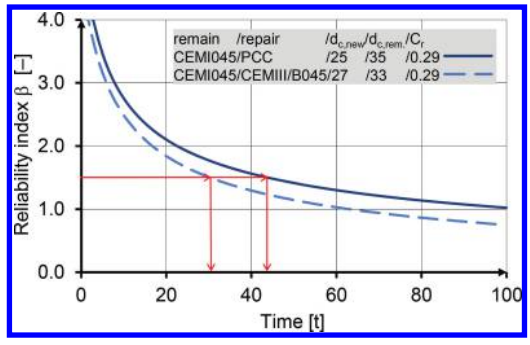

Figure 10. Residual service life according to the probabilistic approach presented in this paper for an exemplary case in which repair materials with high diffusion resistance against chlorides are used.

result shows that there is a very good correlation between the results of the simplified approach and those of the numerical calculations. The probabilistic approach presented in this paper thus enables the chloride transport to be described with a degree of accuracy that is sufficient to deliver reliable prognoses of the service life.

3.5 *Application limits of the approach*

In the approach presented here for estimating the residual service life of structural elements after repair, the residual chloride profile is only taken into account by considering the chloride concentration at the rebar surface. Neither the gradient of the residual chlorides nor its redistribution is considered. This means that the approach does not apply to cases in which the residual chloride profile fails to reach the depth at which the rebar surface is located (cf. Figure 9).

One possibility of estimating the residual service life after repair in such cases is as follows. Assuming a low residual chloride concentration at the rebar surface, e.g. $C_r = 0.10$ wt.-%/c, the approach presented here must be used to calculate the residual service life. The period of time that must elapse before the residual chloride profile at the rebar surface reaches a concentration of 0.10 wt.-%/c must be estimated conservatively and added to the residual service life previously calculated.

4 CONCLUSIONS AND PRACTICAL APPLICATIONS

This paper has described a simplified probabilistic approach for estimating the residual service life of concrete structural elements after repair. The repairs consisted of replacing the concrete cover either partially or entirely with a cement-based repair material. In particular, the presence of any residual chloride contamination in the remaining concrete layer was considered.

Table 2. Input parameters of the repair materials for the reliability analysis in Figure 10.

	Distribution & values	
Parameter	PCC	CEM III/B045
$D_{RCM}(t_0)$ [$\cdot 10^{-12}$ m²/s]	ND (2.3/0.46)	ND (1.9/0.38)
ageing factor α [–]	βD (0.51/0.18/0/1)	βD (0.45/0.20/0/1)

The approach presented here was validated with the aid of analytical calculations and numerical investigations.

The most frequently used repair materials in the event of chloride-induced corrosion of the reinforcing steel are polymer-modified cement-based systems; PCC (Polymer modified Cement Concrete) and SPCC (Sprayed Polymer modified Cement Concrete). The performance of such materials, whose composition is not generally revealed by the manufacturers, and their long-term behaviour have not yet been investigated. The parameters needed for a performance-based assessment of the efficiency of such materials were determined in *Rahimi et al. (2014.09)* on the basis of ongoing investigations of selected materials. The parameters and the probabilistic approach presented in this paper were used to determine the residual service life for a design case by way of illustration (repair material PCC I from *Rahimi et al. (2014.09)*, remaining concrete layer and residual chloride profile, see Figures 5 and 10, action see Table 1). The calculated β-t-run is shown in Figure 10. The desired reliability index of $\beta = 1.5$ is reached approx. 45 years after repair.

By comparison, Figure 10 shows also the β-t-run for the same design case, differing only in the repair material used. The material selected was a CEM III/B concrete (w/c = 0.45) which is known to has a high diffusion resistance against chlorides. In this case, the service life for $\beta = 1.5$ is reached after approx. 30 years. The material parameters used in the analyses are shown in Table 2.

REFERENCES

BAW Code of Practice MCL "Resistance of Concrete to Chloride Penetration" 2012.

CEN/TS 12390-11 (2010). Testing hardened concrete—Part 11: Determination of the chloride resistance of concrete, unidirectional diffusion.

Carslaw H. S., Jaeger J. C. 1959. Conduction of Heat in Solids, Clarendon Press, Oxford, UK.

Crank J. 1975. The Mathematics of Diffusion, Clarendon, Oxford,UK, 2nd edition.

COMSOL Multiphysics®—Multiphysics Modeling, Finite Element Analysis, and Engineering Simulation Software, www.comsol.com.

EN 1990:2002 – Eurocode 0. Bases of structural design. CEN, Brussels.

fib bulletin 34 (2006). Model Code for Service Life Design, prepared by *fib* Task Group 5.6.

fib MC (2010). Model Code for concrete structures.

Gehlen C. 2000. Probability-based service life design of reinforced concrete structures—Reliability studies for prevention of reinforcement corrosion. DAfStb Heft 510, Berlin, Beuth (in German).

ISO 16204:2012. Durability—Service life design of concrete structures.

Maxima—A Computer Algebra System. Energy Science and Technology Software Center. http://maxima.sourceforge.net

NT Build 492 (1999). Nordtest method: Concrete, Mortar and Cement-Based Repair Materials: Chloride Migration Coefficient from Non-Steady-State Migration Experiments.

NT Build 443 (1995). Nordtest method: Concrete, hardened: accelerated chloride penetration.

Rahimi A., Gehlen C., Reschke T., Westendarp A. 2015. Chloride transport in concrete structural elements after repair. Proceeding of the International fib symposium 2015 "Concrete—Innovation and Design", 18.-20. May, Copenhagen, Denmark.

Rahimi A., Gehlen C., Reschke T., Westendarp A. 2014.09. Efficiency of materials used for repair measures of concrete structures exposed to chlorides. 5th International Conference on Concrete Repair—Concrete Solutions, 01.-03. September 2014.

Rahimi A., Gehlen C., Reschke T., Westendarp A. 2014.01. Approaches for Modelling the Residual Service Life of Marine Concrete Structures. International Journal of Corrosion 1/2014, http://www.hindawi.com/journals/ijc/2014/432472/abs/.

STRUREL—A structural reliability analysis program system by RCP GmbH (Reliability Consulting Programs), www.strurel.de.

Concrete Repair, Rehabilitation and Retrofitting IV – Dehn et al. (Eds)
© 2016 Taylor & Francis Group, London, ISBN 978-1-138-02843-2

Relationships between defects and inventory data of RC bridges and culverts in the Western Cape, South Africa

T.D. Mbanjwa & P. Moyo
Department of Civil Engineering, University of Cape Town, Cape Town, South Africa

ABSTRACT: Annually, road and rail authorities are able to only replace a fraction of their ageing network infrastructure owing to lack of funding. Bridge Management Systems have been developed to aid the prioritization of bridges and culverts according to their urgency for repair and rehabilitation. Their databases contain significant data which could be used to identify, if any, relationships between data of an area of interest. Thus, this paper presents findings from several logistic regression analyses and data mining activities conducted on inventory and inspection data of reinforced concrete bridges and culverts in the Western Cape Province of South Africa. The study investigates defects, their predominance, their spatial distributions as well as their relationships with inventory data such as the location of structures (in terms of district municipalities); types of structures; age and span length/width. Further, average condition indices are provided as a means to quantify their average state.

1 INTRODUCTION

Bridges and culverts form critical links within transportation networks and society has always relied on transportation for survival. The earliest bridges were made of fallen trees and vines and with the evolution of technology, tailored to facilitate mechanized transportation of people and goods (Tang, 2007). The performance of bridges and culverts should be of great concern as transportation systems not only have an impact on the country's economy, they also affect society's everyday lives (Adhiikare, Moselhi & Bagchi, 2013).

Bridges and culverts are prone to defects resulting from chemical, mechanical and physical mechanisms. For example in South Africa during 1996, the legal axle load was increased from 8.2 tonnes to 9 tonnes (Nordengen and De Fleuriot, 1998); deterioration of transportation infrastructure was consequently expected to increase. Furthermore, according to Schraven et al. (2011), Bien, Elfgren and Olofsson (2007), society's expectations for infrastructure managers to meet new demands are steadily increasing. These demands include higher axle loads, higher speeds, safety, less disturbances, reduced maintenance costs and increased availability and reliability of network structures. Thus, for reasons such as these it is important that transportation authority's monitor and maintain the performance and condition of their ageing network infrastructure.

Schraven et. al. (2011) indicate that in the past public agencies were able to allocate large budgets for maintenance, renovations and the reconstruction of infrastructure. However, in the last decade, agencies have been confronted with budgetary constraints. As a result of these, the quantity of structures receiving maintenance works decreased and the quantity of structures requiring repairs and rehabilitation increased. Attention shifted from structural maintenance to structural preservation (Nordengen & Nell, 2005). Recently, many of the road and rail authorities within Southern Africa did not have network infrastructure management systems in place; hence they adopted the Struman BMS (Nordengen & De Fleuriot, 1998). The BMS is a defects-based system which employs a prioritization algorithm on data derived from visual inspections to rank bridges and culverts in order of importance for rehabilitation and repair.

The Provincial Government of the Western Cape (PGWC) has also adopted this system. They are responsible for 16 000 km of road; 6000 km of paved road and 10 000 km of unpaved road. These networks of road are also inclusive of approximately 2 400 bridges and culverts (Nordengen and Nell, 2005).

The visual inspection data collected for these structures has been solely used to prioritize them for remedial work activities. These data contain useful information pertaining to structures defects and condition. Thus, further analysis of these data could provide an indication of the predominant/reoccurring bridge and culvert defects, their spatial distributions and their relationships with inventory data such as location (in terms of district munici-

palities), structure type, age and span length/width. Subsequently, findings may be used to improve decision making during resource allocation; forecast deterioration and inform future bridge and culvert design.

The paper will therefore discuss findings from an analysis conducted on the PGWC Struman BMS database with the intention to gain a deeper understanding of the relationships that exist between the defects and inspection data of the RC network structures in the Western Cape Province (see Figure 1).

2 INVENTORY AND INSPECTION DATA

A total of 2 419 structures were in the BMS database; about 35% of these structures were classified as bridges and 65% was classified as culverts. RC structures constituted of 92% of the bridges and 88% of the culverts. An indication of their distribution is provided in Figure 2.

About 81% of the RC bridges were simply supported and 90% of the culverts were portal frame culverts. The RC structures had an average age of 42.8 years. Lastly, the average span length for the RC bridges was 8.3 m whereas the average width for RC culverts was 3.1 m.

Figure 1. The Western Cape Province of South Africa.

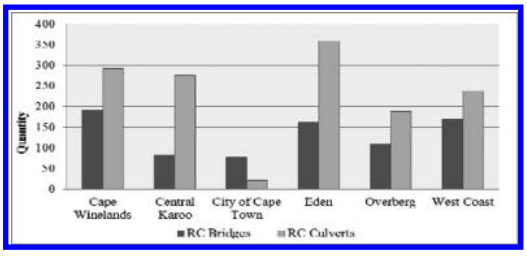

Figure 2. The Western Cape Province of South Africa.

2.1 *Predominant structural defects*

Several defects were investigated of which those identified as the most predominant have been listed, in order of predominance, in Table 1.

Cracking, included cracking due to settlement, torsion, shear stress, bearing stress, prestress restraint etc.(structural and non-structural) and spalling were identified to be the most predominant defects of both RC bridges and culverts when compared to the other defects. The largest percentage of RC bridges with cracking were in the Central Karoo (80.7%) followed by the City of Cape Town (73.1%) and Overberg (71.3%). The percentage of bridges with cracking in Eden (59.9%) and the West coast (59.5%) were relatively similar. The Cape Winelands had the least percentage of RC bridges with cracking (45.6%). On the other hand, the largest percentage of RC culverts with cracking was in the Eden (63.3%) followed by the Overberg (51.6%). The percentage of RC culverts with cracking in the City of Cape Town (36.4%), Cape Winelands (34.5%) and West coast (34.0%) were relatively similar. The Central Karoo had the least percentage of RC culverts with cracking (22.9%). The percentage of RC bridges with spalling was generally higher for district municipalities with higher percentages of RC bridges with cracking and lower for those with lower percentages of RC bridges with cracking. However, for culverts the cracking and spalling was more random.

The cracking, spalling and reinforcement corrosion were assumed linked and their variations attributed to exposure to the marine environment. The far interior is semi-arid, whereas, the West Coast, bordered by the Atlantic Ocean, and the South Coast, bordered by the Indian Ocean, experience varying climatic conditions; from Mediterranean to mild maritime, respectively (Gumbi and van Weele, 2013). In addition to this, the atmosphere in costal environments is laden with salts rich in chloride ions which are transported to RC structures through wind action and ingress the RC structures upon deposition on their surfaces. These chloride ions facilitate reinforcement corrosion

Table 1. Predominant defects on RC structures.

Structure	
RC Bridges	RC Culverts
Cracking	Cracking
Spalling	Spalling
Joint defects	Defective concrete
Surface erosion	Scour
Movement/ Rotation	Movement/Rotation
Reinforcement Corrosion	Reinforcement Corrosion

and consequently cracking and spalling (Alao, Alexander and Beshausen, 2014). The mechanism of chloride penetration varies with the RC structure's distance from the sea and is also influenced by humidity, temperature, wind and solar radiation (Ghods et al., 2005). For this reason, more of the RC bridges and the RC culverts located along the coastal district municipalities were expected to have reinforcement corrosion when compared to those located more inland such as in the Cape Winelands and Central Karoo; a more semi-arid environment. The joint defects were attributed to small movements such as daily thermal cycles; traffic induced movements; faulty installation of materials; lack of routine maintenance resulting in debris collecting in the seals and poor surface drainage. These were also assumed to have contributed to the observed movement and/or rotation defects. The surface erosion was attributed to environmental factors; the defective concrete to poor mix designs and or construction practices and techniques and the scour to increased outlet velocities experienced downstream during seasons of heavy rainfall (Urbonas, 2001). The Western Cape experiences moderately high rainfall during winter and the culverts are therefore expected to be saturated as well as experience large variations in vortices and eddy currents over the intensely heavy rainfall days resulting in an increased likelihood of undermining and scour.

3 RELASHIONSHIPS BETWEEN INVENTORY AND INSPECTION DATA

Logistic regression analysis was used to investigate relationships between the independent variables and the binary dependent variables. The independent categorical variables were that of the various locations and structure types. Age and span length were classified as independent continuous variables and the predominant defects as dependent variables. The analyses were conducted at the 0.05 level of significance characterized by p-values less than 0.05; 95% confidence intervals of odds ratios not containing 1 and odds ratios differing from 1. It may be noted that only the statistically significant relationships identified from logistic regression are presented in this paper. However, all those identified from data mining activities have been provided.

3.1 *Relationships between predominant defects and location*

Two models were developed to measure the significance of location on the dependent variables relative to the base category; an RC bridge or RC culvert in the Cape Winelands. The results are provided in Table 2 and 3, respectively.

A RC bridge in the Central Karoo was 5.06 times more likely to have cracking in comparison to a RC bridge in the Cape Winelands. Subsequently, a RC culvert in the Central Karoo was 9.09 times more likely to have cracking in comparison to a RC culvert in the Cape Winelands. Interpretation for the rest of the logistic regression analyses tables throughout the paper followed the same reasoning.

The mean age of the RC structures as well as the standard deviation as per district municipality, were investigated provided in Table 4 and 5. Also, the average conditions of the structures as per district municipalities were investigated and provided in Figure 3.

The RC bridges in the Central Karoo not only had the higher odds ratios they also had a higher mean age and the lowest average CI. Thus their condition was attributed to their higher mean age which also had the smallest deviation from the mean.

The consequences of employing poor construction practices and techniques in a semi-arid

Table 2. Results from logistic regression analysis between predominant defects and location of RC bridges.

	Cracking		
Variable	z	Odds ratio	p-value
Central Karoo	5.06	4.90	0.000
City of Cape Town	4.77	4.85	0.000
Eden	3.05	1.95	0.002
Overberg	2.89	2.08	0.004
West Coast	2.48	1.69	0.013
Spalling			
West Coast	–5.16	0.29	0.000
Joint defects			
City of Cape Town	6.50	7.70	0.000
Eden	4.17	3.02	0.000
Overberg	4.22	3.42	0.000
Surface erosion			
Central Karoo	7.20	16.8	0.000
City of Cape Town	5.54	9.62	0.000
Eden	4.52	5.48	0.000
West Coast	1.34	1.76	0.000
Movement and/or rotation			
City of Cape Town	–4.00	0.12	0.000
Eden	–5.59	0.12	0.000
Overberg	–4.52	0.15	0.000
Reinforcement corrosion			
Central Karoo	3.12	2.48	0.002
Eden	–2.64	0.41	0.008

Table 3. Results from logistic regression analysis between predominant defects and location of RC culverts.

	Cracking		
Variable	z	Odds ratio	p-value
Central Karoo	10.9	9.09	0.000
Eden	7.16	3.25	0.000
Overberg	3.75	2.05	0.000
Spalling			
Central Karoo	5.71	3.00	0.000
Eden	4.42	2.27	0.000
Overberg	3.94	2.31	0.000
Defective concrete			
Central Karoo	10.5	9.85	0.000
Overberg	–3.11	0.24	0.002
West Coast	3.14	2.11	0.002
Scour			
Central Karoo	4.93	7.79	0.000
Eden	5.83	10.5	0.000
Overberg	4.66	7.52	0.000
Movement and/or rotations			
Central Karoo	4.71	2.91	0.000
Eden	–4.01	0.24	0.000
Overberg	–3.42	0.12	0.000
Reinforcement Corrosion			
Central Karoo	4.42	3.13	0.000

environment such as that of the Central Karoo were assumed to have also contributed to poorer condition of the RC structures in this region.

3.2 *Relationships between predominant defects and structure type*

The significance of location on the dependent variables relative to the base category; an RC bridge or RC culvert in the Cape Winelands, was measured. The results for RC bridges and RC culverts were provided in Table 6 and 7, respectively.

A RC bridge in the Central Karoo was 5.06 times more likely to have cracking in comparison to a RC bridge in the Cape Winelands. Subsequently, a RC culvert in the Central Karoo was 9.09 times more likely to have cracking in comparison to a RC culvert in the Cape Winelands. Interpretation for the rest of the logistic regression analyses tables throughout the paper followed the same reasoning.

The mean age of the RC structures as well as the standard deviation as per district municipality, were investigated provided in Table 8 and 9. Also,

Table 4. Mean age and standard deviation for RC bridges.

	Mean age	Standard deviation
Cape Winelands	47.2	18.2
Central Karoo	50.1	11.8
City of Cape Town	29.9	14.7
Eden	44.0	16.0
Overberg	50.4	18.5
West Coast	51.5	14.6

Table 5. Mean age and standard deviation for RC culverts.

	Mean age	Standard deviation
Cape Winelands	44.3	18.3
Central Karoo	49.0	10.0
City of Cape Town	18.7	20.1
Eden	25.2	23.6
Overberg	34.1	23.9
West Coast	46.3	24.4

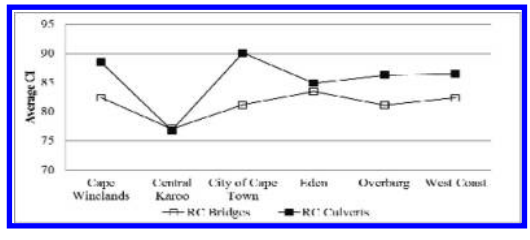

Figure 3. Average CIs for RC bridges and RC culverts as per district municipality.

the average conditions of the structures as per district municipalities were investigated and provided in Figure 3.

The RC bridges in the Central Karoo not only had the highest odds ratios they also had a higher mean age and the lowest average CI. Thus their condition was attributed to their higher mean age which also had the smallest deviation from the mean. On the other hand, the RC culverts in Eden had a much lower mean age when compared to the RC culverts of the other district municipalities. Even though a large percentage of these had cracking (63.3%) and spalling (35%), they were not in the worst condition (see Figure 3).

The low average CI of the RC structures in Central Karoo was in line with the findings from the logit models which suggested the RC structures in this area generally had higher likelihoods of containing the

Table 6. Results from logistic regression analysis between predominant defects and location of RC bridges.

	Cracking		
Variable	z	Odds ratio	p-value
Central Karoo	5.06	4.90	0.000
City of Cape Town	4.77	4.85	0.000
Eden	3.05	1.95	0.002
Overberg	2.89	2.08	0.004
West Coast	2.48	1.69	0.013
Spalling			
West Coast	–5.16	0.29	0.000
Joint defects			
City of Cape Town	6.50	7.70	0.000
Eden	4.17	3.02	0.000
Overberg	4.22	3.42	0.000
Surface erosion			
Central Karoo	7.20	16.8	0.000
City of Cape Town	5.54	9.62	0.000
Eden	4.52	5.48	0.000
West Coast	1.34	1.76	0.000
Movement and/or rotation			
City of Cape Town	–4.00	0.12	0.000
Eden	–5.59	0.12	0.000
Overberg	–4.52	0.15	0.000
Reinforcement corrosion			
Central Karoo	3.12	2.48	0.002
Eden	–2.64	0.41	0.008

Table 8. Mean age and standard deviation for RC bridges.

	Mean age	Standard deviation
Cape Winelands	47.2	18.2
Central Karoo	50.1	11.8
City of Cape Town	29.9	14.7
Eden	44.0	16.0
Overberg	50.4	18.5
West Coast	51.5	14.6

predominant defects. The consequences of employing poor construction practices and techniques in a semi-arid environment such as that of the Central Karoo were assumed to have also contributed to poorer condition of the RC structures in this region.

When the subset of the dominant RC bridge structure type, the simply supported RC bridges, was compared for to the dominant RC culvert structure type, simply supported portal frame RC culverts, it was noted that the RC bridges (61%) affected by cracking were almost equivalent to the

Table 7. Results from logistic regression analysis between predominant defects and location of RC culverts.

	Cracking		
Variable	z	Odds ratio	p-value
Central Karoo	10.9	9.09	0.000
Eden	7.16	3.25	0.000
Overberg	3.75	2.05	0.000
Spalling			
Central Karoo	5.71	3.00	0.000
Eden	4.42	2.27	0.000
Overberg	3.94	2.31	0.000
Defective concrete			
Central Karoo	10.5	9.85	0.000
Overberg	–3.11	0.24	0.002
West Coast	3.14	2.11	0.002
Scour			
Central Karoo	4.93	7.79	0.000
Eden	5.83	10.5	0.000
Overberg	4.66	7.52	0.000
Movement and/ or rotations			
Central Karoo	4.71	2.91	0.000
Eden	–4.01	0.24	0.000
Overberg	–3.42	0.12	0.000
Reinforcement Corrosion			
Central Karoo	4.42	3.13	0.000

Table 9. Mean age and standard deviation for RC culverts.

	Mean age	Standard deviation
Cape Winelands	44.3	18.3
Central Karoo	49.0	10.0
City of Cape Town	18.7	20.1
Eden	25.2	23.6
Overberg	34.1	23.9
West Coast	46.3	24.4

RC culverts affected by cracking (59%). However, more RC bridges contained spalling (45%) and reinforcement corrosion (18%) as opposed to culverts. Continuous RC bridges, which accounted for 12% of total quantity of bridges; the second largest structure type group, were found to have cracking (58%), spalling (38%), and only a third of the total fraction affected by the other defects. The other structure types combined constituted 6% of the total bridges and were affected mostly by cracking and spalling with less than 25% of them exhibiting movement/rotation and rebar corrosion. The frequent defects on precast portal frame culverts,

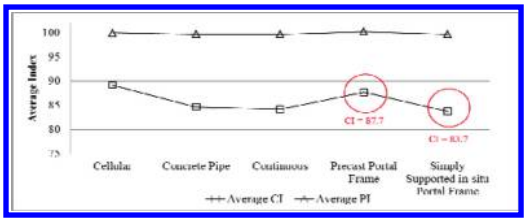

Figure 4. Average CIs for RC bridges and RC culverts as per structure type.

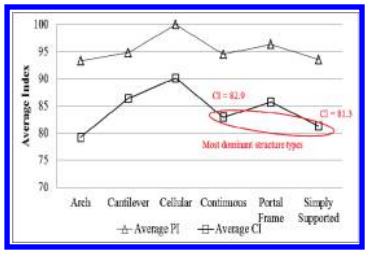

Figure 5. Average CIs for RC bridges and RC culverts as per structure type.

which constituted 18% of the total culverts, were that of cracking (40%) and spalling (32%) followed by defective concrete (27%). The other RC culvert structure types constituted 10% of the total quantity of culverts of which below half of these (40%) were concrete pipes. These concrete pipes were found to have the highest percentage, by structure type, of scour which was approximately 20%. The average Condition of the RC bridges and RC culverts was investigated and the results graphically represented in Figure 4 and 5.

The simply supported RC bridge structure type (simply supported RC bridges) had the one of the lowest average CIs. The differences in the average CI of the in-situ and precast portal frame culverts was assumed characteristic of casting on site as opposed to pre-casting; more care is generally given to precast structures as opposed to those cast in-situ.

3.3 *Relationships between predominant defects and age*

A total of 514 RC bridges (65%) and 266 RC culverts (19%) had known construction dates and therefore their ages could be determined. Significant relationships were tabulated in Table 10 and 11.

Thus, a unit increase in age would increase the likelihood of cracking on an RC bridge by 2.98. and similarily for the RC culverts.

Relationships between increasing age for the RC structures have been represented in Figure 6 and 7.

Table 10. Results from logistic regression analysis between predominant defects and age of RC bridges.

Dependent variable	RC Bridges		
	z	Odds ratio	p-value
Cracking	2.98	1.01	0.003

Table 11. Results from logistic regression analysis between predominant defects and age of RC culverts.

Dependent variable	RC Culverts		
	z	Odds ratio	p-value
Cracking	4.50	1.01	0.000
Spalling	2.49	1.01	0.013
Scour	2.36	1.01	0.018

The graphs in Figure 6 and 7 exhibited general increases in the percentages of RC structures with predominant defects with increasing age categories.

Subsequently, the average conditions of the RC bridges and RC culverts were investigated and the relationships illustrated in Figures 8.

The average CIs graphs for both the RC bridges and the RC culverts showed a clear decrease with increasing age categories between 0 and 50 years. The age category of 40 to 49 years was the turning point for both graphs. A large percentage of the RC bridge (25%) and RC culverts (43%) from this age category were from the Central Karoo; hence the lower CI. The average CIs showed an increase for the age category of 50 to 69 years. The peaking of the graphs at age category 60 to 69 was assumed characterized by the smaller quantity of RC structures (47% less RC bridges and 48% less RC culverts) constructed during this period compared to the successive age category.

3.4 *Relationships between predominant defects and span length/width*

Lastly, relationships between span length/width for over 95% of the RC bridges and RC culverts were investigated and the findings tabulated in Tables 12 and 13.

RC bridge span length was only found to be significant for predicting the likelihood of joint defects. Thus a unit increase in span length increased the likelihood of joint defects by 1.03.

RC culvert width was found significant for predicting the likelihood of cracking and joint defects. Correspondingly, a unit increase in width increased the likelihood of these defects by 1.11 and 1.03.

Figure 9 depicts the relationships between defects and span length for RC bridges.

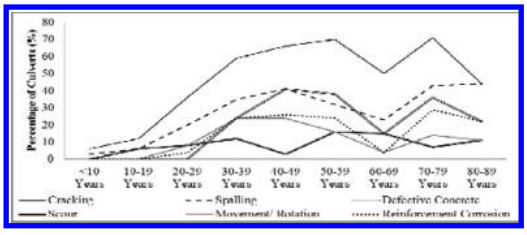

Figure 6. Relationship defects and age for RC bridges.

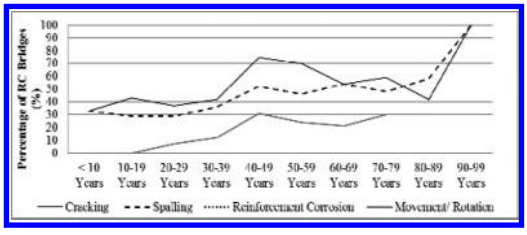

Figure 7. Relationship defects and age for RC culverts.

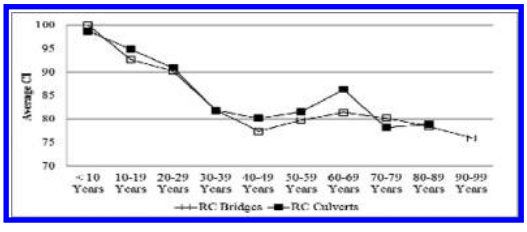

Figure 8. Average CIs for RC bridges and RC culverts as a function of age.

Table 12. Results from logistic regression analysis between predominant defects and span length of RC bridges.

Dependent variable	RC bridges		
	z	Odds ratio	p-value
Joint defects	2.56	1.03	0.010

Table 13. Results from logistic regression analysis between predominant defects and width of RC culverts.

Dependent variable	RC culvert		
	z	Odds ratio	p-value
Cracking	2.11	1.11	0.035
Defective concrete	2.56	1.03	0.003

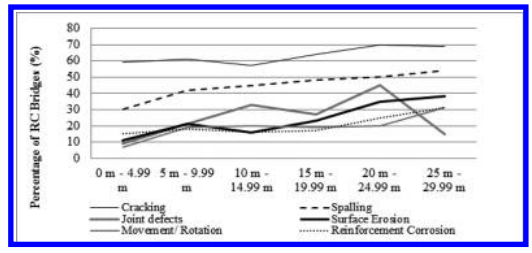

Figure 9. Relationships between span length and identified predominant defects for RC bridges.

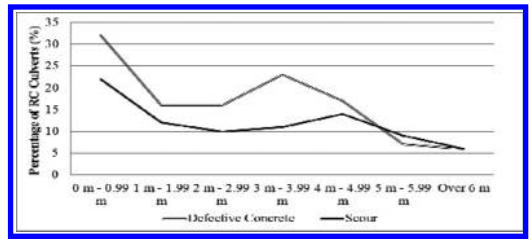

Figure 10. Relationships between defective concrete and scour for RC culverts.

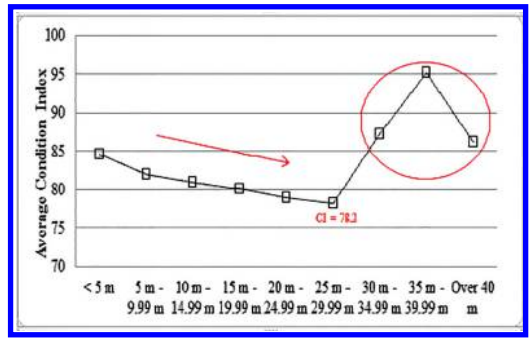

Figure 11. Average CIs for RC bridges as a function of span length.

The percentage of RC bridges and most RC culverts with the predominant defects generally increased with increasing span length/width. However, the percentage of RC culverts with scour and movement and/rotation generally decreased with increasing width as seen in Figure 10.

The condition of the structures with increasing span length and width was investigated and the findings graphically illustrated in Figure 11 and 12.

The average CIs for the RC bridge span lengths between 0 m and 30 m showed a decrease with increasing span length categories. The lowest RC bridge span length was that of 78.2 for span length category between 25 and 30 m. The average span length for RC bridges of span length between 30 and 40 m increased with increasing span length

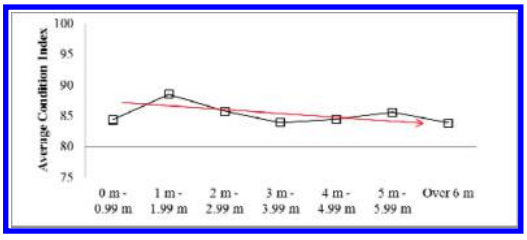

Figure 12. Average CIs for RC culverts as a function of span length.

and thereafter decreased for bridges over 40 m. It may be noted that because the quantity of RC bridges over 30 m only constituted 2% of the total RC bridges, the high average CIs computed for these RC bridges may also be regarded as a result of the very small sample.

On the other hand, the average CIs for the RC culverts were fairly constant and showed a slight decrease with increasing age categories.

4 CONCLUSION

To enhance the knowledge of the state and condition of the RC bridge and RC culvert structures of the Western Cape Province, an analysis of the Struman BMS database was presented in this paper. The investigations between the identified predominant defects and location showed that cracking and spalling were most frequent on the RC structures. These were attributed mostly to the mechanism of chloride ingress; very common in the Western Cape Province. The RC structures had similar defects and it therefore follows that they had similar deterioration mechanisms.

Location (in terms of district municipality), structure type, age and span length/width were found to all be important contributors to the prevalence of the predominant defects. It may be concluded that location better explains the prevalence of predominant defects when consider with the mean age of the structures and the standard deviation of the age.

Simply supported RC bridges and simply supported in-situ portal frame RC culverts constituted too large a portion to be able to draw conclusions on the other structure types. Furthermore, although there were no statistically significant relationships between defect and structure type, it may be noted that the dominant structure types were in the worst condition.

Moreover, the percentage of RC structures with defects general increase with increasing age and span length/width. Hence it follows that there is an overall decrease in condition with increasing age and span length/width.

Finally, considering the average CIs of the entire RC structure population, the RC bridges and RC culverts were considered to be in an acceptable and good condition.

ACKNOWLEDGEMENTS

The author wishes to thank the National Research Foundation (NRF) as well as the Concrete Materials and Structural Integrity Research Unit (CoMSIRU) for the financial and academic support.

REFERENCES

Adhikari, R., Moselhi, O. & Bagchi, A. (2013) A study of image-based element condition index for bridge inspection. *Proceedings of the 30th International Symposium on Automation and Robotics in Construction (ISARC)*. Montreal, Canada.

Alao, O., Alexander, M. and Beshausen, H. (2014). Understanding the influence of marine micro-climates on the durability performance of RC structures. University of Cape Town.

Bien, J., Elfgren, L. and Olofsson, J. Eds. (2007) Sustainable bridges: Assesment for future traffic demands and longer lives. Dolnośląskie Wydawnictwo Edukacyjne, Poland.

Ghods, P., Chini, M., Alizadeh, R., Hoseini, M. & Ramezanianpour, A. (2005). The effect of different exposure conditions on th chloride diffusion into concrete in the Persian Gulf region. *Proceedings of the 3rd International Conference on Construction Materials: Performance, Innovations and Strucural Implications,* Vancoucer, Canada, pp 10.

Nordengen, P. (2012). Bridge management systems: an asset management tool for road structures. *Proceedings of the 4rd CSIR Biennial Conference: Real Problems Relevant solutions*. Pretoria, South Africa.

Nordengen, P. & Fleuriot, E. (1998). The development and implementation of a bridge management system for South Africn road and rail authorities. *Proceedings of the '98 Conference: Investigating in Transport*. Sydney, Australia.

Nordengen, P. & Nell, A. (2005) The development and implementation of a bridge management system for the Provincial Government of the Western Cape. *Proceedings of the 5th International Conference on Bridge Management*. Gildford, United Kingdom, 243–250.

Roux, M., Nordengen, P., Tekie, S. & Rittmann R. (2005). The Namibian bridge management system: A tool for preservation of structures on the road network. Windhoek, Namibia.

Scharven, D., Hartmann, A. & Dewulf, G. (2011). Effectiveness of infrastructure asset management: challenges for public agencies. *Journal of Built Environment Project and Asset Management*, 1(1), 61–74.

Tang, M. (2007). Evolution of bridge technology. *IABSE Symposium Report*. Weimar. 38–48.

Urbonas, B. Ed. (2001). Urban drainage and flood control district. Denver, Colarado.

Concrete Repair, Rehabilitation and Retrofitting IV – Dehn et al. (Eds)
© 2016 Taylor & Francis Group, London, ISBN 978-1-138-02843-2

Safety assurance of problematic concrete bridges by automated SHM: Case studies

K. Islami & N. Meng
mageba SA, Bulach, Switzerland

ABSTRACT: This paper presents a number of recently installed Structural Health Monitoring (SHM) systems of concrete bridges, which measure high-frequency parameters and thus enable a proper understanding of the structures' behavior. This greatly reduces uncertainties relating to material properties and structural capacity, and optimizes inspection and maintenance programs. The diverse range of applications presented, designed in collaboration with structure owners and design engineers, includes concrete box girder bridges in a subsidence area, an old arch bridge subject to structural retrofitting and a cracked concrete railway viaduct. These case studies, based on both static and dynamic approaches, demonstrate the usefulness and ease of use of such systems, and the enormous gains in efficiency they offer over alternative manual monitoring methods.

1 INTRODUCTION

Observed deterioration of structures, updating of structural codes and the intrinsic weakness of some structural elements have shown that many existing bridges and other structures offer inadequate structural performance and must be upgraded to comply with current seismic and other design codes. In the case of new structures, the use of advanced finite element method (FEM) design has pushed the use of materials to the limit, so a direct verification of the real behavior of a completed structure can be very useful in enabling the responsible engineers to have confidence in its performance.

Both above-mentioned cases need to be controlled by advanced technologies that allow real-time observations and permit to respond effectively in case of critical conditions. Such technology generally takes the form of an automated SHM system. SHM systems typically consist primarily of a data acquisition unit and a number of sensors, together with data processing and data transmission capabilities as may be required.

The implications of the development of techniques of monitoring, of statistical modeling of the response of structures, and of gathering and processing data in real time, are important—especially in the context of particularly sensitive structures. It is desirable to verify whether the effects of various environmental variables measured in situ influence the static or dynamic behavior of the structure. Therefore, it is important to eliminate the influence of these factors, so that small changes due to damage can be detected. This is made possible by the use of regression models, which can determine the static variables starting from a predefined input.

All of these techniques have been used in the present study, and more importantly, have been applied to important concrete bridges that were in danger of settlements, were suffering deterioration or were being structurally modified.

2 MONITORING OF SETTLEMENT OF SEVEN CONCRETE BOX GRIDER BRIDGES ON THE HUNTER EXPRESSWAY, AUSTRALIA

The Hunter Expressway, recently constructed in Branxton, New South Wales, is situated in a mining area. The bridges on the new road are at risk of settlement due to mining subsidence, so it was decided to permanently monitor seven structures. The structures are mainly concrete box girder bridges with lengths of 155m, 155m, 337m, 257m, 257m, 200m and 200m respectively (Figure 1).

The principal purpose of this project is to measure the differential settlements of piers and abutments and the horizontal displacements of abutments (Islami et al., 2013). A permanent monitoring system has been installed to fulfil this purpose. The system's principal sensors include: ultrasonic sensors to measure horizontal movements at the abutments; hydrostatic tube balance sensors to measure differential settlements at piers and abutments (Figure 2); and air temperature and humidity sensors and structural temperature

Figure 1. Views of monitored structures of the Hunter Expressway.

sensors in order to relate the movements to environmental effects.

All measurements are accurately gathered in a double database and immediately visible in the project's SHM web interface. Figure 3 shows one of the cockpits that the end-user can access day or night. The measurements on two bridges are shown: west and east structures. On each abutment or pier, the following data is measured and recorded:

- At the abutments: displacement in longitudinal and transverse direction of the expansion joint, settlements and temperature

Figure 2. Installation of the monitoring system inside the concrete box girders of the Hunter Expressway.

- At the piers: settlements relative to the right or left abutment and temperature
- Additionally, the level of the reservoir is measured to ensure an appropriate accuracy.

Not only can the responsible engineers check settlements at any time, they can also view the entire time history of the measurements graphically (Figure 4). Any abnormal settlements will be immediately recognizable, enabling safety precautions to be implemented. To ensure that the information is immediately recognized by the engineers, even when not in the office, the system also includes an alarm feature which will provide immediate notification of such an occurrence by email or SMS.

It is interesting to observe the displacements and settlements in Figure 4, where 17 months of measurements are presented. Together with Figure 5, this shows that longitudinal displacements at the bridge's expansion joints are highly dependent on temperature. Furthermore, it can be seen (Fig. 6) that settlements at every pier and abutment are similarly influenced by environmental parameters (to a lesser degree), as might be expected. Fortunately, since the installation took place, the SHM

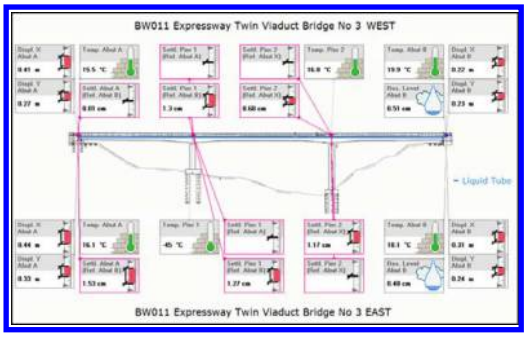

Figure 3. Web interface "cockpit" of the Hunter Expressway SHM system.

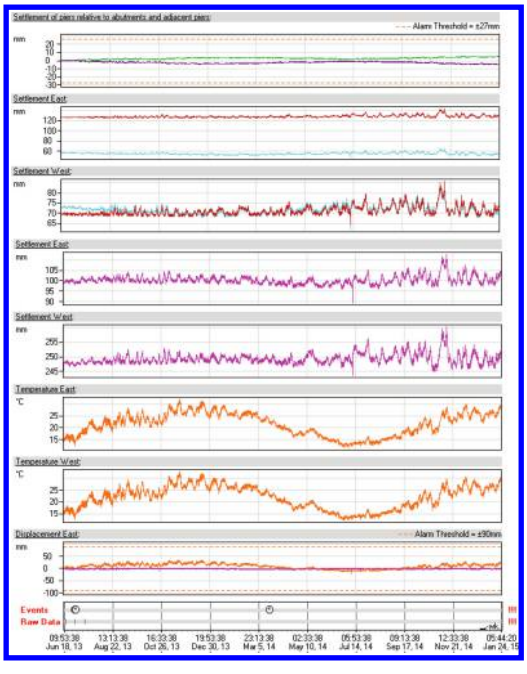

Figure 4. Data records for one and a half years' settlement measurements at one of the bridges.

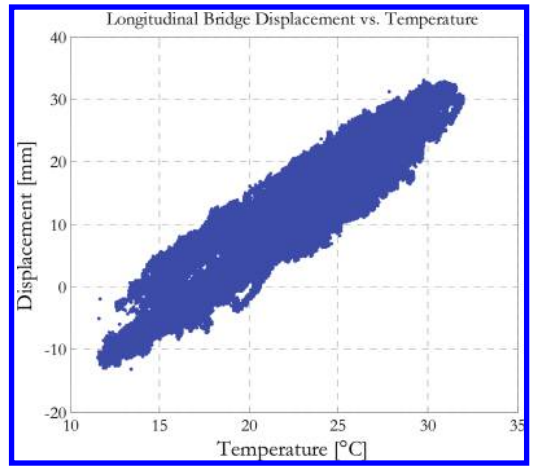

Figure 5. Relationship between longitudinal displacement and temperature at one abutment of one of the bridges.

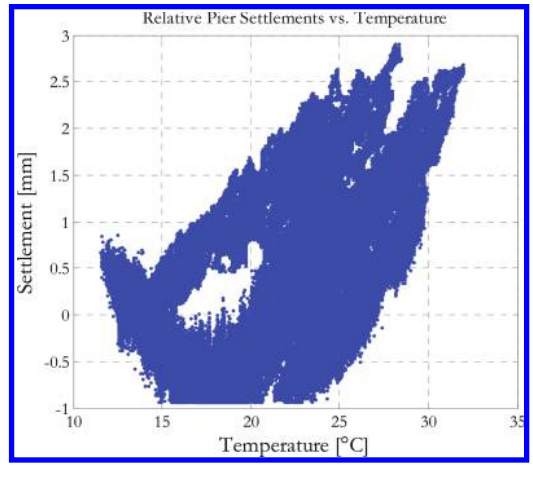

Figure 6. Relationship between settlement of piers and temperature at one abutment of one of the bridges.

system has been able to confirm that no significant settlement has occurred.

3 MONITORING FOLLOWING BRIDGE MODIFICATION WORKS—PONTE NANIN, SWITZERLAND

The twin arch bridges of Ponte Nanin (Figure 7) were constructed in 1967 to create an important new connection serving the San Bernardino Pass in the Swiss Alps. During refurbishment work some thirty years later, modifications were carried out to accommodate increased traffic demands. These changed the static system of the bridge, with several of the bridge's pillars newly monolithically connected to its deck, meaning that all movement now occurs at one end. Considerable impacts on the bridge's bearings and joints were expected. Some of the bearings, which were originally designed to allow sliding movement of the deck, were modified to now act as fixed bearings, resisting the forces that would have caused movements in the past.

In order to provide ongoing confirmation that the impacts of the changes to the bridge's

Figure 7. Ponte Nanin in the Swiss Alps.

Figure 8. Load monitoring at Ponte Nanin bearing.

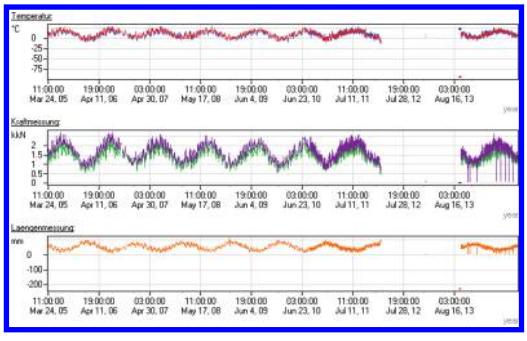

Figure 9. Ten years of measurements at Ponte Nanin.

structural system were as anticipated, and that the structure continues to function properly and safely, a monitoring regime was instigated. Benefiting from the most suitable modern technology available, a remote monitoring system was installed in 2005 to monitor the adapted load transfer through the structure and its bearings (Moor et. al., 2013). This would ensure that the performance of the structure is fully understood and that any changes in the structure, which could affect its performance or safety, are immediately recognized, allowing appropriate action to be taken.

It was decided during consultations with the bridge engineer that records of forces and movements within the structure at 15-minute intervals would in general provide an appropriate level of information. In order to fulfil these objectives, a low-frequency permanent Robo®Control system was determined to provide the optimal solution.

The system measures the loads carried by bearings (Fig. 8 and Fig. 9) at both abutments. It also monitors the movements experienced by the structure's expansion joints, by means of ultrasonic displacement sensors which continually determine the position of the last lamella beam of each joint. The monitoring system is also equipped with meteorological devices to measure air temperature and humidity and concrete temperature (Fig. 9).

The remoteness of the bridge's location had a significant impact on the selection and low-frequency design of the monitoring solution. The lack of fixed line telecommunications resulted in the need to transmit data from the bridge to the system's central server via the available mobile telephone network—limiting the amount of data which should be transmitted in order to avoid excessive transmission costs. And the absence of a local power supply necessitated the use of a solar panel to satisfy energy requirements—limiting the power that would be available to the system, and thus the amount of data that could be recorded and transmitted. The low frequency of measurements required and facilitated by the system's design limits the volume of data arising, making powering by solar panel and transmission of data both sufficient and economical. However, to accommodate special needs, the system is also designed to enable an authorized user, from the comfort of his/her office, to increase the frequency of measurements being recorded and transmitted for analysis.

The main concern following the refurbishment of the bridge related to the "flow of the forces" through the structure. By measuring the loads in the bearings and observing the force distribution in the bridge structure, this concern could be immediately allayed after initial measurements. Since the system's installation, ongoing measurements have been used to assess the thermal behavior of the structure and the effects of increasing traffic (Fig. 10, Fig. 11). And as an added benefit,

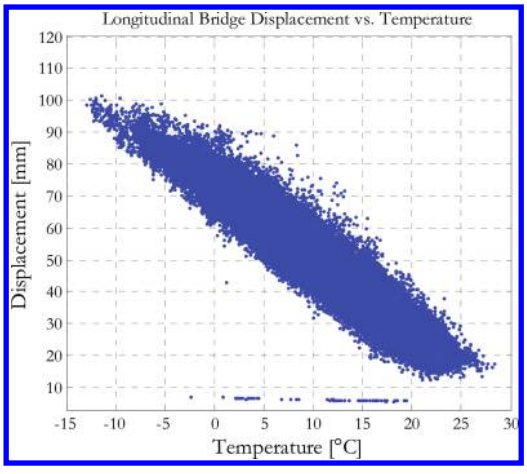

Figure 10. Relationship between displacement and temperature measurements at Ponte Nanin.

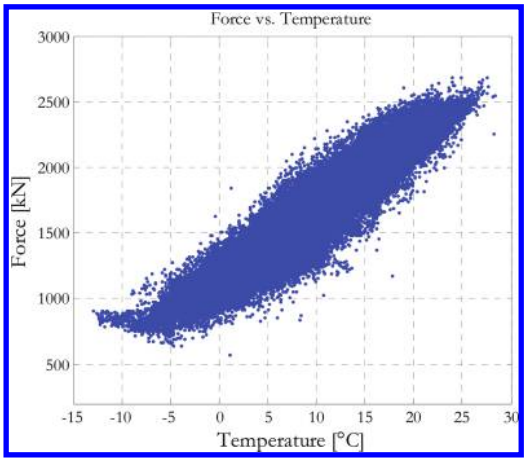

Figure 11. Relationship between force and temperature measurements at Pont Nanin.

the system also features an alarm capability which automatically sends notification, by email and SMS, when the pre-defined boundary value of any variable is exceeded. This allows the bridge owner to have confidence that any changes in the condition of the bridge will be immediately recognized, enabling action to be taken to ensure the safety of the bridge and its users.

The monitoring system, initially installed in March 2005, still provides confidence on an ongoing basis that the structure continues to function safely and well (after 10 years). It therefore confirms the design of the engineers who were faced with the challenge of adapting the static system of an existing structure. The system thus validates the approach which was deemed most suitable for economic reasons, but which necessitated such validation in order to minimize all residual risks, more thoroughly and efficiently than could be achieved by any manual inspection regime.

Figure 12. View of the continuous concrete box girder viaduct.

4 CONTROLLING THE CRACKS OF A CONCRETE BOX GIRDER VIADUCT

After some years in operation, this railway viaduct had revealed cracks on the upper plate of the its box girder. The single span concrete box girder has a total length of 35 meters, and supports two train tracks on top.

It was decided to install a monitoring system in order to follow the evolving of the problem and evaluate the influence of the overpassing rail traffic. The goal of the monitoring project is the measurement and monitoring of the crack movements and crack behavior under traffic and environmental loads, over a period of two years. The system measures different parameters on the structure at frequencies of 100 Hz and 200 Hz, using different measuring principles, and presents the data online. The system is designed to fulfil four major tasks, including monitoring of environmental influences (temperature, humidity), monitoring of strain behavior, monitoring of the structure's temperature and monitoring of the vibrations of the cantilever section of the girder.

Figure 12 shows the long box girder bridge while Figure 13 shows the sensor layout used to control the different structural parameters. A dense grid of sensors (Fig. 14 and Fig. 15) has been installed in order to accurately analyze the conditions of the bridge.

Figure 16 presents the entire two years of measurements: environmental temperature and

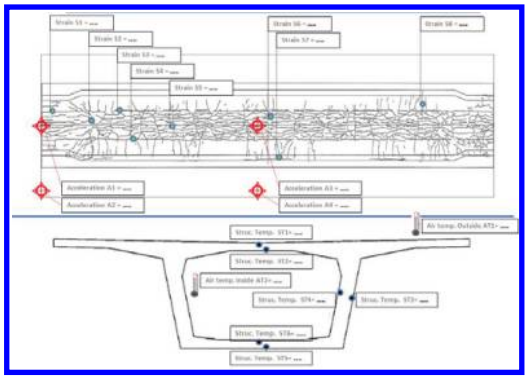

Figure 13. Layout of acceleration, strain and temperature sensors in one of the spans.

Figure 14. Structural temperature sensors installed inside the concrete structure.

humidity at several locations on the bridge, structural temperature inside the concrete, micro-displacements at several locations (few are shown for clarity) and accelerations in different parts of the bridge. In general, the opening/closing movements of cracks are in line with the environmental influences. It can be observed from Figure 16 that accelerations on the deck are also in line with temperature, except for one which decreases notably. During the two years there is no sign of deterioration, with no significant opening of the cracks.

It is also interesting to observe the opening of cracks due to actual loads on the bridge. Figure 17 shows this during the passage of a high-speed train. As expected, there is an evident influence on the displacement sensor but the scale of movements make them quite negligible.

Further data analysis has also been performed. Figure 18 shows the Root Mean Square (RMS) of continuous high frequency (100 Hz) acceleration measurements during a period of five days. This is

Figure 15. Crack displacement sensor installed on the upper deck of the concrete box girder.

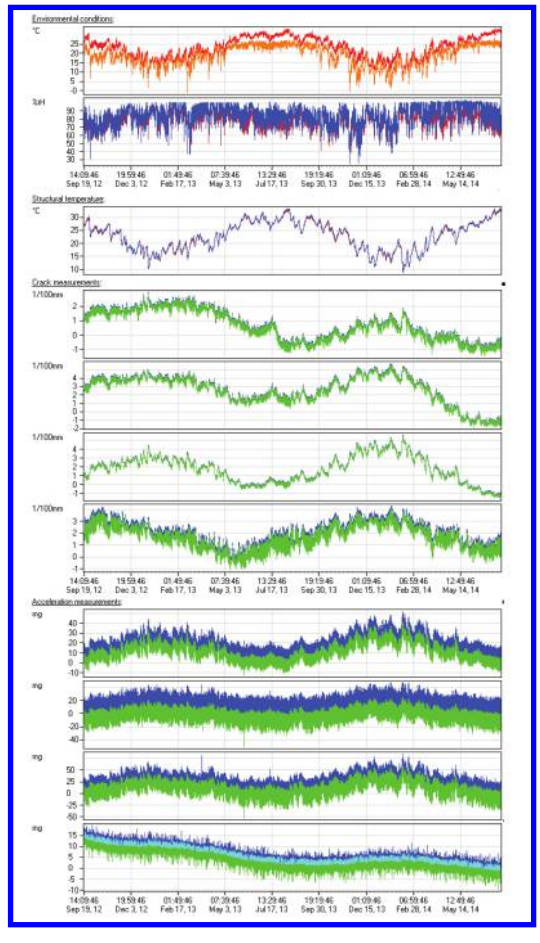

Figure 16. Measurements from two years of monitoring.

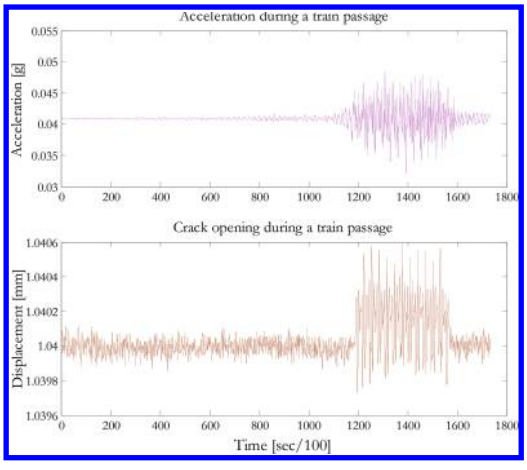

Figure 17. Train passage effects, in close view, on the accelerations and on the crack openings of the bridge.

a statistical measure of the magnitude of a varying quantity, especially useful when variants are positive and negative (Islami & Modena, 2013). The plot shows how the intensity of accelerations varies not only in accordance with the day/night intensity of trains over the bridge but also in accordance with the day/night temperature change. During the daytime, trains travel more frequently and the RMS has a high value (peak at around 10 am), while at nighttime, the frequency is quite low. On the other hand, the vibrations are higher when the bridge is elongating due to temperature, and lower during the night. This method of data analysis can also be used to the actual traffic on the viaduct using accelerometers.

Figure 18 shows the opening and closing of the crack during several days of continuous measurements. Generally this phenomena depends on temperature, but numerous maximum displacement values are also found to appear during the passage of a train.

The main purpose of the system was achieved by providing the responsible structural engineers with valuable data of vibrations and crack opening for a period of two years. The correlation of such parameters with train types and temperature could be used to determine the current state of the structure and to plan future structural refurbishment works.

5 CONCLUSIONS

SHM systems offer many benefits over traditional manual observation and measurement methods. They are typically much more efficient, having

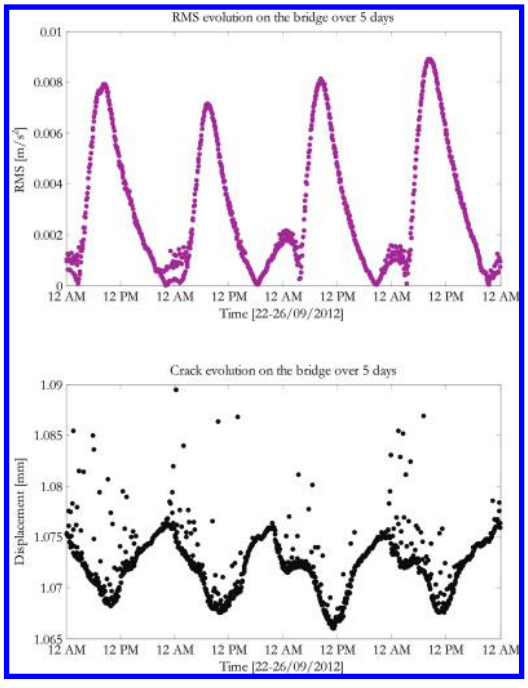

Figure 18. Continuous 100 Hz measurements during several days: RMS and crack opening.

far lower "running costs", and are capable of an extraordinary level of detail and accuracy, e.g. in measuring high-frequency vibrations that would scarcely be registered by human touch. They can also be set up to operate 24 hours a day, 7 days a week, for as long as required, and can thus be relied on to immediately record and report unexpected/serious events, no matter when they might occur. Whether used during installation, inspection, maintenance or replacement works, or to facilitate assessment of unexpected events or planned modifications, automated monitoring systems are thus sure to be increasingly used on bridges in years to come.

REFERENCES

Islami K. & Modena C., 2013, Life-cycle assessment by dynamic diagnosis and long term monitoring of old bridges in northeastern Italy, *ISHMII, Hong Kong.*

Moor G., Meng N. & O'Suilleabhain C., 2013, Remote structural health monitoring systems for bridge expansion joints and bearings, SMAR 2013, Istanbul.

Islami K. et al., 2014, Life-cycle monitoring and maintenance of bridges: The role of remote SHM systems, Istanbul Bridge Conference, Istanbul.

Concrete Repair, Rehabilitation and Retrofitting IV – Dehn et al. (Eds)
© 2016 Taylor & Francis Group, London, ISBN 978-1-138-02843-2

The Tannery bridge: A case study in structural health monitoring and rehabilitation of structures

L. Tassinari & Jérôme Sordet
Kung et associés, Payerne, Switzerland

M. Viviani
HEIG-VD HES-SO, Yverdon-Les-Bains, Switzerland

ABSTRACT: Evaluating the structural health of a bridge is a complex activity. Small and medium bridges constructed in urban areas often undergo too many changes during their service life. Partial reconstruction, increased traffic loads, a new structural schema are some of the changes occurred in the Tannery bridge (Switzerland) over time. These changes were only partially documented. Therefore it was necessary to understand the structure and its behavior prior to assessing its load carrying capacity and the pathologies, before proposing a refurbishment strategy. Furthermore, some important elements were documented but not constructed as stated in the plans. No transition slabs were ever planned and the ramps constructed to access the bridge were rapidly deforming due to the low quality of the soil. Although the concrete deck is not in critical conditions, some degradation is visible and rapidly progressing. The curbs and barrier types obliged the engineers to plan the demolition and to change these important details. This article presents the analyses and the design process for the rehabilitation of the Tannery Bridge, an urban bridge that, in about 5 decades, was completely changed and resisted to unexpected loads such a number of heavy military tanks. Furthermore it will be shown how, sometimes, minor problems may become the real challenge, at least from the financial point of view.

1 INTRODUCTION

1.1 *The Tannery bridge in La Sarraz*

The "Tannery bridge" is a key structure of the fast growing town of La Sarraz (about 42% population growth between 2006 and 2011). An ancient truss steel arch bridge built in 1887 (see figure 1) was deeply modified in the 1976.

The 1976 bridge is a mixed structure with two simply supported steel beams, spanning 51.3 m. The concrete deck is 9.5 m wide (see figure 2).

Some of the old features of the arc bridge remain visible: the abutments in stone masonry and the traces of the arch hinges. The tannery, located under the bridge, is today an industrial laundry service facility. Two major events have brought this bridge to the attention of the authorities and of the engineers: the new Swiss code for roads, that today allows the transit of vehicles weighting up to 40 tons (previous limit was 28 tons) and the ownership of the bridge that passed from the state (canton) to the city of La Sarraz. In 2010, the need of reinforcement was evaluated: after calculations, the engineers stated that no adaptation was necessary and the bridge can stand the new loads as it is.

2 PROJET DESCRIPTION AND DETAILS

2.1 *Introduction*

As all inspections on an existing structure, the first step is having a preliminary inspection of the structure to collect as much information as possible. Information was collected first in the form of the original 1976 executions plans, the 2010 calculation of the bearing capacity of the bridge and finally as a number of interviews with people living in the town. The first fact collected was that in recent years a number of army tanks (probably weighting each more than 40 tons) transited the bridge, severely damaging the joints (chains were covered by rubber bands and yet damage occurred). The second fact was that the final part of one of the ramps leading to the bridge was supposed to be a kind of a transition slab (see figure 3), simply supported on concrete columns (referred as "candles") casted inside regularly spaced niches cut into the stone masonry. On the top of the concrete candles, a so-called "kilcher" bearing had to permit a certain rotation degree.

A number of manhole covers suggested the presence of a number of ducts passing under the

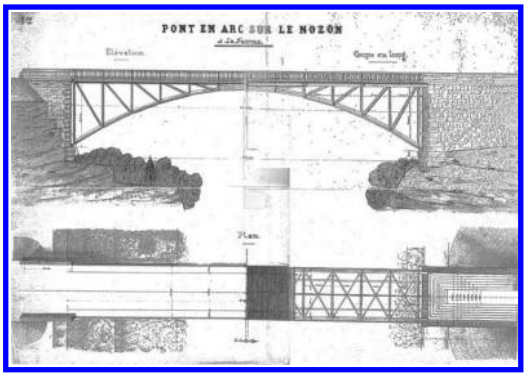

Figure 1. The Tannery bridge in 1887.

Figure 2. The Tannery bridge today.

transition slab. The bearings were regular inspected but just using a binocular. There were no hints of problems on the steel beams. As a matter of fact, the engineer that designed the bridge in its actual form and that directed and inspected the construction process declared that:

1. There are no candles supporting the slab, the abutment was filled with ground and concrete slab was just poured on the top of it.
2. There were indeed a water pipe of the city inside the ground and, according to his knowledge it was unprotected.
3. One of the manhole was abandoned and inside there were nothing.
4. The ground of the ramps was not changed in 1976.

Acquired this knowledge, a plan for a detailed visual inspection was set and executed.

2.2 *Visual inspection and needs for repair/ maintenance*

The visual inspection highlighted immediately that the bridge does not present any pressing safety

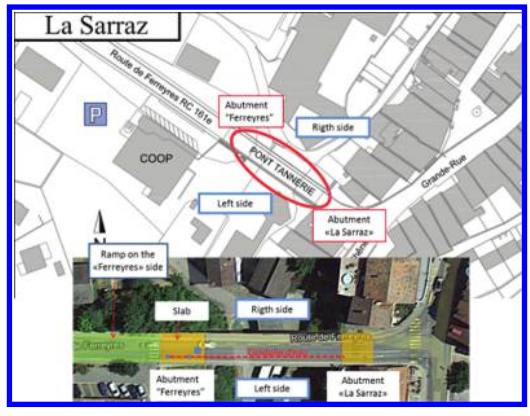

Figure 3. Features of the Tannery bridge.

Figure 4. Right side bearing of the "la Sarraz" abutment.

issue. Beams and other structural elements had some problems on the paint in zones were welding in field occurred. Bearings were inspected and the rubber tested by specialists. They did not present any serious degradation. Retainers of the fix bearing are in need of a general control, cleaning and painting and the concrete of the abutment needs some repair work (see figure 4).

While bearings were in good conditions, the joints were not. "RUB" type joints, installed in a position nearly impossible to thoroughly inspect, were not watertight any longer so that water and

Figure 5. “Ferreyres” joint, right side.

Figure 6. “La Sarraz” joint.

Figure 7. Masonry of the” Ferreyres” abutment.

Figure 8. ”Ferreyres” joint, left side, displacement.

deicing salts could severely damage the surrounding concrete. The “Ferryeres” joint was visible on the sides: whereas severely damaged, the engineers’ main concern remained the severe degradation of the concrete due to deicing salts and freeze-and thaw (see figure 5). Lack of water tightness of the joint is a problem, aggravated by some Styrofoam panels let in place when the joints were installed.

Only the top of the “La Sarraz” joint was visible: the damage produced by the chain links of the army tanks was severe because “extracted” a thick steel plate, one of the main elements of the joints. Furthermore, the water pooled on top of the joint suggesting a damage of the surrounding concrete similar to the one observed in the “La Sarraz” joint. Replacement of the joint and refurbishment of the surrounding reinforced concrete was suggested (see figure 6).

The abutments are original from the 1887 and they are “untouched” except for regular maintenance. In 1976 the ensemble of the stone masonry was inspected and refurbished. The masonry did not present any alarming problem but in many places the mortar of the joint was degraded by the combined action of the freeze and thaw and environmental actions. Some large stone blocks are today supported by spacers used while placing or replacing the joint mortar (see figure 7). Although there is not any risk of rotation of the masonry, it is necessary to replace the joint mortar and correct the position of certain blocks. The Tannery bridge is an urban infrastructure with residential and commercial activities close by and under it. A masonry element falling would possibly arrive to the roof of the industrial laundry facility.

Whereas all these degradations were not alarming the engineers, others did; certainly not for safety reasons but because of the cost to mend them. The first problem was related to the “Ferreyres” ramp and slab. Fig 8 explains that a severe deformation occurred at the interface between the ramp and the slab.

The same phenomenon was observed on the right side of the bridge (see figure 9) were it could be observed also a slight damage to some equipment attached to the deck.

This discovery lead to a further inspection on the type of soil by coring and the engineers agreed that the most appropriate solution will be the construction of a transition slab. This increased the budget necessary for refurbishment of some hundredth thousandth CHF.

The second problem concerned a water pipe passing under the slab « Ferreyres » side and fastened

Figure 9. "Ferreyres" joint, right side, displacement.

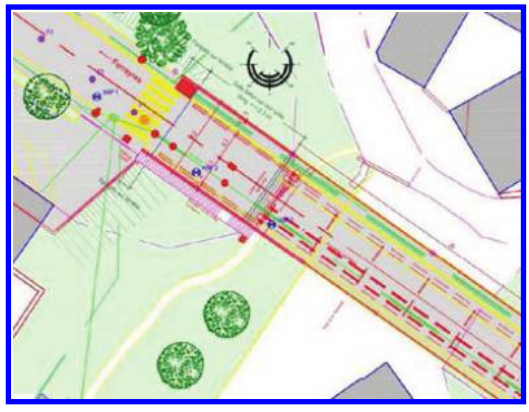

Figure 11. Position of the cores.

Figure 10. Water pipe behind the bearings "Ferreyres" abutment.

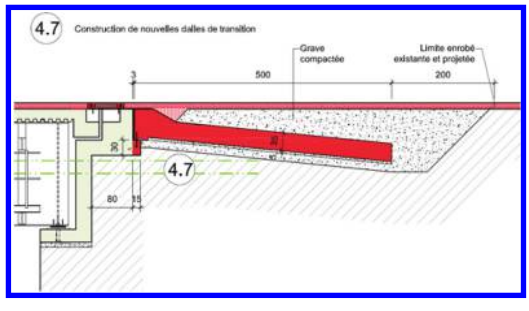

Figure 12. The new transition slab.

under the bridge deck. As it was discovered that this pipe belonged to the city water system, it became clear that only a few meters were encased in a plastic pipe, while most of the pipe was in contact with a mixture of soil and rock (see figure 10).

Although nothing so far happened, the concern of the engineers was that a rock might damage the pipe and the leaking water might fill the ground inside the abutment with catastrophic effect on the masonry walls. It was agreed that the pipe had to be protected for all its length under the abutment and made accessible for inspection.

2.3 *The refurbishment project*

Refurbishment projects have to abide to different codes, to the field conditions and meet a certain number of objectives. In Switzerland the norms and technical documents of the SIA and the directives of the OFROU (Federal highway office) are used. The objectives are to ensure safety and serviceability and to guarantee a suitable durability (extension of the service life).

As soon as the services of a design firm were retained, the project begun. The documentation was thorough and yet some details were not clear. One of the main point of the project was the verification of the bridge safety and serviceability: a review of the old projects highlighted some discrepancies on the thickness of the web of the steel beams. Although the bridge had undergone to severe loads, it is of capital importance that all details match. These details will be clarified when the work on the slab of the Ferreyres abutment will begin. If the real thickness will be even lower that the minimum found on the projects, this would lead to a new verification of the bearing capacity of the beams under the load cases provided by the norms, SIA (2003–2013).

In view of the problems highlighted by the visual inspection on the Ferreyres ramp, a series of soil samples were cored (see figure 11).

The result clearly indicated that the substrate is very compressible and not of the best quality. No viable alternatives to an approach (transition) slab were found. The transition slab has been conceived

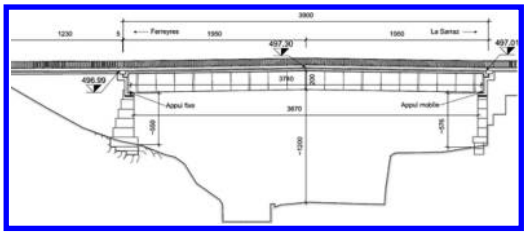

Figure 13. A side view of the bridge.

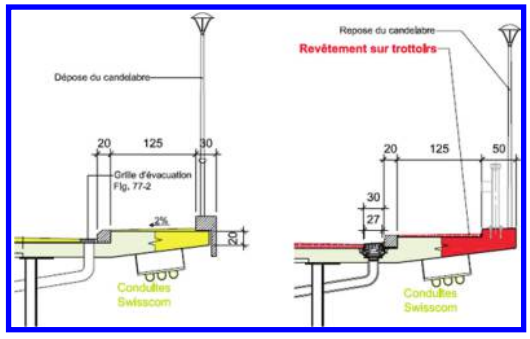

Figure 14. The new fascia.

according to the standards of the OFROU, see figure 12, ASTRA (2006), that has been satisfactorily used in many bridges.

The RUB joints are not any longer in the market so a replacement will not be possible. Furthermore, the new "gap" joints meet high standards of performances and they have reduced noise (an interesting characteristic in an urban areas). The actual bridge was originally cambered by welding to straight half beams and therefore did not offer a good comfort to users (see figure 13).

In order to mend this problem the asphalt will be replaced with a modern material that will also permit to change the actual pitched shape with a curved one.

One of the main challenges in this project was to find a suitable technique to replace the fascia. Tannery bridge deck is equipped of prefabricated fascia that bears a safety fence (see figure 11). Fascia water tightness was long lost and the water dripped on the deck, damaging the concrete and promoting the corrosion of rebars. Furthermore, the fence was simply embedded in concrete without protection and therefore rusting damaged also the fascia. A solution is indicated in figure 14.

The prefabricated fascia will be substituted by a monolithic element casted on place once refurbishment of the concrete deck will be completed.

2.4 *Field organization.*

Repair of a bridge such as the Tannery bridge requires an attentive planning. Days of complete closure of the bridge must be minimized and it must be guaranteed that pedestrians can cross the bridge in order to shop in the large grocery store and to access the bank situated close to the Ferryres abutment. Vehicle traffic will be deviated in a tiny road that passes inside the valley (see figure 3).

3 CONCLUSIONS

The Tannery Bridge is rich of story and had accompanied the growth of La Sarraz for more than a century. The actual bridge is 50 years old and given the rapid change of the surrounding world is in good (structural) health. However, the degradation phenomena are accelerating and many equipment are in critical conditions. A careful visual inspection and a refurbishment project were undertaken. The conclusion of both studies is that today the refurbishment cost will be relevant, approaching one million CHF. The decision to undertake this refurbishment has been taken because the costs would be much higher in the medium term, if the degradation mechanisms are not stopped and the damages are not repaired.

REFERENCES

SIA 260. 2003. Loading conditions for structures.
SIA 261. 2003. Actions on structures.
SIA 262. 2012. Concrete structures.
SIA 269. 2013. Maintenance of structures.
SIA 269/2 2013. Maintenance of concrete structures.
ASTRA 2006 Guideline 12002. Monitoring and maintain ace of highways infrastructures.

Concrete Repair, Rehabilitation and Retrofitting IV – Dehn et al. (Eds)
© 2016 Taylor & Francis Group, London, ISBN 978-1-138-02843-2

Evaluation of concrete structures durability under risk of carbonation and chloride corrosion

L. Czarnecki
Building Research Institute, Warsaw, Poland

P. Woyciechowski
Warsaw University of Technology, Warsaw, Poland

ABSTRACT: Authors The mechanism of reinforced concrete structures degradation under the risk of carbonation and chloride corrosion and its relation to the life cycle of the structure are shown. The models of carbonation progress and chloride migration in concrete are analyzed. Preferences of hyperbolic model of carbonation and the special role of its asymptote as the limit defining the depth of carbonation have been shown. Conditions for the initiation of corrosion in concrete elements with particular attention to the critical chloride concentration are defined. Various methods of determining the distribution profile of chlorides in concrete with particular emphasis on the diffusion coefficient of chloride are discussed. Four possible procedures of determining apparent diffusion coefficient are shown. The first is a computational method based on theoretical equation of chloride distribution in concrete space between surface and maximal depth of measurements. The second one is based on the determination of chloride distribution model using "best fitting curve" method. The third one is estimative—graphical way of determining of diffusion coefficient and the fourth is the calculation of the expression erfc(b) from the equation of diffusion, on the basis of experimentally measured values of chloride concentration, and then, by using the tabularized values of erfc—determining the value of its argument (in parenthesis) and finally the value D0. Examples of using this procedures and threat of possible errors and mistakes are shown also. On this basis an algorithm for predicting the durability of concrete structures under conditions of potential corrosion has been elaborated. The examples of the use of this algorithm are shown.

1 INTRODUCTION

Structure durability is considered by Eurocode 0 [1] as one of the three basic assumptions in the process of design and substantially affects the adopted design and material solutions. According to the findings [1] "The structure shall be designed and installed in such a way that in the intended period of use (...) all the forces and influences expected during the implementation and use can be taken, and it remains useful to the intended use. The structure should be designed in such a way that the load-bearing capacity, serviceability and durability was appropriate. (...) The structure must be designed in such a way that the changes which occurs, during service life, taking into account the influence of the environment and the expected level of maintenance, don't decrease the performance of the structure below the required level". In order to meet these requirements, in the Programme Structural Eurocode (including Eurocode 2 – Construction of concrete) as the basis for the design according to the EC 0 [1], the concept of the limit states (including: capacity that relate to "human security and/or safety construction" and serviceability, which relate to "function of the structure or structural component under normal use, user comfort") was adopted. According to Eurocode 2 [2], "Durable construction should meet throughout the period of use the requirements on serviceability, load capacity and stability, without significant reduction of the usefulness or excessive, unforeseen costs". Therefore, durability will be maintained, if the structure meets in service life the defined functions in terms of serviceability (limit states associated with reducing stress, cracks and deflections), load capacity and stability (capacity limit states – EQU, STR, GEO and FAT). Proper design of construction meet the service requirements at least for the expected service life. In fact however, the durability of the existing structure is affected by a level of uncertainty resulting on defects in design from one side, and execution and material on the other—with limited predictability of impacts related to the conditions of use. Predicting remaining useful life—the residual time of

use (Figure 1) is often taken in the framework of technical expertise as part of the assessment of comfort of use, serviceability requirements and, consequently, also as part of the cost analysis or an element of repairs design.

In the case of the construction of reinforced concrete, one of the main threats to the durability is the corrosion of reinforcement. In practice, the corrosion of rebars is a major—beside the frost corrosion—the cause of the destruction of concrete structures [3,4] in the case of structures elements exposed at atmospheric conditions. Steel reinforcement in the concrete environment is protected against corrosion with concrete cover till the moment of the protection ability loose. This stage of degradation of the structure, called the stage of initiation (Fig. 1), usually takes many years and can be treated as life of the structure. Time of initiation of reinforcement corrosion can be identified with the depletion of serviceability limit state, but it does not mean the depletion of load-bearing capacity. Then, the steel corrosion proceeds at a certain rate, leading to disruption of the cover and exposure of the rods surface, and as a result the fast reduction of cross section of the reinforcement, up to the loss of load-bearing capacity of the structure. Corrosion of reinforcement in concrete can be caused by various factors, but the most common causes are the carbonation of concrete (dealcalisation of cover) and the impact of chloride ions migrating through the concrete cover to the reinforcement. Both effects lead to the destruction of the passive film on the steel surface; it initiates corrosion. Most reinforced concrete structures with not protected surface are exposed to the impact of environments classified in groups of exposure classes XC (carbonation) and XD or XS (chlorides). Most concrete structures are charged under different exposure classes simultaneously, which according to EN 206-1 requires consideration of the necessity of increasing the level of material protection by one level in relation to the most stringent requirements under the different exposure classes.

This paper presents a proposal for the use of carbonation process model (own model [5,6,7,8,9,10])

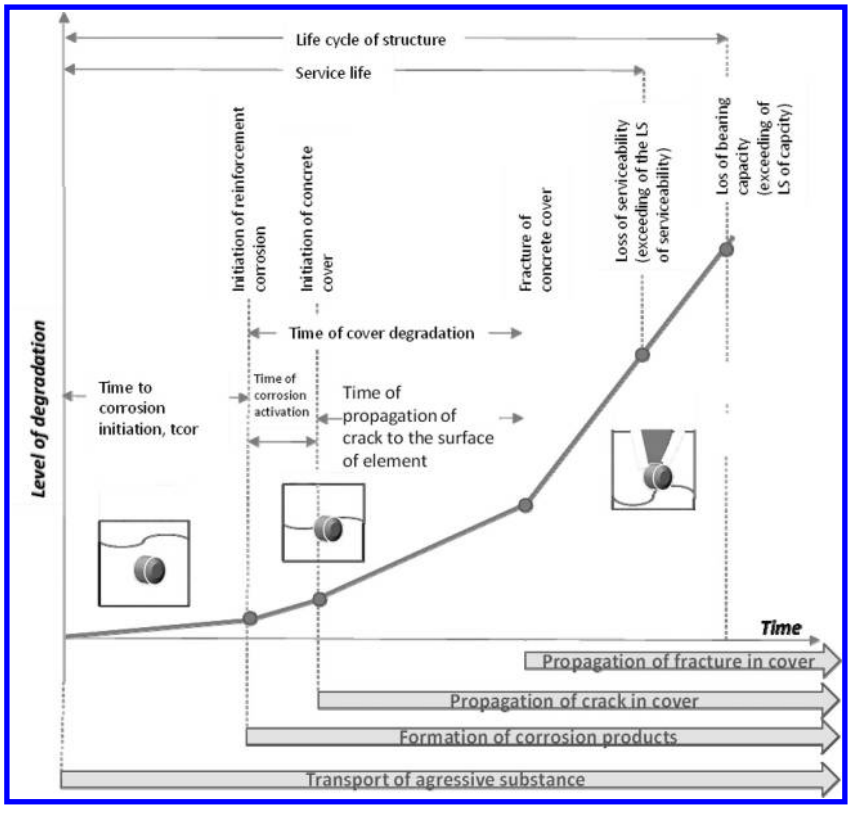

Figure 1. Degradation level of reinforced element as an effect of reinforcement corrosion (on the basis of [3,4,45]).

and the model of migration of chlorides in concrete coating to evaluate the durability of reinforced concrete elements.

2 CARBONATION AND CHLORIDE AGGRESSION AS THE FACTORS AFFECTING CONCRETE ELEMENTS DURABILITY

2.1 *Concrete carbonation—the effect on reinforced concrete, factors controlling the course, models of progress in time, idea of self-terminating nature of carbonation repairing the new file with the correct template*

Concrete carbonation can be defined as complex physicochemical changes in concrete under long-term influence of carbon dioxide. Carbon dioxide is permanently present in atmospheric air, outside and inside of buildings. Volumetric content of CO_2 in the air is ca. 0.03%, but in industrial zones and along main roads it could be up to 0.3%, or locally more, so that carbonation can progress continuously, especially in concrete with no surface protection [2,3]. This primarily concerns the elements of engineering structures such as bridges, viaducts, tunnels, road pavements, car parks etc.

Main chemical mechanism of carbonation is reaction of atmospheric CO_2 with calcium hydroxide from cement hydration with release of calcium carbonate and water:

$$Ca(OH)_2 + CO_2 \rightarrow CaCO_3 + H_2O$$

Others concrete compounds, such as lime from hydrated aluminosilicates, can be partially carbonated, but this process is possible only in a high CO_2 concentration and its influence on concrete is limited. Basic carbonation product—calcium carbonate—crystallizes in concrete pores. Small quantities of silica, alumina and ferrous oxide are also produced as products of CSH carbonation. The rate of carbonation—progress in time depends on external conditions as well as on concrete properties and processes of structure execution. Main negative effect of carbonation is decreasing of concrete pH, which is one of most frequent cause of reinforcement corrosion and ferrocement destruction. Carbonation can be considered as one of the most important factors causing concrete structures destruction [3,4].

The rate of carbonation is determined by different internal and external factors. Between external factors very important are: CO_2 concentration, humidity and air temperature. Internal factors are related to concrete composition, type and content of binder and water-cement ratio, which determine tightness of concrete microstructure. Also an early curing of concrete plays important role. Generally rate of carbonation:

- increases proportionally to square root from CO_2 concentration in the air,
- increases with increase of relative humidity up to 70–80%, but if pores are fully water saturated, speed of carbonation decreases,
- increases with cyclic changes of temperature and pressure,
- increases with increase of water-cement ratio,
- decreases with tightening of concrete structure,
- decreases with increase of cement content in concrete.

Prognosis of changes of depth of carbonation in time is possible with use of mathematical models of carbonation progress in time. Such models were presented by many authors—Wieczorek [5], Slopkova [6], Papadakis [7], Ishida/Maekawa/Soltani [8] and others. Foundation of their models was Fick`s low, which describes speed of diffusion. Final result of carbonation modeling is power function of time with exponent ½.

$$h = A\,(t)^{1/2} + B \tag{1}$$

where h – depth of carbonation, t – time of exposition, A, B – coefficients which depends on internal and external factors.

Different researchers show in their works different forms of such a model, with use of supplementary variables, such as w/c, time of early curing, binder characteristics and others. Presumption that carbonation process is a power function of time of exposition, is equivalent to find a process as unlimited in time, and it is unlimited in depth of concrete. Fick`s law refers to gas diffusion through substance immutable in time and for such a case formula (1) would be justified. But concrete is a material in which deep physicochemical changes occur in time, due to carbonation process. Changes of pores structure, overgrowth of carbonation products in pores, lead to changes of CO_2 diffusive ability in time, which can bring a decreasing of carbonation process intensity, down to stabilize a constant depth of carbonation. This nature of phenomenon was mentioned by Fagerlund [9], Fiertak [12].

Scientific research were conducted within many years in the Department of Building Materials Engineering on Warsaw University of Technology under the guidance of L.Czarnecki and were published in [6,9,10,19], being a basis of Więcławski`s PhD Thesis [10,11,12,13] and monographic publication of Woyciechowski [7].

Those works conclude that concrete carbonation in urban-industrial conditions can be described with hyperbolic function of time (reciprocal square root of time), which have asymptotic value parallel to time axis. This asymptote is a limit of carbonation depth. Traditional and hyperbolic models of carbonation are showed on fig 2. Hyperbolic carbonation model has a following form:

$$h = a(w/c) + b(cp) + c(t^{-0,5}) \quad (2)$$

where: h – depth of carbonation, mm, w/c – water-cement ratio, cp – early curing time, days, t – time of exposition, years, a,b,c – coefficients which describes relevance of influence of w/c, early curing and exposition time on depth of carbonation. It was stated that parameters (a,b,c) mainly depend on binder properties, presence of mineral additives and, especially, on CO_2 concentration. Similar models were elaborated for different types of concrete, particularly with use of Portland cement and cement incorporating slag and fly ash. SEM analysis shows different density of concrete structure in carbonated and non-carbonated zone. It was stated that all results are in accordance with hyperbolic model $h = f(1/t^{0,5})$, regardless of binder composition, but various function characteristic coefficients were obtained for various cements. Determination of carbonation hyperbolic model allows to specify a maximum depth of carbonation and compare it with the thickness of reinforcement cover in the analyzed element.

This allows to assume if there is a risk of corrosion due to the carbonation and to estimate the time when the carbonation front will reach the reinforcement, which can be considered as a time of corrosion initiation (fig. 1).

2.2 *Chloride aggression—effect on reinforced concrete, source of chloride, factors regulating migration, model of chloride diffusion in concrete*

Chloride ions Cl^- are highly aggressive to steel reinforcement. Chloride concentration growth on steel surface up to critical value leads to corrosion cell formation and rapid change of steel potential. This is associated with passive layer damage by Cl^- ions. Chloride critical concentration level depends on hydroxyl ions content in concrete, which is related to cement type, additives and progress of carbonation, resulting in the OH^- ions content decreasing. Usually, it is assumed that steel depassivation in concrete takes place when Cl^- ions content to OH^- ions content ratio exceeds 0.6 [13].

Chloride corrosion of reinforcement is pitting type and leads to cross-section reduction with

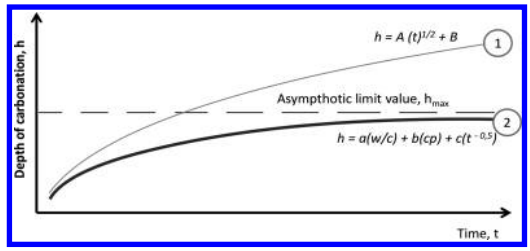

Figure 2. Power (1) and hyperbolic (2) models of carbonation.

simultaneous deposition of corrosion products in anodic zone. The corrosion products have a larger volume then initial bar volume, so the mechanical destruction of concrete cover takes place. The critical presence of chlorides in concrete components is limited by the requirements of the standards for the aggregates, cement type, admixtures and additives. The impact of chloride from the external environment is typical for marine structures, but also for objects exposed to chemicals winter maintenance of roads, i.e., the elements of bridges, tunnels, viaducts, trestle bridges, paving roads and parking lots. Contamination of the gaseous chlorides or solutions, is also found in many industrial buildings.

To predict the progress of chloride corrosion, model of Cl^- ions migration in concrete is needed. Diffusion of chlorides in concrete is the complex process and changes over time. Partially ions can be bound by concrete components (e.g. Friedel salt formation) but release of ions bounded in concrete components is also possible [14]. Necessary condition for chloride diffusion is moisture in capillary pores, wherein the higher is the degree of pores saturation with water—the faster is the diffusion. In air-dry pores chloride migration ceases. In the literature [2,3,14,15,16] a model of chloride diffusion is given.

The penetration of chloride ions into the concrete by diffusion is generally described by the equation of chloride concentration distribution (C) derived from the Fick's law (Fig. 3) as

$$C(x_i,t_i) = C_i + (C_0 - C_i)\,\mathrm{erfc}\left(\frac{0.5x_i}{\sqrt{t_i D_0}}\right) \quad (3)$$

where:

- C_i – initial chloride concentration in concrete ($t = 0$, in points $x > 0$),
- C_0 – chloride concentration on concrete surface (at point $x = 0$),%
- $C(x_i\ t_i)$ – chloride concentration at a distance x_i from surface after migration time t_i, %

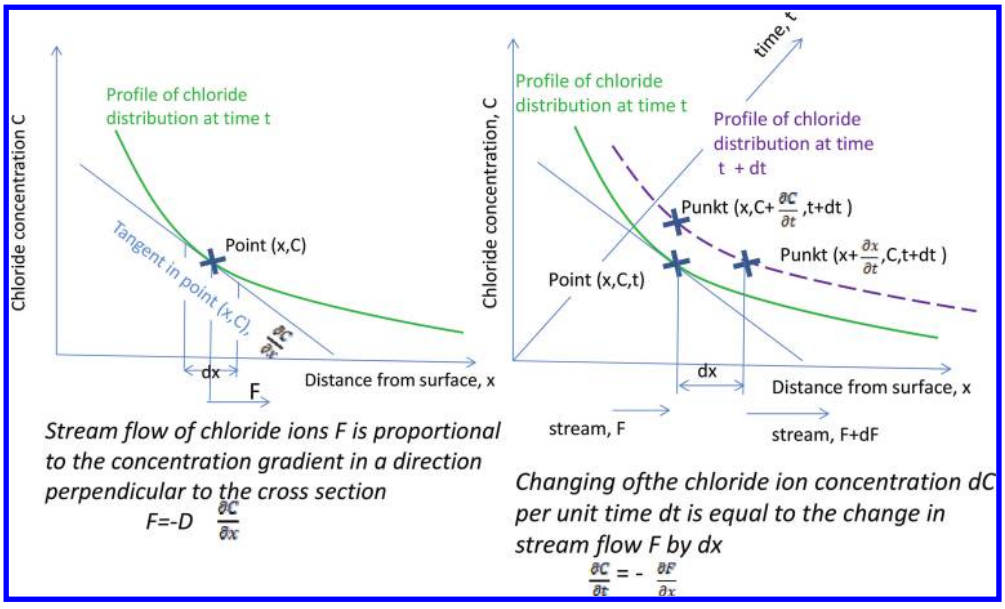

Figure 3. Graphical interpretation of the first (A) and second (B) equation of Fick's Laws, underlying the distribution of concentrations of chloride ions in concrete (inspired after [25]).

– D_0 – diffusion coefficient, cm^2/s
– t – migration time, *s*

This model allows to determine the apparent diffusion coefficient for the concrete in construction on the basis of chloride penetration test and determines the time when the critical concentration would reach the depth of reinforcement [17].

Equation (3) is based on a number of simplifying assumptions:

– $t_i = 0$ - means the time of first contact of the concrete surface with chloride ions;
– Concrete is the quasi-homogeneous, semi-infinite medium;
– $D_0 = \text{const}$, in stabile material and environmental conditions;
– $C_0 = \text{const}$, in the time from $t = 0$ to $t = t_i$;
– $C_i = \text{const}$, in the concrete area from $x = 0$ to $x = x_i$.

This simplification defines an area of the uncertainty of estimation of chloride ions diffusion into the concrete by means of equation (3). Nevertheless, it is a good tool for engineering assessment of chloride corrosion risk for reinforcement concrete structures.

General scheme of the procedure of forecasting is as follows:

1. experimental determination of the profile of chlorides distribution in concrete;
2. the appointment with mathematical methods based on the resulting profile—the value of apparent diffusion coefficient D_0;

3a. determination of chloride concentration in the reinforcement zone according to equation (3) adequate to the time of service life (durability), or alternatively

3b. determination—from the transformed equation (3) – the time when the critical concentration will be achieved in reinforcement zone.

The chloride distribution profile as a function of distance from the exposed surface can be determined by various methods, including: the taking of thin layers of concrete (concrete dust) from different distances from the surface and then measuring the chloride content in the samples (the chloride content—that is soluble in water or the total content—that is soluble in acid).

There are also colorimetric method based on applying a silver nitrate solution, which reacting with free chloride ions forms silver chloride. Due to the fact that $AgNO_3$ changes color under UV radiation it is possible to determine the zone contaminated with chlorides [22,26,27].

Investigation of chloride ion concentration distribution in the concrete may also be conducted using a variety of electrochemical methods described inter alia in [21,27,28,29,30]. The tests may be carried out in relation to the concrete samples treated with the chlorides in the laboratory, in

which idealized course of diffusion is obtained, taking into account only the material factors (including the presence of cations in the concrete, which slow down the rate of diffusion of chloride anions) and external concentration of Cl-ions [23]. In case of testing by extraction, carried out on the samples collected from the structure, distribution profile of chloride ions obtained from investigation is more representative because it takes into account all other disruption of diffusion which occurs during the lifetime of the analyzed element. First of all the effect of stress state in the course of diffusion is integrated in profile of chloride diffusion[44].

Chloride concentration measured at different depths can be the basis of determination of distribution profile of concentration Cx in the space between 0 (surface of element) and x (maximum depth of measurement). The general model form assuming as a result of the equation (3) is as follow:

$$C = C_i + (C_0 - C_i)\operatorname{erfc}\left(\frac{0.5x}{\sqrt{tD_0}}\right) \tag{4}$$

Determination of the apparent diffusion coefficient is possible in several procedures.

The first is a computational method, and involves the use of the equation (4). This function has a horizontal asymptote (equation $C = C_i$). It could be noted that at the point of the ordinate $(0, C_0)$ tangent to the function (4) can be expressed by the equation $\frac{\partial C_x}{\partial x} = -\frac{C_0 - C_i}{\sqrt{\pi t D_0}}$, and intersecting the horizontal asymptote of the function (4) at the point with abscissa $a = \sqrt{\pi t D_0}$. So the equation of the tangent to the curve of the profile at the point $(0, C_0)$ can be determined, then the value a, and then—knowing the exposure time t, one can calculate the value of the diffusion coefficient D_0 as:

$$D_0 = \frac{a^2}{\pi t} \tag{5}$$

The difficulty of such a procedure is related to the lack of formulas of the error function erf or complementary error function erfc in libraries of standard statistical programs. However, taking into consideration that the function erfc (x) is defined as:

$$erfc(z) = \frac{2}{\sqrt{\pi}}\int e^{-z^2}\mathrm{d}z \tag{5a}$$

the formula (4) can be simplified to the formula (6)

$$C = C_t + (C_0 - C_t)e^{bx}, \tag{6}$$

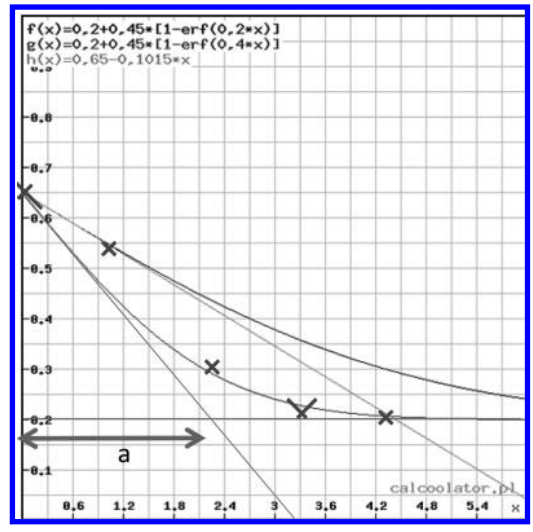

Figure 4. An example of the determination of the diffusion coefficient using the second procedure for a set of measurements; $C_0 = 0.65$, $C_i = 0.2$; $f(x)$ and $g(1)$ - functions (6) for two values of parameter a (0.2 and 0.4); $h(x)$ - the equation of the tangent to the curve g (x) best fit to the results; crosses—results of measurements.

where $b = \frac{0.5}{\sqrt{tD_0}}$, which can be used for analysis according to the "best fitting curve" method. It is the basis of procedure two (fig. 4). For equation (6) it can be calcualted tangent line in point $(C_0, 0)$ and coordinates (C_i, a) of point of its crossing with asymptote C_i for equation (6). Then, using formula (5) diffusion coefficient D_0 can be determined.

The third procedure is also possible [25], by estimative—graphical—way of determining the tangent in point (C_0, x_0) and an a value (fig. 5).

A common practice is also the fourth method, i.e. the calculation of the entire expression $erfc\left(\frac{0.5x}{\sqrt{tD_0}}\right)$ on the basis of experimentally measured values of C_0 and C_i, and then, by using the values of the function *erfc*—determining the value of its argument, z and finally the value D_0. The averaged results for a number of pairs of values (C_i, x_i) is taken as the diffusion coefficient of the concrete under certain conditions. This method is possible to use even in the case of two pairs of values (C_i, x_i), which makes it a very practical tool but usually not enough accurate.

It should be stressed that further simplification of equation (6) by assuming $b = 1$, which leads to formula (6a):

$$C = C_t + (C_0 - C_t)e^{x} \tag{6a}$$

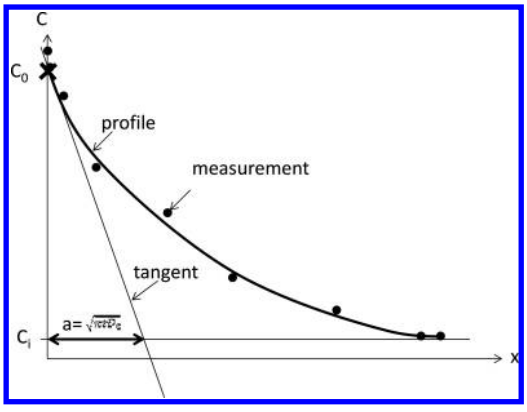

Figure 5. Graphical determination of diffusion coefficient based on the distribution profile of chlorides (procedure three).

is unjustified, and usually wrong in result. This assumption causes the a value being independent from C_i (fig. 6), which is against the physical sense of diffusion as an effect of concentration gradient.

2.3 *Conditions of corrosion initiation in concrete elements*

It is believed [3,4,31] that the moment of the initiation of corrosion means the loss of durability, although this doesn`t necessary mean the exceeding of ultimate state of capacity. It can therefore be assumed that the effective life of the element is equal to the time of initiation of corrosion (Tcor). This assumption is strictly true in the case of prestressed concrete elements, in which both the design of the reinforcement (the bundle of thin tendons) and the effects of corrosion (sudden destruction),

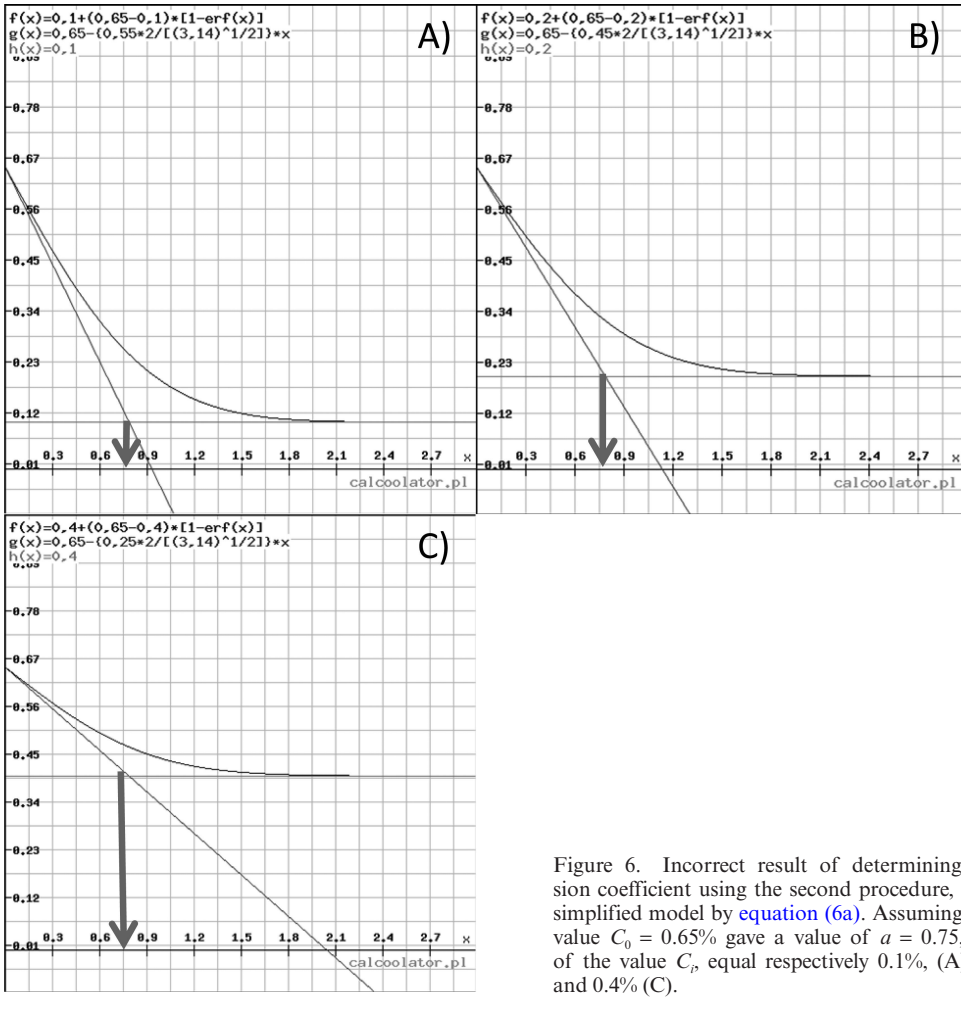

Figure 6. Incorrect result of determining the diffusion coefficient using the second procedure, assuming a simplified model by equation (6a). Assuming a constant value C_0 = 0.65% gave a value of a = 0.75, regardless of the value C_i, equal respectively 0.1%, (A), 0.2% (B) and 0.4% (C).

argue in favor of such a strict criteria of durability. In reinforced concrete structures is also possible to consider the further progress of corrosion of reinforcement after the initiation—loss of the steel-concrete bond, the reduction in the area of reinforcement cross-section till the loss of capacity.

Depth of carbonation—range of decreased pH value vs concrete cover thickness.

The real risk of corrosion of reinforcement due to carbonation is associated with a reduction in the pH of the concrete cover to a critical level, that is, pH level at which the depassivation of steel occurs. Even a slight reduction of the natural pH of the concrete causes deterioration of the protective cover. Already pH level of approx. 11,5 is considered to be dangerous for reinforcement. In practice, however, a lower critical value of pH is adopted. Standardized methods for measuring the carbonation [32,33,34] use the deep purple indicator (phenolphthalein), which allows to determine the range of the front of pH = 8,3. With such a low pH value the level of reinforcement corrosion is already intense. In the diagnostic activities the use of other color indicators is also recommended, for determining the intermediate pH levels (e.g. thymolphthalein—a pH of about 10,5; thymol-phenolphthalein – pH = ca. 9,5) or even universal indicator (called "rainbow test"), which allows to estimate the distribution of the pH in the concrete cover [35]. Time after which the critical pH reaches a reinforcement is the time of initiation of corrosion. The time of this process varies with carbonation level significantly. So to estimate the time when the front of the carbonation reaches the reinforcement, this rate should not be taken as a constant value, although this approach is also indicated in the literature [4,11]. A more correct procedure requires investigation of the course of carbonation and developing of a model of the process for the concrete. The model can be determined by an accelerated method in a increased concentration of CO_2 (to 1% [33]; to 4% [34]). The rate of carbonation in such conditions is higher than under natural conditions, but the maximum value—asymptote of the model (2)—as shown by the study [7], in a case of accelerated carbonation is slightly higher than that obtained in natural conditions. Thus, the adoption of the asymptote obtained in accelerated research in predicting the final depth of carbonation leads to increasing the safety margin in estimation.

Predicting durability under the corrosion caused by carbonation requires the adoption of two basic assumptions which determine both the predicting methodology and its outcome (Table 1):

- critical pH initiating corrosion of reinforcement,
- the method of determining a maximum depth of carbonation.

Each of the concepts presented in Table 1 can be used to predict the durability, while the limitations identified in the table 1 can be regarded as an element of uncertainty of the prognosis.

Chloride ions—critical concentration in different conditions

Risk of chloride corrosion is associated with the migration of chlorides through the pores of the concrete until the critical concentration of Cl-ions reaches the surface of the steel reinforcement. The critical chloride content which initiates corrosion is expressed in the reference documents as a percentage of weight of cement in the concrete or a weight of concrete. The critical values are defined as the total chloride content of all concrete ingredients (aggregates, cement, water, additives and admixtures) and chlorides from external sources. These values vary from reference documents [36,37,38,39,40,41], both because of the different research methods, as well as due to the properties of the element and exploitation conditions (Table 2). Application of the test methods by dissolving in water or in acid leads to significant differences in the results. The higher critical concentrations are achieved by dissolution in acid. Differentiation of requirements depending on the characteristics of the element comprises a type of reinforcement (reinforced concrete, pre-stressed concrete, post-tensioned concrete) and the conditions of production and exploitations (wet conditions of use, external access of chlorides, heat treatment in the production). Initiation of corrosion involves primarily damage of the passive layer on the steel occurring after exceeding the critical values of molar concentrations of Cl–¬¬- and OH-. Assumption of the critical concentration of chlorides on the basis of guidelines given in Table 2 is a necessary step in predicting the durability of elements [42].

Acceptable chloride level (A_c in table 2) is specified without taking into account the effect of mineral additives presence in concrete. It is well known from many published results, that "acceptable chloride level" would decrease as the fly ash content increases in concrete [46]. The effect of ground granulated blast furnace slag is opposite—the presence of slag in concrete increases acceptable chloride level [47]. Very useful for comparison of different concretes durability under chloride aggression could also be a ratio of acceptable chloride level and chloride diffusion coefficient, described by Cheewaket et al. [46].

Table 1. Basic assumptions for predicting durability under the risk of reinforcement corrosion caused by concrete cover carbonation [7].

Acceptable chloride level (A_c in table 2) is specified without taking into account the effect of mineral additives presence in concrete. It is well

Table 1. Basic assumptions for predicting durability under the risk of reinforcement corrosion caused by concrete cover carbonation [7].

Assumption 1: Critical pH value for corrosion initiation		
pH values		**Brief SWOT analysis**
1	8,3 (phenolphthalein)	- value much lower than actual limit of corrosion initiation - testing procedure is standardized (PN EN 14630) - low variability of testing results
2	9,6 (thymol-phenolphthalein)	- value slightly lower than real limit of corrosion initiation - lower variability of tests results than for tyhmolphthalein indicator
3	10,5 (tyhmolphthalein)	- a value close to the actual limit of corrosion initiation - high variability of testing results
4	Rainbow test (wide range of pH values)	- opportunity to measure few pH limits on one concrete break - blurred limits between colors corresponding to neighboring pH values, which makes measurement less accurate
Assumption 2: The method of determining the time at which the carbonation front reaches the reinforcement		
Method		**Brief SWOT analysis**
1	Developing a model based on results of accelerated laboratory carbonation tests performed on samples made of specified concrete	- precise prediction of carbonation depth after at any time of exposition - the need of making laboratory samples from the same concrete as in the construction - testing time min. 3 months
2	Developing a model based on results of accelerated laboratory carbonation tests performed on samples taken from construction	- precise prediction of carbonation depth after at any time of exposition - unknown influence of „shock" change of carbonation rate on results - testing time min. 2 months
3	Adopting an average rate of carbonation on the basis of knowledge about the composition and characteristics of concrete, and data from the literature	- no need to carry out tests, which significantly reduces time of prognosis developing - average rate of carbonation from literature is burdened with high error,
4	Measurement of the depth of carbonation in element and calculation the rate of carbonation on the basis of current exploitation time	- „in situ" test allows to refer estimation to the actual state of concrete in construction - calculation assuming linear progress of carbonation in time, which is burdened with significant error, which is the greater if the shorter would be time of carbonation

known from many published results, that "acceptable chloride level" would decrease as the fly ash content increases in concrete [46]. The effect of ground granulated blast furnace slag is opposite—the presence of slag in concrete increases acceptable chloride level [47].

Very useful for comparison of different concretes durability under chloride aggression could also be a ratio of acceptable chloride level and chloride diffusion coefficient, described by Cheewaket et al. [46].

3 ALGORITHM OF CONCRETE CONSTRUCTION DURABILITY PREDICTION UNDER THE RISK OF CORROSION

Durability of construction or element is usually needed to be predicted when the deterioration process, which could shorten service life of element, is observed. The main aim of the prognosis is to adopt the appropriate structure management options, according to EN 1504–9

Table 2. Classes of chloride content in concrete.

No.	Reference document	The criterion for selection of chloride content class	Chloride content classes	Property adopted as a criterion	Maximum limit value A_c, %
1	European standard: EN 206-1	With no reinforcement steel or other metal except corrosion-resistant handles	Cl 1.0	The maximum permissible content of Cl^- relative to the mass of the cement, defined as the sum of the chloride content in concrete components (without specifying the test method)	1.0
		With steel reinforcement or other metal	Cl 0.20		0.20
			Cl 0.40		0.40
		With pre-stressed steel reinforcement	Cl 0.10		0.10
			Cl 0.20		0.20
2	German national complementary standard to DIN- EN 206-1: DIN 1045-2	With no reinforcement steel or other metal except corrosion-resistant handles	Cl 1.0		1.0
		With steel reinforcement or other metal	Cl 0.40		0.40
		With pre-stressed steel reinforcement	Cl 0.20		0.20
3	British national complementary standard to BS-EN 206-1: BS 8500-1	Pre-stressed concrete or reinforced heat curing concrete	Cl 0.10		0.10
		Post-tensioned concrete	no data		Determine individually
		Reinforced concrete with sulfate resistant Portland cement	Cl 0.20		0.20
		Concrete reinforced with ordinary steel	Cl 0.30		0.30
			Cl 0.40		0.40
4	ACI 318-05 Building code requirements for structural concrete	Pre-stressed concrete	-	The maximum permissible content of Cl^- soluble in water, relative to the mass of the cement	0.06
		Reinforced concrete expose to chloride in service	-		0.15
		Reinforced concrete used in dry conditions and protected from moisture	-		1.00
		Other reinforced concrete constructions	-		0.30
5	ACI 222R-01 Protection of metals in concrete against corrosion	Pre-stressed concrete	-	The maximum permissible content of Cl^- soluble in water or acid, relative to the mass of the cement	water 0.06 acid 0.08
		Reinforced concrete used in wet conditions	-		0.08 0.10
		Reinforced concrete used in dry conditions	-		0.15 0.20

[26]. This standard (in section 5) provides different options of structure management, ranking from "do nothing for a certain time but monitor", through "re-analyze the structural capacity, possibly leading to downgrading in function", "prevent or reduce further deterioration", "strengthen or repair and protect all or part of the concrete structure" to "reconstruct or replace all or part of the concrete structure" or "demolish all or part of the concrete structure". Prognosis of durability is thus an important tool for decisions on repair principle and repair design according to the requirements of standards EN 1504 series.

Recommended approach to the durability prognosis could help not only to manage the construction during its service life but also to create construction robustness at the stage of designing. This would involve different scenarios of construction life.

The algorithm of prognosis (figure 2) includes "in situ" diagnostic tests and laboratory tests on

the samples taken from the structure and computational analysis, conducted on the basis of the obtained results. Prognosis, as a rule, is carried out, assuming that no repair will be done. In the first stage it is necessary to identify the main structural parts of the object and determine its technical condition, including, in particular, defects and damage affecting durability. Then the environment conditions for the elements should be identified, including classes of exposition according to EN 206-1[20] and EN1992-1-1[27]. Based on the analysis of the findings above and the analysis of the design documentation, it shall be determined which components of the structure are the most at risk of corrosion. For the selected elements the subsequent analysis of durability is carried out, independently for carbonation and chloride aggression risk.

With regard to the risk of carbonation, predicting the durability involves estimation of time Tcarb, when the carbonation front reaches a depth of the steel reinforcement, using methods and indicators given in Table 1. Obtained time Tcarb is the residual service life of the element until the initiation of corrosion caused by carbonation. In case of significant cracks in element, it is recommended to check the depth of carbonation in cracks, in which the rate of carbonation is usually greater than in non-cracked place.

With regard to the risk of chloride aggression, predicting the durability involves:

- determination of the critical concentration of Cl- or a given element (the element type, conditions of element production and exploitation, methods of determination of Cl- content),
- determination of diffusion coefficient of Cl- ions in the concrete, based on measurements of chloride concentrations at the surface and in the depth of concrete, with use of methods specified in Chapter 2.2,
- identification of possible routes of chlorides penetration to the reinforcement. External sources of Cl- should be established, places where they are in contact with an element, routes of their transport, including the flow of polluted water, which is in many cases the main source of chlorides. Knowing the critical concentration, diffusion coefficient and migration routes, the times to reach the critical concentration for reinforcement (tCl1, tCl2,... tCln) can be determined for different routes of migration. The time of the shortest value, calculated as:

$$TCl = \min (tCl1, tCl2,... tCln) \quad (7)$$

is considered a residual service life of the element, remaining to initiate chloride-induced corrosion. Minimum of Tcarb, tCl1, tCl2,... tCln, allows to estimate the expected residual service life (Tcor) under conditions of corrosion caused by chlorides and carbonation:

$$Tcor = \min (TCl, Tcarb). \quad (8)$$

Following the above analysis based on measurements in the construction and on samples taken from the construction, ensures that the synergistic effect of chloride migration processes and carbonation will be taken into account. Synergism of carbonation processes and migration of chloride, affects the characteristics of concrete examined in the construction (carbonation depth, diffusion coefficient). Therefore, it is included in the prognosis through the adoption of real concrete properties to the modeling and prediction. In the case of predictions based solely on the basis of laboratory tests or indicators drawn from the literature, the prognosis is subject to greater error, resulting not only from the approximate values of adopted characteristics, but also from difficulties in taking into account the synergy effect.

Knowledge of Tcor and Tw (current time of exploitation) values allows to calculate a reduction of element durability Tr, % as follows:

$$Tr = [1- (Tw+Tcor)/Td] \times 100 \quad (9)$$

where Td is designed service life durability of element.

4 EXAMPLES OF THE DURABILITY PREDICTION OF THE COMPONENTS EXPOSED TO THE RISK OF CHLORIDE CORROSION

There will be two examples presented of residual service life prediction of floor slabs exposed to chloride corrosion. In the first case, the subject of analysis is the pre-stressed hollow core slab and in the second case—similar reinforced concrete slab. With regard to the first example, the methodology according to the fourth procedure (discussed in Section 2.2.) was carried out, because of having an insufficient number of measurement points at different depths of concrete. In the second example the second method for dispatching the measurement results for the five concentrations of chloride depths was used.

Example 1

The floor was made of the pre-stressed hollow core slabs, which were placed on the prefabricated beams and pillars. On the surface of HC slabs the layer of concrete topping was performed, finished with the thin epoxy resin coating on top as a protective layer (Figure 8).

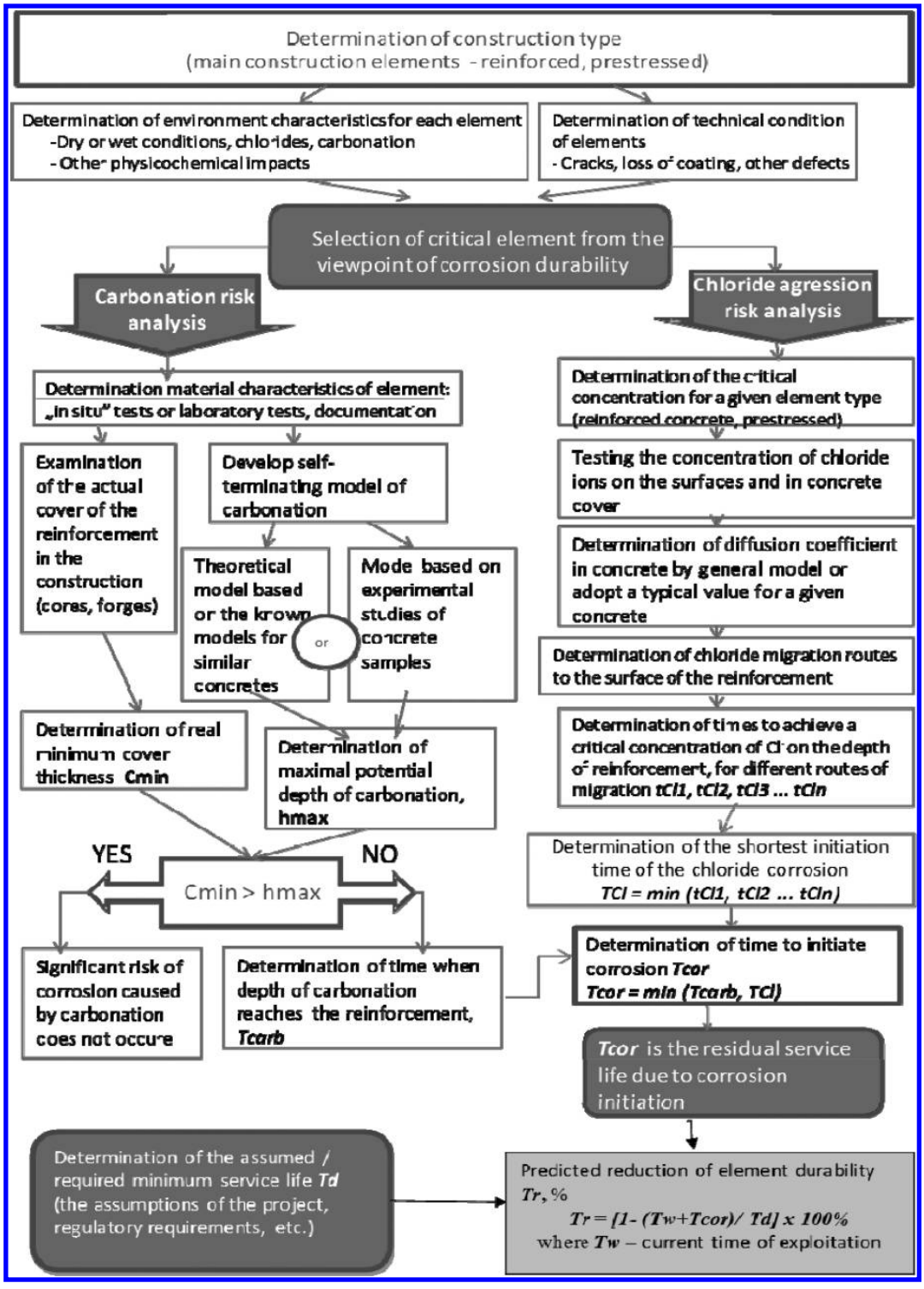

Figure 7. Algorithm of concrete construction durability prediction under the risk of corrosion [8].

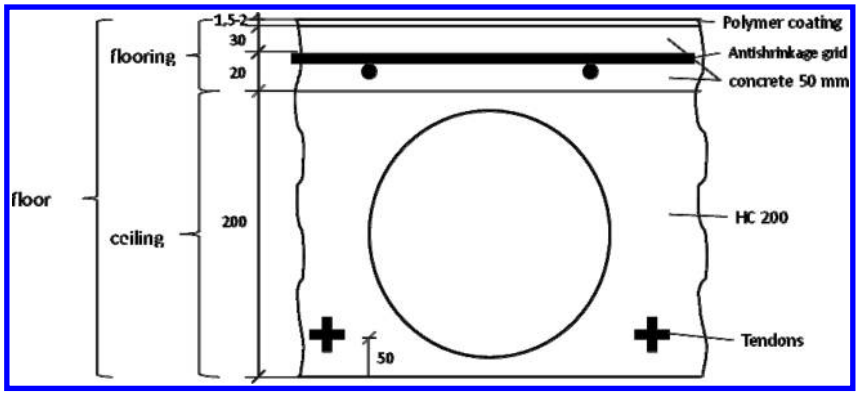

Figure 8. Floor construction.

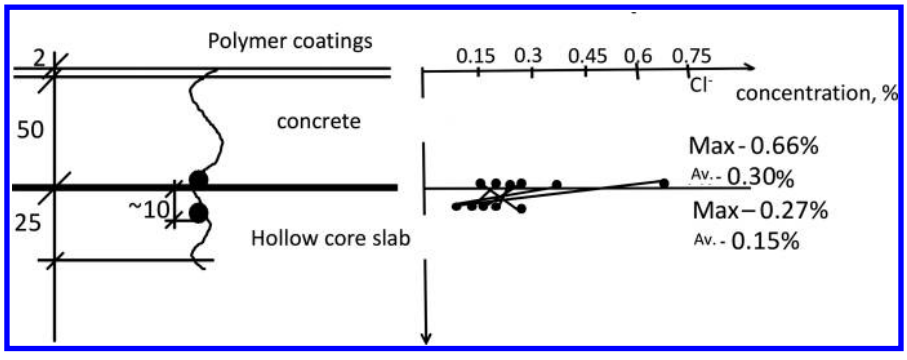

Figure 9. Chloride concentration on the surface and in the upper zone of hollow-core pre-stressed slab, dimensions in [mm].

After 5 years of exploitation, cracks and other damage have been observed on the surface of the floor. Some cracks were through the whole thickness of the slab and topping cover. Improper shaping falls on the floor resulted in stagnant water, often contaminated by the de-icing agents. Cracks were the migration ways through the surface of precast concrete and further into the hollow cores in the pre-stressed slabs. Analysis of the construction has showed that the most vulnerable is the corrosion of the pre-stressed tendons in slabs. The tests were performed on the cores drilled in the concrete topping and the top part of the precast elements.

It was found that the extent of carbonation of concrete top layer (tested thymolphtalein indicator) in cracks reached or exceeded the level of the antishrinkage fabric and effect of corrosion was visible. This process applies not structural element, which can be treated as interchangeable, so its destruction does not affect the durability of the structure. There has also been studied the depth of carbonation of concrete slabs and found out that it was negligibly small at the measurement accuracy of 1 mm. It was found that the risk of reducing the durability of the structure only as a result of carbonation is negligible.

The chloride ions concentration was tested on the surface and inside the concrete of floor slab on the depth of 10 mm from the top surface (Fig. 9). It was found the presence of chloride ions of similar concentration to the upper surface as well as on the side surfaces (in the joints between neighboring plates) and inside the channel. Using equation (6) diffusion coefficient for various sections of the floor slab was determined by the fourth procedure. The fourth method was selected for each profile because only two concentration values at the surface and at a depth of 10 mm were known. Evaluated diffusion coefficient was in the uncracked section $D1 = 1 \times 10^{-8}$ and cracked in section $D2 = 2.0 \times 10^{-7}$cm^2/s

Possible migration paths to the tendons were determined for chlorides by analyzing the structure of the floor (Fig. 10). A critical concentration of Cl^- ions was assumed as equal to 0.1%, as for the precast elements produced using the heat treatment (class Cl 0.10, pos. 3, Table 2).

Finally, for durability estimation following assumptions were done:

- Critical Cl^- concentration in concrete Ccrit = 0.1% m. c.
- Initial Cl^- concentration in concrete C_i = 0,01% m.c.

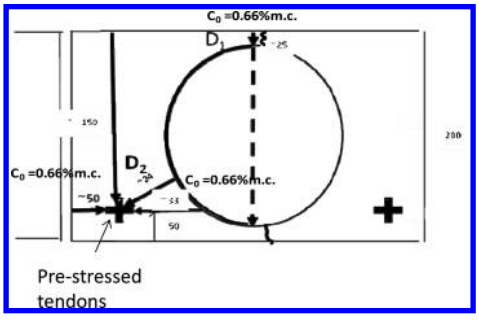

Figure 10. Possible routs of chloride migration, dimensions in [mm].

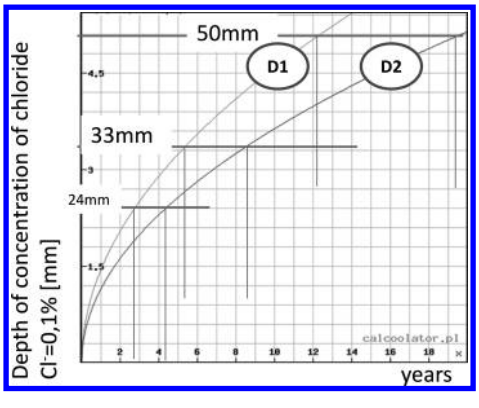

Figure 11. The changes in time of the front of chloride concentration of 0.1% mass of cement, in the case of the value of the diffusion coefficient D1 and D2, respectively.

- Diffusion coefficient in cracked concrete cross-sectionD1 = 2.0 × 10–7 cm^2/s
- Diffusion coefficient in uncracked precast concrete element D2 = 1.0 × 10-8 cm^2/s
- Maximum Cl^- concentration on the surface of the precast element C_0 = 0.66% m.c.

On the basis of the determined values, the time tCln to obtain a concentration of 0.1% Cl on the tendon surface (Table 3), was determined using the formula (6) - figure 11.

Risk analysis of chloride aggression, shows that the remaining time (Tcor) of ceiling use in the pessimistic scenario is equal to TCl = 3 years (Table 3). It is likely, if chloride ions will permeate the hollow void to the tendons (minimum 24 mm). If we assume that migration will take place from the joints between the panels to the tendon (minimum 50 mm), this period may be extended up to 19 years.

In the case of load-bearing elements such as ceilings, expected life in accordance with the Eurocodes [1,2] should not be less than 50 years (Td = 50 years). Taking into account the period of 5 years of exploitation (TW = 5 years) and the calculated values of the residual time of use (Tcor = 3 to 19 years old), it can be estimated that there was a 55–80% reduction in the durability of the floor.

Example 2

The element under consideration is a reinforced HC concrete slab (Fig. 12), exposed to the aggression of the chloride from the top surface, wherein the chloride concentration determined empirically to a depth of 6 cm after 1,5 years of exposure are shown in the graph (Fig. 13). It was assumed that the starting chloride content of the concrete match the class Cl0,20, was 0.2% m.c.

The second procedure was adopted for determining the coefficient of diffusion—the equation of the fitted curve (correlation = 0.94 al) and determined value of a = 2.25 is shown on Figure 13. For the values of a = 2.25 and exposure time t = 1.5 years diffusion coefficient $D_0 = 3{,}4 \times 10^{-8} cm^2/s$ was

Table 3. Estimation of initiation time of pre-stressed tendons corrosion $C(x,t)$ = 0.1% m.c., $D_1 = 2.0 \times 10^{-7}$ cm^2/s $D_2 = 1.0 \times 10^{-8}$ cm^2/s C_0 = 0.66% m.c.

	Through the upper flange of slab and from the bottom of the hollow void to the tendon	From the joints between slabs to the tendon	From the bottom of the hollow void to the tendon	Shortest way from the hollow void to the tendon
	Rout of migration, mm/diffusion coefficient			
Conditions of migration	25/D1+33/D2	50/D2	33/D2	24/D2
Time to reaching concentration Cl = 0,1% m.c. on the level of tendons, tCln, years	12	19	6	3

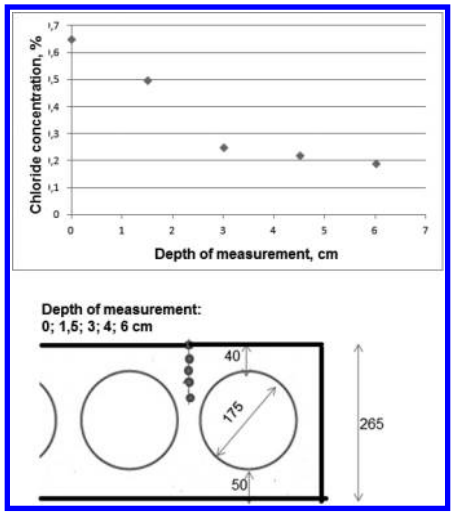

Figure 12. Results of testing chloride ions concentration at different distance from the surface of element.

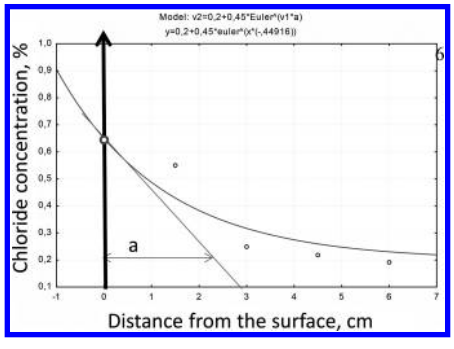

Figure 13. Best fitting curve acc. to formula (6), fitted to the results showed on the figure 12.

determined. Further procedure is similar to the first example, and requires consideration of the location of the reinforcement in the slab and estimation of the migration paths of chlorides.

It is worth noting that it is essential for the result of this modeling, which value is accepted as a starting chloride content of the concrete uncontaminated, i.e. before occurring of the outside chloride aggression. It can be specified such a value on a sample taken from a suitably deep zone of concrete (which the chloride ions have not yet reached).

5 CONCLUSIONS

It is common to assume that the durability of structures in corrosive environments is adequate to reaching the front of carbonation and chlorides the zone of reinforcement. This assumption is someway arbitral but a safety base for the prognosis. From the moment of inhibition of rebar corrosion the further structure life time is determined by the steel corrosion rate. A concrete crack inhibition occurs due to the overgrowth of corrosion products of rebars; a consequences are the loss of concrete adhesion to reinforcement and the propagation of crack in the concrete cover. Subsequently the reinforcement cross-section area is reduced down to the loss of the bearing capacity.

This assumption is also justified by practical considerations, as it often marks the end of the possibility of the repair action.

It is obvious in the light of presented study, that the moment of initiation of steel corrosion is simultaneously the start moment of the occurrence of structure duration threat. Two models of estimation of steel corrosion initial moments have been presented separately in case of carbonation and chloride corrosion risk. The structure residual life time and expected reduction of durability under the given conditions could be evaluated with use of author`s algorithm.

REFERENCES

[1] EN 1990:2004 (Eurocode 0).
[2] EN 1992-1-1:2008 (Eurocode 2), Design of concrete structures – Part 1-1: General rules and rules for buildings.
[3] Czarnecki L. Emmons P.H. Repair and protection of concrete structures, Polski Cement, Kraków 2002 (in Polish).
[4] Ściślewski Z. Protection of reinforced concrete structures. Arkady, Warszawa 1999 (in Polish).
[5] Więcławski R. Concrete carbonation in urban-industrial area, doctroral thesis Politechnika Warszawska, Warszawa 2002 (in Polish).
[6] Czarnecki L. Więcławski R. Concrete carbonation as limited process, Matbud`2003, Kraków 2003 (in Polish).
[7] Woyciechowski P., Model of concrete carbonation, Scientific works. Buildings. Issue 157, Politechnika Warszawska 2013 (in Polish).
[8] Czarnecki L., Woyciechowski P., Application of self-terminating carbonation model and chloride diffusion model to predict reinforced concrete construction durability, Bulletin of the Polish Academy of Science—Technical Sciences, vol. 61, No 1, 2013, 173–181.
[9] Czarnecki L., Woyciechowski P., Durability of concrete according to the European Standard EN 206-1, International Congress on Concrete Durability, Trondheim, June 2012, article A13–1, 11 s.
[10] Czarnecki L., Woyciechowski P., Concrete carbonation as a limited process and its relevance to CO_2 sequestration, ACI Materials Journal vol. 109, No 3, May-June 2012, s. 275–282.
[11] Łakomy T., Reinforcement corrosion in Bridges, doctoral thesis, Politechnika Warszawska, Warszawa 2009 (in Polish).

[12] Fiertak M., Nowak K., Depth of carbonation in structures—theoretical models verification. Ochrona przed Korozją 5s/A/2008, 51–56 (in Polish).
[13] Wieczorek G. Reinforcement corrosion initiated by chlorides or carbonation, Dolnośląskie Wydawnictwo Edukacyjne, Wrocław 2002 (in Polish).
[14] Slopkova K. Observing of state of steel reinforcement in concrete and process of its corrosion by effect of carbonization, Proceedings of KONTRA 2002, Zakopane 2002.
[15] Papadakis V., Vayenas C., Fardis M., Experimental investigation and mathematical modeling of the concrete carbonation problem, Chemical Engineering Science 46 (1991), pp. 1333–1339.
[16] Tetsuya Ishida, Koichi Maekawa, Masoud Soltani, Theoretically identified strong coupling of carbonation rate and thermodynamic moisture states in micropores of concrete. Journal of Advanced Concrete Technology Vol 2 (2004), No 2 pp 213–222.
[17] Fagerlund G. Concrete structures durability, Arkady, Warszawa 1997 (in Polish).
[18] Bakker R.F.M., Initiation period, in P. Schiessl (Ed), Corrosion of steel in concrete: Report of the Technical Committee 60 – CSC RILEM, Chapman and Hall, London, 1988, s. 22–54.
[19] Czarnecki L., Woyciechowski P. Model of concrete carbonation as limited process—experimental investigations of fluidal ash concrete, Proceedings of Brittle Matrix Composites 9, Woodhead Publ. Ltd.,183–194, Warsaw, October 2009.
[20] Tikalsky P.J., Pustka D., Marek P. Statistical variations in chloride diffusion in concrete bridges, ACI Structural Journal, May-June 2005, 481–486.
[21] Raupach M., Corrosion of reinforcement in concrete, Woodhead Publisher, 2007.
[22] Angst U., Critical chloride content in reinforced concrete—A review, Cement and Concrete Research, 2009.
[23] Koter S., Theory of electrolytes transport through ion exchange membranes, Theory and practice Mikołaj Kopernik University, Issue 3, 2006.
[24] Zhang J., Cheung M.M.S., Modeling of chloride-induced corrosion in reinforced concrete structures, Materials and Structures 46, 2013, 573–586.
[25] Poulsen E., Mejlbro L., Diffusion of Chloride in Concrete: Theory and Application, Taylor&Francis, 2010.
[26] Angst U., Chloride induced reinforcement corrosion in concrete. Concept of critical chloride content—methods and mechanism, Ph.D. thesis, NTNU, Trondheim 2011.
[27] Zybura A., Jaśniok M., Jaśniok T., Diagnostic of reinforced concrete structures, PWN, Warszawa 2011 (in Polish).
[28] Kuziak J. Electrochemical investigation of inhibitors influence on steel corrosion in concrete, doctoral thesis, Politechnika Warszawska, 2009.
[29] Czarnecki L., Łukowski P., Repair of concrete structures exploited in chemical aggression threat, Materiały Budowlane 12/2005 (in Polish).
[30] Angst U., Chloride induced reinforcement corrosion: electromechanical monitoring of initiation stage and chloride threshold value, Corrosion Science, 2011.
[31] Czarnecki L. et al., Evaluation of effectiveness of migrating inhibitors of steel corrosion in concrete Politechnika Warszawska, Warszawa 2008, (in Polish).
[32] EN 14630:2007 Products and systems for the protection and repair of concrete structures. Test methods. Determination of carbonation depth in hardened concrete.
[33] EN 13295:2004 Products and systems for the protection and repair of concrete structures—Test methods—Determination of resistance to carbonation.
[34] CEN/TS 12390-12 Testing hardened concrete—Part 12: determination of the potential carbonation resistance of concrete: Accelerated carbonation method, 2010.
[35] Czarnecki L., Woyciechowski P. Methods of concrete carbonation testing, Materiały Budowlane 2/2008, 5–7 (in Polish).
[36] EN 206-1:2015 Concrete Part 1: Part 1: Specification, performance, production and conformity.
[37] PN-B-06265:2004, Complementary polish standard to PN-EN 206–1:2003.
[38] DIN 1045-2: 2008, Anwendungsregeln zu DIN EN 206-1: Tragwerke aus Beton, Stahlbeton und Spannbeton—Teil 2: Beton—Festlegung, Eigenschaften, Herstellung und Konformität.
[39] BS 8500-1:2006 Concrete. Complementary British Standard to BS EN 206-1. Method of specifying and guidance for the specifier.
[40] ACI 318-05 Building code requirements for structural concrete, ACI Committee 318, 2005.
[41] ACI 222R-01 Protection of metals in concrete against corrosion, ACI Committee 222, 2001.
[42] Woyciechowski P., Kuziak J., Królikowski A., Chloride ions concentration in concrete as a threat of reinforcement corrosion, Ochrona przed korozją Nr 6, 2012, s. 286–288; (in Polish).
[43] PN-EN 1504-9:2010 Products and Systems for the Protection and Repair of Concrete Structures—Definitions, Requirements, Quality Control and Evaluation of conformity Part 9: general rules for systems and products applications.
[44] Zaborski A., Modeling of structural concrete elements degradation with use of cellular automata, Ochrona przed korozją 2010, (in Polish).
[45] Krykowski T., Modelling of concrete cover damage due to reinforcement corrosion, Studia z zakresu inżynierii nr 78, KILIW PAN, Warszawa 2012 (in Polish).
[46] Cheewaket T., Jaturapitakkul T., Chalee W., Concrete durability presented by acceptable chloride level and chloride diffusion coefficient in concrete: 10-years results in marine site, Materials and Structures (2014) 47: 1501–1511.
[47] Garcia, V., François R., Carcasses M., Gegout Ph., Potential measurements to determine the chloride threshold concentration that initiates corrosion of reinforcing steel bar in slag concrete, Materials and Structures (2014) 47: 1483–1499.

Concrete Repair, Rehabilitation and Retrofitting IV – Dehn et al. (Eds)
© 2016 Taylor & Francis Group, London, ISBN 978-1-138-02843-2

Using existing inspection data to probabilistically estimate the time-to-rehabilitation for concrete bridges exposed to deicing salts and humidity

Filippos Alogdianakis, Dimos C. Charmpis & Ioannis Balafas
Department of Civil and Environmental Engineering, University of Cyprus, Nicosia, Cyprus

ABSTRACT: Being able to reliably predict the time-to-rehabilitation of aging bridges is a major issue in cost-effectively maintaining these in safe and operational condition. This task is seriously hindered by the high uncertainties that govern the deterioration rate and the lifetime of bridges. In the present work, a method is proposed to probabilistically estimate the time-to-rehabilitation of a bridge. For this purpose, data from a large-scale database of the US Federal Highway Administration are utilized, which include age and structural condition information for several thousands of bridges. This information reveals the effect of bridge exposure to environmental factors such as deicing salts, humidity and chlorides, among others. According to the proposed method, the available data are first appropriately processed and adjusted using shifting and scaling procedures. Weibull distribution functions are then fitted to the data to evaluate condition probabilities and estimate the time-to-rehabilitation. The method is successfully tested on a real sample of 33,810 concrete bridges of various ages, which are exposed to deicing salts and humidity.

1 INTRODUCTION

During the last decades vast budgets have been spent to maintain aging infrastructures all over the world. The 20th century's increased construction activity has led, in particular, to the accumulation of bridges, forming stocks, which are deteriorating with age. Aging bridges need continuous interventions either in the form of maintenance or major rehabilitation. Reliably estimating the deterioration rate and the lifetime of bridges are essential aspects in determining optimal programs regarding maintenance and/or rehabilitation. This could assist decision makers in both elongating the useful life of bridges and controlling their structural safety in a cost-effective manner. However, the structural performance of bridges in time is governed by high uncertainties, which need to be quantitatively treated, in order to be able to make rational decisions regarding maintenance and rehabilitation.

An essential step toward the effective handling of such uncertainties is the gathering and exploitation of respective data. Typically, the data collected refer to current bridge conditions and are used in conjunction with Bridge Management Systems (BMS) to decide on the necessity and degree of priority of any potential intervention and to allocate corresponding funds (Ryall 2001). Frequent inspections ensure that the BMS is up-to-date regarding the structural condition of the stock. However, in order to estimate future needs and optimally allocate available budgets, models to predict the future stock condition are essential. Various deterioration models exist and vary from simple linear regression models (Fitzpatrick et al. 1981) to much more involved Markov chain models (Madanat et al. 1995, Ng & Moses 1996). Recently, in order to improve the prediction accuracy for bridge conditions, new approaches were applied, such as Weibull Analysis (Agrawal et al. 2010), Artificial Neural Networks (Huang 2010) and Bayesian Dynamic Beliefs (Rafiq et al. 2015). These deterioration models use previous years' structural condition data to trace condition changes and estimate the probability of transition from a condition rating to another.

In the present work, a novel method is presented to probabilistically estimate the future structural condition of a bridge. For this purpose, real data maintained by the Federal Highway Administration (FHWA) for USA bridges are exploited. The National Bridge Inventory (NBI) of FHWA, which is updated annually, contains a considerable amount of information and describes the structural condition of over 500,000 bridges (FHWA 1995). The new method presented herein uses the NBI database of a single year to calibrate a probabilistic model for predicting the structural condition of a bridge over time. Thus, all bridges in the data-stock processed are used, based on their ages, to represent the condition of a single bridge during its lifetime. Hence, the portion of bridges being in a certain age and condition represent the probability of the bridge under study to be in the

same condition at that age. This way, curves relating bridge age with cumulative probability for each structural condition can be assembled. Certain time-shifts and scalings are then applied to achieve predictions for bridge ages not covered by available data. By fitting Weibull distribution functions to the original and shifted data and specifying some criteria for deciding bridge rehabilitation, the time left for a bridge until it reaches a structural condition, that induces a need for rehabilitation, can be probabilistically evaluated.

The proposed method is tested on a sample of 33,810 concrete bridges of various ages, which are exposed to deicing salts and elevated humidity. The calculated rehabilitation time predictions are presented and compared to corresponding existing data, which span over a century.

2 THE NATIONAL BRIDGE INVENTORY (NBI)

Inspections are performed on bridges to monitor the infrastructure's stock condition. The FHWA of USA maintains an up-to-date inventory (NBI), which includes over 500,000 bridges in its territory. The NBI contains a considerable amount of information; this includes 116 coded items to describe each bridge. An updated NBI is published annually, as each bridge must be inspected visually biennially. Bridge condition ratings are recorded on a scale 0–9, with 9 representing 'perfect' and 0 'failed' conditions. Inspections are carried out by qualified personnel complying with standard procedures set out in National Bridge Inspection Standards (NBIS) (FHWA 1995). The condition information recorded reveals the effect of bridge exposure to environmental factors, such as deicing salts, traffic loads, earthquakes, humidity and chlorides, among others.

Condition coded with 5 can be regarded as a threshold for rehabilitation. This corresponds to a 'fair' bridge condition (FHWA 1995): all primary structural elements are sound but may have minor section loss, cracking, spalling or scour. Rehabilitating a bridge in that condition is important, before further deteriorating to a 'poor' (code 4), 'serious' (code 3), 'critical' (code 2), 'imminent failure' (code 1) or 'failed' (code 0) condition.

3 MAIN ASSUMPTION OF THE PROPOSED METHOD

Bridges age with different rates, depending on internal and external factors. Internal factors include materials and all the quality embodied through the construction process. External factors, such as deicing salts, earthquakes etc., can cause bridge condition to deteriorate. The effects of both internal and external factors are functions of time. Bridges age and deteriorate due to the duration of exposure to those factors. On the other hand, maintenance can decelerate deterioration (Dunker & Rabbat 1995). As the scope of a deterioration model is to describe a generalized aging-deterioration relation, the selection of a proper sample is crucial.

A bridge is built following certain constructional characteristics depending on age. Performed inspections evaluate the condition of the structure to present criteria. Hypothetically, if inspection data since 1900 existed, then bridge deterioration evolution with age could be described by condition distributions of bridges with similar age. Additionally, the duration of a bridge being at a certain condition could be estimated and transition distributions could then be described. The validity of such method is affected by the changings of the NBIS. Similar inspector standards would ensure that annual evaluations are objective and consistent; however the inspector's subjectivity still remains. The drawn data could be linked to a Markov chain to form bridge stocks distributions and estimate condition probabilities.

In the present work, it is assumed that the NBIS are kept frozen, leaving only the inspectors' subjectivity to create defects. A single annual inspection database is taken into account. The probability of a bridge to be in a certain condition is calculated from the stock's condition distributions with bridge age.

4 STEPS OF THE PROPOSED METHOD

In the present work, a novel method is proposed to probabilistically estimate the time needed for a bridge to reach condition 5 using the aforementioned condition data. Initially, the probability for a bridge of a certain age to be in a specific structural condition (0–9) is calculated. Then, the residual time to condition 5 is estimated by performing time-shifts to future years from condition distributions >5. While shifting, the time axis is scaled appropriately. Weibull distribution functions are finally fitted to the original and shifted/scaled data to evaluate condition probabilities and estimate the time-to-rehabilitation. A specific case study is used to facilitate the description of the method.

4.1 *Case study: Selection of a bridge stock sample*

A specific case study is considered to facilitate the description of the proposed method. The focus of

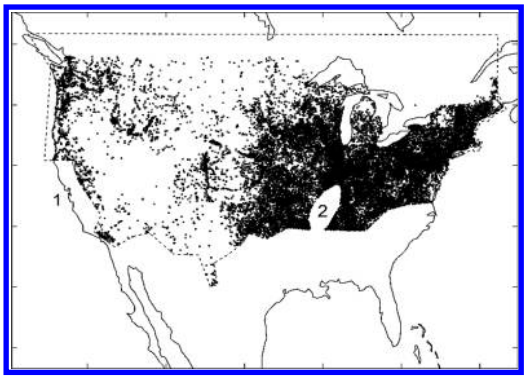

Figure 1. Concrete bridges exposed to deicing salts and humidity. High seismic hazard areas are excluded from the analysis (areas 1 and 2 noted on the figure).

this work is to study bridge deterioration with age, e.g. due to corrosion. Deicing salts are known to accelerate deterioration especially in combination with humidity (Alogdianakis et al. 2014). To locate bridges exposed to chlorides, information from FHWA on the areas of USA using deicing salts have been exploited. The bridges identified are illustrated on the USA map of Fig. 1. To ensure the presence of humidity, the sample was limited to bridges with water passing underneath the structure. Moreover, to limit the structural and material effect on deterioration, only simply supported concrete bridges entered the sample. Finally, cases have been excluded from the selected sample, which correspond to deterioration of a bridge regardless of age. Such cases include earthquakes, accidental actions (e.g. collisions, vandalism), etc. According to the United States Geological Survey (USGS 2014), areas 1 and 2 shown in Fig. 1 represent high seismic hazard regions, which have been excluded from the analysis under study.

Rehabilitated bridges have also been ruled out, as their effect on the sample can be misleading. This is due to the fact that a question arises as to which age to use, based on the year reconstructed or on the year built. In both cases the condition cannot be matched to the rest of the sample, as it is either presented worse or better, respectively.

After the above exclusions the final sample analysed counted 33,810 bridges.

4.2 *Calculation of cumulative condition probabilities based on NBI data*

The proposed method uses the Cumulative Condition Probability (CCP), which calculates the probability of a bridge of a certain age being equal or below a certain condition. Bridges are categorized in age groups forming sub-stocks of the global

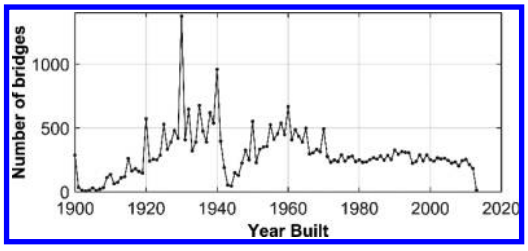

Figure 2. Concrete bridges exposed to deicing salts and humidity constructed at each year.

bridge stock; the CCP of each sub-stock is independently calculated. CCPs for conditions ≤9 to ≤0 are calculated through:

$$CCP_i(t) = \frac{N_{c,i}(t)}{N_{c,\text{tot}}(t)} = \frac{\sum_{j=0}^{i} N_j(t)}{\sum_{j=0}^{9} N_j(t)} = \frac{N_0(t) + \cdots + N_i(t)}{N_0(t) + \cdots + N_9(t)}, \quad (1)$$

where: $CCP_i(t)$ is the CCP for bridge condition ≤i of the sub-stock at age t; $N_{c,i}(t)$ is the total number of bridges at condition ≤i of the sub-stock at age t; $N_{c,\text{tot}}(t)$ is the total number of bridges of the sub-stock at age t (at any condition 0–9); $N_i(t)$ is the total number of bridges at condition i of the sub-stock at age t. Thus, $N_{c,i}$ and $N_{c,\text{tot}}$ are 'cumulative' numbers; this is denoted by the subscript 'c' used.

The total number of bridges of each bridge sub-stock (i.e. of each year) are shown in Figure 2, while the corresponding CCPs are illustrated in Figure 3. Specifically, CCPs for conditions ≤9 to ≤3 are shown in Figure 3.

In this paper, the bridge conditions considered in the analysis are ≤7, ≤6 and ≤5. Condition 4 describes bridges in a far more critical condition to those in need of rehabilitation. In Figure 3, it can be noticed that the probabilities (CCPs) calculated through Equation (1) are not monotonic, but vary within a range, which tends to widen as the bridge sub-stock becomes older. This can be attributed to the smaller samples of constructed bridges available for older years (Fig. 2). It should also be noted that the year of construction may be relevant to the current age of each bridge, but the connection between age and condition has to include the year of inspection. Thus, the actual bridge age that should be considered for calculating CCPs is the year of inspection subtracted from the year built. By applying this transformation, the graph of Figure 4 is obtained, in which the variation range of probabilities seems to be lower than in Figure 3.

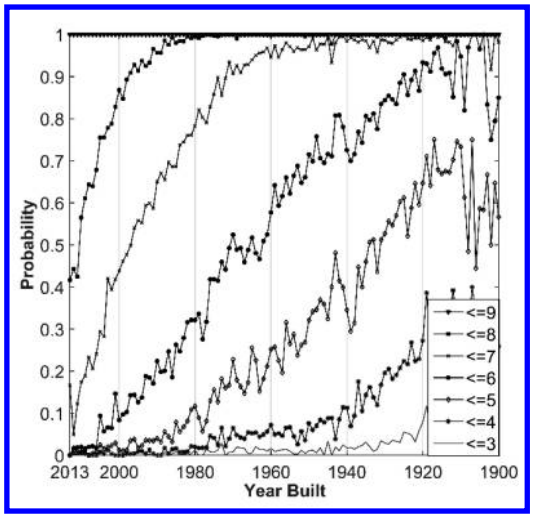

Figure 3. Computed probabilities (CCPs) for each year bridge sample. The 'Year Built' axis is reverse.

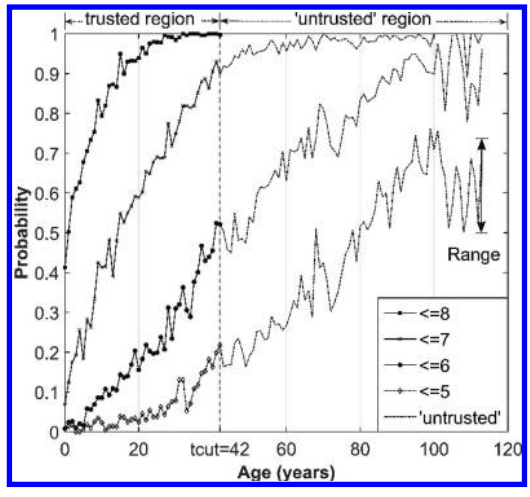

Figure 4. Transformation of probabilities (CCPs) using the year of last inspection; t_{cut} is used to determine the size of the trusted region.

4.3 *Determination of 'trusted' sample*

To separate the bridge ages with acceptable variation ranges of calculated CCPs, a threshold age t_{cut} ('cutting age') is determined to define the 'trusted' part of the overall bridge sample (Fig. 4). Probabilities corresponding to bridge sub-stocks older than t_{cut} are considered to have unacceptably high variation ranges and are therefore 'untrusted'. In Figure 4, t_{cut} = 42 years is selected, separating the trusted CCP-points from the 'untrusted'. The particular t_{cut}-value is selected as a characteristic cutting age to illustrate the steps of the proposed method. An analysis for various t_{cut}-values is presented in section 5.

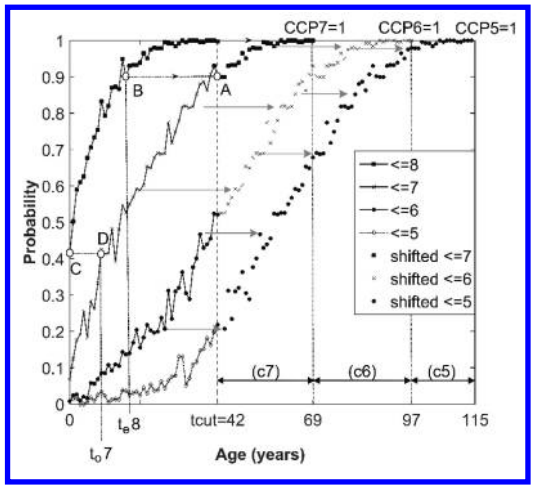

Figure 5. Shifting and scaling procedures; application lengths for each scaling coefficient (c_7, c_6 and c_5).

4.4 *Data shifting*

Data-shifts are performed to copy data from higher CCPs to lower CCPs, where no trusted data are available. The shifting procedure is illustrated in Figure 5. Referring to the CCP-curve for condition ≤7, in order to complete the data beyond the threshold age t_{cut}, data from the CCP-curve for condition ≤8 are used. Hence, point A is first identified, which is the point with probability $CCP_7(t_{cut})$ at age $t = t_{cut}$. By drawing a line parallel to the age axis from point A toward the higher CCP-curve, point B is determined, which is the point of the CCP-curve for condition ≤8 that has the same probability with point A. Point B has probability $CCP_8(t_{e8}) = CCP_7(t_{cut})$ at age $t = t_{e8}$, thus the age t_{e8} can be calculated (obviously, $t_{e8}<t_{cut}$). Then, the points of the higher CCP-curve from point B and beyond are horizontally shifted to the lower CCP-curve at point A, i.e. the aforementioned part of the higher CCP-curve is moved toward the lower CCP-curve by t_{cut}-t_{e8}, as shown by the arrows in Figure 5. This way, data to have a complete CCP-curve for condition ≤7 are created.

The same procedure is performed for every incomplete CCP-curve, in order to be completed beyond the age $t = t_{cut}$. Hence, to complete the data of the CCP-curve for bridge condition ≤i, the probability $CCP_i(t_{cut})$ is found for the age $t = t_{cut}$; then, for equal probability $CCP_{i+1}(t_{e,i+1}) = CCP_i(t_{cut})$, the age $t = t_{e,i+1}$ is determined, which specifies the part of the CCP-curve for bridge condition ≤i + 1 to be

horizontally shifted to the CCP-curve for bridge condition ≤*i*. After performing the required shifts to complete all incomplete curves, all CCP-curves must eventually reach the probability-value of one.

When this shifting procedure is applied as described above, it produces unrealistic high deterioration rates, because data are shifted from higher CCP-curves, which have smaller overall durations (until reaching the probability-value of one). Thus, a scaling procedure needs to be also applied, in order to properly adjust the inclination of the part of a CCP-curve that is shifted to complete a lower CCP-curve. The employed scaling procedure is described in the next subsection.

It should be mentioned that shifts and scalings similar to the ones adopted in the present work are applied to data acquired from accelerated tests performed on materials to evaluate long-term material properties (Alwis & Burgoyne 2008).

4.5 *Data scaling*

As can be verified from Figures 3 and 4, the inclinations of different CCP-curves cannot be the same, because they describe bridge deterioration at different conditions. Normally, lower slopes are generally expected for lower CCP-curves than for higher CCP-curves. However, with the shifting of the previous subsection, curve-parts with the same inclination are generated for different CCP-curves.

To overcome this problem, the inclinations of CCP-curves are adjusted by horizontally spreading the shifted data. This adjustment is performed with an age scaling procedure, which is realized by introducing the scaling coefficient c_i given by:

$$c_i = \frac{t_{cut} - t_{o,i}}{t_{e,i+1}}. \tag{2}$$

The age $t_{o,i}$ is evaluated as follows. Referring, for example, to the CCP-curve for condition ≤7 in Figure 5, point C is first identified, which is the point of the higher CCP-curve for condition ≤8 at age $t = 0$. At point C, the probability is $CCP_8(0)$. By drawing a line parallel to the age axis from point C toward the lower CCP-curve, point D is determined, which is the point of the CCP-curve for condition ≤7 that has the same probability with point C. Hence, point D has probability $CCP_7(t_{o7}) = CCP_8(0)$ at age $t = t_{o7}$, thus the age t_{o7} can be calculated. Thus, in general, to evaluate the age $t_{o,i}$ of the CCP-curve for bridge condition ≤*i*, the probability $CCP_{i+1}(0)$ of the CCP-curve for condition ≤*i*+1 at age $t = 0$ is found; then, for equal probability $CCP_i(t_{o,i}) = CCP_{i+1}(0)$, the age $t = t_{o,i}$ is determined. An age $t_{o,i}$ and a corresponding coefficient c_i are calculated for each CCP-curve for condition ≤*i* having shifted data to be scaled.

Using the calculated scaling coefficients, the spreading of the shifted data can be performed for all CCP-curves. Hence, the age range of the shifted data attached to the CCP-curve for condition ≤*i* is simply multiplied by the coefficient c_i. Then, the shifted points are spread uniformly within the new, expanded age range resulting in an adjustment of the inclination of the respective CCP-curve. Note that coefficient c_i modifies only the shifted age-values and *not* the corresponding CCP-values, i.e. only age scaling is performed and the spreading of the shifted points is carried out in a horizontal manner.

Table 1. Weibull parameter values and goodness-of-fit information.

Bridge condition	α (years)	β	R^2
≤7	20.14	1.010	0.9858
≤6	58.34	1.475	0.9945
≤5	95.38	1.991	0.9958

4.6 *Fitting of Weibull distribution to the original and shifted/scaled data*

With the purpose of simultaneously obtaining a smooth CCP-curve and also achieving a good description of the respective data, a Weibull distribution (Yang 2007) can be fitted to the set of CCP-points available for bridge condition ≤*i*. Weibull distributions are extensively used for deterioration modelling and BMS (Agrawal et al. 2010). The standard (two-parameter) Weibull Cumulative Distribution Function (CDF) is given by (Yang 2007):

$$F(t) = 1 - \exp\left[-\left(\frac{t}{\alpha}\right)^{\beta}\right], \quad t \geq 0, \tag{3}$$

where $\alpha > 0$ is the scale parameter, which has the same unit as t, while $\beta > 0$ is the unitless shape parameter. Hence, for each CCP-curve, a nonlinear regression is performed to determine the Weibull parameters α and β and produce a least-squares fit based on the CDF of Equation (3).

For the cutting age adopted, Table 1 presents the Weibull parameter values calculated, as well as the coefficient of determination R^2 attained by applying the fitting procedure to the properly completed CCP-data for bridge conditions ≤7, ≤6 and ≤5. The very high R^2-values reported indicate that a very good fit has been achieved between Equation (3) and the available data. Figure 6 graphically

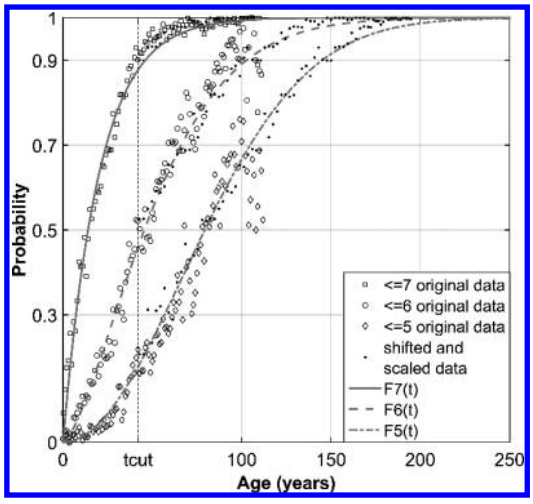

Figure 6. Weibull distributions fitted to the sample data assuming $t_{cut} = 42$ years. Original trusted and 'untrusted' data (before shifting/scaling), as well as shifted/scaled data, are shown for comparison.

illustrates the three Weibull CDFs obtained and shows a comparison of these curves with the original data. The three CDFs are graphical representations of Equation (3) using the Weibull parameter values of Table 1. These successful CDF-fits are due to the adequate size of the utilized sample, which exhibits low variation in the available data. In other cases employing lower-quality data, reduced R^2-values are observed.

5 STATISTICAL VALIDATION OF THE PROPOSED METHOD

The method proposed in the previous section uses recorded, trusted data to predict future condition probabilities. The selection of a cutting age t_{cut} is a subjective decision, which specifies the trusted part of the available data ($t \le t_{cut}$), but also creates the need to predict the condition probabilities for $t > t_{cut}$. In this section, the effectiveness of the proposed method is assessed with respect to the selected value of t_{cut}. Hence, Weibull CDFs are fitted to the same data using various t_{cut}-values and comparisons are made with the original data.

For the case study processed in this paper, original data are available until the bridge age of 114 years (Fig. 4). When a t_{cut}-value is chosen, the data recorded for $t > t_{cut}$ are excluded from the analysis. Thus, age t_{cut} represents the 'new' known present and the excluded data represent the 'unknown' future. The method's predictions for $t > t_{cut}$ can then be compared with the respective recorded data, which were excluded from the analysis. Hence, for each t_{cut}-value considered, the method of the previous section is applied to obtain a Weibull CDF for each of bridge conditions ≤7, ≤6 and ≤5. Then, two coefficients of determination can be calculated to evaluate the goodness-of-fit achieved:

- the standard coefficient of determination R^2, which compares the attained Weibull CDF with the original data for $t \le t_{cut}$ and the shifted/scaled data for $t > t_{cut}$; the R^2-value for $t_{cut} = 42$ years is reported in Table 1;
- the modified coefficient of determination R_m^2, which compares the attained Weibull CDF with the original data (before shifting/scaling) for $t \le 114$ years ($t_{cut} \to \infty$); Figure 6 provides a graphical representation of the original data (along with the Weibull CDFs identified for $t_{cut} = 42$ years).

Hence, the comparison with the attained Weibull CDF is performed using the original and shifted/scaled data actually used to calculate the Weibull parameter values (for R^2) or with the original unshifted/unscaled (trusted and 'untrusted') data (for R_m^2). In general, higher values for R^2 than for R_m^2 are expected.

Under real circumstances, R_m^2 cannot be calculated, because all trusted data are exploited to derive Weibull parameter values; there is no meaning in comparing the fitted CDF curve with the part of the data that cannot be trusted. However, the sample processed in this section includes data that are of acceptable quality over the whole range of bridge ages $t \le 114$ years (Fig. 4), i.e. there are actually no untrusted data. Thus, by selecting various values for t_{cut}, we can compare the resulting Weibull CDFs with original *trusted* data for bridge ages up to 114 years. In other words, we predict bridge condition probabilities for t_{cut}-114 years beyond the age t_{cut}, for which we have actual *trusted* data to compare against and can therefore calculate a meaningful value of R_m^2. This allows an objective assessment of the method proposed in the present paper.

The results obtained from fitting Weibull CDFs on the sample described in subsection 4.1 assuming various values of t_{cut} are reported in Figure 7. In particular, the upper graphs of Figures 7(a-c) show the R^2 and R_m^2-results attained for various values of t_{cut}. These results verify that the proposed method predicts satisfactorily the recorded data for various values of t_{cut}, as high R^2-values and at least adequate R_m^2-values are achieved. In general, better fits are attained for larger ages t_{cut}, because richer CCP-data are exploited. When the trusted CCP-data covers probability values (almost) up to 1, the proposed method maximizes its fitting capability

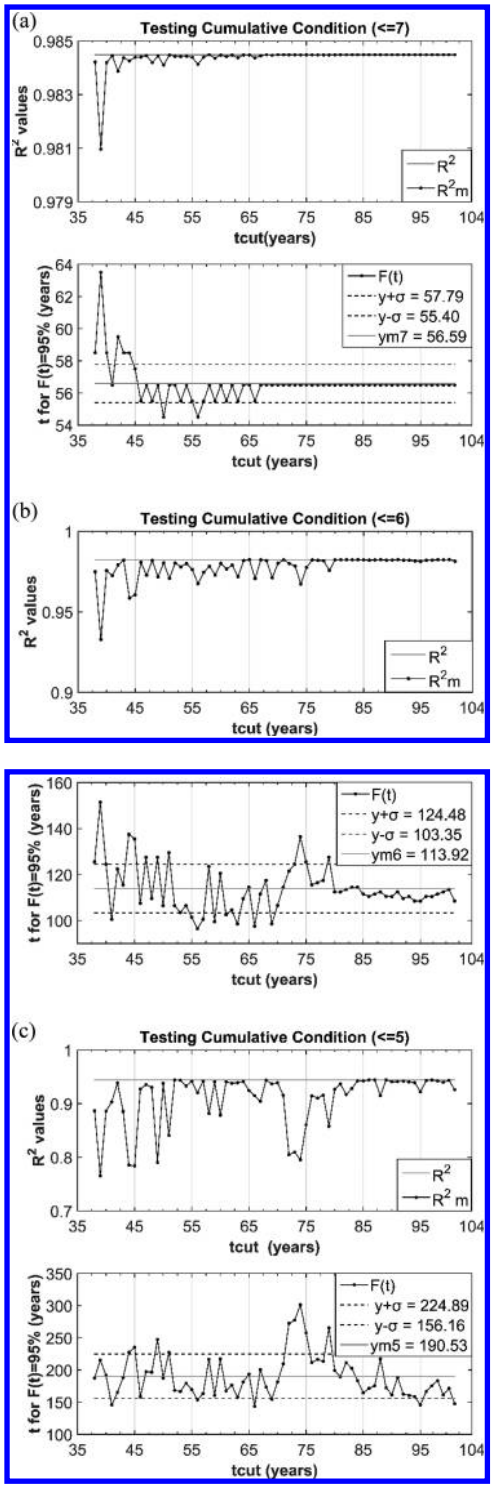

Figure 7. Statistical evaluation of the proposed method by varying the cutting age t_{cut}.

and the obtained R_m^2-value tends to be equal to the corresponding R^2-value (see Figs. 7(a),(b) for bridge conditions ≤7 and ≤6, respectively). Even in the case of bridge condition ≤5, which involves trusted CCP-data that cover probabilities up to values considerably lower than 1, high R_m^2-values are achieved for large ages t_{cut} (Fig. 7(c)).

The proposed method can be also evaluated with respect to the consistency of its results by focusing on a specific probability value $F(t)$ to reach a bridge condition. Hence, for various values of t_{cut}, the lower graphs of Figures 7(a-c) show the bridge age, at which condition ≤7, ≤6 or ≤5 is reached with probability $F(t) = 95\%$. These figures include lines that indicate the mean value and standard deviation calculated from the results for the various t_{cut}-values processed. The results of these figures demonstrate small variations around the mean age for bridge conditions ≤7 and ≤6 and acceptable variation for bridge condition ≤5.

Furthermore, Figure 8 presents analogous results in the form of boxplots for various $F(t)$-values (from 0.01% to 99.9%). Hence, for each $F(t)$-value and for all t_{cut}-values considered, the variation of the bridge age to reach condition ≤7, ≤6 or ≤5 is illustrated. It is interesting to note that a non-symmetric distribution of age predictions appears to be yielded for each $F(t)$-value. In general, a higher prediction variation is associated with a higher probability $F(t)$. Nevertheless, the selected t_{cut}-value does not seem to excessively influence the calculated age predictions.

6 PROBABILISTIC ESTIMATION OF THE TIME-TO-REHABILITATION

Using a Weibull distribution fitted to the set of CCP-points available for bridge condition ≤5, the time-to-rehabilitation can be probabilistically estimated. That is, any time-to-rehabilitation given is accompanied by a probability for the bridge considered to have reached condition ≤5, which is assumed to induce the need for rehabilitation.

The Weibull CDF for bridge condition ≤5 (Table 1, Fig. 6) provides the sought probabilistic information for the time-to-rehabilitation of a concrete bridge exposed to deicing salts and humidity: by selecting a probability of reaching bridge condition ≤5, the respective time-to-rehabilitation for the bridge is determined. Table 2 gives the time-to-rehabilitation for selected probability-values. Note that, as the term 'time-to-rehabilitation' is used herein, it counts from the year a bridge is built, i.e. this is the 'age-to-rehabilitation'. The actual time-to-rehabilitation is easily calculated by subtracting the current age of a bridge from its 'age-to-rehabilitation'. Using such information, a decision maker can make

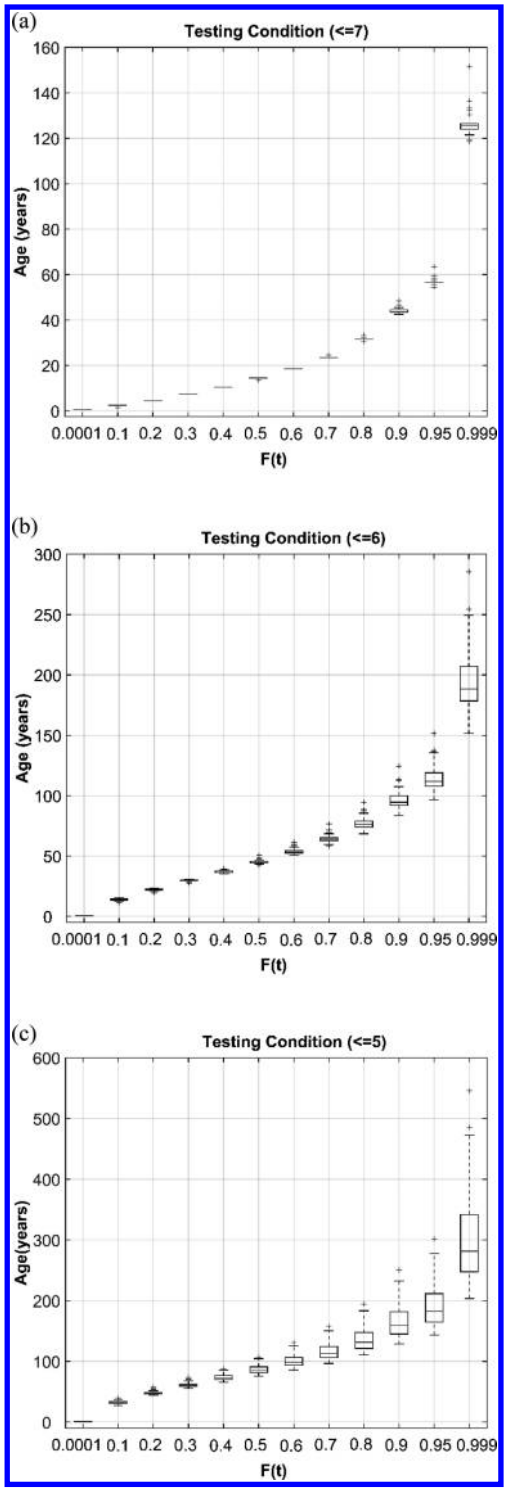

Figure 8. Boxplots for each $F(t)$-value and for all t_{cut}-values considered.

Table 2. Time-to-rehabilitation for selected probabilities of a bridge to have reached condition ≤5.

Probability to reach condition ≤5	Time-to-rehabilitation(years)
30%	57
50%	79
70%	105
90%	145

a rational schedule for bridge rehabilitations, which takes into account not only available or anticipated funds, but also risks associated with the uncertain deterioration rate of bridges.

7 CONCLUSIONS

In this paper, real condition data from the NBI database of USA' FHWA were utilized for predicting the deterioration of bridges. Specifically, probabilistic results were obtained for concrete bridges exposed to deicing salts and humidity that allow the quantitative estimation of the time-to-rehabilitation. To accomplish this task, a new method was presented for identifying a reliable probabilistic description of bridge deterioration over time. In general, reasonable deviations between original data and data predicted with the new method were observed for a large number of test configurations considered.

The procedure followed herein can be applied to any type of bridges exposed to various environmental effects, provided that respective data are available. Enriching our knowledge on the deterioration rate of bridge stocks is a key aspect in cost-effectively handling and maintaining such important infrastructures.

REFERENCES

Agrawal, A.K., Kawaguchi, A., Chen, Z. 2010. Deterioration rates of typical bridge elements in New York. *ASCE Journal of Bridge Engineering* 15:419–429.

Alogdianakis, F., Balafas, I., Charmpis, D.C. 2014. Environmental effects on bridges—Statistical durability study based on existing inspection data. *2nd International Conference on Innovations on Bridges and Soil-Bridge Interaction (IBSBI 2014)*, Athens, Greece, pp. 161–168.

Alwis, K.G.N.C., Burgoyne, C.J. 2008. Accelerated creep testing for aramid fibres using the stepped isothermal method. *Journal of Materials Science* 43(14):4789–4800.

Dunker, K.F., Rabbat, B.G. 1995. Assessing infrastructure deficiencies: The case of highway bridges. *ASCE Journal of Infrastructure Systems* 1(2):100–119.

Federal Highway Administration (FHWA). 1995. *Recording and coding guide for the structure inventory and appraisal of the nation's bridges*, Report No. FHWA-PD-96–001, Washington D.C.: U.S. Department of Transportation.

Fitzpatrick, M.W., Law, D.A., Dixon W.C. 1981. Deterioration of New York State highway structures. *60th Annual Meeting of the Transportation Research Board*, Washington D.C., USA, pp. 1–8.

Huang, Y.H. 2010. Artificial neural network model of bridge deterioration. *ASCE Journal of Performance of Constructed Facilities* 24(6):597–602.

Madanat, S., Mishalani, R., Ibrahim, W.H.W. 1995. Estimation of infrastructure transition probabilities from condition rating data. *ASCE Journal of Infrastructure Systems* 1(2):120–125.

Ng, S.K., Moses, F. 1996. Prediction of bridge service life using time-dependent reliability analysis. *3rd International Conference on Bridge Management*, University of Surrey, Guildford, UK, pp. 26–33.

Rafiq, M.I., Chryssanthopoulos, M.K., Sathananthan, S. 2015. Bridge condition modelling and prediction using dynamic Bayesian belief networks. *Structure and Infrastructure Engineering* 11(1):38–50.

Ryall, M.J. 2001. *Bridge management*. Oxford, UK: Butterworth-Heinemann.

United States Geological Survey (USGS). 2014. *National seismic hazard maps*. http://earthquake.usgs.gov/hazards/.

Yang, G. 2007. *Life cycle reliability engineering.* Hoboken, NJ, USA: John Wiley & Sons.

Concrete Repair, Rehabilitation and Retrofitting IV – Dehn et al. (Eds)
© 2016 Taylor & Francis Group, London, ISBN 978-1-138-02843-2

Orphan sustainable sensor system for monitoring chlorides or CO_2 ingress in reinforced concrete

F. Barberon & P. Gegout
Pôle Ingénierie Matériaux, Bouygues Travaux Publics, France

ABSTRACT: Depassivation and corrosion of steel bars are the most severe threat of degradation for reinforced concrete elements. Actual available monitoring systems require contact or wired instrumentation, which can lead to delay in the measurement of the penetration front or create preferential path for the ingress of the deleterious agents.

The present system is designed to anticipate the corrosion of reinforcement and consists of isolated, wireless and embedded steel sheets which dimension are about 100 µm thick and few centimeters diameter. The sensors are placed into the freshly poured concrete and positioned at different depth between the surface and the first raw of steels. The sheets are oriented perpendicularly to the diffusion front. When in contact with chlorides or CO_2 the sheets are oxidized in the same manner as the reinforcement.

The principle is to use the thermal properties of iron to check its oxidation state. When the metallic iron is subjected to a variable magnetic induction, a current is created at the surfaces (Lenz's law) with a sudden and important raise of temperature of the iron sheet (Ohm's law).

The embedded sheets are warmed-up by induction from the surface of the concrete element. The thermal response is then measured with an infrared reader, from the surface of the concrete, and the signal analyzed to assess the state of oxidation. Indeed, dissimilar to a sound sheet, the oxidized one will provide with a different thermal response, which signal is of low amplitude and rapid decay. The position and the depth of the sheets being previously located in the structure, it is thus possible to determine, at any given time, the front of diffusion.

It is believed that the proposed non destructive method permits to anticipate the level of propagation of chlorides or CO_2 and promote mitigation measures prior the depassivation of the reinforcement steel and need of major repair.

1 INTRODUCTION

Among the main pathologies of the reinforced concrete, corrosion of reinforcement remains the most important by the number of works concerned, and certainly by the costs associated with their repair. The corrosion comes from CO_2 or chlorides, which progress by diffusion into the concrete. To ensure the maintenance and select repair methods, it is important to establish a diagnosis as accurate as possible, and as soon as possible too. Generally, the appearance of rust, or even spalling on surface, is evidences of a corrosion already widely initiated within the concrete.

If semi destructive sampling and analysis method are often necessary to refine the assumptions from the initial observations carried out on site, we can observe nowadays the development of non-destructive detection techniques, non to minimally invasive, allowing to maintain the work integrity, whether it is structural or aesthetic reasons. The principles of measurements are optical, acoustic, or electrical. Potential measurement on steels, associated to a prior location by radar, allows, for already several years, to obtain relevant information on the state of damage of steel (Dollet & Taché et al. 2010). Acoustic emission measurements (EA), for their part, record the micro cracks in the corrosion of steels, but cannot, in the same way confirm the start of the phenomenon (Idrissi et al. 2010), as well as measurement of the deformation by optical fibers (Mc Cartera 2004, Habel et al. 2005).

Apart from EA, these methods require however a physical connection between the steels and the data recording system. These wired connections create interfaces, and, in the case of measurements over long periods, notably in less accessible areas, they are likely to 'interfer'. In addition, the recent results on the initiation of corrosion by chlorides show that the nature of the binder impacted strongly on the measurement, resulting in an actual diagnosis error (Garcia 2013). Finally, these methods do provide information on the state of the reinforcement at a given moment, but don't allow anticipation.

The goal of our approach is to follow the ingress of the front, and not the state of corrosion of reinforcement. So it is possible to locate this front in the coating at any moment, without contact or wired connection from the outside. The measure would also be simple to carry out. The method consists of measuring the thermal properties of the iron that evolve depending on its oxidation state. The determination is carried from the surface of the concrete, not on the reinforcement steels, but on metal elements- the sensors- correctly arranged within the concrete cover and playing a role of fuses.

Of course and contrary to the actual systems being applicable on hardened concrete structures, this new patented system requires the positioning of the sensors in the freshly poured concrete.

2 TECHNOLOGICAL CHOICES

2.1 *Existing systems*

Existing systems so far are mostly based on potential measurement (Schiessl 1991, Raupach 1996, Raupach & Schiessl 1997, AFGC 2005). Each of them has advantages and disadvantages, for the lifetime of the sensors used either the reliability of measurement, which can be disrupted by the surrounding conditions, such for example as the local humidity conditions, changing the resistivity of the material. The costs of such systems can be prohibitive and limit the number of installations, which in the end may provide with a result unrepresentative of the overall condition of the structure. Very recently, the work of Garcia (2010) has shown that the nature of binders, especially those made with slag cements, could impact considerably the potential of corrosion of reinforcement. The research showed that while considering a cement replacement of 30% and more the potential loss was not necessarily correlated with an initiation of the corrosion of the steels.

2.2 *Proposed system*

The proposed principle is based on the association of two elements: the initial positioning of 'sensors' within the coating, and the use of the thermal properties of metallic iron in its oxidation state.

2.3 *Position of the sensors into the concrete*

The sensors are circular or square metal sheets about 100 µm thick with a surface of the order of a few square centimeters. They are arranged during the pouring of concrete and geographically identified by any means available, physical mark on the concrete surface or mapped by GPS. They are sufficiently spaced laterally to avoid interference between each other, and positioned by depth approximately every centimeter (Figs. 1, 2).

Tests have shown that once arranged (for a not too fluid concrete) the process of concrete compaction does not significantly displace or change the position of the sensor. However, attention shall be paid to avoid moving the sensor with the vibrating needle.

Chloride and CO_2 progress by diffusion in the concrete. This front is going through the cement paste towards the forefront of reinforcement steels. When chloride or CO_2 reaches the sensor, it behaves like steel and will corrode. The sensors are orphan, i.e. not connected physically with any device between them, nor to an external system. Individually response of each of the sensors, allows to precisely locate the front of aggression. The cost of the sensors being only a few euros, it is possible to lay a number of sensors enough in supposed strategic and sensitive locations and therefore

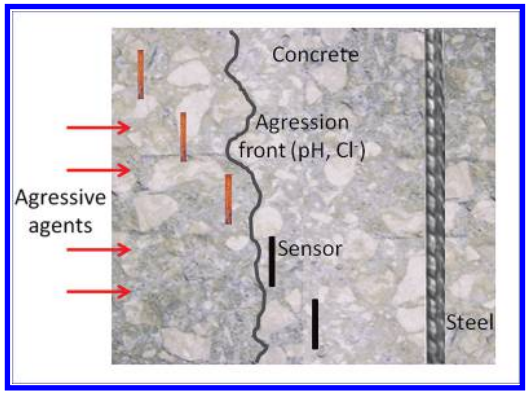

Figure 1. Vertical view of the layout of the sensors into the concrete between surface and first rebar.

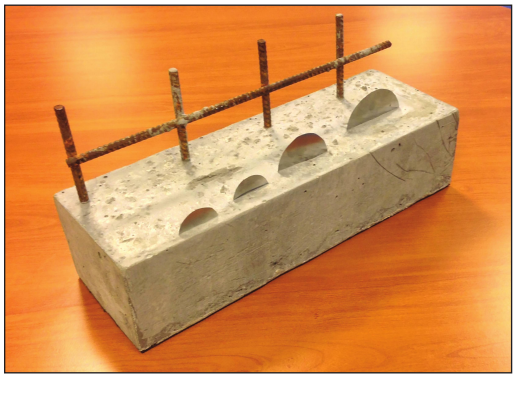

Figure 2. Example of position of sensors between surface and steel in concrete prism.

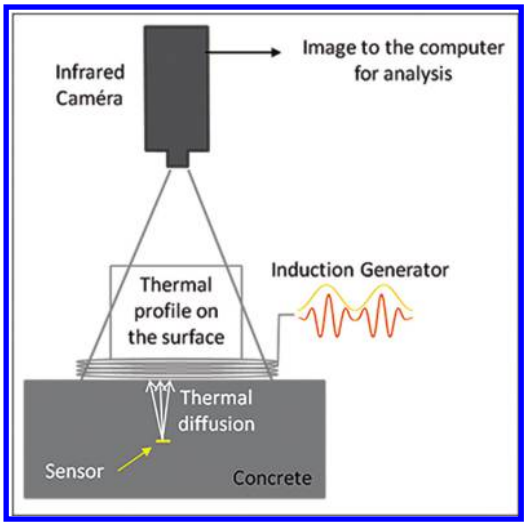

Figure 3. Principle of measurement of the state of corrosion of the sensor.

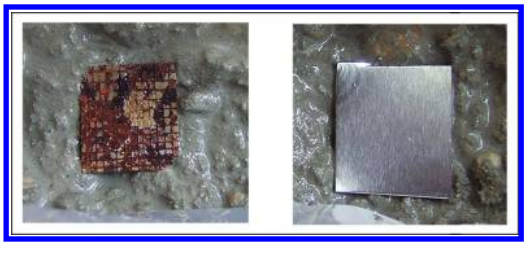

Figure 4. Example of sensors: artificially corroded (left) and healthy (right).

obtain a sufficient and reliable statistical picture of the penetration front of chlorides or CO_2.

2.4 *Measurement principle*

The principle of measurement is visible in figure 3.

The measurement of the corrosion level of the metal sheets is based on the thermal properties of the iron and its oxidation state. The principle is to excite the sensor, from the surface of the concrete, by magnetic induction (Lenz's law). This magnetic induction mobilizes electrons on the surface of the metallic sheet, according to its conductivity (Eddy currents). If the sheet is sound, it is very conductive and heat up by Joule's effect (Ohm's law), while a corroded sensor warms up to a lower level. Thus, by studying the temperature response of a sensor embedded in the concrete through an infrared camera, it is possible to estimate its state of corrosion.

To verify the thermal response of sensors after warm-up, tests were previously conducted on sound and artificially corroded sensors by attack in acid solution (Fig. 4).

3 EXPERIMENTS AND RESULTS

Trials were conducted to assess the optimal thermal response versus different size of the sensors embedded into the concrete.

In the above experiment, 2 sensors were introduced at a depth of 2 cm in one mortar prism size $15 \times 6 \times 4$ cm. The prism was excited during 50 s by magnetic induction under a few micro Tesla field. The thermal response in the prism surface measured by infrared thermography, just after induction, but also 1 min, 2 min and 4 min after induction are presented in figure 5.

On the one hand, the intensity of the hot spot corresponding to the partially corroded sensor is lower than the one corresponding to the sound sensor; and, on the other hand the hot point associated to the partially corroded sensor disappears much faster. The static and dynamic responses can be therefore considered as a sensitive and discriminating indicator between sound and corroded sensor.

After the induction period, the infrared camera allows in front of each sensor to record the evolution of temperature of the surface of concrete. As an example, we can see on figure 6, the repartition of temperature of a sound sensor in a concrete prism.

A series of complementary tests allowed defining the optimal size of the sensors and the heating power needed to achieve a workable response (Fig. 7). These tests enabled to find a compromise between the duration of induction required to raise the temperature of a few degrees in a sound sensor and the surface area of the sensor at various depth/concrete cover. The optimum is respectively 2 minutes and 50 cm² maximum for the most distant sensors.

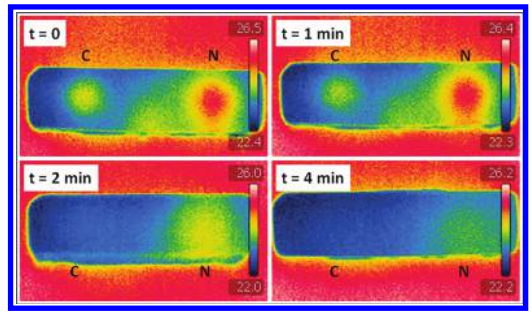

Figure 5. Infrared images just after excitement then 1 min, 2 min and 4 min. of corroded (C) and not corroded (N) sensors. On corroded sensor (C) we observe a low intensity which decreases quickly during time. On not corroded sensor (N), the intensity is strong and decreases slowly. The central hot spot on the first two images matches fingerprints of the operator on the concrete surface of the sample.

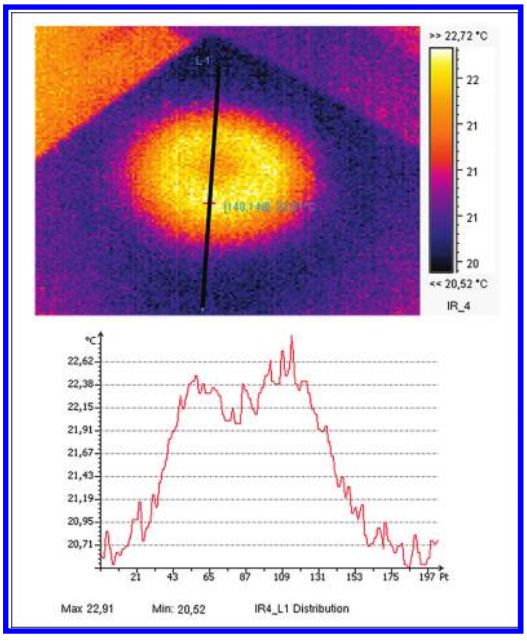

Figure 6. Repartition of the temperature at the surface of the concrete in front of a sound sensor after application of magnetic induction. Top: infrared photography from the camera; Bottom: temperature along the diameter of the sensor (black line). The difference between initial and maximal temperature is about 2°C.

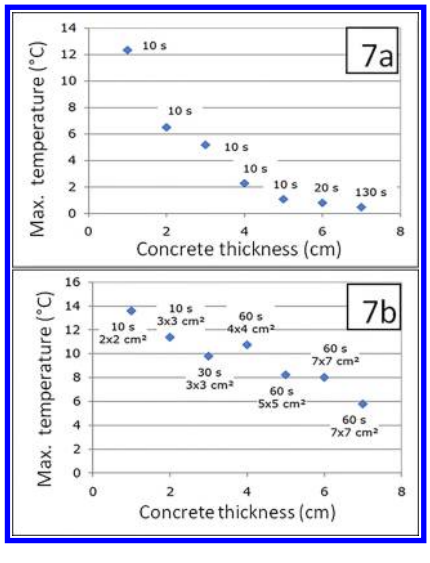

Figure 7. Examples of thermal responses of healthy and corroded sensors for various depths, with the same induction power. The values on each point correspond to the same induction: 7a: at the time of induction, in seconds, for a same surface of the sensor (here 2 cm^2); 7b: on the surface of the sensor, cm^2, associated with a specified induction time.

For the same sensor surface (2 × 2 cm) and the same power of induction, the achieved maximum temperature elevation decrease with the depth of the sensor (Fig. 7a). After 7 cm depth, the thermal response becomes very small and the induction duration need to be high (130 s).

For a better thermal signal, we need to increase the surface of the sensors when the thickness of concrete becomes too important. On figure 7b, we can see the temperature elevation and the influence of the surface of the sensor and the duration of induction before infrared measurement. For a surface of sensor about 50 cm^2 and a duration of 60 seconds of induction, we still measure 6°C temperature raise at the concrete surface.

So, up to 7 cm deep, it is possible to record a significant thermal signal according to the state of corrosion of a sensor, with a compromise between time of induction and surface of the sensor. Smaller sensors will be placed near the surface, under about 3 cm, with a good thermal response, and larger will be used deeper.

4 CONCLUSIONS

The patented system presented in this article makes use of the thermal properties of metallic iron to follow the diffusion front of CO_2 or chloride through the concrete structure cover; and aims to anticipate the initiation of corrosion of reinforcement.

Sensors are orphans and have no connection with the outside world. Excited by induction through an external magnetic field, their heat-up response is related to the state of corrosion. These sensors in fact play a role of fuses. With their positioning in chevron in the coating, it is thus possible to relatively well identify the forehead of the CO_2 diffusion or chlorides until it reaches the first rebars. Actual tests allow to use these sensors up to a depth of approximately 7 cm, for a duration of measurement which is of the order of a few minutes maximum. A compromise needs to be found between surface of the sensor and induction duration.

From 2013, a hundred sensors were installed in a concrete structure exposed to sea spray to try to follow diffusion front during time in a real situation. Follow-up actions are planned in the coming years and will make a return of experience and refine the method if necessary.

ACKNOWLEDGMENT

The authors thank J. Lopez-Rios (Ciprian) for active participation on development of the method,

and Y. Taibi (Bouygues TP) for helping on durability concrete.

REFERENCES

AFGC 2005: *Méthodologie d'évaluation non destructive de l'état d'altération des ouvrages en béton*. Association française de génie civil, Presses de l'école nationale des Ponts et Chaussées, ISBN: 2-85978-405-5.

Dollet A. et Taché G. 2010: *Méthodes de diagnostic du béton armé, in Anticorrosion et durabilité dans le bâtiment et le génie civil*, S. Audisio et G Béranger, pp. 659–668. Presses polyt. et univ. Romandes ed.

Garcia V., 2013: *Contribution du taux de chlorures pour l'amorçage de la corrosion des armatures du béton armé*. Thèse Univ. de Toulouse 3 Paul Sabatier, LMDC.

Idrissi H., Lenain JC, Proust A., Watson J., 2010: *Détection de la corrosion des armatures de béton armé par émission acoustique, in Anticorrosion et durabilité dans le bâtiment et le génie civil*, S. Audisio et G Béranger, pp. 659–668. Presses polyt. et univ. Romandes ed.

Mc Cartera W.J., Ø. Venneslandb, 2004: *Sensor systems for use in reinforced concrete structures* (Review), Construction and Building Materials, 18, 20, 351–358.

Nathan N., Habel W.R., Wolfbeis O.S, 2005: Fiber optic pH sensor for early detection of danger of corrosion in steelreinforced concrete structures. *Smart Structures and Materials* 2005, proc of SPIE.

Raupach M., 1996: Chloride-induced macrocell corrosion of steel in concrete-theoretical background and practical consequences. *Construction and Building Materials*, Vol. 10, 5, pp. 329–338.

Raupach M., Schiessl P. 1997: Monitoring system for the penetration of chlorides, carbonation and the corrosion risk for the reinforcement. *Construction and Building Materials*, Vol. 11, 4, pp. 207–214.

Schiessl P., 1991: *Corrosion measuring cell*. Patent, US5015355, 04/05/1991.

Education, research and specifications

Concrete Repair, Rehabilitation and Retrofitting IV – Dehn et al. (Eds)
© 2016 Taylor & Francis Group, London, ISBN 978-1-138-02843-2

Numerical modeling of basic creep of concrete under different types of load

N. Ranaivomanana, S. Multon, A. Turatsinze & A. Sellier
Université de Toulouse, UPS, INSA, LMDC, Grenoble, France

ABSTRACT: Despite a relative abundant literature on the topic, delayed mechanical behaviour of concrete remains a problematic of contemporary research. Underestimating concrete creep during the designing phase may lead to well-known consequences such as excessive strains, losses of prestress and even sometimes failure. This study aims to a better understanding of concrete's delayed mechanical behaviour by means of the modeling of basic creep of concrete under different types of load namely direct tension, compression and bending. For the purpose, an original model was developed; it takes into account physical phenomena, namely consolidation and damage induced by creep, to reproduce experimental findings. Such an approach allows a better understanding of the coupling between shrinkage, damage and creep in concrete.

1 INTRODUCTION

Concrete has a very complex mechanical behaviour. Creep (increase in strain with time when the load is maintained constant) is an important part of this behaviour. Underestimating creep during designing phase of concrete elements may lead to the well-known consequences such as excessive strain (or displacements) in concrete members, losses of prestress, redistribution of stress and even sometimes failure. Creep of concrete was highlighted for the first time by Hyatt in USA in 1907 and by Freyssinet in France some years later, more exactly in 1912, regardless the works of Hyatt (Pons & Torrenti 2008). Before that, design rules concerning reinforced concrete structures such as the French one (the circular of 1906) supposed that the elastic modulus of concrete, as that of steel, is practically constant. This is no longer the case of design codes currently in force (Eurocode 2, ACI209, etc.). For example, in order to take into account creep, the European standard Eurocode 2 considers an equivalent coefficient (steel/concrete elasticity modulus ratio) greater than or equal to 15. In the same context, some empirical formulas to estimate delayed strain are also proposed. However, in particular cases, long term management of civil engineering concrete structures requires finite elements modeling which may be more accurate than standards predictions, especially when dealing with exceptional structures such as dams, nuclear power plants, nuclear waste storage tunnels, etc. Phenomenological models based on linear viscoelastic principles using rheological elements are widely used in creep modeling. However, their application to the case of concrete has not always proved relevant. For example, they fail to reproduce the creep of concrete under different type of load (namely in direct tension and in compression) by means of a single formulation, without introducing additional parameters that have no physical meaning (Reviron 2009). Concrete has a very complex delayed behaviour, including delayed strain occurring under loading (creep) and without loading (shrinkage). A common way to carry out measurements is to split delayed strains of concrete into different components including autogenous shrinkage, drying shrinkage, basic creep and drying creep, which assumes a decoupling of underlying phenomena (Rilem TC-107 1998). Actually, there is a strong coupling between these components, which has to be taken into account in the modeling and one of the most appropriate framework for that is the poro-mechanics one. Thus, from the poro-mechanics point of view, shrinkage (autogenous or drying shrinkage) results from water effects on the viscoelastic solid skeleton whereas basic creep is the effect of effective stresses. Their coupling is then implicitly assumed. In its original variant, poro-mechanics cannot however explain the additional strain observed when a concrete specimen is subjected to mechanical loading along with drying (the so-called "Pickett effect"). This explains why some authors (Bazant 2001, Benboudjema et al. 2005) have chosen to add a further component to poro-mechanics models to take this phenomenon into account. This approach, more phenomenological than physical, points out a gap in physical

comprehension of involved mechanisms and consequently in the poro-mechanics formulation. Another aspect which characterizes basic creep of concrete and not taken into account in most of models is the non-linearity of delayed strains magnitude with regards to the applied stress, which occurs for high load-levels. If this aspect is not accurately modeled, the risks that tertiary creep-induced failure occurs can be overestimated. In this study, an original approach for modeling the basic creep of concrete is developed (Sellier et al. 2012). The originality of the model relies on physical phenomena taken into account, namely consolidation (allowing creep potential depletion under hydro-mechanical loading to be reproduced) and damage induced by creep. Such an approach allows a better understanding of the coupling between shrinkage, damage and creep. Finally, a comparison of the model prediction with basic creep of concrete under different types of load (in direct tension, in compression and in bending) is proposed.

2 DESCRIPTION OF THE MODEL

2.1 *Principles of the modified poro-mechanics formulation*

As stated above, classical poro-mechanics formulation allows different aspects of delayed behaviour of concrete such as shrinkage or basic creep to be explained. In this formulation, the total stress tensor σ can be expressed as follows:

$$\sigma = \sigma' - b_0 \pi \tag{1}$$

where σ' represents the effective stress tensor corresponding to the stress part supported by the solid skeleton, b_0 the Biot tensor representing the part of pressure transmitted to the solid skeleton and π the equivalent pressure which depends on the saturation state of the porosity and defined by:

$$\pi = S_l P_l + S_g P_g - \frac{\partial(U\phi)}{\partial\phi} \tag{2}$$

In this expression, S_l and S_g are respectively the saturation degree of the porosity ϕ by liquid and gaz at the pressure P_l and P_g, U is the liquid-gas interface free-energy. Equation (2) can be rewritten as follows:

$$\pi = S_l P_l + (1 - S_l) P_g - \frac{\partial(U\phi)}{\partial\phi} \tag{3}$$

$$\pi = -S_l (P_g - P_l) + P_g - \frac{\partial(U\phi)}{\partial\phi} \tag{4}$$

In general case, the gaz pressure P_g which is in equilibrium with atmospheric pressure can be neglected until the dimensions of the structure are not so important. This is also the case of the variation of interfaces free-energy considering a monotonic hydraulic path. In these conditions, the expression of the equivalent pressure becomes:

$$\pi \approx -S_l (P_g - P_l) = -S_l P_c \tag{5}$$

With P_c the equivalent capillary pressure taking into account the coupling between capillary pressure and disjunction force (Powers 1968).

From equation (5), equivalent pressure π can thus be expressed in function of the saturation degree S_l, knowing the sorption-desorption isotherm (Bazant 1972, Benboudjema 2002, Powers 1968).

To make easy the model implementation in finite elements codes, a simplified approach as that used by (Sellier & Buffo-Lacarrière 2009) to simulate shrinkage was adopted. Equivalent capillary pressure P_c is assumed to vary linearly in function of water content w (by volume) as shown in the following expression, obtained by neglecting the contribution of the pore volume variation due to the volumetric deformation of the solid skeleton:

$$P_c \approx -M_{shr}(w - \phi) \tag{6}$$

M_{shr} is a parameter equivalent to a Biot modulus. This expression allows the shrinkage of concrete to be simulated up to a saturation degree of about 50%.

The classical poro-mechanics formulation does not however allow "Pickett Effect" to be reproduced. Drying creep phenomenon is usually interpreted as a structural effect. Due to concrete microstructure heterogeneity, a very complex stress state can result from the different types of shrinkage of the matrix or more generally from an overall deformation. At local scale, micro-cracks will occur if the local tensile stress exceeds the tensile strength of the material. When no load is applied to a concrete specimen (such as a specimen undergoing free shrinkage), the micro-cracks will be oriented randomly. Now, if a compressive stress is applied, the stress in the loaded direction is shifted to the compression domain. Consequently, the risk for micro-damage formation is reduced in the compressive loading direction but remains important in the non-loaded one, so that micro-damage state becomes anisotropic (Sellier et al. 2012). On the other hand, the application of a compressive load leads to the re-closure of some of micro-cracks induced by shrinkage. Actually, only the non-damaged part of the matrix is able to transmit its shrinkage to the macro-scale. Thus, a loaded specimen will exhibit a more pronounced shrinkage that a non-loaded one and this structural effect can

explain a great part of the "Pickett Effect". From a statistical point of view, the probability of existence of tensile zones decreases in the direction which was loaded in compression. The application of a compressive stress σ (negative value by convention) will therefore increase the equivalent pressure in the loaded direction and this can be expressed by the following modified poro-mechanics formulation (Sellier et al. 2012):

$$\sigma = \sigma' - b_0\left(1 - \frac{\sigma}{\sigma_{dc}}\right)\pi \tag{7}$$

The previous relation introduces a modulation of the Biot tensor with the aim to take account the pressure effect rising in the loaded direction. σ_{dc} is a material parameter considering both the stress field heterogeneity and its effect on the equivalent pressure amplitude.

2.2 *Basic creep modeling*

The effective stress σ' can be assessed by means of a basic creep model. Delayed strains result from the combined effects of the external loading σ and the equivalent pressure π. In general, geomaterials exhibit behaviour which can be split in 3 parts: instantaneous reversible strain, reversible delayed strain and irreversible delayed strain. Consequently, the viscoelatic solid skeleton is modeled by a Burger chain represented in figure 1. The Hooke element (superscript e) allows instantaneous elastic response ε^e to be simulated, the Kelvin-Voigt element (superscript KV) is associated with reversible viscous strain ε^{KV} and the Maxwell element (superscript M) is associated with irreversible viscous strain ε^M. This scheme is applied separately to each component of σ′ tensor. Compressibility coefficients k are used for the spherical part of σ′ while shear coefficients μ are used for the deviatoric part of σ′.

2.2.1 *Constitutive equations*

The set of differential equations to be solved for spherical branch is the following:

$$\begin{cases} \sigma'^{s} = k^e \varepsilon^{e(s)} \\ k^e \varepsilon^{e(s)} = k^{KV} \varepsilon^{KV(s)} + \eta^{KV(s)} \dot{\varepsilon}^{KV(s)} \\ k^e \varepsilon^{e(s)} = \eta^{M(s)} \dot{\varepsilon}^{M(s)} \end{cases} \tag{8}$$

For the deviatoric branch, one can obtain the following system:

$$\begin{cases} \sigma'^{d} = 2\mu^e \varepsilon^{e(d)} \\ 2\mu^e \varepsilon^{e(d)} = 2\mu^{KV} \varepsilon^{KV(d)} + \eta^{KV(d)} \dot{\varepsilon}^{KV(d)} \\ 2\mu^e \varepsilon^{e(d)} = \eta^{M(d)} \dot{\varepsilon}^{M(s)} \end{cases} \tag{9}$$

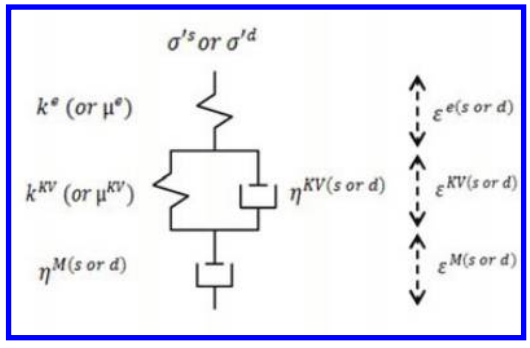

Figure 1. Rheological scheme used for basic creep modeling.

The differential equations are solved numerically using a "step by step" temporal integration scheme. The originality of the model relies on the Maxwell level presented in the following sections, the two upper levels being usual.

2.2.2 *Consolidation and basic creep induced damage*

Experimental results obtained over a long term period point out that creep rate slows down progressively with time, and more precisely with delayed stain (creep and/or shrinkage) undergone by a concrete specimen. During a creep experiment, viscous phases of the cement matrix (mainly C-S-H gel) are progressively interlocked by the other non-viscous phases (other hydrated phases, aggregates, etc.) according to the "consolidation theory" (Sellier & Buffo-Lacarrière 2009). This progressive creep sites depletion corresponding to a "creep potential decrease" is taken into account in the model by an increase of the apparent viscosity of the Maxwell element η^M. A simple way to represent this consolidation phenomenon is:

$$\eta^M = \eta^0 C_C \tag{10}$$

Where η^0 is the viscosity at the beginning of the loading and Cc the consolidation coefficient defined by:

$$C_C = \exp\left(\frac{\varepsilon^{eq}}{\varepsilon^k}\right) \tag{11}$$

In this expression which allows very long term strain evolution to be reproduced, ε^{eq} is the equivalent strain which quantify the cumulated viscous strains undergone by concrete during its history and ε^k a parameter playing the role of a creep strain potential. When the equivalent strain ε^{eq} is large compared with ε^k, the consolidation coefficient increases and then the creep rate decreases

to simulate interlocking phenomena. ε^{eq} is taken proportional to the viscous dissipation ϕ^v, the expression of which is:

$$\phi^V = \int (\varphi^s + \varphi^d) dt \tag{12}$$

where φ^s and φ^d are respectively the spherical and the deviatoric instantaneous viscous dissipation:

$$\begin{cases} \varphi^s = \vec{\sigma}^{M(s)} \cdot \vec{\dot{\varepsilon}}^{M(s)} \\ \varphi^d = \vec{\sigma}^{M(d)} \cdot \vec{\dot{\varepsilon}}^{M(d)} \end{cases} \tag{13}$$

On the other hand, during the interlocking process between viscous and non-viscous phases mentioned above, the part of viscous stresses supported by viscous phases is progressively transferred to the non-viscous phases. Such stress redistribution leads to stress concentration on non-viscous sites, able to damage them and then liberates new creep sites. This "creep-induced damage" d^{bc} is a function of the load level and also of the consolidation state because consolidation is responsible for stress transfer. The only condition that d^{bc} has to fulfil to be in agreement with thermodynamic principles is the one indicated in (14):

$$\dot{d}^{bc} \geq 0 \tag{14}$$

If d^{∞} represents the asymptotic creep-induced damage reached theoretically for an infinite time (i.e. when $Cc \to \infty$), the evolution law of d^{bc} can be written as follow:

$$d^{bc}(t) = d^{\infty}\left(1 - \frac{1}{C_C(t)}\right) \tag{15}$$

Creep-induced damage d^{bc} can be represented in function of its associated "thermodynamic force" namely the damage strain energy release rate Y:

$$d^{bc} = f(Y) \tag{16}$$

d^{∞} is expressed as function of the maximum creep-induced damage which can be reached d^{max} as follows:

$$d^{\infty} = \frac{d^{\max}}{Y^{\max}} Y \tag{17}$$

The equation (17) allows d^{max} to be expressed as a material parameter independent of the compressive strength of the material R_c which is present in Y^{max} (see equation 19).

The damage strain energy release rate can be expressed as follows:

$$Y = \frac{J_2}{2\mu} + \frac{1}{2k}\left(\frac{I_1}{3}\right)^2 \tag{18}$$

where I1 and J2 are respectively the first invariant of the effective stress tensor (from the point of view of damage mechanics) and the second invariant of the effective stress deviatoric tensor. Y^{max} is a fitting parameter such that d^{max} is reached when the loading allows $Y = Y^{max}$ to be obtained.

$$Y^{\max} = \frac{1}{2}\frac{R_C^2}{E} \tag{19}$$

Finally, the creep potential ε^k can be defined from the asymptotic creep-induced damage d^{∞} by:

$$\varepsilon^k = \varepsilon^0 \frac{d^{\infty}}{d^{\max}} \tag{20}$$

In equation (20), ε^0 is the characteristic strain for the consolidation process, which is a parameter independent of loading.

Therefore, the poro-mechanics formulation (7) has to be modified to take into account the coupling between creep-induced damage and poro-mechanical loading as follows:

$$\sigma = (1 - d^{bc})\sigma' - b_0\left(1 - \frac{\sigma}{\sigma_{dc}}\right)\pi \tag{21}$$

Equation (21) allows a great part of the non-linearity of creep amplitude in relation to load level to be explained. It is important to mention that the different components of delayed concrete strains can thus be reproduced by means of a single formulation thanks to a "unified approach" (Sellier & Buffo-Lacarrière 2009).

2.3 *Calibration parameters*

Three steps are required to simulate the delayed strains of concrete under different types of load (in our case, in direct tension, compression and bending) by means of the model:

1. The M_{shr} parameter is first calibrated to simulate a free-shrinkage test. This first step is essential since it defines the consolidation state of the material before an external loading.

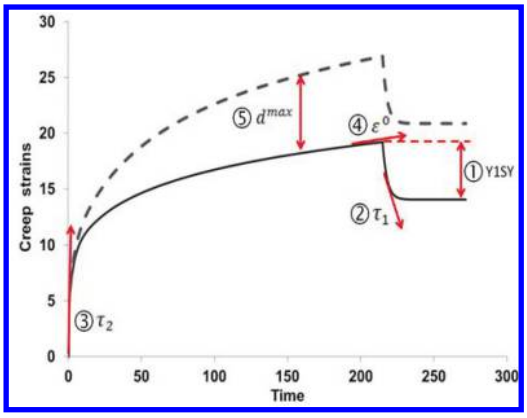

Figure 2. Rheological parameters calibration steps.

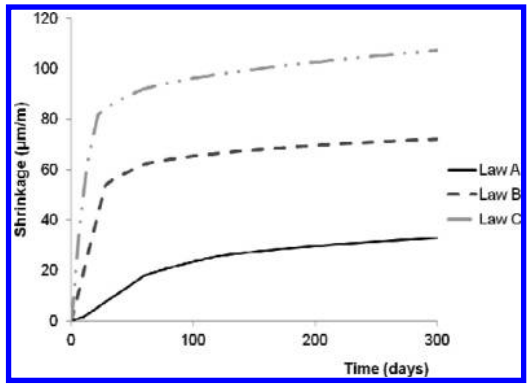

Figure 3. Simulated shrinkage strains obtained by means of the three evolution laws.

2. The basic creep parameters are then calibrated by means of compressive basic creep test simulations.
3. The final validation is carried out by simulating tensile creep tests (in direct tension and in bending) and by comparing simulated results with experimental ones.

The calibration of the creep model parameters in compression includes 5 steps described above as represented in the figure 2.

- The amplitude ① and the kinetics ② of the recovery supply respectively the compressibility/shear coefficient and the viscosity coefficient of the Kelvin-Voigt level by means of the parameters Y1SY and τ_1. Y1SY corresponds to the ratio k^{KV}/k^e while τ_1 is the characteristic time of the Kelvin-Voigt level. The amplitude of the reversibe part of the creep decreases when the value of Y1SY increases.
- The characteristic time of the Maxwell element τ_2 ③ which defines the initial viscosity η^0 is adjusted until the initial rate of simulated creep curve match initial rate of experimental results.
- The value of the characteristic strain for the consolidation process ε^0 is calibrated to obtain the amplitude at the end of the loading. The more important the value of ε^0, the greater the final amplitude because an increase in creep potential leads to slow-down the consolidation process.
- The previous parameters are obtained by fitting experimental creep results where damage is not significant, for example for a 30% load level which is generally the reference for creep tests. The value of the parameter d^{max} ⑤ is such that experimental creep test results for higher load level (50% in the case of this study) can be reproduced without changing the values of other parameters.

3 APPLICATION OF THE MODEL TO PREDICT BASIC CREEP OF CONCRETE UNDER DIFFERENT TYPES OF LOADING

3.1 *Free-shrinkage simulation*

This paper is devoted to the simulation of basic creep of concrete under mechanical load. However, as mentioned in the introduction, creep and shrinkage of concrete are coupled and they cannot be simply dissociated. This highlights the impact of shrinkage, particularly the built-in consolidation phenomenon, in the creep modeling. One have to note that the concrete used in this study (Ranaivomanana et al. 2013) is the same that the one used by Brue (2010) in her PhD. M_{shr} is then determined from the slope of the desorption isotherm of Brue expressed as the capillary pressure in function of the water content. A M_{shr} of 1500 MPa has been found and will be used in the following calculations.

A parametric study is then conducted to have three different consolidation states before loading in order to analyze its impact on creep strain for the different types of loading. For that purpose, three shrinkage final amplitudes were considered by means of three water content evolution laws (called evolution laws A, B and C in the following). The shrinkage amplitude calculated after 300 days are respectively about 35 µm/m, 70 µm/m and 110 µm/m for the laws A, B and C respectively as shown in figure 3. The amplitude of viscous strain undergone by the material is actually the most important aspect to be taken into account with regard to

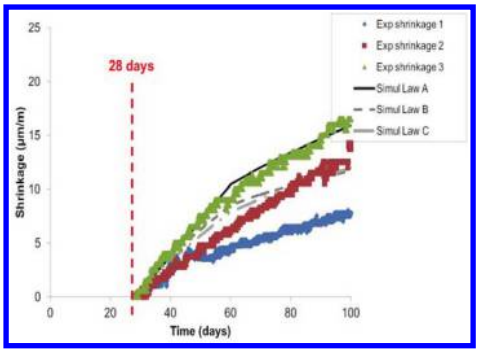

Figure 4. Predicted shrinkage strain from 28 days by means of the 3 evolution laws compared with experimental results.

Table 1. Materials parameters used to simulate compressive creep test at 30% and 50%.

Parameter	Origin	Notation	Value
Elastic modulus (MPa)	measured	E	41617
Poisson coefficient	usual	υ	0.2
Comp. strength (MPa)	measured	Rc	68.2
Tens. Strength (MPa)	measured	Rt	3.0
Pick strain in comp.	usual	ε^c	2×10^{-3}
Pick strain in tens.	usual	ε^t	1.3×10^{-3}

the consolidation phenomenon. As it can be seen in figure 4, the three evolution laws show that the model prediction and the experimental shrinkage measured after 28 days are in a good agreement.

3.2 *Compressive basic creep modeling*

The compressive basic creep simulations are carried out by considering the three previous assumptions on shrinkage. As in practice, shrinkage is deduced from total strains to get creep strains. The parameters calibration process was explained in above section. The value of parameter σ_{dc} was fixed to 27 MPa according to a previous study conducted in desiccation conditions (Sellier et al. 2012). Table 1 summarizes the material parameters and the values used for the simulations of the 30% and 50% compressive basic creep with their origin. The specimens were loaded at 28 days while unloading has been carried out after 215 days of loading.

The model parameters allowing reproducing the experimental results for each assumption on water content evolution law are presented in table 2. The predicted results are reported on figures 5, 6 and 7.

As can be seen on these figures, a good restitution of the experimental results can be obtained by means of the three assumptions on shrinkage and it is thus impossible for now to reject any of these

Table 2. Rheological parameters used to simulate compressive creep test at 30% and 50%.

Parameter	Law A	Law B	Law C
Y1SY	6	6	6
τ_1 (days)	3	3	3
τ_2 (days)	80	200	200
ε^0	4×10^{-4}	3.7×10^{-4}	2.7×10^{-4}
d^{max}	0.58	0.52	0.38

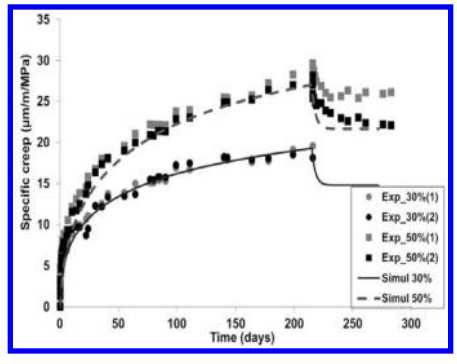

Figure 5. Simulated compressive creep curve at 30% and 50% obtained with law A.

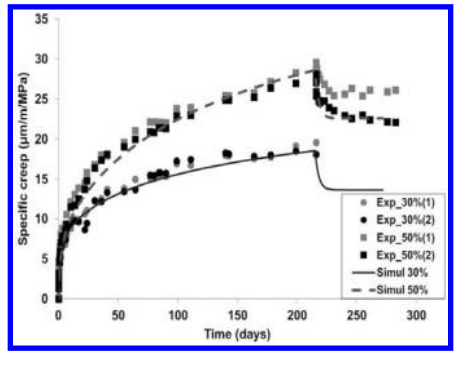

Figure 6. Simulated compressive creep curve at 30% and 50% obtained with law B.

assumptions. Some comments can also be made about the apparent non-linearity which is actually the effect of micro-damage acting as follows:

- Creep-induced damage increases the effective stress (from the point of view of the damage mechanics) which is responsible for creep strain and which increases in turn the creep amplitude.
- Application of a compressive loading tends to re-close microcracks allowing a better transmission of pressure in the loaded direction. This supplementary shrinkage explains another part on the non-linearity given that the cracks re-closure and

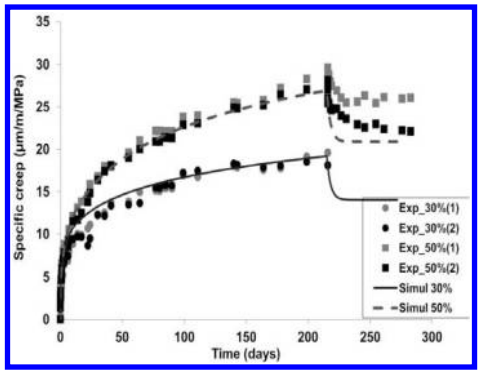

Figure 7. Simulated compressive creep curve at 30% and 50% obtained with law C.

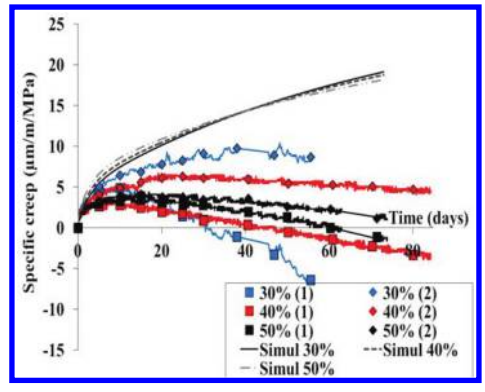

Figure 8. Simulated tensile creep curve at 30%, 40% and 50% obtained with law A.

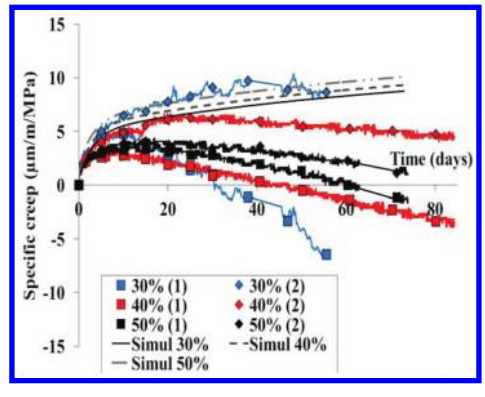

Figure 9. Simulated tensile creep curve at 30%, 40% and 50% obtained with law B.

then the micro-damage attenuation depends on the loading intensity. Consequently, only a damage value of about 38% is required when using the law C where water effects on solid skeleton is the most important instead of a damage value of about 58% when using the law A.

However, this creep-induced damage seems to have only very little effects on the instantaneous mechanical characteristics and on creep recovery as pointed out by experimental results. On this aspect, more testing using for example non-destructive techniques such as acoustic emission will help to identify the real nature of this damage.

3.3 *Tensile basic creep simulation*

Simulation of basic creep tests in tension were carried out by keeping the set of parameters determined above. It allows the relevance of the assumptions made on shrinkage to be validated. For that purpose, three load levels are tested, namely 30%, 40% and 50% of tensile strength. The results obtained by taking law A, B and C are presented in figures 8, 9 and 10 respectively.

The dissymmetrical creep behaviour observed between tension and compression can be explained by dissymmetrical creep potentials. In the model, this aspect is taken into account by the fact that the creep potential ε^k is expressed as a function of the ratio of the applied stress and the compressive stress R_c according to equations 17 to 20. Consequently, the creep potential is lower in tension than in compression so that tensile creep is more sensitive to shrinkage than compressive creep in relation to the consolidation phenomenon.

In the case of simulation performed with law A, the low amplitude of shrinkage is such that concrete is not enough consolidated and that tensile creep strain is more important that experimental measured strains. However, when the consolidation degree is enough (case of simulation performed with law B and C), the simulated curves are well located in the area delimited by experimental curves.

An aspect not taken into account in the model is the negative slope observed experimentally. Physically, it could correspond to free-water consumption due to the hydration of anhydrous grains (phenomenon of self-healing crack) which increases the amplitude and the kinetics of self-drying shrinkage (Ranaivomanana et al. 2013, Rossi et al. 2012). A modification of the Biot tensor modulation to take into account this aspect should be proposed in the future.

Given that laws B and C seem to be relevant to simulate direct tensile creep, we have conducted simulation of bending basic creep only using law C. Symmetry considerations lead to consider only the quarter of a $10 \times 10 \times 50$ cm concrete beam. On the other hand, cubic finite elements with 20 Gauss nodes were used. A view of the 3D mesh is proposed in figure 11.

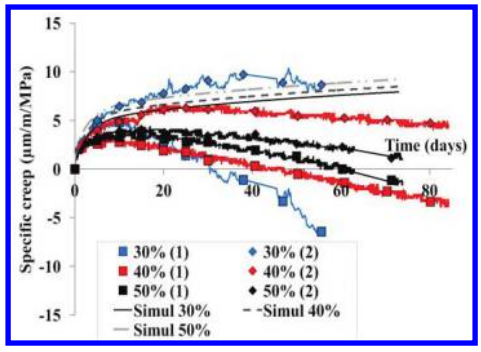

Figure 10. Simulated tensile creep curve at 30%, 40% and 50% obtained with law C.

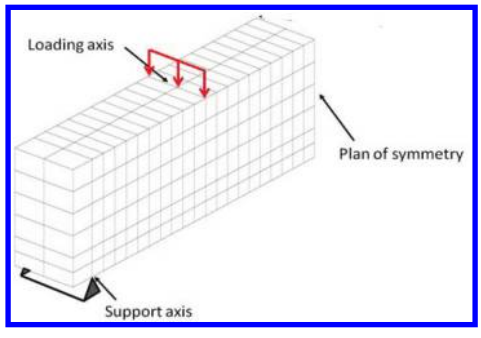

Figure 11. 3D-view of the mesh used for bending creep simulation.

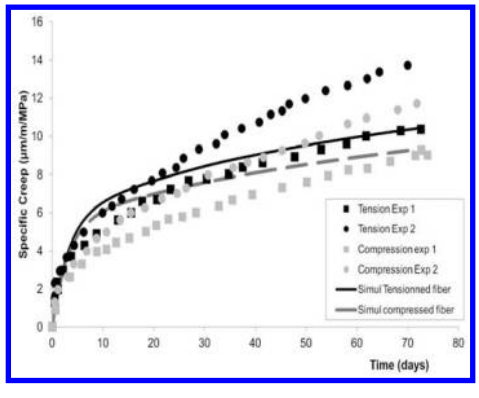

Figure 12. Experimental results and predicted ones of bending specific creep at 50%.

The strains obtained on most compressed and the most tensioned fiber of the beam are represented in figure 12 where only simulations corresponding to 50% are presented. As it can be seen, experimental results and predicted ones are in a good agreement.

4 CONCLUSIONS

A numerical model has been used in this study to analyze the basic creep of concrete. The reproduction of the delayed behaviour of concrete under different types of loading, namely in direct tension, in compression and in bending by means of a single formulation was possible. The originality of the model relies on physical phenomena taken into account which are consolidation allowing creep-site depletion under hydro-mechanical loading and creep-induced damage to be taken into account. This study points out the role played by shrinkage in the creep modeling. Such an approach allows thus a better understanding of the coupling between shrinkage, damage and creep in concrete. Finally, one have to note that this model is actually in progress and ongoing modifications will certainly be brought in the future to address missing aspects.

REFERENCES

Bazant, Z. 1972. Thermodynamics of hindered adsorption and its implications for hardened cement paste and concrete. *Cement and Concrete Research* 2:1–16.

Bazant, Z. 2001. Prediction of concrete creep and shrinkage: past, present and future. *Nuclear Engineering and Design* 203:27–38.

Benboudjema, F. 2002. Modeling of the delayed strains of concrete under biaxial loading. Application to the containment vessels of nuclear power plants. PhD Thesis (In French).

Benboudjema, F., Meftah, F. & Torrenti, J.M. 2005. Interaction between drying, shrinkage, creep and cracking. *Engineering Structures* 27:239–250.

Brue, F. 2009. Roles of temperature and composition on the THM coupling in concretes. PhD Thesis (In French).

Pons, G. & Torrenti, J.M. 2007. Shrinkage and creep. In Ollivier, J.P. & Vichot, A. (eds), Durability of concrete; Presses de l'école nationale des Ponts et Chaussées. (In French)

Powers, T.C. 1968. The thermodynamics of volume change and creep. *Materials and Constructions* 1(6):487–507.

Ranaivomanana, N., Mutlon, S. & Turatsinze, A. 2012. Basic creep of concrete under compression, tension and bending. *Construction and Building Materials* 38:173–180.

Reviron, N. 2009. Study of the creep of concretes in tension. Application to the containment vessels of REP nuclear power plants. PhD Thesis (In French).

Rilem TC-107 CSP. 1998. Measurement of time-dependent strains in concrete. *Materials and structures* 31:507–512.

Sellier, A. & Buffo-Lacarrière, L. 2009. Towards a simple and unified modeling of basic creep, shrinkage and creep in desiccation of concrete. *French review of Civil Engineering* 13:1161–1182.

Sellier, A., Buffo-Lacarrière, L., Multon, S., Vidal, T. & Bourbon, X. 2012. Non-linear basic creep and drying creep modeling. In *Proc. intern. Symp. Conference on Strategies for Sustainable Concrete Structures*. Aix-en-Provence (France).

Concrete Repair, Rehabilitation and Retrofitting IV – Dehn et al. (Eds)
© 2016 Taylor & Francis Group, London, ISBN 978-1-138-02843-2

Distributions of bond stress between plain round bars and low strength concrete under cyclic loadings

H. Araki
Hiroshima Institute of Technology, Hiroshima, Japan

C. Hong
Constec Engi, Co., Tokyo, Japan

ABSTRACT: The purpose of this study is to determine the bond characteristics of plain round bars in low strength concrete. Cyclic pull-out loadings were subjected to both ends of the bar embedded in the concrete prisms. Bond stress started to occur from the loaded end when the pull-out load increased at the first cycle, while adhesive force remained near unloaded end of the bar. Slip at the unloaded end started after the adhesion force vanished along the bar. The distribution of the bond stress along the bar converged to an anti-symmetric shape due to the residual tensile stress along the bars. It is estimated that the friction force was relatively larger than the restoring force of the bar in the low strength concrete. The local bond characteristics were similar to the average bond characteristics regardless of the bond length of bars.

1 INTRODUCTION

Seismic evaluations in Japan have found many RC buildings to have very low strength concrete (Sakamaki 2001), and there has been several research projects concerning the seismic performance of those RC members (Taniguchi 2008). It has been reported that the strength of those members with plain round bars do not reach the flexural strength due to bond slip failure of the main bars before yielding. In order to investigate the bond strength of the plain round bars embedded in low strength concrete, the authors performed monotonic pull-out loading tests (Araki and Kagawa 2010). The relationship between the average bond stress obtained dividing the pull-out load by the bond area of the bar, and the slip measured at the unloaded end of the bar were discussed. They concluded that the bond strengths were very scattered and were much lower than the allowable bond strength recommended in the current standard. To obtain the proper strength of those RC members it is necessary to clarify the distribution of bond stress along bars and the transition of the distribution in the reversal loadings.

Distributions of bond stress of reinforcing bars in concrete have been performed all over the world (Watstein 1947and Mains 1951), and the distributions of the bond stress obtained from the measured tensile strains along the deformed bars have been investigated. The results were focused on the bond splitting mechanism of the deformed bars, not the bond slipping mechanism of the plain round bars. Resistance of the bond mechanism of the plain round bars, that was adhesion force and friction force at the surface of the bar, was different from the mechanical interlock in the deformed bar. Therefore, it is impossible to apply the results of the deformed bars to the plain round bars. Recently, to obtain fundamental knowledge on the rehabilitation of existing RC buildings, the distribution of the bond stress and the restoring force characteristics of plain round bars have been investigated by using normal strength concrete (Fledman 2007 and Verderme 2009). They proposed a bond slip model between the plain round bars and normal strength concrete through monotonic pull-out loading tests. It is very important to investigate the bond characteristic of the plain round bars in low strength concrete because the bond mechanism of the bar is significantly influenced by the concrete strength.

The purpose of this study is to determine the distribution and the bond characteristics of plain round bars in low strength concrete. Cyclic pull-out loadings were performed using bars embedded in concrete prisms with strength less than 13.5 N/mm^2. The local tensile and compressive stresses of the bar were obtained by strain gauges mounted inside the bar, as per the references. The main parameter being considered is the length of the embedded bars. By calculating the tensile force along the bar, the relative slip in the bar is also investigated.

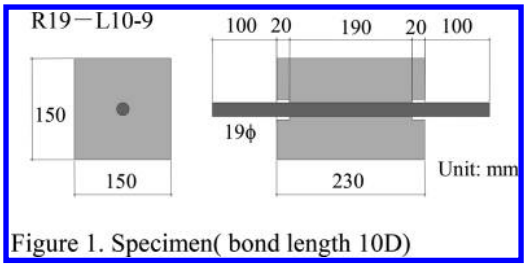

Figure 1. Specimen(bond length 10D).

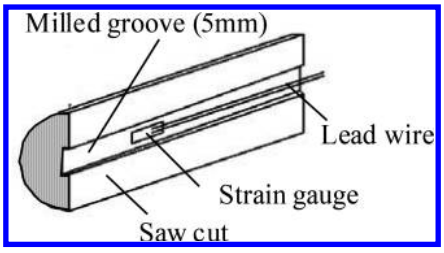

Figure 2. Method of making test bar.

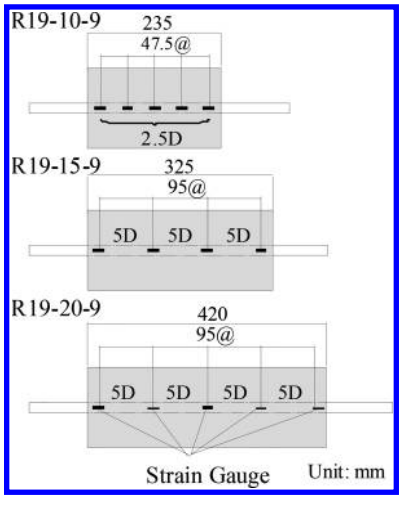

Figure 3. Mounted strain gauges.

2 OUTLINE OF EXPERMENTAL WORK

2.1 *Specimens*

Plain round bar of diameter 19mm was embedded in concrete prism of section 150mm × 150mm. Three lengths of the embedment were prepared at 10D, 15D and 20D (D is diameter of the bar). The lengths of the concrete prisms were 210mm ~ 430mm depending on the length of the embedded bar. The specified concrete strength was 9N/mm^2 to represent low strength concrete of the existing RC buildings. (The Standard for Seismic Evaluation of Existing Reinforced Concrete Building (2010) sets 13.5 N/mm^2 as the recommended lower limit of concrete strength). The concrete prisms were not reinforced against splitting failure assuming that bond slipping failure occurred ahead of the splitting of the concrete. Both ends of the embedded length were isolated 20mm from the concrete to avoid the influence of the concrete being compressed with the reaction force of the pull-out load. The specimen of embedment length (10D) is shown in Figure 1.

The concrete prisms were stored in open air. Cyclic pull-out loading tests were performed at concrete age of 28 days. Referring to the experimental procedure (Mains 1951) to measure the local strain of the bar, strain gauges were mounted in the milled groove of the half plain round bar. This half of the bar was milled to provide a 5mm wide groove for the gauges and lead wires. Two gauges were mounted at the relative position to minimize the effect of local bending of the bar. Two processed halves of the bar were bonded to each other with epoxy resin. The method of making the plain round bar is shown in Figure 2. The gauge length was 5mm. Eight or ten gauges were equally spaced within the concrete prisms shown in Figure 3, spaced at 2.5D for the bond length 10D and 5D for the bond length 15D and 20D.

2.2 *Material*

The mix properties of low strength concrete were defined by the preliminary mixing tests. The only parameter considered in the mixing tests was the water/cement ratio, which is the predominant factor influencing concrete strength. The water/cement ratio in this paper was 110% using a high-range water reducing additive to avoid segregation in the fresh concrete. The mixing properties of concrete are shown in Table 1. The compressive tests of the concrete were performed before and after the pull-out loading tests. The average strength and the modulus of elasticity of concrete were 10.4 N/mm^2 and 22.1 kN/mm^2 respectively. The yield strength of the main bar 19ϕ was 331 N/mm^2. The test bars were calibrated under tension with the gauge before they were embedded in the concrete prisms. The mechanical properties of the test bars before and after processing are almost the same. Two relationships between the tensile stress and the average strain are shown in Figure 4.

2.3 *Loading and measurement procedure*

The test setup is shown in Figure 5. The bar was subjected to reversal tensile loads with center-hole jack. A bearing was set between the jack and the

Table 1. Mix properties of concrete.

Specified Strength	W/C (%)	Sand Percentage (%)	Additive (kg/m^3)	Slump (cm)
Fc9	110	55.0	1.17	18

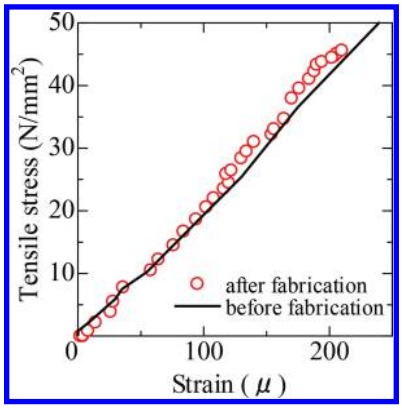

Figure 4. Characteristics of test bar.

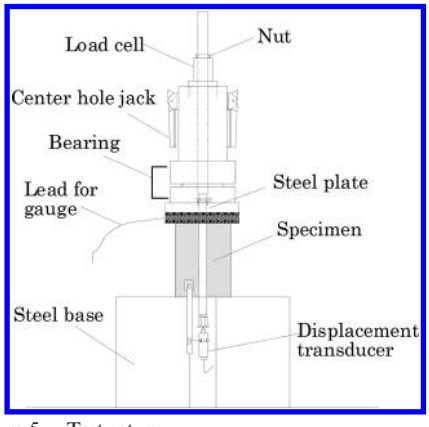

Figure 5. Test setup.

specimen to avoid an eccentric pull-out load. All leads of the gauges were passed through the inside of the bar and were drawn out on the verge of the one end of the bar. A linear viable differential transducer (LVDT) was mounted at the unloaded end of the bar to measure the slip displacement of the bar end. The cyclic loadings were controlled by the measured slip displacement. The target slip displacements of each cycle were 0.2mm, 0.5mm and 1mm. After slip length of 1mm, the target displacement was increased for each 1 mm to 5mm. After the positive loading, the specimen was reversed and the bar was pulled out at the opposite side. Assuming that the bond stress along the bar was constant the bond stress is calculated as:

$$\tau = \frac{P}{\phi \cdot L} \tag{1}$$

where, P is the pull-out load, L is the bond length, and ϕ is the circumferential length of the plain round bar. The local tensile stress σ_n of the bar is obtained by multiplying the modulus of elasticity E_s to the strain ε_n as measured by strain gauges. The local bond stress τ_n is expressed as the difference between the adjacent tensile stresses ε_n. The local tensile stress σ_n and bond stress τ_n are calculated as:

$$\sigma_n = E_s \cdot \varepsilon_n \tag{2}$$

$$\tau_n = \frac{E_s \cdot A_s \left(\varepsilon_n - \varepsilon_{n-1}\right)}{\phi \cdot \Delta L} \tag{3}$$

where, ΔL is the distance between the adjacent gauges, and A_s is the cross sectional area of the plain round bar.

2.4 *Loading and measurement procedure*

The distributions of the local tensile stress and the bond stress are discussed separately in the four loading schemes in Figure 6 (a) ~ (d). The slip did not occur until the pull-out load reached point A because the adhesion force was partially alive along the bar in Figure (a). The pull-out load reached the maximum at point B soon after the slip started to occur and decreased gradually until point C as shown in Figure (b). Point C was the target slip displacement at the first loading cycle. The first target slip displacement was determined to be 0.2mm. From the test results of low strength concrete (Araki and Kagawa 2010), it was confirmed that the maximum bond stress occurred within a slip displacement of 0.2mm. In a previous experimental study concerning the bond characteristics (Abram 1913), it was reported that slip at the maximum bond stress of normal strength concrete was approximately 0.1inch (0.254mm). In a more recent study (Verderame 2009), slip at the maximum bond stress was distributed from 0.1mm to 0.34mm. The bond strength of the low strength concrete reached its maximum when the slip displacement was relatively small. From point C the pull-out load decreased to zero at point D while the slip displacement did not change. From point D the pull-out load was subjected to the bar end of the opposite side until slip started in the opposite direction at point E as shown in Figure (c). From point E the slip increased in the opposite

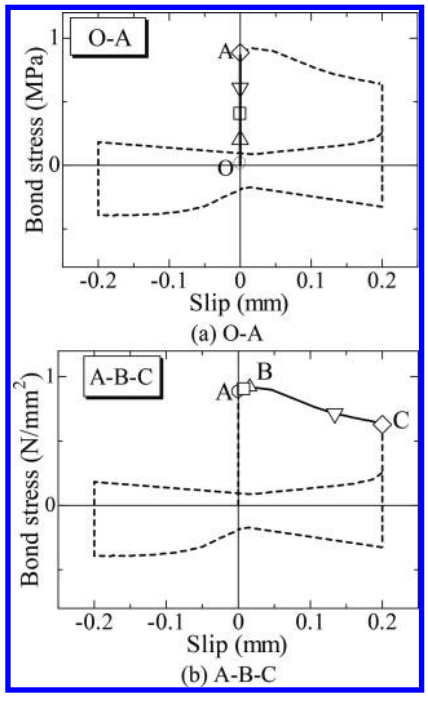

Figure 6. Loading program.

direction while the pull-out load slightly decreased until the slip displacement was zero at point F. It is estimated that the slight decrease of pull-out load toward a slip displacement of zero is due to the decrease of the friction force of the bar which re-entered the concrete prism (Verderame 2009). After point E the pull-out load again increased slightly to the next target slip displacement G.

3 TEST RESULTS AND DISCUSSIONS

3.1 *Distributions of tensile stress and bond stress*

The distributions of the local tensile stress and the local average bond strength of the specimen (the bond length 15D) through the reversal loadings are illustrated in Figure 7. The distributions of the other specimens (10D and 20D) were approximately the same as the specimen (15D).

3.1.1 *Phase O-A*

The distributions of tensile stress and bond stress under the monotonic pull-out loading are shown in Figure 7 (a). Each point is the local tensile stress and the local average bond stress at the loading points shown in Figure 6. The distribution shape is smoothed by 3-dimensional curves (Mains 1951 and Mizuno1963). In the tensile stress distribution, the peak stress shifted to the center of the bar while the pull-out load increased as shown in Figure 7 (a). The peak tensile stress in the distribution was 60 N/mm^2 which was relatively small due to the low strength concrete. Tensile stress was not observed at the opposite side of the loading. In the bond stress distribution, the peak of the bond stress shifted to the opposite side of the loading in the early stage of the pull-out loading. The resistance of the adhesion force rapidly vanished from the loaded end. Therefore, the bond stress due to the friction force near the loading side was approximately zero. The pull-out load was close to point A and bond stress in the opposite direction was observed at the loaded end because the embedded bar at this end was affected by the concrete compressed by the reaction force of the pull-out load. In previous studies (Abram 1913) concerning bond stress it was reported that the average bond stress was not only influenced by the concrete strength, but also various factors; the mix properties of concrete, curing, construction method and diameter of the bar. In this study the maximum bond stress in the distribution was approximately 2MPa regardless of the bond length.

3.1.2 *Phase A-C*

The distributions from point A to C in Figure 6 (b) did not change significantly as shown in Figure 7 (b). The peak tensile stress continued to stay at the

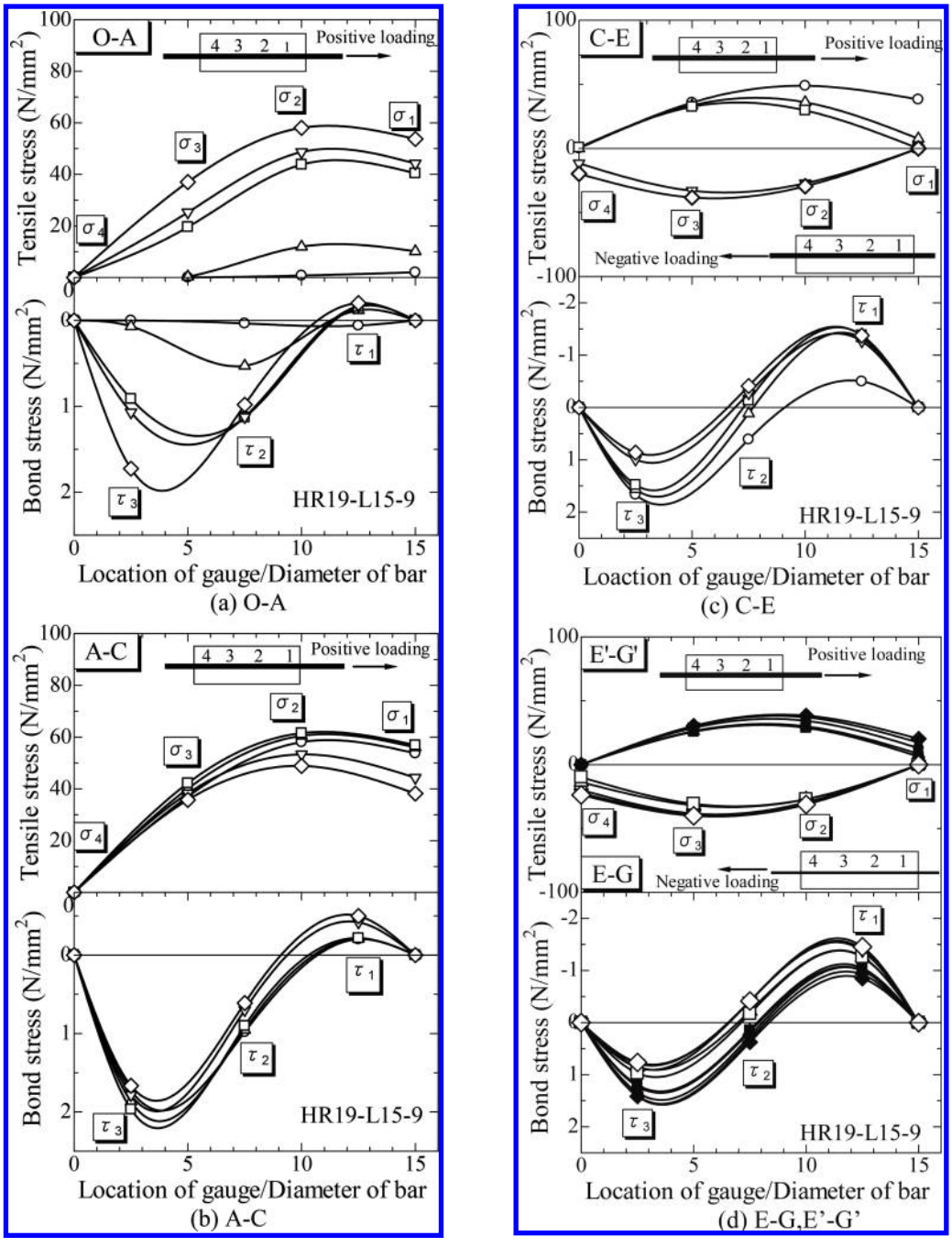

Figure 7. Distributions of tensile stress and bond stress along bond length(15D).

same location. The tensile stress decreased toward the unloaded end. The peak of the bond stress did not change through the loading point A to C. Bond stress in the same direction as the pull-out load was observed near the loaded end. In the monotonic pull-out loading tests for the plain round bars, the transition of the distributions of the tensile stress and the bond stress were consistent with the results of the previous studies (Feldman 2007 and Mizuno 1963).

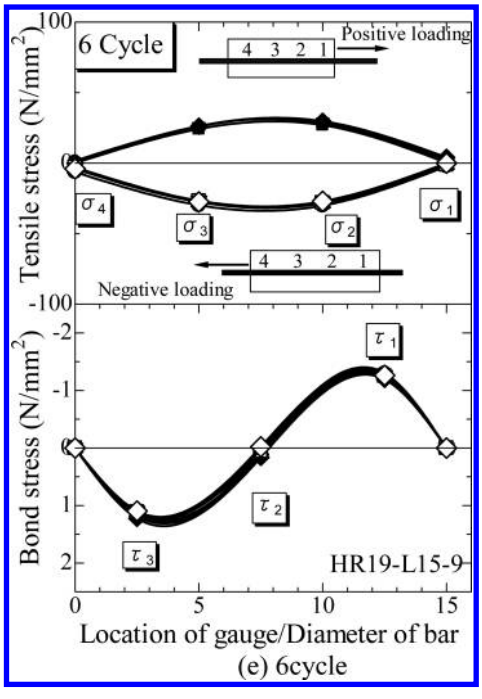

Figure 7. *Continued.*

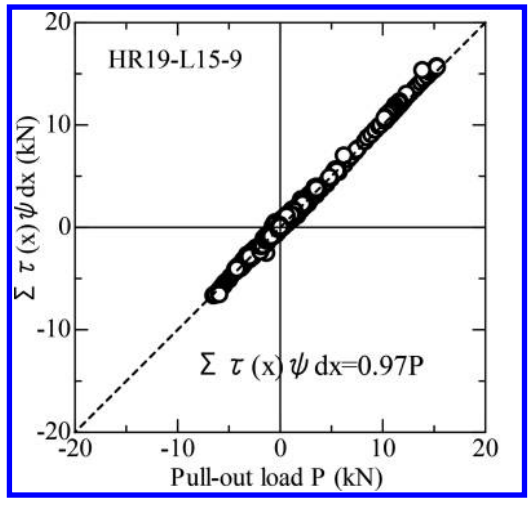

Figure 8. Pull-out laod versus summation distributed bond stress along bond length(15D).

3.1.3 *Phase C-E*

From the unloading point C in Figure 6 (c), the local tensile stress at the loaded end decreased to zero at point D while residual tensile stress was observed in the middle area of the bar, although the tensile stresses of both ends of the bar were zero as shown in Figure 7 (c). It is estimated that those residual tensile stresses were due to the friction force between the concrete and the surface of the plain round bars. Therefore, the bond stresses still remained even though the external pull-out load was zero. The residual bond strengths existing at the right and left sides of the bar were fully balanced. At point D the specimen was reversed and was subjected to pull-out loading in the opposite direction. The distributions of the tensile stress are shown in the lower part of Figure 7 (c). The tensile stress increased at the loaded end (left side of the distributions). The peak of the bond stress shifted to the unloaded end (right side of the distributions), while the pull-out load increased.

3.1.4 *Phase E-G and G'-E'*

The distributions of the tensile stress and the bond stress as shown in Figure 7 (d) from point E to G was approximately the same because the pull-out load was not significantly changed as shown in Figure 6 (d). After the reverse from the negative loading to the positive loading, the bond stress through point E' to G' slightly shifted to the unloaded end.

3.1.5 *Phase 6 cycle*

The distributions of the tensile stress and the bond stress of in the 6 cycle reversal loading converged to the same shapes shown in Figure 7 (e). The slight transitions of the distribution of the bond stress were corresponding to the very low pull-out loads.

3.2 *Relation between pull-out load and distributed bond stress*

The relationships of the pull-out load P and the summation of the local bond stress in the bond length are illustrated in Figure 8. Bond stress between the adjacent gauges was assumed to be constant. The relationship between both values had an extremely high linearity and the summation of the local bond strength was 0.97 times of the pull-out load by the least-square analysis. It is confirmed that the summation of the bond strength approximately coincides with the pull-out load through the reversal loadings. The maximum positive pull-out load of 15.7kN occurred during the first cycle at point B in Figure 6 (b). The maximum negative pull-out load was 6.65kN in the same cycle at point G because the adhesion force had already vanished in the positive loading.

3.3 *Local bond stress and relative slip*

It was reported that the relative slip in the bond area was different from the slip displacement at

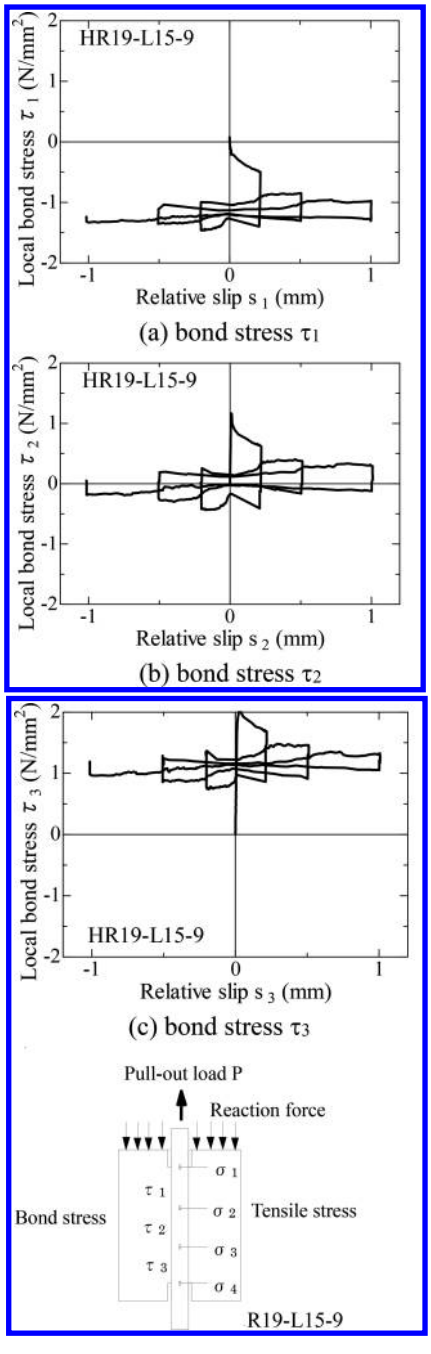

Figure 9. Local bond stress versus relative slip.

the unloaded end of the bar due to the elongation of the bar. Slip displacement is derived as shown below (Feldman 2007). Elongation $e_s(x)$ in the embedded length is calculated as:

$$e_s(x) = \int_0^x \frac{T(x)}{A_s \cdot E_s} dx \tag{4}$$

where $T(x)$ is the force in the bar, A_s is the sectional area of the bar and E_s is the modulus of elasticity of steel. The contraction of concrete prism is calculated as:

$$e_c(x) = \int_0^x \frac{f_c(x)}{E_s} dx \tag{5}$$

where $f_c(x)$ is the compressive stress of the concrete prism at point x and E_c is the modulus of elasticity of concrete. The compressive stress $f_c(x)$ of the concrete by reaction force of the pull-out load is calculated as:

$$f_c(x) \cong -\frac{T_c(x)}{A_c} \tag{6}$$

where A_c is the effective sectional area of concrete. The relative slip $s(x)$ is calculated as:

$$s(x) = e_s(x) - e_c(x) = \left(\frac{1}{A_s \cdot E_s} + \frac{1}{A_c \cdot E_c} \right) \int_0^x T(x) dx \tag{7}$$

After slip at the unloaded end s_0 occur the relative slip $s(x)$ is obtained adding s_0 to the relative slip due to the elongation of steel and the contraction of concrete as:

$$s(x) = s_0 + \left(\frac{1}{A_s \cdot E_s} + \frac{1}{A_c \cdot E_c} \right) \int_0^x T(x) dx \tag{7}$$

The rate of relative slip due to the elongation of the steel and the contraction of concrete was small in this study because the existing tensile force $T(x)$ in the bar was very low as shown in Figure 7. It is estimated that the relative slip of the bar in the embedded area (the second term in equation (7)) was significantly small because the local tension force $T(x)$ was very low. The relationship between the local bond stress and the relative slip of the test specimen (bond length 15D) is illustrated in Figure 9. The bond stress τ_1 at the loading side moved to the negative load area in the early stage of the pull-out loading. The center of the restoring force characteristics was a bond stress of minus 1.1 N/mm² as shown in Figure 9 (a). The bond stress τ_3 moved to the positive side on the contrary τ_1. The difference between τ_1 and τ_3 is derived from the distribution of the residual

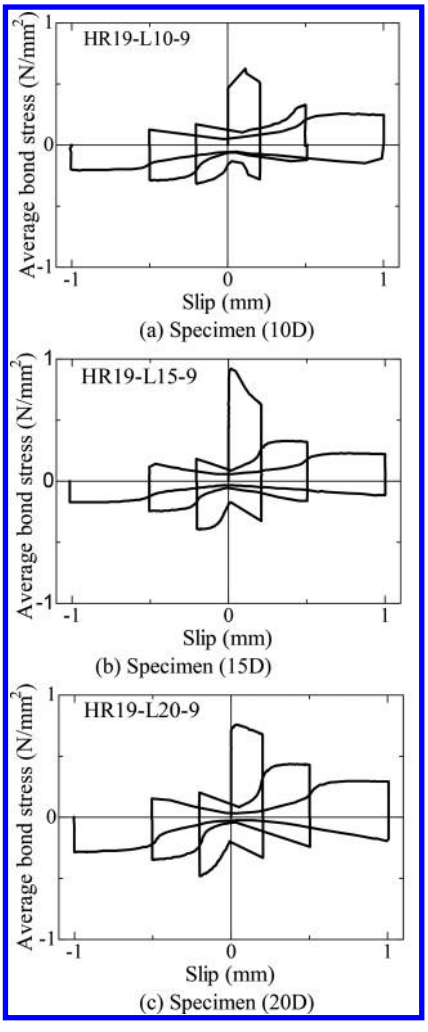

Figure 10. Average bond stress versus slip.

tensile stress. The restoring force characteristics of the bond stress τ_2 at the center of the embedded length is similar to the relationship between average bond stress and the slip s_0 measured at the unloaded end of the bar as shown in Figure 10. The average bond strength was less than 1.0 N/mm^2 while the local bond stress was 2 N/mm^2.

4 CONCLUSIONS

Based on the results of the pull-out tests using the plain round bar and low strength concrete the following conclusions are made;

1. The distributions of the tensile stress and bond stress have the same characteristics regardless of the bond length.
2. The peak of bond stress shifted to the unloaded end when the pull-out load increased until the slip occurred.
3. The distributions of the tensile stress and the bond stress do not change significantly although the bond characteristics deteriorated due to the cyclic loadings.
4. The characteristics of local bond stress are approximately the same as the average bond stress along the bond length.

ACKNOWLEDGEMENTS

This research has been supported by the Japan Ministry of Education, Culture, Sports, Science and Technology under Grant-in-aid No.21360268. The authors would like to thank the staff and graduate students of the Structural Earthquake Engineering Lab. of Hiroshima University, Japan.

REFERENCES

Abrams, D.A. 1913. Tests of Bond Between Concrete and Steel, *University of Illinois Bulletin No.71, University of Illinois at Urbana-Champaign, Ulbana.IL.*

Araki, H., and Kagawa, J. 2010. Bond Strength of Plain Round Bars Repaired by Epoxy Resin Injection. *the 34th IABSE Symposium*, Italy, Venice.

Feldman L.R. and Bartlett F.M. 2007. Bond stresses along plain steel reinforcing bars in pullout specimens. *ACI Structural Journal,* 104(6), 685–692.

Japan Building Disaster Prevention Association 2001. Standards of seismic diagnosis of existing RC buildings" Revised Edition.

Mains, R.M. 1951. Measurement of the Distribution of Tensile and Bond Stresses Along Reinforcing Bars, *Journal. of ACI*, Vol,23, No.5, Nov,225–252.

Mizuno T. and Watanabe A. 1963. On the bond stress distribution along round bars, deformed bars and twisted deformed bars, *Journal of Japan Society of Civil Engineering*, No.93, 23–30.

Morita S. and Sumi T. 1975. Bond-slip relationship under repeated loading, *Transactions of the Architectural Institute of Japan*, No.229, 15–24.

Sakamaki, K., Hirosawa, M., Shimizu, Y.,and Zhou, J, 2001. Research on concrete strength of existing reinforced concrete buildings (Part1, Part2), *Summaries of technical papers of the annual meeting of Architectural Institute of Japan*, 801–804.

Taniguchi, H., Yasojima, A., and Araki, H. 2008. Seismic Performance of Reinforced Concrete Beams with Low Strength Concrete," *The 14th World Conference on Earthquake Engineering*, October, 12–17, Beijing, China.

Verderame, G.M., Ricci P., De Carlo G., Manfredi, G. 2009. Cyclic bond behaviour of plain bars. Part I: Experimental investigation, 3499–3511, Part II: Analytical investigation, 3512–3522, *Construction and Building Materials* 23.

Watstein, D. 1947. Distribution of Bond Stress in Concrete Pull-out Specimens, *Journal of ACI*, Vol.18, No.11, 1041–1052.

Concrete Repair, Rehabilitation and Retrofitting IV – Dehn et al. (Eds)
© 2016 Taylor & Francis Group, London, ISBN 978-1-138-02843-2

Damage evaluation of RC columns subjected to seismic loading by energy dissipation using 3D lattice model

M.R. Simão & T. Miki
Kobe University, Kobe, Japan

ABSTRACT: This study is aimed at the application of the 3D lattice model, which based on discretization of concrete in truss and arch analogy is able to express the shear resisting mechanism of RC structures in order to perform damage range evaluation of RC columns. Nonlinear dynamic analysis is performed using the new multi-directional 3D lattice model for circular cross section columns. Damage range evaluation is proposed in terms of energy dissipation capacity. A new damage index that is based on the elemental strain energy of concrete and steel reinforcement is proposed. The applicability of the model is verified by performing dynamic analysis on a circular cross section RC column that has been tested by the E-Defense. The results show acceptable agreement in hysteretic response after cracking and localized damage concentration based on the amount of energy dissipated in RC columns is observed.

1 INTRODUCTION

Reinforced concrete (RC) structures exhibit a highly nonlinear behavior in the event of an earthquake. Grasping this behavior is at the top of priorities in many analytical techniques currently developed to study seismic behavior. In current seismic design, large consideration is given to issues of strength and deformation capacity, but it is recognizable that in structural damage analysis energy dissipation capacity is one of the key factors in structural damage.

The essence of earthquake damage to structures is the process of energy input, conversion and dissipation. In bridge structures, excessive displacement and high degree of destruction can be observer in bridge piers under repeated cyclic loading in the most extreme cases; therefore modeling column behavior with a relative simplicity nonetheless accuracy can be useful.

A 2D lattice model has been proposed by Niwa et al. (1995) and further enhance by Miki & Niwa (2004), which allows reasonable prediction behavior of RC structural members under seismic loading with reduced degrees of freedom by adopting the arch and truss analogy in structural discretization. Based on the above considerations, this study is focused on the applicability of the 3D lattice model to perform damage evaluation of RC columns with circular cross section having consideration for the energy dissipation characteristics of columns under seismic excitation.

2 ANALYTICAL MODEL

2.1 *Outlines of the 3D lattice model*

The development of the 3D lattice model is based on the 2D lattice model (Miki & Niwa 2004). Figure 1 shows the schematic representation of RC column using the 3D lattice model, which allows the representation of elements in terms of concrete and reinforcement. In the 3D lattice model, the concrete region is divided in arch and truss part and the shear resisting mechanism is represented by truss and arch action, and it is assumed that the arch action is defined by four arch members that connect the loading point with the bottom of the column at the opposite corner. The truss action can be seen as an idealized compressive strut.

2.2 *Multi-directional polygonal 3D lattice model*

Circular reinforced concrete columns are favored for bridge piers, because of relative simplicity of construction as well as omnidirectional strength characteristics under wind and seismic loads (Ang et al. 1989). However, under these circumstances the columns' flexural and especially shear resistance are very important. Based on previous studies (Miki & Niwa 2004) the 3D lattice model has shown satisfactory capabilities of prediction of shear behavior of RC structural members with relative simplicity in analytical procedure. Based on the above an analysis concept has been developed using the 3D lattice model for circular cross section RC columns based on more realistic

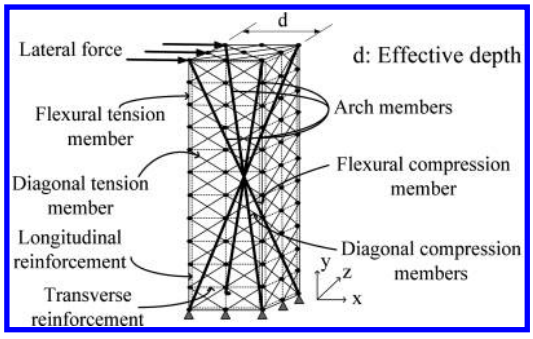

Figure 1. Diagram of 3D lattice model (Miki & Niwa 2004).

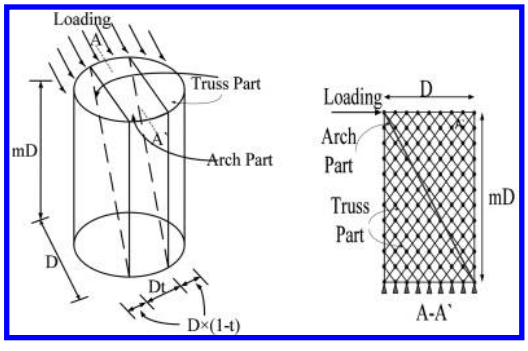

Figure 2. Arch and truss discretization in the 3D lattice model for circular column.

multi-directional polygonal discretization. The modeling will be further explained.

2.2.1 *Modeling of lattice model members*

In the multi-directional polygonal 3D lattice model the resisting mechanism is based upon the arch and the truss analogy presented in Figure 2. The discretization from solid concrete to the 3D lattice model is performed so that the actual cross-sectional diameter, D of the analytical model corresponds to that of the target, that means that the target defines mesh size and model height.

Figure 2 illustrates a schematic representation of arch members for a circular cross section column as well as truss members in 3D space. The representation of vertical and horizontal members is detailed in Figure 3. The detailed representation of the diagonal members is shown in Figure 4. The diagonal members which include a part of representation of truss action consist of three parts, which are inner diagonal members (IDM), surface diagonal members (SDM) and diagonal members in transverse direction (DMT) respectively.

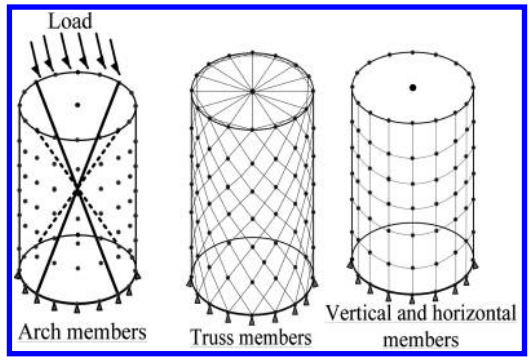

Figure 3. Schematic diagram of multi-directional polygonal 3D lattice model.

In the model the inner diagonal members are assumed to be modeled as the truss action in the RC column. It is assumed that the modeling of diagonal members is preceded by the distribution of sixteen peripheral nodes for every horizontal layer. The distance between two adjoin nodes is equal to the half of cross-sectional diameter, $0.5D$, the in-plane nodal positions are set according to their polar coordinates defined by $x = r\cos\phi$ and $y = r\sin\phi$ in an orthogonal system, where r is the radius of cross-section and ϕ is the internal angle on the cross section defined by a triangle formed by joining two successive node to each other and the center node. The distribution of truss elements within the nodes is detailed in Figure 4.

Longitudinal reinforcement is represented as vertical reinforcement member along the sixteen nodes per layer defining the geometry of the model. Regarding transverse reinforcement, it is represented in the form of horizontal reinforcement members uniformly distributed at intervals of $0.5D$ throughout the model as the intervals of arrangement are not taken into account.

2.2.2 *Cross-sectional area of lattice members*

The determination of cross-sectional area of arch and diagonal members in the multi-directional 3D lattice model is performed considering that the diameter of the model is invariant for the definition of geometry properties of the analytical model, which are the height, mesh size and distribution of nodes. Therefore the notion of analytical diameter is introduced. An analytical diameter of column cross section is the defined as the diameter obtained from analytical conditions to calculate the cross-sectional area of arch and truss members.

The analytical diameter is obtained considering the effect of effective stiffness in dynamic response of RC columns. For that, the reduction of the flexural stiffness EI thought the inertia of the column is considered. In this study, reduction factors

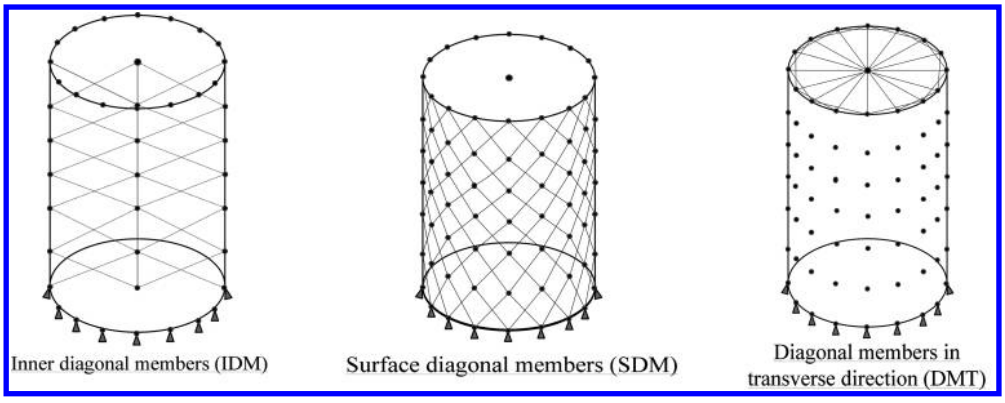

Figure 4. Representation of the truss elements.

of moment of inertia ranging from 0.4 to 0.7 times gross moment of inertia are considered (Pique & Burgos 2008). For the determination of the stiffness matrix in the arch members, it is assumed that a single arch member is representative of the stress flow for analysis purposes. The equivalence of global stiffness of structural systems in 2D and 3D is assumed (Miki & Niwa 2004). The cross sectional area of arch members is given as presented in Equation 1.

$$A_{arch-3D} = \left\{ \frac{2+m^2}{1+m^2} \right\}^{3/2} \cdot A_{arch-2L} \quad (1)$$

$$A_{arch-2D} = D^2_{ana}\, t \cdot \sin\theta \quad (2)$$

where $A_{arch\text{-}3D}$ = Cross sectional area of arch member in 3D; $A_{arch\text{-}2D}$ = Cross sectional area of arch member in 2D; D_{ana} = Analytical diameter; t = Ratio of width of arch to truss members; m = Set so that $m \times D_{ana}$ = Model height; and θ = Inclination of the arch member.

The determination of the cross sectional area of the diagonal members is given as follows:

$$A_{IDM} = A_{SDM} = \frac{D_{ana}(1-t)}{2} \cdot \frac{D_{ana}}{2} \sin 45° \quad (3)$$

$$A_{DMT} = \frac{a}{2m} \cdot \frac{D_{ana}}{2} \sin 45° \quad (4)$$

where A_{IMD} = Inner diagonal members; A_{SMD} = Surface diagonal members; A_{DMT} = Diagonal members in transverse direction; D_{ana} = Analytical diameter of the column model; t = Ratio of width of arch to truss members; and m is set so that $m \times D_{ana}$ = Model height.

It is noticeable in Equation 3 that cross sectional area of inner diagonal members and surface diagonal members is calculated using the same equation. This simplification is due to the fact that in the pre-analysis process, it was verified that omnidirectional properties of a circular cross section meant that a single formula for the diagonal members in longitudinal direction to the transverse plane could be adopted for simplification of analytical procedure.

2.2.3 *Material constitutive models*

2.2.3.1 Concrete

For the arch and diagonal members of concrete, the compression model accounts for lateral restraint effect by shear reinforcement. In this model in order to consider the effect of confinement by transverse reinforcement, the stress-strain relationship proposed by Mander et al. (1988) is used. The compressive softening behavior of cracked concrete is given according to Vecchio & Collins (1986) who proposed that the ability of fully cracked concrete to resist compressive stress decreases as the transverse tensile strain ε_t increases.

The flexural compression member is assumed to be cover concrete that is unconfined and becomes ineffective after the compressive strength is reached. The stress-strain relationship of un-cracked concrete is here represented by a quadratic curve (Vecchio & Collins 1986) and an exponential curve.

The flexural tension members of concrete are assumed to be located near reinforcement. In this region, the concrete behaves with the reinforcements and continues to contribute tensile force even after cracking due to the bond effect between the concrete and reinforcements. Therefore, after cracking, the tension stiffening model (Rokugo et al. 1989) is applied to the flexural tension members. On the other hand, for the diagonal tension members that consist of concrete far from reinforcement the tension softening curve, the so-called 1/4 model proposed by Uchida et al. (1991) is applied. The fracture energy of concrete G_F, is as sumed to be 0.1 N/mm.

2.2.3.2 Reinforcing bar

The envelope stress-strain relationship of reinforcement is modeled as a bi-linear. The tangential stiffness after yielding is set as $0.01E_s$, where E_s denotes the Young's modulus of reinforcement. After yielding, the stiffness of reinforcement decreases when the stress stage changes from tension to compression, while similar behavior is observed when the stress stage changes from compression to tension. In the analysis, this phenomenon due to the Bauschinger effect is considered by using a numerically improved model of reinforcement by Fukuura & Maekawa (1997).

3 ENERGY DISSIPATION OF RC COLUMNS AND DAMAGE RANGE EVALUATION

3.1 *Hysteretic energy dissipation*

Tembulkar & Nau (1987) stated that damage attained by a RC member under dynamic loading can be assessed by a well-constructed hysteretic model. Furthermore, with well-defined parameters, energy based hysteresis models may successfully represent seismic response considering the deteriorating behavior of RC members.

On the other hand, Bousias et al. (1995) reported that the strong coupling between the two transverse plane directions of columns produces an apparent reduction of strength and stiffness in each of the two transverse plane directions when considered separately, but also an increase in hysteretic energy.

With that, the cumulative hysteretic energy dissipation is a very important notion in the analysis of cyclic behavior of RC structures, because it relates to the global damage potential and energy capacity. The hysteretic energy is calculated considering the area of each loading cycle in the X (longitudinal) and Y (transverse) direction for the lateral force and displacement relationships, and the total energy dissipation is calculated as the sum of these two parts. Equations 5–7 express the analytical relationships.

$$Ed_x = \int F_x d_x \tag{5}$$

$$Ed_y = \int F_y d_y \tag{6}$$

$$Ed_{total} = \int F_x d_x + \int F_y d_y \tag{7}$$

where Ed_x = Energy dissipation in X direction; Ed_y = Energy dissipation in Y direction; Ed_{total} = Total energy dissipation; F_x = Force in X direction; F_y = Force in Y direction.

3.2 *Elemental energy dissipation*

The 3D lattice model offers some unique characteristics in terms of analytical capacity of the composing analytical elements. Because of the truss and arch analogy, the analytical response is obtained individually for every component of the system. The lattice model comprises several elements, and it is assumed that an average stress and strain relationship governs each one of them. In other words, the stress and strain relationships define the strain energy for each element in the lattice model.

This definition can be very useful for the calculation of strain energy after the target of analysis has reached the yielding point, and especially because of highly nonlinear behavior of concrete after cracking. That way, the strain energy is defined as presented in equation 8.

$$E_{strain} = \frac{1}{2}\left(\sigma_i + \sigma_{i-1}\right)\left(\varepsilon_i - \varepsilon_{i-1}\right) \tag{8}$$

where E_{strain} = Strain energy; σ_i = Stress in *i* node; σ_{i-1} = stress in *i*-1 node; ε_i = Strain in *i* node; and ε_{i-1} = Strain in *i*-1 node.

By taking into account the energy dissipation in individual elements, the distribution of energy dissipation in a RC column can be evaluated by the dynamic lattice model. Based on this assumption the energy dissipated in each element can be calculated from the product of the strain energy dissipated in each element, where the strain energy is the area enclosed by the stress-strain relationship for the unloading and reloading curves, and the elemental volume. RC member accumulated energy dissipation will be the sum of all the elemental energy dissipation histories as shown in equation 9 below.

$$E_{dissip} = \sum_{i=1}^{n}\left(Es_i \times V_i\right) \tag{9}$$

where E_{dissip} = Acumulated energy dissipation at the member Es_i = Strain energy in element *I*; V_i = Volume of element *i.*

3.3 *Damage range evaluation*

The evaluation of seismic damage of concrete structures is very important in order to take countermeasures, such as repair and strengthening the deteriorated structures after severe earthquakes. However, global damage condition of a structure can only be assessed using energy methods if there is knowledge about the total energy capacity.

Based on the arch and truss assumption used in the lattice model it is possible to determine from an elemental level the expected energy capacity of single elements and compare them to the response obtained from the analysis

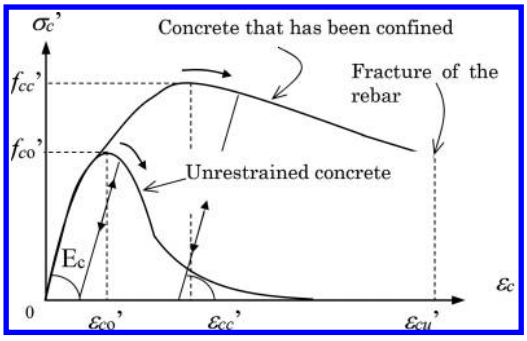

Figure 5. Compressive model of concrete (Mander et al. 1980).

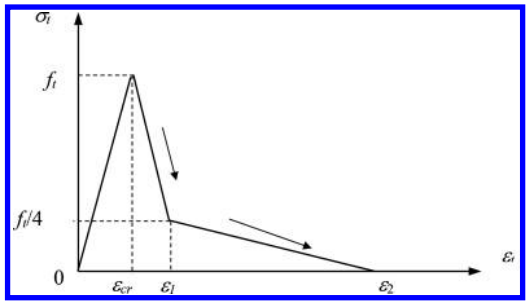

Figure 6. Tension softening model (Uchida et at. 1991).

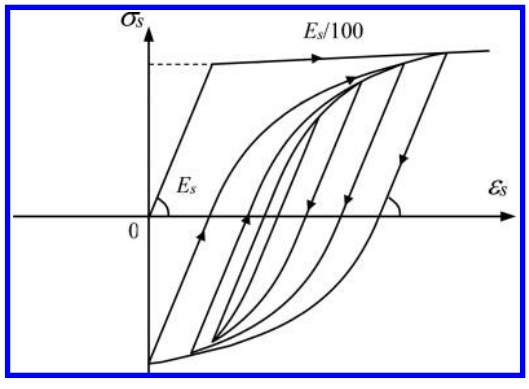

Figure 7. Stress-strain relationship of steel reinforcement (Fukuura & Maekawa 1997).

3.3.1 *Assessment of seismic damage using damage index*

In order to use the energy dissipated as an indicator of seismic damage in concrete structures, the total energy dissipated must somehow be normalized so as to compare the results of different size specimens (Inoue 1994).

Furthermore, the key questions of how much seismic energy dissipation capacity that a structure possesses as well as localization of damage are essential in damage range evaluation. In this study, the damage range evaluation is performed from the material point of view, which means that the stress-strain relationships of the RC structural members are used to determine energy dissipation capacity and ultimately damage range. Since reinforced concrete is composed of concrete and reinforcing steel, its damage can be defined by the composition of the damage sustained by concrete and by reinforcing steel as shown in Equation 10 below.

$$D_{RC} = D_{concrete} + D_{steel} \tag{10}$$

where D_{RC} = Damage in reinforced concrete; $D_{Concrete}$ = Damage in concrete; and D_{steel} = Damage in steel reinforcement.

Here the assumption is that the material`s ultimate energy dissipation capacity is calculated from the constitutive model of material, within certain set strain parameters. In that manner, for concrete in compression is used the model proposed by Mander et al. (1980) shown in Figure 5, concrete in tension proposed by Okamura & Maekawa (1991) and Uchida et al. (1991) shown in Figure 6, and reinforcement proposed by Fukuura & Maekawa (1997) shown in Figure 7. In the case of concrete the maximum strain in compression is assumed to be 0.0035 when concrete crushes and the maximum compressive stress corresponds to 0.002 of compressive strain and the maximum tensile strain is calculated using the 1/4 model by Uchida et al. (1991).

Damage index in the material will be derived as the ratio between the analytical response energy dissipation and the energy dissipation calculated using the constitutive models, assuming that they represent the maximum energy dissipation capacity of a material under the conditions previously explained.

Since elemental energy dissipation has been defined as the product between strain energy and elemental volume, the damage index in material can be expressed as the ratio between strain energy of analysis response and strain energy obtained using the constitutive models. The damage relationships are presented in Equation 11.

$$D_{concrete} = D_{steel} = \frac{Es_{response}}{Es_{constitutive}} \tag{11}$$

here $D_{Concrete}$ = Damage in concrete; D_{steel} = Damage in steel reinforcement, $Es_{response}$ = Strain energy

obtained from analytical response; and $Es_{constitutive}$ = strain energy obtained from the constitutive models.

Seismic performance objectives can be defined as the coupling of expected performance levels with expected levels of seismic ground motion. According to Li-Dejian et al. (2013) and Huanjun et al. (2013), structural damage conditions can be assessed from 0–1. In this notation, damage condition 0 means no damage at all, while damage condition 1 means total failure of structure. In this study, this convention will also be applied at the material level.

However, the performance indexes between 0–1 shall be defined in a different manner. The critical values for performance are defined using the constitutive models of materials, especially having in mind that in real structures they are the best approximation available to the expected global performance of structures. In that manner critical damage point correspond to the point where damage potential changes from moderate to high and are defined as follows:

$$CDP_{concrete} = \frac{Es_{compression} + Es_{tensile}}{Es_{concrete-total}} \quad (12)$$

$$CDP_{steel} = \frac{Es_{yielding}}{Es_{steel-total}} \quad (13)$$

here, $CDP_{concrete}$ = Critical damage point in concrete; CDP_{steel} = Critical damage steel point in steel reinforcement; $Es_{compression}$ = Strain energy at maximum compression point, assumed in this study to correspond to a compressive strain of 0.002; $Es_{tensile}$ = Strain energy at cracking of concrete in tension; $Es_{yielding}$ = Strain energy at yielding of reinforcement; $Es_{coconcrete-total}$ = Total strain energy of concrete; and $Es_{steel-total}$ = Total strain energy in steel reinforcement.

In the other hand as previously stated, the accumulated damage in a reinforced concrete structures results from the composition of damage in concrete and damage in steel reinforcement. In most RC structures, even in the event of total failure or collapse damage tends to be localized, therefore it is important to focus the evaluation of damage at the regions of most potential for damage that leads failure.

Simão & Miki (2014) reported that on a cantilever bridge column, about 50% of damage is concentrated below the column mid-height. Based on that, it is reasonable to assume that the most significant concentration of damage at the bottom is very representative of damage condition. In this study, concentrated damage in cantilever columns should be focus on the column bottom.

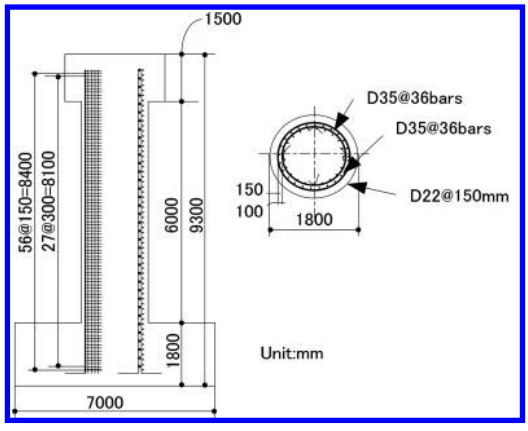

Figure 8. C1-5 specimen details (Kawashima et al. 2010).

4 DAMAGE EVALUATION OF RC COLUMNS WITH CIRCULAR CROSS-SECTION

4.1 *Analytical target (Kawashima et al. 2010)*

The analytical target is a circular cross section column named C1-5 tested using a shake-table by E-Defense.

The specimen, shown in Figure 8 is a cantilever circular column with diameter 2000 mm. The heights of the column and footing correspond to 7500 mm and 1800 mm respectively.

The longitudinal and transverse reinforcement have a nominal strength of 345 MPa (SD345) and the design concrete strength of 27 MPa. Sixty four deformed 35 mm diameter longitudinal bars are presented in two layers, while deformed 22 mm circular ties are set at 150 mm and 300 mm intervals in the outer and inner longitudinal bars.

Column C1-5 was excited using a near-field ground motion which was recorded at the JR Takatori Station during the 1995 Kobe earthquake. Taking into account the soil/structure interaction, a ground motion with 80% of the original intensity of JR Takatori name E-Takatori was imposed as command to the table in the experiment.

In the experimental program, C1-5 has been excited under different conditions, however in this study the analysis will focus on C1-5(1) corresponding to 100% E-Takatori and C1-5(3) corresponding to 125% E-Takatori accelerations, respectively. In order to analyze column C1-5, an analytical model shown in Figure 9 was used. Localized damage evaluation is performed in case C1-5(1). The height of the column portion is 1000 mm corresponding to the first layer of lattice model elements.

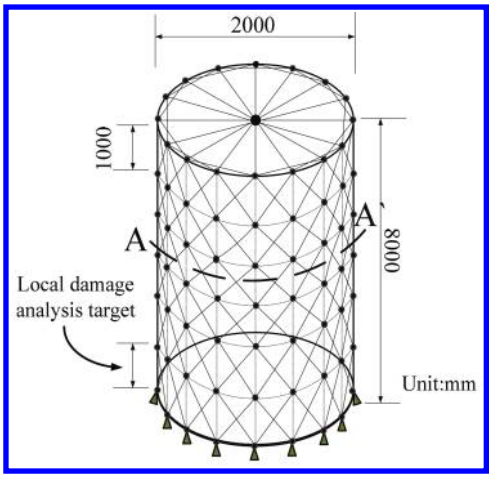

Figure 9. Analytical model.

Table 1. Hysteretic energy dissipation of column.

Hysteretic Energy dissipation KN-m	C1-5(1)	C1-5(3)
Analysis (1)	353	2466
Experimental (2)	283	2808
(1)/(2)	1.24	0.87

Table 2. Local damage evaluation of C1-5(1).

		Concrete	Steel
Strain energy KN/mm^2	Analysis	28.02	15.86
	Constitutive	84.07	253.87
Energy dissipation KN-m	Analysis	3.20	6.21
	Constitutive	10.99	96.50
Critical damage point (CDP)	Analysis	0.30	0.06
	Constitutive	0.56	0.34
Damage index		0.33	0.06

4.2 *Analytical results and discussion*

The analytical results of cases C1-5(1) and C1-5(3) are presented in Figure 10 for load-displacement relationships and Table 1 for the energy dissipation evaluation. Table 2 presents the results regarding local damage evaluation of C1-5(1).

Looking at Figure 10, the analytical results present acceptable hysteretic agreement with the experimental results after cracking of concrete in both directions for C1-5(1) and in longitudinal direction for C1-5(3).

In transverse direction however, for C1-5(3) although the behavior is generally agreeable between analysis and experiment, the analysis underestimates the maximum displacement. On the other hand in the hysteretic response of both C1-5(1) and C1-5(3), there is an overestimation in initial stiffness because of the number of members needed to correctly represent the geometry of the column. A circular cross-section column to be represented using the 3D lattice model requires more detailing than an equivalent rectangular cross-section column (Simão & Miki 2014), thus is by tendency stiffer before cracking of concrete.

In Table 1, the hysteretic energy dissipation relation calculated for the analytical and experimental cases show that for case C1-5(1) the analytical energy dissipation is 24% bigger than the experimental case. Looking at both directions, the distribution of energy is very similar for both experimental and analytical results. However in the case of C1-5(3), the analytical energy dissipation is 23% smaller than the experimental energy dissipation. In the analysis, the hysteretic response in transverse direction underestimates the maximum displacement visible. Although differences are observed in the energy dissipation capacity predicted, the general results are acceptable for the pre-established strain conditions.

In Table 2, the details of damage localization analysis for column C1-5 (1) show the energy based behavior of concrete and steel individually. The results show that response strain energy of concrete is about a third of constitutive strain energy of concrete, while in reinforcement the analytical strain energy is sixteen times smaller than the constitutive. This reinforces the idea that energy the energy dissipation potential of steel reinforcement is by large most significant than that of concrete.

The energy dissipation capacity obtained from the analysis for concrete shows that about 30% of energy is dissipated in the target region, while reinforcement dissipates less than 1%. This means that by large in the given conditions, the damage potential is bigger in concrete than in steel.

Furthermore, concrete and reinforcement do not reach the critical damage point, however the analytical CDP of concrete compared to the constitutive CDP suggests that cracking of concrete as already occurred based on the fact that in concrete tensile strain energy is smaller than compressive strain energy and further confirmed by reports on experimental results by Kawashima et al. (2010). In reinforcement however, based on comparison of CDP analytical and constitutive damage range is very small.

Looking at the damage index of materials, it is clear that concrete sustained some level of damage, but not critical, while steel suffered little damage and contributed more to seismic response of column.

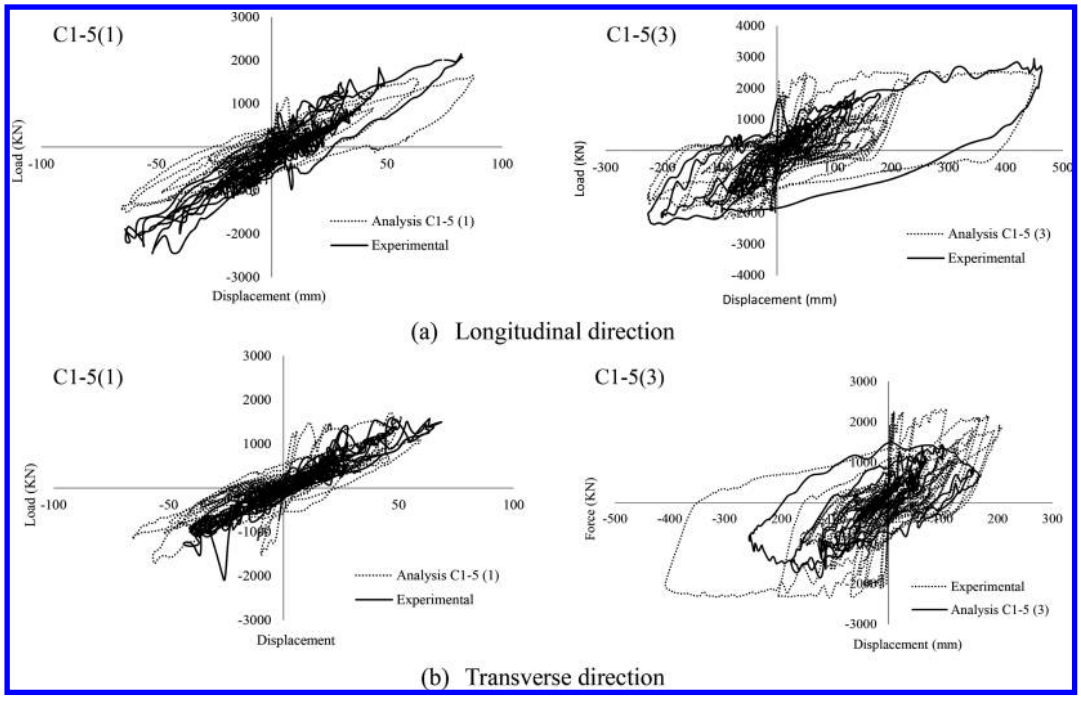

Figure 10. Load-displacement relationship computed using analytical model.

5 CONCLUSIONS

1. The applicability of the 3D lattice model to perform damage evaluation of reinforced concrete columns with circular cross section is proposed using the multi-directional polygonal 3D lattice model. The analytical results confirm the applicability of the model, especially the hysteretic response after cracking of concrete.
2. Damage evaluation has been proposed from the material point of view considering the accumulated energy dissipation of concrete and reinforcement, which are dependent on strain energy. Analytical results show that by large scale, steel reinforcement is the most dominant material in seismic resistance capacity.
3. The analysis of damage considering the critical damage (CDP) condition point, allowed the reasonable prediction of real structure damage condition. At this point in this research, suffices to assume that damage range potential between 0 and CDP is moderate, while damage range from CDP to 1 is consistent with more severe damage potential, especially for concrete which presents less ductility capacity when compared to steel reinforcement.

REFERENCES

Ang, B. G. Priestley, M. J. N. and Paulay, T. 1989. Seismic Shear Strength of Circular RC Columns. *ACI structural journal*, Vol. 86, No.1: 45–59.

Bousias, S.N. Verzeletti, G. Fardis, M.N. and Gutierrez, E. 1995. Load-Path Effect in Column Biaxial Bending With Axial Force. J*ournal of Engineering Mechanics*: 596–605.

Fukuura, N. and Maekawa, K. 1997. Computational Model of Reinforcing Bar Under Reversed Cyclic Loading for RC Nonlinear Analysis. *Journal of Materials, Concrete Structures and Pavements,* JSCE,Vol. 564, No.35:291–295.

Huanjun, J. Bo, F. and Linzhi, C. 2013. Damage-control seismic design of moment-resisting RC frame buildings, *Journal of Asian architecture and building engineering:* 49–55.

Inoue, S. 1994. *Ductility and energy dissipation of concrete beam members and their damage evaluation based on hysteretic energy dissipation,* Kyoto: Kyoto University Press.

Kawashima, K. Sasaki, T. Ukon, H. Kajiwara, K., Unjoh, S. Sakai, J. Kosa, k. Takahashi, Y. Yabe, M. and Matsuzaki, H. 2010. Evaluation of seismic performance of a circular reinforced concrete bridge column designed in accordance with the current design code based on E-Defence excitation, *Journal of JSCE*, Vol. 66, No. 2: 324–343.

Li, D. Peng, Y. Ning, M. and Long, G. 2013. A New Strategy to Assess the Seismic Energy Dissipation Safety of Reinforced Concrete bridge Piers, *International Journal of Energy Engineering*, Vol.3: 55–61.

Mander, J. B. Priestley, M. J. and Park, R. 1988. Theoretical stress-strain model for confined concrete, *Journal of Structural Engineering*, ASCE, Vol. 114, No.8: 1804–1826.

Miki, T. and Niwa, J. 2004. Nonlinear analysis of RC structural members using 3D lattice model, *Journal of advanced concrete technology*, Vol.2, No.3: 343–358.

Niwa, J. Choi, I. C. and Tanabe, T. 1995. Analytical study for shear resisting mechanism using lattice model, *Concrete library of JSCE*: 95–109.

Pique, J. R., Burgos, M. 2008. Effective rigidity of reinforced concrete elements in seismic analysis and design, *Proc. of 14th World Conference on Earthquake Engineering*: Beijing.

Rokugo, K. Iwasa, M. Suzuki, T. and Koyanagi, W. 1989. Testing method to determine tensile strain softening curve and fracture energy of concrete, *Journal of Fracture toughness and fracture Energy*: 153–163.

Simão, M.R. & Miki, T. 2014. Seismic Damage Range Evaluation of RC Columns with Circular Cross Section by Energy Dissipation Using 3D Lattice Model. *Proc. 2014 JSCE International Summer symposium:* Osaka.

Tembulkar, J.M. and Nau, J.M. 1987. Inelastic Modeling and Seismic Energy Dissipation. *Journal of Structural Engineering*, Vol. 113, No. 6.

Uchida, U., Rokugo, K., and Koyanagi, W. 1991. Determination of Tension Softening Diagrams of Concrete by Means of Bending Tests, *Journal of Materials, Concrete Structures and Pavements*, JSCE, No.426, Vol.14: 203–212.

Vecchio, F. J. and Collins, M.P. 1986. The modified compression-field theory for reinforced concrete elements subjected to shear, *ACI Journal*, vol. 83, No.2: pp. 219–231.

Concrete Repair, Rehabilitation and Retrofitting IV – Dehn et al. (Eds)
© 2016 Taylor & Francis Group, London, ISBN 978-1-138-02843-2

Influence of aggregate size and the effect of superplasticizer on compression strength

H. Aljewifi
Materials Research Laboratory, University of Omar Al-mukhtar, Albida, Libya

X.B. Zhang
Institut Pascal, Université Blaise Pascal de Clermont-Fd, Montluçon, France

J. Li
Université Paris XIII, LSPM, CNRS UPR, France

ABSTRACT: The aggregate is used as a principal element in concrete because it presents a ratio of not less than 60–78% as size and 63–85% as weight. Furthermore, the aggregate is needed for manufacture of concrete from economic point of view because it allows to reduce the level of link (cement), which is more expensive, from technically point, it increases the stability of the dimensions (shrinkage, creep) and be more resistant than the cement. This paper describes firstly, the effect of all size of aggregates on the compressive strength of the ordinary concrete used in buildings. The importance of this effect is determined by conducting laboratory experiments on ordinary concrete prepared using aggregates of different size (but same type: limestone) without varying water cement ratio in this phase. Physical properties of aggregates classified using the initial experiments such as: sieves analysis, the water content test; coefficient of absorption, bulking of sand test, cleaning of aggregate, porosity and real volume bulk density. In addition, Micro Deval test used to determine Los Angles coefficient. In the first phase of this research and the same as, for all size of aggregates, ordinary concrete prepared using smaller size of aggregates demonstrated higher compressive strength values. Secondly, this paper studied the effect of HAA Dynamon and Adricete BVF admixture on the compressive strength of the ordinary concrete with vary water cement ratio, in terms of reducing the water content within the normal concrete, according to the specific proportions of cement weight and classification of the mechanical properties of fresh and solid concrete at 28 days and examined the benefits of admixture in terms of improving the compression resistance.

1 INFLUENCE OF AGGREGATE SIZE

1.1 *Introduction*

Identification of the constituents of an aggregate is essential to know the performance the aggregates tested before they are used in concrete. The most commonly used aggregates—sand, gravel, crushed stone, and air-cooled blast-furnace slag produce freshly mixed normal-weight concrete with a density (unit weight) of 2200 to 2400 kg/m^3 (140 to 150 lb/ft^3). Shape of aggregate used in manufacturing of pervious concrete has remarkable bearing on compressive strength and permeability of pervious concrete. The magnitude of this effect is determined by conducting laboratory experiments on mixes of pervious concrete prepared using aggregates of different shape with varying water cement ratio (Jain et al. 2011). They indicated that strength and permeability of pervious concrete vary as a function of shape of the aggregate along with size of aggregate and water cement ratio in the mix which leads to the conclusion that shape of aggregate shall be considered as an important parameter in deciding the suitability of course aggregate to prepare pervious concrete.

The influence of aggregate shape on the fracture energy, tensile strength and elasticity modulus in concrete is considered (Rocco & Elices, 2009). The compressive strength of concrete depends on the water to cement ratio, degree of compaction, ratio of cement to aggregate, bond between mortar and aggregate, and grading, shape, strength and size of the aggregate (Abdullahi, 2012). Anastasios et al. 2006 examined the effects of coarse aggregate type and size on the mechanical properties of concrete, in an effort to develop more cost-efficient mixes for pavements and other highway structures. They studied if the cement efficiency of standard Ohio Department of Transportation (ODOT) concrete mixes for pavements and

other transportation structures can be improved by the use of larger sized coarse aggregates. They showed that coarse aggregate properties often did not have a significant effect on the mechanical properties of concrete. Aginam et al. 2013 used in their investigation, crushed granite, washed gravel, and unwashed gravel. They found that the 28 day strengths of the concretes made with crushed granite, washed gravel, and unwashed gravel were 25.1 N/mm^2, 20.0 N/mm^2, and 16.9 N/mm^2 respectively. Consequently, it was concluded that the strength of concrete depends greatly on the internal structure, surface nature and shape of aggregates.

This research studies influence of various size of limestone aggregates on compression strength at 28 days.

1.2 *Materials*

Cement: according to Egyptian code, an ordinary Portland cement (CEM I 52.5) was used. Apparent volume bulk density measured in laboratory is 1.254 g/cm^3.

Sand: sand used in the search is fetched from the apse area Aljabal. Where it found a large proportion of harmful impurities concrete resulting from the lack of clean sand was told to sell it, according to global standards. Sieve analysis showed that this sand size is 0–2 mm. Apparent volume bulk density measured in laboratory is 1.77 g/cm^3.

Aggregate: source, four aggregate samples were taken from area Aljabal of the quarries (breaker) near the Quba area.

1.2.1 *Morphology of aggregates*

In collaboration with the Department of Micro Scoop a microscope was used to check the aggregates samples before and after their introduction in concrete. Figure 1 shows the physical properties of the granules observed by electron microscope. The magnification microscope scale is 1/40, but we have encountered some problems in the full recognition of these properties and the reason is the weakness of possibilities that exist in the workplace, which has the process of conducting this experiment Laboratory.

Surface broken: the surface is irregular due to abrasion and take slant to rotate the shape (fig 1a), the form is semi-round, either the surface of the granulate almost free of soft material (see fig 1b).

Surface broken: figure 2a shows the granule form that takes non-regular shape, while in figure (2b), the surface has a beloved distortions with no soft materials.

Figure 3 shows the surface of the grain only the lack of a soft material and the presence of heterogeneity on the surface.

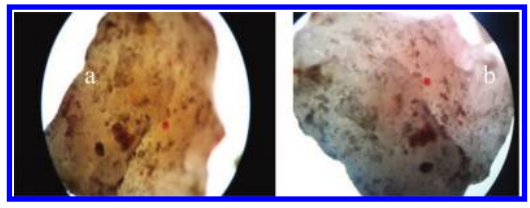

Figure 1. Granulate form, size is 1/19 mm.

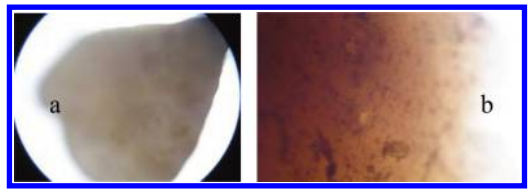

Figure 2. (a) Granule form; (b) the surface of the grain, size is 1/25 mm.

1.2.2 *Physical properties of aggregate*

sieve analysis: it allows the identification and determination of various diameter of the granules that form aggregates. Therefore, the sieve analysis works on the separation and classification with the help sift these granules under their own diameter. Sieve curve obtained from the analysis of the note and allows investment this information simply. Experiment steps are subjected to the European Code NF P 18 560.

This code is applicable for the diameter of aggregate larger than 100 micrometers.

After applied sieve analysis on dry aggregates, we found that the type of aggregates is limestone, so the diameters of the aggregates from sieve analysis were (8/37.5), (1/25), (1/19) and (1/62.5).

The vibration is not enough to work landing soft material at the bottom, so the code permits to wash the aggregate on smaller sieves. In fact, the water works to drag soft material with him. Using smaller sieve analysis only ensures the carry of soft material with him through the sieve. So the process of washing is not the aim of cleaning the aggregate, on the other hand, it is important to be clean grain but this does not mean removing soft material because they are a part of the soft-grain components of the aggregate. This means must be taken in account the percentage of soft material weight. Figure 4 shows the washing process.

Figure 5 shows sieve analysis curves for the sand (0–2 mm) and different sizes of aggregates.

For sand fineness modulus is 2.96. Fig (5a) shows the following points:

- curve (1/19mm) convergence properties of aggregates with a diameter 1/25, continuously curved, the particle size isn't tight;

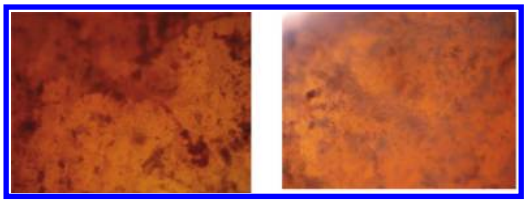

Figure 3. Surface of grain, size is 8/37.5 mm.

Figure 4. Washing process on smaller sieves.

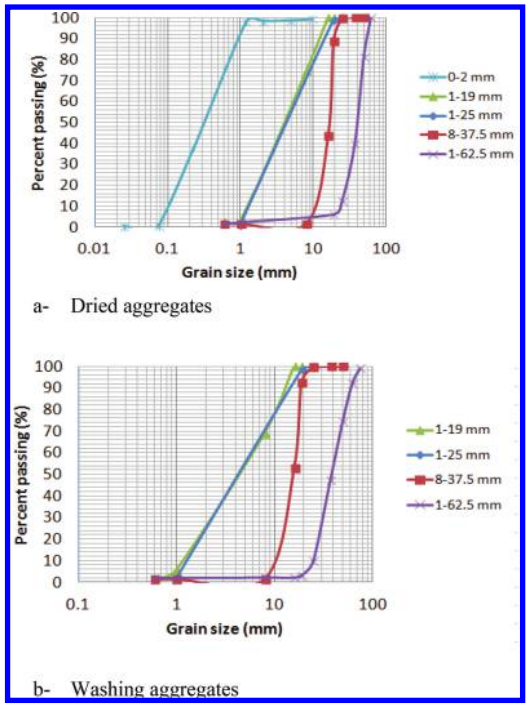

Figure 5. Grain size analysis curve of aggregates.

- curve (1/25mm) continuous gradation, good gradient and granulate almost be different sizes;
- curve (8/37.5mm) curved inclined to continuity, and inclined to be vertical, is curved weak gradient and sizes close;
- curve (1/62.5mm) continuously curved inclined to be vertical, has a approached grain sizes;
- curve (sand) note that sand has a low ratio of a fin materials and the quality of sand is normal.

After washing the aggregates, the percent of fin materials diminishes and overall the curve presented in fig (5b) has approached behavior than fig (5a).

Real volume bulk density and coefficient of absorption until constant mass: according to EN 1097-6, the real volume density of aggregate was determined by immersing the aggregates in a bowl during 24h under the water. By measuring immerged weight, dried and saturated weight, we can find mean real volume density ($\rho_{constant}$ mass).

Real volume bulk density by graduated test tube: this is a simple test depending on the measure of the difference between the volume V1 (water volume in graduated test tube) and V2 (granulate inside the same test tube) while taking into account the elimination of air bubbles, we can find mean real volume density (ρ_{tube})..

Real volume bulk density by using the balloon: this method depends on the using glass bowl in form of balloon filled with water and covered with a glass lid with a rectangular shape. From the measured weight of bowl with and without the aggregates in presence the water, we can find mean real volume density ($\rho_{balloon}$).

Real volume bulk density by using trellised basket: according to NFEF 1097-6, in this method, it is necessary to determine immersed weight of aggregates under the water during 24h in trellised and leave immersed in a bigger bowl with water so that the water level is at least 50mm from the top. After it is dried sample surface quietly on the first piece of cloth and then transferred to another soft cloth and absorber when the first piece does not absorb water again. Is published aggregates so exposed to the open air until the water surrounding each granule disappears and is taking the weight, we can find mean real volume density ($\rho_{trellised}$).

The following tables illustrate some of the basic properties of aggregates, information through previous experiences:

Bulking of sand test: with increasing the size of the water content in the sand, the size of the soft material in the sand begins to increase. In fact, the materials used for the manufacture of concrete at the site from which the material aggregates do not always have good storage (storage under the open sky) volumetric weight of the wet sand lead

Table 1. Real volume bulk density values.

Size mm	ρ(constant mass) g/cm³	ρ(tube) g/cm³	ρ(balloon) g/cm³	ρ(trellised) g/cm³
1–19	2.57	2.41	2.39	–[2]
1–25	2.45	2.93	2.54	–[2]
8–37.5	2.61	2.52	2.21	–[2]
1–62.5	–[1]	2.63	–[1]	2.41

* (1): big size; (2): small size

Table 2. Physical properties of aggregates.

Size mm	Mean real volume Bulk density g/cm³	Coefficient of absorption %	Porosity %	Water content %
1–19	2.47	2.45	16.6	4.60
1–25	2.64	2.88	8.4	4.19
8–37.5	2.48	2.04	6.1	4.84
1–62.5	2.50	2.49	14.5	5.32

in mixing concrete to a lack of soft material and this produce has negative effects on the quality of the concrete.

The goal is to measure variables in the virtual weight of the sample volume of sand from the gradual increase of the water content. In this test, we used following percent of water content: 2%, 3%, 4%, 5%, 6%, 7% and 10%.

Figure 6 shows that for the addition of water there is an increase in volume due to the membrane that are the grains of sand, which reached its peak at 3.2%, but with increase the water content broke (water bridge) or membrane, causing the adhesion of sand grains directly with each other and the expulsion until the air particles, which caused the reduction in size from the original size of the sample, a trend that appears in the negative values. If added to the sand or water was wet, the thin layer of water-jacketed grains of sand, and pay-grained away from each other due to the impact tensile surface phenomenon and thus increases the sand size and stop those volumetric increase of sand on the amount of moisture to some extent and then less than if increased humidity where under the influence of surface tension gradually to that sand back to its original size and value rises volumetric increase the smaller the grains of sand, and that due to the increased surface area (the effect of increasing the tensile surface).

Cleaning of aggregate: overall quality aggregates used in the concrete to be an important factor, in addition to a good distribution of aggregates, acceptable to granulate and shape provides satisfactory cleanliness. In fact, if the granulate be submerged by surpassing the amount of soft component which is usually of mud, it prevents the coalescence well with the cement past also cause decreasing in the mechanical resistance of concrete.

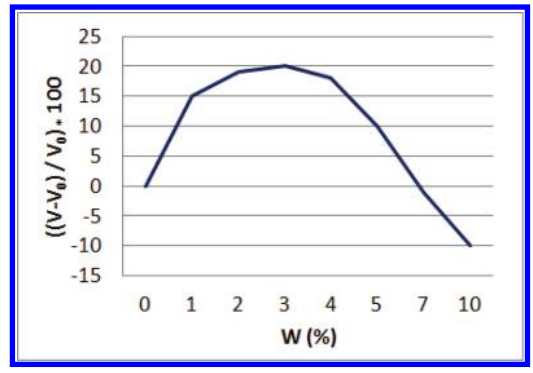

Figure 6. Increase in volumetric mass relative initial volume in function of the water content.

Figure 7. Aggregates after the failure process.

In this test it is necessary to determine soft-containing materials in the granulate appoint laboratory, by cleaning the granulate on 0.5 mm sieve using clean water, and the ratio obtained be specific after dry process remaining on this sieve. The percent obtained from this test are: 1-19(0.13%), 1-25(0.11%) and 8-37.5(0.03%). According to the XP P 18_540 code on the surface cleanliness small aggregates in concrete are:

1. granulate of a few or is unbroken: 1.5%
2. broken rocky granulate: 3%

We can ignore the cleanliness of the granulate in the Alabel due to geological between Europe and Libya.

1.2.3 *Determination of the mechanical properties of the aggregates*

Los Angles abrasion value test is used. Measuring the amount of material lower than 1.6 mm resulting from the refraction and the failure of the aggregate of balls found in the interior of the cylinder rotation. Usually this experience is important for granulate roads. In fact the frequent passage of vehicles leads to sharp refinement of the granulate and to lower docking between wheels on the asphalt as well as assess the quality of aggregates used in concrete preparation. introduced with precaution took mass M = 5000 g and the charge of the particle size range balls after 500 rotations of the machine with a regular speed between 30–33 tr/min granulates collect and sift 1.6 mm, the percentage of refuse compared the initial mass present the coefficient Los Angles equal to 68% (see fig 7). Then from NFP18_573 code the classification of aggregate is limestone.

Water

For preparation of mix and curing of concrete samples, potable water supplied from a tube well located in the campus was used.

1.3 *Mix proportions*

To obtain high strength of concrete, we used the general proportion in construction at Aljabel town. W/C ratio can be in the range of 0.54. The quantity of sand used is 810 kg/m^3. The increase of cement content leads to the increase of the compressive strength of concrete. The total cementations material content is 350 kg/m^3. Furthermore, one type (limestone) and four sizes of aggregates (1/19, 1/25, 8/37.5 and 1/62.5 mm) were used to conduct the study, aggregate content 910 kg/m^3.

1.4 *Manufacture of composite*

The preparation of concrete is mixed following weight components ratios mentioned before. It is dry mixing of aggregates, cement and sand respectively for 3 minutes and then water is added and confused for two additional minutes so that the total mixing time does not exceed 5 minutes are taking into account wetting surface of mixture before mixing.

Four concrete mixtures of normal concrete varied in size of aggregates have prepared, the form of concrete was cubic samples (size: 150 × 150 × 150 mm) and cylindrical samples (size: 160 × 320 mm).

Specimens have removed from the mold after 24h and they were immersed under the water of 20°C, time curing 28 days.

1.5 *Test methods*

1.5.1 *Fresh concrete*

Standard slump test is used. The essential property of fresh concrete workability is making capable of performing only import what volume. Many factors affect workability of them form aggregates and grain size. The variable characterizing the workability is its consistency measurement can be performed easily on site with slump test, is a subsidence of a volume of truncated concrete test according to NF P 18-451.

Flow test: is to set the percentage of the flow and the workability of concrete, to characterize the fluidity of the concrete after mixing, we proceeded to the measurement of the flow on a smooth surface using the pre-moistened mold to place the fresh concrete. The flow can also be expressed in% of the variation in the diameter of the wafer formed by the diameter of the mold according to ISO 9812 following experimental formula:

$$E = (D_f - D_i)/D_i \tag{1}$$

where D_f is the final diameter of the wafer formed by the fresh concrete and D_i is the inside diameter the mold as showed in fig 5.

Apparent volume density: on fresh concrete allows knowledge of changes resulting from the addition of the aggregate in concrete on apparent volume density. It is simple test to achieve at the site then it determines measuring the weight of fresh concrete fills a mold 1L. All test realized at 28 days.

1.5.2 *Hard concrete*

Apparent volume density: The same measure method is used for hard concrete as that used for fresh concrete.

Compression test: according to SIA162 code we measured maximum strength of concrete and Young's modulus. Figure 9 shows the extensometer used to measure vertical deformation.

Indirect tension test: according to NFP 18-408 code.

Speed of sound: This is one of the non-important experiments that allow knowledge of several properties of concrete once, such as: the homogeneity of concrete, the possible existence of voids or cracks out. This test is realized according to 13311 IS (part 1 1992). The principle of the test consists in measuring the speed of sound within the concrete. This rate is higher as the concrete is stronger.

Sclerometer test: according to NF P 18-417, this test is realized on cylindrical and cubic concrete sample. In fact it is to test the surface hardness of hardened concrete (project). This hardness

Figure 8. The variable concrete workability according to the diameter of aggregates.

Figure 9. Measuring longitudinal deformation using extensometer.

increases as the concrete is more resistant, it helps to have an order of magnitude of the damage resistance concrete at a given age.

2 RESULTS AND DISCUSSION

2.1 *Fresh concrete*

Aggregate size has major influence on slump test than subsidence values increase with. For flow test (E) it has been found that the percent of wafer size increases with aggregate volume. Furthermore, apparent volume density (ρ_{av}) corresponds to the mass of aggregate and to its volume. But in the volume, we count the voids. More aggregates are large voids are more important because the aggregates do not fit perfectly and the bigger they are the less they fit and therefore more occupy the empty volume.

Table 3. Experimental results on fresh concrete.

Size mm	Slump test mm	Flow test %	(E) ρ_{av} g/cm^3
1–19	180	37.5	2.65
1–25	225	70.0	2.69
8–37.5	220	92.5	2.70
1–62.5	245	145	3.01

Table 4. Mechanical results on hard concrete.

Size mm	ρ_{av} g/cm^3	ε mm/mm	$\sigma_{cyli.}$ MPa	E GPa	σ_{cubic} MPa
1–19	2.32	0.0338	27.71	8.10	35.06
1–25	2.42	0.0029	26.97	9.65	34.11
8–37.5	2.35	0.0031	25.49	8.40	34.18
1–62.5	2.36	0.0017	21.67	14.5	26.11

Table 5. Strength and elastic module values.

Size mm	F_c MPa	V_m km/s	R_c MPa	E_b kN/mm^2
1–19	–	3.9	29.5	31582
1–25	–	4.6	72.5	46403
8–37.5	1.98	4.2	39.5	37388
1–62.5	–	4.7	90.0	47613

* (–): non measured.

We note that 1/62.5 mm specimens give high values due to the heterogeneity of the concrete, see table 3.

2.2 *Hard concrete*

We have observed the convergence of the values of the apparent volume density ($\rho_{av)}$ due to the compaction process. Mechanical behavior of cylindrical samples appeared that maximum stress (σ_{cyli}) tends to increasing with smaller size of aggregates; and the longitudinal deformation diminishes with 1–62.5 mm size; Elastic module remains approached except with 1–62.5 mm size of aggregate. For cubic samples, the maximum stress (σ_{cubic}) is greater than that of cylindrical samples and they give the same results as cylindrical samples, see table 4.

Table 5 gives the strength values and elastic module of sound test. The results obtained from the test indicate that the wave speed with excellent properties of concrete, considering that the wave speed is greater than 4000 m/s. Also the resistance

Figure 10. Cracking on the surface of grain, size is 1/19 mm.

of concrete, according to the relationship used to be very high in addition to the model of Young. These values are considered estimates, considering that this concrete resistance to compression to exceed 30 MPa. The maximum strength measured of indirect tension test (Fc) only for one specimen size 8/37.5mm is in order of 1.98 MPa, see table 5.

Sclerometer test results appeared that mean values of cylindrical samples 26.5 MPa of aggregate size 8/37.5 mm with angle 0°. And for cubic samples is between 25MPa and 27MPa with angle (0°, –90°).

We are interested in the surface of aggregates after compression test. Figure 10 shows the surface after the age of 28 days grain sample removed from the concrete mix, and it shows also the cracks on the surface of the granule with deformation after the pressure test.

In Figure (11a) no hydrate process as a result of their interaction on the surface of the cement, and figure (11b) shows the adhesion of the cement paste large construction appears on the surface of the granule rubble process.

3 INFLUENCE OF SUPERPLASTIZIER

3.1 *Dynamon HAA*

Is a liquid admixture based on highly effective harding accelerators, free of chlorides. Dynamon HAA can be used as following:

- used to get particularly for very high mechanical resistance early on, even when used under low temperatures. It accelerates the development of mechanical strength in self-compacting concrete, in this case the product must be used in conjunction with superplasticizer from the dynamo range.

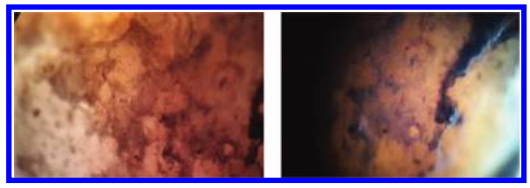

Figure 11. (a): The heterogeneity of the surface, (b): A large incision at the surface of grain, size is 8/37.5 mm.

- It may also be used to speed the removal of form work and to reduce the movement times during the production of vibro_compressed concrete.

The dosage used is 1.25% by weight of cement (W/C = 0.54) and 1L/100 kg by weight of cement (W/C = 0.47). In this case one size of aggregates has been used (1/19mm).

3.2 *Adicrete BVF*

It is a high range water reducing and superplasticizer concrete admixture, an admixture for concrete, brown liquid solution, ready to use directly with concrete soluble in water and based on selective polymers. It is used to produce high early strength in prestressed concrete, precast concrete, bridges and cantilever structures. The dosage used is 4%, 5% and 6% by weight of cement with W/C = 0.47. One size of aggregates has been used (1/19 mm). Mix proportions as description in 2.2 just we mixed the admixture with the water and add to dry compound material. Total mix time was 5 min. Specimens have removed from the mold after 24h and they were immersed under the water of 20°C. The time curing is 28 days. In this case, cubic and cylindrical samples are prepared.

3.3 *Test methods*

All mechanical tests presented in the section 2.4 on fresh and hard concrete were applied on the concrete with different percent of admixture.

3.4 *Results*

Table 6 showed the mechanical results obtained from flow test, slump test on fresh concrete and apparent volume density on hard concrete. It can be noted that Dynamon HAA reduces stretching or flow in the concrete from which reduces the workability. Adricete BVF gives high values of flow test and 4% BVF give low values of slump test when 5% and 6% provided high values.

Figure 12 shows the comparison between compression strength without addition of an admixture and with HAA and BVF. Compression strength

Table 6. Influence of introduction of HAA and BVF mixed on fresh and hard concrete.

Mixed	Percent %	E %	Slump test mm	ρ_{av} g/cm^3
HAA	1.25	37.5	70	-
	1L/100kg	22.5	200	2.37
BVF	4	17.5	35	2.37
	5	70.0	235	2.39
	6	27.5	70	2.33

* (–): non measured.

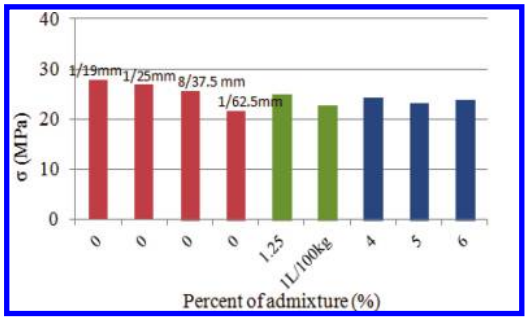

Figure 12. Influence introduce the admixture on compression stress at 28 days.

increases with decreasing size of aggregates and without using an admixture. For the same size (1/19 mm), we note that approached behavior with or without introducing an admixture. Consequence, introduce Dynamon HAA and Adicrete BVF does not carry great influence on mechanical strength.

4 CONCLUSION

From the analysis of results obtained and the discussion above, compression strength varies inversely with the sizes of aggregates. Compared to the case without admixture, we note that the addition of an admixture leads to diminish the flow values; the workability remains important with increasing the percent of admixture except with 6% due to wettability phenomena. Apparent volume density diminishes compared to without admixture due to the homogeneous in compound of concrete. It's important to remark the effect of HAA and BVF on ρ_{av} at state hard concrete.

REFERENCES

Abdullahi, M. 2012. Effect of aggregate type on compressive strength of concrete. International journal of civil and structural engineering 2(3).

Aginam, C. H., Chidolue, C. A. & Nwakire, C. 2013. Investigating the effects of coarse aggregate types on the compressive strength of concrete. International journal of engineering research and applications (ijera) 3, issue 4.

Anastasios M. Ioannides & Jeff C. Mills. 2006. Effect of larger sized coarse aggregates on mechanical properties of Portland cement Concrete pavements and structures. State Job.

Jain, A. K. & Chouhan, J. S. 2011. Effect of shape of aggregate on compressive strength and permeability properties of pervious concrete. International journal of advanced engineering research and studies, ijaers, vol. i, issue i, October—december, 2011.

Prepared in cooperation with the Ohio Department of Transportation and the U.S. Department of Transportation, Federal Highway Administration. No.: 14803(0).

Rocco, C.G. & Elices, M. 2009. Effect of aggregate shape on the mechanical properties of a simple concrete", engineering fracture mechanics 76(2): 286–298.

Concrete Repair, Rehabilitation and Retrofitting IV – Dehn et al. (Eds)
© 2016 Taylor & Francis Group, London, ISBN 978-1-138-02843-2

Bond of reinforcing bars in cracked concrete

P. Desnerck, J.M. Lees & C. Morley
Engineering Department, University of Cambridge, Cambridge, UK

ABSTRACT: Cracks are inherent in reinforced concrete structures. The origin of cracks can be manifold. At early stages they can be caused by plastic settlement, shrinkage, drying shrinkage, etc. Typically, the most severe forms of cracking in reinforced concrete structures are those caused by the corrosion of the reinforcing bars. Corrosion products are expansive in nature and tend to generate tensile stresses in the concrete surrounding the corroding bars. As soon as these stresses exceed the tensile capacity of the concrete, cracks around and along the reinforcing bars are formed.

In assessing existing structures engineers often notice severe cracking due to corrosion or longitudinal cracks due to plastic shrinkage e.g. in the anchorage zones. The section loss of these bars can easily be taken into consideration when performing load bearing capacity checks, but questions arise with respect to the remaining bond capacity of the rebars in the cracked concrete.

This study aims to quantify the influence of different parameters on the bond strength of reinforcing bars in cracked concrete. Rather than performing accelerated corrosion tests, it focuses on the effect of cracking itself (in absence of corrosion products) so the results can be used for non-corrosion related cases as well. Parameters under investigation include the confinement, concrete cover, crack direction and crack extension. Results show that single cracks as narrow as 0.03 mm can have a significant influence on the obtained bond strengths.

1 INTRODUCTION

Concrete is an inhomogeneous material with a relatively low tensile strength. Therefore it is often used in combination with steel reinforcement so that the steel can resist tensile stresses after cracking. The load bearing capacity of reinforced concrete structures depend highly on the interaction between reinforcing bars and the surrounding concrete (Task Group Bond Models 2000). Over time the bond can degrade due to deterioration of the reinforcement.

Cracks are inherent in reinforced concrete structures and are caused by a number of different types of actions (BRE Centre for Concrete Construction 2000). One of the most severe forms of cracking in reinforced concrete is the result of the corrosion of the reinforcing bars. Due to carbonation and chloride ingress a favourable environment is created for corrosion to initiate and corrosion products to be formed (BRE Centre for Concrete Construction 2000). Fib bulletin No. 10 (Task Group Bond Models 2000) categorises the effects of corrosion into 3 potential consequences:

- loss of reinforcing bar section
- creation of a weak interfacial layer at the reinforcing bar/concrete interface
- volumetric expansion of the reinforcing bar

The last two phenomena have a direct influence on the bond of the reinforcing bar. On one hand, a weak interface layer of brittle corrosion products surrounding the reinforcing bar increases the relative displacement of the bar with respect to the concrete at certain load levels. On the other hand corrosion products are expansive in nature and tend to generate tensile stresses in the surrounding concrete. At low levels this expansion may be advantageous but once these stresses exceed the tensile capacity of the concrete, cracks around and along the reinforcing bars develop (Task Group Bond Models 2000). The reduction in confinement due to these cracks then leads to a progressive reduction in the bond strength. Hence, understanding of the link between corrosion rates, the induced cracking (and crack widths) and the reduction in bond capacity is essential.

To investigate crack formation due to corrosion, researchers (Rodriguez et al. 1994; Andrade et al. 1993; Al-Sulaimani et al. 1990; Clark & Saifullah 1994; Almusallam et al. 1996; Clark & Saifullah 1993; Alonso et al. 1998) have undertaken accelerated corrosion tests on reinforced concrete specimens where impressed currents of 0.003 to 10 mA/cm^2 were applied. Table 1 summarizes results found in literature on the corrosion levels to cause cracking of the concrete cover. The corrosion levels are expressed as a percentage of bar cross-sectional area loss (section loss expressed as a uniform metal

Table 1. Overview of reported corrosion levels to cause concrete cover cracking.

Study	ϕ [mm]	Cover ratio [–]	Section loss [%]	Corrosion Penetration × [mm]
(Al-Sulaimani et al. 1990)	10	7.50	5.00	0.130
	14	5.36	3.00	0.110
	20	3.75	2.00	0.100
(Clark & Saifullah 1993)	8	0.50–2.00	0.40–1.30	0.008–0.026
(Andrade et al. 1993)	16	1.25–1.88	0.40–0.50	0.015–0.020
(Rodriguez et al. 1994)	16	2.00–4.00	0.40–1.00	0.015–0.040
(Clark & Saifullah 1994)	8	1.00	0.30–0.55	0.006–0.011
(Almusallam et al. 1996)	12	5.00	4.00	0.120
(Alonso et al. 1998)	8–16	1.25–7.00	0.19–1.30	0.015–0.065

loss around the circumference of the reinforcing bar) and corrosion penetration depth × radially into the bar. Although there is some scatter on the obtained values, all studies agree that a relatively low corrosion penetration depth, ranging from 0.008 to 0.130 mm, causes cracking.

Rodriguez et al. (Rodriguez et al. 1994) found that cracks were initiated for corrosion levels associated with bar radius reductions as low as 0.015 mm to 0.040 mm.

One issue with accelerated corrosion bond tests is that they study the combined effect of cracking and the formation of a soft layer of corrosion products around the reinforcement. While these effects co-exist in practice, it leads to difficulties in analysing the processes at a fundamental level. Furthermore the results cannot be applied to situations in which cracks are present in the absence of corrosion (e.g. plastic shrinkage cracks in congested reinforcement lay-outs).

Therefore this study aims to quantify the bond strength of reinforcing bars in cracked concrete. Rather than performing accelerated corrosion tests, it focuses on the more fundamental effect of the cracking itself (in absence of corrosion products). To achieve this aim, a novel test method is developed.

2 CRACK GENERATION

When assessing existing structures, engineers often observe severe cracking due to corrosion. Some common corrosion induced crack patterns are shown in Figure 1.

As discussed, most studies on the bond properties of cracked concrete specimens have used accelerated corrosion techniques. However, these techniques have the tendency to lead to less controllable crack patterns and a wide range of obtained crack widths.

In this study the principles of a controlled split tensile test is applied to pre-crack specimens. In this way rough crack surfaces are then formed along a predefined cracking plane running through

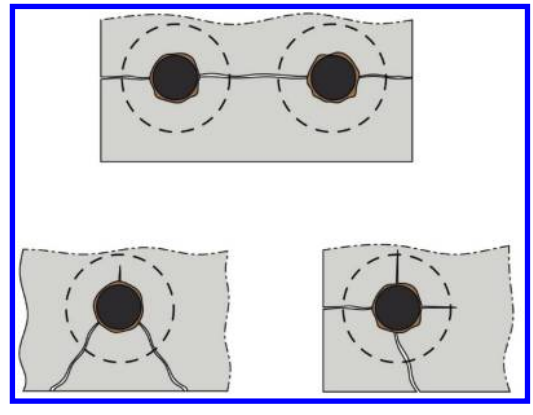

Figure 1. Possible cracks patterns in reinforced concrete due to corrosion.

the axis of the reinforcing bar. To avoid brittle failure and provide some post-cracking confinement, the specimen can be cast within a plastic ring. This ring can remain in place during both the pre-cracking and pull-out phases. With this technique, single or double cracks can be generated to represent observed crack patterns in existing structures.

Of particular interest are the bond reductions during the early stages of corrosion and thus the onset of cracking. The splitting tests seek to achieve 0.03 to 0.04 mm crack widths. These crack widths are relatively small compared to the allowable crack widths of 0.20 to 0.30 mm according to reinforced concrete design guidance (European Committee for Standardization 2004).

3 EXPERIMENTAL PROGRAM

3.1 *Experimental specimens and overview of test method*

In order to represent common crack patterns (as illustrated in Figure 1) and determine the bond

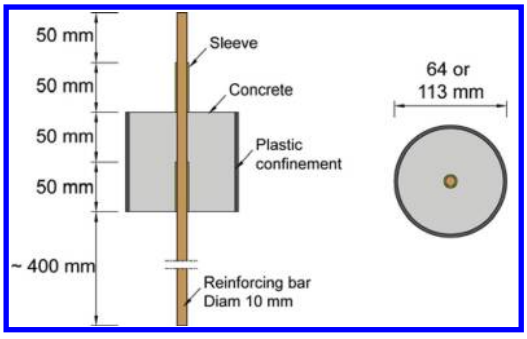

Figure 2. Specimen geometry.

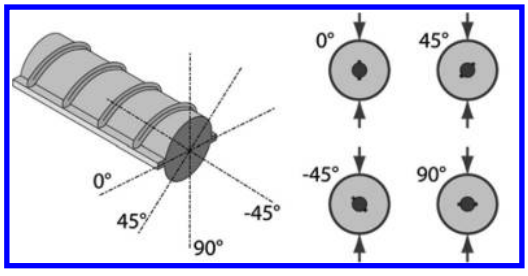

Figure 3. Applied crack orientations with respect to the reinforcing bars rib pattern.

strength of reinforcing bars in cracked, the test method includes one or two pre-cracking phases followed by standard bond strength "pull-out tests" (RILEM TC 1970).

In the pre-cracking phase(s) the specimens are subjected to a split cylinder test. Two line loads are applied on the specimen on opposite sides and along the axis of the concrete cylinder until first cracking of the concrete, at which point the specimen is unloaded. For double cracked specimens, the specimen is rotated 90 degrees after the first pre-cracking experiment and the same procedure is repeated to induce the second crack. Pull-out tests are then conducted on the cracked specimens to determine the influence of the cracks on the bond behaviour.

Cylindrical specimens with a diameter of either 107 mm or 60 mm, and a height of 100 mm are used. A reinforcing bar with a diameter of 10 mm is centrally placed in the specimen, resulting in a cover-to-diameter ratio of 4.8 or 2.5. The specimens are cast with a bond length of 5 times the bar diameter. The bond length itself is reduced by providing a sleeve over the bar in the lower 50 mm (Figure 2). The specimens are cast in a plastic cylindrical mould which was used as confinement for the specimen during the pre-cracking phases and in many cases also remained in place for the pull-out tests.

3.2 *Main parameters*

Based on the afore mentioned studies, the following parameters were selected for investigation: single or double cracking (number of cracks), the crack orientation relative to the reinforcing bar rib pattern, the confinement and the concrete cover.

As reinforced concrete structures are currently primarily constructed with ribbed reinforcing bars, the crack itself can cross the rib pattern of the bar at different angles. Cracks running along to the longitudinal ribs, leaving the concrete around the transverse rib intact, might have a less detrimental impact on the bond compared to cracks that hit the transverse ribs. Whether this crack angle influences the bond behaviour is currently unknown.

Crack widths are often governed by the amount of transverse reinforcement. For longitudinal cracks running along the longitudinal reinforcing bars, the transverse reinforcement is providing a form of confinement transferring forces from one crack face to another and reducing the crack width. As more confinement is provided, the hoop stresses induced during pull-out of a longitudinal reinforcing bar might be counteracted and in this way provide sufficient resistance for the anchorage force to build up (Tepfers 1976).

In cases where the confinement is limited these hoop stresses might induce higher stresses in the transverse reinforcement, leading to cracks opening up and decreases in the bond properties.

Similar to the confinement provided by transverse reinforcement, the concrete cover can also provide confinement. Increasing the concrete cover leads to a bigger influence zone around the reinforcing bar that might resist the hoop stresses being built up and thereby increase the bond strength of the bar.

3.3 *Test series*

A total of 4 series of experiments are undertaken. Each series consists of 4 sets of 5 identical specimens. The entire test matrix, for the total of 80 tests carried out, is shown in Table 2.

In Series 1 the angle of a single crack with respect to the rib pattern of the bar is varied. Different angles are achieved through different orientations of the specimens relative to the applied split tensile load. In addition to a reference uncracked set, a single cracked set with crack angle of 0 degrees, 45 degrees and 90 degrees is tested. The crack angle itself is measured with respect to the plane running through the bar axis and the longitudinal ribs.

Series 2 focusses on double cracked specimens where the crack orientation relative to a reference

Table 2. Overview of parameter combinations for the tested specimen series.

		Confinement		Diameter [mm]		Single crack angle			Double crack angle		
Series	Set	No	Yes	60	107	0	45	90	0&90	–45&45	90&0
1	A		X		X						
	B		X		X	X					
	C		X		X		X				
	D		X		X			X			
2	A		X		X						
	B		X		X				X		
	C		X		X					X	
	D		X		X						X
3	A	X			X						
	B	X			X	X					
	C	X			X			X			
	D	X			X				X		
4	A		X	X							
	B		X*	X*	X*	X					
	C		X	X		X					
	D		X	X					X		

* Pre-cracked specimen of 60 mm cast in a 107 mm specimen.

plane through the bar axis and longitudinal ribs varies. A reference set, a set with cracks orientated at 0 degrees and 90 degrees relative to reference plane, and a set with –45 degrees combined with 45 degrees cracks are tested. As the cracks are formed by applying a splitting test, the crack faces of the first crack are compressed during the second splitting phase. To investigate the potential influence of this sequence, a fourth set of specimens where the cracks at 90 degrees are formed first followed by cracking along the 0 degrees axis has been tested.

Series 3 consisted of specimens where the plastic tube confinement was removed after the cracking phase

In the last series, Series 4, the concrete cover was reduced by casting the specimens in a cylindrical tube with an inner diameter of only 60 mm, reducing the original cover by 23 mm and resulting in a cover-to-diameter ratio of 2.5. An uncracked reference set, a set of specimens with single crack (crack angle 0 degrees) and a set of double cracked specimens (0 degrees combined with 90 degrees) are tested. The final set consisted of specimens of diameter 60 mm single cracked at 0 degrees after which the plastic confinement was removed. The specimen was then placed in the centre of a 107 mm diameter plastic tube and concrete was cast in the annulus between the specimen and the tube. As a result a 23 mm thick concrete ring was formed around the cracked specimen. This scenario simulates a situation in which the crack starts to grow around the rebar but does not yet extend to the outer surface.

Table 3. Concrete properties.

	$f_{c,cub}$ [MPa]		f_c [MPa]		$f_{ct,sp}$ [MPa]
Series	21d	28d	21d	28d	21d
1	29.5	31.3	22.8	23.3	2.4
2	29.0	30.5	20.0	20.0	2.6
3	25.3	27.6	20.2	22.5	2.5
4	28.4	29.0	23.4	23.8	2.7

3.4 *Materials*

A concrete with a 28-day cube compressive strength of about 30 MPa is selected for the tests. The water-to-cement ratio of the mixture is 0.6 and the sand-to-aggregate ratio is 0.45. The concrete is made with an early-strength Portland cement with limestone, type CEM II/A LL 32.5 R (European Committee for Standardization 2011). The aggregates are a natural sand with a maximum grain size of 4 mm and specific gravity of 2.65 and a gravel with maximum grain size of 10 mm with specific gravity of 2.65. The compressive and tensile strengths of the concrete are determined at 21 days (time of pre-cracking) and 28 days (time of bond tests). For the determination of the compressive strength, cubes with sides of 100 mm ($f_{c,cub}$) and cylinders with a height of 200 mm and a diameter of 100 mm (f_c) are used. The splitting tensile strength $f_{ct,sp}$ is measured from cylinders with a diameter of 100 mm and a height of 200 mm. The mean results for the four series are summarized in Table 3.

Figure 4. Instrumentation and test set-up for the pull-out experiments.

The steel bar diameter is fixed for the test program at 10 mm. The yield stress f_y and tensile strength f_u of the high-strength hot-rolled reinforcing bars, are measured in the laboratory as 520 MPa and 606 MPa respectively.

The confinement consisted of a plastic tube with an outer diameter of 113 mm with a wall thickness of 3.2 mm or a tube with a diameter of 64 mm and a wall thickness of 2.1 mm. Both tube diameters showed a similar behaviour under tensile loads.

3.5 *Test procedure and instrumentation*

At an age of 21 days the specimens are subjected to a split cylinder test. During the splitting test, the applied force as well as the strain on the surface of the plastic tube is recorded. The tube confining strain is measured with strain gauges on opposite sides of the specimens at mid-height.

The obtained crack width is measured using a crack microscope with an accuracy of 0.01mm at both sides of the reinforcement bar at a distance of 30 mm from the rebar in case of 107 mm specimens and at 20 mm for specimens with a diameter of 60 mm.

The pull-out tests are performed at 28 days in a 150kN closed loop tensile load frame. During the pull-out tests, the specimens are loaded at a constant displacement rate of 0.04 mm/s until a total relative displacement between the tested reinforcing bar and the surrounding concrete of at least 12.5 mm is reached.

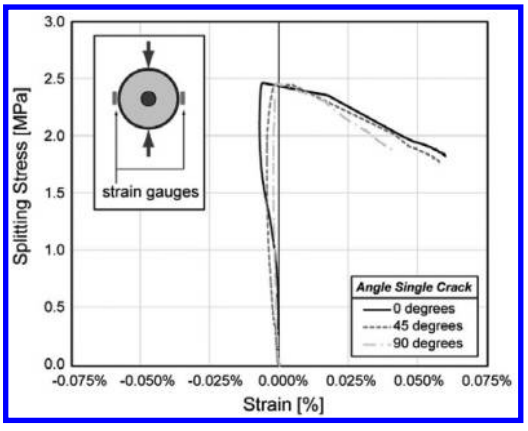

Figure 5. Confinement strains during pre-cracking tests for single cracked specimens.

The slip of the bar, at the passive as well as the active side, is recorded using 2 sets of 2 linear variable differential transducers (LVDT). These LVDT's are secured to the bar by means of a steel collar mounted to the reinforcing bar (Figure 4).

After unloading of the specimens the crack widths are measured again.

4 RESULTS AND DISCUSSION

4.1 *Pre-cracking of the specimens*

For the pre-cracking stage, the measured applied forces at first cracking induce splitting stresses of around 2.3 MPa (DEV = 0.2 MPa).

Figure 5 shows one of the measured splitting stress—confinement strain responses for a Series 1 – set B, C and D specimen (single crack oriented at either 0, 45 or 90 degrees relative to the longitudinal rib). The response of the other specimens was comparable. The final strain in the confinement after cracking is in the 0.04% to 0.06% range which corresponds to confinement stresses of 1.8 MPa to 2.3 MPa in the plastic confinement ring.

The crack widths w after splitting for the pre-cracked specimens are shown in Figure 6 for the different series and sets. The obtained values are around 0.03 mm but there is significant scatter. For the double cracked specimens (Series 2) the average of the two (phase 1 and phase 2) obtained crack widths is plotted. All crack patterns obtained for specimens within the same parameter combination were comparable. No anomalies were detected.

5 BOND STRENGTH

From the pull-out experimental results, values of the bond stress can be derived. Assuming a uniform stress distribution along the short bond length, the force F_s in the reinforcing bar is transferred to the concrete over the embedment length l_d resulting in mean bond stresses τ_d of:

$$\tau_d = \frac{F_s}{l_d \cdot \pi \cdot \phi} = \frac{\sigma_s}{4 \cdot k} \quad (1)$$

where l_d can be defined as a parameter k multiplied by the bar diameter ϕ (k.ϕ) and σ_s the tensile stress in the reinforcing bar.

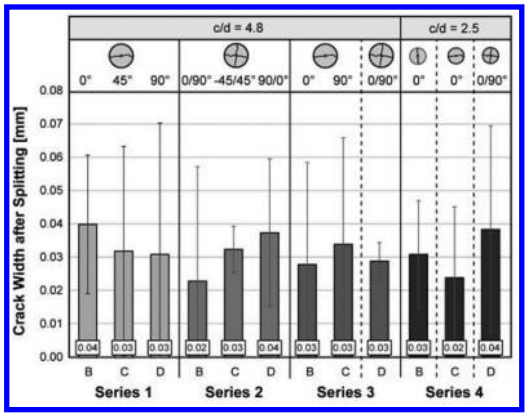

Figure 6. Crack widths *w* after pre-cracking phase.

Two values are of particular interest: the ultimate bond strength τ_R and the so-called characteristic bond strength τ_M. The ultimate bond strength is defined as the bond stress corresponding to the ultimate load recorded during testing. The characteristic bond strength τ_M is calculated as the mean value of the bond stresses corresponding to a slip of 0.01 mm, 0.10 mm and 1.00 mm.

The slip at the ultimate bond strength s_u is of interest with respect to the ductility of the bond failure.

The highest ultimate bond strengths are recorded for the reference uncracked specimens, as was to be expected. The three sets of 107 mm diameter reference specimens (c/d = 4.8) all gave ultimate bond strengths of about 19.2 MPa (DEV = 1.4 MPa). The bond strength of the bars tested with a smaller cover (c/d = 2.5 for the 60 mm diameter specimens), turned out to be 14.3 MPa (DEV = 0.8 MPa) as the dominant failure method in this case was splitting failure (due to the limited reinforcement cover). The ultimate bond strengths of the pre-cracked specimens were all lower than the equivalent reference specimens. The same observations can be made for the characteristic bond strength.

In the analysis hereafter the results of the bond stresses and strengths will be expressed in terms of a bond reduction factor. This factor is defined as the ratio of the actual strength of a specific set to the mean bond strength of the equivalent uncracked reference specimens in that series. In this way direct comparisons of the test results within and between series can be made.

Table 4. Experimental results of pull-out test.

			□R [MPa]		□M [MPa]		su [mm]		wu [mm]	
Series	Set		Mean	DEV	Mean	DEV	Mean	DEV	Mean	DEV
1	A	Reference	20.2	1.3	11.0	0.9	0.95	0.09	0.00	0.00
	B		11.4	0.4	5.5	0.3	0.56	0.09	0.16	0.06
c/d = 4.8	C	Single	11.5	0.5	6.1	0.3	0.58	0.11	0.19	0.06
Confined	D		11.1	0.6	5.6	0.2	0.57	0.10	0.18	0.08
2	A	Reference	19.6	1.0	11.1	1.4	0.89	0.09	0.00	0.00
	B		8.7	0.6	4.0	0.4	0.65	0.13	0.08	0.04
c/d = 4.8	C	Double	9.5	0.6	4.3	0.4	0.63	0.12	0.07	0.01
Confined	D		9.0	0.8	4.4	0.5	0.69	0.13	0.07	0.03
3	A	Reference	17.9	0.9	10.3	1.0	0.92	0.14	0.00	0.00
	B	Single	8.0	0.7	2.9	0.4	0.41	0.12	2.02	0.70
c/d = 4.8	C		8.1	1.0	3.4	1.0	0.54	0.12	1.62	0.49
Unconfined	D	Double	6.4	1.2	2.3	0.6	0.38	0.05	0.89	0.37
4	A	Reference	14.3	0.8	8.2	1.1	0.45	0.23	0.12	0.03
	B*	Single	16.1	0.6	9.3	1.7	0.43	0.24	0.36	0.59
c/d = 2.5	C	Single	10.6	0.9	7.1	1.5	0.31	0.12	0.13	0.01
Confined	D	Double	8.4	0.9	4.5	0.6	0.61	0.20	0.08	0.02

* Re-cast = specimen with c/d = 2.5 pre-cracked and re-casted to achieve c/d = 4.8

5.1 *Crack orientation*

The influence of the crack orientation in single cracked specimens was investigated in Series 1. Three different crack angles were considered, 0, 45 and 90 degrees, with respect to the longitudinal ribs. The results clearly show that the obtained bond strengths are all lower than the reference bond strength. A t-test with a significance level of 95% confirmed this difference to be significant. The differences between the studied crack angles is small and statistically insignificant. Therefore it can be concluded that the orientation of the crack relative to the longitudinal rib has little to no effect on the bond strength. The presence of a single crack however results in a significant reduction in the ultimate bond strength of 44% for the tested specimens.

5.2 *Multiple cracks*

As was the case for the single cracked specimen, the orientation relative to the longitudinal rib is insignificant, as the 0–90 degree and -45–45 degree double cracked specimens gave similar results. In both series the cracks led to ultimate bond strengths that are 54% lower than the uncracked specimens.

The similarity of the set 2-B and 2-D results (double crack with angles 0 and 90 degrees, and 90 and 0 degrees resp.) suggests that the order in which the cracks were formed also had little effect on the bond performance, as was to be expected from the results of the crack orientation tests. In comparison to the single cracked specimens, the double cracks tend to provide an additional reduction in bond strength of about 10%.

5.3 *Confinement*

The cracked specimens tested without confinement all tended to fail due to splitting of the specimen rather than a pure pull-out failure as was the case for the other sets. As the ultimate bond strength is reached, the crack width increases drastically leading to a relatively brittle failure of the bond and hence a sudden decrease in the bond stresses with increasing slips. The larger ultimate crack widths w_u associated with this behaviour are evident from the results.

The unconfined reference specimens provided similar bond strengths to equivalent confined specimens. As the bond failure for both sets was a pure pull-out failure this was to be expected. No cracks were observed on the outer surface of the concrete.

The beneficial effect of the confinement has been reported in earlier studies by (Gambarova et al. 1989) and is confirmed in this experimental program. The absence of any external confinement further reduces the bond capacity of the 10 mm reinforcing bars. For single cracked specimens, an additional reduction of 11% is measured whereas for the double cracked specimens this reduction is 20%.

5.4 *Concrete cover*

As the concrete cover is reduced in Series 4 to a cover-to-diameter ratio of 2.5, the failure mode of the reference specimens shifts from a pull-out failure to a splitting failure, hence a reduction in the ultimate bond strength from 19.2 to 14.2 MPa. The single cracked and double cracked specimens show a reduction relative to the reference of 25 and 41% respectively, which is slightly less than for the counterparts with a 4.8 cover-to-diameter ratio. This difference can be attributed to the changed failure mode.

For the specimens which originally have a cover-to-diameter ratio of 2.5 on pre-cracking, but are recast to give a cover-to-diameter ratio of 4.8, an increase in bond strength is measured. Compared to the original uncracked specimens, the increase is 21%. The concrete ring with a thickness of 23 mm is sufficient to carry the hoop stresses built up during the pull-out test and hence prevent a splitting failure. Failure in these specimens occurs due to pull-out. The cracks in the inner cylinder do not extend to the surface of the uncracked concrete. Comparing these specimens to the original specimens with a cover-to-diameter ratio of 4.8, shows that the re-cast specimens are stronger than the single cracked specimens. This suggests that the bond strength is less affected by partial cracking than in the case where the cracks extend to the other surface of the concrete. However, the bond strength is lower than measured for uncracked specimens.

6 CONCLUSION

Reinforcement corrosion can result in a severe form of concrete cracking. As cracks due to corrosion run along the concrete—rebar interface, the force transfer between the two materials, and more specifically the bond behaviour, is influenced.

To study the effect of the crack angle (relative to a plane running through the axis of the bar and the longitudinal ribs), extent of cracking, confinement and cover depth on the bond properties of reinforcing bars embedded in concrete, an experimental test program was conducted. Cylindrical specimens were pre-cracked by applying split tensile forces. Pull-out tests were then carried out on the cracked specimens to determine the bond properties.

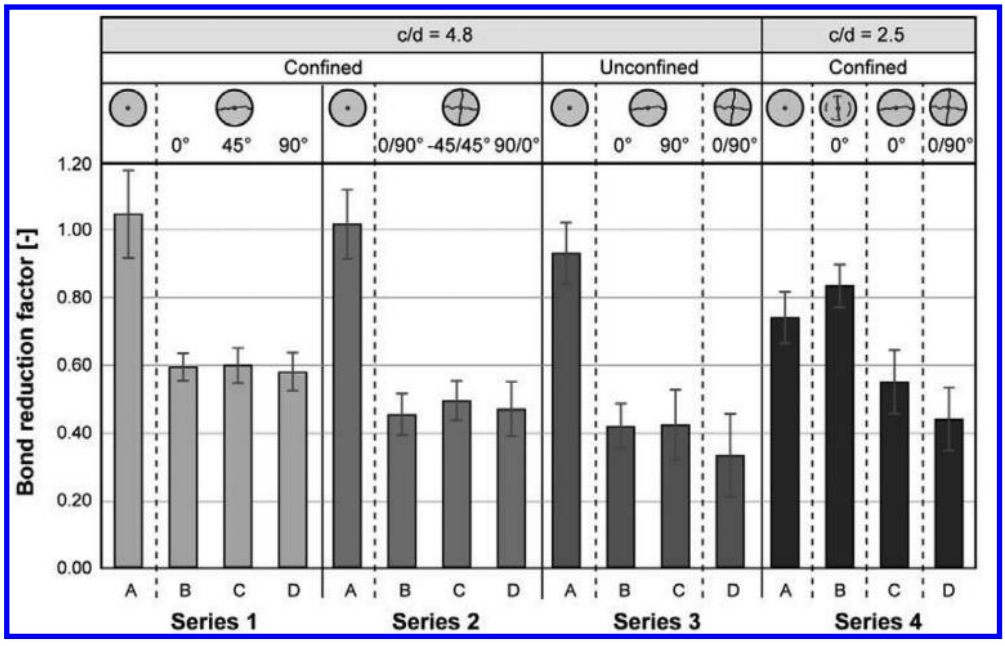

Figure 7. Bond reduction with respect to uncracked reference specimens.

The presence of cracks, even with minor crack widths of 0.03 to 0.04 mm, result in a significant reduction of the bond strength. For specimen with a single crack the reduction was on average 44% and for double cracked specimens the reduction was 54%. The measured values for single and double cracked specimens are within the relatively wide range of values reported by other researchers in the past.

The crack orientation with respect to the rib pattern of the reinforcing bars has little or no effect on the obtained bond properties. Three different crack orientations were tested and the results showed similar ultimate bond strengths.

For double cracked specimens the order in which the cracks are formed (linked to the test method) has no significant influence on the bond behaviour.

Confinement influences the ultimate bond strength of a pre-cracked specimen. In the absence of a restraining force, existing cracks can open up fully enabling the reinforcing bar to more easily slip out of the specimens. The reduction of bond capacity between confined and unconfined specimens was an additional 11% for a given parameter combination.

When the concrete cover is reduced, the residual bond strength after cracking is reduced as well. For smaller covers the failure mode of the uncracked concrete is shifted from a pull-out failure to a splitting failure.

The bond strength of reinforcing bars in cracked cylinders embedded in an uncracked concrete ring of 23 mm is 18% lower than the original uncracked specimens with the same total concrete cover.

The obtained test results indicate that the presence of longitudinal cracks can significantly influence the bond behaviour of ribbed reinforcing bars in concrete. This suggests that bond reduction factors are necessary for cracks that run along the reinforcement bars when undertaking load bearing capacity checks of existing reinforced concrete structures.

ACKNOWLEDGEMENTS

The authors would like to gratefully acknowledge the financial support of the UK Engineering and Physical Sciences Research Council (EPSRC) through the EPSRC Project 'Reinforced concrete half-joint structures: Structural integrity implications of reinforcement detailing and deterioration' [Grant no. EP/K016148/1].

REFERENCES

Almusallam, A. et al., 1996. Effect of reinforcement corrosion on bond strength. *Construction and building Materials*, 10(2), pp.123–129.

Alonso, C. et al., 1998. Factors controlling cracking of concrete affected by reinforcement corrosion. *Materials and Structures*, 31, pp.435–441.

Al-Sulaimani, G., Kaleemullah, M. & Basunbul, I., 1990. Influence of corrosion and cracking on bond behavior and strength of reinforced concrete members. *ACI Structural Journal*, 87(2), pp.220–231.

Andrade, C., Alonso, C. & Molina, F., 1993. Cover cracking as a function of bar corrosion: Part I-Experimental test. *Materials and structures*, 26, pp.453–464.

BRE Centre for Concrete Construction, 2000. Corrosion of steel in concrete—Durability of reinforced concrete structures. *Digest*, 444(February), p.12.

Clark, L. & Saifullah, M., 1993. Effect of corrosion on reinforcement bond strength. In M. Forde, ed. *Proceedings of the conference on structural faults & repair*. Edinbrugh, UK: Engineering Technics Press, pp. 113–119.

Clark, L. & Saifullah, M., 1994. Effect of corrosion rate on the bond strength of corroded reinfrocement. In R. Swamy, ed. *Proceedings of the international conference on corrosion and corrosion protection of steel in concrete*. Sheffield, UK: Sheffield Academic Press, pp. 591–602.

European Committee for Standardization, 2011. *EN 197–1:2011 - Cement – Part 1: Composition, specifications and conformity criteria for common cements*, Brussels, Belgium: European Committee for Standardization.

European Committee for Standardization, 2004. *EN 1992-1-1 Eurocode 2: Design of concrete structures—Part 1-1: General rules and rules for buildings*, European Committee for Standardization.

Gambarova, P., Rosati, G. & Zasso, B., 1989. Steel-to-concrete bond after concrete splitting: test results. *Materials and Structures*, 22(1), pp.35–47.

Rilem TC, 1970. Bond test for reinforcing steel: 2. Pull-out test. *Materials and structures*, 3(15), pp.175–178.

Rodriguez, J., Ortega, L. & Garcia, A., 1994. Assessment of structural elements with corroded reinforcement. In R. Swamy, ed. *Proceedings of the international conference on Corrosion and corrosion protection of steel in concrete*. Sheffield, UK: Sheffield Academic Press, pp. 171–185.

Task Group Bond Models, 2000. *fib Bulletin No. 10 - Bond of Reinforcement in Concrete,* Lausanne.

Tepfers, R., 1976. *A theory of bond applied to overlapped tensile reinforcement splices for deformed bars 2nd ed.*, Goteborg: Chalmers University of technology.

Concrete Repair, Rehabilitation and Retrofitting IV – Dehn et al. (Eds)
© 2016 Taylor & Francis Group, London, ISBN 978-1-138-02843-2

Improved formulation for compressive fatigue strength of concrete

E.O.L. Lantsoght
Universidad San Francisco de Quito, Quito, Ecuador
Delft University of Technology, Delft, The Netherlands

C. van der Veen
Delft University of Technology, Delft, The Netherlands

A. de Boer
Ministry of Infrastructure and the Environment, Utrecht, The Netherlands

ABSTRACT: Understanding the behavior of concrete in fatigue is essential for understanding the behavior of concrete bridges subjected to repeated loads. The Dutch National Annex to the Eurocode prescribes a different expression for the Wöhler curve for compression fatigue than the Eurocode itself, and does not have a smooth transition for 10^6 load cycles. A new expression for concrete in compression fatigue is thus necessary. This new expression should be valid, yet not overly conservative, for high strength concrete. Therefore, a database of experiments on (ultra) high strength concrete tested in compressive fatigue is used to validate the new proposal. A proposal for the assessment of the fatigue strength of existing structures is prepared. For design, a simplified method is proposed. An expression for the fatigue strength of concrete under compression, suitable for high strength concrete, is now available, which can replace the previous fatigue expressions used in The Netherlands.

1 INTRODUCTION

Fatigue is of importance for structures subjected to repetitive loading, such as bridges (fib, 2012). Fatigue cracking in concrete is not as easy and straightforward to determine as fatigue cracks in, for example, steel. As such, it is difficult to identify fatigue distress in concrete structures (CEB Committee GTG 15, 1988).

The compressive strength of concrete decreases as an element is subjected to cycles of loading. In a typical fatigue test for concrete in compression, a concrete specimen (typically a cylinder) is loaded between a lower and upper stress limit. These limits are expressed as a fraction of the concrete compressive strength, and can be written as $S_{min}f_{ck}$ and $S_{max}f_{ck}$. The values of S_{min} and S_{max} are thus between 0 and 1. The upper limit for S_{max} in experiments is typically 0.95 and S_{min} can be as low as 0.02.

The result of fatigue tests on concrete cylinders in compression is the so-called Wöhler-curve, or *S-N* curve. In this graph, a (linear) relation is found between the logarithm of the number of cycles N and the maximum fraction of the static compressive strength S_{max}. From experiments, it is known that the *S-N* curve for concrete is approximately linear starting at 100 cycles (Kim and Kim, 1996).

The expression for concrete under compression subjected to cycles of loading from NEN-EN 1992-2+C1:2011 (CEN, 2011a) is more conservative than previously used expressions in the Netherlands. Therefore, different expressions are given in the National Annex NEN-EN 1992-2+C1:2011/NB:2011 (Code Committee 351 001, 2011a). The *S-N* relationship given in the Dutch National Annex consists of two equations: the first branch is valid for $N \leq 10^6$ cycles and the second branch for $N > 10^6$ cycles. The transition between these two expressions is not smooth, but instead causes a jump in the Wöhler-curve. Because of this anomaly in the current code provisions, it is necessary to propose a new expression for concrete under cycles of compressive loading. Moreover, the proposed expression should be valid, yet not overly conservative, for high strength concrete.

2 LITERATURE SURVEY

2.1 *Parameters affecting the fatigue strength*

The fatigue strength depends on the maximum as well as on the minimum stress in the cycle. An increase of the minimum stress level S_{min} typically results in an increased fatigue strength for a given

number of cycles (CEB Committee GTG 15, 1988). Sometimes the stress ratio $R = S_{min}/S_{max}$ is used.

The scatter on the number of cycles to failure for a given stress level can be explained by the scatter on the static compressive strength (Holmen, 1982). This scatter is nonetheless significant, and therefore it is necessary to test a number of specimens at each of different levels of S_{max} to determine the *S-N* curve. The static strength is usually determined from tests in which the rate of load application may be several orders of magnitude less than the rate of loading in the fatigue test (CEB Committee GTG 15, 1988).

Variables such as water-cement ratio, cement content, amount of entrained air, curing conditions and age at loading do not seem to influence the fatigue strength when expressed as S_{max} and S_{min}. These conclusions were based on extensive experimental research for concrete compressive strengths up to 60 MPa (CEB Committee GTG 15, 1988).

Most fatigue experiments are tested by alternating stresses continuously until failure. Some research studied the effect of rest periods. The results of this research, in which repeated rest periods up to 5 minutes after each set of 4500 cycles are used, indicate that rest periods increase the fatigue strength, and that some recovery occurs during the rest periods. In practice, concrete elements are subjected to cycles of loading of random and varying amplitudes. Typically, the Palmgren-Miner hypothesis, which states that damage accumulates linearly with the number of cycles applied at a certain level, is used (CEB Committee GTG 15, 1988).

A last parameter that has an influence on the fatigue life is the frequency of loading in experiments. A common conclusion is that a frequency between 1 and 15 Hz has little effect on the fatigue strength, provided that the maximum stress level is less than about 75% of the static strength. At higher stress levels the fatigue strength decreases with decreasing frequency (CEB Committee GTG 15, 1988). It was also found that compressive fatigue tests on concrete prisms varying the loading rate from 0.5 to 50 MPa/s resulted in a tenfold increase in the mean fatigue life expressed as cycles for $S_{max} > 0.75$. This suggests that accelerated fatigue tests on concrete structures may give an overestimate of their true fatigue life under loading rates that occur in service (CEB Committee GTG 15, 1988).

2.2 *Fatigue life of high strength concrete*

Currently, there seems to be a disagreement in the literature on whether or not the fatigue strength of concrete under compression decreases as the compressive strength of the concrete increases, or, in other words, if the *S-N* curve should be steeper and reducing more quickly for higher strength concrete.

Experiments done in Norway (Petkovic et al., 1990) led to the conclusion that no difference in the fatigue behavior between normal and high strength concrete could be observed. Other research (Hordijk et al., 1995) led to similar conclusions. In these experiments, the difference between gravel and limestone aggregates was studied. Failure of the specimens occurred in an explosive way.

An overview of previous research (Kim and Kim, 1996) mentions that high strength concrete was more brittle than normal strength concrete under fatigue loading. The test results show that the fatigue life decreased with increasing the concrete strength, and the authors proposed a model for the *S-N* relationship considering the effect of the concrete strength. The concrete compressive strength of the specimens varied between 26 MPa and 103 MPa; the maximum stress was applied from 75% to 95% of the static compressive strength as determined before the fatigue tests.

Experiments on UHPC (Ultra-High Performance Concrete) (Lohaus et al., 2011) showed that for all the investigated lower stresses S_{min} larger stress ranges could be attained than in similar experimental investigations on normal strength concrete specimens that were used to develop the Model Code 1990 (CEB-FIP, 1993). Heat treatment gave UHPC samples a better fatigue life (Lohaus and Anders, 2006). The influence of the testing frequency is disputed: some authors argue that the number of cycles to failure increases when the frequency is increased for a constant stress-level (Hsu, 1981), while this effect was reversely observed for UHPC (Lohaus and Anders, 2006). It was found that fiber reinforcement does not affect the fatigue strength, and the authors mentioned that UHPC might be more sensible to fatigue loading compared to normal strength concrete (Lohaus and Anders, 2006).

Other research indicates that, for the larger upper stress limit S_{max}, the fatigue strength of higher strength concrete is smaller than of normal strength concrete. For $S_{max} > 0.6$; the *S-N* curve has a steeper tangent than normal strength concrete (Tue and Mucha, 2006). The researchers also found that the influence of S_{max} on the fatigue behavior is larger for high strength concrete than for normal strength concrete, which could be explained by the larger brittleness of high strength concrete.

After reviewing the currently existing literature, *fib* task group 8.2 concluded that HPC has a lower fatigue limit compared to normal strength concrete mainly due to a lower water-cement ratio, and it was mentioned that one has not yet succeeded in finding adequate design rules for the fatigue behavior taking into consideration the special properties of HPC (fib Task Group 8.2, 2008).

Table 1. Comparison between authors.

Source	$f_{c,mean,max}$ (MPa)	Influence f_c?
Petkovic et al., 1990	95 MPa	No
Kim & Kim, 1996	103 MPa	Yes
Hordijk et al., 1995	78.2 MPa	No
Lohaus et al., 2011	170 MPa*	No
Lohaus & Anders, 2006	145 MPa*	Yes
Tue & Mucha, 2006	65 MPa	Yes

Note: * is used for samples with fiber reinforcement.

As can be seen from the previous paragraphs, there is no consensus on whether or not increasing the concrete compressive strength reduces the fatigue life for compression. A brief overview of the different sources and their stated influence of the concrete compressive strength on the fatigue life is given in Table 1. In Table 1, $f_{c,mean,max}$ is the maximum measured concrete compressive strength used in the series of experiments for which the citation is given in the first column of the table. The last column of Table 1 shows the final conclusions of the research: whether ("yes") or not ('no") the experiments indicated that the fatigue life of high strength concrete is lower than the fatigue life of normal strength concrete under compression.

3 CURRENT CODE PROVISIONS

3.1 *NEN 6723:2009*

The fatigue reference strength $f'_{b,v}$ in the Dutch national code NEN 6723:2009 (Code Committee 351 001, 2009) is the following for concrete classes above C25/30:

$$f'_{b,v} = \frac{f'_{b,rep,v}}{\gamma_m} \tag{1}$$

$$f'_{b,rep,v} = 0.5\left(f'_{b,rep,k} - 0.85\times 30\right) + 0.85\times 30 \tag{2}$$

where γ_m = 1.2; $f'_{b,rep,k}$ = the characteristic value of the uniaxial short term concrete compressive strength $0.85f'_{ck}$, in [MPa] and $f'_{brep,v}$ = the characteristic value of the concrete compressive strength in the limit state of fatigue, in [MPa].

According to NEN 6723:2009 §9.6.2.1, the number of cycles to failure N_i for given compressive stresses $\sigma'_{b,d,max}$ and $\sigma'_{b,d,min}$ can be determined as:

$$Log\left(N_i\right) = \frac{10}{\sqrt{1-R}}\left(1 - \frac{\sigma'_{b,d,max}}{f'_{b,v}}\right) \text{ for } \frac{\sigma'_{b,d,max}}{f'_{b,v}} > 0{,}25 \tag{3}$$

Table 2. Overview of statistical parameters of tested to predicted values, comparing the experiments from the database and the proposed methods.

Method	$\gamma_{c,fat}$	AVG	STD	COV	Char	5%
design	1.5	1.27	0.139	10.9%	1.044	1.089
existing	1.5	1.15	0.112	9.7%	0.965	1.004

where $R = \sigma'_{b,d,min}/\sigma'_{b,d,max} = S_{min}/S_{max}$ = the stress rate, with $\sigma'_{b,d,min}$ = design value of the minimum compressive stress in the concrete, in [MPa] and $\sigma'_{b,d,max}$ = the design value of the maximum compressive stress in the concrete, in [MPa].

3.2 *NEN-EN 1992-1-1+C2:2011*

The design fatigue strength according to NEN-EN 1992-1-1+C2:2011 (CEN, 2011b) §6.8.7 is prescribed as:

$$f_{cd,fat} = k_1\beta_{cc}(t_0)f_{cd}\left(1 - \frac{f_{ck}}{250}\right) \tag{4}$$

$$\beta_{cc}(t_0) = \exp\left\{s\left[1 - \left(\frac{28}{t_0}\right)^{0.5}\right]\right\} \tag{5}$$

where $\beta_{cc}(t_0)$ = a coefficient for the concrete strength at first load application, as given in §3.1.2(6); t_0 = the time of the start of the cyclic loading on concrete in days; s depends on the strength class of the cement, eg. for 42.5N, $s = 0.25$; and $f_{cd} = f_{ck}/\gamma_{c,fat}$ with $\gamma_{c,fat}$ = 1.5 for fatigue as recommended in Table 2.1 from NEN-EN 1992-1-1:2005+C2:2011. The Dutch National Annex NEN-EN 1992-1-1+C2:2011/NB:2011 (Code Committee 351 001, 2011b) §2.4.2.4(1) prescribes $\gamma_{c,fat} = 1.35$.

The value for k_1 can be found in the National Annex. The recommended value for $N = 10^6$ cycles is $k_1 = 0.85$, as given in NEN-EN 1992-1-1+C2:2011/NB:2011 §6.8.7(1), and this recommendation is followed in the Dutch National Annex NEN-EN 1992-1-1+C2:2011/NB:2011.

According to NEN-EN 1992-1-1+C2:2011 §6.8.7(1), Eq. (6.72), a satisfactory fatigue resistance may be assumed for concrete under compression, if the following condition is fulfilled:

$$E_{cd,max,equ} + 0{,}43\sqrt{1 - R_{equ}} \le 1 \tag{6}$$

for which $R_{equ} = E_{cd,min,equ}/E_{cd,max,equ}$ = the stress ratio; $E_{cd,max,equ} = \sigma_{cd,max,equ}/f_{cd,fat}$ = the maximum compressive stress level; $E_{cd,min,equ} = \sigma_{cd,min,equ}/f_{cd,fat}$ = the minimum compressive stress level; $f_{cd,fat}$ = the design fatigue strength; $\sigma_{cd,max,equ}$ = the upper stress of the ultimate amplitude for N cycles and $\sigma_{cd,min,equ}$ = the

lower stress of the ultimate amplitude for N cycles.

The number of cycles N can be found in the National Annex. The recommended value, also used in The Netherlands, is $N = 10^6$ cycles. In other words, NEN-EN 1992-1-1+C2:2011 uses a damage-equivalent check for fatigue for one single number of cycles and does not describe a Wöhler diagram.

3.3 *NEN-EN 1992-2+C1:2011*

According to NEN-EN 1992-2+C1:2011 (CEN, 2011a) §6.8.7 (101), the number of cycles to failure can be determined based on nationally prescribed *S-N* diagrams, or based on Eq. 6.72 of NEN-EN 1992-2+C2:2011, here Eq. (6), in which the coefficient 0.43 is replaced by $\log N_i/14$ and the inequality in the expression is omitted. Sufficient resistance against fatigue for concrete under compression can then be assumed when (Eqs. 6.105–6.109):

$$\sum_{i=1}^{m} \frac{n_i}{N_i} \le 1 \tag{7}$$

with m = the number of cycles of constant amplitude; n_i = the number of cycles with a constant amplitude at interval i and N_i = the number of cycles to failure with a constant amplitude at interval i, for which:

$$N_i = 10^{\left(14\frac{1-E_{cd,max,i}}{\sqrt{1-R_i}}\right)} \tag{8}$$

where R_i = the stress ratio; $E_{cd,min,i}$ = the minimum stress level; $E_{cd,max,i}$ = the maximum stress level and $f_{cd,fat}$ = the design value of the fatigue capacity of concrete according to Eq. (6.76) from NEN-EN 1992-1-1+C2:2011, here given as Eq. (4).

The bridge code NEN-EN 1992-2+C1:2011 thus requires a more elaborate study of fatigue and describes the Wöhler diagram, which the general code NEN-EN 1991-2-2+C2:2011 does not consider.

3.4 *NEN-EN 1992-2+C1:2011/NB:2011*

In the Dutch National annex NEN-EN 1992-2+C1:2011/NB:2011 (Code Committee 351 001, 2011a), separate equations for the *S-N* curve are given. Sufficient capacity against fatigue is assumed when Palmgren-Miner's rule (Eq. (7)) is fulfilled, with N_i:

$$N_i = 10^{\left(\frac{6}{1-0.57k_1\left(\frac{1-f_{ck}}{250}\right)}\left(\frac{1-E_{cd,max,i}}{\sqrt{1-R_i}}\right)\right)} \text{ for } N_i \le 10^6 \tag{9}$$

$$N_i = 10^{\left(\frac{1-E_{cd,max,i}}{\sqrt{1-R_i}}\right)} \text{ for } N_i > 10^6 \tag{10}$$

$$E_{cd,min,i} = \frac{\sigma_{cd,min,i}}{f_{cd}\left(0.9+\frac{\log N_i}{60}\right)} \text{ for } N_i \le 10^6 \tag{11}$$

$$E_{cd,min,i} = \frac{\sigma_{cd,min,i}}{f_{cd,fat}} \text{ for } N_i > 10^6 \tag{12}$$

$$E_{cd,max,i} = \frac{\sigma_{cd,max,i}}{f_{cd}\left(0.9+\frac{\log N_i}{60}\right)} \text{ for } N_i \le 10^6 \tag{13}$$

$$E_{cd,max,i} = \frac{\sigma_{cd,max,i}}{f_{cd,fat}} \text{ for } N_i > 10^6 \tag{14}$$

The value of k_1 in Eq. (4) should be taken as 1 according to the Dutch National Annex NEN-EN 1992-2+C1:2011/NB:2011 §6.8.7(101), which deviates from the recommended value of $k_1 = 0.85$. The stress f_{cd} is based on $\gamma_{c,fat} = 1.35$ instead of $\gamma_c = 1.5$. The compressive strength at 1 cycle is taken as 0.9 f_{cd} according to the Dutch National Annex. This value of $f_{cd} = f_{ck}/\gamma_{c,fat}$ instead of $f_{cd} = f_{ck}/\gamma_c$, so that the value of the compressive strength at 1 cycle equals the static compressive strength.

NEN-EN 1992-2+C1:2011/NB:2011 uses an expression that is different before and after 10^6 cycles, and at 10^6 cycles, both expressions result in different values, so that a jump occurs in the Wöhler-diagram.

3.5 *fib Model Code 2010*

In the *fib* Model Code 2010 (fib, 2012), the fatigue reference compressive strength is calculated as (Eq. 5.1-110 in §5.1.11.1.1):

$$f_{ck,fat} = \beta_{cc}(t)\beta_{c,sus}(t,t_0) f_{ck}\left(1-\frac{f_{ck}}{400}\right) \tag{15}$$

with f_{ck} = the characteristic concrete compressive strength;

$$\beta_{cc}(t) = \exp\left\{s\left[1-\left(\frac{28}{t}\right)^{0.5}\right]\right\}$$

from Eq. 5.1-51 describes the strength development with time, in which s depends on the strength class of the cement, eq. for 42.5N, $s = 0.25$ and t = the concrete age in days, corrected for temperature:

$$t_T = \sum_{i=1}^{n} \Delta t_i \exp\left(13.65 - \frac{4000}{273+T(\Delta t_i)}\right)$$

with Δt_i = number of days with temperature T; $T(\Delta t_i)$ = temperature during time period Δt_i; $\beta_{c,sus}(t,t_0) = 0.85$ for fatigue.

The factor 400 in Eq. (15) is changed with respect to the Model Code 1990 (CEB-FIP, 1993) and the subsequently developed Eurocodes (see Eq. (4)), in which 250 was used for this factor. This change was necessary to accommodate compressive strengths larger than 125 MPa and corresponds better to experimental results on higher strength concrete specimens (Fehling et al., 2013).

The S-N relations are given as (Eq. 5.1-107 – 5.1-109, for $0 \le S_{c,min} \le 0.8$):

$$\log N_1 = \frac{8}{Y-1}\left(S_{c,max} - 1\right) \tag{16}$$

$$\log N_2 = 8 + \frac{8\ln(10)}{Y-1}\left(Y - S_{c,min}\right)\log\left(\frac{S_{c,max} - S_{c,min}}{Y - S_{c,min}}\right) \tag{17}$$

$$Y = \frac{0.45 + 1.8S_{c,min}}{1 + 1.8S_{c,min} - 0.3S_{c,min}^2} \tag{18}$$

$$S_{c,max} = \frac{|\sigma_{c,max}|}{f_{ck,fat}} \tag{19}$$

$$S_{c,min} = \frac{|\sigma_{c,min}|}{f_{ck,fat}} \tag{20}$$

$$\Delta S_c = |S_{c,max}| - |S_{c,min}| \tag{21}$$

If $\log N_1 \le 8$, then $\log N = \log N_1$ and if $\log N_1 > 8$, then $\log N = \log N_2$. If $S_{c,min} > 0.8$ the S-N relations for $S_{c,min} = 0.8$ should be used. These expressions are valid for concrete stored in a constant environment of approximately 20°C, 65% RH. The S-N relationships were developed based on experiments with ultra-high strength concrete (up to C200) and validated for high strength and normal strength concrete. The curves have been verified with experiments up to 10^7 load cycles to failure. For $\log N > 8$ the curves asymptotically approach the minimum stress level of the respective curve. For high strength concrete, Model Code 2010 allows higher strengths for a given number of cycles than Model Code 1990. It can be noted that the reduction of the fatigue life for higher strength concrete classes is smaller than as recommended by the other codes. The *fib* Model Code 2010 is the most recent code, and is the first code to be based on experiments on high strength concrete specimens. As such, a more realistic impression of the influence on the concrete compressive strength on the reduction of the fatigue life can be expected from this code.

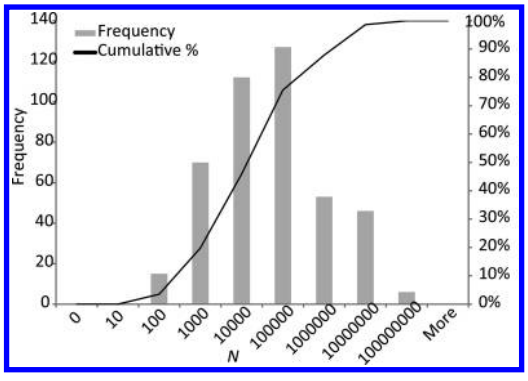

Figure 1. Histogram of number of cycles in the experiments from the database.

4 DATABASE OF TEST RESULTS

To develop a new proposal for the fatigue strength of concrete under compression, a database of fatigue tests is compiled, with an emphasis on recent test results on high strength concrete. The full database can be found in the background report of this research (Lantsoght, 2014). In total, 429 experiments are in the database, of which 234 experiments do not contain fibers in the concrete mix (maximum compressive strength of 145 MPa) and of which 195 experiments contain fibers and have a maximum compressive strength of 226 MPa. An additional 165 test results of normal strength concrete are used for verification purposes of the proposed formulas. The test results are taken from the literature (Petkovic et al., 1990, Fehling et al., 2005, Kim and Kim, 1996, Hordijk, 1994, Hordijk et al., 1995, Saucedo et al., 2013, Lohaus et al., 2011, Lohaus and Anders, 2006, Tue and Mucha, 2006, Wefer, 2010, CUR Committee C 33, 1993, Klausen, 1978). As the range of a low number of cycles to failure is interesting for applications in bridge engineering, a histogram showing the distribution of the number of cycles to failure for the 429 experiments from the database is given in Figure 1.

5 PROPOSED METHODS

5.1 *For design*

For the design of new structures, a method should be proposed that is easy to use and does not require iterations. The expression from NEN-EN 1992-2+C1:2011 (CEN, 2011a), Eq. (8), is used as a starting point to develop this new method. As the Eurocode expression from Eq. (8) leads to very conservative results when compared to the experiments from the database (Lantsoght, 2014),

$k_1 = 1$ can be used instead of the recommended value of $k_1 = 0.85$. The conservativism of the Eurocode expression from Eq. (8) increases even more for higher strength classes of concrete. Therefore, the term $f_{ck}/250$ can be replaced by $f_{ck}/400$ as used in the *fib* Model Code. Using different partial factors γ_c and $\gamma_{c,fat}$ leads to confusion in practice. As such, $\gamma_c = \gamma_{c,fat} = 1.5$ in the proposed model.

$$f_{cd,fat} = k_1 \beta_{cc}(t_0) f_{cd} \left(1 - \frac{f_{ck}}{400}\right) \tag{22}$$

$$N_i = 10^{\left(14 \frac{1 - E_{cd,max,i}}{\sqrt{1 - R_i}}\right)} \tag{23}$$

$$R_i = \frac{E_{cd,min,i}}{E_{cd,max,i}} \tag{24}$$

$$E_{cd,min,i} = \frac{\sigma_{cd,min,i}}{f_{cd,fat}} \tag{25}$$

$$E_{cd,max,i} = \frac{\sigma_{cd,max,i}}{f_{cd,fat}} \tag{26}$$

In Eq. (22), the value of β_{cc} is taken according to Eq. (5).

5.2 *For existing structures*

For existing structures a new method is developed. The following iterative procedure is recommended:

$$\log N_i = \frac{6(S_{max} - 1)}{S_{max,EC} - 1} \text{ for } S_{max} \geq S_{max,EC} \tag{27}$$

$S_{max,EC}$ is here the value of S_{max} which is found for 10^6 cycles, and can be expressed as:

$$S_{max,EC} = \left(1 - \frac{f_{ck}}{400}\right)\left(1 - \frac{3}{7}\sqrt{1 - R_i^*}\right) \tag{28}$$

with f_{ck} in MPa and $R_i^* = S_{min}/S_{max,EC}$ and

$$\log N_i = 14 \frac{1 - E_{cd,max,i}}{\sqrt{1 - R_i}} \text{ for } N_i > 10^6 \tag{29}$$

$$R_i = \frac{E_{cd,min,i}}{E_{cd,max,i}} \tag{30}$$

$$E_{cd,max,i} = \frac{\sigma_{cd,max,i}}{f_{cd,fat}} \text{ for } N_i > 10^6 \tag{31}$$

$$f_{cd,fat} = k_1 \beta_{cc}(t_0) f_{cd} \left(1 - \frac{f_{ck}}{400}\right) \tag{32}$$

with $\beta_{cc}(t_0)$ from Eq. (5), $k_1 = 1$ and $\gamma_c = \gamma_{c,fat} = 1.5$. These equations have the following characteristics:

- for 1 loading cycle, the static compressive strength is found
- at 10^6 cycles, the connection between Eqs. (27) and (29) is smooth
- for higher strength concrete classes, the method is not overly conservative.

The disadvantage of this method is the need for iterations to determine $S_{max,EC}$. This method is recommended for the assessment of existing structures (Lantsoght et al., 2013). Note that when an existing structure is assessed and the measured concrete compressive strength is taken into account, the measured scatter on the tested cores needs to be taken into account to find the characteristic value of the concrete compressive strength f_{ck}.

6 COMPARISON BETWEEN METHODS AND EXPERIMENTS

A full comparison between the test results from the database and the proposed methods can be found in the research report (Lantsoght, 2014). A comparison between the proposal for design and the test results from the database with $S_{min} = 0.05$ is given in Figure 2. In Figure 2, the *S*-N curves for different concrete classes are shown (lines), as well as test results from the database (datapoints) for their respective concrete classes. A similar comparison with the proposal for existing structures is shown in Figure 3.

An overview of the statistical parameters for the ratio of tested to predicted values for the proposed methods is given in Table 2. The best predictions are found when using the method for existing structures, which requires iterations. This method gives the smallest coefficient of variation, which indicates the lowest amount of scatter on the predicted values as compared to the experimental results. The 5% lower bound is determined based on the assumption of a normal distribution ("Char") as well as based on the 5% lower bound in the histogram with the results of tested to predicted values for S_{max} ("5%"). Since the real distribution of these results does not follow a normal distribution, a more conservative lower bound is found when a normal distribution is assumed, and therefore checking based on the real distribution can be used, which leads to satisfactory results for the presented proposals.

A similar comparison is given for each concrete class separately in the background report (Lantsoght, 2014). From these results, it can be seen that the conservativism of the method increases slightly as the concrete compressive strength increases, as

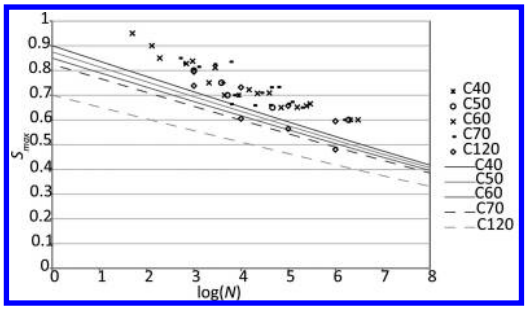

Figure 2. S-N curves from Eq. (23) and comparison to test results with $k_1 = 1$ and $S_{min} = 0.05$.

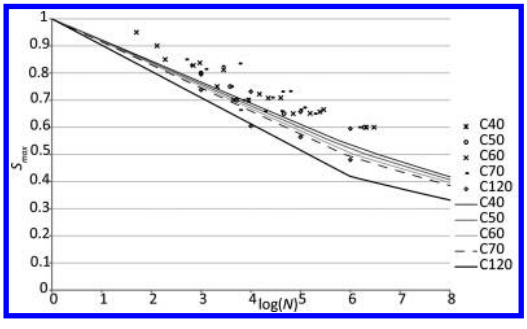

Figure 3. S-N curves from Eqs. (27) and (29) and comparison to test results with $S_{min} = 0.05$.

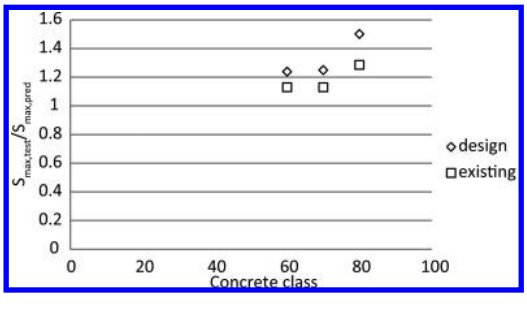

Figure 4. Comparison between unity checks (average value) for different concrete classes, without the C2 results from Saucedo et al. (2013) for C60 concrete.

shown in Figure 4. In Figure 4, $S_{max,test}$ is the value for S_{max} in the experiments for a given number of cycles N and $S_{max,pred}$ is the value of S_{max} found based on the proposed methods for design of new structures of assessment of existing structures for a given number of cycles N.

Finally, the experimental results on normal strength concrete (CUR Committee C 33, 1983, Klausen, 1978) were used to confirm the validity of the proposed methods. This analysis can be found in the background report (Lantsoght, 2014).

Additionally, for concrete specimens tested under water in compressive fatigue, it was observed that the fatigue life is shorter than for dry concrete (CUR Committee C33, 1983, CUR Committee C 33, 1993). For concrete under water (with its application to structures that are in or under water, such as offshore structures), the method described by Eqs. (22) - (26) can be used with $k_1 = 0.85$.

7 SUMMARY AND CONCLUSIONS

When designing and analyzing bridges, which are subjected to repeated loads, the fatigue strength needs to be considered. Traditionally the fatigue behavior of concrete under compression is expressed based on the Wöhler-diagrams, also called the *S-N* curves. The Dutch National Annex to the Eurocode for concrete bridges prescribes different formulas from those recommended in the Eurocode for concrete bridges. The disadvantage of these expressions, however, is that the *S-N* curves show a discontinuity for 10^6 cycles.

A survey of the literature about the fatigue strength of high strength concrete under compression shows that different authors find different results whether or not the concrete compressive strength has an influence on the fatigue life of concrete under compression. A safe approach, as used in the codes under analysis, is thus to reduce the fatigue capacity for high strength concrete. The codes that are analyzed for the current study are the previously used Dutch code NEN 6723:2009, the Eurocode for concrete structures NEN-EN 1992-1-1+C2:2011 and its Dutch National Annex NEN-EN 1992-1-1+C2:2011/NB:2011, the Eurocode for concrete bridges NEN-EN 1992-2+C1:2011 and its Dutch National Annex NEN-EN 1992-2+C1:2011/NB:2011, as well as the *fib* Model Code 2010. The Model Code is the most recent code, and takes new test results on high strength concrete under repeated compression loads into account.

To compare the code methods and the proposed methods to experimental data, a database of 429 test results of mostly high strength concrete is compiled. Moreover, a database with 165 test results of normal strength concrete is compiled for verification purposes. These experiments on normal strength concrete were used to develop the current codes (Dutch code and Eurocodes).

Two new methods are proposed to replace the *S-N* curves from the Dutch National Annex to the Eurocode of concrete bridges NEN-EN 1992-2+C1:2011/NB:2011, in which a discontinuity for 10^6 cycles was observed. One method is an improvement of the expressions from NEN-EN 1992-2+C1:2011, and can be used for the design of new structures. The other method requires

iterations and is developed within the scope of the current research. The latter method is recommended for the assessment of existing structures. Based on a statistical analysis of the comparison between the experimental results from the database and the proposed methods, it is found that the methods are safe, and that the scatter of the results of tested to predicted values is acceptable for the outlined purposes.

ACKNOWLEDGMENTS

The authors wish to express their gratitude and sincere appreciation to InfraQuest for financing this research work and coordinating the cooperation between Delft University of Technology, Rijkswaterstaat and the research institute TNO.

REFERENCES

Ceb Committee GTG 15 1988. Fatigue of Concrete Structures. CEB Bulletin d'information No 188. Lausanne, Switzerland: European Concrete Committee.

CEB-FIP 1993. *Model Code 1990*. Lausanne, Switzerland: European Concrete Committee and International Federation for Prestressing.

CEN 2011a. Eurocode 2: Design of concrete structures - Concrete bridges - Design and detailing rules. NEN-EN 1992-2+C1:2011. Brussels, Belgium: European Committee for Normalization.

CEN 2011b. Eurocode 2: Design of Concrete Structures - Part 1-1 General Rules and Rules for Buildings. NEN-EN 1992-1-1+C2:2011. Brussels, Belgium: European Committee for Normalization.

Code Committee 351 001 2009. Regulations for concrete - Bridges - Structural requirements and calculation methods, NEN 6723:2009. Delft, The Netherlands: Dutch Institute for Normalization. (in Dutch)

Code Committee 351 001 2011a. National Annex to NEN-EN 1992-2+C1, Eurocode 2: Design of concrete structures - Concrete bridges - Design and detailing rules. NEN-EN 1992-2+C1:2011/NB:2011. Delft, The Netherlands: Dutch Institute for Normalization. (in Dutch)

Code Committee 351 001 2011b. National Annex to NEN-EN 1992-1-1+C2, Eurocode 2: Design of concrete structures – Part 1-1: General rules and rules for buildings NEN-EN 1992-1-1+C2:2011/NB:2011. Delft, The Netherlands: Nederlands Normalisatie-instituut.

Cur Committee C 33 1983. Fatigue of concrete, part 1: compression. CUR Report 112. Gouda, The Netherlands: CUR. (in Dutch)

Cur Committee C 33 1993. Fatigue of concrete, part 4: compression (2). CUR Report 163. Gouda, The Netherlands: CUR. (in Dutch)

Fehling, E., Schmidt, M., Teichmann, T., Bunje, K., Bornemann, R. & Middendorf, B. 2005. Development, Durability and Calculation of Ultra High Performance Concrete (UHPC). Universität Kassel. Kassel, Germany. (in German)

Fehling, E., Schmidt, M., Walraven, J., Leutbecher, T. & Fröhlich, S. 2013. Concrete Yeabook: IX - UHPC. Berlin, Germany: Ernst & Sohn. (in German)

FIB 2012. Model code 2010: final draft, Lausanne, Switzerland: International Federation for Structural Concrete.

FIB Task Group 8.2 2008. Constitutive modelling of high strength/ high performance concrete. Lausanne, Switzerland: International Federation for Structural Concrete.

Holmen, J. O. 1982. Fatigue of concrete by constant and variable amplitude loading. *ACI SP-75: Fatigue of Concrete Structures*, 71–110.

Hordijk, D. A. 1994. Comparitive research in material properties of gravel concrete and limestone concrete. Phase II: Fatigue. Delft, The Netherlands: TNO. (in Dutch)

Hordijk, D.A., Wolsink, G. M. & Vries, J. D. 1995. Fracture and fatigue behaviour of a high strength limestone concrete as compared to gravel concrete. *Heron,* 40, 125–146.

Hsu, T. T. C. 1981. Fatigue of plain concrete. *Journal of the American Concrete Institute,* 78(4), 292–305.

Kim, J. K. & Kim, Y. Y. 1996. Experimental study of the fatigue behavior of high strength concrete. *Cement and Concrete Research,* 26(10), 1513–1523.

Klausen, D. 1978. *Strength and damage of concrete after repeated stress cycles.* PhD thesis, Darmstadt, Geramny: Technische Hochschule Darmstadt.(in German)

Lantsoght, E. O. L. 2014. Fatigue of concrete under compression: database and proposal for high strength concrete. Stevin Report 25.05-14-04. Delft, The Netherlands: Delft University of Technology.

Lantsoght, E. O. L., van der Veen, C., de Boer, A. & Walraven, J. C. 2013. Recommendations for the Shear Assessment of Reinforced Concrete Slab Bridges from Experiments *Structural Engineering International,* 23(4), 418–426.

Lohaus, L. & Anders, S. 2006. High-cycle Fatigue of Ultra-High Performance Concrete – Fatigue Strength and Damage Development. *Proceedings of the 2nd fib International Congress.* Naples, Italy.

Lohaus, L., Wefer, M. & Oneschkow, N. 2011. Design model for the fatigue behaviour of normal strength, high strength and ultra-high strength concrete. *Beton- und Stahlbetonbau,* 106(12), 836–846. (in German)

Petkovic, G., Lenschow, R., Stemland, H. & Rosseland, S. 1990. Fatigue of high-strength concrete. *ACI SP-121: High-strength concrete*, 505–525.

Saucedo, L., Yu, R. C., Medeiros, A., Zhang, X. & Ruiz, G. 2013. A probabilistic fatigue model based on the initial distribution to consider frequency effect in plain and fiber reinforced concrete. *International Journal of Fatigue,* 48(3), 308–318.

Tue, N. V. & Mucha, S. 2006. Fatigue behaviour of high strength concrete under compression. *Bautechnik,* 83(7), 497–504.(in German)

Wefer, M. 2010. *Material behavior and Experimental Results of ultra-high strength concrete subjected to uniaxial fatigue.* PhD Thesis, Hannover, Germany: Leibniz Universitat Hannover.

Concrete Repair, Rehabilitation and Retrofitting IV – Dehn et al. (Eds)
© 2016 Taylor & Francis Group, London, ISBN 978-1-138-02843-2

Determination of diffusivities of dissolved gases in saturated cement-based materials

Quoc Tri Phung
Belgian Nuclear Research Centre, Ghent University, Belgium
Magnel Laboratory for Concrete Research, Ghent University, Belgium

Norbert Maes, Diederik Jacques, Elke Jacops & Arno Grade
Institute for Environment, Health, and Safety, Belgian Nuclear Research Centre (SCK•CEN), Belgium

Geert De Schutter
Magnel Laboratory for Concrete Research, Ghent University, Belgium

Guang Ye
Microlab, Delft University of Technology, Delft, The Netherlands

ABSTRACT: Diffusion is an important property for characterizing concrete durability because it governs the penetration of aggressive substances (Cl^-, SO_4^{2-}, O_2, CO_2) responsible for degradation. However, data on the diffusion of substances (other than Cl^-) in concrete are very scarce due to time and resource consuming measurements. This work describes a method to determine the diffusion coefficients of dissolved gases in saturated cement-based materials in order to study the effects of degradation on the transport properties. The proposed method is adapted from the technique used to determine the diffusivity of clay materials. The method is based on a through-diffusion methodology and allows simultaneous determination of diffusivities of two dissolved gases diffusing in opposite directions. A cement plug is mounted between two water reservoirs pressurized by two different gases at equal pressure (~1 MPa) to avoid advection. The changes in the dissolved gas concentration (at the opposite sides) are measured indirectly via gaseous phases which are in equilibrium with aqueous phases according to Henry's law. Additionally, a simple 1-D diffusive transport model (based on 1st and 2nd Fick's laws) is developed to interpret the experimental data. The concentrations at outlet and inlet are used as inputs for the model, and the diffusivity is obtained by a fitting procedure.

Experiments were performed on intact and carbonated cement (CEM I) paste samples with a gas combination: He and Xe. The results showed that the proposed method is providing reliable results within a reasonable experimental time and is useful to study the effects of degradation on the transport properties of cementitious materials. Carbonation resulted in a lower diffusivity.

Keywords: diffusion; cementitious materials; dissolved gas; measure; modelling

1 INTRODUCTION

Diffusion of chemical substances plays an important role in many degradation processes (e.g. corrosion of steel bars; chloride & sulphate attack). Knowledge of diffusion coefficients helps to better design and evaluate durability of concrete structures. Diffusion is a mass transport induced by the random Brownian motion of substance. The diffusion coefficient (diffusivity) is the capacity of a medium to transfer substances (gases, dissolved gases, ions) under a concentration gradient expressed by Fick's first law (1-D):

$$J = -D\frac{\partial C}{\partial x} \tag{1}$$

where J is the substance flux [kg/m^2.s]; $\partial C / \partial x$ is the concentration gradient [kg/m^4]; and D is the diffusion coefficient [m^2/s]. In porous materials, diffusion is affected by the characteristics of pore network (porosity ϕ [-], tortuosity τ[-], constrictivity δ[-]) which leads to the need to define different diffusion coefficients for practical application (García-Gutiérrez et al., 2006). The pore diffusivity, D_p, is smaller than the diffusivity in free water or ideal solutions D_0, which takes into account the

effects of tortuosity (defined as the ratio between the actual length of flow path to the straight length of a sample) and constrictivity (a dimensionless parameter depending on the ratio of the size of diffusion species and pore size) and is expressed as:

$$D_p = D_0 \frac{\delta}{\tau^2} \tag{2}$$

The effective diffusivity, D_e [m^2/s], takes into account the volume of porous media available for diffusion and is defined as:

$$D_e = \phi D_p = D_0 \frac{\phi\delta}{\tau^2} \tag{3}$$

The apparent diffusivity, D_a [m^2/s], takes into account the sorption/binding which retards the diffusion and is linked to the pore diffusivity through a retardation factor (≥1), R_e as follows:

$$D_a = \frac{D_p}{R_e} = D_0 \frac{\delta}{R_e \tau^2} \tag{4}$$

Diffusion generally depends on the pore network characteristics of the cementitious materials, mainly controlled by water/cement ratio, cement type, admixtures, and the age of hardened cementitious materials. Due to the importance of diffusion, many methods to determine diffusivity have been proposed. The diffusion coefficients can be obtained under steady state or transient state conditions. The steady state method requires a long-time experiment compared to the transient method, but it might be accelerated by some means such as using an electrical gradient (Maes et al., 1999).

Published data on the diffusion of gases in cementitious materials are scarce. The diffusion coefficients obtained are decreasing with curing time and increased with w/c ratio. Daimon et al. used a through-diffusion method (see section 2) to measure the diffusion of hydrogen and nitrogen in dried OPC mortars with different curing time and w/c ratios (Daimon et al., 1971). The diffusion coefficients obtained are decreasing with curing time and increasing with w/c ratio. After 28-day curing, the diffusion coefficients are 4.8×10^{-7} and 1.9×10^{-7} m^2/s for w/c ratios of 0.65 and 0.5, respectively. Sercombe et al. studied the diffusion of hydrogen and xenon in cement paste at different relative humidity, w/c ratios and cement types (Sercombe et al., 2007). Results show that gas diffusion decreases with the increase of RH, especially when RH is higher than 55%. The hydrogen diffusion coefficient is found to decrease 4 orders of magnitude when RH is increased from 3% to 93%.

The data on diffusion of dissolved gases in saturated cement-based materials are even scarcer in literature. The measurements are extremely time-consuming as the diffusion of dissolved gas in saturated media is much slower than of gas (in gaseous phase) in unsaturated media. However, knowledge of the diffusion of certain dissolved gases is very important, especially the case of dissolved oxygen which is involved in the corrosion process of steel bars in reinforced concrete. The effective diffusion coefficients of dissolved oxygen are usually determined by an electrochemical method involving cathodic consumption of the diffused oxygen. This technique is much quicker to obtain steady state compared to through-diffusion. Tittarelli studied oxygen diffusion through hydrophobic and normal cement-based materials which were fully immersed in water (Tittarelli, 2009). It is reported that the effective diffusion coefficient of hydrophobic concrete with w/c of 0.8 is 5×10^{-8} m^2/s which is almost 3 orders of magnitude faster than concrete without hydrophobic admixture (7×10^{-11} m^2/s). The author attributed this difference to that dissolved oxygen directly diffuses as a gaseous phase through the empty pores of a hydrophobic cement matrix. In a comparative study of chloride and oxygen diffusion in saturated cement pastes, Yu et al. (Yu and Page, 1991) reported that dissolved oxygen diffuses faster than chloride due to surface charge effect of chloride diffusion, even though the two species have very similar diffusivities in infinitely dilute solution. The retardation increases with decrease of water/binder ratio, at water/binder ratio of 0.5 the diffusion coefficient of oxygen is about 1×10^{-11} m^2/s which is 2 times faster than one of chloride. Castellote et al. (Castellote et al., 2001) have drawn the same conclusion in a study on cement paste with w/c of 0.4. The effective diffusion coefficient of dissolved oxygen determined by electrochemical method is 9.5×10^{-12} m^2/s which is also about 2.5 times faster than one of chloride determined by either electrochemical or migration tests.

Probably for concrete materials, the main concern on ionic diffusion is the migration of the chloride ion. This is due to the extent of reinforcement corrosion damage due to de-icing and exposing to marine environment. A large number of methodologies have been proposed to determine the chloride diffusion coefficient. Most of the methods have been applied for saturated materials, few studies focused on partially saturated concretes (Olsson et al., 2013, Guimaraes et al., 2011). The measured chloride ion apparent diffusion coefficients are of the order of 10^{-11} m^2/s for saturated materials while the apparent diffusion coefficients are significantly decreased with the decrease of saturation degree. At a saturation degree of 50%, the apparent diffusion coefficient drops about one

order of magnitude compared to saturated material (Guimaraes et al., 2011). Besides chloride ions, sulphate ions are also of relevance, as sulphate attack is one of the coherent durability problems in coastal concrete structures. The diffusion coefficient of sulphate ions is normally measured by in-diffusion method in which the sample is located between a sodium sulphate solution (5%) at one side and pure water at the other side (Sun et al., 2013). A similar migration test protocol for chloride can also be applied for the determination of sulphate diffusion coefficient (Moon et al., 2002, Tumidajski and Turc, 1995). The measured chloride ion diffusion coefficients are of the order of 10^{-12} m^2/s (Moon et al., 2002, Condor et al., 2011).

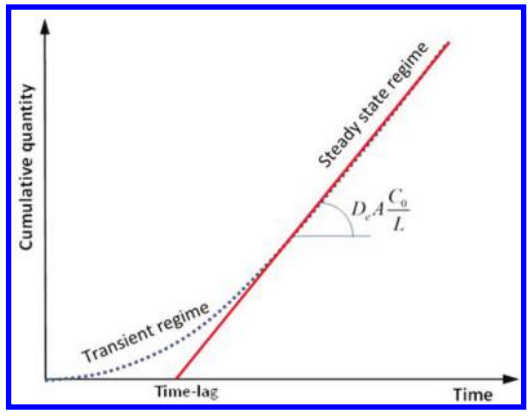

Figure 1. Cumulative quantity in the upstream over time.

2 EXISTING METHODS TO DETERMINE DIFFUSIVITIES OF DIFFERENT SPECIES

2.1 *Gas/dissolved gas diffusion*

The diffusion of gases is normally determined by through-diffusion technique. The setup is quite simple: a thin sample is located in between two compartments. The setup usually allows measuring the diffusivity of only one gas (Sercombe et al., 2007) by injecting the testing gas to the upstream compartment and the sweep gas to the downstream compartment. The sweep gas is needed to balance the pressure in two compartments which prevents the advective transport. Gas concentrations are determined regularly (by gas chromatography) until steady state is reached.

Fig. 1 shows a typical concentration profile of a diffusing gas over time. When steady state condition is reached, the concentration profile becomes a straight line which means the diffusive flux across the sample is constant. Therefore, Fick's first law can be applied to calculate the cumulative quantity $Q(t)$ [kg] of testing gas passed through a sample with a cross-sectional area A [m^2]:

$$Q(t) = \int_0^t -D_e A \frac{\partial c}{\partial x} dt' = D_e A \frac{C_0}{L} t \tag{5}$$

where L [m] is the length of sample; C_0 [kg/m^3] is the concentration of testing gas in the upstream compartment. Note that the concentration of testing gas is neglected compared to C_0. The effective diffusivity is then easy to compute from the slope of $Q(t)$ curve. In case of no sorption/binding ($R_e = 1$), the accessible porosity of the sample can be determined from the time-lag t_{lag} [s] which is the intercept of the straight line with the x axis in Fig. 1. However, it is found that the porosity determined from time-lag is less precise (García-Gutiérrez et al., 2006).

$$\phi = \frac{6 D_e t_{lag}}{L^2} \tag{6}$$

Keeping the concentration gradient constant is difficult because of sampling which decreases the pressure (thereby concentration) of the testing gas. However, a small variation in the concentration gradient can be permitted (García-Gutiérrez et al., 2006). If the pressure in the compartments is dropping too much, a numerical approach is needed to fit the effective diffusion coefficient.

2.2 *Ionic diffusion*

Diffusion of ionic species is probably the most significant transport process which affects the chemical degradation of cementitious materials because most degradation occurs in the presence of water in which ionic species can migrate through concrete driven by concentration gradients. The diffusion of ions is more complex than dissolved gases due to its possibility to interact with solid phases of the porous medium (charge repulsion/attraction) and effects of the presence of other ionic species. In general, the effective diffusion coefficients of ionic species can be measured by through-diffusion (as discussed above), in-diffusion or electro-migration methods (often referred to as "migration" tests).

Instead of waiting until steady state like through-diffusion, in-diffusion is a transient method which is less time-consuming. The technique is based on the measurement of concentration profile of the testing ion by cutting the sample into small slices at a given time. Experiments are usually designed in the way that the source concentration of testing

ionic species is kept constant and the sample is long enough to be considered as a semi-infinite medium. The apparent diffusion coefficient is then obtained by fitting the concentration profile with solution of the Fick's second law (Crank, 1975):

$$C(x,t) - C_0 = (C_s - C_0)erfc\left(\frac{x}{2\sqrt{D_a t}}\right) \quad (7)$$

where $C(x,t)$ is concentration at depth x [m] and time t[s]; C_0 and C_s are the initial and source concentrations, respectively [mol/m^3]; and $erfc$ is the complementary error function.

Electro-migration tests have been developed to accelerate the ionic transport by applying an electrical field. The setup is quite simple. A thin sample is located between two electrodes. A testing ionic species is added to the upstream compartment. A constant electrical potential difference is applied across the sample. In steady-state migration tests, the evolution of the concentration of a given ionic species in the downstream compartment is monitored until steady state is reached. In non-steady state migration tests, the concentration profile of ionic species within the sample is measured after a given period. the calculation of the diffusion coefficient is based on the Nernst–Planck Equation (Bockris and Reddy, 1974).

$$J(x) = -D\frac{\partial C}{\partial x} - DC\frac{zF}{RT}\frac{\partial \Psi}{\partial x} + CV(x) \quad (8)$$

where C is the concentration [mol/m^3]; D is the diffusion coefficient [m^2/s]; z is the valence number [-]; F is the Faraday constant [coulomb/mol]; R is the ideal gas constant [J/mol.K]; T is the absolute temperature of the liquid [K]; Ψ is the electrical potential [V], and $V(x)$ is the bulk velocity of the fluid along x direction [m/s]. On the right side of Eq. (8) the first term stands for diffusion, the second term stands for (electro)migration and the last term stands for convection. Note that chemical activity effects are neglected in this expression. Under steady state flow and with assumption that migration is the dominant transport process, it is possible to calculate the effective diffusion coefficient as follows:

$$D_e = \frac{J(x)RTL}{zFC_s\Delta\Psi} \quad (9)$$

where C_s is the source (boundary) concentration [mol/m^3]; L is the length of sample [m]; and $\Delta\Psi$ is the potential difference [V]. The flux $J(x)$ can be calculated from the concentration evolution in the downstream compartment. In non-steady state regime, the concentration of the ion in the sample changes with time. Fick's second law is applied to solve the problem:

$$\frac{\partial C}{\partial t} = -\frac{\partial}{\partial x}\left(-D\frac{\partial C}{\partial x} - DC\frac{zF}{RT}\frac{\partial \Psi}{\partial x} + CV(x)\right) \quad (10)$$

If the convection term is negligible, for semi-infinite media an analytical solution of Eq. (10) can be obtained by (Luping and Nilsson, 1993)

$$C = \frac{C_s}{2}\left[e^{ax}erfc\left(\frac{x + aDt}{2\sqrt{Dt}}\right) + erfc\left(\frac{x - aDt}{2\sqrt{Dt}}\right)\right] \quad (11)$$

where $a = zF\Delta\Psi / RTL$. Note that D in Eq. (11) is referred as apparent diffusion coefficient because in transient state the physical/chemical interactions have not been completed. The diffusion coefficient is obtained by fitting the calculated concentration profile to the one measured during the migration test. For clays, Maes used an adapted electromigration technique to determine diffusion coefficients of radionuclides (Maes et al., 1998).

3 DETERMINATION OF DIFFUSIVITIES OF DISSOLVED GASES

3.1 *Sample preparation and experimental setup*

The diffusion experiments were performed on two intact samples S1 (water/powder = 0.425, limestone filler/powder = 0%) and S2 (water/powder = 0.375, limestone filler/powder = 10%). These samples had quite similar w/c ratios, i.e. 0.425 for S1 and 0.416 for S2. Furthermore, the change in diffusivity due to carbonation was determined on carbonated sample S1 (named as S1C). Type I ordinary Portland cement (CEM I 52.5 N) was used. This cement has Blaine specific surface area of 435 m^2/kg and density of 3100 kg/m^3. Table 1 gives a summary of the chemical composition. Limestone fillers (Calcitec 2001S) has Blaine specific surface of 3500 cm^2/g and $CaCO_3$ content of 98.30%. Other chemical and physical properties are shown in the Table 2. Superplasticizer Glenium 27 was added to the mix with content of 0.5% with respect to mass of cement.

Cement paste was poured in a cylindrical PVC tube with inner diameter of 97.5 mm. The sample was then rotated during 24 hours to prevent segregation. Afterwards, the sample was cured in a sealed condition in a temperature controlled room (22 ± 2°C) for 27 days. The 28-day-cured cement paste was sawn into 25 mm thick slices. The disks were then embedded into the polycarbonate part of the permeability cells. It took 24 hours for the resin

Table 1. Chemical composition and some properties of the cement CEM I 52.5 N (from manufacturer fact sheet).

Determinant	Percent	Determinant	Percent
CaO	63.0%	Chromium(VI)	$<2.10^{-4}$%
SiO_2	20.0%	Cl-	0.06%
Fe_2O_3	3.0%	Na_2O eq.	0.85%
Al_2O_3	5.0%	Loss on ignition	1.60%
Sulphate SO_3	2.9%	Insoluble residue	0.50%

Table 2. Chemical and physical properties of limestone fillers (from manufacturer fact sheet).

Density	2.7 g/cm^3	$CaCO_3$	98.30%
Blaine specific surface	3500 cm^2/g	MgO	0.36%
Particle size distribution:		SiO_2	0.75%
Passing 2mm	100.0%	Al_2O_3	0.25%
Passing 500µm	99.9%	Fe_2O_3	0.10%
Passing 125µm	97.0%	Na_2O eq.	0.05%
Passing 63µm	77.0%	pH	9.5
D_{50} (50% passing)	10.1µm		

to dry before polishing to obtain the final sample thickness of 25 mm. The samples were afterwards saturated under vacuum conditions (Phung et al., 2013). For carbonated sample, the sample S1C was carbonated by applying a pressure gradient of 5 bar pure CO_2 for 28 days (Phung et al., Under review). Prior to diffusion test, the carbonated sample needs to be saturated after carbonation test. Thanks to the flexibility of the primary cell, the sample/cell can be easily switched/disconnected from the carbonation setup and mounted/connected to the diffusion setup by means of quick connect couplings.

The gas couple He-Xe was used for all diffusion experiments. In order to obtain the effective diffusion coefficients, the accessible porosity was determined by a combination of MIP and N_2-adsorption experiments (Phung, 2015). The MIP experiments determined the porosity down to the pores with minimum diameter of 7.35 nm (corresponding to maximum intrusion pressure of 200 MPa). The porosity in pore size range of 3.17 – 7.35 nm was determined by N_2-adsorption experiments. The BJH method was used to calculated pore volume.

A schematic view and a picture of the experimental setup are presented in Figs. 2 and 3, respectively. The setup is the same as the one used for clay materials (Jacops et al., 2013) except for the diffusion cell which is exactly the same of the permeability cell. Two precise pressure transducers

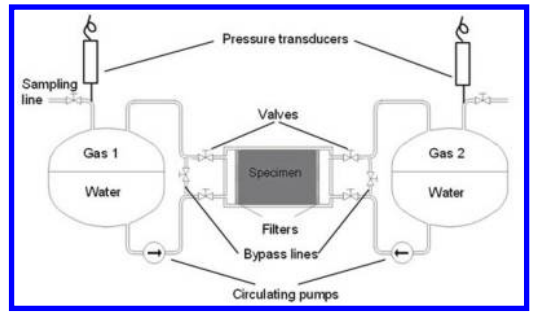

Figure 2. Schematic experimental setup of diffusion (adapted from (Jacops et al., 2013)).

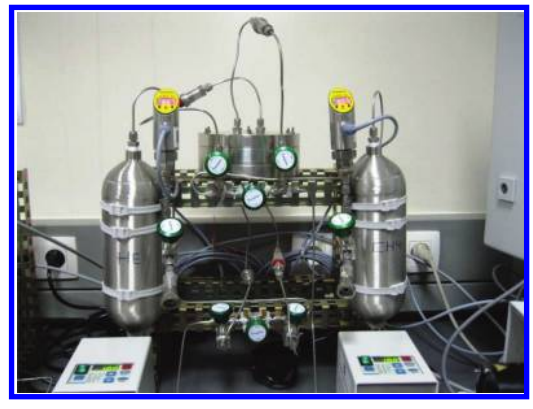

Figure 3. Image of the diffusion experiment.

(TURCK, Plymouth, USA) were used to measure gas pressure in the pressurized water vessels. The water with the dissolved gas was circulated over the contact filter in the cell by means of magnetic coupled gear pumps (ISMATEC, Glattbrugg, Switzerland). The diffusion cell was connected to the system through quick connectors.

3.2 *Experimental procedure*

The experiment was performed in a temperature controlled room at 21 ± 2°C. Prior to the diffusion measurement, the sealing of the whole system was checked by applying a gas pressure of 12 bar and following the pressure evaluation over time (few weeks). The entire setup is considered to be gas-tight if the pressure is stable. The air or residual gas from previous tests in the system was removed as much as possible by flushing the system with the testing gases. During flushing, bypass lines were opened while all valves connected to the sample were closed to prevent diffusion proceeding at this step. Care must be taken to avoid testing gas contamination of each vessel (i.e. gas 1 present in

vessel 2 and vice versa). Subsequently, a volume of 0.5 litre of degassed water was added to each vessel, whereafter they were pressurized by the respective gases to a similar pressure of about 10 bar to prevent advective transport. Prior to the measurement, a sample was taken to determine the initial gas composition of both vessels and referred as the sample at the time zero. In order to start the test, all valves connected to the sample were opened, the bypass lines were closed. At that moment, the pressures in both vessels slightly dropped due to small volume increase of the system, but still in balance. Gas samples were regularly (generally every 2 weeks) taken via external samplers until enough data points were collected to obtain diffusivity (few months). To avoid a too large pressure drop due to sampling, the sample volumes taken were only 6 ml. The gas composition was analysed with a CP4900 micro gas chromatograph (VARIAN, Palo Alto, USA).

3.3 *Data analysis*

In order to interpret the experimental data, a 1-D diffusive transport model was developed (Jacops et al., 2013). Fick's laws were used to describe the diffusion of the dissolved gases.

$$J_{dg} = -D_e \frac{\partial C_{dg}}{\partial x} \tag{12}$$

$$\phi R_e \frac{\partial C_{dg}}{\partial t} = D_e \frac{\partial^2 C_{dg}}{\partial x^2} \tag{13}$$

where J_{dg} [mol/m^2.s] is flux of dissolved gas; D_e [m^2/s] is the effective diffusion coefficient; ϕ[-] denotes porosity; R_e denotes the retardation factor which takes into account the interactions of dissolved gas and the medium. Note that in most cases, the retardation factor R_e of inert gas is one.

C_{dg} [mol/m^3] denotes concentration of dissolved gas in the porous medium; t[s] denotes time and x[m] denotes length. With constant boundary conditions, Eq. (13) can be analytically solved using the inverse Laplace method (Crank, 1975). However, during sampling the concentration at the upstream was decreased. As such boundary conditions are not easily implemented in the analytical solution; a numerical method was chosen to solve the problem.

At the upstream, the dissolved gas concentration was imposed as boundary condition. The dissolved gas concentration was calculated from the gas pressure above the water, which was regularly measured, by Henry's law.

$$C_{dg}^u = K_H P^u \tag{14}$$

where C_{dg}^u [mol/m^3] is concentration of dissolved gas at the upstream; K_H [mol/m^3.atm] is Henry constant; P^u [atm] denotes gas pressure. At the downstream, the concentration was considered to be zero because of the extremely small value compared to the concentration at the upstream (approved by experimental results). The quantity $Q_{out}(t)$ [mol] of dissolved gas diffused out of the sample was calculated as follows:

$$Q_{out}(t) = A\int_0^t J(L,t')dt' \tag{15}$$

where A [m^2] and L are cross section and length of the sample, respectively; $J(L,t')$ is the flux at the downstream boundary. The quantity $Q_{out}(t)$must be equal the total amount of testing gas $Q_{mea}(t)$ at the downstream (in water and gas phase) which can be determined by measuring the partial pressure P^d[atm] of the testing gas above the water at the downstream according to Clapeyron equation and Henry's law for ideal gas .

$$Q_{out}(t) = Q_{mea}(t) = K_H P^d V_l + \frac{V_g P^d}{RT} \tag{16}$$

where V_l and V_g [L^3] are water and gas volumes at the downstream, respectively; R denotes universal gas constant [J/mol.K] and T [K] denotes temperature. Initially, the concentration of dissolved gas was zero in the sample. The diffusion problem was numerically solved in COMSOL Multiphysics. The effective diffusion coefficient was obtained by using a least squares fitting procedure of the diffused quantity $Q_{out}(t)$ to the measured one $Q_{mea}(t)$with the MATLAB Optimization Toolbox.

The changes in effective diffusivity of cementitious materials are due to the alterations of porosity, tortuosity and constrictivity resulting from degradation processes. In order to estimate the effects of carbonation/leaching on the changes of effective diffusion coefficients of other substances, a lumped parameter $\tau^2 / \phi\delta$ can be calculated as follows:

$$\frac{\tau^2}{\phi\delta} = \frac{D_0}{D_e} \tag{17}$$

4 RESULTS AND DISCUSSION

4.1 *Intact samples*

Despite the quite similar w/c ratios, the accessible porosity of sample S2 was 16.8% which is relatively

Table 3. Microstructural parameters and bulk density of intact and carbonated samples determined by N_2-adsorption and MIP combination – "C" denotes carbonated sample.

Sample	**S1**	**S1C**	**S2**
w/p	0.425	0.425	0.375
ls/p	0	0	0.1
Accessible porosity,%	19.7	17.0	16.8
Critical pore diameter, nm	32.0	33.0	36.4
Threshold pore diameter, nm	1000	100	200
Bulk density, g/cm³	1.78	2.14	1.85

lower than sample S1, 19.7%, due to limestone filler addition (Table 4).

It is assumed that there is no adsorption for He and Xe due to its inert characteristics as noble gases. Thus the retardation factor R_e was set to one. Due to lower diffusivity of Xe compared to He (5 times lower in free water), the concentration of Xe at the outlet was not high enough to be detected reliably by gas chromatography within the experimental time (4–5 months). Therefore only the data of He diffusion are presented for the intact samples. Figure 4 shows the fitted and measured partial pressure profiles of He at the outlet for intact samples S1 and S2. Good correlation coefficients were obtained for both cases. The effective diffusion coefficients of samples S1 and S2 were 2.32×10^{-11} m²/s and 1.22×10^{-11} m²/s, respectively. The limestone filler addition improved the microstructure which resulted in a decrease of diffusivity of about 50%. Ramezanianpour et al. (Ramezanianpour et al., 2009) also reported a significant decrease in chloride diffusion due to limestone filler addition for the cases of OPC concrete with w/c ratio of 0.45 and concrete with w/p ratio of 0.37 and 20% limestone filler replacement (w/c = 0.46). However, when w/c ratio was increased to 0.55, the reduction effect in diffusion was not clear. Note, if the comparison is only based on the same w/p ratio, Ramezanianpour showed an increase in diffusion if the limestone filler replacement was higher than 10% which was also observed by Bonavetti et al. (Bonavetti et al., 2000).

From the obtained effective diffusion coefficients the square of tortuosity/constrictivity ratios can be calculated by Eq. (17). Diffusion coefficients for other gases can be calculated if one considers that they exhibit similar τ^2/δ ratio. We calculated the diffusivity of Xe which we were not able to determine because of limited time as shown in Table 4. It can be seen that the effective diffusion coefficient of Xe is quite small compared to He (5 times lower). Therefore, the time needed for collecting enough data to extract Xe effective diffusion coefficient is relatively longer for the case of He.

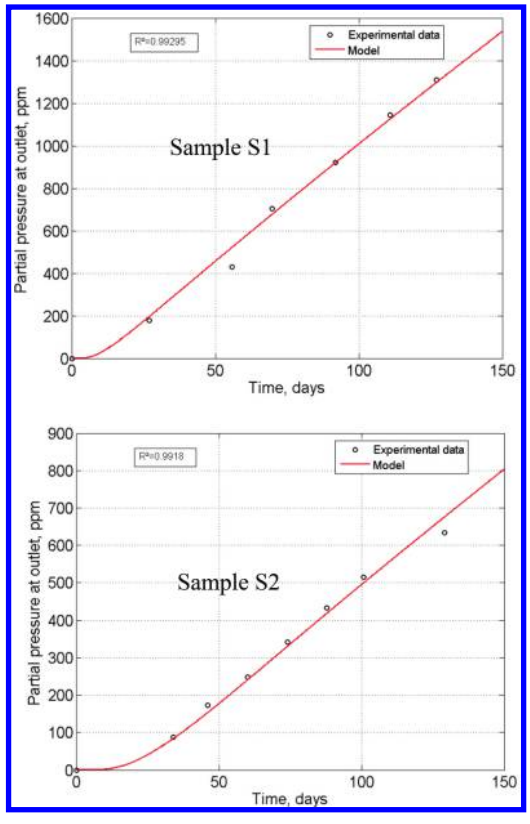

Figure 4. Increase in He partial pressure at the downside compartment in the through-diffusion experiment with dissolved gases - Comparison between experiment and model for intact samples S1 and S2.

4.2 *Carbonated sample*

The diffusion experiments were performed on carbonated sample S1C (w/p = 0.425, ls/p = 0%). As seen in Table 3, the accessible porosity of the carbonated zone (within 3 mm from the reactive surface) was relatively decreased due to carbonation; the critical pore diameter (which is the most frequently occurring pore size in interconnected pores) was almost unchanged. However, the threshold pore diameter was significantly reduced. Note that the porosity of the carbonated sample (not carbonated zone) is not the same over the depth of sample. The average porosity of the entire carbonated sample was calculated by weighted average method as follows:

$$\phi_a = \frac{\phi_{car} d_{car} + \phi_{ref}(d - d_{car})}{d} \tag{18}$$

where ϕ_a, ϕ_{car} and ϕ_{ref} [-] denote the average porosity of the entire carbonated sample, the porosity

Table 4. Estimation of effective diffusion coefficient [m²/s] for Xe from information of tortuosity and constrictivity obtained from He diffusion experiment – (*) obtained from (Jähne et al., 1987).

	Sample S1		Sample S2	
	He (mea.)	Xe (cal.)	He (mea.)	Xe (cal.)
$D_0^{(*)}$	7.22×10^{-9}	1.47×10^{-9}	7.22×10^{-9}	1.47×10^{-9}
D_e	2.32×10^{-11}	4.73×10^{-12}	1.22×10^{-11}	2.49×10^{-12}
ϕ, %	19.7	19.7	16.8	16.8
τ^2/δ	61.2	61.2	99.1	99.1

Table 5. Estimation of effective diffusivity of carbonated zone using series model.

D, m²/s	D_{un}, m²/s	D_{car}, m²/s	D_{un}/D_{car}
1.64×10^{-11}	2.32×10^{-11}	4.72×10^{-12}	4.92

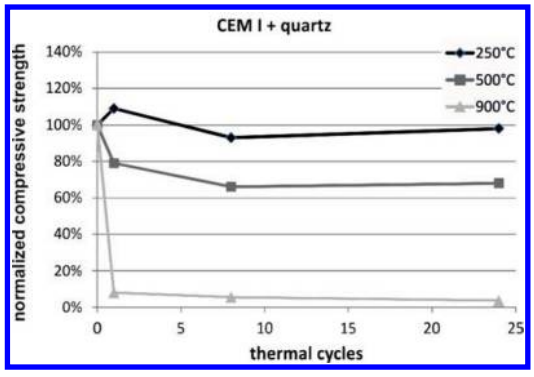

Figure 5. Comparison of the He partial pressure at the outlet obtained from experiment and model for carbonated sample S1C after 28 days of carbonation.

of the carbonated zone and the porosity of the intact sample, respectively; d_{car} and d [m] denote the thicknesses of carbonated zone and the sample, respectively. Furthermore, the porosity might be decreased due to the continuous hydration of the sample during long time diffusion experiment. However, this effect was not counted in this calculation. The retardation factor R_e was again set at one. Fig. 5 shows the fitted and measured partial pressure profiles of He at the outlet for carbonated sample S1C. A good correlation was obtained (r^2 = 0.9919). The effective diffusion coefficient of S1C was 1.64×10^{-11} m²/s, which is 30% lower than the effective diffusion coefficient of the intact sample.

It is worth mentioning that the effective diffusion coefficient of the carbonated sample (D) should be treated as the composite (overall) effective diffusion coefficient. Therefore, the series model (Phung, 2015) was applied for the calculation of the effective diffusion coefficient of the carbonated zone with an assumption that the effective diffusion coefficient of sound zone equals to the one of the intact sample. Estimation of the effective diffusion coefficient of the carbonated zone (D_{car}) resulted in a value of 4.72×10^{-12} m²/s, which is 5 times lower than the effective diffusion coefficient of the intact sample (D_{un}).

5 CONCLUSIONS

In the present work, a promising method to determine the diffusion coefficients of dissolved gases in saturated cement-based materials was described. The proposed method enabled to measure the diffusivities of two dissolved gases in a single experiment and was integrated to the other setups in order to study the effects of degradation on the transport properties. A 1-D diffusive transport model accounting for the pressure drop was used to better interpret the experimental results.

The method proves its reliability through its good correlation coefficients between the measured and modelled partial pressures. However, its accuracy cannot be evaluated because, to the knowledge of the author, this is the first time that data on diffusion of dissolved He in cement-based materials were reported. Oxygen is the only dissolved gas for which diffusion data in cement-based materials can be found in literature (Castellote et al., 2001, Tittarelli, 2009).

It was observed that the addition of limestone filler had significant influences on diffusivity. With a similar w/c ratio, adding 10% of limestone filler reduced the diffusivity of cement paste by 50%. The square of tortuosity/constrictivity ratio calculated from the measured gas (He) can be used to estimate the diffusion coefficients for other gases.

The carbonation exhibited a significant decrease in diffusivity resulting from the changes in microstructure. A series model was used to estimate the diffusivity of the carbonated zone. Estimations showed that the diffusivity of the carbonated zone were significantly decreased (factor of 5) compared to the composite diffusivity (only 30% decrease).

ACKNOWLEDGEMENTS

The financial support by Belgium Nuclear Research Centre (SCK•CEN) is gratefully acknowledged.

REFERENCES

Bockris, J. O. M. & Reddy, A. K. N. 1974. *Modern Electrochemistry: An Introduction to an Interdisciplinary Area, Plenum Press.*

Bonavetti, V., Donza, H., Rahhal, V. & Irassar, E. 2000. Influence of initial curing on the properties of concrete containing limestone blended cement. *Cement and Concrete Research,* 30, 703–708.

Castellote, M., Alonso, C., Andrade, C., Chadbourn, G. A. & Page, C. L. 2001. Oxygen and chloride diffusion in cement pastes as a validation of chloride diffusion coefficients obtained by steady-state migration tests. *Cement and Concrete Research,* 31, 621–625.

Condor, J., Asghari, K. & Unatrakarn, D. 2011. Experimental Results of Diffusion Coefficient of Sulfate Ions in Cement Type 10 and Class G. *10th International Conference on Greenhouse Gas Control Technologies,* 4, 5267–5274.

Crank, J. 1975. *The mathematics of diffusion*, Clarendon Press.

Daimon, M., Akiba, T. & Kondo, R. 1971. Through Pore Size Distribution and Kinetics of the Carbonation Reaction of Portland Cement Mortars. *Journal of the American Ceramic Society,* 54, 423–428.

García-Gutiérrez, M., Cormenzana, J. L., Missana, T., Mingarro, M. & Molinero, J. 2006. Overview of laboratory methods employed for obtaining diffusion coefficients in FEBEX compacted bentonite. *Journal of Iberian Geology,* 32, 37–53.

Guimaraes, A. T. C., Climent, M. A., De Vera, G., Vicente, F. J., Rodrigues, F. T. & Andrade, C. 2011. Determination of chloride diffusivity through partially saturated Portland cement concrete by a simplified procedure. *Construction and Building Materials,* 25, 785–790.

Jacops, E., Volckaert, G., Maes, N., Weetjens, E. & Govaerts, J. 2013. Determination of gas diffusion coefficients in saturated porous media: He and CH_4 diffusion in Boom Clay. *Applied Clay Science,* 83–84, 217–223.

Jähne, B., Heinz, G. & Dietrich, W. 1987. Measurement of the diffusion coefficients of sparingly soluble gases in water. *Journal of Geophysical Research: Oceans,* 92, 10767–10776.

Luping, T. & Nilsson, L.-O. 1993. Rapid Determination of the Chloride Diffusivity in Concrete by Applying an Electric Field. *ACI Materials Journal,* 89, 49–53.

Maes, N., Moors, H., De Canniere, P., Aertsens, M. & Put, M. 1998. Determination of the diffusion coefficient of ionic species in boom clay by electromigration: Feasibility study. *Radiochimica Acta,* 82, 183–189.

Maes, N., Moors, H., Dierckx, A., De Canniere, P. & Put, M. 1999. The assessment of electromigration as a new technique to study diffusion of radionuclides in clayey soils. *Journal of Contaminant Hydrology,* 36, 231–247.

Moon, H.-Y., Lee, S.-T., Kim, H.-S. & Kims, S.-S. 2002. Experimental Study on the Sulfate Resistance of Concrete Blended Ground Granulated Blast-furnace Slag for Recycling. *Geosystem Engineering,* 5, 67–73.

Olsson, N., Baroghel-Bouny, V., Nilsson, L.-O. & Thiery, M. 2013. Non-saturated ion diffusion in concrete – A new approach to evaluate conductivity measurements. *Cement and Concrete Composites,* 40, 40–47.

Phung, Q. T. 2015. Effects of Carbonation and Calcium Leaching on Microstructure and Transport Properties of Cement Pastes. *Department of Structural Engineering.* Belgium, Ghent University.

Phung, Q. T., Maes, N., De Schutter, G., Jacques, D. & Ye, G. 2013. Determination of water permeability of cementitious materials using a controlled constant flow method. *Construction and Building Materials,* 47, 1488–1496.

Phung, Q. T., Maes, N., Jacques, D., Bruneel, E., Driessche, I. V., Ye, G. & Schutter, G. D. Under review. Effect of limestone fillers on microstructure and permeability due to carbonation of cement pastes under controlled CO2 pressure conditions. *Construction and Building Materials*.

Ramezanianpour, A. A., Ghiasvand, E., Nickseresht, I., Mahdikhani, M. & Moodi, F. 2009. Influence of various amounts of limestone powder on performance of Portland limestone cement concretes. *Cement & Concrete Composites,* 31, 715–720.

Sercombe, J., Vidal, R., Galle, C. & Adenot, F. 2007. Experimental study of gas diffusion in cement paste. *Cement and Concrete Research,* 37, 579–588.

Sun, C., Chen, J., Zhu, J., Zhang, M. & Ye, J. 2013. A new diffusion model of sulfate ions in concrete. *Construction and Building Materials,* 39, 39–45.

Tittarelli, F. 2009. Oxygen diffusion through hydrophobic cement-based materials. *Cement and Concrete Research,* 39, 924–928.

Tumidajski, P. J. & Turc, I. 1995. A rapid test for sulfate ingress into concrete. *Cement and Concrete Research,* 25, 924–928.

Yu, S. W. & Page, C. L. 1991. Diffusion in cementitious materials: 1. Comparative study of chloride and oxygen diffusion in hydrated cement pastes. *Cement and Concrete Research,* 21, 581–588.

Concrete Repair, Rehabilitation and Retrofitting IV – Dehn et al. (Eds)
© 2016 Taylor & Francis Group, London, ISBN 978-1-138-02843-2

Comparison of residual strengths of concretes with quarzitic, limestone and slag sand constituents after cyclic high-temperature exposure

S. Anders
Institute of Structural Engineering, Construction Materials, Bergische Universität Wuppertal, Wuppertal, Germany

ABSTRACT: A series of experiments was conducted in order to investigate the effects of different types of cements, different types of aggregates, increased number of thermal cycles and different storing climates on concrete mixtures. It is demonstrated that the compressive strength starts to decrease at temperatures above 250°C. The decrease in strength is governed by the type of aggregate used. Thermal cycles up to 24 cycles do not further decrease the mechanical properties. The decrease in strength seems to be governed by the maximum temperature instead of the number of thermal cycles. The way and duration of storing the concrete mixtures after high-temperature exposure also seems to affect the residual strength. After being exposed to 250°C storing decreases the residual strength, whereas the residual strength increases for some of the mixtures tested after exposure of 900°C.

1 INTRODUCTION

Many experiments and results have been published on the topic of "hot strength" of concrete that means its behavior if subjected to high-temperatures e.g. in case of fire. These results are also well documented in different codes and regulations. But only little information can be found on the "residual strength" of concrete which has cooled down after a high-temperature exposure. This information is for instance needed if the residual load-bearing capacity of structural members has to be evaluated after an event of fire. Even less results can be found in literature if the question of cyclic high-temperature is dealt with. This question can occur e.g. in foundries or steelworks.

Furthermore, it is commonly known that the behavior of concrete subjected to high-temperatures differs in terms of aggregate: calcitic aggregate/limestone or quarzitic aggregate. In this study the type of aggregate will be extended to slag sand, because it has already been subjected to temperatures of about 1.200°C during its production process e.g. in steelworks. The majority of papers dealing with effects of aggregates on the concrete behavior were published before cements were blended using limestone powder. Even effects of using blast-furnace cement instead of ordinary Portland cement have not been reported so far to the author's knowledge. Therefore, the second major topic of this paper are the effects of different types of cements on the residual strength of concrete. As third question it will be dealt with different storing conditions after high-temperature exposure.

2 LITERATURE REVIEW

2.1 *Behavior of aggregates in high temperatures*

As commonly known, the type of aggregate in concrete significantly affects its behavior if subjected to high-temperatures.

As an example the following Figure 1 displays the thermal expansion of limestone, basalt and quarzitic sandstone (Reinhardt 2005). The increase in thermal expansion of quarzitic sandstone is primarily attributed to the quartz inversion at 573°C which goes along with an expansion of the quartz. Basalt shows a more or less linear thermal expansion due to its magmatic origin. Limestone shows a contraction if the temperature is higher than about 800°C because it starts to deacidificate, which means that calcium carbonate outgases carbon dioxide leaving behind highly reactive and water attracting burnt limestone (carbon oxide). In concrete, limestone cannot only be found as aggregate but also as part of the cement in blended cements (e.g. CEM II/A-LL), limestone powder e.g. in self-compacting concrete or both. If burnt limestone gets in contact with liquid water for instance as forge water or attracts air moisture after an event of fire, it can chemically expand and further damage the concrete matrix.

On the other hand, cement can contain blast-furnace slag which can either chemically react to Calcium-Silicate-Hydrate phases (CSH) in the alkaline environment in concrete or function as aggregate if it is used as sand fraction. Therefore, these phases are affected by high temperature in

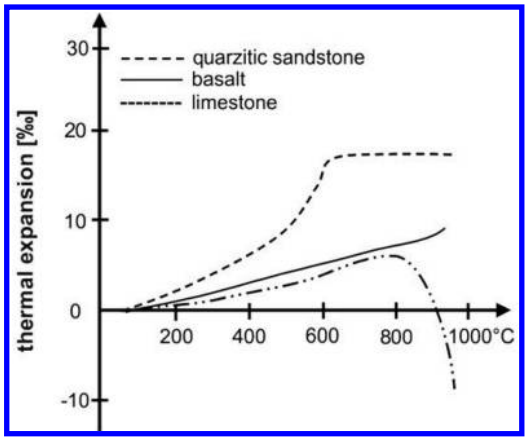

Figure 1. Thermal expansion of limestone, quarzitic sandstone and basalt (Reinhardt 2005).

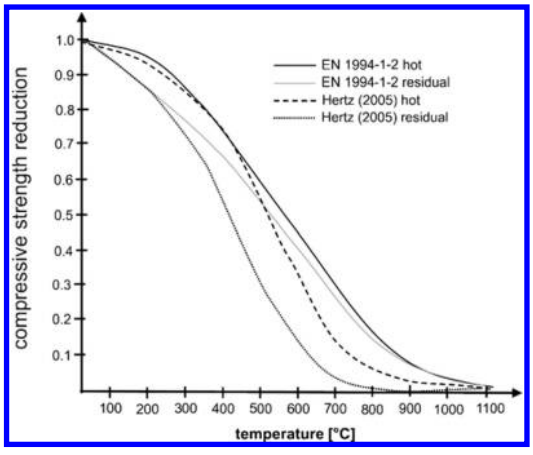

Figure 2. Comparison of hot compressive strength and residual compressive strength by Hertz (2005) and EN 1994-1-2 for quarzitic aggregate.

the same way as the hydration products of ordinary cement are.

2.2 *Residual strengths of concrete after high-temperature exposure*

Concerning the residual strength of heated concrete information have been given e.g. by Hertz (2005) or can be found in the European code EN 1994-1-2. A comparison of the different approaches has been published by Frangi et al. (2006). Figure 2 displays the differences in terms of reduction of the hot compressive strength and residual compressive strength. It can be seen that the curves given by EN 1994-1-2 and Hertz for the hot compressive strength only differ little. In the case of the residual compressive strength EN 1994-1-2 shows curves with a further reduction of compressive strength after cooling down of roughly 10% as long as the temperature is below about 600°C. After exposure in higher temperatures than 600°C the differences are even lower.

In contrast, the curves given by Hertz show a further reduction of about 30% in a temperature range from 300°C to 600°C. The residual strength is zero from about 750 °C onwards.

Frangi et al. explain the differences in the values given by EN 1994-1-2 and Hertz with differences in the stress level during heating which significantly affects the hot compressive strengths.

Some first tests on the cyclic behavior of normal strength concrete and high-strength concrete were done by Wellenberg (2010) and Lenz (2011). They used normal strength concrete and high-strength concrete with steel and carbon fibers and applied temperature cycles on the different mixtures. The maximum temperature was 400 °C and the minimum temperature was 20 °C. The heating rate was 5K/min for all tests. These tests offer some interesting information on the cyclic behavior, but the maximum temperature stays within the range without major chemical or mineralogical changes in the concrete matrix.

Both found that the deterioration of the concrete matrix as well as the mass loss reach a nearly constant value after 5 thermal cycles at the latest.

Basing on this information the experimental program described in the following has been developed.

3 EXPERIMENTAL PROGRAM

The performed experimental program aimed at the determination of effects on the mechanical properties of concrete of different cement types, types of filler/aggregate, number of thermal cycles and finally storing climate after one cycle of high-temperature exposure.

3.1 *Concrete mixtures*

In order to simulate the effects of different cement types an ordinary portland cement CEM I (mixture 1) was applied as reference. In two further mixtures firstly a CEM III/A cement was used (mixture 2) and additionally slag sand was added which completely replaced the quarzitic aggregate (mixture 3).

Furthermore, a CEM II/A-LL (mixture 4) was used in order to get information in which way the limestone powder blended to the cement affects the mechanical properties. In addition, in one concrete

Table 1. Overview on the tested concrete mixtures.

	mix 1	mix 2	mix 3	mix 4	mix 5
Water [kg/m³]	264	264	265	264	264
CEM I [kg/m³]	512	–	–	–	–
CEM III/A [kg/m³]	–	512	512	–	–
CEM II/A-LL [kg/m³]	–	–	–	512	512
quartz sand [kg/m³]	1468	1461	–	1461	1371
limestone powder [kg/m³]	–	–	–	–	100
slag sand [kg/m³]	–	–	1373	–	–
w/c-ratio [–]	0.52	0.52	0.52	0.52	0.52
Initial compressive strength [MPa]	44.0	33.8	32.9	33.1	35.7
Density (fresh) [kg/dm³]	2246	2238	2150	2238	2249

mix additional limestone powder was added replacing some of the quartz sand (mixture 5).

An overview on the composition of the concrete mixtures is given in the following Table 1. The aim was to test normal strength concrete and thus to avoid further effects such as spalling which might have occurred for higher strength concretes.

As specimens, ordinary cement prisms with dimensions of 40 mm × 40 mm × 160 mm were used for all tests. This was possible because the maximum grain size was limited to 4 mm.

3.2 *Temperature*

In order to differentiate between the different chemical and mineralogical effects which were described in Chapter 2.1, the temperature levels were chosen as 250 °C, 500 °C and 900 °C. The number of thermal cycles varied between 1, 8 and 24 cycles.

During the high-temperature tests the heating rate was 5 K/min in the ascending branch of the curve. After the maximum temperature was reached it was kept constant for 4 hours. The cooling down process was free cooling down, because active cooling was not possible in the oven used for the 900 °C level. This cooling down phase took about 10 hours. The next thermal cycle was started when the temperature in the oven had reached between 50 °C and 60 °C.

3.3 *Storing climates*

In terms of storing conditions after high-temperature exposure only specimens were tested which were heated only once. The following climates were chosen:

"Climate A" was cooling down in the oven and immediate testing after having cooled down.

"Climate B" was storing the specimens for 7 days in 20°C and 65% r.h. after having cooled down in the oven. This climate was chosen to simulate the residual strength of concrete 7 days after fire exposure.

"Climate C" means submerging the concrete for 5 minutes after having cooled down and storing it afterward for 7 days as in climate B. These conditions are supposed to simulated structural concrete members which were in contact with forge water.

"Climate D" is the extension of climate B up to 28 days.

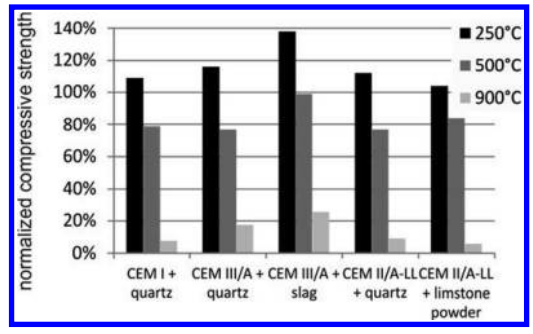

Figure 3. Effect of different types of cement on the residual compressive strength after one thermal cycle.

4 RESULTS AND DISCUSSION

4.1 *Effects of different cements*

In order to characterize the effects of different types of cements the compressive strength and the flexural strength were compared.

Figure 3 displays the effect of the type of cement on the compressive strength at the different temperature levels. The specimens were only subjected to one thermal cycle and tested after cooling down. The values are normalized using the compressive strength of the mixture at room temperature without thermal exposure.

It can be seen that all mixtures show a more or less pronounced increase in compressive strength after 250 °C. After 500 °C all mixtures loose about 20% of strength except for the CEM III/A with slag sand, which can keep up the strength at room temperature. After 900 °C again the mixture 3 containing slag sand performs best. The other mixes have lost about 90% of their initial strength.

One possible explanation for the significantly better performance of the mixture containing CEM III/A and slag sand is that no aggregates are used which undergo chemical reactions, such as limestone, or mineralogical changes, such as quartz. The thermal stability of the slag sand seems to be the reason for the good performance. One could expect that comparable good results

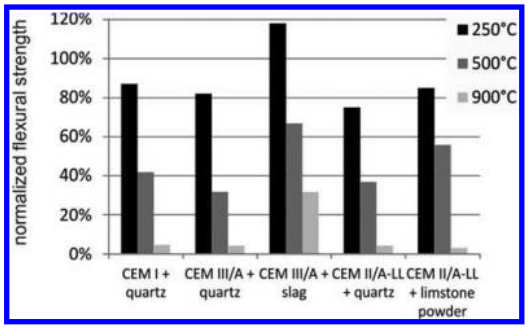

Figure 4. Effect of different types of cement on the residual flexural strengths after one thermal cycle.

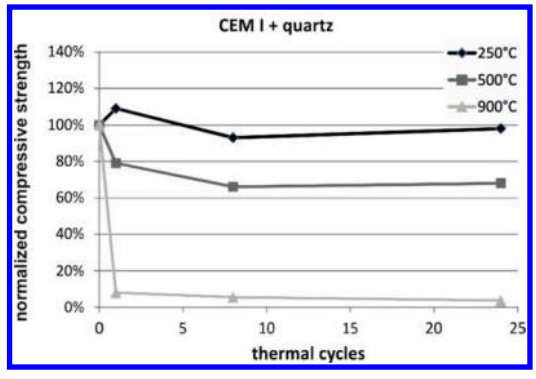

Figure 5. Effect of thermal cycles on the compressive strength on the mixture CEM I + quartz (reference mixture).

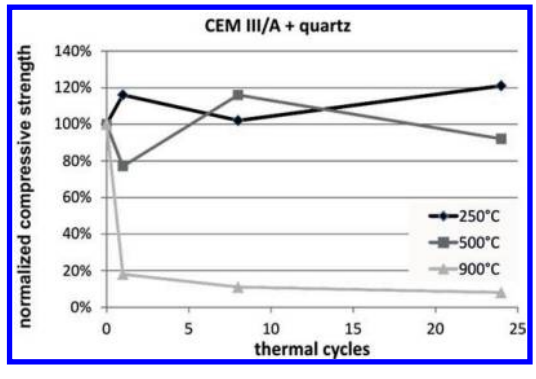

Figure 6. Effect of thermal cycles on the compressive strength on the mixture CEM III/A + slag sand.

could be determined if basalt aggregates were used instead of slag sand.

The mixtures containing CEM I and CEM III/A but quarzitic aggregates show a nearly similar performance which indicates that the type of aggregate seems to be a dominating factor for the residual strengths.

These results have also got to be compread to the values given in literature and which are displayed in Figure 2 for the EN 1994-1-2 as well as Hertz (2005). Both postulate a decrease in compressive strength from 100 °C onwards. The increases in compressive strengths at temperatures up to about 250 °C are not covered. Neither in terms of hot compressive strength nor in terms of residual compressive strength. At a level of 500 °C EN 1994-1-2 and Hertz mention about 55% and 30% respectively for the residual compressive strength. In this study significantly higher residual compressive strengths were found. On the average after exposure to 500 °C the residual compressive strength was about 80% of the strength at room temperature. For the temperature level of 900 °C in this study about 6% to 20% were found. EN 1994-1-2 and Hertz mention 10% and about 0% respectively.

In terms of the flexural strength most of the characteristics mentioned for the compressive strength apply as well. Exceptions are that after an exposure to 250°C only the CEM III/A with slag sand can increase its strength compared to the cold flexural strength. The other mixtures loose about 20% of their initial strength.

4.2 *Effect of thermal cycles*

In the following Figure 5 the effect of thermal cycles on the mixture containing CEM I and quartz aggregate is displayed. It can be seen that after temperatures up to 250 °C the residual compressive strength remains nearly on the level of the strength at room temperature. After cycles up to 500 °C the residual compressive strength decreases to about 65% and further decreases to about 5% if the thermal cycles are up to a temperature of 900 °C. It can additionally be seen that there seems to be no further deterioration of the concrete matrix if the number of cycles is increased. The loss in compressive strength seems to depend only on the maximum temperature level and not on the number of thermal cycles. Comparable results were found by Wellenberg (2010) and Lenz (2011) for normal strength concrete and high-strength concrete respectively.

These remarks are also applicable to the mixture containing CEM III/A and slag sand, with one exception: The loss in strength is considerably lower if slag sand is used as aggregate instead of quartz sand. Even after about 24 thermal cycles the residual compressive strength is comparable to the initial compressive strength at room temperature. These results are in accordance with the explanations given for residual compressive strength after one thermal cycle.

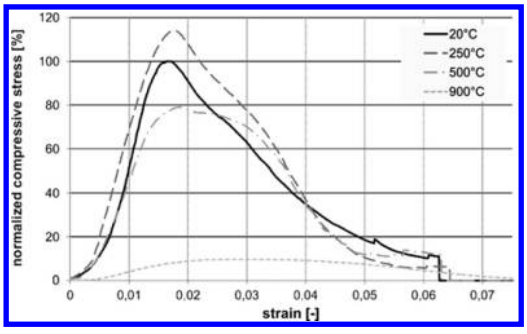

Figure 7. Development of stress-strain behavior exemplarily for CEM II/A-LL + quartz.

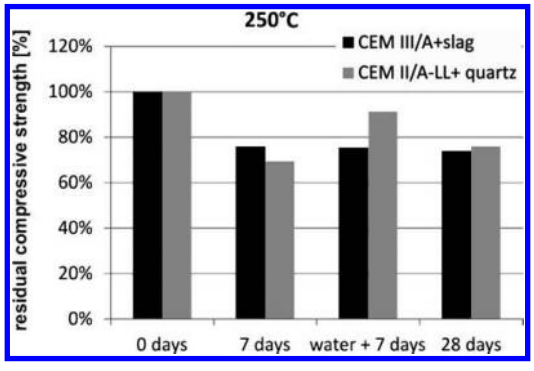

Figure 8. Effect of storing climate after exposure to 250 °C exemplarily for mixtures CEM III/A + slag sand and CEM II/A-LL + quartz.

Shown in the following Figure 7 is the development of the stress-strain behavior is comparable to many other investigations. In Figure 7 the stress was normalized using the compressive strength of the specimens tested at room temperature without thermal exposure. In accordance with the above mentioned, deterioration seems to primarily depend on the maximum temperature and not on thermal cycles, the stress-strain relations only differ slightly after several thermal cycles on one temperature level.

4.3 *Effects of different storing climates*

Interestingly, the effect of different storing climates after thermal exposure seems to depend on the maximum temperature. Not all of these tests are finished at the moment. Figure 8 displays the residual compressive strengths after different storing climates normalized using the climate "0 days" (immediate testing after one thermal cycle and cooling down to room temperature) as reference.

Obviously, any further storing of the specimens seems to further reduce the residual compressive

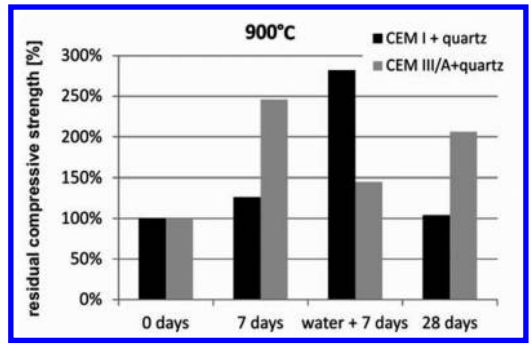

Figure 9. Effect of storing climate after exposure to 900 °C exemplarily for mixtures CEM I and quartz and CEM III/A + quartz.

strength. For the displayed mixtures CEM III/A with slag sand as well as CEM II/A-LL and quarzitic aggregate the residual compressive strengths reduce to roughly 80% on the average. One should bear in mind, that the compressive strength at this temperature level was about 140% for the CEM III/A with slag sand mix so that the resulting compressive strength after storage is still little above the cold compressive strength. For the CEM II/A-LL the resulting compressive strength is about 80% of the compressive strength at room temperature.

If the specimens of the mixtures CEM I and quartz sand as well as CEM III/A and quartz sand are stored in different climates after thermal exposure to 900 °C the storage seems to have healing effects on the concrete structure, resulting in increased compressive strengths

In the case of the CEM III/A mixture the compressive strength increases to about 150% to 250%. One should bear in mind that on the other hand the residual compressive strength of this mixture was only about 20% of the compressive strength at room temperature.

A sound explanation for this differing behavior cannot be given at the moment. Additionally, the results of the mixtures containing CEM II/A-LL which were heated up to 900 °C will be very interesting, because it can be expected that the strengths after storing will be even lower than the strengths after thermal exposure due to the formation of highly reactive calcium oxide during the heating process.

5 SUMMARY

In this experimental study the behavior of different concrete/mortar mixtures was studied which were subjected to cyclic high-temperatures. The

following parameters were changed: type of cement, type of aggregate, number of thermal cycles, type of storage after thermal exposure.

From the experiments the following conclusions can be drawn:

- The residual compressive strength does not differ significantly from the compressives strength at room temperature as long as the maximum temperature does not exceed 250 °C.
- The flexural strength decreases even at temperatures of 250 °C.
- At higher temperature levels the mixture containing CEM III/A as cement and slag sand as aggregate performs significantly better than mixtures containing quazitic aggregates. Therefore, the type of aggregates plays obviously a dominant role.
- Thermal cycles seem not to deteriorate the concrete structure further after some initial thermal cycles. Thus, the damage in the concrete structure seems to depend on the maximum temperature and not on the number of thermal cycles. This behaviour could be observed in terms of the compressive strength, flexural strength as well as development of stress-strain relations.
- Storing the specimens after an exposure to 250 °C as a maximum seems to decrease the residual compressive strength by about 20%. The type and duration of the storing does not seem to have a significant effect on the strength reduction.
- If the specimens were heatd up to 900 °C storing the specimens in climate seems to increase the residual compressive strength compared to an immediate testing after cooling down of the specimen.

Concerning the effects of storing in climate the tests are not finished yet. Maybe cements blended with carbonate will show a different behavior.

REFERENCES

EN 1994-1-2 (Eurocode 4). Bemessung und Konstruktion von Verbundtragwerken aus Stahl und Beton – Teil 1-2: Allgemeine Regeln – Tragwerksbemessung im Brandfall. Beuth, Berlin, 2005.

Frangi, A. & Tesar, C. & Fontana, M. Tragwiderstand von Betonbauteilen nach dem Brand. In *Bauphysik*, Volume 28, No. 3, Ernst & Sohn, Berlin, 2006.

Hertz, K. Concrete strength for fire safety design. In *Magazine of Concrete Research*, Vol. 57, No. 8, London: Thomas Telford Ltd.

Lenz, C. Untersuchungen zur Dauerhaftigkeit von ultrahochfestem Beton (UHPC) bei Temperaturzyklen. Master Thesis at the Bergische Universität Wuppertal, Wuppertal 2011.

Reinhardt, H.W. Beton. In *BetonKalender 2005*, Part 2, Ernst & Sohn, 10245 Berlin, Germany.

Wellenberg, N. Untersuchungen zur Dauerhaftigkeit von Beton bei Temperaturzyklen. Master Thesis at the Bergische Universität Wuppertal, Wuppertal 2010.

Concrete Repair, Rehabilitation and Retrofitting IV – Dehn et al. (Eds)
© 2016 Taylor & Francis Group, London, ISBN 978-1-138-02843-2

Author index